

L A S E R S

Anthony E. Siegman

Professor of Electrical Engineering
Stanford University

University Science Books
Mill Valley, California

University Science Books
20 Edgehill Road
Mill Valley, CA 94941

Manuscript Editor: Aidan Kelly

Designer: Robert Ishi

Production: Miller/Scheier Associates, Palo Alto, CA

TEXpert: Laura Poplin

Printer and Binder: The Maple-Vail Book Manufacturing Group

Copyright © 1986 by University Science Books
Reproduction or translation of any part of this work
beyond that permitted by Sections 107 or 108 of the
1976 United States Copyright Act without the permission of
the copyright owner is unlawful. Requests for permission
or further information should be addressed to
the Permissions Department, University Science Books.

Library of Congress Catalog Card Number: 86-050346

ISBN 0-935702-11-5

Printed in the United States of America

This manuscript was prepared at Stanford University using the text editing facilities of the Context and Sierra DEC-20 computers and Professor Donald Knuth's TEX typesetting system. Camera-ready copy was printed on an Autologic APS-μ5 phototypesetter.



CONTENTS

Preface	xiii
Units and Notation	xv
List of Symbols	xvii

BASIC LASER PHYSICS

1. An Introduction to Lasers	1
2. Stimulated Transitions: The Classical Oscillator Model	80
3. Electric Dipole Transitions in Real Atoms	118
4. Atomic Rate Equations	176
5. The Rabi Frequency	221
6. Laser Pumping and Population Inversion	243
7. Laser Amplification	264
8. More On Laser Amplification	307
9. Linear Pulse Propagation	331
10. Nonlinear Optical Pulse Propagation	362
11. Laser Mirrors and Regenerative Feedback	398
12. Fundamentals of Laser Oscillation	457
13. Oscillation Dynamics and Oscillation Threshold	491

OPTICAL BEAMS AND RESONATORS

14. Optical Beams and Resonators: An Introduction	558
15. Ray Optics and Ray Matrices	581
16. Wave Optics and Gaussian Beams	626
17. Physical Properties of Gaussian Beams	663
18. Beam Perturbation and Diffraction	698
19. Stable Two-Mirror Resonators	744
20. Complex Paraxial Wave Optics	777
21. Generalized Paraxial Resonator Theory	815
22. Unstable Optical Resonators	858
23. More on Unstable Resonators	891

LASER DYNAMICS AND ADVANCED TOPICS

24. Laser Dynamics: The Laser Cavity Equations	923
25. Laser Spiking and Mode Competition	954
26. Laser Q -Switching	1004
27. Active Laser Mode Coupling	1041
28. Passive Mode Locking	1104
29. Laser Injection Locking	1129
30. Hole Burning and Saturation Spectroscopy	1171
31. Magnetic-Dipole Transitions	1213



LIST OF TOPICS

Preface	xiii
Units and Notation	xv
List of Symbols	xvii

BASIC LASER PHYSICS

Chapter 1 An Introduction to Lasers

1.1	What Is a Laser?	2
1.2	Atomic Energy Levels and Spontaneous Emission	6
1.3	Stimulated Atomic Transitions	18
1.4	Laser Amplification	30
1.5	Laser Pumping and Population Inversion	35
1.6	Laser Oscillation and Laser Cavity Modes	39
1.7	Laser Output-Beam Properties	49
1.8	A Few Practical Examples	60
1.9	Other Properties of Real Lasers	66
1.10	Historical Background of the Laser	74
1.11	Additional Problems for Chapter 1	76

Chapter 2 Stimulated Transitions: The Classical Oscillator Model

2.1	The Classical Electron Oscillator	80
2.2	Collisions and Dephasing Processes	89
2.3	More on Atomic Dynamics and Dephasing	97
2.4	Steady-State Response: The Atomic Susceptibility	102
2.5	Conversion to Real Atomic Transitions	110

Chapter 3 Electric Dipole Transitions in Real Atoms

3.1	Decay Rates and Transition Strengths in Real Atoms	118
3.2	Line Broadening Mechanisms in Real Atoms	126
3.3	Polarization Properties of Atomic Transitions	135
3.4	Tensor Susceptibilities	143
3.5	The “Factor of Three”	150
3.6	Degenerate Energy Levels and Degeneracy Factors	153
3.7	Inhomogeneous Line Broadening	157

Chapter 4 Atomic Rate Equations

4.1	Power Transfer From Signals to Atoms	176
-----	--------------------------------------	-----

4.2	Stimulated Transition Probability	181
4.3	Blackbody Radiation and Radiative Relaxation	187
4.4	Nonradiative Relaxation	195
4.5	Two-Level Rate Equations and Saturation	204
4.6	Multilevel Rate Equations	211

Chapter 5 The Rabi Frequency

5.1	Validity of the Rate Equation Model	221
5.2	Strong Signal Behavior: The Rabi Frequency	229

Chapter 6 Laser Pumping and Population Inversion

6.1	Steady-State Laser Pumping and Population Inversion	243
6.2	Laser Gain Saturation	252
6.3	Transient Laser Pumping	257

Chapter 7 Laser Amplification

7.1	Practical Aspects of Laser Amplifiers	264
7.2	Wave Propagation in an Atomic Medium	266
7.3	The Paraxial Wave Equation	276
7.4	Single-Pass Laser Amplification	279
7.5	Stimulated Transition Cross Sections	286
7.6	Saturation Intensities in Laser Materials	292
7.7	Homogeneous Saturation in Laser Amplifiers	297

Chapter 8 More On Laser Amplification

8.1	Transient Response of Laser Amplifiers	307
8.2	Spatial Hole Burning, and Standing-Wave Grating Effects	316
8.3	More on Laser Amplifier Saturation	323

Chapter 9 Linear Pulse Propagation

9.1	Phase and Group Velocities	331
9.2	The Parabolic Equation	339
9.3	Group Velocity Dispersion and Pulse Compression	343
9.4	Phase and Group Velocities in Resonant Atomic Media	351
9.5	Pulse Broadening and Gain Dispersion	356

Chapter 10 Nonlinear Optical Pulse Propagation

10.1	Pulse Amplification With Homogeneous Gain Saturation	362
10.2	Pulse Propagation in Nonlinear Dispersive Systems	375
10.3	The Nonlinear Schrödinger Equation	387
10.4	Nonlinear Pulse Broadening in Optical Fibers	388
10.5	Solitons in Optical Fibers	392

Chapter 11 Laser Mirrors and Regenerative Feedback

11.1	Laser Mirrors and Beam Splitters	398
11.2	Interferometers and Resonant Optical Cavities	408
11.3	Resonance Properties of Passive Optical Cavities	413

11.4	“Delta Notation” for Cavity Gains and Losses	428
11.5	Optical-Cavity Mode Frequencies	432
11.6	Regenerative Laser Amplification	440
11.7	Approaching Threshold: The Highly Regenerative Limit	447

Chapter 12 Fundamentals of Laser Oscillation

12.1	Oscillation Threshold Conditions	457
12.2	Oscillation Frequency and Frequency Pulling	462
12.3	Laser Output Power	473
12.4	The Large Output Coupling Case	485

Chapter 13 Oscillation Dynamics and Oscillation Threshold

13.1	Laser Oscillation Buildup	491
13.2	Derivation of the Cavity Rate Equation	497
13.3	Coupled Cavity and Atomic Rate Equations	505
13.4	The Laser Threshold Region	510
13.5	Multiple-Mirror Cavities and Etalon Effects	524
13.6	Unidirectional Ring-Laser Oscillators	532
13.7	Bistable Optical Systems	538
13.8	Amplified Spontaneous Emission and Mirrorless Lasers	547

OPTICAL BEAMS AND RESONATORS

Chapter 14 Optical Beams and Resonators: An Introduction

14.1	Transverse Modes in Optical Resonators	559
14.2	The Mathematics of Optical Resonator Modes	565
14.3	Build-Up and Oscillation of Optical Resonator Modes	569

Chapter 15 Ray Optics and Ray Matrices

15.1	Paraxial Optical Rays and Ray Matrices	581
15.2	Ray Propagation Through Cascaded Elements	593
15.3	Rays in Periodic Focusing Systems	599
15.4	Ray Optics With Misaligned Elements	607
15.5	Ray Matrices in Curved Ducts	614
15.6	Nonorthogonal Ray Matrices	616

Chapter 16 Wave Optics and Gaussian Beams

16.1	The Paraxial Wave Equation	626
16.2	Huygens’ Integral	630
16.3	Gaussian Spherical Waves	637
16.4	Higher-Order Gaussian Modes	642
16.5	Complex-Argument Gaussian Modes	649
16.6	Gaussian Beam Propagation in Ducts	652
16.7	Numerical Beam Propagation Methods	656

Chapter 17 Physical Properties of Gaussian Beams

17.1	Gaussian Beam Propagation	663
17.2	Gaussian Beam Focusing	675
17.3	Lens Laws and Gaussian Mode Matching	680
17.4	Axial Phase Shift: The Guoy Effect	682
17.5	Higher-Order Gaussian Modes	685
17.6	Multimode Optical Beams	695

Chapter 18 Beam Perturbation and Diffraction

18.1	Grating Diffraction and Scattering Effects	698
18.2	Aberrated Laser Beams	706
18.3	Aperture Diffraction: Rectangular Apertures	712
18.4	Aperture Diffraction: Circular Apertures	727

Chapter 19 Stable Two-Mirror Resonators

19.1	Stable Gaussian Resonator Modes	744
19.2	Important Stable Resonator Types	750
19.3	Gaussian Transverse Mode Frequencies	761
19.4	Misalignment Effects in Stable Resonators	767
19.5	Gaussian Resonator Mode Losses	769

Chapter 20 Complex Paraxial Wave Optics

20.1	Huygens' Integral and <i>ABCD</i> Matrices	777
20.2	Gaussian Beams and <i>ABCD</i> Matrices	782
20.3	Gaussian Apertures and Complex <i>ABCD</i> Matrices	786
20.4	Complex Paraxial Optics	792
20.5	Complex Hermite-Gaussian Modes	798
20.6	Coordinate Scaling with Huygens' Integrals	805
20.7	Synthesis and Factorization of <i>ABCD</i> Matrices	811

Chapter 21 Generalized Paraxial Resonator Theory

21.1	Complex Paraxial Resonator Analysis	815
21.2	Real and Geometrically Stable Resonators	820
21.3	Real and Geometrically Unstable Resonators	822
21.4	Complex Stable and Unstable Resonators	828
21.5	Other General Properties of Paraxial Resonators	835
21.6	Multi-Element Stable Resonator Designs	841
21.7	Orthogonality Properties of Optical Resonator Modes	847

Chapter 22 Unstable Optical Resonators

22.1	Elementary Properties	858
22.2	Canonical Analysis for Unstable Resonators	867
22.3	Hard-Edged Unstable Resonators	874
22.4	Unstable Resonators: Experimental Results	884

Chapter 23 More on Unstable Resonators

23.1	Advanced Analyses of Unstable Resonators	891
------	--	-----

23.2	Other Novel Unstable Resonator Designs	899
23.3	Variable-Reflectivity Unstable Resonators	913

LASER DYNAMICS AND ADVANCED TOPICS

Chapter 24 Laser Dynamics: The Laser Cavity Equations

24.1	Derivation of the Laser Cavity Equations	923
24.2	External Signal Sources	932
24.3	Coupled Cavity-Atom Equations	941
24.4	Alternative Formulations of the Laser Equations	944
24.5	Cavity and Atomic Rate Equations	949

Chapter 25 Laser Spiking and Mode Competition

25.1	Laser Spiking and Relaxation Oscillations	955
25.2	Laser Amplitude Modulation	971
25.3	Laser Frequency Modulation and Frequency Switching	980
25.4	Laser Mode Competition	992

Chapter 26 Laser *Q*-Switching

26.1	Laser <i>Q</i> -Switching: General Description	1004
26.2	Active <i>Q</i> -Switching: Rate-Equation Analysis	1008
26.3	Passive (Saturable Absorber) <i>Q</i> -Switching	1024
26.4	Repetitive Laser <i>Q</i> -Switching	1028
26.5	Mode Selection in <i>Q</i> -Switched Lasers	1034
26.6	<i>Q</i> -Switched Laser Applications	1039

Chapter 27 Active Laser Mode Coupling

27.1	Optical Signals: Time and Frequency Descriptions	1041
27.2	Mode-Locked Lasers: An Overview	1056
27.3	Time-Domain Analysis: Homogeneous Mode Locking	1061
27.4	Transient and Detuning Effects	1075
27.5	Frequency-Domain Analysis: Coupled Mode Equations	1087
27.6	The Modulator Polarization Term	1092
27.7	FM Laser Operation	1095

Chapter 28 Passive Mode Locking

28.1	Pulse Shortening in Saturable Absorbers	1104
28.2	Passive Mode Locking in Pulsed Lasers	1109
28.3	Passive Mode Locking in CW Lasers	1117

Chapter 29 Laser Injection Locking

29.1	Injection Locking of Oscillators	1130
29.2	Basic Injection Locking Analysis	1138
29.3	The Locked Oscillator Regime	1142
29.4	Solutions Outside the Locking Range	1148

29.5	Pulsed Injection Locking: A Phasor Description	1154
29.6	Applications: The Ring Laser Gyroscope	1162

Chapter 30 Hole Burning and Saturation Spectroscopy

30.1	Inhomogeneous Saturation and “Hole Burning” Effects	1171
30.2	Elementary Analysis of Inhomogeneous Hole Burning	1177
30.3	Saturation Absorption Spectroscopy	1184
30.4	Saturated Dispersion Effects	1192
30.5	Cross-Relaxation Effects	1195
30.6	Inhomogeneous Laser Oscillation: Lamb Dips	1199

Chapter 31 Magnetic-Dipole Transitions

31.1	Basic Properties of Magnetic-Dipole Transitions	1213
31.2	The Iodine Laser: A Magnetic-Dipole Laser Transition	1223
31.3	The Classical Magnetic Top Model	1228
31.4	The Bloch Equations	1236
31.5	Transverse Response: The AC Susceptibility	1243
31.6	Longitudinal Response: Rate Equation	1249
31.7	Large-Signal and Coherent-Transient Effects	1256

Index1267

PREFACE



This book presents a detailed and comprehensive treatment of laser physics and laser theory which can serve a number of purposes for a number of different groups. It can provide, first of all, a textbook for graduate students, or even well-prepared seniors in science or engineering, describing in detail how lasers work, and a bit about the applications for which lasers can be used. Problems, references and illustrations are included throughout the book.

Second, it can also provide a solid and detailed description of laser physics and the operational properties of lasers for the practicing engineer or scientist who needs to learn about lasers in order to work on or with them.

Finally, the advanced sections of this text are sufficiently detailed that this book will provide a useful one-volume reference for the experienced laser engineer or laser researcher's bookshelf. The discussions of advanced laser topics, such as optical resonators, Q-switching, mode locking, and injection locking, extend far enough into the current state of the art to provide a working reference on these and similar topics. References for further reading in the recent literature are included in nearly every section.

One unique feature of this book is that it removes much of the quantum mystique from "quantum electronics" (the generic label often applied to lasers and laser applications). Many people think of lasers as quantum devices. In fact, however, most of the basic concepts of laser physics, and virtually all the practical details, are classical in nature. Lasers (and masers) of all types and in all frequency ranges are simply electronic devices, of great interest and importance to the electronics engineer.

In the analogous case of semiconductor electronics, for example, the transistor is not usually thought of as a quantum device. Mental images of holes and electrons as classical charged particles which accelerate, drift, diffuse and recombine are used both by semiconductor device engineers to do practical device engineering, and by solid-state physics researchers to understand sophisticated physics experiments. These classical concepts serve to explain and make understandable what is otherwise a complex quantum picture of energy bands, Bloch wavefunctions, Fermi-Dirac distributions, and occupied or unoccupied quantum states. The same simplification can be accomplished for lasers, and laser devices can then be very well understood from a primarily classical viewpoint, with only limited appeals to quantum terms or concepts.

The approach in this book is to build primarily upon the classical electron oscillator model, appropriately extended with a descriptive picture of atomic energy levels and level populations, in order to provide a *fully accurate, detailed and physically meaningful* understanding of lasers. This can be accomplished

without requiring a previous formal background in quantum theory, and also without attempting to teach an abbreviated and inadequate course in this subject on the spot. A thorough understanding of laser devices is readily available through this book, in terms of classical and descriptively quantum-mechanical concepts, without a prior course in quantum theory.

I have also attempted to review, at least briefly, relevant and necessary background material for each successive topic in each section of this book. Students will find the material most understandable, however, if they come to the book with some background in electromagnetic theory, including Maxwell's equations; some understanding of the concept of electromagnetic polarization in an atomic medium; and some familiarity with the fundamentals of electromagnetic wave propagation. An undergraduate-level background in optics and in Fourier transform concepts will certainly help; and although familiarity with quantum theory is not required, the student must have at least enough introduction to atomic physics to be prepared to accept that atoms do have quantum properties, especially quantum energy levels and transitions between these levels.

The discussions in this book begin with simple physical descriptions and then go into considerable analytical detail on the stimulated transition process in atoms and molecules; the basic amplification and oscillation processes in laser devices; the analysis and design of laser beams and resonators; and the complexities of laser dynamics (including spiking, Q-switching, mode locking, and injection locking) common to all types of lasers. We illustrate the general principles with specific examples from a number of important common laser systems, although this book does not attempt to provide a detailed handbook of different laser systems. Extensive references to the current literature will, however, guide the reader to this kind of information.

There is obviously a large amount of material in this book. The author has taught an introductory one-quarter "breadth" course on basic laser concepts for engineering and applied physics students using most of the material from the first part of the book on "Basic Laser Physics" (see the Table of Contents), especially Chapters 1–4, 6–8 and 11–13. A second-quarter "depth" course then adds more advanced material from Chapters 5, 9, 10, 30, 31 and selected sections from Chapters 24–29. A complete course on optical beams and resonators can be taught from Chapters 14 through 23.

I am very much indebted to many colleagues for help during the many years while this book was being written. I wish it were possible to thank by name all the students in my classes and my research group who lived through too many years of drafts and class notes. Special thanks must go to Judy Clark, who became a *TeX* and computer expert and did so much of the editing and manuscript preparation; to the Air Force Office of Scientific Research for supporting my laser research activities over many years; to Stanford University, and especially to Donald Knuth, for providing the environment, and the computerized text preparation tools, in which this book could be written; and to the Alexander von Humboldt Foundation and the Max Planck Institute for Quantum Optics in Munich, who supplied the opportunity for the manuscript at last to be completed. Finally, there are my wife Jeannie, and my family, who made it all worthwhile.

Anthony E. Siegman

UNITS AND NOTATION



The units and dimensions in this book are almost entirely mks, or SI, except for a few concessions to long-established habits such as expressing atomic densities N in atoms/cm³ and cross sections σ in cm². Such non-mks values should of course always be converted to mks units before plugging them into formulas.

In general, lower-case symbols in bold-face type such as $\mathbf{E}(r, t)$, $\mathbf{b}(r, t)$, $\mathbf{h}(r, t)$, and so on refer to electromagnetic field quantities as real vector functions of space and time, while $E(r, t)$, $b(r, t)$, $h(r, t)$, etc., refer to the scalar counterparts of the same quantities. Bold-face capital letters \mathbf{E} , \mathbf{B} , \mathbf{H} , etc., refer to the complex phasor amplitudes of the same vector quantities with $e^{j\omega t}$ variations, while \tilde{E} , \tilde{B} , \tilde{H} , etc., are the complex phasor amplitudes of the corresponding scalars. As illustrated here, complex quantities are sometimes, but not always, identified by a superposed tilde.

In writing sinusoidal signals and waves, waves propagating toward positive z are written in the “electrical engineer’s form” of $\exp j(\omega t - \beta z)$ rather than the “physicist’s form” of $\exp i(kz - \nu t)$. (This of course does not imply that $i \equiv -j$!) Linewidths Δf , $\Delta\omega$, $\Delta\lambda$ and pulsedwidths Δt , τ or T , unless specifically noted, always mean the full width at half maximum (FWHM).

In contrast to much of the published literature, an attenuation or gain coefficient α in this book always refers to an *amplitude* or *voltage* growth rate, such as for example $\mathcal{E}(z) = \mathcal{E}(0) \exp \pm \alpha z$. Signal powers or intensities in this book, therefore, always grow or attenuate with exponential growth coefficients 2α rather than α .

The notation in the book has a few other minor idiosyncrasies. First, we are often concerned with signals and waves inside laser crystals, in which the host crystal itself has a dielectric constant ϵ and an index of refraction n even without any atomic transition present. To take the dielectric properties of a possible host medium into account, the symbols ϵ , c and λ in formulas in this text always refer to the dielectric permeability, velocity of light and wavelength of the radiation in the dielectric medium if there is one. We then use c_0 and λ_0 in the few cases where it is necessary to refer to these same quantities specifically in vacuum. The advantage of this choice is that all our formulas involving ϵ , c and λ remain correct with or without a dielectric host medium, without needing to clutter these formulas with different powers of the refractive index n .

The other special convention peculiar to this book is the nonstandard manner in which we define the complex susceptibility $\tilde{\chi}_{at}$ associated with a resonant atomic transition. In brief, we define the linear relationship between the induced polarization \tilde{P}_{at} on an atomic transition in a laser medium and the electric field \tilde{E} that produces this polarization by the convention that $\tilde{P}_{at} = \tilde{\chi}_{at}\epsilon\tilde{E}$ where ϵ is the dielectric permeability of the host laser crystal rather than the vacuum value ϵ_0 usually used in this definition. The merits of this nonstandard approach are argued in Chapter 2.

LIST OF SYMBOLS



Throughout this text we attempt to follow a consistent notation for subscripts, using the conventions that:

- a = either *atomic*, as in atomic transition frequency ω_a or homogeneous atomic linewidth $\Delta\omega_a$; or sometimes *absorption*, as in absorption coefficient α_a .
- c = *cavity*, as in cavity decay time τ_c or cavity energy decay rate γ_c ; also, *carrier*, as in carrier frequency ω_c .
- d = *doppler*, as in doppler broadening with linewidth $\Delta\omega_d$, and by extension any other kind of inhomogeneous broadening.
- e = *external*, as in cavity external coupling factor δ_e or external decay rate γ_e ; also, sometimes, *effective*, as in effective lifetime or pumping rate.
- m = *molecular* or *maser*, generally used to refer to atomic or maser or laser quantities, e.g., laser gain coefficient α_m or laser growth rate γ_m .
- o = *ohmic*, referring generally to internal ohmic and/or scattering losses, as in the ohmic loss coefficient α_0 or ohmic cavity decay rate γ_0 . Also used in several other ways, generally to indicate an initial value; a thermal equilibrium value; a small-signal or unsaturated value; a midband value; or a free-space (vacuum) values, as in c_0 , ϵ_0 , and λ_0 .
- p = *pump*, as in pumping rate R_p or pump transition probability W_p .

We also frequently use $ax \equiv axial$; $avail \equiv available$; $circ \equiv circulating$; $eff \equiv effective$; $eq \equiv equivalent$; $inc \equiv incident$; $opt \equiv optimum$; $out \equiv output$; $refl \equiv reflected$; $rt \equiv round-trip$; $sat \equiv saturation$; $sp \equiv spontaneous$ or *spiking*; $ss \equiv small-signal$ or *steady-state*; and $th \equiv threshold$ as compound subscripts.

A partial list of symbols used in the text then includes:

- α = exponential gain or loss coefficient for amplitude (or voltage); also, amplitude parameter for gaussian optical pulse
- α'' = second derivative of $\alpha(\omega)$ with respect to ω
- $\tilde{\alpha}_n$ = complex amplitude of n -th order Hermite-gaussian mode
- α_m = maser/laser/molecular gain (or loss) coefficient
- α_0 = ohmic and/or scattering loss coefficient
- β = propagation constant, including host dielectric effects, but usually not loss or atomic transition effects; also, chirp parameter for gaussian pulse; relaxation-time ratio in multilevel laser pumping systems; Bohr magneton
- β_I = Nuclear magneton
- β', β'' = first and second derivatives of $\beta(\omega)$ with respect to ω
- $\Delta\beta_m$ = added propagation constant term due to reactive part of an atomic transition

- γ = in general, an energy or population decay rate
 γ_c = decay rate for cavity stored energy ($\equiv 1/\tau_c$)
 γ_i = total downward population decay rate from energy level E_i
 γ_{ij} = population decay rate from upper level E_i to lower level E_j
 γ_{nr} = nonradiative part of total decay rate for a classical oscillator or an atomic transition
 γ_{rad} = radiative decay rate for classical electron oscillator or real atomic transition
 $\tilde{\gamma}$ = complex eigenvalue for optical resonator or lensguide
 $\tilde{\gamma}_{mn}$ = complex eigenvalue for mn -th order transverse eigenmode
 $\Gamma = \alpha + j\beta$ = complex propagation constant for an optical wave
 $\Gamma = \alpha - j\beta$ = complex gaussian pulse parameter
 δ = coefficient of (logarithmic) fractional power gain or loss, per bounce or per round trip
 δ_c = total (round-trip) power loss coefficient due to cavity losses plus external coupling
 δ_e = cavity loss coefficient due to external coupling only
 δ_m = power gain coefficient due to laser atoms
 δ_0 = cavity loss coefficient due to internal (ohmic) losses only
 Δ_m = AM or FM modulation index
 ϵ = dielectric permeability of a medium
 ϵ_0 = dielectric permeability of free space (vacuum)
 η = efficiencies of various sorts; also, characteristic impedance $\sqrt{\mu/\epsilon}$ of a dielectric medium
 η_0 = characteristic impedance of free space (vacuum)
 λ = optical wavelength (in a medium); also, eigenvalue for optical ray matrix
 λ_0 = optical wavelength in vacuum
 λ_a, λ_b = eigenvalues of periodic lensguide or $ABCD$ matrix
 Λ = spatial period of optical grating
 μ = electric or magnetic dipole moment; also, magnetic permeability of a magnetic medium
 μ_e = electric dipole moment
 μ_m = magnetic dipole moment
 μ_0 = magnetic permeability of free space
 ρ = amplitude reflection or transmission of optical mirror or beamsplitter; also, distance between two points; $\rho(\omega)$ = cavity mode density
 $\tilde{\rho}$ = complex amplitude reflection or transmission of optical mirror or beam-splitter
 σ = ohmic conductivity; also, transition cross section, standard deviation
 σ_{ij} = cross section for stimulated transition from level E_i to E_j
 τ = lifetime or decay time
 τ_c = cavity decay time due to all internal losses plus external coupling
 τ_i = total lifetime (energy decay time) for energy level E_i
 θ, ϕ, ψ = phase shifts and phase angles of various sorts
 $\psi(r, t)$ = Schrödinger wave function

- ψ_{mn} = Guoy phase shift for an mn -th order gaussian beam
 $\tilde{\chi}$ = susceptibility of a dielectric or magnetic medium = $\chi' + j\chi''$
 χ', χ'' = real and imaginary parts of $\tilde{\chi}$
 $\tilde{\chi}_{at}$ = susceptibility of a resonant atomic transition
 $\tilde{\chi}_e, \tilde{\chi}_m$ = electric (magnetic) dipole susceptibilities
 ω = frequency (in radians/second)
 ω' = in general, a frequency that has been shifted, pulled, or modified in some small manner
 ω_a = atomic transition frequency
 ω_b = a beat frequency (between two signals)
 ω_c = cavity or circuit resonant frequency; also, carrier frequency
 $\omega_i(t)$ = instantaneous frequency of a phase-modulated signal
 ω_m = generally, a modulation frequency of some sort
 ω_q = resonant frequency of q -th axial mode
 ω_R = Rabi frequency on an atomic transition
 ω_{sp} = Spiking or relaxation-oscillation frequency
 $\delta\omega_q$ = frequency pulling of axial mode frequency ω_q
 $\Delta\omega$ = linewidth, or frequency tuning, in radians/sec
 $\Delta\omega_a$ = atomic linewidth (FWHM) in radians/sec
 $\Delta\omega_{ax}$ = axial mode spacing between adjacent axial modes
 Ω = solid angle; also, radian frequency or rotation rate

 \tilde{a}_i, \tilde{b}_i = normalized wave amplitudes
 A = area
 A_{ji} = Einstein A coefficient on $E_j \rightarrow E_i$ transition
 $ABCD$ = matrix elements for optical ray matrix or paraxial optical system
 b = magnetic field as real function of space and time; also, confocal parameter for gaussian beam
 \mathbf{b} = magnetic field as real vector function of space and time; also, confocal parameter for gaussian beam
 B = magnetic field; also, pressure-broadening coefficient or "B integral" for nonlinear interaction
 \tilde{B} = phasor amplitude of sinusoidal B field
 c = velocity of light in a material medium
 c_0 = velocity of light in vacuum
 C = in general, an unspecified constant; also, electrical capacitance; coupling coefficient in mode competition analysis
 CC = complex conjugate (of preceding term)
 CEO = classical electron oscillator model
 d = electric displacement as real function of space and time; also, distance or displacement
 \mathbf{d} = electric displacement as real vector function of space and time
 D = dimensionless dispersion parameter
 \tilde{D} = phasor amplitude of sinusoidal electric displacement
 e = magnitude of electronic charge
 \mathcal{E} = electric field; usually, real field $\mathcal{E}(x, t)$ as function of space and time

- \tilde{E} = phasor amplitude of sinusoidal E field
 $E_n(t)$ = amplitude of n -th mode in a normal mode expansion
 f = frequency in Hz (\equiv cycles/sec); also, lens focal length
 $f^\#$ = lens f -number
 Δf = linewidth, or frequency detuning, in Hz
 Δf_a = atomic transition linewidth (FWHM) in Hz
 Δf_d = doppler or inhomogeneous linewidth (FWHM) in Hz
 F = oscillator strength for an atomic transition; also, lens f -number
 \mathcal{F} = finesse, of interferometer or laser cavity
 $\tilde{F}(x)$ = Fresnel integral function
 F_{ji} = oscillator strength of $E_j \rightarrow E_i$ atomic transition $\equiv \gamma_{\text{rad},ji}/3\gamma_{\text{rad},\text{ceo}}$
 g = amplitude (or voltage) gain, as a number; also, gaussian stable resonator parameter; magnetic resonance g value
 $g(v), g(\omega)$ = normalized lineshapes
 \tilde{g} = complex amplitude (or voltage) gain, as a (complex) number
 g_i, g_j = degeneracy factors for quantum energy levels E_i and E_j
 g_I = nuclear magnetic resonance g value
 \tilde{g}_{rt} = round-trip voltage gain inside an optical cavity
 G = power gain (as a number); also, electrical conductance
 G_{dB} = power gain in decibels
 h = magnetic intensity as real function of space and time; also, Planck's constant
 $\hbar = h/2\pi$
 \mathbf{h} = magnetic H field as real vector function of space and time
 h_n = n -th order polynomial function
 \tilde{H} = phasor amplitude of sinusoidal H field
 H_n = n -th order hermite polynomial
 I = intensity (power/unit area) of an optical wave; also sometimes, loosely, total power in the wave
 I_m = modified Bessel function of order m
 I_{sat} = amplifier (or absorber) saturation intensity
 j = current density as real function of space and time; also, $\sqrt{-1}$
 \mathbf{j} = current density as real vector function of space and time
 \tilde{J} = phasor amplitude of sinusoidal current density
 J_m = Bessel function of order m
 \mathbf{k} = propagation vector of optical wave $= \omega/c$
 K = scalar constant in various equations (especially coupled rate equations); also, spring constant in classical oscillator model
 L = length; electrical inductance
 m = electron mass; also, magnetization (magnetic dipole moment per unit volume) as real function of time
 \mathbf{m} = magnetization (magnetic dipole moment per unit volume) as real vector function of space and time
 m, \tilde{m} = half-trace parameter for ray or $ABCD$ matrix
 M = proton mass; molecular mass

- \tilde{M} = phasor amplitude of sinusoidal magnetic dipole moment
 M = optical ray matrix or $ABCD$ matrix
 n = refractive index; also, photon number $n(t)$ (number of photons per cavity mode)
 n_2 = optical Kerr coefficient n_{2E} or n_{2I}
 N = atomic number or level population; usually interpreted as atoms per unit volume, sometimes as total number of atoms
 ΔN = population difference, or population difference density, on an atomic transition ($\Delta N_{ij} \equiv N_i - N_j$)
 N = Fresnel number $a^2/L\lambda$ for an optical beam or resonator
 N_c = collimated Fresnel number for an unstable optical resonator
 N_{eq} = equivalent Fresnel number for an unstable optical resonator
 N_i = population, or population density, in atomic energy level E_i
 p = perimeter, period or round-trip path length, for cavities or periodic lensguides; also, electric polarization (electric dipole moment per unit volume) as real function of time, and laser mode density or mode number
 \mathbf{p} = electric polarization (electric dipole moment per unit volume) as real vector function of space and time
 p_m = path length (round-trip) through an atomic or laser gain medium
 P = power, in watts; also, pressure, in torr
 $P_n(t)$ = polarization driving term for n -th order cavity mode in coupled-mode expansion
 \tilde{P} = phasor amplitude of sinusoidal electric polarization
 q = axial mode index
 \tilde{q} = complex gaussian beam parameter or complex radius of curvature
 \hat{q} = reduced gaussian beam parameter, \tilde{q}/n
 r = amplitude reflectivity of mirror or beamsplitter; also, dimensionless or normalized pumping rate; displacement off axis of optical ray
 r' = reduced slope $n dr/dz$ for optical ray
 \mathbf{r} = shorthand for spatial coordinates x, y, z
 \tilde{r}_{ij} = complex scattering matrix element, or mirror or beamsplitter reflection coefficient
 r_p = dimensionless pumping rate or inversion ratio, relative to threshold pumping rate or threshold inversion density
 dr = volume element, dV or $dx dy dz$
 R = power reflectivity of mirror or beamsplitter ($\equiv |r|^2$); also, electrical resistance; radius of curvature for mirror, dielectric interface, or optical wave
 \hat{R} = reduced radius of curvature R/n
 R_p = pumping rate in atoms per second and, usually, per unit volume
 s = spatial frequency (cycles/unit length)
 \mathbf{s} = shorthand for transverse spatial coordinates x, y
 ds = transverse area element dA or $dx dy$
 S = multiport scattering matrix (matrix elements S_{ij})

LIST OF SYMBOLS

- t = time; also, amplitude transmission through mirror, beamsplitter, or light modulator
 \tilde{t} = complex amplitude transmission coefficient through mirror, beamsplitter or light modulator
 \tilde{t}_{ij} = complex scattering matrix element, or mirror/beamsplitter transmission coefficient
 T = power transmission of mirror or beamsplitter ($\equiv |t|^2$); also, cavity round-trip transit time, or temperature (K)
 \mathbf{T} = dimensionless susceptibility tensor
 T_b = laser oscillation build-up time
 T_{nr} = temperature of “nonradiative” surroundings
 T_{rad} = temperature of radiative surroundings
 T_1 = energy decay time, population recovery time, longitudinal relaxation time
 T_2 = dephasing time, collision time, transverse relaxation time
 T_2^* = effective T_2 or dephasing time for inhomogeneous (gaussian) transition
 \hat{u} = complex (and usually normalized) optical wave amplitude
 U = energy or, more commonly, energy density (energy per unit volume)
 U_a = energy density in a collection of atoms or atomic energy level populations
 U_{bbr} = energy density of blackbody radiation
 v = velocity of an atom, an electron, or a wave
 \tilde{v} = complex spot size for Hermite-gaussian modes
 v_g = group velocity
 v_ϕ = phase velocity
 V, V_c = volume (of a cavity mode or field pattern)
 w = gaussian spot size parameter ($1/e$ amplitude point)
 w_{ij} = total relaxation transition probability (per atom, per second) from level E_i to level E_j
 W_{ij} = stimulated transition probability (per atom, per second) from level E_i to level E_j
 W_p = pumping transition probability (per atom, per second)
 $x(t)$ = displacement of electronic charge in classical electron oscillator model
 z_D = dispersion length for dispersive pulse broadening
 z_R = Rayleigh range for a gaussian or collimated optical beam
 Z = atomic number
 2^* = dimensionless population saturation factor, with values between $2^* = 1$ (lower level empties out rapidly) and $2^* = 2$ (lower level bottlenecked)
 3^* = dimensionless polarization overlap factor for atomic interactions, with numerical value between 0 and 3

L A S E R S



AN INTRODUCTION TO LASERS

Lasers are devices that generate or amplify coherent radiation at frequencies in the infrared, visible, or ultraviolet regions of the electromagnetic spectrum. Lasers operate by using a general principle that was originally invented at microwave frequencies, where it was called microwave amplification by stimulated emission of radiation, or *maser* action. When extended to optical frequencies this naturally becomes light amplification by stimulated emission of radiation, or *laser* action.

This basic laser or maser principle is now used in an enormous variety of devices operating in many parts of the electromagnetic spectrum, from audio to ultraviolet. Practical laser devices in particular employ an extraordinary variety of materials, pumping methods, and design approaches, and find a great variety of applications. The study of laser and maser devices and their scientific applications is often referred to as the field of *quantum electronics*.

From an electronics-engineering viewpoint, the developments that followed the operation of the first ruby laser in 1960 suddenly pushed the upper limit of coherent electronics from the millimeter-wave range, using microwave tubes and transistors, out to include the submillimeter, infrared, visible, and ultraviolet spectral regions (and soft X-ray lasers are now on the horizon). All the familiar functions of coherent signal generation, amplification, modulation, information transmission, and detection are now possible at frequencies up to a million times higher, or wavelengths down to a million times shorter, than previously. But it has also become possible for engineers and scientists, in fields of technology ranging from microbiology to auto manufacture, to perform an almost unlimited variety of new and unexpected functions made possible by the short wavelengths, high powers, ultrashort pulsewidths, and other unique characteristics of these laser devices.

In the twenty-odd years since the first appearance of coherent light, lasers have become widespread and almost commonplace devices. The importance and the excitement of the laser and its applications, however, still can hardly be overestimated. The objective of this book is to explain in detail how lasers work, what the performance characteristics of typical lasers are, and how lasers are employed in a wide variety of applications. Our goal in this opening chapter is

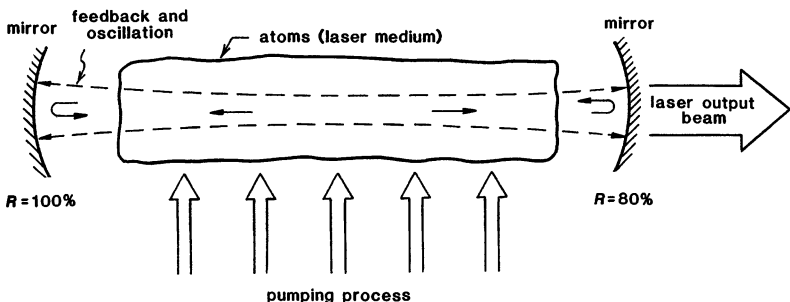


FIGURE 1.1
Elements of a typical laser oscillator.

to give an abbreviated overview of these same points, as a synopsis of what will be presented in much more detail in the remainder of the book.

1.1 WHAT IS A LASER?

Lasers, broadly speaking, are devices that generate or amplify light, just as transistors and vacuum tubes generate and amplify electronic signals at audio, radio, or microwave frequencies. Here “light” must be understood broadly, since different kinds of lasers can amplify radiation at wavelengths ranging from the very long infrared region, merging with millimeter waves or microwaves, up through the visible region and extending now to the vacuum ultraviolet and even X-ray regions. Lasers come in a great variety of forms, using many different laser materials, many different atomic systems, and many different kinds of pumping or excitation techniques. The beams of radiation that lasers emit or amplify have remarkable properties of directionality, spectral purity, and intensity. These properties have already led to an enormous variety of applications, and others undoubtedly have yet to be discovered and developed.

Essential Elements of a Laser

The essential elements of a laser device, as shown in Figure 1.1, are thus: (i) a *laser medium* consisting of an appropriate collection of atoms, molecules, ions, or in some instances a semiconducting crystal; (ii) a *pumping process* to excite these atoms (molecules, etc.) into higher quantum-mechanical energy levels; and (iii) suitable *optical feedback elements* that allow a beam of radiation to either pass once through the laser medium (as in a laser amplifier) or bounce back and forth repeatedly through the laser medium (as in a laser oscillator).

These elements come in a great variety of forms and fashions, as we will see when we begin to examine each of them in more detail.

Laser Atoms and Laser Pumping

For simplicity we will from now on use “atoms” as a general term for whatever kind of atoms or molecules or ions or semiconductor electrons may be used as the laser medium. A pumping process is then required to excite

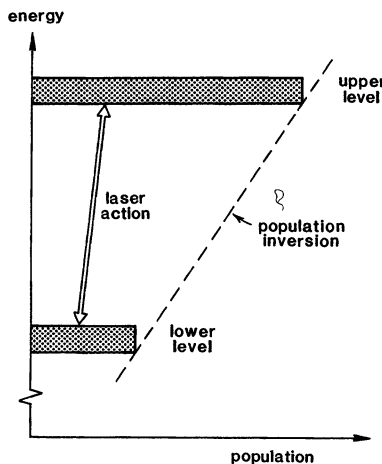


FIGURE 1.2
Population inversion between two quantum-mechanical energy levels.

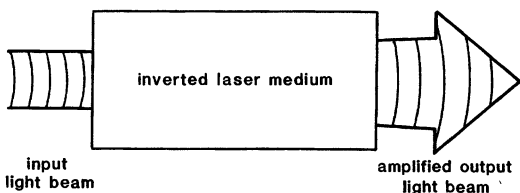


FIGURE 1.3
Laser amplification.

these atoms into their higher quantum-mechanical energy levels. Practical laser materials can be pumped in many ways, as we will describe later in this text.

For laser action to occur, the pumping process must produce not merely excited atoms, but a condition of *population inversion* (Figure 1.2), in which more atoms are excited into some higher quantum energy level than are in some lower energy level in the laser medium. It turns out that we can obtain this essential condition of population inversion in many ways and with a wide variety of laser materials—though sometimes only with substantial care and effort.

Laser Amplification

Once population inversion is obtained, electromagnetic radiation within a certain narrow band of frequencies can be coherently amplified if it passes through the laser medium (Figure 1.3). This amplification bandwidth will extend over the range of frequencies within about one atomic linewidth or so on either side of the quantum transition frequency from the more heavily populated upper energy level to the less heavily populated lower energy level.

Coherent amplification means in this context that the output signal after being amplified will more or less exactly reproduce the input signal, except for a substantial increase in amplitude. The amplification process may also add some small phase shift, a certain amount of distortion, and a small amount of

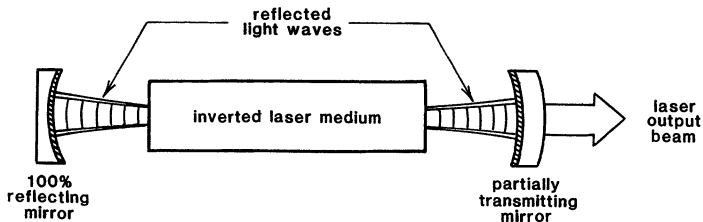


FIGURE 1.4
Laser oscillation.

amplifier noise. Basically, however, the amplified output signal will be a coherent reproduction of the input optical signal, just as in any other coherent electronic amplification process.

Laser Oscillation

Coherent amplification combined with feedback is, of course, a formula for producing oscillation, as is well known to anyone who has turned up the gain on a public-address system and heard the loud squeal of oscillation produced by the feedback from the loudspeaker output to the microphone input. The feedback in a laser oscillator is usually supplied by mirrors at each end of the amplifying laser medium, carefully aligned so that waves can bounce back and forth between these mirrors with very small loss per bounce (Figure 1.4). If the net laser amplification between mirrors, taking into account any scattering or other losses, exceeds the net reflection loss at the mirrors themselves, then coherent optical oscillations will build up in this system, just as in any other electronic feedback oscillator.

When such coherent oscillation does occur, an output beam that is both highly directional and highly monochromatic can be coupled out of the laser oscillator, either through a partially transmitting mirror on either end, or by some other technique. This output in essentially all lasers will be both extremely bright and highly coherent. The output beam may also in some cases be extremely powerful. Just what we mean by "bright" and by "coherent" we will explain later.

REFERENCES

The first stimulated emission devices, before lasers, were various kinds of masers, which operated on essentially the same basic physical principles, but at much lower frequencies and with much different experimental techniques. For an overview and unified approach to all these devices, see my earlier texts *Microwave Solid-State Masers* (McGraw-Hill, 1964) and *An Introduction to Lasers and Masers* (McGraw-Hill, 1971).

Some other good books on lasers can be found. A more elementary introduction, with good illustrations, is D. C. O'Shea, W. R. Callen, and W. T. Rhodes, *Introduction to Lasers and Their Applications* (Addison-Wesley, 1977). A good general coverage is also given in O. Svelto, *Principles of Lasers* (Plenum Press, 1982). Two well-known texts by A. Yariv are *Introduction to Optical Electronics* (Rinehart and Winston, 1971) and the more advanced *Quantum Electronics* (Wiley, 1975).

For full quantum-mechanical treatments of lasers, two good choices are M. Sargent III, M. O. Scully, and W. E. Lamb, Jr., *Laser Physics* (Addison-Wesley, 1977), and H. Haken, *Laser Theory* (Springer-Verlag, 1983).

A useful short bibliographic survey of laser references, aimed particularly at the college teacher, can be found in "Resource Letter L-1: Lasers," by D. C. O'Shea and D. C. Peckham, *Am. J. Phys.* **49**, 915–925 (October 1981).

For more advanced information on various laser topics, the four-volume *Laser Handbook*, edited by F. T. Arecchi and E. O. Schulz-Dubois (North-Holland, Amsterdam, 1972), provides an encyclopedic source with detailed articles on nearly every topic in laser physics, devices, and applications. If you'd like to look at some of the important original literature on lasers for yourself, well-chosen selections can be found in F. S. Barnes, ed., *Laser Theory* (IEEE Press Reprint Series, IEEE Press, 1972), or in D. O'Shea and D. C. Peckham, *Lasers: Selected Reprints* (American Association of Physics Teachers, Stony Brook, N. Y., 1982).

If you would like to do experiments with a home-made laser or just see how one might be constructed, a useful collection of articles from the "Amateur Scientist" section of *Scientific American* has been reprinted under the title *Light and Its Uses*, with introduction by Jearl Walker (W. H. Freeman and Company, 1980). Topics covered include simple helium-neon, argon-ion, carbon-dioxide, semiconductor, tunable dye, and nitrogen lasers, plus experiments on holography, interferometry, and spectroscopy.

Problems for 1.1

1. *Diagramming the electromagnetic spectrum.* On a large sheet of paper lay out a logarithmic frequency scale extending from the audio range (say, $f = 10$ Hz) to the far ultraviolet or soft X-ray region (say, $\lambda = 100$ Å). Mark both frequency and wavelength below the same scale in powers of 10 in appropriate units, e.g., Hz, kHz, MHz, and m, mm, μm . (You might also mark a "wavenumber" scale for $1/\lambda$ in units of cm^{-1} , and an energy scale for $\hbar\omega$ in units of eV.) Above the scale indicate the following landmarks (plus any other significant ones that occur to you):

- Audio frequency range (human ear) (20–15000 Hz)
- Standard AM and FM broadcast bands (535–1605 kHz, 88–108 MHz)
- Television channels 2–6 (54–88 MHz) and 7–13 (174–216 MHz)
- Microwave radar "S" and "X" bands (2–4 and 8–12 GHz)
- Visible region (human eye)
- Important laser wavelengths, including:

HCN far-IR laser (311, 337, 545, 676, 744 μm)

H_2O far-IR laser (28, 48, 120 μm)

CO_2 laser (9.6–10.6 μm)

CO laser (5.1–6.5 μm)

HF chemical laser (2.7–3.0 μm)

Nd:YAG laser (1.06 μm)

He-Ne lasers (1.15 μm , 633 nm)

GaAs semiconductor laser (870 nm)

Ruby laser (694 nm)

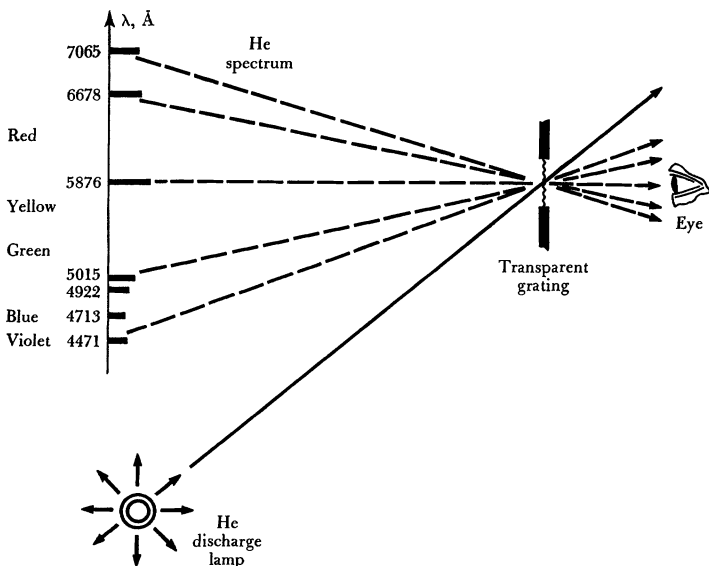


FIGURE 1.5
Helium discharge spectrum observed through an inexpensive replica transmission grating.

Rhodamine 6G dye laser (560–640 nm)

Argon-ion laser (488–515 nm)

Pulsed N₂ discharge laser (337 nm)

Pulsed H₂ discharge laser (160 nm)

1.2 ATOMIC ENERGY LEVELS AND SPONTANEOUS EMISSION

Our objective in this section is to give a very brief introduction to the concepts of atomic energy levels and of spontaneous emission between those levels. We attempt to demonstrate heuristically that atoms (or ions, or molecules) have quantum-mechanical energy levels; that atoms can be pumped or excited up into higher energy levels by various methods; and that these atoms then make spontaneous downward transitions to lower levels, emitting radiation at characteristic transition frequencies in the process. (Readers already familiar with these ideas may want to move on to Section 1.3.)

The Helium Spectrum

Figure 1.5 illustrates a simple experiment in which a small helium discharge lamp (or lacking that, a neon sign) is viewed through an inexpensive transmission diffraction grating of the type available at scientific hobby stores. (If you have never done such an experiment, try to do this demonstration for yourself.)

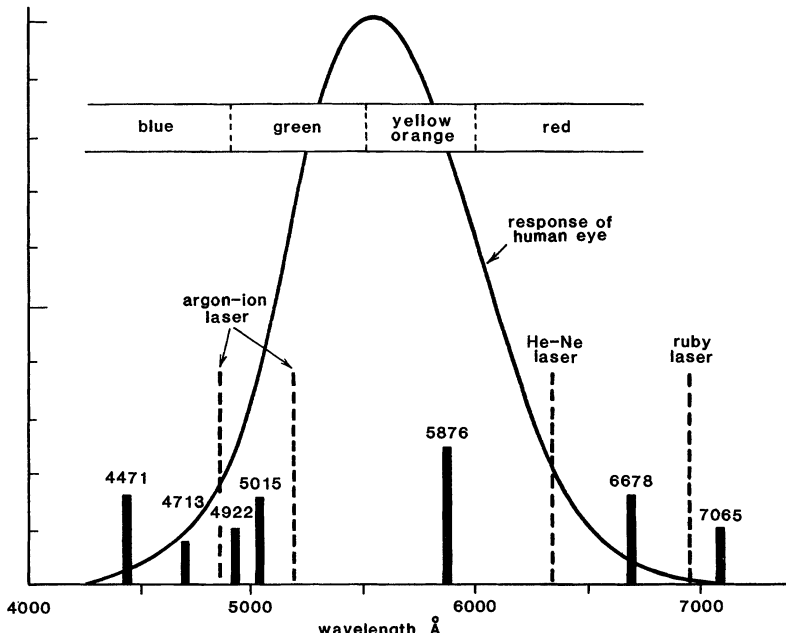


FIGURE 1.6

Helium spectral lines, four common laser lines, and human visual sensitivity.

When viewed directly the discharge helium lamp appears to emit pinkish-white light. When viewed through the diffraction grating, however, each wavelength in the light is diffracted at a different angle. Upon looking through the grating, you therefore observe multiple images of the lamp, each displaced to a different discrete angle, and each made up of a different discrete wavelength or color emitted by the helium discharge. A strong yellow line at 5876\AA (or 588 nm) is particularly evident, but violet, green, blue, red, and deep red lines are also readily seen. These visible wavelengths are plotted in Figure 1.6, along with (as a matter of curiosity) the relative response of the human eye, and the wavelengths of four of the more common visible lasers.

These different wavelengths are, of course, only a few of the discrete components in the fluorescence spectrum of the helium atoms. In the helium discharge tube a large number of neutral helium atoms are present, along with a small number of free electrons and a matching number of ionized helium atoms to conduct electrical current. The free electrons are accelerated along the tube by the applied electric field, and collide after some distance with the neutral helium atoms. The helium atoms are thereby excited into various higher *quantum energy levels* characteristic of the helium atoms. A small fraction are also ionized by the electron collisions, thereby maintaining the electron and ion densities against recombination losses, which occur mostly at the tube walls.

After being excited into upper energy levels, the helium atoms soon give up their excess energy by dropping down to lower energy levels, emitting spontaneous electromagnetic radiation in the process. This *spontaneous emission* or *fluorescence* is the mechanism that produces the discrete spectral lines.

The Discovery of Helium

Helium was first identified as a new element by its fluorescence spectrum in the solar corona. During the solar eclipse of 1868 a bright yellow line was observed in the emission spectrum of the Sun's prominences by at least six different observers. This line could be explained in relation to the known spectral lines of already identified elements only by postulating the existence of a new element, helium, named after the Greek word Helios, the Sun. This same element was later, of course, identified and isolated on Earth.

Quantum Energy Levels

Figure 1.7 shows the rather complex set of quantum energy levels possessed by even so simple an atom as the He atom. The solid arrows in this diagram designate some of the spontaneous-emission transitions that are responsible for the stronger lines in the visible spectrum of helium. The dashed arrows indicate a few of the many additional transitions that produce spontaneous emission at longer or shorter wavelengths in the infrared or ultraviolet portions of the spectrum, lines which we can "see" only with the aid of suitable instruments.

Every atom in the periodic table, as well as every molecule or ion, has its own similar characteristic set of quantum energy levels, and its own characteristic spectrum of fluorescent emission lines, just as does the helium atom. Understanding and explaining the exact values of these quantum energy levels for different atoms and molecules, through experiment or through complex quantum analyses, is the task of the spectroscopist. The complex labels given to each energy level in Figure 1.7 are part of the working jargon of the spectroscopist or atomic physicist. In this text we will not be concerned with predicting the quantum energy levels of laser atoms, or even with understanding their complex labeling schemes, except in a few simple cases. Rather, we will accept the positions and properties of these levels as part of the data given us by spectroscopists, and will concentrate on understanding the dynamics and the interactions through which laser action is obtained on these transitions.

Planck's Law

The relationship between the frequency ω_{21} emitted on any of these transitions and the energies E_2 and E_1 of the upper and lower atomic levels is given by Planck's Law

$$\omega_{21} = \frac{E_2 - E_1}{\hbar}, \quad (1)$$

where $\hbar \equiv h/2\pi$, and Planck's constant $h = 6.626 \times 10^{-34}$ Joule-second.

In this text, as in real life, optical and infrared radiation will sometimes be characterized by its frequency ω , and sometimes by its wavelength λ_0 expressed in units such as Ångströms (Å), nanometers (nm), or microns (μm). Quantum transitions and the associated transition frequencies are also very often characterized by their transition energy or photon energy, measured in units of electron volts (eV), or their inverse wavelength $1/\lambda_0$ measured in units of "wavenumbers"

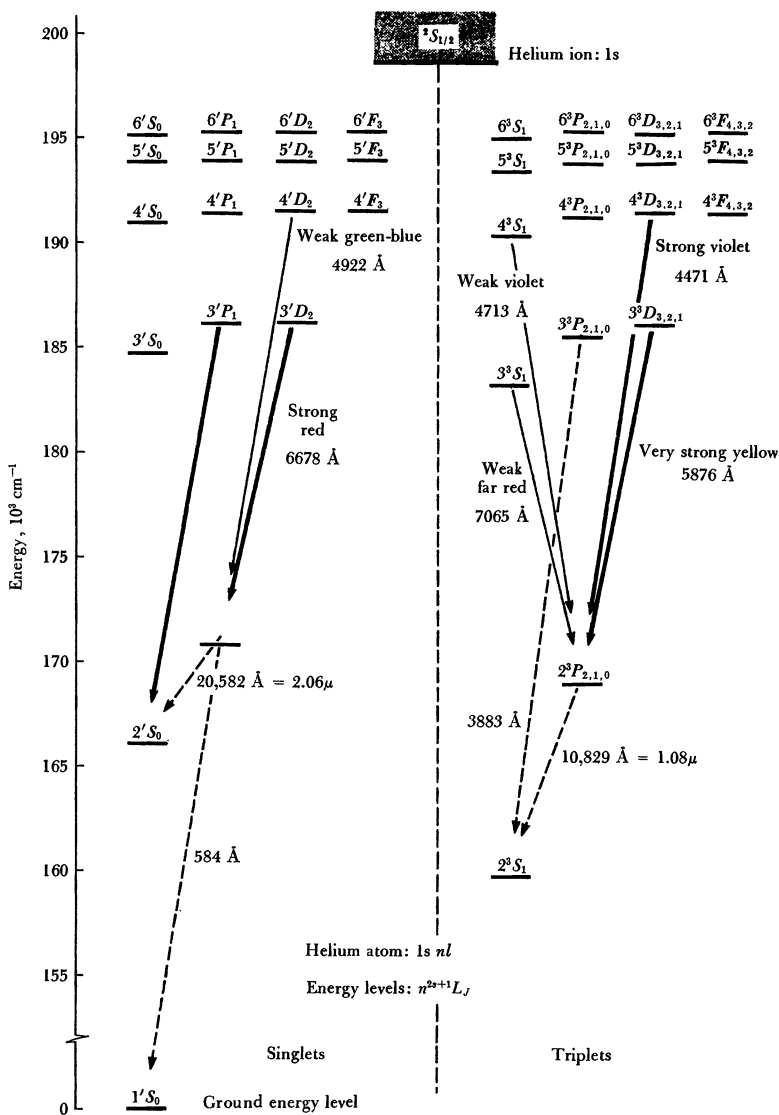


FIGURE 1.7

An energy-level diagram for the helium atom, showing the transitions responsible for the strong visible spectrum, as well as various ultraviolet and infrared transitions.

or cm^{-1} . Since we will be jumping back and forth between these units, it will be worthwhile to gain some familiarity with their magnitudes. Some useful rules of

thumb to remember are that

$$1 \text{ } \mu\text{m} \text{ ("one micron")} \equiv 1,000 \text{ nm} \equiv 10000\text{\AA} \quad (2)$$

and that, in suitable energy units,

$$[\text{transition energy } E_2 - E_1 \text{ in eV}] \approx \frac{1.24}{[\text{wavelength } \lambda_0 \text{ in microns}]} \quad (3)$$

Hence 10000\AA or $1 \mu\text{m}$ matches up with $10,000 \text{ cm}^{-1}$ or $\sim 1.24 \text{ eV}$. A visible wavelength of 500 nm or 5000\AA or $0.5 \mu\text{m}$ thus corresponds to a photon energy of $20,000 \text{ cm}^{-1}$ or $\sim 2.5 \text{ eV}$. Note that this also corresponds to a transition frequency of $\omega_{21}/2\pi = 6 \times 10^{14} \text{ Hz}$, expressed in the conventional units of cycles per second, or Hertz.

Energy Levels in Solids: Ruby or Pink Sapphire

As another simple illustration of energy levels, try shining a small ultraviolet lamp (sometimes called a “mineral light”) on any kind of fluorescent mineral, such as a piece of pink ruby or a sample of glass doped with a rare-earth ion, or on a fluorescent dye such as Rhodamine 6G. These and many other materials will then glow or fluoresce brightly at certain discrete wavelengths under such ultraviolet excitation. A sample of ruby, for example, will fluoresce very efficiently at $\lambda \approx 694 \text{ nm}$ in the deep red, a sample of crystal or glass doped with, say, the rare-earth ion terbium, Tb^{3+} , will fluoresce at $\lambda \approx 540 \text{ nm}$ (bright green), and a liquid sample of Rhodamine 6G dye will fluoresce bright orange.

Since ruby was the very first laser material, and is still a useful and instructive laser system, let us examine its fluorescence in more detail. Figure 1.8 shows a more sophisticated version of such an experiment, in which a scanning monochromator plus an optical detector are used to examine the ruby fluorescent emission in more detail. The lower trace shows the two very sharp (for a solid) and very closely spaced deep-red emission lines that will be observed from a good-quality ruby sample cooled to liquid-helium temperature. (At higher temperatures these lines will broaden and merge into what appears to be a single emission line.)

Figure 1.9 shows the crystal structure of ruby. Ruby consists essentially of lightly doped sapphire, Al_2O_3 , with the darker spheres in the figure indicating the Al^{3+} ions. (The lattice planes shown in the figure are $\sim 2.16\text{\AA}$ apart.) Sapphire is a very hard, colorless (when pure), transparent crystal which can be grown in large and optically very good samples by flame-fusion techniques. The transparency of pure sapphire in the visible and infrared means that its Al^{3+} and O^{2-} atoms, when they are bound into the sapphire crystal lattice, have no absorption lines from their ground energy levels to levels anywhere in the infrared or visible regions. Indeed, no optical absorption appears in pure sapphire below the insulating band gap of the crystal in the ultraviolet.

We can, however, replace a significant fraction (several percent) of the Al^{3+} ions in the lattice by chromium or Cr^{3+} ions. The sapphire lattice as a result acquires a pink tint at low chromium concentrations, or a deeper red color at higher concentrations, and becomes what is called “pink ruby.” The individual chromium ions, when they are bound into the sapphire lattice, have a set of quantum energy levels that are associated with partially filled inner electron shells in the Cr^{3+} ion. These energy levels are located as shown in Figure 1.10.

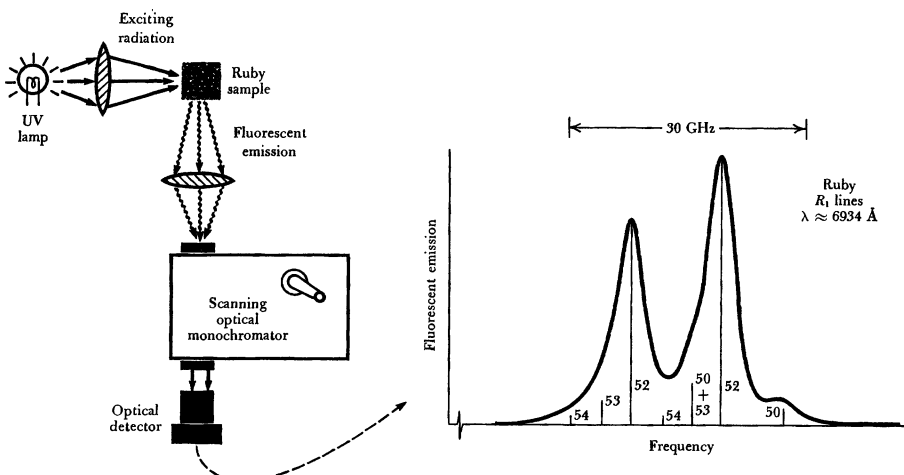


FIGURE 1.8

Fluorescent emission from a ruby crystal. The numbers under the spectrum indicate the slightly shifted transition frequencies corresponding to different isotopes of chromium.

The chromium ions can then absorb incident light in broad wavelength bands extending across much of the visible and near ultraviolet, by making transitions upward from the ground or 4A_2 Cr^{3+} energy level to the series of broad bands or groups of levels labeled 4F and 2F in Figure 1.10. The chromium ions that are excited up into these levels then drop down by rapid nonradiative processes (which we will discuss shortly) to the two sharp 2E levels shown in the figure. From there, these ions relax across the remaining energy gap down to the ground state by almost totally radiative relaxation, emitting the deep-red fluorescent emission characteristic of ruby. (The two sharp 2E levels are often called the R_1 and R_2 levels, with most of the fluorescent emission coming from the lower or R_1 level. The two very sharp emission lines shown in Figure 1.10 then represent the separate transitions from the R_1 level down to the two closely spaced sublevels of the 4A_2 ground level.)

Synthetic Sources of Pink Ruby

Sapphire, or rather pink ruby, was first grown in large amounts for use as jewels in the Swiss watch industry (it is said the pink color was added to make the tiny jewels easier to see and handle). Note that the energy levels of the Cr^{3+} ion in ruby are very strongly shifted by Stark effects associated with the bonding of the Cr^{3+} ion to the surrounding lattice ions. Hence these levels are very different from what would be the energy levels of an isolated Cr^{3+} ion in free space. Many other colors of sapphire can also be created by adding other impurities, such as Fe, Mn, or Co, but only chromium-doped sapphire makes a good laser material.

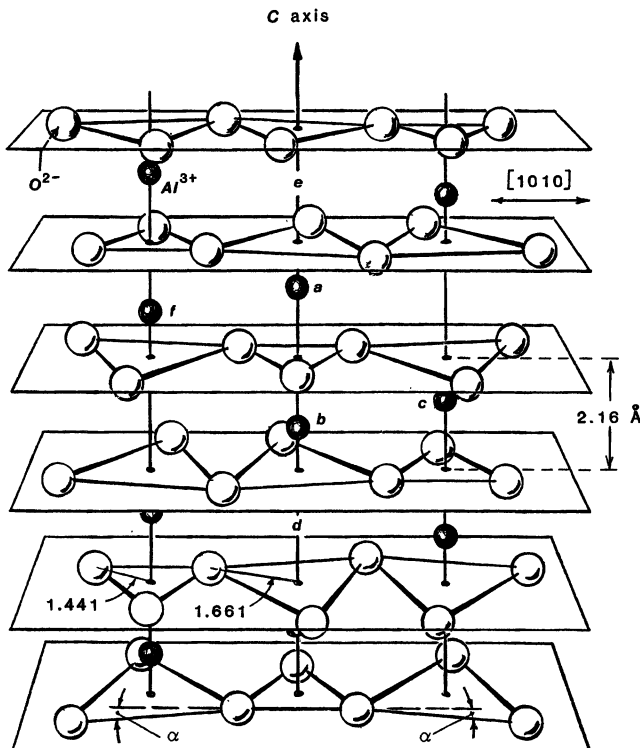


FIGURE 1.9
Sapphire crystal lattice.

Energy Levels in Solids: Rare Earth Ions

Figures 1.11 and 1.12 show how a typical rare-earth ion such as Nd^{3+} or Tb^{3+} can be bonded into an irregular glassy lattice structure, together with the quantum energy levels associated with a trivalent terbium Tb^{3+} ion when such an ion is dispersed at low concentration, either in a glass or in a crystal structure (for example, CaF_2).

Note that the energy levels of rare-earth ions such as Tb^{3+} or Nd^{3+} are associated with the electrons in the partially filled $4f$ inner shell of the rare-earth atom. In nearly all solid materials, these inner electrons are well shielded, by surrounding outer filled electron shells, from the crystalline Stark effects caused by the bonds to surrounding atoms in the crystal or glass material. Hence the quantum energy levels of such rare-earth ions are almost unchanged in many different crystalline or glass host materials.

Almost any material containing small amounts of Tb^{3+} , for example, will fluoresce with the same brilliant green color around 540 nm, and materials containing Nd^{3+} all fluoresce strongly around 1.06 μm in the near-infrared. There are also several other such rare-earth ions, including Dy^{2+} , Tm^{2+} , Ho^{3+} , Eu^{3+} , and Er^{3+} , that make good to excellent laser materials.

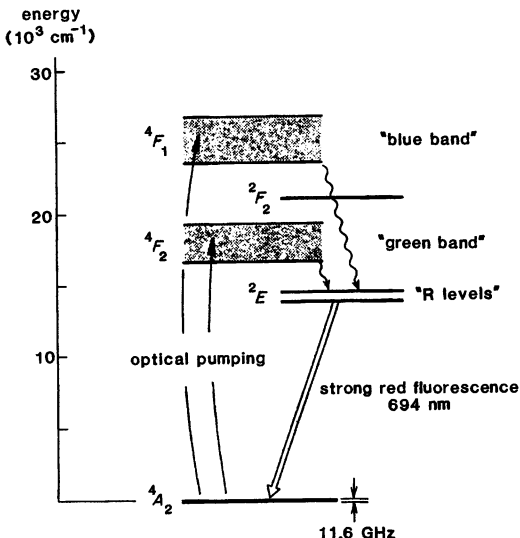


FIGURE 1.10
Quantum-mechanical energy levels of the Cr^{3+} ions in a ruby crystal.

Optical Pumping of Atoms

All of these minerals illustrate another basic method for pumping or exciting atoms into upper energy levels, that is, through the absorption of light at an appropriate pumping wavelength. The high-pressure mercury lamp used as the excitation source in a "mineral light" emits a broad continuum of visible and ultraviolet wavelengths. As shown in Figures 1.8 and 1.12, some of these wavelengths will coincide with the transition frequencies from the lowest or ground levels of the chromium or terbium ions (nearly all the ions are located at ground level when in thermal equilibrium) up to some of the higher energy levels of these ions.

These ions can thus absorb radiation ("absorb photons") from the UV light source at these particular frequencies, and as a result be lifted up to various of the upper levels. This excitation is enhanced by the fact that in solids the higher energy levels are often rather broad bands of levels. The absorption linewidths of the ruby and terbium absorption lines are thus relatively broad, permitting reasonably efficient absorption of the continuum radiation from the mercury lamp.

Once they are lifted upward by this so-called "optical pumping," the ions in each case then relax or fluoresce down to lower energy levels, as shown in Figure 1.12, emitting a relatively sharp fluorescence at two or three visible wavelengths as they drop from upper to lower levels.

Spontaneous Energy Decay or Relaxation

Let us discuss a little more the spontaneous decay or relaxation process we have introduced here. Suppose that a certain number N_2 of such atoms have been pumped into some upper energy level E_2 of an atom or molecule, whether

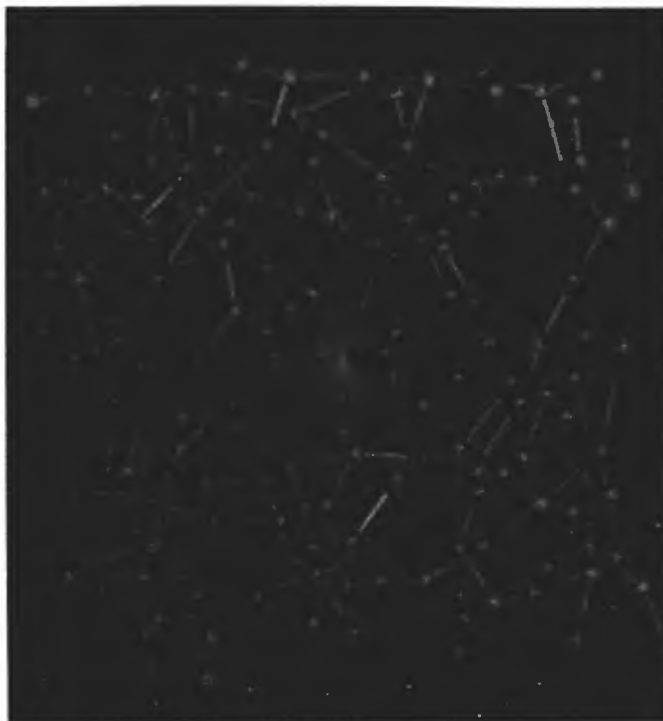


FIGURE 1.11

A single rare-earth ion (largest sphere) imbedded in a BaF_2 glass matrix. The larger spheres in the matrix represent barium, the smaller fluorine.

by electron collision in a gas like helium, or by optical pumping in a solid like ruby, or by some other mechanism. These atoms will then spontaneously drop down or relax to lower energy levels, giving up their excess internal energy in the process (Figure 1.13). (We will see where this energy goes in a moment.)

The rate at which atoms spontaneously decay or relax downward from any upper level N_2 is given by a spontaneous energy-decay rate, often called γ_2 , times the instantaneous number of atoms in the level, or

$$\left. \frac{dN_2}{dt} \right|_{\text{spont}} = -\gamma_2 N_2 \equiv -N_2/\tau_2. \quad (4)$$

If an initial number of atoms N_{20} are pumped into the level at $t = 0$, for example, by a short intense pumping pulse, and the pumping process is then turned off, the number of atoms in the upper level will decay exponentially in the form

$$N_2(t) = N_{20} e^{-\gamma_2 t} = N_{20} e^{-t/\tau_2}, \quad (5)$$

where $\tau_2 \equiv 1/\gamma_2$ is the lifetime of the upper level E_2 for energy decay to all lower levels.

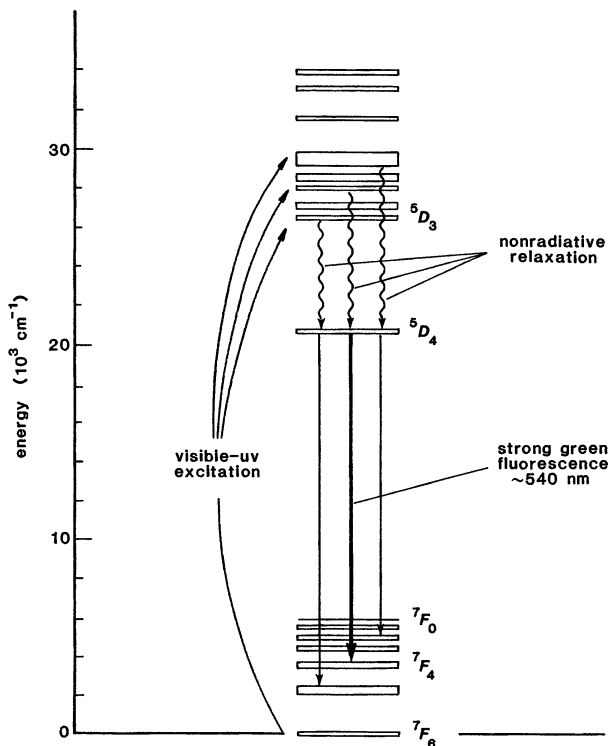


FIGURE 1.12
Optical pumping of the upper quantum-mechanical energy levels in the rare-earth ion terbium, Tb^{3+} .

The lifetime of the R levels in the ruby crystal happens to be long enough (about 4 msec), and the visible fluorescence strong enough, that we can rather easily demonstrate this kind of exponential decay by using the simple apparatus shown in Figure 1.15. The pulsed stroboscopic light source emits a broadband flash of visible and ultraviolet light about 60 μsec long. This flash of light optically pumps the Cr^{3+} ions in the ruby sample up to upper levels, from which they very rapidly decay to the metastable R levels. These levels then decay to the ground level by emitting visible red fluorescence with a decay time $\tau \approx 4.3$ msec. (Similar fluorescence lifetime measurements can also be made for any of the other materials we have mentioned, but some of the lifetimes are much shorter, and the fluorescent intensities much smaller, making the experiment more difficult.)

Radiative and Nonradiative Relaxation

There are actually two quite separate kinds of downward relaxation that occur in these solid-state materials, as well as in most other atomic systems. One mechanism is *radiative relaxation*, which is to say the spontaneous emission of electromagnetic or fluorescent radiation, as we have already discussed. We

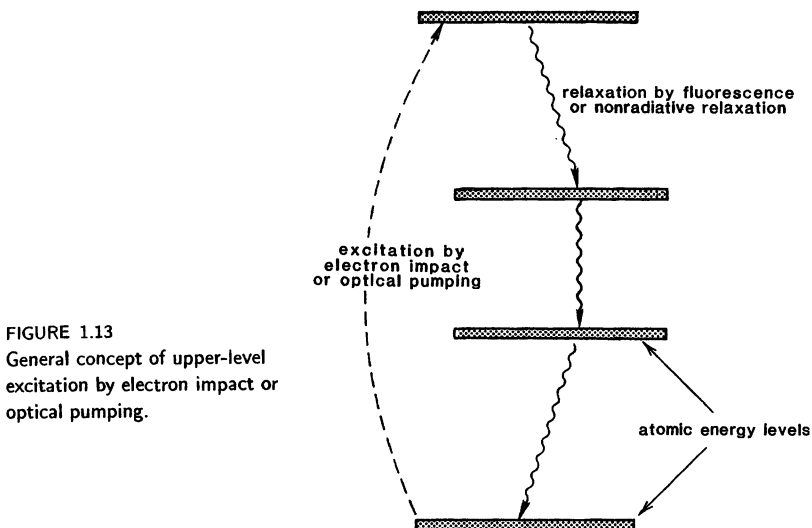


FIGURE 1.13
General concept of upper-level excitation by electron impact or optical pumping.

can usually measure this emitted radiation directly, with some suitable kind of photodetector.

The other mechanism is what is commonly called *nonradiative relaxation*. In terbium, for example, when the terbium ions relax from higher energy levels shown in Figure 1.12 down into the 5D_4 level, they get rid of the transition energy not by radiating electromagnetic radiation somewhere in the infrared, but by setting up mechanical vibrations of the surrounding crystal lattice. To put this in another way, the excess energy is emitted as *lattice phonons*, or as heating of the surrounding crystal lattice, rather than as electromagnetic radiation or *photons*—hence the term *nonradiative relaxation*. This kind of nonradiative emission is usually difficult to measure directly, since it mostly goes into a very small warming up of the surrounding medium. This same kind of nonradiative relaxation process also allows excited ruby atoms to relax down into the 2E levels.

The total relaxation rate γ on any given transition will thus be, in general, the sum of a *radiative* or *fluorescent* or *electromagnetic* part, described by a purely radiative decay rate that we often write as γ_{rad} ; plus a *nonradiative* part, with a nonradiative decay rate that we often write as γ_{nr} . The total or measured decay rate for atoms out of the upper level will then be the sum of these, or $\gamma_{\text{tot}} \equiv \gamma_{\text{rad}} + \gamma_{\text{nr}}$. The actual numerical values for these rates, and the balance between radiative and nonradiative parts, will in general be different for every different atomic transition, and may depend greatly on the immediate surroundings of the atoms, as we will discuss in much more detail later. The one certain thing is that atoms placed in an upper level will decay downward, by some combination of radiative and/or nonradiative decay processes.

Nonradiative relaxation can be a particularly rapid process for relaxation across some of the smaller energy gaps for rare-earth ions and other absorbing ions in solids, as we will see in more detail later. For example, in terbium as in many other rare-earth ions, there may be many rather closely spaced levels or bands at higher energies; but then the energy gap down from the lowest of these

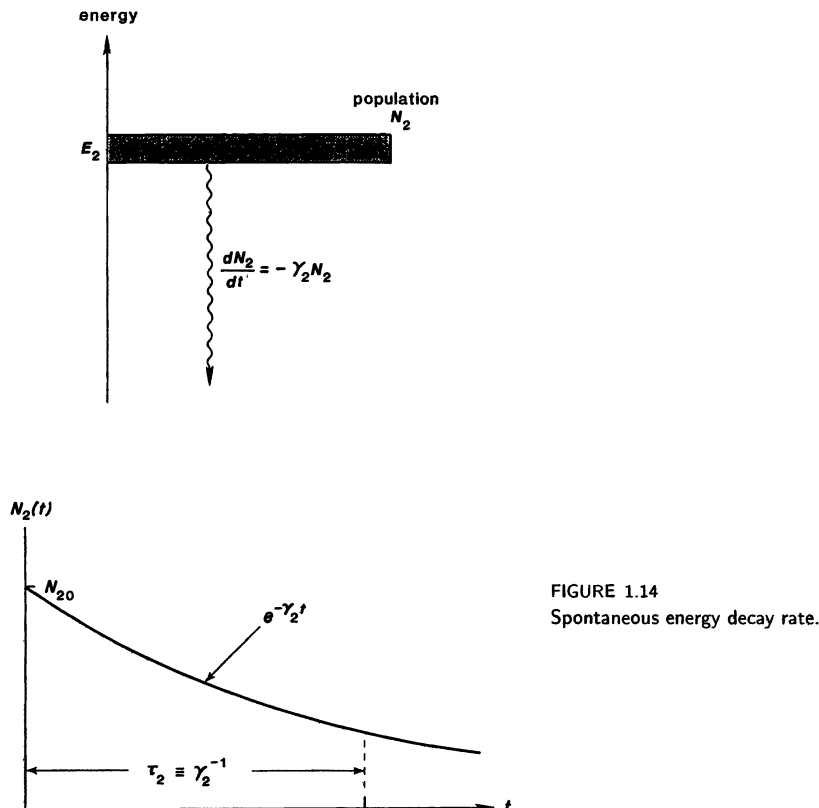


FIGURE 1.14
Spontaneous energy decay rate.

upper levels (the 5D_4 level in terbium) to the next lower group of levels may be larger than the frequency $\hbar\omega$ of the highest phonon mode that the crystal lattice can support.

As a result, the terbium ion cannot relax across this gap very readily by nonradiative processes, i.e., by emitting lattice phonons, since the lattice cannot accept or propagate phonons of this frequency. Instead the atoms relax across this gap almost entirely by radiative emission, i.e., by spontaneous emission of visible fluorescence. Across other, smaller gaps, however, the nonradiative relaxation rate is so fast that any radiative decay on these transitions is completely overshadowed by the nonradiative rate.

This behavior is typical for many other rare-earth ions in crystals and glasses. Following optical excitation to high-lying levels, the atoms relax by rapid nonradiative relaxation into some lower *metastable level*, from which further nonradiative relaxation is blocked by the size of the gap to the next lower level. Efficient fluorescent emission from here to the lower levels then occurs, followed by further fast nonradiative relaxation across any remaining energy gaps to the ground level. The nonradiative decay time of the atoms via phonon emission across the smaller energy gaps may be in the subnanosecond to picosecond range—too fast

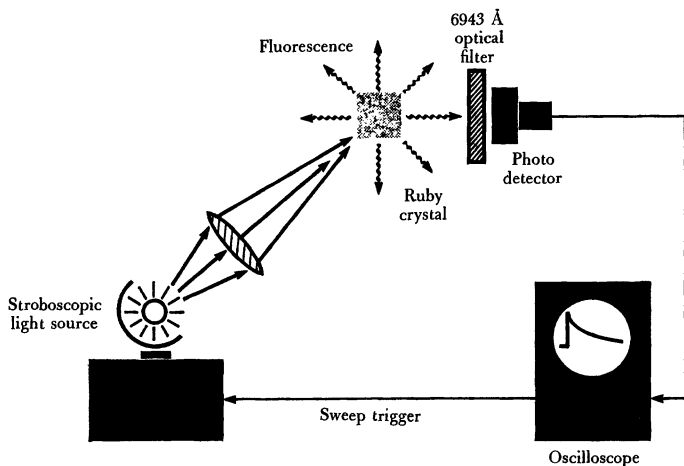


FIGURE 1.15
Measurement of ruby fluorescent lifetime.

to be easily measured—and the average lifetime of the same rare-earth ions in their metastable levels, before they radiate away their energy and drop down, is typically between a few hundred μ sec and a few msec.

We will see later that in many rare-earth samples it is possible, by pumping hard enough, to actually build up enough of a population inversion between the metastable level and lower levels to permit laser action on these transitions. Several different rare-earth atoms can thus be used as good optically pumped solid-state lasers (though terbium itself is not among the best of these).

REFERENCES

Brief but useful introductions to the whole range of spectroscopy, on many different kinds of atomic systems, in widely different frequency ranges and using widely different experimental techniques, can be found in D. H. Whiffen, *Spectroscopy* (John Wiley, 1966), or in Oliver Howarth, *Theory of Spectroscopy* (Halsted Press, John Wiley, 1973).

There exist innumerable books on the theory and practice of atomic and molecular spectroscopy, of which two recent examples are H. G. Kuhn, *Atomic Spectra* (Academic Press, 1969), and J. I. Steinfeld, *Molecules and Radiation: An Introduction to Modern Molecular Spectroscopy* (Harper and Row, 1974).

For tables of detailed data on energy levels of isolated atoms, the standard reference sources are the National Bureau of Standards *Tables of Atomic Energy Levels*, edited by Charlotte E. Moore (U.S. Government Printing Office, 1971).

1.3 STIMULATED ATOMIC TRANSITIONS

Having introduced spontaneous (downward) transitions, we will now look at the stimulated (upward and downward) transitions that are the essential processes in all kinds of laser and maser action.

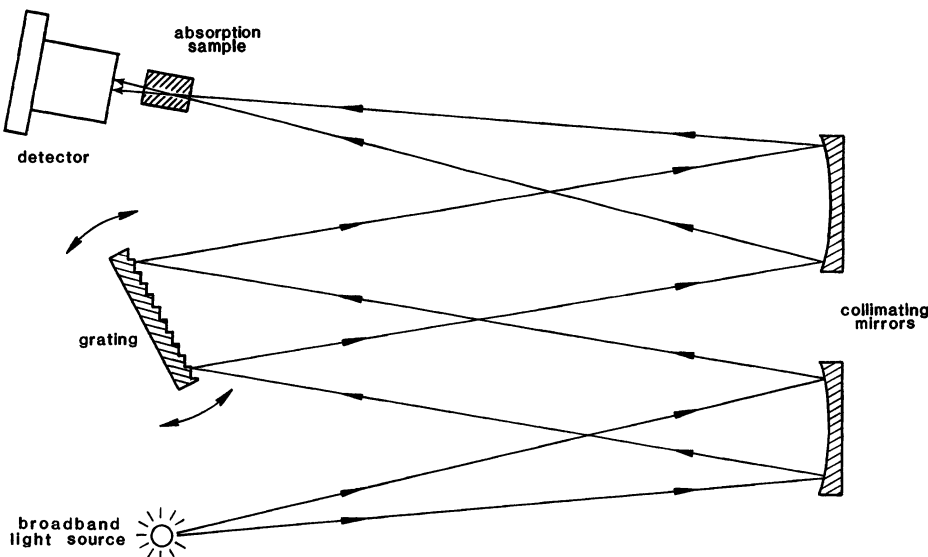


FIGURE 1.16
An elementary grating spectrometer.

Atomic Absorption Lines

Suppose we now examine more carefully the absorption of radiation by a collection of atoms as a function of the wavelength of the incident radiation. Figure 1.16 shows a very elementary example of a grating spectrometer such as might be used for such measurements. (A tunable laser would be a very useful alternative, if one were conveniently available.)

In this spectrometer the radiation from a broadband continuum light source is collected into a roughly parallel beam by a collimating mirror, and is then reflected from a diffraction grating located on a rotatable mount. At any one orientation of the grating, only one wavelength (rather, a finite but narrow band of wavelengths) is reflected at the correct angle to be collected by another curved mirror, focused down through a narrow slit, and passed through the experimental sample onto a detector. By rotating the grating, we can tune the wavelength of the radiation that passes through the sample and thereby measure the transmission through the sample as a function of frequency or wavelength. (Figure 1.17 shows a more compact in-line version of such an instrument.)

The result of such an experiment will often appear as shown schematically in Figure 1.18. The atomic sample will have absorption transitions from the lowest energy level to higher energy levels; so it will exhibit discrete absorption lines—that is, narrow bands of frequency in which the sample exhibits more or less strong absorption—at exactly those wavelengths. These wavelengths will correspond through Planck's law to the energy gaps between the lowest and higher levels. If there happen to be some atoms already located in higher-lying levels, then absorption lines from those levels to still higher levels may also be seen, as illustrated by transition *C* in the figure. These excited-state absorptions, how-

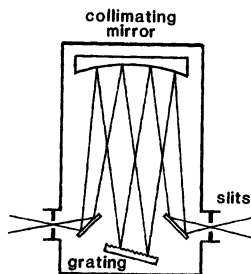


FIGURE 1.17
A compact in-line grating monochromator.

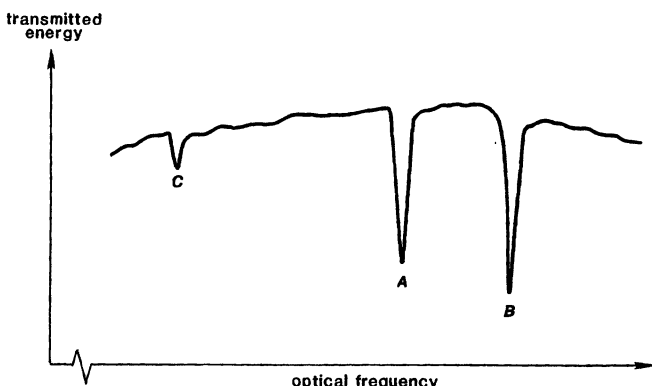
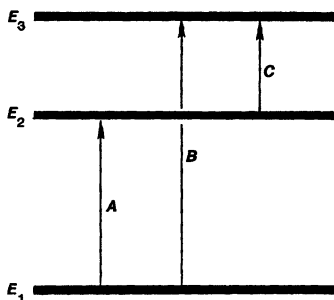


FIGURE 1.18
Absorption transitions (top) and absorption lines (bottom).

ever, will usually appear substantially weaker, simply because there will normally be many fewer atoms in the higher energy levels.

As a specific illustration of atomic absorption, Figure 1.19 shows some of the sharp absorption lines observed when radiation at wavelengths around 540 nm in the visible is transmitted through a crystal of lanthanum fluoride (LaF_2)

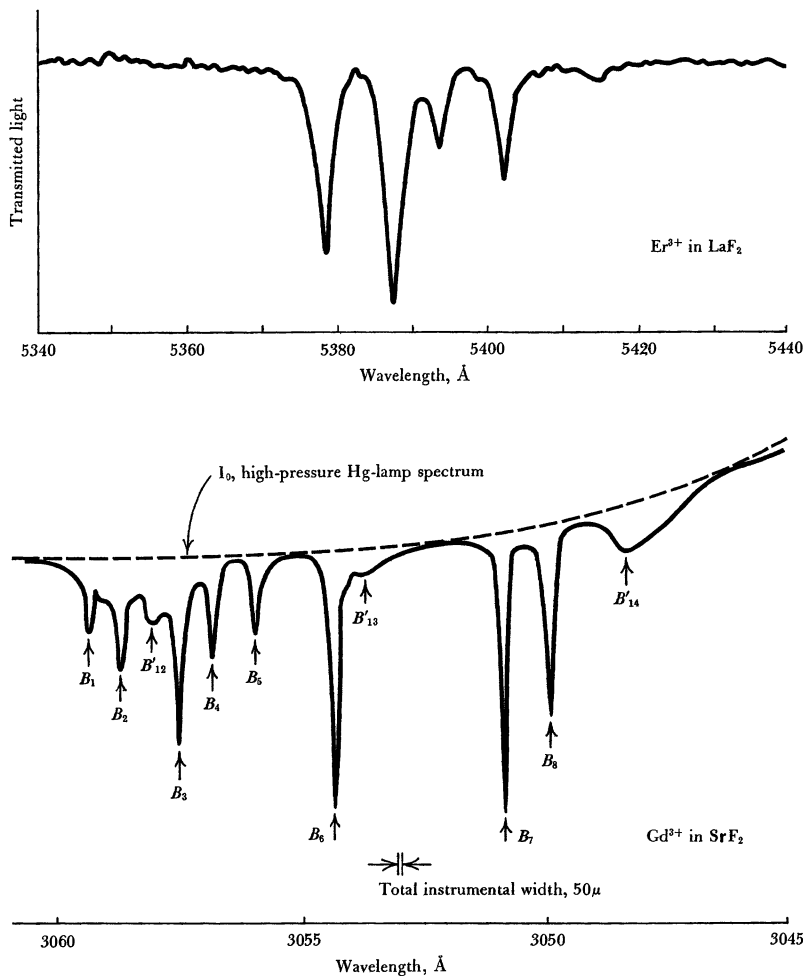


FIGURE 1.19

Light transmission versus wavelength through crystals of lanthanum fluoride (LaF₂) containing a small amount of the rare-earth ion erbium Er³⁺ (upper trace), and strontium fluoride (SrF₂) containing a small amount of the rare-earth ion gadolinium Gd³⁺ (lower trace).

containing a small percentage of the rare-earth ion erbium, or when radiation at wavelengths around 300 nm in the near ultraviolet is transmitted through a crystal of strontium fluoride (SrF₂) containing a small percentage of the rare-earth ion gadolinium. These absorption lines all represent different transitions from the lowest or ground levels of the Er³⁺ or Gd³⁺ ions to higher-lying levels, exactly analogous to the terbium levels shown in Figure 1.13. Of course, if a pure lanthanum or strontium fluoride crystal is grown without any erbium or gadolinium present, no such absorption lines are observed.

Absorption Lines in Gases, and Molecular Spectroscopy

Absorption experiments of this sort are, of course, by no means limited to solids or to rare earths. Isolated atoms or ions in gases will exhibit such absorption lines in the visible, and especially the UV. Molecules in gases, liquids, and solids will exhibit an extremely rich spectrum of absorption lines, notably in the infrared as well as in the visible and ultraviolet. The absorption lines of atoms and molecules in gases are typically sharper or narrower than those in solids or liquids, since the energy levels in gases are not subject to some of the perturbing influences that tend to broaden or smear out the energy levels in liquids or solids.

As just one more example to illustrate absorption spectroscopy, Figure 1.20 shows a few of the sharp absorption lines characteristic of the formaldehyde molecule H_2CO in a narrow range of wavelengths near $3.57\text{ }\mu\text{m}$. This particular spectrum was taken by using a continuously tunable laser source (a cw injection diode laser using a lead/cadmium sulfide diode) rather than an incoherent spectrometer. The dashed envelope in Figure 1.20(a) is the power output of the tunable laser versus wavelength, over a tuning range that is extremely large in absolute terms ($\sim 3 \times 10^{10}\text{ Hz}$), yet extremely narrow ($\sim 0.04\%$) relative to the center frequency. The solid line is the power transmitted through the vapor-filled cell.

Many different molecules exhibit exactly such characteristic sharp lines, specific to the individual molecules, in rich profusion through the near and middle infrared regions. These sharp lines are extremely useful not only as potential laser lines, but as characteristic signatures of different molecules, for use in chemical diagnostics or in identifying the presence of specific pollutant molecules or hazardous chemicals. Note that the sensitivity and the laser scanning rate in the experiment allow a small portion of the formaldehyde absorption spectrum to be displayed on an oscilloscope in real time.

Emission spectroscopy, using the spontaneous emission lines radiated from an excited sample as in Figure 1.5, is thus one way of observing and learning about the discrete transitions and the quantum energy levels of atoms, ions, and molecules. *Absorption spectroscopy*, as briefly described here, is another and complementary method of obtaining the same kind of information. These methods are in fact complementary in their utility, since emission spectroscopy tends to give information about downward transitions emanating from high-lying levels, whereas absorption spectroscopy tends to give information about upward transitions from the ground level or low-lying atomic levels. The formaldehyde example illustrates the possibilities for applying tunable lasers to spectroscopy, to analytical chemistry, and to practical applications such as pollution detection.

Stimulated versus Spontaneous Atomic Transitions

We have now seen that there are two basically different kinds of transition processes that can occur in atoms or molecules.

First, there are *spontaneous emission* or *relaxation transitions*, in which atoms spontaneously drop from an upper to a lower level while emitting electromagnetic and/or acoustic radiation at the transition frequency. *Fluorescence*, *energy decay*, and *energy relaxation* are other names for this process. When atoms emit this kind of fluorescence or spontaneous electromagnetic radiation, each individual atom acts almost exactly like a small randomly oscillating antenna—in

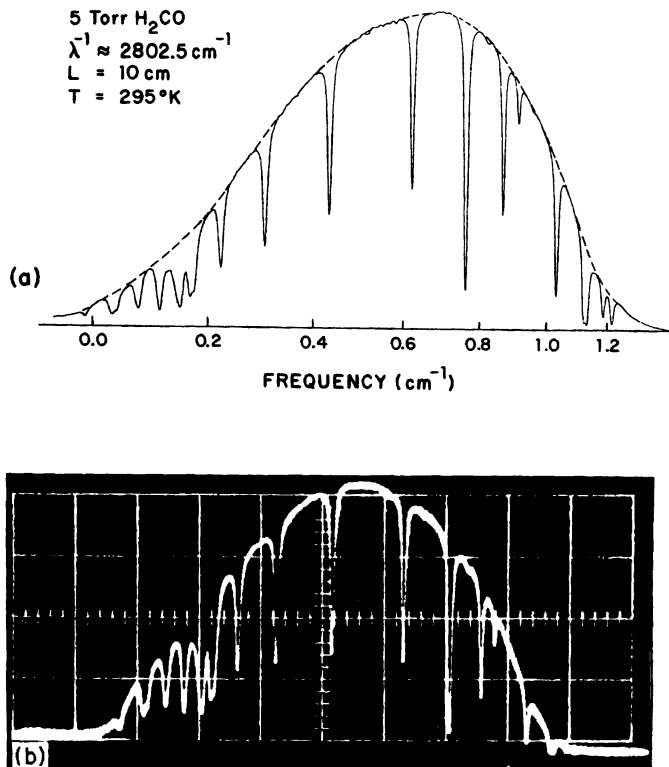


FIGURE 1.20
Absorption spectroscopy of formaldehyde using a tunable laser source near $\lambda = 3.57\mu\text{m}$.

most common cases, a small *electric dipole antenna*—internally driven at the transition frequency. Each individual atom radiates independently, with a temporal phase angle that is independent of all the other radiating atoms. Thus, the total fluorescent emission from a collection of spontaneously emitting atoms is noise-like in character (Figure 1.21), even though it will be limited in spectral width to the comparatively narrow linewidth of the atomic transition. Indeed, such spontaneously emitted radiation has all the statistical properties of narrowly bandlimited gaussian noise. We usually refer to it as *incoherent* emission.

Second, there are the *stimulated responses* or *stimulated transitions*—both stimulated absorption and stimulated emission—that occur when an external radiation signal is applied to an atom. In these transitions each individual atom acts like a miniature passive resonant antenna (again, usually an *electric dipole antenna*) that is set oscillating by the applied signal itself. That is, the internal motion or oscillation in the atom is not random, but is driven by and coherent with the applied signal.

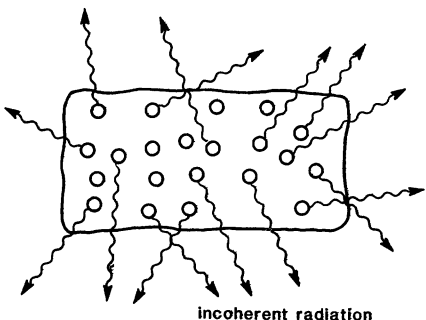


FIGURE 1.21

Spontaneous emission is incoherent or noise-like, emerging randomly in all directions.

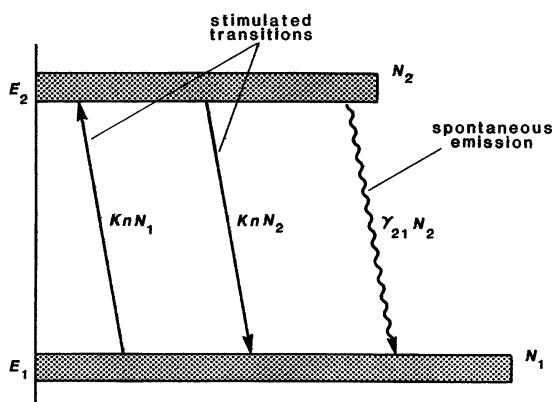


FIGURE 1.22

An energy-level population diagram, showing spontaneous emission plus stimulated transitions.

Atomic Rate Equations

Suppose we have very many identical atoms, each of which has two just energy levels, E_1 and E_2 . (Real atoms will undoubtedly have many other energy levels as well, but we will ignore other levels for the moment.) Suppose that $N_1(t)$ of the atoms present are in level E_1 and $N_2(t)$ atoms are in level E_2 . This situation can be illustrated by an energy-level population diagram, as in Figure 1.22.

We have already stated that the spontaneous-relaxation rate down from level E_2 to level E_1 is directly proportional to the upper-level population $N_2(t)$ and is not influenced at all by the lower-level population $N_1(t)$. Hence the spontaneous-emission rate out of level 2 and into level 1 is given by

$$\frac{dN_2(t)}{dt} \Big|_{\text{spontaneous}} = - \frac{dN_1(t)}{dt} \Big|_{\text{spontaneous}} = -\gamma_{21}N_2(t), \quad (6)$$

where γ_{21} indicates the total spontaneous-transition rate or decay rate (radiative plus nonradiative) from level 2 to level 1.

Suppose now an optical signal is applied to these atoms to cause stimulated transitions, as in the optical pumping or absorption spectroscopy experiments we have just discussed. This signal must, of course, be tuned in frequency close to the transition frequency of interest, i.e., $\omega \approx \omega_{21} \pm \Delta\omega_a$, where $\Delta\omega_a$ is the linewidth of the atomic transition. We might then characterize the strength of this signal by its intensity I (dimensions of power per unit area), or by the strength of its E or H fields. In discussions of stimulated transitions, however, the applied signal intensity or energy density is often expressed in units of the number of signal photons $n(t)$ per unit volume in the applied signal. This does not necessarily imply anything about photons as being billiard-ball-like point particles; it merely means that $n(t)$ is the electromagnetic energy density of the applied signal divided by the quantum energy unit $\hbar\omega$.

Such an applied signal will cause atoms initially in the lower energy level to begin making *stimulated transitions* or “jumps” upward to the upper energy level, at a rate proportional to the applied signal intensity (or power density) times the number of atoms in the starting level. The number of stimulated upward transitions per unit time caused by the applied signal can then be written as

$$\left. \frac{dN_2(t)}{dt} \right|_{\substack{\text{stimulated} \\ \text{upward}}} = K n(t) N_1(t). \quad (7)$$

That is, the stimulated upward transition rate is directly proportional to the photon density n of the applied signal. Each such upward transition absorbs one quantum of energy from the applied signal and—at least in an elementary description—transfers it to one of the atoms which is lifted upward. This is the process of *stimulated absorption*.

But the essential point is that the same applied signal will also cause any atoms initially in the *upper energy level* to begin making similar stimulated transitions or jumps *downward* in energy, at a rate which is again proportional to the applied signal intensity times the number of atoms in the initial (i.e., upper) level. The number of stimulated downward transitions per unit time can thus similarly be written as

$$\left. \frac{dN_2(t)}{dt} \right|_{\substack{\text{stimulated} \\ \text{downward}}} = -K n(t) N_2(t). \quad (8)$$

This is the process of *stimulated emission*. The atoms in this case jump downward, giving up energy. This energy must go into the stimulating optical signal, which is therefore strengthened or amplified.

The constant K in each of these equations is just a proportionality constant that measures the absolute strength of the stimulated response on the particular atomic transition. A fundamental and essential point, however, is that *this proportionality constant necessarily has exactly the same value for transitions in either direction*. This constant K will also be largest for an applied signal tuned exactly to the atomic transition frequency, and will rapidly become small to negligible as the signal frequency ω is tuned away from the transition frequency ω_{21} by more than a linewidth or so.

The *total rate equation* for the atomic populations in this simple example, including stimulated plus spontaneous transitions, is thus given by

$$\begin{aligned} \frac{dN_2(t)}{dt} \Big|_{\text{total}} &= \frac{dN_2(t)}{dt} \Big|_{\substack{\text{stimulated} \\ \text{upward}}} + \frac{dN_2(t)}{dt} \Big|_{\substack{\text{stimulated} \\ \text{downward}}} + \frac{dN_2(t)}{dt} \Big|_{\text{spontaneous}} \\ &= Kn(t) \times [N_1(t) - N_2(t)] - \gamma_{21}N_2(t) = - \frac{dN_1(t)}{dt} \Big|_{\text{total}} \end{aligned} \quad (9)$$

where $n(t)$ is directly proportional to the applied signal intensity or power density.



Quantum Derivation of the Spontaneous Emission Process

In a quantum-mechanical analysis the constant K in the stimulated-transition rate $Kn(t)N(t)$ is usually derived by using a *semiclassical quantum analysis*, in which the atoms are treated quantum-mechanically but the applied electromagnetic signal is treated classically. The spontaneous emission processes described by the spontaneous-relaxation probability $\gamma_{21}N_2(t)$ can, however, only be derived from a fully quantum electrodynamic analysis in which both the atoms and the electromagnetic field itself are treated quantum-mechanically.

Some people note that there is a correspondence in quantum theory between the spontaneous-emission rate, which corresponds to the downward stimulated-transition rate that would be caused by one extra photon, and the presence of zero-point fluctuations in the quantum electromagnetic fields, with a magnitude equivalent to an energy of one photon per mode; and deduce from this that zero-point fluctuations “cause” or “stimulate” the spontaneous emission. This can be a convenient way to calculate the spontaneous-emission rate or the quantum noise magnitude in a laser calculation, but attributing a causal relation to the zero-point fluctuations is a more dubious proposition. Zero-point fluctuations and spontaneous emission are both predicted, separately and independently, by quantum field theory, but nothing in the theory says that either one *causes* the other: they each arise independently of the other, from the commutation properties of the quantum field operators.

Stimulated Transitions and Laser Amplification

The total rate at which atoms make signal-stimulated transitions between two energy levels (i.e., “up” minus “down”) is thus given by $Kn(t) \times [N_1(t) - N_2(t)]$. Each upward transition transfers $\hbar\omega$ of energy from the signal to the atoms; each downward transition does the reverse.

But this implies that the net rate at which energy per unit volume is absorbed *from* the signal *by* the atoms is then given by this net flow rate times the energy $\hbar\omega$ per jump. That is, the net energy transfer rate to the atoms is

$$\frac{dU_a}{dt} = Kn(t) \times [N_1(t) - N_2(t)] \times \hbar\omega, \quad (10)$$

where U_a is the energy density in the forced internal oscillation of the atoms.

This same energy must at the same time be coming out of the signal. Hence the energy density $U_{\text{sig}}(t) = n(t) \times \hbar\omega$ in the applied signal must be decreasing with time according to the reverse expression

$$\frac{dU_{\text{sig}}}{dt} = -K[N_1(t) - N_2(t)] \times n(t) \times \hbar\omega = -K[N_1(t) - N_2(t)] \times U_{\text{sig}}(t) \quad (11)$$

or, in terms of photon density,

$$\frac{dn}{dt} = -K[N_1(t) - N_2(t)]n(t). \quad (12)$$

The signal energy density $U_{\text{sig}}(t)$, or the photon density $n(t)$, may thus either decay or grow with time, depending on the sign of the population difference $\Delta N(t) = N_1(t) - N_2(t)$ in the square brackets.

The signal growth rate described by Equation 1.12 leads to the essential concept of laser amplification. This equation says that if an external signal is applied to a collection of atoms where there are more atoms in the lower energy level than in the upper, or where $N_1(t) > N_2(t)$, then the net transition rate or net flow of atoms between the levels will be upward. In this case net energy is being supplied to the atoms by the applied signal; so the applied signal must become absorbed or attenuated.

If, however, we can somehow produce a condition of *population inversion*, in which there are more atoms in the upper level than in the lower, or $N_2 > N_1$, then both the quantity $N_1 - N_2$ and hence the net energy flow between signal and atoms will change sign. The net stimulated-transition rate for the atoms will now be in the downward direction. Net energy will then be given up by the atoms, and taken up by the applied signal. This energy flow will in fact produce a *net amplification* of that signal, at a rate proportional to the population difference and to the strength of the external signal.

Boltzmann's Principle

One of the fundamental laws of thermodynamics, Boltzmann's Principle, states that when a collection of atoms is in thermal equilibrium at a positive temperature T , the relative populations of any two energy levels E_1 and E_2 are given by

$$\frac{N_2}{N_1} = \exp\left(-\frac{E_2 - E_1}{kT}\right), \quad (13)$$

which of course means that

$$\Delta N \equiv N_1 - N_2 = \left(1 - e^{-\hbar\omega/kT}\right) N_1. \quad (14)$$

Thus for a collection of atoms in equilibrium at a normal positive temperature T , an upper-level population is always smaller than a lower-level population (much smaller if the energy gap $E_2 - E_1$ is an optical-frequency gap).

The total stimulated-transition rate on such an equilibrium transition is thus always absorptive or attenuating rather than amplifying. To create laser amplification, we must find some pumping process which will put more atoms into an upper level than into a lower level, and thus create a nonequilibrium condition

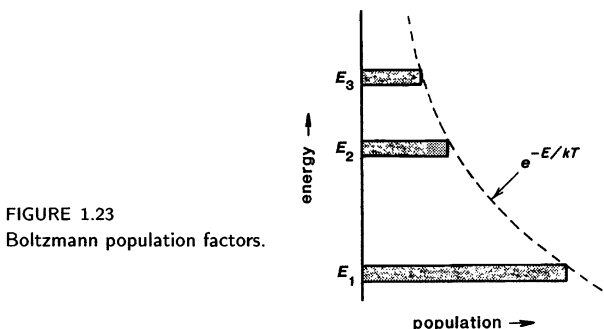


FIGURE 1.23
Boltzmann population factors.

of population inversion. In Section 1.5 we give some information on how this can be done in practice.

Coherence in Stimulated Transitions

If we want, we can think of the basic stimulated transition process as the sum of two separate processes: in one, atoms initially in the lower energy level are stimulated by the applied signal to make transitions upward; in the other, atoms initially in the upper energy level are stimulated by the applied signal to make transitions downward. It is vital to understand, however, that the stimulated-transition probability produced by an applied signal (probability of transition per atom and per second) is always exactly the same in both directions. The net flow of atoms is thus always from whichever level has the larger population at the moment, to whichever level has the smaller population.

There is also no conceivable way to "turn off" one or the other of the stimulated absorption or emission processes separately. If the lower level is more heavily populated, the signal is attenuated. If the upper level is more heavily populated, the signal is amplified. This is the essential amplification process in all lasers and other stimulated-emission devices.

It is also essential to keep in mind that the stimulated transition process we have been introducing here results from a resonant response of the atomic wave function, or of the atomic charge cloud in each individual atom, to the applied signal. That is, the internal induced oscillation or dipole response that is produced in each atom is stimulated by and thus fully coherent with the applied signal.

The net amplification (or attenuation) process is thus a fully *coherent* one, in which the atomic oscillations follow the driving optical signal coherently in amplitude and phase. The output signal from an amplifying laser medium is a linear reproduction of the input signal, and of any amplitude modulation or phase modulation that may be on the input signal, except that (i) the output signal is amplified or increased in magnitude; (ii) the signal modulation may be decreased somewhat in bandwidth because of the finite bandwidth of the atomic response; and (iii) the signal in general has a small amount of spontaneous emission noise added to it.

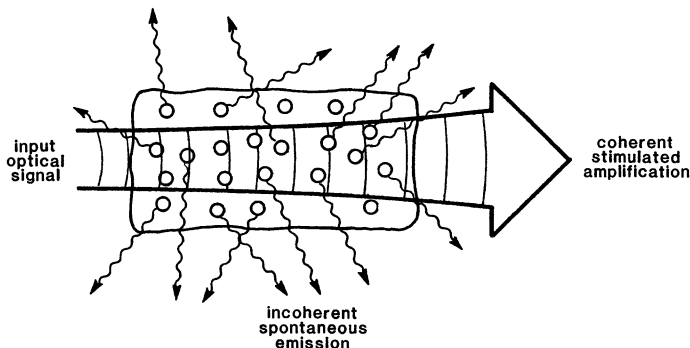


FIGURE 1.24

Incoherent spontaneous emission and coherent stimulated amplification occur simultaneously and in parallel in the laser medium.

Spontaneous Versus Stimulated Transitions

Note also that in a collection of laser atoms with a population inversion, and with an applied signal present, both the spontaneous transitions and the stimulated transitions will occur simultaneously and essentially independently. The stimulated-transition rates and the spontaneous-relaxation rate can be simply added together. The spontaneous emission, however, will emerge in all directions, as in Figure 1.24, and will have the spectral and statistical character of narrowband random noise; whereas the stimulated emission (and absorption) will all be in the same direction and at the same frequency as the applied signal.

In a laser amplifier the input signal will thus be amplified by the stimulated transitions. At the same time, a small amount of the spontaneous emission (in essence, that portion traveling exactly parallel to the applied signal) will be added to the output signal by the spontaneous emission process. The spontaneous emission in this situation thus acts essentially like a small additive amplifier noise source insofar as the stimulated amplification process is concerned. Unless the applied signal is very small, approaching the noise limit of the laser amplifier, the added spontaneous-emission noise can normally be ignored in discussions of the basic stimulated amplification process.

REFERENCES

The basic concepts of the stimulated emission process and the possibility of coherent "negative absorption" from atoms in the upper level of an atomic transition were clearly outlined by A. Einstein in "On the quantum theory of radiation," *Physikalische Zeitschrift* 18, 121 (1917), and again by R. C. Tolman, "Duration of molecules in upper quantum states," *Rev. Mod. Phys.* 23, 693-709 (June 1924).

An interesting and instructive early study on purely spontaneous emission from atoms is reported by E. Gaviola in "An experimental test of Schrödinger's theory," *Nature* 122, 772 (1928). Gaviola observed the spontaneous emission lines from a mercury discharge at 435.8 nm and 404.6 nm from a common 2^3S_1 upper level down to the 2^3P_1 and 2^3P_0 lower levels, under widely varying conditions of pressure and with various added buffer gases. The relative populations of these levels could then be ex-

pected to vary widely under these different conditions. Although Gaviola had no way to measure any of these populations, he could observe that the ratio of the intensities on the 435.8 nm and 404.6 nm lines always remained fixed, even though their absolute intensities changed widely. This strongly implied that the emission rates on these transitions depended only on their common upper-level population and not on either of the lower-level populations.

The first successful demonstration of amplification and oscillation using stimulated emission, employing an inverted population in ammonia at a microwave frequency, was accomplished by J. P. Gordon, H. J. Zeiger, and C. H. Townes, as reported in "The maser—new type of microwave amplifier, frequency standard, and spectrometer," *Phys. Rev.* 18, 1264-1274 (August 15, 1955). Other references to the early history of stimulated emission devices are given in Section 1.10.

1.4 LASER AMPLIFICATION

Using the principles of stimulated emission outlined in the preceding section as a foundation, we next outline briefly how a laser material with an inverted atomic population produces useful laser amplification.

Signal Absorption and Attenuation

Suppose first that we send a wave of tunable optical radiation through a collection of absorbing atoms, as illustrated in Figure 1.25, with this radiation tuned to a frequency ω near the transition frequency ω_{21} between two energy levels E_1 and E_2 of the atoms. Let the populations of these energy levels be N_1 and N_2 as shown earlier. (The symbols N_1 and N_2 nearly always in this book mean *population densities*; i.e., they have dimensions of atoms per unit volume inside the laser medium.)

For an absorbing population difference, we will find that this wave will be absorbed or attenuated with distance in passing through the atoms, in the form

$$\mathcal{E}(z) = \mathcal{E}_0 \times \exp[-\alpha(\omega)z]. \quad (15)$$

For many atomic transitions the attenuation coefficient $\alpha(\omega)$ due to the atoms will be given (as we will derive later) by an expression of the general form

$$\alpha(\omega) = \frac{\lambda^2}{4\pi} \frac{\gamma_{\text{rad}}}{\Delta\omega_a} \frac{N_1 - N_2}{1 + [2(\omega - \omega_{21})/\Delta\omega_a]^2}. \quad (16)$$

This expression contains factors such as the transition wavelength λ (in the laser material); the radiative decay rate γ_{rad} of the transition; and the transition linewidth $\Delta\omega_a$. Most important, it contains the population difference $N_1 - N_2$, and a lineshape factor (in the final term) giving the frequency lineshape of the transition. This lineshape will in general be a sharp resonance curve, as illustrated in Figure 1.25, with a finite linewidth or bandwidth $\Delta\omega_a$.

The particular lineshape given by Equation 1.16 is known as a *lorentzian lineshape*, and is characteristic of many real atomic transitions. Other transitions, for various reasons, may have somewhat different lineshapes, for example, a doppler-broadened or gaussian lineshape. The general dependence of the gain coefficient on the important atomic parameters for any real atomic transition

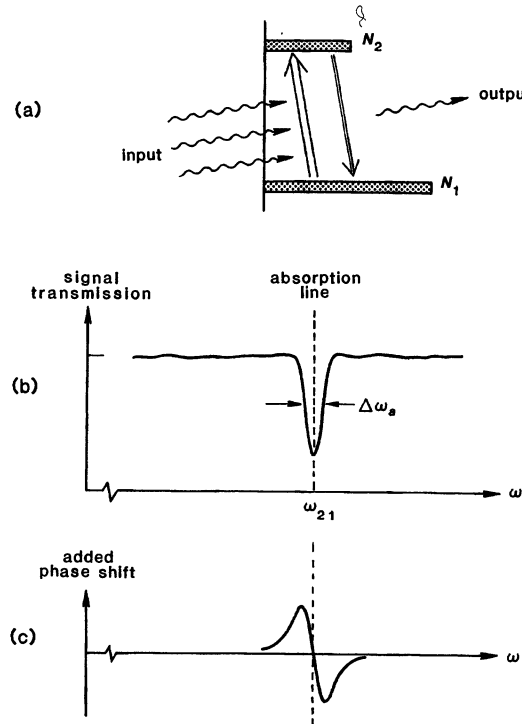


FIGURE 1.25
Stimulated absorption on an uninverted atomic transition.

will still be very much like Equation 1.16, even though the exact lineshape is somewhat different.

The signal wave passing through such an absorbing laser medium will also experience a small frequency-dependent *phase shift* due to the atoms, as shown by Figure 1.25(c). This atomic phase shift can have practical implications (such as laser frequency-pulling effects), which we will discuss in later chapters.

Attenuation Coefficients

Note that the power flow carried by the wave passing through the atoms, or the wave intensity $I(z)$ (in units of power per unit area), is given by

$$I(z) = |\mathcal{E}(z)|^2 = I_0 \exp[-2\alpha(\omega)z]. \quad (17)$$

Hence the power or intensity attenuates with distance in the form $dI(z)/dz = -2\alpha(\omega)I(z)$. Thus in our notation the power-attenuation coefficient is given by $2\alpha(\omega)$. We will consistently use α in this text to represent an amplitude or “voltage” attenuation (or gain) coefficient, and 2α to represent a power or intensity coefficient. In the journal literature, however, α by itself is often used to represent a power-attenuation or power-gain coefficient.

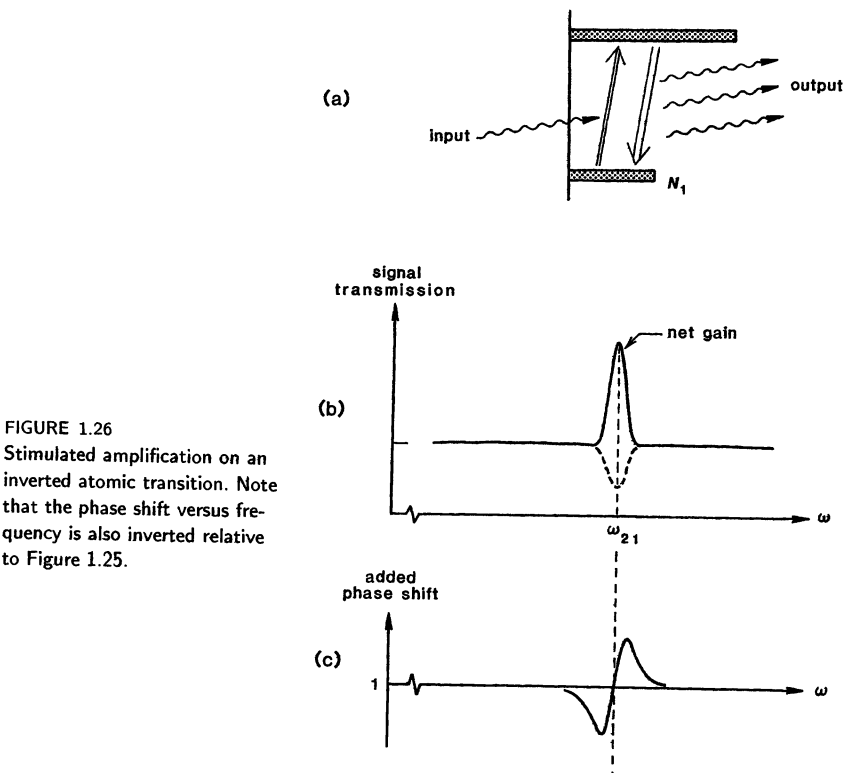


FIGURE 1.26

Stimulated amplification on an inverted atomic transition. Note that the phase shift versus frequency is also inverted relative to Figure 1.25.

Laser Amplification

Suppose now the population difference on an atomic transition can, through some “pumping” process, be made to change sign, creating a *population inversion*. The same expression for the absorption coefficient $\alpha(\omega)$ as in Equation 1.16 then remains valid, except that the *population difference and absorption coefficient are both reversed in sign*. To emphasize this, let us rewrite Equation 1.16 in the form

$$-\alpha(\omega) \equiv \alpha_m(\omega) = \frac{\lambda^2 \gamma_{\text{rad}}}{4\pi \Delta \omega_a} \frac{N_2 - N_1}{1 + [2(\omega - \omega_{21})/\Delta \omega_a]^2}, \quad (18)$$

where $\alpha_m(\omega)$ means the “molecular” or “maser” or “laser” amplification coefficient. The wave amplitude and power will now *grow* or *amplify* with distance in the form

$$\mathcal{E}(z) = \mathcal{E}_0 \exp[+\alpha_m(\omega)z] \quad \text{and} \quad I(z) = I_0 \exp[+2\alpha_m(\omega)z] \quad (19)$$

as shown in Figure 1.26(b). The energy for this amplification comes, of course, from the inverted atoms—that is, the upper-level atoms supply energy to the wave, whereas the lower-level atoms still absorb energy. But since there are more upper-level atoms, the net effect is amplification rather than attenuation.

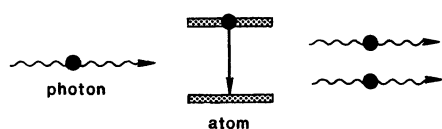
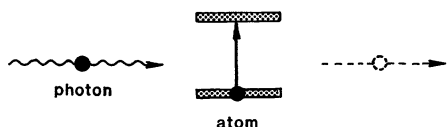


FIGURE 1.27
Photon description of stimulated absorption (top) and stimulated emission (bottom). (This viewpoint is not recommended!)

The laser amplification coefficient $\alpha_m(\omega)$ thus has exactly the same lineshape and all other properties as the absorption coefficient $\alpha(\omega)$ for the same transition without inversion. The only difference between stimulated absorption and stimulated emission is in the sign of the population difference. The net atomic phase shift, in fact, also changes sign as the population difference goes from absorbing to amplifying.

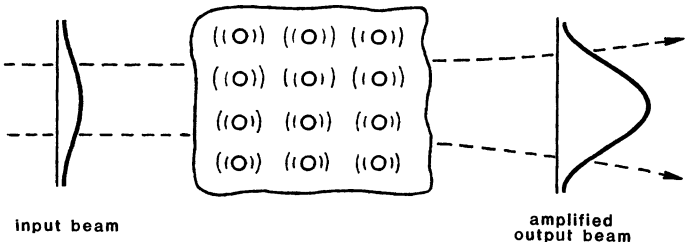
Coherence and “Photons”

We have hardly mentioned *photons* yet in this book. Many descriptions of laser action use a photon picture like Figure 1.27, in which billiard-ball-like photons travel through the laser medium. Each photon, if it strikes a lower-level atom, is absorbed and causes the atom to make a “jump” upward. On the other hand, a photon, when it strikes an upper-level atom, causes that atom to drop down to the lower level, releasing another photon in the process. Laser amplification then appears as a kind of photon avalanche process.

Although this picture is not exactly incorrect, we will avoid using it to describe laser amplification and oscillation, in order to focus from the beginning on the *coherent* nature of stimulated transition processes. The problem with the simple photon description of Figure 1.27 is that it leaves out and even hides the important *wave* aspects of the laser interaction process. A photon description leads students to ask questions like, “How do we know that the photon emitted in the stimulated emission process is coherent with the stimulating photon?” The answer is that the whole stimulated transition process should be treated not as a “photon process” but as a coherent or wave process. These coherence effects are present, and must be considered, in at least two different ways.

First, when an electromagnetic signal wave passes through a collection of atoms, a much more accurate description of the stimulated transition process is that the electromagnetic fields in the wave cause the electronic charges inside the atoms to begin vibrating or oscillating in a coherent relationship to the driving signal fields. The atoms in fact both respond and reradiate like miniature atomic antennas. The fields reradiated by the individual atoms combine coherently with the incident signal fields to produce absorption or amplification (and also phase

(a)



(b)

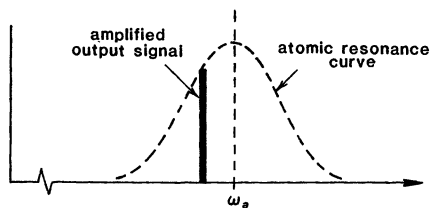
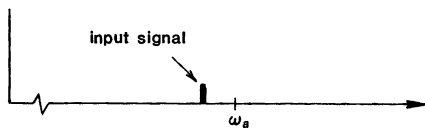


FIGURE 1.28

(a) The stimulated emission or reradiation from each laser atom is spatially coherent or spatially in phase with the incident signal radiation. (b) The stimulated emission is also temporally coherent with, and at the same frequency as, the incident signal radiation.

shift) in a manner that is both *spatially* and *spectrally* coherent, as illustrated in Figure 1.28.

Quantum mechanics tells us in fact that these atoms respond very much like little classical electronic dipole oscillators (as we will discuss in great detail in a later chapter), except that atoms initially in the lower energy level respond in a way that tends to cancel or absorb the incident signal, whereas atoms initially in the upper level respond in exactly opposite phase to the applied signal. The waves reradiated by the upper-level atoms thus tend to *add to* the driving signal wave, and amplify it, whereas the wavelets reradiated by lower-level atoms tend to *add out of phase* to the driving signal and thus attenuate it. Other than this phase difference, the stimulated absorption and emission processes are identical.

Quantum Description of Stimulated Transitions

A second important aspect of stimulated transitions can also be obscured by the photon picture. In a fully correct quantum description, most atoms are not likely to be exactly “in” one quantum level or another at any given instant of time. Rather, the instantaneous quantum state of any one individual atom is usually a time-varying *mixture* of quantum states, for example, the upper and lower states of a laser transition. The populations N_1 and N_2 do not really represent discrete integer numbers of atoms in each level. Rather, each individual atom is partly in the lower level and partly in the upper level (that is, its quantum state is a mixture of the two eigenstates); and the numbers N_1 and N_2 represent averages over all the atoms of the fractional amount that each atom is in the lower or the upper quantum state in its individual state mixture.

Applying an external signal therefore does *not* cause an individual atom to make a sudden discrete “jump” from one level to the other. Rather, it really causes the quantum-state mixture of each atom to begin to evolve in a continuous fashion. Quantum theory says that an atom initially more in the lower level tends to evolve under the influence of an applied signal toward the upper level, and vice versa. This changes the state mixture or level occupancy for each atom, and hence the averaged values N_1 and N_2 over all the atoms. Individual atoms do not make sudden jumps; rather, the quantum states of all the atoms change somewhat, but each by a very small amount.

We should emphasize, finally, that laser materials nearly always contain a very large number of atoms per unit volume. Densities of atoms in laser materials typically range from $\sim 10^{12}$ to $\sim 10^{19}$ atoms/cm³. This density is sufficiently high that laser amplification is an essentially smooth and continuous process, with very little “graininess” or “shot noise” associated with the discrete nature of the atoms involved.

Problems for 1.4

1. *Numerical values for the Boltzmann ratio.* The relative numbers of atoms N_1 and N_2 in two energy levels E_1 and E_2 separated by an energy gap $E_2 - E_1$ are given at thermal equilibrium by the Boltzmann ratio. To gain some feeling for real situations, evaluate the ratio N_2/N_1 for the following cases:
 - (a) an optical transition, $\lambda = 500$ nm, at room temperature, 300 K;
 - (b) a microwave transition, $f = 3$ GHz, at room temperature;
 - (c) a 10 GHz transition at liquid-helium temperature, 4.2 K.

For an optical transition at $\lambda = 500$ nm to have $N_2/N_1 = 0.1$, what temperature is required? What is the energy kT corresponding to room temperature, expressed in wave numbers?

1.5 LASER PUMPING AND POPULATION INVERSION

Let us now examine in elementary terms the kind of pumping process that can produce the population inversion needed for laser amplification.

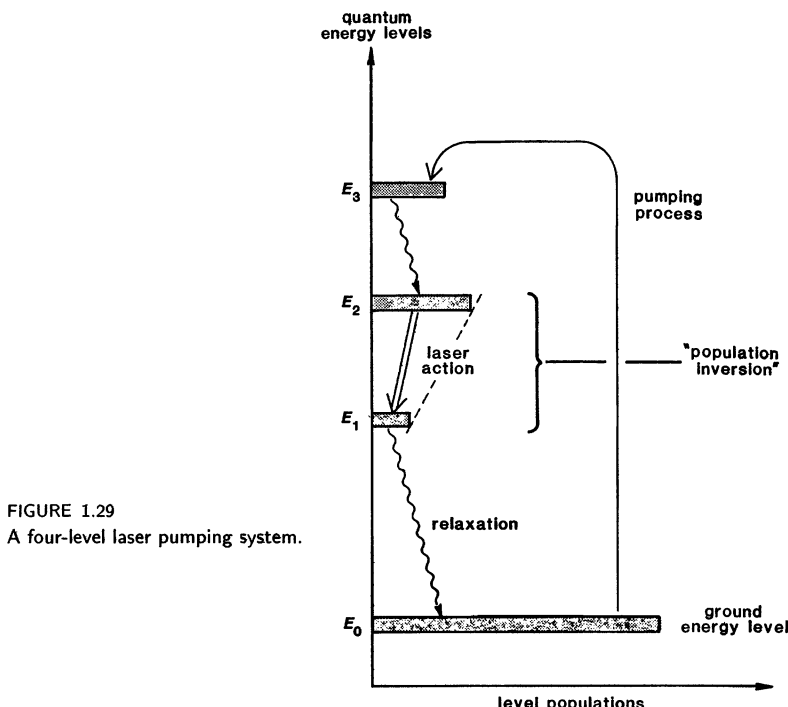


FIGURE 1.29
A four-level laser pumping system.

Four-Level Pumping Model

As a simplified but still quite realistic model of many real laser systems, we can consider the four-level atomic energy system shown in Figure 1.29. We assume here that there is a lowest or ground energy level E_0 and two higher energy levels E_1 and E_2 , between which laser action is intended to take place, plus a still higher level, or more often a group of higher levels, into which there is effective pumping from the ground level E_0 . We can for simplicity group all these higher levels into a single upper pumping level E_3 . At thermal equilibrium, under the Boltzmann relation, essentially all the atoms will be in the ground energy level E_0 .

We then assume that there is a pumping rate R_{p0} (atoms/second) from the ground level E_0 into the upper pumping level or levels E_3 . This pumping rate may be produced by electron impact with the ground-level atoms in a gas discharge, as in many gas lasers; or by pumping with intense incoherent light from a pulsed flashlamp or a cw arc lamp, as in many optically pumped solid-state lasers; or by several other mechanisms we have not yet discussed. In any event, the properties of atoms do permit selective excitation from a lowest level primarily into certain selected upper levels, as assumed in this example.

It is then a realistic description of many practical lasers that a certain fraction η_p of the atoms excited upward will relax down, perhaps through a series of cascaded steps, from the upper pumping level E_3 into the intended upper laser

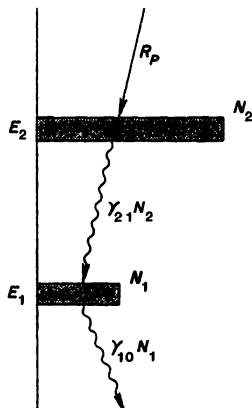


FIGURE 1.30
Rates of flow between atomic energy levels in an ideal four-level laser system.

level E_2 . We might call η_p the pumping efficiency for the laser system, since the effective pumping rate into the upper laser level (again in atoms/second) is $R_p = \eta_p R_{p0}$. This pumping efficiency can be close to unity in some solid-state and organic dye lasers, and only parts per thousand or less in many gas laser systems.

We can also assume in the simplest case that atoms relax from level E_2 down to level E_1 with a relaxation rate γ_{21} and from level E_1 down to level E_0 with a relaxation rate γ_{10} . The relaxation processes between these levels may be a combination of the radiative and nonradiative processes we have described in preceding sections. In many practical lasers the fractional number of atoms lifted up out of the ground level E_0 into all the upper excited levels also remains small, so that the ground-level population remains essentially unchanged whether the pumping process is on or not.

The flow of atoms between energy levels under the influence of these pumping and relaxation processes (but not laser action for the minute) can then be described by atomic rate equations which we will discuss in much more detail in later chapters. For example, the rate equations describing the laser-level populations in the system shown in Figure 1.29 may be written as (Figure 1.30)

$$\frac{dN_2}{dt} \approx R_p - \gamma_{21} N_2. \quad (20)$$

and

$$\frac{dN_1}{dt} \approx \gamma_{21} N_2 - \gamma_{10} N_1. \quad (21)$$

These equations include the upward pumping rate and the downward relaxation rates into and out of levels E_1 and E_2 .

If the pumping process is applied in a continuous fashion and the system comes to a steady-state equilibrium in which $dN_1/dt = dN_2/dt \equiv 0$, we can solve these equations for the steady-state populations and population difference on the laser transition, in the form

$$N_{2,ss} = R_p / \gamma_{21} \quad \text{and} \quad N_{1,ss} = (\gamma_{21} / \gamma_{10}) N_{2,ss}, \quad (22)$$

and hence

$$(N_2 - N_1)_{ss} = \frac{R_p(\gamma_{10} - \gamma_{21})}{\gamma_{10}\gamma_{21}} = R_p\tau_{21} \times (1 - \tau_{10}/\tau_{21}), \quad (23)$$

where $\tau_{21} \equiv 1/\gamma_{21}$ and $\tau_{10} \equiv 1/\gamma_{10}$.

This formula shows that if the lower-level decay rate γ_{10} is fast compared to the upper-level decay rate γ_{21} , so that $\tau_{10} < \tau_{21}$, then there will inevitably be a population inversion on the $2 \rightarrow 1$ laser transition produced by the pumping process. Whether this inversion will be large enough to permit continuous laser amplification or oscillation on this transition is another question, obviously depending in part on the pumping efficiency and on how hard we can pump.

Conditions for Population Inversion

The basic physical requirement to obtain continuous population inversion in this system is that atoms should relax out of the lower laser level E_1 down to still lower levels faster than atoms relax into this level from the upper laser level E_2 . The absolute strength of the population inversion also depends on a strong pumping rate R_p and a long upper-level lifetime $\tau_{21} \equiv 1/\gamma_{21}$; but the essential condition for population is still that the relative relaxation rates obey the condition that $\gamma_{10} > \gamma_{21}$.

The rate equations for real laser systems can become considerably more complicated, and involve more energy levels and relaxation rates than this simplest example; but the essential features will still be quite similar. The upper levels in many real lasers, for example, are more or less *metastable*—that is, they have comparatively long lifetimes. If we can pump efficiently into such a longer-lived upper level, and if there is a lower energy level with a short lifetime or rapid downward relaxation rate, then a population inversion is very likely to be established between these levels by the pumping process.

As we have mentioned, gas discharges and optical pumping are the two most widely used laser pumping processes. The gas discharges may be continuous (usually in lower-pressure gases) or pulsed (typically in higher-pressure gases). Direct electron impact with atoms or ions, and transfer of energy by collisions between different atoms, are the two main mechanisms involved in gas discharge pumping.

Optical pumping techniques may also be continuous or pulsed. The sources of the pumping light may be continuous-arc lamps, pulsed flashlamps, exploding wires, another laser, or even focused sunlight. Other more exotic pumping mechanisms include chemical reactions in gases, especially in expanding supersonic flows; high-voltage electron-beam pumping of gases or solids; and direct current injection across the junction region in a semiconductor laser.

Problems for 1.5

1. *Slightly more complicated laser pumping system.* Add a third relaxation rate directly from level 2 to level 0 in Figure 1.29, with a downward rate on this transition given by $\gamma_{20}N_2$. Write out and solve the new rate equations including this term, and discuss the new conditions that are now necessary for population inversion.

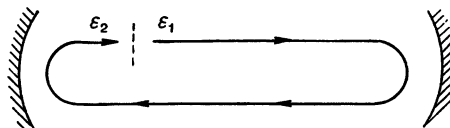


FIGURE 1.31
Round-trip amplification in a laser cavity.

1.6 LASER OSCILLATION AND LASER CAVITY MODES

Adding laser mirrors and hence signal feedback, as we will do in this section, is then the final step necessary to produce coherent laser oscillation and thus to obtain a working laser oscillator.

Condition for Build-Up of Laser Oscillation

Suppose in fact that we have a laser rod or a laser tube containing atoms that are properly pumped so as to produce population inversion and amplification on a certain laser transition. To make a coherent oscillator using this medium, we must then add partially reflecting, carefully aligned end mirrors to the laser medium, as shown in Figures 1.1 or 1.4.

Suppose that we do this, and that a small amount of spontaneous emission at the laser transition frequency starts out along the axis of this device, being amplified as it goes. This radiation will reflect off one end mirror and then be reamplified as it passes back through the laser medium to the other end mirror, where it will of course again be sent back through the laser medium (Figure 1.31).

If the round-trip laser gain minus mirror losses is less than unity, this radiation will decrease in intensity on each pass, and will die away after a few bounces. But, if the total round-trip gain, including laser gain and mirror losses, is greater than unity, this noise radiation will build up in amplitude exponentially on each successive round trip; and will eventually grow into a coherent self-sustained oscillation inside the laser cavity formed by the two end mirrors. The *threshold condition* for the build-up of laser oscillation is thus that the total round-trip gain—that is, net laser gain minus net cavity and coupling losses—must have a magnitude greater than unity.

Steady-State Oscillation Conditions

Net gain greater than net loss for a circulating wave thus leads to signal build-up at the transition frequency within the laser cavity. This exponential growth will continue until the signal amplitude becomes sufficiently large that it begins to “burn up” some of the population inversion, and partially saturate the laser gain.

Steady-state oscillation within a laser cavity, just as in any other steady-state oscillator, then requires that net gain just exactly equal net losses, or that the total round-trip gain exactly equal unity, so that the recirculating signal neither grows nor decays on each round trip, but stays constant in amplitude.

In mathematical terms, using the more detailed model shown in Figure 1.32, the steady-state oscillation condition for a linear laser cavity with spacing L between the mirrors is that the total voltage gain and phase shift for a signal

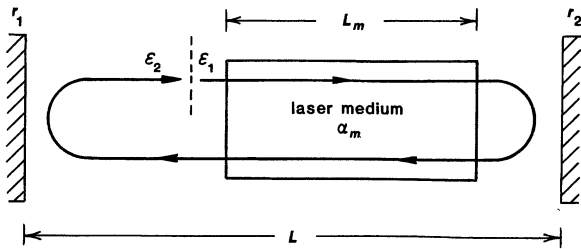


FIGURE 1.32
More detailed model of a linear or “standing-wave” laser oscillator.

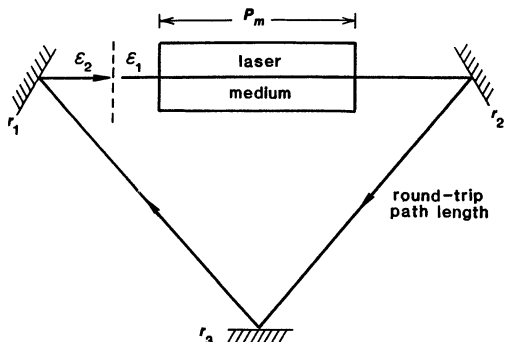


FIGURE 1.33
Analytical model of a ring laser oscillator.

wave at frequency ω in one complete round trip must satisfy the condition that

$$\mathcal{E}_2/\mathcal{E}_1 \equiv r_1 r_2 \exp(2\alpha_m L_m - j2\omega L/c) = 1 \quad \text{at steady state,} \quad (24)$$

where the coefficients r_1 and r_2 ($|r| \leq 1$) are the wave-amplitude or “voltage” reflection coefficients of the end mirrors; $\exp(2\alpha_m L_m)$ is the round-trip voltage amplification through the laser gain medium of length L_m ; and $\exp(-2j\omega L/c)$ is the round-trip phase shift around the laser cavity of length L . (For simplicity we have left out here any internal losses inside the laser cavity, and also any small additional phase-shift effects caused by the laser atoms or the cavity mirrors.)

If the laser employs instead a ring cavity of the type shown in Figure 1.33—as is becoming more common in laser systems—then this condition becomes instead

$$\mathcal{E}_2/\mathcal{E}_1 = r_1 r_2 r_3 \exp(\alpha_m p_m - j\omega p/c) = 1 \quad \text{at steady state,} \quad (25)$$

where now p is the perimeter or full distance around the ring, and p_m is again the single-pass distance through the laser medium.

Round-Trip Amplitude Condition

Either of these conditions on steady-state round-trip gain then leads to two separate conditions, one on the amplitude and the other on the phase shift of the round-trip signal transmission. For example, the magnitude part of the steady-state oscillation condition expressed by Equation 1.24 requires simply

that

$$r_1 r_2 \exp(2\alpha_m L_m) = 1 \quad \text{or} \quad \alpha_m = \frac{1}{4L_m} \ln\left(\frac{1}{R_1 R_2}\right), \quad (26)$$

where $R_1 = |r_1|^2$ and $R_2 = |r_2|^2$ are the power reflectivities of the two end mirrors.

This condition determines the net gain coefficient or the minimum population inversion in the laser medium that is required to achieve oscillation in a given laser system. Using Equation 1.18 for the laser gain coefficient, we can convert this to the often-quoted *threshold inversion density*

$$\Delta N \equiv N_2 - N_1 \geq \Delta N_{th} \equiv \frac{\pi \Delta \omega_a}{\lambda^2 \gamma_{rad} L_m} \ln\left(\frac{1}{R_1 R_2}\right). \quad (27)$$

This expression on the one hand gives the minimum or threshold population inversion ΔN_{th} that must be created by the pumping process if oscillation build-up toward sustained coherent oscillation is to be achieved. On the other hand, Equations 1.26 and 1.27 also give the saturated gain coefficient α_m or the saturated inversion density ΔN (atoms per unit volume) that must just be maintained to have unity net gain at steady state.

A laser oscillator will always start out with inversion somewhat greater than threshold. It will then build up to an oscillation level that just saturates the net laser gain down to equal net loss. This saturation occurs (as we will show in more detail later) when the laser oscillation begins to use up atoms from the upper level at a rate which begins to match the net pumping rate into that level; and it is just this gain saturation process which stabilizes the amplitude of a laser oscillator at its steady-state oscillation level.

Equation 1.27 makes clear that reaching laser threshold will be easiest if the laser has a narrow transition linewidth $\Delta \omega_a$, and low cavity losses, including $R_1, R_2 \rightarrow 1$. Note also that laser action generally gets more difficult to achieve as the wavelength λ gets shorter—irradiated lasers are often easy, ultraviolet lasers are hard.

Round-Trip Phase or Frequency Condition

Equations 1.24 or 1.25 also express a round-trip *phase shift condition* which says that the complex gain in these equations must actually be equal to unity modulo some large factor of $e^{-j2\pi}$; so for a linear cavity,

$$\exp(-j2\omega L/c) = \exp(-jq2\pi) \quad \text{or} \quad \frac{2\omega L}{c} = q2\pi, \quad q = \text{integer.} \quad (28)$$

In other words, the round-trip phase shift $2\omega L/c$ inside the cavity must be some (large) integer multiple of 2π , or the round-trip path length must be an integer number of wavelengths at the oscillation frequency.

In the linear cavity case this phase condition is met at a set of discrete and equally spaced *axial-mode frequencies* given by

$$\omega = \omega_q \equiv q \times 2\pi \times \left(\frac{c}{2L}\right). \quad (29)$$

The phase shift condition thus leads to a *resonance frequency condition* for the laser cavity, or equivalently to an *oscillation frequency condition* for the laser oscillator. The set of frequencies ω_q are called *axial modes* because they represent

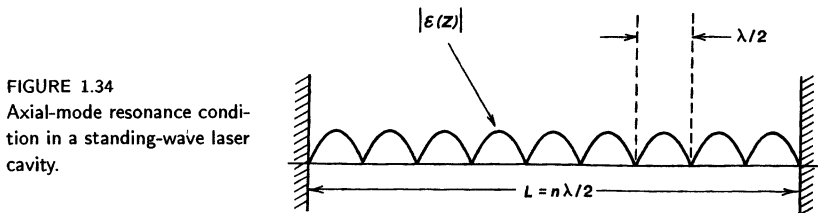


FIGURE 1.34
Axial-mode resonance condition in a standing-wave laser cavity.

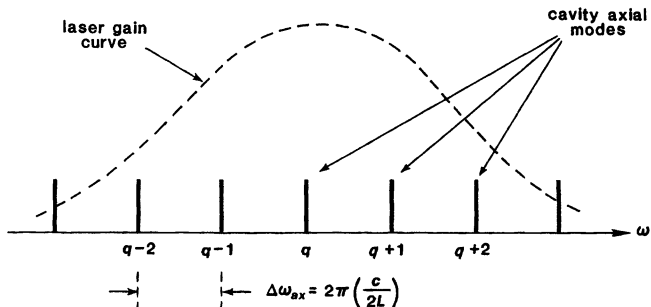


FIGURE 1.35
Multiple axial-mode frequencies under the atomic gain profile in a typical laser system.

the resonant frequencies at which there are exactly q half-wavelengths along the resonator axis between the laser mirror in the linear or standing-wave case.

This same round-trip phase shift condition becomes $\omega p/c = q2\pi$ in the ring cavity case, and the resonant frequencies $\omega_q = q \times 2\pi \times (c/p)$ are then the frequencies at which the ring perimeter p is an integer number of full wavelengths. The axial-mode integer q is typically a very large number in any real laser; e.g., for the standing-wave case

$$q = \frac{\omega_q L}{\pi c} = \frac{2L}{\lambda_q} = \frac{p}{\lambda_q} \approx 10^5 - 10^6, \quad (30)$$

since L (or p) is always $\gg \lambda$ for any except very unusual laser cavities.

The axial resonant modes of the laser cavity are thus equally spaced in frequency, with axial-mode separation $\Delta\omega_{ax}$ given by

$$\begin{aligned} \Delta\omega_{ax} &\equiv \omega_{q+1} - \omega_q = 2\pi \times \frac{c}{2L} = 2\pi \times \frac{c}{p} \\ &\approx 2\pi \times 300 \text{ MHz} \quad \text{for} \quad L = 50 \text{ cm.} \end{aligned} \quad (31)$$

For many (though not all) practical lasers, this mode spacing is smaller than the atomic linewidth $\Delta\omega_a$; and hence there will be several axial-mode cavity resonances within the atomic gain curve, as shown in Figure 1.35. The laser may then oscillate, depending on more complex details, on just the centermost one of these axial modes, or on several (or even many) axial modes simultaneously.

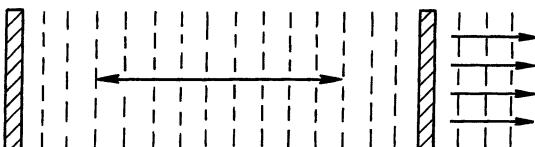


FIGURE 1.36
Plane-wave model for laser oscillation.

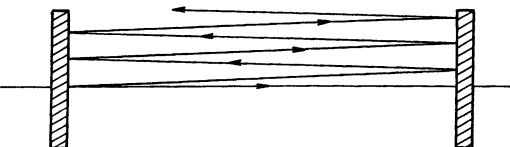


FIGURE 1.37
Walk-off effect for an off-axis wave.

Transverse Spatial Properties: The Plane Mirror Approximation

We need to consider also the *transverse variation* of the optical fields in the laser cavity—that is, the variation over the cross-sectional planes perpendicular to the laser axis—since it is this variation that determines the *spatial coherence* or the *transverse-mode properties* of the laser oscillator.

In the simplest description, a laser will oscillate in the form of a more or less uniform, quasi-plane-wave optical beam bouncing back and forth between carefully aligned mirrors at the two ends of the laser resonator, as in Figure 1.36. The earliest successful lasers, and even some practical lasers today, in fact used flat or planar mirrors carefully aligned exactly parallel to each other and perpendicular to the axis of the laser.

If the optical wave in Figure 1.36 travels at even a slight angle to the resonator axis running perpendicular to the two mirrors, the radiation will walk out the open sides of the cavity, past the mirror edges, after some small number of bounces, as in Figure 1.37. This will represent a large “walk-off” loss from the laser cavity, so that only waves that are very accurately aligned with the resonator axis will remain within the cavity and be able to oscillate. Hence the beam direction for the oscillating waves will lie very accurately along the cavity axis. (This of course also requires strictly parallel alignment of the two mirrors.)

To the extent that the oscillating beam then approximates a finite diameter beam with a nearly planar (or possibly slightly spherical) wavefront, the phase of the emerging wavefront will be essentially uniform across the output mirror, a condition sometimes referred to as a “uniphase” wavefront. There will also then be a very high degree of coherence between the instantaneous phase of the wavefront emerging from widely separated points across the output mirror (but within the overall envelope of the laser beam); and so we can also say that there is a very high degree of “spatial coherence” to the laser output. The laser output beam coming through a partially transmitting end mirror, at least in this simplified description, will thus be a highly directional beam with a uniform phase across the mirror surface and hence essentially perfect spatial coherence in the output beam.

Transverse Modes in Real Laser Cavities

In a real laser cavity, any such quasi-plane wave, as it bounces back and forth, will of course spread transversely because of diffraction, so that some of its energy will spill over the edges of the finite laser mirrors. This spillover will represent a diffraction loss mechanism, which becomes part of the overall round-trip losses of the laser cavity.

It is even more important to recognize, however, that such a wave, as it bounces back and forth between two mirrors, will also undergo distortion of its transverse amplitude and phase profile in each trip around the laser cavity because of these same diffraction effects. A uniform plane wave coming from a finite aperture, for example, will acquire significant Fresnel diffraction ripples in even one pass down the laser cavity. When this rippled beam bounces off a finite-aperture end mirror and the truncated wavefront travels back the other way along the laser cavity, it will acquire still further distortion because of additional diffraction and propagation effects.

The simple bouncing-plane-wave description of Figure 1.36 therefore cannot be fully correct, first because the uniform plane waves will spread and distort because of diffraction, and second because real laser cavities most often employ spherically curved mirrors, as in Figure 1.38, rather than flat or planar mirrors, for reasons we will soon consider. These mirrors have finite transverse widths or diameters, which effectively act as apertures for the circulating laser beam; and in addition there are often additional apertures elsewhere along the laser axis, either deliberately added or caused by the finite diameter of the laser tube or other intracavity elements.

To understand the transverse beam properties in real laser cavities, therefore, we must examine more carefully what happens to a propagating optical wave with a given transverse amplitude and phase pattern when it propagates through one complete round trip around a laser cavity, including all the focusing, aperturing, and diffraction effects in the round trip.

Self-Reproducing Transverse Mode Patterns

The round-trip wave propagation in a real laser cavity can be studied by carrying out analytical or computer calculations of the manner in which the transverse field pattern of the optical beam changes on repeated round trips within a given resonator. Optical resonator mode calculations of this type were first pioneered in the early 1960s by A. G. Fox and T. Li at the Bell Telephone Laboratories, and are often referred to as "Fox and Li" calculations.

Such calculations are usually carried out with the laser gain omitted for simplicity. It then turns out that for any given laser cavity, employing either finite-diameter planar or (more usually) finite-diameter curved end mirrors, one will always find a certain discrete set of transverse eigenmodes, or distinct amplitude and phase patterns for the circulating beam in the cavity, which *will reproduce themselves in form, though slightly reduced in overall amplitude, after one round trip*. A typical example of such a self-reproducing transverse beam pattern is shown in Figure 1.38. These self-reproducing transverse field patterns represent the characteristic set of *lowest-order and higher-order transverse eigenmodes or transverse spatial modes* characteristic of that particular laser resonator.

These self-reproducing transverse eigenmodes, with amplitude and phase patterns that depend on the specific curvature and shape of the laser mirrors,

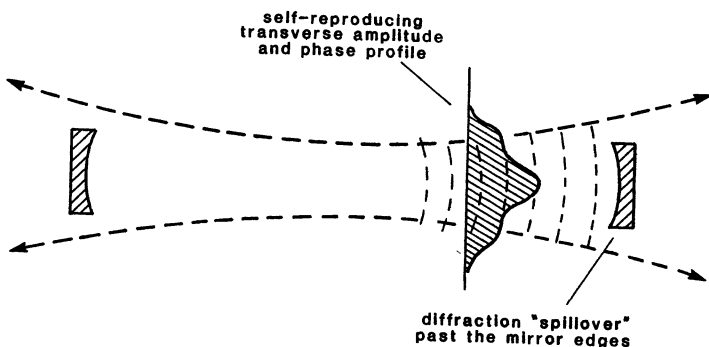


FIGURE 1.38

Example of a self-reproducing transverse mode pattern with finite diffraction losses in a typical real laser cavity.

are analogous to the transverse modes in a closed waveguide, or even more closely analogous to the lowest-order and higher-order propagation modes in a leaky optical lensguide. Indeed, we can view the repeated round trips in either a standing-wave or a ring laser resonator as essentially equivalent to passage through repeated sections of an iterated periodic lensguide, with reflection from the finite-aperture cavity mirrors being replaced by transmission through equivalent finite-aperture lenses having the same focal power.

These transverse eigenmodes can then provide self-consistent oscillation beam patterns for an oscillating laser. The amplitude reduction on each pass—which is generally different for each such transverse mode—simply represents the diffraction or spillover losses for that particular mode, caused by whatever finite apertures are present in the cavity. If the laser then begins oscillating in one of these patterns, and if the laser medium can maintain sufficient round-trip gain to overcome the diffraction losses of that particular transverse mode, along with all the other losses in the cavity, this will be one possible steady-state beam pattern or beam profile for the laser oscillation.

Planar Resonator Modes

In any reasonably well-designed laser cavity with finite-width or finite-diameter end mirrors, we will normally find that there is one such lowest-order transverse mode pattern, which is usually reasonably smooth in its transverse amplitude and phase profile, and which has the lowest diffraction loss of all the self-reproducing transverse mode patterns in that particular resonator.

In a properly aligned planar resonator, for example, the lowest-order transverse mode will generally have an amplitude profile which looks something like the upper part of figure 1.39. That is, this mode will typically look something like the central lobe of a $J_0(r)$ Bessel function across the mirror for circular end mirrors, or like a single lobe of a cosine wave, that is $\mathcal{E}(x, y) \approx \cos(\pi x/a) \cos(\pi y/b)$ for rectangular mirrors of width $2a$ by $2b$. The exact amplitude pattern of this lowest-order mode will, however, also have diffraction ripples, as in the upper part of Figure 1.39, whose amplitude and spacing depend on the finite mirror size; and the quasi-Bessel function or cosine variation will not drop quite to zero

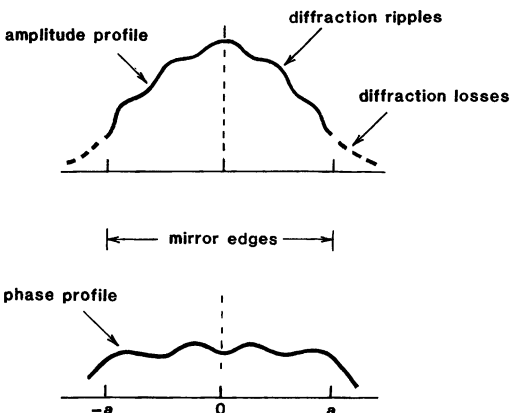


FIGURE 1.39
A typical lowest-order transverse mode profile in a planar-mirror cavity like Figure 1.36.

at the mirror edges, in agreement with the inevitable diffraction losses in such an open-sided resonator.

The phase variation of the lowest-order mode in a typical planar resonator will also exhibit some small Fresnel diffraction ripples, along with some small curvature of the wavefront along the outer edges of the resonator, as in the lower part of Figure 1.39; but over the major portion of the mode the wavefront will in fact be a very good approximation to a planar wavefront. A plane-mirror cavity oscillating in this lowest-order transverse mode will thus in fact have output beam properties very close to those of the simple plane wave described earlier.

The unwanted diffraction losses past the mirror edges for this lowest-order transverse mode will also typically be very small, unless the mirror sizes are made very small. The lower-order self-consistent transverse modes in almost any type of resonator in fact exhibit an uncanny ability to shape their amplitude and phase patterns in ways that minimize their diffraction losses on each round trip.

Higher-Order Modes

This same laser cavity will generally also have many higher-order transverse modes. These will generally have larger diffraction losses and also more complex transverse amplitude and phase variations, like the higher-order transverse modes in waveguides. And they will generally have several transverse nulls and phase reversals, with either even or odd symmetry in simple cases. Their transverse spread inside the cavity is generally larger, which makes their diffraction losses larger than those of the lowest-order transverse mode; and their diffraction spread or beam spread outside the cavity is also generally larger than that for the lowest-order transverse mode. For these reasons, laser oscillation in these higher-order modes is generally considered undesirable. We will analyze the mode properties of these transverse modes in great detail in Chapters 14 through 23.

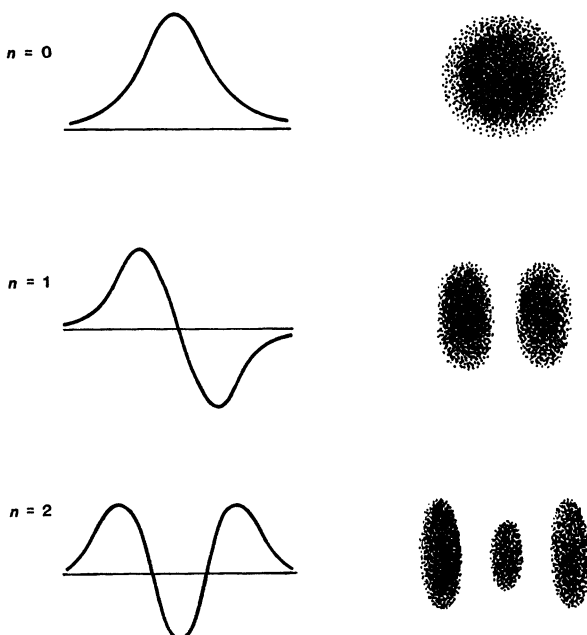


FIGURE 1.40
Hermite-gaussian transverse-mode patterns in a stable laser resonator.

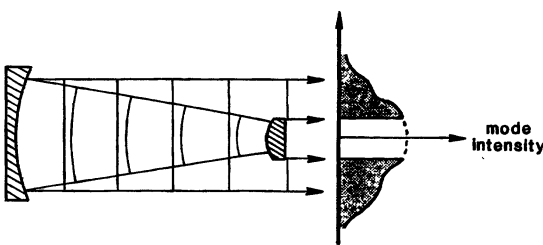
Stable and Unstable Laser Resonators

Practical laser cavities most often employ curved rather than planar end mirrors, in order to shape the transverse modes of the cavity and control the diffraction losses. There is one broad class of such curved-mirror resonator designs, the so-called *stable laser resonators*, in which the diffraction losses are generally very small, and the lowest-order and higher-order modes have the form (very nearly) of Hermite-gaussian functions, as in Figure 1.40, with the lowest-order mode having a gaussian transverse profile of the form $\mathcal{E}(r) = \exp(-r^2/w^2)$. Such gaussian modes and the resulting gaussian output beams are particularly easy to handle both analytically and in experiments, and practical lasers are very often designed in this fashion.

On the other hand, these Hermite-gaussian modes in realistic laser cavities do turn out to be very slender in diameter, so that they do not readily fill all the volume of larger-diameter laser tubes or rods. The laser must then oscillate in a mixture of lowest-order and higher-order modes (which tends to spoil the beam collimation properties) in order to fill and extract all the available power from the laser volume.

There is also a class of so-called *unstable optical resonators*, which make use of deliberately diverging laser wavefronts as shown in Figure 1.41. These resonators have transverse mode patterns that much more readily fill large laser volumes, but still suppress higher-order transverse modes. These unstable optical resonators necessarily have much larger output coupling or lower effective mirror reflectivity than stable resonators, since the diffraction spread past the output

FIGURE 1.41
A typical unstable resonator
transverse-mode profile.



mirror edges is used as the output coupling mechanism. This property limits the usefulness of unstable resonators for low-gain laser systems.

The mode properties of such unstable resonators are also rather more complex and esoteric than the simple Hermite-gaussian stable modes. (Note that the "stability" referred to in these resonator classifications is that of geometrical rays bouncing back and forth in the cavity designs in question, and has nothing directly to do with the stability or instability of the laser oscillation in the resulting transverse eigenmodes.) Perhaps the most useful class of laser resonator modes in the future will be the geometrically unstable but still Hermite-gaussian modes that can be obtained in so-called "complex paraxial" resonators by using variable reflectivity mirrors, as will be described in Chapter 23.

General Transverse-Mode Oscillation Properties

Each different optical-resonator design, whether planar, stable, unstable, or still more complex, will thus possess some lowest-order transverse mode pattern which can circulate repeatedly around the laser cavity without changing its amplitude or phase profile. The phase profile of this lowest-order transverse mode will usually be comparatively smooth and regular across the output mirror of the laser cavity (as well as at any other transverse plane within the cavity). The phase front is often quasi spherical across the output plane of the laser, but this spherical curvature can be removed by a simple lens to convert the output beam into a fairly well-collimated plane wave.

A laser cavity which oscillates only in this lowest-order transverse mode will thus generally produce an output beam with good transverse characteristics and with a nearly uniphase character across the output mirror. If the laser oscillates simultaneously in several transverse modes, however, as can readily happen in real lasers, the output wavefront will no longer be "uniphase," and the collimation and focusing properties of the beam will generally deteriorate.

Forcing laser oscillation to occur only in the lowest-order transverse mode is thus a practical design objective, which is achieved in some though not all practical lasers. The primary obstacle to achieving single-transverse-mode oscillation in higher-power (or higher-gain) lasers is that the diffraction losses of the lowest- and higher-order modes in a large-diameter cavity are all small and nearly identical; so there is little or no loss discrimination between the different transverse modes. A designer must then add mode-control apertures, employ unstable resonator designs, or use other tricks to suppress the unwanted higher-order transverse modes.

Note also that the transverse mode properties we have just been discussing, and the axial mode or resonant frequency properties we discussed earlier, are almost independent of each other. There are some important secondary connections between these properties, and we will discuss them in detail in later chapters. In simplified terms, however, the round-trip propagation length determines the resonant axial-mode frequencies of the laser, whereas the focusing and diffraction effects associated with mirrors and apertures in the round-trip propagation determine the transverse mode patterns.

REFERENCES

The original reference on the Fox and Li approach to optical resonator modes is A. G. Fox and T. Li, "Resonant modes in a maser interferometer," *Bell Sys. Tech. J.* **40**, 453–458 (March 1961); with later and more extensive results in "Modes in a maser interferometer with curved and tilted mirrors," *Proc. IEEE* **51**, 80–89 (January 1963).

A good review of standard stable resonator theory is given by H. Kogelnik and T. Li, "Laser beams and resonators," *Proc. IEEE* **54**, 1312 (October 1966) and *Appl. Optics* **5**, 1550–1567 (October 1966). Unstable resonators are reviewed in A. E. Siegman, "Unstable optical resonators," *Appl. Optics* **13**, 353 (February 1974).

1.7 LASER OUTPUT-BEAM PROPERTIES

The output beam from a laser oscillator thus basically consists of electromagnetic radiation, or light, that is not fundamentally different in kind from the radiation emitted by any other source of electromagnetic radiation. There are several important and fundamental differences in detail, however, between the "incoherent" light emitted by any thermal light source, such as the flashlight in Figure 1.42, and the "coherent" light emitted by a laser oscillator.

The output beams produced by laser oscillators in fact have much more in common with the outputs of conventional low-frequency electronic oscillators, such as transistors or vacuum tubes, than they do with any kind of thermal light sources. Laser beams are often described as being different from ordinary light sources in being both *spatially coherent* and *temporally or spectrally coherent*. These rather vague phrases refer to some characteristic laser output-beam properties that we will review briefly in this section.

An important point to keep in mind is that all these coherence properties arise primarily from the *classical resonant-cavity properties* of the laser resonator, as we described in the preceding section, rather than from any of the quantum transition properties of the laser atoms.

Ideal Laser Monochromaticity and Frequency Stability

The flashlight shown in Figure 1.42, like any other thermal light source, emits a generally broadband continuum of light at many different wavelengths. There are light sources, such as discharge lamps, that emit only comparatively few spectral lines or narrow bands of wavelengths, but the spectral widths of the light emitted by even the best such sources are still limited by the linewidths of the atomic transitions in the discharge atoms.

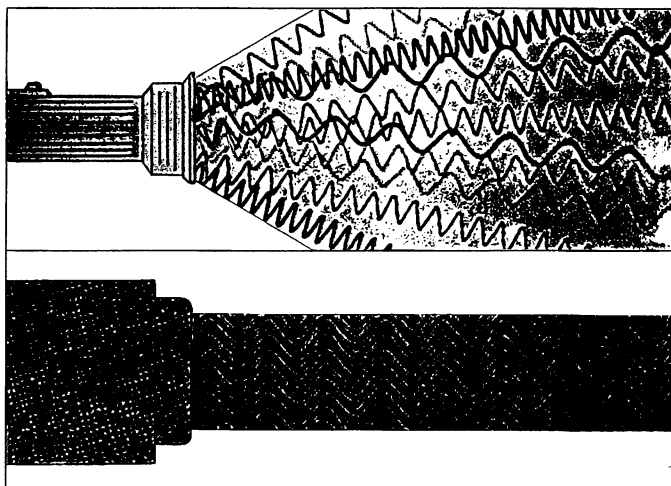


FIGURE 1.42

Incoherent light from a flashlight (top) and coherent light from a laser (bottom).

The output beams from most lasers can be, by contrast, *highly monochromatic*, and in ideal lasers can consist almost entirely of a *single frequency*. That is, the output signal from a near-ideal laser will be a nearly pure, constant-amplitude, highly stable, single-frequency sine wave, exactly like the signal generated by a highly stable electronic oscillator in any other frequency range.

Atomic transitions typically have fractional atomic linewidths $\Delta\omega_a/\omega$ ranging from 1 part in 100 (broadband dye or semiconductor materials) to narrower than 1 part in 10^6 (narrow-line atomic transitions in gases); and it is this linewidth that characterizes the spontaneous or fluorescent emission from such atoms. In absolute terms such linewidths range from a few GHz (as in typical doppler-broadened gas lasers in the visible) to a few tens or hundreds of GHz (as in typical solid-state lasers). The short-term spectral purity of a good-quality single-frequency laser oscillator, by contrast, can range from a few tens of MHz (in a moderately well-stabilized gas laser) down to only a few Hz in a very highly stabilized system.

As we have said, it is the laser cavity and not the laser atomic transition that is primarily responsible for these spectral properties. Continuous oscillations can be sustained in a laser resonator only at those discrete axial-mode frequencies where the round-trip phase shift inside the laser cavity is an integer q times 2π . The laser atomic transition then serves primarily to provide gain at these cavity resonance frequencies, not to determine the oscillation frequency (except for small, second-order frequency-pulling effects that we have not yet discussed).

Spectral Purity in Practical Lasers

Both the short-term frequency jitter and the long-term frequency drift of a laser oscillator usually result primarily from mechanical vibrations and noise, thermal expansion, and other effects that tend to change the length L of the

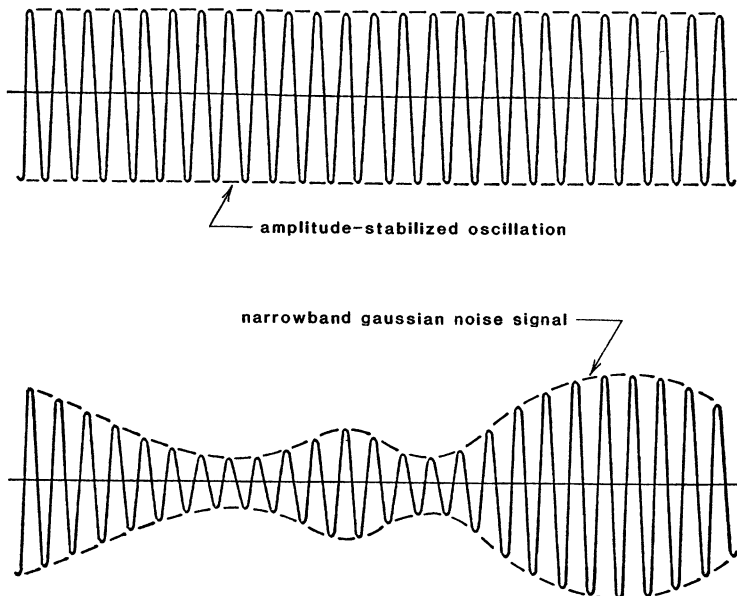


FIGURE 1.43

Sine wave from a coherent oscillator (top) and "noise wave" from a narrowband thermal source (bottom).

laser cavity. Very highly stabilized laser oscillators can nonetheless have long-term absolute frequency stabilities better than 1 part in 10^{10} , and short-term spectral purities as high as 1 part in 10^{13} , making them equal to or better than the best atomic clocks available in any frequency range.

The ultimate limit on laser spectral purity is finally set by quantum noise fluctuations caused by the spontaneous emission from the atoms inside the laser cavity. These quantum noise effects, which are described by the so-called "Schawlow-Townes formula," can be observed with great difficulty only on the very best and most highly stabilized laser oscillators.

Laser Statistical Characteristics

In addition to being highly frequency-stable, a good-quality laser oscillator will generally have all the other statistical and amplitude-stabilization properties associated with a coherent electronic oscillator in any frequency range.

The most basic of these properties is that the instantaneous optical field in a single oscillating cavity mode will be essentially a pure optical-frequency sine wave, whose amplitude remains closely stabilized to the steady-state value at which the saturated laser gain just equals the net mode losses. This is usually a self-stabilizing situation: if the gain increases slightly above the loss because of some random fluctuation, the oscillation amplitude begins to grow slightly, and the slightly increased signal amplitude pulls the gain back down. Conversely, if the amplitude fluctuates slightly above its average value, this pushes the gain down below the loss, and pulls the oscillation amplitude back down.

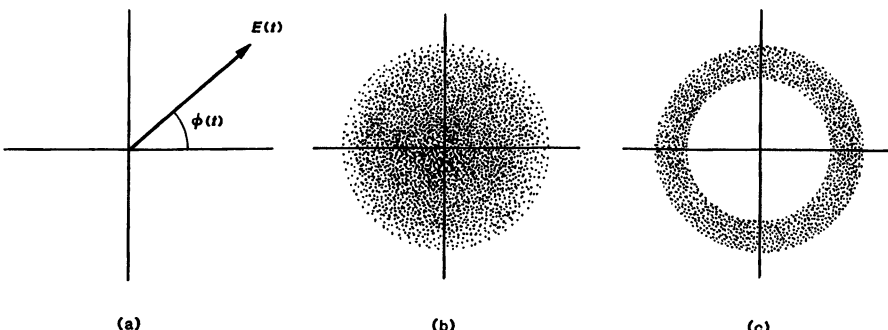


FIGURE 1.44

(a) The complex phasor amplitude of a sinusoidal signal at any one instant of time, and its statistical distributions for (b) a narrowband gaussian noise source, and (c) an amplitude-stabilized oscillator.

A well-stabilized single-frequency laser can in fact have almost negligible amplitude fluctuations, limited mostly by random fluctuations in the pumping rate and the cavity parameters. The output signal from a well-stabilized high-quality single-frequency laser can thus be best described as an optical sine wave with a highly stabilized amplitude and frequency, whose amplitude changes very little, but whose absolute phase drifts randomly and slowly through all possible values, because of small random environmental fluctuations and ultimately because of quantum noise.

Laser Signals Versus Narrowband Incoherent (Thermal) Signals

The output signal from such a high-quality laser will also differ in another quite fundamental way from the spontaneous emission emitted by any thermal or “incoherent” light source. Suppose that the output signal from some very bright thermal light source could be first filtered through some extraordinarily narrowband optical filter, and then amplified through some very high-gain linear optical amplifier (perhaps a laser amplifier), so that the resulting signal was both as narrowband and as powerful as a typical high-quality laser beam. (Though this conceptual experiment would be extremely difficult in practice, there is no fundamental barrier to it in principle.) This output will then also look like an optical-frequency sine wave, but this sine wave will not have constant amplitude or phase, no matter how narrowly filtered it may be. Rather, it will always look something like the incoherent narrowband noise wave in the lower part of Figure 1.43.

Suppose that we write the instantaneous electric field for both the signals in Figure 1.43 in the form $\mathcal{E}(t) = E(t) \cos[\omega_0 t + \phi(t)]$, where ω_0 is the midband or carrier frequency, and $E(t)$ and $\phi(t)$ are the slowly varying amplitude and phase of the signals. We can then represent each signal during any short interval of time by its instantaneous phasor amplitude $E(t)e^{i\phi(t)}$, where this phasor amplitude moves around in time in the complex plane as shown in Figure 1.44(a).

For a thermal noise source, the instantaneous phasor amplitude will then move slowly but randomly through many different phase angles and amplitudes, tracing out a two-dimensional random walk as shown in Figure 1.44(b). The

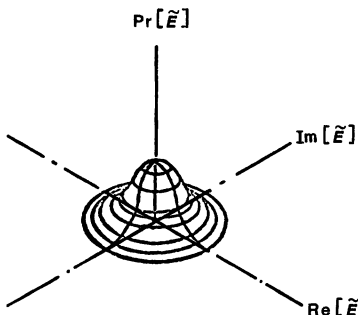


FIGURE 1.45

In three dimensions, the distribution in Figure 1.44(b) is a "gaussian molehill."

bandwidth of the noise signal, no matter how narrow, will determine only how rapidly the phasor moves around within this region—not how far it moves, or with what probability distribution. This noise signal, though having the same power and bandwidth (and hence the same power spectral density) as the laser, will still have the statistical character of narrowband gaussian noise. That is, both the phase and the amplitude of this thermal signal will fluctuate slowly with time, at a rate given essentially by the inverse bandwidth of the signal. The probability distribution for the instantaneous phasor amplitude of the thermal signal will be a "gaussian molehill" (Figure 1.45), with the x and y axes corresponding to the amplitudes of the $\sin(\omega_0 t)$ and $\cos(\omega_0 t)$ components of the signal, and the height of the molehill corresponding to the probability of the signal having these sin and cos components at any instant.

However, the laser oscillator signal, like any other conventional oscillator, will fluctuate primarily only in phase, with only small fluctuations in amplitude about its steady-state value. Its phase angle will wander slowly but randomly through all possible phase angles, in a manner corresponding to its small residual frequency uncertainty; but its amplitude will not. Its probability distribution will thus be a "gaussian molerun" (Figure 1.46) rather than a molehill.

Amplitude Fluctuations in Semiconductor Diode Injection Lasers

The active volume in a semiconductor diode is very small; the passive cavity Q is comparatively low; the atomic lifetimes are fairly short; and the atomic linewidth is very wide compared to most other lasers. As a result of all these characteristics, spontaneous emission effects or fundamental quantum noise fluctuations are generally more significant in semiconductor lasers than in many other types of lasers, and the resulting amplitude and phase fluctuations are larger and more easily observed than in most other lasers. A particularly clean illustration of amplitude-fluctuation effects in semiconductor injection lasers is given, for example, by P.-I. Liu, et. al., in "Amplitude fluctuations and photon statistics of InGaAsP injection lasers," *IEEE J. Quantum Electron.* **QE-19**, 1348-1351 (September 1983). One of the conclusions of this study is that the output signal from a laser oscillator can be very accurately described as the combination of a coherent (highly stabilized) sinusoidal oscillation, plus an additive

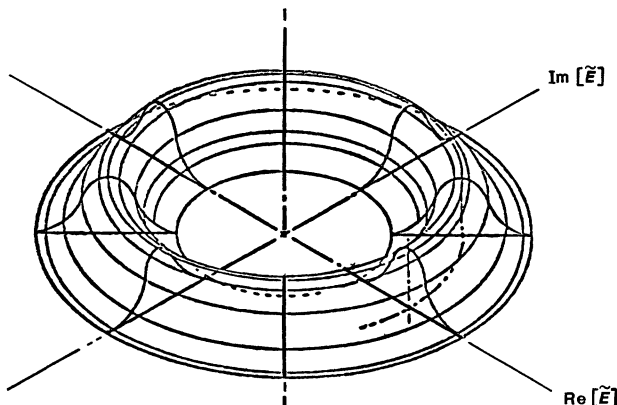


FIGURE 1.46

In three dimensions, the distribution in Figure 1.44(c) is a "gaussian molerun."

gaussian noise component which represents the net effect of spontaneous emission from the inverted laser medium inside the cavity.

Laser Temporal Coherence

The preceding descriptions make more precise what is generally meant by the "temporal coherence" of a laser output signal. However, the term "coherence" is often used carelessly, both in discussions of lasers and in other situations, and this has led to some confusion. The term coherence necessarily refers not to one property of a signal at a single point in space and time, but to a *relationship*, or a *family of relationships*, between one signal at one point in space and time, and the same or another signal at other points in space and time.

There are, for example, certain precise mathematical definitions of coherence functions as used in coherence theory. These functions give the degree of correlation, described in a specific mathematical fashion, between two signals observed at different points in space and/or time. More colloquially, a signal is called "temporally coherent" if there is strong correlation in some sense between the amplitude and/or phase of the signal at any one time and at earlier or later times.

Both the amplitude and the phase of a good-quality laser oscillator will in fact change only slowly with time, so that the amplitude and phase of the output sine wave from the laser at any one time will be strongly correlated with the amplitudes and phases at considerably earlier or later times. A good laser beam might thus be said to be temporally coherent because of this strong correlation between the amplitudes and phases of the signal at not very different points in time. Much the same might be said, however, of the narrowband noise signal described earlier, since there is considerable coherence between the signals at any two times that are less than one reciprocal bandwidth apart. In fact, a high degree of coherence in the formal mathematical sense does not by itself imply

that signals are the kind of “clean” and amplitude-stable sinusoidal oscillation signal generated by a good laser oscillator. Two highly disorderly or irregular signals can still have a very high degree of coherence between themselves.

Laser Spatial Coherence

We have already noted that a good-quality laser oscillator can also oscillate in a single transverse-mode pattern, which has a definite and specific amplitude and phase pattern across any transverse plane inside the laser, and particularly across the output mirror. In this situation there is a very high degree of correlation between the instantaneous amplitudes, and especially between the instantaneous phase angles, of the wavefront at any two points across the output beam. We can then also say that the output beam possesses a very high degree of “spatial coherence” (in the transverse direction) as well as the temporal coherence discussed above.

Often this lowest-order output-beam pattern will vary reasonably smoothly in amplitude, and its phase variation will approximate reasonably closely either a plane wave or a spherical wave (which can be converted into a plane wave with a simple lens). In contrast, if there are badly distorted optical elements inside the laser cavity, the amplitude and especially the phase profile across the beam may be badly distorted. But if this pattern still represents a single transverse cavity mode, however badly distorted, then there will still be a high degree of coherence between the wavefront phasor at different transverse points; i.e., this beam will still be “spatially coherent” in some sense. In principle, we could therefore design a complex “deabberating lens” or deabberating spatial filter that can convert this distorted but stationary wavefront into a smooth and uniphase wavefront of the type that is desirable in a laser output beam.

Laser Beam Collimation

Thermal light sources not only usually emit many wavelengths, but also emit them quite randomly, in essentially all directions. Even if we capture some fraction of this radiation and collimate it with a lens or mirror, as in a searchlight or in the flashlight in Figure 1.42, the resulting degree of collimation, or the amount of radiation emitted per unit solid angle, is still much smaller than in even a very poor quality laser oscillator.

A single-transverse-mode laser oscillator can produce (usually in practice, and always in principle) an output beam that is more or less uniform in amplitude and constant in phase (“uniphase”) across its full output aperture of width or diameter d . Such a beam can propagate for a sizable distance with very little diffraction spread; will have a very small far-field angle at still larger distances; and can be focused into a spot only a few wavelengths in diameter.

Elementary diffraction theory says, for example, that a uniphase plane wave coming from an aperture of diameter d will have a minimum angular diffraction spread $\Delta\theta$ in the far field (Figure 1.47) given by

$$\Delta\theta \approx \frac{\lambda}{d} \quad (\text{in radians}). \quad (32)$$

For a visible laser with $\lambda = 0.5 \mu\text{m}$ and an output aperture of, say, $d = 0.5 \text{ cm}$, this gives an angular spread of $\Delta\theta \approx 10^{-4}$ radians, which we might alternatively express as 0.1 milliradians or 100 μrad .

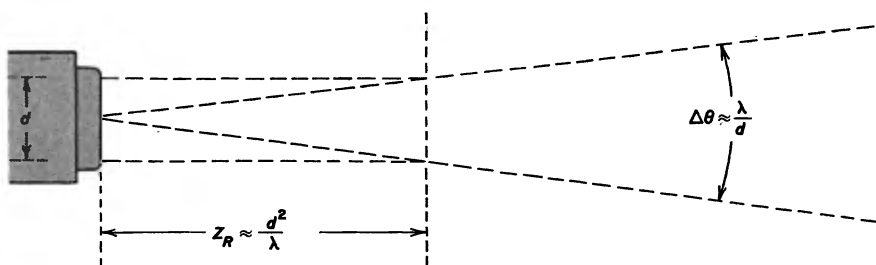
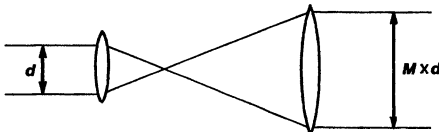


FIGURE 1.47
Laser beam collimation and diffraction spreading.

FIGURE 1.48
Beam-expanding telescope.



The axial distance over which this same beam will stay approximately parallel and collimated before diffraction spreading begins to significantly increase the beam size—sometimes called the Rayleigh range—is then given (see Figure 1.47) by $d/z_R \approx \lambda/d$, or

$$z_R \approx d^2/\lambda. \quad (33)$$

A visible beam with a diameter of 5 mm thus has a Rayleigh range of $z_R \approx 50$ meters.

Suppose this same uniphase beam is magnified by a 20-power telescope attached to the laser output and focused to infinity, as in Figure 1.48. Then the source aperture diameter is increased to $d = 10$ cm, and these results change to $\Delta\theta \approx 5 \mu\text{rad}$ and $z_R \approx 20$ km. Uniphase laser beams can be propagated for very large distances with very small diffraction spreads.

Laser Beam Focusing

Suppose this same uniphase laser beam with initial diameter d is focused down to a spot of diameter d_0 by means of a simple lens of focal length f . The diameter d_0 of the focused spot can then be calculated by applying the same angular spread condition in reverse, to obtain

$$\Delta\theta \approx \frac{\lambda}{d_0} \approx \frac{d}{f} \quad (34)$$

or

$$d_0 d \approx f \lambda, \quad (35)$$

since the focal point will occur essentially one focal length f beyond the lens.

Suppose we follow the common practice in optics of defining the “ f -number” or “ f -stop” of the focusing lens by $f^* \equiv f/d$, i.e., focal length over diameter. (We

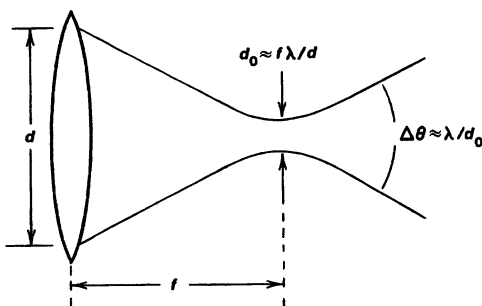


FIGURE 1.49
Laser-beam focusing.

are really defining this quantity in terms of the input beam diameter rather than of the lens diameter, but this of course determines the minimum lens diameter that can be employed.) The approximate diameter of the focused spot can then be written as simply

$$d_0 \approx f^{\#} \lambda. \quad (36)$$

Photography buffs will know that lenses with $f^{\#} \geq 10$ are fairly easy to obtain; lenses with $f^{\#}$ less than about 2 become expensive; and lenses with $f^{\#}$ approaching unity become very expensive.

All the power in a truly uniphase laser beam can thus be focused into a spot a few laser wavelengths in diameter, if we use a powerful lens. (Microscope objectives are usually used for this purpose, at least for laser beams that are not too high in power. A focusing lens for single-wavelength laser radiation of course requires no correction for chromatic aberration, which helps.)

Nonideal Laser Oscillators: Multimode and Multifrequency Oscillation

Many real lasers can produce output beams which come very close to the ideal temporal and spatial behavior described in the preceding paragraphs. Other lasers, however—especially including some of the higher-power laser systems—are more likely to oscillate in both multiple axial and multiple transverse cavity modes. The coherence properties, both temporal and spatial, of such lasers then necessarily deteriorate relative to more ideal single-mode lasers; and the effort to obtain both single-axial-mode (or single frequency) oscillation, and single-transverse-mode (or “diffraction limited”) beam quality, provides a continuing struggle for those who design and construct lasers.

Forcing a practical laser to oscillate in only a single centermost axial mode within the atomic linewidth is most easily accomplished if the laser cavity is made short in order to increase the $c/2L$ axial mode spacing, and if the atomic linewidth is narrow. The laser transition should also preferably be “homogeneously” rather than “inhomogeneously” broadened (we will define these specialized terms later). Special mode-selection techniques employing intracavity etalons and other special filters can also be used to reinforce one selected axial mode and suppress others.

Many practical lasers, however, actually oscillate in several axial modes simultaneously, usually in only a few, but perhaps in a few hundred in extreme

cases. The outputs from such lasers, though no longer single-frequency, can still be quite narrowband compared to incoherent light sources; and multi-axial-mode oscillation is not a serious defect for many practical laser applications.

In such multi-axial-mode lasers there are more likely to be large random fluctuations of individual mode amplitudes, as individual mode frequencies drift across the gain profile because of thermal cavity expansion, and as individual modes compete with each other. The total intensity in all the axial modes is, however, somewhat more likely to remain constant. Real laser devices can also be operated in various internally modulated and pulsed forms, and may be subject to various kinds of instabilities and relaxation oscillations, such as "spiking," which we will discuss in more detail in later chapters.

The output signals from such less-than-perfect lasers may thus usually be described as the summation of several simultaneous and independent oscillation frequencies, and may have substantial random variations in amplitude and frequency for each separate oscillation. Such a rather random multifrequency output, though not really the same as a gaussian random noise signal, may appear much like random noise according to various statistical and spectral measures.

Real Laser Oscillators: Multiple-Transverse-Mode Oscillation

Many real lasers produce output beams which also approach the desirable single-transverse-mode character. A laser beam having the necessary single-mode and uniphase character is often said to be "diffraction limited," since its far-field diffraction angle and focal spot size will approach the ideal limits given just above; whereas beams whose far-field angular spread or focused spot size are k times larger than this are said to be k times diffraction-limited in performance.

More detailed diffraction calculations show that the far-field beam spread of a nonideal beam from an aperture of diameter d is not greatly affected by the exact amplitude pattern of the beam across the aperture; that is, it does not matter greatly whether the amplitude pattern is uniform, gaussian, cosine, or Bessel function, nor do moderate amplitude ripples on the beam lead to serious far-field beam spreading. However, phase variations across the beam wavefront, whether random or regular in character, do begin to substantially increase the far-field beam spread or the focal spot size as soon as they approach the order of 90° phase shift—a distortion of more than a quarter of an optical wavelength—anywhere across the beam width.

A rough argument for the deterioration in beam quality that results from multiple-transverse-mode operation can be developed as follows. Let us call the number of simultaneously oscillating transverse modes in some real laser N_{tm} . Then the far-field angular spread of the output beam from that laser will usually be $\sim N_{tm}^{1/2}$ times larger than the ideal value for a uniphase beam coming from an aperture of the same size, and the focused spot diameter will be $\sim N_{tm}^{1/2}$ times larger than for an ideal beam. (The spot area will, of course, be $\sim N_{tm}$ times larger.)

The ratio $N_{tm}^{1/2}$ is sometimes referred as the "times diffraction limited" or "TDL" ratio of the real laser oscillator. This TDL ratio may range from about 1 up to a few factors of ten in real lasers. (In practice, a designer can often insert some suitable aperture inside a real laser cavity to improve the transverse beam quality, at the price of a corresponding reduction in total output power.)

REFERENCES

In using this text, you may wish to have an optics text handy as a reference. A list of good optics books includes:

C. L. Andrews, *Optics of the Electromagnetic Spectrum* (Prentice-Hall, 1960). Good especially for simple descriptions of diffraction, interference, and optical wave phenomena, using microwave demonstrations. Not very mathematical.

Max Born and Emil Wolf, *Principles of Optics* (Pergamon Press, 1959). The classic advanced-level optics text, found on every laser worker's bookshelf.

Earle B. Brown, *Modern Optics* (Reinhold, 1965). Largely nonanalytical, giving extensive detailed illustrations of practical optical instruments and devices as used in practice.

R. W. Ditchburn, *Light* (Wiley, 1952/1963). Another classic optics text, not as advanced as Born and Wolf, but very extensive and newly revised in 1962.

Grant R. Fowles, *Introduction to Modern Optics* (Holt, Rinehart, and Winston, 1968). Very good elementary optics text, modern and well illustrated.

Max Born, *Optical Physics* (Academic Press, 1965). Not really an optics text; concerned rather with topics in physics that involve optical radiation, including thermal radiation, atomic spectra, and the interaction of optical radiation with matter.

Eugene Hecht and Alfred Zajac, *Optics* (Addison-Wesley, 1974). Another modern basic optics text, including elementary introductions to lasers and holography.

Miles V. Klein, *Optics* (Wiley, 1970). Modern introductory text focused primarily on interference and diffraction.

A. Nussbaum and R. A. Phillips, *Contemporary Optics for Scientists and Engineers* (Prentice-Hall, 1976). Modern coverage of geometrical and physical optics, emphasizing matrix optics and the Fourier analysis approach, plus holography, interferometry, and nonlinear optics.

John M. Stone, *Radiation and Optics* (McGraw-Hill, 1963). More analytical, detailed, and mathematically sophisticated, and with more emphasis on atomic phenomena than the other basic texts in this list.

Robert W. Wood, *Physical Optics* (Dover Publications, 1967). Though many parts of this classic book have become outdated by the passage of four decades since its last revision, this Dover reprint is still valuable for clear descriptions, physical and historical insights, and ingeniously simple demonstrations of optical phenomena.

Problems for 1.7

1. *Fraunhofer (far field) aperture diffraction patterns.* From an optics text find the Fraunhofer diffraction patterns for (a) a square aperture of width d , or (b) a circular aperture of diameter d , when illuminated by a uniform plane wave. Let the beam width of either of these diffraction patterns be defined arbitrarily as the full width between the first nulls in each pattern. Determine the angular width (in radians) and the full solid angle (in steradians) of either far-field pattern as a function of wavelength and aperture area. Compare with the λ/d rule of thumb developed in this chapter.
2. *Huygens' integral and the on-axis intensity in the far field.* Look up a mathematical statement of Huygens' principle in its simplest form. Then suppose a collimated plane wave (i.e., uniform intensity and phase) emerges with total power P_0 through a transmitting aperture of total area A_0 . Using Huygen's integral, show that optical intensity or power density (Watts per unit area) on the beam

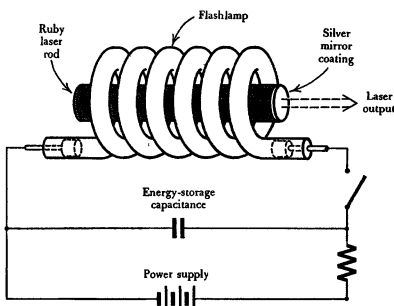


FIGURE 1.50
Design of the first pulsed ruby laser.

axis at large distance z in the far field will be $I = A_0 P_0 / (z\lambda)^2$ independent of the shape of the transmitting aperture. Verify that this is compatible with the far-field angular spread $\Delta\theta \approx \lambda/d$ asserted in this section.

1.8 A FEW PRACTICAL EXAMPLES

Let us look at just a few practical examples of real lasers that illustrate some of the points we have been discussing, notably the ruby solid-state laser, and the helium-neon gas laser.

The Ruby Laser

The first laser of any type ever to be operated was in fact the flash-pumped ruby laser demonstrated by T. H. Maiman at the Hughes Research Laboratory in early 1960. We have already shown in Figure 1.10 the quantum energy levels associated with the unfilled $3d$ inner shell of a Cr^{3+} ion when this ion replaces one of the Al^{3+} ions in the sapphire or Al_2O_3 lattice. Up to $\sim 1\%$ of such replacements can be made in the sapphire lattice to create pink ruby.

By placing such a ruby rod shaped roughly like a slightly overweight cigarette inside a spiral flashlamp filled with a few hundred Torr of xenon (Figure 1.50), and then discharging a high-voltage capacitor bank through this lamp, Maiman was able to use the blue and green wavelengths from this lamp to optically pump atoms from the $^4\text{A}_2$ ground level of the Cr^{3+} ions in the lattice into the broad $^4\text{F}_2$ and $^4\text{F}_1$ bands of excited levels. In ruby, atoms excited into these levels will relax very rapidly, and with close to 100% quantum efficiency, down into the comparatively very sharp ^2E levels, or R_1 and R_2 levels, lying $\sim 14,400$ cm or 694 nm (~ 1.8 eV) above the ground level.

The ruby laser is, however, a three-level laser system, in which the lower laser level is also the ground energy level. By pumping hard enough, we can nonetheless cycle more than half of the Cr^{3+} ions from the ground level up through the pumping bands and into the highly metastable upper laser level, with its fluorescent lifetime of $\tau \approx 4.3$ msec. Thus, even though ruby is a three-level system rather than a four-level system, which is usually very unfavorable,

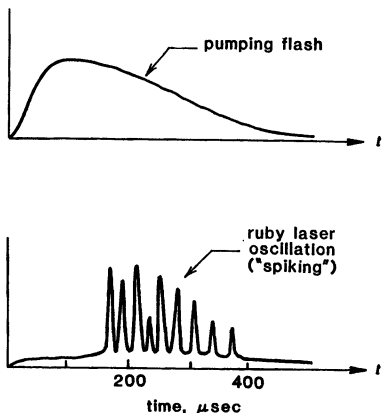


FIGURE 1.51
Output versus time from a typical "long-pulse" ruby laser oscillator.

with sufficiently hard pumping Maiman was able to produce a powerful burst of laser action from the ruby rod.

In a small flash-pumped laser such as ruby, or others, the flashlamp may be connected to a capacitor bank of perhaps 10 to 100 microfarads charged to a prebreakdown voltage of perhaps 1,000 to 1,500 volts, corresponding to ~ 5 to 50 J of stored energy. The lamp itself is then triggered or ionized by a high-voltage pulse, so that it becomes conducting. The capacitor energy then discharges through the lamp with a typical pulse length of perhaps 200 μ sec, peak currents of up to a few hundred amperes, and peak electrical power input of 25 to 250 kW. The laser rod may convert the pump light in a typical solid-state laser into laser energy with $\sim 1\%$ efficiency, leading to laser output energies of 50 mJ to 0.5 J per shot, and average powers during the pulse of 2.5 to 25 kW. (We will discuss later the technique of "Q-switching," which can extract the same laser energy in a very much shorter pulse with very much higher peak power.)

The laser action in ruby actually occurs not as a clean and continuous laser action during the pulse, but as a series of short "spikes" or relaxation-oscillation bursts during the entire pumping time (see Figure 1.51). We will discuss this spiking behavior in more detail in a later chapter.

Other Solid-State Lasers

There are many such solid-state lasers besides ruby (though unfortunately not many in the visible region). The most common of these are the rare-earth ions in crystals or glasses, with by far the most widely used examples being Nd³⁺ lasers using Nd:YAG (Nd³⁺ ions in yttrium aluminum garnet) and Nd:glass materials. The spiral flashlamp and diffusely reflecting pump enclosure used in Maiman's first ruby laser is now almost always replaced by one or more straight lamps placed parallel to the rod along the axes of an elliptical pump cavity (Figure 1.52).

In the first ruby lasers, partially transparent metallic silver mirrors were evaporated directly onto the polished ends of the laser rod (though such metallic mirrors are quite sensitive to optical damage at higher powers). Later solid-state lasers quickly shifted to the use of external dielectric-coated mirrors, just as in gas

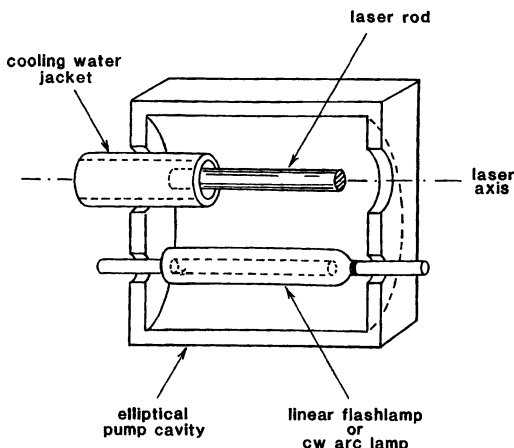


FIGURE 1.52
Elliptical pump cavity used in many optically pumped solid-state lasers.

lasers. The round-trip gains in ruby and other solid-state lasers are often much higher than in gas lasers—up to round-trip power gains of 10X and higher—so that mirrors with much lower reflectivity or higher transmission output can be employed.

Pulsed solid-state lasers are used for a variety of smaller-scale laser cutting, drilling, and marking applications; as military rangefinders and target designators; and in an enormous variety of scientific and technological experiments. By taking advantage of improved lamp efficiencies and laser materials, as well as the fact that most other materials are four-level lasers, we can also operate several solid-state lasers continuously at cw power outputs in the 1–100 W range with efficiencies of $\sim 1\%$ or slightly higher, using electrical inputs of 100 W to 10 kW into xenon or krypton-filled arc lamps. (Both laser rod and lamps must, of course, be carefully water-cooled.) Even ruby can, with some difficulty, be made to oscillate on a cw basis. We will discuss the very useful Nd^{3+} laser system in detail in later chapters.

The Helium-Neon Laser

Another of the most common and familiar types of laser is the helium-neon gas laser developed at the Bell Telephone Laboratories in 1960 and 1961. The laser tube in a He-Ne laser consists of a few Torr of helium combined with approximately one-tenth that pressure of neon inside a quartz plasma discharge tube, which is usually provided with an aluminum cold cathode and an anode, as in Figure 1.53. This discharge tube may be 10 to 50 cm long and a few mm in diameter in a typical small laser. To avoid broadening of the laser transition by isotope shifts (and for other more complex reasons), a mixture of single-isotope He^3 and Ne^{20} is usually employed; and it is found empirically that the optimum pressure-diameter product pd in such a laser is a few Torr-mm and that the optimum gain per unit length varies inversely with tube diameter d .

This tube is then excited with a dc discharge voltage typically of order 1,000 to 1,500 vdc, producing a dc current typically of order ~ 10 mA from a special

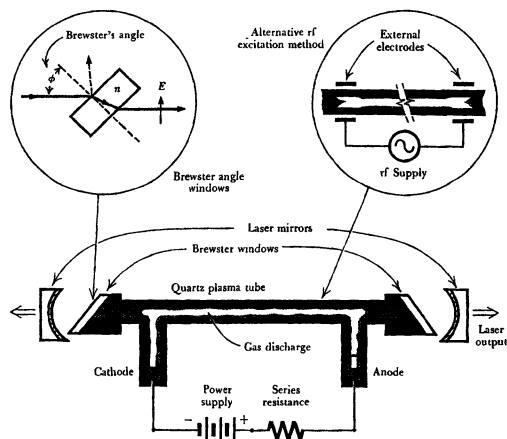


FIGURE 1.53
Elementary design for a helium-neon laser.

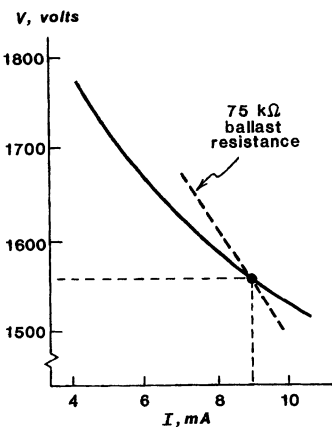


FIGURE 1.54
The glow discharge in a He-Ne laser tube has a negative-resistance I - V curve.

high-purity aluminum cold cathode. (Radio-frequency excitation through external electrodes was also employed in many early lasers, but has been found to be generally less convenient.) Because a dc glow discharge in this pressure range has a negative-resistance I - V curve (Figure 1.54), a ballast resistance in series with the dc voltage supply is necessary to stabilize the discharge; and an initial higher-voltage spike must be supplied to ionize the gas and break down the gas discharge each time the tube is turned on.

The discharge tubes in many gas lasers (especially with longer lasers, or lasers for research purposes) may be provided with Brewster-angle end windows which transmit light of the proper linear polarization with essentially zero reflection loss at either face. (Because of the very low gain in the He-Ne system, reflection losses of several percent at each of the air-dielectric interfaces would be totally intolerable.) In many small inexpensive internal-mirror He-Ne lasers, however,

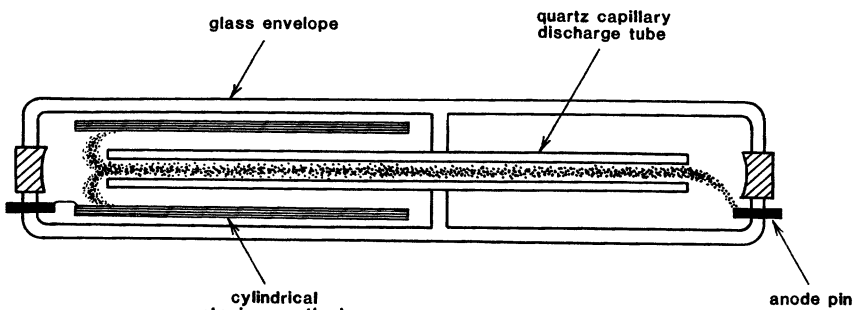


FIGURE 1.55
An internal-mirror He-Ne laser design.

the end mirrors are sealed directly onto the discharge tube, as part of the laser structure (Figure 1.55). Extreme cleanliness and purity of the laser gas fill is vital in the inherently low-gain He-Ne system; the tube envelope must be very carefully outgassed during fabrication, and a special aluminum cathode employed, at least in long-lived sealed-off lasers. The end mirrors themselves are carefully polished flat or curved mirrors with multilayer evaporated dielectric coatings, having as many as 21 carefully designed and evaporated layers to give power reflectivities in excess of 99.5% in some cases.

The pumping mechanism in the He-Ne laser is slightly more complex than those we have discussed so far. The helium gas, as the majority component, dominates the discharge properties of the He-Ne laser tube. Helium atoms have in fact two very long-lived or metastable energy levels, generally referred to as the 2^1S ("2-singlet-S") and 2^3S ("2-triplet-S") metastable levels, located ~ 20 eV above the helium ground level. Free electrons that are accelerated by the axial voltage in the laser tube and that collide with ground-state neutral helium atoms in the laser tube then can excite helium atoms up into these metastable levels, where they remain for long times.

There is then a fortuitous—and very fortunate—near coincidence in energy between each of these helium metastable levels and certain sublevels within the so-called $2s$ and $3s$ groups of excited levels of the neutral neon atoms, as shown in Figure 1.56. (The atomic energy levels in neon, as in other gases, are commonly labeled by means of several different forms of spectroscopic notation of various degrees of obscurity.)

When an excited He atom in one of the metastable levels collides with a ground-state Ne atom, the excited He atom may drop down and give up its energy, while the Ne atom simultaneously takes up almost exactly the same amount of energy and is thus excited upward to its near-coincident energy level. This important type of collision and energy-exchange process between the He and Ne atoms is commonly referred to as a "collision of the second kind." Any small energy defect in the process is taken up by small changes in the kinetic energy of motion of one or the other atom.

This process thus amounts to a selective pumping process, carried out via the helium atoms, which efficiently pumps neon atoms into certain specified excited energy levels. As Figure 1.56 shows, laser action is then potentially possible from these levels into various lower energy levels in the so-called $2p$ and $3p$ groups.

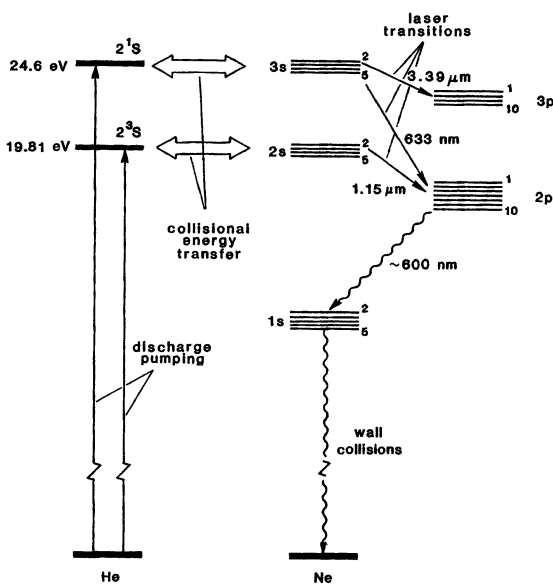


FIGURE 1.56
Energy levels in the He-Ne laser.

The first successful laser action in any gas laser was in fact accomplished by A. Javan and co-workers at Bell Labs in late 1960 on the $2s_2 \rightarrow 2p_4$ transition of helium-neon at 1.1523 microns in the near infrared. Shortly thereafter A. D. White and J. D. Rigden discovered that the same system would lase on the familiar and very useful $3s_2 \rightarrow 2p_4$ visible red transition at 633 nm (or 6328 Å), as well as on a much stronger and quite high-gain set of $3s \rightarrow 3p$ transitions near 3.39 microns. (A half-dozen or so different nearby transitions within each of these groups can actually be made to lase, with the strongest transition in each group being determined in part by the relative pumping efficiencies into each sublevel and in part by the relative transition strengths of the different transitions.)

Characteristics of Gas Lasers

The laser gain in the He-Ne 633 nm system is quite low, with perhaps $2\alpha_m \approx 0.02$ to 0.1 cm^{-1} (often expressed as “2% to 10% gain per meter”); and the typical power output from a small He-Ne laser may be 0.5 to 2.0 mW. With a dc power input of $\sim 10 \text{ W}$, this corresponds to an efficiency of $\sim 0.01\%$. Several manufacturers supply inexpensive self-contained laser tubes of this type for about \$100 retail and considerably less in volume production. Such lasers are very useful as alignment tools in surveying, for industrial and scientific alignment purposes, supermarket scanners, video disk players, laser printers, and the like. (The dominance of the He-Ne laser in such applications may soon be ended by even cheaper and simpler semiconductor injection lasers.) Larger He-Ne lasers

with lengths of 1 to 2 meters that can yield up to 100 mW output at comparable efficiencies are also available.

There are also scores of other gas lasers that are excited by using electrical glow discharges, higher-current arc discharges, hollow-cathode discharges, and transverse arc discharges. One notable family of such lasers are the rare-gas ion lasers, including argon, krypton, and xenon ion lasers, in which much larger electron discharge currents passing through, for example, a He-Ar mixture can directly excite very high-lying argon levels to produce laser action in both singly ionized Ar^+ and doubly ionized Ar^{++} ions. Such ion lasers are generally larger than the He-Ne lasers, and even less efficient, but when heavily driven can produce from hundreds of milliwatts to watts of cw oscillation at various wavelengths in the near infrared, visible, and near ultraviolet. Longer-wavelength molecular lasers, such as the CO_2 laser, and shorter-wavelength excimer lasers are other examples of important gas laser systems.

REFERENCES

For a recent summary of practical laser systems and many of their applications, see, for example W. W. Duley, *Laser Processing and Analysis of Materials* (Plenum Press, 1983).

1.9 OTHER PROPERTIES OF REAL LASERS

Practical lasers in fact come in a great variety of forms and types, using many different kinds of atoms, molecules, and ions, in the form of gases, liquids, crystals, glasses, plastics, and semiconductors. These systems oscillate at a great many different wavelengths, using many different pumping mechanisms. Nearly all real lasers have, however, certain useful properties in common.

Temporal and Spatial Coherence

As we have discussed in some detail in earlier sections, nearly all lasers can be:

(a) *Very monochromatic.* Real laser oscillators can in certain near-ideal situations oscillate in a single, essentially discrete oscillation frequency, exactly like a coherent single-frequency electronic oscillator in more-familiar frequency ranges. This oscillation will, as with any other real oscillator, still have some very small residual frequency or phase modulation and drift, because of mechanical vibrations and thermal expansion of the laser structure and other noise effects, as well as small amplitude fluctuations due to power supply ripple and the like. Such a high-quality laser can still be, however, one of the most spectrally pure oscillators available in any frequency range.

More typically, a real laser device will oscillate in some number of discrete frequencies, ranging from perhaps 5 or 10 simultaneous discrete axial modes in narrower-line lasers up to a few thousand discrete and closely spaced frequencies in less well-behaved lasers with wider atomic linewidths.

Real lasers will also in many cases jump more or less randomly from one oscillation frequency to another, and the amplitudes and phases of individual modes will fluctuate randomly, because of mode competition combined with the kinds of unavoidable mechanical and electronic perturbations mentioned above. Nonetheless, the degree of temporal coherence in even a rather bad laser will generally be much higher than in any purely thermal or incoherent light source, and especially in any thermal source providing anywhere near the same power output as the laser's oscillation output power.

(b) *Very directional.* The output beam from a typical real laser will also be very directional and spatially coherent. This occurs because, with properly designed mirrors, many lasers can oscillate in a cavity resonance mode which is essentially a single transverse mode; and this mode can approximate a more or less ideal quasi-plane wave bouncing back and forth between carefully aligned end mirrors.

As we discussed in the preceding section, the resulting output beam from the laser can then be a highly collimated or highly directional beam, which can also be focused to a very tiny spot. Such a beam can be projected for long distances with the minimum amount of diffraction spreading allowed by electromagnetic theory. It can also be focused to a spot only a few wavelengths in diameter, permitting all the power in the laser beam to be focused onto an extremely small area.

Even lasers with nonideal spatial properties (perhaps because of distorted laser mirrors or, more commonly, because of optical aberrations and distortions in the laser medium or in other elements inside the laser cavity) will typically oscillate in only some moderate number of transverse modes, representing some lowest-order transverse mode and a number of more complicated higher-order transverse modes.

Note again that the longitudinal-mode or frequency properties and the transverse-mode or spatial properties of most laser oscillators are more or less independent, so that, for example, even wide-line or multifrequency lasers can very often have well-controlled transverse mode properties and can oscillate in a nearly ideal single transverse mode.

Other Real Laser Properties

Besides these two basic properties, specific individual lasers can be:

(c) *Very powerful.* Continuous powers of kilowatts or even hundreds of kilowatts are obtained from some lasers, and peak pulse powers exceeding 10^{13} Watts are generated by other lasers. (It is interesting to note that this peak power is an order of magnitude more than the total electrical power-generating capacity of the United States—but of course for a very short time only.)

(d) *Very frequency-stable.* Both the spectral purity and the absolute frequency stability of certain lasers can equal or surpass that of any other electronic oscillator; so these lasers can provide an absolute wavelength standard with an accuracy exceeding that of any other presently known technique.

(e) *Very widely tunable.* Although most common lasers are limited to fairly sharply defined discrete frequencies, those of the spectral lines of the specific atoms employed in certain lasers (e.g., organic dye lasers and to a lesser extent semiconductor lasers) can be tuned over enormous wavelength ranges, and so are extremely useful for spectroscopic and chemical applications.

(f) **Very broadband.** Many laser transitions, though very narrowband in fractional terms, have extremely wide linewidths compared to those of conventional radio or microwave frequencies. Hence, such lasers can provide very broadband amplification and, more important, can generate and amplify extraordinarily short optical pulses. Laser pulses as short as a few picoseconds in duration are relatively commonplace, and some mode-locked lasers can generate light pulses as short as 30 femtoseconds (30×10^{-15} seconds) in length.

(g) **Very efficient.** The efficiency of most common lasers is smaller than designers would like, ranging from ~ 0.001 to 0.1% in many gas lasers, up to typically 1 or 2% in optically pumped solid-state lasers. A few selected lasers, such as the CO₂ laser and the semiconductor injection lasers, can have efficiencies as high as 50% to 70% in converting electrical power directly into coherent radiation.

Examples of Practical Laser Systems

It is impossible to catalog all the laser devices that have been demonstrated to date, especially since the variety of laser materials, laser pumping methods, and laser experimental techniques is almost endless. The *Laser Handbook* (see the References at the end of this section) gives a comprehensive list of most current laser systems. Some laser systems that are particularly well-known, particularly useful for practical applications, or particularly interesting for other reasons will be discussed in more detail later in this text.

The overall situation at present is that at least 10^5 , and up to 10^6 , distinct laser transitions that have been demonstrated, at wavelengths ranging from $\lambda \geq 600 \mu\text{m}$ (0.6 mm) in the far infrared to the present short-wavelength record (1983) of $\lambda = 1160\text{\AA}$ from the pulsed-discharge H₂ laser in the near ultraviolet. At still longer wavelengths, besides more familiar vacuum tubes and semiconductor devices, there are several varieties of millimeter-wave and microwave masers, including molecular beam masers, solid-state electron paramagnetic resonance masers, and nuclear magnetic resonance (NMR) masers. These last devices in fact carry the stimulated-emission principle down to frequencies below 100 Hz. Lasers operating in the X-ray region do not yet seem to have been successfully demonstrated, though several candidates in the soft X-ray region (100–200 \AA) appear very promising.

A critical study by Bennett in 1979 identified a total of 1,329 distinct laser wavelengths coming from 51 different elements, considering only neutral atoms and ions in gases (no molecules). This data was culled from a source file of 30,000 (!) literature articles. There were, for example, 203 identified laser lines from neutral neon alone, grouped into the clusters of transitions shown in Figure 1.57. Another study identified 270 new lasing lines on various vibrational-rotational transitions in a limited wavelength range for the CO molecule alone. When we consider the enormous diversity of potential molecular species, and the very large number of distinct rotational-vibrational transitions in any one such molecule, it is not impossible that the number of potential distinct molecular laser lines could exceed one million.

Laser action has been obtained thus far in atoms, molecules, and ions in vapor (gas) phase; in atoms, ions, or molecules in crystals, glasses, and liquid solutions; in organic dye molecules in liquids, vapors, gels, and plastics; in semiconductors of several varieties; and in molecules and molecular radicals in planetary atmospheres and in interstellar space.

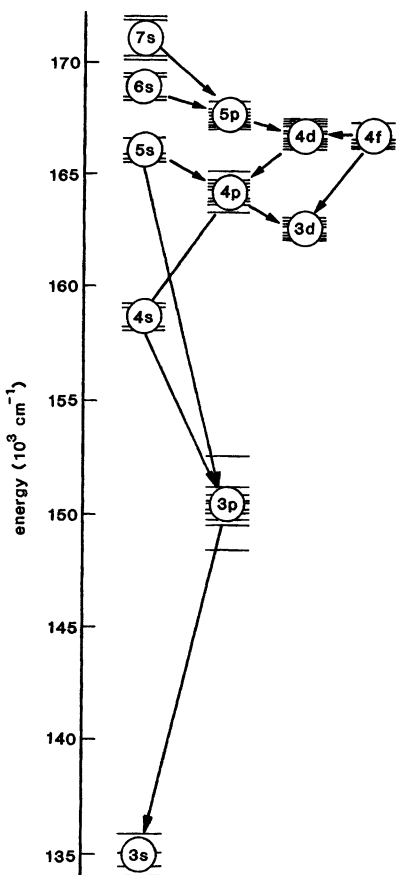


FIGURE 1.57
Groups of available laser transitions in the energy-level spectrum of atomic neon.

Commercially Available Lasers

Of the laser systems mentioned so far, those that are now readily available in routine commercial production include the He-Ne 633 nm laser; many different sizes of both cw and TEA CO_2 lasers at 9 to 11 μm ; various argon, krypton, and other noble-gas ion lasers in the visible and UV; the pulsed N_2 laser at 377 nm; the blue cadmium ion laser; the Nd:YAG laser (including many *Q*-switched, mode-locked, and wavelength-doubled versions); similar ruby, Nd:glass, and alexandrite solid-state lasers; various KrF and other excimer lasers; several varieties of flash-pumped, N_2 -laser-pumped, YAG-laser-pumped, and cw-argon-laser-pumped tunable dye lasers; and of course many versions of the GaAs injection laser.

In addition there is much development work in government, industrial, and university laboratories on large Nd:glass laser systems and on the atomic iodine laser for laser fusion systems, and on various chemical lasers (HF, DF, CO, CO_2)

for military applications. There are also development efforts to a lesser extent on the copper vapor laser, various hollow-cathode visible gas lasers, and a few others. Most of the other known laser systems are available only as (expensive) custom prototypes, or by constructing one's own "home-built" version. (Many chemists, biologists, solid-state physicists, and spectroscopists have now become expert amateur laser builders.)

Commercial development of many other lasers has been rather slow, because the expensive engineering effort to develop a commercially engineered product cannot be justified until a market has been clearly identified. At the same time, commercially significant applications for certain lasers cannot be easily developed if the lasers are not available in commercially developed form.

Laser-Pumping Methods

The list of successful laser-pumping methods that have been demonstrated to date includes the following.

- *Gas discharges*, both dc, rf, and pulsed, including glow discharges, hollow cathodes, arc discharges, and many kinds of pulsed axial and transverse discharges, and involving both direct electron excitation and two-stage collision pumping.
- *Optical pumping*, using flashlamps, arc lamps (pulsed or dc), tungsten lamps, semiconductor LEDs, explosions and exploding wires, other lasers, and even gas flames and direct sunlight.
- *Chemical reactions*, including chemical mixing, flash photolysis, and direct laser action in flames. It is instructive to realize that the combustion of one kg of fuel can produce enough excited molecules to yield several hundred kilojoules of laser output. A chemical laser burning one kg per second, especially if combined with a supersonic expansion nozzle, can thus provide several hundred kW of cw laser output from what becomes essentially a small "jet-engine laser."
- *Direct electrical pumping*, including high-voltage electron beams directed into high-pressure gas cells, and direct current injection into semiconductor injection lasers.
- *Nuclear pumping* of gases by nuclear-fission fragments, when a gas laser tube is placed in close proximity to a nuclear reactor.
- *Supersonic expansion of gases*, usually preheated by chemical reaction or electrical discharge, through supersonic expansion nozzles, to create the so-called *gasdynamic lasers*.
- *Plasma pumping in hot dense plasmas*, created by plasma pinches, focused high-power laser pulses, or electrical pulses. There are also widely believed rumors that X-ray laser action has in fact been demonstrated in a rod of some laser material pumped by the ultimate high-energy pump source, the explosion of a nuclear bomb.

In general, any nonequilibrium situation that involves intense enough energy deposition is reasonably likely to produce laser action, given the right conditions. Schawlow's Law (attributed to A. L. Schawlow, but apparently thus far unpublished) asserts in fact that anything will lase if you hit it hard enough. Schawlow himself has attempted to illustrate this by building, and then consuming, the

first edible laser—a fluorescein dye in Knox gelatine, “prepared in accordance with the directions on the package” and then pumped with a pulsed N_2 laser. The fumes of Scotch whiskeys are also rumored to give molecular laser action in the far infrared when pumped with CO_2 radiation at $10.6\ \mu m$; and Israeli ingenuity has demonstrated a gasoline-fueled chemical laser which is ignited by an automobile spark plug (kilojoules per gallon and resulting pollution problems not identified).

Lasers and Masers as Carnot-Cycle Heat Engines

A microwave laser or maser can be pumped in principle—and even in practice—by connecting a very hot, purely thermal source to the pumping transition, and connecting much colder thermal reservoirs to the other transitions (other than the laser transition) on which efficient downward relaxation is required. In practice, connecting a thermal source only to the pumping transition can mean either varying the emissivity versus wavelength of the pumping source, or putting appropriate wavelength filters between the pumping source and the laser medium, so that the laser medium “sees” the pumping source only within the desired pumping bands.

The maser or laser then functions as a heat engine, extracting energy from the hot pumping source, and converting it partly into coherent oscillation or work, and partly into waste heat delivered to the cold thermal reservoirs with which the other transitions must be in contact. The elementary thermodynamics of this have been discussed by H. E. D. Scovil and E. O. Schulz-DuBois, “Three-level masers as heat engines,” *Phys. Rev. Lett.* **2**, 262–263 (March 15, 1959), who show that the limiting efficiency of these engines is exactly given by the Carnot-cycle efficiency between the hot pumping source and the cold reservoirs. For an experimental example, see J. M. Sirota and W. H. Christiansen, “Lasing in N_2O and CO_2 isotope mixtures pumped by blackbody radiation,” *IEEE J. Quantum Electron. QE-21*, 1777–1781 (November 1985),

Scovil and Schulz-DuBois also point out that a multilevel atomic system can be used as an atomic refrigerator, in which coherent radiation is applied to one of the transitions in order to reduce the Boltzmann temperature appropriate to some other transition in the same atomic system. Atomic refrigeration experiments of this sort have in fact been demonstrated, using another laser or coherent oscillator as the pump.

Laser Performance Records

Much ingenuity as well as much sophisticated physics and engineering have thus far gone into laser research and development. As a result of this, plus the enormous flexibility of the stimulated-emission principle, in nearly every performance characteristic that we can define, the world record for any type of electronic device can be claimed by some laser device or laser system (generally a different laser for each characteristic). Different lasers can claim the current performance records in the following areas.

(a) *Instantaneous peak power.* A rather modest amplified mode-locked solid-state laser system can generate a peak instantaneous power in excess of

$\sim 10^{13}$ W—or several times the total installed-electrical generating capacity of the United States—though only for a few picoseconds.

(b) *Continuous average power.* The unclassified power outputs from certain infrared chemical lasers are in the range of several hundred kilowatts to one-half megawatt of continuous power output. The classified figures for cw power output are, at a guess, probably several megawatts cw or greater.

(c) *Absolute frequency stability.* The short-term spectral purity of a highly stabilized cw laser oscillator can be at least as good as $1:10^{13}$. The absolute reproducibility of, for example, a He-Ne $3.39\text{ }\mu\text{m}$ laser stabilized against a methane absorption line will exceed 1 part in 10^{10} , and may become much better. The absolute standard of time at present is already an atomic stimulated absorption device, the cesium atomic clock. This may be replaced in the future as an absolute standard for both frequency and time by a very stable laser, stabilized against an IR or visible absorption line.

(d) *Short pulsedwidth.* Mode-locked laser pulses shorter than 1 ps (10^{-12} sec) in duration are now fairly routine. The current record is in fact a mode-locked and then compressed dye laser pulse with duration (full width at half maximum) of $\tau_p \approx 12$ femtoseconds, or 1.2×10^{-14} seconds. Since this corresponds to a burst of light only ~ 6 optical cycles in duration, further sizeable improvements may be difficult.

(e) *Instantaneous bandwidth and tuning range.* Most common lasers are limited to sharply defined discrete frequencies of operation that depend on the transitions of the specific atoms employed in the laser, and to fairly narrow tuning ranges that depend on the linewidths of these atomic transitions. Both organic dye lasers in the visible and semiconductor lasers in the near infrared can offer, however, instantaneous amplification bandwidths of order $\Delta\lambda \approx 200\text{\AA}$. This corresponds, for the former, to a frequency bandwidth $\Delta f \approx 24 \times 10^{12}$ Hz, or 24,000 GHz, or about one telephone channel for every person on Earth.

(f) *Antenna beamwidths.* The diffraction-limited beamwidth of a visible laser beam coming from a telescope 10 cm in diameter is considered easy to obtain. In order to obtain such a beamwidth at even a high microwave frequency of 30 GHz ($\lambda = 1$ cm), we would have to use diffraction-limited microwave antenna two kilometers in diameter.

(g) *Noise figure.* Laser amplifiers actually do not offer particularly good noise-figure performance in the usual sense of this term, because of the unavoidable added noise that comes from spontaneous emission in the laser medium. (It is simply not possible to have an inverted laser population without also having spontaneous emission from the upper level.)

This comparatively poor noise performance is, however, really an inherent limitation of the optical-frequency range rather than of the laser principle. That is, it can be shown that no coherent or linear phase-preserving amplifier of any kind can be a highly sensitive receiver or detector at optical frequencies, because “quantum noise” imposes a rather poor noise limitation, equivalent to an input noise of one photon per inverse amplifier bandwidth, on any such optical amplifier, no matter how it operates. Spontaneous emission is the putative source of this noise in a laser device, but any other conceivable optical amplifier with the same performance characteristics will have some equivalent noise source. (This noise limitation can be viewed as representing, if you like, the quantum uncertainty principle appearing in another guise.) Real lasers can, however, operate very close to this quantum noise limit.

Maser amplifiers can, in any case, provide noise figures in the microwave and radio-frequency ranges that are lower than those for any other electronic types of

amplifiers at the same frequencies (though both cooled parametric amplifiers and even microwave traveling-wave tubes can come very close to the same values).

Natural Masers and Lasers

It is also very challenging to realize that naturally occurring molecular masers and lasers with truly enormous power outputs have been oscillating for eons in interstellar space, on comets, and in planetary atmospheres in our own solar system.

Naturally occurring maser action was first identified from observations that certain discrete molecular lines in the radio emission coming from interstellar clouds had enormously large intensities (equivalent to blackbody radiation temperatures of 10^{12} to 10^{15} K), but at the same time had very narrow doppler linewidths, corresponding to kinetic temperatures below 100 K. The radiation was also found to be sometimes strongly polarized, and to occur only on a very few discrete lines in the complex spectra of these molecules.

The only reasonable explanation is that these emissions represent naturally occurring microwave maser action on these particular molecular transitions. Such astronomical maser amplification has been seen on certain discrete vibrational and rotational transitions of molecules, such as the hydroxyl radical (OH^- , 1,600 to 1,700 MHz), water vapor (H_2O , ~ 22 GHz), silicon monoxide (SiO , mm wave region), and a few others. The pumping mechanism responsible for producing inversion is still uncertain, but may involve either radiative pumping by IR or UV radiation from nearby stellar sources or collision pumping by energetic particles. There is of course no feedback; so the observed radiation represents highly amplified spontaneous emission or "ASE" rather than true coherent oscillation.

More recently, amplified spontaneous-emission lines corresponding to population inversion on known CO_2 laser transitions near 10.4 and $9.4\ \mu\text{m}$ have similarly been observed coming from the planetary atmospheres, or mesospheres, of the planets Mars and Venus. The pumping mechanism is believed to be absorption of sunlight by the CO_2 molecules. The net gains through the atmospheric layers are remarkably small ($\leq 10\%$) but the total powers involved quite large, because of the large volumes involved in these "natural lasers."

REFERENCES

The edible laser medium is reported by T. W. Hänsch, M. Pernier, and A. L. Schawlow, "Laser action of dyes in gelatine," *IEEE J. Quantum Electron.* **QE-7**, 45-46 (January 1971).

The list of atomic laser lines comes from W. R. Bennett, Jr., *Atomic Gas Laser Transition Data: A Critical Evaluation* (Plenum Press, 1979). The reference to the carbon-monoxide laser lines is from D. W. Gregg and S. J. Thomas, "Analysis of the CS^2-O^2 chemical laser showing new lines and selective excitation," *J. Appl. Phys.* **39**, 4399 (August 1968).

For other extensive listings of most known laser transitions, see the Chemical Rubber Company *Handbook of Laser Science and Technology*, Vol. I: *Lasers and Masers and Vol. II: Gas Lasers*, ed. by M. J. Weber (CRC Press, 1982); or B. Beck, W. Englisch, and K. Gürs, *Table of (> 6000) Laser Lines in Gases and Vapors* (Springer-Verlag, 3d ed., 1980).

A good review of the important basic atomic and plasma processes in gas discharge lasers is given in C. S. Willett, *Introduction to Gas Lasers: Population and Inversion Mechanisms* (Pergamon Press, 1974). For an introduction to gasdynamic laser pumping see S. A. Losev, *Gasdynamic Laser* (Springer-Verlag, 1981).

Good reviews of naturally occurring masers are given by W. H. Kegel, "Natural masers: Maser emission from cosmic objects," *Appl. Phys.* **9**, 1-10 (1976); by M. J. Reid and J. M. Moran, "Masers," *Ann. Rev. Astron. Astrophys.* **19**, 231-276 (1981); and by M. Elitzur, "Physical characteristics of astronomical masers," *Rev. Mod. Phys.* **54**, 1225-1260 (October 1982).

Recent reports of natural laser action can be found in M. J. Mumma et. al., "Discovery of natural gain amplification in the 10 μm CO_2 laser bands on Mars: A natural laser," *Science* **212** 45-49 (1981); and in D. Deming et. al., "Observations of the 10- μm natural laser emission from the mesospheres of Mars and Venus," *Icarus* **55**, 347-355 (1983).

1.10 HISTORICAL BACKGROUND OF THE LASER

Readers of H. G. Wells' novel *The War of the Worlds* might quite reasonably conclude that the first laser device to be operated on Earth was in fact brought here by Martian invaders a century ago, at least according to the description that:

"In some way they (the Martians) are able to generate an intense heat in a chamber of practically absolute nonconductivity.... This intense heat they project in a parallel beam against any object they choose, by means of a polished parabolic mirror of unknown composition.... However it is done, it is certain that a beam of heat is the essence of the matter. What is combustible flashes into flame at its touch, lead runs like water, it softens iron, cracks and melts glass, and when it falls upon water, that explodes into steam."

(From *Pearson's Magazine*, 1897.)

Those who have seen the effects produced by the beam from a modern multikilowatt CO_2 laser will not be surprised at the recent discovery that the atmosphere of Mars consists primarily of carbon dioxide, and that natural laser action occurs in it!

Whether or not Martians operated CO_2 lasers in 1897, the first man-made stimulated-emission device on Earth came in early 1954, when Charles H. Townes at Columbia University, assisted by J. P. Gordon and H. Zeiger, operated an ammonia beam maser, a microwave-frequency device that oscillated (very weakly) at approximately 24 GHz. This was closely followed by a similar development by N. G. Basov and A. M. Prokhorov in the Soviet Union. The Columbia group coined the name *maser* to represent microwave amplification by stimulated emission of radiation.

There was then much discussion and some experimental work in subsequent years on radio and microwave-frequency maser devices, using both molecular beams and magnetic resonance in solids, and also on theoretical developments toward an optical-frequency maser or laser. Perhaps the most important of these developments was when Nicolaas Bloembergen of Harvard University in 1956 suggested a continuous three-level pumping scheme for obtaining a continuous

population inversion on one microwave resonance transition, by pumping with continuous microwave radiation on another transition.

Bloembergen's ideas were quickly verified in other laboratories, leading to a series of microwave paramagnetic solid-state masers. These microwave masers were useful primarily as exceedingly low noise but rather complex and narrow-band microwave amplifiers. They are now largely obsolescent, except for a few highly specialized radio-astronomy experiments or deep-space communications receivers.

The extension of microwave maser concepts to obtain maser or laser action at optical wavelengths was being considered by many scientific workers in the late 1950s. A widely cited and influential paper on the possibility of optical masers was published by Charles Townes and A. L. Schawlow in 1958. Much recent attention has been given to a series of patent claims based on notebook entries recorded at about the same time by Gordon Gould, then a graduate student at Columbia.

The first experimentally successful optical maser or laser device of any kind, however, was the flashlamp-pumped ruby laser at 694 nm in the deep red operated by Theodore H. Maiman at the Hughes Research Laboratories in 1960. The very important helium-neon gas discharge laser was also successfully operated later in the same year by Ali Javan and co-workers at the Bell Telephone Laboratories. This laser operated initially at 1.15 μm in the near infrared, but was extended a year later to the familiar helium-neon laser transition oscillating at 633 nm in the red.

An enormous number of other laser devices have of course since emerged, not only in the first few years following the initial demonstration of laser action, but steadily during the more than two decades since that time. The variety of different types of lasers now available is enormous, with several hundred thousand different discrete wavelengths available, from perhaps close to a thousand different laser systems. Commercially important and widely used practical lasers are very much fewer, of course, but still numerous. Some of the more interesting and/or useful laser systems have been described earlier in this chapter.

REFERENCES

A useful summary of the early history of masers and lasers is given by B. A. Lengyel, "Evolution of lasers and masers," *Am. J. Phys.* **34**, 903-913 (October 1966). Additional details are in an excellent survey on laser work at IBM by P. P. Sorokin, "Contributions of IBM to laser science—1960 to present," *IBM J. Res. Develop.* **23**, 476-489 (September 1979); and a more personal account of work at General Electric by R. N. Hall, "Injection lasers," *IEEE Trans. Electron Devices* **ED-23**, 700-704 (July 1976).

The widely cited early article by A. L. Schawlow and C. H. Townes setting forth some of the fundamental considerations for laser action is "Infrared and optical masers," *Phys. Rev.* **112**, 1940-1949 (December 15, 1958). Related personal details are given in A. L. Schawlow, "Masers and lasers," *IEEE Trans. Electron Devices* **ED-23**, 773-779 (July 1976); and in R. Kompfner, "Optics at Bell Laboratories—optical communications," *Appl. Optics* **11**, 2412-2425 (November 1972).

The first successful laser operation was published (after a rather ludicrous series of publication misadventures) by T. H. Maiman in *Nature* **187**, 493 (August 6, 1960).

Two news stories on the emergence of Gordon Gould's early patent claims are by Nicholas Wade, "Forgotten inventor emerges from epic patent battle with claim to

laser," *Science* **198**, 379-381 (October 28, 1977), with a reply by A. J. Torsiglieri and W. O. Baker, "The origins of the laser," *Science* **199**, 1022-1026 (March 10, 1978), and by Eliot Marshall, "Gould advances inventor's claim on the laser," *Science* **216**, 392-395 (April 23, 1982).

W. E. Lamb, Jr., has written a scholarly and detailed study of some of the ideas behind the laser in "Physical Concepts in the Development of the Maser and Laser," in *Impact of Basic Research on Technology*, edited by B. Kursunoglu and A. Perlmutter (Plenum Publishing Corporation, 1972), pp. 59-111. Another book covering some of the same material is M. Bertolotti's *Masers and Lasers: An Historical Approach* (Adam Hilger, 1983).

Soviet views on the early laser contributions of V. A. Fabrikant are in an encomium published on his 70th birthday by the editors of *Optics and Spectroscopy (USSR)* **43**, 708 (December 1977).

Finally, an excellent series of historical reminiscences by pioneers in the laser and maser field will be found in the "Centennial Papers" in a Centennial Issue of the *IEEE J. Quantum Electron.* **QE-20**, 545-615 (June 1984).

1.11 Additional Problems for Chapter 1

1. *Energy storage and Q-switching in a solid-state laser.* Solid-state lasers (and some gas lasers) can be operated in a useful fashion known as "Q-switching," in which laser oscillation is prevented by blocking (or misaligning) one of the cavity end mirrors, and building up a very large population inversion in the laser medium using a long pump pulse. At the end of this pumping pulse, the mirrors are suddenly unblocked, and the laser then oscillates in a short but very intense burst that "dumps" most of the energy available in the inverted atomic population.

Pink ruby of the type used in ruby lasers contains $\sim 2 \times 10^{19}$ chromium Cr³⁺ ions/cm³. In a typical Q-switched ruby laser, almost all the ions in the laser rod can be pumped into the upper laser level while the mirrors are blocked, by a flashlamp pump pulse lasting ~ 1 ms. Since the resulting Q-switched pulse when the mirrors are unblocked typically lasts only ~ 50 ns, there will be no further pumping or repumping once the Q-switched pulse begins. What will be the maximum possible energy output in such a single-shot Q-switched burst from a cylindrical ruby rod 7.5 cm long by 1 cm diameter? What will be the peak laser power output (approximately)?

2. *Optical intensity in a focused laser-beam spot.* If the laser pulse in the preceding problem is focused onto a circular spot 1 mm in diameter, what will be the peak power density (in W/cm²) in the spot? What will be the optical *E* field strength in the spot?
3. *Stimulated transition rate for molecules in a CO₂ laser.* A typical low-pressure glow-discharge-pumped CO₂ laser uses a mixture of He, N₂, and CO₂ with an 8:1:1 ratio of partial pressures for the three gases and a total gas pressure at room temperature of 20 Torr (though this may vary somewhat depending on tube diameter). The cw laser power output at $\lambda = 10.6 \mu\text{m}$ from an optimized CO₂ laser tube 1 cm in diameter by 1 meter long might be 50 W. At this power output, how many times per second is an individual CO₂ molecule being pumped upward to the upper laser level and then stimulated downward to the lower laser level by stimulated emission? Note that the relation between pressure *p* and density *N* in a gas is $N(\text{molecules/cm}^3) = 9.65 \times 10^{18} p(\text{Torr})/T(\text{K})$.

4. **Stored energy and energy output in a TEA CO_2 laser.** A CO_2 laser at $10.6\mu\text{m}$ can be operated at low gas pressures, in the range of 20 to 50 Torr, as a low-to medium-power cw gas laser pumped by a cw glow discharge. It can also be operated at much higher gas pressures, in the range of 1 to 10 atmospheres (1 atmosphere = 760 Torr) as a pulsed laser with much higher peak power output. Since it is impossible to maintain a stable glow discharge at such high gas pressures, and since the discharge voltage per unit length goes up rapidly with increasing gas pressure, such a laser must be pumped with a very short high-voltage discharge, lasting perhaps a few microseconds, which is usually applied transversely across the laser tube rather than along the tube. A laser of this type is thus referred to as a *Transverse Electric Atmospheric*, or TEA, type of laser.

Suppose every CO_2 molecule in such a laser is lifted up to the upper laser level and then drops down by laser action just once during a single laser pulse. Calculate the resulting pulse energy output in Joules per 1,000 cm^3 of gas volume per Torr of CO_2 gas pressure. Calculate also the total energy output per pulse from a laser 1 meter long by 2 cm diameter operating with 760 Torr partial pressure of CO_2 .

Real TEA CO_2 lasers more typically yield ~ 40 Joules of output per liter-atmosphere of gas volume during a laser oscillation pulse lasting from a few hundred nanoseconds to perhaps half a microsecond. How many times on average does each CO_2 molecule circulate up through the upper laser level during the pulse?

5. **Heating effects due to focused laser beams.** We wish to gain some feeling for the heating effects of focused laser beams, by calculating these effects for some highly idealized (and hence not fully realistic) examples, as follows.

(a) A 1-Joule, 100-nanosecond pulse from a *Q*-switched Nd:glass laser is focused onto a metallic surface and totally absorbed in a volume of material 20 microns in diameter by 10 nm (100\AA) deep. Neglecting surface losses and heat conduction into the material, what will be the initial rate of rise of the temperature in the absorbing volume?

(b) A 1-Watt laser beam (perhaps from a 1-Watt cw Nd:YAG laser) is focused by a good-quality lens into the same spot. If both heat conduction and vaporization of the material are ignored (which is clearly *not* realistic), what will be the predicted steady-state temperature of the surface in the focused spot?

(c) Suppose a 100-Watt cw beam is used, and all the laser power goes into vaporizing material in and near the spot, so that the laser beam tunnels a hole with a constant $50\ \mu\text{m}$ diameter into the medium. What is the drilling rate in meters/second?

In each of (a) to (c), assume for simplicity a material density of $2\ \text{gms}/\text{cm}^3$, a material specific heat of $1\ \text{cal}/\text{gm}\cdot\text{deg}\ \text{K}$, and in (c) a vaporization temperature of $1,800\ \text{K}$.

6. **Laser fusion: laser design and fundamental economics.** Fusion researchers hope it may be possible in the future to heat and compress tiny nuclear-fuel pellets with short, intense laser pulses until nuclear fusion occurs inside the compressed pellet. Such a process would release useful energy in the form of neutrons emitted from a nuclear micro-explosion. This potentially unlimited energy source faces many practical difficulties, however. Some estimates say laser pulses of $\sim 10^5$ Joules in $\sim 100\ \text{psec}$ may be needed even to reach "scientific break-even," i.e., the point where nuclear energy released just equals laser energy incident.

Preliminary laser fusion experiments use a small mode-locked neodymium-YAG laser oscillator to generate a 10 mJ input pulse at $\lambda = 1.06 \mu\text{m}$, followed by a chain of successively larger Nd:glass amplifiers to amplify the pulse to the required final energy. The amplifier material consists of a special glass doped with $\sim 5\%$ by weight of Nd_3O_5 to give $\sim 4.6 \times 10^{20} \text{ Nd}^{3+}$ ions/cm³. The laser transition is between two excited energy levels of the Nd ions. Some of the design considerations for a Nd:glass fusion laser are as follows.

- (a) As a reasonable estimate, perhaps 10% of the available Nd ions can be pumped into the upper laser energy level, and then 1% of those excited ions can be stimulated to make downward transitions by the ultrashort laser pulse as it passes down the amplifier chain. What minimum total volume of laser glass will be required in the amplifier chain?
- (b) The laser glass when fully pumped has a power gain coefficient $2\alpha_m \approx 0.1 \text{ cm}^{-1}$. What overall length of glass will be required in the amplifier chain?
- (c) Laser glass may be permanently damaged if the optical power density in a short optical pulse exceeds $\sim 10^{10} \text{ W/cm}^2$. What aperture size will be required at the output of the final amplifier stage?
- (d) The energy efficiency of this type of laser, from electrical energy initially stored in the power supply to potential laser energy stored in the upper energy level, is about 1% ; and then only $\sim 1\%$ of this is usefully extracted by a short pulse. If energy-storage capacitors for laser power supplies cost about 10 cents per Joule of energy stored, what will the capacitor bank for this system cost?
- (e) Suppose things go well, and each pellet releases 10^8 Joules (1 MJ) of energy when it is “zapped” by the laser. If the price of electricity is currently 10 cents per kilowatt-hour, what is the retail value of the fusion energy produced per shot?

7. *Thermal light sources versus coherent light sources.* To gain some appreciation for the differences between a thermal and a laser light source, we can compare the visual brightness of a weak laser beam and of a powerful searchlight beam as seen by a distant observer standing in the center of each beam and looking back toward the source.

- (a) Consider first a 10-mW 6328Å Ne-Ne laser with a beam expansion telescope attached. The beam from such a laser usually has a gaussian transverse intensity profile; but let's assume for simplicity that the output beam has a uniform plane-wave distribution across an output aperture 1 cm in diameter. What will be the power density (W/m^2) at the center of this beam as a function of distance in the far field, i.e., at large distances from the source? Note that such a laser will require an electrical power input of perhaps 100 Watts.

A human eye can, under optimum conditions, detect as little as 100 photons per second entering a fully dark-adapted eye with an entrance pupil diameter of ~ 8 mm. From how far away could this laser be seen (assuming you are standing in the center of the beam in the far field)?

- (b) Consider next a simple searchlight consisting of a spherical hot spot (for example, an electric arc) located at the focal point of a large lens or, more likely, a large spherical mirror. Assume the hot spot can be modeled as a thermally emitting ball-shaped blackbody radiator 1 cm in diameter with a temperature of 6,000 K. (Note: melting point of tungsten $\sim 3,700$ K and of carbon $\sim 3,850$ K.) What is the total thermal radiation in Watts from the surface area of this ball

at this temperature (which is also the minimum electrical input power required to drive the searchlight)?

Assume that roughly 15% of this total radiated power falls within the 100-nm-wide band of visible wavelengths. Let both the searchlight mirror diameter and its focal length be 1 meter. What fraction of the total visible emitted radiation is then collimated by the searchlight mirror, and what is the far-field beamspread of this collimated radiation? When all factors are included, what is the far-field visible power density as a function of distance in the searchlight beam? How do the small milliwatt laser and the large kilowatt searchlight compare in far-field brightness?

- (c) How do these comparisons change (i) if another 10-power telescope expands the laser beam initially to 10 cm in diameter? (ii) If the diameter of the searchlight hot spot is increased to 2 cm? (iii) If the searchlight mirror is changed to 2 meters diameter with the same focal length for the mirror? (iv) If the searchlight mirror diameter and its focal length are both doubled, so that the f -number stays the same?
8. *Legal and illegal laser applications.* How many methods (legal or illegal) can you think of to measure the height of a tall building using a laser—*without turning on the laser?*
-

2

STIMULATED TRANSITIONS: THE CLASSICAL OSCILLATOR MODEL

Our first major objective in this text is to understand how optical signals act on atoms (or ions, or molecules) to excite resonance responses and to cause transitions between the atomic energy levels. In later chapters we will examine how the excited atoms or molecules react back on the optical signals to produce gain and phase shift. Eventually we will combine these two parts of the problem into a complete, self-consistent description of laser action. For the minute, however, all we want to consider is what optical fields do to atoms.

The effect of a near-resonant applied signal on a collection of atoms can be divided into two parts. First, there is a resonance *excitation of some individual transition in the atoms*. This can be modeled by a resonant oscillator model, which leads to a resonant atomic susceptibility, among other things. In this chapter we will develop the classical electron oscillator model for an atomic resonance, and show how this model can lead to equations that describe all the essential features of a single atomic transition. In Chapter 3 we will show in more detail how this purely classical model can in fact describe and explain even the most complex quantum-mechanical aspects of real atomic transitions.

The second aspect of the atomic response in real atoms is that, under the influence of an applied signal, atoms begin to make stimulated transitions between the upper and lower levels involved in the transition, so that the atomic level populations begin to change. These stimulated transition rates are described by the *atomic rate equations* that we introduced in the opening chapter of this book. We will discuss these rate equations in more detail in several later chapters.

2.1 THE CLASSICAL ELECTRON OSCILLATOR

Let us first review some of the important physical properties of real atoms. Note that throughout this text, we will speak of “atoms” as a shorthand for simple free atoms, ions, or molecules in gases; or for individual laser atoms, ions, or molecules in solids or in liquids (such as the Cr^{3+} ions in ruby, or the Rhodamine 6G dye molecules in a laser dye); or even for the valence and

conduction electrons responsible for optical transitions in semiconductors. Some of the important background facts about real atoms are as follows.

- Atoms consist in simplified terms of a massive fixed nucleus plus a surrounding *electron-charge distribution*, whether we think of this distribution as a fuzzy charge cloud, or as a set of electronic orbits, as shown in Figure 2.1(a), or as a quantum wavefunction.
- Atoms exhibit *sharp resonances* both in their spontaneous-radiation wavelengths and in their stimulated response to applied signals.
- These resonances are usually *simple harmonic resonances*—that is, there are usually no additional responses at exactly integer multiples of these sharp resonant frequencies.
- Most (though not all) atoms respond to the *electric field* of an applied signal rather than the magnetic field. In more technical terms, the strongest atomic transitions, and those most important for laser action, are usually of the type known as *electric dipole transitions*. (There do exist other types of atomic transitions, including some laser transitions, that are classified as magnetic dipole, electric quadrupole, or even higher order. Magnetic dipole transitions are described, using a different classical model, in a later chapter of this text.)

All these properties lead us to use the *classical electron oscillator (CEO) model* shown in Figure 2.1 as a classical model to represent a single electric-dipole transition in a single atom. With some simple extensions, which we will describe later, this CEO model will give a complete and accurate description of every significant feature of a real atomic quantum transition.

Analysis of the Classical Electron Oscillator Model

The CEO model envisions that the electronic charge cloud in a real atom may be displaced from its equilibrium position with an instantaneous displacement $x(t)$, as shown in Figure 2.1(b). Because of the positive charge on the nucleus, this displacement causes the electronic charge cloud to experience a linear restoring force $-Kx(t)$. The electronic charge cloud is thus in many ways similar to a point electron with mass m and charge $-e$ that is located in a quadratic potential well, with potential $V = Kx^2(t)$, or that is attached to a spring with spring constant K . An externally applied signal with an electric field $\mathcal{E}_x(t)$ may also be applied to this charge cloud.

The classical equation of motion for an electron trapped in such a potential well, or suspended on such a spring, and subjected to an applied electric field $\mathcal{E}_x(t)$, is then

$$m \frac{d^2x(t)}{dt^2} = -Kx(t) - e\mathcal{E}_x(t), \quad (1)$$

which we may write in more abstract form as

$$\frac{d^2x(t)}{dt^2} + \omega_a^2 x(t) = -(e/m)\mathcal{E}_x(t), \quad (2)$$

The frequency ω_a is then the classical oscillator's resonance frequency, given by $\omega_a^2 \equiv K/m$. We will equate this resonance frequency for the CEO model with the

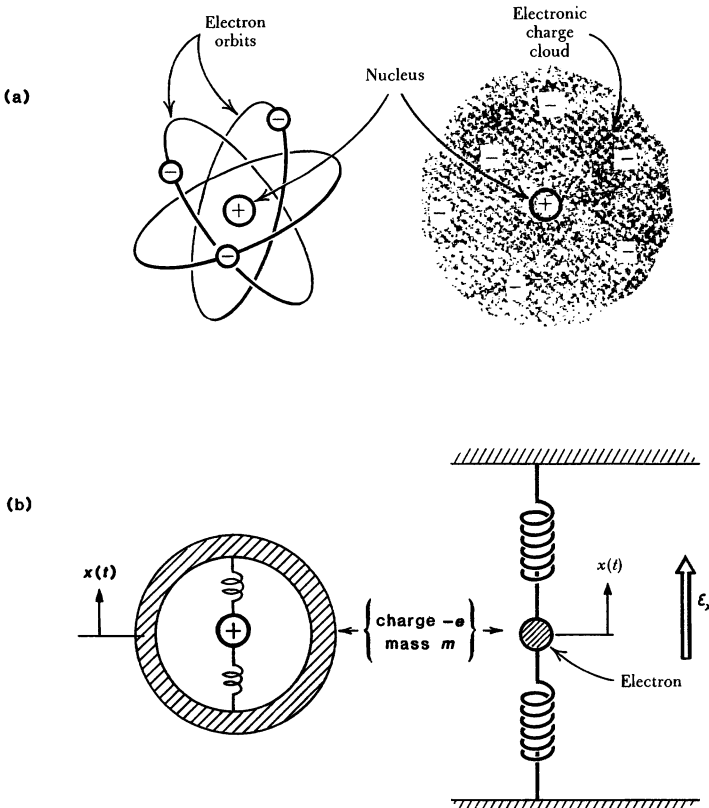


FIGURE 2.1

(a) Electronic models for a real atom. (b) The classical electron oscillator model.

transition frequency $\omega_{21} \equiv (E_2 - E_1)/\hbar$ of a real atomic transition in a real atom. More generally, we will identify any one single transition in an individual atom with a corresponding classical electron oscillator, so that from here on we will refer to real atoms or to individual classical oscillators almost interchangeably.

Damping and Oscillation Energy Decay

The oscillatory motion of the electron in the CEO model, or of the charge cloud in a real atom, must be damped in some fashion, however, since it will surely lose energy with time. Hence we must add a damping term to the equation of motion in the form

$$\frac{d^2x(t)}{dt^2} + \gamma \frac{dx(t)}{dt} + \omega_a^2 x(t) = -\frac{e}{m} \mathcal{E}_x(t), \quad (3)$$

where γ is a damping rate or damping coefficient for the oscillator. The electronic motion $x(t)$ without any applied signal will then oscillate and decay in the fashion

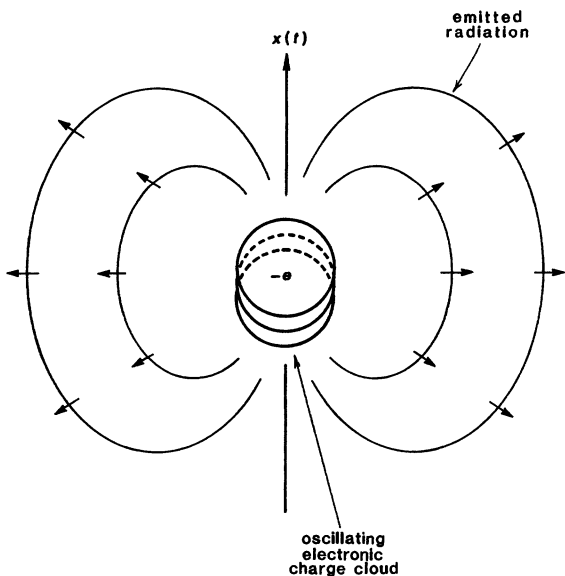


FIGURE 2.2
Emission of electromagnetic radiation by a sinusoidally oscillating electronic charge.

$$x(t) = x(t_0) \exp[-(\gamma/2)(t - t_0) + j\omega'_a(t - t_0)], \quad (4)$$

where ω'_a is the exact resonance frequency given by

$$\omega'_a \equiv \sqrt{\omega_a^2 - (\gamma/2)^2}. \quad (5)$$

The Q of an optical frequency transition in an atom will always be high enough to allow us to simplify life from now on by ignoring the difference between ω_a and ω'_a . The energy associated with the internal oscillation in the CEO model, which we will write as $U_a(t)$, thus decays as

$$U_a(t) = \frac{1}{2}Kx^2(t) + \frac{1}{2}mv_x^2(t) = U_a(t_0)e^{-\gamma(t-t_0)} \equiv U_a(t_0)e^{-(t-t_0)/\tau}. \quad (6)$$

The decay rate γ is thus the *energy decay rate*, and the lifetime $\tau \equiv \gamma^{-1}$ is the *energy decay time* for the oscillator model.

Both classical electron oscillators and real atomic transitions will always lose energy in part by radiating away electromagnetic radiation, in what we call *spontaneous emission* or *fluorescence*, at the transition frequency ω_a . This radiation of electromagnetic energy from the oscillating charge cloud, as shown in Figure 2.2, leads to a *purely radiative* part of the decay rate γ , which we will call γ_{rad} .

Real atomic transitions in many cases, however, also lose additional oscillation energy by other “nonradiative” mechanisms, such as collisions with other atoms, or the emission of heat vibrations into a surrounding crystal lattice. This additional energy loss leads to an additional *nonradiative* part of the total decay rate, which we will denote by γ_{nr} . The total energy decay rate is then generally

given by

$$\gamma \equiv \frac{1}{U_a} \frac{dU_a}{dt} = \gamma_{\text{rad}} + \gamma_{\text{nr}}. \quad (7)$$

Note that the energy U_a we are talking about here is the energy associated with the *internal charge cloud oscillation within the atom*. This energy is quite distinct from other kinds of energy the atom may also possess, such as the kinetic energy of motion of the same atom may possess if the atom as a whole is moving rapidly in a gas.

The energy decay rate for an atomic transition may thus include both radiative and nonradiative parts. Radiative decay, which is exactly the same thing as spontaneous electromagnetic emission or fluorescent emission from the atom, is always present, though sometimes very weak. Nonradiative decay can also be present, sometimes much more strongly and sometimes much less strongly than the radiative part of the total decay, depending on individual circumstances. The causes of nonradiative decay can include inelastic collisions of atoms with each other, or with the walls of a laser tube, so that the internal oscillating energy of the atoms gets converted into kinetic energy of the gas atoms, or goes into heating up the tube walls. Nonradiative decay in solids or liquids can also involve the loss of energy from the electronic oscillation of the atoms into lattice vibrations and hence into heat in the surrounding crystal lattice in a solid. *The general property of all nonradiative atomic relaxation or decay mechanisms is that energy is lost from the internal oscillatory motion of the individual atomic charge clouds, and that this energy goes into simple heating up of surrounding gas atoms or tube walls or crystal lattices.*

Radiative Decay Rates

The purely radiative decay rate or spontaneous emission rate for a classical electron oscillator can be calculated from classical electromagnetic theory (see Problems). The sinusoidally oscillating electron radiates energy outward exactly like an oscillating dipole antenna or an oscillating current source; and this energy is the spontaneous emission. The resulting decay rate for a classical electron oscillator imbedded in an infinite medium of dielectric permittivity ϵ is given by

$$\gamma_{\text{rad,ceo}} = \frac{e^2 \omega_a^2}{6\pi\epsilon mc^3}. \quad (8)$$

Note that according to the conventions used in this text, ϵ and c are the dielectric permeability and the velocity of light in any surrounding dielectric medium, and not necessarily the free-space values ϵ_0 and c_0 . (You might now review the discussion of units and notation for this text given in the Introduction.) This classical oscillator radiative decay rate has a value $\gamma_{\text{rad,ceo}} \approx 10^8 \text{ sec}^{-1}$ for a visible frequency oscillator, compared to an oscillation frequency of $\omega_a \approx 4 \times 10^{15} \text{ sec}^{-1}$. Hence, the decay rate is very small compared to the oscillation frequency.

Real atomic transitions have radiative decay rates that are determined by quantum considerations. These rates for real atoms are different from the classical expression just given, and are different for each different atomic transition. For many transitions, however, the real atomic decay rates for so-called *strongly allowed* transitions are of the same order of magnitude as the purely classical radiative decay rate for a CEO with the same resonance frequency.

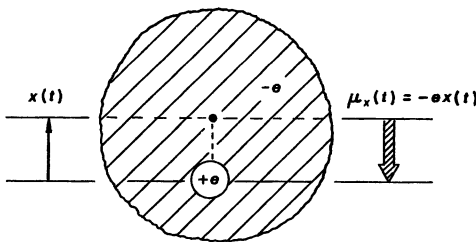


FIGURE 2.3

Microscopic electric-dipole moment in an atom with a displaced electron-charge cloud.

More On Radiative Damping.

The radiative damping process for a classical oscillating electron has other, more complex aspects that we have avoided discussing here. These properties are discussed, for example, in Chapter 25 of W. K. H. Panofsky and M. Phillips, *Classical Electricity and Magnetism* (Addison-Wesley, 1955), or in Chapter 12 of J. M. Stone, *Radiation and Optics* (McGraw-Hill, 1963). An advanced discussion is given by F. Rohrlich, *Classical Charged Particles* (Addison-Wesley, 1965). Other interesting discussions can be found in R. G. Newburgh, "Radiation and the classical electron," *Am. J. Phys.* **36**, 399 (May 1968); in W. L. Burke, "Runaway solutions: Remarks on the asymptotic theory of radiation damping," *Phys. Rev. A* **2**, 1501 (October 1, 1970); and in G. N. Plass, "Classical electrodynamic equations of motion with radiative reaction," *Rev. Mod. Phys.* **33**, 37 (January 1961). A short summary can also be found on pp. 70–71 of A. E. Siegman, *An Introduction to Lasers and Masers* (McGraw-Hill, 1971).

Microscopic Dipole Moments and Macroscopic Polarization

The next important step we must take is to go from microscopic individual atoms, represented by individual electron oscillators, to macroscopic electromagnetic effects in real laser materials. We do this by adding up the *microscopic electric dipole moments* from many individual atoms or classical oscillators to produce a *macroscopic electromagnetic polarization* in the laser material.

We first note that displacement of the electronic charge cloud of an atom away from its equilibrium position around the nucleus by an effective distance $x(t)$ means that there is a displacement of the center of the negative electronic charge, with value $-e$, away from the matching positive charge $+e$ of the heavy and nearly immobile nucleus. This displacement creates a microscopic electric dipole moment $\mu_x(t)$ associated with that individual oscillator or atom, which is given by

$$\mu_x(t) = [\text{charge}] \times [\text{displacement}] = -ex(t) \quad (9)$$

as shown in Figure 2.3.

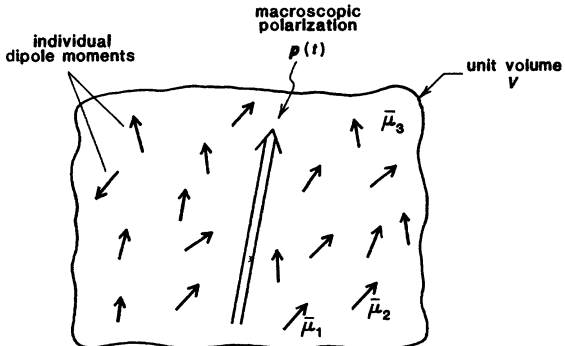


FIGURE 2.4

Macroscopic electric polarization produced by a collection of individual dipole moments.

Let us then recall that in electromagnetic theory Maxwell's equations are written in the form

$$\nabla \times \mathcal{E}(\mathbf{r}, t) = -\frac{\partial \mathbf{b}(\mathbf{r}, t)}{\partial t}, \quad (10)$$

$$\nabla \times \mathbf{h}(\mathbf{r}, t) = \mathbf{j}(\mathbf{r}, t) + \frac{\partial \mathbf{d}(\mathbf{r}, t)}{\partial t},$$

together with the definitions

$$\mathbf{d}(\mathbf{r}, t) = \epsilon_0 \mathcal{E}(\mathbf{r}, t) + \mathbf{p}(\mathbf{r}, t), \quad (11)$$

$$\mathbf{b}(\mathbf{r}, t) = \mu_0 \mathbf{h}(\mathbf{r}, t) + \mathbf{m}(\mathbf{r}, t),$$

in which $\mathbf{p}(\mathbf{r}, t)$ and $\mathbf{m}(\mathbf{r}, t)$ are the *electric and magnetic polarizations, or dipole moments per unit volume*, at point \mathbf{r} and time t .

The electric polarization $\mathbf{p}(\mathbf{r}, t)$ at any point in an atomic medium is thus, by definition, the net *electric dipole moment per unit volume* in a small differential volume surrounding that point. In a laser medium in particular, this polarization \mathbf{p} must be calculated by *adding up the vector sum of the individual dipole moments μ_x of all the atoms in that unit volume*.

Consider, for example, a tiny volume of a laser medium containing a very large number of microscopic atoms or classical oscillators, as shown schematically in Figure 2.4. (Note that in a typical laser medium the density of atoms may be anywhere from 10^{12} to 10^{19} laser atoms/cm³; so there may be anywhere from 10^3 to 10^{10} atoms even in a tiny cube only 10 optical wavelengths on a side.) Let each atom in this volume be labeled by an index i , and let each atom have an instantaneous *electric dipole moment* $\mu_{xi}(t) = -ex_i(t)$.

This medium will then have a macroscopic electric polarization \mathbf{p} around that point \mathbf{r} in the medium whose x component is given by

$$p_x(\mathbf{r}, t) \equiv V^{-1} \sum_{i=1}^{NV} \mu_{xi}(t). \quad (12)$$

The volume V here can represent any small unit volume (but still containing many dipoles) surrounding the point \mathbf{r} , and N is the density of individual dipoles in that volume, so that NV is the total number of dipoles.

We could, to be more general, write both the microscopic dipole moments and the macroscopic polarization in this formula as vector quantities, in which case the macroscopic polarization \mathbf{p} would be the vector sum over all individual dipoles μ_i within that volume. However, for now we are focusing only on the linearly polarized x components of $\mathbf{p}(\mathbf{r}, t)$ and $\mu_i(t)$. Also, in real materials both the applied field $\mathbf{E}(\mathbf{r}, t)$ and the polarization $\mathbf{p}(\mathbf{r}, t)$ will in general be functions of position \mathbf{r} , though the changes in value will be very small compared to interatomic spacings. We will not be worrying about the spatial variation of this macroscopic polarization until later, however.

The step we have just taken, of going from individual microscopic atomic dipole moments μ_{xi} to a macroscopic electric polarization p_x , is a crucial step in the theoretical analysis of laser action. To analyze the response of a laser material, we use quantum theory—or as a substitute we use the CEO model—to calculate the microscopic dipole moments of individual laser atoms. These responses are then summed over large numbers of such atoms per unit volume in a real laser medium to produce the macroscopic polarization. This polarization then goes into Maxwell's equations to produce laser absorption, gain, and/or phase shift (as we will see later). We measure in the laboratory, or employ in laser devices, only the macroscopic effects of this atomic polarization. We seldom if ever observe the minute microscopic effects produced by one tiny single atom acting alone.

Discussion

The primary concept introduced in this section is that we can use the classical electron oscillator model, with resonance frequency ω_a , as a substitute for a single atomic transition with transition frequency ω_{21} in a single real quantum atom. The very great utility of the CEO model for this purpose will become apparent in following sections. The essential accuracy of this simple classical model can, however, be further illustrated by the following point.

Suppose a classical oscillating electric dipole antenna is placed close to a reflecting metallic surface, or close to one or more dielectric layers or surfaces. The spatial radiation pattern, the radiative decay rate, and even the resonance frequency of the classical dipole will then all be changed by significant amounts. This occurs, in classical terms, because the radiating dipole is influenced by its own radiated fields reflected back from the nearby surfaces. These effects are strongest, of course, when the oscillator is close to the surface, within one wavelength or less.

Experimental studies of exactly these same effects have also been carried out on real atomic transition dipoles, using real radiating atoms placed very close to dielectric or metal surfaces, with exactly the same results being obtained for the real atoms. Such experiments have been carried out, for example, by using thin monomolecular layers of radiating dye molecules adsorbed onto dielectric films one wavelength or less thick attached to a reflecting silver surface or to another dielectric surface or layer. The observed changes in the radiative behavior of these real atomic (or molecular) dipoles have been found to agree completely with theoretical calculations using purely classical models for both the radiating atoms and the electromagnetic fields.

REFERENCES

The CEO model, often referred to as the Lorentz model of an atom, has a long history and has been widely used. An early reference, still worth reading, is the second edition of H. A. Lorentz, *The Theory of Electrons*, (reprinted in paperback by Dover Publications, 1952), especially Chapter III, Sections 77–81. Other discussions can be found in, for example, M. Garbuny, *Optical Physics* (Academic Press, 1965); in B. Rossi, *Optics* (Addison-Wesley, 1957); and in J. M. Stone, *Radiation and Optics* (McGraw-Hill, 1963), where a particularly extensive discussion is given. An interesting short discussion of some fine points of the CEO model is given in L. Mandel, “Energy flow from an atomic dipole in classical electrodynamics,” *J. Opt. Soc. Am.* **62**, 1011–1012 (August 1972).

For further information on microscopic dipole moments and macroscopic polarization, consult any good text on electromagnetic theory, such as W. K. H. Panofsky and M. Phillips, *Classical Electricity and Magnetism* (Addison-Wesley, 1955), pp. 20–35 and 117–118; D. T. Paris and F. K. Hurd, *Basic Electromagnetic Theory* (McGraw-Hill, 1969), pp. 65–70; R. S. Elliott, *Electromagnetics* (McGraw-Hill, 1966), Chapter 6; or S. Ramo, J. Whinnery, and T. H. Van Duzer, *Fields and Waves in Communication Electronics* (Wiley, 1965), pp. 63–64 and 131–149. An extensive review of much the same elementary ideas as in this chapter is given in R. W. Christy, “Classical theory of optical dispersion,” *Am. J. Phys.* **40**, 1403 (October 1972).

For interesting references on oscillating atomic dipoles close to surfaces, see K. H. Drexhage in *Scientific American* **222**, March 1970, p. 108; and also in *Progress in Optics*, Vol. XII, edited by E. Wolf (North Holland, Amsterdam, 1974). Other clever experiments done by W. Lukosz and R. E. Kunz are described in “Changes in fluorescence lifetimes induced by variations of the radiating molecules’ optical environment,” *Optics Commun.* **31**, 42–46 (October 1979). See also R. R. Chance, A. Prock, and R. Silbey, *Phys. Rev. A* **12**, 1448 (1975); J. P. Wittke, “Spontaneous-emission-rate alteration by dielectric and other waveguiding structures,” *RCA Rev.* **36**, 655–665 (December 1975); and P. W. Milonni and P. L. Knight, “Spontaneous emission between mirrors,” *Optics Commun.* **9**, 119–122 (October 1973).

Problems for 2.1

1. *More detailed classical electron oscillator model.* A more detailed semiclassical model of an atom might picture the electronic charge cloud as a rigid, uniform, spherical distribution of negative charge with total charge $-Ze$, total mass Zm , and diameter $2a$, surrounding a point nucleus of mass ZM and charge $+Ze$, where Z is the atomic number, m the electron mass, M the proton mass, and $-e$ the charge on an electron. Suppose this rigid electronic charge cloud is displaced slightly from a concentric position about the nucleus (the charge cloud is assumed to be “transparent” to the nucleus, so that they can easily move with respect to each other).

Find the net restoring force on the displaced charge cloud (or, alternatively, find the resulting change in total potential energy of the system) for small displacements of the charge cloud with respect to the nucleus; and then find the classical resonance frequency at which the charge cloud will oscillate about the nucleus. (It may be assumed that only the electronic charge cloud will move appreciably, since $M \gg m$.)

In the simplified Bohr model of the hydrogen atom, the radius of the first electron orbit is $a_0 = 0.53\text{\AA}$ ($1\text{\AA} = 10^{-10}\text{ m}$ or 0.1 nm). Using twice this value as a first

guess for the outside radius of the charge cloud in a typical atom, compute a numerical value for the resonance frequency derived above. To what wavelength does this correspond?

2. *Q-value for a classical electron oscillator.* One way (though not the most general way) of defining the Q or “quality factor” of any resonant system is as the ratio of its resonant frequency to its energy decay rate. At what frequency and what wavelength will the Q of a classical electron oscillator be reduced to unity, provided that purely radiative decay is the only energy decay mechanism that is operative?
 3. *Classical derivation of the radiative decay rate.* The time-averaged rate (averaged over a few cycles) at which power is radiated into the far field in all directions by a dipole antenna or by a sinusoidally oscillating charge with an electric dipole moment $\mu_x(t) = \mu_1 \cos \omega t$ is, from classical electromagnetic theory, $P_{\text{av}} = \omega^4 \mu_1^2 / 12\pi c^3$. Use this formula to verify Equation 2.8 for the radiative decay rate γ_{rad} of a classical electron oscillator.
-

2.2 COLLISIONS AND DEPHASING PROCESSES

The next important concept that we have to introduce—a particularly fundamental and important concept—is the effect of *dephasing events*, such as atomic collisions, on the oscillation behavior of classical oscillators or of real atoms.

Coherent Dipole Oscillations

Any single microscopic electric dipole oscillator, when left by itself, obeys the equation of motion

$$\frac{d^2 \mu_x(t)}{dt^2} + \gamma \frac{d\mu_x(t)}{dt} + \omega_a^2 \mu_x(t) = (e^2/m) \mathcal{E}_x(t) \quad (13)$$

which is obtained by multiplying $-e$ into both sides of Equation 2.3 and using Equation 2.9. Hence the oscillating moment of a single atom with no applied field \mathcal{E}_x present has the exponentially decaying sinusoidal form

$$\mu_x(t) = \mu_{x0} \exp [-(\gamma/2)(t - t_0) + j\omega_a(t - t_0) + j\phi_0], \quad (14)$$

where μ_{x0} is the magnitude and ϕ_0 the phase (at time t_0) of the initial oscillation that has been set up in the dipole oscillator, perhaps by some pulsed applied signal.

We have already pointed out that even a small volume of laser material may contain a large number of laser atoms, or tiny oscillating dipoles. We might therefore label each individual atom or dipole by an index i , and write the oscillating dipole moment of the i -th atom as

$$\mu_{x,i}(t) = |\mu_{x0,i}(t_0)| \exp [-(\gamma/2)(t - t_0) + j\omega_a(t - t_0) + j\phi_i], \quad (15)$$

where ϕ_i is the phase angle of the i -th dipole oscillator at the starting time t_0 .

Now suppose first that these dipoles are all oscillating together, all at the same frequency, and more importantly all initially in phase—that is, all with the

same value of ϕ_i at the same reference time t_0 . Then the total dipole moment due to the vector sum of all these moments in some small volume will be

$$\mu_{x,\text{tot}}(t) = \sum_{i=1}^{NV} \mu_{x,i}(t) = NV \mu_x(t) \quad \left\{ \begin{array}{l} \text{all dipoles} \\ \text{oscillating} \\ \text{in phase} \end{array} \right. \quad (16)$$

where $\mu_x(t)$ is the moment of any one dipole; N is the density of dipoles (i.e., the number per unit volume); and NV is the total number of dipoles in a small volume V . The macroscopic polarization, or the dipole moment per unit volume, will then be given by $p_x(t) = \mu_{x,\text{tot}}(t)/V$, or

$$p_x(t) = N \mu_{x0} \exp [[-(\gamma/2) + j\omega_a] (t - t_0) + j\phi_0] \quad \left\{ \begin{array}{l} \text{all dipoles} \\ \text{oscillating} \\ \text{in phase} \end{array} \right. \quad (17)$$

The macroscopic polarization $p_x(t)$ in the atomic medium will thus have the same natural oscillation frequency ω_a and the same energy decay rate $\gamma/2$ as the individual dipoles. In this example its magnitude will also be N times as large as any one individual dipole—but if (and only if) the individual dipoles all keep oscillating unperturbed and with the same phases.

This macroscopic polarization when all the dipoles are oscillating in time-phase with each other may be rather large in real situations. The dipoles are then said to be oscillating *coherently*, or *fully aligned* with each other.

Dephasing Effects: Random Collisions

This is not the usual situation with real atoms, however. There are almost always perturbation effects, or *dephasing effects*, which scramble or randomize the time-phases ϕ_i of individual dipole oscillators, and which thereby cause the macroscopic polarization $p_x(t)$ to become much smaller than the result given by the two preceding equations. To understand this, let us look first at a very simple example of how a particular type of dephasing process, namely, randomly occurring and instantaneous dephasing events or “collisions,” might operate to destroy the macroscopic polarization or coherent dipolar oscillation in a collection of atoms.

Figure 2.5 shows three assumed dipole moments, which we label $\mu_{x,1}(t)$, $\mu_{x,2}(t)$, and $\mu_{x,3}(t)$, all oscillating initially in phase and at the same oscillation frequency. The total moment $\mu_{x,\text{tot}}(t)$, as shown at the bottom of the figure, is then initially three times as large as the moment of any one dipole. Suppose, however, that after random time intervals first one and then another of the dipoles suffers an instantaneous dephasing event or “collision,” which does not reduce the amplitude of the oscillating moment, but does shift it to a new phase angle in time.

After each such collision the amplitude of the total moment is reduced, because the individual moments no longer add in phase. (The individual dipole oscillations will also slowly decay in amplitude themselves because of energy decay, as discussed in the previous section; but we have not illustrated this point here.) Random collisions thus gradually destroy the macroscopic polarization, even without any energy decay.

Figure 2.6 illustrates in another manner this difference between dipole oscillators that are “aligned” or oscillating coherently in phase, and randomly phased

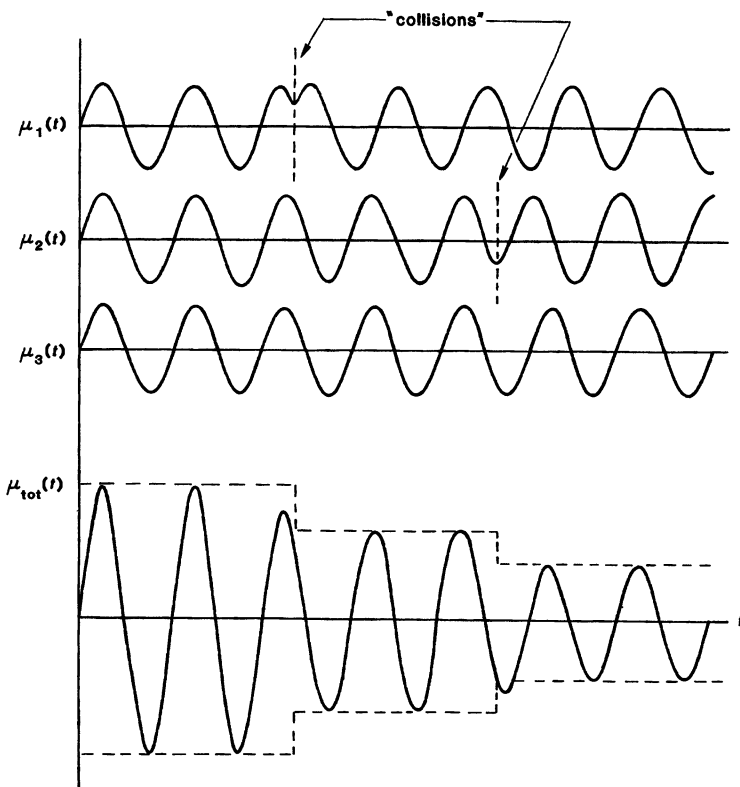


FIGURE 2.5

Decay of the total dipole moment resulting from random dephasing collisions in a collection of oscillating dipoles.

dipole oscillators, by showing the results of adding up three phasors that represent the amplitude and instantaneous time-phase of the three separate individual dipole oscillators. In (a) the three phasors are fully aligned; in (b) and (c) they are gradually shifted in phase or “dephased” to produce a smaller and smaller resultant sum. Note that these are *phasor* diagrams, in which the horizontal and vertical axes for each vector are the real and imaginary parts of the phasor amplitudes of the oscillating moments, or the cosine and sine parts of the sinusoidal oscillations. These axes do not represent the vector coordinates of the dipoles in space, since we are talking here for the moment only about the x component of the dipole oscillations $\mu_x(t)$.

Large Numbers of Dipoles

Suppose that we add up the phasor amplitudes of a large number NV of dipoles, but with the phase angles ϕ_i randomly distributed over all values between 0 and 2π . This then becomes the standard statistical problem of adding up many randomly phased sine waves, and we can find that the resulting total

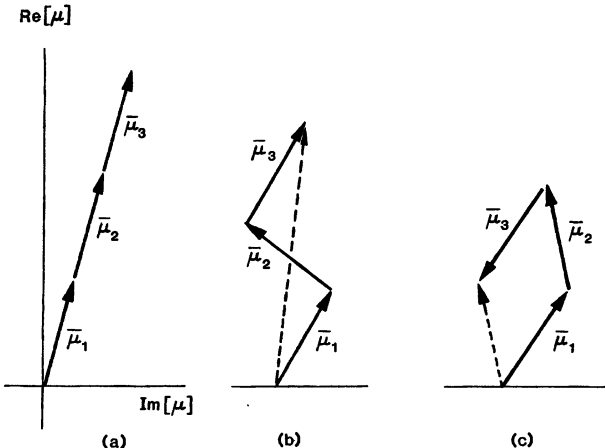


FIGURE 2.6
Addition of phasors. (a) All three phasors in phase. (b) Partially randomized phases. (c) More completely randomized.

dipole moment $\mu_{x,\text{tot}}(t)$ in any small volume V will now be a random quantity; i.e., its amplitude and phase will vary randomly from one small volume to another. Moreover, the total dipole moment in any small volume will have a mean value of zero, i.e.,

$$\langle \mu_{x,\text{tot}}(t) \rangle = 0 \quad (\text{randomly phased dipoles}), \quad (18)$$

but will have a root-mean-square value given by

$$\langle \mu_{x,\text{tot}}^2(t) \rangle^{1/2} = (NV)^{1/2} |\mu_x(t)| \quad (\text{randomly phased dipoles}), \quad (19)$$

where $|\mu_x|$ refers to the value for any one single dipole by itself.

The quantity NV will be a very large number even for very small volumes V . Hence the rms moment, or rms macroscopic polarization, for the randomly phased case, which is proportional to $(NV)^{1/2} |\mu_x|$, will be very much smaller than the possible coherent polarization of order $NV |\mu_x|$ that could be produced by the same number of dipoles oscillating in phase. (The rms polarization in the randomly phased case is in fact essentially random noise; and this noise is essentially the same thing as the spontaneous emission from a collection of quantum atoms, although we will not discuss this topic here.)

Dephasing Mechanisms

The crucial point, then, is that any effect which tends to randomize the oscillation phases ϕ_i in a large collection of individual dipoles (such as are present in even a small volume of laser material) will act to destroy any coherent macroscopic polarization that may be present in this collection of dipole oscillators. Such dephasing effects do exist in real atomic systems, and understanding these additional dephasing effects is our primary task in this section.

These dephasing effects that cause the oscillation phases of individual atomic oscillators to become randomized, even though each dipole continues to oscillate

with the same decaying amplitude and average frequency, are often referred to for simplicity as *collisions*. However, the actual physical processes that can cause dephasing of the individual internal atomic oscillations in a collection of atoms can include the following.

- Atoms (or ions or molecules) in gases, moving with their normal thermal or Brownian motion, can in fact make *random physical collisions* with each other, or with other gas atoms, or with the walls of the laser tube. Even if these collisions are elastic—that is, even if they do not take any energy away from the internal electronic oscillation energy of the atoms—in general such collisions between atoms will scramble and randomize the phases of the electronic oscillations inside the colliding atoms.
- For laser atoms in solids, the quantum energy-level spacings and hence the exact transition frequencies ω_a of the laser atoms are affected by nearby host atoms, and hence depend on the exact distances to nearby atoms in the host crystal lattice. *Thermal vibrations of the crystal lattice* will modulate these distances slightly, and thus modulate the atomic transition frequencies ω_a by small but random amounts with time. This is called *phonon broadening*, and it produces in turn a random phase modulation and hence a “phase smearing” of the dipole oscillations in the laser atoms.
- In materials where the laser atoms are sufficiently dense, the local time-varying electric (or magnetic) fields produced by any one oscillating dipole may spread out to, and be felt by, other neighboring laser atoms. The individual oscillating dipoles are then no longer totally independent, but become weakly coupled to each other through what is called *dipolar coupling*. This kind of weak coupling between individual resonant systems, even if they are all identical, always tends to randomize and to broaden the overall response of the collection. (This is true of weakly coupled resonant electric circuits, as well as weakly coupled resonant atoms.) This process of dipolar coupling is thus still another mechanism for producing random phase smearing in the atomic dipoles. Moreover, this dipolar coupling itself will be randomly modulated in atoms by the thermal motion of the atoms, whether by gas kinetics in gases or lattice vibrations in solids.

Whatever may be the physical cause, the net result of each of these physical processes is to randomize or “dephase” the phases of individual atomic oscillators with respect to each other. The coherent dipole oscillations get converted eventually into *incoherent oscillations*.

More on Collision Broadening.

In a more sophisticated description of collision broadening in gases, the discrete collision between two atoms in the gas is not really instantaneous. Rather, when two quantum atoms in a gas come very near each other, their quantum wavefunctions overlap. The presence of each atom then causes a small but not insignificant shift in the

quantum energy levels of the other atom. (More precisely, we must calculate the shifted quantum levels of the two atoms taken together as a single combined quantum system.) The resonance frequency of each atom is thus shifted by a small, time-varying amount as the atoms pass near each other. The collision interval during which the atoms are close enough to influence each other is short enough ($\approx 10^{-13}$ sec) to be “instantaneous” on a practical time-scale; yet it is long enough for the accumulated shifts in optical frequency cycles to leave the final phases of the oscillators essentially randomized relative to their initial phases. This brief interaction acts for all practical purposes, then, like an instantaneous randomizing collision.

Exponential Decay: The Dephasing Time T_2

A simple formula for the rate at which a macroscopic polarization $p_x(t)$ will be destroyed by random dephasing events can be developed as follows. Suppose that not just a few dipoles, as in the preceding examples, but a very large number of individual (but identical) oscillators are involved. Suppose also that the dephasing events for individual dipoles happen randomly both in their times of occurrence and in the phase changes they produce. Let there then be some large number N_0 of dipoles in a unit volume, all initially oscillating in phase, so that the magnitude of the initial polarization at a starting time t_0 is

$$p_x(t_0) = N_0 \mu_{x0}. \quad (20)$$

At any later time $t > t_0$, we can then divide these N_0 dipoles into (a) a decreasing number of dipoles $N(t)$ that have not yet suffered any collisions at all; and (b) an increasing number $N_0 - N(t)$ of dipoles that have suffered at least one collision, and perhaps more. The $N(t)$ dipoles that have not yet undergone any collisions or dephasing events will then continue to oscillate in phase and to produce a macroscopic polarization

$$p_x(t) = N(t) \mu_x(t) = N(t) \mu_{x0} \cos \omega_{at}. \quad (21)$$

Those dipoles that have suffered even one collision, however, will have phases that are entirely random (assuming, as is normally done, that the phase of a dipole oscillation is entirely randomized after each collision). Hence those dipoles will add up to produce no coherent polarization at all, on the average.

The coherent polarization after any time $t > t_0$ thus comes entirely from the remaining uncollided dipoles. [A more precise statement is that the N dipoles oscillating coherently in phase will add up to produce a macroscopic polarization proportional to $N \mu_{x0}$, whereas the $N_0 - N$ dipoles oscillating with random phases will add up to produce a macroscopic sum with a mean value of zero and an rms value proportional to $(N_0 - N)^{1/2} \mu_{x0}$. Since the number of atoms involved in any atomic system is always very large, the latter quantity is negligible compared to the coherent part of the oscillation; and we can neglect the contribution from the randomly phased dipoles in the latter group.]

The number of uncollided dipoles $N(t)$ will of course decrease steadily with time. How can we calculate the rate at which the number of uncollided atoms $N(t)$ decreases? Let us suppose that collisions occur at a random rate of $1/T_2$ collisions per atom per second. Then, the total number of collisions dN that

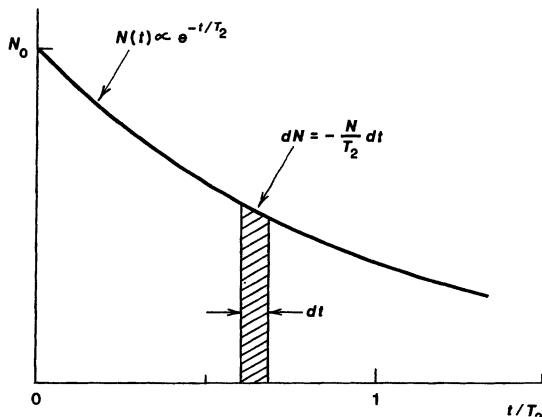


FIGURE 2.7
Decay of the number of uncollided dipoles.

members of this uncollided group will undergo in a little time interval dt about time t , or the loss rate from the uncollided group $N(t)$ in time dt , will be given by

$$dN(t) = -\frac{N(t)}{T_2} dt. \quad (22)$$

The size of the uncollided group will thus decay as

$$N(t) = N_0 e^{-(t-t_0)/T_2}, \quad t > t_0. \quad (23)$$

The coherent macroscopic polarization produced by these still uncollided oscillators will therefore also decay as

$$\begin{aligned} p_x(t) &= N(t)\mu_x(t) \\ &= N_0 e^{-(t-t_0)/T_2} \times \mu_{x0} \exp [-(\gamma/2)(t-t_0) + j\omega_a(t-t_0) + j\phi_0] \\ &= p_{x0} \exp [-(\gamma/2 + 1/T_2)(t-t_0) + j\omega_a(t-t_0) + j\phi_0]. \end{aligned} \quad (24)$$

In other words, the amplitude decay rate $\gamma/2$ appropriate for the individual dipoles must be replaced by $\frac{1}{2}\gamma + T_2^{-1}$ as the effective amplitude decay rate for the coherent polarization $p_x(t)$, or

$$\left(\frac{\gamma}{2}\right) \left(\begin{array}{c} \text{single-dipole} \\ \text{decay rate} \end{array}\right) \Rightarrow \left(\frac{\gamma}{2} + \frac{1}{T_2}\right) \left(\begin{array}{c} \text{macroscopic} \\ \text{polarization} \\ \text{decay rate} \end{array}\right). \quad (25)$$

It may seem slightly odd that in this substitution the dephasing rate $1/T_2$ gets added to the quantity $\gamma/2 \equiv 1/2\tau$, which is *half* the energy decay rate. The reason for this difference of a factor of two—which will continue to be with us—is essentially that $1/T_2$ and $1/2\tau$ are both decay rates for sinusoidal *amplitudes* like $\mu_x(t)$ or $p_x(t)$; whereas γ itself is an energy decay rate for the quantity $|\mu_x(t)|^2$.

Summary

The primary conclusion of this section, therefore, is that although the macroscopic polarization $p_x(t)$, has the same resonance frequency as the individual microscopic dipole oscillations $\mu_x(t)$, it may have a faster decay rate because of dephasing effects. Individual atomic dipole oscillations, in the intervals between dephasing events, can thus be described as obeying the equation of motion

$$\frac{d^2\mu_x(t)}{dt^2} + \gamma \frac{d\mu_x(t)}{dt} + \omega_a^2 \mu_x(t) = (e^2/m) \mathcal{E}_x(t) \quad (26)$$

with an amplitude decay rate $\gamma/2$. But the coherent polarization $p_x(t)$ must be described as obeying the equation

$$\frac{d^2p_x(t)}{dt^2} + (\gamma + 2/T_2) \frac{dp_x(t)}{dt} + \omega_a^2 p_x(t) = (Ne^2/m) \mathcal{E}_x(t), \quad (27)$$

where there is an additional factor of $1/T_2$ in the amplitude decay rate because the dephasing processes cause the oscillations of individual atoms to become randomized in phase at a rate $1/T_2$. (Note again the difference of a factor of 2 between the γ and $1/T_2$ terms.)

In the analysis we have presented here—which is in fact very similar to the approach in much more sophisticated quantum treatments—the time constant T_2 thus has the physical significance of the mean time between dephasing events or collisions for any one individual atom, so that $1/T_2$ is the *collision frequency* for any one individual atom. The time constant T_2 is thus often called the *collision time*. This same time constant is often referred to more broadly as the *dephasing time*, or even the *dipolar interaction time* for $p_x(t)$. In quantum analyses or in the Bloch equations for magnetic resonance, T_2 is also called the *off-diagonal* or *transverse relaxation time*.

REFERENCES

The concepts of collisions and dephasing as presented here were apparently first introduced by H. A. Lorentz in the *Proceedings of the Amsterdam Academy of Science* **8**, 591 (1906). The number of discussions of collisions and line broadening in the literature is now extremely large. We will give many references to these in Section 3.2, where we discuss collision broadening and line broadening in real atoms in more detail.

Problems for 2.2

1. *Collision broadening with a different kind of collision statistics.* Consider a somewhat unusual collection of atoms, in which each individual atom suffers its dephasing collisions at absolutely regular intervals, spaced by an intercollision time T_c , so that the collisions for a given atom occur at instants $t = t_0, t_0 + T_c, t_0 + 2T_c$, and so forth, with the intercollision time T_c being the same for all the atoms. (You might think of each individual atom as bouncing back and forth between two walls at the same constant velocity, not hitting any other atoms, but being dephased each time it hits the walls.) The reference time or “first-collision time” t_0 is different for each atom, however, with values uniformly distributed between

0 and T_c (i.e., the atoms at any instant are uniformly distributed in the space between the walls).

Suppose that a group of atoms with these oddball collision properties are all set oscillating internally, with their internal oscillations initially in phase at $t = 0$. Describe how the macroscopic polarization $p_x(t)$ will decrease with time, including both energy decay and this oddball dephasing; and plot $p_x(t)$ versus t/T_c for values of the parameter $\gamma T_c = 0.1, 1$, and 10.

2.3 MORE ON ATOMIC DYNAMICS AND DEPHASING

Since dephasing effects are a particularly important aspect of atomic dynamics, let us look a bit further at some of the additional consequences and varieties of dephasing effects in real atomic systems.

Dephasing Effects Plus Applied Signals

One basic assumption in discussions of dephasing is that dephasing effects and applied signal fields such as $\mathcal{E}_x(t)$ will act on individual dipoles simultaneously and independently—that is, we can simply add up their effects in computing the total internal motion of individual atoms. What, then, are the relative strengths of these two effects? To explore this, let us consider, for example, the response of a single dipole oscillator subjected to an on-resonance sinusoidal applied field $\mathcal{E}_x(t) = E_1 \cos \omega_a t$ during the period just after this atom has suffered a randomizing collision at $t = t_0$. How rapidly can the applied signal $\mathcal{E}_x(t)$ “pull” the individual dipole moment $\mu_x(t)$ back into a coherent phase relationship with the applied signal, following a dephasing collision?

The problem here is clearly to solve the single-dipole equation of motion (Equation 2.26) with the specified applied signal and with an arbitrary initial condition on the phase (i.e., the position and velocity) of the oscillator at time $t = 0$. This can be done straightforwardly, although the exact solution is a bit messy. We know, however, that an equation of this type has a transient or homogeneous solution, independent of $\mathcal{E}_x(t)$, of the form

$$\mu_x(t) = \mu_{x0} \exp [-(\gamma/2)(t - t_0) + j\omega_a(t - t_0) + j\phi_0]. \quad (28)$$

(There is a minor approximation in this expression, namely, the replacing of ω_a' by ω_a .) We will also show in Section 2.4 that an on-resonance applied signal will produce a steady-state or forced sinusoidal solution of the form

$$\mu_x(t) = \text{Re} \left[-j \frac{e^2 E_1}{m \omega_a \gamma} e^{j\omega_a t} \right] = \text{Re} [\tilde{\mu}_{ss} e^{j\omega_a t}], \quad (29)$$

where $\tilde{\mu}_{ss} \equiv j(e/m\omega_a\gamma)E_1$ is the steady-state phasor amplitude of the motion produced by the field E_1 . Suppose we also define $\tilde{\mu}_0 \equiv \mu_{x0} \exp j\phi(0)$ as the complex phasor amplitude (magnitude and phase) of the sinusoidal motion of $\mu_x(t)$ immediately after the collision. (The phase $\phi(0)$ will take on random values for different dipoles after different collisions.)

The total solution for $\mu_x(t)$ following any given collision will then be a linear combination of the forced plus transient solutions, with just enough transient

solution included to meet the initial boundary condition at t_0 , or

$$\mu_x(t) = \text{Re} \left[\tilde{\mu}_{ss} + (\tilde{\mu}_0 - \tilde{\mu}_{ss}) e^{-(\gamma/2)(t-t_0)} \right] e^{j\omega_a(t-t_0)}. \quad (30)$$

This says, in effect, that we can write $\mu_x(t)$ in the form

$$\mu_x(t) = \text{Re} \left[\tilde{\mu}(t) e^{j\omega_a(t-t_0)} \right], \quad (31)$$

where $\tilde{\mu}(t)$ is a slowly changing complex phasor amplitude given by

$$\tilde{\mu}(t) = \tilde{\mu}_{ss} + [\tilde{\mu}_0 - \tilde{\mu}_{ss}] e^{-(t-t_0)/2\tau}. \quad (32)$$

In other words, following a collision the phasor amplitude $\tilde{\mu}(t)$ of the sinusoidal motion “pulls in” from the initial random post-collision value $\tilde{\mu}_0$, toward the forced or steady-state value $\tilde{\mu}_{ss}$, with an exponential time constant 2τ . Note that this pull-in time constant does not depend at all on the strength of the applied field.

Now, we will see later that for most real laser transitions the dephasing time T_2 is usually much shorter than the energy decay time τ ; so the dephasing time constant T_2 is also much shorter than the pull-in time constant τ (or 2τ). Any individual atom is, therefore, very likely to be dephased again by another collision, after a short time $\approx T_2$, well before it gets pulled completely into phase by the applied signal $\mathcal{E}_x(t)$. In real laser systems, therefore, even with applied signals present, the motions of the individual dipoles are mostly dephased, or randomly phased, by the dephasing processes. A coherent applied signal $\mathcal{E}_x(t)$ can usually only struggle to impose a small amount of phase ordering on this unruly bunch of oscillators.

Exceptions to this usual situation occur only for applied signals that are strong enough to produce the kind of Rabi flopping behavior that we will discuss in Chapter 5. Most signals in common lasers are “weak signals” which do not produce this kind of behavior; and the dipole motion in these system will be mostly random, with a small fractional amount of signal-imposed coherent ordering.

Dephasing by Random Frequency Modulation

Let us also look in a bit more detail at another type of dephasing that occurs in many solid-state laser materials.

The most graphic way of picturing dephasing effects in any collection of atoms is probably the kind of sudden, sharp, discrete, randomly occurring dephasing events or “collisions” that we have described above. An important alternative dephasing process for atoms, however, especially in crystals and other solids, is *phonon broadening*, or phonon frequency modulation of the atomic transitions, rather than genuine collisions between different atoms as in a gas.

In systems with phonon broadening (or with dipolar coupling as well) the dephasing process results not from sudden collisions, but from a more continuous but still random frequency modulation of each individual dipole’s oscillation frequency. The net result, however, is essentially the same: dipoles that begin oscillating in phase gradually end up, after a time on the order of T_2 , with their phases completely randomized.

Consider, for example, the chromium Cr^{3+} ions in a ruby crystal or the neodymium Nd^{3+} ions in a Nd:YAG crystal or glass lattice, such as we showed in Chapter 1; and suppose the internal electronic charges of several such ions have been set oscillating in an internal dipole oscillation with the same initial phase. Now, the surrounding lattice itself will also be vibrating slightly at any finite temperature, because of thermal agitation; so the spacing between each ion and its nearest neighbors in the lattice will be changing slightly in a random way that is different for each ion. But for ions in solids, small changes in the lattice spacing will cause very small but finite shifts in the exact resonance frequency ω_a of the transition in each ion. The sinusoidal dipole oscillations of the various ions, as a result, will proceed at slightly different and randomly changing frequencies; and the dipole oscillations will thus drift slowly and randomly out of phase with each other.

This same argument can hold for dipole oscillations in a crystal lattice, in a glassy solid, in a liquid, or in any condensed atomic medium. Dipoles initially oscillating in phase will eventually be converted to random phases. It is not so evident here that this will lead to an exponential decrease in the coherent polarization component. The fact is, however, that the same assumption of exponential decay that we made for the macroscopic polarization is just as good an approximation for these situations also.

Note on Phonon Broadening.

The shifts in resonance frequencies of ionic transitions in solids due to changes in the local lattice spacing can be demonstrated experimentally simply by squeezing the crystals to compress the lattice spacing slightly, and noting that there are small but finite *pressure shifts* for the transition frequencies of the ions in the crystals. These pressure shifts may be viewed as small changes in the *Stark shifts* of the atomic energy levels which are produced by the electric fields associated with the bonds between atoms in the crystal lattice.

Some Typical Numbers for Dephasing Effects

The magnitudes of the dephasing effects and the values of the dephasing time T_2 exhibit very large variations in different kinds of atomic media. Recall first that visible transitions have oscillation frequencies on the order of 6×10^{14} Hz and thus oscillation periods of the order of 10^{-15} sec.

The collision frequencies for atoms in real gases can vary over a wide range, depending on gas pressure; but values in the range of $1/T_2 \approx 10^8$ to 10^9 sec $^{-1}$, or dephasing times of $T_2 \approx 10^{-8}$ to 10^{-9} sec at low pressures, are not uncommon. Energy decay times in the range of $\tau \equiv \gamma^{-1} \approx 10^{-5}$ to 10^{-7} sec for transitions of interest are also reasonable. The general conclusion is thus that there are always an enormous number of optical cycles between each collision or dephasing event. The collision rate is usually an order of magnitude or more higher than the energy decay rate; so the $1/T_2$ term in the polarization decay often dominates over the $\gamma/2$ part of the decay.

For atoms in solids, the lattice vibrational frequencies that are excited by thermal agitation, and that cause the thermal frequency dephasing, range from zero up to $\approx 10^{13}$ Hz. The lattice modulation of the atomic transition frequencies is thus in general very fast compared to any measurements we might try to make on the atoms, but still slow compared to the actual transition frequencies ω_a . We must then ask not only how rapidly the lattice atoms vibrate, but also how strongly they modulate or shift the transition frequencies ω_a . The answer in typical lasers (e.g., ruby or Nd:YAG) is that these frequencies are shifted randomly by amounts on the order of 10^{11} to 10^{12} Hz.

Now, two dipoles having a random frequency difference of $\omega_{a2} - \omega_{a1}$ will get 2π out of time-phase with each other after an interval of $2\pi/(\omega_{a2} - \omega_{a1})$ seconds. The effective T_2 dephasing times for ionic transitions in solids are thus often of the order of 10^{-11} to 10^{-12} sec. The energy decay times in solids on good laser transitions are sometimes as slow as 10^{-3} to 10^{-4} sec. Again, the $1/T_2$ dephasing component dominates, generally by a very large amount, over the $\gamma/2$ energy decay rate.

Coherent Versus Incoherent Decay

Suppose, as a final mental exercise, that a large number of atoms N_0 are initially all oscillating and radiating together in phase, as we described earlier. (Preparing a group of atoms in this coherently phased initial condition is not always easy to accomplish, as we will see later. It generally requires very strong applied signals, applied in very short pulses.)

Given this initial preparation, all these atoms or oscillators will then radiate together as one giant coherent dipole. The initial value of this dipole will be $N_0\mu_{x0}$, where μ_{x0} is the dipole moment of one individual atom; and the rate at which this collection of coherently oscillating atoms radiates energy will be proportional to $N_0^2|\mu_{x0}|^2$. The essential point is that all the dipoles are radiating coherently, that is, in time-phase with each other.

This coherence will, however, be destroyed by dephasing processes in a time of order T_2 , which for real atomic transitions is often very short (from nanoseconds down to less than picoseconds). Once the coherent oscillation is destroyed, after a few dephasing times T_2 , the individual dipoles will in general still be oscillating and radiating energy, since their energy decay time $\tau \equiv \gamma^{-1}$ is generally longer (sometimes much longer) than the dephasing time T_2 . The individual dipoles will continue, in fact, to radiate energy through the γ_{rad} and γ_{nr} processes, but they now radiate individually and *incoherently*, with random phase relationships between the dipoles. The radiation that now comes out from the sample is essentially narrowband noise, or spontaneous emission, or fluorescence centered at the atomic transition frequency ω_a . It comes out in all directions, and with a narrowband but essentially noise-like spectrum. The power radiated is simply the sum of the individual powers radiated by the N_0 individual dipoles, and hence is now proportional to $N_0|\mu_{x0}|^2$ rather than to $N_0^2|\mu_{x0}|^2$.

Suppose we perform an experiment in which we set a collection of atomic dipoles oscillating coherently, perhaps using some kind of pulsed applied signal, and then observe how the atoms radiate afterward. We can expect to see two transients: first the coherent transient radiation, which may be strong but very fast (time constant $\approx T_2$); and then the incoherent transient radiation, generally much weaker but longer-lived, corresponding to normal spontaneous emission or fluorescence (time constant $\approx T_1$). So-called *coherent pulse* or *coherent free-*

induction decay experiments displaying the first type of behavior can be performed on atoms at optical frequencies. These experiments are generally rather difficult, however, requiring short but intense coherent laser pulses for excitation, together with high-speed detectors for the coherently radiated signals.

Much more common are ordinary *fluorescent lifetime experiments*, such as we will illustrate later. In these, a group of atoms are again set oscillating, but the excitation mechanism is some form of incoherent excitation, such as a pulse of broadband light from an incoherent flashlamp, or a short burst of current through a collection of gas atoms. There is no initial phase coherence to the excitation in these cases, and hence no coherent initial polarization to either radiate coherently or decay at the T_2 rate. The radiation in this case comes entirely from incoherent spontaneous emission or fluorescence, and the measured decay rate will be simply the energy decay rate $\gamma \equiv \gamma_{\text{rad}} + \gamma_{\text{nr}}$. Understanding the distinction between these coherent and incoherent types of processes is extremely important in understanding the atomic phenomena involved in lasers.

Problems for 2.3

1. *Dephasing by random frequency modulation.* It is claimed in this section that a continuous but random modulation of the resonance frequencies of a system can lead to a net exponential result for dephasing behavior. To examine this basic idea in more detail, consider a large number of individual dipole oscillators all having the same natural oscillation frequency ω_a , and all oscillating initially in phase with each other in the general form $\cos \omega_a t$. Suppose, however, that each oscillator is randomly phase-modulated (or frequency-modulated) by some external perturbation, so that after a time t any individual oscillator oscillates as $\cos[\omega_a t + \phi_i(t)]$, where $\phi_i(t)$ is a random phase angle for the i -th oscillator after time t .

If the individual oscillators randomly diffuse in phase angle with increasing time, the probability density distribution of oscillation phases for different oscillators after a time t may take on the gaussian form $\text{Pr}[\phi_i] = \exp[-\phi_i^2/2\sigma^2(t)]/\sqrt{2\pi\sigma^2(t)}$. If, for example, the phases of different oscillators diffuse as a random-walk process, standard statistical arguments say that the random phases will have just this kind of gaussian probability distribution, and that the variance σ^2 of this distribution will increase linearly in time in the form $\sigma^2(t) = 2Dt$, where D is a diffusion coefficient for the phases.

Using this probabilistic model, evaluate how the macroscopic polarization $p(t)$ obtained by summing over a large number of microscopic dipoles $\mu_i(t)$ per unit volume will decay in time, assuming all the dipoles start out oscillating in phase (i.e., with $\phi_i(0) = 0$). Hints: The expected value or average value for some function $f(y)$, where y is a random variable with probability distribution $\text{Pr}[y]$, is given by $\langle f \rangle \equiv \int f(y) \text{Pr}[y] dy$. A useful formula to remember is that

$$\int_{-\infty}^{\infty} e^{-Ay^2 - 2By} dy = \sqrt{\pi/A} e^{B^2/A}.$$

This formula holds for A and B complex, provided only that $\text{Re}[A] > 0$.

2.4 STEADY-STATE RESPONSE: THE ATOMIC SUSCEPTIBILITY

Our next task is to compute the steady-state response of a collection of oscillators or atoms to a sinusoidal applied signal, and to express this response as a linear resonant electric susceptibility.

Phasor Analysis

Suppose that the electric field $\mathcal{E}_x(t)$ applied to a collection of classical oscillators, or electric dipole atoms, is a sinusoidal signal with frequency ω , which we write in the form

$$\mathcal{E}_x(t) = \text{Re}[\tilde{E}_x e^{j\omega t}] = \frac{1}{2}[\tilde{E}_x e^{j\omega t} + \tilde{E}_x^* e^{-j\omega t}]. \quad (33)$$

In electrical engineering jargon the complex quantity \tilde{E}_x is a “phasor” whose magnitude and phase angle give the amplitude and phase of the real quantity $\mathcal{E}_x(t)$. Suppose, for example, that the complex phasor \tilde{E}_x has the magnitude and phase angle $\tilde{E}_x \equiv |\tilde{E}_x|e^{j\phi}$. Then the real field $\mathcal{E}_x(t)$ will be given by $\mathcal{E}_x(t) = \text{Re}[|\tilde{E}_x|e^{j(\omega t+\phi)}] = |\tilde{E}_x| \cos(\omega t + \phi)$, so that obviously $|\tilde{E}_x|$ is the magnitude and ϕ the phase angle (in time) of the sinusoidal signal.

The steady-state response from a linear atomic system will then have the same sinusoidal form, i.e.,

$$p_x(t) = \text{Re}[\tilde{P}_x e^{j\omega t}] = \frac{1}{2}[\tilde{P}_x e^{j\omega t} + \tilde{P}_x^* e^{-j\omega t}], \quad (34)$$

so that a similar description will obviously prevail for the magnitude and phase angle of the real polarization $p_x(t)$ and its complex phasor amplitude \tilde{P}_x .

Both the $e^{j\omega t}$ and the $e^{-j\omega t}$ terms in these phasor expansions are needed to give the complete real fields; but in any *linear* system with a linear differential equation, such as we are considering here, the $\tilde{E}_x e^{j\omega t}$ part of the applied field will be connected only to the $\tilde{P}_x e^{j\omega t}$ part of the induced polarization, and similarly for the $\tilde{E}_x^* e^{-j\omega t}$ and $\tilde{P}_x^* e^{-j\omega t}$ parts of these quantities. Moreover, these separate responses in any real physical system will be simply the complex conjugates of each other, so that the complex-conjugate or $e^{-j\omega t}$ terms really contain no additional information over and above the $e^{j\omega t}$ terms.

Following the usual practice in phasor analyses, therefore, we will focus only on the $e^{j\omega t}$ terms from now on. Moreover, for simplicity we will generally leave off the “Re” notation from now on and write the real fields in the form $\mathcal{E}_x(t) = \tilde{E}_x e^{j\omega t}$, with the operation of taking the real part being understood.

If we put these sinusoidal phasor expansions into the equation of motion for $p_x(t)$, Equation 2.27, and separate out the $e^{j\omega t}$ terms, we obtain a relation between the complex phasor amplitudes:

$$[-\omega^2 + j\omega(\gamma + 2/T_2) + \omega_a^2] \tilde{P}_x = \frac{Ne^2}{m} \tilde{E}_x, \quad (35)$$

which we will rearrange into the form

$$\frac{\tilde{P}_x}{\tilde{E}_x} = \frac{Ne^2}{m} \frac{1}{\omega_a^2 - \omega^2 + j\omega(\gamma + 2/T_2)}. \quad (36)$$

This is the linear steady-state relationship between the phasor polarization \tilde{P}_x induced in the collection of oscillators or atoms and the field \tilde{E}_x applied to them. In linear-system terms, it is the *transfer function* for the response of the atomic medium.

Electric Polarization and Susceptibility: Standard Definitions

This transfer function is more commonly known as the *electric susceptibility of the atomic medium*, as produced by the polarization response of the atoms or oscillators. We can recall that the electric field \tilde{E} , the electric polarization \tilde{P} , and the electric displacement \tilde{D} in any arbitrary dielectric medium are related under all circumstances by the basic definition from electromagnetic theory

$$\tilde{D} = \epsilon_0 \tilde{E} + \tilde{P}. \quad (37)$$

In the more restrictive case of a linear and isotropic dielectric medium, the polarization \tilde{P} and the electric field \tilde{E} will also be related, by an expression which is conventionally written in the form

$$\tilde{P}(\omega) = \tilde{\chi}(\omega) \epsilon_0 \tilde{E}(\omega), \quad (38)$$

so that the quantity $\tilde{\chi}(\omega)$ defined by

$$\tilde{\chi}(\omega) \equiv \frac{\tilde{P}(\omega)}{\epsilon_0 \tilde{E}(\omega)} \quad (39)$$

is the *electric susceptibility* of the medium, with ϵ_0 being the dielectric permeability of free space. We will adopt a slightly modified version of this definition a few paragraphs further on.

The relationship between the electric displacement \tilde{D} and the electric field \tilde{E} in a linear medium can then be written, using the standard definition of Equation 2.39, as

$$\tilde{D} = \epsilon_0 [1 + \tilde{\chi}] \tilde{E} = \tilde{\epsilon} \tilde{E}, \quad (40)$$

which means that the complex dielectric constant $\tilde{\epsilon}(\omega)$ is given by

$$\tilde{\epsilon}(\omega) \equiv \epsilon_0 (1 + \tilde{\chi}). \quad (41)$$

For a completely general description, the field quantities \tilde{D} , \tilde{E} , and \tilde{P} really should be treated as vector quantities in these relations; and in the more general linear but anisotropic case the susceptibility $\tilde{\chi}$ then becomes a tensor quantity. For simplicity, however, let us stick with scalar notation at this point.

The electric susceptibility relating the applied signal \tilde{E}_x and the atomic polarization \tilde{P}_x in an atomic medium is very important in calculating laser gain, phase shift, and many other properties, as we will see shortly. Before going further with this discussion, however, we must introduce a slightly nonstandard definition of the electric susceptibility $\tilde{\chi}$, which is peculiar to this book, but which will turn out to be very useful in simplifying later formulas.

Atomic Susceptibility: A Modified Definition

In a sizable fraction of the laser materials of interest to us, the resonant oscillators or the laser atoms that produce the resonant polarization \tilde{P}_x are not located in free space. Rather, these atoms are imbedded in a laser crystal, or perhaps in a glass or a liquid host material. In the laser material ruby, for example, the Cr^{3+} laser atoms that are responsible for the laser behavior are dispersed (at $\approx 1\%$ density) in a host lattice of colorless Al_2O_3 , or sapphire. In dye laser solutions the dye molecules, for example, Rhodamine 6G, are dissolved at perhaps 10^{-3} molar concentration in a liquid solvent such as water or ethanol.

In all these devices, the host materials in the absence of the laser atoms are transparent dielectric materials that are nearly lossless at the laser wavelength, but have a relative dielectric constant ϵ/ϵ_0 or an index of refraction n that is significantly greater than unity. These materials will possess, therefore, a large nonresonant linear electric polarization P_{host} that is associated with the host material by itself, and that has no direct connection with the generally much weaker resonant polarization P_{at} that comes from the resonant response of the classical oscillators or from the resonant transitions in the laser atoms.

We can therefore write the total displacement vector in such a material in more detail as

$$\tilde{D} = \epsilon_0 \tilde{E} + \tilde{P}_{\text{host}} + \tilde{P}_{\text{at}}. \quad (42)$$

In this equation \tilde{P}_{host} refers to the large, broadband, linear nonresonant polarization associated with the host material by itself; whereas \tilde{P}_{at} refers to the weak, narrowband, linear resonant polarization produced by the classical oscillators or atoms imbedded in the host material. Following conventional electromagnetic notation, we can then define a nonresonant susceptibility $\tilde{\chi}_{\text{host}}$ and a dielectric constant ϵ_{host} for the host material according to the usual definitions, in the form

$$\tilde{P}_{\text{host}} = \tilde{\chi}_{\text{host}} \epsilon_0 \tilde{E} \quad \text{and} \quad \epsilon_{\text{host}} = \epsilon_0 (1 + \tilde{\chi}_{\text{host}}). \quad (43)$$

The total polarization can therefore be written as

$$\tilde{D} = \epsilon_0 [1 + \tilde{\chi}_{\text{host}}] \tilde{E} + \tilde{P}_{\text{at}} = \epsilon_{\text{host}} \tilde{E} + \tilde{P}_{\text{at}}. \quad (44)$$

Note that in typical laser crystals or liquids the host dielectric constant (at optical frequencies) will have magnitude $\epsilon_{\text{host}}/\epsilon_0 \approx 2$ to 3, so that the dimensionless host susceptibility will have magnitude $\tilde{\chi}_{\text{host}} \approx 1$ to 2. To put this in another way, the index of refraction of typical laser host materials, given by $n_{\text{host}} \equiv \sqrt{\epsilon_{\text{host}}/\epsilon_0}$, will have values of $n_{\text{host}} \approx 1.5$ to 2.0 for typical liquids or crystals.

Suppose now that we were also to define a separate susceptibility $\tilde{\chi}_{\text{at}}$ for the atomic or resonant oscillator part of the response in the laser medium, using the same conventional definition as given earlier, namely,

$$\tilde{\chi}_{\text{at}} = \tilde{P}_{\text{at}} / \epsilon_0 \tilde{E} \quad \begin{pmatrix} \text{conventional} \\ \text{definition} \end{pmatrix}. \quad (45)$$

Then we would end up with a result of the form

$$\tilde{D} = \epsilon_{\text{host}} \tilde{E} + \tilde{\chi}_{\text{at}} \epsilon_0 \tilde{E} = \epsilon_{\text{host}} [1 + (\epsilon_0 / \epsilon_{\text{host}}) \tilde{\chi}_{\text{at}}] \tilde{E} \quad \begin{pmatrix} \text{conventional} \\ \text{definition} \end{pmatrix}. \quad (46)$$

Now, there will be many times in later chapters when we will want to expand the bracketed factor involving $\tilde{\chi}_{\text{at}}$ to various orders in $(\epsilon_0 / \epsilon_{\text{host}}) \tilde{\chi}_{\text{at}}$, since this

quantity is always small compared to unity. If we follow this conventional definition for $\tilde{\chi}_{\text{at}}$, using ϵ_0 , we will end up carrying along perpetual factors of $\epsilon_0/\epsilon_{\text{host}}$ to various powers in all these expressions.

To avoid this, we will instead consistently use in this book an alternative nonstandard definition for $\tilde{\chi}_{\text{at}}$ which we obtain by writing

$$\tilde{P}_{\text{at}} \equiv \tilde{\chi}_{\text{at}} \epsilon_{\text{host}} \tilde{E} \quad \begin{pmatrix} \text{this book's} \\ \text{definition} \end{pmatrix}, \quad (47)$$

so that the atomic resonance part of the susceptibility is defined by the expression

$$\tilde{\chi}_{\text{at}} \equiv \frac{\tilde{P}_{\text{at}}(\omega)}{\epsilon_{\text{host}} \tilde{E}(\omega)} \quad \begin{pmatrix} \text{this book's} \\ \text{definition} \end{pmatrix}. \quad (48)$$

Note that we are not rewriting any laws of electromagnetic theory by doing this—we are merely introducing a slightly unconventional way of defining $\tilde{\chi}_{\text{at}}$ for an atomic transition, in which ϵ_{host} is used as a normalizing constant in the denominator, rather than ϵ_0 as in the standard definition. If we use this definition, as we will from here on, the total electric displacement in any laser material is then given by the simpler form

$$\tilde{D} = \epsilon_{\text{host}} \tilde{E} + \tilde{P}_{\text{at}} = \epsilon_{\text{host}} [1 + \tilde{\chi}_{\text{at}}] E \quad \begin{pmatrix} \text{this book's} \\ \text{definition} \end{pmatrix}. \quad (49)$$

This alternative form avoids the factor of $\epsilon_0/\epsilon_{\text{host}}$ in Equation 2.46. For simplicity, from here on we will also drop all the “host” subscripts and simply write ϵ_{host} as ϵ .

To keep all this straight, just remember: from here on ϵ is the dielectric constant of the host lattice or dielectric material *without* the laser atoms; whereas $\tilde{\chi}_{\text{at}}$, defined according to the alternative definition of Equation 2.48, is the additional (weak) contribution due to the resonant atomic transition in the laser atoms. Of course, if the laser material is a dilute gas with $\epsilon_{\text{host}} = \epsilon_0$, there is no difference anyway.

Resonant Susceptibility: The Resonance Approximation

With this definition we can write the general susceptibility $\tilde{\chi}_{\text{at}}$ for the resonant response in a collection of resonant oscillators or atoms by combining Equations 2.36 and 2.48 to obtain

$$\tilde{\chi}_{\text{at}}(\omega) \equiv \frac{\tilde{P}_x}{\epsilon \tilde{E}_x} = \frac{Ne^2}{m\epsilon} \frac{1}{\omega_a^2 - \omega^2 + j\omega\Delta\omega_a}. \quad (50)$$

We have introduced here the important quantity

$$\Delta\omega_a \equiv \gamma + 2/T_2, \quad (51)$$

which we will shortly identify as the *atomic linewidth* (FWHM) of the atomic resonance. Since both γ and $2/T_2$ are always small compared to optical frequencies, this linewidth $\Delta\omega_a$ is very small compared to the center frequency ω_a for essentially all transitions of interest in lasers—never more than 10% at absolute most, and usually much, much narrower. (In fact, fractional linewidths greater than a fraction of a percent occur in practice only in semiconductor injection lasers and organic dye lasers.)

We are most often interested only in the response of the atoms to signal frequencies ω that lie within a few linewidths of either side of the resonant frequency ω_a . Within this region we can make what is called the **resonance approximation** by writing

$$\omega^2 - \omega_a^2 = (\omega + \omega_a)(\omega - \omega_a) \approx 2\omega_a(\omega - \omega_a) \approx 2\omega(\omega - \omega_a), \quad (52)$$

so that the frequency-dependent part of the susceptibility expression becomes

$$\frac{1}{\omega_a^2 - \omega^2 + j\omega\Delta\omega_a} \approx \frac{1}{2\omega(\omega_a - \omega) + j\omega\Delta\omega_a} \approx \frac{1}{2\omega_a(\omega_a - \omega) + j\omega\Delta\omega_a}. \quad (53)$$

By using this we can then convert Equation 2.50 into the simpler resonant form

$$\tilde{\chi}_{\text{at}}(\omega) = \frac{-jNe^2}{m\omega_a\epsilon\Delta\omega_a} \frac{1}{1 + 2j(\omega - \omega_a)/\Delta\omega_a}. \quad (54)$$

It is evident that this response will decrease rapidly compared to its midband value as soon as the frequency detuning $\omega - \omega_a$ becomes more than a few times the linewidth $\pm\Delta\omega_a$; and hence it really does not matter at all whether we use ω or ω_a in the denominator in the first part of this expression, so long as we do not tune away from ω_a by more than, say, $\pm 10\%$.

The Lorentzian Lineshape

The right-hand part of Equation 2.54 exhibits a very common frequency dependence known as a *complex lorentzian lineshape*. Since we will be seeing this frequency dependence over and over in the remainder of this text, let us gain a little familiarity with its properties.

Suppose that, for simplicity, we define a normalized frequency shift away from line center by

$$\Delta x \equiv 2 \frac{\omega - \omega_a}{\Delta\omega_a}, \quad (55)$$

so that $\Delta x = 0$ corresponds to midband and $\Delta x = \pm 1$ corresponds to a frequency shift of half a linewidth away from line center on either side. Then the complex lorentzian lineshape is given by

$$\tilde{\chi}_{\text{at}}(\omega) = -j\chi_0'' \frac{1}{1 + 2j(\omega - \omega_a)/\Delta\omega_a} = -j\chi_0'' \frac{1}{1 + j\Delta x}, \quad (56)$$

where

$$\chi_0'' \equiv \frac{Ne^2}{m\omega_a\epsilon\Delta\omega_a} \quad (57)$$

is the magnitude of the negative-imaginary value at midband.

Readers familiar with Fourier transforms will recognize that this complex lorentzian lineshape is simply the Fourier transform in frequency space of the exponential time decay of the polarization $p_x(t)$. (Whether the $-j$ factor in front of the $1/(1 + j\Delta x)$ frequency dependence is to be considered part of the complex lorentzian lineshape or not is entirely a matter of style.) Note once again that in examining the frequency dependence of lorentzian transitions—for example, in solving some of the problems at the end of this section—the frequency dependence of the constant χ_0'' can be entirely ignored; i.e., it makes

no practical difference whether we use ω or ω_a in the denominator of Equation 2.57. This constant in front can be treated as entirely independent of frequency within the resonance approximation.

The real and imaginary parts of this complex lorentzian lineshape then have the forms

$$\tilde{\chi}_{\text{at}}(\omega) \equiv \chi'(\omega) + j\chi''(\omega) = -\chi_0'' \left[\frac{\Delta x}{1 + \Delta x^2} + j \frac{1}{1 + \Delta x^2} \right], \quad (58)$$

where $\tilde{\chi}'(\omega)$ and $\tilde{\chi}''(\omega)$ are the real and imaginary parts of this function, as plotted in Figure 2.8. The imaginary part of this response, or $\chi''(\omega)$, has a resonant response curve of the form

$$\chi''(\omega) = -\chi_0'' \frac{1}{1 + [2(\omega - \omega_a)/\Delta\omega_a]^2} = -\chi_0'' \frac{1}{1 + \Delta x^2}. \quad (59)$$

This lineshape is conventionally called the *real lorentzian lineshape*, with a response centered at $\Delta x = 0$ or $\omega = \omega_a$, and with a full width between the half-power points $\omega - \omega_a = \pm\Delta\omega_a$ given by

$$\Delta\omega_a = \gamma + 2/T_2. \quad (60)$$

The linewidth $\Delta\omega_a$ is thus the *full width at half maximum (FWHM) linewidth* of the atomic transition. We will shortly identify $\chi''(\omega)$ as the absorbing (or amplifying) part of the atomic response.

The real part of the lorentzian susceptibility, or $\chi'(\omega)$, has the frequency dependence

$$\chi'(\omega) = -\chi_0'' \frac{2(\omega - \omega_a)/\Delta\omega_a}{1 + [2(\omega - \omega_a)/\Delta\omega_a]^2} = -\chi_0'' \frac{\Delta x}{1 + \Delta x^2}, \quad (61)$$

which has the antisymmetric or roughly first-derivative form shown in Figure 2.8. We will shortly identify this $\chi'(\omega)$ part as the reactive, or phase-shift, or dispersive part of the atomic response.

Note that the literature on atomic transitions and lasers uses many different linewidth definitions for $\Delta\omega$, Δf , $\Delta\lambda$, etc., which in different publications are sometimes defined as the half widths of resonance lines; sometimes as the full widths, as here; and sometimes even as rms linewidths, or $1/e^2$ linewidths, or other exotic widths. We will be consistent in this text in always using a FWHM definition for any linewidth $\Delta\omega$, Δf , or $\Delta\lambda$, unless we explicitly say otherwise.

Magnitude of the Steady-State Atomic Response

Let us emphasize once more that the atomic response of a collection of atoms to an applied signal is *coherent*, in the sense that the steady-state induced polarization $\tilde{P}(\omega)$ follows, in amplitude and time-phase, the driving signal field $\tilde{E}(\omega)$ in the manner described by the complex susceptibility or transfer function $\tilde{\chi}(\omega)$. The susceptibility $\tilde{\chi}(\omega)$ given by Equations 2.50, 2.54 or 2.56 is a dimensionless quantity. We will see later that in essentially every case of interest to us, the numerical value of this quantity is very small compared to unity. Only for very large atomic densities, very strongly allowed transitions, and very narrow linewidths does the numerical magnitude of $\tilde{\chi}$ approach unity; and these conditions are not normally all present at once in laser materials.

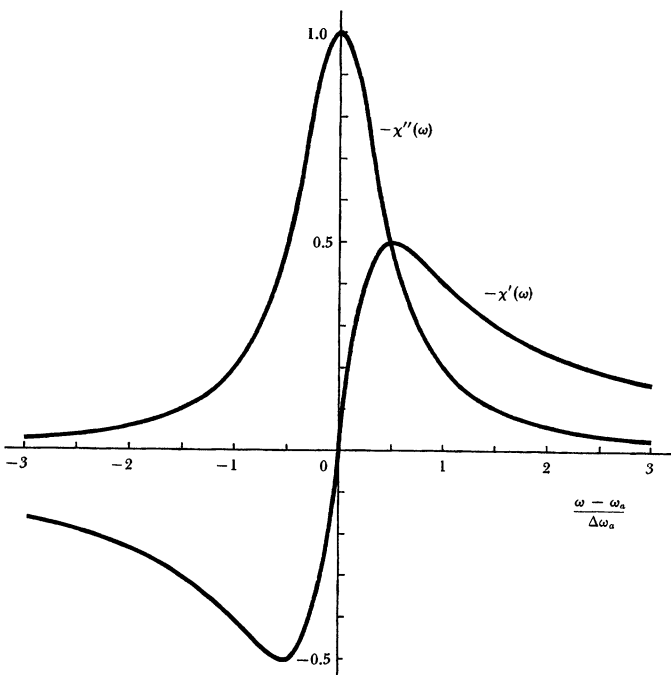


FIGURE 2.8
Real and imaginary parts of the complex Lorentzian lineshape.

We might also note that the magnitude of the atomic susceptibility at mid-band is proportional to the inverse linewidth $1/\Delta\omega_a$, where the linewidth $\Delta\omega_a$ for classical oscillators is given by

$$\Delta\omega_a = \gamma_{\text{rad}} + \gamma_{\text{nr}} + 2/T_2. \quad (62)$$

As the dephasing time T_2 becomes smaller, this linewidth becomes larger, and hence the relative strength of the induced atomic response decreases in direct proportion to the dephasing processes as measured by $2/T_2$.

If there were no dephasing processes, so that $T_2 \rightarrow \infty$, then the applied signal field \tilde{E} could drive all the individual atomic dipoles to oscillate completely in phase, and would produce the largest possible induced response, limited only by the dipole energy decay rate. The dephasing processes associated with any finite T_2 value, however, operate to "fight" the coherent phasing effects of the applied signal, and to reduce the coherent polarization that can be developed. The usual situation in most (though not all) laser materials is that the $2/T_2$ dephasing term dominates over the energy decay rate γ ; as a result, the applied signal can produce only a small fractional coherent ordering of the dipole oscillation's steady state, working against the randomizing effects of the dephasing processes.

Problems for 2.4

1. *Radiative decay rate at the He-Ne laser transition frequency.* Evaluate the radiative decay rate and the radiative lifetime for a classical electron oscillator with the same resonance frequency as the He-Ne 6328Å laser line. Also evaluate the atomic linewidth $\Delta\omega_a$ that would apply if this were the only damping or line-broadening effect present. (Note: The actual 6328Å transition in neon is much weaker, i.e., has a much slower radiative decay rate; and other broadening mechanisms, including both collision and doppler-broadening, are present in the real He-Ne laser.)
2. *Classical-mechanics description of power transfer from field to atoms.* Describe, using suitable plots, the magnitude and phase of the induced dipole response $\mu_x(t)$ of a classical electron oscillator to a sinusoidal applied field $\mathcal{E}_x(t)$ as a function of the driving frequency ω , from well below to well above resonance. Using the fact that the work done by a force $f_x(t)$ pushing on an object moving with velocity $v_x(t)$ is given by $dW/dt = f_x(t)v_x(t)$, explain in mechanical terms the steady-state power transfer from the applied signal to the oscillating dipole, both for frequencies near resonance and in the reactive regimes well away from resonance.
3. *Lorentzian lineshape for a resonant electrical circuit.* Show that the electrical impedance $Z(\omega)$ as a function of frequency for a resistance R , an inductance L , and a capacitance C connected in parallel can also be approximated by a complex lorentzian lineshape.
4. *Lorentzian lineshape locus in the complex plane.* The complex lorentzian susceptibility $\tilde{\chi}(\omega)$ can be plotted as a contour in the complex plane with χ' and χ'' as the horizontal and vertical axes, respectively, and ω as a parameter along this contour. Plot a few points to trace the geometric form of this contour. Can you give a simple analytic form for the contour (in the resonance approximation)?
5. *Range of validity for the resonance approximation.* The resonance approximation leading to the lorentzian lineshape for a high- Q classical oscillator is said to be valid “near resonance.” How far from resonance on either side can you in fact vary the frequency tuning $\omega - \omega_a$ before the magnitude of the difference between the exact form and the approximate lorentzian form for the complex susceptibility of a classical electron oscillator becomes as large as 10 percent?
6. *Derivative spectroscopy.* Some types of spectrometers used to study atomic resonances give an output signal proportional not to the atomic absorption line $\chi''(\omega)$ itself as a function of ω , but rather to its first derivative $d\chi''(\omega)/d\omega$. This first-derivative curve has two peaks of opposite sign centered about ω_a . Find the spacing $\Delta\omega_{pk}$ between these two peaks in terms of the usual FWHM atomic linewidth $\Delta\omega_a$ for a high- Q lorentzian line.
7. *Overlapping lineshapes: maximally flat condition.* Suppose an atomic medium contains two groups of resonant oscillators with the same linewidth, density, and other parameters, but with slightly different resonant frequencies ω_{a1} and ω_{a2} . Using the resonance approximation for each line, plot the total susceptibilities $\chi'(\omega)$ and $\chi''(\omega)$ versus ω due to both groups of atoms combined, for frequency separations $\omega_{a2} - \omega_{a1}$ of 0.2, 0.5, 1, 2, and 5 times the linewidth $\Delta\omega_a$. What

frequency separation will cause the first derivative $d\chi'(\omega)/d\omega$ to be exactly zero at the midpoint between the two lines?

2.5 CONVERSION TO REAL ATOMIC TRANSITIONS

The classical electron oscillator results derived in the preceding sections can be converted into *quantum-mechanically correct* formulas for real atomic transitions in real atoms by making a few simple and almost obvious substitutions. These substitutions are briefly introduced in this section, and then discussed in more detail in the following chapter.

Substitution of Radiative Decay Rate

The first step in converting from the CEO model to real atomic transitions is to notice a similarity between the constant in front of the classical oscillator susceptibility expression of Equation 2.57 in the preceding section, which has the form

$$\chi_0'' \equiv \frac{Ne^2}{m\omega_a \epsilon \Delta\omega_a}, \quad (63)$$

and the classical oscillator radiative decay rate that we introduced in Equation 2.8, which is given by

$$\gamma_{\text{rad,ceo}} = \frac{e^2 \omega_a^2}{6\pi\epsilon mc^3}. \quad (64)$$

In fact, if we substitute the second of these into the first, we can write the amplitude of the classical oscillator susceptibility at midband in the form

$$\chi_0'' = \frac{3}{4\pi^2} \frac{N\lambda^3 \gamma_{\text{rad,ceo}}}{\Delta\omega_a}. \quad (65)$$

In this form all the atomic and electromagnetic constants appearing in the classical oscillator model (charge e , mass m , and the dielectric constant ϵ) drop out; and the resulting expression depends only on directly measurable properties of the classical oscillator, namely, the transition wavelength λ , the density of oscillators N , the radiative decay rate $\gamma_{\text{rad,ceo}}$, and the linewidth $\Delta\omega_a$ of the transition itself. This expression is a more fundamental and useful way of writing the susceptibility, since it is now equally valid for either classical oscillators or real atoms, provided only that we use the appropriate values of λ , γ_{rad} , and $\Delta\omega_a$ in each case.

Introduction of Population Difference

The second and more fundamental step in converting from classical oscillators to real atoms is to notice that the classical electron oscillator response we have derived here is proportional to the number density N of the classical oscillators. But we learned in Chapter 1 that the response on real quantum transitions is proportional to the *population difference density* $\Delta N_{12} = N_1 - N_2$ between

the populations (atoms per unit volume) in the lower and upper levels of the atomic transition.

That is, a collection of classical oscillator “atoms” can only absorb energy, at least in steady state. Both quantum theory and experiments show, however, that when a signal is applied to a collection of real quantum atoms, the steady-state response is always such that the lower-level atoms absorb energy through upward transitions, but the upper-level atoms emit energy through downward transitions. The lower-level atoms thus act essentially like conventional classical oscillators, but the upper-level atoms act somehow like “inverted” classical oscillators.

The single most crucial step in converting our classical oscillator results to accurate quantum formulas for real atomic transitions is thus to replace the classical oscillator density N by a quantum population difference $\Delta N_{12} \equiv N_1 - N_2$, where N_1 and N_2 are the number of atoms per unit volume, or the “level populations,” in the lower and upper energy levels. This substitution is the primary point where quantum theory enters the classical oscillator model.

Quantum Susceptibility Result

If we make both of these substitutions, and also for simplicity leave off all the classical oscillator labels, then the resonant susceptibility expression for either a collection of classical oscillators or a real atomic transition is given by the same expression, namely,

$$\tilde{\chi}_{\text{at}}(\omega) = -j \frac{3}{4\pi^2} \frac{\Delta N \lambda^3 \gamma_{\text{rad}}}{\Delta \omega_a} \frac{1}{1 + 2j(\omega - \omega_a)/\Delta \omega_a}. \quad (66)$$

It will often be convenient to write this expression for the complex lorentzian susceptibility in the form

$$\begin{aligned} \tilde{\chi}_{\text{at}}(\omega) &= -j \chi_0'' \times \frac{1}{1 + 2j(\omega - \omega_a)/\Delta \omega_a} \\ &= -\chi_0'' \left[\frac{2(\omega - \omega_a)/\Delta \omega_a}{1 + [2(\omega - \omega_a)/\Delta \omega_a]^2} + j \frac{1}{1 + [2(\omega - \omega_a)/\Delta \omega_a]^2} \right], \end{aligned} \quad (67)$$

where $-j\chi_0''$ is the given midband susceptibility, with magnitude given by

$$\chi_0'' = \frac{3}{4\pi^2} \frac{\Delta N \lambda^3 \gamma_{\text{rad}}}{\Delta \omega_a}. \quad (68)$$

This expression then becomes an essentially quantum-mechanically correct expression for the resonant susceptibility of any real electric-dipole atomic transition, provided simply that we use in these formulas the real (i.e., measured) values of the parameters λ , γ_{rad} , $\Delta \omega_a$, and ΔN for that particular atomic transition.

Discussion

The preceding results thus say that the linear response to an applied signal, as expressed by $\tilde{\chi}(\omega)$, for a collection of classical oscillators or for a real atomic transition, depends only on the following.

- For the classical case the *number of oscillators* $N\lambda^3$, or for the quantum case the *net population difference* $\Delta N\lambda^3$, contained in a volume of one wavelength cubed, where $\lambda \equiv \lambda_0/n$ is the wavelength in the host crystal medium.
- The *radiative decay rate* γ_{rad} characteristic of that particular oscillator, or of that particular atomic transition. This is a very fundamental and important point: different transitions in real atoms will have very different strengths, as measured by their radiative decay rates. We see here that the *induced* or *stimulated* response on each such transition will be directly proportional to the *spontaneous* emission rate on that same transition. Oscillators that radiate strongly also respond strongly.
- The *inverse linewidth* $1/\Delta\omega_a$ of that transition. This says in effect that there is a characteristic area under each such resonance (with a magnitude proportional to $\Delta N\lambda^3\gamma_{\text{rad}}$). Transitions that are broadened or smeared out by dephasing effects, or by other line-broadening mechanism, then have proportionately less response at line center.
- And finally, there is the *complex lorentzian lineshape* that gives the frequency variation of the atomic response as a system is tuned on either side of the resonance frequency.

Each of these points is fundamental, and will reoccur many times in discussions of real atomic responses later on.

The Quantum Polarization Equation of Motion

We can also make the same substitutions in the differential equation of motion for $p(t)$ in the time domain, and rewrite Equation 2.27 in the form

$$\frac{d^2p_x(t)}{dt^2} + \Delta\omega_a \frac{dp_x(t)}{dt} + \omega_a^2 p_x(t) = \frac{3\omega_a \epsilon \lambda^3 \gamma_{\text{rad}}}{4\pi^2} \Delta N(t) \mathcal{E}_x(t), \quad (69)$$

after which *this also becomes an essentially quantum-mechanically correct equation for the induced polarization response $p(t)$, or at least for its quantum expectation value, on a real atomic transition*. We will make further use of this quantum equation in later chapters.

Notice that after making this conversion to the quantum case, we now have a situation in which the population difference $\Delta N(t)$ on the right-hand side of the equation may itself be an explicit function of time, as a result of stimulated transitions, pumping effects, and/or relaxation processes, rather than being a constant value N as in the classical case. This makes the quantum equation essentially nonlinear, as contrasted with the essentially linear character of the classical oscillator model.

We will see later that in most cases of interest in lasers, the rate of change of the population difference $\Delta N(t)$ is slow compared to the inverse of the atomic linewidth $\Delta\omega_a$. This represents the so-called *rate-equation limit*, in which we can validly solve the polarization differential equation of motion in a linear fashion, just as we did in this chapter, and thereby obtain the linear resonant sinusoidal susceptibility given above.

There are other situations, however, in which the applied signal becomes strong enough (or the transition linewidth is narrow enough) that we move into a large-signal regime where the time-variation of $\Delta N(t)$ does become important.

In this large-signal regime it is no longer possible to solve Equation 2.69 as a simple linear differential equation; and hence the linear susceptibility $\tilde{\chi}(\omega)$ is no longer an adequate description of the atomic response. We must instead solve the nonlinear polarization equation for $p(t)$, Equation 2.69, together with a separate rate equation for the time variation of $\Delta N(t)$ that we will derive in a later chapter, in order to get the full large-signal atomic behavior. The result in the large-signal limit is a more complex form of behavior, commonly referred to as *Rabi flopping behavior*, which we will describe in more detail in a later chapter.

The polarization equation of motion is thus more general than the sinusoidal susceptibility results, which are valid only within the so-called “rate-equation limits.” Most laser devices in fact operate in the rate-equation regime; but there are also more complex large-signal phenomena, often referred to as “coherent pulse phenomena,” which occur only in the Rabi-frequency regime. Such coherent pulse effects can be demonstrated experimentally using appropriate high-power laser beams and narrow-line atomic transitions.

Additional Substitutions

Let us finally give a brief but complete list of all the other steps that are necessary to convert the classical oscillator results derived in this chapter into the completely correct quantum results for any real electric-dipole atomic transition. Converting the classical oscillator formulas to apply to a real atomic transition requires the following steps.

1. *Transition frequency.* Any single kind of atom will of course have numerous resonant transitions among its large number of quantum energy levels E_i . The classical electron oscillator can model only one such transition between two selected levels, say E_i and $E_j > E_i$, at a time. To treat several different signals applied to different transitions at different frequencies simultaneously, we must in essence employ multiple CEO models, one for each transition. The level populations $N_i(t)$ in the different levels involved are then interconnected by rate equations, as we will discuss in a later section.

The classical resonance frequency ω_a must be replaced by the actual transition frequency ω_{ji} in the real atom, i.e.,

$$\omega_a \Rightarrow \omega_{ji} = \frac{E_j - E_i}{\hbar}. \quad (70)$$

The actual transition wavelength λ , measured in the laser host medium, must of course also be used.

2. *Atomic population difference.* The population difference must be replaced by the population difference on that particular transition, i.e.,

$$\Delta N \Rightarrow \Delta N_{ij} = N_i - N_j, \quad (71)$$

where N_i is the lower-level and N_j the upper-level population density.

3. *Radiative decay rate.* The radiative decay rate γ_{rad} must be replaced by a quantum radiative decay rate appropriate to the specific $i \rightarrow j$ transition under consideration, i.e.,

$$\gamma_{\text{rad}} \Rightarrow \gamma_{\text{rad},ji}. \quad (72)$$

Every real atomic transition between two energy levels E_i and E_j will have such a characteristic spontaneous-emission rate, which is the same thing as the Einstein A coefficient on that transition, i.e., $\gamma_{\text{rad},ji} \equiv A_{ji}$.

4. *Transition linewidth.* The linewidth $\Delta\omega_a$ must be replaced by a linewidth $\Delta\omega_{a,ij}$ characteristic of the real transition in the real atoms, i.e.,

$$\Delta\omega_a \Rightarrow \Delta\omega_{a,ij}. \quad (73)$$

This involves using real-atom values for the linewidth contributions of both the energy decay rate, i.e., γ_{ij} , and the dephasing time $T_{2,ij}$ on that particular transition, as well as any other broadening mechanisms that may be present. We will say more later about what these real-atom values mean and how they are obtained. Note also that different $i \rightarrow j$ transitions in a given atom may have quite different linewidths $\Delta\omega_{a,ij}$.

5. *Transition lineshape.* More generally, the complex lineshape of $\tilde{\chi}_{\text{at}}(\omega)$ for a real atomic transition may not be exactly lorentzian, although many real atomic transitions are. It may be necessary for some transitions to replace the lorentzian frequency dependence with some alternative lineshape or frequency dependence for $\tilde{\chi}(\omega)$. Whatever this lineshape may be, however, the real and imaginary parts $\chi'(\omega)$ and $\chi''(\omega)$ near resonance will almost always have line-shapes much like those in Figure 2.8.

6. *Tensor properties.* We assumed in previous sections a classical oscillator model that was linearly polarized along the x direction. We have thus derived essentially only one tensor component of the linear susceptibility, that is, the component defined by

$$\tilde{P}_x(\omega) = \tilde{\chi}_{xx}(\omega)\epsilon\tilde{E}_x(\omega). \quad (74)$$

The response of a real atomic transition may involve a more complicated and anisotropic (though still linear) response of all three vector components $\mathbf{P}(\omega) = [\tilde{P}_x, \tilde{P}_y, \tilde{P}_z]$ to the vector field components $\mathbf{E}(\omega) = [\tilde{E}_x, \tilde{E}_y, \tilde{E}_z]$. The susceptibility $\tilde{\chi}(\omega)$ must then be replaced by a tensor susceptibility $\chi(\omega)$, i.e.,

$$\tilde{\chi}(\omega) \Rightarrow \chi(\omega). \quad (75)$$

where $\chi(\omega)$ is a 3×3 susceptibility tensor defined by

$$\mathbf{P}(\omega) = \chi(\omega)\epsilon\mathbf{E}(\omega). \quad (76)$$

We discuss the resulting tensor properties of real transitions in more detail later.

7. *Polarization properties.* The magnitude of the response of an atomic transition to an applied signal in the tensor case will also depend on how well the applied field polarization \mathbf{E} lines up or overlaps with the tensor polarization needed for optimum response from the atoms. If the applied field is not properly polarized or oriented with respect to the atoms, the observed response will be reduced. We can account for this by replacing the numerical factor of 3 that appears in the susceptibility expression with a factor we call “three star,” i.e.,

$$\frac{3}{4\pi^2} \Rightarrow \frac{3^*}{4\pi^2}, \quad (77)$$

where the numerical value of this 3^* factor (to be explained in more detail in the following chapter) is $0 \leq 3^* \leq 3$.

8. *Degeneracy effects.* What appears to be a single quantum energy level E_i may be in many real atomic systems some number g_i of *degenerate energy levels*, i.e., separate and quantum-mechanically distinct energy states all with the same or very nearly the same energy eigenvalue E_i . To express the net small-signal response summed over all the distinct but overlapping transitions between these degenerate sublevels, the population-difference term $N_i - N_j$ for systems with degeneracy must be replaced by

$$\Delta N_{ij} = (N_i - N_j) \Rightarrow \Delta N_{ij} = (g_j/g_i) N_i - N_j, \quad (78)$$

where E_i is the lower and E_j the upper group of levels; g_i and g_j are the statistical weights or degeneracy factors of these lower and upper groups of levels; and N_i and N_j are the *total* population densities in the degenerate groups of lower and upper levels.

9. *Inhomogeneous broadening.* Finally, additional line-broadening and line-shifting mechanisms, the so-called “inhomogeneous” broadening mechanisms, will often broaden and change the lineshapes of real atomic resonances, over and above the broadening due to energy decay and dephasing as expressed in the linewidth formula $\Delta\omega_a = \gamma + 2/T_2$. The *homogeneous linewidth* $\Delta\omega_a$ then gets replaced (at least for certain purposes) by an *inhomogeneous linewidth* $\Delta\omega_d$, i.e.,

$$\Delta\omega_a \Rightarrow \Delta\omega_d. \quad (79)$$

When this happens, the lineshape often gets changed also, from lorentzian to something more like gaussian in shape; and the $3^*/4\pi^2$ numerical factor in front of the susceptibility expression may be increased by $\approx 50\%$. What is meant by inhomogeneous broadening, and how these additional broadening mechanisms affect real atomic resonances, is described in the final section of the following chapter.

Further details on all the topics introduced in this section are given in the next chapter. With these conversion factors included, the basic polarization equation of motion and the resulting linear susceptibility formula for a real homogeneously broadened atomic transition become quantum-mechanically and quantitatively correct for real quantum atomic transitions.

REFERENCES

An interesting historical review of early attempts to develop purely classical theories of atomic and molecular absorption of radiation, and of their connections to quantum mechanics, including dipole moments, collision broadening, and sum rules, is given by J. H. Van Vleck and D. L. Huber, “Absorption, emission, and linebreadths: A semihistorical perspective,” *Rev. Mod. Phys.* **49**, 939–959 (October 1977).

Problems for 2.5

1. *Classical oscillator model for the index of refraction in gases.* Can the classical oscillator model be used to explain not only the resonance behavior of atomic

transitions, but also the low-frequency dielectric properties of gases and solids? For example, the *CRC Handbook of Chemistry and Physics* gives the values shown in the following table for the low-frequency relative dielectric constant ϵ/ϵ_0 for some simple gases at 0°C and atmospheric pressure (760 torr), measured from dc through radio and microwave frequencies, as well as the optical index of refraction n measured across the visible region.

Gas	$(\epsilon/\epsilon_0 - 1) \times 10^4$	$(n - 1) \times 10^4$
He	0.6	0.36
Ar	5.1–5.4	2.8
H ₂	2.5	1.3–1.4
CO ₂	9.2	4.5
Air	5.3	2.9

Can these values be explained, at least as to order of magnitude, using a simple CEO model for the atoms involved?

To answer this question, we must realize that in simple gases such as He, the strongest upward electric-dipole transition from the atomic ground state is usually to some first excited level that is located well into the ultraviolet. Such an atom can then be modeled for many purposes by a classical electron oscillator with a resonance frequency ω_a located somewhere in the ultraviolet. The low-frequency dielectric constant, as well as the index of refraction through the visible region, are then both caused primarily by the low-frequency “tail” of this first strong ultraviolet transition, with both of these quantities being only very slightly larger than unity in numerical value.

To demonstrate this analytically, suppose a dc electric field E_0 is applied to a collection of such classical oscillators with the same density N as a standard gas at room temperature and atmospheric pressure (which implies a density $N \approx 2.5 \times 10^{19}$ atoms/cm³). Assume these oscillators have a resonance frequency ω_a corresponding to $\lambda_a = 100$ nm, which is in the vacuum ultraviolet. Using the CEO model, what will be the induced dc polarization P_0/E_0 in this gas? What will be its dc dielectric constant ϵ compared to the value of ϵ_0 for a vacuum, and by how much will its index of refraction $n = \sqrt{\epsilon/\epsilon_0}$ differ from unity? Why does argon have a larger value than helium, and why do the molecular gases also have significantly larger values?

2. *Classical oscillator model for the index of refraction in solids.* Let us now apply the same argument as in Problem 2 to a solid material. The host crystal in a typical solid-state laser material, for example, itself consists of atoms, and these atoms (in the crystalline form) usually have their lowest atomic resonance frequency in the near ultraviolet. Can the CEO model also give a reasonable explanation of the dielectric polarization properties of the host laser material itself, independent of any laser atoms that may be present in the material?

To test this, evaluate the dielectric polarization P and the relative dielectric constant $\epsilon_{\text{host}}/\epsilon_0$ at visible and near-infrared wavelengths for a medium consisting of a collection of classical oscillators, if the classical oscillators have a resonance

frequency ω_a in the near ultraviolet, say, at $\lambda = 300$ nm (which is not an unrealistic value for the band edge or ultraviolet edge in typical solid materials). Find the numerical value of this relative dielectric constant, assuming the oscillators have a density N comparable to typical solid densities, e.g., 10^{22} atoms/cm³.

3

ELECTRIC-DIPOLE TRANSITIONS IN REAL ATOMS

In the previous chapter we developed the classical electron oscillator model for an atomic transition, and showed how it could lead to quantum-mechanically correct expressions for the equation of motion and for the resonant susceptibility on a single atomic transition in a real quantum atom. In this chapter we continue this discussion to show how, with some simple extensions, this same purely classical model can explain even the most complex quantum-mechanical aspects of real atomic transitions. We also give some typical numerical values and experimental examples of these properties in real laser transitions.

3.1 DECAY RATES AND TRANSITION STRENGTHS IN REAL ATOMS

This section discusses in more detail the energy decay rates and the transition strengths of real atomic transitions, and their relationship to the purely classical oscillator model introduced in Chapter 2.

Energy Decay Processes in Real Atoms

Real atoms of course have a large number of quantum energy levels, with many transitions and decay rates among these levels. The atoms in an upper energy level E_j in a collection of real atoms will relax to many different lower levels E_i via both radiative and nonradiative decay mechanisms, as illustrated in Figure 3.1. The total rate at which atoms will decay from an upper energy level E_j through all downward relaxation paths may be expressed by a “rate equation” of the form

$$\frac{dN_j}{dt} = - \sum_{E_i < E_j} \gamma_{ji} N_j = -\gamma_j N_j = -N_j / \tau_j, \quad (1)$$

where τ_j is the total lifetime of the excited state E_j , and γ_j is its total decay rate. The total decay rate γ_j is given by the sum over all the downward decay

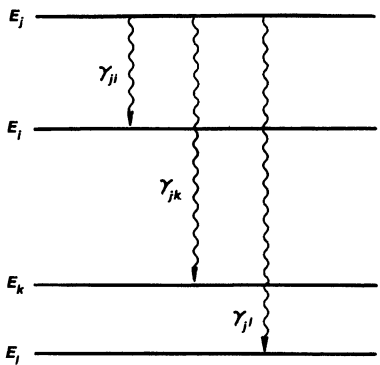


FIGURE 3.1
Downward relaxation of atoms from an upper energy level.

paths, i.e.,

$$\gamma_j \equiv \frac{1}{\tau_j} = \sum_{E_i < E_j} \gamma_{ji} = \sum_{E_i < E_j} [\gamma_{\text{rad},ji} + \gamma_{\text{nr},ji}], \quad (2)$$

so that this sum includes both radiative and nonradiative rates to all lower levels $E_i < E_j$.

In the absence of any applied signals, the population $N_j(t)$ of the upper level will thus decay with time in the exponential form

$$N_j(t) = N_j(t_0) e^{-\gamma_j(t-t_0)} = N_j(t_0) e^{-(t-t_0)/\tau_j}. \quad (3)$$

The decay rate γ_j given by these equations is the quantum analog for level E_j of the energy decay rate γ in the classical oscillator model.

Fluorescent Lifetime Measurements

The lifetime τ_j of an upper energy level can be measured by observing the fluorescent emission from the upper level E_j to any other lower level E_i immediately after a short pulse of pumping light applied to a solid-state laser material, or a short current pulse sent through a gaseous atomic system, has lifted an initial number of atoms up into the upper level. Figure 3.2 illustrates this kind of fluorescent lifetime measurement on a ruby sample, using a stroboscopic light source that produces repeated pumping pulses a few tens of μs long, and an optical filter that blocks most of the excitation light, so that only the exponentially decaying ruby fluorescence ($\tau \approx 4.3 \text{ ms}$) reaches the detector.

The measured intensity of the fluorescent emission on some specific $j \rightarrow i$ transition will be proportional to the radiative decay rate $\gamma_{\text{rad},ji}$ on that transition and to the upper-level population as a function of time, i.e.,

$$I_{\text{fl}}(t) = \text{const} \times \gamma_{\text{rad},ji} N_j(t). \quad (4)$$

Since the upper-level population $N_j(t)$ decays with an exponential decay rate equal to the total decay rate γ_j , the measured exponential behavior for the fluorescent emission will be like

$$I_{\text{fl}}(t) = \text{const} \times N_j(t) = \text{const} \times e^{-t/\tau_j}. \quad (5)$$

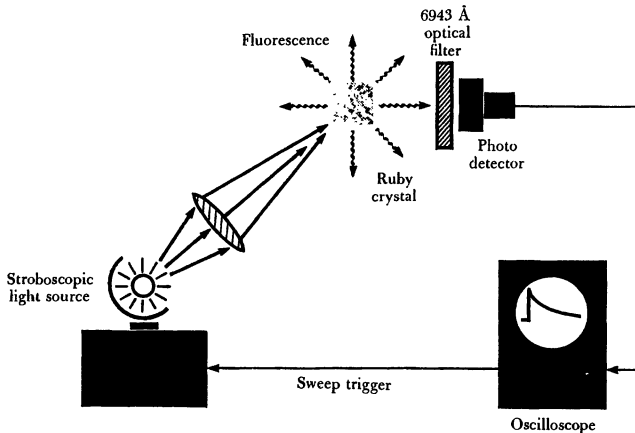


FIGURE 3.2

Fluorescent lifetime measurement using a pulsed light source.

A fluorescence decay measurement thus measures only the *total lifetime* τ_j of the upper level E_j , not the radiative decay rate $\gamma_{\text{rad},ji}$ on any individual transition (even though it is this radiative decay rate that produces the observed fluorescent emission).

Nonradiative Decay Rates

It is important to distinguish between the radiative and the nonradiative parts of the total energy decay rate γ_{ji} on each downward transition. The total decay rate, just as for a classical oscillator, is the sum of both mechanisms; so the total decay rate on the $j \rightarrow i$ transition is

$$\gamma_{ji} = \gamma_{\text{rad},ji} + \gamma_{\text{nr},ji}. \quad (6)$$

The radiative part of this decay represents spontaneous emission of electromagnetic radiation, which is physically the same thing as fluorescence. Radiative decay is always present (although sometimes very weak) on any real atomic transition.

The nonradiative part of the decay represents loss of energy from the atomic oscillations into heating up the immediate surroundings in all other possible ways, such as into inelastic collisions, collisions with the laser tube walls, lattice vibrations, and so forth. Nonradiative decay may or may not be significant on any specific transition, and its magnitude may change greatly for different local surroundings of the atoms (e.g., the nonradiative decay rate can be quite different for the same solid-state laser ion in different host lattices).

Purely Radiative Decay in Real Atoms

The radiative part of the total decay rate on a real atomic transition has a very close analogy to the radiative decay rate of a classical oscillator. An oscillating atom, like an oscillating classical dipole, will radiate electromagnetic

energy (photons) at its discrete oscillation frequencies; this radiation will decrease or decay with time; and many real atomic transitions will radiate with an electric-dipole-like radiation pattern.

The radiative decay rate for a real atomic transition is exactly the same thing as the *Einstein A* coefficient for that transition, i.e. $\gamma_{\text{rad},ji} \equiv A_{ji}$, where E_j is the upper and E_i the lower energy level involved. The numerical value of A_{ji} or $\gamma_{\text{rad},ji}$ on any real atomic transition is given by the quantum-mechanical integral

$$A_{ji} = \frac{8\pi^2}{e\hbar\lambda^3} \left| \iiint \psi_j^*(\mathbf{r}) e\mathbf{r} \psi_i(\mathbf{r}) d\mathbf{r} \right|^2, \quad (7)$$

which involves the dipole moment operator $e\mathbf{r}$ and the product of the quantum wave functions of the two quantum states involved. Hence the quantum radiative decay rate for a real atomic transition can in principle always be calculated (though not always easily) if the quantum wave functions ψ_i and ψ_j of the two levels are known. Calculated values for simpler atoms and molecules can also be found in handbooks and in the literature.

We pointed out earlier that the classical electron oscillator has a radiative decay rate given by

$$\gamma_{\text{rad,ceo}} = \frac{e^2 \omega_a^2}{6\pi\epsilon mc^3} \approx 2.47 \times 10^{-22} \times n f_a^2, \quad (8)$$

where n is the index of refraction of the medium in which the oscillator is imbedded, and the oscillation frequency is measured in Hz (\equiv cycles/second). A useful rule of thumb is that the purely radiative lifetime for a classical oscillator is approximately given by

$$\tau_{\text{rad,ceo}}(\text{ns}) \approx \frac{45 \times [\lambda_0(\text{microns})]^2}{n}, \quad (9)$$

where n is again the index of refraction and λ_0 is the free-space wavelength in μm . (These two equations are among the few formulas in this book where an index of refraction term is explicitly needed.) For example, at the visible wavelength $\lambda_0 = 500 \text{ nm}$ or $0.5 \mu\text{m}$, the classical oscillator lifetime is $\tau_{\text{rad,ceo}} \approx 11 \text{ ns}$, or $\gamma_{\text{rad,ceo}} \approx 10^8 \text{ sec}^{-1}$. Note also the wavelength-squared dependence of this lifetime: infrared oscillators will have substantially longer lifetimes than UV or especially X-ray oscillators.

Oscillator Strength

It is then a general rule that the radiative decay rate for any real atomic or molecular transition will always be slower than, or at best comparable to, the radiative decay rate for a classical oscillator at the same frequency, so that $\gamma_{\text{rad},ji} \leq \gamma_{\text{rad,ceo}}$, or $\tau_{\text{rad},ji} \geq \tau_{\text{rad,ceo}}$. We can also recall that the induced response to an applied signal of either a real atomic transition or a classical electron oscillator will be directly proportional to the radiative decay rate γ_{rad} , with essentially the same proportionality constant in each case.

Because of this, it has become conventional to define a dimensionless *oscillator strength* as a measure of the strength of the response on a real atomic transition relative to the response of a classical electron oscillator at the same frequency.

This oscillator strength is defined formally for a transition from level j down to level i by

$$\mathcal{F}_{ji} \equiv \frac{\gamma_{\text{rad},ji}}{3\gamma_{\text{rad,ceo}}} = \frac{\tau_{\text{rad,ceo}}}{3\tau_{\text{rad},ji}}. \quad (10)$$

A factor of 3 appears in this definition because of the polarization properties of real atoms compared to classical oscillators, in a fashion which will emerge later.

TABLE 3.1
Typical Radiative Decay Rates

Transition	Wavelength	Radiative decay rate	Oscillator strength	Comments
<i>Atomic sodium resonance lines:</i>				
$3s \rightarrow 3p$	589 nm	$6.3 \times 10^7 \text{ s}^{-1}$ (1.6 ns)	0.33	Strong sodium D line
$3s \rightarrow 4p$	330 nm	$2.9 \times 10^6 \text{ s}^{-1}$ (350 ns)	0.0047	Weaker UV transition
<i>He-Ne laser transitions:</i>				
$3s_2 \rightarrow 2p_4$	633 nm	$1.4 \times 10^6 \text{ s}^{-1}$ (0.7 μs)	0.0084	Red laser line
$2s_2 \rightarrow 2p_4$	$1.153 \mu\text{m}$	$4.4 \times 10^6 \text{ s}^{-1}$ (0.23 μs)	0.09	Near IR laser
$3s_2 \rightarrow 3p_4$	$3.392 \mu\text{m}$	$9.6 \times 10^5 \text{ s}^{-1}$ (1.04 μs)	0.17	Middle IR laser
<i>Selenium quasi forbidden laser lines:</i>				
$^1S_0 \rightarrow ^3P_1$	489 nm	7.7 s^{-1} (130 ms)	3×10^{-8}	Magnetic-dipole transition
$^1S_0 \rightarrow ^1D_2$	777 nm	2.3 s^{-1} (430 ms)	2×10^{-9}	Electric-quadrupole
<i>Neodymium YAG laser transition:</i>				
$^4F_{3/2} \rightarrow ^4I_{3/2}$	$1.064 \mu\text{m}$	820 s^{-1} (1.22 ms)	$\approx 8 \times 10^{-6}$	Measured τ_2 is 230 μs
<i>Ruby laser transition:</i>				
$^2E \rightarrow ^4A_2$	694 nm	230 s^{-1} (4.3 ms)	$\approx 10^{-6}$	Decay is almost purely radiative
<i>Rhodamine 6G dye laser transition:</i>				
$S_1 \rightarrow S_0$	620 nm	$3 \times 10^8 \text{ s}^{-1}$ (3.3 ns)	≈ 1.1	Decay is almost purely radiative

Some typical oscillator strengths for real atomic transitions are given in Table 3.1. Note that strongly allowed transitions starting from the ground level of a simple atom in a gas to the first excited level of opposite parity—for example, the $3s \rightarrow 3p$ transition in Na, or the $2s \rightarrow 2p$ transition in a Li atom—have oscillator strengths very close to unity, and hence radiative decay rates close to the classical oscillator values. These transitions are sometimes called the resonance *lines* of the atoms, since they show up very strongly in both the spontaneous emission and the absorption spectra of these atoms. Other allowed electric-dipole transitions in the same atoms may be from 10^{-2} to 10^{-5} times weaker, and magnetic-dipole and electric-quadrupole transitions may have oscillator strengths of $\mathcal{F} \approx 10^{-7}$ or smaller. Laser transitions in solids or in gaseous molecules typically have similarly weak oscillator strengths, whereas the strong visible singlet-to-singlet transitions in organic dye molecules, such as the Rhodamine 6G dye laser molecule, may have oscillator strengths near unity, and hence radiative decay rates close to the classical oscillator value (e.g., radiative decay times of several nanoseconds).

A strongly allowed atomic transition with oscillator strength of the order of unity will thus have a stimulated response to an applied signal of the same magnitude as a classical electron oscillator at the same frequency. Very weakly allowed atomic transitions, on the other hand, may have an oscillator strength or response ratio as small as $\mathcal{F} \approx 10^{-6}$ to 10^{-7} times weaker. So-called “forbidden transitions,” or atomic transitions on which virtually no response can be obtained, will have $\gamma_{\text{rad},ji} \ll \gamma_{\text{rad,ceo}}$ and hence $\mathcal{F}_{ji} \rightarrow 0$ in principle, although in fact the decay rate is never absolutely zero.

Sum Rules, and Oscillator Strengths for Degenerate Transitions

When the upper and lower energy levels are degenerate, with degeneracy factors g_j and g_i (to be explained in a later section), the upward and downward oscillator strengths for a given transition are usually defined more precisely by

$$\mathcal{F}_{ji}|_{\text{down}} = -\frac{\gamma_{\text{rad},ji}}{3\gamma_{\text{rad,ceo}}} \quad \text{and} \quad \mathcal{F}_{ij}|_{\text{up}} = +\frac{g_j}{g_i} \frac{\gamma_{\text{rad},ji}}{3\gamma_{\text{rad,ceo}}}. \quad (11)$$

With these more precise definitions also go *quantum-mechanical sum rules*, which say that the numerical sum of the oscillator strengths $\sum_{j \neq i} \mathcal{F}_{ji}$ (including sign) from a given level E_j to all other levels above and below it in the same atom has some simple value, which is usually close to unity.

Example: The Nd:YAG Laser Transition

The $1.06 \mu\text{m}$ transition in the Nd:YAG laser is not only of great practical importance, but can provide a good illustration of many of the practical factors that determine the radiative decay rate and the oscillator strength for a real atomic transition.

The solid arrow in Figure 3.3 shows the strong laser transition at $\lambda_0 = 1.0642 \mu\text{m}$ on the $^4F_{3/2}$ to $^4I_{11/2}$ group of transitions in Nd:YAG. (The dashed lines on the left in this figure indicate other transitions near $1.35 \mu\text{m}$ and 880 nm on which useful laser oscillation can also be obtained; the transitions from the $^4F_{3/2}$ to $^4I_{15/2}$ levels, with wavelengths near $1.8 \mu\text{m}$, are very weak and oscillate only with difficulty if at all.)

The measured fluorescent lifetime of the $^4F_{3/2}$ upper energy level (call this level E_2) in this material is $\tau_2 \approx 230 \mu\text{s}$; so the total decay rate for this compound

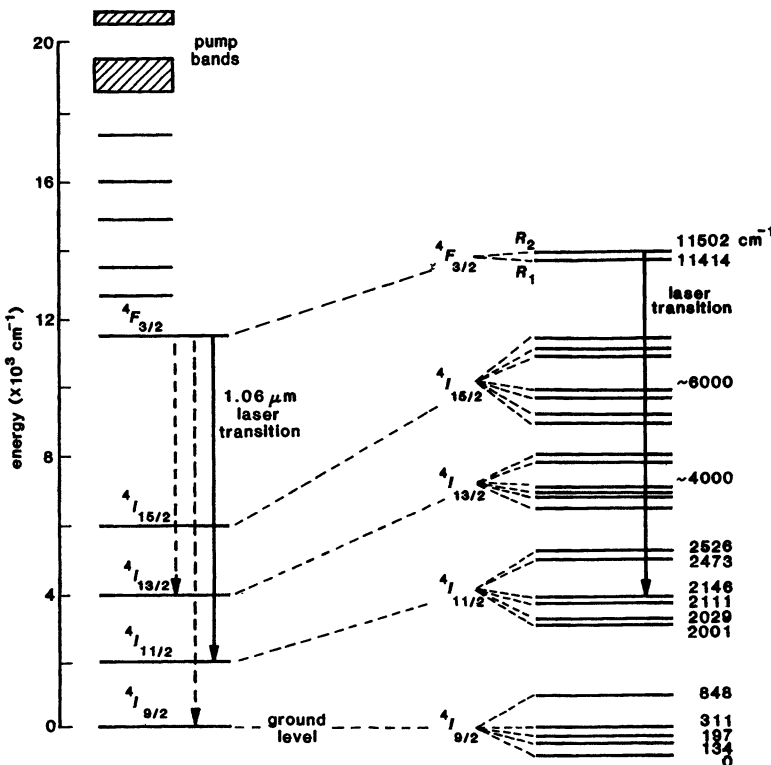


FIGURE 3.3
Quantum-mechanical energy levels of the Nd^{3+} ion in a Nd:YAG laser crystal.

level or group of levels is $\gamma_2 = \gamma_{\text{rad}} + \gamma_{\text{nr}} \approx 4350 \text{ s}^{-1}$. The measured quantum efficiency for this level, however, defined as the ratio of radiative decay (photons emitted) to total decay (i.e., total atoms relaxing down) turns out to have an experimental value

$$\frac{\text{radiative decay rate}}{\text{total decay rate}} = \frac{\gamma_{\text{rad}}}{\gamma_{\text{rad}} + \gamma_{\text{nr}}} \approx 0.56; \quad (12)$$

so the purely radiative decay rate is $\gamma_{\text{rad}} \approx 0.56 \times 4350 \approx 2435 \text{ s}^{-1}$. (The quantum efficiency is measured by shining a calibrated light source onto the crystal, and making a difficult measurement of the total number of input photons absorbed compared to total fluorescent photons emitted.)

The upper level E_2 in Nd:YAG really consists, however, of two distinct but closely spaced and partially overlapping levels (call them E_{2a} and E_{2b}), which are sometimes called the R_1 and R_2 levels, and which have an energy spacing of $\approx 80 \text{ cm}^{-1}$. The upper level E_{2b} is the actual upper laser level. These two levels at room temperature will have Boltzmann population ratios $N_{2b}/N_2 \approx 0.4$ and $N_{2a}/N_2 \approx 0.6$, and will be held to these ratios by fast relaxation processes between the two levels. Both of these levels will then radiate spontaneously with different strengths to six different lower levels; so there are actually 12 closely

spaced fluorescent lines from the two upper levels to the six lower levels in the 1.06 μm group, with the relative strengths of these lines varying by more than an order of magnitude.

The branching ratio, or the amount of spontaneous radiation on the actual 1.0642 μm laser transition, relative to the total radiative emission from both $^4F_{3/2}$ levels to all lower levels, has been measured to be

$$\frac{\gamma_{\text{rad}}(1.0642 \mu\text{m} \text{ laser line}) \times N_{2b}}{\gamma_{\text{rad}}(\text{all } 1.06 \mu\text{m lines}) \times N_2} \approx 0.135. \quad (13)$$

Hence we can finally deduce that the purely radiative decay rate for the isolated YAG laser transition by itself is

$$\gamma_{\text{rad}}(1.0642 \mu\text{m}) \approx (0.135/0.40) \times 2.435 \times 10^3 \approx 820 \text{ sec}^{-1}. \quad (14)$$

This corresponds to a purely radiative lifetime of $1/820 \text{ sec} \approx 1.22 \text{ ms}$ (to be compared to the measured fluorescent lifetime of 230 μs).

The numbers quoted here represent a current best estimate, at the time of writing, for the value of $\gamma_{\text{rad},ji}$ that should be used in formulas for the response on this particular Nd:YAG laser transition. However, even in a system as heavily studied as Nd:YAG, these numbers are uncertain, largely because of the experimental difficulties of measuring accurately such quantities as the branching ratio and the absolute fluorescent quantum efficiency. There is no observable physical quantity anywhere in this system that actually decays with this radiative lifetime of 1.22 ms.

REFERENCES

The concept of an effective oscillator strength for each real atomic transition traces back at least to R. Ladenburg in *Zeitschrift für Physik* 4, 451 (1921). For early but still interesting reviews of this subject, see S. A. Korff and G. Breit, "Optical dispersion," *Rev. Mod. Phys.* 4, 471–502 (July 1932); or R. Ladenburg, "Dispersion in electrically excited gases," *Rev. Mod. Phys.* 5, 243–256 (October 1933).

Calculations of oscillator strengths or decay rates for real atomic transitions in real environments are very complex. You may have to search a wide variety of scientific literature to find whatever numbers are available for any specific laser system. In practice, these rates are either measured or simply estimated. Tabulations of oscillator strengths and radiative decay rates for individual transitions in isolated atoms (at least the simpler ones) are published in such references as the National Bureau of Standards' volumes on *Atomic Transition Probabilities, Volume I: Hydrogen Through Neon*, by W. L. Wiese, M. W. Smith, and B. M. Glennon, and *Volume II: Sodium Through Calcium*, by Wiese, Smith, and B. M. Miles, available from the U. S. Government Printing Office.

Atomic transitions in isolated atoms are also of great interest to plasma physicists and astrophysicists, and the literature in these fields includes many useful references. Two outstanding examples are H. R. Griem, *Plasma Spectroscopy* (McGraw-Hill, 1964); and the extensive compilation of formulas and data in C. W. Allen, *Astrophysical Quantities* (London: Athlone Press, 1973).

A good example of how oscillator strengths and transition probabilities are calculated for a rare-earth ion in various crystals is M. J. Weber *et al.*, "Optical transition probabilities for trivalent holmium in LaF_3 and YAlO_3 ," *J. Chem. Phys.* 57, 11–16

(July 1, 1972). The oscillator strengths for the various transitions of this ion all turn out to have values of 10^{-6} to 10^{-7} , typical of such rare-earth ions.

As we said, the numbers given in the literature for the basic properties of the Nd:YAG laser transition are by no means all in agreement, despite the widespread use of this laser material. The most extensive and detailed review of all aspects of the Nd:YAG laser is probably the chapter on "Progress in Nd:YAG Lasers" by H. G. Danielmeyer in Vol. 4 of *Lasers: A Series of Advances*, edited by A. K. Levine and A. J. DeMaria (Marcel Dekker; 1976), pp. 1–71. The numbers given in this section come primarily from the careful measurements and analysis by S. Singh, R. G. Smith, and L. G. Van Uitert, "Stimulated-emission cross section and fluorescent quantum efficiency of Nd^{3+} in yttrium aluminum garnet at room temperature," *Phys. Rev. B* **10**, 2566–2572 (September 15, 1974).

As if to illustrate the difficulty of accurate optical measurements, a more recent publication by M. Birnbaum, A. W. Tucker, and C. L. Fincher, "Laser emission cross section of Nd:YAG at 1064 nm," *J. Appl. Phys.* **52**, 1212–1215 (March 1981), argues that the stimulated transition cross section and the quantum efficiency for Nd:YAG are both about twice the values previously given by Singh *et al.*

Problems for 3.1

1. *Quantum calculation: Hydrogen-atom oscillator strengths.* The energy eigenstates for the hydrogen atom, and the formula for calculating the transition strength or the Einstein A coefficient of a transition given the upper and lower quantum wave functions, can be found in any standard quantum-theory text. Using these, calculate the oscillator strengths for the three allowed transitions from the $n = 1$, $l = 0$, $m = 0$ ground state of the hydrogen atom to the $n = 2$, $l = 1$, $m = -1$, 0, and +1 levels (taken together, these transitions form the 1216 Å Lyman α transition). Note: This calculation is straightforward, but becomes a bit messy.
-

3.2 LINE-BROADENING MECHANISMS IN REAL ATOMS

Let us now consider a few of the more important line-broadening mechanisms responsible for the atomic linewidths $\Delta\omega_a$ in real atoms. All of these mechanisms are, as we will see, basically extensions of those derived for the classical electron oscillator. In this section we give more information on homogeneous line-broadening mechanisms in real atoms, and on how these relate to the CEO model.

Homogeneous Broadening

All the line-broadening mechanisms we have considered thus far produce what is called *homogeneous broadening*. This means simply that all the energy-decay and dephasing mechanisms we have discussed thus far act on all the dipoles in a collection in the same way, so that the response of each individual oscillator or atom in the collection is broadened in the same fashion. The homogeneous lorentzian linewidth (FWHM) that we derived for the stimulated response of a

collection of classical oscillators is then

$$\Delta\omega_a = \gamma + 2/T_2, \quad (15)$$

where γ is the energy decay rate and $1/T_2$ the rate at which “dephasing events” occur, whatever may be the cause of these dephasing events. There do exist additional and basically different types of broadening effects called *inhomogeneous broadening effects*, which we will introduce in the last section of this chapter. Doppler broadening is one primary example of such an inhomogeneous broadening mechanism.

Lifetime Broadening in Real Atomic Transitions

That part of the homogeneous linewidth $\Delta\omega_a$ caused by the total energy decay rate $\gamma \equiv \gamma_{\text{rad}} + \gamma_{\text{nr}}$ is called *lifetime broadening*. Lifetime broadening is basically a Fourier-transform effect. An exponentially decaying signal of the form $\mathcal{E}(t) = \exp[-(\gamma/2 + j\omega_a)t]$ for $t > 0$ has a complex lorentzian Fourier transform of the form $\bar{\mathcal{E}}(\omega) = 1/[1 + 2j(\omega - \omega_a)/\gamma]$, which has a FWHM linewidth $\Delta\omega_a = \gamma$.

If dephasing effects are absent, only this lifetime broadening will remain. If in addition all nonradiative mechanisms are turned off, then only radiative decay will be left, and the linewidth will take on its minimum possible value $\Delta\omega_a = \gamma_{\text{rad}}$. This is called *purely radiative lifetime broadening*. This purely radiatively broadened condition may sometimes occur for real atoms in very low-pressure gases, where the atoms are highly isolated, and where no collisions or nonradiative effects can occur (although doppler broadening, to be discussed later, will also be present and of great importance in such a gas).

In a collection of real atoms, the transition at frequency ω_{ji} between two energy levels E_j and E_i with total decay rates γ_j and γ_i , respectively, will generally have a lifetime-broadening contribution that is given in a more exact analysis by

$$\Delta\omega_a = \gamma_i + \gamma_j + 2/T_{2,ij}, \quad (16)$$

where $2/T_{2,ij}$ is the dephasing rate appropriate to that particular transition. The main point here is that in most cases the γ term in the classical oscillator linewidth is replaced by the sum of the upper-state and lower-state energy decay rates $\gamma_i + \gamma_j$, so far as lifetime-broadening effects are concerned.

We have noted previously that energy decay rates γ_j for real atomic transitions take on widely different values, depending on both radiative and nonradiative processes. For strong visible-wavelength atomic transitions in gases, γ_{rad} may become as large as $\approx 10^7$ to 10^8 s⁻¹, leading to a lifetime-broadening contribution $\Delta\omega_a/2\pi$ ranging from a few MHz to a few tens of MHz. This can be a significant source of homogeneous line broadening for a transition in a low-pressure gas.

For the Nd:YAG laser on the other hand, the upper-level energy decay time is $\tau_j \approx 230 \mu\text{s}$. This gives a lifetime-broadening contribution of only 700 Hz, which is absolutely insignificant compared to the enormously larger phonon-broadening dephasing contribution of $\Delta\omega_a/2\pi \approx 120$ GHz.

Dephasing Collisions and Pressure Broadening in Gases

The primary dephasing events for atoms or molecules in gases are real collisions between the radiating atoms or molecules and various collision partners. In

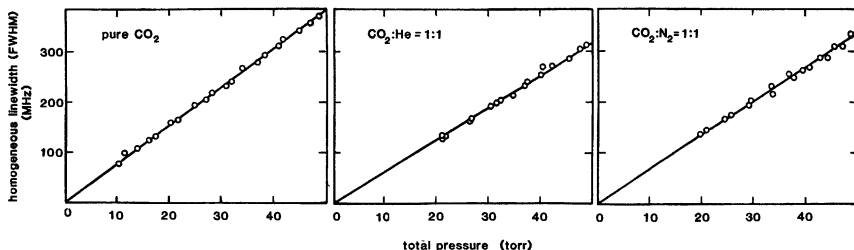


FIGURE 3.4
Pressure broadening of the CO_2 laser transition in various gas mixtures. (Adapted from R. L. Abrams, *Appl. Phys. Lett.* **25**, 609–611, November 15, 1974.)

a typical gas mixture atoms may collide with other atoms of the same kind (called “self-broadening”); with atoms of different kinds (called “foreign-gas broadening”); or with the tube walls (generally not of importance at optical frequencies). The total collision-broadening contribution to the homogeneous linewidth of a given atomic transition will then be directly proportional to the density, or to the partial pressure, of each species that is present. The homogeneous linewidth will therefore increase linearly with total gas pressure (assuming a constant gas mixture) in the general form

$$\Delta\omega_a = A + BP, \quad (17)$$

where A and B are constants that are different for different atomic transitions and gas mixtures. This behavior is naturally referred to as *pressure broadening*, and Equation 3.17 is sometimes referred to as the *Stern-Vollmer equation*. (The coefficients A and B used here have nothing at all to do with the Einstein A and B coefficients).

Figure 3.4 illustrates some measured homogeneous pressure-broadening results for the $10.6 \mu\text{m}$ laser transition in CO_2 caused by CO_2 molecules colliding with other CO_2 molecules and also with He atoms or N_2 molecules in various gas mixtures. Note that here (as in many other common gases) a few tens of torr of total pressure gives a few hundreds of MHz of pressure broadening. Note also that the lifetime-broadening contribution in these mixtures is apparently negligible, as indicated by the essentially zero intercept of the pressure-broadening curves at zero pressure.

Typical Numerical Values

The amount of dephasing and line broadening that actually occurs in a real collision between two atoms (or molecules, or ions) depends on how close the two partners come to each other; how their quantum wave functions overlap and interact with each other during the collision; and (to a slight extent) how fast the atoms are traveling. The atomic wave functions that are involved are, of course, different for different energy states E_i or E_j of the colliding partners. Therefore the amount of pressure broadening, or the constant factor B in the

Stern-Vollmer formula, can often be different for different transitions even in the same atom.

TABLE 3.2
Typical pressure-broadening coefficients

Wavelength	Collision partners	Pressure broadening
<i>Mercury resonance line:</i>		
2537 Å	Hg + Ar, N ₂ , CO ₂	10–20 MHz/torr
<i>Sodium resonance line:</i>		
589 nm	Na + Na	≈ 2000 MHz/torr
<i>He-Ne laser transitions:</i>		
633 nm	He+Ne	≈ 70 MHz/torr
3.39 μm	He+Ne	50–80 MHz/torr
<i>CO₂ laser transition:</i>		
10.6 μm	CO ₂ + CO ₂	7.6 MHz/torr (5.8 GHz/atm)
10.6 μm	CO ₂ + N ₂	5.5 MHz/torr (4.2 GHz/atm)
10.6 μm	CO ₂ + He	4.5 MHz/torr (3.5 GHz/atm)
10.6 μm	CO ₂ + H ₂ O	2.9 MHz/torr (2.2 GHz/atm)

Pressure-broadening coefficients are often expressed in practice in units of MHz/torr or, in some cases, GHz/atmosphere, as in Table 3.2. Collision-broadening coefficients are also sometimes given in the literature as frequency broadening (in various units) versus gas density N rather than gas pressure P . It is then convenient to remember that

$$N(\text{atoms/cm}^3) = 9.65 \times 10^{18} \frac{P(\text{torr})}{T(K)} \quad (18)$$

for the relation between partial pressure and density of each species in a gas mixture.

The results for the CO₂ laser transition in Table 3.2 and in Figure 3.4 also illustrate how the pressure-broadening coefficient, or the effective cross section of a gas molecule for dephasing collisions, can be different for different collision partners. In a typical He:N₂:CO₂ laser gas mixture, the total pressure broadening

of the 10.6 micron CO_2 laser transition must be written as an expression like

$$\Delta\omega_a(\text{CO}_2) = A + B_{\text{He}}P_{\text{He}} + B_{\text{N}_2}P_{\text{N}_2} + B_{\text{CO}_2}P_{\text{CO}_2}, \quad (19)$$

where each P_x is the partial pressure of a different gas, and the pressure-broadening coefficients B_x have different values for each different collision partner.

Nonlorentzian Lineshapes in Collision Broadening.

It can be shown from various statistical arguments that dephasing collisions that have zero duration and that completely randomize the oscillation phases after each collision should in theory produce an exponential polarization decay, and hence an associated exact lorentzian lineshape. It can also be shown that zero-duration collisions that shift the oscillation phases by very small but randomly distributed amounts ($\delta\phi \ll 2\pi$ after each collision) should also produce a lorentzian lineshape. Collisions that last for a short but finite duration, however, may lead to small but observable deviations from the ideal lorentzian lineshape.

The simplest form of extended theory for finite-duration collisions predicts a modified lorentzian lineshape, in which the linewidth $\Delta\omega_a$ itself becomes frequency-dependent, with a midband value $\Delta\omega_{a0}$ plus an added term of the form $-C \times (\omega - \omega_a)$ at frequencies away from line center. Hence the lineshape deviates increasingly from an exact lorentzian with increasing detuning from line center, with this deviation becoming most observable in the outer wings of the atomic line, many linewidths from line center.

Clearcut measurements of this small deviation in the wings of the sodium D_1 and D_2 lines at ≈ 589 nm, caused by collisions with He, Ne, Ar, Kr, and Xe atoms, have recently been made by observing the scattering of a tunable single-frequency laser beam from a sodium cell. Results in good agreement with an extended theory are reported by R. E. Walkup, A. Spielfiedel, and D. E. Pritchard, "Observation of non-lorentzian spectral lineshapes in Na-noble-gas systems," *Phys. Rev. Lett.* **45**, 986-989 (September 22, 1980).

Phonon Broadening (FM Broadening) of Real Atoms in Solids

Another kind of homogeneous line broadening that is important for many solid-state laser transitions is *phonon broadening*. Phonon broadening refers to a rapid and random frequency modulation of the instantaneous atomic-transition frequency for an atom in a solid (or liquid) caused by high-frequency lattice vibrations in the surrounding crystal lattice. This process is physically quite different from a discrete collision-type process having a mean time T_2 between collisions, but the net result in terms of randomizing the phases and broadening the response of a collection of oscillators is very much the same, and can in fact be described by an effective dephasing time T_2 .

Phonon broadening does not depend directly on atomic density N as does pressure broadening. It does, however, depend strongly on lattice temperature,

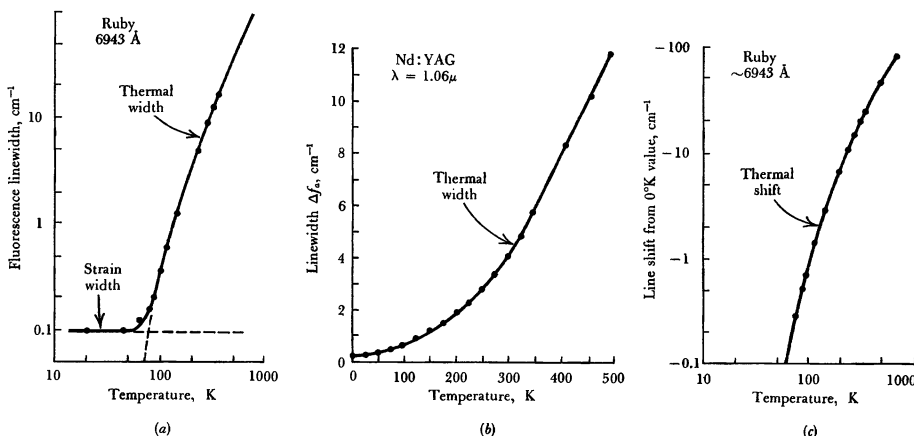


FIGURE 3.5
Phonon broadening and resonance frequency shifting versus temperature in two solid-state laser materials. (From D. E. McCumber and M. D. Sturge, *J. Appl. Phys.* **34**, 1682, June 1963.)

since the lattice vibrations result from thermal excitation of the lattice modes. Figure 3.5 shows, for example, the linewidths of two common solid-state laser transitions plotted versus temperature. The 694 nm laser transition in ruby shows a residual inhomogeneous strain broadening at lower temperature, changing over to thermal FM or phonon broadening at higher temperatures, whereas the linewidth of the 1.06 μm laser transition in Nd:YAG shows strongly temperature-dependent thermal phonon broadening over essentially the entire range plotted.

The phonon-broadening contribution will become very small for temperatures below a few tens of degrees Kelvin. There may then be a residual linewidth contribution of inhomogeneous type, which arises from residual static strains and imperfections in the solid-state material. This residual strain broadening may be quite different from sample to sample, depending on the perfection of individual crystal samples.

Note also that besides phonon broadening in these solids, there may also be a significant *thermal shift* of the exact center frequencies of the transitions, which can sometimes be useful (and sometimes not so useful).

Dipolar Broadening

A third important mechanism that produces homogeneous dephasing and line broadening in certain materials at higher densities is *dipolar broadening*. Dipolar broadening results from the random interaction and coupling between nearby atoms through their overlapping dipolar electric or magnetic fields (Figure 3.6). The random perturbation of each dipole oscillator by the random fields from its neighbors can cause a time-varying frequency shift in the exact resonance frequency of each such dipole; and this in turn leads to an effective dephasing and line broadening in a fashion somewhat similar to phonon broadening.

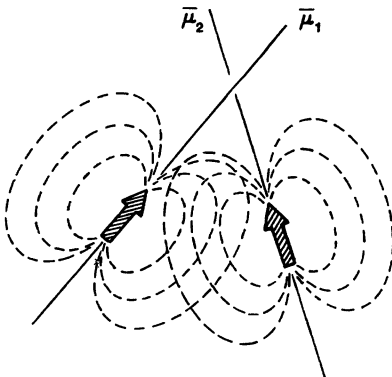


FIGURE 3.6
Dipole-dipole coupling between two nearby electric or magnetic dipoles.

Dipolar broadening is not commonly of great importance in laser materials, since they do not usually have the combination of high atomic density and strong atomic dipoles needed to make dipolar broadening predominate over the collision or thermal phonon-broadening mechanisms. However, dipolar broadening can be observed, for example, in rare-earth pentaphosphates and certain other solid-state materials that can have a high intrinsic density of rare-earth atoms, and that are sometimes used for miniature optically pumped solid-state lasers. If these materials are carefully prepared and cooled to liquid-helium temperatures, where thermal phonon broadening becomes negligible, dipolar-broadened linewidths of a few kHz can be observed by various sophisticated experiments.

Transit-Time Broadening

There can be some experiments in which the atoms in a gas move across the full width of the optical beam with which they are interacting in a transit time T_{tr} , which is small compared with either the energy decay lifetime $\tau = 1/\gamma$ or the dephasing time T_2 of the atoms. In such a situation, it is this transit time which limits the duration of the coherent interaction between the atoms and the applied signals, and which thus determines a kind of effective lifetime broadening. This is generally referred to as *transit-time broadening*, with an effective linewidth contribution on the order of $\Delta\omega_a \approx 1/T_{tr}$.

Since the thermal velocity of an atom or molecule in a gas is typically on the order of $\approx 10^5$ cm/s, transit-time broadening will produce only a few hundred kHz of broadening for a beam width or interaction length even as small as a few mm. Transit-time broadening thus becomes significant only in special situations, for example, very high-resolution molecular-beam experiments involving tightly focused optical beams and high-speed molecules. Transit-time broadening must also sometimes be considered with larger gas cells in experiments using extraordinarily high-resolution laser frequency standards, very low-pressure gases, and very long-lived molecular absorption lines.

Coherent Pulse Experiments: Dephasing Versus Energy Decay

As we have noted in earlier discussions, it is important, and somewhat subtle, to distinguish clearly between those effects involved in *energy decay* and those involved in *line broadening* and *dephasing* of real atoms.

We described earlier, for example, an excited-state lifetime measurement in which atoms were excited into an upper energy level E_j , and the spontaneous emission or fluorescence on a downward transition $E_j \rightarrow E_i$ was then observed. This fluorescent emission is purely spontaneous emission, that is, incoherent random noise with a narrow spectrum (of width $\Delta\omega_a$) centered at the transition frequency ω_{ji} . The excitation mechanism (pumping light or electric current) excites the atoms into level E_j in an incoherent fashion. The atoms then oscillate spontaneously at frequencies like ω_{ji} , but with no phase coherence between individual atoms. We add the radiated powers from each atom (not the voltages) to get the total spontaneous emission. This emission comes out randomly in all directions, and has the statistical and spectral characteristics of narrowband random noise.

It is also possible, though usually much more difficult, to perform a more complicated experiment to demonstrate coherent atomic emission and the effects of dephasing on this coherent emission. Suppose some incoherent excitation mechanism, such as a flash of light or a current pulse in a gas, excites some of the atoms in an atomic medium up into some excited level E_j or E_i , or maybe even into a mixture of both. Spontaneous emission will then start. But before the populations N_j or N_i have decayed away, let us send a strong but short coherent signal pulse at the transition frequency ω_{ji} through the atoms. This pulse will then excite a coherent response $p(t)$ in the atoms on the $j \rightarrow i$ transition.

This induced polarization $p(t)$ will be given by the transient solution of the polarization equation of motion (Equation 2.69), taking into account the applied signal pulse. The applied signal pulse may be too short for the steady-state solution $\tilde{P}(\omega)$ given by the linear susceptibility to be reached. But nonetheless, after the signal pulse passes through the collection of atoms, they will be left with a *coherently oscillating macroscopic polarization* $p(t)$ in the medium. The atoms have all been driven in phase by the same applied signal; and after it passes they will continue to oscillate coherently and in phase at least for a brief while.

In the jargon of quantum electronics, we say that the atoms have been “coherently prepared” or “transversely aligned” by the strong signal pulse. They will then continue to radiate coherently and in the same direction as the applied signal pulse. This radiation, like the applied signal, will be spatially and temporally coherent radiation, not noise. The atoms will have some memory of how they were coherently excited by the signal pulse; and we must add vectorially the radiated voltage, not power, from each oscillating atomic dipole.

The amplitude of this coherent oscillation and radiation will, however, decay away at a total rate $(\gamma/2 + 1/T_2)$ because of the dephasing plus lifetime processes. This decay will be faster—often very much faster—than the energy decay rates γ_i or γ_j of the level populations. If the dephasing rate $1/T_2$ is rapid compared to γ_i and γ_j , the coherent radiation will rapidly disappear, leaving behind the much weaker but longer-lasting incoherent spontaneous emission.

This kind of more sophisticated experiment is referred to generally as a “coherent pulse” experiment. The presence of a coherent initial signal pulse to set up the transient coherent polarization $p(t)$ is essential. The exponentially decaying coherent radiation after the coherent signal pulse is turned off is often called

“free induction decay.” Note that a very narrow atomic transition in a gas might have a linewidth $\Delta\omega_a/2\pi \approx 1$ MHz, so that $T_2 \approx 300$ ns. Optical signal pulses shorter than this can be generated, and lifetimes this short can be measured with fast photodetectors; hence coherent-pulse measurements on such a transition are feasible.

In Nd:YAG, the 1.06 μm laser transition has an upper-level energy-decay lifetime of $\tau_2 \approx 230$ μs . The transverse dephasing time of this transition (its inverse phonon-broadened linewidth) is, however, more like $T_2 \approx 1$ psec at room temperature. This is simply too fast to be either excited or observed with conveniently available optical tools.

REFERENCES

The descriptions of collisions, dephasing processes, and energy decay that we have presented have been largely “phenomenological”—that is, we have added reasonable terms to the equations of motion for atomic phenomena in order to make theoretical predictions that agree reasonably well with the phenomena observed in real atoms. Essentially the same phenomenological approach is also used, however, even in more sophisticated and detailed quantum analyses of atomic behavior and atomic transitions. See, for example, R. G. Breene, Jr., *The Shift and Shape of Spectral Lines* (Pergamon Press, 1970), which uses this same approach to the theory of collision broadening. A newer and more advanced book on this topic by the same author is *Theories of Spectral Line Shape* (Wiley, 1981).

An early but very clear review of the same semiclassical theory of collision broadening may be found in H. Margenau and W. W. Watson, “Pressure effects on spectral lines,” *Rev. Mod. Phys.* **8**, 22 (January 1936). A more recent review is given by A. Ben-Reuven, “The meaning of collision broadening of spectral lines: the classical analog,” in *Advances in Atomic and Molecular Physics*, Vol. 5, ed. by D. R. Bates and I. Estermann (Academic Press, 1969).

In real gases, collisions between atoms can lead not only to broadening of the transition, but also to a somewhat smaller shifting of the atomic transition frequency, usually to a lower frequency (a “red shift”). These pressure shifts often amount to as much as $\approx 30\%$ to $\approx 50\%$ of the line broadening. A good discussion of the physics underlying both collision broadening and shifting of atomic lines in gases is given in Chapter 4 of A. C. G. Mitchell and M. W. Zemansky, *Resonance Radiation and Excited Atoms* (Cambridge University Press, 1961). Various theories and confirming experimental data for gaseous transitions are reviewed in S. Y. Chen and M. Takeo, “Broadening and shifting of spectral lines due to the presence of foreign gases,” *Rev. Mod. Phys.* **29**, 20 (January 1957).

More advanced reviews of collision broadening and shifting include an excellent review by H. M. Foley, “The pressure broadening of spectral lines,” *Phys. Rev.* **69**, 616 (1946); as well as W. R. Hindmarsh and Judith M. Farr, “Collision broadening of spectral lines by neutral atoms,” in *Progress in Quantum Electronics*, Vol. 2, ed. by J. H. Sanders and S. Stenholm (Pergamon Press, 1974), pp. 141–214. A similar reference is H. van Regemorter, “Spectral line broadening,” in *Atoms and Molecules in Astrophysics*, ed. by T. R. Carson and M. J. Roberts (Academic Press, 1972), pp. 85–119. The most recent and extensive review is perhaps that by N. Allard and J. Kielkopf, “The effect of neutral nonresonant collisions on atomic spectral lines,” *Rev. Mod. Phys.* **54**, 1103–1182 (October 1982).

Problems for 3.2

1. *Derivative spectroscopy on a variable-pressure gas sample.* A spectrometer of the type that measures $d\chi''(\omega)/d\omega$ versus ω is used to study an atomic transition in a gas for different gas pressures in the sample cell of the spectrometer. The atomic transition exhibits lifetime broadening plus pressure broadening of the Stern-Vollmer type. When all pressure-dependent factors are included, what is the optimum pressure for obtaining the strongest peak-derivative signal in the spectrometer? Explain physically.
-

3.3 POLARIZATION PROPERTIES OF ATOMIC TRANSITIONS

The transitions between quantum energy levels in real atoms exhibit anisotropic vector characteristics, or tensor characteristics, in both their spontaneous emission behavior and their stimulated response; and we need to understand the tensor nature of this behavior in order to fully understand real atomic transitions. In the simplest case, the response of a real atomic transition may be either *linearly polarized* or *circularly polarized* on different transitions. In the most general case, any single transition in an atom or molecule may have an *elliptically polarized response* relative to some specific set of (x, y, z) axes. The induced response in all these situations must then be described by a *tensor susceptibility* connecting the vector signal field and the vector atomic polarization.

We can gain a great deal of insight into these tensor properties by examining the transitions in a collection of single free atoms (not molecules) when these atoms are placed in a dc magnetic field. The dc field then both provides a reference axis and also Zeeman-splits the energy levels to eliminate all degeneracy in the system. In this section we will examine the behavior of such Zeeman-split transitions; in the next section we will introduce the general tensor-analytical method.

Zeeman-Split Atomic Transitions

The simplest example of a real atomic transition is probably the transition between a single lower energy level E_1 that is an S state, having quantized angular momentum $J = 0$, and an upper level E_2 that is a P state, having quantized total angular momentum $J = 1$. (Such states are characteristic of isolated single atoms in gases.) An angular-momentum value greater than 0 means that the upper level really consists of $2J + 1 = 3$ distinct quantum levels, which are degenerate in energy in zero magnetic field. These levels will, however, be split apart by a dc magnetic field B_0 into 3 distinct energy levels labeled by $M_J = 1, 0$, and -1 , as illustrated in Figure 3.7. (This splitting into separate energy levels is, of course, known as Zeeman splitting.) There are then three separate and distinct transitions from the upper levels to the lower level, at three slightly different transition frequencies as illustrated in Figure 3.7. Figure 3.8 shows some real spectral lines recorded on photographic plates in a high-resolution spectrometer for various spontaneous emission lines from excited zinc or sodium atoms,

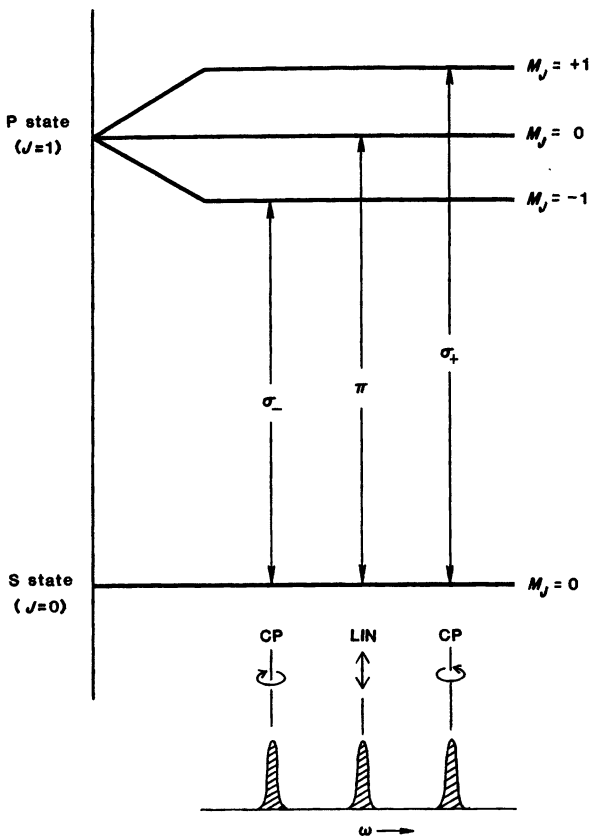


FIGURE 3.7

Zeeman splitting of atomic energy levels in a simple case.

with and without dc magnetic fields, illustrating both the simplest and more complicated types of Zeeman splitting.

Pi and Sigma Transitions

If we study the polarization behavior of the central transition (from $M_J = 0$ to $M_J = 0$) in the example shown in Figure 3.7, we will find that this transition behaves exactly like a dipole oscillator that is linearly polarized along the direction of the dc magnetic field, both in its spontaneous radiation and in its stimulated response to an applied signal. That is, on this particular transition the atoms act just like our linearly polarized CEO model, with their linear axis along the dc field. No spontaneous emission comes out in the direction directly along the dc field axis, for example, since a linearly oscillating dipole does not radiate along its polarization axis; and there will be no stimulated response to applied E fields perpendicular to that direction. Such a linearly polarized $\Delta M_J = 0$ transition is often called a π transition.

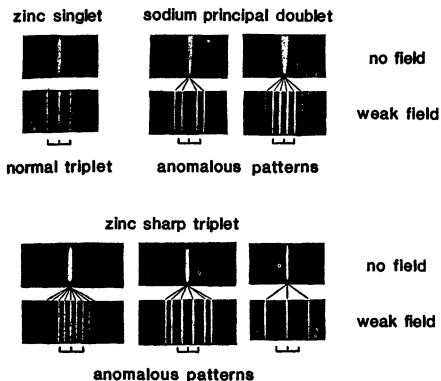


FIGURE 3.8

Spectral lines emitted on certain transitions from excited zinc and sodium atoms, with and without dc magnetic fields applied, showing both normal and anomalous Zeeman splitting.

The outer two lines in Figure 3.7 (connected to the $M_J = +1$ and -1 levels) are then found to be circularly polarized with respect to the magnetic field axis, with opposite senses of circularity in both their spontaneous emission and their stimulated responses. These circularly polarized lines are called σ_+ and σ_- transitions.

We will need to use tensors to describe the susceptibility properties of these transitions. Before we discuss this, however, a brief summary of some of the quantum properties of these atomic transitions may be very useful in understanding both their polarization properties and the relationship between the quantum theory and the classical models of these transitions. Readers with limited backgrounds in quantum theory should skim the next few paragraphs, and not be concerned if all the details are not clear to them.

Quantum Description of Atomic Transitions

In quantum theory, the quantum state of any real atom at time t is completely specified by a quantum wave function $\psi(\mathbf{r}, t)$, where \mathbf{r} indicates a general position in space. The evolution of this wave function in space and time is governed, according to quantum theory, by Schrödinger's equation of motion. We can, at least in principle, solve Schrödinger's equation to find $\psi(\mathbf{r}, t)$ for a given atom with given initial conditions and a given applied signal; and we will then know everything there is to know physically about that atom.

Any isolated quantum system such as a single atom will also have a special set of quantum energy eigenstates or "stationary states" with associated quantum wave functions $\psi_j(\mathbf{r})$. These wave functions $\psi_j(\mathbf{r})$ are time-independent solutions of Schrödinger's equation with no applied signal present. Each such eigenstate corresponds to one of the energy levels and energy eigenvalues E_j of the atom. These stationary eigenstates then provide a basis set, or a set of normal modes, for expanding any quantum state of the atom at any time.

A real atom at any instant of time will in general not be in a single energy eigenstate or energy level. Rather, it will be in a time-varying quantum state mixture of two or more such eigenstates. The wave function for a single atom at

any instant of time may then be written in general as

$$\psi(\mathbf{r}, t) = \tilde{a}_1(t)e^{-iE_1 t/\hbar}\psi_1(\mathbf{r}) + \tilde{a}_2(t)e^{-iE_2 t/\hbar}\psi_2(\mathbf{r}) + \dots, \quad (20)$$

where E_1 , E_2 , etc., are the energy eigenvalues. In the absence of an applied signal or any other external perturbation, the complex-valued expansion coefficients $\tilde{a}_1(t)$, $\tilde{a}_2(t)$, ... in this expansion will be constant in time, and there will be only the $\exp(-iE_j t/\hbar)$ frequency factor associated with each eigenstate.

One key idea here is that an atom is generally *not* in just one energy level. Rather, each atom is generally in a mixture of levels. An individual atom with a quantum state like that in Equation 3.20 then has a probability $|\tilde{a}_1|^2$ of being found in level E_1 ; a probability $|\tilde{a}_2|^2$ of being found in level E_2 ; and so forth. Averaging these probabilities over many atoms gives the same net effect as if N_1 atoms were in level E_1 , N_2 atoms in level E_2 , and so on.

A second key point is that these state mixtures are “stationary,” in the sense that the \tilde{a}_j ’s do not change with time unless there is an external signal or external perturbation applied to the atom. The time-varying phase rotation factor $\exp(-jE_j t/\hbar)$ associated with each term in the expansion is necessary to make $\psi(\mathbf{r}, t)$ satisfy the Schrödinger equation in the absence of an applied signal; but these phase factors do not, of course, change the magnitudes of the coefficients.

Physical Interpretation of the Quantum State

One physical interpretation for the wave function $\psi(\mathbf{r}, t)$ of an electron charge cloud surrounding a fixed nucleus is that $|\psi(\mathbf{r}, t)|^2$ gives the probability density for finding an orbital electron at point \mathbf{r} at time t . More generally, we can say that $\rho(\mathbf{r}, t) \equiv -e|\psi(\mathbf{r}, t)|^2$ gives the value (more precisely, the “quantum expectation value”) of the local charge density in the electron charge cloud around the atom. If the wave function $\psi(\mathbf{r}, t)$ is a mixture of, say, two energy states, the charge density in the atom has the form

$$\begin{aligned} \rho(\mathbf{r}, t) &= \left| \tilde{a}_1(t)e^{-iE_1 t/\hbar}\psi_1(\mathbf{r}) + \tilde{a}_2(t)e^{-iE_2 t/\hbar}\psi_2(\mathbf{r}) \right|^2 \\ &= |\tilde{a}_1(t)|^2 |\psi_1(\mathbf{r})|^2 + |\tilde{a}_2(t)|^2 |\psi_2(\mathbf{r})|^2 \\ &\quad + \tilde{a}_1(t)\tilde{a}_2^*(t)\psi_1(\mathbf{r})\psi_2^*(\mathbf{r})\exp[i(E_2 - E_1)t/\hbar] \\ &\quad + \tilde{a}_1^*(t)\tilde{a}_2(t)\psi_1^*(\mathbf{r})\psi_2(\mathbf{r})\exp[-i(E_2 - E_1)t/\hbar] \\ &= \rho_{dc}(\mathbf{r}) + \rho_{ac}(\mathbf{r}, t). \end{aligned} \quad (21)$$

The key observation here is that the atomic charge density contains both two *static* parts, proportional to the individual level occupancies $|\tilde{a}_j(t)|^2 |\psi_j(\mathbf{r})|^2$, and a *sinusoidally oscillating component* given by the mixed term or cross term

$$\rho_{ac}(\mathbf{r}, t) = \text{Re} [\tilde{a}_1(t)\tilde{a}_2^*(t)\psi_1(\mathbf{r})\psi_2^*(\mathbf{r})e^{i\omega_{21}t}]. \quad (22)$$

This oscillating component inherently oscillates at the transition frequency $\omega_{21} = (E_2 - E_1)/\hbar$ between the two levels involved. *There is in effect a natural quantum oscillating dipole moment in the real quantum atom*, which can be compared with the oscillating moment $\mu_x(t)$ of the CEO model. This is a *quantum-mechanically predicted oscillation* in the atom, at the transition frequency between any two occupied levels.

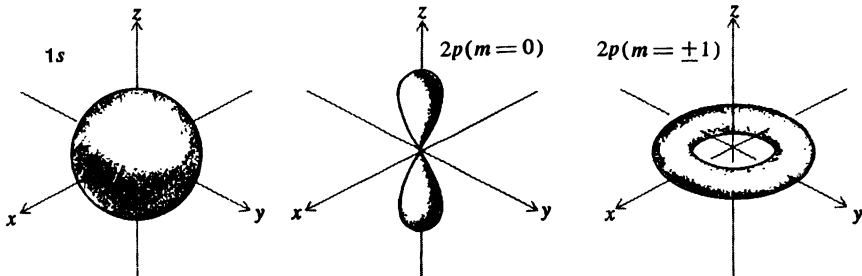


FIGURE 3.9

Schematic representations of the electronic charge distributions for Zeeman-split quantum eigenstates.

The magnitude of this oscillating component is proportional to the cross term $\tilde{a}_1(t)\tilde{a}_2^*(t)$ between the two level occupancies, and it obviously decays away as the level occupancy coefficients $\tilde{a}_1(t)$ and $\tilde{a}_2(t)$ decay away, just as $\mu_x(t)$ decays at rate γ in the classical oscillator. The phase ϕ_i of the atomic oscillation in the i -th atom depends on the *phase-angle difference* of the complex coefficients $\tilde{a}_1 = |\tilde{a}_1|e^{-i\phi_1}$ and $\tilde{a}_2 = |\tilde{a}_2|e^{-i\phi_2}$ in the combination $\tilde{a}_1\tilde{a}_2^* = |\tilde{a}_1\tilde{a}_2|e^{i(\phi_2-\phi_1)}$. This phase can be randomized by dephasing processes that randomize the individual phases of \tilde{a}_1 and \tilde{a}_2 , without necessarily changing the occupancies $|\tilde{a}_1|^2$ or $|\tilde{a}_2|^2$ of either level.

Zeeman Transitions: Linear and Circular Dipoles

As a specific example of such an oscillating charge pattern and oscillating dipole moment in a real atom, let us examine the simple but realistic Zeeman-split example described earlier. We will look in the following paragraphs at simplified three-dimensional representations of the volume charge distributions $\psi(r, t)$ that correspond to various eigenstates and state mixtures, keeping in mind that $\psi(r, t)$ itself is a complex function with a sign or phase angle as well as a magnitude at each point in space.

Figure 3.9 shows in schematic form, for example, the wave functions $|\psi(r, t)|^2$ for a $J = 0$ eigenstate or S state (a spherically symmetric charge cloud); for a $J = 1, M_J = 0$ or P_0 eigenstate (dumbbell shape); and for a $J = 1, M_J = \pm 1$ or $P_{\pm 1}$ eigenstate (toroidal ring). Note that in the dumbbell the wave function $\psi(r)$ has opposite sign in the upper and lower lobes, whereas in the $M_J = \pm 1$ states the wave function has an $\exp(\pm j\theta)$ phase variation around the torus.

Linearly Polarized (π) Transition

Suppose, then, that the quantum state $\psi(r, t)$ of an atom is a mixture of, say, the $1S$ and the $2P_0$ states of the hydrogen atom (the ball and the dumbbell in Figure 3.9; the transition between these two levels in the hydrogen atom is, in fact, the Lyman α line at 1216\AA). When the phases of the complex coefficients $\tilde{a}_1(t)$ and $\tilde{a}_2(t)$ are included, the complex-valued wave functions $\tilde{a}_1\psi_1(r)$ and $\tilde{a}_2\psi_2(r)$ associated with these states may interfere constructively and/or

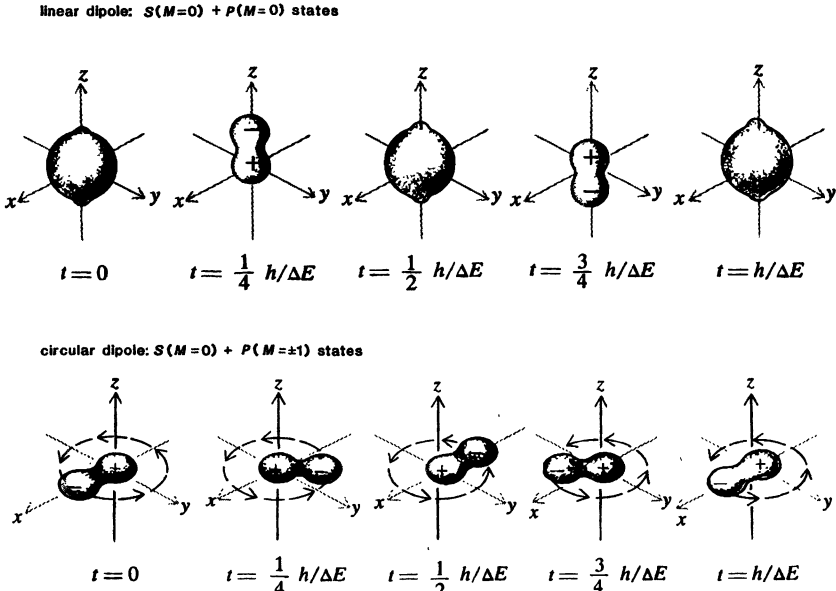


FIGURE 3.10

Upper part: Oscillating charge distribution in the coherent state mixture $1S + 2P_0$ as a function of time for a quantum atom. The atom acts as a linearly oscillating dipole. Lower part: Corresponding probability density, or quantum charge distribution, for a quantum state mixture of $1S + 2P_1$ states. This quantum state mixture acts like a rotating, circularly polarized electric dipole. (Adapted from G. R. Fowles, *Introduction to Modern Optics*, Holt, Rinehart, and Winston, 1968.)

destructively at different points to create the total wavefunction $\psi(\mathbf{r}, t)$; and this interference will, moreover, rotate through all possible phases at the transition frequency ω_{21} because of the $\exp(-iE_j t/\hbar)$ terms.

The upper part of Figure 3.10 shows what the total wave function $|\psi(\mathbf{r}, t)|^2$ produced by summing and squaring the $1S$ and the $2P_0$ states will look like at successive times during one oscillation cycle of the $\exp(j\omega_{21}t)$ variation. The center of charge of the total atomic charge cloud clearly oscillates back and forth linearly along what is here labeled the z axis. The quantum atom with this particular mixture of $1S + 2P_0$ states acts exactly like a linearly oscillating dipole.

Circularly Polarized (σ) Transitions

The lower part of Figure 3.10 shows the same type of result when the lower state E_1 is again a $1S$ state, but the upper level E_2 is now a $2P_1$ state with $M_J = +1$. Because of the $\exp(+j\theta)$ variation of the P_1 state wave function

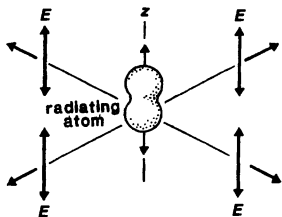
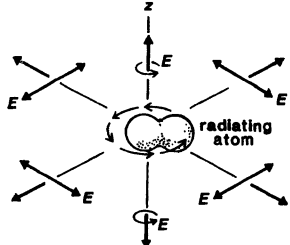
π transitions σ transitions

FIGURE 3.11
Polarization properties and oscillation characteristics of simple Zeeman-split atomic transitions.

around the equatorial plane, the wave functions ψ_1 and ψ_2 corresponding to the "ball" and the "torus" interfere constructively on one side and destructively on the other side of the rotational axis, producing a cancellation on one side and a "bulge" on the other side.

As the coefficients $\tilde{a}_1 e^{-iE_1 t/\hbar}$ and $\tilde{a}_2 e^{-iE_2 t/\hbar}$ rotate in time-phase, however, the resulting bulge in the quantity $|\psi_1(\mathbf{r}) + \psi_2(\mathbf{r})|^2$ rotates about the z axis at the transition frequency ω_{21} . The atom radiates like an oscillator that is circularly polarized in the x, y plane. The polarization of this rotation will be of opposite sense (opposite circularity) depending on whether the magnetic quantum number $M_j = +1$ or -1 in the upper level.

Figure 3.11 summarizes the polarization properties and the radiation characteristics into various directions of these simple Zeeman-split oscillating-electric-dipole charge distributions. These results represent the quantum-mechanical polarization properties of real atomic transitions. They obviously can be very well represented, however, by the kinds of purely classical electron oscillator models we have been developing.

These polarization properties of the quantum oscillations in the atomic wave functions determine both the spontaneous and the stimulated properties of the real atoms. That is, an atom whose charge distribution can oscillate only in a certain direction on a given transition will obviously respond only to applied fields that have the same direction or sense of polarization. Hence Figure 3.11 illustrates equally well both the stimulated response and the spontaneous emission properties of these transitions.

Elliptically Polarized Transitions

Many real atomic transitions, particularly the transitions of isolated single atoms in gases, as well as many molecular transitions, will have either pure linear or pure circular polarization properties exactly like those illustrated in Figures 3.10 and 3.11. Atomic transitions in crystals or in complex molecules may, however, have more complex polarization properties. It turns out (though we will not attempt to illustrate this in detail here) that the most general possible polarization for either an electric-dipole or a magnetic-dipole type of atomic transition is an *elliptical polarization* in an arbitrarily oriented plane of polarization, with arbitrary ellipticity and arbitrary orientation of the elliptical axes in that plane. Linear and circular polarization are then elementary limiting cases of this general form.

REFERENCES

The sketches of oscillating atomic dipoles in this section are adapted from the excellent text by G. R. Fowles, *Introduction to Modern Optics* (Holt, Rinehart and Winston, 1968), especially Chap. 7. See also G. R. Fowles, "Quantum dynamical description of atoms and radiative processes," *Am. J. Phys.* **31**, 407-409 (June 1963).

Problems for 3.3

1. *Two-dimensional Zeeman-split classical oscillator model.* Let us see if it is possible to develop a purely classical oscillator model that will reproduce in more detail some of the circular polarization and Zeeman-splitting properties of the real atomic transitions described in this section.

To do this, consider a *two-dimensional* classical electron oscillator, consisting of a point electron that is free to move in two dimensions on an x, y plane. Assume that there is a central restoring force such that the restoring force terms in the two transverse directions are $f_x = -Kx$ and $f_y = -Ky$. Assume that there is also a dc magnetic field B_0 normal to the x, y plane. Such a field will cause forces $-eB_0(dy/dt)$ in the x direction and $+eB_0(dx/dt)$ in the y direction. Assume also that there are equal damping factors γ in both directions, in exact analogy to the one-dimensional case.

Assuming then a sinusoidal \tilde{E}_x field applied (for simplicity) only in the x direction, find the resulting steady-state displacements $\tilde{X}(\omega)$ and $\tilde{Y}(\omega)$ of the oscillator as a function of the applied frequency. Discuss the resonance behavior of the response, and identify the resonance frequencies of the oscillator. (Note that you will need to solve two coupled equations of motion, and that the resulting equation for the resonance frequencies will be quartic rather than quadratic as for the simple one-dimensional classical electron oscillator.)

Discuss also, with appropriate sketches, the nature of the induced steady-state electron motion $x(t)$ and $y(t)$ for signals tuned to one or the other of the Zeeman-split resonance peaks. The behavior calculated should be similar to the Zeeman splitting of real atomic resonances when a dc magnetic field is applied. Discuss also the induced electron motion at ω_a , exactly halfway between the peaks.

Hints: It will be convenient to define a cyclotron frequency $\omega_c \equiv eB_0/m$, and to make the assumptions that $\gamma \ll \omega_c \ll \omega_a$. (These assumptions imply that the magnetic field splitting, or Zeeman splitting, of the resonance at ω_a will be large compared to the damping γ but still small compared to the unperturbed center frequency ω_a .) The algebra involved in this problem will also be easier if you use a resonance approximation, as well as the other approximations noted above, as early as possible in the calculations.

2. *Computer plots of oscillating atomic charge distributions (research problem).* Using whatever computer graphics facilities may be available to you, carry out further computer investigations of the oscillating charge density distributions for quantum state mixtures like those shown in this section. Try making, for example, contour plots or three-dimensional display plots at different phases in the oscillation cycle, to illustrate the dynamic motion of the charge density—and please send me copies of any particularly good results! You might also investigate such plots for simpler one-dimensional cases, such as an electron in a one-dimensional quadratic or square well potential.
-

3.4 TENSOR SUSCEPTIBILITIES

Real atomic transitions thus have a tensor character that must be taken into account to give a complete and accurate description of the stimulated response on these transitions. In this section we summarize these tensor aspects of electric (or for that matter magnetic) dipole transitions in real atoms.

Tensor Susceptibility: Linear Dipole Oscillators

Suppose that a sinusoidal signal with frequency ω on or near a single atomic transition is applied to a collection of real electric-dipole atoms. Then the steady-state vector polarization $\mathbf{P}(\omega)$ induced in the collection of atoms must be related to the vector field $\mathbf{E}(\omega)$ by a tensor equation of the form

$$\mathbf{P}(\omega) = \chi(\omega)\epsilon\mathbf{E}(\omega), \quad (23)$$

where $\chi(\omega)$ is a 3×3 tensor form of the susceptibility $\tilde{\chi}(\omega)$, with components $\tilde{\chi}_{xx}(\omega)$, $\tilde{\chi}_{xy}(\omega)$, and so forth. Let us first examine the tensor character of this susceptibility for some simple examples, to get a feeling for the nature of these tensor responses.

The most elementary example is the linear classical electron oscillator. For the classical oscillator we calculated the x component of polarization \tilde{P}_x induced by an x -polarized field component \tilde{E}_x . In tensor notation this gives us only the xx tensor component of χ , or

$$\tilde{P}_x(\omega) = \tilde{\chi}_{xx}(\omega)\epsilon\tilde{E}_x(\omega). \quad (24)$$

It is physically evident that no \tilde{P}_y or \tilde{P}_z polarization components will occur in the linear oscillator model (since the electron is by definition not free to move along those coordinates in the linear model); and also that no response will be induced in the linear model by field components \tilde{E}_y or \tilde{E}_z . Hence we can write

this response in expanded tensor or matrix form as

$$\mathbf{P}(\omega) = \begin{bmatrix} \tilde{P}_x(\omega) \\ \tilde{P}_y(\omega) \\ \tilde{P}_z(\omega) \end{bmatrix} = \tilde{\chi}(\omega)\epsilon \begin{bmatrix} 3 & 0 & 0 \\ 0 & 0 & 0 \\ 0 & 0 & 0 \end{bmatrix} \begin{bmatrix} \tilde{E}_x(\omega) \\ \tilde{E}_y(\omega) \\ \tilde{E}_z(\omega) \end{bmatrix}. \quad (25)$$

Following a pattern that we will use repeatedly in this section, we have separated the right-hand side of this equation into a dimensionless tensor part with a trace of magnitude 3, plus a purely scalar (but still complex) susceptibility $\tilde{\chi}(\omega)$.

The scalar susceptibility part of this expression for a homogeneously broadened lorentzian transition will then have the usual form

$$\tilde{\chi}(\omega) = -j \frac{1}{4\pi^2} \frac{\Delta N \lambda^3 \gamma_{\text{rad}}}{\Delta \omega_a} \frac{1}{1 + 2j(\omega - \omega_a)/\Delta \omega_a} \quad (26)$$

in which the factor of 3 has been left with the dimensionless tensor for reasons that will become apparent later. Subscripts ij might also be attached to each factor in Equations 3.25 and 3.26 if necessary to identify the specific transition in a real atom that is involved.

Note that the choice of the x axis for the direction of the linear response here is entirely arbitrary. We might choose to label the linear response as being along the y or the z axes, or along some more arbitrary linear axis. If we made this last choice, the tensor would become more complicated in form, corresponding to an arbitrary rotation of the coordinate axes with respect to the x, y, z axes. It would still be, however, a purely real tensor.

Circularly Polarized (Gyrotropic) Responses

Let us next consider circularly polarized transitions, such as the σ_{\pm} transitions we saw in the previous section. For a transition that is circularly polarized in the x, y plane (which is true of many simple transitions in free atoms), the tensor susceptibility becomes

$$\mathbf{P} = \begin{bmatrix} \tilde{P}_x \\ \tilde{P}_y \\ \tilde{P}_z \end{bmatrix} = \tilde{\chi}(\omega)\epsilon \times \frac{3}{2} \begin{bmatrix} 1 & \mp j & 0 \\ \pm j & 1 & 0 \\ 0 & 0 & 0 \end{bmatrix} \begin{bmatrix} \tilde{E}_x \\ \tilde{E}_y \\ \tilde{E}_z \end{bmatrix}. \quad (27)$$

where $\tilde{\chi}(\omega)$ is exactly the same as in Equation 3.26, and the factor of $3/2$ is attached to the tensor part of this circularly polarized expression, in order to make its trace (i.e., its diagonal sum) have the same value of 3 as for the linearly polarized expression.

Suppose that the applied signal in this case is linearly polarized along the x axis, i.e.,

$$\tilde{E}_x = \tilde{E}_0 \quad \text{and} \quad \tilde{E}_y = \tilde{E}_z = 0. \quad (28)$$

Then the induced polarization components will be

$$\tilde{P}_x = (3\tilde{\chi}\epsilon/2)\tilde{E}_0 \quad \text{and} \quad \tilde{P}_y = \mp j(3\tilde{\chi}\epsilon/2)\tilde{E}_0, \quad (29)$$

where $(3/2)\tilde{\chi}\epsilon$ is in general a complex-valued quantity. Hence the real polarization terms will be of the form

$$\begin{aligned} p_x(t) &= \operatorname{Re} \left[\tilde{P}_x e^{j\omega t} \right] = |(3\chi\epsilon/2)E_0| \cos(\omega t + \theta), \\ p_y(t) &= \operatorname{Re} \left[\tilde{P}_y e^{j\omega t} \right] = \pm |(3\chi\epsilon/2)E_0| \sin(\omega t + \theta), \end{aligned} \quad (30)$$

where θ is the net phase angle of $(3\tilde{\chi}\epsilon/2)\tilde{E}_0$. Although the applied signal field is linearly polarized, the induced polarization $\mathbf{p}(t)$ is *circularly polarized* in the x, y plane, rotating from x to y for the + sign or from x to $-y$ for the - sign.

The circularly polarized tensor form given in Equation 3.27 inherently leads to circularly polarized behavior of the induced polarization. This form is characteristic of σ -type electric-dipole transitions and many simple magnetic-dipole transitions, and is often referred to as a *gyrotropic tensor response*. As before, rotation to a different coordinate orientation will make the tensor appear more complicated, but the essential character will remain the same.

Elliptically Polarized Responses

Suppose a sinusoidal electric field $\tilde{\mathbf{E}}$ is applied to an arbitrary two-level nondegenerate electric-dipole transition in a real atom. Such a transition will have a *quantum dipole matrix element* $\tilde{\mu}_{21}$ given by the integral

$$\tilde{\mu}_{21} = -e \iiint \psi_2^*(\mathbf{r}) \times \mathbf{r} \times \psi_1(\mathbf{r}) d\mathbf{r} \equiv \begin{bmatrix} \tilde{\mu}_x \\ \tilde{\mu}_y \\ \tilde{\mu}_z \end{bmatrix} \quad (31)$$

between the upper and lower levels of the transition. That is, $\tilde{\mu}_{21}$ may be interpreted as a column vector with elements given by the x, y, z vector components of the integral. The hermitian conjugate $\tilde{\mu}_{21}^\dagger$ of this column vector is then a row vector whose elements $[\tilde{\mu}_x^*, \tilde{\mu}_y^*, \tilde{\mu}_z^*]$ are the complex conjugates of the elements in the column vector.

An exact quantum analysis then says that the expectation value for the phasor amplitude $\tilde{\mu}$ of the dipole moment induced in the atom by the applied field will be given by

$$\begin{aligned} \tilde{\mu} &= \text{const} \times (\tilde{\mu}_{21}^\dagger \cdot \tilde{\mathbf{E}}) \times \tilde{\mu}_{21} \\ &= \text{const} \times [\tilde{\mu}_x^* \quad \tilde{\mu}_y^* \quad \tilde{\mu}_z^*] \cdot \begin{bmatrix} \tilde{E}_x \\ \tilde{E}_y \\ \tilde{E}_z \end{bmatrix} \times \begin{bmatrix} \tilde{\mu}_x \\ \tilde{\mu}_y \\ \tilde{\mu}_z \end{bmatrix}, \end{aligned} \quad (32)$$

where the dot product is taken in the usual matrix-multiplication fashion between the row vector $\tilde{\mu}_{21}^\dagger$ and the column vector $\tilde{\mathbf{E}}$ with elements $[\tilde{E}_x, \tilde{E}_y, \tilde{E}_z]$.

The induced macroscopic polarization $\tilde{\mathbf{p}}(\omega)$ in a collection of atoms will then be just the microscopic dipole moment $\tilde{\mu}$ in each individual atom, as given by Equation 3.32, summed over all the atoms in any small unit volume. Equation 3.32 contains a scalar constant, times a scalar dot product, times the column vector $\tilde{\mu}_{21}$, which is the net vector quantity on the right-hand side of the equation. Equation 3.32 says, therefore, that the induced response $\tilde{\mu}$ or $\tilde{\mathbf{p}}$ of the atoms will always have exactly the same polarization properties as the transition's dipole matrix element $\tilde{\mu}_{21}$, regardless of the polarization properties of the applied signal

$\tilde{\mathbf{E}}$. That is, you can drive the atoms with any polarization $\tilde{\mathbf{E}}$ you want; but they will always respond with their own fixed, characteristic form of polarization, as given by $\tilde{\mu}_{21}$.

The *magnitude* of this induced response, however, will depend on the dot product between the applied field \mathbf{E} and the hermitian conjugate of the moment μ_{21} ; and this dot product is mathematically the same thing as matrix multiplication between these two quantities. By invoking the associative properties of matrix and vector multiplication, therefore, we can reorder Equation 3.32 into the alternative form

$$\tilde{\mu} = \text{const} \times \tilde{\mu}_{21} \times \tilde{\mu}_{21}^\dagger \times \tilde{\mathbf{E}} = \text{const} \times \begin{bmatrix} \tilde{\mu}_x^* \\ \tilde{\mu}_y^* \\ \tilde{\mu}_z^* \end{bmatrix} \times \begin{bmatrix} \tilde{\mu}_x^* & \tilde{\mu}_y^* & \tilde{\mu}_z^* \end{bmatrix} \times \begin{bmatrix} \tilde{E}_x \\ \tilde{E}_y \\ \tilde{E}_z \end{bmatrix}. \quad (33)$$

In this reorganized form, the middle product $\tilde{\mu}_{21} \times \tilde{\mu}_{21}^\dagger$ can now be interpreted as the matrix product, computed according to the usual rules, of the two vector (or matrix) quantities $\tilde{\mu}_{21}$ and its hermitian conjugate. But the result of this multiplication will be a 3×3 matrix or tensor \mathbf{T} , often called a *dyadic product*, which we will write as

$$\mathbf{T} \equiv \text{const} \times \tilde{\mu}_{21} \times \tilde{\mu}_{21}^\dagger = \text{const} \times \begin{bmatrix} \tilde{\mu}_x^* \\ \tilde{\mu}_y^* \\ \tilde{\mu}_z^* \end{bmatrix} \times \begin{bmatrix} \tilde{\mu}_x^* & \tilde{\mu}_y^* & \tilde{\mu}_z^* \end{bmatrix} = \begin{bmatrix} \tilde{t}_{xx} & \tilde{t}_{xy} & \tilde{t}_{xz} \\ \tilde{t}_{yx} & \tilde{t}_{yy} & \tilde{t}_{yz} \\ \tilde{t}_{zx} & \tilde{t}_{zy} & \tilde{t}_{zz} \end{bmatrix}, \quad (34)$$

where the constant is some suitable normalization constant. Note that the nm -th element of the \mathbf{T} matrix is obtained in the usual matrix-multiplication way, by multiplying the n -th row of the $\tilde{\mu}_{21}^\dagger$ column vector (just one element) times the m -th column of the $\tilde{\mu}_{21}$ row vector (also just one element).

Hence we can write the macroscopic polarization in a general tensor form as

$$\tilde{\mathbf{p}}(\omega) = \text{const} \times \tilde{\mu}_{21} \tilde{\mu}_{21}^\dagger \times \tilde{\mathbf{E}}(\omega) = \tilde{\chi}(\omega) \epsilon \times \mathbf{T} \times \tilde{\mathbf{E}}(\omega), \quad (35)$$

where the most general form of the susceptibility tensor \mathbf{T} for a dipole transition is given by the dyadic product

$$\mathbf{T} = \text{const} \times \tilde{\mu}_{21} \tilde{\mu}_{21}^\dagger. \quad (36)$$

Suppose the transition matrix element $\tilde{\mu}_{21}$ is a column vector with elements $[1, -j, 0]$ corresponding to RHCP motion in the x, y plane. The hermitian conjugate $\tilde{\mu}_{21}^\dagger$ is then a row vector with elements $[1, +j, 0]$, and the tensor susceptibility has the form

$$\mathbf{T} = \frac{3}{2} \times [1 \ -j \ 0] \times \begin{bmatrix} 1 \\ j \\ 0 \end{bmatrix} = \frac{3}{2} \times \begin{bmatrix} 1 & j & 0 \\ -j & 1 & 0 \\ 0 & 0 & 0 \end{bmatrix}. \quad (37)$$

This is, of course, just the RHCP gyrotropic result given in Equation 3.27.

Most General Tensor Form

Simple linearly polarized and circularly polarized responses are the most common and elementary forms for the tensor responses of electric-dipole and magnetic-dipole atomic transitions. To obtain the most general possible form for a dipole susceptibility tensor, we can note that the quantum transition moment

$\tilde{\mu}_{21}$ can have at most three complex-valued vector components, namely, $\tilde{\mu}_x$, $\tilde{\mu}_y$, and $\tilde{\mu}_z$, or six independent real numbers. Using these values, we can then carry out the matrix multiplication of the dyadic product as defined in Equation 3.34 to obtain the most general tensor form \mathbf{T} .

It can then be shown that for any such dipole transition the most general allowed form of this dyadic-product response will be an *elliptically polarized tensor response*, with the resulting induced polarization $\tilde{P}(\omega)$ having some arbitrary (but fixed) degree of ellipticity and arbitrary orientation of the elliptical axes in some reference plane which is itself arbitrarily oriented with respect to the x, y, z axes. This behavior is inherent in the mathematical form itself, independent of physical properties of the transitions.

There seems to be little point in writing out this general elliptical tensor form in more detail here. If you wish to know what the resulting tensor looks like, first add together the tensor responses for two independent linear responses along the x and y axes, but with an arbitrary amplitude ratio and arbitrary phase angle between them. This will produce the tensor form for an arbitrary elliptical response in the x, y plane. Performing a conventional coordinate rotation from the x, y, z axes to an arbitrarily oriented set of new x', y', z' axes will then generate the most general possible form for the susceptibility tensor.

Note that the degree of ellipticity of the original ellipse, plus the orientation of this ellipse in space, accounts for four real parameters. The normalization condition that the trace of the resulting tensor should be normalized to three, i.e., $\tilde{t}_{xx} + \tilde{t}_{yy} + \tilde{t}_{zz} = 3$, then accounts for the remaining two of the six real numbers mentioned above. (Alternatively, we could require only that the magnitude of the trace be unity, leaving an arbitrary overall phase shift in all the tensor elements.) There are thus really only four adjustable real parameters among the nine complex elements of the normalized susceptibility tensor.

Tensor Axes

But what determines the direction of the relevant axes of polarization and the degree of ellipticity for a real transition in a real atom? A simplified answer is as follows.

Single atoms floating freely in a gas always have degenerate electronic energy levels, for example, the Zeeman levels described earlier (except, of course, for $J = 0$ or S states, which are not degenerate). In this situation we must apply some static perturbation, such as a dc magnetic field (Zeeman splitting) or a dc electric field (Stark splitting), to "break" this degeneracy and to separate the individual transitions into distinct transition frequencies. Each of these separate Zeeman-split transitions will then have a distinct type and direction of tensor polarization.

The direction of the static perturbation in this situation will determine one of the reference axes for the tensor susceptibility; this direction is often chosen to be the z direction. The dc field direction will thus serve as the reference axis for the tensor responses on these transitions. For free atoms in such a static field, the response is then always either linear along this z axis (π transitions) or else circularly polarized about it (σ transitions), so that no unique choice for the x and y axes is either necessary or possible.

Atoms in a crystal will have a more complex environment, with more clearly determined reference axes, but often with a lower order of symmetry. In a crystal, each individual atom will be imbedded in some surrounding lattice structure

with a distinctive orientation in space. The orientation of this lattice structure gives the reference axes against which the polarization-tensor properties of the atomic transitions can be uniquely evaluated. The most general possible result, as already noted, is an elliptically polarized tensor response with respect to these axes.

Finally, in molecules the structural axes of the molecular structure itself give reference axes for the electronic transitions of the electron charge cloud of the molecule. As the molecule rotates, these axes rotate with it. If a simple molecule has only a single axis of symmetry (e.g., a diatomic molecule like N_2), all its electronic transitions are either linear along this axis or circular about it.

Isotropic Responses?

An important observation is that it is *not* physically possible for the tensor response of a single, nondegenerate atomic or molecular transition to be isotropic (that is, to be linear and equal in all directions). That is, a single nondegenerate transition cannot have a tensor response of the form

$$\begin{bmatrix} \tilde{P}_x \\ \tilde{P}_y \\ \tilde{P}_z \end{bmatrix} = \tilde{\chi}(\omega)\epsilon \times \begin{bmatrix} 1 & 0 & 0 \\ 0 & 1 & 0 \\ 0 & 0 & 1 \end{bmatrix} \times \begin{bmatrix} \tilde{E}_x \\ \tilde{E}_y \\ \tilde{E}_z \end{bmatrix}. \quad (38)$$

A response that is effectively isotropic in this fashion can, however, be obtained by averaging over a collection of atoms. There are two different ways in which this can occur, as follows.

- The response of each individual atom in a collection may be anisotropic, with one of the nondegenerate tensor forms given earlier; but the atoms may have their reference axes randomly oriented in all directions. This would be expected in a randomly oriented collection of gas molecules, for example, or in a noncrystalline material, such as a liquid, a powder, or a glass, in which the local surroundings for different atoms may be randomly oriented. Averaging over all directions of the atomic axes leads to an isotropic overall response as in Equation 3.38.
- The observed response may be the summation over a complete set of degenerate atomic transitions that are not resolved in frequency, because no external perturbation has been applied to break the degeneracy. These degenerate transitions all coincide in frequency, and hence cannot be separately excited. Adding up the small-signal tensor responses of such a complete set of overlapping degenerate transitions then leads to an isotropic response here also. (Or we could say that there is no way to define any unique reference axes in the atoms; so the atoms are in effect randomly oriented.)

In either situation the tensor response will have the apparently isotropic form given in Equation 3.38, where the scalar $\tilde{\chi}(\omega)$ is again the same as in Equation 3.26, that is, without the factor of 3 in front.

To look at this in another way, suppose we have a collection of randomly oriented atoms, so that $N/3$ of them will be in effect oriented along each axis. The linear response due to these atoms will then be the value of $\tilde{\chi}(\omega)$ derived in the previous chapter, including the initial factor of 3, but with a population (or

population difference) of only $N/3$ instead of N . Therefore, the response along each axis will be given by the scalar $\tilde{\chi}(\omega)$ formula in the form we have used in this section *without the initial factor of 3 that appeared in $\tilde{\chi}(\omega)$ in earlier chapters.*

The isotropic tensor form of Equation 3.38 is thus both mathematically simple and characteristic of certain common physical situations. It also has a trace equal to three—at least if we give the diagonal elements the simplest value of unity. It is largely for this reason that we have adopted the convention that $\text{Tr}[T] \equiv 3$ in writing all of the preceding normalized tensor susceptibilities. The significance of this factor of 3 is discussed in more detail in the following section.

Problems for 3.4

1. *Negative circular polarization response of a gyrotropic tensor.* Using the gyrotropic form of tensor response, verify that if you apply a circularly polarized \vec{E} field which has one sense of circular polarization to an atom whose natural response is the opposite sense of circular polarization, then this applied \vec{E} field will produce no atomic response at all.
2. *Tensor response of an anisotropic two-dimensional classical oscillator.* Suppose that you have a two-dimensional classical electron oscillator in which the electron moves in an anisotropic potential well in such a way that the restoring force in the x direction is $-K_x x$, but in the y direction is $K_y y$, where K_x and K_y differ by an amount that is small compared to their average value, but large compared to the fractional linewidth of the atomic transitions. The damping and collision-broadening rates for motion along both axes are the same, and no magnetic field is present. Write the classical electron oscillator susceptibility, including the tensor form, for a macroscopic collection of such oscillators.
3. *Tensor response of a three-dimensional Zeeman-split classical oscillator.* Consider as a classical model for an electric-dipole atom an electron that can move in the x , y , and z directions about a nucleus with a linear central restoring force, where a dc magnetic field B_0 is also present in the z direction as in Problem 1 of Section 3.3. Using the same notation and results as in that problem (except that the electron is now also free to move in the z direction), derive a general expression for the tensor electric susceptibility of a collection of these classical atoms. As in the earlier problem, work out the three separate resonance frequencies of this system (corresponding to separate atomic transitions). Then, making the reasonable assumptions that $\omega_0 \gg \omega_c \gg \Delta\omega_a$ (i.e., small Zeeman splitting, but even smaller atomic linewidths), discuss the tensor character of $\tilde{\chi}(\omega)$.
4. *Field patterns in a “twisted-mode” laser cavity.* Circularly polarized optical signals can be confusing but interesting. Consider, for example, a uniform optical wave that is right-hand circularly polarized looking along its direction of propagation (that is, at any single transverse plane, the field \mathcal{E} of this particular wave rotates from x into y as time t increases). Suppose this wave passes through a quarter-wave plate (QWP); bounces off a mirror at normal incidence; and passes back out through the QWP along the same optical axis, but propagating in the opposite direction.

[A quarter-wave plate is an optical element made of an anisotropic or birefringent material, e.g., crystal quartz, that has two transverse axes; call them the x and y

or “fast” and “slow” axes. When an optical wave passes through such an element in the z direction, the \mathcal{E}_y component of the optical field vector \mathcal{E} sees a slightly higher index of refraction n_y than the value n_x seen by the \mathcal{E}_x field component. A quarter-wave plate has a thickness d such that $(n_y - n_x)\omega d/c_0 = (\pi/2)$, i.e., the optical path length through the QWP is one quarter-wavelength longer for one polarization component than the other.]

- (a) Develop a “snapshot” of the vector field pattern $\mathcal{E}(z, t)$ in the standing-wave region on the side of the QWP away from the mirror, showing how the \mathcal{E} fields appear at any single instant of time t , with whatever amount of analysis or explanation is needed to support this “snapshot.” How does this resulting field pattern differ from a RHCP propagating wave?
- (b) In an ordinary standing-wave laser cavity with linearly polarized \mathcal{E} fields, there are nulls in the standing-wave field pattern every half-wavelength along the cavity. Laser atoms located at or near these nulls are thus essentially unaffected by the optical signal, and in particular deliver no power or gain to the optical signal, leading to a phenomenon referred to as “spatial hole burning.” Would the vector field pattern analyzed above eliminate the problems caused by spatial hole burning?
5. *More on the twisted-mode cavity.* A laser cavity with no Brewster angle surfaces, with a quarter-wave plate at each end of the cavity, and with the principal axes of the two quarter-wave plates rotated by 45° with respect to each other, was invented once as a means of eliminating spatial inhomogeneity effects in lasers. Analyze the axial modes in this cavity, and explain why it may be useful for this purpose. (See my article, “Historical note on spatial hole burning and twisted-mode laser resonators,” *Opt. Commun.* **24**, 365, March 1978).

3.5 THE “FACTOR OF THREE”

One of the more confusing and often-argued aspects of atomic transitions is the “factor of three” that appeared in Equations 3.10 and 3.11, in the definition of oscillator strength, as well as in the trace of the tensor susceptibility in the preceding section. This section gives a brief but accurate explanation both of how this factor arises and of how it must be included in the appropriate theoretical formulas.

Tensor Power Transfer Rates

We showed in Section 3.4 that the tensor susceptibility for a real atomic transition can be written in the form

$$\chi(\omega) = \tilde{\chi}(\omega)\mathbf{T} = -j\chi_0''\mathbf{T} \quad (\text{at midband}), \quad (39)$$

where $\tilde{\chi}(\omega)$, or its midband value $-j\chi_0''$, is a scalar susceptibility formula (without the numerical factor of 3); and \mathbf{T} is a dimensionless tensor that we will always normalize to make

$$\text{Tr}[\mathbf{T}] = 3. \quad (40)$$

Let us now do some energy-storage and power-transfer calculations. For example, the time-averaged rate of energy transfer per unit volume from an applied field $\mathcal{E}(t)$ to a collection of atoms through the induced polarization $\mathbf{p}(t)$ may be written as

$$\frac{dU_a}{dt} = \left\langle \mathcal{E}(t) \cdot \frac{d\mathbf{p}(t)}{dt} \right\rangle. \quad (41)$$

For a steady-state sinusoidal response given by $\mathbf{P}(\omega) = \chi(\omega)\epsilon\mathbf{E}(\omega)$, this leads at midband, $\omega = \omega_a$, to the time-averaged result

$$\frac{dU_a}{dt} = -\frac{\omega_a \chi_0'' \epsilon [\mathbf{E}^* \cdot \mathbf{T} \mathbf{E} + \mathbf{E} \cdot \mathbf{T}^* \mathbf{E}^*]}{4}. \quad (42)$$

The multiplications on the right-hand side of this equation must be carried out using the standard rules for matrix multiplication, with vectors to the right of the dots considered as column vectors and quantities to the left of the dots considered as row vectors.

The time-averaged stored energy per unit volume in the same signal fields is, however,

$$U_{\text{sig}} = \left\langle \frac{1}{2} \epsilon |\mathcal{E}(t)|^2 \right\rangle = \frac{\epsilon [\mathbf{E}^* \cdot \mathbf{E}]}{2}. \quad (43)$$

Hence a ratio of energy transfer rate (to the atoms) over energy stored (in the signal fields) may be written as

$$\frac{1}{U_{\text{sig}}} \frac{dU_a}{dt} = \omega_a \chi_0'' \times \left[\frac{\mathbf{E}^* \cdot \mathbf{T} \mathbf{E} + \mathbf{E} \cdot \mathbf{T}^* \mathbf{E}^*}{2 \mathbf{E}^* \cdot \mathbf{E}} \right]. \quad (44)$$

When the dimensionless ratio in the brackets on the right-hand side of this equation is calculated for various forms of the susceptibility tensor \mathbf{T} , as given in the previous section, and for various signal field polarizations \mathbf{E} , its value always turns out to be somewhere between a maximum of 3 and a minimum of 0. (Some examples are shown in Table 3.3. Work a few of these out for practice, using the tensor forms from Section 3.4.)

TABLE 3.3
Normalized tensor responses

Saturated Tensor Form	Gain Applied Field Polarization	Normalized Response
Circular, $x \rightarrow \pm y$	Circular, $x \rightarrow \pm y$	3
Circular, $x \rightarrow \pm y$	Circular, $x \rightarrow \mp y$	0
Circular, $x \rightarrow \pm y$	Linear (x or y)	1.5
Circular, $x \rightarrow \pm y$	Linear (x)	0
Circular, $x \rightarrow \pm y$	Random	1
Linear (x)	Linear (x)	3
Linear (x)	Linear (angle θ from x)	$3 \cos^2 \theta$
Linear (x)	Circular, $x \rightarrow \pm y$	1.5
Linear	Random	1
Linear (x)	Linear (y or x)	0
Isotropic	Arbitrary	1

The Factor of "Three-Star"

The dimensionless factor that multiplies $\omega_a \chi_0''$ in Equation 3.44 thus always ranges between 0 and 3, depending on the nature of the signal polarization and the normalized tensor response. In fact, for different situations this dimensionless factor takes on values as follows.

- For *aligned atoms*—that is, for any collection of atoms that have a non-degenerate transition, and all of whose atomic axes are aligned in parallel to give an identical tensor response—there is always some optimum signal field polarization that will give this dimensionless factor its maximum value of 3, and thus make $(1/U_{\text{sig}})(dU_a/dt) = 3 \times \omega_a \chi_0''$.
- For such aligned atoms there is always also an “anti-optimum” signal polarization, for which the corresponding value is identically zero. (Linear dipole transitions have, in fact, an entire plane in which the induced response is identically zero.)
- Combining aligned atoms with any other signal polarization between the optimum and anti-optimum forms gives a value for the dimensionless factor somewhere between $3 \times \omega_a \chi_0''$ and $0 \times \omega_a \chi_0''$.

- For *nonaligned* (which is to say, randomly aligned) atoms, and hence an isotropic tensor response, the dimensionless response always has the value of unity, so that $(1/U_{\text{sig}})(dU_a/dt) = 1 \times \omega\chi_0''$.
- In a similar manner, for *randomly polarized* signal fields combined with any atomic alignment, the dimensionless response is also always unity.

In our discussions from here on, it would be nice if we did not have to keep track of the explicit vector nature of the signals or the tensor nature of the atomic responses. In order to do this, while allowing for the tensor nature of the atomic response, we will give this dimensionless factor in Equation 3.44 a name, and include it in the atomic susceptibility expression from now on. That is, we will from now on in this book often write the susceptibility expression for a homogeneous lorentzian atomic transition in the form

$$\tilde{\chi}(\omega) = -j \frac{3^*}{4\pi^2} \frac{\Delta N \lambda^3 \gamma_{\text{rad}}}{\Delta\omega_a} \frac{1}{1 + 2j(\omega - \omega_a)/\Delta\omega_a}, \quad (45)$$

where the parameter 3^* ("three-star") indicates what we will from now on call the "factor of three." This parameter, depending on circumstances, may have the numerical values:

- $3^* = 3$ for fully aligned atoms plus optimally polarized fields; or
- $3^* = 1$ either for randomly aligned atoms with arbitrarily polarized fields, or for randomly polarized fields with any atomic alignment; or
- $3^* = 0$ for fully aligned atoms and "anti-optimum" fields; or
- $0 \leq 3^* \leq 3$ for any intermediate case.

This notation will prove very convenient, especially since, as we will see, this same factor of 3^* carries over into many other stimulated-transition and gain formulas as well.

Problems for 3.5

1. *Averaging $\cos^2 \theta$ over 4π steradians.* Show by direct integration that the average value of $\cos^2 \theta$ averaged over all directions—that is, the value of $(4\pi)^{-1} \int \int \cos^2 \theta d\Omega$, where $d\Omega$ is the integral over all solid angles—is $1/3$.
-

3.6 DEGENERATE ENERGY LEVELS AND DEGENERACY FACTORS

In many real atomic systems, what appears to be a single atomic resonance in a collection of atoms, with a single transition frequency ω_{21} between upper and lower energy levels E_2 and E_1 , may in fact be the summation of a number of overlapping transitions, with different strengths and polarization properties, between distinct but degenerate sublevels of the upper and lower levels. It is still possible in discussing the small-signal response of such a system to treat such a

set of degenerate transitions as a single transition with an isotropic susceptibility. This section shows, however, that we must modify the definition of population inversion on such a degenerate transition by adding certain lower-level and upper-level degeneracy factors, in order to take into account the unresolved degeneracies of both the upper and lower levels.

Degeneracy Factors

Suppose, to be specific, that two apparently discrete energy levels E_1 and E_2 really each consist of g_1 and g_2 quantum-mechanically distinct sublevels, respectively, as shown in Figure 3.12. The integers g_1 and g_2 are then called the *statistical weights* or *degeneracy factors* of the levels. Let N_1 and N_2 be the *total* populations in levels E_1 and E_2 . At thermal equilibrium the atoms in each level will then be divided equally among the sublevels, with populations N_1/g_1 or N_2/g_2 in each of the respective sublevels. (There are, moreover, very rapid relaxation processes that usually act to rapidly equalize the populations of degenerate sublevels, even if they are somehow perturbed from equal populations, for example, by a strong applied signal.)

Boltzmann's Law, which relates the relative populations of an upper and lower energy level at thermal equilibrium, then applies rigorously to each distinct energy sublevel. In other words, it says that for any pair of such sublevels the population ratio at thermal equilibrium must be

$$\frac{N_2/g_2}{N_1/g_1} = \exp\left(-\frac{E_2 - E_1}{kT}\right). \quad (46)$$

Hence for the *total* level populations the Boltzmann ratio really must be written in the form

$$\frac{N_2}{N_1} = \frac{g_2}{g_1} \exp\left(-\frac{E_2 - E_1}{kT}\right). \quad (47)$$

This is a more precise generalization of the Boltzmann Law. Note that as a consequence of this, a highly degenerate upper level might possibly have, at thermal equilibrium, a larger total population than a lower level that is less degenerate (that is, if $g_2/g_1 > \exp[(E_2 - E_1)/kT]$). This is not a population inversion in any sense, however—for example, it does not lead to net stimulated emission or gain, as we will now show.

Net Susceptibility of a Degenerate Transition

To evaluate the overall stimulated response on a degenerate transition, we must sum over all the individual subtransitions, as shown in Figure 3.12. Let us label all the upper sublevels by an index m that runs from $m = 1$ to $m = g_2$, and all the lower sublevels by a similar index n . The total response on the transition is then the sum over n and m of all transitions between all the sublevels E_{1n} and E_{2m} .

The tensor susceptibility on any one such transition between level E_{1n} and level E_{2m} may then be written in the form

$$\chi_{1n,2m}(\omega) = \tilde{g}(\omega) \times \gamma_{\text{rad},2m \rightarrow 1n} \times \left(\frac{N_1}{g_1} - \frac{N_2}{g_2}\right) \times \mathbf{T}_{1n,2m}, \quad (48)$$

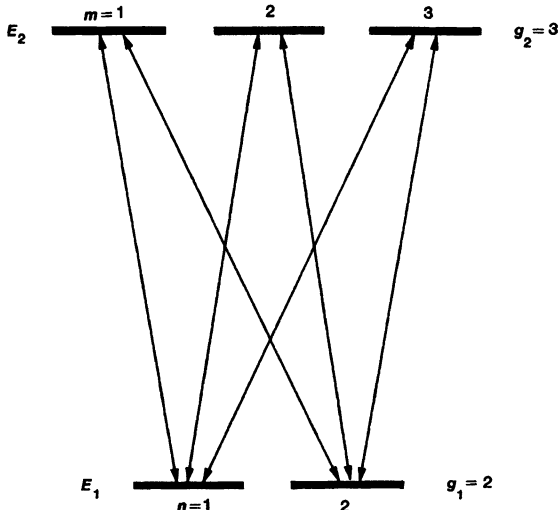


FIGURE 3.12
Degenerate sublevels of two quantum energy levels E_1 and E_2 . Each sublevel is a separate and distinct quantum energy eigenstate, but the degenerate sublevels all have the same energy eigenvalue.

where $T_{1n,2m}$ is the tensor response on that particular transition; $N_1/g_1 - N_2/g_2$ gives the population difference on that particular transition; $\gamma_{\text{rad},2m \rightarrow 1n}$ gives the strength of that particular transition; and the lineshape function $\tilde{g}(\omega)$ can usually be assumed to be the same for all transitions, namely,

$$\tilde{g}(\omega) = -j \frac{1}{4\pi^2} \frac{\lambda^3}{\Delta\omega_a} \frac{1}{1 + 2j(\omega - \omega_a)/\Delta\omega_a}. \quad (49)$$

(If different subtransitions have different linewidths, this will complicate the following analysis, but probably not change the results.)

The total response on all the $1n \rightarrow 2m$ transitions can then be written as

$$\begin{aligned} \chi_{\text{tot}}(\omega) &= \sum_{n=1}^{g_1} \sum_{m=1}^{g_2} \chi_{1n,2m}(\omega) \\ &= \tilde{g}(\omega) \times \sum_{n=1}^{g_1} \sum_{m=1}^{g_2} \gamma_{\text{rad},2m \rightarrow 1n} \left(\frac{N_1}{g_1} - \frac{N_2}{g_2} \right) \times T_{\text{av}}, \end{aligned} \quad (50)$$

where T_{av} is some averaged tensor susceptibility over all the transitions involved. This tensor will simply be isotropic if the average is over a complete set of degenerate transitions.

At the same time, the total radiative decay rate downward out of the upper level E_2 will be given by

$$\frac{dN_2}{dt} = - \sum_{n=1}^{g_1} \sum_{m=1}^{g_2} \gamma_{\text{rad},2m \rightarrow 1n} \left(\frac{N_2}{g_2} \right). \quad (51)$$

That is, we must sum over all radiative decay rates from all upper sublevels to all lower sublevels. This total downward rate may then be equated to an averaged

or measured radiative decay rate that we will call $\gamma_{\text{rad},2 \rightarrow 1}$, defined by

$$\frac{dN_2}{dt} = -\gamma_{\text{rad},2 \rightarrow 1} N_2. \quad (52)$$

This will be the measured radiative decay rate for level E_2 viewed as a single effective level without degeneracy taken into account. Since the level populations can be taken outside the sums in all the preceding equations, this averaged decay rate is given by

$$\gamma_{\text{rad},2 \rightarrow 1} \equiv \frac{1}{g_2} \sum_n \sum_m \gamma_{\text{rad},2m \rightarrow 1n} \quad (53)$$

Combining Equations 3.48 to 3.53 then gives

$$\chi_{\text{tot}}(\omega) = \tilde{g}(\omega) \times \gamma_{\text{rad},2 \rightarrow 1} \times \left(\frac{g_2}{g_1} N_1 - N_2 \right) \times T_{\text{av}}. \quad (54)$$

If we absorb the tensor properties into a factor 3^* as in the previous section, this may be written as a scalar susceptibility

$$\tilde{\chi}_{\text{tot}}(\omega) = -j \frac{3^*}{4\pi^2} \frac{\lambda^3 \gamma_{\text{rad},2 \rightarrow 1}}{\Delta\omega_a} \left(\frac{g_2}{g_1} N_1 - N_2 \right) \frac{1}{1 + 2j(\omega - \omega_a)/\Delta\omega_a}, \quad (55)$$

where T_{av} will normally be isotropic and 3^* will be equal to unity.

This final result now looks exactly like the nondegenerate susceptibility expression in earlier sections, except that the population difference ΔN is replaced by

$$\Delta N \Rightarrow \left(\frac{g_2}{g_1} N_1 - N_2 \right). \quad (56)$$

A more precise condition for population inversion and gain on an atomic transition is thus

$$\frac{N_2}{g_2} > \frac{N_1}{g_1} \quad (57)$$

and not just $N_2 > N_1$. In physical terms, there must be true population inversion on the individual sublevels, and not simply $N_2 > N_1$.

For degenerate transitions in gases, with randomly aligned atoms, the averaged tensor susceptibility T_{av} will in fact always be isotropic, leading to $3^* = 1$ in Equation 3.55. For degenerate transitions in solids the situation may be somewhat more complex, and a degenerate transition may still have some anisotropic character to its tensor response T_{av} .

Discussion

The main result of this section, then, is that the small-signal steady-state response on a degenerate transition is exactly the same as for a nondegenerate transition, except that the effective value of $\gamma_{\text{rad},2 \rightarrow 1}$ must be employed, and the effective population difference becomes $\Delta N \equiv (g_2/g_1)N_1 - N_2$ rather than just $N_1 - N_2$. We will use this result where appropriate in future sections.

This result does assume that the various sublevels of each main level remain equally populated, so that we can assign an equal fraction N_j/g_j of the level population to each one of them. For very strong signals, and perhaps also for very

short pulses (short compared to T_2), some of the transitions between sublevels E_{1n} and E_{2m} will respond more strongly to an applied signal than will others, because of substantially different values of $\gamma_{\text{rad},2m \rightarrow 1n}$, as well as different polarization properties. A strong applied signal will then cause atoms to flow from certain sublevels E_{1n} to other sublevels E_{2m} at quite different rates; and this difference will tend to unbalance the otherwise equal sublevel populations, especially if for some reason the relaxation between the sublevels is slowed down. This kind of selective pumping between lower and upper sublevels, especially when the degeneracy has been slightly broken, is in fact an essential element of a spectroscopic technique referred to as *optical pumping*.

Unless the degeneracy between sublevels is at least partially broken, however, there will usually also be relaxation processes between sublevels that will tend to rapidly return the sublevel populations to equality. These so-called "cross-relaxation" processes can be especially fast, because no energy change is required to relax an atom from one sublevel to another sublevel within the same degenerate main level. Strong applied signals can thus override these relaxation processes, but only temporarily.

The general warning to be taken is the following: In considering the effects of very strong (or very short-pulse) signals, for example, in so-called "coherent pulse" experiments, a degenerate transition can no longer be treated as a slightly modified single transition. It must instead be treated in detail as a set of multiple, independent, though still closely coupled transitions all at the same frequency.

REFERENCES

A good readable discussion of some of the limitations warned about in the last paragraph is A. Dienes, "On the physical meaning of the 'two nondegenerate levels' atomic model in nonlinear calculations," *IEEE J. Quantum Electr.* **QE-4**, 260-263 (May 1968). See also B. W. Shore, "Effects of magnetic sublevel degeneracy on Rabi oscillations," *Phys. Rev. A* **17**, 1739-1746 (May 1978).

Self-induced transparency is one of the large-signal situations in which the behavior with degeneracy present is considerably different from that in the simple nondegenerate case. This is discussed in detail by C. K. Rhodes, A. Szöke, and A. Javan, "The influence of level degeneracy on the self-induced transparency effect," *Phys. Rev. Lett.* **21**, 1151-1155 (October 14, 1978).

Rather complex equations result if we take full account of the level degeneracies in a gas laser, especially if we include the small Zeeman splitting of the nearly degenerate transitions that results when either a longitudinal or a transverse dc magnetic field is applied. One example from among the extensive literature on this topic is M. Sargent III and W. E. Lamb, Jr., "Theory of a Zeeman laser. I and II," *Phys. Rev.* **164**, 436-465 (December 10, 1967).

3.7 INHOMOGENEOUS LINE BROADENING

As the final step in describing the resonant response of real atomic transitions, we must introduce an additional and important type of line broadening known as *inhomogeneous broadening*, of which doppler broadening is the premier example.

Homogeneous Broadening

The steady-state response of a homogeneously broadened transition in a collection of oscillators or atoms is given by the complex lorentzian formula

$$\tilde{\chi}_h(\omega; \omega_a) = -j \frac{3^*}{4\pi^2} \frac{\Delta N \lambda^3 \gamma_{\text{rad}}}{\Delta \omega_a} \frac{1}{1 + 2j(\omega - \omega_a)/\Delta \omega_a}. \quad (58)$$

We have attached a subscript h to indicate that this is the usual form for a *homogeneous* transition; and we have added the second argument to $\tilde{\chi}_h(\omega; \omega_a)$ to indicate the explicit dependence on the resonance frequency ω_a along with the applied frequency or signal frequency ω . This kind of broadening is called *homogeneous broadening* because the response of each individual atom in the collection is equally and homogeneously broadened. Many real atomic transitions, under appropriate conditions, exhibit exactly this lineshape.

Inhomogeneous Broadening

In many other real atomic situations, however, different atoms in a collection of nominally identical atoms may, for various reasons, have slightly different resonant frequencies ω_a , such that the ω_a values for different atoms are randomly distributed about some central value ω_{a0} . We must then think of the resonance frequencies ω_a for different atoms as being randomly shifted by small but different amounts for each atom in the collection.

An applied signal passing through such a collection of atoms will then see only a total response due to all the atoms—it will have no way to pick out only those atoms with certain specific frequency shifts. If the random shifting of the individual center frequencies is sizable compared to the linewidth $\Delta \omega_a$ of each individual response, any measurement of the overall response from all the atoms in the collection will then give a smeared-out or broadened summation of the randomly shifted responses of all the individual atoms (see Figure 3.13). The overall response of the collection of atoms will be substantially broadened, and the response at line center will be substantially reduced in amplitude. This general type of behavior is referred to as *inhomogeneous broadening*.

Spectral Packets

That subgroup of atoms whose resonant frequencies ω_a all fall within a range of roughly one homogeneous linewidth $\Delta \omega_a$ about a given value of ω_a is often referred to as a single *spectral packet* (or *spin packet* in magnetic-resonance jargon). All the atoms in a single packet have essentially the same (homogeneous) response to an applied signal. The total response of an inhomogeneously broadened line is then the sum of the individual responses of all the spectral packets, each at a different resonance frequency.

If the individual packets are spread out in frequency about ω_{a0} by an amount large compared to their individual homogeneous widths $\Delta \omega_a$, as in Figure 3.13, the line is said to be *strongly inhomogeneous*. If the inhomogeneous shifting is small compared to the homogeneous packet widths, the line will remain essentially homogeneous, and the amount of inhomogeneous broadening that does exist will be of little importance.

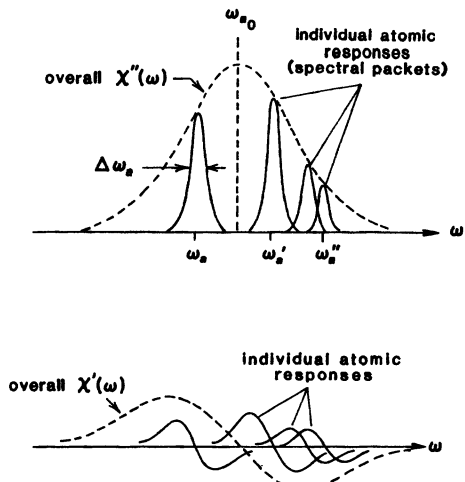


FIGURE 3.13
Individual atomic responses, or "spectral packets," within an inhomogeneously broadened atomic transition.

Causes of Inhomogeneous Broadening

There are several possible causes of random resonance-frequency shifting and thus of inhomogeneous broadening in typical atomic systems.

- In gases, different atoms will have different kinetic velocities through space. This kinetic motion produces a doppler shift in the frequency of an applied signal as seen by the atom, or alternatively a doppler shift in the apparent resonance frequency ω_a of the atom as seen by the applied signal. This so-called *doppler broadening* is an important and widespread source of inhomogeneous broadening for optical-frequency transitions in atomic and molecular gases.
- In solids, laser atoms at different sites in a crystal may see slightly different local surroundings, or different local crystal structures, because of defects, dislocations, or lattice impurities. This produces slightly different values for the exact energy levels of the atoms, and thus slight shifts in transition frequencies. To the extent that the local lattice surroundings are similar for every atom but vibrate rapidly and randomly in time, they produce a dynamic *homogeneous phonon broadening*. To the extent that the surroundings are different from site to site but static in time, they produce a static *inhomogeneous lattice broadening* or *strain broadening*.

Other types of inhomogeneous broadening also exist (for example, inhomogeneous dc magnetic fields in magnetic resonance experiments), but these are two of the most important for optical transitions.

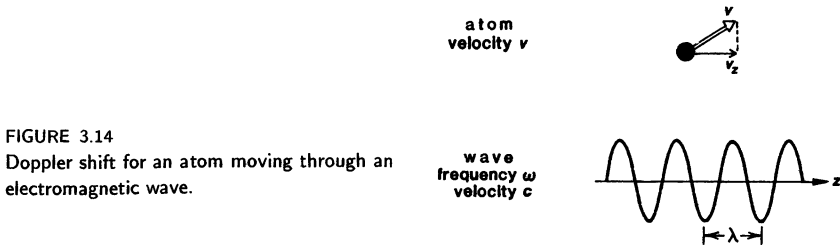


FIGURE 3.14
Doppler shift for an atom moving through an electromagnetic wave.

Doppler Broadening

One of the most common examples of inhomogeneous broadening is *doppler broadening* of the resonance transitions in gases. The atoms in an atomic or molecular gas will have, in addition to their internal oscillations, thermal or Brownian kinetic motion through space, with a Maxwellian distribution of kinetic velocities. When an atom moving with velocity v_z as in Figure 3.14 interacts with a wave of signal frequency ω traveling at velocity c along the z direction (for example, a wave traveling down the axis of a laser tube), the frequency of the wave as seen by the atom will be doppler-shifted to a new value ω' given by

$$\omega' = (1 - v_z/c) \omega. \quad (59)$$

Resonance of the applied signal with the atomic transition in that particular atom will then occur when the doppler-shifted signal frequency $\omega' = \omega(1 - v_z/c)$ seen by the moving atom equals the atom's internal resonance frequency ω_{a0} .

From an alternative viewpoint, resonance will occur when the signal frequency ω measured in the laboratory frame equals the shifted resonance value $\omega_{a0}(1 + v_z/c)$. In other words, as seen from the lab the resonance frequency of the atom appears to be doppler-shifted to a new value,

$$\omega_a = (1 + v_z/c) \omega_{a0}. \quad (60)$$

For an atom or molecule of mass M in a gas at temperature T , the kinetic velocity v_z has a mean-square value given by $M \langle v_z^2 \rangle \approx kT$. Hence the average doppler shift for a moving gas atom will be of order

$$\frac{\omega_a - \omega_{a0}}{\omega_{a0}} \approx \sqrt{\frac{kT}{Mc^2}} \approx 10^{-6} \quad \left(\begin{array}{l} \text{for typical atomic} \\ \text{masses and temperatures} \end{array} \right). \quad (61)$$

The amount of doppler broadening in a real gas thus depends (but only rather slowly) on the kinetic temperature T of the gas and on the molecular weight of the atom or molecule involved.

Doppler Lineshape

To be more precise, the distribution of axial velocities v_z in a gas at thermal equilibrium will be a Maxwellian, or gaussian, probability distribution given by

$$g(v_z) = \left(\frac{1}{2\pi\sigma_v^2} \right)^{1/2} \exp \left(-\frac{v_z^2}{2\sigma_v^2} \right) \quad (62)$$

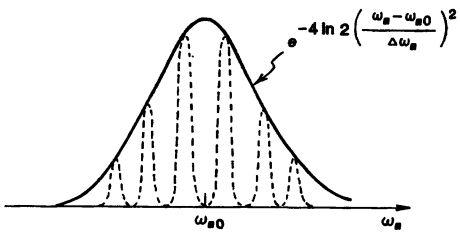


FIGURE 3.15

A gaussian inhomogeneous atomic lineshape, such as is produced by doppler broadening in atoms.

with an rms spread given by $\sigma_v^2 = kT/M$. The inhomogeneous distribution of shifted resonant frequencies, call it $g(\omega_a)$, for a doppler-broadened atomic transition will then similarly have a gaussian form that can be written as

$$g(\omega_a) = \left(\frac{4 \ln 2}{\pi \Delta \omega_d^2} \right)^{1/2} \exp \left[-\left(4 \ln 2 \right) \left(\frac{\omega_a - \omega_{a0}}{\Delta \omega_d} \right)^2 \right] \quad (63)$$

as illustrated in Figure 3.15. This expression has been written so that ω_{a0} is the center frequency; and following our standard convention, the linewidth $\Delta\omega_d$ has been defined to be the FWHM linewidth of the gaussian distribution, which means it must take on the form

$$\Delta\omega_d = \sqrt{\frac{(8 \ln 2) kT}{Mc^2}} \omega_{a0}. \quad (64)$$

It is useful to remember that in units of electron volts, kT at room temperature is 1/40 of an electron volt or 25 meV; and Mc^2 is the rest-mass energy of the atom, which for a single proton is $\approx 10^9$ eV. For an atom or molecule with an atomic number of 20, the fractional doppler broadening is thus

$$\frac{\Delta\omega_d}{\omega_{a0}} = \sqrt{\frac{(8 \ln 2) kT}{Mc^2}} \approx \sqrt{\frac{5.5 \times 25 \times 10^{-3}}{20 \times 10^9}} \approx 2.6 \times 10^{-6} \quad (65)$$

or typically a few parts per million. A visible laser transition will have a center frequency on the order of $\omega_a/2\pi \approx 6 \times 10^{14}$ Hz, and a doppler broadening on the order of $\Delta\omega_d/2\pi \approx 2 \times 10^9$ Hz \approx 2 GHz. The room-temperature doppler broadening of the He-Ne laser transition at 633 nm, in fact, is just about $\Delta\omega_d/2\pi \approx 1,500$ MHz.

General Analysis of Inhomogeneous Broadening

As a more general approach to inhomogeneous broadening, suppose we consider a large collection of nominally identical atoms, with the fractional number of atoms whose exact resonant frequency is between some value ω_a and $\omega_a + d\omega_a$ being given by

$$dN(\omega_a) = Ng(\omega_a) d\omega_a, \quad (66)$$

where N is the total number of atoms. (We really should use the population difference ΔN here, but let's write N instead for simplicity.) The function $g(\omega_a)$ is thus the probability density distribution over the resonant frequencies ω_a , with

the normalization that

$$N^{-1} \int_0^\infty dN(\omega_a) = \int_{-\infty}^\infty g(\omega_a) d\omega_a = 1. \quad (67)$$

The function $g(\omega_a)$ is always very narrowly clustered about the center frequency ω_{a0} , so any portion of the analytic function $g(\omega_a)$ extending below $\omega_a = 0$ can be ignored. It therefore makes negligible difference whether the lower limit in this normalization integral is actually 0 or $-\infty$.

To calculate the overall complex susceptibility of any such collection of atoms, we must then multiply the homogeneous response $\tilde{\chi}_h(\omega; \omega_a)$ produced by any one atom whose resonance frequency is ω_a by the fractional number of atoms $g(\omega_a) d\omega_a$ that have the same resonance frequency ω_a , as illustrated in Figure 3.13, and then integrate that response over all values of ω_a in the form

$$\tilde{\chi}(\omega) = \int_{-\infty}^\infty \tilde{\chi}_h(\omega; \omega_a) g(\omega_a) d\omega_a. \quad (68)$$

Suppose the distribution $g(\omega_a)$ is gaussian, as it often is. The full-blown equation for the complex small-signal susceptibility of an inhomogeneously broadened transition thus becomes a gaussian distribution of frequency-shifted lorentzian lines. If we write this out in full, it takes the general form

$$\begin{aligned} \tilde{\chi}(\omega) = & -j \frac{3^*}{4\pi^2} \sqrt{\frac{4 \ln 2}{\pi}} \frac{N \lambda^3 \gamma_{\text{rad}}}{\Delta\omega_a \Delta\omega_d} \int_{-\infty}^\infty \frac{1}{1 + 2j(\omega - \omega_a)/\Delta\omega_a} \\ & \times \exp \left[-(4 \ln 2) \left(\frac{\omega_a - \omega_{a0}}{\Delta\omega_d} \right)^2 \right] d\omega_a. \end{aligned} \quad (69)$$

This rather messy integral must be evaluated each time an accurate calculation is needed of the susceptibility of an atomic transition in which doppler broadening is important. (Even this integral still ignores certain large-signal saturation and “hole-burning” effects that we will discuss in a later chapter.)

Inhomogeneous broadening in general, whether due to doppler broadening or to other mechanisms, is usually caused by some kind of random distribution of velocities, or defects, or whatever; and random distributions, whatever their cause, are very often gaussian in form (as sometimes expressed in the Central Limit Theorem). We will therefore interpret the gaussian expression for doppler broadening in Equation 3.63 somewhat more broadly, and use it as a general expression for $g(\omega_a)$ in any kind of inhomogeneous broadening. Similarly, we will use $\Delta\omega_d$ as a general notation for the inhomogeneous linewidth of an inhomogeneously broadened distribution, whether this is due to doppler broadening or to some other cause.

Strongly Homogeneous Limit

The integral in Equation 3.69 cannot be evaluated analytically, at least not for arbitrary ratios of inhomogeneous broadening $\Delta\omega_d$ to homogeneous broadening $\Delta\omega_a$. The limiting cases of strongly homogeneous broadening and strongly inhomogeneous broadening can, however, be handled, at least approximately, as follows.

Let us suppose first that the inhomogeneous broadening effects are small, which means either that the resonance frequencies of individual packets are

shifted by very little compared to the homogeneous linewidth $\Delta\omega_a$, or alternatively that the individual packets have a wide homogeneous linewidth $\Delta\omega_a$ compared to the inhomogeneous linewidth $\Delta\omega_d$. The inhomogeneous distribution, whether gaussian or otherwise, is then essentially a delta function, i.e.,

$$g(\omega_a) \approx \delta(\omega_a - \omega_{a0}) \quad \text{if } \Delta\omega_d \ll \Delta\omega_a. \quad (70)$$

The integral in Equation 3.69 is now trivial, and physically obvious: the overall response is simply the unperturbed homogeneous form $\tilde{\chi}_h(\omega; \omega_{a0})$. In effect there is no inhomogeneous or doppler broadening. This is commonly known as the *strongly homogeneous limit*.

As one practical example of this, consider the 10.6 μm TEA CO₂ laser operating at atmospheric pressure. The inhomogeneous doppler broadening for this long-wavelength transition is $\Delta\omega_d/2\pi \approx 60$ MHz, whereas the homogeneous pressure broadening at one atmosphere is $\Delta\omega_a/2\pi \approx 6$ GHz or 6,000 MHz. The individual packets are thus ≈ 100 times wider than the doppler broadening, and the line is essentially homogeneous.

Strongly Inhomogeneous Limit

Now suppose instead that the inhomogeneous linewidth $\Delta\omega_d$ is large enough to shift the spectral packets widely in frequency compared to their homogeneous linewidth $\Delta\omega_a$, so that there are many packets within the overall linewidth. It is then possible in this limit to obtain an analytic approximation to Equation 3.69 that is reasonably accurate for the imaginary part $\chi''(\omega)$ of the overall inhomogeneous susceptibility, though not for the $\chi'(\omega)$ part.

The approximation for the absorptive part of the overall susceptibility is obtained by expanding the complex lorentzian $\tilde{\chi}_h(\omega; \omega_a)$ inside the general integral into its real and imaginary parts. In the limit as $\Delta\omega_a$ becomes small, the χ''_h part of the homogeneous function becomes roughly like a delta function, i.e.,

$$\frac{2}{\pi\Delta\omega_a} \frac{1}{1 + [2(\omega - \omega_a)/\Delta\omega_a]^2} \approx \delta(\omega - \omega_a) \quad \text{if } \Delta\omega_a \ll \Delta\omega_d. \quad (71)$$

This lorentzian curve is not a very good delta function, since its wings fall off only as $1/(\omega - \omega_a)^2$ far from line center, but it is adequate here. Putting this into the general equation and integrating over the delta function then gives for the $\chi''(\omega)$ part of the susceptibility

$$\chi''(\omega) \approx -\sqrt{\pi \ln 2} \frac{3^*}{4\pi^2} \frac{\Delta N \lambda^3 \gamma_{\text{rad}}}{\Delta\omega_d} \exp \left[-(4 \ln 2) \left(\frac{\omega - \omega_{a0}}{\Delta\omega_d} \right)^2 \right] \quad (72)$$

in the strongly inhomogeneous limit where $\Delta\omega_d \gg \Delta\omega_a$.

This expression for a strongly inhomogeneous absorption line has the following interesting features in comparison with the usual homogeneous lorentzian absorption line.

- It has a gaussian, not a lorentzian, lineshape for the absorption profile of $\chi''(\omega)$, with a FWHM linewidth of $\Delta\omega_d$, not $\Delta\omega_a$.

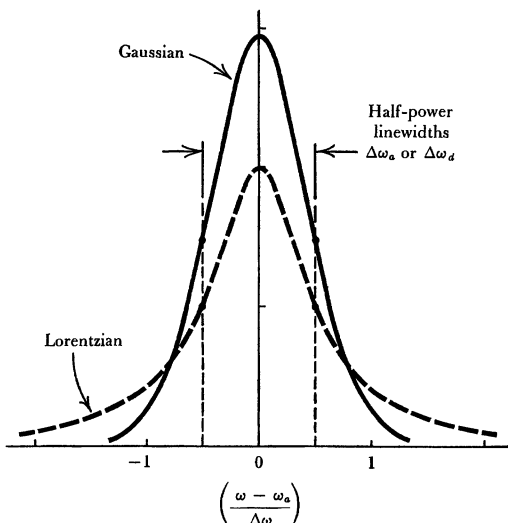


FIGURE 3.16
Comparison of gaussian and
lorentzian lineshapes having the
same half-power linewidth and
the same total area.

- It has essentially the same constant factors in front as does the homogeneous lorentzian response for $\chi''(\omega)$, except that the response now varies as $1/\Delta\omega_d$, instead of $1/\Delta\omega_a$.
- But it has an extra numerical factor of $\sqrt{\pi \ln 2} \approx 1.48$ in front of the other factors that appear in the lorentzian expression.

In fact, these three simple modifications convert the $\chi''(\omega)$ susceptibility expression for a homogeneous lorentzian transition into the corresponding expression for a strongly inhomogeneous gaussian or doppler-broadened transition.

Figure 3.16 shows lorentzian and gaussian (i.e., strongly homogeneous and strongly inhomogeneous) susceptibilities $\chi''(\omega)$ normalized to the same FWHM linewidth and the same area. Note that the gaussian absorption curve $\chi''(\omega)$ has a peak value that is $\approx 50\%$ higher, but that it drops off much faster in the wings than does the lorentzian. The integrated area under each curve is the same, since the smaller area in the wings of the gaussian profile is balanced by the 50% larger peak intensity at the center.

It is also interesting to note that the homogeneous packet linewidth $\Delta\omega_a$ actually does not appear at all in the strongly inhomogeneous expression given in Equation 3.72. *Measuring the $\chi''(\omega)$ response of a strongly inhomogeneous line tells you $\Delta\omega_d$, but it does not give any information about the homogeneous linewidth $\Delta\omega_a$ of the packets buried within the line—at least not to first order.*

Complex Susceptibility in the Strongly Inhomogeneous Limit

It is not possible to develop a similar approximation for the reactive part of the susceptibility, $\chi'(\omega)$, in the strongly inhomogeneous limit. The reason is essentially that although $\chi''(\omega)$ varies like $1/(1 + \omega^2)$ in frequency, which is a weak delta function, the real part $\chi'(\omega)$ varies like $\omega/(1 + \omega^2)$, which is not a delta

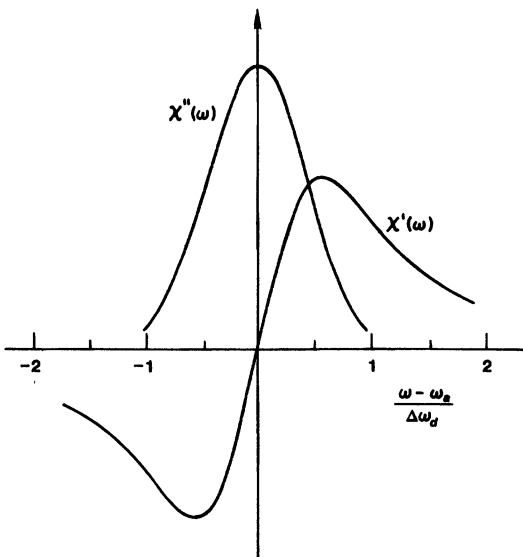


FIGURE 3.17
Exact plots of the real and imaginary parts of the complex susceptibility for a strongly inhomogeneous gaussian transition.

function at all. There is thus no analytic approximation to the exact integral of Equation 3.69 for $\chi'(\omega)$ even in the strongly inhomogeneous limit.

Figure 3.17 does show numerically computed plots of both $\chi'(\omega)$ and $\chi''(\omega)$ for the strongly inhomogeneous gaussian limit, $\Delta\omega_d \gg \Delta\omega_a$. The inhomogeneous susceptibility $\chi'(\omega)$, though it cannot be analytically approximated, looks in general very much like the lorentzian case; i.e., it is antisymmetric and looks generally (though not exactly) like the first derivative of the $\chi''(\omega)$ curve.

Intermediate Region: Voight Profiles and Their Uses

In the intermediate region where $\Delta\omega_a \approx \Delta\omega_d$ and neither of the limiting approximations is valid, the general expression for $\tilde{\chi}(\omega)$ in Equation 3.69 can only be integrated numerically and then plotted for different ratios of $\Delta\omega_a/\Delta\omega_d$. The lineshapes for the $\chi''(\omega)$ curves that are obtained in this region are obviously intermediate between lorentzian and gaussian lineshapes, and are generally referred to as *Voight profiles*. The exact shape of the Voight profile depends on both the homogeneous and the inhomogeneous linewidths, or, more precisely, on the ratio of these two linewidths.

Figure 3.18 shows, for example, the measured absorption profile for a molecular transition in carbon monoxide (the $v'' = 0, J'' = 11$ to $v' = 1, J' = 10$ transition) at a wavelength of $\lambda = 4.76 \mu\text{m}$ or $1/\lambda = 2,099 \text{ cm}^{-1}$, as measured with a tunable laser in a 10:2:88 mixture of $\text{CO}_2:\text{H}_2:\text{Ar}$ at a temperature of 3,340 K and a pressure of 0.195 atm. (These rather unusual conditions were obtained in a special shock-tube measuring apparatus.) This absorption profile is clearly best matched by a Voight profile somewhere intermediate between a gaussian and a lorentzian.

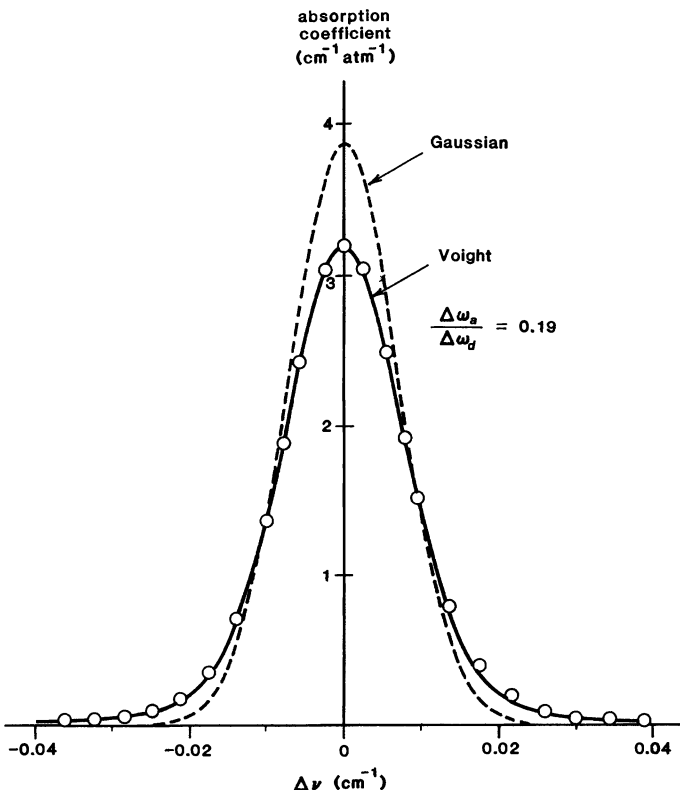


FIGURE 3.18

Measured values of the absorption profile for carbon monoxide (circles) compared with gaussian and Voight functions having the same half-power values.

If we have an experimental plot of $\chi''(\omega)$ for a transition in this intermediate region that has been measured with sufficient accuracy, we can in fact deconvolve the lorentzian and gaussian contributions by fitting the measured curve to numerically a computed Voight profile with the proper ratio of $\Delta\omega_a/\Delta\omega_d$. Since we can predict the doppler linewidth for a given transition in a gas fairly accurately from the theoretical expression in Equation 3.64, we can then use the ratio of $\Delta\omega_a/\Delta\omega_d$ from this kind of Voight profile determinations to derive the homogeneous linewidth $\Delta\omega_a$, provided it is not too small compared to $\Delta\omega_d$. Figure 3.19 shows, for example, absorption data for various pressures of pure CO_2 taken with a tunable CO_2 laser and fitted to Voight profiles. (The absorption measurement technique used here was actually a more effective way of measuring weak absorptions, called photoacoustic spectroscopy.) The top trace shows the laser tuning curve, and the middle traces show raw data, with frequency markers every 30 MHz of frequency tuning. The lower plot shows this data normalized and fitted to a series of Voight profiles with increasing amounts of lorentzian pressure broadening.

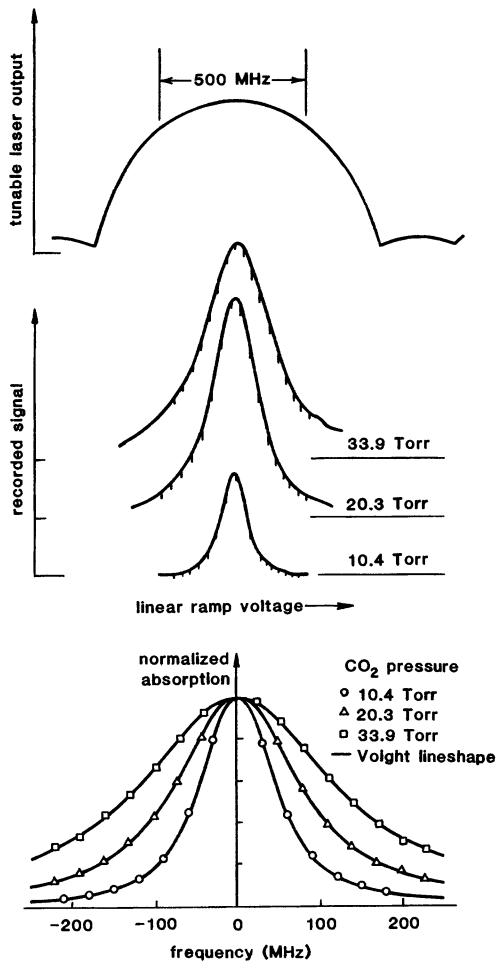


FIGURE 3.19
 Top: The power output from a tunable CO₂ laser versus frequency tuning. Middle: Three absorption profiles for pure CO₂ at different pressures measured using this laser. Bottom: This same data fitted to Voight profiles with different degrees of inhomogeneous broadening.

The Transition From Doppler to Pressure Broadening

If we gradually increase the gas pressure in an absorption cell, the measured absorption profile of a transition in the gas atoms will change over from being doppler-broadened at low pressures ($\Delta\omega_a \ll \Delta\omega_d$) to being pressure broadened at high pressures ($\Delta\omega_a \gg \Delta\omega_d$).

Figure 3.20(a) shows, as one example, an apparatus for making accurate measurements of the absorption profiles of various CO₂ gas mixtures at different pressures using a tunable CO₂ laser. In (b) we see direct midband absorption data versus total gas pressure measured on a typical He:N₂:CO₂ gas mixture, and (c) shows the atomic linewidth deduced from this data. Both curves illustrate the changeover from inhomogeneous doppler broadening at low pressures to homogenous pressure (collision) broadening at high pressures. Figure 3.21 which

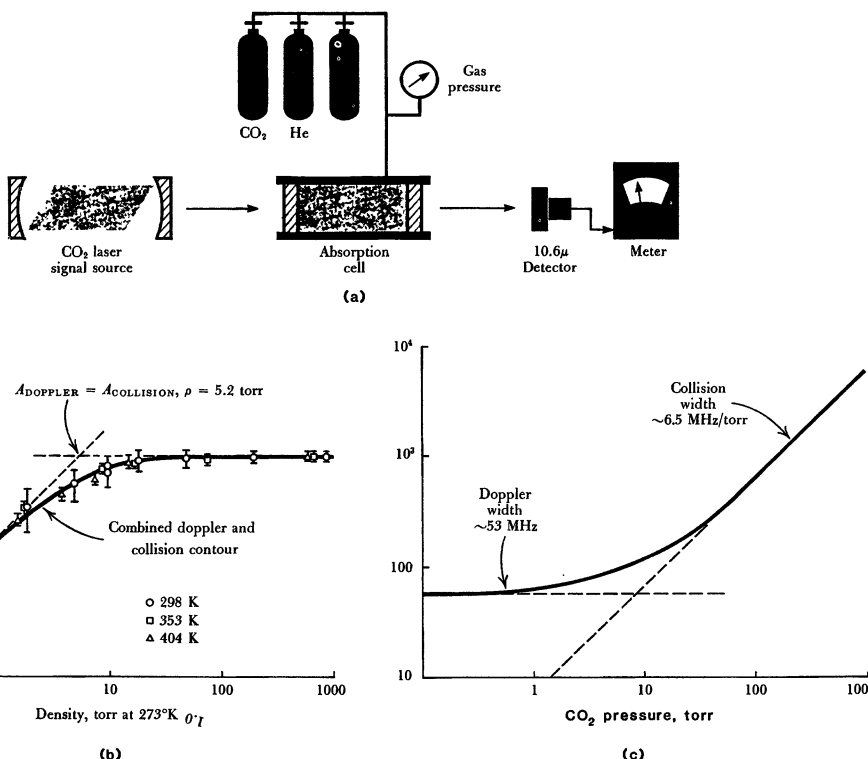


FIGURE 3.20

(a) Apparatus using a tunable CO₂ laser to measure absorption versus frequency in a variable-pressure CO₂ cell. (b) Midband (peak) absorption versus gas pressure; and (c) linewidth versus pressure in a typical He:Ne:CO₂ mixture, showing changeover from doppler broadening at low pressures to pressure (collision) broadening above about 10 torr total pressure. (Data from E. T. Gerry and D. A. Leonard, *Appl. Phys. Lett.* 8, 227, May 1, 1966.)

shows a very similar variation with pressure of the absorption coefficient on a certain chemical laser transition in the mid-IR using deuterium fluoride (DF) molecules (see Problems).

An Alternative Notation: T_2 and T_2^*

The lorentzian and gaussian lineshapes that we have developed in this section are often expressed in an alternative notation, which we can briefly summarize as follows.

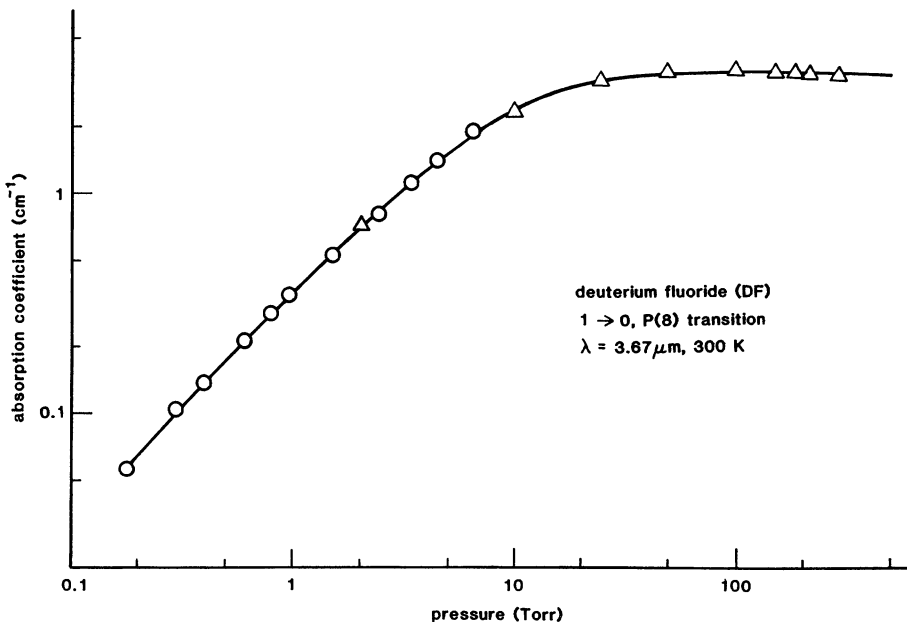


FIGURE 3.21

Midband absorption coefficient versus pressure on a deuterium fluoride (DF) transition, showing the transition from doppler broadening at low pressures to pressure broadening at higher pressures.

In the scientific literature on magnetic resonance, where inhomogeneous broadening was first studied, as well as in other areas of resonance physics, the complex homogeneous lorentzian lineshape is often written in the alternative notation

$$\tilde{\chi}_{\text{lor}}(\omega) = -j\chi_0'' \frac{1}{1 + jT_2(\omega - \omega_a)}, \quad (73)$$

and the real lorentzian lineshape for a homogeneous absorption line is then commonly written in normalized form as

$$g_{\text{lor}}(\omega) = \frac{2}{\pi\Delta\omega_a} \frac{1}{1 + [2(\omega - \omega_a)/\Delta\omega_a]^2} \equiv \frac{T_2}{\pi} \frac{1}{1 + T_2^2(\omega - \omega_a)^2} \quad (74)$$

with the same normalization that $\int g_{\text{lor}}(\omega) d\omega = 1$. In this notation the FWHM homogeneous linewidth is usually written in the simpler form

$$\Delta\omega_a \equiv 2/T_2 \quad (75)$$

rather than as $\Delta\omega_a = \gamma + 2/T_2$. In essence, the γ contribution to the homogeneous linewidth has been absorbed into an expanded definition of $2/T_2$ that includes both the dephasing and lifetime-broadening contributions. (We will occasionally use this expanded definition of T_2 later in this book.)

Then, in order to make the gaussian lineshape function $g_{\text{gauss}}(\omega)$ have the same algebraic constants in front for the same normalization, the inhomogeneous

function is written in the analogous form

$$g_{\text{gauss}}(\omega) \equiv \left(\frac{T_2^*}{\pi} \right) \exp \left[-\frac{T_2^{*2}(\omega - \omega_a)^2}{\pi} \right], \quad (76)$$

which satisfies the same normalization that $\int g_{\text{gauss}}(\omega) d\omega = 1$. The parameter T_2^* that has been introduced here is the inhomogeneous analog to the dephasing time T_2 in the homogeneous case. It is related to the gaussian inhomogeneous linewidth $\Delta\omega_d$ by

$$\Delta\omega_d \equiv \frac{\sqrt{4\pi \ln 2}}{T_2^*} \approx \frac{3}{T_2^*}. \quad (77)$$

The quantity $T_2^* \approx 3/\Delta\omega_d$ is thus the inhomogeneous (or gaussian) analog to the quantity $T_2 = 2/\Delta\omega_a$ for the homogeneous (or lorentzian) lineshape.

Physical Significance of T_2 and T_2^*

If we leave out the complications involving the additional γ contribution, the time constant T_2 is what we identified earlier as the *homogeneous dephasing time*. It defines the average time duration within which the coherent oscillations of two different atomic dipoles are likely to be permanently and irreversibly randomized by collisions, or by other homogeneous dephasing events.

The time constant T_2^* can be given an analogous interpretation as the *inhomogeneous dephasing time* due to inhomogeneous broadening mechanisms for a group of oscillating atoms. Consider, for example, two atoms located in different spectral packets within a gaussian inhomogeneous line. The natural oscillation frequencies ω_{a1} and ω_{a2} of these two atoms will differ by an amount $\omega_{a1} - \omega_{a2}$ that will typically be of order $\approx \Delta\omega_d$. Even without any homogeneous dephasing events, therefore, these two oscillating dipoles will get out of phase by one half-cycle after a length of time δt given by $(\omega_{a1} - \omega_{a2})\delta t = \pi$, or $\delta t = \pi/(\omega_{a1} - \omega_{a2}) \approx \pi/\Delta\omega_d \approx T_2^*$.

The time constant T_2^* is thus the time duration after which different packets within an inhomogeneous line are likely to have become dephased because of their different oscillation frequencies, even without any collisions or similar dephasing events. The condition for a strongly inhomogeneous atomic line can be written in either of the alternative forms

$$\text{strongly inhomogeneous line: } \Delta\omega_d \gg \Delta\omega_a \quad \text{or} \quad T_2^* \ll T_2. \quad (78)$$

Thus in a strongly inhomogeneous line the T_2^* dephasing of different packets because of different oscillation frequencies will happen much more rapidly than the homogeneous dephasing within each packet that is caused by T_2 .

In practical experiments, therefore, if all the different atoms or packets within a strongly inhomogeneous line are initially set oscillating coherently and in phase by means of some suitable initial preparation pulse, the coherent macroscopic polarization $p(t)$ in the collection will disappear after the shorter time T_2^* , not the longer homogeneous dephasing time T_2 , because of the inhomogeneous frequency-difference effects. In an inhomogeneous line under small-signal conditions, T_2^* and not T_2 is the significant dephasing time.

For example, in the He-Ne 633 nm laser transition the doppler linewidth is $\Delta f_d \approx 1,500$ MHz, and the inhomogeneous dephasing time is thus $T_2^* \approx 3/(2\pi\Delta f_d) \approx 320$ psec. This must be compared with a homogeneous linewidth

for individual packets of more like $\Delta f_a \approx 100$ MHz, and hence a homogeneous dephasing time of $T_2 \approx 1/\Delta\omega_a \approx 3.2$ ns.

One vitally important difference between strongly homogeneous and strongly inhomogeneous systems, however, is that the inhomogeneous dephasing after the time T_2^* is fundamentally reversible: the different oscillation phases $\omega_{a1}t$, $\omega_{a2}t$, and so forth, that develop for different atoms after a time t can in principle be "unwound" by certain sophisticated large-signal or coherent-pulse techniques. We will discuss these later, in connection with coherent photon echo experiments.

Inhomogeneous Strain Broadening: Glass Laser Materials

Inhomogeneous broadening is also of considerable importance in certain solid-state laser transitions. Random strains, defects, and other site-to-site variations in solid-state laser materials can significantly change the local crystal fields seen by laser ions that are imbedded in these materials, and this in turn can randomly shift the exact resonance frequencies of laser atoms in those materials, sometimes by quite large amounts.

This type of inhomogeneous broadening predominates in inhomogeneous materials such as laser glasses at room temperature, or in more organized crystalline laser materials at very low temperatures (approaching liquid-helium temperatures), where it is no longer masked by the much larger phonon-broadening effects. Since this kind of broadening, often called *strain broadening*, is caused basically by random defects in the laser material, its magnitude may depend strongly on material growth and perfection, impurities, and annealing. It is thus not possible to give any general formulas, since the amount of strain broadening may vary from sample to sample of the same material.

If these random strains and defects have a gaussian distribution, the resulting inhomogeneous broadening effects can look and act much like doppler broadening, even though the underlying physical mechanism is totally different. The ratio of homogeneous linewidth $\Delta\omega_a$ to inhomogeneous linewidth $\Delta\omega_d$ will still be the crucial parameter in determining whether the transition will be strongly homogeneous, strongly inhomogeneous, or somewhere in between.

For example, the widely used yttrium aluminum garnet (YAG) crystal can be grown with high crystal quality. The linewidth of the Nd^{3+} ion in Nd:YAG laser crystals therefore exhibits only a small amount of inhomogeneous strain broadening. The laser transition is primarily phonon broadened and thus homogeneous at room temperature. Reducing the temperature to below liquid-nitrogen temperature (77 K) greatly reduces the phonon broadening and makes the residual strain broadening observable.

On the other hand, the same Nd^{3+} ion placed in a Nd:glass laser material, with its much larger amount of structural randomness, has a much larger inhomogeneous strain-broadening component, which is significant even at room temperature. This broadening is due to variations in the local crystal fields seen by the laser ions at different sites within the glassy material. The ratio of inhomogeneous to homogeneous broadening in Nd:glass laser materials is not fully understood and varies considerably (by at least a factor of three) from one glass composition to another.

The inhomogeneous linewidths in different glasses at room temperature, for example, vary over a linewidth range of from at least 40 to 120 cm^{-1} . (Linewidths this wide are more often expressed in units of cm^{-1} or wavenumbers than in

more conventional units; remember that $1 \text{ cm}^{-1} \equiv 30 \text{ GHz}$.) The homogeneous linewidth in the same materials varies over a range from 20 to 75 cm^{-1} , and is strongly correlated (for reasons that are not well understood) with the velocity of sound in the glass. This homogeneous linewidth reduces to $\ll 1 \text{ cm}^{-1}$ at 4.2 K , where the lattice vibrations and hence the homogeneous phonon broadening are reduced to nearly zero.

As a general rule, therefore, Nd:glasses are found to fall somewhere in the intermediate or mixed category between homogeneous and inhomogeneous broadening, with ratios of $\Delta\omega_a/\Delta\omega_d$ ranging from 0.16 to 1.9 in different glasses.

Far Outside the Resonance Linewidth: All Lines Become Homogeneous

Suppose we go out into the far wings of any atomic resonance transition, homogeneous or inhomogeneous, and measure the atomic response at 5 or 10 linewidths out from the line center. (Note that in any usual atomic transition we can do this and still be well within the “resonance approximation” we introduced earlier, so that the lorentzian and gaussian lineshapes will still apply.)

The gaussian response characteristic of an inhomogeneous transition—for example, a doppler-broadened transition—will then fall off as $\approx \exp[-(\omega - \omega_a)^2]$, whereas the lorentzian response characteristic of a homogeneous transition—or of a homogeneous packet within an inhomogeneous transition—will fall off only at the much slower rate of $\approx 1/(\omega - \omega_a)^2$ for the χ'' part of the susceptibility, or the even slower rate of $\approx 1/(\omega - \omega_a)$ for the χ' part of the susceptibility. Figure 3.22 shows, for example, the $\chi''(\omega)$ parts of the susceptibility plotted on the same frequency scale for a gaussian transition with a given linewidth $\Delta\omega_d$ and for a lorentzian line—or a lorentzian packet within the gaussian line—whose linewidth $\Delta\omega_a$ is only $1/5$ as large as the gaussian linewidth $\Delta\omega_d$.

This example makes it clear that if we go far enough out from line center, the lorentzian response, though it may be 20 or 30 dB down from the midband value, will clearly dominate over the gaussian response. In other words, *far enough out in the wings, all transitions—even strongly inhomogeneous transitions—once again appear to be homogeneous in character*. If we tune away from an inhomogeneous transition by a sufficient number of inhomogeneous lineshapes, the atomic response will be very weak, though possibly still measurable; and the lineshape of that response will look like a homogeneous lineshape characterized by the $\Delta\omega_a$ of the individual spectral packets, rather than the $\Delta\omega_d$ of the inhomogeneous frequency spreading. For sufficiently strong transitions, this homogeneous response far out in the wings of an inhomogeneous transition can still be of interest, as we will see later on.

Summary

The differences between homogeneous and inhomogeneous broadening in the central part of the atomic line play a very significant role in the performance of a laser material, especially when saturation effects are taken into account. Many practical laser materials, particularly gases, are strongly inhomogeneous, but others are strongly homogeneous. We will return to the detailed “hole burning” properties of inhomogeneous laser systems in a later chapter.

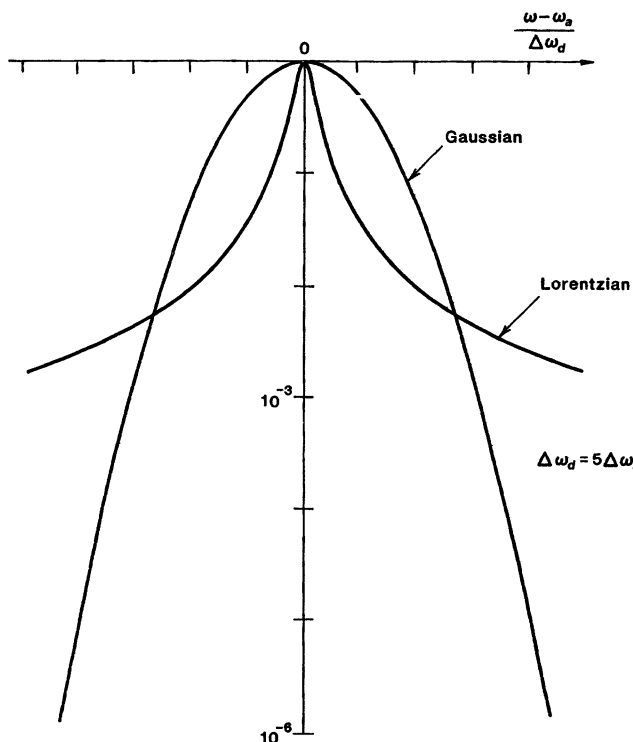


FIGURE 3.22
Comparison of lorentzian and gaussian lineshapes in the wings far from line center.

REFERENCES

The concepts of inhomogeneous broadening and of spectral packets (originally called "spin packets") were first originated in magnetic resonance, notably in the pioneering paper by A. M. Portis, "Electronic structure of F centers: saturation of the electron spin resonance," *Phys. Rev.* **91**, 1071 (1953).

The exact integral for the inhomogeneous susceptibility in the Voight region, with mixed homogeneous and inhomogeneous broadening, can be transformed mathematically into a closed expression involving an error function of complex argument (which doesn't help much). One of many references on this is W. J. Surtrees, "Calculation of combined doppler and collision broadening," *J. Opt. Soc. Am.* **55**, 893 (1965).

The experimental results in Figure 3.20 and nearby illustrations are from E. T. Gerry and D. A. Leonard, "Measurement of $10.6 \mu\text{m}$ CO_2 laser transition probability and optical broadening cross sections," *Appl. Phys. Lett.* **8**, 227 (May 1, 1966); from R. K. Hanson, "Shock tube spectroscopy: advanced instrumentation with a tunable diode laser," *Appl. Optics* **16**, 1479 (1977); and from R. L. Abrams, "Broadening coefficients for the P(20) CO_2 laser transition," *Appl. Phys. Lett.* **25**, 609-611 (November 15, 1974).

For an example of the use of Voight profiles in a solid—specifically in ruby at low temperature, when the linewidth is a combination of homogeneous phonon broadening

and inhomogeneous strain broadening—see D. F. Nelson and M. D. Sturge, “Relation between absorption and emission in the region of the *R* lines of ruby,” *Phys. Rev.* **137**, A1117–A1130 (February 15, 1965).

Problems for 3.7

1. *Inhomogeneous broadening with a lorentzian (rather than gaussian) inhomogeneous distribution.* Most inhomogeneous broadening mechanisms, such as doppler broadening, lead to a gaussian probability distribution of resonance frequencies, for reasons associated with the Central Limit Theorem of statistics. Suppose, however, we could create a collection of atoms having a lorentzian rather than gaussian inhomogeneous distribution of resonance frequencies, i.e., a distribution given by

$$g(\omega_a) = \frac{2}{\pi \Delta \omega_d} \frac{1}{1 + [2(\omega_a - \omega_{a0})/\Delta \omega_d]^2}.$$

The linewidth $\Delta \omega_d$ of this distribution is then exactly analogous to $\Delta \omega_d$ in the doppler case. (The reason for considering such a distribution is primarily because it will make the mathematics easier.)

Using such a lorentzian inhomogeneous distribution, calculate the inhomogeneously broadened small-signal susceptibility $\tilde{\chi}(\omega)$ of a collection of atoms or oscillators, assuming the usual homogeneous complex lorentzian response for each individual atom or spectral packet. (Hint: This calculation is easily done if you know how to evaluate contour integrals in the complex plane using the residue method; if you’re not familiar with this, ask an acquaintance.) Discuss the resulting general inhomogeneous lineshape, its real and imaginary parts, and their overall linewidth for various values of the inhomogeneity parameter $\Delta \omega_a / \Delta \omega_d$.

2. *Inhomogeneous broadening with a uniform inhomogeneous distribution.* There might exist an oddball laser crystal with a distribution of defects such that the atomic frequency shifts produced by these defects were uniformly distributed between some maximum positive and negative shift values about the unshifted center frequency ω_{a0} . (Or there might be an even more remarkable gas in which the axial velocities, instead of having a Maxwellian distribution, were uniformly distributed between a minimum and a maximum value.) Either of these unusual situations would lead to an inhomogeneously broadened transition with a rectangular inhomogeneous lineshape $g(\omega_a)$, rather than the much more common gaussian lineshape discussed in the text.

Let $\Delta \omega_d$ here mean the full width of this rectangular distribution. Find an exact analytic expression for the complex susceptibility $\tilde{\chi}(\omega)$, and plot $\chi'(\omega)$ and $\chi''(\omega)$ versus $(\omega - \omega_a)/\Delta \omega_d$ for different degrees of homogeneous versus inhomogeneous broadening, for example, for $\Delta \omega_d / \Delta \omega_a = 1/20, 1$, and 20 . Find also the midband value $\tilde{\chi}(\omega_{a0})$ in the limits of very large and very small inhomogeneous broadening. (Hint: You may have to do some thinking about how to interpret the natural logarithm of a complex argument.)

3. *Ditto with a triangular distribution.* Repeat the previous problem with a triangular inhomogeneous lineshape having FWHM linewidth $\Delta \omega_d$ and base width $2\Delta \omega_d$.

4. *Midband absorption versus pressure in a gas.* Why does the midband absorption value shown in Figure 3.20 at first increase with increasing pressure and then saturate in the form shown?
5. *Chemical lasers, and absorption versus pressure in a deuterium fluoride gas cell.* By burning deuterium with fluorine to get chemically excited molecules of deuterium fluoride (DF), and then letting the resulting molecules expand through a supersonic nozzle, we can make a very powerful chemical laser (hundreds of kilowatts cw) at wavelengths around $\lambda = 3.6$ to 4.1 microns in the near infrared. Such lasers have been considered as military weapons (if the laser beam doesn't get you, the toxic chemicals will). The quantum transitions in deuterium fluoride molecules are thus of some interest.

Figure 3.21 shows the measured signal-absorption coefficient 2α at midband ($\omega = \omega_a$) versus pressure on a certain DF transition at $\lambda = 3.67$ microns starting from the ground state (lowest energy level) of the DF molecule. The power absorption coefficient 2α is related to the transition susceptibility χ'' by $2\alpha(\omega) = (2\pi/\lambda)\chi''(\omega)$ (as we will learn later). The midband absorption is plotted against gas pressure in a cell containing unexcited DF molecules at room temperature. The DF transition is presumably pressure-broadened, lorentzian, and homogeneous at high gas pressures; but doppler-broadened, gaussian, and inhomogeneous at low gas pressures (pure lifetime broadening will be negligible in all cases).

Explain the shape of this experimental curve, and use it to deduce as much as you can about the properties and numerical coefficients of this particular DF transition. Some useful numbers: molecular weight of a DF molecule = 21; mass of a proton, $M = 1.67 \times 10^{-27}$ kg; Boltzmann constant $k = 1.38 \times 10^{-23}$ in mks units; gas density $N(\text{molecules/cm}^3) = 9.65 \times 10^{18} P(\text{torr})/T(\text{K})$; room temperature ≈ 300 K; and 1 atmosphere = 760 torr.

6. *Inhomogeneous Voight profiles far out in the wings.* Using any suitable numerical procedure, calculate the Voight profile for $\chi''(\omega)$ versus ω for $\Delta\omega_d/\Delta\omega_a = 10$, extending the calculations out to several inhomogeneous linewidths from line center. Plot the results on a log amplitude scale, and compare the exact Voight profile to a gaussian curve that matches the Voight profile near line center. Are there significant differences in the outer wings? Explain.

4

ATOMIC RATE EQUATIONS

Applying a sinusoidal signal to a collection of atoms, with the frequency ω tuned near one of the atomic transition frequencies ω_a , will produce a coherent induced polarization $p(t)$ or $\tilde{P}(\omega)$ in the collection of atoms, as we have described in the preceding two chapters. The strength of this induced response will be proportional to the instantaneous population difference ΔN on that particular transition.

At the same time, however, this applied signal field will also cause the populations $N_1(t)$ and $N_2(t)$ in the collection of atoms to begin changing slowly because of *stimulated transitions between the two levels E_1 and E_2* , as we will discuss in this chapter. The rates of change of the populations are given by *atomic rate equations*, which contain both stimulated terms and relaxation or energy-decay terms (and possibly also other kinds of pumping terms). Deriving the quantum form for these stimulated and relaxation terms is the primary objective of this chapter.

These atomic rate equations are of great value in analyzing pumping and population inversion in laser systems. Solutions of the rate equations for strong applied signals also lead to population saturation effects, which are of very great importance in understanding the large-signal saturation behavior of laser amplifiers and the power output of laser oscillators. Solving the atomic rate equations and understanding these solutions for some simple cases will therefore be the principal objective of Chapter 6.

4.1 POWER TRANSFER FROM SIGNALS TO ATOMS

We will derive the stimulated transition rates for an atomic transition in this chapter by examining the power flow or the energy transfer between an applied optical signal and an atomic transition. To get started on this, let us learn something about the rate at which power is transferred from an applied signal to any material medium, including a collection of resonant oscillators or atoms.

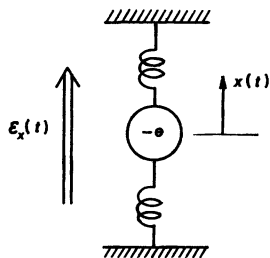


FIGURE 4.1

Mechanical model for a classical electron oscillator with an applied \mathcal{E} field.

Power Transfer to a Collection of Oscillators: Mechanical Derivation

When an electric field $\mathcal{E}_x(t)$ acts on a moving charge, it delivers power to (or perhaps receives power from) that moving charge. In a single classical oscillator (as in Figure 4.1), a purely mechanical argument says that the amount of work dU done by a force f_x acting on the electron, when the electron moves through a distance dx is

$$dU = f_x dx = -e\mathcal{E}_x dx. \quad (1)$$

The instantaneous rate at which power is delivered by the field to the classical oscillator is then

$$\frac{dU(t)}{dt} = -e\mathcal{E}_x(t) \frac{dx(t)}{dt} = \mathcal{E}_x(t) \frac{d\mu_x(t)}{dt}, \quad (2)$$

where $\mu_x(t)$ is, of course, the dipole moment of the oscillator.

If we sum this power flow over all the oscillators or atoms in a small unit volume V , this result says that the average power per unit volume, dU_a/dt , delivered by the field to the atoms or oscillators is

$$\frac{dU_a}{dt} = V^{-1} \mathcal{E}_x(t) \sum_{i=1}^{NV} \frac{d\mu_{xi}(t)}{dt} = \mathcal{E}_x(t) \frac{dp_x(t)}{dt}. \quad (3)$$

This equation, although derived from a mechanical argument, is a very general electromagnetic or even quantum-mechanical result. That is, this equation still holds true whether $p_x(t)$ represents the sum of a large number of classical oscillator dipoles with a number density N , or whether $p_x(t)$ represents the effect of a large number of quantum dipole expectation values proportional to a population difference ΔN .

Time-Averaged Power Flow

To obtain the time-averaged power delivered to a collection of atoms by a sinusoidal signal field, we can write the applied signal and the resulting polarization in phasor form as

$$\mathcal{E}_x(t) = \frac{1}{2} [\tilde{E}(\omega) e^{j\omega t} + \tilde{E}^*(\omega) e^{-j\omega t}] \quad (4)$$

and

$$p_x(t) = \frac{1}{2}[\tilde{P}(\omega)e^{j\omega t} + \tilde{P}^*(\omega)e^{-j\omega t}]. \quad (5)$$

The steady-state sinusoidal polarization $\tilde{P}(\omega)$ on an atomic transition will then be related to the applied field by

$$\tilde{P}(\omega) = \tilde{\chi}(\omega)\epsilon\tilde{E}(\omega) = [\chi'(\omega) + j\chi''(\omega)]\epsilon\tilde{E}(\omega). \quad (6)$$

(Remember that we use the host dielectric constant ϵ and not ϵ_0 in this relation, for the reasons explained in the previous chapter.)

If we substitute these phasor forms into Equation 4.3 and take the time average (by dropping the $e^{\pm 2j\omega t}$ terms) we obtain a useful result for the average power absorbed from the fields, by the atoms, per unit volume, namely,

$$\frac{dU_a}{dt} \Big|_{av} = \frac{j\omega}{4} (\tilde{E}^* \tilde{P} - \tilde{E} \tilde{P}^*) = -\frac{1}{2}\epsilon\omega\chi''(\omega)|\tilde{E}(\omega)|^2. \quad (7)$$

The most important point here is that the power absorption (or emission) by the atoms depends only on the $\chi''(\omega)$ part of the complex susceptibility $\tilde{\chi}(\omega)$. This is the “resistive” or lossy part of $\tilde{\chi}(\omega)$, whereas $\chi'(\omega)$ is the purely reactive part.

The minus sign in the final term of Equation 4.7 merely means that if we use the definition $\tilde{\chi} \equiv \chi' + j\chi''$, then the quantity χ'' for an absorbing medium will turn out to be a negative number, as indeed we have already found for the classical electron oscillator. (Some authors, attempting to avoid this minus sign, use instead the definition that $\tilde{\chi} \equiv \chi' - j\chi''$.)

Poynting Derivation of Energy Transfer

The results for power transfer obtained above are in fact general electromagnetic results, having nothing directly to do with the particular atomic or quantum process that creates the polarization $p_x(t)$. To verify this, let us carry through a standard electromagnetic derivation of this same result, starting by writing Maxwell's equations

$$\begin{aligned} \nabla \times \mathcal{E} &= -\partial \mathbf{b} / \partial t, & \nabla \times \mathbf{h} &= \mathbf{j} + \partial \mathbf{d} / \partial t, \\ \mathbf{d} &= \epsilon_0 \mathcal{E} + \mathbf{p}, & \mathbf{b} &= \mu_0 (\mathbf{h} + \mathbf{m}), \end{aligned} \quad (8)$$

and then substituting them into the vector identity

$$\mathbf{h} \cdot (\nabla \times \mathcal{E}) - \mathcal{E} \cdot (\nabla \times \mathbf{h}) \equiv \nabla \cdot (\mathcal{E} \times \mathbf{h}). \quad (9)$$

Note that all the vector quantities here, for example, $\mathcal{E}(\mathbf{r}, t)$, are general vector functions of space and time at this point.

Equation 4.9 can then be integrated over an arbitrary volume V , bounded by a closed surface S as in Figure 4.2, using the additional vector identity that

$$\int_V \nabla \cdot (\mathcal{E} \times \mathbf{h}) dV = - \int_S (\mathcal{E} \times \mathbf{h}) \cdot d\mathbf{S}, \quad (10)$$

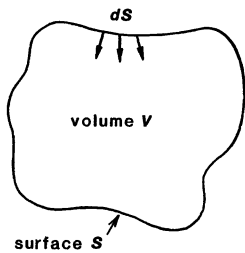


FIGURE 4.2
Volume V with a surface S for the evaluation of electromagnetic power flow.

where $d\mathbf{S}$ is an inward unit vector normal to the surface S . Rearranging terms then gives as a general formula

$$\begin{aligned} \int_S (\mathcal{E} \times \mathbf{h}) \cdot d\mathbf{S} &= \frac{d}{dt} \int_V \left(\frac{1}{2} \epsilon_0 |\mathcal{E}|^2 + \frac{1}{2} \mu_0 |\mathbf{h}|^2 \right) dV \\ &\quad + \int_V (\mathcal{E} \cdot \mathbf{j}) dV \\ &\quad + \int_V \left(\mathcal{E} \cdot \frac{dp}{dt} + \mu_0 \mathbf{h} \cdot \frac{dm}{dt} \right) dV. \end{aligned} \quad (11)$$

We can give a physical interpretation to each term in this equation.

The surface integral on the left-hand side of this equation gives the integral over the closed surface S of the inwardly directed instantaneous Poynting vector $\mathcal{E} \times \mathbf{h}$. According to the standard interpretation of electromagnetic theory, this Poynting integral gives the total electromagnetic power being carried by fields \mathcal{E} and \mathbf{h} and flowing into the volume V at any instant.

The terms on the right-hand side of Equation 4.11 tell where this power is going. The volume integral on the right-hand side of the first line is a purely reactive or energy-storage term. It gives the instantaneous rate of increase or decrease in the stored electromagnetic field energy terms $\frac{1}{2} \epsilon_0 \mathcal{E}^2$ and $\frac{1}{2} \mu_0 \mathbf{h}^2$ in the volume V . (These are vacuum energy density terms—that is, they do not include any energy going into atomic polarizations $\mathbf{p}(t)$ or $\mathbf{m}(t)$ in the volume V .)

The integral on the right-hand side of the second line gives the instantaneous power per unit volume being delivered by the \mathcal{E} field to any currents \mathbf{j} , whether these currents come from ohmic losses ($\mathbf{j} = \sigma \mathcal{E}$) or any other real currents $\mathbf{j}(r, t)$ that may be present in the volume.

The integral on the right-hand side of the final line of Equation 4.11 then accounts for the instantaneous powers per unit volume $\mathcal{E} \cdot (dp/dt)$ and $\mu_0 \mathbf{h} \cdot (dm/dt)$ that are being delivered by these fields to any electric and magnetic polarizations $\mathbf{p}(r, t)$ and $\mathbf{m}(r, t)$ that may be present, as a consequence of any kind of atomic or material medium. The $\mathcal{E} \cdot (dp/dt)$ term represents in particular the vector generalization of the simple mechanical derivation we gave at the beginning of this section.

Reactive Versus Resistive Power Flow

Note that power transfer from the signal fields to these atomic polarization terms does not necessarily mean this power is being *dissipated* in the atoms. If

the medium has a purely reactive susceptibility, with $\chi'' = 0$, then there can be no time-averaged power transfer, because $\mathcal{E}(t)$ and $\mathbf{p}(t)$ will be 90° out of time-phase, and the time-averaged value of the $\mathcal{E} \cdot d\mathbf{p}/dt$ term will be zero: energy will flow from the signal into the medium during one quarter cycle, and back out during the following quarter cycle.

The energy transfer into the polarization in this situation is basically reactive stored energy, which flows into the atoms during one half-cycle and back out during the following half-cycle. This reactive energy flow could be combined with the first integral on the right-hand side of Equation 4.11. If this were done, the expanded first term would become the time derivative of the more familiar expressions $\frac{1}{2}\epsilon|\mathcal{E}|^2$ and $\frac{1}{2}\mu|\mathbf{h}|^2$, which give the total electromagnetic energy stored in a medium rather than in vacuum.

We can also see that the rate of change of polarization $d\mathbf{p}/dt$ in the $\mathcal{E} \cdot d\mathbf{p}/dt$ term plays the same role as the current density \mathbf{j} in the $\mathcal{E} \cdot \mathbf{j}$ term. It is sometimes convenient to define a “polarization current density” \mathbf{j}_p by

$$\mathbf{j}_p \equiv d\mathbf{p}/dt, \quad (12)$$

which can be added to the real current density \mathbf{j} in Maxwell's equations. From Chapter 3 we realize that this polarization current simply represents the sloshing back and forth of the bound but oscillating atomic charge clouds that lead to the oscillating dipole moments $\mathbf{\mu}(t)$ in each atom and to the macroscopic polarization $\mathbf{p}(t)$ in the collection of atoms. To the extent that this current is in phase with the $\mathcal{E}(t)$ term [that is, comes from the $\chi''(\omega)$ part of the susceptibility], it represents additional resistive loss or dissipation in the medium; to the extent that it is 90° out of phase [the $\chi'(\omega)$ part], it represents reactive energy storage.

Quality Factor

The absorptive susceptibility χ'' in an atomic medium can be interpreted as a kind of inverse Q or quality factor for the ratio of signal energy stored in a volume to signal power dissipated in that volume, in just the same fashion as the Q factor is defined for a mechanical system or an electrical circuit. That is, the time-averaged stored signal energy per unit volume associated with a sinusoidal signal field in a host medium of dielectric constant ϵ can be written as

$$U_{\text{sig}} = \frac{1}{2}\epsilon|\mathcal{E}|^2. \quad (13)$$

The inverse Q factor for this little volume can then be defined as

$$\frac{1}{Q} \equiv \frac{\text{energy dissipated}}{\omega \times \text{energy stored}} = \frac{1}{\omega U_{\text{sig}}} \frac{dU_a}{dt} = -\chi''. \quad (14)$$

The dimensionless atomic susceptibility χ'' , as we have defined it in this text, is thus essentially an inverse Q factor describing the average power absorption per unit volume, by the atoms, from the signal. Of course for an amplifying transition, this Q becomes a negative number.

For real laser transitions this Q is always very high, since in all practical laser situations $|\chi''| \ll 1$. We usually think of a high Q value in a system as being in some sense “good”. Here, however, a high Q means a *weak* susceptibility, and hence a small gain in an amplifying laser medium, which is generally *not* what we would like to have.

Tensor Formulation of Power Flow

Real laser transitions may have a linear but anisotropic response, in which the induced polarization must be described by a tensor susceptibility. To describe the power transfer properly in this case we must employ a more sophisticated form for the analysis in terms of the *hermitian* and *antihermitian* parts of this susceptibility tensor.

To do this, we note that the full vector formula for instantaneous power delivered per unit volume is

$$\frac{dU_a(t)}{dt} = \mathcal{E} \cdot d\mathbf{p}/dt. \quad (15)$$

The time-averaged power flow in an atomic medium with a tensor atomic susceptibility χ is then given by

$$\frac{dU_a}{dt} \Big|_{av} = \frac{j\omega\epsilon}{4} [\mathbf{E}^* \cdot \chi \mathbf{E} - \mathbf{E} \cdot \chi^* \mathbf{E}^*] = \frac{j\omega\epsilon}{4} \sum_{i=1}^3 \sum_{j=1}^3 \bar{E}_i^* (\bar{\chi}_{ij} - \bar{\chi}_{ji}^*) \bar{E}_j, \quad (16)$$

where i and j are both summed over the three directions x, y, z . If χ happens to be an isotropic or even a diagonal tensor, then these sums reduce directly to our previous scalar results. For a general anisotropic tensor susceptibility, however, we must separate the complex tensor χ not into its real and imaginary parts, but into its *hermitian* and *antihermitian* parts, as given by

$$\chi \equiv \chi_h + j\chi_{ah}, \quad (17)$$

where χ_h and χ_{ah} are defined by

$$\chi_h \equiv (1/2) (\chi^\dagger + \chi) \quad \text{and} \quad \chi_{ah} \equiv (j/2) (\chi^\dagger - \chi), \quad (18)$$

with χ^\dagger being the hermitian conjugate of χ . Note that χ_h and χ_{ah} are not necessarily the same as the real and imaginary parts of χ , since χ^\dagger and χ are in general not simply the complex conjugates of each other.

It can then be shown that the time-averaged power transfer is given by

$$\frac{dU_a}{dt} \Big|_{av} = -\frac{1}{2} \omega \epsilon \mathbf{E}^*(\omega) \chi_{ah}(\omega) \mathbf{E}(\omega). \quad (19)$$

In the general tensor case it is the *antihermitian* part $j\chi_{ah}$ of the susceptibility tensor, and not just the imaginary part χ'' , that is the resistive or power-absorbing part.

4.2 STIMULATED-TRANSITION PROBABILITY

We will next use these results to derive a stimulated-transition probability, which gives the stimulated-transition rate at which atoms make transitions back and forth between quantum energy levels under the influence of an applied signal. We will do this by considering the rate at which an applied signal will deliver energy to a collection of real quantum atoms, and the manner in which these atoms can accept this energy.

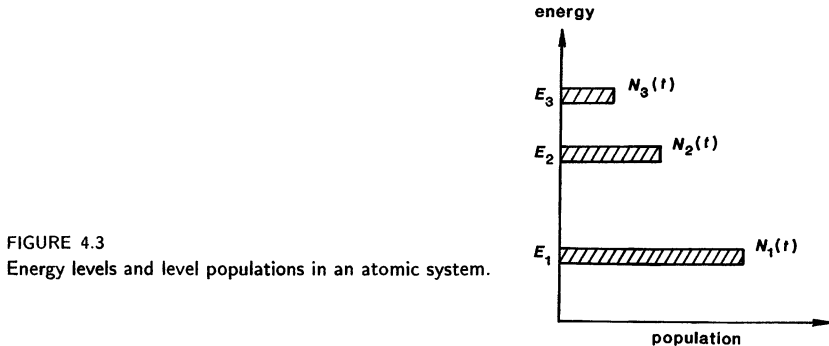


FIGURE 4.3
Energy levels and level populations in an atomic system.

Energy Transfer From Signal To Atoms

We have learned that when a sinusoidal signal field $\tilde{E}(\omega)$ produces a steady-state polarization $\tilde{P}(\omega)$ on a transition in a collection of atoms, the time-averaged power transfer per unit volume from the signal to the atoms must be given by

$$\frac{dU_a}{dt} = -\frac{1}{2}\omega\chi''(\omega)\epsilon|\tilde{E}|^2, \quad (20)$$

where the susceptibility for a homogeneous lorentzian atomic transition is given from the previous chapter by

$$\chi''(\omega) = -\frac{3^*}{4\pi^2} \frac{\Delta N \gamma_{\text{rad}} \lambda^3}{\Delta\omega_a} \frac{1}{1 + [2(\omega - \omega_a)/\Delta\omega_a]^2}. \quad (21)$$

(For an inhomogeneous gaussian transition exactly the same expression as Equation 4.21 would apply, except that the homogeneous linewidth $\Delta\omega_a$ would be replaced by the inhomogeneous linewidth $\Delta\omega_d$; the lorentzian frequency dependence would be replaced by a gaussian; and an additional factor of $\sqrt{\pi \ln 2} \approx 1.48$ would appear in front.)

The rate of energy transfer from the signal to the atoms can thus be written in the general form

$$\frac{dU_a}{dt} = \left[\frac{3^*}{8\pi^2} \frac{\gamma_{\text{rad}}}{\Delta\omega_a} \frac{\omega\epsilon|\tilde{E}|^2\lambda^3}{1 + [2(\omega - \omega_a)/\Delta\omega_a]^2} \right] (N_1 - N_2). \quad (22)$$

Note that this energy absorption is directly proportional to the population difference $\Delta N \equiv N_1 - N_2$.

Energy Storage by the Atoms

Now, what will the atoms do with this energy, or how can they accept this energy from the applied fields? From a quantum viewpoint, the total oscillation energy stored in a collection of atoms is given by the number of atoms N_j in each quantum energy level, times the energy eigenvalue E_j associated with that level, summed over all the energy levels E_j , as in Figure 4.3. In a collection of

identical two-level atoms, for example, the total oscillation energy density U_a (energy per unit volume) is given by

$$U_a(t) = N_1(t)E_1 + N_2(t)E_2, \quad (23)$$

where N_1 and N_2 are the populations in levels E_1 and E_2 . More generally, the total energy in a collection of multilevel atoms is the sum over all levels

$$U_a(t) = \sum_{j=1}^M N_j(t)E_j. \quad (24)$$

Since the energy eigenvalues E_j are fixed quantities, if the collection of atoms is to accept energy the level populations N_j must change, with atoms flowing from a lower energy level to a higher energy level.

In the classical oscillator model the energy of each oscillator was associated with the internal oscillatory motion $|x(t)|^2$. In a quantum description, however, the internal energy of each atom must be calculated from the level populations and energy eigenvalues as above. These two descriptions are not unrelated—for example, we noted earlier that an atom in a mixture of populations at levels E_1 and E_2 has an internal oscillating dipole moment $\mu(t)$ at the transition frequency ω_{21} that is associated with that mixture of populations.

In any event, if energy is to be delivered from a signal to a collection of atoms, the only way in which the atoms can accept this energy and change their total internal energy $U_a(t)$ is by changing the populations $N_j(t)$ in the collection of atoms. The signal field, as we have seen in the previous chapter, induces a dipole moment in each atom, and thus produces a coherent macroscopic polarization proportional to the population difference $\Delta N \equiv N_1 - N_2$. But, it must also cause the quantum state of each individual atom to begin to change in such a way that the populations $N_1(t)$ and $N_2(t)$ in the collection of atoms also begin to change.

Stimulated Transition Probabilities

We can emphasize this point by rewriting Equation 4.22 in the alternative form

$$\frac{dU_a}{dt} = W_{12}N_1\hbar\omega_a - W_{21}N_2\hbar\omega_a, \quad (25)$$

where either of the quantities $W_{12}\hbar\omega_a = W_{21}\hbar\omega_a$ corresponds to the collection of factors inside the set of square brackets in Equation 4.22. By rewriting Equation 4.22 in this alternative form, however, we make the energy flow from the signal to the atoms seem to be produced by two flows of atoms, one upward from level 1 to level 2 at an upward stimulated-transition rate given by $W_{12}N_1$ (units of atoms per second), as shown by the upward arrow in Figure 4.4; plus an opposite flow of atoms downward from level 2 to level 1 at a downward stimulated-transition rate given by $W_{21}N_2$.

In other words, the energy transfer from the signal to the atoms, as given by Equation 4.25, can be accounted for by a net flow rate of atoms across the gap, upward minus downward, given by

$$\frac{dN_2}{dt} \Big|_{\text{stim}} = - \frac{dN_1}{dt} \Big|_{\text{stim}} = W_{12}N_1 - W_{21}N_2, \quad (26)$$

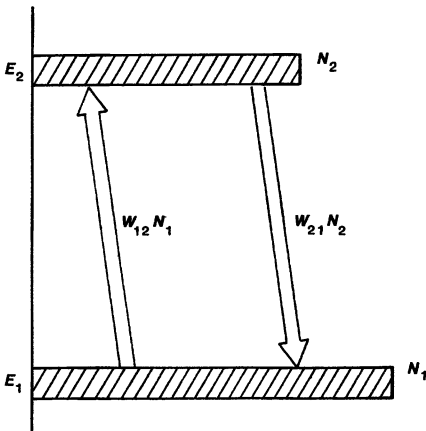


FIGURE 4.4

Upward and downward stimulated transitions between two energy levels.

as illustrated in Figure 4.4. Both of these flow rates are expressed in units of atoms per second. To get the net energy flow, each of these rates must be multiplied by the transition energy or photon energy $\hbar\omega_a$, since each transit of one atom across the energy gap represents a net absorption or emission of one quantum of energy by the atoms.

The quantities W_{12} and W_{21} are then referred to as the *upward and downward stimulated-transition probabilities*, per atom and per unit time, produced by the applied signal acting on the lower-level and upper-level atoms, respectively. By equating Equations 4.22 and 4.25, we can see that these stimulated-transition probabilities are given by

$$W_{12} \equiv W_{21} = \frac{3^*}{8\pi^2} \frac{\gamma_{\text{rad}}}{\hbar\Delta\omega_a} \frac{\epsilon|\tilde{E}|^2\lambda^3}{1 + [2(\omega - \omega_a/\Delta\omega_a)]^2}. \quad (27)$$

With this interpretation we may say that *the applied signal gives each atom in the lower level E_1 a probability W_{12} per unit time of making a stimulated transition to the upper level, absorbing a quantum of energy in the process; similarly, the applied signal gives each atom in the upper level an equal probability W_{21} per unit time of making a transition downward to the lower level, giving up one quantum of energy to the signal in the process.*

Equations 4.25 through 4.27 provide an important and general result, sometimes referred to as “Fermi’s Golden Rule”, which is usually derived only with the aid of quantum theory. We have obtained the correct quantum answer, however, from a simple energy argument, thus further illustrating the power of the classical oscillator arguments used in this text. The reader might reasonably ask, however, since $W_{12} = W_{21}$, why didn’t we describe them both by a single symbol? The answer is, first of all, that later on in writing multilevel rate equations it may help to keep various terms straight if we use W_{ij} to mean a transition probability from level i to level j , and W_{ji} to mean the same transition probability in the reverse direction. In addition, there are some slight additional complications for the rate equations between degenerate energy levels, as we will see in a moment.

Quantum Description of Stimulated Transitions.

These signal-stimulated transition rates for atoms between two energy levels are often described in simplified fashion as a process in which the applied signal causes individual atoms to make discrete jumps back and forth between the two levels under the influence of the applied signal, exchanging one photon with each jump. This is the “billiard-ball” or photon model of laser amplification.

A much more correct description, however, even in quantum theory, is to say that each individual atom in the collection of atoms, rather than making a discrete “jump” or transition from one level to the other, in fact really only changes its quantum state by a small amount in response to the applied signal. We have pointed out earlier that the quantum state of an atom involved in a transition between two levels E_1 and E_2 can be written in the general form

$$\psi(\mathbf{r}, t) = \tilde{a}_1(t)e^{-iE_1 t/\hbar}\psi_1(\mathbf{r}) + \tilde{a}_2(t)e^{-iE_2 t/\hbar}\psi_2(\mathbf{r}). \quad (28)$$

where the expansion coefficients $\tilde{a}_1(t)$ and $\tilde{a}_2(t)$ are constant (stationary) in the absence of an applied signal. The time evolution of this quantum state in each individual atom in the presence of an applied signal must then be calculated in a proper quantum analysis by solving the Schrödinger equation of motion for the atom in the presence of the signal field.

The net result of such a calculation will be that, under the influence of an applied signal, the expansion coefficients $\tilde{a}_1(t)$ and $\tilde{a}_2(t)$ of each individual atom will begin to change *slowly but continuously* with time. In other words, the quantum state makeup of each individual atom will begin to shift by a small but continuous amount from quantum state ψ_1 towards quantum state ψ_2 or vice versa. The probability of finding each atom in one level or the other begins to change by a small amount; and when these probabilities for individual atoms are averaged over the entire collection, it appears as if the population in one level has decreased and in the other has increased.

For many purposes, however, it is acceptable to summarize the results of this calculation by simply saying that, in the presence of an applied signal, atoms begin to make stimulated transitions or jumps back and forth between the two levels E_1 and E_2 , thus changing $N_1(t)$ and $N_2(t)$. The final result averaged over the collection of atoms is basically the same whether we think of each individual atom changing its quantum state by a small amount (which is what really happens), or whether we think of a small fraction of the atoms making discrete “jumps” from one level to the other (which is how the situation is often described).

General Atomic Transition With Degeneracy

To take care of the more general case in which we have transition rates between two arbitrary energy levels E_i and $E_j > E_i$, where these levels may have degeneracy factors g_i and g_j , we must note that the complex susceptibility on such a transition is given by

$$\tilde{\chi}_{ij}''(\omega) = -\frac{3^*}{4\pi^2} \frac{\gamma_{\text{rad},ij} \lambda_{ij}^3}{\Delta\omega_a} \frac{[(g_j/g_i)N_i - N_j]}{1 + [2(\omega - \omega_{ji})/\Delta\omega_{a,ij}]^2}, \quad (29)$$

Hence, the power transfer from signal to atoms can be written, first in electromagnetic form, and then in rate-equation form, as

$$\begin{aligned}\frac{dU_a}{dt} &= \left[\frac{3^*}{8\pi^2} \frac{\gamma_{\text{rad},ji}}{\Delta\omega_a} \frac{\omega|\tilde{E}_{ij}|^2\lambda_{ij}^3}{1 + [2(\omega - \omega_a)/\Delta\omega_a]^2} \right] \left(\frac{g_j}{g_i} N_i - N_j \right) \\ &= W_{ij} N_i \hbar\omega_{ji} - W_{ji} N_j \hbar\omega_{ji}.\end{aligned}\quad (30)$$

By equating these two forms, we see that the general expression for the stimulated transition probabilities in this case becomes

$$W_{ji} \equiv \frac{g_i}{g_j} W_{ij} = \frac{3^*}{8\pi^2} \frac{\gamma_{\text{rad},ji}}{\hbar\Delta\omega_{a,ij}} \frac{\epsilon|\tilde{E}_{ij}|^2\lambda_{ij}^3}{1 + [2(\omega - \omega_{ji})/\Delta\omega_{a,ij}]^2}, \quad (31)$$

where \tilde{E}_{ij} is the electric field of the applied signal on the $i - j$ transition.

Again the flow of atoms upward from level E_i to level E_j is given by the number of atoms in the lower level N_i times an upward stimulated-transition probability W_{ij} , and the quantity W_{ji} is similarly the probability of an upper level atom being stimulated to make a downward transition. The stimulated-transition probabilities W_{ij} and W_{ji} in the two directions are, however, related in general by

$$g_i W_{ij} = g_j W_{ji}. \quad (32)$$

A very fundamental point is that the stimulated-transition probabilities in the two directions are still identical, except for the minor complication of the degeneracy factors g_i and g_j .

Fundamental Properties of the Stimulated-Transition Probabilities

From Equations 4.27 or 4.31, the important physical parameters involved in these signal-stimulated transition probabilities W_{ij} and W_{ji} are evidently

- The applied signal strength, or the signal energy per wavelength cubed, as measured by $\epsilon|\tilde{E}|^2\lambda^3$.
- The relative strength of the atomic transition, measured by its radiative decay rate or Einstein A coefficient, γ_{rad} .
- The inverse atomic linewidth, $1/\Delta\omega_a$.
- The frequency of the applied signal ω relative to the atomic transition frequency ω_a , as measured by the atomic lineshape. Applied signals tuned away from line center are less effective in producing stimulated transitions.
- And, finally, the tensor alignment between the applied field and the atoms, as measured by the factor $0 \leq 3^* \leq 3$.

For an inhomogeneous gaussian transition the formulas in Equations 4.27 or 4.31 must be modified by replacing $1/\Delta\omega_a$ by $1/\Delta\omega_d$; replacing the lorentzian frequency dependence by a gaussian; and adding a factor of $\sqrt{\pi} \ln 2 \approx 1.48$ in front.

Note also that in the preceding analysis we speak of the upward and downward stimulated rates $W_{12}N_1$ and $W_{21}N_2$ as if they were separate and distinct processes. It is, however, only the net transition rate between levels, $W_{12}N_1 - W_{21}N_2$, that really counts. There is no way to "turn off" one of these rates and produce only the other one. They are physically identical or at least physically inseparable.

The transition rates discussed in this section are called *stimulated transition rates* because they are caused by applied signals producing changes in the populations $N_1(t)$ and $N_2(t)$. Populations of atomic levels also change with time because of pumping effects, and because of energy decay or relaxation transitions between the levels. These relaxation processes produce additional terms in the rate equations, which we must describe in subsequent sections. The stimulated and relaxation terms must be added together in the total rate equations to describe how the populations change with time.

REFERENCES

Nearly all the discussions in this book will speak of atoms being acted upon by optical fields that are part of some traveling wave or beam of light. The atoms really respond, however, to the local E field strength of the optical signal (at least in an electric-dipole transition), without caring whether these fields are part of a propagating wave or perhaps of an evanescent field distribution, as in frustrated total internal reflection, or in the evanescent fields outside the core of an optical fiber. Experiments to show that the stimulated-transition probability is in fact exactly the same either for propagating photons or for evanescent fields have been carried out by C. K. Carniglia, L. Mandel, and K. H. Drexhage, "Absorption and emission of evanescent photons," *J. Opt. Soc. Am.* **62**, 479-486 (April 1972).

4.3 BLACKBODY RADIATION AND RADIATIVE RELAXATION

The next objective in this chapter must be to understand how thermal fluctuations, or blackbody radiation fields, can also cause stimulated transitions between atomic energy levels. We will then go on to show how these "noise-stimulated" transitions are related to the spontaneous emission or radiative decay processes we have discussed earlier, and how they provide a very important part of the relaxation processes in an atomic system.

Blackbody Radiation Density

One of the most basic conclusions of thermodynamics is that any volume of space that is in thermal equilibrium with its surroundings must contain a *blackbody radiation energy density*, made up of noise-like *blackbody radiation fields*. Furthermore, the magnitude of these fields depends only on the temperature of the region and of its immediate surroundings and not at all on the shape or construction of the volume (provided only that the volume is large compared to a wavelength of the radiation involved). The electromagnetic fields that make up this blackbody radiation energy are real, measurable, broadband, noise-like E and H fields, with random amplitudes, phases, and polarization, which are present everywhere in the volume.

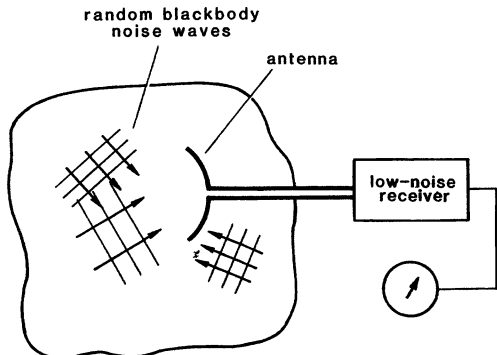


FIGURE 4.5

Measurement of the blackbody radiation fields inside an arbitrary enclosure.

The amount of blackbody radiation energy per unit volume that is present within a region at temperature T_{rad} , at frequencies within a narrow frequency range $d\omega$ about ω , is given in fact by the *blackbody radiation density*

$$dU_{\text{bbr}} = \frac{8\pi}{\lambda^3} \frac{\hbar d\omega}{\exp(\hbar\omega/kT_{\text{rad}}) - 1}. \quad (33)$$

In more precise terms, $dU_{\text{bbr}}/d\omega$ is the spectral density of the blackbody radiation energy, i.e., the amount of energy per unit volume and per unit frequency range centered at frequency ω . We write the temperature as T_{rad} in this expression to indicate that it is the temperature of the “radiative surroundings” of this region—that is, the temperature of the nearest electromagnetically absorbing walls or boundaries—that determines the blackbody radiation energy density in the region.

The energy density dU_{bbr} in any narrow frequency range $d\omega$ will have associated with it a mean-square electric field intensity $d|\tilde{E}_{\text{bbr}}|^2$ given by

$$dU_{\text{bbr}} = \frac{\epsilon}{2} d|\tilde{E}_{\text{bbr}}|^2. \quad (34)$$

That is, there will be real measurable electric fields of noise-like character associated with the blackbody energy within the frequency range $d\omega$, and these fields will have a root-mean-square phasor amplitude \tilde{E}_{bbr} given by

$$d|\tilde{E}_{\text{bbr}}|^2 = \frac{16\pi}{\lambda^3} \frac{\hbar d\omega}{\exp(\hbar\omega/kT_{\text{rad}}) - 1}. \quad (35)$$

With a sensitive enough antenna or probe and a receiver with a low enough noise figure (Figure 4.5), these noise-like fields can be detected and measured as a function of center frequency ω and temperature T_{rad} inside the enclosure.

Blackbody-Stimulated Atomic Transitions

Any atoms that may be present in the region under consideration are then exposed to these entirely real though noise-like \tilde{E}_{bbr} fields. These E fields will in fact act on the atoms just like signal fields, and will cause stimulated transitions and power absorption at exactly the same rate as would be caused by any other

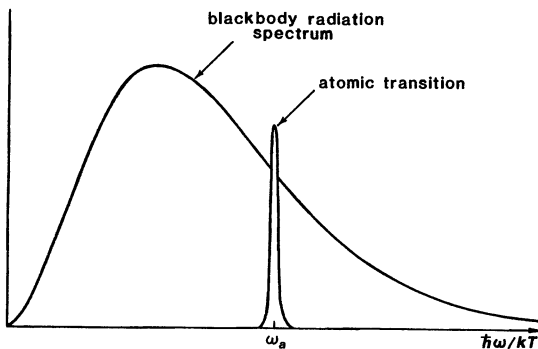


FIGURE 4.6
Blackbody radiation spectrum, and the absorption spectrum of a single narrow atomic transition.

applied signal fields with the same mean-square amplitude. We can calculate the stimulated-transition rates that will be caused by these blackbody radiation fields by means of the following argument.

Figure 4.6 illustrates how the broadband continuum spectral distribution of the blackbody noise fields will overlap with the narrow atomic lineshape of a typical atomic transition. The amount of stimulated-transition probability dW_{12} that will be caused in a two-level atomic system by those blackbody radiation components lying within a small frequency bandwidth $d\omega$ centered at ω within the atomic linewidth will then be given (for a lorentzian transition) by exactly the same stimulated-transition probability expression as was derived in the previous section, namely,

$$dW_{12,\text{bbr}} = dW_{21,\text{bbr}} = \frac{3^*}{8\pi^2} \frac{\gamma_{\text{rad}}}{\hbar\Delta\omega_a} \frac{\epsilon d|\tilde{E}_{\text{bbr}}|^2 \lambda^3}{1 + [2(\omega - \omega_a)/\Delta\omega_a]^2}, \quad (36)$$

with $d|\tilde{E}_{\text{bbr}}|^2$ given by Equation 4.35. Because these blackbody \tilde{E} fields will be randomly polarized, the 3^* factor will have an averaged value of unity; so we will drop it from here on.

The total transition rate on the $1 \rightarrow 2$ transition due to blackbody radiation fields at all frequencies is then easily calculated by integrating the contribution from each narrow range $d\omega$, as given by Equation 4.36, over all the blackbody signals that are present at all frequencies, in the form

$$W_{12,\text{bbr}} = W_{21,\text{bbr}} = \int dW_{12,\text{bbr}} = \int_{-\infty}^{\infty} \left[\begin{array}{l} \text{radiation density} \\ \text{at frequency } \omega \end{array} \right] \times \left[\begin{array}{l} \text{transition response} \\ \text{at frequency } \omega \end{array} \right] d\omega. \quad (37)$$

For any reasonable atomic transition, the atomic linewidth will always be very much narrower than the blackbody spectral distribution, as in Figure 4.6. It is then an entirely valid approximation to give the blackbody distribution function its value at the line center, $\omega = \omega_a$, and take it outside the integral over $d\omega$. The

integral of Equation 4.36 over the lineshape then reduces to the simple form

$$W_{12,\text{bbr}} = W_{21,\text{bbr}} = \frac{\gamma_{\text{rad}}}{\exp(\hbar\omega_a/kT_{\text{rad}}) - 1} \int_{-\infty}^{\infty} \frac{2}{\pi\Delta\omega_a} \frac{d\omega}{1 + [2(\omega - \omega_a)/\Delta\omega_a]^2}. \quad (38)$$

But the integral on the right-hand side of this equation has unity area independent of its linewidth $\Delta\omega_a$; hence we obtain the very simple and fundamental result that

$$W_{12,\text{bbr}} = W_{21,\text{bbr}} = \frac{\gamma_{\text{rad}}}{\exp(\hbar\omega_a/kT_{\text{rad}}) - 1}. \quad (39)$$

These blackbody-stimulated transition rates turn out to be independent of any properties of the atomic transition except its radiative decay rate γ_{rad} .

The very basic result that we obtain here is thus that the *stimulated transition rate between any two atomic levels caused by blackbody fields depends only on the radiative decay rate for that transition, and on the Boltzmann factor at the temperature of the radiation, and on nothing else*. In particular this result does not depend at all on the linewidth, or even the lineshape, of the transition.

Power Absorption from the Surroundings?

This argument says that even without any externally applied signals, thermal-noise-stimulated transitions or “jumps” will be continually taking place in both directions between any two energy levels E_1 and E_2 , with stimulated-transition probabilities $W_{12,\text{bbr}}$ and $W_{21,\text{bbr}}$ given by Equation 4.39. More precisely, for two energy levels E_i and $E_j > E_i$ having level degeneracies g_i and g_j , respectively, these thermally stimulated transition rates will be given by

$$W_{ji,\text{bbr}} = \frac{g_i}{g_j} W_{ij,\text{bbr}} = \frac{\gamma_{\text{rad},ji}}{\exp(\hbar\omega_{ji}/kT_{\text{rad}}) - 1} \quad (40)$$

These transitions are caused entirely by the unavoidable blackbody radiation fields in which the atoms are always immersed (unless the electromagnetic surroundings can be cooled all the way to absolute zero).

But this in turn implies that there will necessarily be net power absorption, proportional to the atomic population difference $\Delta N = N_1 - N_2$, from the blackbody fields to the atoms. In other words, the blackbody fields will be continuously delivering energy, or heat, to the atoms through these stimulated transitions. But this in turn raises serious questions about thermal equilibrium between the atoms and the surroundings. How can a collection of atoms, which are nominally in thermal equilibrium, remain in equilibrium if they are continually absorbing energy from their surroundings? Even more serious, how can a collection of atoms which are supposedly at an atomic temperature T_a (defined by the Boltzmann ratio) continually absorb energy from surroundings that might be at a different thermodynamic temperature T_{rad} —especially if the surrounding temperature T_{rad} might in some cases be colder than the atomic temperature T_a ?

Power Emission to the Surroundings

The answer to these questions comes in remembering that there will also be in any atomic system purely spontaneous and entirely downward transitions, due to the spontaneous emission or radiative decay from the upper-level atoms;

and these spontaneous transitions or purely radiative decays will transfer power from the atoms back to the electromagnetic surroundings, with a spontaneous decay rate given by γ_{rad} .

These spontaneous downward transitions in the atoms are to be viewed as genuinely “spontaneous” and not as “noise-induced” transitions, at least in the approach we are taking here, since they simply occur spontaneously in a manner explainable only by quantum theory. However, we will see that these spontaneous-emission transitions from the atoms to the surroundings can and do exactly balance the noise-stimulated absorption from the surroundings to the atoms, when the atoms are in thermal equilibrium with their electromagnetic surroundings. (Some people find it helpful to describe the spontaneous downward transitions as being “one-way stimulated transitions” which are stimulated by quantum zero-point fluctuations in the electromagnetic field; but we will not get involved in that argument here.)

Thermal Balance with the Electromagnetic Surroundings

Figure 4.7 shows schematically the overall transfer of energy that takes place in both directions between a collection of atoms and their “electromagnetic surroundings,” through stimulated absorption and emission of blackbody radiation, plus spontaneous emission of energy from the atoms to the surroundings.

Each arrow in Figure 4.7 indicates the direction and magnitude of an energy flow. The ratio of energy flow from the atoms into the surroundings caused by blackbody-stimulated plus spontaneous emission, compared to energy flow in the reverse direction due to blackbody-stimulated absorption, is given by

$$\begin{aligned} \frac{\text{energy flow out of atoms}}{\text{energy flow into atoms}} &= \frac{(W_{21,\text{bbr}} + \gamma_{\text{rad}}) N_2}{W_{12,\text{bbr}} N_1} \\ &= \frac{W_{21,\text{bbr}} + \gamma_{\text{rad}}}{W_{12,\text{bbr}}} \times \frac{N_2}{N_1}. \end{aligned} \quad (41)$$

Now, the population ratio in a collection of two-level atoms can be described at any instant by an “atomic temperature” T_a , in the sense that the Boltzmann ratio between the energy-level populations is given by

$$\frac{N_2}{N_1} = \exp\left(-\frac{\hbar\omega_a}{kT_a}\right). \quad (42)$$

At the same time, by using Equation 4.39 the ratio of spontaneous and noise-stimulated emission rates to noise-stimulated absorption rates is related to the temperature T_{rad} of the electromagnetic surroundings by

$$\frac{W_{21,\text{bbr}} + \gamma_{\text{rad}}}{W_{12,\text{bbr}}} = \exp\left(\frac{\hbar\omega_a}{kT_{\text{rad}}}\right). \quad (43)$$

The ratio of the energy flow rates in the two directions is thus given, in terms of the temperatures of the atoms and the surroundings, by

$$\frac{\text{energy flow out of atoms}}{\text{energy flow into atoms}} = \exp\left(\frac{\hbar\omega_a}{kT_{\text{rad}}} - \frac{\hbar\omega_a}{kT_a}\right). \quad (44)$$

electromagnetic surroundings

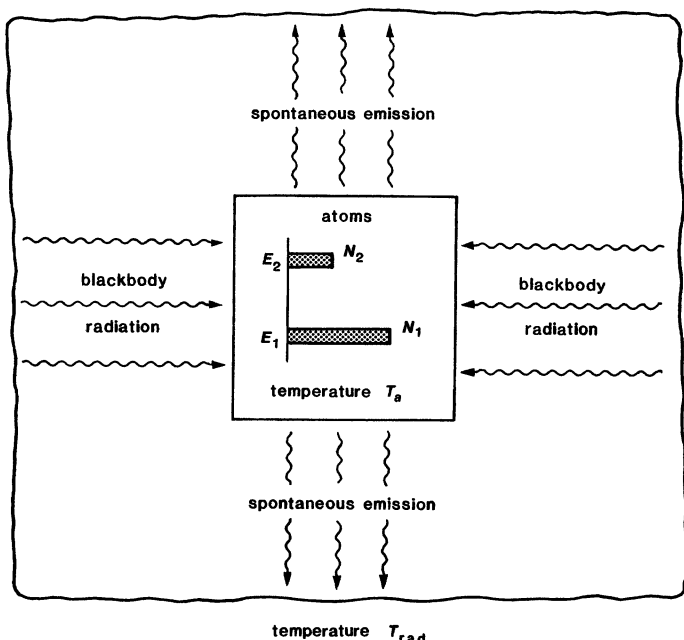


FIGURE 4.7

The blackbody radiation fields inside any volume whose surroundings are at temperature T_{rad} will produce stimulated transitions, and thus power absorption, in a collection of atoms; the atoms in turn will radiate power back to the surroundings through spontaneous emission.

These rates will be equal and opposite if and only if the atomic temperature T_a exactly equals the surrounding electromagnetic temperature T_{rad} .

The net energy received by the atoms from the blackbody fields will thus, at thermal equilibrium, exactly equal the energy radiated back to the surroundings by the atoms. There will be no net flow of atoms between levels E_1 and E_2 , and no net power transfer between atoms and surroundings—as should certainly be the case at thermal equilibrium.

Discussion: Thermal Equilibrium

There are several very fundamental conclusions that can be drawn from the preceding analytical results. First, the existence of a spontaneous, purely downward emission in any collection of atoms appears to be essential, if for no other reason than to maintain energy balance with the atomic surroundings at thermal equilibrium. A collection of atoms in thermal equilibrium at any finite temperature will always have a net power absorption on its atomic transitions; and the volume containing these atoms will always have finite blackbody signals

to be absorbed by the atoms (unless the surroundings are at absolute zero). The atoms will therefore always absorb energy from the blackbody fields, producing a net flow of atoms into the upper energy levels.

These upper-level atoms must then spontaneously drop down and radiate away energy at a rate given by γ_{rad} times the number of atoms in the upper level. This energy reradiation will exactly equal the energy that the same atoms inevitably absorb from the blackbody radiation fields in which they are immersed, if the atoms and the surroundings are at the same temperature.

In the more general situation, the atomic temperature T_a of a collection of atoms and the electromagnetic temperature T_{rad} of their surroundings might be different, at least on a temporary basis. That is, the atoms might be in internal thermal equilibrium at a temperature T_a , in the sense that all the phases of individual atomic oscillations are fully dephased or randomized, and all level populations satisfy the Boltzmann ratios with this temperature value. This temperature might, for example, be relatively hot because the atoms have been immersed in a hot environment. These atoms might then be suddenly moved into an enclosure which has walls at a substantially colder (or hotter) temperature T_{rad} .

The atoms will now form one thermal reservoir at temperature T_a , and the walls and the blackbody radiation will form another reservoir at $T_{\text{rad}} \neq T_a$. Whichever is hotter, energy will flow from the hotter system to the colder. The total system will eventually come to a thermal equilibrium at some temperature in between the initial temperatures, depending on the relative heat capacities of the two systems. This kind of “atomic transition calorimetry” can in fact be carried out experimentally, on nuclear magnetic transitions, for example.

Detailed Balance

Overall thermal equilibrium requires, in fact, that the blackbody absorption and spontaneous emission rates be in exact equilibrium *transition by transition*, for each one of the $E_i \rightarrow E_j$ pairs in a collection of multilevel atoms. This necessity for the net absorption and spontaneous emission to be in balance on each individual transition at thermal equilibrium is sometimes referred to as “detailed balance.” Detailed balance applies, in fact, not just transition by transition, but also frequency component by frequency component within any single transition: the net absorption rate by the atoms at any frequency ω and the spontaneous emission in a very narrow range $d\omega$ about that same ω must also balance. An atomic transition must, therefore, by fundamental thermodynamic arguments, have exactly the same atomic lineshape for spontaneous emission as it does for stimulated absorption, whether this lineshape be lorentzian, gaussian, or whatever.

The simple relationship derived in Equation 4.39 between $W_{ij,\text{bb}}^*$ and $\gamma_{\text{rad},ji}$ is therefore hardly accidental. This relation is rather a basic and necessary condition for thermal equilibrium to ensue. The same relation between $W_{ij,\text{bb}}^*$ and $\gamma_{\text{rad},ji}$ must hold generally for any kind of stimulated transition, with any lineshape or form of tensor response, and any order of electric or magnetic dipole or multipole character. The direct proportionality we noted earlier between the stimulated response $\tilde{\chi}(\omega)$ and the spontaneous emission rate γ_{rad} for an atomic transition is also a necessary consequence of the balance between net blackbody absorption and spontaneous emission that is required to reach thermal equilibrium.

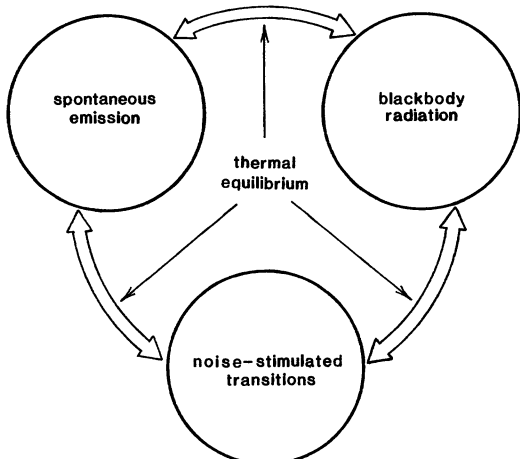


FIGURE 4.8

Stimulated atomic transitions, spontaneous emission, and blackbody radiation are connected by the right sort of circular argument: given any two of them we can calculate the third.

The logical arguments we have developed here might be represented by Figure 4.8. The stimulated-transition circle indicates the processes of noise-stimulated absorption and emission in a collection of atoms. These noise-stimulated processes can be derived by a *semiclassical derivation*—that is, a derivation in which the atoms are quantized but the electromagnetic fields are not. The blackbody-radiation and spontaneous-emission circles then indicate the existence of these two phenomena, either of which can be derived independently of the other, but only by employing a full quantum electrodynamical calculation in which the electromagnetic field itself is quantized.

The connecting arrows then indicate that we can use the existence of any two of these phenomena, plus the criterion of thermal equilibrium, to derive the existence and magnitude of the third. It is a matter of choice, for example, whether we begin with the existence of blackbody radiation, and then use this to imply the necessity for spontaneous emission; or whether we take some other direction around the circle. Any two of these processes imply the third.

REFERENCES

An early paper which develops almost exactly the same argument as in this section is R. C. Tolman, "Duration of molecules in upper quantum states," *Rev. Mod. Phys.* **23**, 693–709 (June 1924). This paper is interesting and instructive to read even now because of how clearly Tolman understands (and presents) the fundamental ideas, despite the confusion over the quantum theory which still prevailed in 1924; and also because he mentions experimental evidence which confirms the theory. Tolman also clearly foresees the possibility of coherent "negative absorption" and hence laser amplification.

Problems for 4.3

1. *Thermal equilibration in a two-level atomic system: purely radiative case.*

Suppose a collection of two-level atoms has a specified radiative decay rate γ_{rad} ,

and no nonradiative decay, $\gamma_{nr} = 0$. The atoms are pre-cooled to absolute zero for long enough to come into equilibrium with $N_2 = 0$, and then are suddenly moved at $t = 0$ into an enclosure with walls held at a finite temperature T_{rad} . Find formulas for the populations $N_1(t)$ and $N_2(t)$, and for the temperature $T_a(t)$ of the collection of atoms for $t > 0$.

4.4 NONRADIATIVE RELAXATION

The total energy-decay rates for quantum energy levels in atoms can involve both radiative and nonradiative transfer of energy from atoms to their surroundings. In a broader viewpoint, therefore, we must really be concerned with the *total atomic relaxation processes* that result from interactions between the atoms and their thermal surroundings, both through electromagnetic or “radiative” interactions and through nonelectromagnetic or “nonradiative” interactions. In this section we will try to make clear how an atomic transition interacts with both its electromagnetic and its nonelectromagnetic surroundings; how these interactions lead to both radiative and nonradiative decay; and how these in turn lead to two different but similar kinds of relaxation transitions associated with these two mechanisms.

Radiative Relaxation Rates and Transition Probabilities

In the preceding section we obtained the remarkable and very fundamental result that blackbody radiation from the “electromagnetic surroundings” of a nondegenerate two-level atom will cause “blackbody stimulated transitions” with upward and downward transition probabilities given by

$$W_{12,bb} = W_{21,bb} = \frac{\gamma_{rad}}{\exp(\hbar\omega_a/kT_{rad}) - 1}, \quad (45)$$

where T_{rad} is the temperature of the electromagnetic surroundings. This is a very fundamental relationship. We can view it as being imposed by the necessity for thermal equilibrium between the rate at which an atom spontaneously radiates energy and the rate at which it absorbs energy from blackbody fields.

The transition rates $W_{12,bb}$ and $W_{21,bb}$ are thus from one viewpoint stimulated transitions caused by the real (if weak), random, omnipresent blackbody radiation fields. The existence of these fields depends only on the temperature of the surroundings, however, and on nothing else. There is nothing we can do in practice to control or modify these blackbody fields (short of cooling everything in the vicinity down toward absolute zero). Hence we may just as well think of the blackbody-stimulated transition rates as being part of the *relaxation mechanisms* which are always present among the atomic-level populations, independent of anything that we ourselves do.

In earlier chapters we spoke for simplicity only of energy decay, i.e., only of spontaneous downward relaxation from upper levels to lower levels. The possibility of “upward relaxation,” caused by energy coming back from the thermal surroundings to the atoms, was not mentioned. We are now seeing that, in a complete and accurate description, when an atom is coupled to external surroundings it can do more than just relax downward and give energy to those surroundings,

as we said earlier. It can also (but with inherently lower probability) receive energy from its thermal surroundings and be lifted or relaxed upward in energy. This is directly related to the fact that in thermal equilibrium there are always some numbers of atoms, given by the Boltzmann ratios, in upper energy levels (though these may be very small numbers). At any temperature greater than absolute zero, the atoms never relax completely into the lowest energy level, as would always happen if only downward relaxation occurred.

Of course, for optical-frequency transitions at room temperature, the Boltzmann ratio is enormously small ($\approx 10^{-36}$). Both the upper-level populations and the upward relaxation rates are truly negligible, and only downward relaxation need be considered. For lower frequencies and more closely spaced levels, however, Boltzmann ratios and upward relaxation rates do need to be taken into account, and therefore we do need to understand the full situation described here. For microwave and lower-frequency transitions, in fact, the Boltzmann ratio becomes nearly unity, and upward and downward relaxation rates become very nearly equal.

Nonradiative Relaxation Rates and Transition Probabilities

Blackbody relaxation and energy-exchange mechanisms represent, however, only the interactions of the atoms with their *electromagnetic* surroundings, acting through the blackbody radiation and the radiative decay rate. These interactions are shown in a schematic form in the top part of Figure 4.9.

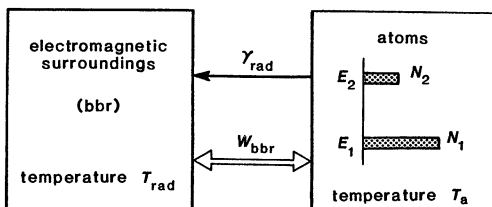
We must recognize, however, that real atoms will usually also be in thermal contact with what we will refer to, in general terms, as “other surroundings” or “nonradiative surroundings,” as shown schematically in Figure 4.9(b). These nonradiative surroundings, to which the atoms can also be coupled, can include a crystal lattice in which the laser atoms are imbedded; or a surrounding liquid medium in which the laser molecules are dissolved; or other atoms or walls with which the atoms of interest are colliding in a gas.

The atoms may then exchange energy with these “nonradiative surroundings” by means of the nonradiative decay processes that are included in the nonradiative decay rate γ_{nr} , in essentially the same way as the atoms exchange energy with the “electromagnetic surroundings” through the purely radiative processes that are involved in γ_{rad} . But this necessarily implies, from the same kind of thermodynamic reasoning we employed earlier, that these “nonradiative surroundings” must also be able to cause “nonradiatively stimulated transitions” between the atomic levels, with stimulated-transition probabilities $W_{12,nr}$ and $W_{21,nr}$, in a manner exactly analogous to the blackbody transitions $W_{12,bbr}$ and $W_{21,bbr}$ described earlier.

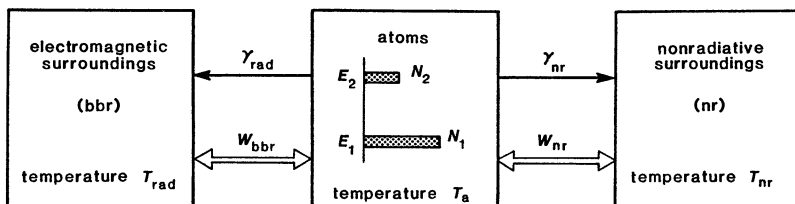
These additional transitions we will refer to generally as *nonradiative relaxation transitions*. The basic physics involved in the nonradiative interaction of a collection of atoms with their “nonradiative surroundings” will then be the same in every important aspect as that of the radiative interaction of these same atoms with their electromagnetic surroundings.

Example: Phonon Interactions in Crystal Lattices

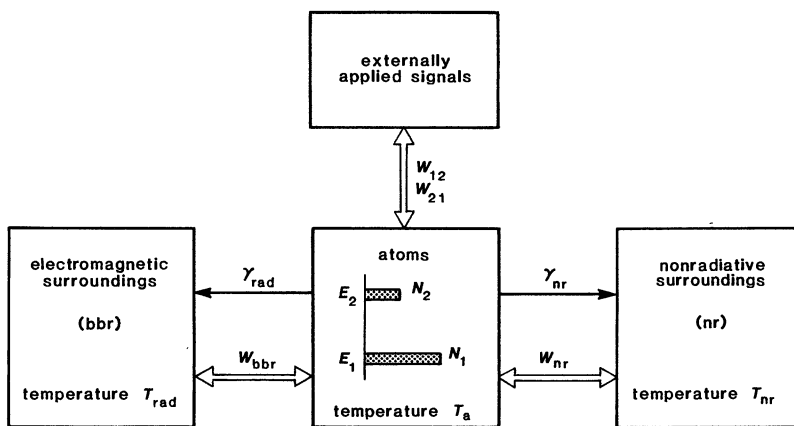
As a specific example of this, let us consider the interaction between a collection of laser or maser atoms and the lattice vibrations in a surrounding host crystal lattice, since this is one important type of “nonradiative surroundings.”



(a)



(b)



(c)

FIGURE 4.9

- (a) Interaction of a collection of atoms with the "electromagnetic surroundings" only.
 (b) Interaction with both "electromagnetic" and "nonradiative" surroundings (which may in general be at different temperatures). (c) Interaction with both of these types of surroundings, and with an externally applied signal.

A crystal lattice containing laser atoms can propagate acoustic waves, often referred to as *phonons*, at many different frequencies and in many different directions, just as a vacuum or dielectric medium can propagate electromagnetic waves, or *photons*. Moreover, like electromagnetic waves, these acoustic waves can interact with atomic transitions of atoms contained in the crystal lattice, and can produce stimulated transitions and induced atomic responses.

That is, there will generally be some weak coupling or interaction between the quantum wave function of an atom imbedded in a crystal lattice and the acoustic vibrations in the surrounding crystal lattice. This coupling is very analogous to the weak electric-dipole coupling between the atomic wave functions and the electromagnetic vibrations (fields) in the surrounding electromagnetic "ether." The basic physical principles that apply to *electromagnetic interactions* with atoms therefore apply in almost exactly the same way to what we may call *generalized acoustic interactions* with the atoms.

For example, a coherent acoustic signal in the form of a lattice vibrational wave at a frequency ω near an atomic transition frequency ω_a can be absorbed or amplified through its interaction with the atoms, just like an electromagnetic wave; and this absorption or amplification of the acoustic wave will depend on the atomic population difference (and the atomic linewidth and lineshape) exactly like an electromagnetic wave interaction. It is entirely possible to use an inverted atomic population to amplify acoustic waves and to produce acoustic-wave oscillation in a crystal at the atomic transition frequency. Such "acoustic lasers" or "acoustic masers" have been experimentally demonstrated at microwave frequencies, using some of the same pumping methods and maser materials used to produce electromagnetic maser oscillation at the same frequencies on the same transitions.

Acoustic Transition Rates

Of more importance to us here is the fact that at any finite temperature such a crystal lattice will have thermal lattice vibrations, or "blackbody acoustic radiation," which is exactly analogous in character to blackbody electromagnetic fields (although the appropriate energy density formulas are somewhat different). These thermally induced vibrations represent the heat content of the crystal lattice, and as such can be characterized by a lattice temperature which we will label more generally as T_{nr} , with the subscripts standing for "nonradiative surroundings". The lattice vibrations of course go to zero only if the lattice temperature T_{nr} itself goes to absolute zero.

A critically important point is that the atoms will then be affected by these thermal lattice vibrations in the surrounding crystal, in basically the same way that they are affected by the blackbody radiation in the electromagnetic surroundings. To describe this interaction we must use exactly the same arguments as for the electromagnetic surroundings, but now we refer to interactions with the "nonradiative" or lattice surroundings rather than with the "electromagnetic surroundings."

Generalized Nonradiative Interaction Processes

In fact, by invoking the necessity for detailed thermal balance in the energy transfer processes between the atoms and the lattice acoustic modes, we can argue that these acoustically stimulated transition rates $W_{12,nr}$ and $W_{21,nr}$ must

be related to the nonradiative decay rate γ_{nr} by exactly the same fundamental relationship as Equation 4.45 for the radiative case, namely,

$$W_{12,\text{nr}} = W_{21,\text{nr}} = \frac{\gamma_{\text{nr}}}{\exp(\hbar\omega_a/kT_{\text{nr}}) - 1}. \quad (46)$$

Only if these relations hold will the power delivered to the atoms by the surrounding lattice through the $W_{12,\text{nr}}$ and $W_{21,\text{nr}}$ transitions always be exactly balanced, under thermal equilibrium conditions, by the power delivered from the atoms back to the nonradiative lattice surroundings through γ_{nr} . This equation applies, in fact, in a completely general fashion, not just to the interaction of atoms with acoustic lattice surroundings in crystals, but also to the nonradiative interactions of a collection of quantum atoms with any kind of nonradiative thermal surroundings.

That is, suppose the upper-level atoms in a collection of atoms do in fact lose some of their excitation energy by transferring energy into any kind of "nonradiative surroundings," whether to a surrounding crystal lattice or cell walls, or by collisions with other atoms in a gas mixture. Suppose this energy loss rate is described by a nonradiative decay rate γ_{nr} times the upper-level population, and that the surroundings which receive this energy are describable by a temperature T_{nr} .

These other surroundings must then necessarily produce upward and downward thermally stimulated transitions on the same transition in the collection of atoms, with thermally stimulated transition probabilities $W_{12,\text{nr}}$ and $W_{21,\text{nr}}$ exactly as given by Equation 4.46. We use the notations W_{nr} and T_{nr} in this equation, and in Figure 4.9(b), to emphasize that the net interaction with any "nonradiative thermal surroundings" is completely analogous to the interaction of the same atoms with the blackbody radiation surroundings, even though electromagnetic radiation and blackbody radiation fields in the usual sense are not involved.

Radiative Plus Nonradiative Surroundings

The nonradiative decay rate γ_{nr} thus plays the same role in interacting with any kind of "nonradiative surroundings" as the radiative decay rate γ_{rad} plays in interacting with the radiative or electromagnetic surroundings. The generalization of Equation 4.46 to degenerate transitions is also the same as for the electromagnetic case, namely,

$$W_{ji,\text{nr}} = \frac{g_i}{g_j} W_{ij,\text{nr}} = \frac{\gamma_{\text{nr},ji}}{\exp(\hbar\omega_{ji}/kT_{\text{nr}}) - 1}. \quad (47)$$

The combined influence of radiative and nonradiative interactions for any collection of atoms (actually for any single transition in a collection of atoms) can then be illustrated by an expanded diagram like Figure 4.9(b), in which we indicate separately the interactions and the relaxation transition rates for the radiative and the nonradiative surroundings. The only significant parameters in these interactions are the two relaxation rates γ_{rad} and γ_{nr} , and the associated temperatures of the surroundings T_{rad} and T_{nr} , respectively.

These two temperatures T_{rad} and T_{nr} will usually have the same value; but in special cases the temperature T_{nr} of the "nonradiative surroundings" could be different from the temperature T_{rad} of the electromagnetic surroundings. Suppose the crystal lattice of an atomic medium is essentially lossless and transparent to

electromagnetic radiation at all frequencies of interest, so that the lattice itself is not part of the electromagnetic surroundings. The temperature T_{nr} characteristic of the lattice vibrations when the crystal is cooled, for example, in a liquid helium bath, may be much colder than the temperature T_{rad} of the warmer electromagnetic surroundings seen by the atoms through the windows of the helium dewar.

Another Nonradiative Example: Inelastic Collisions in Gases

As another example of nonradiative interactions, suppose that excited atoms of type A in a mixture of two different gases can lose some of their excitation energy through inelastic collisions with atoms of type B , with this energy going into heating up the kinetic motion of the type B atoms. This is a form of nonradiative decay for the excited atoms of type A , which can be accounted for by a nonradiative decay rate γ_{nr} (which will probably be directly proportional to the pressure or density of the atoms of type B).

From the same arguments as before, these same collisions must then also produce collision-stimulated transitions in both directions between the levels of the type A atoms, with transition rates $W_{12,\text{nr}}$ and $W_{21,\text{nr}}$ given by Equation 4.47, and with T_{nr} given by the kinetic temperature of the type B atoms. The physical details of how the kinetic motion of the type B atoms can react back to produce collision-stimulated upward and downward transitions in the type A atoms may not be particularly obvious; and it is certainly not at all clear how we might use a population inversion in the type A atoms to “amplify” the type B kinetic motion.

The general rule is, however, that if a collection of excited atoms can deliver energy in any fashion to some part of their nonradiative surroundings, then they are in some way coupled to those surroundings. As a result, these “other surroundings” are necessarily coupled back to the atoms, and thermal fluctuations in these “other surroundings” can cause upward and downward thermally stimulated transition rates in the atomic system by acting through the same nonradiative interaction mechanisms.

Note in this instance that collisions between atoms in a gas may contribute to the homogeneous line broadening of transitions in these atoms in either of two distinct ways. *Elastic collisions* between atoms cause dephasing effects, and thus give a homogeneous line-broadening contribution $2/T_2$ which is directly proportional to the collision frequency and thus to the gas pressure. *Inelastic collisions* may cause both additional dephasing and an additional nonradiative energy decay term γ_{nr} , which will in turn give an additional pressure-dependent lifetime broadening contribution.

Total Relaxation Transition Rates

It is important to understand how there can be separate but essentially similar relaxation effects produced by both the radiative and the nonradiative surroundings, as illustrated in Figure 4.9(b). Once we understand the underlying physics, however, it is then much simpler to combine these two effects (including the spontaneous relaxation effects) into a single pair of *thermally stimulated relaxation transition probabilities*, which we will henceforth denote by w_{12} and w_{21} , and which are defined as follows.

Let the transition rate or flow rate (in atoms/second) in the downward direction due to all these interactions be written in the form

$$\left. \left| \frac{dN_2}{dt} \right| \right|_{\substack{\text{downward} \\ \text{relaxation}}} = (W_{21,\text{bb}} + \gamma_{\text{rad}} + W_{21,\text{nr}} + \gamma_{\text{nr}}) N_2 \quad (48)$$

$$\equiv w_{21} N_2,$$

and let the corresponding flow rate in the upward direction be written as

$$\left. \left| \frac{dN_1}{dt} \right| \right|_{\substack{\text{upward} \\ \text{relaxation}}} = (W_{12,\text{bb}} + W_{12,\text{nr}}) N_1 \quad (49)$$

$$\equiv w_{12} N_1.$$

Obviously we then have

$$w_{21} \equiv W_{21,\text{bb}} + W_{21,\text{nr}} + \gamma_{\text{rad}} + \gamma_{\text{nr}} \quad (50)$$

in the downward direction, and

$$w_{12} \equiv W_{12,\text{bb}} + W_{12,\text{nr}} \quad (51)$$

in the upward direction. The downward relaxation transition probability w_{21} includes both the thermally stimulated downward transitions and the spontaneous emission transitions from both radiative and nonradiative mechanisms, whereas the upward transition probability w_{12} represents the thermally stimulated upward transitions due to both mechanisms.

Figure 4.10 illustrates these net relaxation rates between any pair of atomic levels. For an arbitrary pair of levels E_i and $E_j > E_i$, the downward relaxation probability must be written as

$$w_{ji} \equiv W_{ji,\text{bb}} + W_{ji,\text{nr}} + \gamma_{\text{rad},ji} + \gamma_{\text{nr},ji} \quad (52)$$

and the upward relaxation probability on the same transition is written as

$$w_{ij} \equiv W_{ij,\text{bb}} + W_{ij,\text{nr}}. \quad (53)$$

We will from here on use these lowercase notations w_{12} and w_{21} , or more generally w_{ij} and w_{ji} , as defined above, to indicate the *total relaxation transition probabilities (per atom and per unit time)* in the upward and downward directions between any two levels i and j , due to all the purely thermal interactions plus energy decay processes connecting the atoms to their surroundings.

Also, from now on we will restrict the uppercase symbols W_{12} and W_{21} , or more generally W_{ij} and W_{ji} , to indicate *signal-stimulated transition probabilities* that are produced by external signals or pumping mechanisms that we either deliberately apply to the atoms, or that we allow to build up in a laser cavity, as shown schematically in Figure 4.9(c). That is, from here on the uppercase W_{ij} 's signify deliberately induced transition probabilities that we can turn off or suppress; the lowercase w_{ij} 's are relaxation transition probabilities that we can in essence do nothing about (except possibly by cooling the surroundings).

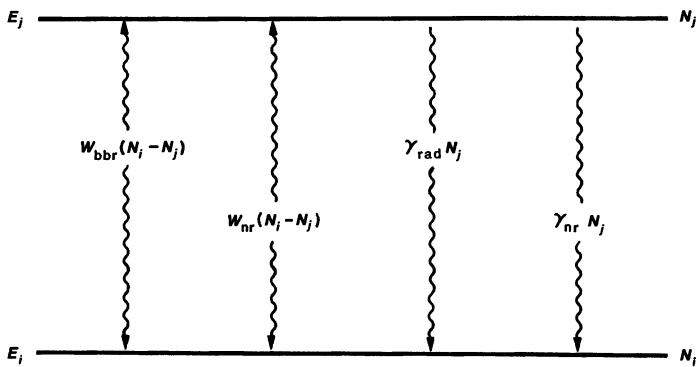


FIGURE 4.10

Total thermally stimulated plus spontaneous-emission transition rates between two energy levels, including both blackbody or radiative relaxation rates and nonradiative relaxation rates.

Boltzmann Relaxation Ratios

Note that if the surroundings of an atom, radiative and nonradiative, are both at the same equilibrium temperature $T_{nr} = T_{rad} = T$, then the preceding expressions show that the ratio between upward and downward relaxation probabilities is always given by the Boltzmann ratio

$$\frac{w_{12}(\uparrow)}{w_{21}(\downarrow)} = e^{-\hbar\omega_a/kT} \quad (54)$$

or, more generally,

$$\frac{w_{ij}}{w_{ji}} = \frac{g_j}{g_i} \exp\left(-\frac{E_j - E_i}{kT}\right), \quad (55)$$

where T is the temperature of the thermal surroundings. The upward thermally induced relaxation rate is always smaller (and on optical-frequency transitions usually much smaller) than the combination of downward thermally induced relaxation plus energy decay.

This Boltzmann relation does not depend on the nature or the strength of the radiative and/or nonradiative relaxation mechanisms that may be present; it will hold if they are all at the same temperature T . If the radiative and nonradiative surroundings are somehow at different temperatures, however, each interaction must be considered separately, and this ratio becomes somewhat more complicated.

Optical Frequency Approximation

A convenient rule of thumb for visible frequencies is that the equivalent temperature corresponding to $\hbar\omega_a/k$ is $\approx 25,000$ K. For any reasonable temperature T of the surroundings, therefore, the Boltzmann ratio at optical frequencies is always very small, on the order of

$$\exp(-\hbar\omega_a/kT) \approx \exp(-25,000/300) \approx 10^{-36}. \quad (56)$$

The thermally stimulated terms in the relaxation rates, either upward or downward, are then totally negligible compared to the spontaneous emission rates, and the relaxation transition probabilities in the two directions can be approximated by

$$w_{ij}(\uparrow) \approx 0 \quad (\text{upward direction}) \quad (57)$$

and

$$w_{ji}(\downarrow) \approx \gamma_{ji} \equiv \gamma_{\text{rad},ji} + \gamma_{\text{nr},ji} \quad (\text{downward direction}). \quad (58)$$

When we write out the rate equations for lower-frequency transitions, such as for magnetic resonance or microwave maser experiments, where the photon energy $\hbar\omega$ is $\ll kT$, then the relaxation terms in both upward and downward directions must be included; and we must use the more complete formulation involving the relaxation probabilities w_{ij} and w_{ji} in both upward and downward directions. The simplified notation using only γ_{ji} terms and including relaxation or energy decay in the downward direction only is more commonly employed in optical-frequency and laser analyses, where the optical-frequency approximation is almost always valid. Infrared and submillimeter laser transitions fall somewhere in between, and may require use of the more complete formulation on at least some of the transitions.

REFERENCES

We refer in this section to the possibility of maser amplification of coherent acoustic signals rather than electromagnetic signals. Coherent amplification of microwave phonons using an inverted atomic transition was first demonstrated by E. B. Tucker, "Amplification of 9.3-kMc/s ultrasonic pulses by maser action in ruby," *Phys. Rev. Lett.* **6**, 547 (1961). A more lengthy review of these kinds of experiments is given in E. B. Tucker, "Interactions of phonons with iron-group ions," *Proc. IEEE* **53**, 1547 (October 1965).

Problems for 4.4

1. *Thermal equilibration: radiative and nonradiative contributions.* A collection of two-level atoms in a crystal is coupled both to the electromagnetic surroundings with radiative decay rate γ_{rad} and to the crystal-lattice surroundings with decay rate γ_{nr} . Suppose the electromagnetic surroundings are somehow held at a fixed temperature T_{rad} which is different from the fixed temperature T_{nr} of the crystal lattice. Derive a formula for the steady-state equilibrium value of the Boltzmann temperature T_a for the level populations of the two-level atoms in this case, as a function of the two surrounding temperatures T_{rad} and T_{nr} , the normalized energy gap $\hbar\omega/k$, and the ratio $\gamma_{\text{rad}}/\gamma_{\text{nr}}$.
-

4.5 TWO-LEVEL RATE EQUATIONS AND SATURATION

The stimulated transition probabilities and relaxation transition probabilities derived in the preceding sections of this chapter can now be used to write the

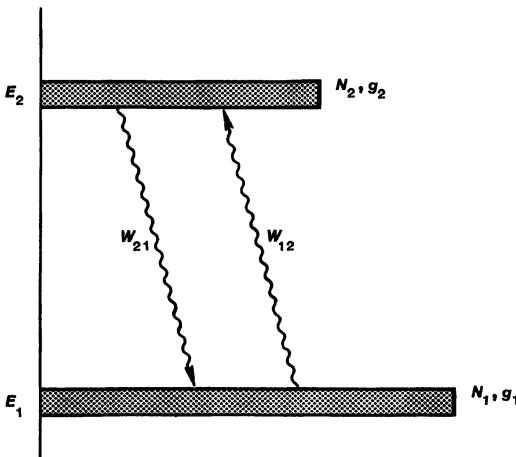


FIGURE 4.11
Total relaxation rates plus
signal-stimulated transition rates
between two energy levels.

general rate equations for any atomic system, taking into account both applied signals and relaxation processes. In this section we will explore the rate-equation solutions for an ideal two-level system. This will allow us to introduce a number of useful concepts, particularly the idea of *saturation* of the population difference ΔN at high enough applied signal levels.

Two-Level Rate Equation

In a simple two-level atomic system with an applied signal present, atoms flow from level 1 to level 2 at a rate $(W_{12} + w_{12}) N_1$, and from level 2 to level 1 at a rate $(W_{21} + w_{21}) N_2$, as illustrated in Figure 4.11. The total rate equation for the level populations N_1 and N_2 in this system is

$$\frac{dN_1(t)}{dt} = -\frac{dN_2(t)}{dt} = -[W_{12} + w_{12}]N_1(t) + [W_{21} + w_{21}]N_2(t). \quad (59)$$

If the energy levels have no degeneracy, the stimulated-transition rates are related by $W_{12} = W_{21}$, and the relaxation rates are related by $w_{12}/w_{21} = \exp(-\hbar\omega_a/kT)$, where T is the temperature of the surroundings of the atoms.

For a two-level system, however, it is usually more convenient to work with the total number of atoms $N_1(t) + N_2(t) = N$ and the population difference $N_1(t) - N_2(t) = \Delta N(t)$. Since the thermal equilibrium populations N_{10} and N_{20} with no signal present are related by the Boltzmann ratio $N_{20}/N_{10} = \exp(-\hbar\omega_a/kT)$, the population difference ΔN_0 on a nondegenerate two-level transition at thermal equilibrium, with no applied signal, can be written as

$$\Delta N_0 \equiv N_{10} - N_{20} = \frac{w_{21} - w_{12}}{w_{12} + w_{21}} N = N \tanh(\hbar\omega_a/2kT). \quad (60)$$

For a simple system with just two levels and a fixed total population, only one rate equation for the population difference $\Delta N(t)$ is then really needed. The equations for $dN_1(t)/dt$ and $dN_2(t)/dt$ can be combined into a single rate

equation in the form

$$\frac{d}{dt} \Delta N(t) = -(W_{12} + W_{21}) \Delta N(t) - (w_{12} + w_{21}) \left(\Delta N(t) - \frac{w_{21} - w_{12}}{w_{12} + w_{21}} N \right). \quad (61)$$

We can make this equation appear even simpler by using the fact that $W_{12} = W_{21}$ for the signal-stimulated transition probability, and by defining a two-level energy relaxation time or population recovery time T_1 by

$$w_{12} + w_{21} \equiv 1/T_1. \quad (62)$$

If we also recognize that the final term in Equation 4.61 is just the thermal-equilibrium population difference ΔN_0 for the atoms in equilibrium with the surroundings at temperature T_{rad} , then this two-level rate equation takes on the particularly simple and yet very general form

$$\frac{d}{dt} \Delta N(t) = -2W_{12} \Delta N(t) - \frac{\Delta N(t) - \Delta N_0}{T_1}. \quad (63)$$

This particularly simple form for the ideal two-level case with fixed total population turns out to be very useful and important for describing a great variety of laser and maser phenomena.

Physical Interpretation: The Population Recovery Time T_1

Understanding this two-level rate equation is important for understanding many subsequent aspects of laser behavior. For example, the relaxation term on the right-hand side of Equation 4.63, namely, $-[\Delta N(t) - \Delta N_0]/T_1$, obviously causes the population difference $\Delta N(t)$ to relax toward its *thermal equilibrium* value ΔN_0 in the absence of an applied signal, with an exponential time constant T_1 . This time constant T_1 is therefore often called the *population recovery time* or the *energy relaxation time* of the system.

Suppose the two-level transition is an optical-frequency transition with $\hbar\omega_a \gg kT$. The upward relaxation probability w_{12} is then essentially zero, whereas the downward relaxation probability w_{21} is essentially the upper-level energy decay rate γ_{21} as, we discussed earlier. The definition of T_1 therefore becomes

$$1/T_1 \equiv w_{12} + w_{21} \approx \gamma_{21} \equiv 1/\tau_{21}. \quad (64)$$

In the optical-frequency limit, the time constant T_1 is thus the same thing as the total lifetime or energy decay time τ_{21} of the upper energy level.

Steady-State Atomic Response: Saturation

In contrast, the stimulated signal term $-2W_{12} \Delta N(t)$ on the right-hand side of Equation 4.63 obviously acts to drive the population difference $\Delta N(t)$ toward zero, that is, to *saturate the population difference*. The stimulated-transition probability W_{12} is, of course, proportional to the strength of the applied signal, and so the rate at which $\Delta N(t)$ is driven toward zero is proportional to the applied signal intensity. Note that the factor of 2 appears in front of this stimulated term because the transition of a single atom from level 1 to level 2 both reduces

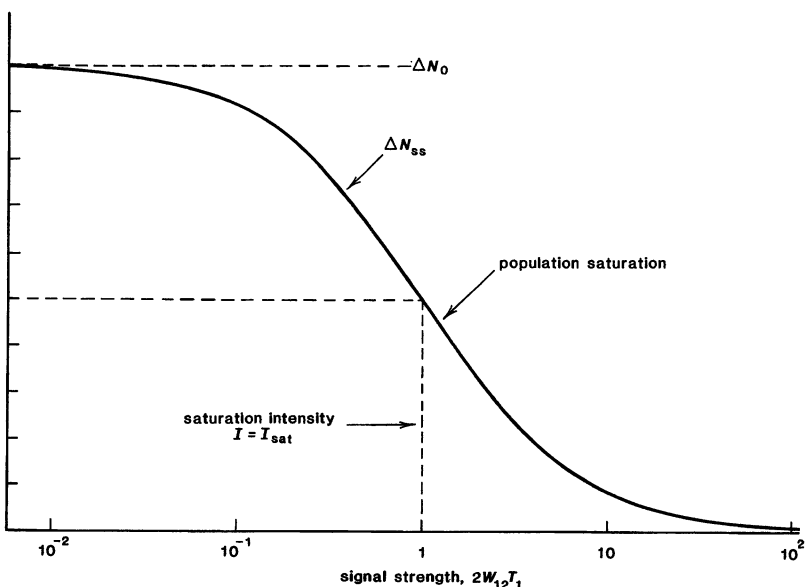


FIGURE 4.12

Saturation of the population difference ΔN with increasing applied signal strength in a two-level atomic transition.

$N_1(t)$ by one and increases $N_2(t)$ by one, and thus changes $\Delta N(t)$ by twice that much.

The steady-state behavior of the population difference ΔN in the presence of an applied signal W_{12} must be a balance between these competing population-recovery and population-saturation effects. To obtain the steady-state solution, we can set the total time derivative in the rate equation equal to zero, i.e.,

$$\frac{d}{dt} \Delta N = 0 = -2W_{12}\Delta N - \frac{\Delta N - \Delta N_0}{T_1} \quad (65)$$

and obtain from this the steady-state population difference

$$\Delta N = \Delta N_{ss} \equiv \Delta N_0 \times \frac{1}{1 + 2W_{12}T_1}. \quad (66)$$

The ratio of the steady-state value ΔN_{ss} with signal present to the thermal-equilibrium value ΔN_0 with no applied signal is plotted versus applied signal strength W_{12} in Figure 4.12.

We see that as the applied signal strength or stimulated-transition rate W_{12} increases, the steady-state population difference ΔN_{ss} is driven below the small-signal or thermal-equilibrium value ΔN_0 , and eventually is driven toward zero at large enough applied signal levels. This steady-state value of the population difference results from a balance between the stimulated-transition term, which acts to transfer atoms from the more heavily populated level N_1 toward the less heavily populated level N_2 , and thus tends to equalize the populations, and the

relaxation term, which tends to pull ΔN back toward its thermal-equilibrium value ΔN_0 .

This reduction in the steady-state population difference with increasing signal strength has the general form

$$\frac{\Delta N_{ss}}{\Delta N_0} = \frac{1}{1 + W_{12}/W_{sat}} = \frac{1}{1 + \text{const} \times \text{signal power}}, \quad (67)$$

where $W_{sat} \equiv 1/2T_1$ is the value of the stimulated-transition probability at which the population difference is driven down to exactly half its initial or small-signal value. This form of reduction in population difference with increasing signal strength is generally referred to as *homogeneous saturation of the population difference* on the two-level transition.

Saturation in Real Laser Systems

This general type of saturation behavior is extremely important in laser theory. Gain coefficients and loss coefficients in laser materials are directly proportional to the population difference on the laser transition. We will see later on that in a great many atomic systems the population difference on the atomic transition will very often saturate with increasing signal strength in the form given by Equation 4.67, even for initially inverted population differences produced by laser pumping.

As a result, either the attenuation coefficient or the gain coefficient α_m in an atomic medium will very often saturate with increasing signal intensity I in the general fashion given by

$$\alpha_m = \alpha_m(I) = \alpha_{m0} \times \frac{1}{1 + I/I_{sat}} = \alpha_{m0} \times \frac{1}{1 + \text{const} \times \text{signal power}}, \quad (68)$$

where α_{m0} is the small-signal (unsaturated) attenuation or gain coefficient; I is the applied signal intensity (usually expressed as power per unit area); and I_{sat} is a saturation intensity at which the gain or loss coefficient is saturated down to half its initial value α_{m0} .

This form of saturation behavior is often referred to as *homogeneous saturation*, since it is characteristic of homogeneously broadened transitions. Inhomogeneously broadened transitions, such as doppler-broadened lines, exhibit a more complex saturation behavior, including “hole burning” effects, which we will describe in a later chapter.

Saturable Absorption and Saturable Gain

Materials specially chosen to operate as saturable absorbers are often used in laser experiments for Q -switching, mode-locking, and isolation from low-level leakage signals. On the other hand, saturation of the inverted population difference and hence the gain in an amplifying laser medium is what determines a laser’s power output. When a laser oscillator begins to oscillate, the oscillation amplitude grows at first until the intensity inside the cavity is sufficient to saturate down the laser gain exactly as we have described. Steady-state oscillation then occurs when the saturated laser gain becomes just equal to the total cavity losses, so that the net round-trip gain is exactly unity. Gain saturation is thus

the primary mechanism that determines the power level at which a laser will oscillate.

Note that the reactive susceptibility $\chi'(\omega)$, and hence the phase shift on an atomic transition, is also directly proportional to the population difference ΔN . An atomic transition will thus exhibit both *saturable absorption or gain* and *saturable phase shift* as the applied signal strength is increased.

Transient Two-Level Solutions

Let us also look at the transient response of a two-level atomic system to an applied signal. Suppose a two-level system has some initial population difference $\Delta N(t_0)$ at time t_0 (where this initial value may or may not be the same as the thermal-equilibrium value ΔN_0); and assume that an applied signal with constant amplitude W_{12} is then turned on at $t = t_0$. The transient solution to the rate equation for $t > t_0$ is then

$$\Delta N(t) = \Delta N_{ss} + [\Delta N(t_0) - \Delta N_{ss}] \exp [-(2W_{12} + 1/T_1)(t - t_0)], \quad (69)$$

where ΔN_{ss} is the steady-state or saturated value of ΔN given earlier. This transient response is plotted for a few typical cases in Figure 4.13.

With no applied signal present, so that $2W_{12}T_1 = 0$, the population $\Delta N(t)$ relaxes from the initial value $\Delta N(t_0)$ toward the thermal-equilibrium value ΔN_0 with exponential time constant T_1 . When a constant applied signal is present, however, the population difference $\Delta N(t)$ relaxes—more accurately, is driven—toward the saturated steady-state value $\Delta N_{ss} < \Delta N_0$. Increasing the signal strength also speeds up the rate $(2W_{12} + 1/T_1)$ at which the population difference approaches this saturated condition.

Two-Level Systems With Degeneracy

The same simple results derived above can also be obtained, though with slightly more algebraic complexity, even if the two-level system has degeneracies g_1 and g_2 in its lower and upper energy levels. To verify this we can recall that if degeneracy factors g_1 and g_2 are present, the stimulated transition rates are related by $g_1W_{12} = g_2W_{21}$, and the relaxation rates are related by $w_{12}/w_{21} = (g_2/g_1) \exp[-(E_2 - E_1)/kT]$. For the degenerate case, it also makes the most sense to define the population difference ΔN on the two-level transition in the form

$$\Delta N(t) \equiv (g_2/g_1)N_1(t) - N_2(t), \quad (70)$$

since this is the population difference that appears in the complex susceptibility $\chi(\omega)$, and hence in any absorption or gain expressions.

The population difference ΔN_0 at thermal equilibrium must also now be written, using these definitions, in the slightly more complicated form

$$\Delta N_0 \equiv (g_2/g_1)N_{10} - N_{20} = N \frac{1 - \exp[-\hbar\omega_a/kT]}{1 + (g_1/g_2) \exp[-\hbar\omega_a/kT]}. \quad (71)$$

Here we must also define the effective signal-stimulated transition probability W_{eff} by

$$W_{\text{eff}} \equiv \frac{1}{2} (W_{12} + W_{21}) \quad (72)$$

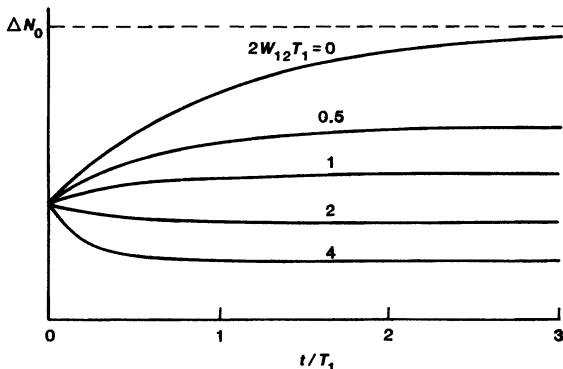
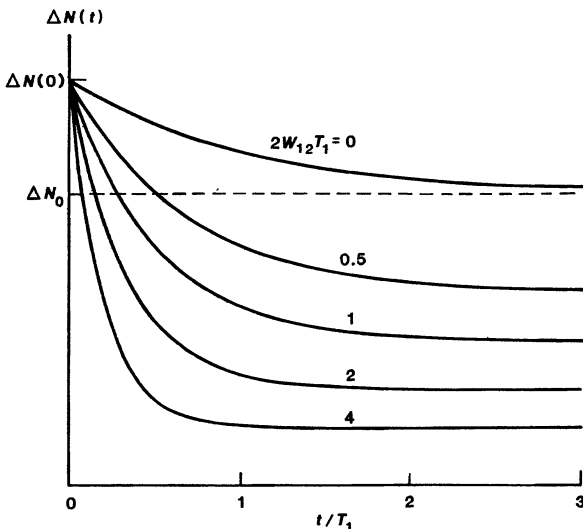


FIGURE 4.13
Transient saturation behavior following sudden turn-on of an applied signal.

and the energy relaxation time T_1 in the same fashion as above, namely, $w_{12} + w_{21} \equiv 1/T_1$. The two-level rate equation with degeneracy then takes on exactly the same simple form as in Equation 4.63, namely,

$$\frac{d}{dt} \Delta N(t) = -2W_{\text{eff}} \Delta N(t) - \frac{\Delta N(t) - \Delta N_0}{T_1}. \quad (73)$$

A two-level system even with degeneracy thus behaves exactly like an ideal non-degenerate two-level system, and all the results we have just derived remain valid, provided that we use the special definitions of $\Delta N(t)$ and W_{eff} that we have just introduced.

Atomic Time Constants: T_1 , T_2 , and τ

The notation T_1 that we have introduced for the two-level rate equation in this section is one example of several different notations for atomic time constants that will appear frequently in the rest of this text, as well as in many analyses of atomic behavior in the scientific literature. It is important to keep track of the physical meanings of these time constants, as well as the distinctions between them.

The symbol T_1 is used rather widely in the scientific literature as we have used it here, namely, to indicate in general the time constant with which a population $N(t)$ or a population difference $\Delta N(t)$ will return to its equilibrium value or—what is essentially the same thing—the time constant with which an atomic system will exchange energy with its surroundings. The time constant T_1 is thus generally equivalent to the population recovery or energy decay times τ or γ^{-1} often used in other analyses. For a two-level optical-frequency transition in particular, this time constant is essentially the same as the upper-level lifetime or energy-decay lifetime τ_{21} . This same time constant T_1 is also, for reasons that we will learn later, sometimes referred to as the *longitudinal relaxation time*, especially in Bloch equation analyses, or the *on-diagonal relaxation time* in quantum analyses of atomic systems.

This time constant T_1 stands in contrast to the quite different time constant T_2 we introduced in an earlier chapter to describe the elastic dephasing of the coherent macroscopic polarization $p(t)$. The time constant T_2 is also widely used in the scientific literature, and is sometimes called the *atomic dephasing time*, the *transverse relaxation time*, or the *off-diagonal relaxation time* of the same atomic transition. In most situations the energy decay or population recovery time T_1 is substantially longer than the dephasing time T_2 (although for highly isolated individual atoms, as in a very low-pressure gas cell, the usual dephasing mechanisms may be nearly eliminated, and then, in the usual notation, $T_2 \approx T_1$).

The notations T_1 and T_2 are most commonly used to indicate these two different time constants in magnetic resonance and Bloch equation analyses, and for analyses on two-level atomic systems; the alternative notations τ or γ and sometimes $\Delta\omega_a = 2/T_2$ are also commonly used, especially in optical-wavelength and multilevel laser calculations. We will jump back and forth between these alternative notations in different parts of this text, depending on what seems to match up best with the usual scientific literature.

Problems for 4.5

1. *Signal-power absorption by a collection of atoms:* Where does the absorbed power go? Consider the net steady-state power per unit volume that is absorbed by the atoms, from the applied signal, in a simple two-level atomic system as a function of the applied signal strength $W_{12} = W_{21}$ (ignore degeneracy effects for simplicity). Plot how this absorbed power varies with signal strength W_{12} , and discuss the behavior especially at very small and very large W_{12} . Where does the absorbed power go?—and how does it get there?
2. *Effect of a sinusoidally modulated saturating signal: linearized analysis.* Suppose a time-varying signal is applied to a collection of nondegenerate absorbing two-level atoms. Assume this signal is tuned exactly to the transition frequency ω_a , but is weakly amplitude-modulated in time at a low frequency ω_m , so that

$W_{12}(t) = W_{21}(t) = W_a + W_b \cos \omega_m t$. Assume the modulation depth is small, $W_b \ll W_a$, and the modulation frequency is low, $\omega_m \ll \omega_{21}$ or $\Delta\omega_a$. The modulation frequency ω_m may, however, be of the same order as the inverse relaxation rate $1/T_1 = w_{12} + w_{21}$.

Try putting this time-modulated transition probability into the two-level rate equation and solving for the time-varying population difference $\Delta N(t)$, including saturation effects. Hints: Assume the population difference will vary like $\Delta N(t) = \Delta N_a + \Delta N_b(t)$, with $\Delta N_b \ll \Delta N_a$, and then linearize the equation by neglecting cross-products of the small terms W_b and ΔN_b . Find out in particular how the phase lag ϕ between the signal modulation $W_{12}(t)$ and the population modulation $\Delta N(t)$ will change with the modulation frequency ω_m .

The instantaneous population of the upper level $N_2(t)$ in this experiment might be monitored as a function of time by observing the spontaneous emission $\gamma_{\text{rad}} N_2(t)$ from the upper level with a suitable detector. By using a variable modulation frequency ω_m and a phase meter to measure the phase lag ϕ versus ω_m , could someone use this technique to measure the lifetime T_1 (or τ) of the two-level system?

3. *Effects of a square-wave modulated saturating signal.* The power level of the signal applied to a two-level atomic transition is modulated back and forth between two steady levels, say, $W(t) = W_a$ and W_b , in square-wave fashion, spending a length of time T at each level before switching to the other level. Carry out an analysis to find the population difference $\Delta N(t)$ as a function of time through one complete cycle of this process, after many cycles have taken place. With the aid of a calculator if necessary, calculate and plot the peak-to-peak variation of $\Delta N(t)$ versus the quantity T/T_1 for various values of the quantities $2W_a T_1$ and $2W_b T_1$.

Verify that your answers go to the correct limiting values in the limits of $T/T_1 \ll 1$ and $T/T_1 \gg 1$.

4.6 MULTILEVEL RATE EQUATIONS

A real atomic system will, of course, have a very large number of energy levels E_i , with different degeneracies g_i and time-varying populations $N_i(t)$. Signals may then be applied to this atomic system simultaneously at frequencies near several different transition frequencies $\omega_{ji} = (E_j - E_i)/\hbar$; and relaxation transitions will occur in general between all possible pairs of levels in the system. We will now show how to write the complete rate equations applicable to such a multilevel, multisignal, multifrequency case.

Multilevel Atomic Systems

Figure 4.14 shows a typical multienergy-level atomic system to which several different signals tuned near different transition frequencies may be simultaneously applied. We assume for simplicity that all the transitions to which signals are applied have resonance frequencies ω_{ji} that differ from each other by at least a few atomic linewidths. This ensures that each applied signal is in

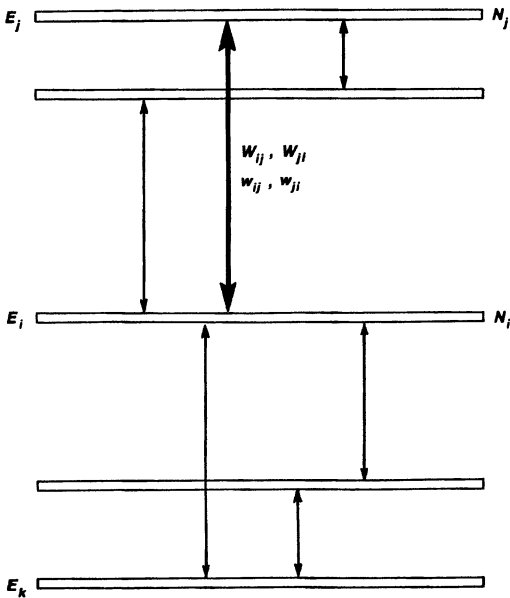


FIGURE 4.14
Multienergy-level rate equations.

resonance with (and thus affects) only the one transition to which it is tuned. We also assume that all the applied signals will be weak enough that a rate equation approach is valid. This is a point that will be discussed in more detail in a later chapter.

Consider first just the flow of atoms between some given level E_i and some other higher-lying level E_j . If a signal is applied to this particular transition, the flow rate in the upward direction out of level E_i will be $(W_{ij} + w_{ij}) N_i$, and the flow rate in the downward direction into level E_i will be $(W_{ji} + w_{ji}) N_j$. The net flow rate between these two levels will thus be expressed by the rate equation terms

$$\frac{dN_i}{dt} = -\frac{dN_j}{dt} = -W_{ij}N_i + W_{ji}N_j - w_{ij}N_i + w_{ji}N_j \quad (74)$$

for any pair of i and j levels.

The stimulated transition rate produced by the applied signal on this particular transition will have the same general form as Equation 4.31, namely,

$$W_{ji} = \frac{g_j}{g_i} W_{ij} = \frac{3^*}{8\pi^2} \frac{\gamma_{\text{rad},ji}}{\hbar \Delta\omega_{a,ij}} \frac{\epsilon |\tilde{E}_{ij}|^2 \lambda_{ji}^3}{1 + [2(\omega - \omega_{ji})/\Delta\omega_{a,ij}]^2}, \quad (75)$$

where all the quantities have values appropriate to that particular $i \rightarrow j$ transition. This expression assumes a lorentzian homogeneous transition. An appropriately modified version must be substituted if the transition is a gaussian inhomogeneous transition. All atomic transition parameters such as $\gamma_{\text{rad},ji}$ and $\Delta\omega_{a,ij}$, as well as the applied signal field \tilde{E}_{ij} , will of course have different values for each transition in the system.

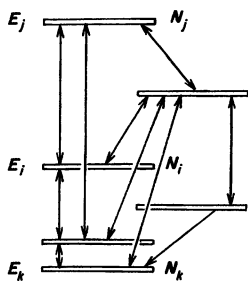


FIGURE 4.15

Example of multiple stimulated and relaxation transitions in a multilevel atomic system.

The relaxation transition probabilities w_{ij} and w_{ji} between an arbitrary pair of levels usually cannot be calculated in any simple fashion, and their numerical values are most often either measured or just guessed at. These numerical values may differ (widely!) for different transitions in any given system, and may depend strongly on gas pressure, crystal-lattice temperature, or other properties of the atomic surroundings. These probabilities on any given transition will, however, be related, as always, by the Boltzmann ratios

$$\frac{w_{ij}}{w_{ji}} = \frac{g_j}{g_i} \exp\left(-\frac{E_j - E_i}{kT}\right) \quad (76)$$

for any pair of levels E_i and E_j .

Multilevel Rate Equations

When multiple signals are present simultaneously on several different transitions, each applied signal will produce stimulated transitions that affect only the populations N_i and N_j of the two levels involved in that particular transition. The population changes produced by multiple signals are then taken into account by simply summing the stimulated transition rates produced by each applied signal on its particular transition, plus the relevant relaxation rates, as given by the preceding equations. The signals on different transitions do not (to first order) interfere with each other, even if they happen to terminate on the same energy level. The relaxation transition rates between all the levels are similarly taken into account simply by adding their independent effects on each energy-level population.

Suppose as a general example that energy level E_i is acted on by several applied signals each close to a different transition frequency $|\omega_{ji}| = |E_j - E_i|/\hbar$ as illustrated in Figure 4.15. (The other levels E_j may be below or above level E_i .) The general rate equation for the population $N_i(t)$ on this particular level is then

$$\frac{dN_i}{dt} = \sum_{j \neq i} (-W_{ij}N_i + W_{ji}N_j) + \sum_{j \neq i} (-w_{ij}N_i + w_{ji}N_j). \quad (77)$$

The first sum gives the stimulated transition rates to all other levels E_j for which appropriate signals tuned at or near $|\omega_{ji}|$ are present. Each such signal will produce appropriate stimulated-transition probabilities related by $g_j W_{ij} = g_i W_{ji}$. The second sum gives the relaxation rates to and from all the other levels

E_j of the atom, or at least all other levels E_j for which the relaxation terms $w_{ij}N_i$ and $w_{ji}N_j$ have any appreciable magnitude.

In general, then, for an M -level atomic system we can write M separate rate equations of the form in Equation 4.77, one for each level population $N_i(t)$ for $i = 1$ to $i = M$. The three rate equations for a 3-level atomic system, for example, have the form

$$\begin{aligned} dN_1/dt = & - (W_{12} + W_{13} + w_{12} + w_{13}) N_1 \\ & + (W_{21} + w_{21}) N_2 + (W_{31} + w_{31}) N_3, \\ dN_2/dt = & - (W_{21} + W_{23} + w_{21} + w_{23}) N_2 \\ & + (W_{12} + w_{12}) N_1 + (W_{32} + w_{32}) N_3, \\ dN_3/dt = & - (W_{31} + W_{32} + w_{31} + w_{32}) N_3 \\ & + (W_{13} + w_{13}) N_1 + (W_{23} + w_{23}) N_2, \end{aligned} \quad (78)$$

if we assume that applied signals may be present on all three possible transitions.

Note that we organized these equations by systematically writing the stimulated plus relaxation terms in each equation, first for the level N_i itself, and then for all the other levels N_j connected to this level. It would be equally possible to organize the terms in each equation in a pair-wise fashion, for example, for level N_2 ,

$$\begin{aligned} dN_2/dt = & - (W_{21}N_2 - W_{12}N_1) - (W_{23}N_2 - W_{32}N_3) \\ & - (w_{21}N_2 - w_{12}N_1) - (w_{23}N_2 - w_{32}N_3), \end{aligned} \quad (79)$$

where we first write all the stimulated terms and then all the relaxation terms, for each other level to which level E_2 is connected. The important point is obviously to include all the (necessary) terms, and then to organize them in a fashion which makes their solution the easiest.

Conservation of Atoms

If the total number of atoms in all the energy levels is constant, however, there will also be a “conservation of atoms” equation, namely,

$$\sum_{i=1}^M N_i = N_1 + N_2 + \cdots + N_M = N, \quad (80)$$

where M is the total number of energy levels in the system. But if this condition applies, then only $M - 1$ of the M rate equations will be linearly independent, since any one of the M rate equations can be obtained as the negative sum of the other $M - 1$ equations.

We will really have, therefore, $M - 1$ rate equations for individual level populations, plus the conservation of atoms equation, to give a total of M independent equations in the M unknown populations $N_i(t)$, $i = 1$ to M .

Multilevel Systems: Steady-State Behavior

We will employ general multilevel rate equations of the type described here to analyze several different laser pumping and signal saturation processes in future chapters. In the remainder of this chapter, however, let us look at some general characteristics of these multilevel equations and their solutions, without going into the details of any specific problems or specific examples.

Let us consider first the steady-state behavior of such a multilevel system when one or more signals of constant amplitude are applied to different transitions in the system. In particular, how will the populations and population differences in a multilevel system saturate or move away from their thermal-equilibrium values in the presence of one or more strong applied signals, and how will this compare to the simple two-level saturation result?

To find out how the steady-state level populations $N_{i,ss}$ will vary in a multilevel system with a set of constant-intensity applied signals W_{ij} , we must solve the appropriate set of $M - 1$ rate equations like those just described, with the time derivatives set equal to zero, plus the supplementary condition given by conservation of the total number of atoms. This gives a set of M coupled linear algebraic equations of the general form

$$\begin{aligned} \hat{W}_{11}N_{1,ss} + \hat{W}_{12}N_{2,ss} + \dots + \hat{W}_{1M}N_{M,ss} &= 0, \\ \hat{W}_{21}N_{1,ss} + \hat{W}_{22}N_{2,ss} + \dots + \hat{W}_{2M}N_{M,ss} &= 0, \\ \dots &+ \dots + \dots + \dots = 0, \\ N_{1,ss} + N_{2,ss} + \dots + N_{M,ss} &= N \end{aligned} \quad (81)$$

where each of the \hat{W}_{ij} elements is a linear combination of (constant) W_{ij} and w_{ij} factors. The first $M - 1$ of these equations come from the $M - 1$ rate equations, and the final one comes from the conservation of atoms. (These equations could, of course, be rearranged into any arbitrary order.)

The available methods for solving such a set of M coupled algebraic equations in all their glory, in order to find the steady-state populations in an M -level system, are merely those used for solving any set of M linear algebraic equations—and the calculations that are required, especially for $M \geq 3$, become just as messy. If you have not done this kind of calculation recently, try carrying out an explicit solution of the full-blown coupled equations for the 3-level system (Equations 4.78). It will rapidly become obvious how intractably messy the algebra becomes even for just three energy levels, let alone any case with $M > 3$.

Real laser problems do sometimes involve, however, atomic or molecular systems having anywhere from four to several dozen simultaneous coupled rate equations of this type. Possible methods for attacking these M -level steady-state problems then include the following.

- Adopt some standard algebraic algorithm, such as Cramer's Rule, and keep tirelessly turning the crank until algebraic solutions emerge. (However, Cramer's Rule is well known to be a poor procedure for numerical computer calculations, because of round-off error in the repeated additions and subtractions that are involved.)
- Use a computer with a good packaged linear-equation routine other than Cramer's rule (such as gaussian elimination).
- Eliminate as many terms from the equations as possible by means of physical arguments (for example, eliminate levels you know have negli-

gible populations or terms corresponding to negligible relaxation rates); and then be clever in substituting the remaining equations into each other.

- Give up and substitute some alternative attack.

The second of these methods is the only feasible one if you have a really big multilevel problem and it really has to be solved. The third approach is the only useful one for most other simple cases.

Saturation in Multilevel Systems

If we do solve one of these multilevel systems for the steady-state populations as a function of relaxation rates and applied signal strengths, what will the saturation behavior on any particular transition look like?

We found in the previous section that the steady-state population difference ΔN_{12} in a two-level system saturates with increasing signal intensity W in a simple homogeneous fashion. We will also find quite generally in any multilevel system that increasing the signal strength W_{ij} applied to any $i \rightarrow j$ transition will cause the population difference on that transition to saturate in essentially the same fashion, that is, in the form

$$\Delta N_{ss,ij} = \Delta N_{0,ij} \frac{1}{1 + W_{ij}/W_{sat,ij}}, \quad (82)$$

where $W_{sat,ij}$ is a saturation value or saturation intensity for that particular transition under those particular circumstances.

The initial inversion $\Delta N_{0,ij}$ on this transition might be, for example, the small-signal population inversion on the lasing transition in a system which is being pumped on some other transition. Both the initial inversion $\Delta N_{0,ij}$ and the saturation intensity $W_{1j,sat}$ will then depend in a complicated way on the relaxation rates of the system and the signals applied to any other transitions in the system. So long as these are fixed in amplitude, however, turning on and increasing the strength of a signal W_{ij} applied to the $j \rightarrow i$ transition will cause the population difference $\Delta N_{ss,ij}$ on that particular transition to saturate in exactly the same homogeneous fashion as for the two-level system. The saturation behavior on the inverted $i \rightarrow j$ transition will be formally identical to the saturation behavior of a two-level system, even though many other relaxation rates or other applied (fixed-intensity) signals may be present in the system.

Proof of Saturation Behavior

The point that we have just made concerning saturation in a multilevel system is best illustrated by solving the multilevel rate equations for a few simple but still realistic practical cases, and examining the solutions, as we will do in later chapters. This point can also be proven in a slightly messy but quite general way, which we will outline here. Readers willing to accept this point may want to move on to the next subheading.

We first note that if a signal W_{ij} is applied to a certain $i \rightarrow j$ transition, the rate equation for either of the two levels N_i or N_j involved in that transition

may be rewritten at steady-state ($d/dt \equiv 0$) in the form

$$\frac{dN_i}{dt} = -W_{ij}N_i + W_{ji}N_j + f_i(N_k, w_{ik}, W_{ik}) = 0, \quad (83)$$

where $f_i(N_k, w_{ik}, W_{ik})$ is a complicated function of all the other level populations N_k , relaxation rates w_{ik} , and applied signals W_{ik} on all the other levels in the system (but not W_{ij} or W_{ji}).

Now, if the signal intensity on this one transition is turned up to a very large value, so that W_{ij} and W_{ji} approach ∞ , the function f_i must approach a finite limiting value, since all the factors in the f_i expression remain finite. Hence, to keep the first pair of terms in Equation 4.83 finite as W_{ij} and $W_{ji} \rightarrow \infty$, the population difference on the transition must decrease in the limiting form

$$\Delta N_{ij} \equiv \left(\frac{g_j}{g_i} N_i - N_j \right) \approx \frac{(g_j/g_i)f_i}{W_{ij}} \quad (W_{ij}, W_{ji} \rightarrow \infty). \quad (84)$$

To examine this in more detail, we can note that since the rate equations are a linear coupled set, their steady-state solutions (for $dN_i/dt = 0$) for any of the steady-state level populations N_k , expressed in terms of any one particular transition probability $W_{ij} \equiv (g_j/g_i)W_{ji}$, must be of the general form

$$N_{ss,k} = \frac{a_{kij} + b_{kij}W_{ij}}{c_{ij} + d_{ij}W_{ij}}, \quad (85)$$

where the constants a_{kij} , b_{kij} , etc., will in general be complicated mixtures of all the other relaxation probabilities w_{pq} and transition probabilities W_{rs} that are present in the system for all the pq and rs transitions other than W_{ij} and W_{ji} . (These coefficients might be found, for example, by expanding the steady-state solution of the rate equations using Cramer's rule; and noting that all the population expressions N_k will have the same denominator $c_{ij} + d_{ij}W_{ij}$.) As W_{ij} and W_{ji} become arbitrarily large, each of the level populations will approach some saturated steady-state value given by $N_k \rightarrow b_{kij}/d_{ij}$ as $W_{ij} \rightarrow \infty$.

Consider in particular the limit of the $i \rightarrow j$ population difference ΔN_{ij} as $W_{ij} \rightarrow \infty$. This can be gotten by subtracting two expressions like Equation 4.85 with $k = i$ and $k = j$. But then the infinite signal limit implies that the factors $(g_j/g_i)b_{iij}W_{ij}$ and $b_{jij}W_{ij}$ involved in these two expressions must exactly cancel. Hence ΔN_{ij} must have the form (for all values of W_{ij})

$$\Delta N_{ss,ij} = \frac{(g_j/g_i)a_{iij} - a_{jij}}{c_{ij} + d_{ij}W_{ij}}. \quad (86)$$

Note again that all the constants in this expression, like a_{iij} and c_{ij} , depend on all the other w_{pq} 's and W_{rs} 's, but not on W_{ij} or W_{ji} .

The conclusion of the derivation just given is that the saturated population difference for a strong signal applied to any one single transition in a multilevel system can be written in the general form

$$\Delta N_{ss,ij} = \frac{\Delta N_{0,ij}}{1 + (d_{ij}/c_{ij})W_{ij}}. \quad (87)$$

This is exactly like the saturation of a two-level system as derived in the preceding section.

Transient Response of Multilevel Systems

We can also say some general things about the transient response of a multilevel atomic system, for example when an applied signal is suddenly turned on or turned off. The $M - 1$ coupled rate equations given earlier, plus the conservation of atoms equation, form a set of M coupled linear differential equations for the level populations $N_i(t)$ versus t (or at least these equations are linear so long as the applied signals W_{ij} have either zero or constant values). Linear coupled differential equations lead in general either to exponentially decaying or possibly to oscillating transient solutions. A two-level system exhibits, for example, a single exponential recovery with decay rate $1/T_1$ for no applied signal or $(W_{12} + W_{21} + 1/T_1)$ for a constant applied signal (cf. Equation 4.69).

The transient solutions for an M -level atomic system will similarly exhibit $M - 1$ transient terms with $M - 1$ exponential time constants, very much like the transient response of a multiloop RC electrical circuit containing $M - 1$ independent capacitances. Each time constant of the multilevel system will in general be some complicated combination of all the w_{ij} 's and W_{ij} 's in the system. These time constants, or rather the corresponding decay rates, will be the multiple roots of a polynomial equation formed from the secular determinant for the coupled set of linear equations. Standard techniques such as Laplace transforms can be used to find these decay rates and transient solutions.

As a practical matter, however, in most multilevel systems one or two relaxation rates dominate in determining the transient behavior of any given level. Experimental results for the time behavior of any one level population $N_i(t)$ usually show either just one predominant time constant or perhaps in more complex cases a double-exponential type of transient behavior.

Optical-Frequency Approximation

As we noted earlier, most laser systems at optical frequencies have $\hbar\omega/kT \gg 1$ for all the transitions involved. To express this in still another way, the energy gap corresponding to visible-frequency radiation is $\hbar\omega \approx 2$ eV, as compared to $kT \approx 25$ meV at room temperature, so that $\hbar\omega/kT \approx 40$.

In this limit, all upward relaxation probabilities w_{ij} can be ignored, and all downward relaxation probabilities can be written as energy decay rates in the form $w_{ji} \approx \gamma_{ji}$. We can therefore use γ_{ji} as an alternative notation for the downward relaxation probability from any level E_j to any lower level E_i in the rate equations, and there are no upward relaxation processes.

The relaxation terms for any given level E_i in the general rate equations can then be simplified to the form

$$\frac{dN_i}{dt} \Big| = - \sum_{k < i} \gamma_{ik} N_i + \sum_{k > i} \gamma_{ki} N_k, \quad (88)$$

where the first sum represents relaxation out of level E_i into all lower levels E_k , and the second sum represents relaxation down into level E_i from all higher levels E_k . If we consider only the first term, the net energy-decay rate from level E_i to all lower levels is

$$\frac{dN_i}{dt} \Big| = - \sum_{k < i} \gamma_{ik} N_i = -\gamma_i N_i. \quad (89)$$

The total decay rate γ_i and the net lifetime τ_i for level E_i are thus given by summing over all the radiative and nonradiative decay rates from level E_i to all lower levels E_k , i.e.,

$$\gamma_i \equiv \frac{1}{\tau_i} = \sum_{k < i} \gamma_{ik}. \quad (90)$$

In the absence of pumping effects or relaxation from upper levels, an initial population $N_i(t_0)$ in level E_i will decay as

$$N_i(t) = N_i(t_0)e^{-\gamma_i(t-t_0)} = N_i(0)e^{-(t-t_0)/\tau_i}. \quad (91)$$

Note again that multiple decay processes acting in parallel combine by summing the decay rates, or summing the *inverse lifetimes* associated with each process.

REFERENCES

An early paper which discusses multilevel rate equations and the saturation behavior of multilevel systems, without any optical-frequency approximations, is J. P. Lloyd and G. E. Pake, "Spin relaxation in free radical solutions exhibiting hyperfine structure," *Phys. Rev.* **94**, 579 (May 1, 1954). A systematic procedure for solving rate equations and finding the transient populations $N_j(t)$ in a sequence of cascading energy levels, using the optical-frequency approximation, is given by L. J. Curtis, "A diagrammatic mnemonic for calculation of cascading level populations," *Am. J. Phys.* **36**, 1123 (December 1968).

A general proof that the populations of an M -level system will return to equilibrium in the form of a sum of $M - 1$ decaying exponentials is given in M. W. P. Strandberg and J. R. Shaw, "General properties of thermal-relaxation rate equations," *Phys. Rev. B* **7**, 4809 (1973).

Problems for 4.6

1. *Saturation of the lower transition in a general three-level atomic system.* Suppose a signal that produces a stimulated transition probability $W_{12} = W_{21}$ (no degeneracy) is applied to the $1 \rightarrow 2$ transition of a three-level system. Solve the complete steady-state rate equations to obtain the saturation behavior of the population difference ΔN_{12} without making any optical-frequency approximation. In general terms, how does this saturation resemble or differ from the saturation of a simple two-level system?
2. *Ditto for saturation of the upper transition in a three-level system.* Repeat the previous problem for a signal W_{23} applied only to the $2 \rightarrow 3$ transition. Compare the saturation behavior in this case to the ideal two-level case.
3. *Saturation of the 1-3 transition in a three-level system: no optical approximation.* Suppose a signal producing a stimulated transition probability $W_{13} = W_{31}$ (no degeneracy) is applied to the $1 \rightarrow 3$ transition of a 3-level system. Using the full rate equations (no optical-frequency approximation), calculate how the population difference $\Delta N_{13} \equiv N_1 - N_3$ on the signal transition will saturate with increasing signal intensity W_{13} . What does the general answer reduce to if all

relaxation rates have very nearly the same value $w_{ij} \approx w_{ji} \approx 1/2T$ for all i and j ?

4. *Ditto, using the optical approximation.* Repeat the previous problem, assuming that the optical approximation applies; i.e., all downward rates w_{ji} are finite and all upward rates $w_{ij} \approx 0$.
5. *Rate-equation analysis of a thermally pumped laser (research problem).* We mentioned in Chapter 1 that a laser or maser can be pumped by a purely thermal or blackbody source, and that a laser oscillator of this sort is really a kind of heat engine with a limiting efficiency that should be equal to the Carnot-cycle efficiency between the pumping and relaxation temperature. Let us try to develop this analysis further.

As an idealized model for this analysis, let us consider a collection of identical atoms having just three energy levels E_0 , E_1 , and E_2 ; and suppose that this collection of atoms has very strong and primarily *radiative* decay on the 0–2 transition, and has very strong and primarily *nonradiative* decay on the 0–1 and 1–2 transitions. Suppose also that the effective temperature T_{rad} of the electromagnetic surroundings for the 0–2 radiative transition is very hot, but the effective temperature T_{nr} for the nonradiative surroundings of the 0–1 and 1–2 transitions is much colder. It may then be possible to achieve a thermally pumped laser inversion on the 2–1 transition; in fact, this situation sounds very much like a description of an idealized sun-pumped laser.

Suppose a laser signal that produces a stimulated transition probability W_s on the 2–1 transition is also present. Solve the rate equations for this system to evaluate the steady-state populations N_0 , N_1 , and N_2 , and evaluate under what conditions a population inversion can in fact be produced on the 2–1 transition. Then evaluate both the net rate at which energy is extracted from the laser medium by the laser signal, as given by $W_s(N_2 - N_1)\hbar\omega_{21}$, and also the net rate at which the thermal radiative pumping source delivers energy to the laser medium on the 0–2 transition.

Considering this device as a kind of heat engine, which converts thermal energy from the hot source at T_{rad} into work in the form of coherent radiation, evaluate the conversion efficiency in this device as a function of the applied signal level W_s . Can the resulting efficiency be made to look anything like a Carnot-cycle efficiency in any reasonable limit?



THE RABI FREQUENCY

Both the linear susceptibility approach and the rate equation analysis we have developed in the past several chapters are approximations—though usually very good approximations—to the exact dynamics of an atomic system with an external signal applied.

If a very strong (or very fast) signal is applied to an atomic transition, however, the exact nonlinear behavior of the atomic response becomes more complicated, and the rate-equation approximation is no longer adequate to describe the atomic response. In this chapter, therefore, we explore the conditions under which the rate-equation approximation will remain valid, and some of the interesting new effects—particularly the very important Rabi flopping behavior—that a resonant atomic transition will display in response to a strong enough applied signal.

The material discussed in this chapter, though essential for understanding large signals and so-called “coherent transient” effects, is not essential for most straightforward laser amplification and oscillation effects. Readers who are primarily interested in the latter may therefore want to skip over this chapter.

5.1 VALIDITY OF THE RATE-EQUATION MODEL

Let us first do a quick review of the basic equations which lead to rate equations, and of the approximations involved in writing the rate equation for a simple two-level atomic system.

The Resonant-Dipole Equation

The classical electron oscillator model, with suitable quantum extensions, led us in Chapter 2 to the “resonant-dipole equation”

$$\frac{d^2p(t)}{dt^2} + \Delta\omega_a \frac{dp(t)}{dt} + \omega_a^2 p(t) = K\Delta N(t)\mathcal{E}(t), \quad (1)$$

where the constant K is given by

$$K \equiv \frac{3^* \omega_a \epsilon \lambda^3 \gamma_{\text{rad}}}{4\pi^2}. \quad (2)$$

We emphasize once more that this equation is a *quantum-mechanically correct* equation for the expectation value of the polarization $\langle p(t) \rangle$ in a two-level quantum system.

To derive the linear susceptibility $\tilde{\chi}(\omega)$ for the atomic transition, we solved this equation for sinusoidal steady-state signals, treating the population difference $\Delta N(t)$ as a constant. This susceptibility turns out to be, of course, directly proportional to the population difference ΔN .

In Chapter 4 we then used these linearized sinusoidal results, based on assuming that the level populations are *constant*, to derive the rate equations that predict a *time rate of change* for the populations $N_1(t)$, $N_2(t)$, and $\Delta N(t)$. To do this, we made the assumption that both the linear susceptibility description (based on constant ΔN) and the rate-equation results (which describe a time-varying $\Delta N(t)$) will remain valid provided that the time rate of change of the population difference $\Delta N(t)$ is “slow” in some meaningful sense. The conditions for this approximation to be valid are essentially the following.

Transient Response of the Resonant Dipole Equation

The resonant-dipole equation 5.1 is basically a linear second-order resonant equation, with a linewidth $\Delta\omega_a$ or response time $2/\Delta\omega_a$ (often written as T_2). To examine its transient behavior, let us suppose that the population difference $\Delta N(t)$ is indeed constant, or nearly so, and that the applied signal $\mathcal{E}(t)$ is a cosinusoidal signal at $\omega = \omega_a$ that is turned on at $t = 0$ in the form

$$\mathcal{E}(t) = E_1 \sin \omega_a t, \quad t \geq 0. \quad (3)$$

The induced response $p(t)$ will then be given, very nearly, by

$$p(t) \approx -K \frac{\Delta N E_1}{\omega_a \Delta\omega_a} [1 - e^{-\Delta\omega_a t/2}] \cos \omega_a t \quad (4)$$

as illustrated in Figure 5.1.

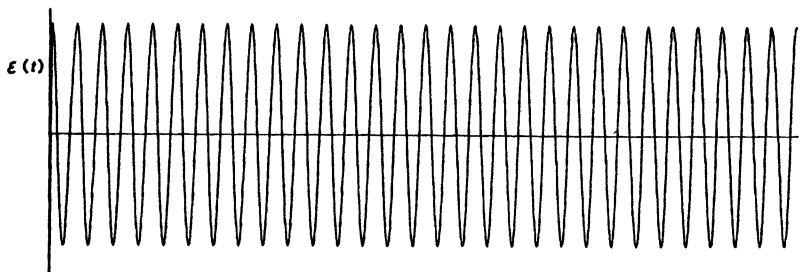
If the $2/T_2$ term dominates in the linewidth expression $\Delta\omega_a = \gamma + 2/T_2$, as is often the case, or if we simply absorb the γ contribution into a broadened definition of $2/T_2$, this may be written as

$$p(t) \approx -K \frac{\Delta N E_1}{\omega_a \Delta\omega_a} [1 - e^{-t/T_2}] \cos \omega_a t. \quad (5)$$

The transient response is thus a forced cosinusoidal oscillation that builds up to a steady-state value with a time constant $2/\Delta\omega_a$, often written as just T_2 for simplicity.

The important conclusion to be drawn here is the following. We already know that the forced response of the atomic polarization $p(t)$ to a sinusoidal driving signal $\mathcal{E}(t)$ will in general be very small unless the driving signal frequency ω is at or close to the resonance frequency ω_a of the system. We now see that this forced sinusoidal response of $p(t)$ will follow any amplitude (or phase) variations in the envelope of the sinusoidal driving term $\mathcal{E}(t)$ with a transient time delay that is approximately $2/\Delta\omega_a \approx T_2$.

sinusoidal signal input:



induced polarization response:

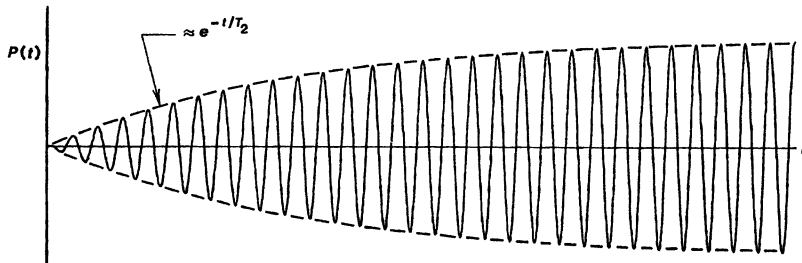


FIGURE 5.1

Transient build-up of induced polarization in response to a weak sinusoidal signal input which is suddenly turned on at $t = 0$.

It will therefore be a valid approximation to solve the resonant-dipole equation 5.1 and use it to find both the steady-state and transient responses of $p(t)$, making the approximation that $\Delta N(t)$ is a constant, provided that the transient rate of change of $\Delta N(t)$ itself is slow compared to the time constant $2/\Delta\omega_a \approx T_2$. It is the slow variation of $\Delta N(t)$ that is essential—not necessarily the slow variation (or weak amplitude) of $\mathcal{E}(t)$.

Note also that within this approximation, variations in either the phase or the amplitude of a signal field $\mathcal{E}(t)$ that are rapid compared to T_2 will simply not be “seen” or responded to by the atomic system. To put this in another way, the atomic transition has a finite bandwidth $\Delta\omega_a$, and rapid variations in phase or amplitude of $\mathcal{E}(t)$ represent frequency sidebands that are outside the linewidth $\Delta\omega_a$ of the atomic response. Hence these sidebands will induce little or no response (in the small signal limit).

The Population Difference Equation

Let us now see what determines the time-variation of $\Delta N(t)$ itself, especially under the influence of stronger applied signals. From an energy-conservation argument, we showed in Chapter 4 that the population equation

for a simple two-level quantum system may be written in the form

$$\frac{d\Delta N(t)}{dt} + \frac{\Delta N(t) - \Delta N_0}{T_1} = - \left(\frac{2}{\hbar\omega} \right) \mathcal{E}(t) \cdot \frac{dp(t)}{dt}. \quad (6)$$

The population difference $\Delta N(t)$ is essentially a measure of the energy in the atomic system; and the term on the right-hand side of this equation gives the instantaneous power delivered by the field $\mathcal{E}(t)$ to the atomic polarization $p(t)$, expressed in photon units. (The factor of 2 is present here for the same reason given in Section 4.5.)

This equation, written in this form, is also a *quantum-mechanically correct* equation for the expectation value of the energy, or the population difference ΔN , in a two-level quantum system. To make this be generally true even at large signals, however, the right-hand side of this equation must be kept in the more general and fundamental form given here, rather than in the stimulated transition form $-2W_{12}\Delta N$, because we are now *not* limiting ourselves to the usual steady-state amplitude and phase relationship between $\mathcal{E}(t)$ and $p(t)$ that leads to the rate equations.

Quasi-sinusoidal Applied Signals

Suppose we write the applied signal $\mathcal{E}(t)$ in a somewhat more general form, namely

$$\mathcal{E}(t) = \text{Re } \tilde{E}(t) e^{j\omega_a t}. \quad (7)$$

That is, we assume that $\mathcal{E}(t)$ is basically a sinusoidal signal somewhere near the resonance frequency ω_a , but with a possible amplitude or phase modulation that is contained in the time-varying complex amplitude $\tilde{E}(t)$. Similarly, we can write the resulting polarization in the same general form

$$p(t) = \text{Re } \tilde{P}(t) e^{j\omega_a t}. \quad (8)$$

Let us put these signals into the right-hand side of the population difference equation 5.6. This right-hand side then becomes

$$\begin{aligned} -\frac{2}{\hbar\omega} \mathcal{E}(t) \frac{dp(t)}{dt} &= -\frac{j}{2\hbar} \left(\tilde{E} e^{j\omega_a t} + \tilde{E}^* e^{-j\omega_a t} \right) \times \left(\tilde{P} e^{j\omega_a t} - \tilde{P}^* e^{-j\omega_a t} \right) \\ &= \frac{j}{2\hbar} \left(\tilde{E} \tilde{P}^* - \tilde{E}^* \tilde{P} \right) - \frac{j}{2\hbar} \left(\tilde{E} \tilde{P} e^{2j\omega_a t} - \tilde{E}^* \tilde{P}^* e^{-2j\omega_a t} \right). \end{aligned} \quad (9)$$

The driving term on the right-hand side of the population equation will thus contain both *quasi constant or dc terms proportional to the imaginary part of $\tilde{E}\tilde{P}^*$* and *second harmonic or $\pm 2\omega$ terms proportional to the imaginary part of $\tilde{E}\tilde{P}$* .

Harmonic-Generation Terms

Let us first consider these $\pm 2\omega$ terms, which are essentially harmonic-generation terms. The response of the population difference $\Delta N(t)$ in Equation 5.6 is fundamentally a sluggish response, because of the normally very long relaxation time T_1 that appears on the left-hand side. We can expect therefore that the response of this equation to the second harmonic or $\pm 2\omega$ terms will be

very small, compared to the response to the quasi-dc terms on the right-hand side.

To put this in another way, changes in $\Delta N(t)$ will result from the integration over time of the terms on the right-hand side of Equation 5.6. But those terms with a time-variation of the form $e^{\pm 2j\omega t}$ will tend to integrate to zero within a few optical cycles, whereas quasi-dc terms will tend to integrate into a significant change with time. The 2ω terms on the right-hand side of Equation 5.6 can therefore normally be dropped.

At high enough signal levels, the harmonic terms appearing in Equation 5.6, which we are now discarding, will produce some small but nonzero modulation at 2ω of the population difference $\Delta N(t)$. These small second-harmonic terms in $\Delta N(t)$ will then carry back into the right-hand side of the resonant-dipole equation 5.1 for $p(t)$, where they will mix with the $\pm\omega$ terms in $\mathcal{E}(t)$ to produce both $\pm 3\omega$ driving terms, and small additional $2\omega - \omega = \omega$ terms. The $\pm 3\omega$ driving terms will then produce third harmonic terms in the polarization $p(t)$, and these terms may in turn radiate and generate third-harmonic optical signals. This chain of harmonic effects can continue to higher orders as well, though the effects grow rapidly weaker with increasing order.

Large enough driving signals will, therefore, potentially produce even-order harmonic responses in $\Delta N(t)$, which in turn will feed back to produce odd-order harmonic responses in $p(t)$, and vice versa. These various higher-order harmonic responses can be observed as *harmonic generation and intermodulation or mixing effects* that occur at large signal intensities in atomic systems. These harmonic-generation effects are one part of the rich repertoire of large-signal nonlinear effects that can be observed in atomic systems, and that form the basis of the very useful field of nonlinear optics.

Conventional Rate-Equation Approximation

If we ignore these weak harmonic terms, however, the population difference equation 5.6 simplifies to

$$\frac{d\Delta N(t)}{dt} + \frac{\Delta N(t) - \Delta N_0}{T_1} = -\frac{j}{2\hbar} [\tilde{E}(t)\tilde{P}^*(t) - \tilde{E}(t)^*\tilde{P}(t)]. \quad (10)$$

Now, if the linear-susceptibility or rate-equation condition holds, we can relate \tilde{P} and \tilde{E} to a good approximation by

$$\tilde{P} \approx \tilde{\chi}\epsilon\tilde{E} \approx (\chi' + j\chi'')\epsilon\tilde{E}, \quad (11)$$

where $\tilde{\chi}$ itself is directly proportional to ΔN . The right-hand side of this equation then simplifies still further to become

$$\frac{d\Delta N(t)}{dt} + \frac{\Delta N(t) - \Delta N_0}{T_1} \approx (\epsilon/\hbar)\chi''|\tilde{E}|^2 \approx -2W_{12}\Delta N(t). \quad (12)$$

But this is, of course, simply the standard two-level rate equation.

Conditions for Rate-Equation Validity

Having derived this rate equation for $\Delta N(t)$ on the assumption that any changes in $\Delta N(t)$ will be slow, we can then solve it for the predicted variation of $\Delta N(t)$ and see if the rate of change will in fact be slow. As we have seen

in earlier chapters, a typical transient solution to the rate equation, assuming a constant-amplitude signal W_{12} suddenly turned on at $t = t_0$, is

$$\Delta N(t) = \Delta N_{ss} + [\Delta N(t_0) - \Delta N_{ss}] \times \exp[-(2W_{12} + 1/T_1)(t - t_0)], \quad (13)$$

where ΔN_{ss} is the partially saturated, steady-state value of $\Delta N(t)$ as $t \rightarrow \infty$.

The condition that the time rate of change of the population, or $(d/dt)\Delta N(t)$, be slow compared to the time constant $2/\Delta\omega_a$ in the resonant-dipole equation reduces to the condition that

$$[2W_{12} + 1/T_1] \ll [\Delta\omega_a \equiv 1/T_1 + 2/T_2]. \quad (14)$$

One general condition for this to be satisfied, and for a rate equation to be valid, is that $1/T_1 \ll 1/T_2$, or that the energy relaxation time T_1 be long compared to the dephasing time T_2 . To put this another way, the atomic transition should have a significant amount of broadening due to dephasing, as compared to the purely lifetime broadening in the system. This condition is generally true for most laser transitions.

Of more significance, once this condition is met, is that the signal strength must be weak enough so that

$$W_{12} \ll \Delta\omega_a. \quad (15)$$

In other words, the stimulated-transition rate W_{12} must be small compared to the transition linewidth $\Delta\omega_a$. For electric dipole transitions this can be converted into a condition on the applied signal strength given by

$$|\tilde{E}|^2 \ll \frac{(\hbar\Delta\omega_a)^2}{\epsilon\hbar\gamma_{rad}\lambda^3}. \quad (16)$$

In a quantum analysis we can show that this condition is equivalent to requiring that *the quantum-mechanical perturbation of the energy of the atom caused by the applied field strength \tilde{E} must be small compared to the homogeneous linewidth $\hbar\Delta\omega_a$ of the atom expressed in energy units*. We will express this condition in another and more meaningful way in the following section.

Rate-Equation Validity in Typical Laser Systems

The great majority of signals present in even high-power laser systems will in fact satisfy the criteria expressed by Equations 5.14 through 5.16, and the rate-equation approximation will thus be valid. Higher-power laser systems, in fact, commonly use materials that have wider atomic linewidths, which helps to preserve this condition.

For example, the atomic linewidths in gas lasers may range from a few hundred MHz up to a few GHz, and solid-state linewidths are typically 10^{11} to 10^{12} Hz. The corresponding transient response times T_2 for the polarization equation are in the range from 10^{-8} to 10^{-12} sec. The stimulated-transition rates in these same lasers can be estimated by equating the actual laser power density extracted per unit volume from the laser medium to the inverted population density ΔN per unit volume, times $\hbar\omega$, times a signal-stimulated-transition rate W_{ij} . The resulting stimulated-transition rates are typically in the range from 10^3 to 10^7 sec^{-1} , and thus readily meet the criterion just given.

The level populations $N_j(t)$ in an atomic system also change with time as a result of relaxation and laser pumping. In practice, in useful laser materials population changes due to either relaxation or pumping are slow—in fact, most often very slow—compared to the inverse linewidth. As an elementary example, the relaxation and pumping time constants w_{ij}^{-1} and W_{ij}^{-1} in solid-state laser materials commonly range from milliseconds (e.g., ruby) to a few hundred microseconds (e.g., Nd:YAG or Nd:glass); whereas inverse linewidths in these materials are in the range $1/\Delta\omega_a \approx 10^{-11}$ seconds. In organic dye lasers the relaxation and stimulated transition times can be much faster, e.g., a few nanoseconds (10^{-9} sec) down to even a few picoseconds (10^{-12} sec). However, the inverse linewidths for these materials are even shorter, e.g., typically $1/\Delta\omega_a \approx 10^{-13}$ sec.

Saturation Condition

We might also ask if we can obtain the saturation condition for a population difference ΔN , as discussed in Chapter 4, while still remaining within the range of validity of the rate equation approach. The signal intensity required to achieve saturation in, for example, a simple two-level atomic system is given by $2W_{12}T_1 \geq 1$ or $W_{12} \geq 1/2T_1$, and the condition for remaining within the rate-equation regime is given in Equation 5.14. Combining these two equations then yields the double condition

$$[1/2T_1] \leq W_{12} \ll [\Delta\omega_a \equiv 1/T_1 + 2/T_2]. \quad (17)$$

This says that a population difference can be saturated without violating the rate-equation limitation only if the time constants T_1 and T_2 satisfy the condition, $1/T_1 \ll \Delta\omega_a$ or $T_2 \ll T_1$. This condition is met in virtually all useful laser materials: the energy relaxation rates are nearly always slow compared to the atomic linewidth, since the latter is determined primarily by dephasing (or even inhomogeneous) mechanisms that are substantially larger than pure lifetime broadening.

Large-Signal Effects in Multilevel Systems

The classical oscillator or resonant-dipole model and the associated linear susceptibility, on the one hand, and the multilevel rate equations, on the other hand, provide two complementary sets of equations for analyzing the complete response not merely of a two-level system, but of a multilevel atomic system as well.

In a multienergy-level system, a separate resonant-dipole model must be applied to each individual atomic transition, with the associated populations $N_j(t)$ and $N_i(t)$ taken as quasi constants. The resulting polarization and susceptibility on each transition can then be used directly in Maxwell's equations, and can describe accurately the amplitude, phase, polarization, and even tensor characteristics of the atomic response on that particular transition. Note that the resonant-dipole equation for each transition is a second-order equation, as well as potentially a vector equation. Hence it can give both amplitude and phase, as well as tensor properties, of the response on that transition.

The rate equations, by contrast, treat only the energy flow, or the intensity part of the atomic response, with no phase information being available. However, they do provide a set of simple coupled first-order equations that can tie together

the populations of all the energy levels in an atomic system, including relaxation and pumping mechanisms, as well as all the simultaneous signals applied to the system.

As a general approach, then, given a multilevel system with multiple signals applied, we can use the susceptibility and polarization results on each individual transition to find phase shifts, gains, and reactions back on the applied signals, and the rate equations to find the resulting populations on those transitions. Combining these two approaches provides a more or less complete, accurate, and self-consistent description of the atomic response.

There are, of course, situations in which applied signals may violate the rate-equation conditions. We can then expect to find nonlinear effects, including nonlinear mixing, intermodulation, harmonic signals, and the Rabi flopping behavior we will describe in the following section. Detailed analysis of these effects in a multilevel system requires more general analytical methods, of which the "density matrix" approach of quantum theory is among the most useful and widely employed. The Bloch equations of magnetic-resonance theory are also very useful for analyzing large-signal and nonlinear effects in simple two-level atomic systems.

REFERENCES

An interesting discussion of when simple rate equations do and do not apply, including the reaction of the atoms back on the signal field, is given by C. L. Tang, "On maser rate equations and transient oscillations," *J. Appl. Phys.* **34**, 2935 (October 1963).

A few representative references on large-signal harmonic-generation and intermodulation effects in atomic systems include J. R. Fontana, R. H. Pantell, and R. G. Smith, "Parametric effects in a two-level electric dipole system," *J. Appl. Phys.* **33**, 2085 (June 1962); C. L. Tang and H. Statz, "Nonlinear effects in the resonant absorption of several oscillating fields by a gas," *Phys. Rev.* **128**, 1013 (1962); W. J. Tabor, F. S. Chen, and E. O. Schulz-DuBois, "Measurement of intermodulation and a discussion of dynamic range in a ruby traveling-wave maser," *Proc. IEEE* **52**, 656 (June 1964); F. Bosch, H. Rothe, and E. O. Schulz-DuBois, "Direct observation of difference frequency signal in a traveling-wave maser," *Proc. IEEE* **54**, 1243 (October 1964); A. Javan and A. Szoke, "Theory of optical frequency mixing using resonant phenomena," *Phys. Rev.* **137**, A536 (1965); and D. H. Close, "Strong-field saturation effects in laser media," *Phys. Rev.* **153**, 360 (January 10, 1967).

Problems for 5.1

1. *Harmonic response of a two-level atomic system.* To gain some feel for the nonlinear harmonic response of an atomic system, retain the second-harmonic terms on the right-hand side of the population equation for a two-level electric dipole system, and evaluate the steady-state $\pm 2\omega$ component ΔN_2 of the population difference $\Delta N(t)$ that will be produced by these second-harmonic driving terms, using the steady-state fundamental-frequency solutions for \bar{E} and \bar{P} . (Assume for simplicity that the fundamental-frequency applied signal \bar{E} is exactly on resonance.)

Then put this second-harmonic component of $\Delta N(t)$ into the resonant-dipole equation on the right-hand side, and evaluate how large a $\pm 3\omega$ component of

polarization \tilde{P}_3 will be produced at steady state by mixing between the $\pm 2\omega$ components of $\Delta N(t)$ and the $\pm\omega$ components of the applied signal \tilde{E} . (This analytical process of computing and matching up successively higher powers of ω on both sides of a set of equations is sometimes referred to as “harmonic balancing.”)

Verify that at low signal levels the third-harmonic component of the polarization will be weaker than the fundamental component by a ratio with a functional dependence like $\tilde{P}_3/\tilde{P}_1 \propto (\omega_R/\omega_a)^2$, where $\omega_R \ll \omega_a$ is the Rabi frequency defined in the following section.

5.2 STRONG-SIGNAL BEHAVIOR: THE RABI FREQUENCY

What happens to the atomic behavior when an applied signal is strong enough that the rate-equation approximation is no longer valid? Much additional insight into the range of validity of the rate equations, and into the quantum behavior of an atomic transition outside this range, can be obtained from a simplified analysis we will present in this section to describe the large-signal response of an elementary two-level electric dipole system. This analysis will introduce an important new concept, the *Rabi frequency* for a stimulated atomic transition.

Students who read this section on the large-signal behavior of electric dipole transitions may also want to read Chapter 31 on magnetic dipole transitions, especially the final section of that chapter, which shows how these same large-signal and Rabi-frequency effects can alternatively be described in magnetic dipole terms.

Simplified Large-Signal Analysis: The Polarization Equation

To carry out a large signal analysis in a simplified and yet meaningful way, we will make three simplifying, though really not very limiting, assumptions. First, we will assume an on-resonance applied signal, which we will write as $\mathcal{E}(t) = E_1(t) \exp(j\omega_a t)$, where $E_1(t)$ is the slowly varying amplitude of this applied signal. Later on we will assume that this amplitude is constant, although it may be very strong, and may be turned on suddenly at $t = 0$.

Second, we will allow for possible large-signal and transient effects in the atomic response by writing the polarization $p(t)$ in the form

$$p(t) = \operatorname{Re} [\tilde{P}_1(t) e^{j\omega_a t}] = \operatorname{Re} [-j P_1(t) e^{j\omega_a t}]. \quad (18)$$

That is, the polarization amplitude $\tilde{P}_1(t)$ is itself assumed to be a time-varying quantity, to account for the transient dynamics of the atomic response. Because we know from experience that in the limiting case of an on-resonance applied signal $p(t)$ will turn out to be -90° out of time-phase with $\mathcal{E}(t)$, we also write this phasor quantity as a real (but time-varying) amplitude $P_1(t)$ with a constant factor of $-j$ in front, corresponding to a fixed 90° phase shift,

Substituting Equation 5.18 into the resonant-dipole equation 5.1, and separating the $e^{+j\omega_a t}$ and $e^{-j\omega_a t}$ terms leads us to an equation of motion for the

phasor amplitude $P_1(t)$, namely,

$$\frac{d^2 P_1(t)}{dt^2} + (2j\omega_a + \Delta\omega_a) \frac{dP_1(t)}{dt} + j\omega_a \Delta\omega_a P_1(t) = jK E_1(t) \Delta N(t). \quad (19)$$

Now, it is certainly true that $\Delta\omega_a \ll \omega_a$; so we can probably drop the $\Delta\omega_a$ factor in front of the $dP_1(t)/dt$ term. In addition, we can reasonably assume that the time-variation of $P_1(t)$ itself, though it may approach in magnitude the quantity $\Delta\omega_a P_1(t)$, will surely be slow compared to $\omega_a P_1(t)$. In simple terms, the phasor amplitude $P_1(t)$ may change significantly within a time of the order of one reciprocal linewidth, or $1/\Delta\omega_a$, but not in one optical cycle, or $1/\omega_a$.

As a result of this, we can drop the second-derivative term $d^2 P_1(t)/dt^2$ relative to the $2\omega_a dP_1(t)/dt$ term, and simplify the transient equation for $P_1(t)$ to

$$\frac{dP_1(t)}{dt} + \frac{\Delta\omega_a}{2} P_1(t) \approx \frac{K}{2\omega_a} E_1(t) \Delta N(t). \quad (20)$$

This approximation is commonly referred to as the *slowly varying envelope approximation* (SVEA). Note that it is a much less restrictive approximation than the rate-equation approximation—that it, it allows much faster time-variations and much stronger signals than in the rate-equation limit.

The Population Difference Equation

Along with this slowly varying envelope approximation for the resonant-dipole equation, we must also use the population equation of motion (Equation 5.6). We have already noted that the transient response of that equation will be governed by the generally very slow relaxation time T_1 . Therefore, as a third approximation we will use on the right-hand side of Equation 5.6 the time-averaged value of $\mathcal{E} \cdot dp/dt$, with the time average being taken over at least a few cycles of the sinusoidal quantities $\mathcal{E}(t)$ and $p(t)$. This approximation then takes out the second-harmonic factors, but still allows for relatively rapid envelope variations in either the signal $\mathcal{E}(t)$ or the polarization $p(t)$.

With this further approximation the population equation becomes

$$\frac{d\Delta N(t)}{dt} + \frac{\Delta N(t) - \Delta N_0}{T_1} \approx -\frac{1}{\hbar} E_1(t) P_1(t). \quad (21)$$

All complex conjugates have been dropped, since we will find that $P_1(t)$ always turns out to be purely real for the on-resonance case, $\omega = \omega_a$, which is all we are considering here.

Large-Signal Solutions: The Rabi Frequency

These last two equations are the basis for our large-signal atomic analysis. Suppose we now assume a constant signal amplitude E_1 which is turned on suddenly at $t = 0$. The large-signal polarization and population equations 5.20 and 5.21 with E_1 constant form a simple pair of *linear coupled first-order differential equations* for the quantities $P_1(t)$ and $\Delta N(t)$ under the influence of the constant signal field E_1 . By substituting one of these equations into the other, we can combine the two first-order equations to obtain a single second-order equation

for $\Delta N(t)$, namely,

$$\frac{d^2\Delta N(t)}{dt^2} + \left(\frac{\Delta\omega_a}{2} + \frac{1}{T_1} \right) \frac{d\Delta N(t)}{dt} + \left(\frac{\Delta\omega_a}{2T_1} + \frac{KE_1^2}{2\hbar\omega_a} \right) \Delta N(t) = \frac{\Delta\omega_a}{2T_1} \Delta N_0. \quad (22)$$

Now, the quantity $KE_1^2/2\hbar\omega$ appearing in the second set of brackets in this equation has the dimensions of a frequency squared. Suppose we define this frequency to be the *Rabi frequency* ω_R , given by

$$\frac{KE_1^2}{2\hbar\omega_a} = \frac{3^*}{8\pi^2} \frac{\gamma_{\text{rad}}\epsilon\lambda^3}{\hbar} E_1^2 \equiv \omega_R^2 \quad (23)$$

This Rabi frequency ω_R is proportional to the applied signal field strength E_1 , and also depends on the transition strength as measured by γ_{rad} . It has a very important physical significance, which we will develop in the following paragraphs.

Using this notation, we can rewrite the population difference equation in the form

$$\left[\frac{d^2}{dt^2} + \left(\frac{\Delta\omega_a}{2} + \frac{1}{T_1} \right) \frac{d}{dt} + \left(\frac{\Delta\omega_a}{2T_1} + \omega_R^2 \right) \right] \Delta N(t) = \frac{\Delta\omega_a}{2T_1} \Delta N_0. \quad (24)$$

We can also write the $P_1(t)$ equation in exactly the same form

$$\left[\frac{d^2}{dt^2} + \left(\frac{\Delta\omega_a}{2} + \frac{1}{T_1} \right) \frac{d}{dt} + \left(\frac{\Delta\omega_a}{2T_1} + \omega_R^2 \right) \right] P_1(t) = \frac{KE_1}{2\omega_a T_1} \Delta N_0, \quad (25)$$

which has exactly the same form as the $\Delta N(t)$ equation, except for a constant on the right-hand side.

Large-Signal Limit: Rabi-Frequency Oscillations

Let us consider first the limiting case in which either the applied signal amplitude E_1 is extremely strong or the relaxation times T_1 and T_2 are very long and the linewidth $\Delta\omega_a$ is very narrow. We can then make the large-signal assumption that the Rabi frequency is large compared to all of these other rates, i.e., $\omega_R \gg \Delta\omega_a$ and $\omega_R \gg 1/T_1$. The differential equations 5.24 and 5.25 for the population difference $\Delta N(t)$ and the polarization amplitude $P_1(t)$ then reduce to the very much simplified forms

$$\frac{d^2\Delta N}{dt^2} + \omega_R^2 \Delta N \approx 0 \quad (26)$$

and similarly

$$\frac{d^2P_1}{dt^2} + \omega_R^2 P_1 \approx 0. \quad (27)$$

The first of these equations has an elementary solution of the form

$$\Delta N(t) = \Delta N_0 \cos \omega_R t, \quad (28)$$

and the polarization amplitude $P_1(t)$ then has a matching solution of the form

$$P_1(t) = \sqrt{K\hbar/2\omega_a} \Delta N_0 \sin \omega_R t = P_m \sin \omega_R t. \quad (29)$$

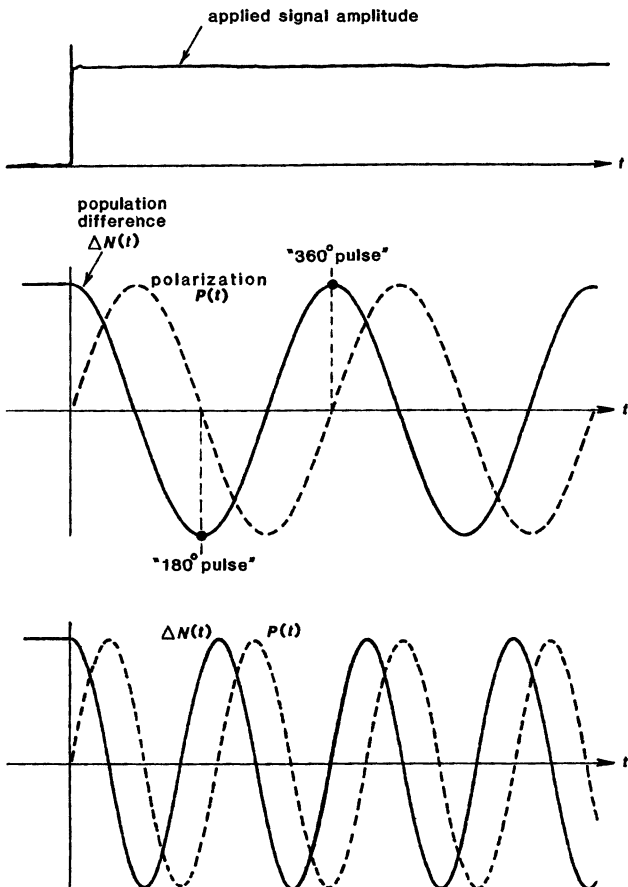


FIGURE 5.2

Rabi flopping behavior in response to a sudden and very strong sinusoidal signal input.

where P_m is the maximum value of the oscillating polarization. Figure 5.2 shows the population difference $\Delta N(t)$ and the envelope of the polarization $P_1(t)$ as given by these very-large-signal solutions.

It is apparent that in this very-strong-signal limit, the atomic behavior is very different from the rate-equation limit. The population difference $\Delta N(t)$, rather than going exponentially toward a saturated value ΔN_{ss} as it does in the rate-equation limit, instead continually oscillates back and forth between its initial value and the opposite of that value, at the Rabi frequency ω_R . At the same time, the induced polarization amplitude $P_1(t)$, instead of catching up to the applied signal with a time constant $\approx T_2$, continually chases but never catches up with the sinusoidal ringing of the population difference $\Delta N(t)$, so that the magnitude of $P_1(t)$ also oscillates sinusoidally, but lags behind $\Delta N(t)$ by $1/4$ of a Rabi cycle.

Discussion of the Rabi Flopping Behavior

This overall behavior of $\Delta N(t)$ and $P_1(t)$ is generally referred to as *Rabi flopping behavior*. It is a common result of quantum as well as classical analyses of large-signal atomic response.

The Rabi frequency ω_R in this very-large-signal limit is, by assumption, large compared to either $\Delta\omega_a \approx 2/T_2$ or to $1/T_1$. An essential feature of this regime is therefore that the population difference $\Delta N(t)$ oscillates through many Rabi cycles in a time interval short compared to either T_1 or (more important) T_2 . This Rabi oscillation frequency will still, however, be very small compared to the optical carrier frequency ω_a , so that there will still be very many optical cycles within each Rabi cycle. The slowly varying envelope approximation for $\Delta N(t)$ and $P_1(t)$ compared to ω_a is therefore still entirely valid.

It is also important to note that the Rabi frequency ω_R at which these oscillations occur depends directly on the applied signal amplitude E_1 , and on the square root of the transition strength as determined by the γ_{rad} value. Turning up the applied signal intensity will therefore give an even more rapid oscillation of the atomic population. The two lower plots in Figure 5.2 show two different applied signal strengths, with the stronger applied signal leading to a larger Rabi frequency. We emphasize again that all this oscillatory behavior occurs during a time interval short compared to either T_1 or T_2 , and is entirely different from the rate-equation behavior at much lower applied signal levels.

Note also that the polarization amplitude oscillates with a 90° time lag relative to $\Delta N(t)$, so that the maximum value of $|P_1|$ occurs when $|\Delta N| = 0$, in sharp contrast to the usual rate-equation behavior, in which $|\tilde{P}(\omega)|$ is directly proportional to $\Delta N(t)$. What this means physically is that the oscillating dipoles are all fully aligned in phase in this situation (since the T_2 dephasing mechanisms are weak compared to the applied signal); in addition, the oscillatory quantum component $\tilde{a}_1 \tilde{a}_2^*$ that we discussed earlier has its maximum value, subject to the constraint that $|\tilde{a}_1|^2 + |\tilde{a}_2|^2 = 1$, at the midway point when $|\tilde{a}_1| = |\tilde{a}_2| = \sqrt{1/2}$.

This Rabi flopping behavior is thus, once again, *totally different from the usual rate-equation behavior*. It represents the most fundamental type of transient large-signal behavior that can be produced in either an isolated atom or a collection of atoms in which the applied signal is strong enough to override all the relaxation and dephasing processes.

Large-Signal Case: Limiting Behavior at Long Times

To gain further insight into the distinction between small-signal and large-signal atomic behavior, we can write down the exact solutions to the full differential equations for $\Delta N(t)$ and $P_1(t)$, assuming a signal E_1 of arbitrary (but constant) amplitude that is again turned on at $t = 0$.

Let us first look, however, at the long-term steady-state solution to these equations. If we set all time derivatives to zero in the full differential equations 5.24 or 5.25, the eventual steady-state value of $\Delta N(t)$, when $d/dt = 0$, is given by

$$\lim_{t \rightarrow \infty} \Delta N(t) = \Delta N_{ss} \equiv \frac{\Delta N_0}{1 + 2(\omega_R^2 / \Delta\omega_a)T_1}. \quad (30)$$

But this is exactly the same as the rate-equation saturation result for a two-level system, namely,

$$\Delta N_{ss} = \frac{\Delta N_0}{1 + 2W_{12}T_1}. \quad (31)$$

Comparing these two equations that the stimulated-transition probability W_{12} which is valid in the small-signal or rate-equation regime can be related to the Rabi frequency ω_R and the transition linewidth $\Delta\omega_a$ by the very simple and useful form

$$\text{stimulated transition probability, } W_{12} \equiv \frac{\omega_R^2}{\Delta\omega_a}. \quad (32)$$

(The reader can verify this formula by making use of the exact formulas for ω_R and W_{12} given earlier.) We will make more use of this interesting result a little later.

Even in the very-large-signal or Rabi-flopping regime, so long as there is any finite T_1 and T_2 , no matter how small, the Rabi flopping behavior will eventually die out. The population difference in our simple two-level mode will eventually saturate (possibly after many Rabi cycles) to a steady-state (and highly saturated) value given by

$$\lim_{t \rightarrow \infty} \Delta N(t) = \Delta N_0 \frac{1}{1 + 2W_{12}T_1} = \Delta N_0 \frac{1}{1 + S}, \quad (33)$$

where S is the “saturation factor” given by

$$S \equiv 2W_{12}T_1 = I/I_{\text{sat}} = \frac{2T_1}{\Delta\omega_a} \times \omega_R^2. \quad (34)$$

This factor is, of course, directly proportional to the applied signal power, and will be very much greater than one for any signal falling in the very-large-signal or Rabi-flopping regime.

Exact Solutions: Transient Response

The differential equations 5.20 and 5.21 (or 5.24 and 5.25) for $\Delta N(t)$ and $P_1(t)$ can, of course, be solved exactly, without approximations, for any level of signal strength. As a practical hint, the algebra involved in doing this becomes much easier if you convert the equations to a suitable set of normalized variables. A convenient choice is to normalize the time scale to the dephasing time T_2 by writing $t' = t/T_2$; to define a normalized signal amplitude by $R = \omega_R T_2 = 2\omega_R/\Delta\omega_a$, and a time-constant ratio by $D = T_2/T_1$ (note that D will normally be a small number); and then to use normalized quantities $\hat{n} = \Delta N/\Delta N_0$ and $\hat{p} = P_1/P_0$, where $P_0 = \sqrt{\hbar K/2\omega_a} \Delta N_0$. The two coupled equations then become

$$\frac{d\hat{n}}{dt} + D(\hat{n} - 1) = -R\hat{p},$$

$$\frac{d\hat{p}}{dt} + \hat{p} = R\hat{n}.$$

Since these are linear coupled equations, the exact solutions will have a transient behavior that will take on either overdamped or oscillatory forms, depending on

the ratio of R to $(1 - D)/2$, which in real terms corresponds to the ratio of ω_R^2 to the quantity $(\Delta\omega_a/4 - 1/2T_1)^2$. Let us examine each of these limits in turn.

1. *The overdamped or weak-signal regime.* In the weak-signal regime the applied signal strength is small enough that $\omega_R < (\Delta\omega_a/4 - 1/2T_1)$, which means that the Rabi frequency is small compared to the atomic linewidth $\Delta\omega_a$ (and so the stimulated-transition probability W_{12} is small compared to $\Delta\omega_a$ also). The exact solution is then overdamped, and has two exponential decay components given by

$$-\alpha \pm \beta = -\left(\frac{\Delta\omega_a}{4} + \frac{1}{T_1}\right) \pm \sqrt{\left(\frac{\Delta\omega_a}{4} - \frac{1}{2T_1}\right)^2 - \omega_R^2}, \quad (36)$$

so that $\beta < \alpha$. This condition corresponds to the usual rate-equation limit, as we will now see.

If we assume for simplicity that the atomic system is initially at rest, so that $P_1(0) = 0$ and $\Delta N(0) = \Delta N_0$ when the signal is first turned on, then the solution in this limit may be written as

$$\Delta N(t) = \Delta N_{\text{sat}} [1 + S e^{-\alpha t} (\cosh \beta t + (\alpha/\beta) \sinh \beta t)], \quad (37)$$

where ΔN_{sat} and the saturation factor S are as defined earlier. For the limiting case of a very weak signal, $\omega_R \ll \Delta\omega_a$, and also slow energy decay, $1/T_1 \ll \Delta\omega_a$, the two time constants approach the limits

$$\alpha + \beta \approx \Delta\omega_a/2 \quad \text{and} \quad \alpha - \beta \approx (2W_{12} + 1/T_1); \quad (38)$$

so Equation 5.37 can be approximated by

$$\Delta N(t) \approx \Delta N_{\text{sat}} \{1 + S \exp[-(2W_{12} + 1/T_1)t]\}. \quad (39)$$

But this is exactly the same as the transient two-level behavior developed in Section 4.5 using rate equations. This result thus verifies that the Rabi-frequency behavior blends smoothly into rate-equation behavior in the appropriate weak-signal limit.

2. *The oscillatory or strong-signal regime.* For signals strong enough that $\omega_R > (\Delta\omega_a/4 - 1/2T_1)$, the equations become underdamped, and we must use instead a pair of complex conjugate time constants given by

$$-\alpha \pm j\beta = -\left(\frac{\Delta\omega_a}{4} + \frac{1}{T_1}\right) \pm j \sqrt{\omega_R^2 - \left(\frac{\Delta\omega_a}{4} - \frac{1}{2T_1}\right)^2}. \quad (40)$$

The imaginary part β in particular now corresponds to a kind of modified Rabi frequency ω'_R given by

$$\beta = \omega'_R \equiv \sqrt{\omega_R^2 - \left(\frac{\Delta\omega_a}{4} - \frac{1}{2T_1}\right)^2} \quad (41)$$

when the effects of damping and dephasing are included.

In terms of these quantities, the exact solution for the same initial conditions then becomes

$$\Delta N(t) = \Delta N_{\text{sat}} \{1 + S e^{-\alpha t} [\cos \beta t + (\alpha/\beta) \sin \beta t]\}. \quad (42)$$

This result is a more exact form of the large-signal Rabi flopping limit given earlier, with the effects of weak relaxation terms $\Delta\omega_a$ and T_1 included.

To illustrate how the transient response of the atomic system changes as the applied signal amplitude increases from the weak-signal or rate-equation regime to the large-signal or Rabi-flopping regime, Figure 5.3 shows the calculated behavior of $\Delta N(t)$ and $P_1(t)$ from these exact solutions plotted versus t/T_1 in a two-level system, assuming that the dephasing time T_2 is $1/5$ of the energy decay rate $1/T_1$ and that the Rabi frequency ranges from 0.15 to 2.2 times the atomic linewidth $\Delta\omega_a$. This obviously covers a range from the weak-signal regime, exhibiting essentially rate-equation behavior, into the lower end of the strong-signal regime, exhibiting a significant amount of Rabi flopping behavior.

In the intermediate regime between weak and very strong applied signals, the population clearly oscillates back and forth at a modified Rabi frequency $\beta \equiv \omega'_R$ that is somewhat lower than ω_R . This Rabi flopping behavior eventually dies out, however, as the dephasing effects described by $\Delta\omega_a$ gradually destroy the coherently driven transient behavior.

Summary

There are two points concerning the results derived in this chapter that we should especially emphasize here.

- All the results we have developed in this section are *quantum-mechanically correct* (at least for an ideal two-level quantum system), since the initial polarization and population difference equations from which we started were quantum-mechanically correct. The Rabi flopping behavior is a very general and characteristic quantum phenomenon, readily predicted from Schrödinger's equation for any strongly perturbed two-level system.
- Even in the weak-signal regime where no Rabi flopping behavior is occurring, the Rabi frequency ω_R still provides a natural measure of the strength of the applied signal field, relative to the transition frequency ω_a . In quantum-mechanical terms, $\hbar\omega_R$ is a measure of the *perturbation hamiltonian* caused by the applied field acting on the atom, just as $\hbar\Delta\omega_a$ is a measure of the random perturbation hamiltonian caused by the relaxation mechanisms and the dephasing or phonon-broadening mechanisms acting on the atoms, and $\hbar\omega_a$ is a measure of the static or unperturbed hamiltonian of the atom.

This point is especially illustrated by the fact that the stimulated-transition probability W_{12} in any two-level system (electric dipole or any other kind) can always be written in terms of the Rabi frequency ω_R for that transition, in the form

$$W_{12} = \frac{\omega_R^2}{\Delta\omega_a}, \quad (43)$$

where $\Delta\omega_a$ is the homogeneous linewidth for that transition. The condition for rate-equation behavior, which we said earlier was $W_{12} \ll \Delta\omega_a$, translates into the condition that

$$\omega_R \ll \Delta\omega_a. \quad (44)$$

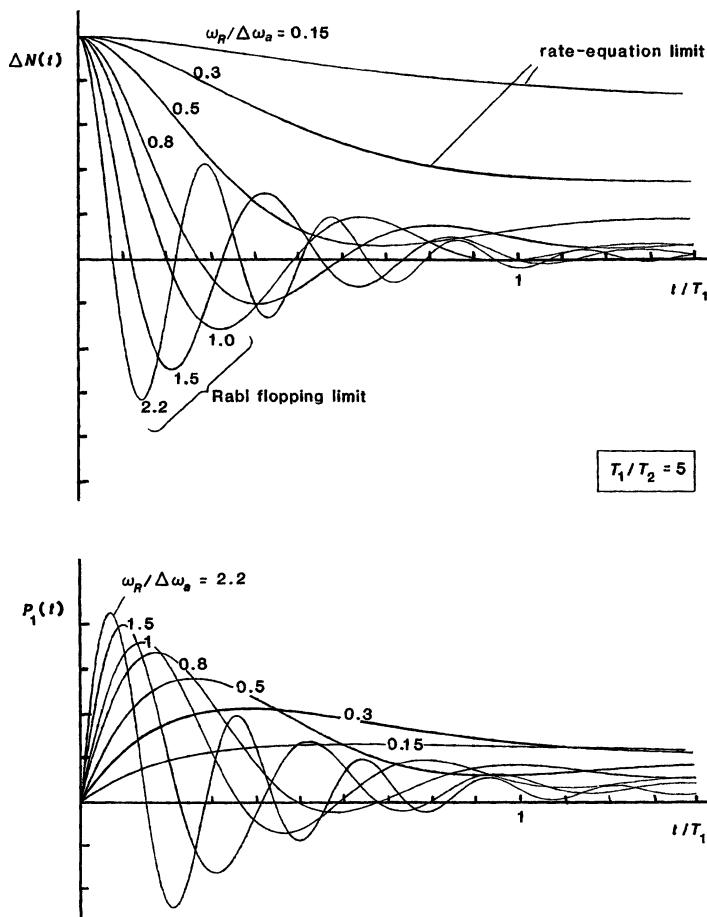


FIGURE 5.3

Exact solutions for the induced polarization $P_1(t)$ and the population difference $N(t)$ in a two-level system produced by sinusoidal applied signals of varying strengths that are suddenly turned on at $t = 0$. The parameters for the various curves are $\Delta\omega_a T_1 = 10$ (or $T_1 = 5T_2$) and $\omega_R/\Delta\omega_a$ ranging from 0.15 up to 2.2. The behavior changes over from weak-signal or rate-equation behavior for $\omega_R \ll \Delta\omega_a$ to strong-signal or Rabi flopping behavior for $\omega_R > \Delta\omega_a$.

In other words, in order to be in the rate-equation regime, the Rabi frequency ω_R itself must be much less than the linewidth $\Delta\omega_a$.

In physical terms, rate-equation behavior results when the signal strength and hence the Rabi frequency are small enough that a dephasing event or a relaxation event is sure to occur, and to break up the Rabi flopping behavior, before even a fraction of a Rabi cycle is completed. So-called coherent or large-signal Rabi-flopping effects occur, on the other hand, when the atoms can be

driven through one or several Rabi cycles in a time short compared to either of the relaxation times T_1 or T_2 .

Coherent Pulse Effects

Rabi flopping behavior, and other strong-signal effects and departures from elementary rate-equation behavior, are most easily observed by using pulsed signals and transient detection methods. This is both a practical matter, in that strong applied signals are more easily obtained in pulsed form, and a consequence of the fact that the nonlinear Rabi-frequency kind of behavior shows up most clearly in transient rather than steady-state behavior of the atoms. Hence a number of different pulsed large-signal experiments have been developed to demonstrate such coherent transient behavior; these are commonly referred to as “coherent pulse” experiments.

As one example, the Rabi flopping behavior predicts that if we apply a sufficiently strong signal pulse with a duration T_p such that $\omega_R T_p \equiv \pi$ to an initially uninverted and absorbing two-level atomic transition, this pulse can flip the initially absorbing population difference ΔN_0 over into a completely inverted and hence amplifying condition $-\Delta N_0$ at the end of the pulse. We simply turn off the applied signal in the Rabi flopping behavior at the point where the initial population inversion has been completely inverted, and then let this inverted population slowly decay back to equilibrium with time constant T_1 .

This is commonly known as a “ π pulse” or “180° pulse” experiment. It provides one way (though in practice not a very useful way) to obtain pulsed inversion in a two-level system. Note that there is an inverse relationship between the signal amplitude E_1 and the pulse duration T_p needed to produce an exactly 180° pulse.

Similarly, a pulse with an “area” (that is, an $\omega_R T_p$ product) such that $\omega_R T_p = 2\pi$ will first invert the atomic population difference, and then flip it exactly back to its initial condition, as illustrated in Figure 5.4. As a result such a “ 2π pulse” or “360° pulse” will deliver no energy at all to the atoms (at least, not to first order). This means that a sufficiently strong pulse with this area can travel essentially unattenuated through an absorbing atomic medium which is otherwise opaque for lower-intensity signals. This phenomenon is known as “self-induced transparency” and has been demonstrated experimentally.

Self-Consistent Coherent Pulse Analyses

More rigorous analysis of these coherent pulse experiments requires us to take into consideration not only the effect of the signal on the atoms, but also the reaction of the resulting induced atomic polarization $p(t)$ back on the signal. For instance, in self-induced transparency the first half of the signal pulse delivers energy from the signal to the atoms, but in the second half of the pulse the atoms radiate energy back to the signal. As a consequence the signal pulse soon distorts from a square pulse, or whatever its initial shape may be, into a unique self-consistent pulse shape. Also, the pulse velocity is reduced much below the free propagation velocity of the electromagnetic wave, in essence because the pulse energy spends a significant fraction of the time stored in the atoms rather than in the wave.

A detailed calculation of pulse propagation through a simple two-level absorbing medium has been carried out by Davis and Lin, using essentially the

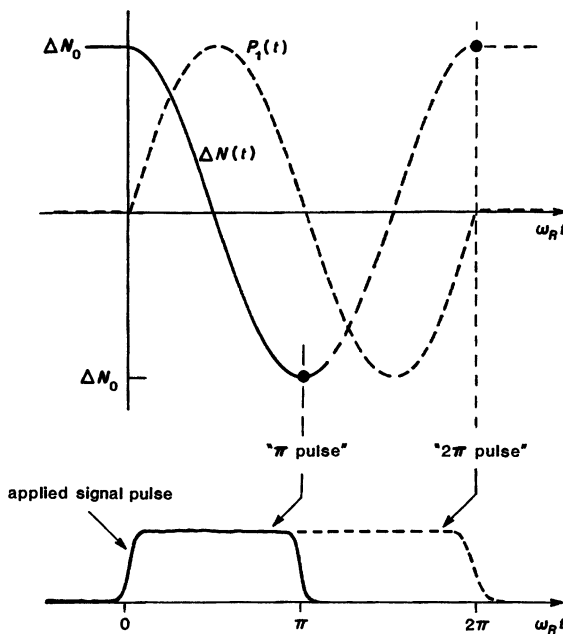


FIGURE 5.4
Large-signal “ π ” and “ 2π ” pulses applied to an atomic system.

atomic equations presented in this section, combined with Maxwell's equations for the propagation of the signal pulse itself. Figure 5.5 illustrates some typical results from their calculations.

The left-hand plots show the initial smooth pulse sent into the absorbing medium (plotted as E field amplitude, not intensity), and also the resulting modified pulseshapes at two different distances into the absorbing medium. The time scale for the modified pulses has been delayed in each case by the propagation time from the input plane to the observation plane, so that the two pulses will line up. The input pulse duration (≈ 5 ps) is much shorter than the assumed value of T_2 for the atomic medium, and the pulse intensity is large enough that the Rabi frequency at the peak is large compared to both the atomic linewidth and the inverse pulse duration. The right-hand plots show the time-variation of the population difference $\Delta N(t)$ at these same two observation planes, on the same delayed time scale, as the pulse sweeps past each plane.

In the top pair of plots, corresponding to the first observation plane, the early portion of the pulse (up to about 1.5 ps) has been strongly absorbed by the medium; but beyond that time the accumulated pulse energy has been enough to strongly saturate the absorber, so that the trailing edge of the pulse is nearly unattenuated. The right-hand plot also shows that the pulse intensity near the peak is more than adequate to produce significant Rabi flopping behavior in the atomic system. Note also that the population difference begins to recover toward its unsaturated value (plotted downward) with time constant T_1 as the pulse intensity dies away.

By the time the pulse reaches the second observation plane, which is five times further into the absorbing medium, the oscillatory Rabi behavior of the

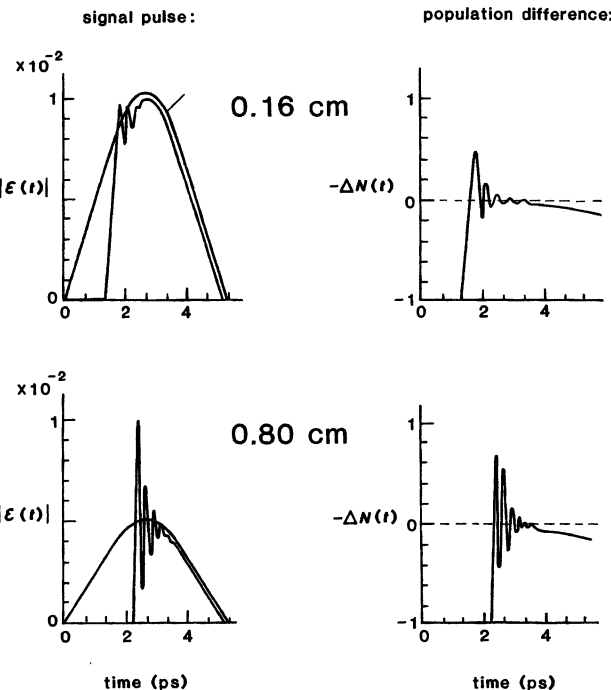


FIGURE 5.5

Results of numerical calculations for propagation of an intense optical pulse through a two-level absorbing medium, including both the non-linear response of the atoms, and the reaction of the medium back on the intensity and phase of the pulse. The left-hand plots show the input pulseshape, and the partially absorbed and reshaped pulses at two different distances into the medium. The right-hand curves show the time-variation of the population difference at the same reference planes inside the medium as the pulse passes by in each case. From L. W. Davis and Y. S. Lin, *IEEE J. Quant. Electr.* **QE-9**, 1135-1138 (December 1973).

atomic polarization has begun to react back on the propagating pulse; and the pulse itself has acquired a strong oscillatory behavior as well. The first full cycle in the pulse oscillation has become, in fact, almost a full 2π pulse, sufficient to flip the population difference more than 60% of the way to complete inversion to the opposite sign. If this pulse were to propagate further, it would in fact break up into one or several such 2π pulses.

There exist a great many such transient, large-signal, coherent-pulse effects which can be demonstrated on atomic transitions using appropriate pulsed signals. These transient responses can be described analytically using either an electric-dipole model for the atomic transition, or a magnetic-dipole model, which often provides more insight into the transient behavior even for what are really electric-dipole transitions. We will therefore consider these transient responses in more extensive detail in Chapter 31, after we have introduced the magnetic-dipole model for atomic transitions.

Multilevel Systems: Mixing and Intermodulation

Strong cw or long-pulse signals can also produce significant harmonic generation and intermodulation effects in a real atomic system, as we mentioned in the previous section. Suppose, for example, that two cw signals are simultaneously applied to the same atomic transition, with at least one of the signals being strong enough to violate the rate approximation conditions and produce significant Rabi flopping effects. Alternatively, suppose that this strong signal is applied to one transition, say, the $i \rightarrow j$ transition, and a weak signal is simultaneously applied to another transition which shares a common energy level, say, the $j \rightarrow k$ transition.

Then in either case, to give a somewhat simplified description, the strong signal will modulate the populations $N_i(t)$ or $N_j(t)$ in time according to the modified Rabi frequency. This modulation of the populations will then modulate the net absorption or emission seen by other, weaker signals on the same or on connecting transitions. In general, we can expect to see intermodulation and distortion products appearing in any strong-signal multiple-frequency experiment, with the weaker signals being modulated at something like the Rabi frequency produced by the stronger signal.

These mixing and intermodulation effects rapidly become very complicated when several energy levels or several applied frequencies are involved. Proper analysis of these effects usually requires carrying out what is called a multilevel quantum-mechanical density-matrix analysis. Fortunately, intermodulation effects of this type are usually small in most practical laser systems, although they can sometimes be observed. The general criterion for observing them is applying unusually strong signals to an atomic system that has unusually narrow linewidths and strong transitions, so that the Rabi frequencies involved can become larger than the linewidths. Some references on effects of this type are given below.

REFERENCES

Discussions of the Rabi frequency will be found in many quantum-mechanics texts and books on atomic transitions and resonance physics. One example (although the discussion happens to be framed in magnetic-dipole or Bloch-vector terminology) is L. Allen and J. H. Eberly, *Optical Resonance and Two-Level Atoms* (Wiley-Interscience, 1975), pp. 52–60. Another is M. Sargent III, M. O. Scully, and W. E. Lamb, Jr. *Laser Physics* (Addison-Wesley, 1974).

Problems for 5.2

1. *The slowly varying envelope approximation.* When you apply the slowly varying envelope approximation to the second-order resonance equation, why isn't it possible to simply drop the d^2p/dt^2 derivative term right from the beginning?
2. *Analysis of off-resonance Rabi flopping behavior.* Carry through the same derivation of large-signal atomic response as in the text for a constant but large-amplitude E_1 field applied to a two-level system, but assume that the applied signal frequency ω may be tuned well off the resonance frequency ω_a , by an amount $(\omega - \omega_a) \approx \omega_R$ or greater. Describe in particular how the effective Rabi

flopping frequency changes as the signal frequency is tuned away from ω_a . [Hint: You will need to treat $\tilde{P}(t)$ as a complex quantity, and to make a resonance approximation along with the slowly varying envelope approximation.]

3. *Coherent transients: The 90° pulse.* In addition to 180° and 360° pulses, coherent transient experimenters often make use of 90° pulses. What sort of atomic behavior would occur in an atomic system following a 90° applied signal pulse, and what sort of experimental uses might this behavior have?
4. *Large-signal atomic response: Two-frequency mixing and intermodulation effects.* Suppose that an applied signal with two steady-state sinusoidal frequency components, $\mathcal{E}(t) = \tilde{E}_1 e^{j\omega_1 t} + \tilde{E}_2 e^{j\omega_2 t}$, where ω_1 and ω_2 are both near ω_a , is applied to a two-level atomic system. Try expanding both $\Delta N(t)$ and $p(t)$ in the form, for example,

$$\Delta N(t) = \sum_{n,m} \Delta N_{nm} \exp j(n\omega_1 + m\omega_2)t,$$

and then substituting these into the exact atomic equations and applying harmonic balance to find the coefficients ΔN_{nm} and P_{nm} .

Find in particular the magnitudes of the $n = 1, m = 1$ (sum frequency) and $n = -1, m = -1$ (difference frequency) components in $\Delta N(t)$, and the $n + m = \pm 3$ components in $p(t)$, as nonlinear functions of the signal amplitudes E_1 and E_2 .

5. *Quantum transition matrix element for an electric-dipole atom.* In quantum theory, applying an electric field \mathcal{E} to an atom produces a perturbation hamiltonian $\mathcal{H}' = -\mu_{\text{op}}\mathcal{E}$ where μ_{op} is a quantum-mechanical electric-dipole operator. In terms of this operator, an electric-dipole transition matrix element μ_{12} between any two atomic levels can then be calculated from an overlap integral $\mu_{12} \equiv \int \psi_1^*(\mathbf{r})\mu_{\text{op}}\psi_2(\mathbf{r}) d\mathbf{r}$; where ψ_1 and ψ_2 are the quantum eigenstates for the two energy levels involved. This transition matrix element gives a quantum measure of the strength of the electric dipole response on that transition. One can show, for example, that the Rabi frequency produced by a sinusoidal field E_1 acting on that transition is given by

$$\omega_R \equiv \frac{\mu_{12}E_1}{\hbar}$$

This is the form in which the Rabi frequency is most often written in the scientific literature.

(a) By equating this form to the expressions for ω_R derived in this section, show that under strong Rabi-flopping conditions the maximum induced polarization P_m of Equation 5.29 has the value $P_m = \Delta N_0 \mu_{12}$. In physical terms, this means that at the maximum points of $P_1(t)$, the applied field E_1 has set the quantum state of every single atom in the population difference ΔN_0 oscillating in exactly the same phase, with an induced dipole moment per atom just equal to the quantum transition dipole matrix element μ_{12} .

(b) Find the analytical connection between the radiative decay rate γ_{rad} and the electric-dipole matrix element μ_{12} as two alternative ways of expressing the strength of any allowed electric-dipole transition; and again, if possible, give a physical interpretation of this.



LASER PUMPING AND POPULATION INVERSION

The atomic rate equations introduced in the two previous chapters are of great value in analyzing laser pumping, population inversion, and gain saturation in laser systems. The primary objective of this chapter is to illustrate this point by solving the atomic rate equations and examining these solutions for some simple but important atomic systems.

6.1 STEADY-STATE LASER PUMPING AND POPULATION INVERSION

One of the most common applications for rate equations is in analyzing laser pumping. In this section, therefore, we will develop and solve the rate equations to analyze steady-state laser pumping in simplified four-level and three-level laser systems.

Elementary Four-Level Laser System

Figure 6.1 shows a complicated multienergy-level system typical of many real laser systems; this one is for a solid-state laser system using the Nd^{3+} ion in Nd:YAG or Nd:glass. The upward arrows indicate upward pumping rates to various higher levels produced by flashlamp pumping on strong absorption lines from the ground state; the downward arrow indicates the widely used $1.064 \mu\text{m}$ laser transition from the $^4F_{3/2}$ level to the $^4I_{11/2}$ level. (There are actually at least eight different laser transitions of widely varying strengths between these two clusters of closely spaced levels, with wavelengths extending from 1.0520 to $1.1226 \mu\text{m}$. In addition, generally weaker laser action is possible from the same $^4F_{3/2}$ levels to the cluster of $^4I_{9/2}$ levels at four wavelengths between 0.89 and $0.9462 \mu\text{m}$; to the $^4I_{13/2}$ levels at four wavelengths between 1.319 and $1.358 \mu\text{m}$; and—very weakly—at $1.833 \mu\text{m}$ to one of the $^4I_{15/2}$ levels slightly above the lowest or ground level in this cluster.)

Figure 6.1 does not show the numerous downward radiative and nonradiative relaxation paths among all these levels. As in many other rare-earth and other solid-state laser systems, however, atoms excited into the higher excited levels in this material will nearly all relax, primarily by fast nonradiative relaxation, into the sharp and long-lived $^4F_{3/2}$ metastable level that provides the upper laser

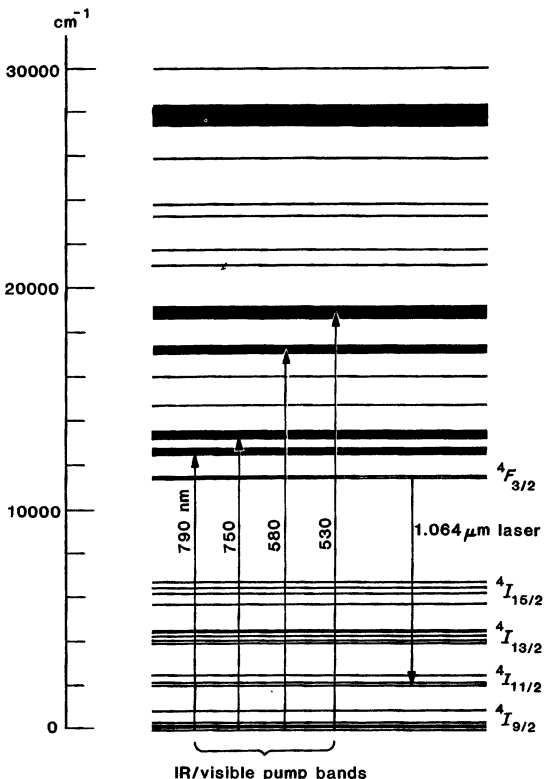


FIGURE 6.1
Important pump bands and the dominant $1.06 \mu\text{m}$ laser transition in the Nd:YAG or Nd:glass laser medium.

level in this system. A sizable population density can thus build up in this upper laser level.

For purposes of analysis this complicated set of levels can then be simplified into the idealized four-level laser system shown in Figure 6.2. This four-level model will in fact provide a simple but surprisingly accurate analytical model for many real laser systems. In this model level 4 represents the combination of all the levels lying above the upper laser level in the real atomic system. It is desirable that many of these levels be in fact broad absorption bands, so that the optical pumping into these levels by a broadband pump lamp can be very efficient.

Level 3 represents the upper laser level, usually a fairly sharp and long-lived level, with a large gap below it. Level 2 then represents the lower laser level, and level 1 the lowest or ground level. Other low-lying levels that may be present in the material, both above and below the lower laser level, are ignored in the model because they play no real role in the laser action. They act only as temporary way stations through which atoms may pass in relaxing from the other levels to the ground level E_1 .

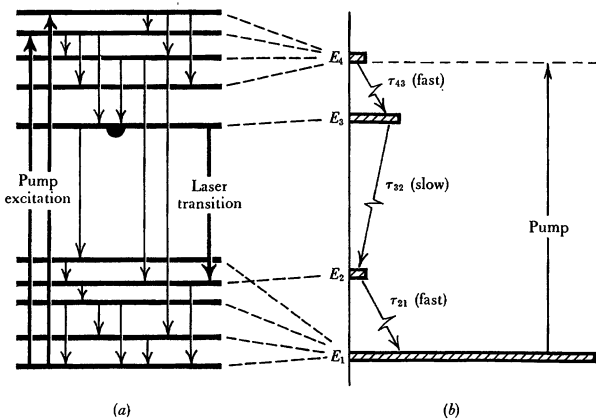


FIGURE 6.2

An idealized four-level pumping system which replaces the more complex scheme of Figure 6.1.

Four-Level Pumping Analysis

To analyze this system we will write down the relevant rate equations one after another, using the model shown in Figure 6.3, and then solve for their steady-state solutions, making reasonable approximations as we go along. Since the condition $\hbar\omega/kT \gg 1$ is usually very well satisfied for all transitions in a visible laser system, we will write all of the following rate equations using the “optical approximation” introduced in Section 4.4.

We begin by assuming that the laser pumping process, whatever its physical cause, produces a stimulated pump transition probability $W_{14} = W_{41} = W_p$ between levels 1 and 4. The rate equation for level 4 in the optical approximation is then

$$\begin{aligned} \frac{dN_4}{dt} &= W_p(N_1 - N_4) - (\gamma_{43} + \gamma_{42} + \gamma_{41})N_4 \\ &= W_p(N_1 - N_4) - N_4/\tau_4, \end{aligned} \quad (1)$$

where the lifetime τ_4 given by

$$\frac{1}{\tau_4} \equiv \gamma_4 = \gamma_{43} + \gamma_{42} + \gamma_{41} \quad (2)$$

is the total lifetime for decay of level 4 to all lower levels. The steady-state population of level 4, when $dN_4/dt = 0$, is then given by

$$N_4 = \frac{W_p \tau_4}{1 + W_p \tau_4} N_1 \approx W_p \tau_4 N_1 \quad \text{if } W_p \tau_4 \ll 1. \quad (3)$$

The normalized pumping rate $W_p \tau_4$, which will appear in many of the following expressions, will in fact have a value much less than unity in many (though not all) practical laser systems.

Direct pumping up from the ground level into the upper laser level 3 in this model can very often be assumed negligible, either because the $1 \rightarrow 3$ transition

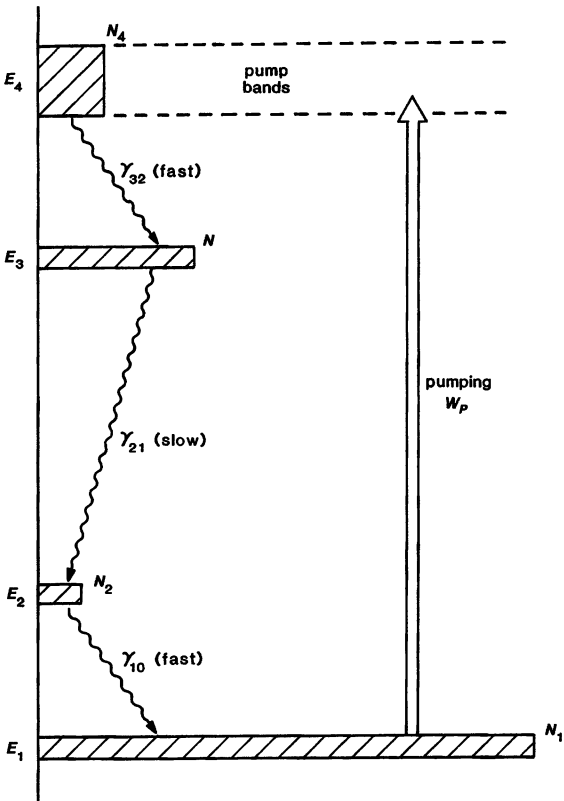


FIGURE 6.3
The idealized four-level pumping scheme of Figure 6.2 shown in more detail.

will have a weaker absorption cross section than the collected $1 \rightarrow 4$ transitions, or because this transition will be much narrower than the strong absorption bands from the ground level to the groups of levels that make up level 4. The rate equations for the two levels N_3 and N_2 are then

$$\frac{dN_3}{dt} = \gamma_{43}N_4 - (\gamma_{32} + \gamma_{31})N_3 = \frac{N_4}{\tau_{43}} - \frac{N_3}{\tau_3} \quad (4)$$

and

$$\frac{dN_2}{dt} = \gamma_{42}N_4 + \gamma_{32}N_3 - \gamma_{21}N_2 = \frac{N_4}{\tau_{42}} + \frac{N_3}{\tau_{32}} - \frac{N_2}{\tau_{21}}. \quad (5)$$

The first of these then gives at steady state ($d/dt = 0$)

$$N_3 = \frac{\tau_3}{\tau_{43}}N_4. \quad (6)$$

In a good laser system the $4 \rightarrow 3$ relaxation rate will be very fast, but the upper laser level 3 will have a long lifetime by comparison, so that $\tau_3 \gg \tau_{43}$ and hence $N_3 \gg N_4$.

Combining Equation 6.5 and 6.6 then gives the result

$$N_2 = \left(\frac{\tau_{21}}{\tau_{32}} + \frac{\tau_{43}\tau_{21}}{\tau_{42}\tau_3} \right) N_3 = \beta N_3, \quad (7)$$

where the parameter β is defined to be

$$\beta \equiv \frac{\tau_{21}}{\tau_{32}} + \frac{\tau_{43}\tau_{21}}{\tau_{42}\tau_3}. \quad (8)$$

This parameter β thus depends only on relaxation-time ratios, not absolute values. If this quantity is less than unity, the steady-state result will be $N_2 < N_3$, which means there will be the desired population inversion on the $3 \rightarrow 2$ transition.

In a good laser system the upper levels E_4 will relax primarily into the upper laser level E_3 , so that $\gamma_{42} \approx 0$ or $\tau_{42} \approx \infty$. In this case $\beta \approx \tau_{21}/\tau_{32}$, and the condition for population inversion becomes simply

$$\beta \equiv \frac{N_2}{N_3} \approx \frac{\tau_{21}}{\tau_{32}} \ll 1. \quad (9)$$

In other words, to have good inversion on the $3 \rightarrow 2$ transition, atoms should relax out of the lower laser level E_2 down into lower levels much faster than atoms relax into E_2 from above. Even if level 4 does not relax only into level 3, if the upper laser level has a long lifetime (both τ_{32} and τ_3 long) and the lower laser level has a short lifetime (τ_{21} short), then population inversion on the $3 \rightarrow 2$ transition is virtually certain.

Whether this population inversion will be large enough to give sufficient gain to achieve laser action in a practical cavity is another matter. Nonetheless, these conditions are met and laser action can be produced on many transitions in many real atomic systems.

Fluorescent Quantum Efficiency

Another dimensionless parameter often used in evaluating laser materials is the *fluorescent quantum efficiency* η , defined as the number of fluorescent photons spontaneously emitted on the laser transition divided by the number of pump photons absorbed on the pump transition(s) when the laser material is below threshold. For the four-level system this quantum efficiency is given by

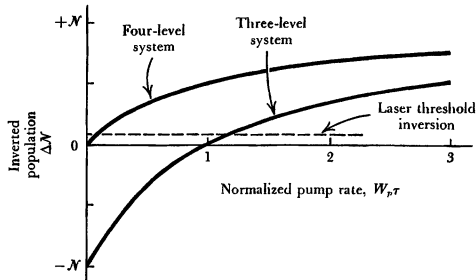
$$\eta = \frac{\gamma_{43}}{\gamma_4} \times \frac{\gamma_{\text{rad}}}{\gamma_3} = \frac{\tau_4}{\tau_{43}} \times \frac{\tau_3}{\tau_{\text{rad}}}, \quad (10)$$

where $\gamma_{\text{rad}} \equiv \gamma_{\text{rad}}(3 \rightarrow 2)$ is the radiative decay rate on the $3 \rightarrow 2$ transition. The first ratio in this expression tells what fraction of the total atoms excited to level 4 relax directly into the upper laser level 3, rather than bypassing 3 and dropping to lower levels, and the second ratio tells what fraction of the total decay out of level 3 is purely radiative decay to level 2.

Four-Level Population Inversion

With the aid of the parameters β and η , plus the conservation of atoms condition that $N_1 + N_2 + N_3 + N_4 = N$, we can solve for the population inversion

FIGURE 6.4
Laser population inversion
versus normalized pumping
rate for idealized four-level
and three-level laser
systems.



$N_3 - N_2$ versus pumping strength on the four-level system. After some algebra we can obtain

$$\frac{N_3 - N_2}{N} = \frac{(1 - \beta)\eta W_p \tau_{\text{rad}}}{1 + [1 + \beta + 2\tau_{43}/\tau_{\text{rad}}]\eta W_p \tau_{\text{rad}}}, \quad (11)$$

where $\tau_{\text{rad}} \equiv \tau_{\text{rad}}(3 \rightarrow 2)$ is the radiative decay rate on the laser transition itself. In a good laser material the lifetime τ_{43} from the upper pump level into the upper laser level will be short compared to this radiative decay time, and this expression can then be simplified into

$$\frac{N_3 - N_2}{N} \approx \frac{(1 - \beta)\eta W_p \tau_{\text{rad}}}{1 + (1 + \beta)\eta W_p \tau_{\text{rad}}} \approx \frac{W_p \tau_{\text{rad}}}{1 + W_p \tau_{\text{rad}}} \quad \text{if } \beta \rightarrow 0. \quad (12)$$

The optimum situation is obviously $\beta \approx \tau_{21}/\tau_{32} \rightarrow 0$.

Figure 6.4 shows a plot of the inversion $N_3 - N_2$ on the four-level laser transition versus the normalized pumping rate $W_p\tau$, assuming $\beta = 0$. For a four-level system, the population inversion on the $3 \rightarrow 2$ transition increases linearly with the pumping intensity W_p at lower pump levels, but then approaches a limiting value for $W_p\tau \gg 1$ as the ground state E_1 is depleted and a large fraction of the atoms are lifted into the upper laser level.

This four-level pumping model provides a surprisingly good analytical model for understanding the behavior of a large number of real laser systems, as we will show in later sections.

Three-Level Laser System

Figure 6.5 illustrates how a three-level laser system can be similarly employed as a model for the real energy levels of the familiar ruby laser, just as the four-level system provided a model for the Nd:YAG and many similar solid-state and dye lasers.

A three-level laser differs from the four-level system in that the lower laser level is the ground level E_1 . This is a serious disadvantage, since more than half the atoms initially in the ground state must be pumped through the upper pumping level E_3 into the upper laser level E_2 before any inversion at all is obtained on the $2 \rightarrow 1$ transition. Three-level lasers are, therefore, usually not as efficient as four-level lasers. One reason for analyzing the three-level system,

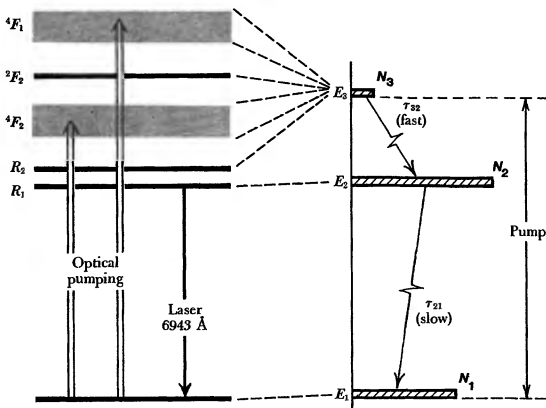


FIGURE 6.5

The relevant quantum energy levels in the laser material ruby, and an idealized three-level model for this system.

nonetheless, in addition to general background knowledge, is that the 694 nm ruby laser—the first laser ever to be operated and still a useful solid-state laser—is a nearly ideal three-level laser system.

Suppose the pumping process in a three-level system produces a stimulated transition probability $W_{13} = W_{31} = W_p$. Then the rate equations for the two upper levels are

$$\frac{dN_3}{dt} = W_p(N_1 - N_3) - \frac{N_3}{\tau_3} \quad (13)$$

and

$$\frac{dN_2}{dt} = \frac{N_3}{\tau_{32}} - \frac{N_2}{\tau_{21}}. \quad (14)$$

There is also the usual conservation equation $N_1 + N_2 + N_3 = N$, and it is again useful to define a fluorescence quantum efficiency given by

$$\eta = \frac{\tau_3}{\tau_{32}} \times \frac{\tau_{21}}{\tau_{\text{rad}}(2 \rightarrow 1)}. \quad (15)$$

The important relaxation-time ratio in this model is given by

$$\beta \equiv \frac{N_3}{N_2} = \frac{\tau_{32}}{\tau_{21}}. \quad (16)$$

The steady-state population difference on the $2 \rightarrow 1$ transition can then be found to be

$$\frac{N_2 - N_1}{N} = \frac{(1 - \beta)\eta W_p \tau_{\text{rad}} - 1}{(1 + 2\beta)\eta W_p \tau_{\text{rad}} + 1}. \quad (17)$$

Inversion in the three-level system can be obtained only if $\beta < 1$, and even then inversion can occur only when the pumping rate exceeds a threshold value given

by

$$W_p \tau_{\text{rad}} \geq \frac{1}{\eta(1 - \beta)}. \quad (18)$$

The optimum situation obviously occurs when the relaxation from the upper pumping level 3 into the upper laser level 2 is very fast, so that $\beta \rightarrow 0$, and when the relaxation from the upper laser level 1 down to the ground level 1 is purely radiative, so that $\eta \rightarrow 1$. The inversion versus normalized pumping strength then reduces to

$$\frac{N_2 - N_1}{N} \approx \frac{W_p \tau_{\text{rad}} - 1}{W_p \tau_{\text{rad}} + 1} \quad \text{if } \eta \rightarrow 1 \text{ and } \beta \rightarrow 0. \quad (19)$$

The significant differences in inversion versus pumping for a three-level and a four-level system are illustrated in Figure 6.4. Other things being equal, a four-level laser system should have a much lower pumping threshold than a three-level laser system.

More on the Ruby Laser

The well-known ruby laser is a special case that overcomes the inherent disadvantages of the three-level laser, since the ruby laser can in fact have a moderately low pulsed laser threshold, and can even (with some difficulty) be operated as a cw laser. The ruby laser works as well as it does because of an unusually favorable combination of other factors, including:

- Unusually broad and well-located pump absorption bands that make very efficient use of the broadband radiation from standard flashlamps.
- A fluorescent quantum efficiency η very close to unity.
- An unusually narrow atomic linewidth for the laser transition.
- An unusually long and almost purely radiative lifetime $\tau_{21} \approx 4.3$ ms for the upper laser level.
- The availability of ruby synthetic crystals with very good optical quality, good thermal conductivity, and high optical power handling capability.

The ruby laser has been particularly useful because it has an oscillation wavelength located in (or at least on the edge of) the visible region, where more sensitive photodetectors are generally available, in contrast to the infrared wavelengths of most of the solid-state rare-earth lasers. On the other hand, modern flashlamp-pumped dye lasers also give good laser action all across the visible region.

Problems for 6.1

1. *Three-level system with two pumping signals applied.* Consider a three-level atomic system with no degeneracies ($g_1 = g_2 = g_3 = 1$) and with two separate pumping signals applied to give $W_{12} = W_{21} = W_a$ and $W_{13} = W_{31} = W_b$. Using the optical-frequency approximation, find the population difference $N_2 - N_3$ as a function of pumping and relaxation rates. Suppose that W_a and W_b can have variable amplitudes but always with a fixed ratio of W_a/W_b . Describe and plot the variation of $(N_2 - N_3)$ with pumping strength for some illustrative cases.

2. *Population inversion versus pumping in an “upper-level” three-level laser system.* It is possible (though not likely in practice) to have a three-level laser system which is pumped on the $1 \rightarrow 3$ transition and in which cw laser action takes place on the $3 \rightarrow 2$ rather than the $2 \rightarrow 1$ transition (no such real system is known). Suppose that level 3 in such a system is long-lived with lifetime τ_3 ; level 2 has a short relaxation time to the ground state; and the system is pumped with transition probability W_p on the $1 \rightarrow 3$ transition.

Carry through the rate-equation analysis (in the optical approximation) necessary to find the population inversion on the $3 \rightarrow 2$ transition as a function of pumping power W_p . Compare the ΔN versus W_p curve for this system to those for the four-level and three-level models shown in Figure 6.4.

3. *Cascade pumping of a four-level laser system.* Suppose a four-level system is “cascade pumped” with two separate pumping transition probabilities $W_{13} \equiv W_A$ and $W_{34} \equiv W_B$. The optical approximation $\hbar\omega \gg kT$ applies for all transitions, and there are significant downward relaxation rates γ_{ji} between all levels.

Solve for the population difference $\Delta N_{42} \equiv N_4 - N_2$ in this system as a function of the two pumping powers W_A and W_B , using the γ_j and γ_{ji} notations for the downward relaxation rates. Discuss what conditions are needed for an inversion on the $4 \rightarrow 2$ transition, and how this inversion depends on the two pumping powers.

4. *Analysis of a five-level laser system.* Consider a five-level atomic system in which the optical approximation applies between all levels. Assume that this system is pumped on the $1 \rightarrow 5$ transition with a pumping transition probability $W_{15} = W_{51} + W_p$, and that each upper level in the system relaxes only into the level immediately beneath it. Evaluate the population difference on the $3 \rightarrow 2$ transition as a function of W_p , and discuss the dependence of this population difference on various interlevel relaxation rates.

5. *Laser refrigeration?* In an earlier chapter we considered an analysis of the population inversion and energy transfer in a thermally pumped laser or maser system. The reverse of this, which is also physically possible, is an optically pumped “laser refrigerator.”

To see how such a refrigerator might operate, consider applying a strong coherent signal to the $1 \rightarrow 2$ transition in a three-level system. With the right ratios of relaxation times, we can then achieve a steady-state population difference on the $2 \rightarrow 3$ transition which is considerably “colder” than the Boltzmann ratio on the same transition before the signal was turned on. The atoms now look significantly colder to the thermal surroundings, at least in the frequency band at and around the $2 \rightarrow 3$ transition frequency. In other words, this becomes a *refrigerator*, which uses coherent work (the applied signal on the $1 \rightarrow 2$ transition) to achieve cooling of the atoms, and maybe even the atomic surroundings, at and near the $2 \rightarrow 3$ transition frequency.

Assume again that, with the use of suitable filters, the atoms can see quite different physical surroundings at different frequency bands (this is a perfectly reasonable assumption). What sort of refrigeration efficiencies might we achieve? What relaxation time ratios and other conditions do we need to achieve high efficiency? Can we ever approach the thermodynamic limit?

6.2 LASER GAIN SATURATION

In many real laser systems laser action takes place between two excited levels that are located high above the ground level, and the population density in these excited laser levels always remains small compared to the total density of atoms in the lowest energy level E_0 (as we will label the ground level in this section). This is particularly true in gas lasers, where linewidths are narrow, transitions are relatively strong, and only small inversion densities are necessary to give significant gain. It may be less true in solid-state lasers, such as the ruby example of the preceding section, where large fractions of the total atomic density may sometimes be pumped into the upper laser levels.

In any event, in this section we will use this as a simplified model to develop some further rate equation analyses, showing in particular how the laser gain itself saturates with increasing signal power in typical laser systems.

Laser Gain Saturation Analysis

Figure 6.6 gives a simplified but yet realistic model for many laser systems of this type. Atoms are pumped by some pumping mechanism from the ground level E_0 into some upper level E_3 . They then relax down (perhaps by cascade processes) into the upper laser level E_2 , from where they relax or make stimulated laser transitions down to the lower laser level E_1 , and thence back to ground. Note that we have specifically included a laser signal, corresponding to laser amplification or laser oscillation, and represented by the stimulated transition probability W_{sig} in this diagram.

Suppose the upper-level populations all remain small compared to the initial ground-state population. Then the pumping rate from the ground level E_0 into the upper atomic level E_3 caused by a pumping transition probability $W_{03} = W_{30} = W_p$ may be written as

$$\left. \frac{dN_3}{dt} \right|_{\text{pump}} = W_p(N_0 - N_3) \approx W_p N_0, \quad (20)$$

where $N_0 \approx N$ is very nearly the total density of laser atoms in the system.

In this situation there is essentially no “back-pumping” from E_3 to E_0 , since very few atoms accumulate in the upper levels and hence $N_3 \ll N_0$. It is then common and convenient practice to speak not of a pumping transition probability W_p (probability per atom per second), but of a *net pumping rate* (atoms per second, per unit volume) being lifted up out of the ground level, as given by $W_p N_0 \approx W_p N$.

This pumping rate $W_p N_0$ in a real laser system will be more or less directly proportional to the pump light intensity (in an optically pumped laser), or to the discharge current density (in a discharge-pumped gas laser), or to a chemical reaction rate (in a chemically pumped laser). Moreover, in many real lasers some fixed fraction η_p of the atoms pumped into an upper energy level will decay, often through some cascade process, down into the longer-lived upper laser level E_2 . The number of atoms per second reaching the upper laser level is then given by an effective pumping rate $R_p = \eta_p W_p N_0$, where η_p represents the quantum efficiency for pump excitation into this upper laser level. (This pumping efficiency may be quite high, even approaching unity, for many solid-state and organic dye lasers, and may be very small for many typical discharge-pumped gas lasers.)

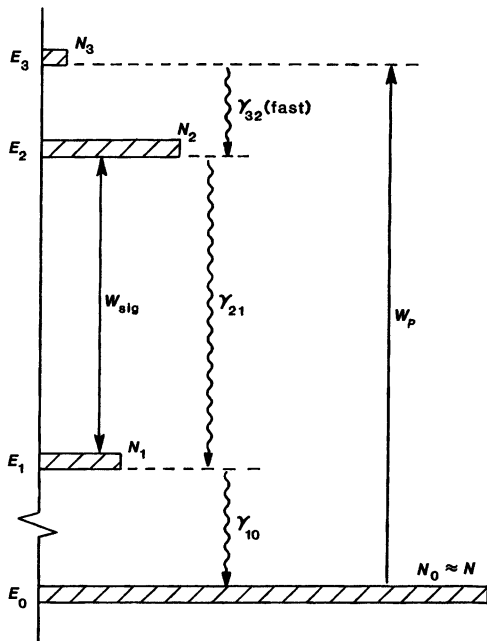


FIGURE 6.6
Simplified model for laser pumping and gain saturation between two high-lying energy levels E_1 and E_2 .

With these generally valid assumptions, the rate equations for the excited laser levels E_2 and E_1 , including a laser signal with stimulated transition probability $W_{12} = W_{21} = W_{\text{sig}}$ on the laser transition, may be written as

$$\frac{dN_2}{dt} = R_p - W_{\text{sig}}(N_2 - N_1) - \gamma_2 N_2 \quad (21)$$

and

$$\frac{dN_1}{dt} = W_{\text{sig}}(N_2 - N_1) + \gamma_{21} N_2 - \gamma_1 N_1, \quad (22)$$

where $\gamma_2 = \gamma_{21} + \gamma_{20}$ is the total decay rate downward from the upper laser level E_2 to all lower levels.

The steady-state solutions to these equations are then given by

$$N_1 = \frac{W_{\text{sig}} + \gamma_{21}}{W_{\text{sig}}(\gamma_1 + \gamma_{20}) + \gamma_1 \gamma_2} R_p, \quad (23)$$

$$N_2 = \frac{W_{\text{sig}} + \gamma_1}{W_{\text{sig}}(\gamma_1 + \gamma_{20}) + \gamma_1 \gamma_2} R_p.$$

Note particularly that only the two rate equations 6.21 and 6.22 were used in obtaining these results. No “conservation of atoms” condition stating that $N_1 + N_2$ remains constant was necessary or even possible in this case, since in fact $N_1 + N_2$ does not remain constant in this system when either the pump rate R_p or the signal strength W_{sig} changes. Two rate equations for the populations at

the two levels are thus both necessary and also sufficient in this particular type of rate-equation calculation.

Gain Saturation Behavior

The steady-state population difference $\Delta N_{21} \equiv N_2 - N_1$ on the laser transition is then given by

$$\Delta N_{21} \equiv N_2 - N_1 = \left(\frac{\gamma_1 - \gamma_{21}}{\gamma_1 \gamma_2} \right) \times \frac{R_p}{1 + [(\gamma_1 + \gamma_{20})/\gamma_1 \gamma_2] W_{\text{sig}}}. \quad (24)$$

The inverted population difference in this simple example varies with both pumping rate and signal intensity in the simple form

$$\Delta N_{21} = \Delta N_0 \frac{1}{1 + W_{\text{sig}} \tau_{\text{eff}}}, \quad (25)$$

where ΔN_0 is a small-signal or unsaturated population inversion given by

$$\Delta N_0 = \frac{\gamma_1 - \gamma_{21}}{\gamma_1 \gamma_2} R_p = (1 - \tau_1/\tau_{21}) \times R_p \tau_2 \quad (26)$$

and τ_{eff} is an effective recovery time or lifetime for the signal gain given by

$$\frac{1}{\tau_{\text{eff}}} = \frac{\gamma_1 \gamma_2}{\gamma_1 + \gamma_{20}} \quad \text{or} \quad \tau_{\text{eff}} = \tau_2 (1 + \tau_1/\tau_{20}), \quad (27)$$

If the upper laser level E_2 relaxes primarily into the lower laser level E_1 and not directly down to any lower levels E_0 , then the expression for the population inversion reduces to simply

$$\Delta N_{21} \approx R_p (\tau_2 - \tau_1) \times \frac{1}{1 + W_{\text{sig}} \tau_2} \quad (28)$$

where we have used the approximation that $\gamma_2 \approx \gamma_{21}$ and $\gamma_{20} \approx 0$.

Discussion

The analytical results in Equations 6.24 through 6.28 illustrate several typical aspects of laser behavior, including:

- The crucial requirement for obtaining inversion on this transition is that the time-constant ratio τ_{21}/τ_1 should be > 1 , or that the condition $\gamma_1 > \gamma_{21}$ be satisfied. In physical terms, this means that inversion is obtained only if atoms relax downward out of the lower level E_1 at rate γ_1 faster than they relax in at rate γ_{21} from the upper level.
- If this condition is met, the small-signal or unsaturated population difference ΔN_0 between the two laser levels is then directly proportional to the pump rate R_p times an effective “population integration time,” which is basically the upper-level lifetime τ_2 reduced by the factor $(1 - \tau_1/\tau_{21})$.
- The effective recovery time τ_{eff} , which determines the signal saturation behavior in Equation 6.25, is in general a combination of the various inter-level relaxation rates or lifetimes in the system. If the lower-level lifetime becomes short enough, $\tau_1 \rightarrow 0$, so that little or no population

can accumulate in the lower level E_1 , then τ_{eff} becomes just the upper-level lifetime, $\tau_{\text{eff}} \approx \tau_2$.

- Finally, in this system as in many real lasers, the saturation intensity of the inverted population depends only on the relaxation lifetimes between the atomic levels, and does not depend directly on the pumping intensity R_p . That is, the signal intensity W_{sig} needed to reduce the population inversion or laser gain to half its initial value does not depend at all (at least in this example) on how hard the atoms are being pumped.

The final point implies in particular that turning up the pump intensity will not increase the saturation intensity of the material, or the signal level required to reduce the gain to half its small-signal value. Turning up the pump intensity does increase the unsaturated population inversion ΔN_0 and hence the unsaturated gain, so that the laser must oscillate harder to bring the saturated gain down to match the losses; but the value of W_{sat} or I_{sat} is basically independent of how hard the system is pumped. This same behavior is characteristic of most real laser systems.

The Factor of 2*

We showed earlier that in a simple two-level system with a constant total population, or $N_1 + N_2 = N$, the rate equation for the absorbing population difference $\Delta N \equiv N_1 - N_2$ takes the general form

$$\frac{d}{dt} \Delta N = -2W_{12} \Delta N - \frac{\Delta N - \Delta N_0}{T_1} \quad (29)$$

and so the saturation behavior takes the form

$$\Delta N = \Delta N_0 \frac{1}{1 + 2W_{12}T_1}, \quad (30)$$

where T_1 is the recovery time for the population difference.

Suppose instead that we have a pumped and possibly inverted two-level system like that just discussed, in which the total population is no longer necessarily constant; and let us suppose in addition that the relaxation rate γ_{10} out of the lower level is extremely rapid, so that essentially no atoms ever collect in level 1, and that $N_1 \approx 0$ under all circumstances. According to the preceding results, the rate equation for the inverted population difference $\Delta N \equiv N_2 - N_1 \approx N_2$ becomes

$$\frac{d}{dt} \Delta N \approx -W_{\text{sig}} \Delta N - \frac{\Delta N - \Delta N_0}{\tau_2} \quad (31)$$

and so the saturation behavior is

$$\Delta N \approx \Delta N_0 \frac{1}{1 + W_{\text{sig}}\tau_2}, \quad (32)$$

where τ_2 is the upper-level lifetime; $W_{\text{sig}} \equiv W_{12}$; and $\Delta N_0 \equiv R_p\tau_2$. These two situations thus lead to exactly the same basic equations except that there is an additional factor of 2 in the stimulated-transition term in one case and not the other. This factor occurs in the simple two-level absorbing system because the transition of one atom between levels reduces the population difference ΔN by two.

Now, there are also many inverted laser systems in which an atom that is stimulated to make a downward transition from level 2 to level 1 remains for some considerable lifetime in level 1 before relaxing down to still lower levels. If the lifetime in level 1 is particularly long, we sometimes say that the atoms are more or less “bottlenecked” in level 1. The stimulated transition of one atom from N_2 to N_1 thus again reduces the population difference $\Delta N \equiv N_2 - N_1$ by two, and we must write the stimulated-transition term as $(d/dt)\Delta N \approx -2W_{\text{sig}}\Delta N$ here also. If level 1 is not bottlenecked, however, and its population empties out very rapidly, so that $N_1 \approx 0$ at all times, we can write the stimulated term as $(d/dt)\Delta N \approx -W_{\text{sig}}\Delta N$, where $\Delta N \approx N_2$ as above.

To handle both of these situations in a single notation, and also to take account of the fact that the population difference most often recovers to some small-signal or unsaturated value ΔN_0 with an effective time constant τ_{eff} , we can write the saturation equation for the inverted population in many different practical laser systems (and also the absorbing population difference in many absorbing systems) in the general form

$$\frac{d}{dt}\Delta N(t) = -2^*W_{\text{sig}}\Delta N(t) - \frac{\Delta N(t) - \Delta N_0}{\tau_{\text{eff}}}, \quad (33)$$

where 2^* is a numerical factor with a value somewhere between $2^* = 2$ (for strongly bottlenecked systems) and $2^* = 1$ (for systems with no bottlenecking). We will use this simple form several times later on to analyze the gain saturation and atomic dynamics in many laser problems, although a more complex rate-equation analysis may be needed to evaluate the actual values of 2^* and τ_{eff} . The effective value of 2^* will turn out to make a significant difference in the energy and power outputs of laser devices. (In general, the absence of bottlenecking, or $2^* \approx 1$, is good; and the presence of bottlenecking, or $2^* \approx 2$, is not so good.)

Problems for 6.2

1. *Transient response in the simplified laser-pumping model.* Find the transient (time-varying) solutions for the laser populations $N_1(t)$ and $N_2(t)$ in the same simplified atomic model discussed in this section, assuming that both the pump rate R_p and the signal intensity W_{sig} are turned on to constant values at $t = 0$. Discuss: (a) the transient build-up of $\Delta N(t)$ when R_p is first turned on, assuming $W_{\text{sig}} = 0$; (b) the transient decay when R_p is turned off, again assuming $W_{\text{sig}} = 0$; and (c) the transient behavior of $\Delta N(t)$ if W_{sig} is suddenly turned on or changed, assuming R_p is constant.
2. *Laser inversion and saturation including degeneracies.* Repeat the pumping and saturation calculations of this section assuming the same pumping rate R_p and relaxation rates γ_{ji} as in the text, but taking into account the existence of degeneracies g_1 and g_2 of the lower and upper energy levels and their effects on the definitions of W_{12} , W_{21} , and ΔN_{21} .
3. *Optically pumped laser absorber.* In a three-level atomic system with levels E_1 , E_2 and E_3 , for which the optical-frequency approximation is valid, pumping radiation producing a stimulated-transition rate $W_{12} = W_{21} = W_p$ is applied to the $1 \rightarrow 2$ transition, and signal radiation with $W_{23} = W_{32} = W_{\text{sig}}$ is applied to the $2 \rightarrow 3$ transition. The pump thus lifts atoms from level 1 to level 2, and creates a

kind of optically pumped laser absorption rather than laser amplification for the signal on the $2 \rightarrow 3$ transition. (Who knows?—it might be good for something.)

Find the population difference ΔN_{23} as a function of the pumping intensity W_p , the signal intensity W_{sig} , and the various downward relaxation rates in this system. Discuss in particular the signal saturation behavior of ΔN_{23} as a function of signal intensity W_{sig} at fixed pump intensity W_p .

4. *Simultaneous pumping into both the upper and the lower laser levels.* Consider a laser transition between two upper energy levels E_1 and E_2 in an atomic system similar to that discussed in this section. Assume, however, that there is pumping up from the ground level into *both* the laser levels E_1 and E_2 , at pumping rates R_1 and R_2 , respectively. (Note: these are pumping *rates*, not transition probabilities.) Assume there is also a laser signal W_{sig} on the $2 \rightarrow 1$ transition, as in this section.

Solve the steady-state equations for the population difference $\Delta N_{21} = N_2 - N_1$ in this system, and put the answer into a form that illustrates the dependence on pumping rates and on signal saturation. Discuss briefly (a) the pumping-rate and relaxation-time conditions for obtaining an inversion at all in this system; and (b) the form of the signal saturation behavior, and how it compares to simpler systems.

5. *Signal saturation behavior in the ideal three-level laser system.* Consider a three-level laser system like the ruby laser analyzed in a preceding section, assuming for simplicity that the only relaxation processes present are γ_{32} , which is very fast, and γ_{21} , which is slow and purely radiative. In addition to a pump transition probability on the $1 \rightarrow 3$ transition, add a signal transition probability W_{sig} on the $2 \rightarrow 1$ transition. Analyze the steady-state population inversion on the $2 \rightarrow 1$ transition as a function of W_p and W_{sig} . In particular, is the signal-saturation behavior produced by W_{sig} , for a fixed value of W_p , homogeneous in form? Does the saturation value for W_{sig} depend on how hard the system is being pumped? If so, is there a physical explanation why this is different from the gain saturation behavior analyzed in this section?

6.3 TRANSIENT LASER PUMPING

The full transient solution to a set of multilevel rate equations can become very complicated, as we noted in Chapter 4, since there will be in general $M - 1$ transient decay terms for an M -level atomic system. The transient solution for the build-up of inversion in a multilevel pulse-pumped laser can, therefore, also become a complicated problem. We will illustrate one or two such transient situations in this section, however, using very simplified models, in order to give some idea of the kind of behavior to be expected.

Transient Rate-Equation Example: Upper-Level Laser

As a first example, let us consider the “upper-level” laser model shown in Figure 6.6 and described in Equations 6.20 through 6.23. To simplify this still further, assume that no signal is present on the E_2 to E_1 transition, and that the relaxation rate out of the lower E_1 level is sufficiently fast that $N_1 \approx 0$ under all

conditions. The transient pumping equation for the upper laser level population $N_2(t)$ is then

$$\frac{dN_2(t)}{dt} = R_p(t) - \gamma_2 N_2(t) \quad (34)$$

where $R_p(t)$ is the (possibly) time-varying pump rate (in atoms lifted up per second) applied to the atomic system. A formal solution to this equation is

$$N_2(t) = \int_{-\infty}^t R_p(t') e^{-\gamma_2(t-t')} dt' \quad (35)$$

This equation says, of course, that of the number of atoms $R_p(t') dt'$ lifted up during a little time interval dt' , only a fraction $e^{-\gamma_2(t-t')}$ will remain in the upper level at a time $t - t'$ later. Suppose we put in a square pump pulse with constant amplitude R_{p0} and duration T_p , i.e., $R_p(t) = R_{p0}$, $0 \leq t \leq T_p$. The maximum upper-level population, reached just at the end of the pumping pulse, is then given by

$$N_2(T_p) = R_{p0}\tau_2 \left[1 - e^{-T_p/\tau_2} \right] \quad (36)$$

where $\tau_2 \equiv 1/\gamma_2$ is the lifetime of the upper laser level. This tells us that in a pulse-pumped laser of the type in which one first pumps up the upper-level population, and then “dumps” this population by Q -switching, it is of very little use to continue the pump pulse for longer than about two upper-level lifetimes or so, since beyond that point the upper-level population no longer increases much with further pumping. Alternatively, we might define a pumping efficiency η_p for this case as the ratio of the maximum number of atoms stored in the upper level, just at the end of the pumping pulse, to the total number of pump photons sent in or atoms lifted up during the pump pulse. Since the total number of atoms lifted up during the pump pulse is $R_{p0}T_p$, this pumping efficiency is given by

$$\eta_p = \frac{N_2(t = T_p)}{R_{p0}T_p} = \frac{1 - e^{-T_p/\tau_2}}{T_p/\tau_2} \quad (37)$$

In other words, this efficiency depends only on the ratio of pump pulselength T_p to upper-level time constant, τ_2 . A little work with your pocket calculator will show that if these time constants are equal, i.e., $T_p = \tau_2$, then the pumping efficiency is only about $\eta_p \approx 63\%$. For the pumping efficiency to reach 90% requires $T_p/\tau_2 \approx 0.2$, i.e., the total pump energy must be delivered in a pulse whose width T_p is only about 1/5 of the upper-level time constant τ_2 .

Transient Rate-Equation Example: Pulsed Ruby Laser

A transient solution for the simplified three-level ruby laser model given earlier in this chapter can also rather easily be obtained and used to demonstrate both the techniques of rate-equation analysis and the good agreement with experiment that can be provided by even a simple rate-equation description.

In ruby the γ_{32} relaxation rate is so fast ($> 10^{10} \text{ sec}^{-1}$) that atoms pumped into level 3 may be assumed to relax instantaneously into level 2. Hence we may assume that $N_3 \approx 0$ at all times, even with the strongest practical pump powers that we can apply. The three-level rate equations for a ruby laser, including

pumping but not signal terms, can then be reduced to the single rate equation

$$\frac{dN_1}{dt} = -\frac{dN_2}{dt} \approx -W_p(t)N_1(t) + \frac{N_2(t)}{\tau} \quad (38)$$

combined with the conservation of atoms condition that $N_1(t) + N_2(t) \approx N$. Here the lifetime τ is the total (and, in ruby, mostly radiative) decay time of approximately 4.3 ms for relaxation downward from level 2 to level 1.

These two equations can then be combined into a single rate equation for the inverted population difference $\Delta N(t) = N_2(t) - N_1(t)$ in the form

$$\frac{d}{dt}\Delta N(t) = -[W_p(t) + 1/\tau]\Delta N(t) + [W_p(t) - 1/\tau]N. \quad (39)$$

For the special case of constant pump intensity, this can be written in the even simpler form

$$\frac{d}{dt}\Delta N = -(W_p + 1/\tau) \times [\Delta N(t) - \Delta N_{ss}]. \quad (40)$$

This equation has exactly the same form as the relaxation of an elementary two-level system toward thermal equilibrium, except that the population difference $\Delta N(t)$ here relaxes toward a nonthermal steady-state equilibrium value ΔN_{ss} given by

$$\Delta N_{ss} \equiv \frac{W_p\tau - 1}{W_p\tau + 1} N, \quad (41)$$

and the relaxation rate toward this value is $(W_p + 1/\tau)$ rather than simply $1/\tau$. If the pumping rate is above threshold, or $W_p\tau > 1$, then $\Delta N(t)$ of course actually relaxes toward an inverted value of ΔN_{ss} .

Pulsed Inversion

Suppose a square pump pulse with constant pump intensity W_p is turned on at $t = 0$ in this particular system. (Some sort of pulse-forming network rather than just a single charged capacitor will be required to produce such a square pulse with a standard flashlamp.) The population inversion as a function of time during the pump flash is then given by the transient solution to the preceding equations with the initial condition that $\Delta N(t = 0) = -N$. This solution is

$$\frac{\Delta N(t)}{N} = \frac{(W_p\tau - 1) - 2W_p\tau \exp[-(W_p\tau + 1)t/\tau]}{W_p\tau + 1}. \quad (42)$$

Suppose that this pumping rate is left on for a pump pulse time T_p which is short compared to the atomic decay time τ ; and that the pumping rate $W_p\tau$ is $\gg 1$, which says that if the pump rate were left on for a full atomic lifetime τ , it would create a very strong inversion. The inversion just at the end of the pump pulse, or $t = T_p$, is then given to a good approximation by

$$\frac{\Delta N(T_p)}{N} \approx 1 - 2e^{-W_p T_p} \quad (T_p \ll \tau \text{ and } W_p\tau \gg 1). \quad (43)$$

This then says that (a) the inversion at the end of the pump pulse depends only on the total energy $W_p T_p$ in the pulse, and not on its duration (or even shape);

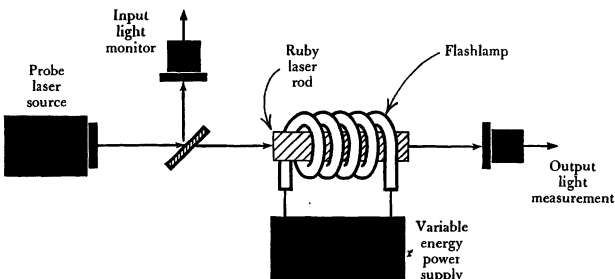


FIGURE 6.7
Pulsed laser gain measurement system.

and (b) the pulsed pump can produce complete inversion of the system, if the pumping energy is large enough ($W_p T_p \gg 1$).

Figure 6.7 illustrates a ruby-laser amplifier experiment in which a square pump pulse of length T_p short compared to the atomic decay time τ was used to pump a ruby amplifier rod without end mirrors. (Practical values for the pumping circuit might be a flashlamp pulse length $T_p \approx 200 \mu\text{s}$, compared to a ruby fluorescent decay time of $\tau = 4.3 \text{ ms}$.) A separate probe ruby laser was then used to measure the single-pass gain through the ruby rod just at the end of this pump pulse.

We will learn later that the gain or loss through a laser amplifier measured in dB is directly proportional to the laser population difference ΔN . For $T_p \ll \tau$ as in these experiments, the ratio of gain G_{dB} just after the pump pulse to initial loss L_{dB} just before the pump pulse is predicted from the preceding equation to be

$$\frac{G_{\text{dB}}(t = T_p)}{L_{\text{dB}}(t = 0)} = \frac{\Delta N(t = T_p)}{\Delta N(t = 0)} \approx 1 - 2e^{-W_p T_p}. \quad (44)$$

Figure 6.8 shows experimental data for this ratio for different values of the total flashlamp pump pulse energy, which is in turn directly proportional to the normalized pump quantity $W_p T_p$. The experimental results are in excellent agreement with the simple theoretical formula. Note in particular that a sufficiently powerful and rapid pump pulse can come very close to complete inversion of the ruby transition; i.e., it can pump essentially all of the Cr^{3+} atoms into the upper laser level.

Laser Oscillation Time Delay

Figure 6.9 shows another simple experimental examination of the transient behavior of populations in a pumped laser system. The small insert in this figure shows the oscillation output from a typical flash-pumped ruby laser, including the time delay t_d between the start of the pump flash and the onset of laser oscillation. The pumping pulse $W_p(t)$ requires a certain amount of time, or a certain amount of integrated pumping energy, before it can pump enough atoms up to the upper laser level to create a population inversion, especially in a three-level system such as ruby. Once a net population inversion is created, however, the laser oscillation then builds up extremely rapidly, as illustrated by the sharp

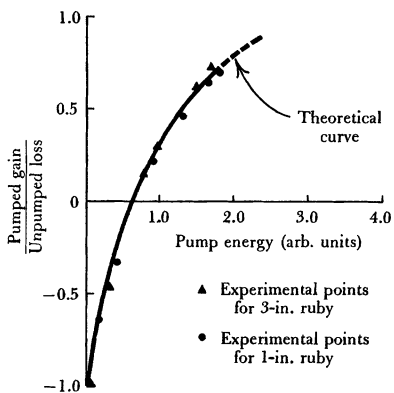


FIGURE 6.8

Experimental data for ruby laser gain versus pumping energy, obtained by using the experimental setup of Figure 6.7. (From J. E. Geusic and H. E. D. Scovil, *Bell. Sys. Tech. J.* **41**, 1371, July 1962.)

leading edge of the laser oscillation. (Note also the strong characteristic spiking behavior in the oscillation output.) The smoothly rising curve before the oscillation starts represents pump light leakage and preoscillation fluorescence from the laser rod.

This figure also shows how the reciprocal of the oscillation time delay varies with the total energy in a long flashlamp pulse. For a long square-topped pump pulse, the time delay t_d to the onset of oscillation can be estimated from the transient solution for $\Delta N(t)$ by finding the time $t = t_d$ at which $\Delta N(t)$ passes through zero (assuming that the oscillation signal will build up very rapidly once inversion is obtained). This time delay to inversion is given for constant pumping by

$$t_d = \frac{\tau \ln[2W_p\tau/(W_p\tau - 1)]}{W_p\tau + 1}. \quad (45)$$

There is a minimum value of pumping intensity W_p below which the laser will not reach oscillation threshold at all. If the pumping pulse has a pulse length T_p several times longer than the upper laser level lifetime τ , then this threshold pump intensity is given by $W_{p,\text{th}} \approx 1/\tau$ for $T_p \gg \tau$. For pump intensities below this value, inversion is never reached no matter how long the pump pulse continues.

The reciprocal oscillation time delay t_d normalized to the upper-level lifetime τ can then be written as

$$\frac{\tau}{t_d} = \frac{r + 1}{\ln[2r/(r - 1)]}, \quad (46)$$

where the parameter r represents the normalized pumping energy above threshold, i.e., $r \equiv W_p/W_{p,\text{th}}$. This simple expression gives a moderately good fit to the experimental data in Figure 6.9.

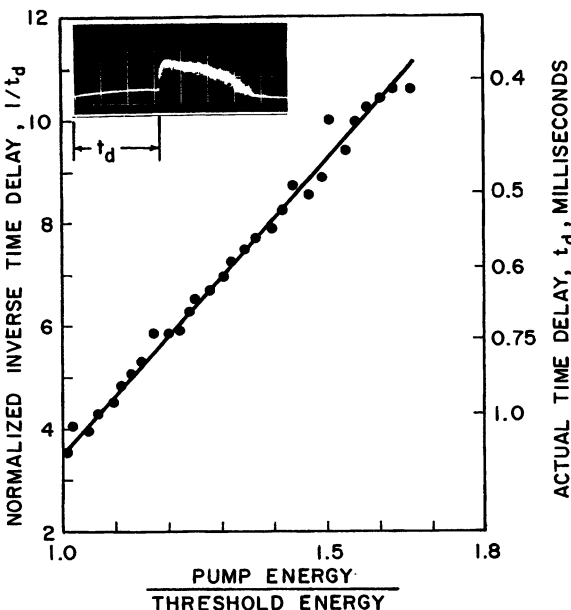


FIGURE 6.9

Time delay for oscillation buildup in a ruby laser versus pump pulse energy. The inset shows the power output versus time (200 μ sec per division) from a flash-pumped ruby laser, and the experimental points show how the reciprocal of the oscillation time delay t_d varies with energy input to the pumping flash lamp. (From A. E. Siegman and J. W. Allen, *IEEE J. Quantum Electron.* **QE-1**, 386-393, December 1965.)

Problems for 6.3

1. *Transient pumping with a gaussian time-varying pump pulse.* Derive an analytical formula for the upper-level population $N_2(t)$ in the simplified upper-level laser model discussed at the start of this section, assuming a gaussian rather than a square time-varying pump pulse $R_p(t)$. Hint: A very useful approximate formula for the error function $\text{erf}(x)$, accurate to $\approx 0.7\%$, is $\text{erf}(x) \approx [1 - \exp(-4x^2/\pi)]^{1/2}$.
2. *Ditto with an exponentially varying pump pulse.* Repeat the previous problem for a single-sided exponential pump pulse, i.e., $R_p(t) = (R_{p0}/T_p) \exp(-t/T_p)$ for $t \geq 0$.
3. *Peak population inversion versus normalized pump pulselwidth.* For either of the previous problems, plot the peak inversion that is produced versus the parameter T_p/τ_2 . For the exponentially varying pump pulse, show that you must make the pump pulse time constant a lot shorter than the upper-level decay time if you want the pumping efficiency to come anywhere close to unity.

4. *Ruby laser gain analysis including degeneracy and R_1 - R_2 level splitting.* In a more exact model of the ruby laser than given in the text, the ground-energy level E_1 is found to have a total degeneracy of $g_1 = 4$. The upper laser level E_2 is split into two so-called R_1 and R_2 levels, separated by $\Delta E = E_{2b} - E_{2a} = 39 \text{ cm}^{-1}$ with separate degeneracies $g_{2a} = g_{2b} = 2$. The relaxation between these two levels is extremely rapid, and so we can always assume that the relative populations of the two levels will remain fixed in the appropriate Boltzmann ratio $\exp(-\Delta E/kT)$ corresponding to room temperature, even during laser pumping and laser oscillation. Since this Boltzmann ratio is not negligible, the R_2 population will be smaller than the lower-lying R_1 population by a significant amount, and the R_1 rather than the R_2 transition always oscillates unless special steps are taken.

Taking these splittings and degeneracy factors into account, but otherwise making the same idealized three-level assumptions as in the text, calculate the effective population difference from the R_1 level to the ground level as a function of pumping power. Also, develop an expression for inverted gain after a pumping pulse compared to absorption before the pumping pulse analogous to the expression given in the text, but with the degeneracy and Boltzmann effects taken into account.



LASER AMPLIFICATION

In this chapter we begin examining the other side of the laser problem—that is, what laser atoms do to applied signals, rather than what applied signals do to atoms. This chapter and the following chapter are concerned primarily with continuous-wave or “cw” laser amplification: how inverted atomic transitions amplify optical signals; what determines the magnitude and bandwidth of this gain; how it saturates; and what phase shifts are associated with it. In Chapters 9 and 10 we will consider pulse propagation and pulsed laser amplification; and then in Chapters 11 and 12 we will add the laser mirrors to these amplifying atoms, and (finally!) be able to discuss laser oscillation and the generation of coherent laser radiation.

7.1 PRACTICAL ASPECTS OF LASER AMPLIFIERS

Let us begin with a few words about the practical interest in lasers as optical amplifiers, rather than as oscillators. Single-pass (and sometimes double-pass) laser amplifiers are used in many practical situations, primarily as power amplifiers, and seldom if ever as weak-signal preamplifiers. The reasons for this are generally the following.

Laser Power Amplifiers

Large laser devices very often face severe stability problems associated with large electrical power inputs, optical damage problems, mechanical vibrations, cooling and heat-dissipation problems, acoustic noise, and other sources of what in the Soviet literature is called “technical noise.” One common way to obtain high laser power output, simultaneously with good beam quality, short pulse length, excellent frequency stability, and good beam control, is to generate a stable input laser signal from a small but well-controlled laser oscillator. This signal can then be amplified through a chain of laser amplifiers, in what is commonly known as a master-oscillator-power-amplifier or MOPA system. Figure 7.1 shows, as one rather extreme example, the sequence of parallel cascaded Nd:glass laser amplifiers used in a giant laser fusion system, in which a four-story-high “space frame” supports some twenty parallel Nd:glass laser amplifier chains. Very

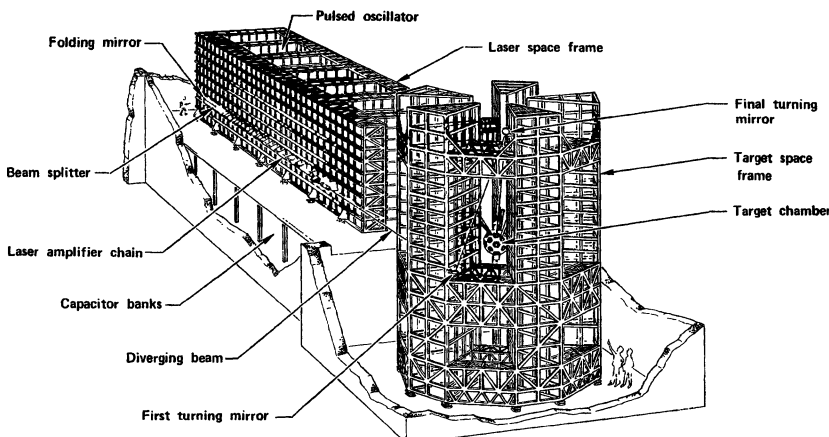


FIGURE 7.1

Laser space frame used with very large laser fusion system at Lawrence Livermore National Laboratory. The four-story-high space frame supports twenty parallel chains of cascaded Nd:glass laser amplifiers.

large high-power CO₂ laser amplifiers are also used in laser fusion experiments; and much smaller but very high-gain pulsed dye laser amplifiers and pulsed solid-state laser amplifiers are used to amplify tunable dye laser pulses or mode-locked solid-state laser pulses in many laboratory experiments.

The output signals in these devices will probably be much more stable than if the same laser amplifiers were converted into a single very high power laser oscillator. The primary defect in the MOPA approach, as we will see later, is that it is generally much less effective in extracting the available power in the large amplifier devices than if the large amplifiers were themselves converted into powerful but hard-to-control large oscillators.

Lasers as Weak Signal Amplifiers

Laser amplifiers are in fact almost always used as power amplifiers, especially for pulsed input signals, almost never as preamplifiers to amplify weak signals in optical receivers, for reasons related primarily to noise figure, and secondarily to the narrow bandwidth of most laser amplifiers.

There exists, as a result of fundamental quantum considerations, an unavoidable quantum noise level in any type of coherent or linear amplifier, at any frequency, whether it be laser, maser, transistor, or vacuum tube. (By a coherent amplifier we mean one which preserves all the phase and amplitude information in the amplified signal; this includes any kind of linear coherent heterodyne detection.) This quantum noise level is roughly equivalent to one noise photon per second per unit bandwidth at the input to the amplifier.

The physical source of this quantum noise in a laser amplifier is the unavoidable spontaneous emission in the laser system, from the upper energy level of the laser transition, into the signal to be amplified. There is, however, some equivalent source of spontaneous-emission-like noise in every other linear ampli-

fication mechanism, no matter what its physical nature. (If there were not, it would be possible to use such an amplifier to make physical measurements that would violate the quantum uncertainty principle.) This “quantum noise” source is normally negligible at ordinary radio or microwave frequencies, but becomes much more significant at optical frequencies. As a result, any coherent optical amplifier, including a laser amplifier, is generally unsuitable for detecting very weak optical signals. An incoherent detection mechanism, such as a photomultiplier tube, can detect much weaker optical signals, though of course at the cost of losing all phase information contained in the signal.

As we will see in this and following chapters, laser amplifiers also generally have a quite narrow bandwidth, especially if any regenerative feedback is added to increase the laser gain. As a consequence of both noise and bandwidth considerations, therefore, laser amplifiers are not used to any significant extent in optical communications receivers or other weak-signal-detection applications.

REFERENCES

A useful survey of the state of the art for designing and building Nd:glass laser amplifiers for pulsed laser fusion systems will be found in David C. Brown, *The Physics of High Peak Power Nd:Glass Laser Systems* (Springer-Verlag, 1980).

A good illustration of the noise properties of laser amplifiers is given by R. A. Paananen et al., “Noise measurement in an He-Ne laser amplifier,” *Appl. Phys. Lett.* **4**, 149–151 (April 15, 1964). More extensive discussions of spontaneous emission and noise in laser amplifiers and electrical systems generally are given in my earlier books *Introduction to Lasers and Masers* (McGraw-Hill, 1971), Chap. 10; and *Microwave Solid-State Masers* (McGraw-Hill, 1964).

7.2 WAVE PROPAGATION IN AN ATOMIC MEDIUM

Our first formal step toward understanding laser amplification will be to analyze the propagation of an ideal plane electromagnetic wave through an atomic medium which may contain laser gain or loss, as well as atomic phase-shift terms and possibly ohmic losses or scattering losses.

The Wave Equation in a Laser Medium

We begin with Maxwell’s equations for a sinusoidal electromagnetic field at frequency ω . The two basic Maxwell equations are

$$\nabla \times \mathbf{E} = -j\omega \mathbf{B}, \quad \nabla \times \mathbf{H} = \mathbf{J} + j\omega \mathbf{D}, \quad (1)$$

where the real vector field $\mathcal{E}(\mathbf{r}, t)$ as a function of space and time is given by

$$\mathcal{E}(\mathbf{r}, t) = \frac{1}{2} [\mathbf{E}(\mathbf{r}) e^{j\omega t} + \text{c.c.}] \quad (2)$$

and similarly for all the other quantities. If these fields are in a linear dielectric host medium which has dielectric constant ϵ , and which possibly contains laser atoms as well as ohmic losses, these quantities will also be connected by

“constitutive relations” which may be written as

$$\mathbf{B} = \mu \mathbf{H}, \quad \mathbf{J} = \sigma \mathbf{E}, \quad \text{and} \quad \mathbf{D} = \epsilon \mathbf{E} + \mathbf{P}_{\text{at}} = \epsilon [1 + \chi_{\text{at}}] \mathbf{E}, \quad (3)$$

where \mathbf{P}_{at} and χ_{at} represent the contribution of the laser atoms imbedded in the host dielectric medium. The material parameters appearing in these equations include:

- The optical-frequency dielectric permeability ϵ of the host medium, not counting any atomic transitions due to laser atoms that may be present.
- The magnetic permeability μ of the host medium (which will be very close to the free-space value μ_0 for essentially all common laser materials at optical frequencies).
- The conductivity σ , which is included to account for any ohmic losses in the host material.
- The resonant susceptibility $\chi_{\text{at}}(\omega)$ associated with the transitions in any laser atoms that may be present, where this $\chi_{\text{at}}(\omega)$ is defined in the slightly unconventional fashion we introduced in Section 2.4.

We will assume here that the atomic transition in these atoms is an electric-dipole transition, and thus contributes an electric polarization \mathbf{P}_{at} in the medium. A magnetic-dipole atomic transition would contribute instead an atomic magnetic polarization \mathbf{M}_{at} and thus a magnetic susceptibility χ_m in the $\mathbf{B} = \mu \mathbf{H}$ expression. The net result in the following expressions would be essentially the same, however, as you can verify for yourself.

Substituting Equations 7.1–7.3 into a vector identity for $\nabla \times \nabla \times \mathbf{E}$, and then assuming that $\nabla \cdot \mathbf{E} = 0$, gives

$$\begin{aligned} \nabla \times \nabla \times \mathbf{E} &\equiv \nabla(\nabla \cdot \mathbf{E}) - \nabla^2 \mathbf{E} \\ &= -j\omega\mu\nabla \times \mathbf{H} \\ &= -j\omega\mu[\sigma + j\omega\epsilon(1 + \chi_{\text{at}})] \mathbf{E} \\ &= \omega^2\mu\epsilon[1 + \chi_{\text{at}} - j\sigma/\omega\epsilon] \mathbf{E}. \end{aligned} \quad (4)$$

We can assume that $\nabla \cdot \mathbf{E} = 0$ provided only that the properties of the medium are spatially uniform (see Problems); and for simplicity we can drop the tensor or vector notation for χ and \mathbf{E} . This vector equation then reduces to the scalar wave equation

$$[\nabla^2 + \omega^2\mu\epsilon(1 + \tilde{\chi}_{\text{at}} - j\sigma/\omega\epsilon)] \tilde{E}(x, y, z) = 0, \quad (5)$$

where $\tilde{E}(x, y, z)$ is the phasor amplitude of any one of the vector components of \mathbf{E} .

This equation will be the fundamental starting point for the analyses in this chapter. We can immediately note as one important point that the atomic susceptibility term $\tilde{\chi}_{\text{at}} \equiv \chi' + j\chi''$ and the ohmic loss term $-j\sigma/\omega\epsilon$ appear in exactly similar fashion in this expression.

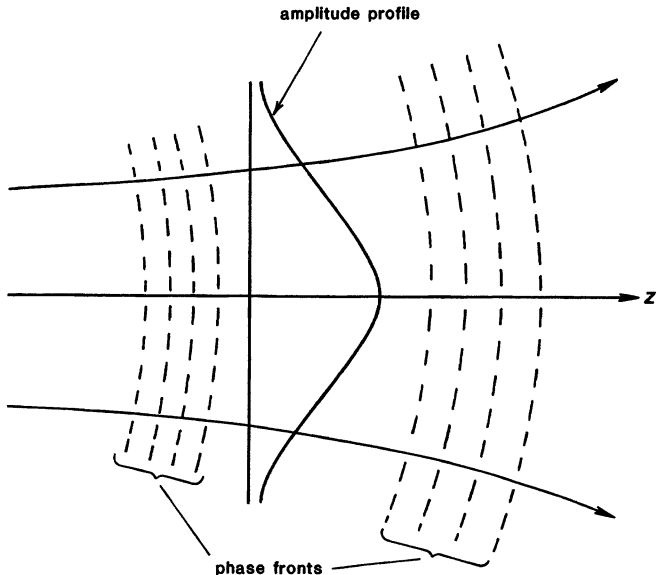


FIGURE 7.2

A propagating optical wave with a reasonably smooth transverse amplitude and phase profile.

Plane-Wave Approximation

Let us consider now either an infinite plane wave propagating in the z direction, so that the transverse derivatives are identically zero, i.e., $\partial/\partial x = \partial/\partial y = 0$, or a finite-width laser beam traveling in the same direction (see Figure 7.2). For a laser beam of any reasonable transverse width (more than a few tens of wavelengths) the transverse derivations will be small enough, and the transverse second derivatives even smaller, so that we can make the approximation

$$\left| \frac{\partial^2 \tilde{E}}{\partial x^2} \right|, \left| \frac{\partial^2 \tilde{E}}{\partial y^2} \right| \ll \left| \frac{\partial^2 \tilde{E}}{\partial z^2} \right| \quad (6)$$

(we will justify this in more detail in the following section).

With this approximation, Equation 7.5 will reduce to the one-dimensional scalar wave equation

$$\left[\frac{d^2}{dz^2} + \omega^2 \mu \epsilon (1 + \tilde{\chi}_{at} - j\sigma/\omega \epsilon) \right] \tilde{E}(z) = 0. \quad (7)$$

We will also for simplicity drop the subscripts on the atomic susceptibility $\tilde{\chi}_{at}$ from here on.

Lossless Free-Space Propagation

Let us now consider the traveling-wave solutions to this equation, first of all without any ohmic losses or laser atoms. We will generally refer to this as "free-

space" propagation, although we are in fact including the electric and magnetic permeabilities ϵ and μ of the host dielectric medium if there is one.

For $\chi_{\text{at}} = \sigma = 0$ the one-dimensional wave equation reduces to

$$[d^2/dz^2 + \omega^2 \mu \epsilon] \tilde{E}(z) = 0. \quad (8)$$

If we assume traveling-wave solutions to this equation of the form

$$\tilde{E}(z) = \text{const} \times e^{-\Gamma z}, \quad (9)$$

where Γ is a complex-valued propagation constant, then the wave equation reduces to

$$[\Gamma^2 + \omega^2 \mu \epsilon] \tilde{E} = 0. \quad (10)$$

The allowed values for the complex propagation factor Γ are thus given by

$$\Gamma^2 = -\omega^2 \mu \epsilon \quad \text{or} \quad \Gamma = \pm j\omega \sqrt{\mu \epsilon} = \pm j\beta, \quad (11)$$

where the quantity $\beta \equiv \omega \sqrt{\mu \epsilon}$ is the plane-wave propagation constant in the host medium.

The complete solution for the \mathcal{E} field in the medium may thus be written as

$$\begin{aligned} \mathcal{E}(z, t) = & \frac{1}{2} \left[\tilde{E}_+ e^{j(\omega t - \beta z)} + \tilde{E}_+^* e^{-j(\omega t - \beta z)} \right] \\ & + \frac{1}{2} \left[\tilde{E}_- e^{j(\omega t + \beta z)} + \tilde{E}_-^* e^{-j(\omega t + \beta z)} \right]. \end{aligned} \quad (12)$$

In this expansion the first line on the right-hand side represents a wave traveling to the right (i.e., in the $+z$ direction) with a complex phasor amplitude \tilde{E}_+ , and the second line represents a wave traveling to the left with phasor amplitude \tilde{E}_- . The student should be sure that the distinction between these two waves is clear and well-understood.

The "free-space" propagation constant β for these waves may then be written in any of the various alternative forms:

$$\begin{aligned} \beta &= \omega \sqrt{\mu \epsilon} = \frac{\omega}{c} = \frac{n\omega}{c_0} \\ &= \frac{2\pi}{\lambda} = \frac{2\pi n}{\lambda_0}, \end{aligned} \quad (13)$$

where the refractive index n of the host crystal is given by

$$n \equiv \sqrt{\mu \epsilon / \mu_0 \epsilon_0} \approx \sqrt{\epsilon / \epsilon_0} \quad \text{if} \quad \mu \approx \mu_0. \quad (14)$$

Note again that in the notation used in this text, c_0 and λ_0 are the velocity of light and the wavelength of the radiation in vacuum, whereas $c \equiv c_0/n$ and $\lambda \equiv \lambda_0/n$ always indicate the corresponding values in the dielectric medium. When we identify particular laser transitions we normally give the value of the wavelength in air, e.g., $\lambda_0 = 1.064 \mu\text{m}$ for the Nd:YAG laser. (Note also that in very precise calculations there will even be a slight difference, typically on the order of $\sim 0.03\%$, between the exact vacuum wavelength of a transition and the commonly measured value of the wavelength in air.)

Propagation With Laser Action and Loss

Let us now include laser action (i.e., an atomic transition) and also ohmic losses in the wave propagation calculation. The one-dimensional wave equation then becomes

$$\left[\frac{d^2}{dz^2} + \beta^2 (1 + \tilde{\chi}_{at} - j\sigma/\omega\epsilon) \right] \tilde{E}(z) = 0 \quad (15)$$

If we assume a z -directed propagation factor Γ in the same form as before, this propagation factor now becomes

$$\Gamma^2 = -\omega^2 \mu\epsilon [1 + \tilde{\chi}_{at} - j\sigma/\omega\epsilon] = -\beta^2 [1 + \tilde{\chi}_{at} - j\sigma/\omega\epsilon] \quad (16)$$

or

$$\Gamma = j\beta \sqrt{1 + \tilde{\chi}_{at} - j\sigma/\omega\epsilon} = j\beta \sqrt{1 + \chi'(\omega) + j\chi''(\omega) - j\sigma/\omega\epsilon}. \quad (17)$$

We include the specific dependence of $\chi'(\omega)$ and $\chi''(\omega)$ on frequency to emphasize that, at least for atomic transitions, this quantity will normally be complex and will have a resonant lineshape, with frequency-dependent real and imaginary parts.

Under almost all practical conditions, both the susceptibility $\tilde{\chi}_{at}(\omega)$ and the loss factor $\sigma/\omega\epsilon$ will have magnitudes that are $\ll 1$. Hence the square root in Equation 7.17 can, with negligible error, be expanded in the form $\sqrt{1 + \delta} \approx 1 + \delta/2$ to give

$$\Gamma \approx j\beta \times \left[1 + \frac{1}{2} \chi'(\omega) + j\frac{1}{2} \chi''(\omega) - j\sigma/2\omega\epsilon \right]. \quad (18)$$

From here on we will separate this into the four individual terms

$$\begin{aligned} \Gamma(\omega) &= j\beta + j\beta\chi'(\omega)/2 - \beta\chi''(\omega)/2 + \sigma/2\epsilon\epsilon \\ &= j\beta + j\Delta\beta_m(\omega) - \alpha_m(\omega) + \alpha_0, \end{aligned} \quad (19)$$

where each of the factors on the first line matches up with the corresponding factor on the second line. The propagation of a $+z$ traveling wave thus takes on the form

$$\mathcal{E}(z, t) = \text{Re } \tilde{E}_0 \exp \{j\omega t - j[\beta + \Delta\beta_m(\omega)]z + [\alpha_m(\omega) - \alpha_0]z\} \quad (20)$$

when the effects of ohmic losses and an atomic transition are included.

Propagation Factors

The significant factors in this complex wave propagation behavior are the following.

1. *The basic plane wave propagation constant.* This is the *basic wave propagation coefficient* β in the host medium, which is given by

$$\beta = \beta(\omega) = \omega\sqrt{\mu\epsilon} = \omega/c \quad (21)$$

This propagation constant leads to a fundamental phase variation $\phi(z, \omega) \equiv \beta z = \omega z/c = 2\pi z/\lambda$. This phase shift with distance is large (many complete

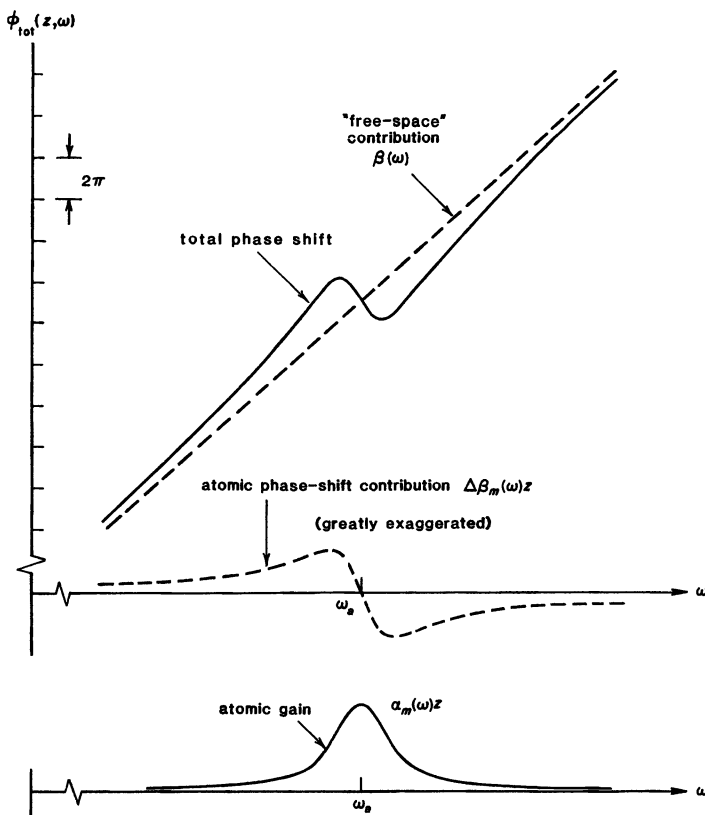


FIGURE 7.3

Phase shift and gain versus frequency in a resonant atomic medium. The atomic phase shift contribution is greatly exaggerated.

cycles) for any propagation length $z \gg \lambda$, and increases linearly (and rapidly) with frequency as shown by the dashed straight line in Figure 7.3.

2. *The additional atomic phase shift.* There is an *added phase-shift factor* $\Delta\phi(z, \omega) \equiv \Delta\beta_m(\omega)z$ due to the atomic transition, where $\Delta\beta_m(\omega)$ is given by

$$\Delta\beta_m = \Delta\beta_m(\omega) = (\beta/2)\chi'(\omega). \quad (22)$$

This phase shift is caused by and has essentially the same lineshape as the reactive part of the atomic susceptibility, $\chi'(\omega)$, as illustrated by the additional asymmetric contribution to the total phase shift in Figure 7.3.

Note that the sign of this term depends on the sign of the population difference ΔN , just as does the atomic gain or loss coefficient α_m . We have drawn the phase shift in Figure 7.3 assuming an inverted or amplifying population difference.

3. *The atomic gain or loss coefficient.* There is an *atomic gain (or loss) coefficient* $\alpha_m(\omega)$ due to the atomic transition, given by

$$\alpha_m = \alpha_m(\omega) = (\beta/2)\chi''(\omega). \quad (23)$$

This gain (or loss) has the lineshape of $\chi''(\omega)$ as illustrated in the bottom curve of Figure 7.3.

We noted in an earlier chapter that if we followed the definition $\tilde{\chi}_{\text{at}} \equiv \chi' + j\chi''$, an absorbing transition produced a negative value of χ'' . We see here also that an amplifying transition will imply positive values for both χ'' and α_m , but an absorbing atomic transition will imply negative values for both these quantities. Of course, we can always associate a suitable \pm sign with $\alpha_m(\omega)$ to give it the proper sign for either absorbing or amplifying media.

4. *The ohmic or background loss coefficient.* Finally, there is an *ohmic or background loss coefficient* α_0 due to the host medium itself. For pure ohmic conductivity in the host medium, this loss term is given by

$$\alpha_0 = \frac{\beta}{2} \frac{\sigma}{\omega\epsilon} = \frac{\sigma}{2\epsilon c}. \quad (24)$$

We will extend the interpretation of the coefficient α_0 in later equations, however, to represent any kind of broadband, background absorption or loss that may be present for the signal in the laser medium, whether this loss is due to ohmic conductivity in the host crystal, or to other loss mechanisms such as scattering or diffraction losses. This loss usually has no significant variation with frequency across the range of interest for a single laser transition.

The preceding four expressions summarize the laser amplification or atomic absorption properties, as well as the phase-shift properties, of any real atomic medium. Recall that in cases of interest to us $\tilde{\chi}_{\text{at}}(\omega)$ is virtually always caused by a very narrow resonant transition, with bandwidth $\ll 1\%$. Hence the linear frequency dependence of $\beta(\omega)$ across the narrow linewidth of $\tilde{\chi}_{\text{at}}(\omega)$ can be neglected in the $(\beta/2)\chi'(\omega)$ and $(\beta/2)\chi''(\omega)$ products, and only the midband value of β need be used. Each of these terms will show up in more detail in later sections.

Experimental Example

A set of measurements of absorption and phase shift made by Bean and Izatt on the 694 nm laser transition in ruby, without pumping or laser inversion, will give a particularly clean and striking experimental confirmation of the results we have just derived.

Let us recall that the laser transition in the ruby energy-level system terminates on the ground level, so that this transition will have a strongly absorptive population difference in the absence of any laser pumping. We have also noted earlier that the 4A_2 ground state of the Cr^{3+} ion in ruby is actually two energy levels which are split, even in zero magnetic field, into two closely spaced sublevels separated by $\Delta E = 0.38 \text{ cm}^{-1} = 11.4 \text{ GHz}$, as illustrated in Figure 7.4. (Each of these two sublevels is in fact also a doublet, which can be further split into two Zeeman levels using a dc magnetic field of a few hundred to a few thousand gauss.)

At liquid-nitrogen temperature the phonon broadening in a good sample of ruby becomes small enough ($\Delta\omega_a \leq 2\pi \times 6 \text{ GHz}$) that the separate absorption lines from the two ground levels can be clearly resolved in the optical absorption

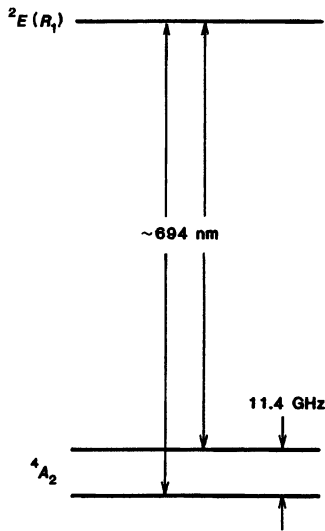


FIGURE 7.4
Absorption transitions near 694 nm from the two ground-state sublevels in ruby to the first excited level.

spectrum of ruby. Bean and Izatt have in fact made careful measurements of the transitions from this split ground state to the first excited or R_1 level in a ruby sample, measuring both the absorption coefficient $\alpha_m(\omega)$ versus frequency, which is directly proportional to $\chi''(\omega)$, and the change in index of refraction $\Delta n(\omega)$ relative to the background index n_0 , which is directly proportional to $\chi'(\omega)$. Typical results of their experiments are shown in Figure 7.5.

These independent measurements of $\chi''(\omega)$ and $\chi'(\omega)$ can then be fitted very closely by simply summing two partially overlapping complex lorentzian lineshapes, as illustrated both in Figure 7.5 and in the double-lorentzian curves in Figure 7.6. These latter curves represent the sum of two elementary lorentzian lines with a relative peak amplitude of 1.29 to 1, a resonance frequency spacing $\omega_{a2} - \omega_{a1} = 2\pi \times 11.5$ GHz, and equal linewidths $\Delta\omega_a = 2\pi \times 5.88$ GHz.

The close agreement between theory and experiment that is obtained here demonstrates both the validity of the lorentzian lineshape analysis and the close relationship between the $\chi'(\omega)$ and $\chi''(\omega)$ parts of the atomic response.

Larger Atomic Gain or Absorption Effects

The analytical results in this section (and indeed in most of the rest of this book) are based on the approximation that $|\tilde{\chi}_{\text{at}} - j\sigma/\omega c| \ll 1$. There are in fact only a few optical situations where this approximation is not valid, and where the related Taylor approximation for the complex propagation constant Γ will no longer be valid. These include:

1. *Absorption in metals and semiconductors.* For propagation into a semiconductor or a metal (or reflection from their surfaces) at wavelengths shorter than the band edge, or frequencies $\hbar\omega$ greater than the bandgap energy E_g , the effective conductivity σ and the $-j\sigma/\omega c$ term can become very large. Exact expressions for both the propagation factor Γ and the wave impedance must

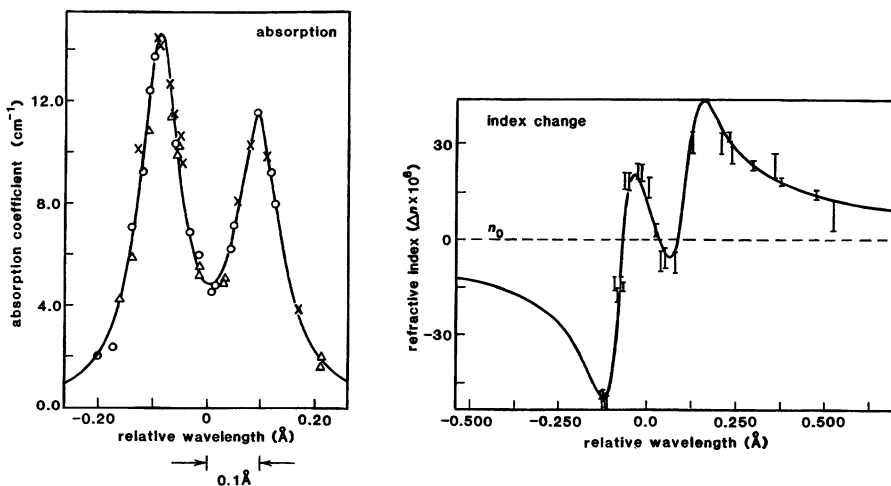


FIGURE 7.5
Measured absorption coefficient and index change for the ground-state absorption line in a ruby crystal at 95 K. (Adapted from B. L. Bean and J. R. Izatt, *J. Opt. Soc. Am.* **63**, 832-839, July 1973.)

then be employed to calculate absorption coefficients and phase shifts (as well as surface reflectivities).

2. *Absorption on strong resonance lines in metal vapors.* Another and more interesting situation where the atomic susceptibility term $\tilde{\chi}$ can become quite large compared to unity is ground-state absorption on the very strong visible or near-UV resonance lines of alkali metal vapors, such as sodium or rubidium, or other metal vapors such as Hg or Cd, at vapor pressures of a few torr or even lower. One particularly common example of this is the pair of sodium D lines at 589.0 and 589.6 nm in the green portion of the visible spectrum. The special features in these situations are that the transitions are very strongly allowed (with oscillator strengths approaching unity); they are relatively narrow, being broadened by doppler broadening only; and they are all ground-state absorption lines, so that all the atoms are in the lower level of the absorbing transition.

As a result, the absorption per unit length at line center on one of these transitions can be extremely large. For example, at the inside surface of a window in a cell containing a moderate vapor pressure of Na or Rb or Hg, the vapor will be so highly absorbing that it will appear essentially metallic and very highly reflecting. This will hold true, however, only within the very narrow range of frequencies within the atomic linewidth (typically a few GHz).

Interesting experiments on optical propagation and atomic transition phenomena can often be done in such vapors, using tunable dye lasers to tune at or very close to these transitions. The practical applications of these phenomena are somewhat limited, however, by the narrow bandwidths, and also by the voracious appetite of the alkali metal vapors for consuming and destroying almost

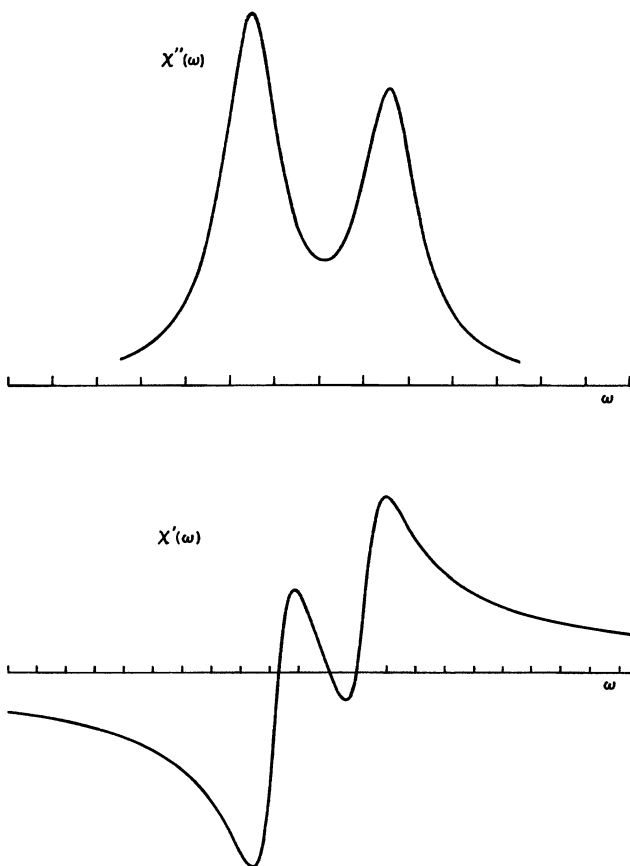


FIGURE 7.6

The summation of two complex Lorentzian lines with slightly shifted center frequencies closely matches the experimental data of Figure 7.5.

any conveniently available transparent window materials (not to mention seals and even the metal walls of the vapor cells).

Problems for 7.2

1. *Lineshapes for absorption and phase shift in ruby.* Reproduce the theoretical double-Lorentzian absorption and phase-shift curves shown for the ruby example in this section.
2. *The $\nabla \cdot \mathbf{E} = 0$ approximation in deriving the wave equation.* Disputatious students always question the wave-equation approximation that $\nabla \cdot \mathbf{E} = 0$, since the rigorous form of Gauss's law is actually $\nabla \cdot \mathbf{D} = \rho$, where ρ is the free charge

that may be present. The free charge ρ and convection current \mathbf{J} are, however, also connected by an equation of continuity which says that $\nabla \cdot \mathbf{J} + \partial \rho / \partial t = 0$. Using these two equations plus the assumption of an ohmic conductivity, i.e., $\mathbf{J} = \sigma \mathbf{E}$, show that $\nabla \cdot \mathbf{E} = 0$ is indeed strictly valid provided only that the quantity $(\tilde{\chi} - j\sigma/\omega\epsilon)$ is spatially uniform within the medium.

3. *Extending the Taylor approximation to higher-order terms in high-loss materials.* Consider a lossy medium having a finite conductivity σ but, for purposes of this problem, no laser susceptibility $\tilde{\chi}_{\text{at}}(\omega)$. First-order expressions for the propagation coefficient β and the attenuation coefficient α for this case are derived in the text by a Taylor-series approximation in $\sigma/\omega\epsilon$. Extend this approximation to get the next higher-order corrections to both β and α . How large will the power attenuation have to become (in the first-order approximation) before either of these higher-order corrections amounts to 10% of the first-order expressions? Express your answer in units of dB of power attenuation per wavelength of distance traveled.
-

7.3 THE PARAXIAL WAVE EQUATION

The next step in accuracy beyond the plane-wave approximation of Section 7.2 is the *paraxial wave equation*. This equation, which we will derive in this section, in fact leads to exactly the same results for axial propagation as in Section 7.2, but also makes it possible to handle transverse variations and diffraction effects of the optical beam profile.

The paraxial wave equation is, in fact, complete enough to describe essentially all laser amplification and laser propagation problems of practical interest in lasers; so it is used in a wide variety of laser and nonlinear optical calculations. It seems worthwhile therefore to derive the paraxial equation at this point, even though we will not need to use it until later in this book.

Paraxial Wave Derivation

The full vector form of the wave equation from Section 7.2 is

$$[\nabla^2 + \beta^2(1 + \tilde{\chi} - j\sigma/\omega\epsilon)] \mathbf{E}(x, y, z) = 0, \quad (25)$$

where β is the plane-wave propagation constant in the host medium, disregarding losses and/or atomic transitions. Suppose we now write any given vector component of this complex \mathbf{E} vector in the form

$$\tilde{E}(x, y, z) \equiv \tilde{u}(x, y, z) e^{-j\beta z}. \quad (26)$$

This says that the field $E(x, y, z)$ is basically a traveling wave of the form $\exp(-j\beta z)$ in the $+z$ direction. (We would, of course, write this as $e^{+j\beta z}$ if the wave were traveling instead in the $-z$ direction; so reversing the wave direction is the same thing as reversing the sign of β in all the following equations.)

This traveling wave may, however, have a transverse amplitude and phase variation, i.e., a dependence on x and y as contained in $\tilde{u}(x, y, z)$; and this transverse profile $\tilde{u}(x, y, z)$ will in general change slowly with propagation distance z as the wave grows, spreads, and/or changes in shape because of absorption

and/or diffraction effects, as illustrated for a typical case in Figure 7.2. The very rapid phase variation $\exp(-j\beta z) = \exp(-j2\pi z/\lambda)$ due to the traveling-wave part of the propagation has, however, been factored out of $\tilde{u}(x, y, z)$.

Putting the above form into the wave equation then yields

$$\nabla^2 \tilde{E} = \left[\frac{\partial^2 \tilde{u}}{\partial x^2} + \frac{\partial^2 \tilde{u}}{\partial y^2} + \frac{\partial^2 \tilde{u}}{\partial z^2} - 2j\beta \frac{\partial \tilde{u}}{\partial z} - \beta^2 \tilde{u} \right] e^{-j\beta z}. \quad (27)$$

Now, we know in advance (or at least we can verify shortly) that the transverse beam profile $\tilde{u}(x, y, z)$ for any reasonably well-collimated optical beam will change only rather slowly with distance z along the beam. That is, the effects of both diffraction and atomic gain or loss on the beam profile $\tilde{u}(x, y, z)$ will be fairly slow, at least compared with the variation of one complete cycle in phase that occurs in one optical wavelength λ because of the $\exp(-j2\pi z/\lambda)$ term. Hence we will make the *paraxial approximation* that the z dependence of $\tilde{u}(x, y, z)$ is particularly slow, especially in its second derivative, so that

$$\left| \frac{\partial^2 \tilde{u}}{\partial z^2} \right| \ll \left| 2\beta \frac{\partial \tilde{u}}{\partial z} \right| \equiv \frac{4\pi}{\lambda} \left| \frac{\partial \tilde{u}}{\partial z} \right| \quad (28)$$

and also that

$$\left| \frac{\partial^2 \tilde{u}}{\partial z^2} \right| \ll \left| \frac{\partial^2 \tilde{u}}{\partial x^2} \right|, \quad \left| \frac{\partial^2 \tilde{u}}{\partial y^2} \right|. \quad (29)$$

We will show shortly that these approximations can in fact be very well justified for beams of interest in lasers.

Making these approximations then allows us to drop the $\partial^2 \tilde{u} / \partial z^2$ term in the preceding equation, and thus reduce the wave equation to the so-called paraxial form

$$\nabla_t^2 \tilde{u} - 2j\beta \frac{\partial \tilde{u}}{\partial z} + \beta^2 (\tilde{\chi}_{\text{at}} - j\sigma/\omega\epsilon) \tilde{u} = 0, \quad (30)$$

where the laplacian operator in the transverse plane is denoted by

$$\nabla_t^2 \equiv \frac{\partial^2}{\partial x^2} + \frac{\partial^2}{\partial y^2}. \quad (31)$$

This paraxial form is the desired and widely used *paraxial wave equation*.

Diffraction Effects Versus Propagation Effects

The paraxial wave equation may also be turned around into the equivalent form

$$\frac{\partial \tilde{u}(x, y, z)}{\partial z} = -\frac{j}{2\beta} \nabla_t^2 \tilde{u}(x, y, z) - [\alpha_0 - \alpha_m + j\Delta\beta_m] \tilde{u}(x, y, z), \quad (32)$$

where the loss term α_0 and the atomic susceptibility terms $\alpha_m(\omega)$ and $j\Delta\beta_m(\omega)$ are defined exactly as in Section 7.2. Equation 7.32 neatly separates the axial rate of change of the complex wave amplitude $\tilde{u}(x, y, z)$ into two terms: the $\nabla_t^2 \tilde{u}$ term, which represents *diffraction effects*; and the α_0 , α_m and $j\Delta\beta_m$ terms, which represent *ohmic and atomic gain, loss, and phase shift effects* caused by σ and $\tilde{\chi}_{\text{at}}$.

Since these diffraction and gain or phase-shift effects appear in the differential equation as separate and independent terms for the z variation of the beam profile, we can conclude that the atomic gain and phase-shift effects for a finite laser beam are to first order unaffected by diffraction effects, and are the same as for an infinite plane wave; and also that the diffraction effects on such a beam are to first order unaffected by *spatially uniform* atomic gain or phase-shift effects. Note also that the paraxial results for the gain and phase shift α_m and $\Delta\beta_m$ are exactly the same as the plane-wave results derived by expanding the square-root function for Γ to first order in χ_{at} and in $\sigma/\omega\epsilon$. The paraxial approximation invokes essentially the same physical approximation concerning z -axis propagation as does the Taylor expansion of the square root in Equation 7.18.

Validity of the Paraxial Approximation

A simple analytical example may give somewhat more insight into the validity of the paraxial approximation. Many real laser beams have a gaussian transverse profile of the form

$$|\tilde{u}(x)| = \tilde{u}_0 \exp\left(-\frac{x^2}{w^2(z)}\right), \quad (33)$$

where the gaussian spot size $w = w(z)$ is a slowly varying function of axial distance z . (The complex field will have some similar transverse phase variation or phase curvature as well, but for simplicity let us leave this out of the following discussion.) The transverse derivatives of this beam profile at any fixed plane z are then given by

$$\frac{1}{\tilde{u}} \frac{\partial \tilde{u}}{\partial x} = \frac{2x}{w^2} \quad \text{and} \quad \frac{1}{\tilde{u}} \frac{\partial^2 \tilde{u}}{\partial x^2} = \left(\frac{2}{w^2} - \frac{4x^2}{w^4}\right) \approx \frac{2}{w^2}, \quad (34)$$

where the final approximation is valid both on the optic axis and over most of the main part of the gaussian beam profile.

Suppose now that the gaussian spot size w equals 1 mm (which is a fairly slender beam), at a visible wavelength of $\lambda = 500$ nm. The term that represents diffraction effects in the paraxial wave equation will then have an approximate numerical magnitude

$$\left| \frac{1}{\tilde{u}} \frac{\partial \tilde{u}}{\partial z} \right| \approx -j \left| \frac{1}{\beta \tilde{u}} \frac{\partial^2 \tilde{u}}{\partial x^2} \right| \approx \frac{\lambda}{\pi w^2} \approx 10^{-1} \text{ m}^{-1}. \quad (35)$$

In other words, this small but rather smooth beam will propagate about 10 meters or so before diffraction effects cause any major change in the beam profile $\tilde{u}(x, y, z)$.

Suppose also that the amplitude gain or loss in the axial direction due to the α_m or α_0 terms has an *e*-folding length somewhere between 10 cm and 1 m (which implies a rather large power gain or attenuation, of between 10 and 100 dB/meter). The gain term in the paraxial equation then has a magnitude

$$\left| \frac{1}{\tilde{u}} \frac{\partial \tilde{u}}{\partial z} \right| \approx \alpha_m \approx 1 \text{ to } 10 \text{ m}^{-1}. \quad (36)$$

In this example at least, diffraction spreading occurs somewhat more slowly than amplification.

The normalized first axial derivative $(1/\tilde{u})(\partial\tilde{u}/\partial z)$ that results from either gain or diffraction effects thus occurs at a rate somewhere between 10^{-1} and 10^1 m^{-1} . The second derivative $(1/\tilde{u})(\partial^2\tilde{u}/\partial z^2)$ in the axial direction will then have a magnitude corresponding to (at most) this rate squared, say,

$$\left| \frac{1}{\tilde{u}} \frac{\partial^2 \tilde{u}}{\partial z^2} \right| \approx 10^{-2} \text{ to } 10^2 \text{ m}^{-2}. \quad (37)$$

Therefore the axial derivative contribution produced by this second derivative term, which we dropped in deriving the paraxial equation, if expressed in the same fashion as Equation 7.37, would be about

$$\left| \frac{1}{2\beta\tilde{u}} \frac{\partial^2 \tilde{u}}{\partial z^2} \right| \approx \frac{\lambda}{4\pi} \left| \frac{1}{\tilde{u}} \frac{\partial^2 \tilde{u}}{\partial z^2} \right| \approx 5 \times 10^{-10} \text{ to } 5 \times 10^{-6} \text{ m}^{-1}. \quad (38)$$

The normalized second derivative given in Equation 7.38 is thus many orders of magnitude smaller than the other derivative terms given in Equations 7.35 through 7.37. The basic paraxial approximation is clearly very well-justified in this example, even for a wide range of different axial growth rates.

Problems for 7.3

1. *Applying the paraxial-wave approximation to gaussian beam propagation.* A more accurate form for the gaussian transverse profile in real laser beams is $\mathcal{E}(x, y, z) = A(z) \exp[-jk(x^2 + y^2)/2\tilde{q}(z)] \exp(-j\beta z)$, where $A(z)$ and $\tilde{q}(z)$ are functions of z only, not of x or y . (We will see later that the parameter $\tilde{q}(z)$ is a kind of complex gaussian radius of curvature plus spot size.) Using the paraxial wave equation, including atomic susceptibility and loss terms, find differential equations for $A(z)$ and $\tilde{q}(z)$, and discuss their meaning.

For example, will $\mathcal{E}(x, y, z)$ remain gaussian as the wave propagates? How do $A(z)$ and $\tilde{q}(z)$ change with distance, and why? Note that the factor $A(z)$ might be replaced by $A(z) \equiv \exp a(z)$, or $a(z) \equiv \ln A(z)$, and one could then get a differential equation for $a(z)$ instead.

7.4 SINGLE-PASS LASER AMPLIFICATION

Let us look next at some of the practicalities of single-pass, small-signal amplification for a wave passing through an inverted laser medium

Laser Gain Formulas

If a quasi-plane wave propagates through a length L of laser material, as in Figure 7.7, the complex amplitude gain or “voltage gain” in an inverted laser

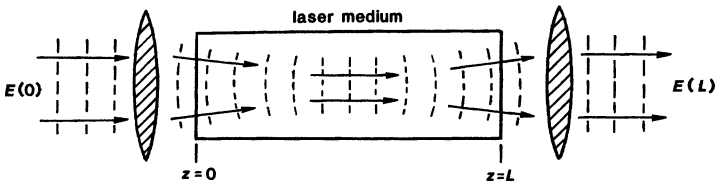


FIGURE 7.7

An elementary single-pass laser amplifier.

medium will be

$$\tilde{g}(\omega) \equiv \frac{\tilde{E}(L)}{\tilde{E}(0)} = \exp \{-j[\beta + \Delta\beta_m(\omega)]L\} \times \exp \{[\alpha_m(\omega) - \alpha_0]L\}. \quad (39)$$

The first exponent on the right-hand side represents the total phase shift through the amplifier, and the second is the amplitude gain or loss.

Because signal power or intensity $I(z)$ is proportional to $|\tilde{E}(z)|^2$, the single-pass power or intensity gain going through the laser medium is

$$G(\omega) \equiv \frac{I(L)}{I(0)} = |\tilde{g}(\omega)|^2 = \exp [2\alpha_m(\omega)L - 2\alpha_0L]. \quad (40)$$

(Note again that in this text symbols like α_m and α_0 will always denote gain coefficients or loss coefficients for the field amplitude or “voltage” of a wave; and hence we will always write 2α for a power gain coefficient. In other books and papers in the literature, the symbol α by itself often means the power gain or loss coefficient.)

In most useful laser materials the ohmic insertion loss coefficient α_0 will be small compared to the laser gain coefficient α_m ; so for simplicity we will leave out the $2\alpha_0L$ loss factor in most of the following equations. Also, for many transitions the laser lineshape will be lorentzian, so that the imaginary part of the susceptibility is given by

$$\chi''(\omega) = \frac{\chi_0''}{1 + [2(\omega - \omega_a)/\Delta\omega_a]^2}, \quad (41)$$

where χ_0'' is the midband value. The power gain $G(\omega)$ then has the frequency lineshape

$$G(\omega) = \exp \left[\frac{\omega L \chi_0''}{c} \times \frac{1}{1 + [2(\omega - \omega_a)/\Delta\omega_a]^2} \right], \quad (42)$$

where c is the velocity of light in the laser medium. Note that in this gain expression, the lorentzian atomic lineshape appears in the exponent. If the atomic lineshape were inhomogeneous and gaussian, then the gaussian lineshape would similarly appear in the exponent.

The quantity $G(\omega)$ is power gain expressed as a number. To convert this to power gain in decibels, or dB, as often used in engineering discussions, we must use the definition that

$$G_{dB}(\omega) \equiv 10 \log_{10} G(\omega) = 4.34 \log_e G(\omega) = \frac{4.34\omega_a L}{c} \chi''(\omega). \quad (43)$$

Therefore the power gain measured in dB has the same lineshape as the atomic susceptibility $\chi''(\omega)$, whether this lineshape is lorentzian, gaussian, or whatever.

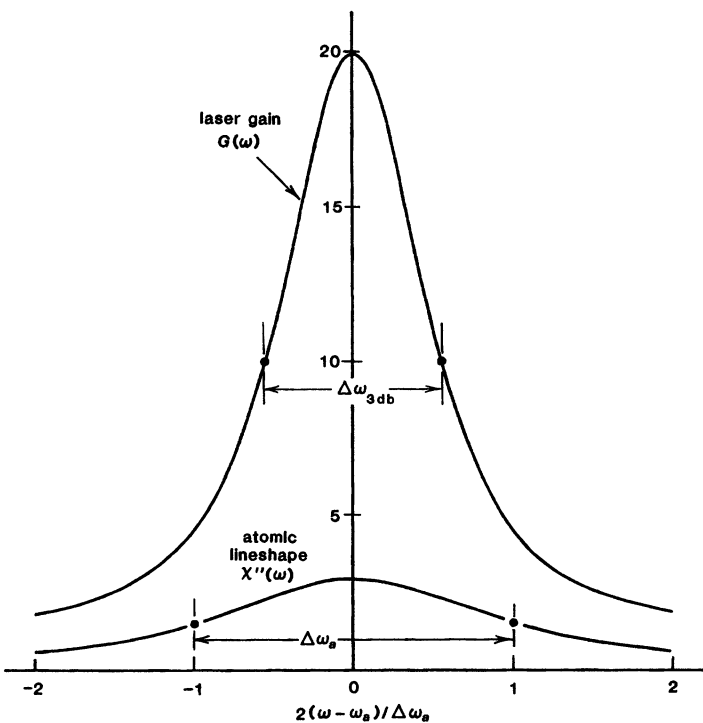


FIGURE 7.8
Gain narrowing in a single-pass laser amplifier.

Amplification Bandwidth and Gain Narrowing

Because the frequency dependence of $\chi''(\omega)$ appears in the exponent of the gain expression, the exponential gain falls off much more rapidly with detuning than the atomic linewidth itself. The bandwidth of a single-pass laser amplifier is thus generally narrower than the atomic linewidth (see Figure 7.8); and this bandwidth narrowing increases (that is, the bandwidth decreases still further) with increasing amplifier gain.

The conventional definition for the bandwidth of any amplifier is the full distance between frequency points at which the amplifier power gain has fallen to half the peak value. This corresponds to “3 dB down” from the peak gain value in dB, if we recall that $10 \log_{10} 0.5 = -3.01$. For a lorentzian atomic line the amplifier 3 dB points are thus defined as those frequencies ω for which

$$G_{dB}(\omega) = \frac{G_{dB}(\omega_a)}{1 + [2(\omega - \omega_a)/\Delta\omega_a]^2} = G_{dB}(\omega_a) - 3 \quad (44)$$

or

$$(\omega - \omega_a)_{3dB} = \pm \frac{\Delta\omega_a}{2} \sqrt{\frac{3}{G_{dB}(\omega_a) - 3}}. \quad (45)$$

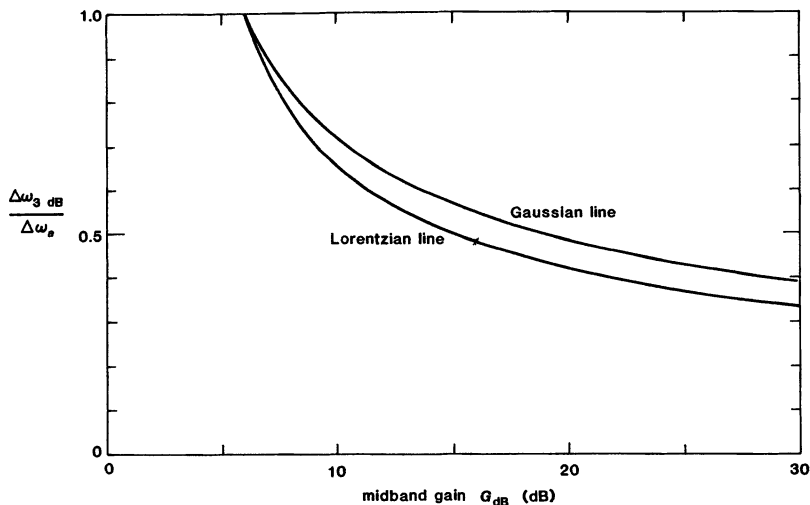


FIGURE 7.9
Reduction of amplifier bandwidth compared to atomic linewidth for single-pass amplifiers using gaussian and lorentzian atomic lines.

The full 3-dB amplifier bandwidth between these points is then twice this value or

$$\Delta\omega_{3dB} = \Delta\omega_a \sqrt{\frac{3}{G_{dB}(\omega_a) - 3}}. \quad (46)$$

Figure 7.9 plots this amplifier bandwidth, normalized to the atomic linewidth, as a function of the midband gain $G_{dB}(\omega_a)$ for both lorentzian and gaussian atomic lineshapes.

The 3-dB amplification bandwidth is substantially smaller than the atomic linewidth, dropping to only 30% to 40% of the atomic linewidth at higher gains. This so-called *gain narrowing* at higher gains is significant in reducing the useful bandwidth of a high-gain laser amplifier.

Amplifier Phase Shift

The total phase shift for a single pass through a laser amplifier can be written as $\exp[-j(\beta + \Delta\beta_m)L] \equiv \exp[-j\phi_{tot}(\omega)]$, where the total phase shift $\phi_{tot}(\omega)$ is given by

$$\phi_{tot}(\omega) \equiv \beta(\omega)L + \Delta\beta_m(\omega)L = \frac{\omega L}{c} + \frac{\beta L}{2}\chi'(\omega). \quad (47)$$

The first term gives the basic “free-space” phase shift $\beta(\omega)L = \omega L/c = 2\pi L/\lambda$ through the laser medium. This term is large and increases linearly with increasing frequency. The second term is then the small added shift $\Delta\beta_m(\omega)L$ due to the atomic transition, as illustrated earlier in Figure 7.3.

Note that the magnitude of the added phase shift through a laser amplifier or absorber is directly proportional to the net gain or attenuation through the same atomic medium. For a lorentzian atomic transition we can in fact relate the added phase shift in radians to the amplitude gain (or loss) factor $\alpha_m L$ (the value of which is often said to be measured in units of *nepers*) by the relation

$$\begin{aligned}\Delta\beta_m(\omega)L &= \left(2\frac{\omega - \omega_a}{\Delta\omega_a}\right) \times \alpha_m(\omega)L \\ &= \frac{G_{\text{dB}}(\omega_a)}{20\log_{10}e} \times \frac{2(\omega - \omega_a)/\Delta\omega_a}{1 + [2(\omega - \omega_a)/\Delta\omega_a]^2}.\end{aligned}\quad (48)$$

In practical terms, the peak value of the added phase shift $\Delta\beta_m L$ occurs at half a linewidth, or $\pm\Delta\omega_a/2$, off line center on each side; and the added phase shift in radians at these peaks is related to the midband gain in dB by $(\Delta\beta_m L)_{\text{max}} = G_{\text{dB}}/40\log_{10}e \approx G_{\text{dB}}/17.4$.

Absorbing Media

The results just discussed are for an amplifying laser medium. The same formulas and physical ideas apply equally well to an absorbing (uninverted) atomic transition, however, if we simply reverse the sign of $\tilde{\chi}_{\text{at}}(\omega)$ and hence of both $\alpha_m(\omega)$ and $\Delta\beta_m(\omega)$. Figure 7.10 plots, for example, the power transmission $T(\omega) = \exp[-2\alpha_m(\omega)L]$ versus frequency through a material with a lorentzian absorbing atomic transition. [In this terminology the power transmission $T(\omega)$ is the same as the power gain $G(\omega)$, but with a magnitude less than unity, not greater than unity.] Note that for very strong absorption the transmission curve “touches bottom” and then broadens with increased absorption strength. An absorbing transition thus has “absorber broadening” rather than the “gain narrowing” discussed earlier (see Problems).

REFERENCES

A very useful even if rather early work is E. U. Condon and G. H. Shortley, *The Theory of Atomic Spectra* (Cambridge University Press, 1935; reprinted 1963).

An early but still quite clear and detailed discussion of a laser amplifier experiment (using a ruby laser rod) is given by J. E. Geusic and E. O. Schulz-DuBois, “A unidirectional traveling-wave optical maser,” *Bell Sys. Tech. J.* **41**, 1371–1397 (July 1962). An early analysis of bandwidth narrowing in a doppler-broadened laser, including saturation effects, is D. F. Hotz, “Gain narrowing in a laser amplifier,” *Appl. Opt.* **34**, 527–530 (May 1965).

An interesting experimental verification of strong phase-shift effects in a high-gain, narrow-line laser amplifier can be found in C. S. Liu, B. E. Cherrington, and J. T. Verheyen, “Dispersion effects in a high-gain 3.39 μm He-Ne laser,” *J. Appl. Phys.* **40**, 3556 (August 1969).

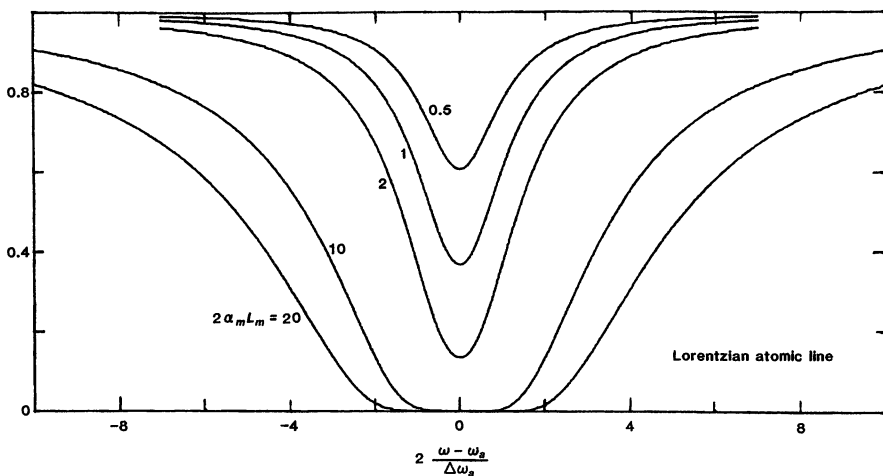


FIGURE 7.10

Power transmission versus frequency through an absorbing medium with a lorentzian atomic lineshape, for increasing degrees of midband absorption. (Adapted from E. U. Condon and G. H. Shortley, *The Theory of Atomic Spectra*, Cambridge Univ. Press, 1935, p. 111.)

Problems for 7.4

1. *Amplification bandwidth for a gaussian atomic transition.* Derive an analytic expression for the 3-dB bandwidth $\Delta\omega_{3dB}$ of a single-pass laser amplifier which has a gaussian rather than a lorentzian linewidth, as plotted in this section.
2. *Absorption linewidth for an absorbing atomic transition.* Consider the curves of power transmission $T(\omega) = \exp[-2\alpha_m(\omega)L]$ through an atomic medium with a lorentzian resonant transition, plotted versus normalized frequency detuning $(\omega - \omega_a)/\Delta\omega_a$ for various values of the midband absorption factor $2\alpha_m(\omega_a)L$, as shown in this section. Suppose an “absorption linewidth” $\Delta\omega_{abs}$ is defined as the full width of the power transmission profile $T(\omega)$ at a level halfway down into the dip, i.e., halfway between the midband value $T(\omega_a)$ and the far-off-resonance value $T = 1$. Derive an expression for this linewidth $\Delta\omega_{abs}$ as a function of the midband absorption $2\alpha_m(\omega_a)L$, and examine its limiting values for very small and very large absorptions.
3. *An alternative bandwidth definition for low-gain amplifiers.* The conventional definition of the 3-dB linewidth as discussed in the text ceases to have meaning for a laser amplifier whose peak gain is less than 3 dB, i.e., when $G(\omega_a) < 2$. Extend the linewidth calculation of the previous problem to the amplifying case (i.e., change the sign of $2\alpha_m L$), and compare the amplifier linewidth calculated in this way to the definition of 3 dB given in the text, assuming the atomic line has a lorentzian lineshape.

4. *Testing for a gaussian atomic lineshape.* How might you plot experimental data on the single-pass gain $G(\omega)$ of a laser amplifier versus frequency detuning $\omega - \omega_a$ to see immediately if the atomic lineshape of the amplifying medium is gaussian?
5. *Gain versus frequency for a cascaded amplifier plus absorber.* A tunable optical signal is passed through a linear single-pass laser amplifier having midband gain coefficient $\alpha_1 L$ and lorentzian atomic linewidth $\Delta\omega_{a1}$, followed by a linear single-pass laser absorber—that is, a collection of absorbing atoms—having midband absorption coefficient $\alpha_2 L$ and atomic linewidth $\Delta\omega_{a2}$, with both transitions centered at the same resonance frequency and with $\alpha_1 > \alpha_2$. What condition on the relative atomic linewidths $\Delta\omega_{a1}$ and $\Delta\omega_{a2}$ will just lead to a double-humped rather than single-humped curve of overall power gain versus frequency for the two atomic systems in cascade? (Hint: You can solve this problem by differentiating the power-transmission expression a couple of times, but there's an easier approach also.)
6. *Continuation of the previous problem: general evaluation of passband broadening in a laser amplifier.* Consider the approach outlined in Problem 5 in more detail, as a possible method of broadening the amplification bandwidth of a single-pass laser amplifier. Give a short analysis and summary of the passband broadening that might be obtained, what this costs in midband gain reduction and in gain variation across the passband, and what conditions on the absorber are required in some typical cases. Note: The allowable gain variation between the two peaks and the midband value in a practical amplifier depends on the application for which the amplifier is to be used; but usually cannot exceed somewhere between 1 dB and 3 dB of peak-to-peak ripple.
7. *Continuation of the previous problem: relationship between midband gain and phase shift derivatives?* In Problem 6, what relationship if any is there between having a maximally flat gain profile at line center and the slope of the phase variation $\Delta\beta_m(\omega)L$ versus ω at line center (where $\Delta\beta_m$ includes both the amplifier and absorber phase-shift contributions)?
8. *“Linewidth modulation spectroscopy”: a new experimental technique.* A low-frequency pressure modulation or mechanical squeezing, when applied to certain organic host crystals, will modulate the atomic linewidth $\Delta\omega_a$ of an absorbing transition in the organic crystal by a small amount about its average value, without changing any other parameters of the transition. Suppose we modulate the linewidth $\Delta\omega_a$ in this fashion by a very small amount at some low modulation frequency, perhaps in the audio range, and then measure the resulting ac modulation of the transmitted intensity of an optical signal transmitted through the absorbing medium, while we slowly scan the optical frequency ω of the signal across the absorption line. The resulting ac signal in the detector will be proportional to the first derivative $d\chi''/d\Delta\omega_a$ at each frequency ω across the absorption profile. (This general type of technique, in which we slowly scan the optical measuring frequency ω across a line, while modulating some parameter of the line at a low modulation frequency and measuring the resulting ac output, is often called *modulation spectroscopy*.)

Derive and plot the lineshape that we will see for the magnitude and phase of this low-frequency modulation signal versus the optical frequency ω , and give a brief physical explanation for its form.

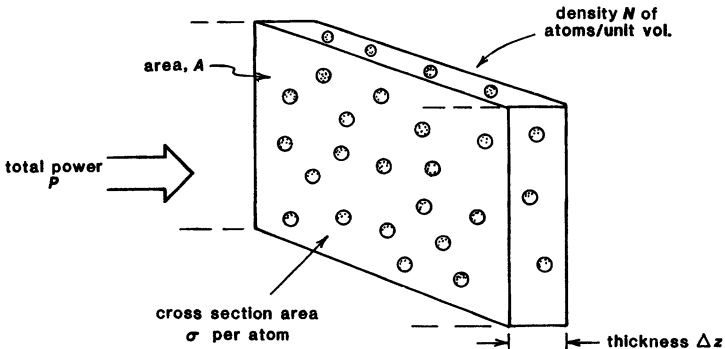


FIGURE 7.11

A collection of atoms with small but finite absorption cross sections distributed throughout a thin slab.

7.5 STIMULATED-TRANSITION CROSS SECTIONS

A very useful concept which we will next introduce for describing both stimulated transitions in absorbing atoms and laser amplification in laser media is the *stimulated-transition cross section* of a laser atom. If you have encountered the idea of a cross section previously in some other connection, you will find this concept straightforward; if not, you may have to pay close attention at first.

Absorption and Emission Cross Sections

Suppose a small black (i.e., totally absorbing) particle with a capture area or "cross section" σ is illuminated by an optical wave having intensity or power per unit area $I \equiv P/A$. The net power ΔP_{abs} absorbed by this object from the wave will then be its capture area or cross section σ times the incident power per unit area in the wave, or

$$\Delta P_{\text{abs}} = \sigma \times (P/A) = \sigma I. \quad (49)$$

(In this text we attempt to always use P to represent total power in watts, and I to represent intensity in watts per unit area. When given in conversation or in texts, values for laser beam intensities are almost universally expressed in dimensions of watts/cm², although the correct mks unit for substitution into formulas is watts/m².)

Consider next a thin slab of thickness Δz and transverse area A , as in Figure 7.11, containing densities N_1 and N_2 of atoms in the lower and upper energy levels of some atomic transition. Suppose we say that each lower-level atom has an effective area or cross section σ_{12} for power absorption from the wave, and similarly each upper-level atom has an effective cross section σ_{21} for "negative absorption" or emission back to the wave (since upper-level atoms must emit power rather than absorb it).

The total number of lower-level atoms in this slab will then be $N_1 A \Delta z$, and the total absorbing area that results from all the lower-level atoms will be the total number of atoms times the cross section per atom, or $N_1 \sigma_{12} A \Delta z$. (We

assume the slab is thin enough and the atoms small enough that shadowing of any one atom by other atoms is negligible.) Similarly, the total effective “emitting area” that results from all the upper-level atoms will be $N_2\sigma_{21}A\Delta z$. The net power absorbed by the atoms in the slab from an incident wave carrying a total power P distributed over the area A will then be

$$\Delta P_{\text{abs}} = (N_1\sigma_{12} - N_2\sigma_{21}) \times P \Delta z. \quad (50)$$

Note that the area factors in the slab volume $A\Delta z$ and in the power density P/A just cancel.

The quantities σ_{12} and σ_{21} that we have introduced here are the *stimulated-transition cross sections* of the atoms on the $1 \rightarrow 2$ transition, with σ_{12} being the *stimulated-absorption cross section* and σ_{21} the *stimulated emission cross section*. These cross sections, which have dimensions of area per atom, provide a very useful way of expressing the strength of an atomic transition, or the size of the atomic response to an applied signal.

Cross Sections and Amplification Coefficients

The net growth or decay with distance caused by an atomic transition for a wave carrying power P or intensity I through an atomic medium can then be written as

$$\frac{dP}{dz} = - \lim_{\Delta z \rightarrow 0} \left(\frac{\Delta P_{\text{abs}}}{\Delta z} \right) = - (N_1\sigma_{12} - N_2\sigma_{21}) \times P. \quad (51)$$

The relationship between upward and downward cross sections on a possibly degenerate transition is in fact given by $g_1\sigma_{12} = g_2\sigma_{21}$, and so the preceding equation, if converted into units of intensity $I(z)$ and population difference ΔN , can be written as

$$\frac{1}{I} \frac{dI}{dz} = -\Delta N_{12}\sigma_{21} = -[(g_2/g_1)N_1 - N_2]\sigma_{21}, \quad (52)$$

where $\Delta N_{12} = (g_2/g_1)N_1 - N_2$ as usual.

But the growth or decay rate for a wave passing through an absorbing or amplifying atomic medium may also be written as $I(z) = I(z_0) \exp[-2\alpha_m(z - z_0)]$, which corresponds to the differential relation

$$\frac{1}{I} \frac{dI}{dz} = -2\alpha_m(\omega). \quad (53)$$

Hence we obtain the simple but very useful expression for the absorption (or amplification) coefficient α_m on the $1 \rightarrow 2$ transition in terms of only the population difference and cross section, namely,

$$2\alpha_m(\omega) = \Delta N_{12}\sigma_{21}(\omega). \quad (54)$$

To specify the loss or gain per unit length on an atomic transition, all we need to know is the atomic density and the transition cross section. Note that the absorption coefficient $\alpha_m(\omega)$ and the cross section $\sigma_{21}(\omega)$ must necessarily have the same dependence on the atomic lineshape; i.e., there is an atomic lineshape contained in $\sigma_{21}(\omega)$, although usually only the numerical value at midband is stated as so many cm^{-2} .

In practice the gain coefficient $2\alpha_m$ is commonly expressed in cm^{-1} , the density N in atoms/ cm^3 , and the cross section σ in cm^2/atom , which makes Equation 7.54 dimensionally consistent even without use of mks units. Both ΔN and α_m will, of course, change sign on an inverted laser transition.

Formula for the Cross Section

One way to obtain a theoretical expression for the cross section σ of a transition is to combine Equation 7.54 with the gain formula 7.23 to obtain

$$\begin{aligned} 2\alpha_m(\omega) &= \Delta N \sigma(\omega) = \frac{2\pi}{\lambda} \chi''(\omega) \\ &= \frac{3^*}{2\pi\lambda} \frac{\Delta N \lambda^3 \gamma_{\text{rad}}}{\Delta\omega_a} \times \frac{1}{1 + [2(\omega - \omega_a)/\Delta\omega_a]^2}. \end{aligned} \quad (55)$$

The population difference ΔN can then be canceled from both sides to give the midband result

$$\sigma(\omega_a) = \frac{3^*}{2\pi} \frac{\gamma_{\text{rad}}}{\Delta\omega_a} \lambda^2. \quad (56)$$

The more general form of the cross-section expression for an arbitrary $i \rightarrow j$ transition, including degeneracy, is

$$\sigma_{ji}(\omega_a) = \frac{g_i}{g_j} \sigma_{ij}(\omega_a) = \frac{3^*}{2\pi} \frac{\gamma_{\text{rad},ji}}{\Delta\omega_a} \lambda^2. \quad (57)$$

These expressions give the midband value of the stimulated-emission cross section for a lorentzian atomic transition. For a gaussian transition, we must replace $\Delta\omega_a$ by $\Delta\omega_d$ and put an additional numerical factor of $\sqrt{\pi \ln 2} \approx 1.48$ in front. Note again that the degeneracy factors appear in such a way that the expression $N_i \sigma_{ij} - N_j \sigma_{ji}$ converts neatly into the form $\Delta N_{ij} \sigma_{ji}$, where we use the degenerate form of the population difference $\Delta N_{ij} = (g_i/g_j)N_i - N_j$ as defined earlier, and where σ_{ji} is the cross section in the downward direction.

The effective cross section $\sigma_{21}(\omega)$ then decreases off line center with precisely the same lineshape as the absorption susceptibility $\chi''(\omega)$ or the stimulated-transition probability $W_{21}(\omega)$. That is, we may have either the lorentzian expression

$$\sigma(\text{lorentzian}) = \frac{3^*}{2\pi} \frac{\gamma_{\text{rad}} \lambda^2}{\Delta\omega_a} \frac{1}{1 + [2(\omega - \omega_a)/\Delta\omega_a]^2} \quad (58)$$

or the gaussian expression

$$\sigma(\text{gaussian}) = \sqrt{\pi \ln 2} \frac{3^*}{2\pi} \frac{\gamma_{\text{rad}} \lambda^2}{\Delta\omega_d} \exp \left[-(4 \ln 2) \left(\frac{\omega - \omega_a}{\Delta\omega_d} \right)^2 \right] \quad (59)$$

corresponding to the homogeneous or inhomogeneous limiting cases.

Maximum Value of the Transition Cross Section

The stimulated-emission (or absorption) cross section provides a convenient and useful way to express the apparent “size” of an atom for interacting with an optical wave, as well as a convenient way to calculate the expected gain in laser systems. Let us look first at the maximum possible value that any such cross section can have. The cross section will be maximal for a transition that has purely radiative lifetime broadening only, and no other line-broadening effects, so that $\Delta\omega_a \equiv \gamma_{\text{rad}}$. If the atoms all have their transition axes aligned and the incident fields are optimally polarized, so that $3^* \equiv 3$, the cross section is then

$$\sigma_{\text{max}} = \frac{3\lambda^2}{2\pi} \approx \frac{\lambda^2}{2}. \quad (60)$$

This says that the maximum cross section is roughly one wavelength square. For a visible transition this means

$$\sigma_{\text{max}} \approx 0.5 \times (5000 \text{\AA})^2 \approx 10^{-9} \text{ cm}^2. \quad (61)$$

Now, the actual physical size of an atom, as measured, say, by the radius of its outermost Bohr orbit, is only a few Ångstroms; yet its effective cross section for capturing radiation can be thousands of Ångstroms in diameter. The physical explanation for this is essentially that the atom has an internal resonance which makes it act like a miniature dipole radio antenna, whose effective cross section for receiving radio or optical waves can be very much larger than the physical dimensions of the antenna, or the atom, by itself.

Real Atomic Cross Sections

For more realistic atoms with realistic line-broadening effects and random orientations ($3^* = 1$), the effective cross section at midband is given by values more like

$$\sigma(\text{lorentzian}) \approx \frac{\lambda^2}{2\pi} \frac{\gamma_{\text{rad}}}{\Delta\omega_a} \quad (62)$$

or by

$$\sigma(\text{gaussian}) \approx \frac{\lambda^2}{4} \frac{\gamma_{\text{rad}}}{\Delta\omega_d}. \quad (63)$$

Note that the wavelength λ in these expressions is, as always, the wavelength *in the laser medium*. Table 7.1 gives some typical cross-section values for a few of the more useful laser transitions.

TABLE 7.1
Typical Laser Transition Cross Sections

Laser system	Transition cross section σ
Gas lasers in the visible and near IR	10^{-11} to 10^{-13}cm^2
Low-pressure CO ₂ laser (10.6 μm)	$3 \times 10^{-18}\text{cm}^2$
Organic dye laser (Rhodamine 6G)	1 to $2 \times 10^{-16}\text{cm}^2$
Nd ³⁺ ion in Nd:YAG	$4.6 \times 10^{-19}\text{cm}^2$
Nd ³⁺ ion in Nd:glass	$3 \times 10^{-20}\text{cm}^2$
Cr ³⁺ ion in ruby	$2 \times 10^{-20}\text{cm}^2$

For example, on a strong but doppler-broadened visible laser transition in a gas with oscillator strength $\mathcal{F} \approx 1$, a radiative decay rate $\gamma_{\text{rad}} \approx 10^8 \text{ s}^{-1}$, and a doppler linewidth $\Delta\omega_d/2\pi \approx 2 \times 10^9 \text{ Hz}$, the cross section will be $\sigma \approx 5 \times 10^{-12} \text{ cm}^2$. Experimentally this would be regarded as a very large cross section; the oscillator strengths and cross sections for transitions in real single atoms in gases are typically one to three orders of magnitude smaller.

Visible and near IR laser transitions in solid-state laser materials have much smaller cross sections, in the range $\sigma = 10^{-18}$ to 10^{-20} cm^2 . For a typical rare-earth laser transition in a solid, the wavelength might be $\lambda = \lambda_0/n \approx 0.6 \mu\text{m}$; the radiative decay rate might be 500 sec^{-1} ; and the linewidth might be 4 cm^{-1} or $\Delta\omega_a \approx 2\pi \times 4 \times 30 \text{ GHz}$. The resulting cross section will be $\sigma \approx 4 \times 10^{-19} \text{ cm}^2$. Visible transitions in the organic molecules used as laser dyes have very wide linewidths, but also very strong radiative decay rates, with oscillator strengths close to unity. This leads to considerably larger cross sections, in the range of $\sigma \approx 1$ to $5 \times 10^{-16} \text{ cm}^2$.

Transition Strength

The cross section σ is a measure of the strength of an atomic transition, as modified by the line-broadening effects of whichever linewidth mechanism $\Delta\omega_a$ or $\Delta\omega_d$ is dominant in determining the linewidth of the atomic response. If the cross section as a function of frequency is integrated across the entire linewidth, however, we obtain a so-called *transition strength* given by

$$S \equiv \int \sigma(\omega) d\omega = \frac{3^* \gamma_{\text{rad}} \lambda^2}{4}, \quad (64)$$

which is the direct measure of the strength of the transition and is entirely independent of the lineshape of $\sigma(\omega)$, whether it be lorentzian, gaussian, or

otherwise. With degeneracy factors included this expression becomes

$$\int \sigma_{ji}(\omega) d\omega = \frac{g_i}{g_j} \int \sigma_{ij}(\omega) d\omega = \frac{3^* \gamma_{\text{rad},ji} \lambda^2}{4}, \quad (65)$$

where j is the upper and i the lower level. Measuring (carefully) the integrated absorption or cross section across the full linewidth of an atomic transition is thus one practical way of determining the radiative decay rate or Einstein A coefficient for that transition. Calculated or measured values of the integrated line strengths for different transitions are often given in handbooks and tables of atomic properties.

Problems for 7.5

1. *Practical expression for atomic oscillator strength.* Develop a general formula for the cross section of a gaussian atomic transition in the form $\sigma = K\mathcal{F}/\Delta\nu$, where K is a numerical constant (which you should evaluate); \mathcal{F} is the oscillator strength of the atomic transition; and $\Delta\nu$ is the doppler linewidth of the transition expressed in units of wavenumbers or cm^{-1} .
2. *Design considerations for a high-energy-storage laser medium.* Laser designers often face the following problem. Suppose you want to build a large high-energy single-pass amplifier for laser pulses. To accomplish this you must pump the laser medium up to an inverted condition, which takes a substantial pumping time; and then “dump” this inversion into the amplified pulse in a very short time. In the inverted condition you want to have the gain coefficient fairly low, to avoid parasitic oscillations in the large inverted volume; and yet you must have a large stored energy density in the laser medium to get large energy output. If you were evaluating different laser media for this application, what specific characteristics (cross section, lifetime, etc.) of the laser atomic transition would you look for? Outline briefly the reasoning behind your choice of specifications.
3. *Measuring an inverted laser transition cross section.* Measuring the cross section σ of an inverted laser transition by simply measuring the small-signal power gain $G = \exp(N\sigma L)$ is not straightforward, because of the difficulty of measuring in any direct way the inverted population difference N . One practical way of bypassing this problem is to measure the gain for a weak signal pulse of total energy U passing through the amplifier, while monitoring the sidelight fluorescence intensity I from the inverted laser atoms. The signal pulse is made powerful enough to cause a small but observable change ΔI in the fluorescence intensity from just before to just after the pulse passes; i.e., the pulse causes a small change in the inverted population N , but not enough to represent any significant gain saturation.

We then measure the pulse energy gain G in the amplifier; the net energy ΔU acquired by the laser pulse; and the fractional change $\Delta I/I$ in the sidelight fluorescence (which does not require any absolute calibration of the fluorescent intensity). Show that the cross section for the laser transition is then given by $\sigma = (\hbar\nu/\Delta U)(\Delta I/I) \ln G$, and discuss why this can be a practical method for a real measurement using available apparatus. (See B. S. Guba et al., “Measurement of cross section for induced transitions in neodymium glasses,” *Opt. and Spectrosc.* **47**, 67–69, July 1979.)

4. *Energy storage in a Nd:YAG rod.* A Nd:YAG laser rod 6.4 mm diameter by 75 mm long is to be pumped to have a maximum one-way power gain of 20. How many joules of laser energy can this rod potentially deliver in a single short pulse (no repumping during the pulse)? [Hint: You know the transition cross section for this material].
 5. *Gain through a thin atomic layer near a mirror.* A very thin layer of inverted laser atoms is located half an optical wavelength in front of a perfectly conducting metal mirror. The layer has N atoms per unit cross-sectional area, and each atom has a stimulated-emission cross section σ . A signal wave is incident perpendicular to the atoms and the mirror. What will be the net gain of the wave after double-passing the thin layer?
-

7.6 SATURATION INTENSITIES IN LASER MATERIALS

The amplification coefficient for a signal wave passing through a laser amplifier is proportional to the population difference on the amplifying transition. At the same time, however, for a strong enough input signal the stimulated transition rate may become large enough to saturate the population difference, and thus reduce the gain coefficient seen by the signal. This process is commonly referred to as *saturation of the gain* (or absorption) coefficient by the applied signal.

Saturation behavior in a laser amplifier (or for that matter an atomic absorber) can be expected therefore whenever the signal strength becomes strong enough for the signal itself to reduce the signal growth or attenuation rate. Understanding this kind of saturation behavior, which is very important in determining the performance of practical laser systems, is our objective here.

Saturation of the Population Difference

A wave traveling through an atomic medium will grow or decay in intensity with distance through the medium according to the differential formula

$$\frac{dI}{dz} = \pm 2\alpha_m I = \pm \Delta N \sigma I, \quad (66)$$

where σ is the stimulated-transition cross section and the \pm signs apply to inverted or absorbing population differences. We have also shown that the population difference ΔN , whether emitting or absorbing, will often saturate with increasing signal strength in the homogeneous form

$$\Delta N = \Delta N_0 \times \frac{1}{1 + W\tau_{\text{eff}}} = \Delta N_0 \times \frac{1}{1 + I/I_{\text{sat}}}, \quad (67)$$

where ΔN_0 is an unsaturated or small-signal inversion value; τ_{eff} is an effective lifetime or recovery time for the transition; and I_{sat} is the *saturation intensity*, or the value of signal intensity passing through the laser medium that will saturate the gain (or loss) coefficient down to half its small-signal or unsaturated value.

The saturation intensity is thus a parameter of great importance in practical laser materials; and our first task in this section is to derive a simple formula and some typical values for this quantity. (Note also that in writing the $W\tau_{\text{eff}}$ term

we have omitted the factor of 2 that appears in the $1 + 2WT_1$ denominator for the ideal two-level case, because the condition that $N_1 + N_2 = \text{constant}$ does not apply on most laser transitions as it does for a simple ideal two-level system.)

The Stimulated-Transition Probability

Obviously, the stimulated-transition probability W must be directly proportional to the signal intensity (power per unit area) I inside the laser medium, with a proportionality factor that can be obtained by the following argument. The net power absorbed by the atoms in a thin slab of thickness Δz from an incident wave carrying total power P uniformly distributed over a transverse area A will be

$$\Delta P_{\text{abs}} = (N_1\sigma_{12} - N_2\sigma_{21}) P \Delta z. \quad (68)$$

(Note that N_1 and N_2 are, as usual, atoms per unit volume, and that the area factors in the slab volume $A \Delta z$ and the power density P/A just cancel.) But from a rate-equation analysis the net power absorption by the atoms in the same slab can also be written as

$$\Delta P_{\text{abs}} = (W_{12}N_1 - W_{21}N_2) A \Delta z \hbar\omega_a, \quad (69)$$

where the energy per photon $\hbar\omega$ must be included to convert the net stimulated transition rate in atoms/second into a net power-absorption rate.

Equating these two expressions, including possible degeneracy factors, then gives the relation

$$W_{21} = \frac{g_1}{g_2} W_{12} = \frac{\sigma_{21}}{\hbar\omega} \frac{P}{A} = \frac{\sigma_{21}}{\hbar\omega} \times I \quad (70)$$

or in simple terms

$$W \equiv \frac{\sigma I}{\hbar\omega}. \quad (71)$$

This is a very useful and general relation which connects the cross section σ , intensity I , and stimulated transition probability W . For degenerate transitions the upward and downward stimulated transition cross sections must obey the same relationship $g_1\sigma_{12} = g_2\sigma_{21}$ as do the stimulated-transition probabilities $g_1W_{12} = g_2W_{21}$.

Saturation Intensity Derivation

The gain or absorption coefficient $2\alpha_m$ for a homogeneous atomic transition will thus commonly saturate with increasing signal intensity in the form

$$2\alpha_m = \frac{2\alpha_{m0}}{1 + I/I_{\text{sat}}} = \frac{\Delta N_0 \sigma}{1 + (\sigma\tau_{\text{eff}}/\hbar\omega) I}. \quad (72)$$

The *saturation intensity* that reduces the small-signal absorption coefficient $2\alpha_{m0} \equiv \Delta N_0 \sigma$ down to half its small-signal value is thus given by

$$I = I_{\text{sat}} \equiv \frac{\hbar\omega}{\sigma\tau_{\text{eff}}}. \quad (73)$$

From this formula, the saturation intensity is inversely proportional to the transition cross section σ ; that is, the larger the cross section, the easier the transition is to saturate. The saturation intensity is also inversely proportional to the recovery time τ_{eff} , because the longer the recovery time (the slower the recovery rate), the easier the transition is to saturate. In fact, an intensity $I = I_{\text{sat}}$ basically means one photon incident on each atom, within its cross section σ , per recovery time τ_{eff} .

Of course, if the signal being applied to either an amplifying or an absorbing atomic transition is tuned off line center, the stimulated transition rate and hence the degree of saturation produced by that signal will decrease in proportion to the atomic lineshape, since for a given intensity I the applied signal will be less effective in inducing transitions and thus causing saturation. Suppose the transition has a homogeneous lorentzian lineshape, and suppose we use the normalized variable $y = 2(\omega - \omega_a)/\Delta\omega$ as a shorthand for the frequency detuning. The effective saturation of the atomic gain or loss coefficient α_m by a signal of intensity I applied off line center will then be given by

$$2\alpha_m(\omega, I) = \frac{2\alpha_{m0}(\omega)}{1 + (I/I_{\text{sat}}) \times \frac{1}{1 + y^2}}, \quad (74)$$

where I_{sat} is the saturation intensity appropriate to a signal at midband. (Note that α_{m0} here indicates the unsaturated or small-signal gain, not the midband gain.)

We must then take this frequency dependence into account either by retaining the explicit frequency dependence $1/(1 + y^2)$ in this formula in all further calculations, or by assuming that the saturation intensity itself becomes frequency dependent, with the effective saturation intensity for an off-resonance signal increasing by the amount

$$I_{\text{sat}}(\omega) = I_{\text{sat}}(\omega_a) \times \left[1 + \left(2 \frac{\omega - \omega_a}{\Delta\omega_a} \right)^2 \right]. \quad (75)$$

The effective saturation intensity goes up off line center, because the applied signal fields are less effective in inducing transitions; so a larger signal intensity is needed to produce a given amount of saturation. The most common procedure is to give a number for the midband-saturation intensity value, and then to include the frequency dependence explicitly in Equation 7.74.

Saturation Broadening or Power Broadening

Suppose we tune a signal of fixed intensity I across an absorption line or a gain profile, and measure the saturated loss or gain coefficient $\alpha_m(\omega, I)$ versus ω using this fixed-intensity signal. Then the complete frequency dependence for the gain coefficient (or the absorption coefficient) on a homogeneous atomic transition will include both the real lorentzian lineshape or frequency dependence of the atomic response itself, which will have the form $1/(1 + y^2)$, and the frequency dependence of the saturation behavior, which we have given in Equation 7.74. Suppose we include both of these frequency dependences explicitly in the gain coefficient $\alpha_m(\omega, I)$. We can then rewrite Equation 7.74 in terms of the midband

gain coefficient and saturation intensity, with the explicit frequency dependences

$$\begin{aligned} 2\alpha_m(\omega, I) &= \frac{2\alpha_{m0}(\omega_a)}{1+y^2} \times \frac{1}{1+(I/I_{\text{sat}})(1/1+y^2)} \\ &= \frac{2\alpha_{m0}(\omega_a)}{1+I/I_{\text{sat}}+y^2}. \end{aligned} \quad (76)$$

This can then be further rewritten in the equivalent form

$$2\alpha_m(\omega, I) = \frac{2\alpha_{m0}(\omega_a)}{1+I/I_{\text{sat}}} \times \frac{1}{1+[2(\omega-\omega_a)/\Delta\omega_b]^2}, \quad (77)$$

where $\Delta\omega_b$ is a power-broadened or saturation-broadened linewidth given by

$$\Delta\omega_b \equiv \sqrt{1+I/I_{\text{sat}}} \times \Delta\omega_a. \quad (78)$$

That is, the measured lineshape for $\alpha_m(\omega, I)$ will still be lorentzian, but it will now appear to have a broadened linewidth given by $\Delta\omega_b$ rather than $\Delta\omega_a$. Note that the homogeneous linewidth of the transition has not really been broadened in any fundamentally new way; but the absorption lineshape measured by means of a tunable signal of fixed intensity I appears to be broadened because of stronger saturation and hence flattening down of the gain or loss coefficient at the middle of the line. This type of power broadening of the atomic response appears in other laser situations as well.

Numerical Values for Saturation Intensities

This saturation intensity, measured in watts per unit area, is very important in determining the large-signal saturation behavior of laser amplifiers and oscillators, as well as saturable absorbers. A laser amplifier will become saturated and give little or no additional gain when the signal intensity passing through the laser material becomes of the order of the saturation intensity. Similarly, the power level in a laser oscillator, at least under steady-state conditions, is going to build up to at most a few times the saturation intensity, at which point the gain in the laser medium will be saturated down to equal the losses in the laser cavity. The saturation intensity is thus a very important measure of the amount of power per unit cross-sectional area that can be extracted from a practical laser device.

In practical terms a visible gas-laser transition might have, very approximately, $\hbar\omega \approx 10^{-19}$ J, $\sigma \approx 10^{-13}$ cm², $\tau_{\text{eff}} \approx 10^{-6}$ s, and hence $I_{\text{sat}} \approx 1$ W/cm². The oscillation power outputs from visible cw gas lasers do typically range from milliwatts to perhaps a few watts at most. A solid-state laser, on the other hand, might have $\sigma \approx 10^{-19}$ cm², $\tau_{\text{eff}} \approx 10^{-3}$ sec, and hence $I_{\text{sat}} \approx 1$ kW/cm². A good cw Nd:YAG laser oscillator with an area $A \approx 0.3$ cm² can have a cw power output of a few hundred watts. Note that a typical liquid-dye laser might have $\sigma \approx 10^{-16}$ cm², and $\tau_{\text{eff}} \approx 10^{-9}$ sec, giving $I_{\text{sat}} \approx 1$ MW/cm².

Note also that the saturation-intensity value in general does not depend on the pumping intensity applied to the laser medium, since neither the cross section σ nor the effective recovery time (in most materials) depends directly on the pumping rate. Pumping a laser medium harder generally creates more small-signal gain, which has to be saturated down further; but it does not change the saturation intensity involved in the saturation expression.

 Problems for 7.6

1. *Saturation intensity for a three-level atomic absorber.* A system with three energy levels has transition frequencies ω_{32} , ω_{21} , and ω_{31} ; total decay rates γ_{32} , γ_{21} , and γ_{31} ; and stimulated-transitions probabilities $\sigma_{32} = \sigma_{23}$, $\sigma_{21} = \sigma_{12}$, and $\sigma_{31} = \sigma_{13}$ between its levels. The “optical frequency approximation” is valid for all transitions. What will be the saturation intensity I_{sat} for a signal passing through this collection of atoms with frequency ω tuned to the transition frequency ω_{31} ?
2. *Saturation lineshape for the reactive part of a homogeneous two-level atomic transition.* How will the atomic phase shift $\Delta\beta_m L$, as contrasted to the atomic gain or absorption coefficient $\alpha_m L$, saturate in a homogeneous atomic medium?

To examine this, suppose that a signal wave having fixed intensity I but variable frequency ω is transmitted through a thin slab of lorentzian, homogeneously saturable absorbing medium of thickness L ; and the added phase shift $\Delta\beta_m(\omega)L$ caused by the atoms is measured as a function of ω . Let the absorption in the cell be fairly small, say, $2\alpha L = 0.1$, so that the intensity $I(z)$ is essentially constant throughout the cell. Plot the variation of $\Delta\beta_m(\omega)L$ versus ω for selected values of I/I_{sat} both < 1 and > 1 . How does the spacing between the peaks of $\Delta\beta_m(\omega)L$ change with increasing intensity?

3. *Saturation behavior in a two-level absorber including excited-state absorption.* A certain molecule has two lowest energy levels E_1 and E_2 with stimulated-transition cross section $\sigma_{12} = \sigma_{21}$ between them. The energy decay time from level E_2 back to level E_1 is T_1 .

These same molecules also absorb at the same wavelength, with a stimulated-transition cross section $\sigma_{23} = \sigma_{32}$, from level E_2 up to a higher level (or group of levels) E_3 . (This would be referred to as an *excited-state absorption transition*.) One can assume, however, that the relaxation rate from the upper levels E_3 back to E_2 is so fast as to be essentially instantaneous, so that the approximation $N_3 \approx 0$ prevails under all conditions.

Evaluate the absorption through a thin slab of this medium as a function of the incident signal intensity I and find its saturation behavior with increasing intensity.

If you could measure the intensity transmission $T(I)$ through a thin slab of this material over a wide range of incident intensities I , what information could you gain (from this data alone) about the relative cross sections σ_{12} and σ_{23} ?

4. *Power balance versus intensity in a two-level saturable absorber.* This problem combines the saturation-intensity concepts of this section with the fundamental rate equation discussed in earlier chapters. Suppose an optical signal with adjustable intensity I is applied to a collection of elementary two-level atoms in an optically thin slab (net attenuation through the slab is small). The slab has total volume V , and the atoms have cross section σ , relaxation time T_1 , and total density of N atoms per unit volume. The optical approximation does *not* apply.

Evaluate the steady-state power balance in this slab by evaluating (a) the net power absorbed by the atoms, from the signal, (b) the net power absorbed by the atoms from their “thermal surroundings,” and (c) the net power spontaneously

radiated by the atoms to their surroundings, all as a function of signal intensity I .

7.7 HOMOGENEOUS SATURATION IN LASER AMPLIFIERS

As an optical signal passes through a laser amplifier, the signal intensity $I(z)$ grows more or less exponentially with distance along the length of the amplifier. However, when the signal intensity begins to approach the saturation intensity for the laser medium, the population difference and hence the gain coefficient in the laser material begin to be saturated; the rate of signal growth with distance begins to decrease; and the signal intensity thus grows more slowly with distance.

In a single-pass laser amplifier such saturation effects begin first at the output end of the amplifier (see Figure 7.12), but only when the input signal is large enough that the amplified signal level at the output end has approached the saturation intensity of the laser medium. This saturation at the output end then causes the growth rate to decrease near the output end, and this in turn reduces the overall saturated gain from input to output as compared to the small-signal or unsaturated gain of the amplifier.

As we increase the input intensity to a laser amplifier, the intensity $I(z)$ will reach the saturating range at an earlier point along the amplifier; the saturation region moves toward the input end as the input power is increased. The net result of this saturation behavior is that large-signal output is not a linear function of large-signal input. In this section we will analyze this behavior in a simple lossless single-pass amplifier, assuming cw signals and homogeneous saturation of the laser gain coefficient.

Homogeneous Saturation Analysis

Suppose the laser gain coefficient in a single-pass laser amplifier saturates homogeneously, with unsaturated gain coefficient $2\alpha_{m0}$, saturation intensity I_{sat} and, for simplicity, no linear losses, so that $\alpha_0 = 0$. The basic differential equation governing the growth rate for the signal intensity along the amplifier thus becomes

$$\frac{1}{I(z)} \frac{dI(z)}{dz} = 2\alpha_m(I) = \frac{2\alpha_{m0}}{1 + I(z)/I_{\text{sat}}}, \quad (79)$$

where α_{m0} is the unsaturated gain coefficient and I_{sat} the saturation intensity of the laser medium. Obviously we can not simply integrate this equation to obtain an overall gain $G = \exp(2\alpha_m L)$, since the gain coefficient α_m varies with intensity I and hence with distance z along the amplifier length.

If, however, we assume an input intensity I_{in} at the input end $z = 0$ and an output intensity I_{out} at the output end $z = L$, then this equation can be rearranged into the form

$$\int_{I=I_{\text{in}}}^{I=I_{\text{out}}} \left[\frac{1}{I} + \frac{1}{I_{\text{sat}}} \right] dI = 2\alpha_{m0} \int_{z=0}^{z=L} dz. \quad (80)$$

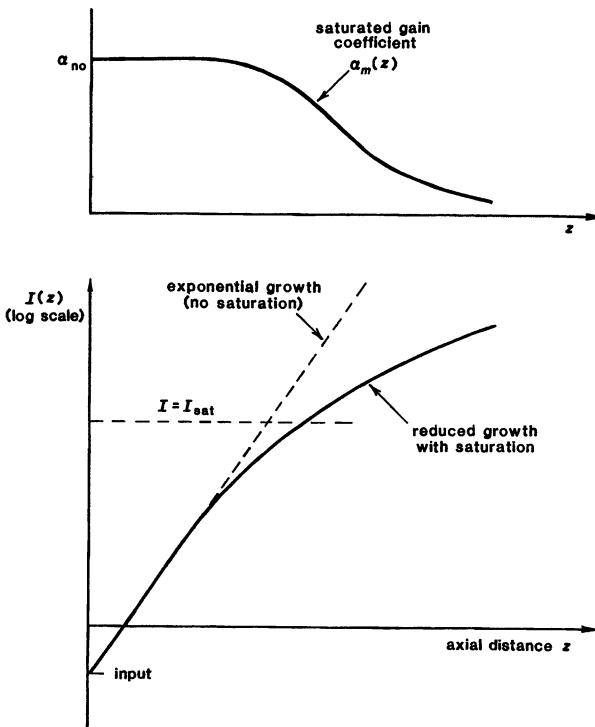


FIGURE 7.12
Gain saturation as a function of distance along a single-pass laser amplifier.

Both sides of this equation can then be integrated to obtain the expression

$$\ln \left(\frac{I_{\text{out}}}{I_{\text{in}}} \right) + \frac{I_{\text{out}} - I_{\text{in}}}{I_{\text{sat}}} = 2\alpha_m L = \ln G_0, \quad (81)$$

where $G_0 \equiv \exp(2\alpha_m L)$ is the small-signal or unsaturated power gain through the amplifier.

As it stands this result gives us an implicit relationship between the input and output intensities, the saturation intensity, and the unsaturated power gain G_0 for the amplifier. We can then obtain useful numbers from this equation in the following fashion. Suppose we define the actual power gain of the amplifier as the ratio of output over input, or $G \equiv I_{\text{out}}/I_{\text{in}}$, under arbitrary saturation conditions. This gain cannot be written as $\exp(2\alpha_m L)$, and its value in fact depends on the intensities I_{in} or I_{out} . We can, however, use Equation 7.81 to write this overall power gain in the form

$$G \equiv \frac{I_{\text{out}}}{I_{\text{in}}} = G_0 \times \exp \left[-\frac{I_{\text{out}} - I_{\text{in}}}{I_{\text{sat}}} \right], \quad (82)$$

which says that the value of the saturated gain G at a given value of I_{in} (or I_{out}) is reduced below the unsaturated value G_0 by a factor that depends exponentially on the extracted intensity $I_{\text{out}} - I_{\text{in}}$ relative to the saturation intensity I_{sat} .

These results can then be manipulated into a variety of forms that can be used in different ways. For example, Equation 7.82 can be rewritten in the forms

$$G \equiv \frac{I_{\text{out}}}{I_{\text{in}}} = G_0 \times \exp \left[-\frac{(G-1) I_{\text{in}}}{I_{\text{sat}}} \right] = G_0 \times \exp \left[-\frac{(G-1) I_{\text{out}}}{G I_{\text{sat}}} \right]. \quad (83)$$

The first of these forms can then be turned around to give the relationship

$$\frac{I_{\text{in}}}{I_{\text{sat}}} = \frac{1}{G-1} \ln \left(\frac{G_0}{G} \right), \quad (84)$$

which gives the input intensity in terms of the unsaturated gain G_0 and saturated gain G . But using the second form (or just multiplying both sides of Equation 7.84 by G) also gives the result

$$\frac{I_{\text{out}}}{I_{\text{sat}}} = \frac{G}{G-1} \ln \left(\frac{G_0}{G} \right) \quad (85)$$

which gives the output intensity as a function of the same quantities. For any given value of unsaturated gain G_0 we can then plug different values of saturated gain in the range $1 < G < G_0$ into Equations 7.84 and 7.85 to obtain paired values of normalized input intensity $I_{\text{in}}/I_{\text{sat}}$ and output intensity $I_{\text{out}}/I_{\text{sat}}$.

Figure 7.13 illustrates the resulting amplifier input-output intensity curves for two different small-signal gain values. Note that for each value, the actual gain G begins to be saturated below its small-signal value G_0 even at output intensities well below the saturation intensity. At high enough input intensities the gain always saturates down toward the limiting value $G = 1$, or 0 dB. For high intensities the amplifier transmission saturates down, not toward zero transmission, but toward unity transmission—that is, the amplifier (which is assumed to have zero ohmic losses) becomes essentially transparent at high enough input intensities.

Power Extraction and Available Power

We might next ask *how much intensity, or how much power per unit cross-section area, can be extracted from such an amplifier at different input-signal levels?* By manipulating the preceding equations we can find that the power per unit area extracted from the amplifier—that is, the output power minus the input power, or the power really supplied to the wave by the amplifier—is given by

$$I_{\text{extr}} \equiv I_{\text{out}} - I_{\text{in}} = \ln \left(\frac{G_0}{G} \right) \times I_{\text{sat}}. \quad (86)$$

The values of this quantity are illustrated by the dashed lines in Figures 7.13 and 7.14.

Note that for low input intensity and high gain ($G \approx G_0$), the output power and the extracted power are essentially the same—that is, we are putting in very little power at the input end compared to what we are getting out at the output end. As the amplifier begins to saturate, however, the extracted power approaches a limiting value, which is the maximum power available to be extracted from the

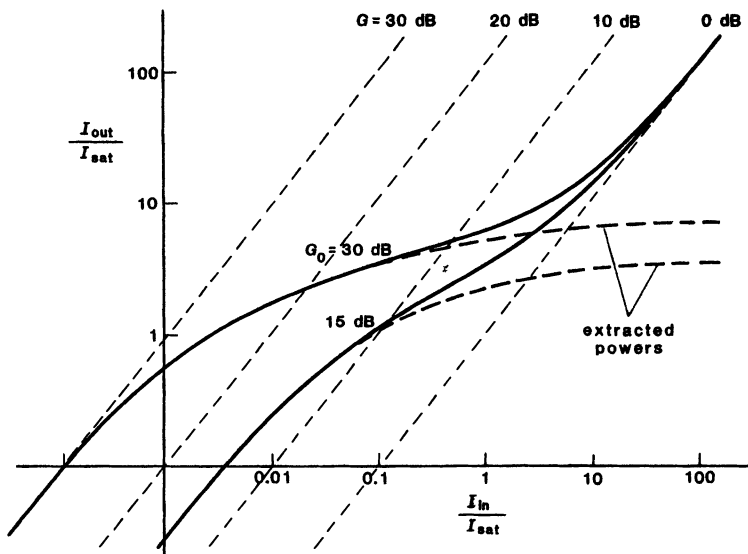


FIGURE 7.13
Amplifier output versus input curves for two different values of small-signal gain.

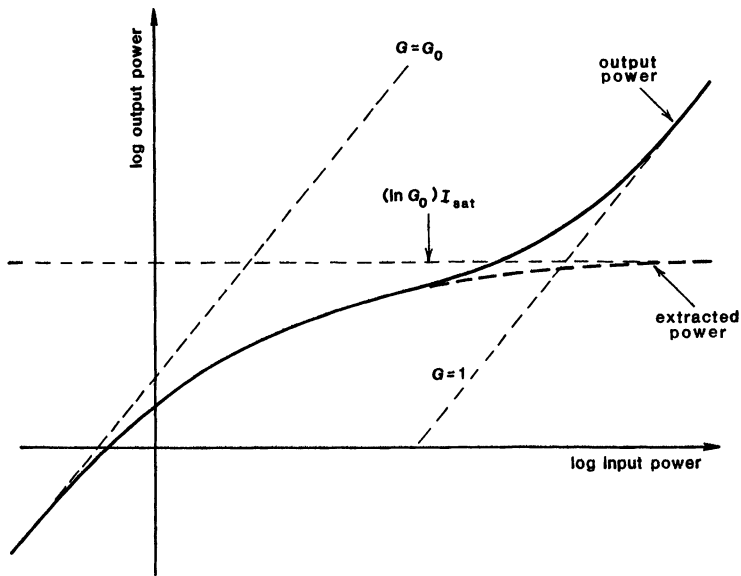


FIGURE 7.14
Power input, power output, and power extraction from a saturating laser amplifier.

amplifying medium. This *maximum available power from the amplifier* (per unit area) is given by the limiting value

$$I_{\text{avail}} = \lim_{G \rightarrow 1} \ln \left(\frac{G_0}{G} \right) \times I_{\text{sat}} = (\ln G_0) I_{\text{sat}}. \quad (87)$$

This is the maximum power per unit area that is available in the laser medium to be given up to the amplified signal.

This expression for the available intensity in the laser medium has a simple physical interpretation. It can be rewritten, using earlier formulas, as

$$I_{\text{avail}} = 2\alpha_{m0}L \times I_{\text{sat}} = (\Delta N_0 \sigma L) \times \left(\frac{\hbar\omega}{\sigma\tau_{\text{eff}}} \right). \quad (88)$$

Since intensity is already power per unit area, we can reduce this to available power per unit volume by writing it as

$$\frac{I_{\text{avail}}}{L} \equiv \frac{P_{\text{avail}}}{V} = \frac{\Delta N_0 \hbar\omega}{\tau_{\text{eff}}}. \quad (89)$$

This says that *the maximum power output per unit volume that we can obtain from the laser medium is given by the initial or small-signal inversion energy stored in the medium, or $\Delta N_0 \hbar\omega$, times an effective recovery rate $1/\tau_{\text{eff}}$.* In other words, we can obtain the initial inversion energy $\Delta N_0 \hbar\omega$ once in every effective relaxation or gain recovery time τ_{eff} , which makes good physical sense.

Power-Extraction Efficiency

A major practical problem, however, is that this available power can be fully extracted only by heavily saturating the amplifier, in essence, by saturating the amplifier gain down until its saturated gain is reduced close to $G = 1$. Suppose we calculate the input and output power, and the associated gain and extracted power, for a hypothetical single-pass amplifier having an unsaturated gain $G_0 = 1,000 = 30$ dB and an available power $P_{\text{avail}} = (\ln G_0) A I_{\text{sat}} = 1$ kW/cm². With this amplifier we might hope to put in an input of 1 W and obtain an amplified output of 1,000 times larger, or close to 1 kW. The actual numbers for this case are, however, those shown in Table 7.2. Note in particular that by the time the device is putting out 800 W, the actual gain has already been reduced from a small-signal gain of 1,000 or 30 dB down to 9 dB or approximately 8. Hence, to obtain this output of 800 W, we must drive the amplifier with an input not of 0.8 W but of 100 W. To get an actual output power equal to the nominally available 1,000 W, we must provide 220 W of input; that is, we already need a fairly high-power preamplifier, just to extract the available power from this power amplifier.

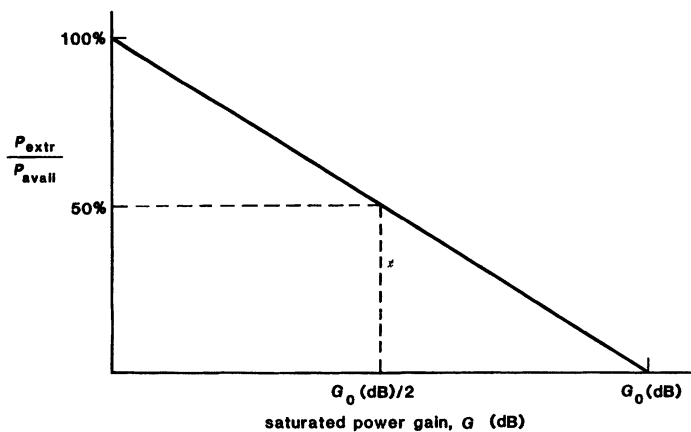


FIGURE 7.15

Power-extraction efficiency versus saturated power gain in a homogeneously saturating laser amplifier.

TABLE 7.2
Actual gain versus input power in a CO₂ amplifier^a

<i>P</i> _{in}	<i>P</i> _{out}	<i>P</i> _{extr}	Saturated gain <i>G</i>	Gain <i>G</i> in dB
~ 0	~ 0	~ 0	1,000	30 dB
0.1	64	64	643	28 dB
1	220	219	220	23 dB
10	457	447	46	17 dB
100	800	700	8	9 dB
220	1,000	780	4.5	7 dB
~ ∞	~ ∞	1,000	1	0 dB

^a*G*₀ = 30 dB, *P*_{avail} ≡ (ln *G*₀) *P*_{sat} = 1,000 W.

An instructive way to demonstrate this same point is to define an energy-extraction efficiency as the ratio of actually extracted power to available power, or

$$\eta_{\text{extr}} \equiv \frac{I_{\text{extr}}}{I_{\text{avail}}} = \frac{\ln G_0 - \ln G}{\ln G_0} = 1 - G_{\text{dB}}/G_{0,\text{dB}}. \quad (90)$$

This energy-extraction efficiency, if plotted versus actual or saturated gain *G* in dB, is thus a straight line (see Figure 7.15). To extract even half the power potentially available in a cw amplifier, one must give up half the small-signal dB gain of the amplifier.

Driving a single-pass amplifier hard enough to extract most of the energy potentially available in the laser medium is thus a difficult problem, and this difficulty in obtaining full energy extraction is the principle defect in MOPA applications. One way around this difficulty is to use multipass amplification, with the same beam sent through the amplifier medium several times, possibly from slightly different directions. Another solution (with its own difficulties) is to convert the amplifier into an oscillator, since oscillators are generally more efficient at extracting the available energy from a laser medium, as we will see in a later chapter.

Saturable Amplifier Phase Shift

If the intensity $I(z)$ at any plane in an amplifier is sufficient to cause saturation of the population difference and thus the gain coefficient α_m , then it will also cause a similar saturation of the atomic phase-shift coefficient $\Delta\beta_m$. The total phase shift through a linear amplifier may thus also change under saturation conditions. To analyze this, we can note that the differential equation for the net phase shift $\phi(z)$ for a signal of frequency ω as a function of distance z along the amplifier can be written as

$$d\phi(\omega, z) = \frac{\omega dz}{c} + \Delta\beta_m(\omega, z) dz. \quad (91)$$

The atomic phase-shift term $\Delta\beta_m$ will depend on the degree of saturation or on the intensity $I(z)$, and thus will vary with distance z along the amplifier. For a homogeneous lorentzian atomic transition, by using the relationship between saturated gain and the saturated value of $\Delta\beta_m$ we can integrate this equation and show that the overall phase shift is related to the input and output intensities in the form

$$\phi_{\text{tot}}(\omega, L) = \frac{\omega L}{c} + \frac{\omega - \omega_a}{\Delta\omega_a} \times \ln \left(\frac{I_{\text{out}}}{I_{\text{in}}} \right) \quad (92)$$

where I_{in} and I_{out} are the actual (saturated) values of input and output intensity at frequency ω . There is, of course, no atomic phase-shift contribution exactly at line center.

REFERENCES

All the results presented in this section, plus more detailed analyses taking into account finite-bandwidth applied signals, are discussed by A. Y. Cabezas and R. P. Treat, "Effects of spectral hole-burning and cross relaxation on the gain saturation of laser amplifiers," *J. Appl. Phys.* **37**, 3556-3563 (August 1966).

More detailed analyses of saturation effects can also be found in W. W. Rigrod, "Gain saturation and output power of optical masers," *J. Appl. Phys.* **34**, 2602-2609 (September 1963), and "Saturation effects in high-gain lasers," *J. Appl. Phys.* **36**, 2487-2490 (August 1965).

A representative example of the measurement of saturation intensity in a laser material is T. S. Lomheim and L. G. DeShazer, "Determination of optical cross sections by the measurement of saturation flux using laser-pumped laser oscillators," *J. Opt. Soc. Am.* **68**, 1575-1579 (November 1978).

A good source on saturable absorption effects, including experimental results, is A. Zunger and K. Bar-Eli, "Nonlinear behavior of solutions illuminated by a ruby laser. II," *IEEE J. Quantum Electron.* **QE-10**, 29–36 (January 1974).

Suppose two independent signals are sent through an amplifier separately but simultaneously. Then the saturation effects due to one signal can change the gain seen by the other signal, and vice versa. This can lead to interesting and potentially useful cross-modulation or cross-saturation effects, some of which are discussed and analyzed by R. W. Gray and L. W. Casperson in "Optooptic modulation based on gain saturation," *IEEE J. Quantum Electron.* **QE-14**, 893–900 (November 1978).

Problems for 7.7

1. *Input-output intensity curves for a saturable amplifier off line center.* The typical curves of output intensity versus input intensity for a homogeneous single-pass laser amplifier given in this section assume a signal tuned to the atomic line center. Explain clearly (with sketches) exactly how these curves will change, for the same amplifier and the same plot, as the signal frequency is tuned off line center. How will the plot of energy extraction efficiency η versus net power gain G change with the same detuning?
2. *Input versus output intensities for a saturable atomic absorber.* All the equations in this section should apply equally well, with an appropriate change of sign, to saturable atomic absorbers. Consider a single-pass, saturable, traveling-wave atomic attenuator (rather than amplifier) using a homogeneously saturating atomic system. Analyze the output intensity versus input intensity for this device, and plot intensity out versus intensity in on log scales for several different unsaturated loss values, say 10 dB, 20 dB, and 30 dB.
3. *Signal penetration and saturation depth versus signal intensity in a homogeneous saturable absorber.* A weak cw laser beam injected into one end of a very long cell containing a homogeneously saturable absorbing medium will be almost totally attenuated within a few absorption lengths. A strong enough input signal, with $I_{\text{in}} > I_{\text{sat}}$, on the other hand, will saturate the absorption and "burn" its way some longer distance into the absorbing cell before being absorbed. Calculate and plot the signal intensity $I(z)$ on a log scale, and the saturated population difference $\Delta N(z)/\Delta N_0$ on a linear scale, both versus distance z through the cell, for input signals that are 1, 10, 100, and 1,000 times the saturation intensity. Can you give an approximate rule of thumb for how far into the cell a strong beam will "burn" its way if $I_{\text{in}} \gg I_{\text{sat}}$?
4. *Obtaining an amplifier output intensity just equal to the available intensity of the laser medium.* A single-pass, homogeneously saturable laser amplifier has an available intensity $I_{\text{avail}} = 1 \text{ kW/cm}^2$. Suppose you want to obtain an actual output intensity equal to the same value, i.e., $I_{\text{out}} = 1 \text{ kW/cm}^2$, with an actual (saturated) power gain of $G = 10 = 10 \text{ dB}$. What must be the unsaturated gain G_0 of the amplifier (either as a number, or in dB)? /itemIn general, if you want to obtain an actual output I_{out} from an amplifier which is just equal to the available intensity I_{avail} , with a specified actual gain G , what is a relationship for the required unsaturated gain G_0 ?

5. *Power output stabilization factor in a partially saturated laser amplifier.* It is sometimes desirable that the output power I_{out} from a laser amplifier remain as nearly constant as possible when the input power I_{in} fluctuates by a small amount ΔI_{in} . A useful measure of this output-power stabilization is the stabilization factor S , defined as $\Delta I_{\text{in}}/I_{\text{in}}$ divided by $\Delta I_{\text{out}}/I_{\text{out}}$ evaluated in the limit as $\Delta I_{\text{in}} \rightarrow 0$. Evaluate this stabilization factor as a function of operating conditions for a single-pass homogeneously saturating laser amplifier. Suppose you want to achieve a specified output level $I_{\text{out}}/I_{\text{sat}}$, a specified saturated gain G , and a specified stabilization factor S in a practical laser system. Discuss the design procedure you would follow.
6. *Cross-saturation of a transversely double-pass laser amplifier.* A laser beam with input power I_1 is sent through a single-pass laser amplifier going in the z direction; and the output beam I_2 is then transversely expanded in one direction and brought around to pass through the amplifier sideways in, say, the x direction. Assume the rectangular laser medium has length L in the z direction and width d in the x direction, and the length-width (L/d) ratio of the amplifier is such that it will have a high unsaturated gain G_0 in the z direction, but only small net gain in the transverse direction. Develop an expression relating the input and output intensities I_1 , and I_2 in this system, taking saturation into account. Indicate how you could calculate and plot a curve of I_2 versus I_1 for the system.
7. *Amplifier input-output curves for other forms of laser saturation.* Suppose that certain unusual laser media saturate with the intensity dependences either $1/[1 + (I/I_{\text{sat}})^2]$ or $1/[1 + (I/I_{\text{sat}})]^2$ instead of the usual $1/[1 + I/I_{\text{sat}}]$. Evaluate and plot the output versus input intensities (on log scales) for single-pass amplifiers using these media, and compare to a standard homogeneous laser system for $G_0 = 30$ dB.
8. *Signal transmission through two intermingled saturable absorber transitions.* Suppose a saturable absorber system contains a mixture of two independent homogeneously saturating atomic absorbers, with absorption coefficients α_{m1} and α_{m2} and saturation intensities I_{s1} and I_{s2} , respectively. Show that the power transmission G through a length L of this dual absorber (where $G \leq 1$) is related to the input intensity I_{in} by the implicit relation $\ln(G/G_0) = C_1 \ln[(1 + C_2 I_{\text{in}})/(1 + C_2 G I_{\text{in}}) + C_3(1 - G)I_{\text{in}}]$, where $G_0 \equiv \exp(2\alpha_{m1}L + 2\alpha_{m2}L)$ is the unsaturated transmission through the absorber cell. (The algebra involved in this calculation is undeniably a bit messy. The problem is also treated by L. Huff and L. G. DeSazer, "Saturation of optical transitions in organic compounds by laser flux," *J. Opt. Soc. Am.* **60**, 157-165, February 1970.)
9. *Saturation effects on transverse beam profiles.* Suppose a collimated laser beam with a smooth transverse amplitude profile (for example, a gaussian transverse amplitude profile) is passed through a thin layer of a rather highly absorbing, homogeneously saturable atomic absorbing medium. Let us consider what happens not to the power level but to the *shape* and the *angular spreading* (or focusing) of the beam.

In experiments like this, we find that in fact both the shape and the focusing properties of the beam coming out of the absorbing slab depend on both the intensity of the incident beam and its frequency ω relative to the resonance frequency ω_a of the absorbing atoms.

List the significant physical effects or processes that might be responsible for these sorts of effects; and predict in general terms the sort of behavior (e.g., additional beam spreading, or beam focusing) that might be expected under various experimental conditions.



MORE ON LASER AMPLIFICATION

We extend the discussion of laser amplification in this chapter to examine a few more advanced aspects of cw laser amplification, including the transient response of laser amplifiers; spatial hole-burning or standing-wave grating effects in laser amplifiers; and some more details on saturation in laser amplifiers.

8.1 TRANSIENT RESPONSE OF LASER AMPLIFIERS

Let us look first at the very interesting topic of the *linear transient response* of a laser amplifier, for example, to a step-function or a delta-function type of signal input.

To understand what a laser amplifier does on a transient basis, we have to recall what the atoms in the laser amplifier do on a transient basis. The induced polarization on an atomic transition is linear in the applied signal field, at least within the rate-equation approximation. A laser amplifier is thus a linear system in its response to an applied signal, at least at low enough signal levels that no saturation effects occur. The impulse response of a laser amplifier to a delta-function-like input pulse should therefore be the Fourier transform of the transfer function, or the complex voltage gain function $\tilde{g}(\omega)$, of this linear system; and the response to a fast-rising step-function input should be the integral of this impulse response. In this section we will illustrate what this means for both passive absorbers and laser amplifiers.

Step Response of an Atomic Absorption Cell

We can obtain a very instructive picture of the transient response both of an atomic cell and of the atoms themselves, by examining an ingenious optical-pulse generation experiment carried out by Eli Yablonovitch at Harvard University, using a CO₂ laser and an atomic absorption cell filled with absorbing (that is, unpumped) hot CO₂ vapor.

Imagine first that a step-function optical signal with carrier frequency tuned to the resonance frequency ω_a is sent into an absorption cell having a large total attenuation $2\alpha_m L$, where α_m is the midband absorption coefficient for the atomic transition in the cell. Suppose that the rise time for the leading edge of

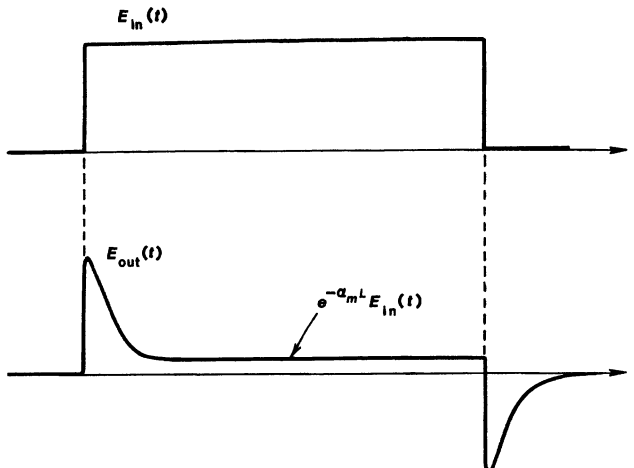


FIGURE 8.1

The step response of an atomic absorber to an input signal which is suddenly turned on, and just as suddenly turned off.

this optical signal is fast compared to the inverse linewidth $T_2 \equiv 1/\Delta\omega_a$ of the atomic transition (but not compared to the optical carrier frequency ω_a of the signal). As the leading edge of the signal pulse sweeps past each point in the cell, there will then be a time delay of order $\approx T_2$ before the absorbing atoms at that cross section can begin to respond to the applied signal, that is, before the induced sinusoidal polarization $\hat{P}(\omega)$ can build up to its steady-state value.

As a result, the leading edge of the pulse will sweep through the full length of the cell with essentially no attenuation. Only after the atoms have begun to respond can the cell begin to function as an absorber, and begin to attenuate the applied signal. The output response of an absorbing cell to a step input with fast enough rise time will thus be a short pulse as shown in Figure 8.1, with essentially the same peak amplitude as the leading edge of the input signal, and with a duration that corresponds roughly to the time constant T_2 before the atomic response and hence the attenuation of the cell can develop.

Transient Response to Signal Turn-Off

An even more interesting observation is that an essentially similar pulse, again of duration $\approx T_2$ but now of opposite sign, will also emerge from the cell just after the termination of the input signal, if we can suddenly turn off the input signal with a similarly fast fall time. The physical interpretation of this trailing-edge pulse is particularly instructive.

As one way of understanding it, consider the total signal that will be seen by an optical detector looking at the total transmitted output from the absorption cell. This detector in our example will see essentially no signal under steady-state conditions, during the main part of the input pulse, since we assume that the attenuation through the absorber cell is large.

One instructive (and correct) way of describing this situation is to say that the detector is actually seeing the superposition of the full original signal field

that would be generated at the detector location *by the input signal source without the absorber cell present*, plus the additional fields that are produced at the detector *by radiation from the induced polarization $p(r, t)$ in the absorber cell itself*. This induced polarization is coherently related to the applied signal; and because we assume an absorbing medium or an absorbing transition, the induced polarization reradiates in a way that will cancel (or nearly cancel) the original applied signal at the detector. (For a strongly absorbing cell this induced polarization exists, with steadily decreasing amplitude, only in the first few absorption lengths at the input end of the cell, after which the total field, applied plus reradiated, becomes small to negligible for the rest of the cell length.)

Suppose we suddenly turn off the applied signal, with a very fast fall time. After an appropriate time delay, corresponding to the travel time at the velocity of light from the applied signal source to the detector, the component of the applied signal field due to the applied signal source itself will thus suddenly vanish. The atomic dipoles, however, will at that instant still be oscillating and radiating in coherent fashion; and, as we have described earlier, they will continue to oscillate and reradiate until the coherent polarization dies out with time constant T_2 because of an appropriate combination of dephasing and energy decay.

Just before the applied signal is turned off, the net signal reaching the detector is essentially zero, since the applied signal field is almost totally canceled by the fields radiated by the absorber-induced polarization (for high insertion loss). Just after the signal turnoff the applied signal component is gone; but the atomic polarization $p(t)$ and its dipole radiation contribution remains, at least for a time of order T_2 . The net signal at the detector, or at the absorber output, will thus suddenly jump up to an amplitude essentially equal to the unattenuated input signal, but with a phase 180° out of phase with the applied signal, as shown in Figure 8.1. In other words, suddenly turning off the input will also produce a short transient pulse at the output.

Experimental Results

Turning an optical signal on or off with a rise time short compared to an atomic response time T_2 requires an unusually fast electrooptic modulator and/or a very narrow atomic absorption line; so experiments of the type described here are not in general easy. Yablonovitch developed an ingeniously simple and also useful way to carry out such a demonstration, using the experimental system shown in Figure 8.2.

In this experiment the output from a pulsed TEA CO₂ laser, which generates a 10.6 μm laser pulse with a pulsedwidth of about 100 ns and a peak power of about 100 MW, was passed first through a lens pair which focused the incident beam down to a focal spot less than two wavelengths in diameter. The beam diverging from this focal spot was then recollimated by the second lens, and transmitted through an absorption cell several meters long and containing hot CO₂ vapor, which automatically absorbs at the CO₂ laser wavelength. The absorbing cell was heated in order to thermally populate the lower level of the CO₂ absorption line, and the pressure could be changed in order to vary the pressure-broadened linewidth and hence the response time T_2 .

When this type of TEA laser is fired, the input intensity to the absorbing cell rises quite slowly, following the build-up time of the TEA laser itself, which has a rise time much too slow (≈ 100 ns) to produce any of the transient pulse effects we have discussed here. At a certain power level, however, the optical intensity

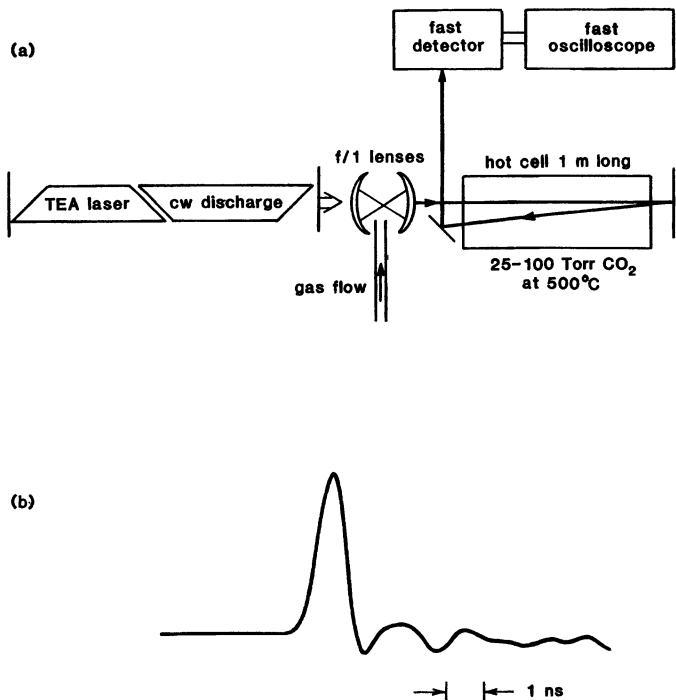


FIGURE 8.2

(a) Apparatus employed to demonstrate fast signal truncation with a gas breakdown cell, followed by short pulse generation in a linear absorber cell. (b) Short pulse generated in the CO_2 absorber cell (rise time of the pulse is limited by the oscilloscope response time). (From E. Yablonovitch and J. Goldhar, *Appl. Phys. Lett.* **25**, 580-582, November 15, 1974.)

in the focal spot can become sufficient to produce very rapid gas breakdown in air, leading to the almost instantaneous creation of a high-density plasma or "laser spark" (accompanied by a very loud sound wave). The electron density in this plasma almost immediately becomes so high that its index of refraction drops almost instantaneously to zero. This plasma spark then acts like a tiny but highly reflecting ball, which scatters essentially all the laser energy out of the beam. The gas breakdown thus provides in essence a self-actuated optical switch, which can completely shut off the transmitted laser beam with a fall time of less than 30 psec in practice.

Shutting off the incident signal using this technique produced the transient output pulse from the CO_2 absorber cell shown in Figure 8.2(b). This pulse not only is interesting as a demonstration of laser dynamics, but can also be useful for subsequent experiments, since it has a peak power nearly equal to the incident TEA laser signal, and a pulselength which can be varied simply by changing the gas pressure in the absorber cell in order to change the time constant T_2 .

Mathematical Analysis: The Step-Function Spectrum

To obtain a simple mathematical description of this pulse-generation process, consider a sinusoidal signal of the form $\mathcal{E}_1(t) = E_s(t) \exp(j\omega_a t)$, where $E_s(t)$ is a unit step-function, so that the carrier signal is suddenly turned on (or off) with zero rise time at $t = 0$. Such a signal has an optical spectrum, or Fourier transform, of the form

$$\tilde{E}_s(\omega) = \int_0^{\infty} e^{-j(\omega - \omega_a)t} dt = \frac{1}{j(\omega - \omega_a)}. \quad (1)$$

When this spectrum passes through an absorber cell with a lorentzian lineshape, the output spectrum is this input spectrum multiplied by the transfer function of the absorber cell or

$$\tilde{E}_2(\omega) = \tilde{E}_s(\omega) \times \exp\left[\frac{-\alpha_m L}{1 + jT_2(\omega - \omega_a)}\right], \quad (2)$$

where we use the simplified formula that $\Delta\omega \equiv 2/T_2$ to define T_2 . The output signal is then given by the inverse Fourier transform

$$\begin{aligned} \mathcal{E}_2(t) &= \frac{1}{2\pi} \int_{-\infty}^{\infty} \tilde{E}_2(\omega) e^{j\omega t} d\omega \\ &= e^{j\omega_a t} \int_{-\infty}^{\infty} \frac{\exp[j2\pi st - \alpha_m L/(1 + j2\pi T_2 s)]}{j2\pi s} ds. \end{aligned} \quad (3)$$

If we write this as $\mathcal{E}_2(t) = E_2(t) \exp(j\omega_a t)$, where $E_2(t)$ is the output envelope for a step-function input, then Yablonovitch and Goldhar have noted that this integral can be evaluated in terms of Bessel functions J_m in the form

$$E_2(t) = e^{-\alpha_m L} - e^{-t/T_2} \sum_{m=0}^{\infty} \left(\frac{t}{T_2 \alpha_m L}\right)^{m/2} J_m \left(2\sqrt{\frac{\alpha_m L t}{T_2}}\right), \quad t \geq 0, \quad (4)$$

for the boundary conditions corresponding to the fast turn-off case.

(In doing this analysis we have left out the $e^{-j\omega L}$ phase shift through the amplifier length L , since this would merely produce a propagation time delay $t = L/c$ in the output pulse; i.e., the output signal given in Equation 8.21 should really occur starting at $t \geq L/c$ and not $t \geq 0$.)

Step-Function Spectrum

This Fourier analysis says in physical terms that turning a monochromatic signal on or off very rapidly will give the signal a spectrum with frequency components extending far into the wings on both the high-frequency and the low-frequency side of the carrier frequency ω_a . This spectral broadening following the breakdown point was confirmed in the Yablonovitch experiments by using an infrared spectrometer to show that the sharply truncated signal following the breakdown point had a much wider power spectrum than the input TEA laser signal. Figure 8.3 illustrates the resulting long and approximately $1/\omega^2$ tails in the measured spectral density on both high-frequency and low-frequency sides of the CO_2 laser wavelength.

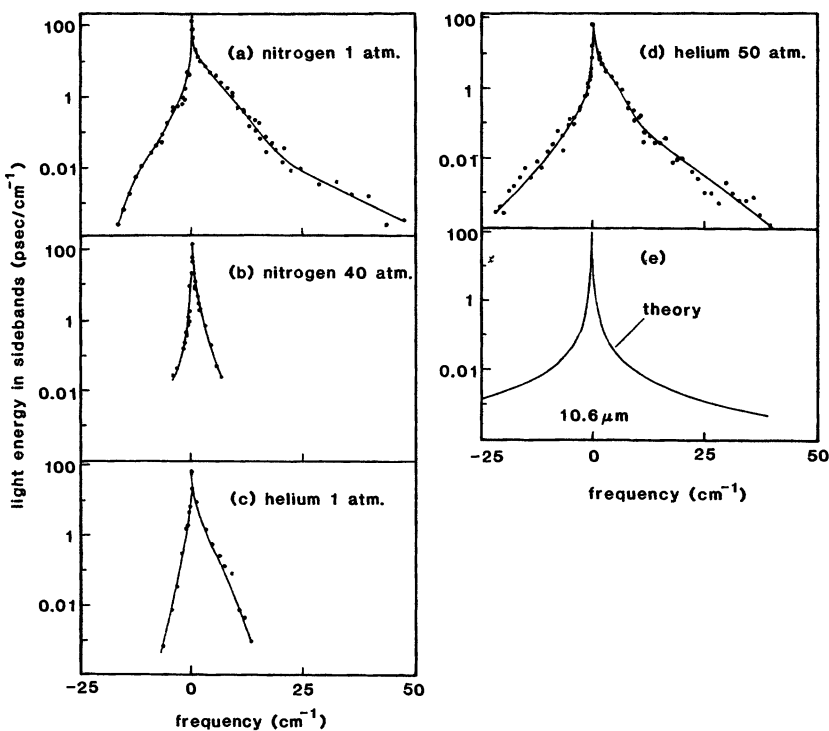


FIGURE 8.3
Spectral broadening of an initially monochromatic CO_2 laser signal that is suddenly truncated by plasma breakdown in various gases. (From E. Yablonovitch, *Phys. Rev. Lett.* **32**, 1102–1104, May 20, 1974.)

An alternative physical approach to understanding the pulse-formation process on either the leading or trailing edges is thus the following. When the spectrally broadened signal shown in Figure 8.3 is transmitted through the absorber cell, the comparatively narrowband CO_2 absorption cuts out only the narrow central portion of the spectrum, within about one linewidth $\Delta\omega_a$ about the carrier frequency. In frequency terms, it is the unattenuated spectral wings that are transmitted through the absorber cell, with a hole cut out of the center, that produce the leading and/or trailing edge pulses.

It is also important to realize that this pulse behavior results entirely from the *linear or small-signal transient behavior* of the absorber cell—no nonlinear or large-signal or Rabi flopping phenomena are involved in these particular results. The trailing-edge pulse in particular is a classic example of what is generally referred to as *free induction decay*—that is, after the signal turnoff the oscillating dipoles are still freely oscillating, initially in phase but with decaying total macroscopic polarization, and in the process are inducing a matching pulse of decaying radiation out the end of the absorption cell. The Yablonovitch experiment thus gives a highly instructive illustration of the linear response behavior of an atomic transition, and of how this behavior can be variously interpreted using

a transient time-domain viewpoint, a Fourier or frequency-domain viewpoint, or an interpretation based on the reradiation from an induced atomic polarization.

Impulse and Step Responses of Laser Amplifiers

Essentially the same transient effects can also be produced in an inverted laser amplifier using an input signal that is either a short enough pulse (quasi delta function) or a step-function having fast enough rise or fall times. For the amplifier it is perhaps more instructive, in fact, to begin with the impulse response of the amplifier to a very short input pulse.

If the input signal to a laser amplifier has the form $\mathcal{E}_1(t) = E_i(t)e^{j\omega_a t}$, where the envelope $E_i(t) \approx \delta(t)$ is a very short delta-function-like pulse, then the Fourier spectrum of this input signal will be essentially flat. The output signal, or the impulse response of the laser amplifier, will then be essentially the Fourier transform of the amplifier's complex voltage gain function, or

$$\tilde{E}_2(\omega) = \exp \left[\frac{+\alpha_m L}{1 + jT_2(\omega - \omega_a)} \right] \quad (5)$$

(assuming that the amplifier has a lorentzian lineshape). An analysis by Bridges, Haus, and Hopf then shows that the inverse transform of this spectrum is given by $\mathcal{E}_2(t) = E_2(t)e^{j\omega_a t}$, where the output envelope $E_2(t)$ is given by

$$E_2(t) = \delta(t) + \sqrt{\frac{\alpha_m L}{T_2 t}} I_1 \left[2\sqrt{\alpha_m L t / T_2} \right] e^{-t/T_2}, \quad t \geq 0, \quad (6)$$

with I_1 being the modified Bessel function of first order. (Changing the sign of the atomic absorption from $-\alpha_m$ to $+\alpha_m$ in the $\sqrt{\alpha_m L t / T_2}$ argument changes the Bessel function from the oscillatory J_m 's given in Equation 8.4 to a growing I_1 -type modified Bessel function.)

The physical interpretation of the first term in this analytical result, as shown in Figure 8.4, is that the impulse function itself will travel through the amplifier essentially unchanged—that is, neither attenuated nor amplified—since the atoms simply do not have time to respond or to build up oscillation and begin reradiating in steady-state fashion as the impulse rushes past. The sinusoidal fields during the impulse do, however, give a finite impulse or “kick” to the atomic dipoles even during the brief passage of the pulse, so that the atoms are left with some induced oscillation or polarization $p(t)$ following the passage of the pulse. The atomic dipoles then continue radiating, and thus produce the decaying free-induction tail which follows the impulse, as shown in Figure 8.4. Because the atoms are inverted or amplifying, this induced tail is in phase with the impulse function, rather than 180° out of phase like the absorber turn-off tail. (In a certain sense, all the gain experienced by the input impulse occurs after the impulse itself has swept past.)

Amplifier Step Response

The step response of a laser amplifier to a fast-rising input signal will be given by the integral of the impulse response. In other words, if $E_2(t)$ as given in Equation 8.6 is the impulse response, then the output response produced by

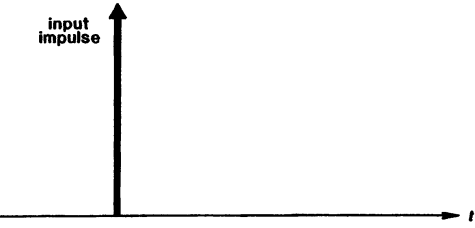


FIGURE 8.4

Linear impulse response of a laser amplifier. The free-induction "tail" on the output pulse actually contains all the energy or power gain which the amplifier gives to the input pulse.

a step input will be given by

$$E_2(t)|_{\text{step}} = \int_0^t E_2(t')|_{\text{impulse}} dt'. \quad (7)$$

Integrating over the delta-function part of the impulse response will cause the output step response to jump instantaneously from 0 to the input value at $t = 0$, as shown in Figure 8.5. This obviously represents the fast-rising leading edge sweeping through the amplifier with neither gain nor attenuation, just as in the absorber.

Integrating over the free-induction "tail" will then cause the output signal to continue to grow up to the steady-state amplified output value of $e^{\alpha_m L}$, also as shown in Figure 8.5. Again, obviously the net gain of the amplifier comes in integrating over the area of the tail; and in fact the net voltage gain is just the total area in the impulse plus the tail, compared to the area in the impulse only.

Experimental Results

Careful measurements of the step response of a laser amplifier have been made and compared with a similar but more detailed analysis in work done by Bridges, Haus, and Hopf. These measurements were made using a low-pressure CO₂ laser amplifier having a pressure-broadened homogeneous atomic linewidth of around 120 MHz or a T_2 of ≈ 2.6 ns. A fast-rising input pulse with less than 1 nanosecond rise time was obtained by passing a low-power cw laser beam through an electrooptic light modulator, and this signal was then reflected back and forth for five passes through the amplifier in order to obtain a net gain of greater than 20 dB. Since the gain-narrowed 3 dB bandwidth of the low-pressure CO₂ amplifier was reduced to about 50 MHz, the 1 ns pulse rise time was short enough to approximate a step-function input, and the ≈ 15 ns rise time of the

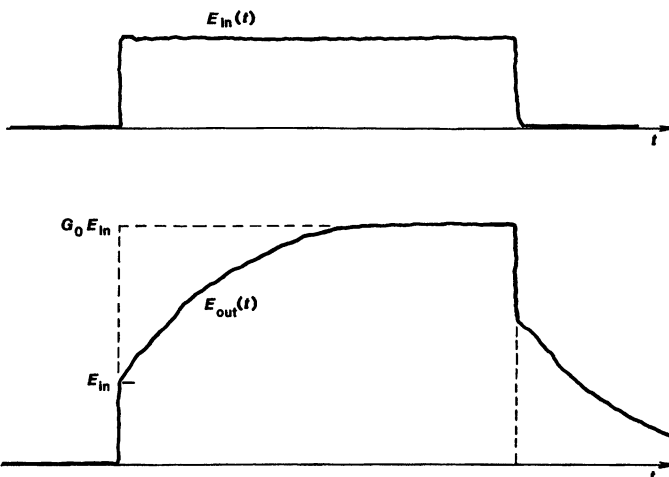


FIGURE 8.5

Linear step response of a laser amplifier. It requires a time $\approx T_2$ for the output signal to build up to the full amplified input value.

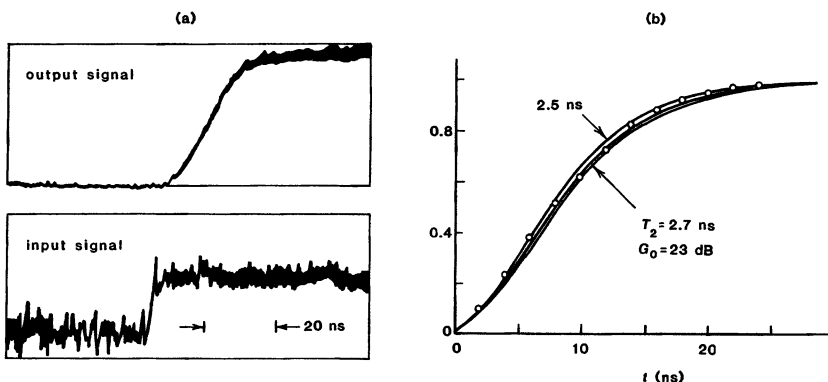


FIGURE 8.6

(a) Measured step response of a CO₂ laser amplifier (input signal, lower trace; output signal, upper trace). (b) Comparison of measured output with theory for two different assumed values of T_2 . (From T. J. Bridges, H. A. Haus, and P. W. Hoff, *IEEE J. Quantum Electron.* **QE-4**, 777-782, November 1968.)

amplifier's output signal could then be observed with a fast infrared detector and oscilloscope, as illustrated in Figure 8.6.

The results in this experiment are closely fit by a more exact version of the theory outlined above, as illustrated by the theoretical plot in Figure 8.6(b). In fact, several measurements of this type using different amplifier gas pressures yielded both the pressure-broadening coefficient for the CO₂ laser transition, and the zero-pressure Doppler-broadened intercept of ≈ 59 MHz.

REFERENCES

The transient turn-off experiments for the CO₂ absorber cell described in this section come from E. Yablonovitch and J. Goldhar, "Short CO₂ laser pulse generation by optical free induction decay," *Appl. Phys. Lett.* **25**, 580–582 (November 15, 1974). The background physics of gas breakdown and the resultant spectral broadening with a CO₂ laser are described in E. Yablonovitch, "Self-phase modulation of light in a laser-breakdown plasma," *Phys. Rev. Lett.* **32**, 1101–1104 (May 20, 1974); and "Self-phase modulation and short-pulse generation from laser-breakdown plasma," *Phys. Rev. A* **10**, 1888–1895 (November 1974).

Further measurements on the same system are in H. S. Kwok and E. Yablonovitch, "30-psec CO₂ laser pulses generated by optical free induction decay," *Appl. Phys. Lett.* **30**, 158–160 (February 1, 1977), and "CO₂ oscillator-pulse shaper-amplifier system producing 0.1 J in a 500 psec laser pulse," *Rev. Sci. Instrum.* **46**, 814–816 (July 1975). The same scheme is applied to the 1.315 μm iodine laser by E. Fill, K. Hohla, G. T. Schappert, and R. Volk, "100-ps pulse generation and amplification in the iodine laser," *Appl. Phys. Lett.* **29**, 805–807 (December 15, 1976).

The earlier work on amplifier step-response measurements discussed in this section comes from T. J. Bridges, H. A. Haus, and P. W. Hoff, "Small-signal step response of laser amplifiers and measurement of CO₂ laser linewidth," *IEEE J. Quantum Electron. QE-4*, 777–782 (November 1968), and "CO₂ laser linewidth by measurement of step response," *Appl. Phys. Lett.* **13**, 316–318 (November 1, 1968).

Interesting extensions to the impulse response of a laser amplifier, including double-pulse inputs and nonlinear large-signal responses, are discussed and illustrated in S. M. Hamadani, N. A. Kurnit, and A. Javan, "Coherent optical pulse evolution in a CO₂ amplifier," *Opt. Commun.* **17**, 32–37 (April 1976).

Problems for 8.1

1. *The leading-edge pulse in a Yablonovitch-type experiment.* Find the analytical expression for the leading-edge pulse in a Yablonovitch-type experiment, assuming an infinitely fast signal turn-on. Hint: Use superposition.
 2. *Asymptotic expressions for amplifier or absorber transient responses.* Using the asymptotic expressions for Bessel functions for very small or very large arguments, show that the Yablonovitch and Goldhar analytical result checks out for (a) a weakly absorbing cell, $\alpha_m L \ll 1$; and (b) a very strongly absorbing cell, $\alpha_m L \gg 1$, for the limit as $t \rightarrow \infty$.
-

8.2 SPATIAL HOLE BURNING, AND STANDING-WAVE GRATING EFFECTS

When two waves traveling in different directions are simultaneously present in a laser medium, interference between these two waves will produce both frequency beating effects and standing-wave patterns in the optical intensity. These interference effects in turn may produce both temporal modulation and spatial variations in the amount of saturation in the laser medium.

Interference between two waves at the same frequency but traveling in different directions in particular can produce spatial hole burning effects, which can

modify the saturation behavior of each wave independently, as well as induced grating effects, which can couple the two initially independent waves to each other. Nonlinear coupling between waves can in turn significantly modify the behavior of certain laser systems. In this section we will therefore introduce the fundamentals of spatial hole burning, and analyze the first-order coupling effects that spatial hole burning can produce in elementary two-wave situations.

Wave Interference Effects

Consider a general situation in which two propagating waves with complex amplitudes \tilde{E}_1 and \tilde{E}_2 , frequencies ω_1 and ω_2 , and propagation vectors β_1 and β_2 are simultaneously present in an atomic medium. The total \mathcal{E} field intensity at any point in the atomic medium must then be written as

$$\begin{aligned}\mathcal{E}(z, t) &= \mathcal{E}_1(z, t) + \mathcal{E}_2(z, t) \\ &= \operatorname{Re} \left[\tilde{E}_1(z) \exp j(\omega_1 t - \beta_1 z) + \tilde{E}_2(z) \exp j(\omega_2 t - \beta_2 z) \right]\end{aligned}\quad (8)$$

and so the total optical intensity $I(z, t)$, at any point z and any instant of time t , must then in general be written in the form

$$\begin{aligned}I(z, t) &= |\mathcal{E}(z, t)|^2 = \left| \tilde{E}_1(z) \right|^2 + \left| \tilde{E}_2(z) \right|^2 \\ &\quad + \tilde{E}_1^*(z) \tilde{E}_2(z) e^{j[(\omega_2 - \omega_1)t - (\beta_2 - \beta_1)z]} + \text{c.c.}\end{aligned}\quad (9)$$

We see that the local intensity will contain, in addition to the average intensities $|\tilde{E}_1|^2$ and $|\tilde{E}_2|^2$ associated with the two waves separately, an interference term proportional to the dot product $\tilde{E}_1^* \tilde{E}_2$. This interference term contains both a time-variation, at the “beat frequency” or difference frequency $\omega_{\text{beat}} = \omega_2 - \omega_1$ between the two signals, and a spatial variation, with a spatial periodicity given by $\beta_2 - \beta_1$.

Temporal Interference Terms

The interference between two signals with different frequencies ω_1 and ω_2 will thus produce a time-varying intensity at each point in the atomic medium, with a sinusoidal frequency equal to the beat frequency ω_{beat} . What this time-varying intensity does to the atomic medium, and particularly to the local population difference $\Delta N(t)$, depends on the difference frequency ω_{beat} and especially on its value relative to the atomic time constants T_1 and T_2 .

Often this sinusoidal modulation can be neglected, for several reasons. Suppose the difference frequency $\omega_2 - \omega_1$ between the two modes is large compared to any of the population recovery times τ or T_1 , as it often is. (This difference frequency may, for example, represent an axial-mode beat frequency of several hundred megahertz or larger.) Then the time-varying part of this modulation will be so rapid that the atomic population difference will simply not respond to this frequency; and hence all the terms oscillating sinusoidally in time can be ignored.

In other situations the two waves \tilde{E}_1 and \tilde{E}_2 may have orthogonal polarizations, so that the vector dot product between them is zero. The interference terms that vary in time and space will then all be identically zero.

Finally, sometimes there may be not just two such ideal sine waves but in fact many such waves, with a significant spread in frequency. If this spread in frequency is sufficiently large—in other words, if the overall temporal coherence of the optical signal is not large—then the temporal interference effects between the multiple signals will tend to be washed out on the average, and only the total time-averaged intensity of the signals will be important.

Cross-Modulation Effects

Note, however, that if any of the atomic properties, such as the gain or loss or phase shift in the atomic medium, do become significantly modulated at the difference frequency $\omega_{\text{beat}} = \omega_2 - \omega_1$, either by time-varying saturation effects or by other nonlinear mixing effects in the atomic medium, then the resulting modulation effects will produce frequency sidebands on both of the applied signals. In fact, the modulation of the ω_2 optical signal by the time-variations at ω_{beat} will produce both an upper sideband at $\omega_2 + \omega_{\text{beat}} = 2\omega_2 - \omega_1$ and a lower sideband at $\omega_2 - \omega_{\text{beat}} = \omega_1$; while the ω_1 signal will similarly acquire an upper sideband at $\omega_1 + \omega_{\text{beat}} = \omega_2$ and a lower sideband at $\omega_1 - \omega_{\text{beat}} = 2\omega_1 - \omega_2$.

In other words, *any type of nonlinear modulation or cross-saturation effects in the atomic response produced by the two signals will react back to couple or cross-modulate the two signals to each other* (as well as to produce new nonlinear mixing frequencies in the system). These nonlinear mixing or cross-modulation effects can become extremely complex, and also quite important in coupling together different frequency signals either in a laser medium or in other kinds of nonlinear optical materials.

Standing-Wave Interference Effects

Even if the two optical waves are at the same frequency, they will still produce spatial (though not temporal) cross-modulation and cross-coupling effects. That is, even if $\omega_1 = \omega_2$ the intensity I in Equation 8.26 will have a spatial variation of the form

$$I(z) = I_1(z) + I_2(z) + 2\sqrt{I_1 I_2} \cos[(\beta_2 - \beta_1)z + \phi], \quad (10)$$

where I_1 and I_2 are the intensities of the two waves separately, and the sinusoidal standing-wave portion has a spatial phase angle ϕ related to the relative phases of the two E fields.

If an intensity pattern of this form is present in a homogeneously saturable atomic medium, it will presumably produce a spatially varying saturation of the form

$$\frac{\Delta N(z)}{\Delta N_0} = \frac{1}{1 + I(z)/I_{\text{sat}}} = \frac{1}{1 + [I_1 + I_2 + 2(I_1 I_2)^{1/2} \cos(\Delta\beta z)]/I_{\text{sat}}}, \quad (11)$$

as illustrated in Figure 8.7. This spatial variation can then considerably complicate the analysis of gain saturation, as well as introduce complex wave-coupling effects in laser problems. The spatial variation of the gain (or loss) saturation in an atomic medium, as illustrated in Figure 8.7(b), is commonly referred to as *spatial hole burning* in the medium.

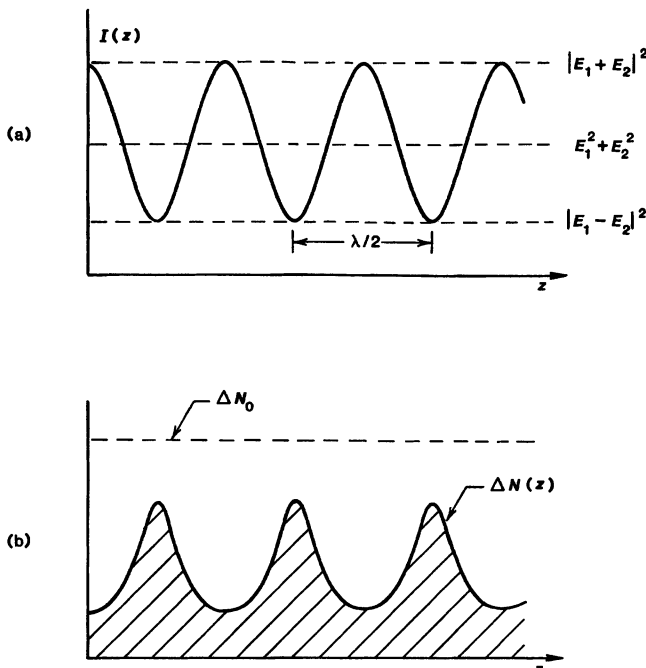


FIGURE 8.7

(a) Spatial intensity pattern produced by interference between two oppositely traveling waves having the same optical frequency. (b) Resulting spatial hole burning or saturation grating pattern of the population difference $\Delta N(z)$.

There are many ways in which the spatial interference effects between two or more waves can be washed out, however, so that we can merely add intensities—that is, merely write $I(z) = I_1 + I_2$, without the cross term—in order to calculate the total atomic saturation, as we will do in a number of later analyses.

First of all, if the waves are in fact at different frequencies, then the interference fringes or standing-wave patterns produced by the two beams will move, or sweep through the material, because of the temporal part of the interference effect. If the beat frequency is large and the material response is slow—that is, if $\omega_{\text{beat}} \gg 1/T_1$, as it often is—then the spatial saturation effects tend to be washed out. Crossed polarizations will also eliminate interference effects—in isotropic though not in anisotropic materials.

Finally, if not just two ideal plane waves are present, but instead many components with different k vectors, then the standing-wave patterns between different waves can become sufficiently complex that many of the cross-coupling effects tend to be washed out on the average, and again only the average intensity in all the waves is significant.

Two-Wave Coupling Effects

There are many situations, however, in which spatial coupling effects, or “induced grating effects,” between signals can be quite important. Let us look somewhat further at an analysis of the most elementary form of this coupling.

The situation we will analyze here is the elementary case of two coherently related uniform plane waves at the same optical frequency passing in opposite directions through a homogeneously saturable atomic medium. The superposition of these two oppositely traveling waves in the medium produces a standing wave with intensity fringes whose period is equal to half the optical wavelength of either wave, as shown in Figure 8.7. If this intensity pattern occurs inside a saturable amplifying or absorbing medium, the net result is to create a greater degree of saturation at the peaks of the intensity profile and a lesser degree of saturation at the nulls.

The saturable medium thus develops a stratified character, and becomes in effect a volume interference grating or a volume hologram. (Such a grating produced by two waves traveling in more or less exactly opposite directions is sometimes referred to as a Lippman grating.) A simple analysis of this case will both demonstrate how to analyze nonlinear wave-interaction problems, and lead to some useful and not entirely obvious conclusions concerning the interaction between these two waves.

The general one-dimensional wave equation that applies in this situation can be written as

$$\frac{d^2 \tilde{E}(z)}{dz^2} + \beta^2 \tilde{E}(z) = -\omega^2 \mu \tilde{P}(z), \quad (12)$$

where $\tilde{E}(z)$ is the total electric field and $\tilde{P}(z)$ is the polarization in the atomic medium. The two waves traveling in the $+z$ and $-z$ directions are then written in the form

$$\mathcal{E}(z, t) = \text{Re} \left[\tilde{E}_1(z) e^{j(\omega t - \beta z)} + \tilde{E}_2(z) e^{j(\omega t + \beta z)} \right], \quad (13)$$

where we allow the possibility that each complex wave amplitude $\tilde{E}(z)$ may change with distance. Note that the plus sign in front of the propagation constant β in the second term means that this wave is traveling to the left or toward $-z$.

We also assume that the atomic medium is a homogeneously saturable gain medium (or absorption medium) in which the signal is exactly on resonance. Hence the sinusoidal polarization $\tilde{P}(z)$ at any position z can be written as

$$\tilde{P}(z) = \tilde{\chi}(\omega_a, z) \epsilon \tilde{E}(z) = j \chi''(\omega_a, z) \epsilon \tilde{E}(z), \quad (14)$$

where the susceptibility $\chi''(\omega_a, z)$ at any point will be the saturated value given by the expression

$$\chi''(\omega_a, z) = \frac{\chi_0''}{1 + I(z)/I_{\text{sat}}}. \quad (15)$$

Note that $I(z)$, the total intensity at position z , will contain a sinusoidal standing-wave variation of the type we have written above.

Small-Saturation Approximation

To proceed further at this point, we must make the approximation that the degree of saturation produced in the atomic medium is comparatively weak, so

that we can use the mathematical approximation $1/(1 + I/I_{\text{sat}}) \approx 1 - I/I_{\text{sat}}$ for $I/I_{\text{sat}} \ll 1$. We can then write the saturated susceptibility as

$$\chi''(\omega_a, z) \approx \chi_0'' \times [1 - I(z)/I_{\text{sat}}], \quad I/I_{\text{sat}} \leq 0.2. \quad (16)$$

We make this approximation partly because it is often physically reasonable, but also because it would be much more difficult to proceed if we did not make it.

Putting the exact form for the intensity as given in Equation 8.9 into the wave equation 8.12 then expands this equation into the form

$$\begin{aligned} \left[\frac{d^2 \tilde{E}_1}{dz^2} - 2j\beta \frac{d\tilde{E}_1}{dz} \right] e^{-j\beta z} + \left[\frac{d^2 \tilde{E}_2}{dz^2} + 2j\beta \frac{d\tilde{E}_2}{dz} \right] e^{+j\beta z} &\approx -\beta^2 \chi_0'' \\ \times \left[1 - \frac{\left| \tilde{E}_1 \right|^2 + \left| \tilde{E}_2 \right|^2 + \tilde{E}_1^* \tilde{E}_2 e^{+2j\beta z} + \tilde{E}_1 \tilde{E}_2^* e^{-2j\beta z}}{I_{\text{sat}}} \right] & \quad (17) \\ \times \left[\tilde{E}_1 e^{-j\beta z} + \tilde{E}_2 e^{+2j\beta z} \right]. \end{aligned}$$

We can drop both of the second-derivative terms on the left-hand side of this equation, on the basis of the slowly varying envelope approximation, and then multiply out and match up the $e^{-j\beta z}$ and $e^{+j\beta z}$ traveling-wave terms on each side of this equation.

When we do this, we note that there is a product term between the $\tilde{E}_1 \tilde{E}_2^* e^{-2j\beta z}$ interference term in the saturation expression for $\chi''(\omega, z)$ and the left going wave term $\tilde{E}_2 e^{+j\beta z}$, and that this product term leads to an additional right going term $\tilde{E}_1 \tilde{E}_2 \tilde{E}_2^* e^{-j\beta z}$ on the right-hand side of the equation. Similarly, there is a product of $\tilde{E}_1^* \tilde{E}_2 e^{+2j\beta z}$ times $\tilde{E}_1 e^{-j\beta z}$, which leads to an additional $\tilde{E}_1^* \tilde{E}_1 \tilde{E}_2 e^{+j\beta z}$ term on the right-hand side. When all these cross-coupling and saturation terms are sorted out, the result is the pair of coupled equations

$$\frac{d\tilde{E}_1}{dz} \approx \pm \alpha_{m0} \left[1 - \frac{|\tilde{E}_1|^2 + 2|\tilde{E}_2|^2}{I_{\text{sat}}} \right] \times \tilde{E}_1 \quad (18)$$

and

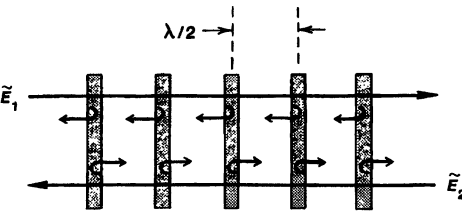
$$\frac{d\tilde{E}_2}{dz} \approx \mp \alpha_{m0} \left[1 - \frac{2|\tilde{E}_1|^2 + |\tilde{E}_2|^2}{I_{\text{sat}}} \right] \times \tilde{E}_2, \quad (19)$$

where we have used $(1/2)\beta\chi_0'' = \alpha_{m0}$, and where the upper or lower signs apply depending on whether the atomic medium is an amplifying or absorbing medium.

These equations are sometimes referred to as a *third-order expansion* for the atomic response, since the derivative terms for, say, the wave amplitude \tilde{E}_1 contain not only a linear or first-order term proportional to \tilde{E}_1 , but also third-order nonlinear terms of the form $\tilde{E}_1 \tilde{E}_1^* \tilde{E}_1$ and $\tilde{E}_2 \tilde{E}_2^* \tilde{E}_1$. If we want to keep track of intensities only, we can also use these equations to obtain

FIGURE 8.8

Two waves traveling in opposite directions through a nonlinear medium can create an induced grating (as in Figure 8.7) which can scatter each wave into the direction of the other wave, as shown in this figure.



$$\frac{dI_1}{dz} \approx \pm 2\alpha_{m0} \left[1 - \frac{I_1 + 2I_2}{I_{\text{sat}}} \right] \times I_1 \quad (20)$$

and

$$\frac{dI_2}{dz} \approx \mp 2\alpha_{m0} \left[1 - \frac{2I_1 + I_2}{I_{\text{sat}}} \right] \times I_2. \quad (21)$$

The most interesting thing to note here is the extra factor of 2 that appears in each of the cross-saturation terms, as compared to the self-saturation terms, in the preceding equations. These terms represent an important (and perhaps unexpected) result that emerges from this analysis. For some reason the cross-saturation between waves—that is, for example, the degree of gain saturation for wave #1 produced by the intensity of wave #2—is exactly twice the self-saturation of each wave by its own intensity.

Grating Backscattering Effects

It is evident, in fact, both physically and from the way in which these terms arise in the equations, that the excess part of this cross-saturation effect is not additional “saturation” caused by the other wave, but results from a *grating backscattering effect*. That is, in physical terms the oppositely traveling waves \tilde{E}_1 and \tilde{E}_2 combine to produce a standing wave, which in turn produces a set of stratified layers or a thick grating in the partially saturated medium. This grating has exactly the correct spacing so that a portion of wave #1 gets backscattered into wave #2 and vice versa (see Figure 8.8).

This physical picture of backscattering from a standing-wave grating also makes it physically reasonable that the excess cross-saturation effect should wash out if waves \tilde{E}_1 and \tilde{E}_2 are sufficiently incoherent. If waves \tilde{E}_1 and \tilde{E}_2 contain different frequency components, or have a partially incoherent spatial pattern, the clean standing-wave grating pattern will tend to wash out or average out, and the associated backscattering or wave-coupling effects will be reduced or eliminated.

Standing-wave grating effects can play a significant role in saturable absorber mode locking of lasers, and especially in the mode competition between simultaneously oscillating modes traveling in opposite directions in a ring laser cavity, as well as in other laser experiments.

REFERENCES

For a typical discussion of spatial hole burning and its effects, see T. Kimura, K. Otsuka, and M. Saruwatari, "Spatial hole-burning effects in a Nd^{3+} :YAG laser," *IEEE J. Quantum Electron.* **QE-7**, 225–230 (June 1971).

Problems for 8.2

1. *Effects of drift or spatial offset in a grating or wave-coupling experiment.* Suppose for purposes of analysis that in a certain atomic medium the saturation effects are basically homogeneous, except that the saturation effect produced by the local signal intensity $I(z)$ at point z tends to drift in space by a small amount ϵ , so that the saturation produced by $I(z)$ actually occurs at point $z + \epsilon$. (Something like this might happen in a real system if the atomic medium is moving or flowing, so that the atoms move by a distance $\approx \epsilon$ before they decay; or if the medium is, for example, a semiconductor with strong internal fields that cause carriers to move in a certain direction.)

For the coherent standing-wave grating discussed in this section, this would mean a spatial displacement by distance ϵ between the intensity standing wave $I(z)$ and the resulting spatial grating of $\chi(\omega, z)$. Analyze what this would do to the coupling between the two oppositely traveling waves, and discuss any new or interesting effects that may arise from this. (Note: certain so-called photo-refractive materials have refractive index gratings that are spatially displaced from the light intensity which produces them, and can as a result produce very interesting wave-coupling and wave-interaction effects.)

8.3 MORE ON LASER AMPLIFIER SATURATION

This section will present some additional details on laser amplifier saturation, including the effects of nonsaturable amplifier losses, saturation behavior in inhomogeneously broadened amplifiers, and transversely varying saturation effects.

Amplifiers With Saturable Gain and Loss

Many practical laser amplifier systems will have both a homogeneously saturable gain coefficient α_m and a smaller but nonsaturating "ohmic" loss coefficient α_0 due to host-crystal absorption, impurities, scattering losses, excited-state absorption, and other effects. The differential equation for signal growth along the amplifier then becomes

$$\frac{dI}{dz} = \frac{2\alpha_{m0}I}{1 + I/I_{\text{sat}}} - 2\alpha_0I. \quad (22)$$

If this equation is integrated through an amplifier of length L , as we did for the lossless amplifier of Section 7.7, the more complicated relation connecting input

and output signal intensities becomes

$$\ln \left[\frac{I_{\text{out}}}{I_{\text{in}}} \right] = 2\alpha_{m0}L - 2\alpha_0L + \left(\frac{\alpha_{m0}}{\alpha_0} \right) \ln \left[\frac{\alpha_{m0} - \alpha_0(1 + I_{\text{out}}/I_{\text{sat}})}{\alpha_{m0} - \alpha_0(1 + I_{\text{in}}/I_{\text{sat}})} \right] \quad (23)$$

or, in an alternative form,

$$\ln \left[\frac{G_0}{G} \right] = \left(\frac{\alpha_{m0}}{\alpha_0} \right) \ln \left[\frac{\alpha_{m0} - \alpha_0(1 + I_{\text{in}}/I_{\text{sat}})}{\alpha_{m0} - \alpha_0(1 + I_{\text{out}}/I_{\text{sat}})} \right], \quad (24)$$

where $G \equiv I_{\text{out}}/I_{\text{in}}$ is the saturated gain at a given input intensity and $G_0 \equiv \exp(2\alpha_{m0}L - 2\alpha_0L)$ is the net unsaturated gain minus loss. Either of these equations must be solved implicitly to find the input-output intensity relationship for an amplifier with given small-signal gain coefficient $2\alpha_{m0}L$ and loss coefficient $2\alpha_0L$.

Maximum Effective Amplifier Length

The deleterious effects of even relatively small amounts of loss in a laser amplifier can be appreciated, however, without making detailed input-output plots, by noting that if we make an arbitrarily long amplifier using such a medium, the effective gain coefficient given by

$$\frac{dI}{dz} = \left(\frac{2\alpha_{m0}}{1 + I/I_{\text{sat}}} - 2\alpha_0 \right) I = 2\alpha'_m I \quad (25)$$

will eventually saturate down to give zero further growth, i.e., $\alpha'_m \rightarrow 0$, as the intensity flux in the amplifier approaches a maximum value I_{max} given by

$$I_{\text{max}} = (\alpha_{m0}/\alpha_0 - 1) I_{\text{sat}}. \quad (26)$$

In other words, for a given small-signal gain α_{m0} and loss α_0 , there is a maximum possible signal flux which can build up in the amplifier. Alternatively, there is a maximum useful amplifier length given approximately by

$$L_{\text{max}} \approx \frac{1}{2(\alpha_{m0} - \alpha_0)} \ln \left[\frac{\alpha_{m0} - \alpha_0}{\alpha_0} \times \frac{I_{\text{sat}}}{I_{\text{in}}} \right]. \quad (27)$$

Beyond this length the signal intensity never increases, because all the additional energy given to the signal by the inverted medium through stimulated emission is immediately absorbed and dissipated by the ohmic loss mechanisms.

Ohmic loss considerations can become important in solid state amplifiers when we wish to obtain particularly high gains and high pulsed flux densities. Losses due to scattering from materials imperfections, or to absorption by either weak ground-state or excited-state absorptions, can then limit the available gain and power output. Similar considerations apply also to dye laser amplifiers, and to high-power visible and ultraviolet gas laser devices, such as excimer lasers, in which both high power and high efficiency are very desirable.

High-power gas lasers in particular often employ moderately high-pressure mixtures of several different gases which are very highly excited by intense transverse arc discharges or electron-beam pumping. There may well be previously unknown or unexpected excited-state absorption lines in these mixtures that unfortunately overlap the desired laser transition; more than one originally

promising high-power gas laser system has been eliminated by such unpleasant discoveries.

Inhomogeneously Saturating Amplifiers

Although many high-power lasers do have the kind of homogeneous broadening that we have assumed in the discussion of saturation thus far, other useful laser materials (including most low-pressure doppler-broadened gas lasers) can be inhomogeneously broadened. We will learn in Chapter 30 that when a strongly inhomogeneous transition is subjected to a strong monochromatic signal, the gain (or loss) for that signal saturates in the inhomogeneous form

$$\frac{dI}{dz} = \frac{2\alpha_{m0}I}{(1 + I/I_{\text{sat}})^{1/2}}. \quad (28)$$

The square root in the denominator comes about (as we will show in Chapter 30) because in an inhomogeneous line the applied signal saturates not only the spectral packet with which it is in exact resonance, but also other adjoining packets with which it has weaker interactions, thus “burning a hole” in the inhomogeneous line.

The analog to the input-output relationship for the homogeneous amplifier that we derived in the previous section then becomes

$$\int_{I=I_{\text{in}}}^{I=I_{\text{out}}} \left(\frac{1}{I^2} + \frac{1}{I/I_{\text{sat}}} \right)^{1/2} dI(z) = \int_{z=0}^{z=L} 2\alpha_{m0} dz. \quad (29)$$

Performing the complicated integration in this case leads to the result

$$\begin{aligned} \frac{\sqrt{1 + I_{\text{out}}/I_{\text{sat}}} - 1}{\sqrt{1 + I_{\text{out}}/I_{\text{sat}}} + 1} &= \frac{\sqrt{1 + I_{\text{in}}/I_{\text{sat}}} - 1}{\sqrt{1 + I_{\text{in}}/I_{\text{sat}}} + 1} \\ &\times \exp \left[2\alpha_{m0}L - 2\sqrt{1 + I_{\text{out}}/I_{\text{sat}}} + 2\sqrt{1 + I_{\text{in}}/I_{\text{sat}}} \right] \end{aligned} \quad (30)$$

This expression provides an implicit (and somewhat complex) way of computing I_{out} versus I_{in} for specified values of G_0 and I_{sat} in the inhomogeneous case.

Transversely Varying Saturation

The discussions of amplifier saturation thus far have also all been phrased in terms of the intensity (power per unit area) of the amplifying beam. If a beam has a flat transverse intensity profile, then we can simply multiply the intensity $I(z)$ by the cross-sectional area A of the beam to get the total power $P(z)$ at any plane.

Real laser beams, however, typically have nonuniform transverse intensity profiles, with the gaussian transverse intensity profile being a common example. When a nonuniform beam passes through a saturable amplifier, the more intense parts of the beam saturate more rapidly than the weaker portions. The beam profile can thus be distorted, with in general the higher-intensity peaks being flattened out relative to the weaker parts.

The transverse profile of the amplifying beam may also change with distance because of diffraction effects as the beam propagates through the amplifier. Usu-

ally, however, amplifiers will be short enough and/or the beam diameters large enough that the beam will not have significant diffraction spreading; so diffraction effects will be far less important than spatially nonuniform saturation effects in the amplifier. To gain some insight into the latter, let us consider a few simple points about such saturation effects, using an elementary gaussian beam profile.

Gaussian Beam Saturation

The transverse intensity distribution in a cylindrically symmetric gaussian beam with spot size w may be written as

$$I(r) = \frac{2P}{\pi w^2} \exp\left(-\frac{2r^2}{w^2}\right). \quad (31)$$

(The factor of 2 appears in the exponent because w is conventionally defined as the $1/e$ radius for the E field amplitude.) The peak intensity of the gaussian is thus the same as if the total power P were uniformly distributed over an area $A = \pi w^2/2$; and indeed we can show that if we consider a uniform-intensity beam having the same total power and the same intensity as the central peak intensity of the gaussian, then the effective area for this equivalent uniform beam appears to be $A_{\text{eff}} = \pi w^2/2$. This may not, however, be the best choice of effective area for a gaussian beam when we want to calculate saturation and power extraction effects.

Let us assume, as is often reasonable, that the amplifying beam is collimated and that diffraction effects are small. Then in essence each elemental cross-sectional area of the beam amplifies and saturates according to its own local intensity $I(r, z)$, independently of all other points in the cross section. The equation for local intensity in a homogeneously saturating amplifier will be

$$\frac{\partial I(r, z)}{\partial z} = \frac{2\alpha_{m0}I(r, z)}{1 + I(r, z)/I_{\text{sat}}}, \quad (32)$$

and the relation between input and output intensity profiles will be the same as in Equation 7.81, namely,

$$\ln\left[\frac{I_{\text{out}}(r)}{I_{\text{in}}(r)}\right] + \frac{I_{\text{out}}(r) - I_{\text{in}}(r)}{I_{\text{sat}}} = \ln G_0. \quad (33)$$

Given an input beam profile $I_{\text{in}}(r)$, we must in general solve this equation numerically for $I_{\text{out}}(r)$, and then integrate to find the total input and output powers P_{in} and P_{out} .

Suppose, however, that an amplifier with a gaussian input profile is either short enough or heavily saturated enough that its overall saturated gain is small. Then the beam profile will not change greatly with distance, and we may assume that the beam remains gaussian at every plane z through the amplifier. This differential gain equation may then be integrated over the amplifier cross section

to give the result

$$\begin{aligned}\frac{dP(z)}{dz} &= \int_0^\infty \frac{\partial I(r, z)}{\partial r} 2\pi r \, dr \\ &= \frac{8\alpha_{m0}P(z)}{w^2} \int_0^\infty \frac{r \exp(-2r^2/w^2) \, dr}{1 + [2P(z)/\pi w^2 I_{\text{sat}}] \exp(-2r^2/w^2)} \quad (34) \\ &= \pi w^2 \alpha_{m0} I_{\text{sat}} \ln \left[1 + \frac{2P(z)}{\pi w^2 I_{\text{sat}}} \right].\end{aligned}$$

Consider first the short and weakly saturated case, where the gaussian beam power P is small compared to the quantity $\pi w^2 I_{\text{sat}}/2$. Then by expanding the logarithm to second order, we can calculate that the power extraction in a short length Δz will vary with incident power P in the form

$$\Delta P \approx 2\alpha_{m0}P [1 - P/\pi w^2 I_{\text{sat}}] \Delta z \quad \begin{cases} \text{gaussian profile,} \\ \text{weak saturation.} \end{cases} \quad (35)$$

The analogous result for power extraction by a uniform beam having area A and total power P , in the small-saturation limit, would be

$$\Delta P = \frac{2\alpha_{m0}P \Delta z}{1 + P/AI_{\text{sat}}} \approx 2\alpha_{m0}P [1 - P/AI_{\text{sat}}] \Delta z \quad \begin{cases} \text{uniform profile,} \\ \text{weak saturation.} \end{cases} \quad (36)$$

By comparing these two equations, we may conclude that in the weak-saturation limit the effective area of a gaussian beam for power extraction is not $\pi w^2/2$ but $A_{\text{eff}} \approx \pi w^2$. In physical terms, the outer wings of the gaussian beam (where much of the power is carried) are at low intensity, and thus do not saturate the laser medium. The gaussian beam therefore acts as if its area were larger than we might expect.

Consider next the heavily saturated (and hence still low-gain) gaussian amplifier when $P(z) \gg (\pi w^2/2)I_{\text{sat}}$. The power extracted from the laser medium in an incremental length Δz may then be written as

$$\Delta P \approx \pi w^2 \alpha_{m0} I_{\text{sat}} \ln \left[1 + \frac{2P_1}{\pi w^2 I_{\text{sat}}} \right] \Delta z \quad \begin{cases} \text{gaussian profile,} \\ \text{strong saturation.} \end{cases} \quad (37)$$

The corresponding expression for a uniform beam in the high-saturation limit will be

$$\Delta P \approx A \times I_{\text{avail}} \Delta z \approx 2\alpha_{m0} I_{\text{sat}} A \Delta z \quad \begin{cases} \text{uniform profile,} \\ \text{strong saturation.} \end{cases} \quad (38)$$

By comparing these we can get a rough idea of how the effective saturation area of the gaussian beam increases at high intensities, as more and more of the gaussian beam profile rises above the saturation-intensity level.

REFERENCES

The effects of amplifier losses and the concept of maximum useful amplifier length are discussed in A. Y. Cabezas, G. L. McAllister, and W. K. Ng, "Gain saturation in neodymium:glass laser amplifiers," *J. Appl. Phys.* **38**, 3487-3491 (August 1967).

An extensive analysis plus experimental results for the combination of saturable gain plus nonsaturating loss will be found in S. M. Curry, R. Cubeddu, and T. W. Hänsch, "Intensity stabilization of dye laser radiation by saturated amplification," *Appl. Phys.* **1**, 153-159 (1973).

Another reference on amplifier saturation, including inhomogeneous systems with hole broadening, is Kazantsev, Rautian, and Súrdutovich, "Theory of a gas laser with nonlinear saturation," *Sov. Phys. JETP* **27**, 756 (1968).

Problems for 8.3

1. *Maximum available power in an inhomogeneously broadened laser amplifier.* Evaluate the available power that can be extracted from an inhomogeneously broadened single-pass laser amplifier in the limit of very large signals when $I_{\text{in}} \gg I_{\text{sat}}$. Comment on differences between this case and the homogeneous case, and give a physical explanation of the difference. (You may need to refer to the discussions of hole burning and inhomogeneous saturation given in later chapters.)
2. *Power output versus power input for a gaussian beam profile in a homogeneously saturable amplifier.* Consider a collimated laser beam with a gaussian transverse profile passing through a homogeneously saturable single-pass laser amplifier. Assume that diffraction effects in passing through the amplifier length are small, so that each element of the beam cross section saturates essentially independently based on its local intensity. Set up a computer program to integrate the output intensity $I_{\text{out}}(r)$ across the output beam cross section to get the total output power P_2 for general values of unsaturated gain G_0 and normalized input power $P_1/\pi w^2 I_{\text{sat}}$. Evaluate in particular the extracted power $P_{\text{extracted}} \equiv P_2 - P_1$ versus P_1 , and discuss the variation of the effective cross section of the gaussian beam for extracting energy as a function of the input power for some typical values of G_0 .
3. *Behavior of a combined saturable amplifier and saturable absorber system.* Suppose an atomic medium contains both a saturable atomic gain with small-signal gain coefficient α_m and saturation intensity I_m ; and a saturable atomic loss with small-signal loss coefficient α_0 and saturation intensity I_0 . Describe with the aid of appropriate sketches the behavior of the intensity $I(z)$ of a wave passing through such a medium (especially the behavior at large z) for all possible relative values of α_m and α_0 , and I_m and I_0 , and for an arbitrary initial input intensity $I(0)$. (A quantitative and graphic description, rather than any mathematical analysis, is what is wanted here.)
4. *Improving laser amplifier energy extraction by reshaping the laser medium: continuous.* Suppose a single-pass homogeneous cw laser amplifier is to be operated with a fixed input-signal power that falls in the saturating range for the laser amplifier. For such a situation the unsaturated input end of the amplifier gives full gain but inefficient energy extraction, whereas the more heavily saturated output end of the amplifier gives efficient energy extraction but not much gain.

It might seem that we could improve the overall performance of an amplifier using the same total volume of laser material by arranging to have a constant degree of gain saturation and energy extraction all through the amplifier. This might be done by tapering the cross-sectional area of the signal beam and the amplifier in such a way that, as the signal grows in power, it also grows in area, so that the intensity $I(z)$ just stays constant.

Suppose appropriate optics are provided to let us continuously expand the diameter of both the laser beam and the laser medium along the amplifier, in such a way that the laser intensity $I(z)$ (i.e., the power per unit area) stays constant with distance along the amplifier. Analyze this case to find the necessary change in amplifier cross section with distance and the resulting saturated power input-output relationship for the amplifier.

Compare the performance of this variable-cross-section amplifier to a constant-cross-section amplifier, assuming the same laser material with the same unsaturated gain coefficient α_{m0} and saturation intensity I_{sat} , the same overall amplifier length L , the same total volume V of laser material, and the same signal power input P_1 .

[For a related reference, see J. H. Jacob, et al., "Expanding beam concept for building very large excimer laser amplifiers," *Appl. Phys. Lett.* **48**, 318–320 (3 February 1986).]

5. *Improving laser amplifier energy extraction by reshaping the laser medium: in two steps.* Repeat the previous problem, but use only two fixed-diameter amplifier stages rather than a continuous variation.

That is, suppose a single-pass, homogeneous, cw, saturating amplifier of length L is divided into two sections each of length $L/2$, with the same basic gain medium and hence the same total unsaturated gain through the two sections, but with different cross-sectional areas for the two sections. Assume the output beam from the first stage is appropriately magnified or demagnified by a suitable telescope between stages to match the change in area between the two stages. Since the cost of the power supplies and pumping hardware for a laser is likely to be more or less directly proportional to the volume of laser material that must be pumped, assume that the total volume of the two stages remains constant and equal to the original single-stage amplifier, but that the relative areas of the two stages may be changed.

Develop an analysis for the power output versus power input of this two-stage amplifier in the presence of saturation, allowing for different distributions of area between the two stages. Suppose the original single-stage amplifier is intended to operate with a certain specified power input sufficient to produce significant saturation in the single-stage device. Is it possible by going to two stages to increase the saturated gain and power output, as compared to the single-stage values, for the same specified power input?

6. *General analysis of output-power improvement by amplifier reshaping (research problem).* As an extension of the preceding problems, consider the more general question: Can we redistribute a given volume of laser material to obtain better overall performance than we get from a constant-cross-section amplifier, and how much better a performance can be obtained in this way? As design constraints for this question, assume: (a) a homogeneously saturating laser material with fixed gain coefficient α and saturation intensity I_{sat} ; (b) a fixed overall amplifier length

L (and hence fixed total small-signal gain); (c) fixed total amplifier volume V (and hence fixed total materials cost and pumping-power requirements); and (d) fixed signal input power P_1 . Assume, however, that optics can be provided to achieve any desired change in beam cross section along the amplifier. Consider then what sorts of tapered or axially varying amplifier cross sections might improve amplifier performance, especially for situations you can analyze either numerically or in closed form. What progress can you make in obtaining improved performance (at least in theory), either by increasing the saturated gain for a given energy extraction, or by increasing the energy extraction for a given saturated gain? (Note: this question leads to some interesting and not entirely expected answers.)



LINEAR PULSE PROPAGATION

Extraordinarily short optical pulses can be generated in mode-locked lasers, and these pulses can then be amplified to very large energies in subsequent laser amplifiers. Such pulses can be used for laser ranging (laser radar, or lidar); for pulse-modulated optical communications, both in free space and especially along optical fibers; and as measurement probes for studying a very wide variety of ultrafast physical, chemical, and biological processes, in what has come to be known as picosecond spectroscopy.

Pulse propagation both in passive optical propagation systems and in laser amplifiers is therefore a subject of considerable practical interest. Understanding the propagation of optical pulses through both linear and nonlinear systems is also important in mode-locked lasers, in optical fibers and other propagation systems, and in picosecond spectroscopic applications.

In this chapter we first introduce some of the fundamental ideas of pulse propagation in linear systems, including the concepts of group and phase velocities, and pulse compression and broadening in linear dispersive systems and laser amplifiers. In the following chapter we will discuss some elementary concepts in the amplification and distortion of optical pulses caused by saturation in laser amplifiers, and also some of the interesting and useful effects, such as nonlinear pulse compression and soliton propagation, that occur in nonlinear dispersive fibers and other propagation systems.

9.1 PHASE AND GROUP VELOCITIES

In this section we will analyze some of the fundamental effects that can arise in pulse propagation through linear systems, especially systems with either group velocity or gain dispersion. Fundamental concepts we will examine include *pulse delay*, *group velocity*, and *pulse compression or group velocity dispersion effects*.

Gaussian Pulses

The concepts we will introduce in this section occur for pulses of any shape. The analysis of these effects becomes particularly simple, however, with little if any of the physics being lost, if we analyze these effects using primarily gaussian

pulses. Such pulses are simple, mathematically tractable, and clearly exhibit all the essential physical features. Many real systems such as actively mode-locked lasers generate pulses that are very close to complex gaussian pulses.

We consider as our basic model, therefore, an optical pulse with a carrier frequency ω_0 and a complex gaussian envelope written in the form

$$\mathcal{E}(t) = \exp(-at^2) \exp j(\omega_0 t + bt^2) = \exp(-\Gamma t^2) \exp j\omega_0 t. \quad (1)$$

The complex gaussian parameter describing this pulse is thus

$$\Gamma \equiv a - jb. \quad (2)$$

(This Γ has nothing to do with the axial wave propagation constant Γ we used in an earlier chapter.) The instantaneous intensity $I(t)$ associated with this pulse can be written as

$$I(t) = |\mathcal{E}(t)|^2 = \exp(-2at^2) = \exp[-(4 \ln 2)(t/\tau_p)^2], \quad (3)$$

so that the pulselwidth τ_p , defined in the usual FWHM fashion, is related to the parameter a by

$$\tau_p = \sqrt{\frac{4 \ln 2}{2a}}. \quad (4)$$

Note that this is the FWHM pulselwidth for the intensity $I(t)$, and not for the signal amplitude $\mathcal{E}(t)$.

Instantaneous Frequency

The time-varying phase shift or phase rotation of the sinusoidal signal within this gaussian pulse is given by

$$\mathcal{E}(t) \propto \exp j(\omega_0 t + bt^2) = \exp[j\phi_{\text{tot}}(t)], \quad (5)$$

so that the total instantaneous phase of the signal is

$$\phi_{\text{tot}}(t) = \omega_0 t + bt^2 \quad (6)$$

What then is the “instantaneous frequency” $\omega_i(t)$ of this sinusoidal signal?

The total phase variation in this case can obviously be written in the form $\phi_{\text{tot}}(t) = \omega_0 t + bt^2 = (\omega_0 + bt)t$. We might therefore be led to say that the instantaneous frequency of the pulse at time t should be written as $\omega_i(t) = \omega_0 + bt$. This is not, however, a correct interpretation.

The instantaneous radian frequency of an oscillating signal, in the way this term is usually interpreted, should instead be *the rate at which the total phase of the sinusoidal signal rotates forward*, or alternatively *2π times the number of cycles completed per unit time*, as measured in any small time interval. In other words, the instantaneous frequency in radians per second is properly defined as

$$\omega_i(t) \equiv \frac{d\phi_{\text{tot}}(t)}{dt}. \quad (7)$$

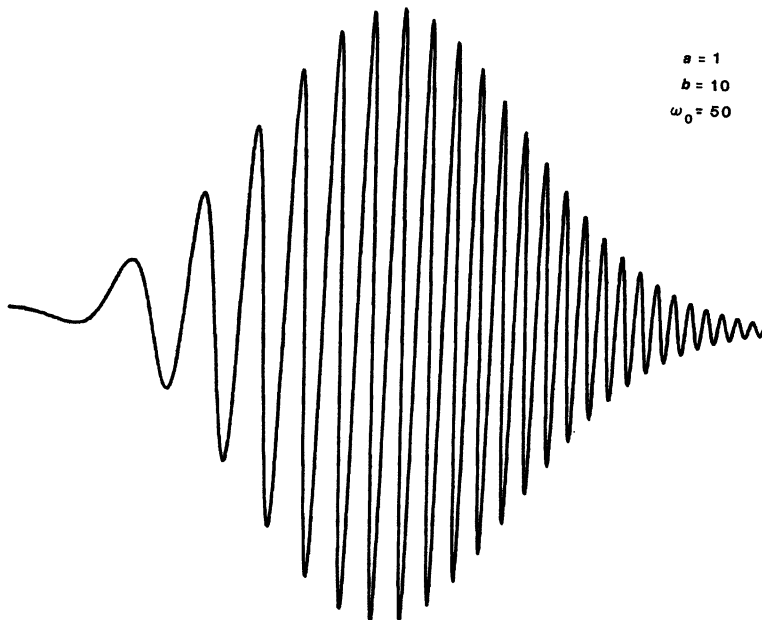


FIGURE 9.1
A chirped gaussian signal pulse.

In the complex gaussian case this gives

$$\omega_i(t) \equiv \frac{d}{dt}(\omega_0 t + bt^2) = \omega_0 + 2bt. \quad (8)$$

The factor of 2 in the time-varying part of this expression is important.

A gaussian pulse with a nonzero imaginary part b thus has a linearly time-varying instantaneous frequency. Such a signal is often said to be *chirped*, with the parameter b being a measure of this chirp. Figure 9.1 shows a rather strongly chirped gaussian pulse with a sizable variation of the instantaneous frequency within the pulse.

Gaussian Pulse Spectrum

One of the major virtues of the gaussian pulse approach is that a gaussian pulse in time immediately Fourier-transforms into a gaussian spectrum in frequency, in the form

$$\mathcal{E}(t) = \exp(-\Gamma t^2 + j\omega_0 t) \quad \Rightarrow \quad \tilde{E}(\omega) = \exp\left[-\frac{(\omega - \omega_0)^2}{4\Gamma}\right]. \quad (9)$$

The exponent in the Fourier transform thus has a complex-quadratic dependence on frequency of the form

$$\tilde{E}(\omega) = \exp \left[-\frac{1}{4} \left(\frac{a}{a^2 + b^2} \right) (\omega - \omega_0)^2 - j \frac{1}{4} \left(\frac{b}{a^2 + b^2} \right) (\omega - \omega_0)^2 \right]. \quad (10)$$

A signal with a linear frequency chirp (or quadratic phase chirp) in time automatically also has a quadratic imaginary component or quadratic phase shift of its Fourier spectrum in frequency, as given by the $b/(a^2 + b^2)$ factor.

The power spectrum, or power spectral density, of this pulse is then given by

$$\begin{aligned} |\tilde{E}(\omega)|^2 &= \exp \left[-\frac{1}{2} \left(\frac{a}{a^2 + b^2} \right) (\omega - \omega_0)^2 \right] \\ &= \exp \left[-(4 \ln 2) \left(\frac{\omega - \omega_0}{\Delta\omega_p} \right)^2 \right], \end{aligned} \quad (11)$$

where $\Delta\omega_p$ is the FWHM spectral width (in radians/second) of the pulse. We can convert this into a pulse bandwidth measured in Hz by writing

$$\Delta f_p \equiv \frac{\Delta\omega_p}{2\pi} = \frac{\sqrt{2 \ln 2}}{\pi} \sqrt{a[1 + (b/a)^2]}. \quad (12)$$

For a given pulsewidth in time as determined by the real parameter a , the presence of a frequency chirp as determined by the imaginary parameter jb increases the spectral bandwidth $\Delta\omega_p$ by a ratio $\sqrt{1 + (b/a)^2}$, as compared to an unchirped pulse with the same pulsewidth in time.

Time-Bandwidth Products, and Transform-Limited Pulses

Combining the preceding equations shows in fact that the gaussian pulse has a *time-bandwidth product* given by

$$\Delta f_p \tau_p = \left(\frac{2 \ln 2}{\pi} \right) \times \sqrt{1 + (b/a)^2} \approx 0.44 \times \sqrt{1 + (b/a)^2}. \quad (13)$$

The minimum or unchirped value of time-bandwidth product for a gaussian pulse is thus $\Delta f_p \tau_p \approx 0.44$. The presence of chirp increases this time-bandwidth product to a value given, in the limit of large chirp, by $\approx b/a$ times the minimum value.

This particular time-bandwidth product is the gaussian-pulse, FWHM version of a general Fourier theorem which says the time-bandwidth product of any pulsed signal is constrained by the uncertainty principle $\Delta f_{\text{rms}} \Delta t_{\text{rms}} \geq 1/2$, where Δf_{rms} and Δt_{rms} are the root-mean-square widths of the signal in frequency and in time. If one uses the rms definitions of Δf and Δt , the time-bandwidth product for a chirped gaussian pulse is in fact the same as Equation 9.13, except that the 0.44 factor is replaced by exactly 0.5. More generally, the exact value of time-bandwidth product $\Delta f \Delta t$ for an arbitrary pulse shape depends on:

- the exact shape of the pulse (gaussian, square, exponential, etc.);
- how Δf and Δt are defined (rms, FWHM, etc.); and
- especially on the amount of chirp or other amplitude or phase substructure within the pulse.

Pulses with little chirp or other internal substructure will have a time-bandwidth product close to the value of ≈ 0.5 . Such pulses are often referred to as *transform-limited pulses*. If separate measurements of pulsed width and spectral width on a pulsed signal give a time-bandwidth product close to this limit, the pulsed signal must have little or no amplitude or phase substructure within the pulse duration. (See Problem 9.1-1 for some other examples of time-bandwidth products.)

Dispersive Systems and “Omega-Beta Curves”

Consider now a dispersive atomic medium, or any other kind of dispersive wave-propagating system, such as a transmission line, waveguide, or optical fiber. By “dispersive” in this context we mean any linear system in which the propagation constant $\beta(\omega)$ as a function of frequency has any form other than a straight line through the origin, i.e., $\beta = \omega/c$.

We have shown plots in earlier chapters of the propagation constant $\beta(\omega)$, or the total phase shift $\phi(\omega) = \beta(\omega)L$, plotted versus frequency ω for various atomic systems. In discussing dispersive systems, however, it is convenient to plot ω versus β , rather than β versus ω , as shown in Figure 9.2. Such an “omega-beta plot” may represent the dispersive effect of an atomic transition or of the background index in a host medium, in which case it is called *material dispersion*. Alternatively, it may represent the propagation characteristics of a guided mode in some waveguiding system such as a microwave waveguide, an optical fiber, or a general filter network, in which case the dispersion is commonly referred to as *waveguide dispersion* or *modal dispersion*.

Suppose we are concerned with narrowband signals having frequency components primarily near some center frequency ω_0 . Then the propagation constant of a dispersive system can be conveniently expanded about its value at ω_0 in the form

$$\beta(\omega) = \beta(\omega_0) + \beta' \times (\omega - \omega_0) + \frac{1}{2}\beta'' \times (\omega - \omega_0)^2, \quad (14)$$

where the derivatives $\beta' \equiv d\beta/d\omega$ and $\beta'' \equiv d^2\beta/d\omega^2$ are both evaluated at $\omega = \omega_0$.

Besides the frequency-dependent propagation constant $\beta(\omega)$, we might at the same time consider the effects of a frequency-dependent gain or loss coefficient $\alpha = \alpha(\omega) = \alpha(\omega_0) + \alpha' \times (\omega - \omega_0) + \frac{1}{2}\alpha'' \times (\omega - \omega_0)^2$ in the same system. Both of these frequency variations will distort or modify a pulse propagating through the system. We wish to focus at this point, however, on pulse propagation and pulse-compression phenomena due only to velocity dispersion. We will therefore ignore for now any frequency-dependent gain coefficient, and assume that any gains or losses are either zero or at least independent of frequency.

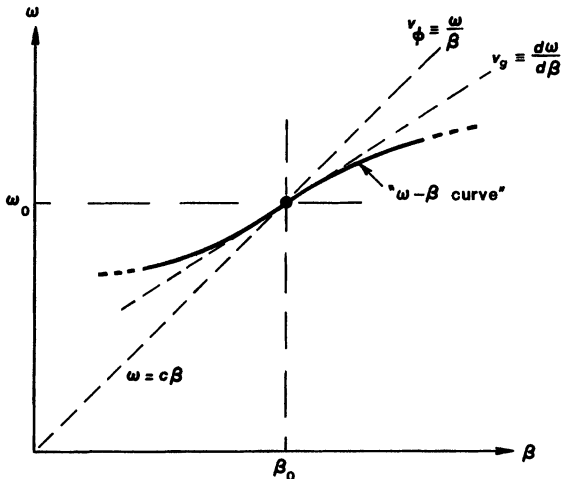


FIGURE 9.2
An "omega-beta" dia-
gram for a dispersive wave-
propagating system.

Gaussian Pulse Propagation Through a Dispersive System

Suppose then that we put a gaussian pulse of the form

$$\mathcal{E}_0(t) = \exp(-\Gamma_0 t^2 + j\omega_0 t), \quad \tilde{\mathcal{E}}_0(\omega) = \exp\left[-\frac{(\omega - \omega_0)^2}{4\Gamma_0}\right], \quad (15)$$

into such a dispersive system, where $\Gamma_0 \equiv a_0 - jb_0$ is the initial pulse parameter at the input to the system. The output pulse spectrum $\tilde{\mathcal{E}}(z, \omega)$ after propagating a distance z through such a system will be the input spectrum $\tilde{\mathcal{E}}_0(\omega)$ of Equation 9.9, multiplied by the frequency-dependent propagation through the system, or

$$\begin{aligned} \tilde{\mathcal{E}}(z, \omega) &= \tilde{\mathcal{E}}_0(\omega) \times \exp[-j\beta(\omega)z] \\ &= \exp\left[-j\beta(\omega_0)z - j\beta' z \times (\omega - \omega_0) - \left(\frac{1}{4\Gamma_0} + \frac{j\beta'' z}{2}\right) \times (\omega - \omega_0)^2\right]. \end{aligned} \quad (16)$$

The output pulse in time from this system will be the inverse Fourier transform of the output spectrum, or

$$\mathcal{E}(z, t) \equiv \int_{-\infty}^{\infty} \tilde{\mathcal{E}}(z, \omega) e^{j\omega t} d\omega. \quad (17)$$

With some minor manipulations, this integral can be put into the form

$$\mathcal{E}(z, t) = \frac{e^{j[\omega_0 t - \beta(\omega_0)z]}}{2\pi} \int_{-\infty}^{\infty} \exp\left[-\frac{(\omega - \omega_0)^2}{4\Gamma(z)} + j(\omega - \omega_0)(t - \beta' z)\right] d(\omega - \omega_0). \quad (18)$$

where $1/\Gamma(z) \equiv 1/\Gamma_0 + 2j\beta''$. In this form, the carrier-frequency time and space dependence have been moved out in front, so that the integral part of this expression gives the time and space dependence of the output pulse envelope. The

output pulse is still a gaussian pulse, but with an altered gaussian pulse parameter $\Gamma(z)$ at the output of the system.

To interpret this mathematical result, we can carry out the integration explicitly using “Siegman’s lemma,” namely,

$$\int_{-\infty}^{\infty} e^{-Ay^2 - 2By} dy \equiv \sqrt{\frac{\pi}{A}} e^{B^2/A}, \quad \operatorname{Re}[A] > 0 \quad (19)$$

or we can simply note that the integral in Equation 9.18 is obviously the Fourier transform of a gaussian pulse of the form $\exp(-\Gamma t^2)$, with a shift in time by $t - \beta' z$ included. From either approach, the output pulse after traveling any arbitrary distance z through the system is given by

$$\begin{aligned} \mathcal{E}(z, t) &= \exp[j(\omega_0 t - \beta(\omega_0)z)] \times \exp[-\Gamma(z) \times (t - \beta' z)^2] \\ &= \exp\left[j\omega_0\left(t - \frac{z}{v_\phi(\omega_0)}\right)\right] \times \exp\left[-\Gamma(z) \times \left(t - \frac{z}{v_g(\omega_0)}\right)^2\right], \end{aligned} \quad (20)$$

where $\Gamma(z)$ is the modified gaussian pulse parameter after traveling a distance z , and where $v_\phi(\omega_0) \equiv \omega_0/\beta(\omega_0)$ and $v_g(\omega_0) \equiv 1/\beta'(\omega_0)$.

Phase Velocity

The first exponent in each line of Equation 9.20 says that in propagating through the distance z , the phase of the sinusoidal carrier frequency ω_0 is delayed by a midband phase shift $\beta(\omega_0)z$, or by a midband phase delay t_ϕ (in time) given by

$$\text{phase delay, } t_\phi = \frac{z}{v_\phi(\omega_0)} = \frac{\beta(\omega_0)}{\omega_0} z. \quad (21)$$

This says that the carrier-frequency cycles, or the sinusoidal waves within the pulse envelope, will appear to move forward with a *midband phase velocity* $v_\phi(\omega_0)$ given by

$$\text{phase velocity, } v_\phi(\omega_0) = \frac{z}{t_\phi} = \frac{\omega_0}{\beta(\omega_0)}. \quad (22)$$

The midband phase velocity is thus determined by the propagation constant $\beta(\omega_0)$ at the carrier frequency ω_0 .

Group Velocity

The second exponent in each line of Equation 9.20 says, however, that the *pulse envelope*, which remains gaussian but with a modified pulse parameter $\Gamma(z)$, is delayed by the *group delay time* t_g given by

$$\text{group delay, } t_g = \frac{z}{v_g(\omega_0)} = \beta' z. \quad (23)$$

That is, the pulse envelope appears to move forward with a *midband group velocity* $v_g(\omega_0)$ given by

$$\text{group velocity, } v_g(\omega_0) = \left. \frac{1}{(d\beta/d\omega)} \right|_{\omega=\omega_0} = \left(\frac{d\omega}{d\beta} \right)_{\omega=\omega_0}. \quad (24)$$

If we could take instantaneous “snapshots” of the pulse fields $\mathcal{E}(z, t)$ from Figure 9.1 as the pulse propagated through the system, we would see the (invisible) pulse envelope moving forward at the group velocity $v_g(\omega_0)$, while the individual cycles within the pulse envelope moved forward at the phase velocity $v_\phi(\omega_0) \equiv \omega_0/\beta(\omega_0)$. For $v_g(\omega_0) < v_\phi(\omega_0)$, for example, we would appear to see cycles of the carrier frequency walking into the pulse envelope from the back edge and disappearing out through the front edge of the pulse envelope, while the envelope itself moved forward at a slower velocity.

Pulse Compression

Finally, the gaussian pulse parameter $\Gamma(z)$ at distance z , relative to the value Γ_0 at the input, is given from Equations 9.16 and 9.18 by

$$\frac{1}{\Gamma(z)} = \frac{1}{\Gamma_0} + 2j\beta''z. \quad (25)$$

The change in $\Gamma(z)$ is determined by β'' , the second derivative of the propagation constant at line center. We will discuss the meaning of this formula, which includes *pulse compression* in particular, in much more detail in the following section.

Summary

The successive coefficients in the power series expansion of $\beta(\omega)$ thus have the meanings

$$\begin{aligned} \beta &\equiv \beta(\omega)|_{\omega=\omega_0} = \frac{\omega_0}{v_\phi(\omega_0)} \equiv \frac{\omega_0}{\text{phase velocity}}, \\ \beta' &\equiv \left. \frac{d\beta}{d\omega} \right|_{\omega=\omega_0} = \frac{1}{v_g(\omega_0)} \equiv \frac{1}{\text{group velocity}}, \\ \beta'' &\equiv \left. \frac{d^2\beta}{d\omega^2} \right|_{\omega=\omega_0} = \frac{d}{d\omega} \left(\frac{1}{v_g(\omega)} \right) \equiv \frac{\text{“group velocity}}{\text{dispersion.}} \end{aligned} \quad (26)$$

The physical interpretation of these coefficients in terms of group and phase velocities, although derived here using gaussian pulses, is very general, and applies to any sort of pulse signal. If a pulsed signal has a carrier frequency ω_0 within a pulse envelope of any shape, and this pulse propagates through any lossless linear system that has a midband propagation constant $\beta(\omega_0)$ and a first-order linear variation $\beta' \times (\omega - \omega_0)$ across the pulse spectrum, then the carrier-frequency cycles within the pulse will move forward at the phase velocity v_ϕ , while the pulse envelope itself will move forward at the group velocity v_g evaluated at the center of the pulse spectrum. The pulse envelope itself may also change in shape with distance because of the β'' term, as we will discuss in the following section.

REFERENCES

For an excellent survey of ultrashort optical pulses and the various ways of generating, artificially compressing, and applying them, see the various chapters included

in *Ultrashort Light Pulses*, ed. by S. L. Shapiro (Topics in Applied Physics, Vol. 18, Springer-Verlag, 1977).

There are many discussions in the literature of dispersive wave propagation, group and phase velocities, and pulse velocity and pulse distortion. A collection of classic early papers by A. Sommerfeld and L. Brillouin is given in L. Brillouin, *Wave Propagation and Group Velocity* (Academic Press, 1960).

For a list of more recent references, work backward starting from S. C. Bloch, "Eighth velocity of light," *Am. J. Phys.* **45**, 538–549 (June 1977).

Problems for 9.1

1. *Time-bandwidth products for various optical pulseshapes.* Evaluate the time-bandwidth products, using both rms and FWHM definitions of pulselwidth and bandwidth, for (a) a square pulse of width T in time; (b) a double-sided exponential pulse $\mathcal{E}(t) = \exp(-|t/T|)$; (c) a single-sided exponential pulse $\mathcal{E}(t) = \exp(-t/T)$ for $t > 0$ and $\mathcal{E}(t) = 0$ for $t < 0$; and (d) a secant-squared pulse $\mathcal{E}(t) = \text{sech}^2(t/\tau_p)$. (Note: There are some unanticipated difficulties in this problem.)
-

9.2 THE PARABOLIC EQUATION

There is an alternative and somewhat more general way to derive the linear pulse propagation results we are presenting in this chapter, by using the so-called "parabolic wave equation." This parabolic equation is widely used in the professional literature, and it also brings out an interesting analogy between dispersive pulse spreading and diffractive optical beam spreading. We will therefore give a brief derivation of the parabolic equation in this section, although we will not make any further direct use of it here. Readers in a hurry for results may therefore want to skip over this short section.

Derivation of the Parabolic Equation

The basic wave equation for a one-dimensional signal in a dispersive medium, or on a dispersive transmission line, may be written as

$$\frac{\partial^2 \mathcal{E}(z, t)}{\partial z^2} - \mu_0 \epsilon_0 \frac{\partial^2 \mathcal{E}(z, t)}{\partial t^2} = \mu \frac{\partial^2 p(z, t)}{\partial t^2}, \quad (27)$$

where $p(z, t)$ is the potentially dispersive but linear polarization of the medium or transmission line. (In more sophisticated problems, a nonlinear polarization may be included here also.) Suppose we write this field $\mathcal{E}(z, t)$ in the form

$$\mathcal{E}(z, t) \equiv \text{Re } \tilde{\mathcal{E}}(z, t) e^{j[\omega_0 t - \beta(\omega_0) z]}, \quad (28)$$

where ω_0 is again a carrier or midband frequency for the signal, with propagation constant $\beta(\omega_0)$ at this midband frequency, and $\tilde{\mathcal{E}}(z, t)$ is taken to be the complex envelope of the pulsed signal.

We can write the polarization $p(z, t)$ in terms of its Fourier transform $\tilde{P}(z, \omega)$ in the form

$$p(z, t) = \frac{1}{2\pi} \int_{-\infty}^{\infty} \tilde{P}(z, \omega) e^{j\omega t} d\omega. \quad (29)$$

Assume this polarization arises from a linear but possibly dispersive response in the medium or transmission line. Then, we may write it in terms of the electric field in the form

$$\tilde{P}(z, \omega) = \tilde{\chi}(\omega) \epsilon_0 \tilde{E}(z, \omega), \quad (30)$$

where $\tilde{E}(z, \omega)$ is the Fourier transform of $E(z, t)$ given by

$$\begin{aligned} \tilde{E}(z, \omega) &= \int_{-\infty}^{\infty} E(z, t) e^{-j\omega t} dt \\ &= \int_{-\infty}^{\infty} \tilde{E}(z, t) e^{j(\omega_0 - \omega)t} dt \end{aligned} \quad (31)$$

and where $\tilde{\chi}(\omega)$ is the dispersive susceptibility of the propagation system.

By using these definitions, plus standard Fourier transform theorems, we can write the polarization term on the right-hand side of Equation 9.27 as

$$\begin{aligned} \frac{\partial^2 p(z, t)}{\partial t^2} &= -\frac{1}{2\pi} \int_{-\infty}^{\infty} \omega^2 \tilde{P}(z, \omega) e^{j\omega t} d\omega \\ &= -\frac{\epsilon_0}{2\pi} \int_{-\infty}^{\infty} \omega^2 \tilde{\chi}(\omega) e^{j\omega t} d\omega \int_{-\infty}^{\infty} \tilde{E}(z, t') e^{j[\omega_0 t' - \beta(\omega_0)z]} dt' \end{aligned} \quad (32)$$

The derivation of the parabolic equation then proceeds by expanding the quantity $\omega^2 \tilde{\chi}(\omega)$ in Equation 9.32 about its midband value in the form

$$\begin{aligned} \omega^2 \tilde{\chi}(\omega) &\approx \omega_0^2 \tilde{\chi}(\omega_0) + \frac{d}{d\omega} [\omega^2 \tilde{\chi}(\omega)] \times (\omega - \omega_0) \\ &\quad + \frac{1}{2} \frac{d^2}{d\omega^2} [\omega^2 \tilde{\chi}(\omega)] \times (\omega - \omega_0)^2 + \dots \end{aligned} \quad (33)$$

with all derivatives evaluated at $\omega = \omega_0$. This is of course exactly the same approximation as in the expansion of $\beta(\omega)$ in the previous section. It is then possible to evaluate the polarization integral of Equation 9.32 by making use of the convenient identities

$$\frac{1}{2\pi} \int_{-\infty}^{\infty} e^{j(\omega - \omega_0)(t - t')} d\omega \equiv \delta(t - t') = \delta(t' - t) \quad (34)$$

as well as

$$\frac{1}{2\pi} \int_{-\infty}^{\infty} (\omega - \omega_0) e^{j(\omega - \omega_0)(t - t')} d\omega \equiv j\delta^{(1)}(t - t') = -j\delta^{(1)}(t' - t) \quad (35)$$

and

$$\frac{1}{2\pi} \int_{-\infty}^{\infty} (\omega - \omega_0)^2 e^{j(\omega - \omega_0)(t - t')} d\omega \equiv -\delta^{(2)}(t - t') = -\delta^{(2)}(t' - t). \quad (36)$$

In these relations, $\delta^{(n)}(t)$ indicates an n -th order derivative of the Dirac delta function, with the useful property that

$$\int_{-\infty}^{\infty} \delta^{(n)}(t - t_0) f(t) dt \equiv \left. \frac{d^n f(t)}{dt^n} \right|_{t=t_0} \quad (37)$$

when applied to any reasonable function $f(t)$. We will also use the various identities that

$$\beta^2(\omega) \equiv \omega^2 \mu_0 \epsilon_0 + \mu_0 \epsilon_0 \omega^2 \bar{\chi}(\omega) \quad (38)$$

as well as

$$2\beta \frac{d\beta}{d\omega} \equiv 2\omega \mu_0 \epsilon_0 + \mu_0 \epsilon_0 \frac{d}{d\omega} [\omega^2 \bar{\chi}(\omega)] \quad (39)$$

and

$$\left(\frac{d\beta}{d\omega} \right)^2 + \beta \frac{d^2 \beta}{d\omega^2} \equiv \mu_0 \epsilon_0 + \frac{\mu_0 \epsilon_0}{2} \frac{d^2}{d\omega^2} [\omega^2 \bar{\chi}(\omega)], \quad (40)$$

where $[d\beta(\omega)/d\omega]_{\omega=\omega_0} \equiv v_g(\omega_0)$ is the midband group velocity in the system; and we will use the slowly varying envelope approximation to drop second derivatives of the pulse envelope $\tilde{E}(z, t)$ with respect to distance z .

When all these approximations are inserted and all the algebra is cleared away, the basic wave equation for $\mathcal{E}(z, t)$ given in Equation 9.27 reduces to the *parabolic equation for the pulse envelope* $\tilde{E}(z, t)$ given by

$$\frac{\partial \tilde{E}(z, t)}{\partial z} + \frac{1}{v_g} \frac{\partial \tilde{E}(z, t)}{\partial t} - j \frac{\beta''}{2} \frac{\partial^2 \tilde{E}(z, t)}{\partial t^2} = 0. \quad (41)$$

where v_g and β'' are both evaluated at midband, $\omega = \omega_0$. This equation is called the parabolic equation both because of the parabolic expansion of $\omega^2 \bar{\chi}(\omega)$ used in deriving it, and because of the second-derivative term in t which appears as a consequence of this approximation.

Group Velocity and Group Velocity Dispersion

We can note first that if the second-derivative term $\beta'' \equiv 0$, then this equation is obviously satisfied by any solution of the form $\tilde{E}(z, t) \equiv \tilde{E}(z - v_g t)$, where v_g is the midband value at $\omega = \omega_0$ as defined in Equations 9.23 and 9.24. This shows that the group velocity concept for propagation of the pulse envelope $\tilde{E}(z, t)$ applies to much more than just the gaussian pulses discussed in the preceding section. For any reasonably narrowband pulsed or modulated signal, the pulse or modulation envelope moves forward at velocity v_g , whereas the individual optical cycles move forward at velocity v_ϕ .

If the $d^2\beta/d\omega^2$ term is nonzero, however, the propagation system will have a “group velocity dispersion,” or a variation of group velocity with frequency, as we will discuss in the following sections. The $j(\beta''/2) \partial^2 \tilde{E} / \partial t^2$ term in Equation 9.41 then acts like a kind of generalized complex diffusion term for the pulse envelope $\tilde{E}(z, t)$ in the time coordinate. This “complex-valued diffusion” leads to pulse broadening, pulse compression, and pulse reshaping effects that we will discuss in more detail in the following sections.

Alternative Form

There is also an alternative form for the parabolic equation, in which we begin with a pulseshape defined as

$$\begin{aligned}\mathcal{E}(z, t) &\equiv \operatorname{Re} \tilde{E}(z, \eta) e^{j(\omega_0 t - \beta(\omega_0)z)} \\ &= \operatorname{Re} \tilde{E}(z, t - z/v_g) e^{j(\omega_0 t - \beta(\omega_0)z)},\end{aligned}\quad (42)$$

so that $\eta \equiv t - z/v_g$ is a displaced time coordinate whose origin $\eta = 0$ is centered at the time of arrival of the pulse at each plane z . The parabolic equation (9.41) then simplifies to the form

$$\frac{\partial \tilde{E}(z, \eta)}{\partial z} - \frac{j}{2} \left(\frac{d^2 \beta}{d\omega^2} \right) \frac{\partial^2 \tilde{E}(z, \eta)}{\partial \eta^2} = 0. \quad (43)$$

Obviously if the dispersion term $d^2/d\omega^2 \equiv 0$, then the pulse shape $\tilde{E}(z, \eta)$ becomes independent of z , or $\tilde{E}(z, \eta) \equiv \tilde{E}_0(\eta) \equiv \tilde{E}_0(t - z/v_g)$, as we have discussed. This form offers a slightly simpler way to express the same ideas.

Space-Time Analogy

The parabolic equation derived in this section has exactly the same mathematical form as the paraxial wave equation used in optical beam propagation analyses (Chapter 16), if we identify the delayed time coordinate $t - z/v_g$ (or η) in the parabolic equation with either of the transverse spatial coordinates x or y in the paraxial equation. The dispersive or second-derivative term that leads to broadening (or compression) of a pulse's time envelope with distance z in the parabolic equation then plays exactly the same role as the diffractive term that leads to transverse spreading of a laser beam's transverse profile with distance z in the paraxial equation. There is thus a very close analogy between signal pulse distortion with propagation distance in the dispersive equation, and changes in transverse beam profile with propagation distance due to diffraction effects in the paraxial situation. An optical wavefront with positive or negative wavefront curvature (imaginary quadratic dependence on x or y in the exponent) is directly analogous to an optical signal with positive or negative chirp (imaginary quadratic dependence on t in the exponent); and this wavefront curvature may lead to a converging or diverging optical-beam profile, just as chirp may lead to pulse compression or expansion with distance.

As another example, an initially square signal pulse propagating on a dispersive transmission line will broaden into a $(\sin t)/t$ pulseshape after a long enough distance, exactly as a uniform plane wave coming through a rectangular slit in the near field will broaden into a $(\sin x)/x$ beam pattern in the far field. This general approach can give useful insights into the relationship between pulse-distortion effects on dispersive lines and beam-spreading effects in diffractive propagation.

REFERENCES

The space-time analogy between dispersive pulse compression in time and optical-beam focusing in space is clearly illustrated in E. B. Treacy, "Optical pulse compression with diffraction gratings," *IEEE J. Quantum Electron.* **QE-5**, 454-458 (September 1969).

This same analogy is also developed in more detail, and applied to both linear and nonlinear examples, by S. A. Akhmanov, A. P. Sukhorukov, and A. S. Chirkin, "Stationary phenomena and space-time analogy in nonlinear optics," *Sov. Phys. JETP* **28**, 748-757 (April 1969). Another paper by the same group is "Nonstationary nonlinear optical effects and ultrashort light pulse formation," *IEEE J. Quantum Electron.* **QE-4**, 598-605 (October 1968).

Problems for 9.2

1. *Parabolic equation derivation.* Carry through the detailed steps leading from Equation 9.27 to 9.41 in this section.
-

9.3 GROUP VELOCITY DISPERSION AND PULSE COMPRESSION

If a pulse propagates through a system in which the group-velocity dispersion term $\beta'' \times (\omega - \omega_0)^2$ has a significant amplitude, then we must consider not only the phase and group velocities as discussed in the preceding sections, but also the fact that the pulseshape itself will be significantly changed in propagating through the system. Interesting and useful effects, such as pulse compression, pulse spreading, and pulse reshaping, can result from such second-order dispersion effects. Once again it is very convenient to derive and illustrate such effects using a chirped gaussian pulse model, as we will show in this section.

Gaussian Pulse Propagation

From the analysis of the preceding section, if we put a pulse with initial pulse parameter $\Gamma_0 = a_0 - jb_0$ through a dispersive propagation system whose propagation constant has nonzero second derivative β'' at the carrier frequency of the pulse, then the change in the complex pulseshape parameter $\Gamma(z)$ with propagation distance z through the system will be given by

$$\begin{aligned} \frac{1}{\Gamma(z)} &= \frac{1}{\Gamma_0} + 2j\beta''z = \frac{a_0}{a_0^2 + b_0^2} + j \left(\frac{b_0}{a_0^2 + b_0^2} + 2\beta''z \right) \\ &= \frac{1}{a(z) - jb(z)} = \frac{a(z)}{a^2(z) + b^2(z)} + j \frac{b(z)}{a^2(z) + b^2(z)}. \end{aligned} \quad (44)$$

This result can be interpreted graphically by noting that the quantity $1/\Gamma(z)$ moves along a vertical straight-line trajectory in the complex $1/\Gamma$ plane with increasing propagation distance $2\beta''z$, starting from an initial point $1/\Gamma_0$, as indicated in Figure 9.3.

Since the real part of $1/\Gamma(z)$ determines the pulse bandwidth, it is evident from the left-hand part of Figure 9.3 that the pulse bandwidth stays constant, as it obviously should do in the absence of gain narrowing. This trajectory in the $1/\Gamma$ plane can then be converted to a trajectory in the $a - jb$ plane (or more conveniently in the $a + jb \equiv \Gamma^*$ plane) by simply inverting each complex point through the origin. An inversion of this form always converts a straight line in

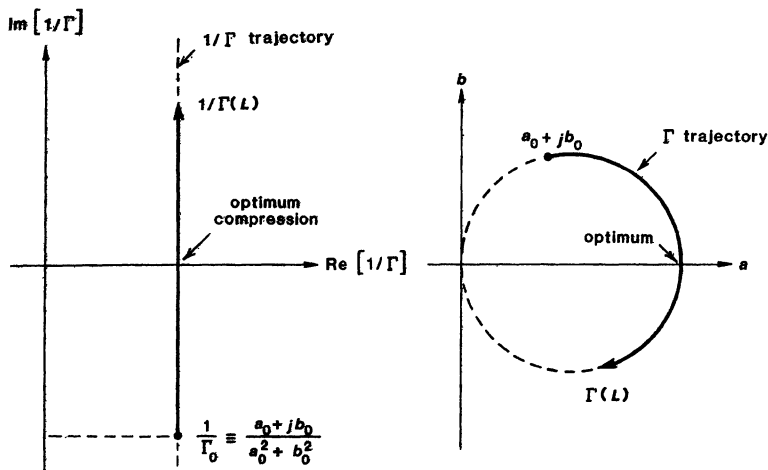


FIGURE 9.3

Trajectories for dispersive pulse propagation and pulse compression in the Γ and $1/\Gamma$ planes.

the $1/\Gamma$ plane to a circle in the Γ or Γ^* plane. Propagation through a distance $2\beta''z$ now represents propagation about an arc of this circle, as illustrated on the right-hand side of Figure 9.3.

Differential Approach

These same results can also be derived using a differential approach. If we differentiate the complex beam parameter $\Gamma(z)$ with respect to distance along the system, we obtain the differential equation

$$\frac{d\Gamma(z)}{dz} = -2j\beta'' \times \Gamma^2(z) \quad (45)$$

and this in turn separates into the two equations

$$\frac{da(z)}{dz} = -4\beta''a(z)b(z), \quad \frac{db(z)}{dz} = 2\beta''[a(z)^2 - b(z)^2]. \quad (46)$$

The solutions to these equations are a family of circular trajectories, such as the trajectory indicated in Figure 9.3.

Pulse Compression

The pulse parameters at the output of a length z of the dispersive line are

$$a(z) = \frac{a_0}{(1 + 2\beta''zb_0)^2 + (2\beta''za_0)^2} \quad (47)$$

and

$$b(z) = \frac{b_0(1 + 2\beta''zb_0) + 2\beta''za_0^2}{(1 + 2\beta''zb_0)^2 + (2\beta''za_0)^2}. \quad (48)$$

The point where the trajectory of $\Gamma(z)$ crosses the positive real axis in either the Γ or $1/\Gamma$ plots obviously corresponds to the maximum value of the output parameter $a(z)$, and hence to the minimum value of the output pulselength $\tau_p(z)$. As the pulse propagates from the initial value Γ_0 to this point, the pulse is being compressed in width, or shortened in time, at least with the choice of parameters we have used in Figure 9.3. Beyond this point, the pulse broadens again in time. This pulse compression for a chirped pulse passing through a dispersive propagation system can be very useful in a wide variety of not only optical but also microwave and radio frequency applications, as we will see later.

Optimum Compression Length

Suppose we can adjust the total dispersion $2\beta''z$, by changing either the group velocity dispersion β'' or the distance z that is traveled. The size of this parameter is related to the distance traveled along the straight-line trajectory or, in a more complicated way, to the arc length traveled along the circle in Figure 9.3. What dispersion length $2\beta''z$ is then needed to reach the minimum pulselength point, starting with a given input pulse parameter Γ_0 ? Differentiating the quantity $a(z)$ with respect to the parameter $2\beta''z$ shows that the maximum value of $a(z)$ occurs for an optimum propagation distance related to the input pulse parameters by

$$(2\beta''z)_{\text{opt}} = -\frac{b_0}{a_0^2 + b_0^2} \approx -\frac{1}{b_0} \quad \text{if } b_0 \gg a_0. \quad (49)$$

The output pulse parameters at this optimum distance are given by

$$a_{\text{opt}} = a_0 [1 + (b_0/a_0)^2] \approx b_0^2/a_0 \quad \text{and} \quad b_{\text{opt}} \equiv 0. \quad (50)$$

After propagating an optimum distance through the system, the output pulse is compressed in time down to a minimum pulselength $\tau_{p,\text{min}}$ which is related to its input pulselength τ_{p0} and to its initial pulse parameters a_0 and b_0 by

$$\frac{\tau_{p,\text{min}}}{\tau_{p0}} = \sqrt{\frac{1}{1 + (b_0/a_0)^2}} \approx \left| \frac{a_0}{b_0} \right| \quad \text{if } b_0 \gg a_0. \quad (51)$$

A large initial chirp compared to the pulselength, or $b_0 \gg a_0$ —which is the same thing as a large initial time-bandwidth product—leads to the possibility of large pulselength compression (Figure 9.4); whereas an initial condition such that $b_0 \leq a_0$ permits only a negligible pulse compression. It is also evident that at the optimum compression point $b_{\text{opt}} = 0$, meaning that all the chirp has been removed. A gaussian pulse will be compressed all the way down to its minimum time-bandwidth product $\Delta f_p \tau_{p,\text{min}} = 0.44$ at the optimum point.

Again these results, although derived for a gaussian pulse, are in fact quite general conclusions, which by no means apply only to gaussian pulses. All signals with large initial time-bandwidth products are potentially compressible; signals with near-transform-limited initial time-bandwidth products are not.

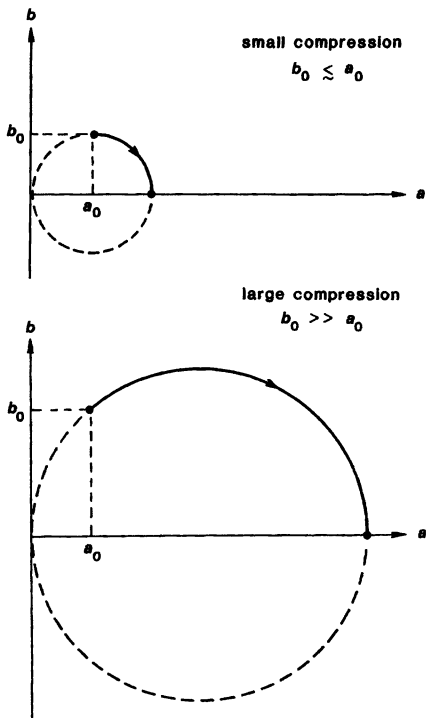


FIGURE 9.4
Optimum pulse compression with the same initial pulsewidths but smaller and larger initial time-bandwidth products.

Physical Interpretation

We can give a physical interpretation of the preceding results as follows. A quadratic variation in $\beta(\omega)$ means that the group velocity, which is related to the linear variation of $\beta(\omega)$, must itself vary significantly across the pulse spectrum. The dispersion parameter β'' is related in fact to the so-called group-velocity dispersion $dv_g(\omega)/d\omega$ by

$$\beta'' = \frac{d}{d\omega} \left(\frac{1}{v_g(\omega)} \right) = -\frac{1}{v_g^2(\omega_0)} \frac{dv_g(\omega)}{d\omega}. \quad (52)$$

Hence the group velocity $v_g(\omega)$ as a function of the frequency deviation of a signal away from ω_0 will be given by

$$v_g(\omega) \approx v_g(\omega_0) - \beta'' v_g^2(\omega_0) \times (\omega - \omega_0); \quad (53)$$

i.e., the group velocity itself is frequency dependent.

Consider then a strongly chirped pulse whose instantaneous frequency varies with time in the form $\omega_i(t) = \omega_0 + 2bt$ at the input plane to a linear system. Instead of thinking of this as a single pulse with carrier frequency ω_0 , let us mentally break this pulse up into a number of segments or subpulses, each with a slightly different carrier frequency, and hence a slightly different group velocity.

Suppose in particular that the center portion of the pulse, which has the central frequency ω_0 , leaves $z = 0$ at $t_0 = 0$, and travels a distance z with a group delay given by $t_{d0} = z/v_g(\omega_0)$. Any other part of the pulse starting at some slightly earlier or later time t_1 has an instantaneous carrier frequency $\omega_1 \approx \omega_0 + 2b(t_1 - t_0)$. Hence we can, in a crude way, say that this other portion of the pulse will travel with slightly different group velocity $v_g(\omega_1)$.

Let us assume that the chirp b_0 is > 0 , so that the instantaneous frequency ω_1 is greater than ω_0 for $t_1 > t_0$ (i.e., the part of the pulse that starts late). Then we can say that this part of the pulse travels at a velocity

$$v_{g1} \approx v_g(\omega_0) - 2\beta''v_g^2(\omega_0)b_0(t_1 - t_0). \quad (54)$$

Hence it travels the distance z in a time

$$t_{d1} \approx \frac{z}{v_g(\omega_0) - 2\beta''v_g^2(\omega_0)b_0(t_1 - t_0)} \approx \frac{z}{v_g(\omega_0)} [1 - 2\beta''v_g(\omega_0)b_0(t_1 - t_0)]. \quad (55)$$

In order for the reduction in travel time for this portion of the pulse to just match the amount $t_1 - t_0$ by which it started late, so that it will exactly catch up with the center of the pulse, we should have

$$t_{d0} - t_{d1} = t_1 - t_0 \quad (56)$$

Substituting the above equations into this leads to the condition

$$2\beta''L \approx -1/b_0. \quad (57)$$

which is the same as the optimum result for large chirp given above.

We can thus view the pulse-compression process as one in which different parts of a chirped pulse, which start out down the line at slightly earlier or later times, also have slightly different frequencies. They can then travel slightly more slowly or rapidly down the line because of group-velocity dispersion, in such a way that they just exactly catch up with the central portion of the pulse.

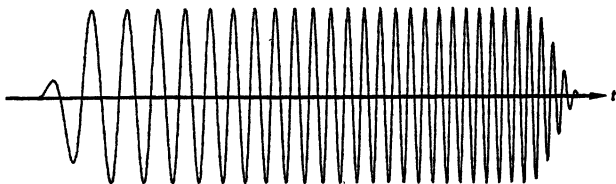
Pulse Compression With Other Pulses: Chirp Radars

We have discussed pulse compression for the analytically tractable case of a gaussian pulse. In other cases, however, it may be necessary to work with other pulseshapes.

In certain radar systems, for example, it is easy to generate rectangular pulses which have constant output amplitude during a long time duration, thus combining low peak power with large total energy per pulse. Suppose we then give these same pulses a linear frequency chirp within the pulse as shown in Figure 9.5. A pulse like this, after propagating through a properly designed dispersive system, can also be substantially compressed in time (by roughly its initial time-bandwidth product). However it will also be distorted in shape, and generally will acquire side-lobes something like a sinc function, as illustrated in Figure 9.5.

Pulses much like this are often used in microwave chirped radar systems, since they can combine a comparatively long low-intensity pulse, easily obtainable from a microwave transmitter, with the much sharper range resolution achieved by using substantial pulse compression in the microwave receiver. Such systems are commonly referred to as *chirped radar systems*. The name dates back to an early classified memo during World War II which described such systems under

chirped input pulse



compressed output pulse

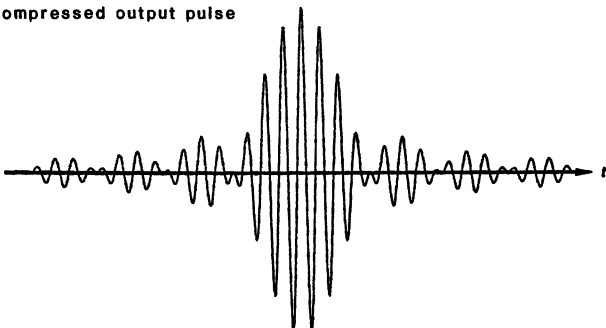


FIGURE 9.5

Pulse compression and reshaping with a square input pulse envelope.

the title “Not With a Bang But a Chirp.” The echo-locating properties of bats are also related to a form of sonic chirped radar.

Other Dispersive Optical Systems

In addition to dispersive atomic media, and to dispersive propagation effects in waveguiding systems such as optical fibers, various other dispersive optical systems have been invented and used, particularly to compress naturally or deliberately chirped laser pulses.

One such system is the Gires-Tournois interferometer (Figure 9.6). This device is simply a lossless etalon with a partially reflecting front surface and a 100% reflecting back surface, so that there is regenerative interference between the front and back surfaces. If the back surface is truly 100% reflecting, and the material between the surfaces is sufficiently lossless, then this device must have a reflectivity magnitude equal to unity at all frequencies. The interference between the front and back surfaces leads, however, to a periodic phase-versus-frequency curve for the complex reflectivity, which varies periodically with the axial mode spacing of the etalon. Portions of this phase-versus-frequency curve can then exhibit the correct dispersion to be used as a pulse-compression method. It is

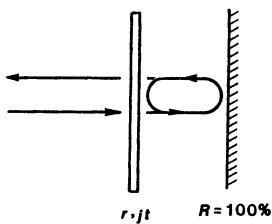


FIGURE 9.6

A Gires-Tournois interferometer has 100% amplitude reflectivity, but a frequency-dependent phase variation.

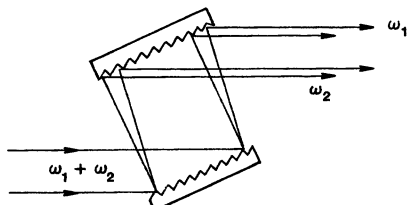


FIGURE 9.7

A pair of diffraction gratings used as a dispersive optical element.

physically obvious, however, that the interferometer itself must be physically very thin compared to the physical length of the laser pulse, or it will obviously break a single laser pulse into two or more multiply reflected pulses, rather than compressing it.

Another and much more useful dispersive system consists of a pair of gratings arranged as shown in Figure 9.7. Different frequencies or wavelengths have a different geometrical propagation distance through this system because they diffract from the gratings at slightly different angles. Such grating pairs have been used very successfully to compress short chirped optical pulses in several different experiments, as will be discussed later.

Still another kind of dispersive system is a sequence of prisms as shown in Figure 9.8. Since the angular dispersion from a prism is generally smaller than from a diffraction grating, prism systems generally produce considerably smaller dispersion effects than grating pairs. On the other hand the insertion losses are also much smaller with prisms. Systems such as Figure 9.8 can thus be placed inside laser cavities to provide small corrections to the round-trip group velocity dispersion which are important in controlling the mode-locking behavior in very short-pulse lasers.

Sign of the Group-Velocity Dispersion

The second derivative of the dispersion parameter β with respect to frequency can be related to other frequency or wavelength derivatives in the forms

$$\beta'' \equiv \frac{d^2\beta(\omega)}{d\omega^2} = \frac{4\pi^2 c_0}{\omega^3} \frac{d^2 n(\lambda_0)}{d\lambda_0^2} = -\frac{1}{v_g^2} \frac{dv_g(\omega)}{d\omega}, \quad (58)$$

where c_0 and λ_0 are the velocity of light and the optical wavelength in free space, and $n(\lambda_0)$ is the index versus wavelength in a dispersive medium.

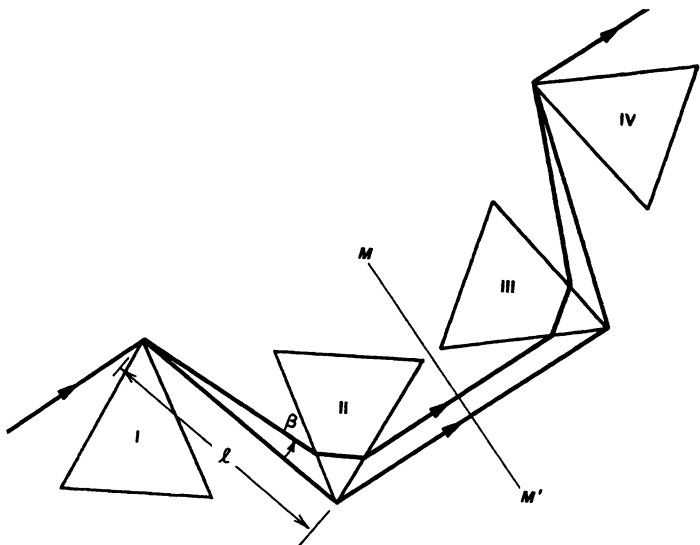


FIGURE 9.8

A sequence of prisms which can be adjusted to give a negative value of group velocity dispersion.

The usual practice in optics texts has been to plot index of refraction $n(\lambda_0)$ of a dispersive medium versus free-space wavelength λ_0 , and then to speak of regions where this plot is concave upward (positive $d^2n/d\lambda_0^2$) as regions of *positive dispersion*, and regions of opposite sign as regions of *negative dispersion*. Positive dispersion in this sense thus means positive values for both β'' and $d^2n/d\lambda_0^2$, but a negative derivative for $dv_g/d\omega$, i.e., for group velocity versus frequency. Most common optical materials exhibit positive dispersion in the visible region, turning to negative dispersion somewhere in the near infrared.

With the recent advent of extremely short (femtosecond-time-scale) pulses, as well as growing realization of the role that self-chirping and pulse compression play in the mode-locked lasers that generate these pulses, there is growing interest in low-loss dispersive systems which can generate dispersion of either sign. The prism configuration in Figure 9.8 can be designed to give either negative or positive dispersion, with the additional advantages that the beams enter and leave the prisms at Brewster's angle, and there is neither displacement nor deviation of the input and output beam paths.

REFERENCES

A detailed survey of microwave chirped radar concepts is given by J. R. Klauder, A. C. Price, S. Darlington, and W. J. Albersheim, "The theory and design of chirp radars," *Bell Sys. Tech. J.* **39**, 745-808 (July 1960). See also C. E. Cook, "Pulse compression—key to more efficient radar transmission," *Proc. IRE* **48**, 310-316 (1960); M. L. Skolnik, *Introduction to Radar Systems* (McGraw-Hill, 1962), pp. 493-500; and S. C. Bloch,

"Introduction to chirp concepts with a cheap chirp radar," *Am. J. Phys.* **41**, 857–864 (July 1973).

The first suggestions for the chirping of optical pulses and then their subsequent compression seem to have come from F. Gires and P. Tournois, "Interféromètre utilisable pour la compression d'impulsions lumineuses modulées en fréquence," *Compt. Rend. Acad. Sci. (Paris)* **258**, 6112–6115 (June 1964); and J. A. Giordmaine, M. A. Duguay, and J. W. Hansen, "Compression of optical pulses," *IEEE J. Quantum Electron.* **QE-4**, 252–255 (May 1968).

One of the earliest experiments was by M. A. Duguay and J. W. Hansen, "Compression of pulses from a mode-locked He-Ne laser," *Appl. Phys. Lett.* **14**, 14–16 (January 1969).

For a description of optical pulse compression using diffraction grating pairs, see E. B. Treacy, "Optical pulse compression with diffraction gratings," *IEEE J. Quantum Electron.* **QE-5**, 454–458 (September 1969); or J. Desbois, F. Gires, and P. Tournois, "A new approach to picosecond laser pulse analysis, shaping and coding," *IEEE J. Quantum Electron.* **QE-9**, 213–218 (February 1973).

The prism configuration shown in Figure 9.8, and other related designs, are outlined in R. L. Fork, O. E. Martinez, and J. P. Gordon, "Negative dispersion using pairs of prisms," *Opt. Lett.* **9**, 150–152 (May 1984), and J. P. Gordon and R. L. Fork, "Optical (ring) resonator with negative dispersion," *Opt. Lett.* **9**, 153–155 (May 1984).

Problems for 9.3

1. *Phase shift versus frequency analysis for the Gires-Tournois interferometer.* Assuming that the voltage reflection coefficient of a Gires-Tournois interferometer can be written as $\tilde{g}_{\text{ref}}(\omega) = \exp[-j\phi(\omega)]$, calculate and plot a few curves of $\phi''(\omega) \equiv d^2\phi(\omega)/d\omega^2$ versus ω over one full free spectral range for two or three different values of the front mirror power reflectivity $R \equiv r^2$. Derive approximate analytical formulas for the maximum value of $\phi''(\omega)$, and the value of ωT at which this occurs, where $T = 2L/c$ is the round-trip transit time inside the interferometer.
 2. *Usefulness of the Gires-Tournois interferometer?* Extend the results of the previous problem to show that the Gires-Tournois interferometer is in fact a fairly lousy pulse-compression device in practical terms.
-

9.4 PHASE AND GROUP VELOCITIES IN RESONANT ATOMIC MEDIA

Particularly strong and interesting dispersion effects can occur when signals are tuned close to the transition frequency of a narrow atomic resonance in an absorbing or amplifying atomic medium. In this section we give a brief description of these atomic dispersive effects, showing how they confirm both the absorption and especially the phase-shift properties of a resonant atomic transition.

Phase and Group Velocities Near Atomic Transitions

The total phase shift for a wave making a single pass through a laser amplifier (or an absorbing atomic medium) can be written as $\exp[-j\phi_{\text{tot}}(\omega)] = \exp[-j(\beta(\omega) + \Delta\beta_m(\omega))L]$, where the total phase shift consists of

$$\phi_{\text{tot}}(\omega) \equiv [\beta(\omega) + \Delta\beta_m(\omega)]L = \frac{\omega L}{c} + \frac{\beta L}{2}\chi'(\omega), \quad (59)$$

The first term gives the basic “free-space” phase shift $\omega L/c$ through the laser medium, a phase shift which is large and linear in frequency; the second term is the small added shift $\Delta\beta_m(\omega)L$ due to the atomic transition. The phase velocity $v_\phi(\omega)$ of the wave in the medium is then given by

$$v_\phi(\omega) = \frac{\omega L}{\phi_{\text{tot}}(\omega)} \quad (60)$$

and the group velocity $v_g(\omega)$ by

$$v_g(\omega) = \frac{L}{d\phi_{\text{tot}}(\omega)/d\omega} = \frac{L}{(d/d\omega)[\beta(\omega) + \Delta\beta_m(\omega)]}. \quad (61)$$

The phase velocity in a medium with an atomic transition is thus given by

$$v_\phi(\omega) = \frac{\omega}{\beta(\omega) + \Delta\beta_m(\omega)} = \frac{c}{1 + \chi'(\omega)/2}, \quad (62)$$

and the group velocity is given by

$$v_g(\omega) = \frac{v_\phi(\omega)}{1 - (\omega/v_\phi)(dv_\phi/d\omega)}. \quad (63)$$

Figure 9.9 shows these quantities for a wave passing through a resonant amplifying laser medium, with the atomic or $\chi'(\omega)$ contributions very much exaggerated.

The group velocity over the central portion of the amplifying bandwidth in a laser medium is slightly *slower* than the free-wave velocity in the medium. A physical explanation for this is that as a pulse travels through the medium, the leading edge of the pulse must first build up a coherent induced polarization in the inverted atomic transition, before this polarization can begin radiating back into the input pulse to amplify it. This build-up, however, requires a short but finite build-up time, on the order of T_2 , as described in the preceding chapter. The leading edge of the pulse thus gets slightly “under-amplified” compared to the steady-state gain of the medium, and by similar arguments the continuing reradiation of the oscillating atoms slightly “over-amplifies” the trailing edge of the pulse. The net pulse envelope in an amplifying medium thus appears to travel slightly more slowly than the free-space wave velocity.

Group Velocities Faster Than the Velocity of Light?

The phase and group velocities in Figure 9.9 are associated with an amplifying atomic medium. Going from an amplifying to an absorbing medium will reverse the signs of both χ'' and χ' , and thus reverse the sign of all the atomic phase-shift contributions in this figure.

The careful reader may then note that for a strongly absorbing atomic transition the group velocity at the center of the transition can apparently become

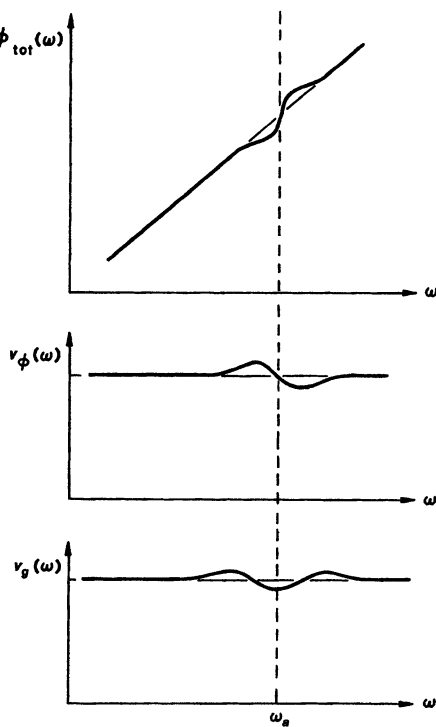


FIGURE 9.9
Phase shift, phase velocity, and group velocity versus frequency for propagation through an inverted atomic transition.

faster than the velocity of light c in the host medium, and also the group velocity off line center can become negative for strong enough absorbing transitions. In fact, for a strong enough transition in a gas, v_g might even become greater than the velocity of light c_0 in vacuum. But this would seem to be in serious conflict with a fundamental axiom of relativity, that no signal or information can ever be transmitted at a velocity greater than c_0 .

The resolution to this apparent paradox lies in the fact that the group velocity v_g , as defined here, can significantly exceed c_0 only at the center of a very strongly absorbing transition. But this is also a situation in which any incident signal will be both strongly attenuated and distorted by this attenuation. Both detailed calculations and experimental measurements for a pulsed signal sent into a strongly absorbing atomic medium, with a carrier frequency anywhere within the absorption line, have been carried out in recent years (see References). These results have shown that when a smooth pulse is sent into a strongly absorbing medium, the observed signal-pulse envelope will indeed appear to travel at very close to the group velocity $v_g \equiv d\omega/d\beta$ in almost all cases, with very little distortion of the pulse shape, even when v_g has values that are greater than c_0 , or even negative (i.e., the peak of the pulse appears to come out of the absorbing sample before it goes in).

This is not a violation of special relativity, however, nor does it mean that the signal is transmitted at greater than the (vacuum) speed of light. The pulses used for all such calculations (and measurements) necessarily always have long

tails that are weak but finite. In passing through the lossy medium, different portions of the pulse spectrum are attenuated and phase-shifted very differently, in such a way that the peak of pulse envelope appears to move faster than c . In reality, however, the pulse is being severely modified under the envelope; and no part of it is actually moving faster than light.

When such calculations are done for an input signal with a sharp discrete leading edge, it is always found that no output ever emerges at the output face at a time earlier than the transit time L/c_0 through the system at the vacuum velocity of light. (For more discussion of this point, see some of the references at the end of this section.)

Group Velocities Much Slower Than Light

The dispersion in the wings of a strongly absorbing transition can produce a group velocity much less than the phase velocity c in the medium (and also obviously less than c_0 in free space); and if the entire signal spectrum of a pulse is sufficiently far out in the wings, the net absorption for the pulse may simultaneously be made very small. With a sufficiently strong and narrow transition, one can thus obtain a very large slowing of the group velocity of a pulse, even while there is very small net absorption of the pulse energy.

As an example of this, cells filled with alkali vapor (such as rubidium or sodium) have been used to produce some rather large (though comparatively narrowband) dispersive effects at wavelengths on the sides of the strong resonance absorption lines in these atoms. In experiments done at the IBM Laboratories, Yorktown Heights, N.Y., the pulse-envelope group delay was measured when short pulses from a tunable dye laser were sent through a gas absorption cell one meter long. By using pulses whose center frequencies were located far out on the wings of a very strongly absorbing transition (i.e., by operating at $|\omega - \omega_a| \gg \Delta\omega_a$), the experimenters were able to obtain a power absorption loss of only $\approx 20\%$ per pass, and yet have a group velocity as slow as 1/10 to 1/15 the velocity of light.

REFERENCES

A detailed analysis of pulse propagation and apparent group velocity in strongly absorbing or amplifying media is given by C. G. B. Garrett and D. E. McCumber, "Propagation of a gaussian light pulse through an anomalous dispersion medium," *Phys. Rev. A* **1**, 305-313 (February 1970).

The series of striking experiments demonstrating group velocities much less than the velocity of light, obtained by operating far from line center on very strongly absorbing atomic transitions in sodium and rubidium vapor cells, are described by D. Grischkowsky in "Adiabatic following and slow optical pulse propagation in rubidium vapor," *Phys. Rev. A* **7**, 2096-2102 (June 1973). See also *ibid.*, "Compression of low-intensity, phase modulated light pulses," *IEEE J. Quantum Electron.* **QE-10**, 723 (September 1974), and "Optical pulse compression," *Appl. Phys. Lett.* **25**, 566-568 (November 15, 1974); and J. K. Wigmore and D. Grischkowsky, "Temporal compression of light," *IEEE J. Quantum Electron.* **QE-14**, 310-315 (April 1978).

Similarly striking experiments showing greatly modified and even negative pulse velocities produced by a strong exciton absorption line in a semiconductor (nitrogen-

doped GaP) are reported by S. Chu and S. Wong, "Linear pulse propagation in an absorbing medium," *Phys. Rev. Lett.* **48**, 738-741 (March 15, 1982).

The strong dispersion in the refractive index of a semiconductor near the band gap is also demonstrated in J. P. van der Ziel and R. A. Logan, "Dispersion of the group velocity refractive index in GaAs double heterostructure lasers," *IEEE J. Quantum Electron.* **QE-19**, 164-169 (February 1983).

Problems for 9.4

1. *Analysis of group-velocity slowing in the wings of a strong atomic transition.* Analyze the type of experiment discussed in the text, in which the group delay of a gaussian pulse is measured when the pulse is sent through a strongly absorbing atomic transition with the pulse carrier frequency tuned quite far out on the wings of the absorption line. What conditions are necessary (i.e., what values of midband absorption, atomic linewidth, and detuning off line center) to obtain a absorption loss of only about 20% per pass, and yet have a group velocity as slow as 1/10 or 1/15 the velocity of light? Note: You may want to refer back to the discussion in Section 3.7 which pointed out that far enough from line center, even inhomogeneous doppler-broadened transitions appear to be essentially homogeneous or lorentzian in their lineshapes.
 2. *Phase and group velocity versus frequency in a mixed laser amplifier and atomic absorber medium.* In an earlier chapter we considered a linear single-pass laser amplifier with midband gain coefficient $\alpha_1 L$ and lorentzian atomic linewidth $\Delta\omega_{a1}$, followed by a linear single-pass laser absorber—that is, a collection of absorbing atoms—having midband absorption coefficient $\alpha_2 L$ and atomic linewidth $\Delta\omega_{a2}$, with both transitions centered at the same resonance frequency; and we asked what relative gain coefficients α_1 and α_2 and relative atomic linewidths $\Delta\omega_{a1}$ and $\Delta\omega_{a2}$ would just lead to a double-humped rather than single-humped curve of overall power transmission versus frequency for the two atomic systems in cascade.

Suppose that these two atomic media are mixed together to produce a medium with both an amplifying and an absorbing transition at the same frequency. Consider the variation in phase and group velocity versus frequency across this compound transition, and especially the derivatives of phase shift and group velocity versus frequency at line center. Does there seem to be any fundamental connection between having a maximally flat gain profile at line center and having either the group velocity or phase velocity derivatives be zero at line center?

 3. *Sensitivity of pulse compression to disperser length.* A chirped gaussian pulse whose initial time-bandwidth product is N times the transform-limited value, where $N \gg 1$, is to be compressed by passage through an optimum length of some dispersive system. Evaluate the sensitivity of the pulse-compression process to the length L of the dispersive system by finding the length tolerance about the optimum value L_{opt} that will cause the output pulse length to increase by $\sqrt{2}$ from the optimum value.
-

9.5 PULSE BROADENING AND GAIN DISPERSION

Pulses can be broadened as well as compressed in a propagation system having significant group-velocity dispersion, and this broadening can be very important both in measurement applications of picosecond optical pulses and in the transmission of such pulses through optical fibers. In this section, therefore, we extend the discussion of the previous sections to cover pulse broadening in such dispersive systems.

In addition, pulses will also be broadened—and more rarely narrowed—in passing through systems with *gain dispersion*, that is, in passing through amplifiers with a finite bandwidth. In this section therefore we also consider the complementary effects of gain or absorption dispersion in a propagating system.

Dispersive Pulse Broadening

Gaussian pulses starting out in the lower half-plane in Figure 9.3 will be initially compressed as they propagate through the dispersive system. On the other hand, pulses starting out—or moving into—the upper half-plane will be broadened (unless, of course, the sign of β'' is reversed, in which case the arrowheads on the trajectories must be reversed). Group-velocity dispersion can thus either *compress a pulse* with the right initial chirp, or *broaden a pulse* with the wrong initial chirp. In particular, a pulse with no initial chirp will begin to acquire a growing amount of chirp and then be broadened in any such system.

Consider for example an initially unchirped pulse, with $b_0 = 0$. Its gaussian pulse parameter after propagating a distance z through a dispersive medium becomes

$$a(z) = \frac{a_0}{1 + (2\beta''z)^2 a_0^2}. \quad (64)$$

Reduction in $a(z)$ means that the pulselwidth $\tau_p(z)$ has broadened, as given by the expression

$$\tau_p^2(z) \equiv \frac{2 \ln 2}{a(z)} = \tau_{p0}^2 + \left(\frac{(4 \ln 2) \beta'' z}{\tau_{p0}} \right)^2 = [1 + (z/z_D)^2] \times \tau_{p0}^2. \quad (65)$$

The initial unchirped pulselwidth τ_{p0} will increase by a factor of $\sqrt{2}$ after a propagation distance z_D given by

$$z = z_D \equiv \frac{\tau_{p0}^2}{(4 \ln 2) \beta''}. \quad (66)$$

This “dispersion length” z_D is a kind of Rayleigh length for pulse broadening in time, analogous to the Rayleigh range for transverse beam spreading we will meet in a later chapter.

It is convenient to rewrite this dispersion length in the form

$$z_D = \frac{(\omega_0 \tau_{p0})^2}{8 \ln 2} \times \frac{\lambda}{D}, \quad (67)$$

where the quantity

$$D \equiv \frac{\omega_0^2 \beta''}{\beta(\omega_0)} \quad (68)$$

is a dimensionless group-velocity dispersion parameter for a propagating system or an atomic medium. The first factor in the z_D expression depends only on pulse parameters—it is essentially the number of optical cycles in the pulse squared—and the second factor is the wavelength in the medium, $\lambda = \lambda_0/n$, divided by the dimensionless dispersion parameter D .

Dispersive Broadening in Real Materials

We might want to evaluate this dispersion parameter, for example, for an ultrashort optical pulse propagating through a typical optical material with a frequency-dependent index of refraction, so that the propagation constant is given by

$$\beta(\omega) = \frac{n(\omega)\omega}{c_0}. \quad (69)$$

A common form for the variation of the index of the refraction across the visible region in transparent optical materials is the Sellmeier equation

$$n^2(\omega) - 1 = \frac{A\omega_e^2}{\omega_e^2 - \omega^2}. \quad (70)$$

For typical optical glasses and crystals A has a value between 1 and 2, and ω_e corresponds to an effective resonant frequency or absorption band edge for the material, often located in the ultraviolet at a wavelength λ_e somewhere between 1000 and 2000 Å. (For semiconductors this wavelength generally corresponds to the band-gap wavelength, and the Sellmeier equation then gives the index of refraction for the semiconductor in the transparent region at wavelengths longer than the band-gap wavelength.)

We can then find that for many typical transparent materials the magnitude of the dimensionless dispersion parameter is given by

$$D \equiv \frac{\omega_0^2 \beta''}{\beta(\omega_0)} \approx 0.10 \text{ to } 0.20. \quad (71)$$

If we assume a value of $D \approx 0.10$ and an index of refraction $n = 1.5$, the approximate $\sqrt{2}$ broadening lengths for initially unchirped pulses of different initial pulsedwidths τ_{p0} are given by

τ_{p0}	100 fs	1 ps	10 ps	100 ps	
z_D	~ 1 cm	~ 100 cm	~ 100 m	~ 10 km	

(72)

This type of dispersive pulse broadening becomes very important in the use of picosecond and femtosecond optical pulses from mode-locked lasers. Pulses ≤ 20 femtoseconds long have already been generated in mode-locked dye lasers. Such a pulse obviously cannot propagate more than a few mm through a typically dispersive medium before it will be significantly broadened by the self-broadening effect.

Dispersive Broadening in Optical Fibers

The pulse-broadening effects caused by group-velocity dispersion in optical fibers are also of great importance in determining the maximum distance that a

pulse of given width can be propagated through an optical-fiber communications systems before being significantly broadened. A 100 ps visible-wavelength pulse, for example, can propagate only a few km in a typical single-mode fiber before being significantly broadened (the situation in multimode fibers is much worse, because of mode-mixing effects). Dispersive pulse broadening can become the primary factor limiting the potential data rate for long-distance communication in low-loss high-capacity optical fibers.

The dispersive behavior of an optical fiber is usually a combination of *materials dispersion*, associated with the index variation of the glass in the fiber, and *waveguide or modal dispersion* associated with the propagating normal mode patterns in the fiber. In typical fibers this net dispersion passes through zero at a wavelength around $1.3 \mu\text{m}$, so that in principle very short pulses tuned to this wavelength could be propagated for very long distances without dispersive spreading.

It can be difficult to match the transmitted wavelength exactly to the zero dispersion point, however, and in addition the lowest-loss wavelength for optical fibers is typically closer to $\lambda = 1.5 \mu\text{m}$ (at which wavelength the absorption and scattering losses in real fibers can have values as extraordinarily small as $\approx 0.2 \text{ dB/km}$). To transmit a pulse with the minimum possible input and output pulselwidth through a given length of such a fiber, we should launch a pulse with an input pulselwidth $\tau_p \equiv \sqrt{2}\tau_{p0}$ and just the right amount of initial compressive chirp into the fiber, where the fiber length is given by $z = 2z_D$, and τ_{p0} and z_D are connected by the analytical relations given in Equations 9.65 and 9.66. This pulse will then compress down to τ_{p0} at the middle of the fiber and broaden back to τ_p at the output end. For a small enough value of normalized dispersion—perhaps $D \approx 0.005$, which might be typical of a single-mode quartz fiber at $\lambda_0 = 1.5 \mu\text{m}$ —the relationship between fiber length and minimum input-output pulselwidth will have typical values given by

$z = 2z_D$	2	5	10	20	50	100	km
$\tau_p = \sqrt{2}\tau_{p0}$	11	16	23	33	53	74	ps

(73)

Note that a data transmission rate of 10 Gbits per second, such as optical-fiber communications designers hope to achieve, requires a pulselwidth at least as short as 100 ps, and preferably somewhat less.

(One very interesting alternative approach for accomplishing the propagation of very much shorter optical pulses in fiber communications systems is the use of nonlinear solitons in optical fibers, as described briefly in the following chapter.)

Pulse-Broadening Effects of Gain Dispersion

Velocity or phase-shift dispersion, which is produced by a frequency-dependent propagation constant $\beta(\omega)$, causes one set of pulse distortion effects. Gain dispersion, by which we mean a frequency-dependent gain coefficient $\alpha(\omega)$, produces a different set of effects. The primary effects that result when a pulse passes through a linear but frequency-dependent gain medium (now leaving out dispersion effects) are pulse-broadening in time, due to finite bandwidth of the gain medium, and possibly more complex frequency-shifting and time-shifting effects that can occur if the gain medium has a linear variation of gain with frequency across the pulse spectrum.

In this section we will consider only quadratic or pulse-broadening effects, since they are the most fundamentally important, leaving the more complex effects of linear frequency dependence to an exercise. We therefore consider again a gaussian pulse with carrier frequency ω_0 and initial pulse parameter Γ_0 , which now passes through a linear gain medium whose gain coefficient has the quadratic frequency dependence

$$\alpha_m(\omega) = \alpha_{m0} - \frac{1}{2}\alpha''_m(\omega_0) \times (\omega - \omega_0)^2, \quad (74)$$

where $\alpha''_m \equiv -d^2\alpha_m(\omega)/d\omega^2$ evaluated at midband. The first term in this expansion gives a uniform amplitude gain which applies equally to all frequency components and hence simply increases the pulse amplitude uniformly without changing its shape. The α''_m term, however, leads to a change in the gaussian pulse parameter given by

$$\frac{1}{\Gamma(z)} = \frac{1}{\Gamma_0} + 2\alpha''_m(\omega_0)z. \quad (75)$$

The trajectory of $\Gamma(z)$ now moves horizontally in the $1/\Gamma$ plane, rather than vertically as in Figure 9.3. For $\alpha''_m > 0$ (that is, a gain peak at line center) this increases the real part of $1/\Gamma$ and hence, as is physically obvious, decreases the spectral bandwidth of the pulse. The result is commonly, though not universally, to broaden the pulse in time as it propagates through the amplifier.

Pulse Broadening in Amplifiers

Consider as a particular example a lorentzian atomic transition with linewidth $\Delta\omega_a$ and a spectrum centered at $\omega_0 \equiv \omega_a$. The gain variation around line center may be written to a first approximation as

$$\alpha_m(\omega) = \frac{\alpha_{m0}}{1 + [2(\omega - \omega_a)/\Delta\omega_a]^2} \approx \alpha_{m0} - \alpha_{m0} \times \left(\frac{2}{\Delta\omega_a}\right)^2 \times (\omega - \omega_0)^2. \quad (76)$$

A length z of such an amplifier then produces an output pulse parameter given by

$$\frac{1}{\Gamma(z)} = \frac{1}{\Gamma_0} + \frac{16\alpha_{m0}z}{\Delta\omega_a^2}. \quad (77)$$

Laser amplifiers with finite bandwidths will then usually broaden pulses in time, just as occurs in any other finite bandpass system.

Consider, for example, an input pulse with no initial chirp, i.e., with $\Gamma_0 = a_0$ and $b_0 = 0$. Equations 9.75–9.77 then convert into the simple pulselwidth broadening result

$$\tau_p^2(z) = \tau_{p0}^2 + \frac{(16 \ln 2) \ln G_0}{\Delta\omega_a^2}. \quad (78)$$

where $G_0 = \exp(2\alpha_{m0}z)$. In a Nd:YAG laser amplifier with $\Delta\omega_a/2\pi \approx 120$ GHz and the very high (possibly multipass) gain $G_0 = 10^5$, this gives approximately

$$\tau_p^2 \approx \tau_{p0}^2 + (\sim 15 \text{ ps})^2. \quad (79)$$

Such an amplifier will convert an ideal delta-function input pulse into an ~ 15 ps output pulse, and will broaden a 50 ps input pulse to ~ 52 ps at its output.

Also, the initially unchirped pulse develops an added chirp in passing through the amplifier. These kinds of results are important in understanding the amplification of short pulses in a laser amplifier, and, as we will see in a later chapter, in understanding mode-locking in laser oscillators.

Pulse Narrowing in a Chirped Laser Amplifier

Laser amplifiers with finite bandwidths can also, under certain special circumstances, shorten chirped pulses in time. Suppose the input pulse also has a significant initial chirp b_0 . The general result for the pulselwidth parameter $a(z)$ after an amplification distance z is then

$$a(z) = \frac{a_0(1 + Ka_0) + Kb_0^2}{(1 + Ka_0)^2 + (Kb_0)^2}, \quad (80)$$

where $K \equiv 2\alpha_m''z = 8 \ln G_0 / \Delta\omega_a^2$. Suppose for simplicity that the bandwidth-broadening factor K is small compared to $1/\Gamma_0$ or $1/\Gamma$. Equation 9.80 expanded to first order in K then becomes

$$a(z) \approx a_0 [1 - Ka_0 + Kb_0^2/a_0]. \quad (81)$$

This shows the first-order pulselwidth-broadening effect due to the $-Ka_0$ term, but also a pulselwidth-narrowing term in the Kb_0^2/a_0 term.

The physical interpretation of this effect is the following. If the pulse has a sizable chirp during its time duration (i.e., $b_0 \gg a_0$), we may think approximately of the pulse frequency sweeping across the gain profile of the amplifying transition. The center section of the pulse (in time) is at line center and hence gets maximum amplification, whereas the frequencies in both the leading and trailing edges of the pulse are somewhat off line center and get less amplification; hence the pulseshape gets somewhat narrowed in time.

This last explanation mingles time and frequency descriptions in a way that is not rigorously correct, but which still gives a reasonably correct physical picture of the result for $b_0 \gg a_0$. Note that the pulse narrowing or compression here is independent of the sign of the chirp, as is compatible with our physical reasoning.

Problems for 9.5

1. *Pulse broadening on passing through a Fabry-Perot etalon.* A paper by Albrecht and Mourou [IEEE J. Quantum Electron. QE-17, 1709-1712 (September 1981)] describes a laser pulse that circulates around repeatedly inside a laser cavity containing an intracavity Fabry-Perot etalon, and gives the formula

$$\tau_{\text{final}}^2 = \tau_{\text{initial}}^2 + 16(\ln 2) \left[\frac{g}{\Delta\omega_p^2} + \left(\frac{Fd}{\pi c} \right)^2 \right] \times N$$

for the FWHM pulselwidth after N round trips. (The $-$ rather than $+$ sign that appears inside the brackets in the original reference must be incorrect.) In this formula the etalon is characterized by its finesse F and thickness d , and the laser gain medium by its gain coefficient per pass g and bandwidth $\Delta\omega_p$.

Derive this same formula; interpret what the authors must mean by the symbols employed; and also explain the next equation in the paper, which says that the

9.5 PULSE BROADENING AND GAIN ...

final pulselwidth after many round trips will be given by $\tau_{\text{final}} \approx 3.5 \times 10^{-11} F d \sqrt{N}$, which depends only on the etalon and not on the laser medium.

2. *Pulse propagation through mixed group-velocity dispersion and gain dispersion.* Consider in more detail the propagation of a complex gaussian pulse with an arbitrary input pulse parameter Γ_0 through a long transmission line (or an extended laser medium) that has both finite group-velocity dispersion β'' and also finite gain dispersion α'' . Illustrate this by plotting contours of pulse propagation in the $1/\Gamma$ (or $1/\Gamma^*$) plane for various ratios of α'' to β'' .

Under which conditions can a system that produces bandwidth narrowing in the frequency domain (i.e., a system with $\alpha'' > 0$) still produce pulselwidth narrowing in the time domain?

3. *Pulse propagation and distortion tuned on the side of an amplifying atomic transition.* The carrier frequency ω_a of a gaussian pulse might be tuned off to the side of an amplifier's passband (that is, $\omega_0 \neq \omega_a$), so that the gain dispersion across the pulse spectrum would need to be written as

$$\alpha(\omega) = \alpha_0 + \alpha' \times (\omega - \omega_0) - \frac{1}{2} \alpha'' \times (\omega - \omega_0)^2$$

with $\alpha' \equiv d\alpha/d\omega$ at $\omega = \omega_0$, and α_0 being the gain value at $\omega = \omega_0$ (not the midband value at $\omega = \omega_a$). Analyze and describe the resulting pulse-propagation effects in this situation, including trajectories in the Γ and $1/\Gamma$ planes, and physical effects on the pulse parameters.



NONLINEAR OPTICAL PULSE PROPAGATION

All the propagation phenomena described in Chapter 9 are *linear propagation effects*, produced by the linear response of the propagating systems. In this chapter we will give a brief survey of a few of the most important *nonlinear propagation phenomena* that occur with optical pulses. These effects include in particular: gain saturation in pulsed amplifiers (which is a relatively weak form of nonlinearity); optical pulse propagation through nonlinear dispersive systems in general; and the especially interesting topic of nonlinear pulse propagation in optical fibers, including the fascinating topic of soliton propagation in optical fibers.

10.1 PULSE AMPLIFICATION WITH HOMOGENEOUS GAIN SATURATION

As we mentioned earlier, laser amplifiers are much more commonly used for amplifying optical pulses than for amplifying cw optical signals. Common examples of pulsed laser amplification include flash-pumped Nd:YAG and Nd:glass amplifiers at $1.06\text{ }\mu\text{m}$; electron-beam-pumped TEA CO_2 laser amplifiers at $10.6\text{ }\mu\text{m}$; excimer lasers in the visible; and pulsed dye laser amplifiers, which are themselves often pumped by another pulsed laser, and which can amplify across broad bandwidths in the visible and near infrared.

Short pulses passing through laser amplifiers will be broadened and distorted by the effects we discussed in Chapter 9. These effects are, however, entirely linear effects, and generally require quite short pulses and sizable dispersions to be significant. Let us now consider an entirely separate form of weakly nonlinear pulse distortion that can arise with much longer pulses, as a result of *time-varying gain saturation effects* when a higher energy pulse is amplified in a homogeneously saturable laser amplifier.

Pulse Energy Saturation in Amplifiers and Absorbers

In order to obtain efficient energy extraction from a laser amplifier, an amplified pulse must be intense enough to cause significant saturation of the population inversion during its passage through the amplifier. But this means that the amplifier gain must necessarily be reduced from a large initial value to a small residual value during the passage of the pulse; hence this time-dependent

saturation during the passage of the pulse must also lead to time-varying gain reduction and pulseshape distortion.

In the same fashion, when a strong enough pulse is sent through a saturable absorber medium, the signal energy in the pulse may partially or completely saturate the atomic absorption and thus increase the energy transmission, leading to an analogous though oppositely directed pulse distortion. Such pulse propagation through saturable absorbers is widely used to shorten mode-locked pulses in passively mode-locked lasers. Again, the pulse itself must change the transmission of the saturable absorber during the passage of the pulse. The fundamental physics is the same as it is for the saturable amplifier, except for a change of sign in going from saturable amplification to saturable absorption.

In order to explain both of these effects, this section presents an analysis of the population saturation and the pulseshape distortion that results when a sufficiently intense pulse passes through a homogeneously saturable, single-pass laser amplifier, or saturable absorber. The physical approximations made in this section are thus significantly different from the linear pulse propagation analysis of Chapter 9. The pulsedwidths we are concerned with here are generally long enough, and the propagation lengths short enough, that pulse compression or expansion effects due to finite amplification bandwidths or to group velocity or gain dispersion effects are generally of minor importance. Our emphasis is thus entirely on the time-varying *saturation effects* in the atomic material.

Homogeneous Saturation Approximations

Two physical approximations help to simplify this analysis. First, although pulse amplification often involves short pulses with fast time-variation and high intensities, usually the rate-equation approximations are still valid, and a purely rate-equation analysis can be employed. Second, in most situations of interest for laser pulse amplification, the amplified pulse durations are short enough that we can neglect both any pumping effects and any upper-level relaxation during the transit time of the amplified pulse. Hence in this section we will analyze a short pulse propagating through a prepumped and inverted laser medium, without including any pumping or relaxation effects during the pulse interval.

Analysis of Homogeneous Pulse Amplification

We consider therefore a short pulse with signal intensity $\hat{I}(\hat{z}, \hat{t})$ traveling in the $+\hat{z}$ direction through a laser medium with inverted population difference $\Delta\hat{N}(\hat{z}, \hat{t})$, where \hat{z} and \hat{t} are the usual laboratory coordinates. (The reason for the “hats” on all these quantities will become apparent in a moment.) We neglect any transverse intensity variations to simplify the analysis.

The basic differential equations for this situation can then be developed as follows. Let us denote the electromagnetic energy density in the optical signal pulse, measured in J/m^3 , by $\hat{\rho}_{\text{em}}(\hat{z}, \hat{t})$. The instantaneous intensity $\hat{I}(\hat{z}, \hat{t})$ in W/m^2 being carried by the pulse through any plane \hat{z} at time \hat{t} is then given by $\hat{I}(\hat{z}, \hat{t}) = \hat{\rho}_{\text{em}}(\hat{z}, \hat{t}) \times v_g$, where v_g is the group velocity in the laser medium. This velocity is normally very close to the phase velocity c in most laser media; so for simplicity we will write $v_g = c$ in the following analysis.

Consider then a short segment of length $\Delta\hat{z}$ in the laser medium, as shown in Figure 10.1. The rate of change of stored signal energy in the length $\Delta\hat{z}$ is given by the energy flux into one end minus the energy flux out the other end of

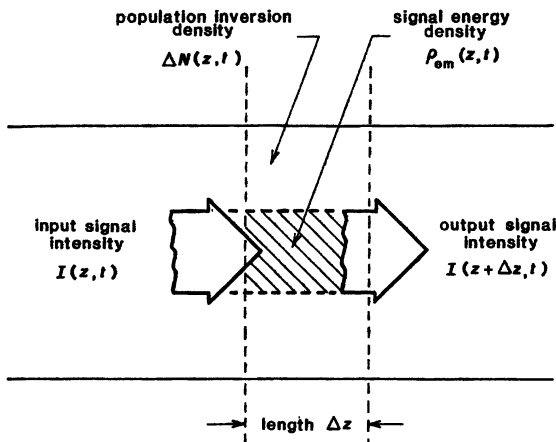


FIGURE 10.1
Optical intensity passing
through a short segment of
a saturable pulse amplifier.

the segment, plus the net rate of stimulated emission within the segment, or

$$\frac{\partial}{\partial \hat{t}} [\hat{\rho}_{\text{em}}(\hat{z}, \hat{t}) \Delta \hat{z}] = \hat{I}(\hat{z}, \hat{t}) - \hat{I}(\hat{z} + \Delta \hat{z}, \hat{t}) + \sigma \Delta \hat{N}(\hat{z}, \hat{t}) \hat{I}(\hat{z}, \hat{t}) \Delta \hat{z}, \quad (1)$$

where σ is the stimulated-transition cross section of the laser medium. Using $\hat{I}(\hat{z}, \hat{t}) = c \hat{\rho}_{\text{em}}(\hat{z}, \hat{t})$ and combining this with the rate equation for the inverted population inside the same segment then gives the two basic equations of this pulse saturation analysis, namely,

$$\frac{\partial \hat{I}(\hat{z}, \hat{t})}{\partial \hat{t}} + c \frac{\partial \hat{I}(\hat{z}, \hat{t})}{\partial \hat{z}} = \sigma c \Delta \hat{N}(\hat{z}, \hat{t}) \hat{I}(\hat{z}, \hat{t}) \quad (2)$$

and

$$\frac{\partial}{\partial \hat{t}} \Delta \hat{N}(\hat{z}, \hat{t}) = - \left(\frac{2^* \sigma}{\hbar \omega} \right) \Delta \hat{N}(\hat{z}, \hat{t}) \hat{I}(\hat{z}, \hat{t}). \quad (3)$$

Note that no pumping or relaxation terms are included in the atomic rate equation. We use the convention mentioned earlier that the “saturation factor” $2^* \equiv 1$ if the lower laser level empties out rapidly compared to the pulse duration; but $2^* \equiv 2$ if the lower-level population accumulates or “bottlenecks” during the pulse.

Transformation to Moving Coordinates

These two basic equations can then be solved with the aid of a few minor tricks, as follows. We first make a change of variables to a coordinate system that moves with the forward-traveling pulse, as defined by the transformation

$$z \equiv \hat{z} \quad \text{and} \quad t \equiv \hat{t} - \hat{z}/c. \quad (4)$$

That is, whereas \hat{z} and \hat{t} are ordinary laboratory coordinates, for the remainder of this section z and t refer to coordinates in the moving pulse frame. Note that

the delayed time coordinate t is essentially centered on the pulse's arrival time at each plane z . For example, if the pulse starts out at an input plane $\hat{z} = 0$ centered at time $\hat{t} = 0$, and arrives at some plane \hat{z} centered about time $\hat{t} = \hat{z}/c$, then the pulse written in the delayed time coordinate t is centered on $t = 0$ at every plane along the amplifier.

We also rewrite the pulse intensity and the population difference in the new coordinate system in the modified forms

$$I(z, t) \equiv \hat{I}(\hat{z}, \hat{t}) \quad \text{and} \quad N(z, t) \equiv \Delta \hat{N}(\hat{z}, \hat{t}), \quad (5)$$

where we use $N(z, t)$ instead of $\Delta N(z, t)$ from here on merely to simplify the formulas. The basic equations for the pulse intensity and the population inversion are then transformed into the significantly simpler forms

$$\frac{\partial I(z, t)}{\partial z} = \sigma N(z, t) I(z, t) \quad (6)$$

and

$$\frac{\partial N(z, t)}{\partial t} = -\left(\frac{2^* \sigma}{\hbar \omega}\right) N(z, t) I(z, t), \quad (7)$$

where these equations are now expressed in the *transformed* or *moving* coordinate system.

Solution of the Pulse Equations

The first of these equations can then be rearranged and integrated over the length of the amplifier in the form

$$\int_{I=I_{\text{in}}(t)}^{I=I_{\text{out}}(t)} \frac{dI}{I} = \sigma \int_{z=0}^{z=L} N(z, t) dz, \quad (8)$$

where $I_{\text{in}}(t)$ is the input pulse intensity at the input plane to the amplifier, and $I_{\text{out}}(t)$ is correspondingly the signal intensity at the output plane, both measured in the delayed time coordinate t . It will then be convenient to define the integral on the right-hand side of this equation as a kind of "total number of atoms" $N_{\text{tot}}(t)$ in the amplifier, in the form

$$N_{\text{tot}}(t) \equiv \int_{z=0}^{z=L} N(z, t) dz. \quad (9)$$

The first of the basic equations can then be expressed in the simple form

$$I_{\text{out}}(t) = I_{\text{in}}(t) e^{\sigma N_{\text{tot}}(t)} = G(t) I_{\text{in}}(t), \quad (10)$$

where $G(t) \equiv \exp[\sigma N_{\text{tot}}(t)]$ is the time-varying or partially saturated gain at any instant within the pulse.

The second of the basic pulse equations can also be integrated over the amplifier length and then rewritten, using the first equation, in the form

$$\frac{\partial}{\partial t} \int_{z=0}^{z=L} N(z, t) dz \equiv \frac{dN_{\text{tot}}(t)}{dt} = -\left(\frac{2^*}{\hbar \omega}\right) \int_{z=0}^{z=L} \frac{\partial I(z, t)}{\partial z} dz, \quad (11)$$

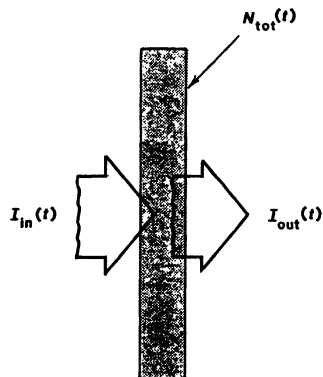


FIGURE 10.2

Thin-slab model for a homogeneously saturating laser pulse amplifier.

which simplifies to

$$\frac{dN_{\text{tot}}(t)}{dt} = -\frac{2^*}{\hbar\omega} [I_{\text{out}}(t) - I_{\text{in}}(t)]. \quad (12)$$

The two basic equations thus reduce to two coupled equations in the delayed time coordinate t only. These will be the fundamental working equations from this point on.

Physical Interpretation

With this change of coordinates *the equations take on the same form as if the total number of atoms $N_{\text{tot}}(t)$ were condensed into an arbitrarily thin slab*, as in Figure 10.2. Equation 10.10 is then a standard exponential gain equation, showing that the input signal $I_{\text{in}}(t)$ is exponentially amplified by $N_{\text{tot}}(t)$ to become the output signal $I_{\text{out}}(t)$; and Equation 10.12 is essentially a conservation of energy equation, showing how $N_{\text{tot}}(t)$ is burned up by the amplification of $I_{\text{in}}(t)$ to produce $I_{\text{out}}(t)$.

Note that the output pulse $I_{\text{out}}(t)$ is actually delayed in real time \hat{t} with respect to the input pulse $I_{\text{in}}(t)$ by the transit time through the amplifier, since a particular point t in the output pulse occurs L/c later than the same point t in the input pulse. Also, the “number of atoms” $N_{\text{tot}}(t)$ is actually not a physical number of atoms that exists at any instant of time \hat{t} , or that could be seen by some snapshot of the amplifier at any single time \hat{t} . It is rather a measure of the total space-integrated (or time-integrated) population difference $\int N(z, t) dz$ seen by any one small segment of the pulse centered at time t , as that segment passes through each successive plane $z \equiv \hat{z}$ of the amplifier at the local time t . The net result, however, still reduces to an equivalent thin slab in which everything seems to happen simultaneously in the delayed time coordinate t .

Analytic Solutions

Several useful explicit solutions to these equations can be obtained as follows. We start by substituting Equation 10.10 into Equation 10.12 to obtain

either of the alternative forms

$$\begin{aligned}\frac{dN_{\text{tot}}(t)}{dt} &= -\frac{2^*}{\hbar\omega} \{ \exp[\sigma N_{\text{tot}}(t)] - 1 \} \times I_{\text{in}}(t) \\ &= -\frac{2^*}{\hbar\omega} \{ 1 - \exp[-\sigma N_{\text{tot}}(t)] \} \times I_{\text{out}}(t).\end{aligned}\quad (13)$$

Suppose the total initial inversion N_0 in the laser medium, at a time \hat{t}_0 prior to the arrival of any input pulse energy, is given by

$$N_0 \equiv \int_{z=0}^{z=L} \hat{N}(\hat{z}, \hat{t}_0) d\hat{z}. \quad (14)$$

The initial single-pass power gain of the amplifier is then $G_0 = \exp[N_0\sigma]$.

We will also write the accumulated signal energies per unit area $U_{\text{in}}(t)$ and $U_{\text{out}}(t)$ in the input and output pulses, from starting time t_0 up to normalized time t as

$$U_{\text{in}}(t) \equiv \int_{t_0}^t I_{\text{in}}(t) dt \quad \text{and} \quad U_{\text{out}}(t) \equiv \int_{t_0}^t I_{\text{out}}(t) dt. \quad (15)$$

These pulse energies per unit area are sometimes referred to as *energy fluences*. It is also convenient to define a saturation energy per unit area U_{sat} (sometimes called a *saturation fluence*) for the atomic medium by

$$U_{\text{sat}} \equiv \frac{\hbar\omega}{2^*\sigma}. \quad (16)$$

This quantity is clearly the pulsed analog to the saturation intensity $I_{\text{sat}} \equiv \hbar\omega/\sigma\tau$ we saw for continuous amplification. If a signal energy fluence U_{sat} flows by an atom in a time much less than the atom's recovery time τ , the atom has essentially a 50% chance of making a stimulated transition from one level to the other during the pulse. (As an example, a Nd:YAG laser, with cross section $\sigma \approx 5 \times 10^{19} \text{ cm}^2$, has a saturation fluence of $\approx 0.4 \text{ Joules per cm}^2$.)

The first of the differential forms in Equation 10.13 can then be integrated in the form

$$\int_{N_0}^{N_{\text{tot}}(t)} \frac{dN_{\text{tot}}}{\exp(\sigma N_{\text{tot}}) - 1} = -\frac{2^*}{\hbar\omega} \int_{t_0}^t I_{\text{in}}(t) dt = -\frac{2^*}{\hbar\omega} U_{\text{in}}(t) \quad (17)$$

to give the useful relation

$$U_{\text{in}}(t) = U_{\text{sat}} \times \ln \left\{ \frac{1 - \exp[-\sigma N_0]}{1 - \exp[-\sigma N_{\text{tot}}(t)]} \right\} = U_{\text{sat}} \times \ln \left[\frac{1 - 1/G_0}{1 - 1/G(t)} \right], \quad (18)$$

where again $G(t) = \exp[\sigma N_{\text{tot}}(t)] = I_{\text{out}}(t)/I_{\text{in}}(t)$ is the time-varying partially saturated gain within the pulse interval. This expression thus connects the cumulative input energy $U_{\text{in}}(t)$ to the net remaining inversion $N_{\text{tot}}(t)$ or the time-varying power gain $G(t)$ at any instant of (normalized) time t within the pulse.

The second differential relation in Equation 10.13 can be similarly integrated to give the complementary relation

$$U_{\text{out}}(t) = U_{\text{sat}} \times \ln \left\{ \frac{\exp[\sigma N_0] - 1}{\exp[\sigma N_{\text{tot}}(t)] - 1} \right\} = U_{\text{sat}} \times \ln \left[\frac{G_0 - 1}{G(t) - 1} \right], \quad (19)$$

where $U_{\text{out}}(t)$ is similarly the cumulative energy in the output pulse up to time t (in delayed time coordinates).

Gain Saturation

Either one of these results can then be inverted to express the instantaneous inversion and gain within the pulse in terms of either of the input or output pulseshapes, $U_{\text{in}}(t)$ or $U_{\text{out}}(t)$. For example, Equation 10.18 can be rewritten in the form

$$\sigma N_{\text{tot}}(t) = \ln \left[\frac{G_0}{G_0 - (G_0 - 1) \exp[-U_{\text{in}}(t)/U_{\text{sat}}]} \right], \quad (20)$$

which gives

$$G(t) = \exp[\sigma N_{\text{tot}}(t)] = \frac{G_0}{G_0 - (G_0 - 1) \exp[-U_{\text{in}}(t)/U_{\text{sat}}]}. \quad (21)$$

For a given input pulseshape $I_{\text{in}}(t)$ and a given initial gain G_0 we can use this to calculate the output pulseshape $I_{\text{out}}(t) = G(t) \times I_{\text{in}}(t)$.

Alternatively, if we want to specify a desired output pulseshape $I_{\text{out}}(t)$ in the presence of saturation, we can calculate the necessary gain versus time from the output pulseshape, using

$$G(t) = 1 + (G_0 - 1) \exp[-U_{\text{out}}(t)/U_{\text{sat}}], \quad (22)$$

and then find the required input pulseshape from $I_{\text{in}}(t) = I_{\text{out}}(t)/G(t)$. How to synthesize the required input pulseshape—which will be different for different output pulse energy levels or degrees of saturation—is, of course, a separate problem.

Pulseshape Distortion

Figure 10.3 illustrates the kind of output pulse distortion that is produced by amplifier gain saturation assuming typical input pulseshapes. In Figure 10.3, where we assume a square input pulse with a perfectly sharp leading edge, the initial gain right at the leading edge of the pulse is the unsaturated value G_0 . This gain immediately begins to saturate, however, falling rather slowly for a weak input pulse and thus producing only a certain amount of “droop” in the output pulse, as in (a), but dropping much more strongly for a strong input pulse, as in (b). The result is then a rapid decrease in the output signal, leaving a large spike on the leading edge of the amplified pulse.

This short pulse formation might seem potentially useful as a means of pulse sharpening, in order to obtain a shortened output pulse from a much longer input pulse. Its practicality is limited, however, because in order to obtain strong pulse sharpening the leading edge of the input pulse must have a rise time substantially shorter than the desired output pulse length. If a practical modulator is unable to create the desired short pulse to begin with, it may be no more capable of generating an input pulse with the required rise time on the leading edge.

A gaussian pulseshape, or any other shape with rounded leading and trailing edges, is generally a more realistic model for saturable pulse amplification. Figure 10.4 illustrates how the gaussian pulseshape (plotted on a log scale) changes as we increase the input energy level to an amplifier with an initial gain $G_0 = 10,000$

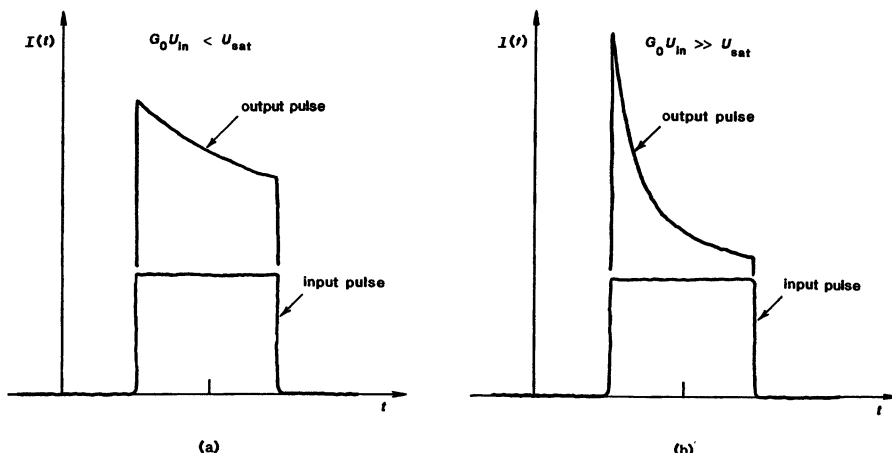


FIGURE 10.3

Output pulshape distortion for square input pulses with small and large input energy.

($\equiv 40$ dB), keeping the input gaussian pulshape constant. Significant saturation effects begin to occur when the amplified output energy disregarding saturation, or $G_0 U_{in}$, begins to approach the saturation energy U_{sat} . Even for input energies well above this value, however, the output pulselwidth appears to be very little changed from the input pulselwidth, even with quite strong saturation, although the pulse does seem to move forward slightly in time.

The output pulse is substantially changed, nonetheless, since there clearly is substantial gain saturation during the pulse. This saturation shows up primarily as an apparent advance in time of the peak of the output pulse. The pulse is not really advanced in time, but merely appears so because the leading edge receives essentially full amplification, whereas the gain is substantially reduced during the peak and trailing-edge portions of the pulse.

Figure 10.5 also plots the total pulse output energy U_{out} integrated over the full pulselwidth versus total pulse input energy U_{in} for the particular case of a homogeneously saturable amplifier with $G_0 = 1,000 = 30$ dB. This plot clearly shows how the pulse energy gain saturates down as the output pulse energy increases much above U_{sat} . (Note that these results are independent of the actual shape of the pulses.)

Pulse Energy Extraction and Energy Gain

The efficiency with which a signal pulse extracts the available energy from a laser pulse amplifier can be calculated in a simple fashion as follows. Subtracting the two earlier expressions for $U_{in}(t)$ and $U_{out}(t)$ gives

$$\frac{U_{extr}(t)}{U_{sat}} \equiv \frac{U_{out}(t) - U_{in}(t)}{U_{sat}} = \ln \left[\frac{G_0}{G(t)} \right] \quad (23)$$

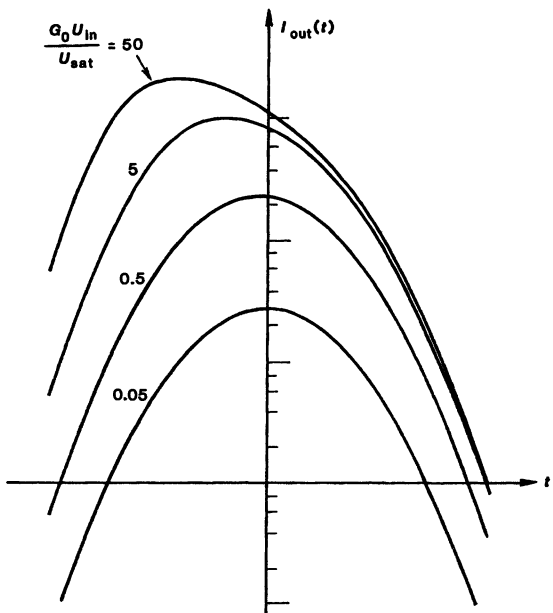


FIGURE 10.4
Pulse shape distortion for gaussian input pulses with different input energies into a high-gain amplifier. The FWHM pulsewidth is very little changed, but the pulses appear to move forward in time at higher input energies.

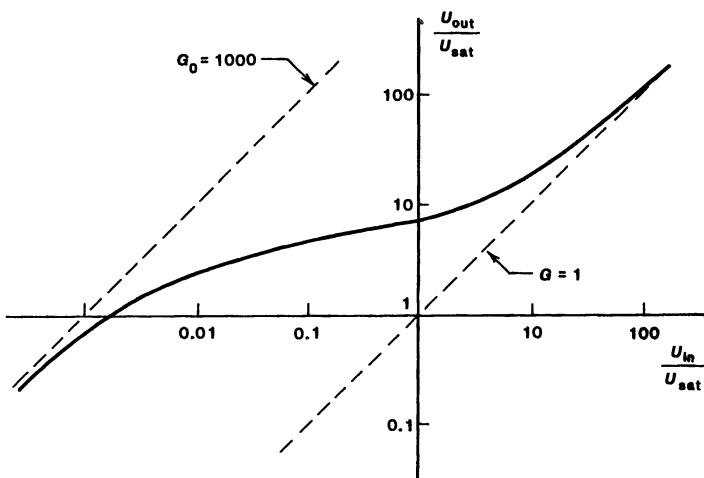


FIGURE 10.5
Pulse output energy versus pulse input energy for a homogeneously saturable amplifier with initial gain $G_0 = 1,000 = 30$ dB.

Let U_{in} and U_{out} without a specific time-dependence henceforth denote the total energies in the complete input and output pulses, i.e., the limits of $U_{in}(t)$ and $U_{out}(t)$ as $t \rightarrow +\infty$; and similarly let G_f denote the final value of $G(t)$ after the pulse has passed, i.e., the limit of $G(t)$ as $t \rightarrow \infty$. The total energy extracted

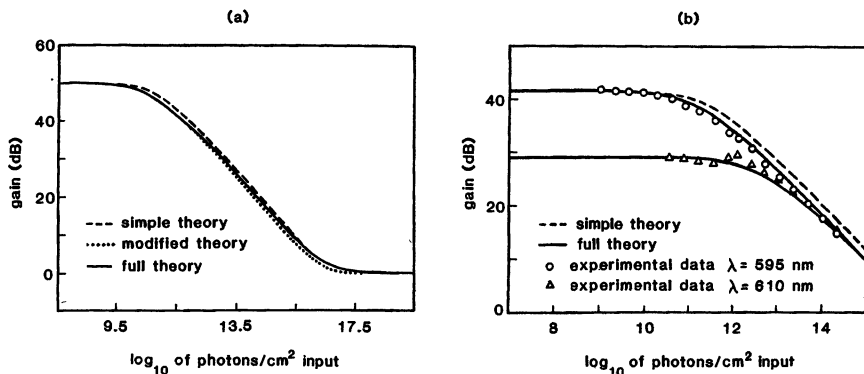


FIGURE 10.6

Pulse energy gain (integrated over the full pulse) versus input pulse energy: (a) theoretical curves for an initial gain $G_0 = 50$ dB; (b) experimental results and theoretical curves for two somewhat lower initial gains in a dye-laser pulse amplifier (from T. L. Koch, L. C. Chiu, and A. Yariv, *Opt. Commun.* 40, 364–368, February 1982).

from the gain medium by the complete pulse is then given by

$$U_{\text{extr}} \equiv U_{\text{out}} - U_{\text{in}} = U_{\text{sat}} \times \ln \left(\frac{G_0}{G_f} \right). \quad (24)$$

The maximum available energy from the amplifier is obviously obtained when the residual gain is saturated all the way down to $G_f \rightarrow 1$. The maximum available energy that can be extracted from the amplifier, assuming an input pulse strong enough to completely saturate the initial inversion, is thus given by

$$U_{\text{avail}} = U_{\text{sat}} \times \ln G_0 = \frac{N_0 \hbar \omega}{2^*}. \quad (25)$$

The right-hand expression confirms the physically obvious result that the available energy from the amplifier is either the total initial inversion energy, $N_0 \hbar \omega$, or half that value, depending on whether the lower level does or does not empty out rapidly during the pulse.

We might also define an overall or pulse-averaged “pulse energy gain” G_{pe} as the ratio of the total pulse energy output U_{out} to the total pulse energy input U_{in} , or

$$G_{\text{pe}} \equiv \frac{U_{\text{out}}}{U_{\text{in}}} = \frac{\ln [(G_0 - 1)/(G_f - 1)]}{\ln [(G_0 - 1)/(G_f - 1)] - \ln [G_0/G_f]}. \quad (26)$$

Figure 10.6 shows theoretical and experimental examples for the reduction in laser pulse energy gain with increasing input pulse energy for one particular experiment using a picosecond-pulse dye laser amplifier.

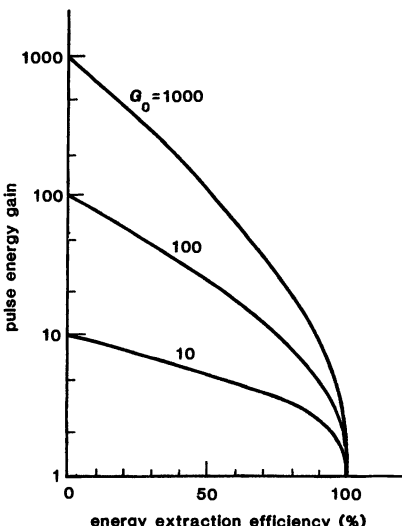


FIGURE 10.7

Integrated pulse energy gain versus energy-extraction efficiency for pulse amplifiers with different initial gains G_0 .

Pulse Energy Extraction Efficiency

Equations 10.23 through 10.26 can also be manipulated in various other ways that may be useful. For example, we might define an energy extraction efficiency η as the ratio of the energy actually extracted from the laser medium to the maximum energy available in the medium, or

$$\eta \equiv \frac{U_{\text{out}} - U_{\text{in}}}{U_{\text{avail}}} = \frac{\ln G_0 - \ln G_f}{\ln G_0}. \quad (27)$$

Inverting this tells us that the final gain G_f can be related to the initial gain G_0 and the energy extraction efficiency η in a simple fashion by

$$G_f = G_0^{1-\eta}. \quad (28)$$

Obviously, if the energy extraction efficiency approaches anywhere near 100%, the final saturated gain G_f at the end of the pulse will be much less than the unsaturated gain G_0 at the beginning of the pulse.

Putting this result into Equation 10.26 then gives a general relationship between the initial or unsaturated power gain G_0 , the time-averaged pulse energy gain G_{pe} , and the energy extraction efficiency η , entirely independent of input or output pulseshapes. Figure 10.7 illustrates how the pulse energy gain is rapidly saturated downward as we attempt to obtain increased energy extraction from an amplifier (i.e., by putting in stronger and stronger input pulses).

Summary

This section has presented the simplest possible rate-equation analysis of pulsed amplifier saturation (often referred to as the Frantz-Nodvik analysis; see the References). More complicated analyses can, of course, be developed to

take into account transverse intensity variations, finite pumping and relaxation times, large-signal and Rabi-flopping effects in the atoms, dispersive wave propagation effects, and other complications; some of these effects are treated in the references.

All of these results for pulse amplification are obviously similar in character to the power extraction and efficiency results we obtained for continuous amplification in Chapter 7. As usual, efficient energy extraction is obtained only at the cost of substantial reduction in effective energy gain integrated over the full pulse. Except for relatively smooth pulses, like gaussian pulses, efficient energy extraction can also mean severe distortion of the output pulseshape.

All the results given in this section also apply directly to pulse propagation through a saturable absorber, if we simply invert the signs of N_0 and $N_{tot}(t)$ in all the expressions. We will apply these results to passive saturable absorber mode locking in a later chapter.

REFERENCES

An extensive and detailed discussion of the behavior of a pulse sent into a strongly absorbing or amplifying medium, including "negative group delay effects," is given in a lengthy paper by E. O. Schulz-DuBois, "Pulse sharpening and gain saturation in traveling-wave masers," *Bell Sys. Tech. J.* **43**, 625-658 (1964). One of the most complete and detailed reviews of nearly all aspects of laser pulse amplification and saturation, using both rate-equation and resonant-dipole approaches, and covering both simple saturable-absorption aspects and more complex coherent-pulse and self-induced-transparency aspects, is given in P. G. Kryukov and V. S. Letokhov, "Propagation of a light pulse in a resonantly amplifying (absorbing) medium," *Sov. Phys. Uspekhi* **12**, 641-672 (March-April 1970).

There are numerous other analyses of optical pulse amplification and propagation in the published literature. Some of the more useful articles include the following.

R. Bellman, G. Birnbaum, and W. G. Wagner, "Transmission of monochromatic radiation in a two-level material," *J. Appl. Phys.* **34**, 780-783 (April 1963). A compact rate-equation analysis of pulse absorption and/or amplification in saturable two-level absorbers and/or amplifiers.

L. W. Davis and Y. S. Lin, "Propagation of optical pulses in a saturable absorber," *IEEE J. Quantum Electron.* **QE-9**, 1135-1138 (December 1973). A resonant-dipole calculation of pulse propagation and attenuation in a saturable absorber, going beyond the rate-equation limits, and showing how coherent ringing and optical-nutation effects also occur at large enough input pulse intensities.

E. Fill and W. Schmid, "Amplification of short pulses in CO₂ laser amplifiers," *Phys. Lett.* **45A**, 145-146 (September 10, 1973). A resonant-dipole calculation of short pulse amplification including both coherent-pulse effects and effects of rotational relaxation in CO₂. Shows how the pulse leading edge steepens and then breaks up into optical nutations at large enough intensity.

L. M. Frantz and J. S. Nodvik, "Theory of pulse propagation in a laser amplifier," *J. Appl. Phys.* **34**, 2346-2349 (August 1963). A detailed rate-equation analysis of energy amplification and pulse sharpening in saturable two-level amplifiers, similar to the discussions in this section.

A. Icsevgi and W. E. Lamb, Jr., "Propagation of light pulses in a laser amplifier," *Phys. Rev.* **185**, 517-545 (September 10, 1969). Extensive and detailed analysis of

pulse propagation using density matrix atomic equations and including inhomogeneous (doppler) broadening effects, with extensive numerically calculated solutions.

A. E. Siegman, "Design considerations for laser pulse amplifiers," *J. Appl. Phys.* **35**, 460–461 (February 1964). A simplified rate-equation derivation of the energy extraction efficiency results for pulse amplification.

J. P. Wittke and P. J. Warter, "Pulse propagation in a laser amplifier," *J. Appl. Phys.* **35**, 1668–1672 (June 1964). Analysis of pulse propagation in homogeneously saturable laser amplifiers with a nonsaturable loss also present, using the Bloch form for the atomic equations. Shows that with loss included a steady-state pulseshape develops at large enough gain or long enough propagation distance.

One practical application of pulsed saturable absorbers is in stabilizing very high-gain pulsed amplifier systems against parasitic oscillations. A good example of the practical complexities this entails in a real application can be found, for example, in R. F. Haglund, Jr., A. V. Nowak, and S. J. Czuchlewski, "Gaseous saturable absorbers for the Helios CO₂ laser system," *IEEE J. Quantum Electron.* **QE-17**, 1799–1808 (September 1981). Another practical application of pulsed saturable absorbers is in nonlinear pulse compression, with a good practical example being a paper by J. E. Murray, "Temporal compression of mode-locked laser pulses for laser-fusion diagnostics," *IEEE J. Quantum Electron.* **QE-17**, 1713–1723 (September 1981).

Problems for 10.1

1. *Pulse input energy to saturate the pulse energy gain down to just half the initial unsaturated gain.* A laser amplifier with large initial power gain, $G_0 \gg 1$, is to be used to amplify a pulse having just enough energy so that the final gain after the pulse has passed is half the initial (numerical) gain. Show that the required input energy is $U_{\text{in}} \approx U_{\text{sat}}/G_0$, the resulting output energy is $U_{\text{out}} \approx (\ln 2)U_{\text{sat}}$, and hence the pulse energy gain is $G_{\text{pe}} \approx (\ln 2)G_0$.
2. *Leading-edge spike width for an infinitely sharp square input pulse.* A square input pulse with an infinitely sharp leading edge when sent into a high-gain saturable pulse amplifier produces a sharp spike on the leading edge of the output pulse. Develop an expression for the width of this spike (FWHM) as a function of the unsaturated amplifier gain, amplifier initial stored energy or available energy, and the power level of the input pulse step.
3. *Calculating input-output pulse profiles for gaussian input pulses of varying pulse energy.* A pulse with total energy U_{in} and gaussian pulse width τ_p (FWHM) is sent through a homogeneous saturable laser amplifier with small-signal gain $G_0 = \exp(2\alpha_0 L)$. Plot the input and output pulseshapes $I_{\text{in}}(t)$ and $I_{\text{out}}(t)$ on log scales versus t for gains $G_0 = 3, 10$, and 100 , and for various values of input energy, such as $U_{\text{in}}/U_{\text{sat}} = 0.001, 0.01, 0.1$, and 1.0 . Repeat for a saturable absorber with small-signal transmission $T_0 = \exp(-2\alpha_0 L) = 0.1$ and 0.01 . Try square instead of gaussian pulse with the same parameters.
4. *Pulse energy transmission through a saturable atomic absorber.* A pulse of input energy U_{in} is sent through a homogeneous saturable absorber having a small-signal transmission $T_0 = \exp(-2\alpha_0 L)$. Plot the net energy transmission $T =$

$U_{\text{out}}/U_{\text{in}}$ through the absorber versus input pulse energy U_{in} for $T_0 = 0.1, 0.01$, and 0.001 .

5. *Measuring pulse saturation energies using photoacoustic spectroscopy.* If a short pulse of laser energy is passed through a very weakly absorbing gas mixture ($2\alpha_m L \ll 1$), then a technique called photoacoustic or optoacoustic spectroscopy can be used to measure accurately, at least on a relative scale, the very small amount of energy ΔU absorbed by the gas. This technique works in essence by measuring the sound impulse that this sudden heat input produces, using an ordinary microphone inside the atomic cell.

Suppose we plot the measured $1/\Delta U$ (in arbitrary units) versus the reciprocal input pulse energy $1/U_{\text{in}}$ in the range $U_{\text{in}} \leq U_{\text{sat}}$. Show that the results of these measurements should be a straight line, which we can extrapolate to find the saturation energy U_{sat} without needing to know either $\alpha_0 L$ or the absolute calibration factor on the measurement of ΔU . (See E. A. Ryabov, "Method for measuring the saturation energy of weakly absorbing gases," *Sov. J. Quantum Electron.* 5, 81–82, July 1975.)

6. *Penetration depth versus energy for pulses traveling into a saturable absorber.* A short laser pulse is injected into one end of a long cell containing a homogeneously saturable absorbing medium. Make plots of the saturation absorption coefficient versus depth into the cell just after the pulse has gone past, for different amounts of input pulse energy, from well below to well above the saturation energy density of the absorbing medium. What is an approximate "rule of thumb" for how far into the cell a strong pulse will penetrate?
7. *Pulse input-output and pulse energy extraction for a partially bottlenecked lower energy level (research problem).* Consider a saturable pulse amplifier of the type analyzed in this section, but assume that the relaxation rate γ_1 out of the lower laser level may be on the same time scale as the pulselength (although the pulse is still assumed very short compared to the upper-level relaxation or pumping times). Develop the necessary set of three coupled rate equations (cavity, upper laser level, lower laser level) to describe this situation, and see if you can make any progress on solving these equations in order to predict, for example, pulse output versus pulse input.
-

10.2 PULSE PROPAGATION IN NONLINEAR DISPERSIVE SYSTEMS

When an optical pulse propagates through any kind of nonlinear system, we can expect to see at least some nonlinear distortion of the pulseshape with propagation distance, with stronger effects for larger amplitude pulses. When such nonlinear distortion is combined, however, with linear dispersive pulse distortion effects such as those discussed in the Chapter 9, even more complex and interesting effects can be expected to occur—especially since the nonlinear distortion effects may in general tend either to *combine with* or to *cancel out* the linear dispersive effects. In this section we will introduce several such nonlinear and dispersive effects that are of particular importance in real laser systems.

Nonlinear Pulse Propagation in Atomic Systems

Let us first make some general observations about the large-signal propagation of an optical pulse through an atomic medium which contains a resonant atomic transition, such as a typical laser medium.

When a pulsed signal with an electric field variation $\mathcal{E}(z, t)$ propagates through any kind of atomic medium, the electromagnetic aspects of the pulse behavior are governed by the electromagnetic wave equation. This equation is a fundamentally *linear* equation for the electric field $\mathcal{E}(z, t)$ in terms of the polarization $p(z, t)$ in the atomic medium. If the polarization term on the right-hand side of this wave equation in turn represents an induced polarization which is also *linear in the applied signal field*, then the overall response of this system will be entirely linear; and the pulse propagation and distortion behavior in the system can be completely described by the dispersion curve for the atomic medium, or the ω - β curve for the wave-propagating system.

Suppose however that the polarization $p(z, t)$ arises from a resonant atomic transition, and also that the applied signal fields are strong enough to produce significant nonlinear or “Rabi flopping” behavior (as described in Chapter 5). The polarization response $p(z, t)$ is then more complicated and no longer linear in the applied signal. The polarization response must be described instead by (at least in simple cases) a resonant dipole equation for the polarization response, together with an additional equation for the population difference $\Delta N(z, t)$ on the relevant transition as a function of space and time. Both of these equations are basically nonlinear equations, at least at larger signal levels.

To find the complete pulse propagation behavior for a large-amplitude wave passing through a resonant atomic system, all three of these equations must then be solved simultaneously and in a self-consistent fashion, taking full account of both the effects of the pulse fields on the atoms and the effects of the atomic polarization back on the pulses. For larger signals where these equations become more strongly nonlinear, the resulting solutions will generally be quite complicated, in themselves and in how they depend on the pulse intensity. As a result there are many complicated analyses of such phenomena in the scientific literature. (Only the atomic equations are nonlinear; Maxwell’s equations and hence the electromagnetic wave equation are entirely linear in \mathcal{E} and p .)

The results that come out of these analyses (and experiments) include purely linear behavior, such as free induction decay, and other types of pulse propagation and distortion behavior, such as Rabi flopping behavior, “self-induced transparency,” and “ π and 2π pulse propagation.” We will not attempt to review any of these resonant-atom pulse phenomena in detail here, since such discussions are unavoidably lengthy and complex, and since the resulting large-signal phenomena, though sometimes experimentally interesting, do not seem to have major practical applications. (We have given a brief description of large-signal pulse propagation in Chapter 5, where we introduced the concept of Rabi flopping behavior).

Nonlinear Optical Polarization: The Optical Kerr Effect

There is, however, another fundamental type of nonlinear polarization response that occurs in essentially all transparent optical materials, not just on resonant atomic transitions, and that can be of considerable practical importance in many laser situations. This is a nonlinear change in the dielectric constant or

index of refraction of almost any optical material with increasing optical intensity, often referred to as an *optical Kerr effect*. In the rest of this section we will examine several of the important propagation effects produced by this optical Kerr effect.

When an electric field \mathcal{E} is applied to a transparent dielectric medium, the force associated with this field produces a distortion of the electron-charge clouds in that medium, and also a possible reorientation of the molecular axes of molecules in a liquid medium, since such molecules generally like to line up with an applied field. Both effects in turn lead to a macroscopic polarization p in the medium that in first order will be linear in the applied \mathcal{E} field. This linear response in a low-loss or transparent dielectric is, of course, just the linear dielectric constant or index of refraction of the medium.

If the applied field is strong enough, however, the polarization response of the medium may become nonlinear in the applied field. (The distortion of the electron-charge clouds, or the realignment of the molecular axes, becomes nonlinear—usually weakly nonlinear—in the applied field strength.) This is very often expressed in a somewhat simplified but still fairly general fashion by writing the polarization as a series expansion in the applied field in the form

$$p = \chi_{(1)}\epsilon_0\mathcal{E} + \chi_{(2)}\mathcal{E}^2 + \chi_{(3)}\mathcal{E}^3 + \dots, \quad (29)$$

where $\chi_{(1)}$ is the linear susceptibility, and $\chi_{(2)}$ and $\chi_{(3)}$ (which have quite different dimensions) represent weak higher-order nonlinearities in the dielectric response of the medium. (In a more accurate picture, all three of the χ quantities should be tensor quantities, and all three should have frequency dependences that become increasingly complex for the higher-order terms.)

Second-Order Susceptibility: Harmonic Generation and Modulation

The $\chi_{(2)}\mathcal{E}^2$ term—sometimes written in an alternative notation as $d_2\mathcal{E}^2$ —represents a second-order nonlinearity, which can be responsible for second-harmonic generation, optical rectification, optical parametric amplification, and other useful nonlinear effects. By symmetry arguments, however, this effect must be identically zero in any material that has a centrosymmetric arrangement of atoms. Effects of this type are found therefore primarily in certain special crystals having a noncentrosymmetric crystal structure—in essence, only in those materials that are also piezoelectric.

This includes, for example, barium titanate or BaTiO_3 , crystal quartz, potassium dihydrogen phosphate (KDP), ammonium dihydrogen phosphate (ADP), cesium dihydrogen arsenate (CDA), and lithium niobate (LiNbO_3); these are some of the nonlinear optical crystals most widely used in optical modulators and harmonic generators.

The Third-Order Susceptibility

The third-order susceptibility term $\chi_{(3)}\mathcal{E}^3$ can be present, however, with varying strength, in essentially *all optical materials of any crystal structure or class*, including liquids and gases. If we include this term in the polarization p , the total electric displacement d in the medium can then be related to the applied field \mathcal{E} in the form

$$d = \epsilon_0[1 + \chi_{(1)}]\mathcal{E} + \chi_{(3)}\mathcal{E}^3 = \epsilon_0[1 + \chi_{(1)} + \epsilon_0^{-1}\chi_{(3)}\mathcal{E}^2]\mathcal{E}. \quad (30)$$

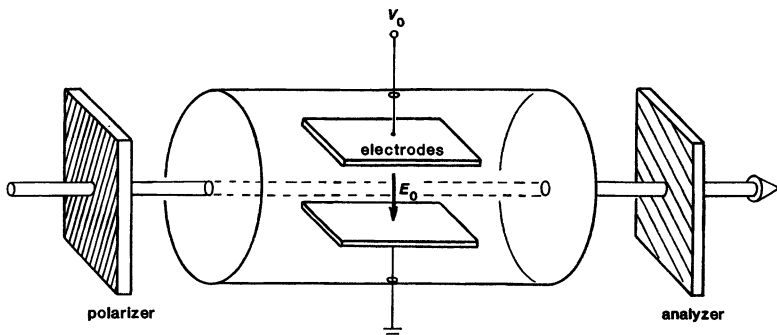


FIGURE 10.8
A Kerr cell light modulator.

Hence the dielectric constant $\tilde{\epsilon}$ is now a nonlinearly varying quantity given by

$$\tilde{\epsilon} = \epsilon_1 + \epsilon_2 \mathcal{E}^2, \quad (31)$$

in which $\epsilon_1 \equiv \epsilon_0(1 + \chi_{(1)})$ is the linear or first-order dielectric constant, and $\epsilon_2 \mathcal{E}^2 \equiv \chi_{(3)} \mathcal{E}^2$ is the nonlinear change in the dielectric constant, produced by the applied field.

Since the optical index of refraction n is related to the optical-frequency value of ϵ by $n = \sqrt{\tilde{\epsilon}/\epsilon_0}$, we can also view this as a nonlinear dependence of the index of refraction on applied signal strength, as given by

$$n = n_0 + n_{2E} \mathcal{E}^2, \quad (32)$$

where $n_0 = \sqrt{\epsilon_1/\epsilon_0}$ is the linear value and $n_{2E} \mathcal{E}^2$ the nonlinear variation of the index of refraction.

Kerr Cell Light Modulators

Suppose we construct a liquid cell containing CS_2 or nitrobenzene or some similar liquid, as in Figure 10.8, to which we apply both a strong low-frequency modulation field E_0 (by using suitable electrodes) and a much weaker optical-frequency field \mathcal{E} (in the form of a traveling optical wave). A strong enough modulation field will then change the index of refraction seen by the optical wave according to the relationship

$$n = n_0 + n_{2E} E_0^2, \quad (33)$$

and this provides a way of phase modulating the light beam.

To be slightly more accurate, the modulation field E_0 usually causes an increase in index of refraction for optical \mathcal{E} fields polarized parallel to the dc field, and a decrease in index of refraction for fields polarized perpendicular to E_0 . This then creates an *induced birefringence* in the modulation cell, with a magnitude proportional to the modulating voltage squared. This birefringence can in turn be converted into amplitude modulation by placing the modulation cell between suitable crossed polarizers. This physical effect is known as the *Kerr effect*, and the resulting device is a *Kerr cell modulator*.

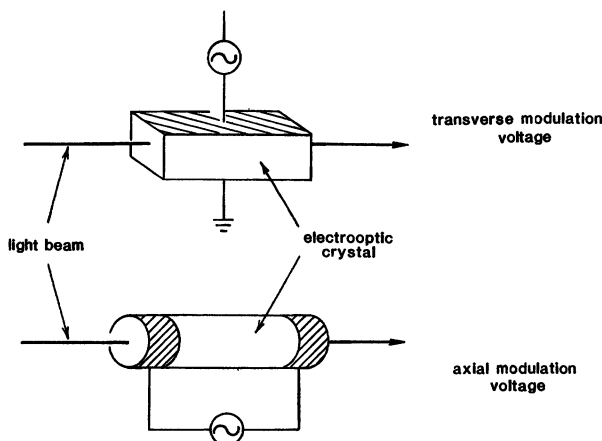


FIGURE 10.9
Alternative ways of constructing a Pockels cell light modulator.

Pockels Cell Light Modulators

Practical Kerr cells, when they are used at all, usually employ one of the molecular liquids mentioned earlier, since the reorientation of the molecules in these liquids under the influence of the applied field E_0 produces the strongest available Kerr coefficient, or change of index with voltage. Even with these liquids, however, voltages on the order of 25,000 volts are necessary to produce sizable amplitude-modulation effects.

Most of the electrooptic modulators used with lasers, therefore, are instead *Pockels cell modulators*, which use one of the noncentrosymmetric crystals mentioned earlier, and produce the index change or birefringence through the second-order nonlinearity term $\chi_{(2)}E_0^2$. The induced birefringence is then linear rather than quadratic in the modulation field E_0 , and adequate modulation can be obtained in practice with modulation voltages of a few thousand volts, or even less in some especially favorable cases. Figure 10.9 shows two examples of simple Pockels cell modulator designs.

Optical Kerr Effect

Suppose, however, we consider an optical signal with a sufficiently strong optical field strength that we can have a significant $\chi_{(3)}\mathcal{E}^3$ or $n_{2E}\mathcal{E}^2$ term produced by the optical beam itself. If $\mathcal{E}(t)$ is in fact an optical-frequency signal, at frequency ω , then this term will produce two effects. On the one hand the $\chi_{(3)}\mathcal{E}^3$ term will produce a third-harmonic polarization $p(t)$ at frequency 3ω ; this may radiate—typically very weakly—at the third harmonic of the applied optical frequency ω . We will neglect this third-harmonic generation process here, since it is usually very weak; is not of direct interest at this point; and will not be properly phase-matched in most situations.

On the other hand, this same $n_{2E}\mathcal{E}^2$ effect will also produce a zero-frequency or time-averaged signal-induced change in the refractive index for the signal field,

which can be written as

$$n = n_0 + n_{2E} \langle \mathcal{E}^2 \rangle = n_0 + n_{2I} I, \quad (34)$$

where $\langle \mathcal{E}^2 \rangle$ represents the time-averaged value of the field squared, and $I \equiv \sqrt{\epsilon/\mu} \langle \mathcal{E}^2 \rangle$ represents the optical intensity. This change in the average value of the optical refractive index produced by the optical signal itself is commonly referred to as the *optical Kerr effect*.

Such an optical Kerr effect will be present, with a positive sign ($n_{2I} > 0$), in nearly all optical materials. A representative value for the optical Kerr coefficient in a typical glass (such as might be used in an optical fiber) might be $n_{2E} \approx 10^{-22} \text{ m}^2/\text{V}^2$ or $n_{2I} \approx 10^{-16} \text{ cm}^2/\text{W}$. Certain strongly polarizable molecular liquids, such as CS_2 or certain long-chain organics, can have values 10 to 20 times larger than this. (Essentially all condensed materials have an *electronic optical Kerr effect* of roughly comparable magnitude; the strongly enhanced response in molecular liquids comes from an *orientational Kerr effect* similar to that produced by low-frequency electric fields).

We will review several nonlinear phenomena produced by this optical Kerr effect in subsequent paragraphs. We can estimate, however, that this optical Kerr effect might produce significant effects if it produces an additional path length $\Delta n L$ of half a wavelength, or an additional half cycle of phase shift, in a path length of, say, $L = 1 \text{ cm}$, or $2\pi n_{2I} I L / \lambda = \pi$. If we use $L = 1 \text{ cm}$ and $\lambda = 0.6 \text{ nm}$, then a significant nonlinear effect will occur for an optical intensity of $I \approx 1 \text{ to } 10 \text{ GW/cm}^2$, depending on the value of n_{2I} . It is in fact in this range of intensities that significant optical Kerr effects do occur in optical systems like high-power laser rods, focusing lenses, and other optical elements.

Note, however, that intensities in this range will occur for a total input power of less than 1 watt in a $4 \mu\text{m}$ -diameter optical fiber; moreover, in an optical fiber it may take kilometers rather than centimeters for the resulting phase-modulation effects to accumulate. This can make possible very strong and useful nonlinear optical effects in optical fibers, as we will see in more detail in the following section.

Whole-Beam Self-Focusing Effects

As a first illustration of an important effect produced by the optical Kerr effect, we can consider so-called *self-focusing* of an optical beam. Suppose an optical beam with a moderate intensity I and a smooth transverse profile passes through a medium having a finite and positive optical Kerr coefficient n_{2I} , as in Figure 10.10. The higher intensity in the center of the beam will then cause an increase in the index of refraction seen by the center of the beam, as compared to the wings; in other words, the optical medium will be given a focusing power, or converted into a weak positive lens.

If this self-focusing effect in propagating through a given length of the medium exceeds the diffraction spreading of the optical beam in the same length, the optical beam profile will begin to be focused inward as the beam propagates. But, inward focusing then increases the intensity in the center of the beam, and makes the sides of the beam profile steeper; and this in turn increases the strength of the self-induced lens. The beam will then continue to be focused ever more strongly inward, in an essentially runaway fashion.

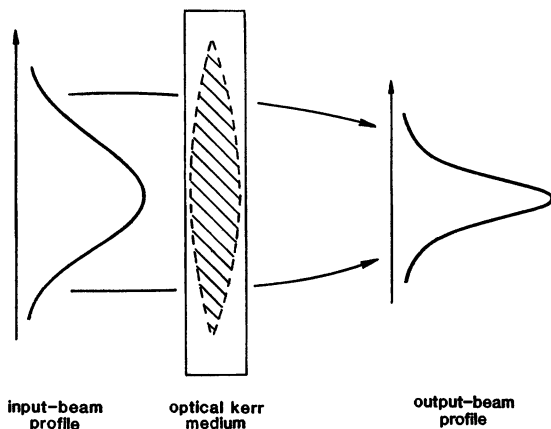


FIGURE 10.10
Whole-beam self-focusing
in an optical Kerr medium.
The light beam itself in-
duces a weak focusing lens
in the optical medium.

This type of self-focusing of the entire beam profile is known as *whole-beam self-focusing*. A more detailed analysis shows that, when the effects of self-focusing and diffraction spreading are both taken into account, runaway whole-beam self-focusing will begin to occur when the total power in a beam with a smooth transverse profile exceeds a certain critical power P_{crit} , independent of the diameter of the beam. Typical values of P_{crit} range from a few tens of kilowatts in strong Kerr liquids to a few megawatts in materials with typical weak Kerr coefficients.

Small-Scale Self-Focusing Effects

There is a similar phenomenon known as *small-scale self-focusing*, in which any small-amplitude variations or ripples on a transverse beam profile will begin to grow in amplitude exponentially with distance because of the optical Kerr effect. In essence the transverse spatial variation of the optical beam intensity produces a transverse spatial variation in refractive index, or a refractive index grating. This grating diffracts some of the optical beam energy into small-angle scattering, and this diffracted light interferes with the original beam in exactly such a way as to make the initial intensity ripples on the beam profile grow in amplitude with distance.

Figure 10.11 shows the dramatic results of an experiment in which initially small-amplitude ripples were put on the transverse amplitude profile of an optical beam, and the beam then sent through a strong optical Kerr medium with an intensity sufficient to cause significant growth in these ripples after a few tens of cm. The runaway growth of the periodic amplitude variations is evident.

In general, if either whole-beam or small-scale self-focusing becomes significant, this self-focusing will continue in a runaway fashion. The optical beam may then rapidly collapse with distance into one or several very small filaments or self-focused focal spots. Once this happens, not only does the beam become badly distorted in its transverse profile, but the power density also usually becomes large enough to cause optical damage, optical breakdown, or other undesirable nonlinear effects to ensue.

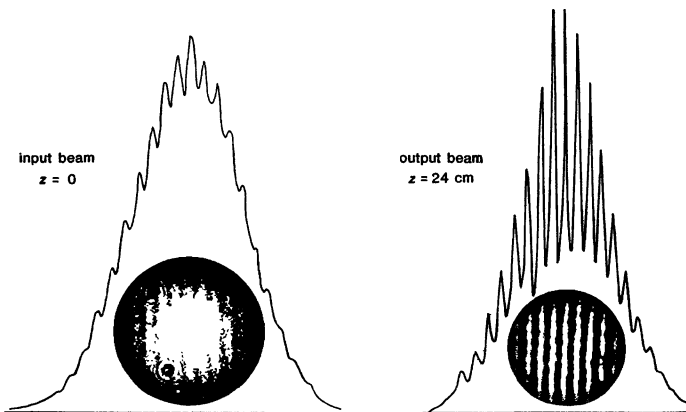


FIGURE 10.11

An experimental demonstration of small-scale self-focusing, or the exponential growth with distance of small periodic intensity ripples on the transverse profile of an optical beam.

The type of nonlinear self-focusing produced by the optical Kerr effect can thus be a major problem in many high-power lasers, especially pulsed lasers, as well as in scientific experiments using focused high-power laser beams.

Self-Phase Modulation

The optical Kerr effect can also produce a very similar *self-phase-modulation* effect, which occurs for pulsed or modulated signals in the time rather than the spatial domain. To demonstrate this, we can next suppose that an optical pulse with some given intensity variation $I(t)$ in time propagates through a certain length L of a medium with a finite optical Kerr coefficient n_{2I} , and that the pulse amplitude is large enough to produce a significant index change $\Delta n(t) \equiv n(t) - n_0 = n_{2I}I(t)$ and a significant change in optical path length $\Delta n(t)L$, at least near the peak of the pulse. (Assume for now that the transverse beam profile is uniform, or that we somehow otherwise avoid the self-focusing effects just discussed.)

The pulse fields will then experience a time-varying phase shift or phase modulation $\exp[j\Delta\phi(t)] = \exp[-j2\pi\Delta n(t)L/\lambda] = \exp[-j2\pi n_{2I}I(t)L/\lambda]$ produced by the intensity variation of the pulse itself. If the optical Kerr coefficient is positive ($n_{2I} > 0$), as it usually is, this self-phase modulation will represent in effect a lowering of the optical frequency of the pulse during the rising or leading edge of the pulse, since $dn/dt > 0$ and hence $\Delta\omega_i(t) = (d/dt)\Delta\phi(t) < 0$. (In physical terms, the medium is getting optically longer; so the arrival of optical cycles is delayed or slowed down.) Similarly there will be an increase in the instantaneous frequency of the pulse signal during the trailing or falling edge of the pulse. The maximum frequency shift will occur at the points of maximum slope or maximum $dI(t)/dt$.

A pulse with a smooth time envelope, as in Figure 10.12, will thus acquire a more or less linear frequency chirp across the central region of the pulse, as

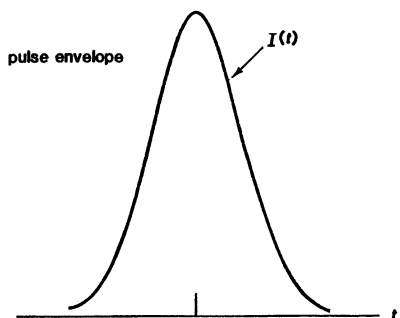
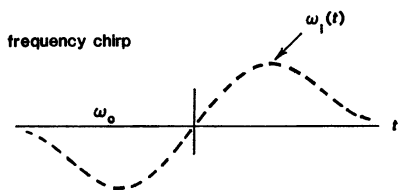


FIGURE 10.12

The initial effect of intensity-dependent self-phase modulation is to lower the frequency on the leading edge and raise the frequency on the trailing edge of a pulse, thus producing a chirp.



shown in the lower plot. The magnitude of this chirp will increase more or less linearly with distance through the medium, at least as long as the pulse intensity profile remains unchanged.

In most practical situations, however, the optical medium will also have a certain value of group-velocity dispersion $dv_g(\omega)/d\omega$. The different portions of the pulse, with their slightly different optical frequencies, will thus begin to travel at slightly different group velocities; and as a result the pulseshape will begin to change by an increasing amount with increasing distance. Depending on circumstances, this effect can lead to at least three different types of behavior: severe pulse distortion and breakup, soliton formation and propagation, or pulse broadening and enhanced frequency chirping. We can discuss each of these in turn.

Approximate Analysis of Self-Phase Modulation

We can develop an approximate analysis to indicate the magnitude of these self-phase modulation effects as follows. Suppose an initially unchirped gaussian input pulse has the time-variation

$$\mathcal{E}(t) = \mathcal{E}_0 e^{-at^2} \quad \text{or} \quad I(t) = I_0 e^{-2at^2}. \quad (35)$$

The net phase shift for this pulse in passing through a length L of nonlinear medium will then be

$$\phi(t) = \frac{2\pi(n_0 + n_2 I)L}{\lambda}, \quad (36)$$

and hence the phase-shift derivative will be

$$\frac{d\phi}{dt} = \frac{2\pi n_{2I} L}{\lambda} \frac{dI(t)}{dt} \approx \frac{4\pi a n_{2I} L I_0}{\lambda} \times t e^{-2at^2}, \quad (37)$$

where we assume for simplicity that to first order the pulseshape $I(t)$ is not changed in passing through the length L .

But this phase modulation corresponds to giving the pulse a frequency chirp at the center of the pulse which is given (in our earlier gaussian pulse notation) by

$$\frac{d\phi}{dt} = 2bt \approx \frac{4\pi a n_{2I} L I_0}{\lambda} t. \quad (38)$$

This means that the pulse will acquire a chirp parameter $b = a$, and thus increase its time-bandwidth product by a factor of $\sqrt{2}$, after passing through a length of nonlinear medium given by

$$\frac{2\pi n_{2I} L I_0}{\lambda} = 1. \quad (39)$$

That is, the pulse will acquire a significant amount of self-phase modulation in length L if its peak intensity exceeds a value given by

$$I_0 = \frac{\lambda}{2\pi n_{2I} L}. \quad (40)$$

If we take $n_{2I} = 3 \times 10^{-16} \text{ cm}^2/\text{W}$, $L = 10 \text{ cm}$, and $\lambda = 0.5 \mu\text{m}$, this gives a threshold intensity for significant self-phase modulation of $I_0 \approx 3 \text{ GW/cm}^2$, which is close to the damage threshold in most optical materials. Suppose, however, we consider a single-mode optical fiber with a diameter of $4 \mu\text{m}$ and a length of $L = 10 \text{ m}$. Its threshold intensity of 30 MW/cm^2 is reached with a total power in the fiber of $\approx 3 \text{ W}$.

Pulse Distortion and Breakup Effects

We can recall that the group velocity in a dispersive medium is given by $1/v_g(\omega) = d\beta(\omega)/d\omega \equiv \beta'(\omega)$. Hence the variation of group velocity with frequency is given by

$$\frac{dv_g}{d\omega} = -v_g^2 \frac{d^2\beta}{d\omega^2} = -v_g^2 \beta'', \quad (41)$$

where $\beta'' \equiv d^2\beta/d\omega^2$ is commonly referred to as the *group-velocity dispersion* of the medium. A negative value of β'' , which corresponds to negative dispersion according to this conventional definition, thus means that the group velocity increases with increasing frequency.

Suppose that an optical Kerr medium in fact has such a negative dispersion, so that v_g increases with increasing ω . This means physically that the leading edge of the chirped pulse in Figure 10.12 will begin to travel more slowly, and to fall back against the main part of the pulse, while the trailing edge of the pulse will begin to travel faster and to catch up with the main part of the pulse. In other words, the pulse will generally become compressed as it propagates, as a consequence of the self-phase-modulation process.

As the pulse becomes more compressed, however, its peak intensity will increase, on the one hand, and its rise and fall times will become shorter, on the other hand. Both effects will then combine to greatly increase the self-chirping effects on the leading and trailing edges of the pulse, and this in turn will increase the pulse compression, in another runaway type of process.

If the dispersion in the medium is of opposite sign, an initially smooth pulse will become broadened in time rather than compressed (as we will discuss in more detail in a later section). Even in this situation, however, the pulse will also acquire a growing amount of chirp, and its spectrum will be continuously broadened by the combination of nonlinear effects plus dispersion. (Note also that the analog to dispersion for pulse distortion in time is diffraction for pulse distortion in space—i.e., in the transverse coordinates—and this diffractive dispersion always has a sign corresponding to pulse compression in space for positive n_{2r} . Self-focusing thus always leads to beam compression in the transverse direction.)

In either situation, if the time envelope of either a pulsed or a cw signal contains any significant amount of initial amplitude (or phase) modulation or pulse substructure—that is, if either the phasor amplitude or the phase angle of the signal field has significant time modulation within the overall pulse envelope—this will increase these nonlinear distortion effects. The phase substructure will represent additional chirp, and the amplitude structure will reinforce the self-phase-modulation effect. The result will often be that the envelope of a high-power laser beam will not retain a smooth shape, if indeed it initially has one, but will begin to break up into increasingly complex subpulses within the main pulse envelope. This increasingly strong phase and amplitude modulation will also broaden the frequency spectrum of the pulse (but not the overall time envelope) by an amount that can increase rapidly with increasing distance.

Pulse Breakup in Practical Laser Systems: The B Integral

These pulse-breakup and spectral-broadening effects, especially when accompanied and intensified by self-focusing effects, can be a source of considerable difficulty in many high-power lasers, and particularly in mode-locked lasers, where the peak power can be very high even though the total energy or the average power may be quite low. As we have said, the effects of nonlinear modulation and dispersion will grow exponentially as a laser signal begins to break up, because the time-variation becomes faster across the substructure within the pulse, and because the pulse energy gets compressed into shorter subpulses with higher peak intensities.

Self-phase-modulation and self-focusing effects are thus especially strong “runaway” effects in such devices as multistage Nd:glass laser amplifier chains and mode-locked Nd:glass laser oscillators. In both the pulse is continually being further amplified, and the laser medium has a broad enough atomic linewidth to continue amplifying the pulse even after its spectrum has been substantially broadened by the nonlinear effects. When a mode-locked Nd:glass laser is pumped too strongly, for example, the early pulses in the mode-locked and Q -switched burst may be reasonably clean and well-formed, but the pulses near and after the peak of the Q -switched burst often become severely distorted and spectrally broadened.

Self-phase modulation of this type is often accompanied by, and reinforced by, self-focusing effects in the same system. It is also a common characteristic of such self-phase modulation that the pulse spectrum gets greatly broadened, generally

in a one-sided fashion, to the low-frequency side of the original carrier frequency; and catastrophic optical damage may occur, often in small self-focused spots, if the peak intensity is not limited.

As a generalization of the self-phase-modulation criterion we developed a few paragraphs back, it has become conventional to define the “*B* integral” for a multipass laser system as a cumulative measure of the nonlinear interaction, where this integral is given by

$$B \equiv \frac{2\pi}{\lambda} \int_0^L n_{2I}(z) I(z) dz, \quad (42)$$

taking into account the changes in diameter and power level of the laser beam through the complete system. A generally accepted criterion for high-power laser systems is that the cumulative *B* integral must be kept somewhere below the value $B \leq 3$ to 5 to avoid serious nonlinear damage and distortion effects due to either self-phase modulation or self-focusing.

REFERENCES

The literature on self-focusing and self-phase-modulation effects is very extensive. A review article covering many aspects of the subject is S. A. Akhmanov, R. V. Khokhlov, and A. P. Sukhorukov, “Self-focusing, self-defocusing and self-modulation of laser beams,” in *Laser Handbook*, edited by F. T. Arecchi and E. O. Schulz-Dubois (North-Holland, 1972), pp. 1151–1228.

An early paper on the concept of whole-beam self-focusing is P. L. Kelley, “Self-focusing of optical beams,” *Phys. Rev. Lett.* **15**, 1005–1008 (December 27, 1965). For a recent and rather clean experimental example of whole-beam self-focusing effects, see J. E. Bjorkholm and A. Ashkin, “CW self-focusing and self-trapping of light in sodium vapor,” *Phys. Rev. Lett.* **32**, 129–132 (January 28, 1974).

The earliest discussion of small-scale self-focusing effects seems to be by V. I. Bespalov and V. I. Talanov, “Filamentary structure of light beams in nonlinear liquids,” *Sov. Phys.—JETP* **3**, 307–310 (1966), and the associated analysis is often referred to as the “Bespalov-Talanov analysis.” See also V. I. Talanov, “Focusing of light in cubic media,” *Sov. Phys.—JETP* **11**, 199–201 (1970).

An extended version of this theory is given by B. R. Suydam, “Self-focusing of very high power laser beams: II,” *IEEE J. Quantum Electron.* **QE-10**, 837–843 (November 1974); and the deleterious effects of both whole-beam and small-scale self-focusing are discussed in B. R. Suydam, “Effect of refractive-index nonlinearity on the optical quality of high-power laser beams,” *IEEE J. Quantum Electron.* **QE-11**, 225–230 (June 1975).

Definitive experimental demonstrations of small-scale self-focusing are given by A. J. Campillo, S. L. Shapiro, and B. R. Suydam, “Periodic breakup of optical beams due to self-focusing,” *Appl. Phys. Lett.* **23**, 628–630 (December 1, 1973); and “Relationship of self-focusing to spatial instability modes,” *Appl. Phys. Lett.* **24**, 178–180 (February 15, 1974).

One of the first experiments to combine nonlinear chirping via self-phase modulation with subsequent pulse recompression is R. A. Fisher, P. L. Kelley, and T. K. Gustafson, “Subpicosecond pulse generation using the optical Kerr effect,” *Appl. Phys. Lett.* **14**, 140–143 (February 15, 1969).

An extensive discussion of the *B* integral and its application in multistage amplifier design is given in D. C. Brown, *The Physics of High Peak Power Nd:Glass Laser Systems* (Springer-Verlag, 1980).

10.3 THE NONLINEAR SCHRÖDINGER EQUATION

The basic equation of motion for analyzing signal propagation through a weakly nonlinear optical medium, or along a nonlinear transmission line (such as an optical fiber with an optical Kerr coefficient), is a nonlinear extension of the parabolic equation we derived in Chapter 9. We can derive this nonlinear form in a simplified manner as follows.

Derivation of the Nonlinear Schrödinger Equation

Consider an optical signal of the form $\mathcal{E}(z, t) \equiv \tilde{E}(z, t) \exp j[\omega_0 t - \beta(\omega_0)z]$ traveling in the $+z$ direction, where $\tilde{E}(z, t)$ is the slowly varying amplitude of this signal. If we Fourier-transform this signal $\tilde{E}(z, t) e^{j\omega_0 t}$ into its frequency spectrum $\tilde{E}(z, \omega)$ at any arbitrarily chosen plane z , propagate each frequency component forward by a small distance dz using the frequency-dependent and intensity-dependent propagation constant $\beta(\omega)$, and then Fourier-transform these components back into the time domain, we can find that the signal envelope $\tilde{E}(z, t)$ at the plane $z = z + dz$ is given by

$$\tilde{E}(z + dz, t) = \frac{1}{2\pi} \int_{-\infty}^{\infty} d\Delta\omega \int_{-\infty}^{\infty} dt' \tilde{E}(z, t') e^{j\Delta\omega(t-t')} e^{-j\Delta\beta dz}, \quad (43)$$

where $\Delta\omega \equiv \omega - \omega_0$ and $\Delta\beta \equiv \beta(\omega) - \beta(\omega_0)$.

The partial derivatives of the signal $\tilde{E}(z, t)$ with respect to time can be calculated by multiplying the integrand in Equation 10.43 by $\partial/\partial t \equiv j\Delta\omega$, and with respect to distance by either expanding in powers of dz or by multiplying the integrand by $\partial/\partial z \equiv -j\Delta\beta$. We can also suppose that the propagation constant $\beta(\omega)$ has the weakly nonlinear and dispersive form

$$\beta(\omega) = \beta(\omega_0) + \beta_2 \langle \mathcal{E}^2 \rangle + \beta'(\omega_0) \times (\omega - \omega_0) + \frac{1}{2} \beta''(\omega_0) \times (\omega - \omega_0)^2, \quad (44)$$

where β' and β'' are the first and second derivatives of β with respect to ω , and where

$$\beta_2 \langle \mathcal{E}^2 \rangle \equiv \frac{2\pi\omega_0 n_2 E}{c} \quad (45)$$

gives the (small) change in midband propagation constant due to the optical Kerr effect. We can then show, after some algebra, that the integral form for $\tilde{E}(z, t)$ in Equation 10.43 is equivalent to the differential equation

$$\left[\frac{\partial}{\partial z} + \beta' \frac{\partial}{\partial t} - j \frac{\beta''}{2} \frac{\partial^2}{\partial t^2} + j \frac{\beta_2 |\tilde{E}|^2}{2} \right] \tilde{E}(z, t) = 0, \quad (46)$$

where we have used $\langle \mathcal{E}^2 \rangle \equiv \frac{1}{2} |\tilde{E}|^2$ for a sinusoidal signal.

Discussion

Equation 10.46 is a generalization of the parabolic equation 9.41 derived in Chapter 9, with a nonlinear optical Kerr effect term added. (This approach to its derivation also illustrates another way of arriving at Equation 9.41.) Equation 10.46 has the form of a *nonlinear Schrödinger equation*, with a nonlinear potential function, except that z and t are interchanged from the roles they usually play in the conventional Schrödinger equation.

This same equation arises in other physical situations, including deep-water wave propagation, ion-acoustic waves in plasma physics, superconductivity, and vortex motions; so many techniques for its solution have been developed. Note again that the group-velocity dispersion term β'' in the propagation constant translates into what is essentially a complex diffusion term $j\beta''\partial^2/\partial t^2$ in the differential equation. Since this diffusion coefficient can have either sign, it can correspond to either pulse spreading or pulse compression in different situations. Its effects must, however, be balanced against the nonlinear propagation effects, as we will see further in the following section.

REFERENCES

For references on the solutions to this equation, see the works by Akhmanov and coworkers cited at the end of Section 9.2, and the works on the analysis of solitons cited in the final sections of this chapter.

10.4 NONLINEAR PULSE BROADENING IN OPTICAL FIBERS

To illustrate the importance of self-phase-modulation effects in fiber optics, we can consider what happens when a low- to moderate-power optical pulse (e.g., a few hundred milliwatts to a few watts peak power) of very short time duration (picoseconds to femtoseconds) is injected into a very low-loss single-mode optical fiber, typically a few microns in diameter.

Self-focusing effects will then be effectively eliminated by the strong waveguiding properties of the optical fiber; at the same time, the low losses and small area of the fiber will permit strong self-phase-modulation and dispersion effects to accumulate over very long distances in the fiber, at energy and power levels well below those that will produce optical damage. This permits the demonstration of some very interesting and useful nonlinear propagation effects, including in particular pulse self-chirping and subsequent compression, and optical soliton propagation.

Dispersive Effects in Optical Fibers

We need first to describe the dispersion effects versus wavelength in an optical fiber, especially a single-mode optical fiber. Figure 10.13 shows the typical variation of the index of refraction versus wavelength or frequency across the visible and near-infrared regions, and the resulting variations of β' and β'' across the same regions, for typical transparent optical materials such as quartz or glass. The group-velocity dispersion parameter β'' changes from being positive at shorter wavelengths or higher frequencies to negative at longer wavelengths.

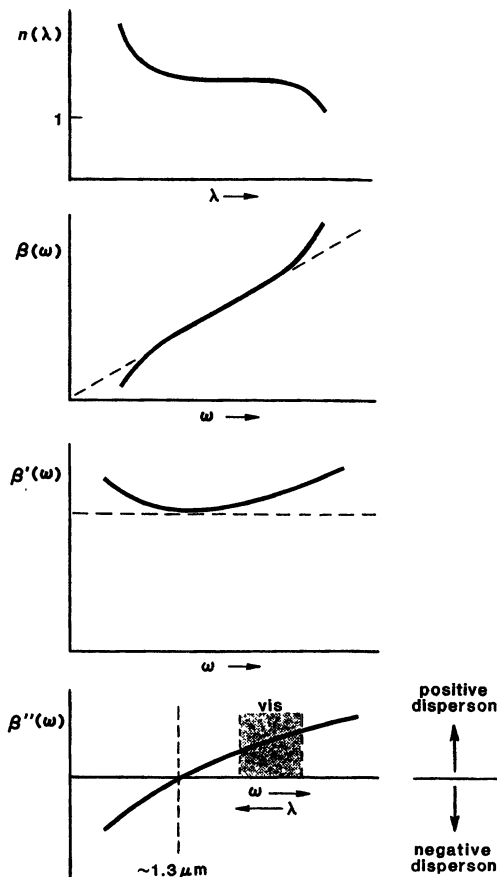


FIGURE 10.13
Optical dispersion versus frequency or wavelength in a typical optical fiber. The dispersion parameter β'' is usually positive in the visible region, becoming negative somewhere in the near infrared.

There is some confusion in the literature over how dispersive properties should be labeled; but the situation where $\beta'' > 0$, which is equivalent to $dv_g/d\omega < 0$ or $dv_g/d\lambda > 0$, is usually referred to as *positive or normal dispersion*, and the opposite case is referred to as *negative or anomalous dispersion*.

The effective dispersion values for a propagating wave in a single-mode optical fiber will differ somewhat from the purely material dispersion properties, because of *modal dispersion effects*, or waveguide propagation effects, which depend in essence on the mode shape, and on how the fields of the propagating mode are distributed between the core and the cladding of the optical fiber. The general rule for quartz optical fibers, however, is that the group-velocity dispersion is positive (according to the preceding definition) across the visible region, goes through zero in the vicinity of $1.3 \mu\text{m}$, and becomes increasingly negative at longer wavelengths. Note that the lowest-loss region for such optical fibers occurs, however, in the vicinity of $1.5 \mu\text{m}$, where the dispersion has become significantly negative.

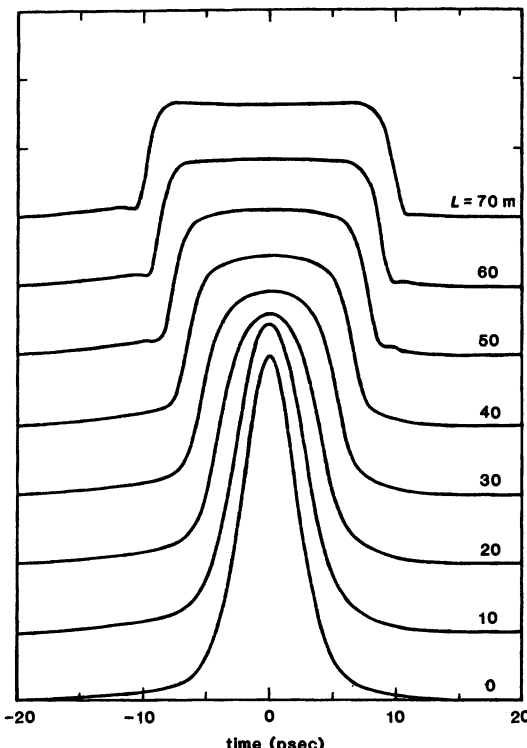


FIGURE 10.14
 Pulse broadening produced by self-phase modulation plus positive dispersion for a 5.5 ps, 10 W input pulse at $\lambda_0 = 590$ nm traveling through increasing lengths of single-mode fiber.

Nonlinear Pulse Broadening and Self-Chirping

Let us first consider the propagation properties of an optical fiber in the visible region, where the group-velocity dispersion is positive. From the arguments given two sections back, this means that the frequency chirp produced by the optical Kerr effect across the center of an optical pulse with a smooth time envelope will lead to *broadening* of the pulse envelope in time. It also turns out that such a pulse, as it propagates, will not only broaden, but acquire a growing amount of frequency chirp.

Suppose a short optical pulse propagates through an optical fiber at a wavelength in the visible region where the group-velocity dispersion in glass fibers is positive. Propagation of this pulse can then be calculated by the nonlinear Schrödinger equation derived in the preceding section, with an appropriate sign for the group-velocity-dispersion parameter. It is found that an initially smooth input pulse gradually broadens out to acquire an essentially rectangular shape, with increasing width and increasingly sharp rising and falling edges at increasing distances. Figure 10.14 shows predicted pulseshapes if we transmit a 5.5-ps pulse with 10 W peak power at 590 nm through increasing lengths ranging from 0 to 70 meters of a typical 4 μm -diameter single-mode optical fiber. The self-broadening effect on the pulse profile is evident.

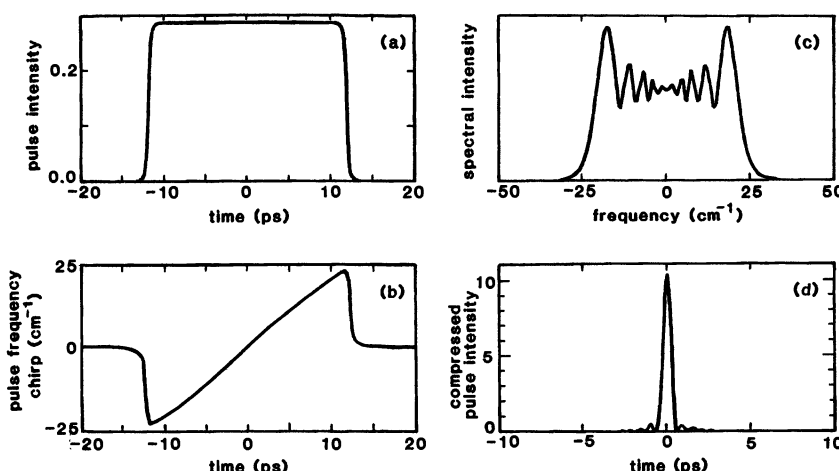


FIGURE 10.15

Self-broadening of an initial 6-ps 100-W pulse after propagation through 30 m of single-mode fiber. (a) Output pulse intensity versus time. (b) Output frequency chirp. (c) Output pulse spectrum. (d) Result of linear dispersive compression of this chirped pulse.

Figure 10.15 shows more details from a similarly calculated result for an initially 6-ps 100-W pulse propagated through 30 m of single-mode fiber. The pulse has broadened from a initial smooth hyperbolic secant pulse with initial pulsewidth of 6 ps to a rectangular pulse ≈ 24 ps in duration as shown in (a). This pulse has also acquired a nearly linear frequency chirp over the full pulse duration as shown in (b). In agreement with this, the pulse spectrum has broadened from the initial transform limit of $\approx 2.5 \text{ cm}^{-1}$ to a characteristic phase-modulation spectrum nearly 50 cm^{-1} wide, as shown in (c). Plot (d) shows the greatly shortened pulse that could result from taking the self-chirped pulse in this particular theoretical example and compressing it externally using an optimum linear dispersive element.

Chirped Pulse Recompression

It was in fact realized and demonstrated by Grischkowsky and co-workers at the IBM Research Laboratories that this kind of strongly self-chirped pulse is an essentially ideal input signal for subsequent pulse recompression using any type of auxiliary dispersive medium following the fiber, such as the diffraction grating pair shown earlier.

Figure 10.16 illustrates an experiment in which an initial pulse from a mode-locked laser is first self-chirped and broadened using a length of optical fiber, and then compressed to less than a tenth of its initial pulsewidth by using a simple grating pair of the type described in an earlier section as the auxiliary linear dispersive element. (Note that Grischkowsky and colleagues in fact used a retroreflective prism to achieve the desired dispersion with only a single grating.)

By cascading two stages of this type of self-broadening and linear recompression, this group has in fact converted initial 5.9-ps pulses into 0.09-ps (or 90-fs) pulses, as illustrated in Figure 10.17. In other experiments, Shank and co-workers

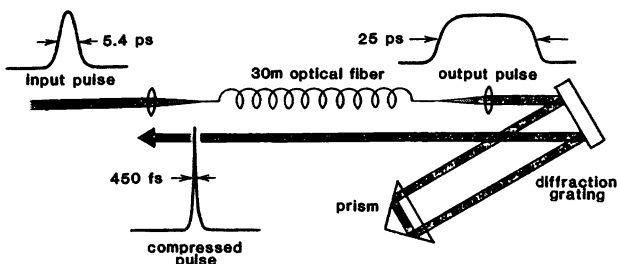


FIGURE 10.16

Experimental system for first broadening a pulse using an optical fiber, and then compressing it with a diffraction grating system.

have used a single stage to convert initial 90-fs pulses from a colliding-pulse mode-locked dye laser into 30-fs optical pulses. These pulses are approximately 14 optical cycles long, and are the shortest pulses known to date.

REFERENCES

One of the earliest articles on pulse self-broadening and compression in optical fibers is H. Nakatsuka, D. Grischkowsky, and A. C. Balant, "Nonlinear picosecond-pulse propagation through optical fibers with positive group-velocity dispersion," *Phys. Rev. Lett.* **47**, 910-913 (September 28, 1981).

Other recent articles from this same group include D. Grischkowsky and A. C. Balant, "Optical pulse compression based on enhanced frequency chirping," *Appl. Phys. Lett.* **41**, 1-3 (July 1, 1982); B. Nikolaus and D. Grischkowsky, "12 \times pulse compression using optical fibers," *Appl. Phys. Lett.* **42**, 1-3 (January 1, 1983); and B. Nikolaus and D. Grischkowsky, "90 fsec tunable optical pulses obtained by two-stage pulse compression," *Appl. Phys. Lett.* **43**, 228-230 (August 1, 1983).

Application of the same technique to femtosecond dye laser pulses is also described by C. V. Shank *et al.*, "Compression of femtosecond optical pulses," *Appl. Phys. Lett.* **40**, 761-763 (May 1, 1982).

10.5 SOLITONS IN OPTICAL FIBERS

In 1834 John Scott Russell, then a young Scottish university scientist and later to become a famous Victorian engineer and shipbuilder, recorded the following observations from the banks of the Glasgow-Edinburgh canal, where he first developed many of the fundamental principles of hydrodynamics and of ship's hull design: "I was observing the motion of a boat which was rapidly drawn along a narrow channel by a pair of horses, when the boat suddenly stopped—not so the mass of water in the channel which it had put in motion; it accumulated round the prow of the vessel in a state of violent agitation, then suddenly leaving it behind, rolled forward with great velocity, assuming the form of a large solitary elevation, a rounded, smooth and well-defined heap of water, which continued its course along the channel apparently without change of form or diminution of speed. I followed it on horseback, and overtook it still rolling on at a rate of some

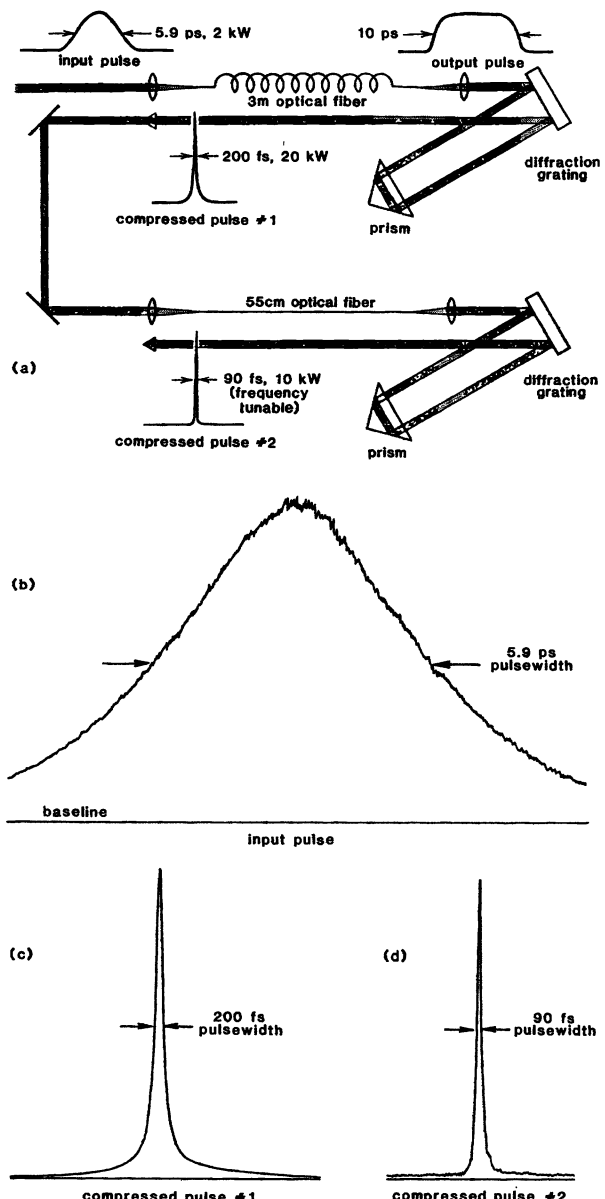


FIGURE 10.17

(a) Two-stage pulse compression system. (b) Autocorrelation trace of 5.9-ps initial input pulse. (c) Output of first compression stage (450 fs). (d) Output of second stage (90 fs).

eight or nine miles an hour, preserving its original figure some thirty feet long and a foot to a foot and a half in height. Its height gradually diminished, and after a chase of one or two miles I lost it in the windings of the channel. Such, in the month of August 1834, was my first chance interview with that singular and beautiful phenomenon . . ."

This represented one of the first detailed observations of a *solitary wave*, or *soliton*, a special large-signal solution to some nonlinear dispersive propagation equation, which either propagates with a certain fixed and unchanging steady-state pulseshape over very long distances, or else displays a slow periodic oscillation with distance between a certain set of similar characteristic pulseshapes.

Solitons having these properties represent a very interesting and useful physical phenomenon, with applications in many fundamental areas of physics. It has very recently been realized that very short optical pulses in optical fibers can also propagate as solitons, at very modest power levels; and that these soliton pulses may be very important for carrying pulsed optical communications signals through such fibers over very long distances and at very high data rates. In this section therefore we will briefly review some of the basic concepts of solitons, and particularly of their properties in single-mode optical fibers.

Solitons in General

A soliton is in general any member of a class of solutions to some nonlinear equation or nonlinear propagation problem, in which each such solution is characterized by a certain amplitude or power level and a certain pulseshape, with these two usually being interrelated; and in which these solutions can either propagate with an unchanging pulseshape over an indefinite distance, or else display a slow periodic oscillation with distance through a set of recurring characteristic pulseshapes. Depending on the particular nonlinear equation, the soliton pulses may have different shapes; and the velocities of propagation and the distances for periodic recurrence generally depend on both the nonlinear equation and the pulse amplitude.

(According to a more precise classification, any solution to a nonlinear equation which will propagate with unchanged shape, or will repeat its shape periodically in distance, is known as a *solitary wave*; but only those classes of solitary waves which can collide or pass through each other and then resume their solitary propagation without change of shape after such a collision are called *solitons*. Hence not all solitary-wave solutions are solitons.)

Three nonlinear equations which are known to have soliton solutions are the *Korteweg-deVries equation*, the *Sine-Gordon equation*, and the *nonlinear Schrödinger equation* already introduced in this chapter. Equations like these arise in many physical situations, including shallow- and deep-water wave propagation, waves in plasmas, lattice waves in solids, superconductivity, vortex motions in liquids, and propagation in optical fibers.

Solitons in Optical Fibers

At wavelengths longer than $\lambda_0 \approx 1.35 \mu\text{m}$, the group-velocity dispersion in quartz single-mode optical fibers has the appropriate sign (namely, $\beta'' < 0$) such that the chirp produced by self-phase modulation through the optical Kerr effect will lead, at least at first, to time-compression of the central part of the optical pulse, rather than to pulse broadening as described in a preceding section.

A smooth pulse of sufficient amplitude will thus be steadily compressed, and also progressively distorted in shape, at least until it becomes sufficiently short that higher-order nonlinear effects begin to compete with the dispersive pulse compression.

It is found, in fact, that such a pulse can approach a limiting pulseshape which does not change further with distance, and which represents in fact the *lowest-order soliton solution* to the nonlinear Schrödinger equation that governs the nonlinear wave propagation in the fiber. This solution has a sech dependence of the pulse amplitude on time, in the form

$$\mathcal{E}(z, t) = \mathcal{E}_0 \operatorname{sech} \left(\frac{t - t_0 - z/v_g'}{\tau_0} \right) \exp[j(\Omega t - \kappa z)], \quad (47)$$

where the peak amplitude \mathcal{E}_0 , the pulsewidth τ_0 , the modified group velocity v_g' , the (small) frequency shift Ω , and the wavenumber shift κ are all interrelated. Different values for these parameters thus describe a continuous family of solutions that have the same basic shape but different amplitudes and pulsewidths, that carry different amounts of energy per pulse, and that travel at very slightly different group velocities.

For example, such a pulse in a single-mode fiber might have a width of 3 ps and a peak power of 100 mW, and thus carry a total energy of ≈ 0.3 pJ. Lower peak powers mean longer pulsewidths, and the converse.

Higher-Order Soliton Solutions

There also turn out to be higher-order soliton solutions, characterized by an index $N \geq 1$, which do not propagate with constant shape, but which instead, if launched with a proper initial shape and amplitude will return to that same initial shape at periodic distances along the fiber. Analytical solutions for these periodically recurring solitons are difficult to obtain, and they are often studied by means of large-scale numerical simulations.

These higher-order solutions generally require higher amplitudes and energies than the lowest-order soliton, and the soliton period generally decreases with increasing pulse amplitude. They have also now been seen experimentally (see References).

Fermi-Pasta-Ulam Recurrence

One of the counterintuitive properties of these higher-order periodic soliton solutions in certain systems—including optical fibers—is that the frequency spectrum of the nonlinear pulse signal, starting from a narrow and even transform-limited initial pulse, can first broaden out substantially with distance (or with time), but then can later condense back again to the same narrow initial spectrum. This seems quite counter to what might be an initial expectation, that nonlinear and intermodulation effects should generally always act to continually broaden a signal spectrum.

This spectral broadening and subsequent recondensation is sometimes referred to as “Fermi-Pasta-Ulam recurrence”; these three men carried out an early set of calculations on the first large-scale computers at Los Alamos in order to trace the long-term dynamics of a computer model of nonlinear springs and discrete masses having many nonlinearly coupled resonant modes. Instead

of displaying a long-term trend from initial order toward eventual quasi random thermalization, as had been expected, these computer simulations frequently revealed a mysterious periodic recurrence behavior, which was not understood, and which is now sometimes explained as the excitation of periodically recurring solitons in the nonlinear system.

The Soliton Laser

The circulating pulses in some of the narrowest-pulse mode-locked lasers are in fact probably solitons, in the sense that nonlinear chirping and dispersion in the various laser elements begins to play a significant role in the reshaping of the pulses. This reshaping can be beneficial, if it leads to narrower pulses, or deleterious, as in the pulse break-up effects discussed earlier. There is an even more interesting way of using solitons in a mode-locked laser, which is accomplished as follows.

Suppose a length of fiber is connected to one end of a laser cavity in such a fashion that a pulse can come out the end of the laser, propagate down the fiber and reflect at the far end, and come back and enter the laser cavity again; and suppose the fiber length corresponds to the periodic recurrence or reshaping distance for a certain optical soliton. If the laser operates at a wavelength where the fiber supports soliton propagation, and if the laser energy is properly adjusted, it is possible for the pulse to travel through the laser medium as a comparatively wide pulse in time, with a correspondingly narrow bandwidth that remains within the amplification bandwidth of the laser medium; but then it enters the fiber to propagate as a higher-order soliton ($N > 1$). As the pulse travels down the fiber and back, it can thus narrow in time and broaden in bandwidth, and then reverse this process as it returns back to the laser. This makes it possible to generate mode-locked pulses which are much narrower than can normally be supported by the finite amplification bandwidth of the mode-locked laser medium. This important (and very recent) development is referred to as the "soliton laser."

REFERENCES

The quotation from John Scott Russell which opens this section comes from his "Report on Waves," *Proceedings of the Royal Society of Edinburgh*, 319 (1844). It is reprinted in a recent and extensive review paper with many references on "The soliton: A new concept in applied science," by A. C. Scott, F. Y. F. Chu, and D. W. McLaughlin, *Proc. IEEE* **61**, 1443-1483 (October 1973).

The initial suggestion for soliton propagation in optical fibers was made by A. Hasegawa and F. Tappert, "Transmission of stationary nonlinear optical pulses in dispersive optical fibers: I, Anomalous dispersion; II, Normal dispersion," *Appl. Phys. Lett.* **23**, 142-144 and 171-172 (August 1 and 15, 1973). More detailed theoretical discussions are given in A. Hasegawa and Y. Kodama, "Signal transmission by optical solitons in monomode fiber," *Proc. IEEE* **69**, 1145-1150 (September 1981).

The first experimental confirmation of their prediction was L. F. Mollenauer, R. H. Stolen, and J. P. Gordon, "Experimental observation of picosecond pulse narrowing and solitons in optical fibers," *Phys. Rev. Lett.* **45**, 1095-1098 (September 29, 1980). More recent experimental observations include R. H. Stolen, L. F. Mollenauer, and W. J. Tomlinson, "Observation of pulse restoration at the soliton period in optical

fibers," *Opt. Lett.* **8**, 186–188 (March 1983); and L. F. Mollenauer, R. H. Stolen, J. P. Gordon, and W. J. Tomlinson, "Extreme picosecond pulse narrowing by means of soliton effect in single-mode optical fibers," *Opt. Lett.* **8**, 289–291 (May 1983). See also L. F. Mollenauer and R. H. Stolen, "The soliton laser," *Opt. Lett.* **9**, 13–15 (January 1984).

The literature on solitons in other physical systems unfortunately seems to be far more mathematical than physical in approach. For further general discussions of nonlinear waves and solitons, see, for example, G. B. Whitham, *Linear and Nonlinear Waves* (Wiley, 1974), *Solitons in Action*, edited by K. Lonngren and A. Scott (Academic Press, 1978), or G. L. Lamb, Jr., *Elements of Soliton Theory* (Wiley, 1980).

The original Fermi-Pasta-Ulam recurrence phenomena can be found in *The Collected Papers of Enrico Fermi* (University of Chicago Press, 1962), II, 978–988.

11

LASER MIRRORS AND REGENERATIVE FEEDBACK

In previous chapters we have described what optical signals do to laser atoms, including resonant atomic response, laser pumping, and population inversion; and what laser atoms do back to optical signals, including the amplification of signals in a single pass through a laser medium. In this and the following two chapters we will bring in the laser mirrors and resonant cavities needed to provide regenerative feedback and eventually oscillation in laser devices.

Because the mirrors are the critical new elements, and regenerative feedback is the critical new physical process, we will first examine in this chapter some basic physical properties of mirrors and optical beam splitters, as well as the resonant properties of optical cavities, or etalons, or interferometers. We then explore the regenerative feedback and amplification effects that occur in a resonant laser cavity *below* threshold. Besides introducing some useful new concepts and devices, this will give us an understanding of cavity resonant frequencies and axial modes, and show us how lasers behave just below the oscillation threshold that we will (finally!) reach in the following chapter.

11.1 LASER MIRRORS AND BEAM SPLITTERS

Laser mirrors and beam splitters have certain fundamental properties that are important to understand. Before discussing the use of mirrors in laser cavities, let us therefore review the more important of these properties.

Single Dielectric Interface

The simplest example of a partial mirror or beam splitter is the interface between two dielectric media, as shown in Figure 11.1. Suppose we write the normalized fields for the incident and reflected waves on the two sides of this interface (labeled by subscripts $i = 1, 2$) in the form

$$\mathcal{E}_i(z, t) = \text{Re} \left\{ \tilde{a}_i \exp[j(\omega t \mp \beta_i z)] + \tilde{b}_i \exp[j(\omega t \pm \beta_i z)] \right\}, \quad i = 1, 2, \quad (1)$$

where β_1 is the propagation constant in the dielectric medium on the left side of the interface, \tilde{a}_1 is the normalized wave amplitude of the *incident* wave and

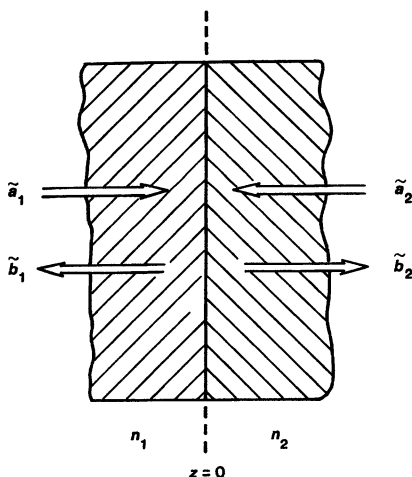


FIGURE 11.1
Reflection and transmission of optical waves
at a dielectric interface.

b_1 is the normalized wave amplitude of the reflected wave on that side of the interface, and the same expressions with subscript $i = 2$ apply on the right-hand side of the interface. The field amplitudes \mathcal{E}_i are normalized so that $|\mathcal{E}_i|^2$ gives the intensity or power flow in the medium on either side of the interface.

Note that the upper signs in front of the β_i terms in the exponents apply on the left-hand side of the interface, so that \tilde{a}_1 represents the complex amplitude of the incident wave traveling to the right (toward $+z$), and \tilde{b}_1 represents the reflected or left-traveling wave. The lower signs apply on the right-hand side of the interface, so that \tilde{a}_2 is again the incident but now left-traveling wave and \tilde{b}_2 the right-traveling wave.

The amplitude reflection and transmission properties for a simple dielectric interface at normal incidence can then be written as

$$\begin{aligned}\tilde{b}_1 &= r \tilde{a}_1 + t \tilde{a}_2, \\ \tilde{b}_2 &= t \tilde{a}_1 - r \tilde{a}_2,\end{aligned}\tag{2}$$

or in matrix notation

$$\begin{bmatrix} \tilde{b}_1 \\ \tilde{b}_2 \end{bmatrix} = \begin{bmatrix} r & t \\ t & -r \end{bmatrix} \times \begin{bmatrix} \tilde{a}_1 \\ \tilde{a}_2 \end{bmatrix},\tag{3}$$

where the reflection and transmission coefficients r and t are given for this particular interface by

$$r = \frac{n_1 - n_2}{n_1 + n_2} \quad \text{and} \quad t = \frac{2\sqrt{n_1 n_2}}{n_1 + n_2},\tag{4}$$

and the lossless nature of the interface is expressed by $r^2 + t^2 = 1$. Note that in writing these relations we are implicitly locating the $z = 0$ plane, or the reference plane for the fields given in Equation 11.1, exactly at the dielectric interface. The \tilde{a}_i and \tilde{b}_i coefficients thus express the complex wave amplitudes exactly at the interface between the two dielectrics.

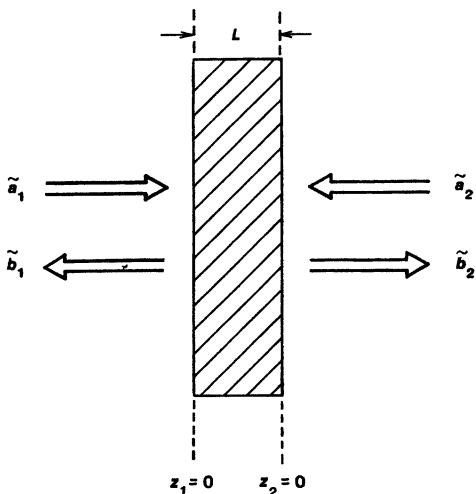


FIGURE 11.2

Reflection and transmission of optical waves from a thin dielectric slab.

For this particular interface, and this particular choice of reference plane, the coefficients r and t are purely real numbers. The reflection coefficients have opposite signs, however, depending on the direction from which the wave approaches the interface. This change of sign can be understood in physical terms because a medium with a very high index of refraction acts essentially like a metallic surface or like a very large shunt capacitance across a transmission line. Going from a low-index to a high-index medium ($n_2 > n_1$) is thus like the reflection from the end of a short-circuited transmission line, with a 180° phase shift on reflection or $r < 0$, whereas reflection from a low index medium acts like an open-circuited transmission line, with a reflection coefficient $r > 0$.

Thin Dielectric Slab

As a more realistic model for a real laser mirror, we might consider next the reflection and transmission properties of a thin lossless dielectric slab of thickness L and index n as shown in Figure 11.2, assuming, for simplicity, air or vacuum on both sides of this slab.

We will again write the fields on both sides of the slab as in Equation 11.1, using \tilde{a}_i and \tilde{b}_i coefficients for the incident and reflected waves, except that we will now measure the incident waves and the reflected waves using separate $z = 0$ planes that are located at the outer surfaces of the slab on each side, so that the reference planes on opposite sides of the slab are offset by the thickness of the slab.

With a little calculation we can find that the general relationship between incident and reflected waves in this case can be written in the general complex matrix form

$$\begin{bmatrix} \tilde{b}_1 \\ \tilde{b}_2 \end{bmatrix} = \begin{bmatrix} \tilde{r}_{11} & \tilde{t}_{12} \\ \tilde{t}_{21} & \tilde{r}_{22} \end{bmatrix} \times \begin{bmatrix} \tilde{a}_1 \\ \tilde{a}_2 \end{bmatrix}, \quad (5)$$

where the complex reflection coefficients are now given by

$$\tilde{r}_{11} = \tilde{r}_{22} = r_0 \frac{1 - e^{-j\theta}}{1 - (r_0 e^{-j\theta})^2} \quad (6)$$

and the complex transmission coefficients by

$$\tilde{t}_{12} = \tilde{t}_{21} = e^{-j\theta} \frac{1 - r_0^2}{1 - (r_0 e^{-j\theta})^2}. \quad (7)$$

In these expressions $\theta = n\omega L/c_0$ is the optical thickness of the slab, and $r_0 = (1 - n)/(1 + n)$ is the single-surface reflection coefficient at either surface of the slab. The scattering matrix is now *complex* but *symmetric*, and the coefficients now obey the complex condition $|\tilde{r}|^2 + |\tilde{t}|^2 = 1$ representing zero losses in the slab.

Purely Real Reflectivity

As one particularly simple example of this type of mirror, we might adjust the optical thickness nL of the slab to be an odd number of quarter wavelengths, so that $\theta = n\omega L/c_0$ is an odd integer multiple of $\pi/2$. The reflection and transmission coefficients for the mirror then take on the particularly simple form

$$\begin{bmatrix} \tilde{b}_1 \\ \tilde{b}_2 \end{bmatrix} = \begin{bmatrix} r & jt \\ jt & r \end{bmatrix} \times \begin{bmatrix} \tilde{a}_1 \\ \tilde{a}_2 \end{bmatrix}, \quad (8)$$

where r and t are again purely real and subject to $r^2 + t^2 = 1$.

The reflection coefficients from the two sides of this slab are now symmetric and purely real. In writing down the reflection equations we no longer have to worry about whether we are approaching this mirror or beamsplitter from its "high index side" or its "low index side." The transmission factors in this example, however, now have an additional factor of j , or a phase shift of 90° , associated with them. This phase shift arises essentially from the fact that we measure the waves at two different reference planes, on opposite sides of the slab and separated by the (small) thickness of the slab.

Note that we can, at least in principle, always adjust the index n and the thickness L of such a slab separately to obtain any desired values of θ and r_0 , and hence any desired values for the magnitudes of r or t . This thin-slab model might therefore be a particularly simple and symmetric model for any real lossless dielectric mirror.

Scattering Matrix Formalism

The formalism we have been using here is obviously a *scattering matrix formalism* of the kind used in circuit theory or in describing waveguide or transmission-line junctions. From this viewpoint a partially transmitting mirror is simply a two-port network connected between two waveguides or transmission lines; and the matrices we have written represent simple examples of the 2×2 scattering matrix S that might describe such a two-port network in transmission-line theory.

This scattering matrix approach is of course not limited to two-port cases. Figure 11.3 shows, for example, a partially transmitting mirror or optical beam

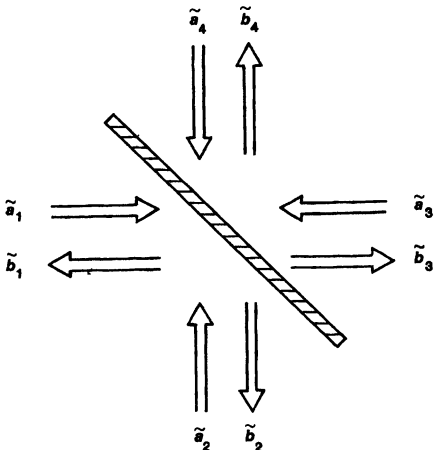


FIGURE 11.3
A partial mirror or optical beamsplitter at off-normal incidence.

splitter used at off-normal incidence, so that it now has four incident and outgoing waves. This is equivalent to a general four-port network, and would require a 4×4 scattering matrix, which we would have to write in the form

$$\begin{bmatrix} \tilde{b}_1 \\ \tilde{b}_2 \\ \tilde{b}_3 \\ \tilde{b}_4 \end{bmatrix} = \begin{bmatrix} \tilde{r}_{11} & \tilde{t}_{12} & \tilde{t}_{13} & \tilde{t}_{14} \\ \tilde{t}_{21} & \tilde{r}_{22} & \tilde{t}_{23} & \tilde{t}_{24} \\ \tilde{t}_{31} & \tilde{t}_{32} & \tilde{r}_{33} & \tilde{t}_{34} \\ \tilde{t}_{41} & \tilde{t}_{42} & \tilde{t}_{43} & \tilde{r}_{44} \end{bmatrix} \times \begin{bmatrix} \tilde{a}_1 \\ \tilde{a}_2 \\ \tilde{a}_3 \\ \tilde{a}_4 \end{bmatrix}. \quad (9)$$

In more compact notation we can write Equations 11.2, 11.5 or 11.9 as

$$\mathbf{b} = \mathbf{S} \times \mathbf{a}. \quad (10)$$

The column vectors \mathbf{a} and \mathbf{b} then contain the incident and reflected wave amplitudes. The diagonal elements of the matrix \mathbf{S} give the (generally) complex reflection coefficients \tilde{r}_{ii} looking into each port of the system, and the off-diagonal elements \tilde{t}_{ij} give the amplitude transmission coefficients from, say, the wave going into port j to the wave coming out of port i .

Multilayer Dielectric Mirrors

We now need to discuss some subtleties concerning the effective reference planes of real laser mirrors, and how we should choose these reference planes in writing scattering matrices and carrying out laser analyses.

So far we have discussed two particularly simple examples of reflecting systems and their resulting scattering matrices. Figure 11.4, however, illustrates a more typical multilayer dielectric mirror of the type often used in lasers. Such a mirror may have as many as twenty or more quarter-wavelength-thick dielectric layers of alternating high and low index of refraction, evaporated onto a transparent substrate. (The opposite surface of this substrate usually has a high-quality antireflection coating; and the two surfaces of the substrate are often wedged by a few degrees to avoid etalon effects from any residual back-surface reflection.)

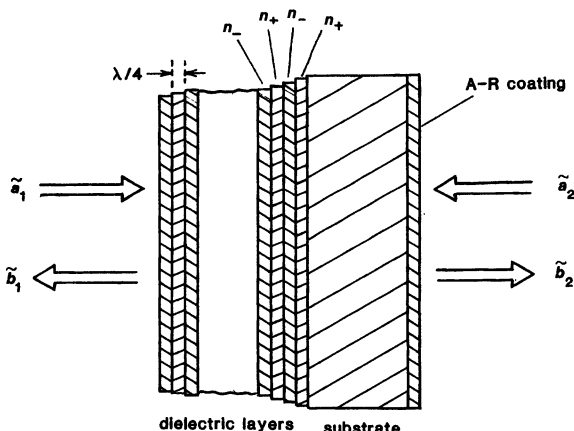


FIGURE 11.4
Reflection and transmission of optical waves from a multilayer dielectric mirror.

In the simple examples we have discussed so far, it may have seemed physically obvious that the reflecting surfaces are located at the physical surfaces of the dielectrics. But where should the effective mirror surface, or the effective reflecting plane $z = 0$, be located in a thick multilayer mirror like Figure 11.4 that is several optical wavelengths thick?

Mirror Reference Planes

In fact, there really is *no* unique plane which we can (or need to) identify as the exact reflecting surface, or the unique reference plane, for such a multilayer mirror. The total reflection of the mirror, as seen from outside the coating layers on either side, builds up gradually through the series of layers, which can be several wavelengths thick overall. The choice of where to locate the reference plane in this (or any other) mirror is entirely arbitrary. We can pick any reasonable reference plane within (or even outside) the multilayer mirror as the reference plane for defining the scattering matrix coefficients. In physical terms, picking such a reference plane simply means choosing the $z = 0$ origin for measuring the electric fields $\mathcal{E}(z, t)$ well outside the mirror, assuming the fields are expanded as in the opening equation of this section.

Even with the single dielectric interface, it is not essential that the mirror reference surface be chosen right at the physical surface between the dielectrics—especially since we very seldom if ever can position any mirror or optical element with an absolute position accuracy of better than a few optical wavelengths. So long as we are concerned only with the amplitudes and phases of the waves $\mathcal{E}(z, t)$ at larger distances — say, more than a few wavelengths—away from the reflecting surface, we can choose the reference surface anywhere near the physically reflecting structure. Shifting the choice of reference plane from one axial position to another location a distance Δz away then merely rotates the phase angles of the complex wave amplitudes \tilde{a}_i and \tilde{b}_i by phase shifts $\exp(\pm j\beta_i \Delta z)$, without changing their amplitudes. This rotation of the phase angles of \tilde{a}_i and \tilde{b}_i in turn merely attaches different phase angles to each of the scattering coefficients \tilde{S}_{ij} .

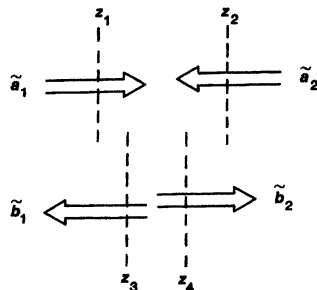


FIGURE 11.5

The reference planes for incident and reflected waves need not be at the same positions.

We can in fact even choose *different reference planes at which to measure the complex incoming and outgoing waves in each of the arms*, as illustrated in Figure 11.5 (although why this would be a useful choice may be open to question). Regardless of the choice of reference plane(s) and the associated phase shifts, however, the scattering matrix elements still have certain fundamental properties, which we must next consider.

Hermitian Matrix Notation

To understand a bit more about the basic properties of mirrors and beam splitters and their scattering matrices, it will be useful to introduce some *hermitian matrix notation*.

We are using the notation \mathbf{b} , for example, to denote a column vector with complex elements b_1, b_2, b_3, \dots running from the top down. We can then define the *hermitian adjoint* or *hermitian conjugate* to this vector, denoted by \mathbf{b}^\dagger , as the row vector with complex conjugate elements $\tilde{b}_1^*, \tilde{b}_2^*, \tilde{b}_3^*, \dots$ running horizontally. Hermitian conjugation converts a column vector into a row vector, or vice versa, and takes the complex conjugate of each individual element.

More generally, suppose we have an $m \times n$ matrix \mathbf{S} with complex elements \tilde{S}_{ij} as given above. Then, the hermitian adjoint or hermitian conjugate \mathbf{S}^\dagger of this matrix will be an $n \times m$ matrix with complex elements given by $(\mathbf{S}^\dagger)_{ij} = (\mathbf{S})_{ji}^*$. The hermitian adjoint or hermitian conjugate is a kind of matrix generalization of the complex conjugate of an ordinary quantity. To calculate the hermitian adjoint of a complex matrix or vector, interchange subscripts and take the complex conjugate. Just as with ordinary complex conjugation, applying this operation twice restores the original matrix or vector, i.e., $\mathbf{S}^{\dagger\dagger} \equiv \mathbf{S}$.

Power Flow Into and Out of a Scattering Matrix System

Matrix notation can then be used to write the total power flowing into or out of a multiport scattering system in a particularly compressed form. We have assumed that the wave amplitudes in our examples are normalized, so that the time-averaged power flowing into or out of any single port can be written as $|\tilde{a}_i|^2$ or as $|\tilde{b}_i|^2$, respectively. Assuming we pick the right units for \tilde{a}_i and \tilde{b}_i , the total power flowing out of an optical element, or out of all the ports in an N -port

network, can then be written in the simplified form

$$P_{\text{out}} = \sum_{j=1}^N \tilde{b}_j^* \tilde{b}_j = \left[\tilde{b}_1^*, \tilde{b}_2^*, \tilde{b}_3^*, \dots \right] \times \begin{bmatrix} \tilde{b}_1 \\ \tilde{b}_2 \\ \tilde{b}_3 \\ \dots \end{bmatrix} = \mathbf{b}^\dagger \times \mathbf{b}, \quad (11)$$

where the final term implies matrix multiplication of \mathbf{b}^\dagger times \mathbf{b} , carried out, as in all hermitian adjoint formulas, using the usual rules for matrix multiplication.

By using this notation, plus the usual rules for matrix multiplication, we can then relate the total power flowing out of any scattering system—for example, any optical mirror or beam splitter—to the input waves and the scattering matrix in the form

$$\begin{aligned} P_{\text{out}} &= \mathbf{b}^\dagger \mathbf{b} = (\mathbf{S} \mathbf{a})^\dagger (\mathbf{S} \mathbf{a}) \\ &= (\mathbf{a}^\dagger \mathbf{S}^\dagger) (\mathbf{S} \mathbf{a}) = \mathbf{a}^\dagger (\mathbf{S}^\dagger \mathbf{S}) \mathbf{a}. \end{aligned} \quad (12)$$

In going from the third to fourth and fourth to fifth terms, we have made use of the basic rules that (i) matrix multiplication is associative, i.e., $\mathbf{A}(\mathbf{B}\mathbf{C}) = (\mathbf{A}\mathbf{B})\mathbf{C}$, and (ii) the hermitian adjoint of any product is the product of the individual adjoints taken in reverse order, i.e., $(\mathbf{ABC})^\dagger \equiv \mathbf{C}^\dagger \mathbf{B}^\dagger \mathbf{A}^\dagger$.

Scattering Matrices for Lossless Systems

But, if a mirror or other scattering element is to be lossless, then the output power in Equation 11.12 must equal the input power, which is just $P_{\text{in}} = \mathbf{a}^\dagger \mathbf{a}$. The only way this can be true in general, for arbitrary input signals \mathbf{a} , is for the product $\mathbf{S}^\dagger \mathbf{S}$ in Equation 11.12 to equal the identity matrix; i.e.,

$$\mathbf{S}^\dagger \mathbf{S} = \mathbf{I} \quad \text{or} \quad \mathbf{S}^\dagger \equiv \mathbf{S}^{-1} \quad (13)$$

In this equation \mathbf{I} is the identity matrix (unity elements on the diagonal and all other elements zero), and \mathbf{S}^{-1} denotes the matrix inverse of the \mathbf{S} matrix. In matrix terms, this says that the scattering matrix \mathbf{S} for a lossless network must be a *unitary matrix*, since Equation 11.13 is the definition of unitarity.

Matrix Forms for Lossless and Reciprocal Twoport Networks

It is also a general theorem that the scattering coefficients of a *reciprocal system* must obey $|\tilde{S}_{ij}| \equiv |\tilde{S}_{ji}|$. This result comes from the symmetrical behavior of Maxwell's equations if we reverse either the E or the H fields and also reverse the sign of the time t . Most common optical elements are in fact reciprocal; only elements such as optical isolators containing Faraday rotators or similar elements containing a dc magnetic field can be nonreciprocal.

If all these constraints are applied to a lossless reciprocal two-port network, the result is the set of conditions

$$\begin{aligned} |\tilde{t}_{12}| &= |\tilde{t}_{21}|, \quad |\tilde{r}_{11}| = |\tilde{r}_{22}|, \\ |\tilde{r}_{11}|^2 + |\tilde{t}_{21}|^2 &= |\tilde{r}_{22}|^2 + |\tilde{t}_{12}|^2 = 1, \\ \tilde{r}_{11}\tilde{t}_{12}^* + \tilde{t}_{12}\tilde{r}_{22}^* &= 0 \end{aligned} \quad (14)$$

These are general conditions that must be obeyed by the complex reflection and transmission coefficients of any lossless two-port mirror or beam splitter.

The purely real and the complex symmetric examples we derived earlier in this section, namely,

$$S = \begin{bmatrix} r & t \\ t & -r \end{bmatrix} \quad \text{and} \quad S = \begin{bmatrix} r & jt \\ jt & r \end{bmatrix} \quad (15)$$

with r and t real, are two of the possible ways in which the four conditions of Equation 11.14 can be satisfied for a two-port system. On the other hand, the real and symmetric matrix

$$S = \begin{bmatrix} r & t \\ t & r \end{bmatrix}, \quad (16)$$

is *not an allowable scattering matrix* for a lossless optical mirror or beam splitter.

The conditions of unitarity plus reciprocity will always lead to a set of relationships like Equations 11.14 between the coefficients \tilde{S}_{ij} of any lossless $N \times N$ scattering matrix. We can always rotate the complex phase angles of the different matrix elements for a given physical system by choosing different reference planes in the various input and output arms. The magnitudes of the scattering coefficients of course will not change in this process, since the power transfer from any one arm to any other arm is not changed by a different choice of reference planes. No matter how the reference planes are chosen, however, certain phase relationships between the different coefficients must be maintained, at least for lossless systems.

The exact form of the scattering matrix S for a real mirror or beamsplitter thus depends on where we pick the reference planes; and there is in general no unique or preferred place to pick the reference plane in a real mirror. *For all future analyses of laser cavities and interferometers in this book, however, we will arbitrarily choose the complex symmetric form $S = [r, jt, jt, r]$, with r and t purely real, as the scattering matrix form to describe all mirrors and beam splitters.* This arbitrary choice will make no difference in any of the physical conclusions we reach about laser devices. It seems easier, however, to remember that transmission coefficients always have a factor of j associated with them than to remember which side of each mirror in a laser system is the $+r$ and which is the $-r$ side.

Polarization Effects and Transverse Mode Effects

In all the examples discussed so far, we have implicitly assumed a single sense of polarization in each of the input and output directions. Optical waves can, however, have two orthogonal senses of polarization for the wave in each direction. These may be, for example, two orthogonal linear polarizations, or positive and negative circular polarization, or whatever. If two orthogonal polarizations are present, each is in essence a separately measurable wave, with a separate wave amplitude. If both polarizations are considered separately, therefore, the total number of ports in the scattering matrix must be doubled; i.e., a system with N input and output directions will require a $2N \times 2N$ scattering matrix.

In addition, if we go to more realistic optical beams (or fibers), in which there may be both a lowest-order transverse mode and various higher-order transverse modes, then in essence each such transverse mode is a separate port or beam;

and the dimensionality of the scattering matrix must be expanded to include a separate port for each different transverse mode (with possible coupling between transverse modes inside the scattering system).

Further Discussion

All the analysis in this section may seem an overly complicated approach to the scattering properties of a simple mirror or beam splitter. If we failed to include the unitary properties of beam splitters when we analyze more complex configurations, such as Michelson interferometers or ring-laser cavities, however, it would be easy to invent cavities or optical devices that do not conserve energy, or have other useful properties. (It is by no means unknown for such inventions to be suggested, and even to appear in research proposals.)

The dielectric mirrors and beam splitters used in most laser applications are in fact almost perfectly lossless (though the partially transmitting metal films which were often used as output mirrors for early solid-state lasers were by contrast quite lossy). Higher-power lasers require nearly lossless mirrors if the mirrors are not to be destroyed by the power they absorb; and low-gain lasers need high reflectivity and low mirror losses for good efficiency. Even a lossy mirror can usually be described as a lossless mirror which obeys the preceding restrictions, sandwiched between two thin absorbing layers.

Finally, we might also emphasize that once we choose a specific reference plane in a multilayer mirror, the phase shifts associated with the scattering matrix for that mirror are fixed at any one frequency, but *may have different values at different frequencies*. The different phase shifts in reflecting from a mirror at two different optical wavelengths can be quite significant when we intercompare two optical frequency standards using interferometric methods, since the exact optical length of an interferometer cavity (between the reference planes of the two end mirrors) need not be the same for two different wavelengths.

Mirror phase shifts can also be significant in nonlinear optics experiments, such as double-pass harmonic-generation experiments. Suppose a fundamental wave passes through a phase-matched nonlinear crystal, generating second-harmonic radiation; and both the fundamental and the harmonic then reflect off a mirror and back through the crystal again. This is *not* necessarily equivalent to a nonlinear crystal twice as long, if the relative phases of the fundamental and the harmonic are shifted in bouncing off the mirror.

REFERENCES

Multilayer dielectric mirrors have been produced with accurately measured power reflectivities as high as $R = 99.975\%$ in the visible. Measuring a mirror reflectivity to this accuracy is far from an easy task, as discussed, for example, by J. M. Herbelin and J. A. McKay, "Development of laser mirrors of very high reflectivity using the cavity-attenuated phase-shift method," *Appl. Optics* **20**, 3341-3344 (October 1, 1981).

Problems for 11.1

1. *Scattering matrix for a general dielectric slab.* Derive the general scattering matrix results for a thin dielectric slab, as given in the text.

2. *Changes in the scattering matrix for different reference planes.* Show in detail how the scattering matrix for a planar interface between two different dielectric media can be converted to complex symmetric form by choosing a different reference plane or planes. Indicate specifically where the new reference plane(s) should be located.
3. *Derivation of the necessary matrix element relationships for a lossless reciprocal two-port.* Write out the hermitian adjoint and inverse matrices S^\dagger and S^{-1} in full for the general two-port S matrix given in the text, using the \tilde{r}_{ij} and \tilde{t}_{ij} notations, and show that reciprocity and unitarity lead to the conditions that are stated there.
4. *Scattering matrix for a transmission line junction.* Work out the scattering matrix for a transmission line of characteristic impedance Z_{01} connected to a second transmission line of characteristic impedance Z_{02} , using the connection point as the reference plane; and show that it takes the purely real form given in the text.
5. *Transmission-line junction with a lumped shunt capacitance.* Repeat this calculation assuming a lumped capacitance of value C is connected across the two lines in shunt right at the connection point. Is the scattering matrix still unitary?
6. *Three-port and five-port optical scattering systems?* Invent and sketch some real, physical 3-port and 5-port optical beam splitters.
7. *Impossibility of a completely matched three-port network.* When a wave is sent into any one of the ports of the four-port beam splitter shown in this section, there is no reflected wave directly back out the same port, so that $\tilde{r}_{ii} = 0$ for all i . In transmission line jargon this system is said to be *matched* looking into each of the four ports. Show that it is impossible in principle to devise any kind of lossless three-port network in which all three ports are similarly matched.
8. *Conditions for an N -port equal-amplitude beam splitter.* An N -port optical element is to function as a lossless equal-amplitude beam splitter, dividing the beam coming into any port into two equal beams coming out the next two adjacent ports moving clockwise around the network. All inputs are to be matched, i.e., there is no reflection of the input beam looking into any of the ports. Can you develop an all-real and symmetric form of the scattering matrix for such a system with $N = 4$ ports?
9. *Synthesizing an arbitrary complex optical two-port (research problem).* Suppose you are given the values of all four elements of an arbitrary complex 2×2 scattering matrix, which may be in general neither lossless nor reciprocal. Synthesizing a lumped electrical circuit which will produce this scattering matrix is a classic electric-circuit design problem. How about the optical analog? If you wanted to synthesize an arbitrary 2×2 optical scattering matrix, which elementary “building blocks” might you employ, and how could you synthesize a given arbitrary scattering matrix S from them?

11.2 INTERFEROMETERS AND RESONANT OPTICAL CAVITIES

In this section, we will introduce some of the key ideas concerning the resonance behavior of passive optical cavities, without laser gain. We will use a plane-wave

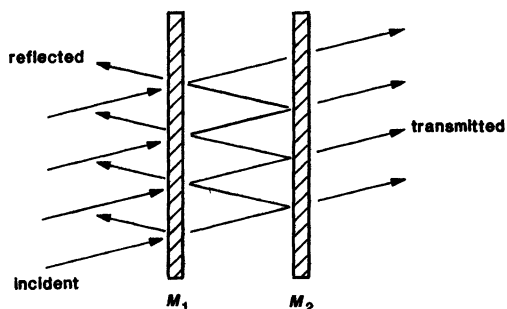


FIGURE 11.6
A Fabry-Perot interferometer (old style) with a slightly off-axis incident wave.

or transmission-line model for the resonators, and discuss both standing-wave and ring optical resonators on an equal footing. In later sections we will then introduce laser gain to produce regenerative amplification and, eventually, laser oscillation in such structures.

Fabry-Perot Interferometers and Etalons

A common optical element, widely used since long before the advent of lasers is the *Fabry-Perot interferometer* or *Fabry-Perot etalon* sketched in Figure 11.6. In its original form, a Fabry-Perot interferometer consisted of two closely spaced and highly reflecting mirrors, with mirror surfaces adjusted to be as flat and parallel to each other as possible. An alternative but conceptually equivalent element is a solid etalon made from some very low-loss material such as fused quartz or sapphire, with its two faces polished flat and parallel and perhaps coated with a metal or dielectric mirror coating. As we will see, such Fabry-Perot interferometers or etalons can have sharp resonances or transmission passbands at discrete optical frequencies. Fabry-Perot interferometers or etalons have thus long been used as narrowband optical filters for measuring the frequency spectrum of particularly narrow optical lines, especially lines whose width was below the resolving power of prism or grating spectrometers.

In their original form, such interferometers used only flat or planar reflecting surfaces, and the spacings between the mirrors were usually smaller than, or at most on the same scale as, the transverse diameters of the mirrors. Moreover, it was usual to illuminate such an interferometer with a converging or diverging beam having a spread of angular directions, and then look at the "Fabry-Perot rings" transmitted through the interferometer in certain discrete angular directions.

Interferometers used in this manner were generally analyzed using an infinite plane-wave model, with the plane waves assumed to be arriving either at normal incidence or at some specified angle to the normal, as in Figure 11.6. The standard formulas in optics texts, as a result, consider the resonant frequencies and the transmission properties of Fabry-Perot etalons as a function of the mirror spacing, the optical wavelength or frequency, and the angle of incidence. The transverse width or shape of the two mirrors is generally not taken into account, and transverse field variations are neglected.

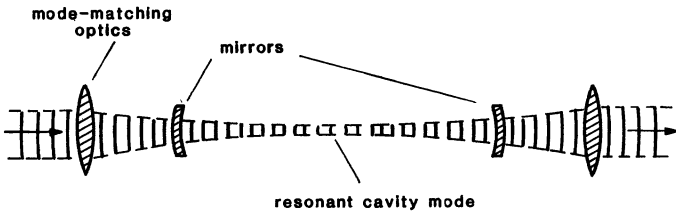


FIGURE 11.7

A typical optical resonator or passive interferometer cavity (new style) with an on-axis resonant cavity mode.

Optical Resonators

As the fundamental ideas of laser devices began to emerge, however, researchers began to consider the properties of interferometers formed by setting up rather small mirrors, spaced by distances large compared to the mirror sizes, as in Figure 11.7. The waves in such long, narrow optical cavities must travel at very small angles to the optical axis of the cavity, or else the waves will very rapidly "walk off" past the edges of the mirrors; hence the off-axis angular properties of such structures are of little interest. It was soon realized, in fact, that such structures are better thought of as optical resonators or *optical cavities*, with properties related as much to microwave waveguide resonators as to optical interferometers. The ideas of transverse as well as longitudinal modes in such structures, and of using curved as well as planar mirror surfaces, then began to be developed.

Modes in Planar and Curved-Mirror Cavities

Figure 11.8(a) shows, for example, a typical optical cavity formed by two partially transmitting mirrors set up facing each other, such as might be used in a regenerative laser amplifier or oscillator, or in a modern optical interferometer, along with two lenses being used to focus a collimated external optical beam into and out of this cavity. The one slightly unrealistic aspect of this drawing is that real laser cavities are often even longer and relatively more slender than shown here.

Most modern optical resonators and laser cavities are also designed using mirrors which are slightly curved rather than planar, as illustrated in Figures 11.7 and 11.8. The use of such curved mirrors generally leads (as we will study in much more detail in later chapters) to the existence of very well-defined and well-behaved, low-loss *transverse-mode patterns* in such cavities. (By loss we mean here the *leakage* or *diffraction* losses caused by the loss of energy out the open sides of the cavity or past the edges of the finite-diameter mirrors.) The transverse-mode patterns in many, though not all, curved-mirror optical resonators take the form of quite smooth and regular transverse patterns that resemble Hermite-gaussian or Laguerre-gaussian cross sections, and that depend to first order only on the curvature and spacing, and not on the transverse size, of the end mirrors.

Optical resonators formed by finite flat or planar mirrors have definite transverse modes also. These modes are generally more irregular than in curved-mirror cavities, and not gaussian in profile; they also typically have somewhat larger

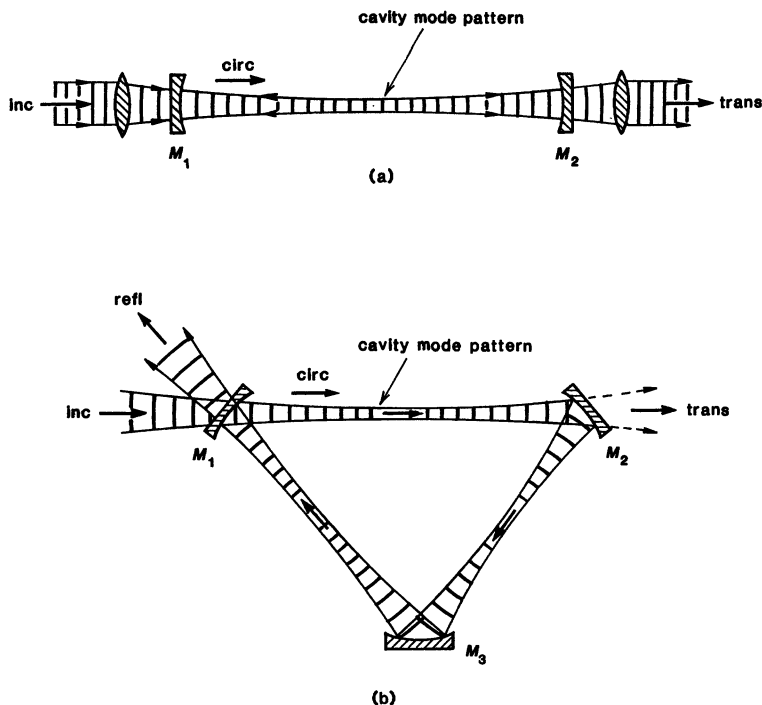


FIGURE 11.8

Simple examples of (a) a linear or standing-wave optical cavity, and (b) a ring or traveling-wave optical cavity.

diffraction losses or power leakage. The details of the transverse mode profiles in planar-mirror cavities also depend rather more critically on the exact size and transverse shape of the mirrors (e.g., circular, square, or whatever).

There also exist so-called *unstable optical resonators*, whose mirrors have a negative or divergent curvature so that the optical waves tend to be spread outward as they bounce back and forth between the end mirrors. These unstable resonators still have definite transverse mode patterns, and in fact are very useful for high-gain lasers, though their mode properties are more complicated and their diffraction losses much higher than in planar or convergent-mirror resonators.

The basic idea that it is possible set up two aligned mirrors to create a resonant optical cavity with clearcut resonant modes may seem straightforward and obvious now, but was in fact one of the key ideas in the development of the laser. The antecedents to this idea were the passive resonant étalons and interferometers used in classical optics; and there are many useful devices in optics today which involve passive optical cavities, or resonant mirror structures without optical gain.

Ring Cavities and Standing-Wave Cavities

The majority of early laser cavities, as well as passive resonant interferometers and etalons, employed just two mirrors set up facing each other to form a resonant structure, as in Figure 11.8(a). Such a cavity is often referred to as a *standing-wave cavity*, since the two waves traveling in the forward and reverse directions in such a cavity form an optical standing wave. In such a standing-wave system, the signal E and H fields will have periodic spatial variations along the axis, with a period equal to one-half the optical wavelength.

(This is strictly true, of course, only if the signal inside the cavity is at a single frequency. If multiple frequencies are present, the standing waves associated with different frequency components will have different periods and spatial locations, and the summation of these will tend to wash out some of the standing-wave character.)

In more recent years, however, many laser cavities, as well as passive optical interferometers, have been designed as *ring resonators*, such as that in Figure 11.8(b). Traveling-wave or ring cavities are not really different in principle from linear or standing-wave cavities, since the round-trip optical path in going once down a standing-wave cavity and back is essentially equivalent to going once around a ring cavity of the same overall path length. Ring resonators do have the special property, however, of having separate and independent resonances in the two opposite directions around the ring. Despite their slightly greater complexity, ring cavities offer several practical advantages in different applications, and are being increasingly used in practical devices (see Section 13.5).

One of these major advantages is that when a ring resonator is driven by an external signal, the cavity is excited with signals going in only one direction around the ring, and there is no reflection directly back into the external signal source. This can be important because many laser devices do not function well when looking directly into a back reflection. Ring laser oscillators can also, with proper design, be made to oscillate in one direction only, so that there is no standing-wave character to the fields inside the cavity; and this can give advantages in power output and in mode stability.

Mode-Matching Optics

To excite any such optical cavity in just one of its transverse modes, it is necessary to shape and focus the input beam using lenses and other so-called *mode-matching optics* in order to couple properly into the desired transverse mode of the cavity. The desired mode is usually the lowest-order transverse mode of the cavity, since this is (by definition) the transverse mode with the most highly confined transverse field pattern and the lowest leakage or diffraction losses.

If the input beam is not properly aligned and mode-matched to the transverse pattern of the lowest-order mode, the input wave will excite some mixture of lowest-order and higher-order transverse modes in the cavity. Since these higher-order transverse modes usually have slightly different resonance frequencies, tuning the input signal may excite a number of separate and frequency-shifted resonances in different transverse modes as the frequency is varied; but since the higher-order modes often have larger diffraction losses and thus lower Q values, the cavity response in the higher-order modes is often weaker than in the lowest-order transverse mode.

Uniform Plane-Wave (Transmission-Line) Approximation

The transverse field patterns inside most practical laser resonators and interferometer cavities, even when excited in a single transverse mode, are still very close to ideal plane waves. The fields propagate along the axial direction of the resonator essentially like uniform plane waves, with only minor or second-order effects due to the finite transverse width and transverse mode profile of the fields.

We will, therefore, in this and several following chapters, disregard all these transverse-mode complications and analyze the resonant properties of the signals inside and outside such cavities or interferometers using only a simple on-axis plane-wave approach. That is, we will consider the variations of the fields only in the axial or z direction, and ignore any variations in the transverse or x and y directions. This is equivalent to using essentially a *transmission-line model* to describe all the cavity resonance effects.

REFERENCES

For much more detailed information on the transverse modes and mode properties of optical resonators and interferometers, see Chapters 14–23 of this text, and the references in those chapters.

11.3 RESONANCE PROPERTIES OF PASSIVE OPTICAL CAVITIES

Let us develop therefore an elementary analysis for the resonance properties of either a linear (standing-wave) or a ring (traveling-wave) optical cavity, using the plane-wave or transmission-line analytical models shown in Figure 11.9.

Basic Cavity Analysis: The Circulating Intensity

To do this, we will suppose that a steady-state sinusoidal optical signal is incident on one of the cavity mirrors, call it mirror M_1 , using the notations \tilde{E}_{inc} and \tilde{E}_{ref} to denote the *incident* and *reflected complex signal amplitudes*, respectively, as measured just *outside* this mirror. We will also use \tilde{E}_{circ} to denote the *circulating signal amplitude* inside the cavity, as measured just *inside* the same mirror.

The circulating signal just inside the input mirror then consists of the vector sum of that portion of the incident signal which is transmitted through the input mirror, and thus has the value $jt_1\tilde{E}_{\text{inc}}$; plus a contribution representing the circulating signal \tilde{E}_{circ} which left this same point one round-trip time earlier, traveled once around the cavity, and has returned to the same point after passing through all the elements (twice, in the standing-wave model) and bouncing off mirror M_1 as well as all the other mirrors in the cavity. The total circulating signal just inside mirror M_1 can thus be written in the form

$$\tilde{E}_{\text{circ}} = jt_1\tilde{E}_{\text{inc}} + \tilde{g}_{\text{rt}}(\omega)\tilde{E}_{\text{circ}}, \quad (17)$$

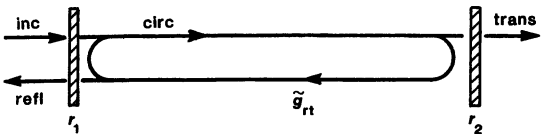
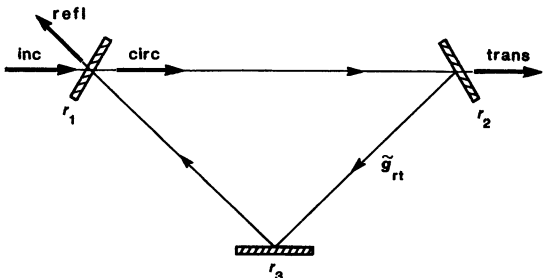


FIGURE 11.9
Elementary models for the incident, reflected, and circulating waves in resonant optical cavities or interferometers.



where $\tilde{g}_{rt}(\omega)$ is the net complex round-trip gain for a wave making one complete transit around the interior of the resonant cavity, whether it be a standing-wave or a ring-type cavity. Equation 11.17 is the key equation for calculating the resonance properties of any resonant optical cavity, optical interferometer, or oscillating laser system.

Passive Lossy Optical Cavities

In analyzing optical cavities we will consistently use L for the one-way length of a standing-wave cavity, and p ($\equiv 2L$) for the perimeter or the round-trip path length in either the ring or the standing-wave cavities. By using this notation, and by always considering round-trip gains, losses, and phase shifts, we can develop a unified analysis that treats standing-wave or ring cavities on an equal footing.

Suppose then that the round-trip optical path in either type of cavity contains material with voltage absorption coefficient α_0 (or possibly other kinds of internal losses), so that the attenuation of the signal amplitude or signal voltage in one round trip is $\exp(-\alpha_0 p) = \exp(-2\alpha_0 L)$, and the round-trip power reduction is $\exp(-2\alpha_0 p) = \exp(-4\alpha_0 L)$.

We are, of course, considering here sinusoidal optical signals with frequency ω and propagation constant $\beta = \beta(\omega) = \omega/c$, where c is the velocity of light in the material inside the cavity. Hence there is also a phase shift or propagation factor $\exp(-j\omega p/c)$ associated with the round trip. (Let's leave out any atomic phase shifts $\Delta\beta_m$ for the moment.)

The circulating signal after one complete round trip in either type of cavity will then return to the reference plane just inside mirror M_1 with a net round-trip transmission factor, or complex round-trip gain, which is given for a passive

lossy cavity by

$$\tilde{g}_{rt}(\omega) \equiv r_1 r_2 (r_3 \dots) \times \exp[-\alpha_0 p - j\omega p/c]. \quad (18)$$

In writing this expression we put the $(r_3 \dots)$ factor inside brackets because there may or may not be a third or fourth mirror in the cavity, depending on whether we are considering a simple two-mirror standing-wave resonator or some kind of multimirror ring (or folded linear) cavity. We refer to \tilde{g}_{rt} as the “complex round-trip gain” inside the cavity, even though of course in any passive optical cavity (or even in any laser cavity below oscillation threshold) the magnitude of this round-trip gain will be less than unity, i.e., $|\tilde{g}_{rt}| < 1$.

We can then write Equation 11.17 as

$$\tilde{E}_{circ} = j t_1 \tilde{E}_{inc} + r_1 r_2 (r_3 \dots) \exp[-\alpha_0 p - j\omega p/c] \tilde{E}_{circ}. \quad (19)$$

This expression then applies equally well to either a ring or a standing-wave cavity, if we simply replace p by $2L$ for the standing wave.

Cavity Resonances

This derivation says we can relate the circulating signal inside the cavity to the incident signal outside the cavity by

$$\frac{\tilde{E}_{circ}}{\tilde{E}_{inc}} = \frac{j t_1}{1 - \tilde{g}_{rt}(\omega)} = \frac{j t_1}{1 - r_1 r_2 (r_3 \dots) \exp[-\alpha_0 p - j\omega p/c]}. \quad (20)$$

What does this equation tell us? To help answer this question, Figure 11.10(a) shows several examples of how the circulating intensity $I_{circ} \equiv |\tilde{E}_{circ}|^2$ inside such an optical resonator varies with frequency ω or round-trip phase shift $\omega p/c$, assuming unit incident intensity, a round-trip internal power loss of $2\alpha_0 p = 2\%$, and symmetric mirror reflectivities $R_1 = R_2 = R$ which vary from $R = 70\%$ to $R = 98\%$.

It is obvious from these plots, as well as from Equation 11.20, that the signal inside the optical resonator exhibits a strong resonance behavior each time the round-trip phase shift $\omega p/c$ equals an integer multiple of 2π , i.e., each time $\omega = \omega_q \equiv q \times 2\pi \times (c/p)$, with q being an integer. In fact, the circulating intensity inside the cavity at these resonances becomes many times larger than the intensity incident on the cavity from outside. As we will discuss in more detail in the following sections, these resonant frequencies are known as *cavity axial modes*, and the frequency interval between resonances is known as the *axial mode spacing* or the *free spectral range* of the cavity.

Rotating Vector Interpretation

The resonance behavior that is evident in these plots can perhaps be most easily understood from the following graphical analysis. The denominator in the ratio of circulating to incident signal amplitudes in Equation 11.20 is given by the complex factor $1 - \tilde{g}_{rt}(\omega) \equiv 1 - r_1 r_2 (r_3 \dots) \exp[-\alpha_0 p - j\omega p/c]$. The quantity $\tilde{g}_{rt}(\omega)$ is a complex vector with a magnitude that is less—but perhaps not much less—than unity. This complex gain has a phase angle $\omega p/c$ such that $\tilde{g}_{rt}(\omega)$ rotates through one complete revolution in the complex plane every time $\omega p/c$ increases by 2π . Since the cavity perimeter p is many optical wavelengths in length, the

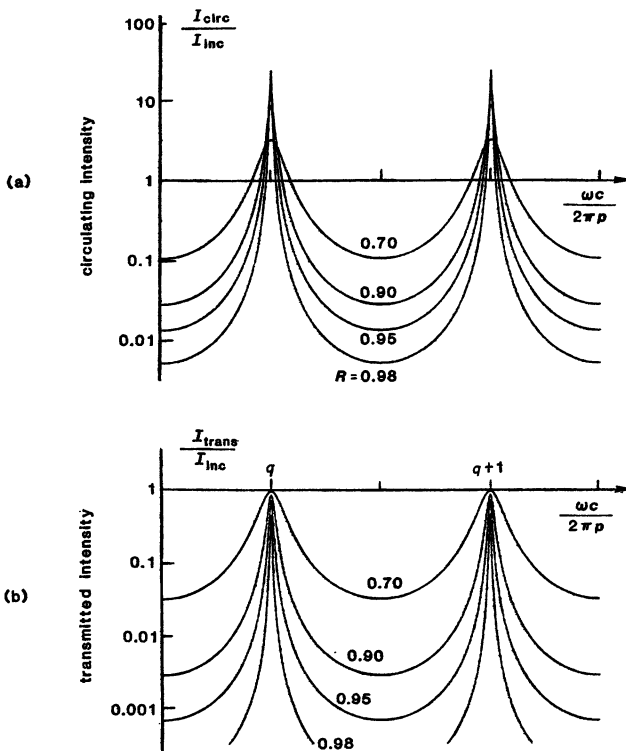


FIGURE 11.10

Circulating (a) and transmitted (b) power in an optical resonator plotted versus frequency or round-trip phase shift $\omega p/c$ and mirror reflectivity $R_1 = R_2 = R$, assuming a fixed internal power loss of 2% per round trip.

rotation of $\omega p/c$ through many complete cycles with increasing frequency is quite rapid.

Suppose we plot this denominator in a complex plane. The complex vector representing $\tilde{g}_{\text{rt}}(\omega)$ then rotates about the point $1 + j0$ as shown in Figure 11.11. Every time the tip of the rotating $1 - \tilde{g}_{\text{rt}}(\omega)$ vector sweeps close to the origin in this sketch, the denominator $1 - \tilde{g}_{\text{rt}}(\omega)$ of the $\tilde{E}_{\text{circ}}/\tilde{E}_{\text{inc}}$ ratio becomes very small, and the value of the circulating field becomes correspondingly large. This occurs, of course, every time $\omega p/c$ passes through another integer multiple of 2π .

Circulating Intensity Magnification

Let us examine how large the circulating signal inside the cavity can become at one of these peaks. Consider as a simple example a symmetric linear cavity with equal end-mirror reflectivities $r_1 = r_2 = r$, and assume negligible internal losses, or $\alpha_0 p \approx 0$. The peak value of the circulating field at resonance is then

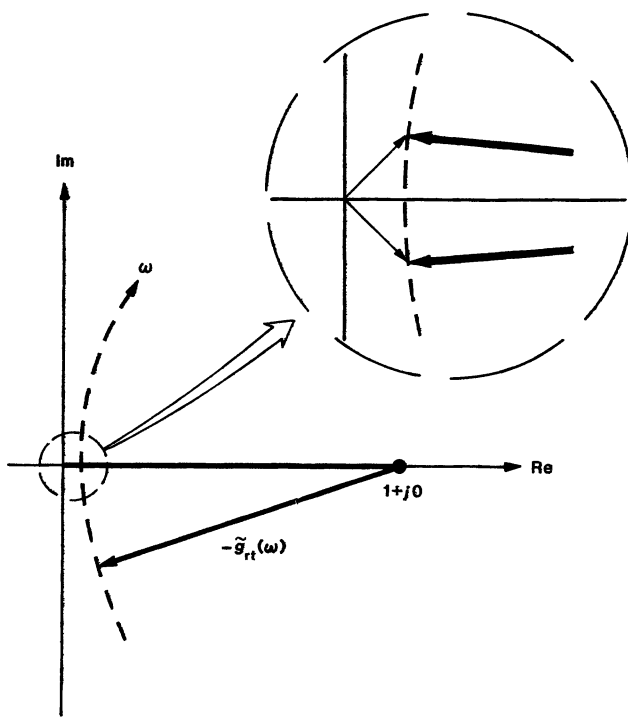


FIGURE 11.11
Graphical diagram to help explain the behavior of an interferometer cavity near resonance.

given by

$$\left. \frac{\tilde{E}_{\text{circ}}}{\tilde{E}_{\text{inc}}} \right|_{\omega=\omega_q} = \frac{jt}{1 - r_1 r_2 e^{-\alpha_0 p}} \approx \frac{jt}{1 - r^2} = \frac{j}{t}, \quad (21)$$

where we have used $t_1 = t_2 = \sqrt{1 - r^2}$ for lossless mirrors. (Note that the 90° phase shift between the incident and circulating fields is inherent in our choice of matrix representation for the partially transmitting mirror.)

The ratio of circulating intensity to incident intensity for a symmetric cavity with negligible internal losses is thus given by

$$\left. \frac{I_{\text{circ}}}{I_{\text{inc}}} \right|_{\omega=\omega_q} \approx \left| \frac{1}{t} \right|^2 = \frac{1}{T}, \quad (22)$$

where $T \equiv t^2$ is the power transmission of either end mirror. If we assume, for example, end mirrors which are 99% reflecting and 1% transmitting, so that $T = 1\% = 0.01$ (note that mirrors are usually characterized by their power reflection and transmission values), then this gives

$$I_{\text{circ}} \approx 100 \times I_{\text{inc}} \quad \text{for} \quad \begin{cases} R_1 = R_2 = 0.99, \\ \alpha_0 p \ll 0.01. \end{cases} \quad (23)$$

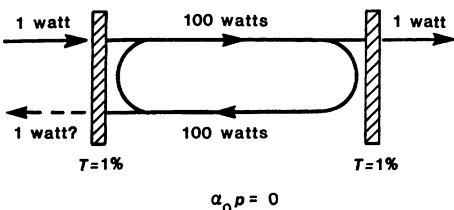


FIGURE 11.12
Magnification of the circulating signal level in a lossless optical cavity at resonance.

In other words, 1 watt of laser power incident on this cavity from outside will build up a circulating power of ≈ 100 watts traveling in each direction inside the laser cavity, as illustrated in Figure 11.12.

The circulating power inside a passive cavity resonator can thus be much larger than the power incident on the cavity end mirror from outside. There is, of course, no way that this magnified circulating power can be usefully extracted (at least not continuously), since energy conservation still must be obeyed! This form of power magnification can be used, however, in testing the damage thresholds of low-loss optical elements placed inside such a cavity. This circulating stored energy can also be switched out of the cavity on a transient basis, using a fast switch, to give a short pulse of energy at the magnified intensity level. The latter technique is sometimes referred to as "cavity dumping".

The intensity magnification in this symmetric and lossless example has a maximum value of $1/t^2 = 1/(1 - R)$, where R is the mirror reflectivity at each end. Finite internal losses or increased mirror transmission will in general reduce this resonance enhancement, the circulating intensity at resonance being given more generally by

$$\frac{I_{\text{circ}}}{I_{\text{inc}}} \Big|_{\omega=\omega_r} = \frac{t_1 t_2}{[1 - r_1 r_2 (r_3 \dots) e^{-\alpha_0 p}]^2}. \quad (24)$$

If, for example, $r_1 r_2 = 0.99$ (and $r_3 \equiv 1$), so that the round-trip power loss through the end mirrors is 1%, then giving the internal losses the same value of 1% by making $\alpha_0 p = 0.01$ will cut the circulating field amplitude in half, and decrease the circulating intensity by four times, or a reduction of approximately 6 dB.

Transmitted Cavity Fields

When the 100 watts of power circulating inside the cavity in Figure 11.12 impinge on the 1% transmitting output mirror, this means that a net transmitted power of 1 watt—equal to the incident signal—must be transmitted out through the output mirror at the opposite end of the cavity, as shown in Figure 11.12. In other words, this particular cavity, at resonance, has a resonant transmission from input to output of essentially unity. As the frequency ω is tuned off resonance, however, both the circulating and the transmitted signal intensities will drop rapidly, as illustrated in Figure 11.10.

To develop a more general formula for the transmitted field \tilde{E}_{trans} coming out the other end or through the other mirror M_2 , in either the ring or the linear example, we can suppose that a portion p_1 of the cavity path is in the leg between mirrors M_1 and M_2 ($p_1 \equiv L$ in the linear example). The transmitted

signal intensity coming out through mirror M_2 will then be given by

$$\tilde{E}_{\text{trans}} = j t_2 \exp[-\alpha_0 p_1 - j \omega p_1 / c] \times \tilde{E}_{\text{circ}}. \quad (25)$$

Hence the net transmission through the cavity or interferometer, from input to output, is given by

$$\frac{\tilde{E}_{\text{trans}}}{\tilde{E}_{\text{inc}}} = \frac{-t_1 t_2 \exp[-\alpha_0 p_1 - j \omega p_1 / c]}{1 - r_1 r_2 (r_3 \dots) \exp[-\alpha_0 p - j \omega p / c]} = \frac{-t_1 t_2 \exp[-\alpha_0 p_1 - j \omega p_1 / c]}{1 - \tilde{g}_{\text{rt}}(\omega)} \quad (26)$$

for the ring example, or by the essentially equivalent formula

$$\frac{\tilde{E}_{\text{trans}}}{\tilde{E}_{\text{inc}}} = \frac{-t_1 t_2 \exp[-\alpha_0 L - j \omega L / c]}{1 - r_1 r_2 \exp[-2\alpha_0 L - 2j \omega L / c]} = -\frac{t_1 t_2}{\sqrt{r_1 r_2}} \frac{\sqrt{\tilde{g}_{\text{rt}}(\omega)}}{1 - \tilde{g}_{\text{rt}}(\omega)} \quad (27)$$

for the standing-wave cavity. The minus sign in front of either expression is a basically irrelevant additional phase shift of π that arises because we insist on making a certain choice of reference planes at each mirror, as discussed in the preceding section.

Both Figure 11.10(b) and Figure 11.13(a) plot the transmitted intensity versus frequency for various choices of mirror reflectivities and losses. It is evident that the resonant cavity acts as a narrowband transmission filter, with a periodically spaced set of transmission passbands whose bandwidth and peak transmission depend on the cavity losses and the balance between input and output coupling to the cavity. Figure 11.13(b) also shows the transmission phase angle versus frequency for a typical case.

Dielectric Etalons

The resonant transmission properties of optical interferometers or Fabry-Perot etalons have long been used as passive optical filters for incoherent light sources. In the laser field, thin dielectric etalons, with or without additional reflective coatings, are also often used as filters *inside* laser cavities, in order to tune the laser, to obtain wavelength or frequency selection, or to reduce the gain bandwidth and thus limit the number of oscillating axial modes inside a laser cavity. The intracavity application of such an etalon is illustrated in Figure 11.14.

In this application the etalon is usually tilted to an angle large enough that the external reflected beams from the etalon are deflected away from the cavity axis, so that they do not set up any unwanted resonances with the other mirrors in the resonator. At the same time the angle is made small enough that the waves bouncing back and forth inside the etalon are shifted transversely by only a very small amount compared to the beam diameter on each bounce, thus keeping the “walk-off losses” of the etalon interferometer small.

The resonant transmission peaks of the etalon can then be tuned by small changes in the etalon angle. (Warning: the peaks tune “the wrong way” with change in angle; see Problem 11.3-2.) By using several etalons of different thickness in cascade, it is possible to combine the narrow linewidth but small free spectral range obtained from a longer etalon, with the wider linewidth but also wider free spectral range of a thinner etalon, as shown in Figure 11.14(b).

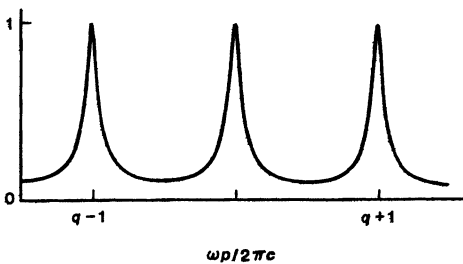
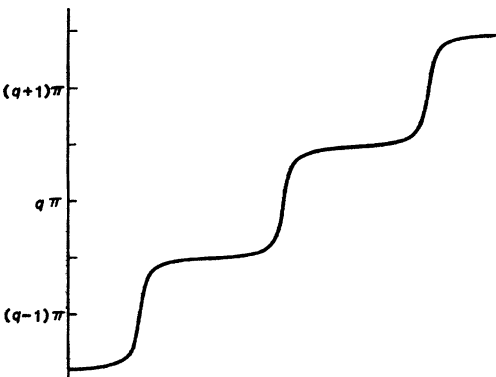


FIGURE 11.13
Transmitted intensity (top curve)
and phase shift (bottom curve)
versus frequency through a typical
interferometer or etalon.



Reflected Cavity Fields

Let us examine finally the reflected wave that comes back from a resonant cavity or etalon at the cavity input mirror, as illustrated in Figure 11.15. Note that in a standing-wave cavity (Figure 11.15(a)) the reflected wave goes straight back along the same direction as the incident wave, and hence presumably straight back into whatever source generated the incident wave; whereas in the ring cavity (Figure 11.15(b)) this reflected wave goes off in a different direction, like a specular reflection from mirror M_1 . This can be a major advantage of a ring as compared to a standing-wave cavity, since many laser devices do not function well when looking into even a relatively weak back-reflection.

Suppose we look first at the reflected wave from the symmetric cavity example with the 100 watts of circulating power in Figure 11.12. Since the input mirror M_1 in this example also has a 1% power transmission, it might appear that at resonance another 1 watt of power must be transmitted back out of the cavity in the reverse direction, because of transmission from the 100 watts of circulating power back through the 1% mirror at the input end. This seems to say that with 1 watt of incident power, 1 watt of power can appear in the reflected wave as well as in the transmitted wave coming out of the cavity. Obtaining 2 watts of total output power in the transmitted plus reflected waves from the cavity, with only 1 watt of input power, does pose some conceptual difficulties, however; and

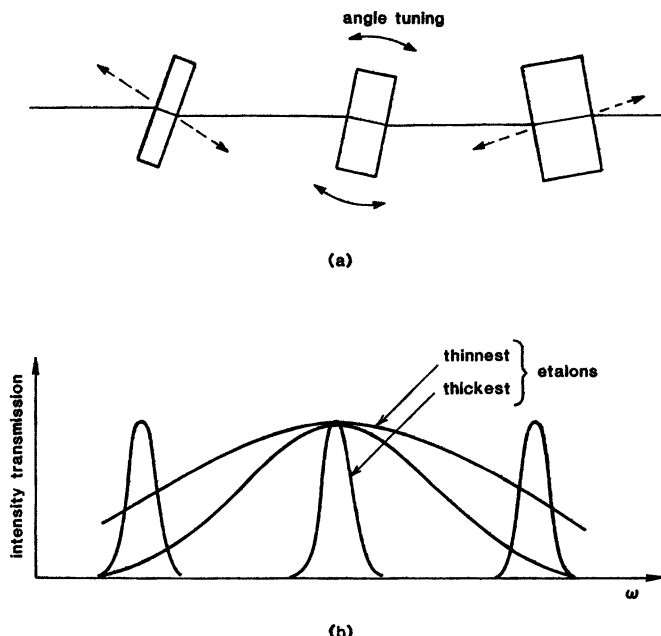


FIGURE 11.14

(a) Tilted Fabry-Perot etalons as intracavity filters or tuning elements, and (b) the sequential transmission curves for etalons of different thicknesses, adjusted so that their transmission peaks coincide at one frequency.

it would seem that ≈ 0 watts in the reflected wave would be a more reasonable result for this example.

Reflected Signal Formulas

The significant point here is, of course, that for both the traveling-wave and standing-wave cases the total “reflected” wave \tilde{E}_{refl} coming from mirror M_1 must consist of a component $r_1 \tilde{E}_{\text{inc}}$ that is due to straightforward reflection from the outer surface of mirror M_1 , plus a second component that represents the circulating signal \tilde{E}_{circ} inside the cavity that is transmitted out through the mirror M_1 into the same direction, as illustrated graphically in Figures 11.15(a) and (b). The latter component comes from the circulating signal \tilde{E}_{circ} that left the reference plane one round-trip time earlier; traveled once around the cavity except for bouncing off mirror M_1 ; and then is transmitted out through the input mirror. The value of this component is thus given by $j t_1 (\tilde{g}_{\text{rt}}/r_1) \times \tilde{E}_{\text{circ}}$. (The round-trip gain must be divided by r_1 because the wave does not bounce off mirror M_1 , it goes through it.)

The total reflected wave thus consists of

$$\tilde{E}_{\text{refl}} = r_1 \tilde{E}_{\text{inc}} + j t_1 (\tilde{g}_{\text{rt}}/r_1) \tilde{E}_{\text{circ}}. \quad (28)$$

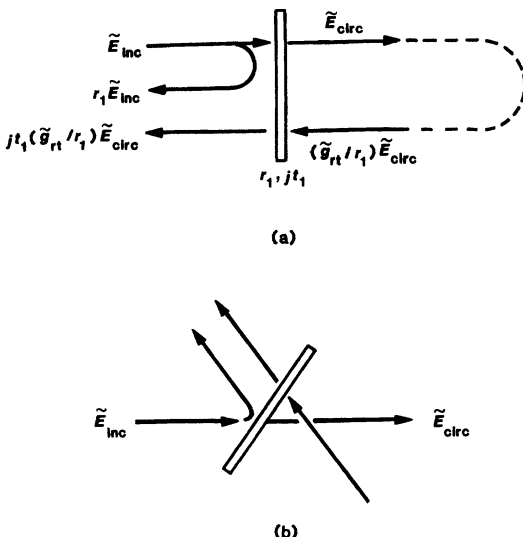


FIGURE 11.15
Externally reflected waves from (a) standing-wave and (b) ring-laser cavities.

Using our earlier expressions for \tilde{E}_{circ} , we can then write the total reflection coefficient from mirror M_1 as

$$\frac{\tilde{E}_{\text{refl}}}{\tilde{E}_{\text{inc}}} = r_1 - \left[\frac{t_1^2 r_2 e^{-\alpha_0 p - j\omega p/c}}{1 - r_1 r_2 (r_3 \dots) e^{-\alpha_0 p - j\omega p/c}} \right] = r_1 - \frac{t_1^2}{r_1} \frac{\tilde{g}_{\text{rt}}(\omega)}{1 - \tilde{g}_{\text{rt}}(\omega)}. \quad (29)$$

These expressions, with their two separate terms, are useful in emphasizing that the reflected signal does consist of the directly reflected component, plus a transmitted component coming from the circulating signal inside the cavity, as shown in Figure 11.15. By using the lossless mirror expression that $r_1^2 + t_1^2 = 1$, however, we can also convert these expressions into the slightly simpler forms

$$\frac{\tilde{E}_{\text{refl}}}{\tilde{E}_{\text{inc}}} = \frac{r_1 - r_2 e^{-\alpha_0 p - j\omega p/c}}{1 - r_1 r_2 e^{-\alpha_0 p - j\omega p/c}} = \frac{1}{r_1} \times \frac{r_1^2 - \tilde{g}_{\text{rt}}(\omega)}{1 - \tilde{g}_{\text{rt}}(\omega)}. \quad (30)$$

The second form of this expression makes it evident that the reflectivity from mirror M_1 of the cavity depends only on the amplitude reflectivity r_1 of that mirror and the round-trip gain $\tilde{g}_{\text{rt}}(\omega)$, and that the reflectivity can go to zero if these become exactly equal at resonance.

Figures 11.16 and 11.17 show several curves of the power reflectivity $I_{\text{refl}}/I_{\text{inc}}$ from a resonant cavity or interferometer versus frequency, assuming a fixed reflectivity R_1 for the front mirror and varying values of the additional losses due to $R_2 e^{-2\alpha_0 p}$. Note that only the product $R_2 e^{-2\alpha_0 p}$ counts; it makes no difference to the total reflectivity at mirror M_1 how the additional losses in the rest of the cavity are divided between the second mirror reflectivity R_2 and the internal losses $e^{-2\alpha_0 p}$.

In plotting Figure 11.17, we have plotted the intensity-reflection curves for $R_1 \geq R_2 e^{-2\alpha_0 p}$ above the axis and the curves for $R_1 \leq R_2 e^{-2\alpha_0 p}$ below the

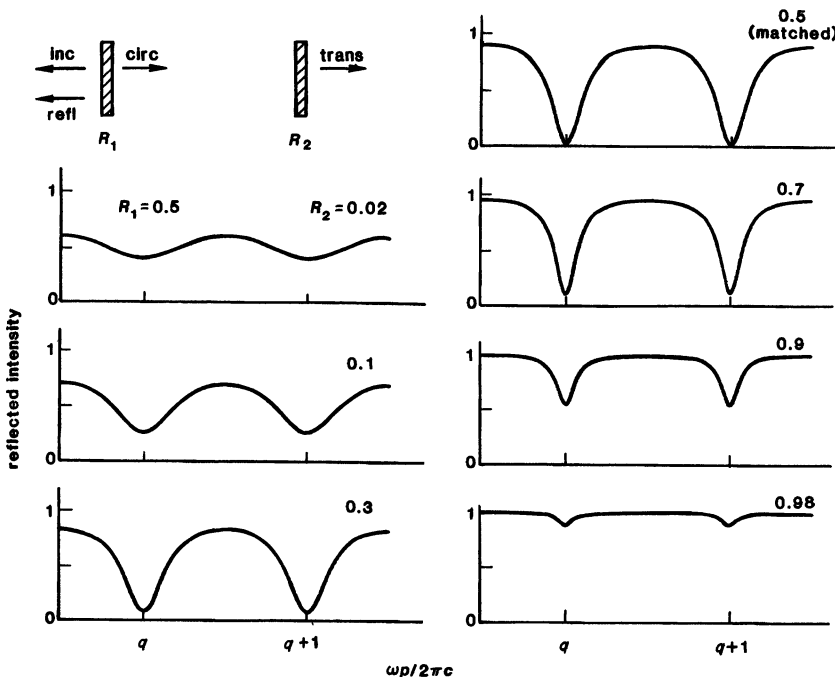


FIGURE 11.16

Reflected intensity versus frequency from one mirror of an interferometer cavity, for different values of the internal cavity loss or the reflectivity of the other mirror.

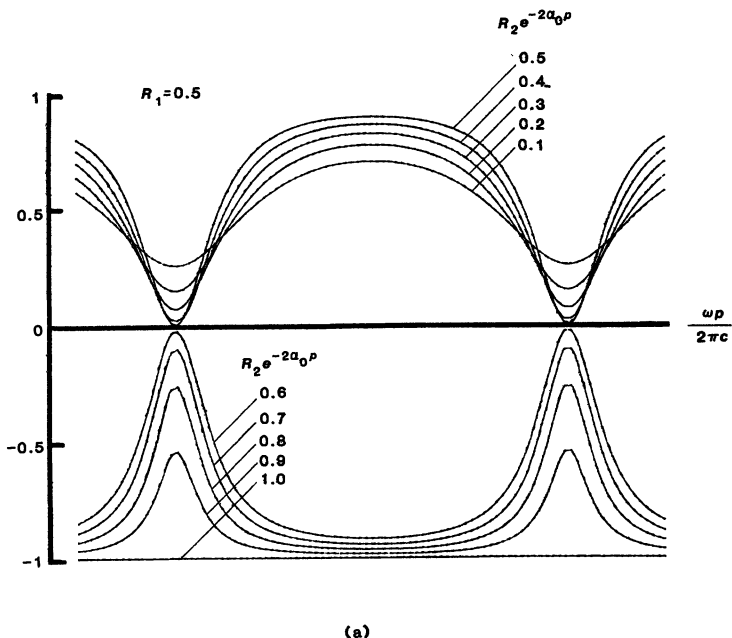
axis, to indicate that there is indeed a 180° phase shift in the total reflectivity at resonance as the interferometer goes from one situation to the other. We have also shown some examples of the rather complex phase-angle variations with frequency exhibited by the reflected wave.

Matched Input Conditions

The special situation when the input mirror reflectivity R_1 exactly equals the additional loss terms given by $R_2 e^{-2\alpha_0 p}$ causes the two terms in the reflection expression to exactly cancel, and the net reflection coefficient to become exactly zero at resonance. This is often called the *impedance-matched* situation, since it corresponds to looking into an impedance-matched resonant circuit or cavity (i.e., load impedance = characteristic impedance) on an ordinary transmission line. The numerical example that we considered in Figure 11.12, with the 100 watts of circulating power, was an input-matched situation, as is any symmetric interferometer (i.e., $r_1 = r_2$) with very small internal losses.

Etalon Mirrors

Even when the reflectivities from each individual mirror surface are comparatively low, i.e., R_1 and $R_2 \ll 1$, the combined reflectivity in the backward



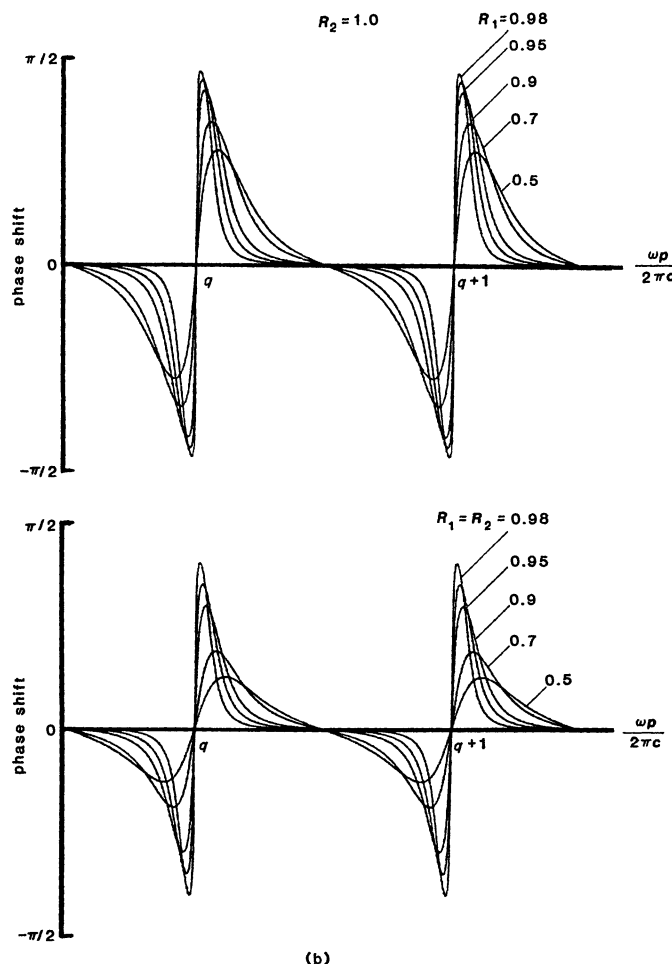
(a)

FIGURE 11.17(a)

Intensity of the reflected signal plotted versus frequency for a cavity with fixed front-mirror reflectivity and various values of the additional cavity losses plus back-mirror reflectivity.

direction from an interferometer cavity over the off-resonance part of the reflection curve can be considerably larger than the individual reflections from either surface alone, as illustrated in Figure 11.18.

As one application of this, polished etalons made from dielectric materials such as quartz ($n \approx 1.46$) or clear sapphire ($n \approx 1.76$) with highly parallel faces are often used as the output mirrors for pulsed high-power solid-state lasers—that is, the lasers are operated with a 100% mirror on one end and a polished etalon a few mm or a cm thick, generally with no additional reflective coatings, as the output mirror on the other end. Since these lasers typically have large round-trip gains, they operate best with low-reflectivity output mirrors, and the uncoated dielectric etalon provides a simple way of achieving the necessary output mirror reflectivity. These uncoated etalons are also simple to fabricate, can have very high optical-damage thresholds, and the reflectivity peaks can serve a useful purpose in narrowing the oscillation bandwidth of a wide-line laser medium, such as a Nd:glass or dye laser. Note that the reflectivity peaks in these mirrors occur not at resonance, but rather half-way between the axial-mode resonances of the etalon itself.



(b)

FIGURE 11.17(b)

Phase angle of the reflected signal plotted versus frequency for a cavity with fixed front-mirror reflectivity and various values of the additional cavity losses plus back-mirror reflectivity.

Transient Cavity Reflections

The fact that the total reflected signal \tilde{E}_{refl} from a resonant cavity is formed from the vector combination of the directly reflected input signal $r_1 \tilde{E}_{\text{inc}}$, plus a transmitted portion of the circulating signal, or $j t_1 (\tilde{g}_{\text{rt}} / r_1) \tilde{E}_{\text{circ}}$, means that the transient response of the cavity reflection, if we suddenly change either one of these signals, can be rather complex. If an input signal is very suddenly turned on, for example, the directly reflected component appears immediately; but the

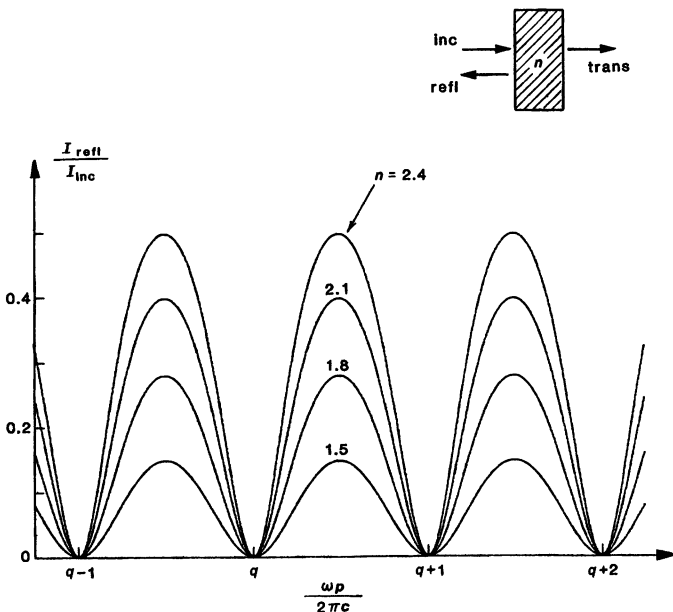


FIGURE 11.18

The back-reflection from a dielectric etalon at frequencies midway between the transmission resonances can be substantially larger than the reflection from either of the etalon surfaces alone.

circulating component only appears more gradually, after the circulating field inside the cavity has time to build up.

This makes it possible to devise various clever schemes for modulating the reflected signal on a transient or pulsed basis. Suppose, for example, that a matched steady-state on-resonance situation with these two terms essentially canceling each other has been established, and that the incident signal is then suddenly turned off by means of some kind of fast electro-optic modulator. The net reflected signal will then suddenly jump from near zero to a value equal to $-r_1$ times the originally incident signal, with a step-function leading edge; and will then gradually die away, with the cavity decay rate ω/Q_c as the stored energy drains out of the resonant cavity.

If we can instead suddenly shift the phase of the incident signal by 180° , the total reflected signal will suddenly jump up to a value $\tilde{E}_{\text{refl}} \approx -2r_1\tilde{E}_{\text{inc}}$, or a reflected power equal to four times the incident power, at least in the leading edge of the resulting transient response.

 Problems for 11.3

1. *Design specifications for a transmission etalon.* A Fabry-Perot etalon is to be used as a transmission filter inside an oscillating laser cavity, as mentioned in this section. A very high peak transmission ($\geq 99.0\%$) is required in order to avoid excessive losses inside the laser, and a finesse ≥ 30 is also needed. What specifications must be given for the etalon mirror reflectivities R_1 and R_2 , and for the internal round-trip power loss $\delta_0 \equiv 2\alpha_{op}$ in the etalon?
2. *Angle tuning of a transmission etalon.* Analyze (or look up in an optics text) the transmission function of a resonant etalon as a function of angle; and discuss how the transmission peak of an intracavity etalon will tune with angle.
At larger angles the apparent thickness or path length through the etalon increases; therefore the etalon should tune to lower frequencies or longer wavelengths with increasing angle—right?
3. *Calculating cavity parameters from measured transmission-reflection curves.* Suppose that by using a tunable laser you can measure fairly accurately the magnitudes of both the transmission coefficient and the reflection coefficient versus frequency for a passive interferometer cavity (i.e., internal losses but no gain medium) across one full axial-mode resonance. Develop formulas by which you can work backward to calculate the reflectivities r_1 and r_2 of the two end mirrors, and also the internal cavity loss α_{op} of the cavity, in terms of the measured midband transmission and reflection factors and their measured bandwidths.
4. *Reflection properties of uncoated dielectric etalon mirrors.* Carry out an analysis of the dielectric-etalon mirrors mentioned in this section, assuming a simple dielectric slab a few mm to a cm thick with polished and parallel front and back surfaces, negligible internal losses, and no additional mirror coatings. Analyze the reflectivity properties versus frequency of these dielectric etalons, and find typical values of peak reflectivity for such etalons both on resonance and midway between resonances. (Note: typical values of index of refraction range from $n \approx 1.45$ for simple typical glasses to $n \approx 1.54$ for quartz, $n \approx 1.76$ for sapphire or $n \approx 3.3$ for GaAs.) Does the maximum reflectivity occur at resonance, or midway between resonances, and how large is this reflectivity compared to the single-surface reflectivities of the same etalons? Discuss in physical terms how the reflection versus frequency behavior can be explained.
5. *Linewidth of a power reflectivity dip.* Suppose we define the “50% linewidth” $\Delta\omega_{50}$ for the power reflection curve from a Fabry-Perot interferometer or lossy regenerative cavity as the full frequency width between the points halfway down into the resonance dip. Find an expression for this linewidth versus the midband loss of the interferometer in dB.
6. *Reflection phase angle versus frequency.* Compute and plot the phase angle versus frequency for the complex interferometer reflectivity $\tilde{E}_{\text{ref}}/\tilde{E}_{\text{inc}}$ for some typical choices of R_1 , R_2 and δ_0 . Consider in particular the case of the Gires-Tournoi interferometer, which has R_1 finite, $R_2 = 100\%$, and $\delta_0 = 0$, so that the magnitude of the overall reflectivity is constant and equal to 1 at all frequencies, but the phase angle of the reflection changes sharply with frequency. (Hint: Consider the phase angles versus frequency for the numerator and denominator separately, and then combine.)

7. *Field magnification inside a resonant cavity.* How much larger is the electric field strength inside the resonant cavity of Figure 11.11, compared to the field strength at any point in the incident laser beam outside the cavity?

11.4 “DELTA NOTATION” FOR CAVITY GAINS AND LOSSES

Before we continue our general discussion of cavity resonance properties, let us introduce in this section a unified notation for describing cavity gain and loss factors that will be useful throughout the rest of this book. We can also then use this notation to simplify some of the formulas from the preceding section.

Mirror Reflectivities: The Delta Notation

The usual practice in optics is to describe mirrors by their *power reflection and transmission* values; “95% reflectivity,” for example, means a mirror with $R_1 = 0.95$ and hence, for a lossless mirror, $T_1 = 1 - R_1 = 0.05$.

In the early days of lasers, the available gains in most laser systems were very small, and oscillation could be obtained only with very high-reflectivity mirrors. It then became conventional to describe the small difference between the mirror power reflectivity and unity by the symbol δ , so that a mirror with 95% reflectivity would be described by $R_1 = 1 - \delta_1 = 0.95$, or $\delta_1 = T_1 = 0.05$.

As a more convenient and general definition, however, one useful for both high- and low-reflectivity mirrors, and hence for either small or large output coupling, we will in the remainder of this text relate the reflectivity R_1 of any mirror to a “mirror coupling coefficient” δ_1 by means of the definition

$$R_1 \equiv e^{-\delta_1} \quad \begin{aligned} & \text{(exact definition, arbitrary } \delta_1\text{),} \\ & \approx 1 - \delta_1 \quad \text{(approximate definition, } \delta_1 \ll 1\text{).} \end{aligned} \quad (31)$$

Thus, if we have a laser cavity with two end mirrors having reflectivities R_1 and R_2 , we will write these as $R_1 \equiv r_1^2 \equiv e^{-\delta_1}$ and $R_2 \equiv r_2^2 \equiv e^{-\delta_2}$. The general definition of δ_i is thus

$$\delta_i \equiv \ln \left(\frac{1}{R_i} \right) = 2 \ln \left(\frac{1}{r_i} \right) \quad (32)$$

for mirrors with arbitrarily low reflectivity and thus arbitrarily large output coupling.

In the high-reflectivity, low-coupling limit we can still write the mirror transmission as $T = 1 - R$, with the approximation that $T \approx \delta$ and hence $t \approx \sqrt{\delta}$ for $\delta \ll 1$. For a mirror having, say, $R = 80\%$ reflectivity and $T = 20\%$ power transmission, the exact value of δ is given by $\delta = \ln(1.25) = 0.223$, not far distant from the approximate value of $1 - R = 0.20$. Hence the approximation that $\delta \approx 1 - R = T$ remains reasonably accurate even for mirror reflectivities as low as $R \approx 80\%$ and $T \approx 20\%$.

Internal Cavity Gain and Loss Factors

If we use this notation for the end-mirror coupling factors δ_1 and δ_2 , the round-trip power gain inside any cavity or interferometer with a perimeter p , internal loss coefficient α_0 , and internal gain coefficient α_m , can be conveniently condensed into the form

$$|\tilde{g}_{rt}|^2 = R_1 R_2 e^{2\alpha_m p_m - 2\alpha_0 p} = e^{\delta_m - \delta_0 - \delta_1 - \delta_2}. \quad (33)$$

That is, we can make a natural extension of the “ δ notation” by also writing the total round-trip power gain and loss in the cavity due to the internal loss coefficient α_0 and the laser gain medium in the forms

$$\delta_0 \equiv 2\alpha_0 p \quad \text{and} \quad \delta_m \equiv 2\alpha_m p_m. \quad (34)$$

As a further extension we can include within the internal loss coefficient δ_0 not only the round-trip power reduction arising from any distributed attenuation $\alpha_0 p$, but also any additional discrete losses that may occur inside the cavity because of lossy interfaces, imperfect Brewster windows, internal scattering elements, or whatever. The significant quantity is thus not α_0 or p separately, but the total internal power loss in one complete round trip, as expressed by $e^{-\delta_0}$.

From here on we will thus generally express any kind of round-trip power gain or power loss in an optical cavity by the notation

$$\delta_x \equiv \ln[\text{power gain, or power loss, ratio per round trip}]. \quad (35)$$

In the small gain or loss limit, δ_x is essentially the fractional power gain or loss per round trip due to mechanism x , and we will often speak loosely of δ_x in those terms, e.g., $\delta_x = 0.20$ means $\approx 20\%$ power gain or loss per round trip.

Total Cavity Gains and Losses

As one final bit of notation, it will often be convenient to combine all the round-trip losses contained in the factor δ_0 —which we will call *internal cavity losses*—with all the loss factors δ_1 and δ_2 due to the cavity mirrors—which we will call *external coupling losses*—to give a *total cavity-loss factor* δ_c defined by

$$\delta_c \equiv \delta_0 + \delta_1 + \delta_2 = 2\alpha_0 p + \ln\left(\frac{1}{R_1 R_2}\right) \quad (36)$$

(plus additional mirror reflectivities R_3 if needed). With this notation the round-trip power gain inside any cavity also containing a laser gain medium can then be written in the simple form

$$|\tilde{g}_{rt}|^2 = e^{\delta_m - \delta_c} \approx 1 + \delta_m - \delta_c \quad \text{if} \quad |\delta_m - \delta_c| \ll 1. \quad (37)$$

The net growth (or decay) rate for a signal circulating around inside the laser cavity (with no injected signal) is thus simply the difference between the total (saturated) laser gain factor δ_m and the total cavity loss factor δ_c .

With all of these gain and loss factors δ_x defined in terms of a *round trip*, most of our formulas will apply equally well to either standing-wave or ring-type laser cavities. Note that similar notation is used in much of the laser literature, but published papers are not always consistent about whether δ_x means power

gain or loss *per one-way pass* or *per round trip*. In consulting the literature, watch out for possible factors of two, depending on which definition is employed.

Cavity Q Values

It can also be useful in some situations to relate cavity gain or loss factors to cavity Q factors, defined in the following manner.

Suppose some initially injected energy is circulating around inside a laser cavity, with no further injected signal being applied. If we consider only a “cold” laser cavity (no gain present), this circulating energy will decrease after a number N of round trips in the exponential fashion

$$I_{\text{circ}}(t) = I_{\text{circ}}(t_0) \times \exp[-N\delta_c] = I_{\text{circ}}(t_0) \times \exp\left[-\frac{\delta_c}{T_{\text{rt}}}(t - t_0)\right], \quad (38)$$

where $T_{\text{rt}} \equiv p/c$ is the round-trip transit time in the laser cavity, and $N = (t - t_0)/T_{\text{rt}}$ is the number of round trips in time $t - t_0$. Another way of expressing this exponential decay that is commonly used in many engineering fields is to write it in the form

$$I_{\text{circ}}(t) = I_{\text{circ}}(t_0) \times \exp\left[-\frac{\omega_a}{Q_c}(t - t_0)\right], \quad (39)$$

where Q_c is sometimes called the “cold cavity Q ” of the laser cavity due to internal losses plus external coupling. This Q value plays the same role in an optical cavity as does, for example, the familiar $Q = \omega L/R$ value characteristic of a series RLC electrical circuit.

The Q factor (sometimes called the “quality factor”) of an optical cavity due to its internal losses plus external coupling through the mirrors can thus be calculated from

$$Q_c = \frac{\omega_a T_{\text{rt}}}{\delta_c} = \frac{2\pi p}{\lambda} \frac{1}{\delta_c}. \quad (40)$$

(We could also define a negative Q_m value representing the laser gain, by replacing the loss factor δ_c by δ_m in this expression.) Real laser cavities typically have very large Q_c values, even in very lossy optical cavities.

Suppose for example that an optical cavity is very lossy, with 90% power loss per round trip, corresponding to $\delta_c = \ln(1/0.1) \approx 2.3$. The Q_c value will then still be very large, even though 90% of the circulating energy is lost out of the cavity on every round trip, because the cavity perimeter p will (except in very special cases) be larger than the optical wavelength λ by a factor typically somewhere between 10^4 and 10^6 . In physical terms, the power loss *per round trip* is large, but the fractional power loss *per cycle* (which determines the Q_c value) is very small.

Field Values in Low-Loss Cavities

By using the delta notation, plus the low-loss approximations, we can write some useful simplified forms of the analytical results given earlier in this chapter. The on-resonance value of the denominator $1 - \bar{g}_{\text{rt}}$ that appears in all the

resonant-cavity expressions can first be simplified to the form

$$1 - \tilde{g}_{rt} \equiv 1 - r_1 r_2 e^{\alpha_m p_m - \alpha_{op}} \approx \frac{\delta_c - \delta_m}{2}. \quad (41)$$

The peak value for the circulating intensity in a purely passive cavity ($\delta_m = 0$) at resonance can then be written as

$$\left. \frac{I_{\text{circ}}}{I_{\text{inc}}} \right|_{\omega=\omega_q} \approx \frac{4\delta_1}{(\delta_1 + \delta_2 + \delta_0)^2} \approx \begin{cases} 4/\delta_1 & \text{if } \delta_2 + \delta_0 \ll \delta_1 \text{ and } \delta_1 \ll 1, \\ 1/\delta_1 & \text{if } \delta_2 + \delta_0 = \delta_1. \end{cases} \quad (42)$$

The power increase of the signals inside the cavity at resonance is thus of order $4\delta_1/\delta_c^2 \approx 1/\delta_c$, where again $\delta_c \equiv \delta_1 + \delta_2 + \delta_0$. For maximum enhancement, the only loss mechanism in the cavity should be the external mirror transmission or coupling δ_1 through which the external signal is injected.

Similarly the peak signal transmission through a passive low-loss interferometer or cavity at resonance can be written in the form

$$\left. \frac{I_{\text{trans}}}{I_{\text{inc}}} \right|_{\omega=\omega_q} \approx \frac{4\delta_1\delta_2}{(\delta_1 + \delta_2 + \delta_0)^2} = \frac{4\delta_1\delta_2}{\delta_c^2}. \quad (43)$$

A little examination shows that this gives $I_{\text{trans}}/I_{\text{inc}} \approx 1$ if $\delta_1 \approx \delta_2$ and $\delta_0 \ll \delta_1, \delta_2$. The peak transmission through a Fabry-Perot etalon can thus approach 100%, provided that (a) the end-mirror reflectivities are closely enough matched, and (b) the internal loss δ_0 is small compared to the end-mirror couplings. The actual mirror-transmission values δ_1 and δ_2 are not important for high peak transmission (though of course they have a critical effect on the bandwidth of the transmission peak).

Reflected Waves For Low-Loss Cavities

The somewhat more complex behavior of the reflected waves for a passive cavity or interferometer can be emphasized for the low-loss situation, where all the δ 's are $\ll 1$, by writing the on-resonance voltage reflectivity in the form

$$\left. \frac{\tilde{E}_{\text{refl}}}{\tilde{E}_{\text{inc}}} \right|_{\omega=\omega_q} \approx \frac{\delta_2 + \delta_0 - \delta_1}{\delta_2 + \delta_0 + \delta_1} \quad \text{if all } \delta \text{'s } \ll 1. \quad (44)$$

This gives the limiting values

$$\left. \frac{\tilde{E}_{\text{refl}}}{\tilde{E}_{\text{inc}}} \right|_{\omega=\omega_q} \approx \begin{cases} +1 & \text{if } \delta_2 + \delta_0 \gg \delta_1, \\ 0 & \text{if } \delta_2 + \delta_0 = \delta_1, \\ -1 & \text{if } \delta_2 + \delta_0 \ll \delta_1. \end{cases} \quad (45)$$

These three limiting cases may be described as follows.

1. If the internal cavity losses plus output mirror coupling are significantly larger than the input mirror coupling, i.e., $\delta_2 + \delta_0 \gg \delta_1$, then this represents an *undercoupled cavity*. The circulating intensity inside the cavity does not build up to a large value, and the net reflectivity for the external signal is essentially just the normal reflectivity $r_1 \approx +1$ due to the input mirror alone.

2. If the input coupling is exactly equal to all the other cavity losses, i.e., if $\delta_1 = \delta_2 + \delta_0$, then this is the *impedance-matched situation*, in which the

normal reflection component of $+r_1$ from the mirror itself is just matched by a net component of $-r_1$ from the circulating energy inside the cavity. The input reflectivity is zero, and all the power delivered by the external source onto mirror M_1 goes into either the internal cavity losses or the transmitted output through mirror M_2 .

3. Finally, in the *overcoupled situation*, all the other losses and coupling are small compared to the coupling at mirror M_1 , i.e., $\delta_2 + \delta_0 \ll \delta_1$. The on-resonance circulating intensity builds up to its largest possible value ($\hat{E}_{\text{circ}}/\hat{E}_{\text{inc}} \approx 4j/\delta_1$); and the out-coupled portion of this circulating intensity completely reverses the $r_1 \approx +1$ term to give a total reflectivity of ≈ -1 instead.

Obviously, all these reflected and transmitted cavity field expressions can be generalized to active laser cavities if we use $\delta_c - \delta_m$ rather than simply δ_c in the denominator; but we leave the examination of these formulas as an exercise for the reader.

11.5 OPTICAL-CAVITY MODE FREQUENCIES

Since the resonance frequencies of optical cavities and interferometers are of particular interest, let us also examine in somewhat more detail the frequency properties of passive optical resonators, including the axial-mode spacing, the resonance bandwidths, and the frequency tuning or scanning possibilities in optical resonators.

Axial-Mode Spacing

The axial modes in a passive optical resonator (without laser gain) occur, as we have already seen, at those frequencies ω which satisfy the round-trip phase condition $\phi(\omega) \equiv \omega p/c = q \times 2\pi$ in a ring cavity of perimeter p , or $\phi(\omega) \equiv 2\omega L/c = q \times 2\pi$ in a standing-wave cavity of length L , with q being a (large) integer. (We have left out any atomic pulling effects at this point, but will include them in the next section.)

The resonant frequencies of the optical cavity are thus given by

$$\omega = \omega_q = q \times 2\pi \times \frac{c}{p} = q \times 2\pi \times \frac{c}{2L}, \quad q = \text{integer.} \quad (46)$$

These axial modes form an equally spaced comb of resonant frequencies labeled by index q , as in Figure 11.19, with each mode separated by the *axial-mode spacing* or *axial-mode interval*

$$\Delta\omega_{ax} \equiv \omega_{q+1} - \omega_q = 2\pi \times \frac{c}{p} = 2\pi \times \frac{c}{2L}. \quad (47)$$

The frequency spacing between the axial modes of a standing-wave cavity, expressed in Hz or cycles/second, is thus $\Delta f_{ax} \equiv \Delta\omega_{ax}/2\pi = c/p$ or $c/2L$. (Since most cavities in the earlier days of lasers were standing-wave cavities, many laser workers routinely speak of the “ $c/2L$ mode spacing” in a laser cavity.) These quantities must be written as c_0/np or $c_0/2nL$ if it is necessary to take explicitly into account the index of refraction of any dielectric material inside the cavity.

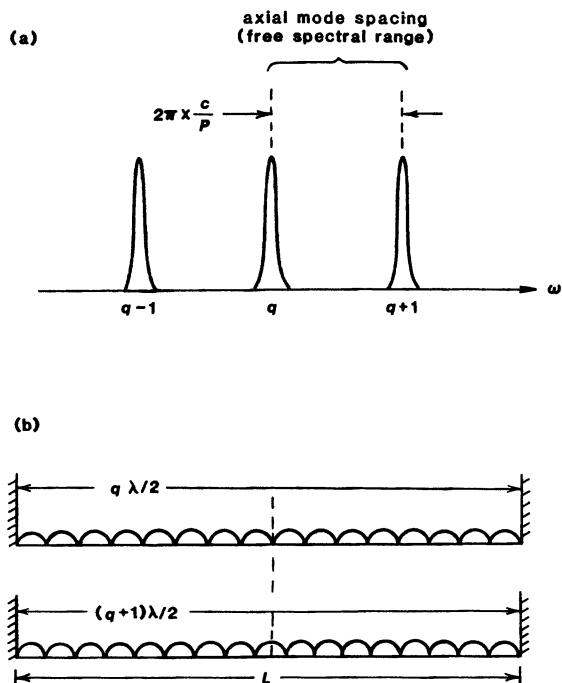


FIGURE 11.19

(a) Axial-mode resonances in an interferometer or laser cavity, and (b) the corresponding electric field distributions along the axis of the cavity.

For typical cavities in laser oscillators, this axial mode spacing will have values in the range

$$\Delta f_{\text{ax}} = \frac{c}{2L} \approx \begin{cases} 150 \text{ MHz} & \text{if } L = 1 \text{ m,} \\ 500 \text{ MHz} & \text{if } L = 30 \text{ cm,} \\ 2,000 \text{ MHz} & \text{if } L = 5 \text{ cm and } n = 1.5. \end{cases} \quad (48)$$

The axial-mode intervals for laser cavities are thus typically a hundred MHz or less for a one- or two-meter-long argon-ion or CO₂ laser cavity; rising to 500 MHz for a shorter, 30-cm-long He-Ne or Nd:YAG laser; and increasing to several GHz for a very short laser a few cm long. An example of the latter category might be a very simple solid-state laser with the mirror coatings evaporated directly on the ends of the rod.

Note also that semiconductor injection lasers (and also certain very short dye-laser cavities) can have cavity lengths L of only a few tens to a few hundreds of microns. These axial modes become so widely spaced that it may make more sense to specify their axial-mode spacing as a wavelength spacing in Å than as a frequency spacing in MHz. A typical GaAs semiconductor diode laser with length $L = 100 \mu\text{m}$ and index of refraction $n = 3.6$ has an axial-mode spacing of $\Delta f_{\text{ax}} \approx 4.2 \times 10^{11} \text{ Hz}$, corresponding to a wavelength interval $\Delta\lambda \approx 10 \text{ \AA}$ at a center wavelength of $\lambda \approx 8600 \text{ \AA}$. Figure 11.20 shows, as a similar example, the amplified spontaneous emission spectrum from a thin film of optically pumped organic dye

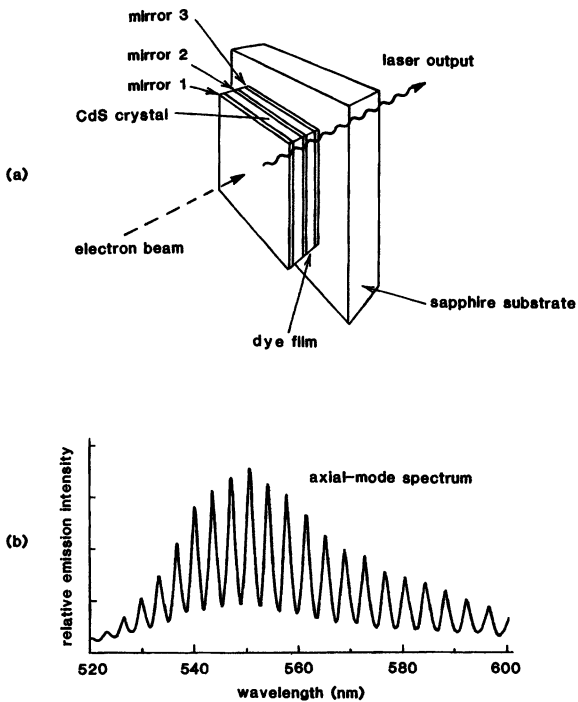


FIGURE 11.20

(a) A "Dagwood sandwich" laser, in which an electron beam pumps a thin CdS semiconductor laser, which in turn pumps a very thin film of dye laser material. (b) Amplified spontaneous emission spectrum from the dye laser segment below oscillation threshold, showing the very widely spaced axial mode resonances. (Adapted from J. R. Onstatt, *Appl. Phys. Lett.* **31**, 818-820, December 15, 1977.)

medium filling the space between two very closely spaced high-reflectivity mirrors (see Problems).

Interferometers and Free Spectral Range

In the jargon of optical interferometry, the c/p or $c/2L$ frequency spacing is commonly called the *free spectral range*, since it represents the frequency interval between transmission peaks of a resonant interferometer. Fabry-Perot etalons, which are often used in laser experiments as resonant mirrors, filters, or bandwidth narrowing elements, typically have lengths ranging from $L = 1$ cm down to $100 \mu\text{m}$, and are often made of materials like fused quartz, with an index of refraction $n \approx 1.46$, or sapphire, with $n \approx 1.76$. Their axial-mode spacings or

free spectral ranges therefore typically have values more like

$$\Delta f_{\text{ax}} = \frac{c_0}{2nL} \approx \begin{cases} 0.33 \text{ cm}^{-1} \approx 10 \text{ GHz} & \text{if } L = 1 \text{ cm,} \\ 3.3 \text{ cm}^{-1} \approx 100 \text{ GHz} & \text{if } L = 1 \text{ mm,} \\ 33 \text{ cm}^{-1} \approx 10^{12} \text{ Hz} & \text{if } L = 100 \text{ } \mu\text{m.} \end{cases} \quad (49)$$

assuming $n = 1.5$ in each case. When mode spacings become this large, it is more convenient to express them in wavenumber units, or

$$\Delta\nu_{\text{ax}} \equiv \Delta \left(\frac{1}{\lambda_0} \right)_{\text{ax}} = \frac{c_0^2}{np} \quad \text{or} \quad \frac{c_0^2}{2nL}. \quad (50)$$

A convenient rule of thumb to remember is that 1 wavenumber or 1 cm^{-1} equals 30 GHz.

Axial-Mode Number

The axial mode index q in an optical cavity or interferometer is given by

$$q = \frac{\omega_q}{\Delta\omega_{\text{ax}}} = \frac{p}{\lambda_q} = \frac{L}{\lambda_q/2}. \quad (51)$$

Since the perimeter p of an optical cavity is typically much longer than the optical wavelength λ , the value of q is typically a very large integer, on the order of 10^6 to 10^7 for typical laser cavity lengths. In a ring cavity the index q represents simply the number of optical wavelengths or optical cycles around the cavity perimeter, and in a standing-wave cavity it represents the number of half-optical-wavelengths along the cavity axis as illustrated in Figure 11.19(b). The values of the mode integer q in very short cavities or thin etalons become more like 10^3 to 10^5 .

Going from mode q to mode $q+1$ thus corresponds to increasing the optical frequency or decreasing the optical wavelength λ just enough to squeeze one more half-wavelength into the standing-wave cavity length, as shown in Figure 11.19(b). Note that the standing-wave patterns of two adjacent axial modes in a linear cavity are spatially in phase at the ends of the cavity, but exactly out of phase at the center of the cavity. The spatial offset of the fields can have important implications for axial-mode competition in various kinds of lasers.

Bandwidth, Resolving Power, and Finesse

Let us next look at the resonance bandwidths of optical cavities or interferometers. The dominant frequency dependence for both the circulating and the transmitted signals in a resonant cavity is obviously contained in the resonance denominator $1 - \tilde{g}_{\text{rt}}(\omega) \equiv 1 - r_1 r_2 (r_3 \dots) e^{-\alpha_0 p - j\omega p/c}$. The magnitudes of $\tilde{E}_{\text{circ}}/\tilde{E}_{\text{inc}}$ and $\tilde{E}_{\text{trans}}/\tilde{E}_{\text{inc}}$ will be decreased by $\sqrt{2}$, or the corresponding intensities reduced to half their maximum values, at those frequencies for which the quantity $|1 - \tilde{g}_{\text{rt}}(\omega)|^2$ doubles compared to its value at a resonance peak. With

a little algebra, this gives a FWHM bandwidth for the resonance peaks of

$$\begin{aligned}\Delta\omega_{\text{cav}} &= \frac{4c}{p} \sin^{-1} \left[\frac{1 - g_{\text{rt}}}{2\sqrt{g_{\text{rt}}}} \right] \\ &\approx \frac{2\pi c}{p} \times \left[\frac{1 - g_{\text{rt}}}{\pi\sqrt{g_{\text{rt}}}} \right] = \left[\frac{1 - g_{\text{rt}}}{\pi\sqrt{g_{\text{rt}}}} \right] \times \Delta\omega_{\text{ax}},\end{aligned}\quad (52)$$

where the assumption in the second line is that the magnitude of the round-trip gain, $g_{\text{rt}} \equiv |\tilde{g}_{\text{rt}}(\omega)|$, is not too much less than unity. The resonance bandwidth in general is obviously only a fraction of the axial-mode spacing or free spectral range, and becomes narrower the closer the round-trip gain \tilde{g}_{rt} comes to unity.

In classical optics the power transmission through an etalon or interferometer is often written in the form

$$\left| \frac{\tilde{E}_{\text{trans}}(\omega)}{\tilde{E}_{\text{inc}}(\omega)} \right|^2 = \frac{T_{\text{max}}}{1 + (2\mathcal{F}/\pi)^2 \sin^2(\pi\omega/\Delta\omega_{\text{ax}})}, \quad (53)$$

where T_{max} is the peak transmission through the etalon; $\Delta\omega_{\text{ax}} \equiv 2\pi c/p$ is the free spectral range or axial-mode interval between resonances; and \mathcal{F} is the so-called *finesse* of the interferometer. By comparing this with Equation 11.27 for $\tilde{E}_{\text{trans}}/\tilde{E}_{\text{inc}}$, we can see that the finesse is in fact just the ratio of the free spectral range to the cavity bandwidth, as given by

$$\text{finesse, } \mathcal{F} \equiv \frac{\pi\sqrt{g_{\text{rt}}}}{1 - g_{\text{rt}}} \approx \frac{\Delta\omega_{\text{ax}}}{\Delta\omega_{\text{cav}}}. \quad (54)$$

The finesse thus gives the *resolving power* of the etalon used as a transmission filter. This resolving power obviously becomes largest in the limit of mirror reflectivities approaching unity ($r_1, r_2 \rightarrow 1$) and very small internal losses ($\alpha_0 p \rightarrow 0$). As a practical matter, a finesse of $\mathcal{F} \approx 100$ for a passive interferometer or optical cavity in the visible is considered extremely good; and a finesse this large clearly requires $1 - g_{\text{rt}} \leq 0.03$, or less than 3% round-trip voltage loss.

If we use the delta factors defined in the preceding section, and include gain as well as cavity losses, the finesse can be written as

$$\mathcal{F} \equiv \frac{\pi\sqrt{g_{\text{rt}}}}{1 - g_{\text{rt}}} \approx \frac{2\pi}{\delta_c - \delta_m}, \quad (55)$$

where $\delta_c \equiv \delta_1 + \delta_2 + \delta_0$ is the total fractional power loss per one round trip in the cavity due to *all* the cavity-loss mechanisms—mirror reflectivities plus internal losses. The laser gain, if any is present, then appears as a kind of “negative loss” term. The resonance bandwidth for the circulating signals then becomes

$$\Delta\omega_{\text{cav}} \approx \frac{\Delta\omega_{\text{ax}}}{\mathcal{F}} = \frac{\delta_c - \delta_m}{2\pi} \times \Delta\omega_{\text{ax}}. \quad (56)$$

Obviously by adding laser gain δ_m to a passive cavity with total losses δ_c we can make the finesse \mathcal{F} approach infinity, and the resonance bandwidth approach zero.

Axial Modes in Dispersive Optical Cavities

The resonance frequency formulas given in Equation 11.46 above become slightly more complicated for *dispersive optical cavities*—cavities in which the velocity of light c or the index of refraction n are themselves functions of frequency. The round-trip phase-shift condition for the q -th axial mode in this case (again with atomic pulling or $\Delta\beta_n$ effects neglected) becomes

$$\frac{n(\omega)\omega p}{c_0} \equiv \frac{2n(\omega)\omega L}{c_0} = q \times 2\pi, \quad (57)$$

where c_0 is the velocity of light in free space and $n(\omega)$ the frequency-dependent refractive index.

Since the fractional spacing between axial modes is normally very small, and the index variation with frequency is also small, we can almost always expand the index of refraction about its value at some central mode ω_q in the form $n(\omega_{q+1}) \approx n(\omega_q) + n'(\omega_q) \times \Delta\omega_{\text{ax}}$, where $n' \equiv dn(\omega)/d\omega$. The axial-mode spacing is then given, to first order of approximation in $n(\omega)$, by

$$\Delta\omega_{\text{ax}} \approx \frac{2\pi c_0}{(n + n'\omega)p} = 2\pi \times \frac{1}{1 + (\omega/n)(dn/d\omega)} \times \frac{c}{p}, \quad (58)$$

where n and $n' \equiv dn/d\omega$ are midband values.

The correction term $(\omega/n)(dn/d\omega)$ for transparent dielectrics is usually positive, so that the effective axial-mode spacing is slightly reduced by this term. The resulting correction factor can become as large as a 10-percent reduction in axial-mode spacing over the $2\pi c/p$ value for the special case of GaAs injection lasers, in which the GaAs crystal fills the entire cavity and has an unusually large dispersion at the lasing wavelength. For most other lasers, even solid dielectric etalons, this correction is very small and is usually neglected.

Optical Cavity Tuning

Very small changes in the length of an optical cavity can be used to tune the resonant frequencies of the cavity by sizable amounts. From the resonant-frequency expressions given earlier, we can see that changing the cavity perimeter by a small amount δp at fixed q tunes each of the axial-mode resonant frequencies by an amount

$$\frac{\delta\omega_q}{\omega_q} \approx -\frac{\delta p}{p} \approx -\frac{\delta L}{L}, \quad (59)$$

which can be rewritten as

$$\delta\omega_q \approx -\frac{\delta p}{\lambda} \times \Delta\omega_{\text{ax}} \approx -\frac{\delta L}{\lambda/2} \times \Delta\omega_{\text{ax}}. \quad (60)$$

In other words, changing the ring-cavity perimeter by one optical wavelength, or the standing-wave cavity length by one half-wavelength, shifts each of the axial modes over by an amount just equal to the spacing between axial modes. A round-trip length change of λ causes mode q to be tuned over to the frequency previously occupied by mode $q \pm 1$, depending on whether the cavity is shortened or lengthened.

Cavity Tuning Methods

Interferometer cavities and laser oscillators are commonly tuned (or stabilized) in absolute frequency by a combination of temperature tuning (to be described below), plus the use of a piezoelectric mounting on one cavity mirror to move the mirror back and forth by a few optical wavelengths, thus scanning the absolute frequency of each axial mode by a few axial-mode intervals.

With typical piezoelectric “stacks,” a few hundred volts applied to the piezoelectric element is usually sufficient to tune each resonance through one axial-mode interval. (Note that moving one of the mirrors in a ring cavity by a distance Δz actually increases the ring perimeter by an amount $\approx 2\Delta z$, depending on how the ring is laid out; so a mirror motion of Δz accomplishes approximately the same frequency tuning in either the ring or the standing-wave cavity.) The absolute amount of frequency tuning for an increase of one wavelength in the cavity perimeter, namely, $\Delta\omega_{\text{ax}}$, is itself inversely proportional to the cavity length; so the absolute amount of frequency tuning can become very large for very short interferometer cavities.

Magnetic drivers—in the simplest case, converted loudspeaker coils—can also be used to obtain larger mirror motions, for example, for long-wavelength infrared lasers. To first order the spacing $\Delta\omega_{\text{ax}}$ between adjacent axial modes is hardly changed by adding a few half-wavelengths $\lambda/2$ to the cavity length L or perimeter p . Hence, to first order, changing the cavity length by a few wavelengths simply tunes the entire comb of axial modes back and forth underneath the atomic line, without noticeably changing the axial-mode spacing.

Temperature Tuning and Thermal Drifts

Note also that in a typical optical cavity or laser structure a temperature change δT of a few degrees or less will produce enough thermal expansion of the cavity to give a δp of one half-wavelength or more. Optical cavities thus generally have a large thermal tuning or thermal drift rate, unless carefully stabilized in temperature.

Highly stable laser cavities are often made with the mirror spacing controlled by a rod of Invar, a steel alloy having small or even zero expansion coefficient at room temperature. Rods of quartz, carbon fiber, or zero-expansion ceramics can also be used for the same purpose. Unwanted tuning and frequency jitter of lasers caused by mechanical vibrations and acoustic noise is another very serious issue in any laser where high-frequency stability is required, and careful shock mounting and acoustic isolation may be required for highest stability.

Scanning Optical Interferometers

Tunable interferometer cavities are often used as passive tunable filters, or as so-called scanning interferometers, for measuring laser output spectra or other optical signals.

To measure a laser signal in this fashion, we can send the signal through a passive optical cavity or scanning interferometer as illustrated in Figure 11.21, and then scan the axial modes of the interferometer back and forth in frequency across the laser spectrum by changing the passive cavity length (typically at an audio frequency rate or slower). A strong optical signal is transmitted through the passive cavity each time one of its axial-mode resonances coincides with an

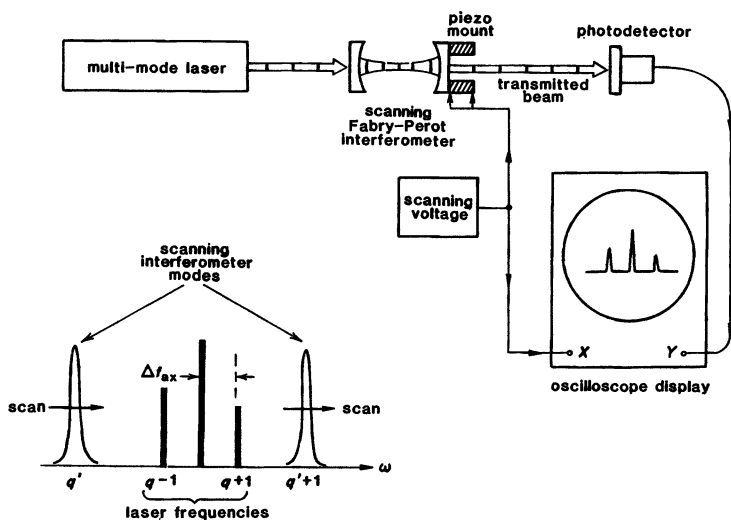


FIGURE 11.21

A scanning Fabry-Perot interferometer used as a tunable filter for observing the frequency output of a multifrequency laser. The laser oscillator has axial modes $q - 1$, q , and $q + 1$, and the interferometer cavity has axial modes q' and $q' + 1$.

input laser signal. This transmitted signal is then detected and displayed on an oscilloscope as illustrated in Figure 11.21.

Note that if the scanning interferometer is scanned by more than one of its free spectral ranges, another transmission resonance will be observed each time another axial mode of the scanning interferometer cavity scans across any one of the incident laser frequencies. Hence to prevent confusion or ambiguity in the results, the axial-mode spacing or free spectral range of the interferometer should be wider than the full oscillation range of the laser signal being measured, as illustrated in Figure 11.21. This requires that the interferometer cavity be shorter than the cavity of the laser generating the signals—and often considerably shorter. The shorter the scanning cavity, however, the wider its resonance linewidth and the poorer its frequency resolution for a given amount of loss. Scanning interferometer design is thus a tradeoff between free spectral range and resolving power, with a high premium given to minimizing the losses in the scanning cavity.

Confocal Fabry-Perot Interferometers

With a conventional Fabry-Perot interferometer using planar or only slightly curved mirrors, the incident laser beam must be very precisely aligned with the axis of the interferometer in order not to excite many higher-order transverse modes of the interferometer cavity, and thus obtain very confused resonance signals. For interferometer cavities which are exactly confocal (meaning that the center of curvature of each mirror lies exactly on the other mirror) this difficulty does not occur, for reasons we will explain in a later chapter. Hence confocal op-

tical cavities, because of their relative freedom from alignment restrictions, are widely used for scanning interferometers, including several commercially available instruments of this type.

REFERENCES

Very strong second-order dispersion effects on the mode spacing in semiconductor injection lasers are demonstrated, for example, by L. F. Johnson, "Mode locking a diode laser," *J. Appl. Phys.* **51**, 6413-6414 (December 1980); or by J. P. van der Ziel and R. A. Logan, "Dispersion of the group velocity refractive index in GaAs double heterostructure lasers," *IEEE J. Quantum Electron.* **QE-19**, 164-169 (February 1983).

Problems for 11.5

1. *Axial-mode spectrum for an optical cavity with an internal dielectric section.* Evaluate the axial-mode spectrum of a standing-wave cavity of total length $L = L_1 + L_2$ assuming that length L_1 of the cavity is filled with a medium having index of refraction n_1 and length L_2 is filled with medium of index n_2 . Neglect any dispersion effects in the two dielectrics, and also any reflections at the interface between the two dielectrics.
 2. *Axial-mode spectrum including dispersion.* Repeat the previous problem assuming that dispersion effects in both dielectrics are in fact significant.
 3. *Resonance properties of an equilateral triangular dielectric prism.* Suppose a prism in the shape of an equilateral triangle is used as a three-mirror reflective ring-type solid etalon, in which an optical beam enters at the midpoint of one face, bounces around inside the prism, reflecting at the midpoint of each of the three faces with an internal angle of incidence 30° of the normal to surface, and emerges at the same point it entered. What will be the finesse of this interferometer (a) if it is made of quartz ($n = 1.46$) and depends only on the air-dielectric reflection at each of the three faces; and (b) if the two faces other than the input-output face are silvered to give $\approx 100\%$ reflectivity?
 4. *Mirror spacing in an optically pumped thin dye laser.* Figure 11.20 shows the fluorescence emission spectrum from a thin "sandwich" of optically pumped organic dye molecules filling the space between two high-reflectivity mirrors, as observed normal to the mirror surfaces. When optically pumped by another laser beam, the dye molecules become inverted and regeneratively amplify their own spontaneous emission. What is the spacing L between the mirrors in this experiment? Assume the dye solution has index of refraction $n \approx 1.5$.
-

11.6 REGENERATIVE LASER AMPLIFICATION

In this section we will finally add laser gain as well as mirrors to a laser cavity, and thus finally achieve true regenerative feedback and regenerative amplification in a laser amplifier. Doing this will bring us closer to the threshold of laser oscillation—a threshold we will finally cross in the following chapter.

Regenerative Gain Formula

Suppose that we add a laser gain medium with gain coefficient $\alpha_m(\omega)p_m$ and added phase shift $-j\Delta\beta_m(\omega)p_m$ to the interferometer model we have already analyzed. Then the formulas we have already developed will all remain valid, except that the round-trip gain $\tilde{g}_{rt}(\omega)$ inside the laser cavity will be modified to

$$\tilde{g}_{rt}(\omega) = r_1 r_2 (r_3 \dots) \times \exp[\alpha_m p_m - \alpha_0 p - j\omega p/c - j\Delta\beta_m(\omega)p_m]. \quad (61)$$

The length p_m here is the total length of the active laser medium in a ring laser cavity, or twice the length of the laser medium (i.e., $p_m = 2L_m$) in a standing-wave laser cavity.

The circulating power in the laser cavity will then still be given by Equation 11.20, except that $\tilde{g}_{rt}(\omega)$ will now be given by Equation 11.61. The overall regenerative gain through the cavity, or the transmission from input to output, will thus be given by

$$\begin{aligned} \frac{\tilde{E}_{\text{trans}}}{\tilde{E}_{\text{inc}}} &= -\frac{t_1 t_2 \exp[(\alpha_m p_m - \alpha_0 p - j\omega p/c - j\Delta\beta_m p_m)/2]}{1 - r_1 r_2 \exp[\alpha_m p_m - \alpha_0 p - j\omega p/c - j\Delta\beta_m p_m]} \\ &= -\frac{t_1 t_2}{\sqrt{r_1 r_2}} \times \frac{\sqrt{\tilde{g}_{rt}(\omega)}}{1 - \tilde{g}_{rt}(\omega)}. \end{aligned} \quad (62)$$

This is the formula for *transmission gain* through the regenerative amplifier. We could write another, slightly more complex formula for the *reflection gain* $\tilde{E}_{\text{refl}}/\tilde{E}_{\text{inc}}$ coming back out the input end of the amplifier (and this reflection gain would in fact be a more useful way to employ a regenerative ring-laser amplifier); but we leave this task as an exercise for the reader (see Problems).

Gain Properties of Regenerative Amplifiers

We are now going to demonstrate that as we turn up the magnitude of the round-trip gain inside the interferometer or laser cavity toward a limiting value of unity, the peak value of the transmission (and also the reflection) gain through the laser cavity will shoot upward toward infinity, as a result of regeneration in the laser cavity.

Figure 11.22 plots the log of the transmitted power gain $|\tilde{E}_{\text{trans}}/\tilde{E}_{\text{inc}}|^2$ versus frequency, as given by Equation 11.62, assuming a fixed gain medium with the rather largish midband gain value $\exp[\alpha_m p_m - \alpha_0 p_0] = 2$, and with increasing end-mirror reflectivities ranging from $R_1 = R_2 = 0$ (i.e., no mirrors) to $R_1 = R_2 \approx 35\%$.

Two aspects of the amplification behavior in this system are immediately apparent. First, when mirrors with even rather small reflectivity are added, the overall power gain $|\tilde{g}(\omega)|^2$ at certain frequencies within the atomic-gain curve can become larger, and eventually very much larger, than the single-pass gain of the laser medium itself; and second, these high-gain frequencies occur only in very narrow bands located at the regularly spaced *axial-mode resonances* of the cavity.

The round-trip cavity length p for these particular calculations has been chosen so that one of the axial-mode resonances lies exactly at the line-center frequency ω_a , and several adjoining axial modes are nearby within the atomic linewidth. The regenerative amplification of these off-line-center axial modes

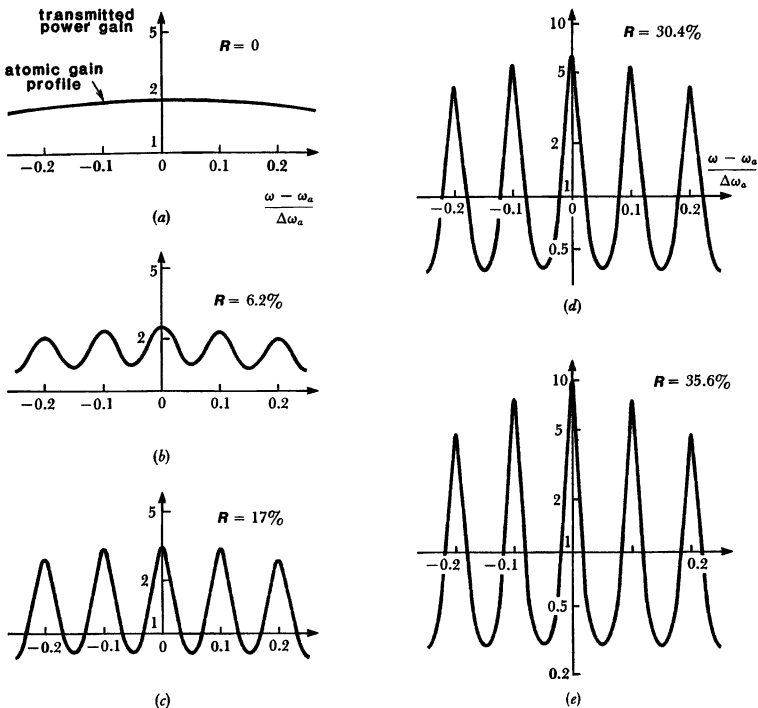


FIGURE 11.22

Regenerative power gain (on log scales) through a regenerative laser cavity versus frequency detuning from atomic line center. Plot (a) shows the single-pass gain through the laser medium alone, without mirrors. Plots (b) through (d) show the overall transmission gain for increasing values of end-mirror reflectivity.

is clearly reduced relative to the centermost mode, especially at higher mirror reflectivities, because of the decreasing atomic gain away from line center. We have used a fairly high atomic-gain value in order to make all the regenerative gain peaks broader and thus easier to plot; and we have used log scales in order to exhibit the large increases that the overall gain can acquire.

Figure 11.23 plots a similar set of transmission gain curves versus frequency, but this time on a linear scale and assuming fixed mirror reflectivities of $R_1 = R_2 = 40\%$, with increasing amounts of internal laser gain. Figure 11.23(a) shows the overall power gain or intensity transmission through the cavity with no internal laser gain and 4% internal round-trip power losses, demonstrating the typical resonance behavior of a passive interferometer cavity or etalon. The peak overall transmission is slightly less than unity, and the transmission peaks are spaced in frequency by the usual free spectral range of the interferometer. Adding small amounts of internal gain then rapidly converts these resonance peaks into overall regenerative gain peaks, with peak gain substantially larger than unity, as shown in Figure 11.23(b).

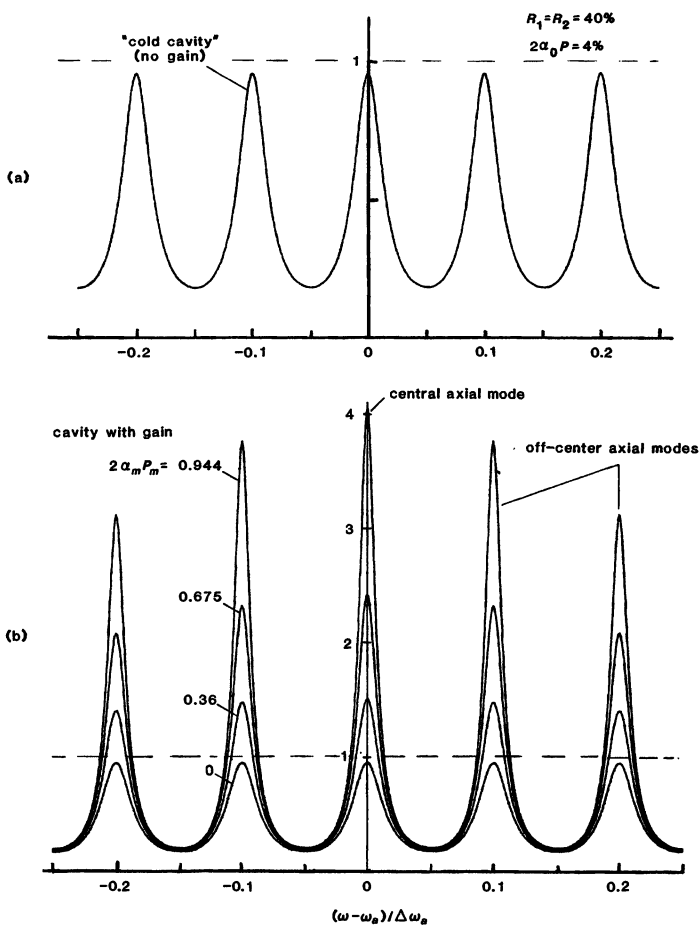


FIGURE 11.23

Plots of regenerative power gain similar to Figure 11.22, but on a linear scale and with fixed mirror reflectivities of $R_1 = R_2 = 40\%$. (a) Transmission through the "cold cavity" or passive interferometer without laser gain. (b) Transmission through the amplifier cavity with increasing amounts of intracavity laser gain.

Regenerative Feedback Model

To readers familiar with regenerative feedback systems, the reasons for the behavior shown in Figures 11.22 and 11.23 will seem obvious. The laser cavity can be modeled by a typical control-system or feedback-system block diagram, as in

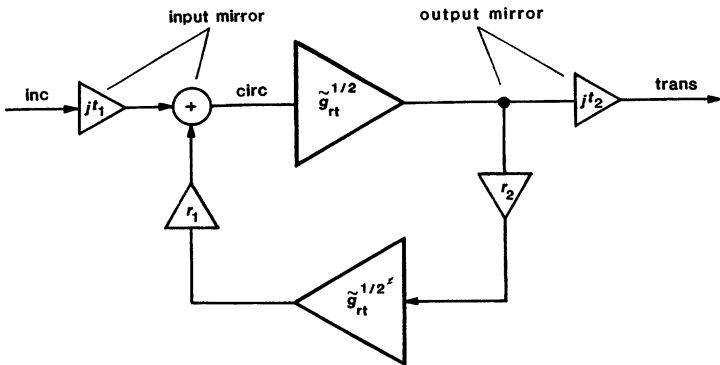


FIGURE 11.24
Feedback diagram describing a regenerative laser cavity.

Figure 11.24. Near the axial-mode resonances the system has a round-trip phase shift which passes through an integer multiple of 2π , thus producing positive or regenerative feedback. This condition reoccurs at each axial mode; and because the round-trip path length in a laser is very long in units of wavelengths, these axial modes are very closely spaced in frequency.

As the magnitude of the round-trip gain in this feedback loop approaches unity, the overall gain from input to output of the feedback system approaches infinity; and the system in fact becomes unstable and breaks into self-oscillation when the round-trip gain just becomes unity.

This same kind of regenerative feedback can always be used to obtain large overall gain in any kind of amplifying system, using a single-pass amplifier with comparatively small gain, but applying positive feedback to obtain a very large overall gain. This feedback mechanism is effective, however, only over a very limited bandwidth, where the feedback signal has the correct phase. For example, at frequencies halfway between the axial modes, the round-trip phase shift changes so that the feedback produces instead negative feedback or degeneration. This in turn actually reduces the overall gain below what would otherwise be the net transmission through the two mirrors and the gain medium. (Note the demonstration of this in Figure 11.22.)

Physical Interpretation: The Approach to Threshold

Another physical interpretation of the large regenerative gain observed at resonance can be given as follows. Suppose as an extreme example that the input mirror to a regenerative amplifier has a large reflectivity, say, $R = 98\%$. It may then appear that 98% of an input signal is immediately reflected back from the laser input and wasted, with only 2% entering the amplifier to be amplified.

The high-reflectivity mirrors plus the internal gain inside the cavity, however, permit any energy inside the cavity to recirculate or reverberate inside the cavity many times, extracting energy from the laser medium on each bounce, so that the recirculating wave also builds up to very large amplitudes inside the cavity, relative to the incident wave amplitude outside the cavity. This build-up plus coherent reinforcement leads to a very large increase of the internal circulating energy relative to the incident energy striking the mirror from outside. On each

successive axial modes

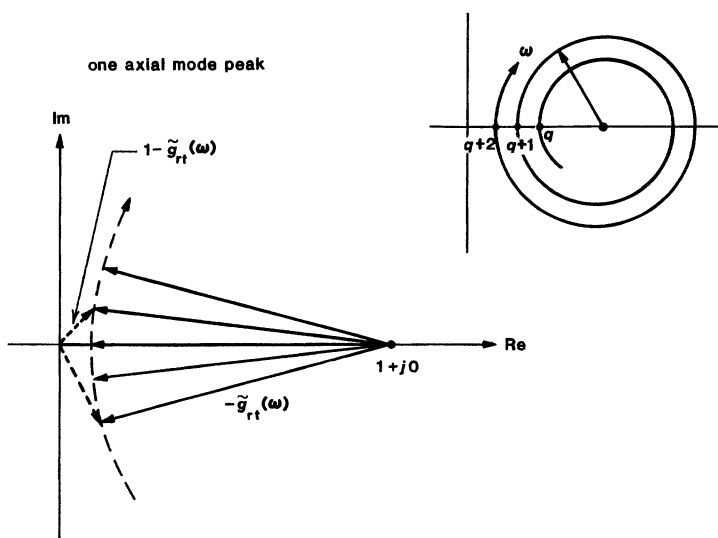


FIGURE 11.25

Geometric interpretation of axial-mode gain peaks.

end-mirror reflection, a portion of this very large circulating energy is also transmitted back out through both the input and the output mirrors, leading to the large overall transmission and reflections gains that occur at resonance.

Geometric Interpretation

Looking again at the vector or geometric interpretation given in Figure 11.11 may also be helpful in explaining the high overall gain obtained at resonance. The crucial aspect of the overall gain expression is again the feedback denominator $1 - \tilde{g}_{rt}(\omega)$. The round-trip gain $\tilde{g}_{rt}(\omega)$ has a magnitude just less than unity (for cavities below threshold), and a phase angle which rotates rapidly with frequency in the complex plane. The length of this vector may also change slowly as it rotates because of the change in laser gain as the frequency is tuned off line center.

Figure 11.25 shows again how this vector is pivoted at the point $1 + j0$ in the complex plane, and rotates rapidly about that point. The cavity transmission gain is inversely proportional to the distance from the origin to the tip of this vector. Hence each time the tip of $1 - \tilde{g}_{rt}(\omega)$ sweeps close to the origin the gain becomes very high—but over only a brief section of the rotation cycle—and another axial-mode resonance is generated.

Experimental Illustration

The existence of axial cavity modes, and especially the regenerative amplification which occurs at axial-mode peaks in a laser cavity below threshold, shows up most dramatically perhaps in semiconductor diode lasers. The widely

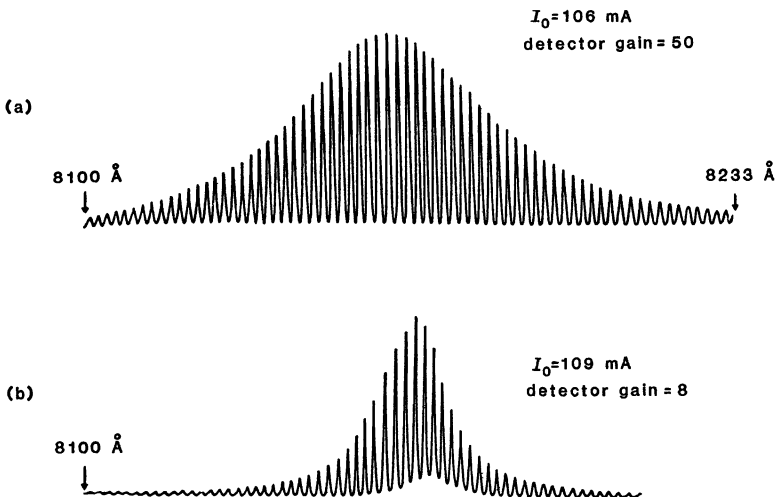


FIGURE 11.26

Regeneratively amplified spontaneous emission spectra from a GaAs semiconductor laser at two levels of regenerative gain just below oscillation threshold. In curve (b) the cavity is closer to oscillation threshold, and the central modes have become much stronger relative to the outer axial modes.

spaced axial modes in these lasers ($\Delta\omega_{ax} \approx 10\text{Å}$) are located within an even wider atomic transition (atomic linewidth greater than 100Å), and it becomes possible to observe these modes with a relatively low-resolution optical spectrometer.

Moreover, rather than making a measurement of regenerative laser gain versus frequency (which requires a tunable signal source and other complexities), we can simply measure the *amplified internal spontaneous emission* coming from within the laser diode itself, as this radiation is regeneratively amplified inside the laser cavity and transmitted through the end mirrors. Measurements of this type are also aided by the particularly strong spontaneous emission in semiconductor lasers.

A typical example of this kind of measurement is shown in Figure 11.26. Note that the curve in part (b) of this figure represents a slightly higher driving current through the laser, which produces slightly more internal gain, thus bringing the laser closer to oscillation threshold. (Note also the difference between the vertical scales of the two parts.) The regenerative increase of the centermost modes relative to the modes further out on the atomic gain curve thus becomes quite marked in part (b).

Note also that this kind of axial-mode structure will develop only in the emission traveling along the axial direction and coming out through the ends of the laser cavity. The spontaneous emission from the atoms coming out through the sides of the laser cavity will not exhibit this structure (except insofar as internal defects or spurious reflections may scatter some of the axial radiation out through the sides of the cavity).

Problems for 11.6

1. *Reflection gain of a regenerative laser amplifier.* The “reflection gain” looking into the input end of a regenerative laser amplifier may be defined as $\tilde{g}_{\text{ref}}(\omega) = \tilde{E}_{\text{ref}}/\tilde{E}_{\text{inc}}$, using the same notation as in the text. Derive a general expression for this reflection gain $\tilde{g}_{\text{ref}}(\omega)$ as a function of the mirror parameters and the round-trip gain of the laser medium, and discuss its behavior as compared to the transmission gain derived in this section.
 2. *Phase angle versus frequency for a regenerative laser cavity amplifier.* The variation of the magnitude of the overall transmission gain $|\tilde{E}_{\text{trans}}/\tilde{E}_{\text{inc}}|$ versus frequency over several axial modes has been plotted and discussed in this section. Give a similar analysis and description of how the *phase angle* of this transmission gain versus frequency varies across a similar range spanning two or three axial modes. You may ignore any small frequency pulling effects due to the $\Delta\beta_m$ term in doing this. (Hints: To understand the phase variation with frequency, consider the rotating-vector picture of regenerative feedback, and evaluate the total phase shift by evaluating the phase shifts of numerator and denominator separately and then subtracting them.)
 3. *Enhanced feedback diagram.* Extend and complete the feedback diagram of Figure 11.24 to include reflection gain from the interferometer cavity, and possible input signals that might be sent into the “output” as well as “input” ends of the interferometer cavity.
-

11.7 APPROACHING THRESHOLD: THE HIGHLY REGENERATIVE LIMIT

As the laser gain is turned up (or the cavity losses are turned down) in a regenerative laser cavity, and the laser cavity approaches oscillation threshold, we can observe that:

- the regenerative gain peaks become *very high* (especially the centermost one);
- these regenerative gain peaks also become *very narrow*; and
- each regenerative gain peak approaches (as we will now show) a *fixed gain-bandwidth product*.

This section analyzes this limiting situation when an optical cavity is highly regenerative and just below threshold.

The Approach to Threshold

Let us note once again that the quantity $1 - \tilde{g}_{\text{rt}}(\omega)$ appearing in the denominator of Equation 11.62 is one minus the round-trip voltage gain for a wave circulating around inside the laser cavity, including bouncing off the mirrors at each end. If this round-trip gain has magnitude less than unity, then the laser cavity is below threshold. This means that unless new energy is continually in-

jected into the cavity by an external injected signal, the recirculating signal energy inside the cavity will decay in amplitude on successive round trips, so that any signals in the cavity will gradually die out. The cavity can thus not oscillate so long as $|\tilde{g}_{rt}| < 1$. It can, however, function as a regenerative amplifier, with potentially very high transmission or reflection gain.

If the magnitude of the internal round-trip gain approaches and then exceeds unity, however, then any circulating signals inside the cavity will grow in amplitude on each successive round trip, eventually building up to unlimited amplitudes. Of course when the signal amplitude inside the cavity grows to a large enough value, the signal fields will begin to saturate the population inversion and reduce the atomic gain. The round-trip gain will then be driven back down toward the value of exactly unity, at which point the circulating signals inside the cavity neither grow nor decay on successive round trips. The laser can then maintain a steady-state self-sustained oscillation, without any externally injected signal. The condition for the build-up of such a steady-state self-sustained oscillation in a laser cavity (starting from an injected signal, or just from spontaneous emission noise) is thus $|\tilde{g}_{rt}| > 1$.

The line where the round-trip gain magnitude $|\tilde{g}_{rt}|$ becomes just equal to unity, as shown in Figure 11.27, thus marks a boundary line between the stable, below-threshold, finite regenerative-gain region, and the unstable, above-threshold region where no steady-state operation is possible. This boundary line thus represents both *oscillation threshold* (where oscillation can just start) and *the steady-state oscillation condition for an oscillating laser*.

The High-Gain Near-Threshold Limit

Some interesting calculations can then be made as the round-trip gain in the cavity approaches the threshold limit from below. To show this, suppose we write the round-trip gain inside a regenerative cavity in the phase-amplitude form

$$\tilde{g}_{rt}(\omega) \equiv g_{rt}(\omega)e^{-j\phi(\omega)}. \quad (63)$$

Then we can generally assume that the *round-trip gain magnitude* $g_{rt}(\omega)$ will be essentially constant across any one axial-mode peak at $\omega = \omega_q$, although the value of $g_{rt,q} \equiv g_{rt}(\omega_q)$ will change from one axial mode peak to the next, depending on where each individual peak is located within the atomic linewidth.

This is equivalent to saying that the laser gain coefficient $\alpha_m(\omega)$ within any one axial-mode peak may be approximated by its value at the center of that peak; i.e., $\alpha_m(\omega) \approx \alpha_m(\omega_q) \equiv \alpha_{mq}$ for $\omega \approx \omega_q$ for the q -th axial mode. We must, however, keep track of the slightly different gain values α_{mq} at different axial modes q , because very small differences in $\exp(2\alpha_{mq}p_m)$ between different axial modes can lead to large differences in the height of the overall gain peaks, especially as the centermost mode approaches threshold.

Near any single high-gain axial-mode peak located at $\omega = \omega_q$, we can also approximate the *round-trip phase shift* inside the cavity by

$$\phi(\omega) \approx \frac{\omega p}{c} = \frac{\omega_q p}{c} + \frac{(\omega - \omega_q)p}{c} = q \times 2\pi + \delta\phi(\omega), \quad (64)$$

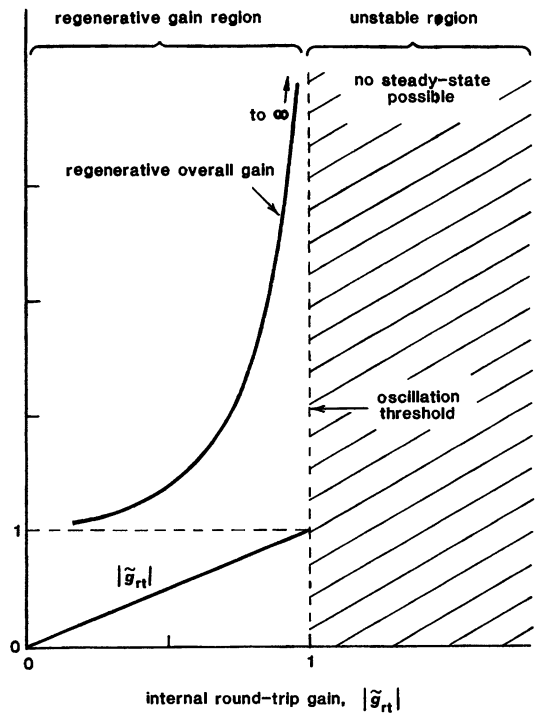


FIGURE 11.27
Regenerative gain versus internal round-trip gain, showing the approach to oscillation threshold.

where $q \times 2\pi$ is the phase shift exactly at the axial-mode peak, and the additional phase shift $\delta\phi(\omega)$ given by

$$\delta\phi(\omega) \equiv \frac{\omega - \omega_q}{c} p \approx 2\pi \times \frac{\omega - \omega_q}{\Delta\omega_{\text{ax}}} \quad (65)$$

is the small phase deviation as we tune away from resonance. In writing these expressions, we have supposed that any small atomic pulling effects due to the $\Delta\beta_m p_m$ term are incorporated into a slightly pulled value for the axial-mode frequency ω_q .

Gain and Bandwidth Near Any One Axial-Mode Peak

Suppose we consider only those frequencies within a narrow bandwidth about one such axial mode, so that $\omega \approx \omega_q$ and $|\omega - \omega_q| \ll \Delta\omega_{\text{ax}}$. We may then make the approximation that

$$e^{-j\phi(\omega)} = e^{-j\delta\phi(\omega)} \approx 1 - j\delta\phi(\omega) = 1 - j2\pi \frac{\omega - \omega_q}{\Delta\omega_{\text{ax}}} \quad (66)$$

The transmission gain given by Equation 11.62 near this one axial-mode peak (assuming for simplicity that the round-trip path length is evenly divided between the forward and reverse paths, as in a standing-wave cavity) can then be

put into the form

$$\begin{aligned} \left. \frac{\tilde{E}_{\text{trans}}}{\tilde{E}_{\text{inc}}} \right|_{\omega \approx \omega_q} &= -\frac{t_1 t_2}{\sqrt{r_1 r_2}} \frac{g_{\text{rt}}^{1/2}(\omega) e^{-j\phi(\omega)/2}}{1 - g_{\text{rt}}(\omega) e^{-j\phi(\omega)}} \\ &\approx -\frac{t_1 t_2}{\sqrt{r_1 r_2}} \frac{g_{\text{rt},q}^{1/2} e^{-j\phi(\omega)/2}}{1 - g_{\text{rt},q} + j(2\pi g_{\text{rt},q}/\Delta\omega_{\text{ax}}) \times (\omega - \omega_q)}. \end{aligned} \quad (67)$$

The overall gain profile for this one axial mode can evidently be well approximated by a *complex lorentzian resonance lineshape*, so that we can rewrite this expression in the form

$$\left. \frac{\tilde{E}_{\text{trans}}}{\tilde{E}_{\text{inc}}} \right|_{\omega \approx \omega_q} = -e^{-j\phi(\omega)/2} \frac{g_{0,q}}{1 + 2j(\omega - \omega_q)/\Delta\omega_{3dB,q}}. \quad (68)$$

The minus sign in front of this expression comes from our convention for mirror transmissions, and the $e^{-j\phi(\omega)/2}$ term is simply a phase shift term representing the net optical path length $\omega L/c$ from mirror M_1 to mirror M_2 . The significant part of this expression is the remaining portion, which is a complex lorentzian lineshape with a peak voltage gain from input to output of $g_{0,q}$ for the q -th axial-mode gain peak, and a FWHM bandwidth of $\Delta\omega_{3dB,q}$ for that same gain peak.

By comparing Equations 11.67 and 11.68, we see that in the highly regenerative limit any single axial-mode peak thus has a midband voltage gain magnitude given by

$$g_{0,q} \equiv \frac{t_1 t_2}{\sqrt{r_1 r_2}} \frac{g_{\text{rt},q}^{1/2}}{1 - g_{\text{rt},q}} \quad (69)$$

and a 3 dB amplification bandwidth given by

$$\Delta\omega_{3dB,q} \approx \frac{1 - g_{\text{rt},q}}{g_{\text{rt},q}} \times \frac{\Delta\omega_{\text{ax}}}{\pi}. \quad (70)$$

As the round-trip gain magnitude $g_{\text{rt},q}$ inside the cavity approaches unity, the corresponding regenerative transmission gain through the cavity obviously becomes very high, so that $g_{0,q} \rightarrow \infty$, and the bandwidth of that gain peak becomes very narrow, so that $\Delta\omega_{3dB,q} \rightarrow 0$.

Gain-Bandwidth Product

But more than this, as the peak gain becomes very large and the bandwidth very small, their product approaches a *fixed gain-bandwidth product* given by

$$[g_0 \Delta\omega_{3dB}]_q \approx g_{\text{rt},q}^{-1/2} \times \frac{t_1 t_2}{\sqrt{r_1 r_2}} \times \frac{\Delta\omega_{\text{ax}}}{\pi}. \quad (71)$$

But since in the high-gain limit $g_{\text{rt},q} \rightarrow 1$, we can further simplify this to

$$g_0 \Delta\omega_{3dB} \approx \frac{t_1 t_2}{\sqrt{r_1 r_2}} \times \frac{\Delta\omega_{\text{ax}}}{\pi}. \quad (72)$$

In this final result, therefore, the dependence on the atomic gain and cavity losses, and even on the axial-mode coefficient q , drops out entirely, leaving only the cavity external-coupling parameters r_1, r_2 and t_1, t_2 in the formula.

We conclude that there is a fixed *gain-bandwidth product* in the high-gain limit for each axial-mode peak. Moreover, this gain-bandwidth product is the same for all axial modes, and depends only on the *cavity coupling* parameters, i.e., on r_1, r_2, t_1 , and t_2 , and not on either the laser gain or the internal cavity losses.

Note that the peak transmission gain values $g_{0,q}$ for the different axial modes across an atomic-gain curve will have significantly different values, because of the slightly different values of α_{mq} or $g_{rt,q}$ in the resonance denominators. The centermost mode will rapidly outstrip the off-center modes as its value of roundtrip gain $g_{rt,q}$ comes closest to unity. Earlier figures have illustrated how the peak gain of the most favored mode races up to infinity, and the bandwidth heads toward zero, as the mode approaches threshold. The off-center axial modes will not come quite as close to the threshold limit, but all will have the same gain-bandwidth product.

Numerical Example

Does this kind of regenerative gain enhancement have practical applications in laser devices? The answer is generally no, first because the practical gain-bandwidth products are too small to be useful, and second because the necessary adjustments of the round-trip gain to achieve high overall gain are too delicate to be controlled in practical applications. Unless a laser medium has enough *single-pass* gain to be used without regeneration, it is probably not useful as a laser amplifier. On the other hand, the theory of regenerative laser amplification is very useful in understanding laser physics and particularly in understanding the manner in which laser oscillators approach oscillation threshold.

As a representative numerical example for gain-bandwidth product, we might consider a typical low-loss laser cavity with the parameters

$$\left. \begin{array}{l} r_1 r_2 = R = 0.97 \\ t_1 t_2 = T = 0.03 \\ L = 30 \text{ cm} \\ \Delta\omega_{ax} = 2\pi \times 500 \text{ MHz} \end{array} \right\} g_0 \Delta f_{3dB} \approx 5 \text{ MHz.} \quad (73)$$

Suppose we want to place a 30-cm-long He-Ne laser tube, which might be able to produce somewhere between 5% and 10% power gain per one-way pass, inside this cavity, and then magnify this up by regeneration to obtain a peak-transmission gain for the centermost axial mode of $g_0 = 10$ or $g_0^2 = 100 = 20$ dB. Since this cavity has about 6% power loss through the end mirrors per round trip, and perhaps a few percent more of internal losses, the He-Ne laser tube will easily be able to bring the cavity arbitrarily close to threshold, and produce the desired 20 dB of overall gain from input to output on the centermost axial mode.

The amplification bandwidth of this axial mode will then, however, turn out to be only $\Delta f_{3dB} \approx 500$ kHz! The usefulness of a bandwidth of a few hundred kHz, even though it may be at an optical carrier frequency, seems dubious. In fact, even to measure this bandpass will require a frequency stability of $\Delta f/f_0 \approx 5 \times 10^5 / 5 \times 10^{14} \approx 1 \times 10^{-9}$ between the signal source and the laser amplifier.

Regenerative optical amplifiers are thus useful as a source of insight into the physics of laser oscillation, but seem not to have practical applications.

The concept of a fixed gain-bandwidth product which we have derived here applies, of course, not only to laser amplifiers, but also to any type of regenerative amplifier in any frequency range. Given any kind of electronic or acoustic or mechanical amplification process, no matter how weak its gain, we can always employ positive feedback to increase the overall gain by any desired amount. If the feedback loop has a long time delay, however, as is inherent in a laser merely from the propagation time around the cavity, the total phase shift in the feedback loop will be large and will change rapidly with frequency. This in turn will inherently limit the bandwidth or, more precisely, the gain-bandwidth product of the regeneratively magnified amplification.

Regenerative Noise Amplification in a Laser

The fixed gain-bandwidth product for a regenerative laser amplifier operating just *below threshold* can be used to derive, at least in a heuristic fashion, one of the most famous formulas in laser theory, the so-called Schawlow-Townes formula for the spectral linewidth caused by quantum noise of a laser oscillator operating *above threshold*.

To derive this, we must first note that a regenerative laser amplifier—or indeed any other kind of coherent optical amplifier—will have a certain finite amount of noise because of spontaneous emission from the upper-laser-level atoms inside the amplifier. For a laser amplifier of any kind, regenerative or single pass, this finite amount can be represented by an equivalent input noise power, which we view as coming into the input of the amplifier, with an input noise power spectral density given by

$$\frac{dP_n}{d\omega} = \frac{N_2}{N_2 - N_1} \times \hbar\omega. \quad (74)$$

In other words, the equivalent input noise power to the amplifier is equivalent to one input photon per second per cycle of bandwidth, multiplied by an excess noise factor $N_2/(N_2 - N_1)$. This excess noise factor is unity if the lower laser level is empty, so that $N_2 - N_1 = N_2$. It becomes larger than unity if N_1 is finite, because then more upper-level atoms and hence more spontaneous emission will be present for the same net inversion and gain.

Consider now a regenerative laser amplifier pumped right up to the oscillation threshold point, with no coherent input signal applied. Even with no input signal present, this laser will still amplify the equivalent input noise within its 3 dB amplification bandwidth $\Delta\omega_{3dB}$. (Really, of course, it is regeneratively amplifying its own spontaneous emission generated *within* the laser cavity.) The effective rectangular bandwidth of a lorentzian amplifier with FWHM bandwidth $\Delta\omega_{3dB}$ is in fact $(\pi/2) \times \Delta\omega_{3dB}$. Hence the total amplified noise output power from the amplifier very close to threshold will be given by

$$\begin{aligned} P_{out} &= G_0 \times \frac{\pi\Delta\omega_{3dB}}{2} \times \frac{dP_n}{d\omega} \\ &= \frac{N_2}{N_2 - N_1} \times \frac{\pi G_0 \Delta\omega_{3dB} \hbar\omega}{2}, \end{aligned} \quad (75)$$

where $G_0 \equiv g_0^2$ is the midband overall transmission gain through the laser cavity.

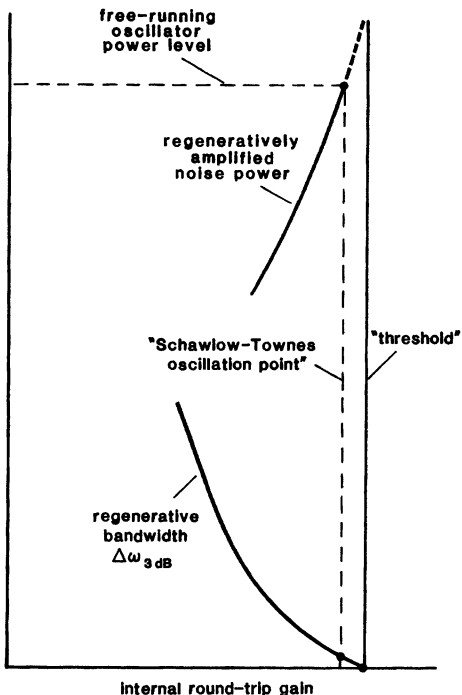


FIGURE 11.28
Schawlow-Townes model of a laser oscillator as a very high-gain, very narrowband regenerative noise amplifier operating just below the threshold point.

As we bring the cavity closer and closer to threshold, the overall gain G_0 will become very large; the bandwidth $\Delta\omega_{3dB}$ will become very narrow; and the noise output from the laser will become an increasingly powerful but increasingly narrowband amplified noise signal. Suppose we bring the cavity extremely close to oscillation threshold, as shown in Figure 11.28. One partially correct, but incomplete, way of describing what happens as the laser comes very close to the threshold point is the following: When the amplified noise output power comes close to the available power that can be extracted from the laser gain medium, then the laser gain medium begins to saturate. As a result of this gain saturation, the overall power gain G_0 will no longer increase beyond the point where the (very) narrowband amplified noise output equals the potential output oscillation power from the laser.

The Schawlow-Townes Formula

From this (partially correct) viewpoint, the laser oscillator is simply a very high-gain, very narrow bandwidth, amplified spontaneous emission noise source operating just the slightest bit below the exact threshold point, with an overall power output given by Equation 11.75, with $P_{out} = P_{osc}$, where P_{osc} is the free-running power output that the laser oscillator can deliver. But we also have a constant gain-bandwidth expression connecting $g_0 \equiv G_0^{1/2}$ and $\Delta\omega_{3dB}$. For sim-

plicity let us assume a laser cavity with very small internal losses and reasonably small external coupling, so that we can write $r_1 r_2 \approx 1$ and $t_1 t_2 \approx \delta_c$, where δ_c is the cavity loss factor derived earlier. By using the cavity Q_c definition from Equation 11.40, we can then rewrite the gain-bandwidth product in the form

$$G_0^{1/2} \Delta\omega_{3dB} \approx \frac{2\omega_a}{Q_c} = 2\Delta\omega_c, \quad (76)$$

where $\Delta\omega_c \equiv \omega/Q_c$ is the “cold cavity” bandwidth of any one axial mode in the laser cavity due to its external coupling.

Combining Equations 11.75 and 11.76 then gives the interesting result that

$$\Delta\omega_{osc} = \Delta\omega_{3dB} \approx (2) \times \frac{N_2}{N_2 - N_1} \times \frac{\pi\hbar\omega\Delta\omega_c^2}{P_{osc}}, \quad (77)$$

where $\Delta\omega_{osc}$ is to be interpreted as the spectral width of the highly amplified noise coming out of the laser operating at or above threshold. This formula for the “noise bandwidth” of the laser output is commonly referred to as the “Schawlow-Townes formula” for a laser oscillator. Note that this linewidth depends only on the cold-cavity bandwidth $\Delta\omega_c$ of the laser cavity, and on the power level P_{osc} at which the laser oscillates above threshold.

More Correct Description

We have put the factor of 2 in Equation 11.77 in brackets to emphasize the way in which this formula is partially correct and partially incorrect. When a laser reaches its oscillation threshold, there is, as we noted in Chapter 1, a qualitative change in the character of the laser output spectrum. The laser changes over just at threshold from being a very narrowband but still essentially *incoherent gaussian noise source*, with large (but slow) fluctuations in both amplitude and phase, to being a *coherent sinusoidal oscillator*, with a highly stabilized phasor amplitude, but still with random noise-like but very slow fluctuations or drifts in the oscillation phase.

If we simply delete the bracketed factor of 2 in Equation 11.77, *this equation still correctly predicts the spectral bandwidth of the coherent laser oscillation above threshold*, as caused by random phase fluctuations in the laser output. In other words, the Schawlow-Townes result, reduced by a factor of two, is still correct in the nonlinear region above threshold, even though it is derived by using a linear below-threshold model.

The phase fluctuations and the consequent oscillation spectral broadening caused by spontaneous emission in a laser oscillator above threshold (along with some small but still observable residual amplitude fluctuations) are commonly referred to as *quantum noise fluctuations* in the laser. These quantum amplitude and frequency fluctuations in ordinary lasers are usually completely masked by much larger fluctuations due to mechanical vibrations, acoustic noise, thermal drift, and other “technical noise sources.” Quantum amplitude and frequency fluctuations have been measured, however, in excellent agreement with the Schawlow-Townes formula, by careful measurements both on highly stabilized gas lasers, and on semiconductor injection lasers, where these fluctuations can be substantially more noticeable.

REFERENCES

Despite the technical difficulties in dealing with such high gains and narrow linewidths, painstaking measurements demonstrating in detail the fixed gain-bandwidth product in a He-Ne laser with a gain-bandwidth product of ≈ 1 MHz were once carried out by G. Herziger, G. Makosch, and J. Weber, "Verstärkung, Bandbreite und Photonendichte beim He-He-Laserverstärker für die Wellenlänge $\lambda = 6328\text{\AA}$," *Z. Physik* **228**, 89–98 (1969). Peak gain in the experiment was varied from $G = 1$ up to $G = 40,000$, and the corresponding bandwidth varied from 1 MHz down to 5 kHz.

Problems for 11.7

1. *Power transmission through a laser cavity halfway between axial modes.* Suppose one sets up two high-reflectivity mirrors in series, but with the mirrors misaligned in angle by enough to destroy any regenerative or resonance effects. The total power transmission through these two mirrors in cascade is then simply $T_1 T_2$. Examination of the results given in this chapter will show that the power transmission through a highly regenerative traveling-wave amplifier at a frequency halfway between two axial-mode resonances turns out to be approximately 6 dB lower than this value for the end mirrors by themselves with no regenerative effects—in other words, regeneration with the wrong phase actually reduces the power transmission from input to output. Verify this, and explain why the reduction factor is roughly 6 dB.
2. *Gain sensitivity of a regenerative laser amplifier.* The gain sensitivity of a laser amplifier to small changes in the active laser medium may be defined as the fractional change $\delta G/G$ in the overall midband power gain divided by the fractional change $\delta \alpha_m/\alpha_m$ in the laser-medium gain coefficient, for small changes $\delta \alpha_m$ and δG . (The change in α_m might be caused, for example, by a small change in the laser's pumping rate.) Calculate and compare the overall gain sensitivities for a round-trip laser amplifier and for a highly regenerative laser amplifier, as a function of the overall midband power gain in each case. (Disregard saturation effects in both cases.)
3. *Skirt selectivity of a regenerative laser amplifier.* In some applications it can be important to know not only the 3 dB bandwidth of an amplifier, but also how fast the amplifier gain falls off outside this bandwidth (for example, in order to find out how much a strong interfering signal outside the amplifier passband will be suppressed). Analyze and discuss this so-called "skirt selectivity" performance for a highly regenerative laser amplifier, considering the maximum rejection halfway between axial modes, and the linewidths for the gain to drop 10, 15, 20 dB, etc., below the peak gain.
4. *Output versus input for a regenerative laser amplifier with saturable internal gain.* The following problem is slightly tricky, but also instructive.

Suppose a highly regenerative ring interferometer cavity has an input mirror reflectivity $R_1 = 95\%$, an internal round-trip voltage attenuation $\alpha_{mp} = -4\% = -0.04$ due to an absorbing atomic transition, and no other internal losses (i.e., $\alpha_0 = 0$). The output mirror reflectivity is $R_2 = 100\%$. The internal atomic absorption α_m saturates in homogeneous fashion with a saturation intensity I_{sat} .

An input signal with intensity I_{inc} tuned to the resonant frequency of the resonant cavity is sent against the input mirror (mirror M_1) of the cavity from outside. The problem is to plot the reflected intensity I_{ref} that is reflected back from the input mirror as a function of the input intensity I_{inc} of the input signal.

Hints: (1) You clearly need to establish a relationship between the input intensity I_{inc} and the intensity I_{circ} inside the cavity, since it is the latter intensity that saturates the atomic absorption. (2) Since the round-trip gain inside the cavity is always close to unity, you can assume that the intensity inside the cavity has essentially the same value all around the cavity. (3) The system may exhibit bistable or bivalued behavior in its output-versus-input relationship.

5. *Regenerative gain peaks for off-line-center axial modes.* In a certain laser the axial-mode spacing $2\pi c/2L$ is exactly one-fifth the lorentzian atomic linewidth $\Delta\omega_a$, and the centermost axial mode (the q -th axial mode, say) is located exactly at line center. The mirror reflectivity at each end of the laser is $R_1 = R_2 = 0.95$, and there are no internal cavity losses. Find and plot the overall power gains at the peaks of the three closest off-line-center axial modes (i.e., the $q+1$, $q+2$, and $q+3$ modes) versus the peak power gain of the centermost axial mode, as the round-trip gain inside the laser cavity is slowly turned up to unity.

You should discover that the peak gains of the off-center modes go to finite values as the gain of the centermost mode goes to infinity (i.e., to oscillation threshold). What gain values in dB do the off-center modes approach as the gain of the central mode approaches infinity?

6. *Transient reflection from a resonant cavity.* Suppose a sinusoidal signal with a step-function turnon (that is, $\mathcal{E}_{\text{inc}}(t) = 0$ for $t < 0$ and $\mathcal{E}_{\text{inc}}(t) = \sin(\omega_0 t)$ for $t \geq 0$) is incident on a highly regenerative optical cavity or interferometer, with the signal carrier frequency ω_0 tuned to one of the axial mode resonances of the cavity. Use the highly regenerative approximation to find the complex voltage reflection coefficient of the cavity as a function of frequency for ω near ω_0 ; and then use Fourier transform or Laplace transform methods to find the reflected signal $\mathcal{E}_{\text{refl}}(t)$ from the cavity as a function of time for $t \geq 0$. Discuss the physical significance of your result, and compare the descriptions of the reflected signal in the time and frequency domains.

(Hint: A signal with a sharp step-function leading edge will have a frequency spectrum which actually spreads out over several axial modes. Using the highly regenerative approximation and considering only the one axial mode with which the signal is in resonance, as in this problem, will in essence filter out the discrete step-wise variation of the reflected signal as the circulating signal travels around and builds up on successive round trips.)

7. *Approach to threshold in the Schawlow-Townes model.* For a typical set of parameters, how close is the round-trip gain magnitude g_{Rt} to unity at the operating point implied by the Schawlow-Townes laser model illustrated in Figure 11.28. What is the fractional deviation of g_{Rt} from unity?



FUNDAMENTALS OF LASER OSCILLATION

This chapter brings us finally to the complete laser oscillator: atoms, plus pumping and population inversion, plus signals and amplification, plus mirrors to provide feedback and oscillation.

In this chapter we will develop formulas for some of the simpler aspects of laser operation, including the population inversion required to reach oscillation threshold; the pumping power density required to produce this inversion; the laser power output, and its dependence on output coupling and pumping power in simple cases; the difference between homogeneously and inhomogeneously broadened lasers; and the atomic-frequency pulling effects in a laser oscillator.

In Chapter 13 we will then develop a set of coupled rate equations which link cavity photons to laser atoms, and laser atoms to cavity photons. Using these equations we will explore laser oscillation buildup and the remarkable threshold properties characteristic of the laser oscillator.

12.1 OSCILLATION THRESHOLD CONDITIONS

The basic requirement either for just reaching laser oscillation threshold, or for maintaining steady-state laser oscillation, is that *the round-trip gain inside the laser cavity, including mirror reflections, must be exactly unity, modulo an integer number of multiples of $e^{-j2\pi}$.* Only if the round-trip gain is exactly unity can the system maintain steady-state oscillation, in which the circulating signal inside the cavity neither grows nor decays on successive round trips. (This assertion does leave out some extremely minute effects due to spontaneous emission or noise in the laser cavity, which are totally negligible in any of the following discussions.)

In the notation developed in Chapter 11, unity round-trip gain requires that

$$\begin{aligned}\tilde{g}_{rt}(\omega) &\equiv r_1 r_2 (r_3 \dots) \times \exp \left[\alpha_m(\omega) p_m - \alpha_0 p - j \frac{\omega p}{c} - j \Delta \beta_m(\omega) p_m \right] \\ &= \exp[-jq2\pi],\end{aligned}\tag{1}$$

where q is an integer. This can in turn be separated into an *amplitude or magnitude condition*, which says that at steady-state the round-trip gain must have

magnitude unity, or

$$r_1 r_2 (r_3 \dots) \times \exp[\alpha_m(\omega) p_m - \alpha_0 p] = 1, \quad (2)$$

and a *phase or frequency condition*, which says that at steady state the round-trip phase shift must be an integer multiple of 2π , or

$$\frac{\omega p}{c} + \Delta\beta_m(\omega) p_m = q \times 2\pi. \quad (3)$$

The first of these conditions determines the population inversion density, and hence the pumping rate, needed to reach oscillation threshold. The second condition determines primarily the frequency ω at which the laser must oscillate.

Threshold Inversion Density

Suppose we rewrite the amplitude condition in terms of the round-trip power gains and losses, since we usually speak of power gains and mirror power reflectivities R_i rather than voltage reflectivities r_i in practical discussions. The gain coefficient required to just reach threshold in the laser cavity is then given by

$$2\alpha_m(\omega) p_m = 2\alpha_0 p + \ln \left[\frac{1}{R_1 R_2 (R_3 \dots)} \right], \quad (4)$$

or, in terms of the “delta notation” we introduced in the previous chapter,

$$2\alpha_m(\omega) p_m \equiv \delta_m(\omega) = \delta_0 + \delta_1 + \delta_2 + \dots \equiv \delta_c. \quad (5)$$

Now, we can recall from earlier chapters that the laser gain coefficient for a lorentzian atomic transition is given by

$$\alpha_m(\omega) = \frac{3^*}{4\pi} \frac{\gamma_{\text{rad}} \lambda^2}{\Delta\omega_a} \frac{\Delta N}{1 + [2(\omega - \omega_a)/\Delta\omega_a]^2} \quad (6)$$

or by a very similar expression for a gaussian atomic transition. The inversion density required either to reach threshold, or to maintain steady-state oscillation, in a cavity mode located at midband ($\omega = \omega_a$) on a lorentzian atomic transition, is thus given by

$$\Delta N = \Delta N_{\text{th}} \equiv \frac{2\pi}{3^*} \times \frac{\Delta\omega_a}{\gamma_{\text{rad}}} \times \frac{1}{\lambda^2} \times \frac{\delta_c}{p_m}. \quad (7)$$

In order to have achieve oscillation with the lowest possible inversion density we want to have a laser system with the following characteristics:

- A narrow atomic linewidth $\Delta\omega_a$.
- A strong radiative decay rate γ_{rad} .
- A long wavelength λ .
- Low cavity losses and output coupling, δ_c .
- A long gain medium p_m .

The dependence on wavelength in particular agrees with the general observation that infrared lasers are usually fairly easy to obtain, whereas visible and UV lasers become progressively more difficult.

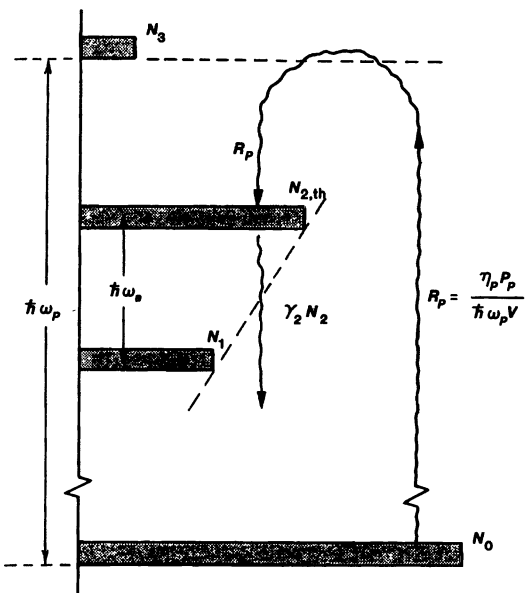


FIGURE 12.1
A general model for calculating pumping power density required in a typical four-level laser oscillator.

Not all of these criteria are essential; some are not even always desirable. For example, many useful laser materials have wide linewidths and small radiative decay rates, and many lasers work best with very large output couplings. They do, however, at least indicate which properties will make achieving laser action more or less difficult.

This same threshold condition can also be expressed much more simply in terms of the transition cross section σ given by $2\alpha_m = \Delta N\sigma$, which leads to the particularly simple result

$$\Delta N_{th} = \frac{\delta_c}{\sigma p_m}. \quad (8)$$

A large transition cross section and a small threshold inversion obviously go together.

Threshold Pump Power Density

Although the threshold inversion density is important, of more practical importance is the *pump power density* required to achieve this threshold inversion in a practical laser. We can express this threshold pump power density in a fairly general form, more or less independent of the particular pumping mechanism that is employed, using the general laser pumping model shown in Figure 12.1.

First of all, obtaining the threshold inversion density given by Equation 12.7 will require achieving an upper-laser-level population density $N_{2,th}$ that is greater than this threshold inversion ΔN_{th} by some ratio that depends, as shown in Figure 12.1, on how much population accumulates in the lower laser level, which depends in turn on how rapidly the lower laser level empties out.

Suppose that in order to achieve inversion atoms are pumped upward by a pumping power density (power per unit volume) P_p/V into one or more upper pump levels E_3 , from which some fraction of these atoms fall down into the upper laser level E_2 , with a net pumping rate of R_p atoms per unit volume per second into this upper laser level. Let the effective energy gap across which atoms must be lifted by the pumping mechanism be given by $\hbar\omega_p$, where ω_p is the "pumping frequency" (whether or not the pumping is actually done optically using photons of energy $\hbar\omega_p$ or by some other mechanism); and let the fraction of excited atoms that actually end up falling into the upper laser level be given by a pumping efficiency η_p . (The remainder of the pumping power is wasted, either in lifting up atoms which drop back down through other paths, or simply in added heat dissipation in the medium.)

The effective pumping rate R_p and the upper level population density N_2 which is created by this pumping rate are then given by

$$N_2 = \frac{R_p}{\gamma_2} = \frac{\eta_p P_p}{\gamma_2 \hbar \omega_p V}, \quad (9)$$

where P_p/V is the total pumping power density (power per unit volume) going into the laser medium, and γ_2 is interpreted as the total downward decay rate out of level 2 due to all decay mechanisms.

By combining this expression with the threshold inversion expression 12.7, we can find that a quite general expression for threshold pump power density is

$$\frac{P_{p,\text{th}}}{V} = \frac{1}{\eta_p} \times \frac{N_{2,\text{th}}}{\Delta N_{\text{th}}} \times \frac{\omega_p}{\omega_a} \times \frac{\gamma_2}{\gamma_{\text{rad}}} \times \frac{4\pi^2}{3^*} \times \frac{\hbar\Delta\omega_a}{\lambda^3} \times \frac{c\delta_c}{p_m}. \quad (10)$$

This is a very important expression for calculating—or at least estimating—the performance characteristics and pumping requirements of a given laser system.

Practical Laser Pumping Requirements

The first four factors in this expression are all dimensionless ratios with values which may vary greatly from laser system to laser system, but which are never smaller than unity. Each factor can thus provide a criterion for searching for good laser systems. Each ratio does in fact come close to unity in certain particularly favored laser systems, though each of them is also more commonly much worse than unity in other systems.

If we look at each of these factors in turn, we can see that the criteria for a good laser medium—or at least one with low pump-power requirements—include, first, a good pumping efficiency η_p in terms of atoms lifted up per unit pump power applied to the medium. Systems which show up well on this criterion include optically pumped dye lasers, solid state lasers, semiconductor lasers, and some gas lasers such as chemical lasers and the CO_2 laser. Systems not favored by this criterion include many common gas-discharge lasers, such as the He-Ne or ion lasers, where only a small part of the pumping energy goes into lifting atoms into the desired upper laser levels.

In a He-Ne or Argon-ion gas laser, for example, the number of atoms actually pumped into the upper laser level is very small compared to photon units of electrical energy dissipated in the gas discharge medium, so that $\eta_p \ll 1$. In these lasers most of the electrical energy input into the laser gas goes either into exciting unwanted atomic levels or just into heating up the gas atoms and the

electrons. In a laser-pumped dye laser, by contrast, the ratio of dye molecules pumped up to the upper laser level to laser pumping photons absorbed can be almost unity. Of course, these laser-generated pumping photons are themselves rather expensive photons to obtain.

A good laser system should also have a lower laser level that empties out rapidly, so that $N_1 \approx 0$ and $\Delta N \approx N_2$ (which, of course, works against three-level lasers like ruby). A good laser system should also have its upper pumping level not far above the upper laser level, and its lower laser level close to (but not right at) the ground level, so that the pump photons can be as small as possible. Again this favors dye lasers, most solid-state lasers, and some gas lasers, and works strongly against other gas lasers like He-Ne and argon lasers, where we must lift the atoms up to levels that are ≈ 20 eV or more above ground level, in order to get out ≈ 2 eV photons across the laser transition.

Finally, we want a laser transition which is as close to purely radiative on the laser transition as possible, with no other radiative or nonradiative decay rates to leak off atoms, so that $\gamma_2 \approx \gamma_{\text{rad}}$. This favors the ruby laser, organic dye lasers, and to a lesser extent other solid-state and gas lasers.

Note in particular that if the condition $\gamma_2 \approx \gamma_{\text{rad}}$ is satisfied, then the actual value of the transition strength γ_{rad} drops out of the pump power density expression. A strong transition with a large γ_{rad} needs a smaller population inversion, according to our above results; but at the same time the faster decay makes this inversion harder to maintain continuously. Hence ruby and Rhodamine 6G are both very good visible laser systems, even though their values of γ_{rad} differ by some 6 orders of magnitude.

After all these factors are taken into account, the remaining factors in obtaining laser inversion are the final two terms in Equation 12.10. Laser action is always harder to obtain the wider the atomic linewidth (though at the same time wide linewidth is essential if we want to have tunable laser action). We also see once again that the difficulty in obtaining laser action goes up very rapidly as the laser wavelength gets shorter, with the pump power density rising, other factors being equal, at least proportional to $1/\lambda^3$. In fact, in doppler-broadened gas lasers the doppler linewidth itself tends to increase as $1/\lambda$, and hence the wavelength dependence of $P_{p,\text{th}}$ will be more like $1/\lambda^4$. A genuine X-ray laser will be very difficult to obtain, both for this reason and because of other factors as well, not the least of these being the lack of good X-ray mirrors.

Finally, the last term in the threshold pumping condition contains the cavity factors, i.e., to reach oscillation in a weak laser system we want the lowest possible cavity losses, and the longest possible gain medium.

Problems for 12.1

1. *Off-resonance regenerative amplification through an oscillating laser?* A standing-wave laser cavity with mirror reflectivities $R_1 = R_2 = R$ is oscillating in steady state at its centermost axial mode. A separate signal tuned off by one-half of an axial-mode spacing is sent into one end of this cavity. What is the overall transmission gain for this signal out the opposite end of the cavity? (The laser medium is homogeneous, and its atomic linewidth is wide compared to the axial mode spacing.) What happens to this transmission gain if the mirror reflectivity R is small? Explain physically.
-

12.2 OSCILLATION FREQUENCY AND FREQUENCY PULLING

Let us next look at the frequency characteristics of laser oscillators: whether a laser will oscillate only in a single mode and at a single frequency, or in many modes at once, and also what the exact frequencies of these oscillations will be if atomic pulling effects are included.

The axial cavity mode whose frequency is located closest to the center of an atomic transition will of course normally see the highest gain, and will thus normally reach oscillation threshold first, before other modes located further from the atomic line center. Suppose, however, that we turn up the gain or the pump power still further, beyond the point where the first cavity mode reaches threshold. Will additional axial (or transverse) modes then also begin oscillating? The answer to this question is that there are in general two idealized or limiting types of laser oscillation behavior for the remaining cavity modes, depending on whether the laser transition is *homogeneously* or *inhomogeneously* broadened. We will first consider these two general classes of laser oscillation, before discussing the atomic pulling effects that occur for either class.

Ideal Homogeneous Lasers: Single Frequency Oscillation

In an ideally *homogeneous* laser transition, the atomic lineshape is fixed and identical for all the atoms in the laser medium. The magnitude of the gain and phase shift measured at any given frequency will move up and down as the population inversion ΔN varies; but the lineshapes of $\chi''(\omega)$ and $\chi'(\omega)$ versus frequency will remain unchanged—in essence the whole lineshape moves up and down together.

Suppose the midband gain in such a homogeneous laser medium is increased until the axial mode closest to line center just reaches threshold (i.e., gain just equals losses), as illustrated in Figure 12.2(a). This mode q can then begin to oscillate, whereas all the other modes ($q - 1$, $q + 1$, and $q + 2$) are still below threshold and cannot oscillate. (Note that the gain actually exceeds the losses in the center portion of the atomic line, but there is no cavity mode located there to build up to oscillation.)

Even if we pump this laser harder, we cannot push the gain profile further up so as to cause the $q + 1$ mode to oscillate, as illustrated by the dashed gain profile in Figure 12.2(a). Such oscillation is not possible, at any rate, on a cw or steady-state basis, because then gain would exceed loss for the q -th mode, and the amplitude of this mode would grow continuously on successive round trips.

It may of course be possible to push the gain for several modes above the steady-state or threshold value on a transient basis, during initial turn-on or pulsed operation of the laser. Note also that the centermost axial mode may not be the first or preferred mode to oscillate, if special mode-control methods are used to increase the losses of this mode relative to another axial mode further out on the atomic gain profile.

An ideally homogeneous laser, therefore, should oscillate under steady-state conditions in only one preferred mode, the first mode to reach threshold; and the gain in the laser medium will be clamped at the level that just causes that mode to reach threshold. Pumping harder will make that preferred mode oscillate more strongly, as we will see very shortly, but will not increase the gain or start new modes oscillating.

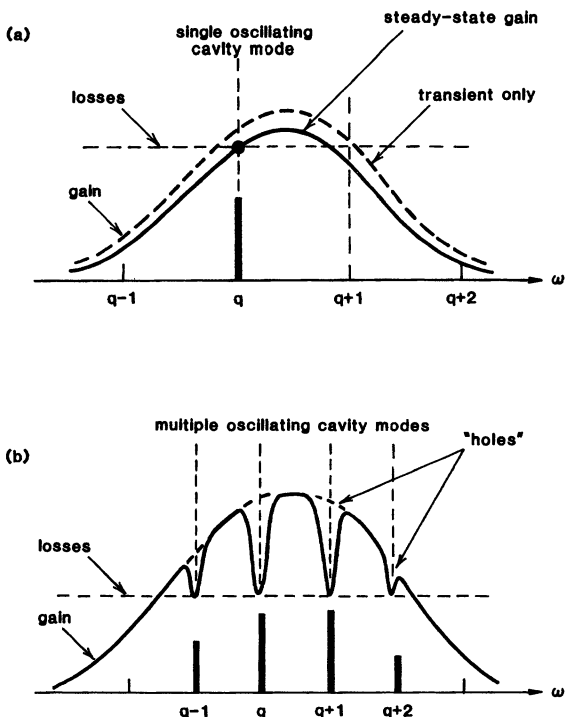


FIGURE 12.2

(a) In an ideal homogeneously broadened laser, the gain profile cannot be pushed above the threshold point for the first oscillating mode—at least not on a steady-state basis—because the first mode would then have a permanently positive growth rate. (b) Multiple axial modes can, however, oscillate with each mode, burning a separate and independent “hole” in the gain profile to make gain equal loss for each mode.

Several practical factors, such as spatial hole burning (Section 8.2), tend to weaken this conclusion in real lasers. In an ideal system, however, and to a sizable extent in many real lasers, a homogeneously broadened laser will tend to oscillate at only a single frequency, on its centermost (or most preferred) axial and transverse mode.

The experimental spectra in Figure 12.3, taken on a semiconductor injection laser, give an excellent illustration of how a single oscillating mode can emerge just above threshold from a cluster of regeneratively amplified axial-mode noise peaks just below threshold. Note the sharp change in the character and intensity of the output spectrum as the diode injection current is increased from $I_o = 155$ mA, just below threshold, to $I_o = 162.5$ mA, just above threshold. The special characteristics of semiconductor diode lasers, including their very small cavity volume, high gain, strong spontaneous emission, broad linewidth, and wide axial-mode spacing, make it comparatively easy to obtain this type of experimental result. In most other types of lasers the below-threshold output is relatively much weaker, and the threshold transition very much sharper, so that similar experiments become very much more difficult.

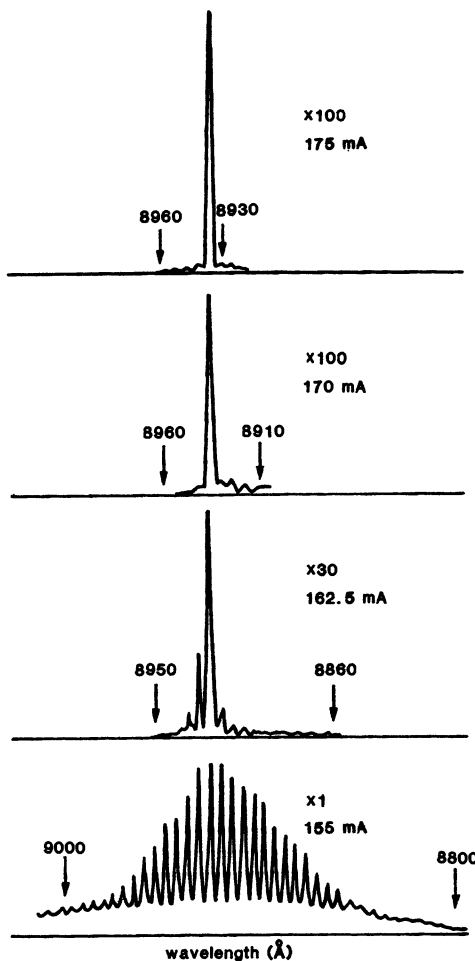


FIGURE 12.3

Single-mode oscillation rises up out of multimode amplified noise as the excitation current is increased in a homogeneous semiconductor diode injection laser. Note changes in vertical scale in the successive curves.

Inhomogeneous Lasers: Multi-Axial-Mode Oscillation

Doppler-broadened gas lasers, and other lasers with *strongly inhomogeneous* transitions, by contrast, can easily oscillate simultaneously on multiple frequencies or multiple axial modes within the atomic linewidth.

As we will show in a later chapter, when the atomic gain in an inhomogeneous transition exceeds the loss, each axial mode for which this occurs saturates only that subgroup of atoms, or that particular spectral packet, whose atomic frequencies are in resonance with that particular oscillation frequency. As a result, the laser “burns a hole” in the gain curve, and saturates the gain down to equal the loss, at each oscillating axial mode separately, as illustrated in Figure

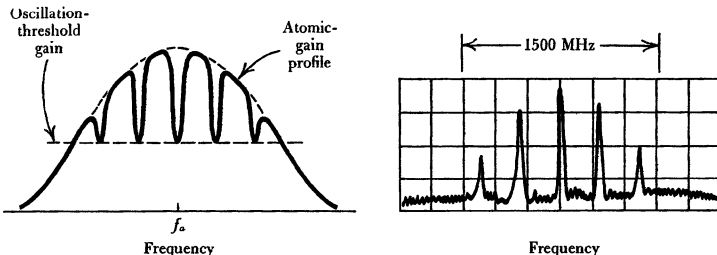


FIGURE 12.4

Multiple simultaneously oscillating axial modes in a He-Ne laser oscillator.

12.2(b). *Inhomogeneous lasers can thus oscillate simultaneously in many axial modes, with each mode oscillating almost independent of all the other modes.*

For many common laser systems, there can be a substantial number of axial cavity modes within the atomic gain profile of the laser. Helium-neon lasers, for example, with a doppler linewidth $\Delta f_d \approx 1,500$ MHz and axial-mode spacings $\Delta f_{ax} \approx 150$ to 500 MHz, will typically have three to ten axial modes within the atomic linewidth; and because the line is strongly inhomogeneous, the laser can oscillate in all of these modes at once. Figure 12.4 shows, for example, five simultaneous axial-mode oscillation frequencies from a typical cw He-Ne laser.

A low-pressure CO₂ laser, on the other hand, with only 60 to 100 MHz of combined doppler and pressure broadening, may have only one axial mode within its atomic linewidth. Far-infrared and submillimeter molecular gas lasers also generally have very narrow atomic lines (because they operate at low gas pressures and because the doppler broadening decreases as the transition frequency decreases); and so they usually have one (or even fewer) axial modes within their atomic linewidth.

A neodymium-YAG laser with an atomic linewidth of $\Delta f_a \approx 4$ cm⁻¹ ≈ 120 GHz will typically have hundreds of axial modes within the atomic gain curve. As a result this type of laser will often exhibit highly multimode oscillation under the transient conditions associated with short-pulse operation. At the same time this laser can oscillate in only one mode or more often a few simultaneous axial modes under continuous-wave or cw conditions, because of the strongly homogeneous character of the atomic transition.

Spatial Hole Burning

The most significant effect leading to multimode operation even in spectrally homogeneous lasers is *spatial inhomogeneity*, and especially *spatial hole burning*, as described previously in Section 8.2, and illustrated in Figure 12.5.

Suppose a linear or standing-wave laser is initially oscillating in the q -th axial mode. This leads to a standing-wave pattern for the field amplitude or optical intensity along the z axis, with peaks and nulls spaced by one-half optical wavelength (between each null). The inverted population in this laser will then be saturated in a similar spatially periodic fashion, as illustrated in Figure 12.5.

One of the effects of this saturation will be to produce a spatial inverted-population grating or gain grating, which will introduce cross-coupling between the forward and backward-traveling wave components of the q -th axial mode. Of more importance at this point, however, is the fact that, at least near the center

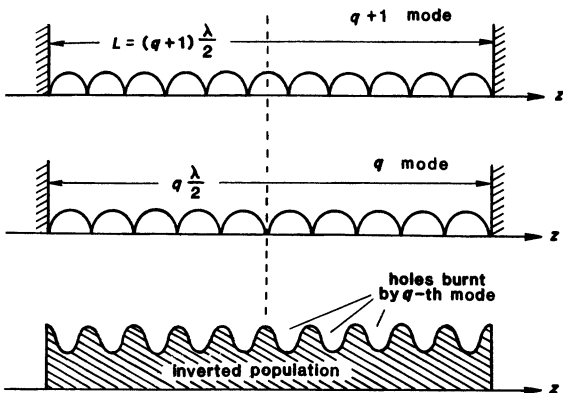


FIGURE 12.5
Spatial hole burning.

of the cavity, the standing-wave pattern of the $(q+1)$ -th mode—which squeezes one more half optical wavelength into the cavity length—will have its maximum intensity located just at the points that are left unsaturated by the q -th mode. [The same point is, of course, equally true for the $(q-1)$ -th axial mode.]

As a result of this, the gain competition between the two adjacent axial modes is much reduced; and both axial modes may well be able to oscillate simultaneously, even with a strongly homogeneous laser medium, by using in essence different groups of atoms. Oscillation with any two adjacent axial modes at equal amplitudes will then saturate the population uniformly, at least in the center of the cavity, possibly discouraging the oscillation of any further axial modes. This behavior is sometimes seen, for example, in solid-state lasers, such as the Nd:YAG laser, which often seem to prefer to oscillate at steady state in just two axial modes.

Unidirectional oscillation in a ring-laser cavity is one way of eliminating this kind of hole burning, thus giving a better chance of obtaining single-frequency operation. Placing a comparatively short section of active laser medium close to one of the end mirrors is another way to reduce the effectiveness of the spatial hole-burning process.

Exact Oscillation Frequencies, and Frequency Pulling Effects

Laser oscillation normally occurs in only a few preferred longitudinal and transverse modes of a laser cavity. The exact oscillation frequency of a laser will, however, be shifted away by a small amount from the resonance frequency of the corresponding “cold cavity” mode—that is, the resonance frequency of the cavity mode without laser material—because of small frequency pulling effects associated with the χ' part of the atomic susceptibility. Let us next look at how these pulling effects can be calculated.

The round-trip phase shift $\phi(\omega)$ in a laser cavity, with the gain medium present, must satisfy the phase shift condition

$$\phi(\omega) \equiv \frac{\omega p}{c} + \Delta\beta_m(\omega)p_m = q2\pi, \quad (11)$$

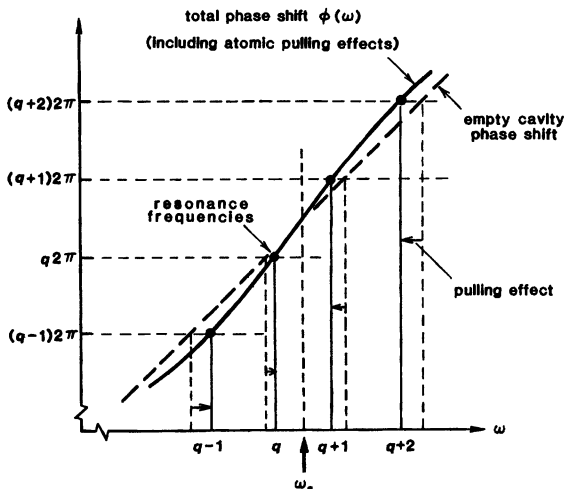


FIGURE 12.6

Atomic frequency pulling effects. (An inverted transition always "pulls" the cavity resonance frequencies toward the atomic line center.)

where the atomic phase shift term is normally given by

$$\Delta\beta_m(\omega) = \frac{\beta\chi'(\omega)}{2} = \frac{\omega\chi'(\omega)}{2c}. \quad (12)$$

We thus obtain a general condition on the laser frequency given by

$$\frac{\omega p}{c} \times \left[1 + \frac{p_m}{2p} \chi'(\omega) \right] = q2\pi. \quad (13)$$

Figure 12.6 shows, in greatly exaggerated form, how the $\Delta\beta_m(\omega)$ or $\chi'(\omega)$ contribution appropriate to an amplifying transition causes a shift in the exact frequency at which the $\phi(\omega)$ curve intersects the $q2\pi$ resonance values.

Frequency-Pulling Expression

The magnitude of the $\chi'(\omega)$ term in Equation 12.13 is usually small compared to unity; and the size of the pulling effect will be still further reduced if the length of the atomic medium p_m is small compared to the overall cavity perimeter p . Given this assumption, we can invert Equation 12.13 and solve for the pulled laser oscillation frequency—let's call it ω'_q —in the form

$$\begin{aligned} \omega = \omega'_q &= \frac{q2\pi c/p}{1 + (p_m/2p) \chi'(\omega_q)} \\ &\approx \frac{q2\pi c}{p} \times \left[1 - \frac{p_m}{p} \frac{\chi'(\omega'_q)}{2} \right] \\ &= \omega_q + \delta\omega_q, \end{aligned} \quad (14)$$

where $\omega_q \equiv q2\pi c/p$ is the unpulled or “cold cavity” resonance frequency, and $\delta\omega_q$ is the pulling of the resonance frequency by the atomic phase-shift effects. We can then write this (usually) small pulling effect as

$$\delta\omega_q \approx -\frac{p_m}{2p} \omega_q \chi'(\omega_q) \approx -\frac{\Delta\beta_m(\omega_q)p_m}{p/c}. \quad (15)$$

But since the axial-mode spacing in the cavity is given by $\Delta\omega_{\text{ax}} = 2\pi c/p$, we may rewrite this as

$$\frac{\delta\omega_q}{\Delta\omega_{\text{ax}}} \equiv \frac{\text{pulling amount}}{\text{axial mode spacing}} \approx -\frac{\Delta\beta_m p_m}{2\pi}. \quad (16)$$

Since the atomic phase-shift term $\Delta\beta_m p_m$ will usually be small compared to 2π , the pulling of each mode will usually be small compared to an axial-mode interval. If this pulling term is also small compared to the atomic linewidth, then we can evaluate the pulling contribution $\chi'(\omega)$ at the unpulled frequency $\omega = \omega_q$ (which is much simpler to do) rather than at the pulled frequency $\omega = \omega_q'$.

The magnitude of the reactive susceptibility $\chi'(\omega)$ in an oscillating laser will, of course, depend on the degree of saturation of the atomic transition, and thus on how strongly the laser is oscillating, as well as on where the oscillating mode (or modes) are located within the atomic linewidth. The phase-shift expressions 12.13 to 12.16 serve primarily, however, to determine the exact frequency at which the laser must oscillate, rather than its power level or other characteristics.

Linear Dispersion Region

Figure 12.6 shows how the $\chi'(\omega)$ term for an amplifying transition tends to shift each axial mode in toward the atomic transition frequency ω_a by an amount $\delta\omega_q$ that depends on distance from the line center. Amplifying transitions always tend to “pull” cavity frequencies toward line center; absorbing transitions have χ' values of opposite sign, and thus tend to “push” the cavity resonances away from line center.

For axial modes within the central part of an atomic line, where the value of $\chi'(\omega)$ increases essentially linearly with the mode offset, modes that are further from line center tend to be pulled proportionately more strongly, in such a way that the axial-mode spacing between successive modes remains nearly constant, though decreased by the mode-pulling effect. This is sometimes referred to as the *linear dispersion region* of the atomic transition (Figure 12.7), in contrast to the *nonlinear dispersion region* further out on the atomic gain profile, where the value of $\chi'(\omega)$ begins to bend over and no longer increases linearly with frequency.

Frequency Pulling for Lorentzian Atomic Transitions

The frequency-pulling term for a lorentzian atomic transition can be rewritten in a particularly simple form by noting that for a lorentzian transition the atomic gain coefficient $\alpha_m(\omega)$ and the atomic phase shift $\Delta\beta_m(\omega)$ are related by

$$\Delta\beta_m(\omega) = 2 \frac{\omega - \omega_a}{\Delta\omega_a} \times \alpha_m(\omega). \quad (17)$$

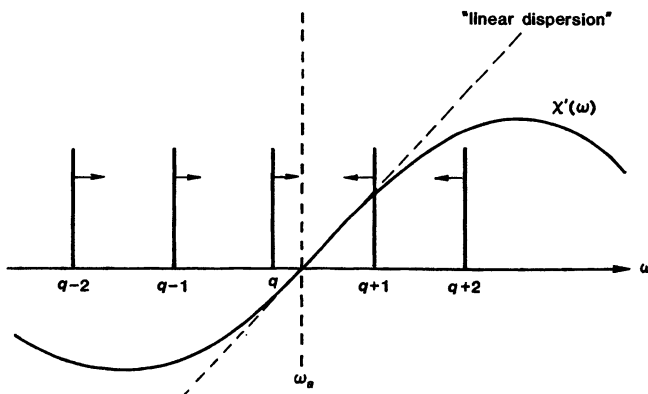


FIGURE 12.7

The pulling effects increase linearly with distance away from line center in the central linear-dispersion region of the atomic line.

Hence the frequency-pulling correction can be written as

$$\frac{\delta\omega_q}{\Delta\omega_{\text{ax}}} \approx -\frac{2\alpha_m(\omega_q)p_m}{2\pi} \times \frac{\omega_q - \omega_a}{\Delta\omega_a}. \quad (18)$$

In most lasers the round-trip power gain coefficient $2\alpha_m p_m$ will be considerably smaller than 2π ; and for those axial modes near line center the quantity $\omega_q - \omega_a$ will be only a few axial-mode intervals, and hence usually small compared to the atomic linewidth $\Delta\omega_a$. Hence the frequency pulling of each mode will be only a small fraction of the axial-mode spacing.

As a numerical example, we might consider a He-Ne laser with 10% power gain per round trip ($2\alpha_m p_m = 0.1$) and ten axial modes within the atomic linewidth ($\Delta\omega_{\text{ax}}/\Delta\omega_a = 0.1$). The fractional pulling for the first axial mode on either side of line center will then be

$$\frac{\delta\omega_q}{\Delta\omega_{\text{ax}}} \approx -\frac{0.1}{2\pi} \times \frac{1}{10} \approx -1.6 \times 10^{-3}. \quad (19)$$

This corresponds to ≈ 100 kHz pulling out of a 150 MHz axial-mode spacing.

It is also possible, however, for pulling effects to become much larger in lasers that have both very high gain and very narrow atomic linewidth. One example of this is the very high gain 3.39 μm transition in narrow-bore He-Ne laser tubes.

Still Another Frequency-Pulling Formulation

Still another version of the frequency-pulling formula is worth presenting briefly, because of the additional insight it gives into frequency-pulling effects. For the lorentzian case we have discussed, we can also rewrite the round-trip phase-shift condition into the form

$$\frac{\omega p}{c} + 2\alpha_m p_m \frac{\omega - \omega_a}{\Delta\omega_a} = q 2\pi \equiv \frac{\omega_q p}{c}, \quad (20)$$

$$\frac{Q_1\omega_1 + Q_2\omega_2}{Q_1 + Q_2}$$

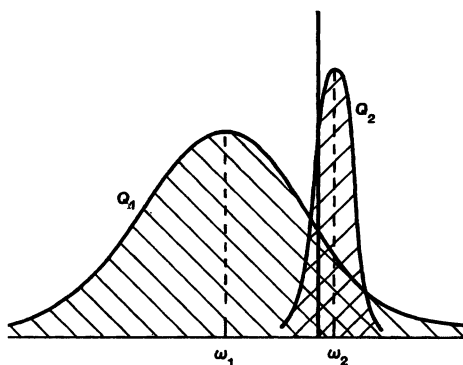


FIGURE 12.8

The oscillation frequency for detuned cavity and atomic resonances will lie between the two resonance frequencies and closer to whichever one has the higher Q value.

where $\omega_q \equiv q2\pi c/p$ is the unpulled or cold cavity frequency. We can then argue that at steady-state oscillation in a homogeneous laser the total cavity gain given by $2\alpha_m p_m$ should just equal the cavity losses, given by δ_c , and so the frequency-pulling expression can be rewritten in the form

$$\frac{\omega_a p}{c\delta_c} \times (\omega - \omega_q) + \frac{\omega_a}{\Delta\omega_a} \times (\omega - \omega_a) = 0. \quad (21)$$

But the quantity $\omega_p/c\delta_c$ that multiplies the first frequency difference in this expression is just the "cold cavity" Q_c value that we have defined earlier (in Section 11.4); and we can for the sake of symmetry define the ratio multiplying the second term as a kind of "linewidth Q_a " given by $Q_a \equiv \omega_a/\Delta\omega_a$.

The frequency condition then takes on the particularly simple form

$$Q_c(\omega - \omega_c) + Q_a(\omega - \omega_a) = 0, \quad (22)$$

where, to make the notation symmetric, we have relabeled the axial-mode frequency ω_q as the "cold cavity" frequency ω_c . This result says that the pulled cavity or oscillation frequency is given by the symmetric expression

$$\omega'_c = \frac{Q_c\omega_c + Q_a\omega_a}{Q_c + Q_a}. \quad (23)$$

This says that, as Figure 12.8 shows, if we couple a cavity resonance with $Q = Q_c$ to an atomic resonance with $Q = Q_a$, the resulting oscillation frequency will lie somewhere between the two resonance frequencies ω_a and ω_c , closer to whichever one has the higher Q . The usual situation in most laser oscillators is that the cavity resonance has much the higher Q value; and hence the oscillation occurs essentially at the cavity frequency ω_c , but pulled slightly toward the atomic frequency ω_a .

Exactly the opposite situation can also occur, for example, in certain microwave masers or atomic clocks that have an extraordinarily narrow atomic line and a much wider cavity linewidth. In these we want the oscillation frequency ω to occur as accurately as possible at the atomic frequency ω_a , with as little perturbation as possible by the cavity frequency ω_c . Equation 12.23 then tells

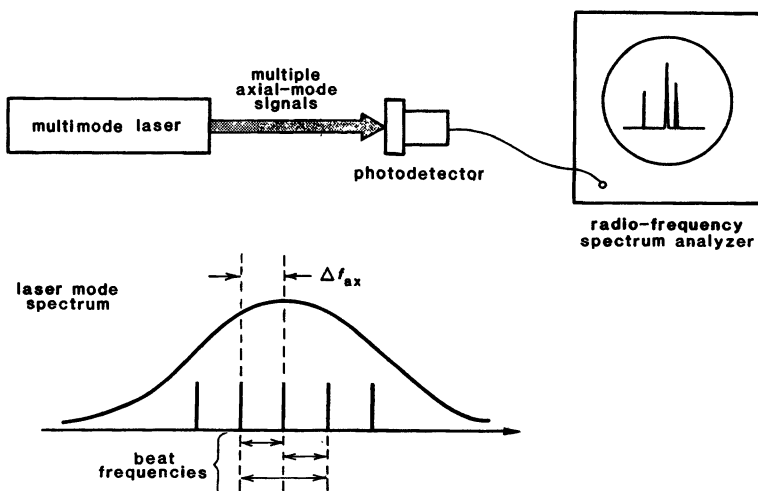


FIGURE 12.9

Measurement system for observing heterodyne beats between axial modes in a laser.

how much error may result if the cavity frequency ω_c is unavoidably detuned by some amount from ω_a .

Frequency Beating Measurements

Laser frequency-pulling effects, although typically very small, can be observed in the laboratory in a number of ways. In practice it can be quite difficult to measure the absolute frequencies of laser oscillators to very high precision (although the frequencies of highly engineered laser frequency standards can at present be measured to an absolute accuracy exceeding 1 part in 10^{10} , and can be stabilized with relative accuracies several orders of magnitude higher). Laser frequency pulling is therefore seldom if ever measured on an absolute basis.

It is much easier, however, to measure relative laser frequencies by observing the difference or beat frequency between two different laser signals, assuming these frequencies are close enough together and stable enough with respect to each other to give a clean beat note, as is true in particular of different axial-mode resonances in the same laser cavity. Difference frequency measurements between two laser oscillations can be accomplished most easily by simply allowing the two laser beams, carefully aligned to be parallel to each other, to fall on any conventional optical detector, such as a photodiode or photomultiplier, and then looking at the photodetector output for signals at the heterodyne or "beat" frequencies between the optical frequencies, as illustrated in Figure 12.9.

Since the optical detector is a square-law device—that is, its signal current is proportional to optical intensity, or to optical E field squared—the detector responds to two optical signals at, say, f_q and f_{q+1} in proportion not only to the dc intensities I_q and I_{q+1} at these two frequencies, but also to a sinusoidal heterodyne beat note of intensity $\sqrt{I_q I_{q+1}}$ at the difference frequency $f_{q+1} - f_q$. (Do not allow the heterodyne jargon here to obscure the elementary fact that the instantaneous amplitude of any signal consisting of the sum of two sinusoidal

carriers at f_q and f_{q+1} is automatically modulated at the difference frequency $|f_{q+1} - f_q|$.)

If we make such a measurement on the output beam from, say, a typical 30-cm long He-Ne laser, using a reasonably fast photodetector and a radio receiver or spectrum analyzer, we can easily detect the 500 MHz beats between several simultaneous axial modes in the laser, as illustrated in Figure 12.9. If the experiment is done using a suitable radio-frequency spectrum analyzer, we can usually see two or three closely spaced beat notes between different pairs of axial modes, with the frequencies of the different axial-mode beats spread out by a few hundred kHz about the expected $\Delta\omega_{\text{ax}}$ value of the laser.

These multiple axial-mode beats result from the slightly different pulling effects that occur for different axial modes in the laser cavity, plus more complicated inhomogeneous cross-pulling effects we have not discussed yet. The observed beat spectral components will in fact jump about in frequency by small amounts as the axial modes shift together across the atomic gain profile because of thermal drift of the laser cavity, and as different modes suddenly turn on or off at the outer edges of the oscillation range. Mode-beating experiments are thus an effective way of observing mode-pulling effects and any other small frequency-shifting effects in laser oscillators.

Frequency Beating Between Two Independent Lasers

Heterodyne beats can be observed between beams from two separate lasers as well, but with somewhat more difficulty. The spatial overlap and especially the angular alignment of the two laser beams must first be adjusted to a very high degree of precision to observe any beats. (In a single laser the angular alignment of different frequency modes is automatic.) The two lasers must then be tuned close enough together in frequency, and the frequency jitter of each laser must be kept small enough, so the beat frequency is within the range of the photodetector and receiver; and we must then scan either the receiver or the lasers until we find where this initially unknown beat frequency is located. Optical heterodyne measurements using sufficiently stable lasers are nonetheless commonly carried out, often with the assistance of automatic frequency control (AFC) loops to stabilize the difference frequency between the two lasers.

REFERENCES

An early but good discussion of spatial hole-burning effects can be found in C. L. Tang, H. Statz, and G. deMars, "Spectral output and spiking behavior of solid-state lasers," *J. Appl. Phys.* **34**, 2289–2295 (August 1963).

For an illustration of mode-pulling and mode-beating effects, see U. P. Oppenheim and M. Naftaly, "Observation of mode pulling in a CO₂ laser," *Appl. Opt.* **23**, 661–664 (March 1 1984).

Problems for 12.2

1. *Number of modes in a doppler-broadened laser.* A doppler-broadened He-Ne lasers ($\Delta\omega_d = 2\pi \times 1,500$ MHz) has a midband unsaturated gain coefficient $2\alpha_{m0}$

of 3% per meter. Assuming the intracavity power losses are 0.5% per one-way pass because of imperfect Brewster windows and the output mirror is to have $R = 99\%$, with $R = 100\%$ for the other mirror, make a plot of the number of modes oscillating versus the length L of the laser. Assume the laser material fills the laser cavity except for 10 cm for the Brewster angle sections at each end, and that the centermost axial mode is located exactly at the atomic line center.

2. *Laser cavity design for at least one and not more than three simultaneous axial modes.* A certain laser system has a midband unsaturated gain coefficient $2\alpha_{m0}$, output coupling δ_e , internal cavity losses δ_0 , and an inhomogeneous gaussian atomic lineshape with linewidth $\Delta\omega_d$. You want to be sure that this laser will always oscillate in at least one axial mode, no matter how the centermost axial mode drifts back and forth with respect to the atomic line center. How long must you make the cavity, at a minimum? What is the maximum length if you want the laser never to reach threshold for three or more modes at once?
3. *Length considerations for He-Ne laser design.* If a He-Ne laser is made too short, not only is the round-trip gain reduced, but there may be situations in which no axial mode is present within the net positive-gain region of the laser. Suppose a typical He-Ne laser has a doppler-broadened gain profile with linewidths $\Delta f_d = 1,500$ MHz and a midband gain coefficient $2\alpha_{m0} = 2.5 \times 10^{-4}$ cm $^{-1}$. Suppose the laser is to use mirrors with 100% and 98% reflectivity at the two ends, and that internal cavity power losses are 0.5% per one-way pass. For mechanical reasons the laser mirrors must be 3 cm beyond the end of the discharge at each end.

While the laser is running, its axial-mode frequencies will slowly drift across the atomic-gain profile because of thermal expansion. Find the allowable range of cavity lengths which will ensure that during such drifts the laser will always oscillate in one or two axial modes, but never in three or more axial modes.

4. *Mode pulling of the axial-mode spacing in different types of lasers.* Calculate by how much the beat frequency between two adjacent axial modes will differ from the “cold cavity” $c/2L$ value as a result of atomic frequency pulling in the linear dispersion regime for the cases: (a) He-Ne 6328 Å laser, $L = 10$ cm, $T = 3\%$ for the output mirror, $R = 100\%$ for the other mirror; (b) Ruby laser at 77K, $L = 5$ cm, one end fully silvered ($R = 100\%$), output end completely unsilvered (air-dielectric reflection only). Hints: The index of refraction for sapphire is $n \approx 1.76$, and data on the atomic linewidth versus temperature for the ruby laser transition is given in Figure 3.5.

12.3 LASER OUTPUT POWER

We will next calculate the *power output* that can be obtained from an oscillating laser, as a function of the output coupling and the pumping power, using a simple laser model. In this section we will limit the derivation to a lightly coupled laser oscillator—that is, a laser in which the reflectivities of the laser end mirrors are not too much less than unity.

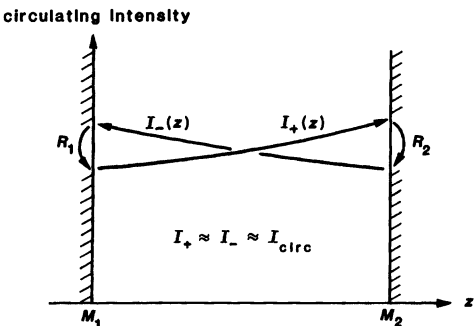
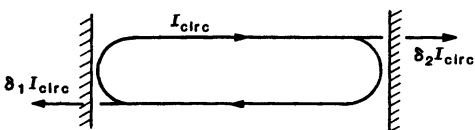


FIGURE 12.10

Left and right-traveling intensities in a laser oscillator with small output coupling.

power output



Steady-State Homogeneous Saturation Equations

We emphasized earlier that the round-trip power gain for the signal intensity inside a laser cavity must be exactly equal to unity under cw steady-state conditions. If we assume, for example, a standing-wave laser cavity with a simple homogeneously saturable gain medium, the growth of the two oppositely traveling waves $I_+(z)$ and $I_-(z)$ inside this cavity will be given by the two equations

$$\frac{dI_+(z)}{dz} = [2\alpha_m(z) - 2\alpha_0] I_+(z) \quad (24)$$

for the forward or $+z$ wave, and

$$\frac{dI_-(z)}{dz} = -[2\alpha_m(z) - 2\alpha_0] I_-(z) \quad (25)$$

for the reverse wave as illustrated schematically in Figure 12.10. (We will carry out all the calculations in this section for a *linear or standing-wave cavity*, leaving it to the reader to carry out the essentially similar calculations of power output and optimum output coupling for a ring-laser cavity.)

For a homogeneously saturable gain medium, which saturates at each transverse plane z according to the sum of the intensities $I_+(z)$ and $I_-(z)$ at that plane, the saturated gain coefficient as a function of position along the axis will be

$$2\alpha_m(z) = \frac{2\alpha_{m0}}{1 + [I_+(z) + I_-(z)]/I_{\text{sat}}}, \quad (26)$$

where α_{m0} is the unsaturated gain coefficient. This assumption neglects in-

terference or standing-wave effects between the right- and left-traveling waves, as discussed earlier in Section 8.2. Nonetheless, it serves as an excellent first approximation, and gives results that agree very well with experiment.

Small Output Coupling Approximation

Suppose now that the end-mirror reflectivities R_1 and R_2 are both close to unity, so that the intensities I_+ and I_- remain nearly constant along the length of the cavity, as in Figure 12.10. (The *unsaturated* gain per pass through the laser medium need not be small; but the net *saturated* gain per pass must be not much greater than unity.) We can then make the approximation that

$$I_+(z) \approx I_-(z) \approx I_{\text{circ}}, \quad (27)$$

where I_{circ} , the one-way circulating intensity inside the laser cavity, is to first order independent of position inside the cavity. The saturated gain coefficient is then similarly independent of position along the cavity, and can be written as

$$2\alpha_m \approx \frac{2\alpha_{m0}}{1 + 2I_{\text{circ}}/I_{\text{sat}}}. \quad (28)$$

The factor of 2 in the denominator arises, of course, because the laser medium sees equal intensities I_{circ} traveling in both directions along the cavity.

Steady-State Oscillation Condition

The threshold and/or the steady-state gain condition for the laser oscillator is then given by

$$2\alpha_m p_m \approx \frac{2\alpha_{m0} p_m}{1 + 2I_{\text{circ}}/I_{\text{sat}}} = 2\alpha_{0p} + \ln\left(\frac{1}{R_1 R_2}\right) \equiv \delta_0 + \delta_1 + \delta_2. \quad (29)$$

The circulating intensity inside the cavity that must build up in order to saturate the gain factor $2\alpha_{m0} p_m$ down to where it just equals the total cavity losses $\delta_0 + \delta_1 + \delta_2$ is thus given by

$$I_{\text{circ}} = \left[\frac{2\alpha_{m0} p_m}{\delta_0 + \delta_1 + \delta_2} - 1 \right] \times \frac{I_{\text{sat}}}{2}. \quad (30)$$

It is often convenient to define a threshold ratio r given by

$$r \equiv \frac{2\alpha_{m0} p_m}{\delta_0 + \delta_1 + \delta_2} = \frac{\text{unsaturated round-trip laser gain}}{\text{total round-trip cavity losses}}. \quad (31)$$

The condition $r = 1$ then corresponds to threshold; and the value of $r \geq 1$ tells by how much the laser gain is pumped above threshold. The circulating intensity inside a standing-wave cavity can then be written as

$$I_{\text{circ}} = (r - 1) \times \frac{I_{\text{sat}}}{2}. \quad (32)$$

This expression, of course, has meaning only so long as the laser is above threshold, so that $r > 1$ or $2\alpha_{m0} p_m > \delta_0 + \delta_1 + \delta_2$.

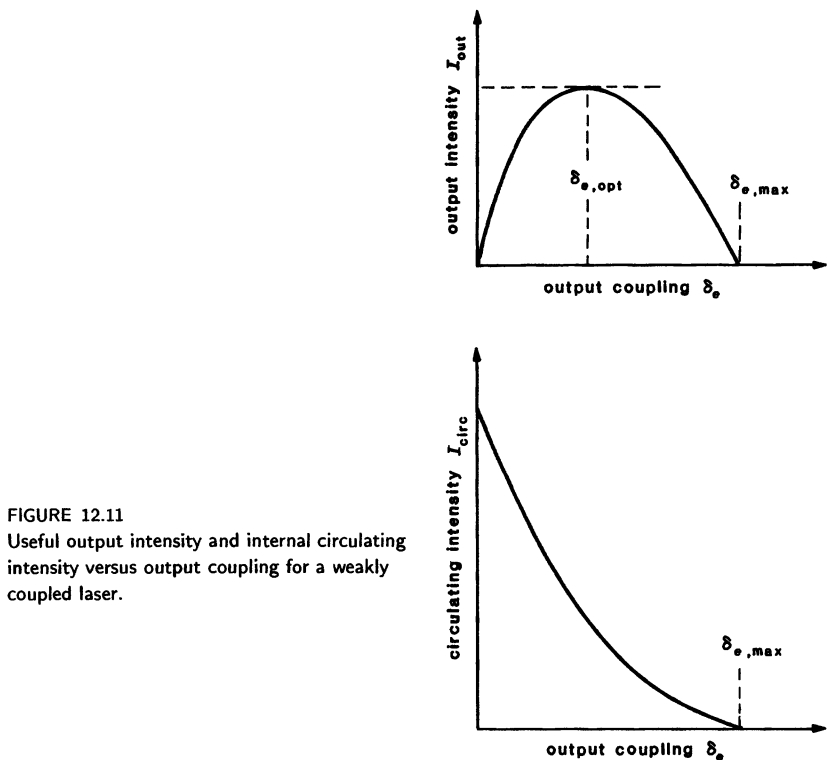


FIGURE 12.11
Useful output intensity and internal circulating intensity versus output coupling for a weakly coupled laser.

Laser Power Output

Now, for a lightly coupled laser cavity, the end-mirror transmissions are given by $T_1 = 1 - R_1 \approx \delta_1$ and $T_2 = 1 - R_2 \approx \delta_2$, so long as both δ_1 and δ_2 are reasonably small compared to unity. Normally in a laser we take the power output from one end of the cavity only. The total potentially useful output intensity (power per unit area) is really the power from both ends of the laser cavity, however, or

$$I_{\text{out}} = (\delta_1 + \delta_2) \times I_{\text{circ}} = \delta_e \times I_{\text{circ}}, \quad (33)$$

where we have defined one additional delta factor δ_e (with "e" standing for "external") by the definition

$$\delta_e \equiv \delta_1 + \delta_2 = \text{external cavity coupling.} \quad (34)$$

The value of δ_e thus represents the total *external coupling*, or *output coupling*, through both ends of the laser cavity. At least for small coupling, δ_e represents the total fractional power coupled out per round trip through the external mirrors (or whatever other output coupling mechanism might be employed).

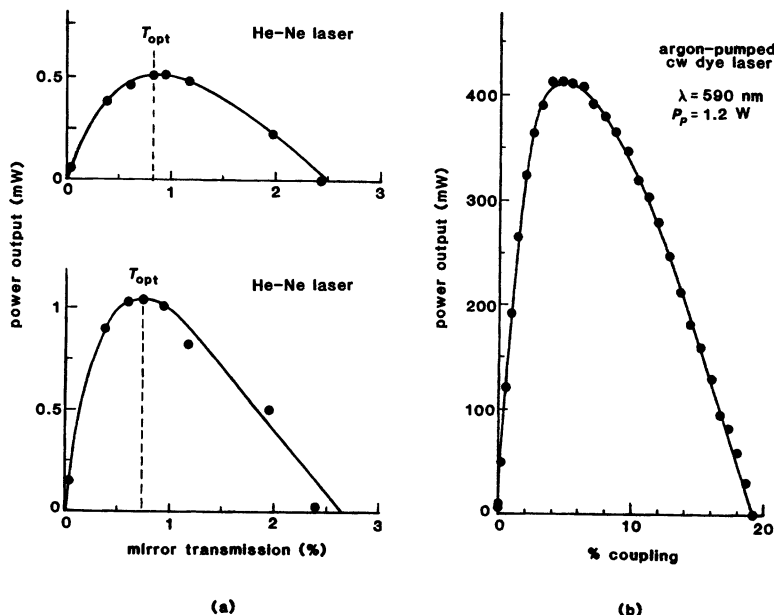


FIGURE 12.12

(a) Typical experimental results for laser power output versus coupling in two low-gain He-Ne lasers. (b) Similar results for a higher-gain cw dye laser. (Adapted from P. Laures, *Phys. Lett.* **10**, 61, May 15, 1964; and from C. V. Shank *et al.*, *Opt. Commun.* **7**, 176–177, March 1973.)

The total output intensity, as a function of the unsaturated gain $2\alpha_{m0}$, the internal cavity losses δ_0 , and this external coupling factor δ_e , then becomes

$$I_{\text{out}} = \delta_e \left[\frac{2\alpha_{m0}p_m}{\delta_0 + \delta_e} - 1 \right] \frac{I_{\text{sat}}}{2}. \quad (35)$$

Figure 12.11 shows a typical example of how both the circulating power and the output power vary with external coupling.

Experimental Verification

Some representative experimental results for power output versus output mirror transmission are shown in Figure 12.12, both for two very low-gain He-Ne lasers, and for a considerably higher-gain argon-laser-pumped Rhodamine 6G dye laser. Note that the results for the dye laser agree very well with the predicted form derived earlier, even though the maximum output coupling of $\approx 20\%$ is becoming significant compared to unity.

Mirrors or output couplers with continuously variable transmission or output coupling are not readily available, especially for small values of output coupling; and performing experiments like those shown in Figure 12.12 with a series of different transmission mirrors on a low-gain, low-coupling laser can be difficult,

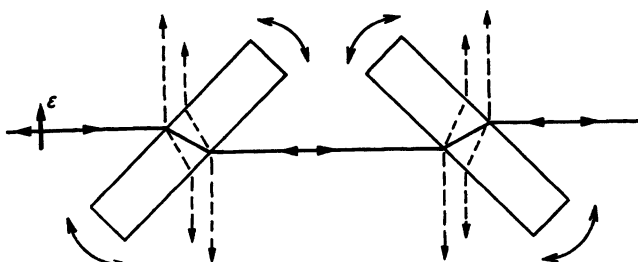


FIGURE 12.13

Device for small variable insertion loss or output coupling. The plates are operated near Brewster's angle, where all the reflections vanish.

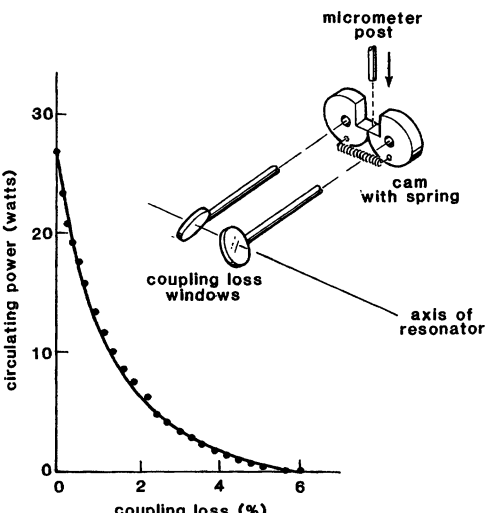


FIGURE 12.14

Circulating power versus coupling loss in a weakly coupled Nd:YAG laser.

because the laser must be readjusted and realigned with each change of mirrors, and because you can never be certain that all the mirrors are equally lossless and defect-free.

Figure 12.13 shows a device that uses two contra-rotating dielectric plates tilted near Brewster's angle, where the output reflectivity from each surface of the plates passes through zero, in order to produce a variable output coupling or insertion loss in a laser cavity. (The same device is also very useful as a separate external optical attenuator; the use of two plates means that the optical axis of the laser beam suffers no net transverse displacement as the plates are rotated in opposite directions.) Figure 12.14 then shows a careful measurement, made using one of these devices, of the circulating power inside a cw Nd:YAG laser, with results in excellent agreement with theory. Note that though the output power from this laser is only a few hundred milliwatts, the circulating power inside the cavity is several tens of Watts.

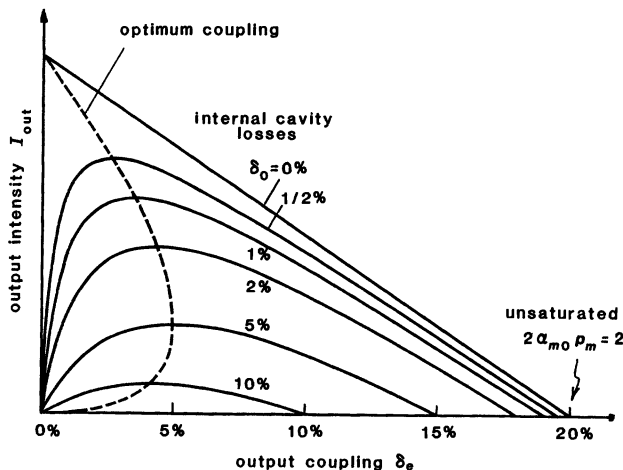


FIGURE 12.15

Laser output intensity versus output coupling δ_e assuming an unsaturated gain coefficient $2\alpha_{m0}p_m = 20\%$ and different values of the internal cavity loss factor $2\alpha_0 p$.

Optimum Output Coupling Factor

For any of the lasers shown in Figures 12.11 or 12.12 there is obviously a maximum allowable output coupling, given by $\delta_{e,\max} \equiv 2\alpha_{m0}p_m - 2\alpha_0 p = \delta_{m0} - \delta_0$, beyond which the cavity is overloaded, so that total cavity losses exceed the available gain, and no oscillation is possible. As the cavity coupling or end-mirror transmission is reduced below this value, both the circulating intensity and the output intensity increase with decreasing coupling. Below a certain optimum coupling factor $\delta_{e,\text{opt}}$, however, the mirror transmission decreases faster than I_{circ} increases, and the power output decreases, eventually becoming zero at zero transmission through the end mirrors. The laser at this point is, of course, still oscillating—in fact, oscillating the strongest of all—but with all its available power being uselessly dissipated in the internal cavity losses.

Figure 12.15 illustrates in more detail how the laser output intensity for a typical laser depends on the cavity output coupling, assuming a fixed value of 20% power gain per round trip, and varying amounts of internal cavity loss. It is evident that for each different value of internal cavity loss there is a different optimum output coupling which maximizes the output power. It is also apparent that the optimum output coupling is always considerably smaller than the available gain, and that even very small internal losses have a very serious effect on the maximum useful output power available from the laser.

It is a straightforward calculation to evaluate the optimum output coupling for given values of unsaturated gain and internal cavity losses. Differentiation of the expression for output intensity given in Equation 12.35 with respect to the output coupling δ_e gives for this optimum coupling

$$\delta_{e,\text{opt}} = \sqrt{2\alpha_{m0}p_m\delta_0} - \delta_0 = \left[\sqrt{\delta_{m0}/\delta_0} - 1 \right] \delta_0. \quad (36)$$

where $\delta_{m0} \equiv 2\alpha_{m0}p_m$. The dashed line in Figure 12.15 indicates the locus of these optimum coupling values.

One slightly unusual aspect evident from Figure 12.15 is that the optimum coupling value apparently goes to zero as the internal cavity losses go to zero, i.e., $\delta_{e,\text{opt}} \rightarrow 0$ as $\delta_0 \rightarrow 0$. In the limiting case of zero internal losses, we would apparently get maximum output by using end mirrors with 100% reflectivity and zero transmission!

The explanation of this minor paradox is, of course, that as both δ_0 and δ_e go to zero, the internal circulating power I_{circ} goes to ∞ ; and the product of zero coupling times infinite circulating power leads to a finite power output. Real laser cavities will, of course, always have some small but finite losses, and so will always require an equally small but finite output coupling.

Optimum Output Power and Power Extraction Efficiency

If one adjusts a standing-wave laser oscillator for optimum output coupling, the output intensity with this optimum coupling is then given by

$$\begin{aligned} I_{\text{out, opt}} &= \left[\sqrt{2\alpha_{m0}p_m} - \sqrt{\delta_0} \right]^2 \frac{I_{\text{sat}}}{2} \\ &= \left[1 - \sqrt{\delta_0/\delta_{m0}} \right]^2 \times [2\alpha_{m0}L_m I_{\text{sat}}], \end{aligned} \quad (37)$$

where we have used $p_m \equiv 2L_m$. But the second term in the second line of this expression can be recognized as the same maximum available intensity from the laser medium that we obtained in our earlier discussion of laser amplification (Section 7.7), that is, $I_{\text{avail}} \equiv 2\alpha_{m0}L_m I_{\text{sat}}$.

We can then identify the remaining factors in the output intensity formula as defining the *power extraction efficiency* η with which the laser oscillator extracts energy from the laser medium and converts it into useful power output. In particular, for a standing-wave laser cavity with arbitrary gain, loss, and output coupling, the extraction efficiency will be given in general by

$$\eta(\delta_0, \delta_e) \equiv \frac{I_{\text{out}}(\delta_0, \delta_e)}{I_{\text{avail}}} = \left[\frac{\delta_e}{\delta_0 + \delta_e} - \frac{\delta_e}{2\alpha_{m0}p_m} \right]. \quad (38)$$

The maximum value of this extraction efficiency with optimum output coupling, or $\delta_e = \delta_{e,\text{opt}}$, then becomes

$$\eta_{\text{opt}} = \left[1 - \sqrt{\frac{\delta_0}{2\alpha_{m0}p_m}} \right]^2, \quad (39)$$

which depends only on the ratio of internal losses to unsaturated gain.

The most significant aspect of these results is the extremely serious effect that even very small internal losses ($\delta_0 \ll 2\alpha_{m0}p_m$) will have on the useful power output. Figure 12.16 shows how this optimum extraction efficiency rapidly decreases as the ratio of internal losses to unsaturated gain increases.

Note, for example, that internal losses only one-tenth as large as the unsaturated gain will reduce the optimized output intensity to less than 50% of its maximum value; and internal cavity losses equal to half the unsaturated gain will reduce the energy extraction efficiency to $\eta_{\text{opt}} \approx 9\%$. To put this another way, in

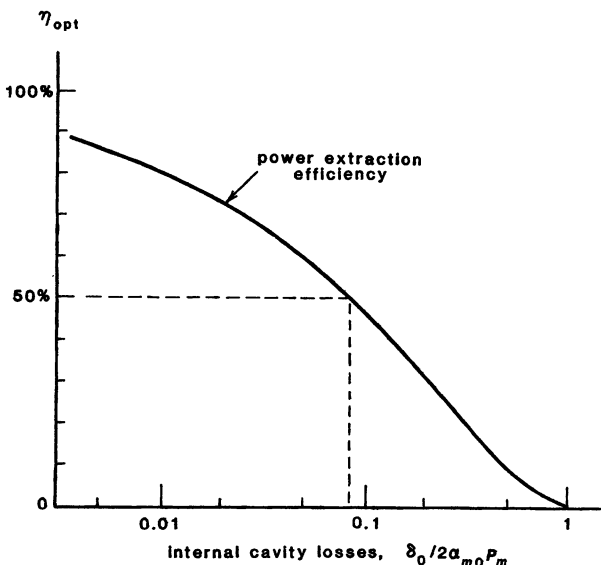


FIGURE 12.16

Even very small internal losses, relative to the laser gain, will cause a large reduction in power extraction efficiency in a low-gain laser oscillator.

a laser with 5% power gain per pass, to extract even 50% of the potentially available power output we must cut the internal cavity losses to $\leq 0.3\%$ —something which can be very difficult to do in a real laser cavity.

If the internal losses can be made sufficiently small, however, then the extraction efficiency of a laser oscillator—in contrast to our earlier results for single-pass laser amplifiers—can approach 100% with optimum coupling. A properly coupled low-loss oscillator can extract nearly all the power that is available in a laser material, something that is much more difficult to do if the same medium is used as a single-pass laser amplifier.

Power Output Versus Pumping

We showed in earlier chapters that in many real laser systems the unsaturated gain coefficient $2\alpha_{m0}$ increases linearly with the pumping power applied to the laser, whereas the magnitude of the saturation intensity I_{sat} is most often independent of the pumping power. If this is so, then we can view the dimensionless gain factor r that we defined earlier as also representing a *dimensionless pumping ratio*, which gives the amount that the laser is pumped above its oscillation threshold, i.e.,

$$r \equiv \frac{2\alpha_{m0}p_m}{\delta_0 + \delta_e} = \frac{R_p}{R_{p,\text{th}}} = \frac{\text{pumping power}}{\text{threshold pump power}}. \quad (40)$$

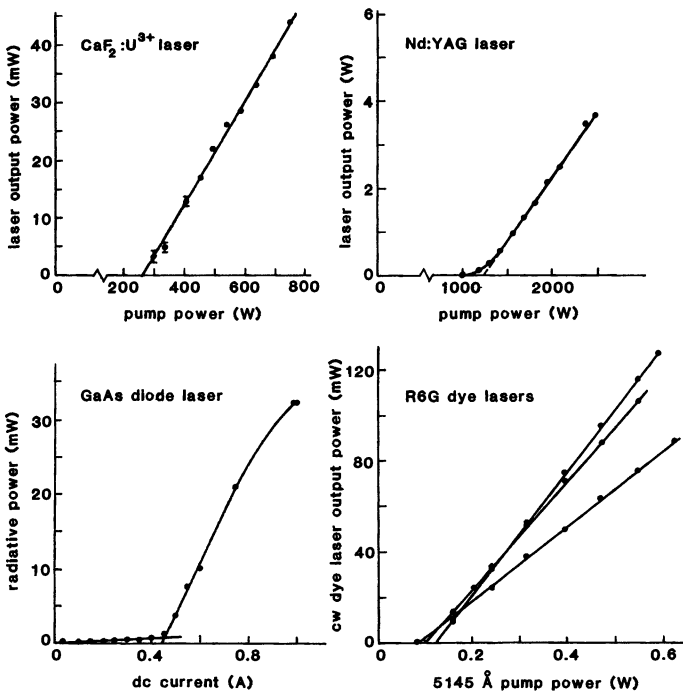


FIGURE 12.17

Laser power outputs versus pumping input for two cw arc-lamp-pumped solid-state lasers, a direct-current-pumped semiconductor diode laser, and a laser-pumped cw dye laser oscillator, all illustrating a similar linear output variation above threshold.

Equation 12.35 laser output intensity then becomes

$$I_{\text{out}} = \frac{(r-1)\delta_e I_{\text{sat}}}{2} = \left[\frac{R_p}{R_{p,\text{th}}} - 1 \right] \times \frac{\delta_e I_{\text{sat}}}{2}. \quad (41)$$

The power output versus pumping power or pumping rate, at fixed coupling, for a great many lasers will therefore be zero up to a certain threshold pumping level corresponding to $r = 1$, and will then rise more or less linearly with pumping rate above this threshold.

To illustrate this point, Figure 12.17 shows the oscillation power outputs versus pump power input for some very different lasers, including two cw lamp-pumped solid-state lasers; a dc-current-pumped semiconductor diode laser; and a laser-pumped cw dye laser, operating with three different end-mirror transmissions on the laser. These results are typical of many different experimental results for many different types of laser devices, all showing more or less linear variation of laser output with pump input for substantial distances above their pump thresholds.

A particularly pretty illustration of several fundamental aspects of laser physics is also shown by the experimental results for two similar narrow-strip

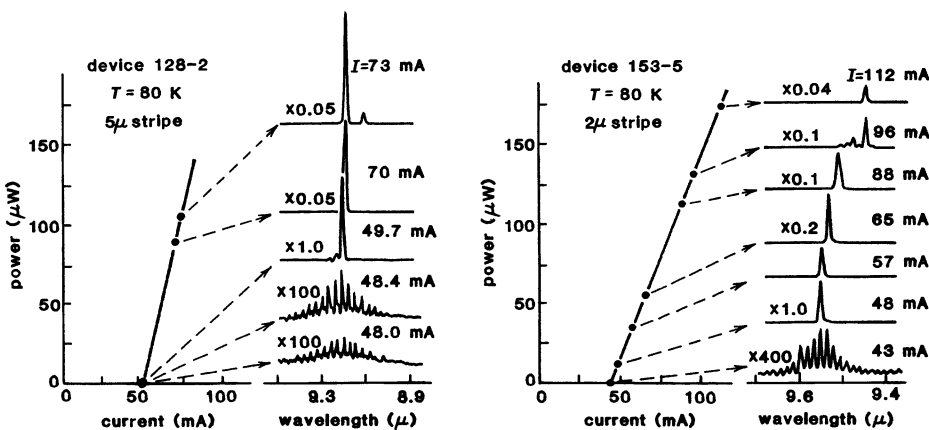


FIGURE 12.18

Power outputs and output spectra versus pumping current for two similar narrow-stripe PbSnTe buried heterostructure laser diodes oscillating near $9.5\text{ }\mu\text{m}$. (Adapted from D. Kasemset and C. C. Fonstad, *Appl. Phys. Lett.*, **39**, 8720-874, December 1, 1981.)

buried heterostructure injection diode lasers shown in Figure 12.18. These lasers are both PbSnTe diodes, fabricated using liquid-phase epitaxy, with active regions 1 to $1.5\text{ }\mu\text{m}$ thick, 2 to $5\text{ }\mu\text{m}$ wide, and 250 to $450\text{ }\mu\text{m}$ long, oscillating in a single transverse mode at wavelengths near $9.5\text{ }\mu\text{m}$. The experimental spectra clearly show (i) the regeneratively amplified spontaneous emission at the axial-mode peaks just at or below threshold; (ii) the sudden changeover to essentially a single oscillating axial mode produced by a very small change in current just at threshold (note the changes in vertical magnification between adjacent spectra); and (iii) the extreme linearity of the power output versus pumping current above threshold. The laser transition is clearly very homogeneous in its spectral behavior.

REFERENCES

Two early laser analyses which include and extend the results of this section, and of the preceding section, are P. A. Miles and I. Goldstein, "Effects of output coupling on optical masers," *IEEE Trans. on Electron Devices* **ED-10**, 314-318 (September 1963); and A. Yariv, "Energy and power considerations in injection and optically pumped lasers," *Proc. IEEE* **51**, 1723-1731 (December 1963).

The YAG circulating power measurements in this section are from R. R. Rice, J. R. Teague, and J. E. Jackson, "Dynamic coupling characteristics of TEM Nd:YAG lasers," *J. Appl. Phys.* **46**, 2716-2720 (June 1975).

Problems for 12.3

1. Optimum coupling analysis for a unidirectional ring-cavity laser. Repeat the small-coupling analysis of this section for a unidirectional ring-cavity laser (i.e., one that oscillates in only one direction around the ring). Find the power out-

put versus coupling, the optimum output coupling, and the power-extraction efficiency.

Suppose that exactly the same laser medium, with a fixed length L_m , fixed gain coefficient α_{m0} , and fixed loss coefficient α_0 (assume all the losses are in the laser medium itself), is to be used in either a standing-wave or a unidirectional ring cavity. Plot the power output versus coupling for each, assuming a 10% one-way unsaturated power gain and a 2% one-way power loss through the laser medium.

2. *Internal losses and optimum coupling in real lasers.* For the various experimental curves of power output versus coupling illustrated in Figure 12.12 can you deduce what the internal losses must have been in each situation, and hence what the power extraction efficiencies at optimum coupling must have been?
3. *Laser power output versus tuning.* Suppose that the frequency of a single axial mode can be tuned across the full gain profile of a homogeneous laser transition at fixed pump power, with all other axial modes suppressed or spaced far outside the gain profile. Show that the power output versus frequency curve for this mode can be written as

$$I_{\text{out}}(\omega) = \left[r - 1 - \left(2 \frac{\omega - \omega_a}{\Delta\omega_a} \right)^2 \right] \times \frac{\delta_e I_{\text{sat}}}{2},$$

and that the full tuning range over which this mode will oscillate is given by $\Delta\omega_{\text{osc}} = \Delta\omega_a \times \sqrt{r - 1}$, where r measures how far above threshold the laser is pumped at line center.

4. *Laser oscillator with both saturable gain and saturable loss.* A laser cavity contains both a saturable gain medium with low-level gain coefficient α_{m0} and saturation intensity $I_{\text{sat},m}$; and a saturable absorbing medium with low-level absorption coefficient α_{a0} and saturation intensity $I_{\text{sat},a}$; and also some nonsaturating losses (such as scattering losses or output coupling losses) represented by a non-saturating absorption coefficient α_0 . Find the steady-state internal intensity I_{circ} at which this laser will oscillate (or possibly will not oscillate) for different relative ratios of α_{m0} , α_{a0} , and α_0 , and also of $I_{\text{sat},m}$ and $I_{\text{sat},a}$. Hint: there are several physically different situations that have to be considered here.
5. *Cross coupling between oscillation power and a separately injected signal.* A low-gain cavity laser with a homogeneously saturable laser medium is oscillating on an axial mode located exactly at line center. A separate laser signal of intensity I_1 tuned exactly to line center is also sent through the same laser medium at a very slight angle so that this external signal misses the laser mirrors but illuminates exactly the same volume of atoms as the oscillation signal inside the laser cavity. Develop an expression for the oscillation power output through the end mirrors of the laser cavity as a function of the externally injected signal level and the usual laser parameters.
6. *Second-harmonic output coupling.* When a laser beam passes through certain nonlinear optical crystals, such as lithium niobate (LiNbO_3) or potassium dihydrogen phosphate (KH_2PO_4), a portion of the incident intensity at the laser frequency ω can be converted into second-harmonic radiation at the doubled frequency 2ω . For small conversion efficiency, the second-harmonic power generated is given by $I(2\omega) = K_2 I^2(\omega)$, where K_2 is the harmonic-generation coefficient. The power converted into second harmonic is of course taken away from the fundamental intensity.

The conversion efficiency from $I(\omega)$ to $I(2\omega)$ with low-power cw laser beams is usually very small (a few percent or less), because the nonlinearity coefficient K_2 in real crystals is typically small. The amount of second-harmonic power obtained from a low-power laser can be increased by placing the nonlinear crystal inside the laser cavity, where the circulating intensity is much larger than outside the cavity. (Special mirrors are used to let the harmonic radiation escape while reflecting the fundamental-frequency laser radiation.) The second harmonic radiation then becomes the useful output coupling from the laser.

Analyze this type of second-harmonic output coupling by considering a ring-laser cavity which contains a homogeneously saturable gain medium; some small internal cavity losses at the fundamental frequency; and a square-law second-harmonic generation crystal whose conversion coefficient K_2 can be adjusted, for example, by changing the nonlinear crystal length or the degree of fundamental beam focusing inside the crystal. Assume the fundamental frequency output coupling is zero, i.e., 100% reflecting mirrors at ω are employed. Find the value of the nonlinearity coefficient K_2 that will maximize the second-harmonic power output from this laser, and discuss in general how the harmonic power output can be optimized, and how the power output at 2ω can compare with the optimum fundamental power that could be obtained from the same laser medium. Will the optimum nonlinearity K_2 change if the laser pumping rate is changed?

For literature references on this subject, see R. G. Smith, "Theory of intracavity optical second-harmonic generation," *IEEE J. Quantum Electron.* **QE-6**, 215-223 (April 1970); D. Frölich, L. Stein, H. W. Schröder, and H. Welling, "Efficient frequency doubling of cw dye laser radiation," *Appl. Phys.* **11**, 97-101 (1976); and A. I. Ferguson and M. H. Dunn, "Intracavity second-harmonic generation in continuous-wave dye lasers," *IEEE J. Quantum Electron.* **QE-13**, 751-756 (September 1977).

12.4 LARGE OUTPUT COUPLING ANALYSIS

The power-output analysis of the previous section was based on a weak-coupling approximation. A more accurate analysis of the power output from a homogeneous laser with arbitrarily large round-trip gain and output coupling was originally developed by W. W. Rigrod at Bell Telephone Laboratories, and is often referred to as the "Rigrod analysis."

As we will demonstrate in this section, for a laser with large unsaturated atomic gain the power output remains fairly constant over a very wide range of output coupling, so that critical adjustment of the output coupling is not as essential for reasonably good energy extraction as it is for a low-gain laser.

Analytical Formulation: The Rigrod Analysis

The analysis we will repeat here assumes a homogeneously saturable gain medium as in Section 12.3, but no distributed losses, so that $2\alpha_0 p \equiv 0$. Following Rigrod's original notation, as shown in Figure 12.19, we use $I_+(z)$ and $I_-(z)$ to indicate the intensities traveling toward $+z$ and $-z$, respectively, in the cavity.

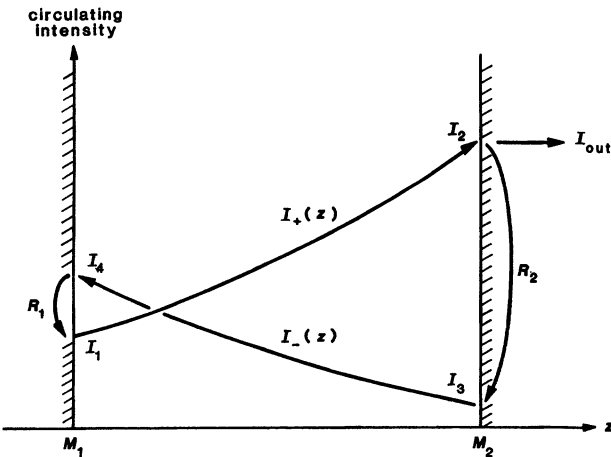


FIGURE 12.19

Left and right-traveling intensities in a laser oscillator with large output coupling.

These intensities then grow with distance according to the equations

$$\begin{aligned}\frac{dI_+(z)}{dz} &= +2\alpha_m(z)I_+(z), \\ \frac{dI_-(z)}{dz} &= -2\alpha_m(z)I_-(z).\end{aligned}\quad (42)$$

(The sign changes in the second equation because the waves are traveling in the $-z$ direction.) For simplicity, let us assume that I_+ and I_- are normalized to the saturation intensity I_{sat} of the medium. The gain coefficient $\alpha_m(z)$ at any plane z then saturates according to the total intensity at that plane in the form

$$\alpha_m(z) = \frac{\alpha_{m0}}{1 + I_+(z) + I_-(z)}. \quad (43)$$

Writing the gain in this form takes into account the spatial variation of both the forward- and the backward-traveling waves in a high-gain cavity, but neglects any spatial hole burning or induced-grating coupling effects caused by standing waves or by interference between the forward- and the backward-traveling waves inside the laser cavity.

By combining the two derivatives in Equation 12.42, we can see that the product of the intensities in the two directions at any plane is constant, i.e.,

$$\frac{d}{dz}[I_+(z)I_-(z)] = -2\alpha_m I_+ I_- + 2\alpha_m I_+ I_- = 0, \quad (44)$$

so that we can write at any plane

$$I_+(z)I_-(z) = \text{constant} = C. \quad (45)$$

The differential equation for, say, the $I_+(z)$ wave can then be written as

$$\frac{dI_+(z)}{dz} = \frac{2\alpha_{m0}I_+(z)}{1 + I_+(z) + C/I_+(z)}, \quad (46)$$

and this can be integrated over the length of the laser medium in the form

$$\int_{I_1}^{I_2} \left(1 + \frac{1}{I_+} + \frac{C}{I_+^2} \right) dI_+ = 2\alpha_{m0} \int_0^L dz. \quad (47)$$

Carrying out the same procedure for the $I_-(z)$ wave, and using the boundary conditions shown in Figure 12.19, then leads to the pair of expressions

$$\begin{aligned} 2\alpha_{m0}L &= \ln \left(\frac{I_2}{I_1} \right) + I_2 - I_1 - C \left(\frac{1}{I_2} - \frac{1}{I_1} \right), \\ 2\alpha_{m0}L &= \ln \left(\frac{I_4}{I_3} \right) + I_4 - I_3 - C \left(\frac{1}{I_4} - \frac{1}{I_3} \right). \end{aligned} \quad (48)$$

In addition we have the mirror power reflection coefficients $I_1 = R_1 I_4$ and $I_3 = R_2 I_2$, and the two product relations at the end surfaces, namely, $I_1 I_4 = I_2 I_3 = C$.

By combining all these relations, together with some minor manipulation, we can eliminate the constant C and obtain the result that, for example, the normalized intensity striking the right-hand mirror is

$$I_2 = \frac{1}{(1 + r_2/r_1)(1 - r_1 r_2)} \left[2\alpha_{m0}L - \ln \left(\frac{1}{r_1 r_2} \right) \right], \quad (49)$$

where $r_1 \equiv R_1^{1/2}$ and $r_2 \equiv R_2^{1/2}$ are the voltage reflection coefficients of the mirror.

Power Output and Power-Extraction Efficiency

Let us now assume that mirror M_2 is the output mirror of the laser, with output coupling T_2 and reflection coefficient R_2 , and that any finite reflectivity R_1 of the other mirror M_1 represents unwanted or unavoidable losses in that mirror. Then the useful output intensity from the laser (with all intensities measured now in real intensity units) will be

$$I_{\text{out}} = T_2 I_2 = \frac{T_2 I_{\text{sat}}}{(1 + r_2/r_1)(1 - r_1 r_2)} \left[\ln G_0 - \ln \left(\frac{1}{r_1 r_2} \right) \right]. \quad (50)$$

We know from previous sections that the maximum intensity that can be extracted from such a laser medium is

$$I_{\text{avail}} = 2\alpha_{m0}L_m I_{\text{sat}} \equiv (\ln G_0) I_{\text{sat}}, \quad (51)$$

and hence the power-extraction efficiency, or the normalized output intensity, of the laser can be written as

$$\eta \equiv \frac{I_{\text{out}}}{I_{\text{avail}}} = \frac{T_2}{(1 + r_2/r_1)(1 - r_1 r_2)} \left[1 + \frac{\ln r_1 r_2}{\ln G_0} \right]. \quad (52)$$

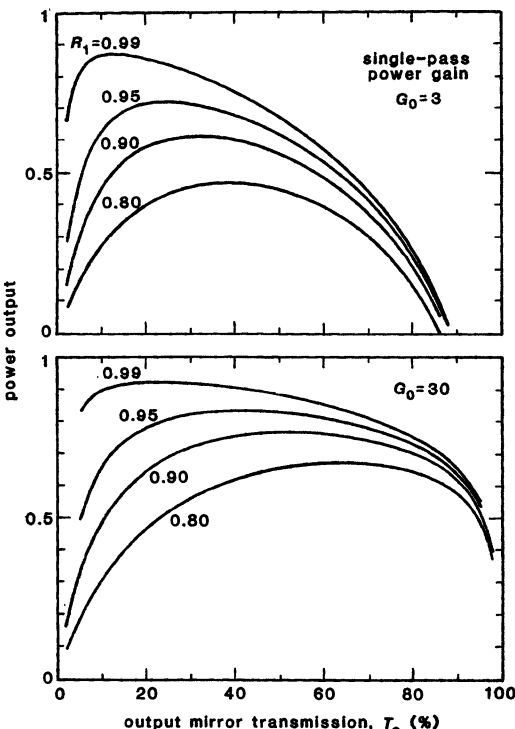


FIGURE 12.20

Normalized power output versus output mirror transmission T_2 for homogeneous high-gain laser oscillators with unsaturated single-pass gains of $G_0 = 3$ and $G_0 = 30$, for varying values of the mirror reflectivity R_1 at the opposite (nonoutput) end, according to the Rigrod analysis.

There are no small-amplitude restrictions on the unsaturated gain G_0 or the output coupling level in this formula.

Typical Results

Examples of power output versus coupling as given by this formula for two comparatively large values of one-way unsaturated power gain G_0 are shown in Figure 12.20. For large values of G_0 and for reflectivity R_1 on the left-hand mirror not too much less than unity, the power output is roughly constant over a very wide range of output couplings. The exact output coupling level applied to a high-gain laser is thus not nearly as critical a factor as it is for a low-gain laser.

At the same time it is evident that even fairly small losses caused by the finite reflectivity $R_1 < 1$ at the left-hand mirror do have a significant effect on the useful power output from the other end. Obtaining the maximum available power output clearly requires minimum internal losses ($R_1 \rightarrow 100\%$), and power output is generally maximized by smaller rather than larger coupling ($T_2 \leq 50\%$).

We could obviously differentiate Equation 12.50 or 12.52 to find the optimum output coupling $T_{2,\text{opt}}$ and the associated optimum output power. This yields, however, a transcendental equation for $T_{2,\text{opt}}$ does not seem useful to discuss in more detail here. Internal cavity losses an internal absorption coefficient $2\alpha_0$



FIGURE 12.21
Measured output energy versus coupling in an atomic iodine photodissociation laser at different buffer gas pressures.

could also be added to the differential equations for the laser, but these equations then become much more difficult to integrate. The general effects of small distributed losses in the laser cavity are best assessed by assuming them to be incorporated as part of the left-hand mirror reflectivity R_1 .

Many experimental examples of measured power output versus coupling in confirmation of the Rigrod analysis can be found in the literature. Figure 12.21 shows, for example, the power output versus output mirror reflectivity for a large atomic iodine photodissociation laser, intended as an amplifier (with a one-way power gain of 200 to 300 times), but used in these tests as an oscillator.

REFERENCES

The analysis in this section is from W. W. Rigrod, "Saturation effects in high-gain lasers," *J. Appl. Phys.* **36**, 2487-2490 (August 1965). A complementary discussion, including inhomogeneous transitions, is W.W. Rigrod, "Gain saturation and output power of optical masers," *J. Appl. Phys.* **34**, 2602-2609 (September 1963); and a more general discussion including distributed internal loss is W. W. Rigrod, "Homogeneously broadened CW lasers with uniform distributed loss," *IEEE J. Quantum Electron.* **QE-14**, 377-381 (May 1978). See also G. M. Schindler, "Optimum output efficiency of homogeneously broadened lasers with constant loss," *IEEE J. Quantum Electron.* **QE-16**, 546-549 (May 1980). A rather opaque Rigrod-type analysis for ring-laser oscillators is A. C. Eckbreth, "Coupling considerations for ring lasers," *IEEE J. Quantum Electron.* **QE-11**, 796-798 (September 1965).

The various simplifying approximations usually made in laser power analyses are examined and estimates of their validity given by L. W. Casperson, "Laser power calculations: sources of error," *Appl. Opt.* **19**, 422-434 (February 1 1980).

Problems for 12.4

1. *Optimum output coupling for a large-gain Rigrod-type laser.* Consider a homogeneous high-gain laser which obeys the Rigrod analysis. Suppose there are no internal losses; the round-trip unsaturated power gain is 5; the non-output mirror has a power reflectivity of 95%; and the output mirror has adjustable coupling with $R+T = 1$ (i.e., no loss in this mirror). What is the optimum output coupling

from this laser, and the power-extraction efficiency at that coupling? (Only the power coming through the output mirror is counted as useful power.)

2. *Total power output from a high-gain laser oscillator.* Develop an analysis for the total power output from both ends of a high-gain Rigrod-type laser, and plot some examples of the total power output versus mirror transmission T_2 for various choices of the opposite reflectivity R_1 . How much difference in efficiency does it make to include the power output from both ends?
3. *Dual output coupling values for a high-gain laser oscillator.* The Rigrod analysis shows that a standing-wave oscillator can have the same power output through mirror M_2 for two very different values of output coupling T_2 . For example, with $G_0 = 10$ and $R_1 = 0.95$ the power output will have the same value for either $R_2 \approx 0.11$ (i.e., very heavy output coupling) or for $R_2 \approx 0.949$ (i.e., very light output coupling). Examine the difference in internal behavior of the laser for these two couplings, and explain in physical terms how these two very different couplings can lead to the same useful power output.
4. *Rigrod analysis of a one-way ring-laser oscillator.* Develop a large-output-coupling analysis of laser output power versus output coupling for a ring-cavity laser oscillator. Assume a three-mirror (triangular) ring cavity with the output mirror having power reflection R_2 . The laser medium is located between the other two mirrors, both of which have power reflection R_1 . Only the power transmitted through the output mirror is useful. Plot power out versus coupling for $G_0 = 10$ and $R_1 = 0.99, 0.95$ and 0.90 , and compare with results for a standing-wave cavity using the same gain medium.
5. *Two-segment ring-laser oscillator.* Extend the preceding problem to a ring laser in which the gain medium is broken into two segments of equal length with a finite reflectivity mirror having reflection coefficient R_1 between the two segments. Assume the output mirror has reflection and transmission coefficients R_2 and T_2 . Compare your results to those for a standing-wave laser, assuming the same total gain medium and same value of R_1 in both.
6. *Gain saturation in a high-gain, double-pass laser amplifier.* A single-pass laser amplifier can be converted to double-pass operation (with twice the dB gain) by sending the input signal through the amplifier once in one direction and then reflecting it back through the same volume of the amplifier in the opposite direction. Two polarizers and a quarter-wave plate can be used to separate the incident and return beams, or the reflected beam can simply be tilted slightly so that the incident and reflected beams overlap within the medium but can be separated externally.

Using the Rigrod formalism, develop a relationship between input and output intensities from a homogeneous cw amplifier operated in this fashion. Evaluate the maximum available power and the power-extraction efficiency, and compare to the same laser medium operated as a single-pass amplifier.

OSCILLATION DYNAMICS AND OSCILLATION THRESHOLD

In this chapter we discuss a number of additional topics related to the elementary properties of laser oscillation. We consider first the oscillation build-up time with which coherent oscillation develops from noise in a laser cavity. From this we develop a set of simple coupled rate equations which link cavity photons to laser atoms, and laser atoms to cavity photons. Using these equations we explore further the laser oscillation buildup and the remarkable threshold properties characteristic of the laser oscillator.

We then examine briefly some of the more complex laser cavities that are useful in practice, including multimirror laser cavities, ring-cavity lasers, bistable laser systems, and “lasers” with no cavity at all.

13.1 LASER OSCILLATION BUILDUP

The primary question to be addressed in this section is: How fast does the coherent oscillation in a laser cavity build up from noise, when the laser is first turned on?

Oscillation Buildup Analysis

To answer this question, consider a laser cavity in which the laser gain exceeds the cavity losses, at least temporarily; and follow any small packet of signal energy through one complete round trip within the cavity, with a round-trip time $T = p/c$, as shown in Figure 13.1. The growth in circulating intensity in one round trip, starting with intensity I_0 at time $t = 0$, is then

$$I(T) = I_0 \times R_1 R_2 (R_3 \cdots) \exp [2\alpha_m p_m - 2\alpha_0 p] = I_0 \exp [\delta_m - \delta_c], \quad (1)$$

where all the notation has been defined in the preceding chapters. The net growth after N round trips will be given by

$$I(NT) = I_0 \times [R_1 R_2 (R_3 \cdots) e^{2\alpha_m p_m - 2\alpha_0 p}]^N = I_0 \exp[N(\delta_m - \delta_c)] \quad (2)$$

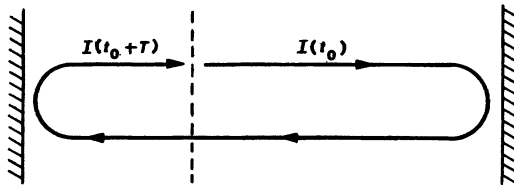


FIGURE 13.1
Round-trip intensity gain and travel time in a laser cavity.

which we can rewrite more generally as

$$I(t) = I_0 \exp \left[\frac{\delta_m - \delta_c}{T} t \right], \quad (3)$$

since the circulating intensity will make N round trips in a time $t = NT$. It can also be convenient to write this as

$$I(t) = I_0 \exp [(\gamma_m - \gamma_c) t], \quad (4)$$

where we define the cavity growth and decay rates by

$$\gamma_m \equiv \frac{\delta_m}{T} = \frac{2\alpha_m p_m}{T} \quad \text{and} \quad \gamma_c \equiv \frac{\delta_c}{T} = \frac{2\alpha_o p + \ln(1/R_{\text{tot}})}{T}, \quad (5)$$

where $R_{\text{tot}} \equiv R_1 R_2 (R_3 \cdots)$. The cavity lifetime or exponential decay time τ_c for optical signals in the cavity in the absence of laser gain is then given by

$$\tau_c \equiv \gamma_c^{-1} = \frac{T}{\delta_c}. \quad (6)$$

Since the round-trip time T for a typical laser cavity is 1 to 10 ns, and the round-trip cavity losses may range from 1% ($\delta_c = 0.01$) to, say, 70% ($\delta_c \approx 1$), typical “cold cavity” decay times (with no laser gain) will range from the order of 1 ns to the order of 1 μ s.

Oscillation Buildup

The signal in a laser cavity following a sudden initial turn-on of the laser gain will thus build up exponentially with time much as shown in Figure 13.2, starting from an initial noise level I_0 which is usually very small, typically corresponding to only a few spontaneous-emission noise photons in the cavity. This buildup will continue until the circulating intensity reaches a steady-state level I_{ss} with a very large number of photons in the cavity. This steady-state level corresponds to the oscillation level at which the laser gain is saturated down enough to just equal the total cavity losses (internal losses plus output coupling).

Figure 13.2 does assume either that the laser gain is very suddenly turned on to its full value at the start of the buildup interval, or else that some added cavity losses are suddenly turned off at this point, with a switching time short compared to the growth rate of the laser intensity. This may not be true in many real lasers. In an He-Ne laser, for example, the turn-on time for the plasma discharge and thus the laser gain will be much slower than the oscillation buildup time. In many other lasers, however, including E-beam-pumped excimer lasers, certain optically pumped lasers, and Q -switched lasers of all types, the gain can be switched on

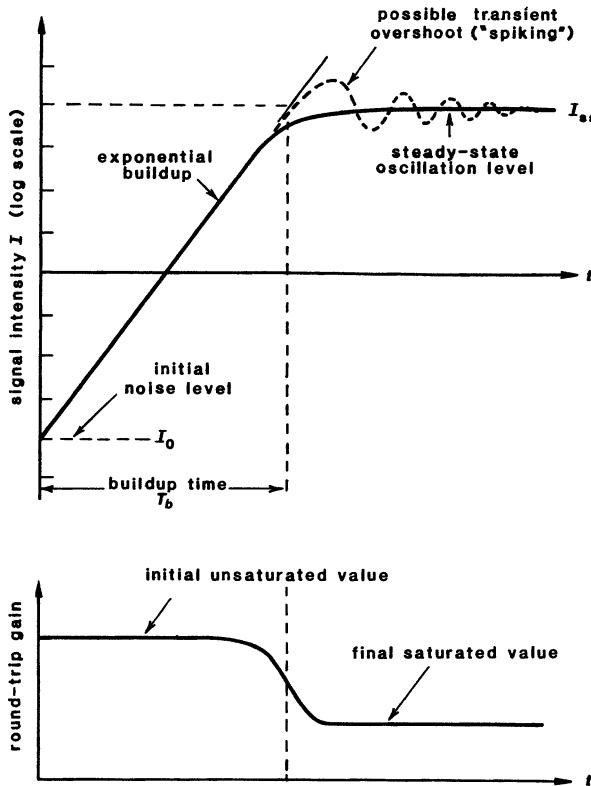


FIGURE 13.2

Exponential buildup of the signal intensity inside a laser cavity following sudden turn-on of the laser gain. The signal intensity starts from an initial noise level which is typically a few initial spontaneous-emission-noise photons, and grows to a very much larger steady-state oscillation level, with an approximate buildup time T_b . Certain lasers may approach the steady-state oscillation level with a transient overshoot or "spiking."

(or added losses switched off) in times short compared to the oscillation buildup time.

Typical Oscillation Buildup Times

It is very convenient in discussions such as these to define a *normalized inversion ratio* r as the ratio of the initial unsaturated gain coefficient δ_{m0} to the cold-cavity loss coefficient δ_c , or

$$r \equiv \frac{\delta_{m0}}{\delta_c} = \frac{\gamma_{m0}}{\gamma_c} = \frac{2\alpha_{m0}p_m}{2\alpha_{0p} + \ln(1/R_{\text{tot}})}, \quad (7)$$

The oscillation buildup rate of Equations 13.3 or 13.4 can then be written in the form

$$I(t) = I_0 \exp \left[\frac{r-1}{\tau_c} t \right]. \quad (8)$$

The total intensity buildup from the initial noise level I_0 to the final steady-state oscillation level I_{ss} is then given, to a good approximation, by

$$I_{ss} \approx I_0 \exp \left[\frac{r-1}{\tau_c} T_b \right] \quad (9)$$

or the buildup time T_b is given by

$$T_b \approx \frac{\tau_c}{r-1} \ln \left(\frac{I_{ss}}{I_0} \right). \quad (10)$$

The ratio of final oscillation level to initial noise level in real lasers may range from $I_{ss}/I_0 \approx 10^8$ to $I_{ss}/I_0 \approx 10^{12}$, depending on the type of laser. Since this ratio appears only logarithmically in the buildup-time expression of Equation 13.10, however, and since its logarithm varies only from $\ln(I_{ss}/I_0) \approx 18$ to $\ln(I_{ss}/I_0) \approx 28$, an exact knowledge of this ratio is not essential.

The general conclusion, in fact, is that the oscillation buildup time T_b may range from ≈ 10 to ≈ 30 cavity decay times τ_c , depending on how far the laser is pumped above threshold. Thus, for a rather long, low-loss He-Ne laser operated not far above threshold, with $L = 1$ m, $T = 6$ ns, $\delta_c = 3\%$, and $r = 1.1$, the buildup time will be $T_b \approx 50$ μ s. For a short, high-gain Nd:YAG laser pumped well above threshold, on the other hand, with $L = 30$ cm, $T = 2$ ns, $\delta_c = 0.5$, and $r = 3$, the buildup time shortens to $T_b \approx 50$ ns.

More Exact Buildup Analysis

In some but by no means all lasers the laser gain will saturate more or less immediately with increasing light intensity $I(t)$. Let us assume this, and also assume that the unsaturated growth rate γ_{m0} is not much greater than the cold-cavity decay rate γ_c , or that the initial inversion ratio r is not much greater than 1, so that the degree of saturation at steady state will remain small.

We can then write the instantaneous growth rate in a standing-wave laser oscillator cavity in the approximate form

$$\gamma_m(t) \approx \frac{\gamma_{m0}}{1 + 2I(t)/I_{sat}} \approx \gamma_{m0} [1 - 2I(t)/I_{sat}], \quad (11)$$

where $\gamma_{m0} \equiv r\gamma_c$ is the unsaturated laser growth rate. A more exact equation for the oscillation buildup, including gain saturation, can then be written in the form

$$\frac{dI}{dt} = \gamma I - \beta I^2, \quad (12)$$

where we have followed the notation commonly used in the literature, with $\gamma \equiv \gamma_{m0} - \gamma_c$ being the unsaturated growth rate and $\beta \equiv 2\gamma_{m0}/I_{sat}$ the saturation coefficient. The solution to this more exact equation is

$$I(t) = \frac{I_0 I_{ss} e^{\gamma t}}{I_{ss} + I_0 (e^{\gamma t} - 1)}, \quad (13)$$

where I_0 is the initial intensity at turn-on, corresponding usually to a few noise photons inside the laser cavity; and $I_{ss} \equiv \gamma/\beta = (1 - \gamma_c/\gamma_{m0}) \times I_{sat}/2$ is the steady-state oscillation level at the end of the buildup period. The time delay following gain turn-on needed to reach, say, half the final intensity is then given from this expression

$$T_b = \frac{1}{\gamma} \ln \left(\frac{I_{ss} - I_0}{I_0} \right) \approx \frac{\tau_c}{r-1} \ln \left(\frac{I_{ss}}{I_0} \right), \quad (14)$$

which is essentially the same result we obtained earlier.

Experimental Results

Figure 13.3 shows two examples of experimental results for oscillation buildup times in gas lasers. In Figure 13.3(a) a helium-neon laser which is initially oscillating at steady state is suddenly quenched by illuminating the He-Ne laser tube with a short but intense pulse of ultraviolet radiation from a xenon flashlamp. This UV radiation efficiently pumps neon atoms from a lower-lying $1s^5$ metastable level up into the lower level of the laser transition, thus destroying the laser gain and suddenly quenching the laser action, without significantly disturbing either the laser cavity or the laser discharge. The gain then recovers rapidly as these atoms relax back out of the lower laser level, and the laser oscillation builds back up again, with varying time delays for different steady-state intensities, as shown. Note that the numerical time delays agree generally with the numerical estimate of $\approx 50\mu\text{s}$ given earlier.

Figure 13.3(b) shows the buildup of oscillation in an optically pumped far-infrared laser that employs formic acid vapor as the laser medium for oscillation at a wavelength of $743\text{ }\mu\text{m}$. The pumping power coming from the $9\text{ }\mu\text{m}$ CO_2 laser that excites this laser is turned on very rapidly in step-function fashion, using an acousto-optic modulator that has a 70-ns rise time, much faster than the buildup time for the far-infrared oscillation. The experimental results shown can then be fitted very accurately into Equation 13.13 using only a single intensity-scaling parameter and a laser gain coefficient α_m that is directly proportional to the optical pumping power.

Spiking Behavior

In many solid-state lasers, as well as other types of lasers, the excess gain that is present during the oscillation buildup period does not saturate immediately with increasing laser intensity, but decreases only after a certain time delay required for the circulating laser intensity $I(t)$ to "burn up" the excess population inversion. Analysis of this situation requires a more exact set of equations, to describe the dynamics of the atomic populations as well as the cavity fields.

The oscillation buildup in this situation may not converge smoothly to the final steady-state value, but may instead exhibit a strong transient overshoot, followed by quasi periodic "spiking" or relation oscillation behavior, as illustrated in Figure 13.2. We will carry out a more detailed examination of this interesting but rather useless spiking behavior in a later chapter.

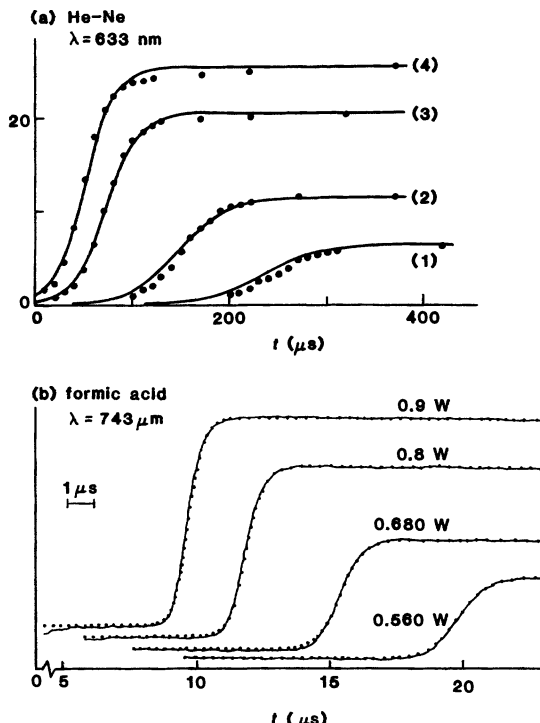


FIGURE 13.3
Laser oscillation buildup times: (a) in a helium-neon laser; (b) in a far-infrared laser.

REFERENCES

The experimental results for laser oscillation buildup shown in this section come from B. Pariser and T. C. Marshall, "Time development of a laser signal," *J. Appl. Phys.* **6**, 232–234 (June 15 1965); and from J. Wascat, D. Dangoisse, P. Glorieux, and M. Lefebvre, "Growth of emission in a far infrared laser," *IEEE J. Quantum Electron.* **QE-19**, 92–95 (January 1983).

For another careful and detailed set of experiments, see F. T. Arecchi and V. De Giorgio, "Statistical properties of laser radiation during a transient buildup," *Phys. Rev. A* **3**, 1108–1124 (March 1971).

For still another typical illustration of laser oscillation buildup, but with a time-varying inversion and gain, see B. K. Garside, E. A. Ballik, and J. Reid, "Pulse delays in TEA CO_2 lasers," *J. Appl. Phys.* **43**, 2387–2390 (May 1972).

Problems for 13.1

1. *Discrete step behavior of laser oscillation buildup.* Suppose a very short optical pulse, like a little "bullet" of light, circulates around inside a laser cavity. The laser cavity is 120 cm long and has end mirrors with power reflectivities $R_1 = 0.35$ and $R_2 = 0.8$. In the exact center of the cavity is a very short laser rod with one-way

power gain of 3 times ($G = 3$). Plot the instantaneous energy in the circulating pulse as a function of time for 3 full round trips around the cavity, starting with unity initial energy. Also evaluate and plot the net exponential growth rate in the cavity, on the same plot. Compare this exponential growth line with the exact energy versus time plot for the circulating pulse.

2. *More complicated discrete buildup calculation.* Repeat the previous problem assuming the end mirrors have reflectivities $R_1 = R_2 = 0.5$, the one-way power gain is 4 times, and there is a uniformly distributed loss inside the laser cavity such that $2\alpha_{op} = 0.4$.
 3. *Cavity lifetime in a semiconductor diode laser.* A typical GaAs injection diode laser cavity may be $200 \mu\text{m}$ long, with an index of refraction $n \approx 3.8$ and an end-mirror reflectivity $R \approx 0.36$ because of the air-dielectric interface. If the internal absorption losses in the cavity are assumed to be small (which may not in fact be true in real injection lasers), what is the cavity lifetime τ_c in such a cavity?
 4. *Exact buildup solution for a typical laser.* Calculate and plot the exact oscillation buildup behavior using the fast-saturation formula (Equation 13.13) given in this section, assuming a steady-state intensity I_{ss} that is 10^8 times the initial noise intensity I_0 and an unsaturated growth rate γ_{m0} that is 1.2 times the cavity decay rate γ_c . Plot both the normalized intensity $I(t)/I_{ss}$ on a log scale, and the instantaneous growth rate $\gamma_m(t)/\gamma_c - 1$ on a linear scale, versus the normalized time t/τ_c .
-

13.2 DERIVATION OF THE CAVITY RATE EQUATION

In this section we will extend the cavity growth-rate calculation developed in the preceding section to derive a “photon rate equation” for the signal intensity or the number of photons in each laser cavity mode, including—for the first time—the effects of spontaneous emission. In the following section we will then combine these cavity rate equations with the atomic rate equations we have developed earlier to obtain a set of coupled cavity plus atomic rate equations which are simple, and yet extremely useful in analyzing many fundamental aspects of laser theory.

Derivation of the Cavity Rate Equation

The exponential growth rate for the signal intensity inside a laser cavity derived in the previous section had the general form

$$I(t) = I_0 \exp [(\gamma_m - \gamma_c)t], \quad (15)$$

If either of the coefficients γ_m or γ_c is time-varying, however—as they well may be in real cases—then we must convert this equation to the more general differential form

$$\frac{dI(t)}{dt} = [\gamma_m(t) - \gamma_c(t)] \times I(t) \quad (16)$$

The parameters γ_m or γ_c might become time-varying, for example, because the gain coefficient saturates, or because we deliberately modulate the cavity losses or cavity output coupling with time. Equation 13.15 is then a correct solution to the more general Equation 13.16 only when the two gain and loss rates are constant. In particular, the gain coefficient γ_m will be directly proportional to the inverted population difference $\Delta N(t) \equiv N_2(t) - N_1(t)$ on the laser transition; and this population difference will very likely change with time in a real laser. We can take this dependence of γ_m on ΔN into account by writing

$$\gamma_m(t) \equiv \frac{2\alpha_m p_m}{T} \equiv K \Delta N(t), \quad (17)$$

where all the other geometrical and atomic parameters of the system are absorbed into the constant K .

At the same time that we do this, we can also conveniently express the total signal energy inside the laser cavity in dimensionless units by defining a “number of photons” $n(t)$ in the cavity by

$$\begin{aligned} n(t) &= \text{“number of photons in the cavity”} \\ &\equiv \left[\frac{\text{total signal energy in the cavity}}{\text{quantum of energy, } \hbar\omega} \right] \\ &= \text{const} \times I_{\text{circ}}(t). \end{aligned} \quad (18)$$

It should be emphasized that we are not focusing any special attention on the photon nature of light by writing this equation—the emphasis in laser analyses should almost always be on the wave rather than the particle nature of light. Rather, we are simply expressing the total signal energy in the laser cavity in the convenient units of $\hbar\omega$. Also, we will not really need any explicit formula for the constant appearing in the last line of Equation 13.18, although if such a formula is wanted, the photon number $n(t)$ in a low-gain standing-wave cavity of length L , cross-sectional area A and circulating intensity I_{circ} can be calculated to a good first approximation from

$$n(t) \approx \frac{2AI_{\text{circ}}(t)L}{\hbar\omega c} = \frac{2V_c}{\hbar\omega_a c} I_{\text{circ}}(t), \quad (19)$$

where $V_c = AL$ is the volume of the cavity mode.

Equations 13.16, 13.17, and 13.18 can then be combined to give the *cavity rate equation*

$$\frac{dn(t)}{dt} = [K \Delta N(t) - \gamma_c] \times n(t) \quad (20)$$

or

$$\frac{dn(t)}{dt} = K [N_2(t) - N_1(t)] n(t) - \gamma_c n(t), \quad (21)$$

where $N_1(t)$ and $N_2(t)$ are the total number of atoms in the lower and upper levels of the laser transition. The first two terms on the right-hand side of Equation 13.21 then represent stimulated emission and absorption between the cavity mode and the atoms, while the third term represents the cavity losses plus output coupling.

Note that in earlier chapters we have consistently used $N_1(t)$ and $N_2(t)$ to indicate atomic densities, or numbers of atoms per unit volume. In writing the

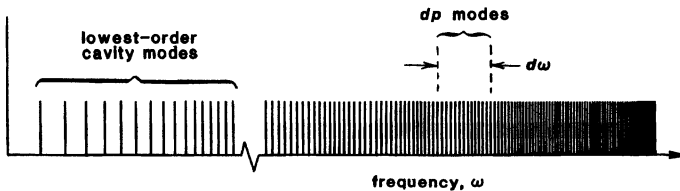


FIGURE 13.4

The lowest and higher-order resonant mode frequencies in a typical closed and lossless resonant cavity.

cavity and atomic rate equations in this and following chapters, however, it will be more convenient to let the symbols $N(t)$ and $\Delta N(t)$ represent the total numbers of atoms inside the laser cavity. The student will have to be a little cautious in interpreting these symbols, therefore, in any formulas from now on in this book.

Value of the Coupling Constant K

By using the formulas derived in earlier chapters for the gain coefficient α_m , we can rewrite the constant K appearing in Equations 13.17, 13.20, and 13.21 in the form (for a lorentzian transition)

$$K \equiv \frac{2\alpha_m p_m}{T \Delta N} = \frac{3^*}{4\pi^2} \frac{\omega_a \gamma_{\text{rad}} \lambda^3}{\Delta \omega_a V_c}, \quad (22)$$

where V_c is the volume of the cavity or, more precisely, of the cavity mode with which the atoms are interacting. Note again that we are now using N_1 and N_2 to indicate the total numbers of atoms in the laser levels, so that $\Delta N(t)/V_c$ is the volume-averaged inversion density with which the cavity mode interacts. Equation 13.22 can be reduced to the particularly simple and useful form

$$K = \frac{3^* \gamma_{\text{rad}}}{p} \quad (23)$$

if we define a parameter p , called the **cavity mode number** (no relation to the laser cavity perimeter p), given by

$$p \equiv \frac{4\pi^2 V_c}{\lambda^3} \frac{\Delta \omega_a}{\omega_a}. \quad (24)$$

This parameter has a very important physical significance, as we will now show.

Frequency Distribution of Resonant Cavity Modes

Suppose we consider some arbitrarily shaped enclosure or cavity having closed and completely reflecting walls. Let us then calculate all the theoretically possible lowest and higher-order electromagnetic modes in this cavity; and plot the resonant frequencies of these modes as tick marks on a frequency scale, as shown in Figure 13.4. Then, at some low frequency, corresponding to a wavelength on the order of the cavity dimensions, we will see the lowest-order resonant mode of the cavity, followed by a succession of higher-order resonant modes with successively higher resonant frequencies, as shown in Figure 13.4.

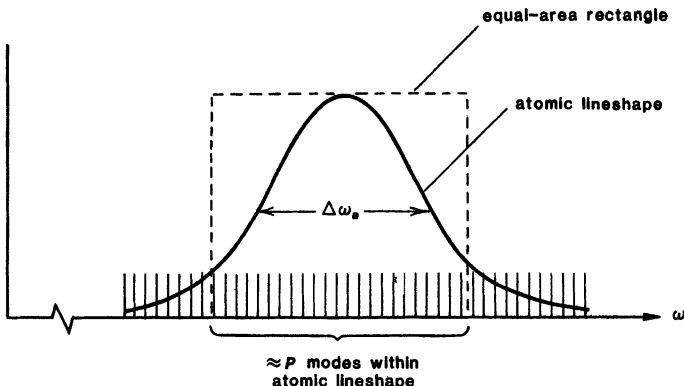


FIGURE 13.5

Physical interpretation of the cavity mode number p . Note that the areas under the lorentzian lineshape with linewidth $\Delta\omega_a$ and the rectangular box of width $(\pi/2) \times \Delta\omega_a$ are the same.

As we go to much higher frequencies, where the cavity dimensions become large compared to the resonance wavelengths, these resonant modes will become more and more closely spaced along the frequency axis, so that the mode distribution in frequency space will become very dense. In fact, it can be shown that in any such enclosure or cavity, regardless of its exact shape, the number of resonant modes falling within a unit (radian) frequency interval, or the resonant mode density $\rho(\omega)$ along the frequency axis, will be given by

$$\rho(\omega) = \frac{dp(\omega)}{d\omega} \equiv \left[\frac{\text{number of cavity modes, } dp}{\text{frequency range, } d\omega} \right] = \frac{8\pi V_c}{\lambda^3} \frac{d\omega}{\omega}. \quad (25)$$

This formula will hold for any cavity shape, whenever the frequencies are high enough that the cavity dimensions become large compared to the resonant wavelengths.

This distribution function can be given another interpretation that does not even require the concept of resonant modes. Suppose we wish to describe an arbitrary electromagnetic field distribution in some large rectangular volume. We can always expand such a field distribution using a Fourier-series expansion in all three spatial coordinates or, to put this in another way, we can expand the fields in a set of waves traveling in all possible directions through the volume. (This process is sometimes referred to as “box normalization” in electromagnetic theory or in quantum mechanics.) The number of independent Fourier components, or of traveling-wave terms, call this number $dp(\omega)$, needed to give a complete description of an arbitrary electromagnetic field within a large rectangular region of volume V_c , assuming this field distribution is made up of frequency components lying within a frequency range $d\omega$, is then given by exactly the same formula $dp(\omega) = \rho(\omega) d\omega$ given in Equation 13.25.

The Cavity Mode Number p

The mode number p appearing in the stimulated transition constant formula (Equations 13.23 or 13.24) can then be understood as the effective number of laser cavity modes lying within the atomic transition linewidth $\Delta\omega_a$, as shown

in Figure 13.5. That is, this number is given by the formula

$$p \equiv \rho(\omega) \times \frac{\pi \Delta\omega_a}{2} = \frac{4\pi^2 V_c}{\lambda^3} \frac{\Delta\omega_a}{\omega_a}. \quad (26)$$

The effective frequency bandwidth multiplying the mode-density function $\rho(\omega)$ in this equation is $(\pi/2)$ times the atomic linewidth $\Delta\omega_a$ rather than just $\Delta\omega_a$, because this is the width of an equivalent rectangular distribution having the same peak height and the same area as a lorentzian lineshape, as shown in Figure 13.5.

The linewidth $\Delta\omega_a$ of any laser transition is always small compared to the transition frequency ω_a , but the cavity volume V_c of a normal laser cavity is always very much larger than a single cubic wavelength. The mode number p is thus normally an extremely large number for ordinary laser cavities, with values typically on the order of $p \approx 10^7$ to $p \approx 10^{10}$. We will learn more about the significance of this parameter very shortly.

Frequency Dependence of the Coupling Coefficient K

Before going on to introduce the concept of spontaneous emission into a cavity mode, we should note that the value of the rate-equation coupling constant K given in Equations 13.22 and 13.23 is obviously the *midband value*, appropriate to a cavity mode tuned to the center of the atomic transition. If we consider instead a cavity mode whose resonant frequency ω_i is tuned off the atomic line center, then the response of the atoms to the cavity fields will be reduced by the atomic lineshape, and hence the coupling coefficient $K(\omega_i)$ for that off-resonance mode will be reduced with a frequency dependence $K(\omega_i) = 2\alpha_m(\omega_i)p_m/T$ that is given for a lorentzian transition by

$$K(\omega_i) = K_0 \times \frac{1}{1 + [2(\omega_i - \omega_a)/\Delta\omega_a]^2}, \quad (27)$$

or for a gaussian transition by

$$K(\omega_i) = \sqrt{\pi \ln 2} \times K_0 \times \exp \left[-4 \ln 2 \left(\frac{\omega_i - \omega_a}{\Delta\omega_a} \right)^2 \right]. \quad (28)$$

where $K_0 \equiv K(\omega_a) \equiv 3^* \gamma_{\text{rad}}/p$.

Suppose we sum the coupling coefficients $K(\omega_i)$ over all the cavity modes ω_i underneath an atomic transition, weighted by their frequency dependences, while also averaging the polarization factor 3^* over all field or atomic polarizations. This sum over all modes is, in essence, an integration over the mode density shown in Figure 13.5, weighted by the atomic transition lineshape shown in that figure, as given in Equations 13.27 or 13.28. Using either of these lineshapes, we can obtain the very fundamental result that

$$\sum_{\text{all modes}} K(\omega_i) \rightarrow \int_0^\infty K(\omega) \times \rho(\omega) d\omega \equiv \gamma_{\text{rad}}. \quad (29)$$

This fundamental result, which says that the sum of $K(\omega_i)$ over all cavity modes under an atomic linewidth is just equal to the γ_{rad} value for that transition, is in fact a very general result, completely independent of the atomic lineshape, the

details of the laser cavity, or any other factors except the radiative decay rate γ_{rad} of the atomic transition.

Introduction of Spontaneous Emission

We have thus far written the cavity rate equation for a single cavity mode in the form

$$\frac{dn}{dt} = K[N_2 - N_1]n - \gamma_c n, \quad (30)$$

where this form includes *stimulated transitions* (that is, stimulated-emission and stimulated-absorption terms), and also *cavity loss terms*, but not yet *spontaneous-emission terms*.

We must now take into account the process of *spontaneous emission* from the upper-level atoms into this cavity mode (as well as into every other cavity mode within the laser cavity volume). That is, the atoms are spontaneously emitting in a noise-like fashion, at a rate directly proportional to the number of upper-level (but not lower-level) atoms, and independent of the number of photons n already in each cavity mode; and a small fraction of this spontaneous emission will have the right direction, polarization and frequency to feed directly into the cavity mode we are considering. The rate equation for each individual cavity mode must thus be extended to the more complete form

$$\frac{dn}{dt} = K[N_2 - N_1]n + K_{\text{sp}}N_2 - \gamma_c n, \quad (31)$$

where K_{sp} is a *spontaneous-emission constant* governing the rate of emission from the upper-level atoms into that particular cavity mode.

But, there is a fundamental result of quantum theory—one of the most fundamental principles of quantum electronics, in fact—which says that the *spontaneous-emission rate from any given set of atoms into any one individual cavity mode is exactly equal to the stimulated-emission rate that would be produced from those same atoms by one photon of coherent signal energy present in the same mode*. For each cavity mode with resonance frequency ω_i , therefore, the *stimulated and spontaneous transition constants* involved in the interaction with a given set of atoms must necessarily be related by

$$K_{\text{sp}}(\omega_i) \equiv K(\omega_i) \quad (32)$$

for each and every cavity mode. Therefore, the cavity rate equation for each separate cavity mode, including spontaneous emission, can also be rearranged into the form

$$\frac{dn}{dt} = KN_2[n + 1] - KN_1n - \gamma_c n. \quad (33)$$

Written in this form the equation seems to say that, whereas the net atomic absorption rate is proportional to the instantaneous number of cavity photons $n(t)$, the net emission rate is proportional to $n(t) + 1$, i.e., the number of cavity photons *plus one*.

Spontaneous Emission: The “Extra Photon”

This “plus one” factor caused by the spontaneous emission sometimes leads laser workers to speak of an “extra photon” in the cavity mode—a photon that somehow causes only downward transitions.

It is important to understand, however, that this additional spontaneous-emission term in the cavity rate equation is much more accurately viewed as an incoherent or noise-like driving term which excites the cavity mode in a random or noise-like fashion, completely uncorrelated with the coherent stimulated-emission terms or with any cavity signal that may already be present. This spontaneous-emission term thus acts as a fundamental *quantum noise source* in the cavity equations. It is this quantum noise source which is responsible for the ultimate noise figure of laser amplifiers, for example, and also for the quantum noise fluctuations in phase and amplitude that are present in even the most ideally stabilized laser oscillators or frequency standards.

One of the practical conclusions stemming from this is that it is impossible to make a laser amplifier—or, in fact, any other kind of amplifier—with an equivalent input noise power less than one noise photon per Hz of bandwidth.

Derivation of the Spontaneous-Emission Coefficient

Let us now verify that this spontaneous emission rate for noise photons into each cavity mode corresponds exactly to the spontaneous atomic emission process that we have already discussed in earlier chapters. We can recall first that the total relaxation rate out of any upper atomic level will normally include two different relaxation processes. First of all, there will normally always be a *purely radiative relaxation rate*, or a *spontaneous emission rate*, $\gamma_{\text{rad}}N_2$ on the $2 \rightarrow 1$ transition we are considering. In addition, there may be (and usually will be) both *nonradiative relaxation rates* from level 2 down to various lower levels and possibly *other purely radiative decay rates* from level 2 down to lower levels *other than level 1*.

The purely radiative or spontaneous emission part of this relaxation on the $2 \rightarrow 1$ transition can then be described in two different but physically equivalent fashions. From a “free-space” viewpoint, each upper-level atom in the cavity volume has a certain probability per unit time γ_{rad} of radiating spontaneously at some frequency within the atomic lineshape, and into some random emission direction. If we look into the open sides of the cavity from any external point, we will see this spontaneous emission coming out from all sides of the cavity, with a lineshape corresponding to the atomic transition lineshape, and with a total emission rate (in photons/second) into all directions given by $\gamma_{\text{rad}}N_2$. Essentially all this spontaneous emission is emitted out through the open sides of a normal laser cavity, although a very minute portion of it is radiated into the low-loss direction exactly along the cavity axis.

From an alternative “cavity mode” viewpoint, however, the atoms can be thought of as spontaneously radiating this same energy, not out into free space, but rather *directly into each of the very large number of resonant cavity modes (mostly very lossy modes) whose frequencies lie within the atomic linewidth*. The total spontaneous-emission fields coming out of the cavity in all directions can then be viewed as the result of the very rapid leakage or diffraction loss from all of these cavity modes out the sides of the cavity.

In considering the total number of modes within a resonant cavity, we must keep in mind that all of the reasonably *low-loss* cavity modes—that is, those lowest and slightly higher-order axial-transverse modes that we have described elsewhere in this text—really represent only a very minute fraction of the total number of cavity modes associated with the cavity volume. There will typically be within an atomic linewidth only a few, or at most a few hundred, low-order axial-plus-transverse modes which describe the radiation traveling in the low-loss directions very close to the cavity axis. There are, however, some $p = 10^7$ to 10^{10} other potential cavity modes, most of them having enormously high losses out the cavity sides, which are needed in principle to describe all possible field configurations traveling in all directions within the cavity volume and within the atomic linewidth.

From the second viewpoint, therefore, each of these laser cavity modes within the atomic linewidth should receive spontaneous emission at a rate given by Equation 13.33, with a K value $K(\omega_i)$ appropriate to that particular cavity mode. But, nearly all of these modes have extremely fast decay rates out the side of the cavity, and hence this energy radiated from the atoms into all these modes is immediately radiated on out of the cavity in all directions.

From this viewpoint we must equate the total spontaneous-emission power coming from the atoms to the total spontaneous-emission power emitted into all these cavity modes. That is, suppose we label each cavity mode by its resonance frequency ω_i . Then we can write for the total spontaneous rate on the $2 \rightarrow 1$ transition

$$\sum_{\omega_i} K_{\text{sp}}(\omega_i) N_2 = \sum_{\omega_i} K(\omega_i) N_2 = \gamma_{\text{rad}} N_2 \quad (34)$$

But, we have already shown in Equation 13.29 that the summation in the middle term of this equation just adds up to the radiative decay rate γ_{rad} , so that this “conservation of total spontaneous emission” is indeed verified.

We can now understand better, as well, why the midband interaction constant K , or K_{sp} , must have the value $3^* \gamma_{\text{rad}}/p$ given in Equation 13.23. If we assume, as is reasonable, that the geometrical and atomic factors determining the spontaneous-emission rate into each mode within the atomic lineshape are likely to be essentially the same, except for polarization factors and for the atomic lineshape itself, then we can approximate the total spontaneous rate into all of the $\approx p$ modes within the main part of the atomic linewidth by

$$\gamma_{\text{rad}} = \sum_{\omega_i} K_{\text{sp}}(\omega_i) \approx p \times K_0, \quad (35)$$

where $K_0 \equiv K(\omega_a) = K_{\text{sp}}(\omega_a)$ refers to the on-resonance value for some preferred lowest-loss cavity mode located near the center of the atomic line. If we put in a polarization factor 3^* , the K_0 value for this preferred mode located close to the line center becomes

$$K_0 = K_{\text{sp}}(\omega_a) = K(\omega_a) = \frac{3^* \gamma_{\text{rad}}}{p}, \quad (36)$$

where 3^* has a value appropriate to that particular mode. But this is just what we started with in Equation 13.23. The p in the denominator simply represents the fact that $1/p$ of the total spontaneous emission from the upper level atoms goes into that one particular cavity mode.

REFERENCES

The spontaneous-emission intensity per mode, or the fraction $\approx 1/p$ of the total spontaneous emission coupled into each individual laser cavity mode, is a particularly important parameter in semiconductor lasers, where the mode number p is comparatively small and the spontaneous emission comparatively strong. For an example of this, see W. Streifer, D.R. Scifres, and R.D. Burnham, "Analysis of diode laser properties," *IEEE J. Quantum Electron. QE-18*, 1918-1929 (November 1982).

The mode-density arguments, and especially the "extra photon" explanations of spontaneous emission in this section, depend in a fundamental way on the modes in question being a set of power-orthogonal electromagnetic modes. The low-order axial plus transverse cavity modes that are commonly used to describe open-sided laser cavities are, however, not power-orthogonal; and as a result the effective spontaneous-emission rate into these modes can appear to be greater than the amount corresponding to one added photon, by a so-called "excess spontaneous-emission factor," which increases the increasing diffraction loss in the cavity.

The existence of such an excess spontaneous-emission factor was first predicted for gain-guided semiconductor diode lasers by K. Petermann, "Calculated spontaneous emission factor for double-heterostructure injection lasers with gain-induced waveguiding," *IEEE J. Quantum Electron. QE-15*, 566-570 (July 1979). A good explanation of how this excess emission factor depends on the non-power-orthogonality of the laser modes, and how it can be reconciled with the fundamental arguments given in this section, can be found in H.A. Haus and S. Kawakami, "On the "excess spontaneous emission factor" in gain-guided laser amplifiers," *IEEE J. Quantum Electron. QE-21*, 63-69 (January 1985).

Problems for 13.2

1. *Cavity photon number in a real laser.* A certain Nd:YAG laser is 1 meter long, has internal power losses of 5% per one-way pass, and end mirrors with reflectivities $R_1 = 100\%$ and $R_2 = 95\%$. The cw power output through mirror M_2 is 1 watt. What is the total number of photons n_{ss} in the laser cavity when it is oscillating?
 2. *Effective width of a lorentzian transition.* Verify that the effective width of a lorentzian lineshape—that is, the width of a rectangular lineshape having the same peak height and the same total area—is in fact given by $(\pi/2) \times \Delta\omega_a$.
 3. *Examples of the cavity-mode density formula.* Derive the cavity-mode density expression $\rho(\omega)$ given in this section for one or more specific simple cavity shapes, such as rectangular or cylindrical cavities, by starting with the standard resonant-mode formulas for microwave cavities and then taking the limit as the wavelength becomes very small compared to the cavity dimensions.
-

13.3 COUPLED CAVITY AND ATOMIC RATE EQUATIONS

We must now proceed to join the *cavity rate equations* developed in the preceding section to the *atomic rate equations* developed in earlier chapters. The result will be a set of coupled cavity plus atomic rate equations that are very useful

in describing laser threshold behavior, laser amplitude modulation, laser spiking and Q -switching, and a wide range of other laser phenomena.

Atomic Rate Equations

The signal and noise photons in the cavity mode discussed in Section 13.2 were assumed to be interacting with a two-level atomic system having total populations $N_1(t)$ and $N_2(t)$ in the lower and upper levels, respectively. Drawing on our results from earlier chapters, we can then write a pair of atomic rate equations for these level populations in the same form as in earlier chapters, that is

$$\begin{aligned}\frac{dN_1}{dt} &= -W_{12}N_1 + W_{21}N_2 + \begin{bmatrix} \text{pumping} \\ \text{terms} \end{bmatrix} + \begin{bmatrix} \text{relaxation} \\ \text{terms} \end{bmatrix}, \\ \frac{dN_2}{dt} &= W_{12}N_1 - W_{21}N_2 + \begin{bmatrix} \text{pumping} \\ \text{terms} \end{bmatrix} + \begin{bmatrix} \text{relaxation} \\ \text{terms} \end{bmatrix}.\end{aligned}\quad (37)$$

The $W_{12}N_1(t)$ and $W_{21}N_2(t)$ terms are the stimulated-transition terms caused by the cavity fields. The exact form of the pumping and relaxation terms in each equation will depend on the details of the particular atomic system and how it is being pumped or excited.

But, we know that the stimulated-transition probabilities W_{12} and W_{21} that appear in these atomic rate equations are themselves directly proportional to the signal energy, or to the cavity photon number $n(t)$, in the resonant cavity mode. We can thus write these stimulated-transition probabilities (leaving out degeneracy effects for simplicity) as being directly proportional to $n(t)$ in the form

$$W_{12} = W_{21} = K'n(t), \quad (38)$$

where K' is again a proportionality constant which contains all the other geometrical and atomic parameters. The stimulated transition terms in the atomic rate equations can thus be written as

$$W_{21}N_2 - W_{12}N_1 = K' [N_2(t) - N_1(t)] n(t). \quad (39)$$

But every time an atom makes a signal-stimulated transition downward in the atomic rate equations, giving up an energy of $\hbar\omega$, this energy must be delivered into one of the cavity modes, so that the cavity photon number must simultaneously go up by one unit of $\hbar\omega$ in the cavity rate equation for that mode. The reverse argument must of course apply equally well to stimulated absorption transitions going in the opposite direction. The stimulated-transition rates $K(N_1 - N_2)n$ and $K'(N_1 - N_2)n$ in the cavity and in the atomic rate equations must therefore be numerically identical; and hence the constants K and K' in front of these terms must be the same, so that in fact $K' \equiv K$ (see the Problems at the end of this section for another way of deriving this same result.)

The form of the pumping and relaxation terms in Equations 13.37 will depend on the exact atomic system being considered. Suppose we now consider, as a simple but specific example, two upper atomic levels E_1 and E_2 such as we have considered in earlier chapters, with a pumping rate R_p into the upper level, and with the usual relaxation rates (in the optical-frequency approximation) from the upper and lower levels downward. The complete atomic rate equations for

this system will then take on the form

$$\begin{aligned}\frac{dN_2}{dt} &= R_p - Kn[N_2 - N_1] - \gamma_2 N_2, \\ \frac{dN_1}{dt} &= Kn[N_2 - N_1] + \gamma_{12} N_2 - \gamma_{10} N_1,\end{aligned}\tag{40}$$

where the coupling coefficient $K = K(\omega_i)$ is exactly the same as in the corresponding cavity rate equation.

Complete Coupled Cavity and Atomic Equations

We have shown in Section 13.32 how to write the cavity rate equation for any one individual cavity mode, including spontaneous emission, and have also pointed out that a real laser system will have $\approx p$ cavity modes, each one of which is, at least in principle, able to interact with the atoms contained within the cavity volume. The final result of this discussion is then that to describe properly, even within the rate-equation approximation, a laser cavity having a large number of resonant modes, each labeled by index i , plus a set of atoms with populations N_1 and N_2 , we must, at least in principle, write down a separate rate equation for each cavity mode individually, in the form

$$\frac{dn_i(t)}{dt} = K_i N_2(t)[n_i(t) + 1] - K_i N_1(t)n_i(t) - \gamma_{ci} n_i(t),\tag{41}$$

where n_i is the cavity photon number, K_i the coupling constant, and γ_{ci} the cavity decay rate for the i -th cavity mode. We must then also write a pair of rate equations for the atomic populations in the general form developed in this section, namely,

$$\begin{aligned}\frac{dN_2(t)}{dt} &= \sum_i K_i n_i(t)[N_1(t) - N_2(t)] + \left[\begin{array}{l} \text{pumping} \\ \text{terms} \end{array} \right] + \left[\begin{array}{l} \text{relaxation} \\ \text{terms} \end{array} \right], \\ \frac{dN_1(t)}{dt} &= - \sum_i K_i n_i(t)[N_1(t) - N_2(t)] + \left[\begin{array}{l} \text{pumping} \\ \text{terms} \end{array} \right] + \left[\begin{array}{l} \text{relaxation} \\ \text{terms} \end{array} \right].\end{aligned}\tag{42}$$

The two atomic levels are, in other words, potentially coupled to the total set of p near-resonant cavity modes, as illustrated in Figure 13.6, as well as to whatever pumping and relaxation processes may be present.

Note that in these equations the stimulated-transition terms for the atoms must be summed over the total stimulated-transition effects produced by the signal fields in *all the cavity modes* acting on the atoms (or at least all those cavity modes that contain any significant number of photons). Note also that no additional spontaneous-emission terms need be added to the atomic rate equations, because the transition rate due to spontaneous emission into all the cavity modes is already included in the purely radiative part of the relaxation terms.

Idealized Single-Mode, Single-Level Rate Equations

Writing out the complete set of cavity rate equations for $p \approx 10^8$ cavity modes would be a daunting task, with or without the assistance of a computer.

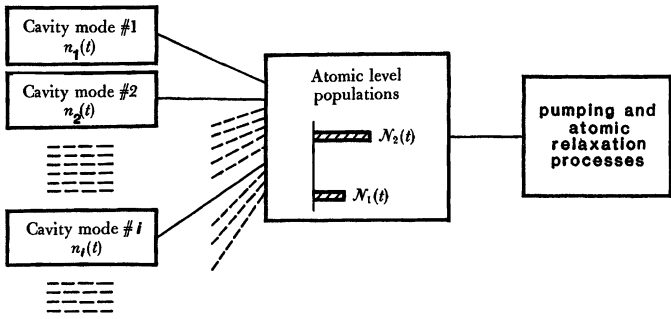


FIGURE 13.6

One set of atoms coupled to many cavity modes within the atomic linewidth.

Fortunately, in most real lasers we only need to write out explicitly the cavity rate equations for one or a few of the most favored or lowest-loss cavity modes, and not for the whole set of p such modes. In fact, one of the most remarkable features of laser action is that a typical laser cavity having perhaps $p \approx 10^8$ individual and distinct cavity resonance modes can still oscillate in just one or a few of these cavity modes. So long as only one or a few cavity modes are excited with any significant number of photons n_i , we need write down the rate equations for only those few modes.

In fact, the simplest possible laser model—but one that still contains all the essential physics—is to assume that there is just *one* lowest-loss (or highest-gain) preferred cavity mode that builds up any significant photon number $n(t)$, so that we need write only *one* cavity rate equation. The atomic rate equations can also be put into their simplest form by assuming that the relaxation rate downward out of level 1 is sufficiently fast that $N_1 \approx 0$ under all circumstances, and that the pumping into level N_2 can be described by a simple pumping rate R_p .

The coupled cavity and atomic rate equations 13.41 and 13.42 will then reduce to their simplest possible combined form, namely,

$$\begin{aligned} \frac{dn}{dt} &= KN_2(n+1) - \gamma_c n, \\ \frac{dN_2}{dt} &= R_p - KN_2n - \gamma_2 N_2. \end{aligned} \tag{43}$$

This simple pair of equations is still surprisingly general, and we will use these two equations extensively to analyze several fundamental aspects of laser behavior in succeeding chapters.

We might also just mention some of the limitations of the coupled cavity plus atomic rate equations for analysing laser behavior, even in the case where we might write a larger number of cavity mode equations. In particular, this approach is necessarily limited to the small-signal or rate-equation atomic regime, as described in earlier chapters. No coherent-pulse effects can be included. More important, this rate-equation approach completely ignores, or hides, all the *phase* information associated with the signal fields in each resonant cavity mode. It also completely leaves out any spatial interference effects between modes, and thus any spatially inhomogeneous saturation effects or “spatial hole burning” that

this may produce in the atomic level populations N_1 and N_2 . Nonetheless, this rate-equation approach can be very useful in laser theory, as we will see.

Problems for 13.3

1. *Alternative derivation of the K coefficient.* Give an alternative derivation of the coefficient K appearing in the coupled cavity and atomic rate equations by starting from the atomic rate equation; writing the stimulated-emission term in the form $K[N_2(t) - N_1(t)]n(t) \equiv W_{12}[N_2(t) - N_1(t)]$; and using the formulas we have developed earlier for the stimulated-transition probability W_{12} . Demonstrate that the final result is the same as given in this section.
2. *Thermodynamic implications of the “extra photon.”* Suppose a laser cavity has no other losses or output coupling, so that $\gamma_c \equiv 0$, but suppose it does contain a set of absorbing atoms whose upper-level population N_2 and lower-level population N_1 are held in thermal equilibrium at a positive temperature T . These atoms then provide in effect a cavity loss, and the electromagnetic fields in the cavity should come to thermal equilibrium with the atoms at this same temperature T . It is also a basic result of quantum thermodynamics that the average number of photons in each resonant mode in a system at thermal equilibrium should be given by $\langle n \rangle = [\exp(\hbar\omega/kT) - 1]^{-1}$.

Write down the cavity rate equation for any one cavity mode in such a cavity, and show that it predicts exactly this result, but only if (i) the “extra photon” is included, and (ii) the spontaneous and stimulated transition coefficients are in fact equal, or $K_{sp} = K$, for each mode individually.

3. *More cavity-mode thermodynamics.* Suppose a cavity like that in the previous problem contains two different sets of atoms, both with the same transition frequency, but with their level populations held at two different temperatures. How would we calculate the effective temperature of the blackbody radiation within the cavity to which these groups of atoms are both coupled?
4. *Initial noise value for laser oscillation buildup (research problem).* We have asserted in an earlier section that oscillation in a laser cavity builds up from a small number of “initial noise photons” present in the cavity when the gain is first turned on. In fact, however, the amount of noise energy initially present in an optical cavity at ordinary temperatures, with no inverted population present, is very much less than one photon; and a more accurate picture is to say that the oscillation builds up from the effects of the spontaneous emission that always accompanies an inverted population, as described in this section. The spontaneous emission that occurs during a short time just before and just after the laser gain is first turned on, before the cavity signal builds up to more than a few stimulated photons, is particularly important in setting the effective initial noise level for the laser oscillator.

To demonstrate this, consider a laser cavity in which the laser gain increases linearly with time in the form $\gamma_m(t) - \gamma_c = KN(t) - \gamma_c = \gamma_c \times t/t_d$. This means that the net growth rate passes upward through zero just at $t = 0$, with t_d being the time it takes the laser gain to rise from zero to just equal the cavity decay

rate γ_c . Using this assumption, solve separately (a) the cavity rate equation $dn(t)/dt = [KN(t) - \gamma_c]n(t)$ without spontaneous emission, but assuming an initial noise value n_0 at $t = 0$; and also (b) the more accurate equation $dn(t)/dt = KN(t)[n(t) + 1] - \gamma_c n(t)$ including spontaneous emission, but assuming an initial condition of zero initial photons in the cavity for $t \ll 0$.

By comparing these solutions, show that they give the same form for $n(t)$ for large positive time, $t \gg 0$, providing an initial photon number $n_0 \equiv (2\pi t_d/\tau_c)^{1/2}$ is assumed in case (a). Discuss the physical interpretation of this formula.

5. *Coupled rate-equation analysis of a transverse flow laser.* Consider a transverse-flow type of gas transport laser in which there is no laser pumping mechanism operating inside the laser cavity itself. Rather, pre-excited upper-level laser atoms flow continuously into one side of the laser cavity, and upper- and lower-level atoms flow out the other side. (Assume there is a bottleneck so that lower-level atoms cannot relax to any still lower levels.)

As a simple model for this laser, assume that:

- (a) the upper- and lower-level population densities inside the laser cavity may be described by volume-averaged densities N_2 and N_1 ;
- (b) the rate at which pre-excited upper-level atoms flow into the cavity is given by an initial density N_0 times the transverse flow velocity v ;
- (c) the rate at which upper- and lower-level atoms flow out of the cavity is given by the average densities inside the cavity times the same flow velocity;
- (d) atoms transfer from level 2 to level 1 inside the cavity as a result of both downward relaxation with a relaxation rate γ_2 and stimulated transitions caused by a cavity photon number n ;
- (e) the cavity may be characterized by a cavity decay rate γ_c (including both internal cavity losses and external output coupling), and a stimulated transition coefficient K .

Taken all together, these assumptions provide at least a rough model for certain kinds of gasdynamic and transverse-flow chemical lasers. Carry through a coupled rate-equation analysis of this system, and find the steady-state level populations N_1 and N_2 and the photon number n inside the cavity as a function of the flow velocity v . What is the minimum or threshold flow velocity v_{th} necessary to reach oscillation threshold, and the laser power output as a function of velocity above threshold? (Note: Spontaneous emission effects may be entirely neglected in this calculation.)

13.4 THE LASER THRESHOLD REGION

The almost discontinuous change in power output that occurs at threshold, when a laser suddenly breaks into oscillation, is one of the most remarkable features of laser behavior. Several of the most significant aspects of this laser threshold behavior can be explained using a remarkably simple rate-equation model, as we will demonstrate in this section.

Idealized Rate-Equation Analysis

To analyze laser threshold behavior we can use the highly idealized, and yet very realistic, laser model developed in Section 13.3, consisting of a single preferred or lowest-loss cavity mode with photon number $n(t)$, plus an ideal two-level laser transition with upper-level population $N_2(t)$. This upper level is assumed to be pumped at a steady (but adjustable) pumping rate of R_p atoms/second, and to have a population decay rate γ_2 . Downward relaxation out of the lower laser level is assumed to be arbitrarily fast, so that $N_1 \approx 0$ under all circumstances.

The coupled rate equations for this system, as developed in Section 13.3, are then

$$\begin{aligned}\frac{dn}{dt} &= K(n+1)N_2 - \gamma_c n, \\ \frac{dN_2}{dt} &= R_p - KnN_2 - \gamma_2 N_2,\end{aligned}\tag{44}$$

where γ_c is the cavity decay rate, and the coupling constant K is given, as in the preceding sections, by $K \equiv 3^* \gamma_{\text{rad}}/p$. As usual, γ_{rad} is the radiative decay rate on the laser transition, and the important quantity p is the (very large) number of resonant cavity modes within the cavity volume and transition linewidth. To simplify the results slightly, we will set $3^* = 1$ from here on.

Steady-State Solutions Below Threshold

The steady-state solutions to Equations 13.44, when $d/dt = 0$ in both equations, can then be manipulated in several different ways. For example, the form that is most useful for understanding below-threshold behavior is to write the steady-state solution to the first of these equations in the form

$$n_{\text{ss}} = \frac{N_{\text{ss}}}{\gamma_c/K - N_{\text{ss}}} = \frac{N_{\text{ss}}}{N_{\text{th}} - N_{\text{ss}}},\tag{45}$$

and the solution to the second in the form

$$N_{\text{ss}} = \frac{R_p}{\gamma_2 + Kn_{\text{ss}}} = R_p \tau_2 \times \frac{1}{1 + (\gamma_{\text{rad}}/\gamma_2) \times (n_{\text{ss}}/p)}.\tag{46}$$

Equation 13.45 then says that the number of steady-state photons n_{ss} in the cavity mode will remain small, somewhere between zero and perhaps a few hundred, until the upper-level population N_{ss} is raised to within a fraction of a percent of a *threshold inversion value* N_{th} , where this threshold inversion value is given by

$$N_{\text{th}} \equiv \frac{\gamma_c}{K} = \frac{\gamma_c}{\gamma_{\text{rad}}} p.\tag{47}$$

This value is the threshold inversion we calculated earlier, at which (or very near which) laser oscillation begins.

Equation 13.46 then says that in this same region, so long as the photon number n_{ss} remains very much less than p , the upper-level population increases essentially in direct proportion to the pumping rate; i.e., $N_2 \approx R_p \tau_2$. The threshold pumping rate, at which the population inversion N_{ss} will just reach the threshold

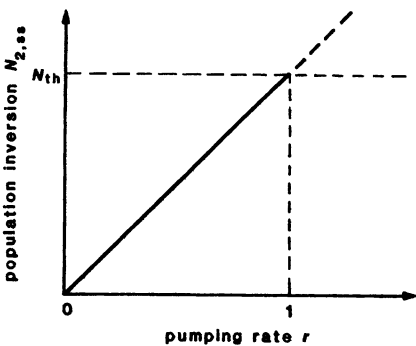


FIGURE 13.7
Laser behavior below threshold.

inversion N_{th} if this continues, is given by

$$R_{p,th} = \gamma_2 N_{th} = \frac{\gamma_2 \gamma_c p}{\gamma_{rad}} \quad (48)$$

It is convenient to define a normalized pumping rate relative to this threshold value by

$$r \equiv \frac{R_p}{R_{p,th}} = \frac{\gamma_{rad} R_p}{\gamma_2 \gamma_c p}. \quad (49)$$

The below-threshold region ($r < 1$) is then described by the approximate results

$$\left. \begin{aligned} n_{ss} &\approx \frac{r}{1-r} \\ N_{ss} &\approx r \times N_{th} \end{aligned} \right\} \quad \text{below threshold, } r < 1. \quad (50)$$

as plotted versus r in Figure 13.7. It is evident that until the pumping rate r becomes very close to the threshold value $r = 1$, the photon number in the cavity will be of order unity or a few orders of magnitude larger. Because the photon number n_{ss} will remain $\ll p$ for $r < 1$, the saturation term $1/(1 + n_{ss}/p)$ in the

denominator of the pumping Equation 13.47 will be negligible, and so N_{ss} will increase linearly with pumping rate R_p below threshold, as shown in Figure 13.7.

Steady-State Behavior Above Threshold

We can also, however, rearrange the steady-state solutions to the same two rate equations 13.44 in the reversed forms

$$N_{ss} = \frac{\gamma_c}{K} \times \frac{n_{ss}}{n_{ss} + 1} = \frac{n_{ss}}{n_{ss} + 1} \times N_{th}, \quad (51)$$

and

$$n_{ss} = \frac{R_p - \gamma_2 N_{ss}}{K N_{ss}} = \frac{\gamma_{rad} p}{\gamma_2} \left[\frac{N_{th}}{N_{ss}} r - 1 \right]. \quad (52)$$

From Equation 13.51 we can see that above threshold, or as soon as the photon number becomes very much greater than unity, the population inversion N_{ss} "clamps" at the threshold value $N_{ss} \approx N_{th}$ (or, more precisely, at just a minuscule amount below N_{th}). At the same time, if N_{ss} is clamped at N_{th} then Equation 13.52 says that for $r > 1$ the cavity photon number is given by

$$n_{ss} \approx (r - 1) \times \frac{\gamma_{rad}}{\gamma_2} \times p. \quad (53)$$

For any reasonable ratio of γ_{rad}/γ_2 and any pumping rate r above threshold, this says that (i) the photon number n_{ss} will increase *linearly* with pumping power above threshold, and (ii) the photon number will be of the same order of magnitude as the mode number p , which we have noted is a very large number (order of 10^8 to 10^{10}) in most laser cavities.

The approximate formulas for the laser behavior above threshold are thus

$$\left. \begin{aligned} N_{ss} &\approx N_{th} \\ n_{ss} &\approx (r - 1) \gamma_{rad} p / \gamma_2 \end{aligned} \right\} \quad \text{above threshold, } r > 1, \quad (54)$$

as illustrated in Figure 13.8. Note that the cavity photon number n_{ss} in the below-threshold region in Figure 13.8 is orders of magnitude smaller than the value above threshold, and does not even show up on the scale of the above-threshold photon number.

Energy Transfer Rates Below and Above Threshold

Below threshold, all of the pumping power used in lifting atoms into the upper laser level is reemitted by the atoms as *incoherent* energy, in the form of radiative relaxation processes (spontaneous emission, or fluorescence), plus non-radiative relaxation processes (lattice phonons, wall collisions, and the like), with a combined relaxation rate of $\gamma_2 N_2 \equiv \gamma_{rad} N_2 + \gamma_{nr} N_2$. The radiative part of this relaxation in particular can be pictured as a process in which the atoms spontaneously emit into all of the $\approx p$ resonant modes within the cavity linewidth, and then the energy spontaneously emitted into these cavity modes immediately leaks out of the cavity into all directions as incoherent spontaneous emission.

As soon as the laser goes above threshold, however, the upper-level population N_{ss} clamps at the threshold value, and hence the incoherent relaxation out of this level (radiative plus nonradiative) also clamps just at the value it had at

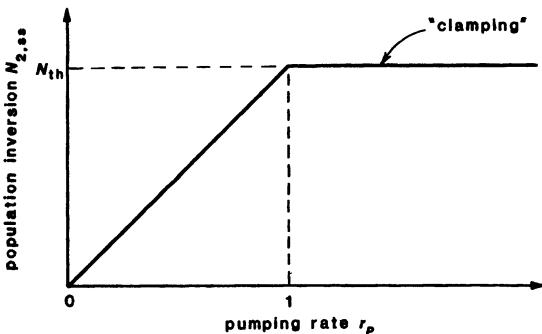
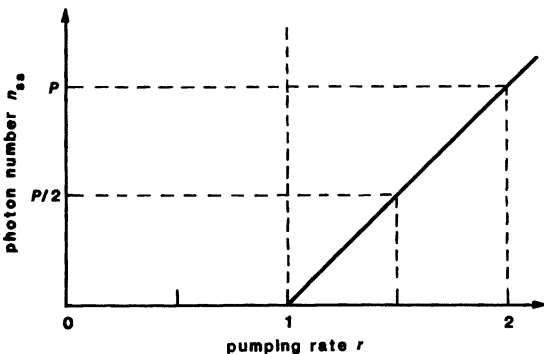


FIGURE 13.8
Laser behavior above threshold.



threshold. All of the additional pumping power fed into the upper laser level above threshold then goes into, or is stolen by, the coherently oscillating cavity mode. The laser thus provides a kind of optical illustration of the maxim that “the rich get richer” (or perhaps “the coherent get more coherent”).

To illustrate this point, let us assume for simplicity that the upper-level relaxation is purely radiative, so that $\gamma_2 = \gamma_{\text{rad}}$, and let us define $P_{\text{th}} \equiv R_{p,\text{th}}\hbar\omega_a$ to be the total pumping power that is fed into the upper laser level just at threshold. The total incoherent or spontaneous emission power P_{fluor} coming out of the atoms as they fluorescence into all directions, and the total coherent oscillation power P_{osc} coming out of the cavity in the one coherently oscillating cavity mode, will then be given, both below and above threshold, by the simple expressions

$$P_{\text{fluor}} \equiv \gamma_2 N_{ss} \hbar\omega \approx \begin{cases} r P_{\text{th}} & r \leq 1, \\ P_{\text{th}} & r \geq 1, \end{cases} \quad (55)$$

and

$$P_{\text{osc}} \equiv \gamma_c n_{ss} \hbar\omega \approx \begin{cases} 0 & r \leq 1, \\ (r-1)P_{\text{th}} & r \geq 1. \end{cases} \quad (56)$$

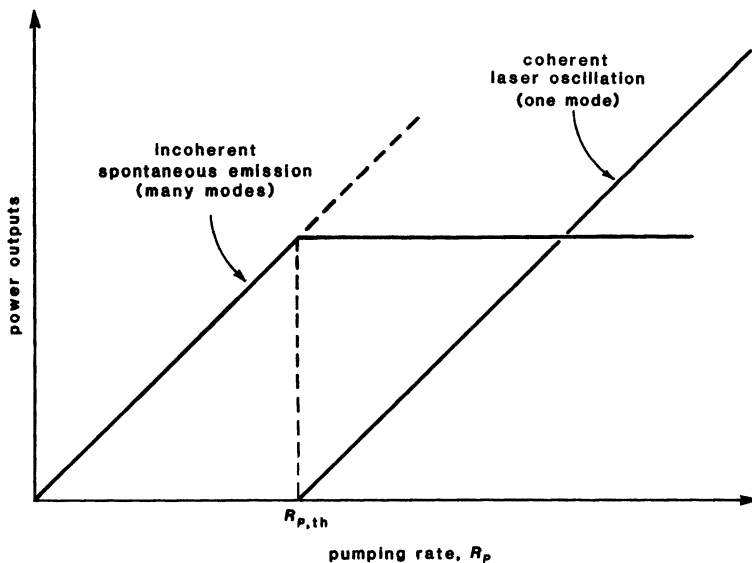


FIGURE 13.9

Coherent and incoherent power outputs.

As illustrated in Figure 13.9, below threshold all the input power goes into incoherent emission; above threshold all the additional pumping power goes into the coherent oscillation output.

Of course, in any real laser system most of the pump power input is not used directly for exciting atoms to the upper laser level, but rather is wasted in pumping atoms up into unwanted levels or in heating up the laser medium. Nonetheless, all of what does go into the upper laser level is then converted into laser oscillation above threshold.

Exact Results for the Threshold Region

The approximate results derived above are very useful for insight into the behavior of laser oscillation below and above threshold. We can, however, also obtain an exact expression for the cavity photon number n_{ss} versus pumping rate r that is valid for all values of r (within the very mild approximations of the rate-equation approach) by eliminating N_2 between the two basic rate equations 13.44 and solving for n_{ss} versus r .

Suppose for simplicity we assume again that $3^* = 1$ and in addition that $\gamma_2 = \gamma_{rad}$, i.e., that the upper level relaxes entirely by radiative relaxation into level 1. Then the exact steady-state solution to the two rate equations 13.44 at the start of this section is the rather innocuous-looking expression

$$n_{ss} = \left[(r - 1) + \sqrt{(r - 1)^2 + 4r/p} \right] \times \frac{p}{2}. \quad (57)$$

Figure 13.10 is a plot of this expression over a range of pumping power centered about $r = 1$, showing how the cavity photon number jumps almost discontinuously from its below-threshold value of order unity, or slightly larger, to numbers

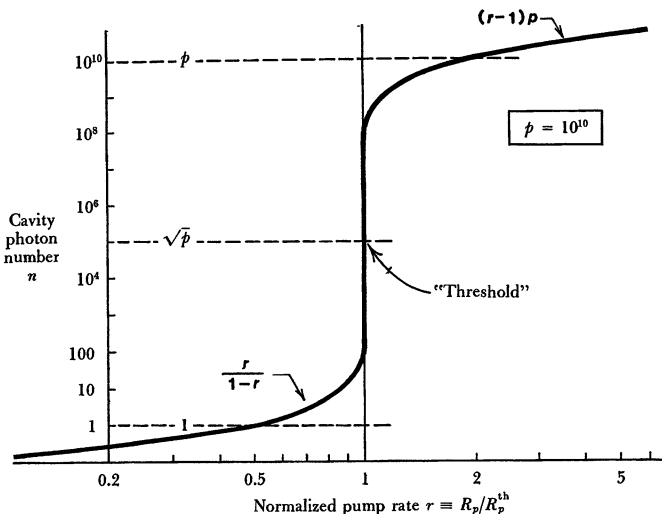


FIGURE 13.10

Cavity photon number n_{ss} versus normalized pumping rate r as given by the exact solution to the single-cavity-mode rate equations.

of order p , as the pumping rate increases by a very small amount, with a change of order $1/p^{1/2}$, at threshold. Note the widely different logarithmic scales on the two axes of this figure.

It is virtually impossible to control the pumping rate R_p in a real laser to a precision of order $1/p^{1/2}$, and it is equally difficult, for that matter, to measure the cavity photon number accurately over a dynamic range covering 8 or 10 orders of magnitude. Hence it is not surprising that when we gradually turn up the pump-power knob in a real laser, the onset of oscillation at the oscillation threshold point, where r passes through one, usually appears as an essentially discontinuous event.

Oscillation Mode Discrimination

The sharpness of the photon number curve versus r , combined with the sudden clamping of the population inversion N_2 at the threshold value (really just *below* the threshold value), also helps to explain how a laser cavity having some $p \approx 10^8$ or 10^{10} potentially oscillating modes can actually oscillate and extract all the additional pumping input in just one preferred oscillating mode.

Suppose, for example, a laser cavity has a resonant mode #1 which is the “most preferred” mode, because it has the lowest losses and/or the best coupling to the laser atoms; plus a second cavity mode #2 which is slightly less preferred because it has higher losses or weaker coupling to the atoms or both. Then, as Figure 13.11 shows, when the population inversion clamps at the threshold inversion for mode #1, the less preferred mode #2 will still be slightly below threshold (at least, in an ideal picture). Hence this second mode will never be able to develop a sizable number of photons. The extraordinary sharpness of the threshold behavior and the large value of p help to explain how the photon number in mode #2 can always remain $\ll p$, no matter how hard the laser is

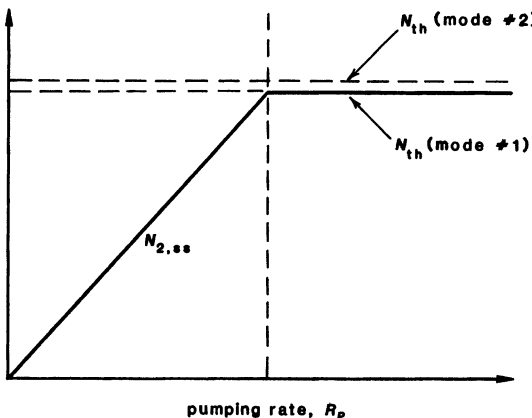


FIGURE 13.11
 "Clamping" of the population inversion due to a slightly preferred mode #1, leading to suppression of oscillation for mode #2.

pumped, unless the difference in losses between the two modes is of order $1/p^{1/2}$ or smaller.

The preceding description is, of course, highly idealized. In particular it neglects the spatial and spectral inhomogeneity effects that we discuss elsewhere in this text. Only the population inversion in those atoms that are fully "seen" by mode #1 will be clamped at threshold. If there are other atoms not fully seen and saturated by mode #1, but seen by mode #2, the population inversion on these other atoms can increase with increased pumping, and can pull mode #2 above threshold.

Most practical lasers will in fact oscillate in several, or even many, cavity modes at pumping levels well above threshold; and controlling or eliminating multimode oscillation is a continuing design problem in lasers. Nonetheless, there are also real lasers which are sufficiently well controlled that they can generate large laser output powers in exactly one single laser cavity mode, in full agreement with our idealized model.

Experimental Threshold Measurements on Injection Diode Lasers

Experimental measurements on lasers just at or below threshold are very difficult, both because of the sharpness of the threshold, and hence the extraordinary stability required in such experiments, and also because of the very weak signals emitted from a cavity containing only a few noise photons below threshold. Semiconductor diode lasers, however, because of their very small cavity volume, can have a smaller than average mode density ($p \approx 10^5 - 10^6$), giving them a comparatively "soft" threshold. Their very efficient direct-current pumping mechanism can also make threshold experiments somewhat simpler.

We have already seen in earlier chapters how a single preferred axial mode can spring into oscillation, rising out of a cluster of amplified axial-mode noise peaks in an injection laser. Figure 13.12 shows a more detailed measurement of how the output power in the dominant axial mode from an injection laser suddenly rises by a large amount as the laser current is increased by a very small amount just at threshold. The light output below threshold in this situation may not represent a fully accurate measure of the photon number in this single

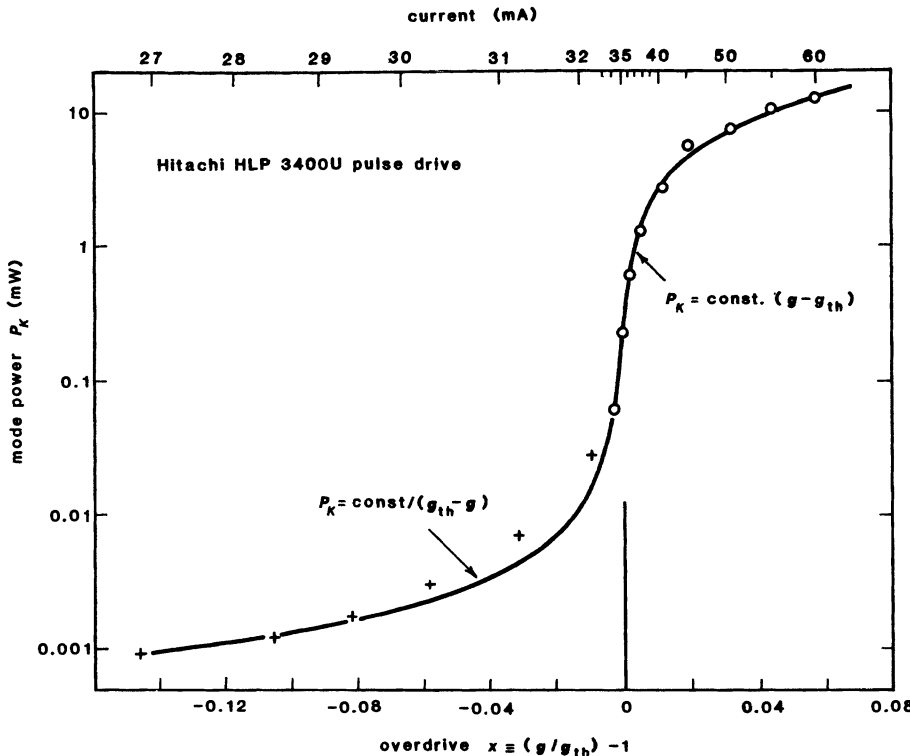


FIGURE 13.12

Output power in the dominant axial mode from a GaAs injection laser as the pumping current is increased through the threshold value (from Sommers).

preferred cavity mode, since the measurement apparatus may detect some of the below-threshold noise emission from other axial or near-axial cavity modes. Nonetheless, the general trend is clear.

Figure 13.13 also shows for two other injection laser diodes the sharp clamping of the upper-level population at threshold, as observed by measuring the spontaneous emission out the side or top of the diode as the diode current passes through threshold. Figure 13.13(b) shows that if the face of the diode is scratched or damaged to prevent laser oscillation, the sharp "knee" at the threshold point disappears and the sidelight fluorescence continues to increase with increasing current.

The energy-level system in a semiconductor injection laser is both very broad and much more complicated than just a simple two-level system. Hence, for example, the fluorescent emission at longer wavelengths than the laser wavelength does not clamp as sharply. This emission presumably comes from electronic levels slightly below the laser levels, whose population is not depleted or controlled as sharply by the laser action.

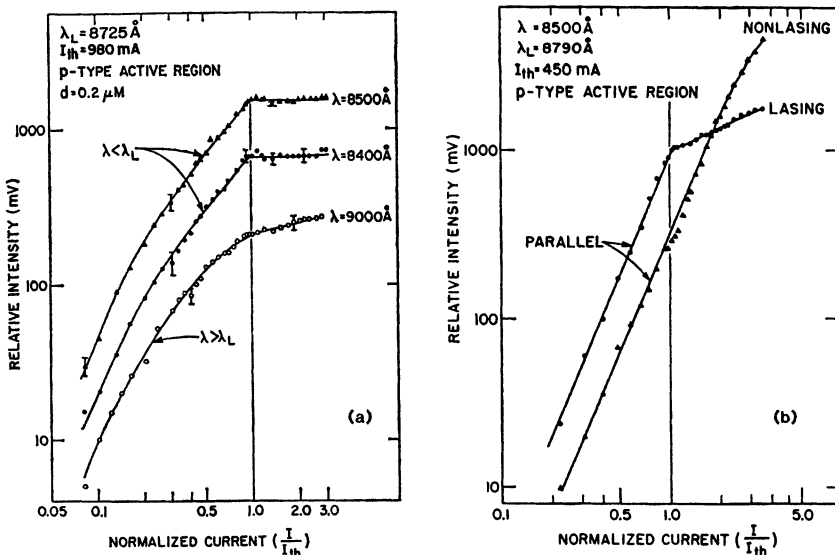


FIGURE 13.13

(a) Sidelight fluorescent emission from an injection diode laser as seen through the top and sides of the lasing region, versus pumping current below and above threshold. The different curves represent spontaneous emission at different wavelengths within the very broad transition characteristic of GaAs injection lasers. (b) Sidelight fluorescent emission from the same laser under lasing and nonlasing conditions (achieved by damaging the cleaved end mirror surfaces).

Other Laser Threshold Measurements

It is also possible, with care, to make threshold measurements in other lasers, for example, in highly stabilized He-Ne lasers. One preferred technique is to stabilize the laser pumping rate at a value well above threshold at the middle of the atomic gain profile; and then tune the cavity-mode frequency out to the point on the side of the atomic-gain curve where gain just equals loss. By tuning the cavity resonance through a very small frequency range centered on this point, using piezoelectric-length tuning, we can pass smoothly and repeatedly from just below to just above threshold.

Figure 13.14 shows the normalized power output from a highly stabilized He-Ne laser (measured by photon counting techniques) as the normalized unsaturated gain or effective pumping rate r is varied about the threshold by ± 2 parts in 10^3 . It is possible to deduce from this data that the mode number for this cavity is $p \approx 5 \times 10^7$ (see Problems).

Finally, as another demonstration of the “clamping” phenomenon, Figure 13.15 shows the fluorescent emission below threshold and the laser emission above threshold (with greatly reduced detector sensitivity) for a group of closely adjacent transitions with a common upper level in an HgCl excimer laser.

The molecules in this laser are created in a $v' = 0$ excited state by a high-voltage electron beam passing through a high-pressure cell containing rare-gas mixtures with small traces of Hg and CCl_4 . The left-hand diagram shows a

FIGURE 13.14

Output intensity from a very carefully stabilized small He-Ne laser as the effective pumping rate r is varied through a range $\delta r = \pm 0.002$ about the threshold value $r = 1$. Note that even the highest points shown on this curve are still very close to threshold, and far below what would be the normal operating level in this laser (from Corti and Digeorgio.)

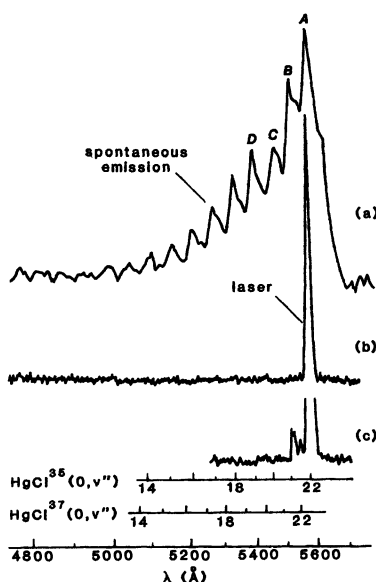
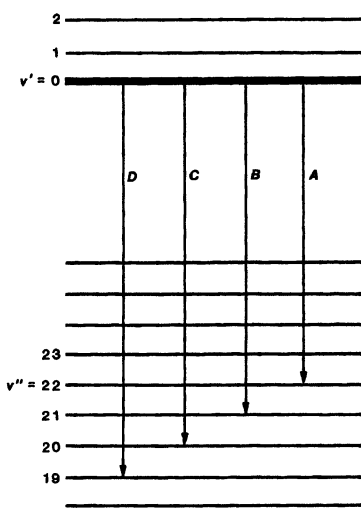
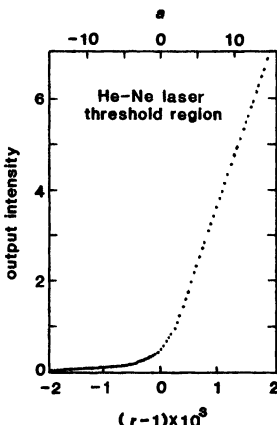


FIGURE 13.15

Spontaneous emission and laser oscillation from HgCl molecules excited by electron-beam pumping in an excimer laser. Curve (a): Spontaneous emission, measured with a sensitive detector below threshold, on several different vibrational-rotational transitions indicated in the adjoining partial energy diagram. Curves (b) and (c): Laser action at increased pumping rates, well above threshold.

small part of the energy-level structure of the HgCl molecule, with several of the spontaneous emission lines identified (note that these are different rotational quantum transitions or lines, not just different axial modes). The $v' = 0$ to

$v'' = 22$ transition is the strongest of these lines in fluorescence (strongest value of γ_{rad}), and it also reaches laser threshold first.

Once this transition oscillates, the population of the upper $v' = 0$ level is then clamped. (The populations of the lower $v'' < 22$ levels may also be increased once oscillations begin by cascading from the $v'' = 22$ level.) The significant point is that, even with very much higher pumping, none of the other lines can be brought to threshold, except possibly for very weak transient oscillation of the next adjoining line at the highest pump level.

Threshold Characteristics

A summary of the changes occurring in the cavity fields and in the output beam as a laser passes through threshold for a single mode thus includes the following.

- A sudden very large rise in power output in the oscillating mode.
- Clamping, more or less completely, of the upper-level population and hence of the sidelight fluorescence.
- A sudden sharp spectral narrowing, in which the frequency width of the signal radiation suddenly changes from broadband spontaneous emission (with essentially the bandwidth of the atomic transition) to emission of all the additional energy in one or a few essentially monochromatic axial modes.
- A sudden sharp spatial or output beam narrowing, in which instead of spontaneous fluorescent emission coming out randomly in all directions, the additional energy emerges as a more or less collimated, spatially coherent beam which is describable by (depending on the cavity) only one or a few transverse cavity modes.
- A hidden but important change in the statistical character of the laser radiation, from essentially gaussian random noise to a coherent amplitude-stabilized oscillation.

None of these last three items emerges directly from the rate-equation model used in this section. However, the fact is that the signal energy in the laser cavity below threshold is essentially random noise, with random phase and with random amplitude that varies about its mean value from instant to instant. We refer to this as gaussian noise, because the instantaneous amplitudes of the cosine and sine frequency components of this noise are random variables with gaussian probability-density distributions and with no correlation between cosine and sine components. (This means that the phase of the instantaneous phasor amplitude has a uniform distribution between 0 and 2π , whereas the magnitude of the phasor amplitude has a Rayleigh distribution.)

Above threshold, on the other hand, the laser oscillates (ideally) in a single mode with a coherent purely sinusoidal oscillation of the instantaneous E field, just like any coherent electronic oscillator at any frequency. The amplitude of the oscillating E field is highly stabilized (by the gain saturation feedback mechanism that stabilizes any laser oscillator), with only very small residual amplitude fluctuations about the mean value. The phase of the optical oscillation is random, in the sense that there is no absolute phase or absolute clock to which a free-running oscillator will be stabilized. However, the phase of a good laser oscillator will stay essentially fixed for long periods of time (an enormous number

of optical cycles), changing only through a slow random walk in absolute phase caused by small residual noise effects in the laser.

REFERENCES

The experimental results for semiconductor injection lasers in this section are from T. Paoli, "Saturation behavior of the spontaneous emission from double-heterostructure junction lasers operating high above threshold," *IEEE J. Quantum Electron.* **QE-9**, 267-272 (February 1973); and H. S. Sommets, Jr., "Spontaneous power and the coherent state of injection lasers," *J. Appl. Phys.* **45**, 1787-1793 (January 1974).

A slightly different theoretical expression for semiconductor laser power output versus pumping, which is experimentally indistinguishable from Equation 13.57 in this section, is given and tested in H. S. Sommers, Jr., "Spectral characteristics of single-mode injection lasers: The power-gain curve from weak stimulation to full output," *J. Appl. Phys.* **53**, 156-160 (January 1982). Sommers has also written a review of this subject in "Threshold and oscillation of injection lasers: A critical review of laser theory," *Solid-State Electron.* **25**, 25-44 (1982).

The He-Ne laser results of Figure 13.14 come from M. Corti and V. Degiorgio, "Analogy between the laser and second-order phase transitions," *Phys. Rev. Lett.* **36**, 1173-1176 (May 17 1976).

The excimer laser results of Figure 13.15 are from J. H. Parks, "Laser action on the $B^2\Sigma_{1/2}^+ \rightarrow X^2\Sigma_{1/2}^+$ band of HgCl at 5576 Å," *Appl. Phys. Lett.* **31**, 192-194 (August 1977).

The next step beyond the idealized single-mode analysis in this section would obviously be to include more than one cavity mode (perhaps many more than one) in the analysis. An expanded rate-equation analysis which includes a large number of modes has been developed by L. W. Casperson, "Threshold characteristics of multimode laser oscillators," *J. Appl. Phys.* **46**, 5194-5201 (December 1975). Casperson shows that in a cavity with a large number of very nearly equal-loss modes the laser threshold becomes "softer" and less abrupt (as might be expected).

The very next case beyond one cavity mode is, of course, two cavity modes; and one convenient way to experiment with two cavity modes is to use the two oppositely directed modes in a ring-laser cavity. Experimental results illustrating the mode competition in such a system are given by M. M. Tehrani and L. Mandel, "Mode competition in a ring laser at line center," *Opt. Lett.* **1**, 196-198 (December 1977).

The transition or change of state that a laser undergoes at threshold has many physical and theoretical similarities to the phase transitions that occur in ferromagnets, superfluids, and superconductors. A brief but readable discussion of this identification is given in R. Salomaa and S. Stenholm, "Observable manifestations of phase transitions in lasers," *Appl. Phys.* **14**, 355-360 (1977).

Other references on this analogy include M. O. Scully, "The laser-phase transition analogy — recent developments," in *Coherence and Quantum Optics*, ed. by L. Mandel and E. Wolf (Plenum Publishing Corp.); and R. Graham, "The phase transition concept and coherence in atomic emission," in *Progress in Optics*, Vol. XII, ed. by E. Wolf (North-Holland, 1974), pp. 235-288.

See also G. Marowsky and W. Heudorfer, "Second- and first-order phase transition analogy in the operation of an organic dye laser," *Opt. Commun.* **26**, 381-383 (September 1978); and A. R. Bulsara and W. C. Schieve, "First-passage time analysis of metastable states in laser phase transitions," *Opt. Commun.* **26**, 384-388 (September 1978).

 Problems for 13.4

1. *Exact solution for the inverted population.* Complete the discussion in the text by analyzing the exact variation of the upper-level population N_{ss} versus R_p or r . Use the simplifying conditions that $3^* = 1$ and $\gamma_2 = \gamma_{rad}$. Develop in addition approximate expressions for N_{ss}/N_{th} to the first order in $1/p$ for r both below and above threshold. How close to threshold can r come (from either side) before these approximate expressions fail?
2. *Cavity mode number in a He-Ne laser.* Using the data in Figure 13.14, deduce that the mode number p in the He-Ne laser cavity used in these experiments must be approximately $p \approx 5 \times 10^7$ modes within the doppler-broadened atomic linewidth. The laser employed was a Spectra-Physics Model 119 frequency-stable laser with an unusually short cavity length of 9.5 cm, bore diameter of around 1 mm, and doppler linewidth of 1,500 MHz. Does the theoretical value for p in this laser check with the value estimated in the preceding (even though the laser is inhomogeneous whereas our analytical model is homogeneous)?
3. *Alternative expression for output-power variation through threshold.* A paper by Huang and Mandel, *Opt. Commun.* **32**, 345–349 (February 1980), gives a more sophisticated formula for the variation of photon number with pumping power both below and above threshold

$$n_{ss} = n_0 \left[a + \frac{2 \exp(-a^2/4)}{\sqrt{\pi}[1 + \operatorname{erf}(a/2)]} \right]$$

where a is some constant times $r - 1$. Relate this formula to the below and above-threshold results derived in this section, and compare its behavior in the threshold region near $r = 1$ with the “exact” formula (Equation 13.57) for the threshold region derived in this section.

4. *Threshold analysis with a partially bottlenecked lower level.* Repeat the derivations in the text for cavity photon number n , populations N_1 and N_2 , and population inversion $N_2 - N_1$ versus pumping rate for pumping levels both below and above threshold, but use a more complicated rate-equation model in which the upper level is pumped at rate R_p and both upper and lower levels have finite relaxation rates γ_2 and γ_1 , with level 2 relaxing partly into level 1 (rate γ_{21}) and partly down to still lower levels (rate γ).
5. *Threshold behavior in a two-mode laser (research problem).* Extend the threshold discussion in the text by considering an idealized laser system in which just two preferred laser cavity modes, with very nearly the same losses, share the same single-level atomic system. Write the necessary rate equations, using the simplifying single-level assumption, and attempt to find exact or approximate solutions for the two cavity photon numbers versus pumping rate. Consider particularly the population in the second (more lossy) mode as the first mode goes through and above threshold. Note also whether there are any significant changes in the general behavior when the difference in mode losses becomes very small. If so, how small, in terms of p ? Compare your results to those given by Tehrani and Mandel cited in the preceding.
6. *Threshold behavior in a partially inhomogeneous two-mode laser (research problem).* As another approach to gain some insight into multimode oscillations in a

laser, consider a cavity having two preferred cavity modes, whose losses differ by some moderate amount, say, 10 percent. As a rough way of modeling for either spatial inhomogeneity or partially overlapping hole burning in the laser transition, assume that the laser atoms are divided into three groups: those seen only by one cavity mode, those seen only by the other mode, and those seen equally by both modes. All the atoms are pumped equally.

Devise a set of laser rate equations for this system, and attempt to solve these to find the oscillation levels of the two modes as the pump level is raised so that first one and then the other mode comes above threshold (assume that each mode is either well above or well below threshold at any given pumping level, and ignore the photon density in either mode when it is below threshold). Explore the resulting behavior for various values of the cavity loss ratio and of the population distribution between the modes (i.e., for different degrees of sharing of atoms between the two modes). *Note:* It may be possible to solve this problem analytically by assuming at various pumping levels that both, one, or neither of the modes oscillates; or numerical solutions with the aid of a computer may be needed.

13.5 MULTIPLE-MIRROR CAVITIES AND ETALON EFFECTS

In this and the following section we consider a number of more complicated multiple-mirror cavity designs which can be used in practical lasers to help obtain various desirable laser properties such as bandwidth narrowing, axial-mode selection, or single-frequency laser operation.

Intracavity Etalons for Frequency Tuning and Mode Control

We have already noted that in many kinds of lasers, including doppler-broadened gas lasers, most solid-state lasers, and organic dye lasers, the atomic gain profile can be much wider than the axial-mode spacing of the laser cavity; and the laser can then oscillate simultaneously over a broad spectrum of multiple axial modes, especially if the gain medium is at all inhomogeneously broadened. It is then common practice, provided the laser gain is not too small, to insert a short, tilted intracavity etalon, or even several such etalons, inside the laser cavity, as shown in Figure 13.16, so that the narrowband frequency transmission of these etalons near resonance can provide frequency tuning and axial mode selection in the laser.

We have analyzed the transmission properties of such simple passive etalons in an earlier section. In this particular situation, the tilt of the intracavity etalon must be kept small enough that it does not seriously reduce the transmission finesse of the etalon through transverse walk-off, yet large enough that the reflected waves from each side of the etalon pass out of the cavity and do not set up additional resonances with the other mirrors of the laser cavity. The center frequency of such an etalon for transmission along the axial direction of the laser can then be varied by angle tuning, temperature tuning, piezoelectric tuning, or sometimes gas-pressure tuning.

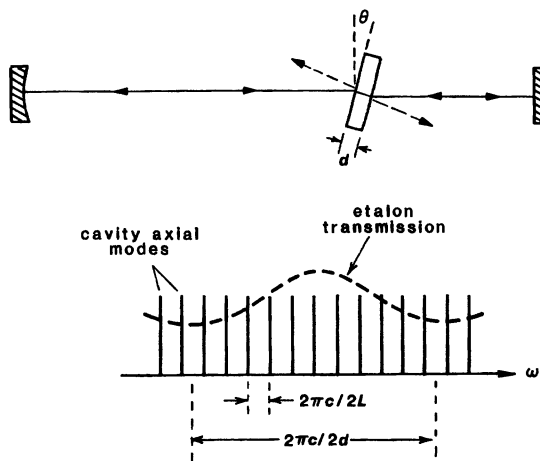


FIGURE 13.16
Laser resonator with intracavity etalon to help achieve axial-mode selection.

Multiple-Mirror Laser Cavities and Interferometers

Sometimes additional mirrors added to laser cavities may be deliberately aligned in resonance with the existing cavity mirrors to obtain *multimirror laser* cavities. The resonance frequency properties of such cavities then become more complicated, in ways that may be useful for various laser purposes. Figure 13.17 illustrates a number of different multimirror cavity and interferometer designs that have been used or studied in connection with laser oscillators.

Basic Analysis of the Three-Mirror Cavity

The simplest form of multimirror cavity is obviously the three-mirror cavity shown in Figure 13.17(a). The properties of such a resonant cavity with three or more mirrors are in general complex, and it may be useful to introduce briefly some of these complexities using a simple analytical model.

Suppose we consider first a general three-mirror cavity as shown in Figure 13.18. (Such a cavity, if two of the mirrors are closely enough spaced, can also be viewed as a two-mirror resonator with an etalon mirror on one end or the other.) As shown in Figure 13.18, let us assume this resonator has mirror reflectivities R_1 , R_2 , and R , and use \tilde{g}_1 and \tilde{g}_2 to describe the round-trip gains inside the two cavity segments, leaving out the mirror reflectivities, so that

$$\tilde{g}_1 \equiv \exp(-\alpha_1 p_1 - j\omega p_1/c) \quad \tilde{g}_2 \equiv \exp(-\alpha_2 p_2 - j\omega p_2/c), \quad (58)$$

with $\alpha_1 p_1$ and $\alpha_2 p_2$ representing the round-trip laser gains or losses, if any, inside each segment of the cavity. (Note that this is different from our earlier notation, where g_{rt} represented the complete round-trip gain inside an interferometer, including the end-mirror reflectivities.)

One simple way to analyze such a cavity is to use our earlier results to write down the complex amplitude reflectivity, call it r'_2 , looking into the R, R_2 section of this interferometer (of length L_2) from the left. We can then use this result

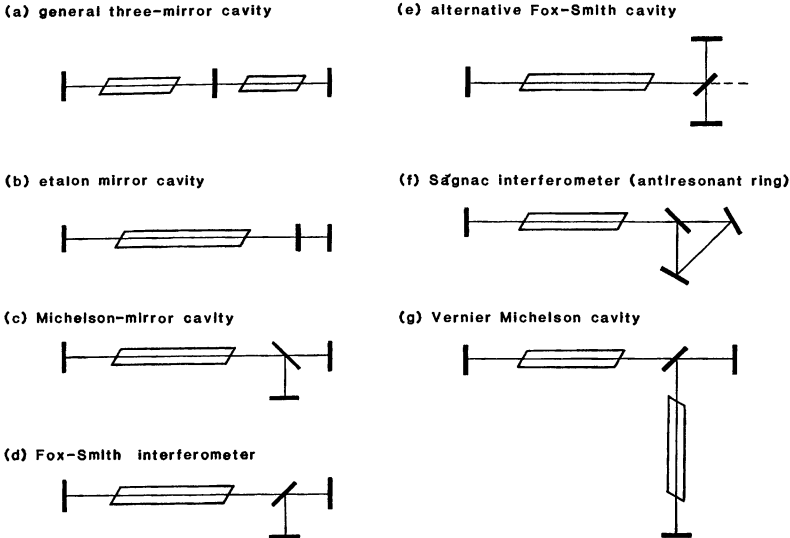
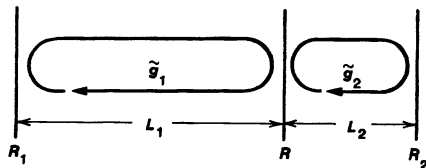


FIGURE 13.17
Examples of multiple-mirror laser cavities and interferometers used for resonance-frequency tuning and axial-mode control in lasers.

FIGURE 13.18
Analytical model for general three-mirror laser cavity.



for r'_2 as the effective end reflectivity to write down the total reflectivity, call it r'_1 , looking into the R_1, R cavity segment (of length L_1) again from the left.

The end result of this is that the total reflectivity looking into the three-section cavity from outside the R_1 mirror can be written as

$$r'_1 = \frac{r_1(1 - rr_2\tilde{g}_2) - \tilde{g}_1(r - r_2\tilde{g}_2)}{1 - rr_1\tilde{g}_1 - rr_2\tilde{g}_2 + r_1r_2\tilde{g}_1\tilde{g}_2}. \quad (59)$$

If we then consider the denominator $D(\omega)$ of this expression as a function of frequency, the complex values of ω that give the roots of this denominator, i.e., that make

$$D(\omega) \equiv r_1r_2\tilde{g}_1(\omega)\tilde{g}_2(\omega) - rr_1\tilde{g}_1(\omega) - rr_2\tilde{g}_2(\omega) + 1 = 0, \quad (60)$$

will define the resonance frequencies and the decay rates for the resonant modes of this cavity.

Basic Properties of Three-Mirror Laser Cavities

Depending on the relative reflectivities and spacings of the cavity mirrors, one might view a three-mirror cavity of this type either as two semi-independent resonant cavities of lengths L_1 and L_2 coupled together by transmission through the central mirror R ; or alternatively one might consider this as a single long cavity of total length $L_1 + L_2$ with an internal perturbation produced by the mirror R ; or as a single cavity of length L_1 with an etalon mirror of length L_2 on one end. Various different analytical approximations can then be used to calculate the cavity resonant frequencies and losses from Equation 13.60.

As a general rule, however, the resonance properties of the three-mirror cavity are sufficiently complex that the use of numerical solutions and computer display techniques can be very helpful, if not essential, in finding and understanding the resulting cavity modes. We will show here only one or two examples of such solutions, to illustrate the type of behavior that can result.

Figure 13.19, for example, shows how the resonant frequencies of a three-mirror cavity shift and how the mode losses change in a typical situation if we vary the reflectivity R of the central mirror, with fixed reflectivities R_1 and R_2 for the end mirrors. The cavity segments are assumed to be lossless in these particular plots, except for the finite mirror reflectivities, and the height of each spectral component is proportional to the energy decay rate for that resonance component.

The longer cavity segment L_1 in this particular situation is assumed to be three times as long as the shorter cavity segment L_2 on a macroscopic length scale, so that the overall axial mode spectrum will repeat periodically with a period corresponding to the axial mode spacing $2\pi \times c/2L_2$ of the shorter cavity. The spectral behavior will also depend strongly, however, on how the axial modes of the two individual cavities are “micro-tuned” with respect to each other. Parts (a) and (b) of Figure 13.19 illustrate the variation in cavity spectrum with central mirror reflectivity R when the two individual cavities are adjusted so that an axial mode characteristic of the short cavity by itself falls either exactly on top of, or halfway in between, the axial modes of the longer cavity. The dashed horizontal lines indicate the mode losses that would occur for the overall cavity $L_1 + L_2$ with no central mirror.

Some examination of Figure 13.19 is worthwhile. There are, of course, four axial modes per repetition period, since the overall cavity length is four times L_2 . It is then evident that the coupling between the two cavity segments produces both large variations in loss, and also strong frequency pulling effects on the modes, and both of these effects depend strongly on how the two cavity segments are tuned relative to each other.

Figure 13.20 similarly shows the variation in mode losses and resonant frequencies for a cavity with fixed mirror reflectivities and macroscopic lengths $L_1 \approx 4L_2$ as the shorter cavity is tuned through one of its separate axial mode intervals. This example corresponds in essence to an etalon-mirror cavity in which the etalon mirror (length L_2) is continuously scanned in frequency through one of its axial mode intervals.

Note that the location of the low-loss region in this spectrum tunes more or less continuously across one full mode interval of the etalon mirror as the etalon

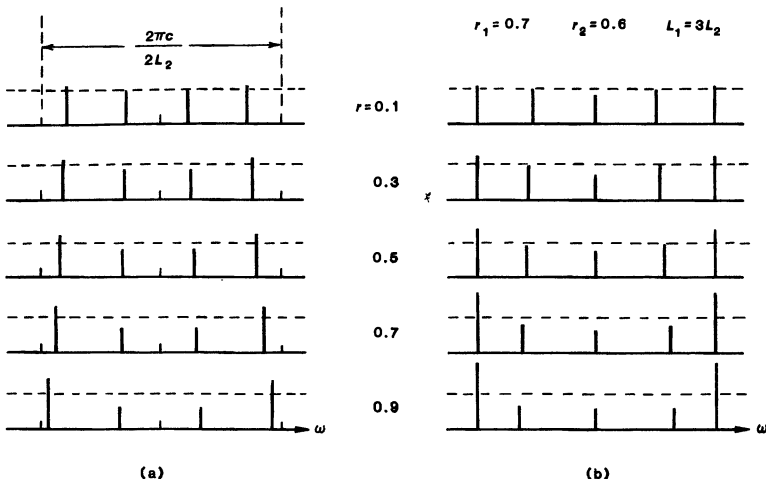


FIGURE 13.19

An illustration of how the mode frequencies and mode losses for a typical three-mirror cavity change as the reflectivity of the central mirror is varied. The two segments of the cavity in this situation have a 3:1 ratio of lengths ($L_1 = 3L_2$), with the two cavities being microtuned so that an axial mode of the shorter cavity is located either (a) exactly coincident with or (b) halfway in between the axial modes of the longer cavity.

is tuned. No single axial mode of the combined cavity tunes in this fashion, however, and there is clearly a discontinuous “mode jump” in the lowest-loss mode in the middle of the tuning range. If we wish to select and tune a single axial mode across the full tuning range in an etalon cavity, it is obvious that simply tuning the etalon mirror is not enough. We must instead somehow tune the lengths of both cavity segments simultaneously, so that the lowest loss mode of the overall cavity tracks the high-reflectivity region of the etalon mirror.

Applications of Three-Mirror Laser Cavities

Simple three-mirror cavities as discussed in the preceding have found some direct applications in lasers. If, for example, we cleave a short semiconductor diode laser into two segments somewhere near the center, carefully maintaining the alignment of the two sections, and then attach separate current leads to the two sections, the result has been called the “cleaved coupled cavity” or C³ type of injection laser. Both the gain and the optical length of each segment can be individually controlled in this situation; and this design has been found to have potential advantages in maintaining a single axial mode, without “mode hopping” effects, over a wide range of injection currents.

Three-mirror or etalon-mirror cavities of this type do not usually provide the optimum design for achieving single-axial-mode operation in low-gain inhomogeneously broadened gas lasers, however, although etalon mirrors are often used in high-gain pulsed solid-state lasers. One reason for this is that, as Figure 13.22

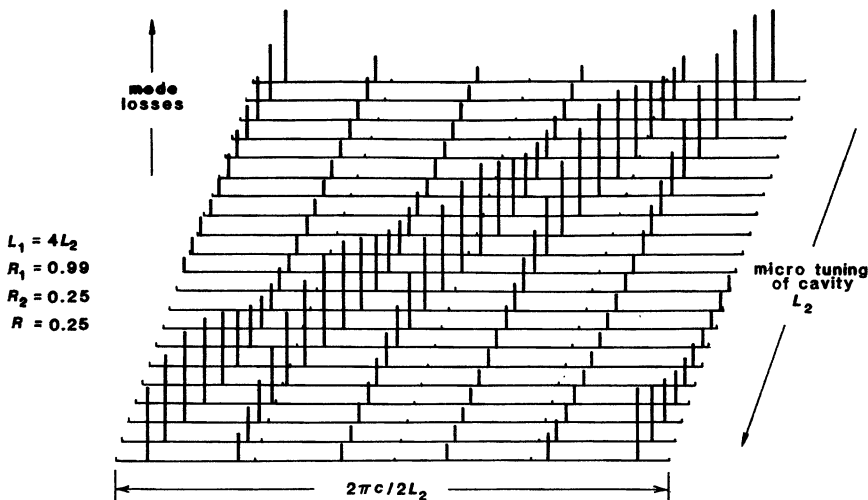


FIGURE 13.20

Another example showing the variations in mode losses and frequencies for a three-mirror cavity with power reflectivities $R_1 = 0.99$, $R_2 = 0.25$, $R = 0.25$, and $L_1 = 4L_2$ as the shorter cavity is tuned through one of its axial mode intervals.

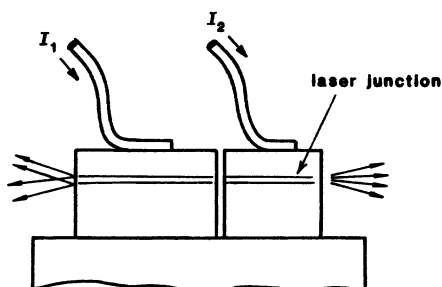


FIGURE 13.21
 C^3 (cleaved-coupled-cavity) injection diode laser.

shows, a high-reflectivity or low-loss etalon normally provides a narrow transmission peak and thus a broad reflection band, whereas what is wanted for axial mode control is a narrow reflection peak. For this same reason, the Michelson-mirror cavity design shown in Figure 13.17(c), which has a sinusoidally varying reflectivity versus frequency, is also usually a less than optimum design.

Fox-Smith Interferometers, and Other Multimirror Designs

More complex but preferred cavity designs for axial mode selection are then provided by one or another of the alternative forms of the Fox-Smith interferometer shown in Figures 13.17 (d) and (e). Note that in both forms most of the signal energy circulating in the primary cavity will be reflected out of this cavity

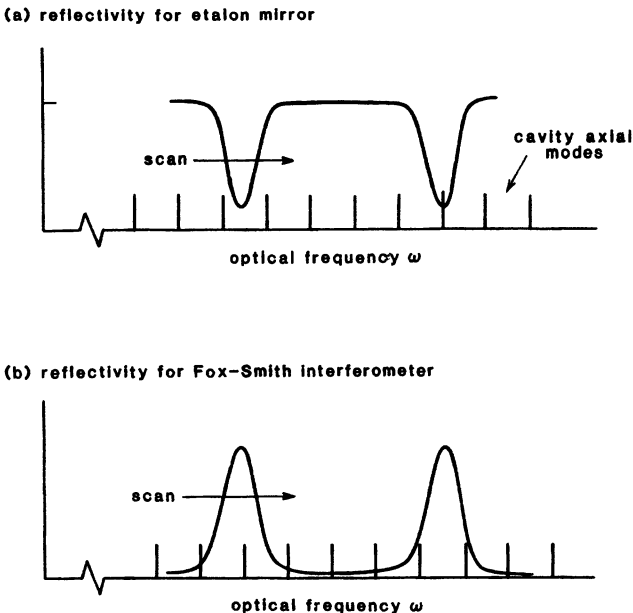


FIGURE 13.22

Reflection coefficients versus frequency for (a) etalon mirror; (b) Fox-Smith interferometer. The arrows indicate how the reflection profile scans as the etalon or interferometer is tuned.

at most frequencies, except at those frequencies where the secondary cavity becomes resonant and builds up a large internal amplitude. This design thus does provide the desired narrow reflection peak as shown in Figure 13.22(b).

Reasonably good mode selection can also be obtained in low-gain lasers using the "vernier Michelson" cavity design shown in Figure 13.17(g). Here, high selectivity is obtained by placing a laser tube in each arm of the Michelson interferometer; and the vernier action results from interference effects between the two long arms, which are made very nearly but not exactly the same length.

Cavity Back-Reflection Effects

We might also note once again that laser cavities are often very sensitive (in power output, frequency tuning, and oscillation stability) to any back-reflection of the laser signal from external optical components directly back into the laser cavity. These back-reflection effects can of course be understood as multimirror cavity effects of the type described in this section, with the external cavity usually being both long and mechanically unstable. If the external back-reflectivity is small, this means that the external cavity segment is very lossy, or has low effective reflectivity; but the very high Q of the oscillating laser cavity segment can still mean that the effects of even weak backscattered signals can be very significant.

REFERENCES

An excellent comprehensive review of multimirror laser cavities and other resonator mode control methods is given in P. W. Smith, "Mode selection in lasers," *Proc. IEEE* **60**, 422-440 (April 1972).

The C³ semiconductor laser concept and some of its advantages are discussed in W. T. Tsang, N. A. Olsson, and R. A. Logan, "High-speed direct single-frequency modulation with large tuning rate and frequency excursion in cleaved-coupled-cavity semiconductor lasers," *Appl. Phys. Lett.* **42**, 650-652 (April 15 1983).

For a recent example of three-mirror cavity-mode calculations, see M. J. Adams and J. Buis, "Two segment cavity theory for mode selection in semiconductor lasers," *IEEE J. Quantum Electron.* **QE-20**, 99-103 (February 1984).

The Sagnac interferometer cavity design is described in A. E. Siegman, "An antiresonant ring interferometer for coupled laser cavities, laser output coupling, mode locking, and cavity dumping," *IEEE J. Quantum Electron.* **QE-9**, 247-250 (February 1973).

As one example from the many papers on the effects of back-reflected signals on lasers, see J. H. Osmundsen and N. Gade, "Influence of optical feedback on laser frequency spectrum and threshold conditions," *IEEE J. Quantum Electron.* **QE-19**, 465-469 (March 1983).

Problems for 13.5

1. **Three-mirror cavity frequency expression.** If we take the limit as the reflectivity R of the internal mirror goes to zero and its transmission goes to 100%, then the expression (Equation 13.60) given in this section for the resonant denominator of a three-mirror cavity goes to $D(\omega) = 1 + r_1 r_2 g_1 g_2$ rather than to $D(\omega) = 1 - r_1 r_2 \tilde{g}_1 \tilde{g}_2$ as we might expect. How come?
2. **Energy distribution in a multimirror cavity.** The different loss rates for different resonant modes in a multimirror cavity, as illustrated in this section, must mean that the relative distribution of stored energy between the individual cavity segments is different from one resonance to another. Carry out a more detailed analysis of the three-mirror (or two-segment) cavity discussed in this section, in order to calculate the relative wave amplitudes of the circulating waves in the two sections of the cavity when the cavity is excited at one or another of its resonant frequencies.
3. **Analysis of the Fox-Smith interferometer.** Carry out a suitable analysis of the Fox-Smith interferometer in either of its forms and discuss the resulting mode selection properties. Consider in particular the requirements on the beam splitter reflection and transmission, and on the losses in the secondary cavity, if the peak reflectivity back into the primary cavity is to be very close to unity. How might we tune either of these cavity designs to obtain tunable single-frequency operation across the full axial mode spacing of the shorter secondary cavity?

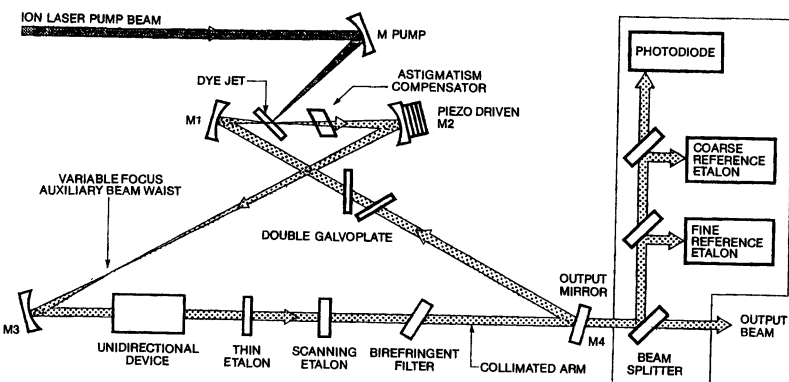


FIGURE 13.23

Example of a ring-laser cavity design with intracavity etalons, filters, and unidirectional devices, as used to provide single-frequency, continuously tunable, high-efficiency operation in a commercially available cw dye laser.

13.6 UNIDIRECTIONAL RING-LASER OSCILLATORS

Ring-laser cavities were understood and demonstrated very early on, and have since been extensively developed for application in ring-laser gyroscopes. Ring-laser cavities possess one unique capability as compared to standing-wave cavities, namely they have the ability to oscillate, simultaneously or independently, in either of two distinct counter-propagating directions.

Ring resonators also possess a number of other attributes which can be very useful in several different laser and passive interferometer applications. Full appreciation of the advantages of ring resonators in optical applications has only emerged more recently, and it seems useful therefore to give a brief summary in this section of the special properties of ring-laser resonators.

Example of a Unidirectional Ring-laser Cavity

Figure 13.23 shows, by way of example, a typical folded ring resonator design as used in a commercially produced cw dye laser. The ring cavity in this example contains not only the dye-jet gain medium, several frequency control etalons and filters, and an astigmatism compensating element, but also a unidirectional device ("optical diode") which allows oscillation to occur in only one direction around the ring. This figure also illustrates the array of diagnostic elements which are used, in conjunction with electronic feedback loops, to control the etalon elements, the piezo mirror control, a double galvoplate, and the birefringent optical filter, all needed to give single-frequency laser operation tunable over a wide tuning range.

The primary advantage to unidirectional oscillation in a ring laser such as this is that the purely traveling-wave rather than standing-wave operation eliminates spatial hole-burning effects, making the laser medium in effect much more homogeneous. This in turn substantially increases the mode competition between adjacent axial modes, making it possible to pump the laser considerably further above threshold while maintaining single-frequency operation. In addition, because the traveling-wave mode saturates the gain medium uniformly, with no

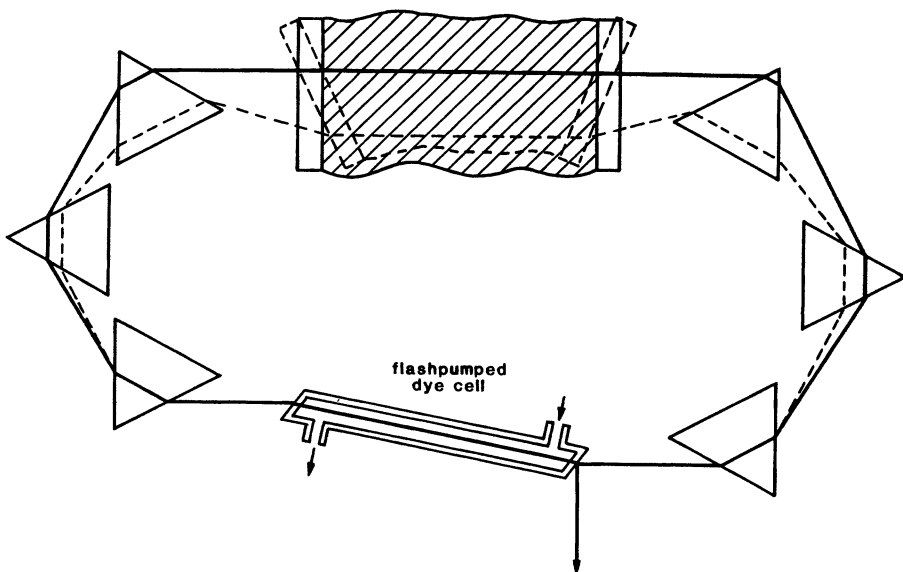


FIGURE 13.24
Prism-type ring resonator. (Adapted from Schäfer and Müller.)

spatial nodes along the axial direction, this mode can extract more power than would otherwise be obtained.

The combined effect can be an increase in single-frequency power output by more than an order of magnitude compared to what can be obtained using a standing-wave cavity in a typical dye laser example. Similar advantages can be obtained in other lasers, for example, pulsed solid-state lasers, as well.

Other Attributes of Ring Resonators

Other potentially useful attributes of ring optical resonators include:

(1) *Increased cavity design flexibility and alignment insensitivity.* We will point out later on, in the resonator chapters of this text, that a ring optical cavity provides increased flexibility in resonator design as compared to a standing-wave cavity, especially for unstable resonator designs. In particular, a ring cavity can easily employ a comparatively short beam expansion section, using readily available short-focal-length optical elements, and then a long collimated beam section at large beam diameter, for obtaining full power extraction from large diameter laser gain media. (Figure 13.23 shows, by contrast, the way in which very small focal spots, for use with intracavity dye jets or modulation elements, can equally easily be obtained inside a ring-laser resonator.)

Ring resonators also offer the possibility of using prisms of various sorts in place of mirrors in forming the ring; and this aspect has been used in ring-laser designs such as Figure 13.24. A planar ring resonator also has the interesting attribute of being first order insensitive to misalignments in the plane of the ring. That is, when any element is misaligned by a small amount in the plane of the ring, the resonator mode can always respond by making small changes in

beam position and direction to find a new closed and aligned path in the plane of the ring.

(2) *Elimination of input feedback, and reduced sensitivity to back reflection.* We have noted earlier that when an external signal is injected into a ring resonator or ring interferometer, the reflected-plus-transmitted signal from the input mirror goes off in a different direction, with no optical feedback directly back into the external signal source. This can be very useful for laser injection locking experiments, where feedback from a high-power locked oscillator back into the much lower-power injection source can be a major experimental problem. A unidirectional ring oscillator can also be less sensitive to feedback from external reflections placed in its output beam, since these reflections go into a non-oscillating direction in the ring.

Similar considerations apply when a passive ring resonator is used as a scanning interferometer or frequency filter for laser diagnostics or frequency stabilization. Elimination of feedback from the passive cavity in this situation can minimize instability effects in the laser being studied.

(3) *Single-pass operation of intracavity elements.* Intracavity elements, such as modulators, harmonic generation crystals, and the like, are excited in only one direction in a unidirectional ring-laser oscillator. While this may in many situations reduce the modulation efficiency or harmonic generation efficiency of the element, it can also simplify certain experiments and permit more accurate measurements on intracavity experimental cells or samples.

The order in which optical elements are encountered is also inherently different going in the two directions around a ring. Going in one direction, for example, a wave may see first the laser-gain medium, then a saturable absorber, and then the output coupler, whereas the order is obviously reversed in the opposite direction. This can be used to control power levels and saturation intensities in different elements, and can be a source of directional nonreciprocity in a ring-laser oscillator.

Ring-laser Disadvantages

The primary disadvantage of the ring resonator for laser applications, leaving aside the additional complexity and structural requirements, is probably that the gain medium is traversed only once. A low-gain laser will thus operate considerably closer to threshold, and have more stringent requirements on reducing the output coupling, and especially the internal losses, if good efficiency is to be maintained. (Of course, other lossy intracavity elements other than mirrors are also encountered only once rather than twice per round trip.)

The astigmatism produced by off-axis reflection from cavity mirrors must also be taken into account in the resonator design. This astigmatism can even be an advantage in some situations, however, and can usually be compensated for when it is not.

Techniques for Obtaining Unidirectional Oscillation

The mode competition between two potentially oscillating modes in a ring laser (or in any other multimode laser situation) is in general a complex problem. As we will show in later sections, depending on mode losses, mode cross-coupling, and mode self-saturation and cross-saturation properties, competition between two modes may lead to stable single-mode operation; to simultaneous

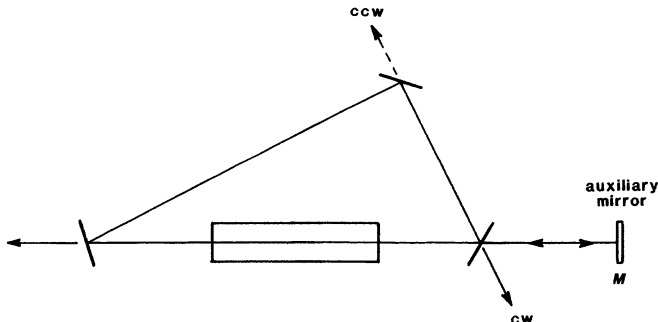


FIGURE 13.25
Use of an external mirror to augment one-way oscillation in a ring laser.

dual-mode operation; or to random jumping back and forth between the two potential modes. This applies especially to the oppositely traveling waves in a ring resonator, and several different techniques for obtaining or improving unidirectional operation in ring resonators have been demonstrated.

One of the simplest of these is to employ an auxiliary external mirror, having partial or complete reflectivity, to reflect part of, say the CCW circulating output back into the CW direction, as illustrated in Figure 13.25. If this cavity attempts to oscillate in the CW direction, the resulting back-reflected signal will serve as an injected signal for the CCW direction, leading to a much stronger oscillation in the CCW direction.

This technique does work as intended, at least crudely and in some situations. If the laser medium is otherwise homogeneous, the preferred CW oscillation does grow at the expense of the CCW oscillation. The CCW oscillation is not fully extinguished, however, but remains as a low-amplitude injection signal to drive the CW oscillation. Intensity ratios between the two directions in the range of 10:1 to 50:1 have been reported in typical situations.

For inhomogeneously broadened materials the technique may not work at all, especially when the centermost axial mode of the ring cavity is not at line center. In this situation the ring may oscillate with equal intensity in both directions, and may also oscillate in several axial modes at once. This scheme is also sensitive to internal backscattering inside the ring, which can interact interferometrically with the external mirror. These interactions make the basic technique fundamentally unsound when finite backscattering is taken into account.

Nonreciprocal Optical Diodes

A much preferable solution is to place a nonreciprocal optical isolator, sometimes referred to as an "optical diode," inside the ring cavity to introduce nonreciprocal losses in the two directions. Figure 13.26 shows the basic elements of such an optical diode.

The primary component is a Faraday rotation device using a transparent material with a finite Verdet constant placed in a dc magnetic field. When a linearly polarized optical wave passes through such an element, its plane of polarization is rotated about the optical axis, with a direction of rotation which depends on the dc magnetic field direction but not on the direction of travel of the wave. To

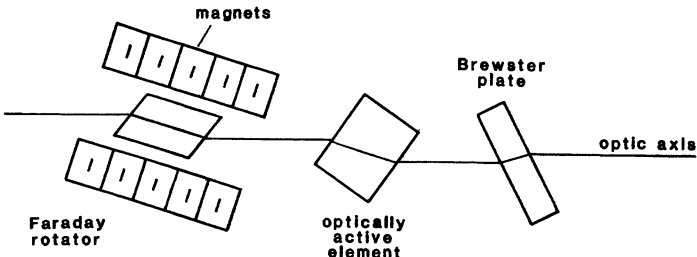


FIGURE 13.26

Nonreciprocal "optical diode" using a Faraday rotator.

make an optical isolator, a second purely reciprocal rotation element is added to cancel out the Faraday rotation going in one direction through the system. This reciprocal element may be an optically active crystal or liquid (e.g., quartz, or a sugar solution), or a birefringent crystal used as a partial wave plate.

The reciprocity properties of this system then mean that the total polarization effects due to the two elements going in the forward direction through the system can cancel each other, giving no net polarization change, whereas the effects of the two elements going in the opposite direction will add to give a finite modification of the wave polarization. A linearly polarized wave going in the forward direction through the system can then pass unattenuated through a Brewster angle plate (or some other type of polarization-sensitive element) on successive round trips, whereas a wave going in the opposite direction, because of the net polarization rotation, will experience added loss on each round trip.

(It should be noted that this additional loss is in general not given simply by calculating first the polarization rotation of a linearly polarized wave in the optically active elements and then the transmission of the resulting wave through the Brewster plate. We must instead use some form of polarization calculus to calculate the total propagation of two orthogonal polarization components around the ring, as well as the cross coupling between these polarization components in each optical element; and the use these results to find the two polarization eigenmodes and associated eigenvalues for the cavity. A cavity which contains birefringent or polarizing elements will in general have two such mixed polarization eigenmodes, neither of which will generally be as lossy as predicted by the simple approach given in the preceding.)

Useful Faraday rotators for optical wavelengths are difficult to obtain in practice, primarily because the physical basis of Faraday rotation is the anisotropic tensor response $\chi'(\omega)$ on the side of some very strong, and Zeeman split, atomic transition. Materials with large Verdet constants (i.e., large polarization rotation per unit of dc magnetic field) are thus most often also highly absorbing, whereas highly transparent materials typically have very small Verdet constants. In practice the optical diodes used in ring lasers typically have Faraday rotations of a few degrees, and differential losses between the two directions of a percent or so. This additional insertion loss in the reverse direction is, however, enough to strongly suppress oscillation in the reverse direction, and produce highly selective oscillation in the forward direction only.

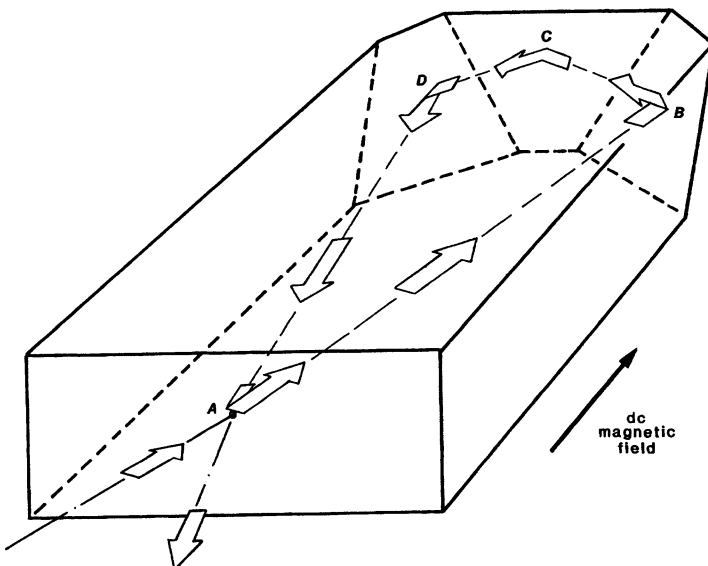


FIGURE 13.27
Unidirectional nonplanar solid-state ring laser. (From Byer et al.)

Nonplanar Ring Resonators

We will also point out later in this text that *nonplanar ring resonators* can provide unique image rotation and also polarization rotation properties. These properties have been employed recently to develop a unique monolithic solid-state laser with inherent unidirectional properties, as illustrated in Figure 13.27.

The material used here is Nd:YAG, which has both laser gain and a finite Verdet constant. A small crystal cut as shown in this figure then provides a nonplanar ring resonator which employs total internal reflection at all but one of its surfaces. The polarization rotation inherent in the nonplanar ring path is then compensated in one direction, but not in the other, by the Faraday rotation produced by a dc magnetic field. The crystal thus oscillates inherently in only one direction around the ring, and as a consequence also achieves high-quality single-frequency operation.

REFERENCES

The use of a traveling-wave ring resonator with a Faraday rotator to eliminate standing waves and thereby obtain single-frequency oscillation was demonstrated at an early date in a ruby laser by C. L. Tang, H. Statz, and G. deMars, Jr., "Spectral output and spiking behavior of solid-state lasers," *J. Appl. Phys.* **34**, 2289-2295 (August 1963).

The use of back reflection from an auxiliary mirror to improve unidirectional operation was also demonstrated not long after by M. Hercher, M. Young, and C. B. Smoyer, "Traveling-wave ruby laser with a passive optical isolator," *J. Appl. Phys.* **36**, 3351 (October 1965). The fundamental properties of this auxiliary mirror concept are

also discussed in F. R. Faxvog, "Modes of a unidirectional ring laser," *Opt. Lett.* **5**, 285–287 (July 1980).

Application of the unidirectional ring resonator concept to dye lasers was first demonstrated by F. P. Schäfer and H. Müller, "Tunable dye ring-laser," *Opt. Commun.* **2**, 407–409 (January 1971); and by J. M. Green, J. P. Hohimer, and F. K. Tittel, "Traveling-wave operation of a tunable cw dye laser," *Opt. Commun.* **7**, 349–350 (April 1973).

For more recent developments in unidirectional ring lasers and Faraday rotators, see, for example, S. M. Jarrett and J. F. Young, "High-efficiency single-frequency cw ring dye laser," *Opt. Lett.* **4**, 176–178 (June 1979); or T. F. Johnston, Jr., and W. Proffitt, "Design and performance of a broad-band optical diode to enforce one-direction traveling-wave operation of a ring laser," *IEEE J. Quantum Electron.* **QE-16**, 483–488 (April 1980).

The monolithic solid-state ring laser is described by T. J. Kane and R. L. Byer, "Monolithic, unidirectional single-mode Nd:YAG ring laser," *Opt. Lett.* **10**, 65–67 (February 1985).

13.7 BISTABLE OPTICAL SYSTEMS

The equations of motion for a laser oscillator, or more generally for any system of coupled fields and atoms, are intrinsically nonlinear (although we often make linear approximations to these equations). It has been increasingly realized in recent years that one can often obtain in such nonlinear systems interesting and fundamental types of *bistable*, *multistable*, *self-pulsing*, and even *chaotic* behavior.

In this section, therefore, we briefly introduce some of the interesting bistability properties of lasers and also of passive optical cavities. These bistability properties may someday find practical applications in optical computers, "optical transistors," or other optical signal-processing devices, although the real practicality of any such all-optical computer systems remains at present still in considerable doubt.

Bistable Laser Oscillation

As the simplest example of a bistable laser oscillator, we can consider a laser cavity containing both a homogeneously saturable gain medium and a homogeneously saturable atomic absorber. Suppose that at small signal levels the combined saturable and nonsaturable losses in this cavity exceed the unsaturated gain, so that the cavity cannot begin oscillating spontaneously starting from noise. The laser thus has one stable operating point in the totally quiescent condition, with no signal present.

Suppose, however, that the cavity losses saturate much more easily with increasing signal intensity than does the laser gain—that is, the absorbing atoms have a lower saturation intensity than do the amplifying atoms. At high-enough signal intensities the saturated round-trip losses can then drop below the saturated round-trip gain, as shown in Figure 13.28. If this laser can ever start oscillating, therefore—perhaps with assistance from some externally injected signal—it will build up to a large circulating intensity and remain oscillating until it is turned off.

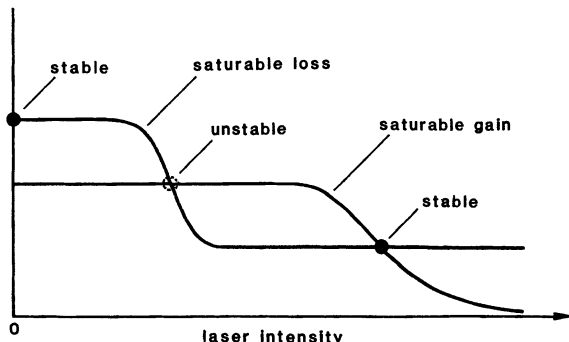


FIGURE 13.28
Gain and loss saturation
versus intensity in a bistable
laser oscillator.

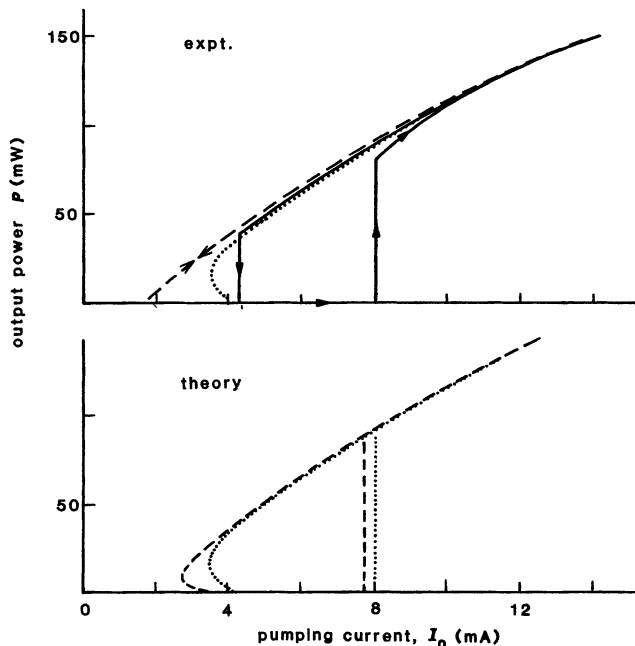


FIGURE 13.29
Hysteresis and bistable operation in the output of a CO₂ laser oscillator
plotted versus excitation current. (Adapted from E. Aromondo and B. M.
Dinelli, *Opt. Commun.*, **44**, 277–282, January 15, 1983.)

This simple system thus exhibits *bistable* behavior, with two stable steady-state operating points, as shown in Figure 13.29. There is also a third potential steady-state operating point where gain also equals loss, at the first crossing of the saturable loss and saturable gain curves. However, it can readily be shown (see Problems) that this is not a stable operating point for the laser.

A laser of this type can also exhibit a strong *hysteresis* in the variation of output power with pumping power, as illustrated in Figure 13.29. The results shown there are for a cw CO₂ laser with an intracavity cell containing 25 mm of gaseous SF₆ as a saturable absorbing medium. When the pumping current I_0 is turned up from zero, laser action cannot start until the laser gain exceeds the laser cavity losses plus the unsaturated losses of the SF₆ cell. Once the laser starts oscillating, however, the SF₆ absorber cell is saturated, and we can then reduce the pumping current to a considerably lower value before the laser will suddenly drop out of oscillation.

Analysis of a Nonlinearly Absorbing Cavity

As an even simpler example of a bistable optical system, we can consider a passive Fabry-Perot interferometer, of either the standing-wave or the ring-cavity type, containing only a simple passive saturable absorber, and driven by an externally applied optical signal.

Suppose such a passive Fabry-Perot cavity has input and output mirrors with reflectivities $R_1 = r_1^2 = \exp(-\delta_1)$ and $R_2 = r_2^2 = \exp(-\delta_2)$, and a round-trip power attenuation coefficient due to a saturable atomic absorber of $\delta_m \equiv 2\alpha_m p_m$. If this cavity is driven by an externally incident signal I_{inc} which is tuned to the cavity resonant frequency, then the internal circulating signal I_{circ} and the transmitted signal field I_{trans} from the cavity will be given by the elementary interferometer relations derived in earlier sections. In particular, if we assume that all of the loss factors are small compared to unity, then the incident, circulating, and transmitted intensities from this cavity will be related by the expressions

$$\frac{I_{\text{trans}}}{I_{\text{inc}}} \approx \frac{4\delta_1\delta_2}{[\delta_1 + \delta_2 + \delta_m(I)]^2} \equiv T(I), \quad (61)$$

and

$$\frac{I_{\text{circ}}}{I_{\text{inc}}} \approx \frac{4\delta_1}{[\delta_1 + \delta_2 + \delta_m(I)]^2} \equiv \frac{T(I)}{\delta_1}, \quad (62)$$

where $T(I) \equiv I_{\text{trans}}/I_{\text{inc}}$ is the intensity-dependent power transmission through the cavity. Let us assume that the internal atomic absorption saturates in the homogeneous fashion

$$\delta_m = \delta_m(I) = \frac{\delta_{m0}}{1 + 2^* I_{\text{circ}}/I_{\text{sat}}} = \frac{\delta_{m0}}{1 + I} \quad (63)$$

with $2^* \equiv 1$ for a ring cavity and $2^* \equiv 2$ for a standing-wave cavity, and where $I \equiv 2^* I_{\text{circ}}/I_{\text{sat}}$. Then by picking successively increasing values of the circulating intensity I_{circ} , we can calculate first the intensity-dependent transmission gain $T(I)$, and then calculate and plot the transmitted intensity I_{trans} versus the incident intensity I_{inc} for the interferometer.

If we assume for simplicity that the input and output couplings are the same, $\delta_1 = \delta_2$, then the power transmission $T(I)$ through the interferometer can be written as

$$T(I) = \left[\frac{1}{1 + R/(1 + I)} \right]^2 = \left[\frac{1 + I}{1 + R + I} \right]^2, \quad (64)$$

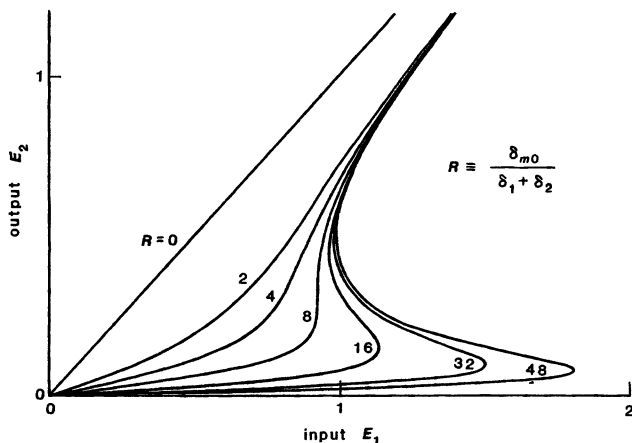


FIGURE 13.30

Nonlinear amplitude transmission through a Fabry-Perot interferometer containing a homogeneous saturable absorber.

where R is the ratio of unsaturated gain to total coupling, as defined by

$$R \equiv \frac{\delta_{m0}}{\delta_1 + \delta_2}. \quad (65)$$

It is further convenient to define normalized input and output signal intensities for the cavity by

$$I_1 \equiv E_1^2 \equiv \frac{2^* I_{\text{inc}}}{\delta_1 I_{\text{sat}}} \quad \text{and} \quad I_2 \equiv E_2^2 \equiv \frac{2^* I_{\text{trans}}}{\delta_1 I_{\text{sat}}}, \quad (66)$$

and then to eliminate the internal circulating intensity $I \equiv 2^* I_{\text{circ}}/I_{\text{sat}}$ between the preceding equations. The input-output field relationship then takes the simple form

$$E_1 = E_2 \left[1 + \frac{R}{1 + E_2^2} \right]. \quad (67)$$

Figure 13.30 shows the nonlinear input-output relationship that is produced by this type of saturable absorber cavity transmission. A multivalued input-output relation occurs in this simple situation only if the ratio of unsaturated losses to total cavity coupling has a value $R \geq 8$.

Absorptive Bistability

A saturable-absorber cavity of this type will, as a consequence, exhibit the general type of bistable input-output hysteresis behavior shown in Figure 13.31. That is, if we turn up the input intensity to this cavity, starting from low values, the circulating intensity inside the cavity will at first not be greatly enhanced, because of the sizable absorption losses and hence low finesse of the interferometer. When the incident signal level reaches a certain value marked

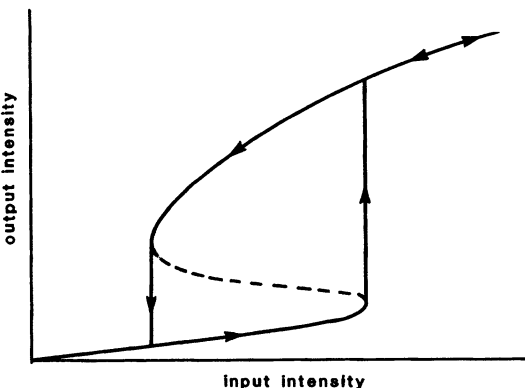


FIGURE 13.31
Hysteresis behavior in a non-linear system such as Figure 13.30.

by the first turning point in Figure 13.31, however, the circulating intensity will become large enough to begin to saturate the absorption.

The cavity finesse will then begin to increase, which means the circulating intensity inside the cavity will also begin to increase for the same incident power level, thus causing a further increase in cavity finesse and in circulating intensity. The cavity operating point will then suddenly jump upward in a discontinuous fashion to the upper branch, where the cavity losses are essentially saturated and the cavity finesse, circulating intensity, and transmitted intensity are all much larger than on the lower branch.

If the incident intensity is then reduced, the much higher finesse of the cavity on the upper branch makes it possible for the internal circulating intensity to remain above the saturation level even with much smaller input intensity. The cavity will thus move back down along the upper branch, until at a certain point it drops discontinuously back to the lower branch. The portion of the input-output curve between these two discontinuities, marked by a dashed line, is unstable and cannot be a steady-state solution.

Dispersive Optical Bistability

An analogous but physically different (and generally more useful) type of bistability can also occur in a passive interferometer cavity containing a nonlinear dispersive rather than absorptive medium.

Consider, for example, a simple ring or standing-wave interferometer cavity containing an optical Kerr type of material in which the optical refractive index n changes as the optical intensity is increased, in the form for example $n(I) = n_0 + n_2 I$, where I is the circulating intensity inside the cavity. As the circulating intensity changes, therefore, the resonant frequency of the cavity will change, and this will in turn change the relationship between the input, circulating, and output intensities in a manner which can lead to a variety of complex bistable and multistable behavior.

The incident signal in this situation need not be tuned to the small-signal resonant frequency of the cavity. The nonlinear behavior in this system can instead be examined using the following simple graphical analysis. If we again

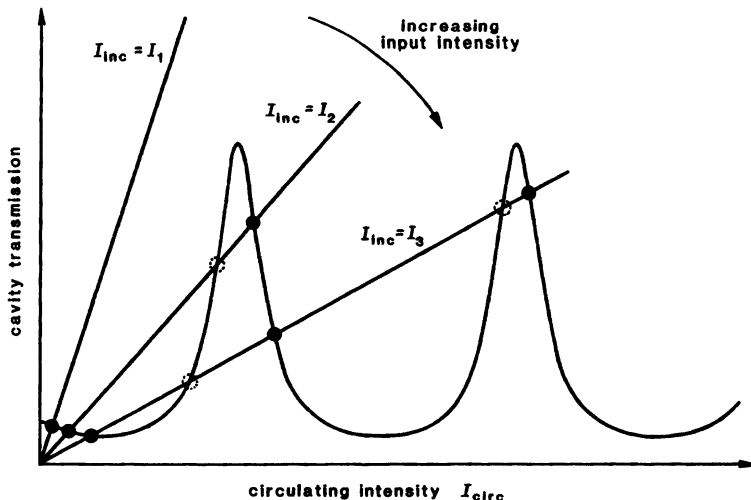


FIGURE 13.32
Graphical interpretation of dispersive cavity bistability.

make use of results from earlier chapters, the power transmission $T(I)$ through the cavity can be written as

$$T(I) \equiv \frac{I_{\text{trans}}}{I_{\text{inc}}} = \frac{1}{1 + F \sin^2 \phi(I)/2}, \quad (68)$$

where F is the finesse of the cavity and $\phi(I)$ is the round-trip phase shift. For a cavity filled with an optical Kerr material and excited at a free-space wavelength λ_0 this phase shift will be given by

$$\phi(I) = \frac{2\pi p}{\lambda_0} [n_0 + n_2 I_{\text{circ}}], \quad (69)$$

where p is the round-trip length in the cavity.

Figure 13.32 plots this transmission gain $T(I)$ through an optical cavity containing a lossless optical Kerr material, assuming that the cavity resonance is tuned well away from the applied signal frequency at small signal levels, and that the intensity is varied over a wide enough range to shift several axial modes of the cavity through the applied signal frequency. This curve will be shifted transversely, depending upon how the incident signal is tuned.

But, in addition the input, circulating, and output intensities are also related by the expressions $I_{\text{trans}} = \delta_2 I_{\text{inc}} = T I_{\text{inc}}$, or $T(I) = \delta_2 I_{\text{circ}}/I_{\text{inc}}$, which corresponds to a set of straight lines in the $T(I)$ versus I_{circ} plot, with slopes which decrease with increasing input intensity I_{inc} .

Figure 13.32 then shows, for example, how for a low incident intensity $I_{\text{inc}} = I_1$ there is only one operating point at which these two formulas intersect. The cavity frequency in this situation is essentially unshifted from its low-intensity value, and the cavity is operating at low transmission, well off resonance.

At a larger incident intensity $I_{\text{inc}} = I_2$, however, there are three potential operating points, one at low transmission well off resonance, and two others

within the high-transmission resonance peak. Only two of these points, however, indicated by the solid circles, represent stable operating points.

At the outermost operating point, for example, the cavity is operating close to one of its axial mode resonances, but with the intensity-shifted cavity resonance frequency slightly below the input signal frequency. If the incident power level increases slightly, then the circulating intensity increases, and this in turn drives the cavity resonance frequency slightly lower (by increasing the value of the intracavity index n). But, this moves the cavity resonance frequency slightly further away from the applied signal frequency, causing the circulating power to decrease and thus partially canceling the effect of the increased incident power. Operating points on the upper sides of the cavity resonances are thus stable, whereas operating points on the lower sides, by a similar argument, are perturbation unstable.

This same plot also shows that if the incident intensity is still further increased to the value $I_{\text{inc}} = I_3$, multistable behavior with three or more potential operating points also becomes possible.

Fluctuations and Self-Pulsing Phenomena

These two examples illustrate the elementary properties of purely absorptive and purely dispersive optical bistability or optical multistability. More generally, if one considers an optical cavity containing a general two-level resonant atomic system, then we will have an even more complex situation, with a mixture of absorptive and dispersive nonlinear properties, depending upon how the atoms and the cavity are tuned. The atomic system may also exhibit either homogeneous or inhomogeneous saturation behavior, depending upon its type; and at larger signal levels we may have to take into account Rabi flopping effects in addition to the nonlinear saturation behavior of the atoms.

The net result of all this is a very rich and complex variety of nonlinear behavior in passively excited optical cavities containing saturable atoms. In addition to the simple bistability and hysteresis behavior illustrated in the preceding, at larger input intensities many of these nonlinear optical systems will exhibit *spontaneous periodic fluctuations*, in which the cavity intensity jumps back and forth at a regular rate between two branches of the input-output curve, thus converting a steady-state input beam into a pulsed output beam.

These jumps have a close conceptual relationship to phase transitions in atomic systems, and to limit cycle behavior in other nonlinear systems. In fact, it has been realized in recent years that many different nonlinear systems, ranging from optical cavities to mechanical systems and fluid-flow problems, can all exhibit broadly similar nonlinear properties. As we turn up the excitation intensity, or some other kind of gain parameter in a nonlinear system, we often see at first some kind of bistable or hysteresis behavior, as illustrated in the preceding. This may be followed by a periodic pulsing behavior, and this periodic behavior may at higher intensities show a discontinuous jump in the pulsation frequency, often to half the previous frequency (referred to as *period doubling*).

At each of these discontinuities if we suddenly switch the incident intensity to a value well above or well below the discontinuity point, then the transition from one form of behavior to another occurs very rapidly. If the incident intensity is only moved a very small amount beyond the transition point, however, then the transition from one branch to the other occurs only very slowly, a phenomenon referred to as *critical slowing down*.

The Transition to Chaos

Finally, such nonlinear systems may often, as the excitation parameter is varied, suddenly jump to a very distinctive new form of behavior referred to, with good reason, as *chaos*. In the chaotic region, even though the equations of motion for the system are entirely deterministic and may contain only a few parameters, and the system input is constant, still the resulting system behavior (e.g., the cavity output intensity) fluctuates wildly with time, in what seems to be a totally random fashion. The power spectrum for the cavity amplitude fluctuations, for example, will apparently have a continuous distribution in frequency, with no observable discrete frequency components.

A passive optical cavity containing an ideal optical Kerr material, for example, with an externally applied cw signal, can pass through discrete regions of bistable behavior, then periodic fluctuations, then various sorts of period doublings, and then various sharply defined regions of chaotic behavior, as the incident signal intensity is slowly increased. The turbulence which invariably develops in a fluid flow above a sharply defined Reynolds number is another elementary illustration of chaos. These chaotic phenomena do not seem to depend on any fundamental noise sources in the system, and exhibit striking similarities across widely different physical systems.

Experimental Results

All of the preceding-mentioned nonlinear phenomena, including bistability, multistability, periodic fluctuations, period doubling, and chaos, have in recent years been both predicted and experimentally observed, although often only with some difficulty, in optical cavities. In general, nonlinear dispersive and mixed-dispersive effects are more easily obtained (as well as more interesting) than purely absorptive effects.

For example, by combining tunable dye lasers with the very strong but narrow resonance transitions in metal vapors, such as sodium or rubidium cells, one can demonstrate many atomic nonlinear phenomena using reasonable input powers and detection speeds. It is difficult to envision practical optical signal-processing devices using this approach, however.

Optical Kerr effects are also often observed using molecular liquids such as CS_2 , although only with comparatively high optical powers and fast pulses. Certain semiconductors, such as GaAs and InSb, and also semiconductor quantum well structures, can also exhibit strong optical nonlinearities at wavelengths near or just beyond their optical absorption edges; and there is much interest in these materials for possibly practical bistable optical systems.

REFERENCES

For some more recent and complex results in laser bistability, see, for example, L. W. Hillman, J. Krasinski, R. W. Boyd, and C. R. Stroud, Jr., "Observations of higher order dynamical states of a homogeneously broadened laser," *Phys. Rev. Lett.* **52**, 1605–1608 (April 30 1984).

For an excellent introductory review of passive optical bistability, see E. Abraham and S. D. Smith, "Optical bistability and related devices," *Rep. Prog. Phys.* **45**, 815–885 (August 1982).

More recent but more theoretical surveys of bistability in driven optical cavities, with numerous references, are given by L. A. Lugiato, "Theory of Optical Bistability," and by J. C. Englund, R. P. Snapp, and W. C. Shieve, "Fluctuations, Instabilities and Chaos in the Laser-Driven Nonlinear Ring Cavity," in *Progress in Optics*, Vol. XXI, ed. by E. Wolf (Elsevier, 1984); pp. 69–216 and 355–428.

For an excellent introduction to the fundamental ideas of nonlinear instabilities and chaos, the student should see "Metamagical Themas," by D. R. Hofstadter in *Scientific American* **245**(5), 16–29 (November 1981). A more formal discussion of the same ideas is given by E. Ott, "Strange attractors and chaotic motions of dynamical systems," *Rev. Mod. Phys.* **53**, 655–671 (October 1981).

A few recent research results on optical bistability and chaos include E. Abraham, W. J. Firth, and J. Carr, "Self-oscillation and chaos in nonlinear Fabry-Perot resonators with finite response time," *Phys. Lett.* **91A**, 47–51 (August 23 1982); M. Maeda and N. B. Abrahamson, "Measurements of mode-splitting self-pulsing in a single-mode Fabry-Perot laser," *Phys. Rev. A* **26**, 3395–3403 (December 1982); and H. Nakatsuka et al., "Observation of bifurcation to chaos in an all-optical bistable system," *Phys. Rev. Lett.* **50**, 109–111 (10 January 1983).

Problems for 13.7

1. *Bistable laser oscillator.* Using a homogeneous rate-equation model, find the potential steady-state operating points for the bistable laser oscillator discussed at the beginning of this section, and show that the first intersection between the loss and gain curves in this model is indeed unstable.
 2. *Critical condition for absorptive bistability.* Show that for the simple absorptive bistable example analyzed in this section, the critical point for the onset of bistability occurs at the operating conditions $R = 8$, $I_{\text{circ}} = 3I_{\text{sat}}$, $I_{\text{inc}} = 27\delta_1 I_{\text{sat}}$, and $I_{\text{trans}} = 3\delta_1 I_{\text{sat}}$.
 3. *Absorptive bistability at large nonlinearity.* Show further that for strong absorptive nonlinearity in an interferometer cavity—that is, for $R \gg 8$ —the turning points in the bistability curve of I_{trans} versus I_{inc} are given by $I_{\text{circ}} = I_{\text{sat}}$, $I_{\text{inc}} = R^2\delta_1 I_{\text{sat}}/4$ and $I_{\text{trans}} = \delta_1 I_{\text{sat}}$ for the first root, and by $I_{\text{circ}} = rI_{\text{sat}}$, $I_{\text{inc}} = 4R\delta_1 I_{\text{sat}}/4$ and $I_{\text{trans}} = R\delta_1 I_{\text{sat}}$ for the second root.
 4. *Bistable ring absorber cavity.* Consider a ring-laser cavity which has only a single input-output mirror with reflectivity $R_1 = \exp(-\delta_1)$, all other mirrors having 100% reflectivity. Evaluate the reflected intensity I_{ref} versus incident intensity I_{inc} from this mirror, assuming the ring cavity contains a homogeneously saturable absorber, and no other losses.
 5. *Inhomogeneous absorptive bistability* Calculate and plot the input-output intensity relationship for a purely absorptive interferometer tuned to resonance, assuming that the absorber saturates inhomogeneously—that is, as $1/(1 + I/I_{\text{sat}})^{1/2}$ —rather than homogeneously.
-

13.8 AMPLIFIED SPONTANEOUS EMISSION AND MIRRORLESS LASERS

Some laser systems have such extremely high gain that they need no mirrors—they can emit very bright and more or less quasi coherent beams out each end of the laser medium simply as a result of very high-gain amplification of their own internal spontaneous emission traveling along the length of the laser-gain medium. Interstellar masers and x-ray lasers must also of necessity operate without mirrors, since no mirrors are available.

Interesting concepts that have been developed in connection with this kind of behavior include such terms as *superradiance*, *superfluorescence*, *coherence brightening*, and *amplified spontaneous emission* (ASE). In this section we will attempt to give a brief classification and explanation of each of these terms, together with a brief summary of the useful properties of mirrorless laser systems.

Coherently Oscillating Dipoles and Free Induction Decay

In developing this topic it may be easiest to begin with the more exotic and strongly coherent forms of behavior, and work down toward the simplest and most common kinds of mirrorless or ASE lasers. The first part of the following discussion will thus be closely related to the coherent-pulse and coherent-dipole types of behavior that we also discuss in other sections of this text.

We have pointed out elsewhere, for example, that if a collection of two-level atoms is prepared such that the individual atomic dipoles are oscillating or precessing at least partly in phase with each other, then the associated macroscopic polarization $p(t)$ in the collection of atoms will emit electromagnetic radiation in a coherent fashion—that is, the emitted radiation will be coherent or sinusoidal in time, with a time-phase determined by the initial preparation of the atoms. This radiation will also have directional or spatially coherent properties determined by the relative phases with which the radiating atoms at different points are initially set oscillating.

Such a coherently prepared atomic system may occupy a volume that is large in terms of optical wavelengths. If the initial atomic oscillations are then prepared using, for example, a traveling optical pulse of sufficiently large intensity, the resulting coherent emission will emerge in the same direction of travel as the preparing pulse.

If the degree of initial coherence imposed on the individual oscillators is comparatively small, and if the atomic populations are initially either not inverted, or at most have small gain, then this coherent radiation, although brighter and more directional than the usual spontaneous emission, will be relatively weak; and the coherently radiated signal will decay in time with the appropriate dephasing time T_2 in homogeneous systems, or T_2^* in inhomogeneous systems, until it disappears into the incoherent spontaneous emission background from the same atoms.

This particular kind of coherent atomic radiation is often referred to as simple *free-induction decay*. Free-induction decay can be demonstrated experimentally both in low-frequency magnetic resonance systems and in optical-frequency atomic systems using pulsed laser excitation, as we describe elsewhere in this text.

Dicke Superradiance

At a time well before the invention of the laser, R. H. Dicke also considered analytically the situation in which a sizable number of atoms contained in a small volume V may all be oscillating with a very *high* degree of coherence between the individual dipole oscillations. If such a volume contains N coherently oscillating atomic dipoles, the macroscopic dipole moment within the volume will have magnitude $N\mu_1$, where μ_1 is the oscillating moment of a single atom. The rate of coherent radiative power emission from this volume will then be proportional to $(N\mu_1)^2$, in contrast to the usual incoherent form of spontaneous emission, where the emission rate is proportional only to the number of atoms N . The coherent emission from this small but coherently excited volume will emerge as a short burst or pulse of radiation with a duration proportional to $1/N$, rather than as an exponential decay with a lifetime τ independent of the number of atoms.

This specific type of small-volume, coherently prepared emission, with strong initial coherence, has come to be known as *Dicke superradiance*. The atoms here are locked together, not only by their initial preparation all in phase with each other, but also by the strong coupling of all the atoms to each other through their common radiation fields. Dicke superradiance of this type has been observed in specially prepared low-frequency magnetic resonance systems, but not, at least in its simplest form, in optical-frequency systems.

Incoherently Prepared Dicke Superradiance

Suppose next that a two-level system having N atoms is initially prepared with a completely inverted population, i.e., $N_1 = 0$ and $N_2 = N$, so that each of the atoms is completely in its upper energy level to start with. The atomic system will then initially possess *no* coherent macroscopic polarization $p(t)$, since the quantum expectation value for the dipole oscillation of each individual atom is zero if the atom is entirely in its upper (or for that matter, its lower) quantum state. (As an alternative, the atoms may be prepared in an only partially inverted state, but with an *incoherent preparation method*, such that all the atomic dipoles are randomly phased and no coherent macroscopic polarization is initially present.)

Each upper-level in this situation will then begin to radiate spontaneously and incoherently through the purely quantum spontaneous emission processes that are represented by the radiative decay rate γ_{rad} . Note that this spontaneous emission process, although it can be modeled by a gaussian quantum noise source, can only be derived from a completely quantum analysis, in which the atoms and the electromagnetic field are both quantized.

Dicke then pointed out in his original paper that if the N atoms prepared in this inverted but incoherent fashion were all contained in a volume small compared to the emission wavelength cubed, the atoms would all be coupled together through their overlapping radiation fields. As a consequence the individual atoms will not in fact continue to radiate independently and incoherently. Rather the initial spontaneous emission from any one atom (or, if you like, a small initial fraction of the spontaneous emission from all of the atoms) will tend to "capture" or entrain the oscillations in all the other atoms, in such a way that the inverted system can develop a very large and almost totally coherent macroscopic polarization.

As a result, this system, although initially incoherent, can still evolve into a coherent superposition, and can emit, after a certain time delay, almost exactly the same sort of $(N\mu_1)^2$ superradiant burst described in the preceding. Because the coherent emission builds up initially from spontaneous emission noise, the phase angle of the radiation will be entirely random from shot to shot, and there will also be small random fluctuations in the delay time between initial preparation of the atoms and emergence of the superradiant burst.

(In terms of the Bloch vector picture developed in a later chapter in this text, the “super Bloch vector” describing the sum of all the dipoles in the small volume is initially oriented essentially antiparallel to the effective dc magnetic field, in the highest-energy, but metastable, orientation. The effect of spontaneous emission is then to give a small initial disturbance, or effectively a small initial tilt angle to this vector. If suitable conditions are met, this Bloch vector will then precess outward, maintaining constant length, so that its tip stays on the surface of a sphere, and will eventually radiate all of its energy into a superradiant burst as the precessing vector passes from the inverted orientation through the equatorial plane and on to the lowest-energy orientation parallel to the effective dc magnetic field.)

Optical Extensions of Dicke Superradiance

In the simplest situation, the emergence of this type of superradiant emission from an initially inverted but *incoherently prepared* atomic system depends on the atoms being contained within a volume $V \leq \lambda^3$, so that there will be very strong coupling between all the atoms through their common radiation field. (Note that this coupling occurs only through the radiation fields; the quantum wavefunctions of the individual atoms need not be overlapping.) This particular type of small-volume incoherently prepared superradiant emission has not yet been demonstrated in any optical system, largely because there seems to be no available atomic medium in which a sufficient number of suitable atoms can be assembled within a volume of the order of λ^3 .

Considerable attention has been given, however, to the more general situation in which a large number of inverted atoms, with strong initial population inversion but with no initial coherent polarization, are prepared in an *extended region of space*, most often in the form of a long cylindrical region, or pencil, having a Fresnel number on the order of unity. This larger volume may then, depending on the size of the inversion, emit either simple *amplified spontaneous emission* (ASE), as we will describe below, or a kind of extended Dicke superradiance which has come to be referred to as *superfluorescence*.

Pure Superfluorescence Behavior

Ideal or pure superfluorescence behavior, as described by a number of theories and experiments (see References), will occur in such systems only under rather specialized conditions in which the atomic transition is strong and narrow enough, and the inversion density large enough, so that the radiative coupling between atoms becomes very strong, in the same sense as in the superradiant experiments described in the preceding, even though the atoms are spread over a volume large compared to the radiation wavelength. The necessary conditions for pure superfluorescent behavior are quite complex, but a key condition seems to be that the atomic gain coefficient must be large and the sample length small com-

pared to the distance that radiation can travel in one inverse atomic linewidth, or one atomic dephasing time T_2 . If all the atoms are to emit cooperatively, they must be able to communicate with each other strongly in a time short compared to their dephasing time. To accomplish this, radiation coming from any one atom must be strongly amplified and transmitted to another atom, and the reverse, before either of these atoms has either radiated spontaneously or been dephased.

The principal experimental features of pure superfluorescence will then be an intense simultaneous burst of quasi coherent radiation coming out in a narrow cone from each end of the inverted pencil of atoms. This pulse will have an intensity proportional to the initial number of atoms squared, and an angular spread which is roughly the aspect ratio of the inverted pencil of atoms. The pulse duration will be inversely proportional to the number of atoms, and the pulse will have a definite time delay following the initial preparation of the inverted atoms. Since this emission will be initiated by random spontaneous emission in the atoms, there will again be small random variations in the time delay of the pulse from one experimental shot to another.

The essential features of pure superfluorescence are thus a delayed emission pulse, with intensity proportional to N^2 , emerging from a large-volume atomic collection that is prepared with *no initial coherent polarization or oscillating dipole moment*.

Superfluorescence Experiments

The conditions needed to demonstrate ideal superfluorescence are fairly hard to obtain, and only a few experiments have displayed this effect in a clear and definite fashion thus far. Perhaps the clearest experiment demonstrating pure superfluorescence was carried out on an upper-level atomic transition having a wavelength of $2.9 \mu\text{m}$ in low-pressure cesium vapor. The upper level of this transition could be selectively populated at a high density by optical pumping from the cesium ground state using a tunable pulsed dye laser at 455 nm . By using a low-pressure cesium cell it was possible to obtain a vapor with minimal collision broadening and long lifetime; and by using Zeeman splitting in a dc magnetic field together with selective pumping it was possible to populate the upper level of only a single strong transition corresponding to a near-ideal two-level atomic system. The results obtained in these experiments were then in excellent agreement with the theoretical concepts outlined preceding.

Amplified Spontaneous Emission (ASE) Lasers

We come finally to the most common form of mirrorless laser behavior, namely, "ordinary" amplified spontaneous emission or ASE, as illustrated in Figure 13.33.

Amplified spontaneous emission as used here refers to any situation in which the spontaneous emission coming from a distribution of inverted laser atoms is linearly amplified by the same group of atoms, with a gain which is sizable in at least one direction through the atoms, but the more complex features of superfluorescence are not present. If the amplification along a long thin cylinder of inverted atoms is sufficiently large, for example, this can produce an output beam from each end of the laser medium which can be quite bright, powerful, and moderately directional, with a fair amount of spatial (but usually not temporal) coherence. This radiation may become strong enough to produce significant

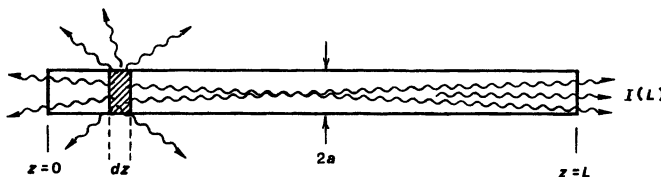


FIGURE 13.33
An amplified-spontaneous-emission or ASE laser.

saturation along the gain medium, and to extract the major portion of the inversion energy into the directional beams. The inverted medium thus acts as a "mirrorless laser," with output characteristics that are intermediate between a truly coherent laser oscillator and a completely incoherent thermal source.

Examples of such mirrorless lasers can include many pulsed excimer lasers and visible and ultraviolet molecular lasers, such as the N_2 laser at 337 nm or the H_2 laser at 120 nm, especially when pumped by fast transverse discharges or by electron beam pumping. Mirrorless laser action also occurs in certain very high-gain infrared gas laser lines, such as the $3.39\ \mu\text{m}$ line in He-Ne or the $3.51\ \mu\text{m}$ line in He-Xe ; in very high-gain dye laser amplifiers; and in high-gain semiconductor diode lasers in which the mirror reflection at the end of the laser is deliberately spoiled. The enormously large and powerful natural masers and lasers which occur in interstellar space are also primary examples of mirrorless or ASE laser systems.

Questions of Terminology

There has in the past been considerable inconsistency in the laser literature in the use of the various terms superradiance, superfluorescence, and amplified spontaneous emission; and many articles still refer to the type of mirrorless laser we are discussing here as "superradiant emission" or as a "superradiant laser system."

In most of the mirrorless lasers of practical interest, however, the laser medium can still be assumed to remain entirely in the rate-equation regime (with population saturation taken into account); and the emerging radiation can be accurately described merely as narrowband amplified gaussian noise. The kinds of pulse delays and large coherent polarizations that are characteristic of superradiance or superfluorescence, and the dependence of peak pulse intensity on N^2 as described in the preceding, do not appear in simple ASE lasers. It seems preferable, therefore, to refer to these simpler systems in general either as *amplified spontaneous emission* systems or as *mirrorless lasers*, and to reserve the terms *superradiance* and *superfluorescence* for the more specialized phenomena described in the preceding.

Practical Characteristics of Mirrorless ASE Lasers

Consider a long slender rod of inverted laser medium with length L and diameter $2a$, as illustrated in Figure 13.33, and assume for simplicity that the laser transition is completely inverted with inversion population density N . The spontaneous emission power going out into all directions from any small unit volume of this medium will then be given by $N\gamma_{\text{rad}}\hbar\omega$.

If we neglect for the minute any gain saturation effects and assume a long slender rod with $L \gg a$, the contribution to the amplified spontaneous intensity dI arriving at the output end of the rod from any small length dz near the input end of the rod can then be written as

$$dI = \frac{\pi a^2 N \gamma_{\text{rad}} \hbar \omega}{4\pi L^2} e^{2\alpha_m(L-z)} dz, \quad (70)$$

where $2\alpha_m \equiv N\sigma$ is the power amplification coefficient in the rod. If we integrate the total spontaneous emission contribution coming from the entire length of the rod, this yields for the total ASE intensity at the output end

$$\begin{aligned} I &\approx \frac{N \gamma_{\text{rad}} \hbar \omega a^2}{4L^2} e^{2\alpha_m z} \int_0^z e^{-2\alpha_m z} dz \\ &\approx \frac{\gamma_{\text{rad}} \hbar \omega a^2}{4\sigma L^2} e^{2\alpha_m L}. \end{aligned} \quad (71)$$

In writing this we have assumed that the total gain $e^{2\alpha_m L}$ along the rod is large, so that we can replace the upper limit of the integral in Equation 13.71 by infinity. Most of the ASE intensity at each end of the rod then comes from just the first gain length $(2\alpha_m)^{-1}$ at the other end of the rod, and the solid angle of this emitting volume as seen from the other end of the rod is essentially constant at $\pi a^2/L^2$.

We have shown earlier that the stimulated transition rate W_{12} produced by a wave of intensity I is given by $W_{12} = \sigma I / \hbar \omega$. Thus, the ratio of the stimulated transition rate caused by the ASE to the spontaneous emission rate in the same atoms at the output end of the rod (in other words, at either end) can be written in the simple form

$$\frac{W_{12}}{\gamma_{\text{rad}}} \approx \left(\frac{a}{2L} \right)^2 e^{2\alpha_m L}, \quad (72)$$

which depends only on the aspect ratio a/L of the rod, and the overall gain coefficient $2\alpha_m L$.

Although the radius to length ratio a/L of a typical laser medium is normally small, the exponential gain factor in Equation 13.72 means that as soon as the gain coefficient $2\alpha_m L$ becomes larger than a few times unity, the stimulated emission rate from the atoms at each end of the laser medium due to amplified spontaneous emission from the other end will begin to exceed the purely spontaneous emission rate by a large ratio. In other words, as soon as $2\alpha_m L \gg 2 \ln(2L/a)$, the presence of ASE will begin to speed up the net emission rate, and thus to shorten the effective inversion lifetime of the laser medium, by a significant amount. Obviously, this *lifetime shortening* due to ASE will become even more serious if the amplification length is large in more than one direction, for example, across the width of a flat gain slab, or across all three dimensions of a spherical or rectangular gain volume.

Since the saturation intensity in a simple homogeneous gain medium can be written at $I_{\text{sat}} = \hbar \omega / \sigma \tau_2$, where τ_2 is the effective lifetime or repumping time for the upper laser level, then we can also write the ratio of the amplified spontaneous emission intensity to the saturation intensity at either end of the rod in the form

$$\frac{I}{I_{\text{sat}}} \approx \left(\frac{a}{2L} \right)^2 \left(\frac{\tau_2}{\tau_{\text{rad}}} \right) e^{2\alpha_m L}. \quad (73)$$

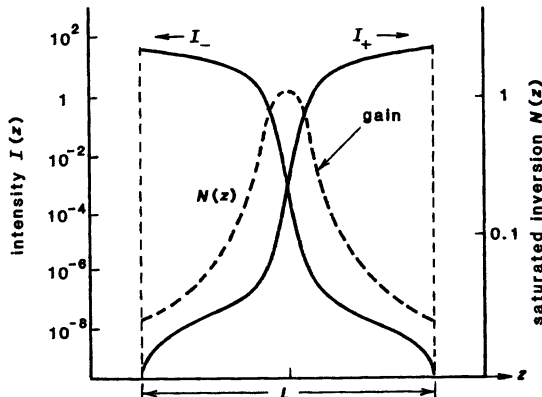


FIGURE 13.34
Gain saturation and traveling-wave intensities in a typical ASE laser.

Again, as soon as the net gain coefficient $2\alpha_m L$ becomes more than a few times unity, the ASE will surely become large enough to produce significant gain saturation and significant power extraction from the inverted gain medium.

Saturation and Power Extraction

Calculating the total power extraction and the exact end-fire emission pattern from such a mirrorless laser system becomes a more complicated problem when gain saturation is taken into account, since we must take into account both the effects of the ASE on the atomic inversion and the effects of gain saturation back on the growth rate for the ASE. Several numerical calculations for problems of this type are listed in the References, and Figure 13.34 illustrates the general type of behavior that occurs in a long narrow high-gain ASE laser when saturation is taken into account.

The basic result illustrated here is that under high-gain conditions, ASE coming from each end of the gain medium tends to heavily saturate the inversion over a sizable region at the opposite end of the medium, leaving a relatively narrow region or band of unsaturated gain only in the central region of the rod. As we increase the pumping level or the initial unsaturated gain value in a system of this type, this central unsaturated gain region becomes narrower and narrower. The growth of the intensities in opposite directions along the rod is also, of course, no longer a simple exponential with distance, although there is still large gain from one end of the system to the other.

Casperon has further calculated the manner in which the total spontaneous emission flux from the ends of an ASE laser increases as we turn up the pumping power, or alternatively the gain length in the laser medium. Typical results for a homogeneously broadened laser medium are shown in Figure 13.35, and generally similar results are obtained for inhomogeneously broadened lasers. The parameter labeling the different curves in this figure is a dimensionless measure of the spontaneous emission rate, related to the value of $1/p$ from our earlier rate-equation analysis. This parameter thus has a value much less than unity for most typical laser systems.

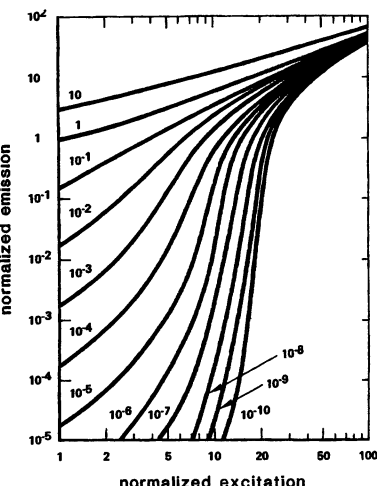


FIGURE 13.35

Total amplified spontaneous emission power output from a long cylindrical homogeneous gain medium. (From L. W. Caspenson, *J. Appl. Phys.* **48**, 256–262, January 1977.)

The primary interpretation to be made here is that, whereas an ASE laser cannot have the kind of extraordinarily sharp threshold behavior produced by the feedback from the mirrors in an ordinary laser cavity, mirrorless lasers can exhibit a kind of “soft threshold behavior” which may not appear too greatly different from true laser action.

Temporal and Spatial Output

The output spectrum from a mirrorless laser, at least at low intensity, will consist of the incoherent spontaneous emission from the laser medium, which has a spectral lineshape corresponding to the atomic lineshape, as amplified by the atomic gain process. The amplification process is also characterized by the same atomic linewidth or bandwidth, however, and we have pointed out earlier that the finite linewidth of the gain medium means that the spectrum will be significantly narrowed, typically down to values 2 to 5 times narrower than the atomic linewidth in a homogeneous system at high gain values.

When saturation effects are taken into account in inhomogeneously broadened media, this narrowing can be significantly reduced, especially at higher gains, because the inhomogeneous gain profile saturates first in the center, and only more gradually in the wings of the line. Typical results have also been calculated by Caspenson, as shown in Figure 13.36.

The temporal output from a mirrorless ASE laser, regardless of its spectral width, will always consist of narrowband, highly amplified but still essentially random gaussian noise, rather than any kind of coherent or amplitude-limited sinusoidal oscillation. Mirrorless lasers thus generally lack most of the important temporal coherence features associated with the sinusoidal amplitude-stabilized oscillation in a true laser oscillator.

The spatial pattern from the ends of an ASE laser will be a narrow cone with a cone angle defined by the aspect ratio of the laser rod, that is with a half-angle $\Delta\theta \approx a/L$. If the rod is very slender, so that it has a Fresnel number

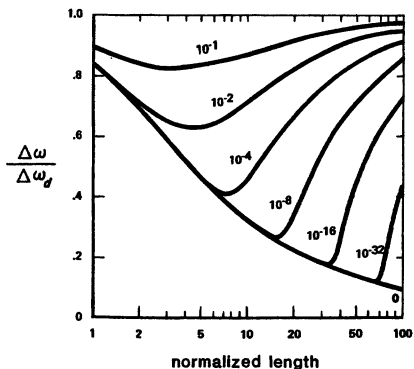


FIGURE 13.36
Normalized amplified spontaneous emission spectral width for an inhomogeneous transmission. (From Caspenson, *loc. cit.*)

$N_f \equiv a^2/L\lambda \approx 1$, then all of the end-fire emission will emerge in essentially a single transverse mode. The output beam from a sufficiently slender mirrorless laser can thus have a large degree of spatial coherence (although perhaps not so much total power because of the small rod diameter).

A larger diameter rod, with $N_f > 1$, will emit its radiation into a random superposition of essentially πN_f^2 transverse modes, as we will discuss in later chapters, and will thus have considerably less ideal spatial coherence (although such a system may still compare not unfavorably with a cavity-type laser having poor mode selection and thus also a large number of transverse modes).

Coherence Brightening and Swept-Gain Operation

This combination of significant spatial coherence with some spectral narrowing is sometimes referred to as *coherence brightening* in the mirrorless laser output. Coherence brightening is not a very precisely defined term, however, and much the same kind of coherence brightening is equally well observed in long slender superradiant or superfluorescent systems.

We can also note that in some laser systems with large spontaneous emission, high gain, and short upper-state lifetimes, the pumping process in the laser medium is carried out using some form of *traveling-wave excitation* which travels down the laser medium in one direction, at a velocity close to the velocity of light. If the total gain is large enough, the traveling excitation pulse soon becomes accompanied by a pulse of amplified spontaneous emission, which travels just behind the excitation pulse, and extracts or "dumps" the inversion energy as fast as it is created.

This type of *swept-gain laser action*, which produces a beam coming out of only one end of the laser, is likely to be characteristic of many X-ray lasers, as well as many fast pulse UV lasers, since the inversion lifetime for the laser medium in these situations may be comparable to or shorter than the transit time for a light pulse down the length of the laser medium.

Parasitic Laser Oscillation and ASE

Amplified spontaneous emission can also play a very much unwanted role in many large high-gain laser systems. In cascaded multisection laser amplifiers,

for example, such as are often used in laser fusion systems, spontaneous emission from the input end of the amplifier chain may, after amplification through the chain, become large enough to deplete the laser inversion, damage the target pellet, or even cause optical damage to components, before the desired optical signal can be sent through the amplifier chain. Saturable absorbers, which absorb the weak spontaneous emission but pass the larger signal pulses, must often be placed between the sections in such amplifier chains in order to avoid severe ASE problems.

Parasitic oscillations which arise from a combination of amplified spontaneous emission and weak unintentional reflections from various internal surfaces can also be a serious problem in any large high-gain laser system. In large glass disk amplifiers, for example, parasitic oscillations and ASE in directions running across the face of the disk, or around the rim of the disk, can be a serious problem; and in general the total energy storage volume of any large high-power laser device is often limited by a combination of parasitic oscillations and ASE.

We might note finally that the emission *improvement* and lifetime *shortening* that occurs in an inverted atomic system is the exact opposite of the emission reduction and lifetime *extension* that has long been known due to *radiation trapping* in strongly absorbing atomic systems. The spectral narrowing in an ASE system is thus the reverse of the *line reversal* that is well known in such radiation trapped systems.

REFERENCES

The basic concept of superradiance was first developed in the article by R. H. Dicke, "Coherence in spontaneous radiation processes," *Phys. Rev.* **93**, 99–110 (January 1954).

A more detailed analysis for the optical situation is given by R. Bonifacio, P. Schwendimann, and F. Haake, "Quantum statistical theory of superradiance. I and II," *Phys. Rev. A* **4**, 302–313 and 854–864 (July and September 1971). Other extensions of this concept to optical systems are also reviewed in J. H. Eberly, "Superradiance revisited," *Am. J. Phys.* **40**, 1374–1383 (October 1972).

Some comments on the distinction between Dicke superradiance and mirrorless lasers are also given by L. Allen and G. I. Peters, "Superradiance, coherence brightening and amplified spontaneous emission," *Phys. Lett.* **31A**, 95–100 (9 February 1970).

The theory of optical superfluorescence is developed by R. Bonifacio and L. A. Lugato, "Cooperative radiation processes in two-level systems: superfluorescence. I and II," *Phys. Rev. A* **11**, 1507–1521 (May 1975) and **12**, 587–598 (August 1975).

Representative experiments demonstrating superfluorescence are described by N. Skribanowitz, I. P. Herman, J. C. MacGillivray, and M. S. Field, "Observation of Dicke superradiance in optically pumped HF gas," *Phys. Rev. Lett.* **30**, 309–311 (February 19 1973); and by H. M. Gibbs, Q. H. F. Vrehen, and H. M. J. Hikspoors, "Single-pulse superfluorescence in cesium," *Phys. Rev. Lett.* **39**, 547–550 (August 29 1977). For an extensive review of this subject, see also Q. H. F. Vrehen and H. M. Gibbs, "Superfluorescence experiments," in *Dissipative Systems in Quantum Optics*, ed. by R. Bonifacio (Springer-Verlag, 1982).

For a general discussion of lasers based on amplified spontaneous emission, see L. W. Casperson, "Threshold characteristics of mirrorless lasers," *J. Appl. Phys.* **48**, 256–262 (January 1977), and references therein.

Other typical calculations on the properties of ASE systems are given by L. W. Caspenson and A. Yariv, "Spectral narrowing in high-gain lasers," *IEEE J. Quantum Electron.* **QE-8**, 80-85 (February 1972); by H. Maeda and A. Yariv, "Narrowing and rebroadening of amplified spontaneous emission in high-gain laser media," *Phys. Lett.* **43A**, 383-385 (March 26 1973); and by U. Ganiel, A. Hardy, G. Neumann, and D. Treves, "Amplified spontaneous emission and signal amplification in dye-laser systems," *IEEE J. Quantum Electron.* **QE-11**, 881-892 (November 1975).

For one recent experimental example of a mirrorless ASE semiconductor laser, see C. S. Wang, *et. al.*, "High-power low-divergence superradiance diode," *Appl. Phys. Lett.* **41**, 587-589 (October 1 1982).



OPTICAL BEAMS AND RESONATORS: AN INTRODUCTION

This chapter and the following several chapters describe the transverse mode properties of laser resonators, and the propagation properties of the optical beams generated by lasers. These are very extensive subjects, and the reader will need to pick and choose with some care, passing over those sections which treat more detailed topics than are of immediate interest. It seems a good idea therefore to give an outline at this point of the contents of these chapters.

Chapter 14: Optical Beams and Resonators: An Introduction. In this chapter we first give a brief overview of what we mean by the transverse modes in an optical resonator, and how these modes should be analyzed. We also summarize briefly some of the most general properties of these modes, to set the stage for the more detailed discussions to follow.

Chapter 15: Ray Optics and Ray Matrices. The basic concepts of ray optics, especially paraxial ray optics and the so-called ray matrices or “*ABCD* matrices,” prove to be very useful in understanding both the stability properties of optical resonators and the propagation properties of optical beams. In fact the ray matrix approach—which at first seems to be limited to geometrical optics only—turns out later to provide the foundation for a sophisticated and powerful treatment of paraxial wave optics and paraxial diffraction theory in general. Chapter 15, therefore, presents a detailed review of ray optics and ray matrices.

Chapter 16: Free-Space Wave Optics. We then follow the ray analysis with another review of the fundamentals of wave propagation and diffraction in free space, including the paraxial wave equation and Huygens integral. We note in particular that Hermite-gaussian (or Laguerre-gaussian) beams are the “eigenmodes of free-space propagation.”

Chapter 17: Gaussian Beams in Free Space. Because of the widespread importance of gaussian beams in lasers, Chapter 17 reviews the practical properties of these free-space gaussian optical beams in some detail.

Chapter 18: Beam Perturbation and Diffraction Effects. The propagation of gaussian beams or of any other beam profiles in free space will be perturbed by the diffraction effects associated either with any kind of hard-edged apertures

or with any kind of scattering or grating elements through which the beam may pass. Since these effects are very important in determining the properties of real optical beams and resonators, we give a brief review of their basic properties here.

Chapter 19: Stable Two-Mirror Gaussian Resonators. Many practical laser resonators consist essentially of two end mirrors with only free space in between. When such a resonator is also “stable” in a certain sense, the resulting resonator modes are very close to free-space gaussian modes. A substantial body of analysis and terminology for such gaussian resonator modes has become part of the basic lore of the laser field. Chapter 19 therefore reviews the basic properties of simple two-mirror stable gaussian resonators.

Chapter 20: Generalized Paraxial Wave Optics. In recent years, on the other hand, a much more general and powerful approach to paraxial wave optics and to optical resonators has been developed, which includes “soft” gaussian apertures and quadratic transverse amplitude variations as part of the formalism. This generalized approach to paraxial wave optics can be expressed in a very powerful fashion using a generalized $ABCD$ matrix approach, which includes complex ray matrices and complex Hermite-gaussian modes. Chapter 20 therefore develops the full complex $ABCD$ matrix formalism, of which the free-space gaussian beam results are a simple limiting case.

Chapter 21: Generalized Paraxial Resonator Analysis. Applying this complex paraxial formalism to optical resonators then enables us to develop a very general analysis of such resonators, and in particular to see how optical resonators can be classified into “real” and “complex” resonators, into “geometrically stable” and “unstable” resonators, and into “perturbation-stable” and “unstable” resonators (which is not the same thing). Chapter 21 therefore develops this more general resonator analysis, and shows how it can be applied to important practical resonators, including multielement stable resonators and the important new class of complex-stable resonators with variable reflectivity mirrors.

Chapter 22: Unstable Optical Resonators, and Chapter 23: More on Unstable Resonators. Finally, the so-called “unstable optical resonators” that we just mentioned are, in fact, a quite different class of resonators which have emerged in recent years to provide very useful resonator designs for a wide variety of high-power and high-gain lasers. Chapters 22 and 23 therefore present an extensive review of the properties of this very useful class of resonators.

14.1 TRANSVERSE MODES IN OPTICAL RESONATORS

Laser cavities differ in several significant ways from the closed microwave cavities that are commonly treated in electromagnetic theory textbooks. Optical resonators first of all usually have open sides, and hence always have diffraction losses because of energy leaking out the sides of the resonator to infinity. Optical resonators are also usually described in scalar or quasi plane-wave terms, with emphasis on the diffraction effects at apertures and mirror edges, rather than in vector terms with emphasis on matching boundary conditions. The distinction between “longitudinal” and “transverse” modes in the resonator is also much sharper in optical than in microwave resonators.

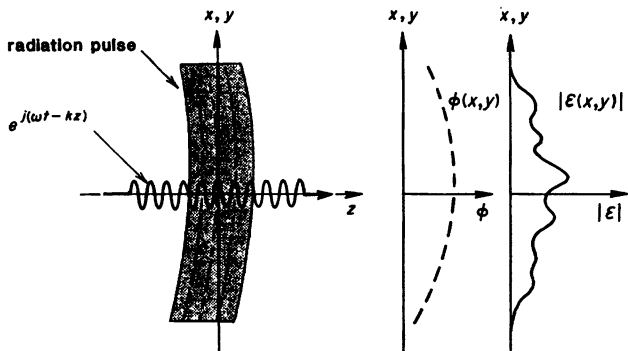


FIGURE 14.1

A traveling pulse or "slab" of optical radiation, propagating in the z direction.

Before beginning any detailed analysis of optical resonators, therefore, it may be useful to introduce some of the fundamental concepts we will use to describe optical resonator modes in rather broad and general terms.

The "Recirculating Pulse" Approach

In earlier chapters we have often emphasized how the optical radiation inside an optical cavity circulates repeatedly around the cavity, bouncing back and forth between the end mirrors (or circulating around the ring in a ring-laser cavity). In these earlier discussions we used only a plane-wave approximation, ignoring the transverse spatial variation of the waves.

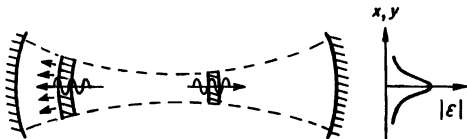
To bring transverse variations into the discussion, let us next consider only that portion of the optical energy traveling in the $+z$ direction and contained within some short axial segment of length Δz within the cavity. We can think of the radiation in this segment as forming a short pulse or a thin "slab" of radiation (see Figure 14.1), whose axial thickness Δz is small compared to the length L of a typical laser cavity but still very large compared to an optical wavelength λ .

The time and space variation of the \mathcal{E} fields within such a circulating pulse or slab as it travels through the resonator, including transverse variations, can then be written in the form

$$\begin{aligned} \mathcal{E}(x, y, z) &= \operatorname{Re} \tilde{E}(x, y, z) e^{j(\omega t - kz)} \\ &= \operatorname{Re} |\tilde{E}(x, y, z)| e^{j(\omega t - kz) + j\phi(x, y, z)}. \end{aligned} \quad (1)$$

By writing the fields in this fashion, we separate out the plane-wave aspects of the wave propagation as given by the $e^{j\omega t - jkz}$ factor, where ω is the optical carrier frequency and $k = \omega/c = 2\pi/\lambda$ the associated plane-wave propagation constant, from the complex phasor amplitude $\tilde{E}(x, y, z)$ which describes the transverse amplitude and phase variation of the beam. The transverse intensity profile of the beam within this particular pulse or slab is then given by $I(x, y, z) = |\tilde{E}(x, y, z)|^2$, whereas the transverse phase variation, or the shape of the optical wavefront is given by the transverse phase variation $\phi(x, y, z)$.

stable resonator



unstable resonator

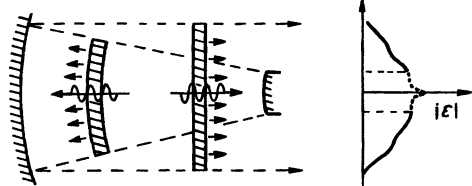


FIGURE 14.2
Circulating pulses ("slabs") in stable and unstable optical resonators.

Although we write the phasor amplitude function $\tilde{E}(x, y, z)$ as a function of x , y and also z , we will see later that the variation of this transverse beam profile with the axial or z coordinate is generally very slow compared to the e^{-jkz} variation that we have separated out. The latter function goes through a complete $e^{\pm j2\pi}$ variation in just one optical wavelength. By contrast, the complex amplitude profile $\tilde{E}(x, y, z)$ will not change much if at all through the thickness of one "slab"; and it will also change only very slowly with distance as a particular slab propagates down the resonator, or through free space outside a resonator.

Pulse Propagation in Stable and Unstable Resonators

If, however, we follow the transverse profile $\tilde{E}(x, y, z)$ of any one such slab as it travels (at the velocity of light) through one complete round trip around a laser cavity, we will definitely see the transverse field pattern in the slab change with distance as the slab propagates, diffracts, bounces off mirrors, and passes through rods, lenses and finite apertures. These changes in the transverse pattern $\tilde{E}(x, y, z)$ of the slab caused by propagation and diffraction are the primary effects that determine the transverse mode properties of optical beams and resonators.

We will see later that optical resonators can usually be divided into either "geometrically stable" or "geometrically unstable" categories (where these terms refer to ray stability within the resonators, and have nothing to do with whether or not the laser is or is not stable against laser oscillation). In such resonators, the recirculating slabs themselves may also acquire a certain macroscopic curvature caused by the focusing effects of the laser mirrors, as shown for either a typical "stable" resonator or an "unstable" resonator in Figure 14.2.

Each such pulse or slab of radiation as it travels around may thus be rather inelegantly described as a "recirculating pancake" of radiation within the resonator. An important point is that the propagation of each such slab is essentially

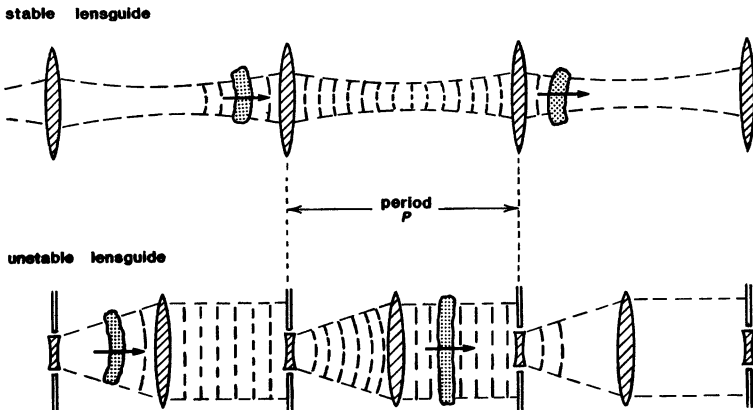


FIGURE 14.3

Propagation through repeated round trips in an optical resonator is physically equivalent to propagation through repeated sections of an iterated periodic lensguide. This lensguide may be, as in Figure 14.2, geometrically stable or unstable.

unaffected by the radiation in the slabs immediately in front of or behind it—the optical radiation in each axial segment or “pancake” is more or less independent of the other pancakes ahead of or behind it in the resonator.

Optical Resonators and Equivalent Periodic Lensguides

Rather than thinking of repeated round trips within a resonator, it can be helpful to think of the pulse or “pancake” as propagating instead through repeated sections of an iterated periodic optical system as in Figure 14.3. In setting up such an iterated periodic lensguide, curved mirrors in the original resonator are replaced by thin lenses of equal focusing power, and all other elements encountered in the lensguide are made the same as those encountered in the original resonator (except that in a standing-wave cavity each element must be included twice to model a complete round trip in both directions).

The diffraction and aperturing effects that the pulse sees in a series of repeated round trips around the original laser cavity will then be the same as in propagating through an equivalent number of segments in the periodic lensguide; and the lensguide itself may be either “stable” or “unstable” in the sense discussed in the preceding. This lensguide approach obviously adds no new physics to the problem, but it does convert the resonator problem into an equivalent waveguide problem, and it can sometimes be helpful in visualizing the behavior in an optical resonator, as we shall see.

Optical Resonator Eigenmodes and Eigenvalues

Let us now look at how this recirculating or traveling pulse approach leads to the concept of *transverse cavity modes* or *eigenmodes* in an optical resonator.

Suppose such a pulse or slab of radiation makes one complete round trip around an optical cavity, or travels through one complete period of the equivalent

lensguide. After one complete round trip, the transverse field pattern $\tilde{E}^{(1)}(x, y)$ within a given slab as it arrives back at its starting plane will in general be different from its starting pattern $\tilde{E}^{(0)}(x, y)$ before the round trip, because of diffraction, reflection and aperturing effects; and after a second round trip the pattern $\tilde{E}^{(2)}(x, y)$ may again be still different. (Note that we have dropped the z dependence in writing these patterns, because we are only considering the transverse variation as observed at one arbitrarily chosen reference plane somewhere within the resonator, or at a set of such planes spaced one period apart in the equivalent lensguide.)

We can then ask if, to put the question in physical terms, there exist any transverse patterns, call them $\tilde{E}_{nm}(x, y)$, such that if a pulse or pancake starts off with one of these transverse patterns, it will return one round trip later with exactly the same pattern? More precisely, we require that the pulse of radiation must return with exactly the same transverse form, but possibly with a reduced amplitude because of diffraction and other losses during the round trip. The wave may in general also return with an arbitrary absolute phase shift, because of the propagation distance p around the resonator at the optical frequency ω of the pancake.

If we can find any such self-reproducing transverse patterns, it certainly seems reasonable to call them *transverse modes* of the resonator, or of the equivalent lensguide. That is, a pulse which is launched with an initial transverse profile matching one of these transverse modes can then propagate repeatedly around the resonator, or propagate indefinitely down the lensguide, always getting weaker in amplitude, but always maintaining the same transverse profile at the same reference plane in the resonator or the lensguide.

In fact, if we add enough laser gain within the resonator to just cancel the diffraction losses, it would seem that the resonator can oscillate indefinitely in any one of these transverse modes. (We will see shortly that this is indeed true, though with some slight complications.)

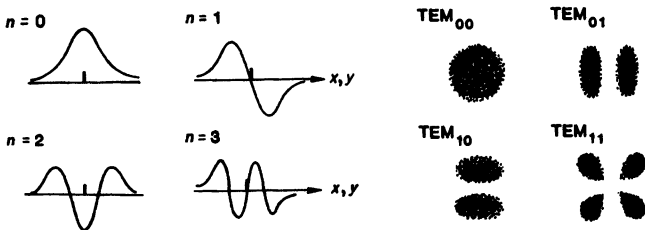
Examples of Optical Resonator Eigenmodes

Do such lossy but self-reproducing transverse eigenmodes then really exist for open-sided and finite-diameter optical cavities—especially the very long slender cavities often used in practical lasers? The answer is that they do indeed exist, and that moreover the lowest-order transverse modes in properly designed (and aligned) laser cavities can have remarkably low diffraction losses, as well as remarkably good propagation properties.

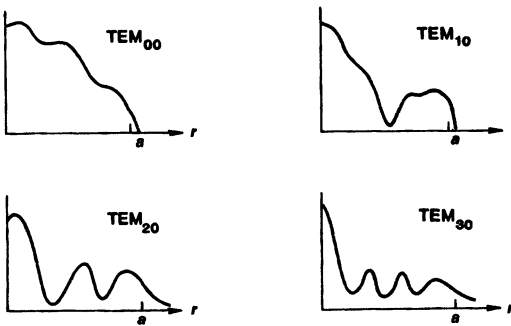
The simplest transverse mode patterns, and the ones that are easiest to analyze, occur in the so-called *geometrically stable* optical resonators or lensguides using properly curved mirrors, such as those we have illustrated earlier. The lowest-order and higher-order modes in stable optical resonators, if expanded in rectangular transverse coordinates, are given almost (but not quite) exactly by Hermite-gaussian functions, such as those exhibited in the top part of Figure 14.4. We will discuss these gaussian modes in much greater detail in subsequent sections.

These modes, like the modes in most other optical resonators, are essentially plane waves, or slightly curved spherical waves, multiplied by the transverse amplitude and phase profiles given by the transverse mode functions $\tilde{E}_{nm}(x, y)$. Although the exact vector expressions for the associated optical beams must then necessarily have some small axial E and H field components, the primary

(a) stable cavity transverse modes



(b) planar cavity modes



(c) unstable cavity modes

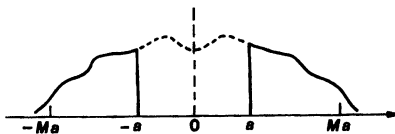


FIGURE 14.4

Examples of the lowest-order and higher-order transverse-mode intensity profiles in some typical (a) geometrically stable, (b) planar (flat mirror), and (c) geometrically unstable optical resonators.

field components in these beams are polarized transverse to the direction of propagation, just as in ideal uniform plane or spherical waves. These waves are very often referred to, therefore, as TEM_{nm} optical waves, and we have used this notation in Figure 14.4. (Note, however, that a truly pure TEM electromagnetic wave can only exist in a transmission line having at least two conductors; and that these TEM_{nm} optical waves must therefore always have some small axial E and H field components.)

Planar and Unstable Resonator Modes

If we set up an optical resonator with two perfectly aligned flat mirrors—for example, two flat circular mirrors—the transverse mode patterns become more difficult to express analytically, but they nonetheless still exist. The first four azimuthally symmetric, or $l = 0$, modes of a typical circular plane-mirror resonator will have radial variations something like those shown in Figure 14.4(b). There also exist a large number of azimuthally varying or $l > 0$ transverse modes which we have not shown here.

Again these are essentially TEM modes, with radial amplitude patterns that in this situation look approximately like lowest and higher-order Bessel functions, with a small amount of irregular diffraction ripple added. Note, however, that these transverse mode patterns, which are viewed in this figure at the end mirror surface, do not quite go to zero at the mirror edges. The amount of energy that is lost past the mirror edges represents the diffraction loss or diffraction spillover from the ends of the resonator.

Finally, there are the even more complicated geometrically unstable resonators, which we will discuss in more detail in Chapter 22. These resonators have modes in which a large amount of energy is lost on each round trip past the edges of the smaller output mirror, as illustrated for a typical situation in the bottom part of Figure 14.4. This energy in fact forms the useful output beam in unstable-resonator lasers, which must typically have large laser gain in order to operate with such large output coupling.

Unstable resonator lasers can on the other hand have important advantages for higher-power lasers, including large mode volume, good discrimination against higher-order transverse modes, all-reflective optics (which can be, for example, water-cooled in very high-power lasers), and good output beam quality. Unstable resonators do have higher-order transverse modes, as well as the lowest-order type of mode pattern illustrated in Figure 14.4(c), but all of these modes are very difficult to express analytically and show large variations in shape with changes in the resonator length and diameter. We have therefore shown only one representative lowest-order example in Figure 14.4.

14.2 THE MATHEMATICS OF OPTICAL RESONATOR MODES

Let us now restate the basic problem outlined in the previous section in mathematical terms, and ask how we can calculate the propagation effects for an optical pulse through one round trip in a resonator, or one period of the periodic lensguide, and how we can find these transverse mode patterns that are self-reproducing after each such round trip or periodic step.

The Round-Trip Propagation Integral

For essentially all the optical cavities of interest to us, the total propagation through one round trip in an optical resonator, or through one period in the equivalent lensguide, can be described mathematically by a propagation integral which will have the general form

$$\tilde{E}^{(1)}(x, y) = e^{-jkp} \iint_{\text{Input plane}} \tilde{K}(x, y, x_0, y_0) \tilde{E}^{(0)}(x_0, y_0) dx_0 dy_0, \quad (2)$$

where k is the propagation constant at the carrier frequency of the optical signal; p is the length of one period or round trip; and the integral is over the transverse coordinates at the reference or input plane. The function \tilde{K} appearing in this integral is commonly called the propagation kernel, since the field $\tilde{E}^{(1)}(x, y)$ after one propagation step can be obtained from the initial field $\tilde{E}^{(0)}(x_0, y_0)$ through the operation of the linear kernel or “propagator” $\tilde{K}(x, y, x_0, y_0)$.

Any arbitrary reference plane within the resonator, or within one period of the equivalent lensguide, may be chosen as the starting plane or reference plane for writing the preceding integral. The exact form of the kernel \tilde{K} will depend on the reference plane that is chosen. If for example, the reference plane is chosen at an aperture, and the only intervening element before the next aperture is simply free space, this propagator will be simply Huygens’ integral for free space, with the integral being evaluated over the aperture at the input end of each period.

More generally the propagation kernel will contain additional factors caused by intervening lenses, apertures, and other optical elements. Evaluating the form of the kernel in Equation 14.2 will be one of our major interests in the following chapters.

In doing resonator analyses, we will usually separate out from the propagation kernel the on-axis phase shift term e^{-jkp} , as has been done in Equation 14.2, since all the necessary information for evaluating transverse field patterns is contained in the remaining kernel $\tilde{K}(x, y, x_0, y_0)$, with the exponential term only furnishing a constant phase shift in front. We will look at propagation kernels of various types in much more detail for specific situations later on. For the present all we need understand is that there is (almost always) a linear relationship like Equation 14.2 between the input field $\tilde{E}^{(0)}(x_0, y_0)$ and the output field $\tilde{E}^{(1)}(x, y)$ after one step.

The Eigenequation for Optical Resonator Modes

In mathematical terms the propagation integral in Equation 14.2 is a *linear operator equation*: that is, the linear propagation operator \tilde{K} acts on the optical field $\tilde{E}^{(0)}(x, y)$ at a reference plane on one round trip to produce a new optical field $\tilde{E}^{(1)}(x, y)$ one round trip or one period later. Given an operator equation such as this, we may then ask whether this equation has a set of *eigensolutions*.

That is, for a given resonator or kernel, does there exist a set of mathematical eigenmodes $\tilde{E}_{nm}(x, y)$ and a corresponding set of eigenvalues $\tilde{\gamma}_{nm}$ such that each one of these eigenmodes after one round trip satisfies the round-trip propagation expression

$$\tilde{E}_{nm}^{(1)}(x, y) \equiv \iint \tilde{K}(x, y, x_0, y_0) \tilde{E}_{nm}^{(0)}(x_0, y_0) dx_0 dy_0 = \tilde{\gamma}_{nm} \tilde{E}_{nm}^{(0)}(x, y), \quad (3)$$

or simply

$$\tilde{\gamma}_{nm} \tilde{E}_{nm}(x, y) \equiv \iint \tilde{K}(x, y, x_0, y_0) \tilde{E}_{nm}(x_0, y_0) dx_0 dy_0, \quad (4)$$

where we can drop the superscript indices.

If eigensolutions that satisfy Equation 14.4 do exist, then these eigensolutions will provide exactly the self-reproducing transverse eigenmodes we seek, for either the optical resonator or the corresponding periodic lensguide. That is, if we launch a “recirculating pancake” in the form of any single one of these eigenmodes $\tilde{E}_{nm}(x, y)$ in the proper direction at the selected reference plane, then after one

round trip the field at that same plane will be

$$\tilde{E}_{nm}^{(1)}(x, y) = \tilde{\gamma}_{nm} e^{-j k p} \tilde{E}_{nm}^{(0)}(x, y). \quad (5)$$

The field after one period will have exactly the same transverse form, both in its phase variation $\phi_{nm}(x, y)$ and in its amplitude variation $|\tilde{E}_{nm}(x, y)|$, although if we do not include any laser gain, the transverse mode pattern will be reduced in amplitude and shifted in absolute phase by the complex eigenvalue $\tilde{\gamma}_{nm}$. This self-reproducing behavior is the mathematical definition of a “transverse mode” of the optical resonator or the periodic lensguide.

Note that these transverse mode patterns $\tilde{E}_{nm}(x, y)$ (if any exist) will have in general a different field pattern $\tilde{E}_{nm}(x, y, z)$ at each transverse z plane within the resonator, i.e., the shape of each transverse mode will change (slowly) with distance as it propagates along the resonator (or returns going in the opposite direction at the same plane in a standing-wave cavity). To put this in another way, the exact form of the kernel $\tilde{K}(x, y, x_0, y_0)$ and hence of the eigenmodes $\tilde{E}_{nm}(x, y)$ will be different if the kernel and the eigenmodes are evaluated at different reference planes, although the round-trip eigenvalues $\tilde{\gamma}_{nm}$ will be the same.

Resonator Eigenvalues and Diffraction Losses

A transverse wave pattern that is bounded within a finite width will always spread out due to diffraction as it propagates. In an open-sided resonator with finite-diameter mirrors, therefore, some of the radiation will spread out past the mirror edges after each round trip, and the magnitudes of the transverse eigenvalues (again neglecting gain) will therefore always be less than unity, i.e., $|\tilde{\gamma}_{nm}| < 1$.

Hence even with perfectly lossless mirrors the nm -th eigenmode of an optical resonator will always have a power loss per round trip given by

$$\text{fractional power loss per round trip} = 1 - |\tilde{\gamma}_{nm}|^2. \quad (6)$$

These losses result from diffraction losses at the mirror edges or at apertures within the cavity, and will continue to occur on all subsequent round trips.

If no laser gain is present the amplitude of a given transverse mode will decay exponentially with successive round trips in the form

$$\frac{\tilde{E}_{nm}^{(k)}(x, y)}{\tilde{E}_{nm}^{(0)}(x, y)} = \tilde{\gamma}_{nm}^k. \quad (7)$$

If we add a laser medium with transversely uniform round-trip voltage gain $e^{\alpha_m p_m}$ inside the optical cavity, the total round-trip amplitude gain and phase shift become

$$\tilde{E}_{nm}^{(1)}(x, y) = \tilde{\gamma}_{nm} e^{\alpha_m p_m - j k p} \tilde{E}_{nm}^{(0)}(x, y). \quad (8)$$

(If the gain itself has a transverse x, y variation, this must become part of the propagation kernel determining the eigenmodes.) The amplitude condition for laser threshold or for steady-state laser oscillation, as in Chapter 5, then becomes

$$\left| \frac{\tilde{E}_{nm}^{(1)}(x, y)}{\tilde{E}_{nm}^{(0)}(x, y)} \right| = |\tilde{\gamma}_{nm} e^{\alpha_m p_m - j k p}| = 1. \quad (9)$$

The lowest-loss eigenmode, i.e., the one with the largest value of $|\tilde{\gamma}_{nm}|$ and smallest value of δ_{nm} , will have the lowest threshold for oscillation and hence will (normally) be the dominant mode in the cavity.

Existence of Resonator Eigenmodes

Many readers of this text may be familiar with the electromagnetic theory of microwave cavities or microwave waveguides, where resonant eigenmodes always do exist. That is, for closed cavities with lossless walls, such as are usually treated in electromagnetic theory texts, the wave equation describing the cavity fields is a hermitian mathematical operator; and the existence of a complete set of normal modes can therefore be rigorously proven. The completeness property then means that any arbitrary field pattern inside the cavity can always be expanded using this set of eigenmodes as the basis set.

There is a serious mathematical difficulty for open-sided optical resonators, however, in that the round-trip propagation kernel $\tilde{K}(x, y, x_0, y_0)$ for such resonators is generally found not to be a hermitian operator. This in turn means that the existence of a complete and orthogonal set of eigensolutions to Equation 14.4 is not automatically guaranteed, whereas it would be for a hermitian kernel. Such eigenmodes may exist, but we cannot guarantee in advance either their existence or, if they do exist, their completeness.

In the early days of lasers, the physical reality as well as the mathematical existence of transverse modes in open resonators was a matter of considerable debate. Even now, in fact, except for a few special situations, rigorous mathematical existence and completeness proofs for optical resonator modes do not exist. Real lasers have never had any difficulty in finding such modes in which to oscillate, however; and from a combination of empirical and experimental evidence, it is now entirely accepted that transverse eigenmodes as we have defined them in the preceding paragraphs do exist, and do provide a physically realistic and meaningful basis for describing laser oscillation in real laser resonators.

Transverse Mode Orthogonality

A related mathematical peculiarity of optical resonator eigenmodes is that they are generally not “normal modes” in the usual sense of this term. That is, because of the nonhermitian kernel the eigenmodes $\tilde{E}_{nm}(x, y)$ of an optical resonator calculated at any plane z are generally not power orthogonal in the usual fashion, i.e., for any two modes we may in general not write

$$\iint \tilde{E}_{nm}(x, y) \tilde{E}_{pq}^*(x, y) dx dy = \delta_{np} \delta_{mq} \quad (\text{wrong}), \quad (10)$$

where δ_{np} is the Kronecker delta function. Rather the set of modes $\tilde{E}_{nm}(x, y)$ are generally *biorthogonal* (without complex conjugation) to an *adjoint* set of modes, let's call them $\tilde{E}_{pq}^\dagger(x, y)$, in the form

$$\iint \tilde{E}_{nm}(x, y) \tilde{E}_{pq}^\dagger(x, y) dx dy = \delta_{np} \delta_{mq} \quad (\text{right}), \quad (11)$$

These adjoint functions $\tilde{E}_{nm}^\dagger(x, y)$ usually represent the transverse modes traveling in the opposite direction in the same cavity. The biorthogonality properties of general optical resonator modes are summarized at the end of Chapter 20.

It is also not in general possible to prove that the transverse eigenmodes of an optical resonator form a complete set. That is, it cannot be rigorously proven in advance that any field pattern within a given resonator can be written in the form

$$\tilde{E}(x, y) \stackrel{?}{=} \sum_{nm} c_{nm} \tilde{E}_{nm}(x, y) \quad (\text{not guaranteed}). \quad (12)$$

However, the Hermite-gaussian or Laguerre-gaussian functions that approximate the eigenmodes in ideal stable resonators certainly do form a complete basis set; and in most practical situations people simply proceed as if the resonator eigenmodes always do form a complete set.

Axial Versus Transverse Resonator Modes

It is important to understand that, once the axial phase shift term e^{-jkp} has been factored out, the propagation kernel $\tilde{K}(x, y, x_0, y_0)$ in a typical optical resonator or lens waveguide depends only very slightly on the exact frequency ω or the exact wavelength λ of the radiation in the recirculating pancake. In physical terms, the diffraction effects experienced by a transverse mode function $\tilde{E}_{nm}(x, y)$ in a round trip will be essentially the same for any carrier frequency (or any axial mode frequency) within the linewidth of a single atomic transition or the oscillation bandwidth of a single laser oscillator. Hence, the transverse mode properties and the axial frequency properties of a given optical resonator can be treated almost completely separately from each other.

The transverse eigenmodes for any given laser can then be calculated based only on the mean laser wavelength; and all of the axial modes within a given laser line will then have the same set of transverse eigenmodes and eigenvalues. The transverse eigensolutions, in fact, might rather be viewed as the transverse propagation modes of the equivalent lensguide, for which axial resonance frequencies have no meaning. If we shift to a different laser line which is, say, 20% different in frequency, then the diffraction effects in one round trip may change somewhat, and we can expect the form of the transverse eigenmodes to change by a noticeable amount.

By launching a continuous stream of "pancakes" one after another, nose to tail so to speak, we can fill an entire laser cavity with radiation all in one given transverse eigenmode, and all at one carrier frequency. To satisfy the round-trip phase-shift condition, or to make the axial variation of the fields continuous completely around the resonator, the carrier frequency of these pancakes would have to be one of the axial mode frequencies of the resonator; and having done this we would have filled the cavity with radiation in a single axial and single transverse mode.

14.3 BUILD-UP AND OSCILLATION OF OPTICAL RESONATOR MODES

Without going into details of the exact modes for any specific resonator, we can now say some additional things about how resonator transverse modes can be calculated numerically; about their exact resonance frequencies; and about how these modes build up, compete, and decay in real lasers.

Calculating The Lowest-Loss Eigenmode

Suppose one of our pulses or “pancakes” with an arbitrary initial field distribution $\tilde{E}^{(0)}(x, y)$ is launched inside a resonator with no laser gain. We will assume, without worrying about rigorous justification, that this initial distribution can be written as a sum of the transverse eigenmodes for that particular resonator, i.e.,

$$\tilde{E}^{(0)}(x, y) = \sum_{nm} c_{nm} \tilde{E}_{nm}(x, y), \quad (13)$$

(and we will not worry about the axial variation of the pulse, since we do not need it to calculate the round-trip propagation.)

Then, on each round trip inside the resonator each transverse mode component will be multiplied by its eigenvalue $\tilde{\gamma}_{nm}$; and hence the field at the same reference plane k round trips later will be given by

$$\tilde{E}^{(k)}(x, y) = \sum_{nm} c_{nm} \tilde{\gamma}_{nm}^k \tilde{E}_{nm}(x, y). \quad (14)$$

The relative amplitude of each transverse mode will thus have attenuated after k successive round trips as $|\tilde{\gamma}_{nm}|^k$.

Suppose we index the transverse eigenmodes so that $nm = 00$ labels the transverse mode with the largest eigenvalue or the smallest loss per round trip. All other nm combinations will then have smaller eigenvalues and hence larger mode losses. Suppose we run the field distribution $\tilde{E}(x, y)$ through many repeated round trips, letting k in Equation 14.14 become large.

Then the amplitudes of the various eigenmodes will attenuate or die out with different rates on repeated round trips (see Figure 14.5). It is apparent that, whatever may be the initial mode distribution, after a sufficient number of round trips the lowest-loss or 00 mode will become dominant compared to all the other transverse modes. There is a chance that two modes will have exactly the same magnitude, and hence both will persist, but we can handle this as an unusual special situation. We can also dismiss as extremely unlikely the chance of any real initial distribution containing no initial component of the 00 mode whatsoever. Starting with any arbitrary initial transverse field pattern and following it through enough round trips in the resonator is thus a prescription for finding the lowest-order transverse mode of an optical resonator or lensguide.

The Fox and Li Approach

This conceptual approach to finding the lowest-order resonator transverse modes is often called the “Fox and Li” approach, since it describes not only the real physical situation in an optical cavity, but also the numerical mode-calculation procedure pioneered by A. G. Fox and T. Li at Bell Telephone Laboratories around 1960, in the earliest days of the laser.

Fox and Li simulated the iterative round trips of a wavefront $\tilde{E}(x, y)$ in a resonator by using numerical computation on a digital computer. In these computations they repeatedly integrated the propagation equation (14.2) using the Huygens’ integral kernels for plane-mirror resonators and other simple situations. Figure 14.6 shows some typical results from this kind of calculation.

Fox and Li’s first calculations were made assuming, for simplicity, a “strip resonator,” that is, a resonator with end mirrors in the form of two parallel flat

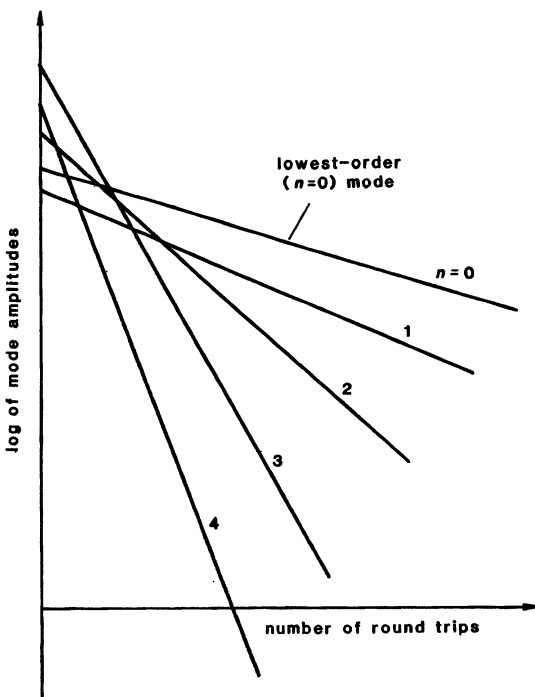


FIGURE 14.5
Attenuation of lowest-order and higher-order transverse modes on successive round trips.

strips having transverse variations in the x direction only (strip width = $2a$), spaced by a distance L in the z direction, and with no variations in the y direction along the strips. The starting field on one end mirror was simply a uniform field pattern $\tilde{E}^{(0)}(x, y) = 1$ across the mirror, as in Figure 14.6(a).

The two curves in Figure 14.6(b) then show the resulting field pattern or diffraction pattern $\tilde{E}^{(1)}(x, y)$ after the first propagation step from one end of the laser cavity to the other. (Fox and Li's initial calculations involved axially symmetrical laser cavities, and were phrased in terms of propagation steps from one end to the other, rather than complete round trips; but the essential ideas remain unchanged.) A beam propagating away from an aperture with sharp edges can be expected to exhibit Fresnel diffraction ripples in its near-field pattern, and the conventional Fresnel diffraction ripples in the field pattern after this first step are very evident.

Convergence to the Lowest-Order Mode

Initially we do not know the eigenmodes $\tilde{E}_{nm}(x)$ of the resonator and we thus have no way of separating an arbitrary starting function $\tilde{E}^{(0)}(x, y)$ into eigenmodes. After a sufficient number of bounces, however, the wavefunction $\tilde{E}^{(k)}(x, y)$ in the computer should converge in form to the lowest-order eigenmode $\tilde{E}_{00}(x, y)$, for the reasons given in the preceding; and the eigenvalue for this mode

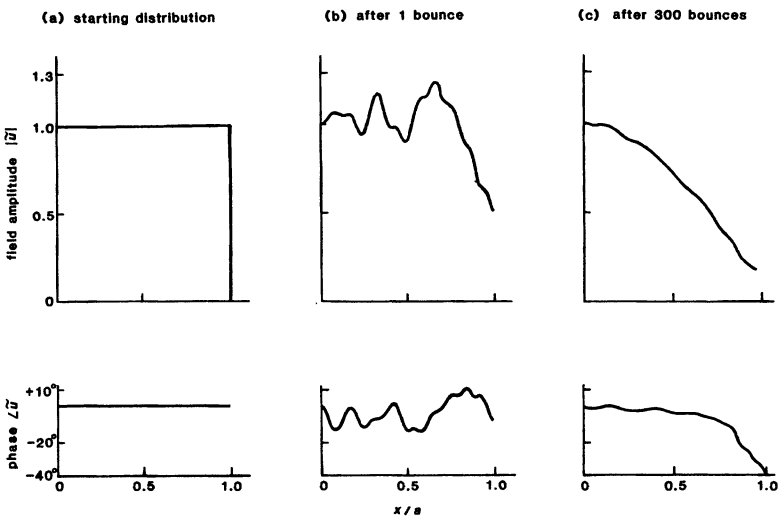


FIGURE 14.6

Typical results from Fox and Li's early numerical mode calculations, showing amplitude and phase variation of the wavefront $\tilde{E}(x)$ across one end mirror of the optical cavity. (a) Uniform initial distribution. (b) Field pattern after one bounce, showing Fresnel diffraction ripples. (c) Steady-state field pattern (\equiv lowest-order mode) after 300 bounces.

should be given from the computer iterations by

$$\tilde{\gamma}_{00} = \lim_{k \rightarrow \infty} \frac{\tilde{E}^{(k+1)}(x, y)}{\tilde{E}^{(k)}(x, y)}. \quad (15)$$

The field distribution $\tilde{E}^{(k)}(x, y)$ in the computer of course decreases steadily in overall amplitude with each successive bounce because of diffraction losses, but this is handled in the calculations simply by rescaling the overall signal level back upward by a constant amount after each iteration, or each few iterations.

Figure 14.6(c) then shows the steady-state, unchanging amplitude and phase pattern that the resonator mode in this particular example settles into after $k \approx 250$ to 300 round trips. (This is a comparatively low-loss resonator, and the higher-order modes only die out quite slowly.) The finite value of the steady-state mode pattern just at the mirror edge indicates that the mode does still have some diffraction losses past the edges of the end mirror. The smoothed shape and tapered profile of the steady-state pattern also indicate, however, that higher spatial frequency components are rapidly lost past the edges of the resonator, and that this lowest-loss transverse mode pattern has a very typical ability to "pull in its edges" and minimize its diffraction losses due to diffraction spreading. The exact shape of this mode pattern changes, and the mode losses decrease or increase, as the width of the planar end mirrors is changed, or the cavity length L is changed.

The primary conclusion from this numerical simulation or "computer experiment" is that even a simple optical resonator consisting only of two flat end mirrors, with completely open sides, still has a lowest-order transverse mode

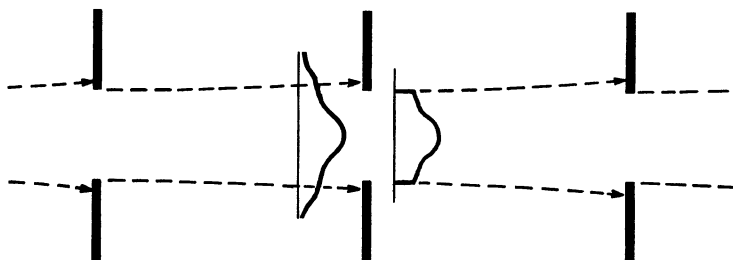


FIGURE 14.7

The field pattern in Figure 14.6 can also be interpreted as the lowest-order transverse mode in a "lensless lensguide" defined only by periodically spaced apertures.

which will reproduce itself on repeated round trips. This mode is in fact almost like a half-cosine in appearance, rather similar to more familiar waveguide cavity modes. The effects of the finite mirror edges and diffraction losses do show up, however, in the small diffraction ripples on the mode wavefront and on the mode amplitude pattern, and in the finite diffraction losses characteristic of the mode.

Note that this same analysis also means that a lens waveguide consisting simply of a series of slit apertures, without any lenses (see Figure 14.7), will also propagate exactly the same transverse mode pattern as a traveling mode pattern in the lensguide. The diffraction effects of the aperture edges in this lensguide are exactly equivalent to the cutting off of the transverse mode pattern on each bounce by the finite mirror width in the Fox and Li resonator calculation.

Fox and Li, and many others since them, have done many more such calculations for resonators with curved mirrors, mirrors of more complex shape, mirrors with central holes, planar but tilted mirrors, and so forth. In every situation a lowest-order mode with some sort of self-reproducing mode pattern and associated eigenvalue has resulted from this sort of calculation.

Finding the Higher-Order Transverse Modes

More sophisticated numerical procedures then allow us to obtain higher-order eigenmodes from the Fox and Li iterative procedure as well. For example, even in the simple Fox and Li procedure if we reach a stage in the iterative calculation where only two dominant modes are left, then there will be only two terms left in Equation 14.14. The field amplitude at any fixed point on the mirror surface will then display a periodic beating between the two modes (see Figure 14.8).

This periodic interference occurs because the fields of the two modes combine with different phases on successive round trips, since the different eigenmodes have eigenvalues $\tilde{\gamma}_{nm}$ with different phase angles ψ_{nm} . The eigenvalue of the next-highest eigenmode can then be deduced from the rate and period with which this "mode beating" between the two modes dies out.

A more sophisticated procedure known as the *Promy method* is one among several numerical techniques that allow us to start with an initial distribution containing a mixture of many eigenmodes, and after N iterations to deduce the N lowest-loss eigenvalues $\tilde{\gamma}_{nm}$ and eigenmodes $\tilde{E}_{nm}(x, y)$.

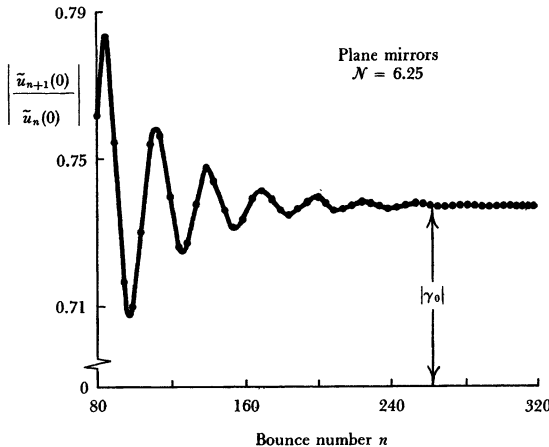


FIGURE 14.8
“Mode beating” in a Fox-and-Li mode calculation.

Resonator Eigenfrequencies

Having found the transverse eigenmodes $\tilde{E}_{nm}(x, y)$ and eigenvalues $\tilde{\gamma}_{nm}$ of a given cavity or lensguide, we can also find the exact resonant frequencies, or axial-plus-transverse mode resonances, of the cavity in the following manner.

The exact resonance frequency of a given axial-plus-transverse mode in a laser cavity is determined by the resonance condition that the round-trip phase shift in the cavity must be an integer multiple of 2π . Suppose a real regenerative laser cavity has round-trip phase shift due to the laser medium given by $\exp[-j\Delta\beta_m p_m]$, and suppose we consider a particular transverse mode $\tilde{E}_{nm}(x, y)$ with a complex eigenvalue $\tilde{\gamma}_{nm} \equiv |\tilde{\gamma}_{nm}| \exp[j\psi_{nm}]$. Regenerative feedback or laser oscillation for this particular transverse mode can occur only at frequencies for which the total round-trip phase shift is given by

$$\exp[-jkp - j\Delta\beta_m p_m + j\psi_{nm}] = \exp[-jq2\pi], \quad (16)$$

where we use ψ_{nm} for the phase angle of $\tilde{\gamma}_{nm}$. The axial phase shift term $e^{-j\Delta\beta_m p_m}$ has been brought back into this expression, with $k = \omega/c$, and q being an axial-mode integer. Equating the phase angles on opposite sides of Equation 14.16 then gives

$$\frac{wp}{c} + \Delta\beta_m p_m - \psi_{nm} = q \times 2\pi. \quad (17)$$

The resonance frequencies ω_{qnm} of the axial-plus-transverse modes in this cavity are thus given by

$$\omega = \omega_{qnm} \equiv \frac{2\pi c}{p} \left[q + \frac{\psi_{nm}}{2\pi} - \frac{\Delta\beta_m p_m}{2\pi} \right]. \quad (18)$$

Since q is normally a very large integer ($\approx p/\lambda$), the transverse mode factor $\psi_{nm}/2\pi$ represents only a small correction to the plane-wave resonance frequency $\omega_q \equiv q \times 2\pi(c/p)$. This correction will be in general slightly different for each specific nm -th transverse mode. As we already know, the $\Delta\beta_m p_m/2\pi$ factor is

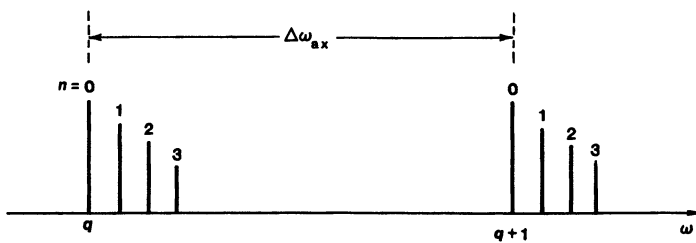


FIGURE 14.9

Transverse-mode frequencies in a typical laser resonator.

an additional (and usually still smaller) atomic frequency pulling effect caused by the reactive or χ' part of the laser susceptibility.

Transverse Mode "Beats"

Different transverse modes \tilde{E}_{nm} thus lead to slightly different resonance frequencies ω_{qnm} , with small relative frequency shifts which are determined by the phase angles of the transverse mode eigenvalues $\tilde{\gamma}_{nm}$ in real laser cavities. Figure 14.9 illustrates how each axial mode frequency ω_q in the plane-wave approximation splits into a set of different axial-plus-transverse mode resonances ω_{qnm} in a typical resonator. (The actual magnitude of this splitting can be quite different for different types of real resonators.)

Heterodyne interference effects or "beats" at the difference frequencies between these transverse modes can often be detected by examining the output signal of a laser oscillator with any kind of standard square-law photodetector (i.e., any detector whose response is proportional to the optical intensity, or to the optical E field squared, such as a photomultiplier tube or solid-state photodiode). These "transverse mode beats" can provide a sensitive test for the presence of multiple transverse modes. In addition, since the inter-mode beat frequency can be easily measured, and since this frequency depends in a sensitive fashion on the phase angles of the mode eigenvalues, the agreement between measured and theoretical frequencies can provide a test for the validity of the transverse mode calculations.

The Buildup of Laser Oscillation

The Fox and Li numerical approach simulates mathematically what actually happens physically in a real optical resonator with an initially injected field distribution and no gain. Each transverse mode component circulates around and dies out at a rate determined by its eigenvalue. With a slight change in viewpoint, this same picture also describes what happens in a real laser oscillator at turn-on.

When a laser oscillator is turned on from a cold start, an initial mode distribution $\tilde{E}^{(0)}(x, y)$ (determined in most real situations by noise or spontaneous emission in the laser cavity) begins to circulate repeatedly around the cavity, and to grow in amplitude if the cavity is above threshold. If the gain medium is spatially uniform so that all modes $\tilde{E}_{nm}(x, y)$ see the same gain, then the lowest-loss or 00 mode grows the fastest, since it has the highest value of net gain minus loss.

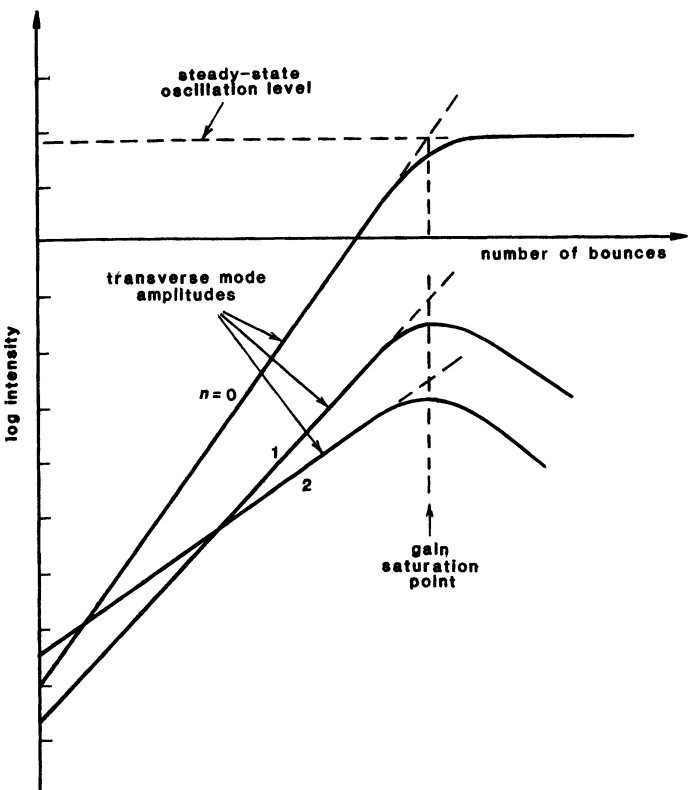


FIGURE 14.10
Buildup of laser transverse modes at laser turn-on.

In simple situations the dominant or 00 mode will eventually grow to a level where it saturates the gain down until the gain for this particular mode just equals the loss. This mode will then stay at a steady-state level, whereas all the higher-loss transverse modes die out, in the same way as sketched earlier. This initial growth and eventual stabilization process is illustrated in Figure 14.10.

Transverse Mode Competition Effects

There are many factors that complicate this picture in real lasers. In a more realistic picture, for example, the $n = 0, m = 0$ mode may still build up most rapidly; but this mode will then saturate the gain medium strongly only in those regions of the transverse plane where the field amplitude $|\tilde{E}_{00}(x, y)|^2$ is large. This may leave unsaturated gain at other transverse positions x, y , and this may allow other higher-order transverse modes to oscillate simultaneously. In very high-gain but short-pulse lasers the entire laser pulse may be over in so few round trips that the 00 mode has insufficient time to grow to where it dominates over higher-order modes. The transverse mode selection may thus be less effective in a *Q*-switched laser than in a cw steady-state laser.

Even in a cw laser, the differences in loss and in growth rate for different eigenmodes \tilde{E}_{nm} may be very small, so that the competition between modes is very weak. The gain may not be uniform across the laser, so that different eigenmodes $\tilde{E}_{nm}(x, y)$ actually see different gains. If the atomic linewidth is particularly narrow, and the laser is tuned so that the lowest-order $q00$ resonant frequency is off line center, whereas some other higher-order qnm transverse mode is tuned closer to line center, the laser may then also see higher net gain in the higher-order mode even though it has higher diffraction losses. Interference effects between the fields of different transverse modes may also modulate the gain differently at different transverse positions and thus cross-couple the different transverse modes. In all these different situations, several transverse modes may then oscillate simultaneously, or the laser may jump back and forth between transverse modes.

Single Transverse Mode Operation

All in all, it is often a considerable struggle to force a large or high-gain laser oscillator to oscillate only in a single lowest-loss transverse mode. One of the main considerations in the design of a practical laser resonator is to have simultaneously both minimum unwanted loss for the lowest-order transverse eigenmode, and also high mode discrimination—that is, a large increase in diffraction losses—for all the higher-order transverse modes. This is often accomplished by putting an adjustable aperture inside the laser cavity and reducing its size until it attenuates and if possible kills the higher-order modes, but still has negligible effect on the desired lowest-order modes. The unstable resonator provides another and somewhat different method for accomplishing the same goal.

Despite these complexities, which we will discuss in more detail in later sections, there are many lasers which do operate in a single lowest-order transverse mode according to the description presented above. Even in more complex situations the transverse eigenmode picture generally provides a solid and useful basis for describing the more complex multimode and coupled-mode phenomena that may occur in real lasers.

Conclusions

Evaluating the round-trip wave propagation in an optical resonator, using the appropriate round-trip kernel or mathematical transformation, is obviously the primary step in evaluating and understanding the transverse modes, their losses, and their resonant frequencies, in any real laser resonator. In the following two chapters we introduce two primary tools for accomplishing this: ray matrix methods for treating ray propagation without diffraction, and paraxial wave optics for treating wave propagation including diffraction in most real laser beams and cavities.

REFERENCES

The original (and still very instructive) reference on the Fox and Li approach to optical resonator modes is A. G. Fox and T. Li, "Resonant modes in a maser interferometer," *Bell Syst. Tech. J.* **40**, 453–458 (March 1961). Later and more extensive results are in

"Modes in a maser interferometer with curved and tilted mirrors," *Proc. IEEE* **51**, 80–89 (January 1963).

For an extension of this work which makes clear many of the basic properties of transverse modes in laser resonators, see also A. G. Fox and T. Li, "Computation of optical resonator modes by the method of resonance excitation," *IEEE J. Quantum Electron.* **QE-4**, 460–465 (July 1968).

Many of the concepts and mathematical solutions of transverse modes for periodic beam waveguides or lensguides were also developed quite independently of lasers, in the context of millimeter wave systems, especially in work by G. Gobau as reviewed in a chapter on "Beam Waveguides," in *Advances in Microwaves*, Vol. 3, edited by L. Young (Academic Press, 1968); pp. 67–126.

For further examples of Gobau's important early contributions to propagation in periodic optical and millimeter-wave systems, see, for example, G. Gobau, "On the guided propagation of electromagnetic wave beams," *IEEE Trans. AP-9*, 248–255 (May 1961); and G. Gobau and J. R. Christian, "Some aspects of beam waveguides for long distance transmission at optical frequencies," *IEEE Trans. MTT-12*, 212–220 (March 1964).

An excellent review of standard stable resonator theory as it developed in the early years of the laser era is given by H. Kogelnik and T. Li, "Laser beams and resonators," appearing both in *Proc. IEEE* **54**, 1312 (October 1966) and *Appl. Opt.* **5**, 1550–1567 (October 1966); see also H. Kogelnik, "Modes in Optical Resonators," in *Lasers: A Series of Advances*, Vol. I, ed. by A. K. Levine (Marcel Dekker, New York, 1966), p. 295. A historical survey of Bell Laboratories work in all aspects of laser optics, with many references, is given by R. Kompfner in, "Optics at Bell Laboratories—optical communications," *Appl. Opt.* **11**, 2412–2425 (November 1972).

A survey of newer types of resonators for high-power lasers is given by A. E. Siegman in, "Unstable optical resonators," *Appl. Opt.* **13**, 353 (February 1974). A somewhat inaccessible reference to Soviet work in resonator theory is L. A. Weinstein, *Open Resonators and Open Waveguides* (Golem Press, Boulder, Colorado, 1969).

Another Soviet reference on laser resonators is Y. Ananiev (or Anan'ev), *Résonateurs Optiques et Problème de Divergence du Rayonnement Laser* (Éditions Mir, Moscow, Russian original 1979, French translation 1982).

Some early references on the mathematical questions involved in nonhermitian resonator integral equations include S. P. Morgan, "On the integral equations of laser theory," *IEEE Trans. MTT-11*, 191–193 (May 1963); W. Streifer and H. Gamo, "On the Schmidt expansion for optical resonator modes," in *Quasi Optics*, ed., by J. Fox (Polytechnic Press, Polytechnic Institute of Brooklyn, 1964), pp. 351–365; D. J. Newman and S. P. Morgan, "Existence of eigenvalues of a class of integral equations arising in laser theory," *Bell Sys. Tech. J.* **43** 113–126 (January 1964); J. A. Cochran, "The existence of eigenvalues for the integral equations of resonator theory," *Bell Sys. Tech. J.* **44**, 77–88 (January 1965); and H. Hochstadt, "On the eigenvalue of a class of integral equations arising in resonator theory," *SIAM Rev.* **8** 62 (January 1966).

More recent references include J. A. Arnaud, *Beam and Fiber Optics* (Academic Press, 1976), pp. 122–123 and 175; I. F. Balashov and V. A. Berenberg, "Nonstationary modes of an open resonator," *Sov. J. Quantum Electron.* **5**, 159–161 (August 1975); and A. E. Siegman, "Orthogonality properties of optical resonator eigenmodes," *Optics Comm.* **31**, 369–373 (December 1979).

The problem of finding optical resonator eigenmodes is very closely related to the earlier mathematical problem of shaping a transmitted beam to obtain maximum power transmission between two apertures. Various aspects of this topic are often referred to as "Luneberg apodization problems," since they were posed, and also converted into

mathematical eigenvalue problems, in R. K. Luneberg, *Mathematical Theory of Optics* (University of California Press, Berkeley, 1964).

Other and more recent references include A. F. Kay, "Near-field gain of aperture antennas," *IEEE Trans. AP-8*, 586-593 (November 1960); G. V. Borgiotti, "Maximum power transfer between two planar apertures in the Fresnel zone," *IEEE Trans. AP-14*, 158-163 (March 1966); H. N. Rexroad and B. J. Henderson, "Maximum power-transfer coefficient between two confocal apertures," *J. Opt. Soc. Am.* **59**, 1415-1421 (November 1969); and T. Ueno and T. Asakura, "Apodization for maximum encircled energy with specified over-all transmittance," *J. Optics (Paris)* **8**, 15-31 (1981).

Problems for 14.3

1. *Higher-order mode suppression during laser turn-on.* A certain laser cavity has a lowest-loss eigenmode \tilde{E}_{00} with eigenvalue $|\tilde{\gamma}_{00}| = 0.9$ and a next-lowest-loss eigenmode \tilde{E}_{01} with eigenvalue $|\tilde{\gamma}_{01}| = 0.8$ (as well as numerous higher-loss eigenmodes). When this laser is first turned on, the unsaturated gain during the initial build-up period is 40% power gain per one-way pass down the laser cavity ($G_1 = |g_1|^2 = 1.4$). How many round trips will it take before the circulating power in the laser cavity has become 99% lowest-order transverse mode, assuming for simplicity that the lowest and next-lowest eigenmodes have equal initial noise amplitudes and that this all takes place during the initial build-up period before gain saturation begins to occur?
2. *Finding the next higher-order transverse mode.* Develop the necessary mathematical formulas and then, using the data from Figure 14.6, find the eigenvalue magnitude $|\tilde{\gamma}_1|$ for the next higher-order transverse mode in this resonator, and its phase angle relative to the lowest-order eigenvalue $\tilde{\gamma}_0$. (Note: The index in this figure is the number of one-way "bounces" in the resonator, rather than the number of two-way round trips.) Hint: Assume that only the $\tilde{\gamma}_0$ and $\tilde{\gamma}_1$ modes are left, and that the complex amplitude of the $\tilde{\gamma}_1$ mode component has become small compared to the $\tilde{\gamma}_0$ mode component.
3. *Higher-order transverse mode beats.* In the previous problem, what will be the beat frequency between the lowest and next lowest-order transverse modes in the resonator of Figure 14.6, assuming that the laser cavity is 1 meter long?
4. *Spectral content of a circulating pulse.* Suppose a "circulating slab" of axial length Δz inside a laser cavity of length L has an axial field variation $\cos(\omega_p t - k_p z)$ [or, if you like $\exp[j(\omega_p t - k_p z)]$] within the slab, where $k_p \equiv \omega_p/c$, and where ω_p (the carrier frequency of the "pancake") is *not* equal to any of the axial mode frequencies $\omega_q = q2\pi(c/2L)$ of the laser cavity. Suppose gain just equals loss, so that this pulse circulates repeatedly inside the cavity, emitting a short pulse of carrier frequency ω_p and duration $\Delta t = \Delta z/c$ through the end mirror every $T = 2L/c$ seconds.

It may then seem that this laser is producing output primarily at frequency ω_p , when lasers are supposed to oscillate only at their axial mode frequencies ω_q . Resolve this apparent paradox by a suitable spectral argument. Hint: Consider the frequency spectrum of a single pulse of carrier frequency ω_p ; of two such pulses separated in time by $T = 2L/c$; of three such pulses; and so forth. Use some simple pulse shape (e.g., square or gaussian); assume ω_p is, say, one-third

of the way between two axial modes; let Δz equal, say, $L/10$; and actually plot the spectral amplitude versus frequency for increasing numbers of pulses.

5. *Output beam characteristics of a multi-transverse-mode laser.* Suppose a laser is oscillating simultaneously in a lowest-order transverse mode that has, say, even symmetry in the transverse x direction and a higher-order transverse mode that has odd symmetry in the same transverse direction. How will the center of gravity of the beam emerging from this laser behave, in the near field and in the far field?

Suppose the output beam is detected by a photodetector large enough to capture all of the energy emerging through the end of this laser. Will this photodetector sense a transverse mode beat? What sort of arrangement will maximize the sensitivity for measuring such beats?

6. *Transverse modes that self-reproduce after several round trips?* The question is sometimes raised: Why does an optical resonator eigenmode \tilde{E}_{nm} have to reproduce itself after only one round trip? Could we not have a transverse eigenmode that was self-reproducing in form only after two, or three, or even k round trips?

Discuss this question, explaining why such a “multipass transverse eigenmode” could not be associated with a single axial mode integer, and why such a “multipass eigenmode” would really consist of a mixture of the “true” single-pass transverse eigenmodes. Hint: Consider not only the transverse and longitudinal field expansion inside the laser cavity, but also the space and time dependence of the beam that would come out the output end of a laser cavity oscillating in such a “multipass eigenmode.”



RAY OPTICS AND RAY MATRICES

Ray optics—by which we mean the geometrical laws for optical ray propagation, without including diffraction—is a topic that is not only important in its own right, but also very useful in understanding the full diffractive propagation of light waves in optical resonators and beams. This chapter, therefore, gives a fairly extensive introduction to ray optics in paraxial optical systems. The following chapter will then give a similar introduction to wave optics in the same systems.

15.1 PARAXIAL OPTICAL RAYS AND RAY MATRICES

Ray matrices or “ABCD matrices” are widely used to describe the propagation of geometrical optical rays through paraxial optical elements, such as lenses, curved mirrors, and “ducts.” These ray matrices also turn out to be very useful for describing a large number of other optical beam and resonator problems, including even problems that involve the diffractive nature of light. Therefore, we begin the discussion of optical beams and resonators with a detailed review of paraxial ray theory and ray matrices.

Optical Rays and Ray Transformations

Consider a ray of light—or equally well a particle, such as an electron—that is traveling approximately in the z direction, but with a transverse displacement $r(z)$ from the axis and also a small slope dr/dz , as in Figure 15.1. If such a ray propagates in free space from a plane at z_1 to a later plane at $z_2 = z_1 + L$, as in Figure 15.2, its input and output ray coordinates will be related by the transformation

$$\begin{aligned} r_2 &= r_1 + L dr_1/dz \\ dr_2/dz &= dr_1/dz. \end{aligned} \tag{1}$$

Suppose the same ray passes through a thin lens of focal length f as in the lower part of Figure 15.2. The input and output ray coordinates just before and after

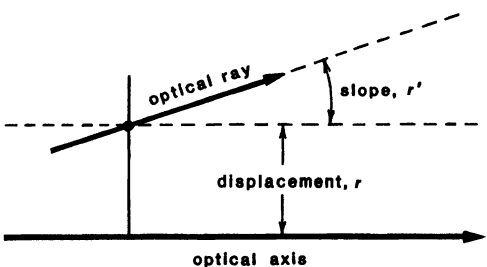
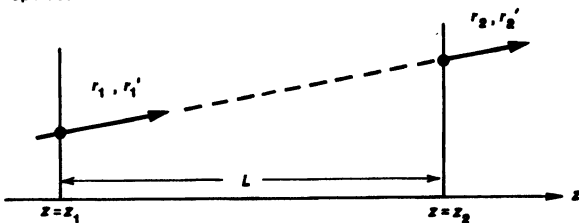


FIGURE 15.1
Definition of an optical ray.

free space:



thin lens:

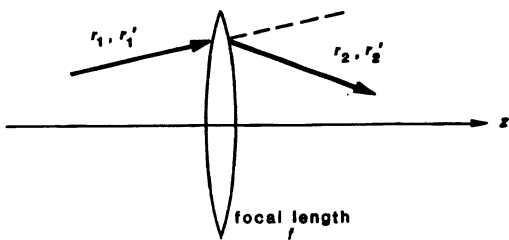


FIGURE 15.2

Optical-ray transformations through free space and through a thin lens.

the lens will then be related by

$$r_2 = r_1 \quad (2)$$

$$dr_2/dz = -(1/f) r_1 + dr_1/dz.$$

(Note that we use a sign convention in which a positive value for f means a positive or converging lens.)

Equations 15.1 and 15.2 both give linear transformations between the input and output displacements and slopes of the rays. In rectangular coordinates, of course, these displacements r and slopes dr/dz can represent equally well either the x -axis quantities x and dx/dz , or the y -axis quantities y and dy/dz .

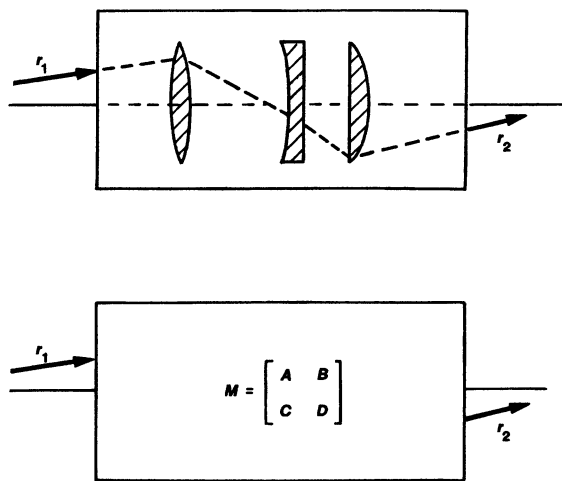


FIGURE 15.3
Example of an overall ray matrix.

Optical Ray Matrices, or *ABCD* Matrices

In fact, the change in displacement and slope of an optical ray upon passing through a wide variety of simple optical elements can be written in the same general form as Equations 15.1 and 15.2. One slight additional complexity should be added, however. In writing ray transformations like these, we will simplify many later results if we define the ray slope variable to be, not the actual slope dr/dz of the ray, but rather *this actual slope multiplied by the local index of refraction at the ray position*. Hence, we will define in the most general situation

$$r'(z) \equiv n(z) \frac{dr(z)}{dz} \quad (3)$$

and similarly for $x'(z) \equiv n(z) dx(z)/dz$ and $y'(z) \equiv n(z) dy(z)/dz$. With these definitions we can connect input and output displacements and slopes in a wide variety of paraxial optical elements by the general form

$$\begin{aligned} r_2 &= Ar_1 + Br'_1 \\ r'_2 &= Cr_1 + Dr'_1. \end{aligned} \quad (4)$$

where we use r'_1 and r'_2 to denote the modified ray slopes at the input and output planes, and where the coefficients A, B, C, and D characterize the paraxial focusing properties of this element. If we need to, we can refer to the derivatives $dr(z)/dz$ and so forth as the *real slopes* and to the quantities $r'(z)$ and so forth as the *reduced slopes*, in situations where we need to be precise.

It is then natural to write Equation 15.4 in matrix form as

$$r_2 \equiv \begin{bmatrix} r_2 \\ r'_2 \end{bmatrix} = \begin{bmatrix} A & B \\ C & D \end{bmatrix} \times \begin{bmatrix} r_1 \\ r'_1 \end{bmatrix} \equiv M r_1, \quad (5)$$

where M is the *ray matrix* for the optical element. Table 15.1 lists the ray matrices for a large number of basic paraxial optical elements, using the actual

displacement and reduced slope variables. Note in particular that if we use the generalized definition for the reduced ray slopes, then the bending of a ray trajectory that occurs at a dielectric interface because of Snell's law is automatically taken into account, and the $ABCD$ matrix for a planar dielectric interface is simply the identity matrix.

With the generalized slope definition of Equation 15.3, it is a general property of all the basic elements in Table 15.1 that the ray matrix determinant is given by

$$AD - BC = 1. \quad (6)$$

(If we do not use the reduced slopes, then we have the more cumbersome relation that $AD - BC = n_1/n_2$ where n_1 and n_2 are the refractive indices at the input and output planes.) Since the determinant of a matrix product is the product of the determinants, Equation 15.6 holds equally well for an arbitrary cascade of optical elements.

Interfaces and Ducts

The fundamental building blocks for all the paraxial systems of Table 15.1 are *curved dielectric interfaces* and *quadratically varying dielectric media* or “ducts”. The general $ABCD$ matrix for a curved interface between two dielectric media can be derived from Snell's law and elementary geometry, and is given in Table 15.1. The corresponding $ABCD$ matrix for a quadratically varying medium can be developed as follows.

First of all, by a “duct” we mean any dielectric medium which has a quadratic transverse variation in its index of refraction, with either a maximum or minimum on axis, as shown in Figure 15.4. We will also extend this concept in later sections to include “complex ducts” in which there may be a quadratic transverse variation of the loss or gain coefficient as well as the real index of refraction.

To analyze ray propagation in a duct, we can consider a ray, or better a light beam of small but finite width, traveling as in Figure 15.5. The inner edge of this beam is at radius r , and the outer edge at radius $r + \Delta r$. Suppose the index of refraction $n(r)$ decreases going radially outward from the system axis, so that the inner edge of this light beam is in a region of slightly higher index. The inner edge of the beam then travels more slowly, whereas the outer edge sees a lower index value and travels faster. As a result the beam tends to be continually turned or bent inward toward the axis.

Suppose that the index of refraction in this medium can be written, or at least approximated, in the quadratic form

$$n(r, z) = n_0(z) - \frac{1}{2}n_2(z)r^2, \quad (7)$$

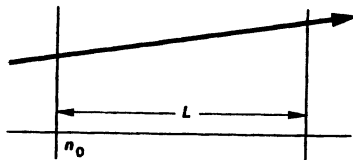
where $n_0(z)$ is the variation along the axis, and the parameter

$$n_2(z) \equiv -\left. \frac{\partial^2 n(r, z)}{\partial r^2} \right|_{r=0} \quad (8)$$

is the downward curvature of the index at the axis. Then, within the paraxial approximation a ray traveling through this medium will follow a trajectory given

TABLE 15.1
Ray Matrices for Paraxial Optical Elements

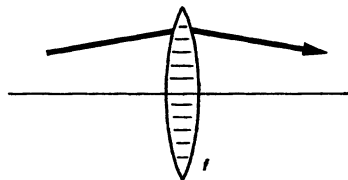
(a) "Free space" region, index n_0 , length L



$$\begin{bmatrix} 1 & L/n_0 \\ 0 & 1 \end{bmatrix}$$

(b) Thin lens, focal length f

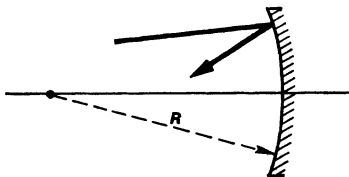
$f > 0$ for converging lens



$$\begin{bmatrix} 1 & 0 \\ -1/f & 1 \end{bmatrix}$$

(c) Curved mirror, radius R , normal incidence

$R > 0$ for concave mirror

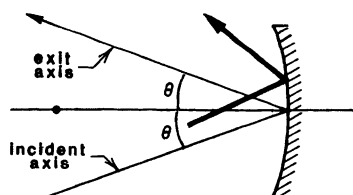


$$\begin{bmatrix} 1 & 0 \\ -2/R & 1 \end{bmatrix}$$

(d) Curved mirror, arbitrary incidence

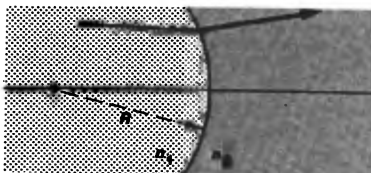
$R_e = R \cos \theta$ in the plane of incidence ("tangential")

$R_e = R/\cos \theta \perp$ to plane of incidence ("sagittal")



$$\begin{bmatrix} 1 & 0 \\ -2/R_e & 1 \end{bmatrix}$$

(e) Curved dielectric interface, normal incidence

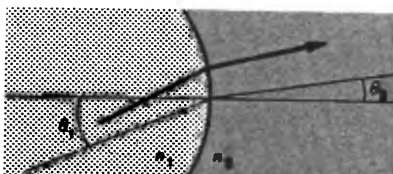
 $R > 0$ for concave surface

$$\begin{bmatrix} 1 & 0 \\ (n_2 - n_1)/R & 1 \end{bmatrix}$$

(f) Curved interface, arbitrary incidence, tangential plane

 $R > 0$ for concave surface; $n_1 \sin \theta_1 = n_2 \sin \theta_2$

$$\Delta n_e = (n_2 \cos \theta_2 - n_1 \cos \theta_1) / \cos \theta_1 \cos \theta_2$$

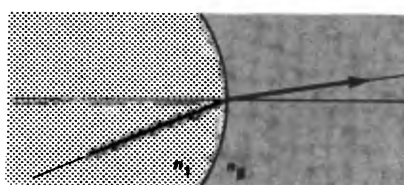


$$\begin{bmatrix} \frac{\cos \theta_2}{\cos \theta_1} & 0 \\ \Delta n_e/R & \frac{\cos \theta_1}{\cos \theta_2} \end{bmatrix}$$

(g) Curved interface, arbitrary incidence, sagittal plane

 $R > 0$ for concave surface; $n_1 \sin \theta_1 = n_2 \sin \theta_2$

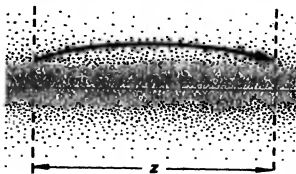
$$\Delta n_e = n_2 \cos \theta_2 - n_1 \cos \theta_1$$



$$\begin{bmatrix} 1 & 0 \\ \Delta n_e/R & 1 \end{bmatrix}$$

(h) "Duct" (radially varying index and gain)

$$n(x) = n_0 - \frac{1}{2} n_2 x^2; \gamma^2 \equiv n_2/n_0$$



$$\begin{bmatrix} \cos \gamma z & (n_0 \gamma)^{-1} \sin \gamma z \\ -(n_0 \gamma) \sin \gamma z & \cos \gamma z \end{bmatrix}$$

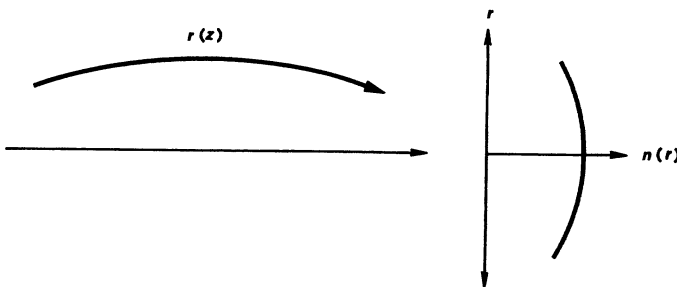


FIGURE 15.4
Ray propagation in a "duct."

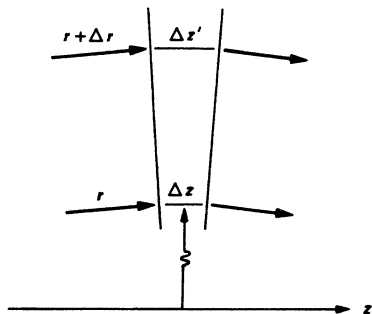


FIGURE 15.5
Ray bending in an index gradient.

by the ray propagation equation

$$\frac{d}{dz} \left[n_0(z) \frac{dr(z)}{dz} \right] + n_2(z) r(z) = 0. \quad (9)$$

Suppose we define the reduced slope for this ray at any plane, as already discussed in the preceding, by

$$r'(z) \equiv n_0(z) \frac{dr(z)}{dz}. \quad (10)$$

Then we can separate the ray propagation equation (15.9) into the pair of equations

$$\frac{dr(z)}{dz} \equiv \frac{r'(z)}{n_0(z)} \quad \text{and} \quad \frac{dr'(z)}{dz} = -n_2(z) r(z), \quad (11)$$

where the first equation is true by definition, and the second accounts for refractive bending in the radially inhomogeneous duct.

Stable Quadratic Ducts

Ray propagation in real quadratic ducts separates naturally into geometrically *stable* and *unstable* ducts. To show this, let us suppose that the on-axis

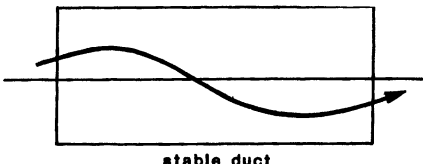
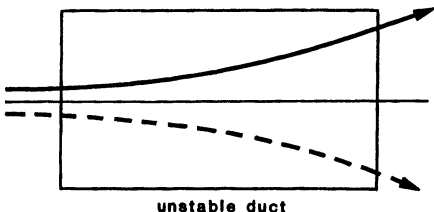


FIGURE 15.6
Ray trajectories in geometrically stable and unstable quadratic ducts.



index value n_0 and the transverse derivative n_2 in Equations 15.11 are both constant with distance. The two ray equations can then be combined to give the single trajectory equation

$$\frac{d^2r(z)}{dz^2} + \frac{n_2}{n_0}r(z) = \frac{d^2r(z)}{dz^2} + \gamma^2r(z) = 0, \quad (12)$$

where γ is given (for positive values of n_2) by

$$\gamma^2 = \frac{n_2}{n_0} \quad \text{or} \quad \gamma = \sqrt{\frac{n_2}{n_0}}. \quad (13)$$

The general solution for ray propagation in this kind of paraxial (quadratic) duct becomes

$$\begin{aligned} r(z) &= r_0 \cos \gamma z + \frac{1}{\gamma} \frac{dr_0}{dz} \sin \gamma z \\ &= r_0 \cos \gamma z + (n_0 \gamma)^{-1} r'_0 \sin \gamma z, \end{aligned} \quad (14)$$

where r_0 and r'_0 are the initial displacement and (reduced) slope of the ray at $z = 0$.

From Equation 15.14 and its derivative, we can see that the general ray matrix for a duct of length z is

$$\mathbf{M} = \begin{bmatrix} \cos \gamma z & (n_0 \gamma)^{-1} \sin \gamma z \\ -n_0 \gamma \sin \gamma z & \cos \gamma z \end{bmatrix}. \quad (15)$$

A duct with an index maximum on axis and a quadratic variation near the axis will trap optical rays so that they will oscillate periodically back and forth across the centerline of the duct, as shown in the top part of Figure 15.6. We will refer to this as a *stable quadratic duct*.

Unstable Quadratic Ducts

The same analysis in Equations 15.12 to 15.15 will apply equally well to a medium in which the index of refraction *increases* quadratically going outward from the axis, so that $n_2 < 0$ or $d^2n/dr^2 > 0$. In this situation, however, the value of γ^2 becomes a negative quantity, and γ must be replaced by

$$\gamma^2 = -\left|\frac{n_2}{n_0}\right| \quad \text{or} \quad \gamma = j\sqrt{\frac{1}{n_0} \frac{d^2n}{dr^2}} = j|\gamma|. \quad (16)$$

The general solution analogous to Equation 15.14 then becomes

$$r(z) = r_0 \cosh \gamma z + (n_0 \gamma)^{-1} r'_0 \sinh \gamma z, \quad (17)$$

and the *ABCD* matrix becomes

$$M = \begin{bmatrix} \cosh \gamma z & (n_0 \gamma)^{-1} \sinh \gamma z \\ -n_0 \gamma \sinh \gamma z & \cosh \gamma z \end{bmatrix}. \quad (18)$$

Such an “anti-duct,” with an index minimum on axis, will diverge (as well as defocus) optical rays. It acts in general in the same way as a thick diverging lens, as shown in the lower part of Figure 15.6.

Ducts thus provide our first illustration of the distinction between *stable ray-propagating systems*, in which rays oscillate periodically back and forth about the ray axis but with bounded excursions; and *unstable ray-propagating systems*, in which rays diverge exponentially outward with distance. We will see many examples of this for more complex types of paraxial focusing systems in later sections.

Examples of Ducts: Optical Fibers and GRIN Rods

The focusing and ray-trapping properties of stable quadratic ducts are of great practical importance. They provide first of all an idealized model for light propagation in the graded-index optical fibers that are now becoming widely used for long distance optical communications. The simplest type of optical fibers are made up of a uniform core surrounded by a lower-index cladding, as in Figure 15.7, so that the radial index variation is a step-function rather than a smooth quadratic variation. A more detailed waveguide type of analysis is then required to give an accurate description of the modes in fibers having this type of discontinuous index variation.

Many fibers are now being made, however, with a smoothly varying radial profile which more or less approximates a quadratic index variation (Figure 15.7, lower part). The simple results given in the preceding equations will then provide a good first-order approximation to the ray behavior in this kind of fiber, regardless of the actual index variation $n(r)$, provided that the index variation has a quadratic leading term near the axis and provided that the ray trajectories are confined close enough to the axis so that higher-order terms in the radial index variation do not become important. More accurate solutions for other index variations—notably the square-topped or stepped index variations in cladded fibers—are also available but rapidly become more complex.

Optical elements that are of poor optical quality, such as imperfect laser rods and nonlinear optical crystals, may also have unintentional ducts, either stable or unstable, built into them due to local variations in optical index. Laser

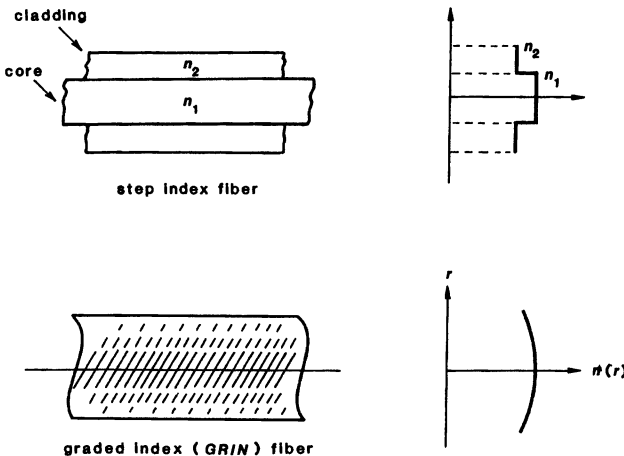


FIGURE 15.7
Examples of step-index and graded-index optical fibers.

oscillations can then be trapped along the stable ducts, and rejected by any unstable “anti-ducts,” in such rods. Early laser rods, particularly ruby rods, often exhibited large random index variations and thus random ducting effects across their transverse cross section, leading to poor optical beam quality and possibly to damage at high optical powers. Modern optical rods are generally much better in this regard.

The intense pumping light in solid-state lasers can also cause a temperature rise on the rod axis, which usually produces an increase in index of refraction on axis. The rod as a whole then becomes a duct which acts like a weak positive focusing lens with a pump-power-dependent focal length. Such thermal focusing effects are usually not desirable, and usually limit the oscillation power available from the rod.

Finally, glass rods and fibers with built-in quadratic ducting properties are now commercially manufactured under such trade names as SEL-FOC (“self-focusing”) or GRIN (“graded refraction index”) rods, and are used as self-focusing laser systems and as specialized lenses for many optical applications.

Axial Index Variations

We can also consider the situation where there is no transverse variation, or $n_2 = 0$, but there is an axial variation of the index in the medium given by $n_0 = n_0(z)$. The relevant ray equation in this situation is

$$\frac{dr'(z)}{dz} = \frac{d}{dz} \left[n_0(z) \frac{dr(z)}{dz} \right] = 0 \quad (19)$$

with the solution

$$r(z) = r_0 + r'_0 \int_{z_0}^z \frac{1}{n_0(z)} dz. \quad (20)$$

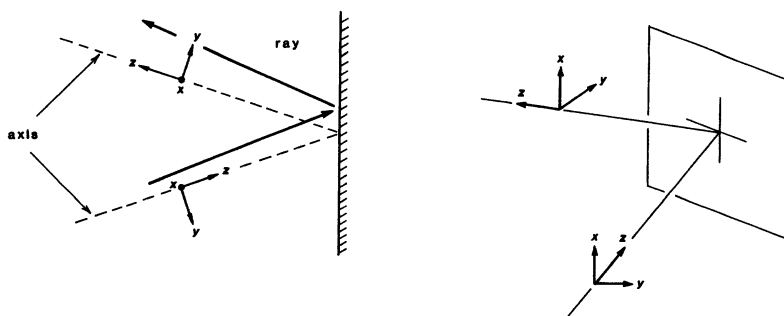


FIGURE 15.8

Ray inversion (or coordinate inversion) on reflection.

This gives for the $ABCD$ matrix through a section of length L starting at $z = 0$

$$M = \begin{bmatrix} 1 & B(L) \\ 0 & 1 \end{bmatrix} \quad \text{where} \quad B(L) \equiv \int_0^L \frac{dz}{n_0(z)}. \quad (21)$$

The ray-bending properties of a segment with an axial index variation are contained in the definition of the reduced slope $r'(z)$.

Ray Inversion

One additional elementary ray operation that we have not considered yet is *ray inversion* of an optical ray with respect to one or the other of its transverse coordinate axes.

Ray inversion necessarily occurs, for example, in one transverse coordinate or the other whenever an optical ray is specularly reflected from a mirror, as shown in Figure 15.8. If we are to retain a right-handed coordinate system looking in the direction of ray propagation both before and after reflection, the ray displacements and slopes in the planes perpendicular to and lying in the plane of incidence must be related before and after reflection by

$$x = x_0, x' = x'_0 \quad \text{and} \quad y = y_0, y' = -y'_0. \quad (22)$$

The ray matrices along the principal axes can thus be written in the form

$$x_2 = I x_1 \quad \text{and} \quad y_2 = -I y_1, \quad (23)$$

where I is the identity matrix. Ray inversion thus represents one particularly primitive kind of astigmatism in an optical system. Ray inversion also means, among other things, that a ring laser having an odd number of mirrors will have a net overall inversion with respect to one or the other of its axes in one round trip.

REFERENCES

The paraxial ray matrix approach, though widely used in the laser field, is not yet as widely taught in elementary optics texts. A short survey of this approach, with

many useful references, is given by Allen Nussbaum in "Teaching of advanced geometric optics," *Appl. Opt.* **17**, 2128–2129 (July 15 1978). One useful recent book not referenced there is A. Garrard and J.M. Burch, *Introduction to Matrix Methods in Optics* (Wiley, 1975).

The detailed mathematical description of ray propagation and ray bending in an inhomogeneous optical medium with arbitrary spatial variation of the index of refraction is a fairly subtle and complex topic, involving such concepts as eikonal functions, hamiltonian characteristic functions, variational principles, and Euler equations. The classic reference book on the subject is R. K. Luneburg, *Mathematical Theory of Optics* (University of California Press, 1964). Other lengthy discussions can be found in M. Born and E. Wolf, *Principles of Optics* (Pergamon Press, 1959); and in J. A. Arnaud, *Beam and Fiber Optics* (Academic Press, 1976).

A more complex and generalized analysis of ray propagation in ducts with both axial and radial index variations is given in K. Tanaka, "Paraxial theory of rotationally distributed-index media by means of Gaussian Constants," *Appl. Opt.* **23**, 1700–1706 (June 1 1984).

The ray matrices for curved dielectric interfaces at oblique incidence are derived by G. A. Massey and A. E. Siegman, "Reflection and refraction of gaussian light beams at tilted ellipsoidal surfaces," *Appl. Opt.* **8**, 975–978 (May 1969).

Graded-index rods or ducts as discussed in this section are of course essentially equivalent to thick optical lenses. Such graded-index or GRIN rods are now used as lenses in a number of commercially important applications, either singly as fiber optical connectors and medical imaging devices, or in large arrays as imaging systems for photocopying machines. A good series of papers reviewing the technology and applications of graded-index optics can be found in *Appl. Opt.* **21** (March 15 1982), **22** (February 1 1983) and **23** (June 1 1984).

Problems for 15.1

1. *Ray matrix for a curved dielectric interface.* Using Snell's law, derive the ray matrix for a curved interface between two dielectrics.
2. *Ray matrix elements for a curved diffraction grating.* Curved diffraction gratings are occasionally employed as end mirrors for laser cavities, as well as in beam-expanding systems and grating spectrometers. Suppose a curved diffraction grating with radius of curvature R has rulings running in the y direction with grating spacing d in the x direction. An incident beam striking this grating at an angle θ_1 from the normal in the x, z plane will then be diffracted in N -th order into angle θ_2 in the same plane given by the grating equation $\sin \theta_1 + \sin \theta_2 = N/d$.

Show that the ray matrix for reflection from this grating has matrix elements $A = 1/D = M$, $B = 0$, and $C = -2/R_t$ in the tangential or x, z plane, where $M \equiv \cos \theta_2 / \cos \theta_1$ is a transverse magnification or beamwidth expansion, and the effective radius of the grating is $R_t \equiv R \cos \theta_1 \cos \theta_2 / (\cos \theta_1 + \cos \theta_2)$. Show also that the matrix elements in the perpendicular or sagittal direction are given by $A = D = 1$, $B = 0$, and $C = -2/R_s$ where $R_s \equiv 2R / (\cos \theta_1 + \cos \theta_2)$.

3. *Limiting case.* Show that the limiting case for a short but very strongly focusing duct is a simple thin lens, and give the focal power of the lens in terms of the duct parameters.
-

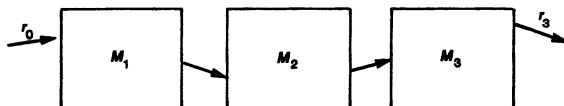


FIGURE 15.9
Ray matrix systems in cascade.

15.2 RAY PROPAGATION THROUGH CASCADED ELEMENTS

Let us next look at how rays propagate through cascade optical systems consisting of several different paraxial elements connected together in cascade. It is one of the most important properties of ray matrices that such cascaded paraxial optical elements can be handled simply by matrix multiplying the individual $ABCD$ matrices for the individual optical elements, arranged in reverse order.

Cascaded Ray Matrices

Suppose several optical elements with ray matrices M_1, \dots, M_n —for example, a free-space section, a thin lens, another free-space section, a dielectric interface, and so on—are arranged in cascade as shown in Figure 15.9. The total ray transformation through this cascaded series of elements can then be calculated from the chain multiplication process

$$\begin{aligned} r_1 &= M_1 r_0 \\ r_2 &= M_2 r_1 = M_2 M_1 r_0 \\ r_3 &= M_3 r_2 = M_3 M_2 M_1 r_0, \end{aligned} \tag{24}$$

and so on up to the general result

$$r_n = [M_n M_{n-1} \cdots M_2 M_1] r_0 = M_{\text{tot}} r_0. \tag{25}$$

The overall or total ray matrix M_{tot} for this system is thus given by

$$M_{\text{tot}} \equiv M_n M_{n-1} \cdots M_2 M_1. \tag{26}$$

A single 4-element ray matrix equal to the ordinary matrix product of the individual ray matrices can thus describe the total or overall ray propagation through a complicated sequence of cascaded optical elements. Note, however, that the matrices must be arranged *in inverse order* from the order in which the ray physically encounters the corresponding elements.

Ray Matrices and Spherical Wave Propagation

Ray matrices and paraxial ray optics provide a general way of expressing the elementary lens laws of geometrical optics, or of spherical-wave optics, leaving out higher-order aberrations, in a form that many people find clearer and more convenient. *Ray optics and geometrical optics in fact contain exactly the same physical content, expressed in different fashion.*

To demonstrate this we can first note that an ideal spherical wave with radius of curvature R can also be viewed as a collection of rays all diverging from a common point, the wavefront's center of curvature C (Figure 15.10). The slope

FIGURE 15.10
Spherical wave as a fan of rays.

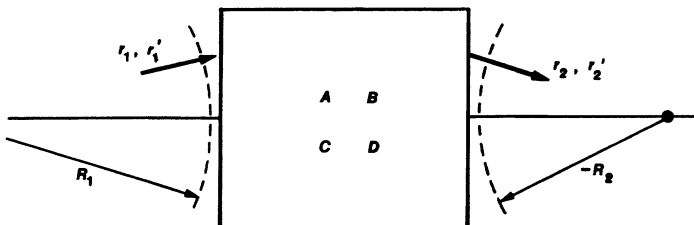
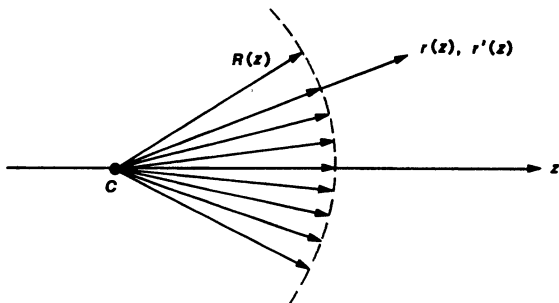


FIGURE 15.11
Spherical wave transformation through an arbitrary paraxial system.

and displacement of each of these rays at the plane z where the radius of curvature is $R(z)$ —that is, at a distance R from the source point—are then related by

$$r'(z) = n(z) \frac{dr(z)}{dz} = \frac{n(z)r(z)}{R(z)} \quad \text{or} \quad R(z) \equiv \frac{n(z)r(z)}{r'(z)}. \quad (27)$$

Equation 15.27 implies a sign convention in which positive R indicates a diverging spherical wave, as drawn, whereas a negative value of R implies a converging spherical wave.

Suppose such a spherical wavefront with radius R_1 passes through a paraxial system with ray matrix $ABCD$ as in Figure 15.11. Then the emerging wavefront at the other end of the $ABCD$ system will also be a spherical wavefront with radius R_2 , which can be calculated from any one of the output rays by writing

$$\frac{R_2}{n_2} \equiv \frac{r_2}{r'_2} = \frac{Ar_1 + Br'_1}{Cr_1 + Dr'_1} = \frac{A(R_1/n_1) + B}{C(R_1/n_1) + D}. \quad (28)$$

(Note that Figure 15.11 shows a converging output wave, which means its radius of curvature R_2 would be a negative number according to our sign conventions.) More generally, if we define a “reduced radius of curvature” by $\hat{R}(z) \equiv R(z)/n(z)$, then Equation 15.28 in terms of the reduced radii becomes simply

$$\hat{R}_2 = \frac{A\hat{R}_1 + B}{C\hat{R}_1 + D}. \quad (29)$$

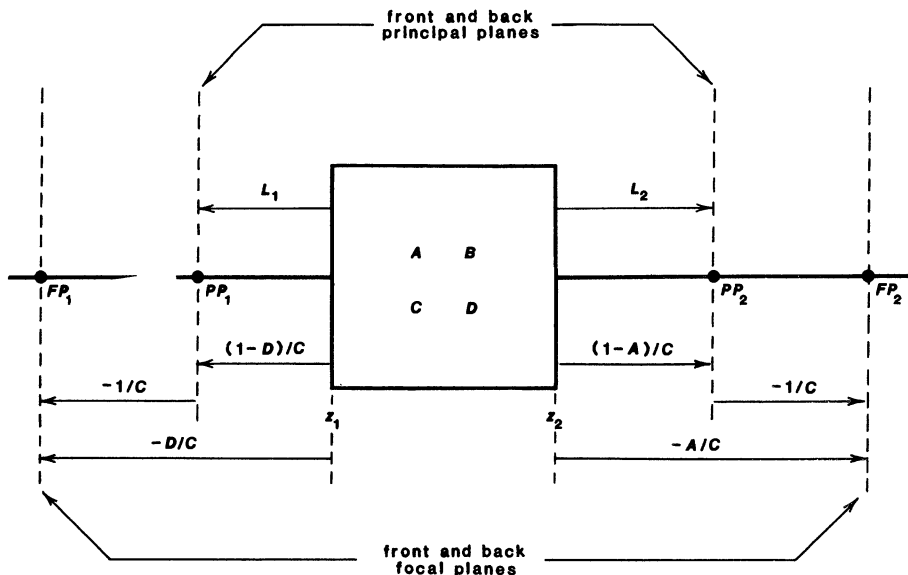


FIGURE 15.12

Front and back principal planes and focal planes for an arbitrary $ABCD$ system treated as a compound lens.

This simple but very general connection between R_1 and R_2 , using only the $ABCD$ matrix, will be very important and useful in later sections. It summarizes all of elementary geometrical optics expressed in ray matrix form.

Thick Lenses and $ABCD$ Matrices

To expand on this last point a bit more, we can note that Equation 15.29 can be manipulated into the alternative form

$$\frac{1}{\hat{R}_2 - L_2} = \frac{1}{\hat{R}_1 - L_1} + \frac{1}{1/C}, \quad (30)$$

with $L_2 \equiv (A - 1)/C$ and $L_1 \equiv (1 - D)/C$. But this expression is obviously just a slightly generalized form of the usual geometrical optics lens formula. It says that the reduced input and output wave curvatures or image and object distances \hat{R}_1 and \hat{R}_2 obey the simple lens law for a thin lens of focal length $f \equiv -1/C$, if these quantities are measured from reference planes located at distances $(1 - D)/C$ and $(A - 1)/C$ behind the input and output planes of the $ABCD$ system.

For simplicity let us consider only the situation where the index of refraction is unity on both sides of the $ABCD$ system, so that $\hat{R} \equiv R$, and the radius R gives the distance to or from the source point for the spherical wave. Then, the two reference planes or *principal planes* for the $ABCD$ system just referred to are located at distances $(1 - D)/C$ and $(1 - A)/C$ behind and in front of the input and output planes z_1 and z_2 of the $ABCD$ system itself, as indicated by the points PP_1 and PP_2 in Figure 15.12. (Note that with our sign convention

for radii of curvature, the output principal plane is located a distance L_2 *behind* the output plane z_2 , or a distance $-L_2 \equiv (1 - A)/C$ in front of it.)

If the input and output rays, or spherical waves, are referenced to these principal planes rather than the original reference planes z_1 and z_2 , the overall $ABCD$ system from input to output principal planes then acts exactly like a thin lens with a focal length $f \equiv -1/C$, as given in Equation 15.30. This lens then also has front and back focal points FP_1 and FP_2 located a distance f outside the principal planes, as indicated in Figure 15.12. Any arbitrary $ABCD$ system with $n_1 = n_2$ is thus equivalent to a thick lens, which can be fully characterized by its two principal planes and its focal length f . If $n_1 \neq n_2$ this conclusion still remains true, but the thick lens must be characterized in a slightly more complex fashion by its *principal*, *focal*, and *nodal* planes; see the Problems at the end of this section for details.

Imaging Properties of $ABCD$ Systems

For the simpler situation of $n_1 = n_2 = 1$, the overall $ABCD$ matrix in Figure 15.12 going from the input to output *principal planes* is then given by

$$M = \begin{bmatrix} 1 & 0 \\ C & 1 \end{bmatrix} \quad \begin{pmatrix} \text{principal plane} \\ \text{to principal plane} \end{pmatrix}. \quad (31)$$

This is the ray matrix for a thin lens with $f = -1/C$. In other words, as we noted in the preceding, the overall $ABCD$ matrix between these planes appears to have an effective length $B = 0$ and a focal power C equivalent to the $ABCD$ matrix itself.

By contrast, the overall $ABCD$ matrix from the input to output *focal planes* is given by

$$M = \begin{bmatrix} 0 & C^{-1} \\ C & 0 \end{bmatrix} \quad \begin{pmatrix} \text{focal plane} \\ \text{to focal plane} \end{pmatrix}. \quad (32)$$

This is the general form of the ray matrix going from focal point to focal point. Note that the apparent length associated with this propagation is $C^{-1} = -f$, even though the actual physical length (for a positive thin lens) is actually $2f$.

More generally, for arbitrary indices, consider an input spherical wave which diverges from an arbitrary *object plane* located at a point OP on the z axis, and is then focused by an arbitrary $ABCD$ system back down to a (real or virtual) *image plane* located at a point IP on the z axis. We can then show that the overall $ABCD$ matrix going from the object plane at OP to the image plane at IP has the general form

$$M = \begin{bmatrix} M & 0 \\ C & 1/M \end{bmatrix} \quad \begin{pmatrix} \text{object plane} \\ \text{to image plane} \end{pmatrix}. \quad (33)$$

Once again the effective length from object plane to image plane is zero, but in the most general situation there will be an *image magnification* M (given in general by $(CR_1 + D)^{-1}$) from any point r_1 in the image plane to the corresponding point r_2 in the output plane. (Note that because the effective length $B \equiv 0$, all the rays leaving from any input point r_1 will pass through the same output point r_2 .)

A *ray-angle demagnification* given by the D element value of $1/M$ is then necessarily associated with this image magnification M . This conclusion repre-

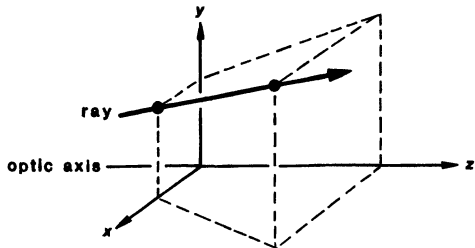


FIGURE 15.13
Ray propagation in two transverse coordinates.

sents, in fact, a paraxial approximation to the more general *sine condition* of optics which says that if a ray leaves a point r_1 in an object plane with angle θ_1 and arrives at a point r_2 in an image plane with an angle θ_2 , these quantities must be related by $n_1 r_1 \sin \theta_1 = n_2 r_2 \sin \theta_2$.

This condition in turn can be given a thermodynamic interpretation: If we collect the blackbody radiation leaving a small area of diameter r_1 and temperature T within a cone angle θ_1 and image it, with lateral magnification M , so that it is incident within cone angle θ_2 onto another small area of diameter $r_2 = Mr_1$, then this incident radiation must just match the blackbody radiation which the second surface area at the same temperature T would emit back into the same cone angle θ_2 . If we take properly into account the difference in blackbody energy densities and velocities in two media with different refractive indices, we can then use the necessity for thermodynamic balance to derive either the more general sine condition, or the ray matrix condition that $AD - BC = 1$.

Ray Matrices in Astigmatic Systems

When cartesian coordinates are used in an optical system, with propagation primarily in the z direction, then a general ray must be described by its transverse displacements in both the x and y directions (Figure 15.13). For simple optical elements the ray matrix formalism just described then applies separately and independently to both the x, x' and y, y' coordinates. If an overall optical system is rotationally symmetric the same $ABCD$ matrices apply equally to both x, x' and to y, y' . If the system contains astigmatic elements, then different $ABCD$ matrices must be used for these elements in the x and y directions, as we will discuss in more detail in a later section.

Other Ray Matrix Properties

Ray matrices have many other interesting and useful properties and applications which we will introduce in this and later chapters. The properties of real ray matrices in periodic systems, in misaligned ray matrix systems, and in nonorthogonal ray matrix systems (systems with “twist”) are discussed in later sections of this chapter. In later chapters we will also show how Huygens’ diffraction integral can be written entirely in terms of ray matrix elements; how ray matrix concepts can be extended and all of paraxial optics explained by generalized or complex ray matrices; and how arbitrary ray matrices can be symmetrized, decomposed and/or synthesized by appropriate transformations.

 Problems for 15.2

1. *Evaluating the focal length of a thin lens.* A thin lens may be regarded as two curved dielectric interfaces with vanishingly small distance between them. Using this viewpoint and the ray matrices for a dielectric interface, find the focal length f of a thin lens in terms of the radii of curvature of the two lens surfaces and the index of refraction n of the lens material.
2. *Replacing an arbitrary “black box” ray matrix with a single lens.* An optical black box has various optical elements inside it, producing a given real $ABCD$ matrix from its input plane to its output plane. We want to replace this black box with a box of physical length L containing only a single lens of focal length f . Can this be done? What length L , focal length f , and lens location within L will be required?
3. *Ray matrix of cascaded elements going in the reverse direction.* A collection of optical elements in series has an overall $ABCD$ matrix going in one direction. Find the $ABCD$ matrix going through the same elements in the reverse direction, i.e., assume the direction of the z axis going through these elements is reversed (or equivalently, assume that the whole system is picked up, turned around, and set back down on the same z axis with all the elements now in reverse order).
4. *Evaluating the total ray matrix for a reflection problem.* A ray passes through a collection of optical elements in series having an overall $ABCD$ matrix; bounces off a mirror of radius R ; and passes back out through the same collection of elements in the reverse direction. What is the total $ABCD$ matrix for the entire round trip?
5. *Replacing an arbitrary ray matrix system with a single mirror.* A certain optical black box has a front entrance plane and various lenses and mirrors inside it, such that a ray entering the entrance plane eventually comes back out through the same plane with a total ray transformation given by a known $ABCD$ ray matrix. Suppose this black box is to be replaced by a single curved mirror of radius R located an appropriate distance L behind (or, if necessary, in front of) the entrance plane of the box. Find the required radius R and position L of the single curved mirror.
6. *Focusing properties of thick-lens $ABCD$ matrices.* Verify the $ABCD$ matrix equations (15.31-15.33) given in the text for transfer between input and output principal planes and between input and output focal planes (for $n_r = 1$), and more generally between object and image planes (for arbitrary n_r).
7. *General formulas for an arbitrary thick lens or $ABCD$ system* The focal, principal and nodal planes for an arbitrary thick lens or $ABCD$ system having input and output reference planes z_1 and z_2 and input and output indices of refraction n_1 and n_2 are defined by the conditions that:
 - (1) An input spherical wave emanating from the input focal point FP_1 and passing through the $ABCD$ system will emerge as an output plane wave; whereas an input plane wave will emerge as a spherical wave which converges to (or appears to diverge from) the output focal point FP_2 .
 - (2) If an input ray r_1 which comes from the input focal point FP_1 , and the output ray r_2 parallel to the output axis which it produces, are extended forward or

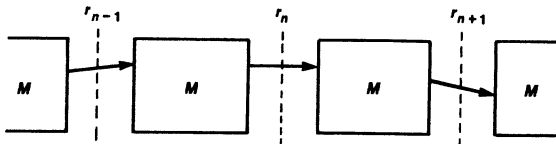


FIGURE 15.14
Analytical model for a periodic focusing system.

backward until they intersect, their intersection point defines the input principal plane PP_1 . Similarly, the intersection of a parallel input ray r_1 and the output ray r_2 which it produces defines the output principal plane PP_2 .

- (3) If an input ray with coordinates r_1, r'_1 produces a parallel output ray, i.e., $r'_2 = r'_1$, then the line connecting the input and output points r_1, z_1 and r_2, z_2 crosses the optical axis at the *optical center OC* of the lens. If extensions of the same entering and exit rays are constructed, these rays then intersect the optical axis at the *front and back nodal planes* NP_1 and NP_2 of the lens.

(To put this in another way, Ditchburn speaks of any pair of planes which are imaged onto each other as *conjugate planes*, and then says, “The plane conjugate to a plane at an infinitely great distance from the system in a positive direction is called the first focal plane . . . In a similar way the second focal plane is conjugate to a plane infinitely distant in the negative direction.” Also, “Any ray which before entering the system is directed toward the first nodal point will emerge with its final direction parallel to the original direction and passing through (or coming from) the second nodal point,” and finally, the principal planes of a thick lens “. . . are conjugate planes of unit positive magnification,” i.e., any input ray which, when projected, intersects the first principal plane at $r_1 = a$ and any slope r'_1 will produce an output ray which intersects the second plane at the same distance $r_2 = a$).

From these definitions, find general formulas for the locations of all these points or planes for an arbitrary $ABCD$ system with $n_1 \neq n_2$, and then illustrate by calculating the actual locations for some representative systems, such as a thick lens with curved front and back faces, or a section of a quadratic duct.

15.3 RAYS IN PERIODIC FOCUSING SYSTEMS

Perhaps the most interesting and important application of ray matrices comes in the analysis of *periodic focusing systems*, i.e., systems in which the same sequence of elements is repeated many times down a cascaded chain or optical lensguide. An optical resonator can be modeled, as we have already shown in Figure 14.3, by such an iterated periodic focusing system. The eigenvalues and “eigenrays” for such periodic focusing systems play an important role in optical resonator theory, particularly in explaining the stable and unstable properties of optical resonators and lensguides. The stability analysis for periodic optical focusing that we will present here will also apply equally well to periodic particle focusing systems, such as electron beams in periodically focused traveling-wave tubes or in linear accelerators.

Eigenvalues and Eigenrays

Let the ray matrix for propagation through one period in such a system, from an arbitrary reference plane in one period to the corresponding plane one period later (see Figure 15.14), be denoted by \mathbf{M} . The ray vectors \mathbf{r}_n and \mathbf{r}_{n+1} at the n -th and $n+1$ -th reference planes are then related by

$$\mathbf{r}_{n+1} = \mathbf{M} \mathbf{r}_n = \mathbf{M}^{n+1} \mathbf{r}_0, \quad (34)$$

where \mathbf{r}_0 is the initial ray at the input plane $p = 0$, and \mathbf{M}^{n+1} is the matrix for one period raised to the $n+1$ -th power.

Any cascaded matrix problem such as this can best be analyzed by finding the eigenvalues and eigensolutions of the matrix \mathbf{M} . That is, we look for a set of “eigenrays” \mathbf{r} and corresponding eigenvalues λ (no connection with optical wavelength λ) which each individually satisfy the eigenequation

$$\mathbf{M} \mathbf{r} = \lambda \mathbf{r}. \quad (35)$$

For a 2×2 ray matrix \mathbf{M} this is equivalent to the equation

$$[\mathbf{M} - \lambda \mathbf{I}] \mathbf{r} = 0 \quad \text{or} \quad \begin{bmatrix} A - \lambda & B \\ C & D - \lambda \end{bmatrix} \begin{bmatrix} r \\ r' \end{bmatrix} = 0, \quad (36)$$

where \mathbf{I} is the identity matrix.

Nonzero solutions to Equation 15.36 are possible if and only if the determinant of the matrix in this equation satisfies the relation

$$\begin{vmatrix} A - \lambda & B \\ C & D - \lambda \end{vmatrix} \equiv \lambda^2 - (A + D)\lambda + 1 = 0, \quad (37)$$

where we have used the fact that $AD - BC = 1$. It is convenient to define an “ m parameter” for the system, equal to half the trace of the $ABCD$ matrix, or

$$m \equiv \frac{A + D}{2}. \quad (38)$$

The ray matrix eigenvalues are then given by the two values

$$\lambda_a, \lambda_b = m \pm \sqrt{m^2 - 1} \quad (39)$$

which obey the general relationship that

$$\lambda_a \lambda_b \equiv 1. \quad (40)$$

There are also two matching eigenrays \mathbf{r}_a and \mathbf{r}_b , which the reader can calculate for herself, such that

$$\mathbf{M} \mathbf{r}_a = \lambda_a \mathbf{r}_a \quad \text{and} \quad \mathbf{M} \mathbf{r}_b = \lambda_b \mathbf{r}_b. \quad (41)$$

The properties of these eigenvalues and eigenrays are fundamental to the theory of stable and unstable optical resonators, as we shall now see.

Eigenray Expansions

It is a fundamental property of these matrix eigensolutions that any arbitrary ray \mathbf{r}_0 at the input to the periodic system (or for that matter at any other plane) can always be expanded as a sum of the two eigenrays of the system in the form

$$\mathbf{r}_0 = c_a \mathbf{r}_a + c_b \mathbf{r}_b, \quad (42)$$

where c_a and c_b are suitable expansion coefficients. The ray vector after any number of sections n will then be given by

$$\begin{aligned} \mathbf{r}_n &= \mathbf{M}^n \mathbf{r}_0 = \mathbf{M}^n \times (c_a \mathbf{r}_a + c_b \mathbf{r}_b) \\ &= c_a \times \lambda_a^n \mathbf{r}_a + c_b \times \lambda_b^n \mathbf{r}_b. \end{aligned} \quad (43)$$

The propagation of each eigenray is thus specified simply by multiplying it by the corresponding eigenvalue raised to the appropriate power. The eigenrays and their matching eigenvalues therefore contain all the information that is needed to fully describe the propagation of any arbitrary ray in the periodic system.

Stable Periodic Focusing Systems

All such periodic focusing systems (with purely real ray matrices) can in fact be neatly divided into either *stable* or *unstable periodic systems*, depending only on the properties of the matrix eigenvalues.

Suppose first that the ray matrix for one period has A and D coefficients such that

$$-1 \leq m \leq 1, \quad \text{or} \quad m^2 \equiv \left(\frac{A+D}{2} \right)^2 \leq 1. \quad (44)$$

In this situation we may write the m parameter as

$$m \equiv \frac{A+D}{2} \equiv \cos \theta, \quad (45)$$

where θ is the angle defined by this expression. The eigenvalues of the system can then be written as

$$\lambda_a, \lambda_b = m \pm j\sqrt{1-m^2} = \cos \theta \pm j \sin \theta = e^{\pm j\theta}. \quad (46)$$

The matrix eigenvalues are thus complex and have magnitude unity. The propagation of any ray in the periodic system then takes the form

$$\mathbf{r}_n = c_a \mathbf{r}_a \times e^{jn\theta} + c_b \mathbf{r}_b \times e^{-jn\theta} = \mathbf{r}_0 \cos \theta n + \mathbf{s}_0 \sin \theta n, \quad (47)$$

where $\mathbf{r}_0 \equiv c_a \mathbf{r}_a + c_b \mathbf{r}_b$ is the input ray vector, and $\mathbf{s}_0 \equiv j(c_a \mathbf{r}_a - c_b \mathbf{r}_b)$ is a kind of "input slope vector."

Any periodic focusing system with $|m| \leq 1$ thus represents a *stable periodic focusing system*, analogous to a stable duct. Rays in the system will oscillate back and forth about the axis, as in Figure 15.15, with a maximum excursion determined entirely by the initial ray parameters \mathbf{r}_0 and \mathbf{s}_0 . The displacement \mathbf{r}_n of any ray at successive reference planes down the system will oscillate periodically about the axis in the form

$$\mathbf{r}_n = \mathbf{r}_0 \cos \theta n + \mathbf{s}_0 \sin \theta n, \quad (48)$$

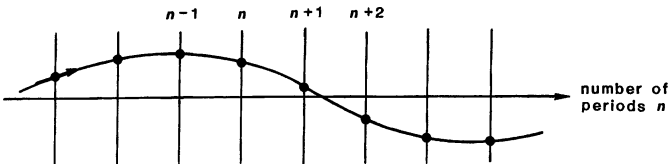


FIGURE 15.15
Ray trajectory in a stable periodic system.

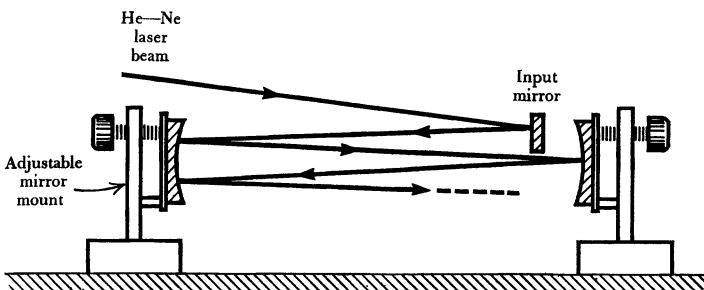


FIGURE 15.16
A simple demonstration of a stable periodic focusing system or optical delay line, using a pair of silvered mirrors and a He-Ne laser beam.

where r_0 and s_0 are the ray initial conditions. Note that it is the index n , and not the angle θ , that is the variable which increases with distance down the chain.

Note also that Equations 15.47 and 15.48 only give the displacement r_n as measured at the successive reference planes—they do not say anything about what happens to the ray inside the periodic section between those reference planes. Viewed only at the successive reference planes, however, the ray appears to oscillate about the axis of the periodic focusing system as in Figure 15.15, with an oscillation period equal to $2\pi/\theta$ periods of the periodic focusing system itself.

Periodic Focusing Demonstration

Any reader who has the opportunity should set up a simple demonstration of such a stable periodic focusing system, using a pair of silvered mirrors perhaps 10 to 15 cm in diameter with a 50 cm to 1 m focal length, as illustrated in Figure 15.16. (Suitable inexpensive mirrors and simple mirror mounts are available from hobby stores or amateur astronomy supply houses.) The beam from a He-Ne laser can be injected at one edge of the resonator, using a small adjustable injection mirror just inside the edge of one of the larger mirrors.

Thoughtful adjustment of the beam injection direction and the mirror spacing and alignment will then lead to various kinds of periodically repeating spot patterns on the end mirrors. A little chalk dust or smoke can make the interlaced beam patterns inside the resonator dramatically visible in a darkened room, although a more effective way to make the beams visible without fouling the mirrors is to attach a few strands of white cord or thin wire to the shaft of a

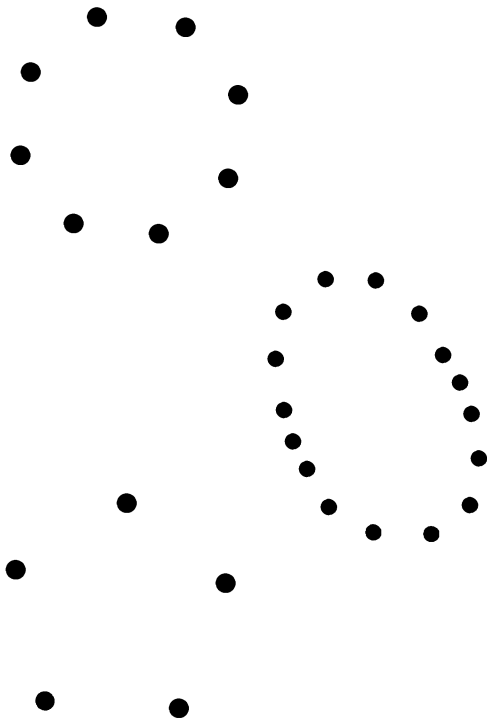


FIGURE 15.17

Depending upon the spacing and alignment of the mirrors, and the injection conditions for the laser beam, the system shown in Figure 15.16 will produce spot patterns on the end mirrors like those illustrated in this figure.

small electric motor so that they sweep transversely across the resonator like a soft buzzsaw.

Note that the periodic solutions derived in Equation 15.47 and 15.48 will apply equally well to both of the transverse displacements x_n and y_n , with appropriate (and in general different) initial conditions in each transverse coordinate. The beam in a stable periodic focusing system should thus oscillate sinusoidally about the axis with the same period in both x and y (assuming no astigmatism in the optical system). The oscillations will however in general have different amplitudes and phases in the two directions, depending upon the initial conditions.

But this is just the necessary condition for producing Lissajou figures, except that the Lissajou figures in this situation will be discrete spot patterns at integer values of n rather than continuous line patterns. In the demonstration apparatus, therefore, the successive spots at which the ray strikes either of the end mirrors will trace out a Lissajou pattern with the same frequency or period in the x and y directions. By adjusting the initial beam conditions to vary the phase and amplitude between the x and y oscillations, we can obtain arbitrary circular, elliptical or linear spot patterns (for examples, see Figure 15.17).

Inspection will also show (and we will later verify analytically) that the gaussian laser beam in such a periodic focusing system does not spread due to diffraction as we might expect, even after a large number of round-trip bounces. The

same stability conditions that make the ray trajectory stable but oscillatory inside the resonator also make the laser beam spot size be periodically refocused at each mirror. The beam spot size at different points may then oscillate periodically, but it also remains bounded and stable over an indefinite number of round trips.

With proper adjustment we can also catch the laser beam and extract it from the cavity with an extraction mirror (or even with the injection mirror) after any integral number of one-way bounces. The optical delay time in such a cavity is ~ 6 nsec per round trip for a 1 m long cavity, and with more expensive high-quality mirrors the power loss per bounce can be quite small. Reentrant optical cavities of this type can thus function as optical delay lines. Such delay lines were once seriously considered as potential high-capacity optical memories (with the cavity filled with coded information in the form of very short optical pulses); and they have also been used a number of times as optical delay lines in various scientific experiments.

Unstable Periodic Focusing Systems

Let us now turn to the opposite example, that of an *unstable periodic focusing system*, in which the ray matrix for one period has instead the property that

$$m^2 \equiv \left(\frac{A + D}{2} \right)^2 > 1 \quad \text{or} \quad |m| > 1. \quad (49)$$

The eigenvalues of the system will then have the values

$$\lambda_a, \lambda_b = m \pm \sqrt{m^2 - 1} = M, 1/M, \quad (50)$$

where M is a “transverse magnification per period,” with the property that $|M| > 1$. The ray displacement in this situation will obey the formula

$$\mathbf{r}_n = M^n \times c_a \mathbf{r}_a + M^{-n} \times c_b \mathbf{r}_b = \mathbf{r}_0 \cosh \theta n + \mathbf{s} \sinh \theta n, \quad (51)$$

where $\theta \equiv \ln M$ and \mathbf{r}_0 and \mathbf{s}_0 again represent initial conditions at the start of the periodic system.

The ray displacement \mathbf{r}_n in this situation will diverge exponentially with distance down the chain, as shown in Figure 15.18, with the displacements and slopes magnifying by a magnification M in each period. There will also be at first a demagnifying component to the trajectories, decreasing as $1/M$ per section, but this will die out after a few sections. Note that the ray position may also oscillate back and forth across the ray axis in alternate periods, depending on whether the magnification has a value $M < -1$ or $M > +1$. Such unstable periodic focusing systems have an important practical application in the unstable laser resonators we will describe later.

REFERENCES

Periodic lens waveguides were once of great interest because of what seemed to be their potential for long-distance communications through underground pipes (optical fibers now seem to have made this concept obsolete). Gas lenses and other interesting concepts were invented for use in these optical lensguides. Records of some of these experiments

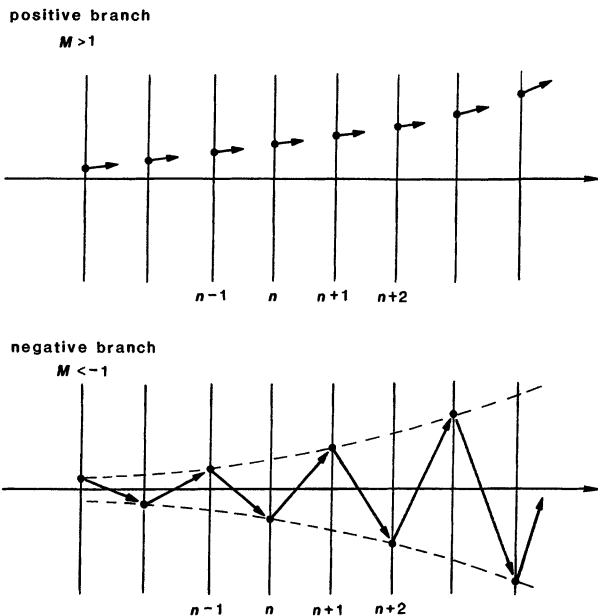


FIGURE 15.18

Unstable periodic focusing systems of the "positive-branch" and "negative-branch" types.

can be found in D. Gloge, "Experiment with an underground lens waveguide," *Bell Sys. Tech. J.* **46**, 721-735 (April 1967); and in D. Gloge and W. H. Steier, "Pulse shuttling in a half-mile optical lens guide," *Bell Sys. Tech. J.* **47**, 767-782 (May-June 1968).

Problems for 15.3

1. *Properties of the eigenrays in a periodic system.* Calculate the two eigenrays r_a and r_b for a periodic focusing system in terms of the $ABCD$ matrix elements. Note that any physically meaningful ray in the periodic system must be purely real, i.e., must have purely real displacement and slope, yet the eigenvectors r_a and r_b for a stable periodic system are in general complex quantities. How can this be true? Under what conditions (if any) can individual eigenrays be individually or separately excited in the periodic system?
2. *Ray properties of an elementary periodic lensguide.* Calculate the ray eigenvalues and eigenrays for the simplest type of lens waveguide, namely repeated identical convergent lenses of focal length f spaced a distance L apart, using the midpoint between lenses as the reference plane. Use the notation $L = 4f(1 - \Delta)$, and discuss the mathematical behavior and the physical significance of the eigenvalues and eigenrays as the lens spacing is increased toward the value $L \rightarrow 4f$ or $\Delta \rightarrow 0$. What would be the optical resonator analog to this limit?

Try repeating this problem working from reference planes located at the mid-planes of the lenses (i.e., half the lens focusing power is placed on each side of the reference plane); and compare the eigenvalues at this reference plane to the eigenvalues at the previous reference plane.

3. *Computer plotting of periodic ray positions.* Write a simple computer program to compute and plot (on some suitable plotter or printer) the x, y positions on one end mirror on successive bounces for a ray bouncing through repeated round trips inside a resonator of length L with two identical end mirrors having radii of curvature R . Allow for arbitrary initial ray injection conditions and also for astigmatic mirrors, i.e., mirrors having different curvatures R_x and R_y in the x and y transverse directions.

Experiment with different spacings, curvatures, and injection conditions to find the kinds of trajectories the spot will follow around the transverse plane on one end mirror, noting particularly how the spot moves around the mirror from bounce to bounce. (You might also plot side or top views of how the rays bounce in the resonator, or examine the spot patterns at planes inside the resonator other than the end mirror.)

4. *Periodic systems with integer numbers of spots.* Suppose you have set up either the computer simulation outlined in the previous problem, or a working optical delay line model using a He-Ne laser and two identical mirrors with variable spacing. Then you can discover that as you change the spacing between mirrors (with fixed mirror radii R), there are certain spacings L for which the beam produces an exactly integral number of spots on each mirror before returning back to the same point where it is injected. (a) Find an expression for the mirror spacings L_n at which there are exactly n spots produced on each mirror, in terms of the radius of curvature R of the two identical mirrors. (b) If the input beam is injected properly the spots on the end mirrors walk around a circular orbit. At any transverse plane in between the mirrors the spots then lie on a circle also, but of smaller diameter than on the end mirrors (the rays lie on a hyperboloid of revolution). Find the ratio between the diameters of the spot circles at the center of the resonator and on the end mirrors.
5. *Alignment procedure for the periodic delay line demonstration.* There is a simple sequence of steps one can follow, using the injected laser beam, to get the optical delay line demonstration initially aligned, with the two mirrors properly aligned to each other, and with the injected beam properly aligned to the resonator. Can you describe how this should be done?
6. *Eigenray solutions for a near-spherical optical resonator.* Find the ray matrix eigenvalues and eigenvectors for a near-spherical resonator (i.e., $R_1 = R_2 \approx 2L$), using the midplane of the resonator as the reference plane. Discuss the physical significance of the results in the limiting situation of an exactly spherical resonator.
7. *Perturbation stability of periodic focusing eigenrays.* Suppose that a ray starts out in a periodic focusing system as primarily one of the eigenrays, say, the \mathbf{r}_a eigenray, but with a small perturbation or a small amount of the other eigenray \mathbf{r}_b mixed in, so that $\mathbf{r}_1 = \alpha_1 \mathbf{r}_a + \beta_1 \mathbf{r}_b$, with $\beta_1 \ll \alpha_1$. Show that on each successive round trip the relative amount of the \mathbf{r}_b component in the ray mixture will grow as λ_b^2 . In other words, show that any small perturbation about either one of the eigensolutions will grow (or decay) with a “perturbation eigenvalue” that is equal to the ray eigenvalue of the other eigensolution squared.

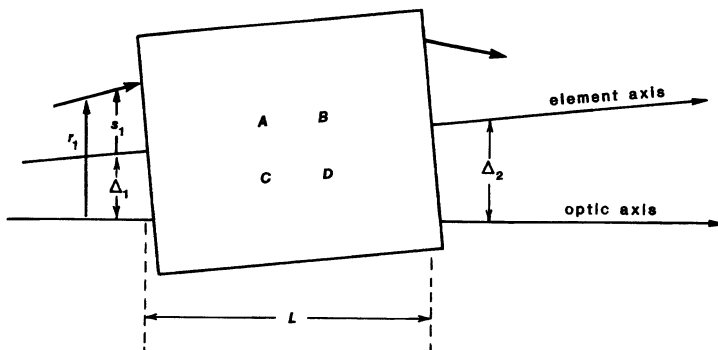


FIGURE 15.19

Notation for analyzing a misaligned paraxial optical element.

8. *Ray intersections inside an optical resonator.* In a multiple-pass optical delay line as described in this section, optical rays on different bounces will intersect each other (at least in one transverse dimension) at certain locations inside the cell. Analyze the locations of these intersections, and find the total number of such intersections within a cell as a function of the multiple-pass cell design. Note that beam intersections within such a cell can be significant where nonlinear optical interactions are important, for example, in the multiple-pass Raman gain cells described by B. Perry, et al., "Controllable pulse compression in a multiple-pass-cell Raman laser," *Optics Lett.* 5, 288–290 (July 1980).

15.4 RAY OPTICS WITH MISALIGNED ELEMENTS

The ray matrix formalism we have used thus far assumes that all the paraxial elements are properly aligned and centered with respect to the optical reference axis. What effects will misalignment or transverse misplacement of individual optical elements have on the overall ray matrix performance?

Analysis of Misaligned Elements

To answer this question let us first consider the effects of misalignment on a single optical element, or perhaps a collection of elements forming a single internally aligned *ABCD* system. In order to analyze this situation, we must from here on distinguish between the real physical axis (the "true optical axis") of any individual paraxial element or *ABCD* system, which we will call its *element axis*, and the reference optical axis we use for analyzing the rays in this optical system, which may be arbitrarily chosen, and which we will call the *reference optical axis* or just the *optical axis*, as in Figure 15.19.

Suppose then that the element axis of some arbitrary *ABCD* system, with overall length *L*, is displaced from the reference optical axis by displacements Δ_1 and Δ_2 at the input and output ends, as in Figure 15.19. The element axis is thus also misaligned in slope with respect to the reference axis by the (small)

angle

$$\Delta' \equiv \frac{\Delta_2 - \Delta_1}{L}. \quad (52)$$

The misalignment of an individual element or collection of $ABCD$ elements with respect to the reference axis can thus be characterized by any two of the three parameters Δ_1 , Δ_2 , Δ' . (Note that Δ' is a real, not a reduced slope.)

We can also express this misalignment of the paraxial system by two “misalignment vectors” at its input and output ends, as given by

$$\Delta_1 \equiv \begin{bmatrix} \Delta_1 \\ \Delta'_1 \end{bmatrix} \quad \text{and} \quad \Delta_2 \equiv \begin{bmatrix} \Delta_2 \\ \Delta'_2 \end{bmatrix}. \quad (53)$$

where $\Delta'_1 \equiv n_1 \Delta'$ and $\Delta'_2 \equiv n_2 \Delta'$ are the reduced values of the element axis slope at each end. The two misalignment vectors will then be connected by

$$\Delta_2 \equiv \begin{bmatrix} \Delta_2 \\ \Delta'_2 \end{bmatrix} = \begin{bmatrix} 1 & L/n_1 \\ 0 & n_2/n_1 \end{bmatrix} \begin{bmatrix} \Delta_1 \\ \Delta'_1 \end{bmatrix} \equiv M_\Delta \times \Delta_1, \quad (54)$$

where M_Δ is shorthand for the 2×2 matrix in this equation.

The coordinates of any general ray vector as measured with respect to the arbitrary reference optical axis we will then continue to denote by r, r' as before, whereas the same ray vector measured with respect to the element axis we will denote by s, s' . These quantities are then related at the input plane by

$$r_1 = s_1 + \Delta_1 \quad \text{and} \quad r'_1 = s'_1 + \Delta'_1, \quad (55)$$

and similarly for r_2 and r'_2 . Hence, in vector notation,

$$r_2 = s_2 + \Delta_2 \quad \text{and} \quad r_1 = s_1 + \Delta_1. \quad (56)$$

(We assume small angles, so that we can simply add the slopes.)

Now, the ray vectors measured with respect to the element axis will transform through the $ABCD$ element in the usual fashion, namely

$$s_2 \equiv \begin{bmatrix} s_2 \\ s'_2 \end{bmatrix} = \begin{bmatrix} A & B \\ C & D \end{bmatrix} \begin{bmatrix} s_1 \\ s'_1 \end{bmatrix} \equiv M \times s_1, \quad (57)$$

where M is the $ABCD$ matrix for the aligned element(s). However, the input and output displacements and slopes measured with respect to the reference optical axis will now be given, in matrix terms, by

$$r_2 = s_2 + \Delta_2 = M s_1 + M_\Delta \Delta_1 = M r_1 + [M_\Delta - M] \Delta_1 \quad (58)$$

which we will rewrite in general terms as

$$r_2 = M r_1 + E. \quad (59)$$

The primary effect of misalignment on a paraxial system is to add to the usual ray matrix transformation what we might call an “error vector” E which is given by

$$E \equiv \begin{bmatrix} E \\ F \end{bmatrix} = [M_\Delta - M] \Delta_1 = \begin{bmatrix} 1 - A & L - n_1 B \\ -C & n_2 - n_1 D \end{bmatrix} \begin{bmatrix} \Delta_1 \\ \Delta' \end{bmatrix} \quad (60)$$

in terms of the usual $ABCD$ matrix elements and the misalignment quantities Δ_1 and Δ' .

Three-by-Three Matrix Formalism for Misaligned Systems

These results for a general misaligned paraxial system can be put into a convenient 3×3 matrix form by adding a third dummy element of value unity to each of the ray vectors, and then writing a 3×3 "ABCDEF" matrix relation in the form

$$\begin{bmatrix} r_2 \\ r'_2 \\ 1 \end{bmatrix} = \begin{bmatrix} A & B & E \\ C & D & F \\ 0 & 0 & 1 \end{bmatrix} \times \begin{bmatrix} r_1 \\ r'_1 \\ 1 \end{bmatrix}, \quad (61)$$

where the two additional ray matrix quantities E and F are given by the results derived in Equation 15.60, namely,

$$E = (1 - A)\Delta_1 + (L - n_1 B)\Delta' \quad \text{and} \quad F = -C\Delta_1 + (n_2 - n_1 D)\Delta'. \quad (62)$$

These 3×3 matrices can then be cascaded, perhaps with the aid of a simple computer program, to handle several such misaligned paraxial elements connected in series.

Cascaded Misaligned Elements

Suppose several successive optical elements or groups of elements are arranged in cascade, with each element or group of elements having a different degree of (small) misalignment, and hence different E_i and F_i elements, as well as the usual A_i , B_i , C_i , D_i elements. (These individual misalignments are all measured relative to a common reference optical axis passing, in a straight line, through the whole collection.) We can then cascade these 3×3 ray vectors and ray matrices (in reverse order, as usual) to propagate rays through any sequence of cascaded, and individually misaligned, paraxial systems, each with its own ABCD elements and its own distinct EF misalignment elements.

Rather than multiplying and manipulating 3×3 matrices, however, we can analyze the same situation in a more convenient fashion by rewriting Equation 15.61 on the partitioned matrix form

$$\begin{bmatrix} r_2 \\ 1 \end{bmatrix} = \left[\begin{array}{c|c} \mathbf{M} & \mathbf{E} \\ \mathbf{O} & 1 \end{array} \right] \begin{bmatrix} r_1 \\ 1 \end{bmatrix}, \quad (63)$$

where \mathbf{M} is the usual 2×2 ABCD matrix; r_1 , r_2 and \mathbf{E} are 2×1 column matrices; \mathbf{O} is a 1×2 row matrix with both elements 0; and 1 is a single "1×1" element. Partitioned matrices of this sort can then be multiplied out analytically by applying the usual rules of matrix multiplication treating each individual submatrix within the partitioned matrix as a fixed element.

Suppose we wish to cascade just two individually misaligned ABCD systems in sequence. The overall 3×3 matrix for the cascaded system can then be calculated from

$$\begin{aligned} \left[\begin{array}{c|c} \mathbf{M}_{\text{tot}} & \mathbf{E}_{\text{tot}} \\ \mathbf{O} & 1 \end{array} \right] &= \left[\begin{array}{c|c} \mathbf{M}_2 & \mathbf{E}_2 \\ \mathbf{O} & 1 \end{array} \right] \times \left[\begin{array}{c|c} \mathbf{M}_1 & \mathbf{E}_1 \\ \mathbf{O} & 1 \end{array} \right] \\ &= \left[\begin{array}{c|c} \mathbf{M}_2 \mathbf{M}_1 & \mathbf{M}_2 \mathbf{E}_1 + \mathbf{E}_2 \\ \mathbf{O} & 1 \end{array} \right]. \end{aligned} \quad (64)$$

As a check the reader may want to multiply out the full 3×3 matrices in non-partitioned form to verify that the final result is indeed

$$\left[\begin{array}{c|c} \mathbf{M}_{\text{tot}} & \mathbf{E}_{\text{tot}} \\ \hline \mathbf{O} & 1 \end{array} \right] = \left[\begin{array}{ccc} A_2 A_1 + B_2 C_1 & A_2 B_1 + B_2 D_1 & A_2 E_1 + B_2 F_1 + E_2 \\ C_2 A_1 + D_2 C_1 & C_2 B_1 + D_2 D_1 & C_2 E_1 + D_2 F_1 + F_2 \\ 0 & 0 & 1 \end{array} \right], \quad (65)$$

or the same as given by the partitioned form.

We see first of all that the 2×2 or $ABCD$ part of the overall cascaded, misaligned system has exactly the same form as the product of the two matrices would have without misalignment, since this part of the product does not depend at all on the misalignment values E_1, F_1 or E_2, F_2 of the individual elements. To phrase this more generally, *the basic ray matrix properties and paraxial focusing properties of a cascaded system are entirely unchanged by small misalignments of individual elements within the system.*

Overall Misaligned Systems

These same conclusions obviously remain true even if we cascade an arbitrary number of arbitrarily misaligned paraxial elements. Suppose we propagate an initial ray r_0 through N such elements or subsystems, each with an individual misalignment described by an error vector $\mathbf{E}_k \equiv [E_k, F_k]$ as referenced to a single straight-line optical axis through the overall system.

The overall transformation through the cascaded system can then be written as

$$\mathbf{r}_N = \mathbf{M}_{\text{tot}} \mathbf{r}_0 + \mathbf{E}_{\text{tot}}, \quad (66)$$

where the overall $ABCD$ matrix is given as usual by the matrix product $\mathbf{M}_{\text{tot}} = \mathbf{M}_N \cdots \mathbf{M}_2 \mathbf{M}_1$, and where the cumulative “error vector” through the entire system is given in terms of the error vectors of the individual elements by

$$\mathbf{E}_{\text{tot}} = [\mathbf{M}_N \cdots \mathbf{M}_2] \mathbf{E}_1 + [\mathbf{M}_N \cdots \mathbf{M}_3] \mathbf{E}_2 + \cdots + \mathbf{M}_N \mathbf{E}_{N-1} + \mathbf{E}_N. \quad (67)$$

The overall misalignment elements E_{tot} and F_{tot} for the cascaded system obviously involve the misalignments E_k, F_k of each individual element in the system, as “propagated” through the $ABCD$ matrices of all the subsequent elements in the system. In a cascaded $ABCD$ system with misaligned individual elements, the overall system will thus appear to have a total misalignment $E_{\text{tot}}, F_{\text{tot}}$ that depends in a complicated way both on the misalignment of individual elements and on the transmission of each of these individual misalignments through the individual $ABCD$ matrices of all later elements.

System Alignment, and the Overall Element Axis

Suppose we do the kind of calculation just outlined, and find the overall misalignment parameters E_{tot} and F_{tot} for some particular cascaded system, using some particular arbitrarily chosen reference optical axis that passes in a straight line through the entire system. The preceding results then imply that the overall system acts as if it is a single properly aligned overall system, but one whose overall element axis has end-plane displacements Δ_0 and Δ_N at its

input and output ends like those in Figure 15.20, measured with respect to the reference optical axis that we used in doing all the calculations.

Any system with misaligned individual elements can thus obviously be converted into an effectively aligned overall system, having $E_{\text{tot}} = F_{\text{tot}} = 0$, either by a physical translation and rotation of the overall system to bring its overall element axis into coincidence with the reference optical axis, or equivalently by a redefinition of the reference optical axis to bring it into coincidence with the system's element axis. That is, any overall values of $E = E_{\text{tot}}$ and $F = F_{\text{tot}}$ for the overall system can be canceled out by physically translating the entire system as a unit downward an amount Δ_0 given by

$$\Delta_0 = \frac{(1 - D)E - (L - B)F}{(1 - A)(1 - D) + (L - B)C}, \quad (68)$$

and then physically rotating it toward the system axis, with center of rotation at the input plane, by the angle

$$\Delta' = \frac{CE + (1 - A)F}{(1 - A)(1 - D) + (L - B)C}, \quad (69)$$

where all the quantities A, B, C, D, E, F and L in these expressions are the overall values for the cascaded system. Once this is done the overall system will look perfectly well aligned, despite the individual misalignments of its various internal elements.

Misaligned Resonators or Periodic Systems

A slightly different viewpoint and approach can also be useful in discussing the ray matrix properties of an optical resonator, or its equivalent iterated periodic focusing system, in the situation where individual optical elements inside the resonator may be misaligned.

Suppose we unfold an optical resonator having one or more misaligned internal elements into an equivalent periodic system. Each individual period of the resulting lensguide, corresponding to one round trip in the resonator, will then have an overall element axis, with respect to which that individual period or round trip will look like an ideal aligned system. *This element axis, however, in general will not come back on itself after one round trip—that is, the element axis in each individual period may be tilted with respect to the reference optical axis running through the repeated sections of the lensguide, so that the element axes in successive periods do not connect to each other.*

Is there then some better or alternative way to define an effective axis in a misaligned resonator or periodic system? To answer this question we might recall that the distinguishing characteristic of the axis in an aligned paraxial system is that a ray vector which starts out exactly aligned along the axis always remains exactly on the axis. We might ask therefore if, starting from any given reference plane within a misaligned resonator or periodic system, there will be some unique “axis ray,” let us label it by r_0 , whose displacement and slope (measured with respect to the reference optical axis) will exactly repeat themselves after one period or one round trip through this ABCDEF system?

Such a ray, which self-reproduces after one round trip, is given by the conditions that

$$Mr_0 + E = r_0 \quad \text{or} \quad r_0 = (I - M)^{-1} E, \quad (70)$$

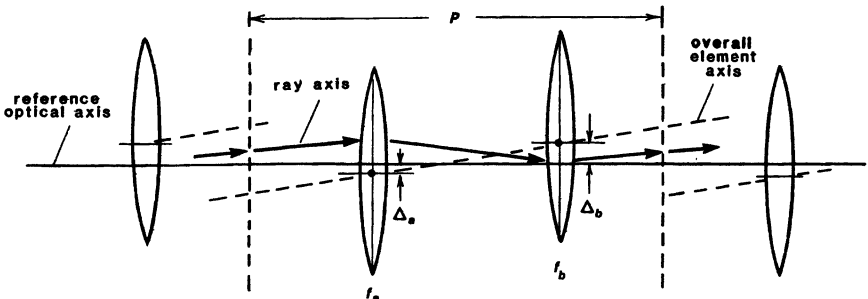


FIGURE 15.20

A misaligned periodic focusing system, in which each period of the system has its element axis misaligned with respect to the reference optical axis of the overall system.

where \mathbf{I} is the identity matrix, and the -1 superscript means the inverse of the matrix within the parentheses. If we carry out the algebra, we can find that the displacement and slope of this “axis ray” are given (at this one particular reference plane) by

$$\mathbf{r}_0 \equiv \frac{(1 - D)\mathbf{E} + B\mathbf{F}}{2 - A - D} \quad \text{and} \quad \mathbf{r}'_0 \equiv \frac{C\mathbf{E} + (1 - A)\mathbf{F}}{2 - A - D}. \quad (71)$$

It is then easy to show that the transformation of any other input ray \mathbf{r}_1 through the misaligned system is given by

$$(\mathbf{r}_2 - \mathbf{r}_0) = \mathbf{M} \times (\mathbf{r}_1 - \mathbf{r}_0), \quad (72)$$

where the $ABCD$ elements are the round-trip elements starting from and coming back to some particular reference plane inside the resonator. This particular ray \mathbf{r}_0 then represents a kind of misaligned “natural optical axis” for the misaligned periodic system, as observed at this particular reference plane.

The resonator or periodic system becomes in effect a well-aligned $ABCD$ system if the input and output ray coordinates are measured relative to the axis ray $\mathbf{r}_0 \equiv [\mathbf{r}_0, \mathbf{r}'_0]$ at the particular reference plane z_0 used to define the $ABCDEF$ matrix elements. If a ray starts around the resonator with input displacement and slope given by \mathbf{r}_0 , it will return to this same position on every successive round trip. Any other ray, however, starting off with different initial values, will oscillate about this ray (or possibly diverge from it) in exactly the stable or unstable periodic fashion described earlier for aligned periodic systems.

Differences Between the Axis Ray and the Overall Element Axis

We note again that the axis ray for a misaligned resonator or periodic system is not the same in general as the “overall element axis” we discussed a few paragraphs back. The overall element axis through a given collection of misaligned elements is a *straight line* through these elements, as in Figure 15.20, such that if the ray displacements and slopes are measured relative to this axis, the overall system will act like an aligned 2×2 matrix from input to output.

The axis ray through the same collection of elements, by contrast, will consist in general of a series of bent or even curving segments, with respect to which

the system again acts like an aligned 2×2 matrix. The axis ray has the property that it comes out parallel to itself after one pass through the system. However, although the axis rays at the input and output planes have the same displacement and slope, and thus are parallel to each other, they do not in general define a single straight line through the system, whereas does the overall element axis does.

In fact, in an optical resonator or periodic system with several individually misaligned elements the axis ray, which acts as the effective optical axis for the periodic system, will trace out a zig-zag course within the $ABCD$ system, shifting or bending from plane to plane within the period or round trip. Moreover, the axis rays going in the forward and reverse directions through a standing-wave resonator may not lie on top of each other (though they must intersect in position, but not necessarily in slope, at the end mirrors); and also the axis ray in a misaligned system may or may not coincide with the element axis of any individual element at the point where it intersects that element. Such an axis ray nonetheless always exists.

Summary

The overall conclusion of this section is clearly that (small) displacements or misalignments of individual paraxial elements are usually not a serious problem. They can be handled with the extended matrix technique of this section if desired, but in general they do not change the basic focusing or stability problems of a paraxial $ABCD$ system. If we are designing an extended beam transmission system and perhaps wish to know the sensitivity of the overall system alignment to misalignments of individual elements, then the techniques of this section can be very useful. If the problem is merely to design and evaluate the stability and spot size properties of a closed resonator, then misalignment effects can be ignored.

REFERENCES

The 3×3 matrix technique we have introduced for handling misaligned systems is also briefly described in Appendix B of the book by A. Garrard and J.M. Burch, *Introduction to Matrix Methods in Optics* (Wiley, 1975).

Problems for 15.4

1. *Error vector for a tilted flat mirror.* What is the error vector \mathbf{E} for a flat mirror which is misaligned (i.e., tilted) by a small angle θ relative to its aligned position (assuming its aligned position is perpendicular to the reference optical axis of the system).
2. *Misaligned optical resonator.* Consider an optical resonator consisting of an aligned flat mirror at the left-hand end; a collection of aligned optical elements having an overall $ABCD$ matrix going in the $+z$ direction from the left-hand mirror to the right-hand mirror; and another planar mirror at the right-hand end which is misaligned by a small tilt angle θ . Find formula for the overall element

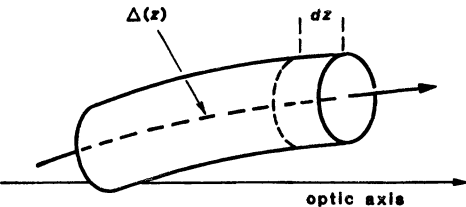


FIGURE 15.21
A curved optical fiber or duct.

axis and axis ray for one round trip in this resonator, or in its equivalent periodic lensguide.

Calculate and sketch the locations of these rays for the specific situation of a resonator of length L with a thin lens of focal length f located at the center of the cavity, for both a stable resonator ($L/4 < f < \infty$) and a positive-branch unstable resonator ($f < 0$).

3. *More misaligned resonators.* Repeat the previous problem assuming the thin lens of focal length f is located just in front of the left-hand mirror, and then just in front of the right-hand mirror. (The stability conditions are different in each of these situations.)
4. *Finding the axis ray in another optical resonator with misaligned elements.* A laser resonator of total length L consists of two intracavity lenses of focal length $f = 2L$ equally spaced between two flat end mirrors. One lens is displaced above the optic axis of the resonator by a small distance $\Delta = \epsilon$; the other is displaced downward by $\Delta = -2\epsilon$. Trace the “axis ray” through this resonator.

15.5 RAY MATRICES IN CURVED DUCTS

As still another example of an interesting ray matrix system, consider a quadratic duct as defined previously, in which the transverse index variation $n = n(r)$ is constant with distance, but assume now that this duct is twisted or bent, so that the axis of the duct at any plane z is displaced from a straight reference axis by a small amount $\Delta(z)$ as in Figure 15.21. (This could represent a curved or twisted optical fiber.) What is the $ABCD$ matrix for this curved duct?

Differential Matrix Analysis

Following the combined approach of the preceding two sections, we can suppose that $\mathbf{M}(z)$ represents the 3×3 $ABCDEF$ matrix for such a system from an input plane z_0 up to plane z , with elements $A(z)$ through $F(z)$. Then from the cascading properties of ray matrices we can write that

$$\mathbf{M}(z + dz) = \mathbf{M}(dz) \times \mathbf{M}(z), \quad (73)$$

where $\mathbf{M}(dz)$ is the ray matrix for the short distance dz from z to $z + dz$.

Now, for a thin segment of transversely displaced duct, as in Figure 15.21, this matrix has the form, in the limit as $dz \rightarrow 0$, of

$$\mathbf{M}(dz) = \begin{bmatrix} 1 & n_0^{-1}dz & 0 \\ -n_0\gamma^2dz & 1 & n_0\gamma^2\Delta(z)dz \\ 0 & 0 & 1 \end{bmatrix}. \quad (74)$$

Multiplying the matrices $\mathbf{M}(dz)$ and $\mathbf{M}(z)$ together and comparing them term-by-term with the matrix $\mathbf{M}(z + dz)$, then gives the differential relations

$$\begin{aligned} \frac{dA(z)}{dz} &= n_0^{-1}C(z), & \frac{dB(z)}{dz} &= n_0^{-1}D(z) \\ \frac{dC(z)}{dz} &= -n_0\gamma^2A(z), & \frac{dD(z)}{dz} &= -n_0\gamma^2B(z), \end{aligned} \quad (75)$$

plus the two additional equations

$$\frac{dE(z)}{dz} = n_0^{-1}F(z) \quad \text{and} \quad \frac{dF(z)}{dz} = -n_0\gamma^2[E(z) - \Delta(z)]. \quad (76)$$

Solving the first four equations, starting from z_0 , gives the overall $ABCD$ matrix as a function of distance in the form

$$A(z) = D(z) = \cos \gamma(z - z_0), \quad n_0\gamma B(z) = -(n_0\gamma)^{-1}C(z) = \sin \gamma(z - z_0) \quad (77)$$

which agrees with what we already know from Equation 15.15. The overall $ABCD$ matrix is again unchanged by curvature or misalignment of the duct.

Effects of Duct Misalignment

The final two equations, which are independent of $ABCD$, however, yield the formal solutions

$$\begin{aligned} E(z) &= \gamma \int_{z_0}^z \Delta(z') \sin \gamma(z - z') dz' \\ F(z) &= n_0\gamma^2 \int_{z_0}^z \Delta(z') \cos \gamma(z - z') dz'. \end{aligned} \quad (78)$$

There is one particular situation where these solutions can be quite important. Suppose the axis displacement $\Delta(z)$ in the duct has a natural periodic component with a spatial variation $\Delta(z) = \cos \gamma_1 z$ or $\sin \gamma_1 z$, and suppose that γ_1 equals or closely matches the natural ray oscillations at $\cos \gamma z$ or $\sin \gamma z$. The integrands in Equation 15.78 will then contain $\cos^2 \gamma z$ or $\sin^2 \gamma z$ factors which will integrate cumulatively with distance z . This then implies that the displacement parameters $E(z)$ and $F(z)$, or in essence the cumulative amount of misalignment in the duct, will grow more or less linearly with distance.

Problems will thus result if the physical curvature or waviness of a duct has a periodic variation that resonates with the natural oscillation period for optical rays about the axis of the duct. The system axis of the duct then seems to diverge by an increasing amount from the physical axis (or element axis) of the duct as we go further down the duct. In more physical terms this means that the periodic oscillations of rays in the duct will appear to grow linearly in amplitude

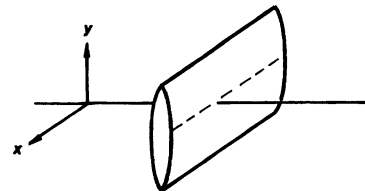


FIGURE 15.22
An astigmatic optical element (cylindrical lens).

with distance, until these rays encounter the edges of the duct, or some other nonlinearity occurs to limit their growth.

If the duct has instead a randomly wavy axis, i.e., with random variations in $\Delta(z)$ along the length of the guide, then the oscillations in off-axis rays will grow as the square root of distance along the guide rather than linearly with the distance z . The growth rate for this process will be proportional to the amplitude of the spatial frequency components of $\Delta(z)$ in the immediate vicinity of the natural wave number γ .

REFERENCES

The basic differential analysis presented in this section comes from A. Hardy, "Beam propagation through parabolic-index waveguides with distorted optical axis," *Appl. Phys.* **18**, 223–226 (1979).

Though the analysis in this section refers to a continuous parabolic duct with a curved or wavy axis, very similar results will apply to an iterated periodic lensguide having perturbations $\Delta(z)$ in the location of the optic elements from section to section along the guide. Understanding of the growth rate for random perturbations in such periodic systems was of considerable importance in pre-fiber-optics times, when periodic optical lensguides were under serious consideration for long-distance optical communications.

An early analysis of this for the periodic lensguide situation was given by J. Hirano and Y. Fukatsu, "Stability of a light beam in a beam waveguide," *Proc. IEEE* **52**, 1284–1292 (November 1964). A later study was D. W. Berreman, "Growth of oscillations of a ray about the irregularly wavy axis of a lens light guide," *Bell Sys. Tech. J.* **41**, 2117–2132 (November 1965). Another interesting analysis is D. Marcuse, "Physical limitations on ray oscillation suppressors," *Bell Sys. Tech. J.* **45**, 743–751 (May–June 1966).

15.6 NONORTHOGONAL RAY MATRICES

We have noted earlier that in optical systems with rotational symmetry the same ray matrices apply equally but separately to the x, x' and the y, y' ray coordinates. In the slightly more complicated situation of optical elements having simple astigmatism, the ray matrices will be different along the x and y coordinates. A thin cylindrical lens having its cylinder axis aligned along the x axis (Figure 15.22), for example, will act as a thin lens with the appropriate $ABCD$ matrix so far as the y transverse coordinate is concerned, but will have no focusing or bending effect on the x displacement of the ray.

Suppose that an overall optical system contains several such astigmatic elements, but these elements all have their principal axes aligned along the same x and y axes. We can then still analyze the ray behavior in each transverse coordinate separately and independently, using separate $ABCD$ matrices for the x and the y directions. Such an astigmatic system, for example, might even be stable in one coordinate and unstable in the other. Systems having only simple astigmatism, and thus describable by separate and independent ray matrices in two principle planes that are 90° apart, are commonly referred to as *orthogonal systems*.

Systems not having this property are said to be *nonorthogonal*. Nonorthogonal systems in general exhibit one or another kind of "twist" or image rotation, which is more complicated than simple astigmatism, and which in general does not permit the ray matrices to be separated into two separate ray matrices along two orthogonal axes. The ray analysis of nonorthogonal paraxial optical systems has not yet been extensively developed, and we can therefore summarize in this section only a few results concerning such systems.

General Analysis of Nonorthogonal Ray Optical Systems

It would be useful, for example, to establish the most general forms that the ray matrices of both orthogonal and nonorthogonal optical systems can assume if we include such operations as arbitrary astigmatism, image rotation, and image inversion. These questions will not be fully answered in this section, although we will derive some of the general properties of nonorthogonal systems by building up from combinations of elementary ray operations and matrices. We are particularly interested in establishing the conditions under which an optical system will remain orthogonal, so that the system can be described by separate and independent ray matrices along two orthogonal transverse directions.

There are first of all two basically different ways in which we might write the 4×4 matrices needed to describe the ray coordinates in both the x and y transverse coordinates. One way is to organize the ray coordinates in the form of displacements and then slopes, e.g.,

$$\begin{bmatrix} x_2 \\ y_2 \\ x'_2 \\ y'_2 \end{bmatrix} = \begin{bmatrix} A_{xx} & A_{xy} & B_{xx} & B_{xy} \\ A_{yx} & A_{yy} & B_{yx} & B_{yy} \\ C_{xx} & C_{xy} & D_{xx} & D_{xy} \\ C_{yx} & C_{yy} & D_{yx} & D_{yy} \end{bmatrix} \begin{bmatrix} x_1 \\ y_1 \\ x'_1 \\ y'_1 \end{bmatrix}, \quad (79)$$

or in shorthand notation

$$\begin{bmatrix} \mathbf{r}_2 \\ \mathbf{r}'_2 \end{bmatrix} = \begin{bmatrix} \mathbf{A} & \mathbf{B} \\ \mathbf{C} & \mathbf{D} \end{bmatrix} \times \begin{bmatrix} \mathbf{r}_1 \\ \mathbf{r}'_1 \end{bmatrix}, \quad (80)$$

where we use the notation in these paragraphs that \mathbf{r} and \mathbf{r}' are column vectors with elements $\mathbf{r} \equiv [x, y]$ and $\mathbf{r}' \equiv [n_x dx/dz, n_y dy/dz]$, and \mathbf{A} , \mathbf{B} , \mathbf{C} and \mathbf{D} are all 2×2 matrices.

For an astigmatic but orthogonal system with its principal axes oriented along the x and y directions, all four of these matrices will then be diagonal, i.e., the xy and yx elements that couple between the x and y axes will all be zero. Any rotation of the coordinate system will make these off-diagonal elements

nonzero, although for orthogonal systems there will be constraints among the diagonal and off-diagonal elements. A general nonorthogonal system will have off-diagonal elements between the x and y directions that cannot be removed by any coordinate rotation.

Expressing the 4×4 problem in the form of Equation 15.79 has a number of advantages, as discussed for example by Nazarathy (see References). If a superscript T indicates the matrix transpose, then it can be shown (see References) that even in the most general nonorthogonal system these 2×2 matrices must satisfy the constraints

$$\begin{aligned} \mathbf{AB}^T &= \mathbf{BA}^T, & \mathbf{B}^T \mathbf{D} &= \mathbf{D}^T \mathbf{B} \\ \mathbf{DC}^T &= \mathbf{CD}^T, & \mathbf{C}^T \mathbf{A} &= \mathbf{A}^T \mathbf{C} \end{aligned} \quad (81)$$

as well as

$$\mathbf{AD}^T - \mathbf{BC}^T = \mathbf{A}^T \mathbf{D} - \mathbf{B}^T \mathbf{C} = \mathbf{I}, \quad (82)$$

where \mathbf{I} is the identity matrix. The last two relations are obviously the nonorthogonal generalizations of the $\mathbf{AD} - \mathbf{BC} = 1$ relation for orthogonal 2×2 ray matrices. There are potentially sixteen elements in the general 4×4 ray matrix, but as a result of these six relations there are only ten independent elements (as also pointed out by Arnaud).

We can also show, following Nazarathy, that with this form for the 4×4 matrices the general form of the Huygens-Fresnel integral that we will introduce in a later chapter can be put into the very beautiful form

$$\tilde{u}_2(\mathbf{r}_2) = \frac{j}{|\mathbf{B}|^{1/2} \lambda} \int_{-\infty}^{\infty} \tilde{K}(\mathbf{r}_2, \mathbf{r}_1) \tilde{u}_1(\mathbf{r}_1) d\mathbf{r}_1, \quad (83)$$

where $|\mathbf{B}|^{1/2}$ is the square root of the determinant of the \mathbf{B} matrix, and \tilde{K} is the exponential part of the Huygens' kernel given by

$$\tilde{K}(\mathbf{r}_2, \mathbf{r}_1) \equiv \exp \left[-j \frac{\pi}{\lambda} (\mathbf{r}_1 \cdot \mathbf{B}^{-1} \mathbf{A} \cdot \mathbf{r}_1 - 2\mathbf{r}_1 \cdot \mathbf{B}^{-1} \cdot \mathbf{r}_2 + \mathbf{r}_2 \cdot \mathbf{B}^{-1} \cdot \mathbf{r}_2) \right], \quad (84)$$

with \mathbf{B}^{-1} being the inverse of the \mathbf{B} matrix. This form of Huygens' integral is then equally valid for orthogonal or nonorthogonal systems.

Alternative Matrix Notation

An alternative notation to Equation 15.79 for ray systems in two transverse dimensions is to organize the coordinates and matrix elements in the form

$$\begin{bmatrix} x_2 \\ x'_2 \\ y_2 \\ y'_2 \end{bmatrix} = \begin{bmatrix} A_{xx} & B_{xx} & A_{xy} & B_{xy} \\ C_{xx} & D_{xx} & C_{xy} & D_{xy} \\ A_{yx} & B_{yx} & A_{yy} & B_{yy} \\ C_{yx} & D_{yx} & C_{yy} & D_{yy} \end{bmatrix} \begin{bmatrix} x_1 \\ x'_1 \\ y_1 \\ y'_1 \end{bmatrix}. \quad (85)$$

As a shorthand notation we will write this equation in the partitioned matrix form

$$\begin{bmatrix} x_2 \\ y_2 \end{bmatrix} = \begin{bmatrix} \mathbf{M}_{xx} & \mathbf{M}_{xy} \\ \mathbf{M}_{yx} & \mathbf{M}_{yy} \end{bmatrix} \begin{bmatrix} x_1 \\ y_1 \end{bmatrix}, \quad (86)$$

where \mathbf{x} and \mathbf{y} are the ray vectors in the x and y coordinates, respectively; \mathbf{M}_{xx} and \mathbf{M}_{yy} are the ordinary 2×2 $ABCD$ matrices applying to the x and y directions; and \mathbf{M}_{xy} and \mathbf{M}_{yx} are the cross-matrices between the x and y directions. We will pursue some applications and consequences of this alternative matrix arrangement in the remainder of this section.

Rotated Astigmatic Optical Systems

Most of the difficulties in nonorthogonal systems arise from questions of rotation, where the term rotation can mean either *coordinate system rotation* or *actual image rotation* of a ray bundle by arbitrary angles about the direction of propagation. Let us therefore examine in some detail the analytical effects that arise from such rotations.

For example, we might begin by organizing the 4×4 ray matrix for an astigmatic but still orthogonal system, aligned along its principle axes, in the form

$$\begin{bmatrix} x_2 \\ x'_2 \\ y_2 \\ y'_2 \end{bmatrix} = \begin{bmatrix} A_x & B_x & & \\ C_x & D_x & & \\ & & A_y & B_y \\ & & C_y & D_y \end{bmatrix} \begin{bmatrix} x_1 \\ x'_1 \\ y_1 \\ y'_1 \end{bmatrix}, \quad (87)$$

where we will follow the convention that any elements not written are zero. The x and y quantities in this situation are entirely uncoupled.

At any position z we can always make a coordinate rotation from our original x_1, y_1 coordinates to a set of axes x_2, y_2 which are rotated about the z axis by an angle θ (Figure 15.23). This is done analytically by applying the general rotation matrix

$$\begin{bmatrix} x_2 \\ x'_2 \\ y_2 \\ y'_2 \end{bmatrix} = \begin{bmatrix} \cos \theta & \sin \theta & & \\ \cos \theta & \sin \theta & & \\ -\sin \theta & \cos \theta & & \\ -\sin \theta & \cos \theta & & \end{bmatrix} \begin{bmatrix} x_1 \\ x'_1 \\ y_1 \\ y'_1 \end{bmatrix}, \quad (88)$$

where subscript 1 refers to the ray coordinates measured in the old coordinate system and subscript 2 refers to the same ray measured in the new (rotated) coordinate system. We can then write this in shorthand notation as

$$\begin{bmatrix} x_2 \\ y_2 \end{bmatrix} = \begin{bmatrix} C_\theta & S_\theta \\ -S_\theta & C_\theta \end{bmatrix} \begin{bmatrix} x_1 \\ y_1 \end{bmatrix}, \quad (89)$$

where C_θ and S_θ (with suitable subscripts) represent the cos and sin of the rotation angle, with each of these understood to be multiplied by the identity matrix which is not written out. Rotation in the opposite direction simply reverses the sign of S_θ .

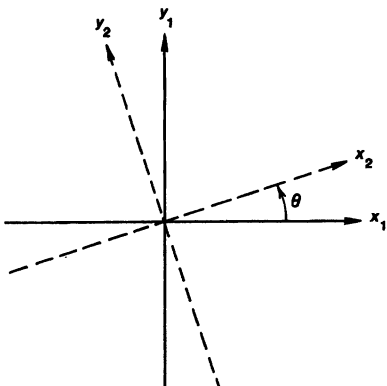


FIGURE 15.23
Coordinate system rotation.

Suppose an orthogonal astigmatic element is physically rotated about the z axis by an arbitrary angle θ , as in Figure 15.23, and that we wish to describe the ray propagation through this element written in the original or unrotated coordinate system. To pass a ray through this rotated element analytically using the original x_1, y_1 axes, we must transform from our original axes into the rotated principal axes of the element; propagate through the element using the $ABCD$ matrices along its principal axes; and then rotate back to our original axes by a rotation of amount $-\theta$. If we carry out this procedure, the ray matrix of the rotated astigmatic element written in the original x, y coordinate axes is the cascade product

$$\begin{bmatrix} C_\theta & -S_\theta \\ S_\theta & C_\theta \end{bmatrix} \times \begin{bmatrix} M_{xx} & \\ & M_{yy} \end{bmatrix} \times \begin{bmatrix} C_\theta & S_\theta \\ -S_\theta & C_\theta \end{bmatrix} \quad (90)$$

which can be manipulated into the form

$$\begin{bmatrix} C_\theta^2 M_{xx} + S_\theta^2 M_{yy} & S_\theta C_\theta (M_{xx} - M_{yy}) \\ S_\theta C_\theta (M_{xx} - M_{yy}) & S_\theta^2 M_{xx} + C_\theta^2 M_{yy} \end{bmatrix}. \quad (91)$$

An orthogonal system rotated to an arbitrary angle θ will thus have a 4×4 matrix of this general form. In particular we can deduce that *in an orthogonal but arbitrarily rotated system, the upper right and lower left 2×2 blocks may not be zero, but they will always be identical*, as illustrated in Equation 15.91.

Two Rotated Elements in Cascade

Suppose next that two individually orthogonal but astigmatic elements or systems are arranged in cascade, and are rotated to arbitrary angles θ_1 and θ_2 about the z axis (see Figure 15.24), with element #1 passed through first. The overall ray matrix of these cascaded elements is then the matrix product of two rotated matrices of the type given in Equation 15.91, with appropriate subscripts to identify the first and second systems (e.g., $S_{\theta_1} \equiv \sin \theta_1$ for the first element; $M_{xx,1}$ is the x -axis ray matrix of the first element in its own principal axes;

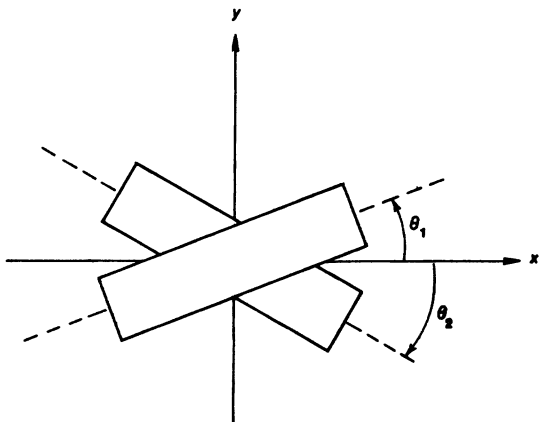


FIGURE 15.24
Rotated astigmatic optical elements.

$M_{yy,2}$ is the y -axis ray matrix of the second element in its own principal axes; and so forth).

The overall matrix product that results from carrying out this multiplication is lengthy and not particularly transparent. But suppose this overall product is written in the shorthand form

$$\left[\begin{array}{c|c} M_{xx} & M_{xy} \\ \hline M_{yx} & M_{yy} \end{array} \right] = \left[\begin{array}{c} \text{overall } 4 \times 4 \\ \text{matrix product} \end{array} \right]. \quad (92)$$

In this situation the 2×2 M_{xx} and M_{yy} matrices are no longer necessarily correct $ABCD$ matrices by themselves, but are merely the upper left and lower right blocks of the overall 4×4 matrix, whereas the M_{xy} and M_{yx} are cross matrices between the x and y coordinates.

Now, if this overall cascaded system is to be an orthogonal system, then the upper right and lower left blocks must be identical, i.e., $M_{xy} = M_{yx}$, in the same way as in the rotated orthogonal system of Equation 15.91. All of these blocks are complicated functions of the rotations θ_1 , θ_2 and the individual system matrices. It can be shown, however, after some algebra, that the upper right and lower left blocks of the cascade product of Equation 15.91 will differ by the amount

$$M_{xy} - M_{yx} = \sin(\theta_2 - \theta_1) \cos(\theta_2 - \theta_1) (M_{xx,1} - M_{yy,1}) (M_{xx,2} - M_{yy,2}). \quad (93)$$

We can deduce from this that a cascaded system of two rotated astigmatic elements will in general be orthogonal only if (i) $\theta_2 - \theta_1 = 0^\circ$ or 90° , which means the two elements have relative rotations such that their principal planes coincide; or else if (ii) $M_{xx,1} = M_{yy,1}$, or $M_{xx,2} = M_{yy,2}$, which means that one or the other of the cascaded systems is not astigmatic (e.g., is rotationally symmetric).

To phrase this in the opposite sense, we can conclude that, except for these very special situations, an optical system having cascaded astigmatic elements rotated at arbitrary angles will in general not be orthogonal. Such a system will not have any pair of transverse coordinates separated by 90° with respect to which a ray can be analyzed by separate and independent $ABCD$ matrices.

FIGURE 15.25
Image inversion in a Dove prism.



Image Rotation

Paraxial optical systems of the most general form can also exhibit *image rotation* in addition to inversion and astigmatism. Image rotation means that the displacement and slope of a ray on passing through an element are actually rotated in the x, y plane in the manner given analytically by the general 4×4 rotation matrix given in Equation 15.88.

We introduced the coordinate rotation notation given above at first to represent simply a purely mathematical transformation of coordinates. In simple situations we may rotate the x, y coordinate system by an angle θ , perhaps in order to line up the coordinate system with the principal axes of an astigmatic element. We may then rotate the coordinate system back by $-\theta$ to the original axes further along the z axis, after passing through the astigmatic element.

However, there are also optical systems which accomplish genuine *physical rotation* of the ray position even with respect to fixed coordinate axes. This image rotation is also given analytically by the same rotation matrix using C_θ and S_θ as given in Equation 15.88, but with the rotation operation now viewed as operating on the rays with respect to fixed coordinate axes. Such image rotation systems often also contain one or more image inversions. A beam passing a partially rotated Dove prism is one simple example of this type. In such a system the rotation matrix only operates once—there is no “reverse rotation” later on.

Nonplanar Ring Resonators

The concepts of coordinate rotation versus image rotation become particularly indistinguishable for a twisted or nonplanar ring resonator (see Figure 15.26). When rays bounce off a mirror at other than normal incidence, as in any ring resonator, it is most natural to use transverse coordinate axes that lie in the plane and perpendicular to the plane of incidence defined by the ray axes just before and after reflection. This is particularly desirable when reflecting off spherical mirrors at other than normal incidence, since the effective radius of curvature of the mirror becomes $R \cos \theta_0$ for rays in the plane of incidence and $R/\cos \theta_0$ for rays perpendicular to the plane of incidence, where θ_0 is the angle between the incident direction and the normal to the mirror.

Analyzing the ray propagation in going around a twisted or nonplanar ring then requires repeated coordinate rotations just before each mirror, in order to bring the transverse x, y axes into agreement with the plane of incidence and reflection of the optical rays on that particular mirror. For a twisted ring, these rotations at each mirror may or in general may not sum to zero net rotation after a complete round trip.

We can then view this situation either as a set of sequential coordinate transformations which do not bring the final coordinate axes back in alignment with the initial axes after one round trip; or alternatively we may view this as a phys-

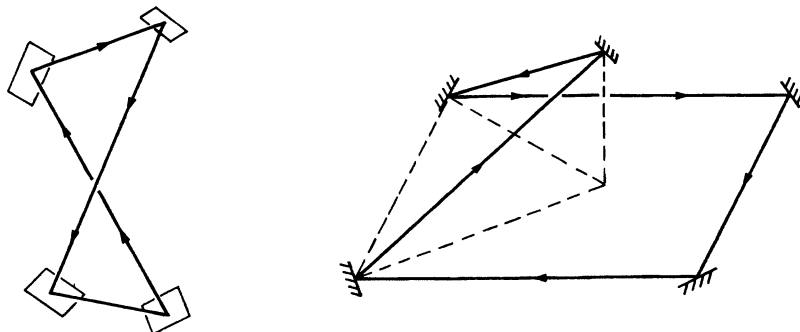


FIGURE 15.26
Nonplanar ring resonators.

ical rotation of the image or of the ray vectors as seen in the original transverse coordinates after one round trip. The result either way is a net nonzero rotation of the ray coordinates in one round trip. An image rotation plus an orthogonal system in cascade will have a net 4×4 matrix in one of the two forms

$$\left[\begin{array}{c|c} C_\theta M_{xx} & S_\theta M_{xx} \\ \hline -S_\theta M_{yy} & C_\theta M_{yy} \end{array} \right] \quad \text{or} \quad \left[\begin{array}{c|c} C_\theta M_{xx} & S_\theta M_{yy} \\ \hline -S_\theta M_{xx} & C_\theta M_{yy} \end{array} \right], \quad (94)$$

depending on whether the rotation or the astigmatic element comes first. Systems with image rotation are clearly not orthogonal.

Summary

The analysis of general nonorthogonal systems, i.e., those having image rotation, inversion, and/or cascaded and rotated astigmatic elements, thus becomes significantly more complicated than for the simple 2×2 ray matrix. Arnaud and others have shown, for example, that the most general 4×4 ray matrix has just ten independent elements out of the sixteen total elements. A general nonorthogonal system can also be separated into independent x and y coordinates in a particular *nonorthogonal* set of x and y axes, i.e., a set of transverse coordinates that are not at 90° to each other. Systems with image rotation generally also rotate the electric field polarization of a real optical wave, leading to added complexities for the polarization eigenmodes of such a resonator.

We will not explore any of these properties of nonorthogonal optical systems further in this text, and the remainder of our discussions in the following chapters will apply only to orthogonal astigmatic systems, with separable and orthogonal x and y axes.

REFERENCES

The theory of ray propagation, paraxial optical propagation, and gaussian beam propagation in nonorthogonal systems has been treated by a number of authors using ray matrix, eikonal, Huygens' integral, and differential operator methods. An important

early reference is S. A. Collins, Jr., "Lens-system diffraction integral written in terms of matrix optics," *J. Opt. Soc. Am.* **60**, 1168–1177 (September 1970).

Other references from this same period include E. E. Bergmann, "Optical resonators with paraxial modes," *Appl. Opt.* **11**, 113–119 (January 1972); and Y. Suematsu and H. Fukinuki, "Matrix theory of light beam waveguides," *Bull. Tokyo Inst. Technol.* **88**, 33–47 (1968).

Extensive discussions have also been given by J. A. Arnaud in a series of papers, including "Degenerate optical cavities," *Appl. Opt.* **8**, 189–195 (January 1969); "Degenerate optical cavities. II: Effects of misalignments," *Appl. Opt.* **8**, 1909–1917 (September 1969); "Gaussian light beams with general astigmatism," (with H. Kogelnik) *Appl. Opt.* **8**, 1687–1693 (August 1969); "Nonorthogonal optical waveguides and resonators," *Bell Sys. Tech. J.* **49**, 2311–2347 (November 1970); and "Mode coupling in first-order optics," *J. Opt. Soc. Am.* **61**, 751–758 (June 1971).

The matrix results using the first of the two formalisms outlined in this chapter come from M. Nazarathy, *Operator Methods in First Order Optics*, D. Sc. Dissertation, Technion, Israel Institute of Technology (1982).

Other relevant references, particularly on nonplanar ring resonators, include S. I. Zavgorodnaya, V. I. Kuprenyuk, and V. I. Sherstobitov, "Unstable resonator with field rotation," *Sov. J. Quantum Electron.* **7**, 787–788 (June 1977); G. B. Al'tshuler, et al., "Analysis of misalignment sensitivity of ring-laser resonators," *Sov. J. Quantum Electron.* **7**, 857–859 (July 1977); and F. Biraben, "Efficacite des systemes unidirectionnels utilisables dans les lasers en anneau," *Optics Comm.* **29**, 353–356 (June 1979), which proposes the use of a nonplanar ring to rotate the plane of polarization for an optical isolator.

Russian theorists have published extensively on field rotation in resonators and nonplanar rings, including papers by V. I. Kuprenyuk and V. E. Sherstobitov, "Calculations on the mirror system of an unstable resonator with field rotation," *Sov. J. Quantum Electron.* **10**, 449–453 (April 1980); M. M. Popov, "Resonators for lasers with unfolded directions of principal curvatures," *Optics and Spectrosc.* **25**, 213–217 (1968); and "Resonators for lasers with rotated directions of principal curvatures," *Optics and Spectrosc.* **25**, 170–171 (1968).

See also E. F. Ishchenko and E. F. Reshetin, "Sensitivity to misalignment of an optical ring resonator with a focusing element," *Optics and Spectrosc.* **46**, 202–207 (February 1979); and Yu. A. Anan'ev, V. I. Kuprenyuk, and V. E. Sherstobitov, "Properties of unstable resonators with field rotation. I. Theoretical principles," *Sov. J. Quantum Electron.* **9**, 1105–1110 (September 1979), and D. A. Goryachkin et al., "II. Experimental results," *Sov. J. Quantum Electron.* **9**, 1110–1114 (September 1979).

Recent Soviet work on nonplanar rings is reported by Yu. I.D. Golyaev, et al., in "Spatial and polarization characteristics..." and "Temporal and spectral characteristics of radiation from a cw neodymium-doped garnet laser with a nonplanar ring resonator," *Sov. J. Quantum Electron.* **11**, 1421–1426 and 1427–1432 (November 1981).

Fundamental formulas for the rotation of an image upon reflection from a plane mirror are given in D. A. Berkowitz, "Design of plane mirror systems," *J. Opt. Soc. Am.* **55**, 1464–1467 (November 1965).

Problems for 15.6

1. *Image rotation in a Dove prism.* Using ray matrices, show that when you physically rotate the Dove prism of Figure 15.25, the image transmitted through the prism rotates twice as fast as the prism itself.
-

16

WAVE OPTICS AND GAUSSIAN BEAMS

A more accurate treatment of optical beams and laser resonators must take into account diffraction and the wave nature of light. Practical laser beams are almost always well enough collimated even under worst conditions, however, that we can describe their diffraction properties using a scalar wave theory, and working in the paraxial wave approximation.

In this chapter, therefore, we introduce the paraxial wave analysis and the equivalent Huygens-Fresnel integral approach for optical beams in free space. We also introduce the lowest and higher-order gaussian mode solutions of these equations as a widely useful set of “normal modes of free space.”

The Hermite-gaussian or Laguerre-gaussian modes which we introduce in this chapter are exact and yet mathematically convenient solutions to the paraxial wave equation in free space. They also provide very close (though not quite exact) approximations for the transverse eigenmodes of stable laser resonators with finite diameter mirrors. Gaussian beams are therefore very widely used in analyzing laser beams and related optical systems. Our approach in this chapter is to focus primarily on the mathematical derivation of these modes, whereas in the following chapter we summarize most of the important practical properties of gaussian beams in considerable detail.

16.1 THE PARAXIAL WAVE EQUATION

One fundamental way of analyzing free-space wave propagation, using a differential approach, is through the *paraxial wave equation*, which we can derive once again here in the following fashion.

Derivation of the Paraxial Wave Equation

Electromagnetic fields in free space (or in any uniform and isotropic medium) are governed in general by the scalar wave equation

$$[\nabla^2 + k^2] \tilde{E}(x, y, z) = 0, \quad (1)$$

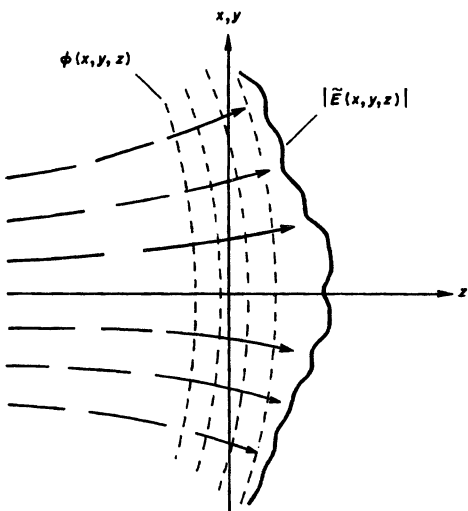


FIGURE 16.1
Transverse amplitude and phase variation of a paraxial optical wave.

where $\tilde{E}(x, y, z)$ is the phasor amplitude of a field distribution that is sinusoidal in time. We will be concerned in this section with optical beams propagating primarily along the z direction, so that the primary spatial dependence of $\tilde{E}(x, y, z)$ will be an $\exp(-jkz)$ variation. This $\exp(-jkz)$ variation has a spatial period of one wavelength λ in the z direction.

In addition, for any beam of practical interest the amplitude and phase of the beam will generally have some transverse variation in x and y which specifies the beam's transverse profile, as shown in Figure 16.1; and this transverse amplitude and phase profile will change slowly with distance z due to diffraction and propagation effects. Both the transverse variations across any plane z , however, and especially the variation in beam profile with distance along the z axis, will usually be slow compared to the plane-wave $\exp(-jkz)$ variation in the z direction for a reasonably well-collimated beam.

It is then convenient to extract the primary $\exp(-jkz)$ propagation factor out of $\tilde{E}(x, y, z)$, by writing each relevant vector component of the field (such as E_x or E_y) in the form

$$\tilde{E}(x, y, z) \equiv \tilde{u}(x, y, z) e^{-jkz}, \quad (2)$$

where u is a complex scalar wave amplitude which describes the transverse profile of the beam. Substituting this into the wave equation 16.1 then yields, in rectangular coordinates, the reduced equation

$$\frac{\partial^2 \tilde{u}}{\partial x^2} + \frac{\partial^2 \tilde{u}}{\partial y^2} + \frac{\partial^2 \tilde{u}}{\partial z^2} - 2jk \frac{\partial \tilde{u}}{\partial z} = 0. \quad (3)$$

Now, we emphasize once again that with the $\exp(-jkz)$ dependence factored out, the remaining z dependence of the wave amplitude $\tilde{u}(x, y, z)$, is caused basically

by diffraction effects, and this z dependence will in general be slow compared not only to one optical wavelength, as in $\exp(-jkz)$, but also to the transverse variations due to the finite width of the beam. This slowly varying dependence of $\tilde{u}(x, y, z)$ on z can be expressed mathematically by the *paraxial approximation*

$$\left| \frac{\partial^2 \tilde{u}}{\partial z^2} \right| \ll \left| 2k \frac{\partial \tilde{u}}{\partial z} \right| \quad \text{or} \quad \left| \frac{\partial^2 \tilde{u}}{\partial x^2} \right| \quad \text{or} \quad \left| \frac{\partial^2 \tilde{u}}{\partial y^2} \right|. \quad (4)$$

By dropping the second partial derivative in z , we thus reduce the exact wave equation 16.3 to the *paraxial wave equation* \star

$$\frac{\partial^2 \tilde{u}}{\partial x^2} + \frac{\partial^2 \tilde{u}}{\partial y^2} - 2jk \frac{\partial \tilde{u}}{\partial z} = 0. \quad (5)$$

More generally we may write this paraxial wave equation as

$$\nabla_t^2 \tilde{u}(s, z) - 2jk \frac{\partial \tilde{u}(s, z)}{\partial z} = 0, \quad (6)$$

where s refers to the transverse coordinates $s \equiv (x, y)$ or $s \equiv (r, \theta)$, depending on what coordinate system (rectangular or cylindrical) we elect to use, and ∇_t^2 means the laplacian operator operating on these coordinates in the transverse plane. This equation will be the primary governing equation for all the analysis of this and the following several chapters.

Paraxial Wave Propagation: Finite Difference Approach

The paraxial wave equation can also be turned around and written in the form

$$\frac{\partial \tilde{u}(s, z)}{\partial z} = -\frac{j}{2k} \nabla_t^2 \tilde{u}(s, z). \quad (7)$$

This equation can then be integrated forward in the z direction in order to compute the forward propagation and diffraction spreading of an arbitrary paraxial optical beam. That is, we can employ any suitable numerical differentiation and integration algorithms, first to evaluate the transverse derivative $\nabla_t^2 \tilde{u}(s, z)$ at a given plane z , and then to step forward to a new plane $z + \Delta z$. We can thus accomplish numerical forward propagation of an arbitrary optical wavefront, making sure to use adequate numbers of sampling points in both the transverse and longitudinal directions.

This numerical approach, sometimes referred to as the “finite difference approach,” has been applied to practical beam propagation problems by several workers. For almost any free-space beam propagation problem that we may consider, however, the integral formulation that we will consider in the next section is probably a better choice for numerical calculations, because of the much greater computational efficiency of fast Fourier transforms that can be employed.

Validity of the Paraxial Approximation

The paraxial wave equation in either of the above forms is fully adequate for describing nearly all optical resonator and beam propagation problems that arise with real lasers. As perhaps the simplest but most effective way to confirm

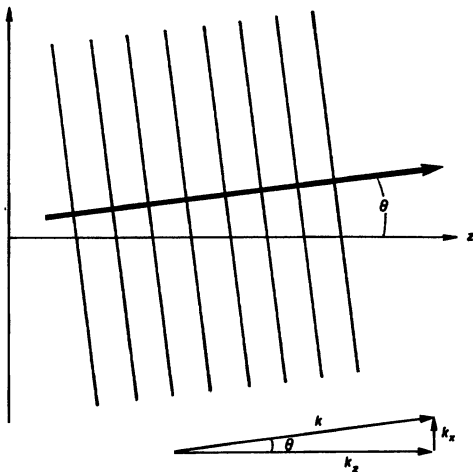


FIGURE 16.2
A plane wave traveling at a small angle θ to the optic axis.

this, and also to illustrate the physical limitations of the paraxial approximation, we can consider the following argument.

Any optical beam can always be viewed as being made up of a superposition of plane wave components traveling at various angles to the z axis. (We will discuss this kind of plane wave expansion more rigorously in a later section.) Consider, for example, a plane wave component $\tilde{E}(x, z)$ traveling at angle θ to the z axis in the x, z plane, as shown in Figure 16.2. (For simplicity we consider only one transverse coordinate.) The axial and transverse variations of this plane wave component are then given by

$$\tilde{E}(x, z) = \exp[-jkx \sin \theta - jkz \cos \theta] = \tilde{u}(x, z)e^{-j kz}. \quad (8)$$

The exact form for the reduced wave amplitude $\tilde{u}(x, y, z)$, and its approximate form within the paraxial approximation, then become

$$\tilde{u}(x, z) = \exp[-jkx \sin \theta - jkz(1 - \cos \theta)] \approx \exp\left[-jk\theta x + jk\frac{\theta^2 z}{2}\right]. \quad (9)$$

The normalized first and second derivatives of $\tilde{u}(x, z)$ in the transverse direction then take on the values

$$\begin{aligned} -j \frac{2k}{\tilde{u}} \frac{\partial \tilde{u}}{\partial z} &= +2k^2(1 - \cos \theta) \approx k^2 \theta^2 \\ \frac{1}{\tilde{u}} \frac{\partial^2 \tilde{u}}{\partial x^2} &= -k^2 \sin^2 \theta \approx -k^2 \theta^2. \end{aligned} \quad (10)$$

However, the second derivative in the z direction takes on the form

$$\frac{1}{\tilde{u}} \frac{\partial^2 \tilde{u}}{\partial z^2} = -k^2(1 - \cos \theta)^2 \approx -\frac{k^2 \theta^4}{4}. \quad (11)$$

This particular derivative is smaller than either of the preceding terms by the ratio $\theta^2/4$ (with θ measured in radians)—a ratio which will be $\ll 1$ so long as θ is $\leq 1/2$ radian.

We can conclude that so long as all (or at least most) of the plane wave components making up any optical beam are traveling at angles $\theta \leq 0.5$ rad, or θ less than about 30° , the $\partial^2\hat{u}/\partial z^2$ terms will be at least an order of magnitude smaller than either of the other two terms, in agreement with the basic paraxial approximation. Paraxial optical beams can thus be focused or can diverge at cone angles up to $\approx 30^\circ$ before significant corrections to the paraxial wave approximation become necessary.

REFERENCES

Corrections to the paraxial optical theory derived in this section do become significant when beams are focused so tightly, or diverged so rapidly, that local wavefronts become tilted by more than about 30° to the beam axis. The next higher-order extensions that are then required are discussed in M. Lax, W.H. Louisell, and W.B. McKnight, "From Maxwell to paraxial optics," *Phys. Rev. A* **11**, 1365–1370 (1975).

Their approach is extended and simplified by L.W. Davis, "Theory of electromagnetic beams," *Phys. Rev. A* **19**, 1177–1179 (March, 1979); and the resulting next-order correction term for gaussian optical beams is discussed by G.P. Agrawal and D.N. Patakyak, "Gaussian beam propagation beyond the paraxial approximation," *J. Opt. Soc. Am.* **69**, 575–578 (April 1979).

16.2 HUYGENS' INTEGRAL

Another equally valid and effective way of analyzing paraxial wave propagation, but now using an integral approach, is to employ *Huygens' principle*, expressed in the *Fresnel approximation*. We can derive this alternative approach to paraxial beam propagation as follows.

Spherical Waves, and the Fresnel Approximation

Let us first note that one very general solution to the exact wave equation, which corresponds physically to a uniform spherical wave diverging from a source point r_0 (Figure 16.3) may be written in the form

$$\tilde{E}(\mathbf{r}; \mathbf{r}_0) = \frac{\exp[-jk\rho(\mathbf{r}, \mathbf{r}_0)]}{\rho(\mathbf{r}, \mathbf{r}_0)}, \quad (12)$$

where $\tilde{E}(\mathbf{r}; \mathbf{r}_0)$ means the field at point \mathbf{r} due to a source at point \mathbf{r}_0 , and where the distance $\rho(\mathbf{r}, \mathbf{r}_0)$ from the source point s_0, z_0 to the observation point s, z is given by

$$\rho(\mathbf{r}, \mathbf{r}_0) \equiv \sqrt{(x - x_0)^2 + (y - y_0)^2 + (z - z_0)^2}. \quad (13)$$

We emphasize that a spherical wavefunction in this form is an exact solution to the full scalar wave equation of the previous section.

Consider, however, a situation in which the source point x_0, y_0, z_0 for this wave is located somewhere not too far off the z axis; and suppose we only wish

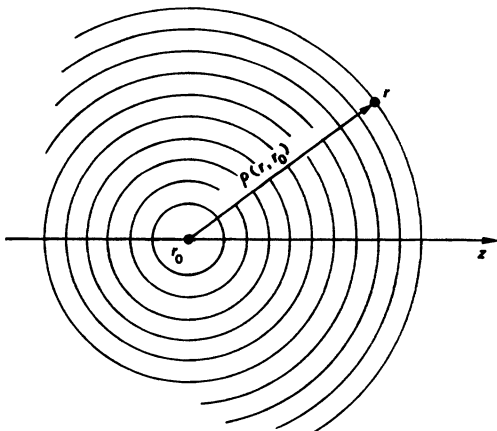


FIGURE 16.3
A general spherical wave.

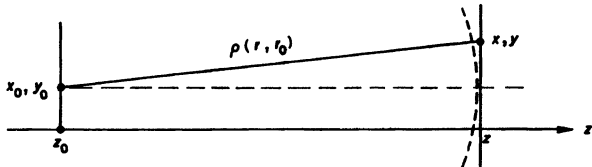


FIGURE 16.4
Fresnel approximation to the spherical wave of Figure 16.3.

to write the resulting field distribution $\tilde{E}(x, y, z)$ or $\tilde{u}(x, y, z)$ of this spherical wave on some transverse plane x, y that is farther along the z axis, for values of x and y that are also not too far off the axis, as in Figure 16.4. The *Fresnel approximation* to diffraction theory says that if we expand the distance $\rho(r, r_0)$ in Equation 16.13 in a power series in the form

$$\rho(r, r_0) = z - z_0 + \frac{(x - x_0)^2 + (y - y_0)^2}{2(z - z_0)} + \dots, \quad (14)$$

then we can drop all terms higher than quadratic in this expression, at least in writing the phase shift factor $\exp[-jk\rho(r, r_0)]$. (We will examine the validity of this assumption in more detail a bit further on.) In the $1/\rho$ denominator of Equation 16.12, on the other hand, we will drop even the quadratic terms, and replace $\rho(r, r_0)$ by simply $z - z_0$.

The spherical wave of Equation 16.12 is then converted, in this Fresnel approximation, into what we might call a “paraxial-spherical wave” given by

$$\tilde{E}(x, y, z) \approx \frac{1}{z - z_0} \exp \left[-jk(z - z_0) - jk \frac{(x - x_0)^2 + (y - y_0)^2}{2(z - z_0)} \right], \quad (15)$$

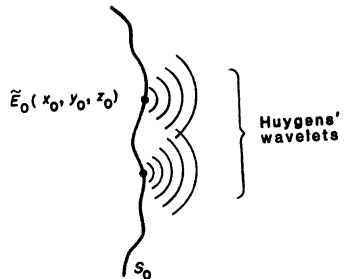


FIGURE 16.5
Huygens' principle.

or

$$\tilde{u}(x, y, z) = \frac{1}{z - z_0} \exp \left[-jk \frac{(x - x_0)^2 + (y - y_0)^2}{2(z - z_0)} \right]. \quad (16)$$

These expressions approximate the spherical wave by a quadratic phase variation as observed on a transverse plane x, y located at a distance $z - z_0$ away from the source point along the z axis, as shown in Figure 16.4. The “paraxial-spherical wave” given by this Fresnel approximation is, as the reader can verify, an exact analytical solution to the paraxial wave equation rather than to the exact wave equation.

Huygens' Integral

We can next connect these spherical-wave and paraxial-spherical-wave ideas to Huygens' integral.

Huygens' integral originated as an intuitive physical principle, which was only later put into more rigorous mathematical terms. This principle says in physical terms that if we are given an incident field distribution $\tilde{E}_0(x_0, y_0, z_0)$ over some closed surface S_0 , we may regard the field at each point on that surface as the source for a uniform spherical wave or “Huygens' wavelet” which radiates from that point on the surface, as illustrated in Figure 16.5. The total field at any other point s, z inside, or beyond, the surface S_0 can then be calculated by summing the fields of all these Huygens' wavelets coming from all the points on the surface S_0 .

Huygens' intuitive ideas concerning this principle were put into more formal mathematical form, first by Fresnel and Kirchoff, and later by Rayleigh and Sommerfeld. The general idea is that each of the Huygens' wavelets should be viewed as a spherical wave with a form like Equation 16.12, leading to Huygens' integral equation in the form

$$\tilde{E}(s, z) = \frac{j}{\lambda} \iint_{S_0} \tilde{E}_0(s_0, z_0) \frac{\exp[-jk\rho(r, r_0)]}{\rho(r, r_0)} \cos \theta(r, r_0) dS_0, \quad (17)$$

where $\rho(r, r_0)$ is the distance between source and observation points as defined earlier. In this formulation dS_0 is an incremental element of surface area at point s_0, z_0 on the surface S_0 , and the factor $\cos \theta(r, r_0)$ is an “obliquity factor” which depends on the angle $\theta(r, r_0)$ between the line element $\rho(r, r_0)$ and the normal to the surface element dS_0 .

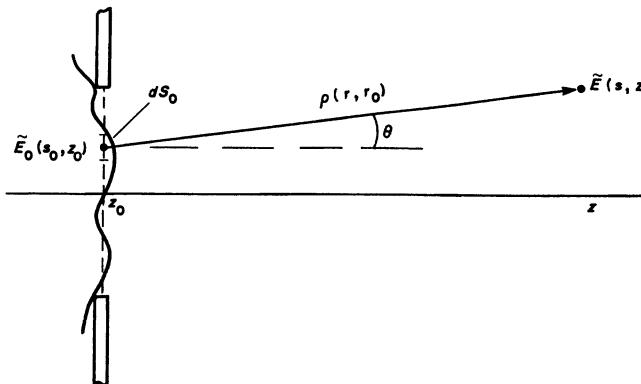


FIGURE 16.6

Geometry for evaluating Huygens' integral in the Fresnel approximation.

Slightly different forms for the obliquity factor in Equation 16.17 are predicted by the Kirchoff-Fresnel or the Rayleigh-Sommerfeld approaches to diffraction theory, although in either situation this factor goes to unity if the angle θ is limited to small values. The j/λ factor in front of Huygens' integral is a normalization factor which comes out of a more detailed approach to the theory, and which is necessary in order to get the correct near-field and far-field dependence from Huygens' integral. (We will also see another physically meaningful explanation for this factor in the following chapter.)

Fresnel Approximation to Huygens' Integral

Suppose now that we are given the input field distribution or beam profile $\tilde{E}_0(x_0, y_0, z_0)$ of a paraxial optical beam across an input transverse plane at $z = z_0$, as in Figure 16.6, and we wish to calculate the output beam profile $\tilde{E}(x, y, z)$ across another plane at distance $z = z_0 + L$, accurate to within the paraxial degree of approximation. We can then make this calculation by using Huygens' principle in the form just given, except that we can replace the exact spherical wave $\exp[-jk\rho]/\rho$ from Equation 16.12 with a "paraxial-spherical wave" in the form derived in Equation 16.15.

If we do this, we obtain *Huygens' integral in the Fresnel approximation*, as given by

$$\tilde{E}(x, y, z) \approx$$

$$\frac{je^{-jk(z-z_0)}}{(z-z_0)\lambda} \iint \tilde{E}_0(x_0, y_0, z_0) \exp \left[-jk \frac{(x-x_0)^2 + (y-y_0)^2}{2(z-z_0)} \right] dx_0 dy_0. \quad (18)$$

We have assumed here that the distance $z - z_0$ between input and output planes in Figure 16.6 is large enough so that the angle of the line element connecting source and observation points is always ≤ 0.5 rad. Hence we can approximate the obliquity factor $\cos \theta$ in Equation 16.17 by unity, as well as using the Fresnel approximation in the exponent.

This formulation of Huygens' integral can equally well be written for the reduced wavefunction $\tilde{u}(x, y, z)$ in the form

$$\tilde{u}(x, y, z) = \frac{j}{L\lambda} \iint \tilde{u}_0(x_0, y_0, z_0) \exp \left[-jk \frac{(x - x_0)^2 + (y - y_0)^2}{2L} \right] dx_0 dy_0, \quad (19)$$

where $L \equiv z - z_0$ is again the distance from input to output plane, and the integrations are over the transverse input plane located at $z = z_0$. We will most often use Huygens' integral in this second form, with the on-axis or plane-wave phase shift $\exp(-jkL)$ or $\exp[-jk(z - z_0)]$ omitted, since it is the transverse variation of $\tilde{u}(x, y)$ that is usually of primary interest. The plane-wave phase factor must be brought back into the calculation if resonant frequencies or total phase shifts are to be calculated.

Validity of the Fresnel Approximation

The reader can verify that the "paraxial spherical wave" given in Equations 16.15 or 16.16 satisfies exactly the paraxial wave equation, just as the exact spherical wave in Equation 16.12 satisfies the exact wave equation. Any field expression for $\tilde{u}(x, y, z)$ given by Huygens' integral in the Fresnel approximation, as given in Equation 16.19 with $L = z - z_0$, will therefore satisfy the paraxial wave equation exactly, and vice versa. *Huygens' integral and the paraxial wave equation represent exactly the same mathematical (and physical) approximations.*

There are, however, some subtleties in the physical interpretation of the Fresnel approximation which it is useful to understand. Suppose we wish to calculate the forward propagation of a paraxial beam through a distance L , from an input wave $\tilde{u}_1(x_1, y_1)$ at plane $z = z_1$ to an output wave $\tilde{u}_2(x_2, y_2)$ at plane $z = z_2 = z_1 + L$. Suppose also that this beam is confined to a width $\approx 2a$, i.e., \tilde{u}_1 and \tilde{u}_2 have negligible values outside of $-a \leq x, y \leq a$.

Now the Fresnel approximation of Equations 16.14 to 16.19 assumes that the quartic and higher-order terms in the expansion of the exponent $e^{-jk\rho}$ can be dropped, because their contribution to the complex exponent will be small compared to, say, $\pi/2$. If we consider either of the transverse coordinates x or y , this condition on the next higher-order terms seems to require that

$$\left| \frac{k(x_2 - x_1)^4}{4L^3} \right| \approx \left| \frac{2\pi}{\lambda} \frac{(2a)^4}{4L^3} \right| \leq \frac{\pi}{2}, \quad (20)$$

since by assumption $|x_2 - x_1| \leq 2a$. This condition can be rewritten in the alternative form

$$\frac{L}{2a} \geq \left(\frac{2a}{\lambda} \right)^{1/3}. \quad (21)$$

In any normal situation, where the beam width is large compared to a wavelength, or $2a \gg \lambda$, this condition apparently says that Huygens' integral in the Fresnel approximation can only be applied to calculate forward beam propagation over lengths that are significantly greater than the beam diameter, or $L \gg 2a$. There seems to be an inconsistency in this limitation, however, in that the paraxial wave equation 16.7 of the previous section can obviously be applied over arbitrarily short forward steps in z , and the paraxial wave equation and the

Huygens-Fresnel integral are supposed to be mathematically equivalent. Is the condition in Equation 16.21 really a limitation on the use of Huygens' integral in the Fresnel approximation?

This question can be answered (in the negative) as follows. Suppose the optical wavefront $\tilde{u}(x_1, y_1, z_1)$ at the input plane z_1 is a freely propagating paraxial beam, without any sharp discontinuities or aperturing at or near that particular plane. Then, the effective sources for this beam are really located at source points x_0, y_0, z_0 that are located far behind (or, for a converging beam, far ahead) of either of the planes z_1 or z_2 . We can then clearly apply the Huygens-Fresnel integral to calculate the wave propagation from plane z_0 to plane z_1 , and we can equally well apply this integral to calculate the propagation from plane z_0 to plane z_2 . But the inherent cascading properties of the Huygens-Fresnel integral (which the reader may want to verify; see the Problems) then imply that the Huygens-Fresnel integral in exactly the same form must also be valid over the distance $z_2 - z_1 = L$, even if this distance is too small to satisfy Equation 16.21, and in fact even if $L \rightarrow 0$.

The essential physical point here is that *the paraxial or Fresnel approximation is a physical property of the optical beam, not a mathematical property of the Huygens-Fresnel formulation*. The paraxial wave equation 16.7 and also the Huygens-Fresnel integral 16.19 can be applied over arbitrarily short distances L if the optical beam itself is truly paraxial.

Sharp-Edged Aperture Effects

We can give a more physical interpretation to this assertion about paraxial beams—which may seem somewhat confusing at first—by the following illustration.

Suppose for example that an input wave $\tilde{u}_1(x_1, y_1)$ does have some sharp discontinuity in its wavefunction at the input plane z_1 , either in amplitude or phase, such as would be caused by a hard-edged aperture or by a discontinuous phase step in the input plane z_1 , say, at radius $x = a$. We will see later that such discontinuities appear to act in effect as sources for quasi spherical diffraction waves or “edge waves” which appear to radiate from the discontinuous edges of the aperture. The criterion of Equation 16.21 must then be applied, not only to the kernel of Huygens’ integral, but also to these “edge waves” as seen at any plane a distance L away from the aperture plane. Huygens’ integral in the Fresnel approximation can thus not be used for distances closer than $L/2a \approx (2a/\lambda)^{1/3}$ beyond such an aperture.

But in fact, neither Huygens’ integral in the Fresnel approximation nor the paraxial wave equation can be applied to this sort of sharp-edged diffraction situation over distances L shorter than given by the preceding condition. The Huygens-Fresnel integral cannot be used because this would violate the Fresnel approximation for those diffracted wavelets which appear to be scattered from the edges of the aperture. The paraxial wave equation cannot be applied accurately in this region, because the rapid changes in $\tilde{u}(x, z)$ with both x and z near the sharp aperture edges violate the approximations inherent in the paraxial wave equation.

The fundamental point, then, is that *paraxial methods*, however they may be formulated, can only be applied to paraxial beams, and a beam diffracted by a sharp-edged aperture does not again become paraxial until we move far enough past the aperture to satisfy Equation 16.21.

Huygens' Integral in One Dimension

Huygens' integral may be rewritten in the general form

$$\tilde{u}(\mathbf{s}, z) = \iint \tilde{K}(\mathbf{r}, \mathbf{r}_0) \tilde{u}_0(\mathbf{s}_0, z_0) d\mathbf{s}_0, \quad (22)$$

where \mathbf{r}_0 and \mathbf{r} indicate points on the input and output transverse planes; $\tilde{K}(\mathbf{r}, \mathbf{r}_0)$ is shorthand for the Huygens kernel of Equation 16.19; and $d\mathbf{s}_0$ indicates an element of area on the input plane. In rectangular coordinates the Huygens-Fresnel kernel separates into a product kernel in the form

$$\tilde{K}(\mathbf{r}, \mathbf{r}_0) = \tilde{K}_1(x - x_0) \times \tilde{K}_1(y - y_0), \quad (23)$$

where the one-dimensional kernel \tilde{K}_1 has the form

$$\tilde{K}_1(x - x_0) = \sqrt{\frac{j}{L\lambda}} \exp\left[-j\frac{\pi(x - x_0)^2}{L\lambda}\right]. \quad (24)$$

If the wavefunction $\tilde{u}(\mathbf{s}, z)$ is also separable in x, y coordinates, the entire integral can be separated into two one-dimensional integrals of the form

$$\tilde{u}(x, z) = \sqrt{\frac{j}{L\lambda}} \int \tilde{u}_0(x_0, z_0) \exp\left[-j\frac{\pi(x - x_0)^2}{L\lambda}\right] dx_0 \quad (25)$$

and the same for $\tilde{u}(y, z)$ and $\tilde{u}_0(y_0, z_0)$. We will frequently write such integrals in only one transverse dimension, in order to simplify the mathematical expressions.

Note that the $j/L\lambda$ factor in front of the three-dimensional Huygens' integral 16.19 reduces to $\sqrt{j/L\lambda}$ if there is only one transverse dimension. If only one transverse coordinate is included, the Huygens' wavelet is in essence a cylindrical wave rather than a spherical wave. Hence its amplitude decreases with distance as $1/\sqrt{\rho}$ or $1/\sqrt{L}$, rather than as $1/\rho$. The phase shift of $\pi/2$ due to the j factor in two dimensions also reduces to $\pi/4$ in one dimension. This phase factor represents in essence an initial phase shift of the Huygens' wavelet compared to the actual field value at the input point. We will see later that this corresponds to a well-known "Guoy phase shift" associated with any wave passing through a focus, or coming from a small enough source point.

REFERENCES

For an excellent introduction to scalar diffraction theory, with earlier references, see Chapter 3 of J. W. Goodman, *Introduction to Fourier Optics* (McGraw-Hill, 1968). Much more extensive discussions will also be found in M. Born and E. Wolf, *Principles of Optics* (Pergamon Press, 1959).

Problems for 16.2

1. *Solid angular spread from a uniformly illuminated aperture.* A transmitting aperture of total area A_0 transmits a collimated wavefront with total power P_0 having (ideally) a uniform intensity distribution over the aperture. Using Huygens' integral, show that the transmitted intensity on axis in the far-field (as $z \rightarrow \infty$)

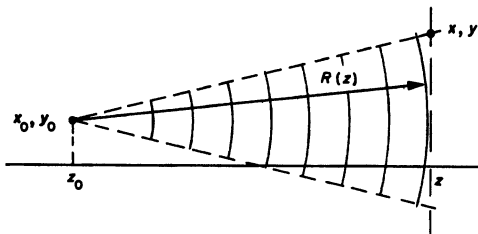


FIGURE 16.7
Spherical waveform coming from a real point source.

will be given in all cases by $I_z = P_0/(z\lambda)^2$, entirely independent of the shape of the aperture. What does this say about the approximate spread in solid angle of the far-field beam diverging from an aperture having total area A_0 but arbitrary shape? Can you give a simple argument why a uniform intensity distribution is optimum?

2. *Cascade properties of the Huygens-Fresnel integral.* Suppose we use the operator notation $\tilde{u}(x_1, z_1) = \tilde{K}(x_1 - x_0; z_1 - z_0) * \tilde{u}(x_0, z_0)$ as shorthand to indicate the operation of propagating an optical field $\tilde{u}(x, z)$ from plane z_0 to plane z_1 using the one-dimensional Huygens-Fresnel integral 16.19. Verify that the cascade of two such steps over successive distances z_0 to z_1 and then z_1 to z_2 is the same as a single step over the combined distance z_0 to z_2 , independent of the length of the individual steps. That is, verify that $\tilde{K}(x_2 - x_0; z_2 - z_0) * \tilde{u}(x_0, z_0) \equiv \tilde{K}(x_2 - x_1; z_2 - z_1) * \tilde{K}(x_1 - x_0; z_1 - z_0) * \tilde{u}(x_0, z_0)$ independent of the spacings between z_0 , z_1 and z_2 .

16.3 GAUSSIAN SPHERICAL WAVES

Our next important step is to derive the analytical form for a gaussian spherical wave, or a so-called “gaussian beam” in free space; and then to show that this gaussian beam is a very useful exact solution to the paraxial wave equation, or to Huygens’ integral in the Fresnel approximation.

Paraxial Spherical Waves

Consider a uniform spherical wave diverging from a source point located at x_0, y_0, z_0 , and observed at an observation point x, y, z , as in Figure 16.7. If the axial distance $z - z_0$ between the source and observation points is sufficiently large compared to the transverse coordinates x_0, y_0 and x, y , then the field distribution produced by this wave at point x, y on the plane located at distance z can be

written, using the paraxial approximation, in the form

$$\begin{aligned}\bar{u}(x, y, z) &= \frac{1}{z - z_0} \exp \left[-jk \frac{(x - x_0)^2 + (y - y_0)^2}{2(z - z_0)} \right] \\ &= \frac{1}{R(z)} \exp \left[-jk \frac{(x - x_0)^2 + (y - y_0)^2}{2R(z)} \right],\end{aligned}\quad (26)$$

where $R(z) = z - z_0$ gives the radius of curvature of the spherical wave at plane z . The phase variation $\exp[-jk\phi(x, y, z)]$ across a transverse plane at fixed z for such a paraxial spherical wave with radius of curvature $R(z)$ thus has the quadratic form

$$\phi(x, y, z) \equiv k \frac{(x - x_0)^2 + (y - y_0)^2}{2(z - z_0)} = \frac{\pi}{\lambda} \frac{(x - x_0)^2 + (y - y_0)^2}{R(z)}. \quad (27)$$

The radius of curvature $R(z)$ of the wave at plane z can be written in a more general form as

$$R(z) = R_0 + z - z_0, \quad (28)$$

with R_0 being the value at the earlier plane z_0 (and with $R_0 = 0$ if the earlier plane is the source plane, as in the present situation). As such a spherical wave propagates forward to any other plane z , the radius of curvature of the wave thus increases linearly with distance.

Note that with our sign convention, a value of $R > 0$ indicates a diverging or expanding wave, whereas $R < 0$ indicates a converging wave moving inward toward the source point. Note also that if the wave is propagating in some dielectric medium, k and λ are the values in that medium, not in free space. This quadratic phase variation of course represents only a paraxial or Fresnel approximation to the true surface of a sphere, so that this form will have a sizable phase error if we move far enough out from the optic axis.

Introducing Complex Source Point Coordinates

A paraxial spherical wave in the form given in Equation 16.26 cannot by itself be a very useful analytical form for a real physical beam, however, because the amplitude of the spherical wave does not fall off with transverse distance from the axis. Such a wave instead extends out to infinity in the transverse direction, and carries infinite energy and power across the transverse plane (as well as having large deviation from a true sphere far off the axis).

A very simple way to overcome these difficulties can be developed, however, as follows. Let us first note that the spherical wave expressions in Equations 16.26–16.28 satisfy the paraxial wave equation, or the Huygens-Fresnel integral, exactly for any arbitrary choice of the source point coordinates x_0, y_0, z_0 . That is, these coordinates are simply constant parameters, which cancel out identically when the spherical wave expression is put into the paraxial wave equation or the Huygens-Fresnel integral. What then will happen if we explore the possibility of employing complex values for these source point coordinates?

In particular, suppose that for simplicity we set x_0 and y_0 to zero, but that we convert the axial location z_0 of the source point into a *complex number*, by subtracting from it an arbitrary complex quantity which we will call \tilde{q}_0 . That is, we replace the purely real value z_0 in the spherical wave expression by the

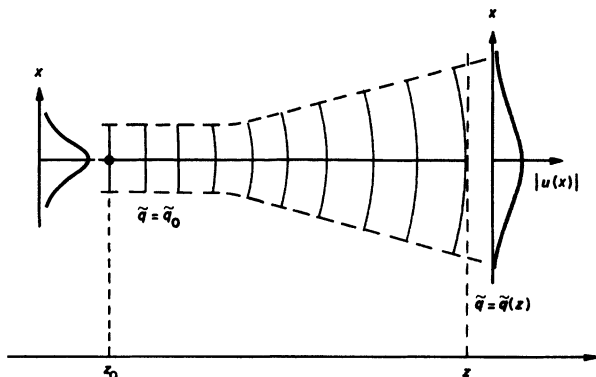


FIGURE 16.8
Gaussian-spherical wave from a complex point source.

complex value $z_0 - \tilde{q}_0$. This amounts to the same thing as replacing the radius of curvature $R(z) = R_0 + z - z_0$ by the complex quantity $\tilde{q}(z) = z - (z_0 - \tilde{q}_0) = \tilde{q}_0 + z - z_0$. [We introduce a new notation $\tilde{q}(z)$ in place of $R(z)$ because this quantity will turn out to be a complex generalization of the purely real spherical-wave radius of curvature $R(z)$.] Note that the value of this new “complex radius” at the source plane $z = z_0$ is just $\tilde{q}(z_0) = \tilde{q}_0$.

The spherical wave diverging from this complex source point is now written, following the same form as Equation 16.26, as

$$\begin{aligned}\tilde{u}(x, y, z) &= \frac{1}{z - z_0 + \tilde{q}_0} \exp \left[-jk \frac{x^2 + y^2}{2(z - z_0 + \tilde{q}_0)} \right] \\ &= \frac{1}{\tilde{q}(z)} \exp \left[-jk \frac{x^2 + y^2}{2\tilde{q}(z)} \right],\end{aligned}\quad (29)$$

where the complex radius $\tilde{q}(z)$ is given by

$$\tilde{q}(z) = \tilde{q}_0 + z - z_0 \quad (30)$$

in direct analogy to the expression 16.28 for $R(z)$.

But if $\tilde{q}(z)$ is complex, then we can separate the exponent in Equation 16.29 into real and imaginary parts, by first separating the quantity $1/\tilde{q}(z)$ into real and imaginary parts in the form

$$\frac{1}{\tilde{q}(z)} \equiv \frac{1}{q_r(z)} - j \frac{1}{q_i(z)}, \quad (31)$$

and then writing the spherical wave expression in the form

$$\tilde{u}(x, y, z) = \frac{1}{\tilde{q}(z)} \exp \left[-jk \frac{x^2 + y^2}{2q_r(z)} - k \frac{x^2 + y^2}{2q_i(z)} \right]. \quad (32)$$

(Note that q_r and q_i as defined here are not in general the real and imaginary parts of $\tilde{q}(z)$, but rather are defined by Equation 16.31.)

The resulting exponent for this complex-source-point beam now has both an imaginary quadratic transverse variation, corresponding to a quadratic phase front, or a spherical wave with a real radius of curvature; and also a purely real quadratic transverse variation, which gives a gaussian transverse amplitude profile or amplitude variation, with a transverse fall-off determined by the imaginary part of $1/\tilde{q}$. Both of these variations are contained in the complex radius of curvature \tilde{q} through Equation 16.31.

Gaussian-Spherical Beams

At this point let us convert this result into the standard notation which is very widely used in the laser field, by rewriting it in the form

$$\begin{aligned}\tilde{u}(x, y, z) &= \frac{1}{\tilde{q}(z)} \exp \left[-jk \frac{x^2 + y^2}{2\tilde{q}(z)} \right] \\ &\equiv \frac{1}{\tilde{q}(z)} \exp \left[-jk \frac{x^2 + y^2}{2R(z)} - \frac{x^2 + y^2}{w^2(z)} \right],\end{aligned}\quad (33)$$

where $R(z)$ is now the radius of curvature and $w(z)$ the so-called “gaussian spot size” of this solution. Equation 16.33 gives the *lowest-order spherical-gaussian beam solution in free space*. We can view this solution if we like as being simply a paraxial-spherical wave diverging from a complex source point, which is located a complex distance $z - z_0 + \tilde{q}_0$ rather than a real distance $z - z_0$ behind the observation plane z .

It is very important to note here that, although we use the same notation for $R(z)$ as before, *this radius of curvature can no longer be calculated by the formula $R(z) = R(z_0) + z - z_0$ from Equation 16.28*. Rather, the radius of curvature $R(z)$ and the spot size $w(z)$ of the wave at any plane z are derived from the complex radius $\tilde{q}(z)$ by the definition that

$$\frac{1}{\tilde{q}(z)} \equiv \frac{1}{R(z)} - j \frac{\lambda}{\pi w^2(z)}. \quad (34)$$

The variation of the complex radius of curvature $\tilde{q}(z)$ with distance is then determined by the formula

$$\tilde{q}(z) = \tilde{q}_0 + z - z_0. \quad (35)$$

The fundamental propagation law for all such gaussian beams in free space is entirely contained in this simple relation for $\tilde{q}(z)$.

Summary

The primary result of this section, then, is that replacing the purely real radius of curvature $R(z)$ for a spherical wave coming from a real source point z_0 with a *complex radius of curvature* $\tilde{q}(z)$, or a *complex source point* $(z_0 - \tilde{q}_0)$, converts the paraxial-spherical wave solution given in the opening paragraphs of this section into the *gaussian-spherical wave solution* given by Equations 16.29–16.35. This gaussian-spherical wave solution is still an exact mathematical solution to either the paraxial wave equation or the Huygens-Fresnel integral. Now, however, it has in addition the physically desirable properties that its amplitude falls off smoothly and rapidly with distances from the z axis; it carries finite total power

across the beam cross section; and it also remains complex gaussian in profile at all later planes z .

This gaussian-spherical solution, together with various higher-order Hermite-gaussian or Laguerre-gaussian extensions, will prove to be extraordinarily useful in the analysis of optical resonators and beams. This gaussian-spherical wave solution and its higher-order extensions for paraxial beams in free space can in fact be derived in at least four different ways, by using:

- (i) The complex source point derivation used in the present section; or
- (ii) A differential equation approach based on the paraxial wave equation, which we will use in the following two sections; or
- (iii) Direct substitution of the spherical-gaussian solution into the Huygens-Fresnel integral; or
- (iv) A plane-wave expansion approach, which we will introduce in several later sections.

The complex-source-point approach we have used here is, despite its simplicity, both subtle and entirely rigorous. We will explore the physical properties of this gaussian mode solution, and its higher-order extensions, in great detail in the following chapter.

REFERENCES

A very good summary of much of the early work on gaussian beams and resonator modes is given by H. Kogelnik and T. Li, "Laser beams and resonators," *Appl. Optics* **5**, 1150-1567 (October 1966).

The concept of a gaussian beam as a spherical wave emanating from a complex-valued source point has been developed in numerous places in the literature. See, for example, G. A. Deschamps, "Gaussian beam as a bundle of complex rays," *Electron. Lett.* **7**, 684-685 (1971); or M. Couture and P-A. Belanger, "From gaussian beam to complex-source-point spherical wave," *Phys. Rev. A* **24**, 355-359 (July 1981).

Problems for 16.3

1. *Changes in wavefront curvature on reflection from a curved mirror.* The phase variation across a transverse plane (i.e., at constant z) for a diverging spherical wave with radius of curvature $|R|$ traveling in the $+z$ direction has the form $\exp[-jkx^2/2|R|]$. What will be the transverse variation of this same wave (a) after reflecting off a planar mirror set up normal to the z axis? (b) After reflecting off a concave spherical mirror with radius of curvature $R_m = |R|$? (c) After reflecting off a concave spherical mirror with the same radius?
2. *Using a reversed coordinate system.* In the previous problem, suppose that in writing the fields of the reflected wave we decide to use a coordinate system in which the z direction is reversed, i.e., we write the reflected fields as $\tilde{E}(x, z')$ where $z' = -z$. What will be the answers to the same questions?
3. *Spherical waves and circular interference rings.* When we work with coherent light sources it is commonplace to observe circular interference rings or "bullseye patterns" in the beam coming from a laser resonator or from some subsequent

optical system. Suppose that a set of such concentric rings with maxima at radii r_n are observed in the output beam pattern from an optical system, and the hypothesis is that these rings must result from interference between two spherical waves coming from different source points within the system. Analyze what the radial spacing of such interference rings would be and discuss how, if you were able to measure a set of such radii r_n in the output beam, you might be able to determine where one or both of the source points were located within the system.

4. *Complex transverse source point coordinates.* Demonstrate that if we introduce complex values for one or both of the transverse source point coordinates—say, a small imaginary value for the transverse coordinate x_0 —as well as a complex value for z_0 , the result is to produce a tilted (and possibly transversely displaced) gaussian-spherical beam which travels at a small angle to the z axis in the x, z plane.
-

16.4 HIGHER-ORDER GAUSSIAN MODES

The gaussian beam expression we introduced in the previous section is really only the lowest-order solution in an infinite family of higher-order solutions to the same Huygens' integral, or the same free-space paraxial wave equation. The higher-order solutions to the same equations can take the form either of Hermite-gaussian functions in rectangular coordinates, or of Laguerre-gaussian functions in cylindrical coordinates. These higher-order gaussian modes are of considerable importance both in practical lasers and in optical beam analyses. Hence we reproduce their mathematical derivation in some detail in this section.

Lowest-Order Mode: The Differential Approach

A slightly more formal way of deriving the expressions we have just given for a lowest-order gaussian beam is to assume a trial solution to the paraxial wave equation of the form

$$\tilde{u}(x, y, z) = A(z) \times \exp \left[-jk \frac{x^2 + y^2}{2\tilde{q}(z)} \right], \quad (36)$$

where $A(z)$ and $\tilde{q}(z)$ are initially assumed to be unknown. If we substitute this trial solution into the paraxial wave equation, we obtain

$$\left[\left(\frac{k}{2} \right)^2 \left(\frac{d\tilde{q}}{dz} - 1 \right) (x^2 + y^2) - \frac{2jk}{\tilde{q}} \left(\frac{\tilde{q}}{A} \frac{dA}{dz} + 1 \right) \right] A(z) = 0. \quad (37)$$

Now, the only way in which this equation can be satisfied for all x and y is to set both of the differential expressions inside the large square brackets to zero. We then have the two differential equations

$$\frac{d\tilde{q}(z)}{dz} = 1 \quad \text{and} \quad \frac{dA(z)}{dz} = -\frac{A(z)}{\tilde{q}(z)}, \quad (38)$$

whose solutions are given by

$$\tilde{q}(z) = \tilde{q}_0 + z - z_0 \quad \text{and} \quad \frac{A(z)}{A_0} = \frac{\tilde{q}_0}{\tilde{q}(z)}. \quad (39)$$

These correspond exactly to the complex-source-point expressions derived in the preceding section.

Higher-Order Solutions in Rectangular Coordinates

We will now show how this same trial solution approach can be extended to find higher-order Hermite-gaussian eigensolutions $\tilde{u}_{nm}(x, y, z)$ or Laguerre-gaussian eigensolutions $\tilde{u}_{pm}(r, \theta, z)$ to the paraxial wave equation.

We will derive first the higher-order Hermite-gaussian solutions to the wave equation in rectangular coordinates. In rectangular coordinates the elementary solutions can be separated into products of identical solutions in the x and y directions, i.e.,

$$\tilde{u}_{nm}(x, y, z) = \tilde{u}_n(x, z) \times \tilde{u}_m(y, z), \quad (40)$$

where $\tilde{u}_n(x, z)$ and $\tilde{u}_m(y, z)$ have the same mathematical form. We can therefore find the solutions in only one rectangular coordinate and bring in the other coordinate by analogy.

The paraxial wave equation in one transverse coordinate reduces to

$$\frac{\partial^2 \tilde{u}_n(x, z)}{\partial x^2} - 2jk \frac{\partial \tilde{u}_n(x, z)}{\partial z} = 0. \quad (41)$$

As one way of looking for higher-order solutions, let us now write a more general trial solution for the wave amplitude $\tilde{u}(x, z)$ in the form

$$\tilde{u}_n(x, z) = A(\tilde{q}(z)) \times h_n\left(\frac{x}{\tilde{p}(z)}\right) \times \exp\left[-jk \frac{x^2}{2\tilde{q}(z)}\right], \quad (42)$$

where $\tilde{q} = \tilde{q}(z)$ is the same as in the preceding; $A(\tilde{q})$ and $h_n(x/\tilde{p})$ are initially unknown functions; and $\tilde{p} = \tilde{p}(z)$ is a distance-dependent scaling factor in the argument of h_n . Diode

Substituting this form into the paraxial wave equation, and assuming that $\tilde{q}(z)$ will continue to obey the propagation rule $d\tilde{q}/dz = 1$, then converts the paraxial wave equation into a differential relation for $h_n(x/\tilde{p})$, namely

$$h_n'' - 2jk \left[\frac{\tilde{p}}{\tilde{q}} - \tilde{p}' \right] x h_n' - \frac{jk\tilde{p}^2}{\tilde{q}} \left[1 + \frac{2\tilde{q}}{A} \frac{dA}{d\tilde{q}} \right] h_n = 0, \quad (43)$$

where h_n' and h_n'' mean the first and second derivatives of h_n with respect to its total argument, e.g., $h_n'(y) = dh_n(y)/dy$, and $\tilde{p}' \equiv d\tilde{p}(z)/dz$. But, Equation 16.43 is very similar to the standard differential equation for the Hermite polynomials $H_n(x/\tilde{p})$, which has the form

$$H_n'' - 2(x/\tilde{p})H_n' + 2nH_n = 0. \quad (44)$$

The two equations for h_n and H_n will in fact become the same if we can find solutions for $\tilde{p}(z)$ and $A(\tilde{q})$ which satisfy simultaneously the two conditions

$$2jk \left[\frac{\tilde{p}}{\tilde{q}} - \frac{d\tilde{p}}{dz} \right] = \frac{2}{\tilde{p}} \quad \text{or} \quad \frac{d\tilde{p}}{dz} = \frac{\tilde{p}}{\tilde{q}} + \frac{j}{k\tilde{p}}, \quad (45)$$

and

$$\frac{-jk\tilde{p}^2}{\tilde{q}} \left[1 + \frac{2q}{A} \frac{dA}{d\tilde{q}} \right] = 2n \quad \text{or} \quad \frac{2q}{A} \frac{dA}{d\tilde{q}} = \frac{2jnk\tilde{p}^2}{\tilde{q}} - 1. \quad (46)$$

Now, there are at least two, and probably many different ways in which Equations 16.45 and 16.46 can be solved, with each solution leading to a different family of higher-order Hermite-gaussian solutions. We will describe in this section one family of such solutions, which we will refer to as the “standard” Hermite-gaussian solutions. In the following section we will describe another alternative set of solutions which we will refer to as the “elegant” solutions.

The “Standard” Hermite Polynomial Solutions

The set of Hermite-gaussian solutions that we will derive in this section are by far the most widely used set of such solutions, as well as being the closest to simple physical solutions in ordinary stable lasers. However, this set is also perhaps the most complicated and inelegant approach from a mathematical viewpoint. This standard approach to Hermite polynomial solutions is obtained by assuming that the scale factor $\tilde{p}(z)$ in the function $h_n(x/\tilde{p})$ will be purely real, and in fact will be related to the gaussian spot size $w(z)$ in the form

$$\frac{1}{\tilde{p}(z)} \equiv \frac{\sqrt{2}}{w(z)}. \quad (47)$$

As motivation for this approach we can note that if this is valid then the higher-order solutions of Equation 16.42, namely

$$\tilde{u}_n(x, z) = h_n \left(\frac{\sqrt{2}x}{w(z)} \right) \exp \left[\frac{-jkx^2}{2R(z)} - \frac{x^2}{w^2(z)} \right], \quad (48)$$

will have the same normalized shape at every transverse plane z . That is, these functions will change in transverse scale like $w(z)$, and will acquire spherical curvature $R(z)$, but their amplitude profiles will remain unchanged in shape at any plane z .

We must first verify that this form for $\tilde{p}(z)$ will satisfy the differential equation 16.45. Since the spot size $w(z)$ is related to $\tilde{q}(z)$ by

$$\frac{1}{\tilde{q}(z)} = \frac{1}{R(z)} - j \frac{\lambda}{\pi w^2(z)} \quad (49)$$

we can use this to obtain

$$\frac{1}{w^2(z)} = \frac{jk}{4} \left[\frac{1}{\tilde{q}(z)} - \frac{1}{\tilde{q}^*(z)} \right] = \frac{jk}{4} \frac{\tilde{q}^*(z) - \tilde{q}(z)}{\tilde{q}(z)\tilde{q}^*(z)}. \quad (50)$$

We can also note that the formulas for $\tilde{q}(z)$ imply the useful relations that

$$d\tilde{q}^*/dz = d\tilde{q}/dz = 1 \quad \text{and hence} \quad \tilde{q}^* - \tilde{q} = \tilde{q}_0^* - \tilde{q}_0. \quad (51)$$

The reader can then verify that the form for $\tilde{p}(z)$ given in Equation 16.47 does indeed satisfy Equation 16.45.

The simplest way to satisfy the equation for $A(\tilde{q})$ is then perhaps to use the definition of $1/\tilde{q}$, and the fact that $d\tilde{q}^* = d\tilde{q}$ to rewrite Equation 16.46 as

$$\frac{dA}{A} = -\frac{1}{2} \frac{d\tilde{q}}{\tilde{q}} + \frac{n}{2} \left(\frac{d\tilde{q}^*}{\tilde{q}^*} - \frac{d\tilde{q}}{\tilde{q}} \right). \quad (52)$$

Integrating this equation then yields

$$A(\tilde{q}) = A_0 \times \left(\frac{\tilde{q}_0}{\tilde{q}(z)} \right)^{1/2} \times \left(\frac{\tilde{q}_0}{\tilde{q}_0^*} \frac{\tilde{q}^*(z)}{\tilde{q}(z)} \right)^{n/2}. \quad (53)$$

A complete set of properly normalized higher-order Hermite-gaussian mode functions for a beam propagating in free-space are thus given, in one transverse dimension, by

$$\begin{aligned} \tilde{u}_n(x, z) = & \left(\frac{2}{\pi} \right)^{1/4} \left(\frac{1}{2^n n! w_0} \right)^{1/2} \left(\frac{\tilde{q}_0}{\tilde{q}(z)} \right)^{1/2} \left[\frac{\tilde{q}_0}{\tilde{q}_0^*} \frac{\tilde{q}^*(z)}{\tilde{q}(z)} \right]^{n/2} \\ & \times H_n \left(\frac{\sqrt{2}x}{w(z)} \right) \exp \left[-j \frac{kx^2}{2\tilde{q}(z)} \right], \end{aligned} \quad (54)$$

where the H_n 's are the Hermite polynomials of order n , and $\tilde{q}(z)$ and $w(z)$ are exactly the same as for the lowest-order gaussian mode.

The Guoy Phase Shift

The most compact and efficient way of writing the higher-order Hermite-gaussian eigenmodes is as in Equation 16.54, using the ratios of $\tilde{q}(z)$ and $\tilde{q}^*(z)$ raised to appropriate powers. This form can also be converted, however, to a more commonly used form involving the real spot size $w(z)$ and a phase angle $\psi(z)$, as follows.

Let us associate a magnitude and especially a phase angle $\psi(z)$ with the complex \tilde{q} parameter at any plane z by writing

$$\frac{j}{\tilde{q}} = \frac{\lambda}{\pi w^2} \left[1 + j \frac{\pi w^2}{R \lambda} \right] \equiv \frac{\exp[j\psi(z)]}{|\tilde{q}|}, \quad (55)$$

so that the phase angle $\psi = \psi(z)$ is given at any plane z by

$$\tan \psi(z) \equiv \frac{\pi w^2(z)}{R(z) \lambda}. \quad (56)$$

We have included the factor of j in Equation 16.55 because it will be convenient later on to have $\psi(z) = 0$ at the "waist" of a gaussian beam, where the spot size w is finite but the radius of curvature R becomes infinite.

If we use this definition, we can then show (after some algebra) that the first part of the $\tilde{q}_0/w_0\tilde{q}(z)$ normalization factor in Equation 16.54 can be written as

$$\frac{1}{w_0} \frac{\tilde{q}_0}{\tilde{q}(z)} = \frac{\exp[j(\psi(z) - \psi_0)]}{w(z)}, \quad (57)$$

where $\psi_0 \equiv \psi(z_0)$ is the initial value of $\psi(z)$ at $z = z_0$. The lowest-order gaussian-spherical wave (Equation 16.33) may then be written in the alternative form

$$\tilde{u}_0(x, z) = \left(\frac{2}{\pi}\right)^{1/4} \sqrt{\frac{\exp j[\psi(z) - \psi_0]}{w(z)}} \exp \left[-j \frac{kx^2}{2\tilde{q}(z)}\right]. \quad (58)$$

In other words, the factor $(1/w_0) \times (\tilde{q}_0/\tilde{q}(z))$ contains the necessary $1/w(z)$ normalization factor in front of the gaussian beam expression, along with an added phase shift term given by $\psi(z) - \psi_0$.

For all higher-order Hermite-gaussian modes we must also include the additional factors given by the term

$$\left[\frac{\tilde{q}_0}{\tilde{q}^*(z)} \frac{\tilde{q}^*(z)}{\tilde{q}(z)} \right]^{n/2} \equiv \exp [jn[\psi(z) - \psi_0]] \quad (59)$$

appearing on the right-hand side of Equation 16.54. This factor gives rise to a pure phase shift. With this factor included, the higher-order Hermite-gaussian mode functions of Equation 16.54 can be written in the alternative form

$$\begin{aligned} \tilde{u}_n(x) = & \left(\frac{2}{\pi}\right)^{1/4} \sqrt{\frac{\exp[-j(2n+1)(\psi(z) - \psi_0)]}{2^n n! w(z)}} \\ & \times H_n \left(\frac{\sqrt{2}x}{w(z)} \right) \exp \left[-j \frac{kx^2}{2R(z)} - \frac{x^2}{w^2(z)} \right]. \end{aligned} \quad (60)$$

We will discuss the physical significance of the so-called “Guoy phase shift term” $\psi(z)$ in the following chapter.

Hermite-Gaussian Mode Expansions

The Hermite-gaussian functions $\tilde{u}_n(x, z)$ we have derived here provide a complete basis set of orthogonal functions characterized by a single complex parameter, the complex \tilde{q}_0 parameter at any arbitrary reference plane z_0 . (We will discuss the physical significance of this parameter in the following chapter.) These functions obey the orthonormality condition

$$\int_{-\infty}^{\infty} u_n^*(x, z) \tilde{u}_m(x, z) dx = \delta_{nm}, \quad (61)$$

independent of either z or of \tilde{q}_0 . They can thus be used as a basis set to expand any arbitrary paraxial optical beam $\tilde{E}(x, y, z)$ in the form

$$\tilde{E}(x, y, z) = \sum_n \sum_m c_{nm} \tilde{u}_n(x, z) \tilde{u}_m(y, z) e^{-jkz}. \quad (62)$$

If we multiply both sides of this by $u_n^*(x, z) u_m^*(y, z)$ and integrate across the full cross section, we can find that the expansion coefficients c_{nm} are given by

$$c_{nm} = \int_{-\infty}^{\infty} \int_{-\infty}^{\infty} \tilde{E}(x, y, z) u_n^*(x, z) u_m^*(y, z) dx dy. \quad (63)$$

The coefficients c_{nm} will depend upon the arbitrary choice of \tilde{q}_0 at z_0 . There is thus in general no unique or necessary way of choosing the waist size w_0 or waist

location z_0 for the basis set to expand a given beam pattern $\tilde{E}(x, y)$. We may attempt to choose these parameters to given an expansion which best fits some other physical constraint in the problem, or which gives an expansion that best fits the actual field $\tilde{E}(x, y, z)$ with the smallest number of terms.

Astigmatic Mode Functions

As we noted earlier, the Hermite-gaussian function $\tilde{u}_n(x, z)$ in one dimension corresponds essentially to a cylindrical wave, and hence has a normalization factor of $1/\tilde{q}^{1/2}(z)$ or $1/w^{1/2}(z)$ rather than $1/\tilde{q}(z)$ or $1/w(z)$. The overall normalization factor for the field function $\tilde{u}_{nm}(x, y, z)$ is then the product of the individual normalization functions for $\tilde{u}_n(x, z)$ and $\tilde{u}_m(y, z)$.

There is no fundamental reason in fact why the complex beam parameters \tilde{q}_{0x} , w_{0x} and z_{0x} associated with the functions $\tilde{u}_n(x, z)$ in the x transverse coordinate cannot have entirely different values from the corresponding parameters \tilde{q}_{0y} , w_{0y} and z_{0y} associated with the functions $\tilde{u}_m(y, z)$ in the y direction. The gaussian beam solutions can thus be converted, where it seems necessary or useful, into a set of somewhat more general astigmatic gaussian beam modes by replacing $\tilde{q}(z)$, and the related quantities $w(z)$ and $\psi(z)$, by separate values for the x and y coordinates wherever these quantities appear in the Hermite-gaussian solutions.

Note in particular that only half of the fundamental Guoy phase comes from each transverse coordinate. The Guoy phase shift for a uniform cylindrical wave through a focus is only 90° rather than 180° , and the phase factor in Huygens' integral in one transverse dimension is \sqrt{j} rather than j .

Cylindrical Coordinates: Laguerre-Gaussian Modes

An alternative but equally valid family of solutions to the paraxial wave equation can be written in cylindrical rather than rectangular coordinates. These solutions are in general the *Laguerre-gaussian solutions* of the form

$$\begin{aligned} \tilde{u}_{pm}(r, \theta, z) = & \sqrt{\frac{2p!}{(1 + \delta_{0m}) \pi (m + p)!}} \frac{\exp j(2p + m + 1)(\psi(z) - \psi_0)}{w(z)} \\ & \times \left(\frac{\sqrt{2}r}{w(z)} \right)^m L_p^m \left(\frac{2r^2}{w(z)^2} \right) \exp \left[-jk \frac{r^2}{2\tilde{q}(z)} + im\theta \right]. \end{aligned} \quad (64)$$

In these solutions the integer $p \geq 0$ is the radial index and the integer m is the azimuthal mode index; the L_p^m functions are the generalized Laguerre polynomials; and all the other quantities \tilde{q} , w and ψ are exactly the same as in the Hermite-gaussian situation.

These solutions are written using the "standard" transverse scaling $r/\tilde{p}(z) = \sqrt{2r}/w(z)$ that we used for the Hermite-gaussian solutions in Equation 16.47 of this section. An alternative set of complex Laguerre-gaussian cylindrical solutions using the complex scaling $r/\tilde{p}(z) = \sqrt{jkr^2/2\tilde{q}(z)}$ which we will introduce in the following section could equally well be developed. In either situation these modes have cylindrical symmetry, with modes having circles of constant intensity in the radial direction and an $e^{im\theta}$ variation in the azimuthal direction. Alternatively linear combinations of the $\pm m$ terms can be formed to give $\cos m\theta$ and/or $\sin m\theta$ variations, leading to $2m$ nodal lines running radial outward from the mode axis. Laguerre-gaussian exhibit the same Guoy phase shift as the rectangular modes.

The Laguerre-gaussian solutions provide an equally general but alternative basis set to the Hermite-gaussian solutions for expanding an arbitrary optical beam $\tilde{u}(r, \theta, z)$ in free space (provided we are knowledgeable about generalized Laguerre polynomials). Since both the Hermite-gaussian and Laguerre-gaussian functions form complete sets, we must be able to expand any Hermite solution in terms of the Laguerre functions and vice versa.

The Laguerre-gaussian functions will perhaps be more convenient for problems having a large amount of cylindrical symmetry, and will probably not provide the most convenient set for expanding any real optical beam having substantial astigmatism between x and y axes. In real lasers the Brewster windows and any other tilted surfaces or distorted elements usually provide a small but inherent rectangular symmetry to the laser cavity. Real lasers, therefore, overwhelmingly elect to oscillate in near-Hermite-gaussian rather than near-Laguerre-gaussian modes. Experiments with very carefully aligned gas lasers having internal mirrors and no Brewster windows have, however, clearly demonstrated oscillations in Laguerre-gaussian modes with higher-order radial and azimuthal symmetry.

REFERENCES

A summary of the standard Hermite-gaussian mode functions and some of their properties is given in A. E. Siegman and E. A. Szkla, "Mode calculations in unstable resonators with flowing saturable gain. I: Hermite-gaussian expansion," *Appl. Optics* **13**, 2775-2792 (December 1974).

More detailed discussions of the vector properties of free-space beam modes can be found in, for example, L. W. Davis and G. Patsakos, "TM and TE electromagnetic beams in free space," *Optics Lett.* **6**, 22-23 (January 1981) and "Comment on 'Representation of vector electromagnetic beams,'" *Phys. Rev. A* **26**, 3702-3703 (December 1982), and the references cited therein.

A very useful reference source for orthogonal polynomials and almost all other special functions is M. Abramowitz and I. A. Stegun, *Handbook of Mathematical Functions* (Dover Publications, Inc., New York, 1965).

Problems for 16.4

1. *Intensity contours for a higher-order Hermite-gaussian mode.* Consider as an example the $\tilde{u}_{22}(x, y)$ higher-order gaussian mode in rectangular coordinates. Develop a formula and write a computer program to trace out the constant-amplitude contours in the xy plane for this mode, and make an isoamplitude contour map or model.
2. *Finding the mode content of an arbitrary optical beam (research problem).* Suppose you have an optical beam made up of an arbitrary, unknown combination of lowest and higher-order Hermite-gaussian modes. How could you *experimentally* separate this beam into its individual Hermite-gaussian components, with each component being directed into a separate single-mode optical fiber?

So far as I know, no good solution to this problem has yet been given. The problem of identifying and measuring the mode content of an arbitrary optical beam is addressed, however, in M. A. Golub, et al., "Synthesis of spatial filters for

investigation of the transverse mode composition of coherent radiation," Sov. J. Quantum Electron. **12**, 1208-1209 (September 1982).

3. *Recursion relation for Hermite-gaussian modes* A standard recursion relation for the Hermite polynomials $H_n(x)$ is $H_{n+1}(x) = 2xH_n(x) - 2nH_{n-1}(x)$. Using this relation derive a similar recursion relation for the normalized Hermite-gaussian functions $\hat{u}_n(x)$ introduced in this section.

16.5 COMPLEX-ARGUMENT GAUSSIAN MODES

The "standard" Hermite-gaussian solutions developed in the preceding section are the most commonly used form for the Hermite-gaussian eigenmodes, and the form most often given in the laser literature. They represent, among other things, the set of Hermite-gaussian modes that are the closest approximation to the actual higher-order modes of finite-mirror stable resonators. These modes are perhaps somewhat inelegant mathematically, however, in that we have a complex scaling factor in the gaussian function but only a real scaling factor in the Hermite polynomials. As a result, Equation 16.54 is somewhat messy, since the inelegant combinations of \tilde{q} and \tilde{q}^* values must be carried along in all the normalization factors.

There are, however, many other alternative choices for $\tilde{p}(z)$ and $A(\tilde{q})$ that will satisfy the differential equations 16.45 and 16.46 for these quantities derived in the preceding section. To illustrate this we will develop one of these alternative families of solutions in this section. The motivation behind this particular solution is to use the same complex scaling factor, that is, the quantity $\sqrt{jkx^2/2\tilde{q}}$, as the argument both in the gaussian exponent and in the Hermite polynomial functions.

The "Elegant" Hermite Polynomial Solutions

To do this we will define the complex scale factor \tilde{p} in the functions $h_n(x/p)$ of the previous section not by $1/\tilde{p} = \sqrt{2}/w$ as in Equation 16.47, but by

$$\frac{1}{\tilde{p}(z)} \equiv \sqrt{\frac{jk}{2\tilde{q}(z)}}. \quad (65)$$

The reader can verify that this choice will also satisfy the differential equation 16.45, and that the differential condition 16.46 for $A(\tilde{q})$ then takes on the significantly simpler form

$$\frac{\tilde{q}}{A} \frac{dA}{d\tilde{q}} = -\frac{n+1}{2}. \quad (66)$$

If we solve this, the Hermite-gaussian eigenfunctions then take on the alternative form

$$\hat{u}_n(x, z) = \hat{u}_0 \left[\frac{\tilde{q}_0}{\tilde{q}(z)} \right]^{n+1/2} H_n \left(\sqrt{\frac{jkx^2}{2\tilde{q}(z)}} \right) \exp \left[-j \frac{kx^2}{2\tilde{q}(z)} \right]. \quad (67)$$

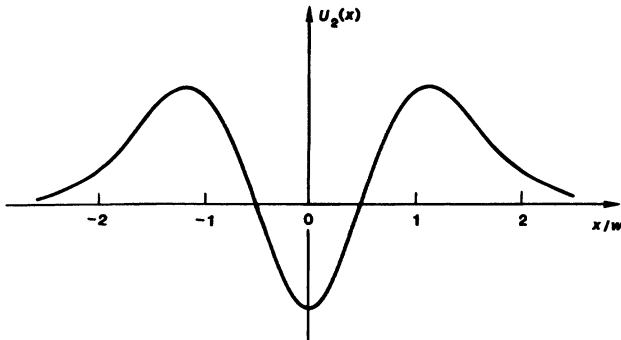


FIGURE 16.9

The "standard" (real-argument) Hermite-gaussian function $\tilde{u}_n(x)$ for $n = 2$.

This alternative solution puts the same complex argument $\sqrt{jkx^2/2\bar{q}(z)}$ into both the Hermite polynomial and the gaussian exponent, and is much simpler than the "standard" solutions given in Equation 16.54.

This alternative set of Hermite-gaussian solutions represents an equally valid complete set of solutions to the paraxial wave equation in free space. This alternative set is more compact and elegant, with some interesting analytical properties, but it is also perhaps less directly useful physically. For example, whereas these alternative functions $\tilde{u}_n(x, z)$ still form a mathematically complete set, they are no longer orthogonal to each other in the usual sense. Rather the alternative functions \tilde{u}_n are *biorthogonal* to a set of adjoint functions \hat{v}_n given by

$$\hat{v}_n(x, z) = H_n \left(\sqrt{\frac{-jk}{2\bar{q}^*}} x \right), \quad (68)$$

(no gaussian factor) with the orthogonality relation now being

$$\int_{-\infty}^{\infty} \hat{u}_n(x, z) \hat{v}_n^*(x, z) dx = c_n \delta_{nm}, \quad (69)$$

where c_n is an appropriate normalization constant.

Properties of the "Elegant" Solutions

The lowest-order or $n = 0$ and $n = 1$ members of the "standard" and the alternative or "elegant" sets of Hermite-gaussian functions given in Equations 16.54 and 16.67 are indistinguishable from each other, since they consist only of the gaussian exponential, or of this exponential multiplied by x . There are, however, significant differences between the higher-order modes in the two sets.

The next higher-order function $n = 2$, for example, uses the Hermite polynomial $H_2(x) = 4x^2 - 2$, so that the "standard" solution $\tilde{u}_2(x)$ has the form

$$\tilde{u}_2(x, z) = \text{const} \times \left[\frac{4x^2}{w^2} - 1 \right] \exp \left[-j \frac{kx^2}{2\bar{q}} \right], \quad (70)$$

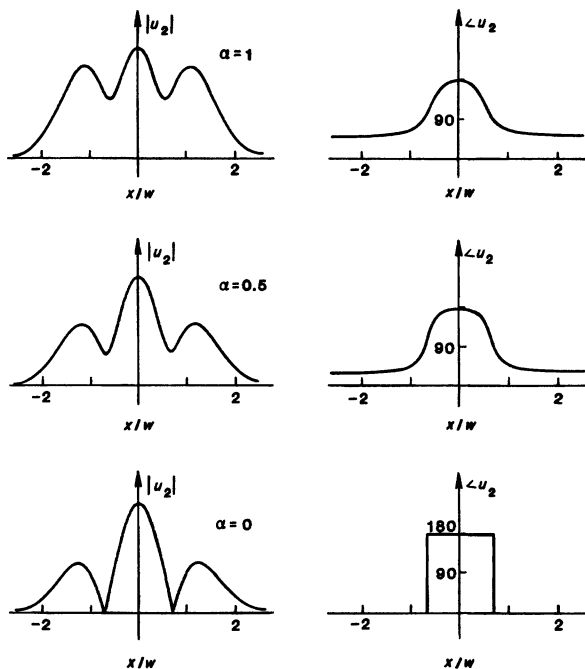


FIGURE 16.10
The “elegant” (complex-argument) Hermite-gaussian function $\hat{u}_n(x)$ for $n = 2$ and for different values of the parameter $\alpha \equiv \pi w^2 / R\lambda$.

whereas the “elegant” solution $\hat{u}_2(x)$ becomes

$$\begin{aligned}\hat{u}_2(x) &= \text{const} \times \left[\frac{jkx^2}{\tilde{q}} - 1 \right] \exp \left[-j \frac{jkx^2}{2\tilde{q}} \right] \\ &= \text{const} \times \left[\frac{2(1+j\alpha)x^2}{w^2} - 1 \right] \exp \left[-j \frac{jkx^2}{2\tilde{q}} \right],\end{aligned}\quad (71)$$

where $\alpha = \pi w^2 / R\lambda$. The two functions are different, though somewhat similar, even for $\alpha = 0$; and for nonzero values of α the complex argument in the polynomial causes the usual nulls in the function to be filled in, as illustrated in Figure 16.10, and also produces an additional phase variation across the beam which is not purely spherical in form, as Figure 16.10 also shows. For $n \geq 2$ the amplitude and phase patterns of the higher-order alternative modes also change in shape with propagation distance z (unlike the “standard” modes) because of the change in $\tilde{q}(z)$ with distance.

Either family of Hermite-gaussian solutions, 16.54 or 16.67, is equally valid as a general basis set for analytic expansions of arbitrary optical beams. Stable laser resonators with spherical mirrors and negligible beam aperturing will generally have real eigenmodes that are much closer to the “standard” or $\sqrt{2}x/w$ family of Hermite-gaussian modes, and hence this form for the Hermite-gaussian solutions

is much more widely used in the laser literature. More general complex paraxial systems including soft gaussian apertures, such as we will discuss later, do lead to Hermite modes with complex arguments, like the “elegant” or $\sqrt{jkx^2/2q}$ family, and this type of solution is now being more extensively considered. In all situations we can develop astigmatic mode solutions with different fundamental parameters in the x and y coordinates if this seems useful.

REFERENCES

The complex Hermite solutions described in this section were introduced in A. E. Siegman, “Hermite-gaussian functions of complex argument as optical-beam eigenfunctions,” *J. Opt. Soc. Am.* **61**, 1093–1094 (September 1973).

More general complex free-space solutions are also given by R. Pratesi and L. Ronchi, “Generalized gaussian beams in free space,” *J. Opt. Soc. Am.* **67**, 1274–1276 (September 1977).

16.6 GAUSSIAN BEAM PROPAGATION IN DUCTS

Gaussian beams in free space always remain gaussian, but do of course spread outward due to diffraction effects as they propagate. In a medium with a quadratic transverse variation of index of refraction, however, it becomes possible to trap and propagate a particular confined gaussian beam which neither spreads nor contracts with distance. We have already discussed the ray-trapping properties of graded-index optical waveguides or ducts. Such ducts are also of substantial practical and analytical interest in gaussian beam optics as well as in ray optics. The two topics are, in fact, essentially identical in concept and in results.

Gaussian Beam Propagation in Ducts

Suppose again that the index of refraction $n(r)$ in a duct has a radial (or transverse) variation given by

$$n(r) = n_0 - \frac{1}{2}n_2r^2. \quad (72)$$

The wave equation 16.1 in a medium with a quadratic transverse variation such as this must then be expanded to the form

$$[\nabla^2 + \omega^2\mu\epsilon[1 - n_2(x^2 + y^2)]]\tilde{E}(x, y, z) = 0. \quad (73)$$

Converting this to the paraxial approximation in the same form as used in deriving Equation 16.5 then gives

$$\left[\nabla_{xy}^2 - k^2n_2(x^2 + y^2) - 2jk\frac{\partial}{\partial z}\right]\tilde{u}(x, y, z) = 0. \quad (74)$$

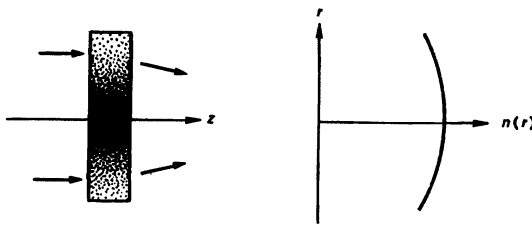


FIGURE 16.11
A short section of a duct.

The reader can verify that a stable solution to this equation is given by the confined or trapped gaussian beam

$$\tilde{u}(x, y, z) = \tilde{u}_0 \exp \left[-\frac{x^2 + y^2}{w_1^2} + j \frac{\lambda z}{w_1^2} \right], \quad (75)$$

where the spot size w_1 is given by

$$w_1^2 = \frac{\lambda}{\pi \sqrt{n_2}}. \quad (76)$$

This solution thus represents a *stable trapped gaussian eigenmode of fixed diameter in the waveguide or duct*. Note that the quadratic exponent for this wave is purely real, i.e., the wavefronts in this guided beam are exactly plane waves. Higher-order modes with Hermite-gaussian or Laguerre-gaussian form can also propagate in the same duct.

Physical Interpretation

One way of understanding this confined mode is the following. In a duct with an index variation like Equation 16.72, each axial segment of length Δz is like a thin lens with focal length $f = 1/n_2 \Delta z$, as illustrated in Figure 16.11. For a gaussian beam with spot size w_1 as given in the preceding, the effects of diffraction spreading in each unit length are just canceled by this focusing effect, so that the beam size remains constant.

Note again that the steady-state gaussian spot size w_1 varies inversely as the strength n_2 of the transverse index variation—the stronger the focusing the smaller the steady-state beam profile that will be propagated in the duct. This gaussian eigenmode also acquires a small added phase shift per unit length, over and above the e^{-jkz} factor, that is expressed by the $+j\lambda z/\pi w_1^2$ term. This indicates that the z -directed propagation constant in the duct, call it k_d , is not the on-axis value of k in the medium but rather a guided-wave value given by

$$k_d = k - \lambda/\pi w_1^2. \quad (77)$$

The added phase shift $\psi(z)$ associated with the $-\lambda z/\pi w_1^2$ per unit length in the duct is just given by $d\psi(z)/dz = \lambda/\pi w_1^2 = 1/z_R$ where z_R would be the Rayleigh range for the guided beam without the ducting effects. This is in fact exactly the same as the derivative $d\psi(z)/dz$ exactly at the waist for the Guoy effect which we will discuss in the following chapter.

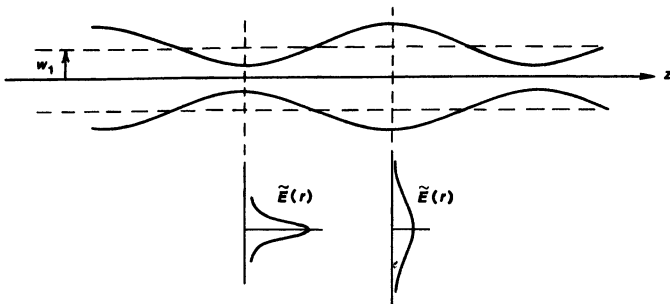


FIGURE 16.12
Beam scalloping in a quadratic duct.

Beam Oscillations or Beam Scalloping in Ducts

Suppose we introduce into such a duct a gaussian beam which does not match the gaussian eigenmode of the duct, either in spot size or in wavefront curvature. Suppose the input beam is initially smaller than the steady-state spot size w_1 . The diffraction spreading for this smaller beam will then be larger than for the steady-state spot size, whereas the refocusing produced by each unit length of the duct will be the same. The spot size will therefore begin to grow, and the gaussian beam will begin to spread with distance.

As soon as its spot size becomes larger than the steady-state value, however, the opposite condition will prevail, and the beam will be refocused again. An input beam with a spot size $w(z)$ either larger or smaller than the steady-state value w_1 will thus oscillate or scallop periodically inward and outward about the steady-state value in sausage-like fashion as it propagates down the guide, as shown in Figure 16.12.

This gaussian beam behavior is very much analogous to the oscillatory behavior of rays trapped in a stable duct, and to first order the beam oscillations will have the same oscillation period as the stable ray solutions we derived earlier. As an equally valid alternative explanation, we can say that the mismatched input beam excites in the duct a mixture of the lowest and higher-order eigenmodes of the duct. These eigenmodes then propagate with slightly different phase velocities, since the added phase shift term $\lambda z / \pi w_1^2$ is different for the lowest-order and for the higher-order eigenmodes. The periodic scalloping behavior then represents a beating phenomena in the axial direction as the higher-order modes propagate and interfere with different phases at different distances along the duct.

Ducts in Real Systems

The paraxial wave solutions in a duct will be exactly gaussian only if the index variation about the axis is exactly quadratic—and a purely quadratic decrease of the index with radius cannot continue indefinitely. The Hermite-gaussian solutions for propagation in a duct are thus generally approximations to the real modes, although they will be quite good approximations if the index variation is in fact approximately quadratic out to at least a few spot sizes w_1 of the trapped gaussian beam (as is quite often the situation). If this approximation

fails, or if the index variation is other than quadratic, then other mathematical forms for the trapped modes must be sought; and there is a very large published literature on such trapped modes, especially of course for the modes in simple optical fibers which have step variations rather than continuous variations in index of refraction.

Transverse index variations leading to duct-like effects occur naturally on a random basis in many situations—for example, in laser rods, in inhomogeneous optical materials, in optical (or radio-wave) propagation through the atmosphere, or in sound-wave propagation through the oceans. Poor quality laser rods in the early days of lasers, in fact, often exhibited highly irregular transverse beam patterns, with many small spots across the face of the rod, due to strong ducting effects at random locations across the rod cross-section. More controlled ducting effects are also now deliberately produced to create waveguiding effects in optical fibers or in laser rods manufactured under such trade names as GRIN (graded refractive index) or SEL-FOC rods. Note that the spot size w_1 of the trapped beam in a duct will almost always be much smaller than the half-width $1/n_2^{1/2}$ of the duct itself, unless the duct is extremely small. Hence it will only be the quadratic or $n_2 \equiv -\partial^2 n / \partial r^2$ variation of the index close to the axis that will usually be important, even if the index profile no longer remains purely quadratic at larger radii.

Larger ducts can also trap an entire family of higher-order Hermite-gaussian or Laguerre-gaussian modes such as we have analyzed in the previous chapter. We will develop a more general theorem of gaussian ducts in Chapter 20, including both quadratic index and loss variations, by using a complex $ABCD$ matrix approach.

REFERENCES

Two examples of more general treatments of optical ducting and guided waves with arbitrary index profiles are C. N. Kurtz and W. Streifer, "Guided waves in inhomogeneous focusing media, Part I and Part II," *IEEE Trans. MTT-17*, 11-15 and 250-253 (January 1969 and May 1969); and W. J. Firth, "Propagation of laser beams through inhomogeneous media," *Optics Commun.* **22**, 226-230 (August 1977).

Many of the optical properties and applications of graded-index or GRIN laser rods and lenses are surveyed in a Special Issue of *Appl. Optics* **21** (March 15 1982).

Problems for 16.6

1. *Practical criteria for trapping a gaussian beam in a duct.* To express the criterion for trapping of a gaussian beam in an index duct in a more visible form, suppose that the index variation across a duct is given by the formula $n(x) = n_a + \Delta n \exp[-(x/a)^2]$ where n_a is the background value in the duct; Δn is the (small) peak value of the transversely varying part of the index; and a is the $1/e$ spot size for this index variation. Show that the spot size w of the gaussian beam that will be trapped in this duct is then given by

$$\frac{w}{a} \approx \left(\frac{n_a}{2\Delta n} \right)^{1/4} \times \left(\frac{\lambda}{\pi a} \right)^{1/2},$$

with the obvious condition that w must be somewhat smaller than a for the gaussian beam theory to be a reasonable approximation.

2. *Lensing or ducting effects in a saturated laser amplifier.* In an experiment carried out at the Bell Telephone Laboratories, a powerful gaussian laser beam was passed through a laser amplifier, and certain interesting power-dependent focusing effects were observed. The incident laser beam was powerful enough to cause at least partial saturation of the amplifying transition in the laser amplifier, and because the signal fields are strongest at the center of a gaussian incident beam, the degree of saturation was largest on the axis of the amplifier tube, decreasing radially outward. When the saturation took place, it was found that the amplifier tube began to act as a (weak) lens, with the sign of this lens effect (convergent or divergent) depending on whether a weak probing beam used to observe lens effect had a frequency slightly above or slightly below the atomic center frequency.

Explain the physical causes of this effect, and in particular whether the lens should be convergent or divergent above and below the laser center frequency. (For simplicity, assume that the gain profile is uniform across the amplifier-tube cross section before saturation, and that the atomic transition is homogeneously broadened.)

3. *Higher-order eigenmodes in ducts.* Find the higher-order Hermite-gaussian modes in a quadratic duct—that is, find the higher-order solutions to the paraxial wave equation given in this section. (Hint: The standard analysis given in quantum-mechanics texts for the quantum wavefunctions of a harmonic oscillator in a quadratic potential well may be useful.)
-

16.7 NUMERICAL BEAM PROPAGATION METHODS

Hermite-gaussian modes, particularly the lowest-order gaussian beams, provide extremely useful tools for analyzing optical beam propagation in simple situations, especially in low-loss stable optical resonators, and in other situations where the physical modes of the problem are close to Hermite-gaussian in character, and where the effects of diffraction by hard-edged apertures are negligible or entirely absent. We can even, if necessary, expand any arbitrary optical beam as a summation of Hermite-gaussian modes; and then calculate the propagation of the arbitrary beam by calculating the propagation of the individual Hermite-gaussian modes.

There are many situations in real optical systems, however—such as unstable resonator problems, for example—where aperture diffraction effects play a major role. We must then treat the effects of edge diffraction, and analyze the propagation of beams with rather arbitrary and irregular amplitude and phase profiles. Numerical calculation methods play a large role in such analyses. The most efficient numerical methods then generally center around the use of Huygens' integral together with various “fast transform” numerical methods. In this section we will review briefly some of the analytical and numerical tools that become important in handling these more messy situations that arise in real-world problems.

Paraxial Wave Propagation: The Finite Difference Approach

We have already mentioned the possibility of calculating the forward propagation of an arbitrary optical beam by writing the paraxial wave equation in the form

$$\frac{\partial \tilde{u}(\mathbf{s}, z)}{\partial z} = -\frac{j}{2k} \nabla_t^2 \tilde{u}(\mathbf{s}, z), \quad (78)$$

and then integrating this equation forward numerically using so-called finite difference methods, first to calculate the transverse derivative of the known wavefunction at one plane, and then to step forward in z to the next plane.

This finite-difference approach to paraxial wave propagation can be of some practical usefulness for calculating beam propagation through inhomogeneous regions, such as perturbed atmospheres or problems involving thermal blooming or an inhomogeneous laser medium. Even in such inhomogeneous situations, however, fast transform methods, properly applied, are probably still superior.

Huygens' Integral: Fourier Transform Interpretation

Huygens' integral provides another straightforward way to propagate an arbitrary optical wavefront from an input plane at z_0 to any later plane z . In doing this, it is particularly useful to note that the one-dimensional Huygens' integral written in rectangular coordinates has exactly the form of a convolution integral.

That is, Huygens' integral as given in Equation 16.25 has exactly the form of a convolution (in x) of the input field $\tilde{u}_0(x_0, z_0)$ with a spherical wavefunction $\exp[-j\pi x^2/(z - z_0)\lambda]$ in the form

$$\tilde{u}(x, z) = \tilde{u}_0(x_0) * \exp[-j\pi x_0^2/(z - z_0)\lambda], \quad (79)$$

where the symbol $*$ indicates the convolution operation. (We leave out the constant in front for simplicity.)

The convolution of two functions, as in Equation 16.79, can be accomplished, however, according to Fourier transform theory, by (i) calculating the Fourier transform of each function individually; (ii) multiplying together the two Fourier transforms point by point to get a product transform; and then (iii) inverse Fourier transforming this product transform to get the desired convolution.

Efficient fast Fourier transform algorithms then provide a very practical way of doing the required transforms in order to numerically convolve two arbitrary functions such as Equation 16.79 on a digital computer. (In doing Huygens' integral calculations in this fashion, the spherical function corresponding to the kernel in Huygens' integral must be transformed only once and then stored.) This approach is generally by far the most efficient way to evaluate the Huygens-Fresnel integral numerically, in order to calculate the propagation and diffraction spreading of an arbitrary optical beam in a numerical calculation, if the work is to be done in rectangular coordinates.

Alternative Fourier Transform Approach

As a slightly different approach, we can also rewrite Huygens' integral for one transverse dimension in the form

$$\tilde{u}(x, z) = \exp\left(\frac{-j\pi x^2}{L\lambda}\right) \sqrt{\frac{j}{L\lambda}} \int_{-\infty}^{\infty} \tilde{u}'_0(x_0, z_0) \times \exp[j(2\pi/L\lambda)xx_0] dx_0, \quad (80)$$

where $L \equiv z - z_0$, and $\tilde{u}'_0(x_0, z_0)$ is a modified input function given by

$$\tilde{u}'_0(x_0, z_0) \equiv \tilde{u}_0(x_0, z_0) e^{-j\pi x_0^2/L\lambda}. \quad (81)$$

But Equation 16.80 simply has the mathematical form of a Fourier transform between the variables x and x_0 . In this form, therefore, the Huygens-Fresnel propagation integral appears as a single (scaled) Fourier transform between the input and output functions \tilde{u}_0 and \tilde{u} . This transform is applied, however, to the modified function $\tilde{u}_0(x_0, z_0) \exp(-j\pi x_0^2/L\lambda)$, and is followed by multiplication by another factor of $\exp(-j\pi x^2/L\lambda)$.

Applying a fast Fourier transform algorithm directly to the evaluation of Equation 16.80 provides another related but different way to do the same propagation calculation, using now a single Fourier transform. However, this transform is now applied to a more complex input function, because of the additional spherical wave factor $\exp(-j\pi x_0^2/L\lambda)$. The total amount of numerical work seems to come out about the same for either approach in most practical situations.

Fourier Transforms and Gaussian Beams

Huygen's integral in the Fresnel approximation thus has the mathematical form either of a convolution of the input wavefront against a spherical wavefunction, or of a Fourier transform of the input wavefront multiplied by a spherical wavefront. Suppose we put a gaussian-spherical beam as the input into either of these mathematical forms. The reader should then know, or learn, that *the convolution of a gaussian function with another (possibly complex) gaussian always gives still another gaussian*. A gaussian beam passing through the convolution process of Equation 16.79 will thus always come out again gaussian, as we already know.

To express this same point in an alternative form, the Fourier transform of a gaussian function is always another gaussian transform (and in fact the Fourier transform of a Hermite-gaussian function is always another Hermite-gaussian function of the same order). All of the gaussian beam properties we have derived earlier and will discuss later are thus deeply imbedded in the self-transforming properties of generalized complex gaussian functions, and their higher-order Hermite-gaussian extensions.

Paraxial Plane Waves and Transverse Spatial Frequencies

The mathematical procedures that are employed in evaluating the Huygens-Fresnel integral by Fourier transform methods can be given a simple and graphic physical interpretation in terms of *an expansion of the optical beam in a set of infinite plane waves traveling in slightly different directions*. The Fourier transforms that are calculated in the convolution procedure correspond, in fact, to the transformation of the beam profile into a "spatial frequency" domain, or into a

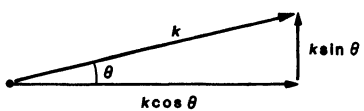


FIGURE 16.13
Off-axis propagation vector.

“ k -vector space” of plane waves traveling at different directions with respect to the z axis, as illustrated earlier in Figure 16.2.

Because this spatial-frequency or k -vector viewpoint is very graphic and because it may give useful physical insights into the nature of beam propagation, we will rederive this plane wave description in some detail in the following paragraphs, even though the final results we obtain will be entirely identical to what we have already obtained merely by applying Fourier theorems to the Huygens-Fresnel integral.

To carry out this derivation, we consider as fundamental building blocks a set of infinite plane waves of the form

$$\tilde{u}_{pw}(x, y, z) \equiv \exp[-jk \cdot r] = \exp[-j(k_x x + k_y y + k_z z)]. \quad (82)$$

The propagation vector $\mathbf{k} = (k_x, k_y, k_z)$ for any such plane wave traveling at angles θ_x and θ_y with respect to the z axis in the x, z and y, z planes has transverse components which we can write (see Figure 16.13) as

$$k_x = k \sin \theta_x \equiv 2\pi s_x \quad \text{and} \quad k_y = k \sin \theta_y \equiv 2\pi s_y. \quad (83)$$

The quantities $s_x \equiv (k/2\pi) \sin \theta_x \approx \theta_x/\lambda$ and $s_y \equiv (k/2\pi) \sin \theta_y \approx \theta_y/\lambda$ are then the transverse spatial frequencies along the x or y axes for a plane wave traveling at a small angle (θ_x, θ_y) away from the z axis toward the x or y directions.

The longitudinal k -vector component for a given plane-wave component can then be written, using the paraxial or Fresnel approximation, in the form

$$\begin{aligned} k_z &= \sqrt{k^2 - k_x^2 - k_y^2} \approx k - (k_x^2 + k_y^2)/2k \\ &= k - \pi\lambda(s_x^2 + s_y^2). \end{aligned} \quad (84)$$

Each individual plane wave component, characterized by its angles θ_x and θ_y , or by its spatial frequencies s_x and s_y , will then have a z propagation given by

$$\tilde{u}_{pw}(x, y, z) = \tilde{u}_{pw}(x, y, 0) \times \exp[-jkz + j\pi\lambda(s_x^2 + s_y^2)z]. \quad (85)$$

Each plane-wave component thus travels with a slightly different propagation constant in the z direction, given (within the paraxial approximation) by the $\pi\lambda(s_x^2 + s_y^2)z$ factor.

Expansion as a Distribution of Plane Waves

We then assume that an arbitrary paraxial optical beam $\tilde{u}(x, y, z)$ can be expanded into a plane-wave or spatial-frequency expansion in the form

$$\begin{aligned}\tilde{u}(x, y, z) &= \iint \tilde{U}_{pw}(s_x, s_y, 0) \times \tilde{u}_{pw}(x, y, z) ds_x ds_y \\ &= \iint \left[\tilde{U}_{pw}(s_x, s_y, 0) e^{-jkz + j\pi\lambda(s_x^2 + s_y^2)z} \right] \times e^{-j2\pi(s_x x + s_y y)} ds_x ds_y \\ &= \iint \tilde{U}_{pw}(s_x, s_y, z) \times e^{-j2\pi(s_x x + s_y y)} ds_x ds_y,\end{aligned}\tag{86}$$

where $\tilde{U}_{pw}(s_x, s_y, 0)$ gives the complex amplitude at plane $z = 0$ of each plane-wave component in the beam having spatial frequencies s_x, s_y , or traveling at angles $\theta_x \approx \lambda s_x$ and $\theta_y \approx \lambda s_y$. In writing the second and third lines we have made use of the fact that each such plane-wave component propagates forward in z with a differential propagation constant given by

$$\tilde{U}_{pw}(s_x, s_y, z) = \tilde{U}_{pw}(s_x, s_y, 0) \times e^{-jkz + j\pi\lambda(s_x^2 + s_y^2)z},\tag{87}$$

so that each component of this spatial-frequency distribution rotates in phase by a slightly different amount as the beam propagates forward.

At any arbitrary input plane $z = z_0$ the beam intensity pattern can thus be written as

$$\tilde{u}(x, y, z_0) = \iint \tilde{U}_{pw}(s_x, s_y, z_0) \times e^{-j2\pi(s_x x + s_y y)} ds_x ds_y.\tag{88}$$

But this expression is exactly a two-dimensional Fourier transform between the transverse spatial coordinates x, y and the spatial frequencies s_x, s_y . If we know the input field distribution $\tilde{u}(x, y, z_0)$ at plane z_0 , therefore, we can evaluate the spatial frequency distribution $\tilde{U}_{pw}(s_x, s_y, z_0)$ by carrying out the inverse Fourier transformation given by

$$\tilde{U}_{pw}(s_x, s_y, z_0) = \iint \tilde{u}(x, y, z_0) \times e^{+j2\pi(s_x x + s_y y)} dx dy.\tag{89}$$

Having transformed $\tilde{u}(x, y, z_0)$ into the spatial-frequency domain, we can then propagate this spatial-frequency distribution forward (or for that matter backward) to any other plane z by multiplying it by the phase shift factor

$$\tilde{U}_{pw}(s_x, s_y, z) = \tilde{U}_{pw}(s_x, s_y, z_0) \times e^{-jk(z-z_0) + j\pi\lambda(s_x^2 + s_y^2)(z-z_0)}.\tag{90}$$

The field distribution $\tilde{u}(x, y, z)$ at the second plane can then be evaluated from the second Fourier transformation

$$\tilde{u}(x, y, z) = \iint \tilde{U}_{pw}(s_x, s_y, z) \times e^{-j2\pi(s_x x + s_y y)} ds_x ds_y.\tag{91}$$

Propagating any arbitrary paraxial wavefunction from plane z_0 to plane z in free space is thus carried out using two Fourier transformations plus one simple multiplication step. Note also that the $e^{-jk(z-z_0)}$ term is just the on-axis or plane-wave phase shift, whereas the $e^{j\pi\lambda(s_x^2 + s_y^2)(z-z_0)}$ factor gives the differential phase rotation of each individual spatial frequency component.

This whole approach, from Equation 16.86 to Equation 16.91, is nothing more than a physical reinterpretation of the convolution or double-Fourier-transform approach to the evaluation of Huygens' integral which we discussed in connection with Equation 16.79. Looking at it in spatial-frequency terms, however, emphasizes again the importance of the small-angle or Fresnel approximation and the quadratic spatial-frequency dependence which this produces in all the exponents.

Huygens' Integral in Cylindrical Coordinates

Huygens' integral 16.19 for free space can also be written in cylindrical coordinates (r, θ, z) , leading to the result

$$\begin{aligned} \tilde{u}(r, \theta) = & \frac{j}{L\lambda} \int_0^\infty r_0 dr_0 \int_0^{2\pi} \tilde{u}_0(r_0, \theta_0) \times \\ & \exp \left\{ -j \left(\frac{\pi}{L\lambda} \right) [r^2 + r_0^2 - 2rr_0 \cos(\theta - \theta_0)] \right\} d\theta. \end{aligned} \quad (92)$$

Suppose the wavefunction has m -th order azimuthal symmetry, so that we can separate the radial and azimuthal variables in the form

$$\tilde{u}(r, \theta) = \tilde{u}_m(r) \times e^{\pm jm\theta} \quad (93)$$

for both u and \tilde{u}_0 . Huygens' integral then reduces to the simpler form

$$\tilde{u}_m(r) = \frac{2\pi j^{m+1}}{L\lambda} \int_0^\infty r_0 \tilde{u}_0(r_0) e^{-j(\pi/L\lambda)(r^2+r_0^2)} J_m(2\pi r r_0/L\lambda) dr_0, \quad (94)$$

where J_m is the m -th order Bessel function.

Huygens' integral in this situation takes the form of a Fourier-Bessel transform, more commonly called a Hankel transform. A quasi "fast Hankel transform" is then available for the carrying out of numerical propagation and diffraction calculations on optical beams in cylindrical coordinates.

REFERENCES

One representative example of the finite-difference method for numerical beam calculations can be found in P.B. Ulrich and J. Wallace, "Propagation of collimated pulsed laser beams through an absorbing atmosphere," *J. Opt. Soc. Am.* **63**, 8 (1973).

The plane-wave or spatial-frequency approach to beam propagation has been discussed, among many other references, in L. M. V. Camargo and I. Palocz, "A new Fraunhofer zone and some of its applications," *Proc. IEEE* **60**, 149 (January 1972).

The fast Fourier transform was first extensively applied to optical beam and resonator calculations by E. A. Szkla and A. E. Siegman, "Diffraction calculations using fast Fourier transform methods," *Proc. IEEE* **62**, 410 (March 1974), and "Mode calculations in unstable resonator with flowing saturable gain. II. Fast Fourier transform method," *Appl. Opt.* **14**, 1873-1889 (August 1975). See also M. M. Johnson, "Direct application of the fast Fourier transform to open resonator calculations," *Appl. Opt.* **13**, 2326-2328 (October 1974); and A. E. Siegman, "How to compute two complex even Fourier transforms with one transform step," *Proc. IEEE* **63**, 544 (March 1975).

Optical resonator and beam propagation calculations using the standard fast Fourier transform algorithm (sometimes called the Cooley-Tukey algorithm) can be speeded

up still further by a newer and even faster FFT algorithm developed by S. Winograd, "On computing the discrete Fourier transform," *Math. of Comp.* **32**, 175-199 (January 1978). This approach is followed, for example, by D. Heshmaty-Manesh and S. C. Tam, "Optical transfer function calculation by Winograd's fast Fourier transform," *Appl. Opt.* **21**, 3273-3277 (September 15 1982).

A "fast Hankel transform" algorithm for carrying out beam calculations in cylindrical coordinates is outlined (in a primitive form) in A. E. Siegman, "Quasi fast Hankel transform," *Optics Lett.* **1**, 13-15 (March 1977); and applied in a more sophisticated form in S-C. Sheng and A.E. Siegman, "Nonlinear optical calculations using fast transform methods: Second harmonic generation with depletion and diffraction," *Phys. Rev. A* **21**, 599-606 (February 1980).

For other ways of calculating Hankel transforms, see A. V. Oppenheim, G. V. Frisk, and D. R. Martinez, "Computation of the Hankel transform using projections," *J. Acoust. Soc. Am.* **68**, 523-529 (1980); S. M. Candel, "Dual algorithms for fast calculation of the Fourier-Bessel transform," *IEEE Trans. ASSP-29*, 963-972 (October 1981); S. M. Candel, "An algorithm for the Fourier-Bessel transform," *Comp. Phys. Commun.* **23**, 343-353 (1981); and P. K. Murphy and N. C. Gallagher, "Fast algorithm for the computation of the zero-order Hankel transform," *J. Opt. Soc. Am.* **73**, 1130-1137 (September 1983).

Problems for 16.7

1. *Center of gravity of a paraxial optical beam.* Given an arbitrary paraxial optical beam $\bar{u}(x, z)$ in free space, prove that the "center of gravity" $\bar{x}(z)$ of this beam as defined by

$$\bar{x}(z) \equiv \frac{\int_{-\infty}^{\infty} x |\bar{u}(x, z)|^2 dx}{\int_{-\infty}^{\infty} |\bar{u}(x, z)|^2 dx}$$

travels in a straight line in the x, z plane. (Hints: Use the wave equation and differential identities; or a plane wave expansion and Fourier transform theorems; or Huygens' integral; or a Hermite-gaussian expansion and the Hermite-gaussian recursion relation.)

What physical interpretation can you give to the formula for the slope of this line? (Each of the preceding techniques in fact gives different and interesting insights into this question.)

2. *Second moment of a paraxial optical beam.* Extend the calculations of the previous problem, using a plane wave expansion, to calculate the second moment and the standard deviation $\langle (x - \bar{x})^2 \rangle$ of an arbitrary paraxial beam as a function of propagation distance. Again, give physical interpretations of the quantities involved, and see if you can develop an uncertainty relation between the standard deviations of the beam in real (x) space and in spatial frequency space.
-



PHYSICAL PROPERTIES OF GAUSSIAN BEAMS

The previous chapter developed the analytical tools needed for calculating optical-beam propagation in free space. We also need to have, however, a physical and intuitive understanding of the propagation of real optical beams—an understanding which the next two chapters attempt to develop.

In particular, the Hermite-gaussian or Laguerre-gaussian modes which we introduced in the previous chapter are both mathematically convenient, and also provide very good (though not quite exact) approximations to the transverse modes of stable laser resonators with finite diameter mirrors. Gaussian or quasi gaussian beams are therefore very widely used in analyzing laser problems and related optical systems. A good physical as well as mathematical understanding of gaussian beam properties is particularly important. In this chapter we thus review most of the important physical properties of ideal gaussian optical beams in free space.

17.1 GAUSSIAN BEAM PROPAGATION

We first look in this section at what the analytic expressions for a lowest-order gaussian beam imply physically in terms of aperture transmission, collimated beam distances, far-field angular beam spread, and other practical aspects of gaussian beam propagation.

Analytical Expressions

Let us assume a lowest-order gaussian beam characterized by a spot size w_0 and a planar wavefront $R_0 = \infty$ in the transverse dimension, at a reference plane which for simplicity we take to be $z = 0$. This plane will henceforth be known for obvious reasons as the *beam waist*, as in Figure 17.1.

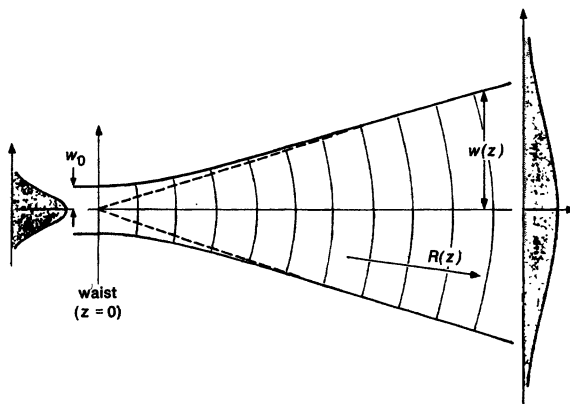


FIGURE 17.1

Notation for a lowest-order gaussian beam diverging away from its waist.

The normalized field pattern of this gaussian beam at any other plane z will then be given by

$$\begin{aligned}\tilde{u}(x, y, z) &= \left(\frac{2}{\pi}\right)^{1/2} \frac{\tilde{q}_0}{w_0 \tilde{q}(z)} \exp\left[-jkz - jk \frac{x^2 + y^2}{2\tilde{q}(z)}\right] \\ &= \left(\frac{2}{\pi}\right)^{1/2} \frac{\exp[-jkz + j\psi(z)]}{w(z)} \exp\left[-\frac{x^2 + y^2}{w^2(z)} - jk \frac{x^2 + y^2}{2R(z)}\right],\end{aligned}\quad (1)$$

where the complex radius of curvature $\tilde{q}(z)$ is related to the spot size $w(z)$ and the radius of curvature $R(z)$ at any plane z by the definition

$$\frac{1}{\tilde{q}(z)} \equiv \frac{1}{R(z)} - j \frac{\lambda}{\pi w^2(z)}. \quad (2)$$

In free space this parameter obeys the propagation law

$$\tilde{q}(z) = \tilde{q}_0 + z = z + jz_R, \quad (3)$$

with the initial value

$$\tilde{q}_0 = j \frac{\pi w_0^2}{\lambda} = jz_R. \quad (4)$$

Note that the value of λ in these formulas is always the wavelength of the radiation *in the medium in which the beam is propagating*.

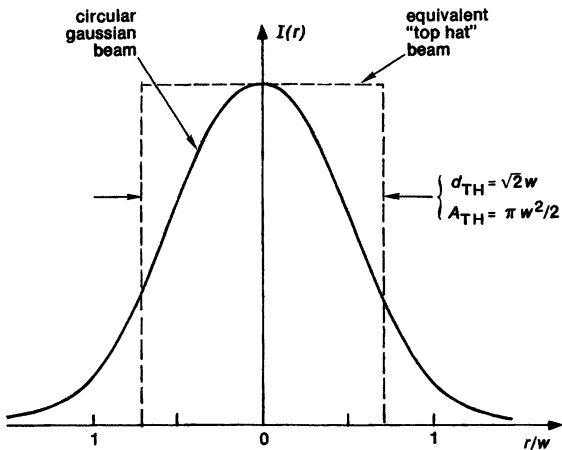


FIGURE 17.2
The equivalent “top hat”
radius for a cylindrical gaussian beam.

All the important parameters of this gaussian beam can then be related to the waist spot size w_0 and the ratio z/z_R by the formulas

$$w(z) = w_0 \sqrt{1 + \left(\frac{z}{z_R}\right)^2},$$

$$R(z) = z + \frac{z_R^2}{z},$$

$$\psi(z) = \tan^{-1} \left(\frac{z}{z_R} \right).$$
(5)

In other words, the field pattern along the entire gaussian beam is characterized entirely by the single parameter w_0 (or \tilde{q}_0 , or z_R) at the beam waist, plus the wavelength λ in the medium.

Aperture Transmission

Before exploring the free-space propagation properties of an ideal gaussian beam, we might consider briefly the vignetting effects of the finite apertures that will be present in any real optical system. The intensity of a gaussian beam falls off very rapidly with radius beyond the spot size w . How large must a practical aperture be before its truncation effects on a gaussian beam become negligible?

Suppose we define the total power in an optical beam as $P = \iint |\tilde{u}|^2 dA$ where dA integrates over the cross-sectional area. The radial intensity variation of a gaussian beam with spot size w is then given by

$$I(r) = \frac{2P}{\pi w^2} e^{-2r^2/w^2}.$$
(6)

The effective diameter and area of a uniform cylindrical beam (a “top hat beam”) with the same peak intensity and total power as a cylindrical gaussian beam will

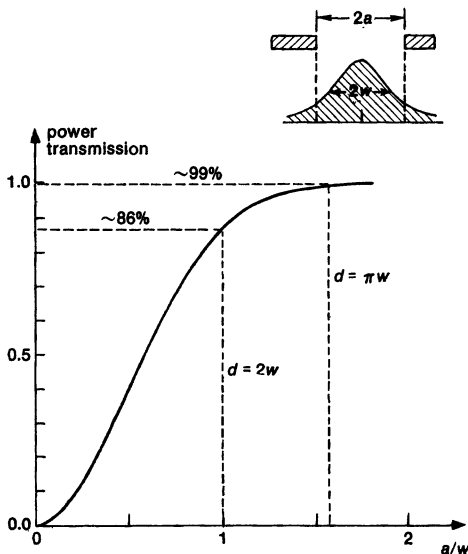


FIGURE 17.3

Power transmission of a cylindrical gaussian beam through a circular aperture.

then be

$$d_{TH} = \sqrt{2}w \quad \text{and} \quad A_{TH} = \frac{\pi w^2}{2} \quad (7)$$

as shown in Figure 17.2.

An aperture significantly larger than this will be needed, however, to pass a real gaussian beam of spot size w without serious clipping of the beam skirts. The fractional power transfer, for example, for a gaussian beam of spot size w passing through a centered circular aperture of diameter $2a$, as in Figure 17.3, will be given by

$$\text{power transmission} = \frac{2}{\pi w^2} \int_0^a 2\pi r e^{-2r^2/w^2} dr = 1 - e^{-2a^2/w^2}. \quad (8)$$

This figure plots this transmission versus aperture radius a normalized to spot size w . An aperture with radius $a = w$ transmits $\approx 86\%$ of the total power in the gaussian beam. We will refer to this as the $1/e$ or 86% criterion for aperture size.

A more useful rule of thumb to remember, however, is that an aperture with radius $a = (\pi/2)w$, or diameter $d = \pi w$, will pass just over 99% of the gaussian beam power. We will often use this as a practical design criterion for laser beam apertures, and will refer to it as the " $d = \pi w$ " or 99% criterion. (A criterion of $d = 3w$ which gives $\approx 98.9\%$ transmission would obviously serve equally well.) Figure 17.4 illustrates just where some of these significant diameters for a gaussian beam will fall on the gaussian beam profile.

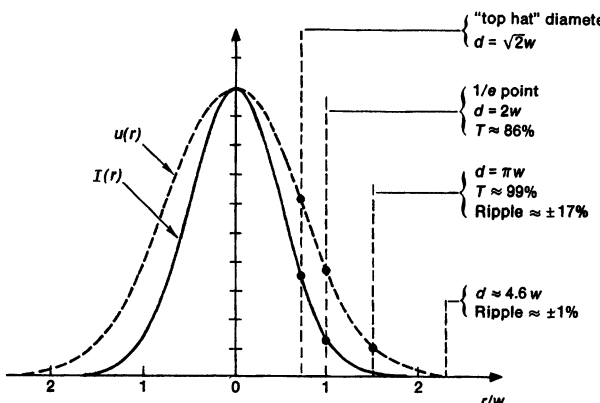


FIGURE 17.4

Significant diameters for hard-edged truncation of a cylindrical gaussian beam. Note that the $d = \pi w$ criterion gives 99% power transmission, but also $\pm 17\%$ intensity ripples and intensity reduction in the near and far fields.

Aperture Diffraction Effects

Optical designers should take note, however, that sharp-edged apertures, especially circular apertures, even though they may cut off only a very small fraction of the total power in an optical beam, will also produce aperture diffraction effects like those shown in Figure 17.5, which will significantly distort the intensity pattern of the transmitted beam in both the near-field (Fresnel) and far-field (Fraunhofer) regions.

We will show in the following chapter, for example, that the diffraction effects on an ideal gaussian beam of a sharp-edged circular aperture even as large as the $d = \pi w$ criterion will cause near-field diffraction ripples with an intensity variation $\Delta I/I \approx \pm 17\%$ in the near field, along with a peak intensity reduction of $\approx 17\%$ on axis in the far field. We have to enlarge the aperture to $d \approx 4.6w$ to get down to $\pm 1\%$ diffraction ripple effects from a sharp-edged circular aperture.

Beam Collimation: The Rayleigh Range and the Confocal Parameter

Another important question is how rapidly an ideal gaussian beam will expand due to diffraction spreading as it propagates away from the waist region or, in practical terms, over how long a distance can we propagate a collimated gaussian beam before it begins to spread significantly?

The variation of the beam spot size $w(z)$ with distance as given by Equation 17.5 is plotted in Figure 17.6 for two different waist spot sizes w_{01} and $w_{02} > w_{01}$, with the transverse scale greatly enlarged. The primary point is that as the input spot size w_0 at the waist is made smaller, the beam expands more rapidly due to diffraction; remains collimated over a shorter distance in the near field; and diverges at a larger beam angle in the far field.

In particular, the distance which the beam travels from the waist before the beam diameter increases by $\sqrt{2}$, or before the beam area doubles, is given simply

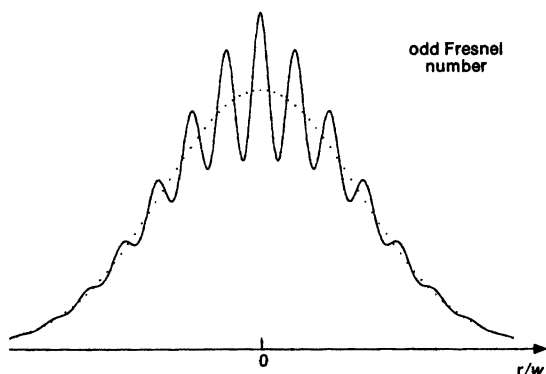


FIGURE 17.5
Near-field Fresnel-diffraction
ripples produced by truncation
of a gaussian beam.

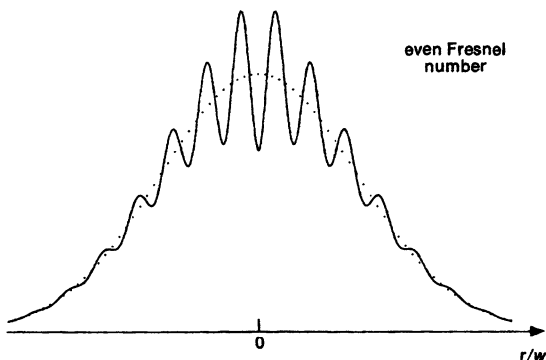
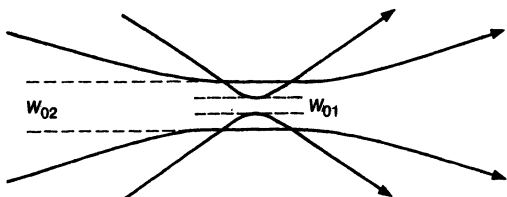


FIGURE 17.6
Diffraction spreading of two gaussian beams with different spot sizes at the waist.



by the parameter

$$z = z_R \equiv \frac{\pi w_0^2}{\lambda} = \text{"Rayleigh range."} \quad (9)$$

The term *Rayleigh range* is sometimes used in antenna theory to describe the distance $z \approx d^2/\lambda$ that a collimated beam travels from an antenna of aperture diameter d (assuming $d \gg \lambda$) before the beam begins to diverge significantly. We have

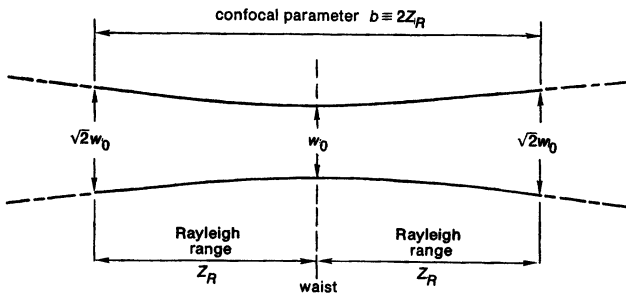


FIGURE 17.7
The collimated waist region of a gaussian beam.

therefore adopted the same term here as a name for the quantity $z_R \equiv \pi w_0^2 / \lambda$. The Rayleigh range marks the approximate dividing line between the “near-field” or Fresnel and the “far-field” or Fraunhofer regions for a beam propagating out from a gaussian waist.

To express this same point in another way, if a gaussian beam is focused from an aperture down to a waist and then expands again, the full distance between the $\sqrt{2}w_0$ spot size points is the quantity b given by

$$b = 2z_R = \frac{2\pi w_0^2}{\lambda} = \text{confocal parameter.} \quad (10)$$

This confocal parameter was widely used in earlier writings to characterize gaussian beams. Using the Rayleigh range $z_R \equiv b/2$, as shown in Figure 17.7, seems, however, to give simpler results in most gaussian beam formulas.

Collimated Gaussian Beam Propagation

Over what distance can the collimated waist region of an optical beam then extend, in practical terms? To gain some insight into this question, we might suppose that a gaussian optical beam is to be transmitted from a source aperture of diameter D with a slight initial inward convergence, as shown in Figure 17.8, so that the beam focuses slightly to a waist with spot size w_0 at one Rayleigh range out, and then reexpands to the same diameter D two Rayleigh ranges (or one confocal parameter) out. We will choose the aperture diameter according to the πw or 99% criterion, i.e., we will use $D = \pi \times \sqrt{2} w_0$ at each end.

The relation between the collimated beam distance and the transmitting aperture size using this criterion is then

$$\text{collimated range} = 2z_R = \frac{2\pi w_0^2}{\lambda} \approx \frac{D^2}{\pi\lambda}. \quad (11)$$

Some representative numbers for this collimated beam range at two different laser wavelengths are illustrated in Figure 17.8 and in Table 17.1. A visible laser with a 1 cm diameter aperture can project a beam having an effective diameter of a few mm with no significant diffraction spreading over a length of 50 meters or more. Such a beam can be used, for example, as a “weightless string” for alignment on a construction project. With the aid of a simple photocell array,

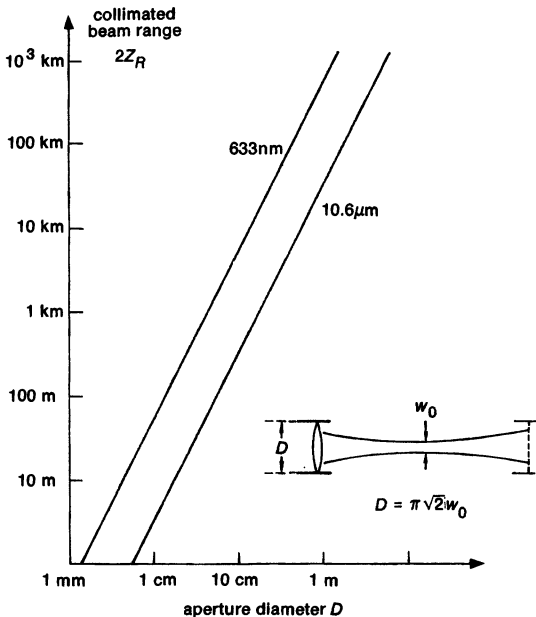


FIGURE 17.8
Collimated gaussian beam ranges versus transmitting aperture diameter D , using the $d = \pi w$ criterion.

TABLE 17.1
Collimated Laser Beam Ranges

Aperture diameter D	Waist spot size w_0	Collimated range, $2z_R$ (10.6 μm)	Collimated range, $2r_R$ (633 nm)
1 cm	2.25 mm	3 m	45 m
10 cm	2.25 cm	300 m	5 km
1 m	22.5 cm	30 km	500 km

the center of such a beam can easily be found to an accuracy of better than $w/20$, or a small fraction of a mm, over the entire distance.

Far-Field Beam Angle: The "Top Hat" Criterion

Suppose we next move out into the far field, where the beam size expands linearly with distance, as in Figure 17.9. At what angle does a gaussian beam spread in the far field, that is, for $z \gg z_R$?

From the gaussian beam equations (17.1-17.5), the $1/e$ spot size $w(z)$ for the field amplitude in the far field for a gaussian beam coming from a waist with spot size w_0 is given by

$$w(z) \approx \frac{w_0 z}{z_R} = \frac{\lambda z}{\pi w_0} \quad (z \gg z_R), \quad (12)$$

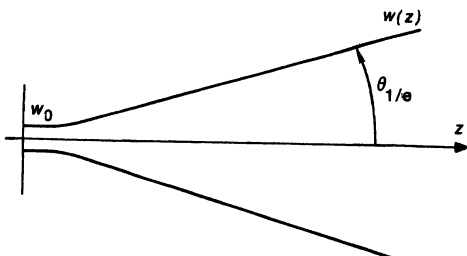


FIGURE 17.9
A gaussian beam spreads with a constant diffraction angle in the far field.

which gives the simple relation

$$w_0 \times w(z) \approx \frac{\lambda z}{\pi} \quad (13)$$

connecting the spot sizes at the waist and in the far field. The far-field angular beam spread for a gaussian beam can then be related to the near-field beam size or aperture area in several different ways, depending on how conservative we want to be.

The on-axis beam intensity in the far field, for example, is given by

$$I_{\text{axis}}(z) = \frac{2P}{\pi w^2(z)} \approx \frac{P}{\lambda^2 z^2 / 2\pi w_0^2}. \quad (14)$$

Hence, the on-axis intensity is the same as if the total power P were uniformly distributed over an area $\pi w^2(z)/2 = \lambda^2 z^2 / 2\pi w_0^2$. The solid angle for an equivalent “top hat” angular distribution in the far field, call it $\Omega_{\text{TH}}(z)$, is thus given by

$$\Omega_{\text{TH}} = \frac{\pi w^2(z)}{2z^2} = \frac{\lambda^2}{2\pi w_0^2}. \quad (15)$$

At the same time, the “equivalent top hat” definition of the source area at the waist is given from Equation 17.7 by $A_{\text{TH}} = \pi w_0^2/2$. The product of these two quantities is thus given by

$$A_{\text{TH}} \times \Omega_{\text{TH}} = \left(\frac{\lambda}{2}\right)^2. \quad (16)$$

The source aperture size (at the waist) and the far-field solid angular spread thus have a product on the order of the wavelength λ squared, although the exact numerical factor will depend on the definitions we choose for the area and the solid angle, as we will see in more detail later.

Far-Field Beam Angle: The 1/e Criterion

Another and perhaps more reasonable definition for the far-field beam angle is to use the $1/e$ or 86% criterion for the beam diameter, so that the far field half-angular spread is defined by the width corresponding to the $1/e$ point for the E field amplitude at large z .

With this definition, the half-angle $\theta_{1/e}$ out to the $1/e$ amplitude points in the far-field beam is given, as shown in Figure 17.9, by

$$\theta_{1/e} = \lim_{z \rightarrow \infty} \frac{w(z)}{z} = \frac{\lambda}{\pi w_0}. \quad (17)$$

Twice this angle then gives a full angular spread of

$$2\theta_{1/e} = \frac{2\lambda}{\pi w_0}, \quad (18)$$

which can be interpreted as a more precise formulation, valid for gaussian beams, of the approximate relation $\Delta\theta \approx \lambda/d$ that we gave in Chapter 1. We can then define the gaussian beam solid angle $\Omega_{1/e}$ on this same basis as the circular cone defined by this angular spread, or

$$\Omega_{1/e} = \pi\theta_{1/e}^2 = \frac{\lambda^2}{\pi w_0^2}. \quad (19)$$

This cone will, as noted in the preceding, contain 86% of the total beam power in the far field.

Suppose we use the same $1/e$ criterion to define the effective radius of the input beam at the beam waist (ignoring the fact that an aperture of radius $a = w_0$ at the waist would actually produce some very substantial diffraction effects on the far-field beam pattern). Then the product of the effective source aperture area $A_{1/e} \equiv \pi w_0^2/2$ and the effective far-field solid angle $\pi\theta_{1/e}^2$ using these $1/e$ definitions becomes

$$A_{1/e}\Omega_{1/e} = \pi w_0^2 \times \pi\theta_{1/e}^2 = \lambda^2. \quad (20)$$

This is a precise formulation for gaussian beams of a very general antenna theorem which states that

$$\iint A(\Omega) d\Omega = \lambda^2 \quad (21)$$

This theorem says in physical terms that if we measure the effective capture area $A(\Omega)$ of an antenna for plane-wave radiation arriving from a direction specified by the vector angle $\Omega = (\theta, \phi)$, and then integrate these measured areas over all possible arrival angles as specified by $d\Omega$, the result (for a lossless antenna of any form) is always just the measurement wavelength λ . This result is valid for any kind of antenna, at radio, microwave or optical wavelengths.

Far-Field Beam Angle: Conservative Criterion

Finally, as a still more conservative way of expressing the same points, we might use the $d = \pi w$ or 99% criterion instead of the $1/e$ criterion to define both the effective source aperture size and the effective far field solid angle. We might then say that a source aperture of diameter $d = \pi w_0$ transmitting a beam of initial spot size w_0 will produce a far-field beam with 99% of its energy within a cone of full angular spread $2\theta_\pi = \pi w(z)/z$. On this basis the source aperture area, call it A_π is $\pi d^2/4$ and the beam far-field solid angle is $\Omega_\pi = \pi\theta_\pi^2$; and these are related by the more conservative criterion

$$A_\pi\Omega_\pi = \left(\frac{\pi}{2}\right)^4 \lambda^2 \approx 6\lambda^2. \quad (22)$$

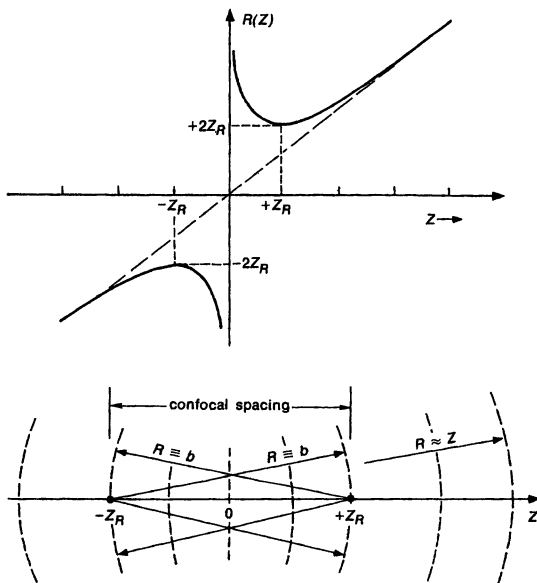


FIGURE 17.10
Radius of curvature for the
wavefront of a gaussian beam,
versus distance from the
waist.

None of the criteria we have introduced here for defining effective aperture size and effective solid angle are divinely ordained, and which of them we use should depend largely on what objective we have in mind.

Wavefront Radius of Curvature

We can next look at how the wavefront curvature of a gaussian beam varies with distance. The radius of curvature $R(z)$ of a gaussian beam has a variation with distance given analytically by

$$R(z) = z + \frac{z_R^2}{z} \approx \begin{cases} \infty & \text{for } z \ll z_R \\ 2z_R & \text{for } z = z_R \\ z & \text{for } z \gg z_R \end{cases} \quad (23)$$

This is plotted against normalized distance in Figure 17.10(a).

The wavefront is flat or planar right at the waist, corresponding to an infinite radius of curvature or $R(0) = \infty$. As the beam propagates outward, however, the wavefront gradually becomes curved, and the radius of curvature $R(z)$ drops rather rapidly down to finite values (see Figure 17.10). For distances well beyond the Rayleigh range z_R the radius then increases again as $R(z) \approx z$, i.e., the gaussian beam becomes essentially like a spherical wave centered at the beam waist. What this means in physical terms is that the center of curvature of the wavefront starts out at $-\infty$ for a wavefront right at the beam waist, and then moves monotonically inward toward the waist, as the wavefront itself moves outward toward $z \rightarrow +\infty$.

Confocal Curvatures

The minimum radius of curvature occurs for the wavefront at a distance from the waist given by $z = z_R$, with the radius value $R = b = 2z_R$. This means that at this point the center of curvature for the wavefront at $z = +z_R$ is located at $z = -z_R$, and vice versa, as illustrated in Figure 17.10.

This particular spacing has a special significance in stable resonator theory. Suppose the curved wavefronts $R(z)$ at $\pm z_R$ are matched exactly by two curved mirrors of radius R and separation $L = R = b = 2z_R$. Since the focal point of a curved mirror of radius R is located at $f = R/2$, the focal points of these two mirrors then coincide exactly at the center of the resonator. The two mirrors are said to form a *symmetric confocal resonator*, thus giving rise to the *confocal parameter* $b \equiv 2z_R \equiv 2\pi w_0^2/\lambda$. Such a resonator has certain particularly interesting mode properties which we will explore later.

REFERENCES

Further discussion of the concept of the “Rayleigh range” can be found in J. F. Ramsay, “Tubular beams from radiating apertures,” in *Advances in Microwaves*, Vol. 3, ed. by L. F. Young (Academic Press, New York, 1968), p. 127.

Earlier considerations of the same ideas by Lord Rayleigh (J. W. Strutt) himself can be found in his papers “On images formed with or without reflection or refraction,” *Phil. Mag.* **11**, 214–218 (1881), and “On pinhole photography,” *Phil. Mag.* **31**, 87–89 (1891).

Problems for 17.1

1. *Gaussian beam transmission through a square aperture.* Find the power transmission for a gaussian beam through a square aperture with sides of length $2a$, in analogy to the circular aperture results given in the text.
2. *Criteria for centering accuracy of a circular aperture.* Suppose a gaussian beam is transmitted through a circular aperture of diameter $d = \pi w$. How critical is the centering of the laser beam axis with respect to the aperture position (or vice versa)? Attempt to evaluate the decrease in beam transmission versus the displacement between beam and aperture centers, using either approximate mathematical methods or computer evaluation.
3. *Setting tolerances on beam collimation and far-field beam angle.* A laser oscillator is designed to give a collimated beam at its output plane with a specified spot size w_0 and a collimated wavefront with radius of curvature $R_0 = \infty$. Due to manufacturing tolerances, however, the actual output wavefront may come out slightly spherical. Suppose we establish as a practical tolerance for good collimation that the far-field beam angle of the laser output beam should not vary by more than 10% from its design value. What is the resulting tolerance on R_0 (or $1/R_0$) at the laser’s output plane for a fixed value of w_0 ? How much wavefront distortion does this represent, expressed in terms of fractional wavelengths of wavefront distortion at the $1/e$ radius of the output beam?
4. *Simulating an annular beam with positive and negative gaussians.* A circularly symmetric beam with a hole in the center can be simulated by superposing

two collimated gaussian beams to give an initial field distribution $\tilde{u}_0(r) = \exp(-r^2/w_1^2) - \exp(-r^2/w_2^2)$ with $w_2 = \beta w_1$ and $0 \leq \beta \leq 1$. Calculate and plot the profile $\tilde{u}(r, z)$ of this beam at different distances z in the near and far fields for different values of β , with distance measured in the normalized coordinate $s \equiv z\lambda/\pi w_1^2 \equiv z/z_{R1}$. How rapidly does the hole in the center of the beam fill in as a function of distance for different values of β ?

- Locating the center of curvature of a gaussian beam. The text describes how the radius of curvature $R(z)$ changes as we move out along the z axis away from a gaussian waist at $z = 0$. Give an analytic expression for how the center of curvature of the same wavefront moves.
- Beam spot size at long distances. Suppose a frequency-doubled Nd:YAG laser ($\lambda = 532$ nm) is transmitted through a 1 meter diameter diffraction-limited telescope, using the $d = \pi$ criterion, to illuminate a spot on the face of the moon ($z \approx 384,000$ km). What will be the $1/e$ diameter of the spot?

As a practical matter, because of beam distortions through the atmosphere, except under very exceptional "seeing conditions" the largest aperture that can be diffraction-limited through the Earth's atmosphere has a diameter more like 10 cm. What will be the spot size for this aperture?

17.2 GAUSSIAN BEAM FOCUSING

Besides propagating collimated gaussian beams over long distances, we are often interested in focusing such beams to very small spots, whether for recording data on optical videodisks or tapes, drilling holes in razor blades, or counting cell nuclei in a laser microscope. (Since the standard demonstration of ruby laser intensity in early days was to zap a hole in one or more razor blades with a single laser shot, pulsed laser energies were occasionally quoted in "Gillettes.") What sort of focused spot sizes and intensities can be achieved with a gaussian beam—or for that matter with any reasonably well-formed optical beam?

Focused Spot Sizes

The usual situation where a collimated gaussian beam is strongly focused by a lens of focal length f , as shown in Figure 17.11, can be viewed as simply the far-field beam problem of Figure 17.9 in reverse. The waist region now becomes the focal spot of spot size w_0 , whereas the focusing lens can be viewed as being in the far field at $z \approx \pm f$. If $w(f)$ is the gaussian spot size at the lens, we then have the same relationship as Equation 17.13 but with a reverse interpretation, namely,

$$w_0 \times w(f) \approx \frac{f\lambda}{\pi}. \quad (24)$$

What does this expression imply in practical terms?

It seems obvious that in a practical focusing problem, the incident gaussian beam should fill the aperture of the focusing lens to the largest extent possible without a severe loss of power due to the finite aperture of the lens (and also without serious edge diffraction effects). As one reasonable criterion for practical

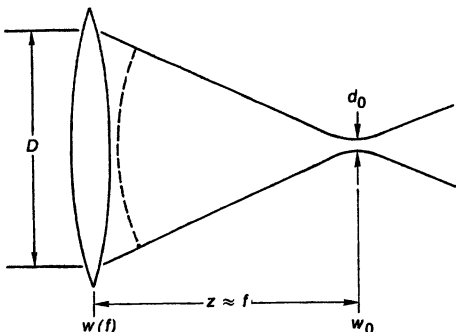


FIGURE 17.11
Focusing of a gaussian beam to a small spot size.

designs, we might adopt the $D = \pi w(f)$ or 99% criterion for the diameter d of the focusing lens, so that we lose $< 1\%$ of the incident energy in this lens. At the same time we might adopt the $1/e$ or $d_0 = 2w_0$ criterion for defining the effective diameter d_0 of the focused spot, since this is a diameter which contains 86% of the focused energy, and at the edges of which the focused intensity is already down to $1/e^2 \approx 14\%$ of its peak value. Combining these criteria then gives

$$d_0 \approx \frac{2f\lambda}{D} \quad (25)$$

for the effective diameter of the focused gaussian spot.

The *f-number* of a focusing lens (also called the *relative aperture* or the *speed* of the lens) is defined by

$$f^\# \equiv \frac{f}{D}. \quad (26)$$

The focal spot diameter, using the rather arbitrary criteria we have just selected, will then be given by

$$d_0 \approx 2f^\#\lambda. \quad (27)$$

As an alternative way of reaching essentially this same conclusion, we can calculate that if a gaussian beam carries total power P and we focus it using a lens of focal length f with the same $D = \pi w$ criterion for the lens diameter, then the peak intensity at the center of the focused spot will be given by

$$I_0 = \frac{2P}{\pi w_0^2} \approx \frac{P}{2(f^\#\lambda)^2}. \quad (28)$$

The peak intensity is thus the same as if all the energy were focused into a circle with an area of $2(f^\#\lambda)^2$, or a diameter of $(8/\pi)^{1/2} f^\#\lambda \approx 1.6 f^\#\lambda$.

Influence of the Lens f Number and the Lens Fresnel Number

Whatever the choice of definitions, it is evident that an ideal gaussian beam can be focused down to a spot that is roughly one to two optical wavelengths in diameter, multiplied by the *f-number* of the focusing lens. Note that a long focal length lens, say, an $f/10$ lens, will generally be simple, inexpensive and easy to

obtain, with quite small aberration coefficients. Lenses with f -numbers less than 2, and especially with $f^{\#} \leq 1$, on the other hand, generally require complex and expensive multielement designs, and can become very expensive.

Some optics workers also like to characterize a simple lens of diameter $D = 2a$ and focal length f by its *lens Fresnel number* N_f , given by

$$N_f \equiv \frac{a^2}{f\lambda}. \quad (29)$$

In terms of this quantity plus our arbitrary criteria for beam and spot diameters, the focal spot diameter and the lens diameter are then related by

$$\frac{d_0}{D} \approx \frac{1}{2N_f}. \quad (30)$$

Whereas the f -number of a given lens is independent of wavelength, the Fresnel number depends on wavelength. The limitation expressed by Equation 17.30 can become significant particularly for longer wavelengths, for example, in focusing infrared beams using IR lenses. Strong focusing, down to a spot size much less than the lens diameter, requires a lens with an adequately large Fresnel number N_f .

A crucial condition for accomplishing strong focusing, regardless of definitions, is that the incident gaussian beam properly fill the focusing lens aperture, since it is the *gaussian beam diameter* and not the *lens diameter* that is the critical dimension in determining the focal spot size of the gaussian beam.

Depth of Focus

The depth of focus of a gaussian beam is obviously given by the Rayleigh range z_R of the gaussian waist, or perhaps by $2z_R$, depending upon just how we want to define the depth of focus. If we use the latter definition, along with the lens diameter criterion $D = \pi w(f)$, then the depth of focus can be written as

$$\text{depth of focus} = 2z_R \approx 2\pi f^{\#2} \lambda \approx \frac{\pi}{2} \left(\frac{d_0}{\lambda} \right)^2 \lambda. \quad (31)$$

If the beam is focused down to a spot N wavelengths in diameter, the depth of focus will be $\approx N^2$ wavelengths in length.

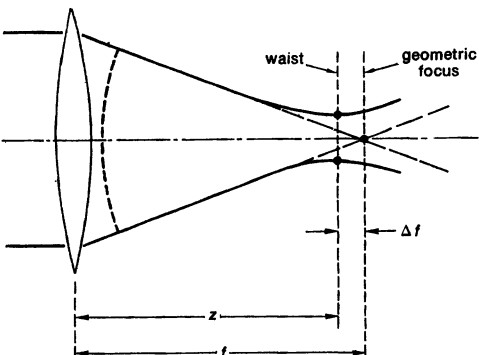
All these expressions for focused spot size and depth of focus do of course assume (a) that the gaussian beam entering the lens is more or less collimated, with a planar wavefront, so that the beam focuses approximately at the focal point f ; and (b) that the beam is in fact "strongly focused," in the sense that $w_0 \ll w(f)$, or $z_R \ll f$, or $N_f \gg 1$. This latter point is equivalent to saying that the lens is in the far field, as seen looking backward from the waist or the focal point. If either of these assumptions is not entirely valid, corrections must be applied in calculating the exact location and size of the focused spot, as illustrated in several of the Problems following this section.

Focal Spot Deviation

When a collimated beam is focused by an ideal lens, the actual focal spot, meaning the position of minimum spot size and maximum energy density, does

FIGURE 17.12

There is a very small (in practice, negligible) shift in position between the geometrical focus of the lens and the actual waist of the focused gaussian beam.



not in fact occur exactly at the geometrical focus of the lens; but rather is located just slightly *inside* the lens focal length. The amount of this focal spot deviation—which is typically very small—can be easily calculated for a focused gaussian beam from Figure 17.12.

Using the notation of Figure 17.12, we can let the distance from the lens to the beam waist, or the actual focal spot, be z , whereas the focal length of the lens is f . A collimated beam passing through a thin lens of focal length f acquires (by definition) a wavefront radius of curvature equal to f . The wavefront curvature just beyond the thin lens must therefore be given, from the combination of gaussian beam theory and lens theory, by

$$R(z) = z + z_R^2/z = f. \quad (32)$$

The difference between the focal length f and the actual distance z to the waist can then be written as

$$\Delta f \equiv f - z = z_R^2/z \approx z_R^2/f. \quad (33)$$

Since the Rayleigh range z_R of the focused beam is normally much less than the focal length f , the focal deviation is generally much less than the depth of focus (which means that in fact it is really quite negligible). One way of expressing this criterion is

$$\frac{\Delta f}{f} \approx \frac{1}{2N_f^2}. \quad (34)$$

As a practical matter, when adjusting an optical setup one very seldom knows the exact value of the lens focal length, or the exact location of the lens focal point, or the exact degree of collimation of the input beam to sufficiently high accuracy that this focal spot deviation is of any practical significance. We usually find the best focal adjustment in any optical system by small experimental adjustments over a small adjustment range, after the system is assembled.

Summary

Essentially all of the results we have given in this section, for collimated beam length, far-field beam angle, focal spot size, depth of focus, and focal spot deviation, although derived here for a gaussian beam, will apply equally

well in fact to any optical beam having a reasonably well-collimated or uniform phase front and a reasonably uniform amplitude profile across the beam. The gaussian beam simply provides a particularly convenient example in which the mathematical expressions for spot size and wavefront curvature are particularly simple. The gaussian beam also has the special characteristic, as distinguished from most other beams, that its transverse profile remains gaussian at every transverse cross section.

Suppose a uniform plane wave is focused to a spot by an ideal thin lens with a circular aperture. The focused spot will then have the form of an Airy disk pattern at the focal plane of the lens; but the spot size and depth of focus of this focused spot will still have essentially the same dependence on lens f -number or Fresnel number as given by Equations 17.24 to 17.31. More detailed calculations will even show that the on-axis intensity will be very slightly higher, and the average beam diameter very slightly smaller, at a transverse cross section just slightly inside the exact focal length; and the position of this plane of tighter focus will be given by the same Equations 17.33 or 17.34 we have just derived for focal spot deviation.

REFERENCES

Some interesting practical methods for measuring small gaussian beam waists can be found in M. B. Schneider and W. W. Webb, "Measurement of submicron laser beam radii," *Appl. Optics* **20**, 1382–1388 (April 15 1981); and in D. K. Cohen, B. Little, and F. S. Luecke, "Techniques for measuring 1- μm diam gaussian beams," *Appl. Opt.* **23**, 637–640 (February 15 1984).

If a gaussian beam is focused strongly enough to begin violating the paraxial approximation, we expect deviations from gaussian beam theory to appear particularly strongly in the focal spot region. Some of these deviations have been calculated and plotted in detail by W. H. Carter, "Anomalies in the field of a gaussian beam near focus," *Optics Commun.* **7**, 211–218 (March 1973).

Problems for 17.2

1. *Focusing for absolute minimum spot size.* A collimated gaussian beam of fixed spot size w is to be focused to the absolute minimum possible spot size (not necessarily a beam waist) on a work piece, using a single lens located a fixed distance L from the work piece. What should be the exact focal length f of this lens, and what will be the exact spot size of the focused spot? What is the waist size and location of the same focused beam?
2. *Focusing a gaussian beam with an astigmatic lens.* A circular gaussian beam with an initially large spot size w_1 is focused using an astigmatic lens which has different focal lengths f_x and f_y in the x and y transverse coordinates. Develop an analysis for the shape and location of the two different waists in the two transverse directions. Discuss in particular how the axial distance between the two waists will relate to the Rayleigh length for each individual waist if the two focal lengths are similar but differ by, say, 10% to 20% in magnitude.
3. *Focusing into a dielectric medium.* A focusing lens of focal length f is located outside a dielectric sample with a flat front surface, at a distance from the sur-

face that is less than the focal length f , so that the focal spot or gaussian beam waist occurs inside the dielectric sample. What is the spot size at this resulting waist; how does it compare to the spot size that would occur without the dielectric present; and where does it occur with respect to the lens position and the dielectric surface? (Warning! You will have to think through rather carefully what happens to a gaussian beam in passing through a planar dielectric surface.)

17.3 LENS LAWS AND GAUSSIAN MODE MATCHING

A common requirement in laser optical systems is to propagate a gaussian beam through a cascaded sequence of lenses, free-space regions, and other optical elements, as shown in Figure 17.14, perhaps in order to match a gaussian beam coming from a waist with specified spot size w_1 at location z_1 into another laser cavity or interferometer requiring waist spot size w_2 at location z_2 . The design steps necessary to accomplish this are usually referred to as *gaussian beam mode matching*.

Such problems if they become at all complicated are probably best handled by the general *ABCD* methods we will introduce later. A quick introduction to elementary gaussian mode matching techniques at this point may, however, be useful.

Lens Laws and Collins Charts

The lens law for purely spherical waves passing through an ideal thin lens of focal length f (Figure 17.13) is

$$\frac{1}{R_2} = \frac{1}{R_1} - \frac{1}{f}. \quad (35)$$

We follow the standard convention in this book of using positive R for diverging waves going in the $+z$ direction, and positive f for *converging* or *positive* lenses. A gaussian spherical beam passing through such a thin lens then has its radius of curvature R changed in exactly the same way, whereas its spot size w is unchanged. The lens law for gaussian beams is therefore the direct analog, that is,

$$\frac{1}{\tilde{q}_2} = \frac{1}{\tilde{q}_1} - \frac{1}{f}, \quad (36)$$

where \tilde{q} is the complex curvature parameter defined in Equation 17.2.

By applying this lens law, plus the propagation rule $\tilde{q}_2 = \tilde{q}_1 + z_2 - z_1$ for a free-space section, we can then propagate a gaussian beam forward or backward through any sequence of thin lenses and spaces. It can be helpful to plot this propagation as a trajectory in the complex $1/\tilde{q}$ plane or, more conveniently, in the complex j/\tilde{q} plane with rectangular coordinates x and y corresponding to $x \equiv \lambda/\pi w^2(z)$ and $y \equiv 1/R(z)$, respectively. From Equation 17.36 the effect of a thin lens is to cause a vertical jump of magnitude $-1/f$ in the j/\tilde{q} plane.

To those familiar with bilateral transformations as used in electrical circuit theory and elsewhere, it will be obvious that the transformation law through a free-space section, as given by $\tilde{q}(z) = \tilde{q}_0 + z = z + jz_R$, corresponds to a

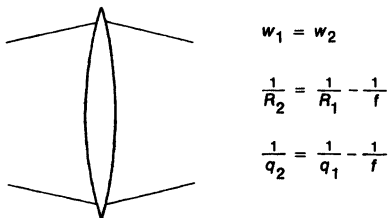


FIGURE 17.13

Gaussian beam transmitted through an ideal thin lens.

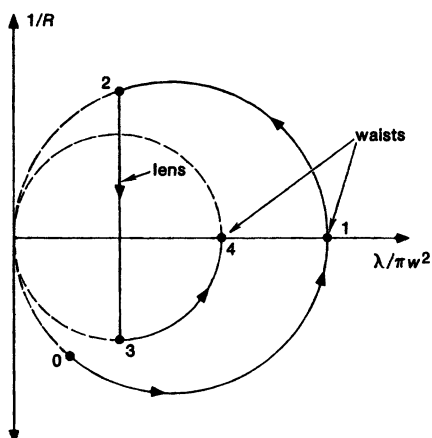
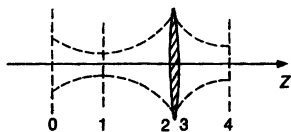


FIGURE 17.14

Gaussian beam propagation through a sequence of optical elements, as diagrammed on a gaussian-beam chart or Collins chart.

transformation around a circular arc in the complex j/\tilde{q} plane, as shown in Figure 17.14. In these so-called gaussian beam charts or *Collins charts*—which are very similar in form to the Smith charts of transmission line theory—different gaussian beam waists correspond to different points $x = 1/z_R$, $y = 0$ on the x axis. Free space propagation then corresponds to circular arcs passing through these points and the origin (which corresponds to the far field at $z \rightarrow \infty$); whereas lines of constant z/z_R for different z_R are also circles passing through the origin. Thin lenses are then vertical transitions on the same chart as shown.

Charts of this type may be of some use for visualizing gaussian beam propagation problems or for diagramming solutions. With widespread access to computers, however, their practical uses as calculational tools are negligible.

REFERENCES

The gaussian beam chart or Collins chart is described in S. A. Collins, Jr., "Analysis of optical resonators involving focusing elements," *Appl. Optics* **3**, 1263–1275 (November 1964); and in T. Li, "Dual forms of the gaussian beam chart," *Appl. Optics* **3**, 1315–1317 (November 1964).

Other references on the same topic include J. P. Gordon, "A circle diagram for optical resonators," *Bell Sys. Tech. J.* **43**, 1826–1827 (November 1964); and T. S. Chu, "Geometrical representation of gaussian beam propagation," *Bell. Sys. Tech. J.* **45**, 287–299 (February 1966).

Another graphical approach to gaussian beam propagation and mode matching is given by P. Laures, "Geometrical approach to gaussian beam propagation," *Appl. Opt.* **6**, 747–755 (April 1967).

Problems for 17.3

1. *Thin-lens imaging formulas for gaussian beams.* A gaussian waist with spot size w_1 , located a distance L_1 to the left of a thin lens with focal length f , is imaged by that lens into a waist with spot w_2 located a distance L_2 to the right of the lens. Evaluate for this situation (a) the relationship between the "object distance" L_1 , the "image distance" L_2 , and the focal length f ; and (b) the linear magnification $M = w_2/w_1$ between object and image, again in terms of L_1 , L_2 and f . Discuss any differences between these gaussian-beam results and the corresponding formulas for purely geometrical optics.

17.4 AXIAL PHASE SHIFTS: THE GUOY EFFECT

The propagation of a gaussian beam also involves a subtle but sometimes important *added phase shift* through the waist region, which we will briefly describe in this section.

Axial Phase Shift

The propagation equation (17.3 or 17.5) for a lowest-order gaussian beam includes both a spot size variation and a cumulative phase shift variation with axial distance z which are given on the optical axis ($x = y = 0$) by the factors

$$\bar{u}(z) \propto \frac{\tilde{q}_0 e^{-jkz}}{\tilde{q}(z)} = \frac{e^{-jkz}}{1 - jz/z_R} = \frac{\exp[-jkz + j\psi(z)]}{w(z)}. \quad (37)$$

In addition to the free-space or plane-wave phase shift given by the e^{-jkz} term, there is also an added axially-varying phase shift $\psi(z)$ given by

$$\psi(z) = \tan^{-1} \left(\frac{z}{z_R} \right) \quad (38)$$

assuming we measure this added phase shift with respect to the beam waist location.

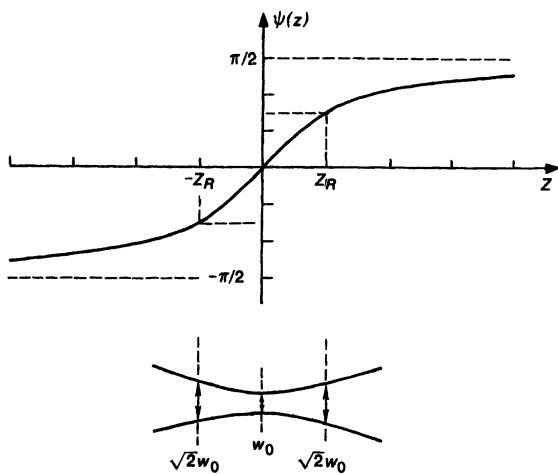


FIGURE 17.15
Guoy phase shift through the waist region of a gaussian beam.

The net effect of this added phase shift $\psi(z)$ for the lowest-order gaussian mode, as plotted in Figure 17.15, is to give an additional cumulative phase shift of $\pm 90^\circ$ on either side of the waist, or a total added phase shift of 180° in passing through the waist, with most of this additional phase shift occurring within one or two Rayleigh ranges on either side of the waist.

This added phase shift means in physical terms that the effective axial propagation constant in the waist region is slightly smaller, i.e., $k_{\text{eq}}(z) = k - \Delta k$, or that the phase velocity and the spacing between phase fronts are slightly larger, i.e., $v_\phi(z) = c + \Delta v$, than for an ideal plane wave. The phase fronts for a gaussian beam passing through a waist will thus shift forward by a total amount of half a wavelength compared to an ideal plane wave, as illustrated in Figure 17.16.

A mathematical understanding of this additional phase shift can be obtained by rewriting the paraxial wave equation (16.7) in the form

$$\frac{\partial \tilde{u}(x, y, z)}{\partial z} = -\frac{j}{2k} \nabla_{xy}^2 \tilde{u}(x, y, z), \quad (39)$$

where ∇_{xy}^2 is the Laplacian in x, y coordinates. The transverse second derivatives of the wave amplitude \tilde{u} thus lead, through the wave equation, to a small but significant additional phase shift per unit length in the axial direction. The resulting increased phase velocity in the axial direction is exactly like the increased phase velocity in a closed waveguide. The transverse derivatives are the largest, and hence the added phase shift term is most significant, within one or two focal depths on either side of a focus, more or less independent of the exact transverse amplitude profile of the focused beam.

The Guoy Effect

This result is in fact simply the gaussian beam version of the Guoy effect, which is valid for any kind of optical (or microwave) beam passing through a focal region. This effect, which was first discovered experimentally by Guoy in

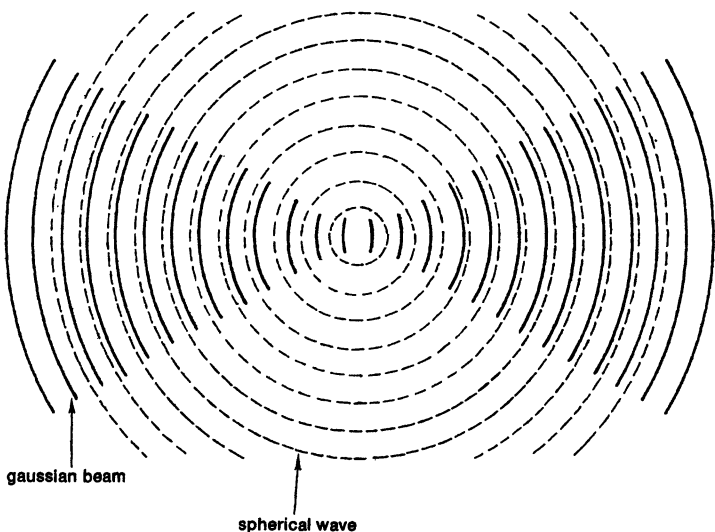


FIGURE 17.16

Alternative picture of the Guoy phase shift through the waist region, as compared to an ideal spherical wave.

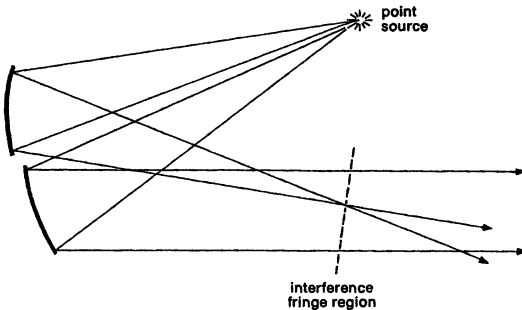


FIGURE 17.17

Experimental apparatus used by Guoy to demonstrate the extra 180° phase shift for an optical beam passing through a focus.

1890, says that a beam with any reasonably simple cross section will acquire an extra half-cycle of phase shift in passing through a focal region.

Figure 17.17 shows the simple apparatus employed by Guoy to demonstrate this effect. In the original experiment the light diverging from a small pinhole was reflected into two overlapping beams reflected from both a planar and a curved mirror. Interference effects between the two beams then produced a set of circular interference fringes between the two beams which could be observed at transverse planes near the first image of the pinhole. Guoy noticed that the centermost fringe in this "bulls-eye pattern" changed sign from dark to light (or vice versa) if he observed the fringes at observation planes just before or just after the focal point. This change of sign implied that the focused beam had somehow picked up an extra π phase shift in passing through the focus.

We will see shortly that higher-order transverse modes, because they have more complicated transverse second derivatives in Equation 17.39, have larger

Guoy phase shifts in passing through the waist region. In fact, if the lowest-order gaussian mode has Guoy phase shift $\psi(zz)$ at any plane z , measured relative to the focal point, then an nm -th order Hermite-gaussian mode with the same \tilde{q} parameter will have a Guoy phase shift of $(n+m+1) \times \psi(z)$. These differing phase shifts are directly responsible for the slightly different resonance frequencies and mode beats of different nm -th order transverse modes in stable laser cavities.

The Guoy phase shift also explains the possibly somewhat puzzling 90° phase shift associated with the factor of j in the $j/L\lambda$ constant that occurs as part of the kernel in Huygens' integral (Equations 16.17 or 16.19). The physical interpretation of Huygens' integral considers the Huygens' wavelets as being ideal spherical wavelets diverging from each source point on the wavefront in the input plane, except that there is apparently a 90° phase shift between the incident wavefront and the diverging wavelet. The Guoy effect says that this occurs because each wavelet will acquire exactly 90° of extra phase shift in diverging from its point source or focus to the far field, thus accounting exactly for the j factor in the $j/L\lambda$ term.

REFERENCES

The original references on the Guoy effect can be found in G. Guoy, *Compt. Rendue Acad. Sci. Paris* **110**, 1251–1253 (1890) and *Ann. de Chim. et Phys.* **24**, 145–213 (1981); cf. also F. Reiche, *Ann. Physik* **29**, 65 and 401 (1909).

The Guoy effect occurs equally well with focused microwave or radio-wave beams as well as with optical beams. A useful discussion and illustration of all these situations can be found in C. L. Andrew, *Optics of the Electromagnetic Spectrum* (Prentice-Hall, 1960), pp. 114–118.

Another useful discussion along lines similar to the present section, and with an extensive summary of earlier references, can be found in R. W. Boyd, “Intuitive explanation of the phase anomaly of focused light beams,” *J. Opt. Soc. Am.* **70**, 877–880 (July 1980).

For a clear theoretical discussion and graphical illustrations of the Guoy effect near the focal region of a nongaussian (uniform) beam, see E. H. Linfoot and E. Wolf, “Phase distribution near focus in an aberration-free diffraction image,” *Proc. Phys. Soc. B* **69**, 823–832 (1956). For theoretical results in the focal region of a gaussian beam, see W. H. Carter, “Anomalies in the field of a gaussian beam near focus,” *Optics. Commun.* **7**, 211–218 (March 1983).

For experimental results, see G. W. Farnell, “Measured phase distribution in the image space of a microwave lens,” *Canadian J. Phys.* **36**, 935 (1958).

17.5 HIGHER-ORDER GAUSSIAN MODES

Let us now look in somewhat more detail at the higher-order Hermite-gaussian modes we derived in the previous chapter. In doing this we will consider only the “standard” set of higher-order Hermite-gaussians discussed in Section 16.4, since they usually match up most closely with the actual higher-order modes in simple optical resonators (at least in optical resonators which do not have “soft” apertures or radially varying gains or losses).

Higher-Order Hermite-Gaussian Mode Functions

The free-space Hermite-gaussian TEM_{nm} solutions derived in the preceding chapter can be written, in either the x or y transverse dimensions, and with the plane-wave e^{-jkz} phase shift factor included for completeness, in the normalized form

$$\tilde{u}_n(x, z) = \left(\frac{2}{\pi}\right)^{1/4} \left(\frac{1}{2^n n! w_0}\right)^{1/2} \left(\frac{\tilde{q}_0}{\tilde{q}(z)}\right)^{1/2} \left[\frac{\tilde{q}_0 \tilde{q}^*(z)}{1 \tilde{q}_0 \tilde{q}(z)}\right]^{n/2} \times H_n\left(\frac{\sqrt{2}x}{w(z)}\right) \exp\left[-jkz - j\frac{kx^2}{2\tilde{q}(z)}\right], \quad (40)$$

where the H_n 's are the Hermite polynomials of order n , and the parameters $\tilde{q}(z)$, $w(z)$ and $\psi(z)$ are exactly the same as for the lowest-order gaussian mode as given in Equation 17.5. These same functions can be written in alternative form, emphasizing the spot size $w(z)$ and Guoy phase shift $\psi(z)$, in the form

$$\tilde{u}_n(x, z) = \left(\frac{2}{\pi}\right)^{1/4} \left(\frac{\exp[j(2n+1)\psi(z)]}{2^n n! w(z)}\right)^{1/2} \times H_n\left(\frac{\sqrt{2}x}{w(z)}\right) \exp\left[-jkz - j\frac{kx^2}{2R(z)} - \frac{x^2}{w^2(z)}\right], \quad (41)$$

where $\psi(z)$ is still given by $\psi(z) = \tan^{-1}(z/z_R)$.

Note the important point that the higher-order modes, because of their more rapid transverse variation, have a net Guoy phase shift of $(n + 1/2)\psi(z)$ in traveling from the waist to any other plane z , as compared to only $\psi(z)$ for the lowest-order mode. This differential phase shift between Hermite-gaussian modes of different orders is of fundamental importance in explaining, for example, why higher-order transverse modes in a stable laser cavity will have different oscillation frequencies; or how the Hermite-gaussian components that add up to make a uniform rectangular or strip beam in one transverse dimension at an input plane located in the near field (at a beam waist) can add up to give a $(\sin x)/x$ transverse variation for the same beam in the far field.

Hermite-Gaussian Mode Patterns

Figure 17.18 illustrates the transverse amplitude variations for the first six even and odd Hermite-gaussian modes. Note that the first few (unnormalized) Hermite polynomials are given by

$$\begin{aligned} H_0 &= 1 & H_1(x) &= 2x \\ H_2(x) &= 4x^2 - 2 & H_3(x) &= 8x^3 - 12x. \end{aligned} \quad (42)$$

These polynomials obey the recursion relation

$$H_{n+1}(x) = 2xH_n(x) - 2nH_{n-1}(x) \quad (43)$$

which can provide a useful way of calculating the higher-order polynomials in numerical computations.

The Hermite-gaussian beam functions alternate between even and odd symmetry with alternating index n . The n -th order function has n nulls and $n + 1$

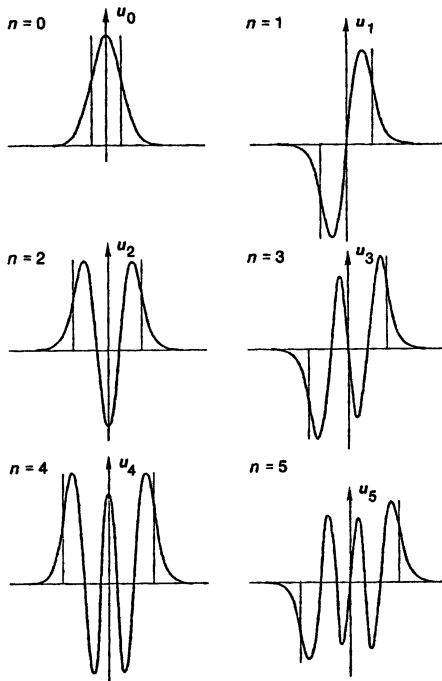


FIGURE 17.18
Amplitude profiles for low-order Hermite-gaussian modes.

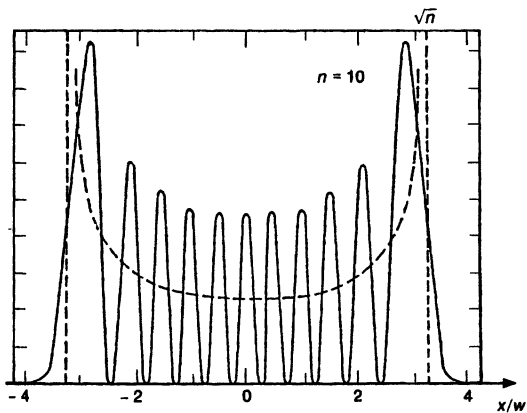


FIGURE 17.19
Intensity profile for the Hermite-gaussian mode pattern with $n = 10$.

peaks. These same Hermite-gaussian functions are also the quantum mechanical eigenfunctions for the linear quantum harmonic oscillator. Figure 17.19 illustrates the intensity variation, or the wave amplitude squared, for the $n = 10$ eigenmode, showing how the wave distribution approaches the classical proba-

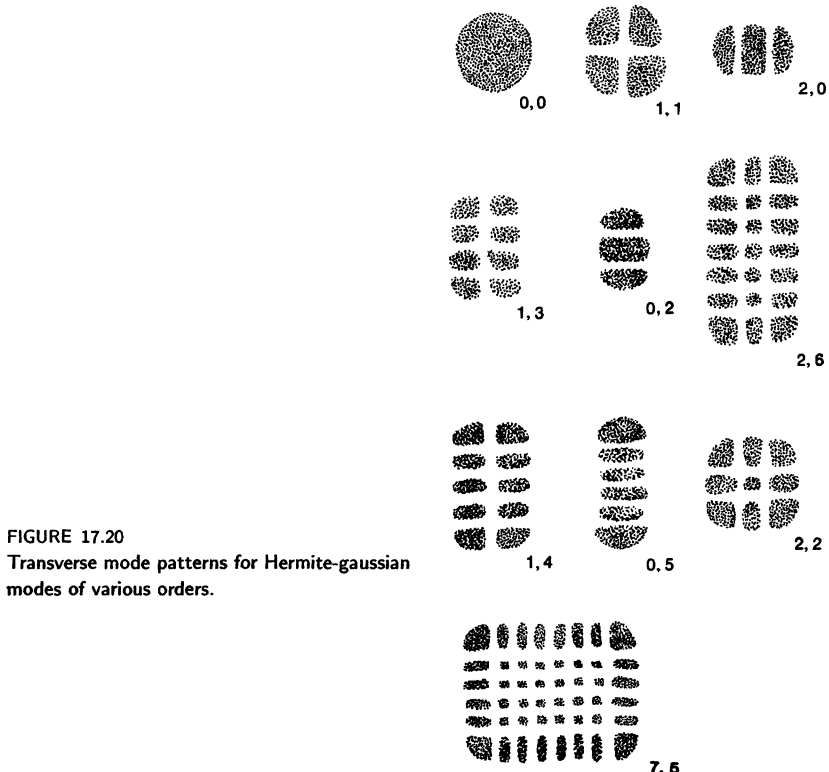


FIGURE 17.20
Transverse mode patterns for Hermite-gaussian modes of various orders.

bility density for a linear harmonic oscillator. It can also be seen that for larger values of n the outermost peaks become noticeably more intense than the inner peaks.

The complete set of Hermite-gaussian transverse modes for a beam in two transverse dimensions can then be written as $\tilde{u}_{nm}(x, y, z) = \tilde{u}_n(x, z) \times \tilde{u}_m(y, z)$, where in the most general situation a different $\tilde{q}(z)$ parameter, and even a different waist location, may apply to the x and the y variations. Figure 17.20 shows how the intensity patterns of various higher-order modes appear if the output beam from a laser oscillating in one of these higher-order modes is projected onto a screen. Note that the Hermite-gaussian functions are everywhere scaled to the spot size w through the arguments x/w and y/w . Hence, the intensity pattern of any given TEM_{nm} mode changes size but not shape as it propagates forward in z —a given TEM_{nm} mode looks exactly the same, except for scaling, at every point along the z axis.

The higher-order Laguerre-gaussian mode patterns also described in Section 16.4 (cf. Equation 16.64) are characterized by azimuthal and radial symmetry, rather than by the rectangular symmetry of the Hermite-gaussian modes, as illustrated in Figure 17.21. As explained earlier, most real lasers prefer to oscillate in modes of rectangular rather than cylindrical symmetry, although with very

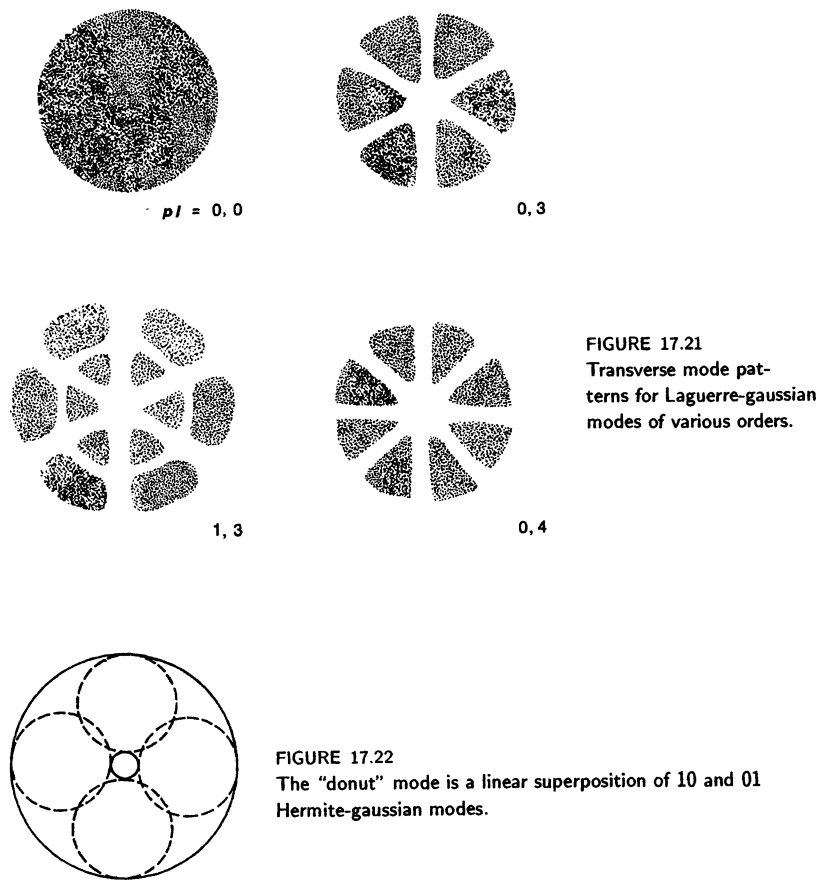


FIGURE 17.21
Transverse mode patterns for Laguerre-gaussian modes of various orders.

careful adjustment, certain internal-mirror lasers can be made to oscillate in the cylindrical Hermite-gaussian modes.

The "Donut Mode"

In many laser experiments with stable laser resonators, the experimental procedure is to stop down an adjustable circular aperture inside the laser cavity until higher-order mode oscillation is completely suppressed and the laser oscillates only in the desired TEM_{00} mode. For aperture diameters slightly larger than this value, lasers are often observed to produce an output beam in the form of a circularly symmetric ring with a dark spot on axis, as illustrated in Figure 17.22.

This mode, often referred to as the "donut mode," cannot be an $m = 0$ mode, since an $m = 0$ Laguerre-gaussian mode can never have a null on axis. It might be interpreted as a higher-order $\tilde{u}_{pm}(r, \theta)$ Laguerre-gaussian mode with $p = 1$ and an azimuthal variation like $e^{jm\theta}$ with $m \geq p$. In most practical lasers, however,

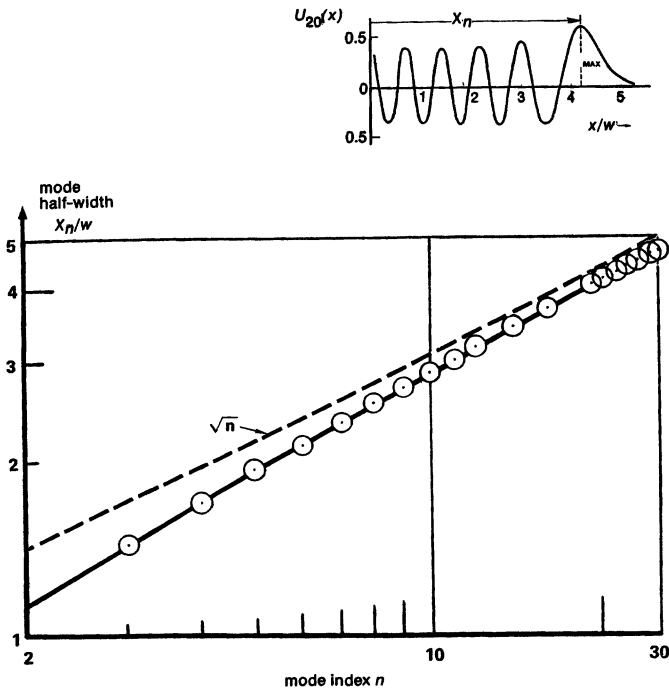


FIGURE 17.23

The outermost peak of an n -th order Hermite-gaussian mode occurs at $x_n \approx \sqrt{n} \times w$. The inset shows the $n = 20$ mode as an example.

this “mode” is more likely to represent a linear combination of the TEM_{10} and TEM_{01} Hermite-gaussian modes oscillating separately and independently, with slightly different oscillation frequencies because of the astigmatism introduced by the Brewster windows in the laser. The time-averaged total power output is then still circularly symmetric about the axis.

Higher-Order Mode Sizes

It is obvious from inspection as well as from analytical approximations that higher-order Hermite-gaussian or Laguerre-gaussian modes spread out further in diameter as the mode index n (or p) increases. The mode pattern of the $n = 10$ mode function shown in Figure 17.23, for example, spreads out considerably farther than the lowest-order or $n = 0$ gaussian mode. This increase in mode diameter with increasing index n can be put on a quantitative footing as follows.

Let us use the peak of the outermost ripple in the Hermite-gaussian pattern, call its location x_n , as a convenient and fairly realistic measure of the spread or half-width of the Hermite-gaussian function. Numerically calculating and plotting the location of this outmost peak versus the mode index n , as in Figure 17.23—or alternatively, exploring more advanced descriptions of the mathematical properties of the Hermite-gaussian functions—then shows that this width

increases with n in approximately the form

$$\text{mode half-width, } x_n \approx \sqrt{n} \times w. \quad (44)$$

In addition, since these higher-order modes have $n/2$ full ripples or periods of approximately equal width across the full width $2\sqrt{n}w$ of an n -th order Hermite-gaussian function, the spatial period Λ_n of the quasi-sinusoidal ripples associated with, or describable by, a Hermite-gaussian function of order n and spot size w is given by

$$\text{spatial period, } \Lambda_n \approx \frac{4w}{\sqrt{n}}. \quad (45)$$

Both of these criteria are very reasonable approximations to the mathematical properties of the Hermite-gaussian functions, especially for larger n .

Higher-Order Transverse Mode Aperturing

To illustrate the use of these quantities, suppose that we have an aperture of width or diameter $2a$, corresponding perhaps to a mode control aperture or an end mirror inside a laser cavity; and that we are considering expanding the amplitude distribution across that aperture using a set of Hermite-gaussian modes of spot size w at the plane of the aperture. It is then obvious that only those Hermite-gaussian modes of orders low enough so that $x_n \leq a$, or with indices n less than the value given by

$$n \leq N_{\max} \approx \left(\frac{a}{w}\right)^2 \quad (46)$$

will pass through this aperture, or oscillate inside this cavity with relatively negligible mode losses. Modes with higher mode indices will spill over past the edges of the aperture; and we can expect a rapid increase in energy losses caused by the aperture for all modes with indices larger than this value. (Obviously this criterion is the most accurate for apertures at least several times larger than w , since the sharpness of the outer edge transition becomes increasingly apparent at higher mode numbers.) Larger-diameter lasers often choose to oscillate in multiple transverse modes extending up to and including the highest-order transverse modes that will "fit" inside the laser tube or the laser mirrors according to this criterion, since all of these transverse modes will have comparatively low diffraction losses at the laser tube walls or mirror edges.

Transverse mode-control apertures are often placed inside stable laser cavities in order to attenuate or block higher-order modes from oscillating while producing minimal loss for the lowest-order TEM_{00} modes. A common rule of thumb for the necessary aperture size in low-gain lasers, such as for example He-Ne lasers, is that the mode control aperture should have an aperture size of diameter $2a \approx 3.5$ to $4.0 \times w$, or slightly larger than the $2a = \pi w$ or 99% criterion we introduced at the beginning of this section.

Numerical Hermite-Gaussian Mode Expansions

Suppose we wish to carry out a numerical expansion of some given (or perhaps unknown) function $f(x)$ across an aperture or strip of width $2a$ using a

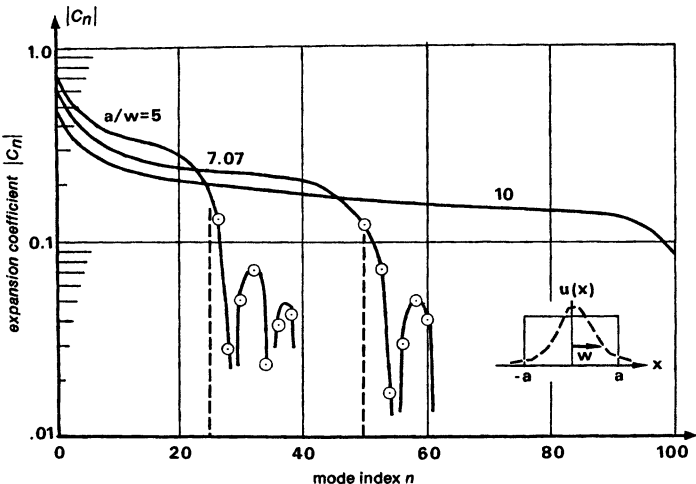


FIGURE 17.24

Expansion coefficient magnitudes $|c_n|$ versus mode index n for expanding a uniform square function of width $2a$ using a Hermite-gaussian basis set, for different choices of the parameter a/w .

Hermite-gaussian basis set in the form

$$f(x) = \sum_{n=0}^N c_n \tilde{u}_n(x; w), \quad -a \leq x \leq a, \quad (47)$$

where $\tilde{u}_n(x; w)$ refers to an n -th order Hermite-gaussian function characterized by spot size w , and N is the maximum index value to be kept in a finite expansion. Let us explore some of the numerical considerations involved in this expansion, such as the optimum choice of the gaussian spot size w (assuming this to be a free parameter), and the number of terms N that we will need to keep in the summation.

The expansion coefficients for a given function $f(x)$ will be given by the overlap integrals

$$c_n = \int_{-a}^a f(x) \tilde{u}_n^*(x) dx. \quad (48)$$

Figure 17.24 shows, for example, how the expansion coefficient magnitudes $|c_n|$ will decrease in amplitude with increasing mode index n if we expand a simple rectangular function of width $2a$ using Hermite-gaussian basis sets of different fundamental spot size w . The dashed lines represent the values $N_{\max} = (a/w)^2$ in each situation. It is obvious from these plots that the amplitude of the expansion coefficients drops off rapidly in each situation as soon as n increases slightly beyond this value. This fall-off obviously occurs because the Hermite-gaussian modes of order higher than this extend past the edges of the aperture, or the square input function, and hence less and less of the Hermite-gaussian function falls within the overlap integral given in the preceding.

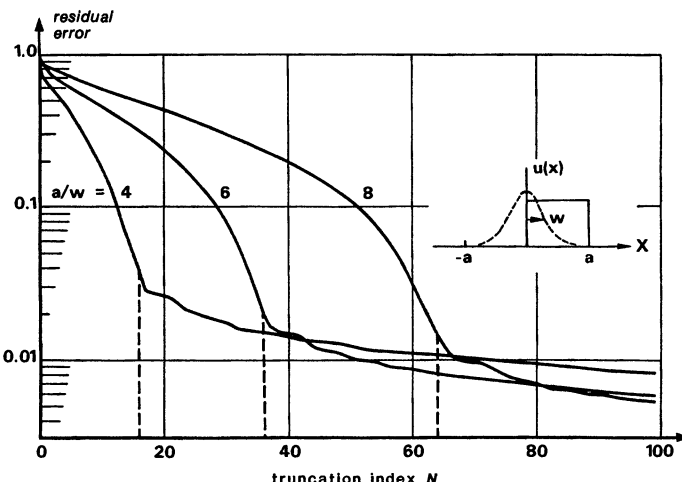


FIGURE 17.25

Residual mean-square error in approximating a half square of width a using a truncated series of Hermite-gaussian functions, plotted versus series truncation index, for different values of a/w .

As a slightly different illustration of the same point, Figure 17.25 shows similar results for the expansion of a half-square (or displaced square) function covering the range $0 \leq x \leq a$ using Hermite-gaussian basis functions. The quantity plotted in this situation is the residual mean-square error in the series approximation to the function $f(x)$ caused by truncating the series expansion at a maximum value N , for different choices of the ratio a/w . Again we see that the maximum error drops rapidly with increasing number of terms in the series expansion, but only up to a rather surprisingly sharp corner at $N \approx N_{\max} = (a/w)^2$. Beyond this value, keeping additional terms only causes a very slow further improvement in the accuracy with which the function is approximated by the finite series.

Spatial Frequency Considerations

Suppose as a more general example that we wish to describe an arbitrary function $f(x)$ across an aperture of width $2a$ with a finite sum of $N+1$ Hermite-gaussian functions $\hat{u}_n(x; w)$, of arbitrary spot size w , for $0 \leq n \leq N$. How then should we select the spot size w to use in the expansion, and the maximum index N at which the series expansion is to be truncated?

To do this sensibly, we must first calculate (from experimental or other evidence) what is the maximum spatial frequency or spatial period Λ of the fluctuations in the function to be expanded across the interval $-a \leq x \leq a$? That is, we must pick a value of Λ such that the significant variations in $f(x)$ will be no more rapid than $\approx \cos 2\pi x/\Lambda$ at most.

We must then select values of w and N so that the highest-order Hermite-gaussian functions to be employed will simultaneously satisfy two criteria: they must at least fill the aperture, and they must at least handle the highest spatial

variations in the signal. But these are equivalent to the two conditions

$$N \geq N_{\max} \equiv \left(\frac{a}{w}\right)^2 \quad \text{and} \quad \Lambda_N \approx \frac{4w}{\sqrt{N}} \leq \Lambda. \quad (49)$$

Satisfying these conditions simultaneously then leads to the spot-size and maximum-index criteria

$$w \leq \sqrt{\frac{a\Lambda}{4}} \quad \text{and,} \quad N \geq \frac{4a}{\Lambda}. \quad (50)$$

The second of these criteria is obviously a Hermite-gaussian version of the familiar sampling theorem of Fourier transform theory, which says that to describe an arbitrary function which is bandlimited to a spatial frequency $2\pi/\Lambda$, we need at least two sample points per spatial period Λ . In the Hermite-gaussian analog we need $N = 4a/\Lambda$ samples in space across a width of $2a$, or equivalently $N = 4a/\Lambda$ coefficients in a Hermite-gaussian expansion.

REFERENCES

The width and divergence properties of higher-order Hermite-gaussian modes have also been analyzed by W. B. Bridges, "Divergence of high order gaussian modes," *Appl. Optics* **14**, 2346-2347 (October 1975). Similar properties for Laguerre-gaussian modes are treated by R. L. Phillips and L. C. Andrews, "Spot size and divergence for Laguerre gaussian beams of any order," *Appl. Optics* **22**, 643-644 (March 1 1983).

Some interesting properties of Laguerre-gaussian modes with zero radial order and high azimuthal orders are given by A. H. Paxton, "Propagation of high-order azimuthal Fourier terms of the amplitude distribution of a light beam: a useful feature," *J. Opt. Soc. Am. A* **1**, 319-321 (March 1984).

Experimental studies of multimode beam divergence are given by H. M. Lamberton and V. G. Roper, "Beam divergence of a highly multimode CO₂ laser," *J. Phys. E: Sci. Instrum.* **11**, 1102-1103 (1978); and J. T. Luxon and D. E. Parker, "Higher-order CO₂ laser beam spot size and depth of focus determined," *Appl. Optics* **20**, 1933-1935 (June 1 1981).

More details on astigmatic higher-order modes and their aberrations are given in S. L. Chao and J. M. Forsyth, "Properties of high-order transverse modes in astigmatic laser cavities," *J. Opt. Soc. Am.* **65**, 867-875 (August 1975).

An experimental method for analyzing the transverse mode content of laser beams is outlined in M. A. Golub, A. M. Prokhorov, I. N. Sisakyan, and V. A. Soffer, "Synthesis of spatial filters for investigation of the transverse mode composition of coherent radiation," *Sov. J. Quantum Electron.* **12**, 1208-1209 (September 1982).

Problems for 17.5

1. *Instantaneous beam profile for the "donut mode."* Suppose you can take a series of instantaneous snapshots of the output beam intensity profile from a laser oscillating in the donut mode, in a situation where there is a finite frequency difference or beat frequency between the TEM₀₁ and TEM₁₀ modes (perhaps because some Brewster windows make the laser cavity slightly astigmatic and

slightly different in length for x -varying and y -varying modes). What will the time variation of the instantaneous intensity profile look like?

2. *Near-field beam with a central hole.* Consider a near-field beam pattern at the beam waist location which has a central hole in it (in one transverse direction), produced by combining $\tilde{u}_0(x)$ and $\tilde{u}_2(x)$ modes with correct amplitude ratio to produce a null value on axis (i.e., at $x = 0$). What will the far field pattern of this beam look like? Will there still be a hole on axis? Explain.
3. *Recursion relation for expanding a half-rectangle in Hermite-gaussian functions.* If you expand an off-center half-square function of width a into Hermite-gaussian functions, the first two expansion coefficients are

$$c_0 = (2\pi)^{1/4} (w/4a)^{1/2} \operatorname{erf}(a/w)$$

$$c_1 = (2\pi)^{1/4} (w/a)^{1/2} [1 - \exp(-a^2/w^2)].$$

Using the recursion and differential relations for Hermite-gaussian polynomials, show that all the higher-order expansion coefficients can be obtained from the recursion relation

$$c_n = \left(\frac{n-1}{n}\right)^{1/2} c_{n-2} - \frac{w}{n^{1/2} a} [\tilde{u}_{n-1}(a; w) - \tilde{u}_{n-1}(0; w)],$$

where the $\tilde{u}_n(x; w)$ are the properly normalized Hermite-gaussian functions of spot size w .

17.6 MULTIMODE OPTICAL BEAMS

Lasers that oscillate in multiple higher-order transverse modes are almost always considered as “bad” lasers, since they will have a far-field beam spread considerably larger than a well-behaved lowest-order single-transverse-mode laser. The quasi analytic results that we have just obtained for Hermite-gaussian mode expansions can also be applied to give a useful description of multimode or non-diffraction-limited laser beams, in the following fashion.

Description of a Multimode or Non-Diffraction-Limited Beam

Suppose that an oscillating laser emits a reasonably well-collimated but obviously multimode optical beam which occupies a width or diameter $2a$ in the transverse direction at the output from the laser. (By “collimated” we mean simply that any overall spherical curvature of the wavefronts emitted from the laser has been corrected by a suitable collimating lens.)

The far-field angular spread of the multimode beam coming from this laser will then be substantially larger than the value $\Delta\theta \approx \lambda/2a$ that would be characteristic of a more or less diffraction-limited optical beam. From another viewpoint, if the output beam from this laser consists of a mixture of a sizable number of different transverse modes, the wavefront at the laser output is likely to be quite random in character, with considerable spatial incoherence or variation in local amplitude and phase from point to point across the aperture.

How can such a strongly non-diffraction-limited laser beam then be described analytically—especially in situations where little information may be available concerning the detailed mode characteristics of the laser, and where all that is known for certain may be the near-field aperture width and the far-field angular spread of this beam?

Hermite-Gaussian Analysis of Multimode Optical Beams

One useful approach can be to analyze this beam as if the output fields in the beam are made up of, or can be analyzed as, a superposition of Hermite-gaussian modes having a characteristic spot size w_0 . This assumption might apply quite well, for example, to the output beam from a laser with a stable gaussian resonator, such as we will describe in the following chapter, in which the natural resonator spot size is w_0 , but the laser tube diameter or mirror diameter $2a$ is substantially larger than w_0 . This laser may then oscillate simultaneously in multiple transverse modes which fill the entire diameter $2a$.

More generally, consider an arbitrary, irregular, multimode beam coming from any kind of laser cavity, stable or not; and assume that this beam has sizable fluctuations in amplitude and especially in phase across its diameter $2a$. Regardless of whether the underlying mode structure in this beam is gaussian, we can still use a set of Hermite-gaussian modes to expand the fields. Following the procedure outlined in the previous section, we can first ask what spot size w_0 and number of modes N we would need to choose so that the spatial frequencies and the spatial resolution of the set of Hermite-gaussian modes would be just adequate to describe the most rapid spatial variations across the aperture of that particular beam. We can then use these values to calculate the basis set of Hermite-gaussian functions which we can employ to describe that particular beam with adequate accuracy.

For an aperture of width $2a$, where a is at least a few times larger than w_0 , the maximum number of Hermite-gaussian modes that will “fit” within the aperture, or the number of modes that will be needed to describe the fields in the aperture, will then be given by

$$N \approx N_{\max} \equiv (a/w_0)^2. \quad (51)$$

The corresponding maximum half-angle spread of the overall beam in the far field, using a near-field spot size of w_0 and modes of index running up to $n = N$, will then be

$$\theta_{\max} \approx \sqrt{N} \times \theta_{1/e} = \frac{N^{1/2} \lambda}{\pi w_0} = \frac{a \lambda}{\pi w_0^2}. \quad (52)$$

If we consider for simplicity a circular aperture of diameter $2a$, then the far field beam will also have a circular cross section of angular diameter $2\theta_{\max}$. The product of the source aperture area $A \equiv \pi a^2$ and the far-field solid angular spread $\Omega \equiv \pi \theta_{\max}^2$ will then be given by

$$A \times \Omega \equiv (\pi a^2) \times (\pi \theta_{\max}^2) \approx (N \lambda)^2. \quad (53)$$

This product for the multimode or non-diffraction-limited beam is then N^2 times the diffraction-limited value $A \times \Omega = \lambda^2$ we derived earlier for an ideal lowest-order gaussian beam.

"Times Diffraction Limited" (TDL)

An irregular or multimode laser beam which can be described in the fashion leading up to Equation 17.53 is often said to be " N times diffraction limited." That is, its far-field angular spread is $\approx N$ times as large in one dimension (or N^2 times in solid angle) as the diffraction-limited angular spread that would be obtained from a uniphase beam with a reasonably regular amplitude variation filling the same aperture. The quantity N is sometimes referred to as the "times diffraction limited" or "TDL" of the beam. Note that if this same beam is focused to a spot with a suitable lens, the diameter of the focused spot will also be $\approx N$ times the spot size that would be obtained with an ideal diffraction-limited beam.

This argument can also be applied in the reverse direction. That is, given a beam known to be N times diffraction limited (based on experimental data on its initial aperture size and its far-field beam spread), we can treat this beam analytically as if it were made up of a mixture of N^2 Hermite-gaussian modes, with spot size given by $w_0 \approx a/N^{1/2}$, and with mode amplitude coefficients assumed to be approximately equal or perhaps randomly distributed in amplitude. The relatively simple mathematical properties of the Hermite-gaussian modes then make it possible to calculate or at least estimate other properties of this beam that might be of interest (for example, perhaps the amount of harmonic generation it would produce in a given crystal).

It may seem somewhat inconsistent here to employ the Hermite-gaussian modes, which are characteristic of rectangular coordinates, and then compute areas and solid angles assuming circular beams, which might more accurately be described using cylindrical coordinates and Laguerre-gaussian functions. The only excuse is that the Hermite-gaussian properties are perhaps simpler and more familiar than the Laguerre-gaussians, and the right answer comes out by using formulas based on a circular aperture.

REFERENCES

For more discussion of these topics see the following chapter, and also the references at the end of the previous section. See also Z. Karny, S. Lavi, and O. Kafri, "Direct determination of the number of transverse modes of a light beam," *Optics Lett.* **8**, 409–411 (July 1983).

For a somewhat different approach to other types of laser beam aberration, see C. B. Hogue, R. R. Butts, and M. Burlakoff, "Characteristics of phase-aberrated nondiffraction-limited laser beams," *Appl. Optics* **13**, 1065–1070 (May 1984).

Problems for 17.6

1. **Beam expansion criteria using Laguerre-gaussian functions.** Look up sufficient information concerning the asymptotic properties of Laguerre polynomials and Laguerre-gaussian functions to calculate the number of Laguerre-gaussian functions of given w_0 that will fit within a circular aperture of radius a , and the number of azimuthal orders that will be involved; and then repeat the "TDL" argument of this section working in cylindrical coordinates.
-

BEAM PERTURBATION AND DIFFRACTION

In this chapter we consider what happens to the transverse profile of an optical beam in free space when the beam is perturbed by a weak disturbance such as a phase or amplitude perturbing screen, or by a hard-edged diffracting aperture, such as a uniform slit or a square or circular aperture. The primary objective in presenting these examples is to gain insight into the effects that can occur when a free-space beam is perturbed in various elementary ways, as well as some familiarity with the common analytical techniques for describing these effects.

18.1 GRATING DIFFRACTION AND SCATTERING EFFECTS

Optical elements in real life are often of good but not perfect quality. Optical beams may then be perturbed by various kinds of weak amplitude or phase perturbations, such as scratches, dust particles or blemishes on lenses or mirror surfaces, or bubbles and defects inside optical components. Optical imperfections of this kind may be modeled in many situations either as a collection of point scatterers, or as weak and more or less random amplitude or phase-perturbing screens or gratings. We will look briefly at both of these descriptions in this section, taking up the grating diffraction approach first.

Consider, for example, a perturbing screen with a random transverse amplitude or phase profile like Figure 18.1. The amplitude and phase variations this element will impose on a uniform beam passing through it can be described by a perturbation transmission function; and the phase and amplitude parts of this transmission function can in turn be expressed as a superposition of sinusoidal components or spatial-frequency components of the form $\sin 2\pi x/\Lambda$ or $\cos 2\pi x/\Lambda$ in the transverse direction. We can analyze the scattering produced by each such spatial component separately, and then for weak gratings add their effects to describe the total scattering produced by the complete perturbation.

Amplitude Gratings

Let us consider first a weak sinusoidal amplitude grating oriented perpendicular to the z axis and having a sinusoidal periodicity of period Λ in the x direction, as in Figure 18.1(b). The amplitude (i.e., field) transmission through

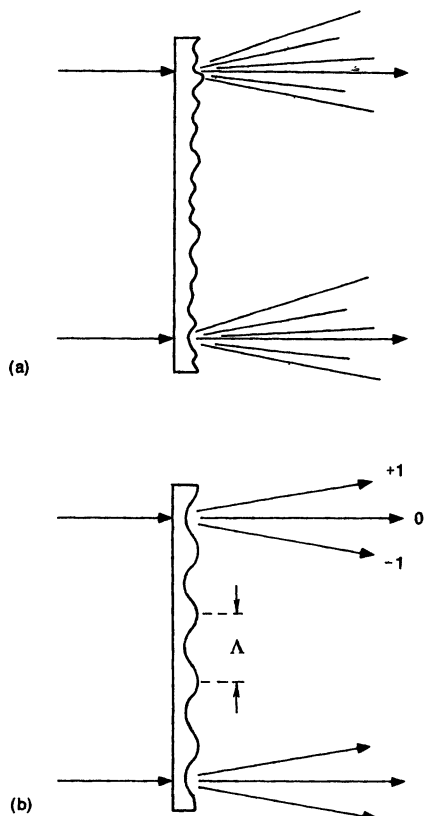


FIGURE 18.1
 (a) A random amplitude or phase-perturbing screen. (b) Sinusoidal amplitude or phase-perturbing element with spatial period Λ .

this grating can then be written in the form

$$\tilde{t}(x) = \exp[-\Delta(1 - \cos k_x(x - x_0))], \quad (1)$$

and the intensity transmission $T(x) \equiv |\tilde{t}(x)|^2$ in the form

$$T(x) = \exp[-2\Delta[1 - \cos k_x(x - x_0)]] = \exp\left[-4\Delta \sin^2 \frac{\pi(x - x_0)}{\Lambda}\right], \quad (2)$$

where $k_x \equiv 2\pi/\Lambda$ is the k -vector of the periodic grating. This intensity transmission is illustrated for different values of Δ in Figure 18.2.

The analytical form of Equation 18.1 is a convenient way of representing a sinusoidal modulation with peak-to-peak modulation depth of 2Δ in amplitude (or 4Δ in intensity), either in a spatial dimension as we are doing here, or for a sinusoidal amplitude modulation in time as we will do in a later chapter. This form has the convenient property that the intensity transmission is always less than or equal to unity, but never goes negative even for very large Δ (although we are most interested in the small- Δ regime in this chapter). This particular

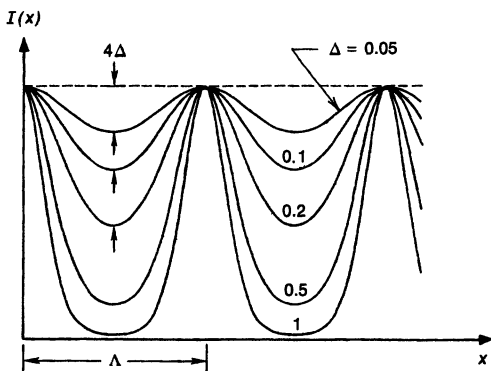


FIGURE 18.2
Intensity transmission versus position for various modulation depths Δ .

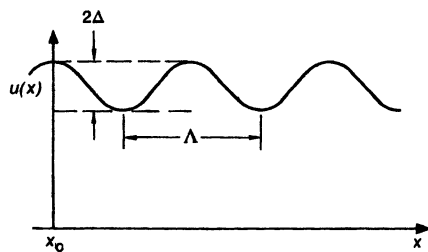
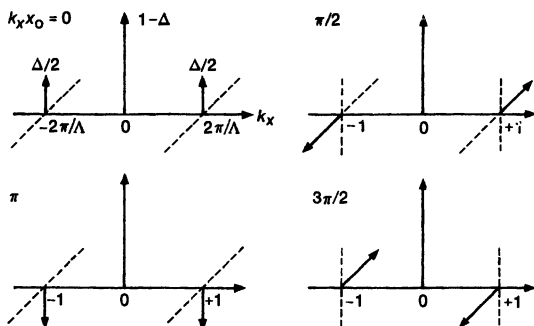


FIGURE 18.3
Relative phase angles of the +1 and -1 sidebands for different transverse positions of a pure amplitude grating.



form also corresponds rather closely to the actual amplitude transmission versus time or space in many practical acoustooptic and electrooptic light modulators.

A uniform plane wave passing through this grating will retain a planar wave-front, but will acquire a transverse intensity profile which we can write as

$$\begin{aligned}\tilde{u}(x) &= \exp[-\Delta[1 - \cos k_x(x - x_0)]] \\ &\approx 1 - \Delta + \frac{\Delta}{2} \exp[-jk_x(x - x_0)] + \frac{\Delta}{2} \exp[+jk_x(x - x_0)] \quad (3) \\ &= \tilde{\delta}_0 + \tilde{\delta}_1 e^{-jk_x x} + \tilde{\delta}_{-1} e^{+jk_x x}, \quad \text{for } \Delta \ll 1.\end{aligned}$$

The second and third lines of this expression show that the primary effect of a weak sinusoidal amplitude grating is to scatter a small part of the original plane wave amplitude into two diffracted components or diffraction orders with transverse k vector components given by $\pm k_x$, where

$$k_x \equiv k \sin \theta_x \equiv 2\pi/\Lambda_x \approx 2\pi\theta_x/\lambda. \quad (4)$$

The amplitudes of these sidebands are given by $\tilde{\delta}_0 = 1 - \Delta$ for the original wave vector component (the "carrier"), and by

$$\tilde{\delta}_1 = \frac{\Delta}{2} \times e^{jk_x x_0} \quad \text{and} \quad \tilde{\delta}_{-1} = \frac{\Delta}{2} \times e^{-jk_x x_0} \quad (5)$$

for the amplitudes scattered into the +1 and -1 diffraction orders, respectively. Note that the transverse position of the amplitude grating with respect to the z axis, as contained in the x_0 parameter, shows up as a *relative phase shift* $\exp(\pm jk_x x_0)$ in the phases of these two sidebands. The various possible relative phase angles for the amplitude grating sidebands caused by different transverse shifts of the grating are sometimes represented graphically by the kind of three-dimensional phasor diagram shown in Figure 18.3.

Phase Grating

Suppose we have instead a weak sinusoidal phase grating, with complex amplitude transmission given by

$$\tilde{t}(x) = \exp[j\Delta \cos k_x(x - x_0)]. \quad (6)$$

(Note that there is no need to add a constant term in front of the cosine in this situation, since the phase shift can equally well go positive or negative.) An initially uniform plane wave passing through this grating will again be diffracted into the components

$$\begin{aligned}\tilde{u}(x) &= e^{j\Delta \cos k_x(x - x_0)} \\ &\approx 1 + j \frac{\Delta}{2} \times [e^{-jk_x(x - x_0)} + e^{+jk_x(x - x_0)}] \quad (7) \\ &= 1 + \tilde{\delta}_1 e^{-jk_x x} + \tilde{\delta}_{-1} e^{+jk_x x}, \quad \text{for } \Delta \ll 1,\end{aligned}$$

where Δ is again the depth of modulation, but now in phase rather than in magnitude.

The transmitted intensity is now constant across the aperture. The same amount of energy has, however, again been scattered (for the same modulation

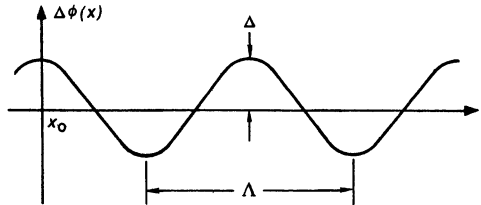
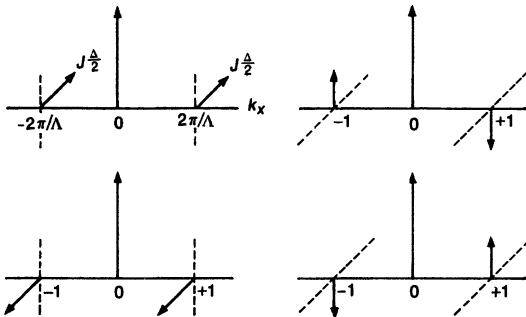


FIGURE 18.4

Relative phase angles of the +1 and -1 sidebands for different transverse positions of a pure phase grating.



depth Δ) into two diffracted orders with the same transverse k vector components, but now with complex amplitudes given by

$$\tilde{\delta}_1 = j \frac{\Delta}{2} \times e^{jk_x x_0} \quad \text{and} \quad \tilde{\delta}_{-1} = j \frac{\Delta}{2} \times e^{-jk_x x_0}. \quad (8)$$

Again the relative phase angles of these two sidebands for different transverse shifts of the phase grating can be represented by different vector diagrams as shown in Figure 18.4. Note, however, the distinguishing phase differences between the amplitude and phase grating results shown in Figures 18.3 and 18.4. If the grating is a pure amplitude grating the two wave amplitudes will be related by the condition

$$\tilde{\delta}_1 \equiv \tilde{\delta}_{-1}^* \quad (\text{amplitude grating}), \quad (9)$$

whereas we have instead the condition that

$$\tilde{\delta}_1 \equiv -\tilde{\delta}_{-1}^* \quad (\text{phase grating}) \quad (10)$$

for a pure phase grating.

General Two-Diffracted-Wave Situation

Suppose a uniform plane wave passes through some general combination of a weak amplitude grating plus a weak phase grating, with both gratings having the same transverse period Λ (though not necessarily the same modulation depth Δ or offset x_0). The transmitted wave just beyond the grating can then still be

written in the general form

$$\tilde{u}(x) \approx \tilde{\delta}_0 + \tilde{\delta}_1 e^{-jk_z x} + \tilde{\delta}_{-1} e^{+jk_z x}, \quad (11)$$

where $\tilde{\delta}_1$ and $\tilde{\delta}_{-1}$ represent the complex amplitudes of the waves scattered or diffracted into the +1 and -1 orders. Any arbitrary relative amplitudes and phases for the two sidebands can then always be generated by the proper combination of a weak amplitude grating plus a weak phase grating, with the resulting total wave amplitudes given by

$$\tilde{\delta}_1 = \tilde{\delta}_{1,\text{am}} + \tilde{\delta}_{1,\text{fm}} \quad \text{and} \quad \tilde{\delta}_{-1} = \tilde{\delta}_{1,\text{am}}^* - \tilde{\delta}_{1,\text{fm}}^*. \quad (12)$$

(Because of the obvious connection between these grating sidebands and the modulation sidebands associated with the time modulation of signals as in AM and FM radio, we use the initials AM and FM as shorthand to represent amplitude and phase gratings, respectively.)

Single-Sideband Gratings

An optical grating may in fact even act like a single-sideband modulator, i.e., it may produce only a single diffracted sideband which may be written in the form

$$\tilde{u}(x) \approx 1 + \tilde{\delta}_1 e^{-jk_z x}. \quad (13)$$

It is evident from the preceding results that such a single sideband represents an equal combination of amplitude and phase gratings, with transverse displacements x_0 between them adjusted to just cancel the total sideband on one side, but reinforce the sidebands on the opposite side. The intensity variation across this beam is then

$$I(x) = |\tilde{u}(x)|^2 \approx 1 + |2\tilde{\delta}_1| \cos(k_z x + \theta_1). \quad (14)$$

The intensity variation in this situation always has a periodic ripple with peak magnitude $2|\tilde{\delta}_1|$ and period corresponding to the grating spacing, independent of the phase angle θ_1 of the single sideband.

Beam Transformations With Distance

From our earlier discussion of plane-wave expansions of optical beams, we know that for a plane wave with transverse k -vector components given by

$$k_x = k \sin \theta_x \approx k \theta_x \quad \text{and} \quad k_y = k \sin \theta_y \approx k \theta_y, \quad (15)$$

the propagation vector component in the z direction will be given by

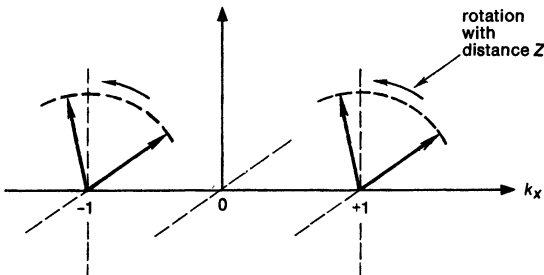
$$k_z = \sqrt{k^2 - k_x^2 - k_y^2} \approx k - \frac{k}{2} [\theta_x^2 + \theta_y^2]. \quad (16)$$

If a grating produces two diffracted components traveling at angles $\pm\theta$ in the x, z plane, these components will both propagate or rotate in relative phase as they travel outward from the grating in the form

$$\tilde{\delta}_{\pm 1}(z) = \tilde{\delta}_{\pm 1}(0) \times \exp[j(k\theta^2/2)z]. \quad (17)$$

FIGURE 18.5

Propagation through distance z rotates both the $+1$ and -1 sidebands of Figures 18.3 and 18.4 in the same direction.



Note that both sidebands rotate in the same direction relative to the carrier, as illustrated in Figure 18.5.

But this rotation will gradually shift the relative phases so as to convert amplitude modulation sidebands into phase modulation sidebands, and vice versa. In fact, the primary result that emerges from this is that after a distance d given by $\exp[jk\theta^2 d/2] = \exp[j\pi/2]$, or

$$d = \frac{\pi}{k\theta^2} = \frac{\lambda}{2\theta^2} = \frac{\Lambda^2}{2\lambda} \quad (18)$$

the sideband components corresponding to a pure phase grating wavefront will have rotated into a phase angle relationship corresponding to a pure amplitude grating wavefront, and vice versa. In other words, a field distribution that starts out as, for example, a pure phase grating or phase-modulated wavefront will be converted after a certain distance into the form of a pure amplitude-modulated wavefront, and vice versa. In addition, after twice this distance the components of either type of grating will return to the same type of grating but exactly reversed in sign.

These conversion distances depend on the square of the angle θ or of the period Λ of the grating components. If we have a more complex grating with several spatial frequency components, each of these components will convert back and forth between amplitude and phase gratings with a different axial period. The general amplitude profile of the beam in the space beyond the multiple grating will thus be quite complicated. If the conversion distances for the different spatial components are incommensurate, then the original beam profile will never be recovered completely at any distance.

Point Scatterers and Spherical Waves

An alternative model to the grating approach for a random scatterer or perturbation in an optical beam—one that can be a better representation for point defects like dust particles or other very small scatterers—is a single point scatterer that reradiates a weak scattered spherical wave. Such a wave then generally interferes with the primary wave to create patterns of interference rings, such as we will analyze in this section.

Consider, for example, a weak spherical wave scattered by a point source and interfering with a primary plane wave, as in Figure 18.6. The total field amplitude at radius r , centered on the transverse location of the point defect,

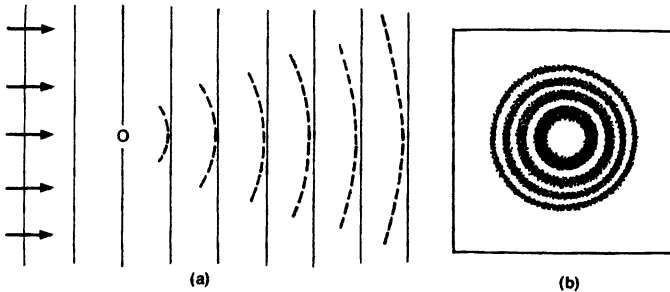


FIGURE 18.6

(a) Quasi spherical wave scattered from a point defect. (b) Concentric ring interference pattern between primary and scattered waves.

can then be written as

$$\tilde{u}(x) = 1 + \tilde{\delta}_1 \exp[-jkr^2/2R(z)] \quad \text{with } |\tilde{\delta}| \ll 1. \quad (19)$$

The intensity across the transverse plane will be given by

$$I(x) \approx 1 + |2\tilde{\delta}_1| \cos[kr^2/2R(z) + \theta_1], \quad (20)$$

where θ_1 is the initial phase angle of the scattered wave referred back to the scattering point. The amplitude of the scattered wave (assumed to be $\ll 1$) will obviously decrease as $1/R$, but we can include this implicitly in the value of $\tilde{\delta}_1$.

The intensity profile in this situation will obviously consist of a “bulls-eye pattern” or series of concentric rings, with the radii r_n of the successive bright rings given by

$$(kr_n^2/2R) + \theta_1 = n2\pi \quad \text{or} \quad r_n = \sqrt{\left(n - \frac{\theta_1}{2\pi}\right) \times 2R\lambda}. \quad (21)$$

Whether the center of the pattern will be a bright ring, a dark ring, or somewhere in between depends on the absolute value of the initial phase angle θ_1 , but not on the distance $R = z - z_0$ along the axis. As we move farther away from the point-source origin of the rings, however, the diameter of the rings will steadily increase in proportion to $z^{1/2}$, until all the rings walk out of a finite-sized beam, leaving only the central bright, or dim, spot filling the entire beam.

REFERENCES

The elementary analysis presented in this section is valid only for optically thin gratings. For optically thick amplitude or phase gratings we must use one of the many advanced analyses of grating diffraction in the literature, of which a widely referenced example is H. Kogelnik, “Coupled wave theory for thick hologram gratings,” *Bell Sys. Tech. J.* 48, 2909–2947 (November 1969).

Problems for 18.1

1. *Doppler shift from a moving grating.* Suppose that the weak amplitude or phase gratings discussed at the beginning of this section are not stationary in time but are moving transversely in space (in the x direction) at velocity v_x (as is the situation in, for example, a traveling-wave acoustooptic phase modulator). This transverse motion will then give a linear time dependence to the $\exp(\pm jk_x x_0)$ phase shifts, which will represent in turn an upward or downward frequency shift for the first-order diffracted sidebands.

Calculate this frequency shift for the two sidebands, and show also that it is essentially equivalent to a doppler shift of the scattered radiation as it “bounces” off the moving fringes of the grating.

18.2 ABERRATED LASER BEAMS

Let us now look briefly at what these properties of diffracted or scattered radiation imply for the overall properties of weakly perturbed or weakly aberrated laser beams.

Scattered Wave Amplitude and Ripple Amplitude

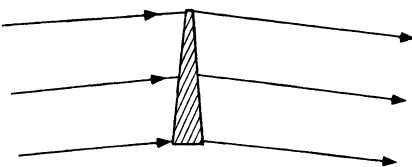
We can first note that in all of these situations, a very small amount of intensity scattered into a diffracted wave will produce a much larger relative variation or ripple amplitude in the total beam intensity. That is, if we have, for example, a scattered wave with a relative field amplitude of $\delta_1 = 0.1$, the various relative quantities then become

- amplitude of scattered wave = $\delta_1 = 0.1$,
- intensity of scattered wave = $\delta_1^2 = 0.01 = 1\%$,
- intensity ripple in total wave $\approx \pm 2\delta_1 = \pm 20\%$.

Only 1% power scattered into a diffracted sideband thus leads to $\pm 20\%$ ripple in the total intensity across the beam profile.

Note that for $\delta_1 < 1$ the intensity in the minima of the interference fringes or in the “dark” rings is not actually zero. The response of the human eye is such, however, that even a fringe pattern or ring pattern with relatively limited visibility, or relatively limited difference between “bright” and “dark” rings, will still appear visually to have a quite high contrast between these two levels. Unless we take great pains, the near-field beam profiles associated with a coherent laser beam in almost any optical system are apt to contain a rich assortment of perturbation or dust-induced fringe patterns and ring patterns. On the other hand, because of this enhanced visibility of interference fringes, what appears to be a terribly rippled and distorted beam profile may really represent only very small power losses into scattered waves diffracted out of the primary beam profile.

wedge



thin lens

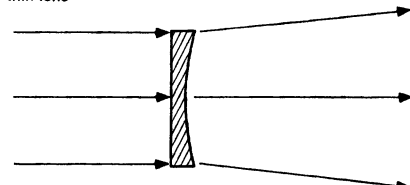


FIGURE 18.7

A wedge, and a thin lens, are the two lowest-order "slow" phase perturbations across an optical beam.

Low-Spatial-Frequency Beam Perturbations

The aberrations, especially phase aberrations, that occur in real laser cavities or laser optical systems can often be separated into two broad classifications. One category consists of those phase aberrations that have only a very slow variation across the beam profile. If these aberrations are sufficiently slow, their effect is relatively trivial and easily corrected.

A linearly varying phase profile across a beam, for example, simply represents a wedge, which bends the beam direction without distorting the beam profile as in the upper part of Figure 18.7. A quadratic phase variation represents a lens which causes focusing, or defocusing, of the beam. This can be corrected by inserting an appropriate compensating lens (possibly an astigmatic lens, if the quadratic aberration is different along two transverse directions).

From another viewpoint a thin lens imposes a quadratic phase "chirp" on the spatial profile of an optical beam. This spatial chirp has many analogies to the temporal phase chirp that we discussed in Chapter 9. In fact the spatial compression and then expansion of a focused beam following a lens (Figure 18.8), is an exact analog in the spatial domain to the pulse compression and expansion in the time domain caused by propagation through a dispersive waveguiding system.

Slow aberrations of order higher than quadratic are then true aberrations—that is, they are not easily analyzed by paraxial techniques, nor corrected by simple lenses or spherical surfaces. These higher-order aberrations are extensively discussed in standard optics texts, and we will not attempt to cover these topics here, except to say that such aberrations with magnitudes much greater than a fraction of a wavelength across a beam profile will have serious distortion effects on a good-quality laser beam profile.

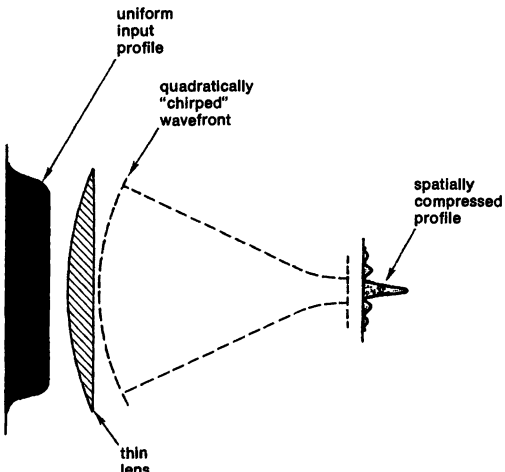


FIGURE 18.8

Free-space propagation converts a quadratically chirped wavefront into a focused, or spatially compressed, beam at the focal point.

High-Spatial-Frequency Beam Perturbations

The opposite limiting situation then consists of those phase or amplitude aberrations that have at least several cycles of variation across the laser beam. Suppose a laser beam which has reasonably good beam quality, or which is reasonably close to diffraction-limited in its transverse profile, is perturbed by phase or amplitude variations whose spatial frequencies are large compared to the inverse of the beam diameter d , so that the spatial periods of these aberrations are given by $\Lambda \leq d/N$, where N is some number (not necessarily an integer) at least several times unity.

If the original laser beam is of reasonably good beam quality, this means that essentially all its energy is contained within a narrow distribution of plane waves, with a spread in k space or in angle θ limited to roughly $\Delta\theta \approx \lambda/d$, where d is the width or diameter of the laser beam. The effect of higher-spatial-frequency aberrations, according to the analysis of Section 18.1, will then be to scatter energy from these plane-wave components into diffracted angles given by

$$\theta \approx \frac{\lambda}{\Lambda} \approx N \times \Delta\theta. \quad (22)$$

These angles are large compared to the original angular spread of the laser beam.

The primary effect of high-spatial-frequency perturbations is thus a scattering of some amount of the original beam energy into a range of angles considerably larger than the diffraction limit for the original beam, leaving the main or central portion of the beam's angular spectrum weakened in amplitude, but otherwise unchanged in shape. Such aberrations are thus likely to weaken the central portion of the far-field profile of a laser beam, but to leave it more or less unchanged in shape. The missing energy will then be found in a broader and more or less random pedestal of scattered energy spread over a much wider angle around the central portion of the beam, as shown schematically in Figure 18.9. The general

weakly perturbed beam

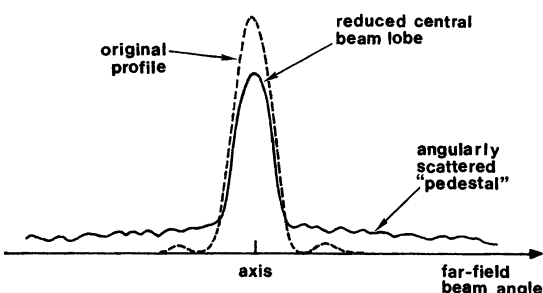


FIGURE 18.9
Far-field beam profile of a weakly perturbed laser beam.

shape and width of this background pedestal will depend on the exact shape and nature of the aberrations.

Note the difference in viewpoint between this discussion and the discussion of strongly distorted or highly multimode beams in Section 17.6. That discussion was concerned with strongly aberrated or highly multimode beams. The present viewpoint can be used as a model for the analytical treatment of weakly aberrated or weakly non-diffraction-limited laser beams.

The Intermediate situation: Serious Beam Distortion

The most difficult situation clearly arises for those aberrations whose spatial variation is roughly comparable to the laser beam diameter. These aberrations are generally too complicated to be corrected by simple lenses or wedges; and at the same time the diffraction angles produced by these aberrations are small enough that the scattered waves remain within the main beam angle, seriously distorting the main beam profile, rather than merely being scattered in a large-angle background surrounding the main laser spot.

The designers of large-aperture laser amplifiers in laser fusion systems, where the beam profile must be very good to permit focusing onto a very small target pellet, have actually made careful point-by-point measurements of the phase aberrations across the entire laser profile, and then added special elements to correct these distortions. Experimenters working with other kinds of high-power laser oscillators have used real-time measurement and correction of beam aberrations by adaptive optical techniques within the laser resonator, for example by servo-controlled deformable laser mirrors.

Amplitude Versus Phase Perturbations

The discussions at the beginning of this chapter demonstrate that weak or *small-amplitude* perturbations with high spatial frequencies do about the same amount of damage to an optical beam—that is, about the same amount of energy is scattered out into larger angles—for either amplitude or phase gratings having the same peak-to-peak modulation index Δ . As beam profile variations or beam perturbing effects become stronger, however, particularly for beam profile variations with slow to intermediate spatial frequencies, a general principle is that *phase perturbations are generally more serious, and cause more reduction in far-field beam intensity, than do amplitude variations.*

If an optical beam with fixed total power is transmitted through an aperture having an arbitrary transverse shape, the highest on-axis intensity in the far field will be obtained if the transmitted power is distributed as a collimated plane wave with uniform intensity over the entire transmitting aperture, regardless of its shape. Suppose, however, that the phase and amplitude distribution in the transmitting aperture is to be modified (keeping the total transmitted power fixed), perhaps in order to obtain other advantages, such as reduced intensity in certain side lobes, or perhaps simply because a uniform intensity distribution is not available from the beam source. In the jargon used by some workers, modification of the amplitude or intensity distribution within the aperture is referred to as *apodization*, whereas modification of the phase profile or wavefront shape is referred to as *(phase) aberration*.

The general rule then is that large but slow amplitude variations or apodization will not greatly reduce the far-field brightness; whereas large but slow phase variations or aberration will quite strongly reduce the on-axis brightness in the far field. To demonstrate this, we can calculate the on-axis far-field intensity for a slit or circular aperture using various transverse or radial amplitude variations, such as $1 - (x/a)^n$ or $\cos^n(\pi x/2a)$ (at fixed total power), and see that the brightness is generally reduced by factors of the order of 50% or less. Large phase variations across the beam, however, represent strong lenses or prisms, which either strongly defocus the beam in the far field, or bend the direction of different parts of the beam to different positions in the far field. It is also possible to show using fundamental mathematical inequalities (see the References) that applying phase aberration to an already apodized beam always makes the far-field brightness become still lower, whereas in the reverse situation, applying apodization to an already phase-aberrated beam can sometimes make the far-field brightness get (somewhat) better. Phase aberrations always make things worse; apodization sometimes can make them even a little better.

Nonlinear Wavefront Perturbations: Small-Scale Self-Focusing

The grating description introduced in this section is particularly relevant to the nonlinear type of self-induced perturbation known as “small-scale self-focusing” which occurs in higher-power laser beams passing through almost any optical material (and which we have also mentioned in an earlier section).

In almost any transparent optical material, the local index of refraction of the material will increase slightly with increasing optical intensity at high enough optical field strengths, in the form $n = n_0 + n_2|\vec{E}|^2$. This is referred to as the optical Kerr effect, since it represents a kind of Kerr effect induced in the medium by the optical fields themselves. The coefficient n_2 is present, though typically very weak, and has a positive sign in nearly all optical materials. (The optical intensities needed to produce a noticeable index change are typically in the range of 1 to 10 Gw/cm².)

Suppose a high-power laser beam has an amplitude profile with some initial weak amplitude ripples, produced by any sort of initial perturbation. These ripples in the optical intensity will then cause a periodic variation in the local index of refraction, thus producing a weak phase grating having the same period, through the $n_2|\vec{E}|^2$ effect. But this phase grating will then diffract additional energy from the main beam into phase-grating sidebands; and these sidebands will, after a certain distance as discussed in the preceding, convert into an additional

amplitude grating, which can produce additional index changes and additional scattering.

Analysis of this effect shows that in fact the feedback in this process is positive: the strength of the amplitude ripples on the beam and of the index perturbation in the material will grow exponentially with distance as the beam propagates forward through the medium. The growth rate itself depends on the intensity of the laser beam. For beams with intensity levels in the range $\geq 1 \text{ Gw/cm}^2$ —which are not uncommon in high-power Nd:glass lasers, for example—this exponential growth can cause initially very small ripples to grow to a level sufficient to destroy the material within a very short distance. Elimination of these small-scale self-focusing effects, both by carefully filtering out the initial ripples and by selecting low Kerr coefficient materials, is one of the primary objectives in designing a high-power and high-intensity laser system.

REFERENCES

A viewpoint on weakly aberrated laser beams very similar to that presented in this section is also expressed in more detail by C. B. Hogge, R. R. Butts, and M. Burlakoff, "Characteristics of phase-aberrated nondiffraction-limited laser beams," *Appl. Optics* **13**, 1065–1070 (May 1974).

This viewpoint is also used to get a rough estimate of aberration effects on laser oscillator power output and beam quality in A. E. Siegman, "Effects of small-scale phase perturbations on laser oscillator beam quality," *IEEE J. Quant. Elect.* **QE-13**, 334–337 (May 1977).

A quite different way of describing aberrated laser beams in circular apertures, which is much more closely related to classical lens aberrations, but much less suited to beam propagation calculations, is to express the beam wavefront in Zernike polynomials. A recent discussion of this approach is given by J. Y. Wang and D. E. Silva, "Wave-front interpretation with Zernike polynomials," *Appl. Opt.* **19**, 1510–1518 (May 1, 1980).

Adaptive optical techniques for correcting optical wavefronts in laser beams and imaging systems are surveyed in a Special Issue of the *J. Opt. Soc. Am.* **63** (March 1977) and in a review paper by J. W. Hardy, "Active optics: A new technology for the control of light," *Proc. IEEE* **66**, 651–697 (June 1978).

For an application of these techniques inside laser resonators see K. E. Oughstun, "Intracavity adaptive optic compensation of phase aberrations. I: Analysis," *J. Opt. Soc. Am.* **71**, 862–872 (July 1981).

A starting point for discussions of apodization and the effects of different aperture distributions is V. N. Mahajan, "Luneberg apodization problem I," *Opt. Lett.* **5**, 267–269 (June 1980).

The original recognition and analysis of small-scale self-focusing traces back to a paper by V. I. Bespalov and V. I. Talanov, "Filamentary structure of light beams in nonlinear liquids," *JETP Lett.* **3**, 307–310 (June 15, 1966).

Interesting experimental demonstrations of the effect are given by A. J. Campillo, S. L. Shapiro, and B. R. Suydam in "Periodic breakup of optical beams due to self-focusing," *Appl. Phys. Lett.* **23**, 628–630 (December 1, 1973), and "Relationship of self-focusing to spatial instability modes," *Appl. Phys. Lett.* **24**, 178–180 (February 15, 1974).

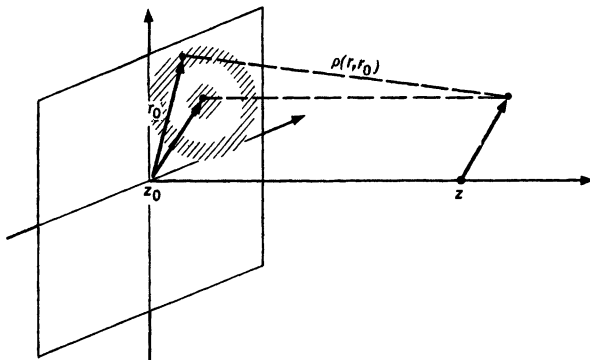


FIGURE 18.10

Geometry for evaluating the Fresnel zones surrounding a projected observation point r .

18.3 APERTURE DIFFRACTION: RECTANGULAR APERTURES

All real optical systems will have finite apertures, with some sort of boundaries or edges. In this section, therefore, we will consider the near-field and far-field diffraction patterns that are produced when paraxial optical beams pass through simple apertures having sharp edges, with emphasis on slits and square or rectangular apertures. (Circular apertures will be taken up in the following section.) The primary objective in presenting these examples is again to gain insight into the kinds of physical diffraction effects that can occur in simple situations, as well as some familiarity with the common analytical techniques for describing these diffraction effects.

Fresnel Diffraction Effects

Much of the material in this section will be a replay of the optics section from the freshman physics curriculum. Let us remind ourselves therefore (at least for those who need reminding) of the elementary physics of Fresnel diffraction and Fresnel zones.

The Huygens-Fresnel integral says, as we have already noted, that the wave amplitude at an observation point $r \equiv (s, z)$ as in Figure 18.10 is produced by the vector sum of wavelets coming from source points $r_0 \equiv (s_0, z_0)$ with a net phase delay, over and above the on-axis phase shift term, given by

$$\exp[-jk\rho(r, r_0)] = \exp\left[-j\frac{\pi|s - s_0|^2}{(z - z_0)\lambda}\right]. \quad (23)$$

Wavelets coming from different source points r_0 thus add with different relative phases depending on the magnitude of this additional phase shift.

One way to visualize this is to drop a perpendicular from the observation point r back to the source plane, as shown in Figure 18.10, and then to imagine the intercept of this line as surrounded by circles of constant $s - s_0$, or constant additional phase shift, as shown in Figure 18.10. All those source points lying within the central circle for which $k\rho \leq \pi$, or $|s - s_0|^2 \leq (z - z_0)\lambda$, will then

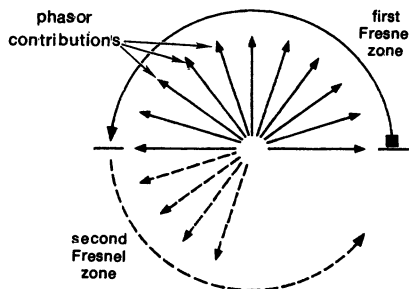


FIGURE 18.11

The phasor contributions from successive Fresnel zones first add and then cancel.

produce phasor contributions that add up at the observation point with phasor angles that are more or less in phase, or at least in the same half-plane, as shown in the phasor diagram in Figure 18.11. However, all those points lying in the next annular region for which $\pi \leq k\rho \leq 2\pi$, or $(z - z_0)\lambda \leq |s - s_0|^2 \leq 2(z - z_0)\lambda$, will add with phasor angles that tend to cancel the contributions coming from wavelets in the inner circle.

Suppose the wave passing through the source plane is a uniform plane wave with constant phase, and that we gradually open up a circular aperture of increasing diameter $2a$ in the source plane surrounding the projected observation point (s, z_0) . Examination of the phasor diagram in Figure 18.11, or a more formal integration of Huygens' integral, will then show that the intensity at the observation point s, z increases steadily with increasing source aperture diameter, up to a maximum value when the aperture just contains the entire inner disk for which $k\rho \leq \pi$. The intensity at the observation point will then decrease as the source aperture is opened further, and in fact will drop entirely to zero when the diameter $2a$ is such that $k\rho = 2\pi$. (A dramatic demonstration of this effect using a microwave source and detector can be found in the optics text by Andrews.)

Fresnel Zones and the Fresnel Number

The intensity at the observation point in fact will oscillate periodically from zero to maximum and back again as successive additional annular rings or *Fresnel zones* are contained within the aperture. The radii s_n that define the boundaries of these successive rings or so-called Fresnel zones about the projected source point s, z_0 are thus given by

$$s_n^2 = nL\lambda, \quad L \equiv z - z_0. \quad (24)$$

An important point here is that each successive Fresnel zone has equal area, so that each contributes an equal positive or negative contribution (assuming the entire circular aperture is uniformly illuminated).

To look at the consequences of this in another way, suppose we consider an observation point situated on the z axis a distance L out from the center of an aperture of width or diameter $2a$. The number of Fresnel zones contained within the aperture, as seen from the observation point, is then given by the *Fresnel*

number defined by

$$N \equiv \frac{a^2}{L\lambda}. \quad (25)$$

The importance of this Fresnel number parameter both for beam propagation problems and for optical resonators will become apparent in this section and in later chapters.

Far-Field Intensity and the Rayleigh Range

A second useful parameter in characterizing the diffraction properties of an aperture is the *Rayleigh range* of a collimated beam emerging from that aperture. Let us consider a definition of this parameter for an aperture of arbitrary cross-sectional shape.

Suppose an aperture of any arbitrary cross-sectional shape is illuminated by a collimated and uniform-intensity plane wave. We can then show quite generally from Huygens' integral that the peak intensity in the far field occurs exactly on the beam axis, and that this on-axis intensity $I(z)$ at distance z is related to the uniform intensity I_0 in the transmitting aperture itself by

$$\frac{I(z)}{I_0} = \left(\frac{A}{z\lambda} \right)^2, \quad (26)$$

where A is the total area of the input aperture.

For a gaussian beam, on the other hand, the peak or on-axis intensities at the beam waist and in the far field ($z \gg z_R$) are related by

$$\frac{I(z)}{I_0} = \left(\frac{z_R}{z} \right)^2, \quad (27)$$

where z_R is the Rayleigh range for a gaussian beam, given by $z_R \equiv \pi w_0^2 / \lambda$ where w_0 is the gaussian spot size at the beam waist.

Now, there does not seem to be any universally accepted way of defining a similar Rayleigh range z_R for other beam profiles or aperture shapes, although it is generally accepted that the Rayleigh range should mark in some sense the boundary between the “near-field” and “far field” diffraction regions for the beam emerging from the aperture. As a convenient and simple definition, we will adopt the convention that the Rayleigh range for a transmitting aperture of any shape is given by equating the two preceding equations for $I(z)/I_0$. That is, for a transmitting aperture of area A , the Rayleigh range is given by

$$z_R \equiv \frac{A}{\lambda} \quad (\text{arbitrary aperture shape}). \quad (28)$$

This definition will lead to slightly different expressions for the relationship between the aperture diameter or width and the Rayleigh range, or between the aperture Fresnel number and Rayleigh range, depending on the exact shape of the aperture, as we will see in later sections. It does, however, seem to be a convenient and meaningful way of defining a Rayleigh range for any shape of aperture.

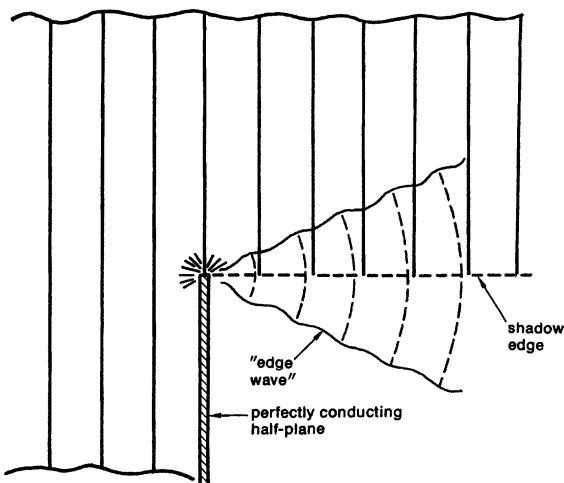


FIGURE 18.12
In the Sommerfeld diffraction theory, a sharp edge appears to be the source point of a cylindrical scattered wave.

Apertures and Scalar Diffraction Theory

Let us now turn to the diffraction properties of sharp-edged apertures. The primary mathematical foundation for this discussion is an analytical solution published by Sommerfeld around 1896 for the diffraction of an infinite plane wave incident at an arbitrary angle on a perfectly conducting half plane. Notable aspects of this Sommerfeld solution (which we will not examine in detail here) are that it is a vector solution to the full electromagnetic problem; it assumes as boundary condition an infinitely thin and perfectly conducting sheet covering half of the transverse plane; part of the diffracted signal appears as a nonuniform cylindrical wave radiating from the discontinuous edge of this half plane; and the results are expressed in terms of Fresnel integral functions of the coordinates. This Sommerfeld solution (along with earlier work by Huygens, Rayleigh, Fresnel, and Kirchoff) provides the mathematical underpinnings for the scalar Huygens-Fresnel integral theory we will use to describe diffraction effects in a variety of situations.

We might note that the Fresnel-Kirchoff and the Rayleigh-Sommerfeld formulations of diffraction theory predict slightly different forms for the obliquity factor as a function of angle in Huygens' integral. These two forms, however, both go to the same limit of unity in the paraxial limit which is of interest to us.

We might also note again that Sommerfeld's theory is based on a diffracting surface which is perfectly conducting and infinitely thin. The diffracting apertures that we encounter in most real diffraction problems, on the other hand, are made from materials that have a finite thickness and are certainly not perfectly conducting. The Huygens-Fresnel integral, however, is calculated using only the incident field values in the open part of the aperture. We normally do not even consider what are the electromagnetic properties of the surrounding material, therefore, and in practice the nature of the aperture does not seem to make any significant difference either in the theory or in the experimental results that are obtained under conditions typical of paraxial optical beams.

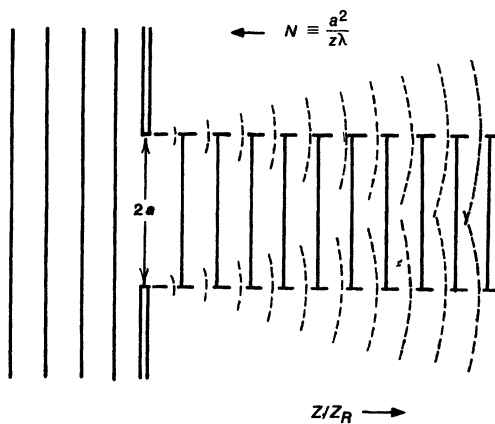


FIGURE 18.13
Single-slit diffraction involves the interplay between two scattered “edge waves.”

Edge Waves or Boundary-Wave Diffraction Theory

One important concept that emerges both in the Sommerfeld theory and in the discussions further on in this section is that diffraction from a sharp-edged aperture creates a series of nonuniform spherical waves (or more precisely, cylindrical waves) that appear to be scattered from line sources exactly along the edges of the aperture, as sketched in Figure 18.12. This concept in fact traces back to suggestions by Young and observations by Newton more than a century earlier, noting that if we observe the diffracted light from an aperture, we can indeed see that the edge of the aperture appears to be a brightly illuminated line source.

The edge-wave interpretation of the Sommerfeld diffraction results was also extended around 1957 by Keller into a more general formulation of diffraction theory entirely in terms of edge waves scattered from aperture boundaries (see References). This interpretation is sometimes referred to as the “Keller edge-wave theory,” or the “boundary diffraction wave theory” of optics. We must use this edge-wave theory with some caution, however, as the simple boundary-wave picture applies rigorously only to edges or apertures that are illuminated with uniform-intensity plane or spherical waves, and not to other more general types of illumination.

Single-Slit Diffraction Formula

One classic problem in diffraction theory is the diffraction of a uniform collimated plane wave by a single slit of width $2a$, as illustrated in Figure 18.13. The Huygens-Fresnel integral in one dimension that applies to this problem is

$$\tilde{u}(x, z) = \sqrt{\frac{j}{z\lambda}} \int_{-a}^a \tilde{u}_0(x_0, z_0) \exp \left[-j \frac{\pi}{(z - z_0)\lambda} (x - x_0)^2 \right] dx_0. \quad (29)$$

Suppose we assume a uniform incident plane wave, and define the normalized variables

$$y \equiv \frac{x}{a} \quad \text{and} \quad N \equiv \frac{a^2}{(z - z_0)\lambda} = \text{Fresnel number}, \quad (30)$$

where N is the number of circular Fresnel zones that will be visible in the slit, as seen from a distance $z - z_0$ beyond the slit. The Huygens-Fresnel integral then takes on the normalized form

$$\tilde{u}(y) = \sqrt{jN} \int_{-1}^1 e^{-j\pi N(y-y_0)^2} dy_0. \quad (31)$$

This expression makes it apparent that the normalized diffraction pattern depends on distance z only through the dimensionless Fresnel number N and no other parameters.

The Complex Fresnel Integral

It is convenient to interpret this single-slit result using the *complex Fresnel integral function* $\tilde{F}(x)$ defined by

$$\tilde{F}(x) \equiv C(x) + jS(x) \equiv \int_0^x e^{j\pi t^2/2} dt. \quad (32)$$

The real and imaginary parts of this are the well-known Fresnel cosine and sine integrals, which are conventionally defined as

$$C(x) \equiv \int_0^x \cos\left(\frac{\pi t^2}{2}\right) dt \quad \text{and} \quad S(x) \equiv \int_0^x \sin\left(\frac{\pi t^2}{2}\right) dt. \quad (33)$$

If we plot the values of these integrals as real and imaginary parts of a contour in the complex plane, with the argument x as a parameter along the contour, we produce the well-known *Cornu spiral* shown in many optics texts and in Figure 18.14. Note that this curve spirals inward in a decreasing circle to the asymptotic points $\pm(1+j)/2$ in the complex plane for large positive or negative arguments.

The complex Fresnel integral has the mathematical property that $\tilde{F}(-x) = -\tilde{F}(x)$, and the asymptotic formulas given by

$$\tilde{F}(x) \approx \begin{cases} x e^{j\pi x^2/2} & \text{for } |x| \ll 1, \\ \frac{1+j}{2} - \frac{j}{\pi x} e^{j\pi x^2/2} & \text{for } |x| \gg 1. \end{cases} \quad (34)$$

The large argument form is particularly useful, and is in fact a quite reasonably good approximation even for arguments only slightly greater than unity.

Delta Function Property of the Fresnel Kernel

The integrand in the Fresnel integral function or in the sine and cosine integrals is obviously a normalized version of the Huygens' integral kernel, and it can be useful to examine briefly the form of this integrand. The functions $\cos(\pi/2)x^2$ and $\sin(\pi/2)x^2$, if plotted versus x , appear as in Figure 18.15. We

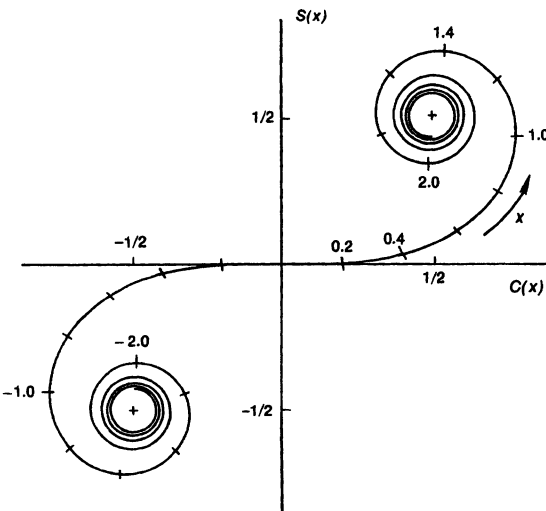


FIGURE 18.14

The Cornu spiral is a map of the complex Fresnel integral $\tilde{F}(x) \equiv C(x) + jS(x)$ in the (C, S) plane.

can note that the total area under either of these functions is finite and also equal, as evidenced by the result that

$$\int_{-\infty}^{\infty} e^{j(\pi/2)x^2} dx = \int_{-\infty}^{\infty} e^{-ax^2} dx \Big|_{a \equiv -j\pi/2} = \sqrt{\frac{\pi}{a}} = \sqrt{2j}. \quad (35)$$

(We obviously have to add a very small positive real part to the constant a , or perhaps to the value of π , to make the integral converge properly.)

This complex Fresnel integrand, moreover, despite the fact that it neither goes to infinity at $x = 0$ nor goes to small values as $x \rightarrow \infty$, still operates something like a rather crude Dirac delta function. If we multiply the curves shown in Figure 18.15 by any slowly varying function $f(x)$ and integrate from $-\infty$ to ∞ , the integral will pick out primarily the value of $f(x)$ within the central lobes of the kernel around $x = 0$. At larger values of x the $\cos(\pi x^2/2)$ and $\sin(\pi x^2/2)$ functions oscillate so furiously between positive and negative values that they average out to 0 over any slow variations of the function $f(x)$. We must emphasize, however, that the Fresnel kernel really is a quite poor delta function, with a considerable response to values of $f(x)$ —and especially to discontinuous changes in $f(x)$ —at values of x well away from zero.

Rational Approximation to the Fresnel Integral

The Fresnel integral function is essentially identical to an error function of complex argument. Analytical expressions and numerical results related to the error function can thus be very useful in working with the Fresnel integral.

Abramowitz and Stegun also give a rational approximation—that is, a purely empirical polynomial approximation—to the Fresnel integral function which can be very useful for numerical calculations. The complex Fresnel integral can first

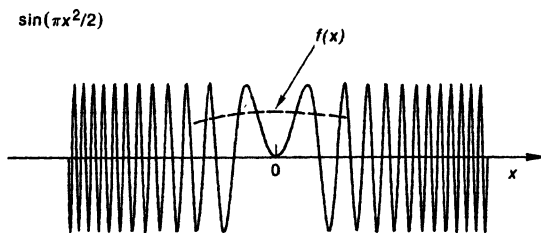
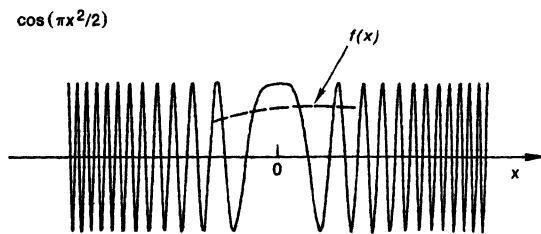


FIGURE 18.15
The cosine and sine functions in the Fresnel integral look like this.

be written as

$$\tilde{F}(x) = \frac{1+j}{2} - [g(x) + jf(x)]e^{j\pi x^2/2}, \quad (36)$$

and the two functions $f(x)$ and $g(x)$ can then be approximated by

$$\begin{aligned} f(x) &\approx \frac{1 + 0.962x}{2 + 1.792x + 3.104x^2}, \\ g(x) &\approx \frac{1}{2 + 4.142x + 3.492x^2 + 6.670x^3}. \end{aligned} \quad (37)$$

The resulting error in the calculation of $\tilde{F}(x)$ is $\leq 2 \times 10^{-3}$ for all values of $0 \leq x < \infty$. (Similar polynomial approximations exist for Bessel functions and many of the other higher transcendental functions.)

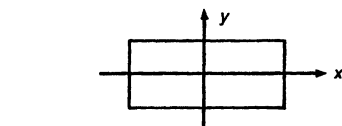
Single-Slit Diffraction Results

The diffraction pattern predicted by Huygens' integral for a uniformly illuminated slit then becomes, in terms of the Fresnel integral function,

$$\tilde{u}(y) = \sqrt{\frac{j}{2}} \left[\tilde{F}^* \left[\sqrt{2N}(1-y) \right] - \tilde{F}^* \left[-\sqrt{2N}(1+y) \right] \right]. \quad (38)$$

From the analytical results for the Fresnel integral function, we can deduce the following characteristics of the single-slit diffraction patterns in the near and far-field regions:

rectangular aperture



far-field diffraction pattern

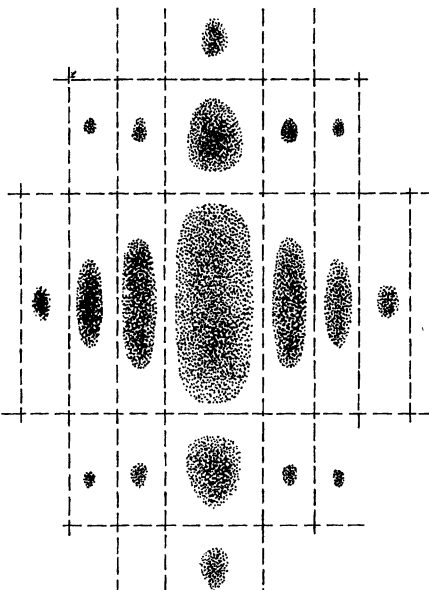


FIGURE 18.16

The far-field diffraction pattern of a uniformly illuminated hard-edged rectangular aperture.

(1) *Far-field diffraction pattern.* In the far-field region, where $z \gg a^2/\lambda$ or $N \ll 1$, the analytical form for the beam pattern becomes

$$\tilde{u}(x) \approx (4jN)^{1/2} \frac{\text{sinc}(2\pi Nx/a)}{2\pi Nx/a} = (4jN)^{1/2} \text{sinc}\left(\frac{2\pi ax}{z\lambda}\right) \quad (39)$$

for $z \gg a^2/\lambda$ or $N \ll 1$. [We use the definition that $\text{sinc}(x) \equiv (\sin x)/x$.] The diffraction pattern thus stabilizes into a single central peak, plus substantially weaker sidelobes, as shown for a rectangular aperture (equivalent to two crossed slits) in Figure 18.16. The width of the central peak is inversely proportional to the slit width, and eventually diverges linearly with increasing distance from the source aperture, yet remains essentially constant in shape.

(2) *Fresnel number and Rayleigh range.* The on-axis field amplitude in the far field can thus be written in the form

$$\frac{\tilde{u}(z)}{\tilde{u}_0} = \sqrt{4jN} = \sqrt{z z_R/z}, \quad (40)$$

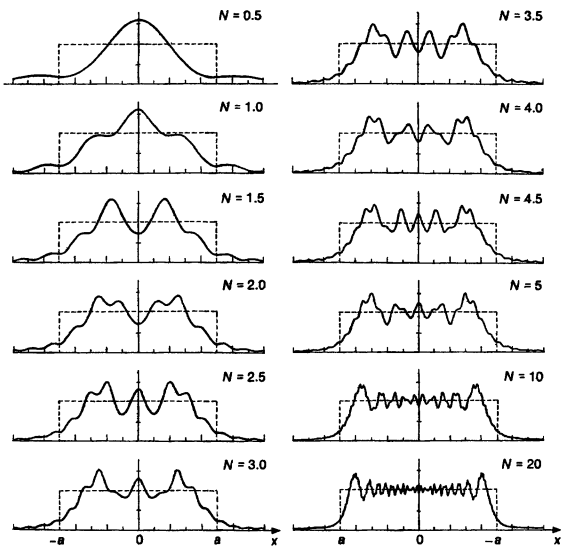


FIGURE 18.17
Near-field intensity profiles from a uniformly illuminated single-slit aperture, plotted versus the Fresnel number N . Note that larger values of N mean that one is moving closer to the source aperture.

where the first equality comes from Huygens' integral and the second from our convention for defining z_R for an aperture. We thus have the relation

$$\frac{z}{z_R} = \frac{1}{4N} \quad \text{or} \quad z_R \equiv \frac{4a^2}{\lambda} \quad (\text{single-slit aperture}) \quad (41)$$

between the Fresnel number and the Rayleigh range for a slit or a square aperture. (Other aperture shapes will give a slightly different numerical constant in this relation, as we will see later.)

(3) *Near-field diffraction ripples.* The near-field diffraction patterns closer in to a uniformly illuminated slit are much more complex and variable than the far-field pattern, which has a constant shape, and merely expands linearly in size with increasing distance.

Figure 18.17, for example, along with Figure 18.18, shows plots of the normalized beam intensity profile $|\tilde{u}(y)|^2$ across the normalized slit width $y = x/a$ at various Fresnel numbers N or normalized distances z/z_R from the input slit. (These results were plotted using the rational approximations given in Equation 18.37; note that the distance z goes *inversely* with the Fresnel number N .)

The diffraction behavior clearly separates into a far-field region where $N \ll 1$ and $z \gg z_R$, and a near-field region for which $N \geq 1$ and $z \leq z_R$. For $N = 0.5$, for example, which is roughly the boundary region between near and far fields, the beam has essentially only one smooth central lobe, similar to the far field, with weak ripples or side lobes in the outer tails. From Figure 18.17 it may seem that in the boundary region around $N \approx 0.5$, the central lobe of the beam appears to be considerably narrower than the slit from which it came, even though no focusing is present, and only diffraction spreading is taking place. A substantial fraction of the beam energy, however, has actually diverged out into the strong tails of the beam, extending well beyond the projected slit width, so that the rms width of the beam continually increases. Figure 18.18 shows that beyond this

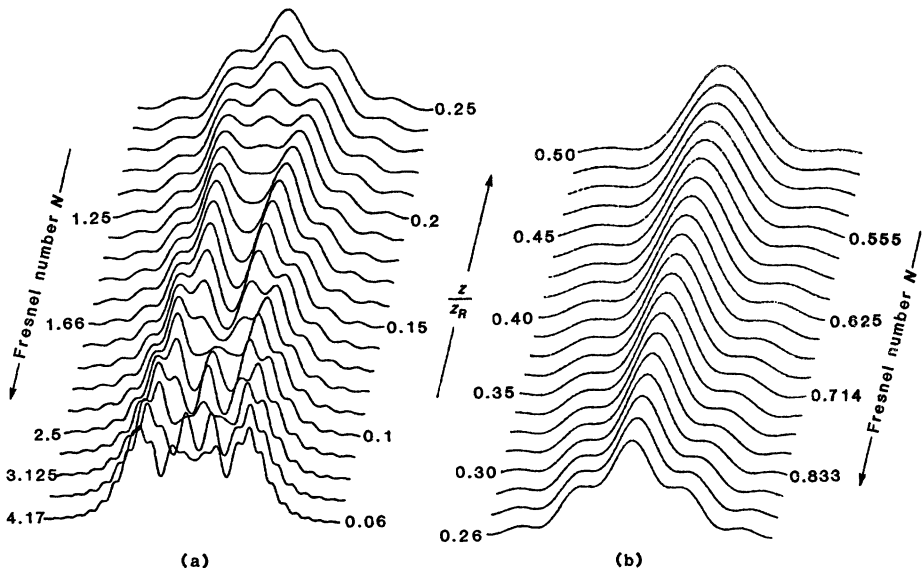


FIGURE 18.18

Intensity patterns for a uniform plane wave coming through a slit of width $2a$, at fixed increments of normalized distance z/z_R beyond the slit. (Note the slight change in axial step size between the left and right plots.)

distance the beam does diverge into a linearly spreading beam with an essentially constant profile.

In the near-field region, on the other hand, as we move closer to the aperture and the Fresnel number N increases, the diffraction patterns acquire an increasingly complex structure, with increasing number of diffraction ripples, or “Fresnel ripples.” The pattern becomes increasing rectangular in shape as we move closer to the aperture, especially for $N \geq 3$ or 4, but the Fresnel ripples remain strong and increase rapidly in frequency as we move in toward the aperture.

(4) *Ripple interpretation.* The strong Fresnel ripples observed on the beam in the near field can be interpreted using the asymptotic form of the Fresnel integral function, as follows. Consider the two terms in the Huygens' integral solution, using the large-argument approximation for the complex Fresnel integral given in Equations 18.34 or 18.36. The two $\exp(j\pi x^2/2)$ terms, when evaluated for $x = \sqrt{2N}(1 \pm 1)$, then have the forms

$$\tilde{u}(y) \approx \exp[-j\pi N(y \pm 1)^2] = \exp\left[-j\frac{\pi(x \pm a)^2}{z\lambda}\right]. \quad (42)$$

But we can recognize these as exactly the analytical forms for two spherical (or, more precisely, cylindrical) waves emanating from the edges of the slit, as in Figure 18.13. That is, Equation 18.43 corresponds to two cylindrical waves coming from source points $x_0 = \pm a$, and observed at an observation point (x, z) beyond the slit.

The Fresnel ripples seen in Figure 18.17 and 18.18 result from the presence of two Sommerfeld edge waves. These waves interfere with the primary geometric part of the transmitted wave (which is represented by the constant term in the asymptotic expansion), producing the large-scale or large-amplitude ripples; and also interfere with each other, thus leading to a complex pattern of finer ripples on top of the coarser ripples.

(5) *Number of ripples.* Inspection will show in fact that for $N \geq 1$, the diffraction patterns in Figure 18.17 have essentially N large-scale ripples across the aperture width. These ripples come, more or less, from each edge wave interfering with the geometric plane wave coming through the aperture on the same side. These larger ripples are then modified by smaller-amplitude but higher-frequency ripples, especially near the outer edges of the aperture. These higher-frequency ripples are clearly produced primarily by interference with the spherical wave that comes from the opposite side of the aperture, so that we are on the $4N$ -th Fresnel zone from that source point or, rather, that source line. (Why is this $4N$ and not $2N$?)

(6) *Geometric shadow terms.* We can also note that if we are inside the projected slit aperture, so that $|x| \leq a$ and hence $|y| \leq 1$, and also in the near-field region where $N \geq 1$ or $z \leq 4z_R$, then both of the arguments in the complex Fresnel integral of Equation 18.38 will be positive. Hence, the two constant terms in the large-argument expansion will add in phase. These two terms combine in fact to give a value just equal to unity, i.e., they give the constant geometric projection of the incident beam through the aperture.

As soon as we move outside the geometric shadow, however, on either side of the beam, one or the other of these arguments changes sign and becomes negative. The two constant terms then cancel, and give the expected value of zero for the geometric value of the amplitude outside of $x = \pm a$ or $y = \pm 1$.

Conclusions: Single-Slit Diffraction Behavior

All in all, the complex diffraction ripples in the near field can thus be viewed as resulting from a complicated interference between the simple geometric transmission of the aperture, and the spherical edge waves scattered from the two edges. As we move in ever closer to the aperture (yet still remain within the underlying paraxial approximation), the beam profile in Figure 18.17 becomes more and more “square” and the Fresnel ripples become higher and higher in frequency, although they never disappear.

The Fresnel ripple behavior near the aperture, in fact, is very analogous to the Gibbs phenomena that occur in the Fourier analysis of a square pulse as we take an increasing number of Fourier components. We can show that for large N the outermost ripple, just inside the beam boundary, is always the largest, and that this ripple has a peak overshoot of $\approx 18\%$ in amplitude or twice this in intensity.

Numerical Beam Calculations: Number of Sample Points

In practical beam or resonator problems, we often want to calculate the exact diffraction pattern produced by some source wave $\tilde{u}_0(x_0)$ which is more complicated than a simple plane wave, after that wave has passed through a

hard-edged aperture such as a slit of width $2a$. We must then evaluate Huygens' integral (Equation 18.29) with the appropriate source function $\tilde{u}_0(x_0)$ included; and the resulting calculations must usually be done numerically.

The Sommerfeld edge waves from the aperture edges will still play a role in the diffraction patterns with apertures other than simple slits, and with source functions other than a simple plane wave. The exact diffraction patterns will be more complex, however, than just a geometric projection of the incident source function, plus edge waves proportional to the amplitude of the source function at the aperture edges. (The Sommerfeld edge waves in some sense have a physical reality as cylindrical waves diverging, or appearing to diverge, from the slit edges; but in a more accurate picture they represent a mathematical effect of sharply truncating a uniform plane wavefunction at the aperture edges.)

From the uniform plane wave solutions discussed in this section, we can at least draw the insight that the diffraction patterns for reasonably smooth source functions passing through apertures of width $2a$ are likely to exhibit on the order of N large-scale ripples across the beam aperture, plus smaller-amplitude ripples with spatial periods ranging down to approximately $2a/4N$. (Again, why $4N$?) From the sampling theorems of transform theory, we then know that to describe the diffracted wave pattern accurately we will need at least 2 sample points per ripple period.

Depending upon the accuracy that is required, we will therefore need somewhere between $2N$ and $8N$ total sample points in each transverse direction across the aperture—or a comparable number of terms in any kind of series expansion—in order to do numerical calculations of the diffraction patterns with adequate accuracy. (We can derive this same criterion by asking how many points we will need to evaluate the kernel in Huygens' integral accurately for all pairs of points across the aperture.)

As we move inward toward a source aperture, the Fresnel number N goes up: *it takes more mathematical work to propagate a beam a short distance beyond an aperture than a long distance!* (assuming that we want to describe the detailed near-field function accurately).

Beam Spillover and Guard Bands

In doing numerical calculations of beam propagation beyond a slit or other hard-edged aperture, we must also realize that the diffracted wave function even in the near-field region spreads out for a sizeable distance into the shadow region outside the aperture width, i.e., into the region $x > a$ or $y > 1$. (Look again at Figure 18.17 to confirm this.) Although the field amplitude obviously dies out as we move transversely outward, a significant amount of energy can reside outside the geometric beam boundary, and this region must be taken into account, particularly if we are making a series of forward propagation steps beyond the aperture.

It is thus necessary to include in the numerical calculations the field values in a “guard band” that extends into the shadow region, out to a distance of perhaps ≈ 1.2 to ≈ 1.5 times the half-width of the aperture itself. Additional guard-band space may also be required by whatever numerical technique is being employed, in order to avoid spurious results due to aliasing effects in the numerical procedure. This additional requirement will increase still further the total number of sample points required in a numerical calculation procedure.

On-Axis Intensity: Square Aperture

It is also often of interest to calculate the field amplitude or the intensity as a function of distance z exactly on the aperture axis in both the near and far fields for a wave diffracted by apertures of various shapes. For a uniformly illuminated single slit, the diffracted amplitude on axis is given in the near and far fields by

$$\begin{aligned}\bar{u}(0, z) &= \sqrt{2j} E^*(\sqrt{2N}) \\ &\approx \begin{cases} \sqrt{4jN} & \text{for } z \gg z_R, \\ 1 + j\sqrt{\frac{j}{2\pi^2 N}} \exp(-j\pi N) & \text{for } z \ll z_r. \end{cases} \quad (43)\end{aligned}$$

The diffraction pattern for a rectangular aperture is then simply the product of diffraction patterns for two slits at right angles with Fresnel numbers $N_x = a^2/z\lambda$ and $N_y = b^2/z\lambda$ in the two transverse directions, as illustrated in Figure 18.16.

The intensity on axis for a square aperture is thus equal to the amplitude for a slit aperture raised to the fourth power. Figure 18.19 shows this on-axis intensity versus normalized distance $z/z_R \equiv (4N)^{-1}$ for both square and circular apertures of width or diameter $2a$. For both apertures the intensity (by definition) asymptotically approaches the value $(z_R/z)^2$ at large z .

For a square aperture (upper plot) the intensity oscillates periodically with period $2N$ as we move inward toward the source aperture, i.e., peaks occur roughly near $N = 1, 3, 5, \dots$ and minima occur near $N = 2, 4, 6, \dots$. The phase factors in the second term of the large-argument expansion for the Fresnel integral show, however, that the extrema will not occur exactly at integer values of N , though the periodicity goes as $N\pi$. Note that in contrast to the circular aperture (which we will discuss shortly), the amplitude of the on-axis variation for the square aperture fades out as we move closer in to the source aperture.

REFERENCES

In addition to the list of optics books given in Chapter 1 of this text, some additional texts on diffraction problems and their analysis by transform methods include J. D. Gaskill, *Linear Systems, Transforms, and Optics* (Wiley, 1978); J. W. Goodman, *Introduction to Fourier Optics* (McGraw-Hill, 1968); and A. Papoulis, *Systems and Transforms With Applications in Optics* (McGraw-Hill, 1968).

An interesting collection of pictures and plots of far-field diffraction patterns from many different sources is given in G. Harburn, C. A. Taylor, and T. R. Welberry, *Atlas of Optical Transforms* (Cornell University Press, 1975).

The Keller edge-wave theory of diffraction is introduced in J. B. Keller, "Diffraction by an aperture," *J. Appl. Phys.* **28**, 426-444 (1957); and J. B. Keller, R. M. Lewis, and B. D. Seckler, "Diffraction by an aperture. II," *J. Appl. Phys.* **28**, 570-579 (1957).

Analytic expressions for another gaussian-beam sharp-edged diffraction problem will be found in T. Takenaka and O. Fukumitsu, "Asymptotic representation of the boundary-diffraction wave for a three-dimensional gaussian beam incident upon a Kirchhoff half-screen," *J. Opt. Soc. Am.* **72**, 331-336 (March 1982).

A rather over-detailed discussion of collimated beam patterns from various forms of apertures, with emphasis on the Rayleigh range concept, can be found in J. F. Ramsey,

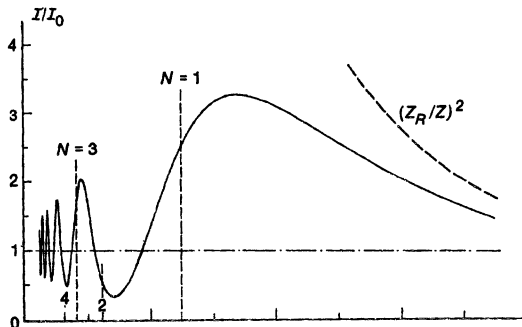
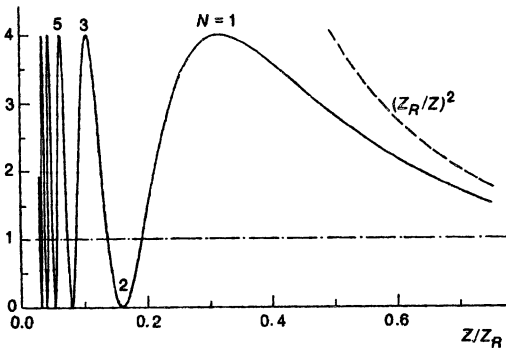


FIGURE 18.19

Variation of the central or on-axis intensity with distance z beyond the aperture for a square aperture (upper plot) and a circular aperture (lower plot), both illuminated with uniform intensity plane waves.



"Tubular beams from radiating apertures," in *Advances in Microwaves*, Vol. 3, edited by L. Young (Academic Press, 1968); pp. 127-221.

Historical references relevant to the "Rayleigh range" include J. W. Strutt (Lord Rayleigh), "On images formed with or without reflection or refraction," *Phil. Mag.* **11**, 214-218 (1881); and "On pinhole photography," *Phil. Mag.* **31**, 87-99 (1891).

Problems for 18.3

1. *Single-slit diffraction pattern exactly at the shadow edge.* Using the complex Fresnel integral properties, find an expression for the field amplitude in a uniformly illuminated single-slit diffraction pattern exactly at the shadow edge, i.e., at $y = 1$, as a function of distance z along the beam, and discuss its behavior for large and small distances.
2. *Far-field slit diffraction pattern.* Missing from our analysis of the single slit results in this section is any formal analysis of the far-field amplitude pattern, i.e., the variation of field amplitude off the axis in the far field (although most readers will probably know that the Fraunhofer diffraction pattern of a single slit has a $\text{sinc } x \equiv (\sin x)/x$ variation with distance off axis, or with angular deviation from the z axis, in the far field).

Using the Fresnel integral function results, fill in this missing discussion of the far-field diffraction pattern for the single-slit situation. Hint: Although the point exactly on axis in the far field falls in the small-argument range of the Fresnel integrals, as soon as you move any significant distance off axis in the far field, or move out to any significant angle from the axis, you are again back in the large-argument range of approximation.

3. *Single slit with gaussian illumination.* Develop an analysis of a single-slit aperture of width $2a$ illuminated by a centered gaussian plane-wave source field with central amplitude \tilde{u}_0 and spot size w_0 at the source plane. Show that the results can be expressed as Fresnel integral functions of complex argument. Discuss in particular the intensity variation $\tilde{u}(z)/\tilde{u}_0$ along the axis as a function of distance z in the near-field region, with different ratios of w_0/a as a parameter.
 4. *Single slit with variable-size gaussian illumination.* Consider the same situation as in the preceding problem, but suppose that the slit has a fixed width $2a$, and the incident gaussian beam has a fixed total power P_0 per unit slit length, but a variable spot size w_0 . (This would correspond to the situation where a given gaussian beam was passed through a collimating telescope of variable magnifying or demagnifying power just before striking the slit.) What value of w_0/a would give the largest far-field on-axis intensity in this situation?
-

18.4 APERTURE DIFFRACTION: CIRCULAR APERTURES

Another classic diffraction problem is the diffraction of a uniform plane wave by a circular aperture of diameter $2a$. We will explore some of the practical implications of this problem for laser-beam behavior in this section.

Circular Aperture With Cylindrical Symmetry

Suppose a circular aperture of diameter $2a$ located at plane z_0 is illuminated by an arbitrary but cylindrically symmetric source function $\tilde{u}_0(r_0)$. The general Huygens' integral giving the field amplitude $\tilde{u}(r)$ at plane z can then be written in radial coordinates in the form

$$\tilde{u}(r) = j2\pi Ne^{-j\pi N(r/a)^2} \int_0^1 \frac{r_0 \tilde{u}_0(r_0) e^{-j\pi N(r_0/a)^2}}{a} J_0\left(\frac{2\pi N r r_0}{a^2}\right) d\left(\frac{r_0}{a}\right), \quad (44)$$

where the Fresnel number N for the circular case is defined by

$$N \equiv \frac{a^2}{(z - z_0)\lambda}. \quad (45)$$

Note that this again depends only on the normalized variable r/a and the Fresnel number N .

Circular Aperture, Noncylindrical Symmetry

If the input function $\tilde{u}_0(r_0, \theta_0)$ is not cylindrically symmetric, we must first expand this input function into a set of functions $\tilde{u}_{0m}(r_0)$ of increasing azimuthal

order m in the form

$$\tilde{u}_0(r_0, \theta_0) = \sum_{m=-\infty}^{\infty} \tilde{u}_{0m}(r_0) e^{jm\theta_0}. \quad (46)$$

The functions $\tilde{u}_{0m}(r_0)$ can be found by Fourier-transforming the source function $\tilde{u}_0(r_0, \theta_0)$ in the azimuthal variable θ_0 in the form

$$\tilde{u}_{0m}(r_0) \equiv (2\pi)^{-1} \int_0^{2\pi} \tilde{u}_0(r_0, \theta_0) e^{-jm\theta_0} d\theta_0. \quad (47)$$

Each individual azimuthal component $\tilde{u}_m(r)$ can then be propagated to distance $z - z_0$ by a generalized form of Equation 18.44, namely

$$\tilde{u}_m(r) = j^{m+1} 2\pi N e^{-j\pi N(r/a)^2} \int_0^1 \frac{r_0 \tilde{u}_{0m}(r_0) e^{-j\pi N(r_0/a)^2}}{a} J_m \left(\frac{2\pi N r r_0}{a^2} \right) d \left(\frac{r_0}{a} \right), \quad (48)$$

where J_m is Bessel function of order m . The final output function is obtained by reassembling the azimuthal components in the same series, i.e.,

$$\tilde{u}(r, \theta) = \sum_{m=-\infty}^{\infty} \tilde{u}_m(r) e^{jm\theta}. \quad (49)$$

The integral transforms involved in these calculations are referred to as the *Fourier-Bessel* or *Hankel transforms*.

No analytical solutions as convenient as the Fresnel integral function exist for these circular aperture situations, even for uniform plane wave excitation. The circular analogs of the Fresnel integral function are the Lommel functions, which are not much discussed in standard references. The general features of the near and far-field diffraction patterns for a circular aperture are, however, generally similar to the slit or square aperture situations, although there are also some very significant differences, as we will now discuss.

Circular Aperture: Far-Field Diffraction Pattern

The properties of circular-aperture mode functions become successively more complex as we go to higher azimuthal orders; and in practice the first effort we make with any laser having cylindrical symmetry is to obtain at least an azimuthally symmetric beam. In the remainder of this section, therefore, we will limit our discussion almost entirely to the lowest-order $m = 0$ or azimuthally uniform beams.

The far-field diffraction pattern for a uniformly illuminated circular aperture, i.e., the solution to Equation 18.44 for $N \ll 1$, can be obtained using the Bessel function relation

$$\frac{d}{dz} [z J_1(z)] = z J_0(z). \quad (50)$$

The result is the well-known *Airy disk* pattern given by

$$\tilde{u}(r, z) \approx j\pi N e^{-j\pi N(r/a)^2} \times \frac{2J_1(2\pi N r/a)}{2\pi N r/a}, \quad (51)$$

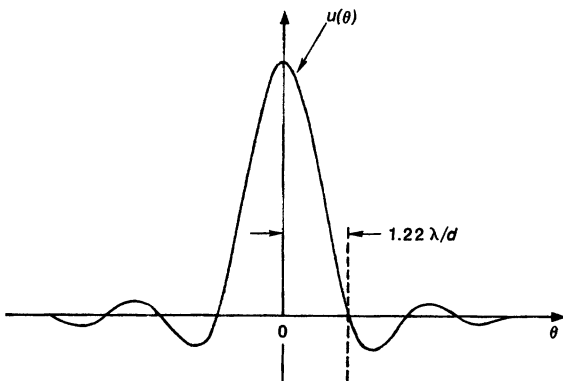


FIGURE 18.20
The far-field or Airy-disk diffraction pattern from a uniformly illuminated circular aperture.

which we can rewrite in terms of the far-field angle θ in the form

$$\tilde{u}(r, z) \approx j4\pi N e^{-j\pi N(r/a)^2} \times \frac{2J_1(2\pi a\theta/\lambda)}{(2\pi a\theta/\lambda)} \quad (52)$$

which is valid in the far field for $z \gg z_R$ or $N \rightarrow 0$. By analogy to the sinc function which is defined as $(\sin x)/x$, this function is sometimes referred to as the “jinc” function, with the definition that $\text{jinc}(r) \equiv 2J_1(r)/r$.

This pattern has a single dominant central lobe, which in the circular situation contains $\approx 86\%$ of the total energy, surrounded by a series of increasingly weaker circular rings, as shown in Figure 18.20. The first null of this pattern occurs at a half-angle θ_1 or a radius r_1 in the far field given by

$$\theta_1 = \frac{r_1}{z} \approx \frac{1.22\lambda}{d}, \quad (53)$$

with successive nulls r_n or θ_n defined by successive zeros of the J_1 Bessel function.

Since the limiting value of the first-order Bessel function for small argument is $J_1(r) \approx r/2$, the far-field on-axis intensity for a circular aperture is given by

$$\frac{I(0, z)}{I_0} = \left(\frac{A}{z\lambda} \right)^2 = \left(\frac{\pi a^2}{z\lambda} \right)^2 = \left(\frac{z}{z_R} \right)^2, \quad (54)$$

where we have again made use of our general definition of Rayleigh range. The relationship between Rayleigh range and Fresnel number for the circular aperture is thus

$$\frac{z}{z_R} = \frac{1}{\pi N} \quad \text{or} \quad z_r \equiv \frac{\pi a^2}{\lambda} \quad (\text{circular aperture}). \quad (55)$$

This differs by a small numerical factor (i.e., $4/\pi$) from the comparable expression given in Equation 18.41 for the square aperture situation.

Circular Aperture: Near-Field Diffraction Patterns

The near-field or Fresnel diffraction patterns for a uniformly illuminated circular aperture, for $N > 1$ or $z < z_R$, consist of a series of circular rings

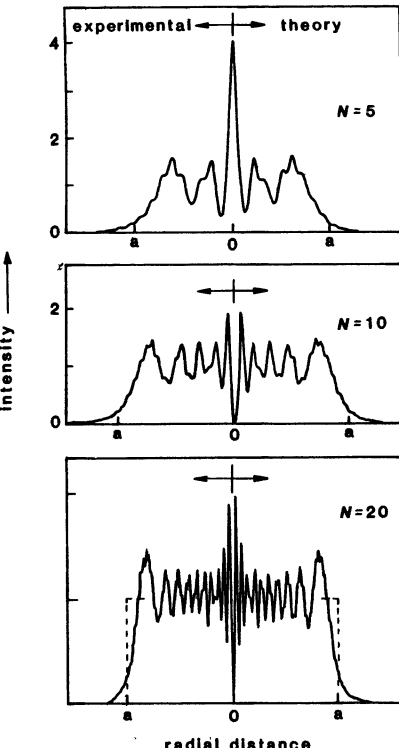


FIGURE 18.21
A few near-field intensity patterns for a uniformly illuminated circular aperture. (Compare with the single-slit diffraction patterns shown in Figure 18.17.)

modulating a constant-amplitude geometric background or “top hat” pedestal, in a fashion generally similar to the single-slit diffraction patterns shown in Figures 18.17 and 18.18. The analogous near-field patterns for the uniformly illuminated circular aperture are somewhat more difficult to calculate, however, and do not seem to be given in many elementary optics texts.

Figure 18.21 shows a few examples of plots of intensity versus radius for near-field diffraction patterns from a circular aperture at various Fresnel numbers greater than unity. (Note that in Figure 18.21 one side of the plot represents a theoretical calculation from the Huygens’ integral, whereas the other side represents a careful experimental measurement for the same conditions using a laser beam setup.)

It is again apparent that these near-field diffraction patterns have approximately N large-amplitude Fresnel ripples across the full width of the beam, and that these larger fringes are then modulated by many smaller-amplitude but higher-frequency Fresnel ripples on top of them. A significant difference from the single-slit situation, however, is that the centermost ripple or spike (which occurs for every odd Fresnel number N) is now significantly larger than all the other Fresnel ripples. The central minimum (which occurs for every even N) is also significantly deeper, and in fact goes exactly to zero. (Recall that in the slit or square aperture situations, the strongest near-field Fresnel ripples occurred at the edges of the aperture.)

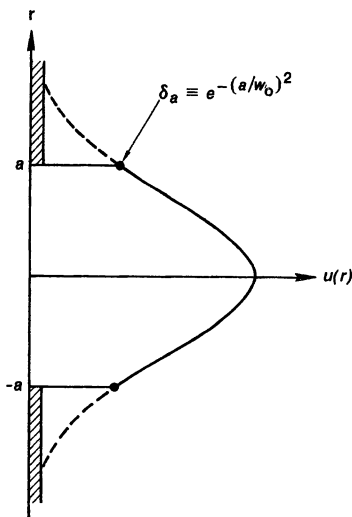


FIGURE 18.22

A circular aperture with gaussian plane-wave illumination.

Circular Aperture: On-Axis Intensity

This difference between rectangular and circular apertures also shows up in the behavior of the intensity on axis, which has already been plotted for both square and circular apertures in Figure 18.19. As we move in toward the uniformly illuminated circular aperture, the on-axis intensity oscillates with increasing frequency between limiting values of zero and of four times the intensity in the transmitting aperture. These peaks and nulls occur exactly at integer values of the Fresnel number N , and the magnitude of these oscillations does not decrease as we get closer in to the aperture, in distinct contrast to the slit or square aperture case. This magnification of the intensity on axis can sometimes cause significant damage problems in higher-power lasers, and we will explore it further below.

General Formula: Circular Aperture With Gaussian Illumination

Before carrying this discussion further, it will be convenient to generalize the azimuthally uniform circular-aperture situation slightly by supposing that the source field in the aperture is a centered *gaussian plane-wavefunction* with a radial amplitude function given by

$$\tilde{u}_0(r_0) = e^{-r_0^2/w_0^2}, \quad (56)$$

as shown in Figure 18.22.

It is then possible, after some manipulation, to expand the general Huygens' integral given in Equation 18.44 into an infinite series of terms containing successively higher-order Bessel functions (see References). The two leading terms

in this series expansion are given by

$$\tilde{u}(rz) \approx \frac{\tilde{q}_0 e^{-j\pi N(r/a)^2}}{\tilde{q}(z)} \times \left[1 - e^{-j\pi N} e^{-a^2/w_0^2} J_0(2\pi N r/a) \right], \quad (57)$$

where $\tilde{q}_0 = j\pi w_0^2/\lambda$, and $\tilde{q}(z) = \tilde{q}_0 + z$ is given by the usual gaussian-beam propagation expressions. This approximation is valid only for values of r near the optical axis, i.e., for $r/a \ll 1$, but it is valid on axis, i.e., at $r = 0$, for any arbitrary distance z in the near or far fields beyond the aperture.

To make Equation 18.57 more transparent, we can define the amplitude $\delta_a \equiv e^{-a^2/w_0^2}$ to represent the wave amplitude of the input gaussian beam at the point where it is cut off at the edge of the circular aperture, as in Figure 18.22. The magnitude of the wave on and near the z axis in the near and far fields then has the form

$$I(r, z) \approx \left[\frac{w_0}{w(z)} \right]^2 \times \left| 1 - \delta_a e^{-j\pi N} J_0(2\pi N r/a) \right|^2 \quad (r \ll a), \quad (58)$$

where $\delta_a \leq 1$, with $\delta_a = 1$ corresponding to a uniform plane-wave input.

Near-Axis Fresnel Ripples: Uniform Illumination

Equation 18.58 says that for either gaussian or uniform plane wave illumination, the wave amplitude on and near the axis consists in essence of the amplitude corresponding to the unperturbed gaussian beam, with a relative magnitude of unity times $\tilde{q}_0/\tilde{q}(z)$, plus a Bessel function contribution of the form $J_0(2\pi N r/a)$ which has relative magnitude $\delta_a \leq 1$, and which adds to the unperturbed beam with relative phase given by $e^{-j\pi N}$.

Consider first the uniform plane-wave situation, with $w_0 \rightarrow \infty$ and $\delta_a \rightarrow 1$. The centermost ripples in the uniform circular-aperture diffraction patterns given in the preceding have the form of a $J_0(r)$ Bessel function centered on the axis whose central lobe has magnitude of unity. This Bessel function subtracts from the background value for even N values, thus giving an exact null on axis, but adds to the background value for odd N values, thus giving twice the amplitude. The central spikes occurring at even Fresnel numbers should thus have an intensity equal to four times the peak intensity in the transmitting aperture itself.

The surrounding rings are substantially weaker than the central spike, because the higher-order maxima of the J_0 function become successively smaller compared to unity. The central spikes continue to reoccur at more and more closely spaced axial distances as we move toward the source aperture, as seen in the near-field patterns in Figure 18.21, and also in the on-axis intensity results for the uniformly illuminated circular aperture given in Figure 18.19. They also become much narrower or sharper as we move in to larger Fresnel numbers, because the $J_0(2\pi N r/a)$ function becomes much narrower as N increases.

Near-Axis Fresnel Ripples: Truncated Gaussian Illumination

We can easily extend this discussion to the circularly truncated gaussian beam situation. The $J_0(r)$ function responsible for the central spike is simply reduced in amplitude in this situation by exactly the relative field strength $\delta_a = \exp(-a^2/w_0^2)$ at the edge of the circular aperture. For $\delta_a < 1$ this smooths out

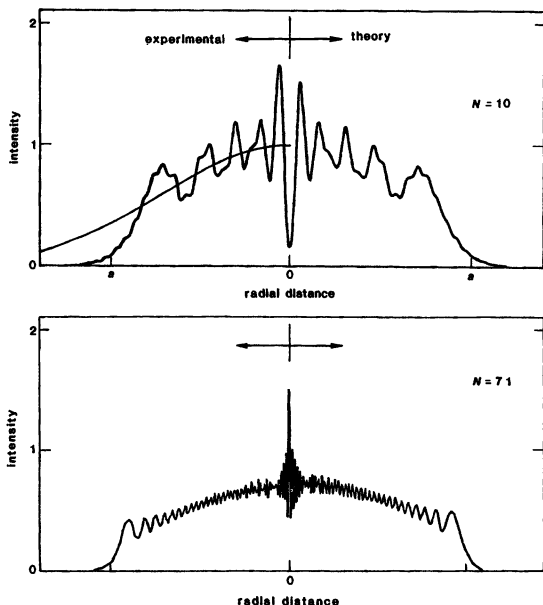


FIGURE 18.23
Near-field intensity patterns
for a circular aperture with
gaussian plane-wave illumina-
tion.

the ripple variation along the z axis in the near field, filling in the nulls and trimming down the peaks.

Figure 18.23 shows a few experimental and theoretical near-field diffraction patterns for the intensity versus radius when a gaussian beam is truncated by a circular aperture at the $1/e$ intensity points (i.e., at $a = w_0/\sqrt{2}$). The central null at even N and central peak at odd N are still apparent, but the null no longer touches bottom, and the peak is now substantially reduced in intensity.

We clearly have here an example of the general point discussed in the previous section: Truncating the gaussian beam at a fractional amplitude given by δ_a , and hence at a much smaller fractional intensity given by δ_a^2 , produces central diffraction ripples in the near-field intensity pattern whose peak-to-peak amplitude variation is given by $1 \pm \delta_a$. The ripples in the near field thus have an intensity variation given by $\approx \pm 2\delta_a$. Truncating the gaussian beam even as far out as its 1% intensity point, for example, corresponding to $\delta_a^2 = 0.01$ or $\delta_a = 0.1$, will still cause an intensity ripple of magnitude $\approx \pm 0.2$ or $\pm 20\%$ in the near field.

Far-field Intensity For a Truncated Gaussian

It is worth noting that in the truncated gaussian situation, the change in on-axis intensity caused by the central diffraction fringe or intensity ripple persists out to arbitrary distance in the far field; and this ripple is a *negative* ripple, or an intensity reduction, as $z \rightarrow \infty$. Truncating a gaussian beam with a circular aperture at the δ_a^2 intensity radius will reduce the on-axis far-field intensity—and in fact the whole central far-field lobe intensity—by a fractional amount $(1 - \delta_a)^2 \approx 1 - 2\delta_a$.

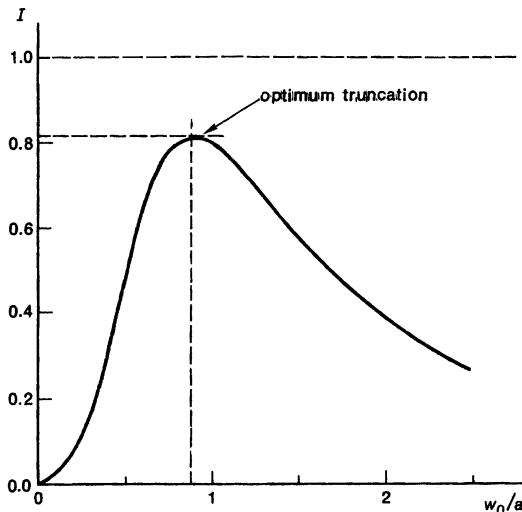


FIGURE 18.24
Optimum truncation of a gaussian beam through a fixed-diameter circular aperture.

Suppose we wish to reduce the intensity ripples in the near field, or the brightness reduction in the far field to $\leq 1\%$. This then requires $\delta_a = \exp(-a^2/w_0^2) \leq 1/200$, which in turn requires an aperture with diameter $d = 2a \geq 4.6w_0$. This is substantially larger than the $d = \pi w_0$ criterion we have introduced earlier on the basis of $\geq 99\%$ power transmission through the aperture itself.

Optimum Aperture for a Gaussian Beam

As an extension of this point, suppose we have a gaussian beam of fixed total power P_0 whose spot size w_0 we can adjust to any desired value by passing this beam through a magnifying or demagnifying telescope. We wish to transmit this beam through a circular aperture whose diameter $2a$ is fixed by practical considerations, such as available lens or mirror sizes, in such a way as to maximize the on-axis intensity in the far-field beam from the aperture. Increasing the beam spot size w_0 to better fill the aperture will thus decrease the far-field angular spread in this situation, but beyond a certain point will also cause increasing power loss as the gaussian beam is truncated by the finite-diameter aperture.

Figure 18.24 illustrates the optimum choice of the ratio w_0/a for optimum far-field intensity in this situation. The maximum far-field intensity is $\approx 81\%$ of what could be obtained if the same total power could be uniformly distributed over the circular aperture; and this condition occurs for $w_0/a \approx 0.89$, or for an aperture diameter $d \approx 2.25w_0$. Note that the amplitude reduction at the aperture edge in this situation has a value of only $\delta_a \approx 0.28$, so that this particular situation will lead to quite substantial near-field ripples.

The Poisson Spot, or the Spot of Arago

Exactly the same kind of intense but narrow on-axis Fresnel structure in the near field that we have discussed in the preceding can also be seen, not only

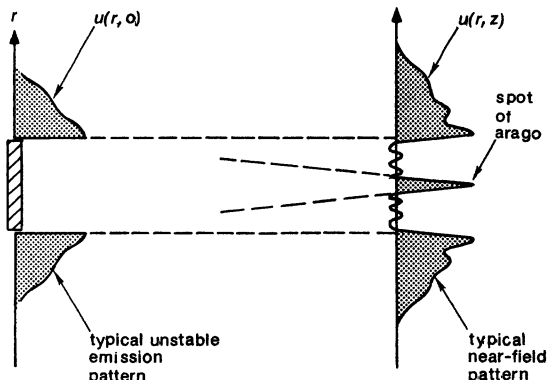


FIGURE 18.25
The Poisson spot or "spot of Arago" behind a circular obstacle.

from a beam passing *through* a circular aperture, but also from the edge-wave diffraction effects when a larger beam is transmitted *past* or *around* a sharp-edged circular obstacle. The resulting sharp narrow spike, with surrounding rings, that appears on the axis in the shadow region behind a circular aperture is generally known either as the *Poisson spot* or, as is becoming more common in recent discussions, *the spot of Arago*.

Suppose a collimated and centered gaussian beam of spot size w_0 is transmitted past an opaque, sharp-edged circular obstacle of diameter $2a$. In accordance with Babinet's principle, the transmitted amplitude in this situation is then equal to the amplitude of the original gaussian beam, *minus* the diffraction pattern that would result from sending the same gaussian beam through a circular aperture of the same diameter. We can then use exactly the same approximate analysis as given in Equation 18.58, except that we no longer have the direct background term. Instead, we see only the scattered Fresnel terms, so that the intensity on and near the axis, in the shadow region behind the obstacle, is given approximately, near the axis, by

$$\tilde{u}(r, z) \approx -\frac{\tilde{q}_0}{\tilde{q}(z)} e^{-j\pi N - a^2/w_0^2} \times e^{-j\pi N(r/a)^2} J_0(2\pi N r/a). \quad (59)$$

This expression produces a central spike of amplitude $\approx \delta_a$, and surrounding Bessel function rings, which are present everywhere along the axis in the exact center of the shadow region of the circular object. The central intense spike is often called the Poisson spot in classical optics texts.

This spot has also come to be called the "spot of Arago" by many laser workers. An example of this spot of Arago for a gaussian beam coming past a circular obstacle is shown in Figure 18.25. Note again that for a beam coming *through* a circular apertures the on-axis bright spot only occurs at distances corresponding to even Fresnel numbers, although these locations become very closely spaced on axis as we move in closer to the aperture. For a beam coming *past* a circular obstacle, however, or for almost any kind of annular aperture, this narrow but intense spot occurs essentially everywhere along the axis in the near field.

Although this spot contains little total energy, its peak intensity as we noted in the preceding can be as high as four times the average intensity in the trans-

mitting aperture. Such spots of Arago have in fact been responsible for many small damage spots and even holes drilled in the center of lenses or optical windows placed in the near-field output region in front of unstable-resonator lasers. Note also that analogous very bright on-axis spots or Fresnel diffraction peaks may occur at certain points along the axis *inside* a laser resonator, where the large circulating intensity may do similar unexpected (and unwanted!) optical damage.

Diffraction Patterns for Annular Apertures

By applying Babinet's principle—that is, by combining the approximate analytic formulas for one or more truncated or untruncated gaussian beams—we can then compute the on-axis and near-axis intensities for a wide variety of annular apertures which have either uniform or radially tapered illumination, and which may be truncated on both their inner and outer edges. Because this type of illumination provides a reasonably good model for the output beam coming from a circular unstable resonator, these results can be of some interest in the design and evaluation of unstable optical resonators.

The kind of annular output beam that comes from a simple hard-edged unstable resonator in fact generally produces both a strong spot of Arago in the near field, and a far-field beam spread which is proportional more to the radial width of the annulus than to the overall beam diameter. Proposals are often made, therefore, to find some way of combining the standard diffraction coupling past the edge of the unstable resonator with partial transmission through the central part of the output mirror. One difficulty with this idea, however, lies in controlling the absolute phase angle which the centrally transmitted wavefront will have relative to the wavefront transmitted past the output mirror edge.

To illustrate the kind of behavior we can expect in these situations, Figure 18.26 shows a few examples of the axial intensity variation we can expect from apertures of this type with different intensities and relative phase angles for the wavefront coming through the central and annular regions of the output aperture.

The Distinction Between Circular and Other Apertures

The intense but narrow on-axis spikes, rings and nulls that we have seen in Figures 18.21, 18.23, and 18.25 are very commonly seen whenever a coherent optical wavefront passes through an aperture having circular symmetry, but are much attenuated for essentially any other aperture shape. A physical explanation for the large increase in sharpness and in peak intensity of these central spike phenomena seen with a circular aperture as compared to other shapes might be argued as follows.

We can note, for example, that in a square aperture the effective Fresnel number or Fresnel phase shift, as seen from an on-axis point, is different in different radial directions, as illustrated in Figure 18.27. For the square aperture, the effective Fresnel number is equal to $a^2/z\lambda$ only exactly along the z or y axes; and the Fresnel phase shift changes as we consider scattered waves coming from points near the corners of the aperture. In other words, the edge waves from various points along the perimeter of a rectangular aperture (or a slit) will arrive at the observation point with somewhat different phase shifts, so that they will not all add in phase.

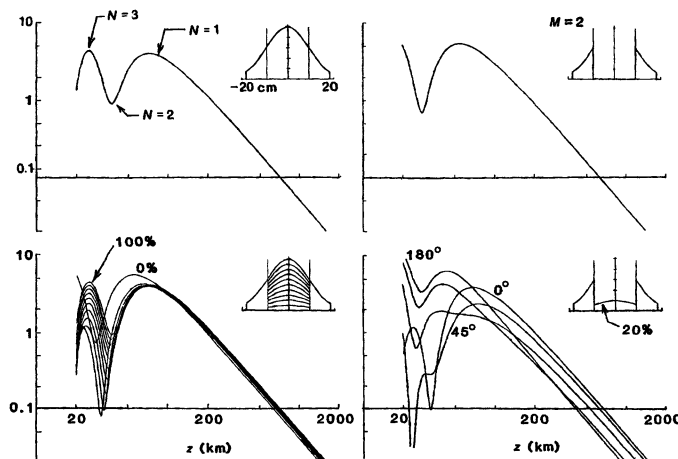


FIGURE 18.26

On-axis intensity versus distance in the near and far fields for a gaussian beam with various types of inner and outer truncation. (a) Gaussian beam truncated only on the outer edge. (b) Annular beam (gaussian beam truncated on inner and outer edges) similar to unstable resonator output with magnification $M = 2$. (c) Same annular beam with central portion partially filled in to various percentage intensity levels. (d) Annular beam with central region filled in to 20% of full amplitude, but with varying phase shifts between central section and annulus.

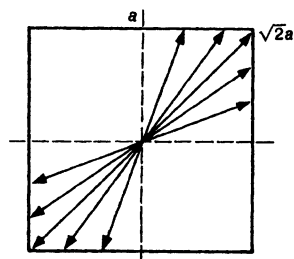


FIGURE 18.27
With a rectangular aperture, the effective Fresnel number is different along different radial directions.

In the circular situation, by contrast—and in fact *only* in this situation—the Fresnel phase shifts between a point on axis and the scattered wavelets coming from the aperture edge are the same for every point around the perimeter of the aperture, since the Fresnel number is independent of azimuth. In a circular aperture, therefore, *all of the edge-wave contributions from the entire perimeter can arrive at an on-axis point exactly in phase*, and thus they can add up to produce the maximum possible Fresnel ripple fluctuation.

The smearing or averaging out of the Fresnel number in other situations seems to be the obvious physical reason for the substantial softening or smoothing out of the on-axis peaks as compared to the circular situation, especially at larger Fresnel numbers. (This smearing out of the Fresnel number along different

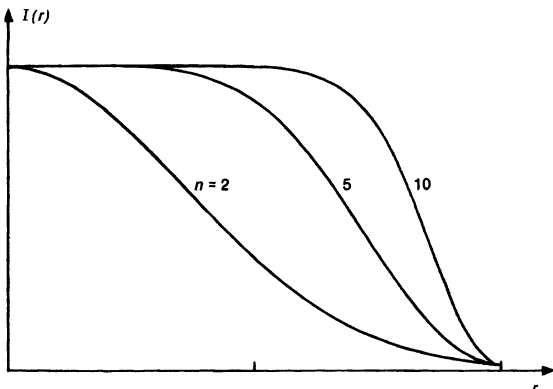


FIGURE 18.28
Supergaussian beam profiles.

azimuthal directions is also responsible for the extrema of the square-aperture on-axis intensity not occurring exactly at integer values of the Fresnel number N .)

Anything that tends to reduce the in-phase vector addition characteristic of the circular aperture will tend to damp out the peak amplitude of the Fresnel ripple effects. Techniques for reducing Fresnel ripple effects can include tapering the aperture transmission at the aperture edge ("soft" versus "hard" apertures); or using any aperture shape other than a perfect circle (rippled or serrated apertures, ellipses, etc.). Several of these approaches have in fact been used in laser beam applications.

"Supergaussians" and Other Smoothed Beam Shapes

As an extension of this idea, we can note that the simple gaussian beam profile, though it may be attractive to the mathematical analyst, is generally not attractive to the designer of laser fusion amplifiers, or other high-power laser systems, for two related reasons. If the gaussian spot size is made relatively small compared to the amplifier aperture, in order to avoid edge diffraction effects, then the energy extraction from the laser medium is poor—the outer part of the beam does not saturate and extract energy from the laser medium, which has been pumped or excited at great trouble and expense. If the gaussian beam is expanded to more effectively fill the aperture, however, this will produce strong edge diffraction ripples, which are not only unsightly but will produce serious self-focusing effects at high powers, thus causing even more troublesome and expensive damage effects.

To get around this, laser designers have explored a variety of other potential transverse beam profiles, which may be more difficult to generate, but which will on the one hand more uniformly fill the aperture, and on the other hand taper smoothly to zero or near-zero at the aperture edge, on the principle that the way to avoid edge waves is to set the optical amplitude δ_a to zero at the aperture edge. (This principle is approximately but not exactly valid.) One set of transverse functions that have been proposed are the "supergaussians," with

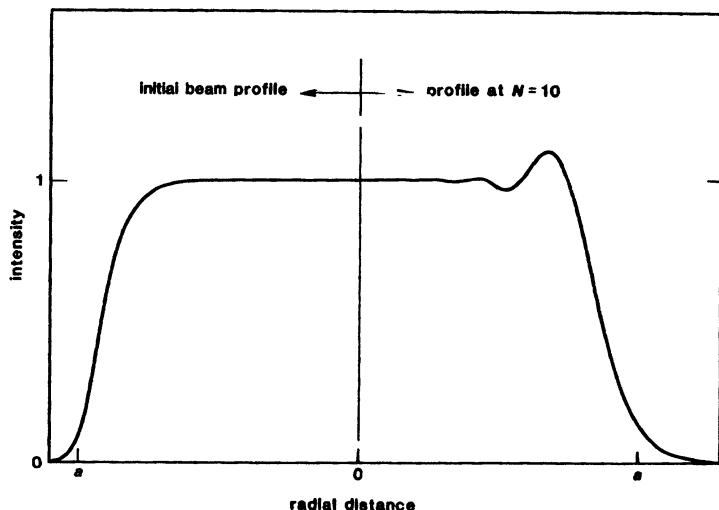


FIGURE 18.29

A smoothed circular beam profile (left side) and its near-field diffraction pattern at Fresnel number $N = 10$ (right side).

the analytical form

$$\tilde{u}(r) = \exp[-c_n r^n], \quad n \geq 2. \quad (60)$$

Intensity profiles for some of these supergaussians are shown in Figure 18.28. Profiles of this type with indices ranging from $n = 5$ to 10 have been analyzed in various laser fusion programs. We can show, for example, that a TEM_{00} gaussian beam profile only fills $\approx 22\%$ of the volume of a laser rod or tube with diameter $d = 3w$, whereas a supergaussian with $n = 8$ will fill $\approx 86\%$ of the rod volume at the same diameter.

Figure 18.29 shows, on one side, another smoothed intensity profile, in this situation one obtained by passing a gaussian beam through a strongly saturating amplifier so that the center of the gaussian is much reduced compared to the outer edges. The other side of Figure 18.29 then shows the calculated near-field diffraction pattern for this input intensity for a particular outer edge truncation, at a distance corresponding to a Fresnel number of $N = 10$. Diffraction ripples still exist, but the elimination of the central spike and general smoothing of the near-field pattern is very evident.

Relay Imaging of Apertured Laser Beams

As an extension of this topic, we can note that multistage laser amplifiers often use beam expanding telescopes between successively higher-power stages, combined with spatial filters consisting of small apertures at the telescope focus which remove the amplitude components scattered or diffracted into larger angles by imperfections, ripples, edges, or small-scale self-focusing in each successive amplifier stage. A concept found very useful in the design of these systems is the use of *image relaying*, as illustrated in Figure 18.30. In this technique, the

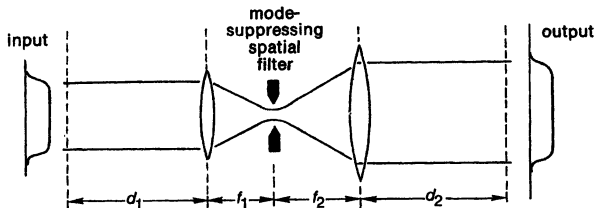


FIGURE 18.30
Combination of image magnification, spatial filtering, and image relaying.

locations and focal lengths of the relay lenses are chosen so that they simultaneously achieve the desired beam magnification, namely, $M = f_2/f_1$, and achieve direct imaging from an object plane located at $-d_1$ to an image plane located at $+d_2$ as shown in Figure 18.30.

This means that, except for the (we hope) small diffraction effects of intervening apertures, the beam profile at the aperture plane or midplane of one amplifier can be imaged as an essentially identical but magnified beam profile at the midplane or image plane of the next amplifier. The intensity cutoff at one aperture is thus automatically converted into an (almost) zero amplitude at the edge of the next aperture. By thus successively relaying the aperture images from amplifier to amplifier through the system, we can hope to fill the diameter of each stage, and yet simultaneously reduce or minimize the edge diffraction effects produced by the finite aperture of each stage.

Far-Field Angular Beam Spread: Arbitrary Aperture Shapes

Finally, for use in predicting the far-field diffraction effects of beams coming from more imperfect or irregular apertures, we can present a rather remarkable expression for the far-field angular beam spread from uniformly illuminated apertures of *arbitrary transverse cross section* which has recently been published by Clark, Howard, and Freniere (see References). The derivation of this formula, which is rather subtle, makes use of the concepts that the normalized intensity near the beam axis in the far field from a uniformly illuminated aperture will be directly proportional to the aperture area A (as we have already shown); but because of edge diffraction effects, the amount of intensity scattered out into larger angles away from the axis should be directly proportional to the *total perimeter length* p of the aperture.

Using this approach, these authors obtain an approximate expression for the fractional encircled power $P(\theta)/P_{\text{tot}}$ contained within a far-field cone of half-angle θ , in the form

$$\lim_{\theta \rightarrow \infty} \frac{P(\theta)}{P_{\text{tot}}} \approx 1 - \frac{p\lambda}{2\pi^2 A} \frac{1}{\theta} = 1 - \frac{1}{2} \frac{\theta_{\text{hp}}}{\theta}. \quad (61)$$

The half-angle θ_{hp} which contains (approximately) half of the total power in the far-field beam will thus be given by

$$\theta_{\text{hp}} \equiv \frac{p\lambda}{\pi^2 A}. \quad (62)$$

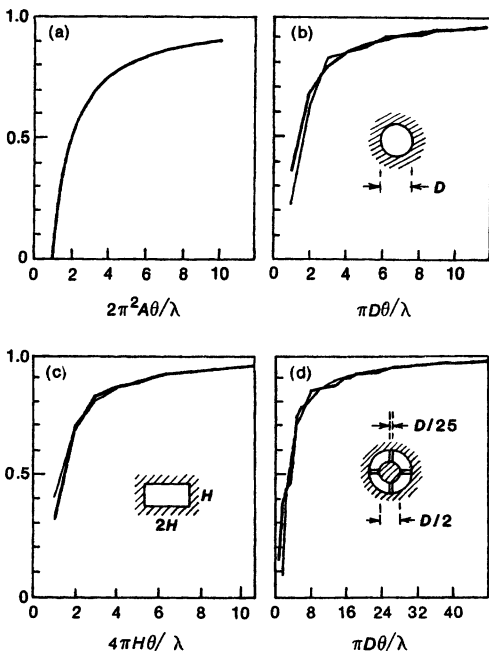


FIGURE 18.31
Fractional encircled energy versus far-field angle (a) Theory (from Equation 18.61) (b), (c) and (d) Theory compared to exact results for various aperture shapes.

If we define a solid angle $\Omega_{hp} = \pi\theta_{hp}^2$ based on this half angle, the product of the transmitting aperture area and the far-field solid angle which contains half of the total power can be written as

$$A \times \Omega_{hp} \approx \frac{(p\lambda)^2}{\pi^3 A} \approx \begin{cases} (4/\pi^2)\lambda^2 \approx 0.41 \times \lambda^2 & \text{(circular aperture),} \\ (16/\pi^3)\lambda^2 \approx 0.52 \times \lambda^2 & \text{(square aperture).} \end{cases} \quad (63)$$

For simple circular or square apertures, therefore, Equation 18.63 gives results in agreement with the Equation 17.21 derived earlier.

Equation 18.61 is more remarkable, however, in that it appears to be quite accurate even at small encircled angles for a variety of different aperture shapes, as illustrated in Figure 18.31. The four different plots show, respectively, the approximate analytical expression, and its comparison with exact encircled energies for a circular aperture, a rectangular aperture, and an annular aperture with four radial struts. Note in particular the substantially larger far-field angular spread for the annular aperture with struts, due to the relatively larger perimeter to area ratio of this aperture.

REFERENCES

The theoretical and experimental sketches of diffracted beam profiles for a circular aperture with uniform or gaussian illumination that are shown in Figures 18.21 and

18.23 come from a very useful paper by A. J. Campillo *et al.*, "Fresnel diffraction effects in the design of high-power laser systems," *J. Appl. Phys.* **23**, 85-85 (July 15, 1973). See also A. I. Mahon, C. V. Bitterli, and S. M. Cannon, "Far-field diffraction patterns of single and multiple apertures bounded by arcs and radii of concentric circles," *J. Opt. Soc. Am.* **54**, 721-732 (June 1964).

The full Bessel-function series expansions for diffraction of a gaussian beam by a circular aperture can be found in G. O. Olaofe, "Diffraction by gaussian apertures," *J. Opt. Soc. Am.* **60**, 1654-1657 (December 1970); and in R. G. Schell and G. Tyras, "Irradiance from an aperture with a truncated-gaussian field distribution," *J. Opt. Soc. Am.* **61**, 31-35 (January 1971).

Conclusions on gaussian-beam circular-aperture diffraction effects similar to those in this section will be found in J. P. Campbell and L. G. DeShazer, "Near fields of truncated-gaussian apertures," *J. Opt. Soc. Am.* **59**, 1427-1429 (November 1969); and in P. Belland and J. P. Crenn, "Changes in the characteristics of a gaussian beam weakly diffracted by a circular aperture," *Appl. Optics* **21**, 522-527 (February 1, 1982).

A discussion and experimental demonstration of relay imaging in a large amplifier chain is given in J. T. Hunt, P. A. Renard, and W. W. Simmons, "Improved performance of fusion lasers using the imaging properties of multiple spatial filters," *Appl. Opt.* **16**, 779-782 (April 1977).

An excellent survey is given by J. E. Harvey and J. L. Forgham of "The spot of Arago: New relevance for an old phenomena," *Am. J. Phys.* **52**, 243-247 (March 1984).

The approximate formula for arbitrary apertures comes from P. P. Clark, J. W. Howard, and E. R. Freniere, "Asymptotic approximation to the encircled energy function for arbitrary aperture shapes," *Appl. Opt.* **23**, 353-357 (January 15, 1984).

Problems for 18.4

1. *Diffraction pattern of circular aperture at the shadow edge.* Show that for a uniformly illuminated circular aperture the diffracted field amplitude exactly at the geometric shadow edge, i.e., at $r = a$, is given analytically as a function of distance z by $\hat{u}(a, z) = (j/2) [J_0(2\pi N)e^{-j2\pi N} - 1]$ where $N \equiv a^2/z\lambda$.
 2. *More on diffraction ripples near the shadow edge.* As the Fresnel number N becomes significantly larger than unity—that is, as we move closer and closer in toward the aperture—the outer Fresnel ripples just inside the shadow edge for a circular aperture begin to look more and more like the same ripples near the shadow edge for a slit or rectangular near-field diffraction pattern. (For example, the peak overshoot of the outermost ripple begins to look about the same in both situations.)
- Indeed, we might suppose that if we look at the first few diffraction fringes in the near vicinity to an aperture edge, it would not make much difference whether the edge was straight (corresponding to a slit or half-plane) or had some slight curvature (corresponding to a large circular aperture). Attempt to justify this similarity by comparing the diffraction formulas for a slit and a circular aperture in the limits of $N \gg 1$ and x or r approaching a from inside.
3. *Central spike for a truncated circular gaussian.* Figure 18.23 shows the near-field diffraction pattern for a gaussian beam truncated at the $1/e$ intensity point and observed at $N = 71$. Explain the numerical value of the observed peak intensity in the central spike.

4. *Simple numerical method for calculating uniform circular aperture diffraction patterns.* One quite simple (if perhaps not very efficient) way to compute the far-field (or even the near-field) diffraction pattern of a circular aperture, without getting involved in Bessel functions, is to break the circular aperture up into a moderate number of narrow rectangular strips and then add up the easier-to-calculate diffraction patterns from each individual strip. Program this on a small personal computer and try a few simple situations.
5. *Optimum gaussian spot size through an aperture.* Verify the result given in the text for the optimum spot size of a gaussian beam if this beam is to be transmitted through a circular aperture of radius a so as to produce the maximum on-axis intensity in the far-field.
6. *Diffraction patterns for partially filled annular apertures.* Set up the necessary analysis to handle the kinds of problems illustrated in Figure 18.26, and reproduce the results shown there, or other similar situations that you find of interest.
7. *Imaging analysis for the relay imaging system.* Set up an $ABCD$ matrix analysis of the relay imaging system shown in this section, and explain how we can simultaneously achieve arbitrary transverse magnification M (for collimated input and output beams) and a zero effective length (i.e., $B \equiv 0$) from input to output planes.
8. *Diffraction pattern for an “inverted” truncated gaussian (research problem).* There seems to be no reason why the approximate result for a gaussian-illuminated circular aperture given in the text cannot also model an inverted or radially growing gaussian beam which is sharply truncated at radius a , but which has $w_0^2 < 0$ and thus $\delta_a > 1$. If so, this could serve as a model for a beam with a sharply truncated quasi annular ring pattern.

Examine whether the approximate formula seems to be valid in this situation, and if so discuss the nature of the near and far-field patterns that would be produced by this kind of illumination.

STABLE TWO-MIRROR RESONATORS

The simplest kind of optical resonator consists of just two curved mirrors set up facing each other. If the curvatures of these two mirrors correspond to a stable periodic focusing system, and if their transverse dimensions are large enough so that we can neglect edge-diffraction effects, then these mirrors can in essence trap a set of lowest-order and higher-order gaussian modes or beams that will bounce back and forth between the two mirrors. These trapped Hermite-gaussian modes form, to a first approximation, a set of resonant modes for the two-mirror cavity.

Simple two-mirror cavities such as this are widely used in practical lasers, and the properties of these stable gaussian resonator modes form part of the basic lore of laser physics. In this chapter, therefore, we give a fairly detailed account of these properties and of how they are derived from gaussian beam theory. In addition we give a brief survey of the (usually) small deviations from ideal gaussian beam behavior that occur because of finite mirror sizes, including in particular the finite diffraction losses in finite-diameter resonators.

In later chapters we will discuss the additional complexities that arise in analyzing multielement resonators which contain, for example, intracavity lenses or gaussian apertures, as well as the quite different and nongaussian modes associated with unstable optical resonators. Even in these situations, however, the stable two-mirror gaussian concepts introduced in this section will prove very useful in understanding and explaining the behavior of these more complex resonators.

19.1 STABLE GAUSSIAN RESONATOR MODES

Suppose we have a gaussian beam with a certain waist size and waist location, as in Figure 19.1, and suppose that we then fit a pair of curved mirrors to this beam at any two points along the beam, as also illustrated in Figure 19.1. If the radii of curvature of the mirrors are exactly matched to the wavefront radii of the gaussian beam at those two points, and if the transverse size of the mirrors is substantially larger than the gaussian spot size of the beam, each of these mirrors will in essence reflect the gaussian beam exactly back on itself, with exactly reversed wavefront curvature and direction.

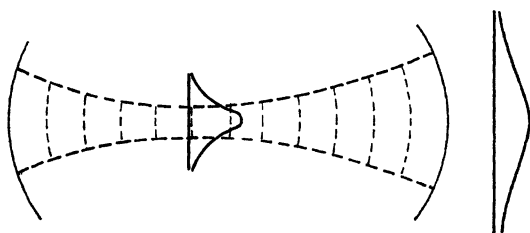


FIGURE 19.1
A gaussian beam can be
trapped by two mirrors of the
proper curvature and spacing.

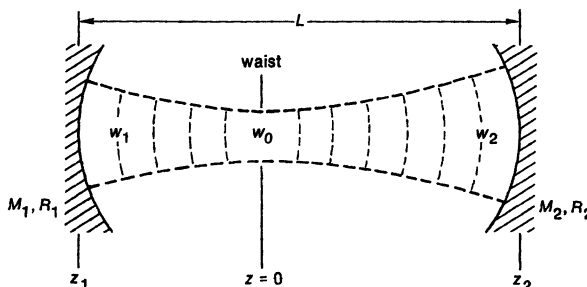


FIGURE 19.2
Notation and analytical model for analyzing a simple stable two-mirror cavity.

These two mirrors can thus trap the gaussian beam as a standing wave between the two mirrors, with, if the mirrors are large enough in size, negligible diffraction or “spillover” losses past the edges of the mirrors. The two mirrors thus form an optical resonator which can support both the lowest-order gaussian mode, and also higher-order Hermite-gaussian or Laguerre-gaussian modes, as resonant modes of the cavity. We will see in this section that this simple description is, in essence, exactly what happens in elementary stable two-mirror gaussian resonators.

Stable Two-Mirror Resonator Analysis

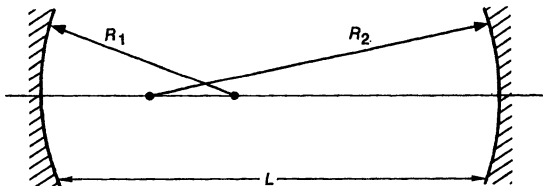
In practice, instead of being given a gaussian beam and asked to fit mirrors to it, we are much more likely to be given two curved mirrors M_1 and M_2 with radii of curvature R_1 and R_2 and spacing L , and asked to find the right gaussian beam that will just fit properly between these two mirrors. To analyze this situation we can use the model in Figure 19.2, assuming that the gaussian beam will have an (initially unknown) spot size w_0 or Rayleigh range $z_R \equiv \pi w_0^2/\lambda$, and that the mirrors will be located at distances z_1 and z_2 from the (initially unknown) location of the beam waist.

The essential conditions are then that the wavefront curvature $R(z)$ of the gaussian beam, as given by gaussian beam theory, must match the mirror curvature at each mirror, taking into account the specified mirror spacing L . This

$$g_1 \equiv 1 - L/R_1$$

$$g_2 \equiv 1 - L/R_2$$

FIGURE 19.3
The resonator g parameters.



provides us with three equations, namely,

$$R(z_1) = z_1 + z_R^2/z_1 = -R_1, \quad (1)$$

$$R(z_2) = z_2 + z_R^2/z_2 = +R_2,$$

and

$$L = z_2 - z_1. \quad (2)$$

The minus sign in the first of these equations arises because of a difference in the sign conventions that we use in describing beam wavefronts or in describing resonator mirrors. The gaussian wavefront curvature $R(z)$ is usually taken as positive for a diverging beam, or negative for a converging beam, traveling to the right; whereas the mirror curvatures R_1 and R_2 are usually taken as positive numbers for mirrors that are concave inward, i.e., as seen looking out from within the resonator, and as negative numbers for mirrors that are convex as seen from inside the resonator.

The g Parameters

We must then invert these three equations in order to find the gaussian beam parameters z_R , z_1 and z_2 in terms of the specified mirror curvatures and spacing R_1 , R_2 and L . Before doing this, however, it is customary to define a pair of “resonator g parameters,” g_1 and g_2 , which were introduced in the early days of laser theory to describe laser resonators, and have since become standard notation in the field. These parameters are given by

$$g_1 \equiv 1 - \frac{L}{R_1} \quad \text{and} \quad g_2 \equiv 1 - \frac{L}{R_2}. \quad (3)$$

We will see more of their physical significance later.

In terms of these parameters we can then find that the trapped gaussian beam in Figure 19.2 will have a unique Rayleigh range given by

$$z_R^2 = \frac{g_1 g_2 (1 - g_1 g_2)}{(g_1 + g_2 - 2g_1 g_2)^2} L^2, \quad (4)$$

and that the locations of the two mirrors relative to the gaussian beam waist will be given by

$$z_1 = \frac{g_2(1 - g_1)}{g_1 + g_2 - 2g_1g_2} L \quad \text{and} \quad z_2 = \frac{g_1(1 - g_2)}{g_1 + g_2 - 2g_1g_2} L. \quad (5)$$

(Note that if mirror M_1 is located to the left of the beam waist, so that the waist is inside the resonator as in Figure 19.2, then z_1 as measured from the waist will be a negative number.)

It is also useful to write out the waist spot size w_0 , which is given by

$$w_0^2 = \frac{L\lambda}{\pi} \sqrt{\frac{g_1g_2(1 - g_1g_2)}{(g_1 + g_2 - 2g_1g_2)^2}}, \quad (6)$$

and the spot sizes w_1 and w_2 at the ends of the resonator, which are given by

$$w_1^2 = \frac{L\lambda}{\pi} \sqrt{\frac{g_2}{g_1(1 - g_1g_2)}} \quad \text{and} \quad w_2^2 = \frac{L\lambda}{\pi} \sqrt{\frac{g_1}{g_2(1 - g_1g_2)}}. \quad (7)$$

These quantities depend only on the resonator g parameters defined in the preceding, and on the quantity $\sqrt{L\lambda/\pi}$ which we will discuss in the following.

Resonator Stability Diagram

It is immediately obvious from Equations 19.4 to 19.7 that real and finite solutions for the gaussian beam parameters and spot sizes can exist only if the g_1, g_2 parameters are confined to a stability range defined by

$$0 \leq g_1g_2 \leq 1. \quad (8)$$

We refer to this as a stability range because this is also exactly the condition required for two mirrors with radii R_1 and R_2 and spacing L to form a stable periodic focusing system for rays, as analyzed earlier in Chapter 15.

In the early days of gaussian resonator theory this stability criterion was immediately translated into the *resonator stability diagram* shown in Figure 19.4. Every two-mirror optical resonator can then be characterized by the parameters $g_1 = 1 - L/R_1$ and $g_2 = 1 - L/R_2$, and hence represented by a point in the g_1, g_2 plane. If this point falls in the shaded stable region, shown in Figure 19.4, the mirrors correspond to a *stable periodic focusing system*, and the resonator (if the mirrors are large enough transversely) will trap a family of lowest and higher-order gaussian modes with gaussian beam parameters given by Equations 19.4 through 19.7. Such a stable resonator will thus have a unique set of gaussian transverse resonator modes.

If the point g_1, g_2 instead falls in any of the unstable regions outside the shaded area, the mirrors will correspond to an *unstable periodic focusing system*, and no gaussian beam that will fit properly between the mirrors can be found. These mirror configurations correspond to the very different (but also very useful) *unstable optical resonators* that we will discuss in a later chapter.

Optical ray theory and gaussian mode theory thus have a close connection, which we will study in more detail later on, even though the diffraction effects that are an integral part of gaussian beam theory are entirely neglected in the

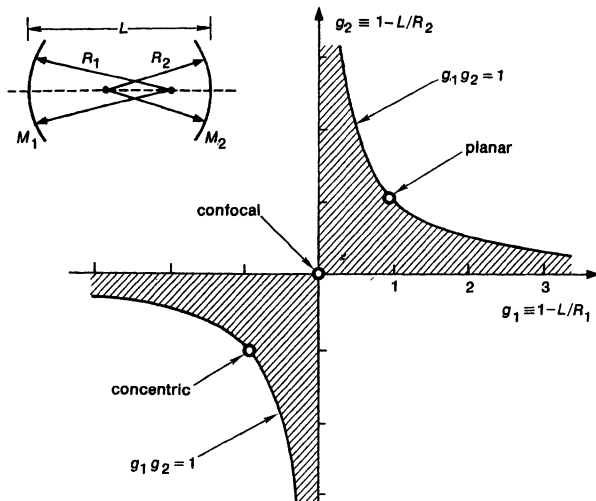


FIGURE 19.4
The stability diagram for a two-mirror optical resonator.

optical ray theory. Note also that these distinctions between stability and instability depend only on the g parameters, and are (to first order) entirely independent of either the optical wavelength or the transverse size or dimensions of the resonator. In the following section we will examine in more detail the various types of resonators that occur in various regions of the stability diagram, and the various practical properties of these resonators.

Resonator Circle Diagrams

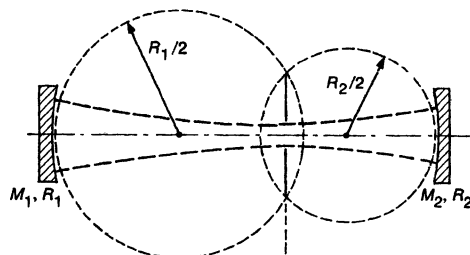
An alternative and less commonly used graphical method for interpreting the gaussian beam parameters in stable two-mirror resonators is the *circle diagram* of Deschamps. Suppose again that two mirrors of radii R_1 and R_2 are set up with spacing L . If we then draw circles with diameters R_1 and R_2 tangent to the concave side of each of these mirrors, as shown in Figure 19.5, the intersection of these two circles is a necessary and sufficient condition for the existence of a stable gaussian mode in the resonator; and moreover the waist location and its relative size in the resonator is determined by the line joining the intersection of these two circles.

REFERENCES

The standard review article in the journal literature on gaussian resonator modes is H. Kogelnik and T. Li, "Laser beams and resonators," *Appl. Optics* 5, 1550–1567 (October 1966). See also the many other references cited therein.

Many of the same ideas on gaussian beams as eigenmodes of stable periodic focusing systems developed quite independently of laser resonator theory, and somewhat

waist inside:



waist outside:

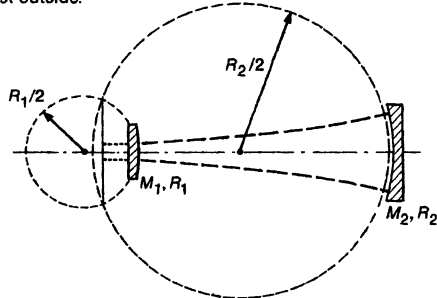


FIGURE 19.5
Circle diagrams for stable optical resonators.

earlier, in the work of Gobau and colleagues on periodic beam waveguides intended as millimeter-wave rather than optical transmission systems. A good review of this work is given in the article by G. Gobau, "Beam waveguides," in *Advances in Microwaves*, Vol. 3, ed. by L. F. Young (Academic Press, 1968), p. 67.

The connections between ray theory and gaussian resonator theory are explored in more detail by I. A. Ramsay and J. J. Degnan, "A ray analysis of optical resonators formed by two spherical mirrors," *Appl. Optics* **9**, 385-398 (February 1970).

The circle diagram described in this section was introduced by G. A. Deschamps and P. E. Mast in *Proceedings of the Symposium on Quasi-Optics*, edited by J. Fox (Brooklyn Polytechnic Press, New York, 1964), p. 379; and has been extended by P. Laures in "Geometrical approach to gaussian beam propagation," *Appl. Optics* **6**, 747-755 (April 1967).

Problems for 19.1

1. **Another graphical representation for resonator mode stability.** Make a series of sketches showing two mirrors facing each other, with the mirror spacing fixed. Assuming that the center of curvature C_2 of the right-hand mirror is located in the following positions, indicate by cross hatching those sections of the axis within which the center of curvature C_1 of the left-hand mirror must be located in order to have a stable resonator:
 - (a) C_2 located between the two mirrors.

- (b) C_2 located to the left of the left-hand mirror.
- (c) C_2 located to the right of the right-hand mirror (i.e., a divergent right-hand mirror).
2. *Symmetric cavity with central thin lens.* A stable optical cavity of length L is to be formed by two symmetric mirrors with radius of curvature R , plus a thin lens of focal length f placed exactly in the center of the cavity. Calculate how to fit a stable gaussian beam within this cavity, and then describe the stability limits of the cavity and the profile of the gaussian beam within the cavity for different choices of f , R , and L . Describe in particular where the waist (or waists) will occur in the cavity under different conditions. Hint: Split the central thin lens into two lenses with half the focal power each, and then put a reference right in the middle between these two thin lenses.
3. *Standing-wave cavity fields.* The standing-wave field $\tilde{u}(x, y, z)$ for a single lowest-order gaussian mode inside an ideal stable laser cavity is the sum of two identical but oppositely traveling gaussian beams. Write down this field expression, in terms of the waist spot size w_0 characteristic of the resonator and the coordinates x, y, z . Do the standing-wave fields oscillate in the same time-phase everywhere inside the laser cavity?

19.2 IMPORTANT STABLE RESONATOR TYPES

To gain more insight into the general properties of stable gaussian resonators, let us now survey some of the characteristics associated with resonators at various different points of interest in the stability diagram introduced in the previous section.

(1) Symmetric Resonators

Perhaps the simplest resonator configurations to analyze are symmetric resonators, which have mirror curvatures $R_1 = R_2 = R$, and hence g parameters $g_1 = g_2 = g = 1 - L/R$. The waist of the gaussian resonant mode is then obviously in the center of the resonator, with waist and end mirror spot sizes given by

$$w_0^2 = \frac{L\lambda}{\pi} \sqrt{\frac{1+g}{4(1-g)}} \quad \text{and} \quad w_1^2 = w_2^2 = \frac{L\lambda}{\pi} \sqrt{\frac{1}{1-g^2}}. \quad (9)$$

All these symmetric resonators obviously lie along the $+45^\circ$ diagonal through the origin in the g plane, with an allowed range from $g = 1$ (planar mirror case), through $g = 0$ (symmetric confocal case), to $g = -1$ (concentric or spherical case).

Figure 19.6 shows how the resonator spot sizes change as the g value is varied along this range, for example, by steadily increasing the mirror curvatures while keeping the mirror spacing fixed.

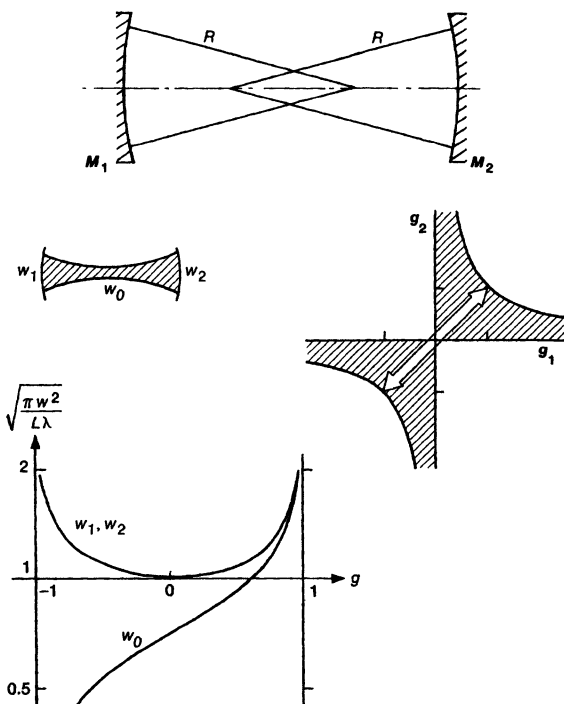


FIGURE 19.6
Symmetric stable resonators lie along the diagonal axis in the g_1, g_2 plane.

(2) Half-Symmetric Resonators

Another elementary system is the half-symmetric resonator of Figure 19.7, in which one mirror is planar, $R_1 = \infty$, and the other curved, so that $g_1 = 1$ and $g_2 = g = 1 - L/R_2$. Such a resonator is obviously equivalent to half of a symmetric system that is twice as long. The waist in this situation will be located on mirror number 1, with spot sizes given by

$$w_0^2 = w_1^2 = \frac{L\lambda}{\pi} \sqrt{\frac{g}{1-g}} \quad \text{and} \quad w_2^2 = \frac{L\lambda}{\pi} \sqrt{\frac{1}{g(1-g)}}. \quad (10)$$

The allowed range for $g_2 = g$ is now from $+1$ to 0 , corresponding to a vertical line between the points $(1, 1)$ and $(1, 0)$ in the stability diagram.

(3) Symmetric Confocal Resonator

The central point in the stability diagram, and in some sense a central type of stable optical resonator, is the *symmetric confocal stable resonator*, which is characterized by the values $R_1 = R_2 = L$ and $g_1 = g_2 = 0$ (Figure 19.8). This is referred to as a confocal resonator because the focal points of the two end mirrors (which are located at $R/2$ out from the mirror) coincide with each other at the center of the resonator. We have already seen in Figure 15.10 that confocality

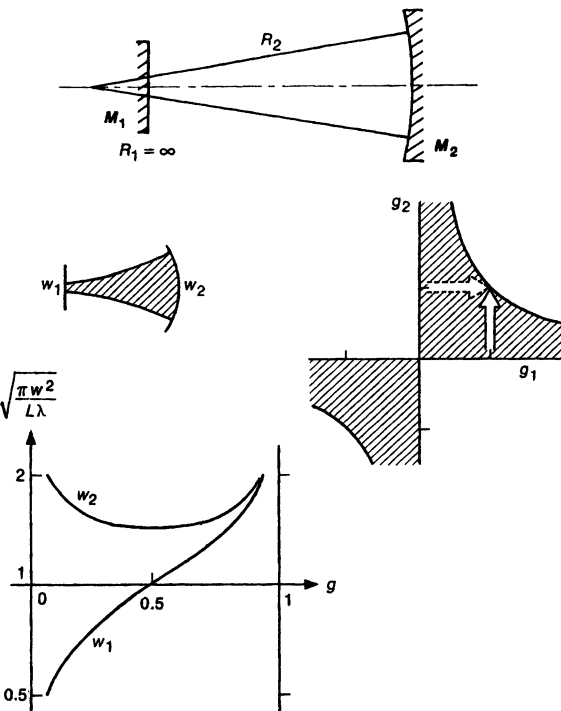


FIGURE 19.7

Half-symmetric resonators have their waist at the plane-mirror end of the cavity.

corresponds to the condition for a gaussian beam in which the center of curvature of each mirror is located exactly on the opposite mirror. The two mirrors are thus spaced from each other by exactly two Rayleigh ranges or by exactly the waist length of the trapped gaussian beam.

The spot sizes at the center and at the end mirrors of a confocal resonator are then given by

$$w_0^2 = \frac{L\lambda}{2\pi} \quad \text{and} \quad w_1^2 = w_2^2 = \frac{L\lambda}{\pi}. \quad (11)$$

The spot sizes on the end mirrors thus correspond exactly to the scale factor $\sqrt{L\lambda/\pi}$ that arises in all types of stable resonators, whereas the spot size at the central waist is smaller by $1/\sqrt{2}$.

Table 19.1 gives some typical values of this spot size for resonators of different lengths at the typical wavelengths of 633 nm for the He-Ne laser and at 10.6 μm for the CO₂ lasers. The Table also shows the laser tube diameter that might be associated with this length of resonator, using the rule of thumb that aperture diameter $d = \pi w$.

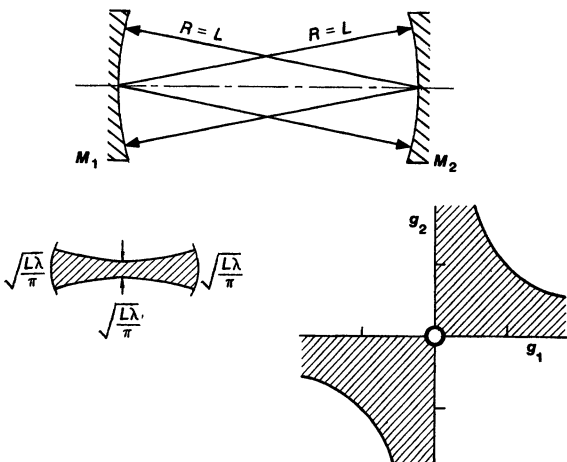


FIGURE 19.8
The symmetric confocal resonator is a special case, located exactly at the origin of the stability diagram.

TABLE 19.1
Confocal Resonator Spot Sizes

Cavity length, L	10 cm	1 m	10 m
Spot size, $w_1 = \sqrt{L\lambda/\pi}$:			
$\lambda = 633 \text{ nm}$	150 μm	0.4 mm	1.5 mm
$\lambda = 10.6 \mu\text{m}$	600 μm	1.7 mm	6 mm
Tube diameter, πw_1 :			
$\lambda = 633 \text{ nm}$	0.4 mm	1.2 mm	4 mm
$\lambda = 10.6 \mu\text{m}$	1.7 mm	5 mm	1.7 cm

These mode diameters are significantly smaller than the diameters of the laser rods or tubes that we might want to use to obtain reasonable laser power outputs at these wavelengths. Finding ways to increase the diameter of the stable gaussian modes (or finding new resonator designs which inherently have larger mode volumes) is one of the primary design objectives in most laser designs.

The confocal resonator in fact has overall the smallest average spot diameter along its length of any stable resonator, although we will see that other resonators may have a smaller waist size at one spot within the resonator. The confocal resonator is also highly insensitive to misalignment of either mirror. Tilting of either mirror still leaves the center of curvature located on the other mirror surface, and merely displaces the optic axis of the resonator by a small amount. The confocal resonator can thus be very useful, for example, as a trial resonator design when we are first attempting to obtain laser oscillation from a laser medium whose gain is small or uncertain. The small mode size then means very small diffraction losses, and the alignment insensitivity means that critical mirror alignment should not be necessary to get the laser to oscillate.

The confocal resonator is also useful for power or energy measurements, in which we simply want to know how much power or energy is available in some laser medium, without consideration of mode control requirements. A confocal

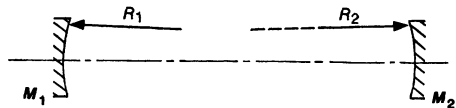
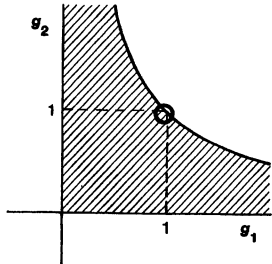
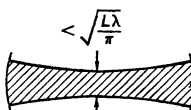


FIGURE 19.9

The long-radius or near-planar resonator can have larger mode volume, but is very sensitive to mirror misalignment.



resonator is then likely to oscillate in a combination of lowest and higher-order modes that will fill the entire volume of the laser medium and extract essentially all the stimulated emission available from the laser medium.

The small average size of the confocal modes, on the other hand, means that the lowest-order or TEM_{00} confocal mode will not be very effective in extracting power from larger-diameter gain media. Multimode oscillation, as in the power measurement situation, will mean large far-field diffraction spreading of the laser output beam.

(4) Long-Radius (Near-Planar) Resonators

Another elementary resonator configuration, and one that was used in many of the earliest laser devices, is the *near-planar* or *long-radius* stable resonator of Figure 19.9. A planar or flat-mirror resonator can be regarded as the limiting situation of a long-radius stable resonator as the radii of curvature of the two mirrors go to infinity. The resonator parameters then become $R_1 \approx R_2 \approx \infty$ and $g_1 \approx g_2 \approx 1$. If we let $R_1 = R_2 = R$, the spot sizes in this situation all become large and essentially equal, in the form

$$w_0^2 \approx w_1^2 \approx w_2^2 \approx \frac{L\lambda}{\pi} \times \sqrt{\frac{R}{2L}} \quad \text{for } R \gg L. \quad (12)$$

In gaussian beam terms the long-radius resonator has a very long and large waist, of which the resonator encompasses only a very short central part. As the mirror radii become infinite the spot sizes become infinite also, though only very slowly, with the radius increasing as $(R/2L)^{1/4}$. The exactly planar resonator occurs right on the stability boundary, at $g_1 = g_2 = 1$, and so the gaussian theory fails at and beyond that point.

Long-radius resonators, although they can have larger mode volumes, are generally avoided in practical laser designs because of their very great alignment difficulties. Since the centers of curvature of the mirrors are cantilevered far out beyond the ends of the resonator, at distances $\pm R$, very delicate angular

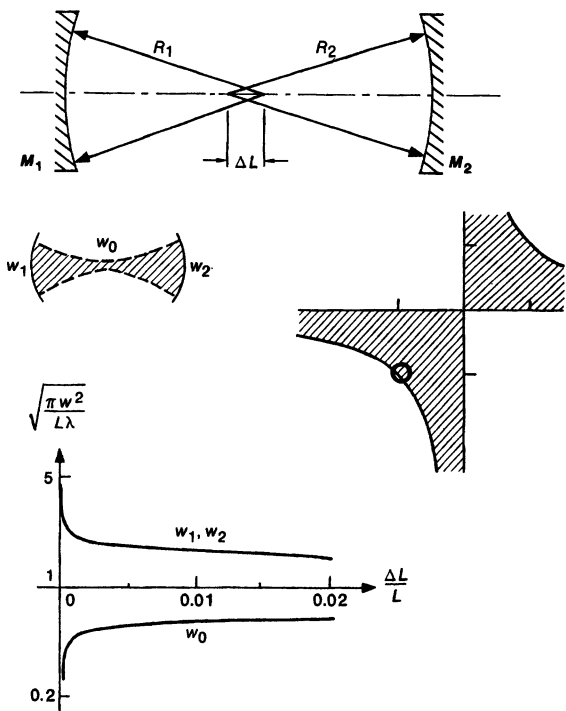


FIGURE 19.10
The near-concentric resonator can have large spot sizes at the ends, but is also very sensitive to misalignment.

alignment of the mirrors becomes necessary if the optical axis of the resonator (which passes through these two centers of curvature) is to be kept aligned within the center of the laser medium itself. Long-radius mirrors are also difficult to manufacture and to test. Note, for example, that for a 2.5 cm diameter mirror with a 50-m radius of curvature, the total sag at the center of the mirror relative to the edges is only $\approx 1.5 \mu\text{m}$. At the same time the spot size enhancement factor for a laser resonator that is $L = 50 \text{ cm}$ long is only $(R/2L)^{1/4} \approx 2.7$.

(5) Near-Concentric Resonators

The near-concentric stable resonator is another design which is on the boundary of the stability region, and which can give large spot sizes at the end mirrors, but now with a vanishingly small spot size in the center of the resonator, as illustrated in Figure 19.10.

For a near-concentric resonator, in which the cavity length L is less than the sum of the two radii $R_1 + R_2$ by the small amount ΔL , the resonator parameters are given by $R_1 \approx R_2 \approx R = L/2 + \Delta L$ and $g_1 \approx g_2 = -1 + \Delta L/R$. The spot size at the central waist is then given by

$$w_0^2 \approx \frac{L\lambda}{\pi} \times \sqrt{\frac{\Delta L}{4L}} \quad \text{for } \Delta L \ll L, \quad (13)$$

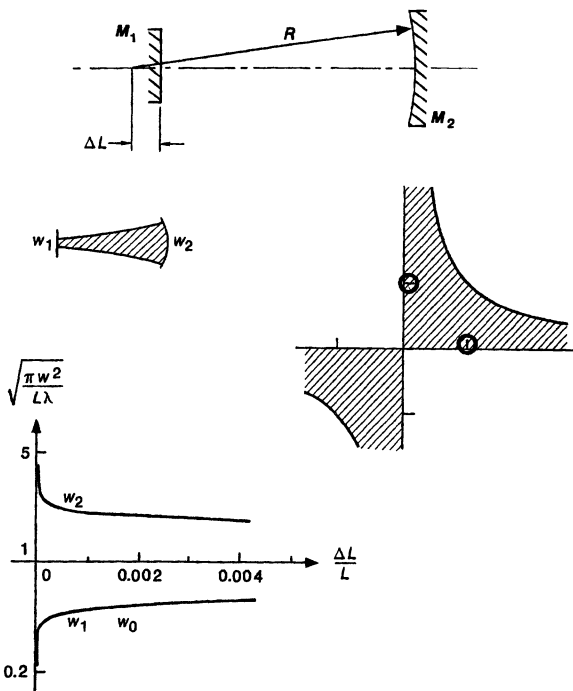


FIGURE 19.11
The near-hemispherical resonator is widely used in practical laser oscillators.

and the end-mirror spot sizes by

$$w_1^2 = w_2^2 \approx \frac{L\lambda}{\pi} \times \sqrt{\frac{4L}{\Delta L}} \quad \text{for } \Delta L \ll L. \quad (14)$$

The mirror radii are now physically reasonable, and the spot sizes can be adjusted in operation by using translatable end-mirror mounts. The mirrors can then be pulled slowly apart in order to bring the resonator closer to or even across the stability boundary, by making the incremental length ΔL small or even negative.

The central portion of the resonator, where the spot size becomes very small, is then not very useful, at least for laser power extraction. More seriously, the mirror centers of curvature now become very close to each other at the center of the cavity, as illustrated in Figure 19.10. Hence this resonator again becomes very sensitive to large axis misalignments caused by very small mirror misalignments.

(6) Hemispherical Resonators

The resonator design that is by far the most commonly used in practical stable-resonator lasers, such as, for example, most medium and low-power gas lasers, is the *near-hemispherical* or *half-concentric stable resonator*, of Figure 19.11, for which the resonator parameters are $R_1 = \infty$ and $R_2 = L + \Delta L$, and hence $g_1 = 1$ and $g_2 = \Delta L/L \approx 0$. This resonator is like half of a near-concentric

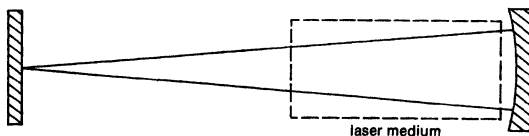


FIGURE 19.12
The active mode volume in a near-hemispherical resonator is essentially cone-shaped.

resonator, with the very small spot size at the plane-mirror end given by

$$w_1^2 = w_0^2 \approx \frac{L\lambda}{\pi} \times \sqrt{\frac{\Delta L}{L}} \quad \text{for } \Delta L \ll L, \quad (15)$$

and the large spot size at the curved mirror end given by

$$w_2^2 \approx \frac{L\lambda}{\pi} \times \sqrt{\frac{L}{\Delta L}} \quad \text{for } \Delta L \ll L. \quad (16)$$

Again by making small adjustments in the resonator length the spot size w_2 at the curved mirror end can be made as large as desired, whereas the spot size $w_1 = w_0$ at the flat mirror end becomes correspondingly tiny.

The mode volume in a near-hemispherical resonator is then essentially in the shape of a cone, as in Figure 19.12. Lasers with near-hemispherical resonators are usually designed with the cavity somewhat longer than the active laser volume, and with the laser tube or rod placed near the large-diameter end of the cavity. Readers may note in typical small internal-mirror He-Ne lasers, for example, that the discharge region is usually stopped well short of the flat-mirror end of the laser; and in some situations a tapered laser bore is even employed.

Hemispherical Laser Construction

The great advantage of the hemispherical design, however, is that the mode alignment difficulties in this design are largely if not completely eliminated. Consider, for example, the construction of an internal-mirror laser structure in which the mirrors are to be attached directly to the laser tube bore, as in Figure 19.13. The mechanical requirements are then first that the bore itself be fabricated with a sufficiently accurate length L compared to the mirror radius R to give the desired ΔL and hence the desired spot size. This is not, in general, a severe requirement. The second requirement is that the flat-mirror end of the bore be sufficiently perpendicular to the bore axis that the mirror normal will travel down the bore, which is again typically not a severe mechanical tolerance.

The curved mirror can thus be brought into alignment with the perpendicular axis through the bore either by angular adjustments, or alternatively by sideways translation of the curved mirror relative to the bore. Gas lasers can thus be aligned on production lines purely by translation of the curved mirror, if this proves simpler than providing an angular adjustment.

For all these reasons hemispherical resonator designs, or slightly more complicated variations, are used in many practical lasers. Lasers with external mirrors usually provide for angular adjustments in both mirror mounts, and possibly a small length adjustment in one of the mounts; whereas many small gas lasers have completely fixed or internally mounted mirrors.

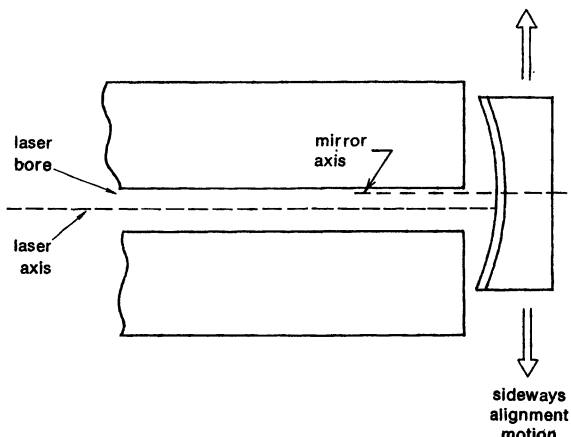


FIGURE 19.13
Alignment of a hemispherical resonator can be accomplished by mirror translation instead of mirror tilt.

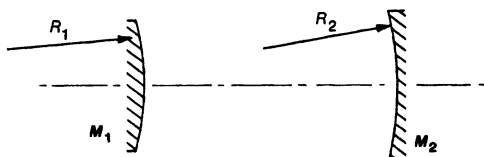
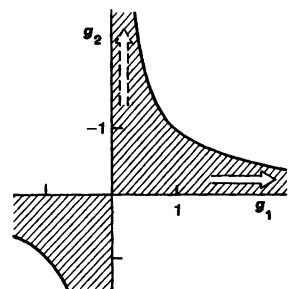
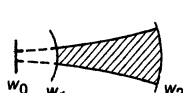


FIGURE 19.14
Convex-concave stable resonators can also provide large mode volumes, but are seldom used in practice.



(7) Concave-Convex Resonators

Even with a hemispherical design, the spot size of the TEM_{00} mode in a stable gaussian resonator is often much smaller than we would like in order to extract energy efficiently from a larger-diameter laser medium. Any design in fact which operates close to the stability boundary can give larger mode sizes, but only at the expense of high sensitivity to small fluctuations in the mirror curvature or spacing. Such resonators are also likely to be highly sensitive to effects such as pump-power dependent thermal focusing effects in solid-state laser rods.

By moving out into the regions of the stability diagram beyond $g_1 = 1$ or $g_2 = 1$, it is possible to have so-called concave-convex stable resonators such as are illustrated in Figure 19.15. In these resonators the waist lies outside the resonator, and the mode volume is comparatively large everywhere inside the resonator. Resonators such as these have found some practical use, but generally tend to require inconveniently long mirror radii and sensitive alignment procedures.

(8) Unstable Confocal Resonators

Finally, it is also possible to have resonators that are confocal but asymmetric, i.e., resonators in which the two mirrors have different radii of curvature R_1 and R_2 but their focal points still coincide, as in Figure 19.15. The spacing for a general asymmetric confocal resonator is

$$R_1/2 + R_2/2 = L, \quad (17)$$

which can be translated into the condition

$$g_1 + g_2 = 2g_1g_2. \quad (18)$$

Examination of the stability diagram will show that this condition corresponds to a contour or locus which is *unstable* everywhere in the g_1, g_2 plane, except at the symmetric confocal point $g_1 = g_2 = 0$, and at the planar symmetric point $g_1 = g_2 = 1$. (The mirror focal points in the latter situation are coincident at infinity.)

All asymmetric confocal resonators are *thus unstable*, as is also evident from the gaussian beam parameters in the previous section. In fact, we will see later that such confocal unstable resonators are of particular interest because one of the circulating beams in such a resonator is always a collimated beam, which can be particularly useful as the collimated output beam from the unstable resonator. The inset in Figure 19.15 shows how a typical ray diverges outward on successive bounces in such a resonator.

The symmetric confocal resonator shown in Figure 19.8 is thus obviously located at a kind of singular point or saddle point in the stability diagram, since small deviations from this point in different directions can take us either into stable or unstable regions of the plane.

REFERENCES

For references on concave-convex resonators, see R. B. Chesler and D. Maydan, "Convex-concave resonators for TEM_{00} operation of solid-state ion lasers," *J. Appl. Phys.* **43**, 2254-2257 (May 1972); and J. Steffen, J-P. Lortscher, and G. Herziger, "Fundamental mode radiation with solid-state lasers," *IEEE J. Quantum Electron.* **QE-8**, 239-245 (February 1972).

Problems for 19.2

1. The "stop band" in near-confocal resonators. When a low-gain laser with two curved mirrors of the same nominal radius R (in reality the two mirrors are

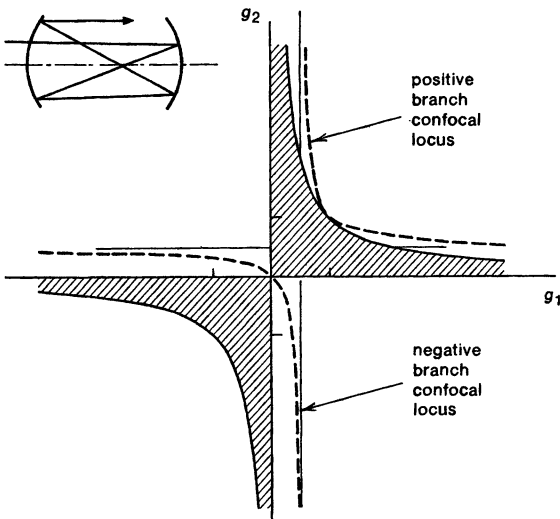
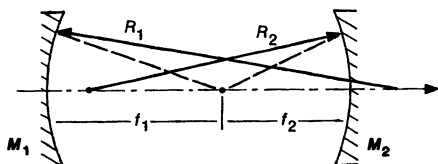


FIGURE 19.15

All asymmetric confocal resonators lie outside the shaded region and are thus unstable.

never exactly identical) and with variable spacing L is set up as a nominally confocal resonator, it is sometimes found that in the region near confocal spacing ($L \approx R$) there is a narrow range of L over which the laser will not oscillate, although it will oscillate quite well at either slightly larger or slightly smaller values of the spacing L . What might be the reason for this somewhat mysterious (but frequently observed) behavior?

2. *Mode matching from one stable resonator into another.* (a) The output beam from a He-Ne laser whose two mirrors have 2 m radii of curvature and are 1 m apart is to be re-focused by a single lens so as to match into the resonant mode of an interferometer cavity having 10 cm radius of curvature mirrors 5 cm apart. The only lens available has $f = 1\text{ m}$. Find the necessary spacings between the laser output mirror, the lens, and the interferometer input mirror. (Hint: Some trial-and-error numerical calculations may be faster than trying to obtain a closed-form analytic solution).
- (b) Suppose instead the laser output mirror and the interferometer input mirror must be exactly 50 cm apart, but a single lens is still to be used. What lens focal length is required and where must this lens be located?

3. *Spot size adjustments in a near-hemispherical resonator.* An He-Ne 6328Å gas laser nominally 1 m long is to be designed with a hemispherical cavity, i.e., one flat mirror and one curved mirror with $R = 1$ m. A micrometer screw is to be used to vary the exact cavity length over a small range, so that the cavity length will be $L = R - \Delta L$, where $\Delta L \ll L$. In this way the spot size w_2 at the curved-mirror end can be varied to fill the 5 mm radius of an aperture at the spherical mirror end of the laser.
- (a) Making use of the fact that $\Delta L \ll L$ and R , write down the simple expression for w_2 as a function of ΔL .
- (b) Over what range of ΔL must the micrometer screw move the curved mirror if w_2 is to vary from 5 mm to all larger values? Plot w_2 versus ΔL over this range.
- (c) When $w_2 = 5$ mm, what will be the value of w_1 at the flat mirror end of the laser?
-

19.3 GAUSSIAN TRANSVERSE MODE FREQUENCIES

Because of the Guoy phase shift and its dependence on Hermite-gaussian mode number, the different transverse modes in a stable gaussian resonator have different resonance frequencies and transverse mode frequency shifts that are sometimes of practical interest. In this section, therefore, we derive and summarize the analytic formulas for these transverse modes.

Transverse Mode Phase Shifts

The total phase shift from one end of the cavity to the other, including the $k(z_2 - z_1) \equiv kL$ term and the Guoy phase shift terms, for an nm -th order Hermite-gaussian mode is given by

$$\phi(z_2 - z_1) = kL - (n + m + 1) \times [\psi(z_2) - \psi(z_1)] \quad (19)$$

where the Guoy phase shifts ψ are related to the gaussian beam parameters by

$$\psi(z_i) = \tan^{-1}(z_i/z_R). \quad (20)$$

If we use Equations 19.5 and 19.6 for z_1 and z_2 in terms of g_1 and g_2 from the first section of this chapter, it is possible to show (after a fair amount of algebra) that the total Guoy phase shift along the resonator length is given in terms only of the g parameters by the formula

$$\psi(z_2) - \psi(z_1) = \cos^{-1} \pm \sqrt{g_1 g_2} \quad (21)$$

where the + sign applies in the upper right quadrant ($g_1, g_2 > 0$) and the - sign applies in the lower left quadrant. (Note that in the lower left quadrant, for example, near the concentric situation $g_1 = g_2 = -1$, the resonator becomes substantially longer than the gaussian beam waist. The beam then picks up essentially the full 180° Guoy phase shift, which means that the cosine of this phase shift must approach -1.)

Transverse Mode Frequencies

The resonance condition for a standing-wave cavity says that this one-way phase shift must be an integer number of half cycles, or the total round-trip phase shift must be an integer multiple of 2π , so that we must satisfy

$$\frac{\omega L}{c} - (n + m + 1) \cos^{-1} \pm \sqrt{g_1 g_2} = q\pi, \quad q = \text{integer.} \quad (22)$$

The resonance frequencies of the axial-plus-transverse modes in the cavity must thus be given by

$$\omega = \omega_{qnm} = \left[q + (n + m + 1) \frac{\cos^{-1} \pm \sqrt{g_1 g_2}}{\pi} \right] \times \frac{2\pi c}{p}, \quad (23)$$

where $p \equiv 2L$ is the round-trip distance or perimeter of the cavity. A little inspection will show that the Guoy phase shift factor appearing in this equation takes on the limiting values

$$\frac{\cos^{-1} \pm \sqrt{g_1 g_2}}{\pi} \approx \begin{cases} 0 & \text{for the near-planar situation, } g_1, g_2 \rightarrow 1, \\ 1/2 & \text{for the near-confocal situation, } g_1, g_2 \rightarrow 0, \\ 1 & \text{for the near-concentric situation, } g_1, g_2 \rightarrow -1. \end{cases} \quad (24)$$

Let us examine these results in a bit more detail.

Near-Planar (Long-Radius) situation

For the near-planar situation the transverse mode frequencies ω_{qnm} associated with a given axial mode q are all clustered on the high-frequency side of the associated axial mode frequency ω_{q00} , as shown in the top line of Figure 19.16, with equal spacings that are small compared to the axial mode spacing. The mode spot size is large in this situation, and the resonator length is short compared to the Rayleigh range for the gaussian beam. The transverse modes therefore pick up very little additional Guoy phase shift. What phase shift they do pick up subtracts from the plane-wave $\omega L/C$ term, and therefore a higher frequency is required to make up the $q\pi$ total phase shift—in other words, the higher-order transverse mode frequencies are always on the high-frequency side of the associated axial mode.

The axial-plus-transverse mode spectrum in the near-planar situation thus appears as the usual axial mode frequencies spaced by $q \times 2\pi c/p$, with higher-order transverse modes clustered as satellite modes on the high-frequency side of each axial mode. If we think, for example, of fixing the resonator length L and gradually increasing the mirror curvatures R to bring the resonator gradually inward from the near-planar situation to the near-confocal situation, then the mode spot size gradually gets smaller; the transverse derivatives get larger; the Guoy phase shift contributions become larger; and the transverse mode spacings gradually broaden out, as illustrated in Figure 19.16. The higher-order transverse modes ω_{qnm} associated with a given axial mode q move out toward, and in fact pass above, the frequencies of the higher-frequency axial modes, e.g., the $q+1, 00$ and $q+2, 00$ and higher axial modes.

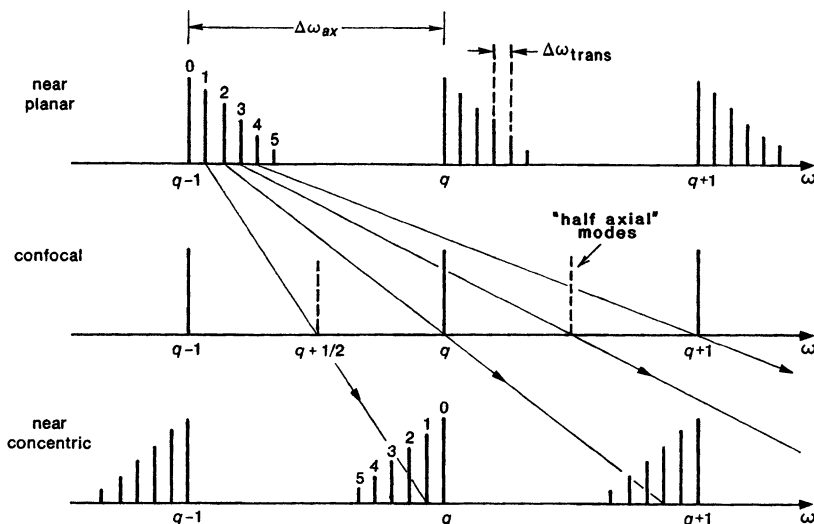


FIGURE 19.16

Transverse mode frequencies in various stable Gaussian resonators.

Confocal Resonators

The confocal resonator represents the situation, in fact, where the 01 and 10 transverse modes associated with the q -th axial mode move out to fall exactly halfway between the q and $q + 1$ axial modes; the $q11$, $q02$ and $q20$ modes of the q -th axial mode move out to coincide with the $q + 2, 00$ mode; and so forth. The confocal resonator thus represents a situation where all the even-symmetry transverse modes of the cavity are exactly degenerate at the axial mode frequencies of the laser; and all the odd-symmetry modes are exactly degenerate at the "half-axial" positions midway between the axial mode locations.

Scanning Fabry-Perot Interferometers

This degeneracy in confocal transverse mode frequencies is of considerable practical importance for scanning Fabry-Perot interferometers or optical frequency tunable filters. A scanning Fabry-Perot interferometer is a passive optical cavity whose length L can be scanned over a few optical half-wavelengths, usually by means of a piezoelectric crystal or piezoelectric stack mounted behind one of the end mirrors. The resonant frequencies of the cavity can thus be scanned over a few axial modes or free spectral ranges of the cavity.

If the output signal from a laser is sent through such a cavity while it is being scanned, and the optical signal transmitted through the scanning interferometer is displayed on an oscilloscope, then a large detected signal will be seen every time the scanning cavity frequency equals one of the oscillation frequencies in the laser output. The scanning interferometer thus provides an electrically tunable filter for examining and displaying the frequency components in the laser signal.

One practical difficulty with such interferometers, however, is the existence of higher-order transverse modes in the scanning interferometer. Suppose the laser input signal has only a single frequency component, but that the input laser beam

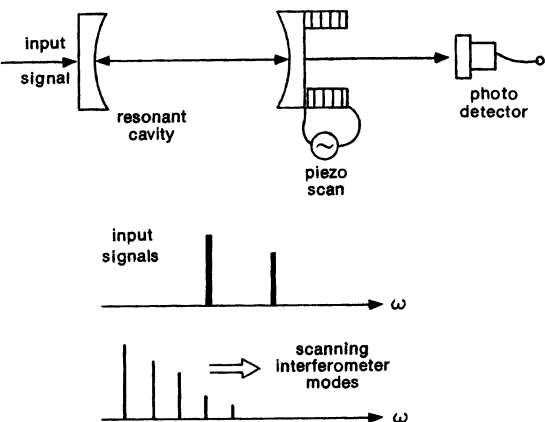


FIGURE 19.17
Operation of a scanning
Fabry-Perot interferometer.

is misaligned or improperly mode matched to the scanning interferometer cavity. Then as the interferometer cavity is scanned, the laser signal will successively come into resonance with and excite different higher-order transverse modes of the interferometer (Figure 19.17); and these in turn will produce transmitted signals in the interferometer output. The single laser input frequency will produce multiple spurious, or at least unwanted, apparent frequency components in the scanning interferometer display.

One way to eliminate these spurious transmission signals is to carefully align and mode-match the laser signal into the interferometer cavity—generally a delicate and difficult task. An alternative and much more practical solution is to make the scanning Fabry-Perot interferometer be an exactly confocal cavity, so that all the higher-order transverse modes are exactly degenerate in frequency. This then means that the input beam to such an interferometer need not be mode-matched into the interferometer in order to excite only a single transmission resonance. Rather the input beam can be misaligned and mismatched to a significant extent, and yet it will still excite resonance transmission at only a single frequency.

Commercial scanning Fabry-Perot interferometers are thus very often designed as confocal resonators. A mismatched input beam to a confocal cavity still excites a mixture of lowest and higher-order transverse modes in the interferometer; but in the confocal situation their resonance frequencies are all exactly degenerate. More precisely, the even-order transverse modes are all degenerate at the axial mode frequencies, whereas the odd-order modes are degenerate halfway in between.

One disadvantage of a confocal scanning interferometer is that the free spectral range of the interferometer is now only half the axial mode spacing, or $c/4L$ in hertzian frequency. The odd-order modes can be eliminated or at least greatly attenuated, however, by at least centering and aligning a spatially coherent input beam to the interferometer, even if proper mode matching is not obtained. Observing how the scanning interferometer signal sharpens up for very small adjustments of the interferometer length about the confocal condition is also an interesting experimental demonstration.

Concentric Resonator situation

If we continue to sharpen the mirror curvature so that the resonator approaches the concentric condition, the $q01$ mode in Figure 19.16 as an example will move out until it approaches the $q + 1, 00$ mode from the low-frequency side; and so forth. In the concentric limit, therefore, the axial-transverse mode spectrum will come again to look like a set of axial modes with closely spaced transverse mode satellites, but with these now clustered on the low-frequency side. It is important to realize, however, that these clusters of modes, although they are closely grouped in frequency, in this limit actually represent different axial as well as transverse mode numbers.

Transverse Mode Beats

One of the best ways to observe experimentally the presence of transverse mode oscillations, in any resonator configuration, is to look for the *transverse mode beats* between whatever axial-transverse modes may be oscillating in a given laser, using a suitable photodetector and radio-frequency receiver or spectrum analyzer.

Suppose a laser is oscillating simultaneously in two such modes with indices $q_1 n_1 m_1$ and $q_2 n_2 m_2$. The output signal from this laser impinging on a suitable photodetector may then be written in the form

$$\mathcal{E}(x, y, t) = \tilde{u}_1(x, y)e^{j\omega_1 t} + \tilde{u}_2(x, y)e^{j\omega_2 t}, \quad (25)$$

where $\tilde{u}_1(x, y)$ and $\tilde{u}_2(x, y)$ are the transverse patterns of these two modes on the photodetector. The total photocurrent or photosignal that this optical field will produce from a typical square-law optical detector is then given by

$$\begin{aligned} i(t) &= \iint |\mathcal{E}(x, y, t)|^2 \, dx \, dy \\ &= \iint |\tilde{u}_1(x, y)e^{j\omega_1 t} + \tilde{u}_2(x, y)e^{j\omega_2 t}|^2 \, dx \, dy \\ &= I_{01} + I_{02} + I_{12}e^{j(\omega_2 - \omega_1)t} + \text{c.c.}, \end{aligned} \quad (26)$$

where the dc currents I_{01} and I_{02} are given by

$$I_{01} = \iint |\tilde{u}_1(x, y)|^2 \, dA \quad \text{and} \quad I_{02} = \iint |\tilde{u}_2(x, y)|^2 \, dA, \quad (27)$$

and the complex phasor amplitude I_{12} is given by

$$I_{12} = \iint \tilde{u}_1^*(x, y) \times \tilde{u}_2(x, y) \, dA. \quad (28)$$

The integrals are taken over the active surface area of the photodevice; and it is assumed that the photodetector response averages over a few optical cycles, so that sum-frequency cross products at $\omega_1 + \omega_2$ can be ignored.

The total output signal from the photodetector thus consists of dc currents I_{01} and I_{02} due to each beam separately, plus a cross product or *beat frequency* term I_{12} between the two signals, in the form

$$i(t) = I_{01} + I_{02} + I_{12} \cos [(\omega_2 - \omega_1)t + \phi_{12}], \quad (29)$$

where $\omega_2 - \omega_1$ is the difference frequency or beat frequency between the two oscillating modes. If several such modes are oscillating, similar beat frequencies between any pair of the oscillating modes may be observed. For a stable gaussian resonator these difference frequencies will be given in general by

$$\begin{aligned}\omega_2 - \omega_1 &= \omega_{q_2 n_2 m_2} - \omega_{q_1 n_1 m_1} \\ &= \left[(q_2 - q_1) + (n_2 - n_1 + m_2 - m_1) \frac{\cos^{-1} \pm \sqrt{g_1 g_2}}{\pi} \right] \times \frac{2\pi c}{p} \\ &= \Delta q \times \Delta\omega_{\text{ax}} + \Delta(n + m) \times \Delta\omega_{\text{trans}},\end{aligned}\quad (30)$$

where $\Delta q = q_2 - q_1$, $\Delta n = n_2 - n_1$, and so on. The beat signal will thus contain components at various integral multiples of the axial mode spacing $\Delta\omega_{\text{ax}}$ and the transverse mode spacing $\Delta\omega_{\text{trans}}$.

Overlap Integrals and Orthogonality

Note that the magnitude of each beat signal will be given by the overlap integral between the transverse modes on the photodetector surface, or

$$I_{12} = \left| \iint \tilde{u}_1^*(x, y) \times \tilde{u}_2(x, y) dx dy \right|. \quad (31)$$

For ideal Hermite-gaussian modes (and to a lesser extent for real resonator modes), this overlap integral between different transverse modes will integrate out to zero because of the transverse orthogonality or near-orthogonality between different transverse modes. This is only true, however, if the integral is taken over the full transverse cross section of the modes. This overlap integral will in general not vanish if the integration is taken only over part of the beam cross section. The area of integration may be limited either because the photodetector itself has a limited area, or because of an aperture inserted in the beam in front of the detector. Inserting such a partial aperture is, in fact, a standard technique for making visible transverse mode beats that are otherwise not seen.

Transverse mode beat frequencies (which are typically in the range from a few MHz to a few hundred MHz) can be measured with great accuracy, since any absolute frequency shifts in the laser oscillation due to mechanical vibrations or thermal expansion are essentially the same for both modes, and cancel out of the difference frequency. Such mode beats thus provide both a convenient diagnostic for the presence of higher-order transverse-mode oscillations, and also a particularly good test for resonator mode theory.

Note that the transverse beat frequencies are directly tied to the Guoy phase shifts of the different modes, which are in turn directly tied to the transverse spatial derivatives and hence the transverse mode patterns of the modes. Experiments that have been done on transverse mode beats in stable gaussian resonators have always yielded results in excellent agreement with theory, and thus have served as at least a strong indirect confirmation of the validity of the gaussian resonator mode theory.

REFERENCES

An excellent and detailed set of measurements on transverse mode frequencies are reported in J. P. Goldsborough, "Beat frequencies between modes of a concave-mirror optical resonator," *Appl. Optics* **3**, 267-275 (February 1964).

For any given set of mirror radii in a stable gaussian resonator there are certain mirror spacings at which there will be exactly an integer number n of transverse modes between each axial mode. In certain multimode doppler broadened gas lasers this can lead to a slight reduction in oscillation power output at these spacings, since the different transverse modes no longer burn holes more or less uniformly across the frequency profile of the gain line, but instead cluster in groups separated by $\Delta\omega_{ax}/n$ between each axial mode. This weak but definite effect is neatly confirmed by G. O. Harding and T. Li in "Effect of mode degeneracy on output of gaseous optical masers," *J. Appl. Phys.* **35**, 475-478 (March 1964).

Problems for 19.3

1. *Relationship between spot size and transverse mode frequency.* Consider a near-hemispherical optical resonator of length L with one plane mirror and one curved mirror of radius R , where $L = R - \Delta L$ and $\Delta L \ll L$. In such a resonator both the output spot size w_2 and the transverse-mode frequency spacing will depend rather strongly on the small length adjustment ΔL , and so we can use measurements of either or both of these quantities to check on the predictions of the gaussian mode theory.

Assume such a laser is allowed to oscillate in several axial and transverse modes, and that f_{beat} is the *lowest* intermode beat frequency that is observed in the laser output (i.e., it is the beat between some $q00$ mode and the nearest adjacent $q+k, mn$ mode). Verify that w_2 and f_{beat} will then satisfy the fixed product $w_2^2 \times f_{beat} \approx c\lambda/\pi^2$, independent of L or R , as ΔL is varied with $\Delta L \ll L$.

2. *Conditions for transverse mode degeneracy.* Under certain conditions there can be a kind of transverse mode degeneracy in a stable gaussian resonator in which exactly an integer number of transverse mode frequencies lie between each axial mode interval, so that transverse modes of different orders from different axial modes all coincide at a discrete set of frequencies. Tuning a laser cavity to this condition can then lead to a small reduction in total power output in certain inhomogeneously broadened lasers.

For an optical resonator of length L with one flat mirror and one curved mirror of radius R , evaluate the length to mirror-curvature ratios L/R at which there will be exactly $2, 3, 4, \dots$ transverse-mode spacings in each axial-mode frequency interval.

19.4 MISALIGNMENT EFFECTS IN STABLE RESONATORS

The effects of mirror misalignments on stable two-mirror resonators can be relatively complicated, since misalignment or misadjustment of either mirror both rotates and translates the optical axis of the resonator. One way to handle such

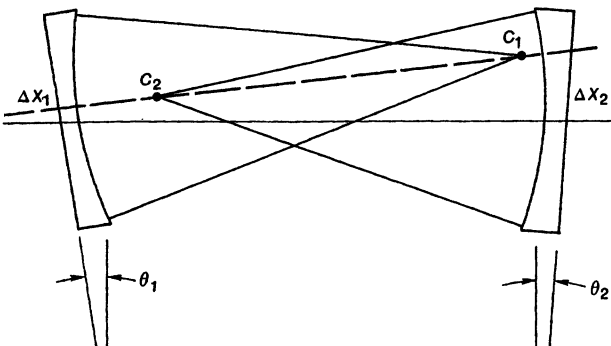


FIGURE 19.18
Geometry for analyzing misalignment and axis displacement in a stable optical resonator.

misalignments is to use the techniques for misaligned ray matrix systems discussed in Section 15.4. We can give in this section, however, a brief description of the axis displacement and misalignment produced in a simple two-mirror cavity by angular misalignment of either end mirror.

Misalignment Analysis

The optical axis in a two-mirror resonator is by definition the line passing through the centers of curvature C_1 and C_2 of the two end mirrors. The quadratic phase curvatures of the two mirrors are centered on or normal to this axis. If the cavity also contains any kind of aperture (including the apertures defined by the mirrors themselves), rotation of an end mirror will translate the optical axis relative to this aperture or, alternatively, will cause the aperture to be effectively off center with respect to the resonator axis. The presence of an off-center aperture will tend to produce resonator eigenmodes which are mixtures of the even and odd eigenmodes of the aligned resonator. Solving for the exact eigenmodes and their exact diffraction losses in this situation becomes a complicated calculation.

Simple geometry can at least tell us how far the optical axis will be translated and rotated by a small angular rotation of either end mirror. Let θ_1 and θ_2 be the small angular rotations of the two end mirrors and Δx_1 and Δx_2 be the small sideways translations of the new or misaligned optical axis at the point where it intercepts the end mirrors, as shown in Figure 19.18. (Alternatively, Δx_1 and Δx_2 can represent the off-center translations of the apertures at those two mirrors.) From Figure 19.18 and some simple geometry, we can then evaluate these displacements as

$$\begin{aligned}\Delta x_1 &= \frac{g_2}{1 - g_1 g_2} \times L \theta_1 + \frac{1}{1 - g_1 g_2} \times L \theta_2 \\ \Delta x_2 &= \frac{1}{1 - g_1 g_2} L \Delta \theta_1 + \frac{g_1}{1 - g_1 g_2} L \Delta \theta_2.\end{aligned}\quad (32)$$

One criterion for judging the seriousness of misalignment effects is then to compare these displacements Δx_1 and Δx_2 with the resonator spot sizes w_1 and w_2 at the same end mirrors.

The angular displacement of the resonator axis (which can be important in evaluating far-field pointing accuracy, for example) can also be evaluated from

$$\Delta\theta \equiv \frac{\Delta x_2 - \Delta x_1}{L} = \frac{(1 - g_2)\theta_1 - (1 - g_1)\theta_2}{1 - g_1 g_2}. \quad (33)$$

Note that the sensitivity of all these measures to angular misalignment blows up as $g_1 g_2 \rightarrow 1$, i.e., as the resonator design approaches the stability boundary on either the planar (long-radius) or the near-concentric sides of the stability region.

REFERENCES

Misalignment effects in stable resonators are treated in more detail, and with supporting experimental results, by R. Hauck, H. P. Kortz, and H. Weber, "Misalignment sensitivity of optical resonators," *Appl. Optics* **19**, 598–601 (February 15, 1980).

Exact calculations of the effects of mirror tilt on resonator losses for planar resonators, with both strip and circular mirrors, are given by J. L. Remo, "Diffraction losses for symmetrically tilted plane reflectors in open resonators," *Appl. Optics* **19**, 774–777 (March 1, 1980).

19.5 GAUSSIAN RESONATOR MODE LOSSES

The gaussian beam results developed in this chapter thus far are based on the assumption that the resonator end mirrors are infinitely wide in the transverse direction, or at least extend out so far compared to the gaussian spot size of the gaussian modes that any aperture diffraction effects are entirely negligible.

Introduction of a finite aperture into a stable gaussian resonator then modifies these results, though generally by a small amount if the aperture diameter is large compared to the gaussian spot size. In this section we will review briefly the mode distortions and diffraction losses that result from introduction of finite apertures or mirror sizes.

Resonator Fresnel Number

A very important parameter for discussing aperture effects in finite-diameter stable (or for that matter unstable) optical resonators is the resonator *Fresnel number* N_f , which is commonly defined as follows. Let $2a$ represent the transverse width of the resonator end mirrors in the x or y directions in a one-dimensional strip mirror situation, or alternatively the diameter of the circular end mirrors in a circularly symmetric situation. The resonator Fresnel number N_f is then defined, just as in the previous chapter, by

$$\text{resonator Fresnel number, } N_f \equiv \frac{a^2}{L\lambda}. \quad (34)$$

This parameter is obviously the number of Fresnel zones across one end mirror, as seen from the center of the opposite mirror. There are also, however, a number of other significant interpretations of this parameter.

We note first that the spot size on the end mirror of a symmetric confocal resonator of length L is given by $w_1^2 = L\lambda/\pi$, and that other stable resonators have spot sizes which differ from this only by some numerical factor which depends on the g values. We can therefore write the simple expression

$$\frac{\text{resonator mirror surface area}}{\text{confocal TEM}_{00} \text{ mode area}} = \frac{\pi a^2}{\pi w_1^2} = \pi N_f. \quad (35)$$

In other words, *the ratio of the resonator mirror area to the area of the lowest-order confocal mode, with the mode area defined for this purpose by πw_1^2 , is given by the resonator Fresnel number multiplied by π .*

We can express much the same point in a slightly different way by recalling from an earlier chapter that the outer radius of an n -th order Hermite-gaussian mode (for $n > 1$) is given to a good approximation by

$$s_n \approx \sqrt{nw_1} \approx \sqrt{nL\lambda/\pi}. \quad (36)$$

We might ask therefore what is the largest-order Hermite-gaussian or Laguerre-gaussian mode (indicated by index N_{\max}) that will still fit within the aperture of width or diameter $2a$? The answer is again

$$N_{\max} = a^2/w_1^2 = \pi N_f. \quad (37)$$

The resonator Fresnel number N_f is thus essentially an indicator of how large the resonator aperture is compared to the confocal mode size in that resonator, or alternatively a measure of the order of transverse modes we can go to before these higher-order modes begin to be significantly perturbed by the aperture edges.

Finite-Diameter Resonator Mode Losses

The exact transverse eigenmodes and eigenvalues of stable gaussian resonators with finite apertures must be calculated by finding the eigensolutions to the resonator integral equation using the appropriate Huygens' kernel with finite limits of integration, as described in earlier chapters. Analytical solutions to these equations with finite mirror diameters are generally not available (with a few limited exceptions), and so the eigensolutions must usually be found numerically. This is most commonly done using some variation of the Fox and Li iterative technique described earlier. The results of some of these calculations will be summarized briefly here, and in the References at the end of this section.

Figure 19.19 shows, for example, the power losses per bounce (that is, per one-way transit) in both confocal and planar resonators having circular finite-diameter mirrors, for the first few azimuthally symmetric and radially varying modes in each situation. (Similar curves could be calculated and plotted for modes of higher azimuthal index m ; they would in general have similar shapes, and show significantly higher losses.)

In the confocal situation, for example, which we already know to be a very small mode diameter or low loss situation, we see that as soon as the resonator Fresnel number becomes greater than about unity, the diffraction losses for the TEM_{00} mode become very small, on the order of 1% per bounce or less. The higher-order TEM_{10} and TEM_{20} modes, which have higher-order radial variations, have larger losses at any given Fresnel number, but all of these losses

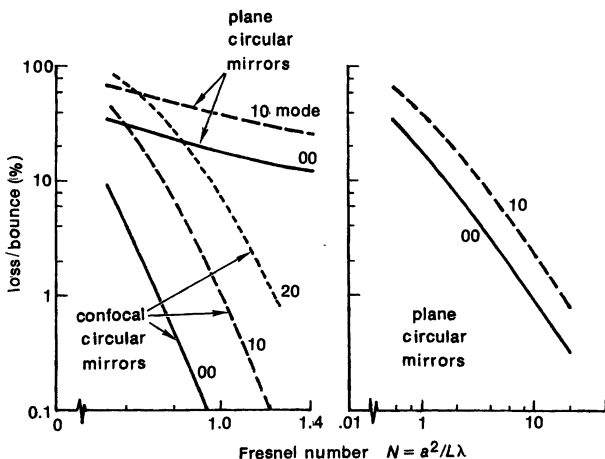


FIGURE 19.19
Exact one-way mode losses due to finite-diameter mirrors in plane-circular and confocal-circular laser cavities.

decrease very rapidly and become very small as the Fresnel number increases much above unity.

For the planar (flat) mirror resonator, by contrast, the losses are significantly larger, although again these losses decrease with increasing Fresnel number. The right-hand plot shows, in fact, that when N becomes greater than about 10, the losses become less than $\approx 1\%$ per bounce and continue decreasing rapidly with increasing Fresnel number.

Finite-Diameter Mode Patterns

The exact mode calculations for the confocal resonator situation will also show that when the Fresnel number becomes greater than about unity, the exact mode pattern over the central portion of the resonator becomes very similar to the gaussian beam pattern predicted by the infinite-mirror gaussian mode theory presented in the preceding sections of this chapter. The exact mode losses in this limit will, however, actually be considerably smaller than the spillover losses that we might calculate by using the gaussian mode patterns and calculating the amount of energy going past the mirror edges on each bounce. In other words, the exact mode patterns will distort near the mirror edges in such a way as to reduce the mode amplitude and the power losses at the mirror edges below even the (small) value predicted by the gaussian beam theory.

The planar resonator mode patterns can not approach such a gaussian limit, since the planar resonator is on the boundary of the stability region, where the gaussian spot size blows up to infinity. The planar resonator mode will, however, have a relatively smooth radial mode pattern, something similar to a $J_n(r)$ Bessel-function pattern with the first (or n -th) null of the Bessel function occurring at the mirror edges. There will also be small Fresnel ripples on top of this pattern and a small but finite value at the mirror edges, with the amplitudes of both the Fresnel ripples and the mirror-edge value becoming increasingly small as the Fresnel number (i.e., the mirror diameter) of the resonator increases.

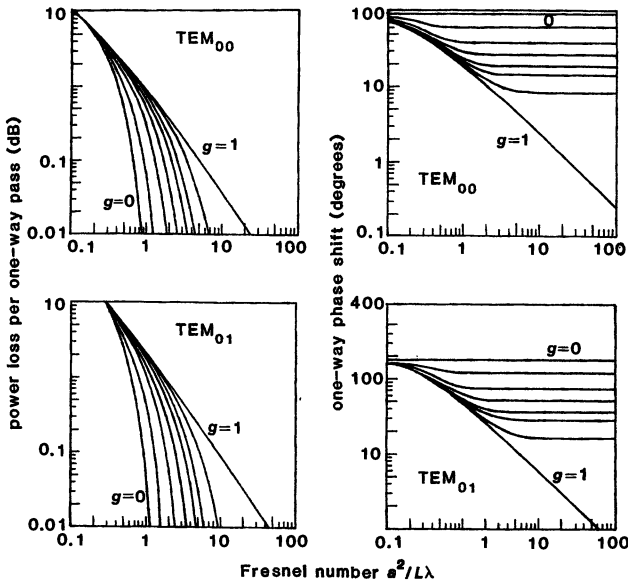


FIGURE 19.20

Power losses per bounce (measured in dB) and additional phase shifts per transit versus Fresnel number for both the TEM_{00} and TEM_{01} modes in two-mirror resonators with g values ranging from $g = 0$ (confocal resonator) to $g = 1$ (planar resonator). The intermediate g values in each plot are $g = 0.5, 0.8, 0.9, 0.95, 0.97$, and 0.99 .

Mode Losses and Phase Shifts

Figure 19.20 shows further results from a large number of additional exact mode calculations for finite-diameter circular-mirror resonators with different g values ranging from $g = 0$ (confocal resonators) to $g = 1$ (planar resonators). Plotted in this situation are both the loss per bounce (expressed in dB) and the phase angle of the one-way resonator eigenvalue, for both the TEM_{00} and TEM_{01} modes, i.e., the lowest-order radial modes for the azimuthal indices $m = 0$ and $m = 1$.

Of particular interest here are the phase shifts of the eigenvalue $\tilde{\gamma}$, where $\tilde{\gamma}$ is the resonator eigenvalue for a one-way pass. These phase shifts are the exact versions of the Guoy phase shifts $\psi(z_2) - \psi(z_1)$ given in the ideal gaussian limit by Equation 19.21. They thus determine the exact transverse mode spacing in the finite-diameter mirrors. We see, for example, that the phase shift for the $g = 0$ confocal TEM_{00} mode is exactly 90° , corresponding to the phase shift through the waist region (from $-z_R$ to z_R) in the confocal situation; whereas the same phase shift for the TEM_{01} situation is 180° , corresponding to $\Delta m = 1$.

More generally, we can see that in both the losses and the phase shifts, as N increases for a given g value, there is a shoulder or break point—admittedly, a rather soft shoulder—above which the mode losses decrease more rapidly, whereas the added phase shift becomes essentially constant at the value predicted by the $\cos \sqrt{g_1 g_2}$ formula for the ideal gaussian situation. This break point

represents the value of N at which the truncation of the gaussian mode fields by the finite-diameter mirrors becomes sufficiently weak that the gaussian approximation for the mode shape is exceedingly good. This diameter increases with increasing g value, and never occurs at all for the plane mirror situation where $g = 1$.

Approximate Formulas for Resonator Losses

A number of approximate or empirical formulas for finite-diameter resonator losses have been developed by various researchers. In general these are formulas for the one-way power loss per pass $\delta \equiv 1 - |\tilde{\gamma}|^2$ where $\tilde{\gamma}$ is the single-pass eigenvalue. Examples of these formulas include:

(1) for confocal square mirrors,

$$\begin{aligned}\delta &\approx 8\pi\sqrt{2N} \exp(-4\pi N) & \text{for } N \geq 0.5, \\ \delta &\approx 1 - 16N^2 \exp[-2(2\pi N/3)^2] & \text{for } N \rightarrow 0;\end{aligned}$$

(2) for confocal circular mirrors,

$$\begin{aligned}\delta &\approx \pi^2 2^4 N \exp(-4\pi N) & \text{for } N \geq 1, \\ \delta &\approx 1 - (\pi N)^2 & \text{for } N \rightarrow 0;\end{aligned}\tag{38}$$

(3) for planar strip mirrors,

$$\delta \approx 0.12N^{-3/2} \quad \text{for } N \geq 1;$$

(4) for planar circular mirrors,

$$\delta \approx 0.33N^{-3/2} \quad \text{for } N \geq 1.$$

More complicated formulas are given in various publications by the Soviet researcher Vainshtein (or Weinstein in some English translations).

Experimental Verification

The numerical results shown in Figure 19.20 may be regarded in a sense as "computer experiments" which serve both to verify the ideal gaussian mode theory and to define its limits. Moreover, numerous measurements that have been made of resonator spot sizes and of transverse mode beat frequencies serve to verify the gaussian mode theory in quite exact detail. (Note that the transverse mode beats in particular represent a subtle but very significant confirmation of the theory.)

Detailed experimental tests of the mode losses predicted by the exact theory have been quite limited, however. Such experiments are difficult because the losses are generally small, and thus easily obscured by other mirror and scattering losses, Brewster window losses, effects of cavity misalignment, and the like.

Figure 19.21 shows the very good comparison between experiment and theory for the TEM_{00} mode losses that was obtained in a near-hemispherical resonator with one flat mirror and curved mirror of radius 60 cm, as the mirror spacing was pulled apart toward the stability boundary at $L = 60$ cm. Note that the exact mirror spacing at which the losses reach some particular loss level as L is increased depends on the diameter or Fresnel number of the resonator, with

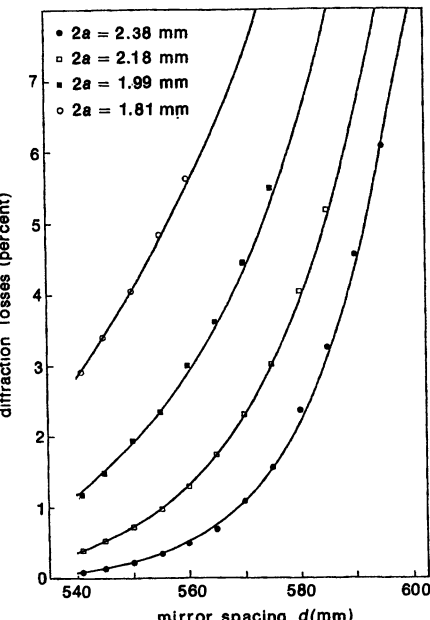


FIGURE 19.21
Experimental tests of mode losses in a near-hemispherical laser cavity.

this value moving out toward the limiting value of $L = 600$ mm as the mirror diameter increases.

We might say, in fact, that the stability diagram of Figure 19.4 has infinitely sharp edges between stable and unstable regions only if the mirror diameter is infinite. For finite-diameter mirrors the boundary line between stable and unstable regions is more like a fuzzy boundary region, where the resonator behavior changes over from ideal gaussian behavior, uninfluenced by the mirror edges, to a region where the mode pattern and mode losses are strongly influenced by the mirror or aperture edges. This boundary region has a width that decreases toward zero as the mirror diameter becomes very large.

Hole-Coupled Resonators

A number of calculations and experiments have also been done on the modes of *hole-coupled resonators*, that is, stable gaussian resonators with coupling holes in the center of the end mirror. Such mirrors can be comparatively simple to fabricate (for example by drilling a central hole in a polished copper or molybdenum mirror), and the use of hole coupling might seem attractive as one way of bypassing the difficulties of finding low-loss transparent mirror substrates and low-loss reflective coatings for high-power IR or UV lasers.

The general conclusion from exact Fox and Li calculations of such resonators, however, is that this is not an effective method for obtaining significant output coupling while simultaneously maintaining good transverse mode performance. As soon as the diameter of a central coupling hole is made large enough to cou-

ple significant power out of the lowest-order gaussian mode in such a resonator, theory and experiment show that the resonator will convert to oscillation in a distorted lowest-order eigenmode—basically, a mixture of higher-order Hermite-gaussian modes—which avoids the central hole and concentrates the modal energy in an annular ring around the hole.

Resonators quite generally, in fact, show a remarkable ability to distort their eigenmodes and, so to speak, “pull in their skirts” to minimize diffraction losses for whatever aperture or distortion may be placed in the resonator. The one form of hole coupling that may be effective is a large number of coupling holes, each individually small compared to the $\sqrt{L\lambda/\pi}$ dimension for the resonator, distributed more or less uniformly over the entire surface of the end mirror.

REFERENCES

Numerical results and asymptotic formulas for losses in real finite stable resonators are reviewed at some length in the review article by Kogelnik and Li referenced in the first section of this chapter. For a typical example of the important early calculations of exact resonator modes from the Bell Laboratories (by other than Fox and Li), see, for example, G. D. Boyd and J. P. Gordon, “Confocal multimode resonator for millimeter through optical-wavelength masers,” *Bell Sys. Tech. J.* **40**, 489–508 (March 1961).

For a review and discussion of losses in strip resonators, see L. Ronchi, “The asymptotic expression for the resonant modes losses of a Fabry-Perot open resonator,” *Appl. Optics* **9**, 733–736 (March 1970).

The experimental results in this section are from J. P. Taché, “Experimental determination of diffraction losses in a near-hemispherical resonator,” *Opt. Quantum Electron.* **16**, 71–76 (1984).

Some of the theoretical calculations on hole-coupled resonators are by D.E. McCumber, “Eigenmodes of a symmetric cylindrical confocal laser resonator and their perturbation by output coupling apertures,” *Bell Sys. Tech. J.* **44**, 333–363 (February 1965); and “Eigenmodes of an asymmetric cylindrical confocal laser resonator with a single output-coupling aperture,” *Bell Sys. Tech. J.* **48**, 1919 (July-August 1969).

Other references on this topic include T. Li and H. Zucker, “Modes of a Fabry-Perot laser resonator with output-coupling apertures,” *J. Opt. Soc. Am.* **57**, 984–986 (August 1967); G.T. McNice and V.E. Derr, “Analysis of the cylindrical confocal laser resonator having a single circular coupling hole,” *IEEE J. Quantum Electron.* **QE-5**, 569–575 (December 1969); and J. M. Moran, “Coupling of power from a circular confocal laser with an output aperture,” *IEEE J. Quantum Electron.* **QE-6**, 93–96 (February 1970).

Further references on this topic include G. Shennagel, “Eigenmodes of a laser resonator with concave mirror and a hole for beam extraction,” *Soviet Physics—Technical Physics* **14**, 1553–1559 (May 1970); Y. Yoshida, H. Ogura, and J-I. Ikenoue, “Fabry-Perot resonator with circular apertures,” *Japan. J. Appl. Phys.* **10**, 754–757 (June 1971); and M. Tsuji, H. Shigesawa, and K. Takiyama, “Eigenvalues of a nonconfocal laser resonator with an output-coupling aperture,” *Appl. Optics* **18**, 1334–1340 (May 1979).

Problems for 19.5

1. “*Spillover losses*” for a gaussian resonator mode. As a rough first estimate for the power losses in stable optical resonators having circular mirrors of finite diameter a , use the standard gaussian field expressions and calculate the fraction of the energy in the assumed gaussian patterns that will be lost by spillover past the edges of the mirrors, as a function of the Fresnel number N and the resonator g parameters.

Note: The losses predicted by this procedure, although small, will still be considerably larger than the real losses. In stable resonators with mirror diameters larger than a spot size or two, the real modes follow the predicted gaussian mode patterns quite accurately over most of the central region of the mirror where the mode amplitude is large, but the exact mode pattern close to the edge of the mirror, where the gaussian is small, deviate from the gaussian patterns and become even smaller, so that the exact mode losses are reduced considerably below the simple gaussian spillover predictions.

2. Criterion for the “shoulder” in finite-diameter resonator loss curves. Using the formulas given in this chapter for resonator spot size, plus the Fresnel number criterion, attempt to develop an approximate criterion for the Fresnel numbers at which the break points in Figure 19.20 occur, as a function of the g values of the resonators.
-



COMPLEX PARAXIAL WAVE OPTICS

A very useful generalized form of paraxial optics has been developed in recent years. This generalized form can handle paraxial wave propagation not only in free space, and in simple lenses and ducts, but also in more general types of paraxial optical systems, including cascaded multielement optical systems (cascaded sequences of paraxial optical elements), and also systems having "soft apertures" or quadratic amplitude as well as phase variations about the axis.

This more general type of paraxial wave theory can be expressed in several mathematically equivalent forms. The approach that seems most convenient describes paraxial wave propagation entirely in terms of complex ray matrices or complex $ABCD$ matrices. This approach is very useful for handling complicated multielement optical resonators, as well as resonators with the very useful variable-reflectivity mirrors that are now being developed.

In the present chapter, therefore, we develop the basic theory for this extended form of paraxial optics using complex $ABCD$ matrices. Topics covered include soft or gaussian apertures; complex $ABCD$ matrices; the expansion of Huygens' integral in complex $ABCD$ matrices; and the complex Hermite-gaussian modes that appear as the eigensolutions for generalized paraxial optical systems. In the following chapter we will apply this approach to develop a generalized analysis of paraxial optical resonators, which will treat in one formalism not only conventional stable and unstable optical resonators, but also two new and useful classes of complex stable and unstable resonators.

The author appreciates many helpful contributions that have been made to the development of these chapters, first by Professor Amos Hardy of the Weizmann Institute of Science and by Dr. Shinan-Chur Sheng, and more recently by Dr. Moshe Nazarathy as a visitor at Stanford University.

20.1 HUYGENS' INTEGRAL AND ABCD MATRICES

The first step in deriving a generalized form of paraxial wave optics is to show how Huygens' integral for propagation through a cascaded series of conventional optical elements can be accomplished in one step, using nothing more than the overall $ABCD$ matrix elements for that system. We will give a tutorial derivation in this section which applies initially only to real $ABCD$ matrices. The general-

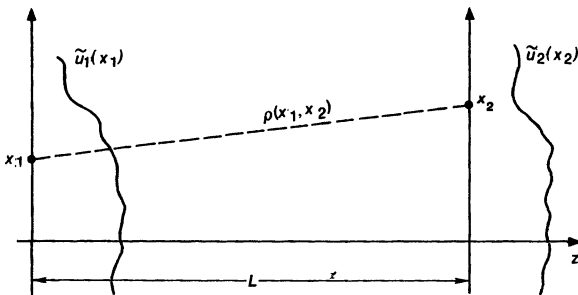


FIGURE 20.1
Huygens' integral in free space.

ized Huygens formula that we will derive will, however, in fact be valid for both real and complex $ABCD$ matrices, as we will show later.

Huygens' Integral in Free Space

Huygens' integral in one transverse dimension for propagation through a distance L in free space can be written in the form

$$\begin{aligned}\tilde{u}_2(x_2) &= e^{-j k L} \int_{-\infty}^{\infty} \tilde{K}(x_2, x_1) \tilde{u}_1(x_1) dx_1 \\ &= \sqrt{\frac{j}{L \lambda}} \int_{-\infty}^{\infty} \tilde{u}_1(x_1) \exp[-jk\rho(x_1, x_2)] dx_1,\end{aligned}\quad (1)$$

where the path length $\rho(x_1, x_2)$ for an optical ray in free space traveling from position x_1 at plane z_1 to position x_2 at plane $z_2 = z_1 + L$ is given in the paraxial approximation by

$$\rho(x_1, x_2) = \sqrt{L^2 + (x_2 - x_1)^2} \approx L + \frac{(x_2 - x_1)^2}{2L}. \quad (2)$$

Huygens' integral always involves this kind of optical path length $\rho(\mathbf{r}_1, \mathbf{r}_2)$, sometimes called the *eikonal function*, from an optical source point at \mathbf{r}_1 to an observation or field measurement point at \mathbf{r}_2 . The Huygens-Fresnel kernel for wave propagation in free space thus takes on the form

$$\tilde{K}(x_2, x_1) = \sqrt{\frac{j}{L \lambda}} \exp\left[-j \frac{\pi(x_2 - x_1)^2}{L \lambda}\right] \quad \begin{pmatrix} \text{free space} \\ \text{propagation} \end{pmatrix} \quad (3)$$

in one transverse dimension, or a product of two such kernels in two transverse dimensions.

Huygens' Integral Through a General Paraxial System

Suppose we consider instead an input wavefunction $\tilde{u}_1(x_1)$ traveling not through free space, but through a cascaded optical system containing an arbitrary collection of real paraxial optical elements (lenses, ducts, etc.) between the

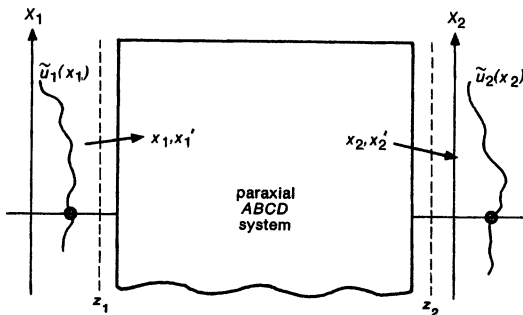


FIGURE 20.2
Huygens' integral through an arbitrary paraxial *ABCD* system.

two planes z_1 and z_2 , as illustrated in Figure 20.2. These cascaded optical elements can be characterized by an overall *ABCD* matrix or ray matrix. We will now show (or at least give a pretty good argument) that the eikonal function and the total Huygens' integral through this complete system can be written in one step, using only the overall *ABCD* matrix elements for the cascaded paraxial system.

To do this, we will again invoke Huygens' principle of viewing the wave function $\tilde{u}_1(x_1)$ at each point on the input plane z_1 as a source of Huygens' wavelets, and evaluating the total amplitude $\tilde{u}_2(x_2)$ at each point on the output plane z_2 by adding up the contributions at x_2 from all the input points x_1 , taking account of the path length or phase delay from each input point x_1 to each output point x_2 . We must therefore be able to calculate the overall path length, or the eikonal function $\rho(x_1, x_2)$, from each point x_1 on plane z_1 in Figure 20.2 to each point x_2 on plane z_2 , going through the complex paraxial system.

To do this, we can try to find the net path length $\rho(x_1, x_2)$ for that particular optical ray which, starting out from transverse displacement x_1 at plane z_1 , will emerge with transverse displacement x_2 at plane z_2 , as in Figure 20.3. This ray will, in general, not travel along a straight line path inside the system between the two end points, but will instead follow some more complicated trajectory within the optical elements making up the *ABCD* system. What will be the optical path length $\rho(x_1, x_2)$, or the eikonal function, for this ray between the input and output points, analogous to the free-space value used in the Huygens' integral in Equation 20.2?

Optical Path Lengths, and Fermat's Principle

We note first that if a ray is to enter at a specified point x_1 and exit at a specified point x_2 , then from the ray relationship $x_2 = Ax_1 + Bx'_1$ the input slope of this particular ray must be given by

$$x'_1 = \frac{x_2 - Ax_1}{B}, \quad (4)$$

and the exit slope must be

$$x'_2 = \frac{Dx_2 - x_1}{B}. \quad (5)$$

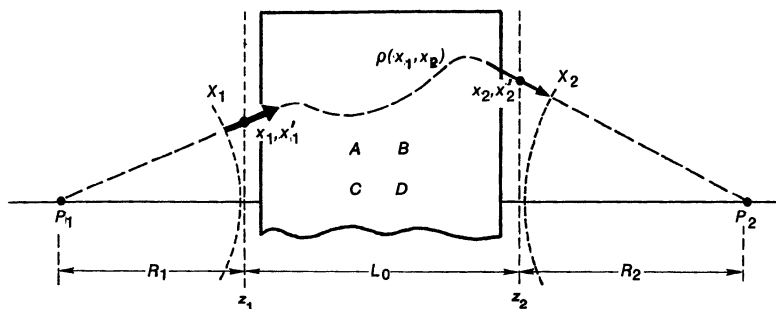


FIGURE 20.3

Fermat's principle says the total path length from object point P_1 to image point P_2 must be the same along the axis or along the ray path indicated by the dashed lines.

The input ray may then be viewed as coming from an on-axis source point P_1 located a distance R_1 behind the input plane, as shown in Figure 20.3. Hence, R_1 is given by

$$\frac{R_1}{n_1} \equiv \frac{x_1}{x'_1} = \frac{Bx_1}{x_2 - Ax_1}. \quad (6)$$

Upon passing through the cascaded paraxial optical system, this input ray is converted into an output ray which can again be associated with a spherical wave having an output radius of curvature R_2 given by

$$\frac{R_2}{n_2} \equiv \frac{x_2}{x'_2} = \frac{Bx_2}{Dx_2 - x_1}. \quad (7)$$

This output ray thus intersects the axis at point P_2 located a distance R_2 behind (or $-R_2$ in front of) the plane z_2 ; and we now have both R_1 and R_2 given in terms only of x_1 and x_2 and the $ABCD$ matrix elements.

Now in optical terms, the points P_1 and P_2 in Figure 20.3 are conjugate points, or object-image points, in the sense that all rays leaving the axis from P_1 will be focused back to the axis at P_2 , or vice versa. But Fermat's principle then says that "all rays connecting two conjugate points must have the same optical path length between these two points." Applied to our system, Fermat's principle requires that

$$\left[\begin{array}{l} \text{ray path from } P_1 \text{ to } P_2 \\ \text{through } X_1 \text{ and } X_2 \end{array} \right] \equiv \left[\begin{array}{l} \text{ray path from } P_1 \text{ to } P_2 \\ \text{along the optical axis} \end{array} \right], \quad (8)$$

where we use X_1 and X_2 to denote the points on planes z_1 and z_2 where the off-axis rays intersect and leave the $ABCD$ system.

Suppose the total optical path length through the paraxial system, from plane z_1 to plane z_2 , for a ray traveling exactly on the axis is denoted by L_0 . In general this length will be given by a summation like

$$L_0 = \sum_i n_i L_i, \quad (9)$$

where each individual element inside the system has physical thickness L_i and index of refraction n_i . If we also assume for complete generality that there are

different indices of refraction n_1 in the region before z_1 and n_2 in the region after z_2 , then the total optical path length along the optical axis from point P_1 to P_2 is given by

$$P_1 P_2 \equiv n_1 R_1 + L_0 - n_2 R_2. \quad (10)$$

(Again, the minus sign is associated with the sign convention for R_2 .)

On the other hand the total distance going along the off-axis ray trajectory through points X_1 and X_2 is given, in the paraxial approximation, by

$$\begin{aligned} P_1 X_1 X_2 P_2 &= P_1 X_1 + X_1 X_2 + X_2 P_2 \\ &= n_1 (R_1^2 + x_1^2)^{1/2} + \rho(x_1, x_2) - n_2 (R_2^2 + x_2^2)^{1/2} \\ &\approx n_1 \left(R_1 + \frac{x_1^2}{2R_1} \right) + \rho(x_1, x_2) - n_2 \left(R_2 + \frac{x_2^2}{2R_2} \right), \end{aligned} \quad (11)$$

where $\rho(x_1, x_2)$ is the path length inside the *ABCD* system. Fermat's principle then requires that the total path length from point P_1 to conjugate point P_2 going along either path be the same, i.e., $P_1 P_2 = P_1 X_1 X_2 P_2$.

Equating 20.10 and 20.11 and using the paraxial approximations, along with 20.6 and 20.7 for R_1 and R_2 , then gives for the desired eikonal function

$$\rho(x_1, x_2) = L_0 - \frac{n_1 x_1^2}{2R_1} + \frac{n_2 x_2^2}{2R_2} = L_0 + \frac{1}{2B} (Ax_1^2 - 2x_1 x_2 + Dx_2^2). \quad (12)$$

The optical path length $\rho(x_1, x_2)$ through the *ABCD* system from point x_1 to point x_2 is thus equal to the on-axis distance L_0 , plus an added optical length which is, within the paraxial approximation, quadratic in the displacements x_1 and x_2 , and otherwise involves only the overall *ABCD* matrix elements for the system. This added length is the generalized eikonal function, or a generalized analog to the added optical distance $(x_2 - x_1)^2/2L$ that appears in the free-space Huygens' kernel between a source point at (x_1, z_1) and an observation point at (x_2, z_2) when $z_2 - z_1 = L$.

Huygens' Integral Through the General *ABCD* System

We can make therefore a (correct) guess that the Huygens' integral for wave propagation all the way through the entire paraxial system, from plane z_1 to plane z_2 , can be written in one step in the same general form as for the free-space situation of Equation 20.1, namely

$$\tilde{u}_2(x_2) = e^{-jkL_0} \iint \tilde{K}(x_2, x_1) \tilde{u}_1(x_1) dx_1, \quad (13)$$

but now with the Huygens kernel in one transverse dimension given by

$$\tilde{K}(x_2, x_1) = \sqrt{\frac{j}{B\lambda_0}} \exp \left[-j \frac{\pi}{B\lambda_0} (Ax_1^2 - 2x_1 x_2 + Dx_2^2) \right] \left(\begin{array}{c} \text{arbitrary} \\ \text{ABCD system} \end{array} \right) \quad (14)$$

with λ_0 being the optical wavelength in free space. The scale factor $\sqrt{j/B\lambda_0}$ in front of the kernel is inserted out of necessity to conserve power, and to make the general Huygens kernel agree with the free space result when the *ABCD* system

consists only of free space. The matrix element B plays the same role in this kernel as the length $L = z_2 - z_1$ in the simple free-space Huygens' integral.

This form for Huygens' integral says that, within the paraxial approximation, an arbitrary optical wave can be propagated through a complete paraxial optical system, including all diffraction effects, using knowledge *only* of the overall $ABCD$ coefficients of the system. (This is assuming no significant apertures or stops within the optical system, between the input and output planes.) A more rigorous derivation to be given later will verify that this is in fact true even for more general paraxial systems having complex-valued $ABCD$ matrices. A still more general version, applying to nonorthogonal systems as well, has been stated without proof in Equation 15.83 of the earlier chapter on ray optics.

If there are apertures within the system, it is necessary to apply Huygens' integral in separate steps from the input up to the first aperture, from that aperture on to the next aperture, and so on. Note also that the on-axis optical length L_0 of the system is not contained in the generalized Huygens' integral, and in fact is not given by the $ABCD$ coefficients. This length represents a separate and independent parameter, outside of the $ABCD$ coefficients. Also, if the paraxial system is astigmatic, we will use different $ABCD$ matrices in the x and y directions.

REFERENCES

The formula for Huygens' integral given at the end of this section can be found in several places in the literature, although it is perhaps not as widely understood as it ought to be. Two important early references are P. Baues, "Huygens' principle in inhomogeneous isotropic media and a general integral equation applicable to optical resonators," *Opto-Electronics* **1**, 37-44 (1969); and S. A. Collins, Jr., "Lens-system diffraction integral written in terms of matrix optics," *J. Opt. Soc. Am.* **60**, 1168 (September 1970).

Several other relevant references by J. A. Arnaud include "Mode coupling in first-order optics," *J. Opt. Soc. Am.* **61**, 751-758 (June 1971); "Hamiltonian theory of beam mode propagation," in *Progress in Optics*, Vol. 11, ed. by E. Wolf (American Elsevier Publishing Co., New York, 1973); and "Nonorthogonal optical waveguides and resonators," *Bell Sys. Tech. J.* **49**, 2311-2348 (November 1970).

For discussions of Fermat's Principle, see any standard optics text, such as, for example, B. Rossi, *Optics* (Addison-Wesley, 1957), p. 100; or R. W. Ditchburn, *Light* (Wiley Interscience, 1963), Sect. 6.58, p. 217.

20.2 GAUSSIAN BEAMS AND ABCD MATRICES

Gaussian beams are the "eigenfunctions of free space", as we have pointed out in Chapter 16, and they may be the eigenfunctions of general complex paraxial wave systems also—especially since the Huygens-Fresnel integrals for free space and for a general paraxial $ABCD$ system are so similar in form.

To explore this point, let us therefore consider next what happens if we transmit a gaussian (or Hermite-gaussian) optical beam through a multielement paraxial optical system that is described only by its real (or possibly complex) $ABCD$ matrix, and see if a Hermite-gaussian beam in produces a Hermite-gaussian beam out.

Gaussian Beam Propagation Formula

For this purpose consider an input beam of the form

$$\tilde{u}_1(x_1) = \exp\left(-j\frac{\pi x_1^2}{\tilde{q}_1 \lambda_1}\right) \quad \text{where} \quad \frac{1}{\tilde{q}_1} \equiv \frac{1}{R_1} - j\frac{\lambda_1}{\pi w_1^2}. \quad (15)$$

(Note that the λ used in writing \tilde{q} is always, by our definition, the wavelength in the medium where the beam is currently located.) If we put such a gaussian beam into the generalized one-dimensional Huygens' integral given in Equation 20.14, we obtain the integral

$$\tilde{u}_2(x_2) = \sqrt{\frac{j}{B\lambda_0}} \int_{-\infty}^{\infty} \exp\left[-j\frac{\pi x_1^2}{\tilde{q}_1 \lambda_1} - j\frac{\pi}{B\lambda_0} (Ax_1^2 - 2x_1 x_2 + Dx_2^2)\right] dx_1, \quad (16)$$

where λ_0 in this formula is the vacuum or free-space wavelength.

This integral contains only linear and quadratic powers of x_1 , and thus is easily evaluated using the lemma ("Siegman's lemma")

$$\int_{-\infty}^{\infty} e^{-ax^2 - 2bx} dx = \sqrt{\frac{\pi}{a}} e^{b^2/a}, \quad (17)$$

where a and b may in general be complex, the only requirement being that a have a slightly positive real part. The result of this integration is that the beam at the output plane will still be a gaussian beam, but now in the form

$$\tilde{u}_2(x_2) = \sqrt{\frac{1}{A + n_1 B / \tilde{q}_1}} \exp\left(-j\frac{\pi}{\tilde{q}_2 \lambda_2} x_2^2\right), \quad (18)$$

where its complex \tilde{q} parameter will have been transformed according to the relationship

$$\frac{\tilde{q}_2}{n_2} = \frac{A(\tilde{q}_1/n_1) + B}{C(\tilde{q}_1/n_1) + D} \quad (19)$$

with $n_2 \lambda_2 = n_1 \lambda_1$. But this is exactly the same as the ray-matrix equation 15.28. In other words, the complex \tilde{q} parameter for a gaussian beam can be transformed through an arbitrary real or complex paraxial system by exactly the same rule as applies to the radius of curvature R for a spherical wave using purely geometric optics.

Discussion

Equation 20.19 is extremely useful. It permits a gaussian beam to be propagated through multiple paraxial elements in sequence, using only the cascaded $ABCD$ matrices for those elements. One can either step the \tilde{q} value through individual elements in sequence, one by one, using the individual $ABCD$ matrices; or alternatively we can cascade-multiply all the $ABCD$ matrices first, and then propagate the gaussian beam through the entire system in one step using the overall $ABCD$ matrix.

We noted earlier that if we defined the *reduced radius of curvature* \hat{R} for a purely spherical wave at any plane by

$$\hat{R}(z) \equiv \frac{R(z)}{n(z)}, \quad (20)$$

where $R(z)$ is the real radius of curvature at that plane, then the fundamental law of geometric optics can be simplified to

$$\hat{R}_2 = \frac{A\hat{R}_1 + B}{C\hat{R}_1 + D} \quad (\text{geometric ray optics only}). \quad (21)$$

Note again that this formula is strictly valid only for purely spherical waves, that is, only in the geometric optics limit. Equation 20.21 does not give correct results for the radius R of a gaussian beam, except in the limit as the spot size w approaches infinity.

Obviously we can also define a reduced \hat{q} parameter, \hat{q} , at any plane z by the corresponding definition

$$\frac{1}{\hat{q}} \equiv \frac{n}{\hat{R}} \equiv \frac{n}{R} - j \frac{n\lambda}{\pi w^2} = \frac{1}{\hat{R}} - j \frac{\lambda_0}{\pi w^2}, \quad (22)$$

where $R(z)$ is the real radius of curvature; $w(z)$ is the real spot size; $\lambda(z) = \lambda_0/n(z)$ is the wavelength in the medium at that plane; and λ_0 is the optical wavelength in vacuum. The paraxial wave transformation rule using the *ABCD* matrix elements and the \hat{q} gaussian beam parameters then becomes

$$\hat{q}_2 = \frac{A\hat{q}_1 + B}{C\hat{q}_1 + D} \quad (\text{full paraxial wave optics}). \quad (23)$$

By using the reduced \hat{q} values we can carry out all calculations using only the *ABCD* matrix elements and the vacuum wavelength, with the local index of refraction $n(z)$ coming into the calculations only when we go from reduced to real variables. Obviously the radius R and the “complex radius” \hat{q} scale by the index n in going from real to reduced variables, whereas the spot size w remains unchanged.

We will make extensive use of this gaussian beam transformation rule in future sections. It remains valid even for complex-valued *ABCD* matrices, to be introduced shortly.

Gaussian Beam Amplitude Transformation

Note also that the complex amplitude coefficient in front of the gaussian beam is transformed in propagating through the *ABCD* system in the form (for one transverse dimension)

$$\frac{\tilde{u}_2(x_2 = 0)}{\tilde{u}_1(x_1 = 0)} = \sqrt{\frac{1}{A + B/\hat{q}_1}}. \quad (24)$$

With some algebraic manipulation this can be converted for purely real-valued *ABCD* elements into the form (again, for one transverse dimension)

$$\frac{\tilde{u}_2(x_2 = 0)}{\tilde{u}_1(x_1 = 0)} = \sqrt{\frac{w_1}{w_2}} \exp(-j\psi/2), \quad (25)$$

where ψ is now the phase angle defined by the complex quantity

$$\frac{A + B/\hat{q}_1}{|A + B/\hat{q}_1|} \equiv \exp(j\psi). \quad (26)$$

This phase shift is a generalization of the Guoy phase shift introduced earlier. The ratio $\sqrt{w_1/w_2}$ is just the amplitude scaling for a one-dimensional or cylindrical wave.

For a beam that has gaussian variations in both transverse dimensions, the ratio $\tilde{u}_2(0)/\tilde{u}_1(0)$ given in Equation 20.25 must be squared, taking account also of any astigmatism in the beam parameters (i.e., \tilde{q}_{1x} , \tilde{q}_{1y}) or in the optical system (A_x , A_y , etc.). The phase shift $\psi/2$, or $(\psi_x + \psi_y)/2$ for the two-transverse-dimension situation, must then be added to the e^{-jkL_0} term which is normally left out of these calculations.

REFERENCES

For an early discussion of the use of the generalized Huygens' integral with gaussian beams, see P. Baues, "The connection of geometric optics with the propagation of gaussian beams and the theory of optical resonators," *Opto-Electronics* **1**, 103–118 (1969).

Relationships between gaussian beams, rays and ABCD matrices are also developed in R. Herloski, S. Marshall and R. Antos, "Gaussian beam ray-equivalent modeling and optical design," *Appl. Opt.* **5**, 1168–1174 (April 15, 1983).

Problems for 20.2

1. *Bilinear transforms for gaussian beams in ABCD matrix systems.* The input to an arbitrary real paraxial optical system is a collimated gaussian beam, with a planar wavefront ($R_1 = \infty$) at the input plane, but with a variable input spot size w_1 . Show that the gaussian beam parameter \tilde{q}_2 at the output plane moves around a complete semicircle in the complex $1/\tilde{q}$ plane as the input spot size varies from $w_1 \rightarrow 0$ to $w_0 \rightarrow \infty$. (The mathematical jargon relevant to this is "bilinear transform.")
2. *Mirror design specification for a small He-Ne laser—ABCD analysis.* You are asked to specify the output mirror design for a small commercial He-Ne laser which is to have one flat high reflectivity mirror and one curved output mirror spaced by exactly $L = 30.0$ cm. The output mirror is actually a cylindrical plug of thickness $t = 0.5$ cm made of quartz (index $n = 1.457$), with the mirror coating on its inner surface. The outer surface of the mirror will be AR (anti-reflection) coated and ground to serve as a collimating lens. The output beam is to have a gaussian spot size $w = 1.0$ mm at the inside mirror surface, and is to be collimated outside the laser. Find the necessary radii of curvature R_1 and R_2 for the inside and outside surfaces of the collimating mirror.
3. *Tolerances on the mirror design specification.* Suppose in the previous problem that the tolerance on the output spot size is actually $w = 1 \pm 0.05$ mm, and the tolerance on the output beam collimation is stated as "the far-field beam angle shall not differ from the collimated-beam value by more than $\pm 10\%$." Establish the manufacturing tolerances that are allowable for the mirror spacing L and

for the two radii of curvature. Note: For simplicity, in solving this problem you may treat the output mirror as a thin lens, i.e., disregard the finite thickness t (although in fact it should probably *not* be disregarded).

4. *Focusing into a dielectric sample—ABCD analysis.* A focusing lens of focal length f is located a distance $L_1 < f$ outside a dielectric sample having a flat front surface, so that this lens focuses a collimated gaussian beam with initial waist size w_1 (before the lens) to a waist with spot size w_0 located inside the dielectric sample. Using an *ABCD* analysis, calculate the spot size w_0 at this waist, and where this waist is located inside the dielectric medium. Compare with the waist spot size and distance that would be produced by the same lens focusing the same input beam without the dielectric present.
-

20.3 GAUSSIAN APERTURES AND COMPLEX ABCD MATRICES

In this section we introduce the very important new concepts of gaussian or “soft” apertures and gaussian ducts, and their description as generalized or complex paraxial elements, described by *complex-valued ABCD* matrices.

Gaussian Apertures

We might first recall that a thin convergent lens of focal length f , gives an optical wave an added quadratic phase shift of the form

$$\tilde{t}(x) \equiv \frac{\tilde{u}_2(x)}{\tilde{u}_1(x)} = \exp\left(+j\frac{\pi x^2}{f\lambda}\right) \quad (27)$$

and is represented by an *ABCD* matrix of the form

$$\begin{bmatrix} A & B \\ C & D \end{bmatrix} = \begin{bmatrix} 1 & 0 \\ -1/f & 1 \end{bmatrix} \quad \begin{array}{l} \text{(ABCD matrix)} \\ \text{for thin lens} \end{array} \quad (28)$$

Let us consider instead a thin optical element consisting of a “soft aperture” (Figure 20.4) which has a quadratic transversely varying wave-amplitude transmission of the form

$$\tilde{t}(x) \equiv \frac{\tilde{u}_2(x)}{\tilde{u}_1(x)} = \exp\left(-\frac{a_2 x^2}{2}\right). \quad (29)$$

This might be the transmission function through a thin apodized filter element, as in Figure 20.4, or the amplitude reflection function from a planar mirror with a radially varying reflectivity, often referred to as a variable-reflectivity mirror or VRM.

We will commonly refer to an optical element with this sort of radially varying transmission or reflection function as a “gaussian aperture” or a “gaussian variable-reflectivity mirror.” Note that the intensity transmission through this element will be $T(x) = |\tilde{t}(x)|^2$, and that a two-transverse-dimensional version will have $\tilde{t}(x, y) = \tilde{t}_x(x)\tilde{t}_y(y)$ along its transverse principal axes.

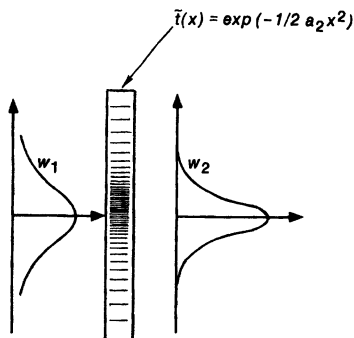


FIGURE 20.4
A gaussian aperture with transversely varying amplitude transmission.

The transmission of a centered gaussian beam through this element is then given (in one transverse dimension) by

$$\tilde{u}_2(x) \equiv \exp\left(-j \frac{\pi x^2}{\hat{q}_2 \lambda_0}\right) = \tilde{t}(x) \times \tilde{u}_1(x) = \exp\left(-\frac{a_2 x^2}{2} - j \frac{\pi x^2}{\hat{q}_1 \lambda_0}\right). \quad (30)$$

Assuming that a_2 is a positive quantity, the gaussian spot size is reduced, and the complex gaussian beam parameter \hat{q} is transformed in passing through a gaussian aperture according to

$$\frac{1}{\hat{q}_2} = \frac{1}{\hat{q}_1} - j \frac{\lambda_0 a_2}{2\pi}. \quad (31)$$

We can put this into a more systematic form by rewriting it as

$$\hat{q}_2 = \frac{\hat{q}_1 + 0}{(-j \lambda_0 a_2 / 2\pi) \hat{q}_1 + 1} = \frac{A \hat{q}_1 + B}{C \hat{q}_1 + D}. \quad (32)$$

A gaussian aperture thus seems to act, at least so far as the \hat{q} parameter of a gaussian beam is concerned, like a complex paraxial element, with a *complex-valued ABCD* matrix given by

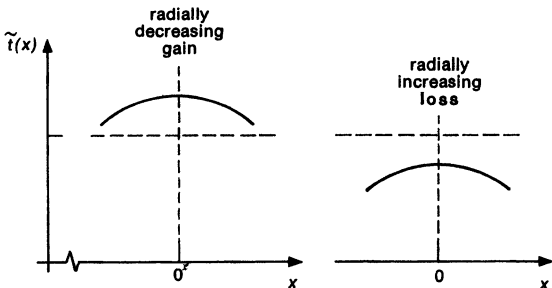
$$\begin{bmatrix} A & B \\ C & D \end{bmatrix} = \begin{bmatrix} 1 & 0 \\ -j \lambda_0 a_2 / 2\pi & 1 \end{bmatrix} \quad \begin{pmatrix} \text{ABCD matrix for} \\ \text{"gaussian aperture"} \end{pmatrix}. \quad (33)$$

The gaussian aperture (with quadratic variation in the real part of the exponent) is thus very much like a thin lens or curved mirror (with quadratic variation in the imaginary part of the exponent), except that its focal length appears to be a purely imaginary quantity.

Gaussian Aperture Plus Thin Lens

As a slightly more general case, we might suppose that the element under consideration combines a thin lens having focal length f with a quadratic transmission variation $a_2 x^2 / 2$ as in Equation 20.27. (This could equally well be a curved variable-reflectivity mirror, with a radius of curvature $R = 2f$ and the

FIGURE 20.5
Either radially increasing loss
or radially decreasing gain
can lead to effectively the same
gaussian aperture.



same amplitude variation.) The complex $ABCD$ matrix then becomes

$$\begin{bmatrix} A & B \\ C & D \end{bmatrix} = \begin{bmatrix} 1 & 0 \\ -1/f - j\lambda_0 a_2/2\pi & 1 \end{bmatrix} \quad \begin{pmatrix} \text{thin lens plus} \\ \text{gaussian aperture} \end{pmatrix}. \quad (34)$$

The complex-valued matrix element shows up only in the lower left corner of this particular matrix. One can easily see, however, that if this $ABCD$ matrix is cascaded with other purely real matrices, the complex values can easily spread to all four elements of the overall $ABCD$ matrix.

Complex $ABCD$ Matrices

So far we have only shown that a complex $ABCD$ matrix like that in Equation 20.34 provides one way to interpret the propagation law for \hat{q} through a gaussian aperture. In the following sections we will prove more generally, however, one of the fundamental principles of generalized or complex paraxial optics — namely, that any paraxial optical system which includes a gaussian (that is, a quadratic-exponent) variation in amplitude transmission across the axis may be considered as a complex paraxial system, and described by a complex-valued $ABCD$ matrix or ray matrix.

It may not be clear what it means physically to have a ray passing through a complex-valued ray matrix—at least, not in a purely geometric ray-optic analysis. We will see shortly, however, that essentially every formula developed for real paraxial systems and $ABCD$ matrices will hold equally well for complex paraxial systems described by complex $ABCD$ matrices.

A transverse variation in transmission (or reflection) amplitude, as described in Equation 20.29, is the basic condition for a complex paraxial system. Such a transverse variation may arise physically from a transverse variation in loss or absorption, or it may equally well represent a transverse variation in laser gain, as illustrated in Figure 20.5. The gaussian aperture described in Equation 20.29, for example, may equally well have the more general form

$$\tilde{t}(x) = \exp \left[-a_0 - \frac{a_2 x^2}{2} \right] = \tilde{t}_0 \exp \left[-\frac{a_2 x^2}{2} \right]. \quad (35)$$

The on-axis transmission may then either be $\tilde{t}_0 < 1$ and hence $a_0 > 0$, representing an on-axis loss which increases radially; or it may be $\tilde{t}_0 > 1$ and $a_0 < 0$, i.e., an on-axis gain which decreases radially. The complex $ABCD$ matrix remains

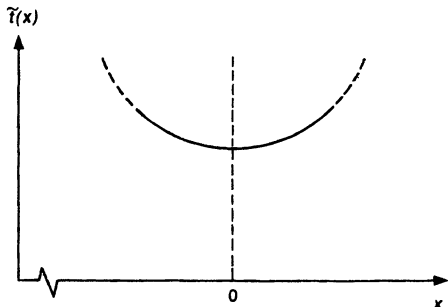


FIGURE 20.6
A “negative gaussian aperture” with radially increasing amplitude transmission.

the same, since it involves only the quadratic part of the transverse variation in either situation.

Other Forms of Aperture Transmission

The complex paraxial analysis developed in this chapter will be mathematically exact (within the limits of the overall paraxial approximation) for systems having only linear or quadratic transverse variations in the exponent, as given in Equation 20.35. (Linear variations in phase or amplitude across the beam represent tilt, misalignment, or a displacement of the center of the beam.) This analysis can also be extended, however, at least as a first approximation, to any transversely varying system whose transmission has a quadratic variation to first order near the optical axis.

That is, consider any “soft” aperture whose transmission varies with transverse coordinate, at least near the axis, in the approximate form

$$\tilde{t}(x) \approx t_0 \times (1 - a_2 x^2/2), \quad (36)$$

where the coefficient a_2 is now defined by the transverse second derivative, i.e.,

$$a_2 \equiv -\frac{1}{t_0} \left| \frac{d^2 \tilde{t}(x)}{dx^2} \right|_{x=0} \quad (37)$$

evaluated at the axis. This aperture may be approximated to first order by a gaussian aperture, and by a complex *ABCD* matrix with the same value of a_2 . The complex paraxial analysis will then remain a good approximation so long as the resulting mode solutions remain confined sufficiently close to the axis so that $|\frac{1}{2}a_2 x^2| \ll 1$ across the main portion of the wave.

The transverse coefficient a_2 may even be a negative number, representing a radially increasing transmission, i.e.

$$\tilde{t}(x) = \exp \left[+\frac{|a_2|x^2}{2} \right], \quad (38)$$

as in Figure 20.6, and the basic analysis will still apply equally well, with appropriate changes of sign. Questions arise, of course, as to how one realizes a radially increasing transmission function in practice, at least over any very large radius; and we will also see shortly that serious mode instability problems arise

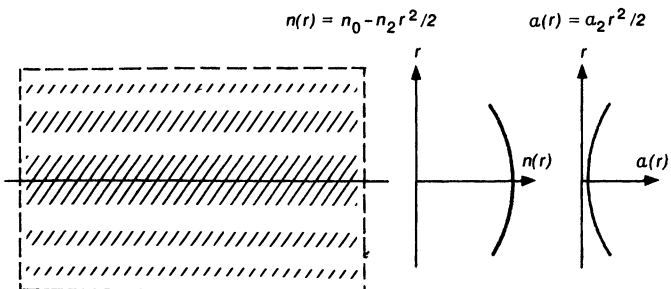


FIGURE 20.7

A complex gaussian duct, with transversely varying refractive index and/or absorption coefficient.

in systems with radially increasing transmission functions. The basic analysis, however, still remains valid regardless of the sign of a_2 .

Gaussian Ducts

As a generalization of the gaussian aperture, or gaussian aperture plus lens, we next introduce the concept of a *complex gaussian duct*. We mean by this an arbitrary length of a dielectric medium which may have in general gaussian transverse variations of either the index of refraction $n(x)$ and/or the loss (or gain) coefficient $\alpha(x)$ about the optical axis. Such a gaussian duct will also lead to a complex $ABCD$ matrix which is a direct extension of the ray matrix for purely real gaussian ducts.

A gaussian duct is thus a transversely inhomogeneous medium in which the refractive index and the absorption coefficient may both vary transversely, in the forms

$$n(x) = n_0 - \frac{1}{2}n_2x^2 \quad \text{and} \quad \alpha(x) = \alpha_0 + \frac{1}{2}\alpha_2x^2. \quad (39)$$

Note that the coefficients α , α_0 and α_2 in this situation are loss coefficients or loss factors per unit length, rather than total loss factors a_0 and a_2 through a discrete aperture as in the previous section. Such a medium is obviously a complex extension of the graded-index ducts that we have considered earlier. The complex propagation constant k in such a duct varies near the axis in the form

$$k^2(x) = k_0^2 - k_0k_2x^2 \quad \text{or} \quad k(x) \approx k_0 - \frac{1}{2}k_2x^2, \quad (40)$$

where the coefficient k_2 corresponds to the transverse second derivative

$$k_2 \equiv -\left. \frac{d^2k(x)}{dx^2} \right|_{x=0} = \frac{2\pi}{\lambda} \left(\frac{n_2}{n_0} + j \frac{\lambda\alpha_2}{2\pi} \right) \quad (41)$$

measured on the axis of the duct. The presence of a small uniform background loss or gain α_0 will also give the on-axis propagation constant a (normally very small) imaginary part, so that k_0 is expanded to $k_0 - j\alpha_0$. Note again that k_0 in this section means the k value on axis, at $x = 0$, and *not* necessarily the free-space or vacuum value.

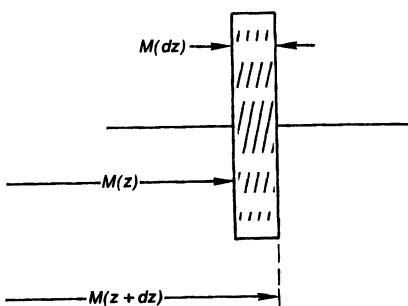


FIGURE 20.8
A short segment of a complex gaussian duct.

Differential Analysis

Consider a small axial segment dz of such a duct, as in Figure 20.8. The results of the preceding section say that this small segment can be considered as a gaussian aperture plus a thin lens, with a complex *ABCD* matrix given by

$$\mathbf{M}(dz) = \begin{bmatrix} 1 & dz/n_0 \\ 0 & 1 \end{bmatrix} \times \begin{bmatrix} 1 & 0 \\ -n_0\tilde{\gamma}^2 dz & 1 \end{bmatrix} = \begin{bmatrix} 1 & dz/n_0 \\ -n_0\tilde{\gamma}^2 dz & 1 \end{bmatrix}. \quad (42)$$

That is, the segment is essentially the combination of a small increment of free space having length $B = dz/n_0$, plus a thin lens-gaussian aperture combination with a complex focal power given by

$$-n_0\tilde{\gamma}^2 dz = -\left(n_2 + j\frac{\lambda_0\alpha_2}{2\pi}\right) dz \quad (43)$$

for the incremental length dz .

Now let $\mathbf{M}(z)$ be the *ABCD* matrix for a complex (but axially uniform) duct from some arbitrary initial plane z_0 up to the plane z , and let $\mathbf{M}(z + dz)$ be the same matrix from z_0 to $z + dz$. From the rules for cascading matrices we can then write

$$\mathbf{M}(z + dz) = \mathbf{M}(dz) \times \mathbf{M}(z), \quad (44)$$

where $\mathbf{M}(z)$ has matrix elements $A(z)$, $B(z)$, etc., and $\mathbf{M}(z + dz)$ has matrix elements $A(z + dz)$, $B(z + dz)$, and so on. If we multiply out this matrix product and take the limit as $dz \rightarrow 0$, we will obtain the same four differential equations as we obtained in Section 15.1, except now with a complex argument $\tilde{\gamma}$. Hence the complex overall *ABCD* matrix is given by the same result we derived in Equations 15.15 and 15.18, namely,

$$\begin{bmatrix} A & B \\ C & D \end{bmatrix} = \begin{bmatrix} \cos \tilde{\gamma}(z - z_0) & (n_0\tilde{\gamma})^{-1} \sin \tilde{\gamma}(z - z_0) \\ -n_0\tilde{\gamma} \sin \tilde{\gamma}(z - z_0) & \cos \tilde{\gamma}(z - z_0) \end{bmatrix}, \quad (45)$$

except that the $\tilde{\gamma}$ parameters are now all complex. This is the general complex *ABCD* matrix for a general gaussian duct.

Discussion

The matrix solution in Equation 20.45 is obviously the complex generalization of the purely real ray matrix results derived earlier for a quadratic-index duct. Since $\tilde{\gamma}$ will in general now be complex (except for the limiting situation of $\alpha_2 \equiv 0$ and $n_2 > 0$), the cosines and sines will now have complex arguments, and must be interpreted as combinations of trigonometric and hyperbolic functions according to the usual rules.

As one limiting situation, suppose the length $\Delta z \equiv (z - z_0)$ of such a duct goes to zero, but the strength $\tilde{\gamma}$ of the transverse variation increases in such a way that $\tilde{\gamma}^2 \Delta z$ remains finite. The $ABCD$ matrix then simplifies to

$$\begin{bmatrix} A & B \\ C & D \end{bmatrix} \approx \begin{bmatrix} 1 & 0 \\ -n_0 \tilde{\gamma}^2 \Delta z & 1 \end{bmatrix} = \begin{bmatrix} 1 & 0 \\ -(n_2 + j\lambda_0 \alpha_2 / 2\pi) \Delta z & 1 \end{bmatrix}. \quad (46)$$

This becomes just the combination of a thin converging lens (for $n_2 > 0$) and a thin gaussian aperture with quadratic coefficient α_2 , as discussed earlier.

We have chosen the definitions for n_2 and α_2 in this section such that $n_2 > 0$ represents an index maximum on axis, whereas $\alpha_2 > 0$ represents a transmission maximum (i.e., a loss minimum, or a gain maximum) on axis. These are the conditions which usually lead to confined and stable resonator or waveguide modes, and hence they are usually the conditions of most interest. Either n_2 or α_2 could change sign, and all of Equations 20.27 to 20.45 would remain valid, provided that we keep proper track of signs and complex phase angles in the various complex-valued formulas.

In an orthogonal but astigmatic system a separate matrix like this can obviously be written for each of the transverse principal axes, with the appropriate and possibly different values of $\tilde{\gamma}$ for the x or y transverse axes.

20.4 COMPLEX PARAXIAL OPTICS

We have argued, though not rigorously proved, in the previous two sections that any general paraxial optical element can be described by a complex-valued $ABCD$ matrix. The most general cascaded, orthogonal, paraxial optical system can then be described by its overall $ABCD$ matrix, which will be the matrix product of the complex matrices of the individual elements. Imaginary parts of the $ABCD$ matrix elements will appear in such systems in general whenever there are components that have a quadratic transverse variation of gain or loss, such as quadratic apertures or ducts.

The primary objectives in this section are to extend this complex ray matrix picture to Huygens' integral, and then to prove in a general way that this picture is indeed a valid representation for any complex-valued quadratic or paraxial system.

Complex Huygens' Integral

We developed in the first section of this chapter a generalized form of Huygens' integral for arbitrary real $ABCD$ systems, namely, (in one transverse

dimension)

$$\tilde{u}_2(x_2) = \sqrt{\frac{j}{B\lambda_0}} \int_{-\infty}^{\infty} \tilde{u}_1(x_1) \exp \left[-j \frac{\pi}{B\lambda_0} (Ax_1^2 - 2x_1 x_2 + Dx_2^2) \right] dx_1 \quad (47)$$

in which $\tilde{u}_1(x_1)$ is the complex input wave at plane z_1 ; $\tilde{u}_2(x_2)$ is the output wave at plane z_2 ; and the $ABCD$ elements are the overall complex ray matrix elements from z_1 to z_2 .

This equation does not include the on-axis phase shift factor $e^{-jk(z_2-z_1)}$. This total phase shift factor will be given in general by a sum of individual terms like

$$k(z_2 - z_1) = \sum_i k_i(z_i - z_{i-1}), \quad (48)$$

where $k_i(z_i - z_{i-1})$ is the on-axis optical path length through the i -th element. This axial phase shift factor is not uniquely determined by the $ABCD$ matrix elements, and must be separately evaluated if its exact value is required.

For simplicity we are writing Huygens' integral and all of the corresponding equations throughout this section in one transverse coordinate only, assuming an orthogonal optical system. It is also assumed throughout that there are no hard apertures that will cause significant diffraction effects anywhere inside the optical system beyond the input plane, other than the soft gaussian apertures represented by the complex parts of the $ABCD$ matrices.

General Proof For Complex Paraxial Systems

We now want to prove in general that the complex form 20.47 for Huygens' integral, and all of the other results given so far in this chapter, will apply to *any arbitrary complex paraxial system*.

In order to do this, we first note that any complex paraxial optical system can be made up of only two basic elements, namely, complex gaussian propagation segments, or "ducts," such as we have previously described; and curved dielectric interfaces, having a spherical radius of curvature R , between such gaussian propagation segments. All other paraxial elements can be formed from combinations and/or limiting situations of these two basic elements. (Note that if we were to use the reduced ray matrix notation discussed in an earlier chapter, even the planar dielectric interfaces would drop out, and we could formulate everything from ducts alone.) The general validity of complex paraxial optics can then be established by

- Showing that the generalized Huygens' integral in the form given in Equation 20.47 is valid for both of these two basic elements individually; and
- Showing that Huygens' integral in this form can be cascaded through multiple elements in sequence simply by using $ABCD$ matrix multiplication.

If Huygens' integral is valid for complex elements, then all the other results that we have established using the general Huygens' integral must also be valid in general for complex $ABCD$ elements.

Huygens' Integral for Complex Ducts

Let us now proceed with these steps. First of all, the general definition of a quadratic propagation medium or duct is any region in which the complex propagation constant k has the quadratic transverse variation

$$k^2(x) = k_0^2 - k_0 k_2 x^2. \quad (49)$$

Although the constants k_0 and k_2 are in general complex when gain or loss are present, the imaginary part of k_0 is usually neglected in the $ABCD$ formulation; and the restriction that $|k_2 x^2| \ll |k_0|$ over the volume of interest is generally assumed.

If we combine this with the usual paraxial approximation that $|\partial^2 u / \partial z^2| \ll |k \partial u / \partial z|$, the paraxial wave equation for propagation in this quadratic duct then becomes

$$\left[\frac{\partial^2}{\partial x^2} - 2jk_0 \frac{\partial}{\partial z} - k_0 k_2 x^2 \right] \tilde{u}(x, z) = 0. \quad (50)$$

Any valid solution for wave propagation in a gaussian duct must satisfy this wave equation.

Suppose we now take Huygens' integral in the form given in Equation 20.47, together with the complex $ABCD$ matrix in the form

$$\begin{bmatrix} A(z) & B(z) \\ C(z) & D(z) \end{bmatrix} = \begin{bmatrix} \cos \tilde{\gamma}(z - z_0) & (n_0 \tilde{\gamma})^{-1} \sin \tilde{\gamma}(z - z_0) \\ -n_0 \tilde{\gamma} \sin \tilde{\gamma}(z - z_0) & \cos \tilde{\gamma}(z - z_0) \end{bmatrix}, \quad (51)$$

where

$$\tilde{\gamma}^2 = \frac{k_2}{k_0} = \frac{n_2}{n_0} + j \frac{\lambda \alpha_2}{2\pi}, \quad (52)$$

and substitute all of this into the extended paraxial wave equation 20.50 for the duct. We can then show—after a considerable amount of algebraic labor—that this combination indeed satisfies Equation 20.50 exactly in any gaussian duct. The kernel of the complex Huygens' integral also reduces to the usual Huygens-Fresnel kernel—that is, to simple spherical wavelets emanating from each source point x_1 —in the limit as $|\tilde{\gamma}| \ll 1$, so that the whole solution is also valid in the free-space limit.

Huygen's integral as given at the beginning of this section, plus the general $ABCD$ matrix as given in Equation 20.51, thus provide general solutions within any gaussian duct. It remains only to prove that these results can be extended to dielectric interfaces, and that they cascade properly.

Huygens' Integral for Dielectric Interfaces

A spherically curved boundary or interface between any two optical elements, and in particular between any two sections of complex gaussian duct, is the other basic paraxial optical element. Such an interface will have a basically real $ABCD$ matrix that is given in general by

$$\begin{bmatrix} A & B \\ C & D \end{bmatrix} = \begin{bmatrix} 1 & 0 \\ (n_2 - n_1)/R & 1 \end{bmatrix}, \quad (53)$$

where n_1 and n_2 are the on-axis propagation constants on the input and output sides of the interface, and R is the radius of curvature of the interface. The sign

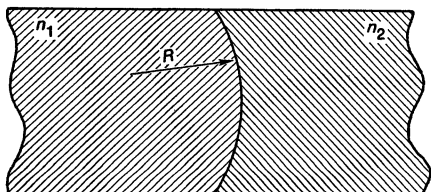


FIGURE 20.9
A curved interface between two dielectric media.

convention for this curvature says that R is positive for a surface concave toward the input medium or medium #1.

The $ABCD$ matrix for an interface is basically purely real, because n_1 and n_2 are essentially real quantities. Any small imaginary part to these on-axis propagation constants, due to an average gain or loss coefficient α_0 , can normally be neglected.

We must now verify that the combination of Huygens' integral plus this interface $ABCD$ matrix reproduces what actually happens at a dielectric interface. If we insert the matrix elements given in Equation 20.51 directly into Huygens' integral, this will lead to a singular integral, because $B \equiv 0$ for a discontinuous interface. We can avoid this difficulty, however, by cascading a short length Δz of the appropriate dielectric medium on each side of the interface, so that the integral then becomes finite.

When we then evaluate Huygens' integral across an interface in the limit as the length Δz of each attached segment goes to zero, we find that the kernel of Huygens' integral acquires a Dirac delta function character; and the effect on the incident wavefront $\tilde{u}_1(x)$ predicted by Huygens' integral becomes in the limit simply

$$\tilde{u}_2(x) = \tilde{u}_1(x) \exp \left[-j \frac{\pi(n_2 - n_1)x^2}{R\lambda} \right]. \quad (54)$$

But this is exactly the expected physical result for a curved interface.

In carrying out beam calculations with cascaded optical elements, it is thus important to remember that even though the optical fields themselves will be continuous across an interface between two different media, the interface still has an $ABCD$ matrix as given in Equation 20.53, which must be included in the calculations. The \tilde{q} value of a gaussian beam changes discontinuously in going through such an interface, for example, because the wavelength in the medium changes, even though the spot size of the beam is continuous. The radius of curvature changes because of Snell's law.

Cascading Huygens' Integral

To complete our proof, we must verify that we can cascade Huygens' integral in the $ABCD$ matrix form off Equation 20.47 using matrix multiplication of the complex $ABCD$ elements. Propagating through any sequence of complex ducts and interfaces can then be done by first multiplying out their cascaded $ABCD$ matrices, and then applying Huygens' integral using the product matrix for the system.

Suppose we want to transform an arbitrary input wavefunction $\tilde{u}_0(x_0)$ from an input plane z_0 to an intermediate wavefunction $\tilde{u}_1(x_1)$ through one paraxial

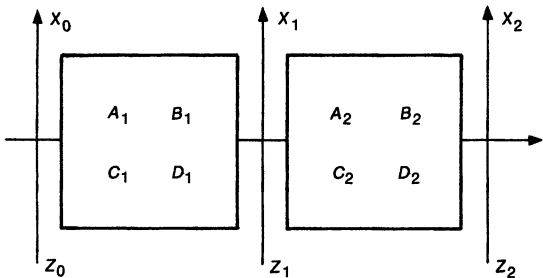


FIGURE 20.10
Cascaded complex $ABCD$ matrix systems.

element, using Huygens' integral with some set of complex matrix elements $\mathbf{M}_1 = (A_1, B_1, C_1, D_1)$; and then (without any intervening aperture) transform from the intermediate wavefunction $\tilde{u}_1(x_1)$ to an output wavefunction $\tilde{u}_2(x_2)$ as in Figure 20.10, again using Huygens' integral through a second set of matrix elements $\mathbf{M}_2 = (A_2, B_2, C_2, D_2)$.

Suppose we do this in straightforward fashion, by writing the cascaded Huygens' integrals

$$\begin{aligned}\tilde{u}_2(x_2) &= \int_{-\infty}^{\infty} \tilde{K}_2(x_2, x_1) \tilde{u}_1(x_1) dx_1 \\ &= \int_{-\infty}^{\infty} \tilde{K}_2(x_2, x_1) \left\{ \int_{-\infty}^{\infty} \tilde{K}_1(x_1, x_0) \tilde{u}_0(x_0) dx_0 \right\} dx_1 \\ &= \int_{-\infty}^{\infty} \left\{ \int_{-\infty}^{\infty} \tilde{K}_2(x_2, x_1) \tilde{K}_1(x_1, x_0) dx_1 \right\} \tilde{u}_0(x_0) dx_0,\end{aligned}\quad (55)$$

where the transition from the second to the third lines requires interchanging the order of integration between dx_0 and dx_1 . Doing this calculation then involves quadratic terms and products in x_0 , x_1 and x_2 that arise from the exponents of the Huygens' kernels. It therefore requires some algebraic exercise in completing squares and using "Siegman's lemma."

But we will find that the final result is exactly the same as we would have gotten by first multiplying together the two matrices to get a product matrix $\mathbf{M}_{20} \equiv \mathbf{M}_2 \times \mathbf{M}_1$ using standard matrix multiplication; writing a Huygens' kernel $\tilde{K}_{20}(x_2, x_0)$ in the usual fashion using these matrix elements; and then evaluating Huygens' integral in one step in the form

$$\tilde{u}_2(x_2) = \int_{-\infty}^{\infty} \tilde{K}_{20}(x_2, x_0) \tilde{u}_0(x_0) dx_0. \quad (56)$$

(Note as usual that the matrices must be multiplied together in reverse order.) Huygens' integral in the generalized $ABCD$ matrix form can thus always be cascaded through multiple sections simply by multiplying together the individual complex $ABCD$ matrices in the appropriate (i.e., reversed) order.

There is one weak mathematical constraint on this proof. Convergence of the intermediate integration over x_2 in Equation 20.55 does require a weak condition on the matrix elements involved, to ensure that the fields do not blow up radially at the intermediate plane if any negative gaussian apertures are present. However,

this does not appear to present a significant limitation for actual physical optical systems.

Conclusions

All the expressions for the $ABCD$ matrices, Huygens' integral, the transformation rule for the gaussian \hat{q} parameter, and in fact all of the other results we have derived in earlier sections and chapters for real $ABCD$ matrices, thus apply equally well to complex paraxial systems and complex $ABCD$ matrices. The reader will note that the fundamental formula $AD - BC = 1$ also applies to all the basic building blocks of complex paraxial analysis, and hence to any complex cascaded system as well. This general approach, employing complex $ABCD$ matrices in the x and y directions separately, seems to provide the most general form for analyzing propagation of any generalized paraxial wave through any generalized or complex paraxial optical system.

There are several other more sophisticated mathematical approaches, besides the complex $ABCD$ matrix approach, through which these same generalized paraxial optical results can be derived and expressed (see References). Some of these alternative approaches express generalized paraxial optics in terms of generalized operators, whereas others employ complex ray functions, eikonal functions, or Green's functions. The generalized $ABCD$ approach of this section seems to the author be the simplest approach, both to learn and to apply, as we will attempt to demonstrate in the following sections and chapters.

REFERENCES

One of the alternative approaches to complex paraxial optics, using differential raising and lower operators, is introduced in partial form by E. E. Bergmann, "Optical resonators with paraxial modes," *Appl. Optics* **11**, 113-119 (January 1972). An extended and generalized version of this approach, with numerous other references, is developed by D. Stoler, "Operator methods in physical optics," *J. Opt. Soc. Am.* **71**, 334-341 (March 1981).

Another very powerful canonical operator approach is outlined by M. Nazarathy and J. Shamir in "First-order optics—a canonical operator representing lossless systems," *J. Opt. Soc. Am.* **72**, 356-364 (March 1982); and in "First-order optics: operator representation for systems with loss or gain," *J. Opt. Soc. Am.* **72**, 1398-1408 (October 1982). See also M. Nazarathy, "Operator Methods in First Order Optics," D. Sc. Dissertation, Technion, Israel Institute of Technology (1982).

Complex ray and complex eikonal approaches are reviewed by J. A. Arnaud in "Nonorthogonal optical waveguides and resonators," *Bell Syst. Tech. J.* **49**, 2311-2348 (November 1970); "Mode coupling in first-order optics," *J. Opt. Soc. Am.* **61**, 751-758 (June 1971); and "Hamiltonian theory of beam mode propagation," in *Progress in Optics*, Vol. 11, ed. by E. Wolf (American Elsevier, 1973). See also M. J. Bastiaans, "The Wigner distribution function and Hamilton's characteristics of a geometrical-optical system," *Optics Commun.* **30**, 321-326 (September 1979).

Complex ray techniques for analyzing general paraxial wave systems (though without including transverse amplitude variations) have also been extensively discussed by G. A. Deschamps, "Ray techniques in electromagnetics," *Proc. IEEE* **60**, 1022-1035 (September 1972); and J. B. Keller and W. Streifer, "Complex rays with an application to gaussian beams," *J. Opt. Soc. Am.* **61**, 40-43 (January 1971).

 Problems for 20.4

1. *Square root of an ABCD matrix.* Show that the square root of an arbitrary $ABCD$ matrix has matrix elements $A_{1/2} = (A + 1)/(A + D + 2)^{1/2}$, $B_{1/2} = B/(A + D + 2)^{1/2}$, and $D_{1/2} = (D + 1)/(A + D + 2)^{1/2}$.
-

20.5 COMPLEX HERMITE-GAUSSIAN MODES

The ordinary Hermite-gaussian modes derived in Chapter 16 form a set of “normal modes of free space.” Any such Hermite-gaussian (or Laguerre-gaussian) mode will propagate through free space retaining its Hermite-gaussian form and changing only in its radius of curvature $R(z)$ and its scale factor or spot size $w(z)$. The propagation of such Hermite-gaussian modes is entirely governed by the free-space propagation law $\tilde{q}(z) = \tilde{q}(z_0) + z - z_0$.

As a very general extension of this free-space gaussian beam theory, a family of *generalized* or *complex Hermite-gaussian modes* will be identified in this section as normal modes for any arbitrary *complex paraxial optical system*. In this section we will develop the formalism and the propagation laws for these complex Hermite-gaussian modes of any order propagating through any complex paraxial $ABCD$ system. The propagation of these complex Hermite-gaussian modes can be completely described, in fact, by simple transformation rules very much like the transformation rules for free space, using only the complex $ABCD$ elements of the system.

Complex Hermite-Gaussian Waves

An n -th order complex Hermite-gaussian mode of the type we wish to consider may be written in its most general form, in one transverse coordinate, as

$$\tilde{u}_n(x) = \tilde{\alpha}_n \tilde{v}^n H_n \left(\frac{\sqrt{2}x}{\tilde{v}} \right) \exp \left(-j \frac{kx^2}{2\tilde{q}} \right), \quad (57)$$

where the three parameters $\tilde{\alpha}_n$, \tilde{v} and \tilde{q} all become *complex quantities* in the most general situation. The complex radius of curvature \tilde{q} is still defined, just as in the free-space situation, by

$$\frac{1}{\tilde{q}} \equiv \frac{1}{R} - j \frac{\lambda}{\pi w^2}, \quad (58)$$

where R and w are the purely real radius of curvature and gaussian spot size. The Hermite polynomial part of Equation 20.57 contains, however, a new complex Hermite scale factor or “complex spot size” \tilde{v} which appears in the argument of the Hermite polynomials. This parameter is basically a new independent complex parameter, representing a generalization on the real gaussian spot size w .

We will henceforth refer to waves of the form in which \tilde{v} is purely real and equal to w as “real” or “ordinary” Hermite-gaussian waves. The same functions

with \tilde{v} complex, or even with \tilde{v} real but different from w , we will refer to as “complex” or “generalized” Hermite-gaussian waves. The distinction between these “ordinary” and “complex” Hermite-gaussians is the primary topic of this section.

We have pointed out in Chapter 16 that there is no meaningful difference between the ordinary and the complex Hermite-gaussian waves for the two lowest-order modes $n = 0$ and $n = 1$, since the factor \tilde{v} drops out of both of these. For modes with $n > 1$, however, a complex argument in the Hermite polynomial produces a transverse phase as well as amplitude variation in the Hermite polynomial part of the function. As a result, the phase front of the mode is no longer purely spherical, but has additional phase distortion or wrinkling due to the complex Hermite factor as well. The transverse mode pattern also changes shape with distance for complex Hermite-gaussians with $n \geq 2$.

Propagation of Complex Hermites Through Complex Systems

Suppose a complex Hermite-gaussian mode function $\tilde{u}_{1n}(x_1)$ in the general form given in Equation 20.57, with subscripts 1 on the quantities $\tilde{\alpha}_{1n}$, k_1 , \hat{q}_1 and \tilde{v}_1 , is sent into a general paraxial optical system characterized by a complex $ABCD$ matrix. (Remember that \hat{q}_1 is the reduced value of the \tilde{q} parameter, as defined earlier.) Propagation of this wave through the complete paraxial system can then be calculated in one step by using the complex Huygens’ integral of Equation 20.47 in terms of the complex $ABCD$ elements. Use of the generating function for the Hermite polynomials, namely,

$$\exp(2xt - t^2) = \sum_{n=0}^{\infty} \frac{H_n(x)t^n}{n!}, \quad (59)$$

allows this Huygens’ integral to be evaluated analytically. The output function for a complex Hermite-gaussian input mode function $\tilde{u}_{1n}(x_1)$ propagating through a complex $ABCD$ system is found to be still a complex Hermite-gaussian mode function of exactly the same order as the input, but with in general new and different values for the parameters $\tilde{\alpha}_{2n}$, \hat{q}_2 and \tilde{v}_2 .

The output value for the \hat{q} parameter after passing through the complex paraxial system is related to the input value by exactly the same transformation rule as for real $ABCD$ systems, namely,

$$\hat{q}_2 = \frac{A\hat{q}_1 + B}{C\hat{q}_1 + D}. \quad (60)$$

In addition, the input and output mode amplitudes are related by the simple rule

$$\frac{\tilde{\alpha}_{2n}}{\tilde{\alpha}_{1n}} = \left(\frac{1}{A + B/\hat{q}_1} \right)^{n+1/2}. \quad (61)$$

Finally, the input and output values of the complex \tilde{v} parameter are related by a new, third rule, namely,

$$\tilde{v}_2^2 = (A + B/\hat{q}_1)^2 \times \tilde{v}_1^2 + j \frac{4B}{k_1} (A + B/\hat{q}_1). \quad (62)$$

This is a new basic rule governing the propagation of the complex spot size parameter \tilde{v} through a general complex $ABCD$ system.

Discussion

The three transformation laws 20.60 to 20.62 are the most general form of the propagation rules for a complex Hermite-gaussian function through a complex paraxial optical system. They involve the complex (reduced) radius of curvature \hat{q} , the complex spot size parameter \tilde{v} , and the complex amplitude (and phase) parameter $\tilde{\alpha}_n$. In terms of these parameters any input Hermite-gaussian of order n transforms into another Hermite-gaussian of the same order after passing through any complex paraxial system. The on-axis phase shift factor $\exp[-jk(z_2 - z_1)]$ is not included in this transformation, but will be the same for all modes of any order n .

We can then show algebraically that each of the transformation rules in Equations 20.60 to 20.62 cascades properly through multiple $ABCD$ systems if we use as the matrix elements for the cascaded system the matrix product of the matrices of the individual cascaded elements. Thus, the cascading property of the complex $ABCD$ matrices holds here as it does in all other situations.

In carrying out the evaluation of Huygens' integral with a general Hermite-gaussian input, there is one mathematical condition that arises, namely, it is necessary for convergence to assume that the imaginary part of the input quantity $k(A/B+1/\hat{q}_1)$ is negative. For real k and real $ABCD$ elements this means that the input and output spot sizes must both be positive and finite. For the complex situation, especially in systems that might have both radially decreasing and radially increasing loss at different points along the system, the physical meaning of this restriction is somewhat obscure. A reasonable hypothesis is that this mathematical restriction may mean that the input wave must be limited to values that keep the output spot size bounded and the beam energy finite everywhere within the overall system.

Applications of the Complex Hermite-Gaussian Functions

The complex-argument Hermite-gaussian functions of Equation 20.57 have not yet found wide application, in optics or elsewhere, and the properties of these functions have not yet become as familiar as the conventional real-argument Hermite-gaussians. It may be helpful, therefore, to present a few examples to illustrate the application of these general propagation rules and their connection with various earlier analyses.

(1) The Complex Hermite-Gaussian Scale Factor

The complex scale factor \tilde{v} appearing in the generalized Hermite-gaussian functions in Equation 20.57 is a complex generalization of the usual gaussian spot size w . The physical relationship between w and \tilde{v} in the general situation is not entirely clear. In fact, it may be that some other way of parameterizing these functions would lead to a clearer separation between w and \tilde{v} . In any case, the transformation rule given in Equation 20.62 for the parameter \tilde{v} may perhaps be made to appear somewhat more plausible as follows.

The usual propagation law for the real gaussian spot size w through a purely real $ABCD$ system may be written, using earlier gaussian beam formulas, as

$$w_2^2 = (A + B/R_1)^2 \times w_1^2 + (2B/k_1)^2(1/w_1^2), \quad (63)$$

where w_1 and R_1 are the real gaussian parameters at the input to the system and the $ABCD$ elements are assumed purely real. With some algebraic manipulation, this result may also be recast in the form (again, for real matrices only)

$$w_2^2 = (A + B/\hat{q}_1)^2 \times w_1^2 + (4jB/k_1)(A + B/\hat{q}_1). \quad (64)$$

This involves the complex factor \hat{q}_1 but gives a real answer. The transformation rule 20.62 for \tilde{v} then appears to be a fully complex generalization of these expressions, applicable to the fully complex situation.

(2) Propagation Eigenmodes of a Complex Quadratic Medium

As one example of the use of the general propagation rules, we can search for the propagation eigenmodes of a complex quadratic medium, i.e., a gaussian duct. That is, we can look for a set of complex Hermite-gaussian eigenmodes $\tilde{u}_n(x, z)$ for which the transverse field distribution will be independent of the axial distance z . Formally this means we must look for input values of \hat{q}_1 and \tilde{v}_1 such that the transformed values of these quantities remain unchanged, or $\hat{q}(z) = \hat{q}_1$ and $\tilde{v}(z) = \tilde{v}_1$, through an arbitrary length of complex gaussian duct.

From the transformation rules for \hat{q} and \tilde{v} plus the matrix elements of a gaussian duct, we can find that the complex Hermite-gaussian parameter values for these eigenmodes are

$$\hat{q}_2^2(z) = \hat{q}_1^2 = -\tilde{\gamma}^{-2}, \quad (65)$$

and

$$\tilde{v}^2(z) = \tilde{v}_1^2 = 2/k_0\tilde{\gamma}, \quad (66)$$

where k_0 is the on-axis propagation constant, $\tilde{\gamma}$ is the complex parameter characterizing the duct as defined in Equation 20.43, and $\tilde{\alpha}_{1n}$ is an arbitrary initial constant. The phase shift and attenuation factor for one of these eigenmodes traveling a distance z down the duct is then given by

$$\frac{\tilde{\alpha}_n(z)}{\tilde{\alpha}_{1n}} = \exp [+j(m + 1/2)\tilde{\gamma}z]. \quad (67)$$

These results are identical with results obtained previously by Marcuse, who solved the inhomogeneous wave equation directly. However, we will also show in a later section that modes with $m \geq 2$ may be unstable in this system, so that only the two lowest eigenmodes may be physically useful.

(3) Complex Gaussian Beams in Purely Real $ABCD$ Systems

A general complex beam with a complex scale factor \tilde{v} can be launched into a purely real ray matrix system. In working with the complex \tilde{v} parameter, it is sometimes useful to define a parameter \tilde{V} as the ratio of the complex to real spot sizes, i.e.,

$$\tilde{V} \equiv \frac{\tilde{v}}{w}, \quad (68)$$

so that the generalized Hermite-gaussian beam has the form

$$\tilde{u}_n(x) = \tilde{\alpha}_n [\tilde{V} w]^n H_n \left(\frac{\sqrt{2}x}{\tilde{V} w} \right) \exp \left(-j \frac{kx^2}{2\tilde{q}} \right). \quad (69)$$

When $\tilde{V} = \pm 1$ the complex Hermite-gaussian reduces to a conventional real Hermite-gaussian.

We can then show that for a purely real $ABCD$ system the propagation rule for \tilde{v} reduces to

$$\frac{\tilde{V}_2^2 - 1}{\tilde{V}_1^2 - 1} = \frac{A + B/\tilde{q}_1}{A + B/\tilde{q}_{1r}^*}, \quad (70)$$

which can be converted to

$$\tilde{V}_2^2 - 1 = (\tilde{V}_1^2 - 1) \times \exp [2j\angle(A + B/\tilde{q}_1)], \quad (71)$$

where $\angle(A + B/\tilde{q}_1)$ means the phase angle of that quantity. This shows that any optical system with real matrix elements will have an output wave with $\tilde{V}_2 = \pm 1$ if and only if the input wave has $\tilde{V}_1 = \pm 1$. Therefore if we start with a purely real gaussian beam there is no optical system with purely real matrix elements that will transform it into a complex gaussian beam.

Conversely, once we have a generalized complex gaussian beam with $\tilde{V}_1^2 \neq 1$, there is no optical system with real matrix elements that can transform it back into a purely real gaussian beam. This can be done only by a complex $ABCD$ system. These conclusions are meaningful only for mode indices $n \geq 2$, since, as we have noted before, there is no meaningful distinction between real or complex modes for $n = 0$ or $n = 1$.

As one specific example, consider the propagation of a complex Hermite-gaussian beam in free space. Suppose that the input plane of the optical system, z_1 , coincides with the waist of the beam. The matrix elements of the system out to any plane z are then $A = D = 1$, $B = z$ and $C = 0$, and we then find

$$\frac{\tilde{V}^2(z) - 1}{\tilde{V}^2(0) - 1} = \frac{1 - j(z - z_1)/z_R}{1 + j(z - z_1)/z_R}. \quad (72)$$

This result is essentially identical to that of Pratesi and Ronchi, who obtained it by solving the wave equation directly.

Beam Expansions In Complex Hermite-Gaussians

Any field distribution $\tilde{u}(x)$ that satisfies the wave equation in a paraxial optical system can be expanded using as a basis set the complex Hermite-gaussian functions

$$\tilde{u}_n(x) = \tilde{\alpha}_n \tilde{v}^n H_n \left(\frac{\sqrt{2}x}{\tilde{v}} \right) \exp \left(-j \frac{kx^2}{2\tilde{q}} \right), \quad (73)$$

where $\tilde{\alpha}_n$ is an appropriate normalization constant, and where \tilde{v} and \tilde{q} may be arbitrarily chosen. The series expansion has the usual form

$$\tilde{u}(x) = \sum_{n=0}^{\infty} c_n \tilde{u}_n(x). \quad (74)$$

The general orthogonality relation for Hermite polynomials is

$$\int_{-\infty}^{\infty} H_n(\sqrt{cx}) H_m(\sqrt{cx}) \exp(-cx^2) dx = \sqrt{\frac{\pi}{c}} 2^n n! \delta_{nm} \quad \text{Re}[c] > 0. \quad (75)$$

Using this we can show that the complex Hermite-gaussian functions $\tilde{u}_n(x)$ are biorthogonal to a set of functions $\phi_n(x)$ given by

$$\phi_n(x) = \beta_n H_n\left(\frac{\sqrt{2}x}{\tilde{v}}\right) \exp\left[j\frac{kx^2}{2\tilde{q}} - \frac{2x^2}{\tilde{v}^2}\right] \quad (76)$$

with the normalization constant given by

$$\beta_n = \left(\frac{2}{\pi}\right)^{1/2} \frac{1}{2^n n! \tilde{\alpha}_n \tilde{v}^{n+1}} \quad (77)$$

in the sense that $\int_{-\infty}^{\infty} \phi_n(x) \tilde{u}_m(x) dx = \delta_{nm}$. The coefficients in the expansion are then given by

$$c_n = \int_{-\infty}^{\infty} \phi_n(x) \tilde{u}(x) dx \quad (78)$$

as in the usual expansion fashion.

If the input wave $\tilde{u}_1(x)$ to a complex *ABCD* system is expanded in this fashion, then the output wave $\tilde{u}_2(x)$ from the system can be found by propagating each Hermite-gaussian wave $\tilde{u}_n(x)$ through the system using the transformation rules of the previous section, and then reexpanding $\tilde{u}_2(x)$ at the output using the same c_n coefficients. In other words the coefficients c_n in the expansion do not change as the wave passes through a general paraxial system. The Hermite-gaussian basis functions themselves change, as given by the transformation rules. This invariance is one of the useful properties of the complex Hermite-gaussian expansion.

REFERENCES

The results presented in this section seem to have been first derived in their most general form in unpublished work by Amos A. Hardy, Shinan-Chur Sheng, and A. E. Siegman at Stanford University. They are also derived, using the "first-order optics" approach, in M. Nazarathy, A. Hardy, and J. Shamir, "Generalized mode propagation in first-order optical systems with loss or gain," *J. Opt. Soc. Am.* **72**, 1409–1420 (October 1982).

Earlier references on the same topic include A. E. Siegman, "Hermite-gaussian functions of complex argument as optical beam eigenfunctions," *J. Opt. Soc. Am.* **63**, 1093–1094 (September 1973); L. W. Casperson, "Beam modes in complex lenslike media and resonators," *J. Opt. Soc. Am.* **66**, 1373–1379 (December 1976); and R. Pratesi and L. Ronchi, "Generalized gaussian beams in free space," *J. Opt. Soc. Am.* **67**, 1274–1276 (September 1977).

The propagation formulas for linear propagation of gaussian beams through complex paraxial media, as developed in these sections, can also be extended to nonlinear media. Nonlinear effects such as thermal defocusing or Kerr effect self-focusing can then be analyzed, at least to a first order of approximation, via the following approach. We first solve for small-signal or unperturbed gaussian-beam propagation in the medium;

then calculate the resulting nonlinear effects and their modifications to the medium; take these modifications into account as modifications to the paraxial elements; recalculate the new propagation behavior; and then iterate this procedure. The resulting calculations represent reasonable approximations so long as the modified beam stays gaussian, i.e., so long as the nonlinear effects are not so strong as to produce severe beam focusing, spherical aberration, or other nonparaxial effects. One example of this type of calculation is presented in A. Yariv and P. Yeh, "The application of gaussian beam formalism to optical propagation in nonlinear media," *Optics Commun.* **27**, 295–298 (November 1978).

More exact solutions for wave propagation in ducts with gaussian (as contrasted to quadratic) transverse gain variations are described by B. N. Perry, P. Rabinowitz and M. Newstein, "Wave propagation in media with focused gain," *Phys. Rev. A* **27**, 1989–2002 (April 1983).

Problems for 20.5

1. *Verifying the cascading properties of complex ABCD matrices.* Verify that each of the transformation rules in Equations 20.60 through 20.62 does cascade properly through two complex ABCD systems in succession, using the matrix product for the two ABCD systems.
2. *Complex gaussian eigenmode of a complex gaussian duct.* More detailed examination shows that a gaussian duct will have a confined and stable lowest-order complex-gaussian eigenmode only when either (a) the transverse loss variation has a value of $\alpha_2 > 0$ (i.e., radially increasing loss), with the radial index variation n_2 being arbitrary, or (b) the transverse loss profile has $\alpha_2 = 0$ and the transverse index variation has $n_2 > 0$ (i.e., a radially decreasing index). Verify that as a result of this, the physically meaningful gaussian eigenmode in any such duct is given by $1/\hat{q}_1 = -j\hat{\gamma}$ and not by the opposite sign.
3. *Biorthogonal modes in gaussian ducts.* Using the result from the previous problem, show that if the complex functions $\tilde{u}_n(x)$ are the propagation eigenmodes of a complex gaussian duct, then the biorthogonal set of modes $\phi_n(x)$ have exactly the same form of gaussian exponent as the $\tilde{u}_n(x)$. [In fact, the modes $\phi_n(x)$ in this situation are really just the same modes $\tilde{u}_n(x)$ propagating in the opposite direction along the gaussian duct.]
4. *Initial excitation of a complex gaussian duct.* Suppose a complex gaussian duct with gaussian eigenvalue $1/\hat{q} = -j\hat{\gamma}$ is excited at an input plane by a lowest-order gaussian input function $\tilde{u}(x) = (2/\pi w_i^2)^{1/4} \exp[-jkx^2/2\hat{q}_i]$ where the \hat{q}_i value for this input wave can be experimentally varied. Evaluate the resulting expansion coefficient c_0 for the lowest-order eigenmode $\tilde{u}_0(x)$ in this situation as a function of the input gaussian parameter \hat{q}_i (keeping the total input power constant). Show in particular that:
 - (a) The magnitude of the lowest-order expansion coefficient c_0 is maximized if the input wave has $\hat{q}_i = -\hat{q}^*$, that is, if $w_i = w$ and $R_i = -R$ (which means that maximum excitation of a *positively* curved eigenwave is accomplished by sending in a *negatively* curved input wave).
 - (b) The power excited into the lowest-order $\tilde{u}_0(x)$ by itself (disregarding the excitation into higher-order modes $\tilde{u}_n(x)$ with $n > 0$) can actually be greater than the incident power in the input wave $\tilde{u}(x)$.

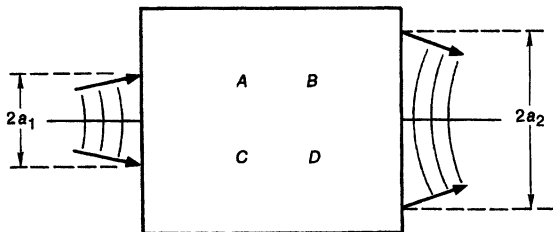


FIGURE 20.11
Propagation and transverse rescaling of a general wave through a complex $ABCD$ system.

- (c) And, the ratio of power carried by $\tilde{u}_0(x)$ to the power injected from $\tilde{u}(x)$ can be greater than unity only if the gaussian duct has a radial loss variation $\alpha_2 > 0$.

20.6 COORDINATE SCALING WITH HUYGENS' INTEGRALS

Once we have the complex $ABCD$ elements, it is possible, for purposes of either analysis or numerical computation, to transform the propagation of any arbitrary beam through any arbitrary complex paraxial system into an equivalent propagation of a near-collimated beam through an equivalent length of free space. We will give both a mathematical derivation and a physical explanation of this transformation in the present section.

Transformation of the General Huygens' Integral

To demonstrate this mathematically, suppose an arbitrary optical beam of approximate width $2a_1$, which may be either diverging or converging, is sent into an arbitrary complex $ABCD$ system, as illustrated in Figure 20.11. For a complicated $ABCD$ system, with multiple internal lenses, gaussian apertures and the like, this beam will then emerge with some different approximate width $2a_2$, and with a wavefront which may be either diverging or converging, as illustrated in Figure 20.11.

The transmission of this beam through the $ABCD$ system is given by the same Huygens' integral as in the preceding sections, namely,

$$\tilde{u}_2(x_2) = \sqrt{\frac{j}{B\lambda_0}} \int_{-a_1}^{a_1} \tilde{u}_1(x_1) \exp \left[-j \frac{\pi}{B\lambda_0} [Ax_1^2 - 2x_1 x_2 + Dx_2^2] \right] dx_1, \quad (79)$$

except that we now suppose that the limits of the integral are set to the values $\pm a_1$, where we choose the input aperture width $2a_1$ either to equal an actual aperture in the input plane, or else just wide enough to comfortably contain all the significant portion of the input beam (including adequate allowance for "spillover").

Suppose we then also chose a scale width $2a_2$ at the output, where a_2 is arbitrary, but is best made wide enough to contain all the significant portion of the output beam. We then define the ratio of these widths as a *magnification scaling factor* $M \equiv a_2/a_1$, where M may in fact be either greater or less than

unity, depending upon what actually happens to the particular beam in going through the paraxial system.

Let us next define normalized transverse coordinates y_1 and y_2 at the input and output planes by

$$y_1 \equiv \frac{x_1}{a_1} \quad \text{and} \quad y_2 \equiv \frac{x_2}{a_2} = \frac{x_2}{Ma_1}, \quad (80)$$

and also define transformed input and output wavefunctions by

$$\tilde{v}_1(y_1) \equiv a_1^{1/2} \tilde{u}_1(x_1) \exp \left[-j \frac{\pi(A - M)x_1^2}{B\lambda} \right] \quad (81)$$

and

$$\tilde{v}_2(y_2) \equiv a_2^{1/2} \tilde{u}_2(x_2) \exp \left[+j \frac{\pi[D - M]x_2^2}{B\lambda} \right]. \quad (82)$$

Obviously, these transformations—which depend in part upon the choice of the magnification M —amount to multiplying the input and output wavefronts by a quadratic phase transformation, as in passing through a thin lens, plus also possibly multiplying them by a gaussian aperture transmission if the A , B or D elements are complex.

The physical effect of these transformations, as we will see in the following, is essentially to convert the input beam, whether diverging or converging, into a quasi collimated input beam, and then to convert the output from the analysis back into the appropriate diverging or converging beam. We will also sometimes refer to this transformation as “extracting out the spherical portion of the input or output wavefront.”

If we make these analytical transformations and plug them into the general Huygens’ integral 20.79, this integral is then transformed into the very simple form

$$\tilde{v}_2(y_2) = \sqrt{jN_c} \int_{-1}^1 \tilde{v}_1(y_1) \exp [-j\pi N_c(y_1 - y_2)^2] dy_1. \quad (83)$$

But this is exactly the normalized form of Huygens’ integral for transmission through a free-space region with a Fresnel number given by

$$N_c \equiv \frac{a_1 a_2}{B\lambda} = \frac{Ma_1^2}{B\lambda}, \quad (84)$$

where N_c is a new kind of “collimated Fresnel number” for this propagation calculation.

The Collimated Fresnel Number

The formal transformation from the original Huygens’ integral to the normalized free-space form in Equation 20.83 is mathematically valid independent of the choice we make for the output scale factor a_2 or the magnification M , so that the values assigned to these quantities are quite arbitrary so far as the mathematical analysis is concerned. The most meaningful choice, however, will be for us to select the value of a_1 so that a_1 either matches the actual input aperture, if there is one, or else is just large enough to match the full width of the input beam. We should then choose M so that a_2 is similarly large enough to just include all the significant portions of the output beam.

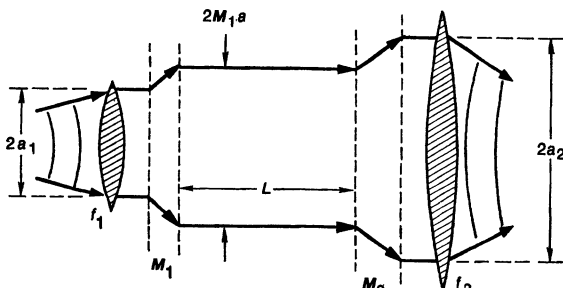


FIGURE 20.12

A more detailed propagation model to represent the general paraxial propagation of Figure 20.11.

If we do this, the normalized functions $\tilde{v}_1(y_1)$ and $\tilde{v}_2(y_2)$ will then both more or less fill up the range ± 1 in the input or y_1 and output or y_2 coordinates, i.e., the optical beam will look more or less like a *collimated beam* confined to the range $\approx \pm 1$ in the dimensionless y coordinate. After the quadratic phase (and possibly quadratic amplitude) variations are extracted out by the transformations given in Equations 20.80 through 20.82, therefore, the diffraction effects of propagating through a complex *ABCD* system are exactly the same as propagating a quasi collimated beam through an equivalent length B/M of free space, as expressed by the Fresnel number N_c . We therefore refer to this Fresnel number N_c as the “collimated Fresnel number” for the system.

This collimated Fresnel number is a primary measure of the amount of numerical work needed to evaluate the wave propagation integral 20.79 or 20.83 using any of the numerical techniques discussed in Section 16.7 (see also Section 18.3). It depends on the paraxial optical system through the parameter B ; on the width $2a_1$ of the input beam; and also on the divergence or convergence of the input beam, through the magnification M that is needed to match the input and output beam widths.

Physical Interpretation

The preceding mathematical analysis can be given a more physical interpretation as follows. Consider again the wave propagation through an arbitrary *ABCD* system as in Figure 20.11. This propagation can always be modeled by the collection of elements shown in Figure 20.12, consisting of a (possibly complex) lens with (possibly complex) focal length f_1 at the input end, which converts the input beam into a quasi collimated beam; a “magnifier” (i.e., a relay imaging system of zero effective length) which magnifies this collimated beam pattern transversely by a magnification M_1 ; a free space section of (as yet unknown) length L ; a second “magnifier” of power M_2 ; and an output lens of (possibly complex) focal length f_2 , which gives the output beam the correct output curvature.

The total transformation through the equivalent model of Figure 20.12 can then be equated to the *ABCD* matrix of the actual paraxial system in Figure

20.11 by evaluating the matrix products

$$\begin{bmatrix} A & B \\ C & D \end{bmatrix} = \begin{bmatrix} 1 & 0 \\ -1/f_2 & 1 \end{bmatrix} \begin{bmatrix} M_2 & 0 \\ 1/M_2 & 0 \end{bmatrix} \begin{bmatrix} 1 & L \\ 0 & 1 \end{bmatrix} \begin{bmatrix} M_1 & 0 \\ 1/M_1 & 0 \end{bmatrix} \begin{bmatrix} 1 & 0 \\ -1/f_1 & 1 \end{bmatrix}, \quad (85)$$

where the $ABCD$ coefficients on the left side are those of the actual paraxial system. If we multiply this out, we get the relationships

$$\begin{aligned} A &= M \times \left[1 - \frac{L_{\text{eq}}}{f_1} \right] \\ B &= M \times L_{\text{eq}} \\ D &= \frac{1}{M} - \frac{ML_{\text{eq}}}{f_2}, \end{aligned} \quad (86)$$

where $L_{\text{eq}} \equiv L/M_1^2$, and where M is now set equal to the total magnification $M_1 \times M_2$ through the model system, which we will presumably adjust to match the actual transverse magnification from input to output beams.

We can then see that for any given choice of M , the three independent elements A , B and D of the actual system can be matched by three adjustable parameters f_1 , f_2 and an “equivalent length” $L_{\text{eq}} \equiv L/M_1^2$ which always appears in combination in Equations 20.86. If we invert these relations, we find that the equivalent free space length and the input and output focal lengths in the model of Figure 20.12 are given in terms of the M value and the parameters of Figure 20.11 by

$$L_{\text{eq}} = \frac{L}{M_1^2} = \frac{B}{M}, \quad \frac{1}{f_1} = \frac{M - A}{B} \quad \text{and} \quad \frac{1}{f_2} = \frac{1/M - D}{B}. \quad (87)$$

Moreover, the collimated free-space region in the center of Figure 20.12—which is the only region where Huygens’ integral need be evaluated—has a width $M_1 a_1$ and a length $L = M_1^2 B/M$. Hence the Fresnel number in this free-space portion of the model is given by

$$N_c = \frac{(M_1 a_1)^2}{L \lambda} = \frac{a_1^2}{(L/M_1^2) \lambda} = \frac{M a_1^2}{B \lambda} = N_c. \quad (88)$$

In other words, the Fresnel number in the collimated region of the model is exactly the same as the result in the purely mathematical analysis in Equation 20.84, independent of how we divide the total magnification M between the input magnification M_1 and the output magnification M_2 . The collimated Fresnel number N_c —which determines the computational difficulty of the propagation task—is indifferent to this choice.

More On the Optimum Magnification

Suppose further that in the system of Figure 20.11 the $ABCD$ matrix elements are purely real, or nearly so, so that we may with reasonable accuracy think about real rays going through the system. In addition, suppose further that the beam coming into the system is more or less similar to a bounded spherical wave with an input width $2a_1$ and an approximate radius of curvature R_1 . The outer edge of this beam can then be delineated by an input ray with displacement $x_1 = a_1$ and slope $x'_1 = a_1/R_1$.

The corresponding output ray, which will delineate the approximate outer edge of the output beam, will then have a displacement $x_2 \approx a_2 = Ax_1 + Bx'_1 = (A + B/R_1)a_1$. Hence, the approximate or geometric magnification of the transverse width for this beam going through the system will be given by

$$M = \frac{a_2}{a_1} \approx A + B/R_1. \quad (89)$$

But if we plug this magnification into Equations 20.87, the resulting focal lengths for the input and output lenses will be

$$\begin{aligned} \frac{1}{f_1} &= \frac{M - A}{B} \approx \frac{1}{R_1} \\ \frac{1}{f_2} &= \frac{1/M - D}{B} \approx \frac{1}{R_2}. \end{aligned} \quad (90)$$

In other words, with the commonsense geometric choice for M , the input and output lenses do just convert from the external diverging or converging beam profiles to an essentially collimated profile internal to the model.

Simple Example

As the simplest possible example of this beam transformation process, let us consider a uniform-amplitude spherical wave of initial radius R_0 diverging away from a hard-edged input aperture of width $2a_1$ and traveling forward through a real distance L , as in Figure 20.13. The $ABCD$ matrix for the paraxial “system” in this situation will just be the free-space matrix

$$\begin{bmatrix} A & B \\ C & D \end{bmatrix} = \begin{bmatrix} 1 & L \\ 0 & 1 \end{bmatrix}, \quad (91)$$

and the magnification from input to output will be

$$M = 1 + L/R_0 = \frac{R_0 + L}{R_0}. \quad (92)$$

This diverging beam problem will then be formally equivalent to a collimated beam problem with a collimated Fresnel number given by

$$N_c = \frac{Ma_1^2}{B\lambda} = \frac{(L + R_0)a_1^2}{R_0 L \lambda} = \frac{a_1^2}{L_{eq}\lambda}. \quad (93)$$

In other words, propagation of the uniform diverging beam through distance L will be formally equivalent to propagation of a uniform collimated beam of the same width a_1 through an equivalent (shorter) length L_{eq} given by

$$L_{eq} = \frac{B}{M} = \frac{R_0 L}{R_0 + L}, \quad (94)$$

as in Figure 20.13.

In physical terms, the Fresnel diffraction profile of the diverging beam at distance L will be exactly the same as the Fresnel profile of the collimated beam at the shorter distance L_{eq} , except for transverse scaling and an underlying wavefront curvature in the former. We might crudely say that the diverging beam in the upper part of the figure suffers less Fresnel diffraction because it

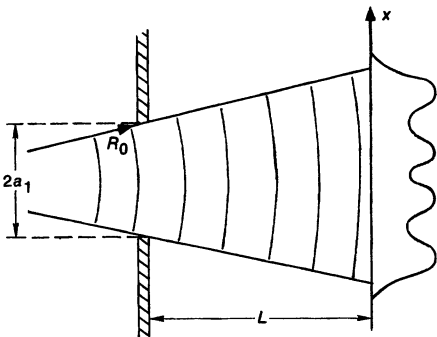
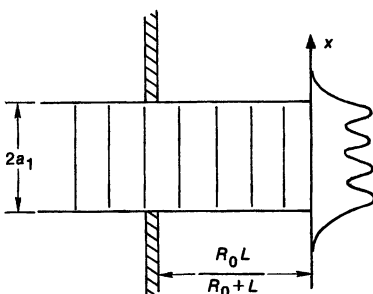


FIGURE 20.13

The two propagation problems shown here are formally equivalent, and the output beam profiles will have the same shape except for a transverse scaling and an underlying wavefront curvature.



keeps getting wider transversely, and thus diffraction effects act more slowly. If the beam is converging, and has a negative value for R_0 , then exactly the opposite is true. In fact, as we know, following a converging beam down to its focus or caustic point is equivalent to following the equivalent collimated beam all the way out to $L_{eq} \rightarrow \infty$.

Conclusion

Use of the coordinate transformation developed in this section makes it evident that propagation and aperture diffraction calculations for diverging and converging beams traveling different physical distances are entirely equivalent, if they are described by the same collimated Fresnel number N_c . In fact, N_c is the only parameter that is relevant for any situation in which a uniform intensity plane or spherical wave, of any curvature, comes through a slit or circular aperture of width or diameter $2a$.

The use of this transformation also makes it possible to handle the diffraction calculations for any paraxial propagation problem, through any paraxial system, with a single computer program which solves the propagation problem only through free space. Such a program is generally best written, as we have said several times, using some sort of fast Fourier or Hankel transform algorithm.

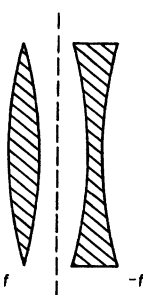


FIGURE 20.14
Self-cancelling thin-lens pair, with equal and opposite focal lengths.

REFERENCES

The coordinate transformation described in this section is a generalization of an earlier version described by E. A. Sziklas and A. E. Siegman, "Diffraction calculations using fast Fourier transform methods," *Proc. IEEE* **62**, 410–412 (March 1974), which in turn was based on a coordinate transformation described by L. C. Bradley and J. Hermann, "Numerical calculations of light propagation in a nonlinear medium," (abstract only) *J. Opt. Soc. Am.* **61**, 668 (May 1971).

Some of the relevant ideas were also developed in A. E. Siegman, "A canonical formulation for analyzing multielement unstable resonators," *IEEE J. Quantum Electron.* **QE-12**, 35–40 (January 1976).

Very similar ideas on transformation and factorization of the overall *ABCD* system have also been expressed in an unpublished memo by D. A. Copeland and D. L. Bullock, "A canonical formalism for wave propagation through a series of paraxial optical elements," Optical Physics Department, TRW, Inc., Redondo Beach, California.

20.7 SYNTHESIS AND FACTORIZATION OF ABCD MATRICES

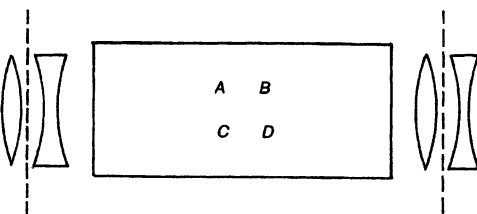
The previous section briefly introduced the concepts of extracting out a quadratic phase and amplitude profile from an arbitrary wavefront, and of synthesizing a given complex *ABCD* system out of elementary paraxial elements. These are very useful analytical techniques, and in this section we add a few additional notes on how they might be generalized and employed.

Curved Reference Planes and Self-Canceling Lens Pairs

One technique for simplifying *ABCD* matrix problems and paraxial propagation calculations is to extract out a quadratic phase front from the actual optical beam by multiplying the actual beam by a given spherical wave function, as we did in the previous section. In general we do this so as to convert a quasi spherical beam that is diverging or converging into a quasi collimated beam. From another viewpoint, this is exactly the same as measuring or observing the optical beam not on a transverse reference *plane* but on a *spherical reference surface* intersecting the optical axis at the given location *z*.

Another way of describing this same technique physically is to think of introducing into the *ABCD* system at any point of interest a self-canceling lens

FIGURE 20.15
Introducing self-cancelling lens pairs before and after an arbitrary $ABCD$ system can transform the matrix elements for that system.



pair—that is, a pair of thin lenses of equal but opposite focal power, as shown in Figure 20.14. The overall $ABCD$ matrix through these two lenses is just the identity matrix, and so introducing this lens pair will do nothing to the overall performance of the $ABCD$ system. Choosing a reference plane located between the two lenses, however, is equivalent to observing the optical beam at that location on a spherically curved reference surface.

The generalization of these ideas is to extract out both a quadratic or spherical phase and a quadratic or gaussian amplitude variation from the optical wavefront, by multiplying the actual wave by an arbitrary complex-quadratic exponential, which is to say, by an arbitrary gaussian aperture. This is equivalent to observing the optical wave on some kind of “complex-spherical” reference surface. Physically it corresponds, of course, to inserting into the $ABCD$ system a self-cancelling thin lens plus gaussian aperture pair, with one aperture having a positive and the other a negative gaussian transmission; and then again observing the optical beam at the reference plane between these two elements.

Transforming the $ABCD$ Matrix

As one example of this technique, let us show how we can transform the elements of an arbitrary $ABCD$ matrix in various ways by putting in such self-cancelling pairs before and after the $ABCD$ system. To do this, we visualize an optical element consisting of a thin lens plus possibly a gaussian aperture, so that this element has a total complex focal power, call it \tilde{p} , given by $\tilde{p} \equiv (1/f + j\lambda a_2/2\pi)$ in the notation of the previous sections. We then introduce a self-cancelling pair of such elements both before and after the arbitrary $ABCD$ system, as in Figure 20.15. Introducing these elements will obviously not change the physical performance of this $ABCD$ system as a periodic focusing or round-trip resonator matrix; and we can go through one period or one round trip from the reference planes between the self-cancelling elements.

Multiplying out the ray matrices will then give a transformed or primed ray matrix in the form

$$\begin{bmatrix} \hat{A} & \hat{B} \\ \hat{C} & \hat{D} \end{bmatrix} = \begin{bmatrix} 1 & 0 \\ \tilde{p} & 1 \end{bmatrix} \begin{bmatrix} A & B \\ C & D \end{bmatrix} \begin{bmatrix} 1 & 0 \\ -\tilde{p} & 1 \end{bmatrix} = \begin{bmatrix} A - B\tilde{p} & B \\ A\tilde{p} - B\tilde{p}^2 + C - D\tilde{p} & D + B\tilde{p} \end{bmatrix}. \quad (95)$$

The ray matrix $\hat{A}\hat{B}\hat{C}\hat{D}$ is then the ray matrix going from one reference plane between the self-cancelling elements to the next such reference plane.

Symmetric Matrix Form

Provided that the B element of the original $ABCD$ matrix is not zero, we can convert the “hat” form of the $ABCD$ matrix into a symmetrized form with $\hat{A} = \hat{D}$ by choosing the complex curvature \tilde{p} to be

$$\tilde{p} = \frac{A - D}{2B}. \quad (96)$$

With this choice of reference plane, the $ABCD$ matrix will take on the symmetrized form

$$\begin{bmatrix} \hat{A} & \hat{B} \\ \hat{C} & \hat{D} \end{bmatrix} = \begin{bmatrix} m & B \\ (m^2 - 1)/B & m \end{bmatrix} \quad \begin{pmatrix} \text{symmetric} \\ \text{matrix form} \end{pmatrix}. \quad (97)$$

Making the \hat{A} and \hat{D} elements equal will complete the square in the exponent of the Huygens’ kernel of the previous section, and it will also simplify some of the resonator results of the following chapter. Note also that for any choice of \tilde{p} , the value of the B element of the matrix—which is essentially the “length” of the paraxial system—remains unchanged.

Canonical Matrix Form

As another example, if we choose $1/\tilde{p}$ to be equal to either of the eigen- \tilde{q} -values of the system, as discussed in the following chapter, namely,

$$\tilde{p} = \frac{1}{B} \left[\frac{A - D}{2} \pm \sqrt{\left(\frac{A + D}{2} \right)^2 - 1} \right] = \frac{1}{\tilde{q}_a} \quad \text{or} \quad \frac{1}{\tilde{q}_b}, \quad (98)$$

then the $ABCD$ matrix will be cast into a canonical form in which $\hat{C} \equiv 0$ and $\hat{A} \times \hat{D} = 1$. The \hat{A} and \hat{D} elements will in fact become equal to the eigenvalues λ_a and λ_b of the system (see the following chapter), and the $ABCD$ matrix can be converted into the simplified form

$$\begin{bmatrix} \hat{A} & \hat{B} \\ \hat{C} & \hat{D} \end{bmatrix} = \begin{bmatrix} \lambda_a & B \\ 0 & \lambda_b \end{bmatrix} \quad \begin{pmatrix} \text{canonical} \\ \text{matrix form} \end{pmatrix}, \quad (99)$$

or else the reverse of this with a and b interchanged.

Once it is in canonical form, the $ABCD$ matrix can then easily be raised to the n -th power by writing

$$\begin{bmatrix} \lambda_a & B \\ 0 & \lambda_b \end{bmatrix}^n = \begin{bmatrix} \lambda_a^n & B_n \\ 0 & \lambda_b^n \end{bmatrix}, \quad (100)$$

where B_n is given by

$$\frac{B_n}{B} = \sum_{k=1}^{k=n} \lambda_a^{n-k} \lambda_b^{k-1} = \sum_{k=1}^{k=n} \lambda_a^{n+1-2k} = \sum_{k=1}^{k=n} \lambda_b^{n+1-2k}. \quad (101)$$

These various kinds of transformation can prove useful in the following chapter.

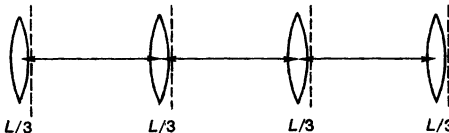


FIGURE 20.16

The system shown here is a factorized version of the identity matrix.

Telescopic Ray Matrices

A ray matrix with $C = 0$ is sometimes called a *telescopic ray matrix*, since any ray coming into such a system parallel to the axis ($x'_1 = 0$) will emerge parallel to the axis ($x'_2 = 0$), which is the property of a telescope focused to infinity. Since the eigenwaves and eigenvalues of any real but geometrically unstable ray matrix system will be purely real, this canonical transformation shows that all such geometrically unstable $ABCD$ systems are telescopic going from one properly chosen real (curved) reference plane to another. Real but geometrically stable systems, by contrast, are telescopic only in a complex ray sense, i.e., only if we extract out a complex gaussian wave from the input and output beams, or go from one “complex-curved reference plane” to another.

Factorization of Arbitrary $ABCD$ Matrices

Other related questions in this same area involve how we might break down or factorize an arbitrary complex $ABCD$ matrix into various subelements, for example, in order to synthesize an arbitrary system from a minimum number of subelements, or to find the n -th root of an arbitrary complex matrix. These questions are closely associated with the basic mathematical properties of matrix theory; and paraxial optical matrices can provide interesting practical examples to illustrate these more general mathematical properties. Some preliminary work on this topic has been done.

Casperon has shown, for example, as an illustration of the possibilities of these techniques, that the triple-cascaded combination of lenses and free spaces in Figure 20.16 has the interesting property that

$$\left\{ \begin{bmatrix} 1 & 0 \\ -3/L & 1 \end{bmatrix} \times \begin{bmatrix} 1 & L \\ 0 & 1 \end{bmatrix} \right\}^3 = I, \quad (102)$$

i.e., each individual section consisting of free space of length L and a thin lens of focal length $L/3$ has an $ABCD$ matrix corresponding to the cube root of the identity matrix. More work on this topic remains to be done.

REFERENCES

Some of the fundamental concepts in the factorization and synthesis of $ABCD$ matrices, including the cube root example in this section, are summarized by L. W. Casperson, “Synthesis of gaussian beam optical systems,” *Appl. Optics* **20**, 2243–2249 (July 1, 1981).

GENERALIZED PARAXIAL RESONATOR THEORY



In this chapter we will use the generalized paraxial-wave concepts of the preceding chapter to analyze the Hermite-gaussian modes of generalized paraxial optical resonators. The resulting analysis will show how all such resonators can be classified into four categories of resonators whose modes are either real or complex gaussian in character, and either stable or unstable in behavior. It will also show how complicated multielement paraxial resonators can be analyzed based on knowledge only of their round-trip $ABCD$ matrices, whether real or complex.

The results of this analysis will provide nearly exact descriptions of the Hermite-gaussian resonator eigenmodes for real and complex stable resonators, and will provide at least a great deal of insight into the mode properties of real and complex unstable resonators. We will also examine some of the special features of multielement real stable resonators, and give an analysis of the general orthogonality properties of optical resonator eigenmodes.

21.1 COMPLEX PARAXIAL RESONATOR ANALYSIS

As a general analytical model for this chapter, we consider either a standing-wave cavity or a ring-laser cavity in which all the optical elements can be described as generalized complex paraxial elements. Any hard-edged stops or apertures in the resonator are thus ignored, or at least their effects are deferred for later consideration. A complete round trip around such a resonator, including any end mirrors or internal soft apertures, can then be completely described by a complex total $ABCD$ matrix.

Self-Consistent Lowest-Order Gaussian Solutions

The analysis of such a resonator then proceeds as follows. We must select some specific reference plane inside the resonator—perhaps just before the output mirror—and then evaluate the total $ABCD$ matrix for one complete round trip inside the cavity, starting from and returning to this reference plane, as illustrated in Figure 21.1. We then ask: is there a complex Hermite-gaussian beam whose \tilde{q}

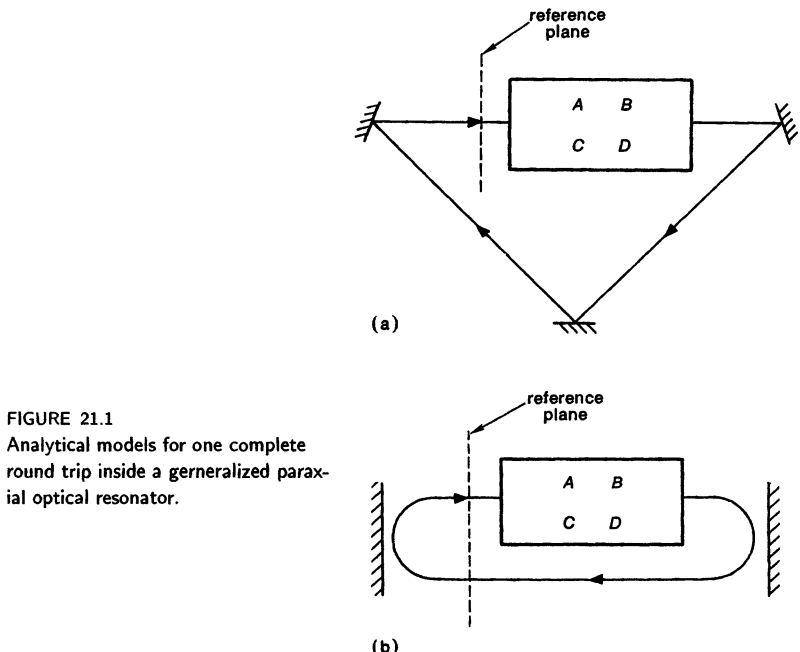


FIGURE 21.1
Analytical models for one complete round trip inside a generalized paraxial optical resonator.

and \tilde{v} values will be *self-consistent*, that is to say, self-reproducing after one trip around this resonator?

Let us focus initially on the lowest-order Hermite-gaussian mode, so that the parameter \tilde{v} is not involved. Also, let us assume in all situations from now on that \tilde{q} means the reduced value of \tilde{q} , if it necessary to make the distinction. We then ask specifically if there is a *self-consistent* value of $\tilde{q} = \tilde{q}_1 = \tilde{q}_2$ such that after one complete round trip this value will return to its initial value, as given by

$$\tilde{q}_2 = \frac{A\tilde{q}_1 + B}{C\tilde{q}_1 + D} = \tilde{q}_1. \quad (1)$$

To find this self-consistent \tilde{q} value, or better the corresponding $1/\tilde{q}$ value, we rewrite this as

$$\left(\frac{1}{\tilde{q}}\right)^2 + \frac{A - D}{B} \left(\frac{1}{\tilde{q}}\right) + \frac{1 - AD}{B^2} = 0, \quad (2)$$

using the relationship $AD - BC = 1$. The solution to this quadratic equation then gives the two self-consistent solutions

$$\frac{1}{\tilde{q}_a}, \frac{1}{\tilde{q}_b} = \frac{D - A}{2B} \mp \frac{1}{B} \sqrt{\left(\frac{A + D}{2}\right)^2 - 1}. \quad (3)$$

These are the *self-consistent* \tilde{q} values or “eigen- \tilde{q} -values” of the resonator, which we will label from now on by the subscripts a and b .

Confined Gaussian Solutions

A second important question is then whether at least one of these solutions represents a *confined gaussian beam solution*. That is, we recall that the exponent in the Hermite-gaussian functions is given by

$$-j \frac{\pi x^2}{\tilde{q}\lambda} \equiv -j \frac{\pi x^2}{R\lambda} - \frac{x^2}{w^2} \quad \text{or} \quad \frac{1}{\tilde{q}} \equiv \frac{1}{R} - j \frac{\lambda}{\pi w^2}. \quad (4)$$

If the fields of the beam are to die off at large radius, one or the other of $1/\tilde{q}_a$ or $1/\tilde{q}_b$ in Equation 21.3 must have a negative imaginary part, corresponding to the $-x^2/w^2$ term with w^2 being a real and positive quantity. If this is not the situation, then the wave fields will not fall off as $\exp(-x^2/w^2)$ at large distances from the axis, and this wave obviously cannot represent a physical solution carrying finite power.

Deciding which if either of the solutions in Equation 21.3 corresponds to a confined solution can become somewhat difficult in the completely general situation where A , B and D may all be arbitrary complex quantities.

Perturbation-Stable Gaussian Solutions

Self-consistency after each round trip, together with a confined mode pattern, might seem to be enough to characterize a Hermite-gaussian wave and to determine whether it provides a physically meaningful eigensolution for an optical resonator or a periodic complex paraxial system. But, as Casperson showed, we must ask still another question, namely, are *these confined and self-consistent eigensolutions stable against perturbations*? That is, if we start a wave around the cavity with an initial \tilde{q} value close to one of these eigensolutions, \tilde{q}_a or \tilde{q}_b , but differing by a small amount $\Delta\tilde{q}$, will this deviation $\Delta\tilde{q}$ increase or decrease after one round trip?

To analyze this, we can put an input beam with an initial value of either $\tilde{q}_1 = \tilde{q}_a + \Delta\tilde{q}_1$ or $\tilde{q}_1 = \tilde{q}_b + \Delta\tilde{q}_1$ into the round-trip propagation formula in Equation 21.1, and evaluate the output \tilde{q}_2 to first order in $\Delta\tilde{q}_1$, in the form

$$\begin{aligned} \tilde{q}_2 &= \frac{A(\tilde{q}_{a,b} + \Delta\tilde{q}_1) + B}{C(\tilde{q}_{a,b} + \tilde{q}_1) + D} \approx \left[\frac{A\tilde{q}_{a,b} + B}{C\tilde{q}_{a,b} + D} \right] + \left[\frac{1}{C\tilde{q}_{a,b} + D} \right]^2 \times \Delta\tilde{q}_1 \\ &= \tilde{q}_{a,b} + \Delta\tilde{q}_2, \end{aligned} \quad (5)$$

where we consider only small perturbations about either of the self-consistent solutions \tilde{q}_a or \tilde{q}_b , so that $\Delta\tilde{q}_1, \Delta\tilde{q}_2 \ll \tilde{q}_a$ or \tilde{q}_b .

The unperturbed portions of \tilde{q}_1 and \tilde{q}_2 cancel out for either of the self-consistent eigensolutions \tilde{q}_a or \tilde{q}_b ; and so the input and output perturbations are related by

$$\Delta\tilde{q}_2 = \left[\frac{1}{C\tilde{q}_{a,b} + B} \right] \times \Delta\tilde{q}_1 \equiv \left[\frac{1}{A + B/\tilde{q}_{a,b}} \right] \times \Delta\tilde{q}_1. \quad (6)$$

But if we plug in the self-consistent values for \tilde{q}_a or \tilde{q}_b , this then leads to perturbation growth ratios that are given for the \tilde{q}_a eigensolution by

$$\left. \frac{\Delta \tilde{q}_2}{\Delta \tilde{q}_1} \right|_{\tilde{q}_1 = \tilde{q}_a} = \left[\frac{1}{A + B/\tilde{q}_a} \right]^2 = \left[\frac{A + D}{2} + \sqrt{\left(\frac{A + D}{2} \right)^2 - 1} \right]^2 \equiv \lambda_a^2, \quad (7)$$

and for the \tilde{q}_b eigensolution by

$$\left. \frac{\Delta \tilde{q}_2}{\Delta \tilde{q}_1} \right|_{\tilde{q}_1 = \tilde{q}_b} = \left[\frac{1}{A + B/\tilde{q}_b} \right]^2 = \left[\frac{A + D}{2} - \sqrt{\left(\frac{A + D}{2} \right)^2 - 1} \right]^2 \equiv \lambda_b^2, \quad (8)$$

where the quantities λ_a and λ_b are in fact just the eigenvalues of the $ABCD$ matrix. We will often speak of λ_a and λ_b as the *perturbation eigenvalues* corresponding to the self-consistent solutions \tilde{q}_a and \tilde{q}_b , respectively, although in fact the respective perturbations actually grow as λ^2 rather than as λ . Note that the \pm signs in the two Equations 21.7 and 21.8 for λ_a and λ_b are exactly reversed from the \mp signs in the corresponding self-consistent Equation 21.3 for \tilde{q}_a and \tilde{q}_b .

The Perturbation Eigenvalues

It will again be a convenient shorthand to define a “complex \tilde{m} value” for a general complex paraxial resonator as

$$\tilde{m} \equiv \frac{A + D}{2}. \quad (9)$$

Note that this \tilde{m} value is half the trace of the ray matrix. As such it is invariant under many transformations—particularly the choice of reference plane within the cavity. The perturbation eigenvalues then take on the simple forms

$$\lambda_a, \lambda_b = \tilde{m} \pm \sqrt{\tilde{m}^2 - 1}, \quad (10)$$

and we can also see that for all values of m

$$\lambda_a \lambda_b \equiv 1. \quad (11)$$

These eigenvalues have the same form as the ray matrix eigenvalues for stable or unstable periodic focusing systems that we developed from a purely geometric ray analysis in an earlier chapter (Equation 15.39), except that they now represent the perturbation-stability eigenvalues, or the eigenvalues for growth and/or decay of small perturbations about the self-consistent waves, in a general complex paraxial optical system. (The reader might also refer back to Problem 7 in Section 15.3.)

Conclusions

The essential requirements for a physically meaningful gaussian mode in a generalized paraxial resonator are thus that:

- The \tilde{q} parameter (and if relevant the \tilde{v} parameter) of the mode must be *self-consistent* in one complete round trip;

- One or the other of the two self-consistent solutions must be *confined* (that is, must have finite spot size) in the transverse direction;
- And, of particular importance, this confined and self-consistent mode must be *perturbation-stable* in the sense developed in the preceding paragraphs.

The general category of paraxial optical resonators (or generalized periodic paraxial waveguides) that we have analyzed here can then be conveniently separated into four distinct physical categories, namely,

- Purely real and geometrically stable resonators (m^2 real and < 1);
- Purely real and geometrically unstable resonators (m^2 real and > 1);
- Complex and perturbation-stable resonators (\tilde{m} complex); and
- Complex and perturbation-unstable resonators (\tilde{m} also complex).

In the following sections we will give a brief review of the differing properties of each of these four fundamental types of resonators.

REFERENCES

The complex *ABCD* matrix and perturbation-stability concepts described in this section were introduced by L. W. Caspenson in "Mode stability of lasers and periodic optical systems," *IEEE J. Quantum Electron.* **QE-10**, 629–634 (September 1974). The same analysis has been formulated in canonical operator form by M. Nazarathy, A. Hardy, and J. Shamir, "Generalized mode theory of conventional and phase-conjugate resonators," *J. Opt. Soc. Am.* **73**, 576–586 (May 1983).

Many of the ideas in these chapters are also contained, although in a rather confusing presentation, in the papers by P. Baues, "Huygens' principle in inhomogeneous isotropic media and a general integral equation applicable to optical resonators," *Opto-Electronics* **1**, 37–44 (1969) and "The connection of geometrical optics with the propagation of gaussian beams and the theory of optical resonators," *Opto-Electronics* **1**, 103–118 (1969).

A nonlinear expansion of the general *ABCD* technique has been developed, in which gaussian modes for a resonator with uniform gain are calculated; these modes are used to calculate a transversely nonuniform gain saturation; the modes are recalculated with the gain nonuniformity included; and the process is iterated to convergence. See A. Hardy, "Gaussian modes of resonators containing saturable gain medium," *Appl. Optics* **19**, 3830–3836 (November 15, 1980).

Problems for 21.1

1. **Resonator analysis using symmetrized matrices.** The derivations of the present section could equally well be done after using the matrix symmetrization techniques introduced in Section 20.7 of the previous chapter to reduce the round-trip *ABCD* matrix for the resonator to symmetric form. Carry out such an analysis, and find the somewhat simpler algebraic expressions that result for the confinement and stability conditions.

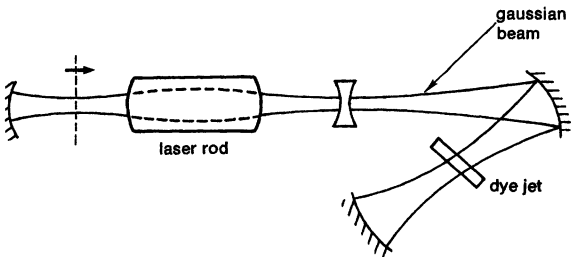


FIGURE 21.2
Example of a stable multielement gaussian resonator.

21.2 REAL AND GEOMETRICALLY STABLE RESONATORS

Let us consider first the situation where the $ABCD$ elements within a resonator are all purely real, i.e., there are no transversely varying gains or losses, and the purely real half-trace or m value of this matrix falls within the range

$$-1 \leq m \leq 1 \quad (\text{geometrically stable situation}). \quad (12)$$

This situation represents a straightforward generalization of the stable two-mirror gaussian optical resonators discussed in an earlier chapter.

Confined Mode in a Real and Stable Resonator

The self-consistent gaussian \tilde{q} values derived in the previous section can be written for this situation as

$$\frac{1}{\tilde{q}_a}, \frac{1}{\tilde{q}_b} = \frac{D - A}{2B} \mp j \frac{\sqrt{1 - m^2}}{B} = \frac{1}{R} \mp j \frac{\lambda}{\pi w^2}, \quad (13)$$

where $(D - A)/2B$ is real, but the second term is in all situations imaginary. Depending upon the sign of B , which can be either a positive or a negative quantity, one or the other of these two solutions then corresponds to a confined gaussian beam solution with a positive real spot size w . In other words, for any multielement optical resonator with a purely real $ABCD$ matrix and $m^2 < 1$, there will be a confined and self-consistent gaussian beam which can be fitted within the multielement paraxial resonator, in exactly the same way that a gaussian beam was fitted between the mirrors of the simple two-mirror resonator. An example of such a gaussian mode for a stable multielement resonator is illustrated in Figure 21.2. The other eigensolution then corresponds to a nonphysical gaussian beam with a transversely increasing intensity, and hence can be ignored.

The radius of curvature of the confined solution (actually, of either the confined or unconfined solutions) at the chosen reference plane is then

$$R = \frac{2B}{D - A}, \quad (14)$$

whereas the spot size is

$$w_2^2 = \frac{|B|\lambda}{\pi} \times \sqrt{\frac{1}{1 - m^2}}. \quad (15)$$

We see that the $|B|$ parameter for the generalized $ABCD$ situation plays something like the same role as the cavity length L in the simple two-mirror resonators of Chapter 19, whereas m (or m^2) plays something like the role of g_1g_2 in the two-mirror resonator.

Eigenvalues for the Real and Geometrically Stable Resonator

Since $|m| < 1$, the perturbation eigenvalues of Equation 21.10 can be written in the form

$$\lambda_a, \lambda_b = m \pm j\sqrt{1 - m^2} = \cos \theta \pm j \sin \theta = \exp(\pm j\theta), \quad (16)$$

where we introduce an angle θ defined by

$$m \equiv \cos \theta \quad \text{or} \quad \theta = \cos^{-1} m = \cos^{-1} \left(\frac{A + D}{2} \right). \quad (17)$$

The eigenvalue for the confined eigensolution is thus either $e^{j\theta}$ or $e^{-j\theta}$, with the choice of sign depending on the sign of B . This notation is exactly the same as the ray eigenvalues in Equations 15.45 and 15.46. Small perturbations to the mode thus do not decrease on successive round trips, but neither do they grow, so that the system is considered stable.

Discussion

We thus have the general conclusion that any paraxial resonator with m real and $|m| < 1$ will have a confined and stable gaussian mode solution, such as that illustrated for a typical situation in Figure 21.2. Such resonators are both geometrically stable (in the periodic focusing sense) and perturbation-stable (in the sense introduced in the previous section). This class of resonators represents a straightforward generalization of the ordinary two-mirror stable resonators considered in Chapter 18.

Note that in a folded but planar multielement resonator (e.g., that in Figure 21.2), there may be some astigmatism; that is, the round-trip $ABCD$ matrices may be different for rays in the plane of the paper and for rays perpendicular to this plane. We must then evaluate the $ABCD$ matrices, eigensolutions and eigenvalues separately and independently in the x and y transverse directions. (As a practical matter, resonators of this particular type are often used in dye lasers and other mode-locked lasers to get tightly focused waists between the two curved mirrors; and the resulting astigmatism in the off-axis mirrors and in various other Brewster angle plates is traded off to obtain near-zero astigmatism in the overall round trip.)

Higher-Order Hermite-Gaussian Modes

These real and geometrically stable resonators will also support a complete family of higher-order real Hermite-gaussian modes of the type described in Chapters 16, 17, and 18, provided that the mirror diameters in the real system are sufficiently large so that the diffraction losses are small. Using the $ABCD$ procedure described here thus makes it easy to find the gaussian mode parameters for multiple-element stable resonators, with any kind of real elements such

as lenses, graded-index ducts, and so forth within the laser cavity. Note that the eigenvalues of the resonator are independent of the choice of reference plane within the cavity, but the eigen- \tilde{q} -values depend upon the reference plane selected.

Modal Oscillations in Real Stable Gaussian Resonators

The fact that the perturbation eigenvalues in this class of resonators have magnitude unity actually means that perturbations in the stable gaussian mode will oscillate on successive round trips, neither growing nor dying out (at least, not in the ideal gaussian situation). This means physically that if we launch a gaussian beam into such a resonator with a \tilde{q} value close to, but not exactly equal to, the confined self-consistent value, then on successive round trips the beam will "scallop" or oscillate about the self-consistent value in the quasi-sinusoidal fashion already shown in Figure 16.12. The angle θ gives the fraction of this oscillation that will be completed in one round trip, so that one complete oscillation of the beam will require essentially $2\pi/\theta$ round trips.

This same behavior can also be described in another basically equivalent fashion. Suppose again that a perturbed input wave near but not equal to the confined perturbation-stable eigenmode is sent into the resonator. Such a perturbed eigenwave can be expanded as a superposition of the correct lowest-order gaussian eigenmode plus a small amount of higher-order Hermite-gaussian or Laguerre-gaussian mode components mixed in.

These various higher-order mode components will then propagate around the resonator with slightly different total phase shifts per round trip, because of the Guoy phase shifts we have discussed earlier. These individual mode phase shifts will in fact differ by integer multiples of the angle θ , and hence the total field, produced by the superposition of these modes, will appear to oscillate or change in shape with a period equal to θ .

As a practical matter, any real stable resonator will have small but finite diffraction losses due to an outer aperture or finite mirror size; and these diffraction losses will be in general larger the higher the mode number. In a real resonator, therefore, the higher-order mode components with $m \geq 1$ will gradually be filtered out, eventually reducing the fields in the resonator to the $m = 0$ component only. The scalloping in a real resonator will thus appear to damp out due to this diffraction filtering after a sufficient number of round trips.

21.3 REAL AND GEOMETRICALLY UNSTABLE RESONATORS

We consider next an equally important but very different class of resonators—that is, those resonators in which the $ABCD$ elements are still all real, but the resonator is *geometrically unstable* in the periodic focusing sense, so that

$$|m| = \left| \frac{A + D}{2} \right| > 1 \quad (\text{geometrically unstable}). \quad (18)$$

This means the half-trace of the matrix is either m greater than +1 (positive branch resonator) or m negative and less than -1 (negative branch resonator).

Unstable Resonator Eigenwaves

The self-consistent eigenwaves in this situation are both purely real, and may be written in the form

$$\frac{1}{\tilde{q}_a}, \frac{1}{\tilde{q}_b} = \frac{D - A}{2B} \mp \frac{\sqrt{m^2 - 1}}{B} = \frac{1}{R_a} \quad \text{or} \quad \frac{1}{R_b}. \quad (19)$$

The formal solutions in this situation correspond to two purely spherical waves with radii of curvature R_a and R_b and with infinite width, i.e., with no gaussian transverse amplitude variation. These waves obviously violate the confinement condition of our analysis. They are still of considerable practical importance, however. As we will see in a later chapter they have a meaningful interpretation as zero-order solutions for the general class of *hard-edged geometrically unstable resonators*.

The matching perturbation eigenvalues for these two spherical waves are now also purely real quantities, i.e.,

$$\lambda_a, \lambda_b = m \pm \sqrt{m^2 - 1} = M \quad \text{or} \quad 1/M, \quad (20)$$

where the geometric magnification M is a real number with magnitude $|M|$ greater than unity. The eigenvalues and eigenwaves for either of these waves can also be rewritten in the alternative forms

$$\frac{1}{R_a}, \frac{1}{R_b} = \frac{D - \lambda_a}{B}, \frac{D - \lambda_b}{B}, \quad (21)$$

and these can sometimes be useful expressions.

Positive Branch Unstable Resonators

The labeling of these geometrically unstable solutions then becomes somewhat complicated, because geometrically unstable resonators must first be divided into *positive-branch* and *negative-branch* unstable resonators, depending upon whether M is greater than +1 or less than -1; and the two geometrical eigensolutions for either of these classes must then be separated into a *magnifying* and a *demagnifying* eigensolution. Which of these waves corresponds to eigenvalue \tilde{q}_a or eigensolution \tilde{q}_b then depends upon which branch the resonator corresponds to.

Consider first the situation of m positive and greater than +1. The two eigenvalues are then

$$\left. \begin{aligned} \lambda_a &= m + \sqrt{m^2 - 1} = M \\ \lambda_b &= m - \sqrt{m^2 - 1} = 1/M \end{aligned} \right\} \quad \begin{pmatrix} \text{positive branch} \\ m > +1 \end{pmatrix}, \quad (22)$$

where the geometric magnification M itself is also positive and greater than +1. The two corresponding eigenwaves then have radii of curvature R_a and R_b as given in Equation 21.19 or 21.21.

Consider next a ray r_a which is perpendicular to the surface of the eigenwave R_a . The displacement and slope of this ray crossing the reference plane at the start of any one round trip will then be related by $r'_{a,1} = r_{a,1}/R_a$. After one round

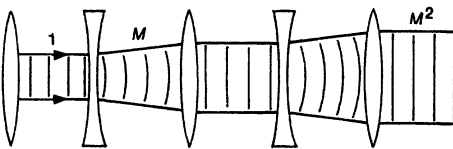
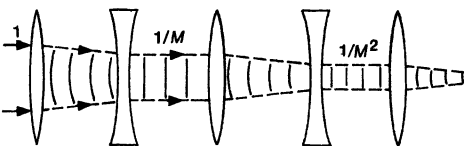
magnifying solution R_b, λ_b 

FIGURE 21.3

The magnifying and demagnifying geometrical eigenwaves in a positive-branch geometrically unstable resonator.

demagnifying solution R_a, λ_a 

trip, therefore, this ray will still be normal to the same spherical wavefront, but its displacement will now be reduced to

$$\begin{aligned} r_{a,2} &= Ar_{a,1} + Br'_{a,1} = (A + B/R_a)r_{a,1} \\ &= r_{a,1}/\lambda_a = r_{a,1}/M \quad (\text{demagnifying eigenwave } R_a). \end{aligned} \quad (23)$$

In other words the transverse position of the ray will be *demagnified* by just the magnification M (Figure 21.3).

For a ray normal to the R_b eigensolution, on the other hand, the ray position will be *magnified* on each round trip by

$$r_{b,2} = r_{b,1}/\lambda_b = M \times r_{b,1} \quad (\text{magnifying eigenwave } R_b). \quad (24)$$

These two results indicate that one of the eigensolutions is a *magnifying eigenwave* R_b which grows in transverse size, but keeps the same radius of curvature, on each round trip; whereas the other is a *demagnifying eigenwave* R_a which decreases in size on each round trip, but also preserves its radius of curvature.

Suppose we send into such a resonator a beam that has wavefront curvature equal to one or the other of the unstable eigenwaves R_a or R_b , but that has either a finite width or else a large gaussian spot size w ; and then follow this beam through one or more trips around the resonator (or equivalently through one or more iterations of the associated $ABCD$ matrix for the periodic system). We will then find that the transverse spread, or the gaussian spot size, of one of these waves (R_b) will *magnify transversely* by essentially the magnification M on each repeated round trip, whereas the other wave (R_a) will *demagnify* in size by the inverse ratio $1/M$ on each round trip, as in Figure 21.3. We will therefore call these the *magnifying and demagnifying eigensolutions or eigenwaves*, for obvious reasons.

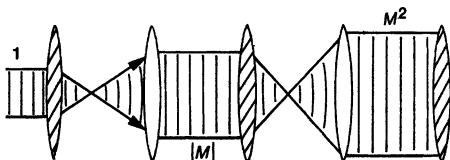
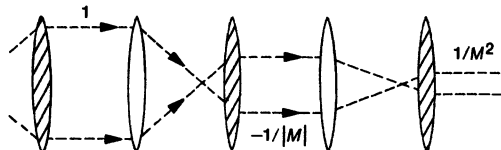
magnifying solution R_a, λ_a demagnifying solution R_b, λ_b 

FIGURE 21.4
Magnifying and demagnifying geometrical eigenwaves in a negative-branch unstable resonator.

Negative Branch Unstable Resonators

Suppose on the other hand that we consider a negative-branch resonator (Figure 21.4) for which m is negative and less than -1 . In this situation we will find that the two eigenvalues are

$$\left. \begin{aligned} \lambda_a &= -|m| + \sqrt{m^2 - 1} = 1/M \\ \lambda_b &= -|m| - \sqrt{m^2 - 1} = M \end{aligned} \right\} \quad \begin{pmatrix} \text{negative branch} \\ m < -1 \end{pmatrix}, \quad (25)$$

where M is now also a negative number in the range $M < -1$. If we again trace the eigenwaves or eigenrays through this system, we will find that in this situation it is the R_a wave that magnifies in size (but inverts in sign) on each round trip, whereas the R_b wave also inverts but demagnifies in sign, as in Figure 21.4.

For both the positive and the negative branch, therefore, one of the two eigenwaves magnifies and the other demagnifies in transverse width on each round trip, as illustrated in Figure 21.4. This is what we mean when we say that the system is geometrically unstable. The negative branch differs from the positive branch only in different ordering of the a or b solutions, and in the fact that the wave inverts about the system axis, as well as becoming magnified after each pass, corresponding to the fact that $M < -1$.

This inversion about the axis on each pass for a negative branch resonator implies that there must be at least one (or in general, an odd number) of focal points inside the cavity, whereas positive branch resonators must have an even number (including zero) of such internal foci. Negative-branch resonators, even though attractive in other ways, must usually be avoided in high-power lasers because of problems with optically induced breakdown at these focal points.

Note also that the magnifying wave going in the forward direction through the equivalent periodic lensguide is precisely equivalent to the demagnifying wave

going in the reverse direction, and vice versa. This point will become important in understanding asymmetric ring unstable resonators in later sections.

Perturbations in Real Unstable Resonators

Further examination of the wave solutions in the real unstable resonator situation will then reveal that in every case it is the *magnifying wave solution* that is associated with the *perturbation-stable eigenvalue*, and the *demagnifying wave solution* that is associated with the *perturbation-unstable eigenvalue*, whether these are the waves labeled by R_a or R_b .

That is, if we send into the system a spherical wavefront with a curvature close to the magnifying wavefront radius, but with some slight perturbation in curvature, that wavefront will grow in size transversely by the magnification M on each successive pass; but the *deviation in curvature* from the exact eigenwave will decrease on each successive pass by the ratio $(1/M)^2$.

Conversely, if the wavefront is initially close to the demagnifying solution but with some slight initial error, this error in the wavefront curvature will grow as M^2 on each successive bounce, until the converging wave essentially “runs away,” and eventually converts over into the diverging or magnifying wavefront. (This conversion generally occurs after only a rather small number of round trips in typical situations.) If we follow the labeling conventions used in the preceding, in the positive-branch situation it is the a eigenwave that is demagnifying but perturbation unstable and the b eigenwave that is magnifying but perturbation stable; whereas for the negative-branch situation these subscripts must be reversed.

This general behavior clearly illustrates how the eigenvalues λ_a and λ_b are associated as much with the *perturbation stability* of the eigenwaves, as with the transverse magnification or demagnification of the waves on successive round trips.

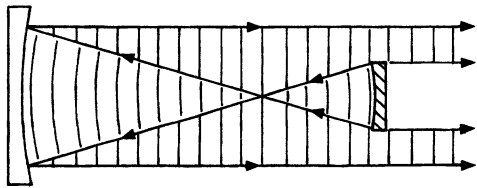
Practical Properties of Real Unstable Resonators

These unbounded spherical-wave solutions for the real but geometrically unstable situation are clearly nonphysical as they stand. They do represent, however, a useful “zeroth-order” approximation to the real nongaussian modes of the so-called *hard-edged unstable optical resonators* (Figure 21.5) that are used in many higher-power lasers. We will discuss this class of resonators in more detail in a later chapter, but for the present we can say the following.

If the magnifying wave expands on each round trip in a geometrically unstable resonator, it must eventually run into the mirror edges or the laser tube walls. These edges will then obviously have major effects on the wave, both in cutting off further transverse growth, and also in producing strong diffraction effects in the wavefront on the next round trip. The resonator edges thus obviously play a very important role in real unstable resonators, and the diffraction effects due to these effects cannot be ignored, even in an approximate theory. A correct analysis of real unstable resonators can thus be carried out in full detail only by doing a full diffraction or Huygens-integral analysis of the unstable resonator.

As we will see in a later chapter, however, experience shows that the magnifying eigenwave predicted by the simple *ABCD* analysis does give a very good first approximation for the basic wavefront radius of curvature (either R_a or R_b) and for the round-trip magnification M in a real hard-edged unstable resonator, even

negative branch confocal



positive branch confocal

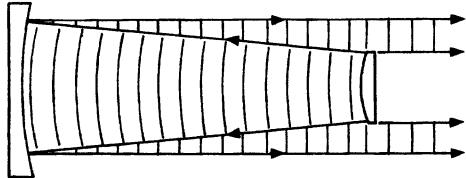


FIGURE 21.5

The geometric modes in real hard-edged unstable resonators correspond to the magnifying eigenwaves shown in Figures 21.3 and 21.4.

when the strong edge-diffraction effects are taken into account. The exact transverse mode shape in such a resonator will look like the geometrically magnifying phase front, with an amplitude profile that has large Fresnel diffraction ripples and that expands by an amount M on each round trip, before being cut off by the finite aperture edges. The detailed amplitude ripples can only be predicted from a full diffraction calculation taking into account the mirror edges, and the exact form of these ripples will depend very strongly on the exact aperture size. These hard-edged unstable resonators can be very useful, and we will describe them in much more detail in the following chapter.

REFERENCES

Geometrically unstable resonators were first analyzed by A. E. Siegman, "Unstable optical resonators for laser applications," *Proc. IEEE* **53**, 277-287 (March 1965). A longer review article is in A. E. Siegman, "Unstable optical resonators," *Appl. Opt.* **13**, 353-367 (February 1974).

The distinction between positive and negative branch unstable resonators was pointed out by W. F. Krupke and W. R. Sooy, "Properties of an unstable confocal resonator CO₂ laser system," *IEEE J. Quantum Electron.* **QE-5**, 575-586 (December 1969).

Problems for 21.3

1. *Convergence and divergence of a gaussian beam in a geometrically unstable system.* Suppose that a gaussian beam with an initially large spot size w_0 and an initial radius of curvature R_0 equal to that of the demagnifying eigensolution is launched into a real unstable ABCD system. Using the positive branch situation

for simplicity, analyze the changes in spot size w_n and radius of curvature R_n for this injected gaussian beam on successive round trips around the resonator (or at successive reference planes along the equivalent lensguide). In particular, show that:

- The spot size will initially demagnify by $w_{n+1} \approx w_n/M$ on each successive round trip.
- The minimum spot size that w_n can reach is then given by $w_{\min}^2 \approx B\lambda/\pi$, and the number of round trips to reach this minimum is given by the (small) number $N \approx \ln(w_0/w_{\min})/\ln M$. (Hint: Use the normalized variables $x_n \equiv \lambda/\pi w_n^2$, $y \equiv 1/R_n$, and $z_n = x_n + jy_n \equiv j/\tilde{q}_n$.)
- Beyond this point the gaussian beam then converts over into a magnifying wave with a limiting behavior that $w_{n+1} \approx M \times w_n$.

Suggestion: Try both some analysis and some purely numerical simulations of specific situations, and see how they compare.

21.4 COMPLEX STABLE AND UNSTABLE RESONATORS

Putting gaussian apertures or similar transverse amplitude variations into an optical resonator will lead in general to complex $ABCD$ systems. The general solutions that we developed in the first section of this chapter for the self-consistent eigenwaves and perturbation eigenvalues in a general complex paraxial resonator will then be given, once again, by

$$\frac{1}{\tilde{q}_a}, \frac{1}{\tilde{q}_b} = \frac{D - A}{2B} \mp \frac{1}{B} \sqrt{\left(\frac{A + D}{2}\right)^2 - 1}, \quad (26)$$

and

$$\lambda_a, \lambda_b = \frac{A + D}{2} \pm \sqrt{\left(\frac{A + D}{2}\right)^2 - 1}, \quad (27)$$

where A , B , and D may all be complex quantities. The conditions for a well-behaved and physically real resonator eigenmode are again that at least one of these eigenwaves should be confined, and that the perturbation eigenvalue associated with that particular wave should have a magnitude $|\lambda| \leq 1$.

When the individual matrix elements in Equations 21.26 and 21.27 may all potentially be complex numbers, it is not usually at all obvious by inspection which of the two eigenwaves is the confined solution; nor is it then obvious by inspection whether the eigenvalue associated with that confined wave has a magnitude less than or greater than unity. In fact, the only way to answer these questions for a completely general complex paraxial resonator seems to be to calculate the complex $ABCD$ elements and then examine the $1/\tilde{q}$ and λ values for a specific system in close detail, to see whether or not they meet the necessary criteria.

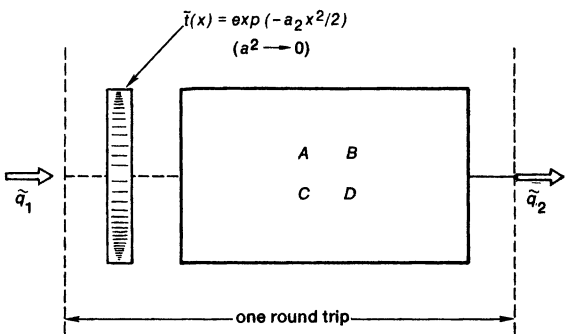


FIGURE 21.6
Inserting a weak gaussian aperture into a purely real $ABCD$ system.

Complex Perturbation-Stable Gaussian Resonators

We can, however, gain considerable insight into complex paraxial resonator systems in the following fashion. It is possible to show quite generally (see the Problems) that if an *arbitrarily small amount of transversely increasing loss* (or transversely decreasing gain) is added anywhere inside any purely real $ABCD$ system, whether geometrically stable or unstable, then one of the eigenwaves for that system will always be modified so as to become both a confined and perturbation-stable gaussian wave.

In other words, an arbitrarily weak gaussian aperture, as in Figure 21.6, will act to convert any purely real resonator—whether it is geometrically stable or unstable to start with—into a *complex perturbation-stable resonator*. Note that *geometric stability* and *perturbation stability* are thus quite separate and distinct concepts in the complex resonator.

Consider first the results for a geometrically stable resonator to which a weak gaussian aperture is added. An initially stable resonator will have one confined and one unconfined eigensolution, which we have indicated by points labeled $1/\tilde{q}_a$ and $1/\tilde{q}_b$ in Figure 21.7(a), together with matching eigenvalues λ_a and λ_b , both of which lie on the unit circle in the complex λ plane. Adding a weak positive gaussian aperture will then cause the eigenwaves and eigenvalues for this situation to move in the directions indicated by the arrows in the plots. In particular, for an initially stable resonator the confined eigensolution will always move so as to remain confined and become perturbation stable.

If, on the other hand, we consider a geometrically unstable system, we initially have two unconfined eigenwaves R_a and R_b and two purely real eigenvalues λ_a and λ_b , with λ_b being the perturbation-stable (and thus magnifying) solution in this example. Adding the weak gaussian aperture will then always cause the perturbation-stable solution to remain perturbation-stable and become confined, as illustrated by the arrows in Figure 21.7(b).

Physical Example

Figure 21.8 shows an example of the kind of complex gaussian eigenmode that results for a resonator where the mirror curvatures by themselves lead to strongly unstable behavior in the geometric sense, but where the complex gaussian modes are perturbation-stabilized by a weak gaussian aperture. One way of

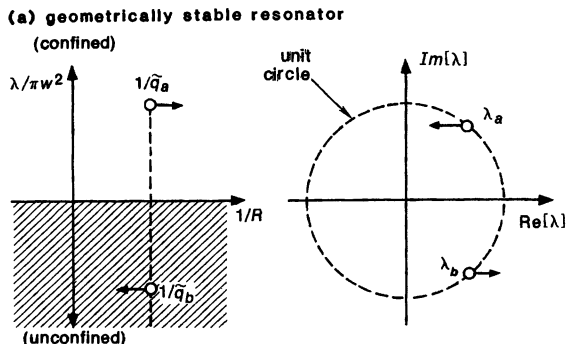
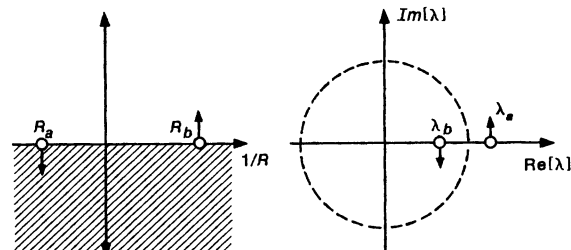


FIGURE 21.7

Inserting a weak gaussian aperture, as in Figure 21.6, will convert either (a) a geometrically stable or (b) a geometrically unstable system into a confined and perturbation-stable system.

(b) geometrically unstable resonator



viewing the behavior of gaussian beams in this kind of resonator is to consider an initially injected gaussian beam with a curvature near the magnifying eigenwave of the unapertured resonator, but with a spot size initially small compared to the gaussian aperture. Such a gaussian wavefront will then be magnified on each round trip by a factor close to the geometric magnification M as a result of the unstable defocusing effects.

This magnifying wave will eventually grow to a large enough diameter, however, that it will begin to run into the gaussian aperture. The divergence or the geometric magnification will then be limited and the wave trimmed back in size on each round trip by the "soft aperture" effects of the gaussian aperture or variable reflectivity mirror. In fact, a gaussian beam with a spot size much larger than the aperture would be rapidly reduced in spot size on the first pass through the aperture. The magnifying eigenwave thus stabilizes to a spot size which is constant (and perturbation-stable) on successive round trips, representing a balance between geometric magnification and soft aperture narrowing.

This particular type of resonator, with a combination of geometric instability for round-trip magnification, plus gaussian aperturing for spot size and eigenwave stabilization, appears to hold very substantial promise for future development of large-diameter but well-controlled laser modes, as we will discuss in more detail in the following chapter. The development of such *complex perturbation-stable gaussian resonators* has been limited to date primarily by the difficulty in

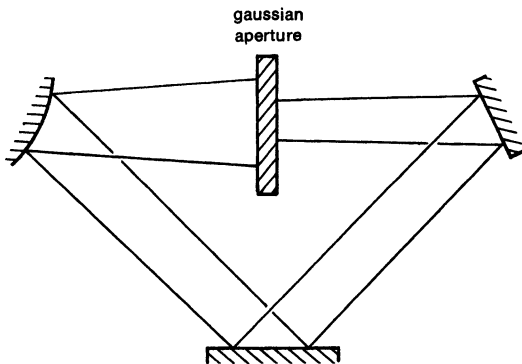


FIGURE 21.8
General behavior of the lowest-order gaussian mode in a geometrically unstable resonator which is stabilized by a weak gaussian aperture.

obtaining practical gaussian apertures, but this is a problem which now seems to be finding practical solutions.

Complex Perturbation-Unstable Resonators

There is also the opposite situation, namely, a resonator with a transversely increasing transmission caused either by transversely decreasing loss or transversely increasing gain. The opposite of the previous generalization then applies, namely, *adding even a small amount of transversely increasing transmission will convert any purely real resonator, geometrically stable or unstable, into a complex and perturbation-unstable resonator.*

Even in this situation there will be one eigenwave which is transversely confined, and which might therefore seem to be a physically useful solution. If transversely increasing gain is present, however, this confined eigenwave will always turn out to be perturbation unstable: if it is disturbed even slightly, it will begin to grow in diameter. The other wave which is perturbation stable, by contrast, will always turn out to be unconfined in the transverse direction. Hence, neither of these waves appears to be physically useful as a real resonator mode, and so such complex perturbation-unstable resonator modes appear to be of little interest for practical laser devices—at least not in their ideal form.

A brief summary of the properties of each of the general types of complex paraxial resonators is presented in Table 21.1.

Practical Considerations for Systems With Radially Increasing Gain

There can be some practical situations in which transversely increasing gain will be present in a resonator, at least over some finite range of diameter. In large-bore CO₂ lasers, for example, increased heating of the laser gas at the center of the laser tube can lead to decreased gain on axis and increasing gain near the tube walls. Gain saturation of almost any gain medium by a gaussian laser beam will also appear to reduce the gain more at the center than at the edges, even in an initially uniform gain medium.

According to the complex resonator theory, even small effects of this type should then, at least in principle, cause even strongly stable real resonators to

TABLE 21.1
Complex Paraxial Resonator Types

Type of resonator:	Real stable	Real unstable	Complex stable	Complex unstable
ABCD elements:	Real	Real	Complex	Complex
Half-trace, m^2 :	$m^2 < 1$	$m^2 > 1$	Complex	Complex
Gain vs. radius:	Flat	Flat	Decreasing	Increasing
Nature of eigenwaves:	Stable gaussian	Unstable spherical	Complex gaussian	Complex gaussian
Modes confined?	Yes/No	No/No	Yes/No	Yes/No
Perturbation stable?	Yes/Yes	Yes/No	Yes/No	No/Yes
Edge effects important?	No	Yes!!	No	Yes

become perturbation unstable. As a practical matter, however, it appears that the focusing effects of the lenses and mirrors in a real stable resonator are of substantially larger magnitude than the defocusing or destabilizing effects of weak radial gain increases. What is probably of even more importance is that even weak diffraction effects from mirror edges or mode control apertures appear to have a stabilizing effect, though this is obviously not directly covered by the ideal *ABCD* theory. The practical implication, therefore, is that weak and transversely bounded radial increases in gain do *not* appear to cause serious perturbations in otherwise stable laser resonators. This entire subject has, however, not as yet been much investigated.

Multiperture Complex Resonators

We might finally, in the most general situation, even encounter resonators containing transversely decreasing transmission elements at some locations in the resonator, and transversely increasing or destabilizing elements at other places, so that both positive and negative apertures are encountered in a complete round trip. Will such a resonator then be overall complex-stable or complex-unstable? It appears to be difficult to give any general answers regarding the resulting resonator behavior, other than by computing the total complex *ABCD* matrices for the resonator of interest, and then finding out by direct inspection into which class the overall system falls.

An additional complication for resonators having *both* positive and negative gaussian apertures at different points around the resonator is the following. It is possible for such a resonator to have a mode which appears to be self-reproducing, confined and perturbation-stable when calculations are made starting from one reference plane within the resonator—for example, a reference plane just after a transversely decreasing aperture—but for the same eigenwave to appear as perturbation-stable but unconfined when the same resonator is analyzed starting from a different reference plane—for example, a reference plane just after one

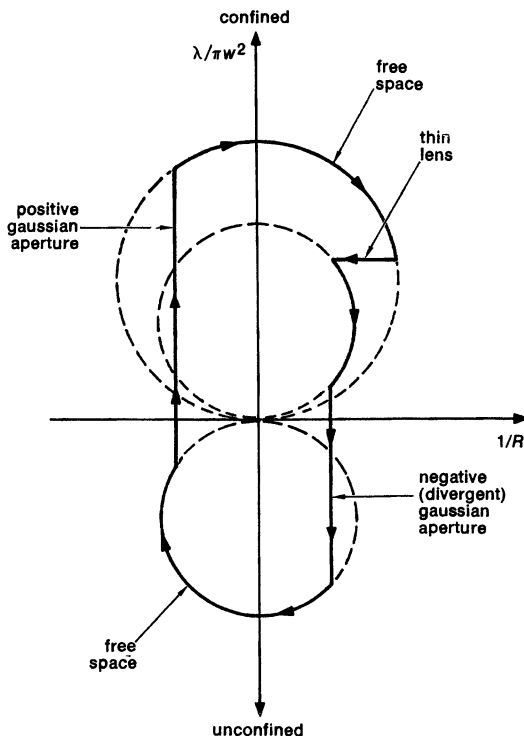


FIGURE 21.9
 Round-trip trajectory for a gaussian beam in a multiaperture resonator which is perturbation-stable around the full trajectory but transversely unconfined in part of the resonator.

of the transversely increasing apertures. The trajectory in the $1/\bar{q}$ plane for one example of such a resonator is shown in Figure 21.9.

One primary point here is that beam power is in general not conserved in going through a gaussian aperture of either sign. In particular, it is possible for a confined gaussian beam having finite power, after passing through a transversely increasing aperture, to be converted into an unconfined beam carrying infinite power. All that is required is that the transverse gain increase more rapidly than the bounded input wave amplitude decreases. Thus, a confined and perturbation-stable gaussian beam, in passing through a transversely increasing aperture, can under some conditions be transformed into an unconfined wave; and then later transformed back into a confined wave by a transversely decreasing aperture.

The conclusion is that in those rare situations where transversely decreasing and increasing apertures are both present in a single resonator, we cannot find out whether the wave is confined at every plane merely by examining the solutions for the eigenwaves and perturbation eigenvalues at one reference plane. The round-trip *ABCD* matrix from only one reference plane does not contain sufficient information to determine this. We must instead follow the selected eigenwave completely round the resonator, step by step, and verify its confinement at every plane.

REFERENCES

The earliest discussion of modes in resonators with gaussian reflectivity mirrors—though done without introducing any *ABCD* matrix concepts—is by H. Zucker, “Optical resonators with variable reflectivity mirrors,” *Bell Sys. Tech. J.* **49**, 2349–2376 (November 1970).

Additional discussions of this situation are presented in A. Yariv and P. Yeh, “Confinement and stability in optical resonators employing mirrors with gaussian reflectivity tapers,” *Optics Commun.* **13**, 370–374 (April 1975); L. W. Casperson and S. D. Lunnan, “Gaussian modes in high loss laser resonators,” *Appl. Optics* **14**, 1193–1199 (May 1975); and U. Ganiel, A. Hardy, and Y. Silberberg, “Stability of optical laser resonators with mirrors of gaussian reflectivity profiles, which contain an active medium,” *Optics Commun.* **14**, 290–293 (July 1975).

Problems for 21.4

1. *Inserting a weak gaussian aperture into an arbitrary ring resonator.* A multielement paraxial ring optical resonator with all real *ABCD* elements is “cut open” at some point and an arbitrarily weak gaussian aperture is inserted. Verify the assertions made in the section that this will always produce a self-consistent, confined, perturbation-stable mode, regardless of whether the initial all-real resonator was geometrically stable or unstable.
2. *Practical design of a large-mode-volume resonator.* A common objective in laser resonator design is to produce a resonator having a large gaussian mode size, in order to efficiently fill a large diameter laser rod or laser tube, and at the same time to have a sizable difference in loss per round trip between the lowest and next higher-order modes, in order to suppress higher-order mode oscillation.

Suppose you are setting out to achieve these objectives, starting from a purely real paraxial optical resonator and adding a weak gaussian aperture. In terms of the resonator parameters introduced in this section, what criteria would you specify? For example, would you start with a resonator that was geometrically stable or unstable? Large or small values of B , m or M ? What value of aperture size relative to other parameters?

3. *Convergence to the final stable mode in a gaussian-aperture-stabilized resonator.* Consider a general complex paraxial resonator with round-trip matrix elements $A = M(1 - j\alpha)$, $B = L$, $C = -j\alpha$ and $D = 1/M$ with $M > +1$. (This corresponds more or less to a geometrically unstable resonator with round-trip magnification M to which has been added a gaussian aperture with strength proportional to α .)

Plot trajectories in the $1/\tilde{q}$ (or $1/\tilde{q}^*$) plane which show how the \tilde{q} value of a beam with an initial complex radius \tilde{q}_0 will evolve on successive round trips, starting with initial values in all different parts of the physically realizable complex half-plane. Discuss the physical interpretation of significant regions in this plane. Use, for example, the values $M = 2$ and $\alpha L = 1/10$.

4. *Same problem, but for a negative branch resonator.* Repeat the previous problem, but with $M < -1$.
5. *Mode parameters in a gaussian-aperture-stabilized two-mirror standing-wave resonator.* Consider a symmetric two-mirror optical resonator of length L having

mirrors with radius of curvature R and transverse amplitude reflectivity variation $|\rho(x)|^2 = \exp(-a_2 x^2/2)$ at each end. Assuming there is enough single-pass gain in the resonator to make up the losses at the mirrors, find the steady-state self-consistent lowest-order mode in which the resonator will oscillate. Consider both stable and unstable curvatures R , noting in particular the spot sizes and wavefront curvatures at the center and at the end of the resonator, as functions of R, L and a_2 .

6. *Gaussian aperture stabilization in a plane-mirror resonator.* A complex paraxial resonator is set up with two plane mirrors spaced by a distance L . Both mirrors are variable-reflectivity mirrors (VRM), one with a transversely decreasing transmission (positive value of a_2), and one with a transversely increasing transmission (negative value of a_2). Assuming that both of these gaussian apertures are very weak (small values of a_2 for each), evaluate the perturbation stability and the confinement properties of the perturbation-stable mode, for the situations where the two a_2 values are both different and exactly equal in magnitude. Note: This problem may be a bit more subtle than it looks, and the situations of equal or different a_2 magnitudes require slightly different treatment.

21.5 OTHER GENERAL PROPERTIES OF PARAXIAL RESONATORS

We can next analyze some further properties of complex paraxial resonators, including round-trip amplitude and phase changes; general properties of standing-wave and traveling-wave (ring) resonators; and the stability properties of higher-order modes in such resonators.

Round-Trip Amplitude Changes and Phase Shifts

We consider next what happens to the complex amplitude coefficients in front of the Hermite-gaussian eigenmodes of a generalized paraxial resonator on each round trip. We showed in the previous chapter that when a generalized Hermite-gaussian mode passes through an arbitrary complex $ABCD$ system, the amplitude coefficient for the wave changes by the complex ratio

$$\frac{\tilde{\alpha}_{2,n}}{\tilde{\alpha}_{1,n}} = \left(\frac{1}{A + B/\tilde{q}_1} \right)^{n+1/2}. \quad (28)$$

But if \tilde{q}_1 corresponds to either of the self-consistent eigenvalues \tilde{q}_a or \tilde{q}_b , as it does for a resonator mode, this result says that the round-trip change in wave amplitude and phase for the mode in the resonator is given by the same factor as the perturbation eigenvalue. If we work in only one transverse dimension, this factor is

$$\left. \frac{\tilde{\alpha}_{2,n}}{\tilde{\alpha}_{1,n}} \right|_{\tilde{q}_1=\tilde{q}_a, \tilde{q}_b} = \left(\frac{1}{A + B/\tilde{q}_{a,b}} \right)^{n+1/2} = \lambda_{a,b}^{n+1/2}, \quad (29)$$

whereas if we consider a complete TEM_{nm} higher-order Hermite-gaussian mode in two transverse dimensions, then we have

$$\left. \frac{\tilde{\alpha}_{2,nm}}{\tilde{\alpha}_{1,nm}} \right|_{\tilde{q}_1 = \tilde{q}_a, \tilde{q}_b} = \left(\frac{1}{A + B/\tilde{q}_{a,b}} \right)^{n+m+1} = \lambda_{a,b}^{n+m+1}. \quad (30)$$

(For Laguerre-gaussian modes $n + m + 1$ can be replaced by $p + m + 1$.) A perturbation-stable mode decreases (or at least stays constant) in amplitude on each round trip, whereas a perturbation-unstable mode increases in amplitude.

Guoy Phase Shifts and Transverse Mode Frequencies

The magnitudes of the eigenvalues λ_a and λ_b thus determine the round-trip losses for the resonator eigenmodes (to be made up by the laser gain in an oscillating laser), whereas the phase angles of the eigenvalues give the phase shifts for the mn -th order Hermite-gaussian modes. For example, in a real stable gaussian resonator the round-trip eigenvalue becomes simply

$$\left. \frac{\tilde{\alpha}_{2,nm}}{\tilde{\alpha}_{1,nm}} \right|_{\tilde{q}_1 = \tilde{q}_a, \tilde{q}_b} = \exp [\mp j(n + m + 1)\theta], \quad (31)$$

where $\cos \theta = m$. The angle θ thus represents the multielement or real- $ABCD$ generalization of the Guoy phase shift ψ for gaussian beams and two-mirror resonators that we discussed in Section 19.3. Higher-order modes once again have this phase shift increased by the factor $n + m + 1$. A real gaussian resonator with no soft apertures has no diffraction losses. Hence, the magnitude of the amplitude coefficient remains unchanged, or the net round-trip amplitude gain is unity, for modes of all orders m or n . There is thus no transverse mode discrimination—at least not until some finite aperture is inserted into the cavity.

For a complex stable resonator, i.e., one which contains soft apertures, the round-trip amplitude and phase shift will be given by the formulas developed in this section, where the applicable eigenvalue will be the perturbation eigenvalue for the confined and perturbation-stable mode. Since this eigenvalue by definition has magnitude $|\lambda| \leq 1$, each higher-order mode is attenuated relative to lower-order modes by this eigenvalue raised to the appropriate power. So long as no hard apertures are present, the perturbation eigenvalues are all that are needed to characterize completely the losses, the phase shifts, and the perturbation stability of Hermite-gaussian modes of all orders.

Higher-Order Hermite-Gaussian Modes

We have considered up to this point only the transformation and the perturbation-stability properties of the gaussian \tilde{q} parameter and of the mode amplitude coefficient $\tilde{\alpha}_{nm}$. For higher-order modes, however, we also have to examine what happens to the complex spot size parameter \tilde{v} on successive round trips.

The general transformation rule for the \tilde{v} parameter on one round trip is, as derived in the previous chapter,

$$\tilde{v}_2^2 = (A + B/\tilde{q}_1)^2 \times \tilde{v}_1^2 + j \frac{4B}{k_1} (A + B/\tilde{q}_1). \quad (32)$$

If \tilde{q}_1 has the values \tilde{q}_a or \tilde{q}_b , then the self-consistent values of $\tilde{v}_2 = \tilde{v}_1 = \tilde{v}$ are given by

$$\tilde{v}_{a,b}^2 = \mp j \frac{B\lambda}{\pi} \times \sqrt{\frac{1}{\tilde{m}^2 - 1}}, \quad (33)$$

where $m \equiv (A + D)/2$, and where the upper and lower signs are consistent with the upper and lower signs in Equations 21.3 and 21.10 for the eigen- \tilde{q} -values and eigenvalues.

If we then look at the perturbation stability of \tilde{v}_a and \tilde{v}_b , we can find that whereas the perturbation stability for the \tilde{q}_a and \tilde{q}_b values is expressed by

$$\left. \frac{\Delta \tilde{q}_2}{\Delta \tilde{q}_1} \right|_{\tilde{q}_1 = \tilde{q}_a, \tilde{q}_b} = \lambda_a^2 \quad \text{or} \quad \lambda_b^2 \quad (34)$$

the perturbation stability analysis for the \tilde{v} values leads to exactly inverse results, namely,

$$\left. \frac{\Delta \tilde{v}_2}{\Delta \tilde{v}_1} \right|_{\tilde{q}_1 = \tilde{q}_a, \tilde{q}_b} = \frac{1}{\lambda_a^2} \quad \text{or} \quad \frac{1}{\lambda_b^2} = \lambda_b^2 \quad \text{or} \quad \lambda_a^2. \quad (35)$$

In other words, any mode which is perturbation-stable in \tilde{q} is perturbation-unstable in \tilde{v} . This would seem to imply that no higher-order modes above $n = 2$ can exist and be simultaneously perturbation-stable in both \tilde{q} and \tilde{v} in a general complex paraxial resonator.

Physical Interpretation

The physical meaning of this result is the following. For purely real and stable systems, the eigenvalues λ_a and λ_b all have unity magnitude in any event. Both lowest and higher-order modes can then propagate with (marginal) stability in both \tilde{q} and \tilde{v} on repeated round trips, although we can expect that as soon as any finite aperture, soft or hard, is added to the resonator, the higher-order modes will begin to be filtered out, since they always spread out further.

In complex but perturbation-stable systems, however, soft apertures are already present; and higher-order Hermite-gaussian or Laguerre-gaussian modes, because they spread farther out, will have higher losses. Consider then the propagation of some higher-order mode $\tilde{u}_n(x)$ with $n \geq 2$, so that both \tilde{q} and \tilde{v} are relevant. Any slight perturbation of this mode can then be described as a coupling of some of the power from this particular n -th order mode into other Hermite-gaussian modes of both higher and lower index n' .

But any lower-order modes that are excited by the perturbation will have lower net losses than the original n -th order mode. Hence, as the beam goes around on successive round trips, the original n -th order mode will gradually die out relative to the lower-order modes; and in the long run only the lowest symmetric ($n = 0$) and antisymmetric ($n = 1$) modes will remain.

The higher-order Hermite-gaussian or Laguerre-gaussian modes are thus a mathematical possibility; but unless we put in specially shaped apertures (wires, point scatters, etc.), they do not represent long-term perturbation-stable solutions in competition with the lowest-order modes. This higher-order mode suppression tendency of the complex stable resonators is, in fact, one of the most attractive features of this class of resonators.

Standing-Wave Resonators Versus Traveling-Wave Resonators

We can point out finally some significant distinctions that can be drawn between the eigenwaves in *standing-wave* and *traveling-wave* optical resonators. These distinctions will supplement, but in no way replace, the various considerations concerning confinement and stability that we have introduced in the previous section.

Consider, for example, standing-wave resonators that are either geometrically stable or unstable. The unit cell for the equivalent lensguide in either situation is then necessarily symmetric about the two reference planes corresponding to the two end mirror surfaces of the standing-wave resonator. If either of these mirror surfaces is taken as the reference plane for the $ABCD$ calculation, the round-trip $ABCD$ matrix necessarily has the symmetry property that $A = D$.

From the analytical results derived earlier, we can see that for a real stable standing-wave resonator the two eigen- \tilde{q} -values are both purely imaginary on the end mirror surfaces, since $D - A \equiv 0$. This means in turn that the phase front of the eigenwaves is always exactly matched in curvature to the end mirror surfaces, and this implies in turn that the forward and reverse traveling waves in the stable standing-wave cavity are matched in curvature everywhere. The standing wave is, in fact, a true standing wave (leaving out the possibility of different amplitudes for the forward and reverse waves due to finite mirror amplitude reflectivity or laser gain).

For real but unstable standing-wave resonators, on the other hand, the condition that $A = D$ on the end mirror reference planes implies that the magnifying and demagnifying waves R_a and R_b (or vice versa) (a) have equal and opposite curvatures at the end mirror surface, and (b) neither of these curvatures matches the end mirror surface. This is in fact a general characteristic of geometrically unstable resonators. We can also see, from a little further examination, that the geometrically demagnifying wave in the standing-wave situation is just the magnifying wave traveling in the reverse direction around the resonator, or in the reverse direction down the equivalent lensguide. The magnifying and demagnifying waves are connected in essence simply by time reversal.

Traveling-Wave Resonators and Eigenmodes

Consider now ring-type or traveling-wave real stable and unstable resonators and their equivalent lensguides. For a ring laser there is in general no necessary requirement that the equivalent lensguides have any symmetry between forward and reverse directions, and hence there need not be any reference plane within the rings or the lensguides where the $ABCD$ matrix will have equal diagonal elements, i.e., in general $A \neq D$ at any plane.

In fact, if we use the same reference plane going in either direction around the ring, the inversion rules for $ABCD$ matrices say that the $ABCD$ matrix elements in the two directions are related by $A_R = D_F$, $D_R = A_F$, $B_F = B_R$ and $C_F = C_R$, where the subscripts refer to forward and reverse directions, respectively. We will see later that the general propagation operators in the two directions, including finite aperture effects, are in general the mathematical transposes of each other. This does not mean that the $ABCD$ matrices in the two directions are the matrix transposes of each other; but rather that when these matrices are inserted into the generalized Huygens' integral operator, this

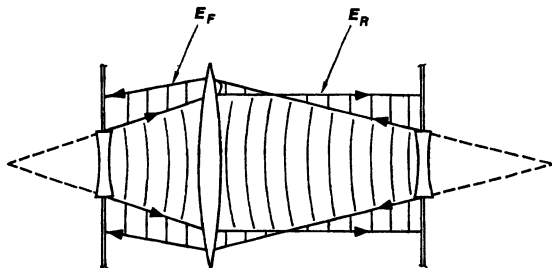


FIGURE 21.10
In an asymmetric geometrically unstable system the forward and reverse eigenvalues are the same, but the forward and reverse eigenvalues are not.

operator in the reverse direction becomes the transpose of the integral operator in the reverse direction.

General Properties of Traveling-Wave (Ring) Resonators

Several general properties of the paraxial eigenmodes going in the two opposite directions around a ring can then be deduced from this. First, since the traces of the $ABCD$ matrices going in the two directions are always identical, we can deduce that for either stable or unstable, real or complex resonators, the eigenvalues in the two opposite directions are always identical. The losses and phase shifts in either direction around a ring laser cavity are always the same, even though the shapes of the eigenwaves in the two directions may be different.

Second, for real stable resonators the perturbation-stable eigenwaves in the two directions are also the same, i.e., the eigenwave in one direction is just the reversed eigenwave in the other direction. On the other hand, for real unstable resonators the magnifying and perturbation-stable eigenwave going in one direction is just the time-reversed demagnifying wave going in the other direction.

In the asymmetric unstable lensguide shown in Figure 21.10, for example, the wave \tilde{E}_F corresponds to the magnifying and perturbation-stable wave going in the forward direction. The wave \tilde{E}_R then corresponds both to the demagnifying and perturbation-unstable wave going in the forward direction and also to the magnifying and perturbation-stable wave going in the reverse direction. Note that although the wavefronts and beam profiles of these two waves are significantly different, the geometric magnifications are in fact the same.

The resonator parameters in Figure 21.10 have been chosen so that the magnifying wave in the forward direction has a collimated wavefront in the magnified section. This is not in general true of all or even most unstable resonators. It occurs here only because the particular wave shown in Figure 21.10 corresponds to a confocal unstable resonator going in the forward direction. The same resonator is then obviously not confocal going in the reverse direction. Note that this kind of directional asymmetry can only be accomplished in a ring resonator. There is no way in which this same situation could be accomplished in a standing-wave resonator.

Resonator Properties With Nonparaxial Apertures

Essentially all of the properties introduced in this section, although derived here only for ideal paraxial resonators with infinite mirrors and at most only soft apertures, remain either partially or completely true even for the exact eigenmodes of much more general resonators with finite mirror diameters or hard-edged apertures.

If, for example, the underlying real paraxial elements in a resonator correspond to a geometrically stable system, then the exact eigenmodes in any standing-wave resonator will still have phase fronts that nearly coincide with the end mirror surfaces, and nearly correspond to pure standing-wave fields, even if the resonator contains finite apertures which produce small but finite diffraction losses. Increasing amounts of diffraction loss will cause progressively increasing departures from these properties.

The exact eigenmodes in geometrically unstable resonators with finite apertures will also, as we have mentioned earlier, still have wavefront curvatures close to the magnifying spherical eigenwave, even for rather large diffraction losses. The forward and reverse eigenmodes in the unstable traveling-wave situation will also continue to correspond to the magnifying and demagnifying forward solutions as described in the preceding, even for large diffraction losses.

The exact eigenmodes in the forward and reverse direction for any traveling-wave resonator, whether geometrically stable or unstable, will also continue to have exactly the same eigenvalues (and hence the same diffraction losses) in both directions even under very general conditions of finite apertures and large diffraction losses. Several of these concepts will be discussed further, for more general resonator models, when we discuss the orthogonality properties of resonator modes in a later section.

REFERENCES

The relation between forward and reverse, and magnifying and demagnifying waves in an asymmetric ring resonator is clearly outlined in P. del Pozzo, R. Polloni, O. Svelto, and F. Zaraga, "An unstable ring resonator," *IEEE J. Quantum Electron.* **QE-9**, 1061 (November 1973).

Problems for 21.5

1. *Magnifying and demagnifying eigenwaves in an unsymmetric ring unstable resonator.* Consider an unstable resonator or lensguide similar to Figure 21.10, consisting of a diverging lens of focal length $-f_1$, free space of length $l_1 = f_2 - f_1$, a converging lens of focal length $f_2 = Mf_1$, and a second free space segment of length $l_2 = \beta l_1$, where M is the geometric magnification, and β is a symmetry parameter which must have the value $\beta = 1$ for a standing-wave cavity, but can have arbitrary values in a traveling-wave or ring cavity.

Solve for and sketch the magnifying and demagnifying eigenwaves in this resonator going in the forward direction, or equivalently the magnifying waves going in the forward and reverse directions, for the situation $M = 2$ and for values of $\beta = 0.6, 0.8, 1, 2$ and 3 .

21.6 MULTIELEMENT STABLE RESONATOR DESIGNS

Many practical laser devices (such as, for example, mode-locked ion lasers, pulsed solid-state lasers, and tunable dye lasers) make use of multielement stable laser resonators which may contain a sizable number of lenses, curved and off-axis mirrors, ducts, Brewster-angle plates, and the like. As we have already noted several times, the stable gaussian modes in these multielement cavities can be analyzed in one pass by multiplying out their round-trip $ABCD$ matrices and then solving for their confined and perturbation-stable gaussian eigenwaves. A simple interactive computer program can be of great assistance both in entering the various elements into such an analysis and then in calculating and displaying the results—especially since this procedure may often have to be done separately but simultaneously in two transverse dimensions.

In complicated resonators of this type, changing the values of different elements can have effects on the stable mode parameters that interact in a complex and sometimes sensitive fashion; so that even with computer assistance the design procedure for synthesizing an optimized laser resonator can be time-consuming and unclear. Some general guidance in approaching the desired design values may then be of help; and this section will briefly review a few general principles for stable multielement resonator design.

Mode Sizes in Real Stable Resonators

In many situations we may wish to obtain a large spot size w at a certain plane inside a laser resonator, in order, for example, to extract maximum energy from a laser rod or tube; whereas in other situations a very small spot size may be needed to obtain maximum energy density in a saturable absorber or a dye laser cell or jet. How can we control in general terms the spot size at selected planes in a multielement optical resonator?

We might first recall that the gaussian spot size w for the stable eigenmode at the selected reference plane in a stable cavity is given by

$$w^2 = \frac{|B|\lambda}{\pi} \times \sqrt{\frac{1}{1-m^2}} = w_0^2 \times \sqrt{\frac{1}{1-m^2}}, \quad (36)$$

where we use the abbreviation $w_0^2 \equiv |B|\lambda/\pi$. We can then observe that the “effective length” $|B|$ for a multielement resonator will depend on the reference plane that is employed, whereas the half-trace m will be the same for all choices of reference plane. In many situations, moreover, the effective round-trip length $|B|$ will be of the same order as the physical cavity length, or shorter, so that w_0 will be comparable to the (small) confocal spot size in a simple two-mirror resonator of comparable length.

To achieve a larger spot size $w \gg w_0$, for example in order to fill a large-diameter laser tube, we must then adjust m^2 fairly close to unity, or close to the stability boundary for the cavity. But we can then show that the sensitivity of this adjustment—that is, the sensitivity δw of the spot size w to small errors δm in the adjustment of the m parameter—will be given by

$$\frac{\delta w}{w} = \frac{m^2}{2} \left(\frac{w}{w_0} \right)^4 \frac{\delta m}{m} \approx \frac{1}{2} \left(\frac{w}{w_0} \right)^4 \times \frac{\delta m}{m} \quad \text{for } m^2 \rightarrow 1. \quad (37)$$

If we want to achieve, for example, a spot size w that is 10 times the “confocal value” w_0 , then the adjustment tolerance for whatever resonator parameter is being adjusted to vary m becomes $\approx 5,000$ times more sensitive than the allowable tolerance in the spot size w itself. It is thus in general a difficult and tricky process to achieve a large spot size with a stable gaussian resonator, unless we can somehow obtain a large B parameter.

To meet the opposite design objective, that is, to obtain an unusually small spot size, it is evident that adjustments of the m^2 parameter offer little room for improvement; and we must find instead an overall resonator design that yields a sufficiently small B parameter at the desired reference plane. We will show how to accomplish either of these objectives shortly.

Intracavity Telescopes

One technique that can be useful for obtaining both small and large spot sizes is the use of an intracavity telescope or magnifier, usually with the focus set to infinity or not too far from there. Consider, for example, a galilean telescope focused at infinity plus two adjoining free-space sections L_1 and L_2 as in the top part of Figure 21.11. The $ABCD$ matrix going in the magnifying direction through this telescope is then

$$\begin{bmatrix} A & B \\ C & D \end{bmatrix} = \begin{bmatrix} M & ML_1 + L_2/M + f_2 - |f_1| \\ 0 & 1/M \end{bmatrix}, \quad (38)$$

where $M \equiv f_2/|f_1|$ is the transverse magnification of the telescope. Note that the effective length on the smaller side of this telescope is equal to the actual physical length L_1 multiplied by the telescope magnification M , whereas the effective length on the larger side is the physical length divided by M .

If we use instead a newtonian telescope, as in the lower part of Figure 21.11, then the $ABCD$ matrix going in the forward direction through the telescope becomes

$$\begin{bmatrix} A & B \\ C & D \end{bmatrix} = \begin{bmatrix} -M & (f_1 + f_2) - (ML_1 + L_2/M) \\ 0 & -1/M \end{bmatrix}, \quad (39)$$

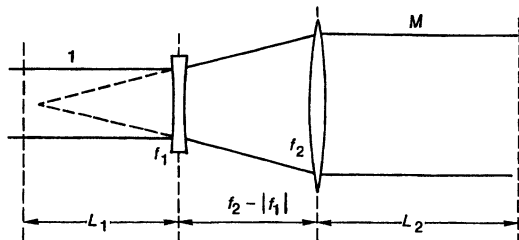
where in this situation $-M \equiv -f_2/f_1$ is the (negative) magnification through the telescope. One significant point here is that if we pick L_1 and L_2 to correspond to conjugate image points we can make the net value of the effective length B through the telescope be zero, or arbitrarily close to zero. This condition obviously corresponds to the image relaying system, with transverse magnification M , that we mentioned in an earlier section.

More generally, an inverting or newtonian telescope can be used to insert a negative value of effective length into a resonator, in order to cancel out positive B contributions from other parts of the resonator. For a resonator to be geometrically stable, the net round-trip magnification must be unity. This can be accomplished more or less automatically in a standing-wave cavity since the telescope will be traversed twice, going in opposite directions, so that the telescope magnification M will be canceled out.

Mode Spot Size Stability Against Internal Perturbations

One common cause of spot size instability in solid-state lasers can be the weak thermal focusing that occurs in solid laser rods when they are heavily

galilean:



newtonian:

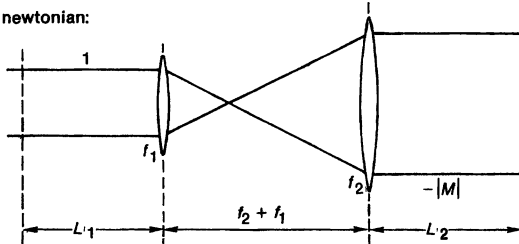


FIGURE 21.11
Galilean and newtonian telescopes, both focused at infinity.

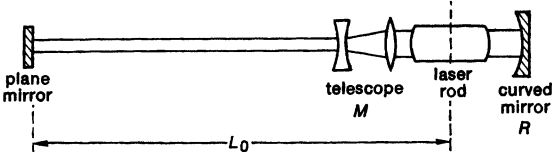
pumped. The combination of temperature rise and thermal expansion at the center of a cylindrical rod will produce an index increase due both to the thermal variation of the index of refraction and to thermally induced stress-optic effects. The rod will then act like a weak index duct, with a sufficiently long focal length that it can usually be approximated as a weak thin lens. For typical Nd:YAG rods, for example, the focal length of this thin lens decreases inversely with pumping power, and has a typical focal length of ≈ 1 m for a few kW of input electrical power to the pumping lamps.

The effect of this pump-power-dependent thermal focusing on mode spot size can then be eliminated to first order, while achieving the desired spot size in the rod, by the use of an intracavity telescope as illustrated in Figure 21.12 (see References). In this cavity design the rod is placed close to a curved mirror of radius of curvature R , with a telescope of magnification M placed close to the rod on the other side, spaced by a larger distance L_0 from a flat mirror at the opposite end of the cavity.

In a typical cavity of this type the rod and telescope will be sufficiently short compared to the remainder of the cavity that we can lump their contribution to the cavity length into the rest of the cavity, and treat them as zero-length elements in a preliminary analysis. The net ray matrix starting from a reference plane at the curved mirror end, going out through the demagnifying telescope to the flat mirror, and back again (but leaving out the curved mirror), will then have an $ABCD$ matrix given by

$$\begin{bmatrix} A & B \\ C & D \end{bmatrix} = \begin{bmatrix} 1/M & 0 \\ 0 & M \end{bmatrix} \times \begin{bmatrix} 1 & 2L_0 \\ 0 & 1 \end{bmatrix} \times \begin{bmatrix} M & 0 \\ 0 & 1/M \end{bmatrix} = \begin{bmatrix} 1 & 2M^2L_0 \\ 0 & 1 \end{bmatrix}. \quad (40)$$

(a) cavity design:



(b) equivalent resonator:

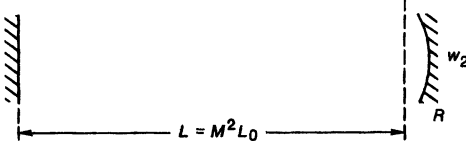


FIGURE 21.12

(a) A typical laser cavity design, and (b) an approximate analytical model for the same cavity.

In other words, the demagnifying telescope plus straight section looks like an equivalent section that is M^2 as long as the actual physical cavity length.

The effect of weak thermal focusing in the rod can then also be approximated as a small variation in the effective radius of curvature R of the right-hand mirror, and we can thus replace the multielement cavity by a simple two-mirror cavity of effective length $L = M^2 L_0$ with one flat and one curved mirror, as shown in Figure 21.12(b). The spot sizes at the left and right-hand ends of the cavity are then given in terms of the equivalent g parameters by

$$w_1^2 = \frac{L\lambda}{\pi} \times \sqrt{\frac{g_2}{g_1(1-g_1g_2)}} \quad \text{and} \quad w_2^2 = \frac{L\lambda}{\pi} \times \sqrt{\frac{g_1}{g_2(1-g_1g_2)}}. \quad (41)$$

Now, the spot size w_2 at the curved mirror end is the spot size that we wish to stabilize against small variations in the effective mirror radius R and hence against small variations in the parameter $g_2 \equiv 1 - L/R_2$. The sensitivity of w_2 to the latter parameter is then given by

$$\frac{\delta w_2}{w_2} = \frac{2g_1g_2 - 1}{4(1-g_1g_2)} \times \frac{\delta g_2}{g_2} \approx 0 \quad \text{for} \quad g_1g_2 = 1/2. \quad (42)$$

For optimum sensitivity against thermal focusing effects, the resonator should therefore be designed to fall on the contour $g_1g_2 = 1/2$ in the stability plane. (Similar but different criteria can be found for elements placed at other locations within the cavity; see Problems.)

A combination of cavity length L_0 , mirror radius R and telescope magnification M can thus be found which will simultaneously give the desired spot size w_2 in the laser rod, and make this spot size stable to first order against thermal focusing in the rod. In a more general version of this design procedure, a telescope focused at other than infinity can be employed, and a portion of the focusing power of the telescope used to change the effective radius R of the output mirror. In a real system we would also want to carry out a more accurate analysis including the physical lengths and focal powers of all the elements, and

examining the sensitivity of the system to, for example, slight changes in focal adjustment of the telescope. The general criterion given here can be used, however, as the starting point for a fundamentally sound solution to this particular design problem.

Other Fundamental Cavity Designs

Various other concepts that are sometimes used in describing or synthesizing multielement cavities (or cavity subsections) with real $ABCD$ matrices include the following:

(1) A real $ABCD$ system with $C = 0$ is often called a *telescopic system*, since any rays coming into the system parallel to the axis ($x'_1 = 0$) will emerge parallel to the axis ($x'_2 = 0$), as in a telescope focused to infinity. We pointed out in the previous chapter that all real and geometrically unstable systems (with $|m| > 1$) will be telescopic going from one properly chosen real (curved) reference plane to another. Geometrically stable systems ($|m| < 1$), by contrast, are telescopic only in a complex ray sense, i.e., only if we extract out a complex gaussian wave from the input and output beams, or go from one “complex-curved reference plane” to another.

(2) Real $ABCD$ systems with $B = 0$ can be referred to as *self imaging* or *image relaying systems*, since they transfer or image all the rays leaving a point x_1 at the input to a point $x_2 = Ax_1$ after one round trip. (Such systems might also be called “round-trip confocal systems,” since they transfer a focal point of the system back to the same focal point after one round trip.) All real self-imaging or round-trip confocal systems are geometrically unstable ($|m| > 1$) except for the marginally stable situation where $A = D = m = \pm 1$.

(3) Cavities having the special limiting values of $A = D = 1$ and $B = C = 0$ are classified by some authors as *degenerate cavities*. They have the general properties that any arbitrary ray returns to its initial value after one round trip; and hence that any input beam pattern or image reproduces itself exactly after one round trip. Systems with $A = D = -1$ and $B = C = 0$ are then *half degenerate*: They repeat after two round trips, and convert into a degenerate cavity if we shift to an arbitrary off-axis ray as the optical axis.

Because such degenerate and half-degenerate cavities can support more or less arbitrary multimode transverse beam patterns, they are useful for applications in active imaging; in “Scan Lasers” whose direction of oscillation can be scanned within the laser cavity; in the regenerative amplification of distorted beam patterns; and in scanning interferometers or filters which do not require transverse mode matching.

(4) Finally, any system that has $A = D = 0$ (and hence $m = 0$) will convert Huygens’ integral into a simple Fourier transformation from the input wave to the output plane, going in either direction through the system. Such systems might thus be referred to as *Fourier transform systems*. Systems with only $A = 0$ or only $D = 0$ accomplish a modified kind of Fourier transform in one direction only, and might thus be called “one-way Fourier transform systems.”

The trace of m value of a system is, of course, invariant to changes in either the curvature or location of the reference plane, but the $ABCD$ values themselves can be modified in various ways by changing either the curvature of the reference plane, as discussed in the previous chapter, or by moving to another reference plane within the system.

REFERENCES

Techniques for designing perturbation-insensitive stable resonators in the manner outlined in this section are discussed in more detail by J. Steffen, J.-P. Lörtscher, and G. Herziger, "Fundamental mode radiation with solid-state lasers," *IEEE J. Quantum Electron.* **QE-8**, 239–245 (February 1972); J.-P. Lörtscher, J. Steffen and G. Herziger, "Dynamic stable resonators: a design procedure," *Opt. Quant. Electr.* **7**, 505 (1975); and D. C. Hanna, C. G. Sawyers, and M. A. Yuratich, "Telescopic resonators for large-volume TEM₀₀-mode operation," *Opt. Quant. Electr.* **13** 493–507 (1981).

A related analysis is given by A. Le Floch, J. M. Lenormand, R. Le Naour, and J. P. Taché, "A critical geometry for lasers with internal lenslike effects," *J. Physique–Lettres* **43**, L493–L497 (July 15, 1982).

A general discussion of cavities in which an arbitrary ray retraces its path after a single round trip is given by J. A. Arnaud, "Degenerate optical cavities," *Appl. Opt.* **8**, 189–195 (January 1969).

Self-imaging unstable resonators were first discussed by A. H. Paxton and T. C. Salvi, "Unstable optical resonator with self-imaging aperture," *Opt. Commun.* **26**, 305–308 (September 1978). The properties of a marginally stable self-imaging cavity (inaccurately referred to as a "Fourier-transform" cavity) are also described by E. Sklar, "Fourier-transform ring laser," *J. Opt. Soc. Am. A* **1**, 537–540 (May 1984).

 Problems for 21.6

1. *Longitudinal magnification of a telescope.* A simple newtonian telescope used as an image relaying system magnifies the transverse size of an image by the magnification $-M$ and also demagnifies beam angles by the ratio $-1/M$. Show that the longitudinal magnification of an image, however, is either M^2 or $1/M^2$, depending upon which direction one goes through the telescope.
2. *Contours of constant m in the stability diagram.* Calculate the contours of constant half-trace m in the g_1, g_2 plane for a simple two-mirror laser cavity.
3. *Perturbation-insensitive cavity design.* Show that the perturbation-insensitive cavity design discussed in this section (spot size at a certain plane insensitive to small focusing perturbations at that same plane) corresponds in general to the condition that $A = -D$ or $m = 0$.
4. *Planar resonator with a single intracavity lens.* A stable optical cavity is to be formed by two flat mirrors spaced by distance L plus a single lens of focal length f placed at an arbitrary location within the cavity. Develop a formula for the spot size at the lens in this cavity, as a function of lens position and focal length, and discuss the stability range and the stable gaussian mode patterns in this cavity.
5. *Mode profile in a stable multielement resonator.* A ring resonator or periodic lensguide consists of alternating lenses of focal lengths f_1 and f_2 separated by distances of L_1 (going from f_1 to f_2) and L_2 (going from f_2 to f_1). Find the stable gaussian beam solution in this system, and sketch the beam profile though one section for various values of the focal lengths and spacings.
6. *Spot size stability against focusing at a different plane.* Suppose we want the output spot size w_2 in a laser cavity to be insensitive to first order to small amounts of thermal focusing for a laser rod placed at the center of a half-symmetric laser cavity consisting of a flat mirror M_1 and a curved mirror M_2 with radius of cur-

vature R_2 . What should be the length of the cavity, and on what contour should it be located in the g_1, g_2 plane, assuming the rod is always at the center of the cavity?

7. *Characteristics of various types of ray systems.* Verify that (a) an even number of Fourier transform systems (not necessarily all identical) in cascade corresponds to an overall self-imaging system; and (b) an odd number of such systems gives an overall Fourier transform system.
-

21.7 ORTHOGONALITY PROPERTIES OF OPTICAL RESONATOR MODES

To finish our discussion of general paraxial resonators, in this section we will consider the orthogonality properties of optical resonator eigenmodes. Our analysis will include not only the ideal complex paraxial resonator model introduced at the beginning of this chapter, but also a more general class of resonators having hard-edged apertures and other quite general nonparaxial apertures and elements. In the derivation as we will carry it out in this section, these nonparaxial elements are all lumped at a single plane within the resonator, and described by a complex aperture transmission function $\tilde{\rho}(s)$. The results we will obtain probably apply, however, to a considerably more general class of resonators than just this single-aperture situation.

"Normal Modes" in Transmission Lines and Resonators

The propagating modes in ordinary waveguides or transmission lines are commonly referred to as "normal modes" of these systems. The usual meaning of this phrase is that these eigenmodes are power-orthogonal to each other across the waveguide cross section, in the sense that

$$\int_A \tilde{u}_n^*(s) \tilde{u}_m(s) ds = \delta_{nm}, \quad (43)$$

where \tilde{u}_n and \tilde{u}_m are two different eigensolutions in the transverse direction. These modes also generally provide a complete set of basis functions for expanding any propagating fields in the waveguide or in a resonant cavity having the same cross-section.

Optical resonator modes, however, are generally *not* orthogonal in this fashion, nor do they necessarily comprise a complete set. Optical modes lack these desirable properties because the fundamental operator of which the optical modes are eigensolutions is not in general a hermitian operator; and nonhermitian operators are not necessarily guaranteed to have a complete and orthonormal set of eigensolutions.

Transverse eigenmodes in open-sided optical resonators and lensguides instead usually obey a *biorthogonality relationship* between the eigenmodes and a related set of transposed or adjoint modes. We will show in this section that these adjoint modes represent in physical terms the transverse eigenmodes traveling in the opposite direction inside the same resonator or lensguide.

TABLE 21.2
Linear Operators and Their Adjoints

Type of operator	Operator L	Transpose L_T	Hermitian adjoint L_H
Matrix:	M_{ij}	$(M_T)_{ij} = M_{ji}$	$(M_H)_{ij} = M_{ji}^*$
Integral:	$K(x, x_0)$	$K_T(x, x_0) = K(x_0, x)$	$K_H(x, x_0) = K^*(x_0, x)$
Differential:	$p_n(x) \frac{d^n}{dx^n} u(x)$	$(-1)^n \frac{d^n}{dx^n} [p_n(x) u(x)]$	$(-1)^n \frac{d^n}{dx^n} [p_n^*(x) u^*(x)]$

Linear Operator Notation: Adjoints and Transposes

By way of introduction, let us first review some general properties of linear but not necessarily hermitian operators. Let L indicate a general linear operator, whether this means a differential, integral, or matrix operator. Such an operator then acts on a function \tilde{u} (or in the matrix situation on a vector \mathbf{u}) to produce some new function \tilde{u}' , in the fashion

$$L\tilde{u} = \tilde{u}'. \quad (44)$$

Associated with any such linear operator L will then also be an *adjoint* or *transposed operator* L_T , and an *hermitian conjugate* or *hermitian adjoint operator* L_H .

The procedures for converting an operator to its transpose or its hermitian conjugate are illustrated in Table 21.2. For example, if L is a matrix operator, then its transposed operator is obtained simply by interchanging the order of subscripts. For an integral operator the transpose is obtained by interchanging coordinates in the operator kernel. For a differential operator the transpose is obtained by modifying each n -th order derivative term in the manner illustrated in the table. The hermitian conjugate or hermitian adjoint operator for each of these situations is then simply the complex conjugate of the transpose operator.

A *hermitian operator* is then by definition an operator which is equal to its *hermitian conjugate*, so that $L_H \equiv L_T^* = L$.

Operator Eigenfunctions and Eigenvalues

Most of the linear operators with which we work, whether hermitian or not, possess some set of eigenfunctions \tilde{u}_n and eigenvalues $\tilde{\gamma}_n$ satisfying the eigenequation

$$L\tilde{u}_n = \tilde{\gamma}_n \tilde{u}_n. \quad (45)$$

If a linear operator is hermitian, then it can be rigorously proven that its eigenvalues $\tilde{\gamma}_n$ will all be purely real, and its eigenfunctions \tilde{u}_n will form a set that is complete and also orthonormal in the sense given earlier, namely,

$$\int \tilde{u}_n^*(s) \tilde{u}_m(s) ds = \delta_{nm}. \quad (46)$$

The integration here is over the full range of the complete set of coordinates s that characterise the eigenfunctions.

If linear operator is not hermitian, however, then these properties cannot be proven in general, and may or not be true in individual specific situations. In this situation, the transposed operator L_T and the hermitian adjoint operator L_H will have separate and different sets of eigensolutions, call them ϕ_n and \tilde{w}_n respectively, which satisfy the separate eigenequations

$$L_T \phi_n = \tilde{\kappa}_n \phi_n \quad \text{and} \quad L_H \tilde{w}_n = \tilde{\xi}_n \tilde{w}_n. \quad (47)$$

Since the two operators L_T and L_H are simply complex conjugates of each other, however, their eigensolutions are essentially the same set, with the relations

$$\phi_n \equiv \tilde{w}_n^* \quad \text{and} \quad \tilde{\kappa}_n \equiv \tilde{\xi}_n^*. \quad (48)$$

It can also be shown that even for a nonhermitian operator, the eigenvalues of all three operators are related by

$$\tilde{\xi}_n^* = \tilde{\kappa}_n = \tilde{\gamma}_n. \quad (49)$$

That is, L and its transpose L_T always have the same eigenvalues even for nonhermitian operators. Their eigenfunctions \tilde{u}_n and ϕ_n will not in general be complex conjugates, however, nor will they have any other simple relationship for a nonhermitian operator.

Biorthogonality

Instead of being power-orthogonal in the sense of Equation 21.43, the eigenfunctions \tilde{u}_n of a nonhermitian operator L will be *biorthogonal* to the eigenfunctions ϕ_n of the corresponding transpose operator, in the form

$$\int \tilde{u}_m(s) \phi_n(s) ds \equiv \int \tilde{u}_m(s) \tilde{w}_n^*(s) ds = \delta_{nm}. \quad (50)$$

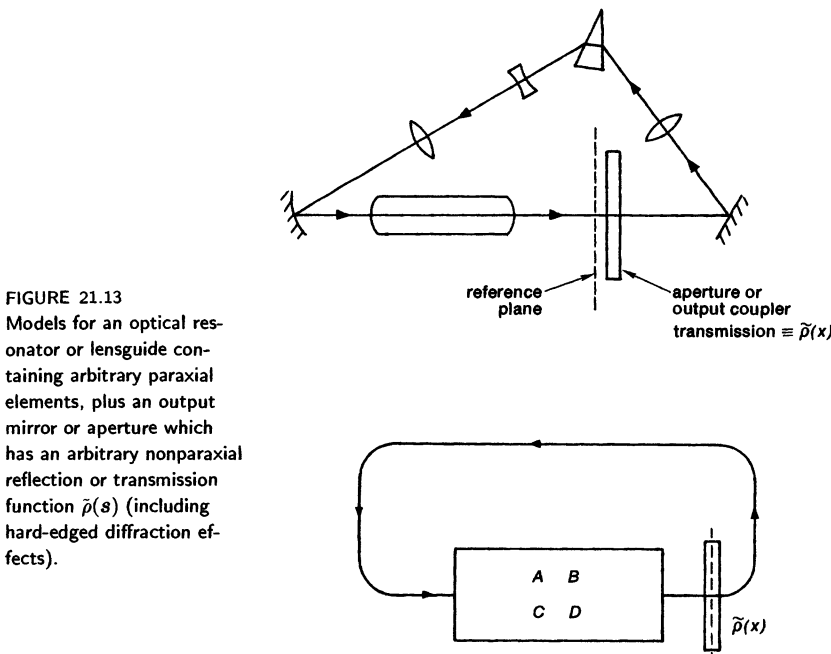
(It is a matter of convenience whether we choose to employ the hermitian adjoint eigenfunctions \tilde{w}_n or the transpose eigenfunctions ϕ_n in this relationship.) A further useful relation between these eigenfunctions is that

$$\sum_n \phi_n(s) \tilde{u}_n(s_0) \equiv \sum_n \tilde{w}_n^*(s) \tilde{u}_n(s_0) = \delta(x - x_0), \quad (51)$$

where the sum is over the full set of eigenfunctions. From this relation, we can show that for either a matrix operator or an integral operator, the sum of the eigenvalues will be

$$\sum_n \tilde{\gamma}_n = \int_A \tilde{K}(s, s) ds = \text{Tr}[L], \quad (52)$$

where Tr means the trace of the matrix operator. This can be very useful for checking numerical calculations of optical resonator eigenmodes.



Optical Resonator Model

To apply these orthogonality or biorthogonality concepts to optical resonators, we will use the slightly idealized model for an optical resonator shown in Figure 21.13.

In this model we consider either a standing-wave cavity, or a ring cavity, or an equivalent periodic lensguide, which may contain an arbitrary collection of complex paraxial elements; but in which all finite mirrors, or hard-edged apertures, or other nonparaxial apertures or output coupling elements are lumped at a single transverse plane. The transmission of the circulating wave through this plane is then described by a transverse transmission or reflection function $\tilde{\rho}(s)$.

That is, for a standing-wave resonator with some kind of finite output mirror, this function describes the transverse reflectivity variation $\tilde{\rho}(s)$ of the output mirror. For a ring resonator or a periodic lensguide with some kind of internal aperture or spatial filter, on the other hand, $\tilde{\rho}(s)$ is the transmission factor of the aperture between successive sections. For a finite mirror or hard-edged aperture this function then has the value $|\tilde{\rho}| = 0$ outside the finite mirror or aperture edges. The remainder of the resonator is assumed to contain only an arbitrary sequence of complex paraxial optical elements. For simplicity, we write the Huygens' integrals in one transverse dimension only, but this is easily generalized.

Forward and Reverse Propagation Operators

Let us first note that the propagation through the paraxial portions of the resonator, starting just after the aperture, traveling in the forward direction around the resonator, and ending just before the aperture, can be expressed by the standard complex paraxial Huygens' kernel

$$\tilde{K}(x, x_0) = \sqrt{\frac{j}{B\lambda_0}} \exp \left[-j \frac{\pi}{B\lambda_0} (Ax_0^2 - 2xx_0 + Dx^2) \right], \quad (53)$$

where A , B and C are the complex matrix elements going around the resonator or along the lensguide in the forward direction. Note that this is not in general a hermitian integral kernel.

Suppose we reverse the direction of travel, however, and propagate the field in the reverse direction between these same two planes. The $ABCD$ matrix elements going in the reverse direction through the same system are then given by $A_R = D$, $B_R = B$, $C_R = C$, and $D_R = A$; and the Huygens' kernel in the reverse direction is thus given by

$$\tilde{K}_R(x, x_0) = \sqrt{\frac{j}{B\lambda_0}} \exp \left[-j \frac{\pi}{B\lambda_0} (Dx_0^2 - 2xx_0 + Ax^2) \right]. \quad (54)$$

But this is just the transpose of the kernel in the forward direction; so we can write (in two transverse directions)

$$\tilde{K}_R(s, s_0) = \tilde{K}(s_0, s) = \tilde{K}_T(s, s_0). \quad (55)$$

We see that (a) the Huygens' integral kernel is not a hermitian operator; and (b) propagating in the reverse direction through a given paraxial system is the transpose of propagating through the same system in the forward direction.

Handling the Nonparaxial Aperture

We can now include the nonparaxial aperture in this same analysis by the following trick, namely, as shown in Figure 21.14, we will use as our initial reference plane a hypothetical plane located "halfway through" the transmitting aperture or reflecting mirror that is characterized by the aperture function $\tilde{\rho}(s)$. That is, we assume that to propagate once around the resonator the initial field $\mathcal{E}_0(s_0)$ at this reference plane must be multiplied by half the mirror reflection function, or $\tilde{\rho}^{1/2}(s_0)$; propagated on around the remainder of the cavity using Huygens' integral; and finally again multiplied by half the mirror reflection, or $\tilde{\rho}^{1/2}(s)$, before becoming the resulting field $\mathcal{E}(s)$ one full round trip later. (For a real curved mirror this is in fact equivalent to taking the reference plane on the mirror surface.)

The propagation operator for one complete trip around the resonator in the forward direction, starting out from and coming back to this reference plane, is then

$$\mathcal{E}(s) = \tilde{\rho}^{1/2}(s) \int \tilde{K}(s, s_0) \tilde{\rho}^{1/2}(s_0) \mathcal{E}_0(s_0) ds_0, \quad (56)$$

where $\tilde{K}(s, s_0)$ is the forward Huygens' integral kernel as given in Equation 21.54, and where the integral is evaluated over the aperture midplane. This integral is

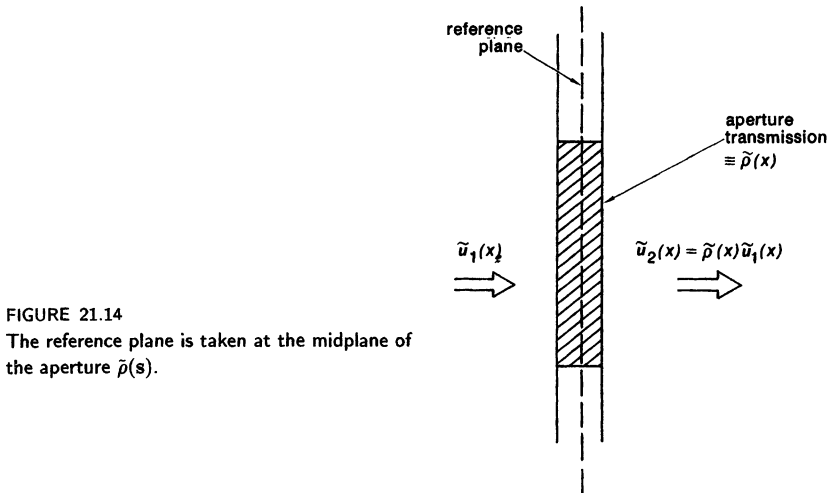


FIGURE 21.14

The reference plane is taken at the midplane of the aperture $\tilde{\rho}(s)$.

obviously over all regions of the aperture or mirror midplane where the optical field is not zero, that is to say, all regions where $|\tilde{\rho}(s)| \neq 0$.

The resonator eigenmode equation going in the forward direction is then

$$\int \tilde{K}_F(s, s_0) \mathcal{E}_n^F(s_0) ds_0 = \tilde{\gamma}_n^F \mathcal{E}_n^F(s), \quad (57)$$

where the overall kernel $\tilde{K}_F(s, s_0)$ in the forward direction is

$$\tilde{K}_F(s, s_0) = \tilde{\rho}^{1/2}(s) \times \tilde{K}(s, s_0) \times \tilde{\rho}^{1/2}(s_0). \quad (58)$$

This is clearly not in general a hermitian integral operator, and the transverse modes of optical resonators are thus in general not guaranteed to be normal modes in the usual sense.

If we go around the ring resonator or travel along the lensguide in the reverse direction, however, then we have potentially a different, transposed round-trip operator, such that the eigensolutions for the resonator or lensguide going in the reverse direction, call them $\mathcal{E}_n^R(s)$, will be given by the eigenmode equation

$$\int \tilde{K}_R(s, s_0) \mathcal{E}_n^R(s_0) ds_0 = \tilde{\gamma}_n^R \mathcal{E}_n^R(s), \quad (59)$$

where the reverse-direction kernel $\tilde{K}_R(s, s_0)$ is given by

$$\begin{aligned} \tilde{K}_R(s, s_0) &= \tilde{\rho}^{1/2}(s_0) \times \tilde{K}(s_0, s) \times \tilde{\rho}^{1/2}(s) \\ &\equiv \tilde{K}_F(s_0, s). \end{aligned} \quad (60)$$

In other words, even with the aperture included, these propagation operators are in general not hermitian, and the integral operator \tilde{K}_R for propagation through the lensguide or resonator in the reverse direction is just the transpose of the operator \tilde{K}_F for propagation in the forward direction.

Biorthogonality of Resonator Eigenmodes

We can conclude therefore that the forward eigenmodes $\mathcal{E}_n^F(s)$ of an optical resonator will in general not be orthogonal among themselves in the usual complex conjugate fashion. Rather, the forward-going transverse modes $\mathcal{E}_n^F(s)$ will be biorthogonal to the transverse modes $\mathcal{E}_n^R(s)$ of the wave going in the reverse direction in the same resonator, as expressed mathematically by

$$\int \mathcal{E}_n^R(s) \mathcal{E}_m^F(s) ds = \delta_{nm}. \quad (61)$$

Note that no complex conjugation is involved in the integrand.

This biorthogonality integral is derived thus far only for the special “mid-aperture” reference plane described by $\tilde{\rho}(s)$. Since the two sets of waves are traveling in opposite directions through the system, however, it is evident that we can shift to a reference plane immediately outside the aperture, on either side, by multiplying one set of modes by the partial reflection factor $\tilde{\rho}^{1/2}(s)$ and dividing the other set by the same factor. The net effect of this leaves the biorthogonality integral unchanged. The integral in Equation 21.61 thus holds immediately outside the aperture also.

In addition, given that the two sets of functions represent propagating waves traveling in opposite directions through a paraxial system, it is then not difficult to use the propagation properties of a general paraxial system to prove that biorthogonality at one transverse plane implies biorthogonality at all other planes within the resonator. The integral in Equation 21.61 thus holds generally, at any plane within the resonator.

Physical Interpretation

This biorthogonality relation between forward and reverse directions has the following physical interpretations for standing-wave and traveling-wave optical resonators. First of all, in a standing-wave optical resonator with a 100% reflecting mirror at one end and the finite output mirror at the other end, the aperture midplane is actually on the surface of the output mirror. The forward and reverse propagation paths around the resonator, starting from this mirror surface, are then equivalent and identical; and the equivalent lensguide is inherently symmetrical in the forward and reverse directions.

A little consideration then shows that in such a standing-wave resonator the biorthogonality property means simply that the fields of the *right-traveling wave component* of any standing-wave eigenmode $\mathcal{E}_n(x, z)$ are biorthogonal to the fields of the *left-traveling wave components* of all the other eigenmodes at the same transverse plane z .

In a ring cavity, on the other hand, the forward and reverse (or clockwise and anticlockwise) directions are physically distinguishable, and can correspond to a directionally asymmetric lensguide. The forward and reverse waves can then have quite separate and distinct sets of eigenfunctions traveling in the two opposite directions around the ring or along the lensguide. Characteristic profiles for the oppositely traveling modes in an asymmetric ring unstable resonator are illustrated in Figure 21.15. The geometric profiles of these modes are significantly different, as shown, with the forward mode in this particular asymmetric situation being confocal and the reverse mode nonconfocal. The actual unstable resonator eigenmodes, which will be Fresnel-distorted variations on these zero-

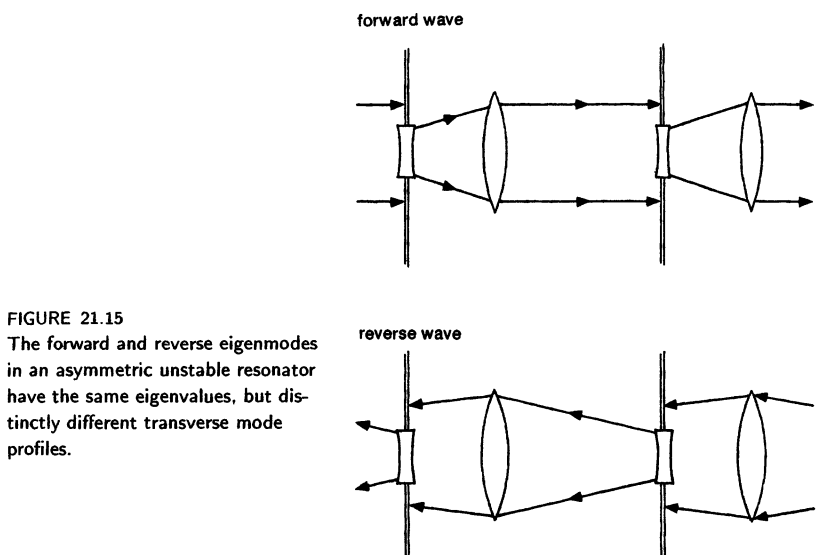


FIGURE 21.15

The forward and reverse eigenmodes in an asymmetric unstable resonator have the same eigenvalues, but distinctly different transverse mode profiles.

order geometric solutions, will have similar variations in the two directions. The eigenvalues will, however, be the same, as illustrated by the fact that the net magnification is $M = 2$ in both directions in Figure 21.15. These two sets of eigenfunctions are then biorthogonal to each other in exactly the fashion given in the preceding.

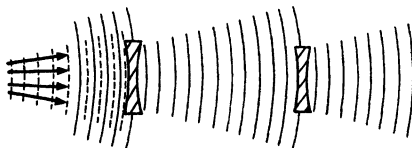
Discussion

The nonhermitian character of the Huygens' integral operator may seem surprising, especially since Huygens' integral is derived from the wave equation operator $[\nabla^2 - \mu\epsilon(\partial^2/\partial t^2)]\hat{u}$, which is clearly hermitian. Suppose we consider, however, an asymmetric unstable lensguide with its forward and reverse modes as shown in Figures 21.10 or 21.15. The significant point is that the forward and reverse eigenmodes deliver power to opposite sides of the aperture. More generally, in any real open-sided resonator there will be radiation leakage or output coupling fields that represent power flow out to infinity.

In terms of the complete wave equation in space and time, therefore, the operator is hermitian but the boundary conditions are not. This difficulty does not arise in simple waveguide problems where all the boundaries are closed and perfectly conducting, or else the fields all die away rapidly enough at infinity. When the optical resonator problem is separated into $\exp(\pm j\omega t)$ terms, however, the individual operator applied only to the $\exp(j\omega t)$ part of the fields turns out to be nonhermitian.

The derivation presented here has also been limited to the paraxial form of the Huygens integral. All that is really necessary, however, is that the appropriate kernel or Green's function for propagation around the resonator obey the reciprocity property $\tilde{K}_R(s, s_0) = \tilde{K}_F(s_0, s)$; and this will be generally true under

(a) mode-matched input signal



(b) adjoint injected signal

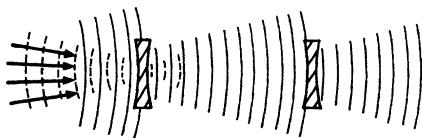


FIGURE 21.16

The largest amplitude for a given propagation eigenmode will be obtained not by sending in a “mode-matched” input signal as in part (a), but an “adjoint injected signal” as in part (b).

a very wide range of conditions. Hence the result presented here will be valid for a comparably wide range of resonator designs.

Excitation of Resonator Eigenmodes

The biorthogonality properties of optical resonator modes can lead to some perhaps surprising conclusions, particularly in unstable resonators. Suppose we wish to excite the maximum amplitude of the dominant mode in an unstable resonator or lensguide, as in Figure 21.16, using an injected signal of fixed total power.

It might then seem that we would use the injected power most effectively by matching it as closely as possible to the wavefront that we want to excite, as shown in Figure 21.16(a). In fact, however, the dominant mode of the unstable system will be excited most effectively, or with the largest mode amplitude, by matching the injected signal to the converging or adjoint wavefront, as shown in Figure 21.16(b), a process sometimes referred to as “adjoint coupling.”

We can understand the necessity for this by supposing that the wave amplitude that is to be excited in the unstable system will be measured only after a large number of round trips, or after the wave has propagated through many sections of the equivalent lensguide, so that only the dominant mode in the system will be left. It then seems more physically evident that if we want to get as much power as possible as far down the system as possible—which means putting as much of the excitation as possible into the dominant or lowest-loss mode—then we indeed want to focus the energy initially into a converging wave which will first travel inward before being spread back out by diffraction effects.

Power Normalization of Biorthogonal Modes

Part of the confusion in this situation arises from our usual concepts that we can compute the excitation of each individual “normal mode” in a system and

then add up the powers given to each normal mode to get the total power carried by the system. In a biorthogonal system, however, we cannot do this because the eigenmodes are not in general power-orthogonal to each other—in fact, they are in general not orthogonal to each other at all, either with or without complex conjugation involved. Hence one cannot compute the total power traveling along a nonhermitian lensguide as simply the sum of the powers in the individual eigenmodes.

We can normalize the individual forward or reverse eigenmodes \mathcal{E}_n^F and \mathcal{E}_n^R in various ways. However, we can also show that if these eigenmodes are biorthogonal in the form given in Equation 21.61, then it is in general not possible to also power-normalize both \mathcal{E}_n^F and \mathcal{E}_n^R such that the integral of $|\mathcal{E}|^2$ is unity for both of these sets of functions separately.

We should perhaps note again that the Hermite-gaussian modes, which provide very close approximations for the real eigenmodes in stable gaussian resonators, are a complete set of normal modes in the usual sense, and hence we can apply all the usual orthonormality properties to these functions. The diffraction losses in stable resonators are usually very small, and as a consequence the real modes in stable gaussian resonators are very nearly “normal modes” in the usual sense.

REFERENCES

The material in this section is an extension of the discussion presented by J. A. Arnaud in *Beam and Fiber Optics* (Academic Press, New York, 1976), pp. 122–123 and 174. Some related ideas on the completeness of optical resonator modes are discussed in I. F. Balashov and V. A. Berenberg, “Nonstationary modes of an open resonator,” *Sov. J. Quantum Electron.* **5**, 151–161 (August 1975).

An abbreviated version of the material in this section, using a rather awkward notation, has been published in A. E. Siegman, “Orthogonality properties of optical resonator eigenmodes,” *Optics Commun.* **31**, 369–373 (December 1979); and also applied to laser calculations in A.E. Siegman, “Exact cavity equations for lasers with large output coupling,” *Appl. Phys. Lett.* **36**, 412–414 (March 15, 1980).

Much more general (though sometimes confusing) discussions of hermitian and non-hermitian operators, adjoints, conjugates, and biorthogonality will be found in P. M. Morse and H. Feshbach, *Methods of Theoretical Physics*, Vol. 1 (McGraw-Hill, 1953).

There has been some controversy over whether the biorthogonality relation presented in this section also applies to optical resonators with several apertures in the cavity, especially if the apertures are asymmetrically spaced [see K. E. Oughstun, “Transverse mode structure properties in multiaperture optical cavities,” *Opt. Comm.* **43**, 41–46 (September 1, 1982); and K. E. Oughstun, P. A. Slaymaker, and K. A. Bush, “Intracavity spatial filtering in unstable ring resonator geometries: Part I – Passive cavity mode theory,” *IEEE J. Quantum Electron.* **QE-19**, 1558–1576 (1983)].

The consensus appears to be that the biorthogonality property as referenced in the preceding applies equally well to multiaperture resonators under a very broad range of conditions: cf. E. M. Wright and W. J. Firth, “Orthogonality properties of general optical resonator eigenmodes,” *Opt. Comm.* **40**, 410–412 (February 15, 1982); E. M. Wright, D. P. O’Brien, and W. J. Firth, “Reciprocity and orthogonality relations for ring resonators,” *IEEE J. Quantum Electron.* **QE-20**, 1307–1310 (1984); and M. Piché and P. A. Bélanger, “On the losses of the counterpropagating modes of ring cavities,” *IEEE J. Quantum Electron.* **QE-20**, 1303–1307 (1984).

Problems for 21.7

1. *Demonstrating the transpose relationship for propagation in opposite directions through a multiaperture resonator.* Suppose a second aperture with an arbitrary wave-amplitude transmission factor $\bar{\rho}'(x)$ is placed at some arbitrary plane inside an optical resonator, in addition to the "end mirror" aperture $\bar{\rho}(x)$. Arbitrary complex paraxial elements occupy both spaces between apertures. Demonstrate that the total propagation kernels from end to end of the resonator in forward and reverse directions still obey the transpose relationship $\tilde{K}_F(x, x_0) = \tilde{K}_R(x_0, x)$.
 2. *Symmetrizing the optical resonator eigenproblem.* Show that if we extract out an appropriate spherical-gaussian wave from both the forward and reverse-traveling waves at the aperture midplane by multiplying each of them by one or the other of the functions $\exp[\mp j(\pi(D - A)/2B\lambda)x^2]$, then the round-trip propagation in either direction (including the aperture) can be represented by the same symmetrized kernel, namely, $\tilde{K}_S(x, x_0) = \sqrt{j\bar{\rho}(x)\bar{\rho}(x_0)/B\lambda} \times \exp\{-j(\pi/2B\lambda) \times [(A + D)(x^2 + x_0^2) - 2xx_0]\}$, and hence these reduced mode functions in the two directions will become identical.
-

UNSTABLE OPTICAL RESONATORS

Unstable optical resonators, of both the “hard-edged” and “soft-edged” varieties, have been found very useful as resonant cavities for laser oscillators, particularly whenever any combination of high gain, large mode volume, high energy or high power is present. In this and the following chapter, therefore, we apply many of the concepts developed in the preceding chapters to a more detailed examination of the somewhat complex properties of unstable optical resonators.

Before reading these chapters, readers may wish to review the fundamental ideas about ray matrices and ray matrix stability, generalized paraxial resonator theory, resonator Fresnel numbers, and aperture diffraction effects that have been discussed in earlier chapters, especially Section 21.3, because these concepts turn out to be fundamental to understanding the sometimes complex and mysterious behavior of unstable optical resonators.

Readers should also be sure to persevere (or if necessary skip) to the final section of the following chapter, which is concerned with soft-edged or variable-reflectivity *unstable resonators*. Resonators of this type seem likely in the long run to provide the optimum resonator designs for almost any variety of low or high-gain laser systems.

22.1 ELEMENTARY PROPERTIES

Before developing a more detailed analysis of unstable resonator eigenmodes, as we will do in following sections, let us look in this section at some of the elementary practical aspects of unstable resonators, including practical coupling methods, and the general structure of the near-field and far-field beam patterns of unstable resonator lasers, using a purely geometric approach.

Figure 22.1 illustrates the general characteristics of the simplest form of hard-edged, single-ended, positive-branch, standing-wave confocal unstable resonator. We have already pointed out that unstable resonators in general:

- Are derived from unstable periodic focusing systems.
- Are characterized by a geometric magnification parameter M , which may be either a positive or negative number with magnitude greater than unity.

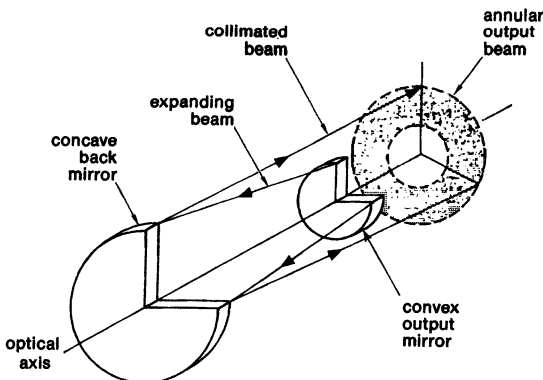


FIGURE 22.1

Simplest form of single-ended confocal positive-branch unstable resonator.

- Can be classified into positive-branch and negative-branch varieties, depending upon the sign of M .
- Have characteristic magnifying (or diverging), and demagnifying (or converging) geometrical eigenwaves according to a purely geometric or paraxial analysis.
- Are perturbation-stable for the magnifying eigenwave and perturbation-unstable for the demagnifying eigenwave, according to the paraxial analysis.
- And, have a set of real transverse eigenmodes with mode properties that are basically similar to the magnifying geometrical eigenwave, but that are strongly influenced by the diffraction properties at the outer mirror or aperture edges in the resonator.

We have also noted that confocal unstable resonators are particularly useful because they produce a collimated output beam, as in Figure 22.1; and that the demagnifying geometrical eigenwave going in one direction through a geometrically unstable system corresponds to a reversed version of the magnifying paraxial eigenwave going in the opposite direction. We will build on these concepts in the following sections.

Output Coupling Methods For Unstable Resonators

One important feature of the hard-edged unstable resonator is that the magnified or diffracted energy coming past the outer edge of the output mirror becomes the useful output from the laser. This means that totally reflecting optics can be employed, thus eliminating the sometimes troublesome problems of finding low-loss dielectric coatings and transparent and low-loss mirror substrates at infrared, mm-wave or ultraviolet wavelengths. In fact, all-metal mirrors with internal water cooling channels are often employed to carry away the heat dissipation associated with mirror reflection losses in very high power lasers.

The output mirror must then be mounted so as to permit the output beam to pass around it. One way to do this is to mount the mirror on a small post extending from an output window behind the mirror, as in Figure 22.2(a). Another

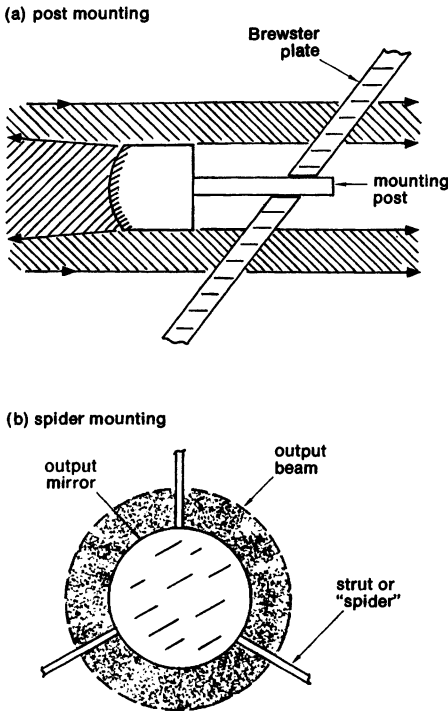


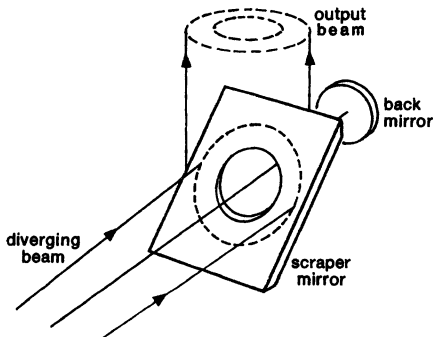
FIGURE 22.2
Practical mirror mounting methods for unstable resonators.

technique is to use a “spider” or arrangement of transverse wires or struts, as in figure 22.2(b). These struts should have as small an area as possible to minimize power losses and unwanted far-field diffraction effects.

A third technique, widely used in higher-power lasers, is to employ a diagonal “scraper mirror” to provide the output coupling, as shown in Figure 22.3. This has the advantages that no struts or posts are required; the output coupling element can be mounted entirely separately from the cavity end mirrors; there are no obstructions in the output aperture; and the output beam direction can even be steered to some extent, without upsetting the cavity alignment. The major practical problems with this approach are the difficulties in cutting an aperture with clean and optically smooth edges in the scraper mirror, and some small difficulties in standing-wave cavities because the circulating beam in the cavity actually strikes the scraper mirror twice, coming from opposite sides.

Geometrical Output Coupling Value

Note that the output coupling from an unstable resonator depends, in the zero-order or geometric approximation, only on the magnification M , and not at all on the transverse mirror diameters or the Fresnel numbers of the resonator. (We will see some more exact corrections to this statement in the following sections, but it is still basically a good approximation.)



negative-branch confocal resonator
with scraper mirror

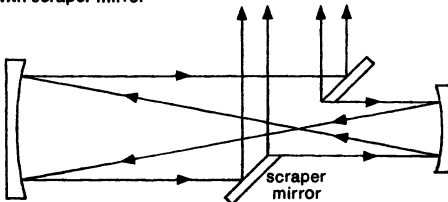


FIGURE 22.3

Output coupling with a "scraper mirror."

In a one-dimensional or strip-mirror resonator, according to the purely geometric picture, the field expands transversely in one dimension by the factor M , and thus decreases in field amplitude by the geometric eigenvalue $\tilde{\gamma}_{\text{geom}} \equiv 1/|M|^{1/2}$ on each round trip. The fractional power loss per round trip is thus given by

$$\text{power loss per round trip} = 1 - |\tilde{\gamma}_{\text{geom}}|^2 = 1 - \frac{1}{M} \quad (\text{strip resonator}). \quad (1)$$

For a two-transverse-dimensional mirror, the area expansion becomes M^2 , so that the geometric eigenvalue is $\tilde{\gamma}_{\text{geom}} \equiv 1/M$ and the fractional power loss per round trip becomes

$$\text{power loss per round trip} = 1 - |\tilde{\gamma}_{\text{geom}}|^2 = 1 - \frac{1}{M^2} \quad (\text{circular resonator}). \quad (2)$$

The reader can verify from geometric arguments, in fact, that even in a double-ended unstable resonator (with output from both ends) the total geometric output coupling per round trip is entirely independent of the transverse shape or alignment of the end mirrors (provided the resonator axis passes through both mirrors), and also of how the total magnification and total coupling may be divided between the two end mirrors.

Since the output coupling, in the geometric approximation, depends only on the magnification and not on the mirror diameters, we can therefore always expand the diameter of the geometric mode in an unstable resonator so as to fill a laser rod or tube of almost any size, at fixed magnification or output coupling,

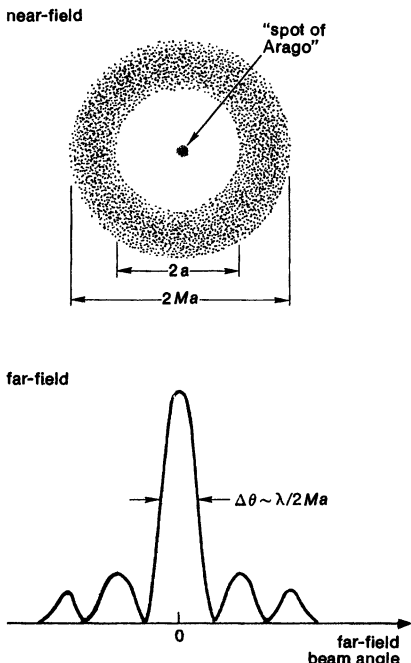


FIGURE 22.4
Near-field and far-field beam patterns for an elementary hard-edged unstable resonator.

simply by expanding the size of the output mirror until the magnified beam diameter more or less fills the active volume of the laser medium. The efficient power extraction which this permits, along with good transverse mode control, is the primary attractive feature of the unstable optical resonator.

Near-Field Output Beam Pattern

The near-field beam pattern just beyond the output mirror for a circular-mirror unstable resonator will then be an annular beam with an outer diameter roughly M times the inner diameter, as shown in Figure 22.4. In the idealized geometric analysis this beam will be uniform in amplitude and spherical in phase across the annular aperture. In real hard-edged unstable resonators, as we will see in the following section, the radial intensity profile in the annular region will often be closer to a radially tapered intensity profile, with circular Fresnel diffraction rings of small to moderate strength imposed upon the average profile.

The phase variation across the output plane in a real resonator will nearly always be very close to the predicted wavefront for the magnifying geometrical eigenwave discussed in Section 21.3, and illustrated in Figures 21.3 and 21.4, with only small Fresnel-ripple deviations from this ideal wavefront. The phase ripples in the real resonator, or the deviation from the ideal geometrical situation, will be sufficiently small compared to an optical wavelength that they will produce little deterioration in the far-field beam pattern compared to the uniform geometric situation.

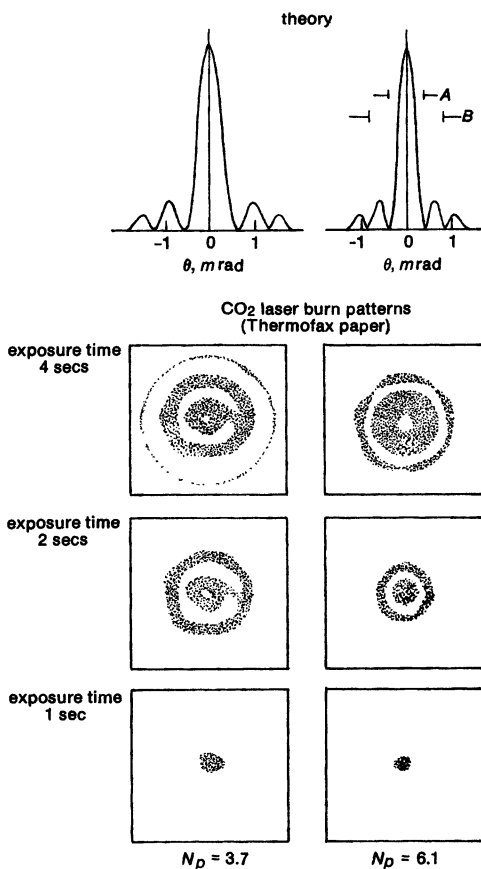


FIGURE 22.5

Experimental results for far-field burn patterns on thermofax paper for a low-power CO₂ laser with two different sets of mirrors.

The near-field pattern will also develop, within a very short distance from the output mirror, a strong but small "spot of Arago" which can, as we have mentioned earlier, cause optical damage or other difficulties if not properly blocked in higher power lasers.

Far-Field Output Beam Pattern

The far-field pattern from an unstable resonator laser, like the far-field pattern from a Cassegrainian telescope, will no longer have a hole on axis as in the near field, but will have a central lobe on axis, surrounded by side lobes or diffraction rings of decreasing amplitude, as shown in Figures 22.4 and 22.5. The angular width of this central lobe will correspond more or less to the diffraction-limited far-field pattern for a slit or circular aperture corresponding to the outer width or diameter of the near-field pattern.



FIGURE 22.6

Reproductions of the burn patterns in a lucite block produced by a very high power CO₂ laser beam, both in the near field (approximately one meter from the output mirror) and in the far field (at the focus of a long focal-length lens). The near-field pattern shows a distinct spot of Arago on axis. The far-field pattern, which is heavily overexposed, shows the narrow central lobe, with a series of surrounding rings similar to an Airy disk pattern.

Because of the finite annular nature of the near-field pattern, however, the surrounding side lobes or rings will spread out over an angular width corresponding roughly to the width of the annulus itself. A laser having low magnification and thus a narrow annulus will have a correspondingly broad distribution of side lobes or rings, with only a limited fraction of the total energy contained in the central lobe. To obtain the narrowest overall far-field distribution for a given near-field aperture diameter, we thus want to use the largest possible magnification, so that the largest possible fraction of the near-field aperture is filled with radiation.

Some examples of the far-field beam patterns from a low-power unstable resonator CO₂ laser, as observed using burn patterns on thermofax paper, are shown in Figure 22.5. Note that in the far-field patterns, the different patterns represent different exposure times, in order to bring out first the narrow central peak and then the surrounding circular ring patterns. Figure 22.6 illustrates burn patterns in lucite blocks from a somewhat higher-power CO₂ laser, again illustrating the annular near field, including a central spot of Arago, and the (much overexposed) far-field pattern.

Advantages of Unstable Laser Resonators

The desire to operate at large magnification, in order to obtain a good far-field beam pattern, means that unstable resonators operate best at large output couplings. The simple hard-edged unstable resonator is thus best suited to laser oscillators that are characterized by *large mode volume* (in technical terms, large Fresnel number), and *large round-trip gain*, so that the oscillator can operate efficiently at large output coupling. Unstable resonators are frequently employed on very high power or high energy lasers as well; but high gain is the primary criterion to make efficient use of the unstable resonator's useful characteristics.

For laser devices that may have large mode volume or large Fresnel number, but only low gain—for example, cw CO₂ lasers—the situation is more difficult. The potential solutions in this situation seem to be to use a low-magnification unstable resonator and live with the output beam problem; or to use a folded

multipass configuration through the gain medium in order to get the effective Fresnel number down and the gain up; or to use either a very long stable cavity or one adjusted perilously close to the stability boundary, in order to get increased stable gaussian spot size; or best of all, if possible, to use the variable-reflectivity-mirror techniques described in the final section of Chapter 23.

The advantages of the unstable resonator concept, when the necessary conditions are met, then include:

- Large, and controllable, mode volume.
- Controllable diffractive output coupling.
- Good transverse mode discrimination.
- Single-ended, all-reflective optics.
- Automatically collimated output beams
- Ease of alignment and adjustment.
- Efficient power extraction.
- Good far-field beam patterns.

Unstable resonators have to date found useful application in flash-pumped solid-state lasers, such as ruby and Nd:YAG lasers; in flash-pumped and nitrogen-pumped dye lasers; in pulsed and cw CO₂ lasers; in optically pumped sub-mm and far infrared lasers; in many very high power chemical and gasdynamic lasers; in many excimer lasers such as KrF and XeF lasers; in pulsed metal vapor lasers such as the Cu vapor laser; in optically pumped Raman lasers; and in semiconductor injection diode lasers.

Additional Discussion

The intuitive feeling of some laser researchers seems to be that an unstable resonator laser, perhaps because it is called "unstable," or because of its use of diffractive rather than transmissive coupling, is in some way special and fundamentally different from a more conventional laser using output coupling through a partially transmitting mirror. It has sometimes been argued, for example, that an unstable resonator laser, especially one with large magnification, "cannot have axial modes." It may be worthwhile asserting, therefore, that *an unstable resonator laser cavity having a certain percentage output coupling will not differ in any fundamental aspect of its behavior from any other kind of laser cavity having the same effective output coupling* (except in the details of their respective mode shapes and volumes).

It is clear in principle—and has many times been verified experimentally—that applying either a stable or an unstable cavity resonator with the same percentage output coupling to the same laser medium will produce essentially the same total power output. Unstable resonator lasers can be and have been internally modulated, Q-switched, mode locked, injection locked, and generally made to demonstrate the same properties as any other type of laser. The unstable resonator, however, because of its much better transverse mode discrimination, will almost always produce a better far field beam profile and higher on-axis brightness in the far field than any other cavity design for those high-gain and large Fresnel number resonators to which it is best suited.

REFERENCES

The unstable resonator concept was first discussed in A. E. Siegman, "Unstable optical resonators for laser applications," *Proc. IEEE* **53**, 277–287 (March 1965), with further analysis in A. E. Siegman and R. Arrathoon, "Modes in unstable optical resonators and lens waveguides," *IEEE J. Quantum Electron.* **QE-3**, 156–163 (April 1967). See also A. E. Siegman and H. Y. Miller, "Unstable optical resonator loss calculations using the Prony method," *Appl. Opt.* **9**, 2729–2736 (December 1970); and A. E. Siegman, "Stabilizing output with unstable resonators," *Laser Focus*, 42–47 (May 1971). An early analysis in terms of ray matrices was also given by W. K. Kahn, "Unstable optical resonators," *Appl. Opt.* **5**, 407–413 (March 1966).

More recent review articles include A. E. Siegman, "Unstable optical resonators," *Appl. Opt.* **13**, 353–367 (February 1974); A. Anan'ev, "Unstable resonators and their applications," *Sov. J. Quantum Electron.* **1**, 565–586 (May–June 1972); and R. A. Chodzko and A. N. Chester, "Optical Aspects of Chemical Lasers," Chapter 3 in *Handbook of Chemical Lasers*, edited by R. W. F. Gross and J. F. Bott (Wiley, 1976).

Books reporting on the extensive Soviet contributions to stable and unstable resonator theory include L. A. Weinstein, *Open Resonators and Open Waveguides* (in English translation from Golem Press, Boulder, Colorado, (1969); and Y. Ananiev (or Anan'ev), *Résonateurs Optiques et Problème de Divergence du Rayonnement Laser* (Éditions Mir, Moscow, Russian original 1979, French translation 1982).

A simple post-mounted end mirror for an unstable resonator is illustrated in R. L. Herbst, H. Komine, and R. L. Byer, "A 200 mJ unstable resonator Nd:YAG oscillator," *Optics Commun.* **21**, 5–7 (April 1977).

Spider mountings that employ curved spokes will produce smaller far-field diffraction effects than similar mountings with straight radial spokes; see, for example, J. L. Richter, "Spider diffraction: a comparison of curved and straight legs," *Appl. Opt.* **23**, 1907–1913 (June 15 1984).

When a scraper mirror is used in a standing-wave cavity, additional diffraction effects can occur because the wave encounters the aperture twice in each round trip. Although these effects are usually small if the coupling aperture is located close to one end of the cavity, some of their possible consequences are explored in W. P. Latham, Jr., and M. E. Smithers, "Diffractive effect of a scraper mirror in an unstable resonator," *J. Opt. Soc. Am.* **72**, 1321–1327 (October 1982).

Techniques for aligning unstable resonators usually involve sending a collimated visible beam back into the unstable cavity in the reverse direction and observing the resulting behavior of the beam spot on successive bounces. Various techniques are discussed in L. V. Koval-chuk and N. A. Sventsitskaya, "Methods of alignment of lasers with unstable resonators," *Sov. J. Quantum Electron.* **2**, 450 (March–April 1973); J. Hanlon and S. Aiken, "Alignment technique for unstable resonators," *Appl. Opt.* **13**, 2461 (November 1974); and S. L. Chao and A. D. Schnurr, "Unstable resonator alignment using off-axis gaussian beam propagation," *Appl. Opt.* **23**, 2115–2121 (July 1, 1984).

 Problems for 22.1

1. *Geometrical output coupling for double-ended unstable resonators.* Verify that even if an unstable optical resonator of overall round-trip magnification M has diffraction-coupled outputs past the edges of both end mirrors, the total round-

trip power loss is still given by the same formula which depends on the overall magnification M only.

22.2 CANONICAL ANALYSIS FOR UNSTABLE RESONATORS

Our next important steps are to calculate the significant parameters and to calculate and examine some of the exact mode properties of unstable optical resonators, taking into account the strong diffraction effects that occur at the mirror edges. Before examining any of these exact results, however, we will develop a simple but very general canonical formulation for analyzing almost all standard unstable resonator designs of interest. We do this by transforming the round-trip Huygens' integral for a general unstable resonator into an equivalent collimated free-space form, and then examining the important physical parameters of this canonical model.

Huygens' Integral for Unstable Resonators

The objective here is to obtain a basic analytical formalism that will cover all but the most exotic forms of real unstable resonators, by considering a general unstable resonator with either a single output coupling mirror in the standing-wave situation, or a single output coupling plane or mirror in the ring situation. Given the $ABCD$ matrix for the full round trip around the cavity (see Figure 22.7), we can then define as usual the half-trace parameter $m \equiv (A + D)/2$, with $|m| > 1$ for unstable resonators. This then leads to the round-trip geometric magnification M given by

$$M \equiv \begin{cases} m + \sqrt{m^2 - 1} & \text{positive branch, } m > +1 \\ -m - \sqrt{m^2 - 1} & \text{negative branch, } m < -1, \end{cases} \quad (3)$$

where $|M|$ is also > 1 for unstable resonators.

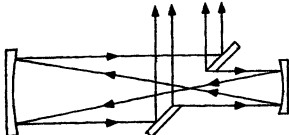
For purposes of analysis, let us choose a reference plane z_0 that is located just *inside* the output mirror or just *before* the coupling aperture, going in the outward direction; and then consider the propagation to a reference plane z_2 at the same location one period or round-trip later, as shown in the bottom plot of Figure 22.7. If we assume that the output mirror or coupling aperture has a finite width of $2a$ in one transverse dimension, we can then write the round-trip Huygens' integral for the resonator in that one transverse direction in the form

$$\tilde{u}_2(x_2) = \sqrt{\frac{j}{B\lambda_0}} \int_{-a}^a \tilde{\rho}(x_0) \tilde{u}_0(x_0) \exp \left[-j \frac{\pi}{B\lambda_0} (Ax_0^2 - 2x_2 x_0 + Dx_2^2) \right] dx_0. \quad (4)$$

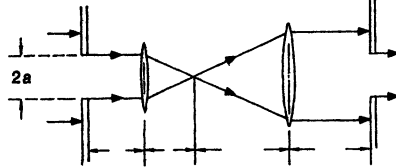
If the output mirror or coupler, rather than being a simple hard-edged aperture, has some form of variable reflection or transmission, we can take this into account by including the transmission function $\tilde{\rho}(x_0)$ which multiplies the input function $\tilde{u}_0(x_0)$ inside the integral, as in the orthogonality discussion in the previous chapter.

In a real circular or other two-transverse-dimension resonator we will have to write the Huygens' integral in both transverse dimensions, and take proper

typical unstable resonator



unfolded lensguide model



ABCD matrix model

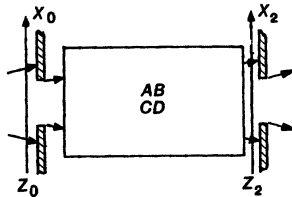


FIGURE 22.7

Evolution of a general analytical model for any unstable resonator with a single output coupling plane.

account of the actual transverse shape of the output mirror or coupler, whether it is square, rectangular, circular, or some more complex shape. To simplify the notation, however, let us write out the expressions here in only one transverse dimension, assuming a simple aperture of half-width (or, if it is circular, of radius) equal to a .

Canonical Formulation

We can now convert the Huygens' integral of Equation 22.4 into a general canonical form by a simple transformation which begins by writing the input and output waves in the forms

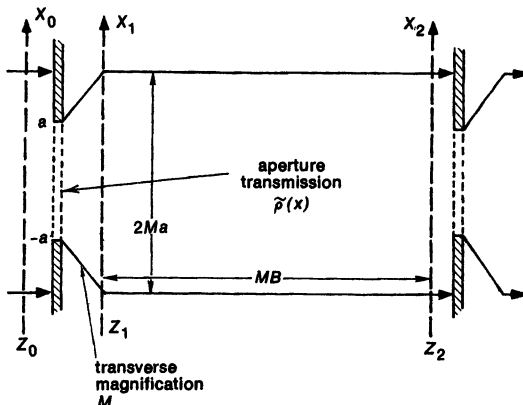
$$\tilde{u}_0(x_0) \equiv \tilde{v}_0(x_0) \times \exp \left[+j \frac{\pi(A - M)x_0^2}{B\lambda_0} \right], \quad (5)$$

and

$$\tilde{u}_2(x_2) \equiv \tilde{v}_2(x_2) \times \exp \left[-j \frac{\pi(D - 1/M)x_2^2}{B\lambda_0} \right]. \quad (6)$$

These transformations are physically equivalent to extracting out the spherical curvature of the unstable resonator modes, thereby converting the magnifying wavefronts into collimated wavefronts at both the input and output ends of the

FIGURE 22.8
Canonical formulation for an arbitrary single-aperture geometrically unstable resonator.



cavity. The Huygens' integral given in Equation 22.4 then becomes

$$\tilde{v}_2(x_2) = \sqrt{\frac{j}{B\lambda_0}} \int_{-a}^a \tilde{\rho}(x_0) \tilde{v}_0(x_0) \exp \left[-j \frac{\pi}{B\lambda_0} (Mx_0^2 - 2x_2 x_0 + x_2^2/M) \right] dx_0. \quad (7)$$

But this form for Huygens' integral corresponds to propagation through a simple collimated telescopic system with a ray matrix of the form

$$\begin{bmatrix} A & B \\ C & D \end{bmatrix} \equiv \begin{bmatrix} M & B \\ 0 & 1/M \end{bmatrix} \equiv \begin{bmatrix} 1 & MB \\ 0 & 1 \end{bmatrix} \times \begin{bmatrix} M & 0 \\ 0 & 1/M \end{bmatrix}. \quad (8)$$

The overall system, with the spherical curvatures extracted out, can thus be factored into the matrix product of a zero-length telescope of magnification M , plus a free-space section of length MB , as indicated by the matrix product in Equation 22.8 and by the drawing in Figure 22.8.

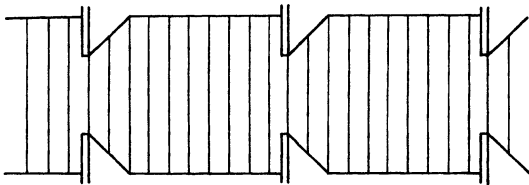
To express this same point in another way, we can move the input reference plane from the location z_0 just before the telescope to a magnified input plane z_1 just after the zero-length magnification step, by making the change of variables $x_1 \equiv Mx_0$ and $dx_1 \equiv M dx_0$. The Huygens' integral of Equation 22.7 can then be converted to the form

$$\tilde{v}_2(x_2) = \sqrt{\frac{j}{MB\lambda_0}} \int_{-Ma}^{Ma} \frac{\tilde{\rho}(x_1/M)\tilde{v}_0(x_1/M)}{M^{1/2}} \exp\left[-j\frac{\pi(x_1 - x_2)^2}{MB\lambda_0}\right] \cdot dx_1 \quad (9)$$

The general Huygens' integral for traveling completely around an arbitrary unstable resonator has thus been converted into the form of a *purely free space Huygens' integral*, which operates through a distance MB and across a full width of $2Ma$, and which is applied to a transversely magnified version of the input wavefunction $\tilde{\rho}(x_0)\tilde{v}_0(x_0)$.

We can use this integral as a canonical form for making calculations on any type of unstable resonator, with any number of intracavity paraxial elements, which falls within the above assumptions.

(a) magnifying wave



(b) demagnifying wave

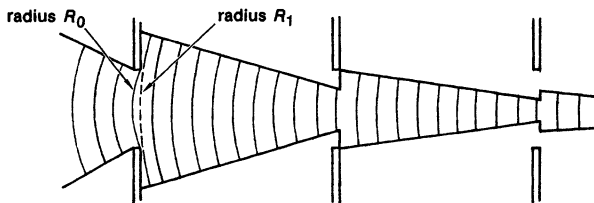


FIGURE 22.9

A purely geometrical analysis predicts both a magnifying and a demagnifying eigenwave in the canonical unstable system.

Collimated Fresnel Number

The effective Fresnel number, call it N_c , which characterizes the effective free-space propagation distance in this canonical model is then obviously given by

$$N_c = \frac{(Ma)^2}{MB\lambda_0} = \frac{Ma^2}{B\lambda_0} \equiv \text{collimated Fresnel number.} \quad (10)$$

This so-called *collimated Fresnel number* N_c will determine the amount of numerical work it takes to propagate a wave once around the resonator. It will also determine the number of Fresnel diffraction ripples that we can expect to see in the output wave across the output aperture of the unstable resonator. It is thus a second primary parameter which, along with the magnification M , characterizes any real hard-edged unstable resonator.

Low-Fresnel-number resonators ($N_c \leq 5$ or 10, say) can generally be handled numerically with reasonable computer programs, whereas large-Fresnel-number resonators ($N_c \geq 100$, say) are very difficult to handle in any sort of exact numerical analysis. Unfortunately, many unstable resonator lasers of practical interest have collimated Fresnel numbers N_c that are as large as this, or even much larger.

The Converging (Demagnifying) Geometrical Wave Solution

The *magnifying* geometrical eigenwave solution for an unstable resonator, viewed in the canonical formulation, is clearly just a collimated plane wave which passes through the aperture (or equivalently bounces off the finite output mirror); is expanded transversely by the magnification M , remaining planar; and then

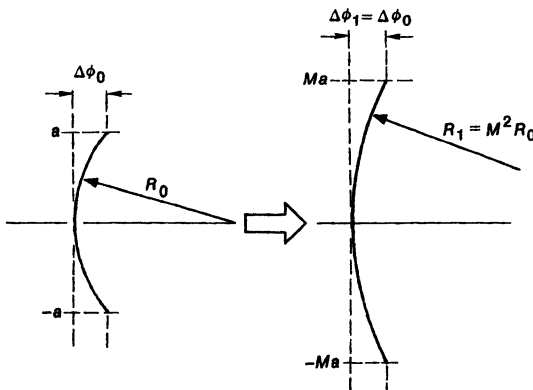


FIGURE 22.10

Transverse magnification by a factor M increases the radius of curvature by M^2 .

propagates through distance MB back to the same reference plane, as shown in the top sketch in Figure 22.9.

This same canonical system also has, however, a demagnifying geometrical eigenwave (or equivalently a magnifying eigenwave going in the opposite direction), which in general is not collimated, but instead has the general form shown in the lower part of Figure 22.9. We can obtain the parameters of this demagnifying solution from a simple geometric analysis as follows.

Consider a spherical wave of radius R_0 viewed at the input reference plane z_0 in the canonical model. When we magnify or stretch such a spherical wave in the transverse direction by a magnification factor M , its radius of curvature is multiplied by M^2 , since the phase lag $\Delta\phi(x)$ at the outer edge of the beam lag should stay the same before and after magnification (Figure 22.10). If we use R_1 for the radius of curvature of the wave at the reference plane z_1 after the magnification step, then we can write this phase lag at the beam edge in each case as

$$\Delta\phi_0(x)|_{x=a} = \frac{\pi a^2}{R_0 \lambda} = \Delta\phi_1(x)|_{x=Ma} = \frac{\pi (Ma)^2}{R_1 \lambda}, \quad (11)$$

so that obviously $R_1 = M^2 R_0$.

But after this spherical wave propagates on through the free-space distance MB in Figure 22.8, it should then come back to the same reference plane z_2 with radius $R_2 \equiv R_0$, as given by

$$R_2 = R_1 + MB = M^2 R_0 + MB = R_0. \quad (12)$$

Hence the radius of the demagnifying eigenwave in Figure 22.9(b) must be given by

$$R_0 = -\frac{MB}{M^2 - 1}, \quad (13)$$

where this is evaluated at the reference plane just before striking the output mirror or aperture. (The radius is negative because the wave is a converging wave.)

Aperture Coupling Between the Geometrical Eigenwaves

The reader should keep in mind that the magnifying and demagnifying geometrical eigenwaves shown in Figure 22.9 are, strictly speaking, eigensolutions only for an unbounded or purely geometrical unstable system—not for a real, hard-edged resonator in which finite beam diameters and edge diffraction effects must be included. The dominant mode pattern in a real unstable resonator is, however, generally quite similar in its basic properties to the magnifying geometrical eigenwave.

Now, when this kind of magnifying wave strikes the edges of the output aperture, we can expect that spherical (or cylindrical) edge waves will be scattered from the aperture edges into all directions, as we have discussed in Chapter 18. Some of this edge-wave energy, in particular, will be scattered into a direction which matches up with the demagnifying eigenwave traveling on beyond the aperture (or if you like, some rays are scattered from the aperture edge into a direction which feeds directly into the demagnifying eigensolution).

We might hypothesize then that the wave energy scattered by the aperture edges from the magnifying eigenwave into the demagnifying eigenwave direction will at first demagnify down toward the “core” of the unstable system, coming closer to the axis on each pass around the system. After a relatively few round trips, however, this energy will have demagnified down into such a small diameter beam that diffraction spreading effects will become very important. After a relatively few round trips, therefore, this “demagnified energy” will be turned back outward by diffraction effects, and in fact will be converted back into the magnifying eigenwave direction. If this simple edge-wave description has any validity, we might then guess that the *relative phase angle* with which the demagnifying wave is excited by the aperture edges and fed back into the primary magnifying wave may be quite significant in determining the mode behavior of a real unstable resonator.

Equivalent Fresnel Number

It turns out, in fact, that this relative phase shift between the magnifying and demagnifying geometrical eigenwaves at the aperture edge is very significant in real unstable resonators. Suppose we calculate this relative phase shift, as shown in Figure 22.11, and then express it in terms of what has become known as the *equivalent Fresnel number* N_{eq} for an unstable resonator, through the definition

$$[\phi_{\text{mag}}(x) - \phi_{\text{demag}}(x)]_{x=a} = \frac{\pi a^2}{R_0 \lambda} \equiv N_{\text{eq}} \times 2\pi, \quad (14)$$

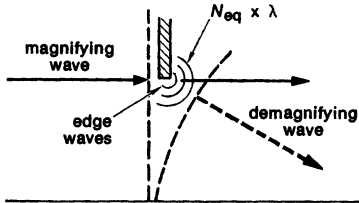
or

$$N_{\text{eq}} = \frac{a^2}{2R_0 \lambda} = \frac{M^2 - 1}{2M} \frac{a^2}{B\lambda_0} = \frac{M^2 - 1}{2M^2} \times N_c. \quad (15)$$

This equivalent Fresnel number N_{eq} turns out to be a very important alternative parameter for the behavior of hard-edged unstable resonators—perhaps more important than the collimated Fresnel number N_c to which it is related.

Equation 22.15, although derived using the canonical model, is quite general. Exactly the same expression for N_{eq} can also be derived, for example, in any

(a) canonical formulation



(b) standing-wave cavity

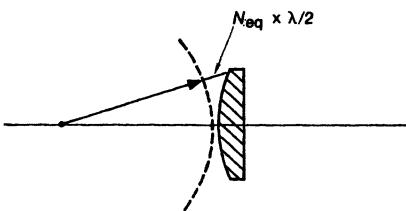


FIGURE 22.11
Geometrical interpretation of the equivalent
Fresnel number N_{eq} .

specific resonator by using

$$\begin{aligned}
 [\phi_{\text{mag}}(x) - \phi_{\text{demag}}(x)]_{x=a} &\equiv \left(\frac{1}{R_b} - \frac{1}{R_a} \right) \frac{\pi a^2}{\lambda} \\
 &= \left(\frac{D - 1/M}{B} - \frac{D - M}{B} \right) \frac{\pi a^2}{\lambda} = N_{\text{eq}} \times 2\pi.
 \end{aligned} \tag{16}$$

A physical interpretation of this formula at the outer edge of the output mirror for a standing-wave unstable resonator is also shown in Figure 22.11(b).

Confocal Unstable Resonators

Design formulas for various kinds of unstable resonators in terms of the three parameters N_{eq} , N_c and M are presented in Table 22.1. In particular, for any confocal unstable resonator (of either positive or negative branch) we can show that the matrix B parameter is given by $B = (M + 1)L/M$. Because of the collimated output beam in this situation, it is also convenient to define an “outer Fresnel number” N_0 for a confocal resonator based on the actual length L and the actual outer diameter $2Ma$ of the resonator, by

$$N_0 \equiv \frac{(Ma)^2}{L\lambda} = \text{outer Fresnel number}, \tag{17}$$

where $2a$ is the width or diameter of the output mirror, or of the hole in the output coupler. This outer Fresnel number is the quantity most directly related

to the diameter and length of the real laser device. The relations between this outer Fresnel number and N_{eq} and N_c are then given in Table 22.1.

REFERENCES

The concepts of positive and negative branch unstable resonators, and the virtues of the confocal unstable resonator design, were first pointed out by W. F. Krupke and W. R. Sooy, "Properties of an unstable confocal resonator CO₂ laser system," *IEEE J. Quantum Electron.* **QE-5**, 575-586 (December 1969).

The canonical formulation presented in this section was first outlined in A. E. Siegman, "A canonical formulation for analyzing multielement unstable resonators," *IEEE J. Quantum Electron.* **QE-12**, 35-40 (January 1976).

The equivalent Fresnel number was first introduced in the paper by Siegman and Arrathoon referenced in the previous section. Its physical interpretation seems to have been first explained clearly by A. Anan'ev and V. E. Sherstobitov, "Influence of the edge effects on the properties of unstable resonators," *Sov. J. Quantum Electron.* **1**, 263-267 (November-December 1971). See also C. R. Bisio, L. Ronchi, and V. Tognetti, "Some considerations about the diffraction loss of open resonators," *IEEE Trans. MTT-19*, 490-491 (May 1971).

A concept similar to the collimated Fresnel number can also be found in W. H. Steier and G. L. McAllister, "A simplified method for predicting unstable resonator mode profiles," *IEEE J. Quantum Electron.* **QE-11**, 725-728 (September 1975).

22.3 HARD-EDGED UNSTABLE RESONATORS

To find the exact eigenvalues and eigenmodes for a hard-edged unstable resonator, we must solve the exact resonator integral equation (preferably after converting it into canonical form). This can be done either by using a Fox-and-Li type numerical procedure or by one of several complicated analytical methods (most of which end up requiring extensive numerical calculations in any case). We will describe in this section a few results of such calculations for typical hard-edged unstable resonators.

Exact Mode Losses

There are only a limited number of published results for unstable optical resonator modes in the literature, partly because, as we will see, the results are complex and somewhat difficult to present, and partly because successful unstable resonator design can usually proceed using only a general understanding of unstable resonator properties, without the need for detailed design curves. Unstable resonator calculations are most often carried out either for one-transverse-dimension "strip" resonators, or for two-transverse-dimension circular-mirror resonators. Strip resonator calculations are considerably more common, probably because the Huygens-integral or Fourier-transform calculations that are involved seem simpler (though it is arguable whether they are really any simpler than the circular situation done right). Square or rectangular-mirror unstable resonators can then be treated as the product of two crossed strip resonators of appropriate widths.

TABLE 22.1
Unstable Resonator Formulas

Each of these cases refers to a two-mirror standing-wave cavity of length L , with mirror radii of curvature R_1 and R_2 taken positive for mirrors concave inward toward the resonator, and with $2a_1$ and $2a_2$ being the mirror widths for strip resonators, or the mirror diameters for circular mirrors. The reference plane is just before the output mirror M_2 , and the basic Fresnel number N is defined by $N \equiv a^2/L\lambda$ where $2a \equiv 2a_2$ is the width or diameter of M_2 .

a. Symmetric double-ended resonator, one-way pass

Mirror radii $R_1 = R_2 = R$; mirror half-widths $a_1 = a_2 = a$

Half-trace parameter $m = g = 1 - L/R$

Positive branch: $R < 0, m > +1, M = m + \sqrt{m^2 - 1}$

Negative branch: $0 < R < L/2, m < -1, M = m - \sqrt{m^2 - 1}$

One-way ray matrix:

$$\begin{bmatrix} A & B \\ C & D \end{bmatrix} = \begin{bmatrix} 1 - 2L/R & L \\ -2L/R & 1 \end{bmatrix} = \begin{bmatrix} 2m - 1 & L \\ 2(m - 1)/L & 1 \end{bmatrix}$$

Fresnel numbers $N_c = MN, N_{eq} = \sqrt{m^2 - 1}N = [(M^2 - 1)/2M]N$

b. Single-ended resonator, full round trip, output mirror M_2

Mirror radii R_1, R_2 arbitrary; mirror half-widths $a_1 = \infty, a_2 = a$

Parameters $g_1 = 1 - L/R_1, g_2 = 1 - L/R_2; m = 2g_1g_2 - 1$

Positive branch: $g_1g_2 > 1, m > +1, M = m + \sqrt{m^2 - 1}$

Negative branch: $g_1g_2 < 0, m < -1, M = m - \sqrt{m^2 - 1}$

Round-trip ray matrix:

$$\begin{bmatrix} A & B \\ C & D \end{bmatrix} = \begin{bmatrix} 4g_1g_2 - 2g_2 - 1 & 2g_2L \\ (4g_1g_2 - 2g_1 - 2g_2)/L & 2g_2 - 1 \end{bmatrix}$$

Fresnel numbers $N_c = [M/2g_2]N, N_{eq} = [(M^2 - 1)/2g_2M^2]N$

c. Confocal unstable resonator, positive or negative branches

Radius condition $R_1 + R_2 = 2L$; mirror half-widths $a_1 = \infty, a_2 = a$

Magnification $M = -R_2/R_1$; half-trace $m = (M^2 + 1)/2M$

Radii $R_1 = -2L/(M - 1), R_2 = 2ML/(M - 1), M > 1$ or < -1

Round-trip ray matrix:

$$\begin{bmatrix} A & B \\ C & D \end{bmatrix} = \begin{bmatrix} M & (M + 1)L/M \\ 0 & 1/M \end{bmatrix}$$

Outer Fresnel number $N_0 = (Ma)^2/L\lambda$

Fresnel number $N_c = [M^2/(M + 1)]N = [1/(M + 1)]N_0$

Fresnel number $N_{eq} = [(M - 1)/2]N = [(M - 1)/2M^2]N_0$

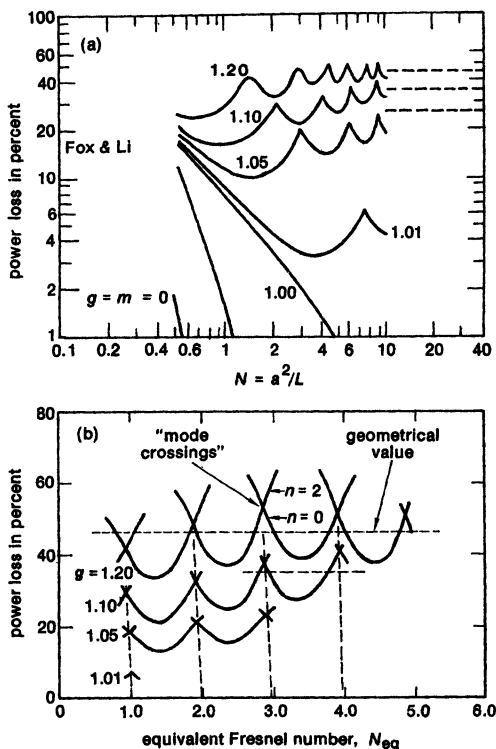


FIGURE 22.12
 (a) Early resonator loss calculations carried out by Fox and Li for a symmetric strip unstable resonator, showing the power loss per one-way bounce versus Fresnel number $a^2/L\lambda$ for a set of both stable and unstable resonators.
 (b) Similar calculations with the results plotted against the equivalent Fresnel number N_{eq} , showing the mode-crossing behavior. The horizontal straight lines in both situations indicate the losses predicted by a purely geometric analysis.

The earliest unstable resonator calculations were published by Fox and Li in a somewhat obscure conference proceedings (see References), at a time before the general properties of the unstable class of resonators were recognized. As shown in Figure 22.12(a), Fox and Li found that as soon as the parameter $g = 1 - L/R$ for a simple symmetric strip resonator was moved outside the stable region $-1 \leq g \leq 1$, the behavior of the resonator diffraction losses with Fresnel number $N = a^2/L\lambda$ changed dramatically. The round-trip diffraction losses, rather than decreasing rapidly with increasing N , approached a roughly constant value, with a periodic ripple about this value.

Repeating these calculations, but plotting them against the equivalent Fresnel number N_{eq} rather than the elementary Fresnel number N , as in Figure 22.12(b), later made it clear that N_{eq} rather than N is indeed the significant parameter in accounting for this periodic loss behavior. Adding lines corresponding to the geometric round-trip loss values $1 - |\bar{\gamma}_{geom}|^2 = 1 - 1/M$ (for the strip situation), as we have done in these figures, also makes clear that the real unstable resonator diffraction losses are similar but by no means exactly equal to the geometrically predicted values.

Mode-Crossing Behavior

In addition, it soon became clear that what appeared to be cusps in the early Fox and Li loss curves were in fact “mode crossings,” or values of M and N_{eq} at which two different modes had exactly the same diffraction losses. The loss curves at these points, when plotted versus N_{eq} , passed through each other, so that what was previously the lowest-order or lowest-loss mode gave up that priority to a separate and distinguishably different mode.

These crossing points are sometimes referred to as “mode degeneracies.” Only the *magnitudes* and not the *phase angles* of the eigenvalues are equal at these crossing points, however. More detailed examination shows that the two complex eigenvalues are always far apart in the complex plane, so that whereas the eigenvalue magnitudes may “cross,” the complex eigenvalues do not “intersect” or become degenerate in any true sense.

This behavior creates some difficulties in devising a sensible labeling scheme for the different eigenvalues, since the lowest-order mode at one value of N_{eq} is generally not the lowest-loss or dominant mode at other values. This is usually resolved by switching indices so that the lowest-loss mode at any given value of N_{eq} is by definition the $n = 0$ mode.

Eigenvalues For Circular-Mirror Resonators

Figures 22.13 and 22.14 show some of the results from an extensive series of eigenvalue calculations carried out by the author and H. Y. Miller on circular mirror hard-edged unstable resonators for a wide range of magnifications and Fresnel numbers. (Note that these calculations plot the eigenvalue magnitude $|\tilde{\gamma}|$ versus N_{eq} whereas the previous figures plotted the loss per bounce $1 - |\tilde{\gamma}|^2$.) These calculations were carried out for modes with both zero and first-order azimuthal variations, i.e., assuming fields of the form $\tilde{u}_{pl}(r, \theta) = \tilde{u}_p(r) \times e^{j\theta l}$ with $l = 0$ and $l = 1$.

These results demonstrate that the periodic crossing of the eigenvalues near integer values of N_{eq} continues indefinitely, up to the largest values of M and N_{eq} that could be handled with the available computational resources. At low Fresnel numbers, which correspond to smaller mirror diameters, only a very few radial modes fit within the unstable resonator, or at least the computations indicate that all higher-order modes have such high losses that their eigenvalues cannot be seen numerically. As the Fresnel number increases, additional modes come up out of the high-loss region, with each such mode eventually becoming the lowest-loss mode and then oscillating and perhaps recurring as the dominant mode at irregular repetition periods.

The phase angles of the eigenvalues obviously rotate continuously through increasing negative multiples of 2π as the Fresnel number increases. This indicates that if we follow the trajectory of any one eigenvalue in the complex plane, each eigenvalue rotates continuously about the origin in a roughly circular orbit with increasing Fresnel number. The dominant eigenvalues, however many of them there are, are always spaced by roughly equal angles in the complex plane.

The Half-Integer “Anti-Crossing Points”

Those values of N_{eq} halfway between the mode crossings, that is, near half-integer values of equivalent Fresnel number in Figures 22.13 and 22.14, might

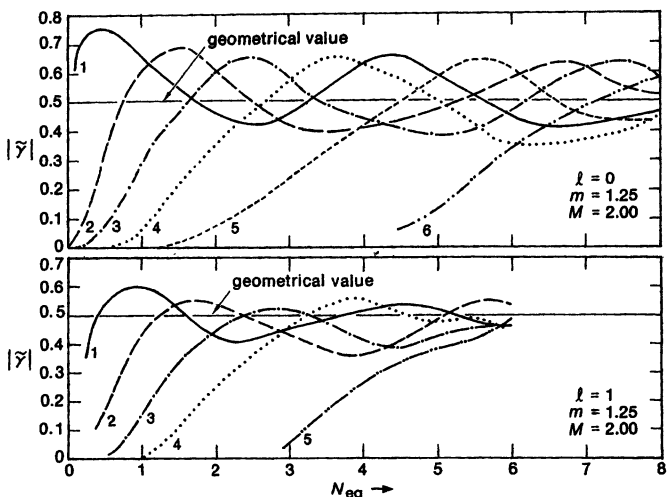


FIGURE 22.13

Plots of the eigenvalue magnitude $|\tilde{\gamma}|$ versus equivalent Fresnel number for the $l = 0$ and $l = 1$ azimuthally varying eigenmodes in a circular-mirror unstable resonator with magnification $M = 2$. In this and the following figure the losses of any higher-order eigenmodes are so large that the eigenvalues cannot be distinguished from the baseline.

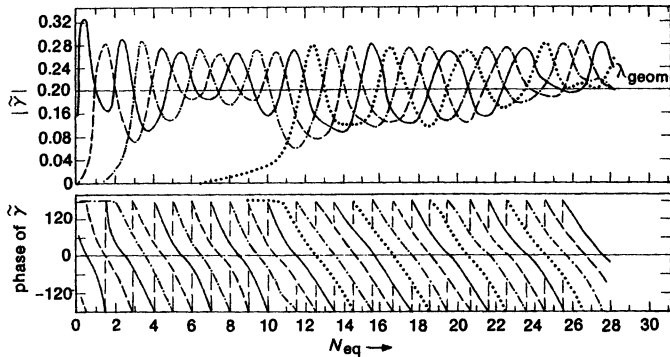


FIGURE 22.14

Magnitude and phase angle of the complex eigenvalue $\tilde{\gamma}$ versus Fresnel number for the $l = 0$ eigenmodes of a circular-mirror unstable resonator with larger magnification ($M = 5$).

seem to be the optimum operating points for an unstable resonator laser, since they combine the largest discrimination between lowest and higher-order modes with the lowest diffraction losses for a given magnification M (which permits operating at a larger magnification for a specified coupling value). This observation is largely true, but has some qualifications, as will be pointed out later.

The general observation is that for circular-mirror unstable resonators the mode crossings and the intervening maximum separation points occur very near

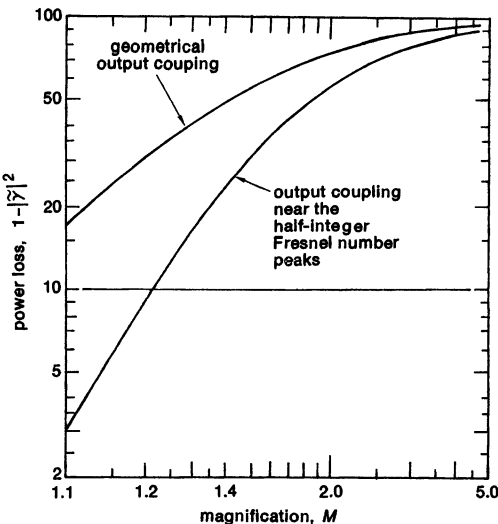


FIGURE 22.15

Geometrical output coupling, and approximate output coupling near half-integer equivalent Fresnel number peaks, versus magnification M for a circular-mirror unstable resonator.

to values of $N_{\text{eq}} \approx k$ and $k + 1/2$, with k integer, whereas for strip resonators these points occur nearer to $N_{\text{eq}} \approx k + 7/8$ and $k + 3/8$. This difference is almost surely due to the fact that a strip resonator actually has different Fresnel numbers along different azimuthal directions, as pointed out in Chapter 18 in connection with slit diffraction effects.

Output Coupling Approximations

The previous results and many similar calculations all show that the resonator diffraction losses or output coupling values at the eigenvalue peaks near the half-integer Fresnel numbers are substantially smaller than predicted by the simple geometric theory; and in fact the diffraction losses for the lowest-order mode at any value of N_{eq} are almost always less than or at most equal to the geometric value. This represents, as we have noted earlier, the strong ability of optical resonator modes to “pull in their skirts” or to shape their eigenmode profiles so as to minimize diffraction losses out the sides of the resonator.

We have already noted that the geometric eigenvalue for a circular resonator is given by $\tilde{\gamma}_{\text{geom}} = 1/M$. A purely empirical formula says that the eigenvalue magnitude near the larger half-integer peaks in the same situation is given approximately by

$$\tilde{\gamma}_{\text{peak}} \approx \sqrt{\frac{2M^2 - 1}{M^4}}. \quad (18)$$

as shown in Figure 22.15. The peak near the lowest value $N_{\text{eq}} \approx 1/2$ generally has a value even slightly larger, or losses even slightly smaller, than this.

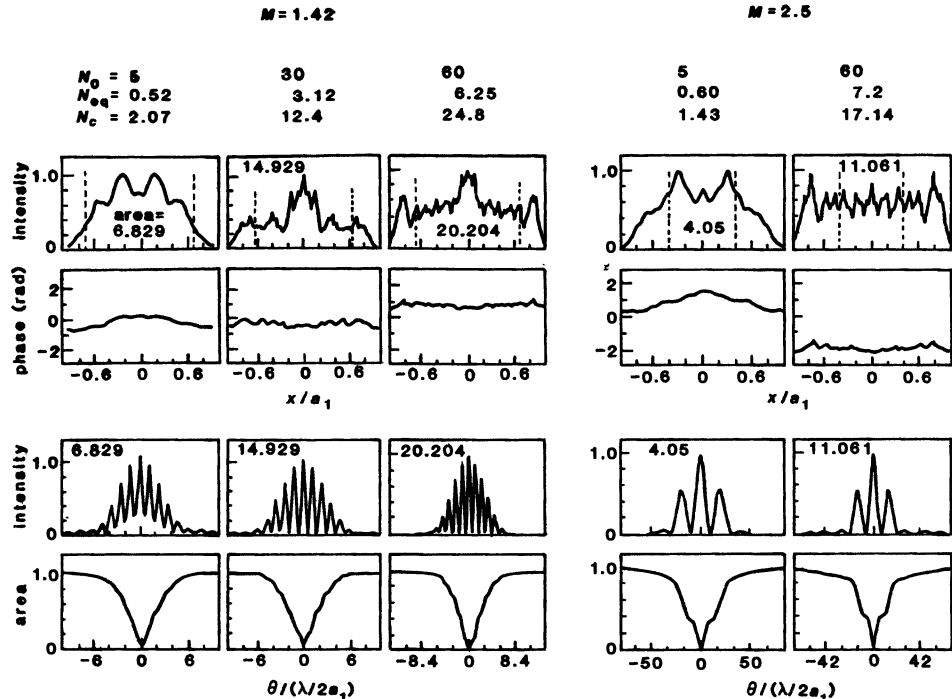


FIGURE 22.16

Transverse variation of the lowest-order eigenmode intensity and phase inside the cavity, and of the far-field beam pattern and cumulative power versus beam angle, for strip unstable resonators with various values of magnification M and equivalent Fresnel number.

Exact Mode Patterns

Figures 22.16 and 22.17 illustrate some of the complicated forms taken on by the lowest-order transverse eigenmodes in a one-dimensional strip resonator for different values of the magnification M and equivalent Fresnel number N_{eq} . The corresponding mode patterns for circular-mirror resonators would be equally if not more interesting, but few detailed calculations for circular-mirror patterns can be found in the literature. The general features will always be very much the same for either the strip or the circular mirror.

The results shown in Figures 22.16 and 22.17 come from early calculations, and may contain some minor inaccuracies, but they correctly illustrate the general features of the unstable resonator lowest-order modes. For each case shown, the top figure illustrates the intensity profile across the strip resonator just inside the output mirror, with the vertical lines indicating the edges of the mirror. The next plot down then shows the phase angle of the same wavefront versus the transverse coordinate.

The complex field amplitude falling outside the vertical bars or mirror edges in these figures determines the near-field pattern that will be coupled out of the resonator past the mirror edges. The third plot indicates the far-field beam pattern versus beam angle that will be produced (in one transverse dimension) by

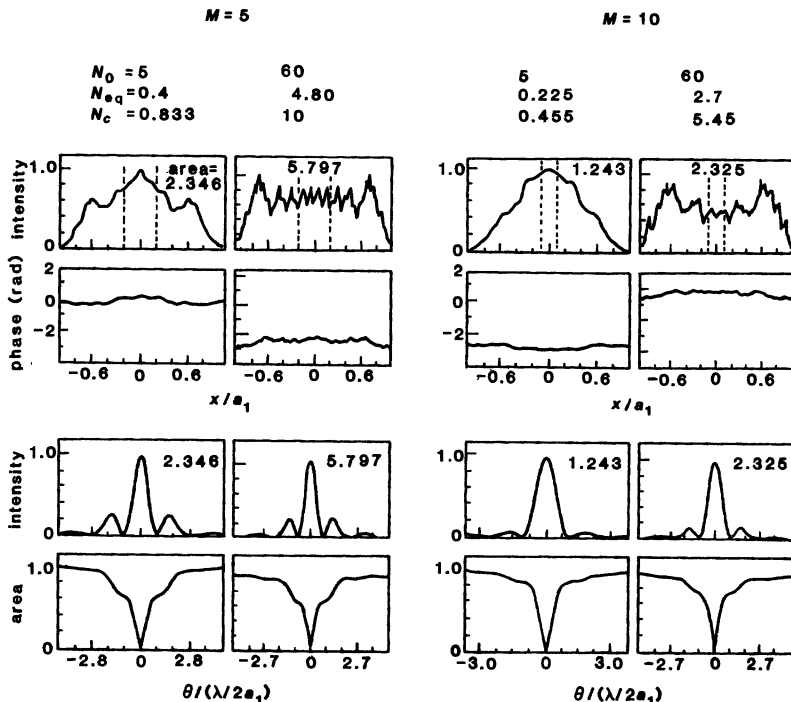


FIGURE 22.17

Transverse variation of the lowest-order eigenmode intensity and phase inside the cavity, and of the far-field beam pattern and cumulative power versus beam angle, for strip unstable resonators with various values of magnification and Fresnel number.

the out-coupled beam pattern. This pattern is essentially the Fourier transform of the out-coupled near-field pattern. Finally, the bottom plot shows the cumulative or integrated power ("power in the bucket") within a given far-field angle.

These plots taken all together illustrate most of the primary features of unstable resonator modes:

(1) *The overall shape of the mode inside the resonator is somewhere between roughly triangular and roughly gaussian for low Fresnel numbers ($N_{\text{eq}} \leq 1$), changing over to a generally squarish shape for large Fresnel numbers ($N_{\text{eq}} \gg 1$), with the intensity pattern extending out to roughly M times the mirror diameter in each case.*

(2) *Superimposed on this basic shape are complex patterns of Fresnel ripples, which become increasingly complex and contain increasingly high spatial frequencies with increasing values of the collimated Fresnel number N_c . In many cases, especially for $N_c \gg 1$, one can see that there are just about N_c large-scale ripples across the full magnified width of the resonator, together with significant amounts of much higher-frequency but small-amplitude ripples superimposed on this.*

(3) *The near-field transverse phase variation shown in the second plot in each group is the transverse phase variation as calculated for a confocal resonator, or equivalently for the canonical formulation. This phase variation represents*

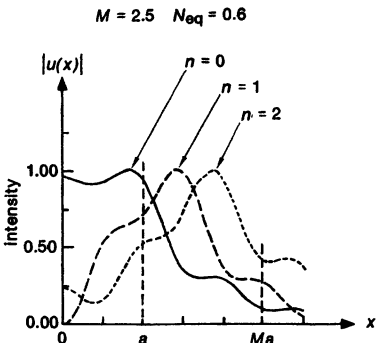


FIGURE 22.18

Amplitude profiles of the three lowest-order eigenmodes for a strip unstable resonator with $M = 2.5$ and $N_{\text{eq}} = 0.60$.

therefore the phasefront difference between the exact unstable eigenmode and the spherical wavefront of the diverging geometrical eigenwave. It is evident that this deviation is small in all situations; i.e., the actual lowest-order wavefront is very close to the purely geometric eigenwave. The finite average value of the phase angle in certain situations simply represents the finite phase angle of the resonator eigenvalue $\tilde{\gamma}$, which has not been subtracted out of these plots.

(4) *The far-field plots make clear the primary weakness of low-magnification unstable resonators: when the near-field output beam is a comparatively narrow annulus, or two comparatively narrow slits as it is here, the far-field pattern contains a large number of side lobes, with only a small fraction of the total beam energy in the centermost lobe.* Note that in all the far-field plots the beam angle is normalized to the diffraction angle $\lambda/2Ma$ characteristic of the full magnified outer width of the near-field pattern; and the first zero of the centermost lobe always occurs at roughly $\theta \approx \lambda/2Ma$. The first break point or change in slope in the integrated power curve indicates the fractional amount of the total output power that is contained in the central lobe. Note that, for example, this central lobe only contains $\approx 15\%$ of the total power for $M = 1.42$, rising to $\geq 70\%$ for $M = 10$.

Also note how little the far-field patterns actually depend on the equivalent or collimated Fresnel numbers—for any given magnification M the far-field patterns, and especially the “power in the bucket” curves, are essentially independent of N_{eq} or N_c .

Higher-Order Modes

Calculations of higher-order unstable resonator modes are also very sparse in the literature. Figure 22.18 shows one example of the three lowest-order symmetric and antisymmetric modes for a very low Fresnel number strip resonator, as calculated using in this case an expansion of the one-dimensional Huygens kernel in linear prolate functions.

We can readily see in Figure 22.18 how the lowest-order or $n = 0$ mode has pulled in its fields so that its diffraction losses are substantially less than would be predicted by the geometric theory. The higher-order modes, by contrast, have substantially larger diffraction spread, and thus greatly increased diffraction losses for the $n = 1$ and $n = 2$ modes.

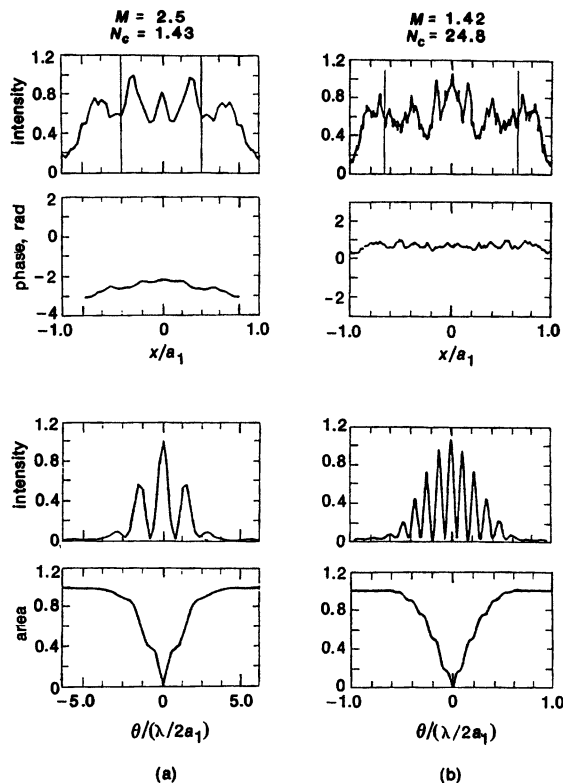


FIGURE 22.19

Calculated near-field and far-field patterns for the steady-state oscillation patterns in two unstable resonators, assuming that a uniform saturable gain sheet with an unsaturated gain equal to ten times the laser threshold value is pasted on the back mirror. Compare with the bare-resonator mode calculations shown in Figures 22.13 and 22.14.

Loaded Resonator Calculations

The question repeatedly arises as to how the modes of a laser cavity will be modified by the effects of a spatially varying gain within the resonator, as well as the effects of gain saturation in the laser medium. To explore this question, Figure 22.19 shows the oscillation mode patterns calculated for two of the same unstable resonators as in Figure 22.13 and 22.14, assuming that a thin saturable "gain sheet" is pasted on the surface of mirror #1 (the back mirror) in the unstable resonator.

In the Fox and Li procedure used for these calculations, the circulating field is multiplied by this gain sheet on each round trip; and then the gain itself is saturated in a homogeneous fashion by the local intensity at each point across the mirror before calculating the next round trip. The resonator fields are then found to converge, after only a very few round trips in most unstable situations, to a self-consistent transverse field and transverse gain pattern which presumably represents the actual oscillating mode that would develop in such a laser.

By comparing these "loaded resonator" results with the corresponding "bare resonator" modes in Figures 22.13 and 22.14, we can see that the general character of the mode is very little changed, the primary difference being that some

of the higher peaks are pushed down in amplitude by the local gain saturation that they produce in the loaded resonator. This seems to be true in most loaded resonator calculations: transverse gain variations and gain saturation have only minor effects on the mode patterns, although any kind of local *transverse phase variations* will have large effect on the mode patterns and on the far-field beam spread in particular.

REFERENCES

The earliest unstable resonator results shown in this section are from A. G. Fox and T. Li, "Modes in a maser interferometer with curved mirrors," in *Quantum Electronics III*, edited by P. Grivet and N. Bloembergen (Columbia University Press, 1964), p. 1263.; and from A. E. Siegman and R. Arrathoon, "Modes in unstable optical resonators and lens waveguides," *IEEE J. Quantum Electron.* **QE-3**, 156-163 (April 1967).

Other early numerical calculations of mode losses and mode patterns for unstable resonators with strip or rectangular mirrors are given in R. L. Sanderson and W. Streifer, "Unstable laser resonator modes," *Appl. Opt.* **8**, 2129-2136 (October 1969), and "Laser resonators with tilted reflectors," *Appl. Opt.* **8**, 2241-2248 (November 1969).

Extensive tabulations of eigenvalues (but not eigenmodes) for circular-mirror unstable resonators are given in A. E. Siegman and H. Y. Miller, "Unstable optical resonator loss calculations using the Prony method," *Appl. Opt.* **9**, 2729-2736 (December 1970). See also D. B. Rensch, "Three-dimensional unstable resonator calculations with laser medium," *Appl. Opt.* **13**, 2546-2561 (November 1974).

The mode patterns for strip resonators given in this chapter come from D. B. Rensch and A. N. Chester, "Iterative diffraction calculations of transverse mode distributions in confocal unstable laser resonators," *Appl. Opt.* **12**, 997-1010 (May 1973). See also

The higher-order eigenfunctions come from M. E. Rogers and J. H. Erkkila, "Resonator mode analysis using linear prolate functions," *Appl. Opt.* **22**, 1992-1995 (July 1, 1983).

For further comments on the use of the Prony method in resonator calculations, see W. D. Murphy and M. L. Bernabe, "Numerical procedures for solving nonsymmetric eigenvalue problems associated with optical resonators," *Appl. Opt.* **17**, 2358-2365 (August 1978). (Has axicon results),

22.4 UNSTABLE RESONATORS: EXPERIMENTAL RESULTS

Detailed experimental studies and comparisons with theory are also surprisingly sparse for unstable resonators, probably due to several reasons. First, many of the development efforts on unstable resonators were focused on very large high-power chemical and gasdynamic lasers in the infrared, where careful diagnostics are technically difficult; and because of the nature of these development projects emphasis was focused on meeting project specifications rather than on detailed exploration of the unstable resonator itself. In addition, there does not seem to be available any convenient, large-bore, high-gain, continuously operating visible laser which could serve as a test bed for careful unstable resonator studies.

The general observation nonetheless is that the experimental performance of unstable resonators agrees very well with theoretical calculations, with no significant disagreements between theory and experiment being found. We will

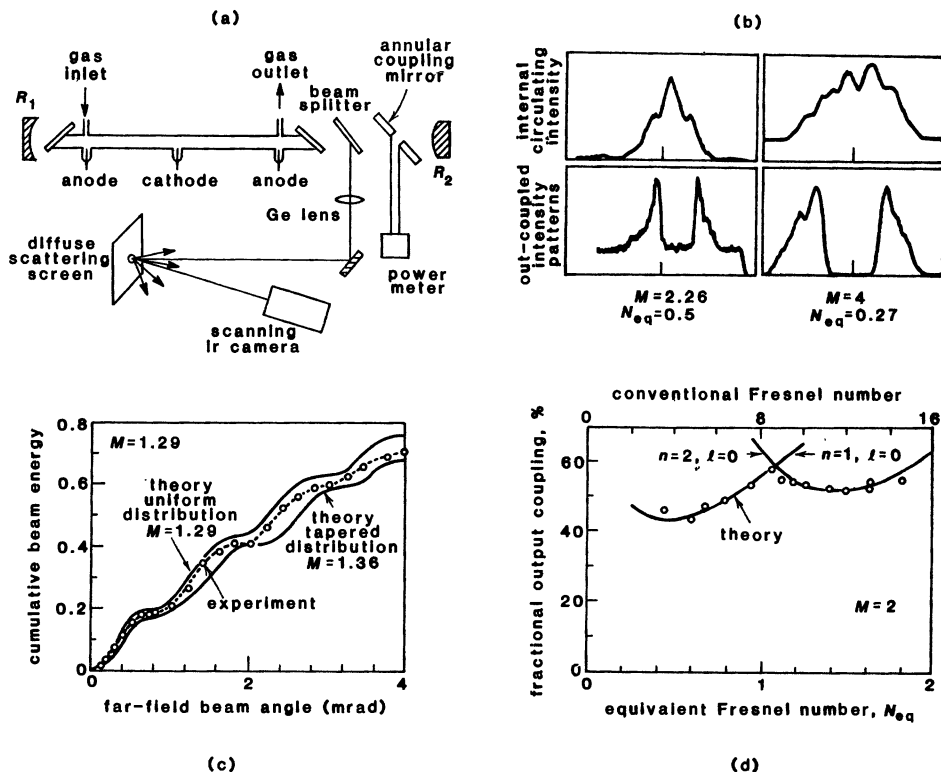


FIGURE 22.20

Measurement system and experimental results for unstable resonator modes on a low-power cw CO₂ laser studied by Freiberg, Chenuasky and Buczek (see References).

review briefly in this section a few of the more significant experimental studies that have been performed on unstable resonators.

Low-Power Unstable Resonator Experiments

Perhaps the most careful and detailed such experimental study was that performed by Freiberg, Chenuasky and Buczek at the United Technologies Research Center on a low-power 10.6 μm CO₂ laser, with results as shown in Figure 22.20.

As shown in part (a) of Figure 22.20, a thin beam splitter was placed inside the laser cavity so that it reflected out a few percent of the circulating intensity just before the output scraper mirror. Insertion of this beam splitter, together with appropriate imaging optics and a scanning IR camera, made it possible to study the circulating mode pattern inside the laser cavity, as well as the near-field and far-field beam patterns coupled out of the cavity.

Figure 22.20(b) shows two typical examples of the internal circulating mode pattern and the near-field beam pattern coming from the scraper mirror, for two different magnifications and (small) values of equivalent Fresnel number. The

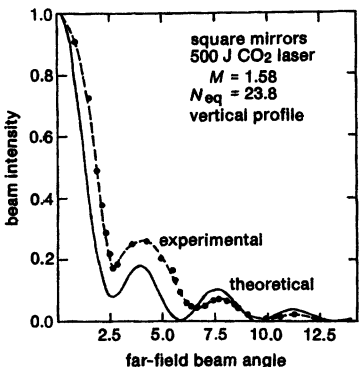


FIGURE 22.21

Theory versus experiment for the far-field beam pattern from a large, pulsed, square-mirror CO_2 laser.

general similarity between these results and the low-Fresnel-number calculations of the previous section is evident.

A typical measurement of integrated far-field energy versus far-field beam angle is shown in Figure 22.20(c). The design value for this resonator was a radial magnification of $M = 1.29$. Both exact calculations and near-field experiments showed, however, that the near-field pattern was closer to a linearly tapered annular radial variation falling to zero at approximately 1.36 rather than 1.29 times the coupling hole diameter. The far-field experimental results have been compared, therefore, to the theoretical far-field patterns for both a uniformly illuminated annular aperture corresponding to $M = 1.29$, and a linearly tapered (but uniphase) annular aperture with $M = 1.36$. It is evident that the far-field beam pattern is not greatly sensitive to the difference between these two distributions, with the actual experimental values falling neatly in between.

Finally, by measuring carefully with an optical power meter both the circulating power inside the cavity just before the coupling mirror and the actual out-coupled power, it was possible to measure experimentally the actual diffraction coupling from the unstable resonator laser under varying experimental conditions. Part (d) of this figure demonstrates the extent to which these measurements agree with the periodic loss variation expected for the unstable resonator near $N_{\text{eq}} = 1$.

Measurements on Higher-Power Lasers

Experimental measurements on higher-power unstable resonator lasers have usually been limited to near-field intensity profiles or burn patterns, which are generally rather uninformative; to measurements of total power or energy output, which generally yield the expected power output for the laser in question; and to observations of the far-field beam patterns, which almost always give something very close to the expected pattern of an intense near-diffraction-limited central spot with surrounding diffraction rings or lines.

Figure 22.21 shows, for example, the variation along one transverse direction of the far-field burn pattern of a very large (≈ 500 J/shot) electron-beam-ionized CO_2 TEA laser having a rectangular laser medium ≈ 1 m long and 15 by 20 cm in cross section, using an unstable resonator with a square output mirror of width

$2a = 9.5$ cm and a magnification $M = 1.58$. The agreement between theory and experiment for the width of the central lobe and the spacing of the diffraction side lobes is very good, considering the nature of this type of experiment. Many other generally similar experimental results for other unstable resonator lasers can be found in the literature, with some of them listed in the following References.

Large-Scale Unstable Resonator Simulations

We might also describe briefly here some of the very large-scale numerical simulations or “computer experiments” that have been carried out for unstable resonator lasers. These calculations are in essence extended versions of the Fox and Li method, in which an optical signal is propagated through repeated round trips inside an unstable resonator, taking into account both the optical beam propagation, as modified by the resonator mirrors, the laser gain medium, internal phase perturbations, and other effects, and also the effects of the optical signals back on the laser medium and the resonator parameters, including gain saturation and repumping, heating and distortion of the laser medium, possible mirror distortions, and other nonlinear effects.

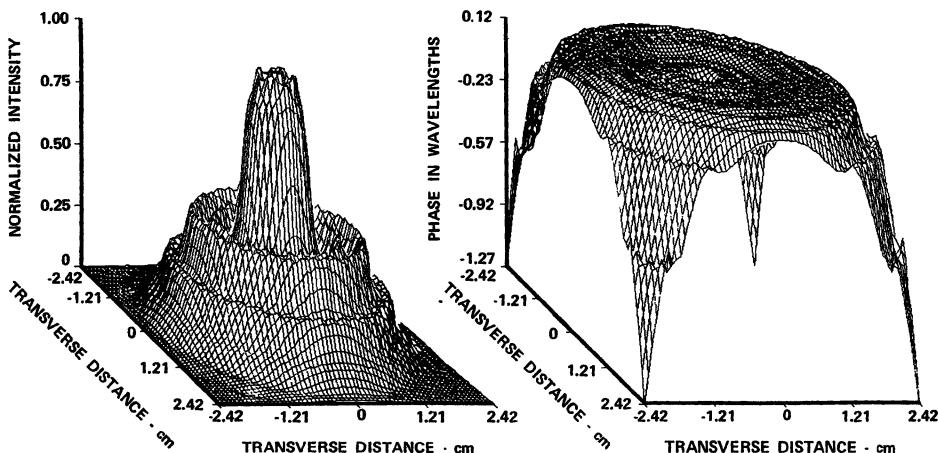
These simulations thus require both large-scale optical codes which propagate the circulating optical field from plane to plane within the unstable resonator, and also atomic, molecular and possibly chemical codes which calculate the nonlinear responses of the gain and phase media inside the resonator. The usual procedure is to divide the laser resonator into several sections in the axial direction and to lump the net laser gain and phase distortion occurring in each section into a thin discrete “gain and phase sheet.” The optical wave is propagated through a free-space length equal to one section, and then multiplied by the lumped gain and phase shift associated with that section, through one complete round trip; after which the gain and phase for each section is recalculated based on the optical intensities in the previous round trip.

Figure 22.22 illustrates the kind of results that can be obtained from such a simulation. The plots in part (a) show the normalized intensity and phase profiles just inside the output coupler for the lowest-order eigenmode in an empty circular-mirror unstable resonator with $N_{eq} = 1.5$ and $M = 2.5$. The circular beam pattern and flat phase front of the mode are evident. The successive plots then show the results of adding a transversely flowing saturable gain medium; flowing gain plus internal phase perturbations from two intra-cavity shock waves; and flowing gain plus a small mirror tilt.

Including the saturable gain clearly produces a large change in the mode intensity profile but only minor changes in the phase profile. Adding to this the phase perturbation due to the weak shock waves causes further severe amplitude distortion, but still only relatively minor phase distortion. Indeed, the far-field beam patterns for all three of these situations are essentially identical, despite the large differences in the near-field intensity patterns.

The primary effect of mirror misalignment is to tilt the output wavefront while leaving it still essentially planar. The far-field beam spot in this situation is steered to one side, but otherwise is essentially unchanged.

We have pointed out earlier that it may take a large number of sample points (perhaps on the order of $8N_c$ points in each transverse direction) to handle adequately even the undistorted bare-resonator modes of an optical resonator. This number can be substantially increased by higher-spatial-frequency distortions within the resonator, and by the necessity to provide adequate “guard bands”

(a) bare resonator: $N_{eq} = 1.5$, $M = 2.5$ 

(b) loaded resonator: flowing gain only

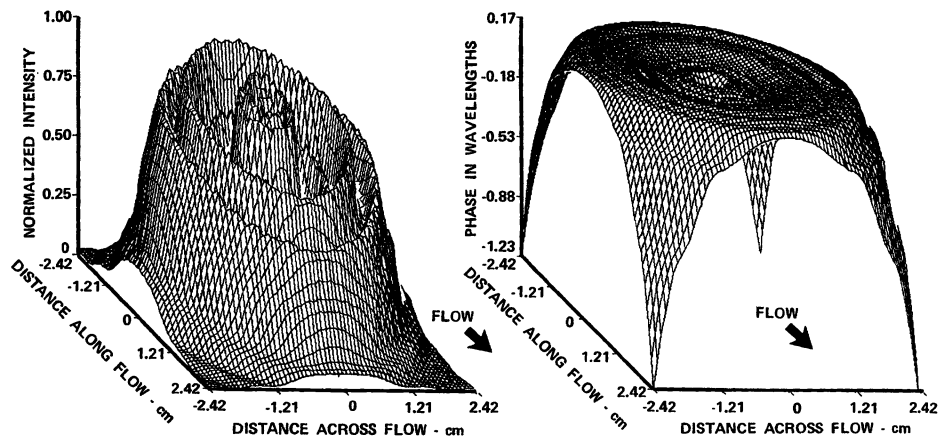
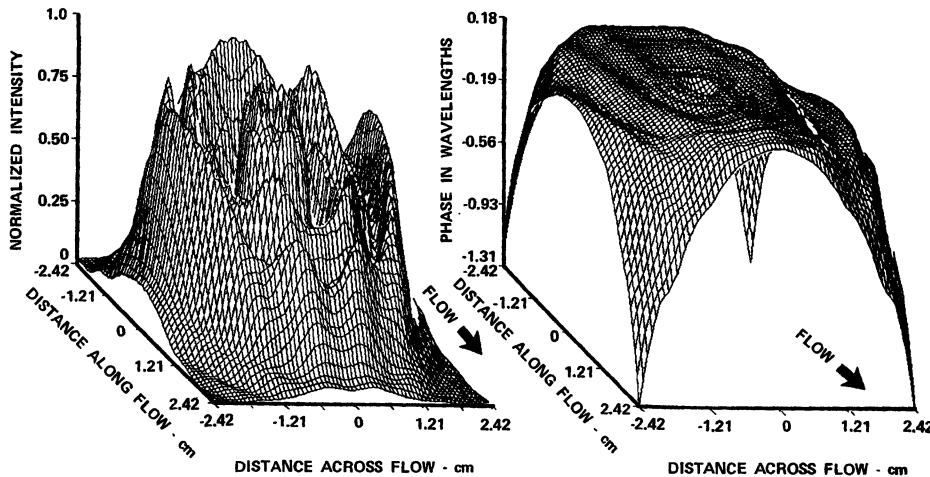


FIGURE 22.22

Near-field intensity and phase profiles from a large-scale computer simulation of a gas-dynamic CO₂ laser. (a) Bare resonator, lowest-order eigenmode. (b) Loaded resonator including transversely flowing saturable gasdynamic gain medium.

outside the resonator edges. The numerical work required in these simulations can thus become very substantial. Fast transform algorithms (fast Fourier or Hankel transforms) seem clearly the optimum way to handle the optical propagation steps. On the fortunate side, the general experience is that large-scale simulations of this type appear to converge in only a small number (e.g., 5 or

(c) loaded resonator: flowing gain, weak shock waves



(d) loaded resonator: flowing gain, 50 μrad mirror tilt

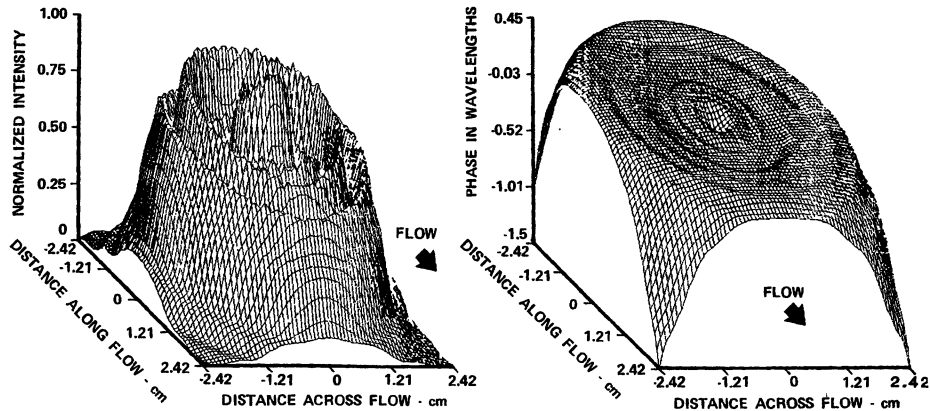


FIGURE 22.22, continued

Near-field intensity and phase profiles from a large-scale computer simulation of a gasdynamic CO₂ laser. (c) Loaded resonator with flowing gain and index perturbations due to two weak shock waves crossing the optical beam inside the cavity. (d) Loaded resonator with flowing gain and no shock waves, but 50 μ rad of mirror tilt.

10) of round trips for most unstable resonators, presumably because of the large transverse mode discrimination associated with unstable resonators.

REFERENCES

Many of the earliest published experimental results for unstable resonators are in the Soviet literature, for example, in Yu. A. Anan'ev, N. A. Sventsitskaya, and V. E. Sherstobitov, "Transverse mode selection in a laser with convex mirrors," *Sov. Phys.—Doklady* **13**, 351–352 (October 1968); Yu. A. Anan'ev, N. A. Sventsitskaya, and V. E. Sherstobitov, "Properties of a laser with an unstable resonator," *Sov. Phys. JETP* **28**, 69–74 (October 1969); and Yu. A. Anan'ev, et. al, "Telescopic-resonator laser," *Sov. Phys. JETP* **31**, 420–424 (September 1970).

The low-power CO₂ results cited in this section are from R. J. Freiberg, P.P. Chenausky, and C. J. Buczek, "An experimental study of unstable confocal CO₂ resonators," *IEEE J. Quantum Electron.* **QE-8**, 882–892 (December 1972); and the high-power pulsed result is from H. Granek and A. J. Morency, "Large effective Fresnel number confocal unstable resonators: an experimental study," *Appl. Opt.* **13**, 368–373 (February 1974).

A representative sample of early references which contain experimental studies of unstable resonator properties in various lasers include W. F. Krupke and W. R. Sooy, "Properties of an unstable confocal resonator CO₂ laser system," *IEEE J. Quantum Electron.* **QE-5**, 575–586 (December 1969); E. V. Locke, R. Hella, and L. Westra, "Performance of an unstable oscillator on a 30-kW CW gas dynamic laser," *IEEE J. Quantum Electron.* **QE-7**, 581–583 (December 1971); J. P. Reilly, "Single-mode operation of a high-power pulsed N₂/CO₂ laser," *IEEE J. Quantum Electron.* **QE-8**, 136–139 (February 1972); P. E. Dyer, D. J. James and S. A. Ramsden, "Single transverse mode operation of a pulsed volume excited atmospheric pressure CO₂ laser using an unstable resonator," *Opt. Commun.* **5**, 236–238 (July 1972); J. Davit and C. Charles, "Performance of an unstable repetitive pulsed O₂ laser oscillator," *Appl. Phys. Lett.* **22**, 248–250 (March 1, 1973); R. A. Chodzko, H. Mirels, F. S. Roehrs, and R. J. Pedersen, "Application of a single-frequency unstable cavity to a CW HF laser," *IEEE J. Quantum Electron.* **QE-9**, 523–530 (May 1973); and V. N. Grebenyuk, V. M. Izgorodin, S. B. Kormer, and K. B. Yushko, "Infrared Raman laser with an unstable resonator," *Sov. J. Quantum Electron.* **8**, 779–781 (June 1978).

The first extensive numerical simulations of a loaded unstable resonator laser, including saturable gain and index perturbations, were reported in A. E. Siegman and E. A. Szklaas, "Mode calculations in unstable resonators with flowing saturable gain. 1: Hermite-gaussian expansion," *Appl. Opt.* **13**, 2775–2792 (December 1974). These calculations were extended to use the FFT approach in E. A. Szklaas and A. E. Siegman, "Mode calculations in unstable resonators with flowing saturable gain. 2: Fast Fourier transform method," *Appl. Opt.* **14**, 1874–1889 (August 1975). Another such calculation is D. B. Rensch, "Three-dimensional unstable resonator calculations with laser medium," *Appl. Opt.* **13**, 2546–2561 (November 1974).

Examples of loaded-resonator calculations from the Soviet literature include L. A. Vasil'ev, V. K. Demkin, Yu. A. Kalinin, and Yu. I. Kruzhilin, "Calculation of the angular distribution of the radiation emitted by a laser with an inhomogeneous active medium and a telescopic resonator," *Sov. J. Quantum Electron.* **5**, 27–29 (July 1975); and Yu. N. Karamzin and Yu. B. Konev, "Numerical investigation of the operation of unstable telescopic resonators allowing for diffraction and saturation in the active medium," *Sov. J. Quantum Electron.* **5**, 144–148 (August 1975).



MORE ON UNSTABLE RESONATORS

Unstable resonators, as a consequence of both their practical utility and their complex analytical properties, have stimulated many clever extensions as well as detailed mathematical analyses. In this chapter we review briefly some of these more advanced analytical techniques and inventions, and then introduce what may eventually become the most useful form of unstable resonator, namely, the "soft-edged" or gaussian variable reflectivity type of geometrically unstable resonator.

23.1 ADVANCED ANALYSES OF UNSTABLE RESONATORS

We first introduce in this section several of the more advanced analytical techniques for treating unstable resonators, along with some more advanced concepts and design ideas related to unstable resonator modes.

Advanced Analytical Techniques for Unstable Resonators

The purely geometric analysis of the unstable resonator, leaving out diffraction or wave-optical aspects, is very simple and provides an excellent zero-order approximation to the wavefronts and mode patterns of the unstable resonator. Numerical solution of the exact integral equation, by contrast, provides an effective but somewhat expensive method for predicting the exact eigenvalues and eigenmode properties of unstable resonators.

We might then attempt to develop some sort of approximate analytical extension to the geometric analysis, putting in diffraction effects to a first-order level of approximation, so as to obtain more accurate answers than in the geometric limit, but in a simpler and more general fashion than purely numerical calculations. We might expect that such a first-order solution would become increasingly valid for larger values of equivalent Fresnel number N_{eq} , or for vanishing values of the optical wavelength λ .

Success in finding any such approximation technique which is simultaneously simple and reasonably accurate has been limited, however. The wave-optical properties of the unstable resonator seem to be inherently complex, so that, for example, the complicated ripple structure of the eigenmodes and the crossing

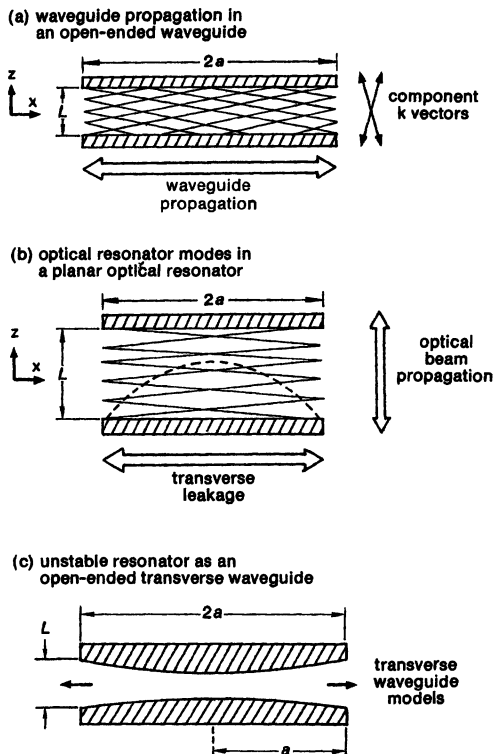


FIGURE 23.1

An optical resonator, with wave propagation in the z direction, can also be viewed as a waveguide, with very-high-order propagation in the x direction.

behavior of the circular-mirror eigenvalues persist even to very large Fresnel numbers N_{eq} , in much the same way that the Gibbs phenomenon in a square-wave Fourier series approximation persists no matter how many terms are kept in the Fourier expansion.

There are, however, a few analytical techniques developed for unstable resonators which we can review briefly, in part because they can be used to obtain useful results, and in part because of the insight they can yield into unstable resonator behavior. These techniques include the so-called *coupled-mode analysis* and several versions of the *asymptotic* or *virtual-source analysis*.

The Coupled Mode or Transverse Waveguide Approach

To introduce this interesting and quite different form of unstable resonator analysis, we can consider the wave propagation in both directions along a finite open-ended length of a conventional microwave waveguide, as shown in Figure 23.1(a). For simplicity let us consider only a two-dimensional strip waveguide formed by two flat metallic planes parallel to the x, y plane, as in Figure 23.1(a). We view this waveguide as having finite length $2a$ in the x or propagation direc-

tion, height L in the transverse or z direction, and (in the simplest situation) no variations in the y direction.

From the conventional waveguide viewpoint the propagation direction in this waveguide is the x direction; and we can view the internal energy as being reflected back and forth between the open ends of the waveguide, which have a finite but not 100% reflectivity. The waveguide section is thus a kind of leaky waveguide cavity, with energy loss out of both ends.

Suppose this waveguide is operated in an *extremely* high-order transverse mode, at a frequency very close to the cutoff frequency for that mode. It is well known in waveguide theory that the fields in the guide will then be made up essentially of plane wave components that are traveling at nearly 90° to the nominal propagation direction or x axis, with their individual k vectors nearly parallel to the z rather than the x axis. These nearly transverse plane waves will combine in such a fashion as to satisfy the transverse boundary conditions at the two metallic planes. In this limit the electromagnetic energy is essentially bouncing back and forth between the two planes and only traveling very slowly in the z direction, in agreement with the well-known fact that the axial group velocity in a waveguide goes to zero at cutoff.

But from an optical-resonator viewpoint, this same truncated waveguide section then looks very much like a very short, very wide optical resonator with its *width* in the x direction and its *length or axial direction* in the z direction, as in Figure 23.1(b). This same structure as seen from the usual optical-resonator viewpoint has propagating waves which bounce back and forth between the two planes in the z direction, with some leakage out the open sides in the x direction.

In fact, the same identical electromagnetic fields can equally well be described either from the waveguide viewpoint as made up of very high-order modes traveling (with very low group velocity) in the $\pm x$ directions, with leakage out the open ends of the structure; or from the optical-resonator viewpoint as optical waves traveling in the $\pm z$ direction with leakage out the open sides of the structure.

Coupled Mode Analysis of Unstable Resonators

A planar optical resonator can thus be analyzed by treating it as a waveguide problem with propagation in the transverse direction; expanding the fields in very high-order x -directed waveguide modes; and then properly evaluating the mode reflectivity, mode conversion, and leakage output which takes place at the truncated open ends of the waveguide. This approach is known as the *coupled mode approach* to optical-resonator theory. Evaluating the complex end reflectivity for an open-ended waveguide is one of the more complicated aspects of this approach.

Conversion from a planar to an unstable (or stable) resonator is accomplished simply by curving the transverse planes as shown in Figure 23.1(c), and then analyzing this situation as a variable-height waveguide. If the waveguide height increases going toward the ends, as shown, this models an unstable resonator; if the height decreases it models a stable resonator. If such a structure is viewed as a pair of curved strips with finite width $2a$ in the x direction and finite average separation L in the z direction, then it obviously corresponds to a strip optical resonator. If the curved surfaces are viewed instead as circular disks with radius a in the y, z plane and spacing L in the z direction, then this is a circular-mirror resonator, in which the waveguide modes must be radial waveguide modes, but such modes are also well-known in waveguide theory.

This coupled-mode waveguide approach to optical resonators has been successfully applied to planar, stable and unstable resonators by several groups in both the U.S. and USSR. It may seem bizarre to analyze the propagating modes in a “waveguide” where the waveguide structure is, say, 5 mm long, 1 meter wide, and operates at a frequency of 5×10^5 GHz; but there is no formal objection to doing so, and in fact the approach does work. The one difficulty is perhaps that the analysis is fairly complicated; and in the end we must do nearly as much numerical work to obtain numerical answers as if we simply did a brute-force Fox and Li calculation.

Asymptotic Analysis of Unstable Resonators

A second analytical approach to unstable resonators, commonly called the *asymptotic approach*, is closer in spirit to the opening paragraphs of this section. It involves expanding the Huygens' kernel in the resonator integral equation in inverse powers of the Fresnel number N , or the equivalent Fresnel number N_{eq} , and then evaluating the Huygens' integral using techniques from the method of stationary phase. The resonator eigenequation is then converted into a polynomial equation whose order depends on the number of terms retained in the expansion. Solving this polynomial leads, after some further algebra, to results for both the eigenvalues and eigenfunctions of the unstable resonator.

The asymptotic approach was developed first in rectangular coordinates, for application to strip resonators. It has since been extended to circular resonators using Bessel function terms in the expansion. It provides a convenient if somewhat tricky way of obtaining solutions at larger Fresnel numbers, with a domain of validity that in fact seems to extend down to Fresnel numbers even as small as unity.

Virtual Source Theory for Unstable Resonators

The most recent, and perhaps most useful, analytical approximation for the unstable resonator is the *virtual source theory*, which is a modified version of the asymptotic approach. In this analysis, one envisions standing, say, just inside the output coupler of an unstable resonator (or just before the aperture plane in an equivalent unstable lensguide), looking back into the resonator or lensguide. One then sees a series of repeated images of the output aperture, with different sizes and at different distances, corresponding to the real output aperture seen after multiple internal reflections in the resonator or multiple periods back down the lensguide.

The field across the output aperture in this model is then approximated by the sum of the geometric field of a plane wave coming from a distant aperture located \mathcal{N} round trips earlier, where \mathcal{N} is some moderately large integer, plus the \mathcal{N} individual edge waves coming from that aperture and all the closer apertures, as seen looking backwards down the equivalent lensguide from the output aperture. Since each of these apertures is seen looking back through a different number of round trips, each such aperture seems to be located at a different distance and with a different transverse magnification.

If the number of terms \mathcal{N} is made large enough, this combination of the plane-wave plus aperture-edge terms becomes a very good analytical approximation for the real field in the resonator, and one can then manipulate this function to obtain a polynomial equation of order \mathcal{N} , which then gives the actual eigenvalues

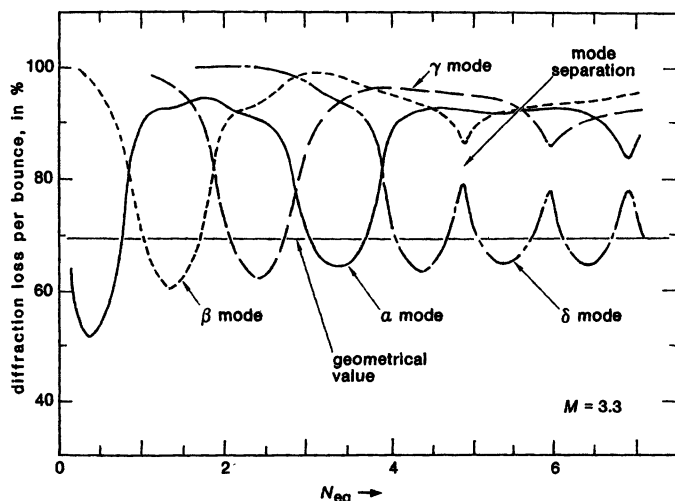


FIGURE 23.2

In rectangular (but not circular) unstable resonators, the lowest-loss eigenvalue will often separate from the remaining intertwined eigenvalues above a certain magnification-dependent value of N_{eq} .

and eigenmodes. A suitable number of terms seems to be

$$\mathcal{N} \approx \frac{\ln(KN_{\text{eq}})}{\ln M}, \quad (1)$$

where K is a constant on the order of a few hundred, and perhaps smaller.

The virtual source technique has been demonstrated first for strip resonators, where the Fresnel-integral edge-wavefunctions can be calculated with relative ease, and more recently for circular-mirror resonators as well. Although the virtual source technique is similar in many ways to the asymptotic approach, it has the considerable advantage that we can attach direct physical significance to each individual term in the mathematical formulation.

Mode Separation Behavior

One striking property of rectangular (but not circular) unstable resonators, which was observed in early numerical calculations and has been confirmed in more recent analyses, is that above some fairly large magnification-dependent value of N_{eq} the eigenvalue for the lowest-loss eigenmode separates off from the other eigenvalues, and no longer continues to exhibit the mode crossing behavior at larger Fresnel numbers, as shown for a typical example in Figure 23.2. The diffraction loss for the lowest-loss mode does continue to exhibit a periodic dependence on N_{eq} , however, leading to what is often referred to as "cusp behavior," as illustrated in Figure 23.2.

Development of the asymptotic analysis for unstable resonators made it possible to explore this mode separation behavior at large Fresnel numbers in more detail. An approximate expression for the critical value of N_{eq} above which mode

separation will occur in strip resonators has been found to be

$$N_{\text{eq}}(\text{crit}) \approx \frac{11.5}{(\ln M)^3}. \quad (2)$$

Even above this value of N_{eq} , however, it is observed that the lowest eigenmode may separate off and remain separated for only 6 or 7 cusping points, after which this mode may drop down in eigenvalue magnitude, and a new lowest-order eigenmode may emerge at a single isolated crossing point. For still larger N_{eq} values there will be a further series of regular cusping points; and so on.

No evidence of any similar mode separation behavior has ever been seen, however, for circular-mirror hard-edged unstable resonators at any values of M or N_{eq} ; and the asymptotic analysis for circular-mirror resonators indicates that the periodic crossing of the eigenvalue magnitudes should apparently continue forever in them. It seems clear that this infinite oscillation is unique to circular-mirror resonators, and is closely related to our earlier discussions in Section 18.4 regarding the unique diffraction properties of circular apertures. Only for a perfectly circular mirror or aperture is the Fresnel number independent of azimuth, so that the edge wave contributions from the entire aperture edge will always add in phase on the system axis or resonator axis.

Eigenmode Behavior at Mode Crossing Points

Another odd aspect of unstable resonator mode behavior brought out by more detailed mode studies is that the eigenmode patterns of the two lowest-loss symmetric eigenmodes in a strip resonator appear to become nearly if not exactly identical at the mode crossing points. At a Fresnel number slightly below a crossing point, for example, the lowest-loss ($n = 0$) mode pattern will generally have more of its intensity concentrated toward the center of the resonator and less in the outer wings, so that the diffraction loss is indeed smaller than the geometric value; whereas the next higher-order ($n = 2$) symmetric mode will have smaller intensity near the center and increasing intensity toward the edges.

As the Fresnel number is adjusted toward a crossing point, however, both mode patterns will change so that at the crossing point they become virtually identical, even to fine details of the Fresnel diffraction structure. On the other side of the crossing point the two mode patterns diverge again, more or less exchanging shapes. This same behavior is also observed at Fresnel numbers above the mode separation limit, where mode crossing no longer occurs. The mode patterns again become very similar at the "cusping points" where the two lowest-mode loss values approach each other, even if they no longer intersect.

Several examples of this behavior are shown in Figure 23.3, which illustrates the $n = 0$ and $n = 2$ lowest-order mode patterns for a strip resonator as calculated using the asymptotic analysis introduced by Horwitz. The mode intensity patterns are plotted from the center to the mirror edges for a magnification $M = 2.9$ and various equivalent Fresnel numbers corresponding to a maximum separation point, a mode crossing point, and a cusping point.

If the two lowest-order mode patterns at a mode crossing point are generally similar (and if both have reasonably good beam quality), then this result implies that it may not be all that essential in unstable resonator design to aim for a half-integer equivalent Fresnel number so as to obtain maximum loss discrimination between modes. Even if the resonator operates at a crossing point, and oscillates

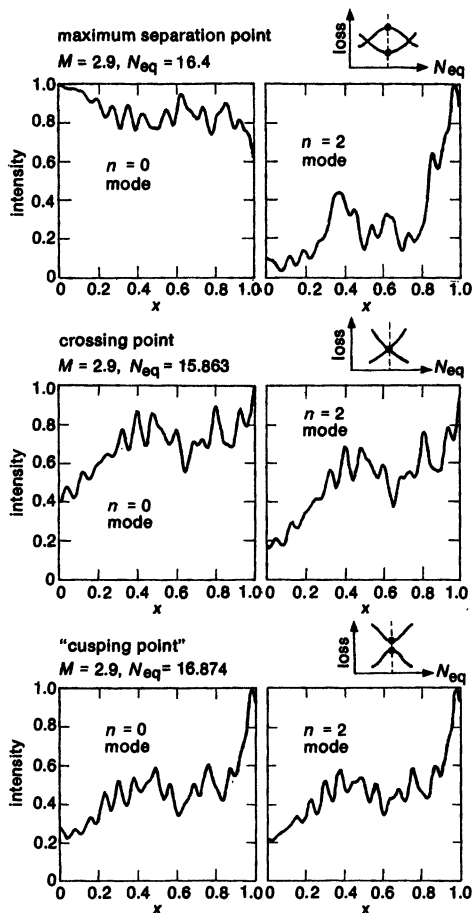


FIGURE 23.3

Whenever the two lowest-order modes in a strip unstable resonator come near a "crossing" (or "cuspingle") point, the mode patterns of the two eigenmodes become nearly identical.

simultaneously in two modes, the far-field beam quality may not be significantly deteriorated by the multi-transverse-mode operation.

Oscillation Build-Up in Pulsed Unstable Resonators

Unstable resonators can be particularly useful for very high-gain, large-volume pulsed lasers, in some of which (such as the pulsed Cu vapor and other metal vapor lasers) the full duration of laser action may only include a few round trips (≤ 10) within the laser cavity. It is then important to understand how rapidly a good transverse mode pattern can be built up within an unstable optical resonator.

The difference in round-trip diffraction losses between the lowest-order mode (or modes) and all the higher-order modes in an unstable resonator is, fortunately, usually quite large. As a result, when laser oscillation begins to build up

from noise in a high-gain unstable resonator, the lowest-order mode, or possibly a few lowest-order modes, will rapidly outstrip all the higher-order and higher-loss transverse modes; and the desired lowest-order mode pattern will be fully established typically within only a few round trips.

An approximate formula for the number of round trips N_{rt} needed to establish a predominantly lowest-order mode distribution in a high-gain unstable resonator of mirror half-width a and length L is given by Anan'ev as

$$N_{rt} \approx \frac{\ln(a^2/L\lambda)}{\ln(M)}. \quad (3)$$

The reader may recognize this from our earlier discussions as essentially the number of round trips that would be required for spontaneous emission coming into the resonator with wavefront equal to the converging eigenwave to be focused down and then converted by diffraction back out into the diverging or magnifying eigenwave. Experiments and numerical simulations by Jones and Perkins demonstrate the general validity of this approximate expression in Equation 23.3. It can thus be used as an estimate for the magnification M needed to ensure that reasonable mode discrimination will be established within the number of round trips n that will be possible in a very short pulse unstable resonator laser.

REFERENCES

The coupled mode or "waveguide near cutoff" technique described in this section is employed in the book by Weinstein cited in Section 22.1, and has been extensively developed by L-W. Chen and L. B. Felsen, "Coupled-mode theory of unstable resonators," *IEEE J. Quantum Electron. QE-9*, 1102-1113 (November 1973).

The asymptotic approach for strip unstable resonators was first developed by P. Horwitz, "Asymptotic theory of unstable resonator modes," *J. Opt. Soc. Am. 63*, 1528-1543 (December 1974). See also P. Horwitz, "Modes in misaligned unstable resonators," *Appl. Opt. 15*, 167-178 (January 1976).

This approach was later extended to circular mirrors by R. R. Butts and P. V. Avizonis, "Asymptotic analysis of unstable laser resonators with circular mirrors," *J. Opt. Soc. Am. 68*, 1072-1078 (August 1978).

The virtual source theory for strip resonators is very clearly outlined in W. H. Southwell, "Virtual-source theory of unstable resonator modes," *Opt. Lett. 6*, 487-489 (October 1981). An extension to circular resonators by the same author is in press as of mid-1986.

Another typical technique for expanding the Huygens' integral in a set of orthogonal functions is demonstrated in M. E. Rogers and J. H. Erkkila, "Resonator mode analysis using linear prolate functions," *Appl. Opt. 22*, 1992-1995 (July 1, 1983).

A fully quantum-mechanical analysis has even been applied to unstable resonators by D. F. Walls and K. J. McNeil, "A quantum multimode approach to unstable laser resonators," *Opt. Commun. 18*, 471-475 (September 1976).

Both the mode separation behavior and the similarity of the mode functions near a crossing point were first noted in the early results for strip mirrors given by R. L. Sanderson and W. Streifer, "Unstable laser resonator modes," *Appl. Opt. 8*, 2129-2136 (October 1969). Further discussion of mode separation behavior is given in the paper by Horwitz cited in the preceding, and the analysis by M. J. Smith, "Simplified calculation of mode degeneracy in unstable strip resonators," *Appl. Opt. 20*, 4148-4149 (December 15, 1981).

The primary theoretical discussion of oscillation build-up in unstable resonators is by Yu. A. Anen'ev, "Establishment of oscillations in unstable resonators," *Sov. J. Quantum Electron.* **5**, 615-617 (June 1975), with extensions and experimental results by R. W. Jones and J. F. Perkins, "Transverse mode formation in low-magnification positive-branch unstable resonators," *Appl. Opt.* **23**, 1361-1368 (May 1, 1984).

Other papers in the Soviet literature include A. A. Isaev, M. A. Kazaryan, G. G. Petrush, and S. G. Rautian, "Converging beams in unstable telescopic resonators," *Sov. J. Quantum Electron.* **4**, 761-766 (December 1974); N. S. Golubeva, L. F. Krinitsyna, L. S. Orbachevskii, and V. I. Rozhdestvin, "Transient processes in *Q*-switched lasers with unstable resonators," *Sov. J. Quantum Electron.* **7**, 25-29 (January 1977); and A. A. Isaev, M. A. Kazaryan, G. G. Petrush, S. G. Rautian, and A. M. Shalagin, "Shaping of the output beam in a pulsed gas laser with an unstable resonator," *Sov. J. Quantum Electron.* **7**, 746-752 (June 1977).

23.2 OTHER NOVEL UNSTABLE RESONATOR DESIGNS

Unstable resonator designs have been modified in many clever ways in various attempts to expand their usefulness. In this section we discuss briefly some of the novel approaches that have been suggested and tried.

Ring Unstable Resonators

Ring unstable resonators, as contrasted to linear unstable resonators, provide much increased design flexibility and a number of design possibilities over and above the advantages possessed by ring resonators for laser applications generally. Several of these aspects are illustrated by Figure 23.4.

A ring unstable resonator can be designed, for example, to have a short telescopic magnification section using conveniently available optical elements with short radii of curvature, and then to have much longer collimated regions which can fill large diameter laser tubes. Negative-branch ring resonators can also be built with internal spatial filters, which can clean up the mode patterns and filter out some of the phase distortion effects caused by inhomogeneous elements in the resonator.

Ring resonators also offer the possibility of unidirectional oscillation, which can eliminate spatial hole burning effects and make injection locking easier. As we have previously pointed out, the bare cavity modes going in opposite directions around a ring resonator will always have exactly the same inherent diffraction losses. The *transverse spatial profiles* for the modes going in opposite directions can be quite different, however, and this can make a substantial difference in how the mode fills a given gain medium or saturable absorber medium in the two directions. The effects that this will have on the mode competition between the two directions in an oscillating laser can be fairly subtle; but this does offer one approach toward achieving unidirectional oscillation in a ring laser.

Ring lasers are often designed using various sorts of folded or "Z" shapes in order to hit at least some of the mirrors at close to normal incidence, since this minimizes astigmatism from curved mirrors and permits standard mirror coatings to be used. Figure 23.4(d) shows one typical example of a folded ring-laser cavity, here for a nitrogen-pumped pulsed dye laser. Folded rings of this sort also minimize the amount of real estate needed for a given cavity length.

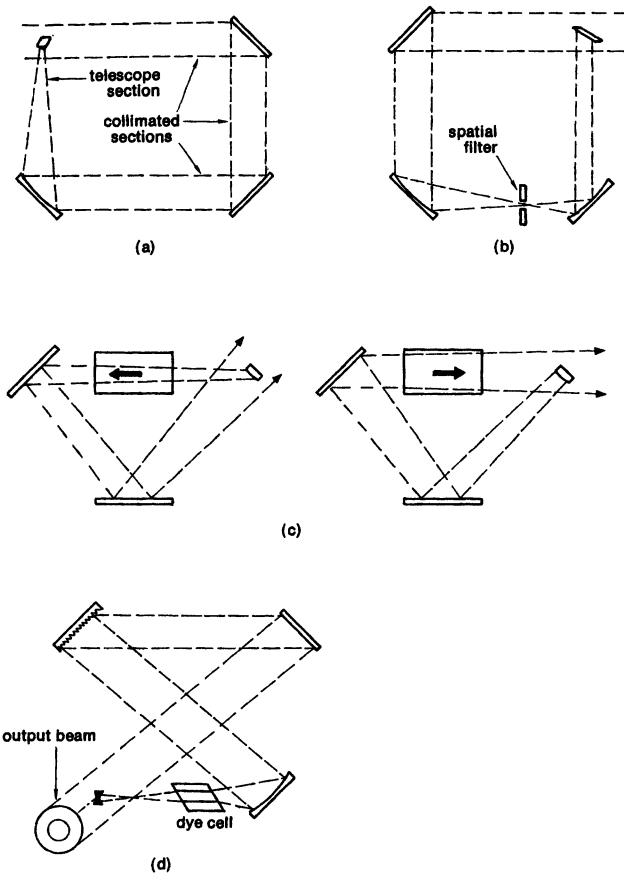


FIGURE 23.4

Examples of ring unstable resonator designs. (a) Unstable ring laser with short telescope section and long expanded regions. (b) Negative-branch unstable resonator with internal spatial filter. (c) Ring cavity with different interaction mode volumes in opposite directions. (d) Example of a ring dye laser design including an intracavity diffraction grating.

Self-Imaging Unstable Resonators

It is possible to design a negative-branch ring unstable resonator (and only a ring resonator) such that each round trip corresponds to an image relay system, which images a magnified version of the coupling aperture back onto itself after each round trip. In the negative-branch confocal ring resonator shown in Figure 23.5, for example, the round-trip $ABCD$ matrix can be written as

$$\begin{bmatrix} A & B \\ C & D \end{bmatrix} = \begin{bmatrix} -|M| & f_1 + f_2 - |M|L_1 - L_2/|M| \\ 0 & -1/|M| \end{bmatrix}, \quad (4)$$

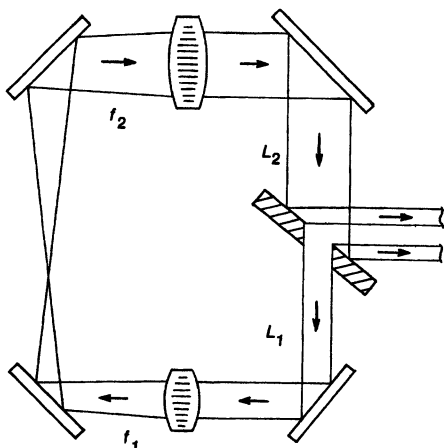


FIGURE 23.5
Self-imaging ring unstable resonator.

where the (negative) value of magnification is given by $M = -f_2/f_1$. If the element spacings in this resonator satisfy the self-imaging condition $f_1 + f_2 = |M|L_1 + L_2/|M|$, then the canonical form of this resonator has $B \equiv 0$ (see also Figure 21.11). Each round trip in this *self-imaging unstable resonator* then has an effective propagation length that is identically zero, and hence the resonator has infinite Fresnel numbers, i.e., $N_c = N_{eq} = \infty$.

The exact eigenmodes of this kind of “self-imaging resonator” are difficult to predict, since it is not clear at present how we should handle the limiting situation of $N_{eq} \rightarrow \infty$ in a mathematical analysis. There is considerable doubt, for example, whether the limiting behavior of the Huygens’ integral problem for $N_{eq} \rightarrow \infty$ really connects smoothly to the geometric limit, particularly in the circular-mirror situation. It is generally believed, however, that the self-imaging situation should give a particularly smooth and uniform lowest-order mode pattern in an unstable resonator.

Off-Axis Unstable Resonators

Another useful if somewhat inelegant variation in unstable resonator design is to use any one of a variety of *off-axis unstable resonator configurations*, as illustrated in Figure 23.6. The primary motivation for any of these off-axis unstable resonator designs is a more uniformly illuminated near-field pattern, so as to increase the intensity in the central lobe and reduce the intensity in the diffraction side lobes in the far field. This objective can in fact generally be achieved, at least to some extent, despite the irregular far-field patterns that we can expect from the kinds of near-field patterns shown.

Off-Axis Mirror Positioning Equals Misalignment

The general properties of these off-axis unstable resonators can be understood from the following argument. Shifting the output mirror of an unstable resonator off axis in either transverse dimension is in fact exactly equivalent to

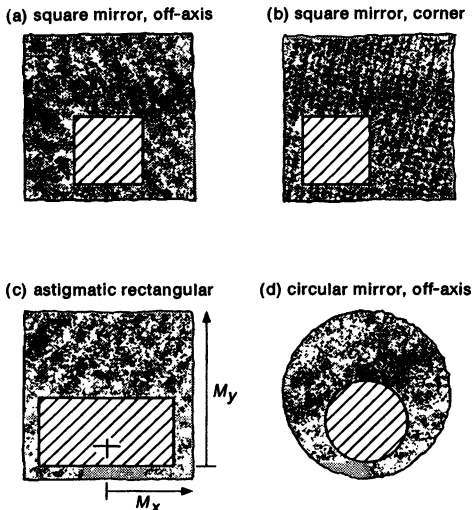


FIGURE 23.6
Unstable resonators with off-axis output mirrors.

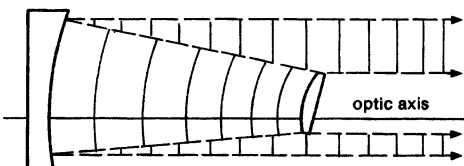


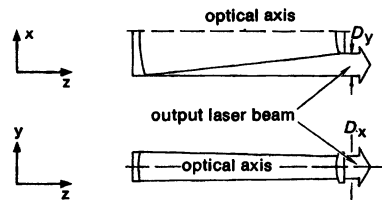
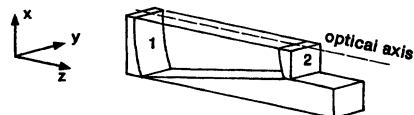
FIGURE 23.7
An off-axis unstable resonator is the same as a misaligned unstable resonator.

misaligning the resonator mirrors (or the resonator optical axis), as shown in Figure 23.7. A misaligned resonator of this type, so long as the optical axis still intercepts the output mirror, can then be viewed, at least approximately, as consisting of two half-resonators on opposite sides of the optical axis, with the two sides having the same magnification but different Fresnel numbers.

Since the mode properties and the output coupling of an unstable resonator depend primarily on the magnification M , and only secondarily on the Fresnel number N_{eq} , we can expect that the near-field pattern for a misaligned unstable resonator will still consist of a roughly uniform (or perhaps tapered) near-field distribution which is magnified outward from the optical axis by the same magnification M on all sides of the output mirror, as illustrated in Figure 23.6. The Fresnel ripple structures within these geometrically predicted patterns, and the exact eigenmodes and mode losses, will certainly depend on the amount of misalignment; but the zero-order near-field and far-field patterns will still be very much as illustrated.

These predictions turn out to be entirely correct. Misalignment of an unstable resonator modifies the exact eigenvalues, and changes the mode crossing behavior, in a complicated but essentially minor fashion. As we might expect, moreover, the nature of these changes is closely related to the equivalent Fresnel numbers of the individual half resonators, e.g., whether the two halves of the res-

(a) off-axis toroidal resonator



(b) stable-unstable slab resonator

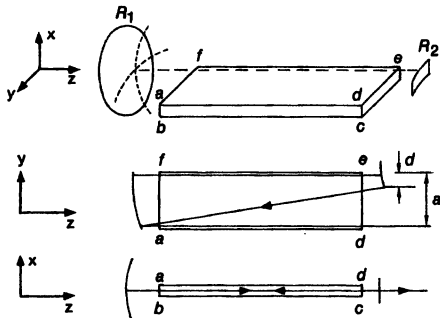


FIGURE 23.8
Two examples of rectangular stable-unstable resonator design.

onator are both at (different) half-integer N_{eq} values, or whether one side is at a half-integer and the other at an integer value. To quote from one of the references at the end of this section (Horwitz, 1976): "The basic conclusion is that rectangular aperture unstable resonators are quite insensitive to misalignment, in the sense that the lowest-loss mode continues to be essentially diffraction limited as long as the feedback mirror remains well within the output beam."

The optimum form of this approach, for a low-gain laser system with rectangular symmetry, might be to use an astigmatic rectangular unstable resonator as shown in Figure 23.6(c), with the magnification in one transverse dimension, say, M_x , made just enough greater than unity to give good mode discrimination and good filling of the mode volume, but very small output coupling. The magnification M_y in the other transverse direction could then be made large enough to give good output coupling, with the resonator misaligned in this direction until the relative amount of power coming past one edge was negligible. The small fractional amount of power coming past three sides of the mirror could then be discarded, and the output power extracted from the fourth side as a completely unobstructed and essentially rectangular output beam.

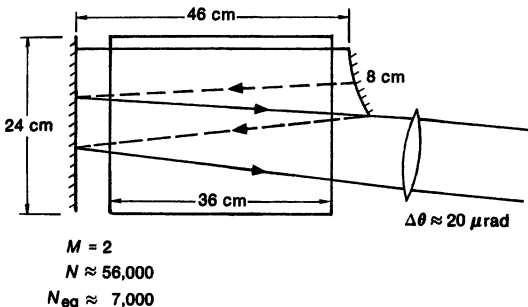


FIGURE 23.9
A large one-sided stable-unstable glass slab laser.

Stable-Unstable Resonators

In a further extension of this concept, there are certain laser systems in which the active medium occurs in the form of a thin slab or gain sheet, which may have a very small equivalent Fresnel number in one transverse direction, and a substantially larger width or equivalent Fresnel number in the other transverse direction. Examples include slab glass or other solid-state lasers; certain flowing chemical lasers where the excited states relax very rapidly after leaving a flat array of supersonic nozzles; certain dye lasers where we might pump a thin flowing sheet of dye with a flashlamp; and various transverse discharge-pumped and e-beam pumped molecular and excimer lasers.

A very effective technique—at the cost of some complexity in optical components—can then be to employ a laser cavity which is stable and supports a lowest-order TEM_0 gaussian mode in one direction, but which is unstable (and probably misaligned in one-sided fashion) in the other dimension. Figure 23.8 shows some examples of how this concept can be applied to various lasers. The Soviet researchers who carried out early experiments using the large glass slab shown in Figure 23.9 reported, for example, diffraction-limited performance ($\Delta\theta \approx 20 \mu\text{rad}$) in the unstable transverse dimension, for a laser resonator with an equivalent Fresnel number of $N_{\text{eq}} \approx 7,000$!

Unstable Resonators in Semiconductor Diode Lasers

Another prime candidate for this type of stable-unstable resonator design would seem to be the semiconductor diode laser or injection laser, in which the gain region is inherently a very thin slab, with stable mode guiding perpendicular to the junction region, and no mode confinement in the plane of the junction (at least in the simplest form of injection diode structure). Use of a curved back mirror to spread out the fields into an unstable mode in the plane of the junction should give simultaneously good transverse mode control and much more power output from a much larger junction area.

Only one Soviet experiment on this type of unstable semiconductor laser action has been published to date, although other efforts may be in progress. There can be some practical difficulties in obtaining a cleaved (or polished) back mirror surface with the necessary unstable curvature on a typically very small injection diode laser.

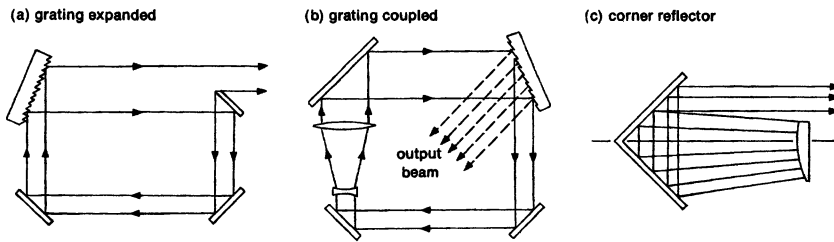


FIGURE 23.10
Design concepts for unstable resonators using diffraction gratings and corner reflectors.

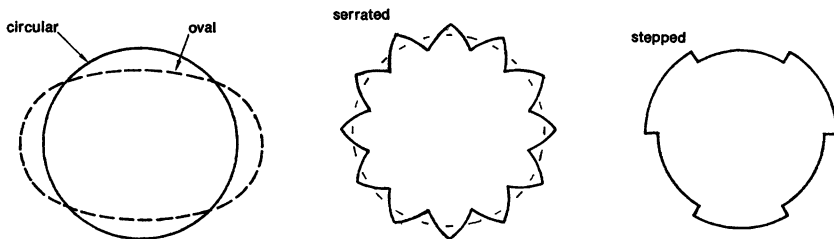


FIGURE 23.11
Shaped mirror edges intended to cancel the edge-wave interference and reduce the near-field diffraction effects.

Grating Expanded Unstable Resonators

Designers of tunable dye lasers realized some years ago that spatially dispersive elements, such as prisms and gratings, could also be used as spatial beam expanders, functioning in essence as one-dimensional pseudo telescopes. Figure 23.10 shows a few of the more exotic proposals for applying this concept to unstable resonators, using the beam-expanding and also output-coupling properties either of diffraction gratings or of dihedral prisms or corner retroreflectors.

Few if any experiments with this type of resonator design seem to have been attempted to date.

Minimizing Edge Wave Effects: Aperture Shaping

We have discussed in earlier sections how the near-field diffraction effects from hard-edged apertures can be minimized by changing the aperture shape so as to more or less cancel the edge waves from different parts of the aperture edges. In our discussion of aperture diffraction, for example, we noted that changing the shape of a hard-edged aperture to anything other than perfectly circular greatly reduces the peak value of the on-axis ripple in the near-field diffraction pattern. Similarly, tapering the actual reflectivity of the edge itself, so that the amplitude or phase of the edge reflectivity varies significantly over a distance corresponding to one full Fresnel zone or more, will greatly reduce the net amplitude of the diffracted edge wave, and thus reduce the Fresnel ripples in the near-field diffraction pattern.

Understanding of these principles has led to various attempts to improve the mode performance of hard-edged unstable resonators by shaping or smoothing

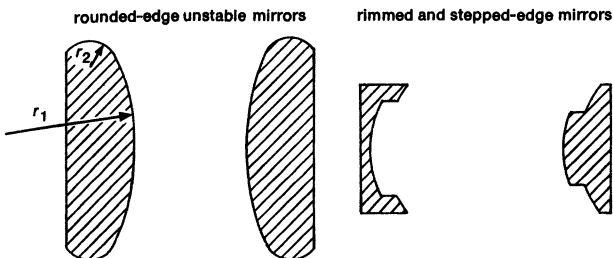


FIGURE 23.12

Unstable resonators with stepped or rounded mirror edges.

the edges of the output mirror or output coupler. Figure 23.11 shows some of the modified circular aperture shapes that have been considered for unstable resonators. The difficulties in fabricating such special mirror shapes, however, as well as the analytical complexities they introduce into any exact mode calculations, make this concept seem relatively unattractive for practical unstable resonator designs.

Unstable Mirrors With Tapered Phase Values

A somewhat more attractive approach to edge-wave cancellation might be to modify or taper the phase angle of the mirror reflection coefficient over a narrow region near the mirror edges, but still retain completely reflective optics. Techniques that have been suggested for this purpose include mirrors with rims or steps near the mirror edges and rolled-over mirror edges, as illustrated in Figure 23.12.

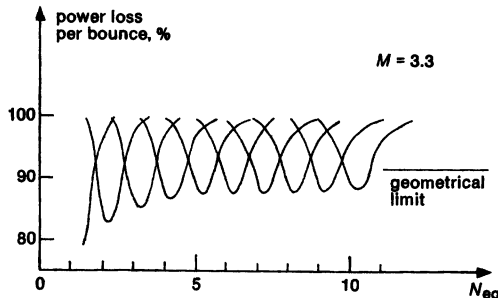
The basic design principle here is to vary the reflection phase through one or more multiples of 2π over a transverse or radial distance which includes at least one or more Fresnel zones as measured by the collimated Fresnel number in the resonator. In general it has been found that this kind of edge modulation applied to one or more of the end mirrors does cause the eigenvalue for the lowest-loss eigenmode in an unstable resonator to separate from the higher-order modes at a lower value of equivalent Fresnel number N_{eq} , as well as reducing the periodic rippling of the eigenvalue or the cavity coupling with increasing N_{eq} , as illustrated for a typical situation in Figure 23.13.

Retroreflected Unstable Resonators

Still another in the list of more unsuccessful attempts to extend the unstable resonator concept is what might be called the “retroreflected unstable resonator,” as illustrated in Figure 23.14.

The general idea here is to use an additional plane mirror to reflect a portion of the emerging beam from an unstable resonator back into the resonator, where it will excite a converging wave that will demagnify down into the center of the resonator and then eventually emerge again as an addition to the magnifying wave. Figure 23.14 shows a design where the inner portion of the annular output beam is retroreflected; an alternative design retroreflects the outer portion of the annulus and lets the inner portion escape.

(a) hard-edged circular unstable resonator



(b) rounded-edge circular unstable resonator

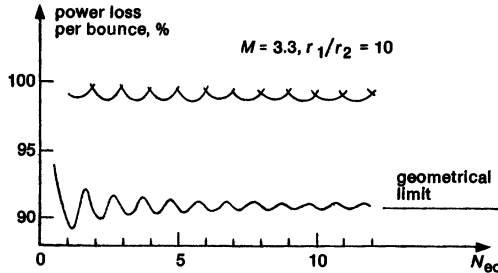


FIGURE 23.13
Rounding the mirror edges, as in Figure 23.12, can lead to a clear separation of the lowest-loss eigenvalue from all the higher-order modes. (From Santana and Felsen.)

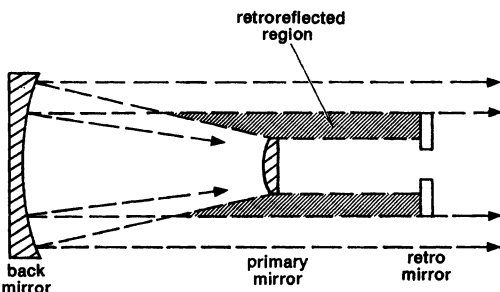


FIGURE 23.14
Retroreflected unstable resonator concept.

Advantages that might be hoped for from this design concept include reduced output coupling for the same magnification, for use with low-gain lasers; and the development of an extended annular region with partially standing-wave fields, which could be useful in coupling to certain kinds of annularly shaped active gain media. This general concept also faces a number of fundamental difficulties, however, including:

- The detailed transverse mode behavior turns out to be (as we might expect) very sensitive to the exact phase with which the retroreflected energy is fed back into the converging paraxial eigenwave. Hence, the resonator performance is sensitive to changes in the relative mirror spacings L_1 and L_2 on the order of a small fraction of an optical wavelength. The cavity is also very sensitive to small changes in the relative angular alignments of the three mirrors.
- Under a wide range of conditions the flat annular mirror and the larger curved mirror at the opposite end of the cavity can form a *stable* two-mirror resonator, which can support a number of high-order Laguerre-gaussian modes with large radial and azimuthal indices in the annular region outside the normal output mirror.
- In contrast to the simplified geometric picture in Figure 23.14, the beams will inherently experience diffraction spreading in traveling down to the annular mirror and back to the normal output mirror. This, along with the increased number of edges and apertures in the resonator, greatly complicates the exact mode behavior (and mode calculations) in the resonator.

All these difficulties have generally made the retroreflection concept seem unattractive after further examination, although we will see even more complex continuations of this idea a few paragraphs further on.

Back-Reflection Effects in Unstable Resonators

The substantial influence on unstable resonator performance of any energy that is fed back into the converging or demagnifying eigenwave has also led other authors to note that unstable resonators can be (1) unusually sensitive to any internal apertures or partially reflecting surfaces (imperfect AR coatings, etc.) which may reflect energy directly back along the laser axis with the correct curvature and direction to go into the converging wave, and also (2) unusually sensitive to external surfaces or optical elements that retroreflect the collimated output beam directly back into an unstable oscillator cavity.

Axiicons, Split-Mode Resonators, HSURIAs, and Other Exotica

Many higher-power laser systems, including especially chemical and gasdynamic lasers, tend naturally to generate a thin annularly shaped gain medium, produced perhaps by radial flow of combusting gases coming out from the outer surface of a cylindrical burner shaped rather like a large oil drum. It is then a particularly difficult challenge to find a resonator structure, perhaps some variant of the unstable resonator, which can extract the energy from a large annular gain region, yet retain good transverse mode control and beam quality. This problem may, in fact, be essentially unsolvable.

Attempts to meet this challenge have led first to the idea of splitting an unstable resonator in half at some point along its optical axis, leading to the concept of the “split-mode unstable resonator”; and then folding these halves back on themselves to create various varieties of coupled half-symmetric unstable resonators. If we accomplish this splitting using an axicon structure with its

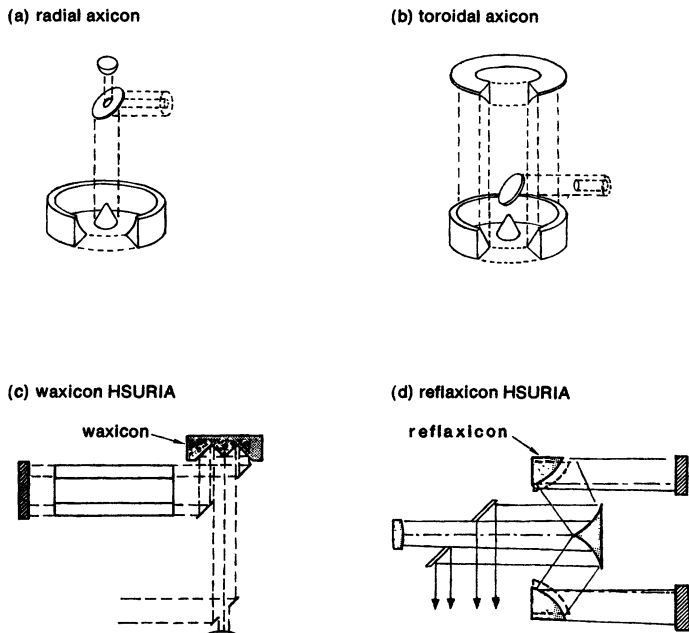


FIGURE 23.15

(a) and (b), Radial and toroidal split-mode resonators with internal axicons.
 (c) HSURIA structure using a waxicon. (d) HSURIA structure with reflexicon.

point located on the optical axis, we can create an increasingly complicated set of exotic radial or annular resonator configurations, a few of which are illustrated in Figure 23.15.

Even the nomenclature for these structures becomes exotic. As an example, the “half-symmetric unstable resonator with internal axicon” becomes known, obviously, as the HSURIA. (The test for whether a laser engineer has received an adequate liberal education is whether this is referred to as “a HSURIA” or “an HSURIA.”) In the jargon that has developed, an axicon that reverses the beam direction (and thereby inverts inner and outer edges) is a “W-axicon” or “waxicon,” whereas a reflective axicon that expands or contracts a beam while sending it on in the same direction is a “reflexicon.” The region where the beam is brought back together again at reduced diameter, and where most of the transverse mode control presumably takes place, is the “compacted region.”

Axicon structures of any type exhibit extremely high sensitivity not only to angular misalignment, but to transverse displacements of even a fraction of a wavelength with respect to the optical axis of the resonator system. If the axicon is to function simultaneously as a telescopic or focusing element, the axicon may also require a surface that is parabolic, toroidal, or some more complex combination. The construction and alignment of any type of practical large high-power laser employing an axicon or other complex resonator design is thus extremely difficult, and may be essentially impossible.

REFERENCES

Design concepts for positive and negative branch ring unstable resonators were first outlined in A. Anan'ev, N. A. Sventsitskaya, and V. E. Sherstobitov, "Properties of a laser with an unstable resonator," *Sov. Phys. JETP* **28**, 69-74 (October 1969). See also A. Anan'ev, N. I. Grishmanova, L. V. Koval'chuk, N. A. Sventsitskaya, and V. E. Sherstobitov, "Possibilities of control of radiation emitted by lasers with telescopic resonators," *Sov. J. Quantum Electron.* **2**, 157-159 (September-October 1972).

The distinctions between forward and reverse and magnifying and demagnifying waves in an asymmetric ring resonator are clearly outlined in P. del Pozzo, R. Polloni, O. Svelto, and F. Zaraga, "An unstable ring resonator," *IEEE J. Quantum Electron.* **QE-9**, 1061 (November 1973), and also "A doubly-confocal unstable ring resonator," *Opt. Commun.* **11**, 115-117 (June 1974).

The virtues of ring resonators are demonstrated experimentally by R. J. Freiberg, P. P. Chenausky, and C. J. Buczek, "Unidirectional unstable ring lasers," *Appl. Opt.* **12**, 1140-1144 (June 1973).

Another interesting example of a ring unstable resonator design is O. Teschke and S. Ribeiro Teixeira, "Unstable ring resonator nitrogen pumped dye laser," *Opt. Commun.* **32**, 287-290 (February 1980).

Self-imaging unstable resonators were first discussed by A. H. Paxton and T. C. Salvi, "Unstable optical resonator with self-imaging aperture," *Opt. Commun.* **26**, 305-308 (September 1978).

The properties of a marginally stable self-imaging cavity (inaccurately referred to as a "Fourier-transform" cavity) are also described by E. Sklar, "Fourier-transform ring laser," *J. Opt. Soc. Am. A* **1**, 537-540 (May 1984).

The analytical questions involved in understanding the limiting values of resonator eigenvalues and eigenmodes at very large Fresnel numbers, as in a self-imaging resonator, and also in understanding the differences between resonators with rectangular and circular mirrors, FLAG remain fairly obscure. One attempt to deal with some of the mathematical issues involved can be found in H. J. Landau, "Loss in unstable resonators," *J. Opt. Soc. Am.* **66**, 525-529 (June 1976).

An excellent experimental demonstration of the virtues of the off-axis unstable resonator approach for a large laser can be found in E. A. Phillips, J. P. Reilly, and D. B. Northam, "Off-axis unstable laser resonator: operation," *Appl. Opt.* **15**, 2159-2166 (September 1976).

The interplay between the equivalent Fresnel numbers for the half-resonators on either side of the optical axis in an off-axis unstable resonator is demonstrated in J. F. Perkins and R. W. Jones, "Effects of unstable resonator misalignment in the cusping domain," *Appl. Opt.* **23**, 358-360 (January 15, 1984).

The far-field pattern from an off-axis unstable resonator will be similar to the far-field diffraction pattern from an aperture with an off-center obstruction. One useful paper on this topic is G. W. Sutton, M. M. Weiner, and S. A. Mani, "Fraunhofer diffraction patterns from uniformly illuminated square output apertures with noncentered square obscurations," *Appl. Opt.* **15**, 2228-2232 (September 1976).

Other related references include M. M. Weiner, "Far-field energy, in the geometric mode limit, of loaded unstable resonators with centered or corner obscurations," *Appl. Opt.* **16**, 1790-1791 (July 1977); and V. N. Mahajan, "Imaging with noncentrally obscured circular pupils," *J. Opt. Soc. Am.* **68**, 742-749 (June 1978).

An early example of an off-axis stable-unstable resonator applied to a very large flat glass slab laser is A. Anan'ev, V. N. Chernov, and V. E. Sherstobitov, "Solid laser with a high spatial coherence of radiation," *Sov. J. Quantum Electron.* **1**, 403-404 (January-February 1972).

The stable-unstable concept is applied to a KrF excimer laser in O. L. Bourne and P. E. Dyer, "A novel stable-unstable resonator for beam control of rare-gas halide lasers," *Opt. Commun.* **31**, 193-196 (November 1979).

A combination of an off-axis unstable resonator in one direction, and a stable gaussian resonator in the other direction is applied to a high-power CO₂ laser in A. Borghese, R. Canevari, V. Donati, and L. Garito, "Unstable-stable resonators with toroidal mirrors," *Appl. Opt.* **20**, 3547-3552 (October 15, 1981).

Some thoughts on the geometric analysis of unstable resonators in which the geometric magnification may vary across the resonator (i.e., using nonspherical mirrors) are given in T. R. Ferguson and M. E. Smithers, "Optical resonators with nonuniform magnification," *J. Opt. Soc. Am. A* **1**, 653-662 (June 1984).

The only published paper in which the unstable resonator concept is applied to a semiconductor diode laser seems to be A. P. Bogatov, P. G. Eliseev, M. A. Man'ko, G. T. Mikaelyan, and Yu. M. Popov, "Injection laser with an unstable resonator," *Sov. J. Quantum Electron.* **10**, 620-622 (May 1980).

The idea may be spreading, however. See, for example, R. R. Craig, L. W. Casperson, G. A. Evans, and J. J. J. Yang, "High loss resonators for semiconductor diode lasers," Postdeadline Paper ThR4-1, Conference on Lasers and Electro-Optics (CLEO '84), Anaheim, Calif., June 1984.

The use of prisms and corner reflectors in unstable resonators was introduced by Yu. A. Anan'ev, "Unstable prism resonators," *Sov. J. Quantum Electron.* **3**, 58-59 (July-August 1973). See also Yu. A. Anan'ev et. al., "Investigations of the properties of an unstable resonator using a dihedral corner reflector in a continuous-flow CO₂ laser," *Sov. J. Quantum Electron.* **7**, 822-824 (July 1977).

The manner in which tapering of the mirror edges could smooth unstable resonator mode performance was first illustrated by A. Anan'ev and V. E. Sherstobitov, "Influence of the edge effects on the properties of unstable resonators," *Sov. J. Quantum Electron.* **1**, 263-267 (November-December 1971). See also V. E. Sherstobitov and G. N. Vinokurov, "Properties of unstable resonators with large equivalent Fresnel numbers," *Sov. J. Quantum Electron.* **2**, 224-229 (November-December 1972).

Further illustrations can be found in G. L. McAllister, W. H. Steier, and W. B. Lacina, "Improved mode properties of unstable resonators with tapered reflectivity mirrors and shaped apertures," *IEEE J. Quantum Electron.* **QE-10**, 346-355 (March 3, 1974); and E. A. Maunders, G. L. McAllister, and W. H. Steier, "Experiments on improved unstable mode profiles by aperture shaping," *IEEE J. Quantum Electron.* **QE-10**, 821-822 (October 1974).

Resonator mode control using various kinds of mirrors with rimmed edges is discussed in M. Lax, W. H. Louisell, C. E. Greninger, and W. B. McKnight, "Transverse mode suppression using rimmed unstable resonators (abstract only)," *IEEE J. Quantum Electron.* **QE-8**, 554 (1972); and in M. Lax, C. E. Greninger, W. H. Louisell, and W. B. McKnight, "Large-mode-volume stable resonators," *J. Opt. Soc. Am.* **65**, 642-648 (June 1975).

Other theoretical calculations of mirror-edge tapering can be found in V. V. Lyubimov and I. B. Orlova, "Effect of mirror-edge shape on the selective properties of unstable cavities," *Opt. Spectrosc.* **41**, 166-168 (August 1976); C. Santana and L. B. Felsen, "Mode losses in unstable resonators with rounded edges," *Appl. Opt.* **17**, 2239-2243 (July 15, 1978); and C. Santana, "Ray-optical calculations of eigenmode behavior of unstable laser resonators with rounded edges," *Appl. Opt.* **20**, 2852-2855 (August 15, 1981).

For still another example of strong mode separation effects produced by a mirror with a stepped edge, see M. E. Smithers, T. C. Salvi, and G. C. Dente, "Unstable resonator with canceling edge waves," *Appl. Opt.* **21**, 729-732 (February 15, 1982);

and M. E. Smithers and G. C. Dente, "Unstable resonator with canceling edge waves: asymptotic analysis," *J. Opt. Soc. Am.* **73**, 76-79 (January 1983).

See also the additional references cited in P. F. Checcacci, A. Consortini, and A. M. Scheggi, "Unstable optical resonators: Comment," *Appl. Opt.* **13**, 1993-1994 (September 1974).

The fundamental ideas of retroreflected unstable resonators are explored in R. A. Chodzko, S. B. Mason, and E. F. Cross, "Annular converging wave cavity," *Appl. Opt.* **15**, 2137-2144 (September 1976).

See also A. H. Paxton and J. H. Erkkila, "Annular converging wave resonator: new insights," *Opt. Lett.* **1**, 166-168 (November 1977); and Yu. A. Anan'ev, D. A. Goryachkin, N. A. Sventsitskaya, and I. M. Petrova, "Investigation of the properties of a laser with an unstable resonator and additional feedback," *Sov. J. Quantum Electron.* **9**, 1043-1044 (August 1979).

The negative effects of retroreflective feedback into an unstable laser oscillator are explored in Yu. A. Anan'ev, N. I. Grishmanova, I. M. Petrova, and N. A. Sventsitskaya, "Internal reflecting surfaces in unstable resonators," *Sov. J. Quantum Electron.* **5**, 1060-1062 (September 1975); and in P. B. Corkum and H. A. Baldis, "Extra-cavity feedback into unstable resonators," *Appl. Opt.* **18**, 1346-1349 (May 1, 1979).

The concept of using an axicon or similar element to split an unstable resonator beam along its axis is introduced and demonstrated by R. J. Freiberg, D. W. Fradin, and P. P. Chenausky, "Split-mode unstable resonator," *Appl. Opt.* **16**, 1192-1196 (May 1977).

Further useful discussions and experimental investigations are given in P. B. Mumola, H. J. Robertson, G. N. Steinberg, J. L. Kreuzer, and A. W. McCullough, "Unstable resonators for annular gain volume lasers," *Appl. Opt.* **17**, 936-943 (March 15, 1978).

Numerical simulations of the HSURIA concept are also given in W. D. Murphy and M. L. Bernabe, "Numerical procedures for solving nonsymmetric eigenvalue problems associated with optical resonators," *Appl. Opt.* **17**, 2358-2365 (August 1978).

Polarization rotation effects caused by the off-axis reflections from the surfaces of the axicons in HSURIA resonators produce complicated effects in which the electric field polarization varies with azimuth around the resonator, rather than having the simple linear polarization characteristic of more elementary resonators. These effects are discussed, for example, in W. P. Latham, Jr., "Polarization effects in a half-symmetric unstable resonator with a coated rear cone," *Appl. Opt.* **19**, 1222-1223 (April 15, 1980).

Other papers on this topic include J. K. Guha, J. L. Martin, R. A. Mickish, and E. E. Pape, "Performance of a coated cone in an annular resonator," *Appl. Opt.* **20**, 3089-3090 (September 15, 1981); and T. R. Ferguson, "Vector modes in cylindrical resonators," *J. Opt. Soc. Am.* **72**, 1328-1334 (October 1982).

See also R. A. Chodzko, S. B. Mason, E. B. Turner, and W. W. Plummer, Jr., "Annular (HSURIA) resonators: some experimental studies including polarization effects," *Appl. Opt.* **19**, 778-789 (March 1980).

Adaptive optical techniques (i.e., deformable mirrors with feedback control) have also been explored to solve the mode control difficulties in HSURIA resonators, as described, for example, in J. B. Shellan, D. A. Holmes, M. L. Bernabe, and A. M. Simonoff, "Adaptive mirror effects on the performance of annular resonators," *Appl. Opt.* **19**, 610-615 (February 15, 1980); and J. M. Spinhirne, D. Anafi, and R. H. Freeman, "Intracavity adaptive optics. 3: Hsuria performance," *Appl. Opt.* **21**, 3969-3982 (November 1, 1982).

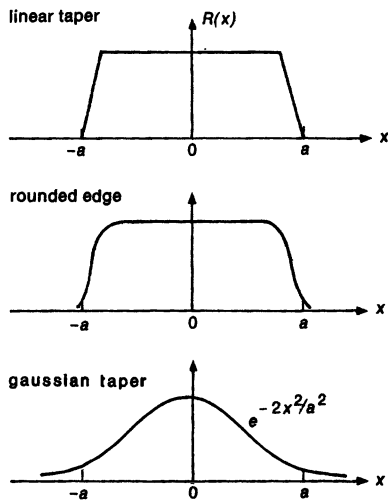


FIGURE 23.16
Various forms of tapered reflectivity for laser resonator mirrors.

23.3 VARIABLE-REFLECTIVITY UNSTABLE RESONATORS

We have saved until last what seems to be the best unstable resonator concept of all—the use of *geometrically unstable resonator optics*, in order to achieve increased mode volume and good transverse mode discrimination, combined with *gaussian variable-reflectivity mirrors* (or variable-transmission output couplers) to control both the mode performance of the unstable resonator and the transverse beam profile of the output beam as well.

Unstable Resonators With Variable Reflectivity Mirrors

An obvious extension of the tapered-edge mirror concepts introduced in the previous section is to taper the *magnitude* of the mirror reflectivity from its maximum value down to zero over some annular region at the outer edge of the output coupling mirror, as shown in Figure 23.16, in order to smear out the edge diffraction effects. Once again it is found both theoretically and experimentally, as shown in Figure 23.17, that this kind of amplitude tapering can lead to substantially improved mode discrimination as well as substantial reduction of the periodic cusping behavior with the equivalent Fresnel number N_{eq} .

Again, however, the primary problem with both phase and amplitude tapering is finding practical methods for tapering the mirror reflectivity which can be fabricated to adequate optical tolerances at reasonable cost, and which will also stand high output powers if necessary. In addition, unwanted phase perturbations associated with an amplitude taper may distort the phase front of the lowest-order mode, so that this mode, although it may have excellent mode separation and mode discrimination against higher-order modes, will have a nonplanar or nonspherical wavefront which cannot easily be converted into a well-collimated output beam.

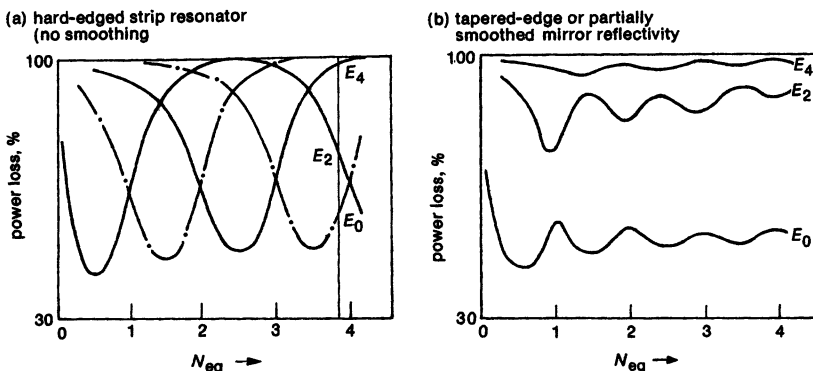


FIGURE 23.17

Typical difference in behavior between (a) a conventional hard-edged unstable resonator, and (b) the same resonator with tapered-reflectivity mirrors. (From Anan'ev and Sherstobitov.)

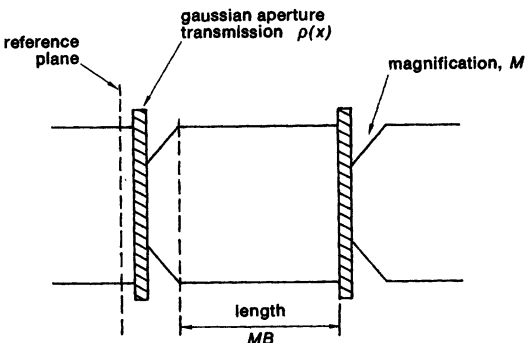


FIGURE 23.18

Canonical formulation for a geometrically unstable resonator with gaussian aperture or gaussian variable-reflectivity mirror.

Gaussian Variable Reflectivity Mirrors (VRM)

If we are going to taper the output-mirror reflectivity, however, then the simplest solution, at least analytically, would seem to be a *gaussian reflectivity taper*—that is, converting the output mirror into effectively a soft gaussian aperture, so that the resonator will become identically a complex gaussian or paraxial resonator of the type already discussed in Section 21.4.

Such a resonator will then have well-understood Hermite-gaussian or Laguerre-gaussian modes, which can be analyzed more or less exactly using the complex *ABCD* methods described in Chapter 21. In the remainder of this chapter we will summarize some of the useful design features of such complex geometrically unstable gaussian resonators, as well as some of the practical methods by which such resonators might be obtained.

Analysis of an Unstable Gaussian-Reflectivity Resonator

To analyze an unstable resonator with a gaussian variable-reflectivity mirror, we can simply replace the hard-edged aperture in the canonical model of Section 22.2 by an aperture with the appropriate amplitude transmission coefficient $\tilde{\rho}(r)$. [The mirror reflection coefficient $\tilde{\rho}(r)$ in the real laser becomes the aperture transmission coefficient in the equivalent lensguide model.] For the ideal gaussian situation we assume this reflection or transmission coefficient is given by

$$\tilde{\rho}(r) = \exp\left(-\frac{a_2 r^2}{2}\right) \equiv \exp\left(-\frac{r^2}{w_a^2}\right), \quad (5)$$

so that

$$\frac{a_2}{2} \equiv \frac{1}{w_a^2} \quad \text{or} \quad w_a \equiv \sqrt{\frac{2}{a_2}}. \quad (6)$$

The radius w_a is then the $1/e$ radius for amplitude transmission, or the $1/e^2$ radius for intensity transmission, through the aperture. (For simplicity, we will consider cylindrically symmetric resonators through the rest of this section.)

The round-trip complex ray matrix for this system is then given by

$$\begin{aligned} \begin{bmatrix} A & B \\ C & D \end{bmatrix} &= \begin{bmatrix} 1 & MB \\ 0 & 1 \end{bmatrix} \times \begin{bmatrix} M & 0 \\ 0 & 1/M \end{bmatrix} \times \begin{bmatrix} 1 & 0 \\ -j\lambda a_2/2\pi & 1 \end{bmatrix} \\ &= \begin{bmatrix} M - j\lambda a_2 B/2\pi & B \\ -j\lambda a_2/2\pi M & 1/M \end{bmatrix}. \end{aligned} \quad (7)$$

Although the gaussian aperture does not have a discrete sharp edge, it is convenient to define an effective Fresnel number for the gaussian aperture, based on the radius w_a and the resonator's effective length B , by the definition

$$N_{ga} \equiv \frac{w_a^2}{B\lambda} = \text{gaussian resonator Fresnel number.} \quad (8)$$

In practice we will usually be interested in resonators with comparatively large mode diameters, or large values of this Fresnel number N_{ga} .

With this notation the $ABCD$ matrix can be written as

$$\begin{bmatrix} A & B \\ C & D \end{bmatrix} = \begin{bmatrix} M - j/\pi N_{ga} & B \\ -j/\pi N_{ga} MB & 1/M \end{bmatrix}, \quad (9)$$

and we can then write the complex \tilde{m} value associated with this resonator as

$$\tilde{m} \equiv \frac{A + D}{2} = \frac{1}{2} \left[M + \frac{1}{M} - \frac{j}{\pi N_{ga}} \right] \equiv m_r - j \frac{1}{2\pi N_{ga}}. \quad (10)$$

The quantity m_r is then the real, geometrically unstable m value that would be associated with this resonator in the absence of the gaussian aperture. It is related to the geometric magnification M by the same formulas used in ordinary unstable resonators, namely,

$$M = m_r + \sqrt{m_r^2 - 1} \quad \text{or} \quad m_r = \frac{M^2 + 1}{2M}, \quad (11)$$

assuming for simplicity that we consider only the positive branch from here on.

Eigenvalues and Eigenmodes

We will also assume for the remainder of this section that the gaussian aperture's Fresnel number N_{ga} will be large enough compared to unity so that the imaginary part $j/2\pi N_{\text{ga}}$ of the complex \tilde{m} expression can be considered as a small first-order perturbation relative to the real m_r part. In practical terms, this means we assume a comparatively weak gaussian aperture. But since in most practical situations we want a comparatively large-diameter mode, this assumption matches the desired design objective.

The complex eigenvalue for the confined, magnifying, perturbation-stable solution in this gaussian resonator can then be approximated by

$$\begin{aligned}\tilde{\gamma} &= \tilde{m} - \sqrt{\tilde{m}^2 - 1} \\ &= m_r - j/2\pi N_{\text{ga}} - \sqrt{(m_r - j/2\pi N_{\text{ga}})^2 - 1} \\ &\approx \left(\frac{1}{M}\right) + j \left(\frac{1}{M^2 - 1}\right) \frac{1}{\pi N_{\text{ga}}} \quad \text{for } m_r \gg 1/2\pi N_{\text{ga}},\end{aligned}\tag{12}$$

whereas the corresponding complex gaussian eigensolution is given by a gaussian beam with \tilde{q} parameter

$$\begin{aligned}\frac{1}{\tilde{q}} &= \frac{D - A}{2B} + \frac{\sqrt{\tilde{m}^2 - 1}}{B} = \frac{D - \tilde{\gamma}}{B} \\ &\approx -j \left(\frac{1}{M^2 - 1}\right) \frac{1}{\pi N_{\text{ga}} B} \equiv -j \frac{\lambda}{\pi w^2} \quad \text{for } m_r \gg 1/2\pi N_{\text{ga}}.\end{aligned}\tag{13}$$

We see that to first order in $1/\pi N_{\text{ga}} B$, adding the gaussian aperture to this unstable resonator leaves the round-trip eigenvalue at $\tilde{\gamma} \approx 1/M$, plus a small imaginary part; whereas it changes the magnifying paraxial eigenwave from an unbounded plane wave (as seen in this canonical formulation) to a gaussian beam which is still collimated, with infinite radius of curvature, but with a finite spot size. This modal spot size w is in fact given by

$$w^2 \approx (M^2 - 1) \times w_a^2 \quad \text{for } m_r \gg 1/2\pi N_{\text{ga}}.\tag{14}$$

The amplitude discrimination between the lowest and higher-order TEM_{mn} modes will thus be roughly $|\tilde{\gamma}|^{m+n} \approx (1/M)^{m+n}$ on each round trip, and the lowest-order TEM_{00} mode will be a clean, collimated gaussian beam inside the laser cavity.

Output Coupling and Output Beam Profiles

Although the transverse profile of the lowest eigenmode will be gaussian inside the laser cavity, the output beam will have this gaussian profile multiplied by the radially varying mirror transmission $T(r) \equiv 1 - R(r)$ outside the cavity. (We will certainly want to use a lossless variable reflection technique, so that $R + T = 1$ everywhere.) The end-mirror reflectivity $R(r)$ will have the general form

$$R(r) \equiv |\tilde{\rho}(r)|^2 = R_0 \exp[-2r^2/w_a^2],\tag{15}$$

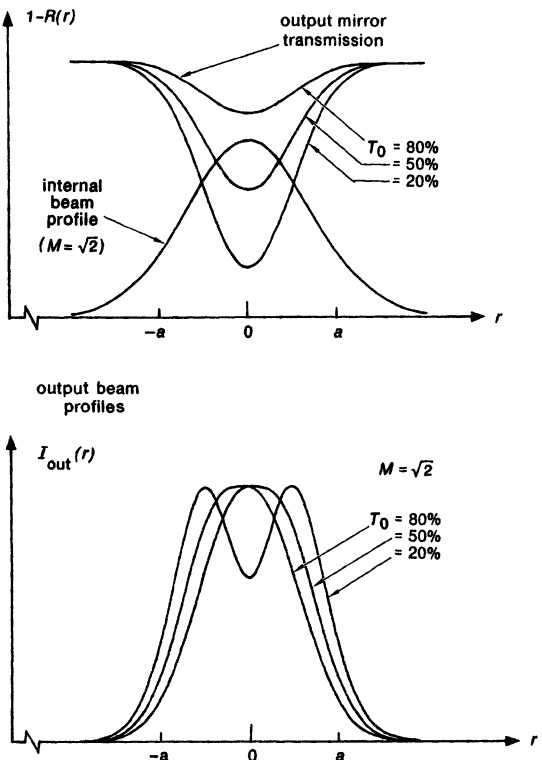


FIGURE 23.19
 Output beam profiles from a VRM resonator with different output mirror transmission factors.

where R_0 is the central value of reflection coefficient and $T_0 \equiv 1 - R_0$ is the power transmission at the center of the mirror.

Multiplying the radially decreasing gaussian beam profile inside the resonator by the radially increasing mirror transmission then gives for the output beam profile

$$I_{\text{out}}(r) = \left[1 - R_0 e^{-2r^2/w_a^2} \right] e^{-2r^2/w^2}, \quad (16)$$

where $w^2 \approx (M^2 - 1)w_a^2$ is the beam spot size in the large-Fresnel-number limit. Figure 23.19 shows plots of the output mirror transmission profile $1 - R(r)$; the gaussian beam profile $I(r) = |\dot{u}(r)|^2$ just inside the output mirror; and the output intensity profiles $I_{\text{out}}(r) = [1 - R(r)]I(r)$ (normalized to the same peak values) for a magnification $M = \sqrt{2}$ and for several different choices of the central mirror reflectivity R_0 . If we want to have an output beam profile without a significant dip in the center, we must use an output mirror or output coupler whose reflectivity at the center is less than unity, so that there is some finite transmission out of the cavity even at the center of the beam.

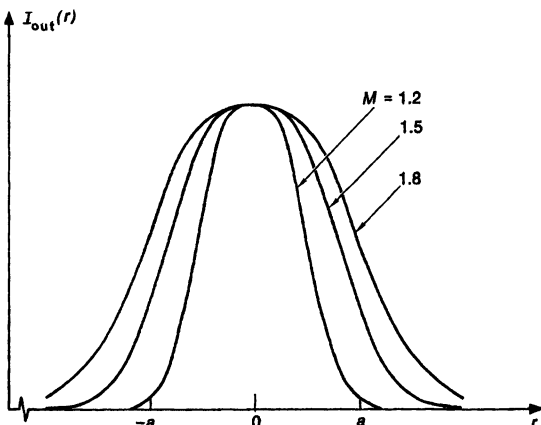


FIGURE 23.20

Maximally flat output beam profiles from VRM lasers with different geometric magnifications.

Radially Averaged Output Coupling

The power output of a laser oscillator depends strongly on the output coupling. The effective output coupling from a gaussian variable-reflectivity-mirror cavity depends upon the effective or average power reflectivity of the end mirror, integrated across the entire mode pattern, as given by

$$\bar{R} = \frac{\int_0^\infty 2\pi r R_0 e^{-2r^2/w_a^2} e^{-2r^2/w^2} dr}{\int_0^\infty 2\pi r e^{-2r^2/w^2} dr} = \frac{R_0}{M^2}, \quad (17)$$

(as we could already have deduced from the fact that the eigenvalue for the resonator is $\tilde{\gamma} \approx 1/M$ and $1 - |\tilde{\gamma}|^2 \equiv \bar{R}$.) The essential point here is that the average reflectivity of the end mirror, or one minus the output coupling, is given by the central reflectivity value R_0 of the output mirror, divided by the magnification M squared. This output coupling value must be adjusted to fall in the optimum output coupling range for the particular type of laser under consideration.

Maximally Flat Output Beam Profiles

The primary tradeoff in designing a gaussian VRM laser is then that if the central reflectivity R_0 is too small the laser oscillator will be overcoupled; whereas if R_0 is greater than a certain value, the mirror transmission will increase with radius faster than the gaussian intensity of the eigenmode itself decreases, so that the output beam will acquire a dip or hole in the center.

For the smoothest and most uniform output beam profile, we might wish to design a gaussian-reflectivity unstable resonator laser so that it operates just at the reflectivity R_0 where the central dip is about to appear. It is then easy to show that the "maximally flat" condition at which the central dip just begins to occur is given by

$$R_0(\text{maximally flat}) = \frac{1}{M^2}, \quad (18)$$

whereas the effective or average reflectivity of the end mirror under maximally flat conditions is given by

$$\bar{R}(\text{maximally flat}) = \frac{1}{M^4}. \quad (19)$$

Figure 23.20 shows examples of these maximally flat output profiles for different values of M .

Gaussian Reflectivity Design Criteria

The design procedure for a gaussian-variable-reflectivity unstable resonator can then be outlined as follows:

- Select a value of geometric magnification M which will achieve an adequate mode intensity discrimination ratio $1/M^2$ per round trip between the lowest-order and next higher-order mode on each round trip.
- At the same time select a value of mirror-center reflectivity R_0 which will, if possible, satisfy the maximally flat criterion $R_0 \leq 1/M^2$ yet still keep the average reflectivity $\bar{R} = R_0/M^2$ high enough for good power extraction from the laser medium.
- Finally, choose the width parameter w_a or the Fresnel number $N_{ga} \equiv w_a^2/B\lambda$ of the gaussian aperture large enough so that the spot size $w^2 = (M^2 - 1)w_a^2$ inside the resonator adequately fills the gain medium.

In low gain lasers, the combination of M and R_0 required to achieve both good mode discrimination and a maximally flat output beam profile may over-couple the laser. In this situation, it may be necessary to increase the central reflectivity R_0 and accept some amount of intensity reduction in the center of the beam. It can then be shown that the intensity reduction at the center of the beam relative to that at the peak of the annular ring (at radius r_p) is given by

$$\frac{I_{\text{out}}(r = 0)}{I_{\text{out}}(r = r_p)} = \frac{M^2(1 - R_0)(M^2 R_0)^{1/(M^2 - 1)}}{M^2 - 1} \quad (20)$$

for values of $R_0 > 1/M^2$.

Practical Variable-Reflectivity Mirrors and Couplers

Any practical form of gaussian aperture or gaussian variable-reflectivity mirror (VRM) which can be employed in this kind of resonator will thus be a very useful optical element. Components of this type which have been proposed or demonstrated to date include:

(1) *Absorbing gaussian apertures.* These can be made using evaporated metal or absorptive coatings, exposed and developed photographic films, or absorptive filters with radially tapered density. Aside from the difficulty of fabricating such apertures, they have the practical problem that they absorb power and hence reduce laser efficiency, and they are likely to be damage-prone in high power lasers.

(2) *Tapered-reflectivity dielectric mirrors.* These can be made by preparing some kind of tapered-reflectivity and hence tapered-transmission, lossless dielectric coating on one end mirror of the laser. Such mirrors, if they became

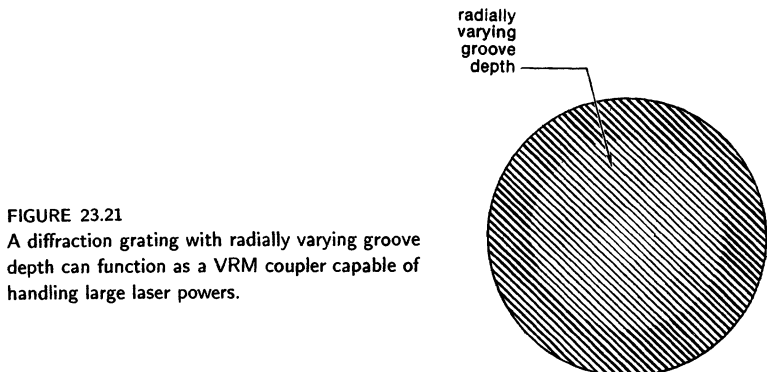


FIGURE 23.21

A diffraction grating with radially varying groove depth can function as a VRM coupler capable of handling large laser powers.

readily available, would be very useful and effective. The principal problem here is that such coatings appear at present to be difficult and expensive to make. There may also be unwanted phase distortions in the transmitted wave due to the tapered coatings.

(3) *Tapered-groove-depth diffraction gratings.* A complex but effective type of variable-reflectivity mirror or coupler can be obtained by etching a diffraction grating into an otherwise 100% reflecting mirror. This grating should be fabricated with a constant grating period and hence diffraction angle, but with a groove depth and hence a diffraction efficiency which varies from center to edge.

We can then use this type of element in either of two ways, with the diffracted beam either providing the mirror feedback and the specular beam the output coupling, or vice versa, as illustrated in Figure 23.10. An element of this kind is obviously difficult to fabricate initially, but once fabricated should be efficient and effective. At least one successful grating-mirror of this type has been prepared by ion beam milling techniques and used with success in a high-power CO₂ laser.

Radially Varying Birefringent Couplers

One of the most promising and effective recent solutions to the variable-reflectivity mirror or coupler problem is the *radially varying birefringent coupling technique* illustrated in Figure 23.22.

In this technique a birefringent element (or, in a ring resonator, an optically active element) with a radially increasing strength or thickness is placed inside a laser cavity. The wave passing through the element will then have its polarization rotated, or converted from linear to elliptical, by an amount which increases with radius from the center of the element. A polarization-sensitive coupling element, such as a dielectric-coated beam splitter, a polarizing crystal, or a Brewster-angle plate, is then used to extract the rotated polarization component with a strength which increases radially at the desired rate.

In more advanced versions of this technique, two polarizing elements of opposite sign, shaped like positive and negative lenses, can be used in cascade to produce the radially varying birefringence yet cancel out any focusing effects due to either element alone. If ordinary birefringent crystals are used, a variety of both radial profiles and central reflection values can be obtained by rotating one

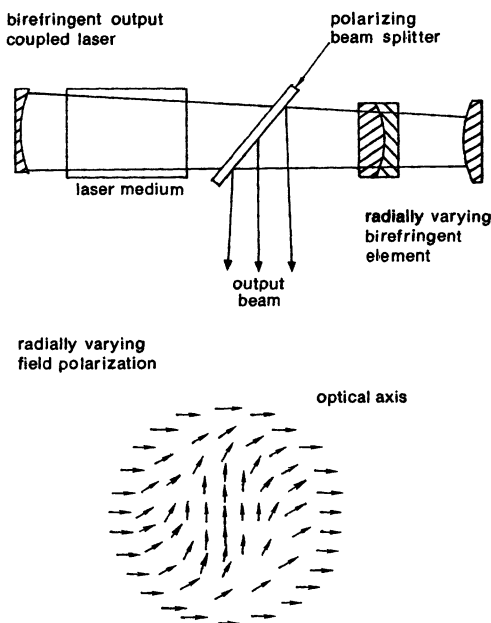


FIGURE 23.22
Radially varying birefringent coupling technique.

or both of these crystals about the resonator axis, as demonstrated by Byer and his co-workers.

This particular technique appears to have great potential, at least for low to medium power lasers in the visible and near IR. The necessary elements can be relatively simple to fabricate and adjust, and can have low insertion losses and relatively high optical-damage thresholds at least in the visible region where suitable optical materials are available. Finding suitable birefringent elements and polarizers does, however, become much more difficult for high average power lasers, especially in the infrared; and alternative solutions to the general variable-reflectivity coupler problem with similarly useful properties would be well worth inventing.

REFERENCES

The earliest discussion of modes in resonators with gaussian variable reflectivity mirrors—though done without introducing any *ABCD* matrix concepts—is by H. Zucker, “Optical resonators with variable reflectivity mirrors,” *Bell Sys. Tech. J.* **49**, 2349–2376 (November 1970).

Another early discussion of unstable resonators with gaussian reflectivity mirrors is given in A. N. Chester, “Mode selectivity and mirror misalignment effects in unstable laser resonators,” *Appl. Opt.* **11**, 2584–2590 (November 1972).

The complex *ABCD* matrix and perturbation-stability formalism for resonators with tapered reflectivity mirrors was first introduced by L. W. Casperson in “Mode

CHAPTER 23: MORE ON UNSTABLE RESONATORS

stability of lasers and periodic optical systems," *IEEE J. Quantum Electron.* **QE-10**, 629-634 (September 1974).

Additional discussions of this topic are presented in A. Yariv and P. Yeh, "Confinement and stability in optical resonators employing mirrors with gaussian reflectivity tapers," *Optics Commun.* **13**, 370-374 (April 1975); L. W. Casperson and S. D. Lunnan, "Gaussian modes in high loss laser resonators," *Appl. Optics* **14**, 1193-1199 (May 1975); and U. Ganiel, A. Hardy, and Y. Silberberg, "Stability of optical laser resonators with mirrors of gaussian reflectivity profiles, which contain an active medium," *Optics Commun.* **14**, 290-293 (July 1975).

The radial birefringent element described in this section is introduced in two papers by G. Giuliani, Y. K. Park, and R. L. Byer, "Radial birefringent element and its application to laser resonator design," *Opt. Lett.* **5**, 491-493 (November 1980); and J. M. Eggleston, G. Giuliani, and R. L. Byer, "Radial intensity filters using radial birefringent elements," *J. Opt. Soc. Am.* **71**, 1264-1272 (October 1981).

Three excellent recent papers on this topic are by N. McCarthy and P. Lavigne, "Optical resonators with gaussian reflectivity mirrors: misalignment sensitivity," *Appl. Opt.* **22**, 2704-2708 (1 September 1983) and (with experimental results) "Large-size gaussian mode in unstable resonators using gaussian mirrors," *Opt. Lett.* **10**, 553-555 (November 1985); as well as P. Lavigne, N. McCarthy, and J-G. Demers, "Design and characterization of complementary gaussian reflectivity mirrors," *Appl. Opt.* **24**, 2581-2586 (15 August 1985).



LASER DYNAMICS: THE LASER CAVITY EQUATIONS

In earlier chapters we analyzed the steady-state behavior of laser cavities using simplified interferometer models, with a few extensions into transient behavior, as in the cavity build-up equations. The objective in this chapter is to give a more complete and systematic derivation of the combined cavity and atomic equations of motion for a real multimode laser. We will then use these equations of motion in later chapters to analyze dynamic phenomena such as spiking, Q -switching, mode locking, and injection locking in lasers.

The laser equations of motion used in the scientific and engineering literature come in several slightly different forms and degrees of approximation. This chapter shows how the basic equations of motion transform into these different versions, and how they relate to each other.

24.1 DERIVATION OF THE LASER CAVITY EQUATIONS

In this opening section we derive the basic laser-cavity equation of motion, using a so-called “Slater normal mode approach” (see References). This approach is independent of the specific form or details of the actual laser cavity. Like essentially every other derivation of the laser-cavity equations in the literature or in other textbooks, this analysis will make certain assumptions about the lossless and orthonormal character of the cavity modes—assumptions which are *not*, in fact, valid for real laser cavities.

Despite this fundamental weakness in the starting approximations, the approach presented here is the standard approach used in the laser field. We reproduce this standard derivation here partly because it will permit students to compare results with the standard laser literature; partly because this derivation also gives many useful insights; but mostly because the final results of this derivation are still essentially correct despite the weakness of the initial assumptions. (For the beginnings of a more rigorously correct approach to the cavity equations, see the references at the end of this section.)

The Vector Wave Equation

We begin the analysis as usual with Maxwell's equations for the real vector electromagnetic fields in the cavity, namely,

$$\nabla \times \mathbf{E}(\mathbf{r}, t) = -\frac{\partial \mathbf{b}(\mathbf{r}, t)}{\partial t} \quad \text{and} \quad \nabla \times \mathbf{h}(\mathbf{r}, t) = \mathbf{j}(\mathbf{r}, t) + \frac{\partial \mathbf{d}(\mathbf{r}, t)}{\partial t}. \quad (1)$$

We add to these the “constitutive relations”

$$\mathbf{b}(\mathbf{r}, t) = \mu_0 [\mathbf{h}(\mathbf{r}, t) + \mathbf{m}_a(\mathbf{r}, t)], \quad \mathbf{d}(\mathbf{r}, t) = \epsilon \mathbf{E}(\mathbf{r}, t) + \mathbf{p}_a(\mathbf{r}, t), \quad (2)$$

and also an assumed ohmic loss relation

$$\mathbf{j}(\mathbf{r}, t) = \sigma \mathbf{E}(\mathbf{r}, t). \quad (3)$$

The field quantities $\mathbf{E}(\mathbf{r}, t)$, $\mathbf{b}(\mathbf{r}, t)$, $\mathbf{j}(\mathbf{r}, t)$, and so on, are all real functions of space and time at this point. The dielectric constant ϵ includes the dielectric permeability of the host crystal lattice or any other dielectric material inside the laser cavity, but does not include the resonant laser transition itself. The polarizations $\mathbf{p}_a(\mathbf{r}, t)$ and $\mathbf{m}_a(\mathbf{r}, t)$ then represent any electric-dipole or magnetic-dipole atomic transitions (e.g., laser transitions) that may be present. The conductivity σ represents ohmic losses inside the laser cavity, extended to include scattering and coupling losses as well.

We then proceed by taking the curl of the first Maxwell equation and combining it with the other equations, plus the vector identity $\nabla \times \nabla \times \mathbf{E} \equiv \nabla(\nabla \cdot \mathbf{E}) - \nabla^2 \mathbf{E}$. We also assume that $\nabla \cdot \mathbf{E} \equiv 0$ inside a closed cavity with no free charges present. The result, after some rearrangement, is the full vector wave equation

$$\frac{\partial^2 \mathbf{E}(\mathbf{r}, t)}{\partial t^2} + \frac{\sigma}{\epsilon} \frac{\partial \mathbf{E}(\mathbf{r}, t)}{\partial t} - \frac{1}{\mu_0 \epsilon} \nabla^2 \mathbf{E}(\mathbf{r}, t) = -\frac{1}{\epsilon} \left[\frac{\partial^2 \mathbf{p}_a(\mathbf{r}, t)}{\partial t^2} + \frac{\partial}{\partial t} \nabla \times \mathbf{m}_a(\mathbf{r}, t) \right]. \quad (4)$$

This is the basic equation for calculating how the cavity fields $\mathbf{E}(\mathbf{r}, t)$ on the left-hand side of Equation 24.4 will be driven or excited by any electric and magnetic atomic polarizations $\mathbf{p}_a(\mathbf{r}, t)$ and $\mathbf{m}_a(\mathbf{r}, t)$ appearing on the right-hand side.

Normal Mode Expansion

We now make the crucial assumption that we can write the fields inside any laser cavity as an expansion in a set of normal modes or eigenmodes $\mathbf{u}_n(\mathbf{r})$ in the form

$$\mathbf{E}(\mathbf{r}, t) = \sum_n E_n(t) \mathbf{u}_n(\mathbf{r}), \quad (5)$$

where the expansion coefficients $E_n(t)$ are scalar functions of time only. The normal modes $\mathbf{u}_n(\mathbf{r})$ in this expansion are assumed to be solutions of Laplace's equation

$$[\nabla^2 + k_n^2] \mathbf{u}_n(\mathbf{r}) = 0 \quad (6)$$

which satisfy the boundary conditions of the particular cavity being analyzed, without the atoms being present. These cavity modes are therefore the eigenmodes of the cavity, which can exist—that is, which can satisfy both the wave

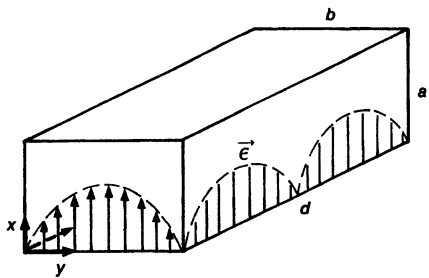


FIGURE 24.1
Resonant eigenmodes of a closed rectangular cavity.

equation and the boundary conditions—only for certain discrete values of the separation constant or eigenvalue k_n . This eigenvalue can in turn be written as

$$k_n \equiv \omega_n \sqrt{\mu_0 \epsilon} = \omega_n / c, \quad (7)$$

where the ω_n 's are the resonance frequencies of the cavity (without laser atoms). The modes u_n and frequencies ω_n are thus the resonant eigenmodes and eigenfrequencies of the empty cavity, leaving out any effects of the atomic polarizations p_a or m_a .

We will also assume that these modes are orthogonal, and that their amplitudes $u_n(r)$ can always be normalized so that they satisfy the orthonormality relation

$$\iiint_{\text{cavity}} u_n(r) \cdot u_m(r) dr = V_c \times \delta_{nm}, \quad (8)$$

where the integral $dr \equiv dx dy dz$ is over the entire cavity volume. An arbitrary normalization factor V_c is included on the right-hand side of this equation. The value of this normalization factor can be arbitrarily chosen, since it merely determines a scale factor for the amplitudes of the cavity modes u_n . The most elementary choice, for example, would be simply to set $V_c = 1$. If, however, this arbitrary normalization factor V_c is chosen to be more or less equal to the volume of the cavity—or, more precisely, to the mode volume occupied by electromagnetic fields in the laser cavity—then the normal mode functions $u_n(r)$ themselves will be dimensionless and will have magnitudes of order unity, i.e.,

$$|u_n(r)| \approx 1 \quad \text{if} \quad V_c \approx \text{actual cavity volume.} \quad (9)$$

With this choice the mode amplitude coefficients $E_n(t)$ will have the dimensions of electric field and magnitudes more or less equal to the actual field $\mathcal{E}(r, t)$ inside the laser cavity.

Eigenmode Example: Closed Rectangular Cavity

Let us take a moment to look at some elementary examples of cavity eigenmodes $u_n(r)$, since this may help to understand the nature of typical cavity eigenmodes.

First of all, it is well-known from microwave theory that closed cavities with lossless boundary conditions will always possess just such a complete set of lossless and orthogonal normal modes for the electromagnetic fields within the cavity.

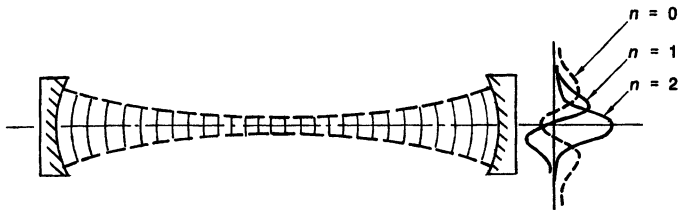


FIGURE 24.2

Hermite-gaussian eigenmodes of an open-sided, stable optical resonator.

For example, in a closed rectangular cavity with perfectly conducting walls (Figure 24.1) there is a set of x polarized transverse-electric (TE) modes which can be written as

$$u_{mnq}(r) = \sqrt{8} \cos\left(\frac{m\pi x}{a}\right) \sin\left(\frac{n\pi y}{b}\right) \sin\left(\frac{q\pi z}{d}\right) x, \quad (10)$$

where x is a unit vector in the x direction, and we have made the arbitrary choice that $V_c = abd$, the cavity volume. The associated eigenvalues are given by

$$k_{mnq}^2 = \left(\frac{\omega_{mnq}}{c}\right)^2 = \left(\frac{m\pi}{a}\right)^2 + \left(\frac{n\pi}{b}\right)^2 + \left(\frac{q\pi}{d}\right)^2. \quad (11)$$

(We will use multiple mode indices, like mnq , where they are useful to identify separate spatial coordinates or axes; but will condense this back to just a single overall index n when we are talking about a general mode expansion or about a single mode in a general expansion.)

The field pattern for a typical mode of this type is shown in Figure 24.1. These x -polarized TE modes, plus a similar set of y -polarized TE modes and a set of TM modes, can be shown to provide a complete set for expanding any electromagnetic field distribution within such a rectangular cavity.

Second Example: Stable Optical Cavity Eigenmodes

As one example of the eigenmodes in an optical or laser cavity, we might consider the transverse and longitudinal eigenmodes in a stable two-mirror optical resonator of length L with mirrors large enough to have negligible diffraction losses, as illustrated in Figure 24.2. These eigenmodes will be given, to a very good approximation, by

$$u_{mnq}(r) \approx H_m\left(\frac{\sqrt{2}x}{w(z)}\right) H_n\left(\frac{\sqrt{2}y}{w(z)}\right) e^{-r^2/w^2(z)} \sin\left(kz + \psi(z) + \frac{\pi r^2}{\lambda R(z)}\right) \quad (12)$$

with eigenvalues given by

$$k_{mnq}^2 = \left(\frac{\omega_{mnq}}{c}\right)^2 \approx \frac{\pi}{L} \left[q + (n + m + 1) \frac{\cos^{-1}(g_1 g_2)^{1/2}}{\pi} \right]. \quad (13)$$

The index q (typically a very large integer) identifies the axial or longitudinal mode number, whereas the indices m and n (typically small integers) identify different transverse mode patterns associated with each longitudinal mode. The gaussian beam parameters g_1 , g_2 , $w(z)$, $R(z)$ and $\psi(z)$ in Equations 24.12 and 24.13 are given by stable gaussian mode formulas that are discussed elsewhere

in this text, and the normalization constant in front of the eigenmode expression has been left out for simplicity.

The fundamental weakness mentioned at the beginning of this section is, however, that real laser cavities like Figure 24.2 are in fact neither closed nor lossless. Real laser cavities usually have a significant power loss out of the cavity through (or past the edges of) at least one end mirror. In addition they normally have open sides, which unavoidably allow some energy to leak out to infinity.

The transverse and axial eigenmodes of conventional laser cavities, therefore, as normally calculated in optical-resonator theory (cf. Chapter 14), are not lossless (against diffraction and coupling losses). In addition, they generally do not satisfy the orthogonality relation given in Equation 24.8 (they obey instead a more general biorthogonality relation derived in Section 21.7). Finally, there are some fundamental mathematical difficulties in even proving that such modes can exist in an open-sided laser cavity, much less that they will form a complete set.

The ideal Hermite-gaussian functions written in Equation 24.12 are in fact lossless and do obey the orthogonality property given in Equation 24.8. The functions in Equation 24.12 are, however, only approximations, though usually very good approximations, to the exact modes of such an open-sided laser cavity. The exact eigenmodes in a stable laser cavity with finite diameter mirrors will differ slightly from these Hermite-gaussian modes, primarily out near the mirror edges, because of the diffraction effects associated with these edges. The Hermite-gaussian modes will be an excellent approximation over most of the resonator volume, so long as the “spillover” losses at the mirror edges are small.

All these mathematical difficulties with real laser cavity modes are generally ignored in conventional laser analyses, and we will ignore them in the present section also. This is not as criminal an act as it might seem—the general form of the derivation, and the final equations resulting from it, are still essentially correct, despite these formal weaknesses in the analytical approach.

Cavity Mode Equation of Motion

The next important step in our derivation is to substitute the normal mode expansion given in Equation 24.5 into the vector wave equation 24.4. From this point on let us also keep only the electric polarization \mathbf{p}_a and drop the magnetic polarization \mathbf{m}_a , since we are most often interested in electric-dipole atomic transitions. Equation 24.4 then reduces to the form

$$\sum_n \left[\frac{\partial^2 E_n(t)}{\partial t^2} + \frac{\sigma}{\epsilon} \frac{\partial E_n(t)}{\partial t} + \omega_n^2 E_n(t) \right] \mathbf{u}_n(\mathbf{r}) = -\frac{1}{\epsilon} \frac{\partial^2 \mathbf{p}_a(\mathbf{r}, t)}{\partial t^2}. \quad (14)$$

Suppose the atomic polarization term \mathbf{p}_a on the right-hand side of this equation happens to be zero. Each term of the left-hand summation can then be independently set to zero, and the free decay of each cavity mode will be given by independent solutions of the form

$$E_n(t) = \text{Re } E_0 \exp \left[-\frac{\sigma}{2\epsilon} t + j\hat{\omega}_n t \right] = \text{Re } E_0 \exp \left[-\frac{\gamma_{0n}}{2} t + j\hat{\omega}_n t \right]. \quad (15)$$

We introduce the notation γ_{0n} to represent the decay rate for the cavity-mode energy due to internal losses. The exact resonant frequency of the cavity mode is then given by

$$\hat{\omega}_n \equiv \sqrt{\omega_n^2 - (\gamma_{0n}/2)^2}. \quad (16)$$

Since the cavity loss rate γ_{0n} is normally many orders of magnitude smaller than the oscillation frequency, we will ignore the very small distinction between ω_n and ω_n from here on.

In the general situation the driving polarization \mathbf{p}_a on the right-hand side will not be zero. We can then multiply both sides of Equation 24.14 by any one particular mode function $\mathbf{u}_n(\mathbf{r})$; integrate over the cavity volume; and make use of the orthonormality relation 24.5 for the cavity modes. If we do this, we obtain a separate equation of motion for the amplitude of that one particular cavity mode, namely,

$$\frac{d^2 E_n(t)}{dt^2} + \gamma_{0n} \frac{dE_n(t)}{dt} + \omega_n^2 E_n(t) = -\frac{1}{\epsilon} \frac{d^2 P_n(t)}{dt^2}, \quad (17)$$

The amplitude of this eigenmode is driven or excited by a polarization term $P_n(t)$ which is given by the overlap integral

$$P_n(t) \equiv \frac{1}{V_c} \iiint_{\text{cavity}} \mathbf{p}_a(\mathbf{r}, t) \cdot \mathbf{u}_n(\mathbf{r}) d\mathbf{r}. \quad (18)$$

A separate cavity-mode equation, with a separate polarization driving term like this, can then be written for each separate normal mode of the cavity. Each such equation has the form of a second-order differential equation, with a characteristic decay rate γ_{0n} , resonance frequency ω_n , and driving polarization $P_n(t)$.

In many practical lasers, multiple cavity modes will oscillate simultaneously. We must then write a separate cavity equation like Equation 24.17 for each such mode. When we include inhomogeneous transitions, saturation, and similar effects, different cavity modes E_n may become coupled to each other, as we shall see later. In mathematical terms this coupling occurs through the polarization terms P_n , i.e., the polarization term P_n for the n -th mode may include contributions proportional to the amplitudes of other modes E_m , as well as the mode E_n itself.

In the simplest situation, however, a laser may operate in only one oscillation mode; and only one cavity equation need then be written. In this situation we will often use the notation ω_c rather than ω_n for the cavity resonant frequency; and we will also drop the subscript n on all other quantities in the equations.

The Polarization Driving Term

The polarization driving term $P_n(t)$ on the right-hand side of Equation 24.17 corresponds to the expansion coefficient for the n -th eigenmode $\mathbf{u}_n(\mathbf{r})$ in an eigenmode expansion of $\mathbf{p}_a(\mathbf{r}, t)$. That is, if we write $\mathbf{p}_a(\mathbf{r}, t)$ as

$$\mathbf{p}_a(\mathbf{r}, t) = \sum_n P_n(t) \mathbf{u}_n(\mathbf{r}), \quad (19)$$

then $P_n(t)$ as defined in Equation 24.18 is just the expansion coefficient in this expansion. In many situations the atomic polarization $\mathbf{p}_a(\mathbf{r}, t)$ will itself be coherently produced by the cavity-mode field $\mathcal{E}(\mathbf{r}, t)$ acting on the atoms in a laser medium. In this situation the polarization $\mathbf{p}_a(\mathbf{r}, t)$ will have more or less the same spatial pattern as the cavity field $\mathbf{u}_n(\mathbf{r})$, at least within the laser medium.

Suppose for example that a laser medium with linear susceptibility χ fills part of the laser cavity, as in Figure 24.3. We can then write the polarization in this laser medium as $\mathbf{p}_a(\mathbf{r}, t) \approx \chi \epsilon \mathcal{E}(\mathbf{r}, t) \approx \chi \epsilon E_n(t) \mathbf{u}_n(\mathbf{r})$. (Writing the polarization

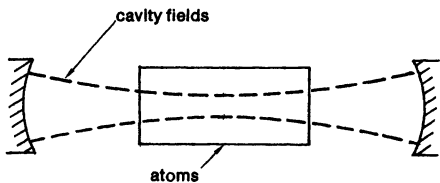


FIGURE 24.3
Overlap integral between cavity fields and laser atoms.

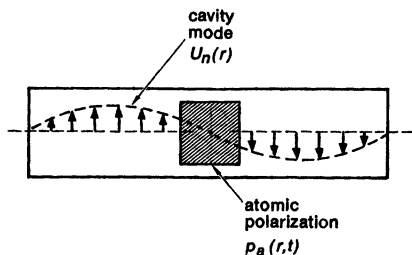


FIGURE 24.4
A situation where the cavity fields and the atomic polarization have nearly zero overlap.

in this form leaves out the phase shift associated with a complex susceptibility $\tilde{\chi}$, which we cannot handle properly until we convert to sinusoidal signals.) The driving polarization then becomes

$$P_n(t) \approx \frac{\chi \epsilon E_n(t)}{V_c} \iiint_{\text{atoms}} \mathbf{u}_n(\mathbf{r}) \cdot \mathbf{u}_n(\mathbf{r}) d\mathbf{r} \approx \eta_c \chi \epsilon E_n(t), \quad (20)$$

where η_c is a filling factor ≤ 1 given by

$$\eta_c \equiv \frac{1}{V_c} \iiint_{\text{atoms}} \mathbf{u}_n(\mathbf{r}) \cdot \mathbf{u}_n(\mathbf{r}) d\mathbf{r}. \quad (21)$$

Because the volume of integration in these integrals extends only over the atoms, and not the full cavity volume, the filling factor has a value $\eta_c \leq 1$ which reduces the effective value of χ on the right-hand side of Equation 24.20.

There can even be situations, as illustrated in Figure 24.4, where the laser atoms or the driving polarization may be located at a node of the electric field. The field then produces no polarization in the material; but even if it did, because of the lack of spatial overlap between the polarization $\mathbf{p}_a(\mathbf{r}, t)$ and the cavity-mode pattern $\mathbf{u}(\mathbf{r}, t)$, this polarization would not couple back into the cavity.

Cavity Lumped Equivalent Circuits

Some people find it helpful to interpret each of the separate resonant modes in a microwave or optical cavity as represented by a lumped resonant electrical circuit, as shown in Figure 24.5. The circuit equation for this lumped resonant circuit is

$$i_a(t) = C \frac{dv(t)}{dt} + G_0 v(t) + \frac{1}{L} \int v(t) dt, \quad (22)$$

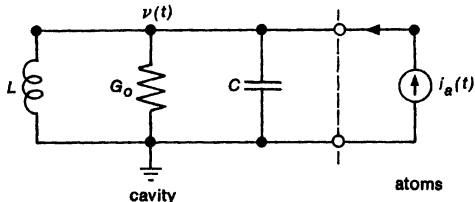


FIGURE 24.5

A lumped-element resonant circuit corresponding to a single resonant cavity mode.

which we can differentiate once more and rewrite as

$$\frac{d^2v(t)}{dt^2} + \gamma_0 \frac{dv(t)}{dt} + \omega_c^2 v(t) = \frac{1}{C} \frac{di_a(t)}{dt}. \quad (23)$$

Then this equation obviously has the same basic form as the cavity equation 24.17 for a single cavity mode.

Noticing the identity in form between the cavity equation 24.17 and the circuit equations 24.23 is the important point here, rather than making an exact connection between the two systems. We can set up at least two relations between the lumped circuit and the real cavity parameters, however, by writing

$$\gamma_{0n} = G_0/C \quad \text{and} \quad \omega_n^2 \equiv \omega_c^2 = 1/LC. \quad (24)$$

Specifying the actual decay rate γ_{0n} and the actual cavity frequency ω_c thus determines any two of the lumped circuit elements G_0 , L and C in terms of the third. The value of the third element is still arbitrary.

We can go further if we wish, however, and relate the cavity-mode amplitude $E_n(t)$ and the equivalent circuit voltage $v(t)$ in a convenient way as follows. The stored electrical energy in the cavity electric fields can be written as

$$U_{\text{cavity}} = \frac{\epsilon}{2} \iiint_{\text{cavity}} |\mathcal{E}(r, t)|^2 dr = \frac{1}{2} \epsilon V_c E_n^2(t) \quad (25)$$

while the stored electrical energy in the lumped circuit can be written as

$$U_{\text{circuit}} = \frac{1}{2} C v^2(t). \quad (26)$$

We will make these two energies numerically equal if we make the identification that

$$v(t) \equiv - \left(\frac{\epsilon V_c}{C} \right)^{1/2} E_n(t). \quad (27)$$

The minus sign in this relation is arbitrary; we insert it merely because the conventional relation between a field E and the voltage v across a distance d is $E = -v/d$.

If we put this into the circuit equation 24.23, then the circuit equation becomes

$$\frac{d^2 E_n(t)}{dt^2} + \gamma_{0n} \frac{d E_n(t)}{dt} + \omega_n^2 E_n(t) = - \left(\frac{1}{\epsilon C V_c} \right)^{1/2} \frac{d i_a(t)}{dt}. \quad (28)$$

But this has exactly the same form as the cavity equation 24.17 provided we make the final identification

$$i_a(t) \equiv \left(\frac{CV_c}{\epsilon} \right)^{1/2} \frac{dP_n(t)}{dt}. \quad (29)$$

If V_c has dimensions of volume (which we have said is a convenient choice for this parameter) then $P_n(t)$ will have the dimensions of electric polarization, or electric dipole moment per unit volume. The first time derivative of $P_n(t)$ will have dimensions of polarization current density, or current per unit area. Since the square-root factor in Equation 24.29 has the dimensions (in mks) of area, the quantity $i_a(t)$ has exactly the proper dimensions of a current.

Conclusion

The net result of all this is that a single cavity mode containing a driving polarization $p_a(r, t)$ can be made formally identical to a simple lumped shunt resonant circuit, with the atomic polarization term $P_n(t)$ represented by an equivalent shunt current generator $i_a(t)$. There are five parameters describing the lumped circuit (G_0 , L , C , v , and i_a), but only four connecting relations between the lumped circuit and the real cavity. Hence, there is an arbitrary scale factor in this relationship, which can be thought of as an arbitrary choice of impedance level for the lumped equivalent circuit. That is, given specified values of the parameters of the real optical cavity, we can arbitrarily choose $C = 1$ fd, say, or perhaps $1/G_0 = 50\Omega$, or any other convenient choice for the lumped circuit. All the other lumped circuit parameters will then be uniquely determined.

Equivalent resonant circuits such as these can be extremely useful, both for purposes of visualization and for understanding the resonance and transient behavior of cavities, and the coupled-mode effects in multimode cavities.

REFERENCES

The type of normal mode expansion developed in this section is sometimes called a "Slater mode expansion" because its use for microwave problems was widely introduced by J. C. Slater in *Microwave Electronics* (Van Nostrand, 1950). It is now the standard approach for microwave electromagnetic problems, as illustrated in R. E. Collin, *Foundations for Microwave Engineering* (McGraw-Hill, 1966), pp. 183-191 and 344-359; or C. C. Johnson, *Field and Wave Electrodynamics* (McGraw-Hill, 1965), esp. Chap. 6, pp. 213-227.

The classic example of applying this approach to laser problems is W. F. Lamb, Jr., "Theory of an optical maser," *Phys. Rev.* **134A**, 1429-1450 (June 15 1964). Another typical example is E. T. Jaynes and F. W. Cummings, "Comparison of quantum and semiclassical radiation theories with application to the beam maser," *Proc. IEEE* **51**, 89 (January 1963).

A more rigorous and exact approach to laser-cavity equations, which takes into account external coupling and the real cavity eigenmodes, has been outlined in A. E. Siegman, "Exact cavity equations for lasers with large output coupling," *Appl. Phys. Lett.* **36**, 412-414 (March 15, 1980).

Problems for 24.1

1. *Cavity equations with a magnetic-dipole driving polarization.* The resonant cavity-mode equation (24.17) derived in this section is a second-order differential equation for $E_n(t)$. As an alternative, show that by using the two expansions $\mathcal{E}(\mathbf{r}, t) = \sum E_n(t) \mathbf{u}_n(\mathbf{r})$ and $\mathbf{h}(\mathbf{r}, t) = \sum h_n(t) \nabla \times \mathbf{u}_n(\mathbf{r})$, we can obtain cavity equations in the form of two coupled first-order differential equations for $E_n(t)$ and $h_n(t)$. Include a magnetic dipole polarization $\mathbf{m}_a(\mathbf{r}, t)$ as well as an electric dipole polarization $\mathbf{p}_a(\mathbf{r}, t)$ in your analysis for completeness.

Note: The vector identity $\nabla \cdot (\mathbf{A} \times \mathbf{B}) = \mathbf{B} \cdot (\nabla \times \mathbf{A}) - \mathbf{A} \cdot (\nabla \times \mathbf{B})$ may be useful; and we can assume the cavity is a closed cavity, with the integral of the Poynting vector over the cavity's outside surface being identically zero.

2. *Equivalent lumped circuit equations.* Identify the two equations derived in the preceding problem with the corresponding equations in an equivalent lumped circuit model.
-

24.2 EXTERNAL SIGNAL SOURCES

A real resonant cavity will normally have some form of coupling to the external world, whether through a partially transmitting end mirror, a coupling hole, or perhaps a partially reflecting beam splitter inside the laser cavity. The cavity modes may then be driven or excited by external signals sent into the cavity through one of these output coupling ports. In this section we develop an analysis of external coupling and external signal injection, using the lumped circuit model as an analytical approach.

Wave Analysis of External Coupling and External Signal Injection

Analyzing the external coupling or external signal injection into a resonant cavity is not always simple or straightforward in a full vector field analysis or in a normal-mode formulation. Figure 24.6 shows, for example, some of the typical cavity coupling methods used for microwave resonant cavities.

One analytical approach often used in microwave problems like these is to treat the coupling hole in a waveguide cavity, or the coupling loop or coupling probe from a coaxial line, as a lumped delta-function polarization. That is, one writes the induced polarization due to the coupling element in the form $\mathbf{p}_e(\mathbf{r}, t) = P_e(t) \delta(\mathbf{r} - \mathbf{r}_e)$ or $\mathbf{m}_e(\mathbf{r}, t) = M_e(t) \delta(\mathbf{r} - \mathbf{r}_e)$, where \mathbf{r}_e is the point at which the coupling occurs, and the amplitudes $P_e(t)$ or $M_e(t)$ are related to the amplitude of the external driving signal.

This polarization due to the external coupling is then added to the right-hand side of the wave equation 24.4 as an additional driving term for the cavity fields. Additional analysis is required to connect the amplitude of the driving polarization terms $P_e(t)$ or $M_e(t)$ to the amplitude of the externally applied signal.

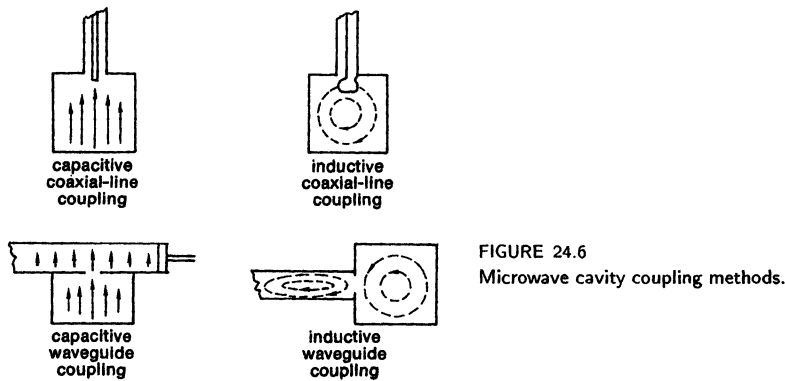


FIGURE 24.6
Microwave cavity coupling methods.

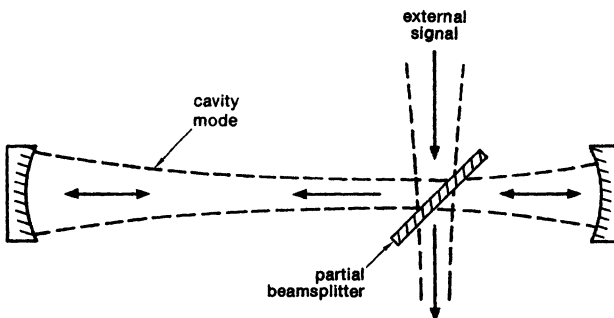


FIGURE 24.7
One possible optical cavity coupling method.

As an optical example of the same approach, suppose a very thin, partially reflecting dielectric beamsplitter with a small reflection coefficient and a large transmission coefficient is put inside a laser cavity to serve as an external coupling element, as shown in Figure 24.8. (Such a very thin beamsplitter, if made from a dielectric film, is sometimes called a *pellicle*.) Suppose a wave coming from an external signal source is sent into this beamsplitter at the correct angle so that a fraction of the external signal wave will be reflected along the cavity axis and will couple into the cavity mode. At the same time, the cavity mode fields propagating back and forth along the cavity axis will be partially reflected into the external coupling direction, and will be coupled out of the laser cavity (in two opposite directions, going both upward and downward, with this particular coupling method). Reflection from this pellicle thus provides both external coupling and external signal injection to the cavity.

From another viewpoint, however, we can say that the external signal fields $\mathcal{E}_e(\mathbf{r}, t)$, in passing through the dielectric beamsplitter, will create a dielectric polarization which we could call $\mathbf{p}_e(\mathbf{r}, t)$ within the volume of the beamsplitter, as shown in Figure 24.8. The magnitude of this polarization depends on the dielectric constant and thickness of the beamsplitter. The presence of this externally driven polarization inside the laser cavity will then provide an additional

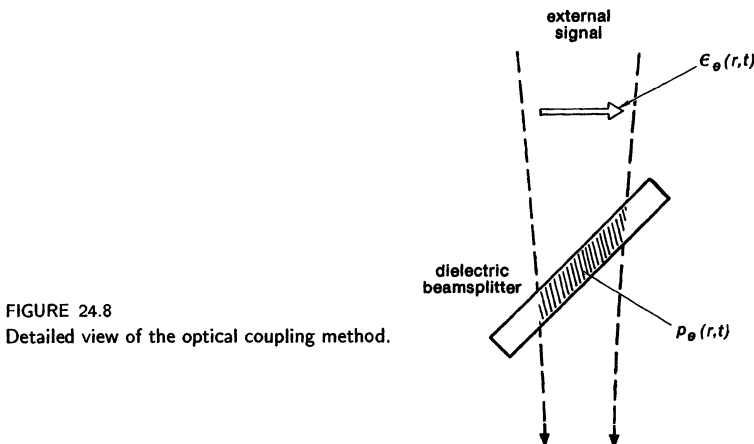


FIGURE 24.8
Detailed view of the optical coupling method.

polarization driving term on the right-hand side of the wave equation 24.4, or of the cavity equation, which will excite or drive the cavity mode amplitude.

Tilting the pellicle to the proper angle to reflect the external wave exactly along the cavity axis ensures that the polarization $p_e(r, t)$ in the pellicle volume will have exactly the optimum overlap integral with the cavity mode $u_n(r)$. Note also that the incident wave should have a transverse mode pattern and wavefront curvature which just matches the cavity transverse mode we want to excite.

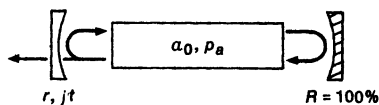
At the same time, the fields $\mathcal{E}(r, t)$ of the cavity mode, in passing through the same pellicle, will induce a similar dielectric polarization in the pellicle volume which will, in part, radiate out of the laser cavity, giving the external coupling out of the cavity illustrated in Figure 24.7. The same pellicle necessarily acts both to couple the external signal into the cavity and to couple internal energy from the cavity mode out of the cavity. Hence, there is a fundamental connection between the decay rate for external coupling or loss out of the cavity, and the coupling strength for coupling of an external signal into the cavity.

How to Calculate External Cavity Coupling and Signal Injection

Given a specific cavity geometry and pellicle geometry, we could calculate both the external coupling and the signal injection for a cavity model like Figure 24.7. This calculation would be somewhat subtle, however, and would require us to assume a specific cavity and coupling geometry (although the results would in fact turn out to be independent of the specific geometry). To analyze external cavity coupling in a manner which does *not* depend on the specific cavity geometry, we will follow instead a (possibly) simpler approach, in which we use the lumped equivalent circuit developed in the previous section as an analog model for analyzing an eternally coupled cavity.

That is, we will derive a general formula for external coupling and external signal injection effects in a resonant system *using the lumped circuit model with an external signal source*; and we will then assume that this same formula will apply equally well to a resonant optical cavity mode (as indeed it does). The

optical cavity



lumped equivalent circuit

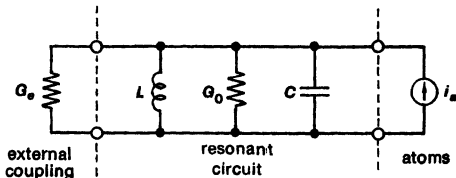


FIGURE 24.9
Circuit model to represent external cavity coupling.

resulting equation will be correct for essentially all types of optical cavities and coupling methods, even though it has been derived from a low-frequency lumped-circuit model.

Lumped Circuit Analysis of External Coupling

In order to follow this line of attack, we first recall that in a real optical cavity with round-trip internal power losses $2\alpha_0 p$ and with one partially transmitting end mirror having power reflectivity $R \equiv r^2$, the circulating energy in the cavity will decay in each round trip with a total energy decay rate γ_c given by

$$\gamma_c = \gamma_0 + \gamma_e = 2\alpha_0 c + \frac{1}{T} \ln(1/R). \quad (30)$$

where T is the round-trip transit time in the cavity. We are following the same convention as in earlier chapters by using the subscript o (for “ohmic”) to refer to internal cavity losses such as absorption or scattering losses; the subscript e to refer to external coupling effects; and the subscript c to refer to total cavity losses including both of these.

Now, an analogous external coupling can be added to the lumped circuit model of Figure 24.5 by adding an “external” conductance G_e across the lumped circuit, as in Figure 24.9, so that the total decay rate in the lumped circuit becomes

$$\gamma_c = \gamma_0 + \gamma_e = \frac{G_0 + G_e}{C}. \quad (31)$$

For the decay rates in the lumped circuit and the real cavity to remain matched, the additional or external conductance should have a value given by

$$G_e = \gamma_e C, \quad (32)$$

just as G_0 was given by $\gamma_0 C$. The conductance G_e then represents the external loading or the external coupling to the real optical cavity.

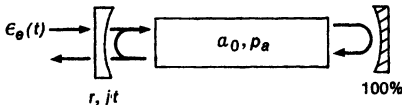
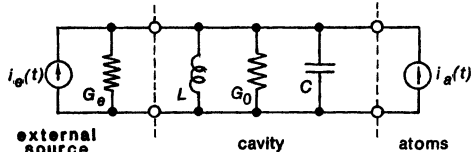


FIGURE 24.10
Circuit model to represent external coupling plus an external signal source.



External Signal Source in the Optical Cavity

Next suppose an externally generated signal wave of amplitude $\mathcal{E}_e(t)$ is sent into the laser cavity from some outside signal source (perhaps another laser), as shown in Figure 24.10, using $\mathcal{E}_e(t)$ to indicate the amplitude of the impinging wave *outside* the cavity mirror. We do not know, yet, how much of this wave will be reflected at the input and how much will be coupled into the cavity. We also assume that $\mathcal{E}_e(t)$ represents only that part of this signal that is properly transverse mode-matched so as to couple into the cavity mode under consideration. (Any remaining part of the incident signal that is not transversely mode matched to the cavity mode in question will have no effect on that mode, but will presumably couple into other transverse modes of the cavity.)

A lumped-circuit analog to such an external signal can then be obtained by adding an external current source $i_e(t)$ in parallel with the external conductance G_e , as shown in the lower part of Figure 24.10. We can relate the amplitude of this external current source $i_e(t)$ in the lumped circuit to the amplitude of the external wave $\mathcal{E}_e(t)$ in the real laser cavity by the following argument.

Suppose we normalize the external wave amplitude $\mathcal{E}_e(t)$ of this incident wave such that the *instantaneous* incident optical power being carried by this incident optical wave (in the mode-matched portion) is given by

$$P(t) \equiv 2\mathcal{E}_e^2(t). \quad (33)$$

We include the factor of 2 in this equation because $\mathcal{E}_e(t)$ will normally represent a quasi-sinusoidal wave, which we will write in the form $\mathcal{E}_e(t) \equiv \text{Re } \tilde{E}_e(t) e^{i\omega t}$; and we can then write the *time-averaged* power being carried by the external wave in the particularly simple form

$$P_{\text{av}} = \left| \tilde{E}_e \right|^2. \quad (34)$$

In electrical circuit jargon, P_{av} represents the *available power from the external source*, i.e., the maximum power that this wave could deliver to a totally absorbing and reflectionless surface.

The particular normalization used in Equations 24.33 and 24.34 is quite arbitrary, and could be chosen differently. Obviously this particular normalization

means that $\mathcal{E}_e(t)$ must be interpreted as an instantaneous normalized wave amplitude, rather than an optical E field. In particular, $E_n(t)$ and $\mathcal{E}_e(t)$ will have different dimensions, because we have chosen to relate them in different ways to the real optical E fields inside and outside the cavity.

External Signal Source in the Lumped Circuit

Now, in the lumped circuit analog of Figure 24.10, the available power from the source current generator $i_e(t)$ in parallel with the source conductance or external conductance G_e is the power which this external source could deliver to an optimum load conductance $G_{\text{load}} = G_e$. (This corresponds to a signal generator delivering power to a matched or nonreflecting load.) This available power from the parallel combination of $i_e(t)$ and G_e can be written as

$$P(t) = \frac{i_e^2(t)}{4G_e} \quad \text{or} \quad P_{\text{av}} = \frac{1}{8G_e} \left| \tilde{I}_e \right|^2, \quad (35)$$

where we again assume that $i_e(t)$ will probably be a quasi-sinusoidal signal in the form $i_e(t) = \text{Re} \tilde{I}_e(t) e^{j\omega t}$.

If we want the external signal source in the real cavity and the external signal source in the lumped circuit model to have the same available power, so that the lumped-circuit model will continue to be a good representation for the cavity, then we must match up Equations 24.33, 24.34, and 24.35 such that the lumped current source $i_e(t)$ will be related to the normalized external wave amplitude $\mathcal{E}_e(t)$ by

$$i_e(t) \equiv -(8G_e)^{1/2} \mathcal{E}_e(t). \quad (36)$$

The minus sign is entirely arbitrary and is inserted only for later convenience.

General Equation for an Externally Excited Cavity

When the external coupling and external signal source are added, Equation 24.23 for the lumped equivalent circuit is expanded to

$$\frac{d^2v}{dt^2} + \left(\frac{G_0 + G_e}{C} \right) \frac{dv}{dt} + \left(\frac{1}{LC} \right) v = \frac{1}{C} \left[\frac{di_a(t)}{dt} + \frac{di_e(t)}{dt} \right]. \quad (37)$$

If we convert this lumped circuit equation to optical-cavity quantities by using all the definitions that we have developed above, then the final result for the lumped circuit is

$$\frac{d^2E_n}{dt^2} + \gamma_c \frac{dE_n}{dt} + \omega_c^2 E_n = -\frac{1}{\epsilon} \frac{d^2P}{dt^2} + \left(\frac{8\gamma_e}{\epsilon V_c} \right)^{1/2} \frac{d\mathcal{E}_e}{dt}. \quad (38)$$

This was derived as a lumped-circuit equation, but it is now expressed entirely in terms of optical-resonator quantities. That is, all of the factors like L , G and C that are specific to the lumped circuit model have canceled out, and only parameters like γ_e , γ_c , ω_c and V_c that apply equally well to the optical cavity are left. We can therefore take Equation 24.38 as representing the general form of the equation of motion for an arbitrary optical cavity mode having internal losses, resonant atoms, external coupling, and an externally injected signal.

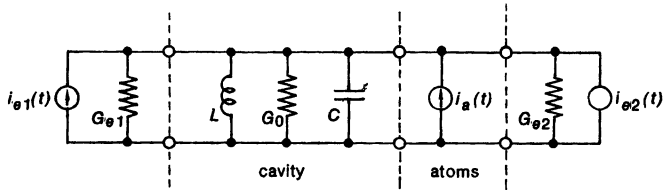
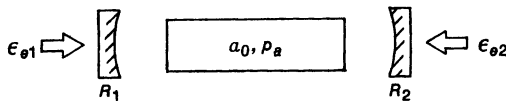


FIGURE 24.11

Circuit model to represent an optical cavity with multiple external coupling ports.

This equation, applied to any arbitrary form of external coupling into an optical or laser cavity, is the primary result of this section.

Discussion

A real optical cavity may have output coupling at several different points, the simplest example being two partially transmitting mirrors with power reflectivities R_1 and R_2 at the two ends of a laser cavity, as illustrated in Figure 24.11. Each such output coupling port must then be represented by a separate external conductance G_{e1} and G_{e2} , as illustrated in the lumped equivalent circuit. If necessary separate current sources $i_{e1}(t)$ and $i_{e2}(t)$ must also be added to represent external signals coming into both of these ports. The complete equation for the cavity mode in the two-port case then takes on the form

$$\frac{d^2 E_n}{dt^2} + \gamma_c \frac{d E_n}{dt} + \omega_c^2 E_n = -\frac{1}{\epsilon} \frac{d^2 P}{dt^2} + \left(\frac{8\gamma_{e1}}{\epsilon V_c} \right)^{1/2} \frac{d \mathcal{E}_{e1}}{dt} + \left(\frac{8\gamma_{e2}}{\epsilon V_c} \right)^{1/2} \frac{d \mathcal{E}_{e2}}{dt}, \quad (39)$$

where $\gamma_c = \gamma_0 + \gamma_{e1} + \gamma_{e2}$; the magnitude of each external conductance is related to the contribution of that output coupling port to the total external-coupling decay rate in the form $\gamma_{e,i} \equiv G_{e,i}/C$; and the external current sources are related to the incident external wave amplitudes by $i_{e,i}(t) = -(8G_{e,i})^{1/2} \mathcal{E}_{e,i}(t)$.

We emphasize again that the lumped circuit model and the cavity equation of motion that we have developed here represent only one cavity resonant mode—that is, if multiple cavity modes are active, each separate transverse and axial laser cavity mode needs a separate mode equation and a separate lumped-circuit model. If several modes are being excited or are oscillating in a real laser, a separate lumped circuit and a separate equation is required for each such mode. Each mode will then have separate mode amplitudes E_n and will in general have different values of internal loss γ_{0n} , external coupling γ_{en} , resonance frequency ω_n , and so forth.

An external signal $\mathcal{E}_e(t)$ must generally have a sinusoidal frequency close to some one cavity frequency ω_c in order to excite a significant response in that mode. In a general multimode analysis, the various frequency components

contained in a possibly broadband external signal $\mathcal{E}_e(t)$ will in general excite separately each of the different laser-cavity modes with which different frequency components are in resonance. To see just how an external signal will excite the cavity mode, and where the input power will go, the reader may want to consider the problems at the end of this section.

REFERENCES

The easiest way to obtain a simple yet general theory of external coupling to resonator modes is through a lumped equivalent circuit approach, as we have just done in this section. A more formal approach which treats coupling loops or holes between microwave cavities as delta-function polarization terms is outlined in standard books on electromagnetic theory. Two basic papers on this subject are H. A. Wheeler, "Coupling holes between resonant cavities or waveguides evaluated in terms of volume ratios," *IEEE Trans. MTT-12*, 231 (March 1964); and H. A. Bethe, "Theory of diffraction by small holes," *Phys. Rev. 66*, 163 (October 1966). A similar approach to external coupling in lasers, using a quasi transmission line approach, is developed by M. B. Spencer and W. E. Lamb, "Laser with a transmitting window," *Phys. Rev. A 5*, 884-892 (February 1972).

Developing a proper quantum theory of the fields in a laser cavity with finite output coupling is even more difficult, since the usual approach to quantization of electromagnetic fields relies on normal modes which are lossless as well as orthogonal. One approach is a one-dimensional cavity model with one 100% reflecting mirror, one lossless but partially transmitting mirror, and then another 100% mirror located a large distance outside the partially transmitting mirror. If this distance is sufficiently large, this system is something like a cavity coupling into free space, and yet we can expand the fields in the closely spaced resonant modes of the lossless region between the two 100% mirrors. This approach has been used, for example, in a series of papers by K. Ujihara, "Theory of a one-dimensional laser with output coupling—linear theory," *Japan. J. Appl. Phys. 15*, 1529-1541 (August 1976); and "Quantum theory of a one-dimensional laser with output coupling. I. through IV.," *Phys. Rev. A 12*, 148-158 (1975) through *Phys. Rev. A 20*, 1096-1104 (1979). The same approach is also used by R. Lang, M. O. Scully, and W. E. Lamb, Jr., in "Why is the laser line so narrow? A theory of single-quasi-mode operation," *Phys. Rev. A 7*, 1788-1797 (May 1973).

Problems for 24.2

1. *Power dissipation in an externally excited cavity.* Suppose a sinusoidal external signal of form $\mathcal{E}(t) = \text{Re } \tilde{E}_e e^{j\omega t}$ with ω equal to the cavity frequency ω_c is applied to a single-ended optical cavity like that discussed in the text, with the cavity having internal losses but, for simplicity, no atomic polarization p_a . Using the laser-cavity equation of motion developed in this section, solve for the steady-state amplitude of the cavity mode, and show that the time-average power P delivered to the internal cavity losses is

$$P = \frac{4\gamma_0\gamma_e}{(\gamma_0 + \gamma_e)^2} P_{\text{avail.}}$$

Verify that this is exactly the same as the power that would be delivered to the conductance G_0 in the equivalent circuit.

Note that when $\gamma_0 = \gamma_e$ the power dissipated inside the cavity becomes equal to the total available power in the external wave, which means that the optical cavity must have a “matched” input, i.e., it must have zero input reflection coefficient. Verify that a single-ended plane-wave interferometer with $\gamma_e = \gamma_0$ does indeed have a zero reflection coefficient looking into the partially transmitting mirror end from outside.

2. *Calculating regenerative cavity gain from the lumped equivalent circuit model.* Insert a negative conductance $-G_m$ connected across a lumped equivalent circuit like Figure 24.11, in parallel with the internal loss conductance G_0 , as a way of representing a laser gain medium inside a laser cavity. Then use this lumped equivalent circuit with external coupling at both ends, plus the internal gain and loss, as a circuit model to calculate the overall regenerative gain (below the oscillation threshold) for a signal coming in one coupling port and going out the other coupling port. Compare the result you obtain from this circuit model with the result obtained using a regenerative plane-wave amplifier model in earlier chapters, and identify the corresponding quantities in the lumped circuit and the regenerative laser cavity.
3. *Alternative derivation of the external coupling term.* Here is an alternative way of deriving the cavity equation of motion, including an external signal, by using another fairly general model. To do this, represent the laser cavity by a simple plane-wave interferometer of the type discussed in Chapter 11. Suppose for simplicity that no atomic polarization p_a is present; but suppose that an external signal wave at a carrier frequency close to one of the axial modes ω_q of the interferometer is incident on the partially transmitting mirror.

We can then say that the wave amplitude traveling to the right just inside the partial mirror, call it $\tilde{E}(t)$, at any instant of time is the sum of the incident wave $j\tilde{E}_e(t)$ being transmitted through the mirror at that same instant, plus the wave amplitude $\tilde{g}_{Ri}\tilde{E}(t - T)$ which left that point one cavity transit time T earlier, traveled around inside the cavity with net round-trip gain and phase shift \tilde{g} , and is being reflected from the partial mirror at time t .

Using the slowly varying envelope approximation plus the approximation that $\tilde{E}(t + T) \approx \tilde{E}(t) + (d\tilde{E}(t)/dt) \times T$, show that you can obtain the SVEA form of the cavity equation using this plane-wave or transmission-line type of model rather than the lumped-circuit model used in this chapter.

4. *Another alternative derivation of the external coupling term.* As still another alternative approach to the previous problem, use the plane-wave or interferometer model employed in earlier chapters to calculate the plane-wave amplitude $\tilde{E}(\omega)$ that will be produced inside an interferometer cavity by an external signal $\tilde{E}_e(\omega)$. This gives you the frequency domain transfer function between $\tilde{E}(\omega)$ and $\tilde{E}_e(\omega)$ at any frequency ω . Using this transfer function with suitable approximations, such as $\omega \approx \omega_q$, together with the standard Fourier transform theorems for the first and second time derivatives of a function, show how you can transform the frequency domain results into the full second-order cavity equation of motion for $E_n(t)$ and $E_e(t)$ derived in this section.

24.3 COUPLED CAVITY-ATOM EQUATIONS

The analysis developed in the preceding two sections, combined with the analyses in earlier chapters, has now given us a full set of coupled cavity and atomic equations that can be used to solve almost any practical laser problem. The purpose of this section and the following section is to combine these equations into a single set, using a unified and consistent notation, and then to show how the resulting set of equations can be simplified and approximated in various useful ways. These simplifications will include the *slowly varying envelope approximation* (SVEA) and the *phase-amplitude form of the equations*, as first introduced by Lamb, and a simplified set of *coupled cavity and atomic rate equations*.

Atomic Polarization Equation

The atomic polarization $p_a(\mathbf{r}, t)$ at any point inside a laser cavity will depend on the signal field $\mathcal{E}(\mathbf{r}, t)$ at that point and perhaps also, as we will see later, on various nonlinear and/or modulation effects occurring inside the cavity. In the simplest situation, for a two-level electric-dipole model as derived in earlier chapters, the atomic polarization at every point \mathbf{r} is coupled to the signal field by the resonant dipole equation of motion

$$\frac{\partial^2 p_a(\mathbf{r}, t)}{\partial t^2} + \Delta\omega_a \frac{\partial p_a(\mathbf{r}, t)}{\partial t} + \omega_a^2 p_a(\mathbf{r}, t) = \kappa \Delta N(\mathbf{r}, t) \mathcal{E}(\mathbf{r}, t), \quad (40)$$

with the constant κ given by

$$\kappa \equiv \frac{3^* \epsilon \lambda^3 \omega_a \gamma_{\text{rad}}}{4\pi^2}. \quad (41)$$

For simplicity we will ignore the tensor nature of the atomic response from here on, since the tensor properties complicate the algebra with little or no gain in physical significance.

Suppose we dot-multiply both sides of Equation 24.40 by one particular mode function $u_n(\mathbf{r})$ and integrate, using the orthonormality properties. The result is a scalar time-varying equation of motion

$$\frac{d^2 P_n(t)}{dt^2} + \Delta\omega_a \frac{dP_n(t)}{dt} + \omega_a^2 P_n(t) = \frac{\kappa}{V_c} \iiint_{\text{atoms}} \Delta N(\mathbf{r}, t) \mathcal{E}(\mathbf{r}, t) \cdot u_n(\mathbf{r}) d\mathbf{r}, \quad (42)$$

where $P_n(t)$ is the same polarization driving term as introduced in the cavity equations 24.17 and 24.18.

Equation 24.42 is still quite general, since it involves the total field $\mathcal{E}(\mathbf{r}, t)$ on the right-hand side. Note also that we must allow for the possibility that the population difference $\Delta N(\mathbf{r}, t)$ as well as the field $\mathcal{E}(\mathbf{r}, t)$ may both be functions of both space and time inside the laser cavity. Suppose, however, that only a single cavity mode $\mathcal{E}(\mathbf{r}, t) = E_n(t) u_n(\mathbf{r})$ is excited, or is oscillating. The right-hand side of Equation 24.42 can then be written as

$$\kappa E_n(t) \times \frac{1}{V_c} \iiint \Delta N(\mathbf{r}, t) u_n(\mathbf{r}) \cdot u_n(\mathbf{r}) d\mathbf{r} \equiv \eta_n \Delta N(t) E_n(t), \quad (43)$$

where $\Delta\mathcal{N}(t)$ is an average population difference density given by

$$\Delta\mathcal{N}(t) \equiv \frac{1}{V_c} \iiint_{\text{atoms}} \Delta N(\mathbf{r}, t) d\mathbf{r}. \quad (44)$$

This quantity is evaluated as if the total number of atoms $\iiint \Delta N(\mathbf{r}, t) d\mathbf{r}$ were uniformly distributed over the cavity volume V_c with a uniform density $\Delta\mathcal{N}(t)$; but then this average density must be multiplied by a filling factor η_n for the n -th mode given by

$$\eta_n \equiv \frac{\iiint \Delta N(\mathbf{r}, t) |\mathbf{u}_n(\mathbf{r})|^2 d\mathbf{r}}{\iiint \Delta N(\mathbf{r}, t) d\mathbf{r}}. \quad (45)$$

This dimensionless filling factor is always ≤ 1 and, together with $\Delta\mathcal{N}(t)$, takes account of the fact that the atoms may not be uniformly distributed inside the laser cavity.

In terms of these quantities the polarization equation (24.42) for any one resonant mode simplifies to

$$\frac{d^2 P_n(t)}{dt^2} + \Delta\omega_a \frac{dP_n(t)}{dt} + \omega_a^2 P_n(t) = \kappa_n \Delta\mathcal{N}(t) E_n(t), \quad (46)$$

where $\kappa_n \equiv \eta_n \kappa$. This equation represents the simplest but yet still fairly general form of the atomic polarization equation for the n -th cavity mode. The filling factor η_n describes how well the field pattern $\mathbf{u}_n(\mathbf{r})$ overlaps the distribution $\Delta N(\mathbf{r}, t)$ of atoms inside the cavity—for example, $\eta_n \rightarrow 0$ if atoms are located only where the fields are not, and $\eta_n \rightarrow 1$ if the atoms are located optimally where the fields are. The numerical value of η_n can in fact most conveniently be absorbed into the definition of the constant $\kappa_n \equiv \eta_n \kappa$, as we will do from now on.

Atomic Population Equation

Besides the polarization equation for $P_n(t)$, we also need an equation of motion for the population difference $\Delta\mathcal{N}(t)$. To derive this, suppose we define the zero level of energy for a two-level atomic system halfway between the lower and upper energy levels E_1 and E_2 , as we can always do. Then the energy density $U_a(\mathbf{r}, t)$ (per unit volume) associated with the energy level populations in the collection of atoms is

$$U_a(\mathbf{r}, t) = [N_2(\mathbf{r}, t) - N_1(\mathbf{r}, t)] \times \hbar\omega/2 = -\frac{1}{2} \Delta N(\mathbf{r}, t) \hbar\omega. \quad (47)$$

The rate of change of this energy density due to stimulated transitions caused by the cavity fields must be just the power density delivered by the signal fields to the atoms. But the power per unit volume delivered to the atoms at any point \mathbf{r} by the field $\mathbf{E}(\mathbf{r}, t)$ acting on the atomic polarization $\mathbf{p}_a(\mathbf{r}, t)$ is $\mathbf{E} \cdot \partial \mathbf{p}_a / \partial t$. Hence in the vicinity of any point \mathbf{r} the equation of motion, or rate equation, for the atomic population difference ΔN , with relaxation included, may be written as

$$\frac{d\Delta N(\mathbf{r}, t)}{dt} + \frac{\Delta N(\mathbf{r}, t) - \Delta N_0(\mathbf{r})}{T_1} = -\left(\frac{2^*}{\hbar\omega}\right) \mathbf{E}(\mathbf{r}, t) \cdot \frac{\partial \mathbf{p}_a(\mathbf{r}, t)}{\partial t}, \quad (48)$$

where T_1 is the effective population relaxation time for the two levels involved; and the factor 2^* depends upon whether the population “bottlenecks” in the

lower level (if so, $2^* = 2$), or whether atoms relax very rapidly out of the lower level to still lower levels (if so, $2^* = 1$).

Suppose we now expand both $\mathcal{E}(\mathbf{r}, t)$ and $\mathbf{p}_a(\mathbf{r}, t)$ in the cavity eigenmodes, and then integrate both sides of Equation 24.48 over the cavity volume. After using the orthogonality properties of the eigenmodes $\mathbf{u}_n(\mathbf{r})$, plus the definition of cavity-averaged atomic density $\Delta\mathcal{N}(t)$ just given in Equation 24.44, we find that Equation 24.48 reduces to

$$\frac{d\Delta\mathcal{N}(t)}{dt} + \frac{\Delta\mathcal{N}(t) - \Delta\mathcal{N}_0}{T_1} = -\frac{2^*}{\hbar\omega} \sum_n E_n(t) \frac{dP_n(t)}{dt}, \quad (49)$$

where the right-hand side is the sum over all cavity modes that are significantly excited. This is the simplest general form of the atomic population equation.

Final Result: The “Neoclassical Equations”

Suppose finally that only a single cavity mode is significantly excited, as can often happen in real laser systems. The complete cavity-plus-atom equations of motion for the laser can then be reduced to just three coupled differential equations connecting the cavity mode amplitude $E(t)$, the atomic polarization amplitude $P(t)$, and the population difference $\Delta\mathcal{N}(t)$ relevant to that particular cavity mode. (We can drop the subscripts n for simplicity).

These equations consist of the cavity equation, the atomic polarization equation, and the population difference equation, or

$$\begin{aligned} \frac{d^2E(t)}{dt^2} + \gamma_c \frac{dE(t)}{dt} + \omega_c^2 E(t) &= -\frac{1}{\epsilon} \frac{d^2P(t)}{dt^2} + \left(\frac{8\gamma_e}{\epsilon V_c} \right)^{1/2} \frac{d\mathcal{E}_e}{dt} \\ \frac{d^2P(t)}{dt^2} + \Delta\omega_a \frac{dP(t)}{dt} + \omega_a^2 P(t) &= \kappa \Delta\mathcal{N}(t) E(t) \\ \frac{d\Delta\mathcal{N}(t)}{dt} + \frac{\Delta\mathcal{N}(t) - \Delta\mathcal{N}_0}{T_1} &= -\frac{2^*}{\hbar\omega} E(t) \frac{dP(t)}{dt}. \end{aligned} \quad (50)$$

These three equations are used as the starting point for a great many laser analyses in the literature. They are sometimes called the “neoclassical formulation of laser theory” based on a series of theoretical papers by Jaynes, since they represent the simplest form of semiclassical quantum theory (i.e., the atoms are quantized, but the electromagnetic field is not) as applied to a single cavity mode and a two-level atomic system. They can in principle be solved with any given initial conditions, taking into account an external driving field $\mathcal{E}_e(t)$. Self-consistent solutions to Equations 24.50 can bring out nearly every significant classical and quantum feature of laser dynamics and of quantum electronic phenomena (except for noise phenomena), at both small and large signal levels.

Note that all the variables in Equations 24.50 are functions of time only, since all spatial variations have been eliminated by using the normal mode formulation. The essential parameters in Equations 24.50 are then the cavity decay rate γ_c , the atomic homogeneous linewidth $\Delta\omega_a$, the population recovery time T_1 , and the coupling coefficient κ between the cavity signal and the atoms. Note also that the arbitrary normalization constant V_c disappears from Equations 24.50, except for its role in establishing the amplitude of the externally injected signal term.

Equations 24.50 can be extended to multi-cavity-mode problems by writing separate cavity and polarization equations for the amplitudes E_n and P_n of each significant cavity mode; and then restoring the summation over these modes on the right-hand side of Equation 24.49. This still does not include, however, one potentially important aspect of multimode behavior, namely, the cross-coupling or cross-saturation effects between modes. If multiple modes are excited, interference effects between modes can cause the degree of saturation of $\Delta N(\mathbf{r}, t)$ to be significantly different at peaks or nulls of the multimode field pattern. This effect can be difficult to include in the preceding analysis, since it shows up primarily as a complicated intensity-dependent change in the filling factor η_n for each different normal mode, caused by changes in the spatial distribution of $\Delta N(\mathbf{r}, t)$. More complicated analytical approaches must be adopted when spatially varying saturation effects become important.

REFERENCES

A typical example of the use of the neoclassical equations is L. W. Davis, "Semiclassical treatment of the optical maser," *Proc. IEEE* 51, 76–88 (January 1963). A more involved discussion of the same topic appears in the article by E. T. Jaynes and F. W. Cummings, "Comparison of quantum and semiclassical radiation theories with application to the beam maser," *Proc. IEEE* 51, 89 (January 1963). In this article and other later publications, Jaynes argued that the neoclassical or semiclassical equations of motion, if solved properly in a fully self-consistent manner, could potentially predict spontaneous emission, Lamb shifts, and other phenomena commonly thought to require a full quantized electromagnetic field analysis. This argument is not now widely accepted, but for a time was heavily debated in the laser field. An article which references many earlier papers on the subject is H. M. Gibbs, "Test of neoclassical radiation theory: incoherent resonance fluorescence from a coherently excited state," *Phys. Rev. A* 8, 456 (July 1973).

24.4 ALTERNATIVE FORMULATIONS OF THE LASER EQUATIONS

The three coupled cavity-plus-atomic equations in Equation 24.50 can be manipulated and simplified into several other useful forms. Two of these forms involve the *slowly varying envelope approximation*, and the *phase-amplitude form* of the coupled equations, both of which are developed in this section.

Slowly Varying Envelope Approximation

Suppose we consider a single-mode laser, and assume, as is almost always reasonable, that the field amplitude $E(t)$ and the polarization $P(t)$ will both be quasi-sinusoidal quantities, with slowly varying amplitudes and phases referenced to some carrier frequency ω . We can then write the ac signal quantities in the slowly varying sinusoidal forms

$$E(t) = \frac{1}{2}[\tilde{E}(t)e^{j\omega t} + \text{c.c.}], \quad \text{and} \quad \mathcal{E}_e(t) = \frac{1}{2}[\tilde{E}_e(t)e^{j\omega t} + \text{c.c.}], \quad (51)$$

and also write the atomic polarization in the same form

$$P_n(t) = \frac{1}{2}[\tilde{P}(t)e^{j\omega t} + \text{c.c.}]. \quad (52)$$

The quantities $\tilde{E}(t)$, $\tilde{P}(t)$ and $\tilde{E}_e(t)$ are thus the slowly time-varying complex phasor amplitudes of these nearly sinusoidal quantities.

Suppose we introduce these expressions into the second-order differential equations for $E(t)$ and $P(t)$, and pick out only the $e^{j\omega t}$ terms on each side of the equations. The equation for $E(t)$, for example, with the external signal term left off for simplicity, then takes on the expanded form

$$\begin{aligned} \frac{d^2\tilde{E}(t)}{dt^2} + [2j\omega + \gamma_c] \frac{d\tilde{E}(t)}{dt} + [\omega_c^2 + \omega_c^2 - \omega^2] \tilde{E}(t) \\ = -\frac{1}{\epsilon} \left[\frac{d^2\tilde{P}(t)}{dt^2} + 2j\omega \frac{d\tilde{P}(t)}{dt} - \omega^2 \tilde{P}(t) \right] + \left(\frac{8\gamma_e}{\epsilon V_c} \right)^{1/2} \left[\frac{d\tilde{E}_e(t)}{dt} + j\omega \tilde{E}(t) \right]. \end{aligned} \quad (53)$$

We can eliminate or simplify a number of the terms in this equation, and in the corresponding equation for $P(t)$, by making the *slowly varying envelope approximation* or SVEA.

This approximation assumes that the time variations of the phasor amplitudes $\tilde{E}(t)$, $\tilde{E}_e(t)$ and $\tilde{P}(t)$ will all be slow compared to the optical carrier frequency ω , and that the cavity decay rate γ_c and the atomic linewidth $\Delta\omega_a$ will also be small compared to ω , ω_a or ω_c . In taking derivatives of the complex phasor amplitudes, therefore, as in Equation 24.53, we can order all of the terms according to the magnitudes

$$\left(\frac{d^2}{dt^2}, \gamma_c \frac{d}{dt}, \Delta\omega_a \frac{d}{dt} \right) \ll \left(\omega \frac{d}{dt}, \omega \gamma_c, \omega \Delta\omega_a \right) \ll (\omega^2, \omega_a^2, \omega_c^2), \quad (54)$$

where ω in the middle term means either ω , ω_c or ω_a . We then drop all the terms of second-order smallness (i.e., d^2/dt^2 or $\gamma_c d/dt$) with respect to terms of first-order or zero-order time variation. We also make the same resonance approximation as in earlier chapters, namely,

$$\omega^2 - \omega_a^2 = (\omega + \omega_a)(\omega - \omega_a) \approx 2\omega(\omega - \omega_a). \quad (55)$$

Finally, we can argue that the whole polarization term on the right-hand side of Equation 24.53 is inherently of first-order smallness, since this term basically represents a comparatively small gain and/or frequency pulling effect on the cavity due to the atoms. We can therefore drop both the $d^2\tilde{P}/dt^2$ and the $2j\omega d\tilde{P}/dt$ terms on the right-hand side as being of second or even third-order smallness, and keep only the $\omega^2\tilde{P}$ term on this side.

If we put all these approximations — which are in fact quite mild approximations — into Equations 24.50, the result is a pair of first-order but now complex equations for the phasor amplitudes $\tilde{E}(t)$ and $\tilde{P}(t)$, plus a modified population

equation for $\Delta\mathcal{N}(t)$, in the form

$$\begin{aligned} \frac{d\tilde{E}(t)}{dt} + [\gamma_c/2 + j(\omega - \omega_c)]\tilde{E}(t) &= -j\frac{\omega}{2\epsilon}\tilde{P}(t) + \left(\frac{2\gamma_e}{\epsilon V_c}\right)^{1/2}\tilde{E}_e(t) \\ \frac{d\tilde{P}(t)}{dt} + [\Delta\omega_a/2 + j(\omega - \omega_a)]\tilde{P}(t) &= -j\frac{\kappa}{2\omega}\Delta\mathcal{N}(t)\tilde{E}(t) \\ \frac{d\Delta\mathcal{N}(t)}{dt} + \frac{\Delta\mathcal{N}(t) - \Delta\mathcal{N}_0}{T_1} &= -j\frac{2^*}{4\hbar}[\tilde{E}(t)\tilde{P}^*(t) - \tilde{E}^*(t)\tilde{P}(t)]. \end{aligned} \quad (56)$$

These three equations are essentially as accurate as the second-order real-amplitude equations 24.50, but they are considerably easier to work with. Hence these simplified SVEA equations are also very widely used.

Discussion of the Slowly Varying Envelope Approximation

Despite its name, the “slowly varying” envelope approximation actually allows for quite fast variations in the complex phasor amplitudes $\tilde{E}(t)$ and $\tilde{P}(t)$. These quantities may have, for example, rapid rates of change compared to the atomic linewidth $\Delta\omega_a$ or to any of the various decay rates γ . The SVEA merely says that the amplitudes and phases of all quantities vary slowly with respect to the *optical carrier frequency ω itself*—and this is virtually always true. This means that the SVEA equations can still accurately describe coherent transients, Rabi frequency behavior, and other large-signal or fast-pulse effects (see Problems). They cannot, however, in their ordinary form, describe harmonic generation or similar effects occurring at totally different optical frequencies.

The reader should also note that in setting up the SVEA equations, the choice of the reference frequency or carrier frequency ω to use in expanding $E(t)$ and $P(t)$, as in Equations 24.51 and 24.52, is essentially arbitrary. As an elementary example to demonstrate this, suppose we use some arbitrary value of ω in writing these quantities, and then solve for the free decay of the cavity fields and the atomic polarization, ignoring the coupling terms on the right-hand sides of Equations 24.56. The solution for the cavity signal phasor will be

$$\tilde{E}(t) = \tilde{E}(0) \exp[-(\gamma_c/2)t - j(\omega - \omega_c)t]. \quad (57)$$

This says that the real cavity-mode amplitude will then oscillate and decay in the form

$$\begin{aligned} E(t) &= \tilde{E}(t) \exp[j\omega t] \\ &= \tilde{E}(0) \exp[-(\gamma_c/2)t - j(\omega - \omega_c)t + j\omega t] \\ &= \exp[-(\gamma_c/2)t + j\omega_c t]. \end{aligned} \quad (58)$$

In other words, the final solution for $E(t)$ will turn out to oscillate at the correct frequency ω_c regardless of the choice of the reference frequency ω used in the initial SVEA expansions. The reader can similarly demonstrate that the free oscillation of $P(t)$ will end up at the correct frequency ω_a , independent of the initial choice of ω .

In the more general situation where we are solving some real laser problem, we can choose any arbitrary value of ω anywhere near ω_c (or ω_a) to set up the SVEA expansion in Equations 24.51 and 24.52; and the SVEA equations will

automatically take this arbitrary choice of ω into account through the $\omega - \omega_a$ and $\omega - \omega_c$ terms in Equations 24.56. Suppose an external signal with some definite frequency ω_e is being applied to a laser. Then it will probably make the most sense to choose the reference frequency ω to be equal to the applied signal ω_e . Suppose on the other hand that the cavity is oscillating as a free-running laser oscillator with no injected signal, and the cavity frequency ω_c and the atomic transition frequency ω_a are not tuned to be equal to each other. Then, the actual oscillation frequency will lie somewhere between these two frequencies and will be initially unknown. The correct procedure in this case is to write all the equations using an initially unknown value of ω , and then solve these equations to calculate what the proper value of $\omega = \omega_{osc}$ should be (see Problems).

Phase-Amplitude Equations of Motion

It can be useful in certain situations to break the complex SVEA equations of motion for $\tilde{E}(t)$ and $\tilde{P}(t)$ into separate equations of motion for the amplitudes and the phases of these quantities. A particularly useful way of doing this was introduced in an important early laser analysis by Willis Lamb, Jr., and this form has since been widely copied.

In this modification the complex signal phasors in the SVEA equations are separated into their magnitudes and phases in the forms

$$\tilde{E}(t) \equiv E_c(t)e^{j\phi_c(t)} \quad \text{and} \quad \tilde{E}_e(t) \equiv E_e(t)e^{j\phi_e(t)}. \quad (59)$$

The atomic polarization $\tilde{P}(t)$ is then written in the slightly more subtle form

$$\tilde{P}(t) \equiv [C(t) - jS(t)] \times e^{j\phi_c(t)}, \quad (60)$$

The $C(t)$ and $S(t)$ functions in this equation evidently give the in-phase and quadrature components—that is, the “cosine” and “sine” parts—of the sinusoidal polarization $\tilde{P}(t)$. These in-phase and quadrature components are measured, however, not with respect to some absolute sine wave, but with respect to the instantaneous phase angle $\phi_c(t)$ of the sinusoidal cavity field $\tilde{E}(t)$ (which may itself be varying substantially with time). The $C(t)$ and $-jS(t)$ parts thus correspond, at least in the linear steady state, to the χ' or reactive and the χ'' or dissipative parts of the atomic susceptibility, respectively.

The SVEA equations from 24.56 now break up into five coupled purely real equations. These consist of the cavity phase and amplitude equations, namely,

$$\frac{dE_c(t)}{dt} + \frac{\gamma_c}{2}E_c(t) = -\frac{\omega}{2\epsilon}S(t) + \left(\frac{2\gamma_e}{\epsilon V_c}\right)^{1/2}E_e(t)\cos[\phi_c(t) - \phi_e(t)] \quad (61)$$

and

$$\frac{d\phi_c(t)}{dt} + \omega - \omega_c = -\frac{\omega}{2\epsilon}\frac{C(t)}{E_c(t)} - \left(\frac{2\gamma_e}{\epsilon V_c}\right)^{1/2}\frac{E_e(t)}{E_c(t)}\sin[\phi_c(t) - \phi_e(t)], \quad (62)$$

plus two equations for the real and imaginary parts of the atomic polarization, namely,

$$\begin{aligned} \left(\frac{d}{dt} + \frac{\Delta\omega_a}{2} \right) C(t) + \left(\frac{d\phi_c(t)}{dt} + \omega - \omega_a \right) S(t) &= 0 \\ \left(\frac{d}{dt} + \frac{\Delta\omega_a}{2} \right) S(t) - \left(\frac{d\phi_c(t)}{dt} + \omega - \omega_a \right) C(t) &= -\frac{\kappa}{2} \Delta\mathcal{N}(t) E_c(t), \end{aligned} \quad (63)$$

and finally the population equation

$$\frac{d\Delta\mathcal{N}(t)}{dt} + \frac{\Delta\mathcal{N} - \Delta\mathcal{N}_0}{T_1} = -\frac{1}{\hbar} E_c(t) S(t). \quad (64)$$

These five equations, though somewhat complicated in appearance, contain a large amount of useful information.

Discussion of the Phase-Amplitude Equations

We can see immediately, for example, that the cavity signal amplitude $E_c(t)$ is driven only by the $S(t)$ or quadrature component of the polarization $\tilde{P}(t)$ —which is the part proportional to χ'' . Similarly, the time-varying phase or frequency expression $d\phi_c(t)/dt + \omega$ is affected only by the in-phase polarization component $C(t)$, or the part proportional to χ' . The final or population equation also makes clear that power transfer from field to atoms involves only the field amplitude $E_c(t)$ times the quadrature component $S(t)$ and not the reactive component $C(t)$ of the polarization.

We can also see that the quantity $d\phi_c(t)/dt + \omega$ always appears in combination in these equations. This is another manifestation of the arbitrary nature for the choice of the reference frequency ω used in making the slowly varying envelope approximation in Equations 24.51 and 24.52. Choosing an incorrect (or inappropriate) value of ω for the initial expansion simply shows up as a compensating linear phase variation of $\phi_c(t)$ with time, which is the same thing as a frequency correction $d\phi_c(t)/dt$ added to ω . (Note also that when we speak of steady-state solutions to a laser problem, we generally mean that the time derivatives $d/dt \equiv 0$ for all *amplitude* quantities; but steady state can still mean $d\phi_c(t)/dt = \text{const}$, or $\phi_c(t) = \text{const} \times t$ for the *phase variation* in a steady-state solution.)

The phase-amplitude equations in the form given in Equations 24.61 to 24.64 were extensively used by Lamb and other authors in laser analyses and in mode-locking calculations in earlier years. They seem to have become less popular in recent years, as compared to the complex SVEA equations. We will use the cavity phase-amplitude equations later on, however, in the study of laser injection locking.

REFERENCES

The original reference on the phase-amplitude form of the laser equations is W. E. Lamb, Jr., "Theory of an optical maser," *Phys. Rev.* **134A**, 1429–1450 (June 15, 1964).

Another extensive discussion and summary of the coupled cavity and atomic equations, including external coupling, and the various ways these equations can be manip-

ulated is given in J. H. Shirley, "Dynamics of a simple maser model," *Am. J. Phys.* **36**, 949–963 (November 1968).

A quite different approach to the problem of a single resonant cavity mode coupled to a single resonant atom is presented in W. L. Lama and L. Mandel, "Source-field approach to the two-level atom in a closed cavity," *Phys. Rev. A* **6**, 2247 (1972).

The slowly varying envelope approximation raises the more general issue of the best way to chose the carrier frequency ω and the complex phasor amplitude $\tilde{E}(t)$ if we want to write a known quasi-sinusoidal signal $E(t)$ in complex phasor form, since specifying a definite real quasi-sinusoidal function does not by itself uniquely determine either the time-varying amplitude or phase for the phasor representation of that function. An analytical procedure which will accomplish this in an optimum manner, according to certain reasonable criteria, is the *analytical signal approach*, first introduced by D. Gabor in "Theory of Communication," *Proc. IEE (London) Ser. 3* **93**, 429–457 (1956).

This approach has since been widely adopted in communication theory, in coherence theory, and in optics, for example, in A. Papoulis, *Systems and Transforms With Applications to Optics* (McGraw-Hill, 1968), p. 83. A recent comment on its use versus alternative formulations is given in L. Mandel, "Carrier frequency and envelope of an electromagnetic wave," *J. Opt. Soc. Am.* **71**, 362–363 (March 1981).

Problems for 24.4

1. *Obtaining previous results using the SVEA equations.* Verify that you can obtain the same results as derived in Chapters 2 and 5 for (a) the complex atomic susceptibility $\tilde{\chi}(\omega)$ and (b) the Rabi frequency ω_R , starting from the SVEA form of the atomic equations.
 2. *Obtaining previous results using the phase-amplitude equations.* Obtain the same results as in the previous problem, including the lorentzian lineshape response for an atomic transition, by using the phase-amplitude form of the cavity-atomic equations. (b) Obtain the Rabi frequency for the same transition from the same equations.
 3. *Calculating atomic response from the phase-amplitude equations.* Assume a strong signal field of amplitude E_0 tuned to the atomic transition frequency (i.e., $\omega = \omega_a$) is suddenly turned on and applied to an atomic transition starting at $t = 0$. Using Lamb's phase-amplitude, but neglecting the reaction of the atoms back on the field (that is, ignoring the cavity equations of motion), calculate the induced response of the atoms in the most general situation (including finite T_1 and T_2) and discuss the form of the resulting atomic motion in small and large-signal situations. (Your solutions will then represent an extension to a slightly higher degree of approximation of the Rabi frequency solutions presented in an earlier chapter.)
-

24.5 CAVITY AND ATOMIC RATE EQUATIONS

In the simplest limit of all, the coupled cavity-plus-atomic equations derived in the preceding sections can be reduced to a pair of *coupled cavity and atomic rate equations* which we will now derive. These rate equations, although valid only

within certain approximations, provide a simple and very useful way of analyzing many significant laser phenomena with more than adequate accuracy, including spiking, Q -switching, mode locking (in most situations), laser power output, and laser threshold behavior.

Cavity Photon Number and Cavity Energy Equation

As a first step we express the electromagnetic signal energy contained in a laser-cavity mode in units of $\hbar\omega$, which is to say, we consider the *number of photons* $n(t)$ in the cavity as defined by

$$n(t) \equiv \frac{\text{cavity energy}}{\hbar\omega} = \frac{\epsilon}{2\hbar\omega} \iiint |\mathcal{E}(\mathbf{r}, t)|^2 d\mathbf{r}. \quad (65)$$

Note that in discussing the number of photons here, we are *not* implicitly assigning any “billiard-ball” particle properties to photons. We are merely expressing the signal energy in the cavity in the convenient units of $\hbar\omega$.

For a single cavity mode with electric field given by $\mathcal{E}(\mathbf{r}, t) = E_n(t)\mathbf{u}_n(\mathbf{r})$ and $E(t) = \frac{1}{2}[\tilde{E}(t)e^{i\omega t} + \text{c.c.}]$, the cavity energy oscillates at frequency 2ω back and forth between the electric and magnetic fields. To obtain the total or time-averaged energy in the cavity, therefore, we must evaluate the integral in Equation 24.65 using either the peak value of $E_n(t)$ (corresponding to those instants in the cycle when all the energy in the cavity is in electric form), or else use twice the time-averaged value of the E -field integral (to account for electric power plus magnetic stored energies).

From either argument the cavity photon number in a given cavity mode is given by

$$n(t) = \frac{\epsilon V_c}{2\hbar\omega} |E_n(t)|_{\text{peak}}^2 = \frac{\epsilon V_c}{2\hbar\omega} |\tilde{E}(t)|^2. \quad (66)$$

If we differentiate Equation 24.66 with respect to time and use the SVEA cavity equation (24.56) for the cavity field $\tilde{E}(t)$, we can show that the rate of change of $n(t)$ is given by

$$\frac{dn(t)}{dt} + \gamma_c n(t) = j \frac{V_c}{4\hbar} \left[\tilde{E}(t)\tilde{P}^*(t) - \tilde{E}^*(t)\tilde{P}(t) \right]. \quad (67)$$

The γ_c term obviously represents photon decay due to cavity losses plus output coupling, whereas the term on the right-hand side gives the time-averaged energy flow (in photon units) delivered by the atomic polarization to the cavity fields. The external signal term has been dropped because external driving signals to a cavity cannot in general be properly accounted for in a purely rate equation analysis.

Atomic Population Equation

If we multiply the average population density $\Delta\mathcal{N}(t)$ by the cavity volume V_c , we get the *total number of atoms* $\Delta N(t) \equiv V_c\Delta\mathcal{N}(t)$ in the cavity. The atomic population equation for this quantity then becomes

$$\frac{d\Delta N(t)}{dt} + \frac{1}{T_1}[\Delta N(t) - \Delta N_0] = -j \frac{2^*V_c}{4\hbar} \left[\tilde{E}(t)\tilde{P}^*(t) - \tilde{E}^*(t)\tilde{P}(t) \right]. \quad (68)$$

The right-hand side of this equation has exactly the same form as in the cavity rate equation 24.67, as it must, since the right-hand side of each equation represents energy flow from the atoms to the fields, or vice versa. The only difference is the factor of 2^* , which we have explained earlier. Note also that the cavity equation for $n(t)$ is not really an independent addition to our earlier set of three coupled Equations 24.56, since it contains no new information over and above the cavity equation for $E_n(t)$ or $\tilde{E}(t)$.

Conversion to Coupled Rate Equations

In many real situations the atomic linewidth $\Delta\omega_a$, which gives the dephasing rate or decay rate for any coherent atomic polarization $P_{\text{tilda}}(t)$, is much faster than the decay rate for the cavity fields, i.e., $\Delta\omega_a \gg \gamma_c$. Even if this is not true, it may still be true that the linewidth $\Delta\omega_a$ is large compared to the rate of change $|d\tilde{E}/dt|$ of the cavity field phasor \tilde{E} . If either of these conditions holds true, this means physically that the transient response time $T_2 \equiv 1/\Delta\omega_a$ with which the polarization $\tilde{P}(t)$ will follow any variation in $\Delta N(t)\tilde{E}(t)$ will be much faster than the rate of variation of the quantity $\tilde{E}(t)$ itself. In other words, the complex polarization $\tilde{P}(t)$ will follow the complex cavity field $\tilde{E}(t)$ with negligible delay on the time scale of variations in $\tilde{E}(t)$.

Within this approximation, which is essentially the linear-susceptibility or rate-equation approximation, we can assume that $\tilde{P}(t)$ will be related to $\tilde{E}(t)$ by the steady-state solution to the SVEA polarization equations, or

$$\tilde{P}(t) \approx -j \frac{2\kappa}{\Delta\omega_a} \frac{1}{1 + 2j(\omega - \omega_a)/\Delta\omega_a} \Delta N(t) \tilde{E}(t). \quad (69)$$

If we put this result into the right-hand sides of the two rate equations 24.67 and 24.68, we will find that both right-hand sides have the form

$$j \frac{V_c}{4\hbar} \left[\tilde{E}(t)\tilde{P}^*(t) - \tilde{E}^*(t)\tilde{P}(t) \right] = -\frac{\kappa V_c}{2\hbar\Delta\omega_a} \frac{\Delta N(t)}{1 + [2(\omega - \omega_a)/\Delta\omega_a]^2} |\tilde{E}(t)|^2. \quad (70)$$

Given the connection between the photon number $n(t)$ and $|\tilde{E}(t)|^2$, we can simplify this further into the form

$$j \frac{V_c}{4\hbar} \left[\tilde{E}(t)\tilde{P}^*(t) - \tilde{E}^*(t)\tilde{P}(t) \right] = -K \Delta N(t) n(t), \quad (71)$$

where the constant K appearing in Equation 24.71 is the same rate-equation K value derived in earlier chapters (note that this constant includes a lorentzian lineshape dependence on the frequency ω).

Hence we obtain, finally, the pair of particularly simple coupled first-order differential equations, namely,

$$\begin{aligned} \frac{dn(t)}{dt} + \gamma_c n(t) &= -K \Delta N(t) n(t) \\ \frac{d\Delta N(t)}{dt} + \frac{\Delta N(t) - \Delta N_0}{T_1} &= -2^* K \Delta N(t) n(t). \end{aligned} \quad (72)$$

These are the coupled rate equations connecting the cavity photon number $n(t)$ and the effective number of absorbing atoms $\Delta N(t)$ in the cavity. These equations state the physically reasonable fact that—within the rate-equation

approximation—the rates of change of $n(t)$ and $\Delta N(t)$ will be proportional to their respective relaxation terms, plus a *stimulated transition term* which is proportional to the product of the number of photons $n(t)$ acting on the population difference $\Delta N(t)$. These rate equations are very widely useful for a broad range of laser problems, including spiking, Q -switching, laser amplitude modulation, and laser mode-locking, where the underlying rate-equation approximation remains valid.

Note that these rate equations discard all knowledge of the phase angles of either the atomic polarization or the cavity field, except for the implicit assumption that $\tilde{P}(t)$ remains coherently driven by $\tilde{E}(t)$. The benefit gained, on the other hand, is simplification to a pair of real, first-order, only slightly nonlinear equations to be solved. We will make extensive use of these equations in subsequent sections.

An Alternative Formulation: Radiative Damping

There is also an opposite limiting situation, considered by Tang and others, in which the cavity mode has a very rapid energy-decay rate and hence a wide bandwidth, whereas the atomic resonance transition is very sharp or narrow, so that the relevant condition is $\gamma_c \gg \Delta\omega_a$. In this limit we can assume that the cavity field $\tilde{E}(t)$ follows the polarization $\tilde{P}(t)$ on a nearly instantaneous basis, rather than the opposite condition as assumed in the preceding paragraphs. In physical terms, the atomic polarization serves as a kind of flywheel, dragging the cavity field along with it, rather than the cavity fields predominantly forcing the atomic oscillations to follow as in the usual rate-equation limit.

In this limit we can solve the SVEA cavity equation of motion in steady-state form, with an atomic polarization present but with no externally applied signal, to get the on-resonance relationship

$$\tilde{E}(t) \approx -j \frac{\omega}{\gamma_c \epsilon} \tilde{P}(t). \quad (73)$$

This is equivalent to assuming that the cavity fields are generated by radiation from the atomic polarization and not by anything else, particularly not by any externally applied signal.

Putting this result into the SVEA polarization equation 24.56 then yields the modified equation

$$\frac{d\tilde{P}(t)}{dt} + \left[\frac{\Delta\omega_a}{2} + \frac{\kappa\omega\Delta N}{2\gamma_c \epsilon} + j(\omega - \omega_a) \right] \tilde{P}(t) = 0. \quad (74)$$

For the noninverted population situation, $\Delta N > 0$, this says that the usual decay or dephasing rate $\Delta\omega_a/2$ for the polarization $\tilde{P}(t)$ is increased by an additional term proportional to ΔN and to the coupling factor κ between the polarization and the cavity. This additional term represents essentially a speeded-up decay of the polarization because $\tilde{P}(t)$ radiates energy into the cavity fields, from where this energy decays more or less instantaneously into the cavity losses. Hence this effect, which occurs only in this special limiting case, is commonly called *radiation damping* from the atoms into the cavity.

This special form of radiation damping represents an increased or extended form of the free-space radiative decay rate γ_{rad} associated with radiating atoms that we discussed in an early chapter of this book. That is, we can recall that for atoms in free space, γ_{rad} is the physical mechanism by which the atoms

radiate away energy to their surroundings. When such atoms are placed inside a sufficiently high- Q cavity, the polarization $\mathbf{p}(\mathbf{r}, t)$ associated with the oscillating atomic dipoles sees a significantly different radiation impedance, because the cavity in effect responds to the radiated fields and reflects them back at the atoms. The radiative decay rate can then be increased because the dipoles are radiating into a cavity impedance which is better matched than simply radiating into free space.

This kind of increased radiative damping is not usually of significance in practical lasers, and we will not have occasion to solve any practical laser problems using this alternative approximation. Significant increased radiative damping can occur in special situations, however, both in certain optical spectroscopy experiments and in low-frequency magnetic resonance experiments (where the concept of radiation damping first originated). Frequency standards and atomic clocks are another example where an atomic transition with a very narrow resonance line may interact with a resonant cavity with a substantially wider cavity linewidth, so that cavity-increased radiative damping can be significant.

REFERENCES

The two limiting situations discussed in this section, of rapid polarization response (rate-equation limit) and of rapid cavity response (radiative damping limit), are also derived and discussed in some detail by C. L. Tang, "On maser rate equations and transient oscillations," *J. Appl. Phys.* **34**, 2935–2940 (October 1963).

The concept of radiation damping of oscillating atoms in cavities was introduced by N. Bloemberger and R. V. Pound, "Radiation damping in magnetic resonance experiments," *Phys. Rev.* **95**, 8–12 (July 1 1954). Other early papers on the same topic include S. Bloom, "Molecular ringing," *J. Appl. Phys.* **27**, 785–788 (July 1956); S. Bloom, "Effects of radiation damping on spin dynamics," *J. Appl. Phys.* **28**, 800–805 (July 1957); and C. Greifinger and G. Birnbaum, "Super-radiation and super-regeneration," *IRE Trans. on Electron Devices ED-6*, 288–293 (July 1959).

More recent references, and an experimental confirmation of radiation damping effects on the spontaneous emission rate of a single atom in a cavity are given in P. Goy, J. M. Raimond, M. Gross, and S. Haroche, "Observation of cavity-enhanced single-atom spontaneous emission," *Phys. Rev. Lett.* **50**, 1903–1906 (June 13, 1983).

A somewhat different approach to describing how the electromagnetic fields produced by a radiating atom will react back on the same atom is given by P. W. Anderson, "The reaction field and its use in some solid-state amplifiers," *J. Appl. Phys.* **28**, 1049–1053 (September 1957).

Problems for 24.5

1. *Deriving the rate equations from the phase-amplitude equations.* Derive the coupled cavity-atom rate equations developed in this section starting from the Lamb phase-amplitude equations developed in Section 24.5.
-

LASER SPIKING AND MODE COMPETITION

In this and the following several chapters we will discuss the transient or dynamic behavior of laser oscillators, especially in response to different kinds of internal modulation. Lasers exhibit several different kinds of characteristic transient or modulation behavior, with some of the most important being:

(a) *Spiking, relaxation oscillations, and gain switching.* These terms all refer to similar kinds of comparatively slow but often large-amplitude relaxation oscillations that are exhibited by many (though not all) kinds of lasers, either when the laser is first turned on, or when the laser is suddenly perturbed by any kind of small fluctuation in gain, cavity loss, or cavity alignment. We will discuss these spiking effects and some related modulation effects in the present chapter.

(b) *Internal Amplitude and Phase Modulation.* This refers usually to internal amplitude or phase modulation applied inside the laser cavity, in such a way as to modulate the oscillation amplitude or frequency of the laser, most commonly at modulation rates which fall within the cavity bandwidth of a single cavity axial mode, so that the resulting modulation spectrum is narrow compared to the spacing between axial modes in the laser.

(c) *Laser Frequency Switching.* This is a very useful technique, which we will describe later in this chapter, in which the instantaneous frequency of a laser can be switched, within one cavity round-trip time, to a completely new value which can be a large distance—even several times the axial mode spacing—away from the initial oscillation frequency.

(d) *Q-Switching.* Q-Switching is a very useful technique employed in many lasers to obtain relatively short and very high-power output pulses. In order to Q-switch a laser, the losses in the cavity are initially held at a very high level, for example, by rotating one end mirror out of alignment, or by inserting a high-loss modulator into the cavity. This prevents the laser from oscillating as the laser pumping process pumps the inversion up to a very high value. The cavity Q in this situation is said to be “spoiled.”

After the population inversion and laser gain have been built up to a high value, the cavity Q is suddenly switched or restored to a low loss value. The laser oscillation in the cavity then builds up very rapidly, and the laser delivers nearly all its energy in a single short, high-intensity burst. This Q-switched mode of operation can be extremely useful, and we will analyze it at some length in the following chapter.

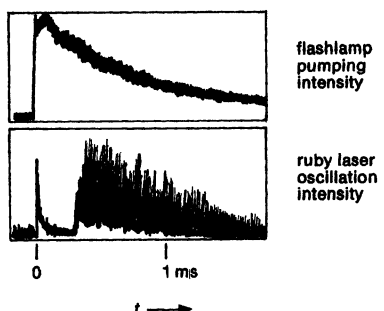


FIGURE 25.1
Spiking behavior in the first ruby laser.

(e) *Laser Cavity Dumping.* This is a technique (sometimes applied in conjunction with either *Q*-switching or mode locking) in which an intracavity light modulator is used to suddenly “open up” the output coupling from the laser cavity, thereby suddenly “dumping” out most or all of the stored optical energy in the cavity, rather than letting this energy come out gradually through a partially transmitting output mirror.

(f) *Mode locking.* Mode locking is another very useful technique in which many simultaneously oscillating axial modes in a laser cavity are locked or coupled together, using an intracavity modulator driven at the axial mode spacing frequency, in order to produce very rapid modulation of the laser output. This mode-locked output usually takes the form of extremely short optical pulses, which circulate around inside the cavity and emerge through one end mirror at a repetition rate corresponding to the round-trip transit time inside the laser cavity. There also exist other less common forms of mode coupling which lead to fast frequency modulation rather than pulsed behavior of the laser oscillation. Laser mode locking will also be discussed at length in later chapters.

In this chapter we will analyze the first three of the above laser modulation techniques; also, because it seems to fit naturally here, we will discuss the competition that may occur between two simultaneously oscillating modes in a laser cavity. In later chapters we will then discuss the remaining topics of *Q*-switching and mode locking in considerable detail, and also analyze the additional and very useful technique of injection locking as applied to laser oscillators.

25.1 LASER SPIKING AND RELAXATION OSCILLATIONS

As soon as the first ruby laser was operated, it was immediately evident that this laser did not wish to oscillate smoothly or continuously during the 1 millisecond or so duration of the pumping flash. Figure 25.1 shows in fact the pumping flash, and the extremely irregular and unstable laser oscillation that resulted, as reported in one of the publications by T. H. Maiman on the first successful operation of the ruby laser. (The initial transient in the laser output trace is electrical leakage from the flashlamp trigger circuitry.)

More careful examination of this laser output intensity on an expanded time scale, using a faster photodetector and oscilloscope, showed that the ruby laser output typically consisted of an irregular sequence of sharp narrow pulses or

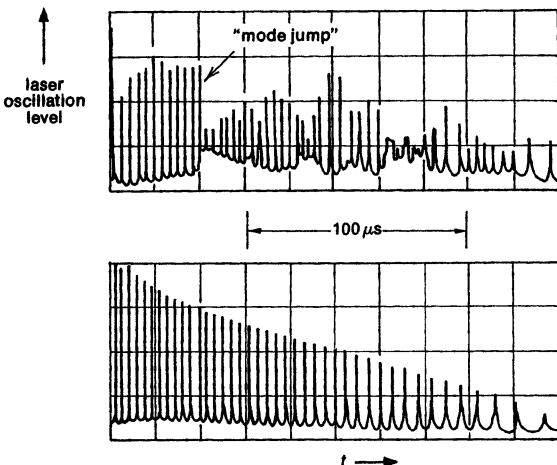


FIGURE 25.2
Ruby laser spiking on an
expanded time-scale.

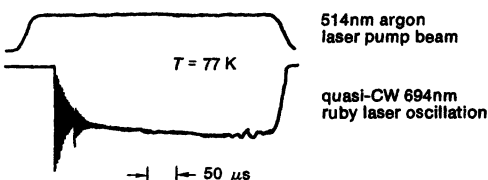


FIGURE 25.3
Attenuated spiking behavior in a
low-temperature cw ruby laser.

"spikes," each a fraction of a microsecond wide and a few microseconds apart, as illustrated in Figure 25.2. Sometimes the spiking behavior jumped erratically and discontinuously as in the upper trace, due presumably to fluctuations or mode jumps in the laser itself; whereas under more stable conditions the spiking behavior appeared to gradually damp out as in the lower trace (which is taken in the trailing edge of the pumping flash).

The ruby laser, for a variety of reasons—primarily because it is a three-level solid-state laser—almost always tends to spike in this very strong and irregular fashion, although under special conditions even ruby laser spiking can be controlled. Figure 25.3 shows, for example, the pumping pulse (upper trace) and the output intensity (lower trace) from a very small ruby laser which is operated under very well-controlled quasi-cw conditions at liquid nitrogen temperature (77 K) and end-pumped by a 514.5 nm beam from a cw argon laser. The laser exhibits a strong spiking response when it first comes on, but this spiking behavior rapidly damps out (with only one visible "glitch") into an essentially cw oscillation.

It was soon found that other and better disciplined four-level solid-state lasers also exhibited a similar spiking behavior when they were first turned on. The initial spiking in these other lasers, however, almost always damps down fairly quickly into a decaying quasi-sinusoidal relaxation oscillation in the laser power

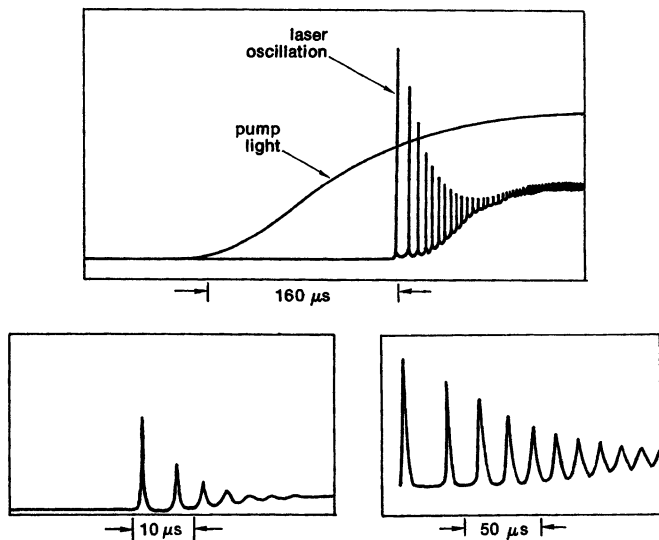


FIGURE 25.4
Spiking turn-on behavior in three typical Nd:YAG lasers.

output. This behavior is well-illustrated in Figure 25.4, which shows typical transient turn-on behavior for three different Nd:YAG lasers.

Large-Amplitude Spiking Versus Relaxation Oscillations

Most lasers that exhibit such spiking, in fact, if they are operated with stable power supplies and in a quiet and stable environment, will eventually settle down to a fairly constant output intensity. Even in this limit, however, any small perturbation, such as a sudden change in pumping rate or cavity loss, will trigger a transient relaxation oscillation of the same general character, which will again die away exponentially in the same oscillatory fashion.

The terminology used to describe this kind of transient laser behavior is not entirely uniform in the laser literature. We will generally use the term "spiking" to refer to the discrete, sharp, large-amplitude pulses that typically occur during the initial turn-on phase of many lasers. We will then use "relaxation oscillations" to describe the small-amplitude, quasi-sinusoidal, exponentially damped oscillations about the steady-state amplitude which occur when a continuously operating laser is slightly disturbed, or into which the initial spiking behavior generally evolves.

Spiking and relaxation oscillations are phenomena that are characteristic of most solid-state lasers, semiconductor lasers, and certain other laser systems in which the recovery time of the excited state population inversion is substantially longer than the laser cavity decay time. Most gas lasers do not satisfy this necessary condition, and as a result spiking and relaxation oscillations are not generally observed in most gas lasers.

Laser Rate Equations

Spiking is an example of laser behavior that can be accurately described using a very simple set of single-mode, single-atomic-level rate equations for the laser. Let us write these equations once again as an equation for the cavity photon number

$$\frac{dn(t)}{dt} = KN(t)n(t) - \gamma_c n(t), \quad (1)$$

and an equation for the population inversion

$$\frac{dN(t)}{dt} = R_p - \gamma_2 N(t) - KN(t)n(t). \quad (2)$$

We are as usual describing the oscillation amplitude in the laser cavity by the photon number $n(t)$ in the oscillating mode, and the instantaneous population inversion by the upper level population or population inversion $N(t)$. The pump rate for the laser inversion is then R_p and the atomic decay rate is γ_2 .

These two coupled equations are nonlinear because of the product term $KN(t)n(t)$ in each equation; and it is therefore not surprising that they may under certain conditions exhibit relaxation oscillations in their evolution toward a steady-state. In fact, these two equations will describe both spiking and relaxation oscillations with more than adequate accuracy in nearly all four-level laser systems. There do not seem to be, however, any simple analytic solutions to Equations 25.1 and 25.2 that apply during the period of strong spiking, when both the population $N(t)$ and particularly the cavity photon number $n(t)$ are changing in a rapid and quite nonlinear fashion.

Elementary Description of Laser Spiking

A reasonably accurate description of the spiking process when a solid-state laser is first turned on can be given by following the graphical argument illustrated in Figure 25.5, which shows the time evolution of a single laser spike. In Figure 25.5 we suppose that the pumping intensity has been turned on somewhat earlier, so that the population inversion $N(t)$ is passing up through the threshold value N_{th} at the starting time t_1 shown in this diagram, whereas the photon number in the laser cavity is still essentially zero at this time. (Note that the buildup time for the population inversion to first reach threshold in solid-state lasers is typically on the order of several hundred microseconds or longer.)

So long as the population inversion $N(t)$ is below the threshold value N_{th} (which represents also the steady-state oscillation value), the photon density in the laser cavity remains essentially at zero (or more accurately at roughly one noise photon per cavity mode). As soon as the population inversion passes through the threshold value N_{th} , however, at time t_1 in the figure, the laser gain then exceeds the loss and the photon number in the cavity begins to build up exponentially from noise.

The exponential growth rate for this build-up is $[N(t)/N_{th} - 1]\gamma_c$, where γ_c is the cavity decay rate as defined earlier, and $N(t)/N_{th}$ is the instantaneous ratio of laser gain to cavity loss. This ratio is continually increasing, as the pump pushes the population inversion further above threshold. The e -folding time for build-up of the photon number $n(t)$ is thus on the order of the cavity decay time τ_c or thereabouts, which might be several tens of nanoseconds in a typical laser cavity. The cumulative time for the cavity photon number to build up from the

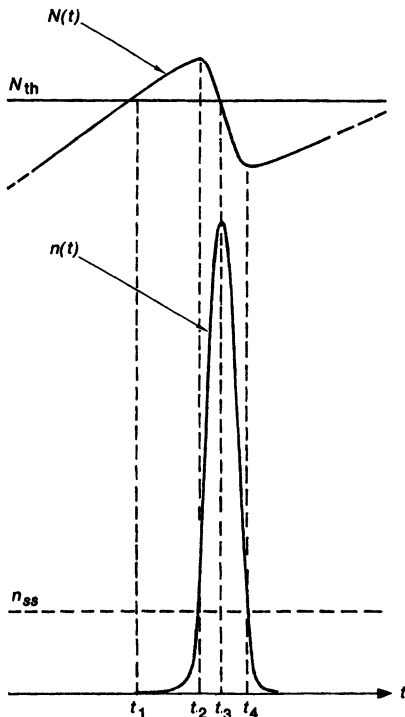


FIGURE 25.5
Chronology of a single laser spike.

initial noise level to an observable output signal corresponding to perhaps 10^8 to 10^{10} photons in the cavity is 20 to 30 times longer than this, in the range of hundreds of nanoseconds to perhaps a few microseconds in typical lasers. The buildup rate for $n(t)$ due to stimulated emission may thus be hundreds of times faster than the buildup rate for $N(t)$ produced by the pumping process.

As soon as the cavity photon number $n(t)$ passes through the steady-state oscillation level n_{ss} —that is, the level which would correspond to continuous steady-state operation in that laser at that pumping rate—the signal intensity in the cavity is large enough to begin burning up excited state atoms at a faster rate than the pump supplies them. Beyond time t_2 in Figure 25.5, therefore, the population inversion $N(t)$ no longer continues to rise, but rather begins to be pulled rather rapidly downward. The population inversion $N(t)$ still exceeds the steady-state value N_{th} , however; so the net gain in the cavity continues to be greater than unity. The cavity photon number therefore continues to rise rapidly. In fact, it is only the last portion of this rise over many orders of magnitude that will be visible on a linear plot, or on a linear oscilloscope display.

The point at which the population inversion $N(t)$ comes back just to the threshold or steady-state value N_{th} , so that gain just equals loss, is also the point at which the photon density $n(t)$ reaches its peak value (time t_3 in the figure) and then begins to fall back downward. There is still a large signal intensity circulating around inside the laser cavity and burning up excited state atoms,

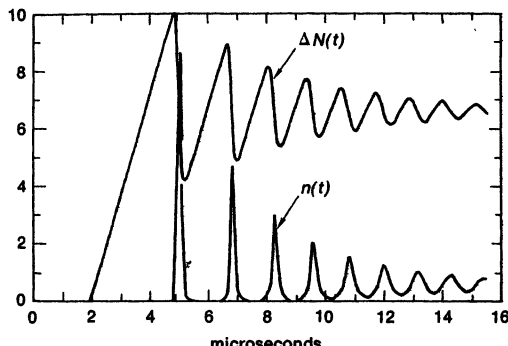


FIGURE 25.6
Computer simulation of laser spiking.

however, so that the population inversion $N(t)$ continues to be driven downward below the steady-state level. The laser gain is now less than the cavity losses, however, so that there is a net loss in the laser cavity. The photon number $n(t)$ therefore drops back down precipitously.

The point where $n(t)$ again reaches the steady-state oscillation level (point t_4 in the figure) is also the point at which the population inversion reaches a minimum, after which the pump can again begin to build up the population inversion toward threshold. The photon number $n(t)$ continues to decrease down to negligible values, however, so the pumping back up of the population inversion by the pump source occurs essentially independently of the photon number in the cavity.

The laser spikes are thus steep and narrow, because of the rapid rates of rise and fall of the photon number $n(t)$ in the cavity, with these rates being related to the cavity decay rate γ_c . The spacing between pulses is somewhat longer, because it is determined by the more lethargic manner in which the pumping source is able to replenish the net population inversion $N(t)$.

This kind of large-signal spiking behavior eventually damps down in most lasers toward a quasi-sinusoidal relaxation oscillation type of behavior. The spiking tends to damp down because neither the cavity photon number $n(t)$ nor especially the population inversion $N(t)$ drops all the way to zero following a spike. Hence each successive spike starts from initial conditions that come closer and closer to the steady-state behavior of the laser.

More accurate and detailed calculations of laser spiking behavior using the rate equations given in Equations 25.1 and 25.2 can only be made by solving these equations with the aid of an analog or digital computer. Figure 25.6 shows calculated results using the rate equations for a hypothetical laser with atomic lifetime $\tau_2 = 5$ ms, cavity lifetime $\tau_c = 16$ ns, and a pumping rate $r \approx 2600$, i.e., the laser is pumped very far above threshold. Note that the interval between the early, large-amplitude spikes changes slightly from spike to spike, but is not greatly different from the period of the damped quasi-sinusoidal behavior toward which the laser system evolves.

Anyone who might undertake these kinds of numerical or computer solutions of the rate equations should note that they involve large and rapid changes of amplitude, particularly in the cavity photon number. Therefore solving Equations 25.1 and 25.2 to obtain accurate predictions on a numerical computer requires

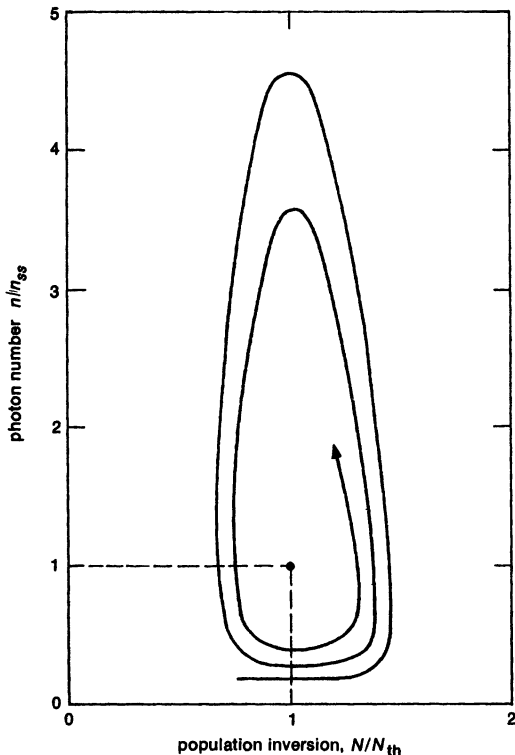


FIGURE 25.7
Phase-plane description of laser spiking.

careful attention to the numerical algorithm and the equation solving procedures that are followed.

Phase Plane Description

Another way to describe spiking behavior analytically is to plot values of the photon number $n(t)$ and the population inversion $N(t)$ as points in a phase plane which has $N(t)$ as, say, the x axis and $n(t)$ as the y axis, as in Figure 25.7. Dividing the two rate equations 25.1 and 25.2 into each other then gives the equation

$$\frac{dn}{dN} = \frac{K(n+1)N - \gamma_c n}{R_p - KnN - \gamma_2 N}, \quad (3)$$

which gives the slope of the trajectory of $n(t)$ versus $N(t)$ passing through any point in the N, n plane.

Figure 25.7 shows the typical convergence toward a steady-state limit point for a moderately “spiky” laser. Starting from any initial point N_0, n_0 in this plane, we can thus follow the spiking trajectory as it circles in toward the final convergence point at $N_{\text{th}}, n_{\text{ss}}$.

Relaxation Oscillations: Linearized Analysis

Once the spiking behavior in a laser oscillator has damped down to what are essentially small-amplitude fluctuations about the steady-state oscillation conditions in the laser, we can carry out a linearized small-signal analysis which gives simple analytic solutions for the relaxation-oscillation frequency and damping rate.

To carry out this analysis we begin with the same rate equations as in Equations 25.1 and 25.2, and recall that the steady-state or dc solutions to these equations above threshold are given by

$$N_{\text{th}} = \gamma_c/K \quad \text{and} \quad n_{\text{ss}} = R_p/KN_{\text{th}} - \gamma_2/K = (r-1)\gamma_2/K. \quad (4)$$

Suppose that in the relaxation-oscillation regime the instantaneous photon number and population inversion in the laser will be not too distant from the steady-state values, so that we can write these quantities in the form

$$\begin{aligned} n(t) &= n_{\text{ss}} + n_1(t), & n_1(t) \ll n_{\text{ss}} \\ N(t) &= N_{\text{th}} + N_1(t), & N_1(t) \ll N_{\text{th}}. \end{aligned} \quad (5)$$

If we substitute Equations 25.5 into the rate equations, the dc or steady-state terms will automatically cancel out of both equations. In addition, we can drop the $KN_1(t)n_1(t)$ terms on the right side of both equations, on the grounds that these cross products of the small fluctuations will be small compared to the products of steady-state values times the small fluctuations.

By using the steady-state solutions, the rate equations can then be reduced to the linearized small-signal form

$$\begin{aligned} \frac{dn_1(t)}{dt} &= (r-1)\gamma_2 N_1(t) \\ \frac{dN_1(t)}{dt} &= -\gamma_c n_1(t) - r\gamma_2 N_1(t). \end{aligned} \quad (6)$$

If we assume that the small quantities $n_1(t)$ and $N_1(t)$ vary as e^{st} , then this leads to the secular determinant

$$\begin{vmatrix} s & -(r-1)\gamma_2 \\ \gamma_c & s + r\gamma_2 \end{vmatrix} = 0 \quad (7)$$

and hence to the secular equation

$$s^2 + r\gamma_2 s + (r-1)\gamma_2 \gamma_c = 0. \quad (8)$$

The natural roots of the system, or the exponential decay rates and oscillation frequencies for the relaxation oscillation behavior, are therefore given by

$$s = s_1, s_2 = -\frac{r\gamma_2}{2} \pm \sqrt{\left(\frac{r\gamma_2}{2}\right)^2 - (r-1)\gamma_2 \gamma_c}. \quad (9)$$

There are two different situations to discuss, depending on the sign of the quantity inside the square root.

(a) *Nonspiking Lasers* : In most gas lasers, to take care of the nonspiking situation first, the atomic lifetime γ_2 and the cavity decay rate γ_c may be of

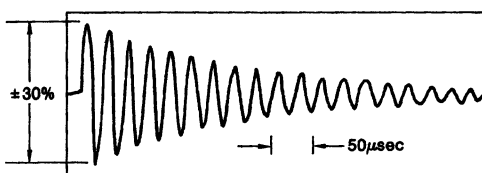


FIGURE 25.8
Relaxation oscillations ("ringing")
in a slightly perturbed Nd:YAG laser
oscillator.

the same order of magnitude. Let us suppose in fact that the cavity decay rate γ_c is somewhat slower, or that the laser is not too far above threshold, so that $(r - 1)\gamma_2\gamma_c$ is smaller than $(r\gamma_2/2)^2$. The two natural roots of this equation are then

$$s = s_1, s_2 \approx \begin{cases} -r\gamma_2 \\ [(r - 1)/r]\gamma_c. \end{cases} \quad (10)$$

The transient response of the oscillating laser to any kind of perturbation in this limit has two exponentially decaying roots, one of which corresponds essentially to a net population repumping rate $r\gamma_2$, whereas the other corresponds to a net cavity build-up rate of $[(r - 1)/r]\gamma_c$. The system is overdamped, so that any fluctuations die out in a double exponential form rather than an oscillatory fashion, with time constants corresponding roughly to the atomic and cavity lifetimes.

When a laser in this category is suddenly turned on, the laser oscillation will generally build up and converge toward the steady-state level with little or no overshoot, or at least without the kind of extreme relaxation oscillations associated with spiking types of lasers.

(b) *Strongly Spiking Lasers* : The alternative situation, which is characteristic of most solid-state and certain other lasers (for example, the iodine photodissociation laser), occurs whenever the atomic decay rate γ_2 is very much slower (with a time constant of perhaps hundreds of microseconds) compared to the cavity decay rate γ_c (which is perhaps hundreds of nanoseconds). In this situation the natural roots for the transient response of the system may be written in the form

$$s_1, s_2 \approx -\frac{r\gamma_2}{2} \pm j\sqrt{(r - 1)\gamma_2\gamma_c - \left(\frac{r\gamma_2}{2}\right)^2} \quad (11)$$

$$\equiv -\gamma_{sp} \pm j\omega'_{sp}.$$

The system clearly has an exponentially damped sinusoidal response of the form

$$n(t) = n_{ss} + n_1 e^{-\gamma_{sp} t} \cos \omega'_{sp} t, \quad (12)$$

in which $\gamma_{sp} \equiv r\gamma_2/2$ gives the decay rate with which the relaxation-oscillation behavior dies out. The small-signal relaxation-oscillation frequency for the laser is then $\omega'_{sp} \equiv \sqrt{\omega_{sp}^2 - \gamma_{sp}^2} \approx \omega_{sp}$, where $\omega_{sp} \equiv \sqrt{(r - 1)\gamma_2\gamma_c}$. (We use the subscript *sp* for these quantities because ω_{sp} is very often referred to as the "spiking frequency," although we are being more precise and calling it the "relaxation-oscillation frequency.") The population inversion $N(t)$ will have similar damped sinusoidal fluctuations about its steady-state value.

If we take typical values for, say, a Nd:YAG laser pumped to 50% above threshold ($r = 1.5$), and assume $\tau_2 \approx 230 \mu\text{sec}$ for the atomic lifetime and $\tau_c \approx 30 \text{ nsec}$ for the cavity lifetime, we find a typical relaxation-oscillation frequency of

$$\omega_{\text{sp}} = \sqrt{(r - 1)\gamma_2\gamma_c} \approx 2\pi \times 40 \text{ kHz.} \quad (13)$$

Figure 25.8 is an oscilloscope trace that shows a classic example of this type of ringing, or transient relaxation oscillation, in a Nd:YAG laser. The dependence of the relaxation-oscillation frequency ω_{sp} on $\sqrt{(r - 1)\gamma_2\gamma_c}$ has been checked experimentally in a number of lasers; indeed, measurements of ω_{sp} have sometimes been used as a way to find values for the parameters r , γ_2 or γ_c .

We can also define a Q factor for the relaxation oscillations, given by

$$Q_{\text{sp}} \equiv \frac{\omega_{\text{sp}}}{\gamma_{\text{sp}}} \approx \sqrt{\frac{4(r - 1)\gamma_c}{r^2\gamma_2}} \approx 10\text{--}100, \quad (14)$$

again in reasonable agreement with observations.

This analysis thus gives the resonant frequency ω_{sp} and the damping rate γ_{sp} in the small-signal relaxation-oscillation regime for an ideal four-level laser system. Note that if we identify the relaxation time or recovery time for the atomic population by $\tau_2 \equiv 1/\gamma_2$, and an effective build-up time or recovery time for the cavity fields by $(r - 1)/\tau_c$, then the relaxation-oscillation frequency is just the geometric mean of these, i.e.,

$$\omega_{\text{sp}} = \sqrt{\frac{r - 1}{\tau_c} \times \frac{1}{\tau_2}}. \quad (15)$$

The repetition rate for the large-amplitude spikes in the strong spiking regime will generally be somewhat different (usually slower) than the small-amplitude relaxation-oscillation frequency ω_{sp} , but not usually by more than a factor of 2 or 3. The damping rate for the large-amplitude spikes will also be different, but ω_{sp} and γ_{sp} at least give a general indication of the resonant frequency and damping rate of the laser even for large-amplitude perturbations.

Ruby Laser Spiking

The ruby laser, since it is a three-level system, has a somewhat more complex set of rate equations than those used in this section. A linearized fluctuation analysis of the ruby laser must thus be carried out using the same approach as in this section but applied to the appropriate equations for the ruby system (see Problems).

Such an analysis shows that the oscillatory behavior in ruby has a quite similar relaxation-oscillation frequency ω_{sp} , but is much less damped than in four-level lasers, as illustrated experimentally by the weak damping observed in the typical ruby laser results shown at the beginning of this section. The sudden random jumps that are typically observed in the ruby spiking behavior can be attributed to various sudden transient fluctuations in the laser, caused by such disturbances as pump fluctuations, acoustic vibrations, thermal expansion of the ruby rod, or the sudden turning on or off of one or more transverse or axial modes within the ruby laser. Special ruby lasers built with very careful transverse mode control, and with unusually long laser cavities to increase the

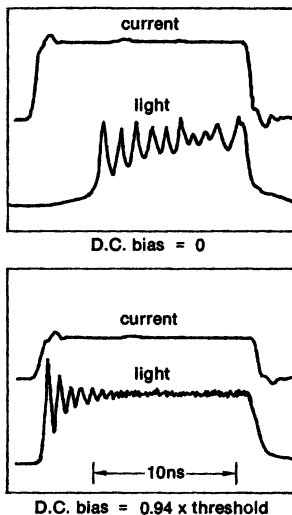


FIGURE 25.9
Transient spiking behavior in pulsed semiconductor diode lasers.

cavity lifetime relative to the upper level lifetime, have been found to give much more regular and smoothly damped spiking behavior.

Spiking in Semiconductor Injection Diode Lasers

Semiconductor injection diode lasers also exhibit essentially the same kind of spiking behavior as ruby and Nd:YAG lasers, but in a very different time or frequency domain, as illustrated by the curves in Figure 25.9. In each of these curves the upper trace shows the driving current pulse through a GaAs injection diode laser, whereas the lower trace shows the laser oscillation output on the same time scale. Note, however, that this time scale is 2 nsec per division, or several orders of magnitude faster than in the previous illustrations.

The physical processes in a typical semiconductor laser are somewhat more complex than, for example, in a Nd:YAG laser, since a typical semiconductor laser will have a large distributed optical loss along the junction; a low mirror reflectivity at each end of the lasers; and a large lower-level absorption as well as a large current-pumped upper level amplification. The spiking behavior in semiconductor lasers can nonetheless be at least roughly described by essentially the same rate equations as in Equations 25.1 and 25.2, but with very different values for the time constants and hence the eventual relaxation-oscillation frequency.

A typical GaAs injection laser may have a cavity which is $L = 300 \mu\text{m}$ long, with an index of refraction $n = 3.35$, and a distributed ohmic loss coefficient along the optical waveguide of $2\alpha_0 \approx 60 \text{ cm}^{-1}$. The end mirror reflectivities due to dielectric reflection at the cleaved ends will then be $R_1 = R_2 \approx 0.3$; the round-trip transit time in the cavity will be $T = 2nL/c_0 \approx 6.7 \text{ psec}$; and the cavity lifetime will be $\tau_c = T/[4\alpha_0 L + \ln(1/R_1 R_2)] \approx 1.1 \text{ psec}$. The upper level lifetime for the inverted population in the p-n junction might be $\tau_2 = \gamma_2^{-1} \approx 3 \text{ nsec}$. It is then clear that $\tau_c \ll \tau_2$, which is the condition for relaxation oscillations and spiking. The relaxation-oscillation frequency for a GaAs pumped to 1.5 times

threshold will then be very roughly given by

$$\frac{\omega_{sp}}{2\pi} \approx \frac{1}{2\pi} \sqrt{\frac{0.5}{3.3 \times 10^{-21}}} \approx 2 \text{ GHz.}$$

This calculated result is in reasonable agreement with typical experimental results for such lasers.

Suppression of Spiking

Various attempts have been made to control or suppress spiking behavior, either by adding some kind of loss mechanism within the laser cavity whose loss increases with increasing photon number $n(t)$ —an optical limiting element, so to speak—or by adding an external feedback loop with a photodetector and loss modulator within the cavity. It can be shown analytically that adding even a small amount of fast-acting limiting effect or saturable gain in a spiking laser will strongly damp the spikes and relaxation oscillations. This approach is limited, however, by the inability to find any good, fast-acting, low-threshold optical limiter which will be effective at the power levels present in typical spiking lasers, and which will not add large amounts of unwanted loss at the normal operating point. (The laser gain medium itself provides a kind of slow-acting optical gain control or AGC; but it is the time delay of this AGC that makes the relaxation oscillations possible.)

The external feedback approach is quite feasible, but generally too complicated and expensive to be worth implementing, given the minor seriousness of the spiking phenomena. Stable mechanical design, acoustic isolation, and power supply stabilization are the keys to avoiding recurrent small-amplitude relaxation oscillations in a practical laser, such as the cw Nd:YAG laser.

Discussion and Summary

Spiking is thus in general more of a nuisance than a useful phenomenon. It does, however, provide a convenient illustration of the validity of the rate-equation theory for laser oscillators. Measurements of the relaxation-oscillation frequency have also been used on occasion to calculate or verify the cavity lifetime τ_c and the atomic lifetime τ_2 in laser oscillators. The spiking behavior in semiconductor injection lasers has also been used to generate a single short pulse (≈ 100 psec or less) from an injection diode laser, by turning on the driving current very rapidly to create a strong initial spike and then turning the current off equally rapidly before the second and later spikes can form. This makes it possible to generate a single optical pulse significantly shorter than the width of the driving current pulse itself.

Gain Switching

Gain switching is another initial-buildup phenomenon in lasers which is generally very similar to spiking. In certain pulsed gas lasers, for example, pulsed or TEA CO₂ lasers, it is possible to turn on the laser gain quite rapidly using a fast pulse of pumping current through the laser tube. (Fast gain turn-on is also accomplished in TEA or electron-beam pumped excimer lasers in the visible or near ultraviolet, and in other laser systems as well.) This fast pumping may cause

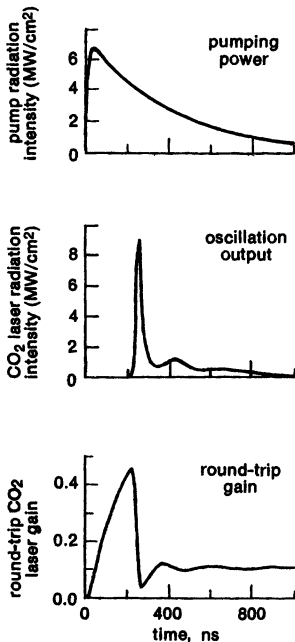


FIGURE 25.10
Calculated gain-switching behavior in a pulsed CO₂ laser at 10.6 μm .

the population inversion and gain to go considerably above threshold before the laser oscillation has time to build up from the initial noise level in the cavity.

The oscillation output of these lasers can then also exhibit a single, rather large initial output spike, possibly followed by a few additional weaker spikes, during the initial turn-on transient. This behavior, which is usually called "gain switching," is similar in character to spiking, and can be described by essentially the same rate equations.

Figure 25.10 illustrates the kind of gain switching behavior that can be observed, for example, in pulsed CO₂ lasers at $\lambda = 10.6 \mu\text{m}$. The plots show the results of theoretical calculations for gain switching in a particular high-pressure CO₂ laser. (These calculations happen to be a laser system in which the pumping power is supplied by a separate pulsed deuterium fluoride or DF laser; the DF laser radiation in the near infrared is absorbed by DF molecules contained in the CO₂ laser gas mixture, and this pumping energy is then transferred to the CO₂ molecules by collisional energy transfer.) The three traces show, from top to bottom, the assumed DF laser pump variation; the calculated CO₂ laser output; and the time-varying average gain in the CO₂ laser. Experimental results on this laser are in general agreement with these theoretical curves.

Figure 25.11 shows experimental results for two different discharge-pumped CO₂ lasers. The left-hand plot shows the 500 nanosecond long current pulse in a typical transversely excited, atmospheric pressure (TEA) CO₂ laser, together with the resulting laser output. In this laser the output more or less follows the fast pumping current pulse, except for a turn-on transient or gain spike on the leading edge.

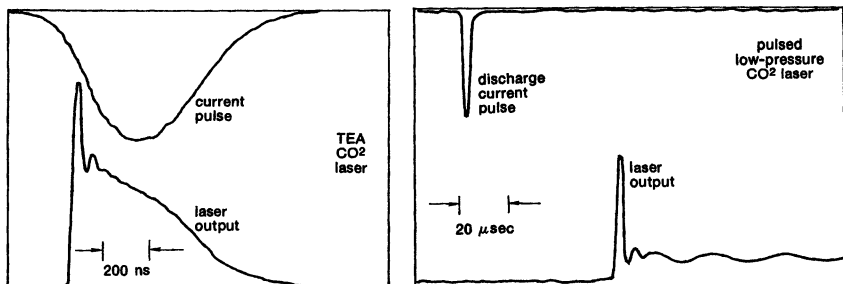


FIGURE 25.11
Examples of "gain switching" in two different pulsed CO₂ lasers.

The right-hand trace shows a somewhat unusual low-pressure CO₂ laser result, in which the longitudinal discharge current is a very short but very intense current pulse only ≈ 50 nsec long. This current pulse produces, however, a sizable population inversion which develops and persists in the low-pressure medium for a long time following the current pulse. The laser thus begins oscillation with a sizable gain-switched pulse that occurs some 70 μ sec after the end of the current pulse, and continues to oscillate for a sizable time after that. (The inversion in this particular laser system is maintained primarily by long-lived vibrationally excited N₂ molecules, which are created in large numbers by the initial current pulse, and which gradually transfer their energy into pumping up the laser CO₂ molecules.)

Because the population lifetimes γ_2 are shorter and closer to the cavity decay times γ_c in these situations than in solid-state lasers, these gain-switched relaxation oscillations are much more heavily damped than the spikes in typical solid-state lasers, and so the spiking behavior typically damps out after one or a very few spikes.

REFERENCES

An inordinate number of experiments and especially of analyses on laser spiking were published in the first few years following the discovery of the laser. Many of these followed on an earlier analysis by H. Statz and G. deMars, "Transients and oscillation pulses in masers," in *Quantum Electronics*, edited by C.H. Townes, (Columbia University Press, 1960), pp. 530-537. The two coupled rate equations used in the present section are thus often referred to as the Statz-deMars equations (though their original paper actually dealt with spiking in microwave ruby masers).

Some of the better subsequent theoretical analyses include papers by R. Dunsmuir, "Theory of relaxation oscillations in optical masers," *J. Electron. Control* **10**, 453-458 (1961); by D. M. Sinnett, "An analysis of the maser oscillator equations," *J. Appl. Phys.* **33**, 1578-1581, and by D. A. Kleinman, "The maser rate equation and spiking," *Bell Sys. Tech. J.* **43**, 1505-1532 (July 1964). A good analysis of small-amplitude relaxation oscillations is D. E. McCumber, "Intensity fluctuations in the output of cw laser oscillators," *Phys. Rev.* **141**, 306-322 (1966).

The experimental result in this section showing cleanly damped spiking from an argon-laser-pumped ruby laser is from M. Birnbaum, P. H. Wendzikowski, and C. L.

Fincher, "Continuous-wave nonspiking single-mode ruby laser," *Appl. Phys. Lett.* **16**, 436-438 (June 1, 1970).

Some interesting early experiments showing how to control or simplify ruby laser behavior with various exotic schemes include D. Roess, "Ruby laser with mode-selective etalon reflector," *Proc. IEEE* **52**, 196-197 (1964), and J. Free and A. Korpel, "Laser emission from a moving ruby rod," *Proc. IEEE* **52**, 90 (1964).

Methods for eliminating spiking by external feedback control are illustrated in H. Statz, et al, "Problem of spike elimination in lasers," *J. Appl. Phys.* **36**, 1510-1514 (May 1965); and the effects of multimode oscillation and mode jumping on ruby laser spiking are treated in C. L. Tang, H. Statz and G. deMars, "Regular spiking and single-mode operation of ruby laser," *Appl. Phys. Lett.* **2**, 222-224 (June 1963), and in H. Statz and C.L. Tang, "Multimode oscillations in solid-state masers," *J. Appl. Phys.* **35**, 1377-1383 (May 1964).

Two selections from the many references in the literature on spiking in semiconductor lasers include V. D. Kurnosov et al., "Self-modulation of emission from an injection semiconductor laser," *JETP Lett.* **4**, 303-305 (1966) (first published observation); and R. Roldan, "Spikes in the light output of room-temperature GaAs injection lasers," *Appl. Phys. Lett.* **11**, 346-348 (December 1967).

Some particularly clean illustrations of predicted multimode spiking behavior in semiconductor diode lasers, including competition between and the gradual suppression of all but one dominant axial mode, are shown in D. Marcuse and T. P. Lee, "On approximate analytical solutions of rate equations for studying transient spectra of injection lasers," *IEEE J. Quantum Electron. QE-19*, 1397-1406 (September 1983).

The DF/CO₂ gain switching calculations shown in this section are from K. Stenersen and G. Wang, "Continuously tunable optically pumped high-pressure DF→CO₂ transfer laser," *IEEE J. Quantum Electron. QE-19*, 1414-1426 (September 1983).

Other detailed calculations and illustrations for gain switching in gas lasers can be found in L. W. Casperson, "Analytic modeling of gain-switched lasers. I. Laser oscillators," *J. Appl. Phys.* **47**, 4555-4562 (October 1976).

A quite different regime of instability which may also cause lasers to "spike," but in a continuous and undamped fashion, has also been predicted for certain inhomogeneously broadened gas lasers in which the product of homogeneous linewidth and cavity lifetime is less than unity. See, for example, L. W. Casperson, "Stability criterion for high-intensity lasers," *Phys. Rev. A* **21**, 911-923 (March 1980).

Relaxation oscillations are a common phenomenon, in many other physical systems besides lasers. For an illustration of rate equations, population depletion, saturation, and "spiking" that involves wolves and moose, rather than photons and atoms, try the article by D. C. Gazis, E. W. Montroll, and J. E. Ryniker, "Age-specific, deterministic model of predator-prey populations: application to Isle Royal," *IBM J. Res. Develop.* **17**, 47-53 (January 1973).

Problems for 25.1

1. *Phase plane description of spiking.* Without actually solving Equations 25.1 and 25.2 for $n(t)$ and $N(t)$ versus t , carry out a graphical analysis of how the spiking trajectories must look in the N, n phase plane by looking for particularly significant loci in the phase plane, such as the lines along which the slope dn/dN is either 0 or ∞ . Use the idealized single-mode four-level laser model, and use numerical values $3^* = 1$, $\gamma_2 = \gamma_{\text{rad}}$, $\gamma_c/\gamma_{\text{rad}} = 5$ and $r = 2$ for purposes of plotting in the phase plane.

2. *Dimensionless form for the spiking equations.* Before carrying out any numerical calculations with the spiking Equations 25.1 and 25.2, it is convenient to reduce them to dimensionless form, for example, by letting $p \equiv n/n_{ss}$ be the dimensionless photon number or oscillation level; N/N_{th} be the dimensionless population inversion; and $\gamma_2 t \equiv t/\tau_2$ be the dimensionless time. Show that the spiking equations then reduce to

$$q' = r - q - (r - 1)pq,$$

$$p' = c(q - 1)p,$$

where p' and q' are the derivatives with respect to the dimensionless time coordinate, and $c \equiv \gamma_c/\gamma_2$ is a large number in a spiky laser.

Since the value of p changes very rapidly and has a wide range of variation, it can also be convenient in numerical calculations to transform from p to the new variable $y = \ln p$. Rewrite these equations in terms of q and y rather than q and p .

3. *Spiking analysis for the ruby laser.* Because the ruby laser is a three-level rather than a four-level laser, it is considerably more difficult to make it oscillate continuously; and its spiking and relaxation-oscillation behavior also differ somewhat in detail from the four-level model analyzed in this section. Carry out the necessary rate-equation analysis to derive the cw oscillation values and also the linearized small-signal relaxation oscillations about that level for the ruby laser. Find the relaxation-oscillation frequency ω_{sp} and spiking decay rate γ_{sp} as functions of the ruby parameters and the pumping rate r above threshold. (Note: It is a valid approximation to treat the relaxation from level E_3 to level E_2 in the ruby system as essentially instantaneous, so that we can assume $N_3 \approx 0$ under all conditions.)
4. *Step response of a “spiky” laser.* The pump power in an operating Nd:YAG laser is suddenly increased from its previous steady-state value of R_p by a small amount ΔR_p at $t = t_0$, with $\Delta R_p \ll R_p$. Evaluate the resulting transient and steady-state changes in the laser power level $n(t)$ and in the upper-laser-level population $N(t)$ for $t > t_0$.
5. *Controlling spiking by an external feedback loop?* Suppose a fast-acting feedback loop is to be added to a strongly spiking laser in an attempt to damp out the relaxation oscillations and stabilize the output power. The proposal is that whenever the instantaneous photon number $n(t)$ in the laser deviates from its steady-state value n_{ss} by any small amount $\delta n(t)$, as sensed by a photodetector monitoring the laser’s output, the feedback loop shall change the instantaneous pumping rate away from its steady-state value R_p by an amount $\delta R_p(t)$ given by

$$\frac{\delta R_p(t)}{R_p} = \beta \frac{\delta n(t)}{n_{ss}},$$

where β is a feedback gain coefficient. Evaluate the resulting transient characteristics of this system for small deviations about steady-state, using an elementary laser rate-equation model. Express your answers as a function of γ_2 , γ_c , β and the steady-state pumping rate normalized to threshold, i.e., $r = R_p/R_{th}$. What value (and sign) should the feedback parameter β have for critical damping (and hence zero overshoot) in the spiking behavior? Are there likely to be any stability problems in this system?

6. *Proof that spiking will always die out in a simple laser system.* The spiking analysis by Sinnett listed in the References [J. Appl. Phys. 33, 1578 (1962)] contains a general proof that the Stazt-deMars rate equations cannot have any undamped large-amplitude limit cycles in the n -versus- N phase plane, and hence that even large-amplitude spiking behavior will always die out eventually. Sinnett also presents a procedure for calculating the damping rate of the large-amplitude spikes, without actually solving the nonlinear rate equations for large amplitudes. Review these analyses and convert them into the notation of this section; and compare the decay rate for large-amplitude spikes from Sinnett's analysis with the damping rate γ_{sp} for small-signal relaxation oscillations from our linearized analysis.
7. *Extended spiking analysis for a semiconductor laser.* A slightly more accurate set of rate equations for an injection diode or semiconductor laser is given by

$$\frac{dn}{dt} = K(N - N_0)n - \gamma_c n,$$

and

$$\frac{dN}{dt} = J - \frac{N}{\tau_2} - K(N - N_0)n,$$

where J is the dc pumping current through the injection diode, measured in appropriately modified units, and the KN_0 terms represent additional loss due to absorption by atoms in the lower laser level. Analyze the dc behavior of these equations, and then carry out a small-signal relaxation oscillation analysis about the steady state, similar to that in the present section. Using the same numbers as given in the text for γ_c and τ_2 , and assuming that the lower-level loss term KN_0 corresponds to an additional loss coefficient of 300 cm^{-1} in the optical waveguide, find a modified prediction for the relaxation-oscillation frequency at a pumping level of $J/J_{th} = 1.25$.

25.2 LASER AMPLITUDE MODULATION

In this section we consider amplitude modulation of laser oscillators produced by modulating either the pumping rate or the cavity losses, for the most part at frequencies small compared to the axial mode spacing of the laser. Other more sophisticated amplitude modulation techniques, such as Q -switching and mode locking, will be considered in later chapters.

Small-Amplitude Pump Modulation

If a laser oscillator is inherently "spiky"—that is, if it has only a weakly damped relaxation oscillation behavior—we can expect that the response of the oscillator to weak modulation of any of the laser parameters will also exhibit a rather strongly resonant response at the natural relaxation-oscillation frequency of the laser. To demonstrate this, suppose we assume the pumping rate applied to the laser is modulated sinusoidally at some low modulation frequency ω_m in the form

$$R_p(t) = R_{p0} + R_{p1} \cos \omega_m t. \quad (16)$$

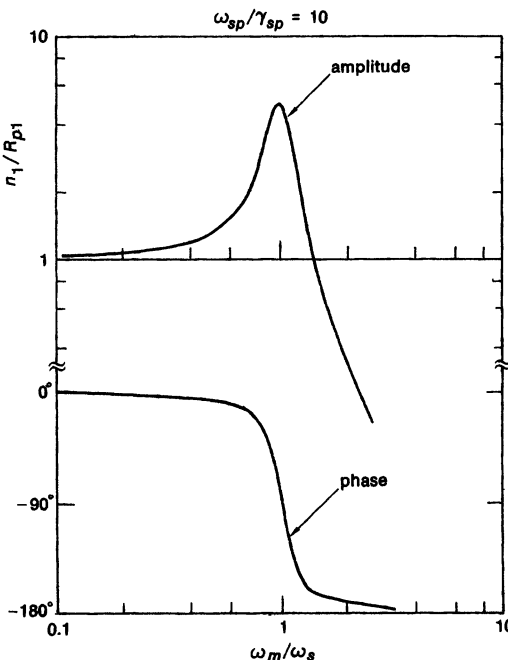


FIGURE 25.12

Theoretical response of a laser to small-amplitude pump modulation at modulation frequencies around the relaxation-oscillation frequency.

We can then also expand the cavity photon number and population inversion in the forms

$$\begin{aligned} n(t) &= n_{ss} + \operatorname{Re} \tilde{n}_1 e^{j\omega_m t}, & |\tilde{n}_1| &\ll n_{ss} \\ N(t) &= N_{th} + \operatorname{Re} \tilde{N}_1 e^{j\omega_m t}, & |\tilde{N}_1| &\ll N_{th}. \end{aligned} \quad (17)$$

By using the same rate equations as in the spiking analysis, and again linearizing by dropping all products of the small sinusoidal terms R_{p1} , \tilde{n}_1 and \tilde{N}_1 , we can obtain a linear transfer function between pump modulation and oscillation amplitude response, namely,

$$\frac{\tilde{n}_1}{R_{p1}} = \frac{\omega_{sp}^2/\gamma_c}{\omega_{sp}^2 - \omega_m^2 + 2j\gamma_{sp}\omega_m}, \quad (18)$$

where $\omega_{sp} = \sqrt{(r-1)\gamma_2\gamma_c}$ and $\gamma_{sp} = r\gamma_2/2$ are the relaxation-oscillation resonant frequency and decay rate defined in the previous section.

Figure 25.12 shows the theoretical variation of the amplitude and phase of the pump modulation response for such a laser in which the relaxation oscillations are relatively undamped ($\omega_{sp}/\gamma_{sp} = 10$). The general form of this response is exactly like the response of any similar underdamped resonant linear system, i.e.,

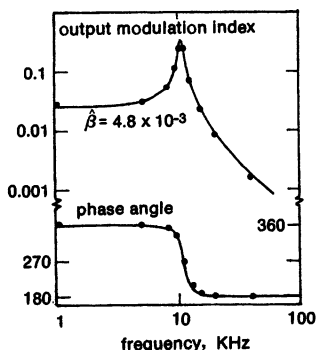


FIGURE 25.13
Measured small-signal pump modulation response in a diode-pumped Nd:YAG laser.

$$\frac{\gamma_c \tilde{n}_1}{R_{p1}} \approx \begin{cases} 1 & \omega_m \ll \omega_{sp}, \\ -j\omega_{sp}/2\gamma_{sp} & \omega_m = \omega_{sp}, \\ -\omega_{sp}^2/\omega_m^2 & \omega_m \gg \omega_{sp}. \end{cases} \quad (19)$$

That is, there is a quasi-dc response well below resonance; a resonance peak with a 90° shift at resonance; and a rapidly decreasing response with a 180° phase shift at frequencies above resonance.

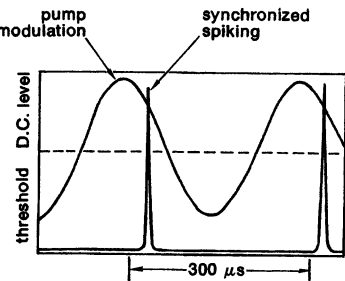
Figure 25.13 shows experimental results for the pump modulation response in a small 1 mW Nd:YAG laser pumped by an array of 64 semiconductor light emitting diodes. (Semiconductor LEDs, excited with a few hundred mA of direct current and emitting efficiently at around 840 nm, can provide an effective pump source for a small Nd:YAG laser oscillating at 1064 nm. Although there are practical problems in obtaining sufficiently powerful and long-lived LEDs and coupling their emission into the Nd:YAG rod, this kind of pumping can provide an efficient, small, portable and rugged YAG laser, which can be directly modulated by modulating the current through the LEDs.)

The results in Figure 25.13 indicate that a modulation index of only 0.48% in the diode pumping current produced a modulation index of $\approx 30\%$ in the laser output near the laser relaxation oscillation frequency of ≈ 12 kHz. Similar experiments on this laser at different dc drive levels also confirm (as has also been done on many other lasers) the $\sqrt{(r-1)\gamma_2\gamma_c}$ formula for the resonance frequency of the relaxation oscillations.

We can expect that the laser oscillation level will be similarly affected by sinusoidal modulation of any other laser parameter, such as cavity loss, output coupling, or mirror alignment. Random noise fluctuations in the laser structure or surroundings or pumping system can thus produce large unwanted resonant fluctuations in the laser oscillation level at frequencies near the natural relaxation-oscillation frequency. In general, if we examine carefully the output spectrum of any naturally spiky laser, we can expect to find enhanced noise sidebands on the output signal at or near the resonance frequency ω_{sp} .

The increased modulation response near the spiking frequency can also become a source of signal distortion in semiconductor diode lasers used in amplitude-modulation communication systems, as we will discuss a little later in this section.

FIGURE 25.14
Synchronized spiking behavior in a Nd:YAG laser with large-amplitude pump modulation.



Large-Amplitude Pump Modulation

The response of a “spiky” laser to cavity modulation or pump modulation will be linear at very small modulation depths, but will become nonlinear for larger modulation depths. For example, by increasing the pump modulation index in the diode-pumped YAG laser of Figure 25.13 to a larger level, and then tuning the modulation frequency anywhere in the range below or up to the resonance frequency ω_{sp} , we can obtain the alternative kind of controlled or entrained spiking behavior shown in Figure 25.14. In this case the current through the pumping diodes is being modulated at a frequency around half the natural resonance frequency ω_{sp} , with a modulation amplitude of $\pm 70\%$ around the threshold level for the laser (shown by the dashed line in the figure). The strong laser spike occurring near the end of each pumping cycle is evident.

In general it is a common characteristic of resonant but nonlinear systems, like spiky lasers, to exhibit complex nonlinear relaxation oscillations, especially when driven with larger excitation amplitudes. Figure 25.15 shows additional forced spiking behavior caused by sinusoidal pump modulation, here in a small diode-laser-pumped $\text{LiNdP}_4\text{O}_{12}$ laser. The average pumping rate in this situation is set at twice the laser threshold, with a peak sinusoidal modulation $R_{p1} = 0.55 \times R_{p0}$ about that level.

The upper left figure shows a locked single-spike behavior at a modulation frequency slightly less than the natural spiking rate in this laser (the sweep rate in all three parts of Figure 25.15 is $20 \mu\text{s}$ per division). In the lower left illustration the modulation frequency has been raised somewhat above the natural spiking frequency, and the laser responds by emitting a spike only every other modulation cycle. In the right-hand trace, at an intermediate frequency, the laser spikes on every cycle, but with an amplitude and timing that shifts every alternate cycle. Other more complex harmonic and subharmonic entrained spiking patterns can be obtained at other modulation frequencies and modulation depths.

Injection Diode Lasers

These types of resonant response and locked spiking behavior become of very direct interest in semiconductor diode lasers, whose natural spiking frequency lies in the GHz rather than kHz range, as we showed in the preceding section. This is especially true when such lasers are operated as directly modulated light sources for optical communication links, with modulation frequencies

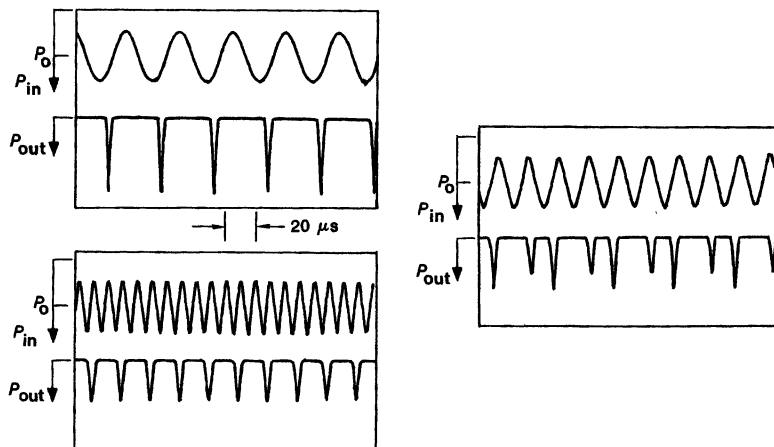


FIGURE 25.15

Examples of synchronized spike trains in a diode-pumped Nd:pentaphosphate laser at different modulation frequencies.

in the same range. The resonance enhancement of the small-signal modulation response near $\omega_m \approx \omega_{sp}$ can then distort sinusoidal communication signals; while the transient response to pulsed current injection becomes of great importance in pulsed binary modulation devices.

In a pulsed binary system we need to know, for example, how much the laser response to one modulation pulse will depend on closely preceding pulses, or whether the laser will respond to a string of several successive closely spaced pulses in a manner different from isolated individual pulses. We can thus find numerous papers in the literature reporting both rate-equation simulations and experimental tests of the effects of spiking and relaxation-oscillation response to current modulation in injection diode lasers.

We illustrated in the previous section the kind of strong initial turn-on spikes that can be produced in an injection diode by a pumping current pulse with a fast-rising leading edge. As an extension of this, if we drive a particularly spiky injection diode laser with a very intense and fast-rise current pulse, and then turn off this current pulse equally rapidly after the first spike, it becomes possible to generate a laser pulse substantially shorter than the driving current pulse (e.g., an optical pulse of duration ≈ 50 ps for a current pulse of duration ≈ 500 ps). This provides a convenient and inexpensive low-power ultrashort optical pulse source for calibrating the response of optical-fiber systems, photodetectors, or fast oscilloscopes, or for measuring other ultrafast physical phenomena.

Cavity Loss and Coupling Modulation

Small-amplitude modulation of the cavity loss rate, i.e., making $\gamma_c = \gamma_c(t)$, should lead to much the same kind of resonance response near the relaxation oscillation frequency as happens for pump power modulation (see Problems); and this type of response has been experimentally demonstrated as well. Large-amplitude modulation of the cavity loss or cavity coupling should also similarly lead to controlled nonlinear spiking behavior under appropriate conditions.

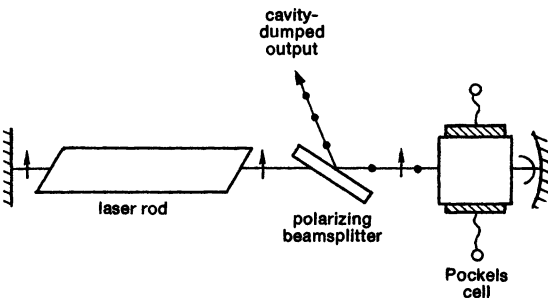


FIGURE 25.16
Electrooptic cavity dumping.

Two of the most common forms of large-amplitude cavity modulation are *cavity dumping*, which we will discuss further in this section, and *Q-switching*, which we will discuss in more detail in the following chapter.

Cavity dumping is a technique in which the output coupling from the laser cavity is suddenly increased to a very large value—essentially as if one of the end laser mirrors had been removed—so that all the circulating energy inside the cavity is “dumped” into an output pulse which, for perfect dumping will be exactly one cavity round-trip time T in length, and contain all the signal energy in the cavity. Figure 25.16 shows one common technique by which this can be accomplished.

This laser cavity contains a polarizing beam splitter which makes the cavity oscillate normally with a vertically oriented linear polarization. In order to dump the cavity energy, the voltage across the electrooptic Pockels modulator is suddenly switched (in a time short compared to T , or typically a few ns) to a value which makes this transparent crystal become birefringent, with a magnitude corresponding to a quarter-wave plate for single pass, or a half-wave plate for double pass. The linearly polarized energy circulating in the cavity, as it passes through this plate going to the right and then coming back to the left, has its polarization converted into circular polarization striking the right-hand mirror, and then on into horizontal polarization coming back out of the Pockels crystal. All the energy in this polarization coming back to the polarizing beam-splitter (which can either be an especially coated dielectric plate, as shown, or a polarizing prism, such as a Glan-Thompson prism) is then dumped out of the cavity as shown.

(As a practical matter, a fixed quarter-wave plate is often added to the Pockels modulator, and the Pockels modulator is then initially biased to the fixed voltage, typically several thousand volts, needed to cancel the fixed quarter-wave plate. Cavity dumping is then accomplished by suddenly switching off the voltage across the Pockels cell, leaving only the fixed quarter-wave plate, since it is often easier to short out or “crowbar” the Pockels cell voltage from a high initial value down to zero in a few ns than it is to switch the same voltage from zero up to the necessary high value in the same length of time.)

Figure 25.17 is an oscilloscope trace that shows the effect of cavity dumping on a laser cavity. This is a low-pressure CO₂ laser pumped by a long current pulse starting at the left end of the trace. The laser oscillation then shows a particularly strong initial gain spike, followed after ≈ 80 μ sec by a cavity dumping transient. The detector in this experiment was observing the energy circulat-

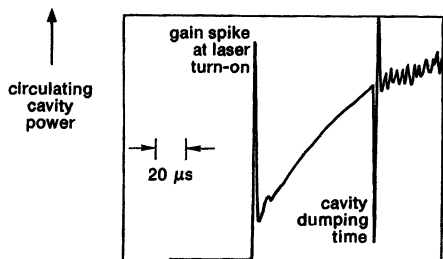


FIGURE 25.17
Cavity dumping of a pulsed CO₂ laser.

ing inside the cavity (via leakage through one of the end mirrors), rather than the energy dumped into the output direction. Hence, the circulating energy is observed to drop nearly to zero, representing nearly complete cavity dumping. The recirculating energy then rapidly recovers with a second gain-switched spike. (The noise on the trace following this point probably represents a combination of electrical pickup noise from the spark gap needed to provide the ≈ 25 kV, 2 ns pulse applied to the CdTe electrooptic modulator crystal, plus acoustic ringing in the CdTe crystal caused by application of the electrical pulse.)

This kind of cavity dumping has the disadvantages of requiring high voltages with fast rise times, applied to a crystal which is typically expensive, often optically lossy, and subject to optical damage at high powers. It can, however, provide fairly complete dumping, with moderately accurate electronic timing, and the ability to handle higher optical powers than most other cavity dumping schemes.

Repetitive Cavity Dumping

If a cw laser oscillator is running in steady-state with a 5% output coupling mirror ($R = 95\%$), the circulating intensity inside the laser cavity is then 20 times as large as the cw output intensity from the laser. If this circulating intensity is suddenly cavity dumped, the peak power output during the dumped pulse can be 20 times as large as the average or cw power output from the laser. (In fact, by reducing the output coupling below its optimum value for maximum average output power, we can make both the circulating intensity and thus the "dumpable" peak power still larger.)

If we further allow the intensity inside the cavity to build back up again, and then again dump the cavity, using *repetitive cavity dumping*, we can obtain most of the available power output from the laser medium in the form of repeated pulses which have substantially higher peak power than the average power from the laser. With proper choice of repetition frequency, the average power in the dumped output can approach the full average power available with optimum coupling in cw operation; but the higher peak powers can make this energy much more effective in cutting, welding, and other nonlinear laser processes.

Cavity dumping in lower power cw lasers, including cw Nd:YAG lasers and gas lasers such as argon-ion lasers, is often accomplished using the kind of acoustooptic modulation arrangement shown (somewhat foreshortened) in Figure 25.18. The acoustooptic modulator consists of a bar of quartz or some other optically low-loss material with a piezoelectric acoustic transducer attached to one end,

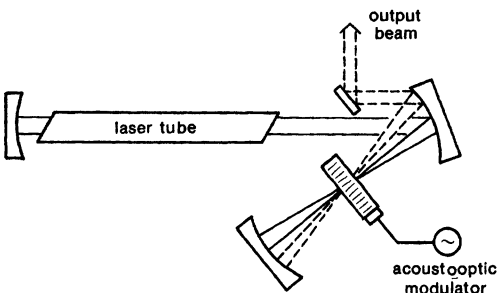


FIGURE 25.18
Acoustooptic cavity dumping.

inserted in the laser cavity at Brewster's angle to minimize optical reflection losses. A radiofrequency pulse with a power level of perhaps 10 to 20 watts, at a frequency typically in the range of 20 to 50 MHz, sends a strong acoustic wave at the same frequency down the bar.

The density and index of refraction variations associated with this acoustic wave then act as a Bragg diffraction grating, deflecting from 50 to 95% of the circulating optical intensity at a small angle, as shown by the dashed lines in the drawing. In the optical arrangement shown in Figure 25.18, the diffracted signals in both directions are recombined to produce the output beam. (By having the acoustic signal normally present and suddenly turning it off, the same arrangement can also function as an acoustooptic *Q*-switching system, as we will discuss in the following chapter.)

In practice, the rise time for the cavity dumping process when the acoustic signal is turned on is limited by the transit time with which the leading edge of the acoustic signal can travel across the width of the laser beam, moving at the speed of sound. To reduce this rise time (which is about 15 nsec per 100 μm of laser beam width), the laser beam is often brought to a focus inside the cavity using the folded arrangement of curved mirrors shown in Figure 25.18. Acoustooptic cavity dumping is thus best suited to relatively long laser cavities.

The recovery time for the intracavity intensity to build back up following a single cavity dumping pulse depends on the laser, but may typically range from a fraction of a microsecond to several microseconds. Repetitive cavity dumping can thus provide a way to get trains of pulses with increased peak power compared to the cw laser output, at repetition rates ranging from kHz to potentially a few MHz. Cavity dumping is also often used in mode-locked lasers to select out a single ultrashort pulse. If a single mode-locked pulse is circulating inside the laser cavity, as is characteristic of mode-locked operation, turning on the cavity dumping modulator can dump that single pulse into the output port of the laser.

REFERENCES

The illustrations of controlled spiking using pump modulation in this section are taken from H. G. Danielmeyer and F. W. Ostermeyer, Jr., "Diode-pump-modulated Nd:YAG laser," *J. Appl. Phys.* **43**, 2911-2913 (June 1972); and K. Kubodera and K. Otsuka, "Spike-mode oscillations in laser-diode pumped LiNdPO₄ lasers," *IEEE J. Quantum Electron.* **QE-17**, 1139-1144 (June 1981).

A few of the many references in the literature concerning the modulation response of injection lasers to injection current modulation include T. Ikegami and Y. Suematsu, "Carrier lifetime measurement of a junction laser using direct modulation," *IEEE J. Quantum Electron.* **QE-4**, 148-151 (1968); G. Arnold and P. Russer, "Modulation behavior of semiconductor injection lasers," *Appl. Phys.* **14**, 255-268 (1977); M. Ito et al., "Dynamic properties of semiconductor lasers," *J. Appl. Phys.* **50**, 6168-6174 (1979); and K. Y. Lau and A. Yariv, "Effect of superluminescence on the modulation response of semiconductor lasers," *Appl. Phys. Lett.* **40**, 452-454 (March 15, 1982).

Good examples of experiment and theory for small-signal cavity loss modulation inside a laser are given by T. Kimura and K. Otsuka, "Response of a CW Nd³⁺:YAG laser to sinusoidal cavity perturbations," *IEEE J. Quantum Electron.* **QE-6**, 764 (December 1970).

The CO₂ laser cavity dumping example in the text, which uses a slightly different electrooptic dumping method, comes from R. Trutna and A. E. Siegman, "Laser cavity dumping using an antiresonant ring," *IEEE J. Quantum Electron.* **QE-13**, 955-962 (December 1977).

The standard literature references on repetitive laser cavity dumping are by R. B. Chesler and D. Maydan, "Calculation of Nd:YAG cavity dumping," and "Q-Switching and cavity dumping of Nd:YAG lasers," *J. Appl. Phys.* **42**, 1028-1034 and 1031-1034 (March 1, 1971). See also R. B. Chesler, M. A. Karp, and J. E. Geusic, "Repetitively Q-switched Nd:YAG-Li₂O₃ 0.53- μ harmonic source," *J. Appl. Phys.* **41**, 4125-4127 (September 1978).

The transition zone between controlled spiking and repetitive cavity dumping is discussed in more detail by H. A. Kruegle and L. Klein, "High peak power output, high PRF by cavity dumping a Nd:YAG laser," *Appl. Optics* **15**, 466-471 (February 1976); and J. M. Moran, "Calculation of the minimum repetition rate of a cavity-dumped four-level laser," *IEEE J. Quantum Electron.* **QE-12**, 639-644 (October 1976).

The standard literature reference describing high-repetition-rate laser Q-switching is R. B. Chesler, M. A. Karr, and J. E. Geusic, "An experimental and theoretical study of high repetition rate Q-switched Nd:YAG lasers," *Proc. IEEE* **58**, 1899-1914 (December 1970).

For a general survey of optical modulation techniques, see R. T. Denton, "Modulation Techniques," Chapter C6 in *Laser Handbook*, edited by T. F. Arecchi and E. O. Schulz-DuBois (North-Holland, 1972), **I**, 703-724.

Problems for 25.2

1. *Linearized small-signal response to laser cavity loss modulation.* The resonance behavior of the cavity photon number for small-amplitude sinusoidal modulation of the pumping rate R_p is analyzed in the text. Carry out a similar analysis to describe small-amplitude sinusoidal modulation of the cavity decay rate γ_c , in the form $\gamma_c(t) = \gamma_{c0} + \gamma_{c1} \cos \omega_m t$. Discuss the resulting behavior of the cavity oscillation amplitude versus modulation frequency ω_m in a laser with strongly resonant relaxation oscillation behavior.
 2. *Linearized small-signal response of the laser population difference.* Calculate and describe the transfer function between sinusoidal pump modulation R_{p1} and the population response \tilde{N}_1 in a strongly resonant laser oscillator.
-

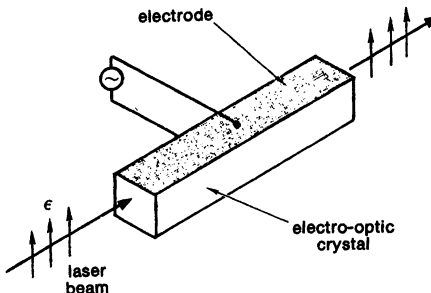


FIGURE 25.19
Pockels-cell phase modulator.

25.3 LASER FREQUENCY MODULATION AND FREQUENCY SWITCHING

Suppose that instead of an amplitude modulator, a *phase modulator* is placed inside a laser cavity. By a phase modulator we mean any device which can add a time-varying phase shift $\phi_m(t)$ to the signal wave passing through it. Such modulators are generally referred to, more or less interchangeably, either as phase modulators or as frequency (FM) modulators, since the effects of such a modulator can be described as producing either frequency modulation sidebands on the laser oscillation signal or as causing a phase shift or frequency jump of the laser oscillation frequency.

We will describe in this section the kinds of frequency modulation and frequency switching behavior that can be produced in a laser oscillator by a phase modulator which is driven either with sinusoidal modulation signals at frequencies that are generally low compared to the axial mode spacing frequency of the laser cavity, or with step-function modulation signals that may be considerably faster. Discontinuous frequency switching of the laser oscillation will then turn out to be one of the more useful forms of such modulation.

There are also more complex types of mode coupling or mode locking behavior that can occur when the phase modulation $\phi_m(t)$ is driven with signals at or near the axial mode frequency interval. These mode-coupling effects will be considered separately in a later chapter devoted to mode locking in general.

Optical Phase and Frequency Modulators

The most common form for an electrooptic phase modulator, as illustrated in Figure 25.19, is a so-called *Pockels cell*, consisting of a crystal of an electrooptic material such as potassium dihydrogen phosphate (KDP), ammonium dihydrogen phosphate (ADP), or lithium niobate (LiNbO_3), with electrodes located so as to apply a transverse voltage across the crystal. (If the material is described as $\text{KD}^* \text{P}$ or $\text{AD}^* \text{P}$, this means the crystal is deuterated, i.e., the dihydrogen is replaced by dideuterium.) Electrooptic materials such as these have the property that applying a transverse or (sometimes) a longitudinal electric field (depending upon the particular crystal) causes a small but significant change in the optical index of refraction and hence in the optical phase shift through the crystal.

Usually applying a voltage causes the index of refraction to increase for optical E fields polarized along one transverse axis, and to decrease for fields polarized along the orthogonal transverse axis, so that the crystal in general acquires

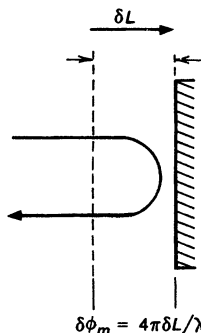


FIGURE 25.20

Optical phase modulation via mirror motion.

an *electrically induced birefringence*. If this electrically induced birefringence is combined with an optical beam that is polarized, for example, between these two axes, then the applied voltage can produce polarization rotation of the optical signal. This rotation, combined with optical polarizers, can then produce *amplitude modulation and switching*, such as we discussed in the previous section.

Alternatively, with proper orientation of the electrooptic crystal, so that the optical signal is polarized along one or the other of the induced axes in the crystal, the net effect on the optical signal can be *pure phase modulation*, with no polarization rotation or amplitude modulation. In Pockels devices this change in the index of refraction, and hence in the optical phase shift through the crystal, is linearly proportional to the voltage applied across or along the crystal. Other useful electrooptic crystals, all of which must lack inversion symmetry in their crystal structure, include gallium arsenide (GaAs) and cadmium telluride (CdTe), both of which are useful for infrared applications.

There also exist *optical Kerr cells* in which an applied voltage produces an optical index change in a transparent but polarizable liquid placed between the electrodes. The index change in such liquid Kerr cells is generally much smaller, but rises as the applied modulation voltage squared.

Cavity Mirror Motions

The simplest way to change the phase of an optical signal at some given point is to change the optical path length the signal must travel to reach that point. One elementary way to accomplish this for a signal which bounces off an optical mirror is to move the mirror forward or backward in some mechanical fashion. A movable mirror is thus the simplest kind of phase modulator. One way to move a mirror electrically is to use either a piezoelectric, magnetostrictive, or magneto-inductive mirror mount (i.e., a solenoid or loudspeaker cone). These electromechanical methods are simple and inexpensive, but are generally limited to low-modulation frequencies (in the audio range), and at least with the piezoelectric mount to very small motions (a few microns at the most).

The simplest form of phase or frequency modulation inside a laser cavity is thus simply to move a cavity end mirror back and forth by an amount δL , as in

Figure 25.20, thereby producing a double-pass phase modulation $\delta\phi_m$ given by

$$\delta\phi_m = \frac{2\omega_0 \delta L}{c} = \frac{2\pi \delta p}{\lambda}, \quad (20)$$

where ω_0 is the unmodulated laser oscillation frequency and $\delta p = 2\delta L$ is the change in the cavity perimeter p . In the static limit this leads to a shift of the oscillation frequency given by

$$\omega_0 + \delta\omega_0 = q \frac{2\pi c}{p + \delta p} \approx \omega_0(1 - \delta p/p), \quad (21)$$

which can be rewritten as

$$\frac{\delta\omega_0}{\Delta\omega_{\text{ax}}} = \frac{-\delta\phi_m}{2\pi} \approx -\frac{\delta p}{\lambda} \approx -\frac{2\delta L}{\lambda}. \quad (22)$$

This emphasizes that a net mirror motion of one-half wavelength in the standing-wave cavity, or an added phase shift of $\delta\phi_m = 2\pi$ in either type of cavity, will shift the laser's oscillation frequency by exactly one axial mode spacing $\Delta\omega_{\text{ax}}$.

Phase-Modulated Laser Cavity Model

What effects are produced if a more general phase modulator of any of the preceding types is placed inside an oscillating laser cavity? To answer this question, we will use a simplified but still generally realistic model of the laser cavity as shown in Figure 25.21. To make the analysis apply equally well to standing-wave or ring resonators, let us define the quantity $\phi_m(t)$ to be the double-pass phase modulation going through the modulator and back again in a standing-wave cavity, or the single-pass phase modulation going once through the modulator in a ring laser. The net round-trip effects in the ring or standing-wave cavities will then be essentially the same, provided that the modulator for the standing-wave is placed immediately adjacent to an end mirror, as is usually done.

Consider then a general time-varying phase modulation $\phi_m(t)$, but suppose for simplicity that the modulation frequencies applied to the phase modulator are on the order of an axial mode spacing or smaller, whereas the laser gain curve is perhaps several axial modes wide. The frequency-modulation sidebands produced by the intracavity modulator acting on the circulating light within the laser cavity will then all fall well within the atomic gain profile. The effect of the finite bandwidth of the laser medium on the modulation sidebands can then be ignored to first order, along with any other dispersion effects in the laser cavity.

Suppose we then consider the time-varying laser oscillation signal at some arbitrary plane inside the laser cavity, for example, the plane just at the output side of the phase modulator, as illustrated in the cavity diagrams. The signal $\mathcal{E}_2(t)$ leaving the phase modulator at time t is then just equal to the signal $\mathcal{E}_1(t)$ incident on the modulator at the same time, multiplied by the modulator transfer function $e^{i\phi_m(t)}$. (We lump all the phase modulation into a plane of zero thickness for simplicity.) But if we assume that the net round-trip gain for the radiation in the remainder of the laser cavity is exactly unity—which is equivalent to our assumption that atomic bandwidth and dispersion effects can be neglected—then the signal $\mathcal{E}_1(t)$ arriving at the modulator at time t is equal to the signal $\mathcal{E}_2(t - T)$ which left the modulator one round-trip transit time T earlier.

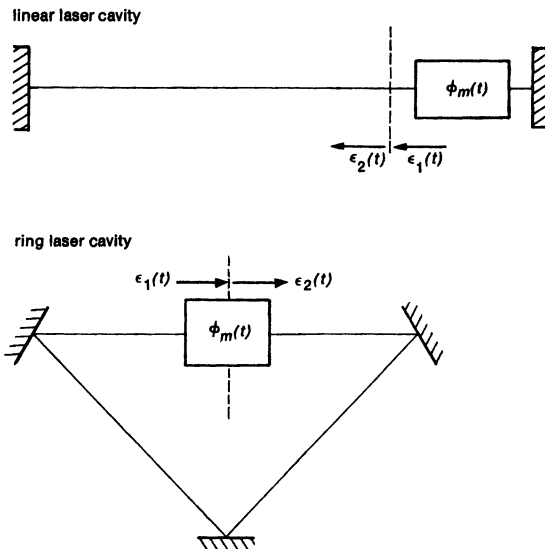


FIGURE 25.21
Cavity models for the analysis of intracavity phase modulation.

Hence we may write the fundamental relationship for phase modulation inside a laser cavity (at least for signals within the atomic linewidth) as

$$\mathcal{E}_2(t) = \mathcal{E}_1(t) \times e^{j\phi_m(t)} \approx \mathcal{E}_2(t - T) \times e^{j\phi_m(t)}. \quad (23)$$

Let us assume that the optical signal inside the laser cavity has the general form

$$\mathcal{E}_2(t) \approx E_0 \exp j[\omega_0 t + \phi_c(t)], \quad (24)$$

where E_0 is the (approximately constant) signal amplitude; ω_0 is the unmodulated oscillation frequency or carrier frequency; and $\phi_c(t)$ is the time-varying phase modulation of the laser cavity signal produced by the phase modulator. Equation 25.23 then translates to the self-consistency condition

$$E_0 \exp j[\omega_0 t + \phi_c(t)] = E_0 \exp j[\omega_0(t - T) + \phi_c(t - T) + \phi_m(t)]. \quad (25)$$

But upon using the fact that (by definition) the frequency ω_0 is an axial mode for which $\omega_0 T = q2\pi$, this reduces to the phase modulation condition

$$\phi_c(t) = \phi_c(t - T) + \phi_m(t). \quad (26)$$

This is the basic equation for analyzing low-frequency phase modulation effects in the laser cavity.

Sinusoidal Phase or Frequency Modulation

Let's consider first pure sinusoidal modulation of the intracavity phase modulator. Suppose the phase modulation is driven sinusoidally at a modulation

frequency ω_m with a peak phase deviation Φ_m in the form

$$\phi_m(t) = \Phi_m \cos \omega_m t. \quad (27)$$

The oscillation signal in the laser cavity will then acquire a similar phase modulation of the form

$$\phi_c(t) = \left(\frac{\Phi_m}{2 \sin \omega_m T/2} \right) \times \sin \omega_m (t + T/2) \quad (28)$$

This result may make more physical sense if we interpret it as a sinusoidal modulation of the instantaneous frequency $\omega_i(t)$ of the laser, where we define instantaneous frequency in the manner introduced in an earlier chapter, namely,

$$\begin{aligned} \omega_i(t) &\equiv \frac{d[\omega_0 t + \phi_c(t)]}{dt} \\ &= \omega_0 + \frac{\Phi_m}{2\pi} \times \frac{\pi \omega_m}{\sin(\pi \omega_m / \Delta \omega_{\text{ax}})} \times \cos \omega_m (t + T/2). \end{aligned} \quad (29)$$

It is clear that an applied *phase modulation* with peak amplitude Φ_m inside the laser cavity produces a *frequency modulation* of the laser signal itself.

This frequency modulation reduces in the low-modulation-frequency limit to

$$\omega_i(t) \approx \omega_0 + \frac{\Phi_m \Delta \omega_{\text{ax}}}{2\pi} \cos \omega_m (t + T/2) \quad \text{if } \omega_m \ll \Delta \omega_{\text{ax}}. \quad (30)$$

The peak frequency deviation of the laser signal is thus given by the quasi static frequency-tuning result $\omega_i \approx \omega_0 + (\Phi_m / 2\pi) \omega_{\text{ax}}$, so long as the modulation frequency ω_m is fairly small compared to the axial mode spacing ω_{ax} .

If, however, the modulation frequency ω_m approaches the axial mode frequency ω_{ax} —which means that the modulation sidebands produced on any one axial mode come close to the adjoining axial mode cavity resonances—then the modulation index and the peak frequency deviation diverge toward very large values, as shown in Figure 25.22. At some point in this limit, the simplified analysis of this section will no longer apply, and we must use instead the kind of axial-mode-coupling analysis that we will develop to describe laser mode locking in a later chapter.

Linear Phase Shift and Instantaneous Frequency Switching

Let us next consider the interesting effects that can be produced by a sudden or fast-rising step-function phase shift applied inside a laser cavity. Suddenly and rapidly moving one end mirror of a laser cavity to a new position is, at least in principle, the simplest way of producing such a fast-rising phase shift. Applying an additional round-trip phase shift of magnitude Φ_m inside a laser cavity will shift the resonance frequency of the cavity, and hence eventually the laser oscillation frequency, over by an amount $(\Phi_m / 2\pi) \omega_{\text{ax}}$. There are interesting experiments in which we might wish to shift the oscillation frequency of a cw laser quite suddenly, by some small or large amount. How fast (and how far) can we actually jump the oscillation frequency inside an oscillating laser cavity?

To understand how we can do this in an ideal fashion, suppose that the intracavity phase modulator $\phi_m(t)$ is changed linearly during one cavity round-trip transit time T from an initial value $\phi_m(0) = 0$ at time $t = 0$, to a final

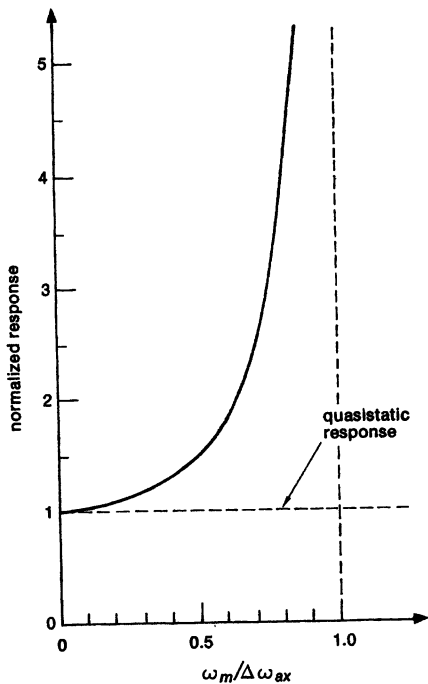


FIGURE 25.22
Modulation response of laser oscillation frequency to sinusoidal cavity phase modulation.

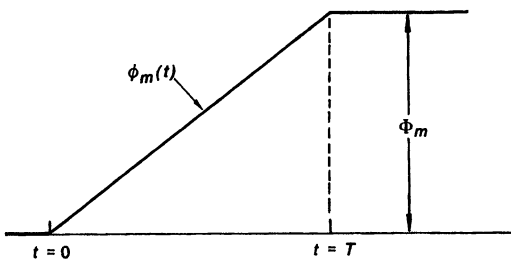


FIGURE 25.23
Ideal linearly ramped cavity phase modulation.

(constant) value $\phi_m(T) = \Phi_m$ exactly one round-trip time later, as illustrated in Figure 25.23. We thus have the phase modulation input

$$\phi_m(t) = \begin{cases} 0, & t < 0 \\ \Phi_m t / T, & 0 < t < T \\ \Phi_m, & t > 0. \end{cases} \quad (31)$$

A little examination will then show that the phase $\phi_c(t)$ of the cavity oscillation signal itself will rise linearly with a time slope $d\phi_c(t)/dt = \Phi_m/T$, beginning at $t = 0$ and continuing indefinitely.

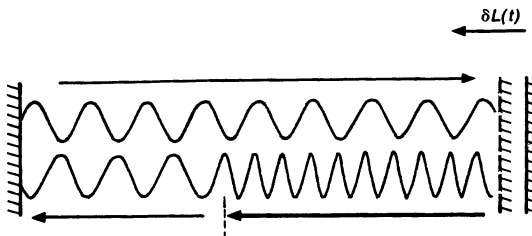


FIGURE 25.24
Doppler frequency shift for a linearly inward-moving cavity end mirror.

But this is the same as saying that the oscillation frequency $\omega_i(t)$ of the laser changes essentially instantaneously at $t = 0$ from its original value ω_0 to a new quasi static value, as given by

$$\omega_i(t) = \begin{cases} \omega_0, & t < 0 \\ \omega_0 + (\Phi_m/2\pi)\omega_{\text{ax}}, & t > 0. \end{cases} \quad (32)$$

With this particular phase modulation input, therefore, we can *instantaneously* shift the oscillation frequency by any desired amount (even by several axial mode spacings if $\Phi_m \gg 2\pi$), provided only that (a) the new phase shift is inserted linearly in time over exactly one round-trip time, and (b) the resulting signal remains within the central part of the atomic gain profile of the laser medium.

Physical Interpretation: Linear Doppler Shift

This conclusion seems to run contrary to the intuition of some laser students. Some people argue, for example, that changing the oscillation frequency of a laser cavity ought to take at least several laser cavity lifetimes τ_c , since “it should take time for the photons at the old frequency to die out, and the new oscillation photons at the new frequency to build up.” Setting aside the introduction into this argument of particle-like photons (which is almost always a mistake in any laser analysis), we can understand this instantaneous frequency shift as follows.

First, consider those portions of the recirculating cavity signal which pass through the phase modulator during the linear ramp interval. These waves receive a linear phase modulation as given by the middle line of Equation 25.31 for $\phi_m(t)$.

Suppose we think of this phase modulation as being provided, for example, by a linearly moving end mirror in a standing-wave cavity (though it would be difficult in practice to move a real mirror this rapidly). Then, the reader can easily determine that the frequency shift of Equation 25.32 is exactly equivalent to a doppler shift off this moving mirror. This linear phase modulation or doppler shift, in fact, frequency shifts the reflected wave by exactly the desired frequency jump between the new and old values.

Figure 25.24 then shows (in greatly exaggerated form) how the optical cycles in the cavity might appear shortly after the end mirror has started moving inward (i.e., shortly after the ramp of phase modulation has begun). That portion of the circulating signal reflected from the mirror has been doppler-shifted upward in frequency by the inward-moving mirror. If the duration of the linear ramp lasts, as in our ideal situation, exactly long enough for all the circulating waves within the laser cavity to come around and be doppler-shifted by the requisite amount

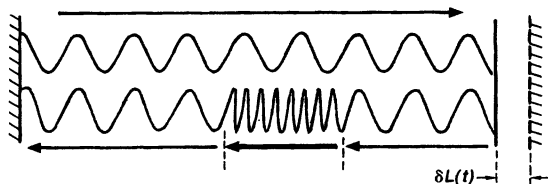


FIGURE 25.25
Pulsed frequency shifting inside a laser cavity for a non-ideal linear ramp.

exactly once, then all of the circulating radiation within the cavity will be shifted to the new frequency. The moving mirror then stops, having just exactly done its job.

The new oscillation frequency need not be an axial mode of the old cavity. It will, however, be automatically an axial mode of the new cavity, with its new cavity length changed by the effective amount $\delta L = -\Phi_m \lambda / 4\pi$.

Note that the results given here only apply to the instantaneous $\mathcal{E}(t)$ field at one particular plane in the cavity, namely, just after the phase modulator. The same frequency shift only arrives at any other planes within the laser cavity after an appropriate transit time delay.

Exact Results: General Analysis

Modulation signals that do not exactly match the ideal ramp waveform of Figure 25.23 will produce more complex frequency shifting effects. Suppose the mirror moves the same total distance in a shorter time (i.e., shorter than the cavity round-trip time). The recirculating signal shortly after the mirror moves will then look something like the drawing in Figure 25.25 (again with the modulation effects greatly exaggerated). We will then need to consider the Fourier transform of the signal circulating inside the cavity, as expanded in axial cavity modes of the new cavity length; and consider how these new axial mode amplitudes will grow or decay in the cavity following the switching time.

An exact analysis of intracavity phase modulation with any waveform $\phi_m(t)$ (still assuming a perfectly flat atomic gain profile) can be obtained as follows. Suppose we define the Fourier transforms of the modulator phase $\phi_m(t)$ and of the resulting cavity signal phase $\phi_c(t)$ in the form

$$\Phi_x(p) = \int_{-\infty}^{\infty} \phi_x(t) e^{-j2\pi p t} dt, \quad (33)$$

with the inverse transform

$$\phi_x(t) = \int_{-\infty}^{\infty} \Phi_x(p) e^{j2\pi p t} dp. \quad (34)$$

where x can be either m for the modulator or c for the cavity signal. From a standard theorem for Fourier transforms we can write the transform of the time-delayed cavity phase as

$$\int_{-\infty}^{\infty} \phi_c(t - T) e^{-j2\pi p t} dt = e^{-j\pi p T} \Phi_c(p). \quad (35)$$

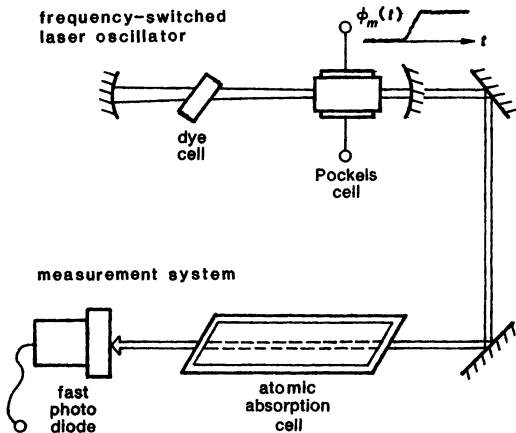


FIGURE 25.26
Spectroscopy system using a frequency-switched laser oscillator.

Hence the basic relationship between $\Phi_c(p)$ and $\Phi_m(p)$ becomes, in the transform domain,

$$\Phi_c(p) = \frac{\Phi_m(p)}{1 - e^{-j2\pi pT}} = \frac{e^{j\pi Tp}\Phi_m(p)}{2j \sin \pi Tp}. \quad (36)$$

We can then invert this transform to find the phase modulation $\phi_c(t)$ of the laser cavity signal produced by any arbitrary phase modulation $\phi_m(t)$.

We may also define $\Omega_i(p)$ to be the Fourier transform of the instantaneous frequency deviation $\omega_i(t) - \omega_0 \equiv d\phi_c(t)/dt$. Another Fourier theorem then tells us that the instantaneous frequency modulation of the laser is given by the inverse transform of

$$W_i(p) = j2\pi\Phi_c(p) = \frac{\pi p e^{j\pi Tp}\Phi_m(p)}{\sin \pi Tp}. \quad (37)$$

Our earlier results are specific examples of what can be produced by specific phase modulations $\phi_m(t)$.

Laser Frequency Switching Spectroscopy

Laser frequency switching, using exactly the electrooptic ramp technique described in Figure 25.23 and Figure 25.24, has become the basis of a very useful form of time-resolved spectroscopy, in which coherent optical transients are excited by fast frequency-switched laser signals. One elementary form for such an experiment is illustrated in Figure 25.26.

The example illustrated here uses a cw dye laser, which has a very wide atomic line, so that it can potentially be frequency switched over a large range. The output from this laser is sent through an atomic absorption cell, with the laser initially tuned at or near the center of the moderately narrow atomic transition in the cell. Hence this signal, during an initial preparation phase, excites a steady-state coherent polarization in the atoms on this transition. (This induced atomic polarization may involve all the atoms in a homogeneously broadened

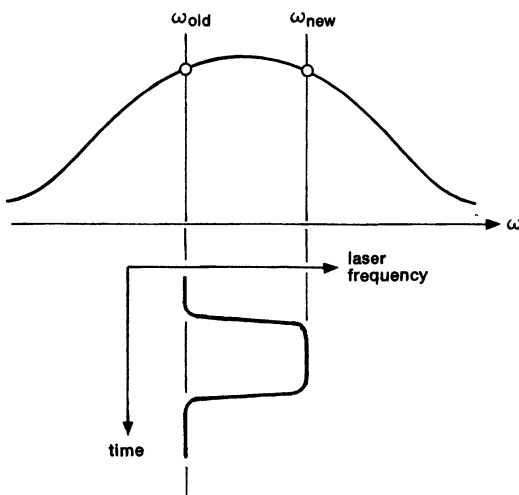


FIGURE 25.27
Frequency-switched laser spectroscopy using the experimental system of Figure 25.26. (The old and new laser frequencies see entirely different spectral packets.)

transition, or just those atoms in a single spectral packet with which the signal is in resonance in an inhomogeneously broadened transition.)

The laser frequency is then suddenly switched to a new value that is either entirely outside the atomic absorption profile, though still within the much wider linewidth of the dye laser itself, or at least that is tuned to a completely different spectral packet in the inhomogeneously broadened absorption cell, as shown in Figure 25.27.

So far as the initially excited atoms in the absorption cell are concerned, the effect of this frequency jump is the same as if the laser signal is suddenly turned off—the laser signal is now shifted so far off resonance as to be irrelevant. The oscillating dipole polarization of these atoms will then continue to oscillate and to radiate at the natural oscillation frequency of the atoms, but this polarization will die out with the decay time T_2 associated with the atomic transition.

A very important aspect of this experiment is that these oscillating atoms were initially excited by the spatially coherent forward-traveling laser beam. Hence they oscillate and continue to radiate in the same forward direction and with the same collimated beam pattern as the exciting laser beam. This spatial as well as temporal coherence of the radiation persists—though its amplitude dies away with time constant T_2 —even after the laser frequency is switched.

Following the switching time the photodetector in this experiment thus sees a linear combination of the frequency-shifted, constant-amplitude laser beam, plus the exponentially decaying radiation from the excited atoms at the original excitation frequency. These two signals mix or heterodyne in the square-law photodetector, with the frequency-shifted laser acting as a frequency offset local oscillator, and the atomic radiation as the signal. The result is a beat frequency output from the photodetector at the difference frequency $\omega_{\text{old}} - \omega_{\text{new}}$, as determined by the laser frequency jump, with an amplitude that decays away in proportion to the decaying radiation from the originally excited spectral packet.

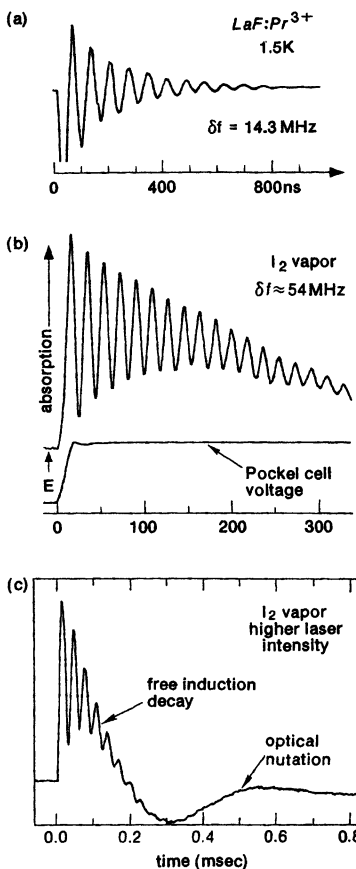


FIGURE 25.28
 Some typical experimental results from frequency-switched spectroscopic experiments

Experimental Results

Figure 25.28 illustrates exactly this kind of result. The top trace shows an essentially ideal free induction decay signal obtained from a very narrow line produced by Pr^{3+} ions in LaF_3 crystals at liquid helium temperature. The beat note between the frequency-shifted laser signal and the initially excited and still radiating atoms is obvious. The laser frequency jump from inside to outside the atomic line is 14.3 MHz in this instance.

In the second and third traces, a cw dye laser signal with a few mW of power at 589.75 nm is passed through a cell containing 30-m torr of I_2 vapor, which has strong narrow atomic lines in the visible. In the second trace the laser frequency has been suddenly frequency shifted by approximately 54 MHz, starting and ending within the doppler-broadened linewidth of one of the discrete optical-frequency rotational-vibrational absorption lines of the I_2 molecule. The decaying oscillation signal is the beat note at 54 MHz between the free-induction

decay radiation from the originally excited molecules and the laser signal at its new frequency.

The third trace is a similar result but with a somewhat higher laser power and a longer time scale. The broader, heavily damped, negative-going oscillation after the free-induction signal has died out represents the “optical nutation” response of the new group of iodine molecules that are being driven into forced oscillation in the spectral packet at the new laser frequency after switching.

The combination of the spatial coherence of the free-induction-decay signal from the originally excited atoms, plus the sensitivity advantage of coherent optical heterodyne detection, plus the relative simplicity of laser frequency switching, all combine to make this a very attractive and important technique for observing coherent transients and measuring various relaxation times in atomic systems. Similar experiments with much faster switching, and switching over much larger frequency jumps, have also been demonstrated.

Other variations on this technique include switching the laser frequency into rather than out of the atomic line, in order to observe the turn-on transient for the atomic response; switching from one packet to another within an inhomogeneous atomic line; and switching away from and then back to a single spectral packet, to observe more complicated atomic dynamics. Detailed observation of the resulting decay profiles can bring out information about hyperfine degeneracies within atomic lines; about the widths and shapes of the holes burnt in inhomogeneous lines; and about many other details of great interest to atomic and molecular spectroscopists.

REFERENCES

An excellent introduction to laser frequency switching and some of its spectroscopic applications is in A. Z. Genack and R. G. Brewer, “Optical coherent transients by laser frequency switching,” *Phys. Rev. A* **17**, 1463–1473 (April 1978).

The practicalities of rapid frequency switching in a CO₂ laser are demonstrated in R. L. Shoemaker, et. al, “Frequency-switchable CO₂ laser: design and performance,” *Appl. Optics* **21**, 961–966 (March 1, 1982).

Problems for 25.3

1. *Verifying the step-function frequency-shift analysis.* Verify that applying the exact form of frequency-domain or Fourier transform analysis developed at the end of this section to the ideal ramp phase shift described earlier in the section will produce exactly the same instantaneous step-function frequency shift as described in the text.
 2. *Frequency shift analysis for a nonideal phase ramp.* Repeat the previous problem for a ramp that takes twice as long (i.e., two round-trip times) to rise to its final value
-

25.4 LASER MODE COMPETITION

We now turn to a rather different but also important kind of laser dynamic behavior, namely, the mode competition between simultaneously oscillating (or potentially oscillating) modes in a laser oscillator.

Most laser cavities have the potential of oscillating in a large number of different modes, including different axial and transverse cavity modes; different directions in ring-laser cavities; and even different senses of polarization in cavities with internal mirrors and no Brewster windows. Different modes will in general have different gains, losses and saturation parameters, and will compete for the available population inversion in the laser. Oscillation in one mode will generally reduce the gain available for another mode, and in some situations may suppress the other mode entirely. The purpose of this section is to introduce some of the elementary concepts and analytical techniques that arise in discussing competition between laser modes.

Mode Competition Effects

Competition between modes in a laser cavity is in general a very complex problem. We may need to take into account among other things:

- Self-saturation and cross-saturation effects between modes, both in the gain medium and in any saturable absorbing media that may be present.
- Possible injection locking and frequency pulling effects between modes caused by scattering effects or by intracavity modulators (as we will discuss in more detail in a later chapter).
- The degree of spatial overlap between modes. Two different transverse or axial modes will in general be partially overlapping and partially separated in space, and thus will have some shared and some separate regions of population inversion.
- The degree of spectral overlap between modes, including whether the competing modes are at the same or different frequencies, and whether the atomic line is homogeneous or inhomogeneous.

In addition we may sometimes need to consider the beating effects between modes at different frequencies, and the population pulsations that this can produce. If two modes of different frequencies are present, the total optical intensity at any point includes both a dc component due to each mode, plus an oscillating component at the difference frequency between modes. The saturation effects due to this time-varying part will be different depending on whether the difference frequency is large or small compared to the atomic relaxation rates for the population inversion.

Self-Saturation and Cross-Saturation Coefficients

To illustrate some of the elementary features of mode competition we will review in the remainder of this section the simplest form of pure intensity or gain competition between just two potentially oscillating modes. We will consider in this discussion only the self-saturation and cross-saturation effects on the respective gains for these two modes, ignoring any back-scattering or cross-scattering

effects that may couple one mode into the other. As in so many other aspects of laser behavior, the fundamental concepts involved in the discussion are much older than the laser, but are particularly well-illustrated by the laser example.

Let us note first that the self-saturation and cross-saturation effects between any two simultaneously oscillating modes in a laser will depend very much both on the spatial overlap of the two modes, and also their spectral overlap and on whether the atomic transition involved is homogeneous or inhomogeneous. For example, in the simplest situation, a completely homogeneous atomic transition being saturated by two incoherently related signals I_1 and I_2 at different frequencies ω_1 and ω_2 , we can in general write the gain saturation for mode #1 in the form

$$\alpha_m(\omega_1) = \frac{\alpha_{m0}(\omega_1)}{1 + \kappa_{11}I_1 + \kappa_{12}I_2} \approx \alpha_{m0}(\omega_1) \times [1 - \kappa_{11}I_1 - \kappa_{12}I_2], \quad (38)$$

and for mode #2 in the form

$$\alpha_m(\omega_2) = \frac{\alpha_{m0}(\omega_2)}{1 + \kappa_{22}I_2 + \kappa_{21}I_1} \approx \alpha_{m0}(\omega_2) \times [1 - \kappa_{22}I_2 - \kappa_{21}I_1]. \quad (39)$$

The coefficients κ_{11} and κ_{22} then represent *self-saturation* of the gains of modes #1 and #2 by their own intensities in each situation, whereas the coefficients κ_{12} and κ_{21} represent the *cross-saturation* of the gain of mode #1 by the intensity of mode #2, and vice versa. The values of these four factors will depend on the inverse of the saturation intensity in the laser medium, but they will also depend on spatial overlaps of the modes with the gain medium and with each other, and on lineshape factors that must be included to take account of how far each of the signals is off the resonance line center. The simplifying approximation in the second term in each equation will then be valid provided the gain coefficient is not too strongly saturated by either signal.

Suppose the two signals are incoherently related (i.e., their intensities can simply be added to get the total intensity in the medium); that both of their frequencies are near the center of a strongly homogeneous atomic gain profile; and that their spatial patterns are essentially identical in the gain medium. We would then expect to find that the four coefficients all have approximately equal values, i.e., $\kappa_{11} \approx \kappa_{22} \approx \kappa_{12} \approx \kappa_{21}$.

Suppose the atomic transition is strongly inhomogeneous, on the other hand, so that the two signals lie within quite different spectral packets or velocity groups. We would then expect to find only very weak cross-saturation effects, so that $\kappa_{12}, \kappa_{21} \ll \kappa_{11}, \kappa_{22}$. In the more general situation of mixed homogeneous and inhomogeneous broadening, the evaluation of the relative self-saturation and cross-saturation effects will require a complicated integration over the partial saturation effects of all the spectral packets, such as we will carry out in a later chapter.

The self-saturation and cross-saturation effects between two modes can thus have quite different relative magnitudes in different situations. We might further recall that for two coherently related signals at the same frequency passing in opposite directions through a completely homogeneous transition, and thus producing significant hole burning and grating backscattering, we have earlier derived the results that the net gain (or absorption) for signal #1 depends on

the two signal intensities (in the small-saturation approximation) in the form

$$\alpha_m(\omega_1) \approx \alpha_{m0}(\omega_1) \times \left[1 - \frac{I_1 + 2I_2}{I_{\text{sat}}} \right]. \quad (40)$$

That is, here the cross-saturation coefficients κ_{12} and κ_{21} are actually larger than the self-saturation coefficients κ_{11} and κ_{22} effects by a factor of 2.

Two-Mode Competition Analysis

To describe the competition between two potentially oscillating modes in a fairly general fashion, therefore, we might write the rate equations, or intensity growth equations, for the two assumed modes in the generalized form

$$\begin{aligned} dI_1/dt &\approx \gamma_{m1}I_1 \times [1 - \kappa_{11}I_1 - \kappa_{12}I_2] - \gamma_{c1}I_1 \\ dI_2/dt &\approx \gamma_{m2}I_2 \times [1 - \kappa_{22}I_2 - \kappa_{21}I_1] - \gamma_{c2}I_2. \end{aligned} \quad (41)$$

This says that the two modes each have unsaturated growth rates γ_{m1} and γ_{m2} and cavity decay rates γ_{c1} and γ_{c2} , respectively. The saturation effects on the growth rate for each mode caused by itself and by the opposite mode are then expressed in terms of the same self-saturation and cross-saturation parameters κ_{ij} , which are inversely proportional to the saturation intensity in the laser medium.

To be consistent with much of the published literature, however, we will instead rewrite Equations 25.41 in a notation used originally by Willis Lamb, and repeated later in the book by Sargent, Scully and Lamb, namely,

$$\begin{aligned} dI_1/dt &= [\alpha_1 - \beta_1I_1 - \theta_{12}I_2] \times I_1 \\ dI_2/dt &= [\alpha_2 - \beta_2I_2 - \theta_{21}I_1] \times I_2. \end{aligned} \quad (42)$$

The coefficients α_1 and α_2 are then obviously the small-signal or unsaturated gains minus losses for each mode, whereas the coefficients β_i and θ_{ij} represent the self- and cross-saturation coefficients. We will now explore the transient and steady-state solutions to Equations 25.42 in some detail.

Steady-State Solutions

Steady-state solutions to Equations 25.42 obviously require either that the saturated gain factor $\alpha_i - \beta_iI_i - \theta_{ij}I_j = 0$, or else that the corresponding intensity $I_i = 0$, in each of Equations 25.42. The condition for zero saturated gain for each mode is given by one of the linear relations

$$I_1 = (\alpha_1/\beta_1) - (\theta_{12}/\beta_1)I_2 \quad \text{and} \quad I_2 = (\alpha_2/\beta_2) - (\theta_{21}/\beta_2)I_1, \quad (43)$$

and each of these relations can in turn be represented by a straight line in the I_1, I_2 plane, as illustrated in Figure 25.29. These two lines then may or may not intersect in the first quadrant of the I_1, I_2 plane, as shown in Figures 25.30 and 25.31.

To develop this analysis further, let us indicate the origin of each of these lines on its own axis by the points $O_1 \equiv \alpha_1/\beta_1$ and $O_2 \equiv \alpha_2/\beta_2$; and the tip or termination of each vector, where it intercepts the opposite axis, by $T_1 = \alpha_1/\theta_{12}$ and $T_2 = \alpha_2/\theta_{21}$. Then, whether or not the two lines intersect, the two points

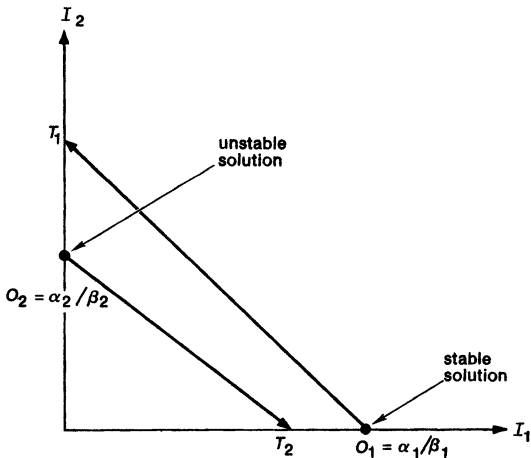


FIGURE 25.29
Single-mode coupled-oscillator conditions.

O_1 and O_2 clearly represent at least potential *single-mode steady-state operating points* for the two-mode laser, corresponding to the operating conditions

$$I_{1,ss} = O_1 = \alpha_1/\beta_1 \quad \text{and} \quad I_{2,ss} = 0 \quad (44)$$

on one hand, and to

$$I_{2,ss} = O_2 = \alpha_2/\beta_2 \quad \text{and} \quad I_{1,ss} = 0 \quad (45)$$

in the other.

If the two vectors also have an intersection point in the first quadrant of the I_1, I_2 plane, as illustrated in Figures 25.30 and 25.31, then that intersection also represents a third potential *two-mode steady-state operating point*, which we can call O_3 . Both modes can potentially oscillate simultaneously at this point, with steady-state intensities given by

$$I_{1,ss} = \frac{\alpha_1 - (\theta_{12}/\beta_2)\alpha_2}{(1 - C)\beta_1} \quad \text{and} \quad I_{2,ss} = \frac{\alpha_2 - (\theta_{21}/\beta_1)\alpha_1}{(1 - C)\beta_2}, \quad (46)$$

where C is a dimensionless coupling factor given by

$$C \equiv \frac{\theta_{12}\theta_{21}}{\beta_1\beta_2}. \quad (47)$$

The question now is, under what conditions will these three potential steady-state solutions be stable against small perturbations?

Perturbation Stability Analysis

To evaluate this we can follow the usual approach of expanding the intensities $I_1(t)$ and $I_2(t)$ about the steady-state intensities in the form

$$I_1(t) = I_{1,ss} + \epsilon_1(t) \quad \text{and} \quad I_2(t) = I_{2,ss} + \epsilon_2(t), \quad (48)$$

and then look for the linearized growth or decay rates of the small perturbations $\epsilon_1(t)$ and $\epsilon_2(t)$ about each potential steady-state operating point.

Let us treat first the single-mode operating point at O_1 , where mode #1 is oscillating alone with intensity $I_1 = \alpha_1/\beta_1$. The linearized differential equations for the small-signal perturbations about this point then become

$$\frac{d\epsilon_1(t)}{dt} \approx -\alpha_1\epsilon_1(t) - \frac{\theta_{12}\alpha_1}{\beta_2}\epsilon_2(t), \quad (49)$$

and

$$\frac{d\epsilon_2(t)}{dt} \approx \left[\alpha_2 - \frac{\theta_{21}\alpha_1}{\beta_1} \right] \epsilon_2(t). \quad (50)$$

The requirement that mode #2 remain stable at zero amplitude at this operating point is clearly determined by the stability criterion that

$$\frac{\theta_{21}\alpha_1}{\beta_1} > \alpha_2 \quad \text{or} \quad \frac{\theta_{21}\alpha_1}{\beta_1\alpha_2} > 1. \quad (51)$$

In geometric terms, this condition says that

$$\frac{O_1}{T_2} = \frac{\alpha_1/\beta_1}{\alpha_2/\beta_{21}} > 1. \quad (52)$$

That is, for single-mode stability the origin O_1 of the zero-gain line for mode #1 must be farther out on the I_1 intensity axis than the tip T_2 of the zero-gain line for mode #2.

The stability criterion for the single-mode solution at O_2 is obviously the same as Equation 25.52, except that the indices are reversed, i.e.,

$$\frac{O_2}{T_1} \equiv \frac{\theta_{21}\alpha_2}{\beta_2\alpha_1} > 1. \quad (53)$$

In geometric terms, it is clear that if the two zero-gain lines do not intersect, as in Figure 25.29, the origin of the outermost of the two vectors (vector $O_1 \rightarrow T_1$ in this illustration) is the stable solution. The laser oscillates only in mode #1, and this mode completely suppresses the less favored mode #2.

Dual-Mode Stability Analysis

When the two zero-gain vectors do intersect, as in Figures 25.30 and 25.31, two quite different situations can occur. First of all, if the origins O_i of both vectors lie inside the tips T_j of the opposite vectors on the I_i axes, as in Figure 25.30, then by the criteria just developed neither of the single-mode solutions O_1 or O_2 can be stable. Hence, the dual-mode solution O_3 must be the only stable solution. The mathematical criterion for this is that both O_1/T_2 and O_2/T_1 must be < 1 , which we can write in the combined form,

$$\frac{O_1}{T_2} \times \frac{O_2}{T_1} = \frac{\theta_{12}\theta_{21}}{\beta_1\beta_2} \equiv C < 1 \quad (\text{weak coupling}). \quad (54)$$

This is generally referred to as *weak coupling* between the two oscillating modes. Both modes can oscillate simultaneously, sharing the same gain medium.

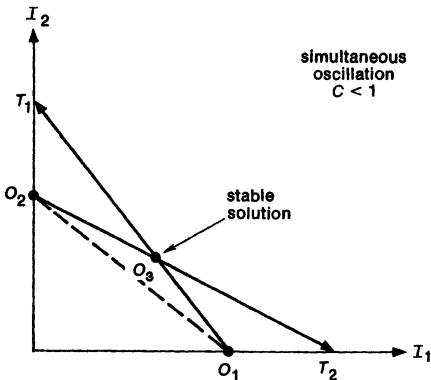


FIGURE 25.30
Weakly coupled oscillator modes ($C < 1$).

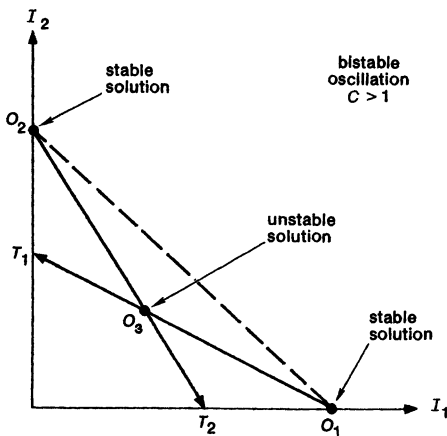


FIGURE 25.31
Strongly coupled oscillator modes
($C > 1$).

For strong coupling, on the other hand, we have the opposite condition, namely,

$$C \equiv \frac{\theta_{12}\theta_{21}}{\beta_1\beta_2} = \frac{O_1}{T_2} \times \frac{O_2}{T_1} > 1 \quad (\text{strong coupling}), \quad (55)$$

and in fact both O_1/T_2 and O_2/T_1 individually > 1 , as illustrated in Figure 25.31. For strong coupling, both of the single-mode solutions O_1 or O_2 are stable, and hence presumably the dual-mode solution O_3 is not.

To verify these conclusions mathematically, we must apply the perturbation expansion about the dual-mode solution at point O_3 . The linearized perturbation equations then become, after some algebra,

$$\begin{aligned} d\epsilon_1/dt &= -\beta_1 I_{1,SS} \epsilon_1 - \theta_{12} I_{1,SS} \epsilon_2, \\ d\epsilon_2/dt &= -\theta_{21} I_{2,SS} \epsilon_1 - \beta_2 I_{2,SS} \epsilon_2. \end{aligned} \quad (56)$$

To see if these equations are stable, we assume potential variations in $\epsilon_1(t)$ and $\epsilon_2(t)$ of the form e^{st} , and then evaluate the resulting secular determinant given by

$$\begin{vmatrix} s + \beta_1 I_{1,SS} & \theta_{12} I_{1,SS} \\ \theta_{21} I_{2,SS} & s\beta_2 I_{2,SS} \end{vmatrix} = 0. \quad (57)$$

This reduces, after some further algebra, to the secular equation

$$s^2 + \left(\frac{\alpha'_1 + \alpha'_2}{1 - C} \right) s + \frac{\alpha'_1 \alpha'_2}{1 - C} = 0, \quad (58)$$

where α'_1 and α'_2 are reduced gains given by $\alpha'_1 = \alpha_1 - (\theta_{12}/\beta_2)\alpha_2$ and $\alpha'_2 = \alpha_2 - (\theta_{21}/\beta_1)\alpha_1$. (These gains represent physically the net gains for mode #1 when mode #2 is oscillating by itself at its full single-mode strength, and vice versa.)

The roots of the secular equation are then given by

$$2s_1, 2s_2 = - \left(\frac{\alpha'_1 + \alpha'_2}{1 - C} \right) \pm \sqrt{\left(\frac{\alpha'_1 + \alpha'_2}{1 - C} \right)^2 - 4 \frac{\alpha'_1 \alpha'_2}{1 - C}}. \quad (59)$$

The weak-coupling situation corresponds to $C < 1$ and $\alpha'_1, \alpha'_2 > 0$, which makes both of the roots in this equation negative. The intersection point O_3 in the weak-coupling situation is therefore a stable dual-mode operating point, as we surmised in the preceding.

The strong-coupling situation, with $C > 1$ and $\alpha'_1, \alpha'_2 < 0$, by contrast causes one of the roots to take on the positive value

$$2s_1 = \left| \frac{\alpha'_1 + \alpha'_2}{C - 1} \right| + \sqrt{\left| \frac{\alpha'_1 + \alpha'_2}{C - 1} \right|^2 + 4 \frac{\alpha'_1 \alpha'_2}{C - 1}}. \quad (60)$$

The dual-mode solution at point O_3 is unstable in this situation. Even if the two modes somehow start oscillating with intensities appropriate to this point, the effect of any small perturbation will cause the laser to move to a condition where only one of the modes (either one) is oscillating by itself. A two-mode laser with strong coupling between modes is, in other words, a bistable system.

Phase-Plane Trajectory Plots

To illustrate the physical behavior of the mode competition in these various situations in a bit more detail, we can follow the lead of Lamb's original paper and plot trajectories for the coupled oscillators in the I_1, I_2 plane. Suppose the two modes are initially set oscillating with initial intensities corresponding to various points in the I_1, I_2 plane (ignoring the practical question of how this might be done).

We can then integrate the basic differential equations of motion for dI_1/dt and dI_2/dt forward in time and follow the trajectory of I_1 and I_2 as these intensities converge to a final steady-state solution in the I_1, I_2 plane. The three plots in Figure 25.32 illustrate the general nature of this behavior for single-mode oscillation, weakly coupled dual-mode oscillation, and strongly coupled or bistable single-mode oscillation. Note how the various trajectories converge toward the stable point or points indicated by the stability analysis given in the preceding.

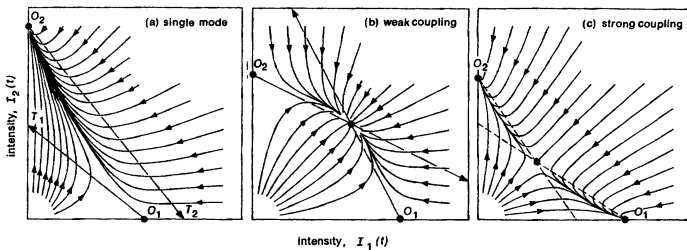


FIGURE 25.32

Oscillator trajectories in the I_1, I_2 plane corresponding to (a) single-mode, (b) weakly coupled dual-mode, and (c) strongly coupled bistable single-mode operation of a pair of competing oscillators.

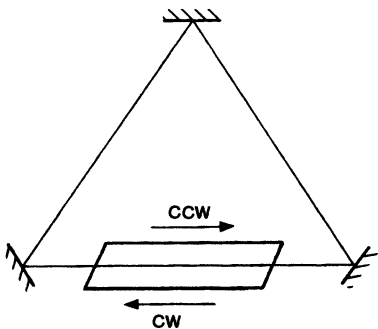


FIGURE 25.33

Competition between oppositely directed waves in a ring laser oscillator.

Examples

A few practical examples may be useful to illustrate the application of these fundamental concepts of mode competition to real lasers:

(1) *Homogeneously Broadened Ring Lasers*: One elementary example of mode competition occurs in ring lasers, where there are two potential modes having the same resonance frequency but traveling in opposite directions around the ring (Figure 25.33). Consider in particular a ring laser in which the gain medium saturates homogeneously, and in which coupling between the two directions produced by backscattering effects inside the ring cavity is negligible.

If the two oppositely traveling waves in such a cavity are at the same frequency, the cross-saturation effect between the two oppositely traveling waves will be larger by a factor of two than the self-saturation effect due to either wave alone, because of the self-induced grating effects we have described in an earlier chapter. A homogeneously broadened ring laser, at least under ideal conditions, will thus correspond to a very strongly coupled situation with $C = 4$. Such a ring should therefore oscillate, at least under ideal conditions, in only one direction at a time. This can be observed experimentally in a number of lasers, although backscattering effects, deviations of the laser medium from ideal homogeneity, and other effects may either partially or completely overcome these strong coupling effects.

Note also that a ring laser with a homogeneous saturable absorber should presumably want to run in both directions simultaneously. This corresponds in fact to the very important situation of colliding-pulse saturable-absorber mode locking, which will be discussed in more detail in a later section.

(2) *Mode competition in inhomogeneously broadened atomic systems:* In an inhomogeneous atomic transition, a strong signal saturates or “burns a hole” in only a single spectral packet, or a small group of atoms with which the signal is nearly or completely in resonance. Another competing mode may interact primarily with atoms in a different, unsaturated spectral packet. Mode competition effects in simple inhomogeneous atomic transitions thus depend very much on whether the two mode frequencies do or do not fall within the same hole, i.e., within roughly one homogeneous linewidth of each other.

If this is not so, and the two modes burn totally separate holes, the coupling can be expected to be weak ($C \ll 1$), in agreement with the common observation of simultaneous multimode oscillation in inhomogeneous lasers. If the two modes come within less than a homogeneous linewidth of each other, the coupling can be expected to approach $C \approx 1$ or neutral coupling. If the two waves are at the same frequency but traveling in opposite directions (as in a ring laser) the coupling in the inhomogeneous situation can potentially become somewhat stronger, and can approach $C \approx 2$ (rather than $C = 4$ as in the analogous homogeneous situation).

(3) *Doppler-broadened lasers, and ring-laser gyroscopes:* Inhomogeneous mode competition effects can become considerably more complex with either standing-wave or ring lasers that employ doppler-broadened inhomogeneous atomic transitions. In the ring laser, for example, if there are two cavity modes with frequencies ω_1 and ω_2 , each mode can burn a single hole at some velocity class in the doppler profile determined by both the frequency detuning $\omega - \omega_0$ of the mode and the direction in which the mode travels around the ring. We must then average the self-saturation and cross-saturation effects over all the velocity classes in the doppler-broadened atomic transition.

Suppose that in a ring-laser gyroscope only a single axial mode falls within the doppler-broadened atomic gain profile, as in Figure 25.34. If the ring-laser gyro is rotated sufficiently rapidly, then this axial mode is split into two frequencies ω_{cw} and ω_{ccw} , corresponding to clockwise and counter-clockwise traveling modes, so long as $|\omega_{\text{ccw}} - \omega_{\text{cw}}|$ is larger than the locking range of the laser gyroscope caused by backscatter within the ring.

If this axial mode, which is split into two simultaneously oscillating modes in opposite directions, is tuned off the center of the doppler gain profile on either side, then the two counter-propagating waves will burn separate and independent holes on opposite sides of the maxwellian velocity distribution. The coupling between the two modes is then weak ($C < 1$), and both modes can oscillate simultaneously, although with a slight intensity preference toward the mode nearest line center, as in the lower part of Figure 25.34.

If the axial mode is tuned near or through the atomic line center, however, the two holes merge. The coupling then moves toward neutral or even toward strong coupling ($C \geq 1$). The result is that one or the other of the oppositely traveling modes goes out just at line center, as shown in Figure 25.34. Note that this is purely an *intensity competition effect*, quite separate from the *injection locking effects* in laser gyroscopes, which are also troublesome and which we will discuss in a later chapter.

In practical ring-laser gyroscopes we want to avoid this mode competition. To accomplish this, most practical helium-neon ring-laser gyroscopes use a laser tube filled with an isotopic mixture of Ne^{20} and Ne^{22} . These two transitions, have

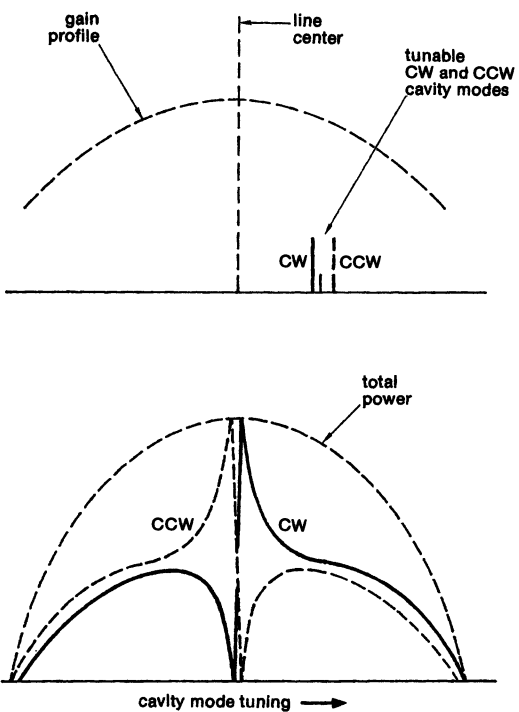


FIGURE 25.34
Mode-competition effects in an inhomogeneous single-frequency ring-laser gyroscope. The lower curve shows the intensity in each direction as a function of where the pair of modes are located underneath the atomic gain profile.

gain curves that overlap, but with center frequencies that are slightly displaced in frequency by an isotopic shift. Thus, a single axial mode can never be at the center of both lines simultaneously. The combined effect of these two transitions is sufficient to avoid the cross-mode suppression since the two modes are never simultaneously at the center of both lines.

(4) *Zeeman lasers*: Some interesting and complicated experiments have also been done to study mode competition in what are called "Zeeman lasers." These are in general gas lasers which use an inhomogeneous doppler-broadened line and a standing-wave cavity, but with no polarization selecting elements. The experiments are normally done using internal mirror lasers, in which there are no Brewster windows, with the mirror surfaces and the mirrors inside the laser carefully selected to avoid even small polarization anisotropies in the mirror reflectivity. A constant dc magnetic field is also applied either across or along the laser tube.

A laser of this type can then oscillate in two different modes representing standing-wave resonances with two different senses of polarization—usually two different senses of circular polarization I_+ and I_- —at the same axial mode frequency. These experimental results also depend on the fact that gas laser transitions will normally have an angular momentum degeneracy, with an angular momentum quantum number J' and hence $2J' + 1$ degenerate transitions for the upper laser level, and $2J'' + 1$ transitions for the lower laser level.

The calculations of the self-saturation and cross-saturation effects in these lasers then become quite complicated since we must include such effects as the superposition of the multiple transitions between each of the degenerate upper and lower levels; the polarization-dependent selection rules for each of these subtransitions; the Zeeman splitting of the upper and lower levels produced by the constant magnetic field; and the doppler velocity distribution for each of these transitions. The resulting calculations, while lengthy, are straightforward, and one can make experimental and theoretical comparisons for a variety of conditions. The results can provide a detailed test of spectroscopic theory, laser theory, and mode competition theory, all within a single experiment.

REFERENCES

The competition between oscillating modes in doppler-broadened lasers is discussed in considerable detail in an important early paper by W. E. Lamb, Jr., "Theory of an optical maser," *Phys. Rev.* **134**, A1429–A1450 (June 15, 1964). Additional results concerning mode competition in doppler-broadened gas lasers and Zeeman lasers are discussed in Chapters 9 through 12 of *Laser Physics* by M. Sargent III, M. O. Scully, and W. E. Lamb, Jr. (Addison-Wesley, 1974).

The competition effects between laser modes can be complicated by noise effects if the amplitudes of the modes involved become very weak. Suppose the pump intensity in a homogeneously broadened ring laser is reduced down very close to threshold, so that both of the two stable single-mode oscillation amplitudes become very weak. At low enough signal levels, quantum fluctuations due to spontaneous emission can then cause the laser to jump randomly between the two stable operating points. Exactly this behavior has in fact been observed in very careful experiments on a cw dye ring laser by P. Lett et al., "Macroscopic quantum fluctuations and first-order phase transition in a laser," *Phys. Rev. Lett.* **47**, 1892–1894 (December 28 1981).

Problems for 25.4

1. *Mode competition with partial spatial overlap.* As a simplified description of mode competition between different transverse cavity modes, suppose that two different laser modes (such as two different transverse modes) share a common laser medium, except that one mode only illuminates a fraction $\eta < 1$ of the transverse cross section of the gain medium, whereas the other illuminates the entire cross section. For simplicity, assume that each mode has a uniform transverse intensity profile in the region that it illuminates; that the gain medium is homogeneous with both modes tuned to line center; and that standing-wave effects and other similar complexities can be ignored.

Develop an analysis for the mode competition in this situation, and discuss the circumstances (i.e., relative values of mode losses) under which such a laser is likely to run single or multiple transverse mode.

2. *Mode competition analysis including coupling or scattering between modes (research problem).* Suppose that a laser cavity or other oscillator has two potentially oscillating modes with field amplitudes (phasor amplitudes) $\tilde{E}_1(t)$ and $\tilde{E}_2(t)$; that the gains or growth rates for these two modes have self-saturation and cross-saturation terms of the forms $\kappa_i |\tilde{E}_i|^2$ and $\kappa_{ij} |\tilde{E}_j|^2$; and that in addition there

are linear coupling terms between the two modes such as might be caused by weak backscattering effects from one direction into the other in a ring laser. To handle these linear cross-coupling effects, one will have to write the differential equations for the field amplitudes $d\tilde{E}_i/dt$ rather than the intensities dI_i/dt , and then include a weak coupling term like $\tilde{c}_{ij}\tilde{E}_j$ in the $d\tilde{E}_i/dt$ equation and vice versa.

Set up the necessary equations for this problem—perhaps in phase-amplitude form?—and then attempt to explore how the combined effects of mode competition and mode coupling will interact. Note: This rapidly becomes a very messy situation, especially if the cavity frequencies ω_1 and ω_2 of the two original modes are different.

3. *Gain saturation with time delay (research problem).* Note that the mode competition analysis presented in this section implicitly assumes that the gain saturation is instantaneous, i.e., that the saturation effects follow the intensities I_1 and I_2 with no time delays. We know that in real lasers, however, the population or gain saturation has a time delay, described by appropriate rate equations for the atomic population inversion; and that if the population response is slow enough (i.e., $\gamma_2 \ll \gamma_c$) then the laser will exhibit the kind of spiking behavior described in the first section of this chapter.

Attempt to extend the analysis of this section by writing *three coupled rate equations* (or should it be four?) which will describe the intensities of two competing laser cavity modes and the population difference in the gain medium which supplies the gain for both modes; and then try to find extended solutions analogous to the mode competition discussion in this section. As part of this, you might, for example, attempt to make plots like the trajectories in the I_1, I_2 plane shown in this section, in the situation where there is enough time delay in the saturation so that the intensities approach their steady-state values in a “spiky” rather than smooth fashion.

LASER Q-SWITCHING

Q-switching is a widely used laser technique in which we allow a laser pumping process to build up a much larger than usual population inversion inside a laser cavity, while keeping the cavity itself from oscillating by removing the cavity feedback or greatly increasing the cavity losses—in effect by blocking or removing one of the end mirrors. Then, after a large inversion has been developed, we restore the cavity feedback, or “switch” the cavity *Q* back to its usual large value, using some suitably rapid modulation method. The result in general is a very short, intense burst of laser output which dumps all the accumulated population inversion in a single short laser pulse, typically only a few tens of nanoseconds long.

There are many practical applications, including laser ranging, laser cutting and drilling, and nonlinear optical studies, where such a short but intense laser pulse is much more useful and effective than the same amount of laser energy distributed over a longer time. The *Q*-switching approach is therefore a technique of great practical importance in many different laser systems. In the present chapter we examine the general characteristics of laser *Q*-switching, and some of the lasers and modulation techniques that are useful for *Q*-switching; and then review some of the fundamental analytical concepts that apply to laser *Q*-switching in actively, passively, and repetitively *Q*-switched lasers.

26.1 LASER Q-SWITCHING: GENERAL DESCRIPTION

The fundamental dynamics of laser *Q*-switching, or giant pulsing, are shown schematically in Figure 26.1. As illustrated there, we assume that the cavity loss in the laser cavity is initially set at some artificially high value—that is, at an artificially low value of the laser cavity Q_c —while the inversion, and hence the gain and the stored energy, in the laser medium are pumped up to a value much larger than normally present in the oscillating laser. In essence, we block one of the laser mirrors to prevent the build-up of oscillation, while the laser pumping process builds up the population inversion over some period of time to a larger than normal value.

The cavity loss is then suddenly lowered to a more normal value—in other words the cavity Q_c is suddenly “switched” to a higher value—with the result

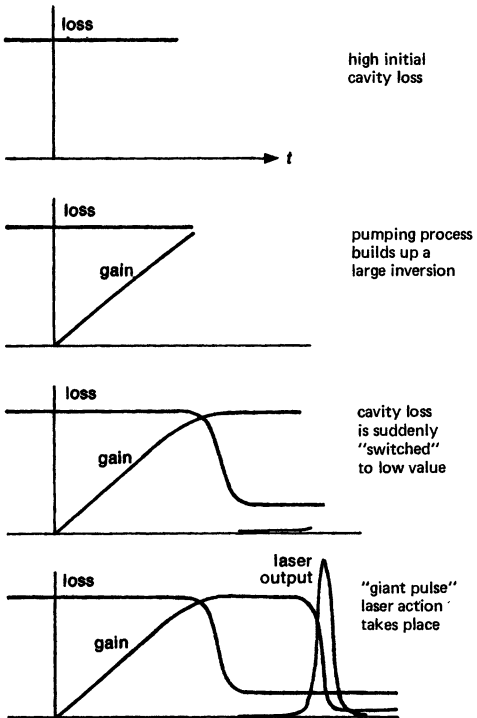


FIGURE 26.1
Laser Q-switching, step-by-step.

that the round-trip gain after switching is much larger than the cavity loss. The initial spontaneous emission or noise level in the laser cavity then immediately begins to build up at an unusually rapid rate, soon developing into a rapidly rising and intense burst, or "giant pulse," of laser oscillation. This oscillation burst rapidly becomes sufficiently powerful that it begins to saturate or deplete the inverted atomic population—in essence to "burn up" the inverted atoms—in a very short time. The oscillation signal in fact rapidly drives the inversion down well below the new cavity loss level, after which the oscillation signal in the cavity dies out nearly as rapidly as it rose. The entire process is somewhat similar to an unusually rapid and intense "spike" of the type we described in the preceding chapter.

The oscillation build-up interval, and particularly the output pulse duration, are generally much shorter than the pumping time during which the population inversion was created. The inversion built up during a long pumping time is thus dumped during a very short pulse duration. The peak power in the Q-switched giant pulse can be three to four orders of magnitude more intense than the cw long-pulse oscillation level that would be created in the same laser using the same pumping rate.

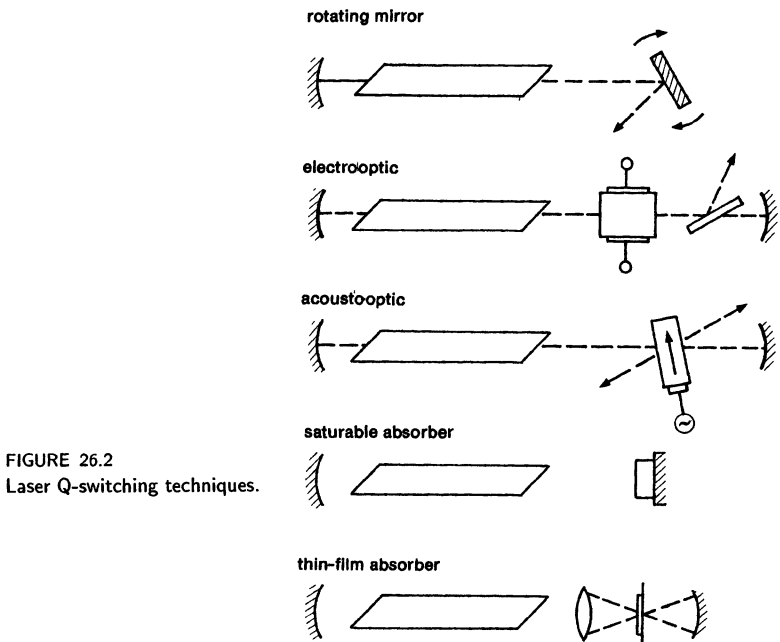


FIGURE 26.2
Laser Q-switching techniques.

Q-Switching Methods

Figure 26.2 illustrates some of the more common *Q*-switching methods that are employed in practical laser systems, including the following standard techniques:

(1) *Rotating Mirror Q-Switching*: The most direct and one of the earliest *Q*-switching methods is simply to mount one end mirror of the laser on a rapidly spinning motor shaft, so that the laser can oscillate only during the brief interval when the mirror rotates through an aligned orientation with respect to the opposite mirror.

This method, although cheap and simple, has numerous practical disadvantages. Even with the highest-speed motors (Waring Blender motors were reputed to be extremely good!) this approach suffers from uncertain timing, slow switching speed, lack of reliability, and vibration and mechanical noise which lead to alignment difficulties in the direction perpendicular to the plane of rotation. To avoid the latter, a rotating 90° prism rather than a rotating mirror was often employed.

This method is now used if at all only on very long laser cavities at very long laser wavelengths—e.g., long CO₂ or far infrared molecular lasers—where mirror alignment is less critical and other modulation techniques may be more difficult.

(2) *Electrooptic Q-Switching*: An electrooptic modulator, as we described in the previous chapter, consists in general of an electrooptic crystal which becomes birefringent under the influence of an applied electrical voltage, plus one or more prisms or other polarizing elements inside the laser cavity. In one form

of electrooptic *Q*-switch, an applied voltage sufficient to make the Pockels crystal into a quarter-wave plate is initially applied. Energy circulating once around the laser cavity then has its polarization rotated by 90° about the cavity axis, so that all the circulating energy is coupled out of the cavity by the polarizing element after just one round trip.

Switching the cavity to a low-loss condition is then accomplished by suddenly turning this voltage off (referred to as “crowbarring” the voltage across the modulator). As an alternative, a fixed quarter-wave element can create the high-loss condition with no voltage applied, and the Pockels cell can then be switched on to cancel this birefringence; but this approach requires an additional element inside the laser cavity.

Electrooptic *Q*-switching provides the fastest form of *Q*-switching (switching time ≤ 10 ns), with precise timing, good stability and repeatability, and a large hold-off ratio (i.e., large insertion loss in the low-*Q* state). This approach requires, however, both a fairly expensive electrooptic crystal and a very fast-rising high-voltage pulse source (at least several kV in a few tens of nanoseconds). Nanosecond rise-time pulses at this voltage level are difficult to obtain, and can produce severe electrical interference in nearby electronic equipment. In addition, this approach needs several elements inside the laser cavity, and these elements (particularly the Pockels crystal) may be both optically lossy and subject to optical damage at the high intensities inside the *Q*-switched laser.

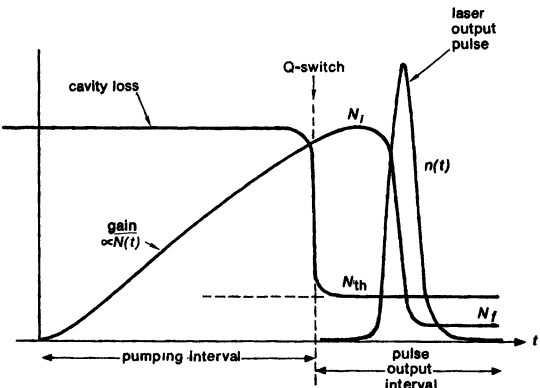
(3) *Acoustooptic Q-Switching*: We also have described in the previous chapter the use of an acoustooptic modulator, in which the index grating produced by an rf acoustic wave Bragg-diffracts light out of the laser cavity. Acoustooptic modulators have the advantages of very low optical insertion loss, relatively simple rf drive circuitry, and ease of use for repetitive *Q*-switching at kHz repetition rates. They have only relatively slow opening times, however, as well as low hold-off ratios. Hence they are primarily employed for lower-gain cw-pumped or repetitively *Q*-switched lasers (as we will describe in more detail in a later section of this chapter).

(4) *Passive Saturable-Absorber Q-Switching*: Passive *Q* switching (also described in more detail in a coming section) uses some form of easily saturable absorbing medium inside the laser cavity. Laser inversion is built up by the pumping process until the gain inside the cavity exceeds this absorption, and laser oscillation begins to develop inside the cavity. This oscillation at some relatively low level then rapidly saturates the absorber and thus opens up the cavity, leading to the development of a rapid and intense oscillation pulse. Saturable absorption using an organic dye solution in an intracavity cell is the most common form of passive *Q*-switching, although there are other systems as well.

Passive *Q*-switching is generally simple, convenient, and requires a minimum of optical elements inside the laser and no external driving circuitry. It is subject to some shot-to-shot amplitude fluctuations and timing jitter, however, and external apparatus must be synchronized to the timing of the laser pulse rather than vice versa. In addition, the absorbing dyes may need careful initial adjustment and may be subject to chemical or photochemical degradation in use. Passive *Q*-switching is nonetheless quite widely used in practical *Q*-switched lasers.

(5) *Thin-Film Q-Switching*: A somewhat unusual form of saturable absorber *Q*-switching is the use of a thin absorbing or metallic layer on a glass or mylar substrate, with the laser energy focused to a small spot on this layer. When laser oscillation first begins to build up in this cavity, the thin absorbing coating very rapidly burns away and is vaporized as the laser oscillation builds up from noise. This makes a particularly simple and fast-opening *Q*-switch which

FIGURE 26.3
Schematic illustration of the Q-switching process in a pulse-pumped and Q-switched laser oscillator. In a real laser the pumping interval will typically be much longer than the pulse output interval



may have applications in low-cost “throwaway” lasers; or it may be practical to obtain repeated shots by moving the absorbing film by a small amount between shots.

26.2 ACTIVE Q-SWITCHING: RATE-EQUATION ANALYSIS

Even though *Q*-switched lasers involve high intensities and moderately short pulses, a simple rate-equation analysis is still virtually always adequate for describing *Q*-switched laser behavior. In this section we derive therefore some simple and yet quite useful results for each of the important stages of laser *Q*-switching, using a simple rate-equation formulation.

Basic Rate Equations

The elementary rate equations for the cavity photon number $n(t)$ and the inverted population difference $N(t)$ in a *Q*-switched laser are, once again,

$$\frac{dn}{dt} = KNn - \gamma_c n \quad \text{and} \quad \frac{dN}{dt} = R_p - \gamma_2 N - 2^* K n N, \quad (1)$$

where $\gamma_c \equiv 1/\tau_c$ is the total cavity decay rate; R_p is the pumping rate and γ_2 is the decay rate or recovery rate for the inverted population difference; and K is the coupling coefficient between photons and atoms as given in earlier sections.

There are two limiting situations for the saturation behavior of the population difference $N(t) \equiv N_2(t) - N_1(t)$ in a *Q*-switched laser. In many *Q*-switched lasers the relaxation out of the lower state will be sufficiently fast that the lower-level population $N_1(t)$ will remain ≈ 0 at all times, even during the *Q*-switched pulse, in which case the parameter $2^* = 1$. In a few situations the lower laser level may be “bottlenecked” so that it cannot empty out during the laser pulse (for example, in *Q*-switched ruby lasers, where the lower laser level is in fact the ground level). The “bottlenecking parameter” then becomes $2^* = 2$ in order to take into account the filling up of the lower level by stimulated transitions from the upper level.

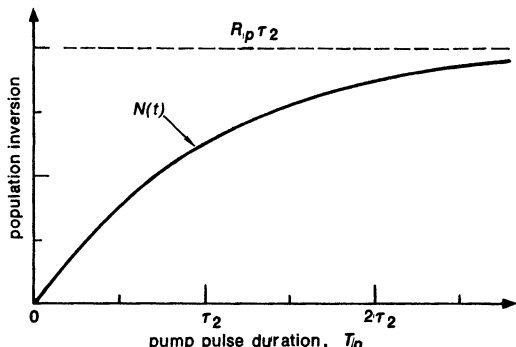


FIGURE 26.4
Energy storage during the pumping interval for a fixed pumping rate.

Figure 26.3 shows in somewhat more detail the various stages in the usual pulse-pumped active *Q*-switching process. As shown in this figure, we can divide the *Q*-switching process into a pumping interval and a pulse output interval, with the latter being subdivided more or less into a pulse build-up interval, and a pulse emission interval. We will now look in more detail at each of these intervals, and give a simplified solution and interpretation of the rate equations for each regime.

Pumping Interval, and Population Build-Up

To model the simplest form of pulsed pumping in a *Q*-switched laser, let us suppose that the cavity feedback is completely blocked during the pumping interval, so that no oscillation occurs and $n(t) \equiv 0$; and that a pump pulse with constant intensity R_p is turned on at $t = 0$. The population rate equation during this interval then reduces to the simplified form

$$\frac{dN(t)}{dt} \approx R_p - N(t)/\tau_2, \quad (2)$$

with the solution

$$N(t) = R_p \tau_2 [1 - \exp(-t/\tau_2)]. \quad (3)$$

The inversion thus builds up toward a maximum inversion value $R_p \tau_2$, as illustrated in Figure 26.4. This inversion may or may not be above the threshold inversion with the cavity blocked; but it preferably will be much above the threshold inversion after the cavity *Q* is switched.

Figure 26.4 makes it clear that there is not much point in supplying pumping power to a *Q*-switched laser for longer than about one or two population decay times τ_2 before the *Q*-switching takes place, since the inverted population no longer continues to grow after this length of time. In fact, at any instant of time, any atoms pumped up more than 1 or 2 lifetimes earlier will already have decayed and no longer be available.

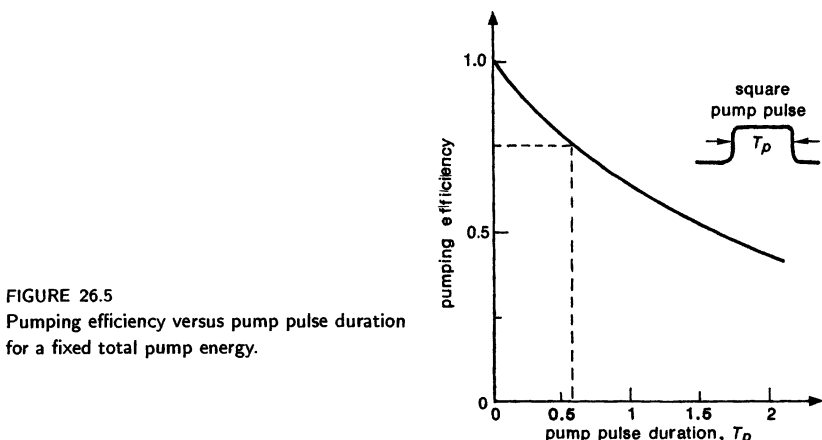


FIGURE 26.5
Pumping efficiency versus pump pulse duration
for a fixed total pump energy.

Pumping Efficiency

We can make this same point in a more practical fashion by assuming a pumping pulse with constant pumping energy and variable pulse duration. Suppose the laser pumping energy (e.g., the energy input to a laser flashlamp) is supplied by a square pump pulse of fixed total energy, although the duration T_p and peak height R_p of this pump pulse may be changed. We can then say that this pumping energy lifts up a total number of inverted atoms given by $N_p = R_p T_p$ during the pumping pulse. The inversion N_i that still remains at the end of the pump pulse, and hence at the initiation of the Q -switching buildup, is given, however, by

$$N_i = N(T_p) = N_p \times \frac{1 - \exp(-T_p/\tau_2)}{T_p/\tau_2}. \quad (4)$$

The normalized inversion N_i/N_p produced by a pump pulse of fixed total energy or fixed $N_p \equiv R_p T_p$ is plotted versus normalized pump pulse duration T_p/τ_2 in Figure 26.5. To get better than 75% efficiency from the pumping pulse, we need to restrict its duration to less than about half of the excited-state lifetime τ_2 .

For typical solid-state lasers with $\tau_2 \approx 200 \mu\text{s}$ to 1 ms, this means we should use pumping pulses with durations not longer than a few hundred microseconds at most. Such pulses can be obtained from typical laser flashlamps, though careful circuit design is required to minimize the inductance in the flashlamp circuitry. The tendency of flashlamps to explode also increases substantially as the pulse duration is decreased below a few hundred μs .

Note also that for most visible gas lasers, as well as organic dye lasers, the population lifetimes τ_2 are typically a few nanoseconds to a few tens of nanoseconds. The time over which population inversion can be built up and stored is then in general less than the time required for a Q -switched pulse to develop. Q -switching of these lasers is thus not a useful or realistic concept, because the storage time for inverted atoms is just too short.

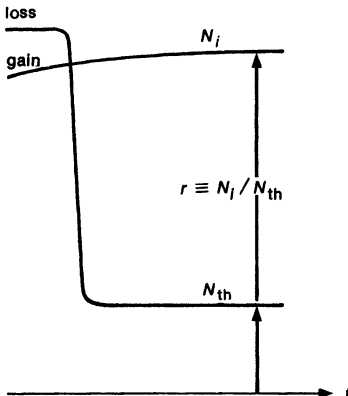


FIGURE 26.6
Inversion values and inversion ratio just after the Q-switch is opened.

Pulse Build-Up Time

At some point near the end of the pumping interval the *Q*-switch will be opened, dropping the cavity losses to a low value; and the *Q*-switched oscillation pulse will then begin to build up. There will be, however, a finite delay time or pulse build-up time, typically of a few tens to hundreds of nanoseconds duration, between the time when the cavity *Q*-switch is opened and when the *Q*-switched pulse appears.

This pulse build-up time is not precisely defined, since the *Q*-switch itself may have a finite opening time, and the resulting pulse has a finite risetime and duration. To make an estimate of the build-up time for a simple situation, however, we can assume that after an initial population inversion has been pumped up, the losses in the laser cavity are switched essentially instantaneously at $t = 0$ (somewhere near the end of the pumping interval) to some much lower value. The laser will at that point have an inversion N_i which is some ratio r times larger than the threshold inversion N_{th} just after switching. That is, this initial inversion ratio r is defined by

$$r \equiv \frac{N_i}{N_{th}} \equiv \frac{\text{population inversion just after switching}}{\text{threshold inversion just after switching}}. \quad (5)$$

as illustrated in Figure 26.6. This initial inversion ratio, plus the cavity lifetime τ_c , are the primary factors controlling the performance of a *Q*-switched laser.

At this point the photon density in the cavity is extremely small, although it will begin to grow rapidly; and so we can neglect the rate at which inverted atoms are burned up by the cavity photons. If the pulse build-up time (a few hundred nanoseconds typically) is also short compared to the upper-level lifetime τ_2 , as it usually will be, then we can neglect relaxation and pumping effects also, and assume that the population inversion $N(t)$ stays approximately equal to its initial value N_i all through the pulse build-up time. The photon rate equation then becomes a good approximation

$$\frac{dn(t)}{dt} \approx K[N_i - N_{th}]n(t) \approx \frac{(r - 1)}{\tau_c}n(t), \quad (6)$$

with the solution

$$n(t) = n_i \exp [(r-1)t/\tau_c]. \quad (7)$$

Unless some artificially injected external signal is present in the laser cavity (as we will discuss in a later chapter on injection locking), the initial noise value in the cavity will be equivalent to $n_i \approx 1$ or a few photons, representing the initial spontaneous-emission noise excitation of the cavity mode.

Let us arbitrarily define the end of the pulse build-up interval as that point on the leading edge of the *Q*-switched pulse where the photon number $n(t)$ just becomes equal to the steady-state photon number n_{ss} that would be present in the laser cavity if the laser could be continuously pumped at a pumping rate r times above its threshold after *Q*-switching. We pick this point because it marks the point where the stimulated emission term $KN(t)n(t)$ first begins to burn up inverted population density at a significant rate. Note that this point is still quite early in the leading edge of the *Q*-switched pulse, since the photon number n_p at the peak of the *Q*-switched pulse will be $n_p \gg n_{ss}$.

The build-up time T_b from the initial photon density n_i to a photon density n_{ss} is then given, from Equation 26.7, by

$$\frac{n_{ss}}{n_i} = \exp \left[\frac{(r-1)T_b}{\tau_c} \right], \quad (8)$$

or, if we invert this,

$$T_b = \frac{\tau_c}{r-1} \times \ln \left(\frac{n_{ss}}{n_i} \right). \quad (9)$$

The ratio of initial to final photon numbers in this expression may vary over the range from $n_{ss}/n_i \approx 10^8$ to 10^{12} . Even a difference of four orders of magnitude in this ratio, however, only makes a difference of $\pm 20\%$ in the logarithm of this ratio. Hence, we may rewrite this result, using an earlier formula for the cavity decay time τ_c , in the form

$$T_b \approx \frac{(25 \pm 5)}{r-1} \times \frac{T}{\delta_c}, \quad (10)$$

where $T = 2L/c$ is the round-trip time inside the laser cavity and δ_c is the fractional power loss per round trip due to cavity losses and output coupling.

As one practical example, we might consider a flash-pumped Nd:YAG laser with a cavity 60 cm long, so that $T = 4$ ns, and an output mirror transmission $1-R = 65\%$, or $\delta_c = \ln(1/R) = 1.05$. If this laser is initially pumped to three times threshold ($r = 3$), the build-up time will be $T_b \approx 50$ ns.

By contrast, a longer cw-pumped Nd:YAG laser or a low-gain CO₂ laser might have a 2 m long cavity with $T = 12$ ns, and only 20% output coupling or $\delta_c = \ln(1/0.8) \approx 0.22$, and be pumped to only 50% above threshold ($r = 1.5$). The build-up time in this situation will be $T_b \approx 3$ μ s.

Pulse Output Interval

We can now in fact develop a quite accurate analytical solution that will describe not only the pulse build-up time, but the entire interval during which the *Q*-switched pulse is generated and the inverted population is “dumped.” This entire period, including pulse build-up and decay, is almost always much

too short for either any significant pumping or relaxation of the inverted atoms to occur. We can therefore leave out the pumping and relaxation terms in the population equation, and approximate the rate equations in this pulse-output interval by

$$\frac{dn(t)}{dt} = K [N(t) - N_{\text{th}}] n(t) \quad \text{and} \quad \frac{dN(t)}{dt} \approx -2^* K n(t) N(t), \quad (11)$$

with the initial conditions that $N = N_i \equiv r N_{\text{th}}$ and $n = n_i \approx 1$ at the switching time $t = t_i$. Dividing these two equations into each other then gives the single relation

$$\frac{dn}{dN} = \frac{N_{\text{th}} - N}{2^* N}. \quad (12)$$

This relation can then be integrated, starting from the time when the cavity Q is switched and going to any arbitrary time t , in the form

$$2^* \int_{n_i}^{n(t)} dn = \int_{N_i}^{N(t)} \left(\frac{N_{\text{th}}}{N} - 1 \right) dN. \quad (13)$$

The initial photon number $n_i \approx 1$ is negligible compared to the very much larger values of $n(t)$ anytime during the laser output pulse. Hence we can set the lower limit on the left-hand integral to zero, and then solve both integrals to obtain the implicit relation

$$2^* n(t) \approx N_i - N(t) - \frac{N_i}{r} \ln \left(\frac{N_i}{N(t)} \right) \quad \text{where} \quad r \equiv \frac{N_i}{N_{\text{th}}}. \quad (14)$$

The only parameters in this expression are the initial inversion N_i , and the ratio $r \equiv N_i/N_{\text{th}}$ by which this initial inversion exceeds threshold. This expression can then be manipulated to yield a large number of useful results concerning the Q -switched pulse.

Q-Switched Pulse Energy

For example, the total energy in the Q -switched pulse is a very important parameter for many applications, such as laser ranging or drilling or cutting. To calculate this, suppose we let the time t in Equation 26.13 run until some final time well after the Q -switched pulse is over, when the pulse energy is well down in the tail of the pulse, so that the photon number approaches a final value $n_f \approx 0$. (This time would be at the far right-hand edge of Figure 26.3, or Figure 26.7.) The pulse inversion $N(t)$ must then also approach a final value N_f , which is given from Equation 26.14 by

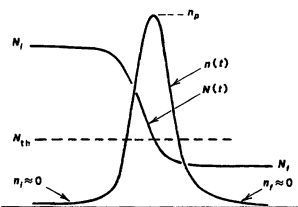
$$N_i - N_f - \frac{N_i}{r} \ln \left(\frac{N_i}{N_f} \right) \approx 0, \quad (15)$$

which can be rewritten as

$$1 - \frac{N_f}{N_i} - \frac{1}{r} \ln \left(\frac{N_i}{N_f} \right) = 0. \quad (16)$$

This formula implicitly gives the ratio of final to initial inversions, N_f/N_i , as a function only of the initial inversion ratio $r = N_i/N_{\text{th}}$, and nothing else.

FIGURE 26.7
Variations of $n(t)$ and $N(t)$ during the pulse output interval.



The initial energy stored in the atoms in the upper laser level just at the end of the pumping pulse, and potentially convertible into laser photons, can be written as $U_{\text{initial}} = N_i \hbar \omega_a$ (we assume $N_{2i} \approx N_i$ and $N_{1i} \approx 0$ at the start); whereas the same energy remaining in the upper energy level at the end of the Q -switched burst will be given by $U_{\text{final}} = (N_i + N_f) \hbar \omega_a / 2^*$ (note that if $2^* = 2$, at most half of the initial energy can be dumped). Since atomic relaxation during the Q -switching interval is negligible, there is no other place that the difference between these initial and final energies can have gone except into Q -switched laser output. The total energy delivered to the Q -switched pulse will thus be just the difference between the initial and final stored energies in the upper laser level, or

$$\text{Q-switched output pulse energy, } U_{\text{out}} = U_{\text{initial}} - U_{\text{final}} = \frac{N_i - N_f}{2^*} \hbar \omega_a. \quad (17)$$

This energy is not necessarily all delivered to *useful* output from the Q -switched laser, since some of it may be dissipated in internal cavity losses. In practice, however, the useful output coupling will typically be substantially larger than the internal cavity losses in most Q -switched lasers, and so most of this energy does come out in the output beam.

Suppose we thus define an energy extraction efficiency η for the conversion of initial stored energy into Q -switched pulse energy, as given by

$$\eta \equiv \frac{\text{Q-switched output energy}}{\text{initial inversion energy}} = \frac{U_{\text{out}}}{U_{\text{initial}}} = \frac{N_i - N_f}{2^* N_i}. \quad (18)$$

Equations 26.16 and 26.18 then combine to give a single implicit relation between the initial inversion ratio r and the energy extraction efficiency η , namely,

$$r = \frac{1}{2^* \eta(r)} \ln \left(\frac{1}{1 - 2^* \eta(r)} \right) \quad \text{or} \quad 1 - 2^* \eta(r) = \exp[-2^* r \eta(r)]. \quad (19)$$

The solution to this implicit equation is plotted in Figure 26.8.

The efficiency with which a Q -switched laser extracts energy from the initial inverted population depends only on the initial inversion ratio r , the bottlenecking parameter 2^* , and nothing else. Note that $2^* \eta(r)$ rapidly approaches 100% for $r \geq 2$. So long as the condition $r \gg 1$ is satisfied, the output energy from a Q -switched laser is largely independent of the exact cavity output coupling or almost any other design parameters, providing the coupling is not so large as to reduce r too close to unity. A Q -switched laser which is only a small amount above threshold ($r \rightarrow 1$) will, on the other hand, leave a large fraction of the initial inversion still in the upper-level atomic population, i.e., it will waste a good deal of the initial inversion.

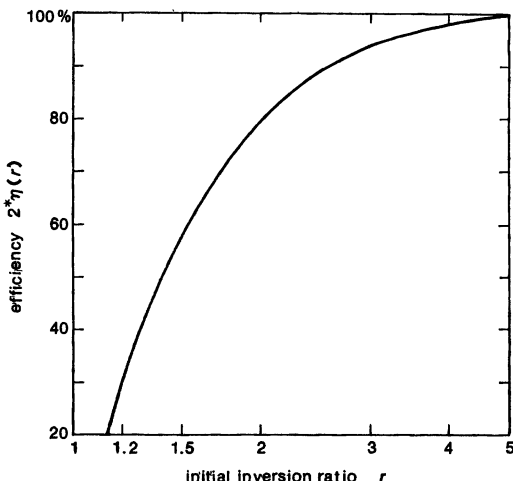


FIGURE 26.8
Energy-extraction efficiency in a Q-switched laser as a function of the initial inversion ratio.

Peak Pulse Power

The power output at the peak of a *Q*-switched laser pulse is also of practical interest. The cavity photon number $n(t)$ obviously reaches its peak value n_p (and the slope dn/dt becomes 0) at the instant when the inversion $N(t)$ passes through the threshold value N_{th} on its way downward in Figure 26.7. If we put these values into Equation 26.14, we can rewrite this equation in either of the forms

$$n_p = \frac{r - 1 - \ln r}{2^* r} N_i \quad \text{or} \quad n_p = \frac{r - 1 - \ln r}{2^*} N_{\text{th}}. \quad (20)$$

The first of these equations says that at the peak of the *Q*-switched pulse the photon number n_p in the cavity is equal to the initial inversion N_i multiplied by a factor which approaches unity for $r \gg 1$ (and $2^* = 1$), as illustrated in Figure 26.9.

In other words, if the initial inversion is very much above threshold, so that there is a very large initial gain and initial signal growth rate, then the *Q*-switched laser in essence first converts virtually all of the initially inverted atoms into photons bouncing around inside the laser cavity. These photons then “leak” out of the cavity, at something like the cavity decay rate γ_c , to produce the *Q*-switched output pulse.

The second form in Equation 26.20 relates the peak power or peak photon number n_p in the cavity to the threshold inversion N_{th} after switching, which is usually a fixed quantity for a fixed cavity output coupling, and also to the initial inversion ratio r , which usually depends linearly on the pumping power or energy applied to the laser. The peak power output from a *Q*-switched laser can be written, using this form, as

$$P_p = \frac{n_p \hbar \omega_a}{\tau_c} = \frac{r - 1 - \ln r}{2^*} \times \frac{N_{\text{th}} \hbar \omega_a}{\tau_c}. \quad (21)$$

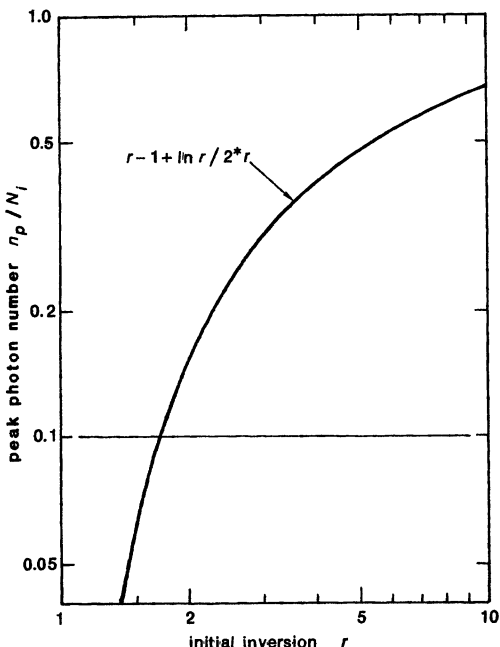


FIGURE 26.9
Peak photon density in a
Q-switched laser.

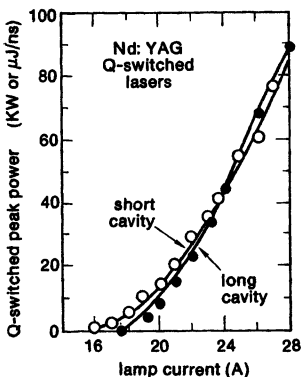


FIGURE 26.10
Experimental results for peak pulse amplitude versus
pump rate.

This form is thus convenient for comparison with experimental results of peak pulse output versus input pump energy W_p or pump rate R_p , such as in Figure 26.10.

The peak pulse powers are actually plotted here versus the pumping lamp current in two similar Nd:YAG lasers pumped by a rather long-pulse low-current flashlamp. The general conclusion is clearly that increasing the initial excitation r increases the peak intensity inside the laser—up to the point, that is, where

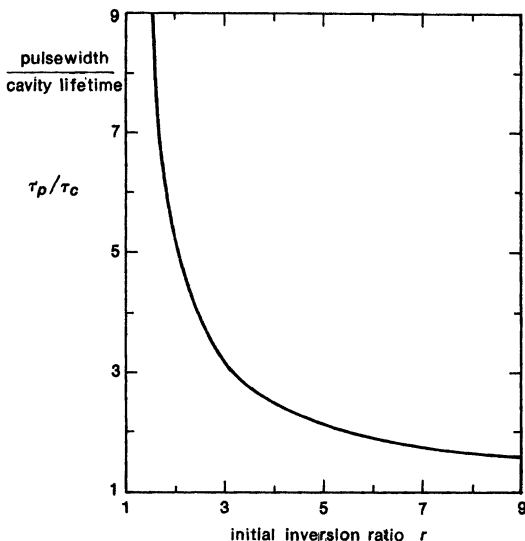


FIGURE 26.11
Q-switched pulsewidth versus initial inversion ratio.

some component inside the cavity suffers optical damage and terminates the experiment.

Q-Switched Pulsewidth

A good approximation to the pulsewidth τ_p for a Q -switched laser pulse can be obtained by dividing the total pulse energy by the peak pulse power to obtain

$$\tau_p \approx \frac{U_{\text{out}}}{P_p} = \frac{r\eta(r)}{r - 1 - \ln r} \times \tau_c, \quad (22)$$

where τ_c is the cavity decay time. The result will not be exactly equal to the FWHM pulsewidth of the pulse, but it will be close enough for most purposes.

Figure 26.11 plots this pulsewidth (which is about 20% smaller than the true FWHM pulsewidth) versus the initial inversion ratio r . The pulsewidth comes down toward a limiting value equal to the cavity lifetime τ_c as the initial inversion r is raised sufficiently far above threshold.

Figure 26.12 shows experimental measurements of the Q -switched pulsewidth versus lamp current in the same two Nd:YAG lasers shown in Figure 26.10. It is evident, as predicted, that the pulsewidth decreases rapidly with increasing pump power or initial inversion r . Moreover, since the two laser cavities use the same laser rod and the same mirror reflectivities, the shorter cavity should have a correspondingly shorter cavity lifetime τ_c and hence a shorter pulsewidth τ_p , exactly as illustrated by the data.

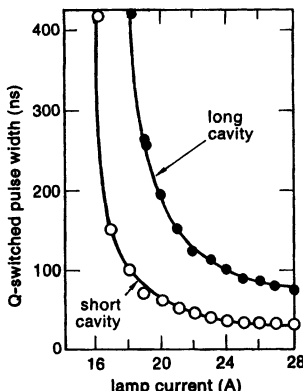


FIGURE 26.12

Pulsewidth versus pumping rate in two typical Q-switched Nd:YAG lasers.

Exact Solutions for the Q-Switched Pulseshape

If we really wish to calculate exact solutions for the *Q*-switched pulse envelope $n(t)$ and the population variation $N(t)$ (exact, at least, within the approximations made earlier in this section), we can substitute Equation 26.14 for $n(t)$ versus $N(t)$ into the rate equation $dN/dt \approx -KNn$ to obtain a single differential expression for $N(t)$ versus t . This equation can then be integrated, starting with $N = N_i$ at the switching time $t = 0$, in the form

$$\gamma_c \int_0^t dt = -N_{th} \int_{N_i}^{N(t)} \frac{dN}{N[N_i - N - N_{th} \ln(N_i/N)]}, \quad (23)$$

which can be converted if desired into the dimensionless integral form

$$\frac{t}{\tau_c} = -\frac{1}{r} \int_1^{\mathcal{N}} \frac{dy}{y[(1-y) + \ln y]}, \quad (24)$$

where $\mathcal{N} \equiv N(t)/N_i$.

No analytical solution for this integral seems to be available. The integral can be evaluated numerically without much trouble, however, to give $N(t)/N_i$ versus t/τ_c ; and these values can then be substituted into Equation 26.14 to give an exact solution for $n(t)$ versus t/τ_c . Figure 26.13 illustrates typical *Q*-switched pulseshapes for different degrees of initial inversion plotted versus t/τ_c (and normalized to the same peak power in each case). The pulseshapes clearly become somewhat asymmetric for larger initial inversions, with a very fast rise time and a slower decay time.

With a very large initial inversion $r \gg 1$, in fact, the leading edge builds up with a growth rate $(r - 1)\gamma_c$ which is substantially faster than the cavity decay rate γ_c during most of the leading edge. Once the pulse reaches its peak, however, the most it can do is to saturate the laser gain down to zero. In the trailing edge, therefore, the pulse intensity dies out with a decay rate which is at most the empty cavity decay rate γ_c . The pulses thus acquire a fast leading edge and a slower trailing edge.

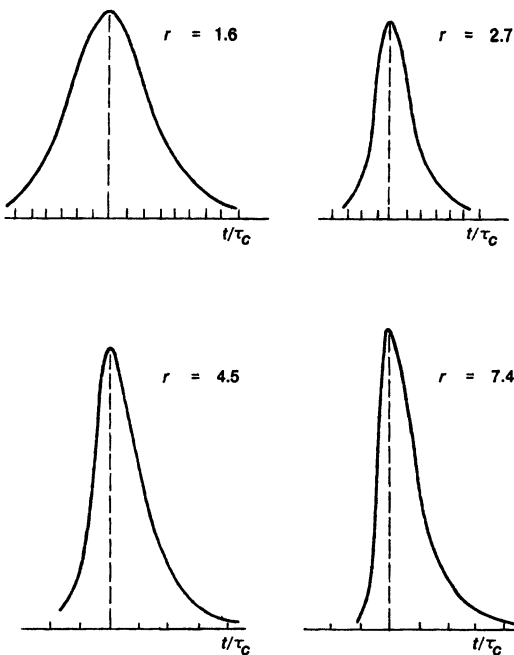


FIGURE 26.13
Exact Q-switched pulse shapes.

Experimental Results

Let's now compare all this analysis with some experimental results. Figure 26.14 reproduces measured data on the pulse delay, or pulse build-up time after *Q*-switching, and also on the *Q*-switched pulse width, for a Nd:YAG laser built at Stanford University by Professor Robert L. Byer. These quantities are plotted versus the electrical pumping energy applied to the flashlamp in the laser, which will be more or less directly proportional to the initial inversion in the rod before the *Q*-switch is opened.

To compare this data with theory, we need to know the exact threshold pumping energy of the laser, in order to calculate the initial inversion ratio r accurately; and it is difficult to obtain this number with precision from the data in its initial form. Since we know from Equation 26.10, however, that the pulse build-up rate scales linearly with inversion ratio, a useful tactic is to invert the measured build-up times and replot them in the form of $1/T_b$ versus pumping energy, as shown in the inset to Figure 26.14. Doing this makes it clear that the threshold pumping energy in this situation (corresponding to $r = 1$) is almost exactly 10 J input to the flashlamp.

The solid lines in Figure 26.14 then represent a simultaneous fit to the theory for both the build-up time and pulselength, assuming that r is proportional to the lamp energy relative to 10 J, and using the known cavity lifetime τ_c for this laser. It appears that the simple theory developed in this section does give a very reasonable description for real *Q*-switched lasers. The slight discrepancies at the

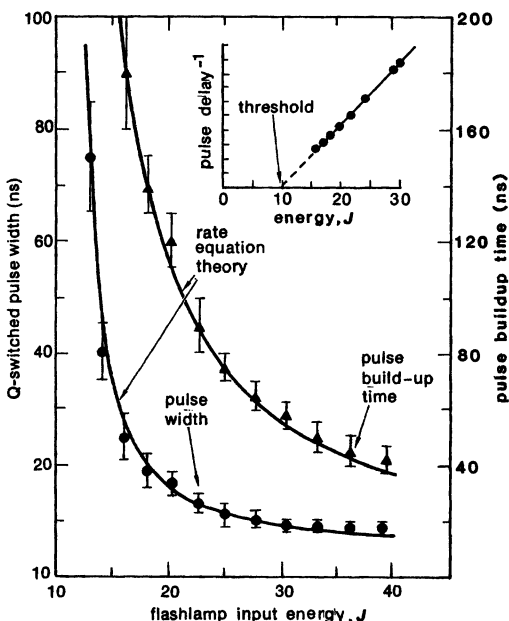


FIGURE 26.14
Q-switching of a Nd:YAG laser: experiment versus theory.

largest energies are expected, in view of the finite Q -switch opening time and the difficulty in measuring the shortest times accurately in the real laser.

Multiple Pulse Problems

A Q -switch which opens too slowly will lead to multiple output pulses from a Q -switched laser. Figure 26.15 (based on computer simulations) shows some typical examples illustrating the effects of a slowly opening Q -switch in a typical laser system.

The cavity loss in these examples starts from an initial value 20% higher than the initial gain, and falls sinusoidally to a value 80% below the initial gain in an adjustable switching time or half-period T_{sw} . The loss then rises back up toward its initial value. In (a), the switching time $T_{sw} = 25$ ns is optimized so that the output pulse occurs just as the cavity loss reaches its minimum value. (Note that the output pulse will not begin to build up at all until the loss drops below the gain, and then will have a continuously increasing growth rate during the build-up interval. The simple analysis of build-up time given earlier, based on constant gain and loss values, thus does not apply here.)

In (b), with $T_{sw} = 50$ ns, the loss drops more slowly, so that the output pulse, though somewhat delayed compared to the first situation, actually occurs before the loss has reached its minimum value. Nearly all the initial inversion is still dumped by the Q -switched pulse, however.

In (c), with T_{sw} increased to the much longer value of 150 ns (note the change in the horizontal time scale), the gain drops so slowly that the effective inversion just before the first Q -switched pulse occurs is only about $r \approx 1.5$. Because of

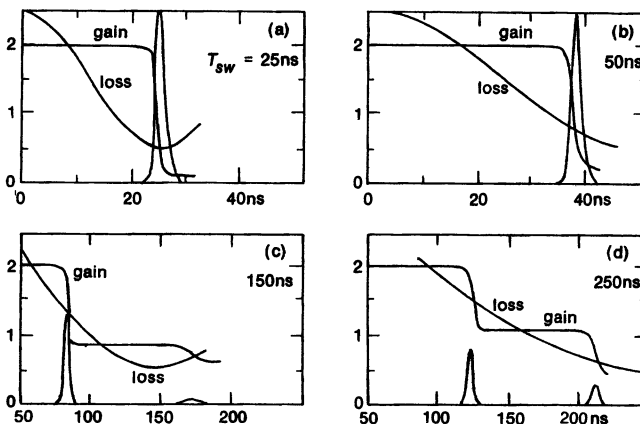


FIGURE 26.15
Multiple pulsing with a slowly opening Q-switch.

this, the initial inversion is only slightly dumped by the first *Q*-switched pulse, leaving a sizable amount of upper-level population and gain remaining after this pulse. The loss then continues to drop, soon falling below the residual gain value remaining in the cavity. The result is a weak but observable second *Q*-switched pulse, which actually occurs after the loss has reached its minimum value and is beginning to rise again.

Finally, (d) shows the same sort of behavior with an even slower *Q*-switch, $T_{sw} = 250$ ns. This situation leads to two clearly defined sequential *Q*-switched pulses, each of which dumps half or less of the initial inversion.

The behavior shown in these examples, though calculated for one particular sinusoidal switching profile, is quite general—a slowly opening *Q*-switch, whether the loss falls linearly, sinusoidally, or in some other fashion with time, will eventually cause the generation of multiple *Q*-switched pulses. The existence of these secondary pulses can, of course, cause timing errors in optical radars, measurement errors in scientific experiments, and a variety of other difficulties in practical applications. A good *Q*-switching device, whatever its nature, should open in a time significantly shorter than the build-up time for the desired output pulse. The opening time required in practical lasers is thus typically a few tens of nanoseconds or faster.

REFERENCES

Early references on *Q*-switching analysis include W. G. Wagner and B. A. Lengyel, "Evolution of the giant pulse in a laser," *J. Appl. Phys.* **34**, 2040 (July 1963); and C. C. Wang, "Optical giant pulses from a *Q*-switched laser," *Proc. IEEE* **51**, 1767 (1963).

Further analyses, especially for slowly opening switches, include A. A. Vuylsteke, "Theory of laser regeneration switching," *J. Appl. Phys.* **34**, 1615 (June 1963); J. E. Midwinter, "The theory of *Q*-switching applied to slow switching and pulse shaping for solid state lasers," *Brit. J. Appl. Phys.* **16**, 1125 (1965); and R. B. Kay and G. S. Waldman, "Complete solutions to the rate equations describing *Q*-spoiled and PTM laser operation," *J. Appl. Phys.* **36**, 1319 (April 1965).

In certain applications we would like to slow down the pulse generation process in a *Q*-switched laser, so as to obtain the same output energy in a longer pulse (perhaps 5 or 10 times longer) with lower peak power. One way to accomplish this is to control the opening rate of the *Q*-switch on a dynamic basis, although this approach requires very fast high-voltage electronics, as described by W. E. Schmid, "Pulse stretching in a *Q*-switched Nd:YAG laser," *IEEE J. Quantum Electron.* **QE-16**, 790-794 (July 1980).

Another method is to place a second-harmonic-generation crystal inside the laser cavity, so that the laser output is coupled out at the second harmonic. Because the harmonic conversion efficiency increases as the fundamental signal intensity squared, this process acts like a coupling mechanism which increases with increasing signal intensity, thereby slowing the growth rate at higher intensities and flattening off the pulse peak. Obtaining sufficient harmonic conversion for pulse stretching is difficult, however, as discussed by J. E. Murray and S. E. Harris, "Pulse lengthening via overcoupled internal second-harmonic generation," *J. Appl. Phys.* **41**, 609-613 (February 1970).

One way of obtaining very large amplification of a weak, short optical pulse (shorter than a cavity round-trip time) in a relatively low-gain laser medium is to place the laser medium between two mirrors to form a closed (and potentially oscillating) laser cavity. The pulse is then injected into this cavity (by means of a fast electrooptic Pockels cell), and allowed to bounce back and forth perhaps 20 to 100 times between the mirrors, being amplified and burning up the inverted laser medium, before being dumped out of the cavity by the same Pockels switch. (This switch also keeps the cavity from self-oscillating before and after the pulse is present.)

The dynamics of this multipass amplifier concept are essentially identical to those of a *Q*-switched laser, except that $n(t)$ now represents the number of photons in the short recirculating pulse. This is illustrated, for example, in W. H. Lowdermilk and J. E. Murray, "The multipass amplifier: Theory and numerical analysis," *J. Appl. Phys.* **51**, 2436-2444 (May 1980). Pulse energy gains as high as 10^{12} are obtained in practice.

Problems for 26.2

1. *Calculating the *Q*-switched energy efficiency.* Derive and test a simple computer routine which uses Newton's method to find the *Q*-switched energy efficiency $\eta(r)$ given r . (It's not as simple as it first seems.)
2. *Two-step, two-pulse *Q*-switching.* Suppose you have a very flexible *Q*-switch which you can open in two successive discontinuous steps to get two independent *Q*-switched pulses. Assume the initial inversion in the atomic system before the first pulse, call it N_i , and the final cavity threshold value after the second pulse, call it N_{th} , are both fixed, with a ratio between them of $r \equiv N_i/N_{th}$; and you want to obtain two *Q*-switched pulses with exactly the same energy (but not necessarily the same peak power or pulselength). To what intermediate value (let's call it N_{int}) should you switch the cavity threshold value on the first pulse in order to accomplish this?

Express your answer as a threshold ratio $r_{int} \equiv N_{int}/N_{th}$ between the intermediate threshold that produces the first pulse and the final threshold that produces the second pulse. Plot the effective inversion ratios r_1 and r_2 and the energy efficiencies η_1 and η_2 on the first and second pulses, as well as the necessary threshold ratio r_{int} , all versus the initial inversion ratio r ; and discuss their limiting values for large r .

3. *Minimizing the Q-switched pulselwidth.* Figure 26.11 shows the ratio τ_p/τ_c going down toward unity with increasing initial inversion ratio r ; hence for a fixed cavity coupling or cavity lifetime τ_c , the Q-switched pulselwidth τ_p will go down toward $\tau_p \approx \tau_c$ as the initial population inversion N_i or the pumping energy to the laser is increased.

Suppose instead you are given a fixed initial inversion value N_i just before the cavity Q is switched, but you can adjust the cavity coupling δ_c and hence the cavity lifetime τ_c or the threshold inversion N_{th} that applies after the Q is switched. Show that in this situation the shortest possible Q-switched pulselwidth τ_p is obtained by adjusting the initial inversion ratio to be $r \approx 3$ and that this minimum pulselwidth is given by $\tau_p \approx 3.1\tau_c$ or $\tau_p \approx 9.4\tau_{mo}$, where τ_{mo} is the exponential build-up time that energy in the cavity would have if the cavity were switched to have zero total losses just after switching.

4. *Q-switching performance versus tuning off line center.* The Nd:YAG laser transition may be described as a homogeneous lorentzian line with a linewidth $\Delta\omega_a$ corresponding to $\approx 4 \text{ cm}^{-1}$ or $\approx 120 \text{ GHz}$. A certain Q-switched Nd:YAG laser with a cavity length of 60 cm and an output coupling of 80% (i.e., power reflectivity $R = 0.2$ for the output mirror) is pumped sufficiently hard to be $r = 5$ times above threshold at line center. Suppose a tunable mode selector is added to this laser cavity which can force the oscillation to build up at an adjustable frequency other than the exact line center. Plot how the Q-switched pulselwidth, peak power, and pulse energy will vary with frequency tuning of this laser, assuming the pumping power or energy remains fixed as the oscillation frequency is tuned.
5. *Linearly opening slow Q-switch.* Suppose the threshold inversion $N_{th}(t)$ in a slowly opening Q-switched laser cavity switches linearly (rather than discontinuously) from an initial high-loss value N_0 at $t = 0$ and earlier, to a final low-loss value N_{min} at $t = T_{sw}$ and after, so that T_{sw} is the Q-switch opening time. The initial inversion in the laser medium at $t = 0$ is N_i . Develop a computer simulation to analyze and plot the pulse build-up time and pulse output energy for the first Q-switched output pulse from this laser as functions of the normalized switching time T_{sw}/τ_c , where τ_c is the cavity lifetime corresponding to the final low-loss threshold value N_{min} . Calculate also the values of T_{sw} for which secondary output pulses will first appear.

Use as parameters in your analysis the inversion ratio $r \equiv N_i/N_{min}$ (i.e., the usual ratio of initial inversion to final threshold value) and also the loss modulation ratio $r_0 = N_0/N_{min}$. Plot results (including second-pulse thresholds) for $r = 5$, $r_0 = 6$ and for $r = 1.5$, $r_0 = 2$ assuming $\ln(n_{ss}/n_i) = 20$.

6. *Sinusoidally opening slow Q-switch.* Repeat the previous problem assuming the cavity loss is sinusoidally modulated so that the cavity threshold varies as $N_{th}(t) = N_0 - (N_0 - N_{min})\sin^2 \pi t/2T_{sw}$ for $t > 0$. Ignore very short switching times T_{sw} less than the build-up time, for which the output pulse will occur after the loss begins to rise back up again.

7. *Double pulsing in a slowly opening Q-switched laser.* Suppose that the threshold inversion for a slowly opening Q-switched laser cavity decreases with time as $N_{th}(t) = N_i - (N_i - N_{min})\sin^2 \pi t/2T_{sw}$ for $t > 0$, where N_{min} is the minimum or lowest-loss cavity threshold, which the cavity reaches after time T_{sw} , and N_i is both the initial high-loss threshold value and the initial inversion of the laser medium at $t = 0$. (That is, the cavity Q begins to be switched sinusoidally

downward just at the instant when the initial inversion equals the initial losses before switching.) What is the earliest time (as a function of the switching time T_{sw} and the inversion ratio $r \equiv N_i/N_{min}$) at which a first Q -switched output pulse can occur, if the laser is not to generate a second (unwanted) output pulse?

26.3 PASSIVE (SATURABLE ABSORBER) Q-SWITCHING

Passive Q -switching, making use of a saturable absorber inside the laser cavity, is another basic approach for generating Q -switched pulses. This approach can be one of the simplest forms of Q switching in practice, since it requires a minimum of elements inside the laser cavity, and no external pulse sources or control circuitry. The Q -switching behavior depends critically, however, on the saturation properties of the gain medium and the saturable absorber, and these can deteriorate with time or with repeated laser shots. In addition, there is no direct control over the timing of the Q -switched pulse—one must synchronize external apparatus to the laser output pulse, rather than the reverse.

The most common examples of saturable-absorber Q -switching are various solid-state lasers Q -switched by organic saturable-absorber dye solutions, such as Nd:YAG or Nd:glass lasers mode-locked with various commercially available dyes having names like Eastman Kodak 9860 or 9740. The possibilities of thin-film single-shot Q -switches for such lasers have also been mentioned. Certain infrared CO_2 lasers are also passively Q -switched using the saturable absorption properties of SF_6 vapor, or hot unpumped CO_2 vapor, or thin p -type Ge slabs.

Rate Equations For Passive Q-Switching

The simplest model for a passively Q -switched laser consists of a laser cavity mode with cavity photon number $n(t)$; a saturable gain medium with population difference and coupling coefficient which we might call $N_g(t)$ and K_g ; and a saturable absorbing medium with population difference $N_a(t)$ and coupling coefficient K_a . The elementary rate equations describing this system are then the cavity photon number equation, which becomes

$$\frac{dn(t)}{dt} = [K_g N_g(t) - K_a N_a(t) - \gamma_c] n(t), \quad (25)$$

plus the usual rate equation for the gain medium, which can be written as

$$\frac{dN_g(t)}{dt} = R_p - \gamma_{2g} N_g(t) - K_g N_g(t) n(t), \quad (26)$$

plus a similar rate equation for the saturable absorber, which we write as

$$\frac{dN_a(t)}{dt} = -\gamma_{2a} [N_a(t) - N_{a0}] - K_a N_a(t) n(t). \quad (27)$$

Obviously γ_{2g} and γ_{2a} now mean the population recovery rates for the gain and the saturable absorber, respectively. The saturable absorber is assumed to relax back toward an unsaturated value N_{a0} with a time constant $\tau_a = 1/\gamma_{2a}$.

Approximate Solution

The solutions to these equations for the passively Q -switched laser are even more strongly nonlinear than for an actively Q -switched laser, since the Q -switching process itself is controlled by the signal buildup in the laser. Simple analytic results like those we derived for active Q switching in an earlier section are thus difficult if not impossible to find. Passive Q -switching is thus more often approached by numerical or experimental methods than by analytical methods.

There is, however, one relatively simple analytical criterion for good passive Q -switching behavior that can be derived from these equations, as follows. Suppose the laser pump power is turned on and begins to pump up the laser gain medium, until the laser gain exceeds the cavity loss plus the unsaturated absorber losses. The photon density $n(t)$ in the cavity will then start to build up from noise, and after a certain time the photon density $n(t)$ will become large enough that it begins to saturate the saturable absorber. Let the point where the saturable absorber just begins to saturate, and the Q -switched pulse just starts to develop, be called $t = 0$ and let the laser inversion just at this point be represented by N_{g0} .

Now, in most Q -switched lasers the pumping and relaxation times for the gain medium are long compared to the Q -switching buildup and decay time (as we have already noted in an earlier section), so that the gain medium equation during the Q -switching interval can be simplified to

$$\frac{dN_g(t)}{dt} \approx -K_g N_g(t) n(t), \quad (28)$$

which has as a formal solution

$$N_g(t) = N_{g0} \exp \left[-K_g \int_0^t n(t') dt' \right]. \quad (29)$$

The physical significance of this approximation is that the gain is depleted by the *integrated* or *cumulative* effect of the photon flux $n(t)$ which passes through the gain medium, rather than by the *instantaneous* intensity in the cavity (at least in the initial stages).

The recovery times τ_a for saturable absorbers are, on the other hand, usually short (in the range of nanoseconds to picoseconds) compared to the Q -switched pulsewidths τ_p in practical lasers (which are typically tens to hundreds of nanoseconds). The absorber's population difference will then be given to a good approximation by the steady-state solution of the absorber rate equation, or

$$N_a(t) \approx \frac{N_{a0}}{1 + (K_a/\gamma_{2a})n(t)}. \quad (30)$$

meaning that the saturable absorber saturates in an essentially instantaneous fashion during the Q -switched pulse.

The initial growth rate for the cavity photon number, just before saturation of either absorber or amplifier occurs, is then given by

$$\frac{dn(t)}{dt} \approx [K_g N_{g0} - K_a N_{a0} - \gamma_c] n(t) = \gamma_{g0} n(t), \quad (31)$$

where $\gamma_{g0} \equiv K_g N_{g0} - K_a N_{a0} - \gamma_c$ is the initial growth rate for the photon number, before any Q -switching has occurred. The photon number $n(t)$ thus

grows initially from a (very small) starting value n_i in the form

$$n(t) \approx n_i \exp(\gamma_{g0}t). \quad (32)$$

The population inversion $N_g(t)$ can then be written, using the approximation of Equation 26.29, in the form

$$N_g(t) \approx N_{g0} \exp[-K_g n(t)/\gamma_{g0}], \quad (33)$$

where this approximation should be valid at least the very early stages of Q -switching.

If the above results for $N_a(t)$ and $N_g(t)$ are used in the rate equation for the cavity photon number $n(t)$, the growth rate of the cavity signal for very early times in the Q -switching period then can be written approximately as

$$\frac{1}{n(t)} \frac{dn(t)}{dt} = K_g N_{g0} \exp\left(-\frac{K_g n(t)}{\gamma_{g0}}\right) - \frac{K_a N_{a0}}{1 + (K_a/\gamma_{2a})n(t)} - \gamma_c. \quad (34)$$

If we expand each of the terms on the right-hand side of this equation to first order in $n(t)$, we can write this to a first approximation as

$$\frac{1}{n(t)} \frac{dn(t)}{dt} \approx \gamma_{g0} + \left(\frac{K_a^2 N_{a0}}{\gamma_{2a}} - \frac{K_g^2 N_{g0}}{\gamma_{g0}} \right) n(t) + \dots. \quad (35)$$

The photon number at first grows as γ_{g0} ; but as $n(t)$ begins to increase, the growth rate changes as determined by the second term on the right-hand side of the equation.

The “Second Threshold” Condition

The criterion that controls the Q -switching behavior is whether the second term on the right-hand side of Equation 26.35 has a positive or a negative sign, so that slope of the growth curve for the signal intensity will turn increasingly upward or downward as the photon number $n(t)$ increases. In physical terms, the question is whether the saturable absorber term will saturate first, thereby allowing the net growth rate to turn upward in an expanding or Q -switching fashion, as shown in Figure 26.16; or whether the gain will begin to saturate first, so that the intensity in the laser will never turn upward, but will only turn downward with increasing $n(t)$, so that a true giant pulse never develops.

An approximate analytical criterion for good Q -switching is thus that the coefficient of the $n(t)$ term on the right-hand side of the preceding equation must be positive. This criterion will be satisfied if

$$\frac{K_a^2 N_{a0}}{K_g^2 N_{g0}} > \frac{\gamma_{2a}}{\gamma_{g0}}. \quad (36)$$

This is a fundamental condition, sometimes called the “second threshold condition,” that must be satisfied for good passive Q -switching. (The “first threshold” is the earlier point in the pumping pulse where the gain first exceeds the unsaturated loss, so that the intensity in the cavity can begin to grow at all; the second threshold is the break point where the growth curve for $n(t)$ turns upward.)

To put this criterion into more readily understandable terms, we can note that the ratio of the initial growth and decay rates $K_g N_{g0}$ and $K_a N_{a0}$ is just the

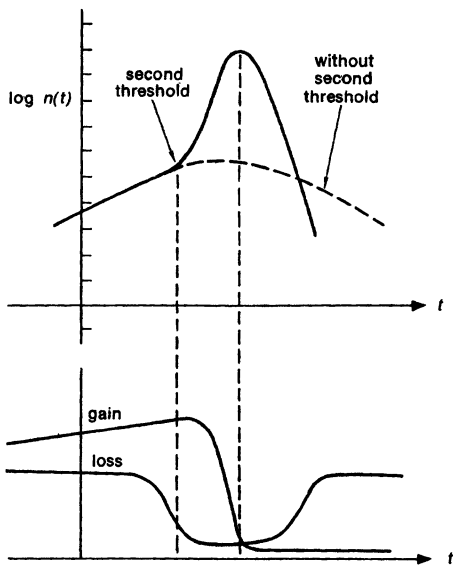


FIGURE 26.16
 Good passive or saturable-absorber Q-switching is dependent on the existence of a "second threshold."

ratio of the initial or unsaturated gain and loss factors $2\alpha_{g0}L_g$ and $2\alpha_{a0}L_a$ in the laser medium and in the saturable absorber cell. These are both experimentally measurable quantities. Also, from the two rate equations we can see that the ratio of the saturation intensities in the two media will be given by

$$\frac{I_{\text{sat,gain}}}{I_{\text{sat,abs}}} \equiv \frac{\sigma_a \tau_a}{\sigma_g \tau_g} = \frac{\gamma_{2g}/K_g}{\gamma_{2a}/K_a} = \frac{K_a \tau_a}{K_g \tau_g}. \quad (37)$$

This tells us the rather obvious fact that the gain and loss coupling coefficients are related by $K_a/K_g \equiv \sigma_a/\sigma_g$, since stimulated transition coefficients K are directly proportional to the stimulated emission or absorption cross sections σ in the two media.

With these interpretations, the criterion for good passive Q -switching reduces to

$$\frac{\gamma_{g0}}{\gamma_{2a}} \times \frac{\sigma_a}{\sigma_g} \times \frac{2\alpha_{g0}L_g}{2\alpha_{a0}L_a} > 1. \quad (38)$$

To put this in still more practical terms, we can note that the saturable absorber's decay rate and lifetime are related by $\gamma_{2a} \equiv 1/\tau_a$. Suppose in addition that the net exponential gain coefficient (power gain coefficient) for one complete round trip around the laser cavity in the initial stage, before any saturation takes place, is denoted by δ_{g0} . That is, we write the initial photon growth rate as

$$\frac{1}{n} \left. \frac{dn}{dt} \right|_{t=0} \equiv \gamma_{g0} = \frac{e^{\delta_{g0}} - 1}{T} \approx \frac{\delta_{g0}}{T}, \quad \delta_{g0} \ll 1, \quad (39)$$

where T is the round-trip transit time. The criterion then becomes, finally,

$$\delta_{g0} \times \frac{\tau_a}{T} \times \frac{2\alpha_{g0}L_g}{2\alpha_{a0}L_a} \times \frac{\sigma_a}{\sigma_g} > 1. \quad (40)$$

The ratio of cross sections σ_a/σ_g in this expression can be quite large (for example, $\sigma_a \approx 10^{-16} \text{ cm}^2$ for a dye absorber versus $\sigma_g \approx 10^{-19} \text{ cm}^2$ for a solid-state laser). The ratio of time constants, on the other hand, is apt to be small ($\tau_a < 0.1 \text{ ns}$, perhaps, whereas $T \approx 5 \text{ ns}$). The ratio of laser gain to saturable absorber loss, or $2\alpha_{g0}L_g/2\alpha_{a0}L_a$, must be greater than unity, but perhaps not by any large factor. Finally, the net initial growth coefficient δ_{g0} in a passively Q -switched laser may be fairly small, as the pump slowly pushes the laser above threshold. Fast pumping, to push δ_{g0} upward rapidly, is thus desirable.

Some readers may wonder why the net growth coefficient δ_{g0} just at the start of the Q -switching process appears in this formula. The answer is that the saturable absorber saturates, in our approximation, on an instantaneous intensity basis, whereas the laser gain medium saturates on a cumulative or integrated intensity basis. We want the laser intensity to grow very rapidly in the initial stages, so that the cavity signal reaches the absorber saturation level before very much of the laser inversion has been burned up.

REFERENCES

The second threshold concept is discussed in a paper by G. H. C. New and T. B. O'Hare, "A simple criterion for passive Q -switching of lasers," *Phys. Lett.* **68A**, 27–28 (September 18, 1978).

An earlier theoretical paper on passive Q -switching is by A. Szabo and R. A. Stein, "Theory of laser giant pulsing by a saturable absorber," *J. Appl. Phys.* **36**, 1562–1566 (May 1965).

26.4 REPETITIVE LASER Q-SWITCHING

Another useful way to operate some lasers is to pump the laser medium on a continuous rather than pulsed basis, and then to repeatedly Q switch the laser cavity at a repetition rate which may range from a few hundred to several thousand pulses per second. Practical examples of repetitively Q -switched lasers include the CO_2 laser, using either a rotating mirror or a GaAs or Ge acoustooptic cell, and the Nd:YAG laser, using a quartz acoustooptic Q -switch. The lower power but higher repetition rate pulses from such lasers can be useful, for example, in micromachining, surgical applications, or scientific experiments.

Characteristics of Repetitively Q -Switched Lasers

Because of practical limitations on the average pump power that can be applied to a laser under cw conditions, the round-trip gain in a cw-pumped and Q -switched laser just before the Q -switch opens is usually rather modest (perhaps 20–40% round-trip power gain in a cw Nd:YAG or CO_2 laser); and the inversion ratio just after the Q -switch opens is similarly modest (perhaps $r \approx 1.2$ to 1.4). As a result the pulse peak powers tend to be much smaller in repetitively Q -

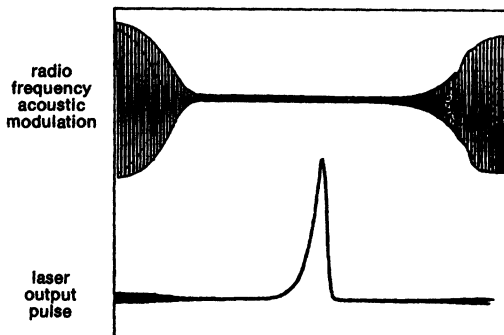


FIGURE 26.17
Repetitive acoustooptic
Q-switching.

switched operation than in flash-pumped and *Q*-switched operation of the same laser, and the pulse build-up times and pulse durations substantially longer (from perhaps several hundred nanoseconds up to a few microseconds).

These lower-intensity pulses can still be very useful, for example, in materials processing applications, where the cutting or drilling effect of even a weak *Q*-switched pulse tends to be much more efficient than the same energy delivered in a cw beam. Repetitively *Q*-switched Nd:YAG lasers can thus be useful for resistor trimming, or for scribing or cutting thin films or integrated circuits. Experiments on nonlinear effects, such as second harmonic generation or stimulated Raman scattering, which depend much more on peak laser power than on average power, are also much more effectively performed with the same total energy delivered as a series of pulses than as a cw beam.

The lower gain and the slower dynamics in the cw-pumped situation make it possible to use *Q*-switching modulators which have smaller hold-off and slower opening times than in the flashpumped situation. The premier example of this type of modulator is the acoustooptic *Q*-switch illustrated in Figure 26.2 of this chapter. Figure 26.17 shows how the radio-frequency signal applied to an acoustooptic modulator can be turned off to "open" the *Q* switch (upper trace), and the resulting *Q*-switched pulse from a low-power Nd:YAG laser (lower trace). The long time delay between the *Q*-switch opening and the output pulse is partly build-up time, but largely acoustic wave propagation time from the acoustic transducer to the laser beam position.

The requirements of repetitively *Q*-switched lasers thus match very well with the capabilities of acoustooptic modulators. In addition the cw-pumped and repetitively *Q*-switched laser tends to retain much the same power stability and good transverse and longitudinal mode stability as characterizes the underlying cw-pumped laser.

Elementary Analysis of Repetitive Q-Switching

To analyze this mode of operation in the simplest situation, we can first note that the time interval needed for the build-up and emission of a *Q*-switched pulse after the *Q*-switch opens will typically be a few microseconds or less, whereas the repumping interval between pulses will almost always be $\geq 100 \mu\text{s}$ (sometimes considerably longer). Therefore we can divide the periodic repetitive operation into a *Q*-switching interval which is essentially of zero length, plus a repumping

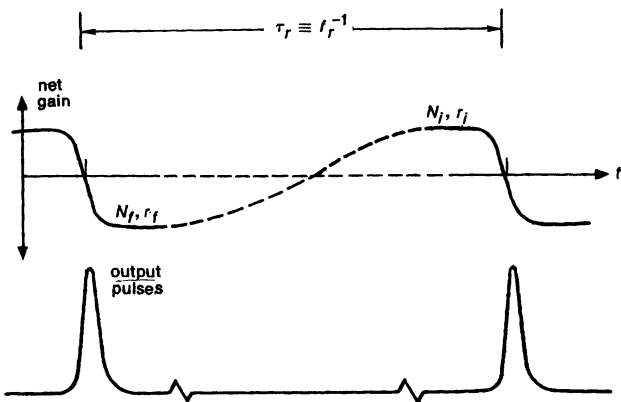


FIGURE 26.18
One period of a repetitive Q-switching cycle.

interval of duration $\tau_r \equiv 1/f_r$ where f_r is the *Q*-switching repetition rate, as illustrated in Figure 26.18.

If we take the simplest possible laser model (single cavity mode, ideal upper laser level, fast-emptying lower level, and fixed cw pumping rate which is r_{cw} times above the cw laser threshold for the low-loss condition), then the laser inversions N_i and N_f just before and just after the k -th *Q*-switched pulse will be given by the *Q*-switching energy relation

$$N_i^{(k)} - N_f^{(k)} = N_{\text{th}} \ln \left(\frac{N_i^{(k)}}{N_f^{(k)}} \right). \quad (41)$$

But the final inversion $N_f^{(k)}$ just after the k -th pulse and the initial inversion $N_i^{(k+1)}$ just before the $k+1$ -th pulse are also connected by the repumping relation

$$N_i^{(k+1)} = r_{\text{cw}} N_{\text{th}} + (N_f^{(k)} - r_{\text{cw}} N_{\text{th}}) e^{-\gamma_2 \tau_r}, \quad (42)$$

where r_{cw} is the normalized cw pumping rate and γ_2 is the population decay rate for the upper laser level. These quantities are illustrated in Figure 26.18.

If we normalize both these inversions to the threshold inversion N_{th} , we can write both of these equations in the dimensionless forms

$$r_i^{(k)} - r_f^{(k)} = \ln \left(r_i^{(k)} / r_f^{(k)} \right) \quad \text{and} \quad r_i^{(k+1)} = r_{\text{cw}} - (r_{\text{cw}} - r_f^{(k)}) e^{-\gamma_2 / f_r}, \quad (43)$$

where $r_i = N_i / N_{\text{th}}$ is the actual inversion ratio just before each *Q*-switched pulse ($r_i \leq r_{\text{cw}}$), as defined in an earlier section; and $r_f = N_f / N_{\text{th}} \leq 1$ is the residual inversion ratio ($r_f \leq 1$) just after each pulse.

Steady-State Solutions

Under steady-state operating conditions, these initial and final inversions will each remain the same on successive pulses, so that we can drop the k and $k+1$ superscripts. Suppose we also define the normalized energy w_{out} dumped

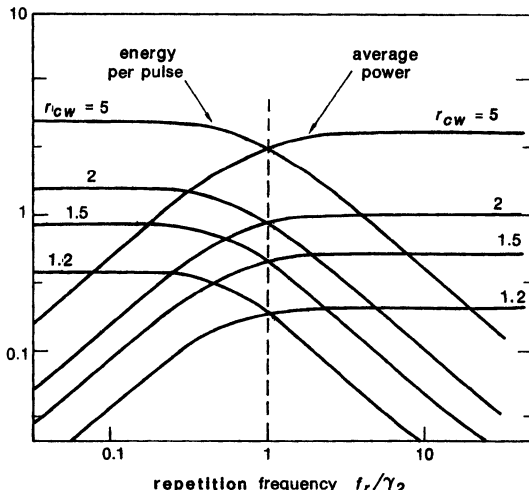


FIGURE 26.19
Variation of pulse energy and average power output with repetition rate in a repetitively Q-switched laser.

in each pulse by

$$w_{\text{out}} \equiv \frac{N_i - N_f}{N_{\text{th}}} = r_i - r_f. \quad (44)$$

In physical terms, this normalized energy w_{out} is the ratio of the population dumped during a single Q -switched pulse to either the population stored in the rod under cw oscillation conditions, or the population pumped up in one lifetime τ_2 when the pump is exactly at threshold. (It is also the same thing as $r_i \eta(r_i)$ where η is the energy extraction efficiency defined in an earlier section.)

This equation can then be recast into the form

$$w_{\text{out}} = r_i (1 - e^{-u_{\text{out}}}), \quad (45)$$

after which Equations 26.41 through 26.45 can be combined to obtain the normalized pulse energy w_{out} for a given pumping rate r_{cw} and normalized repetition frequency f_r / γ_2 . The resulting values of r_i , together with γ_c , will then determine the pulselength and the build-up time of the Q -switched pulse, using the formulas from Section 26.2. Typical results from this calculation are shown in Figure 26.19.

The total energy U_{out} extracted from the laser medium on each Q -switched pulse is then given by

$$U_{\text{out}} = (N_i - N_f) \hbar \omega_a = w_{\text{out}}(r_{\text{cw}}, f_r) \times N_{\text{th}} \hbar \omega_a. \quad (46)$$

The average laser power output is this energy per pulse U_{out} times the repetition rate f_r , or $P_{\text{av}} = f_r U_{\text{out}}$. The average power output from the same laser under cw conditions, on the other hand, would be $P_{\text{cw}} = (r_{\text{cw}} - 1) \gamma_2 N_{\text{th}} \hbar \omega$. The ratio of average power under Q -switching conditions to the potential cw power output is then

$$\frac{P_{\text{av}}}{P_{\text{cw}}} = \frac{f_r}{\gamma_2} \times \frac{w_{\text{out}}(r_{\text{cw}}, f_r)}{r_{\text{cw}} - 1}. \quad (47)$$

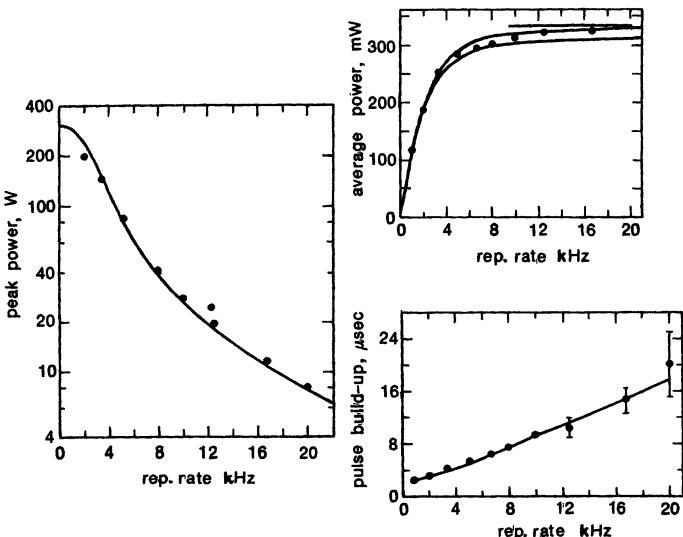


FIGURE 26.20

Experimental results for peak pulse power, average power, and pulse build-up time versus repetition rate in a Q-switched Nd:YAG laser.

(Both of these powers are actually the total power extracted from the laser medium into the oscillating mode; the actual useful output power in both situations will be somewhat less because of internal cavity losses.)

Experimental Results

Figure 26.20 gives some experimental results showing how the peak *Q*-switched pulse power and the average power output depend on repetition rate or repetition frequency f_r for a typical repetitively *Q*-switched Nd:YAG laser. The experimental results compare well with the simple theory just developed.

The obvious conclusions are that at very low repetition rates, $f_r \leq \gamma_2$, the laser acts as a source of fixed-energy *Q*-switched laser pulses with energy corresponding to an inversion ratio $r_i \approx r_{cw}$, and the average power increases directly with repetition rate; whereas at high repetition rates, $f_r \geq \gamma_2$, the laser supplies a fixed average power very nearly equal to the power P_{cw} the same laser would supply under cw operating conditions. The breakpoint between these regimes occurs at or very near the repetition frequency given by $f_r \approx \gamma_2$.

REFERENCES

An excellent and detailed examination of repetitive *Q*-switching can be found in R. B. Chesler, M. A. Karr, and J. E. Geusic, "An experimental and theoretical study of high repetition rate *Q*-switching in Nd:YAG lasers," *Proc. IEEE* **58**, 1899-1914 (December 1970). The experimental results shown at the end of this section are from this paper. See

also R. B. Chesler, M. A. Karp, and J. E. Geusic, "Repetitively *Q*-switched Nd:YAG-LiIO₃ 0.53- μ harmonic source," *J. Appl. Phys.* **41**, 4125-4127 (September 1970).

Repetitive passive *Q*-switching is also possible in a cw-pumped laser with a suitable saturable absorber placed inside the cavity. (The laser dynamics in this situation are in fact much like a sustained spiking behavior which does not damp out with time, because of the destabilizing effect of the saturable absorber.) An illustrative example can be found in H. T. Powell and G. J. Wolga, "Repetitive passive *Q*-switching of single-frequency lasers," *IEEE J. Quantum Electron.* **QE-7**, 213-219 (June 1971).

If a cw-pumped laser is repetitively *Q*-switched at a rate slow compared to the upper-level lifetime, a large fraction of the pumping power is wasted in the intervals between *Q*-switched pulses. It would be more efficient in this situation to build a more complex power supply, which supplies the same average pump power (or perhaps less average power) in repetitive short pump pulses just before the *Q*-switching takes place. A discussion of the resulting behavior can be found in D. G. Carlson, "Dynamics of a repetitively pump-pulsed Nd:YAG laser," *J. Appl. Phys.* **39**, 4369-4374 (August 1968). See also G. A. Badal'yan, V. A. Berenberg, and B. A. Ermakov, "Optimal operating regime for pulsed garnet lasers with a pulse repetition frequency around 1 kHz," *Sov. J. Quantum Electron.* **9**, 1134-1136 (September 1979).

Problems for 26.4

1. *Plotting theoretical curves for repetitively switched lasers.* Use the formulas in this section and in the earlier *Q*-switching analyses to derive and plot theoretical curves for pulse energy, peak pulse power, and average power versus normalized pumping rate r_{cw} in a repetitively *Q*-switched laser operating at steady state.
2. *Transient start-up of a repetitively switched lasers.* If the repetitive *Q*-switching process in a cw-pumped laser is suddenly turned on from an initially nonlasing state, assuming that the pump has been on for some time and has brought the atomic inversion to its full value, but that lasing has been blocked, the first few *Q*-switched pulses from the laser will have higher amplitudes than after the laser settles down to steady-state *Q*-switched operation.

To analyze this, suppose that an ideal single-mode repetitively *Q*-switched laser is being continuously pumped at a pumping rate which is r_{cw} times threshold for the cavity in its low-loss cavity condition. At time $t = 0$ (after the pump power has been on for some time) the cavity then begins to be repetitively *Q*-switched at a repetition frequency f_r . Develop an analysis to show how the energy per pulse varies during the first few *Q*-switched pulses, as the repetitively *Q*-switched laser approaches its steady-state operating conditions. Illustrate the resulting pulse energies versus pulse number for the situations $r_{\text{cw}} = 1.5$ and 2.0 and for repetition rates $f_r = 0.5, 1$ and 2 times the upper-level decay rate γ_2 .

3. *Optimizing the cavity coupling in a repetitively switched laser.* The cavity decay rate γ_c in a repetitively *Q*-switched laser after switching (i.e., after the acoustooptic modulator is turned off) is usually set by the output coupling through the cavity end mirror. The output coupling which is optimum for cw output power from a given laser with a given pumping rate may not be optimum for *Q*-switched operation of the same laser with the same pumping.

Carry out an analysis which predicts the peak *Q*-switched pulse power in a repetitively *Q*-switched laser versus cavity coupling γ_c , keeping all other physical pa-

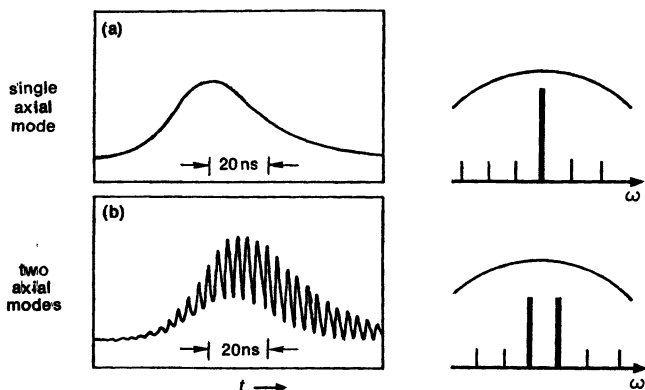


FIGURE 26.21

Axial-mode beating in the output from a Q-switched laser running in two axial modes.

rameters (i.e., real pumping rate r_{cw} , repetition rate f_r , and so forth) constant. Illustrate your conclusions for a typical situation, and compare the coupling for peak pulse power to the optimum coupling for maximum cw oscillation power.

4. *Analytic result for repetition rate equals atomic decay rate.* If the repetition frequency f_r in a repetitively Q-switched laser is set equal to the upper-level decay rate γ_2 , the ratio of average power in the Q-switched situation to unswitched cw power from the same laser approaches a limiting value $P_{\text{av}}/P_{\text{cw}} = 0.9242343\dots$ at vanishingly small pumping above threshold, i.e., as $r_{\text{cw}} \rightarrow 1$. What analytic expression accounts for this number?

26.5 MODE SELECTION IN Q-SWITCHED LASERS

Transverse and axial mode selection processes are generally less effective in Q -switched lasers than in continuous-wave (cw) or long-pulse types of lasers; and Q -switched lasers are therefore more likely than cw lasers to oscillate in several axial and/or transverse modes. Control of these modes can be a significant practical problem in Q -switched lasers used for certain applications.

Axial Mode Discrimination and Axial Mode Beating

When a laser, whether Q -switched or cw, oscillates in two modes simultaneously, the output exhibits "mode beats" at the difference frequency between the two modes. Mode beats of this type are illustrated for a Q -switched solid-state laser in the oscilloscope traces in Figure 26.21. The upper trace shows a clean, smooth Q -switched oscillation pulse corresponding to oscillation in only a single axial mode. The lower trace shows the same output with two axial modes oscillating simultaneously. The two modes in this situation are two adjacent axial modes separated by the observed beat frequency of 150 MHz.

etalon mode selector



narrowband gain cell



external injected signal

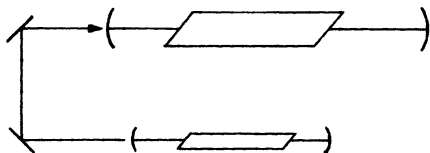


FIGURE 26.22
Mode control methods for Q-switched lasers.

This observed output simply represents the fact that the sum of two sinusoids at closely adjacent frequencies f_1 and f_2 appears to be a single sinusoid at the average frequency $(f_1 + f_2)/2$, whose amplitude is modulated at the difference frequency $f_d = |f_1 - f_2|$. If three or more equally spaced modes are present, the output will still be periodic at the intermode frequency, but with a more complicated periodic waveform.

Note that in *Q*-switched lasers with shorter cavities and/or with wider atomic lines, the mode beats between axial modes may be at very high frequencies, which are outside the passband of the photodetector/amplifier/oscilloscope combination used to observe the laser output. A smooth laser output pulse does not therefore guarantee single-mode operation, unless the photodetection system employed is fast enough to resolve the mode beats within the pulse.

Axial Mode Control

Axial mode beats may be undesirable in some applications, and various techniques are therefore employed to promote single-axial-mode oscillation in *Q*-switched (as also in cw) lasers.

As shown in Figure 26.22, one common technique is to employ one or more resonant etalons within the laser cavity, so as to modulate the cavity losses and provide additional loss for all but the centermost mode, as discussed in an earlier chapter. Another technique, often employed in CO₂ lasers among others, is to place a low-pressure, narrowband gain cell within the same cavity as the high-pressure broadband TEA gain cell that furnishes the primary laser power. The

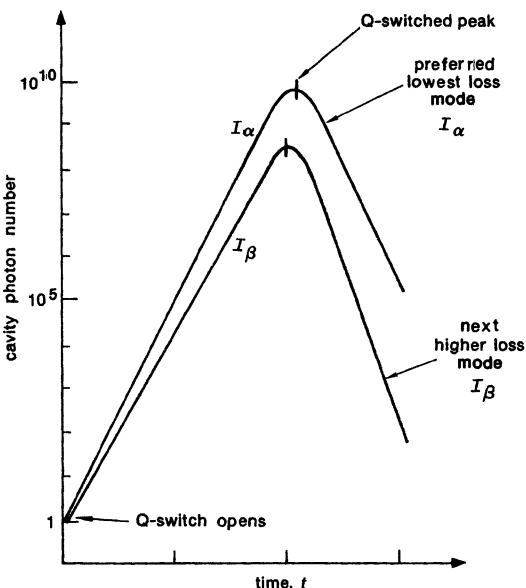


FIGURE 26.23
Mode build-up and mode competition in a Q-switched laser.

low-pressure cell is then operated either in a long-pulse or possibly even cw mode, so as to furnish either a preferential narrowband gain region containing only a single axial mode, or possibly even to produce weak "pre-lasing" before the main *Q*-switch pulse occurs.

More sophisticated single-mode techniques include injecting a weak signal from a separate single-frequency laser into the *Q*-switched laser cavity so that one single cavity mode is given a large preferential initial excitation; or employing various complex feedback systems on the cavity length to ensure that one single axial mode is located exactly at the central gain maximum of the laser medium.

Mode Discrimination in Q-Switched Lasers

A characteristic feature of actively *Q*-switched lasers is that there is little or no gain saturation during the major portion of the oscillation build-up. During the build-up of the oscillation pulse the laser gain is usually large compared to the cavity losses for both the preferred or lowest-loss cavity mode and for some number of higher-loss axial and transverse modes; and so all of these modes tend to grow at comparably rapid rates for most of the pulse build-up time. Only very near the peak of the *Q*-switched pulse is the gain saturated down to near or below the cavity losses.

Figure 26.23 thus illustrates schematically how the preferred or lowest-loss mode (sometimes called the dominant mode) and also the next higher-loss mode may grow to nearly the same amplitude on a log scale during the *Q*-switched burst. As the inversion becomes saturated down by the dominant mode, near the peak of the *Q*-switching process, the gain of the next higher-loss mode also decreases; and this mode will typically pass through its peak value slightly earlier,

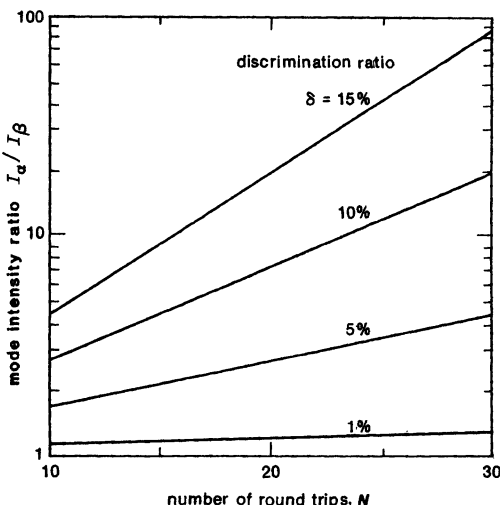


FIGURE 26.24
Ratio of intensities in two competing modes versus number of round trips, for different values of the discrimination parameter δ .

and begin to decay slightly faster than the dominant mode. If the inversion is large, however, and the losses of the two modes nearly the same, the next higher-loss mode may reach nearly the same peak amplitude as the dominant mode.

The axial and transverse mode selection in a Q -switched laser may, therefore, not be as good as in cw or long-pulse lasers, where the mode discrimination process has a longer time to operate. Furthermore, there may be a noticeable improvement in mode discrimination even during the Q -switched pulse itself.

Mode Discrimination Analysis

The conditions necessary to achieve good mode discrimination by the time the peak of the giant pulse occurs can be developed from a simple argument which applies in essentially the same way to mode discrimination between either multiple axial or transverse modes in the laser. To show this, let two different modes in a Q -switched laser cavity be denoted by indices α and β . The ratio of the intensities of these two modes after N round trips during the build-up phase, starting from the same noise level, will then be given by an expression like

$$\frac{I_\alpha}{I_\beta} = \left| \frac{[R_1 R_2 \exp(2\alpha_m p_m - 2\alpha_0 p)]_\alpha}{[R_1 R_2 \exp(2\alpha_m p_m - 2\alpha_0 p)]_\beta} \right|^N = e^{N\delta}. \quad (48)$$

The numerator and denominator of the middle term represent the net round-trip gain minus loss values for the two individual modes; and we then assume that these two net gain minus loss values stand in the ratio e^δ , where $\delta = 0.01$, for example, represents a 1% difference in the two net round-trip gains. This difference may result in practice from either a difference in actual laser gain, as for example with two different axial modes, one of which is farther from line center; or from a difference in cavity losses, as for example with two different transverse modes.

The number of round in a typical Q -switched laser during the build-up phase will typically be on the order of $N \approx 20$ to 30. Figure 26.24 plots the ratio of intensities I_α/I_β that will have developed after a number N of round trips, starting from the same initial noise intensities, for different values of the gain ratio parameter δ . The general conclusion is that if two different modes have only a few percent difference in gain, the mode discrimination between them after even 20 or 30 round trips will be very poor. For good mode discrimination in a Q -switched laser, at least a 10% to 15% difference in mode losses or gains is required.

Transverse Mode Control and Mode Distortions

The suppression of unwanted higher-order transverse modes in Q -switched lasers is much like transverse mode control in cw lasers. That is, the general approach is to use suitable resonator designs and intracavity apertures so that the lowest-order transverse mode has significantly lower diffraction losses than the next higher-order transverse mode. This condition must, however, be more stringently enforced in a Q -switched laser than in a cw laser, for the reasons discussed above.

Transverse mode control may in some situations be more effective in passively rather than actively Q -switched lasers, because the dominant transverse mode which builds up first will preferentially saturate the saturable absorber cell in the transverse region which its fields are most intense. The saturable absorber then becomes a kind of dynamic spatial filter, which lets the lowest-order mode build up while continuing to suppress higher-order modes.

The transverse mode dynamics can also be complicated in a Q -switched laser, however, by dynamic changes in the resonator parameters occurring during the Q -switched pulse, caused by dynamic gain saturation produced by the pulse. The gain medium saturates first in those portions of the transverse cross section where the laser field is most intense. This may cause the high-gain laser medium to act like a rapidly changing aperture, which may modify and distort the transverse profile of the circulating energy on successive round trips. We may then expect dynamic changes in the output beam profile during the pulse itself, produced by both (a) continued filtering out of higher-order transverse modes, and (b) dynamic distortion of all the modes.

REFERENCES

A mode discriminating analysis very similar to that in this section is presented by W. R. Sooy, "The natural selection of modes in a passive Q -switched laser," *Appl. Phys. Lett.* **7**, 36-37 (July 15, 1965).

Dynamic mode distortions are discussed by G. L. McAllister, M. M. Mann, and L. G. DeShazer, "Transverse-mode distortions in giant-pulse amplifiers," *IEEE J. Quantum Electron.* **QE-6**, 44-48 (January 1970).

Problems for 26.5

1. *Gain discrimination requirement for good mode discrimination.* Plot the required gain discrimination in percent needed to obtain a ten to one discrimination in

mode intensities after N round trips versus the number of round trips, for $N = 10$ to 30.

26.6 Q-SWITCHED LASER APPLICATIONS

We can review briefly in this section some typical performance figures for Q -switched lasers, and some of the practical applications for these lasers.

Typical Performance Results

As a practical example of laser Q -switching, we might consider a typical small-to-medium size solid-state laser, such as a Q -switched ruby, Nd:YAG or Nd:glass laser oscillator. The pump power input from the capacitor bank to the flashlamp (or lamps) in such a laser might be 20 to 200 J delivered in a pulse 100 μ s long, corresponding to an electrical power input of 1 to 2 MW to the flashlamps.

This electrical input might be converted to laser output in a typical laser with an efficiency between 0.1% (typical) and 1% (absolute best), so that the laser output energy will be between 20 mJ and perhaps 2 J in a single laser shot. If the laser oscillates in "long pulse mode" (no Q -switching), this corresponds to an average power output between 200 W and 20 kW during the 100 μ s pumping period (although spiking effects may produce peak powers 10 to 20 \times as large).

Suppose the same energy is extracted in a Q -switched pulse which is only 100 ns long. The peak optical output power during this pulse then has a value somewhere in the range from 2 to 200 MW peak, or more than 10 4 larger than the power level from the same laser in long pulse mode (although this may be reduced somewhat by the fact that in general a laser will oscillate more efficiently in long-pulse than in Q -switched operation).

These numbers are quite typical for Q -switched solid-state lasers. If more energy per pulse is needed, either larger diameter rods and flashlamps can be employed or, more commonly, the initial Q -switched laser is followed by one or more stages of laser amplification. Extraction of too much energy from a single oscillator is usually avoided because of self-focusing and optical-damage problems that occur in the laser mirrors, laser rods, and Q -switching elements if the Q -switched energy or peak pulse power is increased much further.

Q-Switched Laser Applications

Important applications for the short pulses and high peak powers provided by Q -switched lasers include:

(a) *Laser radars, or lidars:* The short intense pulses generated by Q -switched lasers are ideal for optical ranging, optical radar, or "lidar" applications, as for example in tank or artillery range-finders. Q -switched solid-state lasers along with the associated detection electronics can be packaged into remarkably small and rugged units, not much bigger than a large pair of binoculars, for military field applications. The pulses from larger Q -switched lasers can be transmitted through large telescopes to permit ranging off corner-cube retroreflector targets in orbiting satellites, or on the surface of the moon. By integrating

over many Q -switched shots, the distance to the moon can in fact be measured with relative accuracy of 10 cm or less, permitting precise calculations of the lunar orbit and of "moon-quakes." By conducting accurately timed ranging experiments on an orbiting satellite from observing stations in different continents, we can calculate the satellite orbit to very high accuracy; we can detect perturbations in the orbit caused by mass perturbations in the Earth itself; and distances between the observing stations can be established with sufficient precision to potentially measure continental drifts. FLAG

(b) *Tunable laser radars:* Laser ranging systems using tunable lasers, whose wavelengths can be tuned to specific atomic or molecular transitions, can be used for pollution detection, aerosol measurement, ranging on clouds and measurement of optical visibility, and similar applications. Similar measurements from orbiting space stations may eventually become possible, leading to world-wide pollution detection and weather forecasting applications.

(c) *Cutting and drilling applications:* The intense pulses from even rather modest sized Q -switched lasers are also extremely effective for optical cutting, welding, and scribing applications. Q -switched lasers can be used for drilling diamonds for wire dies and instrument jewels; scribing semiconductor wafers so that they can be separated into individual chips; welding shut nuclear fuel rods, and trimming resistors and integrated circuits while simultaneously monitoring the electrical properties of these circuits. Unique applications include drilling holes in small rubber baby bottle nipples or in plastic pipes used for trickle irrigation systems.

(d) *Basic scientific experiments, especially nonlinear optics:* Finally, Q -switched lasers have found great many applications in basic physics experiments, particularly where we need to have high-peak power to produce some nonlinear or optical breakdown effect, while still having only relatively small total energy so as to avoid damage effects. Examples of such physical phenomena include optical harmonic generation, stimulated Raman and Brillouin scattering, gas breakdown, and the shock heating of gases and other samples.



ACTIVE LASER MODE COUPLING

Mode locking and related forms of mode coupling in lasers provide important techniques for generating ultrashort light pulses and other useful forms of periodically modulated laser signals, including frequency-swept or so-called “FM-laser” signals.

In this chapter we first introduce some of the general concepts of mode coupling in lasers, and then discuss in particular the kinds of *active mode locking* or *active mode coupling* that can be produced using intracavity amplitude (AM) or phase (FM) modulators. In the following chapter we will describe the ultrashort optical pulses that can be produced using *passive mode locking*, with a saturable absorber element inside the laser cavity.

27.1 OPTICAL SIGNALS: TIME AND FREQUENCY DESCRIPTION

The circulating signal inside an oscillating laser cavity can be described either in the *time domain*, using recirculating pulse concepts, or in the *frequency domain*, using multiple axial-mode concepts. Before introducing any of the mode-coupling techniques that are used in real lasers, therefore, let us describe each of these approaches in turn, and illustrate how they lead to important ideas that are fundamental to mode-locked lasers.

Time Description of Laser Signals

Suppose first of all that we can take a kind of instantaneous “snapshot” of the optical fields circulating inside a laser cavity. As we have pointed out previously, such a snapshot might look something like Figure 27.1.

The fields inside the laser cavity in this example obviously have an irregular structure which does not represent a single oscillation frequency or a single-mode laser. A field pattern such as the one shown would correspond to a laser oscillating in several axial modes with irregular phases, as in a multimode laser or a laser building up from an initial noise pattern.

One point to be emphasized here is that this same circulating field pattern, after being weakened by reflection from the output coupling mirror, will circulate once more around inside the laser cavity and be re-amplified by the laser medium.

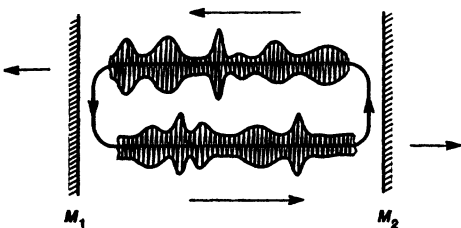


FIGURE 27.1
Optical field pattern circulating inside a laser cavity.

Since the laser amplification process is basically linear and coherent, this circulating pattern will, to first order, be unchanged by the amplification process. The fields within the cavity will thus look essentially the same one round-trip transit time later, with the following minor exceptions:

- The detailed shape of the pattern may be slightly but not greatly changed by the finite bandpass properties of the laser medium (and possibly also by any nonlinearities in the amplifier response).
- The field pattern may be either stronger or weaker on the following round trip if the laser cavity is in either an initial build-up or a decaying phase, with a round-trip gain either greater or less than unity.
- And, a small amount of random noise or spontaneous emission may be added to the pattern due to spontaneous emission from the laser medium.

The final point is usually of negligible importance except for signals approaching the noise limit of the laser device.

Periodic Laser Signals

If the field pattern inside the laser cavity circulates with essentially no change per pass, the output signal coming from the laser cavity will consist of a periodic repetition of the same pattern with a period given by $T = 2L/c$ or $T = p/c$ for a standing-wave cavity of length L or a ring cavity of perimeter p . The repetition frequency or the axial mode spacing frequency of this laser cavity will then be, as we already know,

$$\omega_{ax} \equiv \omega_{q+1} - \omega_q = \frac{2\pi c}{p} = \frac{2\pi}{T}. \quad (1)$$

A typical value of the repetition period and mode-spacing frequency for a laser cavity might be

$$L = 60 \text{ cm} \quad \text{leading to} \quad \begin{cases} T = p/c = 4 \text{ ns}, \\ \omega_{ax} = 2\pi \times 250 \text{ MHz}. \end{cases} \quad (2)$$

One limiting situation of laser oscillation is the single-frequency or single-mode laser, in which only one axial mode is oscillating, so that the circulating pattern within the laser cavity has constant amplitude and frequency everywhere within the cavity, and the number of repeated round trips is indefinitely large.

Another limiting situation is a very high-gain, short pulse type of laser—for example, certain kinds of pulsed excimer lasers or dye lasers—in which the entire laser oscillation burst only lasts for perhaps two or three round trips, and the circulating energy within the cavity may be largely random noise with a bandwidth approaching the atomic linewidth of the laser medium. In certain very high-gain pulsed lasers, for example, the cavity round-trip time may be perhaps 5 or 6 ns, and yet the burst of laser oscillation may last for only 10 or 20 ns.

Periodically Repeated Signal Spectra

The time-domain approach consists in essence of specifying the real laser signal $\mathcal{E}(t)$ that circulates inside the cavity, or that comes out of the cavity output mirror, during one round trip; and then examining what happens to this signal on successive round trips. We need in particular to have a clear understanding of the extent to which steady-state concepts such as cavity axial modes apply, or have any useful meaning, in transient situations such as Q -switched lasers, or in the type of very short pulse lasers we have just mentioned.

To develop this understanding, let us consider the real optical signal $\mathcal{E}(t)$ which may come out of a laser cavity (or transit any reference plane within the laser cavity) during one single round-trip transit time, that is, during the time interval $0 \leq t \leq T$, as shown in Figure 27.2(a), with $\mathcal{E}(t) = 0$ outside that range. Let $\tilde{\mathcal{E}}(\omega)$ then be the Fourier transform of this particular time-limited signal $\mathcal{E}(t)$, as shown in the right-hand part of Figure 27.2(a).

The signal $\mathcal{E}(t)$ in this situation may have almost any form—it may consist, for example, of a short pulse, or burst, of sinusoidal signal, with pulselwidth $\tau_p \ll T$, having a carrier frequency, let us call it ω_c , which may not match up with any of the axial modes ω_q of the laser cavity itself. Suppose that $\mathcal{E}(t)$ has time fluctuations in either amplitude or phase that are rapid compared to the round-trip time T . This implies that its spectrum $\tilde{\mathcal{E}}(\omega)$ will have a spread in radian frequency that is wide compared to $2\pi/T$, and hence compared to the axial-mode interval ω_{ax} . In other words, even if the underlying sine wave in $\mathcal{E}(t)$ looks like a “clean” sine wave with a definite carrier frequency ω_c , the frequency of this signal will not be sharply defined compared to the axial-mode spacing.

Consider now a signal $\mathcal{E}^{(2)}(t)$ that consists of the same signal $\mathcal{E}(t)$ repeated for two round trips, i.e., $\mathcal{E}^{(2)}(t) \equiv \mathcal{E}(t) + \mathcal{E}(t-T)$ as shown in Figure 27.2(b). The Fourier transform of a signal $\mathcal{E}(t-T)$ which is delayed by an amount T in the time domain is given by $\exp(-jT\omega) \times \tilde{\mathcal{E}}(\omega)$ in the frequency domain; and hence the Fourier transform of the two-section signal $\mathcal{E}^{(2)}(t)$ (normalized to unity peak value) is given by

$$\tilde{\mathcal{E}}^{(2)}(\omega) = \frac{1}{2} [1 + e^{-jT\omega}] \times \tilde{\mathcal{E}}(\omega) = \tilde{\mathcal{E}}(\omega) \cos(T\omega/2) \exp(-jT\omega/2). \quad (3)$$

The corresponding intensity or power spectrum is

$$I^{(2)}(\omega) \equiv \left| \tilde{\mathcal{E}}^{(2)}(\omega) \right|^2 = \frac{1}{2} [1 + \cos T\omega] \times I(\omega) = I(\omega) \cos^2 \frac{T\omega}{2}. \quad (4)$$

This two-segment spectrum exactly equals the one-segment spectrum—except for being twice as large in amplitude—at those frequencies where $\omega = \omega_q = q2\pi/T$; but it drops to zero halfway in between.

Figure 27.2(c) then shows the same result for a signal $\mathcal{E}^{(3)}(t)$ and its spectrum $\tilde{\mathcal{E}}^{(3)}(\omega)$ obtained by combining three successive copies of the original signal $\mathcal{E}(t)$.

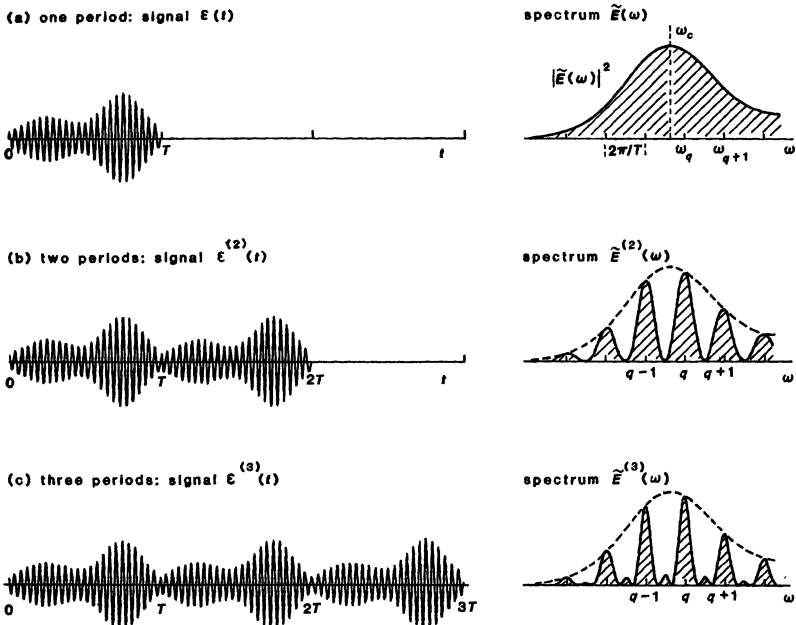


FIGURE 27.2

Examples of a time signal $E(t)$ and its power spectrum for the same signal repeated one, two, or three times in succession. (Note that the carrier frequency ω_c of the sine-wave signal does not coincide with any of the axial modes ω_q .)

It is evident that even after two or three round trips—or after combining only two or three copies of the individual round trip—we have a signal that has already developed a rather broadly defined but clearcut axial-mode spectrum.

The N -Period Spectrum

Suppose in fact we combine N round trips or N identically delayed copies of the time function $E(t)$ such that

$$E^{(N)}(t) \equiv \sum_{n=0}^{N-1} E(t - nT). \quad (5)$$

The Fourier transform of this function is then

$$\tilde{E}^{(N)}(\omega) = \sum_{n=0}^{N-1} e^{-jnT\omega} \times \tilde{E}(\omega) = \frac{1 - e^{-jNT\omega}}{1 - e^{-jT\omega}} \tilde{E}(\omega), \quad (6)$$

and hence the power spectral intensity is given by

$$I^{(N)}(\omega) \equiv \left| \tilde{E}^{(N)}(\omega) \right|^2 = \frac{1 - \cos NT\omega}{1 - \cos T\omega} I(\omega). \quad (7)$$

An illustration of this formula is shown in Figure 27.3 for the case $N = 10$.

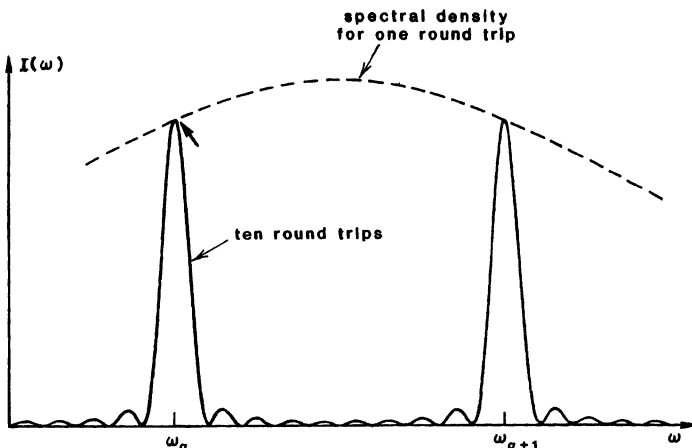


FIGURE 27.3

Power spectral density for the same optical signal repeated 10 times in succession.

Discussion

The interpretation of these results seems clear. It is the fixed time delay or time shift T between successive round trips that gives the axial mode character to a laser output signal, *independent of the detailed waveform $\mathcal{E}(t)$ or of the carrier frequency ω_c that may characterize the optical sine waves under the output signal envelope.*

If a Q -switched or short-pulse laser, for example, puts out a signal that lasts only a few round trips (perhaps $N = 4$ or 5 round trips), then the spectrum of this output will have strong peaks exactly at the steady state axial-mode frequencies ω_q of the cavity. These peaks will not be infinitely sharp, however, but will have a frequency width of order $\delta\omega_q \approx \omega_{\text{ax}}/N$. The total number of axial modes within the spectrum will be essentially the spectral width of the single-pass signal $\mathcal{E}(t)$ divided by the axial-mode spacing ω_{ax} , and will not depend at all on the total number of round trips N . The number of axial modes for a short circulating pulse of width τ_p , or for any circulating signal that has large amplitude or phase fluctuations occurring with time constant τ_p , will be $N_{\text{modes}} \approx T/\tau_p$.

Frequency Domain Description

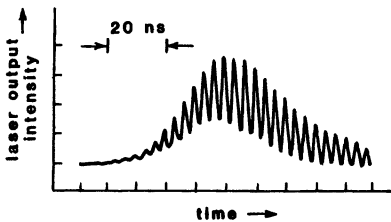
Let us look again at these laser signals, focusing now on the *frequency domain*, in which we speak primarily of the axial modes within a laser cavity.

The simplest situation to consider is that of a laser oscillating in a single axial mode, which means that the signal amplitude, phase and frequency are all constant in time. (Real lasers will always have some random amplitude and phase fluctuations even in a single-mode laser, because of power-supply fluctuations, quantum noise sources, and so forth, but we can ignore these here.)

The next most complicated situation is obviously two oscillating axial modes, for which the output field as a function of time can be written as

$$\mathcal{E}(t) = \text{Re}[E_1 e^{j(\omega_1 t + \phi_1)} + E_2 e^{j(\omega_2 t + \phi_2)}], \quad (8)$$

FIGURE 27.4
Mode beating in a Q-switched laser oscillating in two axial modes.



where taking the real part of the right-hand side is understood. The output intensity from the laser as a function of time then becomes

$$I(t) \equiv |\mathcal{E}(t)|^2 = E_1^2 + E_2^2 + 2E_1E_2 \cos[(\omega_2 - \omega_1)t + \phi_2 - \phi_1], \quad (9)$$

where ϕ_1 and ϕ_2 are the phase angles of the two phasor amplitudes \tilde{E}_1 and \tilde{E}_2 , respectively.

The output intensity from a laser with two axial modes obviously varies sinusoidally with a beat frequency equal to the difference frequency $\omega_2 - \omega_1$ between the two sidebands. This kind of sinusoidal mode beating, as illustrated for a *Q*-switched laser in Figure 27.4, can be seen in the time output of many lasers, and serves as a clear indicator that at least two axial modes are present in the laser spectrum.

The depth of modulation, or visibility, of this sinusoidal beating is 100% if the amplitudes of the two sidebands are equal, and decreases if they are unequal. Note also that changes in the relative phases ϕ_1 and ϕ_2 of the two sidebands will change the time origin for the peak of the mode beating, but will not otherwise change the appearance of the mode beats. As a result, the concept of "mode locking," in the sense of locking together the phases of sinusoidal signals, is not a very meaningful concept for two axial modes only—or perhaps we should say instead that any two sinusoidal signals are always mode-locked, since changes in the relative phases between the two modes can only change the time origin, but not the shape of the resulting signal.

Three Axial Modes

The situation becomes more interesting when we have three or more equally spaced axial modes or sidebands within a laser, as illustrated in Figure 27.5. We show here three sine waves with equally spaced frequencies ω_q , ω_{q+1} , and ω_{q+2} . Suppose that we pick some instant of time when the first two of these sine waves are exactly in phase, and shift the time origin so that this instant corresponds to $t = 0$. Suppose that we then adjust the phase of the third sine wave so that it is exactly in phase with the other two sine waves at this same instant.

The \mathcal{E} field amplitude of the total signal (that is, the sum of the three frequency components) will then appear as in the middle part of Figure 27.5. Note that the peak field amplitude in this situation is 3 times the amplitude of each individual sideband, and hence the peak intensity I_{peak} is nine times the intensity in any single sideband. The average intensity with three equal-amplitude modes will be just three times the intensity in any one mode, so we also have $I_{\text{peak}} = 3I_{\text{av}}$. We have plotted both the field amplitude $\mathcal{E}(t)$ in this situation,

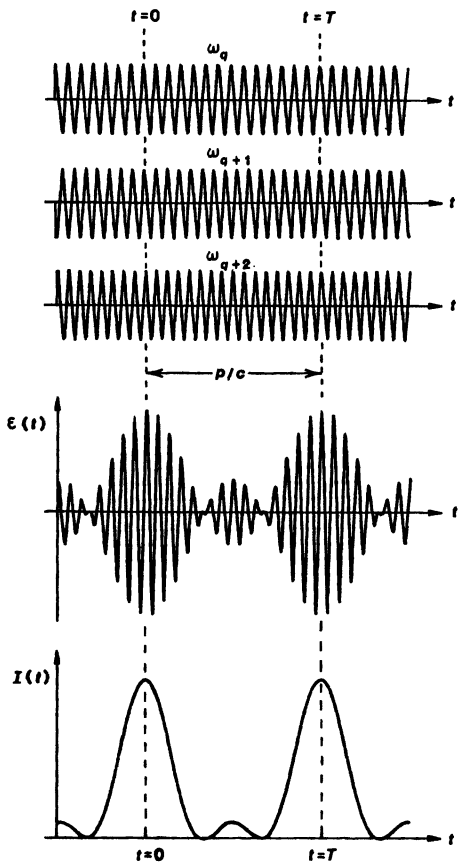


FIGURE 27.5
Superposition of three equally spaced frequency components which are all exactly in phase at $t = 0$.

including its sign, in order to make the weaker central lobe stand out, and to emphasize the 180° phase shift in the center lobe; and also the intensity $I(t)$ versus time to emphasize that even with only three modes we already have a reasonable good “mode-locked” pulse, provided that all three modes are indeed in phase.

Phasor Description

A useful alternative way of describing this same behavior is to represent the complex amplitude and phase of each frequency component in the signal by a complex vector or phasor in the complex plane. Suppose we choose a coordinate system in which the centermost spectral component is stationary, i.e., the coordinate system rotates in real time at the frequency of the centermost spectral component. Higher-frequency or lower-frequency sidebands will then rotate

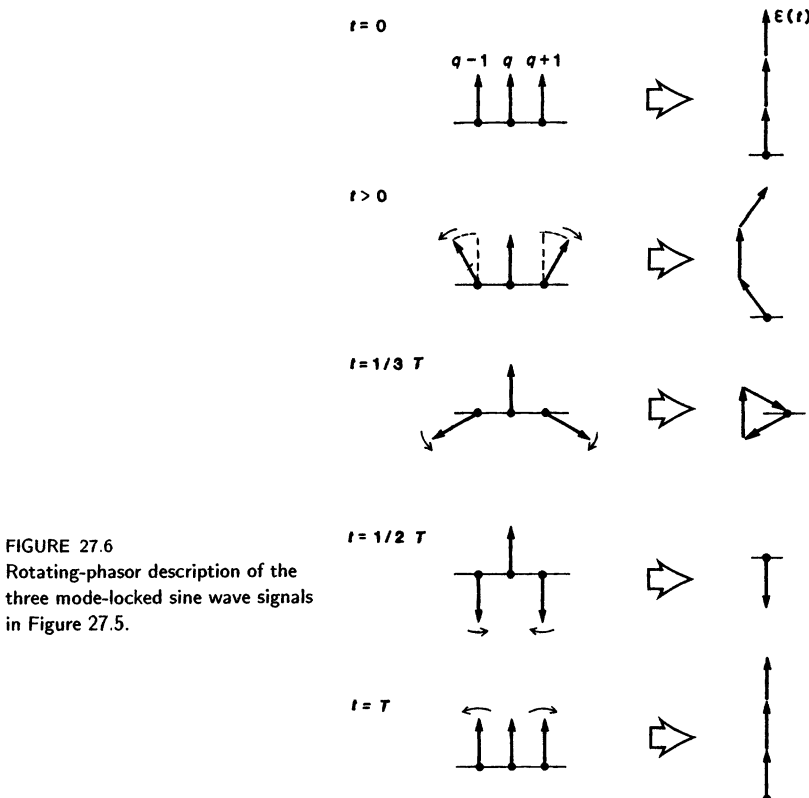


FIGURE 27.6
Rotating-phasor description of the
three mode-locked sine wave signals
in Figure 27.5.

either forward or backward in this coordinate system, at successively faster rates for more distant sidebands.

The instantaneous amplitude and phase of the total electric field or optical signal at any instant t will then be given by the vector sum of these rotating sideband vectors. Figure 27.6 shows, for example, how three vectors can start out initially all in phase, giving the largest possible signal amplitude. One vector then rotates forward in phase with increasing time, whereas the other vector rotates backward, so that after, say, $1/3$ of a beat-frequency period (and also after $2/3$ of a period) the three phasors will have rotated to be 120° out of phase, giving zero output amplitude in the particular situation of three equal-amplitude phasors.

After one complete period of the fundamental beat frequency, however, the three phasors will all add up in phase again, giving another mode-locked pulse; whereas halfway between these pulses the phasors will be arranged with one phasor up and two down, giving an intermediate subpulse as shown in Figure 27.5, in which the phase of the sinusoidal carrier is shifted by 180° relative to the main pulses.

We can also consider situations where the three phasors in Figure 27.6 may have different amplitudes, or different relative phases between themselves. In any

such situation there will always be periodically repeated instants of time spaced by $t = t_0 + nT$ at which any two of the three sidebands will be in phase. We can always pick one of those instants to be $t = 0$ and then measure the phase of the third sideband relative to that origin. Hence, there is really only one *relative* phase difference among the three sidebands in any three-frequency situation like this (or $N - 2$ significant relative phases in an N -sideband spectrum).

The overall time waveform produced by adding up three sine waves will change significantly, however, for other relative phases between the sidebands. The ideally “mode-locked” or “all-in-phase” situation we have described here is only one possible situation. This situation gives the highest-possible peak pulse amplitude, at the periodically recurring instants when all three vectors are in phase. Varying the relative phase of any one of the sidebands will then lead to a continuous family of other waveforms having significantly different time-variations, as we will illustrate later on.

Multiple Axial Modes: Short-Pulsed Mode Locking

The obvious next step is to go to some larger number N of sidebands or equally spaced axial-mode frequencies, where for simplicity we will first assume these sidebands all have the same amplitude. Suppose that we again assume that all these sidebands are lined up exactly in phase at some instant which we define to be $t = 0$. We can then extend the phasor description given in Figure 27.6 to have N phasors rotating in the complex plane at various integral multiples of the axial-mode spacing frequency ω_{ax} , corresponding to N equally spaced sidebands in the signal spectrum.

If there are just N sidebands or axial modes, all in phase, and all of equal amplitude, then we can write the total wave amplitude associated with this signal in the form

$$\mathcal{E}(t) = \sum_{n=0}^{N-1} e^{j(\omega_0 + n\omega_{\text{ax}})t} = \frac{e^{jN\omega_{\text{ax}}t} - 1}{e^{j\omega_{\text{ax}}t} - 1} e^{j\omega_0 t}, \quad (10)$$

so that the intensity is given by

$$I(t) = |\mathcal{E}(t)|^2 = \frac{1 - \cos N\omega_{\text{ax}}t}{1 - \cos \omega_{\text{ax}}t} = \frac{\sin^2 N\omega_{\text{ax}}t/2}{\sin^2 \omega_{\text{ax}}t/2}. \quad (11)$$

The first four plots in Figure 27.7 show the periodic time envelopes that result from Equation 27.11 for the cases $N = 4, 5, 6$, and 8 . There is a complete duality between the time variation that results from adding up N equal frequency sidebands in this situation, and the axial-mode spectral modulation that results from adding up N time periods in the time-description approach introduced in the preceding.

From the phasor viewpoint we can easily see how these short-pulse signals arise. Adding together N equal-amplitude sine waves or complex phasors, all in phase at $t = 0$, produces a peak at $t = 0$, and also again at $t = \pm T, \pm 2T$, and so forth. The \mathcal{E} field amplitude at this peak is N times the amplitude of any one component, or its peak intensity is N times the total time-averaged intensity in all the sidebands together. After a time $\Delta t = \pm T/N$ on either side of these peaks, however, the phasor amplitudes rotate by enough relative to each other to become uniformly distributed in angle, so that the total field amplitude and intensity fall to exactly zero (in the situation of equal phasor amplitudes).

The result is a short intense “mode-locked” pulse, with a full width at the base of $2T/N$, or a FWHM pulselwidth given approximately by $\tau_p \approx T/N$. In between these peaks come $N - 2$ much weaker subsidiary peaks whose width at the baseline is only T/N rather than $2T/N$ as for the main peaks.

Experimental Illustration: Short Pulse Synthesis

The frequency sidebands that make up a mode-locked laser pulse normally come from multiple axial modes within a single laser cavity. Figure 27.8 shows an instructive experiment, however, in which several independent monochromatic signals, derived from independent lasers, were combined to produce artificially synthesized mode-locked pulses.

This experiment made use of a number of small CO₂ waveguide lasers, a type of laser which can provide relatively stable and tunable single-frequency oscillations on the P(20) CO₂ laser transition near 10.6 μm . As shown in Figure 27.8, a portion of the output signal from each of these independently tunable single-frequency lasers was tapped off and independently heterodyned against a master reference laser. By monitoring the rf beat frequency between each oscillator and the reference laser, comparing this to a master radio frequency oscillator, and then using a separate feedback control loop to the piezoelectric mirror adjustment on each laser, it was possible to stabilize each laser's oscillation frequency to a different fixed offset from the reference laser, with each offset being an integer multiple of the same master radio frequency oscillator. (The reference laser itself may then still retain considerable frequency jitter; but if the feedback loops are sufficiently fast and high gain, all the other lasers can be tightly locked at fixed offsets to the reference laser and to each other.)

The lower traces show the pulsed time outputs produced by the combined outputs of three, four, or five such lasers, when the frequency spacings between the lasers were made exactly equal and the phases properly adjusted. Note that the number of secondary maxima between pulses is exactly as expected from the preceding analysis.

This particular experiment represents more a feasibility demonstration than a useful way of generating short optical pulses. It does indicate, however, that at the cost of some complexity we can combine the outputs from N independent lasers to obtain peak power powers N^2 times the output of just one laser. The pulse intervals can also be adjusted to any arbitrary value, entirely independent of the laser lengths. We might, for example, make the frequency offsets small, and thus obtain (rather wide) pulses separated by much more than the round-trip time in the individual lasers.

Other Mode-Coupled Waveforms

The results we have shown so far have all been for the limiting situation of *equal-amplitude* sidebands, with all sidebands exactly *in phase*. There are obviously many other periodic waveforms that can result from adding up equally spaced sidebands with other relative amplitudes and phase angles; and it is important to understand what other kinds of results can also result from other multimode laser signals. Figure 27.8 shows, by way of example, some of the other kinds of periodic signal amplitudes and phases that can be produced if we consider other arrangements of the sidebands.

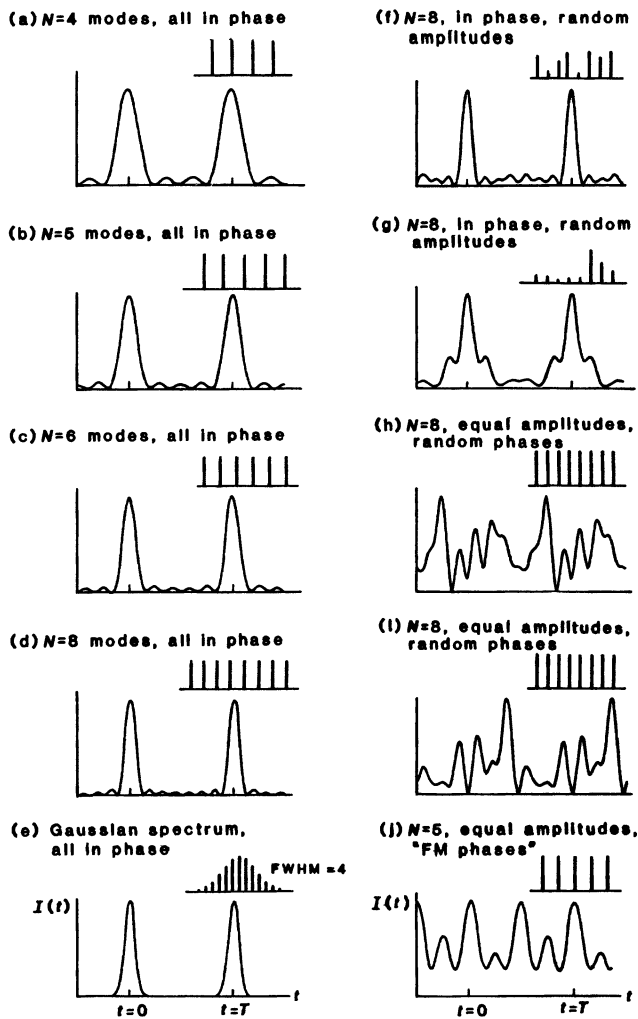


FIGURE 27.7

Examples of the different intensity patterns in time that can be synthesized using N equally spaced frequency components with different relative amplitudes and phase angles.

(1) *Uniform-amplitude sidebands, all in phase.* Figures 27.7(a) through 27.7(d) show the more or less ideal mode-locked pulses that result from a square or *uniform-amplitude spectrum* having N equal-amplitude modes *all in phase*, for various values of N . In each situation there is one primary mode-locked pulse per period, with a FWHM pulselwidth given, roughly, by $\tau_p \approx T/N$; plus $N - 2$ much weaker subsidiary peaks. (Note that these subsidiary peaks, which are not

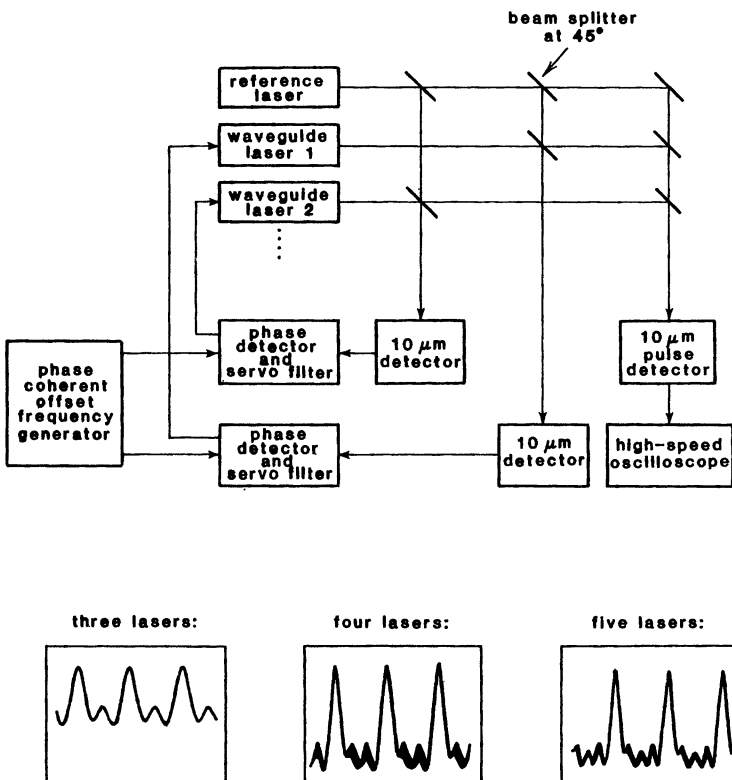


FIGURE 27.8

Short mode-locked 10.6 micron pulses produced by combining and locking together the monochromatic outputs from three, four, or five independent CO₂ laser oscillators. (From Hayes and Laughman, *Appl. Opt.* 16, 263-264, February 1977.)

that far down when measured in decibels, may cause difficulties in, for example, pulsed digital optical communications systems.)

(2) Gaussian-amplitude sidebands, *all in phase*. Figure 27.7(e) shows the time output assuming a gaussian frequency spectrum (gaussian sideband amplitude distribution), with a spectral FWHM corresponding to 4 axial-mode spacings, again with all modes in phase at $t = 0$. Again the result is a train of periodically spaced short pulse, but the pulses now have gaussian shapes in time, with essentially no subsidiary peaks. This illustrates that the Fourier transform of a gaussian spectrum is a gaussian pulse in time, and also that amplitude shaping of the axial-mode spectrum can reduce or eliminate the subsidiary peaks.

(3) Random-amplitude sidebands, *all in phase*. Figures 27.7(f) and (g) then show two examples of the pulses obtained from a spectrum which still has all modes in phase, but which now has random amplitudes over the set of N modes. (Since the sideband amplitudes are random numbers, one obtains a different intensity output profile each time one calculates a case like this.) Periodic pulses are still obtained in this case, but there is an irregular background of sub-pulses

between the main pulses, with the shape of this background varying from case to case.

(4) *Uniform-amplitude sidebands, random phases.* Figures 27.7(h) and (i) show by contrast typical results for a square or *uniform-amplitude spectrum*, but with *random phases* among the sidebands. The signal now consists not of single clean pulses, but of a random set of much weaker impulses—essentially, a noise-like signal—with the impulses distributed throughout the entire round-trip period. The signal is still strictly periodic in time, however, that is, it will repeat exactly after one period T . Note also that the “noise spikes” within each period have a width which is approximately the same as the ideally mode-locked situation, i.e., $\tau_p \approx T/N$ where N is the number of sidebands in the spectrum.

We could also plot other examples of the output waveforms for situations in which *both* the phases and amplitudes of the sidebands are completely random. Such signals would accurately represent in particular the kind of initial noise distribution present in a cavity when it first begins to build up toward oscillation. These results, however, would appear generally very similar to the random-phase but uniform amplitude results shown in Figures 27.7(i) and (j), except that the intensity tends to touch the baseline somewhat more often when both phases and amplitudes are random. The conclusion is that random sideband phases will always lead to noise-like signals, independent of whether the sideband amplitude distribution is random or more orderly.

(5) *Rectangular quasi-FM spectral distribution.* Finally, Figure 27.7(j) shows the output intensity versus time for a rectangular spectrum with $N = 5$ in which the sideband amplitudes are uniform but the sideband phases have been empirically adjusted to give an intensity profile which has reduced peak to peak variation, and which does not go to zero anywhere within the period. This particular result thus represents something close to a *quasi-phase modulation* or *frequency modulation (FM) signal*, with only a minimal amplitude variation during the round-trip period.

“Mode Coupling” Versus “Mode Locking”

Any arrangement of a set of frequency sidebands or axial modes in which the sidebands are exactly equally spaced in frequency, regardless of the relative amplitudes and phases of these sidebands, will thus produce an output signal envelope which is *periodic* in time, with a fundamental period equal to the inverse spacing between adjacent sidebands. Any such situation, regardless of the signal variation within one period, might thus be referred to in general as a *mode-coupled* situation, since the modes are, in some sense, all coupled together with fixed (even if irregular) amplitudes and phases. As a somewhat arbitrary distinction, we might then reserve the term *mode-locked* for only those situations in which the sidebands are arrayed all *in phase*, or nearly so, regardless of their amplitudes; since only these situations lead to the kind of short-pulse output that has become associated with the term “mode locking” in lasers. This at least is the sense in which we will interpret these two terms in the remainder of this chapter.

Summary

An understanding of the points illustrated by each of the preceding examples is very useful for understanding the complex behavior that can occur in

different types of mode-coupled lasers. The essential points that we wish to make in this section include:

- Any laser signal whose time envelope contains variations in amplitude or phase that are rapid compared to the cavity round-trip time—including, but by no means limited to short pulses—will have a frequency spectrum that is wide compared to a single-cavity axial-mode interval.
- The continuous spectrum that corresponds to the time-limited signal during just one round trip then becomes the envelope for a spectrum which begins to exhibit an increasingly sharp axial-mode structure, if the laser signal is repeated any reasonable number of times.
- In fact, any laser signal which continues or repeats for as many as two or three round trips, and which does not change by “too much” from round trip to round trip, will have an axial-mode structure simply due to this repetition. The axial modes will be narrowed by $\approx 1/N$ compared to the axial mode spacing, if the laser action continues for $\approx N$ round trips.
- Any laser signal that has a wide frequency spectrum containing numerous axial modes will necessarily have rapid time-variations in either amplitude or phase or both during one round trip, with the time rate of change for either amplitude, or phase, or both, approximately matching the inverse of the full width of the axial-mode spectrum.
- Any spectrum with the sidebands *all in phase*, even if the amplitude distribution over the sidebands is quite irregular, will generally lead to an output signal in the form of one dominant short pulse per period, usually with weaker side pulses. *Random phasing* of the frequency sidebands will generally produce large and irregular time-variations in both the instantaneous amplitude and phase of the output signal, more or less independent of the amplitude distribution over the sidebands.

In subsequent sections we will see how these concepts play important roles in the performance of different kinds of mode-locked laser systems.

REFERENCES

The synthesized optical-pulse results shown in this section come from C. L. Hayes and L. M. Laughman, “Generation of coherent optical pulses,” *Appl. Opt.* **16**, 263–264 (February 1977). See also C. L. Hayes and W. C. Davis, “High-power-laser adaptive phased arrays,” *Appl. Opt.* **18**, 4106–4111 (December 15, 1979).

Problems for 27.1

1. *Two-pulse laser spectrum.* Suppose the signal inside a laser cavity consists of two short optical pulses separated by one third of the cavity round-trip length (as if there were originally three equally spaced pulses, of which one got lost). For simplicity assume each pulse has a gaussian shape with the same FWHM pulsewidth τ_p and carrier frequency ω_c (no chirp), but let the phases ϕ_{p1} and ϕ_{p2}

of the optical carrier within each pulse be different. Evaluate the Fourier transform spectrum for an indefinitely repeated set of such pulses, and comment on their relative forms, especially for different values of the optical phase difference $\phi_{p2} - \phi_{p1}$ between the sinusoidal carriers under each pulse envelope.

2. *Three-mode signal example.* An optical signal has three equal-amplitude sidebands, equally spaced in frequency, whose absolute phases at $t = 0$ are $-\pi$, 0 and 0. Plot the amplitude and the instantaneous frequency $\omega_i(t)$ of the resulting total optical signal versus time over one full period of the difference frequency or mode spacing between adjacent sidebands.
3. *General three-mode signal spectrum.* Write the total intensity $I(t)$ for an optical signal consisting of three equal-amplitude, equally spaced axial modes having arbitrary phases ϕ_1 , ϕ_2 and ϕ_3 , putting the result into a form which illustrates the dependence of the mode beats on the phase differences between these three axial modes. Discuss the various forms of output which can be obtained.
4. *Another three-mode example.* Calculate and plot the output intensity $I(t)$ versus t for a laser oscillating in three axial modes which are all of equal amplitude and all in phase at $t = 0$, but let these three modes correspond to the axial mode frequencies ω_q , ω_{q+1} and ω_{q+3} (rather than ω_{q+2}). Compare with the corresponding results for three adjacent axial modes q , $q + 1$ and $q + 2$.
5. *Phasor model with N sidebands.* Write a computer program which will plot or display N complex phasors and their vector sum in a complex plane, and then examine how the total vector amplitude and phase angle will vary with time during one beat period if these phasors correspond to the amplitudes of equally spaced sidebands or axial modes, as described in the text.
6. *Mode-locked spectrum with random amplitudes.* Suppose a mode-locked signal has N sidebands all exactly in phase, but that the amplitudes of the individual sidebands are randomly and uniformly distributed between zero and a maximum value E_0 . What will be the expectation values for (a) the average power in the N -mode signal, and (b) the peak power of the dominant mode-locked pulse in each period. What also will be the standard deviation of this peak mode-locked amplitude?
7. *Quasi-FM signal with a square signal spectrum (research problem).* It is well-known that the sideband amplitudes and phases in the spectrum of the pure sinusoidally phase-modulated or frequency-modulated (FM) signal given by $E(t) = \text{Re} \exp j(\omega_0 t + \Delta_m \cos \omega_m t)$, with no amplitude variation, are given by the Bessel functions $J_n(\Delta)$.

Suppose, however, that we must use a rectangular amplitude spectrum, that is, a set of N equal-amplitude and equally spaced sidebands or axial modes; but wish to arrange the phases of these axial modes to obtain the closest possible approximation to a quasi-FM signal, i.e., one which has the smallest possible amplitude variations in some reasonable sense. How should we arrange the phase angles of these N axial modes? What can be said about the significant characteristics of the resulting spectrum, and the associated time signal?

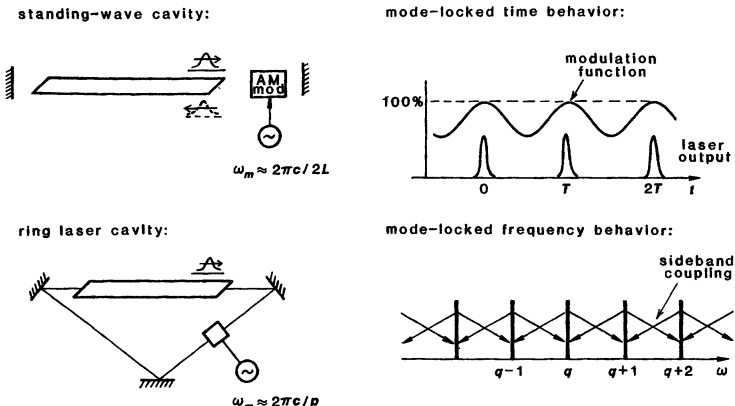


FIGURE 27.9
Active AM mode-locking of a standing-wave or ring-type laser cavity, and its description in the time and frequency domains.

27.2 MODE-LOCKED LASERS: AN OVERVIEW

As an introduction to the more detailed analyses to be given in the remainder of this chapter and in the following chapter, let us first look in a very introductory way at how practical mode-coupling techniques can be applied in practice in various types of mode-locked lasers.

Active Mode Locking

Suppose first that an amplitude (AM) modulator is placed inside either a traveling-wave or a ring-type laser cavity, as shown in the left-hand part of figure 27.9, with this modulator driven at a modulation frequency ω_m that exactly matches the round-trip frequency of the laser cavity (or possibly one of its harmonics). From a time-domain viewpoint it is then reasonable to think that the laser may begin to oscillate in the form of a short pulse which circulates around inside the laser cavity, passing through the modulator on each round trip just at the instant when the modulator transmission is at its maximum, as illustrated in the upper right-hand part of Figure 27.9.

From a frequency-domain viewpoint, by contrast, we can say that each of the oscillating axial modes present in the laser cavity at frequency ω_q will acquire modulation sidebands at frequencies $\omega_q \pm n \times \omega_m$ as a result of the active modulator. The modulator will normally be driven at a modulation frequency ω_m equal or very close to the axial-mode spacing, or one of its integer multiples. Hence the modulation sidebands from each axial mode will fall on top of, or very close to, one of the other axial modes in the cavity, as shown in the lower right-hand part of Figure 27.10. Each of these sidebands will then tend to "injection lock" the axial mode with which it is in resonance; and so the intracavity modulator will tend to couple together, or "mode-lock," each axial mode to one or more of its neighboring modes.

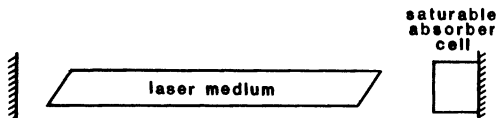


FIGURE 27.10
Saturable-absorber mode locking.

This kind of intracavity modulation, whether viewed in the time or the frequency domain, thus represents the most common form of *active mode locking*, in which the pulse formation process is controlled and synchronized by the applied modulation frequency (which must, however, be tuned very close to the natural round-trip frequency ω_{ax} in the laser cavity). Active mode locking, using a variety of intracavity electrooptic or acoustooptic modulators, can be accomplished in a wide variety of continuous-wave gas lasers and solid-state lasers, and in some pulsed or Q -switched lasers as well.

The shorter the circulating pulse becomes in such an actively mode-locked laser, the less loss it experiences in passing through the modulator—at least until the pulse becomes quite short compared to the modulator period. At the same time, however, the pulse spectrum necessarily becomes wider, and encompasses more axial modes. Since laser media often have very wide atomic linewidths, the laser medium can still continue to provide gain as the pulse becomes narrower, but this gain will decrease as the spectral width of the pulse begins to approach the amplification bandwidth of the laser medium. The limiting pulselength for an actively mode-locked laser therefore usually results from a compromise between the pulselength narrowing effects of the intracavity modulator and the spectral narrowing (or pulselength-broadening) effects of the laser gain medium.

AM and FM Mode Locking, and "FM Laser" Operation

We will see shortly that this kind of mode locking can in fact be produced using either an *amplitude* or a *phase* (or *frequency*) modulator inside the cavity, so that we can have what is referred to as either "AM mode locking" or "FM mode locking," with the output being short pulses in either situation. With an FM modulator, however, it turns out that we can obtain, depending upon details of how the modulator is tuned, either a *pulsed* mode of operation such as we have just described; or a quite different form of constant-amplitude but *frequency-swept* type of operation usually referred to as "FM-laser operation." We will discuss both of these types of operation in later sections of this chapter.

Passive (Saturable-Absorber) Mode Locking

The second primary method that is widely used to obtain short-pulse mode-locked operation is to place a purely passive saturable-absorber element or cell inside the laser cavity, as shown in Figure 27.10. Such an saturable element can be any material—a solid, a liquid solution or a gas—which has an optical absorption that is constant at low intensities, but that saturates and decreases to lower values as the laser intensity rises.

When the laser pumping process is first turned on, this absorption may even be larger than the laser gain, so that no signal can build up in the laser cavity. As the laser gain continues to increase because of continued laser pumping, however, the round-trip gain eventually begins to exceed the total saturable and non-saturable losses in the laser cavity, and an initially weak laser oscillation gradually begins to build up from noise. We can expect that the initial noise distribution in the laser may contain one particular noise spike that has larger intensity than all the other noise spikes within the round-trip time. As the laser oscillation level continues to build up, this particular noise spike can grow to an intensity level where it begins to saturate the loss it encounters in the saturable absorber.

When this begins to happen, this particular noise spike will begin to experience less loss per round trip than other weaker noise spikes which have not yet reached the absorber's saturation level; and hence this particular noise spike will begin to grow preferentially relative to the other noise spikes (which helps it even more in "burning" its way through the saturable absorber). Under proper conditions—which can be in fact rather tricky to obtain—this type of *passive mode locking* process using a saturable absorber can select a single noise pulse, and cause the laser oscillation to build up in the form of a single very short pulse circulating around inside the laser cavity and burning its way through the saturable absorber on each round trip.

Practical Passive Mode-Locked Lasers

Such passive mode locking using many different forms of saturable absorbers is widely used in many different kinds of both pulsed and continuous-wave lasers. In a passively mode-locked laser the modulation effect is produced by the mode-locked laser pulse itself, which means both that the modulation always remains in perfect synchronism with the circulating pulse, and that the modulation effect can become both stronger and faster as the pulse itself becomes shorter. As a result, passive mode locking generally leads to significantly shorter pulses than does active mode locking.

We have emphasized the way in which such a passively mode-locked pulse initially builds up from noise; and indeed there is, unfortunately, a good deal of statistical selection and randomness in the shot-to-shot mode locking behavior of pulsed mode-locked lasers. In certain continuous-wave lasers, however, saturable-absorber mode locking can cause the laser to develop a steady-state mode-locked behavior in which only a single ultrashort pulse circulates repeatedly around the laser cavity, with very high stability. Such a circulating pulse represents the most stable mode of operation for the laser in essence because the round trip loss is significantly less for an intense short pulse, which can saturate its way through the absorber, than for a continuous signal with lower average intensity, which cannot. Continuously operating mode-locked dye lasers of this type have produced the shortest optical (or electrical) pulses yet to be generated, with durations shorter than 30 femtoseconds, corresponding to an optical pulse only a few tens of optical cycles in duration.

Synchronously Pumped Mode Locking

Still another alternative type of modulation that can be used in some lasers is to modulate the laser gain itself at a frequency equal to the cavity-mode

spacing or one of its harmonics, by modulating the pump power applied to the gain medium. This so-called *synchronous pumping* process can be very effectively done in laser-pumped lasers, such as cw dye lasers, by mode-locking the pumping laser at the same repetition frequency. It can also be accomplished very easily and efficiently in semiconductor injection lasers, simply by modulating the pumping current through the injection laser diode.

Homogeneous Versus Inhomogeneous Atomic Transitions

The detailed behavior of either active or of passive mode locking will also be significantly different depending upon whether the laser transition involved is *homogeneously* or *inhomogeneously* broadened.

In an inhomogeneously broadened laser, of which typical examples are any of the visible cw gas lasers such as the He-Ne or argon-ion lasers, the laser will normally oscillate spontaneously in some large number N_0 of free-running axial modes, with mode amplitudes determined primarily by the inhomogeneous saturation and hole-burning properties of the laser transition itself. The primary task of the active modulator in an inhomogeneous laser is then only to pull into synchronism, or lock into phase, these already oscillating modes. If the modulation frequency is tuned close enough to the axial-mode interval, so that the modulation sidebands fall directly on the adjoining axial modes, the modulation sidebands can easily pull the adjoining modes into the necessary phase and frequency synchronism, and the modulation strength required to injection-lock an already oscillating axial mode to its neighbors is quite small.

The oscillation range in an inhomogeneous laser is typically close to the doppler-broadened atomic linewidth $\Delta\omega_d$, so that the number of oscillating modes is given by $N_0 \approx \Delta\omega_d/\omega_m$. From Fourier-transform arguments, therefore, the mode-locked pulsewidth in an inhomogeneous mode-locked laser will typically be given by

$$\tau_p(\text{inhomogeneous}) \approx \frac{0.5}{\Delta f_d} \approx \frac{0.5}{N_0 \Delta f_m}, \quad (12)$$

where Δf_d and f_m are the atomic linewidth and modulation frequency measured in Hz. The value of the mode-locked pulsewidth is thus determined primarily by the atomic linewidth. The modulation index or the modulator drive power is unimportant above a certain minimum (and usually quite small) value needed to pull the modes into synchronism. (A more detailed analysis of the inhomogeneous situation, for example, in a doppler-broadened and mode-locked gas laser, requires a more complicated analysis, including the hole-burning and dispersion properties of the laser transition, as well as the modulator effects. Such an analysis is probably best carried out using the coupled-mode frequency domain approach to be introduced later in this chapter.)

With a strongly homogeneous line, by contrast, the laser prefers to oscillate naturally in only one or a few axial modes located just at line center. The active modulator must then play a stronger role in generating additional modulation sidebands and in causing the laser spectrum to broaden and spread out across more of the atomic linewidth. This leads in general to a quite different dependence of the mode-locked pulsewidth on the modulation strength and the atomic linewidth, which we will describe in detail in Section 27.4.

Transient Versus Steady-State Mode Locking

In any of the mode-locked situations described in the preceding, there is also a finite build-up time, after the modulator or the laser has been turned on, before the active or passive modulator can cause the short pulse to form or can synchronize the axial modes. With practical active modulators this transient build-up time for the mode-locking process is usually many round trip times, and is often longer than the oscillation duration in *Q*-switched or pulsed lasers. The transient characteristics of active mode locking are therefore of considerable importance, and the mode-locking behavior of practical lasers may be significantly different in transient situations than in cw steady-state situations.

Time Versus Frequency Descriptions

The distinction between the time-domain and frequency-domain descriptions of optical signals, as outlined in Section 27.1, translates into two complementary methods of analysis: a differential-equation type of analysis that is carried out primarily in the time domain (with occasional Fourier transforms into the frequency domain); and a coupled-mode type of analysis that is carried out primarily in the frequency domain. Both types of analysis are widely used, and we will give examples of both methods applied to useful laser problems in the following sections.

Harmonic Mode Locking

The modulator in a mode-locked laser is usually driven at or very near the fundamental axial-mode frequency $\omega_m \approx \omega_{ax} = 2\pi/T$, where T is the round-trip cavity time; and this then leads to a single circulating short pulse within the laser cavity. It is entirely possible, however, to drive the modulator at some multiple of this frequency, or $\omega_m \approx N\omega_{ax} = 2\pi N/T$, in what is referred to as *harmonic mode locking*. Harmonic mode locking couples together sidebands which are spaced by N axial-mode intervals apart, and this can lead, depending upon circumstances, to the production of up to N individual pulses following each other around within the laser cavity, separated by equal time intervals of T/N .

Passively mode-locked lasers can also, again depending upon circumstances, oscillate with several distinct pulses circulating within the cavity; and the pulses in this situation need not even be equally spaced, since each pulse can burn its way, more or less independently, through the saturable absorber cell.

Harmonic mode locking is occasionally used in actively mode-locked lasers, either to shorten the mode-locked pulses or to raise the pulse repetition frequency. Multiple-pulse behavior in passively mode-locked lasers is generally unstable and is usually regarded as an undesirable form of behavior.

Summary

If we make a short summary of the major types of physical situations and analytical methods that we have mentioned in this section, we see that we must potentially consider the different properties of:

- Active versus passive mode coupling.
- Amplitude (AM) versus phase or frequency (FM) modulation (or versus synchronous pump modulation).
- Short-pulse versus frequency-swept operation.
- Homogeneous versus inhomogeneous laser transitions.
- Pulsed or transient versus cw or steady-state operation
- Time-domain versus frequency-domain descriptions.

Even leaving out harmonic mode locking and the various subcategories of passive mode coupling, this gives us something like 2^6 or 64 different possible examples to consider. Obviously, in the following sections we will be able to consider only a few of these, perhaps four or five typical examples illustrating each of the major points that have been mentioned. (The wary student may note that this leaves more than fifty additional examples for homework exercises.)

REFERENCES

An excellent survey volume on the basic principles of mode-locked laser pulses and their applications is *Ultrashort Light Pulses: Picosecond Techniques and Applications*, ed. by S. L. Shapiro (Springer-Verlag, 1977).

For more recent advances in this field there is a continuing series of conference proceedings in book form, including *Picosecond Phenomena*, ed. by C. V. Shank, E. P. Ippen and S. L. Shapiro (Springer-Verlag, 1978); *Picosecond Phenomena II*, ed. by R. M. Hochstrasser, W. Kaiser and C. V. Shank (Springer-Verlag, 1980); and *Picosecond Phenomena III*, ed. by K. B. Eisenthal, R. M. Hochstrasser, W. Kaiser and A. Laubereau (Springer-Verlag, 1982).

Other useful review articles and surveys in the laser literature that cover various aspects of mode locking include A. J. DeMaria, D. A. Stetser, and W. H. Glenn, Jr., "Ultrashort light pulses," *Science* **156**, 1557-1568 (June 23, 1967); A. J. DeMaria, W. H. Glenn, Jr., M. J. Brienza, and M. E. Mack, "Picosecond laser pulses," *Proc. IEEE* **57**, 2-25 (January 1969); P. W. Smith, "Mode-locking of lasers," *Proc. IEEE* **58**, 1342-1359 (September 1970); L. Allen and D. G. C. Jones, "Mode locking in gas lasers," *Progress in Optics*, Vol. IX, edited by E. Wolf (North-Holland, 1971); pp. 179-234; A. E. Siegman and D. J. Kuizenga, "Active mode-coupling phenomena in pulsed and continuous lasers," *Opto-electronics* **6**, 43-66 (1974); and W. H. Lowdermilk, "Technology of Bandwidth-Limited Ultrashort Pulse Generation," in *Laser Handbook*, Vol. 3, edited by M. L. Stitch (North-Holland, 1979); Chap. B1, pp. 361-420.

27.3 TIME-DOMAIN ANALYSIS: HOMOGENEOUS MODE LOCKING

In the time-domain approach to laser mode locking, we follow the signal field $\mathcal{E}(t)$ inside a laser cavity through one complete round trip, examining how this signal is changed as it passes through the laser medium, the active or passive modulator, and any other elements inside the cavity. We can then analyze either the transient build-up of a mode-locked signal, or the steady-state form that this recirculating signal must take if it is to remain unchanged from one complete round trip to another.

In this section we will apply this approach to one of the simplest and yet quite important types of mode locking, namely, the active mode locking of a homogeneously broadened laser, using either an intracavity amplitude (AM) or phase (FM) modulator. This particular type of mode locking is of great practical significance in the important Nd:YAG laser, as well as in actively mode-locked CO₂ TEA lasers, and a number of other useful laser systems.

Circulating Gaussian Pulse Analysis

The great convenience of this class of mode-locked lasers is that we can assume quite accurately from the beginning that the pulse circulating inside the laser will be described by a *gaussian pulse envelope*, which we can write in the general form

$$\mathcal{E}(t) = \exp [-\Gamma t^2 + j\omega_0 t], \quad \Gamma \equiv \alpha - j\beta, \quad (13)$$

where $\Gamma \equiv \alpha - j\beta$ is the complex gaussian pulse parameter. This pulse then also has a *gaussian frequency spectrum* given by

$$\tilde{E}(\omega) = \exp \left[-\frac{(\omega - \omega_0)^2}{4\Gamma} \right]. \quad (14)$$

We have already described the propagation properties of such gaussian pulses in considerable detail in Chapter 9. The results obtained there are very directly relevant to the propagation of a gaussian mode-locked laser pulse through repeated round trips in a laser cavity; and the reader may want to review the discussion given in Chapter 9 before proceeding with this chapter.

To analyze the round-trip propagation of such a pulse, let us first transform this pulse into the frequency domain and then pass its Fourier transform through the laser gain function for one complete round trip around the laser cavity by writing

$$\tilde{E}'(\omega) = \tilde{g}(\omega) \tilde{E}(\omega). \quad (15)$$

The transfer function or complex voltage gain $\tilde{g}(\omega)$ for one round trip, including everything except the intracavity modulation function, can then be written in the form

$$\begin{aligned} \tilde{g}(\omega) &= \exp \left[\frac{\alpha_m p_m}{1 + 2j(\omega - \omega_a)/\Delta\omega_a} - j \frac{\omega p}{c} \right] \\ &\approx \exp \left[\alpha_m p_m \left(1 - 2j \frac{\omega - \omega_a}{\Delta\omega_a} - \frac{4}{\Delta\omega_a^2} (\omega - \omega_a)^2 \right) - j \frac{\omega p}{c} \right], \end{aligned} \quad (16)$$

where $\alpha_m p_m$ is the round-trip voltage gain coefficient and $\omega p/c$ the round-trip phase shift in the empty cavity. We will see later that in essentially all situations of practical interest the frequency spectrum $\tilde{E}(\omega)$ of the mode-locked pulse will remain narrow compared to the full atomic linewidth $\Delta\omega_a$ of the laser gain medium, so that the Taylor series expansion used in the second line of Equation 27.16 will be a valid approximation.

Round Trip Transit Time

We have included in this gain expression the phase shift term $\omega p/c$ which accounts for the total phase shift versus frequency of the signal as it propagates once around the laser cavity, taking into consideration everything except the laser transition itself. This means that the length p represents the total optical length taking into account the refractive indices of all the elements, including if necessary the laser host medium, but not including the χ' or χ'' effects of the laser atoms themselves. Let us consider this linear phase shift term in more detail for a moment, before exploring the quadratic pulse shaping effects of the laser medium.

The total linear (in ω) portion of the round-trip phase shift includes the terms

$$\begin{aligned} \frac{\omega p}{c} + \frac{2\alpha_m p_m \omega}{\Delta\omega_a} &= \frac{\omega p}{c} \left[1 + \frac{2\alpha_m p_m}{\Delta\omega_a} \frac{c}{p} \right] \\ &\approx \frac{\omega p}{c} \left[1 + \frac{\omega_{\text{ax}}}{\Delta\omega_a} \frac{\alpha_m p_m}{\pi} \right], \end{aligned} \quad (17)$$

where $\omega_{\text{ax}} = 2\pi p/c$ is the axial-mode spacing. If we recall that a linear phase shift $e^{-jT\omega}$ versus frequency for a signal in frequency space is directly related to a time delay $t - T$ in the time domain, then Equation 27.16 says that the effective time T' for a pulse to make one round trip is increased over the “cold-cavity” transit time $T = p/c$, or the effective round-trip length p' is increased over the cold-cavity perimeter p , by a small fractional amount δ given by

$$\frac{T' - T}{T} \approx \frac{p' - p}{p} \approx \frac{\omega_{\text{ax}}}{\Delta\omega_a} \times \frac{\alpha_m p_m}{\pi}. \quad (18)$$

Alternatively, we can say that the effective group velocity v_g of the pulse is slightly reduced by the atomic dispersion effects, as compared to the phase velocity c , or that the pulled axial-mode frequency interval ω_{ax} is similarly reduced by essentially the same ratio, as expressed by

$$\frac{\omega_{\text{ax}} - \omega'_{\text{ax}}}{\omega_{\text{ax}}} \approx \frac{c - v_g}{c} \approx \frac{\omega_{\text{ax}}}{\Delta\omega_a} \times \frac{\alpha_m p_m}{\pi}. \quad (19)$$

The significant factors here are the ratio of axial-mode spacing ω_{ax} to the atomic linewidth $\Delta\omega_a$, and the ratio of the round-trip gain factor $\alpha_m p_m$ to π .

In a Nd:YAG laser cavity, for example, there may be from 500 to 1,000 axial mode intervals within the atomic linewidth, and the round-trip voltage gain factor under operating conditions may have a value $\alpha_m p_m \approx 0.2$. The fractional change in round-trip cavity length or in modulation frequency thus amounts to approximately 1 part in 10,000, or a frequency shift of ≈ 25 kHz out of a modulation frequency of ≈ 250 MHz.

As a practical matter, we are unlikely to know the exact cavity length or round-trip transit time to this order of precision. The exact synchronism necessary between modulation frequency and laser cavity length is achieved in practice by using a stable modulation signal generator, and then adjusting either the modulation frequency or the cavity length empirically for best mode locking.

We will assume from here on that the modulation frequency ω_m applied to the mode-locking modulator is tuned very precisely to the perturbed or effective round-trip transit frequency ω'_{ax} for the laser pulses—or possibly to an integer multiple of this frequency—taking into account the dispersive effects of the

atomic transition. A circulating laser pulse will thus return to exactly the same position in the modulation cycle on each successive round trip, a condition which is essential for good mode-locking behavior. For simplicity we will usually drop the primes on T' or p' or ω'_{ax} from here on, but the reader should keep in mind that this exact mode-locking modulation frequency ω_m is shifted by this small fractional amount, which is in turn itself somewhat dependent on the round-trip gain in the laser cavity.

Pulse Propagation Through the Laser Gain Medium

The great virtue of the gaussian pulse approximation, combined with the quadratic approximation for the gain medium, is that when we multiply the gaussian pulse spectrum with pulse parameter Γ by the atomic gain function $\tilde{g}(\omega)$ using the quadratic expansion, we simply obtain a new gaussian pulse with a modified pulse parameter Γ' given by

$$\exp\left[-\frac{(\omega - \omega_0)^2}{4\Gamma}\right] \times \exp\left[-\frac{4\alpha_m p_m}{\Delta\omega_a^2}(\omega - \omega_a)^2\right] = \exp\left[-\frac{(\omega - \omega_0)^2}{4\Gamma'}\right], \quad (20)$$

assuming that $\omega_0 = \omega_a$, i.e., that the pulse spectrum is centered on the atomic gain profile. The net change in the gaussian pulse parameter due to passing through the gain medium is thus given by

$$\frac{1}{\Gamma'} = \frac{1}{\Gamma} + \frac{16\alpha_m p_m}{\Delta\omega_a^2}. \quad (21)$$

Since the gain factor $\alpha_m p_m$ is commonly small compared to unity, and the pulse spectrum is also usually narrow compared to the atomic linewidth $\Delta\omega_a$, the fractional change in the gaussian parameter on one pass will normally be small, and Equation 27.21 can be replaced to a very good approximation by

$$\Gamma' - \Gamma \approx -\frac{16\alpha_m p_m}{\Delta\omega_a^2} \Gamma^2. \quad (22)$$

This expression summarizes the *spectral narrowing* of the pulse envelope in the frequency domain, or the *pulse broadening* of the pulse envelope in the time domain, produced by one round-trip transit through the laser medium gain.

Pulse Propagation Through an Amplitude (AM) Modulator

We must next consider the effect of either an amplitude or a phase modulator on the same gaussian pulse parameter. For a simple optical modulator, the net *amplitude* or *voltage transmission* as a function of time for a signal passing through the modulator can be written as

$$\mathcal{E}''(t) = \tilde{t}_m(t)\mathcal{E}'(t), \quad (23)$$

where $\tilde{t}_m(t)$ is the time-varying transmission function. The modulator transmission function for a simple *amplitude* or *AM modulator* can be written in the form

$$\tilde{t}_{am} = \exp[-\Delta_m(1 - \cos\omega_m t)], \quad (24)$$

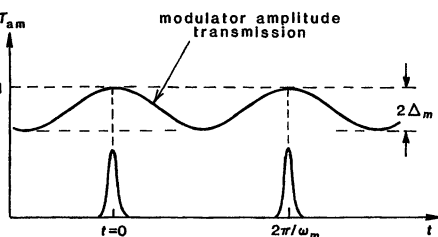


FIGURE 27.11
Pulse transmission through an AM (amplitude) modulator.

where ω_m is some integer multiple of ω_{ax} , and where the quantity $2\Delta_m$ gives the peak-to-peak voltage modulation index, as shown in Figure 27.10. Another form for the AM transmission function sometimes used in the literature is $\tilde{t}_{am}(t) = \cos(\theta_m \sin \omega_m t)$, in which case $\theta_m^2 \equiv \Delta_m$ will give the same transmission function near the transmission peaks.

The usual condition is that the gaussian optical pulse will be short compared to the modulation period, and its passage through the modulator will be centered on the peak of the modulator transmission function, as shown in Figure 27.11. Either of these transmission functions can then be approximated by its quadratic variation about the peak transmission point, as given by

$$\tilde{t}_{am}(t) \approx \exp \left[-\frac{\Delta_m \omega_m^2}{2} t^2 \right], \quad |t| \ll T. \quad (25)$$

This says that the change in the gaussian pulse parameter Γ' in passing through the modulator will be given by

$$\exp[-\Gamma' t^2] \times \exp \left[-\frac{\Delta_m \omega_m^2}{2} t^2 \right] = \exp[-\Gamma'' t^2], \quad (26)$$

or in simpler form

$$\Gamma'' - \Gamma' \approx +\frac{\Delta_m \omega_m^2}{2}. \quad (27)$$

This expresses the pulse narrowing (and hence the spectral broadening) of the pulse produced by passing through the amplitude modulator.

Pulse Propagation Through a Phase (FM) Modulator

For an ideal phase or frequency modulator, we can write a formally very similar expression in which the phase modulation effects of the FM modulator are expressed by the complex transmission function

$$\tilde{t}_{fm}(t) = \exp[j\Delta_m \cos \omega_m t]. \quad (28)$$

The modulation index $2\Delta_m$ in this situation corresponds to the peak-to-peak phase deviation in passing through the modulator, so that $2\Delta_m \omega_m$ will be the peak-to-peak frequency deviation imposed on a cw signal in a single round trip through the modulator.

It turns out, as we will confirm shortly, that the circulating pulse in an FM mode-locked laser always passes through the modulator very near one or the

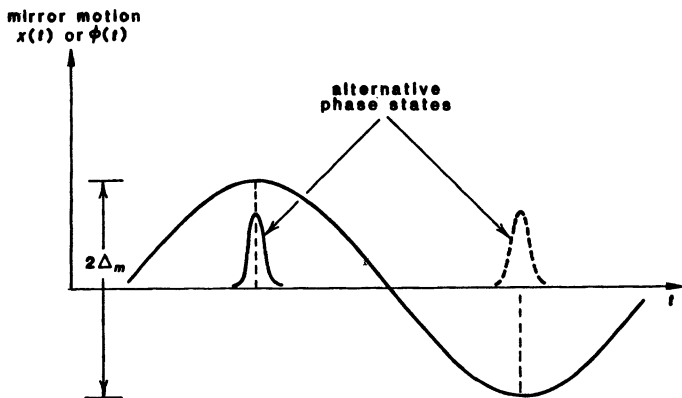


FIGURE 27.12
Pulse transmission through an FM (phase) modulator.

other of the two peaks of the phase modulation cycle, as shown in Figure 27.12. Hence we can again make the quadratic approximation, this time in the form

$$\tilde{t}_{fm}(t) \approx \exp [\pm j\Delta_m(1 - \omega_m^2 t^2/2)]. \quad (29)$$

The static part of this phase shift can be absorbed into a very small net change in the total effective length of the laser cavity, whereas the quadratic part imposes a small chirp on the pulse on each round trip.

The net change in the gaussian pulse parameter on passing through a phase modulator can thus be written in the same fashion as Equation 27.27 for an amplitude modulator, namely,

$$\Gamma'' - \Gamma' \approx \pm j \frac{\Delta_m \omega_m^2}{2}. \quad (30)$$

The only difference is that the change in Γ is purely real for AM, but purely imaginary for FM modulation.

Steady-State Round Trip Solutions

We can thus find that the total change $\Gamma'' - \Gamma$ in the gaussian pulse parameter in one complete round trip around the laser cavity is given by

$$\begin{aligned} \Gamma'' - \Gamma &\approx -\frac{16\alpha_m p_m}{\Delta\omega_a^2} \Gamma^2 + \left\{ \begin{array}{l} 1 \\ \pm j \end{array} \right\} \frac{\Delta_m \omega_m^2}{2} \\ &= 0 \quad \text{for steady-state mode locking.} \end{aligned} \quad (31)$$

The symbol in front of the modulation term on the right-hand side has the value 1 or $\pm j$ depending on whether the intracavity modulator is an AM or an FM modulator.

The net change in Γ in one round trip must be identically zero for a steady-state mode-locked laser, as expressed by the second line of Equation 27.31. The steady-state gaussian pulse parameter in an actively mode-locked homogeneous

laser is thus given by the simple result

$$\Gamma_{ss} = \left\{ \frac{1}{\pm j} \right\}^{1/2} \left(\frac{\Delta_m}{\alpha_m p_m} \right)^{1/2} \frac{\omega_m \Delta \omega_a}{4\sqrt{2}} \equiv \alpha_{ss} - j\beta_{ss}. \quad (32)$$

It is evident that for AM the steady-state gaussian parameter is purely real with a pulselwidth parameter given by

$$\alpha_{ss} = \left(\frac{\Delta_m}{\alpha_m p_m} \right)^{1/2} \frac{\omega_m \Delta \omega_a}{4\sqrt{2}}, \quad (33)$$

and with $\beta_{ss} = 0$, which means no frequency chirp in the AM mode-locked situation. In the FM modulation situation, on the other hand, Γ_{ss} is proportional to the square root of $\pm j$, which has a phase angle of $\pm 45^\circ$ and a magnitude of $1/\sqrt{2}$. The FM situation thus has $\alpha_{ss, fm} = \beta_{ss, fm} = \alpha_{ss, am}/\sqrt{2}$.

Steady-State AM Mode Locking

The FWHM pulselwidth for the pulse intensity $I(t)$ in an AM mode-locked homogeneous laser is then given by the useful expression

$$\begin{aligned} \tau_{p,ss} &\approx \left(\frac{2\sqrt{2} \ln 2}{\pi^2} \right)^{1/2} \left(\frac{\alpha_m p_m}{\Delta_m} \right)^{1/4} \left(\frac{1}{f_m \Delta f_a} \right)^{1/2} \\ &\approx 0.45 \times \left(\frac{\alpha_m p_m}{\Delta_m} \right)^{1/4} \times \left(\frac{1}{f_m \Delta f_a} \right)^{1/2} \end{aligned} \quad (34)$$

whereas the pulselwidth in the FM mode-locked situation is given by the same expression except increased by a factor of $2^{1/4}$. (This factor could equally well be absorbed into a modified definition of the modulation index Δ_m between the AM and FM situations.)

Several useful conclusions can be drawn from this result. First of all, the round-trip gain coefficient $\alpha_m p_m$ in a typical actively mode-locked laser may have a value ranging from 0.1 to perhaps 1 (note that this must be the saturated value of $\alpha_m p_m$ under steady-state operating conditions). The modulation depth Δ_m will typically have a similar range. The ratio of these quantities, reduced to one-quarter power, will then have a value not far from unity in almost all situations; and so the pulselwidth will depend primarily on $1/(f_m \Delta f_a)^{1/2}$.

The modulation index Δ_m in a typical optical modulator varies with the rf power applied to the modulator in one or the other of the forms

$$\Delta_m \propto \begin{cases} P_m^{1/2} & \text{for electrooptic FM modulators,} \\ P_m & \text{for acoustooptic AM modulators.} \end{cases} \quad (35)$$

The mode-locked pulselwidth will thus decrease with increasing modulation power with a variation somewhere between $1/P_m^{1/4}$ and $1/P_m^{1/8}$. This says that the pulselwidth does get shorter, but not very rapidly, as we increase the modulator power.

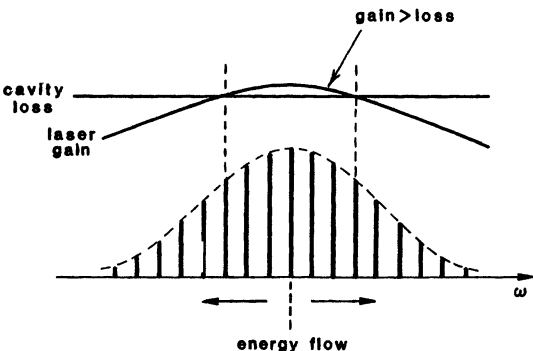


FIGURE 27.13

Energy flow outward in frequency in an actively mode-locked, homogeneously broadened laser.

Comparison With Inhomogeneously Mode-Locked Lasers

The results of this analysis also predict that an actively mode-locked *homogeneous* laser will behave quite differently from an actively mode-locked *inhomogeneously broadened* laser.

We argued in Equation 27.12 that in an inhomogeneous laser, oscillating more or less across its full inhomogeneous linewidth, the mode-locked pulselwidth should have a value of $\tau_p \approx 0.5/\Delta f_d \approx 0.5/(N_0 \Delta f_m)$ where N_0 is the number of axial modes within the atomic linewidth. In the homogeneous mode-locked situation, by contrast, the mode-locked pulselwidth given by Equation 27.34 is related to both the atomic linewidth $2\pi\Delta f_a$ and also to the applied modulation frequency f_m by the dependence

$$\tau_p(\text{homog}) \approx \frac{0.5}{(f_m \Delta f_a)^{1/2}} \approx \frac{0.5}{N^{1/2} f_m}, \quad (36)$$

Since N_0 is typically a large number—for example, on the order of $N_0 \approx 500$ in a Nd:YAG laser—the mode-locked pulselwidth τ_p is broadened compared to the “linewidth-limited” value of $0.5/\Delta f_a$, and the mode-locked spectral width is correspondingly narrowed compared to the atomic linewidth, by the square root of this large number.

The mode-locking behavior in the homogeneous situation obviously represents a balance between spectral narrowing produced by the laser gain medium, which tries to push the laser toward cw single-mode operation, and spectral broadening produced by the active modulator, which in effect attempts to push the sideband distribution outwards in frequency. One consequence of this is that in a fully homogeneous mode-locked laser the centermost group of axial modes will actually have round-trip gains slightly greater than unity, whereas those modes out in the wings of the mode-locked spectrum will have net round-trip losses. A steady-state energy balance is then maintained by the action of the active modulator in transferring or diffusing energy from the stronger central modes to the weaker modes in the wings, as shown in Figure 27.13.

Higher-Order Mode-Locked Pulses.

The gaussian pulse approximation that makes possible the simple analysis presented in this section rests upon the quadratic approximations that can be made for the laser gain as a function of frequency and for the active modulators as functions of time. Any gaussian pulse will then always remain gaussian upon passing through such a system. But there also exists a complete set of higher-order mode-locked pulseshapes that are also self-reproducing under the same quadratic approximations. These higher-order Hermite-gaussian mode shapes all have higher round-trip losses, however, or to express this in a different way, they are all mathematically unstable against small perturbations in shape. The properties of these higher-order mode-locked solutions are discussed by D. M. Kim, S. Marathe, and T. A. Rabson, "Eigenfunction analysis of the mode-locking process," *J. Appl. Phys.* **44**, 1673-1675 (April 1973); and by H. A. Haus, "A theory of forced mode locking," *IEEE J. Quantum Electron.* **QE-11**, 323-330 (July 1975).

FM Mode-Locking Behavior

From the preceding analysis, the steady-state mode-locking performance of a homogeneous laser with an intracavity FM modulator is essentially the same as with an AM modulator, except that the FM mode-locked pulse also acquires a small frequency chirp equal in magnitude to the pulselwidth modulation, i.e., $\beta_{ss, fm} = \pm \alpha_{ss, fm}$. This implies among other things that the time-bandwidth product for the FM mode-locked pulse will be increased by $\sqrt{2}$, i.e., $B_p \tau_p \approx 0.626$ for the FM mode-locked situation, as compared to the ideal gaussian-pulse value of $B_p \tau_p \approx 0.442$ (cf. Chapter 9) for the AM situation.

It may seem surprising that an intracavity phase or frequency modulator should lead to a strongly *amplitude*-modulated or short-pulse type of behavior. A simple physical explanation for this can be given as follows. A phase modulator with peak modulation index Δ_m located near one end of, say, a standing-wave cavity can be viewed in effect as a modulation of the cavity length or of the end mirror position back and forth, with a sinusoidal motion given by $x(t) = x_m \cos \omega_m t = (\Delta_m \lambda / 4\pi) \cos \omega_m t$. Any optical signal which circulates around inside the cavity and strikes this moving end mirror at the same point in its cycle once per round trip, will then in most situations experience a doppler shift on reflection from the moving mirror; and these doppler shifts will accumulate rapidly on successive round trips so as to push the spectrum of the signal entirely outside the atomic gain curve.

A short circulating pulse which strikes the end mirror just at either of the turning points where the mirror reverses direction, however, as shown in Figure 27.12, will not receive such a doppler shift, but only a small quadratic phase modulation or frequency chirp which will tend to broaden its spectrum slightly. Steady-state FM mode locking then represents a condition in which this chirp coming from the FM modulator is just canceled, and in addition a steady-state pulselwidth is just maintained, by the subsequent propagation of the complex or chirped gaussian pulse through the gain medium on each round trip.

One difficulty with the FM mode-locked situation is that the pulses can occur equally well at either of two phase positions that are 180° apart relative to the

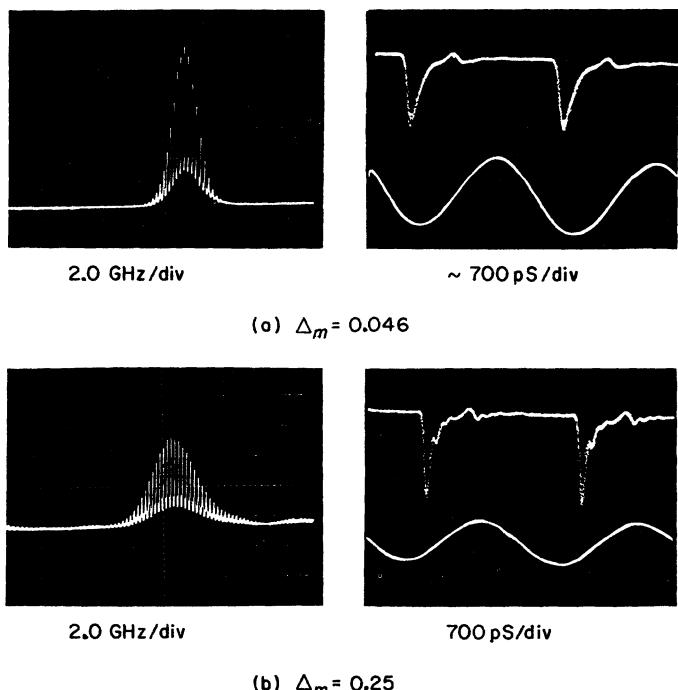


FIGURE 27.14

Experimental results for an actively FM mode-locked Nd:YAG laser, showing both the axial-mode spectrum as observed using a scanning Fabry-Perot interferometer (left column), and the output pulses in time as observed using a fast photodetector (right column), for two different modulation depths Δ_m . The sine wave corresponds to the modulation signal applied to the FM modulator.

modulation signal. In practice FM mode-locked lasers tend to jump back and forth randomly between these two “phase states,” or (less often) even to oscillate in both states simultaneously.

Experimental Results

The analytical results given in the preceding paragraphs have all been closely confirmed by repeated experiments on a variety of different homogeneously broadened lasers. Figure 27.14 shows, for example, the results of early experiments on an actively mode-locked Nd:YAG laser using a lithium niobate FM modulator inside the laser cavity. The upper and lower plots show how the axial-mode spectrum broadens, and the pulsewidth narrows in time, as the modulation depth or the rf power applied to the modulator is increased.

The time profiles of the mode-locked pulses in this figure are considerably distorted by the finite response time of the photodetector and oscilloscope; but the frequency profile of the mode-locked spectrum, as measured with a scanning

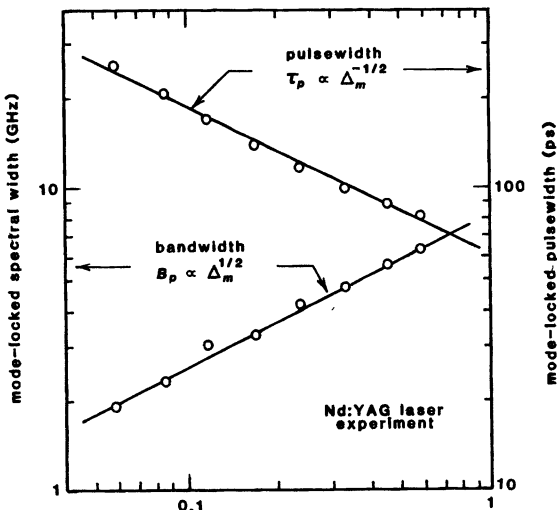


FIGURE 27.15
Experimental results for the pulsewidth and mode-locked spectral bandwidth of an actively mode-locked Nd:YAG laser, confirming the expected dependence on the modulation depth Δ_m of the active modulator.

Fabry-Perot interferometer, is indeed very accurately gaussian, confirming the basic approximation of this section.

If we measure separately the FWHM pulsewidth of the time output and the FWHM bandwidth of the spectral output from a series of experiments such as this, we can also verify quite accurately the expected dependence of both of these quantities on the modulation depth Δ_m , as illustrated in Figure 27.15. Experiments of this type have been done on both AM and FM mode-locked lasers of several different types, with very similar results.

We can also plot bandwidth versus pulsewidth with modulation index as a parameter, and obtain results for a typical FM mode-locked laser such as those shown in Figure 27.16. The agreement with the expected time-bandwidth product of 0.626 then confirms, at least indirectly, the existence of the expected chirp in the FM mode-locked pulse.

Etalon Effects

One important practical consideration in any actively mode-locked laser is that all of the intracavity elements—laser rod, modulator crystal, and so forth—should either use Brewster's angle surfaces, or else be tilted sufficiently with respect to the cavity axis that no unwanted etalon effects can occur in transmission through any of these elements. Such etalon effects if present will cause a periodic variation in transmission, or effectively a periodic variation in the round-trip gain inside the laser cavity, as illustrated in Figure 27.17. An etalon effect of this type which has a spectral period or free spectral range smaller than

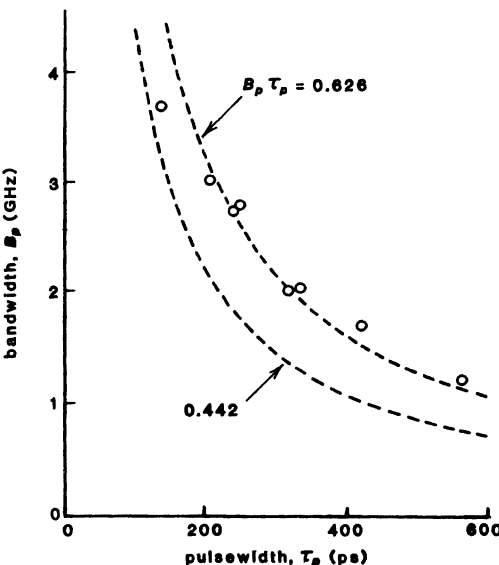


FIGURE 27.16
Confirmation of the time-bandwidth product for an FM-mode-locked Nd:YAG laser.

the atomic linewidth and a transmission peak near line center can then act in effect like a modified gain profile with a much narrower linewidth, even though the peak-to-peak transmission modulation of the etalon may be quite small (see the upper sketch in Figure 27.17).

The spectrum of the mode-locked signal may then be, in effect, trapped in this central quadratic well. The mode-locked laser will still obey the theory of this section, except that the effective linewidth of the atomic gain curve will appear to be drastically reduced, and the mode-locked pulsewidth will be as a result much wider than expected. Such behavior was in fact often observed in early active mode-locking experiments. Ordinary antireflection coatings on the intracavity elements may not be adequate to eliminate these effects; and it may also be necessary in some situations to have the outer surfaces of any output mirrors tilted by a small wedge angle to eliminate etalon effects in the mirror reflectivity.

The experimental trace at the bottom of Figure 27.17 shows a different outcome, for a situation in which the etalon effects were sufficiently weak, and the active modulation sufficiently strong, to push the mode-locked spectrum out of the central well and spread the mode-locked spectral bandwidth over several periods of the etalon effect. The individual axial modes are not well resolved in this photograph, but there are approximately 36 axial modes, or a free spectral range of 36×250 MHz ≈ 9 GHz between the etalon peaks. The very strong effect of even weak etalon gain modulation on the mode-locked spectrum is evident.

A few experiments have also used a thin etalon deliberately tuned with a transmission minimum at line center, in an attempt to cancel part of the laser linewidth curvature and effectively broaden the atomic linewidth, thus obtaining shorter mode-locked pulses. Such experiments, while requiring careful adjustment, have obtained some success.

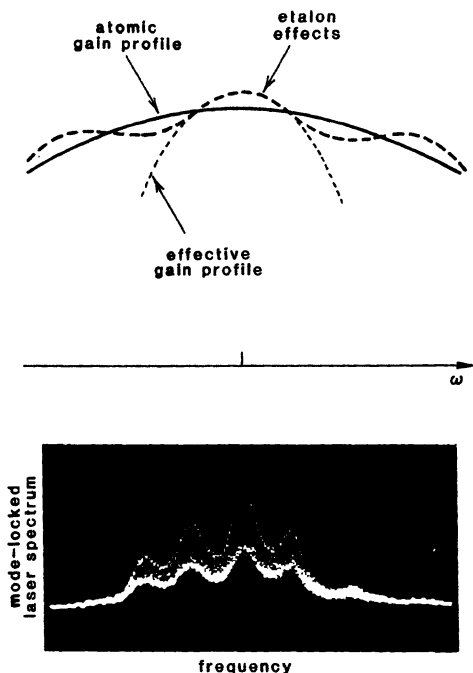


FIGURE 27.17
Etalon effects on the spectral profile of an actively mode-locked laser.

Harmonic Mode Locking

Note that the mode-locked pulselwidth predicted by the preceding analysis varies inversely with the square root of the *modulation frequency* ω_m , rather than the *axial-mode interval* ω_{ax} . Going to a harmonic modulation frequency $\omega_m = N\omega_{\text{ax}}$, with $N > 1$, can thus produce somewhat shorter mode-locked pulses if other parameters are held constant, and this has been observed in practice.

The detailed behavior of such harmonic mode locking is rather complex, however. The sidebands produced by the modulator couple a given axial mode only to its neighbors N axial-mode intervals away on each side. As a result the axial modes become organized into N more or less independent "supermodes" or sets of coupled axial modes, each set consisting only of frequencies spaced N axial-mode intervals apart, with each set shifted by one axial mode interval with respect to the next adjacent set.

These "supermodes" may then oscillate separately and more or less independently, with the competition among them depending upon how the active elements are located in the cavity, and upon spatial and spectral hole burning in the laser gain medium. If only a single supermode oscillates, the result is necessarily N equally spaced pulses circulating inside the laser cavity, and N output pulses per round-trip period. If several of the supermodes oscillate simultaneously, however, the result can be anything ranging from N pulses down to only one pulse per period, depending upon the relative amplitudes and especially phases between the supermodes.

The optimum form of harmonic mode-locking would perhaps be to use a double intracavity modulation system, with one modulator having $N = 1$ to ensure only one pulse per round trip, and a second phase-synchronized modulator with $N \gg 1$ to produce the maximum quadratic curvature about the modulator peak, and thus the shortest possible mode-locked pulses.

REFERENCES

The analytical approach presented in this section comes largely from D. J. Kuizenga and A. E. Siegman, "FM and AM mode locking of the homogeneous laser—Part I: Theory. Part II: Experimental results," *IEEE J. Quantum Electron.* **QE-6**, 694–715 (November 1970). A summary of these and related results, with additional references, is given in A. E. Siegman and D. J. Kuizenga, "Active mode-coupling phenomena in pulsed and continuous lasers," *Opto-electronics* **6**, 43–66 (1974).

Properties of the two possible states in an FM mode-locked laser are discussed by G. W. Hong and J. R. Whinnery, "Switching of phase-locked states in the intracavity phase-modulated He-Ne laser," *IEEE J. Quantum Electron.* **QE-5**, 367–376 (July 1969); and by K. Otsuka and T. Kimura, "Higher order mode-locking and separation of mode-locked states," *Rev. Electr. Commun. Labor. (Japan)* **20**, 682–689 (July–August 1972).

The properties of harmonic mode locking are discussed by M. F. Becker, D. J. Kuizenga, and A. E. Siegman, "Harmonic mode locking of the Nd:YAG laser," *IEEE J. Quantum Electron.* **QE-8**, 687–693 (August 1972).

FM laser mode locking by mechanical modulation of the laser cavity length, using a very long cavity and a high-frequency piezoelectric mirror mount, has in fact been demonstrated experimentally. See, for example, A. L. Pardue, Jr., and G. J. Dezenberg, "CO₂ laser mode locking produced by sinusoidal cavity-length modulation," *IEEE J. Quantum Electron.* **QE-7**, 95–97 (February 1971); and H. J. Schulte, "Optical pulses produced by (He-Ne)-laser length modulation," *J. Appl. Phys.* **37**, 2189 (April 1966).

Problems for 27.3

1. *Steady-state gain condition in an actively mode-locked laser.* A more detailed treatment of the actively mode-locked laser requires calculation of the net changes in the constant, linear in ω , and quadratic in ω terms in the exponent of the gaussian pulse spectrum (or alternatively the changes in the constant, linear and quadratic parts of the pulse exponent in time) in one round trip. Each of these changes must then be separately set equal to zero to find the steady-state operating conditions.

Carry out this type of calculation focusing on the constant factors in the exponent, i.e., on the net change in overall amplitude in the pulse in one round trip. Add a round-trip loss coefficient α_{op} to account for internal cavity losses and output coupling, and explain the physical meaning of any small differences that may be required between this loss coefficient and the steady-state value of the saturated gain coefficient α_{mpm} , in either the AM or the FM mode-locked situations.

2. *Physical basis of FM mode locking.* A complex gaussian pulse with a sizable chirp can actually be narrowed in time, rather than broadened, upon passing through

a homogeneous laser gain medium. Explain this both analytically and in physical terms.

3. *Evaluation of etalon line narrowing effects.* Suppose that a thin lossless dielectric etalon located within a mode-locked laser cavity has an amplitude reflection coefficient ρ_e or a power reflection coefficient $R_e = \rho_e^2$ at each air-dielectric interface; and a free spectral range determined by its thickness d . Evaluate the transmission factor for this etalon versus frequency, and then compare the quadratic line-narrowing effect that transmission through this etalon will have on a gaussian mode-locked spectrum to the quadratic line-narrowing effects of a homogeneous gain medium, as calculated in this section. Under what sort of conditions will the etalon narrowing dominate over the laser gain medium narrowing?
4. *Changes in pulseshape produced by etalon effects.* Figure 27.17 shows a mode-locked pulse spectrum which has been strongly modulated by periodic etalon transmission effects. What will be the corresponding effects on the envelope pulseshape for the same mode-locked pulses in time?
5. *“Supermodes” in harmonically mode-locked lasers.* Suppose a laser is harmonically mode locked with $N = 2$ or $N = 3$. Discuss in more detail how the superposition of two or three supermodes with different relative phases can lead to different oscillation outputs having either one, two or three output pulses per cavity round-trip time.
6. *Research problem: Mode competition among “supermodes” in a harmonically mode-locked laser.*

Using arguments based upon mode competition and spatial hole burning effects, discuss in general terms the types of mode competition and pulse behavior that might be expected in a harmonically AM mode-locked laser with $N = 2$ for different locations of either the active modulator or the laser gain medium within a standing-wave laser cavity.

27.4 TRANSIENT AND DETUNING EFFECTS

As an extension to the previous section, let us look at the transient build-up of mode locking when, for example, the active modulator is suddenly turned on in a homogeneous actively mode-locked laser. We can then ask: how long will it take for the mode-locking condition to develop, and for the actively mode-locked pulse to come to its steady-state solutions? This question is an important one, first of all because it applies directly to specific lasers such as the repetitively Q -switched and actively mode-locked Nd:YAG laser, which is a very useful laser in many practical applications; and second because it answers (negatively) the broader question of how useful active mode-locking (as contrasted to passive or saturable-absorber mode-locking) can be in higher-power pulsed lasers, such as flash-pumped or Q -switched solid-state or organic dye lasers.

We will approach this problem first with a physical discussion, and then with a simplified gaussian pulse analysis. As an extension we will also consider the experimentally important question of just how precisely a mode-locking modulator must be tuned to the cavity round-trip time for good mode-locking behavior to result.

uniform initial distribution:

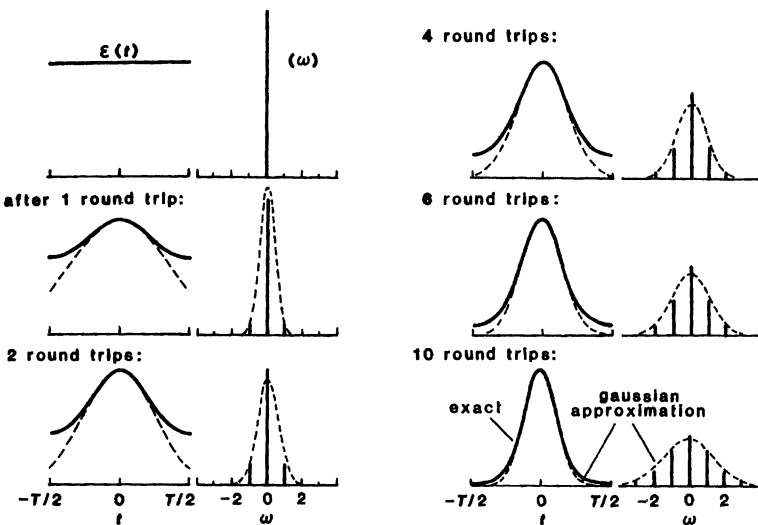


FIGURE 27.18

Evolution of a gaussian pulse shape and pulse spectrum during the first few passes through an amplitude modulator.

Time Development of Active Mode Locking

The time development of active mode locking in a laser will depend to some extent on just how homogeneous or inhomogeneous the laser transition is, and also on just how the laser is turned on—for example, whether the active mode locker is turned on first, before the laser begins oscillating, or whether the laser is already oscillating in a cw steady-state condition when the mode-locking modulator is energized.

Let us consider first an idealized situation in which a strongly homogeneous laser is initially oscillating in only a single axial mode at the time an AM modulator is first turned on. The circulating field $\mathcal{E}(t)$ inside the cavity is then initially constant in time, and the spectrum has only one central axial mode, as shown in the top curve of Figure 27.18.

After just one round trip following modulator turn-on, however, the circulating signal will have been modified to the form $\mathcal{E}(t) = \tilde{t}_{am}(t) = \exp[-\Delta_m(1 - \cos \omega_m t)]$; and after N round trips it will have become $\mathcal{E}(t) \approx \tilde{t}_{am}^N(t) \approx \exp[-N\Delta_m(1 - \cos \omega_m t)]$. Figure 27.18 shows how the resulting pulse envelope will evolve, and also how the corresponding axial-mode spectrum will change during these first few round trips, assuming a peak to peak amplitude modulation index of $2\Delta_m = 0.2$. (These plots also assume, somewhat unrealistically, that the AM modulator itself can be turned on instantaneously, within less than one cavity round-trip time.)

The primary observation here is that within just a few round trips the circulating pulse becomes essentially gaussian in shape, with a pulse envelope given by $\mathcal{E}(t) \approx \exp[-(N\Delta_m \omega_m^2/2)t^2]$; and along with this the axial-mode spectrum also becomes essentially gaussian. The gaussian pulselwidth after the first N round

trips is in fact given by

$$\tau_p \approx \left(\frac{4 \ln 2}{N \Delta_m \omega_m^2} \right)^{1/2} \propto \frac{1}{N^{1/2}}. \quad (37)$$

The spectral width is the gaussian transform of this, and thus increases initially as $B_p \propto N^{1/2}$. Note also that the time-bandwidth product in this situation becomes transform limited and fixed at $B_p \tau_p \approx (2 \ln 2)/\pi \approx 0.44$ after just the first few round trips.

Circulating Gaussian Pulse Analysis

The easiest way to handle this same situation analytically is then to assume that, after a very few round trips, the circulating signal in the cavity—or at least, the time envelope of any circulating noise energy in the cavity—acquires a gaussian envelope shape, and also a gaussian spectrum, as illustrated in Figure 27.18, with a gaussian pulse parameter Γ which changes on each successive round trip. The net change in the gaussian pulse parameter in each round trip, as derived in the preceding section, can then be written in the form

$$\Delta\Gamma \equiv \Gamma'' - \Gamma \approx -\frac{16 \times \alpha_m p_m}{\Delta\omega_a^2} (\Gamma^2 - \Gamma_{ss}^2), \quad (38)$$

where Γ_{ss} is the steady-state gaussian pulse parameter derived in the preceding section. But in most practical situations, for reasonable modulation depths and laser bandwidths, the fractional change in Γ in one round trip will be small, and so Equation 27.38 can be converted to the differential equation

$$\frac{d\Gamma}{dt} \approx \frac{\Delta\Gamma}{T} \approx -\frac{\Gamma^2 - \Gamma_{ss}^2}{\Gamma_{ss} T_{ss}}, \quad (39)$$

where T is the cavity round-trip time, and T_{ss} is a (potentially complex) time constant defined by $T_{ss} \equiv \Delta\omega_a T / 16 \alpha_m p_m \Gamma_{ss}$.

The simplest approach is then to suppose that the laser starts off on its first round trip, at $t = 0$, from a pulse very much wider than its final steady-state value; so we can take $\Gamma(0) \approx 0$. This differential equation can then be integrated in the form

$$\int_0^{\Gamma} \frac{\Gamma_{ss} d\Gamma}{\Gamma_{ss}^2 - \Gamma^2} \approx \frac{1}{T_{ss}} \int_0^t dt, \quad (40)$$

which has the formal solution

$$\Gamma(t) = \Gamma_{ss} \tanh(t/T_{ss}). \quad (41)$$

This solution is formally correct for either the AM or the FM mode-locked situations. Its interpretation is more complicated for the FM situation, however, because the quantities Γ_{ss} and T_{ss} both have complex values for FM. Let us consider therefore only the simpler situation of AM modulation, for which both T_{ss} and Γ_{ss} are purely real.

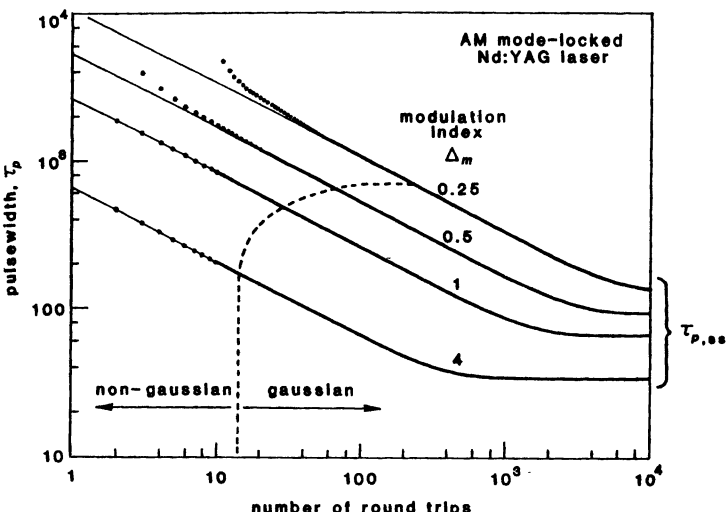


FIGURE 27.19

Mode-locked pulsewidth versus number of round trips after modulator turn-on for different AM modulation indices Δ_m in a typical Nd:YAG laser, starting from uniform single-axial-mode oscillation. The points near the left-hand end of each curve indicate the exact pulsewidth during the early evolution from constant amplitude toward gaussian-shaped pulses.

Time Evolution of AM Mode Locking

It may be more useful to express the time constant T_{ss} in this solution in the form of a number of round trips N_{ss} defined by

$$N_{ss} \equiv \frac{T_{ss}}{T} = \left(\frac{1}{8\alpha_m p_m \Delta_m} \right)^{1/2} \frac{\Delta\omega_a}{\omega_m}. \quad (42)$$

The time evolution of the AM mode-locked pulsewidth following modulator turn-on can then be written as

$$\tau_p(N) = \frac{\tau_{p,ss}}{\tanh^{1/2}(N/N_{ss})} \approx \tau_{p,ss} \times \begin{cases} (N_{ss}/N)^{1/2}, & N \ll N_{ss}, \\ 1, & N \gg N_{ss}, \end{cases} \quad (43)$$

with $\tau_{p,ss}$ being the steady-state AM pulsewidth derived in the preceding section. The AM mode-locked pulsewidth therefore converges toward steady-state in the fashion illustrated for a typical laser with different AM modulation indices in Figure 27.19.

The calculations in this figure have actually been carried out assuming a uniform single-axial-mode field pattern within the cavity just before the first round trip. The individual dots in the left-hand portion of the figure illustrate how the exact pulsewidth (and pulseshape) converge toward the gaussian approximation within a very few round trips for larger modulation indices, and after a somewhat larger number for small modulation index values.

The pulsewidth τ_p in each situation converges to within approximately 20% of its final steady-state value after $N = N_{ss}$ round trips (or to within 5% of

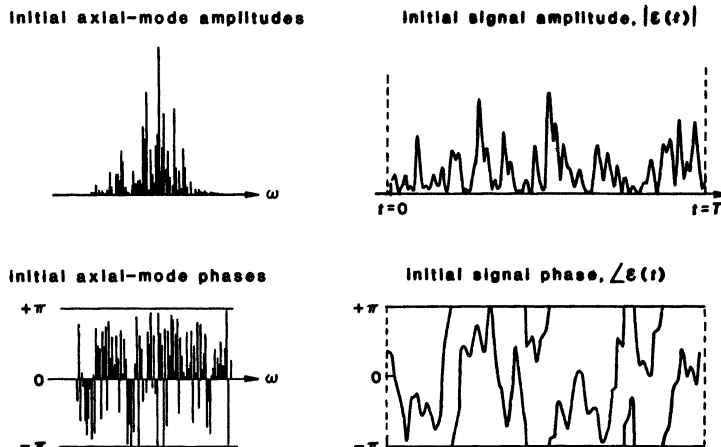


FIGURE 27.20

Initial signal inside a laser cavity having a random distribution of axial-mode amplitudes and phases.

the final value after $N \approx 1.52N_{ss}$ round trips). For typical values in practical lasers, the $(1/8\alpha_m p_m)^{1/2}$ factor in Equation 27.42 for N_{ss} will have a value not too far from unity. The significant factor determining N_{ss} is then once again the atomic linewidth $\Delta\omega_a$ divided by the modulation frequency ω_m . As we have already pointed out, in a typical Nd:YAG laser this ratio may be on the order of $N_{ss} \approx 500$, with much larger values being characteristic of the much broader Nd:glass or organic dye lasers.

The overall conclusion is that it will take somewhere between several hundreds and many thousands of round trips in an actively mode-locked laser for even a rather effective active modulator to pull the mode-locked pulsedwidth down to its final steady-state value. Active mode locking by itself is thus not in general an effective mode-locking technique for short-pulse high-gain lasers, such as flash-pumped solid-state or organic dye lasers. (The combination of weak active mode locking, for initiating and synchronizing the initial pulse build-up, plus a saturable absorber for strong pulse shaping later in the laser burst, can, however, be very effective in so-called active-passive mode-locked lasers.)

Evolution From an Initial Noise Signal

A slightly more complex but not really different situation occurs when active AM mode locking builds up, not from single-frequency oscillations, but from an initial noise-like or multimode situation in a laser cavity. An excellent illustration of this is the widely used cw-pumped, repetitively Q -switched, and actively mode-locked Nd:YAG laser. In this situation, as well as in any kind of flash-pumped and actively mode-locked laser, the active modulator may already be running when the signal in the laser cavity begins to build up; and the signal may then start from noise-like initial conditions produced by, for example, spontaneous emission into multiple axial modes.

Figure 27.20 shows, for example, a typical illustration of the noise-like amplitude and phase distribution that is produced within a laser cavity by a set of

axial modes having randomly distributed amplitudes and phases, such as may be produced by spontaneous emission when the laser oscillation begins to build up. The spectral bandwidth of this spontaneous emission will be approximately the gain linewidth or atomic linewidth $\Delta\omega_a$. Hence, the signal within the cavity will contain rapid amplitude and phase variations, or random pulses in time, having time constants comparable to the inverse bandwidth of the gain medium.

When the amplitude modulator is turned on in this situation, its first effect will be to begin to impose a periodic modulation envelope like that shown in Figure 27.18, on top of the noise-modulated signal already within the cavity. This modulation envelope will then rapidly become gaussian-pulse-like, and will narrow initially as the number of round trips $N^{-1/2}$, in identically the same fashion as described for a cw initial signal in Figure 27.18. The resulting gaussian pulse envelope will contain considerable higher-frequency noise-like internal substructure, however; and thus might be more accurately described as a steadily narrowing noise burst rather than as a clean pulse.

Evolution of the Signal Spectrum

At the same time, the spectral bandwidth of the circulating signal, which is initially comparable to the laser atomic linewidth, will begin to be narrowed on successive round trips by successive passes through the laser amplification process. Indeed, if we make a gaussian approximation for the spectral profile of the laser signal, we can also write a difference or differential equation for the signal bandwidth on successive round trips, and show that it initially decreases as $N^{-1/2}$, just as the envelope width in time decreases initially as $N^{-1/2}$. The signal is, however, nowhere near transform-limited during this build-up stage; and in fact has a time-bandwidth product large compared to unity.

The net result, if this goes on long enough, however, is that the gaussian time envelope of the pulse or noise burst will steadily shorten toward the steady-state mode-locked value; whereas at the same time the noise substructure underneath this pulse envelope will begin to broaden in time because of the spectral narrowing due to the gain medium. Eventually these two trends will meet, and the pulse will evolve into a clean, single, highly gaussian, Fourier-transform-limited pulse, with no remaining internal amplitude or phase substructure.

Experimental Illustrations

In the actively mode-locked and repetitively Q -switched YAG laser that we have mentioned previously, the build-up time for the Q -switched output burst to develop and to dump the laser inversion (typically a few μs) is generally shorter than the number of round-trips needed to obtain full steady-state mode locking. The output burst of mode-locked pulses from this type of laser thus typically occurs in the sloping portion of the curves in Figure 27.19 where $N < N_{ss}$. As a result the mode-locked pulselwidth for fixed build-up time, or for a fixed value of N , decreases with increasing modulation index as $\tau_p \propto \Delta_m^{-1/2}$, rather than having the $\tau_p \propto \Delta_m^{-1/4}$ variation characteristic of the steady state solutions for $N \gg N_{ss}$.

Figure 27.21 shows experimental results for pulselwidth versus modulation index in such a situation, for two different numbers of round trips. The number of round trips needed for the Q -switched burst to build up is controlled in these experiments by varying the cavity losses and the pumping power applied to the

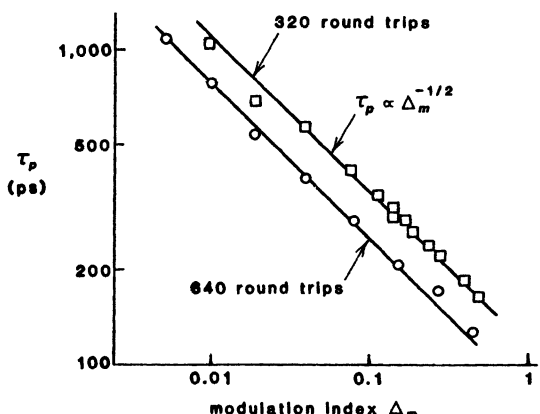


FIGURE 27.21
Pulsewidth versus modulation index for a repetitively Q-switched laser operating in the transient regime where $N < N_{ss}$.

laser rod. The good agreement with theoretical predictions for the dependence both on $\Delta_m^{-1/2}$ and on $N^{-1/2}$ is evident.

Autocorrelation Measurements of Mode-Locked Noise Pulses

One standard method for measuring mode-locked laser spectral characteristics is to measure the autocorrelation function of the output optical pulse against itself using a nonlinear optical process such as optical second-harmonic generation. Figure 27.22 shows the results of three such autocorrelation measurements carried out on a cw-pumped, repetitively *Q*-switched and actively mode-locked YAG laser.

In Figure 27.22(a) the laser is *Q*-switched but not mode locked, so that the output signal is a *Q*-switched pulse envelope with an essentially noise-like internal substructure. The central spike in the autocorrelation function, called a "coherence spike," comes from this noise substructure, and has a width in time comparable to the coherence time of the noise substructure, or to the inverse spectral width of the laser spectrum, as narrowed by repeated passes through the laser gain. The broad background arises from the *Q*-switched laser pulsewidth itself which, at 415 ns, is much wider than the measurement width in these traces.

The central trace shows a *Q*-switched and mode-locked result obtained using a comparatively weak modulation index. The broad gaussian pedestal in this curve indicates that the laser output is indeed a mode-locked pulse envelope with a gaussian pulseshape and a pulsewidth of approximately 530 ps; but the central coherence spike indicates that within this envelope the pulse still contains strong amplitude fluctuations having a much faster time variation.

Finally the bottom trace, obtained using a larger modulation index, shows that the pulsewidth has decreased to ≈ 160 ps, whereas at the same time the internal fluctuations and the coherence spike have broadened somewhat, so that the trace is approaching the clean single gaussian autocorrelation trace, with no separate pedestal or central spike, that we would expect for a clean, fully transform-limited, gaussian mode-locked pulse.

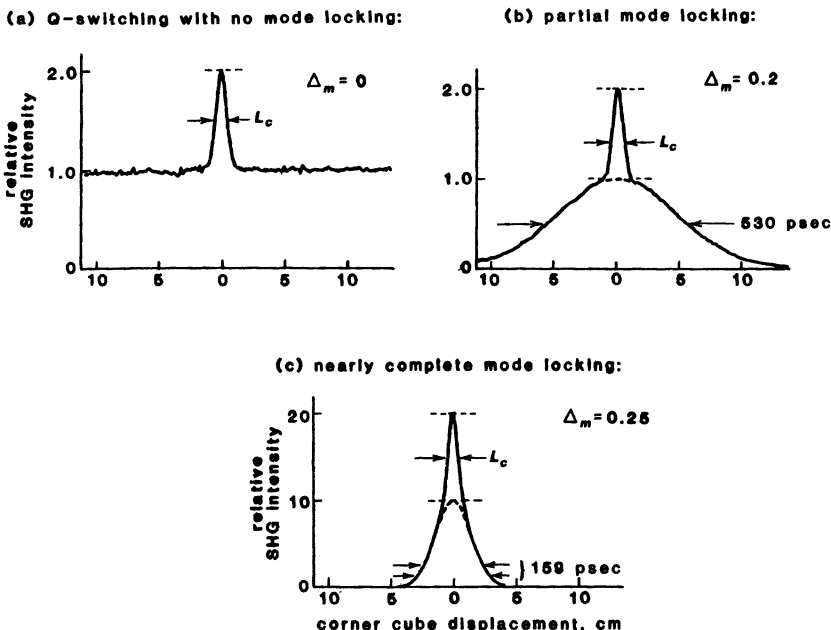


FIGURE 27.22

Autocorrelation traces for a cw pumped, actively mode-locked, and repetitively Q-switched Nd:YAG laser. (a) Q-switched laser alone, without mode locking. (b) Laser mode-locked but with a relatively weak modulation depth, so that the output pulse is not yet fully transform-limited. (c) Mode-locked pulses have nearly reached a fully transform-limited gaussian pulse, without internal substructure. The Q-switching build-up time is $T_b \approx 3 \mu\text{sec}$ in each situation.

Results similar to this have been obtained also for other mode-locked lasers, with a similar interpretation in terms of partial versus complete or transform-limited mode locking.

"Pre-Lasing"

Improved mode-locking in situations of this type can be obtained using the technique of "pre-lasing", in which the opening of the Q-switch is carefully controlled so that the laser can first oscillate weakly, at a low level and without drawing much energy from the laser medium, for a long period before the Q-switch is opened and the Q-switched pulse begins to develop. (The simplest way to do this is to set the loss of the Q-switch in the "off" position at a level where the laser can just oscillate continuously, but very weakly, with the given cw pump power.) The AM modulator is fully energized during this pre-lasing period, however, so that the signal circulating in the cavity has enough time to develop into a fully mode-locked pulse, even though the amplitude of this pulse may be very weak.

When the Q-switch opens, this already well-formed pulse then provides the starting signal that grows into the large-amplitude Q-switched burst. Figure

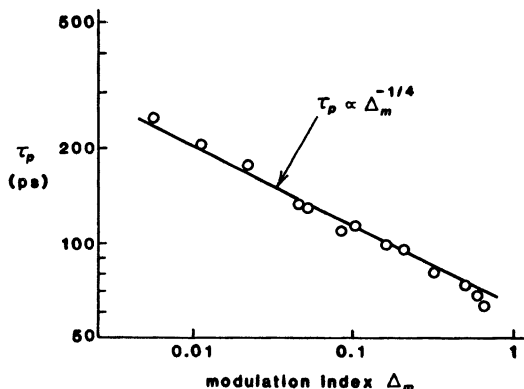


FIGURE 27.23
Results for the laser shown in Figure 27.21, but with pre-lasing.

27.23 illustrates the results if the same laser illustrated previously is converted to pre-lasing operation. The mode-locked pulsewidth is again proportional to $\Delta_m^{-1/4}$, just as in the cw mode-locked situation, and does not depend on the Q -switching build-up time.

Pulse Evolution in the FM Mode-Locked Laser

Let us now turn to the rather different pulse build-up behavior characteristic of a phase-modulated or FM mode-locked laser cavity. The transient evolution of mode locking in an FM mode-locked laser is more complex, and generally much less useful, than for AM.

If an FM modulator is suddenly turned on in an already oscillating laser, whether starting from a single-mode or multimode initial condition, its first effect can only be to produce a phase or frequency modulation on that signal, essentially an increasing sinusoidal chirp on successive round trips, but no pulse-amplitude narrowing of the circulating signal at least within the first few round trips. In fact, only after a much larger number of round trips, when the spectral broadening produced by this phase modulation has become large, will the circulating signal's amplitude profile begin to be changed by the effect of the gain medium acting on this spectrally broadened signal.

If we plot the formal solution for Γ versus number of round trips N in a complex α, β plane for both the FM and AM situations, then the results of Equation 27.41 appear as in Figure 27.24, where the points along each curve give the number of round trips in units of N/N_{ss} . For AM the pulse steadily narrows as the gaussian pulse parameter α moves outward toward the steady-state value α_{ss} . In the FM situation, by contrast, the circulating signal at first acquires only a frequency chirp β . Only after the spectral broadening associated with this chirp has become large enough to interact significantly with the finite bandwidth of the laser gain medium does the pulse begin to narrow and to converge into the steady-state values of α_{ss} and β_{ss} .

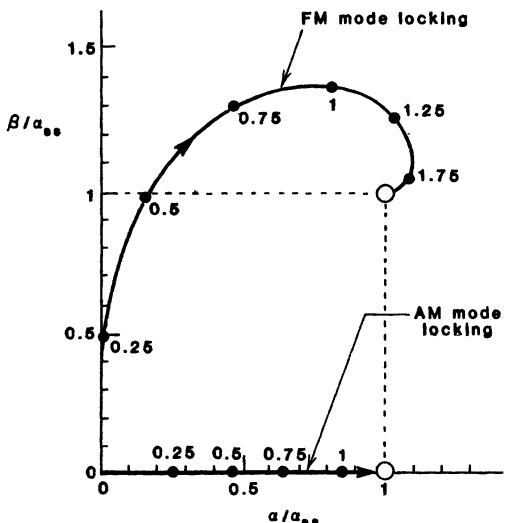


FIGURE 27.24
Transient evolution of the complex gaussian pulse parameter for FM and AM mode locking.

FM mode locking can thus work well enough in a steady-state situation, but appears to have little value for any kind of pulsed or transient mode-locking situation.

Modulation Frequency Detuning Effects

Initial misadjustments in the tuning of the modulation frequency ω_m to equal the axial mode spacing ω'_{ax} , or subsequent slow frequency drifts in the modulation signal generator or thermal changes in the laser cavity length, may cause the round-trip time in a mode-locked laser cavity to be no longer exactly equal to the modulation period of the active modulator, or to a submultiple of this. Such detuning effects will then generally cause substantial deterioration in the mode-locking behavior, especially in cw lasers having particularly short mode-locked pulses.

If the modulation frequency in a mode-locked laser is detuned from exact synchronism by a small amount δf_m , then the mode-locked pulse, instead of arriving back at the modulator at exactly the same point in the modulation cycle after each round trip, will instead arrive with a small time lag or lead δT given for just one round trip by

$$\frac{\delta T}{T} \approx \frac{\delta f_m}{f_m}. \quad (44)$$

This time error will accumulate linearly on successive round trips. The circulating pulse in a typical mode-locked laser makes $\geq 10^8$ round trips per second. An error of even 1 Hz in the modulation frequency synchronism will cause the pulse to walk off synchronism at a rate of one complete modulator period within one second, unless this drift is in some way compensated.

The analysis of such detuning or pulse-walkoff effects is in general complex and somewhat different for the AM and FM mode-locked situations. For example, we can see that as the pulse moves out away from the modulator peak value in the AM modulation situation, the pulse will begin to see an increased average loss, as well as a linear plus quadratic variation in the modulator transmission across the pulse peak. The linear variation of the loss across the pulse envelope will cause a slight distortion in the time envelope of the pulse, which will tend in a very weak fashion to put the pulse center of gravity in time back toward the peak of the modulation function.

The increased average loss will also cause the amplitude of the pulses to decrease, and this, after a time delay will reduce the amount of gain saturation and thus cause the saturated gain to increase. But this in turn will change the amount of atomic dispersion produced by the χ' part of the atomic susceptibility, thereby causing a change in the effective round-trip time T' , which may tend to either cancel or reinforce the initial detuning.

For FM mode locking, as the pulse moves away from exact synchronism it will begin to pick up a linear as well as quadratic phase shift on each pass through the modulator. This will then produce a doppler shift which eventually causes the center of gravity of the mode-locked spectrum to shift sideways out into the wings of the atomic gain curve. This in turn will cause further changes in gain, power output, saturation, and pulse reshaping in the laser medium.

The net result of all these effects is that the mode-locking performance in an actively mode-locked laser is extremely sensitive to very small detuning of the modulation frequency from its exact synchronized value. Both a very well-stabilized laser cavity and a highly stable signal generator are thus required for well-controlled mode locking.

Crude Estimation of Frequency Detuning Effects

No completely satisfactory analysis of mode-locked detuning effects, accompanied by experimental confirmation, seems yet to be available. As a very crude estimate, we might argue that since the active mode-locker requires $\approx N_{ss}$ round trips to shape a mode-locked pulse and pull it into synchronism, one possible criterion is that the pulse should not walk off from its centered position in the modulator by more than some fraction of the steady-state pulselwidth $\tau_{p,ss}$ within N_{ss} round trips, since it may take approximately that many round trips for the modulator to correct the error and pull the pulse back into synchronism.

The synchronism requirement on the pulse round-trip time will then be given, according to this crude argument, by

$$|\delta T| = \frac{|\delta f_m|}{f_m^2} \ll \frac{\tau_{p,ss}}{N_{ss}}. \quad (45)$$

As a practical matter, this says that the modulation frequency must be stable to within a few hundred Hz, or perhaps at absolute most a few kHz, in an actively mode-locked system such as the Nd:YAG laser with its typical pulselwidth of 100 ps or so; and similarly the mode-locked cavity length must be stabilized to within a few μm or better.

These criteria seem to be in agreement with the empirical requirements developed from various experiments. If we attempt to do active mode locking of an even wider line laser, such as a cw dye laser with a potential pulselwidth of 1 ps

or less, the stabilization requirements become more like a frequency stabilization of 1 Hz or better, and a cavity length of a fraction of a μm .

REFERENCES

Theory and experimental results for the transient behavior of AM mode locking are given in D. J. Kuizenga, D. W. Phillion, T. Lund, and A. E. Siegman, "Simultaneous Q-switching and mode-locking in the cw Nd:YAG laser," *Opt. Commun.* **9**, 221–226 (November 1973). See also the more recent experimental results by D. J. Kuizenga, "Generation of short pulses for laser fusion in an actively mode-locked Nd:YAG laser," *Opt. Commun.* **22**, 156–160 (August 1977); and a review by I. V. Tomov, R. Fedosejevs, and M. C. Richardson, "Ultrashort pulse generation in lasers with active mode locking," *Sov. J. Quantum Electron.* **10**, 797–807 (July 1980).

For some instructive numerical simulations showing the detailed transient build-up of active mode locking from noise, see T. W. Chong and P. A. Lindsay, "The generation of picosecond pulses in actively mode-locked c.w. solid-state lasers. IV. The pulse formation," *Int. J. Electron.* **45**, 573–608 (1978).

Some of the complexities of mode-locking detuning analyses are illustrated in A. E. Siegman and D. J. Kuizenga, "Modulator frequency detuning effects in the FM mode-locked laser," *IEEE J. Quantum Electron.* **QE-6**, 803–808 (December 1970); and in W. J. Witteman and A. H. M. Olbertz, "Detuning effects of FM mode-locking in atmospheric CO₂ lasers," *Opt. and Quantum Electron.* **12**, 259 (May 1980).

One way of automatically stabilizing the modulation frequency in an actively mode-locked laser is to detect the axial-mode beat frequency in the laser output with a fast photodetector, and then feed this frequency, properly amplified, back to the active modulator. The practicalities of this self-stabilization approach are well summarized in T. S. Kinsel, "A stabilized mode-locked Nd:YAG laser using electronic feedback," *IEEE J. Quantum Electron.* **QE-9**, 3–8 (January 1973). In particular, proper attention to the radio-frequency phase shift of the feedback signal in this system is essential.

Problems for 27.4

1. *Evolution of FM mode-locked pulses.* Using the analytical solution for the transient build-up in an FM mode-locked laser, verify the transient behavior of Γ versus number of round trips, as illustrated in Figure 27.24.
 2. *Spectral narrowing in a mode-locked laser.* Suppose an actively mode-locked laser starts out with an initial broadband noise spectrum in the laser cavity, as described at one point in this section. Develop an analysis for how the spectral bandwidth is reduced with increasing numbers of passes through the laser gain medium. Using this, describe how the gain-bandwidth product for the mode-locked laser signal will behave as a function of number of round trips in the laser cavity.
-

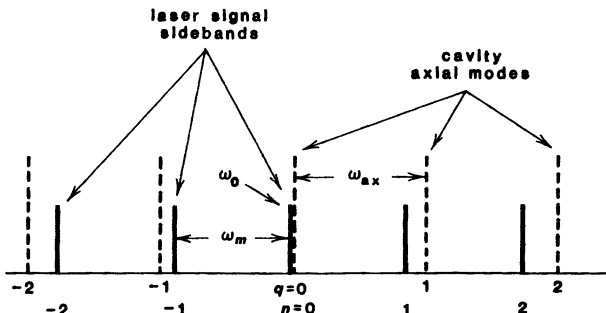


FIGURE 27.25

Cavity resonance frequencies and signal sideband frequencies for use in the coupled-mode analysis.

27.5 FREQUENCY-DOMAIN ANALYSIS: COUPLED-MODE EQUATIONS

The time-domain method of analysis, in which we follow the changes in the laser signal on repeated round trips around the laser cavity, provides one primary way of analyzing laser mode locking. A second primary method, introduced in this section, is the *discrete coupled-mode* type of analysis, in which we analyze the coupling between the multiple axial modes or mode-locked sidebands in a mode-locked laser.

This approach is slightly more formal and complex. However, it also provides a general method for handling more complex situations in a systematic manner. The coupled-mode formalism that we will develop in this system is in fact widely used in the laser literature to analyze not only laser mode locking, but a wide variety of other mode-coupled and multimode laser phenomena.

Coupled-Mode Formulation: Signal and Cavity Frequencies

This analysis begins by recalling that the signal field inside a laser cavity oscillating in multiple axial modes can be written in an axial-mode expansion of the type introduced in earlier sections, namely,

$$\mathcal{E}(\mathbf{r}, t) = \sum_n \tilde{E}_n(t) e^{i\omega_n t} \mathbf{u}_n(\mathbf{r}), \quad (46)$$

where $\tilde{E}_n(t)$ is the complex phasor amplitude of the n -th sideband or axial mode in the slowly varying envelope approximation, and it is understood that we take the real part of the right-hand side. The mode frequencies ω_n must be carefully defined as follows. First, the axial-mode cavity resonances in a laser cavity are given by

$$\omega_q = \omega_{q0} + q\omega_{\text{ax}}, \quad (47)$$

where ω_0 is the centermost axial mode, and the adjacent axial modes are numbered, for simplicity, starting with $q = 0$ at the line center. The axial-mode spacing is $\omega_{\text{ax}} = 2\pi c/p$ without any pulling corrections. (These will be added later.)

On the other hand, in an actively mode-coupled laser with a modulator driven at frequency ω_m , the laser will be oscillating with some central carrier frequency ω_0 plus sidebands produced by the intracavity modulation. The mode-locked signal sidebands actually present in the cavity will then be

$$\omega_n = \omega_0 + n\omega_m. \quad (48)$$

Note that these sidebands will be spaced at the modulation frequency ω_m , even if this modulation frequency is not quite equal to the axial mode spacing frequency ω_{ax} , since it is the active modulator inside the cavity that creates these sidebands on the signal carrier frequency ω_0 .

The actual signal frequencies present will thus be the ω_n 's, whereas the cavity resonances will be the ω_q 's. Each sideband ω_n will, however, generally be very close to a corresponding axial-mode resonance frequency ω_q with $q = n$, so that the n -th order signal sideband will fall within the resonance of the q -th order axial mode, and so forth, as in Figure 27.25. The carrier frequency ω_0 will also be close to but perhaps not exactly identical with the centermost axial resonance ω_{q0} (especially if large detuning or pulling effects are present). It is also convenient to define the detuning ω_d between the (pulled) axial-mode spacing ω_{ax} and the modulation frequency ω_m by

$$\omega_d \equiv \omega_m - \omega_{\text{ax}}. \quad (49)$$

This detuning is generally small (e.g., a few kHz to at most a few MHz), but still very important in mode-locked laser performance.

Cavity Equation and Driving Polarization

The cavity equation for the n -th sideband can then be written, from the slowly varying envelope analysis of Chapter 24, as

$$\frac{d\tilde{E}_n}{dt} + \left[\frac{\gamma_{c,n}}{2} + j(\omega_n - \omega_q) \right] \tilde{E}_n = -j \frac{\omega}{2\epsilon} \tilde{P}_n, \quad (50)$$

where $\gamma_{c,n}$ is the total cavity decay rate for the n -th mode (which may be different for different axial modes); and \tilde{P}_n is that component of the driving polarization in the laser cavity which matches up in spatial variation and in frequency with the n -th cavity mode. It is often convenient to separate the polarization term \tilde{P}_n on the right-hand side into three parts in the form

$$\begin{aligned} \tilde{P}_n = & \text{Linear polarization due to the laser medium} \\ & + \text{Nonlinear polarization due to any nonlinear elements} \\ & + \text{Modulator polarization due to any intracavity modulator.} \end{aligned} \quad (51)$$

The linear part of the polarization term, which is due to the linear response of the laser medium in the cavity, can then be written as

$$\tilde{P}_n = \eta_n \tilde{\chi}(\omega_n) \epsilon \tilde{E}_n = (\chi'_n + j\chi''_n) \epsilon \tilde{E}_n, \quad (52)$$

where $\tilde{\chi}(\omega_n)$ is the linear susceptibility of the laser medium evaluated at the mode frequency $\omega = \omega_n$, and η_n is a filling factor ≤ 1 that takes into account the overlap integral between the cavity fields and the laser atoms, as discussed in an earlier

section. The atomic susceptibility $\tilde{\chi}(\omega_n)$ will in general be the partially saturated value of $\tilde{\chi}(\omega)$, so that the magnitude of $\tilde{\chi}$ may depend on the total intensity $\sum |\tilde{E}_n|^2$ inside the cavity. The form of $\tilde{\chi}(\omega)$ versus ω , or of χ'_n and χ''_n versus n , will also depend very much on whether the laser medium is homogeneous or inhomogeneous.

The nonlinear part of \tilde{P}_n depends on the exact problem being considered. If, for example, a nonlinear optical medium is present in the cavity, we may have a response in which $p(t) \propto \mathcal{E}^2(t)$ for a second harmonic generation medium, or $p(t) \propto \mathcal{E}^3(t)$ for a medium with a so-called cubic nonlinearity. These situations will produce polarization terms at higher harmonics of the signal frequencies ω_n , but they may also cause a sideband at ω_n to mix or “beat” in nonlinear fashion with other sidebands n' , n'' , etc., to produce a nonlinear polarization term \tilde{P}_n at frequency ω_n . These kinds of effects can be important in nonlinear laser calculations, and can be handled using the coupled mode formalism being developed in this section.

Finally, an active modulator present in the cavity at frequency ω_m will act on the cavity fields of the mode at any one sideband, say, E_n , to produce new polarization components at the frequencies of the adjoining modes E_{n+1} and E_{n-1} , and vice versa. The essential function of an intracavity modulator is in fact to mix with or modulate each optical signal component so as to produce sidebands at $\pm\omega_m$. These modulation sidebands from modes $n+1$ and $n-1$ will appear as nonlinear polarization terms \tilde{P}_n at frequency ω_n in the n -th cavity mode equation. Our next task is to calculate the modulation terms \tilde{P}_n in the cavity coupled mode equations.

Modulator Polarization Term

There is a rigorous way to calculate the polarization terms \tilde{P}_n due to an intracavity modulator from a rigorous field theory, which we will develop in the following section. For simplicity, however, we will give a heuristic (but still quite accurate) derivation of the modulator-induced polarization terms here, and then confirm this with the more rigorous derivation in the following section. (Readers of this section might also review the detailed discussion of grating or spatial-modulation sidebands in Section 18.1.)

(1) *Amplitude (AM) modulation sidebands* : Consider first an amplitude modulator placed inside the laser cavity with a time-varying amplitude transmission given by

$$\tilde{t}_{am}(t) = \exp[-\Delta_m(1 - \cos \omega_m t)] \approx 1 - \Delta_m + \Delta_m \cos \omega_m t, \quad \Delta_m \ll 1. \quad (53)$$

The amplitude transmission thus has a peak-to-peak variation of $2\Delta_m$, or a peak-to-peak intensity variation of $4\Delta_m$, as illustrated in Figure 27.26. We will interpret Δ_m to mean the single-pass modulation for a modulator inside a ring cavity, or the double-pass modulation for a standing-wave cavity, since a traveling wave passes through the modulator twice per round trip in the latter situation.

Suppose an optical sine wave of frequency ω_n and complex amplitude \tilde{E}_n passes through this modulator. The output wave, assuming $\Delta_m \ll 1$, is then

$$T(t) \times \tilde{E}_n e^{j\omega_n t} \approx (1 - \Delta_m) \tilde{E}_n e^{j\omega_n t} + \frac{\Delta_m \tilde{E}_n}{2} [e^{j(\omega_n + \omega_m)t} + e^{j(\omega_n - \omega_m)t}]. \quad (54)$$

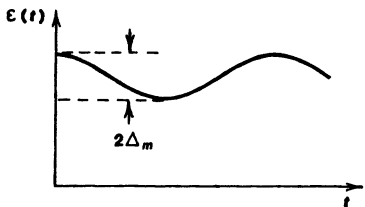


FIGURE 27.26
Modulation sidebands produced when a wave passes through an amplitude (AM) modulator.

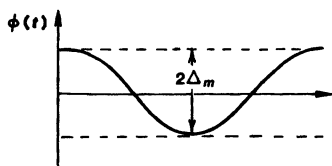
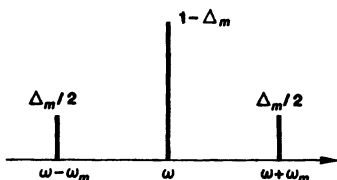
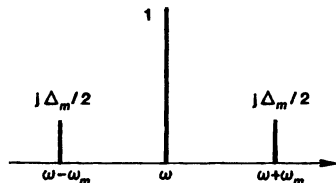


FIGURE 27.27
Modulation sidebands produced when a wave passes through a phase (FM) modulator.



In other words the amplitude modulator attenuates the input sine wave by a factor $(1 - \Delta_m)$, and creates two adjoining sidebands with amplitudes given by $\delta \tilde{E}_{n+1} = \delta \tilde{E}_{n-1} = (\Delta_m/2) \tilde{E}_n$, as shown in Figure 27.26.

(2) *Phase or frequency (FM) modulation sidebands* : Consider on the other hand a phase or FM modulator with transmission given by

$$\tilde{t}(t) = \exp[j\Delta_m \cos \omega_m t] \approx 1 + j \frac{\Delta_m}{2} [e^{j\omega_m t} + e^{-j\omega_m t}], \quad (55)$$

where Δ_m is now the peak phase deviation, or phase modulation index, again for single or double pass in a ring or standing-wave cavity. The sideband generation analogous to the AM situation is now $\delta \tilde{E}_{n+1} = \delta \tilde{E}_{n-1} = j(\Delta_m/2) \tilde{E}_n$.

The sideband generation with either type of modulator can thus be written in the unified form

$$\delta\tilde{E}_{n+1} = \delta\tilde{E}_{n-1} = \left\{ \begin{array}{l} 1 \\ j \end{array} \right\} \frac{\Delta_m \tilde{E}_n}{2}, \quad (56)$$

with 1 for the AM and j for the FM situation.

Modulator Coupled Mode Equations

As an initially sinusoidal signal makes multiple round trips through either type of modulator it will acquire increasingly strong sideband components, and these new sidebands will eventually acquire their own sidebands, and so on. As a simple approximation, however, we can say that the amount of sideband amplitude $\delta\tilde{E}_n$ added or generated per round-trip time T is given by Equation 27.56. Therefore the modulator part of \tilde{E}_n on the right-hand side of Equation 27.50 can be replaced by a $d\tilde{E}_n/dt$ term of the form

$$\left[\frac{d\tilde{E}_n}{dt} \right]_{\text{mod}} \approx \frac{\delta\tilde{E}_n}{T} \approx \left\{ \begin{array}{l} 1 \\ j \end{array} \right\} \frac{\Delta_m}{2T} [\tilde{E}_{n+1} + \tilde{E}_{n-1}], \quad (57)$$

since both of the adjoining mode amplitudes \tilde{E}_{n+1} and \tilde{E}_{n-1} will feed sideband energy into the \tilde{E}_n mode. The final coupled-mode equations will then be the set of equations, one for each sideband \tilde{E}_n , of the form

$$\begin{aligned} \frac{d\tilde{E}_n}{dt} + \left[\left(\frac{\gamma_{c,n}}{2} - \frac{\omega\chi_n''}{2} \right) + j \left(\omega_n - \omega_q + \frac{\omega\chi_n'}{2} \right) \right] \tilde{E}_n \\ = \left\{ \begin{array}{l} 1 \\ j \end{array} \right\} \left(\frac{\Delta_m}{2T} \right) [\tilde{E}_{n+1} + \tilde{E}_{n-1}]. \end{aligned} \quad (58)$$

The bracketed terms on the left-hand side give the loss, the laser gain, the detuning, and the atomic frequency pulling effects for each mode. The terms on the right-hand side give the mode coupling by the AM or FM modulator from the adjacent $n+1$ and $n-1$ modes into the n -th mode.

Note that the cavity frequency pulling effects have appeared in Equation 27.58 in the form of the $\omega\chi_n'/2$ term on the left-hand side. That is, we can write this term instead as $\omega'_q \equiv \omega_q[1 - \chi'_n(\omega_q)/2]$ where ω'_q is the pulled axial-mode resonance frequency.

Equations 27.58 are the fundamental coupled-mode equations used as the starting point for a great many mode locking and other laser calculations. It might seem that in the AM case we should also add a term of the form $-(\Delta_m/T)\tilde{E}_n$ to each $d\tilde{E}_n/dt$ equation to account for the signal conversion out of \tilde{E}_n and into its neighbors \tilde{E}_{n+1} and \tilde{E}_{n-1} by the modulator. Strictly speaking, this is correct. However, the net effect is exactly the same as if the corresponding factor Δ_m/T were added to the cavity loss factor $\gamma_{c,n}/2$; and it is usually assumed that this is what is done. We will show a simple but useful application of these coupled-mode equations in Section 27.7.

REFERENCES

A useful earlier review of mode locking, with emphasis on gas lasers and the coupled-mode approach, is "Mode Locking in Gas Lasers" by L. Allen and D. G. C. Jones, in *Progress in Optics*, Vol. IX, ed. by E. Wolf (North-Holland, 1971).

Two representative examples of the detailed application of coupled-mode theory to mode-locked lasers are S. E. Harris, "Stabilization and modulation of laser oscillators by internal time-varying perturbation," *Appl. Optics* 5, 1639–1651 (October 1966); and O. P. McDuff and S. E. Harris, "Nonlinear theory of the internally loss-modulated laser," *IEEE J. Quantum Electron.* QE-3, 101–111 (March 1967).

See also M. DiDomenico, Jr., "Small-signal analysis of internal (coupling type) modulation of lasers," *J. Appl. Phys.* 25, 2870–2876 (October 1954); and H. Haken and M. Pauthier, "Nonlinear theory of multimode action in loss modulated lasers," *IEEE J. Quantum Electron.* QE-4, 454 (July 1968).

27.6 THE MODULATOR POLARIZATION TERM

In this section we will give a more rigorous derivation of the modulation polarization term \tilde{P}_n that appears on the right-hand side of the cavity equation 27.50 in the previous section, to replace the approximate derivation given in Equations 27.53 through 27.58. Those readers who are willing to accept that simple but essentially correct derivation may want to skip over the more complicated discussion in this section, and go directly to the discussion of the FM laser in Section 27.7.

Modal Analysis

The cavity fields inside a laser cavity are given in the slowly varying envelope approximation (SVEA) by the mode expansion

$$\mathcal{E}(\mathbf{r}, t) = \sum_n \tilde{E}_n(t) e^{j\omega_n t} \mathbf{u}_n(\mathbf{r}), \quad (59)$$

where the $\mathbf{u}_n(\mathbf{r})$ are the eigenmodes (axial plus transverse modes) of the laser cavity. The driving polarization term for the n -th cavity-mode equation in the SVEA approach is then given by

$$\tilde{P}_n(t) e^{j\omega_n t} = \frac{1}{V_c} \int \int \int \mathbf{p}(\mathbf{r}, t) \cdot \mathbf{u}_n(\mathbf{r}) d\mathbf{r}, \quad (60)$$

where $\mathbf{p}(\mathbf{r}, t)$ is the total time- and space-varying electric polarization inside the laser cavity. The cavity eigenmodes are normalized to

$$\int \int \int \mathbf{u}_n(\mathbf{r}) \mathbf{u}_m(\mathbf{r}) d\mathbf{r} = V_c \delta_{nm}, \quad (61)$$

where the integral is over the full cavity volume.

The part of the driving polarization $\tilde{P}_n(t)$ caused by an intracavity phase or amplitude modulator can be calculated as follows. The modulator can be viewed as an intracavity element (see Figure 27.28) whose instantaneous susceptibility is modulated by an externally applied signal such that

$$\tilde{\chi}(\mathbf{r}, t) = \tilde{\chi}_0(\mathbf{r}) + \tilde{\chi}_1(\mathbf{r}) \cos \omega_m t. \quad (62)$$

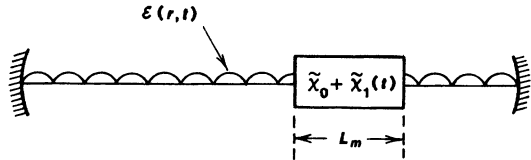


FIGURE 27.28
Time-varying modulation element inside a laser cavity.

where $\tilde{\chi}_0(\mathbf{r})$ and $\tilde{\chi}_1(\mathbf{r})$ are nonzero only inside the modulator element. Strictly speaking, a time-varying linear susceptibility is not a valid concept; but in the present situation the modulation frequency ω_m is so low compared to the optical frequencies of $\mathcal{E}(t)$ and $\mathbf{p}(t)$ that the modulation effects in the modulator may be legitimately approximated by a simple time-variation of $\tilde{\chi}(t)$ in the modulator medium.

The electric polarization in the modulator volume may then be written as

$$\mathbf{p}(\mathbf{r}, t) = \tilde{\chi}(t) \epsilon \mathcal{E}(\mathbf{r}, t) \\ = \left[\tilde{\chi}_0(\mathbf{r}) + \frac{1}{2} \tilde{\chi}_1(\mathbf{r}) (e^{j\omega_m t} + e^{-j\omega_m t}) \right] \epsilon \sum_n \tilde{E}_n(t) e^{j\omega_n t} \mathbf{u}_n(\mathbf{r}). \quad (63)$$

The $\tilde{\chi}_0$ part of this expression is simply a linear susceptibility term. We may drop it out of this expression by supposing that it has already been included in the "empty cavity" calculations used to establish the empty cavity eigenmodes $\mathbf{u}_n(\mathbf{r})$ and eigenfrequencies ω_n .

The time-varying part of Equation 27.63 then contains two components at the particular sideband frequency ω_n , namely,

$$\mathbf{p}(\mathbf{r}, t) = \frac{\epsilon}{2} \tilde{\chi}_1(\mathbf{r}) \left[\tilde{E}_{n+1}(t) \mathbf{u}_{n+1}(\mathbf{r}) + \tilde{E}_{n-1}(t) \mathbf{u}_{n-1}(\mathbf{r}) \right] e^{j\omega_n t}. \quad (64)$$

The two components are the only terms which, when put into the overlap integral for $\tilde{P}_n(t)$, will produce terms at the frequency ω_n corresponding to the n -th eigenmode. The overlap integral in fact becomes

$$\tilde{P}_n(t) = \frac{\epsilon}{2V_c} \tilde{E}_{n+1}(t) \int \int \int \tilde{\chi}_1(\mathbf{r}) \mathbf{u}_{n+1}(\mathbf{r}) \mathbf{u}_n(\mathbf{r}) d\mathbf{r}, \quad (65)$$

plus an exactly identical term involving \tilde{E}_{n-1} and \mathbf{u}_{n-1} . Note that the integral is effectively only over the modulator volume, since only inside the modulator volume is the time-varying polarization $\tilde{\chi}_1$ nonzero.

Evaluation of the Overlap Integral

The overlap integral in Equation 27.65 involves the overlap between the driven polarization $\mathbf{p}(\mathbf{r}, t)$, which varies as $\tilde{\chi}_1(\mathbf{r}) \mathbf{u}_{n+1}(\mathbf{r})$, since it is driven by the $n+1$ -th cavity mode, and the $\mathbf{u}_n(\mathbf{r})$ mode appropriate to the \mathcal{E} field of the n -th cavity mode. These two modes are actually orthogonal over the full cavity volume. However, in the most common situation the modulator fills only a short length L_m located near one end of a cavity of total length L , and the modulated susceptibility $\tilde{\chi}_1(\mathbf{r})$ is essentially constant inside the modulator, i.e., it is not a

function of \mathbf{r} . The axial and transverse mode patterns of $u_n(\mathbf{r})$ and $u_{n+1}(\mathbf{r})$ are then essentially identical inside the modulator, if the two modes represent the same transverse mode, and if the modulator is located close to the end of the cavity.

In this limit the overlap integral is reduced below the mode orthogonality integral by essentially the ratio

$$\frac{1}{V_c} \int \int \int_{\text{mod.}} u_{n+1}(\mathbf{r}) u_n(\mathbf{r}) d\mathbf{r} \approx \frac{L_m}{L}, \quad (66)$$

and the modulator polarization term is given by

$$\tilde{P}_n \approx \frac{\tilde{\chi}_1 \epsilon L_m}{2L} [\tilde{E}_{n+1} + \tilde{E}_{n-1}]. \quad (67)$$

In the more general situation, however, the two modes will have spatial variations which for two adjacent axial modes in a standing-wave cavity will typically look like

$$\begin{aligned} u_q(\mathbf{r}) &\propto \sin q\pi z/L, \\ u_{q+1}(\mathbf{r}) &\propto \sin(q+1)\pi z/L, \end{aligned} \quad (68)$$

The electric field patterns corresponding to two adjacent axial modes will generally be in phase at a reflecting mirror surface; will gradually slip out of phase in their spatial variations as we move toward the cavity center; and will slip in phase by one complete half cycle over the full cavity length. (We might in some situations use a modulation frequency ω_m which was several times, say, k times, the axial-mode spacing ω_{ax} . The two modes u_n and u_{n+k} would then slip by k complete half cycles over the full cavity length.)

The implication of this is that to obtain the most effective coupling of adjacent axial modes in a standing-wave cavity, the modulator must be placed at or near the ends of the cavity. A modulator placed in the center of a standing-wave cavity (or for that matter one filling the entire cavity) will have zero effectiveness in coupling adjacent axial modes.

Connection With Previous Results

Suppose now that a plane wave with carrier frequency passes in one direction through the modulator just described. For a short modulator ($L_m \ll 2\pi c/\omega_m$) the one-way wave propagation through the modulator may be described simply by a time-varying propagation factor

$$T(t) = e^{-j\beta(t)L_m}, \quad (69)$$

where the time-varying propagation constant is given by

$$\beta(t) = \frac{\omega \sqrt{1 + \tilde{\chi}(t)}}{c} \approx \frac{\omega}{c} \left[1 + \frac{1}{2} \tilde{\chi}_0 + \frac{1}{2} \tilde{\chi}_1 \cos \omega_m t \right]. \quad (70)$$

Ignoring for the same reasons as before the purely linear portion of this, we can write the modulated output signal from modulator as

$$\mathcal{E}(t) \approx \exp[j\omega_0 t - j(\omega \tilde{\chi}_1 L_m / 2c) \cos \omega_m t]. \quad (71)$$

If $\tilde{\chi}_1$ is purely real, corresponding to index modulation or phase modulation, then this has the same form as a standard phase modulator with peak phase deviation (in radians) given by

$$\Delta_m = -\frac{\omega L_m}{2c} \tilde{\chi}_1, \quad (72)$$

which exactly matches our earlier result. (The sign is immaterial.) If $\tilde{\chi}_1$ is imaginary, $\tilde{\chi}_1 = \pm j\tilde{\chi}_1''$, then the result in Equation 27.72 corresponds in essence to a sinusoidal amplitude modulator with an amplitude modulation index Δ_m given by the same expression (give or take arbitrary factors of two in the definition of modulation index).

The final result in the usual situation is thus the same as given earlier, namely, that the mode-coupling terms in the SVEA equations have the basic form

$$\frac{d\tilde{E}_n}{dt} \propto -j\frac{\omega}{2\epsilon} \tilde{P}_n = \begin{cases} 1 \\ j \end{cases} \frac{\Delta_m}{2T} [\tilde{E}_{n+1} + \tilde{E}_{n-1}], \quad (73)$$

where the 1 or j apply for AM or FM modulation, respectively.

Problems for 27.6

1. *Cross-coupling between adjacent modes due to gain saturation.* The saturation of the laser gain (or, alternatively, of a saturable absorber) at any point z inside a laser cavity can be expressed to a first approximation by writing the induced polarization $p(z, t)$ at each point as $p(z, t) \approx -j\chi' [1 - \langle \mathcal{E}^2(t) \rangle / I_{\text{sat}}] \mathcal{E}(z, t)$ where $\langle \mathcal{E}^2(z) \rangle$ refers to the time-average value of the total field $\mathcal{E}(z, t)$ at point z . [In other words, for not too strong saturation we can write the homogeneous saturation factor as $(1 + I/I_{\text{sat}})^{-1} \approx 1 - I/I_{\text{sat}}$.] Suppose that $\mathcal{E}(z, t)$ in a standing-wave laser cavity contains just two nearby axial modes \tilde{E}_n and \tilde{E}_{n+k} at frequencies ω_n and ω_{n+k} , where k is some small integer; and suppose the saturable gain (or absorption) cell has length L_m such that on the one hand L_m is long compared to a wavelength λ , but on the other hand L_m is short compared to the cavity length L . Let this cell be located a fraction f of the total cavity length L away from one end mirror where $0 \leq f \leq 0.5$.

What will be the cross-coupling terms between \tilde{E}_n and \tilde{E}_{n+k} appearing in the nonlinear polarization terms \tilde{P}_n and \tilde{P}_{n+k} on the right-hand side of the coupled-mode equations in this situation?

27.7 FM LASER OPERATION

We showed in a previous section that an intracavity phase or FM modulator which is tuned exactly to the round-trip transit time of a laser cavity can lead to a pulsed kind of mode locking in the laser, even though it is the laser cavity phase or frequency, not its amplitude, that is being modulated. This is generally called "FM mode-locked" laser operation.

A laser containing an intracavity phase or FM modulator can, however, also exhibit an interesting frequency-swept mode of operation which represents a

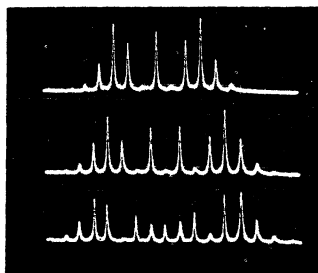


FIGURE 27.29

Axial mode spectra of a He-Ne laser in the FM-laser mode of operation. The individual axial modes are ≈ 150 MHz apart.

different type of mode-coupled operation, quite distinct from the short-pulse operation described earlier. This frequency-swept mode of operation, usually called “FM laser operation”, occurs when the FM modulation frequency ω_m is detuned by a modest amount (e.g., 1% or so) from the exact axial mode spacing ω_{ax} . We analyze this FM laser mode of operation in this section, both for its own interest and as a simple but instructive example of the use of the coupled mode equations for a laser.

Analysis of FM Laser Operation

Suppose a typical cw Nd:YAG laser is operated with an intracavity electrooptic phase modulator (which might use a crystal of LiNbO_3 or KDP), but with the radio-frequency signal ω_m applied to the modulator detuned by ≈ 1 MHz from the axial mode spacing ω'_{ax} . Examination of the laser output with a fast photodiode will then show that the output is not “mode-locked” in the usual short-pulse sense. The laser output amplitude instead appears to be essentially constant, as if the laser were running in a single axial mode.

A photograph of the axial-mode spectrum of the laser, taken using a scanning Fabry-Perot interferometer, may, however, look something like the Figure 27.29, which shows traces taken on the output of a He-Ne laser driven with an internal phase modulator at a modulation frequency near 150 MHz (which happens in this situation to be very nearly twice the axial mode interval).

These spectra should be, and in fact are, very much like the spectral distribution of a pure phase or frequency-modulated (FM) signal, but with a phase modulation index Γ that is very much larger than the single-pass modulation index Δ_m of the intracavity modulation. This index Γ also depends sensitively on the detuning of the modulation frequency ω_m from the axial-mode spacing, or one of its harmonics, as we will now demonstrate.

FM Coupled-Mode Analysis

To show this analytically, we must first note that the basic coupled-mode equations for an FM-modulated laser cavity are

$$\frac{d\tilde{E}_n(t)}{dt} + \left[\left(\frac{\gamma_{c,n} - \omega \chi_n''}{2} \right) + j(\omega_n - \omega_q) \right] \tilde{E}_n = j \frac{\Delta_m}{2T} (\tilde{E}_{n+1} + \tilde{E}_{n-1}), \quad (74)$$

where the dispersive term χ'_n has been absorbed into the definition of the axial mode frequency ω_q . Let us assume steady-state operation, so that $d\tilde{E}_n/dt \equiv 0$, and also assume a significant amount of detuning ω_d between the modulation frequency ω_m and the axial-mode spacing ω_{ax} . We also assume (as is generally correct) that this laser will run with the centermost sideband ω_0 aligned with the centermost axial mode ω_{q0} . We can then write:

$$\begin{aligned}\omega_n - \omega_q &= (\omega_0 + n\omega_m) - (\omega_0 + q\omega_{\text{ax}}) \\ &= n \times (\omega_m - \omega_{\text{ax}}) \\ &= n \times \omega_d.\end{aligned}\quad (75)$$

Typical values for these frequencies in an FM YAG laser might be $\omega_m \approx \omega_{\text{ax}} \approx 2\pi \times 200$ MHz and $\omega_d \equiv (\omega_m - \omega_{\text{ax}}) \approx 2\pi \times 1$ MHz.

FM laser operation can occur in either homogeneous or inhomogeneously broadened lasers. We know that in any kind of steady-state laser oscillator the net gain per pass must equal the total losses per pass. For an inhomogeneously broadened laser with spectral hole burning (as in most visible gas lasers) this condition is satisfied essentially mode by mode, i.e., $\gamma_{c,n} \approx \omega\chi''_n$ for each n individually. We can then drop the $(\gamma_{c,n} - \omega\chi''_n)$ factor in Equation 27.74.

For a homogeneous transition, by contrast, gain equals loss only averaged over all modes. The net loss minus gain, $\gamma_{c,n} - \omega\chi''_n$, is not zero for individual modes; and the net gain or loss for any one individual mode \tilde{E}_n must be balanced by energy transfer between modes produced by the intracavity modulator. For a sufficiently wide homogeneous linewidth, however, such as in Nd:YAG lasers, the gain is very nearly flat with frequency at line center. The net gain versus loss can then be nearly zero even on a mode by mode basis. For either inhomogeneous lines or reasonably wide homogeneous lines, therefore, it becomes possible to make the approximation

$$|\gamma_{c,n} - \omega\chi''_n| \ll n\omega_d, \quad (76)$$

even for rather small values of the detuning frequency ω_d .

Bessel Function Solutions

With this approximation, the coupled-mode equations (27.74) reduce to the steady-state relationship

$$jn\omega_d \tilde{E}_n \approx j \frac{\Delta_m}{2T} (\tilde{E}_{n+1} + \tilde{E}_{n-1}), \quad (77)$$

or

$$\left(\frac{2n\omega_d T}{\Delta_m} \right) \tilde{E}_n \approx \tilde{E}_{n+1} + \tilde{E}_{n-1}. \quad (78)$$

But this relation is exactly the same as a standard recursion relationship for Bessel functions $J_n(\Gamma)$ of argument Γ , namely,

$$\frac{2n}{\Gamma} J_n(\Gamma) = J_{n+1}(\Gamma) + J_{n-1}(\Gamma). \quad (79)$$

A steady-state mode-coupled solution for the “FM laser” with detuning ω_d is thus given by

$$\mathcal{E}(t) = E_0 \sum_{n=-\infty}^{\infty} J_n(\Gamma) \exp[j(\omega_0 + n\omega_m)t], \quad (80)$$

where the factor Γ is given by

$$\Gamma = \frac{\Delta_m}{\omega_d T} = \frac{\omega_{ax}}{\omega_d} \times \frac{\Delta_m}{2\pi}, \quad (81)$$

with ω_{ax} the axial-mode spacing and ω_d the (small) detuning of ω_m from ω_{ax} .

But there is another standard Bessel function identity which says that

$$e^{j\Gamma \sin \omega_m t} \equiv \sum_{n=-\infty}^{\infty} J_n(\Gamma) e^{jn\omega_m t} \quad (82)$$

Hence the laser oscillation signal at any arbitrary reference plane inside the laser cavity—at the end mirror, say—will have the general form

$$\mathcal{E}(t) = E_0 e^{j\omega_0 t} \sum_{n=-\infty}^{\infty} J_n(\Gamma) e^{jn\omega_m t} = E_0 \exp[j\omega_0 t + j\Gamma \sin \omega_m t]. \quad (83)$$

This “FM laser” signal thus has the form of a constant-amplitude oscillation (no pulse), but with a very large amount of sinusoidal modulation of the oscillation phase, at modulation frequency ω_m , and with a modulation index or peak phase deviation Γ .

Instantaneous Frequency Sweep

The behavior of a frequency-modulated or phase-modulated signal of this type can be described either from a spectral viewpoint, leading to Bessel-function sidebands as given in Equation 27.82, or from a temporal viewpoint in which we speak of a sinusoidal frequency sweep of the instantaneous signal frequency. That is, since the instantaneous phase ϕ_{tot} of the laser output signal is given by

$$\phi_{tot}(t) = \omega_0 t + \Gamma \sin \omega_m t, \quad (84)$$

where Γ is the modulation index or the peak phase deviation in radians of the output signal, then the “instantaneous frequency” of this signal is given, according to the usual definition, by

$$\omega_i(t) \equiv \frac{d\phi_{tot}(t)}{dt} = \omega_0 + \Gamma \omega_m \cos \omega_m t. \quad (85)$$

The instantaneous frequency of the laser output signal, from this viewpoint, appears to swing back and forth in sinusoidal fashion at the modulation frequency ω_m , but over a frequency range of $\pm \Gamma \omega_m$, so that the quantity $\Gamma \omega_m$ is the peak upward or downward frequency deviation of the laser signal.

The modulation index Γ for the actual FM laser output signal is then increased over the single-round-trip modulation index Δ_m of the intracavity modulator by the large ratio

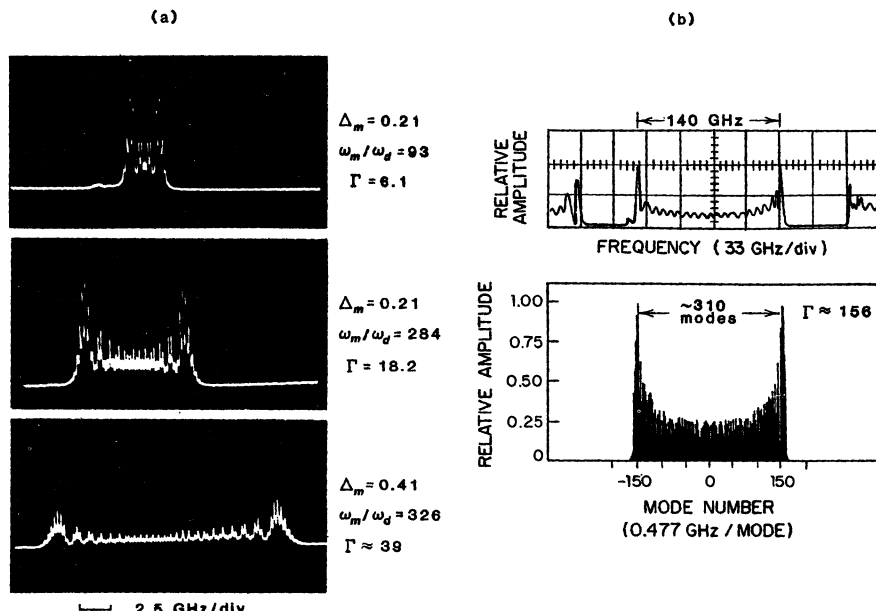


FIGURE 27.30

Axial-mode spectra from two lasers operating in the FM laser mode. (a) Nd:YAG laser with different values of modulation index and modulation frequency detuning. (b) Neodymium-pentaphosphate FM laser with a very large value of Γ .

$$\frac{\Gamma}{\Delta_m} = \frac{1}{2\pi} \frac{\omega_m}{\omega_d} = \frac{1}{2\pi} \frac{\omega_m}{\omega_m - \omega_{\text{ax}}} \quad \text{where} \quad \omega_d \ll \omega_m. \quad (86)$$

This multiplication factor can range up to ≈ 100 or more as the detuning frequency is made small. The frequency sweep of the FM laser output can thus be very much larger than the intracavity modulation frequency.

Experimental Results

Figure 27.30 shows some further experimental results for FM laser operation as observed both in a cw Nd:YAG laser and in a small cw Nd:pentaphosphate laser. In both of these experiments, as in Figure 27.29, we observe the spectral output of the laser using a scanning Fabry-Perot interferometer, so that we measure directly the discrete axial-mode spectrum of the laser.

In the experimental results of Figure 27.30(a) the intracavity modulation index is comparatively small, but by using a small detuning value the phase modulation index of the actual laser output is made much larger. We can then directly observe that the individual axial-mode amplitudes Figure 27.30(a) do have the Bessel-function amplitudes expected for a purely frequency-modulated signal. The sidebands must have the phases characteristic of a phase-modulated rather than an amplitude-modulated or pulsed signal also, since we see no ob-

servable amplitude modulation if the laser output is observed directly with a photodetector and oscilloscope.

Figure 27.30(b) shows additional FM laser results for a small cw neodymium-pentaphosphate laser pumped by a cw dye laser. The atomic linewidth in this laser medium is $\Delta\omega_a/2\pi \approx 25 \text{ cm}^{-1} \approx 750 \text{ GHz}$, or very much wider than the 4 cm^{-1} linewidth characteristic of Nd:YAG, so that a much wider oscillation spectrum can be obtained. For the results shown here the intracavity round-trip modulation index is ≈ 0.8 radians, the axial-mode interval is 480 MHz, and the modulator detuning ranges down to as small as $\approx 400 \text{ kHz}$, giving a maximum output modulation index of $\Gamma \approx 156$. The top curve then shows the measured spectrum (with individual axial modes not resolved) and the bottom curve a computer simulation.

For such very large modulation indices it is a property of the Bessel functions $J_n(\Gamma)$ that the spectral range over which the Bessel-function sidebands have significant amplitude extends out to approximately $\omega_0 \pm \Gamma\omega_m$, and thus the spread of the sidebands in frequency space corresponds more or less directly to the instantaneous frequency variation in the time description. For large modulation index, moreover, the rather irregular Bessel-function spectrum, if sufficiently smoothed, comes to look much like the probability distribution for a sinusoidal oscillator, with most of the spectral energy concentrated in a group of outmost sidebands near the classical turning points of the sinusoidally oscillating instantaneous frequency.

These FM laser spectra thus beautifully illustrate the Bessel-function properties of frequency-modulated signals. (What we have here are perhaps the world's most expensive Bessel function computers!) Note that in the pentaphosphate case the total number of FM sidebands is approximately $2\Gamma \approx 310$ axial modes. Note also that the axial modes in these FM lasers are fully "mode-coupled" in the sense of being fully locked together in relative amplitude and phase by the intracavity modulator. In fact, the spectral range over which axial modes can be tightly locked or coupled is typically much larger in an FM laser than in an AM or FM mode-locked (i.e., pulsing) laser for the same modulation index.

Transition From FM Laser Operation to FM Mode Locking

There is necessarily a transition from FM laser operation to FM mode-locked or pulsed behavior as the detuning ω_d is decreased towards zero from either side. To understand this, we can note that when ω_d becomes very small, the ratio ω_m/ω_d and hence the modulation index Γ become very large, and the FM laser spectrum becomes very wide. As the FM laser sidebands illustrated in figures 27.29 and 27.30 are pushed farther out in frequency from line center, the laser gain decreases (because much of the laser energy moves out to the wings of the gain profile). The laser then becomes unstable, and will eventually cease to oscillate in the FM laser mode.

At very small detunings (typically $< 1\text{--}10 \text{ kHz}$) FM mode-locked or pulsed operation then begins, as illustrated in Figure 27.31. The intermediate detuning region between the two regimes may produce multiple FM laser oscillations with several carriers present simultaneously, or other varieties of noisy or unstable operation.

FM laser operation, despite its interesting features and ease of operation, and despite having been observed in gas, solid-state and dye lasers, has unfortunately yet to find any widespread practical application in lasers.

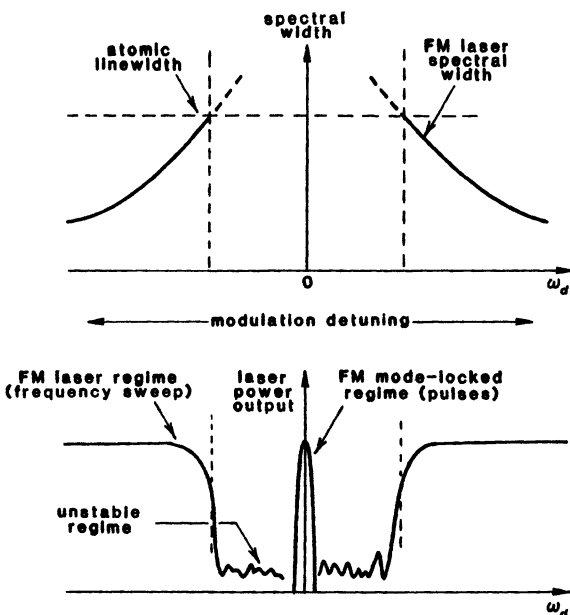


FIGURE 27.31
The transition from FM-laser or frequency-swept operation to FM-mode-locked or pulsed operation.

REFERENCES

Two early papers giving the theory and experimental verification of FM laser operation are by S. E. Harris and O. P. McDuff, "Theory of FM laser oscillation," *IEEE J. Quantum Electron.* **QE-1**, 245-262 (1965); and E. O. Ammann, B. J. McMurtry, and M. K. Oshman, "Detailed experiments on helium-neon FM lasers," *IEEE J. Quantum Electron.* **QE-1**, 263-272 (1965). See also S. E. Harris, "Stabilization and modulation of laser oscillators by internal time-varying perturbation," *Appl. Optics* **5**, 1639-1651 (October 1966).

For examples of FM laser oscillation in wider-linewidth lasers, see D. J. Kuizenga and A. E. Siegman, "FM-laser operation of the Nd:YAG lasers," *IEEE J. Quantum Electron.* **QE-6**, 673-677 (November 1970); or S. R. Chinn and W. K. Zwicker, "FM mode-locked $\text{Nd}_{0.5}\text{La}_{0.5}\text{P}_5\text{O}_{14}$ laser," *Appl. Phys. Lett.* **34**, 647-649 (June 15, 1979).

The temporal and spectral approaches to FM laser signals, as well as to other mode-locked laser signals, can be unified by using a kind of "frequency-plus-time" analytical approach called the Wigner distribution (see Problems). A useful discussion of the Wigner distribution and its properties can be found in a tutorial series by T.A.C.M. Claasen and W.F.G. Mecklenbräker, "The Wigner distribution—a tool for time-frequency signal analysis," *Philips J. Res.* **35**, 217-300 and 372-389 (1980). The origin of the Wigner distribution is in E. Wigner, "On the quantum correction for thermodynamic equilibrium," *Phys. Rev.* **40**, 749-759 (1932).

See also M.J. Bastiaans, "The Wigner distribution function applied to optical signals and systems," *Optics Comm.* **25**, 26-30 (1978); and "Wigner distribution function and its application to first order optics," *J. Opt. Soc. Am.* **69**, 1710-1716 (1979).

 Problems for 27.7

1. *Time-domain derivation of FM laser operations.* Show that the same analytic results for FM-laser oscillation obtained in this section using a coupled-mode analysis can also be derived from a time-domain round-trip analysis. Hints: (1) Assume the circulating laser signal has constant amplitude but time-varying phase; (2) include the finite detuning between the intracavity phase modulation frequency and the cavity round-trip transit time; (3) require self-consistency of phase after one complete round trip; and (4) recognize that your results may appear slightly different depending just where in the cavity you evaluate the circulating field.
2. *Research problem: Single-sideband mode-coupled lasers?* Suppose a single-sideband modulator which produces only a single sideband, say, $\delta\tilde{E}_{n+1}$, to each existing frequency component \tilde{E}_n is placed inside a multimode laser cavity. Can you then predict any interesting mode-coupled type of behavior for the laser, considering either homogeneous or inhomogeneous laser transitions, and either an in-phase or quadrature phase shift for the sideband component. [Note: Single-sideband optical modulators do exist, but the answer to this general mode-coupling question—if there is one—does not seem to have been worked out in the literature].
3. *Wigner distributions for mode-coupled lasers.* The Fourier transform $\tilde{E}(\omega)$ for a time signal $\mathcal{E}(t)$ is a familiar, rigorously defined, and physically meaningful concept.

The Fourier transform $\tilde{E}(\omega)$ for a given signal is a fixed quantity, however, independent of time; whereas physically we may know that the instantaneous frequency of some signal is modulated and changing in some way with time during the signal. An analytical tool that can be useful in situations like this is the symmetrized *Wigner distribution function* $W(\omega, t)$, which can be defined for a signal $\mathcal{E}(t)$ by

$$W(\omega, t) \equiv \int_{-\infty}^{\infty} \mathcal{E}^*(t - \tau/2) \mathcal{E}(t + \tau/2) e^{-j\omega\tau} d\tau,$$

where $\mathcal{E}(t)$ is the analytical form of the signal given by

$$\mathcal{E}(t) = E(t) e^{j[\omega_0 t + \phi(t)]},$$

[i.e., without the “Re” operation being performed]. The Wigner distribution function is then a two-dimensional function of frequency and time, which can be mapped onto the ω, t plane with contours of constant magnitude. Note that if you take an average over all t along any fixed value of ω you have

$$\langle W(\omega, t) \rangle_t = \int_{-\infty}^{\infty} R(\tau) e^{-j\omega\tau} d\tau = |\tilde{E}(\omega)|^2$$

where $R(\tau)$ is the autocorrelation function of $\mathcal{E}(t)$. Hence, averaging $W(\omega, t)$ over t gives you the usual power spectral density $|\tilde{E}(\omega)|^2$. On the other hand, looking at $W(\omega, t)$ versus ω for some fixed t may give you a kind of “quasi power-spectrum” for the signal $\mathcal{E}(t)$ near that particular instant.

The Wigner distribution would seem to be a useful tool for analyzing laser mode locking, especially where a frequency sweep or strong chirp is present. As a start on this, try the following:

- (a) Compute the Wigner function $W(\omega, t)$ for a complex gaussian pulse with $\Gamma \equiv \alpha - j\beta$, and discuss the form of this function in the ω, t plane. (Only the form of the distribution is important, not the constants in front.)
- (b) Describe briefly what happens to $W(\omega, t)$ as a gaussian pulse goes through an AM modulator; an FM modulator; a dispersive delay line (with β''); and a lorentzian gain medium.
- (c) What does the Wigner distribution for a pure FM signal look like?
4. *Transient build-up of FM laser oscillation.* Try developing an analysis of the transient build-up of FM laser oscillation, starting with the laser oscillating in a single axial mode at the time the intracavity phase modulator is turned on. (No such analysis exists in the laser literature, to the author's knowledge.) Assume first an infinitely wide atomic line, i.e., ignore any effects of the finite bandwidth of the laser medium; and then try adding a wide but finite atomic linewidth. Hint: A computer simulation involving a time integration of the coupled mode equations for $d\tilde{E}_n/dt$ for some suitable set of modes \tilde{E}_n may be instructive.
5. *Coupled-mode analysis of AM and FM mode locking.* Show that the Kuizenga-Siegman gaussian-pulse results for homogeneous AM or FM mode locking which were derived in Section 27.3 and 27.4 using a time-domain analysis can equally well be obtained using the coupled-mode analysis developed in this and the preceding two sections. Some hints:
 - (a) If the spectrum of a laser signal is not too wide compared to the atomic linewidth (that is, if $|\omega_n - \omega_a| \leq \Delta\omega_a/2$ for all significant sidebands ω_n), then the susceptibility $\tilde{\chi}(\omega_n)$ can be expanded to only second order in $\omega_n - \omega_a$ about line center.
 - (b) Obviously you will want to do something that matches up powers of ω , or more precisely powers of n , on both sides of the coupled-mode equation (27.58 or 27.74). Now, a gaussian distribution of the form $\tilde{E}_n = \exp(-an^2)$ cannot be represented accurately over its full significant range in n by a Taylor series containing only the first one or two powers of n . However, the function $\tilde{E}_{n+k} = \exp[-a(n+k)^2]$ can be expanded in the first one or two powers of k about \tilde{E}_n or about $k = 0$, in order to relate \tilde{E}_{n+k} to \tilde{E}_n , and this expansion in k will be accurate for any value of n over the entire spectrum.
6. *Research problem: Coupled mode analysis of detuning effects in mode-locked lasers.* Try extending the previous problem to include constant and linear, as well as quadratic, powers of n ; and then using the results to analyze detuning effects in the AM-mode-locked laser, i.e., try to predict the changes in AM-mode-locked performance that will occur as the modulator frequency is slightly detuned from the exact round-trip repetition rate.



PASSIVE MODE LOCKING

Passive mode locking provides an alternative approach to generating ultrashort pulses which is more effective and of more practical importance than active mode locking for use in high-power flash-pumped lasers, and for generating the shortest possible pulses in certain cw mode-locked lasers. This type of mode locking is, however, also generally more difficult to control, particularly if we wish to obtain stable and reliable mode-locked operation.

Passive mode locking, as an inherently nonlinear process, is also rather more complex to describe and less amenable to simple analytical treatments than is active mode coupling. In this chapter, therefore, we will primarily give an overview of the most important forms of passive mode locking, without attempting to carry through the detailed analyses that are necessary to give a complete and accurate picture of passive mode locking.

28.1 PULSE SHORTENING IN SATURABLE ABSORBERS

Since the basic mechanism in nearly all passively mode-locked lasers is pulse shortening during transmission through a saturable absorber element, let us first examine briefly the basic capabilities of this kind of pulse shortening in simple types of saturable absorbers.

Signal Transmission Through Saturable Absorbers

In nearly all situations of practical interest in mode-locked lasers, the time-variation of the mode-locked pulse will still be slow compared to the dephasing time T_2 in the saturable absorbing medium; and the saturation behavior of the absorption will be essentially that of a simple homogeneous atomic transition. Hence we can describe the nonlinear transmission of an optical pulse through such a saturable absorber with sufficient accuracy using only a simple rate-equation approach, without going into more complex resonant-dipole or Rabi-flopping analyses.

The change in pulshape on passing through the absorber will then still depend quite strongly, however, on whether the absorbing medium is a *fast saturable absorber*, that is, one in which the absorption recovery time T_1 is much

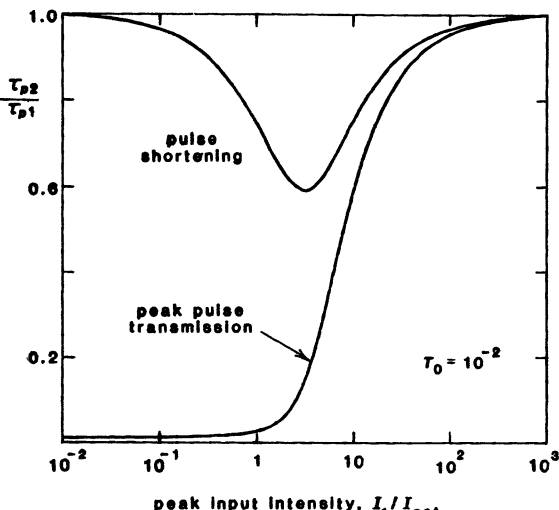


FIGURE 28.1
Pulse shortening in a fast saturable absorber with initial intensity transmission $T_0 = 0.01$ and a gaussian input pulse.

shorter than the pulselength τ_p , so that the absorber saturates in essence on the instantaneous intensity $I(t)$ of the optical pulse; or by contrast whether the absorber is a *slow saturable absorber*, in which τ_p is much longer than the pulselength τ_p , and the absorption saturates primarily on the integrated intensity or energy in the optical pulse. Let us first consider therefore the pulse shortening in the simplest form of fast saturable absorber, and then follow this with the slow-absorber situation.

Pulse Shortening in Fast Saturable Absorbers

For the simplest case of a fast, homogeneously saturable, two-level absorber, illuminated by a beam with a uniform transverse intensity profile, the instantaneous input and output intensities can be related by the cw saturable amplifier equation derived in Section 7.7, namely,

$$\ln \frac{I_2(t)}{I_1(t)} + \frac{I_2(t) - I_1(t)}{I_{\text{sat}}} = \ln T_0, \quad (1)$$

where $T_0 \equiv \exp(-2\alpha_0 L)$ is the small-signal or unsaturated intensity transmission through the absorbing medium. For any given input pulseshape $I_1(t)$ that we send into this medium—for example, an input pulse that is gaussian in time—we can solve Equation 28.1 implicitly for the output pulseshape $I_2(t)$, and then evaluate both the intensity transmission at the pulse peak, and also the FWHM pulselength of this output pulse compared to the input pulse.

Figure 28.1 illustrates the resulting peak pulse intensity transmission and pulselength reduction for a gaussian input pulse after a *single* transit through a fast saturable absorber with a small-signal intensity transmission $T_0 = 10^{-2}$, plotted versus the peak input intensity of the input pulse. Obviously for peak input intensities near or a few times larger than the saturation intensity I_{sat} ,

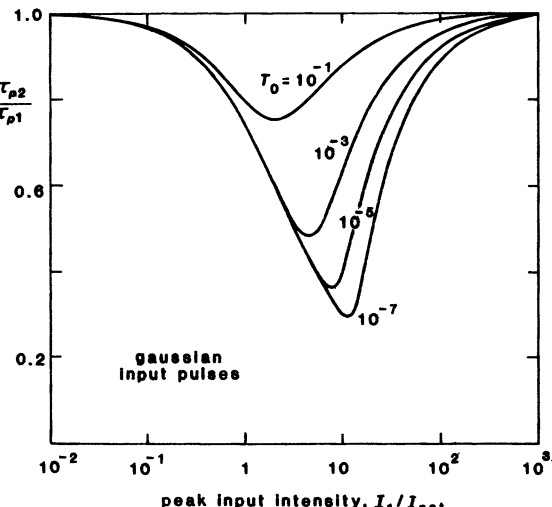


FIGURE 28.2
Pulse shortening as in
Figure 28.1 for a range of
different initial intensity
transmission values.

the pulse transmission rises fairly rapidly from T_0 up toward unity; while at the same time the pulselength of the transmitted pulse is reduced by a maximum ratio of ≈ 0.6 per transit. Note that this reduction factor is independent of the input pulselength, within the fast-absorber approximation that $T_1 \ll \tau_p$.

This pulselength reduction obviously occurs because the stronger central part of the pulse partially “burns through” the saturable absorber and is transmitted with less absorption, whereas the weaker leading and trailing edges of the pulse are more strongly absorbed. This reduction occurs, however, only over a limited range of input intensities: If the input pulse is too weak, no saturation and hence no pulse shortening occurs; whereas if the pulse is too strong, essentially all of the pulse burns through the absorber and again no shortening occurs.

Figure 28.2 shows this same fast-absorber gaussian-pulse reduction factor plotted versus input intensity for saturable absorber cells with different small-signal transmissions ranging from $T_0 = 10^{-1}$ down to $T_0 = 10^{-7}$. The pulselength reduction factor obviously increases from a reduction ratio of only ≈ 0.8 per pass for the 10% transmission cell to a reduction ratio approaching ≈ 0.3 per pass (but occurring at a somewhat higher peak input intensity) for the cell with 10^{-7} small-signal transmission.

These pulselength reduction factors, though calculated for the specific situation of a gaussian input pulse, remain nearly the same for almost any reasonable input pulseshape (other than square; cf. Problems). Figure 28.3 illustrates, for example, the very minor differences in pulse shortening versus peak input intensity between a gaussian pulse and a lorentzian pulse with the same input intensity and input FWHM pulselength, despite the broader peak and wider tails characteristic of the lorentzian situation.

The results just shown will be modified to some extent in practical situations. The transmission through the saturable absorbing medium may not saturate all the way up to unity at large input intensities, due to the effects of excited-state absorption, triplet formation, and similar factors; and the absorbing medium

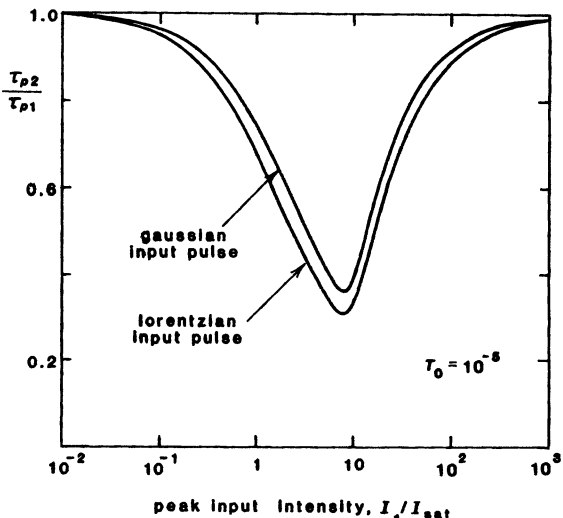


FIGURE 28.3
Pulse shortening versus input intensity in a fast saturable absorber for two different input pulse shapes.

may as a result need to be modeled by a three-level or even more complex rate-equation model. The optical pulses in real lasers will also have some form of finite transverse beam profile, so that the degree of saturation will vary across the transverse beam profile; and this will both modify the pulse shortening and also produce intensity-dependent changes in the beam profile, which will need to be taken into account along the remainder of the optical chain. And in many situations the pulselength τ_p may eventually become comparable to, or even shorter than, the population recovery time T_1 of the saturable absorber, as we mentioned in the preceding.

Pulse Shortening in Slow Saturable Absorbers

The opposite limiting situation, that of a very slow or energy-integrating saturable absorber with $T_1 \gg \tau_p$, is then the exact analog in absorption to the short-pulse saturable amplification we analyzed in Section 10.1; and we can use the same input-output relation we derived there, namely,

$$\frac{I_2(t)}{I_1(t)} = \frac{T_0 \exp[U_1(t)/U_{\text{sat}}]}{1 + T_0[\exp[U_1(t)/U_{\text{sat}}] - 1]}, \quad (2)$$

where T_0 is again the small-signal or unsaturated transmission; $U_{\text{sat}} \equiv I_{\text{sat}} T_1$ is the saturation energy; and $U_1(t) \equiv \int_{-\infty}^t I_1(t) dt$ is the integrated energy up to time t in the input pulse. It is comparatively simple in this situation also, therefore, to pick an arbitrary input pulsedshape and again evaluate the output pulse profile, the peak output pulse intensity transmission, and the output pulselength reduction ratio, all as functions of the small-signal transmission T_0 , the input pulsedshape, and the input pulse intensity.

Typical results from such calculations are not shown here, primarily because in nearly all situations they turn out to be very similar to the fast absorber results

already shown in Figures 28.1 to 28.3 that is, the pulselwidth reduction factors versus T_0 are very nearly the same, the weak dependence on input pulseshape is very similar, and the only major difference is that in general the pulselwidth reduction occurs at somewhat higher input intensities relative to the saturation intensity. (The significant factor in fact is the input pulse *energy*, and not the instantaneous input pulse intensity.)

The actual pulselwidth reduction mechanism for the slow absorber is, nonetheless, significantly different from the fast absorber. The primary mechanism in the slow-absorber situation is that the saturable medium absorbs or “eats away” the leading edge of the input pulse; but then, if there is sufficient energy in the input pulse, the medium becomes bleached part way through the pulse, so that the trailing edge of the pulse is transmitted more or less unchanged. We thus expect the output pulse in this situation to acquire an asymmetry in time, with a faster leading edge, and a more or less unchanged trailing edge.

It is also possible—though more difficult—to carry through similar input-output calculations for an arbitrary ratio of input pulselwidth τ_p to absorber lifetime T_1 . The general result of such calculations is that the amount of pulse shortening obtained at the optimum input intensity remains roughly the same, within a factor of 20% or 30%, as we go from a very fast absorber, with $T_1 \ll \tau_p$, to a very slow absorber with $T_1 \gg \tau_p$. The optimum input intensity, measured relative to I_{sat} , increases by a sizable amount, however, as the absorber changes from a fast instantaneous absorber to a slow integrating-type absorber.

Regenerative and External Single-Pass Pulse Shortening

The most important characteristic of saturable-absorber pulse shortening for use in passively mode-locked lasers is thus that a suitable saturable absorber can continue to shorten an optical pulse by more or less a fixed ratio on each successive pass, even when the pulse becomes very short; but this will occur only if the pulse energy can be reset to somewhere near the optimum energy on each successive pass. The pulse-shortening effects of an active modulator by contrast are most effective when the pulse is wide, and become much less effective as soon as the pulse becomes narrow compared to the sinusoidal period of the modulator. A saturable absorber cell is, in effect, a kind of nonlinear modulator whose modulation depth, or transmission curvature near the peak, is controlled by the optical pulse itself.

The saturable absorber pulse shortening effects described in this section, though most often employed inside passively mode-locked lasers, can also be used—at considerable cost in pulse energy—to shorten available mode-locked pulses still further in *external single-pass operation*. A single-pass absorber cell with $T_0 \leq 10^{-5}$ can, for example, reduce the width of a pulse to less than half its initial value in one pass, though at the cost of having only a few percent of the initial energy remaining in the output pulse. This technique also has the sometimes useful feature that it strips away any background energy or weak subsidiary pulses that may precede or follow the primary input pulse.

A more interesting approach, if suitable fast electro-optic switches are available, is to use a *regenerative pulse-shortening system*. In this approach the input pulse is switched into a laser cavity containing both a roughly balanced saturable absorber cell and a slowly saturating laser gain medium, and then, after a controlled number of round trips, is switched out again. The effective pulse compression obtained in this type of system can be both large and stable, and

the final output pulsedwidth can be controlled by varying the number of round trips in the regenerative cavity (cf. References).

REFERENCES

There are a great many publications in the laser literature on the general problem of pulse shortening in passing through saturable absorbers of different kinds, in long-pulse, Q -switched, and mode-locked lasers. For an early set of experiments studying this process in the picosecond time range, see A. Penzkofer, D. von der Linde, A. Laubereau, and W. Kaiser, "Generation of single picosecond and subpicosecond light pulses," *Appl. Phys. Lett.* **20**, 351-354 (May 1, 1972), along with the more detailed analysis by A. Penzkofer, "Generation of picosecond and subpicosecond light pulses with saturable absorbers," *Opto-electron.* **6**, 87-98 (January 1974).

For a more recent analysis which includes finite absorber lifetimes and also finite transverse spatial variations, see, for example, W. Rudolph and H. Weber, "Analysis of saturable absorbers, interacting with gaussian pulses," *Opt. Commun.* **34**, 491-496 (September 1980).

Another recent publication with good references to earlier work is W. Krause, "A pulse compression analysis for the fast saturable absorber of arbitrary small-signal transmittance," *Opt. Commun.* **48**, 47-52 (November 1, 1983).

Repetitive pulse compression and reamplification inside a regenerative laser cavity is well-demonstrated in J. E. Murray and D. J. Kuizenga, "Regenerative compression of laser pulses," *Appl. Phys. Lett.* **37**, 27-30 (July 1, 1980).

Problems for 28.1

1. *Pulse shortening in fast saturable absorbers.* Set up an analysis and computer program to reproduce the results given in this section for the shortening of gaussian input pulses passing through a fast saturable absorber; and explore in particular the pulse energy loss versus pulse time compression that we obtain operating at the input intensity for optimum pulse shortening in absorbers with different small signal transmissions T_0 .
 2. *Pulse shortening in slow saturable absorbers.* Repeat the previous problem considering instead the situation of a slow saturable absorber, i.e., an absorber which saturates on the integral of the input intensity rather than on the instantaneous input intensity.
 3. *Shortening of square input pulses.* An ideally square input pulse, with arbitrarily sharp leading and trailing edges, will be shortened about as well as any other pulseshape in a slow saturable absorber; but will not be shortened at all in a fast saturable absorber. Explain.
-

28.2 PASSIVE MODE LOCKING IN PULSED LASERS

In this section we will briefly review the passive mode-locking process as it occurs in high-power (and usually also high-gain) pulsed or flash-pumped or Q -switched

lasers, with the premier examples of this type of laser being flash-pumped solid-state lasers such as Nd:YAG, Nd:glass or ruby lasers, or flash-pumped organic dye lasers.

This type of laser is usually made up of the laser mirrors, the laser medium, and a thin saturable absorber cell which is normally placed in close contact with one of the cavity mirrors, although ring-cavity designs employing a thin Brewster angle cell somewhere within the ring are also becoming common. The saturable-absorbing medium in visible and near-infrared lasers is usually some kind of absorbing organic dye with a very short recovery time T_1 . Other kinds of saturable absorbers, including semiconducting materials and molecular gases, are also used in other lasers, especially at longer wavelengths.

This saturable absorbing material usually functions simultaneously as both the passive Q -switch and mode-locking material for the laser, although a separate electro-optic Q -switch may be used along with the passive saturable absorber in some situations.

Development of Pulsed Passive Mode Locking

The growth of laser oscillation and mode locking in this type of laser then generally develops in something like the following five stages:

(1) When the pumping pulse is first turned on, the population inversion builds up at a comparatively slow rate (typically tens to hundreds of microseconds), until the laser passes through a so-called "first threshold" at which the laser gain first equals the total losses due to the unsaturated absorber, the cavity output coupling, and all other internal cavity losses.

(2) At this point the circulating signal energy in the laser cavity begins to build up from a very weak initial noise or spontaneous-emission distribution such as we have described earlier, composed of a large number of axial modes with random initial amplitudes and phases. This kind of initial noise distribution is illustrated in the upper left plot in the computer simulation of Figure 28.4

This initial distribution can equally well be viewed as a random assortment of initial narrow spikes or noise pulses, of randomly varying heights and widths. Since the initial noise emission will have an effective bandwidth essentially the same as the atomic gain profile, the shortest of these initial noise spikes will have a pulselwidth roughly given by the inverse of the atomic linewidth $\Delta\omega_a$.

(3) For some time this initial noise distribution will continue to build up from its very low initial intensity level, while at the same time the individual noise spikes will begin to broaden and to smooth out because of the spectral narrowing produced by repeated round trips through the finite bandpass of the gain medium. This is illustrated in the left-hand column of Figure 28.4. The population inversion and gain may also continue to increase, usually rather slowly, during this initial build-up period.

(4) At some point, under suitable conditions, the laser will reach a "second threshold," similar to the Q -switched situation of Section 26.3, beyond which some one single preferred noise spike within the round trip becomes powerful enough to begin burning its way through the saturable absorber on succeeding round trips. This pulse will then begin to grow more rapidly than its less fortunate surrounding comrades, so that it begins to grow up out of the general noise background, as illustrated by the right-hand three plots in the computer simulation of Figure 28.4.

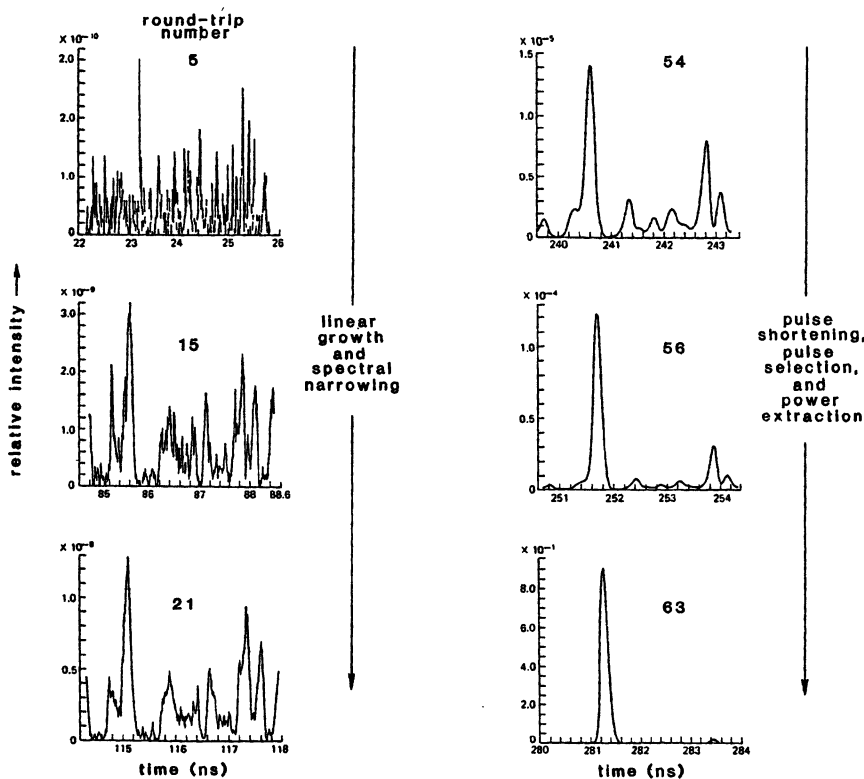


FIGURE 28.4

Computer simulation of the evolution of a single mode-locked pulse from the initial noise spikes in a passively mode-locked laser. Each plot shows the laser output intensity versus time during one round-trip cavity period; successive plots correspond to the output during successively later round trips. Note changes in the vertical intensity scale. (From J. A. Fleck, Jr., *Phys. Rev. B* 1, 84–100, January 1970.)

The streak camera measurements of Figure 28.5, showing the output from a passively mode-locked and *Q*-switched solid-state laser over several 100-nanosecond-duration time intervals before and during the *Q*-switched peak, give some experimental confirmation of these same effects.

(5) Finally, this one preferred pulse will continue to build up in intensity on succeeding round trips, until it reaches a power level such that it extracts all the energy still stored in the laser gain medium in what is essentially a *Q*-switched burst of mode-locked pulses, lasting typically some 10 to 20 or 30 round trips, depending on the exact type of laser. Such a typical *Q*-switched and mode-locked output burst is shown in Figure 28.6. In this experiment, one output pulse near the peak has been selected and switched out using an external single-pulse selector, and this pulse has then been sent into the same photodetector through a different delay path.

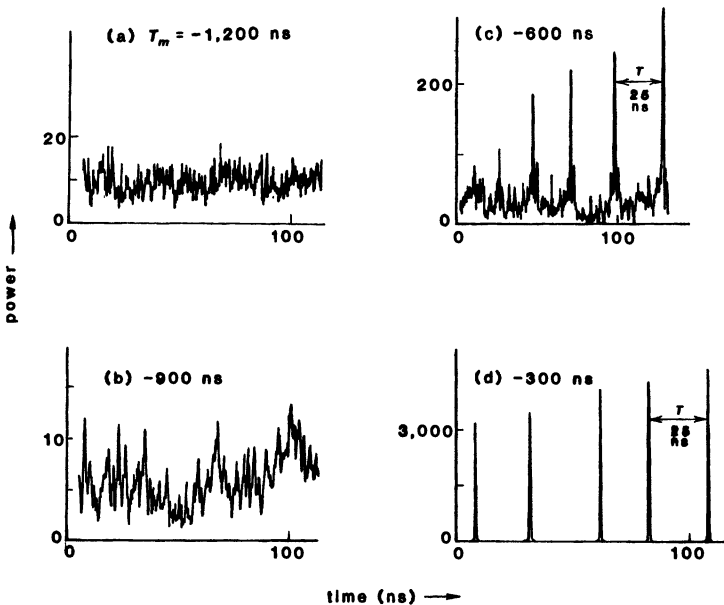
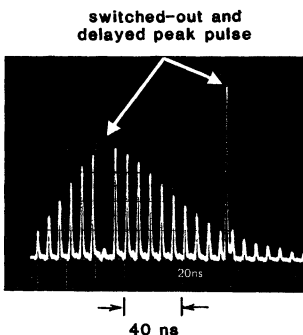


FIGURE 28.5
 Streak camera measurements showing transient build-up of mode locking in a Nd:glass ring laser using #3995 dye in nitrobenzene, over intervals several round trips long at various measurement times T_m before the peak of the Q -switched output burst. (a) and (b): Noise-like signal in the cavity during early linear build-up period. (c) and (d): Emergence and evolution of a single short pulse. (From Chekalin et al.)

FIGURE 28.6
 Output pulse train from a passively mode-locked and Q -switched laser, with one pulse switched out using a single-pulse selector.



Conditions for Good Quality Pulsed Mode Locking

The above is an idealized description of how passive mode locking should work. One desirable condition for good mode locking and pulse generation is

clearly that the saturable absorber should have a short enough lifetime to recover its absorption between individual noise bursts, so that the preferred pulse does not bring several closely following noise spikes up along with it. Another important and somewhat complex condition is that just about the time the preferred pulse begins to burn its way through the saturable absorber, the laser gain should also begin to become at least partly saturated, so that whereas the preferred pulse can continue to grow, all the other weaker pulses will not only grow more slowly, but in fact will begin to decrease on subsequent round trips, leaving only the one strongest pulse. This condition is generally similar to the "second threshold" condition discussed in Section 26.3 in connection with passively Q -switched lasers, but with the more complicated interpretation that only one preferred noise spike should reach this second threshold condition and all the other spikes should not.

Note also that from our discussion in the previous section, a pulse passing through a saturable absorber will be significantly shortened only if it falls in an intensity range roughly a decade or so wide where the pulse compression effects are strongest. We can expect, therefore, that the preferred pulse will be shortened by some ratio in the range from perhaps 0.3 to 0.8 on each round trip during that group of round trips when it builds up through the saturation intensity range of the absorber; but that once the pulse intensity rises beyond this intensity range, it will not be much further shortened on subsequent round trips. (In fact it may be somewhat broadened by the finite bandpass of the laser amplification.) We would thus like the preferred pulse to make as many round trips as possible with its intensity remaining in this pulse-shortening intensity range.

Predicting the Passively Mode-Locked Pulsewidth

The final output pulsewidth will thus depend in a complex way on the width of the initial noise spikes as determined by the atomic linewidth; on the degree of pulsewidth *broadening* that occurs during the initial growth stage following the first threshold; and on the degree of saturable-absorber *narrowing* that occurs during the laser stages around and following the second threshold.

The duration and nature of both of these growth periods will depend in turn in a complex fashion on the pumping rate, the cavity losses, the nature and strength of the saturable absorber, the saturation characteristics of the laser gain, and so forth. In most situations good mode-locked performance, or indeed any mode locking at all, can be obtained only by careful adjustment of all of the laser parameters, including limiting the laser pumping to only a small fractional region above oscillation threshold. Passive mode locking is thus generally a more difficult subject than active mode locking, both experimentally and theoretically; and no simple analytical expressions for passively mode-locked pulsewidth are generally to be had.

Statistical Theories of Passive Mode Locking

Another important point is that mode-locking behavior in the pulsed saturable-absorber case is essentially *statistical* in nature. There are unavoidable statistical variations in the initial noise distribution in the laser cavity, and hence there will be statistical variations in the output pulsewidth and pulse intensity from shot to shot of the same laser. Fortunately, due to the nonlinear limiting characteristics of the laser system, the fluctuations in the output pulse

parameters will generally be less than the completely random nature of the initial conditions.

However, there will inevitably be a certain fraction of shots in any simple passively mode-locked laser in which two (or more) of the initial noise spikes have nearly the same initial advantage, so that the resulting output pulse is either accompanied by one or more somewhat weaker secondary pulses with random time locations ("satellite pulses"); or there are two pulses of essentially equal amplitude and random spacing ("double pulsing"); or in a few situations the laser simply fails to mode-lock at all, and all of the energy comes out in a longer and weaker noise burst ("mis-firing").

The practical experience is that even a well-engineered passively mode-locked solid-state laser may generate a good mode-locked output pulse on only perhaps $\approx 80\%$ of the laser shots. The majority of applications which employ such lasers thus incorporate circuitry which can detect the unsatisfactory shots and reject the experimental data produced by those shots.

Active-passive mode locking, in which we combine the synchronizing and initial pulse-organizing capabilities of an active modulator with the powerful pulse-shortening capabilities of a saturable absorber cell, is one effective method for greatly improving the statistical characteristics of such lasers. Another effective approach is the use of a *stable regenerative laser amplifier*, essentially a passively mode-locked oscillator in which the saturable absorber loss is large enough to keep the laser from achieving self-initiated oscillation under normal pumping. A weak but reasonably well-formed pulse from a second laser is then injected into this laser, with enough intensity to burn partly through the strong saturable absorber on its initial round trip. This pulse will then continue to circulate and build up in intensity so as to dump the energy in the regenerative laser medium. At the same time, because the absorber in this situation can be considerably stronger than is usual in passively mode-locked lasers, a much greater degree of pulse shortening can be achieved.

"Experimental" Results

Given the very short time scales combined with very wide dynamic ranges that are involved in passively mode-locked lasers, experimental studies of the detailed working of such lasers are difficult. Figure 28.7 shows instead a few examples from some very illuminating computer "experiments" closely simulating a passively mode-locked solid-state laser that have been carried out at the University of Graz in Austria.

In these figures, each horizontal slice running from upper left to lower right represents the laser intensity, plotted on a highly compressed logarithmic vertical scale, versus time during one round trip lasting a few ns in the laser cavity. Successive slices from front to back then represent regularly spaced samples from the some 1,000 or more successive round trips during a single mode-locked laser shot. To obtain these plots, laser parameters matching a typical real laser, including a suitable time-varying pump rate, were assumed; and the detailed equations of motion for the cavity fields and the gain medium were solved by an extensive computer simulation. In particular, randomly generated signals corresponding to spontaneous emission were fed into the simulation, not only at the beginning, but continually through the calculations, so that each shot was an independent statistical event.

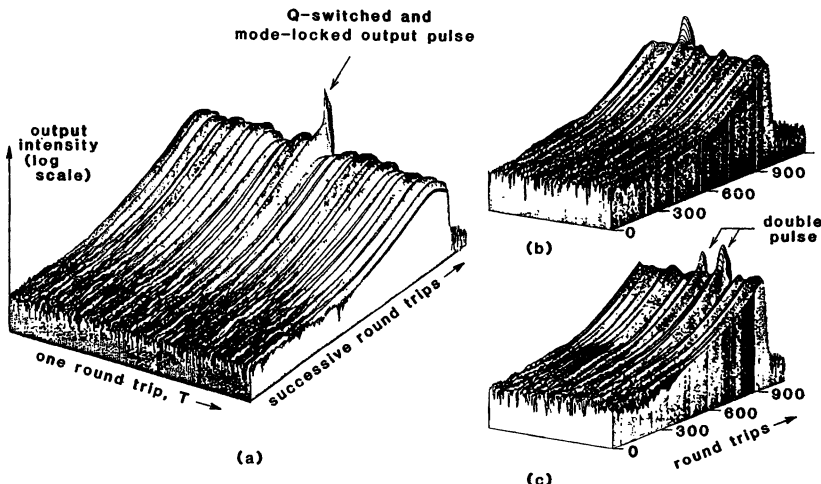


FIGURE 28.7

Detailed numerical simulations of pulse evolution in a passively mode-locked Nd:YAG laser. In each plot, each transverse "slice" from left to right represents one round-trip time; successive slices from front to back represent successive round trips; and the vertical scale represents laser output intensity on a highly compressed logarithmic scale. A realistic time-varying pump intensity, spontaneous emission noise, saturable absorber, cavity characteristics, and saturable gain have all been included in the simulation. (a) Typical result showing good single-pulse mode-locked performance. (b) Another good mode-locked example. (c) Example showing random occurrence of double pulsing. Illustrations courtesy of Professor F. R. Aussenegg, Universität Graz, Austria.

We can clearly see in these calculations the long initial region consisting essentially of noise, while the gain builds up; then the amplitude growth and substantial smoothing of this noise by bandwidth narrowing in the gain medium; then, in a good situation, the sudden emergence of a single mode-locked pulse which is much narrower and has much greater peak intensity than all the rest of the background; and then the very rapid drop in intensity back to noise following the *Q*-switched output burst. Figure 28.7(c) also shows, however, a randomly occurring "double-pulse" event, in which two nearly equal-amplitude pulses both grow and come out during the output period.

Nonlinear and Dispersive Effects

The instantaneous optical intensities inside typical flash-pumped and passively mode-locked lasers at the peak of the mode-locked pulse can easily exceed the intensity level of 1 to 10 GW/cm² at which nonlinear optical Kerr effects become significant in nearly all common optical materials, as described in an earlier chapter on nonlinear pulse propagation. As a result, in many such passively mode-locked lasers the recirculating mode-locked pulse acquires a large and growing *self-phase modulation* during the several tens of round trips it makes at the peak of the *Q*-switched burst.

This self-phase modulation will not at first change the intensity profile of the pulse in time; but it will produce a very large *spectral broadening* in frequency, which will increase rapidly on each successive round trip during the output burst. This nonlinear spectral broadening, or self-induced frequency chirp, will then interact with the dispersive propagation characteristics of the media inside the laser cavity to produce a large and growing amount of irregular amplitude substructure within the mode-locked pulse envelope.

The net result is that although a mode-locked pulse selected from one of the low-intensity round trips early in the output burst may be a relatively clean and near transform-limited pulse, a pulse selected near or after the peak of the burst may have developed a much larger spectral width and also a much larger time-bandwidth product, indicating that a large amount of phase and also amplitude substructure has developed within the pulse. These effects, if strong enough, may even distort the envelope profile of the output burst itself, in those situations where the pulse spectrum becomes wide enough that it can no longer be fully amplified by the finite bandwidth of the laser medium.

At about the same intensity level where self-phase modulation begins, there may also simultaneously appear *self-focusing* effects, which can interact with the focusing properties of the laser cavity to distort the transverse width and beam profile of the recirculating pulse. These self-focusing effects may intensify the self-phase modulation effects. There appears to be no simple way to avoid these problems in high peak power mode-locked lasers, other than keeping the instantaneous intensity level inside the laser just below the (rather sharply defined) level at which these effects become significant.

REFERENCES

The basic concepts involved in saturable absorber mode locking also appear in essentially the same form in much earlier electronic devices, though expressed in different jargon. See, for example, C. C. Cutler, "The regenerative pulse generator," *Proc. IRE* **43**, 140 (February 1955); W. A. Edson, "Nonlinear effects in broadband delay type feedback systems," *Proceedings of the Symposium on Nonlinear Circuit Analysis* (Polytechnic Press, Brooklyn, 1956), pp. 41-53; and V. Met, "On the regenerative pulse generator," *Proc. IRE* **48**, 363 (March 1960).

For detailed descriptions of the pulsed mode-locking process in much the same spirit as in this section, see, for example, P. G. Kryukov and V. S. Letokhov, "Fluctuation mechanism of ultrashort pulse generation by laser with saturable absorber," *IEEE J. Quantum Electron.* **QE-8**, 766-782 (October 1972); or S. V. Chekalin, P. G. Kriukov, Yu. A. Matveetz, and O. B. Shatberashvili, "The process of formation of ultrashort laser pulses," *Opto-electron.* **6**, 249-261 (April 15, 1981), from which Figure 28.6 is taken.

Instructive computer simulations of pulsed passively mode-locked lasers have been carried out by J. A. Fleck, Jr., in "Mode-locked pulse generation in passively switched lasers," *Appl. Phys. Lett.* **12**, 178-181 (March 1, 1968); and in "Ultrashort-pulse generation by *Q*-switched lasers," *Phys. Rev. B* **1**, 84-100 (January 1, 1970), from which Figure 28.4 is taken.

The statistical approach to passive mode locking is also explored by R. Wilbrandt and H. Weber, "Fluctuations in mode-locking threshold due to statistics of spontaneous emission," *IEEE J. Quantum Electron.* **QE-11**, 186-190 (May 1975).

For a practical description of a representative well-engineered solid-state mode-locked laser, see L. S. Goldberg, P. E. Schoen, and M. J. Maronne, "Repetitively pulsed mode-locked Nd:phosphate glass laser oscillator-amplifier system," *Appl. Opt.* **21**, 1474-1477 (April 15 1982).

Some observations seem to show that the statistical probability of obtaining good single-pulse operation in a passively mode-locked laser can be considerably deteriorated by reflection of even a very small fraction ($\leq 10^{-4}$) of the laser output back into the laser cavity, e.g., from external measuring apparatus. See, for example, F. R. Aussenegg, A. Leitner, and M. E. Lippitsch, "Observation of the influence of external feedback on passive mode-locking," *Opt. Commun.* **31**, 231-232 (November 1979).

A further extension of the idea of stable regenerative pulse compression is described in C. H. Brito Cruz, E. De Martini, H. L. Fragnito, and E. Palance, "Picosecond pulse generation by intracavity nonlinear compression in self-injected Nd:YAG laser," *Opt. Commun.* **40**, 298-301 (January 15, 1982).

Successful use of an intracavity "anti-etalon" (an etalon with its transmission minimum tuned to line center) to broaden the effective linewidth in a passively mode-locked laser is described by H. Graener and A. Laubereau, "Shorter and bandwidth-limited Nd:YAG laser pulses," *Opt. Commun.* **37**, 138-142 (April 15 1981).

Active-passive mode locking is described by W. Seka and J. Bunkenburg, "Active-passive mode-locked oscillators at 1.054 μm ," *J. Appl. Phys.* **49**, 2277-2280 (April 1978).

28.3 PASSIVE MODE LOCKING IN CW LASERS

Passive mode locking in pulsed lasers is an important and widely used technique. A second and equally important application of passive mode locking occurs in a rather small set of *continuous-wave* or *cw* lasers, particularly cw mode-locked organic dye lasers and cw mode-locked semiconductor lasers, in which it is possible to generate the shortest optical pulses yet known.

Figure 28.8 shows, for example, a typical layout for a cw mode-locked linear-cavity dye laser pumped by an argon-ion laser. The cavity mode is designed to produce a sharp focal spot or waist with typical diameter $\approx 20 \mu\text{m}$ at both the saturable absorber and the gain medium, in order to produce the high intensities required for saturation in typical organic dyes. The Rhodamine 6G laser medium and the DODCI saturable absorber dye are both contained in thin flowing dye cells, or more commonly in high-speed free-flow jet sheets, in order to prevent the dye from being instantly destroyed by the high optical-power densities at the two focal spots. In other variants of this type of laser the gain medium and the saturable absorber may be combined into a single stream; or the pump laser may be some other form of cw or mode-locked ion laser or a cw mode-locked and frequency-doubled Nd:YAG laser; or the dye laser cavity may be a ring rather than standing-wave cavity, as illustrated in an earlier section on ring lasers.

The theory of passive mode locking in this kind of cw laser system is again rather complex, and we will give in this section only a brief overview of the principal mechanisms involved, and the analytical approach that can be used to describe them.

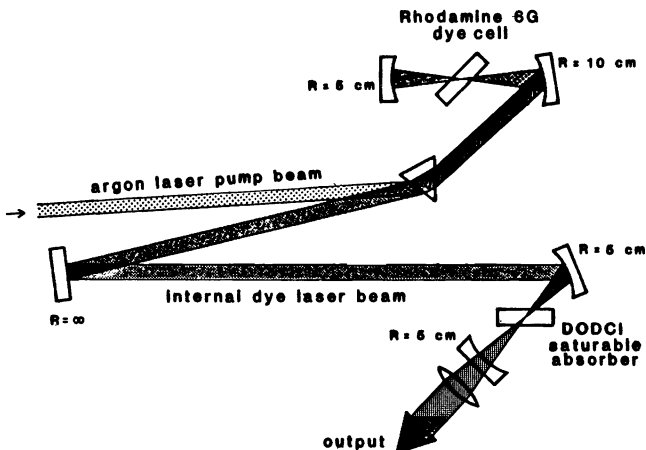


FIGURE 28.8

Typical layout for a cw passively mode-locked linear-cavity dye laser pumped by a cw argon-ion laser.

Description of CW Passive Mode Locking

The mode-locked pulsedwidths in these cw passively mode-locked lasers can become shorter than 100 femtoseconds ($\equiv 0.1$ ps), or much shorter than the recovery time of the saturable absorber medium, so that the theory of slow saturable absorbers is relevant. At the same time, good cw mode locking seems to be limited to those lasers in which the repumping or recovery time for the gain medium is comparable to, or not too much longer than, the round-trip time in the laser cavity, so that at least some gain saturation can also occur during the passage of a single pulse.

Passive cw mode locking has been obtained, for example, in cw organic dye lasers, semiconductor injection diode lasers, and cw CO_2 lasers, all of which meet this condition; but not in cw Nd:YAG lasers, where gain saturation occurs only through the integrated effect of a large number of pulse round trips. The cw mode-locked pulsedwidths are then still very short compared to the recovery time for the gain medium; and so the usual conditions for good cw saturable-absorber mode locking correspond to both a slow saturable absorber and also a slow saturable gain medium.

A simple picture of cw passive mode locking can then be outlined as follows. For simplicity think of the saturable absorber and the gain medium as being combined at a single plane in the laser cavity, and consider the net change in transmission and in pulsedshape as the circulating pulse passes through this plane. For good cw mode locking, at the instant just before the circulating pulse passes through this plane the initial loss value in the saturable absorber, plus the linear cavity losses, must be greater than the initial gain value, so that the leading edge of the pulse sees a net loss and is attenuated, as shown in Figure 28.9. (Note that the initial gain and loss values just before the pulse passage will in general *not* be the small-signal or totally unsaturated gain and loss values; rather they will be partially saturated values that are present as a result of the action of the

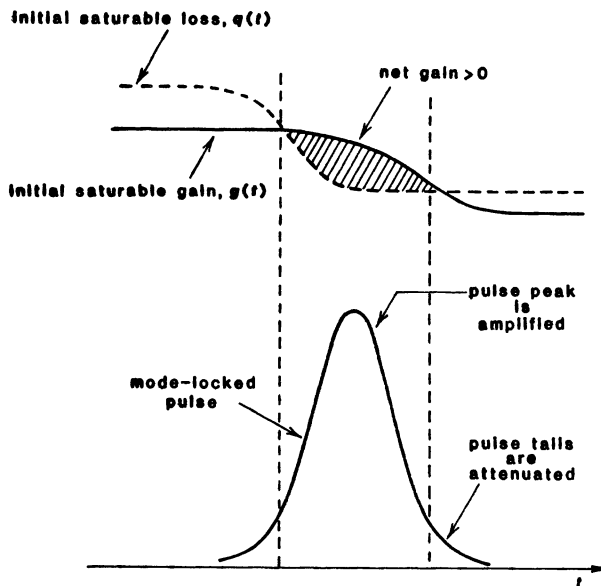


FIGURE 28.9
Gain and absorber saturation on each pass in a cw mode-locked laser.

last preceding pulse, combined with whatever recovery has occurred since the last preceding pulse.)

The optical pulse must then have sufficient energy to saturate the saturable absorption down so that it drops below the initial gain level at some time during the leading edge of the pulse, as shown in Figure 28.9. It is equally essential, however, that the pulse also be able, at a slightly later time during the pulse, to saturate the gain medium also so that the gain again falls below the absorption value during the trailing edge of the pulse.

Only the central portion of the pulse will then see a net energy gain, as shown in Figure 28.9. Net attenuation on both edges of the pulse, leading and trailing, produced by partial saturation of both absorption and gain, seems to be essential (or at least very highly desirable) for the development of stable cw steady-state mode-locking, and for continued compression of the pulselwidth on successive round trips.

To obtain steady-state mode locking, both the partially saturated absorption and gain must then recover back up to their initial values during the round-trip time before the same pulse comes around again. Passive mode locking in a cw laser thus depends on a delicate interplay between the pulse energy, the pumping rate, the cavity losses, the initial values and saturation energies of both the saturable absorption and the gain, and the recovery times for both of these quantities relative to the mode-locked pulse interval. The general observation seems to be that the necessary conditions for good cw mode locking can be met in only a few laser systems, and then only with careful adjustment of the experimental parameters, and usually only for small ranges above the laser threshold pumping value.

Analytical Formulation for CW Mode Locking

A simplified analytical formulation for this type of mode locking has been developed in a series of papers by H. A. Haus (see References). Without reproducing this entire analysis we can develop some useful concepts from it as follows.

Suppose the circulating pulse inside the cavity is described by a signal amplitude $\mathcal{E}(t) = \text{Re } \tilde{E}(t) e^{j\omega_0 t}$ with a Fourier transform $\tilde{E}(\omega)$, so that $\tilde{E}(t)$ is the complex envelope of the pulse with the carrier frequency ω_0 extracted out. We can also normalize these quantities so that $I(t) = |\tilde{E}(t)|^2$ is the instantaneous intensity in the circulating pulse.

We then suppose that in any reasonable cavity the frequency-dependent round-trip transfer function can be approximated by the form

$$\tilde{E}'(\omega) = \tilde{E}(\omega) \times \exp \left[-a_0 - j \frac{a_1}{\omega_c} (\omega - \omega_0) - \frac{1}{\omega_c^2} (\omega - \omega_0)^2 \right], \quad (3)$$

where a_0 represents the linear round-trip loss coefficient (i.e., $a_0 \equiv \alpha_0 p$); the $-ja_1(\omega - \omega_0)/\omega_c$ term represents any linear dispersion or time-delay effects present in the cavity, over and above the simple round-trip time T ; and the $-(\omega - \omega_0)^2/\omega_c^2$ term is the quadratic approximation about line center for whichever bandwidth-limiting effect is most important in the laser cavity.

If the finite linewidth of the laser gain medium itself is the most significant bandwidth-limiting quantity, then this $-(\omega - \omega_0)^2/\omega_c^2$ term will be simply the $-(4\alpha_m p_m / \Delta\omega_a^2) \times (\omega - \omega_a)^2$ term that we introduced in the previous chapter. In most cw mode-locked dye lasers, however, the atomic linewidth $\Delta\omega_a$ is extremely wide; and the $-(\omega - \omega_0)^2/\omega_c^2$ term may represent instead the quadratic variation about the peak transmission for some sort of intracavity etalon inside the mode-locked laser.

Whatever may be the cause of these dispersive and bandwidth-limiting effects, if we assume that their net effect on the pulse in one round trip—that is, the net attenuation, net time-delay, and net bandwidth narrowing—are all small, then we can simplify Equation 28.3 to

$$\tilde{E}'(\omega) \approx \tilde{E}(\omega) \times \left[1 - a_0 - j \frac{a_1}{\omega_c} (\omega - \omega_0) - \frac{1}{\omega_c^2} (\omega - \omega_0)^2 \right]. \quad (4)$$

But from Fourier transform theory we can replace multiplication by $j\omega$ in the frequency domain by differentiation by d/dt in the time domain, and similarly multiplication by $-\omega^2$ in frequency becomes d^2/dt^2 in time. Hence, the net change in the pulse envelope $\tilde{E}(t)$ due to the cavity loss and the linear and quadratic terms can be written as

$$\tilde{E}'(t) \approx \left[1 - a_0 - \frac{a_1}{\omega_c} \frac{d}{dt} + \frac{1}{\omega_c^2} \frac{d^2}{dt^2} \right] \tilde{E}(t). \quad (5)$$

We see once again, as also in earlier chapters on pulse propagation, that bandwidth limiting, which narrows the spectrum in the frequency domain, appears as a second-derivative or diffusion term which inherently broadens the pulse in the time domain.

We then assume that the cavity will also contain saturable (and thus time-varying) gain and loss coefficients, which we write as $g(t) \equiv \alpha_m(t)p_m$ for the saturable gain medium, and as $q(t) \equiv \alpha_a(t)p_a$ for the saturable absorber. If we also assume that the net effect of these factors on the pulse in one round trip is

small (e.g., not more than 20% change per round trip), then we can simply add these time-varying gain and loss effects to the linear loss term a_0 in Equation 28.5 to obtain

$$\tilde{E}'(t) = \left[1 + g(t) - q(t) - a_0 - \frac{a_1}{\omega_c} \frac{d}{dt} + \frac{1}{\omega_c^2} \frac{d^2}{dt^2} \right] \tilde{E}(t) \quad (6)$$

for the net change in one round trip.

Cavity Differential Equation

If we then seek a steady-state or self-consistent solution for the cw mode-locked pulse, we can argue that the net change in the pulse envelope $\tilde{E}(t)$ in one round trip can be at most a small time shift, by an amount $\delta T \ll \tau_p$. The physical interpretation of this time shift is that the round-trip time of flight for the steady-state mode-locked pulse may be slightly different than the cavity round-trip time, by an amount small compared to pulselwidth itself, as a result of the time-varying gain and loss effects $g(t)$ and $q(t)$.

The self-consistency condition for a steady-state pulse mode-locked pulse can then be written as $\tilde{E}'(t) \approx \tilde{E}(t) + (d\tilde{E}/dt) \times \delta T$; and so, from the arguments given in the preceding, the steady-state pulseshape must be a solution of the differential equation

$$\frac{1}{\omega_c^2} \frac{d^2 \tilde{E}}{dt^2} - \left(\frac{a_1}{\omega_c} + \delta T \right) \frac{d\tilde{E}}{dt} + [g(t) - q(t) - a_0] \tilde{E}(t) = 0 \quad (7)$$

with suitably self-consistent forms for the saturable gain $g(t)$ and loss $q(t)$.

Saturable Gain and Loss Terms

We then assume that both $g(t)$ for the gain medium and $q(t)$ for the saturable absorber are produced by appropriate population differences $\Delta N_m(t)$ and $\Delta N_a(t)$, which are in turn governed by simple rate equations of the general form

$$\frac{dq(t)}{dt} = -\frac{1}{T_1} \left[\frac{I(t)}{I_{\text{sat}}} q(t) - [q_1(t) - q_0] \right], \quad (8)$$

and similarly for $g(t)$, where in each situation I_{sat} is the saturation intensity and T_1 the recovery time for the respective medium back to its small-signal or totally unsaturated value of q_0 or g_0 .

We can then analyze either the fast or slow limiting situations within the same analytical framework. If we assume a *fast* saturable absorber, and also a small degree of saturation, then we can write the saturable loss $q(t)$ to first order in the form

$$q(t) \approx q_0 [1 - I(t)/I_{\text{sat}}], \quad I/I_{\text{sat}} \ll 1, \quad (9)$$

with a similar expression for $g(t)$. Alternatively, we can assume a *slow* saturable absorber, for which the saturation behavior will be given by

$$\int_{q_0}^q \frac{1}{q} \frac{dq}{dt} = -\frac{1}{T_1 I_{\text{sat}}} \int_{-\infty}^t I(t) dt \equiv -\frac{U(t)}{U_{\text{sat}}}, \quad (10)$$

and this can then be expanded to second order in the pulse energy $U(t)$, in order to obtain

$$\begin{aligned} q(t) &= q_0 e^{-U(t)/U_{\text{sat}}} \\ &\approx q_0 \left[1 - \frac{U(t)}{U_{\text{sat}}} + \frac{1}{2} \left(\frac{U(t)}{U_{\text{sat}}} \right)^2 \right]. \end{aligned} \quad (11)$$

Again there will also be an exactly analogous solution for the gain $g(t)$.

It then turns out that a formal solution to the basic cavity differential equation (28.7), using either the slow or fast saturation forms as approximated here, can be written as a *hyperbolic secant function* in the form

$$\tilde{E}(t) = E_0 \operatorname{sech}(t/\tau_p) \equiv \frac{E_0}{\cosh(t/\tau_p)}, \quad (12)$$

or

$$I(t) = I_0 \operatorname{sech}^2(t/\tau_p) \equiv \frac{I_0}{\cosh^2(t/\tau_p)}. \quad (13)$$

(This kind of hyperbolic secant, or sech, function turns out to be a useful function in several other areas of laser theory as well.) Note that the parameter τ_p in this function is not the FWHM pulselength, but is related to the FWHM pulselength for the hyperbolic secant squared or $\operatorname{sech}^2(t/\tau_p)$ function by $\tau(\text{FWHM}) \approx 1.76 \times \tau_p$.

This $\operatorname{sech}(t/\tau_p)$ solution, although it can satisfy the relations in Equation 28.7 through 28.11 for $\tilde{E}(t)$, $g(t)$ and $q(t)$, does not immediately yield a unique expression for the pulselength parameter τ_p . Instead, we obtain a set of algebraic relations which interrelate the pulselength parameter τ_p , the peak pulse intensity I_0 , and the pulse time-delay δT in terms of the various parameters of the cavity, the saturable absorber, and the gain medium. In addition, we must use the usual rate-equation solutions, in conjunction with the laser pumping rate, to solve for the recovery behavior of the gain and loss between each successive pulse passage.

All of these relations taken in conjunction then give one or in some cases several different self-consistent solutions in the sech form. We must then investigate further to find out if each (or any) of these solutions: (a) is a stable, self-consistent, and steady-state solution, as outlined in the preceding; (b) is further stable against slow, large-scale relaxation oscillations in the laser output; and (c) is also capable of self-starting (from noise or initial fluctuations) when the laser is first turned on in some physically reasonable manner. We will not attempt to explore the details of any of these solutions in this section; but will simply say that the usual outcome seems to be that all of these conditions can be satisfied simultaneously only within a rather limited range of laser parameters, which seem to be available in only a limited set of lasers. This set, however, fortunately includes the very important cw mode-locked dye laser; the semiconductor diode laser; and a few other less widely used examples.

Experimental Results

Figure 28.10 shows one example of a measured autocorrelation function which provides partial information about the pulseshape for a cw mode-locked

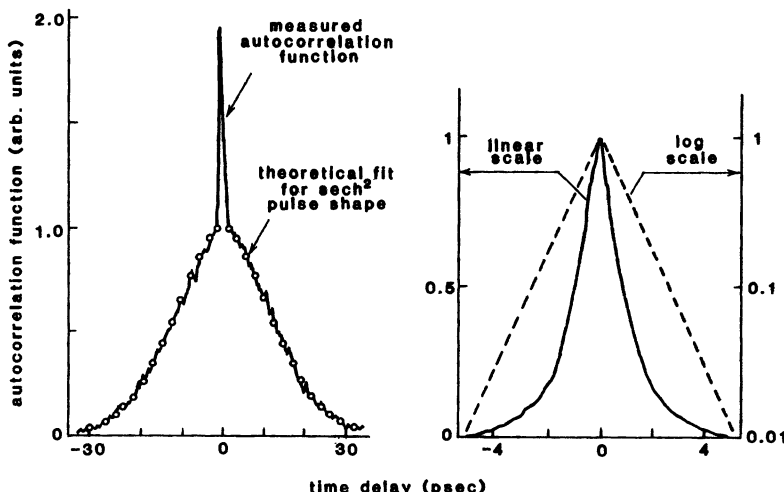


FIGURE 28.10

Measured autocorrelation function for a cw mode-locked dye laser operating both well above threshold (left-hand trace) and very close to threshold (right-hand trace).

laser operating both some distance above oscillation threshold, and also very close to threshold.

The left-hand autocorrelation trace, for operation well above threshold, can obviously be fit very accurately by an assumed hyperbolic secant pulseshape with a pulsewidth parameter $\tau_p = 9.8$ ps, corresponding to a FWHM pulsewidth of 17.6 ps, together with a central correlation spike which indicates the presence of very much faster amplitude substructure within the sech^2 pulse. This substructure may indicate that the dye laser is in reality generating several more or less independent but overlapping hyperbolic secant pulses, with each pulse having a different center frequency located at some different point across the very broad amplification bandwidth of the dye laser.

The right-hand trace in Figure 28.10 shows a significantly sharper pulse that is generated by the same laser operating much closer to threshold. The pulse shape in this situation is clearly no longer hyperbolic secant. It can be tentatively matched, however, by an assymmetric two-sided exponential function; and such a function can in turn be matched against various extensions of the preceding analysis which include higher-order terms in the saturation expansions for $q(t)$ and $g(t)$.

Synchronously Pumped Mode Locking

The round-trip transit time in a cw mode-locked dye laser will typically be in the range from 5 to 12 ns, whereas the upper-state lifetime for the dye gain medium may be more like 3 to 5 ns. Pumping this type of passively mode-locked laser with a cw pump source is then relatively inefficient, since many of the upper-level atoms pumped up during the early part of each round-trip period relax back down and are lost before the next mode-locked pulse comes around.

A reasonably simple solution to this problem can be obtained by actively mode-locking the pumping source, using exactly the same repetition rate as the passively mode-locked laser, so that a short but intense pulse of pumping light arrives at the dye cell immediately before, or just as, the mode-locked pulse arrives to use up the inversion which this pumping pulse will provide. (The circulating pulse in the passively mode-locked laser will synchronize itself more or less automatically to the arriving pump pulses.)

This type of *synchronously pumped mode locking* can in fact be used in many situations to obtain shortened pulses even without any saturable absorber in the pumped laser cavity. Pump pulses with pulsedwidths in the 40 to 300 ps range, for example, can produce synchronously mode-locked pulses with widths in the 1 to 30 ps range from a considerable variety of dye lasers. As a practical matter, the average power obtained from a cw ion laser is typically reduced by 50% or more when the laser is actively mode-locked; but the increased efficiency with which is power can be used means that better mode-locked dye laser operation can still be obtained.

Synchronously pumped dye laser operation can be obtained, at least at present, from a wider range of dyes, and hence of visible and near-infrared wavelengths, than can cw-pumped saturable-absorber mode locking, for which only a few good dye laser and absorber combinations have been found. (The best saturable-absorber mode-locked lasers still give, however, significantly shorter pulses than the best purely synch-pumped situations.)

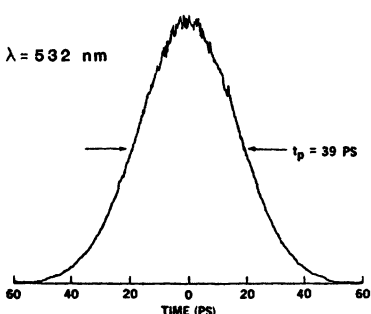
Synchronous Pumping with Nd:YAG Lasers

If a mode-locked Nd:YAG laser is used instead of an ion laser as the synchronous pump source, the mode-locked pumping pulses will be shorter; and the increase in peak power output produced by mode-locking the YAG laser makes it much easier to frequency double the 1.064 μm YAG output with good efficiency into the green at $\lambda = 532$ nm, a wavelength which is ideally suited for pumping many laser dyes. Figure 28.11 shows the measured autocorrelation functions of the accurately gaussian mode-locked and frequency-doubled 532 nm pulses with pulsedwidth of 39 ps that are obtained from a well-engineered cw-pumped Nd:YAG laser; the sech^2 pulses at $\lambda = 575$ nm with pulsedwidth ≈ 1.1 ps that are obtained by using these YAG pulses for pure synchronous pumping of a Rhodamine 6G dye laser; and the still shorter pulses, with pulsedwidths of ≈ 240 and ≈ 150 fs, that are obtained at $\lambda = 620$ nm by combined synchronous pumping and saturable absorber mode locking of this same system, using standing-wave and ring cavities, respectively.

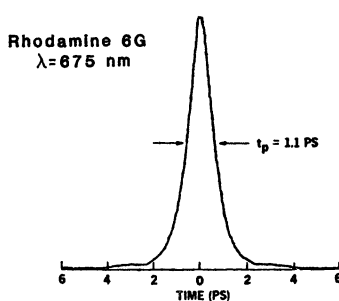
Mode-locked Nd:YAG lasers, which have greater simplicity, durability and power efficiency, as well as shorter mode-locked pulsedwidth, can thus replace ion lasers in many cw synch-pumped dye laser applications. (Flash-pumped and mode-locked YAG lasers can also be used as pump sources for transient *synchronously pumped dye lasers*, thereby producing higher energies and wider tuning ranges but also generally wider pulses.)

The primary practical difficulty with cw synchronously pumped lasers is the necessity for extremely precise synchronization between the round-trip times or pulse repetition rates in the two lasers if the shortest pulses are to be obtained. Length changes in either cavity of a few microns or less around the optimum synchronization point are found to produce rapid deterioration in the short-pulse characteristics. The theoretical treatment of synchronous pumping, with

(a) Nd:YAG laser pump pulses



(b) synchronously pumped dye laser



(c) synchronous pumping plus saturable absorber

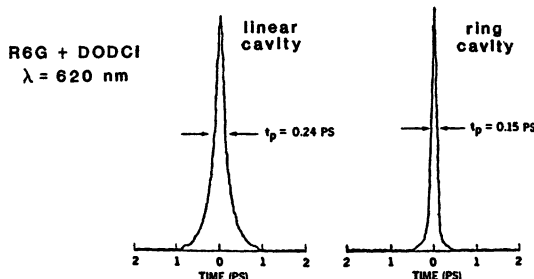


FIGURE 28.11

Autocorrelation traces of (a) cw mode-locked Nd:YAG laser pump source; (b) cw dye laser synchronously pumped with these pulses; and (c) same dye laser with saturable absorber added.

or without a combined saturable absorber, also has much the same complexity and difficulty as for cw passive mode locking in general; and there seem to be some discrepancies in the conclusions of published analyses (see References) even as to the direction in which the pulse characteristics should change as one tunes away from the optimum synchronization point.

Colliding Pulse Mode Locking

It has also been discovered in recent years that in cw mode-locked dye lasers, and perhaps in pulsed lasers as well, significantly shorter pulses can be obtained if the mode-locked cavity is arranged as a *ring* cavity, with pulses traveling in both directions around the ring, rather than as a linear or standing-wave cavity. If such a cavity is arranged as shown in Figure 28.12, with the dye jets for the gain medium and the saturable absorber separated by one-quarter of the round-trip path length, the stable mode of operation consists of two equal-amplitude pulses circulating in opposite directions around the ring such that these pulses collide in the saturable absorber cell and "anti-collide" in the ac-

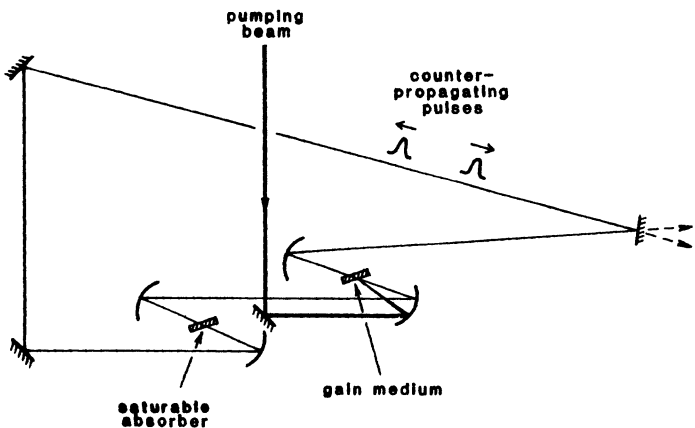


FIGURE 28.12
Layout of a colliding-pulse mode-locked laser.

tive gain medium. This type of *colliding pulse mode locking* in cw-pumped dye lasers has produced the shortest mode-locked laser output pulses to date, with pulselengths (before further external compression) in the range of 50 fs or shorter.

It is clear that in this type of CPML laser, coherent interference between the two colliding pulses will produce a standing-wave grating pattern in the saturable absorber. These grating effects can then both couple the two pulses together (as we have discussed in an earlier section on spatial hole burning effects), and also double the effective saturation efficiency for the colliding pulses as compared to the two pulses passing through the absorber independently. These grating effects may thus play a significant role in the apparently greater effectiveness of CPML for obtaining the shortest possible pulses.

Essentially the same sort of grating effects also occur, however, for a standing-wave cavity having a contacted saturable-absorber dye cell placed directly against one end mirror. It does not yet seem to be entirely clear, therefore, either theoretically or experimentally, whether the improved performance from colliding-pulse mode-locked lasers results from some special attributes of the colliding pulse interaction, or simply from the improved design flexibility and more efficient saturation that the ring cavity can provide.

An alternative cavity form which also permits colliding pulse mode locking without requiring a complete two-way ring is the *antiresonant ring* (or Sagnac interferometer) cavity shown in Figure 28.13. This cavity design has also been used with good success for passive mode-locking of both cw dye lasers and flash-pumped solid-state lasers.

REFERENCES

The necessity for both absorber and amplifier saturation in cw mode-locked lasers is discussed in more detail in G.H.C. New, "Pulse evolution in mode-locked quasi continuous lasers," *J. Quantum Electron.* **QE-10**, 115-124 (February 1974). See also the further computer simulations of G.H.C. New and D.H. Rea, "Rate-equation dynamics

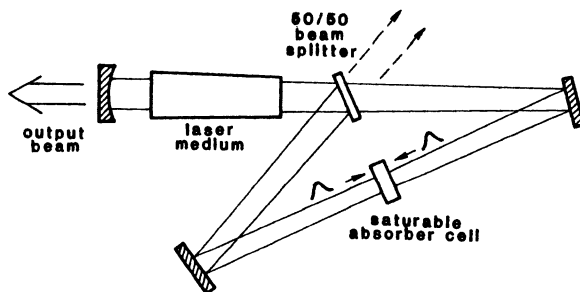


FIGURE 28.13
Antiresonant ring cavity for obtaining colliding-pulse mode locking in a linear laser cavity.

of passively mode-locked quasi continuous lasers: Perturbation theory of a ring laser," *J. Appl. Phys.* **47**, 3107–3115 (July 1976), and in G.H.C. New, K.E. Orkney, and M.J.W. Nock, "Rate equations dynamics of passively mode-locked quasi continuous lasers: Pulse stability and dynamic pulse compression," *Optical and Quantum Electron.* **8**, 425–431 (1976).

The theoretical discussions of cw mode locking by H.A. Haus include "Theory of mode locking with a fast saturable absorber," *J. Appl. Phys.* **46**, 3049–3058 (July 1975); "Theory of mode locking with a slow saturable absorber," *J. Quantum Electron.* **QE-11**, 736–746 (September 1975); and "Parameter ranges for cw passive mode locking," *J. Quantum Electron.* **QE-12**, 169–176 (March 1976). See also H.A. Haus, C.V. Shank, and E.P. Ippen, "Shape of passively mode-locked laser pulses," *Opt. Commun.* **15**, 29–31 (September 1975). A recent extension to this theory is given by O.E. Martinez, R.L. Fork, and J.P. Gordon, "Theory of passively mode-locked lasers including self-phase modulation and group-velocity dispersion," *Opt. Lett.* **9**, 156–158 (May 1984).

For a recent theoretical discussion of synch-pumped laser mode locking, with references to earlier work, see L.M. Davis, J.D. Harvey, and J.M. Pearl, "Rate equation simulation of a synchronously pumped dye laser," *Opt. Commun.* **50**, 49–55 (May 1 1984).

The synchronously pumped results shown in this section come from A.M. Johnson and W.M. Simpson, "Continuous-wave mode-locked Nd:YAG-pumped subpicosecond dye lasers," *Opt. Lett.* **8**, 554–556 (November 1983).

The basic references on colliding pulse mode locking include R.L. Fork, B.I. Greene, and C.V. Shank, "Generation of optical pulses shorter than 0.1 psec by colliding pulse mode locking," *Appl. Phys. Lett.* **38**, 671–672 (May 1, 1981); C.V. Shank et al., "Compression of femtosecond optical pulses," *Appl. Phys. Lett.* **40**, 761–763 (May 1, 1982); R.L. Fork, C.V. Shank, and R.T. Yen, "Amplification of 70-fs optical pulses to gigawatt powers," *Appl. Phys. Lett.* **41**, 223–225 (August 1, 1982); and R.L. Fork, C.V. Shank, C. Hirlmann, and R. Yen, "Femtosecond white-light continuum pulses," *Opt. Lett.* **8**, 1–3 (January 1983). See also C.V. Shank, "Measurement of ultrafast phenomena in the femtosecond time domain," *Science* **219**, 1027–1031 (March 1983).

For theoretical studies of CPML, see D. Kühlke, W. Rudolph, and B. Wilhelm, "Influence of transient absorber gratings on the pulse parameters of passively mode-locked cw ring dye lasers," *Appl. Phys. Lett.* **42**, 325–327 (February 15, 1983); or M. Yoshizawa and T. Kobayashi, "Experimental and theoretical studies on colliding pulse mode locking," *IEEE J. Quantum Electron.* **QE-20**, 797–803 (July 1984).

The antiresonant ring configuration is described in H. Vanherzele, J.L. Van Eck, and A.E. Siegman, "Colliding pulse mode locking of a Nd:YAG laser with an antiresonant ring structure," *Appl. Opt.* **20**, 3483-3486 (October 15, 1981); and applied to cw dye lasers in H. Vanherzele, J-C. Diels, and R. Torti, "Tunable passive colliding pulse mode-locking in a linear dye laser," *Opt. Lett.* **9**, 549-551 (December 1984).

The autocorrelation methods used to measure mode-locked pulsedwidths become particularly important for the ultrashort pulses from cw mode-locked lasers. For an excellent review of these techniques, see the chapter by E.P. Ippen and C.V. Shank, "Techniques for measurement," in *Ultrashort Light Pulses*, ed. by S.L. Shapiro (Springer-Verlag, 1977), pp. 83-122.

For some recent extensions of these methods, see also L.C. Diels, E.W. Van Stryland, and D. Gold, "Investigation of the parameters affecting subpicosecond pulse durations in passively mode-locked dye lasers," in *Picosecond Phenomena*, ed. by C.V. Shank, E.P. Ippen, and S.L. Shapiro (Springer-Verlag, 1978), pp. 117-120; and also T. Mindl, P. Hefferle, S. Schneider, and F. Dörr, "Characterization of a train of subpicosecond laser pulses by fringe resolved autocorrelation measurements," *Appl. Phys. B* **31**, 201-207 (1983).



LASER INJECTION LOCKING

In 1865 Christiaan Huygens (later to become known for the Huygens' integral), while confined to bed by illness, noticed that the pendulums of two clocks in his room invariably locked into synchronism if the clocks were hung close to each other, but became free-running when hung farther apart. He eventually traced the coupling mechanism to mechanical vibrations transmitted through the wall, thus providing one of the first observations of the coupling of two oscillators by injection locking.

Injecting a weak signal into a more powerful free-running oscillator can produce an interesting and useful set of injection locking effects, not only in clocks, but also in lasers and almost any other kind of self-sustained periodic oscillator. These injection-locking effects, besides having important practical applications, provide an excellent illustration both of laser theory and of the fundamental principles of oscillator dynamics.

There are actually two quite different types of behavior that are both (unfortunately) often referred to as injection locking. In one of these, which we might call true injection locking, a weak monochromatic signal is injected into the resonant circuit of another self-sustained oscillator, at a frequency within a narrow locking range around the free-running frequency of that oscillator. The injected signal can then capture or "lock" the subsequent oscillation behavior, so that the oscillator is more or less completely controlled by the injected signal. This kind of injection-locking behavior, which can be produced in almost any kind of coherent oscillator, is analyzed in detail in the first four sections of this chapter.

There are other situations in which a weak external signal is injected into a higher-power pulsed oscillator during the turn-on period when this oscillator is building up from noise. The injected signal in this situation is often too weak or too far off resonance to "lock" the oscillator as described above. It can, however, establish the initial conditions from which the oscillation will build up, and thus exert at least some control over the signal that will develop in the laser. An approach for discussing this kind of pulsed injection locking—which might more accurately be called "injection seeding" or some similar term—is given in a later section of this chapter.

Finally, at the end of the chapter we discuss some practical applications of laser injection locking, including the laser gyroscope, in which injection locking plays an unavoidable but very much unwanted role.

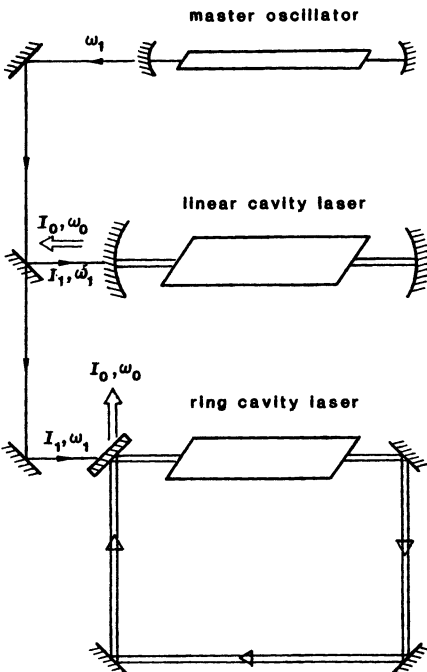


FIGURE 29.1
Laser injection locking techniques.

29.1 INJECTION LOCKING OF OSCILLATORS

As a simple example of “true injection locking,” let us suppose that a self-sustained oscillator of almost any sort—for example, a laser oscillator—is initially oscillating at a free-running oscillation frequency ω_0 and producing a coherent output intensity I_0 at that frequency. This output intensity is presumably the maximum intensity that can be extracted from the amplifying medium inside that oscillator under the given conditions of output coupling, internal gain, and internal losses with which the laser is operating.

Suppose now that a very weak or low-power external signal is injected into this laser oscillator via some suitable coupling method, at a frequency ω_1 which is close to but not exactly coincident with the free-running oscillation frequency ω_0 of the laser. As illustrated in Figure 29.1, the signal from the external master oscillator may be injected either into a linear-cavity laser, with the resulting problem that the injected oscillator also fires its output beam straight back into the master oscillator; or the injected laser may be a ring laser, with the advantage that input and output beams are clearly separated. In either situation, what will happen to this injected signal, and what effects will it have on the original free-running oscillation?

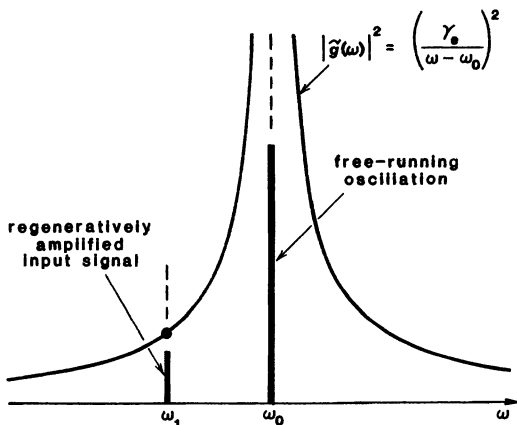


FIGURE 29.2
Regenerative gain versus input frequency ω_1 for a laser cavity oscillating at frequency ω_0 .

Regenerative Amplifier Description of Injection Locking

To answer this question in a simple fashion, we can refer back to the simple model of a laser as a regeneratively amplifying interferometer cavity with partially transmitting end mirrors which we have analyzed in Chapter 11.

We pointed out in those chapters that a laser oscillator below threshold is essentially a regenerative amplifier, with an amplitude gain from input to output which can be written (leaving out a trivial minus sign) in the form

$$\tilde{g}(\omega) = \frac{1 - R}{1 - \mathcal{G}_{rt}(\omega)} = \frac{1 - R}{1 - \mathcal{G}(\omega) \cos \phi(\omega) + j\mathcal{G}(\omega) \sin \phi(\omega)}, \quad (1)$$

where R is the input-output mirror reflectivity, and $\mathcal{G}_{rt}(\omega) \equiv \mathcal{G}(\omega)e^{-j\phi(\omega)}$ is the complex round-trip gain inside the laser cavity, with $\mathcal{G}(\omega)$ being the round-trip gain magnitude including laser gain, internal losses, and finite mirror reflectivities, and $\phi(\omega) = wp/c$ the round-trip phase shift (neglecting small pulling effects). In the highly regenerative limit where $\mathcal{G}(\omega) \rightarrow 1$, this regenerative gain near any one axial-mode frequency ω_0 simplifies to the form

$$\tilde{g}(\omega) \approx \frac{1 - R}{1 - \mathcal{G} + j\mathcal{G}T(\omega - \omega_0)}, \quad (2)$$

where $T = p/c$ is the transit time for one round trip inside the cavity.

Oscillation threshold then occurs when the net round-trip gain magnitude \mathcal{G} inside the laser cavity rises to be exactly unity at the oscillation frequency; and in fact the internal round-trip gain \mathcal{G} clamps at this same value of unity in the steady-state oscillation condition above threshold. Oscillation threshold thus corresponds to the point where the overall regenerative gain goes to infinity for an externally applied signal tuned exactly to the oscillation frequency ω_0 of the laser.

But the fact that \mathcal{G} is clamped at a value of unity also means that the overall regenerative gain for an externally applied signal at any other frequency away from the exact resonance frequency remains finite and limited, as shown in Figure 29.2, even when the laser begins oscillating at its oscillation frequency. In fact

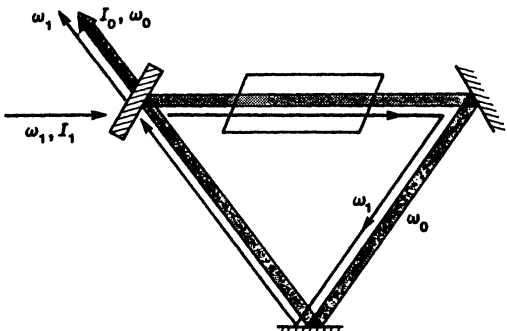


FIGURE 29.3
Simultaneous injected and free-running signals in a ring laser oscillator.

from the gain formula in Equation 29.2, the power amplification from input to output for a signal at $\omega \neq \omega_0$, under oscillating conditions at ω_0 , is given by something very close to

$$|\tilde{g}(\omega)|^2 \approx \frac{\gamma_e^2}{(\omega - \omega_0)^2}, \quad (3)$$

where γ_e is the energy decay rate (and hence also the frequency bandwidth) of the laser cavity due to external coupling. In writing this we have made use of the definition from earlier chapters that the energy decay rate γ_e for a laser cavity due to external coupling through an output mirror of reflectivity R is given by

$$\left[\begin{array}{l} \text{round-trip power decrease} \\ \text{due to external coupling} \end{array} \right] = R = e^{-\gamma_e T} \approx 1 - \gamma_e T \quad \text{if} \quad R \approx 1. \quad (4)$$

The decay rate γ_e and the external cavity Q_e are thus given, at least for small coupling, by

$$\text{external decay rate, } \gamma_e \equiv \frac{\omega}{Q_e} \approx \frac{1-R}{T}. \quad (5)$$

This regenerative power gain blows up to infinity at $\omega \rightarrow \omega_0$, as illustrated in Figure 29.2.

Suppose that a ring-laser cavity is already oscillating at its cavity-resonance frequency ω_0 with an oscillation output level I_0 , as illustrated in Figure 29.3, when a very weak signal of amplitude I_1 at a frequency ω_1 tuned a small amount away from exact resonance is injected into the cavity through one of the end mirrors. If this signal at ω_1 is weak enough, it can circulate around inside the cavity, and be regeneratively amplified by the laser medium, even in the presence of the much stronger oscillation already present at ω_0 .

The injected signal at ω_1 can thus be regeneratively amplified and can produce an amplified power output at this injected signal frequency, essentially independent of the much larger free-running oscillation signal also present inside the cavity. With sufficiently narrowband filters and sensitive detection equipment we could therefore, at least in theory, measure the regenerative amplification of an injected signal at $\omega_1 \neq \omega_0$, entirely independent of the simultaneous oscillation at ω_0 .

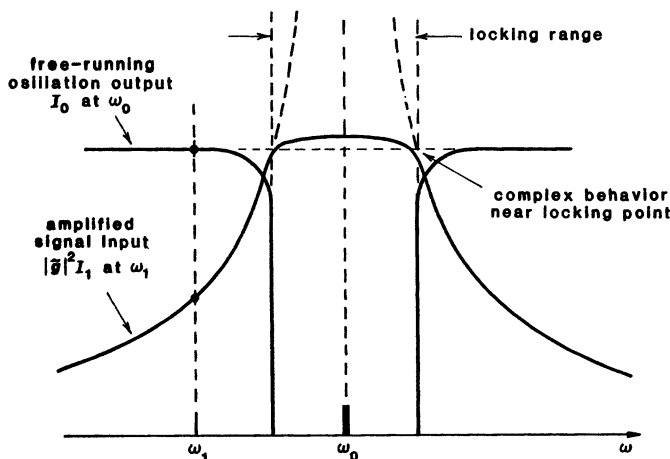


FIGURE 29.4

When an injected signal is tuned outside the locking range on either side, the output from the laser consists of both the amplified and the free-running oscillation signal. When the injected signal is tuned inside the locking range, only a single output wave with the injected frequency is present.

(If the signal at ω_1 is tuned very close to ω_0 , within less than the reciprocal of the population recovery time of the laser gain medium, interference or beating effects between the two signals may drive or excite population fluctuations and even spiking effects in the primary laser oscillation, thus complicating the situation. The detuning range over which this occurs in most atomic systems is extremely narrow, however; and in most situations we can simply assume that both signals, at ω_1 and ω_0 , will be independently amplified by the laser medium inside the cavity, with little or no interference between them so long as the signal at ω_1 is weak enough not to cause additional gain saturation and thus interfere with the laser oscillation at ω_0 .)

Suppression of the Free-Running Oscillation

Suppose now that we fix the incident intensity of the externally injected signal at some small value—call it I_1 —but vary the frequency ω_1 so that it moves continuously closer to the free-running frequency ω_0 from either side. The amplified output intensity $|\tilde{g}(\omega_1)|^2 I_1$ that is extracted from the regenerative cavity, and hence from the laser medium, by this signal then rises up sharply as ω_1 approaches ω_0 , as illustrated by the rising heavy lines in Figures 29.2 and 29.4. The second heavy line in Figure 29.4 is then intended to show that in this region the laser is simultaneously producing a free-running output intensity I_0 at the oscillation frequency ω_0 .

There will come a point, in fact, where the injected signal is tuned close enough to ω_0 that the amplified intensity $|\tilde{g}(\omega_1)|^2 I_1$ begins to approach the free-running oscillation intensity I_0 . We will see in later sections that more or less exactly at this point, on either side of the free-running frequency ω_0 , the amplified signal begins to steal enough gain from the laser medium, or begins to saturate

the laser gain down by just enough, that the free-running laser oscillation at ω_0 is turned off or goes out, leaving only the injected signal at ω_1 .

The amplified power output at the injected frequency ω_1 will, however, no longer continue to rise as ω_1 is tuned further inside this range, because the amplifying medium inside the oscillator simply does not have this much power to supply. Instead, the amplified output at ω_1 will be limited to the free-running oscillation intensity I_0 , or slightly above this to account for the additional signal power that is being injected.

For an injected signal tuned outside this locking point, therefore, the laser output consists of the strong free-running oscillation with intensity I_0 , plus the weaker amplified intensity at the injected signal frequency ω_1 . Inside the locking range, however, the output of the oscillator will consist entirely of the regeneratively amplified but amplitude-limited signal at ω_1 .

Injection Locking Range

We can now ask: for an incident signal of a given intensity I_1 and variable frequency ω_1 , how close to ω_0 can we in fact tune ω_1 before the amplified output $|\tilde{g}(\omega_1)|^2 I_1$ at that frequency will equal the free-running oscillation output, call it I_0 , of this laser. The answer to this is given, at least for small coupling, by

$$|\tilde{g}(\omega_1)|^2 I_1 = \frac{\gamma_e^2}{(\omega_1 - \omega_0)^2} I_1 \approx I_0. \quad (6)$$

The amplified injected signal will thus take over from the free-running oscillation somewhere near the detuning points given by

$$|\omega_1 - \omega_0| \approx \gamma_e \frac{E_1}{E_0} \approx \frac{\omega_0}{Q_e} \sqrt{\frac{I_1}{I_0}}. \quad (7)$$

We will confirm in the following sections that exactly at this point the free-running oscillation, depending on your viewpoint, either goes out and is replaced by the amplified injected signal; or else is completely captured or “locked” by the injected signal.

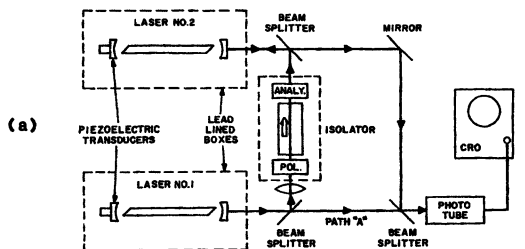
The full locking range for the oscillator is thus twice Equation 29.7, or

$$\Delta\omega_{\text{lock}} \approx 2\gamma_e \frac{E_1}{E_0} = \frac{2\omega_0}{Q_e} \sqrt{\frac{I_1}{I_0}}. \quad (8)$$

Note that this result does not contain any parameters of the specific oscillator device, except for the energy decay rate γ_e , or the “external bandwidth” ω_0/Q_e (sometimes called the “cold cavity bandwidth”) of the resonant circuit used in the oscillator, and the ratio of injected input power to free-running output power (both measured outside the oscillator). It can be shown in fact that this same simple equation applies universally to virtually any kind of injection-locked oscillator, whether laser, electronic, mechanical, or whatever.

Experimental Results

The first clear demonstration of this kind of injection locking of one laser by another, in excellent agreement with the preceding description, was carried



(b)

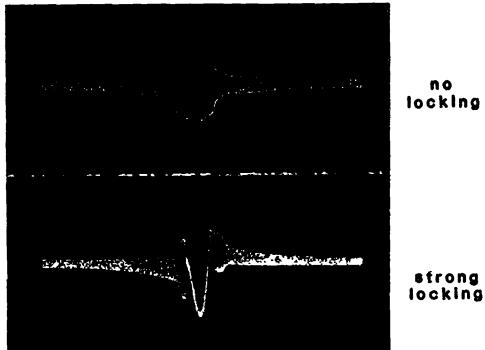


FIGURE 29.5
First experimental demonstration of laser injection locking, by Stover and Steier, *Appl. Phys. Lett.* 8, 91 (1966).

out by Stover and Steier at the Bell Telephone Laboratories, using two single-frequency helium-neon lasers as shown in Figure 29.5.

In these experiments, as outlined in Figure 29.5(a), a portion of the output from one laser was injected back into the other laser through an optical isolator (a one-way Faraday rotation device) which was employed in order to avoid simultaneous feedback from the second laser into the first. Portions of the output beam from each laser were also combined and carefully aligned through a beam splitter and allowed to fall on a photodetector, so that the beat note or interference signal between the two lasers could be detected electronically. Either laser could then be tuned in frequency over a few tens of MHz by changing its cavity length using the piezoelectric mirror mounts on each laser that are shown in Figure 29.5.

To demonstrate injection locking, the frequency of the first laser was scanned through the frequency of the second laser using a linear piezoelectric scan, and the radio-frequency beat note between the two lasers as detected by the photodetector was displayed on an oscilloscope screen versus the horizontal scanning voltage, with results as shown in the two following oscilloscope traces.

In the first of these, the injecting beam path is blocked, so that no injection locking occurs. The beat frequency signal between the two lasers then sweeps from a large difference frequency (perhaps a few tens of MHz) at the left-hand end of the trace down to zero frequency at the middle and back up to a high value at the right-hand end of the trace. Although the individual cycles of the beat signal can not be resolved in the oscilloscope display (except in a very narrow region at the center of the trace), the vertical displacement on the oscilloscope

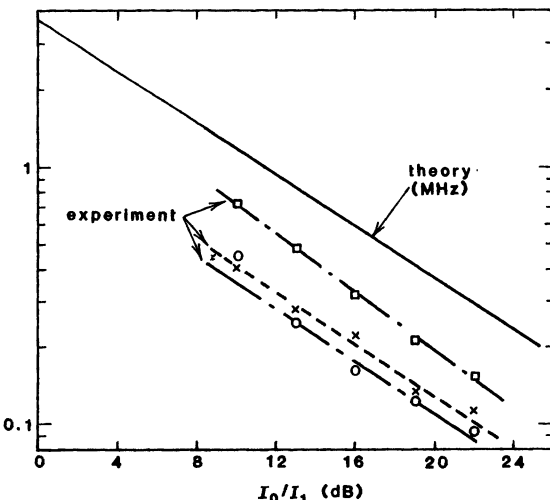


FIGURE 29.6
Measured locking range in MHz versus injected signal level for the experiment of Stover and Steier (Figure 29.5).

screen in effect maps out the audio and radio frequency response versus frequency of the photodetector and oscilloscope combination that was employed.

When the injection path is unblocked, however, as in the lower oscilloscope trace, the beat frequency completely disappears and only a dc response is observed as the two lasers lock together over a significant frequency range in the center of the frequency sweep. (The irregular value of the detected signal within the locking range is an artifact of the dc and low-frequency response in the oscilloscope and photodetector.)

The width of this locking band about zero frequency can then be observed to broaden and narrow as the strength of the injected signal from one laser into the other is increased or decreased. Figure 29.6 shows how the width of this locking range varies as a function of the (inverse) injected signal level in several different experiments. The agreement in functional form between theory and experiment is obviously excellent; and the differences in absolute level can readily be accounted for by uncertainties in the cavity parameters of the two lasers, and by difficulties in obtaining complete alignment and mode matching of the injected beam into the locked laser cavity.

Figure 29.7 shows, finally, a stationary optical interference fringe pattern between the two laser beams which could be observed whenever the two lasers were properly locked (and only then). The interference pattern is circular because the beams from the two lasers had spherical wavefronts with slightly different radii of curvature. Such a stationary interference pattern between two optical wavefronts can be achieved only if the two beams that are being combined to form the interference pattern have exactly the same optical frequency. Shifting the absolute phase of either beam by half a cycle will in fact cause the fringes to shift by half the fringe spacing, so that the center of the pattern will become dark rather than bright.

A frequency difference between the two beams even as small as, say, 1 kHz would then mean that the phase difference between them would increase by 1,000 cycles per second, so that the fringes in the photograph, instead of being sta-



FIGURE 29.7

Stationary interference pattern between two independent but locked laser oscillators, as in Figure 29.5.

tionary, would sweep inward or outward (depending on which laser was higher in frequency) at a rate of 1,000 cycles or fringes per second. In fact, this 1,000 Hz variation, as observed by a photodetector looking only at the center spot in the pattern, would represent precisely the photodetector beat note or optical heterodyne signal described in the preceding. The ability to produce a completely stationary interference pattern of this type thus provides a remarkable confirmation that the two lasers are not merely closely tuned in frequency, but that they are totally locked in both frequency and phase, on a cycle by cycle basis.

Discussion

Across the frequency locking range as derived in this section, therefore, we can view a locked oscillator's power output as being simply the regeneratively amplified but amplitude-limited reproduction of the input signal at frequency ω_1 , with the free-running oscillation at ω_0 having been completely suppressed. Alternatively, we can describe this situation by saying that inside the locking range the free-running oscillation at ω_0 has been completely captured or "injection-locked" by the injected signal at frequency ω_1 . There is no operational difference between the two descriptions, which are simply different ways of looking at the same phenomena.

This brief description using the regenerative amplifier approach contains the essential physics of cw steady-state injection locking in almost any kind of oscillator. There are, however, some more subtle nonlinear effects that can occur very near the edge of the locking range, or in the transient response of an oscillator to an injected signal; and these more subtle effects require a much more complex and detailed analysis, which we will present in the following sections of this chapter.

REFERENCES

The anecdote concerning Huygens' observations of clock synchronization is based on Huygens' letters to his father, cited on p. 52 of *Laser Physics* by M. Sargent III, M. O. Scully, and W. E. Lamb, Jr. (Addison-Wesley, 1974). Later observations by Rayleigh in 1907 of the coupling between two tuning forks on a table top are also described there.

Other striking natural examples of oscillator synchronization, besides the wide range of conventional electronic oscillators and phase-locked loops, include the locking of human circadian rhythms to the length of the day; the synchronized flashing of entire trees full of tropical fireflies; and the synchronization of female menstrual cycles through pheromonal communication.

Two of the earliest discussions of injection locking in an electronic circuit (and still very readable papers even now) are B. Van der Pol, "Forced oscillations in a circuit with a negative resistance," *Phil. Mag. Series 7* **3**, 65 (1927), and "The nonlinear theory of electric oscillations," *Proc. IRE* **22**, 1051 (1934).

A useful series of survey papers on injection locking in different kinds of oscillators, including laser applications, can be found in the October 1973 issue of *Proc. IEEE*. Two particularly good reviews from this issue are K. Kurokawa, "Injection locking of microwave solid-state oscillators," *Proc. IEEE* **61**, 1386 (October 1973); and C. J. Buczek, R. J. Freiberg, and M. L. Skolnick, "Laser injection locking," *Proc. IEEE* **61**, 1411 (October 1973).

The experimental results on the injection locking of one He-Ne laser oscillator by another that are summarized in this section come from H. L. Stover and W. H. Steier, "Locking of laser oscillators by light injection," *Appl. Phys. Lett.* **8**, 91 (1966). Two other papers giving more detailed theory and experimental results on laser injection locking are C. J. Buczek, R. J. Freiberg, and M. L. Skolnick, "CO₂ regenerative ring power amplifiers," *J. Appl. Phys.* **42**, 3133 (1971); and R. J. Freiberg and C. J. Buczek, "The saturated gain-bandwidth of CO₂ regenerative ring amplifiers," *Optics Commun.* **4**, 139 (1971).

For more recent results see C. O. Weiss et. al, "Injection locking of an optically pumped FIR laser," *IEEE J. Quantum Electron.* **QE-16**, 498-499 (May 1980); or T. Urisu et al., "Stabilized injection locking light amplification of a 1.15- μm He-Ne laser," *J. Appl. Phys.* **5**, 3154-3158 (May 1981).

29.2 BASIC INJECTION-LOCKING ANALYSIS

Let us now develop a more rigorous analysis for the injection locking of a laser oscillator, based on the laser equations of motion developed in previous chapters.

Injection-Locking Equations

We will consider in this analysis a single-mode laser oscillator with an external signal applied as discussed in previous sections. It is convenient, though not at all necessary, to think of this as a ring-laser cavity as in Figure 29.3, one advantage being that we then need to keep track of only a single input-output coupling mirror. It is also then easier both analytically and experimentally to separate the injected and the output signals.

Following the same approach as in the derivation of the laser-cavity equations (Chapter 24), let us write the externally generated wave that is incident on the cavity mirror in the phase-amplitude form

$$\text{incident wave amplitude, } \mathcal{E}_1(t) = E_1(t)e^{j[\omega_1 t + \phi_1(t)]}. \quad (9)$$

(From here on we will use subscripts 1 instead of e to denote the externally injected signal quantities.) Similarly, the mode amplitude inside the laser cavity

is written as

$$\text{cavity-mode amplitude, } \mathcal{E}(t) = E_c(t) e^{j[\omega_1 t + \phi(t)]}. \quad (10)$$

Note that both of these are expanded using the *incident or injected frequency* ω_1 as the *carrier frequency*. If the cavity field $\mathcal{E}(t)$ is actually oscillating primarily at the free-running cavity frequency ω_0 , this will have to show up as an appropriate time variation in the cavity phase $\phi(t)$.

Note also that as written these two signal amplitudes have different dimensions and slightly different physical significance. It will be more convenient, as well as simplifying comparisons with experiment, if we can express both of these quantities in the same units of normalized wave amplitudes measured *outside* the laser cavity, as we can do using the following approach. We can first recall that in the normalization used in the derivation of the cavity equations (Sections 24.1 and 24.2), the injected signal is already normalized so that the incident intensity coming toward the cavity from outside is given by

$$\text{injected signal intensity, } I_1 = E_1^2(t). \quad (11)$$

On the other hand, the cavity-mode amplitude is normalized so that the stored signal energy inside the laser cavity is given by

$$\text{stored signal energy, } U_{\text{sig}} = \frac{\epsilon V_c}{2} E_c^2(t). \quad (12)$$

The output intensity emerging from the cavity in the output arm is then given by $I_0 = \gamma_e \times U_{\text{sig}} = \gamma_e \epsilon V_c E_c^2 / 2$. If we define a cavity-wave amplitude $E(t)$ measured just outside the cavity output coupler by

$$E(t) \equiv \sqrt{\frac{\gamma_e \epsilon V_c}{2}} E_c(t) \quad (13)$$

then the emerging or emitted intensity coming out the output coupling port of the cavity can be written in the same format as the incident or injected power, namely,

$$\text{emerging signal intensity, } I(t) = E^2(t). \quad (14)$$

We are now measuring both the incident and output wave amplitudes $E_1(t)$ and $E(t)$ in the same units, and at the same location, just outside the coupling mirror of the laser cavity.

We also assume that the laser oscillator will be operating in the usual linear-susceptibility or rate-equation regime, so that the atomic polarization in the inverted laser medium inside the laser cavity can be related to the cavity field amplitude by

$$P(t) \equiv C(t) - jS(t) = (\chi' + j\chi'')\epsilon E_c(t), \quad (15)$$

where χ' and χ'' are the saturated values of the atomic susceptibility on the laser transition, taking into account the filling factor, and whatever degree of saturation of the laser transition may be present. We can further eliminate the reactive term χ' from the phase-amplitude equations (Section 24.4) by assuming that it will at most produce a small pulling of the cavity frequency, which we can absorb into the definition of the pulled free-running oscillation frequency ω_0 .

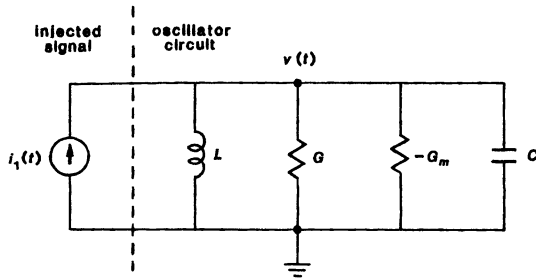


FIGURE 29.8
Lumped equivalent circuit for an injection-locked oscillator.

With these definitions and approximations, the phase-amplitude equations 24.61 and 24.62 give us one equation for the time-varying amplitude $E(t)$ of the cavity signal, namely,

$$\frac{dE(t)}{dt} + \frac{\gamma_c - \gamma_m}{2} E(t) = \gamma_e E_1(t) \cos[\phi(t) - \phi_1(t)], \quad (16)$$

where we use γ_m as a shorthand for the growth rate $\omega\chi''$, plus another equation for the time-varying phase $\phi(t)$, namely,

$$\frac{d\phi(t)}{dt} + \omega_1 - \omega_0 = -\gamma_e \frac{E_1(t)}{E(t)} \sin[\phi(t) - \phi_1(t)]. \quad (17)$$

These are the fundamental injection-locking equations for use in all our further discussion.

Electrical Circuit Analog

We can also show, for whatever insight it may provide, that exactly these same equations can be derived from the simple lumped resonant circuit shown in Figure 29.8. We include in this circuit a negative conductance $-G_m$, which can represent a transistor, vacuum tube, or other active electronic element in an electronic oscillator.

The basic differential equation for this circuit is

$$C \frac{dv(t)}{dt} + [G - G_m]v(t) + \frac{1}{L} \int v(t) dt = i_1(t). \quad (18)$$

Suppose we write the injected signal from the current generator connected to this circuit in the form $i_1(t) = I_1(t) \exp[j(\omega_1 t + \phi_1(t))]$, whereas the voltage that is developed across the circuit has the similar form $v(t) = V(t) \exp[j(\omega_1 t + \phi(t))]$. The integral term associated with the inductance L can then be manipulated via the following widely useful trick. We first replace $v(t)$ with the complex form $\text{Re } V(t) e^{j(\omega_1 t + \phi(t))} \equiv \text{Re } \tilde{V}(t) e^{j\omega_1 t}$, and then integrate this term by parts twice

in succession to obtain the result

$$\begin{aligned} \int_{-\infty}^t \tilde{V}(t) e^{j\omega_1 t} dt &= \frac{-j\tilde{V}(t) e^{j\omega_1 t}}{\omega_1} + \frac{j}{\omega_1} \int_{-\infty}^t \frac{d\tilde{V}(t)}{dt} e^{j\omega_1 t} dt \\ &= \frac{-j\tilde{V}(t) e^{j\omega_1 t}}{\omega_1} + \frac{e^{j\omega_1 t}}{\omega_1^2} \frac{d\tilde{V}(t)}{dt} - \frac{1}{\omega_1^2} \int_{-\infty}^t \frac{d^2\tilde{V}(t)}{dt^2} e^{j\omega_1 t} dt. \end{aligned} \quad (19)$$

We can see that if this process were continued, successive terms in the expansion would become smaller by successively higher derivatives of the slowly varying envelope, divided by successively higher powers of the carrier frequency ω_1 . In fact, only the first two terms in the second line need be kept, whereas the third and higher-order terms can all be dropped in the SVEA approximation.

Putting the slowly varying envelope expansions for $i_1(t)$ and $v(t)$ into the circuit equation, using approximation along with the usual resonance approximation, and separating out the real and imaginary parts of Equation 29.18 then leads directly to the amplitude and phase equations for the resonant circuit, namely,

$$\frac{dV(t)}{dt} + \frac{G - G_m}{2C} V(t) = \frac{1}{2C} I_1(t) \cos[\phi(t) - \phi_1(t)], \quad (20)$$

and

$$\frac{d\phi(t)}{dt} + \omega_1 - \omega_0 = -\frac{1}{2C} \frac{I_1(t)}{V(t)} \sin[\phi(t) - \phi_1(t)], \quad (21)$$

where $\omega_0^2 = 1/LC$. These two equations have exactly the same form as the laser equations 29.16 and 29.17.

Steady-State Solutions Below Threshold

In order to illustrate the validity of these laser equations, let us consider the solution to Equations 29.16 and 29.17 under the assumptions of (i) a constant sinusoidal input signal so that E_1 and ϕ_1 are constants; (ii) a laser cavity below threshold so that the total cavity loss rate γ_c is greater than the laser growth rate $\gamma_m \equiv \omega\chi''$; and (iii) steady-state output conditions so that all derivatives satisfy $dE(t)/dt = d\phi(t)/dt = 0$. Squaring and adding the two equations 29.16 and 29.17 then gives

$$[(\gamma_c - \gamma_m)^2 + 4(\omega_1 - \omega_0)^2] E^2 = 4\gamma_e^2 E_1^2. \quad (22)$$

But this reduces immediately to the power gain versus frequency expression in the large-regeneration limit, namely,

$$\begin{aligned} G(\omega_1) &\equiv \left(\frac{E}{E_1} \right)^2 = \left(\frac{2\gamma_e}{\gamma_c - \gamma_m} \right)^2 \frac{1}{1 + [2(\omega_1 - \omega_0)/(\gamma_c - \gamma_m)]^2} \\ &= g_0^2 \frac{1}{1 + [2(\omega_1 - \omega_0)/\Delta\omega_{3dB}]^2}, \end{aligned} \quad (23)$$

where $g_0 \equiv 2\gamma_e/(\gamma_c - \gamma_m)$ and $\Delta\omega_{3dB} \equiv \gamma_c - \gamma_m$, just as we derived earlier for a ring-type regenerative laser cavity. As we showed earlier, any regenerative amplifier of this type will have a fixed voltage gain-bandwidth product which

is given in this situation by $g_0 \times \Delta\omega_{3dB} = 2\gamma_e$. This gain-bandwidth product, like the injection-locking range, is independent of everything except the external coupling rate $\gamma_e \equiv \omega_0/Q_e$ for the cold laser cavity.

We can also note that the phase equation under these assumptions reduces to

$$\sin(\phi - \phi_1) = -\frac{\omega_1 - \omega_0}{\gamma_e} \times \frac{E}{E_1} \approx -2 \frac{\omega_1 - \omega_0}{\Delta\omega_{3dB}}. \quad (24)$$

This demonstrates once again that the phase angle $\phi - \phi_1$ between the input and output waves in the below-threshold regenerative-amplifier regime swings through approximately 180° , from $+90^\circ$ to -90° , as the injected signal frequency ω_1 is tuned through a narrow range of approximately $\pm\Delta\omega_{3dB}/2$ about the resonance frequency. As the amplifier comes closer to threshold, the bandwidth becomes narrower, and this phase swing becomes sharper, becoming essentially a phase discontinuity at oscillation threshold.

REFERENCES

In addition to the survey papers referenced in the previous section, further analyses of injection locking for lasers have been given by R. H. Pantell, "The laser oscillator with an external signal," *Proc. IEEE* **53**, 474 (1965); H. deLang, "Derivation of the relation between two weakly coupled nonlinear optical oscillators," *Appl. Phys. Lett.* **9**, 205 (1966); C. L. Tang and H. Statz, "Phase-locking of laser oscillators by injected signal," *J. Appl. Phys.* **38**, 323 (1967); R. F. Boikova and E. F. Fradkin, "Laser subject to an external signal," *Optics and Spectrosc.*, 452 (May 1967); and C. C. Wang, "Frequency locking of laser oscillators by injected signal," *Appl. Phys. Lett.* **43**, 158 (1972).

For a more complex analysis starting with quantum theory (but in the end coming to exactly the same classical results) see M. B. Spencer and W. E. Lamb, Jr., "Laser with a transmitting window," *Phys. Rev. A* **5**, 884 (1972), and "Theory of two coupled lasers," *Phys. Rev. A* **5**, 893 (1972).

29.3 THE LOCKED-OSCILLATOR REGIME

Let us now examine the solutions to the injection-locking equations (29.16 and 29.70) in the locked oscillator regime, where the oscillator output is completely controlled or locked by the injected signal.

Steady-State Amplitude Solution

Let us first look for solutions to these equations under steady-state conditions with a steady-state injected signal for which $E_1 = \text{constant}$ and $\dot{\phi}_1 = 0$ for simplicity. We also assume that the injected signal E_1 is very weak compared to the oscillator's free running output level.

The amplitude equation (29.16) then turns out to play a very minor role in determining the injection-locking behavior. We can simply assume that the oscillator will always be delivering an output amplitude $E \approx E_0$ where E_0 is the oscillator's normal free-running output level. This is the oscillation level at which the amplitude growth rate $\gamma_m \equiv \omega y''$ is saturated down to approximately equal the total cavity decay rate γ_c (which includes internal losses γ_0 and external

output coupling γ_e), so that the signal level in the resonant circuit neither grows nor decays with time.

With the time derivative set equal to zero, the amplitude equation (29.16) therefore reduces to

$$\gamma_c - \gamma_m \approx 2\gamma_e \frac{E_1 \cos \phi}{E_0}. \quad (25)$$

This equation is more or less automatically balanced to approximately zero on both sides by the fact that $\gamma_c - \gamma_m \approx 0$ on the left-hand side, whereas E_1 is very small ($E_1 \ll E_0$) on the right-hand side. The laser gain γ_m will actually be very slightly less than the cavity loss γ_c because of the fact that a small amount of external signal energy is being continuously injected into the cavity.

Steady-State Phase Solution: The Adler Equation

With this approximation, the primary equation that describes the injection-locking behavior is the phase equation, 26.17, which can be written in the form

$$\frac{d\phi(t)}{dt} + \omega_1 - \omega_0 = -\frac{\omega_0}{Q_e} \frac{E_1}{E_0} \sin \phi(t) = -\omega_m \sin \phi(t), \quad (26)$$

where $\omega_m \equiv (\omega_0/Q_e)(E_1/E_0)$. The equation in this form is often referred to as the Adler equation (see References). It is this equation that is primarily responsible for explaining the steady-state, and in fact also the transient, injection-locking behavior of an oscillator with an external signal.

According to the Adler equation the requirement for a steady-state locked oscillation, or $d\phi/dt = 0$, is equivalent to the condition that

$$\omega_1 - \omega_0 + \omega_m \sin \phi = 0. \quad (27)$$

But this reduces to the condition on $\sin \phi$ that

$$-1 \leq \left[\sin \phi \equiv \frac{\omega_0 - \omega_1}{\omega_m} \right] \leq 1. \quad (28)$$

This condition can be satisfied for real ϕ only if the injected signal frequency ω_1 remains within the range

$$-\omega_m \leq (\omega_1 - \omega_0) \leq \omega_m, \quad (29)$$

where ω_m is given, as defined in Equation 29.26, by

$$\omega_m \equiv \gamma_e \frac{E_1}{E_0} = \frac{\omega_0}{Q_e} \sqrt{\frac{I_1}{I_0}}. \quad (30)$$

The quantity ω_m is thus the maximum excursion that the injected frequency ω_1 can make about the resonance frequency ω_0 within which the magnitude of $\sin \phi$ can remain less than unity. The full locking range is then twice this or

$$\Delta\omega_{\text{lock}} \equiv 2\omega_m = \frac{2\omega_0}{Q_e} \sqrt{\frac{I_1}{I_0}}. \quad (31)$$

Outside this range a steady-state single-frequency solution is no longer possible, and we must look for more complex solutions. This is exactly the same result we derived in Equation 29.8 using the regenerative viewpoint. We have now,

however, derived it from the more general injection-locking equations, which are valid under any conditions whether the laser is oscillating or not.

Practical Locking Ranges

As a practical example, we might consider a laser cavity 1 m long (round-trip transit time $T = 6$ ns) with an output coupling of $\delta_e = 10\%$. The cavity decay rate will then be $\gamma_e \approx \delta_e/T \approx 1.7 \times 10^7$ sec $^{-1}$, and the full locking range in hertzian frequency units will be

$$\frac{\Delta\omega_{\text{lock}}}{2\pi} \approx 5 \text{ MHz} \times \sqrt{\frac{I_1}{I_0}}. \quad (32)$$

We have already shown experimental results for the injection-locking range in MHz versus the ratio of free-running oscillator power to injected signal power, as measured by Stover and Steier using He-Ne lasers, which fall exactly in this range. The differences in absolute level between theory and the various experimental results in Figure 29.5 represent primarily uncertainties in knowing the losses and coupling coefficients in the lasers, as well as in measuring how accurately the injected signal is aligned and gaussian-mode-matched into the laser cavity.

The general conclusion is that the true locking ranges in laser problems will always be very narrow, in the range from a few MHz down to a few hundred kHz. This imposes severe tolerances in practice, either in tuning the injected signal to within the oscillator's locking range or, in more practical terms, in stabilizing the cavity frequency ω_0 of the injected laser to remain within the locking range about the injected signal ω_1 .

Locked-Oscillation Phase Shift

The solution just given also points out the important fact that the phase angle $\phi = \phi(\omega_1)$ of the output signal E_0 with respect to the injected signal E_1 will shift through 180° as the injected signal is tuned across the locking range, as given by the formula

$$\phi(\omega_1) = \sin^{-1} \left(\frac{\omega_0 - \omega_1}{\omega_m} \right). \quad (33)$$

This behavior is illustrated in Figure 29.9.

As we tune the injected signal across the locking range, in other words, the laser output follows at the same frequency ω_1 , and keeps an essentially constant amplitude $E \approx E_0$; but the phase angle between the injected and output signals continuously shifts as shown. This dependence of phase shift on frequency can have useful applications in the use of locked oscillators or phase-locked loops as frequency demodulators and in other situations, as we will discuss in a later section.

Locked-Oscillation Signal Amplitude

Let us now return to the amplitude equation (29.16) to find a slightly more exact expression for the output power from the locked oscillator within the injection-locked regime. If we have a homogeneous laser medium and not too large output coupling, we can assume that the laser growth rate inside the laser

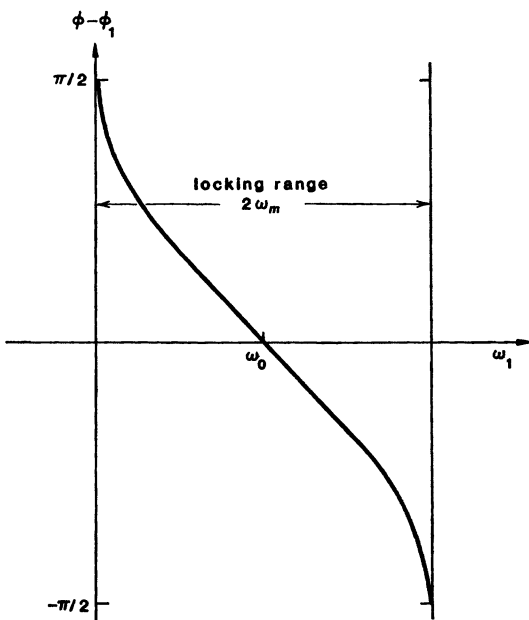


FIGURE 29.9
Relative phase angle versus frequency within the injection-locking range.

cavity will saturate in the homogeneous form

$$\gamma_m = \frac{\gamma_{m0}}{1 + E^2/E_{\text{sat}}^2}. \quad (34)$$

The saturation factor E_{sat}^2 in this expression is directly proportional to the saturation intensity of the laser medium, but also contains some other geometric factors, especially since the field amplitude E^2 in this formula is measured outside rather than inside the laser cavity.

Under conditions of free-running oscillation with no injected signal ($\gamma_m = \gamma_c$ and $E_1 = 0$) the laser output intensity E_0^2 can be written in the usual form

$$E_0^2 = (\gamma_{m0}/\gamma_c - 1) E_{\text{sat}}^2 = (r - 1) E_{\text{sat}}^2 \quad (\text{free-running oscillator}), \quad (35)$$

where $r \equiv \gamma_{m0}/\gamma_c$ is the amount by which the unsaturated laser gain exceeds the losses in the cavity. If we then use Equation 29.34 to relate the unknown quantity E_{sat} to the free-running oscillation output E_0 , we can rewrite the amplitude equation (29.25) under steady-state injection-locked conditions in the more exact form

$$\gamma_c - \gamma_m = \frac{(r - 1)E^2 - E_0^2}{(r - 1)E^2 + E_0^2} \gamma_c = \frac{2\gamma_c E_1 \cos \phi}{E} \quad (\text{locked oscillator}). \quad (36)$$

This equation is cubic in the output amplitude E , and hence somewhat difficult to solve. If we assume, however, that E is not greatly different from E_0 , an approximate first order solution for the power output versus input frequency

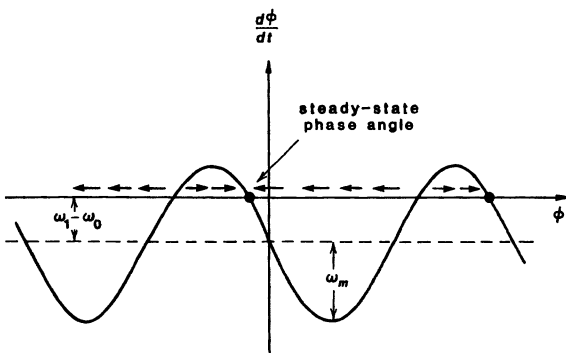


FIGURE 29.10
Graphical illustration of phase pull-in in the injection-locked regime.

tuning is easily found to be

$$E^2(\omega_1) \approx E_0^2 \left[1 + \frac{2r}{(r-1)\gamma_c E_0} \frac{\gamma_e E_1}{\omega_m} \cos \phi(\omega_1) \right]. \quad (37)$$

So long as the injected signal is small, $E_1/E_0 \ll 1$, and the laser pumping ratio not too close to threshold, this solution will be valid. Figure 29.4 shows the slight increase in the power output over and above the free-running oscillation level E_0^2 that is produced across the injection-locking range by the effects of the injected signal.

Transient Pull-In of the Oscillation Phase

Suppose now that an injected signal with constant amplitude E_1 , frequency ω_1 , and phase ϕ_1 is suddenly turned on at time t_1 , when the laser is already oscillating at frequency ω_0 . The transient response with which the signal in the locked oscillator will pull into phase (and frequency) synchronism with the injected signal is again given by the Adler equation (29.26), which must now be written in transient form as

$$\frac{d\phi(t)}{dt} = -(\omega_1 - \omega_0) - \omega_m \sin[\phi(t) - \phi_1]. \quad (38)$$

Figure 29.10 is a plot of the right-hand side of Equation 29.38, showing the sign of $d\phi/dt$ versus $\phi(t)$, with the arrows indicating the direction in which the instantaneous phase $\phi(t)$ will move, starting from any arbitrary initial value.

The phase will obviously always pull in to the steady-state phase angle given by $\sin \phi = (\omega_0 - \omega_1)/\omega_m$ (modulo 2π), so long as $|\omega_1 - \omega_0| \leq \omega_m$. Changing the ratio of $\omega_1 - \omega_0$ to ω_m obviously moves the sine wave in Figure 29.10 up and down with respect to the horizontal axis, making it graphically obvious how the locking range is determined, and how the steady-state phase value changes with $(\omega_1 - \omega_0)/\omega_m$.

A closed analytic solution to the Adler equation (29.26) can also be found. For a frequency detuning $|\omega_1 - \omega_0| \leq \omega_m$, that is, for ω_1 within the locking range,

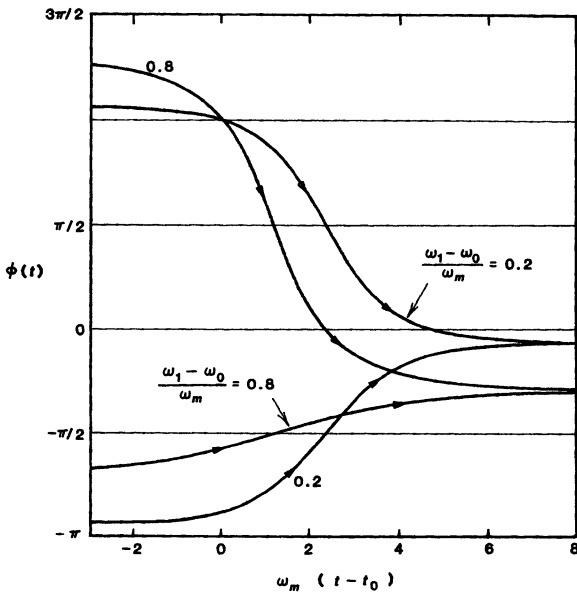


FIGURE 29.11
Transient pull-in behavior in the locked-oscillator regime for two different values of detuning.

this solution is given by the expression

$$\tan \frac{\phi(t) - \phi_1}{2} = \frac{\omega_b}{\omega_1 - \omega_0} \tanh \left[\frac{\omega_b(t - t_0)}{2} \right] - \frac{\omega_m}{\omega_1 - \omega_0}, \quad (39)$$

where $\omega_b \equiv \sqrt{\omega_m^2 - (\omega_1 - \omega_0)^2}$ and t_0 is an adjustable constant needed to match the initial boundary condition on $\phi(t)$. The behavior of this rather complex expression is best illustrated by plotting its solution for various detunings $(\omega_1 - \omega_0)/\omega_m$, as shown for two typical situations in Figure 29.11. Various initial phase values correspond to different starting points in time along these curves.

We can find from such plots, as well as from Figure 29.10, that for injected signals within the locking range, the phase $\phi(t)$ will always pull in smoothly to the steady-state value given by $\sin^{-1}(\omega_0 - \omega_1)/\omega_m$. The time required for the phase to converge close to this value is on the order of a few times the reciprocal locking width ω_m^{-1} . In fact for the limiting situation of zero detuning, $\omega_1 - \omega_0 = 0$, and a small enough initial phase error, the Adler equation (29.26) reduces to simply

$$\frac{d\phi(t)}{dt} \approx -\omega_m \times \phi(t), \quad (40)$$

with the solution

$$\phi(t) \approx \phi(t_0) \exp[-\omega_m \times (t - t_0)]. \quad (41)$$

The transient convergence to the locked condition in this situation is exponential with a convergence rate exactly equal to ω_m . This convergence becomes somewhat slower but is still reasonably rapid for larger values of $\omega_1 - \omega_0$, approaching the maximum detuning ω_m .

REFERENCES

The Adler equation, with its various analytic solutions, comes from a classic paper by R. Adler, "A study of locking phenomena in oscillators," *Proc. IRE* **34**, 351–357 (1946), reprinted in *Proc. IEEE* **61**, 1380 (October 1973). (Trivia buffs may want to note that this same Robert Adler invented the first "Space Command" remote control for Zenith television sets.)

Problems for 29.3

1. *Can the change in instantaneous frequency during the frequency lock-up transient be measured?* A laser is oscillating at its free-running frequency ω_0 when a cw injected signal whose frequency ω_1 is within the locking range is turned on at $t = 0$. Derive an expression for the instantaneous frequency $\omega_i(t)$ of the oscillator signal for $t > 0$, and plot its variation for a few typical situations. Would it be possible to verify this frequency variation experimentally? Why not? [Hint: You may want to read Section 29.5 on the phasor picture of injection locking to help in understanding the solution to this problem.]
-

29.4 SOLUTIONS OUTSIDE THE LOCKING RANGE

Analytical solutions to the Adler equation (29.26) are also available outside the locking range, where both the injected signal and a "free-running" oscillation signal are present. In fact, some particularly complex and interesting phenomena can occur in this range, especially when the injected signal frequency is tuned close to but still just outside the steady-state locking range.

Adler Equation Solutions Outside the Locking Range

Outside the locking range we can still assume that the total laser amplitude $E(t)$ is very close to the free-running oscillation amplitude E_0 , so that the amplitude equation (29.16) is still of minor importance. The important equation is still Adler's equation (29.26), whose exact solution, assuming a constant injected signal amplitude and fixed phase ϕ_1 , is given by a modified form of the solution from the previous section, namely,

$$\tan \frac{\phi(t) - \phi_1}{2} = -\frac{\omega_b}{\omega_1 - \omega_0} \tan \left[\frac{\omega_b(t - t_0)}{2} \right] - \frac{\omega_m}{\omega_1 - \omega_0}. \quad (42)$$

Because the argument of the square root has changed sign for $|\omega_1 - \omega_0| > \omega_m$, the hyperbolic tangent on the right-hand side of Equation 29.39 has now become a

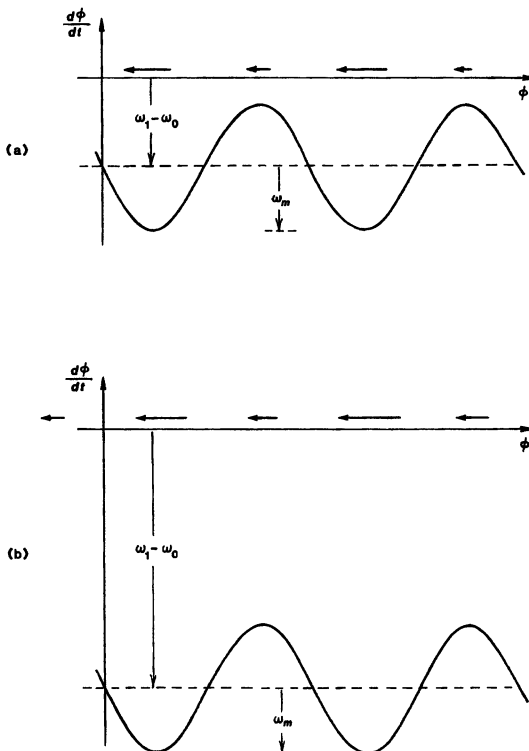


FIGURE 29.12
Plots of $d\phi/dt$ versus ϕ just outside the locking range (upper plot) and well outside this range (lower plot).

trigonometric tangent; and there has also been a change of sign in the definition of the periodic frequency or beat frequency ω_b , which is now given by

$$\omega_b \equiv \sqrt{(\omega_1 - \omega_0)^2 - \omega_m^2}. \quad (43)$$

(Note that Equation 29.42 has a fundamental periodic frequency given by ω_b , despite the factor of two in the denominators, because of the doubly periodic nature of the tangent functions.)

To understand the phase variation given by this rather complex expression, we can plot once again the phase derivative $d\phi(t)/dt$ versus ϕ . Figure 29.12 shows this derivative plotted for conditions in which the injected frequency ω_1 is tuned either just outside the locking range or well outside this range. It is assumed in both situations that the injected frequency ω_1 is tuned on the high side of the locking range, i.e., $\omega_1 > \omega_0 + \omega_m$.

Two things are evident from the direction and magnitude of the arrows in Figure 29.12. First, the phase $\phi(t)$ will have a continuously increasing or cumulative variation with time, toward negative values in these particular examples, and the magnitude of this cumulative variation will increase with increasing values of

the detuning $\omega_1 - \omega_0$ compared to the locking width ω_m . Second, superimposed on this cumulative variation, especially for values of $\omega_1 - \omega_0$ closer to ω_m , will be a periodic modulation of $\phi(t)$ at the beat frequency ω_b .

In fact, it can be shown analytically that the continuously increasing part of the phase variation with time is just given by the linear expression $\phi(t) = -\omega_b t$, where ω_b is the beat frequency defined in Equation 29.43. As a result, the total variation of $\phi(t)$ as given by Equation 29.42 can be written in the general form

$$\begin{aligned}\phi(t) &= -\omega_b t + \sum_n [a_n \cos n\omega_b t + b_n \sin n\omega_b t] \\ &= -\omega_b t + \phi_p(t),\end{aligned}\quad (44)$$

where $\phi_p(t)$ is a bounded periodic variation of the phase containing the fundamental and various harmonics of the frequency ω_b . The beat frequency ω_b is obviously very important in this phase behavior, as we will now demonstrate.

Physical Interpretation of the Phase Variation

In order to understand this phase variation, we should first recall that we began our analysis with an expansion in which the phase $\phi(t)$ was referenced to the injected signal frequency ω_1 and not the free-running oscillator frequency ω_0 . That is, we originally expressed the injected signal as

$$\text{injected signal, } \mathcal{E}_1(t) = E_1 \exp[j\omega_1 t + j\phi_1(t)], \quad (45)$$

and hence the oscillator's output signal was also written as

$$\text{oscillator output signal, } \mathcal{E}(t) = E(t) \exp[j\omega_1 t + j\phi(t)]. \quad (46)$$

But in the unlocked situation, although the injected signal is still at ω_1 , the dominant portion of the laser-cavity signal is likely to be at or close to the free-running oscillation frequency ω_0 .

To see that this is in fact what the analysis predicts, we can rewrite the oscillation signal $\mathcal{E}(t)$ with the linear portion of the time-varying phase $\phi(t)$ attached to the frequency ω_0 , i.e., we rewrite it as

$$\begin{aligned}\mathcal{E}(t) &= E(t) \exp[j\omega_1 t + j\phi(t)] \\ &= E(t) \exp[j(\omega_1 - \omega_b)t + \phi_p(t)],\end{aligned}\quad (47)$$

where $\phi_p(t)$ is the bounded and periodic portion of the instantaneous phase variation given by Equation 29.44. The expansion coefficients a_n and b_n in this sum can be found by suitable analytical expansions of the Adler equation or of the exact solution to 29.42.

Expressing the cavity signal in this fashion makes it clear that the oscillation signal in the cavity consists of a new primary or carrier component with a frequency which we will write from now on as $\omega_{\text{osc}} \equiv \omega_1 - \omega_b$, plus a set of phase modulation components—one of which actually happens to be the injected signal frequency ω_1 —that arise analytically from the periodic phase modulation $\phi_p(t)$ and that are located at integer multiples of $\pm\omega_b$ about this new carrier frequency.

Behavior Well Outside the Locking Range

Let us look more closely at the situation where the injected signal frequency ω_1 is well outside the locking range, i.e., $\omega_1 - \omega_0 \gg \omega_m$. The beat frequency ω_b is then given to good accuracy by the approximation

$$\omega_b \equiv \sqrt{(\omega_1 - \omega_0)^2 - \omega_m^2} \approx \omega_1 - \omega_0 - \frac{\omega_m^2}{\omega_1 - \omega_0}, \quad (48)$$

i.e., the beat frequency is very close to, but still slightly smaller than, the injected frequency offset $\omega_1 - \omega_0$. We will also see shortly that in this limit the periodic phase modulation $\phi_p(t)$ is relatively small. The primary oscillation signal in the cavity is then very nearly a pure sine wave at the slightly shifted or pulled frequency ω_{osc} given by

$$\omega_{\text{osc}} = \omega_1 - \omega_b \approx \omega_0 + \omega_m^2/2(\omega_1 - \omega_0). \quad (49)$$

This is essentially the free-running frequency ω_0 of the laser oscillator, as we would expect, except that it is shifted or pulled by a small amount of frequency pulling of order $-\omega_m^2/2(\omega_1 - \omega_0)$. In the way we have formulated our analysis, *this free-running oscillation signal, which is dominant in the laser for an injected signal well outside the locking range, shows up in the mathematics as a phase modulation sideband, produced by the time-variation of $\phi(t)$, on the injected signal component ω_1 .*

In fact, if we Fourier-analyze the total laser-cavity signal $\mathcal{E}(t)$ in the presence of an injected signal well outside the locking range, the resulting Fourier spectrum will contain a weak sideband at the injected frequency ω_1 ; a much stronger sideband at the slightly pulled “free-running” oscillation frequency $\omega_{\text{osc}} = \omega_1 - \omega_b \approx \omega_0$; and also other, generally very weak sidebands at all the other possible frequencies $\omega_1 + \omega_b$, $\omega_1 + 2\omega_b$, $\omega_1 - 2\omega_b$, and so on. The relative amplitudes of these various spectral components will depend on the exact form of $\phi(t)$, although we already know from physical reasoning that if ω_1 is far outside the locking range, the regeneratively amplified component at ω_1 will be small, and the primary “sideband” near ω_0 will be much larger, approaching the free-running oscillation amplitude E_0 .

This analysis based on the Adler equation thus tells us two interesting pieces of information. First, there will be additional (but probably very weak) sidebands at several other frequencies $\omega \pm n\omega_b$. Secondly, and of more practical importance, the free-running oscillation component at $\omega_1 - \omega_b$ will not be located right at ω_0 , but will in fact be shifted or pulled slightly away from the frequency ω_0 , by the amount $\omega_m^2/2(\omega_1 - \omega_0)$. *The injected signal, even well outside the locking range, causes a pulling of the free-running oscillation away from ω_0 and toward the injected signal frequency.* Figure 29.13 illustrates this pulling effect, and also the manner in which the additional spectral components shift and change in amplitude as the injected frequency ω_1 is tuned closer to the edge of the locking range from outside.

The latter point is particularly important in many practical applications. Laser frequency measurements can in many situations be made with great precision. We now see that even a weak injected signal going into a laser oscillator well outside its locking range can become a source of frequency error through this pulling effect.

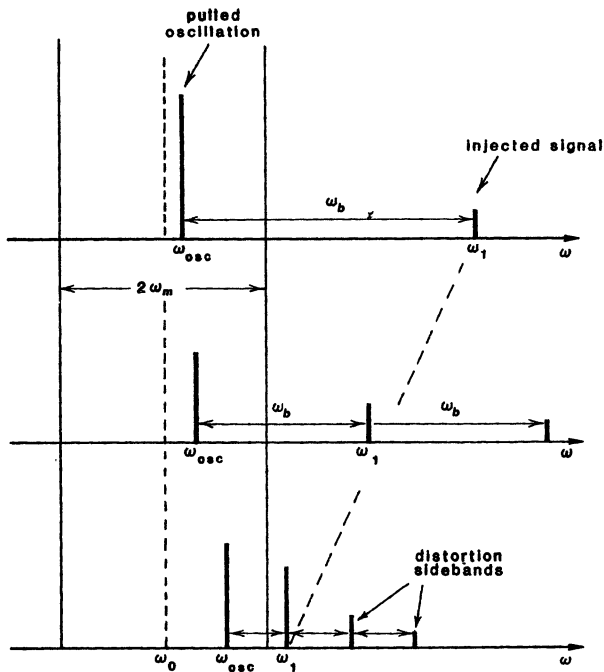


FIGURE 29.13
Frequency components in an oscillator with an injected signal outside the locking range.

Behavior Close to the Locking Edge

Suppose the injected signal frequency ω_1 is tuned closer to the edge of the locking range from outside, so that $|\omega_1 - \omega_0| \rightarrow \omega_m$. The dominant oscillation signal at ω_{osc} then gets more and more strongly pulled away from its free-running value ω_0 and toward the edge of the locking range from inside, as ω_1 approaches this locking range from outside, as illustrated in Figure 29.13.

In fact, if the injected signal is tuned to be just outside the locking range by a small amount ξ , so that we have

$$\omega_1 = \omega_0 + \omega_m + \xi, \quad \text{with } \xi \ll \omega_m, \quad (50)$$

then the oscillation signal is pulled over to be just inside the locking band, at the frequency

$$\omega_{\text{osc}} = \omega_1 - \omega_b \approx \omega_0 + \omega_m - \sqrt{2\omega_m \xi}. \quad (51)$$

As ω_1 approaches the band edge $\omega_0 + \omega_m$ from outside, the oscillation signal approaches it from the inside, until the two merge at $\omega_0 + \omega_m$.

When the injected signal frequency ω_1 is tuned very near the locking band edge coming from the outside, it can be shown that the periodic variation $\phi_p(t)$ in

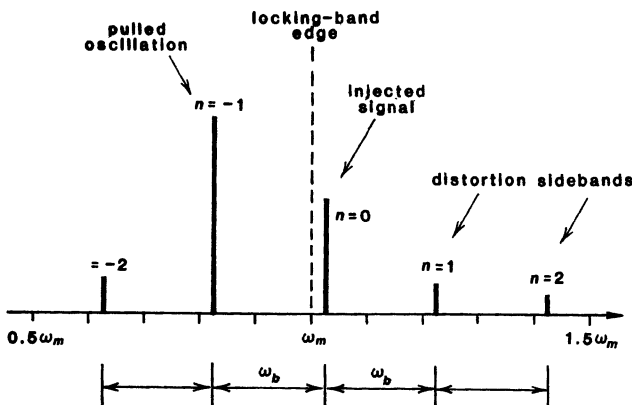


FIGURE 29.14

Additional sidebands appearing as ω_1 come very close to ω_m from the outside.

the total phase $\phi(t)$ becomes larger and more distorted. As a consequence of this large phase variation, the Fourier spectrum of the cavity signal $\mathcal{E}(t)$ (not just the phase modulation $\phi_p(t)$) acquires a growing number of additional sidebands or Fourier components at the other frequencies $\pm n\omega_b t$ as the injected signal is tuned closer to the edge of the locking range. In physical terms, the oscillation signal $\mathcal{E}(t)$ inside the cavity no longer consists simply of the weak injected component at ω_1 plus a stronger pulled-oscillation component at $\omega_{osc} = \omega_1 - \omega_b$. Additional Fourier components or distortion sidebands at the frequencies $\omega_1 + n\omega_b$ for $n \leq -2$ and $n \geq +1$ also become significant in the oscillation spectrum, as illustrated in Figure 29.14. The interference component between these sidebands at the fundamental frequency ω_b is no longer purely sinusoidal but acquires distortion at higher harmonics.

REFERENCES

The basic expressions for injection locking both inside and outside the locking range are very clearly presented in the paper by R. Adler, "A study of locking phenomena in oscillators," *Proc. IRE* 34, 351-357 (1946), reprinted in *Proc. IEEE* 61, 1380 (October 1973). Some useful additional formulas for injection-locking behavior outside the locking region are given in M. Armand, "On the output spectrum of unlocked driven oscillators," *Proc. IEEE* 57, 798 (1969).

Problems for 29.4

1. Fourier signal components near the edge of the locking range. Try substituting the expression $\phi(t) = -\omega_b t + \sum [a_n \cos n\omega_b t + b_n \sin n\omega_b t]$ into the Adler solution for $\phi(t)$ outside the locking range; assuming the higher-order coefficients a_n and b_n are small ($\ll 1$); and then matching up corresponding harmonic components to solve for the magnitudes of at least the first few of these coefficients. (The trigonometric identities $\tan z/2 = (1 - \cos z)/\sin z = \sin z/(1 + \cos z)$ may be

useful in doing this). Having obtained some of the lower-order a_n 's and b_n 's, can you then find the amplitudes of the larger spectral components of the output signal $\mathcal{E}(t)$?

29.5 PULSED INJECTION LOCKING: A PHASOR DESCRIPTION

Injection locking of the type described in the preceding sections is often thought of as a promising way to control the temporal and spatial characteristics not only of cw lasers, but also of high-power pulsed lasers, which are often noisy and unstable, using injected signals from much weaker but much better-behaved cw master oscillators. Much attention has been devoted to the possible use of injection locking for pulsed TEA CO₂ lasers, *Q*-switched Nd:YAG lasers, and pulsed excimer lasers using cw or long-pulse master oscillators of the same type.

The behavior of a high-gain or high-power pulsed oscillator with an external signal is, however, quite different from the classical description of cw injection locking that we have given in previous sections. The injected signal in the pulsed situation is typically so weak or so far off resonance in relation to the free-running pulsed oscillator that the pulsed oscillator is not really "locked" by the injected signal at all. Rather the injected signal can more accurately be viewed as providing an initial condition on the spatial and spectral modes of the pulsed oscillator, from which these modes then grow and develop in the usual fashion, with little continuing influence or control by the injected signal beyond its setting of the initial conditions. We might more accurately refer to this as "injection seeding" of the pulsed oscillator. The term "injection locking" nonetheless continues to be applied, rather inappropriately, to the pulsed situation as well.

The conventional analysis of injection locking given in the previous four sections is thus of little direct relevance to the high-power pulsed situation. In this section we will develop instead some alternative ways of describing and analyzing pulsed laser injection locking. Discussions of this topic very often become very confused, because we must consider highly transient situations, while trying to apply concepts like sinusoidal signals and cavity modes which are basically cw steady-state concepts. It is hoped the discussions in this section will clarify rather than further confuse the situation.

Transient Phasor Analysis of Injected Signals

The injection-locking behavior of a laser cavity with an external signal can perhaps best be understood from a simple phasor picture such as that shown in Figure 29.15.

As shown in this model, let \tilde{E}_{circ} (or \tilde{E}_c in Figure 29.15) be the total phasor amplitude of the circulating optical wave traveling around the cavity, measured at a plane just inside and traveling inward from the output mirror. Let \tilde{E}_{ref} be the portion of that circulating wave that comes from the outward-traveling internal wave reflecting off the output mirror, whereas \tilde{E}_{inj} is the injected signal coming in through the mirror, measured just inside the mirror. (For brevity these waves are labelled as E_c , E_r and E_i in Figures 29.15 through 29.19.) Note that in this discussion all the waves are measured just *inside* the cavity end mirror.

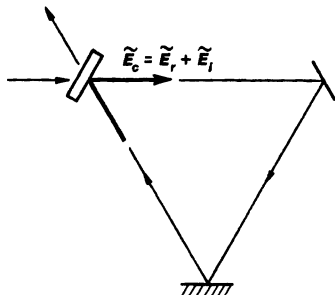


FIGURE 29.15
Analytical model for ring-laser oscillator.

These waves are most easily visualized in a ring cavity as shown, but the analysis we will develop applies equally well to a standing-wave cavity.

These waves must then satisfy two separate physical conditions. First, at every instant of time these complex phasor amplitudes must by definition satisfy the condition that

$$\tilde{E}_{\text{circ}}(t) \equiv \tilde{E}_{\text{refl}}(t) + \tilde{E}_{\text{inj}}(t). \quad (52)$$

Remember that these phasor amplitudes are all defined with respect to the injected signal frequency ω_1 , so that for each of them the real field $\mathcal{E}_x(t)$ at that plane has the form

$$\mathcal{E}_x(t) = \text{Re} \left[\tilde{E}_x(t) e^{j\omega_1 t} \right]. \quad (53)$$

All three complex phasor amplitudes \tilde{E}_{circ} , \tilde{E}_{refl} and \tilde{E}_{inj} may in general be time-varying, within the slowly varying envelope approximation. However, we will normally think of the injected signal \tilde{E}_{inj} as constant, so that it can be represented by a constant phasor at a fixed phase angle in the complex plane.

The second physical condition is that the reflected phasor amplitude $\tilde{E}_{\text{refl}}(t)$ coming off the mirror at any time t is derived from the total circulating field $\tilde{E}_{\text{circ}}(t - T)$ that left that same plane one transit time T earlier, multiplied by the net gain, loss and phase shift for one round trip inside the cavity. To a good approximation this can be written as

$$\tilde{E}_{\text{refl}}(t) = \tilde{E}_{\text{circ}}(t - T) \times e^{\delta_m - \delta_c - jT(\omega_1 - \omega_0)}, \quad (54)$$

where T is the round-trip transit time, and $\omega_1 - \omega_0$ is the amount by which the injection frequency ω_1 is detuned from the cavity resonance frequency ω_0 . (Recall that by definition $\omega_0 T = \omega_0 p/c$ is an exact multiple of 2π .)

Equation 29.54 is strictly true only if the gain and loss factors δ_m and δ_c do not change (at least, not by much) during one round-trip time T . However, even in a rapidly changing situation something close to Equation 29.54 using averaged values of δ_m and δ_c will be valid.

Below-Threshold Cavity Excitation

We can now describe both the steady state and the transient behavior of an injection-locked laser cavity using Equations 29.52 and 29.54 to connect the three

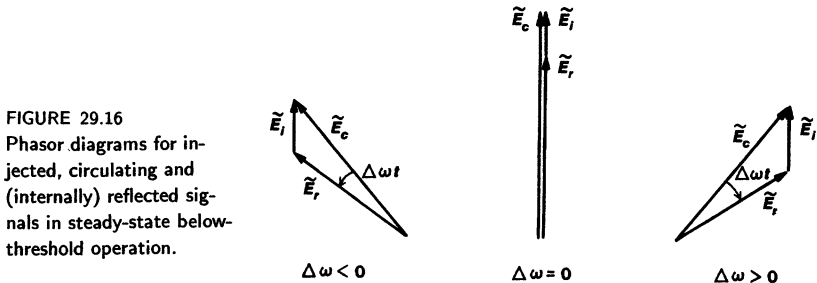


FIGURE 29.16
Phasor diagrams for injected, circulating and (internally) reflected signals in steady-state below-threshold operation.

phasors. As a starting exercise, let us first use this model to analyze steady-state passive-cavity behavior below threshold, primarily to gain some understanding and experience with the model.

In this situation the circulating wave \tilde{E}_{circ} will return after one round-trip as a vector \tilde{E}_{ref} which is smaller than \tilde{E}_{circ} , and which is rotated in phase by a net angle per round trip of $(\omega_1 - \omega_0)T$ if the injected frequency is off cavity resonance. To have steady-state behavior, the injected phasor \tilde{E}_{inj} must then add vectorially to \tilde{E}_{ref} so as to make up the original \tilde{E}_{circ} . The vectorial implications of this are illustrated in Figure 29.16 for injected signals below, at, and above resonance.

Exactly on resonance all three vectors are in phase as shown by the middle sketch in Figure 29.16. The reflected or returned phasor after one round trip, \tilde{E}_{ref} , is in phase with the circulating phasor \tilde{E}_{circ} , but is reduced in magnitude by the amount that the round-trip gain is below unity. The circulating phasor \tilde{E}_{circ} must then adjust its length so that \tilde{E}_{inj} just makes up for the net round-trip loss in \tilde{E}_{circ} . (This is how the net signal level inside the cavity is determined.)

Above or below resonance, however, as illustrated by the two vector diagrams on each side, \tilde{E}_{ref} returns after each round trip both attenuated and rotated in phase by some positive or negative phase shift $(\omega_1 - \omega_0)T \equiv (\omega_1 - \omega_0)p/c$ where p is the round-trip distance. Both \tilde{E}_{ref} and \tilde{E}_{circ} must then be rotated in phase relative to the injected signal \tilde{E}_{inj} , so that \tilde{E}_{inj} can just make up the gap between \tilde{E}_{ref} and \tilde{E}_{circ} , as illustrated by these two diagrams. This demands in general that \tilde{E}_{circ} and \tilde{E}_{ref} must both become smaller and also rotate in absolute phase with respect to the injected phasor \tilde{E}_{inj} .

The two basic Equations 29.52 and 29.54 can be combined in this situation to give the steady-state circulating field \tilde{E}_{circ} produced by an injected field \tilde{E}_{inj} , namely,

$$\begin{aligned}\tilde{E}_{\text{circ}} &= \frac{1}{1 - \exp[-(\delta_c - \delta_m) - jT(\omega_1 - \omega_0)]} \tilde{E}_{\text{inj}} \\ &= \frac{1}{[1 - e^{-(\delta_c - \delta_m)} \cos T(\omega_1 - \omega_0)] + j e^{-(\delta_c - \delta_m)} \sin T(\omega_1 - \omega_0)} \tilde{E}_{\text{inj}},\end{aligned}\quad (55)$$

where $\delta_c - \delta_m$ is the net round-trip loss minus gain due to cavity losses, mirror reflections, laser gain and whatever else is present. This equation, with the differences in notation taken into account, has exactly the same form as the general analytic results derived in earlier chapters for regenerative interferometers

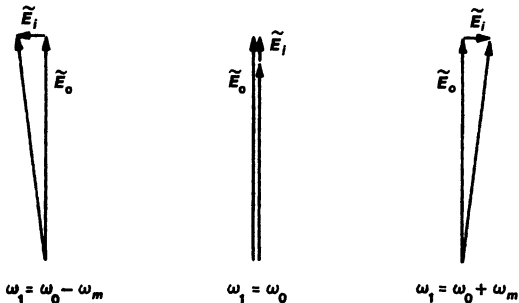


FIGURE 29.17
Phasor diagrams for the injection-locked oscillator, on resonance and at the edges of the locking range.

or below-threshold laser cavities with an external signal. The vector diagrams in Figure 29.16 illustrate graphically how the intracavity signal \tilde{E}_{circ} decreases in amplitude and rotates in phase relative to the external signal \tilde{E}_{inj} as we go off resonance on either side.

Steady-State Injection Locking

Consider now the situation of an above-threshold, cw oscillating and injection-locked laser, as illustrated in Figure 29.17.

In an oscillating laser both \tilde{E}_{circ} and \tilde{E}_{ref} will increase in amplitude to essentially the free-running oscillation level \tilde{E}_0 of the laser oscillator. This is the intensity level at which the laser gain δ_m is saturated down to essentially equal the loss δ_c , so that the difference $\delta_m - \delta_c$ is nearly zero. This free-running level \tilde{E}_0 will normally be very much larger than the injected signal level \tilde{E}_{inj} , especially since these phasors are both measured inside the laser mirror, after the injected signal vector is reduced by the mirror transmission, and before the laser circulating field is reduced by the same amount.

Although the round-trip gain in an oscillating laser is reduced to very close to exactly unity in magnitude, the phase shift $(\omega_1 - \omega_0)T$ will still apply on each round trip. We can see graphically from these diagrams that if the detuning $\omega_1 - \omega_0$ deviates from zero by even a very small amount, the very small phasor \tilde{E}_{inj} must rotate by a rapidly increasing angle with respect to the circulating phasor \tilde{E}_{circ} , in order to close the gap between the two much longer vectors \tilde{E}_{circ} and \tilde{E}_{ref} , which both have magnitudes $\approx \tilde{E}_0$. (To save space we have drawn the two outer diagrams in Figure 29.17 as if the injected phasor \tilde{E}_{inj} rotated in absolute angle, while the longer vectors \tilde{E}_{circ} and \tilde{E}_{ref} stayed vertical, rather than keeping \tilde{E}_{inj} vertical as in Figure 29.16; but obviously it is the relative angle between \tilde{E}_{inj} and \tilde{E}_{circ} that is of importance.)

In fact, the maximum allowable tuning range for the injected signal, $\pm\omega_m$, out to the point where the injected signal \tilde{E}_{inj} and the oscillation vector \tilde{E}_0 will be $\pm 90^\circ$ out of phase, will obviously be given by

$$|T(\omega_1 - \omega_0)| \leq T\omega_m \approx \left| \frac{\tilde{E}_{\text{inj}}}{\tilde{E}_0} \right|. \quad (56)$$

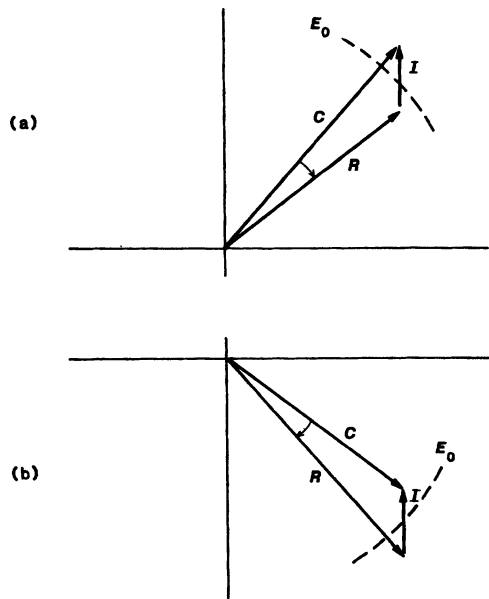


FIGURE 29.18
Stable and unstable solutions to the injection locking equations.

If we translate the phasor amplitudes outside the cavity, where the injected intensity is $I_1 = |\tilde{E}_{\text{inj}}|^2/\delta_e$ whereas the oscillator output intensity is $I_0 = \delta_e|\tilde{E}_{\text{refl}}|^2$, where δ_e is the external coupling factor for the cavity, then we obtain for the half-locking range

$$\omega_m = \frac{\delta_e}{T} \sqrt{\frac{I_1}{I_0}}, \quad (57)$$

which is exactly the same cw result as derived earlier. It indicates graphically that the injection-locking range terminates when the injected signal \tilde{E}_{inj} , even when turned at $\pm 90^\circ$ to the returning phasor \tilde{E}_{refl} , is no longer able to bridge the gap caused by the phase rotation $(\omega_1 - \omega_0)T$ and pull \tilde{E}_{refl} back into phase with \tilde{E}_{circ} . The narrowness of the cw locking range can be traced in essence to the smallness of the injected signal vector $|\tilde{E}_{\text{inj}}| = (\delta_e I_1)^{1/2}$ compared to the free-running oscillation vector $|\tilde{E}_0| = (I_0/\delta_e)^{1/2}$.

The net round-trip gain (i.e., laser gain minus cavity loss) in an oscillating laser is very close to unity, and there seems to be no reason in principle why this gain might not be slightly greater than unity rather than slightly less. It might seem therefore that there could actually be two different possible phase arrangements between the incident, reflected and circulating waves in an oscillating laser at steady state, as illustrated in Figure 29.18. In fact, however, only one of these two situations is stable against perturbations, as the reader may want to demonstrate (see Problems).

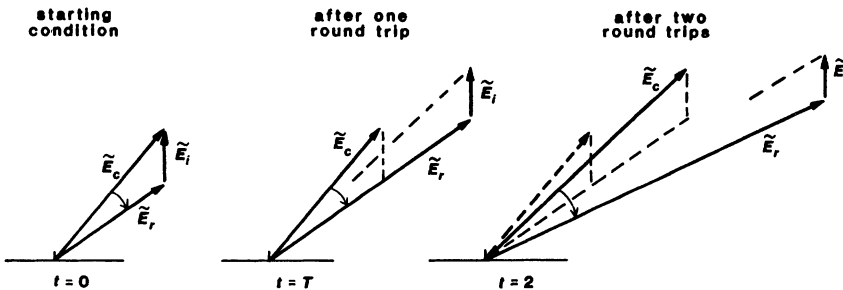


FIGURE 29.19

Phasor evolution on successive round trips during buildup of laser oscillation.

Pulsed Injection Locking

The phasor model thus gives useful new insights into cw injection locking. This same general model is even more useful for pulsed laser injection locking, although the physics and the conclusions are quite different.

The simplest situation to consider here is an ideally Q -switched or gain-switched laser cavity which for $t < 0$ is well below threshold, and is passively excited by an external signal in the manner just described. If this external signal has been turned on for at least two or three cavity lifetimes prior to $t = 0$, the cavity will be at essentially its steady-state, passively excited condition at $t = 0$. The initial condition at $t = 0$ for an injected signal ω_1 well outside a cavity resonance ω_0 —that is, with ω_1 detuned from ω_0 by, say, 20% of the axial-mode spacing—will be a vector diagram with \tilde{E}_{circ} , \tilde{E}_{ref} and \tilde{E}_{inj} making large angles with each other, as shown in earlier diagrams.

Suppose the cavity loss is then suddenly decreased by rapid Q -switching, or the gain is suddenly and greatly increased by gain switching. The description is simplest if we consider such switching as occurring instantaneously, in less than one round-trip time; but the following description will change only in detail for the more realistic situation of slower cavity turn-on.

The circulating vector \tilde{E}_{circ} will then begin to grow and to change rapidly in amplitude and phase on successive round trips, beginning with the first round trip following $t = 0$, as shown in Figure 29.19. Adding the injected phasor $\tilde{E}_{\text{inj}}(t)$ to the returned phasor $\tilde{E}_{\text{ref}}(t)$ no longer restores the original $\tilde{E}_{\text{circ}}(t-T)$ from one round trip earlier, since the cavity is now in a transient and growing situation.

The phasor amplitude inside the cavity thus begins to rotate in phase by an amount $(\omega_1 - \omega_0)T$ per round trip, as well as growing rapidly, on each successive round trip. In fact the magnitudes of \tilde{E}_{ref} and \tilde{E}_{circ} will grow exponentially with successive round-trips, so that within just a few round-trips they will become much larger than the injected phasor \tilde{E}_{inj} . The injected phasor \tilde{E}_{inj} thus becomes of negligible significance after a few round trips.

The Cavity Signal Frequency

It is particularly important to note that the phasors \tilde{E}_{ref} and \tilde{E}_{circ} , once they become large compared to the injected signal \tilde{E}_{inj} , not only continue to grow in amplitude but—in the description given here—they continue to rotate in phase in the complex plane by the factor $\exp[-j(\omega_1 - \omega_0)T]$ per round-trip.

We must remember also that the reference plane in this situation is itself in essence rotating at frequency $-\omega_1$, so that the real field then rotates at frequency $-(\omega_1 - \omega_0) + \omega_1 \equiv \omega_0$.

This means in effect that the actual frequency of the circulating cavity signals is no longer the injected signal ω_1 , with respect to which the complex plane was defined. Rather, the phasors now have a linearly increasing phase factor

$$\phi(t) \approx -(\omega_1 - \omega_0)T \times (t/T) = -(\omega_1 - \omega_0)t, \quad (58)$$

and hence the actual frequency of the signal inside the cavity is

$$\omega_i(t) = \omega_1 + \frac{d\phi(t)}{dt} \approx \omega_0. \quad (59)$$

In other words, as soon as the phasors inside the cavity become significantly larger than the injected phasor \tilde{E}_{inj} , the signal in the cavity automatically and unavoidably changes over to the natural cavity frequency ω_0 rather than the injected signal frequency or seeding frequency ω_1 .

Injection Seeding and Oscillation Mode Control

The essential feature of pulsed injection locking, therefore, is that the initial passive excitation \tilde{E}_{circ} in the cavity before turn-on grows and is very rapidly converted into an essentially free-running normal oscillation in the cavity after turn-on. The signal in any given cavity mode, regardless of how it was initially excited, converts over to the natural resonance frequency ω_0 of that mode within a few round trips (at high enough gain), and retains no memory of the fact that it may have been initially excited at a frequency ω_1 somewhere out on the side of the response curve for that mode.

Pulsed injection locking, or injection seeding, therefore does not really “lock” the oscillation in any mode of the laser. Rather, the essential way in which pulsed injection locking can improve the performance of large multimode lasers is *by controlling the initial excitation of individual modes, and by providing an initial excitation well above the spontaneous emission noise level in one or a small set of desired modes*.

The essential requirement for good behavior of the resulting oscillation is that the initial excitation in the desired spectral and spatial modes be large compared to the noise and spontaneous emission in any other high-gain modes. This will then ensure that the laser signal builds up—at least initially—from this initial excitation and not from noise. If we attempt to lock a pulsed laser in this fashion, in a situation where the unwanted modes have significantly higher gains than the wanted and “seeded” modes, then the wanted modes will start off ahead, and stay ahead for some period of time; but if the laser pulse is too long, the unwanted modes will catch up and take over, and the pulsed injection locking performance will deteriorate.

One essential question, then, is how well an injected signal at frequency ω_1 will initially excite a cavity mode whose resonance is at frequency ω_0 . Reasonably good excitation can be obtained in a passive cavity for a rather large range of injected frequencies ω_1 around an axial-mode resonance ω_0 —the useful range can be a sizable fraction of the axial-mode spacing in typical situations. This range will be much larger than the maximum detuning $\pm\omega_m$ for the true cw

injection locking in the same laser. True injection “locking” generally plays little role in the high-gain pulsed situation.

Frequency Sweeping

The phasor description given in the preceding explains how the frequency of the laser-cavity signals will change within a few round trips from the injected frequency ω_1 to the cavity frequency ω_0 . It is perhaps worth emphasizing, however, that the experimental significance of this frequency change during the transient period is limited.

Suppose that the frequency shift from the injected frequency ω_1 to the cavity frequency ω_0 takes place within N round trips, or during a time-interval of NT , where T is the cavity round-trip time and N is some small integer. Then from the uncertainty relation between frequency and time, the laser frequency is not really precisely defined or measurable within that time-interval to a precision better than about $\Delta\omega \approx \pi/NT$. But the frequency shift $\omega_1 - \omega_0$ is itself at most half the spacing between adjacent axial modes, or $|\omega_1 - \omega_0| \leq \pi/T$ and generally much less. Hence, the frequency shift that occurs is not really measurable within the measuring time that is available. The behavior of the cavity phasor \tilde{E}_{circ} in the complex plane during the transient interval is clear. It's not particularly useful, however, to worry about trying to measure how the cavity frequency gets from ω_1 to ω_0 during the first few round-trips.

Note also that even in a slow turn-on situation, the laser frequency goes from ω_1 to ω_0 as soon as \tilde{E}_{circ} becomes large compared to \tilde{E}_{inj} . This normally occurs in the very early, very low-power portion of the laser's output pulse, before the output signal even becomes visible. Hence, *for practical purposes all the useful power output of the pulsed laser occurs at the cavity frequency ω_0 , not at the injected frequency ω_1 .*

Transient Phasor Equation

The phasor model developed in this section can also be readily converted into an approximate but generally more than adequate cavity differential equation. Suppose we rewrite Equation 29.54 as

$$\begin{aligned}\tilde{E}_{\text{refl}}(t) &= e^{\delta_m - \delta_c - j(\omega_1 - \omega_0)T} \times \tilde{E}_{\text{circ}}(t - T) \\ &\approx [1 + \delta_m - \delta_c - j(\omega_1 - \omega_0)T] \times \tilde{E}_{\text{circ}}(t) - T \times \frac{d\tilde{E}_{\text{circ}}(t)}{dt}.\end{aligned}\quad (60)$$

This equation appears to require an approximation that the net round-trip gain is small, $|\delta_m - \delta_c - j(\omega_1 - \omega_0)T| \ll 1$; but in fact it is probably valid even for quite large gains. The gain can also itself be time varying, even during a round trip. Equation 29.60 then converts to

$$\frac{d\tilde{E}_{\text{circ}}}{dt} + \left[\frac{\delta_c - \delta_m}{T} - j(\omega_1 - \omega_0) \right] \tilde{E}_{\text{circ}} = \frac{1}{T} \tilde{E}_{\text{inj}}. \quad (61)$$

This is essentially the same result as has been obtained from other analytical approaches, and yields essentially all the same results as discussed to date.

REFERENCES

One of the best theoretical and experimental treatments of pulsed laser injection locking to date appears to be J-L. Lachambre, P. Lavigne, G. Otis, and M. Noel, "Injection locking and mode selection in TEA-CO₂ laser oscillators," *IEEE J. Quantum Electron.* **QE-12**, 756-764 (December 1976).

Other useful references include U. Ganiel, A. Hardy, and D. Treves, "Analysis of injection locking in pulsed dye laser systems," *IEEE J. Quantum Electron.* **QE-12**, 704-716 (November 1976); A.J. Alcock, P.B. Corkum, and D.J. James, "A simple mode-locking technique for large-aperture TEA CO₂ lasers," *Appl. Phys. Letters* **30**, 148-159 (February 1, 1977); and I. J. Bigio and M. Slatkine, "Injection-locking unstable resonator excimer laser," *IEEE J. Quantum Electron.* **QE-19**, 1426-1436 (September 1983).

Problems for 29.5

1. *Using the phasor model to obtain additional steady-state locking results.* Use the phasor model of this section to explain the same oscillation frequency pulling and the multiple sideband effects that we derived in earlier sections of this chapter for a cw oscillator with an injected signal that is just outside the locking range
2. *Ambiguity in the phase relationship between injected and oscillating signals?* Figure 29.18 seems to show two equally valid ways of satisfying the phase relationship between the injected (*I*), circulating (*C*) and returning (*R*) phasor amplitudes in a cw injection-locked laser oscillator, given the same off-resonance detuning $\Delta\omega T$, and the same free-running oscillation level \bar{E}_0 . One solution clearly has round-trip gain g_1 slightly less than unity ($\gamma_m < \gamma_c$, but only slightly), whereas the other requires g_1 slightly greater than unity ($\gamma_m > \gamma_c$, but only slightly). Are both solutions really possible? Why, or why not?

29.6 APPLICATIONS: THE RING-LASER GYROSCOPE

Injection-locking phenomena can obviously occur and can be important not only in lasers, but in any kind of coherent oscillator in any frequency range. Injection locking is thus a very basic concept, with essentially the same mathematical description being applicable to lasers at optical frequencies, to microwave solid-state devices, to vacuum tube or transistor audio oscillators, and to almost any other kind of self-sustaining electronic or non-electronic oscillator.

Injection locking can on the one hand be an extremely useful technique for obtaining the clean, well-controlled, and highly stabilized output characteristic of a small and well-stabilized oscillator, while at the same time obtaining the power output and power conversion efficiency characteristic of a large, powerful, but often noisy and unstable power oscillator. Injection locking also plays a significant role in understanding mode-locking effects, as we have seen in an earlier chapter.

Injection-locking effects can also play several unwanted roles in applications such as laser gyroscopes, laser frequency standards, laser communication systems, and other applications where undesirable coupled-oscillator effects can occur as a result of backscatter, either of a laser's output beam back into itself,

or as the result of any other situation in which a weak signal from one signal source is coupled into another oscillator running at the same or nearly the same frequency.

Applications of Injection Locking in Lasers

Important applications of injection-locking concepts that occur particularly in laser oscillators include:

(1) *Stabilization of high-power laser oscillators* . By the use of injection locking, a weak but well-stabilized CW laser can control a much higher-power laser of the same type, where this higher-power laser would be inherently much more noisy and unstable. The power conversion efficiency in this situation, or the conversion ratio from injected signal to controlled oscillator power, can be very high; and at the same time the power extraction efficiency from the large laser operating as an oscillator will generally be much higher than if the same laser medium were operated as a linear amplifier (i.e., a MOPA combination) for the same injected signal source.

(2) *FM demodulators and amplifiers* . A locked oscillator within its locking range provides a system element in which the output amplitude is constant, but the output signal phase varies more or less linearly with the injected signal frequency (at least across the center portion of the locking range). This can be used to accomplish various kinds of demodulation and detection of frequency-modulated (FM) communications signals. This concept is not very important at optical frequencies, but has found application at lower radio frequencies.

(3) *Laser sensitivity to backscatter* . Laser oscillators, especially frequency-stable lasers, are extraordinarily sensitive to the backscattering of even small amounts of their own output beam back into the laser cavity. This is clearly because the backscattered signal is essentially an injection-locking signal which is automatically tuned right to the center of the locking range. If the backscattered signal is phase or frequency modulated (that is to say, doppler-shifted) by reflection from a moving surface (or is phase modulated by air currents in the beam path), this modulation will be translated into a corresponding effect on the oscillation frequency of the laser itself. Lasers in general do not function well when required to look directly into any significant amount of back reflection of their output beams.

(4) *Optical heterodyne experiments* . The standard method for making stable laser frequency measurements is to heterodyne or mix together the beams from two lasers oscillating at slightly different frequencies, in order to measure with precision the difference or "beat" frequency between the two lasers. In such an experiment it is almost impossible to avoid at least some backscattering of the light from each laser into the other. Each laser will experience an injection-locking effect caused by the signal from the other laser. Even if this effect is too weak to produce actual locking, it may be sufficient to produce significant pulling of each laser's frequency outside the locking range, and may thus deteriorate the accuracy of the measurements.

(5) *Ring-laser gyroscopes* . The two oppositely traveling oscillation waves inside a ring-laser gyroscope are supposed to be totally independent and uncoupled oscillators; and the essential requirement in the ring-laser gyro is to measure the very small difference frequency between the independent oscillations in the two directions. Even a very small amount of unavoidable scattering inside the laser cavity will backscatter light from each oscillation into the other, with in-

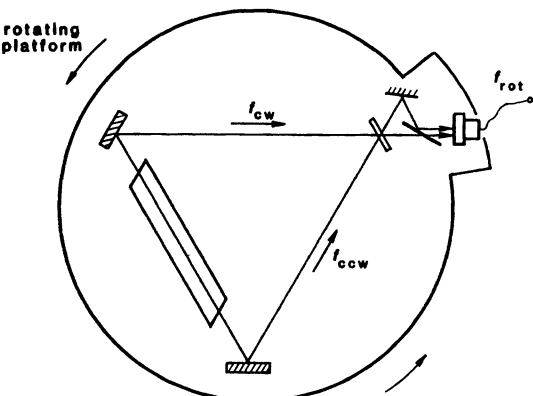


FIGURE 29.20
Three-mirror ring laser gyroscope design.

creased efficiency, in fact, because the scattering occurs right inside the oscillator cavity for each laser. Ring-laser gyros therefore inevitably "lock up," in exactly the fashion described by injection locking, when the difference between the two frequencies becomes small enough to put each oscillator inside the locking range for the other.

(6) *Mode locking* . The intracavity modulator inside a mode-locked laser generates sidebands on each of the axial-mode oscillation frequencies that are present; and these sidebands are normally intended to fall exactly (or almost exactly) on top of other axial-mode frequencies. The process of mode locking in many situations can thus be understood, or at least we can gain insight into the mode-locking process, by viewing it as a situation in which the sidebands generated on each axial mode have an injection-locking effect on the appropriate axial modes separated on either side by the intracavity modulation frequency.

(7) *Coupled oscillators* . Any situation involving two coupled oscillators, where part of the output from each laser is coupled into the other, can be analyzed overall as a dual system with two normal modes, or alternatively as a double injection-locking problem.

The Ring-Laser Gyroscope

Injection-locking effects in a ring-laser cavity play an especially important role in an important practical device, the ring-laser gyroscope. Let us therefore examine this device in slightly more detail.

Figure 29.20 shows a simple, but actually quite realistic, design for a ring-laser gyroscope consisting of a triangular ring-cavity laser mounted on a rotating platform. (In practice, such ring-laser gyros are often made by drilling the three beam paths through a solid block of quartz or low-expansion glass, and then attaching the mirrors directly onto the block at the intersection points between the beam paths.) If backscattering effects inside such a cavity can be made small enough, and also if mode competition effects in the laser medium can be properly arranged, such a ring cavity can oscillate in two separate oscillation signals having the same frequency (if the ring is stationary) but traveling in opposite directions around the ring.

Suppose the ring now begins to rotate about its axis, counterclockwise. In crude terms, the oscillation signal traveling around the ring in the same sense as the rotation will have a slightly longer path to travel in order to "catch its tail," since the ring will rotate slightly during the time the light travels around. Hence the oscillation frequency f_{ccw} for the wave going in this direction will become slightly lower, whereas the frequency f_{cw} for the wave going in the opposite direction will become slightly higher.

If we arrange a detection system that can ride along on the rotating platform and observe the difference frequency between these two oscillations by optical-heterodyning the output signals from the two directions, as shown in Figure 29.20, then we can measure this difference or beat frequency (call it f_{rot}). This frequency will in fact be directly proportional to the rotation rate Ω_{rot} of the ring about its axis in inertial space, i.e.,

$$f_{\text{rot}} \equiv f_{cw} - f_{ccw} = \text{const} \times \Omega_{\text{rot}}. \quad (62)$$

This device functions, in other words, as a gyroscope in inertial space, with an output that has the very convenient form of a frequency that can be measured or counted electronically. For typical optical frequencies and mechanical rotation rates, the observed frequency f_{rot} has an easily measured value in the low audio-frequency range. Note that mechanical vibrations and other disturbances in the ring will affect the frequencies f_{cw} and f_{ccw} equally, and hence have no direct effect on the beat frequency between them.

The Lock-Up Problem

Since the beat frequency between two laser signals can be measured easily and with great accuracy, this new form of gyroscope has great practical appeal. Aside from the advantage of having no moving parts, no bearings and no ultra-precise mechanical assemblies, the laser gyroscope offers important advantages of instant response without warm-up time, and direct sensing of the rotation signal.

The crucial defect in this approach, however, is that even an exquisitely small backscattering signal from one direction of the oscillation into the other direction provides an injection-locking signal that causes the two frequencies to lock together below a certain minimum rotation rate. The plot of beat frequency f_{rot} versus rotation rate Ω_{rot} , instead of going linearly through 0 at $\Omega_{\text{rot}} = 0$, thus shows a locking band or dead band around zero frequency, as illustrated in Figure 29.21, so that the gyro cannot sense small rotation rates. Extraordinary efforts at making ultra-perfect low-scattering mirrors and at eliminating all other backscattering effects can reduce the width of this deadband, but not eliminate it entirely.

There is also an important error in the scale factor $f_{\text{rot}}/\Omega_{\text{rot}}$ of the gyroscope due to the pulling effects we have discussed earlier, which occur for a considerable distance outside the locking range as we have analyzed in the preceding sections. Numerous ingenious methods aimed at avoiding these locking and pulling effects have been proposed, but each such scheme seems to raise new and more complex problems of its own. The standard approach in commercially produced gyros at present, in fact, is the crude but effective technique of dithering or rotating the gyroscope assembly forward and backward with respect to its mounting on a springy torsional support, so that the gyro spends most of its time moving at high positive or negative rotation velocities outside the deadband. Electronic

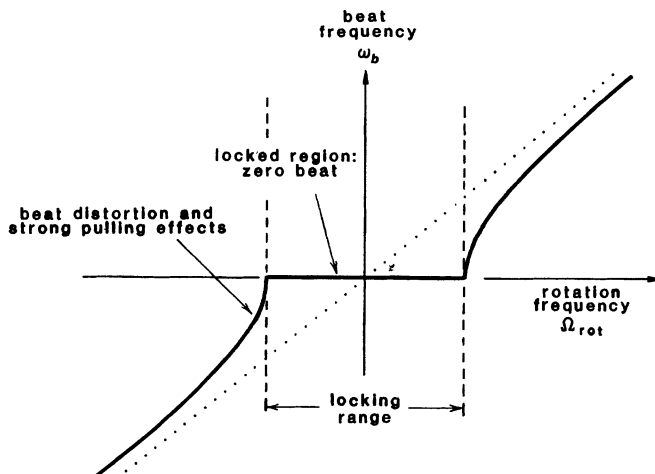


FIGURE 29.21

Dead band and scale factor distortion caused by back-scattering and injection-locking effects in a ring laser gyroscope.

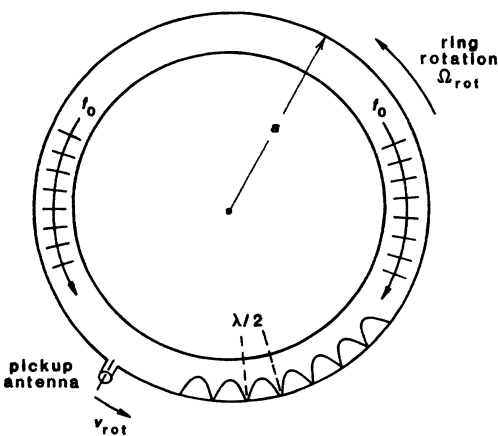


FIGURE 29.22
The pickup antenna, riding on the ring, passes through the optical standing-wave pattern, which remains stationary in inertial space.

counters can easily record the accumulated upward and downward counts during the two directions of rotation, and then subtract them to obtain the much smaller average rotation of the underlying platform.

Simplified Theory of the Ring-Laser Gyroscope

We can give a slightly unusual but still correct derivation of the scale factor and method of operation of such a ring-laser gyroscope as follows.

Rather than a ring cavity using mirrors to form a polygonal path, consider instead a hypothetical perfectly circular loop or path formed from some kind of optical waveguide, as shown in Figure 29.22. This might be a fiber, or a metallic waveguide with extraordinarily smooth and lossless metallic walls formed into a ring, or even a “whispering gallery” type of mode inside a cylindrical ring with lossless metal walls. Suppose two oscillations both at frequency ω_0 are traveling in opposite directions around this ring. The fields in this ring are then equally well describable either as two traveling waves, or as a single standing wave with a periodic intensity variation having a spatial period of $\lambda_0/2$.

Suppose we begin to rotate this ring cavity about its axis. Since there is really nothing to tie the electromagnetic (or optical) fields in the guide to the guide walls—the walls are “slippery” to the fields—we can graphically but accurately view the standing electromagnetic waves as remaining fixed in inertial space, while the ring itself rotates past them.

Assume that there is a very small probe antenna or pick-up device attached to the ring itself, which moves through the standing-wave pattern as the ring rotates, and detects the standing-wave intensity in square-law fashion. As this probe is carried through the standing-wave fields at angular velocity Ω_{rot} , it will measure a frequency (in cycles per second, or Hz) given by

$$f_{\text{rot}} = \frac{v_{\text{rot}}}{\lambda/2} = \frac{2a\Omega_{\text{rot}}}{\lambda}, \quad (63)$$

where v_{rot} is the linear velocity of the probe at the ring perimeter and a is the ring radius. We call this observed frequency f_{rot} because it is exactly the difference frequency introduced earlier, described in a different manner. If we rewrite this frequency in terms of the ring area $A = \pi a^2$ and its perimeter $p = 2\pi a$, the scale factor for this ring gyroscope becomes

$$\frac{f_{\text{rot}}}{\Omega_{\text{rot}}} = \frac{A}{p\lambda}. \quad (64)$$

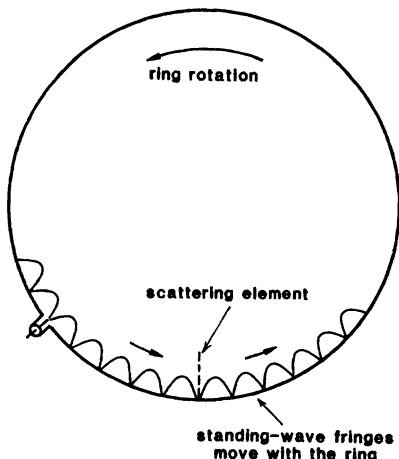
This expression, though derived for a circular ring, is in fact valid for a ring cavity of any shape, where p is again the ring perimeter (followed by the laser beam) and A the area enclosed by that perimeter. (Note that a long narrow ring—or in the limit a standing-wave cavity—has vanishing area and hence vanishing sensitivity.)

As a practical number the Earth's rotation rate about its axis through the poles is 2π radians per 24 hours, or $\Omega_{\text{rot}} \approx 75 \mu\text{rad/sec}$. If we assume a horizontal laser gyroscope with radius $a = 10 \text{ cm}$ and $\lambda = 600 \text{ nm}$, the beat frequency corresponding to Earth rate will then be $f_{\text{rot}} \approx 25 \text{ Hz}$, if measured at the North Pole—the vertical component of Ω_{rot} is 0 at the Equator. Beat frequencies between optical signals in this range are very easily measured, and counted electronically, with great accuracy—if the two optical signals do not lock together. (One group of early laser gyroscope experimenters reported at a scientific meeting that, according to their gyroscope, the Earth was still rotating, although at an uncertain rate.)

Locking Effects in the Circular Ring Model

We can now add locking effects to this picture (as Mother Nature will certainly do even if we do not). Suppose the circular cavity or ring waveguide contains some minute perturbation or scattering element, as in Figure 29.23. If

FIGURE 29.23
A scattering element inside the ring will drag the fringe pattern with it as the ring rotates.



this element is, for example, a small metallic projection, or perhaps a small lossy dust speck, the standing-wave fields in the ring will shift to avoid this element, and to put a null in the standing-wave pattern just at its position.

If we then rotate the ring slowly enough, the standing-wave pattern will be "dragged along" by this perturbation—the fields will rotate with the cavity, and the probe antenna will see no beat frequency. If the ring rotates fast enough, however, the small perturbation will be able to "break loose" from the fields (or vice versa), and be scanned rapidly through the standing-wave cycles. The probe antenna will then again see the beat given by Equation 29.64.

This picture is actually an equally valid description of the locking up of oppositely circulating modes in a ring-laser cavity. With proper extension, it can account for all the same phenomena as the injection locking analysis of earlier chapters.

Fiber Optic Gyroscopes

The circular-cavity-plus-antenna description just given shows how angular rotation can be converted into a beat frequency. It also makes it fairly obvious that extending the ring-waveguide cavity into a multiturn ring with the same basic radius would not change the scale factor—the probe antenna would not move through the standing-wave fringes any more or less rapidly.

There is, however, a competitive form of fiber optic laser gyroscope, in which we send an externally generated signal in both directions around a multiturn loop of optical fiber and measures the differential phase shift of the passive fiber in the two directions. The advantage here is that the optical signal is externally generated and totally independent of the loop, so that locking problems do not arise. The disadvantage is that the differential phase shift which gives the rotation indication in this kind of gyroscope is an extremely minute quantity for the rotation rates of interest. The ring-laser gyroscope converts this minute phase difference per round trip into a frequency difference or a beat frequency, in essence by having the same signal circulate repeatedly around the loop many

many times per second. The fiber-optic gyro, on the other hand, can use a great length of coiled-up fiber—as much as several km of fiber—to magnify the different phase difference through many turns.

At the minute the ring-laser gyroscope is much further along in commercial development, and is in fact being used in the inertial navigation systems of jet airliners, among other things. The fiber gyroscope is newer, very interesting, and may some day reach the same stage of commercial development.

REFERENCES

The use of injection-locked oscillators as FM receivers and demodulators is rather clearly discussed by C. L. Ruthroff in "Injection-locked-oscillator FM receiver analysis," *Bell Sys. Tech. J.* **47**, 1653 (1968); and by T. L. Osborne and C. H. Elmendorf IV, "Injection-locked avalanche diode oscillator FM receiver," *Proc. IEEE* **57**, 214–215 (February 1969).

The general topic of noise in locked oscillators is discussed in considerable detail in papers by M. Kurokawa, "Noise in synchronized oscillators," *IEEE Trans. MTT-16*, 234 (1968); W. O. Schlosser, "Noise in mutually synchronized oscillators," *IEEE Trans. MTT-16*, 732 (1968); and M. E. Hines, J.-C. R. Collinet, and J. G. Ondria, "FM noise suppression of an injection phase-locked oscillator," *IEEE Trans. MTT-16*, 738 (1968).

For a general overview of laser gyroscopes see F. Aronowitz, "The Laser Gyro," in *Laser Applications*, ed. by M. Ross (Academic Press, 1971), or W. Chow, et al., "The ring laser gyro," *Rev. Mod. Phys.* **57**, 61–104 (January 1985).

For a more detailed discussion of locking effects in ring laser, see for example H. A. Haus, H. Statz, and I. W. Smith, "Frequency locking of modes in a ring laser," *IEEE J. Quantum Electron.* **QE-21**, 78–85 (January 1985).

The circular-ring explanation for the laser gyroscope given in this section is also outlined briefly by J.A. Arnaud in *Beam and Fiber Optics* (Academic Press, 1976), pp. 30–31; and was apparently first given by E. O. Schulz-DuBois, "Alternative interpretation of rotation rate sensing by ring laser," *IEEE J. Quantum Electron.* **QE-2**, 299–305 (August 1966).

Problems for 29.6

1. *Locking together of two weakly coupled oscillators.* Two laser oscillators with different cavity parameters, power outputs, and free-running oscillation frequencies (call them ω_1 and ω_2) are set up so that a small fraction η of the output power from laser #1 is fed back into the output port of #2, and vice versa. Analyze the mutual locking effects that the injected signal from each oscillator will have on the other oscillator. Under what conditions can oscillator #1 injection-lock oscillator #2, or #2 lock #1, or both oscillators simultaneously injection-lock each other, so that they both oscillate at a single common frequency? What will be that common frequency, in terms of the laser frequencies, power outputs, and any other relevant parameters?
2. *Frequency pulling of two coupled but unlocked oscillators.* Suppose the two mutually coupled oscillators of the previous problem are outside their locking range. By how much will the exact oscillation frequency of each laser be pulled from its free-running value, as a function of the detuning $\omega_1 - \omega_2$?

3. *Mode coupling due to backscattering.* It is possible to build a lossless but nonreciprocal element in which the optical path length or optical phase shift for light passing through in one direction is longer than for light passing through in the other direction. (Any such nonreciprocal phase shifter must, by symmetry arguments, contain either a dc magnetic field, or some other physical quantity which has a definite sense of direction, in order to distinguish between one direction of travel and the other in the optical element.)

Suppose such a nonreciprocal phase shifter is placed inside a ring-laser cavity which can oscillate simultaneously in both directions. The cavity will then have slightly different oscillation frequencies, call them ω_1 and ω_2 , in the two directions around the ring. (This can serve as a simulation scheme for testing ring-laser gyro behavior.)

Suppose now that a small amount of lossless backscattering (which can be modeled by a weak lossless beamsplitter) is also placed inside the ring cavity, so that a small amount of the signal propagating in each direction around the ring is scattered back into the other direction. What amount of backscattering will be necessary to make the separate oscillations going in the two directions around the ring "lock up" at a common frequency? Analyze this locking behavior as a function of the initial detuning between the two directions, and the usual laser and cavity parameters.

4. *Simultaneous injection of signals at two different frequencies into a free-running oscillator (research problem).* Suppose that two different injection signals, both of them cw sine waves for simplicity, but with different amplitudes and frequencies, are injected into an oscillator. (This might occur when a second and somewhat weaker signal is injected into an oscillator already injection-locked by a somewhat stronger signal; or alternatively when two different signals, both of them outside the locking range, are simultaneously injected into a free-running oscillator, either on the same side or on opposite sides of ω_0 .)

What sorts of behavior can be predicted for these and possibly other situations, as a function of the amplitudes and detunings of the two injected signals?



HOLE BURNING AND SATURATION SPECTROSCOPY

We discussed in an earlier chapter the distinction between homogeneous and inhomogeneous broadening of atomic transitions, and showed how we must calculate the linear susceptibility of an inhomogeneous transition by summing over the responses of all the individual groups of atoms or "spectral packets" with their different resonance frequencies.

This earlier discussion did not, however, take into account any strong-signal saturation effects on the atoms. Inhomogeneously broadened transitions, because of their division into a large number of separate groups of atoms, each with slightly different resonant frequencies, have quite different and substantially more complex saturation properties than do simple homogeneous transitions. Inhomogeneous saturation produces so-called "hole-burning" effects, which allow multimode oscillation in many lasers, and also lead to the very useful technique of saturation spectroscopy. Hole-burning effects also lead to the so-called Lamb dip in the power output of inhomogeneous doppler-broadened gas lasers. In this chapter we develop the analysis of these hole-burning phenomena, and indicate some of their important consequences in laser physics and in atomic and molecular spectroscopy.

30.1 INHOMOGENEOUS SATURATION AND "HOLE BURNING" EFFECTS

The saturation characteristics of an inhomogeneously broadened atomic transition differ greatly from those of a homogeneous transition, and these differences are important. In this section we describe the difference between the two kinds of saturation behavior in some detail.

Homogeneous Saturation Behavior

The essential feature of a homogeneously broadened transition is that every atom in the collection of atoms has both the same center frequency and the same atomic lineshape or frequency response. Hence a signal applied to the transition has essentially the same effects on all the atoms in the collection.

The resulting saturation behavior of a homogeneous transition is perhaps most clearly illustrated by a hypothetical (but entirely realistic) experiment.

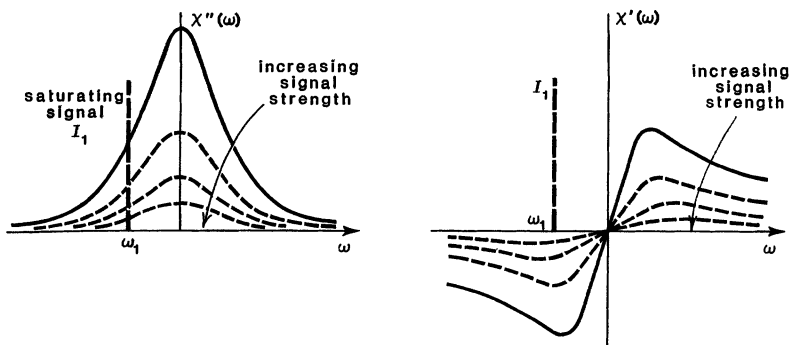


FIGURE 30.1

Saturation of real and imaginary parts of the atomic susceptibility in a homogeneous atomic transition.

Suppose we apply to the atoms a strong saturating signal of intensity I_1 at some fixed frequency ω_1 anywhere within the atomic linewidth, as shown in Figure 30.1, while at the same time we monitor both the reactive susceptibility $\chi'(\omega)$ and the absorptive susceptibility $\chi''(\omega)$ versus frequency ω across the entire linewidth, using a weak tunable probe or test signal which is itself too weak to cause any additional saturation effects.

From our earlier analysis of saturation we know that a strong signal applied to a transition causes the population difference ΔN on that transition to decrease from its small-signal value toward zero for a sufficiently strong applied signal. The atomic responses—both the susceptibilities $\chi'(\omega)$ and $\chi''(\omega)$ —in turn depend directly on the population difference ΔN , and hence saturate with it. The vital point about a fully homogeneous transition is that these susceptibilities will saturate uniformly, or *homogeneously*, across the entire line, under the influence of a sufficiently strong signal applied anywhere within the atomic linewidth.

As the saturating signal strength is increased and the population difference thereby decreased, the measured responses $\chi'(\omega)$ and $\chi''(\omega)$, measured both at the saturating frequency ω_1 and at all other frequencies ω , will decrease in direct proportion to ΔN , without changing in shape or in linewidth.

The transition is most easily saturated (i.e., the least saturating power is required to obtain a given degree of saturation) if the saturating signal frequency ω_1 is tuned exactly to the line center. Nonetheless, a strong saturating signal even well out on the wing of the atomic transition will, if it is strong enough, saturate the entire transition uniformly across its lineshape.

Inhomogeneous Saturation: Hole-burning Effects

The inhomogeneous saturation behavior is more complex. Suppose that this same saturation experiment is repeated for an inhomogeneously broadened transition. Then the major point is that the strong applied signal at frequency ω_1 will saturate the population difference only for those subgroups of atoms, or those spectral packets, whose resonance frequencies are in resonance or nearly in resonance with the applied signal frequency ω_1 . These are the only atoms with which the saturating signal strongly interacts. As the saturating signal increases in strength, only those spectral packets coincident with or immediately adjacent

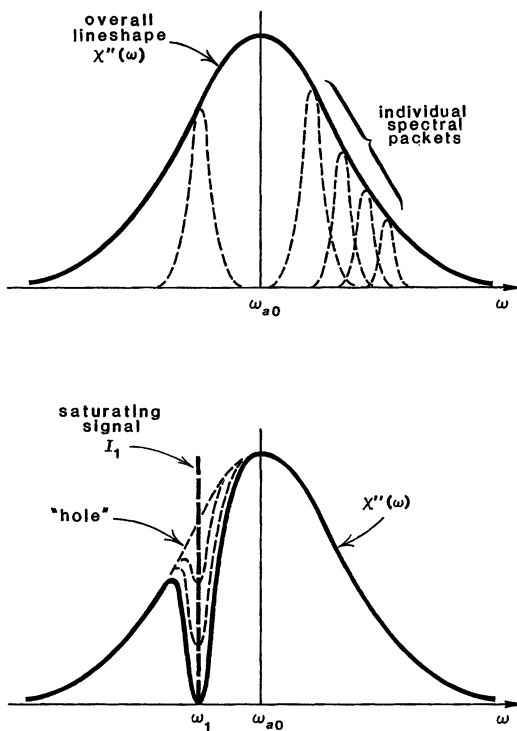


FIGURE 30.2
Burning a hole into the absorption profile of a strongly inhomogeneous transition.

to the strong signal will be saturated. The spectral packets at more distant frequencies will be essentially unchanged.

As a result, with increasing saturating power the strong saturating signal will "burn a hole" in the atomic absorption curve observed by the weak tunable probe signal, as shown in Figure 30.2. We will show shortly that this hole is to first approximation two homogeneous linewidths wide, and becomes steadily deeper with increasing signal strength, as the packet or packets in direct synchronism with the saturating signal become more heavily saturated. The hole eventually "touches bottom," after which the width of the hole increases slowly with further increases in signal strength, since a saturating signal of sufficient strength can saturate packets that are even somewhat more than a linewidth or two away from it.

The understanding of this kind of hole burning originated in nuclear magnetic resonance transitions at radio and microwave frequencies. The same effects are very commonly observed at optical frequencies, however, in doppler-broadened gas transitions, and in some inhomogeneously broadened solid-state atomic materials as well.

Photochemical Hole Burning

As a somewhat exotic but instructive example of hole-burning effects, we can consider the “photochemical hole burning” observed in certain organic crystals. Many complex organic molecules in either gaseous or condensed form will exhibit strong optical absorption lines centered in the visible or the near ultraviolet. If we form a mixed organic crystal or organic glass containing these molecules, then at very low temperatures ($\approx 4\text{ K}$) the homogeneous absorption line for any one molecule can be very narrow ($\leq 0.1\text{\AA}$). (The crystal should be one in which there is weak electron-phonon coupling, so that the homogeneous phonon broadening of the molecular transition is small.)

The overall inhomogeneous absorption line observed in the crystal will, however, typically be very much wider ($\geq 100\text{\AA}$), because each individual molecule's resonance frequency will be randomly shifted by differing local strains and distortions in the immediate environment of each individual molecule. This then provides a classic example of a strongly inhomogeneously broadened atomic (or molecular) system.

When these organic molecules absorb light from, say, a narrowband applied laser signal, there is a finite chance that those molecules which are optically excited will undergo a physical or chemical transformation into a different species. Examples of such optically induced transformations may include *photoisomerization* (the excited molecule twists into a different molecular structure), or *photochemical transformation* (the excited molecule interacts chemically with its surroundings to become a new species), or *triplet state crossing* (the excited molecules transform over into a long-lived triplet electronic state).

At room temperature all these photochemical reactions are reversible, and the excited molecules will rapidly come back to their original form. At helium temperatures, however, the reverse reaction may become very slow (recovery times of hours to days). When a narrowband laser signal at ω_1 is applied to the crystal, therefore, it may photoexcite and eventually destroy those particular molecules that are in resonance with the laser, thus burning a narrow hole in the absorption line of the crystal (since the new species that is created by the photochemical transformation no longer absorbs at the laser frequency, but generally has a new absorption line located elsewhere). All the other out-of-resonance molecules remain unchanged in this process.

Figure 30.3 shows, for example, the photochemical hole burnt in the optical absorption line of the organic molecule quinizarin doped at low density into a transparent organic glass consisting of a 3:1 mixture of ethanol and methanol. (This hole is burnt into the line by a high-intensity fixed-frequency argon laser which provides the saturating signal at ω_1 , and is then measured using a low-intensity tunable dye laser which provides the tunable frequency ω .) When the quinizarin molecules absorb light they make a photochemical transformation between the two forms shown at the top of Figure 30.30. This particular hole was formed by irradiation for 15 minutes with 3 mW of 515 nm radiation from the argon-ion laser. The hole evidently has a lorentzian lineshape with a FWHM linewidth of 1.5 cm^{-1} or $\approx 0.4\text{\AA}$.

Variable Hole Linewidths

These photochemical holes can be erased permanently by warming the crystals up to some temperature approaching 100 K or above, where thermal excitation

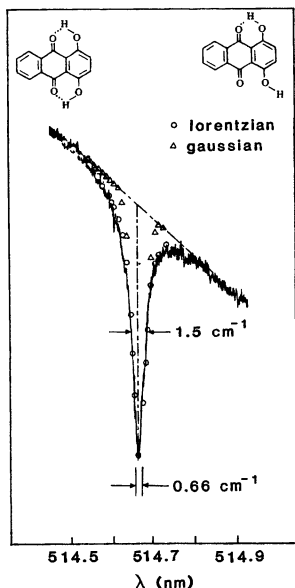


FIGURE 30.3

Photochemical hole burning in an organic glass. Note that the hole is fit much better by a lorentzian than by a gaussian lineshape.

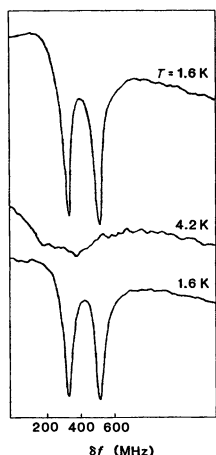


FIGURE 30.4

Effect of temperature cycling from 1.6 K to 4.2 K and back on two closely spaced holes.

can cause the photochemical transformations to be reversed. We can play other games with these systems as well, however.

Figure 30.4 shows two very narrow holes (top trace) with individual linewidths $\Delta\omega_h/2\pi < 100$ MHz, burned 180 MHz apart in another organic sample at 1.6 K. The homogeneous linewidth $\Delta\omega_a$ in this material is a very rapidly

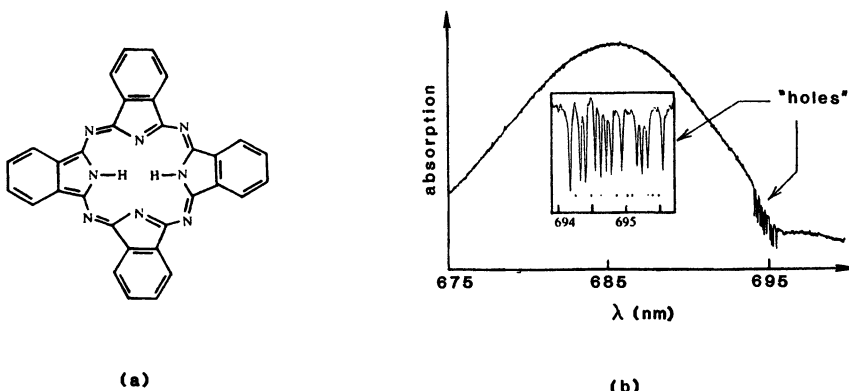


FIGURE 30.5
Optical data storage using photochemical burning in phthalocyanine crystals.

increasing function of temperature. Suppose we "heat" the sample from 1.6 K up to 4.2 K. Then, the hole widths expand, and the holes smear out and become invisible (middle trace). Upon recooling, however, the holes reappear as initially (bottom trace). If the sample temperature is raised much above 30 K, however, the holes anneal out and permanently disappear.

Information Storage With Photochemical Hole Burning

Suppose we burn a spectral hole such as that in Figure 30.4 into a thin film or a bulk crystal of the organic material, but with a spatial variation in hole strength corresponding to a photographic image, or perhaps a holographic fringe pattern. We thus have an image or pattern stored in the material which can be "seen" or read just at this one spectral wavelength. But we can then write another totally different pattern into the material using hole burning at a different wavelength within the broad absorption line. We thus have the possibility, at least in principle, of a very high-density though somewhat complex way of storing many simultaneous images or holograms in a single sample of recording medium. Alternatively, we might store digital bits of information, as in an optical videodisk, but with the possibility of storing multiple bits at each point on the medium using different recording wavelengths.

To illustrate this capability, Figure 30.5(b) shows some dozen closely spaced but independent holes burnt into the long-wavelength end of the absorption line centered at 685 nm that is characteristic of the phthalocyanine molecule H_2Pc dissolved in a polymeric matrix of polymethyl methacrylate at 4.2 K. The photochemical transformation of this molecule, whose structure is also shown in Figure 30.5(a), is believed to result from a light-induced rearrangement of the two central protons within the cage of nitrogen atoms in the center of the molecular structure.

Whether this rather complicated form of information storage will have any practical utility remains to be seen; but it does very clearly demonstrate the elementary physical concepts of hole burning in inhomogeneous absorption lines.

REFERENCES

The original paper introducing the concepts of inhomogeneous versus homogeneous broadening, and of hole burning in inhomogeneous transitions (in the context of electron spin resonance), is A. M. Portis, "Electronic structure of F centers: saturation of the electron spin resonance," *Phys. Rev.* **91**, 1071 (1953).

Hole burning is most commonly observed in doppler-broadened gases, as we will describe in the following sections. For a study of hole burning in a solid-state atomic system, however, including substantial cross-relaxation effects, see P. E. Jessop, T. Muramoto, and A. Szabo, "Optical hole burning in ruby," *Phys. Rev. B* **21**, 926–936 (February 1, 1980).

Another very interesting experiment demonstrating the burning of a hole into the absorption spectrum of p-type germanium using a CO₂ laser at 10.6 μm is described by F. Keilmann in "Tunable-laser-induced grating dip for measuring sub-picosecond relaxation," *Appl. Phys.* **14**, 29–33 (1977).

Two good surveys of the interesting recent developments in hole-burning effects in the absorption lines of organic solids at low temperatures are given by D. M. Burland and B. Haarer, "One- and two-photon laser photochemistry in organic solids," *IBM J. Res. Develop.* **23**, 534–546 (September 1979), and A. R. Gutiérrez, *et al.*, "Multiple photochemical hole burning in organic glasses and polymers: Spectroscopy and storage aspects," *IBM J. Res. Develop.* **26**, 198–208 (March 1982).

For other references on the same subject, see also F. Graf, *et al.*, "Zero-phonon photochemistry of hydrogen bonded hydroxy quinones as studied by photochemical hole burning," *Chem. Phys. Lett.* **59**, 217–221 (November 15, 1978); and R. M. Macfarlane and R. M. Shelby, "Photochemical and population hole burning in the zero-phonon line of a color center—F₃⁺ in NaF," *Phys. Rev. Lett.* **42**, 788–791 (March 19, 1979).

30.2 ELEMENTARY ANALYSIS OF INHOMOGENEOUS HOLE BURNING

Let us next examine analytically how a hole is burnt into in a strongly inhomogeneous transition. That is, let us calculate the saturated susceptibility seen by the weak probe signal at ω , when the strong saturating signal at ω_1 is also present. To do this, we must evaluate both the susceptibility and the degree of saturation of each individual spectral packet, and then integrate these results over all the packets at all the different resonance frequencies.

Elementary Hole-Burning Analysis

In Chapter 2 we showed that the homogeneous susceptibility $\tilde{\chi}(\omega)$ observed at frequency ω due to a single atom with resonant frequency ω_a may be written as

$$\tilde{\chi}_h(\omega; \omega_a) = -j \frac{3^*}{4\pi^2} \frac{\lambda^3 \gamma_{\text{rad}}}{\Delta\omega_a} \frac{1}{1 + 2j(\omega - \omega_a)/\Delta\omega_a}. \quad (1)$$

In writing this we add a subscript h to indicate that this is the *homogeneous* susceptibility; and we add an explicit dependence on the resonance frequency ω_a because from here on different groups of atoms will generally have (slightly) different resonance frequencies. All those atoms with the same value of ω_a , plus or minus roughly one homogeneous linewidth $\Delta\omega_a$, will be referred to as one spectral packet.

For an inhomogeneously broadened transition, the number of atoms with resonant frequencies located in a narrow range $d\omega_a$ about ω_a — that is, the number of atoms in a narrow unsaturated spectral packet of width $d\omega_a$ centered at ω_a —is then given by

$$dN(\omega_a) = N g(\omega_a) d\omega_a, \quad (2)$$

where N (or more correctly ΔN) is the total population of atoms and $g(\omega_a)$ is the inhomogeneous lineshape, or the frequency distribution of packet frequencies. This distribution is normalized such that

$$\int_{-\infty}^{\infty} g(\omega_a) d\omega_a = 1. \quad (3)$$

The lineshape $g(\omega_a)$ is in most situations gaussian, as for example with doppler broadening.

Now, a spectral packet at frequency ω_a , in the presence of one or more strong saturating signals within the inhomogeneous linewidth, will have its effective population reduced by a saturation factor which we will write in general as $S(\omega_a)$. For the particular situation of a single strong saturating signal with intensity I_1 at frequency ω_1 , this saturating factor for the packet at ω_a will be given by

$$S(\omega_a) = \frac{1}{1 + F(\omega_a, \omega_1, I_1, I_{\text{sat}})}, \quad (4)$$

where the factor F is given by

$$F(\omega_a, \omega_1, I_1, I_{\text{sat}}) = \frac{I_1}{I_{\text{sat}}} \times \frac{1}{1 + [2(\omega_1 - \omega_a)/\Delta\omega_a]^2}. \quad (5)$$

This saturation factor $S(\omega_a)$ will then multiply the population difference $N g(\omega_a) d\omega_a$ for the packet located at ω_a . Note that the packet with its signal frequency ω_a located directly on top of or close to the signal frequency ω_1 will be the most heavily saturated as I_1 increases; more distant packets will be only weakly saturated.

To calculate the total susceptibility $\tilde{\chi}(\omega)$ measured at an arbitrary observation frequency ω , in the presence of a strong signal I_1 at a saturating frequency ω_1 , we must then sum over the contributions of all the (partially saturated) packets at all the resonance frequencies ω_a , or

$$\tilde{\chi}(\omega) = N \int_{-\infty}^{\infty} g(\omega_a) S(\omega_a) \tilde{\chi}_h(\omega; \omega_a) d\omega_a. \quad (6)$$

This integral can be written out using the expressions for susceptibility $\tilde{\chi}_h(\omega; \omega_a)$ and saturation factor $S(\omega_a)$ given in Equations 30.1 through 30.5, plus an appropriate expression (usually gaussian) for the inhomogenous lineshape $g(\omega_a)$. The resulting integral is generally quite intractable and not readily solved, even approximately. We can, however, derive several useful approximate formulas in the limiting situation of a strongly inhomogeneous transition.

Change in Susceptibility Due to Hole Burning

The analytic expression in Equation 30.6 does become more tractable if we calculate not the saturated susceptibility directly, but instead calculate the change in susceptibility $\delta\tilde{\chi}(\omega)$ when the saturating signal is turned on. That is,

we calculate only the change or the “hole” $\delta\tilde{\chi}(\omega)$ in $\tilde{\chi}(\omega)$ produced by turning on I_1 . This change is given by

$$\begin{aligned}\delta\tilde{\chi}(\omega) &\equiv \tilde{\chi}_0(\omega) - \tilde{\chi}(\omega) \\ &= N \int_{-\infty}^{\infty} g(\omega_a) [1 - S(\omega_a)] \tilde{\chi}_h(\omega; \omega_a) d\omega_a,\end{aligned}\quad (7)$$

where $\tilde{\chi}_0$ refers to the unsaturated susceptibility with the saturating signal I_1 turned off. This integral is more tractable because the quantity $1 - S$ tends to zero for packet frequencies ω_a distant from ω_1 , whereas the saturation factor S in Equation 30.6 alone does not.

Writing out the integral in Equation 30.7 in full gives the lengthy expression

$$\begin{aligned}\delta\tilde{\chi}(\omega) &= -j \frac{3^* N \lambda^3}{4\pi^2} \frac{\gamma_{\text{rad}}}{\Delta\omega_a} \int_{-\infty}^{\infty} g(\omega_1 + \omega_a - \omega_1) \\ &\quad \times \left[\frac{I_1/I_{\text{sat}}}{1 + I_1/I_{\text{sat}} + [2(\omega - \omega_a)/\Delta\omega_a]^2} \right] \\ &\quad \times \left[\frac{1}{1 + 2j(\omega - \omega_a)/\Delta\omega_a} \right] d\omega_a.\end{aligned}\quad (8)$$

Evaluation of this integral is simplified by introducing the dimensionless ratios

$$\begin{aligned}p &\equiv I_1/I_{\text{sat}} = \text{intensity normalized to saturation intensity,} \\ x &\equiv 2(\omega_a - \omega_1)/\Delta\omega_a = \text{packet frequency } \omega_a \text{ relative to saturation frequency } \omega_1, \\ y &\equiv 2(\omega - \omega_1)/\Delta\omega_a = \text{signal frequency } \omega \text{ relative to saturation frequency } \omega_1, \\ dx &\equiv (2/\Delta\omega_a) d\omega_a = \text{integration over all packets within the line.}\end{aligned}$$

The expression for the hole susceptibility then becomes, in dimensionless variables,

$$\delta\tilde{\chi}(\omega) = -j \frac{3^* N \lambda^3 \gamma_{\text{rad}}}{8\pi^2} \int_{-\infty}^{\infty} g(\omega_1 + \Delta\omega_a x/2) \frac{p}{1 + p + x^2} \frac{1}{1 + j(y - x)} dx. \quad (9)$$

Note again that the variable x is the variable of integration over all packet frequencies ω_a , and the variable y is the dimensionless frequency deviation of ω from ω_1 .

Strongly Inhomogeneous Limit

The integrand of Equation 30.9 contains one purely real lorentzian resonance line in x centered at $x = 0$, and one complex lorentzian in x centered at $x = y$. The first of these implies that the integrand falls off as $1/x^2$ as the variable of integration moves away from $x = 0$; whereas both terms together imply a decrease as $1/x^3$ for large enough x .

At the same time, for a strongly inhomogeneous line with $\Delta\omega_d \gg \Delta\omega_a$ the inhomogeneous lineshape term $g(\omega_a)$ will be quite wide when measured in units of x compared to the other factors in the integrand. It is therefore a valid approximation to set $g(\omega_a)$ equal to its value $g(\omega_1)$ at the center of the hole, i.e.,

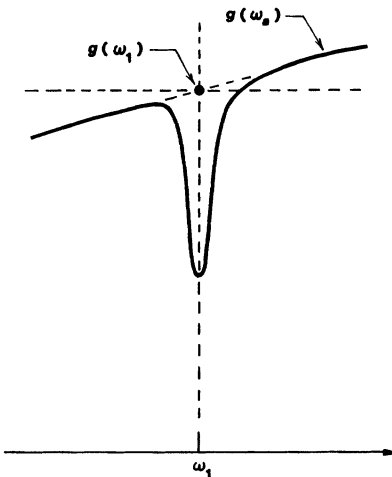


FIGURE 30.6

The strongly inhomogeneous or narrow hole approximation.

at $x = 0$, as in Figure 30.6. We can then take the function $g(\omega_a)$ outside the integral. This approximation will be valid for strongly inhomogeneous lines which have not too wide holes burnt in them.

We then obtain the approximate expression

$$\delta\tilde{\chi}(\omega) \approx -j \frac{3^* N \lambda^3 \gamma_{\text{rad}}}{8\pi^2} g(\omega_1) \int_{-\infty}^{\infty} \frac{p}{1+p+x^2} \frac{1}{1+j(y-x)} dx. \quad (10)$$

This integral is readily evaluated, for example, by contour integration in the complex plane, since it has complex poles at $x = \pm j\sqrt{p+1}$ and $x = y - j$. The contour of integration can be closed in either the upper or lower half of the complex plane, with the resulting value from residue theory being

$$\int_{-\infty}^{\infty} \frac{p}{1+p+x^2} \frac{1}{1+j(y-x)} dx = \frac{\pi p}{\sqrt{1+p}} \times \frac{1}{1+\sqrt{1+p}+jy}. \quad (11)$$

This is basically a complex lorentzian function of y . Putting this result back into Equation 30.9 and converting back to real frequency units gives for the final hole susceptibility

$$\delta\tilde{\chi}(\omega) = j\chi_0''(\omega_1) \times \frac{\sqrt{1+p}-1}{\sqrt{1+p}} \times \frac{1}{1+2j(\omega-\omega_1)/\Delta\omega_{\text{hole}}}, \quad (12)$$

where $\chi_0''(\omega_1)$ is the value of χ'' at $\omega = \omega_1$ in the inhomogeneously broadened line before the hole is burnt, and where $\Delta\omega_{\text{hole}} \equiv [1 + \sqrt{1+p}]\Delta\omega_a$ is the linewidth of the hole. This linewidth is given by

$$\Delta\omega_{\text{hole}} \equiv [1 + \sqrt{1+p}]\Delta\omega_a \approx \begin{cases} 2\Delta\omega_a & I_1 \ll I_{\text{sat}} \\ \sqrt{I_1/I_{\text{sat}}}\Delta\omega_a & I_1 \gg I_{\text{sat}}. \end{cases} \quad (13)$$

The width of the hole is thus approximately two homogeneous linewidths for weak saturation, $I_1 \ll I_{\text{sat}}$, and grows approximately as $\sqrt{I_1/I_{\text{sat}}}$ for $I_1 \gg I_{\text{sat}}$.

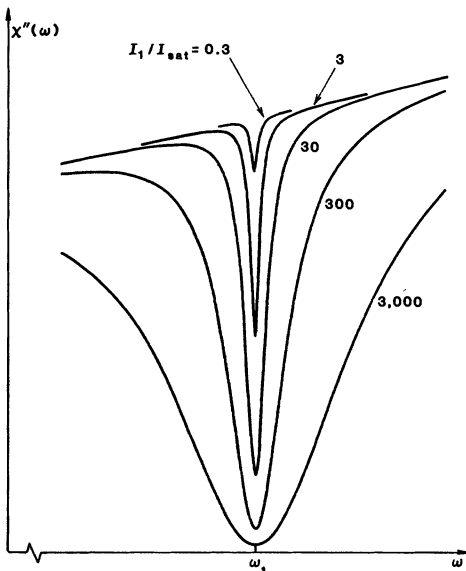


FIGURE 30.7
The hole in the absorption line deepens and broadens as the saturating signal strength is increased.

Complex Hole Susceptibility

The change in susceptibility, $\delta\tilde{\chi}(\omega)$, produced by burning the hole is thus a complex lorentzian line centered at the frequency ω_1 of the strong saturating signal. The change in susceptibility that results is in fact exactly the same as if we had taken away or destroyed a certain number of atoms located right at $\omega = \omega_1$ (or perhaps we should say we have added in some “negative atoms” located at that frequency); except that these atoms act as if they have a homogeneous linewidth equal to the “hole linewidth” $\Delta\omega_{\text{hole}}$ and not the usual homogeneous linewidth $\Delta\omega_a$.

This change thus includes both a reduction in the absorptive part $\delta\chi''(\omega)$ (or, for an inverted transition, a reduction in gain) that is centered at ω_1 , with width $\Delta\omega_{\text{hole}}$; and a change in the reactive part of $\delta\chi'(\omega)$ which is zero at $\omega = \omega_1$ and has peaks of opposite sign on either side in the usual fashion.

The strength, or depth, of the hole burnt in a strongly inhomogeneous line is directly proportional to the unsaturated $\chi_0''(\omega_1)$ value of the line at the center of the hole, multiplied by a “hole strength function” given by

$$\left| \frac{\delta\tilde{\chi}(\omega_1)}{\chi_0''(\omega_1)} \right| \equiv \frac{\sqrt{1+p} - 1}{\sqrt{1+p}} \approx \begin{cases} I_1/2I_{\text{sat}} & I_1 \ll I_{\text{sat}} \\ 1 & I_1 \gg I_{\text{sat}}. \end{cases} \quad (14)$$

The depth of the hole thus increases as $I_1/2I_{\text{sat}}$ for weak saturation and flattens off as the hole “touches bottom” at large intensities, as shown in Figure 30.7. The integrated area of the hole, however, continues to increase as $\Delta\omega_{\text{hole}}$ (or $\sqrt{I_1}$ at large intensities).

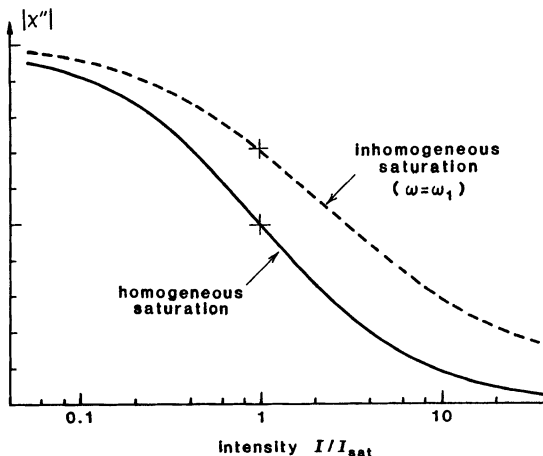


FIGURE 30.8
Comparison of homogeneous and inhomogeneous saturation in response to a strong applied signal.

Inhomogeneous Gain Saturation

The saturated absorption susceptibility seen by the strong saturating signal I_1 itself, right at the center of the hole, is of special interest since this gives the gain saturation or absorption saturation seen by the strong saturating signal itself. This susceptibility is purely imaginary, and is given by

$$\begin{aligned}\tilde{\chi}''(\omega_1) &\equiv \tilde{\chi}_0''(\omega_1) - \delta\tilde{\chi}''(\omega_1) \\ &= \tilde{\chi}_0''(\omega_1) \times \sqrt{\frac{1}{1 + I_1/I_{\text{sat}}}}.\end{aligned}\quad (15)$$

Thus, we have the important result that whereas a homogeneous line saturates (everywhere) like

$$\left. \frac{\chi''}{\chi_0''} \right|_{\text{homog}} = \frac{1}{1 + I_1/I_{\text{sat}}}, \quad (16)$$

an inhomogeneous line saturates (at the center of any one hole) like

$$\left. \frac{\chi''}{\chi_0''} \right|_{\text{inhomog}} = \frac{1}{\sqrt{1 + I_1/I_{\text{sat}}}}, \quad (17)$$

where χ''_0 is the unsaturated gain or absorption value in each situation.

This difference between the linear and square-root dependence in the saturation denominator, as illustrated in Figure 30.8, is the distinguishing difference between homogeneous and inhomogeneous saturation, and we have made use of this difference in several earlier chapters. In physical terms, the inhomogeneous gain or absorption seems to saturate somewhat more slowly at large intensities because the signal can draw energy from an increasingly wider range of packets as the signal intensity increases. This difference can have significant effects on the

saturation behavior, power output, and similar properties of inhomogeneously broadened laser amplifiers and oscillators, as we have seen in earlier chapters.

Summary

The essential features of hole burning in a strongly inhomogeneous line are thus that:

- The hole has a complex lorentzian shape, including both an absorptive part $\delta\chi''(\omega)$ peaked at the hole, and a reactive part $\delta\chi'(\omega)$ which is zero right at the hole and spreads out on either side.
- The hole burned in $\chi''(\omega)$ has a linewidth essentially equal to twice the homogeneous linewidth for weak hole-burning effects, increasing as $\sqrt{I/I_{\text{sat}}}$ for stronger saturation.
- The saturated loss (or gain) seen by the strong saturating signal right at the center of the hole saturates as $1/\sqrt{1+I/I_{\text{sat}}}$ rather than as the $1/(1+I/I_{\text{sat}})$ characteristic of homogeneous transitions.

Experimental results demonstrating these points will be shown in the following sections.

Problems for 30.2

1. *Exact expression for inhomogeneous saturation at line center.* It is possible to derive an exact analytic expression (involving an error function) for the saturated absorption susceptibility seen by a strong saturating signal ω_1 when that signal is tuned exactly to the center frequency ω_0 of a gaussian inhomogeneous transition, for any arbitrary degree of homogeneous or inhomogeneous broadening—that is, for any arbitrary ratio of $\Delta\omega_a$ to $\Delta\omega_d$, or of T_2 to T_2^* . Find this expression, and verify that it reduces to the proper limiting forms for the limiting situations of highly homogeneous ($\Delta\omega_d \ll \Delta\omega_a$) or highly inhomogeneous ($\Delta\omega_d \gg \Delta\omega_a$) broadening.
2. *Exact expression for hole burning in a lorentzian inhomogeneously broadened line.* Inhomogeneously broadened transitions most often have a gaussian distribution of resonance frequencies $g(\omega)$ in real situations. However, for purpose of mathematical analysis it is much easier if we assume a lorentzian distribution of packet frequencies written in the form

$$g(\omega) = \frac{2}{\pi\Delta\omega_d} \frac{1}{1 + [2(\omega - \omega_0)/\Delta\omega_d]^2}.$$

The linewidth $\Delta\omega_d$ is then still the inhomogeneous linewidth, even though the line is no longer either gaussian or doppler, and the distribution is still properly normalized to unit area.

Suppose a transition with such an inhomogeneous resonance frequency distribution has a strong signal of intensity I_1 applied exactly at the atomic line center $\omega_1 = \omega_0$. Evaluate the saturation behavior of the absorption susceptibility χ'' seen by this midband signal at its own frequency ω_1 as a function of the intensity I_1 , doing an exact calculation (i.e., not making the strongly inhomogeneous approximation made in the text). Discuss the saturation behavior for different

amounts of inhomogeneous broadening as measured by the “broadening ratio” $\Delta\omega_d/\Delta\omega_a$, in particular for the homogeneous limit where this ratio is much less than one, and the inhomogeneous limit where it is much greater than one.

Hint: A simple contour integral using the residue theory for complex integration is all the mathematical apparatus required. Note also that although the problem only asks for χ'' with ω_1 at midband, it is not really much harder to do the general situations for both χ' and χ'' with ω_1 anywhere within the line.

3. *Oscillation mode spectrum and power output for a strongly inhomogeneous laser oscillator.* Suppose a laser oscillator has a strongly inhomogeneous atomic transition (inhomogeneous linewidth wide compared to the axial-mode spacing) with a midband gain that increases linearly with the laser pumping rate r . The total cavity loss plus output coupling is small. Develop expressions for the oscillation mode spectrum (i.e., the number of axial modes oscillating) and the total multimode oscillation power as a function of pumping rate above threshold. Plot results for values typical of a He-Ne laser, e.g. an inhomogeneous linewidth $\Delta\omega_d = 2\pi \times 1,500$ MHz, axial-mode spacing $\Delta\omega_{ax} = 2\pi \times 150$ MHz, and total power loss per round trip = 10%, up to the point where at least 9 modes are oscillating. Assume the centermost axial mode is located exactly at line center.

(Note: This is not an entirely realistic calculation for actual He-Ne lasers, since it neglects cross-relaxation effects and, more importantly, the complications of velocity space hole burning in doppler-broadened lines, both of which we will take into account in following sections.)

30.3 SATURATED ABSORPTION SPECTROSCOPY

Spectral hole-burning effects find practical application in the very important technique of high-resolution saturation spectroscopy. This technique is particularly useful for finding the much narrower homogeneous lineshapes that are hidden inside doppler-broadened inhomogeneous transitions in gases.

The analysis of hole-burning effects for doppler-broadened transitions in gases is complicated, however, by the fact that an atom moving in the axial direction will have two equal but opposite doppler shifts depending upon the direction in which the optical wave is traveling along the axis. We will therefore next describe how we must analyze hole-burning effects, saturation spectroscopy, and (in a later section) laser Lamb dips in doppler-broadened atomic transitions.

Doppler-Broadening: Bi-Valued Doppler Shifts

Suppose that an atom in a gas is traveling in the $+z$ direction with velocity v_z , and that it is interacting with an optical wave of signal frequency ω (measured in the laboratory frame), where this wave is traveling at velocity c in either the $+z$ or the $-z$ directions, as shown in Figure 30.9. Then, the apparent signal frequency $\omega'(v)$ seen by the moving atom in its own frame will be one or the other of the two values

$$\omega'(v) = \omega(1 \mp v_z/c), \quad (18)$$

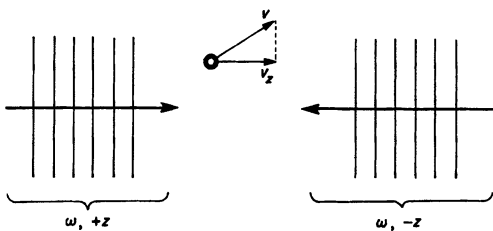


FIGURE 30.9
Moving atom interacting with waves propagating in the $+z$ and $-z$ directions.

with the upper and lower signs corresponding to the $+z$ and $-z$ traveling waves, respectively.

If this frequency $\omega'(v)$ seen by the atom is to be in resonance with the atom's unshifted transition frequency, which we will write as $\omega_0 \equiv (E_2 - E_1)/\hbar$, then the frequency ω in the lab frame must meet the condition that

$$\omega'(v) \equiv \omega(1 \mp v_z/c) = \omega_0, \quad (19)$$

or

$$\omega = \omega_a = \frac{\omega_0}{1 \mp v_z/c}. \quad (20)$$

The apparent resonance frequency of the moving atom, call it $\omega_a(v)$, as measured in the laboratory frame, thus appears to be shifted to one or the other of the doppler-shifted resonance values

$$\omega_a(+v) = \omega_0(1 - v_z/c)^{-1} \approx \omega_0(1 + v_z/c), \quad (21)$$

or

$$\omega_a(-v) = \omega_0(1 + v_z/c)^{-1} \approx \omega_0(1 - v_z/c), \quad (22)$$

depending upon whether the wave is traveling in the $+z$ or the $-z$ direction. The same atom thus has *two different apparent resonance frequencies* when it interacts with waves traveling past it in the two opposite directions.

Inhomogeneous Velocity Distribution

To avoid confusion, therefore, the individual atoms in a doppler-broadened line must be labeled not by their shifted resonance frequencies ω_a , but by their axial velocity values or "velocity classes" v_z . The fractional number of atoms $dN(v)$ with axial velocity v (we drop the z subscript for simplicity) is then given by the maxwellian distribution

$$N^{-1}dN(v) = g(v)dv = (2\pi\sigma_v^2)^{-1/2} \exp[-v^2/2\sigma_v^2]dv. \quad (23)$$

This distribution is gaussian, as shown in Figure 30.10, with a standard deviation which can be related to the atomic mass M and gas kinetic temperature T by $\frac{1}{2}M\langle v_z^2 \rangle \equiv \frac{1}{2}M\sigma_v^2 = kT/2$ or $\sigma_v^2 = kT/M$. This distribution is normalized as usual so that

$$\int_{-\infty}^{\infty} g(v)dv = 1. \quad (24)$$

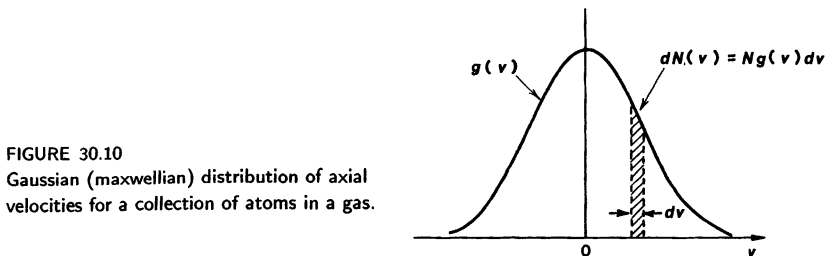


FIGURE 30.10
Gaussian (maxwellian) distribution of axial velocities for a collection of atoms in a gas.

The factor $Ng(v) dv$ is then the number of atoms (or more accurately the unsaturated population difference) in the v -th velocity class.

We can rewrite Equation 30.23 as an inhomogeneous distribution of the atomic resonance frequencies ω_a (for waves going in one direction) in the form

$$g(\omega_a) = \sqrt{\frac{4 \ln 2}{\pi}} \frac{1}{\Delta\omega_d} \exp \left[-4 \ln 2 \left(\frac{\omega_a - \omega_0}{\Delta\omega_d} \right)^2 \right], \quad (25)$$

where we have also converted the scaling factor from the standard deviation σ_v to the doppler-broadened linewidth $\Delta\omega_d$ (FWHM as usual) by writing

$$\Delta\omega_d = \sqrt{8 \ln 2} \frac{\omega_0 \sigma_v}{c} = \omega_0 \times \sqrt{8 \ln 2} \frac{kT}{Mc^2}. \quad (26)$$

Note that the doppler linewidth $\Delta\omega_d$ is directly proportional to the transition center frequency ω_0 , and depends only weakly on atomic mass M and gas kinetic temperature T .

The doppler linewidth of the familiar He-Ne laser transition at 633 nm, for example, with a gas temperature only slightly hotter than room temperature, has the value $\Delta\omega_d/2\pi \approx 1,500$ MHz, whereas the homogeneous or packet linewidth $\Delta\omega_a/2\pi$ may be ≈ 100 MHz or less. The doppler width in an operating argon-ion laser, with shorter wavelength and hotter gas temperature may be $\Delta\omega_d/2\pi = 3$ GHz to 6 GHz. In the $10.6 \mu\text{m}$ CO_2 laser transition, with 20 times longer wavelength, heavier molecular mass M , and moderate temperature T , the doppler-broadening contribution is only $\Delta\omega_d/2\pi \approx 60$ MHz, and is usually overshadowed by pressure broadening effects on the order of $\Delta\omega_a/2\pi \approx 6$ MHz/torr.

Saturation Spectroscopy in Gases

A straightforward measurement of the linear absorption profile for a strongly inhomogeneous transition will simply trace out the doppler-broadened lineshape given in Equation 30.26, with its doppler linewidth $\Delta\omega_d$. Such a measurement will thus yield little or no information about the individual spectral packets that are hidden within that transition, or about their homogeneous linewidths $\Delta\omega_a$. Measurements on individual packets are often desired, however, to study pressure broadening and collision effects, and to find the exact center of the inhomogeneous line to higher accuracy. Measurements of the holes burnt into an inhomogeneous line, as analyzed in the previous section, can give

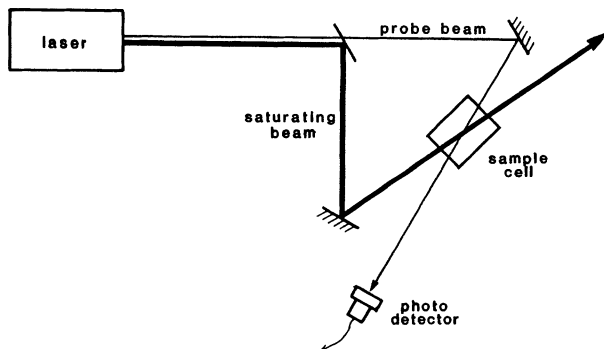


FIGURE 30.11
Crossed-beam saturation-spectroscopy experiment.

all of this information. How this can be done in gases by using an elementary form of *saturation spectroscopy* is illustrated in Figure 30.11.

In this technique a strong saturating beam I_1 at a fixed frequency ω_1 , plus a weak probe beam at a tunable frequency ω , are sent as nearly parallel (or antiparallel) beams through the same volume of the atomic medium. (In practice, the angle between the two beams would be very much smaller than shown in Figure 30.11.) The simplest arrangement for saturation spectroscopy is when the saturating signal and the probe signal both come from the same laser, as in Figure 30.11, and hence both tune together at the same frequency $\omega = \omega_1$. The essential feature is then that the strong saturating signal (strong enough to cause at least partial hole burning) travels in one direction, whereas the weak probe signal (not strong enough to cause any saturation) travels through the same volume of atoms in the opposite direction.

Suppose first that the signal frequency ω is tuned away from the resonant frequency ω_0 of the atoms by at least several homogeneous linewidths $\Delta\omega_a$. The saturating beam will then be in resonance with, and will tend to saturate, those atoms whose axial velocity v is given by

$$v = v_h = \frac{\omega_0 - \omega}{\omega_0} c. \quad (27)$$

The saturating signal will “burn a hole” in the velocity group centered about this resonance velocity, as indicated in the upper part of Figure 30.12 (which assumes that ω is less than ω_0). We are assuming here that the transition is strongly inhomogeneously broadened, with $\Delta\omega_d \gg \Delta\omega_a$, so that the width of the overall velocity distribution is substantially wider than the width of an individual hole. As the saturating beam is chopped on and off, this hole in the velocity distribution will be alternately burned into the line and allowed to heal.

Now the probe wave, because it travels in the opposite direction even though it has the same frequency, will be in resonance with and will interact primarily with an oppositely traveling group of atoms whose velocity is given by

$$v = -v_h = -\frac{\omega_0 - \omega}{\omega_0} c. \quad (28)$$

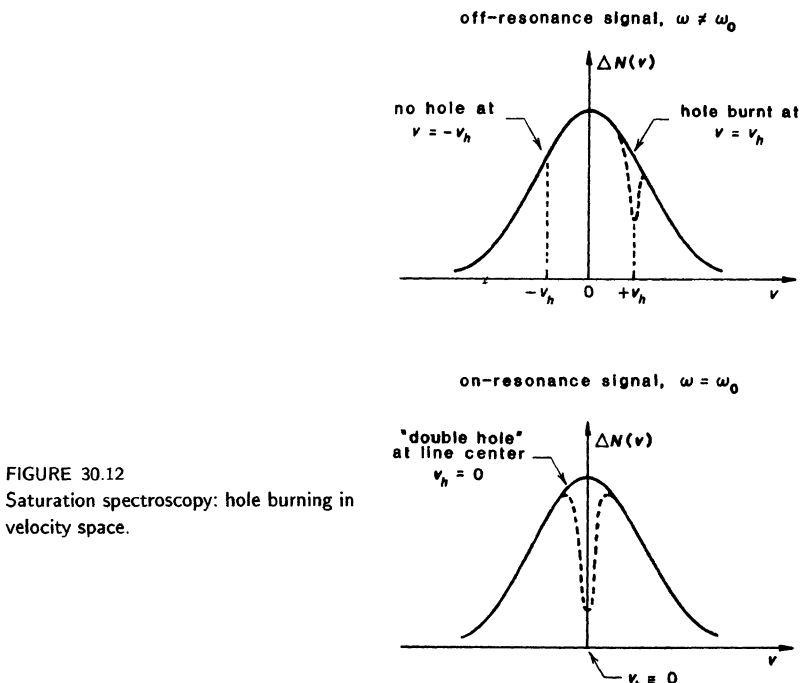


FIGURE 30.12
Saturation spectroscopy: hole burning in velocity space.

This opposite velocity group will be very little saturated by the weak probe signal (assuming the two velocity groups are separated by considerably more than the width of the hole). Hence the absorption saturation produced by the saturating signal will have negligible effect on the absorption of the probe signal—the oppositely traveling saturation and probe waves are “talking to” essentially different groups or velocity classes of atoms.

Suppose, however, that the signal frequency ω is tuned exactly to the unshifted atomic resonance frequency ω_0 , as in the lower part of Figure 30.12. Then both the saturation signal and the probe signal are in resonance with the same group of atoms, namely, the zero-velocity atoms. The saturating signal burns a hole in this zero-velocity group, which means that the attenuation through the cell is partially reduced for both the saturating and the probe signal. Hence the saturating signal absorption may be measurably reduced just at the point where the saturation and probe signals come into coincidence with the zero-velocity group of atoms, i.e., right at line center where $\omega = \omega_1 = \omega_0$. The hole will thus appear right at the line center, independent of any doppler shifts.

Experimental Example

Figure 30.13 shows the doppler-broadened absorption profile of a single vibrational-rotational transition of the H_2O molecule near $5.3 \mu\text{m}$ as measured by the weak tunable probe beam in a saturated spectroscopy experiment like Figure

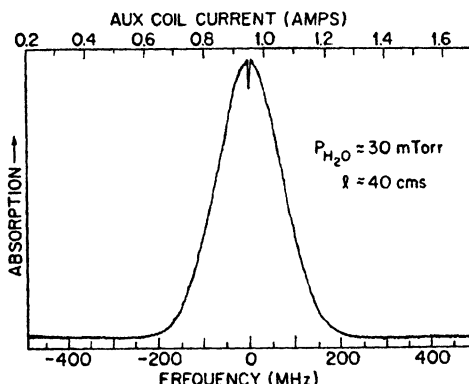


FIGURE 30.13
Absorption profile of a water vapor absorption line near 5.3 microns.
(From Patel.)

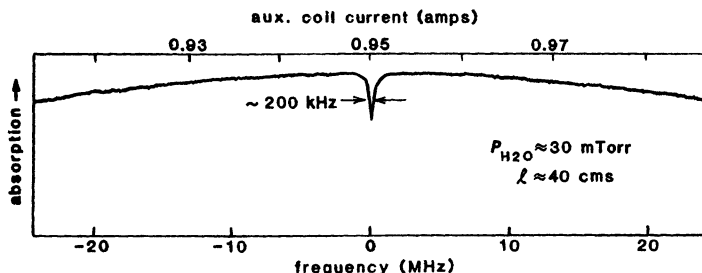


FIGURE 30.14
Expanded view of the saturation dip at the center of Figure 30.13.

30.11, in a cell containing water vapor at 30 mtorr pressure. (The absorption profile was measured by comparing the probe beam transmission through the cell to a reference portion of the same beam which bypassed the cell.) The doppler linewidth for this particular transition is $\Delta\Omega_d/2\pi \approx 165$ MHz.

The cell also had a much stronger saturating beam passing through in the opposite direction, as in Figure 30.11. The presence of this beam produced the very narrow dip in absorption for the probe beam which is barely visible at the center of the doppler line. Figure 30.14 shows this same saturated absorption dip on a greatly expanded frequency scale. The dip is only ≈ 200 kHz wide, out of the full doppler width of ≈ 165 MHz, indicating that this particular line is very strongly inhomogeneously broadened.

The vital feature of the saturated absorption signal in fact is that it locates the unperturbed resonance frequency ω_0 of the atoms to within a precision determined by the homogeneous linewidth $\Delta\omega_a$, rather than the much larger doppler linewidth $\Delta\omega_d$. If we simply measured the linear absorption versus frequency through the gas cell using the same tunable laser, we would trace out only the much broader doppler-broadened profile without the central dip. The potential precision with which the line center can be located is thus much higher, and this can be exploited in high-resolution spectroscopy and in laser frequency standards, as we will see shortly.

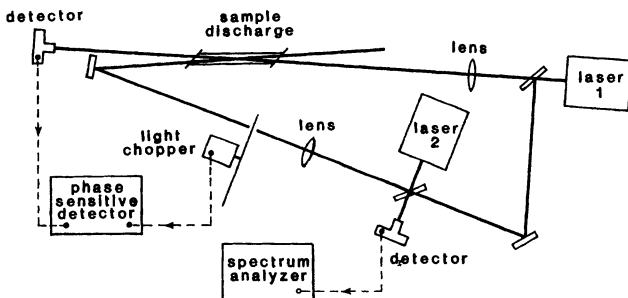


FIGURE 30.15
More detailed layout of a saturated-absorption experiment.

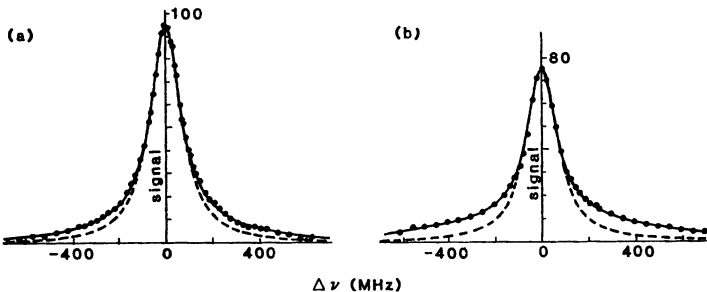


FIGURE 30.16
Experimental results from an experiment such as Figure 30.15. (a) He-Ne mixture, 7:1 ratio, 1.1 torr total pressure. (b) Pure Ne, 2.2 torr total pressure.

AC Saturation Spectroscopy

For the most effective experimental results the strong saturating beam in a saturated spectroscopy experiment, rather than being applied continuously, should be chopped on and off at some low modulation frequency ω_m (say, $\omega_m/2\pi \approx 1,000$ Hz) using a light modulator or "chopper" as in Figure 30.15. The hole in the line is then repeatedly burnt and heals at this repetition frequency. (The chopping frequency ω_m should be slow compared to the T_1 recovery time of the hole in the medium.)

Turning the hole absorption on and off in this fashion then produces a periodic variation in the intensity transmission seen by the weak probe beam at frequency ω . The resulting periodic modulation of the probe beam intensity is detected by a photodetector and ac amplifier tuned to the modulation frequency ω_m . This ac signal becomes largest when the probe signal is tuned exactly to the hole center frequency or $\omega = \omega_1$. The hole, with its linewidth of $\approx 2\Delta\omega_a$, is thus observed directly.

As a practical matter, the use of a phase sensitive detector (or so-called lock-in amplifier) synchronized to the chopping frequency ω_m can eliminate nearly all noise and fluctuations associated with the lasers and the detection apparatus, making possible the measurement of extremely weak holes in a strongly inhomogeneous

geneous line. Two typical experimental curves of this type, measured on a neon absorption transition using a tunable He-Ne laser, are shown in Figure 30.16.

If we have, as we often do, several nearly degenerate transitions all overlapping within a single doppler linewidth, we can then resolve these transitions, and measure their splitting, as separate saturated absorption signals within the single doppler-broadened line. In addition, the saturated absorption technique makes it possible to measure the homogeneous linewidth $\Delta\omega_a$ within the doppler-broadened transition, and thus to find out what the collision rates and pressure-broadening coefficients are on these transitions.

Laser Frequency Stabilization

One of the most important applications for saturated absorption spectroscopy comes in stabilizing the absolute frequency of a laser against suitable atomic or molecular absorption lines. We carefully tune the laser to the central peak of the saturated absorption signal in some suitable absorption cell, and thus stabilize the laser against the unshifted doppler frequency of some selected atomic or molecular transition.

The absorption cell in such an application can be operated at a comparatively low and well-stabilized temperature and pressure, without any buffer gases, electric discharges, magnetic fields, or other perturbations. Hence the effects of pressure broadening and of pressure, Zeeman, or Stark shifts in the saturated absorption cell can be made much smaller than in the laser device itself. At the same time the saturated absorption technique enables us to find the center of the absorbing transition to within the homogeneous linewidth or better. (Electronic techniques usually make it possible to find the center of such a resonance to within 1% or better of the resonance width.)

One of the most important practical systems of this type combines an infrared He-Ne laser operating on a laser transition at $3.39\text{ }\mu\text{m}$ with a very sharp and highly stable absorption line in the spectrum of methane (CH_4). With this system an optical-frequency standard with absolute optical-frequency stabilization better than 1 part in 10^{10} and relative frequency stabilization approaching a few parts in 10^{14} has been demonstrated.

REFERENCES

A lengthy and detailed theory of saturated absorption in inhomogeneous two-level systems is given by S. Haroche and F. Hartmann, "Theory of saturated absorption lineshapes," *Phys. Rev. A* **6**, 1280 (October 1972). A simpler discussion is presented by J. H. Shirley, "Semiclassical theory of saturated absorption in gases," *Phys. Rev. A* **8**, 347-368 (July 1973).

A very large number of experimental results on saturated absorption spectroscopy can be found in the literature. The particularly dramatic results for water vapor shown in Figure 30.13 and 30.14 are from C. K. N. Patel, "Saturation spectroscopy with a tunable spin-flip Raman laser," *Appl. Phys. Lett.* **25**, 112-114 (July 15, 1974); whereas the neon results in Figure 30.16 are from P. W. Smith and T. Hänsch, "Cross-relaxation effects in the saturation of the 6328-Å neon-laser line," *Phys. Rev. Lett.* **26**, 740-743 (March 29, 1971).

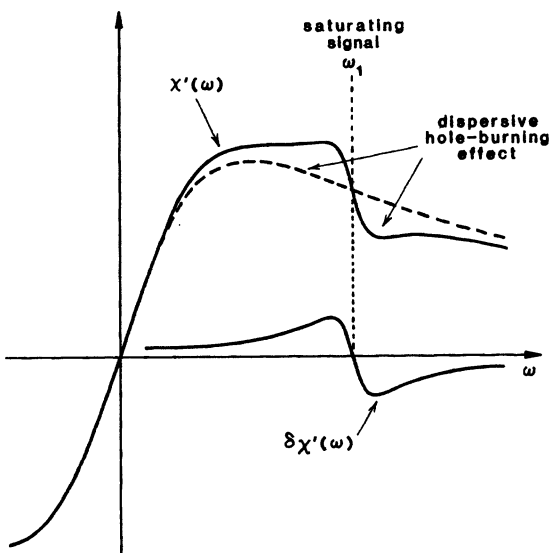


FIGURE 30.17
Effect of hole burning on the reactive susceptibility.

30.4 SATURATED DISPERSION EFFECTS

When a saturating signal is applied to an inhomogeneous transition, a visible “hole” is burned in the absorptive or $\chi''(\omega)$ part of the line. The effects of hole burning on the reactive or $\chi'(\omega)$ part of the atomic response are more complicated.

Reactive Effects of Hole Burning

First of all, the reactive susceptibility $\chi'(\omega)$ for a homogeneous transition is zero at line center. An individual spectral packet therefore makes no contribution to the total $\chi'(\omega)$ value at its own frequency. Thus, saturating a given packet does not change the $\chi'(\omega_1)$ value at the center of that packet.

A spectral packet does contribute, however, to the reactive susceptibility $\chi'(\omega)$ a few homogeneous linewidths away on either side. The contributions are of opposite sign because of the antisymmetric shape of $\chi'(\omega)$. Thus, the effect of saturating a given spectral packet is primarily to change the $\chi'(\omega)$ values at other frequencies located a few packet widths away on either side of the saturated packet, roughly as indicated in Figure 30.17. The change in $\chi'(\omega)$ is exactly the reactive part of the complex change in susceptibility $\delta\chi(\omega)$ contributed by the “negative atoms” referred to a few sections earlier.

Saturated Dispersion Effects

The saturated absorption experiments described in the preceding section measure the change in absorption for a weak probe beam caused by the hole burnt in an inhomogeneous line by a strong saturating signal. The same strong

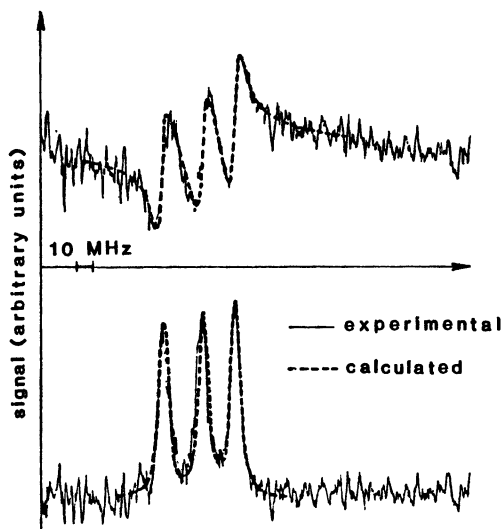


FIGURE 30.18
Inhomogeneous saturation effects produced by three closely spaced iodine resonance lines. Top trace: saturated dispersion, as measured by beam deflection effects. Bottom trace: saturated absorption or hole-burning effects.

saturating signal in these experiments is, however, also changing the *reactive* susceptibility $\chi'(\omega)$, or the index of refraction $n(\omega)$, seen by the probe beam, especially for frequencies a homogeneous linewidth or two away from the saturating signal on either side. This change in index can be measured interferometrically, or by its effects in deflecting or defocusing a probe beam.

Suppose that a probe beam and saturating beam pass through a cell in opposite directions with the probe beam passing just alongside the saturating beam, on the side slope of the transverse intensity profile of the saturating beam. The hole-burning effects produced by the saturating beam will then produce a variation in $\delta\chi'(\omega)$ or in the index of refraction with a similar transverse variation across the probe beam. The probe beam will thus be bent or deflected in one direction or the other, depending upon the sign of $\delta\chi'(\omega)$ as the saturating and probe frequencies are tuned. (If the saturating and probe beams were aligned exactly on top of each other, it would also be possible to observe a small focusing or defocusing of the probe beam caused by the radial variation of the $\delta\chi'(\omega)$ effects across the saturating beam.)

Very clear experiments describing exactly these effects are illustrated in Figure 30.18, which shows a comparison of saturated absorption experiments (lower curve) and saturated dispersion or saturated index experiments (upper curve) on the same gas cell. The bottom curve shows saturated absorption results for three hyperfine transitions of the I_2 molecule located near 590 nm, as measured using a tunable cw dye laser in a cell of iodine vapor at approximately 270 mtorr pressure. Note that the three hyperfine transitions have line centers separated by ≈ 20 MHz, or much less than the doppler-broadened absorption profile that would be produced by the three overlapping transitions.

The top curve then shows saturated dispersion or refractive index effects measured with the same cell and laser by slightly misaligning the saturating and probe beams, inserting a knife edge halfway into the probe beam some distance

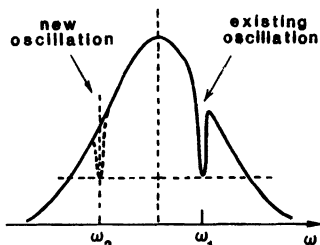


FIGURE 30.19

Dispersive "pushing" of one oscillation by a second oscillation.

beyond the cell, and measuring how much of the probe beam intensity passed this knife edge. The observed signal thus increases or decreases as the probe beam is deflected further onto or off from the knife edge by the $\delta\chi'$ effects associated with hole burning.

These experimental results are particularly outstanding in that they simultaneously demonstrate (a) the ability of saturated-absorption spectroscopy to resolve multiple overlapping atomic transitions within a doppler-broadened line, (b) the fundamental interrelation between $\chi''(\omega)$ and $\chi'(\omega)$ effects, and (c) the manner in which this relationship holds equally well for individual "holes" as for an overall atomic line.

Frequency Pushing Effects

The reactive part of $\delta\chi(\omega)$ can also be responsible for small but still readily observable frequency pushing effects on the simultaneously oscillating modes of a multimode inhomogeneously broadened laser. Consider the dispersive effect on one mode of such a laser produced by the turning on or off of another mode some distance away in frequency, as shown in Figure 30.19. Turning on the second mode will burn a hole, which will change the $\delta\chi'(\omega)$ effects seen by the first mode, which will in turn change its apparent cavity frequency and hence its oscillation frequency by a small but measurable amount (especially if we look at the beam frequencies between different axial modes in the same laser).

Note that the $\delta\chi'(\omega)$ effects produced by burning a hole at ω_1 can be felt at more distant frequency separations than the $\delta\chi''(\omega)$ effects, because the reactive or $\delta\chi'$ effects fall off at large frequency separations only as $1/(\omega - \omega_1)$ compared to $1/(\omega - \omega_1)^2$ for the absorptive or $\delta\chi''$ effects.

REFERENCES

The saturated dispersion results in iodine shown in Figure 30.18 are described in B. Couillaud and A. Ducasse, "Refractive index saturation effects in saturated absorption experiments," *Phys. Rev. Lett.* **35**, 1276-1279 (November 10, 1975).

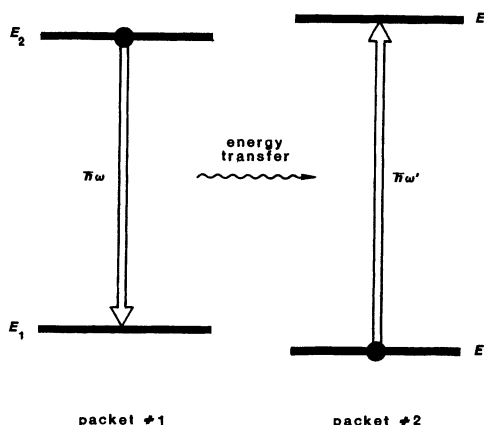


FIGURE 30.20
Energy transfer by "cross-relaxation" between two spectral packets.

30.5 CROSS-RELAXATION EFFECTS

Until now we have implicitly assumed that the individual atoms or spectral packets in an inhomogeneous transition are truly independent of and have no communication with each other. Under the influence of a strong signal at, say, frequency ω_1 , each packet then saturates independently of all the other packets, as described in the preceding section. The analysis of hole burning given in the preceding sections should then be more or less strictly correct.

In many real systems, however, there will be weak but significant effects, often called *cross-relaxation* effects, which can transfer excitation between any one spectral packet and all the other packets. Figure 30.20 illustrates one way of looking at such effects. It shows the slightly different energy level spacings appropriate to two different atoms or two different widely separated packets within an inhomogeneous transition. Suppose that the absorption on packet #1 is slightly saturated, meaning that an excess number of atoms (over the usual thermal equilibrium population) has been lifted into the upper level of this packet. Without any cross-relaxation effects this packet will recover from saturation with the usual longitudinal or energy decay time we have labeled by either T_1 or $\tau \equiv \gamma^{-1}$.

It can also be possible in some situations, however, for an atom in packet #1 to get rid of its excitation energy and return to the lower level by transferring its energy to the upward excitation of an atom in packet #2. This process effectively transfers a part of the excitation and the saturation on packet #1 over to packet #2, through the cross relaxation mechanism, without any net transfer of energy from the atoms to their thermal surroundings.

If cross-relaxation exists between two different spectral packets or groups of atoms, it will generally act in a direction such as to equalize—or at least, attempt to equalize—the atomic temperatures and the degrees of saturation of the two (or more) packets involved. That is, if one packet is being partially saturated (and thus heated up) by an applied signal, cross-relaxation will act to transfer this saturation to other packets, thereby reducing the degree of saturation of the packet in direct contact with the saturating signal. The time constant for this

process to transfer energy out of packet #1 into all other possible packets #2 is commonly called the *cross-relaxation time*, sometimes written as τ_{cr} .

Cross-Relaxation Mechanisms

There are several different physical mechanisms by which cross relaxation can occur in real atoms. Consider first doppler-broadened atoms in a gas. Such atoms undergo collisions in which at least three different effects can happen, separately but simultaneously. First there can be *inelastic collisions*, in which an atom in an upper atomic level transfers some of its internal energy to kinetic energy of the colliding species, in the process dropping down to a lower atomic level. These collisions become part of the energy decay rate γ or $1/T_1$ in the atoms, and contribute to the (homogeneous) lifetime broadening of the collisions.

Second, there can be *elastic dephasing* collisions in which the atomic energy level of the atom is not changed, and the velocity class and hence the doppler shift of the atom is also not changed, but the internal oscillatory motion (or precession) of the atom is randomized in phase. These collisions contribute to the homogeneous dephasing or pressure broadening of the atomic transition, as contained in the dephasing time constant T_2 .

Finally, there can be *elastic but velocity changing collisions*, in which the internal energy of the atom is not changed, but the atom is deflected into a new direction and/or velocity. Hence the atom (carrying along its particular degree of saturation) is transferred over to a new velocity class or spectral packet so far as its doppler shift is concerned. (It then does not really matter whether or not its oscillatory motion is dephased, since it now has a new and randomly determined doppler frequency.) These velocity changing collisions provide exactly a cross-relaxation mechanism.

All three of these collision processes can occur simultaneously, with different effective cross sections and rates, in any real gas or gas mixture. For a near-ideal inhomogeneous transition we want the inelastic and elastic-dephasing collisions to be reasonably weak so that the energy decay and homogeneous broadening are not too strong. Further, we want the velocity changing collisions to be still more infrequent, so that cross relaxation effects are even weaker, though they still may be present. This can be the situation in many real systems.

A second elementary mechanism for cross-relaxation involves communication and energy transfer between atoms through the dipolar interaction between atoms that are close enough to each other in either a gas or a solid for their local dipolar fields to overlap. This mechanism is essentially an extension of the dipolar dephasing and broadening effects we have mentioned earlier. Without going into further details we note that it can also be responsible for cross-relaxation, as can also radiation trapping effects, and energy transfer through phonon coupling mechanisms in solids.

Energy Conservation

The energy transfer between packets shown in Figure 30.20 does not quite conserve energy, since the two atoms have slightly different energy gaps. The fractional difference is generally very small, however, since the packets will be separated by an energy gap corresponding to the inhomogeneous linewidth, or $\hbar\Delta\omega_d$ at most, compared to the total energy gap of $\hbar\omega_a$. The resulting energy difference, or *energy defect*, is $\ll kT$. This energy defect can generally be taken

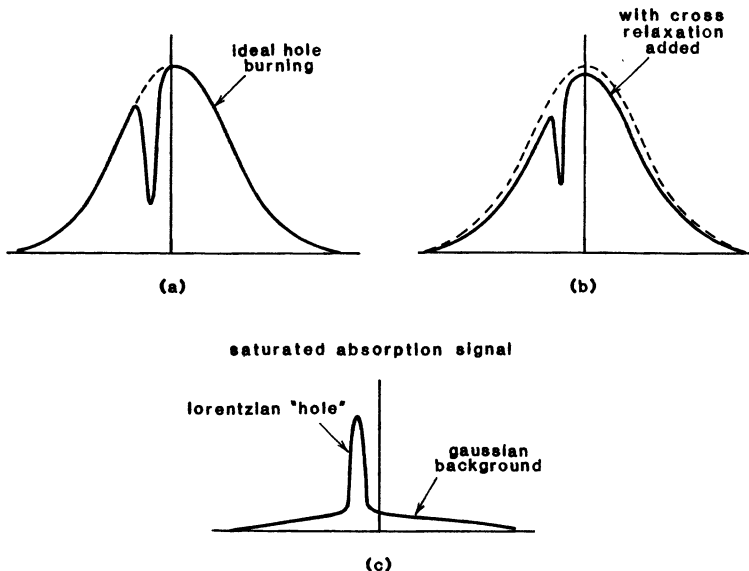


FIGURE 30.21

Hole burning with and without cross-relaxation. (a) No cross-relaxation. (b) Moderate cross-relaxation. (c) Hole lineshape with moderate cross-saturation.

up in the mechanical velocity of colliding gas atoms, or the dipolar or lattice interactions of atoms in solids.

The general effect of cross-relaxation is thus to open up a (weak) energy transfer and thermalizing mechanism between packets. Saturating the population difference on one packet then, in essence, heats up that packet to a higher atomic temperature; and cross-relaxation attempts to transfer this excitation and saturation to other packets located elsewhere within the inhomogeneous line.

Effects of Cross-Relaxation on Hole Burning

The usual assumption for atomic systems with cross-relaxation is that cross-relaxation effects are more or less equally likely to transfer energy from a saturated packet to any other packet anywhere within the inhomogeneous lineshape. That is, there is no great preference for cross-relaxation to packets that are nearby in frequency, as compared to more distant packets.

The implications of this assumption for inhomogeneous hole burning in the presence of weak cross-relaxation are illustrated in Figure 30.21. If there is little or no cross-relaxation, as in Figure 30.21(a), a hole burnt into one packet of a strongly inhomogeneous line has little or no effect on packets some distance away.

In the presence of moderate cross-relaxation, however, part of the saturation of an individual hole is transferred to a weaker but broadband saturation of the packet population differences all across the entire inhomogeneous line, as shown in Figure 30.21(b). In an ac-modulated saturation spectroscopy experiment, this

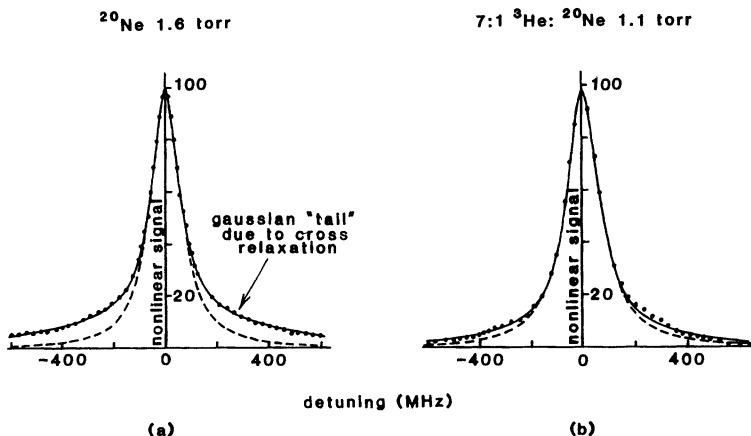


FIGURE 30.22
Saturated absorption results showing (a) strong and (b) weak cross-relaxation effects.

produces a kind of broader pedestal on the hole-burning signal, as illustrated in Figure 30.21(c).

Cross-relaxation within an inhomogeneous transition is sometimes referred to as *spectral diffusion*, since the net effect is as if energy or saturation diffuses out of the saturated packets in the hole, and spreads across the entire inhomogeneous linewidth. In the limit of very fast cross-relaxation obviously the hole would be smeared across the full inhomogeneous linewidth; and the transition would become in effect a homogeneous rather than inhomogeneous line for all practical purposes. The condition for observing cross-relaxation behavior is thus essentially that the cross-relaxation be fast enough to transfer some excitation between packets, but not so fast as to totally smear or wipe out the hole.

Experimental Results

Figure 30.22 shows the effect of cross-relaxation (in this situation by velocity changing collisions) on the results of a saturated absorption. Both parts show the results of ac saturated absorption spectroscopy carried out on the 6328Å transition in an unpumped and uninverted neon cell, using a tunable He-Ne laser. In each situation the dashed line is a lorentzian curve fitted to the center portion of the line, whereas the solid line is a more complicated theory including cross-relaxation effects.

In part (a) the cell contains pure neon only, at a comparatively high pressure of 1.6 torr; cross-relaxation effects due to collisions between neon atoms are strongly visible in the wings of the line. In part (b), the neon pressure has been greatly reduced, decreasing the cross-relaxation collisions in the neon; but a substantial amount of He has been added to the cell to produce dephasing collisions with the neon. As a result the hole widths in the two situations are essentially the same (i.e., same T_2 for the neon transition); but the amounts of cross-relaxation are quite different.

Cross-Relaxation Effects in Amplifying Media

We have described cross-relaxation effects thus far in terms of hole burning and saturation transfer within uninverted or absorptive transitions. All the same mechanisms and concepts apply equally well to inverted amplifying transitions. Cross-relaxation, if present, must then be taken into account in calculating the saturation and power extraction from an inhomogeneous laser transition.

If an amplifying line is homogeneous, for example, an applied signal anywhere within the line can extract the stored energy in the atomic system across the full linewidth; whereas in a completely inhomogeneous line an applied signal can extract only the energy stored in one or two spectral packets within the hole that is burned in the line by a strong signal. We can then expect that saturation behavior in a line with significant cross relaxation will fall somewhere between the $1/(1 + I)$ of an ideal homogeneous transition and the $1/\sqrt{1 + I}$ of an ideal inhomogeneous transition.

REFERENCES

The concept of cross-relaxation originated in the fields of nuclear and paramagnetic resonance, where it applied not only to cross-relaxation between different packets in a single inhomogeneously broadened line, but also to cross-relaxation between two different magnetic resonance transitions having the same or nearly the same resonance frequency (for example, neighboring nuclear or electronic spins located at two slightly different nonequivalent sites in a crystal lattice). Some early references include N. Bloembergen, et al., "cross-relaxation in spin systems," *Phys. Rev.* **114**, 445 (1959); and P.S. Pershan, "Cross relaxation in LiF," *Phys. Rev.* **117**, 109 (1960).

The experimental results for neon shown in this section come from A. V. Otieno, "Homogeneous saturation of the 6328-Å neon laser transition due to collisions in the weak collision model," *Optics Comm.* **26**, 207-210 (August 1978). (Note that the results in Figure 30.16 from P. W. Smith and T. Hänsch, "Cross-relaxation effects in the saturation of the 6328-Å neon-laser line," *Phys. Rev. Lett.* **26**, 740-743 (March 29, 1971) also show observable amounts of cross-relaxation.)

Experiments demonstrating both narrow hole burning and much broader but weaker cross saturation due to spectral cross-relaxation in absorbing ruby samples at very low temperature are also given by P. E. Jessop, T. Muramoto, and A. Szabo, "Optical hole burning in ruby," *Phys. Rev. B* **21**, 926-936 (February 1, 1980).

Fast spectral cross-relaxation such as can occur in a solid-state laser material can have significant effects on the gain saturation and energy extraction in the laser medium. These effects are analyzed in part in A. Y. Cabezas and R. P. Treat, "Effect of spectral hole-burning and cross relaxation on the gain saturation of laser amplifiers," *J. Appl. Phys.* **37**, 3556-3563 (August 1966).

30.6 INHOMOGENEOUS LASER OSCILLATION: LAMB DIPS

In an early and widely read analysis of gas lasers, Willis Lamb predicted, and experimenters soon confirmed, an unexpected aspect of doppler-broadened gas laser oscillation. If we tune the resonance frequency of a single oscillating cavity mode across a doppler-broadened gas laser transition, the curve of oscillation power output versus cavity frequency shows a comparatively sharp and narrow

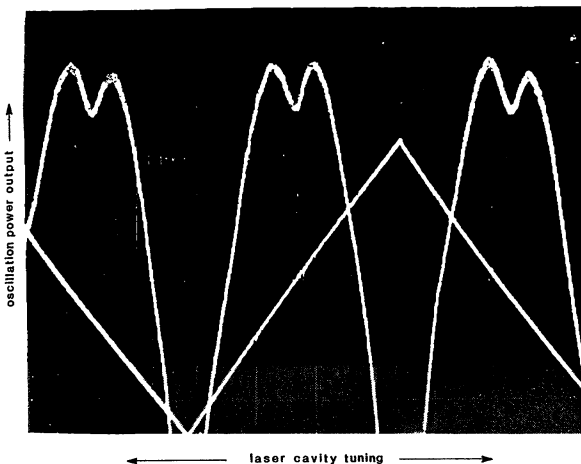


FIGURE 30.23

Lamb dip in the power output versus a He-Ne laser.

dip in power output when the oscillation frequency coincides with the center of the doppler-broadened line. Figure 30.23 shows a typical oscilloscope trace of the measured power output versus oscillation frequency for a single-frequency, single-isotope He-Ne laser at 633 nm. The triangular signal is the ramp voltage applied to the piezoelectric crystal to vary the laser cavity length.

This so-called "Lamb dip" in the power output versus frequency occurs only in standing-wave cavities, and is a consequence of saturation and hole-burning effects in the doppler-broadened line, caused by the two oppositely traveling waves in such a cavity. Measurement of this Lamb dip thus provides both a way of studying inhomogeneous broadening effects and of stabilizing the frequency of doppler-broadened lasers to the exact center of the atomic transition.

Lamb Dip: Physical Explanation

The signal fields inside a conventional standing-wave laser cavity can be divided into two oppositely directed traveling waves which we have referred to as the $+z$ and $-z$ waves. Any single atom with axial velocity v thus sees two oppositely traveling waves, for which it has equal and opposite doppler shifts, even though the two waves are at the same frequency. This leads to double hole-burning effects, and to the occurrence of the Lamb dip we are discussing.

Consider a laser with an inhomogeneous doppler-broadened transition, oscillating in a single-frequency standing-wave axial-mode resonance, with the frequency ω of this resonance detuned from the atomic line center by several inhomogeneous linewidths or hole widths. Then, as illustrated in Figure 30.24, the $+z$ traveling-wave component of the standing-wave cavity fields will interact with and burn a hole in only those atoms in the velocity class given by $v/c = (\omega_0 - \omega)/\omega_0$; while at the same time, the fields in the $-z$ traveling-wave

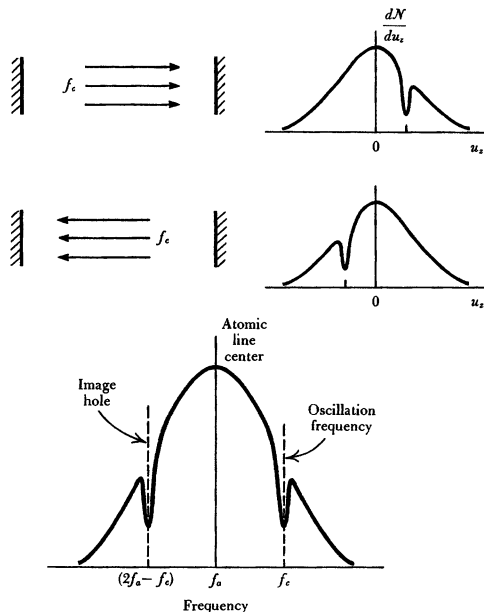


FIGURE 30.24
Traveling waves and resulting velocity holes in a standing-wave laser oscillator.

component will burn an equal and opposite hole in the symmetrically located velocity class at the opposite value of v/c .

Whenever the cavity frequency is well away from line center on either side, therefore, two symmetric holes are burned, and in essence the laser is able to extract power from two separate sets of atoms or velocity classes in the atomic velocity distribution.

If, however, the cavity frequency is tuned exactly to the line center, both the $+z$ and $-z$ waves can interact only with the $v = 0$ velocity class in the doppler distribution. This velocity class is therefore saturated twice as heavily as either of the separate velocity classes in the off-resonance situation, because it sees two signals instead of one. But this means that the laser need only oscillate roughly half as hard to produce the same degree of saturation needed to reduce the gain to equal the cavity losses. In essence the two symmetric holes coalesce into one, and laser power is taken only from the single velocity class at $v = 0$. In an inhomogeneously broadened single-frequency laser, this results in the slight but definite dip in laser power output at line center known as the *Lamb dip*.

Experimental Implications of the Lamb Dip

To obtain a clear and unambiguous Lamb dip, it is important that the inhomogeneously broadened laser oscillate on only a single axial mode within its inhomogeneous linewidth. We can force the laser to do this either by making the laser cavity very short, so that only a single axial mode falls within the inhomogeneous gain profile, or by using mode-control etalons or other techniques to suppress all but one favored axial mode.

The frequency of this one mode can then be scanned across the doppler-broadened atomic line profile, for example, by mounting one of the cavity mirrors on a piezoelectric crystal and changing the cavity length slowly. The resulting curve of single-mode laser power output versus oscillation frequency will look like the result for a typical He-Ne laser shown in Figure 30.23.

The presence or absence of a Lamb dip in a single mode laser thus becomes a sensitive test of whether or not a given laser is inhomogeneously broadened. The center of the Lamb dip, moreover, is directly tied to the $v = 0$ atoms, which have zero doppler shift. The center of the Lamb dip thus becomes a sensitive marker for the exact center of the atomic transition, and can be used for a frequency stabilization reference in frequency-stabilized lasers. Helium-neon lasers using this frequency stabilization technique are commercially available. In addition, the shape and width of the Lamb dip provide a way to measure the homogeneous linewidth in the atomic transition.

Multiple-mode oscillations, however, or the presence of isotopic shifts due to overlapping lines for multiple isotopes, or any other line splitting mechanisms such as Zeeman splitting of the atomic transition, can all smear out and eliminate the Lamb dip even in a strongly inhomogeneous transition. The earliest He-Ne lasers in fact were filled with naturally occurring neon, which has a mixture of Ne^{20} and Ne^{22} isotopes. Both of these contribute to the laser gain and laser oscillation, but with slightly different transition frequencies ω_0 , shifted apart in frequency by approximately 800 MHz, which is smaller than the doppler-broadening, but considerably larger than the homogeneous linewidths in either system. Only after lasers were filled with single-isotope gas mixtures could clearly defined Lamb dips be observed.

Approximate Lamb Dip Analysis

Let us now develop a simplified analysis for the power output versus frequency in a strongly inhomogeneous, single frequency, weakly coupled standing-wave laser, using the following approach.

Suppose the unsaturated midband gain of the laser is pumped above threshold by a dimensionless ratio r given by

$$r \equiv \frac{2\alpha_{m0}p_m}{2\alpha_0p + \ln(1/R_1R_2)}, \quad (29)$$

where α_{m0} is the unsaturated gain coefficient at midband, α_0 is the corresponding internal cavity loss coefficient, and R_1 and R_2 are the end mirror reflection coefficients. The unsaturated gain coefficient $\alpha_m(\omega)$ in a doppler-broadened gain medium then has a frequency dependence given by

$$\alpha_m(\omega) = \alpha_{m0} \exp \left[-4 \ln 2 \left(\frac{\omega - \omega_0}{\Delta\omega_d} \right)^2 \right] = \alpha_{m0} e^{-4\alpha y^2}. \quad (30)$$

In the second part of Equation 30.30 we follow the usual notation in the literature on Lamb dips, by expressing the frequency detuning in the dimensionless form $y = 2(\omega - \omega_0)/\Delta\omega_d$, so that y gives the oscillation frequency tuning off line center measured in units of half the homogeneous linewidth. The dimensionless

quantity

$$\alpha \equiv \left(\frac{\ln 2}{4} \right) \left(\frac{\Delta\omega_a}{\Delta\omega_d} \right)^2 \quad (31)$$

(nothing to do with the gain coefficient α_m) then has a value $\ll 1$ for the strongly inhomogeneous situation $\Delta\omega_a \ll \Delta\omega_d$.

The circulating signal inside the laser cavity for an oscillation frequency ω more than a homogeneous linewidth or so away from the center of the doppler line—in other words, for $y \geq 1$ —will then burn two separate holes in the velocity distribution, one in the velocity class $+v_h/c$ due to the wave going in one direction, and a symmetrically located hole in the velocity class at $-v_h/c$ due to the wave going in the other direction. There will be essentially no interaction between those holes if they are separated by several hole widths or more. From our hole-burning analysis in an earlier section, the gain seen by either of these signals at the center of its own hole will then saturate as

$$\alpha_m(\omega) \approx \alpha_{m0} e^{-4\alpha y^2} \times \sqrt{\frac{1}{1 + I/I_{\text{sat}}}}. \quad (32)$$

The gain for the wave in each direction saturates only on its own intensity (and we assume small output coupling, so that the intensity has essentially the same value I in either direction inside the cavity).

If, however, the oscillation frequency ω is tuned exactly to the line center frequency ω_0 , then the two signals traveling in opposite directions will burn only a single hole at the center of the line, in the $v = 0$ velocity class. This hole is, however, saturated down by the total intensity $2I$ due to the signal waves going in both directions, and thus the gain coefficient for either wave will saturate in the form

$$\alpha_m(\omega_0) \approx \alpha_{m0} \times \sqrt{\frac{1}{1 + 2I/I_{\text{sat}}}}, \quad (33)$$

with an extra factor of 2 in the saturation denominator.

The changeover from one of these forms of saturation to the other will occur as the oscillation frequency ω is tuned away from line center by approximately half the hole width or (roughly) one homogeneous linewidth, which corresponds in normalized form to $y \approx \pm 1$. As a simple way of expressing this analytically, we can then write the basic oscillation condition—which requires that the saturated round-trip power gain just equal the round-trip power losses—in the form

$$\frac{2\alpha_m(\omega)p_m}{2\alpha_0 p + \ln(1/R_1R_2)} = \frac{r \exp(-4\alpha y^2)}{\sqrt{1 + f(y) \times I/I_{\text{sat}}}} = 1, \quad (34)$$

where the factor $f(y)$ multiplying I/I_{sat} in the denominator is given by

$$f(y) \approx \frac{2 + y^2}{1 + y^2}. \quad (35)$$

This factor then changes, as desired, from a value of 2 for $y \ll 1$ to a value of 1 for $y \gg 1$. Inverting Equation 30.34 to obtain the intensity $I = I(y)$ then yields

$$I(y) = \frac{r^2 \exp(-8\alpha y^2) - 1}{f(y)} I_{\text{sat}}. \quad (36)$$

FIGURE 30.25

Predicted Lamb dip profiles at different pumping levels above threshold. Solid lines: simplified theory. Dashed lines: more exact analysis.

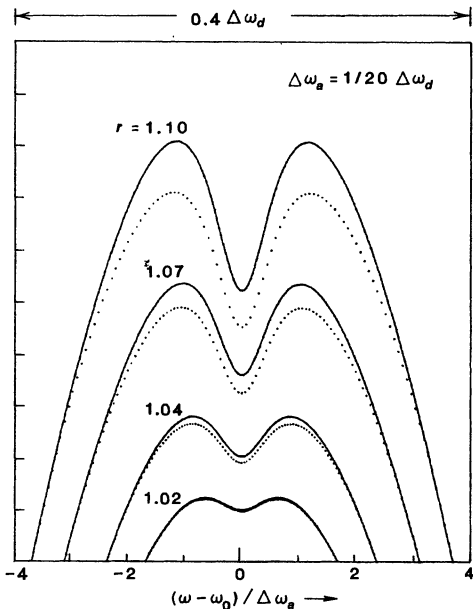


Figure 30.25 shows the oscillation power output versus frequency predicted by Equation 30.35 for various values of pumping level r ranging from 1.02 to 1.10 times threshold, assuming that the homogeneous linewidth $\Delta\omega_a$ is 20 times narrower than the doppler linewidth $\Delta\omega_d$. Note that for pumping levels r that are reasonably well above threshold, the Lamb dip predicted by this simplified analysis should have a fractional depth approaching 50% of the power output off the line center.

Figure 30.26 shows a carefully measured Lamb dip in a single-isotope He-Ne laser, in which the dip approaches although it does not quite reach the fractional depth of 50% for the Lamb dip at line center.

More Exact Analysis

Let us now carry through a somewhat more detailed analysis of the hole burning in a doppler-broadened line, not so much perhaps because of the importance of the answer, as because this will illustrate the analytic approach of integrating over velocity classes that we must follow in such gas laser analyses.

We will analyze therefore the elementary situation of a relatively low-gain and weakly coupled laser oscillating in a single cavity mode on a strongly inhomogeneous doppler-broadened laser medium. The contribution to the round-trip power gain coefficient $\alpha_m(\omega)$ for, say, the $+z$ traveling-wave signal component at frequency ω , produced by all the atoms in a single velocity class $g(v)dv$ at

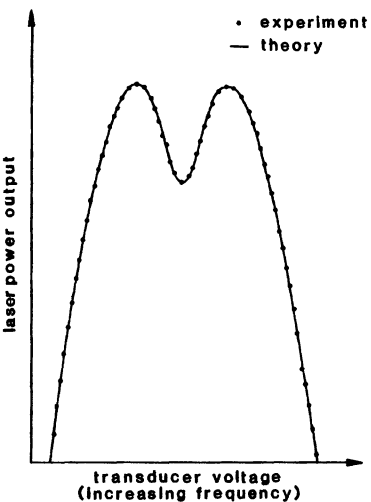


FIGURE 30.26
Carefully measured Lamb dip in a He-Ne laser.

velocity v , can then be written as

$$d\alpha_m(\omega, v) = \frac{K S(v; \omega) g(v) dv}{1 + [2(\omega - \omega_a(v)) / \Delta\omega_a]^2}, \quad (37)$$

where K is a constant factor whose value we will calculate later; $g(v)dv$ is the number of atoms in the v -th velocity class; and the factor $S(v; \omega)$ is the degree of saturation for the v -th velocity class produced by both the $+z$ and $-z$ traveling waves at frequency ω . Remember that the apparent resonant frequency for the atoms in the v -th velocity class as seen by the $+z$ traveling wave is given by $\omega_a(v) = \omega_0(1 + v/c)$, whereas $\omega_a(-v)$ is the resonance frequency seen by the $-z$ wave.

The saturation function $S(v; \omega)$ for the v -th velocity class produced by the waves in both directions can then be written as

$$S(v; \omega) = \frac{1}{1 + [L(+v) + L(-v)] \times I/I_{\text{sat}}}, \quad (38)$$

where $L(v)$ is a lorentzian lineshape function given by

$$L(v) = \frac{1}{1 + [2(\omega - \omega_a(v)) / \Delta\omega_a]^2}, \quad (39)$$

and where I is the intensity of the traveling wave going in either direction inside the laser cavity (assuming small output coupling at either end of the cavity, so that I is nearly the same in either direction). The two lorentzian factors come into Equation 30.38 because *both* the $+z$ and $-z$ waves will in general have a saturation effect on the atoms in the v -th spectral packet, but the amount that these signals will be off resonance depends on whether the wave is traveling in the $\pm z$ direction.

The total round-trip power gain coefficient for the $+z$ wave (or, by symmetry, for the $-z$ wave) at frequency ω is then the integral of the gain contribution at ω due to all the velocity classes, or

$$\alpha_m(\omega) = \int_{-\infty}^{\infty} d\alpha_m(\omega, v) = \int_{-\infty}^{\infty} \frac{K S(v; \omega) g(v)}{1 + [2(\omega - \omega_a(v)) / \Delta\omega_a]^2} dv. \quad (40)$$

Let us adopt the normalized variables

$$p \equiv I/I_{\text{sat}} = \text{normalized oscillation level},$$

$$y \equiv 2 \left(\frac{\omega - \omega_0}{\Delta\omega_a} \right) = \text{detuning of oscillation frequency } \omega \text{ off line center } \omega_0,$$

$$u \equiv 2 \frac{\omega}{\Delta\omega_a} v/c = \text{normalized velocity}.$$

$$L(u) \equiv 1/[1 + u^2] = \text{normalized lorentzian}.$$

Following the custom in the literature we also write the Maxwellian velocity distribution $g(v)$ as

$$g(v) = \exp(-4\alpha u^2), \quad (41)$$

where the dimensionless linewidth parameter α is given as before by

$$\alpha \equiv \left(\frac{\ln 2}{4} \right) \left(\frac{\Delta\omega_a}{\Delta\omega_d} \right)^2. \quad (42)$$

The gain expression given in Equation 30.40 becomes

$$\alpha_m(\omega) = \frac{\alpha_{m0}}{\pi} \int_{-\infty}^{\infty} \frac{\exp(-4\alpha u^2) du}{[1 + (y - u)^2] \times [1 + [L(y - u) + L(y + u)] \times p]}, \quad (43)$$

where α_{m0} is the midband unsaturated gain obtained if we evaluate the integral over u assuming $4\alpha \ll 1$, $y = 0$ and $I = 0$.

Approximate Solution

Steady-state oscillation requires that the saturated gain $\alpha_m(\omega)$ be just sufficient to match the total cavity losses. Hence we must find the intensity $I = I(\omega)$, or $I = I(y)$, which will saturate $\alpha_m(\omega)$ down to just equal the net cavity losses at each different value of the oscillation frequency ω .

The exact integral just given in Equation 30.43 can be evaluated with some difficulty to obtain exact results. This becomes much easier to do, however, with very little loss in physical insight, if we assume that the laser gain is only a small amount (say, $\leq 20\%$) above threshold, as is often the situation in gas lasers. We can then approximate the saturation behavior by

$$\frac{1}{1 + [L(y - u) + L(y + u)]p} \approx 1 - [L(y - u) + L(y + u)]p, \quad (44)$$

where L_+ and L_- are the two lorentzian factors from Equation 30.43.

We will also assume $4\alpha \ll 1$, which says simply that the line is strongly inhomogeneous with $\Delta\omega_a \ll \Delta\omega_d$. We can then note that the $\exp(-4\alpha u^2)$ function is quite slowly varying with u , whereas the denominator of the gain expression in Equation 30.43 contains a comparatively narrow lorentzian resonance which

peaks at $u = y$. Hence the exponential function can be taken outside the integral, and given its value at $u = y$.

With these approximations the general gain integral 30.43 becomes

$$\alpha_m(y) = \frac{\alpha_{m0}e^{-4\alpha y^2}}{\pi} \int_{-\infty}^{\infty} \left[\frac{du}{1 + (y - u)^2} - \frac{p du}{[1 + (y - u)^2]^2} \right. \\ \left. - \frac{p du}{[1 + (y - u)^2][1 + (y + u)^2]} \right]. \quad (45)$$

Each of the terms in the preceding integral is readily evaluated (for example, by the theory of residues), leading to the final result

$$\alpha_m(y) = \alpha_{m0}e^{-4\alpha y^2} \left[1 - \frac{1}{2}f(y)p \right]. \quad (46)$$

where $f(y) = (2 + y^2)/(1 + y^2)$ is the same as defined in Equation 30.34. Suppose that we define the normalized amount that the laser is above threshold exactly at the line center ($y = 0$) by the usual normalized pumping rate r . The steady-state intensity $I(y)$ needed to make gain equal loss is then given by

$$\frac{I(y)}{I_{\text{sat}}} = \frac{2}{f(y)} \times \frac{r \exp(-4\alpha y^2) - 1}{r \exp(-4\alpha y^2)}. \quad (47)$$

This is very similar to the very simple physical approximation we derived previously.

Discussion and Summary

Figure 30.27 shows a set of curves for oscillation power output $I(y)$ plotted versus normalized frequency detuning $(\omega - \omega_0)/\Delta\omega_d$ for pumping levels of $r = 1.05, 1.10, 1.20$ and 1.30 times above threshold, and for homogeneous to inhomogeneous linewidth ratios of $\Delta\omega_a/\Delta\omega_d = 1/5$ and $1/50$.

The general behavior given by Equation 30.47 is quite clear. First, oscillation is possible only over that frequency range for which the doppler-broadened but unsaturated gain exceeds the loss, i.e., for $r \exp(-4\alpha y^2) \geq 1$ or $|y| \leq [(\ln r)/4\alpha]^{1/2}$. Except for very small r , this can cover a moderate range in y if $\alpha \ll 1$.

Second, for frequencies within roughly one homogeneous linewidth of line center, i.e., for $|y| < 1$, there is a saturation factor which is like $1 + 2I/I_{\text{sat}}$ in the denominator of the gain formulas. The factor of 2 in these is present because the active $v = 0$ velocity class in the laser is being saturated by *both* the $+z$ and $-z$ waves. However, as soon as the laser is tuned more than a few hole widths off line center, so that $y^2 > 1$, the active packets at $\pm v$ see only one of the $+z$ or $-z$ waves, and hence saturate only as $1 + I/I_{\text{sat}}$ rather than as $1 + 2I/I_{\text{sat}}$. For the larger values of r and $\Delta\omega_d/\Delta\omega_a$ the depth of the Lamb dip in the limit thus approaches half the peak laser intensity, whereas the width of the Lamb dip is roughly one homogeneous linewidth.

Inverse Lamb Dips

Suppose as an opposite example that a cell containing a *saturable absorber* with a highly inhomogeneous linewidth is placed within the cavity of any type of

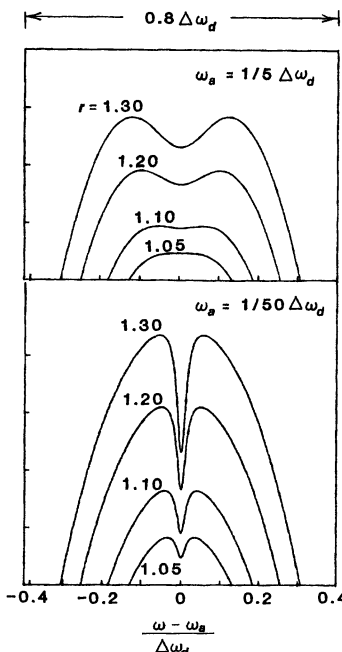


FIGURE 30.27

Theoretically predicted Lamb dips for two different degrees of inhomogeneous broadening.

standing-wave laser oscillator. This cell will then provide a saturable loss rather than a saturable gain, and this loss will be more difficult to saturate when the laser frequency is tuned away from the line center of the absorber, and easier to saturate when the laser frequency happens to coincide exactly with the unshifted resonance frequency or the $v = 0$ velocity class of the absorbing atoms. In other words, this saturable absorber can provide a kind of "inverse Lamb dip" in the power output of the laser, as illustrated in Figure 30.28.

The laser itself may or may not have a normal Lamb dip due to its own gain medium, and the center frequency of the saturable absorber may not necessarily coincide with the center frequency of the laser medium. So long as the absorber's resonance frequency lies within the tuning range of the laser, however, it can provide a small upward pip or inverse Lamb dip, which will mark the center frequency of the absorber, as in Figure 30.28. A molecular absorber such as iodine, which has an extremely complex and dense spectrum of absorption lines in the visible, may in fact produce half a dozen different and independent inverse Lamb dip markers across the tuning range of a single visible gas laser, and these can be used as markers for absolute frequency stabilization of the laser.

This technique can be very useful for laser frequency stabilization, since we can select the laser medium for maximum gain, discharge stability, power output, or other practical considerations, without concern for frequency stabilization considerations. The absorber cell, however, which is purely passive and not required to furnish any power, can be designed for low pressure and hence narrow homogeneous linewidth, and can also be highly temperature stabilized and

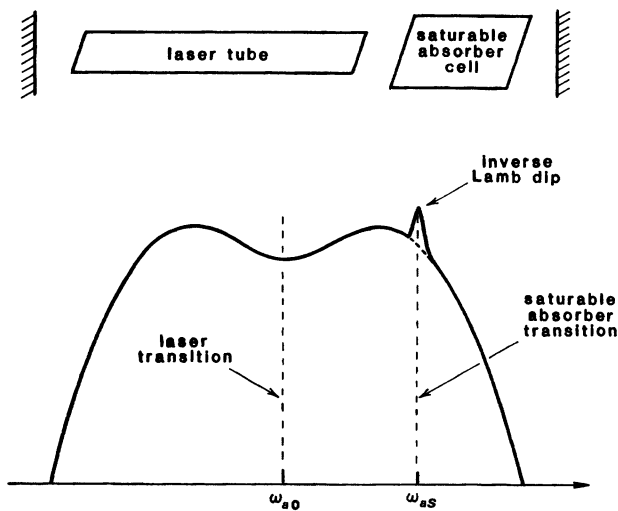


FIGURE 30.28
Inverse Lamb dip produced by an inhomogeneous absorption line within the laser's tuning range.

shielded against stray fields. This technique can thus be used both for sensitive spectroscopy and for laser stabilization.

Dispersive Tuning Effects

Suppose we tune the resonance frequency of a laser cavity mode across the central part of the linewidth of an inhomogeneously broadened laser transition, for example, by changing the cavity length with a piezoelectric mirror mount. If we at first neglect hole-burning effects, then the inhomogeneous transition will have an unsaturated reactive susceptibility $\chi'(\omega)$ which will be zero at line center, positive for $\omega > \omega_0$, and negative for $\omega < \omega_0$. A simple analytic expression for the $\chi'(\omega)$ of even an unsaturated gaussian inhomogeneous transition is not available; but we do know that (a) $\chi'(\omega)$ varies more or less linearly with ω across the central portion of the inhomogeneous line, and (b) for an amplifying transition the sign of $\chi'(\omega)$ is such as to *pull* the cavity frequency toward line center.

If only the unsaturated $\chi'(\omega)$ is included, therefore, the pulled cavity resonance frequency will tune linearly with length change across the central region of the inhomogeneous line; but at a slightly slower tuning rate than would the "cold" or empty cavity resonance without the laser atoms.

Suppose we now include hole-burning effects in a standing-wave laser cavity with a doppler-broadened gain curve. As the laser oscillation frequency is tuned toward the line center, starting from either side of line center, the $+z$ and $-z$ waves will burn the usual two holes in the velocity distribution at $\pm v_h$. In effect the oscillation frequency signal will burn one hole at its own frequency, which has zero pushing or pulling effect on itself; plus a symmetric hole located at an equal distance on the opposite side of line center. This second hole will have a *pushing*

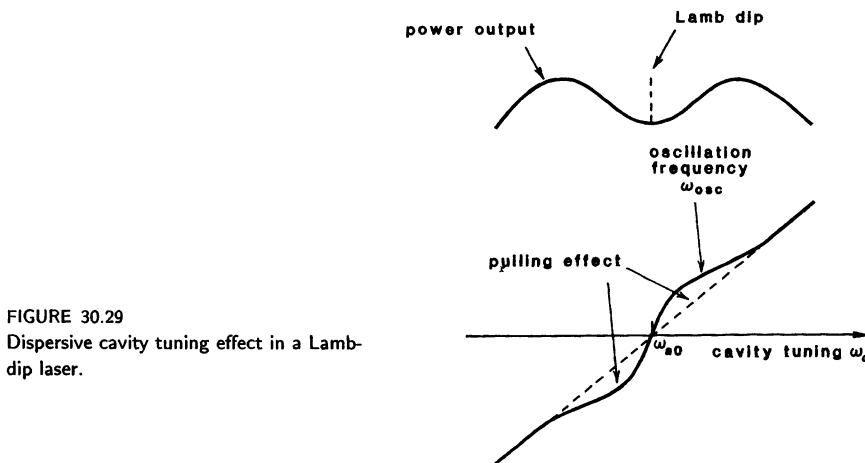


FIGURE 30.29
Dispersive cavity tuning effect in a Lamb-dip laser.

effect on the oscillation frequency, because it represents a reduction in inversion, or in effect the adding of absorption. (In other words, inverted transitions *pull*, but holes in inverted transitions *push*.)

As the laser cavity frequency tunes into the central Lamb dip region, where the holes come close together, this reverse pushing effect will become strongest; but it will then also drop to zero exactly at line center, where the holes completely overlap. The central region of an inhomogeneous laser transition is thus marked both by the Lamb dip in power output, and by a *nonlinear dispersive tuning effect*, as shown (somewhat exaggerated) in Figure 30.29. The center of this dispersive tuning effect has sometimes been used, along with the Lamb dip, as a marker for frequency stabilization of a laser oscillator to the exact center of the atomic transition.

Note that if a laser oscillator contains instead an inhomogeneously broadened saturable absorber, which produces an inverse Lamb dip, then there will be a similar nonlinear dispersive tuning effect of opposite sign centered at the frequency of the inverse Lamb dip. If ω_c is the cold cavity frequency (without pushing or pulling effects), and ω_{osc} is the actual oscillation frequency, then the derivative $d\omega_{osc}/d\omega_c$ can be reduced to zero, or even become negative, at the center of a strong enough inverted Lamb dip. The laser oscillation frequency ω_{osc} thus tends to "hang up," or to become self-stabilized toward the center frequency of the saturable absorber, as the cavity frequency ω_c is tuned into the center of the inverted Lamb dip.

REFERENCES

The original reference predicting the existence of the Lamb dip is W. E. Lamb, Jr., "Theory of an optical maser," *Phys. Rev.* **134**, 1429 (June 15, 1964). The first published observation is by R. A. McFarlane, W. R. Bennett, Jr., and W. E. Lamb, Jr., "Single mode tuning dip in the power output of an He-Ne optical maser," *Appl. Phys. Lett.* **2**,

189–190 (1963). Another early reference showing both the Lamb dip and the nonlinear dispersive tuning effect is W. R. Bennett, Jr., S. F. Jacobs, J. T. LaTourrette, and P. Rabinowitz, “Dispersion characteristics and frequency stabilization of an He-Ne gas laser,” *Appl. Phys. Lett.* **5**, 56–58 (August 1, 1964).

The experimental He-Ne Lamb dip at the beginning of this section is from R. H. Cordover and P. A. Bonczyk, “Effects of collisions on the saturation behavior of the 6328 Å transition of Ne studied with a He-Ne laser,” *Phys. Rev.* **188**, 696–700 (December 10, 1969). Another interesting reference which shows the Lamb dip developing in a 1.5295 μm Hg-He laser as the He pressure is reduced and the Hg laser transition changes from homogeneously pressure-broadened to inhomogeneously broadened is K. A. Bikmikhailov, V. M. Klementev, and V. P. Chebotaev, “Collision broadening of the 1.53 μm line of mercury in an Hg-He, He-Ne mixture,” *Optics and Spectrosc.* **34**, 616–617 (June 1973).

Experimental results on Lamb dips in CO lasers are shown in C. Freed and H.A. Haus, “Lamb dip in CO lasers,” *IEEE J. Quantum Electron.* **QE-9**, 219–226 (February 1973). This useful paper both illustrates the Lamb dip in a different system than the usual He-Ne laser, and also gives an extended analysis of the Lamb dip including asymmetry and cross relaxation.

The concept of putting a low-pressure saturable absorber cell inside a laser cavity to produce a saturated absorption peak, or “inverse Lamb dip,” was first introduced by P. H. Lee and M. I. Skolnik, “Saturated neon absorption inside a 6328-Å laser,” *Appl. Phys. Lett.* **10** 303–305 (June 1, 1967). Detailed analyses of the general situation of a gas laser with an intracavity saturable absorber, including regular and inverted Lamb dips, are given by H. Greenstein, “Theory of a gas laser with internal absorption cell,” *J. Appl. Phys.* **43**, 1732–1750 (April 1972); by J. H. Shirley, “Semiclassical theory of saturated absorption in gasses,” *Phys. Rev. A* **8**, 347–368 (July 1973); and by R. Salomaa and S. Stenholm, “Gas laser with saturable absorber. I. Single-mode characteristics. II. Single-mode stability,” *Phys. Rev. A* **8**, 2695–2726 (November 1973).

The dispersive cavity tuning effects of atomic absorption lines, and their possible application to laser frequency stabilization, are extensively discussed by V. S. Letokhov and B. D. Pavlik, “Method for establishing a quantum frequency standard in the visible range using atomic absorption lines and a cw dye laser,” *Sov. J. Quant. Electron.* **6**, 32–38 (January 1976).

Problems for 30.6

1. *Frequency pulling in an inhomogeneously broadened laser.* Suppose a He-Ne *ring* laser oscillates at two frequencies, ω_1 and ω_2 , located at arbitrary points with the atomic gain profile, with the two oscillations going in opposite directions around the ring so that each burns only one hole in the line. Parameters for the laser are: Total power losses per round trip = 10%; homogeneous linewidth $\Delta\omega_a = 2\pi \times 100$ MHz; inhomogeneous linewidth $\Delta\omega_d = 2\pi \times 1,500$ MHz frequency spacing $\omega_2 - \omega_1 = 2\pi \times 800$ MHz; and axial-mode spacing $\Delta\omega_{\text{ax}} = 2\pi \times 800$ MHz. The laser is running at 20% above threshold, i.e., the unsaturated gain at ω_1 or ω_2 would be 1.2 times the total cavity losses.

Question: By how much (in Hz) is the oscillation frequency of ω_1 pushed (or pulled) by the presence of the oscillation at ω_2 , and vice versa? That is, by how much would either oscillation shift in frequency if the other were turned off or on?

2. *Oscillation spectrum and power output versus pumping in a doppler-broadened gas laser.* The opening section of this chapter has a problem which asks for the number of oscillating modes versus pump level in an inhomogeneously broadened laser. Redo this problem properly for a doppler-broadened gas laser, assuming a standing-wave laser cavity, with the centermost mode tuned to exactly line center.
3. *Anomalous frequency pulling at line center in a doppler-broadened laser.* When the resonance frequency of a standing-wave cavity laser oscillator is tuned through the center of a strongly inhomogeneous doppler-broadened line, we actually observe not only a Lamb dip, but also a frequency pulling effect: that is, the laser oscillation frequency does not track linearly with the cavity tuning as the cavity is tuned through the Lamb dip region. Analyze and describe this frequency pulling effect in the Lamb dip region, using the weak saturation approximation. (You may if necessary neglect the laser intensity variation across the Lamb dip region in calculating this frequency pulling effect.)

Note that this frequency pulling effect can become quite sizable in certain high-gain, narrow-line, inhomogeneous doppler oscillators.

4. *Inverse Lamb dip analysis.* A certain standing-wave-type laser cavity contains a homogeneously broadened laser gain medium whose gain coefficient α_m has a saturation intensity I_{sm} , and an atomic linewidth sufficiently broad that it can be ignored for purposes of this problem. Inside this cavity is also placed a doppler-broadened atomic absorption cell containing a low-pressure gas which has an absorption coefficient α_a , an (inhomogeneous) saturation intensity I_{sa} , and homogeneous and inhomogeneous linewidths $\Delta\omega_a$ and $\Delta\omega_d$, respectively. The cavity also has small but finite losses due to internal cavity losses and cavity coupling.

Analyze the inverse Lamb dip that will be produced in the laser power output in this situation. Assume that the unsaturated laser gain coefficient is r times the cavity losses (that is, the oscillator would be r times above threshold in the absence of the saturable absorber cell), and that similarly the unsaturated loss in the absorber cell is a times the same cavity losses. Discuss in particular the height and width of the inverse Lamb dip above the regular oscillation background level, and what the practical design considerations might be in choosing the relative amounts of gain, normal loss, and saturable loss in designing a laser to be frequency stabilized using such an inverse Lamb dip.



MAGNETIC-DIPOLE TRANSITIONS

In Chapters 2 and 3 of this book we introduced electric-dipole transitions as a category including most though not all important laser transitions. We also introduced the Lorentz electron oscillator model as a classical analog for describing nearly all the important properties of electric-dipole transitions.

Certain atomic and molecular transitions, however, respond directly to the magnetic fields rather than to the electric fields of an applied signal. These transitions are said to be *magnetic dipole* rather than electric dipole in character. The general class of magnetic-dipole transitions includes both a significant number of *optical* and *infrared transitions*, including a few important laser transitions; and also a very large number of *magnetic-resonance transitions* which occur at microwave and radio frequencies between the degenerate (or nearly degenerate) Zeeman sublevels of atomic and molecular energy levels.

In this chapter we describe all these magnetic-dipole transitions using a classical magnetic dipole, or a “magnetized top” as a classical model for understanding magnetic-dipole transitions. This classical magnetic dipole model will be useful in essentially the same way that the classical electron oscillator serves for electric-dipole transitions. This model will lead in particular to the well-known *Bloch equations* for magnetic dipole transitions, which are very important for describing either optical and infrared magnetic-dipole transitions or the much lower-frequency magnetic-resonance transitions.

31.1 BASIC PROPERTIES OF MAGNETIC-DIPOLE TRANSITIONS

The first task in this chapter is to understand how magnetic-dipole properties arise in atomic and molecular transitions. It may be easier to do this by starting from a quantum description than from a classical viewpoint. We are going to show, therefore, using a quantum description, that atoms and molecules can have *magnetic-dipole moments* as well as electric-dipole moments, and that for magnetic-dipole atoms these may include both *static* and *sinusoidally oscillating* magnetic dipole moments.

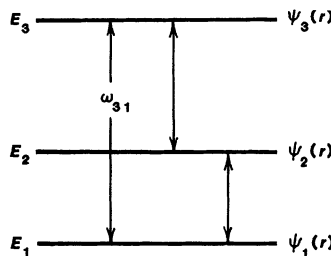


FIGURE 31.1

Quantum energy levels and eigenstates for an atom or molecule.

Quantum Properties of Atoms

Consider a quantized atom or molecule with quantum energy eigenvalues E_1, E_2, \dots and associated quantum energy eigenfunctions $\psi_1(r), \psi_2(r), \dots$, as in Figure 31.1. (The discussion in this section is going to be much like our discussion of the quantum properties of electric-dipole transitions in Section 3.3.)

The total quantum state $\psi(r, t)$ of this atom or molecule at any instant will then in the most general situation consist of a *quantum state mixture* of two or more such energy eigenstates, in the form

$$\psi(r, t) = \tilde{a}_1(t)e^{-iE_1 t/\hbar}\psi_1(r) + \tilde{a}_2(t)e^{-iE_2 t/\hbar}\psi_2(r) + \dots, \quad (1)$$

where the coefficients $|\tilde{a}_n(t)|^2$ give the probability of finding the atom in any particular energy level E_n if we make a measurement at time t ; and the rotating phase terms $e^{-iE_n t/\hbar}$ make this expansion satisfy the Schrödinger equation of motion in the absence of any applied signals. The expansion coefficients $\tilde{a}_1(t)$ and $\tilde{a}_2(t)$ in this expansion will then be constants if the atom is totally isolated, with no applied signals of interactions with other atoms, but will become slowly varying functions of time if the atom is perturbed by any kind of applied signal, or when relaxation effects are included.

Atomic and Molecular Charge Distributions

Given the wavefunction $\psi(r, t)$ describing the quantum states of the electrons in a single atom or molecule, we can then calculate the quantum expectation value for the *quantum charge density* $\rho(r, t)$ in the electron cloud around such an atom or molecule from the formula

$$\begin{aligned} \langle \rho(r, t) \rangle &= -Ze|\psi(r, t)|^2 \\ &= -Ze \left[\sum_i |\tilde{a}_i|^2 |\psi_i|^2 + \sum_{i,j \neq i} [\tilde{a}_i \tilde{a}_j^* \psi_i \psi_j^* e^{i\omega_{ji} t} + \text{c.c.}] \right]. \end{aligned} \quad (2)$$

where Z is the atomic number of the atom or molecule, and the notation *c.c.* refers to the complex conjugate of the preceding term.

Note that Equation 31.2 contains both a series of *static or dc terms* associated with each individual quantum energy level, as given by the summation on the first line, and potentially a series of *oscillating or ac terms*, with amplitudes proportional to the cross-products $\tilde{a}_i \tilde{a}_j^*$, which oscillate at each of the possible

transition frequencies $\omega_{ji} \equiv (E_j - E_i)/\hbar$, as given by the double summation on the second line.

Atomic and Molecular Current Distributions

Now, there also exists in general a space-varying and time-varying *quantum current distribution* $j(\mathbf{r}, t)$ inside any atom or molecule, associated with the charge distribution $\rho(\mathbf{r}, t)$. In fact, according to quantum theory the expectation value for the current density $j(\mathbf{r}, t)$ in the electron cloud is given by the formula

$$\begin{aligned}\langle j(\mathbf{r}, t) \rangle &= -\frac{iZe\hbar}{2m} [\psi(\mathbf{r}, t) \nabla \psi^*(\mathbf{r}, t) - \psi^*(\mathbf{r}, t) \nabla \psi(\mathbf{r}, t)] \\ &= \text{Re} \left[\frac{iZe\hbar}{m} \psi^*(\mathbf{r}, t) \nabla \psi(\mathbf{r}, t) \right].\end{aligned}\quad (3)$$

We could again expand Equation 31.3, in terms of $\tilde{a}_1(t)\psi_1(\mathbf{r})$ and $\tilde{a}_2(t)\psi_2(\mathbf{r})$, and find that there can be in general both static and oscillating components of current, just as there are of charge density.

We can verify also that the quantum charge and current densities given by Equations 31.2 and 31.3 obey the classical continuity equation

$$\nabla \cdot j(\mathbf{r}, t) + \frac{\partial \rho(\mathbf{r}, t)}{\partial t} = 0. \quad (4)$$

This is a conservation of charge equation: it says that the time rate of change of the electronic charge density within any small elemental volume is just equal to the net current flow into and out of that volume element through its enclosing surface area.

Atomic Electric-Dipole Moments

The transition between any pair of atomic or molecular energy levels will then turn out to be either electric-dipole, or magnetic-dipole, or possibly higher-order multipole in character, depending on the quantum charge and current properties of the two energy eigenstates $\psi_1(\mathbf{r})$ and $\psi_2(\mathbf{r})$ that are involved in the transition.

Using the quantum charge density given in Equation 31.2, for example, we can calculate the *quantum electric-dipole moment* $\mu_e(t)$ of a single atom or molecule from the classical formula

$$\mu_e(t) = \iiint \mathbf{r} \rho(\mathbf{r}, t) d\mathbf{r} = -Ze \iiint \psi^*(\mathbf{r}, t) \mathbf{r} \psi(\mathbf{r}, t) d\mathbf{r}, \quad (5)$$

where $d\mathbf{r} = dx dy dz$ is the volume integral over the quantum wavefunction. This atomic dipole moment, like the charge density itself, may contain both static terms, proportional to the level populations $|\tilde{a}_i|^2$, and sinusoidally oscillating terms proportional to the cross-product terms $\tilde{a}_i \tilde{a}_j^*$. These latter terms provide the quantum explanation for the electric-dipole transition properties of real atoms, as we described in some detail in an earlier chapter.

Atomic Magnetic-Dipole Moments

The quantum current density $\mathbf{j}(\mathbf{r}, t)$ inside an atom or molecule can similarly cause each individual atom or molecule to have a *quantum magnetic-dipole moment* $\mu_m(t)$ which can again be related to the classical formula

$$\mu_m(t) = \iiint \mathbf{r} \times \mathbf{j}(\mathbf{r}, t) d\mathbf{r}, \quad (6)$$

where $\mathbf{j}(\mathbf{r}, t)$ is given by the quantum equation 31.3. In a more general quantum analysis, this integral takes the form

$$\langle \mu_m(t) \rangle = \iiint \psi^*(\mathbf{r}, t) \mu_m \psi(\mathbf{r}, t) d\mathbf{r}, \quad (7)$$

where μ_m must be interpreted as a magnetic dipole operator in quantum theory.

In writing Equations 31.5 to 31.7 we are passing over a number of complexities associated with the spin angular momentum and magnetic-dipole properties of both electrons and nuclei. The primary point, however, is that an individual atom or molecule may have both *electric* and *magnetic-dipole moments*, and that these moments may have both static and oscillatory components, depending on the quantum state mixture of the quantum energy levels involved.

General Electric-Dipole Properties of Atoms and Molecules

We are not going to attempt to calculate or to examine these dc and ac components of the electric or magnetic-dipole moments in any detail here for any real atomic eigenstates. (Neither will we attempt to describe in detail the *spin* properties of real atomic eigenstates, though these represent additional quantum magnetic-dipole complexities that are relevant here.) We will summarize, however, the following important points which can be obtained from a careful examination of the quantum equations given above for real atomic systems:

(1) First of all, the quantum charge distribution $\rho(\mathbf{r}) = -Ze|\psi_i(\mathbf{r})|^2$ that is associated with any single energy eigenstate of a real atom or molecule usually does not lead to any constant, or static, electric-dipole moment μ_e . *Isolated atoms or molecules do not normally possess static electric-dipole moments* (although there are a few special molecules that do).

(2) For many pairs of quantum states in real atoms, however, the cross-product term between levels E_i and E_j , as described by the time-varying factor $\psi_i(\mathbf{r})\psi_j^*(\mathbf{r})\exp(j\omega_{ji}t)$, does create a time-varying *electric-dipole moment* $\mu_e(t)$ which oscillates (or precesses) at the transition frequency $\omega_a = \omega_{ji}$. If this is the situation, there is said to be an electric-dipole moment on the $i \rightarrow j$ transition, and this transition then becomes an *electric-dipole-allowed transition*. If the spatial distribution $\psi_i(\mathbf{r})\psi_j^*(\mathbf{r})$ does not produce an oscillating electric dipole moment, then the $i \rightarrow j$ transition is said to be *electric-dipole forbidden*.

General Magnetic-Dipole Properties of Atoms and Molecules

In contrast to the electric-dipole situation, many single atomic and molecular eigenstates $\psi_i(\mathbf{r})$ do have quantum current distributions that generate a *static or dc magnetic dipole moment* even when the atom is in a single quantum level.

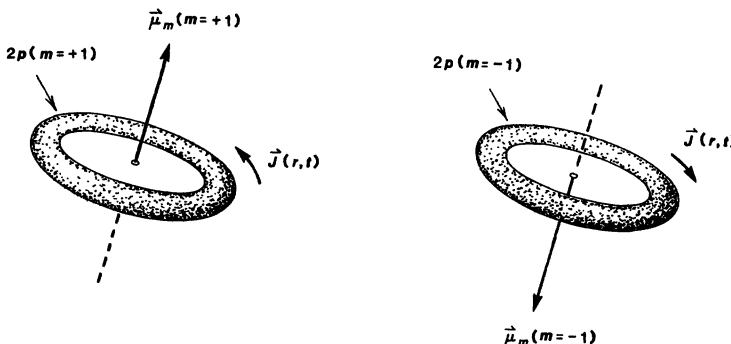


FIGURE 31.2

The $2p(m = \pm 1)$ eigenstates of the hydrogen atom each have a static magnetic dipole moment of opposite sign.

As one such example, consider the charge and current distributions associated with the $2p(m = +1)$ or the $2p(m = -1)$ eigenstates of the hydrogen atom. These eigenstates have a fuzzy toroidal charge distribution, as shown in Figure 31.2. Associated with these charge distributions are quantum current distributions which flow in one direction or the other around the toroid, with the direction depending on whether $m = +1$ or $m = -1$. These quantum current flows then produce *static magnetic-dipole moments* μ_m in the atom, which are perpendicular to the ring and pointing either up or down, as illustrated in Figure 31.2.

Other and more complicated atomic quantum states also lead to similar built-in static magnetic-dipole moments associated with the quantum energy levels in many other kinds of atoms and molecules. There is also an *angular momentum* vector associated with these quantum states, which goes along with the static magnetic-dipole moment.

In addition, just as in the electric-dipole situation, a mixture of two quantum eigenstates $\psi_i(\mathbf{r})$ and $\psi_j(\mathbf{r})$ can lead to a total current distribution $\mathbf{j}(\mathbf{r}, t)$ which produces a *time-varying* or *precessing* magnetic-dipole moment $\mu_m(t)$, which oscillates or precesses at the transition frequency ω_{ji} .

Consider, for example, the superposition of a $2p(m = 0)$ eigenstate (the dumbbell in Figure 31.3) with a $2p(m = +1)$ eigenstate (the toroid). As shown in Figure 31.3, this combination will produce a time-varying magnetic-dipole moment $\mu_m(t)$ which gyrates or precesses in a conical fashion about the symmetry axis at the transition frequency between the $m = 0$ and $m = +1$ energy levels.

Orbital and Spin Magnetic Moments

The magnetic-dipole moments we have illustrated thus far relate only to the *orbital angular momentum* properties of the atom or molecule. Atoms and molecules in general may also possess angular momentum and magnetic-dipole properties due to the *electron spin* of the orbiting electrons, and additional angular momentum and magnetic-dipole properties due to the *nuclear spin* of the nucleus. These spin contributions represent additional quantum contributions to the wavefunctions ψ_i and ψ_j which are not included in Equations 31.1 through

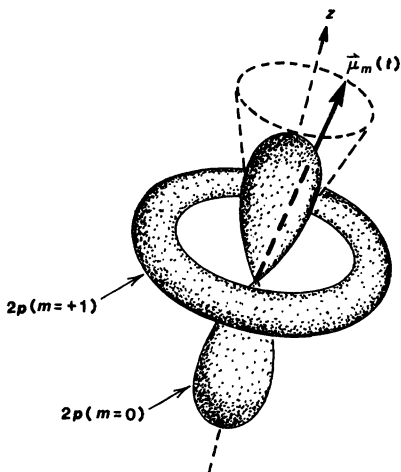


FIGURE 31.3
Linear superposition of the $2p(m = 0)$ and $2p(m = 1)$ eigenstates leads to a sinusoidally precessing magnetic dipole moment.

31.3. We will not attempt to discuss these spin contributions in any further detail here, except to say that in general both the orbital and spin momenta contribute in an important way to the total angular momentum and to the total static and oscillatory magnetic moments associated with quantum states and state mixtures.

The complete energy eigenstates ψ_i , ψ_j , etc., of any real atom or molecule are thus made up in the most general situation of a complex vector summation of the individual electron orbits, the electron spins, the nuclear spins, and, for molecules, the molecular rotation and vibration of the electrons and nuclei in that molecule. When the complete quantum states ψ_i of compound atoms or molecules are built up from individual electrons, protons and neutrons, the individual orbital and spin moments of these particles tend to cancel each other off in pair-wise fashion in many situations. As a result many atomic or molecular eigenstates have small or zero magnetic-dipole moments.

Other atomic or molecular eigenstates, however, will have a finite total angular momentum and magnetic-dipole moment, just as in Figures 31.2 and 31.3. The magnitude of this angular momentum is usually on the order of a few times the basic angular momentum unit \hbar . These same eigenstates then also have a finite magnetic-dipole moment, which is usually on the order of a few times a unit of magnetic moment called the *Bohr magneton* (to be described in a following section), or for nuclear spins is on the order of a few times a much smaller unit called the *nuclear magneton*.

The reader may want to consult any standard text on atomic or molecular spectroscopy, or on the quantum theory of angular momentum, to learn more about the rather complex magnetic-dipole properties of atomic and molecular states. For our purposes here, all we need accept is that (a) some atomic and molecular eigenstates have static magnetic moments, and (b) some pairs of eigenstates lead to oscillating or precessing magnetic moments.

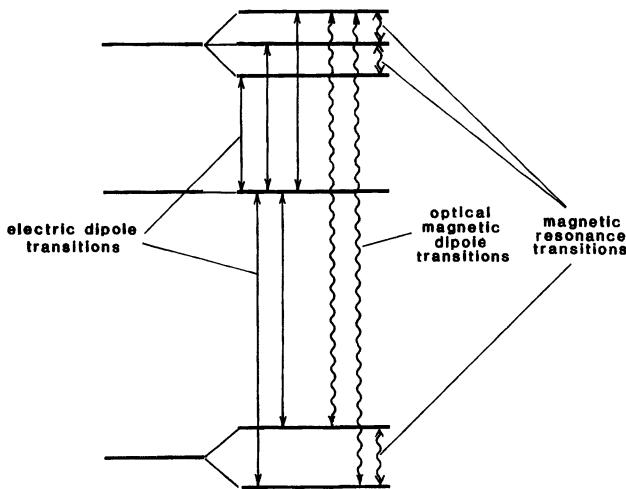


FIGURE 31.4

Different kinds of electric-dipole and magnetic-dipole transitions between different pairs of levels in a typical atom or molecule.

Types of Magnetic-dipole Transitions

Different quantum state mixtures, involving different pairs of energy levels E_i and E_j , may thus display in general either an *oscillating electric-dipole moment* $\mu_e(t)$, or an *oscillating magnetic-dipole moment* $\mu_m(t)$, or in certain situations a still higher-order oscillating quadrupole or multipole moment, at the transition frequency ω_{ji} . *Quantum selection rules* will determine which of these transition moments may be present.

Let us now make a quick survey of the general types of allowed transitions that may arise in different frequency ranges from the electric and magnetic-dipole properties of atoms and molecules. These types of transitions are illustrated in Figure 31.4.

(1) *Electric-dipole transitions.* We have discussed earlier the infrared, optical and ultraviolet electric-dipole transitions that typically occur between electronic energy levels in atoms and molecules. Electric dipole transitions are generally allowed between eigenstates that are of opposite parity, and that have total angular momentum quantum numbers J (or F) differing by ± 1 or 0. In most situations, if the quantum state mixture involved in the transition between two levels produces any significant oscillating electric-dipole moment, then that electric-dipole response is usually dominant; and the transition is primarily *electric dipole* in character.

(2) *Optical-frequency magnetic-dipole transitions.* In those situations where the electric-dipole moment is zero between a pair of levels E_i and E_j , then there may still remain a significant oscillating magnetic-dipole moment between the two levels, and the transition is then *magnetic dipole* in character. Such a transition will radiate spontaneously like an oscillating magnetic, not electric, dipole; and the same transition will respond to the magnetic field part of a si-

nusoidal applied signal at the appropriate transition frequency. The response, however, will be much weaker than for a typical electric-dipole transition.

Real magnetic-dipole transitions can arise first of all between the sublevels of two *different electronic levels* (or possibly two different vibrational levels) in an atom or molecule, where the properties of these states are such that the quantum electric-dipole moment of the transition vanishes, but the magnetic-dipole moment does not. We then observe magnetic-dipole transitions which occur at *optical or infrared or ultraviolet frequencies*. These transitions are very much like electric-dipole optical-frequency transitions, except that the magnetic-dipole transition strength is generally very much weaker than for an electric-dipole transition at the same frequency, usually corresponding to an oscillator strength $F \leq 10^{-6}$.

(3) *Magnetic-resonance transitions.* Magnetic-dipole transitions may also occur at microwave or radio frequencies between closely spaced angular momentum sublevels within a *single electronic level*. These low-frequency magnetic-dipole transitions are commonly called *magnetic-resonance transitions*. They generally have transition frequencies in the microwave, radio, or even audio ranges. Magnetic-resonance transitions may occur between Zeeman-split sublevels of the ground (lowest) electronic state in an atom, or between sublevels of higher excited states (although the latter transitions will become observable only if atoms are somehow first excited upward in order to populate these states).

The energy-level diagram in Figure 31.4 illustrates in a general way how some of the electronic transitions in an atom may be electric dipole in character (straight lines) whereas others may be magnetic dipole in character (wavy lines); and also how optical-frequency magnetic-dipole transitions and low-frequency magnetic-resonance transitions may both be present in a single atomic system. (It is assumed that the degeneracy between all the individual sublevels shown in Figure 31.4 has been lifted by applying a strong dc magnetic field to produce the Zeeman splittings shown.)

Magnetic-resonance Transitions: EPR and NMR

The low-frequency magnetic-resonance transitions within a single electronic level are also quantum-mechanical transitions that can be stimulated by applied signals, and can be used for maser amplification, in exactly the same way as optical laser transitions, though the experimental techniques employed are much different. Microwave cavities and waveguides, or at lower frequencies coils, capacitors and conventional electronic components, replace the optical-frequency mirrors and lenses. The first stimulated emission devices to be discovered were in fact maser devices operating at such lower frequencies.

Depending upon whether these sublevels are determined primarily by the electronic or nuclear angular momentum properties of the atoms, the associated transitions are commonly referred to as *electron paramagnetic resonance* or EPR transitions (usually located in the microwave range), or as *nuclear magnetic resonance* or NMR transitions (usually located in the audio- to radio-frequency range). Magnetic-resonance transitions in ground or excited electronic levels are widely useful in microwave solid-state masers, nuclear magnetic-resonance magnetometers, NMR spectrometers for chemical and biological diagnostics, and in other quantum electronic devices that were developed in the two and one-half decades just before the laser was developed.

Frequency Tuning of Magnetic-resonance Transitions

In most situations, and especially for isolated atoms and molecules in gases, each of the electronic energy levels of an atom or molecule will have some degeneracy, with a degeneracy factor g_i for each energy level E_i . This degeneracy can then be removed, or “broken,” as illustrated in Figure 31.4, by applying a strong enough dc magnetic field to produce significant Zeeman splitting of all the degenerate sublevels involved.

The Zeeman splittings between these sublevels in real atoms and molecules will typically be on the order of a few MHz per gauss of dc magnetic field if electronic orbital or spin moments are involved, or a few kHz per gauss if only nuclear spin is involved. The degenerate energy levels can thus be shifted or tuned by amounts on the order of, say, up to 30 GHz (1 cm^{-1}) in the electronic situation, or up to 40 MHz in the nuclear spin situation, for an applied field of $B_0 = 10,000$ gauss.

The magnetic-resonance transitions within a given electronic level can thus be tuned by varying the dc magnetic field over wide ranges in the microwave and radio-frequency regions, from zero up to frequencies of tens of GHz for EPR, or tens of MHz for NMR. It is thus a common practice in magnetic-resonance experiments to use a fixed-frequency radio or microwave signal source, and to tune the magnetic-dipole transition into resonance using a variable dc magnetic field.

The optical-frequency transitions between sublevels of different electronic levels, as illustrated in Figure 31.4, whether they are electric or magnetic dipole in character, can also be tuned by these same absolute amounts, though this amounts to an almost negligible tuning in fractional or percentage terms.

Summary

There are in summary numerous reasons for studying magnetic-dipole transitions in some detail, as we will do in this chapter:

- First of all, some optical-frequency transitions (including several useful laser transitions), and also many low-frequency magnetic-resonance transitions, are in fact of magnetic-dipole character.
- The low-frequency magnetic-resonance transitions include the fields of both electron paramagnetic or spin resonance (EPR or ESR) and nuclear magnetic resonance (NMR). Magnetic-resonance phenomena form a very useful part of resonance physics and quantum electronics, and have important applications in chemical analysis and diagnostics, in biophysics, in magnetometers and frequency standards, and in microwave masers. Hence they are well worth understanding.
- The study of magnetic-dipole as well as electric-dipole transitions can also give substantial additional understanding and insight into the properties and the dynamics of atomic transitions generally, and particularly into atomic relaxation processes. The magnetic-dipole model gives special insight into the so-called “transverse” and “longitudinal” aspects of atomic transitions, as well as into the polarization aspects of atomic behavior.
- At a very fundamental level, in fact, it can be shown that *the quantum-mechanical equations of motion for any two-level quantum transition*,

whatever its character, can always be transformed mathematically back and forth between an equivalent electric-dipole form or an equivalent magnetic-dipole form. (This is a mathematical transformation—the real transition remains electric dipole, magnetic dipole, electric quadrupole, or whatever, in its physical character.)

The magnetic-dipole model and the resulting Bloch equations can thus describe any purely two-level transition, whatever its real character, equally as well as can the electric dipole model and its equations. This fact has led to the widespread use of magnetic-dipole equations and jargon, even for describing totally electric-dipole types of transitions.

- Finally, there are many large-signal and transient atomic phenomena that were first demonstrated on low-frequency magnetic-resonance transitions, but which are now being widely demonstrated on optical frequency electric-dipole transitions. Examples of such phenomena include so-called 90° and 180° pulses, free-induction decay, adiabatic rapid passage, self-induced transparency, and many other so-called “coherent transient” effects. The magnetic-dipole approach provides both the original and perhaps still the clearest descriptions for explaining and understanding these phenomena, as well as supplying much of the jargon that is widely used for explaining these coherent large-signal effects.

The serious student, after reading this chapter, may thus want to go back and reexamine the electric-dipole discussions of earlier chapters, to see how the same atomic transition phenomena appear alternatively in the electric-dipole or the magnetic-dipole descriptions.

Problems for 31.1

1. *Research problem: magnetic dipole moments in real atoms.* As noted in the text, the probability current density in an atomic wave function is proportional to the real part of $(i\hbar/2m)\psi^*\nabla\psi$ where $\psi(\mathbf{r}, t)$ is the quantum wavefunction of the atom. Evaluate the three-dimensional current density $\mathbf{j}(\mathbf{r}, t)$ for a wave function $\psi(\mathbf{r}, t)$ consisting of a linear mixture of hydrogen-atom $2p(m = 0)$ and $2p(m = 1)$ wavefunctions. Verify that this current distribution will produce a magnetic-dipole moment $\mu_m(t)$ precessing at the transition frequency ω_a in the x, y plane with a fixed component along the z direction. If a three-dimensional graphics plotting capability is available to you, prepare plots illustrating the three-dimensional current distribution (and send copies to me also!).

If you can find solutions in a quantum-theory text for the wave functions of a two-dimensional or three-dimensional simple harmonic oscillator or square-well potential, it would be interesting to calculate the same quantities for these situations also.

2. *Multipole expansion of a real atom.* The multipole expansion procedure used in electromagnetic theory for describing a finite charge and current distribution is explained in more advanced-level electromagnetic theory books. Using the current distribution for superposed $2p(m = 0)$ and $2p(m = +1)$ hydrogen atom wavefunctions as in the previous problem, find the time-varying magnetic-dipole term

$\mu_m(t)$ in the multipole expansions. (Note that this corresponds to the orbital magnetic moment only; the spin magnetic moment is not yet included.)

31.2 THE IODINE LASER: A MAGNETIC-DIPOLE LASER TRANSITION

As one illustration of a practical and important magnetic-dipole laser transition, let us briefly examine some aspects of the iodine photolysis laser (since this will also give us a look at some of the practicalities of laser action, and some of the alternative forms of laser pumping).

The Iodine Photolysis Laser

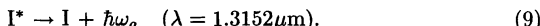
An atomic iodine laser in its simplest form consists of a quartz laser tube containing a few torr to a few hundred torr of an alkyl iodide molecule, such as $\text{C}_3\text{F}_7\text{I}$ (perfluoropropyl iodide), CH_3I or CF_3I , together with a variable pressure of a neutral buffer gas such as argon. This laser tube is pumped by the radiation from a powerful UV flashlamp or, in a larger laser, by an array of such flashlamps.

Organic molecules typically absorb radiation over broad unstructured bands in the ultraviolet, with the UV absorption of these particular molecules extending from ≈ 250 nm to ≈ 300 nm. Upon absorbing a UV photon, such an iodide molecule (often denoted by the abbreviation RI) will then *photodissociate* (or *photolyze*) into a free radical R plus an iodine atom according to the reaction



The iodine atom on the right-hand side of this reaction is denoted by I^* to indicate that it emerges from the photolysis process as an electronically excited atom, located in an upper energy level of the atomic iodine spectrum. The iodine atoms are thus created in an already inverted condition.

Creation of these excited iodine atoms is then followed by either fluorescence or laser action at $\lambda = 1.315 \mu\text{m}$, a process which can be indicated in the same notation by



The fluorescence or laser action in this situation goes directly to the ground level of the iodine atoms.

Because this type of gas-filled, optically pumped laser can be constructed using comparatively low-cost materials, with a large active volume, large inversion densities and energy storage, and moderate efficiency, substantial development work has been carried out on the iodine laser as a potential candidate for laser fusion and other pulsed laser applications.

Atomic Iodine Energy Levels

Figure 31.5 shows the two lowest electronic energy levels, referred to collectively as the $5^2\text{P}_{3/2}$ and $5^2\text{P}_{1/2}$ fine-structure-split ground levels of the iodine atom. (The next higher electronic levels of the iodine atom are a group of 4^P , 4^S and 4^D levels located $\approx 55,000$ to $65,000 \text{ cm}^{-1}$, corresponding to $\approx 1500 \text{ \AA}$,

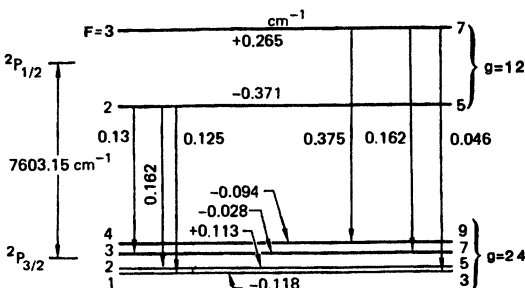
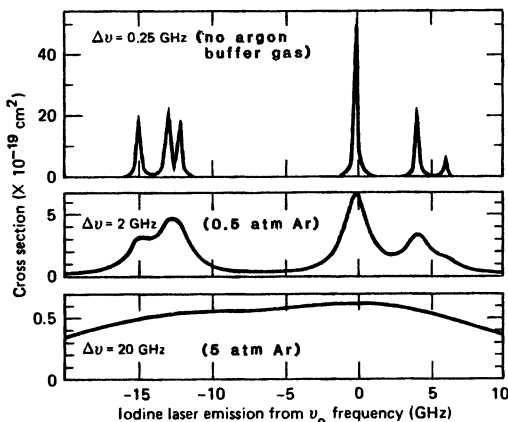


FIGURE 31.5

Upper sketch: The two lowest electronic eigenstates of the neutral iodine atom. Lower sketch: Fluorescent emission spectrum from upper to lower levels at different buffer gas pressures.



above these two levels.) These two electronic levels, which are separated by 7604 cm^{-1} , both have the same orbital angular momentum $L = 1$ (i.e., they are both P states) and thus the same parity, so that electric-dipole transitions between the two groups of levels are totally forbidden. Magnetic-dipole transitions are, however, allowed, thus creating the possibility of a magnetic-dipole-transition laser.

The $5s^25p^5$ electron configuration for the iodine atom in these levels gives in addition a total spin of $S = 1/2$ ($2S + 1 = 2$). The energy levels are thus split by so-called LS coupling into the two groups of levels, with total angular momentum $J = L + S = 3/2$ for the lower level, and $J = L - S = 1/2$ for the upper level. In addition, the iodine nucleus has a nuclear spin $I = 5/2$, which causes still further splitting into sublevels with total angular momentum quantum numbers ranging in integer steps from $F = |J - I|$ to $F = |J + I|$, as shown in the energy-level diagram in Figure 31.5. Each of these levels then has a still further Zeeman-splittable degeneracy given by $g_F = 2F + 1$ as indicated beside each level.

The selection rules for magnetic-dipole transitions in this kind of situation are $\Delta F = 0$ or ± 1 , leading to six allowed transitions of varying relative strength from the upper to the lower group of levels. These transitions cover a frequency

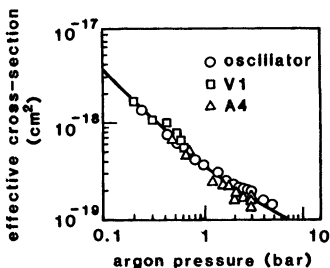


FIGURE 31.6

The iodine laser transition cross section decreases linearly with increasing buffer gas pressures.

spread of about 20 GHz or 0.66 cm^{-1} , as indicated in the lower part of Figure 31.5. The strongest of these transitions is the $F = 3 \rightarrow F = 4$ transition, which contains about 35% of the total transition strength.

Iodine Laser Linewidth

For various practical reasons the iodine laser is usually operated with a large pressure of some buffer gas such as argon, which pressure-broadens the individual laser transitions into a single unresolved line at high enough pressures. The pressure-broadening coefficient for argon on the $1.315 \mu\text{m}$ iodine transition is found to be about 5 MHz/torr or 3.7 GHz/atm, whereas the doppler linewidth is $\approx 0.25 \text{ GHz}$ or 250 MHz.

Operation with an argon buffer pressure of several atmospheres can thus convert the six separate $1.315 \mu\text{m}$ transitions into essentially a single pressure-broadened line with a lorentzian linewidth of $\approx 0.5 \text{ cm}^{-1}$, out of a center frequency of 7604 cm^{-1} , as shown in the bottom curve of Figure 31.5.

Transition Strength

Because this is a magnetic-dipole transition, the transition dipole moment is very small, with a theoretical total radiative decay rate for the upper group of levels of $\gamma_{\text{rad}} \approx 8 \text{ s}^{-1}$, and a measured radiative lifetime τ_{rad} on the order of 150 ms. The individual Einstein A coefficients or radiative decay rates for the six individual transitions between sublevels range from 0.6 to 5 s^{-1} .

Putting this radiative decay rate and the pressure-broadened linewidth into the cross section formula $\sigma = \gamma_{\text{rad}} \lambda^2 / 2\pi \Delta\omega a$ then leads to a transition cross section ranging downward from $\approx 10^{-18} \text{ cm}^2$ at a few hundred torr of argon buffer gas to 10^{-19} cm^2 at 5 to 10 atmospheres, as illustrated in Figure 31.6.

Increasing the argon pressure also reduces the gain per excited atom, making it possible to increase the density of excited molecules and thus the inverted energy storage in large laser volumes, whereas keeping the overall amplifier gain and amplified spontaneous emission at manageable levels. The saturation energy flux for pulse amplification through the medium, given by $U_{\text{sat}} \approx \hbar\omega_a / 2\sigma$, has a value on the order of 1 J/cm^2 at the higher pressures.

Iodine Laser Pumping

Experimentally it is found that virtually all of the iodine atoms come out of the UV photodissociation process into the upper $5^2P_{1/2}$ group of levels. The photolysis pumping scheme in the iodine laser can thus potentially be reasonably efficient.

Depending upon pump cavity design, a laser flashlamp can convert from 30% to perhaps 70% of its electrical input energy into radiation delivered to the laser medium; and about 10% to 20% of the light emission from a xenon flashlamp operated with high currents and short discharge times may fall within the UV absorption bands of the iodine molecules. The internal conversion efficiency from UV photons to excited iodine atoms can be greater than 90%, although the wavelength difference between UV absorption and IR laser action means that the internal energy conversion efficiency is only $\approx 20\%$.

The upper limit for the efficiency of a flashlamp-pumped iodine laser is thus in the range of a few percent. Practical efficiencies approaching 2% have been obtained in small lasers designed for maximum energy efficiency, whereas overall efficiencies of a few tenths of a percent are obtained in large iodine laser pulse amplifiers.

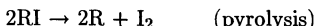
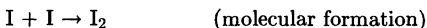
Other Practical Considerations

The gain medium in this laser is very inexpensive, compared to laser crystals or laser glasses, and can readily be provided in very large volumes. In addition, it is essentially free from optical damage, or at least is self-repairing; can be cooled and replenished by gas-flow techniques; and has a very low nonlinear Kerr coefficient compared to solid or liquid lasers. Hence the iodine laser is of substantial interest for high-energy pulsed laser amplifiers.

Figure 31.7 shows a large iodine master oscillator and multistage power amplifier (MOPA) chain built for laser fusion and plasma physics experiments at the Max Planck Institute in Garching, Germany. A typical amplifier in this chain has an unsaturated power gain coefficient $2\alpha_m = 3\%$ to 7% per cm, giving an overall numerical power gain of 250 to 300 in a length of 1 to 2 meters.

The energy dumped into the laser gas mixture by the intense flashlamp illumination in a high-energy-storage iodine laser does lead to rapid and nonuniform gas heating, and this in turn produces strong shock waves that seriously distort the optical path through the amplifiers. Because of this, large iodine laser amplifiers are most commonly used as short pulse amplifiers, with the nanosecond or subnanosecond pulse to be amplified passing through the amplifiers before the shock waves have time to propagate and produce gas density variations.

Photolysis of the iodide molecules does produce both free alkyl radicals and free iodine in the laser tube. These then tend to recombine with varying probabilities according to the formulas



The last reaction in particular is an exothermic “burning” of the alkyl iodides which can take place under intense UV illumination. All these processes tend

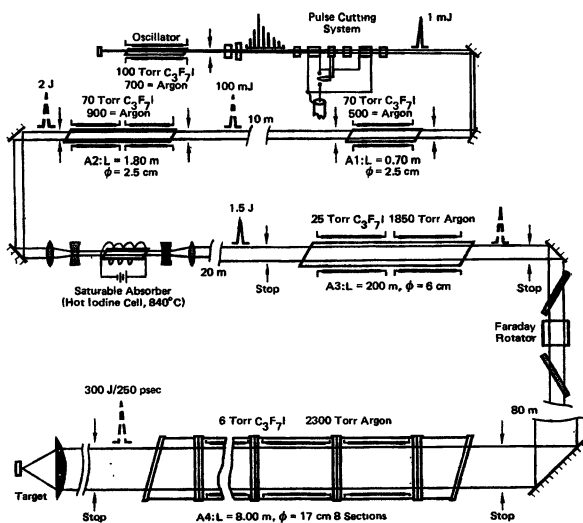


FIGURE 31.7

Schematic of the iodine laser system Asterix III constructed for laser fusion experiments at the Max Planck Institute in Garching, Germany.

both to deplete the supply of laser molecules, as well as making the gas mixture slightly corrosive, and possibly creating unwanted absorption lines in the gas. Methods for recirculating and chemically refreshing the gas fill must thus be provided in practical systems.

Solar Pumped Iodine Lasers?

An intriguing future possibility is the production of cw iodine lasers pumped by focused solar radiation and operating on spacecraft, where the UV radiation from the sun is not absorbed by the atmosphere. Such a solar-pumped laser might provide a means of converting solar energy directly into high-power laser radiation, possibly for transmission to the earth. A long-pulse iodine laser producing a few watts of quasi-cw laser output when pumped with a few kilowatts of simulated sunlight from a solar simulator has in fact been experimentally demonstrated.

Atomic iodine lasers pumped by a plasma discharge created in the iodine laser tube itself, as well as a chemically pumped iodine laser produced by energy transfer from chemically generated excited oxygen molecules have also been reported.

REFERENCES

An early paper reporting this kind of laser action is J. V. Kasper and G. C. Pimentel, "Atomic iodine photodissociation laser," *Appl. Phys. Lett.* **5**, 231-233 (1964).

An excellent survey of the subject is by E. E. Fill, "The High-Power Iodine Laser," in *Developments in High-Power Lasers and Their Applications* (Societe Italiana di Fisica, Bologna, Italy, 1981). A longer discussion can be found in G. Brederlow, E. Fill, and K. J. Witte, *The High-Power Iodine Laser* (Springer-Verlag, 1983).

Problems for 31.2

1. *Iodine laser transition cross section.* Verify that the stimulated transition cross section for the 1.315 μm iodine laser transition given in the text is compatible with the radiative decay rate and linewidth values that are also given.
-

31.3 THE CLASSICAL MAGNETIC TOP MODEL

Let us now return to the dynamics of magnetic-dipole transitions. In the first section of this chapter we outlined a quantum description according to which at least certain energy eigenstates of atoms or molecules may have a finite static magnetic-dipole moment, and also an angular momentum vector, produced by some combination of orbital, electron spin, and nuclear spin effects. Mixtures of two such states may then display an oscillating or precessing magnetic-dipole moment, implying that the transition between those two states is magnetic-dipole allowed for interaction with radiation.

We would now like to develop a simple and purely classical model, analogous to the classical electron oscillator model, to play the same useful role in emulating magnetic-dipole transitions as the classical electron oscillator does for electric-dipole transitions. We can obtain such a model from the following argument.

Orbital Angular Momentum and Magnetic-dipole Moment

With Figure 31.1, showing the hydrogen atom's $2p(m = 1)$ quantum state, in mind, we might adopt as the simplest model for an atomic magnetic dipole a single electron whirling about its nucleus in a circular Bohr orbit of radius a_0 at some very high orbital frequency Ω_0 , as illustrated in Figure 31.8. The classical angular momentum associated with this orbital motion will then be

$$\text{orbital angular momentum} = ma_0^2\Omega_0\mathbf{z} = \hbar\mathbf{L}, \quad (10)$$

where \hbar is a unit of angular momentum and \mathbf{L} a dimensionless orbital angular momentum vector.

But this circulating electron also represents a current loop with current $-e\Omega_0/2\pi$ and area πa_0^2 . Hence it creates a magnetic-dipole moment given by loop current times area, or

$$\text{orbital magnetic-dipole moment} = \mu_{mL} = -\frac{1}{2}e\Omega_0a_0^2\mathbf{z}. \quad (11)$$

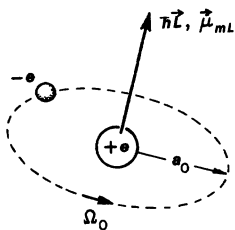


FIGURE 31.8
First Bohr orbit of a one-electron atom.

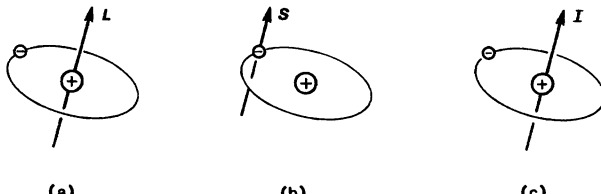


FIGURE 31.9
Orbital, electron-spin, and nuclear-spin momentum vectors.

The angular momentum and the magnetic-dipole moment of this single orbiting electron are thus related by

$$\mu_{mL} = - \left(\frac{e\hbar}{2m} \right) \mathbf{L} \equiv -\beta \mathbf{L}, \quad (12)$$

where the quantity $\beta \equiv eh/2m$ is a standard unit of angular momentum called the *Bohr magneton*, with a value $\beta = 9.27 \times 10^{-24}$ amps per meter squared. Note that both the orbital radius a_0 and the orbital frequency Ω_0 actually drop out of this relationship. Note also that the magnetic moment points in the opposite direction to the angular momentum because of the negative charge of the electron.

Spin Angular Momentum and Magnetic-dipole Moment

This result that we have derived from classical arguments is in fact an accurate representation of the relationship between orbital angular momentum \mathbf{L} and magnetic-dipole moment μ_{mL} for a single electron in a p orbital. Atoms can also have, however, electronic and nuclear spin angular momentum, as illustrated in Figure 31.9; and there is no correspondingly simple classical model to represent the electron spin or nuclear spin moments in real atoms.

For a single electron spin, however, we can show from quantum theory that the relationship between the spin angular momentum $\hbar S$ and its associated magnetic-dipole moment μ_{mS} is given by

$$\mu_{mS} = -2\beta S, \quad (13)$$

where β is the same Bohr magneton. There is a factor of two difference in the quantum scaling factor between angular momentum and dipole moment for pure spin as compared to pure orbital angular momentum.

Total Electronic Angular Momentum and Magnetic-dipole Moment

When both the orbital and spin momenta and their quantum addition rules are taken into account for all the electrons in an atom or molecule, the relationship between the dimensionless total electronic angular momentum (often indicated by the vector quantity \mathbf{J}) and the total magnetic dipole moment for a real atom is usually written in the form

$$\mu_{mJ} = -g\beta\mathbf{J}, \quad (14)$$

where β is again the Bohr magneton. The dimensionless constant g in this expression is the so-called “ g factor” (no relationship to the degeneracy factor introduced earlier). This g factor usually has a value somewhere between 0 and 4, typically not far from 2, depending on just how the orbital and spin contributions of the electrons combine to give the total angular momentum and dipole moment of the complete atomic state.

Nuclear Angular Momentum and Magnetic-dipole Moment

For a still more general discussion the nuclear spin angular momentum, commonly indicated by $\hbar\mathbf{I}$, must also be taken into account. For purely nuclear spin momentum by itself, the relationship between angular momentum and magnetic-dipole moment becomes

$$\mu_{mI} = +g_I\beta_I\mathbf{I}, \quad (15)$$

in which the Bohr magneton β is replaced by the so-called *nuclear magneton* $\beta_I \equiv e\hbar/2M$, which is approximately 1,860 times weaker than the bohr magneton because M is now the proton rather than the electron mass. The nuclear g_I factor is again a dimensionless factor of order unity or slightly larger, characteristic of the particular atomic nucleus involved; and the minus sign in the orbital situation changes to a plus sign in the nuclear situation because the spinning nucleus has a positive rather than negative charge.

In the most general situation of all, when orbital, electron spin, nuclear spin, molecular rotation, molecular vibration, and all other effects are taken into account, the total angular momentum is sometimes written as $\hbar\mathbf{F}$, where $\mathbf{F} = \mathbf{J} + \mathbf{I} = \mathbf{L} + \mathbf{S} + \mathbf{I}$, and an appropriate magnetic-dipole moment is associated with this.

Despite all these complexities, in the end we still have a situation in which the angular momentum of a single atomic eigenstate will be some small integer or half-integer multiple of \hbar , whereas its magnetic-dipole moment will be related to this dimensionless angular momentum by some g value of magnitude not too far from unity multiplying either the Bohr magneton β or, if only nuclear spin is involved, the nuclear magneton β_I . We will therefore adopt the notation $\mu_m = -g\beta\mathbf{J}$ as a general form for describing atomic magnetic dipoles, recognizing that there can be some complications not fully included in this formula.

The Classical Magnetized Top Model

The primary feature in all these situations is that the atom has a linearly related combination of *angular momentum* plus *magnetic-dipole moment*. A classical model for a magnetic-dipole atom could therefore be a *classical magnetized top*.

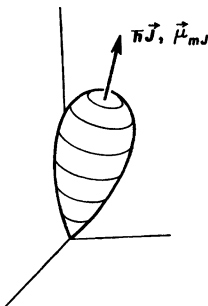


FIGURE 31.10
A classical magnetized rapidly spinning top.

spinning top, as shown in Figure 31.10. This model can be envisioned if you like as a small but heavy, rapidly spinning top pivoted at one end, and made out of something like permanently magnetized soft iron. Hence this top will have both angular momentum $\hbar\mathbf{J}$, and also a permanent magnetic-dipole moment μ_m in agreement with the preceding discussions.

Now, the classical equation of motion for such a top says that the rate of change of its angular momentum equals the torque acting on the top, or

$$\frac{d}{dt} [\text{angular momentum}] = [\text{torque}]. \quad (16)$$

But if a magnetic-dipole μ_m is placed in a magnetic field \mathbf{b} , the vector torque acting on the dipole is $\mu_m \times \mathbf{b}$, and hence the vector equation of motion for the magnetized top becomes

$$\frac{d(\hbar\mathbf{J})}{dt} = -g\hbar\beta \frac{d\mu_m}{dt} = \mu_m \times \mathbf{b}, \quad (17)$$

which we can convert to

$$\frac{d\mu_m}{dt} = \left(\frac{ge}{2m}\right) \mathbf{b} \times \mu_m. \quad (18)$$

This classical equation of motion says that the incremental vector change $d\mu_m$ in the orientation of the dipole moment μ_m in any small time-increment dt is perpendicular to both the instantaneous direction $\mu_m(t)$ and to the direction of the instantaneous \mathbf{b} field. The magnetic-dipole moment therefore wants to precess about the magnetic field direction at a constant cone angle, as shown in Figure 31.11.

Magnetic-dipole Precession

In fact, for the simplest situation, namely, a dc magnetic field $\mathbf{b} = B_0\mathbf{z}$ along the z direction, Equation 31.18 becomes

$$\frac{d\mu_m}{dt} = \frac{geB_0}{2m} \mathbf{z} \times \mu_m = \omega_0 \mathbf{z} \times \mu_m, \quad (19)$$

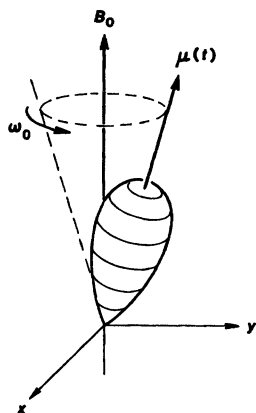


FIGURE 31.11
Precession of a magnetized top in a dc magnetic field.

where the resonance frequency ω_0 is defined by

$$\omega_0 \equiv \frac{ge}{2m} B_0. \quad (20)$$

(By convention the dc field axis in a magnetic-dipole situation is almost always identified as the z axis.)

The reader can then verify that the analytic solution to Equation 31.19 is

$$\begin{aligned} \mu_x(t) &= \mu_+ \cos(\omega_0 t + \phi) \\ \mu_y(t) &= \mu_+ \sin(\omega_0 t + \phi) \\ \mu_z(t) &= \text{const}, \end{aligned} \quad (21)$$

with the additional condition that the dipole length is constant, i.e.,

$$|\mu_m|^2 = \mu_z^2 + \mu_+^2 = \text{constant}. \quad (22)$$

Equations 31.21 and 31.22 describe a positive or right-hand circularly polarized precession in the x, y plane looking along the z axis—hence the use of the “+” subscripts—and the frequency ω_0 is the natural precession frequency of the dipole in the field B_0 .

Connection Between Magnetic Top Model and Real Transitions

The precession frequency ω_0 of this classical model in the magnetic field B_0 we will identify with a real atomic transition frequency ω_a . In fact, for simple magnetic-resonance transitions that are not complicated by so-called “zero-field splittings” and other crystalline field effects, the actual transition frequency between two Zeeman sublevels of a single electronic level will in fact often be given very accurately by the relationship that $\omega_0 = (ge/2m)B_0$. For a pure electronic spin transition with $g = 2$ this Zeeman splitting or tuning factor is given, in

practical units of MHz and gauss, by

$$\frac{f_a}{B_0} \equiv \frac{\omega_0}{2\pi B_0} = \frac{ge}{4\pi m} \approx 2.8 \text{ MHz/gauss.} \quad (23)$$

(This might be written alternatively as 2.8×10^9 Hz/Tesla if we want to use proper mks units.) Typical magnetic fields of 1,000 to 3,000 gauss then give microwave transition frequencies between 3 and 10 GHz.

For pure nuclear spin magnetic resonance (NMR), the spin of a single proton gives $g_J e/4\pi M \approx 4.58$ kHz/gauss. Typical transition frequencies for nuclear magnetic resonance (NMR) thus range widely, varying from ≈ 2 kHz for a proton in the Earth's magnetic field (≈ 0.5 gauss), up to 30 MHz in a typical NMR apparatus for chemical analysis.

For optical or infrared magnetic-dipole transitions, such as those shown in Figure 31.4, the transition frequency ω_0 or ω_{ji} will be very much greater than this, as determined by the optical-frequency energy gap $E_j - E_i$ between the two different electronic states (or possibly, in molecules, on the energy gap between two different vibrational or rotational states). This can be taken into account in the classical model simply by assuming that there is a suitably large virtual or fictitious dc magnetic field in the z direction, given by $(ge/2m)\hat{B}_0 = (E_j - E_i)/\hbar$, which is added to any actual dc field B_0 that may also be applied for Zeeman splitting or tuning of the electronic levels.

Macroscopic Magnetic Polarization

Then, exactly as in the electric-dipole analysis of Chapter 2, we can calculate the *macroscopic magnetic polarization* or *magnetic-dipole moment per unit volume* $\mathbf{m}(t)$ that is created in a collection of many individual magnetic dipoles or magnetic tops by adding up the individual microscope dipole moments $\mu_{mi}(t)$ in a summation of the form

$$\mathbf{m}(t) \equiv \frac{1}{V} \sum_{i=1}^{NV} \mu_{mi}(t), \quad (24)$$

where i is an index labeling the individual dipoles, and the sum is over all the dipoles present with density N in a small unit volume V surrounding the point at which the magnetization \mathbf{m} is being calculated. With the usual dc magnetic field present, this magnetization normally has sinusoidally oscillating transverse components given by

$$m_x(t) = \frac{1}{V} \sum_{i=1}^{NV} \mu_{xi}(t) \quad \text{and} \quad m_y(t) = \frac{1}{V} \sum_{i=1}^{NV} \mu_{yi}(t), \quad (25)$$

and a quasi-dc z component $m_z(t)$ given by a similar sum.

$$m_z = \frac{1}{V} \sum_{i=1}^{NV} \mu_{zi}. \quad (26)$$

Working out the equations of motion for these components of magnetization is our primary task in the remainder of this chapter.

$$\begin{aligned}\text{energy} &= -\mu_m B_0 \cos \theta \\ &= -\mu_z B_0\end{aligned}$$

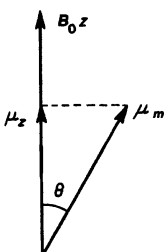


FIGURE 31.12

Orientation angle θ between a magnetic dipole and the dc magnetic field axis.

Oscillation Energy in Magnetic-dipole Atoms

First, however, we should note a few significant differences between the electric and magnetic-dipole classical models that we need to illustrate.

The sinusoidal precession of the oscillating components $\mu_x(t), \mu_y(t)$ or $m_x(t), m_y(t)$ in the classical magnetic top model are obviously the magnetic analog of the sinusoidal oscillation $x(t)$ or $p_x(t)$ of the electric charge in the classical electron oscillator model. However, because of the presence of the permanent magnetic-dipole moment associated with the magnetized top model, the interpretation of the *oscillation energy* in the magnetic dipole situation is quite different from that in the corresponding electric-dipole situation.

In the electric-dipole situation, the stored energy in the atom was related to the oscillatory motion of the electric charge, i.e., $U_a \propto |x(t)|^2$. In the magnetic-dipole situation, however, the magnetic dipole's oscillation energy is *not* given by some constant times the oscillating components, i.e., by something like $\frac{1}{2}[\mu_x^2(t) + \mu_y^2(t)]$. We can note, for example, that we do not have to supply any additional energy to set a classical dipole precessing, or to create $\mu_x(t)$ and $\mu_y(t)$, once that dipole has been oriented at an angle θ to the dc field axis—if we simply turn the dipole to that angle and release it, it will immediately commence precessing by itself, without our “giving it a shove.”

The energy input to the classical dipole thus has nothing to do with the precessing motion represented by $\mu_x(t)$ and $\mu_y(t)$. The work done in establishing a precessing dipole comes rather in initially rotating the dipole out to a finite angle θ away from the dc field in the first place. The energy of a fixed magnetic-dipole moment in a magnetic field is then determined only by its *orientation angle* with respect to the dc magnetic field, or by the *longitudinal* or μ_z *component of the moment*—that is, the component along the dc field axis—through the following argument.

Magnetic dipoles are in a condition of lowest energy when they are aligned parallel to a dc magnetic field. Then, in order to rotate a magnetic dipole μ_m from an initial orientation parallel to B_0 out to some finite value of the angle θ measured relative to the z axis, as in Figure 31.12, we must apply a torque given by $\mu_m \times B_0 z$. This torque must be applied while the dipole is being turned from the initial to the final angle; and thus we must (according to this classical picture) do mechanical work to rotate the dipole out to the angle θ .

It is most convenient to choose the arbitrary zero of energy for the magnetic dipole system to be not at the lowest-energy angle of $\theta_0 = 0^\circ$, but rather at an

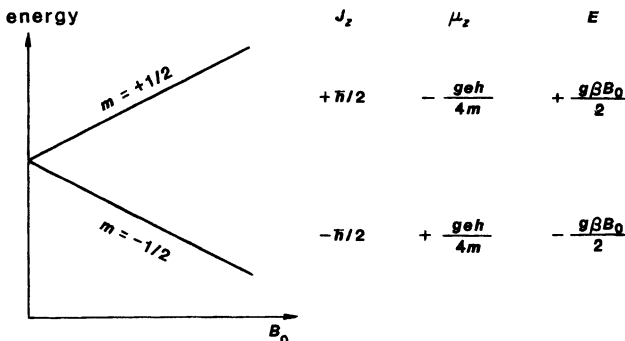


FIGURE 31.13
Angular momentum, axial magnetic moment, and energy in a two-level magnetic-dipole system.

angle $\theta_0 = 90^\circ$, where the dipole is aligned perpendicular to the dc magnetic field. The orientational energy $U_a(\theta)$ of a single dipole μ_m in a field B_0 is then given by

$$U_a(\theta) = -\mu_m \cdot B_0 = -|\mu_m| B_0 \cos \theta \quad (\text{single atom}). \quad (27)$$

The lowest-energy orientation is thus with the dipole parallel to the magnetic field, or $\theta = 0$, corresponding to a negative energy value $-\mu_z B_0$; whereas the highest energy is the opposite value, with the dipole antiparallel to the dc field and $\theta = 180^\circ$.

Magnetic-dipole Energy: Quantum Two-Level Interpretation

The axial or quasi-dc quantity $m_z(t)$ in the magnetic-dipole picture thus determines the stored energy in a collection of microscopic atomic dipoles, and as a result $m_z(t)$ plays the same role in the magnetic-dipole case as does the population difference $\Delta N(t)$ in either the quantum or the electric-dipole picture. We can illustrate this in a genuine quantum system as follows.

The alignment energy for each individual dipole μ_{zi} in a collection of many small dipoles is given by $-\mu_{zi} B_0$. The total stored energy per unit volume in a large collection of magnetic dipoles is then given by

$$U_a = -\frac{1}{V} \sum_{i=1}^{NV} \mu_{zi} B_0 = -m_z B_0 \quad (\text{collection of dipoles}). \quad (28)$$

We can connect this classical result to the quantum picture of a simple two-level atomic magnetic-dipole system in the following way.

The simplest possible quantum magnetic-dipole system is an atom in a degenerate electronic state that has angular momentum quantum number $J = 1/2$ as shown in Figure 31.13. This state is then $(2J+1) = 2$ -fold degenerate, i.e., it has two Zeeman-splittable states with z components of angular momentum given by $J_z = -\hbar/2$ (lower level) and $J_z = +\hbar/2$ (upper level). The z components of magnetic-dipole moment associated with these two states are $\mu_{z1} = ge\hbar/4m$ and $\mu_{z2} = -ge\hbar/4m$; and the associated orientational energies (per atom) are

$E_1 = -g\beta B_0/2$ and $E_2 = +g\beta B_0/2$. (For optical-frequency magnetic-dipole transitions, the magnetic field B_0 in this situation should be considered as including the fictitious field \hat{B}_0 discussed in an earlier paragraph; and we again take the zero of energy halfway between E_1 and E_2 .)

Suppose there are N_1 such atoms per unit volume in the lower Zeeman level and N_2 in the upper level. Then the net z -directed magnetization m_z in the collection of two-level atoms will be

$$m_z = N_1 \mu_{z1} + N_2 \mu_{z2} = (N_1 - N_2) \frac{g\beta}{2} = (g\beta/2) \Delta N, \quad (29)$$

and again the total stored energy per unit volume is

$$U_a = N_1 E_1 + N_2 E_2 = -(N_2 - N_1) g\beta B_0 / 2 = -m_z B_0. \quad (30)$$

The classical model and quantum description for this two-level situation thus agree exactly in their formulas for these quantities.

31.4 THE BLOCH EQUATIONS

In this section we use the classical magnetic top model of the previous section to derive the widely used *Bloch equations* for magnetic-dipole transitions. These equations are of very great importance and usefulness in understanding the relaxation properties and the stimulated transition dynamics for both electric-dipole and magnetic-dipole atomic transitions.

Derivation of the Bloch Equations

Suppose there are a large number of microscopic atomic dipole moments per unit volume in an atomic medium. Then the macroscopic magnetic polarization or magnetization \mathbf{m} in that medium is given, as we have already noted, by

$$\mathbf{m} \equiv \frac{1}{V} \sum_i \mu_{mi}, \quad (31)$$

where the sum is over all the individual dipoles in some small unit volume V . Now all the dipoles in any small enough volume (small compared to a signal wavelength) centered about any given point will see the same value of the applied field \mathbf{b} at that point. Hence the equation of motion for the macroscopic polarization \mathbf{m} at that point can be obtained by adding up the equations of motion for each individual dipole, to obtain

$$\frac{d\mathbf{m}}{dt} = \left(\frac{ge}{2m} \right) \mathbf{b} \times \mathbf{m}. \quad (32)$$

If we break this vector equation into its cartesian vector components, the results are

$$\begin{aligned}\frac{dm_x(t)}{dt} &= \frac{ge}{2m} [b_y(t)m_z(t) - b_z(t)m_y(t)] \\ \frac{dm_y(t)}{dt} &= \frac{ge}{2m} [b_z(t)m_x(t) - b_x(t)m_z(t)] \\ \frac{dm_z(t)}{dt} &= \frac{ge}{2m} [b_x(t)m_y(t) - b_y(t)m_x(t)].\end{aligned}\quad (33)$$

We must now consider the transverse and the longitudinal or z components of these equations separately, and show how different relaxation terms must be added to each of these components.

Behavior of the Transverse Components

The usual situation in magnetic-dipole analyses is to assume that there is a large dc magnetic field B_0 in the z direction, which is responsible for the basic resonance frequency $\omega_a = (ge/2m)B_0$. (As we noted earlier, for optical-frequency magnetic-dipole transitions this magnetic field may consist of a real magnetic field which we apply using some sort of magnet, plus a fictitious magnetic field \hat{B}_0 which we assume is present to account for the large energy gap $E_2 - E_1 = \hbar\omega_a$ between the two electronic energy levels.)

There will generally also be much smaller sinusoidal signal fields which may be applied in the x , y and possibly also the z directions. Suppose initially there are no such signal fields, only the dc field B_0 . Then the transverse or x and y components of the dipole equations (31.33) become the pair of coupled equations

$$\begin{aligned}\frac{dm_x(t)}{dt} &= -(geB_0/2m)m_y(t) = -\omega_a m_y(t) \\ \frac{dm_y(t)}{dt} &= +(geB_0/2m)m_x(t) = +\omega_a m_x(t),\end{aligned}\quad (34)$$

with the sinusoidal solutions

$$m_x(t) = M_+ \cos(\omega_a t + \phi_+) \quad \text{and} \quad m_y(t) = M_+ \sin(\omega_a t + \phi_+). \quad (35)$$

Here the quantity M_+ is a fixed but arbitrary magnitude for the transverse magnetization, and ϕ_+ is an arbitrary phase angle for the righthand circular precession motion.

Coherently Aligned Magnetic-dipoles

Recall that the macroscopic magnetization $\mathbf{m}(t)$ is actually the net summation of a large number of microscopic dipole moments, so that

$$m_x(t) = \frac{1}{NV} \sum_{i=1}^N \mu_{xi}(t) = \frac{1}{NV} \sum_{i=1}^N |\mu_{xi}| \cos(\omega_a t + \phi_i), \quad (36)$$

and similarly for $m_y(t)$. Each individual magnetic dipole will then precess in the same circularly polarized fashion, with the same precession frequency ω_a in the dc field B_0 ; but each individual dipole may have a different and randomly

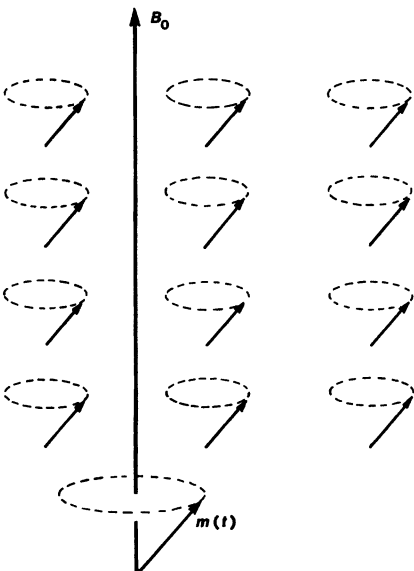


FIGURE 31.14

An aligned magnetic-dipole system, with many individual dipoles all precessing with the same transverse phase angle.

oriented precession phase ϕ_i . As we discussed at length in earlier electric-dipole discussions, there is no reason to think that the individual magnetic dipoles will in general always oscillate with the same precession phase.

It may, however, be possible, with a suitably strong applied signal, to set the individual dipoles in some small unit volume all precessing with the same initial phase, as we have shown in Figure 31.14, and this will then cause all the microscopic $\mu_{xi}(t)$ and $\mu_{yi}(t)$ components to add vectorially into strong macroscopic $m_x(t)$ and $m_y(t)$ components as shown.

Randomly Phased Magnetic Dipoles

However, there are always relaxation mechanisms—collisions, dipolar interactions, phonon modulations—which will tend to scramble and randomize the individual precession phases of $\mu_{xi}(t)$ and $\mu_{yi}(t)$. Hence these mechanisms will tend to attenuate and eventually destroy the transverse macroscopic components $m_x(t)$ and $m_y(t)$, even though the individual dipoles may continue to precess at the same tilt angles and with the same precession magnitudes as before.

Figure 31.14 illustrates in a somewhat exaggerated fashion how individual dipoles all precessing totally in phase will lead to the largest possible transverse macroscopic polarization (for a given dipole density N). Figure 31.15 then shows how the same individual dipoles precessing with totally random phases will lead to no macroscopic transverse magnetization at all, although there can still be a sizable static longitudinal polarization along the z axis.

Note that there is no difference in the atomic energy in these two situations, since the dipoles still have the same net alignment along the z axis. Going from one of these situations to the other thus involves an internal randomization of

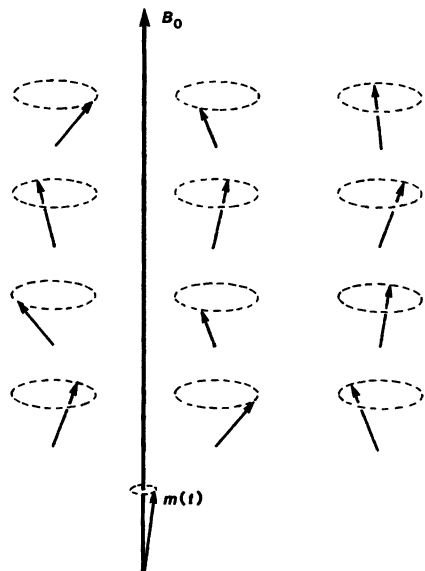


FIGURE 31.15
A randomly phased magnetic-dipole system,
with individual dipoles precessing with randomly distributed transverse phase angles.

the dipole phases, but no net exchange of energy between the dipoles and their surroundings.

Transverse Relaxation or Dephasing

The simplest way to include the effects of phase-randomizing or *dephasing* processes in the Bloch equations, so that an orderly arrangement like Figure 31.14 will gradually be converted into a disorganized arrangement like Figure 31.15 is to add to the macroscopic transverse equations appropriate *transverse relaxation terms* of the form

$$\frac{dm_x}{dt} \Big|_{\text{relax}} = -\frac{m_x}{T_2}, \quad \text{and} \quad \frac{dm_y}{dt} \Big|_{\text{relax}} = -\frac{m_y}{T_2}, \quad (37)$$

where T_2 is a *transverse relaxation or dephasing time* which has essentially the same physical meaning as the dephasing time T_2 that we introduced for electric-dipole transitions in earlier chapters, with the following slight complication.

There is, however, one small complication to this. In the electric-dipole model we distinguished between the *energy decay time* T_1 , and the *elastic dephasing time*, let us call it T_{2e} for the moment (where the e subscript can stand for either “electric dipole” or “elastic dephasing”). Both of these time constants then entered into the atomic linewidth in the form

$$\frac{\Delta\omega_a}{2} = \frac{1}{T_{2e}} + \frac{1}{2T_1} \quad (\text{electric dipole}). \quad (38)$$

We are shortly going to find that the Bloch equations with the relaxation terms given in Equation 31.37 also lead to a lorentzian lineshape, but with a linewidth

that is just

$$\frac{\Delta\omega_a}{2} = \frac{2}{T_{2m}} \quad (\text{magnetic dipole}), \quad (39)$$

where T_{2m} is the magnetic dipole T_2 value appearing in the relaxation terms in Equation 31.37. If we are to make a comparison between the electric-dipole and magnetic-dipole definitions of T_2 , therefore, we must make the identification that

$$\frac{1}{T_{2m}} \equiv \frac{1}{T_{2e}} + \frac{1}{2T_1}. \quad (40)$$

All this really means is that the total relaxation of $m_x(t)$ and $m_y(t)$ in Equation 31.37 really does contain both dephasing and energy decay terms; and the Bloch analysis combines both the lifetime and the elastic dephasing effects given by T_1 and T_{2e} into a single transverse relaxation given by $T_2 = T_{2m}$. As a practical matter, in many magnetic-dipole transitions the dephasing contribution from $1/T_{2e}$ is very much larger than the lifetime broadening term $1/2T_1$, so that the distinction between T_{2m} and T_{2e} is irrelevant anyway. We will not worry about it from here on.

Transverse Decay Times

The immediate consequence of the relaxation terms in Equation 31.37, when added to the basic magnetic-dipole equation of motion, is that the transverse precession of the macroscopic polarization \mathbf{m} , in the absence of any applied signals, now decays in the form

$$\begin{aligned} m_x(t) &= M_+ e^{-t/T_2} \cos(\omega_a t + \phi_+) \\ m_y(t) &= M_+ e^{-t/T_2} \sin(\omega_a t + \phi_+). \end{aligned} \quad (41)$$

The decay time T_2 (or T_{2m}) is variously referred to in different connections as

- the *transverse relaxation time* (in the Bloch equations), or
- the *dephasing time* (with the minor complication just mentioned), or
- the *off-diagonal relaxation time* (in quantum density matrix analyses), or
- the *spin-spin relaxation time* (in magnetic-resonance analyses).

The mechanisms that produce the elastic dephasing part of T_2 are exactly the same as we discussed in the electric-dipole situation: collisions between atoms in gases, or phonon frequency-modulation effects in solids, or dipolar field overlap effects in any medium at high enough density. We will see shortly that the decay time T_2 leads to a homogeneous lorentzian line broadening for the magnetic-resonance transitions, exactly as in the electric-dipole situation.

Longitudinal Magnetic-dipole Moment

Let us now look at the z component of the macroscopic magnetization $\mathbf{m}(t)$. If no transverse magnetic field terms $b_x(t)$ or $b_y(t)$ are present, the longitudinal component of the magnetic-dipole equation of motion 31.33 is zero, i.e., $dm_z/dt = 0$. Hence the z component $m_z(t)$ is, to zeroth order, constant in time, as both the macroscopic magnetization and the individual dipoles precess at their fixed angles with respect to the z axis.

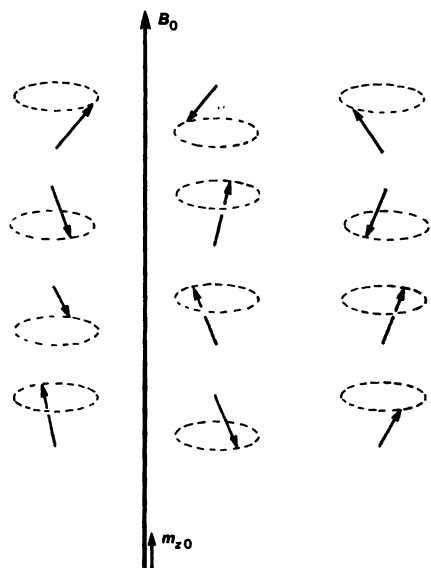


FIGURE 31.16
Magnetic-dipole system at thermal equilibrium, with random transverse phase and (partially) random axial components.

We have already noted also that the longitudinal component m_z in the classical magnetic top model is directly proportional to the energy of the dipoles, or to the population difference $\Delta N \equiv N_1 - N_2$ in the real quantum situation. Since the lowest-energy position for any individual magnetic-dipole moment μ_i is to be aligned parallel to the dc magnetic field, we might suppose that in a classical magnetic-dipole system at rest all of the dipoles would be lined up parallel to B_0 , which would correspond to $m_{z0} = N |\mu_i|$, where m_{z0} is the value of $m_z(t)$ at rest, N is the total density of dipoles, and $|\mu_i|$ is the magnitude of any one individual dipole.

However, we also know from earlier discussions that in any physical system at thermal equilibrium there are always thermal fluctuations; and these thermal fluctuations lead to a Boltzmann thermal equilibrium, which in an atomic system produces a Boltzmann thermal population difference, call it $\Delta N_0 \equiv N_{10} - N_{20}$. The value of this population difference depends only on the temperature through the Boltzmann ratio $N_{20}/N_{10} = \exp(-\hbar\omega_a/kT)$.

Similarly, in the magnetic-dipole situation the thermal equilibrium distribution of the dipoles can be thought of as having random transverse phases, and a distribution of axial components with more dipoles oriented at angles tending to be parallel to the magnetic field (especially as the temperature is lowered), and fewer oriented antiparallel to B_0 . The thermal equilibrium value of the axial magnetization can then be related to the thermal-equilibrium population difference and stored energy per unit volume by

$$U_{a0} = -m_{z0}B_0 = -\Delta N_0 g \beta / 2, \quad (42)$$

as illustrated in Figure 31.16.

Longitudinal Relaxation Behavior

We further know that there are always energy relaxation mechanisms between any collection of atoms and their thermal surroundings, which will act to bring the atoms into thermal equilibrium with their surroundings, with some energy decay rate γ , or after some energy relaxation time T_1 . In a two-level electric-dipole system this leads to a rate-equation relaxation term for $\Delta N(t)$ of the form

$$\frac{d\Delta N}{dt} \bigg|_{\text{relax}} = -\frac{\Delta N(t) - \Delta N_0}{T_1}. \quad (43)$$

In the magnetic-dipole situation we can similarly assume that the longitudinal component $m_z(t)$ will always relax toward its thermal-equilibrium value m_{z0} , with a relaxation time which we will call variously τ or T_1 or γ^{-1} , following the same notation of earlier chapters. To account for this, we will add a longitudinal relaxation term to the $m_z(t)$ equation in the same form

$$\frac{dm_z(t)}{dt} \bigg|_{\text{relax}} = -\frac{m_z(t) - m_{z0}}{T_1}. \quad (44)$$

In the absence of any applied signal $m_z(t)$ will then relax to equilibrium in the (slowly) time-varying form

$$m_z(t) = m_{z0} + [m_z(t_0) - m_{z0}] \exp[-(t - t_0)/T_1]. \quad (45)$$

The time constant T_1 (or τ or γ^{-1}) is called variously

- the *longitudinal relaxation time* (in the Bloch equations), or
- the *energy relaxation time* (in electric or magnetic-dipole situations), or
- the *on-diagonal relaxation time* (in quantum density matrix analysis), or
- the *spin-lattice relaxation time* (in magnetic-resonance analyses).

Whatever they are called, the time constants T_1 and T_2 play essentially the same roles in the electric-dipole and the magnetic-dipole situations, and appear interchangeably in the two analyses.

Spin-Spin Versus Spin-Lattice Relaxation Times

In magnetic-resonance experiments, whether of the nuclear magnetic resonance (NMR) or electron spin resonance (ESR or EPR) variety, the signals are almost always observed on samples containing either nuclear or electron spins, in liquid or solid samples. That is, the *spin* part of the magnetic-dipole moments is usually more important than the *orbital* contribution.

The magnetic-resonance literature therefore conventionally refers to T_1 as the *spin-lattice relaxation time*, since it represents the time constant for energy exchange between the resonant spins and the surrounding lattice, which is the relevant thermal reservoir. The time constant T_2 is then called in magnetic resonance the *spin-spin relaxation time*, since it is the process whereby different spins exchange energy and randomize phases among themselves, but with no net energy transfer from the resonant spin system to the surrounding lattice.

Summary: The Bloch Equations

The final Bloch equations, with all these relaxation terms included, can thus be written as

$$\begin{aligned}\frac{dm_x(t)}{dt} &= \frac{ge}{2m} [b_y(t)m_z(t) - b_z(t)m_y(t)] - \frac{m_x(t)}{T_2} \\ \frac{dm_y(t)}{dt} &= \frac{ge}{2m} [b_z(t)m_x(t) - b_x(t)m_z(t)] - \frac{m_y(t)}{T_2} \\ \frac{dm_z(t)}{dt} &= \frac{ge}{2m} [b_x(t)m_y(t) - b_y(t)m_x(t)] - \frac{m_z(t) - m_{z0}}{T_1}.\end{aligned}\quad (46)$$

These equations were first introduced by Felix Bloch to describe nuclear magnetic resonance in 1946. (The discovery of magnetic resonance in the same year simultaneously by Bloch at Stanford University and by Purcell at Harvard led to their joint Nobel Prize awards in 1952.) The solutions to these equations, and their interpretation, will be the primary topic for the remaining sections of this chapter.

REFERENCES

The original paper introducing the Bloch equations—one still very much worth reading—is F. Bloch, “Nuclear induction,” *Phys. Rev.* **70**, 460–474 (1946). A companion paper which reports the confirming experimental results on nuclear magnetic resonance is F. Bloch, W. W. Hansen, and M. Packard, “The nuclear induction experiment,” *Phys. Rev.* **70**, 474 (1946).

There are also a large number of excellent books available which cover magnetic resonance, and hence the Bloch equations and their derivation and solution. One such book is Charles P. Poole, Jr., and Horacio A. Farach, *Relaxation in Magnetic Resonance* (Academic Press, 1971), which gives extensive discussion of relaxation processes and Bloch equation solutions.

Others include C. P. Slichter, *Principles of Magnetic Resonance* (Harper and Row, New York, 1963; revised edition by Springer-Verlag, 1980); and Robert T. Schumacher, *Introduction to Magnetic Resonance* (W. A. Benjamin, New York, 1970.) The classic reference on NMR is A. Abragam, *The Principles of Nuclear Magnetism* (Oxford, 1961).

31.5 TRANSVERSE RESPONSE: THE AC SUSCEPTIBILITY

We next want to develop the ac steady-state solutions to the Bloch equations for a magnetic-dipole transition in the small-signal regime where linear susceptibility and rate-equation concepts are valid. Large-signal and coherent-transient solutions to the Bloch equations will be taken up in a later section in this chapter.

The small-signal solutions to the Bloch equations separate neatly into *transverse ac components* and *longitudinal quasi-dc components*, as we have already seen. In this section we consider the transverse ac components, in order to derive a linear magnetic susceptibility directly analogous to the dielectric susceptibility derived earlier for electric-dipole transitions. This will then be incorporated into the longitudinal equations in the following section, in order to produce a rate equation for the magnetic-dipole transition.

Linear Small-Signal Approximations

The complete Bloch equations 31.46 in their exact form are inherently nonlinear, because of the product terms such as $b_y(t)m_x(t)$ and $b_y(t)m_z(t)$ that they contain. With suitable approximations, however, we can convert the two transverse Bloch equations into a pair of coupled linear equations, with associated linear small-signal steady-state (or transient) solutions.

We first note that the longitudinal magnetization $m_z(t)$, at least in the absence of any applied signals, is a nearly static or quasi-dc quantity, with only a slow time-variation given by the longitudinal time constant T_1 . We can therefore approximate $m_z(t)$ by a constant, or at least a quasi constant, value on the right-hand side of the two transverse Bloch equations. This approximation has exactly the same physical meaning as the approximation that the population difference $\Delta N(t)$ is constant, or at most only slowly varying, in the earlier derivation of the linear electric-dipole susceptibility.

We have also shown that in the absence of applied signals, the transverse magnetization components $m_x(t)$ and $m_y(t)$ have exponentially decaying sinusoidal solutions of the form

$$m_x(t) = M_+ e^{-t/T_2} \cos(\omega_a t + \phi_+), \quad m_y(t) = M_+ e^{-t/T_2} \sin(\omega_a t + \phi_+). \quad (47)$$

This natural motion in the absence of applied signals is a right-hand circularly polarized precession in the x, y plane with slowly decaying magnitude M_+ and phase ϕ_+ . Since the natural oscillatory motion of the magnetization is contained in the m_x and m_y components, and since the energy exchange between a magnetic field \mathbf{b} and a magnetization \mathbf{m} is given by $\mathbf{b} \cdot d\mathbf{m}/dt$, we may assume that the most efficient signal to apply to the magnetic top model will be an ac magnetic field that is similarly confined to the x, y plane, and that is probably circularly polarized in the same sense.

Suppose we therefore write the applied magnetic fields as

$$\mathbf{b}(t) = B_0 \mathbf{z} + b_x(t) \mathbf{x} + b_y(t) \mathbf{y} \quad (48)$$

so that the longitudinal field contains only the dc field B_0 , whereas the transverse fields are given by the sinusoidal quantities

$$b_x(t) = \text{Re } \tilde{B}_x e^{j\omega t} \quad \text{and} \quad b_y(t) = \text{Re } \tilde{B}_y e^{j\omega t}. \quad (49)$$

It is then natural to write the time-varying magnetization $\mathbf{m}(t)$ also as

$$m_x(t) = \text{Re } \tilde{M}_x e^{j\omega t}, \quad m_y(t) = \text{Re } \tilde{M}_y e^{j\omega t}, \quad m_z = \text{const.}, \quad (50)$$

so that $\mathbf{m}(t)$ also has ac transverse and dc longitudinal components. The $e^{j\omega t}$ components of the two transverse Bloch equations then take the form

$$\begin{aligned} (j\omega + 1/T_2) \tilde{M}_x + \omega_a \tilde{M}_y &= -(ge/2m) m_z \tilde{B}_y \\ j\omega_a \tilde{M}_x + (j\omega + 1/T_2) \tilde{M}_y &= +(ge/2m) m_z \tilde{B}_x. \end{aligned} \quad (51)$$

These two equations form a coupled linear set connecting the sinusoidal transverse magnetization components \tilde{M}_x and \tilde{M}_y to the transverse signal components \tilde{B}_x and \tilde{B}_y . The quantities \tilde{B}_x , \tilde{B}_y and \tilde{M}_x , \tilde{M}_y are, as usual, complex phasor amplitudes with magnitudes and phase angles.

Steady-State Sinusoidal Tensor Solutions

Substituting the sinusoidal expressions into the transverse equations of motion and separating out the $e^{j\omega t}$ terms then gives us a pair of sinusoidal steady-state relations between \tilde{M}_x , \tilde{M}_y and \tilde{B}_x , \tilde{B}_y , which we can write in the form

$$\begin{aligned}\tilde{M}_x &= -j \frac{ge}{2m} \frac{T_2 m_z}{1 + jT_2(\omega - \omega_a)} \times [\tilde{B}_x + j\tilde{B}_y] \\ \tilde{M}_y &= -j \frac{ge}{2m} \frac{T_2 m_z}{1 + jT_2(\omega - \omega_a)} \times [-j\tilde{B}_x + \tilde{B}_y].\end{aligned}\quad (52)$$

Because the natural motion of the precessing magnetization $\mathbf{m}(t)$ has sinusoidal components only in the x , y plane, we can reasonably assume that any sinusoidal field component \tilde{B}_z that might be applied in the z direction will produce no linear or first-order polarization response; and we can similarly assume that neither \tilde{B}_x nor \tilde{B}_y will produce any sinusoidal response \tilde{M}_z in the z direction. Hence we can expand these results into the three-dimensional tensor form

$$\begin{bmatrix} \tilde{M}_x \\ \tilde{M}_y \\ \tilde{M}_z \end{bmatrix} = -j \frac{ge}{2m} \frac{T_2 m_z}{1 + jT_2(\omega - \omega_a)} \begin{bmatrix} 1 & j & 0 \\ -j & 1 & 0 \\ 0 & 0 & 0 \end{bmatrix} \begin{bmatrix} \tilde{B}_x \\ \tilde{B}_y \\ \tilde{B}_z \end{bmatrix}, \quad (53)$$

which we can convert into the tensor susceptibility form

$$\chi_m(\omega) \equiv \frac{\mu_0 \mathbf{M}(\omega)}{\mathbf{B}(\omega)} = -j \frac{ge\mu_0}{2m} \frac{T_2 m_z}{1 + jT_2(\omega - \omega_a)} \begin{bmatrix} 1 & j & 0 \\ -j & 1 & 0 \\ 0 & 0 & 0 \end{bmatrix} \quad (54)$$

It is clear that the tensor form of this magnetic-dipole response has exactly the gyrotrropic right-hand circularly polarized form we developed in Section 3.4 for circularly polarized electric-dipole transitions.

Magnetic-dipole Susceptibility

The scalar part of this tensor magnetic-dipole susceptibility, call it $\tilde{\chi}_m(\omega)$, has the resonant form

$$\tilde{\chi}_m(\omega) = -j \frac{ge\mu_0}{2m} \frac{2m_z}{\Delta\omega_a} \frac{1}{1 + 2j(\omega - \omega_a)/\Delta\omega_a}. \quad (55)$$

This is a complex lorentzian lineshape, with a resonance linewidth $\Delta\omega_a$ given by

$$\Delta\omega_a \equiv \frac{2}{T_2}. \quad (56)$$

The magnetic-dipole susceptibility thus has exactly the same complex lorentzian lineshape as did the electric-dipole susceptibility in Chapters 2 and 3, along with the same $1/\Delta\omega_a$ dependence. Moreover the longitudinal polarization m_z now plays exactly the same role as did N or ΔN in the electric-dipole model.

In fact, the linear susceptibility $\tilde{\chi}_m$ that we have derived here plays exactly the same role for magnetic-dipole transitions, in essentially every interpretation and every formula, as the electric-dipole susceptibility defined in earlier chapters plays for electric-dipole transitions.

Circularly Polarized Notation

Since the response to the Bloch equations is inherently circularly polarized, it can be convenient to convert from cartesian or x, y transverse components into positive and negative circularly polarized vector components. We can do this conveniently by defining a transformation from linear phasor components \tilde{M}_x , \tilde{M}_y to positive and negative circular components \tilde{M}_+ , \tilde{M}_- in the form

$$\begin{aligned}\tilde{M}_+ &\equiv (1/2)(\tilde{M}_x + j\tilde{M}_y) & \tilde{M}_x &\equiv \tilde{M}_+ + \tilde{M}_- \\ \tilde{M}_- &\equiv (1/2)(\tilde{M}_x - j\tilde{M}_y), & \text{or} & & j\tilde{M}_y &\equiv \tilde{M}_+ - \tilde{M}_-\end{aligned}, \quad (57)$$

and similarly for the applied signal field components \tilde{B}_x , \tilde{B}_y , \tilde{B}_+ and \tilde{B}_- . The $+$ and $-$ components can then be identified as the complex phasor amplitudes of the right-hand circularly polarized and left-hand circularly polarized parts of the sinusoidal vectors, respectively.

Suppose that the \tilde{B}_+ component of the applied signal field is finite, whereas the oppositely polarized component $\tilde{B}_- = 0$. The real signal fields are then given by the pure right-hand circular form

$$\begin{aligned}b_x(t) &= \operatorname{Re} \tilde{B}_+ e^{j\omega t} & = |\tilde{B}_+| \cos(\omega t + \phi_+) \\ b_y(t) &= \operatorname{Re} -j\tilde{B}_+ e^{j\omega t} & = |\tilde{B}_+| \sin(\omega t + \phi_+),\end{aligned} \quad (58)$$

where ϕ_+ is the phase angle of the complex quantity \tilde{B}_+ . This clearly corresponds to a right-hand circularly polarized signal, whereas the opposite sign of polarization will occur if \tilde{B}_- is finite while $\tilde{B}_+ = 0$.

Circularly Polarized AC Responses

If we use these transformations, the relations given in Equation 31.52 between \tilde{M}_x , \tilde{M}_y and \tilde{B}_x , \tilde{B}_y can be separated into the two uncoupled equations

$$\begin{aligned}\tilde{M}_+ &= -j \frac{ge}{2m} \frac{T_2 m_z}{1 + jT_2(\omega - \omega_a)} \tilde{B}_+ = \mu_0^{-1} \tilde{\chi}_+(\omega) \tilde{B}_+, \\ \tilde{M}_- &= -j \frac{ge}{2m} \frac{T_2 m_z}{1 - jT_2(\omega + \omega_a)} \tilde{B}_- = \mu_0^{-1} \tilde{\chi}_-(\omega) \tilde{B}_-.\end{aligned} \quad (59)$$

The right-hand circularly polarized and left-hand circularly polarized responses are now seen to be completely decoupled; i.e., the \tilde{B}_+ component produces only an \tilde{M}_+ response, whereas \tilde{B}_- produces only \tilde{M}_- , with separate susceptibilities $\tilde{\chi}_+(\omega)$ and $\tilde{\chi}_-(\omega)$ for right-hand circularly polarized and left-hand circularly polarized signals, respectively.

Further, the $+$ or right-hand circularly polarized susceptibility has a resonant response of the form

$$\tilde{\chi}_+(\omega) \equiv \frac{\mu_0 \tilde{M}_+}{\tilde{B}_+} = -j \frac{ge\mu_0}{2m} \frac{2m_z}{\Delta\omega_a} \frac{1}{1 + 2j(\omega - \omega_a)\Delta\omega_a}, \quad (60)$$

whereas the $-$ or left-hand circularly polarized response has an “antiresonant” response of the form

$$\tilde{\chi}_-(\omega) \equiv \frac{\mu_0 \tilde{M}_-}{\tilde{B}_-} = -j \frac{ge\mu_0}{2m} \frac{2m_z}{\Delta\omega_a} \frac{1}{1 - 2j(\omega + \omega_a)/\Delta\omega_a}. \quad (61)$$

Note the important difference in the denominators for Equations 31.60 and 31.61. Because of this difference, the ratio of these two susceptibilities for a signal frequency ω anywhere near the transition frequency ω_a is

$$\left| \frac{\tilde{\chi}_-}{\tilde{\chi}_+} \right| = \left| \frac{\Delta\omega_a + 2j(\omega - \omega_a)}{\Delta\omega_a - 2j(\omega + \omega_a)} \right| \approx \frac{\Delta\omega_a}{2\omega_a} \ll 1. \quad (62)$$

The left-hand circularly polarized response is seen to be essentially zero compared to the right-hand circularly polarized response, given the usual condition that the linewidth $\Delta\omega_a$ is small compared to the center frequency ω_a .

Rotating Wave Approximation

The physical reason why only the right-hand circularly polarized response is significant is evident from Figure 31.11. The magnetization $\mathbf{m}(t)$ naturally precesses, as we have repeatedly noted, with right-handed circular polarization about the z axis. For a right-hand circularly polarized signal \tilde{B}_+ , the transverse magnetization $\mathbf{b}(t)$ rotates in the same direction, and can thus interact cumulatively with the magnetization \mathbf{m} .

For a left-hand circularly polarized signal \tilde{B}_- , on the other hand, the signal field $\mathbf{b}(t)$ rotates, at frequency ω , in the opposite direction to the natural motion of $\mathbf{m}(t)$. If $\mathbf{m}(t)$ has any initial precession, this means that $\mathbf{b}(t)$ and $\mathbf{m}(t)$ rotate against each other, at opposite rotation frequencies $\pm\omega$, coming into and out of phase with each other twice every period. Any coherent transfer between the \tilde{B}_- component and $\mathbf{m}(t)$ thus rotates through all phases at frequency 2ω , and in general builds up to no cumulative interaction.

The analytic approximation which in the electric-dipole situation we called the *resonance approximation*, and which led there to the lorentzian lineshape, becomes in the magnetic-dipole picture what is called the *rotating-wave approximation*. It consists simply in ignoring the much weaker left-hand circularly polarized response, or $\tilde{\chi}_-(\omega)$, in the analytical results in Equation 31.59, and keeping only the resonant right-hand circularly polarized response or $\tilde{\chi}_+(\omega)$. The procedure for calculating the steady-state sinusoidal magnetic-dipole response in this rotating-wave approximation then becomes:

- Given an arbitrarily polarized applied signal $\mathbf{b}(t)$ with vector components \tilde{B}_x and \tilde{B}_y (and possibly even \tilde{B}_z), separate this signal into its right-hand circularly polarized and left-hand circularly polarized components \tilde{B}_+ and \tilde{B}_- .
- Neglect \tilde{B}_- entirely; and consider only the right-hand circularly polarized response $\tilde{M}_+ = \mu_0^{-1} \tilde{\chi}_+ \tilde{B}_+$ where $\tilde{\chi}_+$ is given by Equation 31.60.
- Finally, convert \tilde{M}_+ back into its cartesian components \tilde{M}_x and \tilde{M}_y , and thence into $\mathbf{m}(t)$ if desired.

The implication of the rotating-wave approximation is that $\tilde{M}_- \approx 0$, and the induced response is always a right-hand circularly polarized response \tilde{M}_+ , regardless of the type of polarization of the input signal.

Summary

The main points developed in this section are thus that:

- A sinusoidal magnetic signal field \tilde{B}_x, \tilde{B}_y produces a linearly related transverse sinusoidal magnetization \tilde{M}_x, \tilde{M}_y . These sinusoidal ac solutions come entirely from the transverse Bloch equations.
- The resulting response has a right-hand circularly polarized natural precession behavior and hence a right-hand circularly polarized gyrotropic tensor response.
- And finally, the resulting response has a complex lorentzian lineshape in frequency, as well as a magnitude proportional to $m_z/\Delta\omega_a$.

In the following section we will see what complementary results arise from the longitudinal Bloch equation.

REFERENCES

A classic early paper on the solution of the Bloch equations, using a rotating coordinate system and the rotating wave approximation, is by I. I. Rabi, N. F. Ramsey, and J. Schwinger, "Use of rotating coordinates in magnetic resonance problems," *Rev. Mod. Phys.* **26**, 167 (April 1954).

Problems for 31.5

1. *Radiative decay rate for a classical magnetic dipole.* A precessing magnetic-dipole moment should have a *classical magnetic-dipole radiative decay rate* γ_{rad} that plays the same role as the electric-dipole radiative decay rate for a classical electron oscillator. Find this classical radiative decay rate for a magnetic-dipole μ precessing at a small angle to a dc magnetic field B_0 , and express it in terms of the precession frequency ω_a and basic physical constants. Discuss similarities and differences to the electric dipole situation. In particular, what is the numerical ratio of the magnetic-dipole and electric-dipole classical radiative decay rates for the same resonance frequency ω_a , assuming ω_a to be in the optical frequency range?

(Some hints: A circularly precessing dipole moment $\mu(t)$ can be broken up into two transverse linearly oscillating moments $\mu_x(t)$ and $\mu_y(t)$, each of which can be considered as being produced by an oscillating current loop perpendicular to the linear direction of the moment. Numerous electromagnetic theory texts will then give formulas for the total signal power radiated by such an oscillating current loop.)

2. *Polarization changes for a circularly polarized wave.* How does the polarization of an optical plane wave change as it propagates through an atomic medium with a circularly polarized response?

To explore this question, consider the case of an inverted, circularly polarized, lorentzian atomic transition which has a right-hand circularly polarized response about the z axis, and a negligible left-hand circularly polarized response. Suppose an optical wave with its ac signal field initially linearly polarized along the x axis is sent through this atomic medium traveling in the $+z$ direction. Describe how the amplitude, and especially the signal polarization, of this signal wave will change with distance, in terms of the midband gain coefficient and the frequency detuning $(\omega - \omega_a)/\Delta\omega_a$ of the signal frequency ω from line center. (Hint: Divide the signal wave into its circularly polarized components and consider the net amplification and phase shift separately for each.)

Describe the behavior in particular for two situations: (a) Signal frequency exactly at line center, for both small and large net gains. (b) Signal frequency a few linewidths off line center, so that the net gain is small or negligible but the reactive phase shift is still significant.

What will be the corresponding results if the transition is absorbing rather than amplifying?

31.6 LONGITUDINAL RESPONSE: RATE EQUATION

The two first-order transverse Bloch equations for the magnetic polarizations $m_x(t)$ and $m_y(t)$, as developed in the previous section, are exactly analogous to the single second-order equation of motion for the electric polarization $p(t)$ as developed for the electric-dipole situation in Chapter 2. We will next show how the *longitudinal* Bloch equation for the longitudinal magnetization $m_z(t)$ is exactly analogous to the two-level rate equation for the population difference $\Delta N(t)$, as developed for the electric-dipole case in Chapters 4 and 5.

Longitudinal Bloch Equation

The z component of the Bloch equation, including relaxation terms, is

$$\frac{dm_z(t)}{dt} + \frac{m_z(t) - m_{z0}}{T_1} = \frac{ge}{2m} [b_x(t)m_y(t) - b_y(t)m_x(t)]. \quad (63)$$

In line with our analysis in the previous section, suppose that $b_x(t)$ and $b_y(t)$, and also $m_x(t)$ and $m_y(t)$, have sinusoidal frequency components at the signal frequency ω . Then the product terms $b_x(t)m_y(t)$ and $b_y(t)m_x(t)$ on the right-hand side of Equation 31.63 will contribute both low-frequency or dc terms at the difference frequency $\omega - \omega = 0$; and also *second harmonic* terms at the sum frequency $\omega + \omega = 2\omega$.

The $m_z(t)$ terms on the left-hand side of Equation 31.63 are then driven by both the dc and the second-harmonic driving terms on the right-hand side. Because of the long time constant or averaging time T_1 on the left-hand side, however, the reader can easily verify that the response of $m_z(t)$ to a 2ω term on the right-hand side will be very much less than the response to a dc driving term. In fact the 2ω response will be less by the very large ratio $(\omega T_1)^{-1}$ which is $\ll 1$ for any reasonable signal frequency ω and relaxation time T_1 .

Conversion to Rate-Equation Form

Let us therefore expand the product terms on the right-hand side of Equation 31.63 using the circularly polarized phasor components \tilde{B}_+ , \tilde{B}_- and \tilde{M}_+ , \tilde{M}_- . (This turns out to be more compact and meaningful than using the cartesian components \tilde{B}_x , \tilde{B}_y , and \tilde{M}_x , \tilde{M}_y .) The products on the right-hand side then take the form

$$\begin{aligned} b_x(t)m_y(t) - b_y(t)m_x(t) = & + (j/2) [\tilde{B}_+^* \tilde{M}_+ - \tilde{B}_+ \tilde{M}_+^*] \\ & - (j/2) [\tilde{B}_-^* \tilde{M}_- - \tilde{B}_- \tilde{M}_-^*] \\ & + (j/2) [\tilde{B}_+ \tilde{M}_- - \tilde{B}_- \tilde{M}_+] \exp[2j\omega t] \\ & + \text{complex conjugate term.} \end{aligned} \quad (64)$$

The first square-bracketed term on the right-hand side of Equation 31.64 is the dc term arising from the product of the \tilde{B}_+ and \tilde{M}_+ terms which have the same sense of rotation. The second such term is another (generally much smaller) dc term arising from the product of the \tilde{B}_- and \tilde{M}_- terms with the opposite sense of rotation.

The final two terms on the right-hand side then give the second-harmonic or 2ω terms that arise from the cross products of the right-hand circularly polarized terms \tilde{B}_+ and \tilde{M}_+ mixing with the left-hand circularly polarized terms \tilde{M}_- and \tilde{B}_- , just as we described in the physical explanation of the rotating wave approximation in the previous section. Suppose we drop these high-frequency or 2ω terms (which will only produce weak second-order nonlinear or harmonic-generation effects), and suppose that we also use the rotating-wave approximation to drop the \tilde{B}_- and \tilde{M}_- dc terms. Then, the longitudinal Bloch equation (31.63) reduces to

$$\frac{dm_z(t)}{dt} + \frac{m_z(t) - m_{z0}}{T_1} = j \left(\frac{ge}{2m} \right) (\tilde{B}_+ \tilde{M}_+^* - \tilde{B}_+^* \tilde{M}_+). \quad (65)$$

The $\tilde{B}_+^* \tilde{M}_+$ and $\tilde{B}_+ \tilde{M}_+^*$ terms on the right-hand side of Equation 31.65 are directly analogous to the time-averaged $\mathcal{E} \cdot dp/dt$ or $E(t)P(t)$ terms on the right-hand side of the rate equations as developed in the earlier electric-dipole chapters.

Magnetic-dipole Rate Equation

Equation 31.65 is still somewhat general in that it allows an arbitrary phase and amplitude relationship between the applied signal \tilde{B}_+ and the precessing magnetization \tilde{M}_+ (such as might be the case in a transient situation). As soon as \tilde{M}_+ settles down to the steady-state sinusoidal result from the previous section, however, as given by

$$\tilde{M}_+ = \mu_0^{-1} \tilde{\chi}_+(\omega) \tilde{B}_+, \quad (66)$$

then the longitudinal Bloch equation becomes

$$\frac{dm_z(t)}{dt} + \frac{m_z(t) - m_{z0}}{T_1} = \left(\frac{ge}{m\mu_0} \right) \chi''_+(\omega) \left| \tilde{B}_+ \right|^2. \quad (67)$$

But this has essentially the same form as the two-level rate equation we discussed in earlier chapters, i.e.,

$$\frac{d\Delta N(t)}{dt} + \frac{\Delta N(t) - \Delta N_0}{T_1} = -2W_{12}\Delta N(t), \quad (68)$$

where W_{12} is the stimulated transition probability between two levels produced by an applied signal. In fact, since χ''_+ in Equation 31.67 depends directly on m_z , we can rewrite Equation 31.67 in the form

$$\begin{aligned} \frac{dm_z(t)}{dt} + \frac{m_z(t) - m_{z0}}{T_1} &= -2 \left(\frac{ge}{2m} \right)^2 \frac{1}{\Delta\omega_a} \frac{1}{1 + [2(\omega - \omega_a)/\Delta\omega_a]^2} \left| \tilde{B}_+ \right|^2 m_z(t) \\ &= -2W_{12}m_z(t). \end{aligned} \quad (69)$$

Comparing the preceding two equations makes it clear that the two-level stimulated transition probability W_{12} in the magnetic-dipole case is given by

$$W_{12}(\text{magnetic dipole}) \equiv \left(\frac{ge}{2m} \right)^2 \frac{1}{\Delta\omega_a} \frac{1}{1 + [2(\omega - \omega_a)/\Delta\omega_a]^2} \left| \tilde{B}_+ \right|^2. \quad (70)$$

This result is exactly parallel to the electric-dipole situation, in which the stimulated transition probability is given by

$$W_{12}(\text{electric dipole}) = \frac{3^* \epsilon \gamma_{\text{rad}}}{8\pi^2 \hbar} \frac{1}{\Delta\omega_a} \frac{1}{1 + [2(\omega - \omega_a)/\Delta\omega_a]^2} \left| \tilde{E} \right|^2. \quad (71)$$

In both cases, the stimulated transition probability is proportional to a lorentzian lineshape; to the inverse linewidth $1/\Delta\omega_a$; and to the applied signal energy density as measured now by $\left| \tilde{B}_+ \right|^2$ rather than by $\left| \tilde{E} \right|^2$.

Saturation Behavior

The Bloch equations will thus lead in steady-state to a saturation of the z -directed magnetization, m_z as given by

$$\begin{aligned} m_{z,ss} &= m_{z0} \times \frac{1}{1 + 2W_{12}T_1} = \frac{m_{z0}}{1 + \text{const} \times \left| \tilde{B}_+ \right|^2} \\ &= m_{z0} \times \frac{1}{1 + I/I_{\text{sat}}}, \end{aligned} \quad (72)$$

exactly like the saturation in the electric-dipole situation. This saturation behavior can be given a simple graphic interpretation, as illustrated in Figure 31.17.

Consider a collection of magnetic dipoles with an equilibrium magnetization $m_z = m_{z0}$ along the z direction in the absence of any applied signal, and suppose a comparatively weak steady-state sinusoidal signal at or near resonance is applied to this collection. When this applied signal is first turned on, the magnetization vector $\mathbf{m}(t)$ will then begin to “open up” into a conical precession about the z axis, driven by the applied signal, as shown in Figure 31.17. The magnetization vector will move out at first by spiraling out on the surface of a sphere of radius equal to the initial equilibrium value m_{z0} of the magnetization.

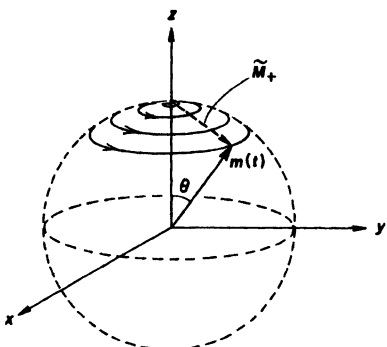


FIGURE 31.17

Applying a sinusoidal signal at resonance initially causes the magnetization vector to spiral out on the surface of a sphere.

The steady-state magnitude of the transverse component of this precession, after the initial transient, can then be written from our earlier results as

$$\tilde{M}_+ = -j \frac{ge}{2m} \frac{T_2 m_z}{1 + jT_2(\omega - \omega_a)} \tilde{B}_+. \quad (73)$$

(We write this using T_2 rather than $\Delta\omega_a$ because it makes some of the subsequent expressions slightly simpler.) Let us define a normalized intensity \mathcal{B}_+ for the applied signal field by

$$\mathcal{B}_+ \equiv (ge/2m)\sqrt{T_1 T_2} |\tilde{B}_+|. \quad (74)$$

The magnitude of the rotating transverse component \tilde{M}_+ relative to the axial m_z component can then be written as

$$|\tilde{M}_+| = \sqrt{T_2/T_1} m_z \mathcal{B}_+. \quad (75)$$

With saturation taken into account, however, the m_z component of the macroscopic polarization must be written as

$$\frac{m_z}{m_{z0}} = \frac{1}{1 + (ge/2m)^2 T_1 T_2 |\tilde{B}_+|^2} = \frac{1}{1 + \mathcal{B}_+^2}. \quad (76)$$

Hence the transverse component \tilde{M}_+ can be related to the unsaturated longitudinal magnetization m_{z0} by

$$\frac{|\tilde{M}_+|}{m_{z0}} = \sqrt{\frac{T_2}{T_1}} \times \frac{\mathcal{B}_+}{1 + \mathcal{B}_+^2} \quad (77)$$

which rises linearly with signal amplitude \mathcal{B} at first, but then decreases at larger amplitudes, with a maximum value of $(1/2)\sqrt{T_2/T_1}$, which is much smaller than unity in most cases.

In other words, in terms of the graphical description of Figure 31.17, the magnetization $m(t)$ does not continue to spiral outward on the surface of the sphere as the applied signal strength \tilde{B}_+ becomes stronger. Rather, the steady-state

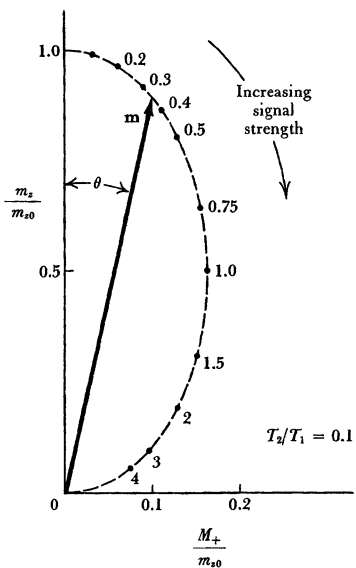


FIGURE 31.18
The steady-state value of the z component of magnetization saturates at larger applied signal levels.

longitudinal component m_z begins to shrink because of saturation, as shown in Figure 31.18, and the magnetization moves down inside the sphere as illustrated graphically in Figure 31.19(b).

If we assume that $T_2 \ll T_1$, as is normally the situation, then the transverse component \tilde{M}_+ will have a maximum possible value $|\tilde{M}_+| = \sqrt{T_2/T_1} \times m_{z0}/2$, which is much smaller than the original static magnetization m_{z0} , as illustrated in Figure 31.18. This maximum value occurs for a signal strength given by $B_+ = 1$, i.e., at the point where the transition, or the population difference on the transition, is exactly halfway saturated.

Physical Explanation

We can also give a physical explanation of this behavior, in terms of the behavior of many little dipoles, and of their dephasing behavior. Before the applied signal is turned on the magnetization $\mathbf{m}(t)$ comes from many little individual dipoles, with N_{10} dipoles pointing "up," and $N_{20} < N_{10}$ dipoles pointing "down," so that there is a net magnetization along the z axis. The dipoles are all precessing with random phases, however, as in Figures 31.15 or 31.16, so that there is no net $m_x(t)$ or $m_y(t)$.

The applied signal, and especially its \tilde{B}_+ component, then begins to pull the precessional motion of these individual dipoles into phase with the applied signal, against the randomizing effects of the T_2 dephasing time. The coherent transverse component \tilde{M}_+ thus grows linearly with \tilde{B}_+ or with B_+ at first. Note that the shorter the dephasing time T_2 , the weaker this coherent response for a given signal field strength \tilde{B}_+ .

The signal field \tilde{B}_+ , as it grows stronger, also begins to tip the individual dipoles over, away from the $\pm z$ axes and toward the 90° or x, y plane. (Note

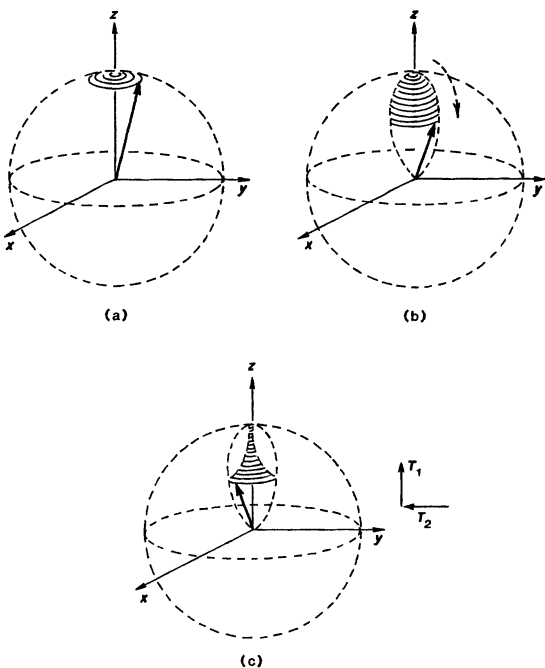


FIGURE 31.19

(a) Initial response when an applied signal is first turned on. (b) Saturation of the m_z component. (c) Transient decay and recovery when the applied signal is turned off.

that the dipoles get tipped toward the equatorial plane whether they were initially pointing up or down along the x axis.) This causes a gradual decrease or saturation in the m_z component.

It also has another effect, however. As the individual dipoles tip closer to the 90° plane the transverse component of the $\mathbf{b} \times \mu_m$ cross product between the applied signal and the dipole becomes progressively weaker, going in fact to zero if the dipoles reach the 90° plane. In other words, as the dipoles get tipped down into the transverse plane by the applied signal, the ability of this same signal to pull the precessional motion of the dipoles into a coherent phase relationship with itself goes toward zero. The transverse magnetization M_+ thus increases at first, but then eventually decreases with increasing signal strength \tilde{B}_+ , as illustrated in Figure 31.18.

Note also from this description that the length of the magnetization vector $|\mathbf{m}(t)|$ does not remain constant, even though the lengths of the individual atomic dipoles μ_i that make up $\mathbf{m}(t)$ remain constant. As we drive the magnetic-dipole system harder, at first $\mathbf{m}(t)$ remains approximately constant in length and simply opens up to larger precession angles with increasing signal strength. However, as the signal becomes strong enough to produce saturation, m_z begins to decrease, and this in turn through the m_z dependence leads to an eventual reduction in the

magnitude of the transverse component \tilde{M}_+ , even though the precession angle keeps opening up all the way down to 90° from the z axis.

Discussion

We will not explore the linear small-signal properties of magnetic-dipole transitions in much further detail, since they are described in many other books (see References) and since we have already discussed most of the basic ideas in detail for the electric-dipole situation. However, some further comments on the relationships between the magnetic-dipole and electric-dipole situations may be useful.

(1) *Circularly polarized response.* The classical magnetic-dipole model we have used has a natural response which is circularly polarized, just as the linear classical electron oscillator had a response which was linearly polarized. We pointed out in earlier chapters that this linear electric-dipole response matched up exactly with the linear polarization of an elementary but real atomic example, namely, an $s \rightarrow p(m=0)$ transition in a simple atom. We also noted that other real electric-dipole transitions could have more general circular or even elliptically polarized responses.

Similarly, the circularly polarized response of the classical magnetic-dipole matches up exactly with any real magnetic-dipole transitions which occur between pure angular momentum states with good quantum numbers m and m' where $m' = m \pm 1$. This includes a great many magnetic-dipole and magnetic-resonance transitions in real atoms and molecules. However, in the presence of crystalline electric fields, or zero-field splittings, or other complications, real magnetic-dipole transitions can also have polarizations other than circular, including elliptical or even linear. To describe these real transitions the magnetic-dipole results must then be suitably modified, essentially by changing the gyrotropic tensor form to whatever other form is required.

(2) *Radiative decay rate.* What may seem a more significant difference between electric and magnetic-dipole situations is that the radiative decay rate γ_{rad} , which played such an important role in the electric-dipole model, does not seem to have played the same important role in the magnetic-dipole analysis.

This difference is, however, apparent rather than real. Magnetic-dipole transitions do have a purely radiative magnetic-dipole energy decay rate γ_{rad} which is directly analogous to the electric dipole radiative decay rate (see Problems). Moreover the susceptibility $\tilde{\chi}_m$, the stimulated transition probability W_{12} , the transition cross section σ , and all the other parameters for a magnetic-dipole transition can be expressed in terms of the magnetic-dipole value for γ_{rad} , exactly as for an electric-dipole transition. (The dependence of these quantities on γ_{rad} is really a fundamental thermodynamic consideration and does not depend at all on the nature of the transition involved.)

The radiative decay rate for a magnetic-dipole transition is, however, extremely weak—approximately 10^6 times weaker than for an electric-dipole transition at the same optical frequency. This rate is especially negligible for magnetic-resonance transitions at their much lower frequencies. Hence the Bloch analysis of magnetic-dipole transitions as it was first developed, primarily for low-frequency magnetic-resonance transitions, simply took no note of the radiative decay rate or its relationship to these transitions. The relationship was simply not of interest, especially since the magnetic-dipole value of γ_{rad} was virtually unmeasurable.

(3) *Transverse relaxation time.* In the magnetic-dipole case we have obtained a lorentzian atomic response with a linewidth given by

$$\frac{\Delta\omega_a}{2} = \frac{1}{T_{2m}}, \quad (\text{magnetic-dipole case}) \quad (78)$$

whereas in earlier chapters we obtained for the electric-dipole case

$$\frac{\Delta\omega_a}{2} = \frac{1}{T_{2e}} + \frac{1}{2T_1}, \quad (\text{electric-dipole case}). \quad (79)$$

All this means is that the decay time T_2 has a slightly different physical interpretation in the electric-dipole and magnetic-dipole cases.

In the electric-dipole case we identified T_1 as representing the energy decay time for the atomic population difference, and T_2 as representing the elastic or energy-conserving dephasing time for the internal atomic oscillations. The atomic response is obviously broadened by both of these effects (although with a difference of a factor of 2 in the way these time constants appears in the atomic linewidth).

In the magnetic-dipole case it was simplest to associate a single decay time with the transverse components $m_x(t)$ and $m_y(t)$, and to call this decay time T_2 . Obviously, however, the T_2 in the magnetic-dipole case contains a combination of both dephasing and energy-decay effects. Hence, to be strictly accurate, it is necessary to make the identification that the T_2 to be used in the transverse Bloch equations (31.46) should be understood have an extended value given by

$$\frac{1}{T_2} \equiv \frac{1}{T_{2e}} + \frac{1}{2T_1}, \quad (80)$$

where T_{2e} is interpreted as the “elastic dephasing” part of T_2 . This distinction is generally recognized in magnetic-resonance textbooks.

Problems for 31.6

1. *Alternative approach to solving the Bloch equations.* An alternative approach to the Bloch equations, which is in some ways neater, is to define “complex-real” field quantities $\tilde{b}(t) \equiv b_x(t) + jb_y(t)$ and $\tilde{m}(t) \equiv m_x(t) + jm_y(t)$ where b_x , b_y , m_x and m_y are the real transverse fields and magnetizations as functions of time. Note that $\tilde{b}(t)$ and $\tilde{m}(t)$ as defined here are not phasor amplitudes, but rather complex combinations of two real vector components.

Show that by using these quantities the Bloch equations (31.46) can be rewritten as only two equations, one of which condenses the two real transverse equations into a single complex transverse equation. Note that for sinusoidal fields at frequency ω these complex quantities may have both $\exp(+j\omega t)$ and $\exp(-j\omega t)$ terms, and that these terms correspond to the right-hand and left-hand circularly polarized parts of the real fields, respectively. Carry through the standard linearized, sinusoidal, small-signal solution of the Bloch equations in this notation, pointing out how the rotating-wave approximation and the saturation of the m_z component occur in this formulation.

31.7 LARGE-SIGNAL AND COHERENT-TRANSIENT EFFECTS

The Bloch equations become especially useful in large-signal transient regimes, where the rate-equation approximations are no longer valid and where the response to an applied signal can no longer be described simply by a linear susceptibility. The dynamic behavior of the magnetic-dipole vector model can then give a particularly vivid physical picture for predicting and explaining many of the Rabi flopping and coherent transient phenomena that were first demonstrated using magnetic resonance, but that have since been demonstrated and extended using optical-frequency transitions and lasers (on electric-dipole equally as well as on magnetic-dipole transitions).

In this section, therefore, we examine briefly some of the analytic and physical predictions of the Bloch vector model in the large-signal and fast-transient regimes, and show how some of the important examples of Rabi flopping behavior, coherent pulse effects, and harmonic generation that we described for electric-dipole transitions in an earlier chapter can equally well be obtained from the magnetic-dipole model.

Rate-equation Response: Transient Behavior

Let us first, just for background, look at the transient behavior we can expect from the magnetic-dipole model if we assume very fast pulses, but signals that are still in the weak signal or rate-equation regime. Suppose that an applied signal with a very fast rise time is suddenly applied to a magnetic-dipole system which is initially at equilibrium, with $m_z = m_{z0}$ and $m_x = m_y = 0$. Then, we can expect the following transient behavior. (We assume for simplicity an on-resonance signal, with $\omega = \omega_a$, turned on at $t = 0$.)

Initially, when the signal field is first turned on, the magnetization vector $\mathbf{m}(t)$ will begin to precess around the dc magnetic field, that is, the z axis, spiralling outward with an increasing cone angle, as illustrated in Figure 31.19(a). This precession will build up rapidly toward a steady-state transverse component given by the sinusoidal steady-state results of an earlier section, with m_z equal to the initial value of the longitudinal magnetization m_{z0} . The build-up from the axis to this steady-state value will be exponential, with time constant given by $T_2 = 1/\Delta\omega_a$. The steady-state cone angle, for signals within the rate-equation regime, will generally be small compared to 90° .

However, if the applied signal is at the same time strong enough to cause significant saturation of the m_z component, as described in the preceding section, the value of m_z will begin to decrease from its initial value m_{z0} as illustrated in Figure 31.19(b), moving down toward whatever steady-state saturated value is appropriate to the applied signal level. The rate at which m_z approaches its final saturated value is given, from the longitudinal rate equation, by the quantity $(2W_{12} + 1/T_1)$. This rate will be, in most situations, substantially slower than the rate $1/T_2$ at which the transverse magnetization component initially spirals outward. This is true at least if $T_2 \ll T_1$, which is the most common situation in atomic transitions.

As m_z saturates downward, it also pulls inward with it the transverse magnetization component \tilde{M}_+ , because of the direct dependence of the ac susceptibility $\tilde{\chi}_+$ on the longitudinal magnetization m_z , as described in the preceding section. The net result is that, in the rate-equation limit, the magnetization $\mathbf{m}(t)$ moves out and then down, ending up not on the surface of a sphere or globe with ra-

dius m_{z0} , but on the surface of a kind of elongated ellipsoid within that globe, as shown in Figure 31.19(b).

Free Induction Decay

Suppose that after the magnetization has come to steady state, we then suddenly turn off the applied signal, with a cut-off time short compared to the transverse decay time T_2 . The precessing magnetization in this situation will then spiral rapidly back in toward the z axis with the transverse time constant T_2 —a process often referred to as *free induction decay*—while at the same time the axial magnetization m_z will begin to recover up to its thermal equilibrium value m_{z0} with the generally slower longitudinal relaxation time T_1 . In other words, the magnetization vector in this situation will move in, and then up, as shown in Figure 31.19(c).

All of these results are in complete accord with the rate equation picture for electric-dipole transitions, where we consider instead the behavior of the polarization $p(t)$ and the population difference $\Delta N(t)$. The motion of the longitudinal and transverse components of $\mathbf{m}(t)$ simply gives an alternative, and perhaps more graphic, way of viewing the atomic dynamics.

Large-Signal Transient Analysis

The transient response of the Bloch equations becomes more complex and interesting for significantly stronger applied signals. To demonstrate this we can next carry out a somewhat simplified but still fairly general analysis of the transient large-signal situation, using the following approach.

Let us suppose that a strong right-hand circularly polarized signal field with a phasor amplitude $\tilde{B}_+ \equiv B_1(t) + jB_2(t)$ is applied to a collection of magnetic-dipole atoms. We can then write the signal fields along the x and y axes as

$$b_x(t) = \text{Re}[B_1(t) + jB_2(t)]e^{j\omega t}, \quad b_y(t) = \text{Re}[-jB_1(t) + B_2(t)]e^{j\omega t}. \quad (81)$$

Within the limits of the rotating wave approximation (which will be a very good approximation virtually always) the induced magnetization $\mathbf{m}(t)$ will be right-hand circularly polarized also, though the magnitude of its right-hand circularly polarized component may vary with time. Hence we also write the transverse portion of $\mathbf{m}(t)$ using a similar notation as

$$m_x(t) = \text{Re}[M_1(t) + jM_2(t)]e^{j\omega t}, \quad m_y(t) = \text{Re}[-jM_1(t) + M_2(t)]e^{j\omega t}. \quad (82)$$

Putting these expressions into either one of the two transverse Bloch equations (31.46) and separating out the real and imaginary parts then leads to the coupled pair of equations

$$\begin{aligned} [d/dt + 1/T_2] M_1(t) - (\omega - \omega_a)M_2(t) &= +\frac{ge}{2m}m_z(t)B_2(t) \\ [d/dt + 1/T_2] M_2(t) + (\omega - \omega_a)M_1(t) &= -\frac{ge}{2m}m_z(t)B_1(t), \end{aligned} \quad (83)$$

while the third or longitudinal Bloch equation, with the harmonic terms dropped, becomes

$$\frac{dm_z(t)}{dt} + \frac{m_z(t) - m_{z0}}{T_1} = -\frac{ge}{2m}[B_1(t)M_2(t) - B_2(t)M_1(t)]. \quad (84)$$

Equations 31.83 and 31.84 represent the magnetic-dipole analog to the large-signal SVEA equations relating $P_1(t)$ and $E_1(t)\Delta N(t)$ which we developed during the electric-dipole discussion of the Rabi frequency in Chapter 5.

Equations 31.83 and 31.84 clearly provide three coupled nonlinear equations in $M_1(t)$, $M_2(t)$ and $m_z(t)$ as driven by $B_1(t)$ and $B_2(t)$. Note that they say that if the applied signal is tuned to resonance, $\omega = \omega_a$, then the magnetization component $M_1(t)$ is coupled to $B_2(t)$, and $M_2(t)$ to $B_1(t)$, i.e., the signal field \tilde{B}_+ tends to produce a rotating magnetization $M_+ \equiv M_1 + jM_2$ which lags behind it by 90° in space (or in precession angle). If the signal is off resonance, however, the in-phase and quadrature components become coupled, and the phase angle becomes more complex.

Rabi Frequency Solutions

If we solve these equations properly, we can obtain and understand not only the weak-signal or rate-equation behavior of the Bloch model, but also the strong-signal or coherent transient behavior as well. In order to look at the very strong signal regime, and to bring out the fundamental Rabi frequency behavior, let us assume for simplicity an applied signal with a constant linearly polarized value of $\tilde{B}_+ \equiv B_1$ (i.e., the signal field is linearly polarized along the x axis), and assume this field is turned on suddenly at $t = 0$. Let us also drop all the relaxation terms involving T_1 and T_2 , by assuming that the signal field B_1 is strong enough so that the $(ge/2m)B_1$ terms in Equations 31.83 and 31.84 are large compared to either the $1/T_1$ or especially the $1/T_2$ terms. (To put this another way, we can say we will look only at the transient behavior for times t short compared to both T_1 and especially T_2 .)

The three Bloch equations then reduce to

$$\begin{aligned} dM_1(t)/dt - \Delta\omega M_2(t) &= 0 \\ dM_2(t)/dt - \Delta\omega M_1(t) &= -\omega_R m_z(t) \\ dm_z(t)/dt &= +\omega_R M_2(t), \end{aligned} \quad (85)$$

where we use $\Delta\omega$ as a shorthand for the off-resonance detuning $\Delta\omega \equiv \omega - \omega_a$, and where ω_R is the *magnetic-dipole Rabi frequency* given by

$$\omega_R \equiv \frac{ge}{2m} \left| \tilde{B}_+ \right| = \frac{ge}{2m} B_1. \quad (86)$$

This Rabi frequency has exactly the same physical significance in the magnetic-dipole case as the electric-dipole Rabi frequency we introduced in Chapter 5. However, we are also including a finite signal-frequency detuning $\Delta\omega$ in these equations, whereas in the electric-dipole case we only calculated the Rabi frequency for on-resonance signals.

If we assume transient solutions of the form e^{st} for $M_1(t)$, $M_2(t)$ and $m_z(t)$, the determinant of Equations 31.85 becomes

$$s[s^2 + \omega_R^2 + \Delta\omega^2] = 0. \quad (87)$$

This clearly has one dc or static root at $s = 0$, plus two imaginary roots at the modified Rabi frequency $s = \pm j\omega'_R$, where

$$\omega'_R \equiv \sqrt{\omega_r^2 + \Delta\omega^2} \approx \begin{cases} \omega_R, & \text{for } \Delta\omega \ll \omega_R \\ \Delta\omega, & \text{for } \Delta\omega \gg \omega_R \end{cases} \quad (88)$$

Tuning the applied signal off resonance obviously increases the effective Rabi frequency for a given applied signal strength.

Suppose we assume that the signal field is turned on suddenly at $t = 0$ in a magnetic-dipole system which is at rest with $M_1(0) = M_2(0) = 0$ and $m_z(0) = m_{z0}$. Then the exact solutions to Equations 31.85 are given by

$$M_1(t) = m_{z0} \times \frac{\omega_R \Delta\omega}{\omega_R^2 + \Delta\omega^2} [\cos \omega'_R t - 1] \quad (89)$$

and

$$M_2(t) = -m_{z0} \times \frac{\omega_R}{\omega'_R} \sin \omega'_R t \quad (90)$$

for the transverse components, and

$$m_z(t) = [(\Delta\omega/\omega'_R)^2 + (\omega_R/\omega'_R)^2 \cos \omega'_R t] m_{z0}, \quad (91)$$

for the axial component.

On-Resonance Rabi Flopping Behavior

Consider first a strong applied signal exactly on resonance. Figure 31.20 then shows how, beginning from its rest position along the B_0 axis, the magnetization $\mathbf{m}(t)$ spirals outward from its initial position along the B_0 axis, but now with its tip remaining on the surface of the sphere of radius m_{z0} . (With relaxation terms ignored, the magnetization vector has constant length.) This vector then spirals all the way down to the $-B_0$ or $-z$ axis (180° pulse); and then spirals back upward again to its starting point (360° pulse). This behavior repeats periodically at the Rabi frequency $\omega_R = (ge/2m)B$.

The primary result is obviously that both the longitudinal magnetization $m_z(t)$ and the 90° out of phase transverse component $M_2(t)$ oscillate periodically in time at the Rabi frequency, as shown in Figure 31.21. This is obviously a direct magnetic-dipole analog to the behavior of $\Delta N(t)$ and $\tilde{P}(t)$ in the electric-dipole large-signal situation. [Note that the transverse magnetization $M_+(t)$ both lags 90° in precession phase behind the rotating signal field $b(t)$ at the optical frequency ω_o , and its magnitude $M_2(t)$ lags 90° behind $m_z(t)$ in the Rabi flopping behavior.]

FIGURE 31.20

In the pure Rabi frequency limit, the magnetization vector spirals outward and downward on the surface of the "globe," precessing about the signal B field.

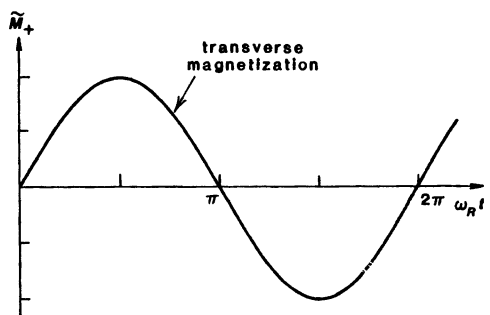
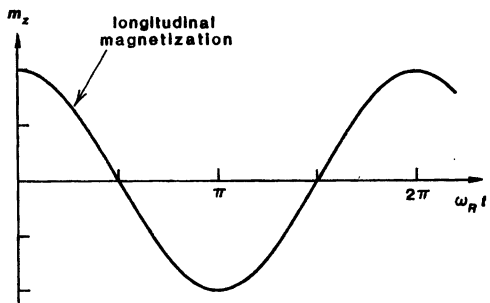
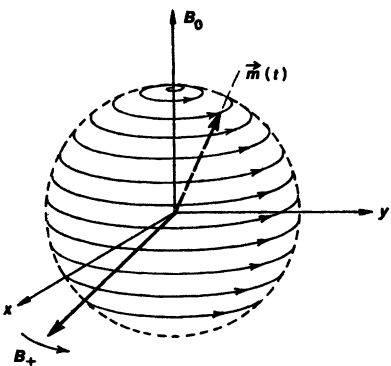


FIGURE 31.21

On-resonance Rabi flopping behavior of the longitudinal and transverse components of the magnetization.

Off-Resonance Rabi Flopping Behavior

If the applied signal is tuned off resonance by increasing amounts $\Delta\omega$ (as measured relative to the on-resonance rabi frequency ω_R), the magnetization vector will still begin to spiral down the surface of the "globe" as in the on-resonance behavior of Figure 31.21. In the off-resonance case, however, before

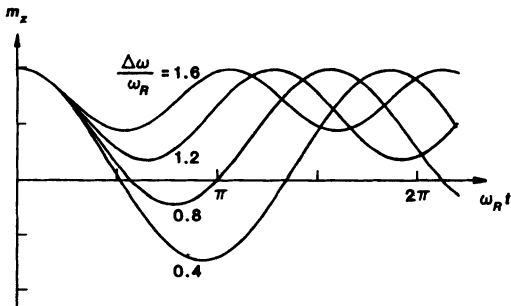


FIGURE 31.22

Off-resonance Rabi flopping behavior of the longitudinal component of magnetization.

the Rabi flopping behavior can carry $\mathbf{m}(t)$ all the way to the bottom, the frequency detuning causes both $M_1(t)$ and $M_2(t)$ components to build up, so that M_+ begins to acquire additional lead or lag relative to \tilde{B}_+ . In essence the rotating magnetization loses the desirable 90° precession phase lag relative to the applied signal. As a result, the Rabi oscillatory motion of $m_z(t)$ turns around and reverses direction before going all the way to the opposite pole—the Rabi flopping behavior is no longer a complete 180° inversion.

The further the applied signal is tuned off resonance, the less complete are the Rabi flopping cycles, as illustrated in Figure 31.22. The effective Rabi flopping frequency also appears to increase, but only because the oscillatory motion is in effect turned back before it can go all the way to the opposite pole. (Note also, however, the implication that essentially complete Rabi flopping behavior can always be obtained, no matter how far the applied signal may be tuned off an atomic resonance line—within reason—provided that we simply increase the applied signal strength until the Rabi frequency $\omega_R = (ge/2m)B_1$ becomes a few times greater than the detuning $\Delta\omega$).

Rabi Flopping Limit Versus the Rate-equation Limit

By comparing this large-signal behavior with the rate-equation behavior derived earlier in this chapter, we can see that for the magnetic dipole situation, just as for the electric-dipole situation, the stimulated transition probability W_{12} is related to the Rabi frequency ω_R by the very simple expression

$$W_{12} = \frac{(ge/2m)^2 |\tilde{B}_+|^2}{\Delta\omega_a} = \frac{\omega_R^2}{\Delta\omega_a}. \quad (92)$$

The condition on the signal strength for the rate-equation approximations to be valid is, just as in the electric-dipole situation, that $W_{12} \ll \Delta\omega_a$. But this is again the same as requiring that the Rabi frequency ω_R be small compared to the atomic linewidth, or to the inverse dephasing time T_2 , i.e.,

$$\left[\omega_R \equiv \frac{ge}{2m} B_1 \right] \ll \left[\Delta\omega_a \equiv \frac{2}{T_2} \right]. \quad (93)$$

In simple physical terms, using the magnetic-dipole vector model, if the signal field B_1 is strong enough to make $\omega_R \gg \Delta\omega_a$, both the individual dipole moments

$\mu(t)$ and the macroscopic magnetization $m(t)$ can make one or several Rabi cycles from $+z$ down to $-z$ and back again, precessing about the *signal* field vector B_1 , before any significant number of collisions occur to break up these large-signal motions. The Rabi flopping behavior will dominate.

In the opposite limit, with $\omega_R = (ge/2m)B_1 \ll \Delta\omega_a$, the individual dipole moments $\mu(t)$ will not be able to make even a fraction of a complete Rabi cycle before collisions randomize their transverse phases and break up the precession about B_1 . Pure rate-equation behavior will then prevail.

Coherent Transient Phenomena

There are a large number of coherent transient atomic phenomena that can be particularly well visualized and explained using the Bloch vector picture of atomic response. This list of coherent transient phenomena that can be explained using the Bloch vector model—but that can be demonstrated experimentally using either magnetic-dipole or electric-dipole transitions—includes:

- **Free induction decay:** This refers to the transient decay of an initially induced polarization at rate $1/T_2$, as we have discussed earlier.
- **Quantum beats:** Free induction decay on a nearly degenerate pair of transitions, so that we see frequency beats between the emission on the two transitions.
- **Optical nutation:** The turn-on transient observed when a medium-strong signal is first applied, demonstrating a combination of Rabi and $1/T_2$ effects.
- **Laser frequency-shifting technique:** We have described this in Section 25.3, in connection with the frequency modulation of laser oscillators.
- **Coherent pulses:** Various combinations of single and multiple 90° , 180° and 360° pulses, as described in earlier chapters.
- **Self-induced transparency:** A combination of coherent-pulse theory with electromagnetic theory to describe large-signal pulse propagation in atomic systems.
- **Adiabatic rapid passage:** Unexpected effects produced when we sweep the frequency ω of a strong applied signal through the atomic resonance frequency ω_a , producing a population inversion on the transition.
- **Photon echo experiments:** Complex pulse experiments that can be produced only on inhomogeneously broadened transitions, by making use of the distinction between the reversible and irreversible dephasing effects associated with T_2 and T_2^* .
- **Multiphoton transient effects:** Still more complex versions of all the preceding, using strong signals at various subharmonics of the transition frequency ω_a .

We will not be able to give full descriptions of any of these here.

Steady-State Nonlinearities: Harmonic Generation

The large-signal transient behavior of the Bloch equations is perhaps the most interesting and dynamic aspect; but there are also other nonlinear harmonic generation effects that can occur even under steady state conditions, and that can be useful for other purposes both in magnetic resonance and at optical frequencies.

There is also another type of nonlinear behavior associated with the Bloch equations (and hence with any two-level atomic transition) leading to the generation of second and higher harmonics of the applied signal frequency. In contrast to coherent transient effects, these harmonic generation effects do not need fast pulses, and can be seen under sinusoidal steady-state conditions—though their magnitude grows comparatively much stronger as the applied signal amplitude is turned up.

The Bloch equations contain nonlinear product terms of the form

$$\begin{aligned}\frac{dm_x}{dt}(t) &\propto [b_y(t)m_z(t) - b_z(t)m_y(t)] \\ \frac{dm_y}{dt}(t) &\propto [b_x(t)m_z(t) - b_z(t)m_x(t)]\end{aligned}\quad (94)$$

in the transverse equations, and

$$\frac{dm_z}{dt}(t) \propto [b_x(t)m_y(t) - b_y(t)m_x(t)] \quad (95)$$

in the longitudinal equation. Suppose that the driving signals $b_x(t)$ and $b_y(t)$ contain only sinusoidal terms at frequency ω , whereas b_z contains only the dc term B_0 , as is most commonly the situation. Then the transverse equations, to first order, will generate components of m_x and m_y at ω , as we have already discussed. These transverse components of $b(t)$ and $\mathbf{m}(t)$ at ω frequency will then mix in the right-hand side of the longitudinal equation to produce components of m_z (or dm_z/dt) at dc ($\omega = 0$), as already discussed, plus additional components in second order at the second harmonic 2ω .

These higher-order components of m_z at 2ω will be much weaker; but if kept track of properly they can then mix back into the transverse equations to produce third-order components of $m_x(t)$ and $m_y(t)$ at the third harmonic or 3ω . These 3ω components will be proportional to $|\vec{B}_+|^3$ rather than to $|\vec{B}_+|$, and thus will be much weaker than the ω components at ordinary signal levels. These components in turn can mix again with the ω dependence of b_x and b_y in the longitudinal to produce terms in m_z at $\omega + 3\omega = 4\omega$, and also additional second-harmonic terms at $3\omega - \omega = 2\omega$; and so on.

By containing in this fashion, we can produce successively higher-order odd harmonics in the transverse components $m_x(t)$ and $m_y(t)$, and even-order harmonics in $m_z(t)$. Applying an even-order signal to the $b_z(t)$ component at, say, 2ω can also assist this process.

The standard procedure if we want to analyze all this in more detail is to write each of the components in a suitable Fourier series, e.g.,

$$\begin{aligned}m_x(t) &= \sum_{k \text{ odd}} m_{x,k} e^{j k \omega t}, \\ m_y(t) &= \sum_{k \text{ odd}} m_{y,k} e^{j k \omega t}, \\ m_z(t) &= \sum_{k \text{ even}} m_{z,k} e^{j k \omega t}.\end{aligned}\quad (96)$$

These are then substituted into the longitudinal and transverse equations in a technique sometimes called “harmonic balance,” evaluating product terms and

keeping as many harmonic factors as seem mathematically necessary. By matching corresponding frequency terms on each side of Equations 31.94 and 31.95 we obtain a set of relations linking the different harmonic components to the applied signals. The third-harmonic components of $m_x(t)$ and $m_y(t)$ will be proportional to the cube of the driving field, or $|\tilde{B}_+|^3$; the fifth-harmonic components to $|\tilde{B}_+|^5$; and so forth. Note also that we can apply a signal at $\omega \approx \omega_0$ and obtain a quasi resonant third harmonic generation at 3ω ; or alternatively we can apply a sub-harmonic driving field at $\omega \approx \omega_0/3$, and obtain another quasi resonant harmonic generation with the output at $3\omega \approx \omega_0$.

REFERENCES

A compact summary of atomic responses and coherent pulse effects is given in a review paper by S. Feneuille, "Interaction of laser radiation with atoms," *Rep. Prog. Phys.* **40**, 1257–1304 (November 1977).

Signal echoes, or photon echoes, are not in fact a peculiarly atomic or even quantum phenomenon; but can occur in any classical system which has (i) a spread of resonance frequencies (inhomogeneous broadening) and (ii) a mild degree of nonlinearity in the system response. A very helpful description of echo effects is given by V. P. Chebotayev and B. Ya. Dubetsky, "A classical model of the photon echo," *Appl. Phys. B* **31**, 45–52 (1983).

The Bloch equations give a very accurate analysis for the response of a two-level atomic system in a great many small-signal and large-signal situations. In certain atomic systems under large-signal conditions, however, it is found that the transverse Bloch equations need to be modified somewhat. In simple terms, working in a rotating coordinate system we can continue to use a T_2 relaxation time for the transverse component along the axis of the circularly polarized applied signal field (call this the x axis); but must use a modified relaxation time T_{2e} along the y axis in the rotating frame, where T_{2e} is a power-dependent relaxation time, ranging from T_2 at low power to T_1 at high applied signal powers.

The original analysis of this effect is in A. F. Redfield, "Nuclear magnetic resonance saturation and rotary saturation in solids," *Phys. Rev.* **98**, 1787–1809 (June 15, 1955). A beautiful experimental demonstration is given by R. G. DeVoe and R. G. Brewer, "Experimental test of the optical Bloch equations for solids," *Phys. Rev. Lett.* **50**, 1269–1272 (April 25, 1983).

Problems for 31.7

1. *Off-resonance Rabi flopping behavior.* Figure 31.22 shows plots of the large-signal solution for $m_z(t)$ with different detunings $\Delta\omega$ in the Rabi flopping limit. Make similar plots of $M_1(t)$ and $M_2(t)$ for the same detunings, and discuss how they relate to the dynamical behavior of the magnetization vector $\mathbf{m}(t)$.
2. *Conversion between electric-dipole and magnetic-dipole models.* See if you can find appropriate mathematical transformations that will convert the Bloch equations more or less exactly into the form of the electric-dipole equations of motion, or vice versa. Hint: Try converting the magnetic-dipole quantities into equivalent electric-dipole quantities by writing $m_x = (d/dt + 1/T_2)p$, $m_y = \omega_a p$, $b_x = 0$, $b_y = \mathcal{E}$; or else do the reverse by writing $m_x + jm_y = (\alpha - j)(d/dt + 1/T_2 + j\omega_a)p$ and $b_x + jb_y = (1 + j\alpha)\mathcal{E}$ where α is an arbitrary constant.

3. *Rabi flopping behavior: alternative derivation.* Repeat the Rabi frequency derivation given in this section using the complex $\tilde{b}(t)$ and $\tilde{m}(t)$ notation suggested in a problem in the preceding section.
4. *Rabi frequency with both detuning and relaxation.* In an earlier chapter we worked out the large-signal Rabi-flopping behavior for the electric-dipole situation, assuming an applied signal exactly on resonance, but keeping the T_1 and T_2 relaxation terms in the solutions; whereas in this section we have worked out the large-signal Rabi-flopping behavior for the magnetic-dipole situation, allowing the signal frequency to be tuned off resonance but dropping the T_1 and T_2 relaxation terms completely.

Try combining these situations by keeping both relaxation terms and allowing off-resonance signals in the magnetic-dipole equations. (Note: It should be adequate to derive the equations of motion and the secular equation, and then find the general form for the normal modes of the system. Trying to fit the boundary conditions for all quantities in all limiting situations would be extremely tedious and not particularly instructive.)

INDEX

A

ABCD matrices, *see* Ray matrices, Complex ray matrices
Aberrated laser beams, 706–711
 See also Multimode optical beams
Absorbing media, 283
 See also Saturable absorbers
Absorption cross section, *see* Transition cross section
Absorptive bistability, *see* Bistable optical systems
Acoustic transitions, 198
 See also Nonradiative transitions, Phonon broadening, Phonon interactions
Acoustooptic *Q* switch, *see* *Q* switches
Active mode locking, 1041–1103
 autocorrelation measurements of, 1081–1082
 chirp in, 1067, 1069–1071
 circulating gaussian pulse analysis of, 1062–1067, 1077–1079
 coupled-mode analysis of, 1087–1092, 1096–1098
 detuning effects in, 1084–1086, 1088
 etalon effects in, 1071–1073
 experimental results for, 1050, 1052, 1070–1073, 1081–103, 1096, 1099–1100
FM laser operation, 1057
FM mode locking, 1069–1071, 1083–1084, 1095, 1100
 general description of, 1056–1061
 harmonic, 1060, 1073–1074
 higher-order solutions for, 1069
 homogeneous versus inhomogeneous, 1059
 modulator polarization term, 1089–1091, 1092–1095
 pre-lasing, 1082–1083
 synchronously pumped, 1058–1059
 time and frequency description of, 1041–1055
 time-domain analysis of, 1061–1067
 transient buildup of, 1075–1081, 1083–1084
 See also Mode locking
Adaptive optics, 709, 711, 912
Adiabatic rapid passage, 1263
 See also Coherent transients
Adjoint modes, 848–849
 See also Linear operators, Orthogonality

Adler equation, 1143, 1147–1149
 See also Injection locking
Airy disk pattern, 679, 728–729
 See also Aperture diffraction
Ammonia maser, 74
Amplification coefficient, *see* Laser amplification
Amplified spontaneous emission (ASE), 547–557
 and lifetime shortening, 552
 and mirrorless lasers, 547–557
 in regenerative cavity, 445, 451–454
 in semiconductor lasers, 445, 463–464
 See also Superfluorescence, Superradiant emission
Amplifier saturation, *see* Saturation
Amplitude modulation of lasers, *see* Laser amplitude modulation
Anomalous dispersion, *see* Dispersion
Antenna theorem, 672
“Anti-etalon” effects, 1072–1073, 1117
Antiresonant-ring interferometer, 1126–1127
 See also Interferometers
Aperture diffraction,
 Airy disk pattern, 728–729
 and relay imaging, 739–740, 742
 by annular apertures, 736, 737
 by circular aperture, 727–743
 by rectangular aperture, 712–727
 by single slit, 716–723
 from arbitrary apertures, 740–742
 of gaussian beams, 667–668, 731–734, 742
 on-axis intensity, 725–726, 731
 special properties of circular apertures, 736–738
 See also Diffraction effects
Aperture shaping, *see* Apodization, Soft apertures, Tapered reflectivity mirrors
Apodization, 578–580, 710, 711
ASE, *see* Amplified spontaneous emission
Astigmatic optical systems, 597, 616–617, 647
 See also Image rotation, Ray matrices, Ray optics
Asymptotic analysis, *see* Unstable optical resonators
Atomic absorption lines, 19–22
Atomic energy levels, 6–18
Atomic linewidth, *see* Line-broadening effects, Linewidths
Atomic phase shift effects, 271–272, 275

Atomic rate equations, 24–28, 37, 176–220, 228, 497–510
 and blackbody-stimulated transitions, 188–190, 195–196
 for four-level system, 245–248
 for magnetic-dipole transition, 1249–1256
 for multiple-energy-level systems, 211–220
 for three-level system, 248–250
 for two-level system, 255
 low- and high-frequency approximations to, 218–219
 transient solutions of, 208, 218, 256, 257–263
 validity of, 225–227

See also Cavity rate equations, Coupled cavity-atomic rate equations, Rabi flopping behavior

Atomic responses,
 quantum description of, 137–142

sinusoidal steady-state, 111–112
See also Classical electron-oscillator model, Rabi flopping behavior, susceptibility

Autocorrelation techniques, 1081–1082, 1122–1123

Available power,
 from laser amplifier, 299–302
 from laser oscillator, 480–481

Axial mode beating,
 in *Q*-switched lasers, 1034–1036, 1046
See also Beat frequencies, Mode beats

Axial modes, 41–42, 432–440, 1041–1054
 in dispersive cavity, 436

for transient signals, 1045

versus transverse modes, 569

See also Modes, Optical resonators

Axicons, in unstable resonators, 908–912

B

B integral, 385–386

Babinet's principle, 736

Backscattering effects,

on laser oscillators, 530, 534, 1163, 1170

on unstable resonators, 906–908, 912

Bandwidth,

for atomic absorber, 284

for single-pass laser amplifier, 281–282, 284

Beam distortion, *see* Aberrated laser beams,

Multimode optical beams

Beam scalloping, 654, 822

See also Ducts, Lensguides

Beat frequency, 317–318, 471–472, 575, 765–766, 767, 1163

See also Mode beats

Bessel functions, 45, 727–729, 742, 1097–1100

Bethe small-hole coupling theory, 939

Bilinear transformation, 680, 785

Biorthogonality, 847, 849–850, 853–854

See also Linear operators, Orthogonality

Birefringent couplers, for variable-reflectivity resonators, 920–922

Bistable optical systems, 538–546

Blackbody radiation, 187–195

Blackbody-stimulated transitions, 188–190, 195–196

Bloch equations,
 derivation of, 1236–1237, 1243
 large-signal solutions of, 1257–1266
 longitudinal, 1240–1242
 longitudinal solutions for, 1249–1256
 Rabi flopping behavior of, 1259–1263
 rotating-wave approximation in, 1247–1248
 saturation behavior of, 1251–1255
 transient solutions of, 1257–1262
 transverse, 1237–1240
 transverse solutions for, 1243–1249

Bloch vector,
 in superradiant emission, 549

Bloembergen three-level maser, 74–75

Bohr magneton, 1218, 1229

Boltzmann's principle, 27–28, 35
 for degenerate levels, 154

Boltzmann ratio, 76, 202–203

Boundary waves, *see* Edge waves

Brewster windows, 63

C

Canonical form,

for Huygen's integral, 805–811

for ray matrix, 813

for unstable resonator, 867–874

for variable-reflectivity resonator, 913–922

Carbon dioxide laser, *see* CO₂ laser

Carnot cycle, 71

Cascade pumping, 251

Cassegrainian telescope, 863

Cavity decay time, *see* Cavity lifetime

Cavity dumping, 975–980

See also Laser amplitude modulation

Cavity frequencies, *see* Optical resonator frequencies

Cavity equation, *see* Cavity rate equation, Laser cavity equations

Cavity frequency pulling, *see* Frequency pulling effects

Cavity lifetime τ_c , 429–430, 492

Cavity mode density, *see* Mode density

Cavity mode number p , 499–501, 502–505

Cavity modes, *see* Optical resonator modes

Cavity Q value, 429–430

See also Cavity lifetime

Cavity rate equation, 497–510

derivation of, 497–505

See also Atomic rate equations, Coupled cavity-atomic rate equations

Chaos, in lasers, 545–546

Chemical lasers, 175

Chirp, 333–334, 345–348, 356

due to self-phase modulation, 382–383

in FM mode-locked lasers, 1067–1071

in spatial frequency domain, 707–708

Chirp radar, 347–348, 350–351

Circuit analogs, *see* Equivalent-circuit models

- Circle diagram, for stable resonators, 748–749
- Circular polarization,
of electric-dipole transition, 136–141, 144–145,
149
of magnetic-dipole transition, 1246–1248, 1255
- Clamping of population inversion, 515–520
- Classical electron-oscillator model, 80–89,
113–117, 227–228
collision broadening of, 93–94
power transfer to, 177–178
two- and three-dimensional, 149
- Classical magnetized top model, 1228–1236
equation of motion for, 1231
precession of, 1231–1232
See also Magnetic dipole transitions
- CO₂ laser, 76, 77, 307–313, 539–540
cross section of, 290
pressure broadening of, 128–129, 163, 166–167
pulse amplification in, 337
transient response of, 314–316
with unstable resonators, 863–864, 885–887,
890
- Coherence, 23, 28, 33–35, 49–60, 66–67, 547
in stimulated transitions, 28
spatial, 43, 55–57, 67
temporal, 54–55, 66–67
- Coherence brightening, 555–556
See also Amplified spontaneous emission
- Coherent pulse effects, *see* Coherent transients
- Coherent transients, 237–341, 547, 1257–1263
- Cleaved-coupled-cavity lasers, 528
- “Cold cavity,” 443, 466
- Colliding-pulse mode locking, *see* Passive mode locking
- Collimated beam propagation, 55–56, 669–670
See also Rayleigh range
- Collimated Fresnel number, 806–808, 870
See also Fresnel number
- Collins chart, 680–681
- Collisions and collision broadening, 90–97,
127–130, 134
elastic versus inelastic, 200, 1196
in classical electron-oscillator mode, 93–94
in real atoms, 99
velocity-changing, 1196
See also Dephasing, Pressure broadening
- Collision rate, in real gases, 99
- Complex ABCD matrix, *see* Complex ray matrices
- Complex gaussian ducts, *see* Ducts
- Complex gaussian pulse shape, 107–109, 169,
331–335
in laser mode-locking theory, 1062
- Complex lorentzian lineshape, 107–109, 169, 1245
- Complex paraxial resonators, 815–857
analysis of, 815–819
complex stable and unstable resonators,
828–829
eigensolutions for, 815–819
higher-order modes, 821–822, 836–837
mode size in, 841–845
multielement, 841–846
- perturbation-stable, 817–818
perturbation-unstable, 831–834, 836–837
real and geometrically stable, 820–822, 841
real and geometrically unstable, 822–828
round-trip phase shifts, 835–836
self-consistent, 816
standing-wave versus traveling-wave, 838–840
types of modes in, 819
with intracavity telescopes, 842–845
- Complex paraxial wave optics, 777–814
and complex Hermite-gaussian beams, 782–785,
798–804
and gaussian apertures, 786–792
and gaussian ducts, 790–792, 793–797
Huygen’s integral for, 777–782, 792–797,
805–811
- Complex radius of curvature \bar{q} , *see* Gaussian beam parameter \bar{q}
- Complex ray matrices, 786–792, 797
and gaussian apertures, 786–788
See also Complex paraxial wave optics
- Complex source point, 638
- Complex spot size \bar{v} , *see* Hermite-gaussian \bar{v} parameter
- Confined modes, *see* Complex paraxial resonators
- Confocal parameter, 669, 674
- Confocal resonator, 438–439, 751–756, 759–760,
771, 873–874
diffraction losses of, 770–774
resonance frequencies of, 763
- Cornu spiral, 717–718
- Coupled cavity-atomic rate equations, 505–510
derivation of, 505–510,
for laser Q switching, 1008
for laser spiking, 958–964, 970
for passive Q switching, 1024
See also Atomic rate equations, Cavity rate equation
- Coupled-mode analysis, *see* Active mode locking,
Unstable optical resonators
- Coupled-mode equations, 1087–1092, 1096–1098
- Critical slowing, 544
- Cross-modulation effects, 318, 1095
- Cross-relaxation effects, 1195–1199
- Cross-saturation effects, *see* Mode competition effects, Saturation
- Cross section,
for atomic transitions, *see* Transition cross section
for collisions, *see* Collisions
- D
- Damping,
coherent versus incoherent, 100
of classical electron oscillator, 82–83
nonradiative, 83–84
radiative, 83
See also Line-broadening effects, Relaxation,
Spontaneous emission
- Decay, *see* Damping, Energy decay rates

- Decibel (definition of), 280
 Degeneracy, of atomic energy levels, 115, 185–186, 256, 287–288
 Degeneracy factors, 115, 153–157, 190, 208–210
 Degenerate optical resonators, 845
 Delta function, see Dirac delta function
 Dephasing,
 by collisions, 90–95
 by dipolar coupling, 93
 by FM modulation, 98–99, 100–101
 by thermal vibrations, 93, 99
 in Bloch equations, 1239–1240
 of classical oscillator model, 93–96
 of electric-dipole transitions, 90–99, 127–130, 134
 of magnetic-dipole precession, 1237–1240, 1255–1256
 plus applied signals, 97–98
 versus energy decay, 133–134
 See also Collisions, Transverse relaxation
 Dephasing time T_2 , 93–96, 210, 222–223, 308–309
 See also Collisions, Dephasing, Transverse relaxation
 Derivative spectroscopy, 109, 135
 Detailed balance, 193–194
 Detuning effects, 1084–1086
 See also Active mode locking
 Dicke superradiance, see Superradiant emission
 Diffraction effects, 277, 635, 698–743
 circular versus other apertures, 736–738
 from arbitrary apertures, 740–741
 on gaussian beams, 667–668, 731–734
 See also Aperture diffraction, Numerical beam propagation methods
 Diffraction losses, see Optical resonators
 Diode lasers, see Semiconductor lasers
 Dipolar coupling, 93, 131–132
 Dipole matrix element, see Transition matrix element
 Dirac delta function, 340
 lorentzian line as, 163
 Fresnel integral as, 717–718
 Dispersion,
 and cavity frequency pulling, 468
 anomalous, 389
 in inhomogeneous transitions, 1192–1194, 1209–1210
 in optical fibers, 357–358
 in optical materials, 356–357
 in resonant atomic systems, 351–355, 376
 in resonant cavities, 436–437
 in wave-propagating systems, 335–339
 nonlinear, 375–386
 Dispersion length z_D , 356–358
 Dispersion parameter D , 356–357
 Dispersive bistability, see Bistable optical systems
 Dispersive pulse broadening, 356–358, 388–392
 in optical fibers, 357–358, 388–392
 in optical materials, 356–357
 “Donut mode,” 688–689
 Doppler broadening, 157, 159, 160–161, 1184–1186

- Doppler shift,
 from moving grating, 706
 from moving mirror, 986–987, 1069
 Double-pulsing,
 in passively mode-locked lasers, 1114–1115
 in Q -switched lasers, 1020–1021
 Ducting, in focusing media, see Ducts
 Ducts,
 beam scalloping in, 654
 complex, 790–794, 801
 definition of, 584
 gaussian beams in, 652–656
 Huygens’ integral for, 793–794
 ray matrix for, 584–592
 stable, 587–589
 unstable, 588–589
 Dyadic product, 146, 147
 Dye lasers, 477, 482, 532, 538
 cw mode-locking in, 1117
 oscillator strength, 122, 123
 saturation intensity, 295
 transition cross section, 290
- E**
- Edge waves,
 in diffraction theory, 716, 723–725
 circular versus rectangular apertures, 736–738
 in unstable resonators, 872–873
 See also Tapered reflectivity mirrors
 Edible laser, 70–71
 Efficiency,
 of cw laser amplifiers, 301–303
 of iodine laser, 1226
 of laser oscillators, 480–481
 of pulsed laser amplifiers, 369–374
 of Q -switched laser, 1010, 1013–1015
 of typical lasers, 68
 Eigenrays, see Periodic focusing systems
 Eigenvalues and eigensolutions,
 for $ABCD$ matrices, 600–604, 813
 for actively mode-locked lasers, 1069
 for complex paraxial systems, 815–819
 for general optical resonators, 562–569
 for linear operators, 848–850
 for periodic focusing systems, 600
 for real geometrically stable resonators, 820–822
 for real geometrically unstable resonators, 822–828
 for stable two-mirror resonators, 744–749
 Fox-and-Li calculations of, 569–578
 Eikonal function, 778, 781
 for unstable resonators, 874–884
 for variable-reflectivity unstable resonator, 916
 Einstein A coefficient, 121, 186
 See also Radiative decay rate
 Electric dipole matrix element, 242
 See also Transition matrix element
 Electric-dipole moment, 85
 definition of, 85

- equation of motion for, 89–90, 96
 quantum expression for, 136–141, 1215–1216
 See also Quantum properties
- Electric-dipole transitions, 81, 118–175, 1219
 Rabi frequency for, 221–242
 stimulated transition probability of, 181–182, 185–186, 213
- Electric polarization,
 decay of, 133–134
 definition of, 86–87
 dephasing of, 94–96
 equation of motion for, 90, 96, 112, 221, 229–230
- Electron oscillator model, see Classical electron-oscillator model
- Electron paramagnetic resonance (EPR), see Magnetic resonance
- Electron spin resonance (ESR), see Magnetic resonance
- Electrooptic *Q* switch, see *Q* switches
- Energy decay rates, 13–18, 118–126
 See also Nonradiative decay, Radiative decay rates, Spontaneous emission
- Energy extraction,
 in cw amplifiers, 301–303
 in laser oscillators, 480–481
 in pulse amplifier, 369–374
- Energy levels, 8–12
 helium atom, 9
 iodine laser, 1223–1224
 Nd, YAG laser, 124, 244
 ruby laser, 13, 249, 273
 terbium ion, Tb^{3+} , 15
- Energy transfer, 176–181, 182
- Equivalent-circuit models,
 for external cavity coupling, 935–939
 for injection-locked oscillator, 1140–1141
 for laser cavity, 929–932
 for regenerative amplifier, 441–443, 940
- Equivalent Fresnel number, 872–873
 See also Fresnel number, Unstable optical resonators
- Equivalent noise input, 72–73, 265–266, 492–494
- Etalon mirrors, 423–427, 528–529
- Etalons, 419, 524
 as mirrors, 423–427, 528–529
 for bandwidth widening, 1072–1073, 1117
 in mode-locked lasers, 1071–1073
 intracavity, 524
 scanning, 438–439, 763–65
 See also Interferometers
- Excimer laser, 519–521, 522
- External signal injection,
 into laser cavity, 932–940
 into laser oscillator, see Injection locking
- “Extra photon,” 503, 509
 See also Photons
- F
- f number, 56–57, 676–677
- Fabry-Perot etalon, see Etalons, Interferometers
- Fabry-Perot interferometer, see Etalons, Interferometers
- “Factor of three,” 150–153
 See also “Three-star”
- Faraday rotator, 535–536
- Far-field beam spread,
 for gaussian beam, 670–673
 for multimode beam, 695–697
 for single-slit diffraction pattern, 720–721
 from arbitrary aperture, 740–741
 See also Rayleigh range
- Far-infrared lasers, 495–496
- Fast Hankel transform, 662
- Feedback, see Regeneration
- Fermat’s principle, 779–782
- Fermi Golden Rule, 184
- Fermi-Pasta-Ulam recurrence, 395–397
- Fiber optic gyroscope, 1168–1169
- Fiber optics, see Optical fibers
- Filamentary effects, see Ducts, Small-scale self-focusing
- Finesse, of interferometer, 435–436
- Finite difference methods, 628, 657, 661
 See also Numerical beam propagation methods
- Fluorescence, 7, 10–12, 22–23
 See also Spontaneous emission
- Fluorescent lifetime, 119
- Fluorescent quantum efficiency, 247
- FM laser operation, 1057, 1095–1103
- FM mode locking, see Mode locking
- Focal phase shift, see Guoy phase shift
- Four-level laser, 36–38, 243–248
- Fourier transform methods, see Numerical beam propagation methods
- Fox and Li mode calculations, 44, 569–575, 577–578, 770–773
 for unstable resonators, 876–877
- Fox-Smith interferometer, 529–530, 531
- Free-induction decay, 307–313, 548, 990–991, 1258
 See also Coherent transients
- Free spectral range, 433–434, 764
- Frequency beating, see Beat frequencies
- Frequency chirp, see Chirp
- Frequency locking effects,
 in coupled oscillators, 1169–1170
 in injected-locked lasers, see Injection locking
 in mode-locked lasers, 1056–1057
 in ring-laser gyroscopes, see Ring-laser gyroscope
- Frequency modulation, see Laser frequency modulation
- Frequency pulling effects,
 due to atomic transition, 466–472, 1063–1064
 due to externally injected signal, 1151–1153
 in coupled oscillators, 1169–1170
 in inhomogeneous transitions, 1194, 1211
- Frequency pushing effects, 1194, 1211
- Frequency stability, 49–51, 66–67, 72
- Frequency switching, see Laser frequency switching
- Frequency switching spectroscopy, 988–981

Fresnel approximation, *see* Huygens' integral
 Fresnel diffraction, 712–714
See also Aperture diffraction, Diffraction effects, Huygens' integral
 Fresnel integral, 717–719
 Fresnel number,
 for gaussian aperture, 915
 in Fresnel diffraction theory, 713–714
 of a lens, 676–678
 of a stable gaussian resonator, 769–770
 of circular versus other apertures, 736–738
 of collimated system, 806–808
 of unstable resonator, 870
See also Collimated Fresnel number, Equivalent Fresnel number
 Fresnel ripples, 721–723, 730, 732–734, 771, 882
 Fresnel zones, 713–714
 Fusion, *see* Laser fusion

G

g parameters, *see* Resonator *g* parameters
g value, *see* Magnetic dipole transitions
 GaAs lasers, *see* Semiconductor laser
 Gain-bandwidth product,
 of regenerative amplifier, 447, 450–451
 Gain coefficient, 272
 Gain dispersion, 358–361
 Gain in dB, 280
 Gain narrowing, 281–282, 284–285
 Gain saturation, *see* Saturation
 Gain switching, 966–968
 See also Laser amplitude modulation
 Gas lasers, 62–66
 Gas lenses, 604
 Gas transport laser, 510
 Gaussian apertures, 786–788
 in unstable resonators, 914–922
 see also Complex paraxial wave optics,
 Complex ray matrices
 Gaussian beam chart, 680–681
 Gaussian beam focusing, 675–680
 Gaussian beam parameter q , 640, 642–643, 664
 eigensolution for, 815–819
 reduced value of, 784
 transformation through paraxial systems,
 783–784
 Gaussian beam profile,
 in saturable amplifiers, 326–328
 Gaussian beam propagation,
 and *ABCD* matrices, 782–786
 collimated propagation of, 669–670
 Collins chart for, 680–681
 deviations from, 679
 in ducts, 652–656
 Rayleigh range for, 667–669, 674
 Gaussian beams, 637–662, 663–697
 analytical expressions for, 663–665
 beam waist of, 663, 669, 675, 679, 683
 confocal parameter of, 669, 674
 depth of focus of, 677

far-field beam angle of, 670–673
 focal spot deviation of, 677–678
 focusing of, 675–680
 mode matching of, 412, 680–682
 multimode, 695–697
 phase shift along, 682–685, 686
 radius of curvature of, 673–674
 top hat criterion for, 665, 667, 670
 transmission through aperture, 665–667,
 731–734
 truncated, 731–734
See also Gaussian resonator modes,
 Gaussian-spherical waves
 Gaussian-hermite modes, *see* Hermite-gaussian modes
 Gaussian-laguerre modes, *see* Laguerre-gaussian modes
 Gaussian lineshape, 160–161, 163–165, 168–170
 See also Doppler broadening, Inhomogeneous broadening
 Gaussian mole run, 53–54
 Gaussian molehill, 53
 Gaussian pulseshape, *see* Complex gaussian pulseshape
 Gaussian resonator modes, 637, 652
 derivation of, 637–652
 higher-order, 642–652, 685–695
 in stable two-mirror resonators, 744–774
 See also Modes, Transverse modes
 Gaussian-spherical waves, 637–642
 complex radius of curvature, 640
 from complex source point, 638–641
 Gaussian \tilde{v} parameter, *see* Hermite-gaussian \tilde{v} parameter
 Geometrical eigenwaves, *see* Unstable optical resonators
 Gires-Tournois interferometer, 348–349
 Glass laser, 171–172, 266, 556
 Gobau lensguide analysis, 748–749
 Gratings, 318, 320, 322, 349, 698–706, 905, 920
 GRIN elements, 589–590, 655
 See also Ducts
 Group velocity, 337–338, 341, 363
 and energy propagation, 363
 dispersion of, 346–350, 383–385, 389
 faster than light, 352–354
 in resonant atomic medium, 351–355
 negative values for, 373
 strongly slowed, 354
 Group velocity dispersion, 341, 346–347, 349–350,
 383–385, 389
 Guoy phase shift, 636, 645–646, 654, 682–686,
 761, 766, 785, 836
 Gyrotropic response, 144–145, 149

H

h and \hbar (Planck's constant), 8
 Hankel transform, 662, 728
 Hard-edged unstable resonators, 826–827, 874–884
 See also Unstable resonators

- Harmonic generation, 224–225, 240–242, 377, 484–485
 in Bloch equations, 1249, 1263–1265
 Harmonic mode locking, 1060, 1073–1074
 See also Active mode locking
- Helium spectrum, 6–9
- Helium-neon (He-Ne) laser, 62–65, 129, 170–171, 465, 477, 495–496, 19–520
 injection locking of, 1134–1137
- Hemispherical resonator, 756–758
- Hermite polynomials, 643, 687, 799, 803
 generating function for, 799
 orthogonality relation for, 803
 See also Hermite-gaussian modes
- Hermite-gaussian mode expansions, 646–647, 691–694, 696, 802–803
- Hermite-gaussian modes, 643–647, 685–695, 798–804, 821–822
 complex form, 798, 803
 complex scale factor \tilde{v} , 798, 800–801
 “elegant” (complex-argument) form, 649–652, 803
 in complex ducts, 801, 804
 in purely real systems, 801–802, 821–822
 “standard form,” 644–647
 transformation through complex paraxial system, 798–804
 widths of, 690–691
 See also Complex paraxial wave optics, Gaussian beams
- Hermite-gaussian \tilde{v} parameter, 798–802, 836–837
- Hermitian adjoint, see Hermitian conjugate
- Hermitian boundary conditions, 854
- Hermitian conjugate, 145–146, 404, 848–849
 See also Linear operators, Orthogonality
- Hermitian matrix, 404–406
- Hermitian susceptibility, 181
- Higher-order modes, 46, 642–652, 685–695, 821–822
 See also Optical resonator modes
- History of the laser, 74–76
- Hole-burning effects, 1171–1184
 and cross-relaxation, 1195–1199
 and inhomogeneous saturation, 1172–1173
 and Lamb dip, 1199–1212
 and saturation spectroscopy, 1184–1194
 change in susceptibility due to, 1178–1181
 elementary analysis of, 1177–1184
 in laser mode locking, 1059
 photochemical, 1174–1177
 strongly homogeneous limit of, 1179–1183
 See also Inhomogeneous saturation, Lamb dips, Spatial hole burning
- Hole-coupled resonators, 774–775
- Hole linewidth, 1180
- Hole susceptibility, 1178–1181
- Homogeneous broadening, 126–135, 158, 162–163, 172
 and laser mode locking, 1059, 1068
 and single-frequency oscillation, 462–463
 See also Dephasing, Line broadening effects
- Homogeneous saturation, see Saturation
- HSURIA, see Unstable optical resonators
- Huygen’s integral, 630–637, 715–717, 1129, 1137
 and ABCD matrices, 618, 777–782
 cascade properties of, 795–797
 for complex paraxial system, 792–797
 for unstable resonator, 867–874
 Fourier transform interpretation, 657–658
 Fresnel approximation to, 633–635
 Guoy phase shift in, 685
 in cylindrical coordinates, 727, 728
 in nonorthogonal systems, 618
 in one dimension, 636
 nonhermitian character of, 854–855
 through general paraxial system, 778–782
 with coordinate scaling, 805–811
- Huygen’s principle, 632
- I
- Image rotation, 619–622
- Image relaying, 739–742, 845
- Incoherent light sources, 52–54, 78–79
- Index of refraction,
 in gases, 115–116
 in solids, 116–117
- Sellmeier equation for, 357
- Inhomogeneous broadening, 15, 157–175, 186
 and laser mode locking, 1059, 1068
 causes of, 159
 effects on laser operation, 464–465
 See also Hole-burning effects
- Inhomogeneous saturation, 1182–1183
 See also Hole-burning effects, Saturation
- Inhomogeneous velocity distribution, 1185–1186
- Initial noise level,
 in laser oscillators, 492–494, 509–510
- Injection lasers, see Semiconductor lasers
- Injection locking, 1129–1170
 Adler equation for, 1143, 1147–1149
 analysis of, 1138–1142
 applications of, 1162–1170
 basic principles of, 1129–1138
 equivalent circuit analog for, 1140–1141
 experimental results for, 1134–1137
 frequency pulling due to, 1151–1153
 in laser mode locking, 1056–1057
 locked-oscillator regime of, 1142–1148
 locking range for, 1134, 1143–1144
 outside locking range of, 1148–1154
 phase shift properties of, 1144
 phasor description of, 1158–1162
 pulsed, 1159–1162
 regenerative description of, 1131–1133
 transient behavior of, 1146–1148, 1158–1162
- Injection seeding, 1154, 1160–1162
- Instantaneous frequency, 332–333
- Interferometers, 408–413, 414–427
 antiresonant-ring, 1126–1127
 basic equation for, 413–414
 circulating intensity in, 415–418, 430–431
 confocal, 438–439

Interferometers, continued

- Fabry-Perot, 409
 - finesse of, 435-436
 - Fox-Smith, 529-530
 - free spectral range of, 433-434
 - Michelson, 529, 530
 - multiple-mirror, 524-531
 - nonlinear, 540-544
 - reflected fields from, 420-427, 431-432, 455
 - resonance properties of, 415-427
 - rotating vector interpretation, 415-417
 - scanning, 438-439, 763-765
 - transmitted intensity, 418-419, 431
- See also* Etalons, Optical resonators, Multiple-mirror cavities, Regenerative amplification

Interstellar masers, 73**Intracavity etalons, 524**

See also Etalons, Interferometers

Inversion, see Laser Inversion**Inversion ratio r , 493, 512**

See also Threshold ratio

Iodine laser, 489, 1223-1228**K****Keller edge waves, see Edge waves****Kerr cell, 378, 981****Kerr effect, 376-378**

See also Optical Kerr Effect

L**Laguerre-gaussian modes, 647-648****Lamb coupled-mode equations, 947-949,**

See also Laser cavity equations, Phase-amplitude equations

Lamb dip, 1199-1212

approximate analysis of, 1202-1204

description of, 1199-1202

dispersive effects of, 1209-1210, 1211

exact analysis of, 1204-1207

frequency stabilization using, 1202, 1208-1209

inverse Lamb dip, 1207-1209, 1212

Laser action in nature, 73**Laser amplification, 3-4, 26-27, 30-35, 264-306**

bandwidth narrowing due to, 281-282, 284-285

delta notation for, 428

gain formula for, 280

in dB, 280

regenerative, *see* Regenerative amplification

saturation behavior, *see* Saturation

Laser amplifiers, 264-306

as power amplifiers, 264-265

as preamplifiers, 265-266

available power from, 299-302

double-pass, 490

for fusion applications, 78, 264-265

inhomogeneously saturating, 325

input-output relation, 298

phase shift in, 282-283

power extraction efficiency of, 301-303

pulse amplification in, 362-375

pulse broadening in, 359-361

saturation of, *see* Saturation

single-pass amplifier, 279-285

transient response of, 307-316

transverse variation in, 325-328

with saturable gain plus loss, 323-325

Laser amplitude modulation, 971-979

in actively mode-locked lasers, 1064-1065, 1089-1090

See also Cavity dumping, Gain switching, Q switching, Laser mode locking, Relaxation oscillations, Spiking

Laser applications, 79**Laser beam focusing, 56-57, 675-680****Laser beams, 49-60****Laser cavities, see Interferometers, Optical Resonators****Laser cavity equations, 923-953**

derivation of, 923-929

equivalent circuit for, 929-932, 935-939

external driving terms for, 932-940

See also Cavity rate equations, Coupled cavity-atomic equations

Laser frequency modulation, 980-991

in actively mode-locked lasers, 1065-1066, 1090-1091

See also FM laser operation, Laser frequency switching, Mode locking

Laser frequency stability, 49-51, 66-67, 72**Laser frequency switching, 984-991**

See also Laser frequency modulation

Laser fusion, 77-78, 264-265**Laser injection locking, see Injection locking****Laser light, 49-60, 66-74**

See also Lasers

Laser mirrors, 2, 39-40, 398-408,

multilayer dielectric, 402-403, 407

reference planes in, 403-404

reflection and transmission properties of, 398-408, 428

Laser mode competition, see Mode competition effects**Laser mode locking, see Mode locking****Laser oscillation, 4-5, 39-49, 457-490, 491-557, buildup of, 39, 260-262, 491-497, 575-577,**

897-898

buildup time for, 493-494

coherence properties of, 28, 33-35, 54-57, 66-67, 521

frequency of, 462-473

in ring cavities, 250, 532-538

initial noise level for, 492-494

mode competition effects in, 992-1003

output power of, *see* Laser output power

parasitic, 555-556

steady-state condition for, 475

threshold conditions for, 457-461

threshold inversion for, 458

threshold pump power for, 459-461

- threshold region for, 447–454, 510–524
- Laser output power, 473–485, 485–490 and homogeneous saturation, 474–475
- Rigrod analysis of, 485–490
- versus coupling, 477
- versus pumping, 481–483
- versus tuning, 484
- with large output coupling, 485–490
- with optimum coupling, 479–481
- with small output coupling, 475–481
- Laser phase modulation, *see* Laser frequency modulation
- Laser pumping, 2–3, 35–38, 70–71, 243–263 for four-level system, 36, 243–248 for three-level system, 248–250 of ruby laser, 258–262 of upper energy levels, 252–257 threshold value of, 459–461 transient build up, 257–263
- Laser *Q* switching, *see* *Q* switching
- Laser radar, *see* Lidar
- Laser refrigeration, 251
- Laser threshold region, *see* Threshold region
- Laser spiking, *see* Spiking
- Laser wavelengths, 5–6, 68–70, 73
- Lasers,
- basic principles of, 1–5, 30–49
 - commercial availability of, 69–70
 - examples of, 60–66, 68
 - history of, 74–76
 - in nature, 73
 - introduction to, 1–79
 - modes in, 41–49
 - oscillation conditions in, 39–42
 - output beam properties of, 49–60
 - performance records for, 71–
 - population inversion in, 35–38
 - pumping methods for, 35–38, 70–71
 - special properties of, 66–74
- Lens Fresnel number, 676–678
- Lens waveguides, *see* Lensguides
- Lensguides, 45, 562, 604, 616, 748–749
- See also* Optical resonators, Periodic focusing systems
- Lidar, 1039–1040
- Lifetime,
- nonradiative, *see* Nonradiative decay rates
 - radiative, *see* Radiative decay rate
- Lifetime broadening, 127
- Line-broadening effects,
- collision, 90–97, 127–130, 134
 - dipolar, 93, 131–132
 - doppler, 157–161, 1184–1186
 - homogeneous, 126–135
 - inhomogeneous, 115, 157–175
 - lifetime, 127
- Linear operators, properties of, 848–849
- Linewidth modulation spectroscopy, 285
- Linewidths,
- FWHM definition of, 107
 - of atomic transition, 107, 108, 114
- See also* Line-broadening effects
- Loaded resonator calculations, 883–884, 887–890
- Locking effects, *see* Frequency locking effects
- Locking range, 1134, 1143–1144
- See also* Injection locking
- Lommel functions, 728
- Longitudinal relaxation time T_1 , 205, 210, 1242
- See also* Relaxation
- Lorentzian lineshape, 30–31, 106–107, 109
- Lumped circuit analogs, *see* Circuit analogs
- Luneberg apodization, 578–580, 711
- M**
- Macroscopic polarization,
- electric-dipole, 86–87
 - magnetic-dipole, 1233
- see also* Electric polarization, Magnetic polarization
- Magnetic-dipole moment,
- equation of motion for, 1218
 - quantum formula for, 1216
- See also* Magnetic-dipole transitions
- Magnetic-dipole transitions, 1213–1266
- ac susceptibility for, 1243–1249
 - at infrared and optical frequencies, 1219–1220
 - at radio and microwave frequencies, 1220
 - basic properties of, 1213–1223
 - Bloch equations for, 1236–1243
 - classical magnetic top model for, 1228–1236
 - coherent transients in, 1256–1266
 - g value for, 1230
 - harmonic effects in, 1263–1264
 - iodine laser as example of, 1223–1228
 - large-signal effects in, 1257–1263
 - longitudinal (rate) equation for, 1249–1256
 - oscillation energy in, 1234–1236
 - quantum properties of, 1214–1217
 - Rabi solutions for, 1259–1263, 1265–1266
 - rate equation for, 1249
- See also* Bloch equations, Magnetic resonance
- Magnetic polarization,
- definition of, 1233
 - dephasing of, 1237–1240
- See also* Magnetic-dipole transitions
- Magnetic resonance,
- electron spin, 1220–1222
 - electronic paramagnetic, 1220–1222
 - nuclear, 1220–1222
- See also* Magnetic-dipole transitions
- Magnification,
- in Huygens' integral, 805–811
 - in image relaying, 739–742
 - in unstable resonators, 860–862, 867
- Masers,
- basic principle, 1
 - history of, 74–76
 - in interstellar space, 73
- Maxwell's equations, 86, 266
- Maxwellian velocity distribution, 1185–1186
- Metal vapors, 274
- Metastable energy levels, 17, 38, 64

- Michelson interferometer, *see* Interferometers
 Mirrors, *see* Laser mirrors
 Mirrorless lasers, 547–557
 See also Amplified spontaneous emission
 Misaligned systems, *see* Ray matrices, Ray optics
 Modal dispersion, 389
 See also Dispersion
 Mode beats, 575, 765–766, 767
 See also Beat frequencies
 Mode competition effects,
 and coupling factor C , 995
 in two-mode laser oscillators, 992–1003
 See also Saturation
 Mode control, *see* Mode discrimination
 Mode coupling versus mode locking, 1053
 See also Mode locking
 Mode crossing behavior, 876–878, 895–897,
 913–914
 See also Unstable resonators
 Mode density $dp(\omega)/dw$, 499–500
 Mode degeneracy, 767
 Mode discrimination,
 in laser oscillator, 462–463, 516–522, 688–689,
 691
 See also Single-frequency oscillation
 Mode locking,
 active, 1041–1103
 autocorrelation measurements of, 1081–1082,
 1122–1123
 coupled-mode equations for, 1087–1092
 FM laser operation, 1057, 1095–1103
 FM mode locking, 1069–1071, 1083–1084, 1095,
 1100
 frequency-domain analysis of, 1087–1103
 frequency-domain description of, 1045–1055
 general description of, 1056–1061
 harmonic, 1060, 1073–1074
 homogeneous versus inhomogeneous, 1059, 1068
 passive (saturable-absorber), 1057–1058,
 1104–1128
 synchronously pumped, 1058–1059, 1123–1125
 time-domain analysis of, 1041–1045, 1061–1086
 transient build-up of, 1075–1086
 transient versus cw, 1060
 See also Active mode locking, FM laser
 operation, Passive mode locking
 Mode matching, 412, 680–682
 Mode number for optical cavity, 499–501, 502–505
 Mode selection, 57–58
 in Q -switched lasers, 1034–1039
 Mode separation behavior, *see* Mode crossing
 behavior
 Mode spot size,
 in real stable resonators, 841–842
 stability of, 842–845
 with intracavity telescope, 842
 Mode separation behavior, *see* Mode crossing
 behavior
 Modes, *see* Optical resonator modes
 MOPA (master-oscillator-power-amplifier),
 264–265, 302, 1163, 1226–1227
 See also Laser amplifiers
- Multilayer dielectric mirrors, 402–403, 407
 Multilevel rate equations, 211–220
 See also Atomic rate equations
 Multilevel atomic system,
 large-signal effects in, 227–228
 rate-equations for, 211–220
 Multimode optical beams, 57–58, 695–697
 See also Aberrated laser beams
 Multiple-mirror cavities, 524–531
- N**
- Natural lasers, 73
 Nd,YAG laser, 171, 292, 359–360, 482–483
 energy levels, 124, 244
 oscillator strength, 123–126
 pulse broadening in, 359–360
 pumping of, 243–245,
 Saturation fluence, 367
 saturation intensity, 295
 transition cross section, 290
 Near-field diffraction patterns, *see* Aperture
 diffraction, Diffraction effects, Unstable
 resonators
 Negative group delay, 373
 Negative-branch unstable resonator, 822, 825–826,
 867, 874
 See also Unstable resonators
 Nodal planes (for thick lenses), 596
 Noise,
 and oscillation buildup, 492–494
 in laser amplifiers, 72–73, 265–266
 Nonlinear dispersion, 375–386
 Nonlinear Schrödinger equation, 387–388
 See also Parabolic equation
 Nonorthogonal optical systems, 616–625
 Nonorthogonal resonator modes, *see*
 Orthogonality
 and collimated Fresnel number, 807
 in unstable resonators, 887–890
 Nonplanar resonators, 537, 622–623
 Nonradiative damping, *see* Nonradiative
 relaxation
 Nonradiative decay rates, 120
 Nonradiative relaxation, 15–18, 195–204
 Nonradiative surroundings, 196–197
 Nonreciprocal devices, 535–536
 Normal mode expansions, 925–929, 931
 Nuclear angular momentum, 1230
 Nuclear magnetic resonance (NMR), *see* Magnetic
 resonance
 Nuclear magnetization, 1218–1221
 Nuclear magneton, 1218, 1230
 Numerical beam propagation methods, 626,
 656–662
 finite-difference method, 628, 657, 661
 Fourier-transform methods, 657–662
 guard bands, 724
 Hermite-gaussian mode expansions, 691–694
 number of sample points, 723–724, 807
 plane-wave expansion, 658–662

O

Off-axis unstable resonators, 901–904, 910–911
 Off-diagonal relaxation time, 1240
See also Dephasing, Transverse relaxation
 Ohmic conductivity, 267
 Ohmic loss, 267, 272
 Omega–beta curve, 335–336
 On–diagonal relaxation time, *see* Longitudinal relaxation time
 Optical axes,
 of misaligned systems, 607, 610–611, 613
 Optical bistability, 538–546
 Optical cavities, *see* Interferometers, Laser cavities, Optical resonators
 Optical delay line, 604
 Optical diode, 535–536
 Optical fibers,
 dispersive pulse broadening in, 357–358
 nonlinear pulse broadening in, 388–392
 solitons in, 392–397
 Optical frequency approximation, 203, 218–219
 Optical harmonic generation, *see* Harmonic generation
 Optical Kerr effect, 376–386, 388
 Optical nutation, 1263
See also Coherent transients
 Optical pumping, 13, 16
 Optical resonator frequencies, 41–42, 574–575, 761–767
See also Axial modes
 Optical resonator modes, 43–49
See also eigenequation for, 566–567
 Fox and Li calculations of, 44, 569–578,
 770–773, 876–877
 large-scale computer simulations of, 883–884
See also Axial modes, Transverse modes
 Optical resonators,
 degenerate, 845
 development of, 410
 employing prisms, 533, 905, 911
 excitation of, 855
 gaussian modes of, 769–776
 general properties of, 558–580
 hole-coupled, 774–775
 introduction to, 558–580
 loaded resonator calculations, 883–884
 modes in, *see* Optical resonator modes
 multielement, 841–846
 multiple-mirror, 524–531
 nonplanar, 537
 orthogonality properties of, *see* Orthogonality
 resonant frequencies of, *see* Axial modes,
 Optical resonator frequencies
 ring-type, 411–412, 532–538
 stable, 563–564, 744–774
 stable two-mirror, *see* Stable two-mirror resonators
 stable-unstable, 903–904
 standing-wave type, 411–412
 telescopic, 845
 thermal focusing in, 842–845

variable-reflectivity, *see* Variable-reflectivity unstable resonators
 with intracavity telescopes, 842–845
 unstable, *see* Unstable optical resonators
 Optimum output coupling, *see* Output coupling
 Orbital angular momentum, 1217, 1228
 Orthogonality,
 of eigensolutions of linear operators, 848–849
 of Hermite–gaussian modes, 646, 650
 of resonator modes, 568–569, 847–857
See also Optical resonators, Transverse modes
 Oscillation, *see* Laser oscillation
 Oscillation build-up, *see* Laser oscillation
 Oscillation frequency, 41–42, 462–473
See also Interferometers, Axial modes
 Oscillation-frequency pulling, *see* Frequency pulling effects
 Oscillation threshold behavior, *see* Threshold region
 Oscillation threshold conditions, 457–461
 Oscillator injection locking, *see* Injection locking
 Oscillator strength, 121–126, 291
 definition of, 121, 123
 for dye lasers, 122, 123
 for Nd,YAG laser, 123–126
 typical values of, 122–123
 Output coupling, 475–481
See also Laser output power
 Overlap integral, 765, 1092–1094

P

p, *see* Cavity mode number
 Parabolic equation, 339–343
See also Nonlinear Schrödinger equation
 Parasitic oscillation, 555–556
 Paraxial wave equation, 276–279, 626–630, 632
 validity of, 278–279, 628–630, 635
 Paraxial wave optics, 777–814
See also Complex paraxial wave optics
 Paraxial-spherical wave, 631–632, 637–638
 from complex source point, 638–641
 Passive mode locking, 1057–1058, 1104–1128
 analysis of (cw), 1120–1122
 anti-etalon effects in, 1117
 colliding-pulse, 1125–1127
 computer simulations of, 1111, 1114–1115
 description of (pulsed), 1110–1111
 double pulsing in, 1114, 1115
 in cw lasers, 1117–1128
 in pulsed lasers, 1109–1117
 nonlinear effects in, 1115–1116
 second threshold in, 1110
 statistical theories of, 1111–1115
See also Mode locking, Saturable absorbers
 Passive *Q* switching, *see* *Q* switching
 Pentaphosphate laser, 1100
 Period doubling, 544
 Periodic focusing systems, 599–607
 eigenrays and eigenvalues, 600
 stability diagram, 748–749

- Periodic focusing systems, *continued*
 stable systems, 601–604
 unstable systems, 604
 with misaligned elements, 611–613
- Periodic lensguide, see Lensguides, Periodic focusing systems
- Perturbation stability, 817–819, 829–831
See also Complex paraxial resonators
- Perturbation-insensitive optical resonators, 842–845,
- Phase-amplitude equations, 947–949, 1138–1140
See also Laser cavity equations
- Phase shift,
 in laser amplifier, 282–283, 303
 in mirrors and beam splitters, 398–407
- Phase perturbations,
 of optical beams, 698–706
- Phase shift through focus, see Guoy phase shift
- Phase transition analogy, 522
- Phase velocity, 337–338
 in resonant atomic medium, 351–355
- Phasors and phasor analysis, 102–103, 1047–1049
- Phonon broadening, 99, 130–131, 171
- Phonon interactions, 198
- Photolysis, 1223
- Photon echoes, 1263
- Photons, 33–35, 498, 502
 and spontaneous emission, 502–505
 “extra photon,” 503, 509
- Pi pulse, 238
See also Coherent transients
- π transitions, 136–140
- Planar resonators, 45–46
- Planck’s constant, 8
- Planck’s law, 8–10
- Plane wave approximation, 268,
- Plane wave expansion, 658–662
- Pockels cell light modulator, 379, 976–977, 980–981
- Poisson spot, see Spot of Arago
- Polarization,
 circular, see Circular polarization
 electric-dipole see Electric polarization
 in cavity equation, see Laser cavity equations
 in optical modulators, see Active mode locking
 magnetic-dipole, see Magnetic polarization
- Polarization properties, 114, 135–143
- Population difference, 110–111
- Population difference equation, 204–205, 223, 231
See also Rate equations
- Population inversion, 27, 32, 35–38
 clamping of, 516–520
 on four-level system, 247–248
See also Laser pumping
- Population recovery time T_1 , see Longitudinal relaxation time
- Positive-branch unstable resonator, 822–824, 867, 874
See also Unstable resonators
- Power broadening, 294–295
 “Power in the bucket”, 882
- Power output, see Laser output power
- Power transfer, 176–181, 182
- Poynting theorem, 178–180
- Poynting vector, 179
- Pre-lasing, in actively mode-locked lasers, 1082–1083
- Pressure broadening, 127–130, 1225
- Precession,
 of magnetic-dipole atoms, 1217–1218, 1234–1235
 of magnetic top, 1231–1232
- Principal planes (for thick lenses), 595–596
- Prisms, in optical resonators, 533, 905, 911
- Propagation constant, 270–272
 in duct, 653
 in free space, 268–269
 in lossy medium, 270
- Pulling effects, see Frequency pulling
- Pulse amplification, 359–361, 362–375
 and pulseshape distortion, 368–369
 energy extraction, 369–372
 slab model for, 366
- Pulse breakup, 384–386
See also Pulseshape distortion
- Pulse broadening,
 and gain dispersion, 358–359
 by laser gain medium, 359–361, 1064
 by self-phase-modulation, 390–392
 dispersive, 356–358
 in optical fibers, 356–358, 390–392
- Pulse compression, 338, 342, 344–351, 391–393
 due to self-phase-modulation, 384–385
 with grating pair, 39–393, 349
- Pulse propagation, 331–361
 and pulse compression, 338, 342, 344–351
 dispersive effects on, 343–351
 in linear systems, 331–361
 in resonant atomic media, 351–355
 of gaussian pulses, 331–335
- Pulse shortening,
 in regenerative system, 1108–1109
 in saturable absorbers, 1104–1109
See also Mode locking
- Pulse synthesis,
 with multiple laser frequencies, 1050–1053
- Pulsed injection locking, see Injection locking,
 Injection seeding
- Pulsed mode locking, see Mode locking
- Pulseshape distortion,
 due to self-phase modulation, 384–386
 in pulse amplifiers, 368–369, 374–375
 in pulse compression, 347–348
- Pumping, see Laser pumping
- Pumping rate, 252–253
- Q**
- \tilde{q} parameter, see Gaussian beam parameter \tilde{q}
- Q , definition of, 180
- Q_c , see Cavity Q value
- Q switches,
 acoustooptic, 1007, 1028

electrooptic, 1006–1007
 rotating mirror, 1006, 1028
 saturable absorber, 1007, 1024–1028
 slowly opening, 1020–1021, 1023–1024
 thin film, 1007–1008
See also *Q* switching and *Q*-switched lasers
Q switching and *Q*-switched lasers, 1004–1040
 applications of, 1039–1040
 axial mode beating in, 1034–1036
 energy efficiency of, 1010, 1013–1015
 exact solution for, 1018–1019
 experimental results for, 1019–1020, 1032
 general description of, 1004–1008
 mode locking of, *see* Mode locking
 mode selection in, 1034–1039
 multiple pulses from, 1020–1021
 passive (saturable absorber), 1007, 1024–1028
 practical methods for, 1006–1008
 pulse output interval of, 1012–1017
 pulsedwidth of, 1017–1018
 pumping interval in, 1009–1012
 rate equation analysis of, 1008–1023
 repetitive, 1028–1034
 second threshold in, 1026–1028
 transverse modes in, 1036–1039
See also *Q* switches
 Quality factor, *see Q*, definition of
 Quantum beats, 1263
 Quantum charge density, 135–138, 1214–1215
 Quantum current density, 1215
 Quantum efficiency, 247
 Quantum electronics, 1
 Quantum energy levels, *see* Energy levels
 Quantum noise fluctuations, 51
See also Schawlow-Townes formula
 Quantum properties,
 of electric-dipole transitions, 1215, 1216
 of magnetic-dipole transitions, 1214–1217
 Quantum states, 137–142

R

Rabi frequency, 221–242, 1259–1260
 relation to stimulated transition probability,
 234, 1262–1263
 Rabi flopping behavior,
 for electric-dipole transitions, 113, 231–242, 376
 for magnetic-dipole transitions, 1259–1263,
 1265–1266
 Radiation damping, of atomic radiation, 952–953
See also Radiative decay rate
 Radiative decay rate,
 for Nd:YAG, 123–126
 of degenerate transition, 155–156
 of atomic transitions, 84–85, 109–110, 120–121
 of classical magnetic dipole, 1248
 of classical electron oscillator, 84
 of magnetic dipole transition, 1255
See also Radiation damping
 Radiative surroundings, 187–193
 Rare-earth ions, 12, 14, 15, 17, 21

Rate equations, *see* Atomic rate equations, Cavity
 rate equation, Coupled cavity-atomic rate
 equations
 Rate equation approximation, 225–227
See also Rate equations
 Ray equation, 587
 Ray inversion, 591
 Ray matrices, 581–625, 777–792, 811–814
 and imaging properties, 596–597
 and gaussian beam propagation, 782–786
 and Huygens' integral, 777–782
 and spherical waves, 593–595
 and thick lenses, 595–599
 canonical form, 813
 complex, *see* Complex ray matrices
 for curved ducts, 614–616
 definition of, 583
 determinant of, 584
 eigenvalues of, 600–604, 813
 factorization of, 814
 for astigmatic systems, 597, 616–617
 for cascaded systems, 593–599
 for misaligned systems, 609, 613
 for nonorthogonal systems, 616–625
 for thick lenses, 595–599
 for gaussian aperture, 786–788
 reduced slope in, 583
 symmetric form, 813
 synthesis of, 814
 table of, 585–586
 telescopic form, 814
 transformation of, 811–814
 Ray optics, 581–625
 and geometrical optics, 593
 and spherical waves, 593–595
 Ray propagation,
 in astigmatic systems, 597, 616–617
 in cascaded systems, 593–599
 in curved ducts, 614–616
 in misaligned systems, 607–614
 in nonorthogonal systems, 616–625
 in periodic systems, 599–607
 Rayleigh range, 667–669, 674, 725, 726
 for circular aperture, 729
 for single slit, 720–721
 for square aperture, 725
 general definition of, 714
 Recirculating pulse approach, 560–565
 Reduced radius of curvature, 594–595, 784
 Reduced slope, 583
 Reflection coefficient, *see* Laser mirrors
 Refractive index, *see* Index of refraction
 Regenerative amplification, 440–447, 447–456,
 1141–1142
 feedback model for, 441–443
 from equivalent circuit model, 940
 gain-bandwidth product, 447, 450–451
 near threshold, 448–454
 of injected signal in free-running oscillator,
 1131–1133
 vector model for, 444–445
 Relay imaging, 739–740, 742, 845

- Relaxation,
longitudinal, 1242
nonradiative, 15–18, 120, 195–204
radiative, 15, 120–121
- Relaxation oscillation frequency, 963–964
See also Relaxation oscillations, Spiking
- Relaxation oscillations, in lasers, 954–971
versus spiking, 957
linearized analysis of, 962–964
See also Spiking
- Repetitive *Q* switching, *see* *Q* switching
- Resonant dipole equation, 96, 112, 221
transient response of, 222–223
- Resonator modes, *see* Optical resonator modes
- Resonator *g* parameters, 746–747
See also Stable two-mirror resonators
- Resonators, *see* Optical resonators
- Retroreflected unstable resonators, *see* Unstable optical resonators
- Rigrod analysis, 485–490
- Ring-laser gyroscope, 1163–1170
locking effects in, 1165–1166, 1167–1168
- Ring lasers, 40, 250, 411–412, 532–538,
nonplanar, 622–623
unstable, 899–900, 910
- Rotating mirror *Q* switch, *see* *Q* switches
- Rotating-wave approximation, 1247–1248
- Round-trip gain, 414–415, 429, 457
- Ruby, 10–11, 18
energy levels of, 249, 273
pumping of, 248–250
spiking in, 955–956
wave propagation in, 272–273
- Ruby laser, 60–61, 122, 131, 258–262, 263
cross section of, 290
spiking in, 955–956, 971, 974–975
- S**
- Sagnac interferometer, 531
- Sapphire, 10–11
See also Ruby
- Saturable absorbers, 207–208, 305, 538,
1104–1109
fast saturable absorption, 1105–1107
pulse propagation in, 240–243
pulse shortening in, 1104–1109
slow saturable absorption, 1107–1108
See also Passive mode locking, Saturation
- Saturable absorber *Q* switch, *see* *Q* switches
- Saturated-absorption spectroscopy, 1184–1191,
1198–1199
- Saturated dispersion effects, 1192–1194
- Saturation,
and spatial hole burning, 316–323, 465–466, 472
cross-saturation effects, 320–322, 992–994
in degenerate system, 208–210
in magnetic-dipole transitions, 1251–1255
in mode-locked lasers, *see* Mode locking
in multilevel system, 216–218, 219–220
in regenerative amplifier, 455
- of amplified spontaneous emission, 553–554
of homogeneous single-pass laser amplifier,
297–306
- of homogeneous transition, 206–208, 474–475,
1171–1172
- of inhomogeneous transition, 1172–1173
- of laser amplifier, 207–208
- of m_z in Bloch equations, 1251–1255
- of pulse amplifiers, 362–375
- of two-level system, 206–208
- with saturable gain and loss, 323–324
See also Hole-burning effects, Mode
competition effects, Spatial hole burning
- Saturation broadening, 294–295
- Saturation factor (2^*), 255–256, 364
- Saturation fluence U_{sat} , 367
- Saturation intensity, 292–297
definition of, 293
frequency dependence of, 294–295
numerical values of, 295
- Scalar diffraction theory, 715–717
See also Aperture diffraction, Diffraction
effects, Huygens' integral
- Scanning optical interferometers, 438–439,
763–765, 1070, 1096
See also Etalons, Interferometers
- Scattering, by point object, 704–705
- Scattering matrices, 401–408
Hermitian notation for, 404–406
for lossless systems, 405–406
reference planes for, 403–404
- Schawlow-Townes formula, 451–454, 456
See also Quantum noise fluctuations
- Scraper mirror, for unstable resonator, 860–861,
866
- sech function, 395, 1122
- Second threshold,
in passively mode-locked lasers, 1110
in *Q*-switched lasers, 1026–1028
See also Passive mode locking, *Q* switching
- SEL-FOC nodes, *see* CRIN elements
- Selection rules, 1224
- Self-canceling lens pairs, 811–812
- Self-chirping, 390–392
See also Self-phase modulation
- Self-focusing, 380–382
in mode-locked lasers, 1115–1116
small-scale, 381–382, 710, 711
whole-beam, 380–381
- Self-imaging unstable resonators, 900–901, 910
- Self-induced transparency, 157, 238, 1263
- Self-phase-modulation, 382–385, 390–392
in mode-locked lasers, 1115–1116
- Sellmeier equation, 357
- Semiconductor lasers, 432–433, 434, 445–446,
463–464, 482, 483, 517–519
amplitude fluctuations in, 53–54
dispersive effects in, 436–437, 439
relaxation oscillations and spiking in, 965–966,
971, 974–975
- threshold behavior of, 463–464, 517–519
- with unstable resonators, 904, 911

- Sidebands,
for amplitude and phase gratings, 700–703
for amplitude-modulated (AM) signals,
1087–1091
for frequency-modulated (FM) signals,
1087–1091
- σ , see Transition cross section
- σ transitions, 136–141
- Single-frequency oscillation, 462–463, 466
See also Laser oscillation, Mode discrimination, Mode selection
- Single-transverse-mode oscillation, 577
- Slater normal mode expansion, 931
- Slowly opening Q switch, see Q switches
- Slowly varying envelope approximation (SVEA)A,
229–230, 241, 944–947, 1258–1259
- Snell's law, 584
- Soft aperture, 738, 786–789, 815, 914–922
See also Tapered reflectivity mirrors,
Variable-reflectivity unstable resonators
- Solar-pumped lasers, 70–71, 1227
- Solid-state lasers, 61–62
- Solitary wave, see Solitons
- Soliton laser, 396, 397
- Solitons, 392–397
in optical fibers, 392–397
- Spatial coherence, see Coherence
- Spatial frequency, 658–659, 707–709
sampling theorem for, 693–694
- Spatial hole burning, 316–323, 465–466, 472
- Spatial Inhomogeneity, see Spatial hole burning
- Spectral packets, 158, 173, 1172–1173, 1177–1178,
1195
See also Hole-burning effects, Inhomogeneous
broadening
- Spectroscopy, 19, 21, 23
by linewidth modulation, 285
- Spherical waves, 630, 704
See also Paraxial-spherical wave, Huygens'
integral
- Spider mounting, for unstable resonators, 860,
866
- Spiking, in laser oscillators, 495, 954–971
versus relaxation oscillations, 957
rate equation analysis of, 958–961, 970
phase-plane description of, 961
in ruby lasers, 955–956, 964–965
in semiconductor lasers, 965–966, 971, 974–975
suppression of, 966, 970
See also Relaxation oscillations
- Spiking frequency, see Relaxation oscillation
frequency
- Spillover losses, 745, 776
- Spin angular moment and magnetic moment,
electronic, 1217–1218, 1229–1230
nuclear, 1230
- Spin-lattice relaxation time, 1242
See also Longitudinal relaxation
- Spin packet, see Spectral packets
- Spin-spin relaxation time, 1240, 1242
See also Dephasing, Transverse relaxation
- Split-mode unstable resonator, 908–912
- Spontaneous emission, 6–18, 22–24, 26, 29,
502–505
and cavity rate equations, 502–505
See also Fluorescence, Radiative decay rate
- Spot of Arago, 734–736, 742, 863
- Stable two-mirror resonators, 744–774
circle diagram for, 748–749
compensation for thermal focusing in, 842–845
concave-convex, 758–759
confocal, 751–754, 763, 765, 770–774
eigensolutions for, 744–749
exact mode patterns, 771
Fresnel number of, 769–770
 g parameters, 746–747
half-symmetric, 751–752
hemispherical, 756–758
long-radius, 754–755, 762
misalignment effects, 767–769
mode losses, 769–776
near-concentric, 755–756
resonant frequencies of, 761–767, 772–773
stability diagram, 747–749
symmetric, 750–751
- Stability diagram, for optical resonators, 747–749
- Stable optical resonators, 47
See also Optical resonators
- Stimulated absorption, 18–26, 30–31
See also Stimulated atomic transitions
- Stimulated emission, 1, 26–27, 32–35
See also Stimulated atomic transitions
- Stimulated transition probability,
due to blackbody radiation, 190, 195, 197
due to nonradiative surroundings, 197, 199
for electric-dipole transition, 181–182, 185–186,
213, 1251
for magnetic-dipole transition, 1251
in degenerate system, 185–186
in multilevel systems, 213
relation to cross section, 293
relation to Rabi frequency, 234, 1262–1263
See also Rate equations
- Stimulated atomic transitions, 18–30
See also Stimulated transition probability
- Strain broadening, 159, 171–172
- Strip resonator, 571, 861, 879
- Stable-unstable optical resonators, 903–904
- Sum rules, 123
- Supergaussian beam profile, 738–739
“Supermodes,” in harmonically mode-locked
lasers, 1073–1074
- Superradiant emission, 548–549, 551, 556–557
See also Superfluorescence
- Susceptibility,
of atomic transition, 111
classical electron oscillator, 102–106
for circularly polarized transitions, 143–150,
1245–1249
for magnetic-dipole transition, 1243–1249
hermitian and antihermitian parts of, 181
modified definition of, 104
of degenerate transition, 153–157
of inhomogeneous hole, 1178–1181

Susceptibility, continued

resonance approximation for, 105–106
strongly inhomogeneous limit, 164–165
tensor properties of, 143–150, 181, 1245

Superfluorescence, 549–550, 551, 556–557
See also Superradiant emission

Swept-gain laser action, 555

Synchronously pumped mode locking, 1058–1059,
1123–1125

See also Mode locking

T

T_1 , *see* Longitudinal relaxation time

T_2 , *see* Dephasing, Dephasing time, Transverse
relaxation

T_2^* , 168–171

Tapered reflectivity mirrors, 905–906, 911–912,
913–917, 919–920

See also Soft apertures, Variable-reflectivity
unstable resonators

TEA lasers, 77, 309–310

Telescopic optical resonator, 845, 869

Temporal coherence, *see* Coherence

Tensor formulation,
of atomic susceptibilities, 143–153, 181,
1245–1247

of power flow, 181

Tensor responses, 114

Thermal equilibrium, 193

Thermal focusing, compensation for, 842–845

Thermal light sources, 52–54, 78–79

Thin film Q switch, *see* Q switches

Three-level laser system, 248–251

Three-level maser scheme, 74–75

“Three-star” (3*), 114, 152–153, 186

Threshold inversion, 41

Threshold ratio r , 475, 481, 512

See also Inversion ratio

Threshold region, 447–454, 457–461, 463–464,
510–524

phase transition analogy, 522

summary of threshold characteristics, 521

See also Laser oscillation

Time-bandwidth product,

definitions, 334–335

in mode-locked lasers, 1071–1072

for gaussian pulse, 334–335

for transform-limited pulse, 335

“Times diffraction limited” (TDL), 58, 696–697

“Top hat” criterion, for gaussian beam, 665, 667,
670

Transform-limited pulses, 335

Transit-time broadening, 132

Transition cross section, 286–292

and gain coefficient, 287

and threshold inversion, 459

for gaussian lineshape, 288, 289

for iodine laser, 1225

for lorentzian lineshape, 288, 289

for magnetic-dipole transitions, 1220, 1225

maximum value, 289

typical values, 288, 289, 1225

Transition matrix element, 145–146, 242

Transition probability, *see* Relaxation transition
probability, Stimulated transition probability

Transition strength, 290, 1225

See also Radiative decay rate, Transition cross
section

Transpose operator, 848–849

See also Linear operators, Orthogonality

Transverse-mode control, 48, 575–577

See also Optical resonator modes, Transverse
modes

Transverse modes, 43–49, 53, 563

beat frequencies of, 575

calculation of, 569–580

competition of, 576–577

diffraction losses, 567

existence of, 568

higher-order, 569–580

of general resonators, 410–411, 559–565

of stable gaussian resonators, 410

of unstable resonators, 411

orthogonality of, 568–569

resonance frequencies of, 762

See also Modes, Gaussian resonator modes

Transverse relaxation,

in Bloch equations, 1239–1240

of magnetic-dipole oscillators, 1237–1240, 1256

See also Collisions, Dephasing

Transverse relaxation time, *see* Dephasing time,

Transverse relaxation

Traveling wave, properties of, 266–275

Traveling-wave amplification, 264–306

basic derivation of, 279–285

saturation of, *see* Saturation

single-pass gain and bandwidth 279–285

Truncated gaussian beam, *see* Aperture

diffraction, Gaussian beams

Tunable lasers, 67, 72

Two-level rate equations, 204–211 *See also* Rate
equations

Two-pi pulses, 238

See also Coherent transients

“Two-star” (2*) factor, 255–256

U

Unidirectional oscillation, 532–538

Uniphase wavefront, 43, 48, 58

Unstable optical resonators, 47–48, 564–565,

759–760, 822–828, 858–922

adaptive optics in, 912

advanced analytic techniques for, 891–899

advantages of, 864–866

aperture shaping effects in, 905–906, 911–922

asymptotic analysis of, 894, 898

axicons in, 908–912

back-reflection effects on, 906–908, 912

canonical form for, 867–874

collimated Fresnel number for, 870

computer simulations of, 883–884, 887–890
 confocal, 759–760, 873–874
 design formulas for, 875
 edge waves in, 872–873, 905–906, 911–922
 elementary properties of, 858–859, 864–866
 equivalent Fresnel number for, 872–873,
 876–878
 experimental results for, 884–890
 Fresnel numbers for, 870, 872–873, 876–878
 hard-edged, 826–827, 874–884
 geometrical solutions for, 860–862, 870–872
 magnification M in, 860–862, 867
 mode crossing and mode separation behavior
 of, 876–878, 895–897, 913–914
 mode losses and mode patterns in, 874–884
 near-field pattern of, 862–864
 negative-branch, 822, 825–826, 867, 874
 off-axis, 901–904, 910–911
 output coupling methods for, 859–861, 879
 positive-branch, 822–824, 867, 874
 references on, 866, 874, 884, 890, 898–899,
 910–912, 921–922
 retroreflected, 906–908, 912
 ring-type, 899–900, 910
 self-imaging, 900–901, 910
 scraper mirror for, 860–861, 866
 semiconductor diode lasers with, 904, 911
 spider output mirror mounting for, 860, 866
 split-mode, 908–912
 stable-unstable, 903–904, 910, 911
 tapered edge effects on, 905–906, 911–922
 virtual source analysis of, 894–895
See also Optical resonators, Variable-reflectivity
 unstable resonators

W

Waist, of gaussian beam, 663, 669, 675, 679, 683
See also Gaussian beams
 Wave equation, 267, 276, 339–343, 626–630
 hermitian character of, 854
See also Paraxial wave equation
 Wave number, 9–10
 Wave propagation,
 in ducts, 653
 in free space, 268–269
 propagation factor, 270–272
 with loss, 270
 Waveguides, optical, see Lensguides
 Whole-beam self-focusing, see Self-focusing
 Wigner distribution function, 797, 1102–1103

Z

Zeeman splitting, 135–137, 149
 Zernike polynomials, 711

V

Variable output coupling, 478
 Variable-reflectivity unstable resonators, 786,
 913–922
 canonical formulation, 914
 design criteria, 919
 eigensolutions for, 916
 Fresnel number for, 915
 output beam profile, 916–919
 output coupling, 916–918
 practical forms of, 919–922
 Velocity-changing collisions, 1196
 Virtual source analysis, for unstable resonators,
 894–895, 898
 Voight profile, 165–168, 173–174, 175
 VRM (variable-reflectivity-mirror) resonators, see
 Variable-reflectivity unstable resonators

Nobel Prize Awards Relevant to Lasers

1902 Pieter Zeeman

Effects of magnetic fields on atomic spectra.

1902 Hendrik Antoon Lorentz

Theory of electromagnetism and atomic transitions.

1904 John William Strutt (Baron Rayleigh)

Fundamental contributions in optics and atomic physics.

1907 Albert Michelson

Precision optical measurements and interferometry.

1908 Gabriel Lippmann

Lippmann photography (a predecessor of holography).

1911 Wilhelm Wien

Blackbody radiation and its relation to thermodynamics.

1915 Sir William Henry Bragg and Sir William Lawrence Bragg

Bragg diffraction and crystal structure.

1918 Max Planck

Planck's Law and the quantization of radiation.

1919 Johannes Stark

The Doppler effect and Stark splitting of atomic transitions.

1921 Albert Einstein

The photoelectric effect, quantum theory and relativity.

1922 Niels Bohr

Atomic structure, Bohr orbital model, correspondence and complementarity principles.

1925 James Franck

Quantum theory of atoms, fluorescence quenching, photochemistry.

1930 Sir Chandrasekhara Raman

The Raman effect and Raman spectroscopy.

1932 Werner Heisenberg

Uncertainty principle, matrix formulation of quantum theory.

-
- 1933 Paul Dirac and Erwin Schrödinger**
Dirac and Schrödinger formulations of quantum theory.
- 1944 Isidor Rabi**
Nuclear magnetic resonance using atomic beam methods.
- 1952 Felix Bloch**
Nuclear magnetic resonance, Bloch equations, spin waves, Bloch wave-functions.
- 1952 Edward M. Purcell**
Nuclear magnetic resonance, and interstellar hydrogen emission.
- 1955 Willis Lamb, Jr.**
The Lamb shift, quantum electrodynamics, quantum laser theories
- 1964 Charles H. Townes,**
The ammonia maser, subsequent developments in masers and lasers.
- 1964 Nikolai G. Basov and Aleksandr M. Prokhorov**
Contributions in masers and lasers.
- 1965 Richard Feynman**
Quantum electrodynamics, generalized Bloch equations.
- 1966 Alfred Kastler**
Optical pumping, double resonance optical spectroscopy.
- 1971 George Herzberg (Chemistry)**
Molecular spectroscopy: infrared and optical spectra of molecules.
- 1971 Dennis Gabor**
Invention of holography.
- 1977 John Van Vleck**
Electric and magnetic susceptibilities, spectroscopy of solids.
- 1978 Arno Penzias and Robert Woodrow Wilson**
Discovery of cosmic background radiation, using a microwave maser receiver.
- 1981 Nicolaas Bloembergen and Arthur Schawlow**
The three-level maser, nonlinear optics, and laser spectroscopy.